

Springer Proceedings in Complexity

Santo Banerjee  
Asit Saha *Editors*

---

# Nonlinear Dynamics and Applications

Proceedings of the ICNDA 2022

 Springer

# **Springer Proceedings in Complexity**



Springer Proceedings in Complexity publishes proceedings from scholarly meetings on all topics relating to the interdisciplinary studies of complex systems science. Springer welcomes book ideas from authors. The series is indexed in Scopus.

Proposals must include the following:

- name, place and date of the scientific meeting
- a link to the committees (local organization, international advisors etc.)
- scientific description of the meeting
- list of invited/plenary speakers
- an estimate of the planned proceedings book parameters (number of pages/articles, requested number of bulk copies, submission deadline)

Submit your proposals to: [Hisako.Niko@springer.com](mailto:Hisako.Niko@springer.com)

Santo Banerjee · Asit Saha  
Editors

# Nonlinear Dynamics and Applications

Proceedings of the ICNDA 2022

 Springer

*Editors*

Santo Banerjee  
Department of Mathematics  
Politecnico di Torino  
Torino, Italy

Asit Saha  
Sikkim Manipal Institute of Technology  
Sikkim Manipal University  
East-Sikkim, India

ISSN 2213-8684

ISSN 2213-8692 (electronic)

Springer Proceedings in Complexity

ISBN 978-3-030-99791-5

ISBN 978-3-030-99792-2 (eBook)

<https://doi.org/10.1007/978-3-030-99792-2>

© The Editor(s) (if applicable) and The Author(s), under exclusive license to Springer Nature Switzerland AG 2022

This work is subject to copyright. All rights are solely and exclusively licensed by the Publisher, whether the whole or part of the material is concerned, specifically the rights of translation, reprinting, reuse of illustrations, recitation, broadcasting, reproduction on microfilms or in any other physical way, and transmission or information storage and retrieval, electronic adaptation, computer software, or by similar or dissimilar methodology now known or hereafter developed.

The use of general descriptive names, registered names, trademarks, service marks, etc. in this publication does not imply, even in the absence of a specific statement, that such names are exempt from the relevant protective laws and regulations and therefore free for general use.

The publisher, the authors, and the editors are safe to assume that the advice and information in this book are believed to be true and accurate at the date of publication. Neither the publisher nor the authors or the editors give a warranty, expressed or implied, with respect to the material contained herein or for any errors or omissions that may have been made. The publisher remains neutral with regard to jurisdictional claims in published maps and institutional affiliations.

This Springer imprint is published by the registered company Springer Nature Switzerland AG  
The registered company address is: Gewerbestrasse 11, 6330 Cham, Switzerland

# Contents

<b>Nonlinear Waves and Plasma Dynamics</b>	
<b>Offset Bipolar Pulses in Magnetospheric Plasma Systems</b> .....	3
Steffy Sara Varghese and S. S. Ghosh	
<b>Forced KdV Equation in Degenerate Relativistic Quantum Plasma</b> .....	15
Geetika Slathia, Rajneet Kaur, Kuldeep Singh, and Nareshpal Singh Saini	
<b>Heliospheric Two Stream Instability with Degenerate Electron Plasma</b> .....	25
Jit Sarkar, Swarniv Chandra, Jyotirmoy Goswami, and Basudev Ghosh	
<b>Bifurcation of Nucleus-Acoustic Superperiodic and Supersolitary Waves in a Quantum Plasma</b> .....	43
Barsha Pradhan, Nikhil Pal, and David Raj Micheal	
<b>Effect of <math>q</math> Parameter and Critical Beam Radius on Propagation Dynamics of <math>q</math> Gaussian Beam in Cold Quantum Plasma</b> .....	55
P. T. Takale, K. Y. Khandale, V. S. Pawar, S. S. Patil, P. P. Nikam, T. U. Urunkar, S. D. Patil, and M. V. Takale	
<b>Study of Quantum-Electron Acoustic Solitary Structures in Fermi Plasma with Two Temperature Electrons</b> .....	63
Shilpi, Sharry, Chinmay Das, and Swarniv Chandra	
<b>Motion of Adiabatic or Isothermal Flow Headed by a Magnetogasdynamic Cylindrical Shock Through Rotating Dusty Gas</b> .....	85
P. K. Sahu	
<b>Structural Variations of Ion-Acoustic Solitons</b> .....	97
Hirak Jyoti Dehingia and P. N. Deka	

<b>Effect of Kappa Parameters on the Modulational Instability in a Polarized Dusty Plasma</b> .....	105
A. Abdikian	
<b>Nonlinear Wave Structures in Six-Component Cometary Ion-Pair Dusty Plasma</b> .....	115
Punam Kumari Prasad, Jharna Tamang, and Nur Aisyah Binti Abdul Fataf	
<b>Cylindrical and Spherical Ion-Acoustic Shock and Solitary Waves in a Nonplanar Hybrid <math>q</math>-nonextensive Nonthermal Plasma</b> .....	127
Subrata Roy, Santanu Raut, and Rishi Raj Kairi	
<b>Formation of Shocks in Ionospheric Plasma with Positron Beam</b> .....	139
Sunidhi Singla, Manveet Kaur, and Nareshpal Singh Saini	
<b>Nonlinear Propagation of Gaussian Laser Beam in an Axially Magnetized Cold Quantum Plasma</b> .....	149
P. P. Nikam, V. S. Pawar, S. D. Patil, and M. V. Takale	
<b>Inelastic Soliton Collision in Multispecies Inhomogeneous Plasma</b> .....	155
K. Raghavi, L. Kavitha, and C. Lavanya	
<b>Propagation of Rarefactive Dust Acoustic Solitary and Shock Waves in Unmagnetized Viscous Dusty Plasma Through the Damped Kadomstev-Petviashvili Burgers Equation</b> .....	167
Tanay Sarkar, Santanu Raut, and Prakash Chandra Mali	
<b>Stability of the Dust-Acoustic Solitons in the Thomas-Fermi Dense Magnetoplasma</b> .....	179
A. Atteya	
<b>Existence and Stability of Dust-Ion-Acoustic Double Layers Described by the Combined SKP-KP Equation</b> .....	193
Sankirtan Sardar and Anup Bandyopadhyay	
<b>Dust-ion Collisional and Periodic Forcing Effects on Solitary Wave in a Plasma with Cairns-Gurevich Electron Distribution</b> .....	203
Anindya Paul, Niranjana Paul, Kajal Kumar Mondal, and Prasanta Chatterjee	
<b>Electron-Acoustic Solitons in a Multicomponent Superthermal Magnetoplasma</b> .....	215
Rajneet Kaur, Geetika Slathia, Kuldeep Singh, and Nareshpal Singh Saini	

**Non-linear Fluctuating Parts of the Particle Distribution Function in the Presence of Drift Wave Turbulence in Vlasov Plasma** ..... 225  
 Banashree Saikia and P. N. Deka

**Effect of Superthermal Charge Fluctuation on Bifurcation of Dust-Ion-Acoustic Waves Under the Burgers Equation in a Magnetized Plasma** ..... 233  
 Jharna Tamang

**Dynamical Aspects of Ion-Acoustic Solitary Waves in a Magnetically Confined Plasma in the Presence of Nonthermal Components** ..... 245  
 Jintu Ozah and P. N. Deka

**Maxwellian Multicomponent Dusty-Plasma with Fluctuating Dust Charges** ..... 259  
 Ridip Sarma

**Effect of Polarization Force on Dust-Acoustic Solitary and Rogue Waves in  $(r, q)$  Distributed Plasma** ..... 275  
 Manveet Kaur, Sunidhi Singla, and Nareshpal Singh Saini

**Dust-Ion-Acoustic Multisoliton Interactions in the Presence of Superthermal Particles** ..... 289  
 Dharitree Dutta and K. S. Goswami

**Fluid Dynamics and Nonlinear Flows**

**Numerical Study of Shear Flow Past Two Flat Inclined Plates at Reynolds Numbers 100, 200 Using Higher Order Compact Scheme** ..... 301  
 Rajendra K. Ray and Ashwani

**On Transport Phenomena of Solute Through a Channel with an Inclined Magnetic Field** ..... 313  
 Susmita Das and Kajal Kumar Mondal

**Unsteady MHD Hybrid Nanoparticle (Au-Al<sub>2</sub>O<sub>3</sub>/Blood) Mediated Blood Flow Through a Vertical Irregular Stenosed Artery: Drug Delivery Applications** ..... 325  
 Rishu Gandhi and Bhupendra K. Sharma

**An Analytical Approach to Study the Environmental Transport of Fine Settling Particles in a Wetland Flow** ..... 339  
 Subham Dhar, Nanda Poddar, and Kajal Kumar Mondal

**Effects of Radiation and Chemical Reaction on MHD Mixed Convection Flow over a Permeable Vertical Plate** ..... 351  
 C. Sowmiya and B. Rushi Kumar

<b>Note on the Circular Rayleigh Problem</b> .....	367
G. Chandrashekhara and A. Venkatalaxmi	
<b>Soret and Chemical Reaction Effects on Heat and Mass Transfer in MHD Flow of a Kuvshinski Fluid Through Porous Medium with Aligned Magnetic Field and Radiation</b> .....	377
Raghunath Kodi and Mohana Ramana Ravuri	
<b>Effect of Reversible Reaction on Concentration Distribution of Solute in a Couette Flow</b> .....	393
Nanda Poddar, Subham Dhar, and Kajal Kumar Mondal	
<b>Mathematical Analysis of Hybrid Nanoparticles (<math>Au - Al_2O_3</math>) on MHD Blood Flow Through a Curved Artery with Stenosis and Aneurysm Using Hematocrit-Dependent Viscosity</b> .....	407
Poonam and Bhupendra K. Sharma	
<b>Response Behavior of a Coaxial Thermal Probe Towards Dynamic Thermal Loading</b> .....	421
Anil Kumar Rout, Niranjan Sahoo, Pankaj Kalita, and Vinayak Kulkarni	
<b>Soret and Dufour Effects on Thin Film Micropolar Fluid Flow Through Permeable Media</b> .....	429
G. Gomathy and B. Rushi Kumar	
<b>Effects of Slip Velocity and Bed Absorption on Transport Coefficient in a Wetland Flow</b> .....	443
Debabrata Das, Subham Dhar, Nanda Poddar, Rishi Raj Kairi, and Kajal Kumar Mondal	
<b>Entropy Analysis for MHD Flow Subject to Temperature-Dependent Viscosity and Thermal Conductivity</b> .....	457
Umesh Khanduri and Bhupendra K. Sharma	
<b>A Numerical Investigation on Transport Phenomena in a Nanofluid Under the Transverse Magnetic Field Over a Stretching Plate Associated with Solar Radiation</b> .....	473
Shiva Rao and P. N. Deka	
<b>Analysis of Solute Dispersion Through an Open Channel Under the Influence of Suction or Injection</b> .....	493
Gourab Saha, Nanda Poddar, Subham Dhar, and Kajal Kumar Mondal	
<b>Mathematical Modelling of Magnetized Nanofluid Flow Over an Elongating Cylinder with Erratic Thermal Conductivity</b> .....	509
Debasish Dey, Rupjyoti Borah, and Joydeep Borah	

**Graphs, Networks and Communication**

**Structure of Protein Interaction Network Associated With Alzheimer’s Disease Using Graphlet Based Techniques** ..... 527  
 Ahamed Khasim, Venkatesh Subramanian, K. M. Ajith, and T. K. Shajahan

**On Divisor Function Even(Odd) Sum Graphs** ..... 535  
 S. Shanmugavelan and C. Natarajan

**A Visible Watermarking Approach Likely to Steganography Using Nonlinear Approach** ..... 545  
 Sabyasachi Samanta

**A New Public Key Encryption Using Dickson Polynomials Over Finite Field with  $2^m$**  ..... 555  
 Kamakhya Paul, Madan Mohan Singh, and Pinkimani Goswami

**Strongly  $k$ -Regular Dominating Graphs** ..... 565  
 Anjan Gautam and Biswajit Deb

**Chaotic Based Image Steganography Using Polygonal Method** ..... 575  
 Dipankar Dey, Solanki Pattanayak, and Sabyasachi Samanta

**On the Construction Structures of  $3 \times 3$  Involutory MDS Matrices over  $\mathbb{F}_{2^m}$**  ..... 587  
 Meltem Kurt Pehlivanoglu, Mehmet Ali Demir, Fatma Büyüksaraçoğlu Sakallı, Sedat Akleylek, and Muharrem Tolga Sakallı

**Fractional System and Applications**

**A Novel Generalized Method for Evolution Equation and its Application in Plasma** ..... 599  
 Santanu Raut, Subrata Roy, and Ashim Roy

**Impact of Fear and Strong Allee Effects on the Dynamics of a Fractional-Order Rosenzweig-MacArthur Model** ..... 611  
 Hasan S. Panigoro and Emli Rahmi

**Stabilization of Fractional Order Uncertain Lü System** ..... 621  
 Manoj Kumar Shukla

**Artificial Intelligence, Internet of Things and Smart Learning**

**The Transfer Trajectory onto the Asteroid for Mining Purposes Using LPG-Algorithm** ..... 633  
 Vijil Kumar and Badam Singh Kushvah



**Prediction of Chaotic Attractors in Quasiperiodically Forced Logistic Map Using Deep Learning** ..... 649  
 J. Meiyazhagan and M. Senthilvelan

**Dynamic Calibration of a Stress-Wave Force Balance Using Hybrid Soft Computing Approach** ..... 659  
 Sima Nayak and Nirranjan Sahoo

**Environment-Friendly Smart City Solution with IoT Application** ..... 669  
 Ayush Kumar, Saket Kumar Jha, and Jitendra Singh Tamang

**Parametric Optimization of WEDM Process on Nanostructured Hard Facing Alloy Applying Metaheuristic Algorithm** ..... 675  
 Abhijit Saha, Pritam Pain, and Goutam Kumar Bose

**Object Detection: A Comparative Study to Find Suitable Sensor in Smart Farming** ..... 685  
 Mohit Kumar Mishra and Deepa Sonal

**Robust Adaptive Controller for a Class of Uncertain Nonlinear Systems with Disturbances** ..... 695  
 Ngo Tri Nam Cuong, Le Van Chuong, and Mai The Anh

**Mathematical Modeling: Trends and Applications**

**Role of Additional Food in a Delayed Eco-Epidemiological Model with the Fear-Effect** ..... 709  
 Chandan Jana, Dilip Kumar Maiti, and Atasi Patra Maiti

**Impact of Predator Induced Fear in a Toxic Marine Environment Considering Toxin Dependent Mortality Rate** ..... 721  
 Dipesh Barman, Jyotirmoy Roy, and Shariful Alam

**Stability Analysis of the Leslie-Gower Model with the Effects of Harvesting and Prey Herd Behaviour** ..... 733  
 Md. Golam Mortuja, Mithilesh Kumar Chaube, and Santosh Kumar

**Modeling the Symbiotic Interactions Between *Wolbachia* and Insect Species** ..... 741  
 Davide Donnarumma, Claudia Pio Ferreira, and Ezio Venturino

**Effect of Nonlinear Harvesting on a Fractional-Order Predator-Prey Model** ..... 761  
 Kshirod Sarkar and Biswajit Mondal

**A Numerical Application of Collocation Method for Solving KdV-Lax Equation** ..... 775  
 Seydi Battal Gazi Karakoc and Derya Yildirim Sucu

<b>Influence of Suspension Lock on the Four-Station Military Recovery Vehicle with Trailing Arm Suspension During Crane Operation</b> .....	783
M. Devesh, R. Manigandan, and Saayan Banerjee	
<b>One-Dimensional Steady State Heat Conduction Equation with and Without Source Term by FVM</b> .....	797
Neelam Patidar and Akshara Makrariya	
<b>Travelling and Solitary Wave Solutions of (2+1)-Dimensional Nonlinear Evolution Equations by Using Khater Method</b> .....	807
Ram Mehar Singh, S. B. Bhardwaj, Anand Malik, Vinod Kumar, and Fakir Chand	
<b>Cosmological Models for Bianchi Type-I Space-Time in Lyra Geometry</b> .....	819
Pratik V. Lapse and Binaya K. Bishi	
<b>A Non-linear Model of a Fishery Resource for Analyzing the Effects of Toxic Substances</b> .....	837
Sudipta Sarkar, Tanushree Murmu, Ashis Kumar Sarkar, and Kripasindhu Chaudhuri	
<b>Analysis for the Impact of HIV Transmission Dynamics in Heterosexuality and Homosexuality</b> .....	849
Regan Murugesan, Suresh Rasappan, and Nagadevi Bala Nagaram	
<b>Exact Traveling Wave Solutions to General FitzHugh-Nagumo Equation</b> .....	861
Subin P. Joseph	
<b>A Multi-criteria Model of Selection of Students for Project Work Based on the Analysis of Their Performance</b> .....	873
Sukarna Dey Mondal, Dipendra Nath Ghosh, and Pabitra Kumar Dey	
<b>Mathematical Modeling of Thermal Error Using Machine Learning</b> .....	883
Rohit Ananthan and N. Rino Nelson	
<b>Establishing the Planting Calendar for Onions (<i>Allium cepa</i> L) Using Localized Data on Temperature and Rainfall</b> .....	895
Jubert B. Oligo and Julius S. Valderama	
<b>Growth of Single Species Population: A Novel Approach</b> .....	907
Suvankar Majee, Soovoojeet Jana, Anupam Khatua, and T. K. Kar	
<b>A Numerical Approximation of the KdV-Kawahara Equation via the Collocation Method</b> .....	917
Seydi Battal Gazi Karakoc and Derya Yildirim Sucu	

**Approximate Solutions to Pseudo-Parabolic Equation with Initial and Boundary Conditions** ..... 925  
 Nishi Gupta and Md. Maqbul

**Mathematical Model for Tumor-Immune Interaction in Imprecise Environment with Stability Analysis** ..... 935  
 Subrata Paul, Animesh Mahata, Supriya Mukherjee, Prakash Chandra Mali, and Banamali Roy

**Dromion Lattice Structure for Coupled Nonlinear Maccari’s Equation** ..... 947  
 J. Thilakavathy, K. Subramanian, R. Amrutha, and M. S. Mani Rajan

**Solving Non-linear Partial Differential Equations Using Homotopy Analysis Method (HAM)** ..... 955  
 Ajay Kumar and Ramakanta Meher

**Nonlinear Modelling and Analysis of Longitudinal Dynamics of Hybrid Airship** ..... 965  
 Abhishek Kumar and Om Prakash

**A New Two-Parameter Odds Generalized Lindley-Exponential Model** ..... 977  
 Sukanta Pramanik

**Stability Switching in a Cooperative Prey-Predator Model with Transcritical and Hopf-bifurcations** ..... 987  
 Sajjan, Ankit Kumar, and Balram Dubey

**Mathematical Model of Solute Transport in a Permeable Tube with Variable Viscosity** ..... 1001  
 M. Varunkumar

**Dynamical Systems: Chaos, Complexity and Fractals**

**Impact of Cooperative Hunting and Fear-Induced in a Prey-Predator System with Crowley-Martin Functional Response** ..... 1015  
 Anshu, Sourav Kumar Sasmal, and Balram Dubey

**Chaotic Dynamics of Third Order Wien Bridge Oscillator with Memristor Under External Generalized Sinusoidal Stimulus** ..... 1027  
 Aniruddha Palit

**The Electrodynamical Origin of the Wave-Particle Duality** ..... 1043  
 Álvaro García López

**Randomness and Fractal Functions on the Sierpinski Triangle** ..... 1057  
 A. Gowrisankar and M. K. Hassan

**Bifurcation Analysis of a Leslie-Gower Prey-Predator Model with Fear and Cooperative Hunting** ..... 1069  
 Ashvini Gupta and Balram Dubey

**Chaotic Behavior in a Novel Fractional Order System with No Equilibria** ..... 1081  
 Santanu Biswas, Humaira Aslam, Satyajit Das, and Aditya Ghosh

**Soliton Dynamics in a Weak Helimagnet** ..... 1093  
 Geo Sunny, L. Kavitha, and A. Prabhu

**Delay-Resilient Dynamics of a Landslide Mechanical Model** ..... 1103  
 Srđan Kostić and Nebojša Vasović

**The Fifth Order Caudrey–Dodd–Gibbon Equation for Exact Traveling Wave Solutions Using the  $(G'/G, 1/G)$ -Expansion Method** ..... 1113  
 M. Mamun Miah

**Results on Fractal Dimensions for a Multivariate Function** ..... 1123  
 T. M. C. Priyanka and A. Gowrisankar

**Stochastic Predator-Prey Model with Disease in Prey and Hybrid Impulses for Integrated Pest Management** ..... 1133  
 Shivani Khare, Kunwer Singh Mathur, and Rajkumar Gangele

**Bifurcation Analysis of Longitudinal Dynamics of Generic Air-Breathing Hypersonic Vehicle for Different Operating Flight Conditions** ..... 1149  
 Ritesh Singh, Om Prakash, Sudhir Joshi, and Yogananda Jeppu

**Multi-soliton Solutions of the Gardner Equation Using Darboux Transformation** ..... 1159  
 Dipan Saha, Santanu Raut, and Prasanta Chatterjee

**Optical Dark and Kink Solitons in Multiple Core Couplers with Four Types of Nonlinearity** ..... 1169  
 Anand Kumar, Hitender Kumar, Fakir Chand, Manjeet Singh Gautam, and Ram Mehar Singh

**Analysis of a Variable-Order Multi-scroll Chaotic System with Different Memory Lengths** ..... 1181  
 N. Medellín-Neri, J. M. Munoz-Pacheco, O. Félix-Beltrán, and E. Zambrano-Serrano

**Effect of DEN-2 Virus on a Stage-Structured Dengue Model with Saturated Incidence and Constant Harvesting** ..... 1193  
 Kunwer Singh Mathur and Bhagwan Kumar

<b>Modulational Instability Analysis in An Isotropic Ferromagnetic Nanowire with Higher Order Octopole-Dipole Interaction</b> .....	1209
T. Pavithra, L. Kavitha, Prabhu, and Awadesh Mani	
<b>Study of Nonlinear Dynamics of Vilnius Oscillator</b> .....	1219
Dmitrijs Pikulins, Sergejs Tjukovs, Iheanacho Chukwuma Victor, and Aleksandrs Ipatovs	
<b>Classical Nonlinear Dynamics Associated with Prime Numbers: Non-relativistic and Relativistic Study</b> .....	1229
Charli Chinmayee Pal and Subodha Mishra	
<b>Other Fields of Nonlinear Dynamics</b>	
<b>Dynamics of Chemical Excitation Waves Subjected to Subthreshold Electric Field in a Mathematical Model of the Belousov-Zhabotinsky Reaction</b> .....	1241
Anupama Sebastian, S. V. Amrutha, Shreyas Punacha, and T. K. Shajahan	
<b>Structural Transformation and Melting of the Vortex Lattice in the Rotating Bose Einstein Condensates</b> .....	1251
Rony Boral, Swarup Sarkar, and Pankaj K. Mishra	
<b>Effect of Internal Damping on the Vibrations of a Jeffcott Rotor System</b> .....	1263
Raj C. P. Shibin, Amit Malgol, and Ashesh Saha	
<b>The Collective Behavior of Magnetically Coupled Neural Network Under the Influence of External Stimuli</b> .....	1275
T. Remi and P. A. Subha	
<b>Excitation Spectrum of Repulsive Spin-Orbit Coupled Bose-Einstein Condensates in Quasi-one Dimension: Effect of Interactions and Coupling Parameters</b> .....	1287
Sanu Kumar Gangwar, R. Ravisankar, and Pankaj K. Mishra	
<b>Empirical Models for Premiums and Clustering of Insurance Companies: A Data-Driven Analysis of the Insurance Sector in India</b> .....	1299
Rakshit Tiwari and Siddhartha P. Chakrabarty	
<b>Variations in the Scroll Ring Characteristics with the Excitability and the Size of the Pinning Obstacle in the BZ Reaction</b> .....	1311
Puthiyapurayil Sibeesh, S V Amrutha, and T K Shajahan	
<b>Periodic Amplifications of Attosecond Three Soliton in an Inhomogeneous Nonlinear Optical Fiber</b> .....	1319
M. S. Mani Rajan, Saravana Veni, and K. Subramanian	

**Analysis of Flexoelectricity with Deformed Junction in Two Distinct Piezoelectric Materials Using Wave Transmission Study** ..... 1329  
 Abhinav Singhal, Rakhi Tiwari, Juhi Baroi, and Chandraketu Singh

**A Review on the Reliability Analysis of Point Machines in Railways** ..... 1341  
 Deb Sekhar Roy, Debajyoti Sengupta, Debraj Paul, Debjit Pal, Aftab Khan, Ankush Das, Surojit Nath, Kaushik Sinha, and Bidhan Malakar

**Application of a Measure of Noncompactness in  $cs$ -Solvability and  $bs$ -Solvability of an Infinite System of Differential Equations** ..... 1353  
 Niraj Sapkota, Rituparna Das, and Santonu Savapondit

**Instabilities of Excitation Spectrum for Attractive Spin-Orbit Coupled Bose-Einstein Condensates in Quasi-one Dimension** ..... 1365  
 Sonali Gangwar, R. Ravisankar, and Pankaj K. Mishra

**The Dynamics of COVID-19 Pandemic**

**Mapping First to Third Wave Transition of Covid19 Indian Data via Sigmoid Function** ..... 1377  
 Supriya Mondal and Sabyasachi Ghosh

**Progression of COVID-19 Outbreak in India, from Pre-lockdown to Post-lockdown: A Data-Driven Statistical Analysis** ..... 1389  
 Dipankar Mondal and Siddhartha P. Chakrabarty

**Analysis of Fuzzy Dynamics of SEIR COVID-19 Disease Model** ..... 1399  
 B. S. N. Murthy, M N Srinivas, and M A S Srinivas

**Covid-19 Vaccination in India: Prophecy of Time Period to Immune 18+ Population** ..... 1409  
 Anand Kumar, Agin Kumari, and Rishi Pal Chahal

**COVID-19 Detection from Chest X-Ray (CXR) Images Using Deep Learning Models** ..... 1417  
 Mithun Karmakar, Koustav Chanda, and Amitava Nag

**Pre-covid and Post-covid Situation of Indian Stock Market-A Walk Through Different Sectors** ..... 1425  
 Antara Roy, Damodar Prasad Goswami, and Sudipta Sinha

<b>A Mathematical Analysis on Covid-19 Transmission Using Seir Model</b> .....	1435
Sandip Saha, Apurba Narayan Das, and Pranabendra Talukdar	
<b>Dynamics of Coronavirus and Malaria Diseases: Modeling and Analysis</b> .....	1449
Attiq ul Rehman and Ram Singh	
<b>Design of Imidazole-Based Drugs as Potential Inhibitors of SARS-Cov-2 of the Delta and Omicron Variant</b> .....	1465
Peter Solo and M. Arockia Doss	

# Contributors

**Abdikian A.** Department of Physics, Malayer University, Malayer, 65719-95863, Iran

**Ajith K. M.** National Institute of Technology Karnataka, Mangaluru, India

**Akleyek Sedat** Ondokuz Mayıs University, Samsun, Turkey

**Alam Shariful** Indian Institute of Engineering Science and Technology, Shibpur, Howrah, West Bengal, India

**Ali Demir Mehmet** Computer Engineering Department, Kocaeli University, Kocaeli, Turkey

**Amrutha R.** Department of Physics, KCG College of Technology, Chennai, India

**Amrutha S. V.** Department of Physics, National Institute of Technology Karnataka, Surathkal, Mangalore, Karnataka, India

**Ananthan Rohit** Mechanical Engineering, Indian Institute of Information Technology, Design and Manufacturing, Kancheepuram, Chennai, India

**Anh Mai The** Vinh University, Vinh city, Nghean, Vietnam

**Anshu** Department of Mathematics, BITS Pilani, Pilani, Rajasthan, India

**Ashwani** School of Basic Sciences, Indian Institute of Technology Mandi, Mandi, Himachal Pradesh, India

**Aslam Humaira** Department of Mathematics, Adamas University, Kolkata, India

**Atteya A.** Department of Physics, Faculty of Science, Alexandria University, Alexandria, Egypt

**Bandyopadhyay Anup** Department of Mathematics, Jadavpur University, Kolkata, India

**Banerjee Saayan** Centre for Engineering Analysis and Design, Combat Vehicles R&D Establishment, DRDO, New Delhi, India



**Barman Dipesh** Indian Institute of Engineering Science and Technology, Shibpur, Howrah, West Bengal, India

**Baroi Juhi** School of Sciences, Christ (Deemed to Be University) Delhi NCR, Ghaziabad, India

**Bhardwaj S. B.** Department of Physics, SUS Govt. College Matak-Majri, Karnal, India

**Bishi Binaya K.** Department of Mathematics, Lovely Professional University, Jalandhar, Phagwara, Panjab, India;

Department of Mathematical Sciences, University of Zululand, Kwa-Dlangezwa, South Africa

**Biswas Santanu** Department of Mathematics, Adamas University, Kolkata, India; Department of Mathematics, Jadavpur University, Kolkata, India

**Borah Joydeep** Department of Mathematics, D. D. R. College, Chabua, AS, India

**Borah Rupjyoti** Department of Mathematics, Dibrugarh University, Dibrugarh, AS, India

**Boral Rony** Department of Physics, Indian Institute of Technology Guwahati, Guwahati, Assam, India

**Büyüksaraçoğlu Sakallı Fatma** Trakya University, Edirne, Turkey

**Chakrabarty Siddhartha P.** Indian Institute of Technology Guwahati, Guwahati, Assam, India

**Chand Fakir** Department of Physics, Kurukshetra University, Kurukshetra, India

**Chanda Koustav** L&T Infotech, Ranaghat, India

**Chandra Swarniv** Jadavpur University, Kolkata, India;

Department of Physics, Govt. General Degree College at Kushmandi, Dakshin Dinajpur, India;

Institute of Natural Sciences and Applied Technology, Kolkata, India

**Chandrashekhara G.** Department of Mathematics, Osmania University, Hyderabad, TG, India

**Chatterjee Prasanta** Department of Mathematics, Siksha Bhavana, Visva-Bharati, Santiniketan, Santiniketan, West Bengal, India

**Chaube Mithilesh Kumar** Dr. SPM IIIT Naya Raipur, C.G., Raipur, India

**Chaudhuri Kripasindhu** Department of Mathematics, Jadavpur University, Kolkata, India

**Chukwuma Victor Iheanacho** Institute of Radioelectronics, Riga Technical University, Riga, Latvia

**Chuong Le Van** Vinh University, Vinh city, Nghean, Vietnam

**Cuong Ngo Tri Nam** Systemtec JSC, Hanoi, Vietnam

**Das Ankush** Department of Electrical Engineering, JIS College of Engineering, Kalyani, West Bengal, India

**Das Apurba Narayan** Department of Mathematics, Alipurduar University, Alipurduar, West Bengal, India

**Das Chinmay** Department of Mathematics, Govt. General Degree College at Kushmandi, Dakshin Dinajpur, India;  
Institute of Natural Sciences and Applied Technology, Kolkata, India

**Das Debabrata** Cooch Behar Panchanan Barma University, Cooch Behar, India

**Das Rituparna** Department of Mathematics, Pandu College, Guwahati, India

**Das Satyajit** Department of Mathematics, Adamas University, Kolkata, India

**Das Susmita** Cooch Behar Panchanan Barma University, Cooch Behar, India

**Deb Biswajit** Department of Mathematics, Sikkim Manipal Institute of Technology, Sikkim Manipal University, East-Sikkim, India

**Dehingia Hirak Jyoti** Department of Mathematics, Dibrugarh University, Dibrugarh, Assam, India

**Deka P. N.** Department of Mathematics, Dibrugarh University, Dibrugarh, Assam, India

**Devesh M.** School of Mechanical Engineering, Vellore Institute of Technology, Chennai, India

**Dey Mondal Sukarna** Department of Mathematics, Dr. B.C. Roy Engineering College, MAKAUT, Kolkata, West Bengal, India

**Dey Debasish** Department of Mathematics, Dibrugarh University, Dibrugarh, AS, India

**Dey Dipankar** Department of Computer Science and Technology, Global Institute of Science and Technology, Haldia, WB, India

**Dhar Subham** Cooch Behar Panchanan Barma University, Cooch Behar, WB, India

**Donnarumma Davide** Università di Torino, Torino, Italy

**Doss M. Arockia** Department of Chemistry, St. Joseph University, Dimapur, India

**Dubey Balram** Department of Mathematics, BITS Pilani, Pilani Campus, Pilani, Rajasthan, India

**Dutta Dharitree** Department of Physics, Anandaram Dhekial Phookan College, Nagaon, Assam, India

**Fataf Nur Aisyah Binti Abdul** Cyber Security Centre, National Defence University of Malaysia (NDUM), Kuala Lumpur, Malaysia

**Félix-Beltrán O.** Faculty of Electronics Sciences, Benemérita Universidad Autónoma de Puebla, Puebla, Mexico

**Gandhi Rishu** Department of Mathematics, Birla Institute of Technology and Science, Pilani, Rajasthan, India

**Gangele Rajkumar** Department of Mathematics and Statistics, Dr. Harisingh Gour Vishwavidyalaya, Sagar, Madhya Pradesh, India

**Gangwar Sanu Kumar** Department of Physics, Indian Institute of Technology, Guwahati, Assam, India

**Gangwar Sonali** Department of Physics, Indian Institute of Technology, Guwahati, Assam, India

**García López Álvaro** Universidad Rey Juan Carlos, Madrid, Spain

**Gautam Anjan** Department of Mathematics, Sikkim Manipal Institute of Technology, Sikkim Manipal University, East-Sikkim, India

**Gautam Manjeet Singh** Department of Physics, Government College, Jind, India

**Ghosh Aditya** Department of Mathematics, Adamas University, Kolkata, India

**Ghosh Basudev** Jadavpur University, Kolkata, India

**Ghosh S. S.** Indian Institute of Geomagnetism, Mumbai, India

**Ghosh Sabyasachi** Indian Institute of Technology Bhilai, Sejbahar, Raipur, Chhattisgarh, India

**Gomathy G.** Department of Mathematics, School of Advanced Sciences, Vellore Institute of Technology, Vellore, Tamilnadu, India

**Goswami Damodar Prasad** Asutosh Mookerjee Memorial Institute, Sivotosh Mookerjee Science Centre, Kolkata, India

**Goswami Jyotirmoy** Jadavpur University, Kolkata, India

**Goswami K. S.** Centre of Plasma Physics—Institute for Plasma Research, Assam, India

**Goswami Pinkimani** Department of Mathematics, University of Science and Technology Meghalaya, Ri-Bhoi, ML, India

**Gowrisankar A.** Department of Mathematics, School of Advanced Sciences, Vellore Institute of Technology, Vellore, Tamil Nadu, India

**Gupta Ashvini** Department of Mathematics, BITS Pilani, Pilani Campus, Pilani, Rajasthan, India

**Gupta Nishi** National Institute of Technology Silchar, Silchar, Assam, India

**Hassan M. K.** Department of Physics, University of Dhaka, Dhaka, Bangladesh

**Ipatovs Aleksandrs** Institute of Radioelectronics, Riga Technical University, Riga, Latvia

**Jana Chandan** Department of Applied Mathematics with Oceanology and Computer Programming, Vidyasagar University, Midnapore, West Bengal, India

**Jana Soovoojeet** Department of Mathematics, Ramsaday College, Amta, Howrah, India

**Jeppu Yogananda** Honeywell Technology Solutions, Hyderabad, Telangana, India

**Joseph Subin P.** Government Engineering College, Wayanad, Thalappuzha, Kerala, India

**Joshi Sudhir** University of Petroleum & Energy Studies, Dehradun, Uttarakhand, India

**Kairi Rishi Raj** Department of Mathematics, Cooch Behar Panchanan Barma University, Cooch Behar, India

**Kalita Pankaj** School of Energy Science and Engineering, Indian Institute of Technology Guwahati, Guwahati, India

**Kar T. K.** Department of Mathematics, Indian Institute of Engineering Science and Technology, Shibpur, Howrah, India

**Karakoc Seydi Battal Gazi** Department of Mathematics, Faculty of Science and Art, Nevsehir Haci Bektas Veli University, Nevsehir, Turkey

**Karmakar Mithun** Department of CSE, CIT Kokrajhar, Kokrajhar, Assam, India

**Kaur Manveet** Department of Physics, Guru Nanak Dev University, Amritsar, India

**Kaur Rajneet** Department of Physics, Guru Nanak Dev University, Amritsar, India

**Kavitha L.** Department of Physics, School of Basic and Applied Sciences, Central University of Tamil Nadu, Thiruvarur, Tamil Nadu, India;

The Abdus Salam International Centre for Theoretical Physics, Trieste, Italy

**Khan Aftab** Department of Electrical Engineering, JIS College of Engineering, Kalyani, West Bengal, India

**Khandale K. Y.** Department of Physics, Shivaji University, Kolhapur, India

**Khanduri Umesh** Department of Mathematics, Birla Institute of Technology and Science, Pilani, Rajasthan, India

**Khare Shivani** Department of Mathematics and Statistics, Dr. Harisingh Gour Vishwavidyalaya, Sagar, Madhya Pradesh, India

**Khasim Ahamed** National Institute of Technology Karnataka, Mangaluru, India

**Khatua Anupam** Department of Mathematics, Indian Institute of Engineering Science and Technology, Shibpur, Howrah, India

**Kodi Raghunath** Department of Humanities and Sciences (Mathematics), Bheema Institute of Technology and Science, Adoni, AP, India

**Kostić Srđan** Geology Department, Jaroslav Černi Water Institute, Belgrade, Serbia

**Kulkarni Vinayak** School of Energy Science and Engineering, Indian Institute of Technology Guwahati, Guwahati, India

**Kumar Bose Goutam** Department of Mechanical Engineering, Haldia Institute of Technology, Haldia, West Bengal, India

**Kumar Dey Pabitra** Department of Computer Applications, Dr. B.C. Roy Engineering College, MAKAUT, Durgapur, West Bengal, India

**Kumar Jha Saket** Department of Electronics and Communication Engineering, Sikkim Manipal Institute of Technology, Sikkim Manipal University, Majitar, Sikkim, India

**Kumar Maiti Dilip** Department of Applied Mathematics with Oceanology and Computer Programming, Vidyasagar University, Midnapore, West Bengal, India

**Kumar Mishra Mohit** Department of Electronics and Communication Engineering, Manipal University, Jaipur, India

**Kumar Sarkar Ashis** Department of Mathematics, Jadavpur University, Kolkata, India

**Kumar Abhishek** Department of Electrical Engineering, Manipal University Jaipur, Jaipur, Rajasthan, India;  
Department of Aerospace Engineering, University of Petroleum and Energy Studies, Dehradun, India

**Kumar Ajay** Department of Mathematics and Humanities, Sardar Vallabhbhai National Institute of Technology, Surat, Gujarat, India

**Kumar Anand** Department of Physics, Chaudhary Ranbir Singh University, Jind, India

**Kumar Ankit** Department of Mathematics, BITS Pilani, Pilani, Rajasthan, India

**Kumar Ayush** Department of Electronics and Communication Engineering, Sikkim Manipal Institute of Technology, Sikkim Manipal University, Majitar, Sikkim, India

**Kumar B. Rushi** Department of Mathematics, SAS, Vellore Institution of Technology, Vellore, Tamil Nadu, India

**Kumar Bhagwan** Department of Mathematics and Statistics, Dr. Harisingh Gour Vishwavidyalaya, Sagar, Madhya Pradesh, India

**Kumar Hitender** Department of Physics, Government College for Women, Gharaunda, India

**Kumar Santosh** Dr. SPM IIIT Naya Raipur, C.G., Raipur, India

**Kumar Vijil** Department of Mathematics and Computing, Indian Institute of Technology (ISM), Dhanbad, Jharkhand, India

**Kumar Vinod** Department of Physics, Chaudhary Devi Lal University, Sirsa, India

**Kumari Agin** Department of Mathematics, Chaudhary Bansi Lal University, Bhiwani, India

**Kurt Pehlivanoglu Meltem** Kocaeli University, Kocaeli, Turkey

**Kushvah Badam Singh** Department of Mathematics and Computing, Indian Institute of Technology (ISM), Dhanbad, Jharkhand, India

**Lavanya C.** Department of Physics, Periyar University, Salem, Tamil Nadu, India

**Lepse Pratik V.** Department of Mathematics, Lovely Professional University, Jalandhar, Phagwara, Panjab, India

**Mahata Animesh** Mahadevnagar High School, Maheshtala, Kolkata, West Bengal, India

**Majee Suvankar** Department of Mathematics, Indian Institute of Engineering Science and Technology, Shibpur, Howrah, India

**Makrariya Akshara** School of Advanced Science-Mathematics, VIT Bhopal University, Bhopal, Madhya Pradesh, India

**Malakar Bidhan** Department of Electrical Engineering, JIS College of Engineering, Kalyani, West Bengal, India

**Malgol Amit** National Institute of Technology Calicut, Kattangal, Kerala, India

**Mali Prakash Chandra** Department of Mathematics, Jadavpur University, Kolkata, India

**Malik Anand** Department of Physics, Chaudhary Ranbir Singh University, Jind, India

**Mamun Miah M.** Department of Mathematics, Khulna University of Engineering & Technology, Khulna, Bangladesh

**Mani Rajan M. S.** Department of Physics, University College of Engineering, Anna University, Ramanathapuram, India

**Mani Awadesh** Condensed Matter Physics Division, Indira Gandhi Centre for Atomic Research, Kalpakkam, Tamil Nadu, India

**Manigandan R.** School of Mechanical Engineering, Vellore Institute of Technology, Chennai, India

- Maqbul Md.** National Institute of Technology Silchar, Silchar, Assam, India
- Mathur Kunwer Singh** Department of Mathematics and Statistics, Dr. Harisingh Gour Vishwavidyalaya, Sagar, Madhya Pradesh, India
- Medellín-Neri N.** Faculty of Electronics Sciences, Benemérita Universidad Autónoma de Puebla, Puebla, Mexico
- Meher Ramakanta** Department of Mathematics and Humanities, Sardar Vallabhbhai National Institute of Technology, Surat, Gujarat, India
- Meiyazhagan J.** Department of Nonlinear Dynamics, Bharathidasan University, Tiruchirappalli, Tamil Nadu, India
- Micheal David Raj** Division of Mathematics, School of Advanced Sciences, Vellore Institute of Technology, Chennai, Tamil Nadu, India
- Mishra Pankaj K.** Department of Physics, Indian Institute of Technology Guwahati, Guwahati, Assam, India
- Mishra Subodha** Department of Physics, Siksha ‘O’ Anusandhan, Deemed to be University, Bhubaneswar, 751030, India
- Mondal Biswajit** Raja N.L. Khan Women’s College (Autonomous), Midnapore, West Bengal, India
- Mondal Dipankar** Indian Institute of Technology Guwahati, Guwahati, Assam, India
- Mondal Kajal Kumar** Department of Mathematics, Cooch Behar Panchanan Barma University, Cooch Behar, West Bengal, India
- Mondal Supriya** MMI College of Nursing, Pachpedi Naka, Raipur, Chhattisgarh, India;  
VY Hospital, Adjacent to Kamal Vihar (Sector 12), Raipur, Chhattisgarh, India
- Mortuja Md. Golam** Dr. SPM IIIT Naya Raipur, C.G., Raipur, India
- Mukherjee Supriya** Department of Mathematics, Gurudas College, Kolkata, West Bengal, India
- Munoz-Pacheco J. M.** Faculty of Electronics Sciences, Benemérita Universidad Autónoma de Puebla, Puebla, Mexico
- Murmu Tanushree** Department of Mathematics, Jadavpur University, Kolkata, India
- Murthy B. S. N.** Department of Mathematics, Aditya College of Engineering and Technology, Surampalem, Andhra Pradesh, India
- Murugesan Regan** Vel Tech Rangarajan Dr. Sagunthala R & D Institute of Science and Technology, Chennai, Tamil Nadu, India
- Nag Amitava** Department of CSE, CIT Kokrajhar, Kokrajhar, Assam, India

**Nagaram Nagadevi Bala** Vel Tech Rangarajan Dr. Sagunthala R & D Institute of Science and Technology, Chennai, Tamil Nadu, India

**Natarajan C.** Department of Mathematics, Srinivasa Ramanujan Centre, SASTRA Deemed University, Kumbakonam, India

**Nath Ghosh Dipendra** Controller of Examinations, Kazi Nazrul University, Asansol, West Bengal, India

**Nath Surojit** Department of Electrical Engineering, JIS College of Engineering, Kalyani, West Bengal, India

**Nayak Sima** Department of Mechanical Engineering, Indian Institute of Technology Guwahati, Guwahati, India

**Nikam P. P.** Department of Physics, Devchand College, Arjunnagar, Kolhapur, India

**Oligo Jubert B.** College of Teacher Education, Nueva Vizcaya State University, Bayombong, Philippines

**Ozah Jintu** Dibrugarh University, Dibrugarh, Assam, India

**Pain Pritam** Department of Mechanical Engineering, Haldia Institute of Technology, Haldia, West Bengal, India

**Pal Chahal Rishi** Department of Physics, Chaudhary Bansi Lal University, Bhiwani, India

**Pal Charli Chinmayee** Department of Physics, Siksha 'O' Anusandhan, Deemed to be University, Bhubaneswar, 751030, India

**Pal Debjit** Department of Electrical Engineering, JIS College of Engineering, Kalyani, West Bengal, India

**Pal Nikhil** Department of Mathematics, Siksha-Bhavana, Visva-Bharati University, Santiniketan, India

**Palit Aniruddha** Department of Mathematics, Surya Sen Mahavidyalaya, Siliguri, India

**Panigoro Hasan S.** Department of Mathematics, State University of Gorontalo, Bone, Bolango, Indonesia

**Patidar Neelam** School of Advanced Science-Mathematics, VIT Bhopal University, Bhopal, Madhya Pradesh, India

**Patil S. D.** Department of Physics, Devchand College, Arjunnagar, Kolhapur, Maharashtra, India

**Patil S. S.** Department of Physics, Vivekanand College, Kolhapur, India

**Patra Maiti Atasi** Directorate of Distance Education, Vidyasagar University, Midnapore, West Bengal, India



**Pattanayak Solanki** Department of Computer Science, Haldia Institute of Management, Haldia, WB, India

**Paul Anindya** Department of Mathematics, Cooch Behar Panchanan Barma University, Cooch Behar, West Bengal, India

**Paul Debraj** Department of Electrical Engineering, JIS College of Engineering, Kalyani, West Bengal, India

**Paul Kamakhya** North Eastern Hill University, Shillong, ML, India

**Paul Niranjan** Department of Mathematics, Siksha Bhavana, Visva-Bharati, Santiniketan, Santiniketan, West Bengal, India

**Paul Subrata** Department of Mathematics, Arambagh Govt. Polytechnic, Arambagh, West Bengal, India

**Pavithra T.** Department of Physics, Central University of Tamil Nadu, Thiruvavur, Tamil Nadu, India

**Pawar V. S.** Department of Physics, Rajer Ramrao Mahavidyalay, Jath, Maharashtra, India

**Pikulins Dmitrijs** Institute of Radioelectronics, Riga Technical University, Riga, Latvia

**Pio Ferreira Claudia** São Paulo State University (UNESP), Botucatu, Brazil

**Poddar Nanda** Cooch Behar Panchanan Barma University, Cooch Behar, WB, India

**Poonam** Department of Mathematics, BITS Pilani, Pilani, Rajasthan, India

**Prabhu A.** Department of Physics, Periyar University, Salem, India

**Prabhu** Department of Chemistry, Periyar University, Salem, Tamil Nadu, India

**Pradhan Barsha** Department of Mathematics, Sikkim Manipal Institute of Technology, Sikkim Manipal University, Majitar, Rangpo, East-Sikkim, India

**Prakash Om** Department of Aerospace Engineering, University of Petroleum and Energy Studies, Dehradun, Uttarakhand, India

**Pramanik Sukanta** Department of Statistics, Siliguri College, North Bengal University, Siliguri, West Bengal, India

**Prasad Punam Kumari** Department of Mathematics, Sikkim Manipal Institute of Technology, Sikkim Manipal University, East-Sikkim, India

**Priyanka T. M. C.** Department of Mathematics, School of Advanced Sciences, Vellore Institute of Technology, Vellore, Tamil Nadu, India

**Punacha Shreyas** Department of Physics, National Institute of Technology Karnataka, Surathkal, Mangalore, Karnataka, India

**Raghavi K.** Department of Physics, School of Basic and Applied Sciences, Central University of Tamil Nadu, Thiruvavur, India

**Rahmi Emli** Department of Mathematics, State University of Gorontalo, Bone, Bolango, Indonesia

**Rajan M. S. Mani** Anna University, University College of Engineering, Ramanathapuram, India

**Rao Shiva** Dibrugarh University, Dibrugarh, Assam, India

**Rasappan Suresh** University of Technology and Applied Sciences- Ibri, Sultanate of Oman, Ibri, Oman

**Raut Santanu** Department of Mathematics, Mathabhanga College, Coochbehar, India

**Ravisankar R.** Department of Physics, Indian Institute of Technology, Guwahati, Assam, India

**Ravuri Mohana Ramana** Department of Basic Science and Humanities (Mathematics), Narasaraopeta Engineering College, Narasaraopeta, AP, India

**Ray Rajendra K.** School of Basic Sciences, Indian Institute of Technology Mandi, Mandi, Himachal Pradesh, India

**Rehman Attiq ul** Department of Mathematical Sciences, BGSB University, Rajouri, India

**Remi T.** Department of Physics, Farook College University of Calicut, Kozhikode, Kerala, India

**Rino Nelson N.** Mechanical Engineering, Indian Institute of Information Technology, Design and Manufacturing, Kancheepuram, Chennai, India

**Rout Anil Kumar** School of Energy Science and Engineering, Indian Institute of Technology Guwahati, Guwahati, India

**Roy Antara** Asansol Institute of Engineering and Management-Polytechnic, Asansol, India

**Roy Ashim** Department of Mathematics, Alipurduar University, Alipurduar, India

**Roy Banamali** Department of Mathematics, Bangabasi Evening College, Kolkata, West Bengal, India

**Roy Jyotirmoy** Indian Institute of Engineering Science and Technology, Shibpur, Howrah, West Bengal, India

**Roy Subrata** Department of Mathematics, Cooch Behar Panchanan Barma University, Cooch Behar, India

**Rushi Kumar B.** Department of Mathematics, School of Advanced Sciences, Vellore Institute of Technology, Vellore, Tamilnadu, India

**Saha Abhijit** Department of Mechanical Engineering, Haldia Institute of Technology, Haldia, West Bengal, India

**Saha Ashesh** National Institute of Technology Calicut, Kattangal, Kerala, India

**Saha Dipan** Advanced Centre for Nonlinear and Complex Phenomena, Kolkata, India

**Saha Gourab** Cooch Behar Panchanan Barma University, Cooch Behar, India

**Saha Sandip** Department of Mathematics, Madanapalle Institute of Technology & Science, Madanapalle, Andhra Pradesh, India;  
School of Advance Sciences (SAS) Mathematics, Vellore Institute of Technology Chennai, Chennai, Tamilnadu, India

**Sahoo Niranjan** Department of Mechanical Engineering, School of Energy Science and Engineering, Indian Institute of Technology Guwahati, Guwahati, India

**Sahu P. K.** Department of Mathematics, Government Shyama Prasad Mukharjee College, Sitapur, Chhattisgarh, India

**Saikia Banashree** Department of Mathematics, Dibrugarh University, Dibrugarh, Assam, India

**Saini Nareshpal Singh** Department of Physics, Guru Nanak Dev University, Amritsar, India

**Sajan** Department of Mathematics, BITS Pilani, Pilani, Rajasthan, India

**Samanta Sabyasachi** Department of Information Technology, Haldia Institute of Technology, Haldia, WB, India

**Sapkota Niraj** Department of Mathematics, Sikkim Manipal Institute of Technology, Sikkim Manipal University, Sikkim, India

**Sardar Sankirtan** Department of Mathematics, Guru Ghasidas Vishwavidyalaya, Bilaspur, India

**Sarkar Jit** Jadavpur University, Kolkata, India

**Sarkar Kshirod** Raja N.L. Khan Women's College (Autonomous), Midnapore, West Bengal, India

**Sarkar Sudipta** Department of Mathematics, Heritage Institute of Technology, Anandapur, Kolkata, West Bengal, India

**Sarkar Swarup** Department of Physics, Indian Institute of Technology Guwahati, Guwahati, Assam, India

**Sarkar Tanay** Department of Mathematics, Jadavpur University, Kolkata, India

**Sarma Ridip** Department of Mathematics, Assam Don Bosco University, Tapesia, Sonapur, Assam, India

**Sasmal Sourav Kumar** Department of Mathematics, BITS Pilani, Pilani, Rajasthan, India

**Savapondit Santonu** Department of Mathematics, Sikkim Manipal Institute of Technology, Sikkim Manipal University, Sikkim, India

**Sebastian Anupama** Department of Physics, National Institute of Technology Karnataka, Surathkal, Mangalore, Karnataka, India

**Sekhar Roy Deb** Department of Electrical Engineering, JIS College of Engineering, Kalyani, West Bengal, India

**Sengupta Debajyoti** Department of Electrical Engineering, JIS College of Engineering, Kalyani, West Bengal, India

**Senthilvelan M.** Department of Nonlinear Dynamics, Bharathidasan University, Tiruchirappalli, Tamil Nadu, India

**Shajahan T. K.** Department of Physics, National Institute of Technology Karnataka, Surathkal, Mangalore, Karnataka, India

**Shanmugavelan S.** Department of Mathematics, Srinivasa Ramanujan Centre, SASTRA Deemed University, Kumbakonam, India

**Sharma Bhupendra K.** Department of Mathematics, Birla Institute of Technology and Science, Pilani, Rajasthan, India

**Sharry** Physics Department, Guru Nanak Dev University, Amritsar, India

**Shibin Raj C. P.** National Institute of Technology Calicut, Kattangal, Kerala, India

**Shilpi** Physics Department, Guru Nanak Dev University, Amritsar, India

**Shukla Manoj Kumar** Lovely Professional University, Phagwara, Punjab, India

**Sibeesh Puthiyapurayil** Department of Physics, National Institute of Technology Karnataka Surathkal, Mangalore, India

**Singh Chandraketu** School of Sciences, Christ (Deemed to Be University) Delhi NCR, Ghaziabad, India

**Singh Tamang Jitendra** Department of Electronics and Communication Engineering, Sikkim Manipal Institute of Technology, Sikkim Manipal University, Majitar, Sikkim, India

**Singhal Abhinav** School of Sciences, Christ (Deemed to Be University) Delhi NCR, Ghaziabad, India

**Singh Kuldeep** Department of Physics, Guru Nanak Dev University, Amritsar, India;  
Department of Mathematics, Khalifa University of Science and Technology, Abu Dhabi, UAE

**Singh Madan Mohan** Department of Basic Sciences & Social Sciences, North Eastern Hill University, Shillong, ML, India

**Singh Ram** Department of Mathematical Sciences, BGSB University, Rajouri, India

**Singh Ram Mehar** Department of Physics, Chaudhary Devi Lal University, Sirsa, India

**Singh Ritesh** Manipal University Jaipur, Jaipur, Rajasthan, India;  
University of Petroleum & Energy Studies, Dehradun, Uttarakhand, India

**Singla Sunidhi** Department of Physics, Guru Nanak Dev University, Amritsar, India

**Sinha Kaushik** Department of Electrical Engineering, JIS College of Engineering, Kalyani, West Bengal, India

**Sinha Sudipta** Burdwan Raj College, University of Burdwan, Burdwan, India

**Slathia Geetika** Department of Physics, Guru Nanak Dev University, Amritsar, India

**Solo Peter** Department of Chemistry, St. Joseph University, Dimapur, India;  
Department of Chemistry, St. Joseph's College (Autonomous), Jakhama, India

**Sonal Deepa** Department of Computer Science, V.K.S. University, Arrah, India

**Sowmiya C.** Department of Mathematics, SAS, Vellore Institution of Technology, Vellore, Tamil Nadu, India

**Srinivas M A S** Department of Mathematics, Jawaharlal Nehru Technological University, Hyderabad, Telangana, India

**Srinivas M N** Department of Mathematics, School of Advanced Sciences, Vellore Institute of Technology, Vellore, Tamilnadu, India

**Subha P. A.** Department of Physics, Farook College University of Calicut, Kozhikode, Kerala, India

**Subramanian K.** Department of Physics, SRM Institute of Science and Technology, Ramapuram Campus, Chennai, India

**Subramanian Venkatesh** National Institute of Technology Karnataka, Mangaluru, India

**Sucu Derya Yildirim** Faculty of Science and Art, Department of Mathematics, Nevsehir Haci Bektas Veli University, Nevsehir, Turkey

**Sunny Geo** Department of Physics, School of Basic and Applied Sciences, Central University of Tamil Nadu, Thiruvavur, India

**Takale M. V.** Department of Physics, Shivaji University, Kolhapur, Maharashtra, India

**Takale P. T.** Department of Physics, Shivaji University, Kolhapur, India

**Talukdar Pranabendra** Department of Mathematics, Alipurduar University, Alipurduar, West Bengal, India

**Tamang Jharna** Department of Mathematics, Sikkim Manipal Institute of Technology, Sikkim Manipal University, Majitar, East-Sikkim, India;  
Department of Mathematics, Sikkim Alpine University, Kamrang, Namchi, South-Sikkim, India

**Thilakavathy J.** Department of Science and Humanities, Jerusalem College of Engineering, Chennai, India

**Tiwari Rakhi** Department of Mathematics, Babasaheb Bhimrao Ambedkar Bihar University, Muzaffarpur, India

**Tiwari Rakshit** Indian Institute of Technology Guwahati, Guwahati-781039, Assam, India

**Tjukovs Sergejs** Institute of Radioelectronics, Riga Technical University, Riga, Latvia

**Tolga Sakallı Muharrem** Trakya University, Edirne, Turkey

**Urunkar T. U.** Department of Physics, Shivaji University, Kolhapur, India

**Valderama Julius S.** College of Arts and Sciences, Nueva Vizcaya State University, Bayombong, Philippines

**Varghese Steffy Sara** Space and Planetary Science Center, Khalifa University, Abu Dhabi, UAE

**Varunkumar M.** Department of Basic Sciences and Humanities, GMR Institute of Technology, Rajam, Andhra Pradesh, India;  
Department of Mathematics, School of Advanced Sciences, VIT-AP University, Amaravati, Andhra Pradesh, India

**Vasović Nebojša** Department of Applied Mathematics and Informatics, Faculty of Mining and Geology, University of Belgrade, Belgrade, Serbia

**Veni Saravana** Department of Physics, Amirta College of Engineering and Technology, Erachakulam Campus, Nagercoil, India

**Venkatalaxmi A.** Department of Mathematics, Osmania University, Hyderabad, TG, India

**Venturino Ezio** Università di Torino, Torino, Italy

**Zambrano-Serrano E.** Facultad de Ingeniería Mecánica y Eléctrica, Universidad Autónoma de Nuevo León, San Nicolás de los Garza, Nuevo León, Mexico

# **Nonlinear Waves and Plasma Dynamics**

# Offset Bipolar Pulses in Magnetospheric Plasma Systems



Steffy Sara Varghese and S. S. Ghosh

**Abstract** The satellite borne electric field instruments have been observed the signatures of Electrostatic Solitary Waves (ESWs) throughout the Earth's magnetospheric boundary layers and have been recorded as localized monopolar, bipolar or tripolar pulses in the electric field (E data). There are also reports of various kinds of electric field structures by the satellites which are different from conventional bipolar pulses. There was no generic theory for them so far. In this work, we are intended to introduce offset bipolar pulses, a possible kinds of non-conventional pulses which can be supported by different kinds of space plasma system. In this regard, we have analyzed a warm multi-ions and two electron temperature plasma model which is quite signifying in magnetospheric studies by adopting the Sagdeev pseudopotential technique. Through rigorous numerical analysis, we have identified and delineated the conditions for the existence of flat top solitary wave, and correlate them with the non-conventional electrostatic solitary wave structures in space plasma observations. It is expected that it will provide a new way of understanding the non-conventional localized pulses in the E-field data recorded during satellite expeditions which are known to be important in determining the microphysics of the Earth's magnetospheric plasma system.

**Keywords** Flat top solitary waves · Electrostatic solitary waves · Offset bipolar pulses

## 1 Introduction

The theory of coherent and organized nonlinear dynamical structures are often found to be relevant in interpreting Electrostatic Solitary Waves (ESWs) which are observed ubiquitously in the Earth's magnetosphere. The large gradient in particle properties

---

S. S. Varghese (✉)

Space and Planetary Science Center, Khalifa University, Abu Dhabi 127788, UAE  
e-mail: [steffystephan28@gmail.com](mailto:steffystephan28@gmail.com)

S. S. Ghosh

Indian Institute of Geomagnetism, Mumbai, India

© The Author(s), under exclusive license to Springer Nature Switzerland AG 2022  
S. Banerjee and A. Saha (eds.), *Nonlinear Dynamics and Applications*,  
Springer Proceedings in Complexity,  
[https://doi.org/10.1007/978-3-030-99792-2\\_1](https://doi.org/10.1007/978-3-030-99792-2_1)



at the magnetospheric boundary layers initiates the perturbations which lead to the generation of stable localized solitary structures. The satellite borne electrical instruments recorded the signatures of localized bipolar and monopolar pulses in the Electric Field (E) data, moving parallel to the background magnetic field. The fast moving positive amplitude bipolar structures are often interpreted as BGK phase space holes for electrons, or, alternatively, as an electron acoustic solitary wave while the low frequency, slowly moving E-field bipolar pulses in the auroral regions are generally interpreted as ion acoustic solitary waves. The monopolar structures, on the other hand, are interpreted as double layers, or shocks, governed by either electron or ion dynamics, and they influence the particle acceleration processes along the field lines.

Advent of high resolution satellite borne instruments, however, identified more kinds of composite and complex organized structures which yet to have a proper theoretical understanding. One such relatively lesser reported structures are the offset bipolar pulses (ofbp) and monopole pairs (mpp) which are the main focus for the present work. The first observational evidence of ESWs was reported in the auroral region by Temerin et al. [1] using S3-3 satellite data. Apart from the conventional bipolar and monopolar structures, they also bore the signatures of ofbp and mpp [2]. For an ofbp, the distance between the bipolar peaks is relatively large compared to the characteristic width of the each peak. Because of their “stretched” look, an ofbp has also been termed as a “stretched bipolar” or a “dispersed bipolar” in the literature. Witt and Lotko [3] theoretically modelled them as paired ion acoustic shocks and showed that they are associated with a square shaped potential well which is different from the conventional bell shaped solitary structures. Their unique theoretical finding, however, didn’t seem to have any subsequent follow ups. Later, fast moving offset bipolar pulses were observed in the day side Polar Cap Boundary Layer (PCBL) [4], the downward current regions of the auroral zone [5, 6], the diffusion region of reconnection [7], and in the magnetosheath [8] by POLAR, FAST, GEOTAIL, and CLUSTER satellites. It was Tsurutani et al. [4] who identified them as unique kinds of coherent localized structures. Following their idea, and incorporating a Bernstein, Greene and Kruskal (BGK) model [5] and Particle In Cell (PIC) simulation [6], ofbp were interpreted as flat shaped electron phase space holes, emerging due to trapping of electrons. Such a theory, however, remain inadequate to explain slow moving ion mode ofbp.

During our theoretical analysis, we have indeed obtained such Flat Top Solitary Wave (FTSW) solutions with square shaped potential profiles [9]. The nomenclature not only describes the unique morphology of the potential profile but also rightly connects it to a more analytical and ideal set of solutions called Flat Top Solitons (FTS). Analogous to a solitary wave vis á vis a soliton solution, an FTSW is the realistic counter part of the FTS which is obtained by using Sagdeev pseudopotential technique. The technique is widely used to predict the existence and characteristics of any nonlinear coherent structure by studying the trajectory of the pseudoparticle in the pseudopotential well without the rigorous solution of any particular NLPDE, as is essential for a soliton, or FTS solution.

Here, for the first time, we have extended the same idea to space plasma for interpreting the ofbp. Rather than being event based, the theory proposes a more

generic approach which correlates the observed ofbp with a more fundamental non-linear dynamical structure called FTS through FTSW where the latter retains all the physical characteristics and the boundary conditions of FTS.

The article is organized as follows. Assuming a simple plasma model, in Sect. 2 we have found an ion acoustic ofbp which we have further validated with the corresponding satellite observations. In Sect. 3 we have explored the generic characteristics of the associated FTSW which is the steady state generalization of an FTS. The concluding remarks are given in Sect. 4

## 2 Analytical Concept

Slow moving ESWs, moving with ion acoustic speed, have been observed in the low altitude auroral region by several spacecraft expeditions. S3-3 recorded slow moving ofbp at an altitude between 6000 and 8000 km [2]. At this altitude, the plasma has been found to have a significant contribution of  $O^+$  ions along with its usual proton ( $H^+$ ) population. Moreover, there is an admixing of hot magnetospheric electrons with a cooler component originated from the ionosphere. Satellite observations have recorded cooler electron temperature  $T_{ec} \approx 0.5-5$  eV. The recorded ambient plasma density of this region is of the order of  $n_0 \approx 5-10$  cm<sup>3</sup>. The tenuous plasma condition and the absence of any physical boundary allow us to assume the plasma to be collisionless, homogeneous, and infinite. Following Temerin et al. [1] we have further assumed that the wave is moving along the ambient magnetic field, making the plasma isotropic and unmagnetized. It is observed that the speed of the ESW in this region is of the order of the ion acoustic speed of the medium, with the wave speed  $V \approx 50$  km/s, which indicates that they are governed by the ion dynamics. To sustain any such wave, the electron temperature should be higher than the corresponding ion temperatures. Besides, they have negligible inertia compared to ions. Theoretically it is well known that a secondary component of electrons is necessary to sustain an ion acoustic DL. The same condition was found to hold true for a Super Solitary Wave (SSW) [10], or an FTSW [9] as well. Hence we have assumed that the plasma has two electron temperatures, both obeying Boltzmann distributions and are separately in thermal equilibrium. The overall plasma is a four component one with warm multi-ion fluids comprising  $H^+$  and  $O^+$  ions so that the corresponding mass ratio  $Q = 1/16$ .

Following Temerin et al. [1], we have chosen an ambient plasma density  $n_0 = 10$  cm<sup>3</sup>, giving rise to an overall proton plasma frequency for  $n_0$  as  $\omega_{pi} = 4.163$  kHz. We have assumed a very low concentration of cooler electrons (viz., 0.12% of  $n_0$ ) and sufficiently small presence of  $O^+$  ions (10% of  $n_0$ ), leading to the normalized ambient densities  $\mu = 0.0012$  for cooler electrons and  $\alpha_h = 0.1$  for  $O^+$  ions, respectively. All the number densities were normalized by the ambient plasma density  $n_0$ . For our convenience, we have chosen  $T_{ec} = 0.5$  eV, and the electron temperature ratio  $\tau = 0.0485$  so that  $T_{ew} = 10.3$  eV. Since both the electrons are taking part in the Debye shielding, we have estimated the effective temperature  $T_{eff} = \frac{T_{ec}T_{ew}}{\mu T_{ew} + (1-\mu)T_{ec}} =$

10.0722 eV which further gives us the estimated effective Debye length  $\lambda_{d_{eff}} = 7.4606$  m and the effective ion acoustic speed for protons  $c_{isl} = 31.06$  km/s. These three parameters, together with  $\omega_{pi}$ , determine the overall scale of our plasma system. This is consistent with the observations of Temerin et al. [1] who have reported a Debye length of  $\lambda_d \approx 5$  m for the said region. For our theoretical analysis, we have normalized all the space variables by  $\lambda_{d_{eff}}$ , time by  $\omega_{pi}^{-1}$ , temperatures by  $T_{eff}$ , and the electrostatic potential  $\phi$  by  $T_{eff}/e$ . All the speeds, along with the wave Mach number  $M$ , are normalized by  $c_{isl}$ .

In the literature, there was a mention of the hotter ion temperature of the order of KeV. Such a high ion temperature would not sustain an ion acoustic wave and it may not be appropriate for the current region. Since ions are necessarily cooler than electrons, we have chosen the lighter ion temperature  $T_{il} = 0.33$  eV which is cooler than the cooler electron temperature. Theoretically we have found that the ion temperature plays a marginal role in determining an FTSW solution compared to the corresponding electronic parameters, such as  $\mu$  and  $\tau$ . Besides, the effect of  $O^+$  ions is expected to be even smaller because of its apparently low concentration. In the absence of any clear mention of the type the ion species for the hotter one, and for our analytical convenience, we have assumed that both the  $H^+$  and  $O^+$  ions have equal temperatures, giving rise to an overall normalized ion temperature  $\sigma = 0.033$ .

To ensure a steady state condition, or a wave frame, we have further assumed  $\eta$  to be the generalized coordinate where

$$\eta = x - Mt \quad (1)$$

The corresponding Sagdeev pseudopotential  $\Psi(\Phi)$  for the chosen plasma model is [10].

$$\begin{aligned} \psi(\Phi) = & - \left[ \left\{ \mu + (1 - \mu)\tau \right\} \left\{ \mu \left( \exp \frac{\Phi}{\mu + (1 - \mu)\tau} - 1 \right) + \frac{1 - \mu}{\tau} \left( \exp \frac{\tau\Phi}{\mu + (1 - \mu)\tau} - 1 \right) \right\} \right. \\ & + \frac{\alpha_l}{6\sqrt{3\sigma_l}} \left\{ [(M + \sqrt{3\sigma_l})^2 - 2\Phi]^{\frac{3}{2}} - (M + \sqrt{3\sigma_l})^3 \right. \\ & \left. \left. - [(M - \sqrt{3\sigma_l})^2 - 2\Phi]^{\frac{3}{2}} + (M - \sqrt{3\sigma_l})^3 \right\} \right. \\ & + \frac{\alpha_h}{6\sqrt{3\sigma_h}} \left\{ \left[ \left( \frac{M}{\sqrt{Q}} + \sqrt{3\sigma_h} \right)^2 - 2\Phi \right]^{\frac{3}{2}} - \left( \frac{M}{\sqrt{Q}} + \sqrt{3\sigma_h} \right)^3 \right. \\ & \left. \left. - \left[ \left( \frac{M}{\sqrt{Q}} - \sqrt{3\sigma_h} \right)^2 - 2\Phi \right]^{\frac{3}{2}} + \left( \frac{M}{\sqrt{Q}} - \sqrt{3\sigma_h} \right)^3 \right\} \right] \quad (2) \end{aligned}$$

which satisfies the following ‘energy equation’

$$\frac{1}{2} \left( \frac{d\Phi}{d\eta} \right)^2 + \Psi(\Phi) = 0 \quad (3)$$

Equation (3) is a modified form of the Poisson’s equation where the slope of the pseudopotential is defined as the associated charge separation, i.e.,  $\frac{\partial \Psi(\phi)}{\partial \phi} = \Delta n(\phi)$

for any  $\phi$ ,  $\Delta n$  being the charge separation. A  $\Psi$  versus  $\Phi$  curve determines the existence of the localized nonlinear coherent structures, like SWs, SSW, or FTSW, provided following boundary conditions are satisfied

$$\Psi(\Phi = 0) = \left. \frac{\partial \Psi}{\partial \Phi} \right|_0 = 0; \quad \frac{\partial^2 \Psi(0)}{\partial \Phi^2} < 0 \quad (4a)$$

$$\Psi(\Phi_0) = 0; \quad \frac{\partial \Psi(\Phi_0)}{\partial \Phi} \neq 0; \quad \Psi(\Phi) < 0 \text{ for } 0 \geq \Phi \geq \Phi_0. \quad (4b)$$

where  $\Phi_0$  is the amplitude of the wave structure.

The last condition in (4a, 4b) ensures the recurrence of the initial state for a soliton, or SW. For a DL, this condition modifies as

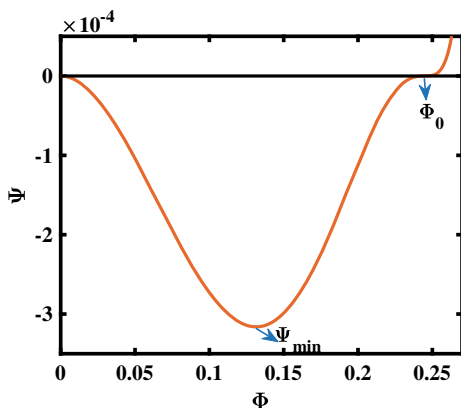
$$\frac{\partial \Psi(\Phi_0)}{\partial \Phi} = \Delta n_d = 0 \quad (5)$$

where  $\Delta n_d$  is the charge separation at the maximum amplitude for DL. Studying the trajectory of the ‘‘pseudoparticle’’ in the said pseudopotential well, and implementing the above mentioned ‘boundary conditions’ for the pseudoparticle, viz., (4a, 4b), the Sagdeev pseudopotential technique enables one to predict the presence of the corresponding steady state nonlinear structure.

For  $M = 1.05663685$ , and for the chosen set of parameters as mentioned above, in Fig. 1 we have plotted the corresponding Sagdeev pseudopotential profile. Since it satisfies (4a, 4b), it represents a SW which is a steady state analog of a soliton. For a FTSW, similar to a regular solitary wave profile the pseudopotential curve shows two extrema and two roots even though, near amplitude the pseudopotential curve meets the zero axis with almost a ‘‘grazing incidence’’. In order to under the significance of such solitary wave structures, we have analysed the corresponding electric field profile and density profile as mentioned below.

To find the corresponding electric field profile, we have deduced the generalized electric field  $E = -\frac{d\Phi}{d\eta}$  from (3). The time duration  $\Delta t$  (non-normalized) is estimated

**Fig. 1** Sagdeev pseudopotential profile corresponding to an FTSW



from the half-width  $W$  assuming  $x = 0$  in (1). The half-width  $W$  is defined from (3) as

$$W = 2\eta_{1/2} = 2 \int_{\Phi_0}^{\frac{\Phi_0}{2}} \left( \frac{1}{\sqrt{(-2\Psi(\Phi))}} \right) d\Phi; \quad \Delta t = \left( \frac{W}{M} \right)' \quad \text{for } x = 0 \quad (6)$$

The normalized half-width  $W = 422.55$  m and the prime ( $'$ ) in (6) denotes the corresponding non-normalized parameters. Figure 2 shows the associated electric field profile in non-normalized parameters. In X-axis we have plotted the time and Y-axis the non-normalized electric field. Comparing the electric field profile with that of observed non-conventional bipolar pulses clearly reveals an offset bipolar pulses (ofbp) [4]. We have further estimated the average  $\left( E_{avg} = \left( \frac{\Phi_0}{W} \right)' \right)$  and the maximum  $\left( E_{max} = -\left( \frac{d\Phi}{d\eta} \right)' \Big|_{\psi=\psi_{min}} \right)$  electric fields analytically, where  $\Phi_0 = 0.2448$  is the normalized potential amplitude and  $\Psi_{min}$  is the minimum value of  $\psi$  for  $0 \leq \phi \leq \phi_0$ , both of them are marked by the respective arrows in Fig. 1. The estimated average electric field across the structure  $E_{avg} = 5.8387$  mV/m, and the estimated time duration  $\Delta t = 12.8746$  ms (Fig. 2). The S3-3 satellite observations have revealed an  $E \leq 15$  mV/m and  $\Delta t = 2-20$  ms which are a close match to our analytical estimations. The analytically estimated peak to peak E-field amplitude  $E_{p-p} = 2 |E_{max}| \approx 37.02$  mV/m, have higher amplitude than the observed E-field. This still remain consistent with the qualitative agreement since a fluid approximation is known to overestimate the amplitude. We have further estimated the speed of the wave structure  $V = 32.83$  km/s from our chosen Mach number  $M (= 1.05663685)$  which is in accordance with the satellite observations, i.e.,  $V \approx 50$  km/s, as mentioned earlier. Table 1 compares shape, size, and speed of an ESW in the auroral region with those estimated analytically for a possible ofbp. The latter shows a com-

**Fig. 2** Non-normalized electric field (E) profile corresponding to an FTSW

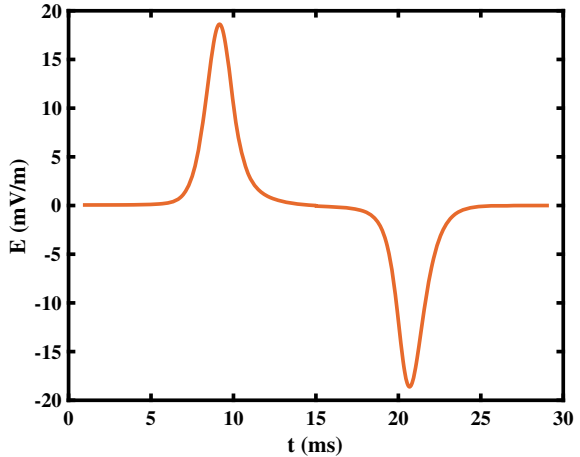


**Table 1** Wave parameters

Theoretical	Observational
$E_{avg} = 5.8387$ mV/m	$E \leq 15$ mV/m
$\Delta t = 12.8746$ ms	$\Delta t = 2-20$ ms
$V = 32.82$ km/s	$V \approx 50$ km/s

paratively wider  $\Delta t$ , as expected from its stretched structure. Our results indicates that the ofbp obtained analytically here using Sagdeev pseudopotential is a feasible candidate to interpret the corresponding satellite observations.

### 3 Physical Properties of FTSW and ofbp

To explore the physical characteristics of an ofbp, we have plotted the corresponding potential (solid line) and charge separation (dotted line) profiles in in Fig. 3. As shown in Fig. 3 the potential profile corresponds to an FTSW confirms a flat top profile. Conceptually, an FTSW can be visualized as an amalgamation of a SW and a DL. It is well evident form the charge separation profile (dotted line), its charge separation near the maximum amplitude turns vanishingly small (dotted line), approaching the condition of a DL (5), although it always remain finite and non-zero, eventually satisfying (4a, 4b) and the solution bounces back to its initial state like any conventional soliton. The modified condition for an FTSW can thus be written as

$$\Psi(\Phi_0) = 0; \quad \left. \frac{\partial \Psi}{\partial \Phi} \right|_{\Phi_0} = \epsilon, \quad \left. \frac{\partial^2 \Psi}{\partial \Phi^2} \right|_{\Phi_0} = \delta; \quad \epsilon, \delta \neq 0; \quad (7)$$

where  $\epsilon, \delta$  are two arbitrarily small, but finite numbers. The grazing incidence (i.e., low slope) of the curve to the  $\Phi$  axis at  $\Phi_0$  satisfies (6) for an FTSW while its finite slope at  $\Phi_0$  satisfies (4a, 4b) as well. This implies that the ‘pseudoparticle’, associated with the solution, leaves  $\Phi = 0$  at rest and reaches its reflection point at  $\Phi_0$  after a prolonged time, as ascertained by the grazing incidence of  $\Psi$ , and then it oscillates back to  $\Phi = 0$  giving rise to an wider, but well localized, coherent structure similar to a conventional SW. The morphology of the structure, however, is different from that of a conventional one as is evident from the associated electric field and potential profiles.

Previously Roth et al. [6] achieved an ofbp by assuming flat top potential profile for their PIC simulation. In the present case, the FTSW and the associated ofbp have been obtained analytically from a simple plasma model without any prior assumption of the potential profile. It was previously indicated that the trapping of electrons in BGK phase space hole may cause an ofbp. Such an assumption will not be valid for an ion mode, positive amplitude ofbp. However, in spite of the differences in the

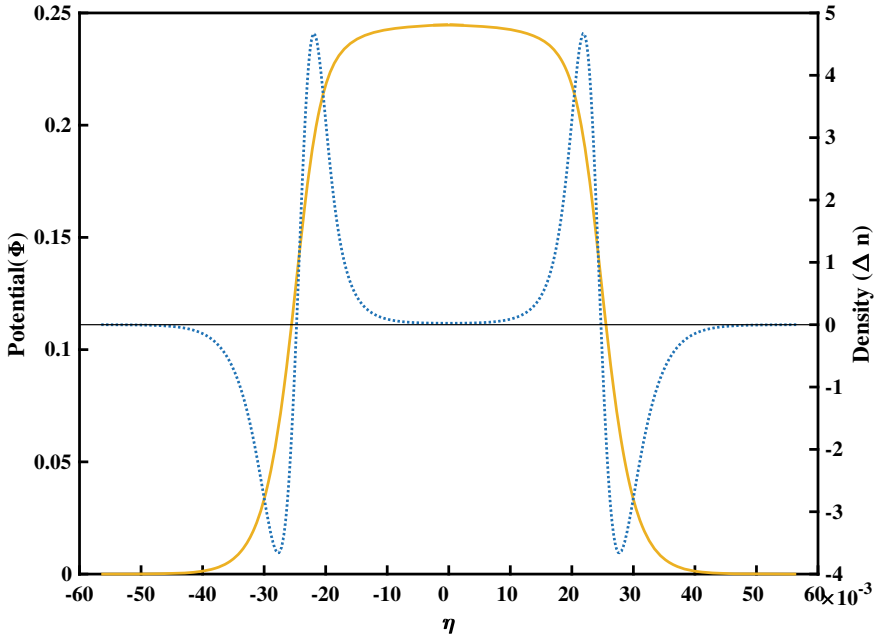


**Fig. 3** Potential profile (solid line) and charge separation profile (dotted line) corresponding to an FTSW

respective plasma models and associated techniques, the charge separation profiles remain the same for both the cases. We have previously observed that, when a Regular Solitary Wave (RSW) transits to a DL in the parameter space, its charge separation at its maximum amplitude drops, becoming ideally zero for a DL. We can here visualize an FTSW as an ‘incomplete DL’ where the solution goes very close to a DL solution but stops short of it and bounces back retaining the characteristics of a SW along with a strong imprint of a DL-like solution as well. This is manifested in the long sustentation of the vanishingly small charge separation which eventually causes the flat top profile. It is the same characteristic which causes the stretching in the localized E-field making it offset bipolar.

It is now evident that the ofbp, and the FTSW, both indicate the same localized coherent structure. The concept now can be extended further to the more ideal solutions called FTS which, as we have discussed earlier, is the mathematical counterpart of an FTSW, in the same way as a soliton is correlated with a more general class of solutions we call as solitary waves. It is well known that the integrable NLPDEs, like Korteweg-de Vries (KdV), govern soliton solutions. Analogously, a modified, or extended form of KdV (eKdV), popularly often known as the Gardner equation, governs FTS solutions depending on its specific boundary conditions [11]. Like eKdV, there are other such modified NLPDEs which also have FTS as one of their possible solutions. As per previous literature, an ofbp has often been described as a

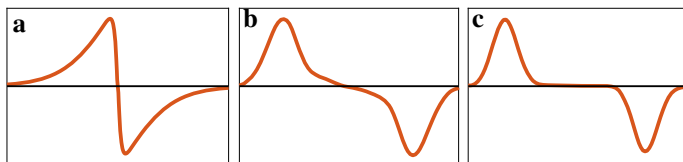


**Fig. 4** Schematic diagram of **a** bipolar E-field pulse **b** offset bipolar E-field pulse and **c** paired monopolar E-field pulse

‘stretched’ or ‘dispersed’ bipolar pulse where it was conjectured that the stretching has been happened due to an extra dispersion in the medium. The solution obtained from an e-KdV or Gardner equation describes the significance of an extra cubic nonlinearity term which results in a secondary resurgence in the nonlinearity” that balances the excessive dispersion maintaining the solitary structure.

To complement our understanding on ofbp, here we recall a schematic diagram in Fig. 4 which explains the characteristics of an ofbp (Fig. 4b) vis á vis a conventional bipolar and a monopole pair (mpp) in Fig. 4a and c respectively. For both an ofbp and an mpp, the distances between the two peaks are relatively large compared to the characteristic width of the each peak. The fine difference between an ofbp and mpp lies in the finite slope of the E-field connecting the two lobes for the former which categorizes it as a solitary wave in general. An mpp, on the other hand, is a pair of two simple monopoles with opposite polarities (Fig. 4c) while the slope of the electric field connecting the two poles goes ideally to zero. The significance of the finite slope in E reflects the low, but non zero slope of the Sagdeev pseudopotential at its maximum amplitude which in turn defines the respective boundary conditions of different nonlinear structures, viz., SW (4a, 4b), DL (5), and FTSW (7). Besides providing a physical explanation for the morphology of an ofbp, it further enhances the candidature of the FTSW to interpret the observed structures.

Recently Qureshi et al. [2] generalized the concept of ofbp beyond the acoustic mode as they predicted both ion acoustic and ion cyclotron ofbp for their theoretical model. Though their results are yet to be validated by the observational data, it indicates that the structure is more generic than it was thought so far. According to the present understanding, the offset bipolars are appearing like a sporadic “deformation” of the conventional bipolar electric field, resulting due to certain arbitrary local conditions at the spot. The proposed theory of FTSW, on the other hand, generalizes an ofbp beyond its local conditions correlating it to an FTS which is, like soliton, is known to exist across different physical situations, even beyond the realm of the plasma physics. Apart from its unique morphology, one common characteristic of an FTS is that they often define a boundary between two phases or nonlinear dynamical processes. Similar characteristic has also been reported for an FTSW as well. During our theoretical analysis, we have found that the FTSW is occurring at the boundary between two types of SSWs, viz. Type I and Type II, where an SSW is characterized by the extra wiggles in their otherwise bipolar electric field [9]. A Type I SSW associates it with a preceding DL/monopole while a Type II emerges



due to a continuous deformation of the bipolar electric field. We here conjecture that, analogous to an FTSW or FTS, an ofbp, too, may define a boundary between two phases, or nonlinear dynamical processes in the space. A more rigorous mathematical derivation of an ofbp from the preliminary FTS solution is beyond the scope of the current paper and may be presented elsewhere.

## 4 Conclusion

Using a simple plasma model, we have analytically estimated the shape, size, and speed of an FTSW which was found to be consistent with the slow moving ofbp observed in the Earth's auroral region. It manifests that ofbps are eventually FTSWs, or even may be FTS where the latter is the more mathematical and ideal counterpart of FTSW. Following the theory of the FTSW and FTS, we have interpreted the ofbp as an amalgamation of SW and DL which determines the boundary of two distinct phases of nonlinear dynamical processes. The proposed theory not only explains the unique morphology of the E-field data but also provide a more generic interpretation for the ofbp which is eventually correlating the mathematical description of a coherent nonlinear dynamical structure with the satellite observations. It is expected to provide a new way of understanding the non conventional localized pulses in the E-field data recorded during satellite expeditions which are known to be important in determining the microphysics of the Earth's magnetospheric boundary layers.

**Acknowledgements** The first author gratefully acknowledges financial support from Khalifa University's Sapce and Planetary Science Center under grant No. KU-SPSC-8474000336.

## References

1. Temerin, M., Cerny, K., Lotko, W., Mozer, F.Z.: Observations of double layers and solitary waves in the auroral plasma. *Phys. Rev. Lett* **48**, 1175–1179 (1982)
2. Qureshi, M.N.S., Shi, J., Torkar, K., Liu, Z.: Theoretical properties of offset bipolar electric field solitary structures in space plasmas. *Adv. Space Res.* **45**, 1219–1223 (2010)
3. Lotko, W., Kennel, C.F.: Spiky ion acoustic waves in collisionless auroral plasma. *J. Geophys. Res.* **88**, 381–394 (1983)
4. Tsurutani, B.T., Arballo, J.K., Lakhina, G.S., Ho, C.M., Buti, B., Pickett, J.S., Gurnett, D.A.: Plasma waves in the dayside polar cap boundary layer: bipolar and monopolar electric pulses and whistler mode waves. *Geophys. Res. Lett.* **25**(22), 4117–4120 (1998)
5. Muschietti, L., Roth, I., Carlson, C.W., Berthomier, M.: Modeling stretched solitary waves along magnetic field lines. *Nonlinear Process. Geophys.* **9**, 101–109 (2002)
6. Roth, I., Muschietti, L., Carlson, C.W., Mozer, F.S., Ergun, R.E.: Stability and interaction of fast auroral solitary structures in three dimensional plasma. *J. Geophys. Res.: Space Phys.* **107**, 13–14 (2002)
7. Deng, X., Tang, R., Matsumoto, H., Pickett, J., Fazakerley, A., Kojima, H., Baumjohann, W., Coates, A., Nakamura, R., Gurnett, D., Liu, Z.: Observations of electrostatic solitary waves associated with reconnection by geotail and cluster. *Adv. Space Res.* **37**, 1373–1378 (2005)

8. Pickett, J., Chen, L.-J., Mutel, R., Christopher, I., Santolk, O., Lakhina, G., Singh, S., Reddy, R., Gurnett, D., Tsurutani, B., Lucek, E., Lavraud, B.: Furthering our understanding of electrostatic solitary waves through cluster multispacecraft observations and theory. *Adv. Space Res.* **41**, 1666–1676 (2008)
9. Steffy, S.V., Ghosh, S.S.: Phase portrait analysis of super solitary waves and flat top solutions. *Phys. Plasmas* **25**, 302 (2018)
10. Steffy, S.V., Ghosh, S.S.: Transitional properties in a two electron temperature warm multi-ion plasma. *Phys. Plasmas* **23**, 082304 (2016)
11. Grimshaw, R., Pelinovsky, D., Pelinovsky, E., Slunyaev, A.: Generation of large-amplitude solitons in the extended Korteweg-de Vries equation. *Chaos: Interdiscip. J. Nonlinear Sci.* **12**, 1070–1076 (2002)

# Forced KdV Equation in Degenerate Relativistic Quantum Plasma



Geetika Slathia , Rajneet Kaur , Kuldeep Singh ,  
and Nareshpal Singh Saini 

**Abstract** The study of heavy ion acoustic solitary waves (HIASWs) in a relativistic degenerate dense plasma (RDDP) having relativistic degenerate lighter ions as well as electrons and inertial heavy ions fluid has been illustrated. By adopting the reductive perturbation method, the forced Korteweg-de Vries (fKdV) equation is obtained to examine the HIASWs. The solution for HIASWs is determined analytically in the presence of external periodic force. It has been observed that the impact of various plasma parameters viz., speed of the wave, frequency and strength of the periodic force significantly alter the basic characteristics of different HIASWs. The findings of this work may be convenient to understand the behaviour of HIASWs in white dwarfs.

**Keywords** Heavy ions acoustic waves · Quantum plasma · Forced KdV equation

## 1 Introduction

Quantum plasma has incited great deal of interest and has attracted many physicists for the comprehensive study to explore different nonlinear waves in white dwarfs, neutron stars and black holes [1–3] owing to its low temperature and extremely large density in dense astrophysical region [4–6]. The various onboard satellite observations [1] have reported that the average particles density per unit volume of the white dwarfs is  $10^6$  to  $10^8$   $\text{gcm}^{-3}$  with average interparticle distance of  $10^{-10}$  to  $10^{-13}$  cm [7]. The prestellar is mainly having heavy nuclei which was compressed

---

G. Slathia (✉) · R. Kaur · K. Singh · N. S. Saini  
Department of Physics, Guru Nanak Dev University, Amritsar 143005, India  
e-mail: [gslathia93@gmail.com](mailto:gslathia93@gmail.com)

K. Singh  
Department of Mathematics, Khalifa University of Science and Technology, Abu Dhabi, UAE

© The Author(s), under exclusive license to Springer Nature Switzerland AG 2022  
S. Banerjee and A. Saha (eds.), *Nonlinear Dynamics and Applications*,  
Springer Proceedings in Complexity,  
[https://doi.org/10.1007/978-3-030-99792-2\\_2](https://doi.org/10.1007/978-3-030-99792-2_2)

into ultra high densities. It is remarkable that the white dwarfs are having number density of heavy nuclei is  $10^{29} \text{ cm}^{-3}$  while the average distance between particle is  $10^{-10} \text{ cm}$  [1]. The estimation of degeneracy of different species is followed by Heisenberg's uncertainty principle where the uncertainty in momenta is extremely large and fast moving degenerate elements yields high pressure, (i.e., degenerate pressure). In quantum regime, as the interspecies distance is comparable to the de Broglie wavelength of species then relativistic effects become important. The characteristics and propagation of nonlinear HIAWs have been explored in different the unmagnetized RDDP models [8–14]. Islam et al. [11] reported the investigation of extremely HIA shock waves in a DRQP system by obtaining Burgers' equation. Singh et al. [12] have examined the characteristics of HIA oscillatory as well as monotonic shocks in dense magnetoplasma. Saini et al. [13] have investigated the dynamics of cnoidal and solitons in a three component magnetised plasma. By incorporating Sagdeev pseudopotential technique, the energy balance equation has been obtained. Kaur et al. [14] have studied the heavy and lighter ions acoustic higher order shock waves in quantum plasma. They have examined that the inclusion of higher order corrections yield dressed shocks.

With the induction of the external periodic force, different kinds of nonlinear waves excite in the plasma system and they characterise completely different which has been investigated by numerous researchers [15–18]. The characteristics of HNA solitary structures in an unmagnetized dense plasma containing of degenerate electrons and lighter ions in a heavy ions fluid along with the source term obtained from various experiments and simulations have been studied [15–18]. A lot of different investigations have been reported which describe about the underlying phenomena of various nonlinear excitations in astrophysical environments [19–21]. Sen et al. [19] illustrated the characteristics of nonlinear waves in the Lower Orbital region of the Earth by deriving fKdV equation under influence of external periodic perturbation. Ali et al. [20] explored the analytical solution and the effect of various plasma parameters on the electron acoustic solitons by obtaining the fKdV equation. Mir et al. [21] illustrated the nonlinear wave mixing obtained from the exact analytical solution of the fKdV equation in the dusty plasma.

In this investigation, the main aim is to explore the dynamics of HIASWs in RDDP comprising of inertial heavy ions with degenerate lighter ions and electrons. To the best of our knowledge, the study of various kinds of nonlinear coherent structures in a RDDP obtained from the fKdV equation in white dwarfs have not been reported so far. The layout of the manuscript is presented as follows: The basic fluid model is provided in Sect. 2. The derivation and analytical solution of fKdV is discussed in Sect. 3. Different kinds of nonlinear structures have been examined and their parametric analysis is given in Sect. 4. The last Sect. 5 presents the conclusions.

## 2 Basic Fluid Equations

We assume unmagnetised RDDP containing relativistic degenerate electrons and lighter ions and inertial heavy ions as fluid. Thus, we have  $N_{e0} = Z_h N_{h0} + Z_l N_{l0}$ , where  $N_{e0}$ ,  $N_{l0}$ ,  $N_{h0}$  are the unperturbed number density of electrons, lighter and heavy ions, respectively. The dynamics of HIAWs is described by the following normalized equations as [12]:

$$\frac{\partial N_h}{\partial t} + \frac{\partial(N_h U_h)}{\partial x} = 0, \quad (1)$$

$$\frac{\partial U_h}{\partial t} + U_h \frac{\partial U_h}{\partial x} = -\frac{\partial \phi}{\partial x}, \quad (2)$$

$$\frac{\partial^2 \phi}{\partial x^2} = (1 + \beta\alpha)N_e - \beta\alpha N_l - N_h + \Theta(x, t), \quad (3)$$

where  $N_i$  (for  $i = h, l, e$ ) is normalised by its equilibrium density  $N_{i0}$ . Here, source term  $\Theta(x, t)$  is an external periodic perturbation which appears in different laboratory experiments. The solitary wave structures or solitons experience external forces such as the resistive wall modes of the plasma when subjected to external magnetic force which may be constant or periodic. The evolution of HIASWs, whose key attributes change with time when subjected to an external perturbations are termed as forced KdV solitary wave structures [20, 22]. The  $\phi$  is normalised by  $\phi_0 = m_e c^2 / e$  and  $U_h$  by  $C_0 = (Z_h m_e c^2 / m_h)^{1/2}$ . The time and space coordinates are normalised by  $\omega_{ph} = (4\pi N_{h0} Z_h^2 e^2 / m_h)^{1/2}$  and  $\lambda_s = (m_e c^2 / 4\pi Z_h N_{h0} e^2)^{1/2}$ , respectively. Where,  $\eta_1 = \eta_l N_{l0}^{\rho_l - 1} / Z_l m_e c^2$  and  $\eta_2 = \eta_e N_{e0}^{\rho_e - 1} / Z_e m_e c^2$ ,  $\alpha = Z_l / Z_h$  and  $\beta = N_{l0} / N_{h0}$ . The expression for lighter ions and electrons in RDDP is given as [12]:

$$N_l = \left(1 - \frac{\rho_l - 1}{\rho_l \eta_1} \phi\right)^{\frac{1}{\rho_l - 1}} = 1 - a_1 \phi + a_2 \phi^2 + \dots \quad (4)$$

$$N_e = \left(1 + \frac{\rho_e - 1}{\rho_e \eta_2} \phi\right)^{\frac{1}{\rho_e - 1}} = 1 + b_1 \phi + b_2 \phi^2 + \dots \quad (5)$$

Now, by putting the (4)–(5) into (3), we get;

$$\frac{\partial^2 \phi}{\partial X^2} = 1 - N_h + c_1 \phi + c_2 \phi^2 + \Theta(x, t), \quad (6)$$

where  $c_1 = b_1 + a_1$  and  $c_2 = b_2 - a_2$ . Here,  $a_1 = \frac{\beta\alpha}{\rho_l \eta_1}$ ,  $b_1 = \frac{1 + \beta\alpha}{\rho_e \eta_2}$ ,  $a_2 = \frac{\beta\alpha(2 - \rho_l)}{2\rho_l^2 \eta_1^2}$  and  $b_2 = \frac{(1 + \beta\alpha)(2\rho_e)}{2\rho_e^2 \eta_2^2}$ .

### 3 Forced KdV Equation and Its Solution

The stretching of variables is given as:

$$X = \epsilon^{\frac{1}{2}}(x - \lambda t) \quad (7)$$

$$T = \epsilon^{\frac{3}{2}}t \quad (8)$$

The expansion of dependent variables is illustrated as

$$N_h = 1 + \epsilon N_{h1} + \epsilon^2 N_{h2} + \dots \quad (9)$$

$$U = \epsilon U_1 + \epsilon^2 U_2 + \dots \quad (10)$$

$$\phi = \epsilon \phi_1 + \epsilon^2 \phi_2 + \dots \quad (11)$$

$$\Theta(x, t) = \epsilon^2 \Theta_2(x, t) + \dots \quad (12)$$

Substituting (7)–(12) into (1)–(2) and (6) and equating the coefficients of smaller powers of  $\epsilon$ , we get the following equations:

$$N_{h1} = \frac{1}{\lambda^2} \phi_1 \quad \text{and} \quad U_1 = \frac{1}{\lambda} \phi_1, \quad (13)$$

$$\lambda = \frac{1}{\sqrt{c_1}} \quad (14)$$

Equation (14) represents the dispersion relation of HIASWs. In limiting case, the phase speed matches with Singh et al. [12]. From the next higher order, we get:

$$\frac{\partial N_{h1}}{\partial T} - \lambda \frac{\partial N_{h2}}{\partial X} + \frac{\partial U_2}{\partial X} + \frac{\partial N_{h1} U_1}{\partial X} = 0, \quad (15)$$

$$\frac{\partial U_1}{\partial T} - \lambda \frac{\partial U_2}{\partial X} + U_1 \frac{\partial U_1}{\partial X} + \frac{\partial \phi_2}{\partial X} = 0, \quad (16)$$

$$\frac{\partial^2 \phi_1}{\partial X^2} = c_1 \phi_2 + c_2 \phi_1^2 - N_{h2} + \Theta(X, T) \quad (17)$$

Equating second order coefficients of  $\epsilon$  and after some algebraic manipulations, we get the following forced KdV (fKdV) equation,

$$\frac{\partial \phi_1}{\partial T} + A \phi_1 \frac{\partial \phi_1}{\partial X} + B \frac{\partial^3 \phi_1}{\partial X^3} = B \frac{\partial \Theta_2(X, T)}{\partial X} \quad (18)$$

where nonlinear coefficient  $A = (\frac{3}{2\lambda} - \frac{\lambda c_2}{c_1})$  and dispersion coefficient  $B = \frac{\lambda^3}{2}$ .

Jun-Xiao and Bo-Ling [23] determined the solutions of the fKdV equation by adopting Hirota bilinear technique. Let us consider  $\Theta_2 = \frac{f_0}{B} X \cos(\omega T)$ , where  $f_0$  represents the strength and  $\omega$  is the frequency of the source. Therefore, (18) becomes;

$$\frac{\partial \phi_1}{\partial T} + A \phi_1 \frac{\partial \phi_1}{\partial X} + B \frac{\partial^3 \phi_1}{\partial X^3} = f_0 \cos(\omega T). \quad (19)$$

This type of source term is deduced from the experimental results. Equation (19) is called fKdV equation. If  $f_0 = 0$ , then (19) reduces the usual KdV equation;

$$\phi_1 = \phi_m \sec h^2 \left( \frac{X - \Lambda T}{W} \right), \quad (20)$$

where  $\phi_m = \frac{3A}{A}$  is the maximum amplitude and  $W = 2\sqrt{\frac{B}{A}}$  is width and  $\Lambda$  is the velocity of the HIASWs. The influence of periodic term  $f_0 \cos(\omega T)$  on the HIASWs we have also determined the momentum conservation law. For small forcing term  $f_0 \cos(\omega T)$ , we obtain;

$$I = \int_{-\infty}^{\infty} \phi_1^2 dX, \quad (21)$$

$$I = \frac{24\sqrt{B}}{A^2} \Lambda^{\frac{3}{2}}(T), \quad (22)$$

and

$$\int_{-\infty}^{\infty} \phi_1 dX = \frac{12\sqrt{B\Lambda(T)}}{A}, \quad (23)$$

where  $\Lambda(T)$  is the speed of the HIASWs of the fKdV equation. Now differentiate (21) w.r.t  $T$ , we get;

$$\frac{dI}{dT} = 2f_0 \cos(\omega T) \quad (24)$$

Putting (22) and (23) into (24) along with  $\Lambda(0) = \Lambda$ , we get;

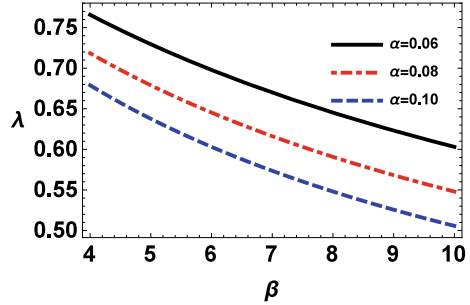
$$\Lambda(T) = \Lambda + \frac{2Af_0}{3\omega} \sin(\omega T). \quad (25)$$

Then, the solution of fKdV equation can be written as;

$$\phi_2 = \phi_m(T) \sec h^2 \left( \frac{X - \Lambda(T)T}{W(T)} \right), \quad (26)$$

where the maximum amplitude and width of HIASWs are time dependent i.e.,  $\phi_m = \frac{3\Lambda(T)}{A}$  and  $W(T) = 2\sqrt{\frac{B}{\Lambda(T)}}$ , respectively.

**Fig. 1** The phase speed ( $\lambda$ ) of HIASWs versus  $\beta$  ( $=N_{l0}/N_{h0}$ ) for different values of  $\alpha$  ( $=Z_l/Z_h$ )



## 4 Parametric Analysis

Here, the parametric analysis has been performed to examine the characteristics of HIASWs in RDDP. We have assumed three species RDDP having relativistic degenerate lighter ions/electrons (viz.,  ${}^1_1H$  or  ${}^4_2He$  or  ${}^{12}_6C$  or  ${}^{16}_8O$ ) and heavy ions (viz.,  ${}^{56}_{26}Fe$  or  ${}^{87}_{37}Rd$  or  ${}^{96}_{42}Mo$ ), and the data is taken from the region of white dwarfs [10, 12, 24].

Figure 1 shows the plot for phase speed ( $\lambda$ ) of HIASWs versus  $\beta$  ( $=N_{l0}/N_{h0}$ ) for different values of  $\alpha$  ( $=Z_l/Z_h$ ). The phase speed of HIASWs enervates with rise in  $\beta$  and  $\alpha$  which means that phase speed gets reduced as the charge and number densities of heavy ions are flourished.

Figure 2 illustrates the plot of nonlinear coefficient  $A$  of HIASWs versus  $\beta$  for different values of  $\alpha$ . The  $A$  is increased with an increment in  $\beta$  and  $\alpha$ . It is remarked that only positive potential (compressive) HIASWs are evolved for  $A > 0$ .

Figure 3 illustrates the plot of the compressive HIASWs profile for different values of  $\alpha$  and  $\beta$ . The amplitude of the HIASWs decreases with the rise in  $\alpha$  and  $\beta$ . It is emphasized that this shrink in the HIASWs amplitude is because of rise in the value of  $A$ .

In Fig. 4, profile of compressive HIASWs for various values of strength ( $f_0$ ) and frequency  $\omega$  of periodic force. It is found that as  $f_0$  increases, the amplitude of the HIASWs is increased and is decreased with increment in  $\omega$ . In Fig. 5, the 3D plot of compressive HIASWs profile of the fKdV equation for different values of  $\alpha$  is given. It is found that as the values of  $\alpha$  is increased, the amplitude of the HIASWs is decreased. Similarly, Fig. 6 shows the 3D plot of compressive HIASWs profile of the fKdV equation versus  $\beta$ . It is noticed that as the values of  $\beta$  is increased, the maximum amplitude of the HIASWs is shrunk.

In Fig. 7, the plot of compressive HIASWs profile versus  $f_0$  for different  $\alpha$  and  $\beta$  is shown. It is noticed that the maximum amplitude of HIASWs decreases with rise in the values of  $\alpha$  and  $\beta$  but increases as the values of  $f_0$  increases.

In Fig. 8, the plot of compressive HIASWs profile vs  $\omega$  for different values of  $\alpha$  and  $\beta$  is shown. It is found that the width of HIASWs decreased with rise in the values of  $\alpha$  and  $\beta$  but enhanced with rise in the values of  $\omega$ .



**Fig. 2** The nonlinear coefficient ( $A$ ) of HIASWs versus  $\beta(=N_{l0}/N_{h0})$  for different values of  $\alpha(=Z_l/Z_h)$

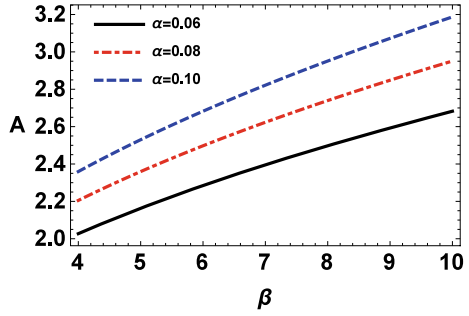


**Fig. 3** The compressive HIASWs profile for different values of  $\alpha = Z_l/Z_h$  and  $\beta = N_{l0}/N_{h0}$

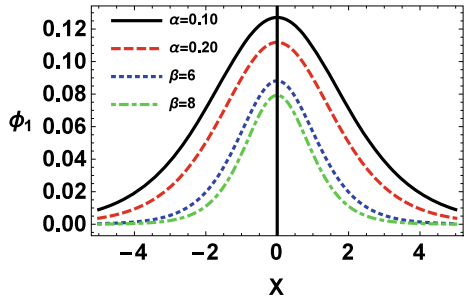
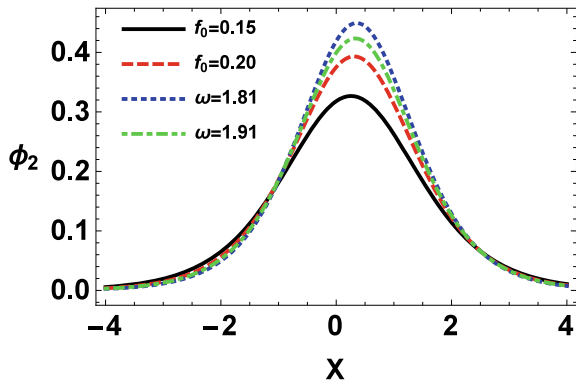


**Fig. 4** The HIASWs profile of the fKdV equation for different values of  $f_0$  and frequency  $\omega$  with fixed values of  $\Lambda = 0.1$ ,  $\alpha = 0.08$ , and  $\beta = 5$



It is stressed that the various plasma parameters have significantly influenced the nonlinear and dispersion effects to modify the characteristics of HIASWs in the RDDP environment.

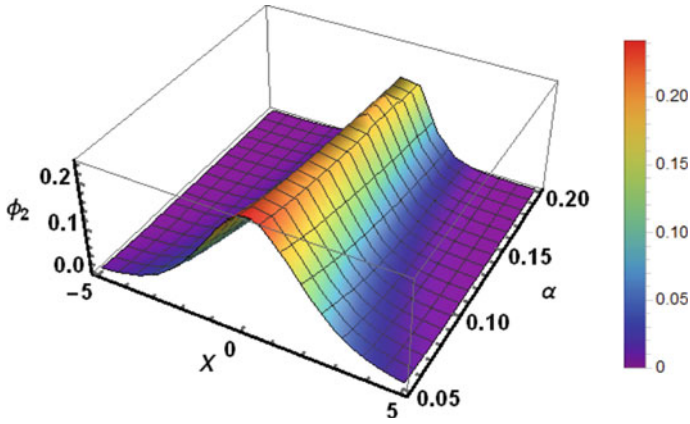


**Fig. 5** The 3D plot of HIASWs profile of the fKdV equation vs  $\alpha$  for  $\Lambda = 0.1$ ,  $f_0 = 0.1$ ,  $\omega = 1.5$ ,  $T = 1.5$

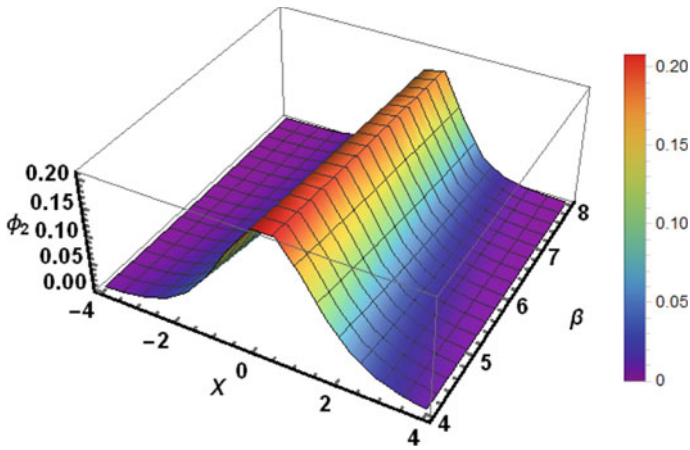


**Fig. 6** The 3D plot of HIASWs profile versus  $\beta$  with  $\Lambda = 0.1$ ,  $f_0 = 0.1$ ,  $\omega = 1.5$ , and  $T = 1.5$

**Fig. 7** The maximum amplitude of HIASWs versus  $f_0$  for different  $\alpha$  and  $\beta$ , other parameters  $\Lambda = 0.1$ ,  $\omega = 1.2$ ,  $T = 1$  are fixed

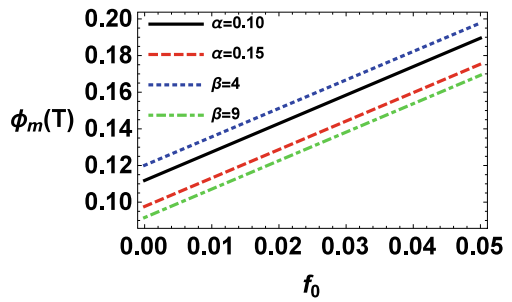
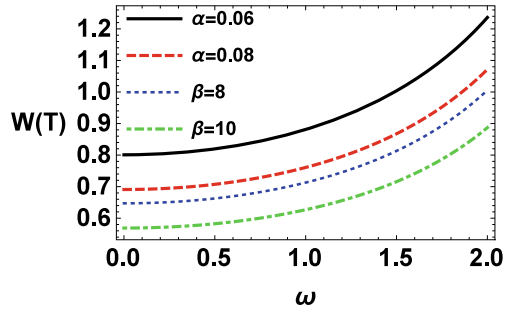


**Fig. 8** The width of HIASWs wrt  $\omega$  of the fKdV equation for different values of  $\alpha$  and  $\beta$ , where other parameters  $\Lambda = 0.1$ ,  $f_0 = 0.7$ ,  $T = 1.1$  are fixed



## 5 Conclusions

In this investigation, we have examined the salient features of HIASWs in RDDP having degenerate lighter ions/electrons and inertial heavy ion fluid. By adopting the reductive perturbation method, the forced Korteweg-de Vries (fKdV) equation is obtained for HIASWs. The solution of fKdV equation is determined to explore the behaviour of HIASWs under the influence of periodic force. Only compressive HIASWs are observed. It is shown that the impact of various plasma parameters like speed and strength of the periodic force significantly modify the basic properties of different HIASWs. The amplitude of HIASWs enervates with the rise in the density ratio while the amplitude of the HIASWs excels with rise in the value of periodic force. The findings of this investigation may highlight the basic features of HIASWs in RDDP in white dwarfs [10, 12, 24].

## References

1. Shapiro, S.-L., Teukolsky, S.-A.: Black Holes, White Dwarfs, and Neutron Stars: The Physics of Compact Objects. Wiley-VCH Verlag, Weinheim (2004)
2. Koester, D., Chanmugam, G.: Physics of white dwarf stars. Rep. Prog. Phys. **53**(7), 837–915 (1990)
3. Koester, D.: White dwarfs: recent developments. Astron. Astrophys. Rev. **11**(1), 33–66 (2002)
4. Drake, R.-P.: High-energy-density physics. Phys. Today **63**(6), 28–33 (2010)
5. Killian, T.-C.: Plasma physics: cool vibes. Newly observed electron-density waves could become useful probes of how electrons behave in this exotic regime. Nature **441**(5), 297–298 (2006)
6. Glenzer, S.-H., Redmer, R.: X-ray Thomson scattering in high energy density plasmas. Rev. Mod. Phys. **81**(4), 1625–1663 (2009)
7. Azam, M., Sami, M.: Many-body treatment of white dwarf and neutron stars on the brane. Phys. Rev. D **72**(7), 024024(1–11) (2005)
8. Mamun, A.-A., Amina, M., Schlickeiser, R.: Nucleus-acoustic shock structures in a strongly coupled self-gravitating degenerate quantum plasma. Phys. Plasmas **23**(9), 094503(1–4) (2016)
9. Mamun, A.-A., Amina, M., Schlickeiser, R.: Heavy nucleus-acoustic spherical solitons in self-gravitating super-dense plasmas. Phys. Plasmas **24**(4), 042307(1–7) (2017)

10. Sultana, S., Islam, S., Mamun, A.-A., Schlickeiser, R.: Modulated heavy nucleus-acoustic waves and associated rogue waves in a degenerate relativistic quantum plasma system. *Phys. Plasmas* **25**(1), 012113(1–9) (2018)
11. Islam, S., Sultana, S., Mamun, A.-A.: Ultra-low frequency shock dynamics in degenerate relativistic plasmas. *Phys. Plasmas* **24**(9), 092308(1–5) (2017)
12. Singh, K., Sethi, P., Saini, N.-S.: Nonlinear excitations in a degenerate relativistic magneto-rotating quantum plasma. *Phys. Plasmas* **26**(9), 092104(1–10) (2019)
13. Saini, N.-S., Kaur, M., Singh, K.: Heavy nucleus acoustic periodic waves in a degenerate relativistic magneto-rotating quantum plasma. *Waves Random Complex Media* **30**, 1–12 (2020)
14. Kaur, R., Singh, K., Saini, N.-S.: Heavy-and light-nuclei acoustic dressed shock waves in white dwarfs. *Chin. J. Phys.* **72**(8), 286–298 (2021)
15. Saha, A., Pal, N., Chatterjee, P.: Dynamic behavior of ion acoustic waves in electron-positron-ion magnetoplasmas with superthermal electrons and positrons. *Phys. Plasmas* **21**(10), 102101(1–10) (2014)
16. Saha, A., Pal, N., Chatterjee, P.: Bifurcation and quasiperiodic behaviors of ion acoustic waves in magnetoplasmas with nonthermal electrons featuring Tsallis distribution. *Braz. J. Phys.* **45**(4), 325–333 (2015)
17. Zhen, H., Tian, B., Wang, Y., Sun, W., Liu, L.: Soliton solutions and chaotic motion of the extended Zakharov-Kuznetsov equations in a magnetized two-ion-temperature dusty plasma. *Phys. Plasmas* **21**(7), 073709(1–7) (2014)
18. Sadiq, S., Mahmood, S., Haque, Q., Ali, M.-Z.: Ion acoustic solitons in dense magnetised plasmas with nonrelativistic and ultrarelativistic degenerate electrons and positrons. *Astrophys. J.* **793**(9), 27(1–12) (2014)
19. Sen, A., Tiwari, S., Mishra, S., Kaw, P.: Nonlinear wave excitations by orbiting charged space debris objects. *Adv. Space Res.* **56**(3), 429–435 (2015)
20. Ali, R., Saha, A., Chatterjee, P.: Analytical electron acoustic solitary wave solution for the forced KdV equation in superthermal plasmas. *Phys. Plasmas* **24**(12), 122106(1–9) (2017)
21. Mir, A.-A., Tiwari, S.-K., Goree, J., Sen, A., Crabtree, C., Ganguli, G.: A forced Korteweg-de Vries model for nonlinear mixing of oscillations in a dusty plasma. *Phys. Plasmas* **27**(11), 113701(1–6) (2020)
22. Chandra, S.: Analytical and simulation studies of forced KdV solitary structures in a two-component plasma. *J. Korean Phys. Soc.* **76**(6), 469–478 (2020)
23. Xiao, Z.-J., Ling, G.-B.: *Commun. Theor. Phys.* **52**(2), 279–283 (2009)
24. Tout, C.-A., Wickramasinghe, D.-T., Ferrario, L.: Magnetic fields in white dwarfs and stellar evolution. *Mon. Not. R. Astron. Soc.* **355**(3), L13–L16 (2004)

# Heliospheric Two Stream Instability with Degenerate Electron Plasma



Jit Sarkar , Swarniv Chandra , Jyotirmoy Goswami ,  
and Basudev Ghosh 

**Abstract** In this paper, we have studied the effect of relativistic degeneracy, electron spin exchange potential and quantum diffraction effect on the electron two-stream instability in a dense stellar body like our Sun. The effect of streaming motion has been studied along with other parameters. We have observed regions of stability and instability in this case considering two oppositely flowing electron jets. Under constrained environments, our findings adjust to traditional results. The results of other researchers in this field also correspond to our findings. We have made use of the Quantum Hydrodynamic Model and also incorporated the one-dimensional thermal anisotropy that slightly modifies the model. Our findings will be helpful in the study of various instabilities and associated phenomena in solar flares, solar storms and similar other indicates in the stellar and nebular environments.

**Keywords** Two stream instability · Electron spin exchange potential · Quantum hydrodynamic model

## 1 Introduction

Over the past few years quantum plasma has attracted much attention in the plasma community. With the growth of study in dense plasma and the ability of experimenting with high power laser beams, the study of quantum tunneling in plasma phenomena has gained utmost importance. Initially pioneering works were carried out by Haas [17], Manfredi [21], Shukla [29], Eliasson [13], Sarkar [26–28], Goswami [15, 16], Brodin [5], Chandra [6–10] on quantum plasmas. Later there were more works with applicability of quantum phenomenon in such dense plasmas. Various types of insta-

---

J. Sarkar · S. Chandra (✉) · J. Goswami · B. Ghosh  
Jadavpur University, Kolkata, India  
e-mail: [swarniv147@gmail.com](mailto:swarniv147@gmail.com)

S. Chandra  
Government General Degree College at Kushmandi, Kushmandi, West Bengal, India

© The Author(s), under exclusive license to Springer Nature Switzerland AG 2022  
S. Banerjee and A. Saha (eds.), *Nonlinear Dynamics and Applications*,  
Springer Proceedings in Complexity,  
[https://doi.org/10.1007/978-3-030-99792-2\\_3](https://doi.org/10.1007/978-3-030-99792-2_3)

bilities and other non-linear effects were observed in them. Quantum hydrodynamic model (QHD) model has been often used to address problem like this.

In plasma physics, the two-stream instability is a very common type of phenomenon which can be induced by an energetic stream of particles injected into the plasma. It can be also obtained by setting a current along with the plasma so that different species (electron & ions; positron and negative ions; etc.) can have different drift velocities depending on their inertia as well as response to the field. Such instability appears immediate when the beams comprise cold particle species with none of the particles being resonant with the wave. Conversely, they can be found from two hot beams in which particles from one or both the streams are resonant with the wave. This kind of instability under various limiting cases evolve into beam plasma instability, beam instability or bump on tail instability. The dispersion relation of the wave showing two-stream instability has two parts, a real and other imaginary. With totally real roots there can be no type of damping. On the other hand with the non-zero imaginary segment of the frequency, there may be either damping or instability(growing). Electron two stream Instability (ETSI) which is driven by oppositely streaming beams was first represented by Bohm and Gross [3] since then various space plasma and experimental instances have reported the existence of ETSI. Such instability produces strong electron heating and coherent plasma emissions at  $\omega_{pe}$  (electron plasma frequency) or its harmonics. As the plasma density varies along the path of the electron beams, the emission frequency drifts. Solar emissions being in the radio band emit 'U' and 'J' type of radio bursts which correspond to various origin of the electrons and contain information about them.

In this paper, we will try to investigate the two-stream instability, its nature and evaluation in a plasma containing streams of electrons moving in the opposite direction in dense quantum plasma. We consider an anisotropy in the direction of propagation of the wave [14] which is more meaningful due to such temperature. The ions are homogeneously distributed to form a neutralising background.

We organised the article in the following way. In Sect. 2 we start with the dynamical equations governing our model plasma. In Sect. 3 we derive the linear dispersion relation. In the next section, we analyzed the result and finally conclude with some remarks concerning recent findings and possible application.

## 2 Finite Temperature Quantum Hydrodynamic Model

Our mathematical model is based on the three dimensional equilibrium Fermi-Dirac distribution for electrons. Due to adiabatic compression, temperature anisotropy occurs in distribution with the motion of a longitudinal electrostatic wave propagating in collision-less plasma. The Fermi-Dirac equilibrium state for Fermions is given by Bransden and Joachain [4] in the following form

$$\begin{aligned}
n_0 &= \frac{1}{2\pi^2} \left( \frac{2m}{\hbar} \right)^{3/2} \int_0^\infty \frac{E^{1/2} dE}{e^{\beta(E-\mu)} + 1} \\
&= -\frac{1}{2\pi^2 \beta^{3/2}} \left( \frac{2m}{\hbar} \right)^{3/2} \Gamma \left( \frac{3}{2} \right) Li_{3/2}(-e^{\beta\mu})
\end{aligned} \tag{1}$$

where  $m$  is the electron mass,  $\hbar$  is the reduced Plank's constant,  $n_0$  is the equilibrium number density,  $\beta = 1/k_B T_{0E}$ ,  $T_{0E}$  is the background temperature of electron,  $\mu$  is the chemical potential and  $Li_\nu(x)$  is the poly-logarithmic function in  $x$  of order ( $\nu$ ). When  $\beta \rightarrow \infty$  i.e, cold temperature of electron, we have  $\mu \rightarrow \varepsilon_F$ , where  $\varepsilon_F$  is the fermi energy, and Eq. (1) becomes

$$n_0 = \frac{1}{3\pi^2} \left( \frac{2m}{\hbar^2} \right)^{3/2} \varepsilon_F^{3/2} \tag{2}$$

or in other way the Fermi energy is

$$\varepsilon_F = (3\pi^2 n_0)^{2/3} \frac{\hbar^2}{2m} \tag{3}$$

Here, we can obtain the Vlasov equations with  $df/dt = 0$  as the fluid is incompressible in phase space. But the incompressibility is compromised by quantum tunneling according to Wigner equation [14], so a non-equilibrium particle distribution function can be represented as

$$f(x, u, t) = \frac{\alpha}{\exp[(\beta m/2)\{(u_x - u_{ex})^2 \eta + u_y^2 + u_x^2\} - \beta\mu] + 1} \tag{4}$$

where  $u_{ex}(x, t)$  is mean velocity of the particles and  $\eta$  is the temperature anisotropy given by  $\eta(x, t) = [n_0/n_e(x, t)]^2$  and  $\alpha = -\frac{n_0}{Li_{3/2}(-e^{\beta\mu})} \left( \frac{\beta m}{2\pi} \right)^{(3/2)}$  (normalization constant). With a constant chemical potential and normalizing  $f$  over velocity space equals  $n_0$ ; when  $\eta = 1$  and  $u_{ex} = 0$ , we get  $f_{max} = \alpha / [\exp(-\beta\mu) + 1]$ .

In the present problem, we consider the dynamics of electrons in positive (+) and negative (-)  $x$  axis. We also considered that the streaming of particles attain such values so as to incorporate relativistic factor ( $\gamma$ ) in the dynamical equations [20]. Now, using Eq. 4, we calculate the zeroth, first and second moments of the distribution function ( $f$ ). So from the zeroth and first moments of the Fermi-Dirac distribution function, we obtain the continuity and momentum equation in the following form:

$$\frac{\partial \gamma_\pm n_\pm}{\partial t} + \vec{\nabla} \cdot (\gamma_\pm n_\pm \vec{u}_\pm) = 0 \tag{5}$$

$$\frac{\partial \gamma_\pm \vec{u}_\pm}{\partial t} + (\vec{u}_\pm \cdot \vec{\nabla}) \gamma_\pm \vec{u}_\pm = \frac{e}{m_e} \vec{\nabla} \phi_E + \frac{1}{m_e n_\pm} \vec{\nabla} \Pi + \frac{\hbar^2}{2m_e^2 \gamma_\pm} \left[ \vec{\nabla} \left( \frac{\nabla^2 \sqrt{n_\pm}}{\sqrt{n_\pm}} \right) \right] \tag{6}$$

Here,  $\Pi$  is the total pressure due to relativistic degeneracy, spin exchange interaction and finite temperature effects ( $\Pi = P_G + P_{ex} + P_{degeneracy}$ ), where  $\gamma_{\pm} = 1/\sqrt{1 - u_0^2/c^2}$ ,  $n_{\pm}$  and  $u_{\pm}$  denote the relativistic factor, electron number density and speeds along  $\pm x$  directions respectively. And  $\phi_E$ ,  $n_{i0}$  refer to the electric potential and ion equilibrium number density. The last term in the momentum equation (6) corresponds to the Bohm potential.

The Relativistic degeneracy potential  $\phi_{ch}$  originates from the degeneracy pressure in dense stellar bodies [11] is given by

$$P_{degeneracy} = \frac{\pi m_e^4 c^5}{3h^3} [R(2R^2 - 3)\sqrt{1 + R^2} + 3 \sinh^{-1} R] \quad (7)$$

Here,  $R = (n/n_0)^{1/3}$  and  $n_0$  is the equilibrium number density of electrons in the plasma. We obtained effective potentials corresponding to relativistic degeneracy as  $(\phi_{ch})[ch \rightarrow \text{Chandrasekhar pressure [11]}$ . The effective potential contribution due to relativistic degeneracy can be simplified as [1]

$$\left. \begin{aligned} \phi_{ch} &= \sqrt{1 + R_0^2 n^{2/3}} && \text{Classical case} \\ \phi_{ch} &= \sqrt{1 + R_0^6 \frac{n^2}{\beta}} && \text{Quantum case} \end{aligned} \right\} \quad (8)$$

Here,  $\beta = \frac{B_0}{B_d}$  with  $B_0$  is the axial magnetic field strength and  $B_d \approx 4.4 \times 10^9$  Tesla is the critical magnetic field intensity of typical strongly magnetised stars. The condition for quantum regime is  $R^2 \ll 2\beta$  whereas  $R^2 \gg 2\beta$  corresponds to classical case.

$$R = \left(\frac{n_e^{cl}}{n_0}\right) \frac{R_0^3}{\beta} \quad (9)$$

corresponds to classical case and

$$R = \left(\frac{n_e^Q}{n_0}\right)^{1/3} R_0 \quad (10)$$

correspond to quantum regime.

Such a correlation can be incorporated by eliminating the exchange potential term ( $\phi_{ex}$ ) and replacing  $\Gamma$  by  $R_0/\sqrt{\beta^2 + \beta R_0^6}$ . This transformation was also checked by Akbari-Moghanjoughi and Ghorbanalilu [2].

The electron spin exchange interaction [ $\phi_{ex}$ ], though small can have significant effects on the electron wave at such high densities. The electron spin exchange potential [25] in generalised terms is given as



$$\left. \begin{aligned} \phi_{ex} &= -\phi_0 [A(\eta) - B(\eta)] \\ A(\eta) &= \left[ \frac{1}{32} (\eta^4 + \eta^{-4}) + \frac{1}{4} (\eta^2 + \eta^{-2}) - \frac{3}{4} (\eta^2 - \eta^{-2}) \ln \eta - \frac{9}{16} + \frac{3}{2} (\ln \eta)^2 \right] \\ B(\eta) &= \left[ -\frac{\eta}{3} \left( \frac{\eta^2 - 1}{\eta^2 + 1} \right) \left\{ \frac{1}{8} (\eta^3 - \eta^{-5}) - \frac{1}{4} (\eta - \eta^{-3}) - \frac{3}{2} (\eta + \eta^{-3}) \ln \eta + \frac{3 \ln \eta}{\eta} \right\} \right] \end{aligned} \right\} (11)$$

where  $\eta = R + \sqrt{1 + R^2}$ ,  $\phi_0 = \frac{2\alpha m_e^4 c^5}{h^3}$  and  $\alpha = e^2/\hbar c$  is the fine structure constant.

This system is bounded by the Poisson's equation

$$\nabla^2 \phi_E = 4\pi e \left( \frac{n_+}{2} + \frac{n_-}{2} - n_{i0} \right) \quad (12)$$

The value of degeneracy parameters for different kinds of plasma is given below [6]:

Degeneracy parameter for different kinds of plasma			
Types of plasma	Density ( $m^{-3}$ )	Temperature (K)	G
Tokamak	$10^{20}$	$10^{18}$	1
Inertial confinement fusion	$10^{32}$	$10^8$	1
Metal and metal clusters	$10^{28}$	$10^4$	1.4
Jupiter	$10^{32}$	$10^4$	1.4
White dwarf	$10^{35}$	$10^8$	4

### 3 Linear Dispersion Relation and Instability Criteria

In order to investigate the linear and non-linear behavior of electron acoustic wave in this three component electron-ion plasma we make the following perturbation expansion for the field quantities  $n_{\pm}$ ,  $u_{\pm}$  and  $\phi_E$  about their equilibrium values:

$$\begin{bmatrix} n_{\pm} \\ u_{\pm} \\ \phi_E \end{bmatrix} = \begin{bmatrix} 1 \\ u_{(0)} \\ 0 \end{bmatrix} + \varepsilon \begin{bmatrix} n_{\pm}^{(1)} \\ u_{\pm}^{(1)} \\ \phi_E^{(1)} \end{bmatrix} + \varepsilon^2 \begin{bmatrix} n_{\pm}^{(2)} \\ u_{\pm}^{(2)} \\ \phi_E^{(2)} \end{bmatrix} + \dots \quad (13)$$

and normalization of the relativity parameter is carried out as  $R \rightarrow \bar{R}R_0$  with  $R_0 = (n_{\pm}/n_0)^{1/3}$ . Now we express  $A(\eta)$  and  $B(\eta)$  in Eq. 11 in terms of  $n_0$  &  $n_{\pm}$  in the following manner

$$\eta = R + \sqrt{1 + R^2} = \left( \frac{n}{n_0} \right)^{1/3} + \left[ 1 + \left( \frac{1}{n_0} \right)^{1/3} (1 + \varepsilon n^{(1)} + \varepsilon^2 n^{(2)})^{1/3} \right]^{1/2} \quad (14)$$

The different orders of  $\eta$  (omitting  $\pm$  sign for brevity) can be obtained as,

$$\left. \begin{aligned} \eta^1 &= P^1 \left[ 1 + \varepsilon \frac{Q}{P} n^{(1)} \right]; & \eta^2 &= P^2 \left[ 1 + 2\varepsilon \frac{Q}{P} n^{(1)} \right]; \\ \eta^3 &= P^3 \left[ 1 + 3\varepsilon \frac{Q}{P} n^{(1)} \right]; & \eta^4 &= P^4 \left[ 1 + 4\varepsilon \frac{Q}{P} n^{(1)} \right]; \\ \eta^5 &= P^5 \left[ 1 + 5\varepsilon \frac{Q}{P} n^{(1)} \right]; & \eta^{-1} &= P^{-1} \left[ 1 - \varepsilon \frac{Q}{P} n^{(1)} \right]; \\ \eta^{-2} &= P^{-2} \left[ 1 - 2\varepsilon \frac{Q}{P} n^{(1)} \right]; & \eta^{-3} &= P^{-3} \left[ 1 - 3\varepsilon \frac{Q}{P} n^{(1)} \right]; \\ \eta^{-4} &= P^{-4} \left[ 1 - 4\varepsilon \frac{Q}{P} n^{(1)} \right]; & \eta^{-5} &= P^{-5} \left[ 1 - 5\varepsilon \frac{Q}{P} n^{(1)} \right]; \\ (\ln \eta)^2 &= -2 \left[ 1 - 4P \left( 1 + \varepsilon \frac{Q}{P} n^{(1)} \right) + 2P^2 \left( 1 + 2\varepsilon \frac{Q}{P} n^{(1)} \right) \right] \end{aligned} \right\} \quad (15)$$

where

$$\left. \begin{aligned} P &= \left\{ \left( \frac{1}{n_0} \right)^{(1/3)} + \frac{1}{2} \left( \frac{1}{n_0} \right)^{(2/3)} \right\} \\ Q &= \left\{ \frac{1}{3} \left( \frac{1}{n_0} \right)^{(2/3)} + \frac{1}{2} \left( \frac{1}{n_0} \right)^{(1/3)} n^{(1)} \right\} \end{aligned} \right\} \quad (16)$$

Putting all values from Eq. 15 omitting  $\pm$  sign corresponding to streaming directions in Eq. 11, we get

$$\left. \begin{aligned} A(\eta) &= R_1 + \varepsilon S_1 n^{(1)} \\ B(\eta) &= V_1 + \varepsilon W_1 n^{(1)} \end{aligned} \right\} \quad (17)$$

where  $R_1 = \frac{1}{32} (P^4 + P^{-4}) + \frac{1}{4} (P^2 + P^{-2}) - \frac{3}{4} \Lambda - \frac{9}{16} + 6 \left( 1 - 4P + P^2 \right)$ ;

$\Lambda = 2 (P^{-2} + P^2) (1 - P)^2$ ;

$S_1 = \left\{ \frac{Q}{8} (P^3 - P^{-5}) + \frac{Q}{2} (P - P^{-3}) + \frac{3}{4} \beta - 24Q + 12QP \right\}$ ;

$V_1 = \left\{ \begin{aligned} &\frac{1}{24} P^4 (P - 1)^2 - \frac{1}{24} P^{-4} (P - 1)^2 - \frac{P^2}{12} (P - 1)^2 (P - P^{-3}) \\ &+ P (P + P^{-3}) (P - 1)^4 - 2P (P - 1)^2 \left( P - 2 + \frac{1}{P} \right) \end{aligned} \right\}$

$W_1 = \left\{ \begin{aligned} &\frac{1}{8} P^3 (P - 1)^2 Q + \frac{5}{24} P^{-5} (P - 1)^2 Q - \frac{1}{12} P (P - 1)^2 Q \\ &+ P (1 - 3P^{-4}) (P - 1)^4 Q - 2P (P - 1)^2 (P + P^{-3}) (1 - P^2) Q \\ &- \frac{1}{3} P (P - 1)^2 \left( \frac{2}{P} - 1 + \frac{1}{P^2} \right) Q + \frac{P^3}{8} T_1 - \frac{P^{-5}}{8} T_1 - \frac{P}{4} (P - P^{-3}) T_1 \\ &+ 3T_1 (P + P^{-3}) (P - 1)^2 - 6T_1 (P^{-1} + 2 + P) \end{aligned} \right\}$

$T_1 = \left\{ \frac{1}{3} (P - 1)^2 Q + \frac{4}{3} (P^4 - P^2) Q \right\}$ ;

$\beta = \left\{ 2P^2 (4QP - 6Q + 2\frac{Q}{P}) - 2P^{-2} (4QP + 2Q - 2\frac{Q}{P}) \right\}$

Using linear perturbations of field quantities like  $n_{\pm} = 1 + n_{\pm}^{(1)} \exp(ikx - \omega t)$ ;  
 $u_{\pm} = u_0 + u_{\pm}^{(1)} \exp(ikx - \omega t)$  and  $\phi_E = \phi_E^{(1)} \exp(ikx - \omega t)$ , the first order terms are obtained as

$$\left. \begin{aligned} n_{\pm}^{(1)} &= \left\{ \frac{-k^2 \phi_E^{(1)}}{\left[ (\omega \mp k u_0)^2 \gamma^3 - k^2 \Gamma - H^2 k^4 \right]} \right\} \\ u_{\pm}^{(1)} &= \left\{ \frac{-(\omega \mp k u_0) k \phi_E^{(1)}}{\left[ (\omega \mp k u_0)^2 \gamma^3 - k^2 \Gamma - H^2 k^4 \right]} \right\} \end{aligned} \right\} \quad (18)$$

where

$$\Gamma = \left\{ \frac{1}{12} \left( \frac{1}{n_0} \right)^{2/3} + \phi_{ex} S_1 - \phi_{ex} W_1 + 3G\beta^2 \right\} \quad (19)$$

Now the linear dielectric function can be written as  $F(\omega, k) = 1 + \chi_{e+} + \chi_{e-}$  where  $\chi_{\pm}$  are the dielectric susceptibilities of counter streaming electron fluids. The dispersion relation is obtained as

$$\frac{2}{R_0^3} + \frac{1}{[k^2\Omega - \gamma^3\omega(\omega + 2kv)]} + \frac{1}{[k^2\Omega - \gamma^3\omega(\omega - 2kv)]} = 0 \quad (20)$$

where  $\Omega = (H^2k^2 - u_0^2\gamma^3 + \Gamma)$

For non-relativistic or weakly relativistic case ( $R_0 \ll 1$ ) with non-relativistic streaming ( $\gamma \rightarrow 1$ ) the Eq. 20 boils down into

$$\omega^2 = R_0^3 + \Gamma k^2 \quad (21)$$

Here we have ignored the finite temperature statistical pressure term. It is justified that if in the classical limit when  $\beta\mu \rightarrow (-\infty)$ , so that  $G \rightarrow 0$ , the dispersion relation (20) corresponds to the Bohm-Gross [3] dispersion relation for hot plasma i.e.;

$$\omega^2 = \omega_{pc}^2 + 3V_{Te}^2 k^2 + \frac{\hbar^2 k^4}{4m^2} \quad (22)$$

Now in the ultra cold limit we have to consider the finite temperature effect as  $\beta\mu \rightarrow \infty$  i.e.;  $G \rightarrow \frac{2}{5}\beta\mu$  &  $\mu \rightarrow \varepsilon_F$ , [ $\equiv \frac{mV_{Fe}^2}{2}$  is the electron Fermi energy]. In this case the dispersion relation takes the form

$$\omega^2 = \omega_{pe}^2 + \frac{3}{5}V_{Fe}^2 k^2 + \frac{\hbar k^4}{4m^2} - \frac{e^2 V_{Fe} k^2}{5\pi\hbar} \quad (23)$$

where the second term of on the right hand side of Eq. 23 corresponds to the finite temperature contribution due to anisotropy, the third term corresponds to the quantum diffraction effect and the forth one is related to the electron exchange pressure. The result may be comparable to high frequency Langmuir oscillations [12]. These results correspond to the previous findings of von Roos and Zmuidzinas [24], Nozieres and Pines [23], Karazawa et al. [19] as well as recent works by Akbari-Moghanjoughi and Ghorbanalilu [2]. The terms in our dispersion relation have the same nature as previous researchers except with certain additional multiplicative terms on the RHS. The expansion of Lindhard dielectric function [18] for phase velocities ( $V_{ph} \leq V_{Fe}$ ) has similar term like the second term in Eq. 23. The quantum diffraction term third on RHS of (23) correspond with the finding of Eliasson and Shukla [14]. The forth term too is relatable with Ekman and others [12] only with  $\frac{3}{5\pi}$  co-factor distinct from Mohammadnejad and Akbari-Moghanjoughi [22]

Before Solving the linear dispersion relation (20), from the survey of the available literature we came to know that there is no well constructed model accounting for relativistic quantum hydrodynamics of finite temperature Fermi plasma. To some extent, we have knowledge on relativistic extension of (QHD) equations incorporating Bohm term from Wigner-Poisson's formulation. However, exchange pressure (Salpeter's [25]) gives a correct density dependence in this relativistic case. Considering all the factors the dispersion relation (20) is solvable and its solution gives four modes (or branches) as,

$$\omega = \pm \sqrt{\frac{[R_0^3 + (4u_0^2\gamma^3 + 2\Omega^2)k^2] \pm \sqrt{[(R_0^2 + 4u_0^2\gamma^3k)^2 + 16u_0^2\gamma^3\Omega k^4]}}{2\gamma^3}} \quad (24)$$

or

$$\omega = \pm \sqrt{\frac{J(k) \pm L(k)}{2\gamma^3}}$$

where  $J(k)=[R_0^3 + (4u_0^2\gamma^3 + 2\Omega^2)k^2]$  &  $L(k)=\sqrt{[(R_0^2 + 4u_0^2\gamma^3k)^2 + 16u_0^2\gamma^3\Omega k^4]}$

The term written within the inner square root can amount to imaginary frequency and hence may be set to zero to find possible real roots. From this above consideration we get a sixth order algebraic equation as

$$16u_0^2\gamma^3 H^2 k^6 + 4\Gamma k^4 + 8R_0^3 u_0^2 \gamma^3 k^2 + R_0^6 = 0 \quad (25)$$

This can be rewritten as

$$A_1 k^6 + B_1 k^4 + C_1 k^2 + D_1 = 0 \quad (26)$$

Equation 25 has no real positive root. Under these algebraic considerations the total term under the square root in Eq. 24 is obviously real for all possible wave-numbers. This does not mean it will be non-negative. Such a negative value of the expression [i.e;  $J(k) \pm L(k) < 0$ ] will correspond to imaginary values of frequency  $\omega$  and determine the range of stable modes.

In order to obtain the wavenumber domain at which the frequency is imaginary, we set the term  $[J(k) \pm L(k)]$  equal to zero and further constraining ourselves within the positive sign of  $\omega$  in Eq. 24, we get the upper mode frequency  $\omega = \sqrt{\frac{R_0^3}{\gamma^3}}$  to be always stable. The instability arises when we consider the negative sign in Eq. 24 i.e.; for  $J(k) \pm L(k)$  quantity.

With these considerations and imposing stability criteria for possible frequency ranges we obtain from Eq. 20 after expanding the squared terms and with some algebraic simplifications.

$$\Omega k^2 [R_0^3 + 8u_0^2\gamma^3 k^2 + 1] = 0 \quad (27)$$

which on further simplification provides

$$k^2(H^2k^2 - u_0^2\gamma^3 + \Gamma)(R_0^3 + 8u_0^2\gamma_0^3k^2 + 1) = 0 \quad (28)$$

This can be rewritten as,

$$A_2k^6 + B_2k^4 + C_2k^2 = 0 \quad (29)$$

$$A_2 = H^28u_0^2\gamma^3, B_2 = H^2(R_0^3 + 1) + (\Gamma - u_0^2\gamma^3)8u_0^2\gamma^3, C_2 = (\Gamma - u_0^2\gamma^3)$$

$$A_2k^6 + B_2k^4 + C_2k^2 = 0 \quad (30)$$

$$\text{or } k^2(A_2k^4 + B_2k^2 + C_2) = 0 \quad (31)$$

$k = 0$  is a root

another roots are obtained by taking  $k^2 = \kappa$

$$\text{or } A_2\kappa^2 + B_2\kappa + C_2 = 0 \quad (32)$$

$$\text{or } \kappa = \frac{-B_2 \pm \sqrt{B_2^2 - 4A_2C_2}}{2A_2} \quad (33)$$

$$\text{or } k = \pm \sqrt{\frac{\sqrt{B_2^2 - 4A_2C_2} - B_2}{2A_2}} \quad (34)$$

We have taken positive values of the square root of the discriminant because otherwise we would have obtained imaginary values. Now using standard techniques, the roots are obtained as  $\kappa_2$  and  $\kappa_3$  where  $(\kappa_1 = 0) < k < \sqrt{\kappa_2}$  and  $\sqrt{\kappa_3} < k$  are the range for unstable states whereas  $\sqrt{\kappa_2} < k < \sqrt{\kappa_3}$  is the stable region in  $k$ -space. A classical correspondence can be drawn for the region of instability for wave number values

$$0 < k < \sqrt{-\frac{\Gamma(R_0^3 + 1)}{(\Gamma - u_0^2\gamma_0^3)8u_0^2\gamma_0^3}} \quad (35)$$

## 4 Analytic Results and It's Physical Interpretations

In Fig. 1, we plot the  $\omega$  versus  $k$  corresponding to Eq. 20 in which we get four different modes in the classical case, in Fig. 2 we plot the dispersion relation corresponding to the quantum range. In both cases, we find a loop kind of structure along the

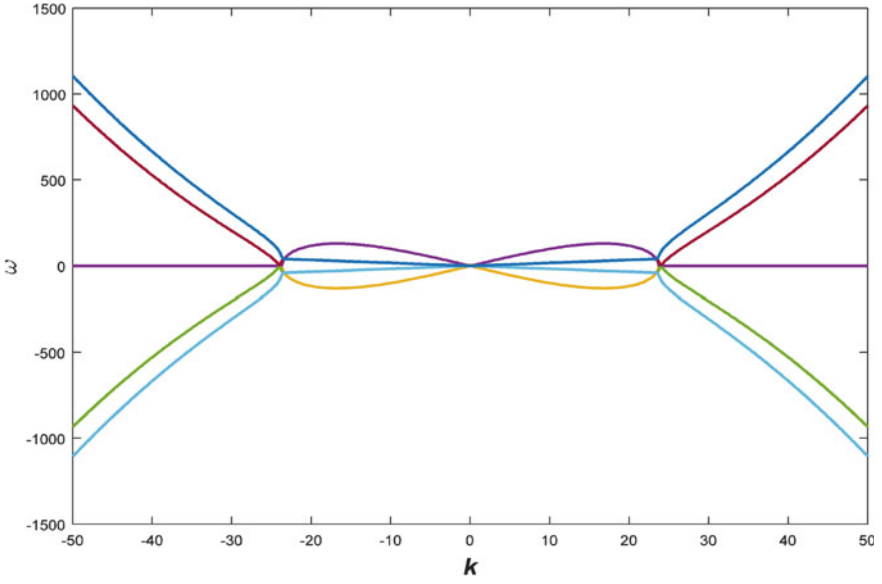


**Fig. 1** Linear dispersion relation for two stream instability in classical regime

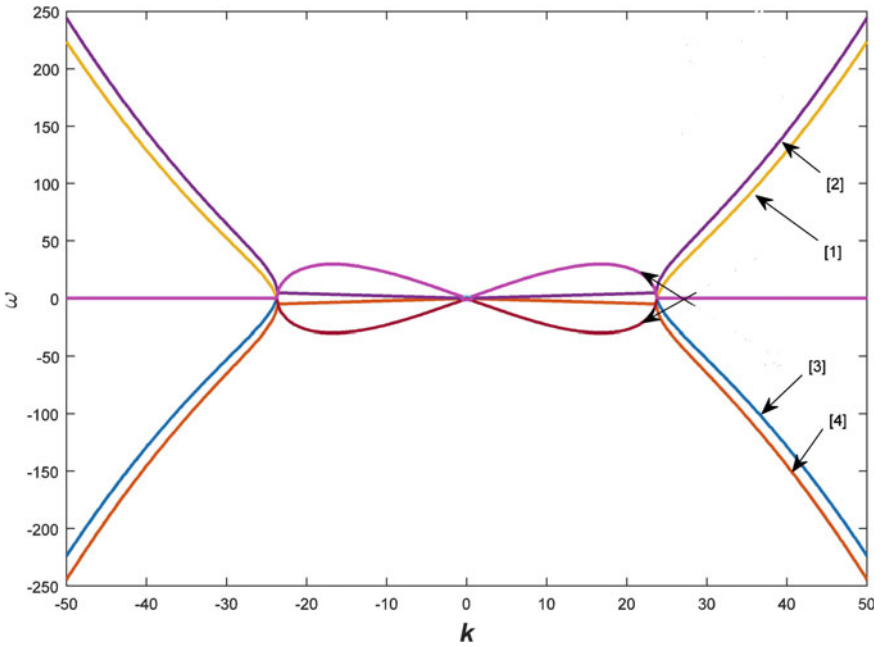


**Fig. 2** Linear dispersion relation for two stream instability in quantum regime

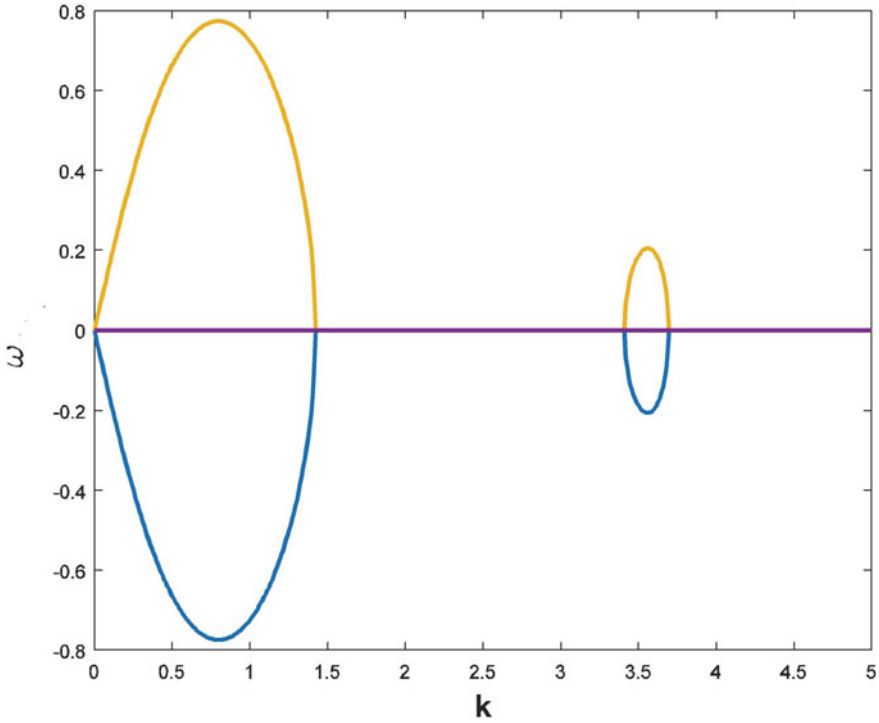


**Fig. 3** Unstable modes with growth rate variation in classical regime

wavenumber axis which corresponds to unstable mode. Just where the unstable mode ceases to exist, we get corresponding curves for the stable modes. This reflects the fact that coupling is exact. In the quantum range, we also get similar behaviours but here the fast modes and the slow modes are not widely separated which means their phase velocity is close by. An electromagnetic wave in such a dispersive medium in which there is a beam of particles with streaming velocity ( $u_0$ ), there can be an exchange of energy from the beam to the wave and vice-versa. When the phase velocity of the wave is slightly smaller than the velocity of the beam, there can be an energy transfer from the beam to the wave resulting in instability of the wave. The fast and slow mode (Figs. 1 and 2) in both cases immediately take up the energy of the beam at higher wavenumber values which means energy is easily dispersed preventing any unwanted instability. Here the perturbation is considered infinitesimally small. However, for a larger value of perturbation bounded solution may be absent. The application of the hydrodynamic model is mere meaningful in such a case where quasi-neutrality, spatial periodicity and stationary stable states can be studied extensively. In such a quantum plasma the instability originates from the free energy source and associated mode coupling resulting in stable and unstable regimes in the wavenumber. It deviates from the classical picture since the quantum effect causes changes in the dielectric

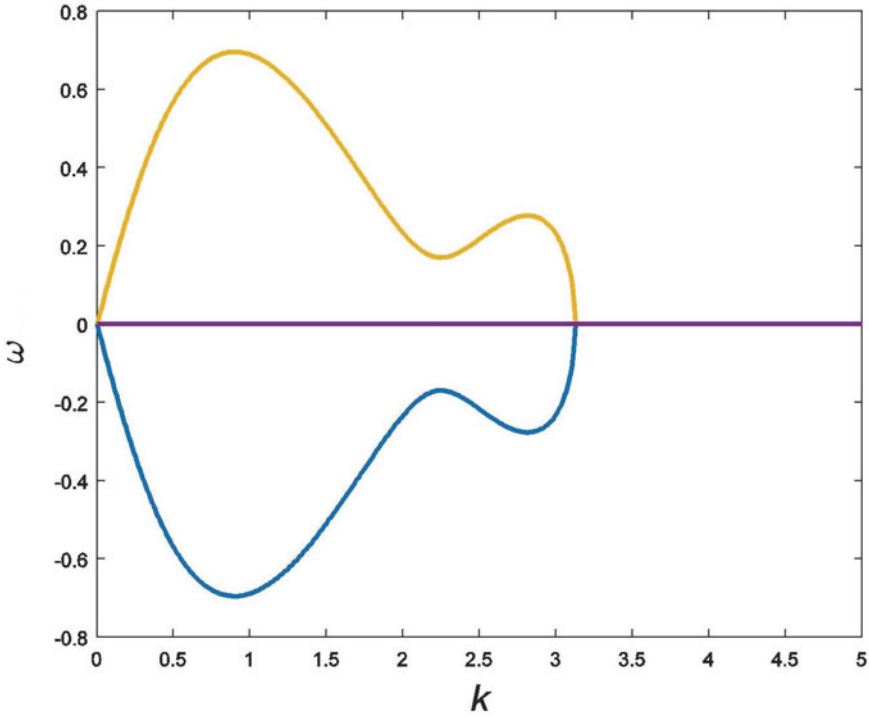


**Fig. 4** Two interacting unstable mode in the quantum regime

function of the plasma. The positive energy modes correspond to the energy being given from the wave to the beam, whereas the negative energy modes are related to the fact the energy is given by the beam to wave. In Fig. 3, two separated loops have been shown corresponding to unstable modes with higher growth of instability at smaller wavenumbers. A small zone of instability appears isolatedly existent. This corresponds to the quick dissipation of energy acquired from the beam to the wave.

Figure 4, shows a semi-classical situation in which two unstable modes are coupled in such a way to exchange between them and give rise to a hybrid model of varying instability growth. Next in Figs. 5 and 6 we show that the quantum regime of all the four modes is stable. Two of them are fast whereas the other two are slow. Here, the wave phase speed is compared with the beam speed. In Figs. 7 and 8, we plot the imaginary roots of dispersion relation i.e; the unstable mode corresponding to parametric variation of quantum diffraction ( $H$ ), relativistic degeneracy factor ( $R_0$ ) and streaming motion ( $u_0$ ). From Fig. 7, it is clear that an increase in the value of  $R_0$  (represented by outward moving curve) increases the instability growth rate in such case the instability ceases to die out with increasing wavenumber. Quantum diffraction negatively affects instability. From the fourth plot of Fig. 7, we can say that 'H' and ' $R_0$ ' have ceratin correlation at higher density in which it fails to contain the



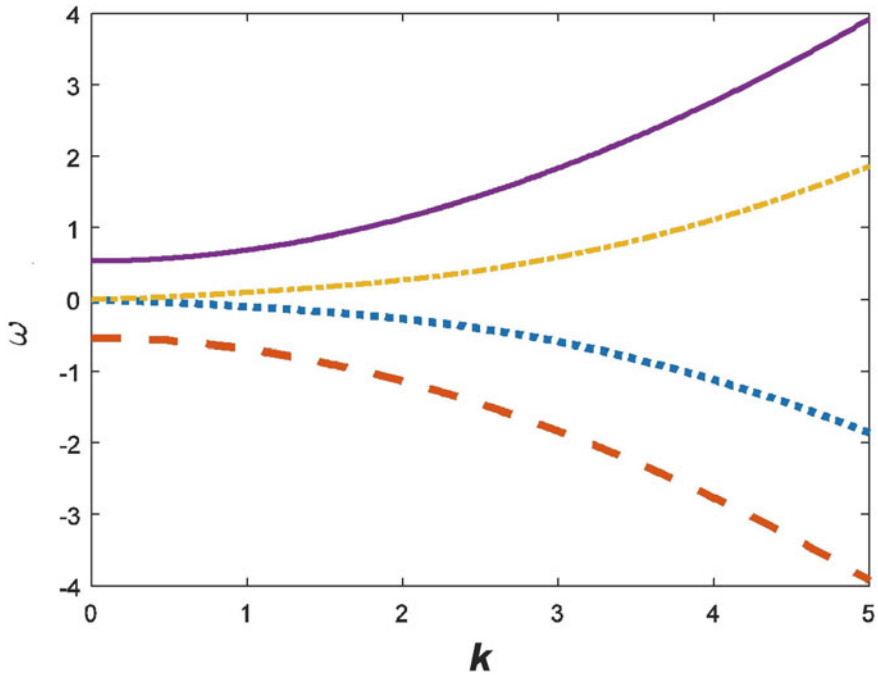


**Fig. 5** Dispersion curve when value of relativistic degeneracy parameter ( $R_0$ ) = 0.8 and quantum diffraction parameter ( $H$ ) = 2

instability at higher wavenumber. From Fig. 8, we conclude, by increasing relativistic streaming velocity, the instability is enhanced but the wave number corresponding to unstable modes are independent of the streaming motion. In Fig. 9, we plot the classical and quantum variation of contour plot in the  $(k - R_0)$  plane. The zone of instability is less in the classical case and is extended in the quantum regime. In Fig. 10, we plot the contour variations in  $(k - R_0)$  plane corresponding to different beam velocities. The curves are almost similar about the wavenumber axis and it is clear from the figure that with the increase in beam velocity the instability zone shrinks. In Fig. 11 we plot the  $R_0$  dependence in the  $(k - u_0)$  plane and conclude that with increasing value of ' $R_0$ ' the zone stability slightly get decreased. All this instability is dominant in the lower wavenumber values which is relatable with Figs. 1, 2 and 3. Our results will find application in interpreting various electrostatic two-stream instability phenomena and associated wave modes that are found to exist in stellar and solar flares. The resulting close correlation with the findings of Akbari, Haas and Eliasson.

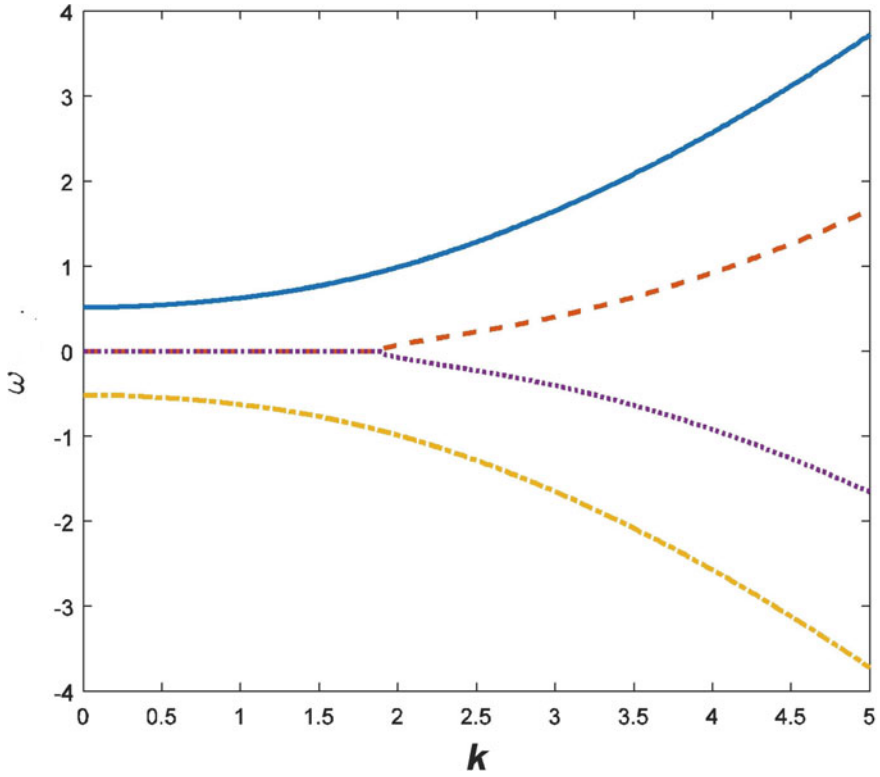


Fig. 6 Unstable modes with growth rate variation in classical regime

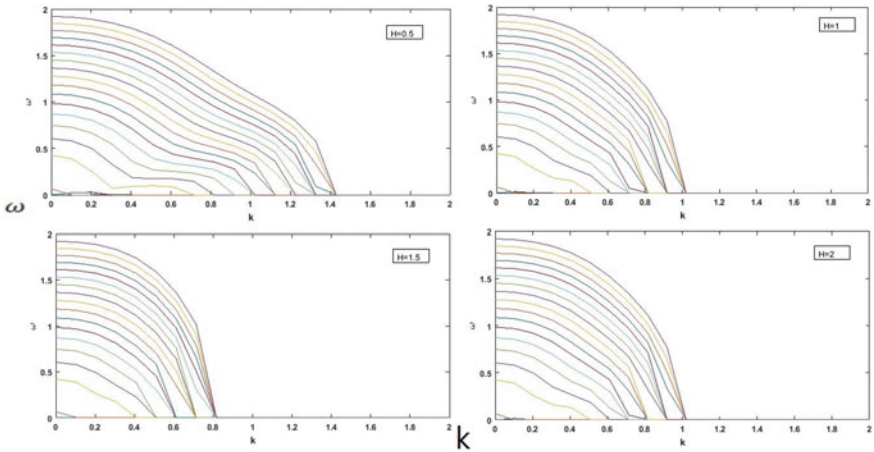
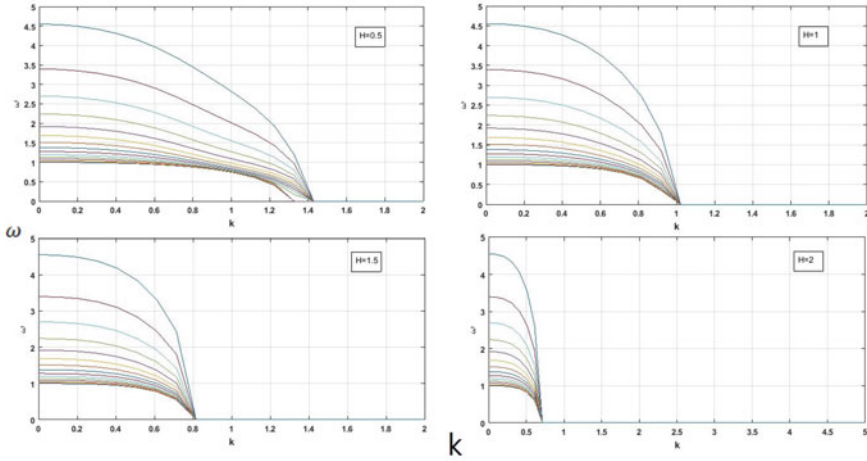
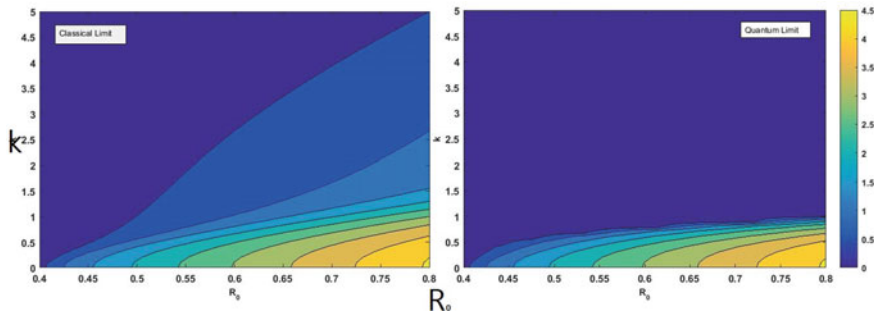


Fig. 7 Two interacting unstable mode in the quantum regime



**Fig. 8** Dispersion curve when value of relativistic degeneracy parameter ( $R_0$ ) = 0.8 and quantum diffraction parameter ( $H$ ) = 2



**Fig. 9** Contour plot ( $k - R_0$ ) plane in classical and quantum limit

## 5 Conclusion

In this study, we investigated analytically the properties encountered in counter-propagating plasma streams that contribute to two-stream instability. We designed the governing equations in a certain way that both classical and quantum regimes may be examined. For this reason, we have employed quantum hydrodynamic model and obtained dispersion characteristics. The physical situation of the problem is related to solar wind and heliospheric plasma. The effects of degeneracy factor, quantum diffraction and streaming motion have been studied with great detail. The stability criterion was encountered to be dependent on the wavenumber's range along with the parameter values. Interacting modes and their domain of interaction have been identified. In a nutshell, this work gives us a better view of the counter streaming instability in a dense plasma.

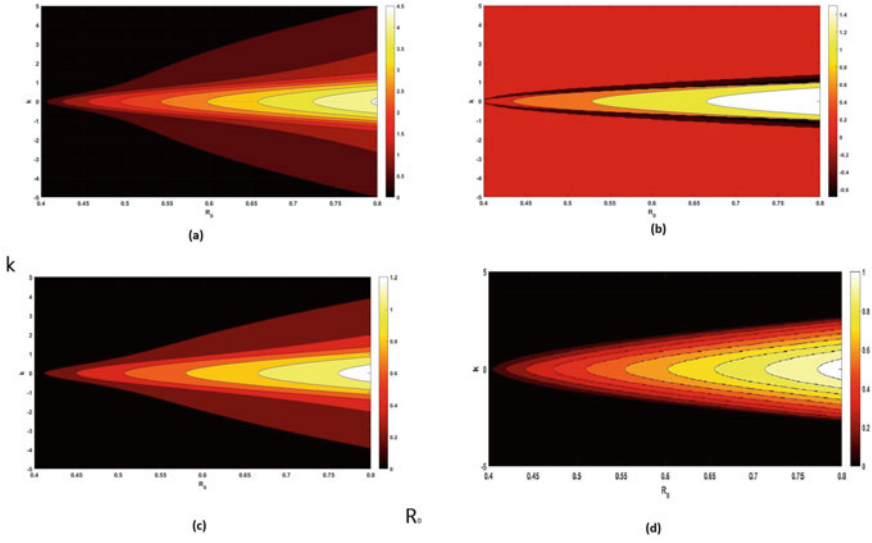


**Fig. 10** Contour plot for different value of  $u_0$  [ $0.8c$  (a),  $0.6c$  (b),  $0.4c$  (c),  $0.2c$  (d)], in  $(k - R_0)$  plane

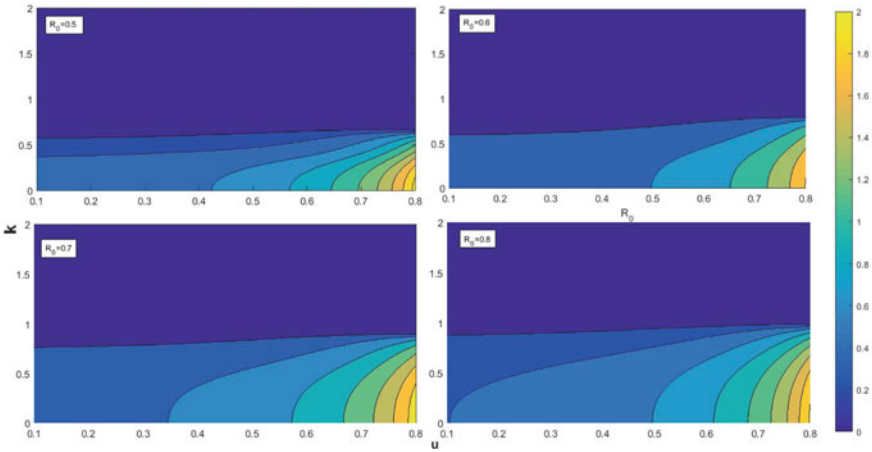


**Fig. 11** Contour plot for different value of  $R_0$  in  $(k - u_0)$  plane

**Acknowledgements** We would like to thank Prof. A. Roy Chowdhuri and Mr. Chinmay Das for their inspiration and support. Authors would like to thank Physics departments of Jadavpur University and Government General Degree College at Kushmandi for providing facilities to carry this work.

## References

1. Akbari-Moghanjoughi, M.: Field-induced degeneracy regimes in quantum plasmas. *Phys. Plasmas* **19**(3), 032703 (2012)
2. Akbari-Moghanjoughi, M., Ghorbanalilu, M.: Energy exchange in strongly coupled plasmas with electron drift. *Phys. Plasmas* **22**(11), 112111 (2015)
3. Bohm, D., Gross, E.P.: Theory of plasma oscillations. b. Excitation and damping of oscillations. *Phys. Rev.* **75**, 1864–1876 (Jun 1949). <https://doi.org/10.1103/PhysRev.75.1864>
4. Bransden, B.H., Joachain, C.J.: *Quantum mechanics*, 2nd edn. (Harlow 2000)
5. Brodin, G., Marklund, M., Manfredi, G.: Quantum plasma effects in the classical regime. *Phys. Rev. Lett.* **100**, 175001 (2008)
6. Chandra, S., Ghosh, B.: Modulational instability of electron-acoustic waves in relativistically degenerate quantum plasma. *Astrophys. Space Sci.* **342**(2), 417–424 (2012)
7. Chandra, S., Ghosh, B.: Non-linear propagation of electrostatic waves in relativistic fermi plasma with arbitrary temperature (2013)
8. Chandra, S., Goswami, J., Sarkar, J., Das, C.: Analytical and simulation studies of forced kdv solitary structures in a two-component plasma. *J. Korean Phys. Soc.* **76**(6), 469–478 (2020)
9. Chandra, S., Goswami, J., Sarkar, J., Das, C., Nandi, D., Ghosh, B.: Formation of electron acoustic shock wave in inner magnetospheric plasma. *Indian J. Phys.* 1–15 (2022)
10. Chandra, S., Sarkar, J., Das, C., Ghosh, B.: Self-interacting stationary formations in plasmas under externally controlled fields. *Plasma Phys. Rep.* **47**(3), 306–317 (2021)
11. Chandrasekhar, S., Chandrasekhar, S.: *An Introduction to the Study of Stellar Structure*, vol. 2. Courier Corporation (1957)
12. Ekman, R., Zamanian, J., Brodin, G.: Exchange corrections in a low-temperature plasma. *Phys. Rev. E* **92**, 013104 (2015)
13. Eliasson, B., Kogelschatz, U.: Modeling and applications of silent discharge plasmas. *IEEE Trans. Plasma Sci.* **19**(2), 309–323 (1991)
14. Eliasson, B., Shukla, P.K.: Nonlinear quantum fluid equations for a finite temperature fermi plasma. *Physica Scripta* **78**(2), 025503 (2008)
15. Goswami, J., Sarkar, J.: Kbm approach to electron acoustic envelope soliton in viscous astrophysical plasma. *Physica Scripta* **96**(8), 085601 (2021)
16. Goswami, J., Sarkar, J., Chandra, S., Ghosh, B.: Amplitude-modulated electron-acoustic waves with bipolar ions and kappa-distributed positrons and warm electrons. *Pramana* **95**(2), 1–10 (2021)
17. Haas, F., Bret, A., Shukla, P.K.: Physical interpretation of the quantum two-stream instability. *Phys. Rev. E* **80**, 066407 (2009)
18. Hu, G., O'connell, R.: Generalization of the Lindhard dielectric function to include fluctuation effects. *Phys. Rev. B, Condensed Matter* **40**, 3600–3604 (09 1989). <https://doi.org/10.1103/PhysRevB.40.3600>
19. Kanazawa, H., Misawa, S., Fujita, E.: Green function method for electron gas. ii: Dispersion relation of plasmons. *Prog. Theor. Phys.* **23**(3), 426–432 (1960)
20. Lee, N.C., Choi, C.R.: Ion-acoustic solitary waves in a relativistic plasma. *Phys. Plasmas* **14**(2), 022307 (2007)
21. Manfredi, G.: *How to Model Quantum Plasmas* (2005)
22. Mohammadnejad, M., Akbari-Moghanjoughi, M.: Two stream ion acoustic wave instability in warm dense plasmas. *Astrophys. Space Sci.* **364**(2), 23 (2019)

23. Nozieres, P., Pines, D.: Correlation energy of a free electron gas. *Phys. Rev.* **111**(2), 442 (1958)
24. von Roos, O., Zmuidzinas, J.S.: Effect of electron exchange on the dispersion relation of plasmons. *Phys. Rev.* **121**(4), 941 (1961)
25. Salpeter, E.E.: Energy and pressure of a zero-temperature plasma. *Astrophys. J.* **134**, 669 (1961)
26. Sarkar, J., Chandra, S., Ghosh, B.: Resonant interactions between the fundamental and higher harmonic of positron acoustic waves in quantum plasma. *Zeitschrift für Naturforschung A* **75**(10), 819–824 (2020)
27. Sarkar, J., Chandra, S., Goswami, J., Das, C., Ghosh, B.: Growth of rt instability at the accreting magnetospheric boundary of neutron stars. In: *AIP Conference Proceedings*, vol. 2319, p. 030006. AIP Publishing LLC (2021)
28. Sarkar, J., Chandra, S., Goswami, J., Ghosh, B.: Formation of solitary structures and envelope solitons in electron acoustic wave in inner magnetosphere plasma with suprathermal ions. *Contrib. Plasma Phys.* **60**(7), e201900202 (2020)
29. Shukla, P.K., Rao, N., Yu, M., Tsintsadze, N.: Relativistic nonlinear effects in plasmas. *Phys. Rep.* **138**(1–2), 1–149 (1986)

# Bifurcation of Nucleus-Acoustic Superperiodic and Supersolitary Waves in a Quantum Plasma



Barsha Pradhan , Nikhil Pal , and David Raj Micheal 

**Abstract** The main motivation of this work is to investigate the existence of arbitrary-amplitude nucleus-acoustic (NA) supernonlinear waves in a degenerate plasma system consisting of light and heavy nuclei and non-relativistic degenerate electrons. To achieve this objective, we plot phase portraits of the dynamical system and their corresponding Sagdeev's pseudopotential curves for different values of Mach number. Distinct topology of phase portraits along with two minima separated by a maxima in Sagdeev's pseudopotential curve ensure existence of NA supernonlinear waves. Further, we discuss influence of Mach number on periodic, superperiodic, solitary and supersolitary wave solutions.

**Keywords** Supersoliton · Supernonlinear periodic trajectory · Supernonlinear homoclinic trajectory · Phase plane analysis

---

Supported by Sikkim Manipal Institute of Technology.

---

B. Pradhan (✉)

Department of Mathematics, Sikkim Manipal Institute of Technology,  
Sikkim Manipal University, Majitar, Rangpo, East-Sikkim 737136, India  
e-mail: [barshapradhan09@gmail.com](mailto:barshapradhan09@gmail.com)

N. Pal

Department of Mathematics, Siksha-Bhavana, Visva-Bharati University, Santiniketan 731235, India

D. R. Micheal

Division of Mathematics, School of Advanced Sciences, Vellore Institute of Technology,  
Chennai, Tamil Nadu, India  
e-mail: [davidraj.micheal@vit.ac.in](mailto:davidraj.micheal@vit.ac.in)

## 1 Introduction

Compact astrophysical bodies have high density (of order  $10^{36} \text{ cm}^{-3}$  in neutron stars and  $10^{29} \text{ cm}^{-3}$  in white dwarf) such that the deBroglie wavelength of particles is comparable to the inter-particle distance [1, 2]. Therefore, roles of quantum effects and degeneracy pressure in such objects become vital. White dwarf mainly contains degenerate electrons, immobile heavy nuclei (e.g.,  $^{56}_{26}\text{Fe}$  and/or  $^{85}_{37}\text{Rd}$  and/or  $^{96}_{42}\text{Mo}$ , etc.) [3–5] and light nuclei (e.g.,  $^1_1\text{H}$  and/or  $^{12}_6\text{C}$  and/or  $^{16}_8\text{O}$ , etc.) [1, 2, 5]. In his work, Chandrasekhar [6, 7] reported that the outward pressure in compact astrophysical objects produced by degenerate electrons balances the inward pull due to gravity. The degenerate electrons follow the equation of state  $P_e = K_e n_e^\gamma$  with  $\gamma = \frac{5}{3}$ ,  $K_e = \frac{3}{5} \frac{\pi \hbar^2}{m_e}$  for non-relativistic (NR) limit and  $\gamma = \frac{4}{3}$ ,  $K_e = \frac{3}{4} \hbar c$  for ultra-relativistic (UR) limit [5–8]. Hence, we can employ either of the two limits for degenerate electrons.

Mammun et al. [9] studied NA waves in which inertia is supplied by nucleus mass density and restoring force is supplied by inertialess degenerate electron pressure which depends solely on electron number density. It is remarkable to note that NA waves exist in cold plasma limit unlike other modes (ion or electron or positron acoustic) which do not exist in cold plasma limits. Nonlinear features such as NA shocks [5, 9, 10] and NA solitons [8, 11] were extensively investigated in the recent years due to its potential implications in dense astrophysical objects. Jannat and Mammun [5] have briefly discussed the application of their results in white dwarfs.

Investigation of nonlinear waves in quantum plasmas by employing the concept of planar dynamical system (PDS) is gaining immense popularity [12–15]. In plasma, Dubinov and Kolotkov [16] developed a new category of nonlinear waves, publicized as supernonlinear waves (SNWs) that are marked by their distinct nonlinear topology of phase plots. Dubinov and Kolotkov [17] initiated the term “supersolitons” in plasmas by taking a model consisting of five components. Afterwards, Verheest et al. [18] verified that three-component in a plasma were sufficient to support supersolitons. Saha and Tamang [19] discussed SNWs using bifurcation theory of planar dynamical system. Since then, arbitrary amplitude SNWs [20, 21] as well as small-amplitude SNWs [15] were investigated in different plasmas using bifurcation theory. Very recently, Saha et al. [22] showed the existence of SNWs in a two-component Maxwellian plasma. But, there is no study of arbitrary amplitude nucleus-acoustic supernonlinear waves in quantum plasmas to the best of our knowledge. In this work, we have employed bifurcation theory to investigate arbitrary amplitude nucleus-acoustic superperiodic and supersolitary waves in a degenerate plasma system consisting of light and heavy nuclei and non-relativistic degenerate electrons.

The layout of this article is as follows: Normalised basic equations are presented in Sect. 2. Formation of planar dynamical system is briefly discussed in Sect. 3. Phase plots of the system are shown in Sect. 4. Section 5 gives the conclusion.



## 2 Normalised Basic Equations

A three-component quantum plasma is considered comprising of stationary heavy nuclei (mass =  $m_h$  and charge =  $Z_h e$ ), non-degenerate mobile, cold, light inertial nuclei (mass =  $m_i$  and charge =  $Z_i e$ ) together with NR degenerate electrons. The mass of stationary heavy nuclei that conserves background neutrality is much greater than the mass of inertial light nuclei that supplies inertia. Charge of light nuclei is greater or equal to unity. On the other hand, non-relativistic inertialess degenerate electrons supplies degenerate pressure that act as a restoring force. The normalized basic equations [8] that describe the dynamics of light nuclei are as follows:

$$\frac{\partial n_i}{\partial t} + \frac{\partial(n_i u_i)}{\partial x} = 0, \quad (1)$$

$$\frac{\partial u_i}{\partial t} + u_i \frac{\partial u_i}{\partial x} + \frac{\partial \phi}{\partial x} = 0, \quad (2)$$

$$K \frac{\partial n_e^\gamma}{\partial x} - n_e \frac{\partial \phi}{\partial x} = 0, \quad (3)$$

$$\frac{\partial^2 \phi}{\partial x^2} - \mu_e (n_e - 1) + n_i - 1 = 0. \quad (4)$$

Here number density  $n_s$  (where indices  $s = h, i, e$  designate heavy nuclei, light nuclei and electron), electrostatic potential  $\phi$  and velocity  $u_i$  are respectively normalized by equilibrium value  $n_{s0}$ ,  $(m_e c^2 / e)$ , where  $e$  is magnitude of protonic charge and  $C_0 = (Z_i m_e c^2 / m_i)^2$ . Light nuclei plasma period  $\omega_{pi}^{-1} = (4\pi e^2 Z_i^2 n_{i0} / m_i)^{-\frac{1}{2}}$  and modified Debye length  $\lambda_m = (m_e c^2 / 4\pi e^2 Z_i n_{i0})^{\frac{1}{2}}$  are used to scale time and space variables respectively. Here  $\mu_e = (n_{e0} / Z_i n_{i0})$  and  $K = (K_e n_{e0}^{\gamma-1} / m_e c^2)$ , where  $K_e$  obeys the equation of state  $P_e = K_e n_e^\gamma$  with  $\gamma = \frac{5}{3}$ ,  $K_e = \frac{3}{5} \frac{\pi \hbar^2}{m_e}$  for NR limit.

Here, we have set  $\frac{Z_h n_{h0}}{Z_i n_{i0}} = \mu_e - 1$  following the quasi-neutrality condition  $Z_h n_{h0} + Z_i n_{i0} = n_{e0}$  in (4). Subsequently, the model equations (1)–(4) absorb the charge state of heavy nuclei  $Z_h$  as a result of normalization.

## 3 Planar Dynamical System (PDS)

Normalized basic equations (1)–(4) are transformed to a PDS by employing travelling wave transformation

$$\xi = x - Mt, \quad (5)$$

where travelling wave velocity  $M$  is taken in positive direction of  $x$ -axis. Applying this transformation to (1)–(3) with boundary conditions  $\phi \rightarrow 0$ ,  $n_i \rightarrow 1$ ,  $u_i \rightarrow 0$  and  $n_e \rightarrow 1$  as  $\xi \rightarrow \pm\infty$ , we acquire

$$n_i = \left(1 - \frac{2\phi}{M^2}\right)^{-\frac{1}{2}}, \quad (6)$$

$$n_e = \left[1 + \left(\frac{\gamma - 1}{k\gamma}\right)\phi\right]^{\frac{1}{\gamma-1}}. \quad (7)$$

Applying transformation (5) to (4) with boundary conditions and substituting (6) and (7), we get

$$\frac{d^2\phi}{d\xi^2} = a\phi + b\phi^2 + c\phi^3 + d\phi^4, \quad (8)$$

with  $a = -\frac{1}{M^2} + \frac{\mu_e}{\gamma K}$ ,  $b = -\frac{3}{2M^4} + \frac{\mu_e(2-\gamma)}{2\gamma^2 K^2}$ ,  $c = -\frac{5}{2M^6} + \frac{\mu_e(2-\gamma)(3-2\gamma)}{6\gamma^3 K^3}$  and  $d = -\frac{35}{8M^8} + \frac{\mu_e(2-\gamma)(3-2\gamma)(4-3\gamma)}{24\gamma^4 K^4}$ .

The system (8) can be expressed as following PDS:

$$\begin{cases} \frac{d\phi}{d\xi} = z, \\ \frac{dz}{d\xi} = a\phi + b\phi^2 + c\phi^3 + d\phi^4. \end{cases} \quad (9)$$

The corresponding Hamiltonian function is:

$$H(\phi, z) = \frac{z^2}{2} - \left(\frac{a}{2}\phi^2 + \frac{b}{3}\phi^3 + \frac{c}{4}\phi^4 + \frac{d}{5}\phi^5\right) = h, \quad (10)$$

say. We consider Sagdeev's equation corresponding to the PDS (9) as

$$\frac{d^2\phi}{d\xi^2} = -\frac{d\psi}{d\phi}, \quad (11)$$

where  $\psi$  is the Sagdeev's pseudopotential. Therefore, from (8) and (11) we get

$$\psi(\phi) = -\left(\frac{a}{2}\phi^2 + \frac{b}{3}\phi^3 + \frac{c}{4}\phi^4 + \frac{d}{5}\phi^5\right). \quad (12)$$

## 4 Phase Plots

To find all equilibrium points the PDS (9), we have  $\frac{d\phi}{d\xi} = 0$  and  $\frac{dz}{d\xi} = 0$ , which give

$$z = 0, \quad \phi(d\phi^3 + c\phi^2 + b\phi + a) = 0, \quad (13)$$

$$\Rightarrow z = 0, \quad \phi(\phi^3 + p\phi^2 + q\phi + r) = 0, \quad (14)$$

where  $p = \frac{c}{d}$ ,  $q = \frac{b}{d}$  and  $r = \frac{a}{d}$ .

(i) If  $\frac{h^2}{4} + \frac{g^3}{27} > 0$ , then there are two equilibrium points of the PDS (9) at  $P_0(\phi_0, 0)$  and  $P_1(\phi_1, 0)$ , where  $\phi_0 = 0$ ,  $\phi_1 = A + B$  with  $A = \sqrt[3]{-\frac{h}{2} + \sqrt{\frac{h^2}{4} + \frac{g^3}{27}}}$ ,  $B =$

$$\sqrt[3]{-\frac{h}{2} - \sqrt{\frac{h^2}{4} + \frac{g^3}{27}}}$$

$g = \frac{1}{3}(3q - p^2)$  and  $h = \frac{1}{27}(2p^3 - 9pq + 27r)$ .

(ii) If  $\frac{h^2}{4} + \frac{g^3}{27} < 0$ , then there are four equilibrium points of the PDS (9) at  $P_0(\phi_0, 0)$ ,  $P_1(\phi_1, 0)$ ,  $P_2(\phi_2, 0)$  and  $P_3(\phi_3, 0)$ , where  $\phi_0 = 0$ ,  $\phi_{2,3,4} = -\frac{p}{3} + 2\sqrt{-\frac{g}{3}}\cos(\frac{\psi}{3} + \frac{2k\pi}{3})$ ,  $k = 0, 1, 2$ , with

$$\cos\psi = -\sqrt{\frac{h^2/4}{-g^3/27}}, \text{ if } h > 0;$$

$$\sqrt{\frac{h^2/4}{-g^3/27}}, \text{ if } h < 0.$$

We denote Jacobian matrix of the system (9) corresponding to the critical point  $P_i(\phi_i, 0)$  by  $J(\phi_i, 0)$ . The critical point  $P_i(\phi_i, 0)$  is a saddle point if  $|J(\phi_i, 0)| < 0$  and a center when  $|J(\phi_i, 0)| > 0$  [23].

Phase plots of a system can differ relying on the number of surrounding separatrix layers [17] and the total number of equilibrium points. For a particular dynamical system, a wave solution can be obtained for a trajectory contained in the phase plot. In this article, we denote nonlinear periodic trajectory by  $NPT_{m,n}$ , nonlinear homoclinic trajectory by  $NHT_{m,n}$ , supernonlinear periodic trajectory by  $SNPT_{m,n}$  and supernonlinear homoclinic trajectory by  $SNHT_{m,n}$ , where  $m$  designates the total number of stable critical points (centres) and  $n$  designates the total number of enveloping separatrix layers. Corresponding to  $NPT_{m,n}$  and  $NHT_{m,n}$ , we can obtain NA periodic wave solution and NA solitary wave solution, respectively, while corresponding to  $SNPT_{m,n}$  and  $SNHT_{m,n}$ , we can obtain NA superperiodic wave solution and NA supersolitary wave solution, respectively.

For our computation we will use the values of dense plasmas [1, 2, 4, 5] consisting of degenerate NR electrons, non-degenerate light nuclei ( $^{12}\text{C}$ ) and heavy nuclei ( $^{85}_{37}\text{Rd}$ ):  $n_{e0} \sim 10^{35} \text{ m}^{-3}$ ,  $n_{i0} \sim 1.666 \times 10^{34} \text{ m}^{-3}$ ,  $\hbar = 1.054 \times 10^{-34} \text{ Js}$ ,  $m_e = 9.10938356 \times 10^{-31} \text{ kg}$ ,  $Z_i = 6$ ,  $c = 3 \times 10^8 \text{ m/s}$  and  $\gamma = \frac{5}{3}$  (NR limit). The calculated values of  $\mu_e$  and  $K$  are 1.0004 and 0.06040810205, respectively. We will use these values of  $\gamma$ ,  $K$  and  $\mu_e$  in this present work.

Figure 1a exhibits phase plot of PDS (9) for  $M = 0.51$ . Here, the critical points  $P_0$  and  $P_1$  are saddle and centre, respectively. A family of periodic trajectories surround  $P_1$  while there is a homoclinic trajectory at  $P_0$ . The plasma system has a family of periodic wave profile given by  $H(\phi, z) = h$ ,  $h \in (0, h_1)$  and a compressive solitary wave profile given by  $H(\phi, z) = 0$ . In Fig. 1b, we present effect of Mach number  $M$  on NA periodic wave solution. One can see from Fig. 1b that only amplitude of NA periodic wave elevates on enhancing  $M$ . The Sagdeev's pseudopotential curve corresponding to Fig. 1a is displayed in Fig. 1c. One can clearly observe a minima at  $P_1$  and a maxima at  $P_0$ .

In Fig. 2a, we present a phase plot of the PDS (9) for  $M = 0.7$ . There exist four equilibrium points  $P_0, P_1, P_2$  and  $P_3$  of the PDS (9), of which  $P_2$  and  $P_3$  are centres and  $P_0$  and  $P_1$  are saddles. There are two families of periodic trajectories enclosing

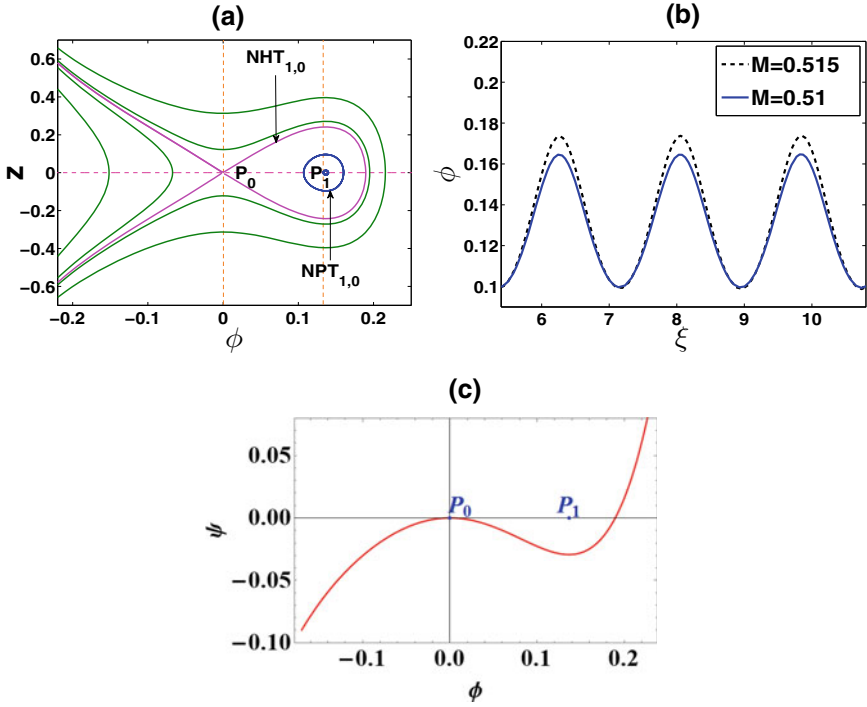


**Fig. 1** **a** Phase portrait of the PDS (9) for  $M = 0.51$ , **b** effect of  $M$  on NA periodic wave solution and **c** Sagdeev pseudopotential  $\psi$  versus  $\phi$  for  $M = 0.51$

$P_2$  and  $P_3$ , respectively, a pair of homoclinic trajectories at  $P_0$ , a family of superperiodic trajectories enclosing these two homoclinic trajectories and a supernonlinear homoclinic trajectory at  $P_1$ . Effect of Mach number  $M$  on NA periodic, superperiodic, compressive solitary, rarefactive solitary and compressive supersolitary wave profiles are shown in Fig. 2b–f, respectively. Heights of NA periodic and rarefactive solitary wave profiles decrease while heights of NA superperiodic, compressive solitary and compressive supersolitary wave profiles increase on enhancing  $M$ . On the other hand, widths of superperiodic and compressive supersolitary wave profiles diminish on enhancing  $M$ . It has been numerically observed that such type of phase plot (Fig. 2a) is possible for this plasma system if  $M$  varies from  $M = 0.666$  to  $M = 0.747$  (approximately). The Sagdeev's pseudopotential curve corresponding to Fig. 2a is depicted in Fig. 2g. Clearly, one can observe two minima at  $P_2$  and  $P_3$  separated by a maxima at  $P_0$ , which is the criteria for SNWs [22].

We show a phase plot of the PDS (9) for  $M = 0.77$  in Fig. 3a that contains four critical points  $P_0, P_1, P_2$  and  $P_3$ , out of which  $P_0$  and  $P_2$  are saddles while  $P_1$  and  $P_3$  are centres. There are two families of periodic trajectories about  $P_1$  and  $P_2$ , respectively, a pair of homoclinic trajectories at  $P_0$ , a family of superperiodic trajectories about these two homoclinic trajectories and a rarefactive supersolitary trajectory at  $P_3$ . We

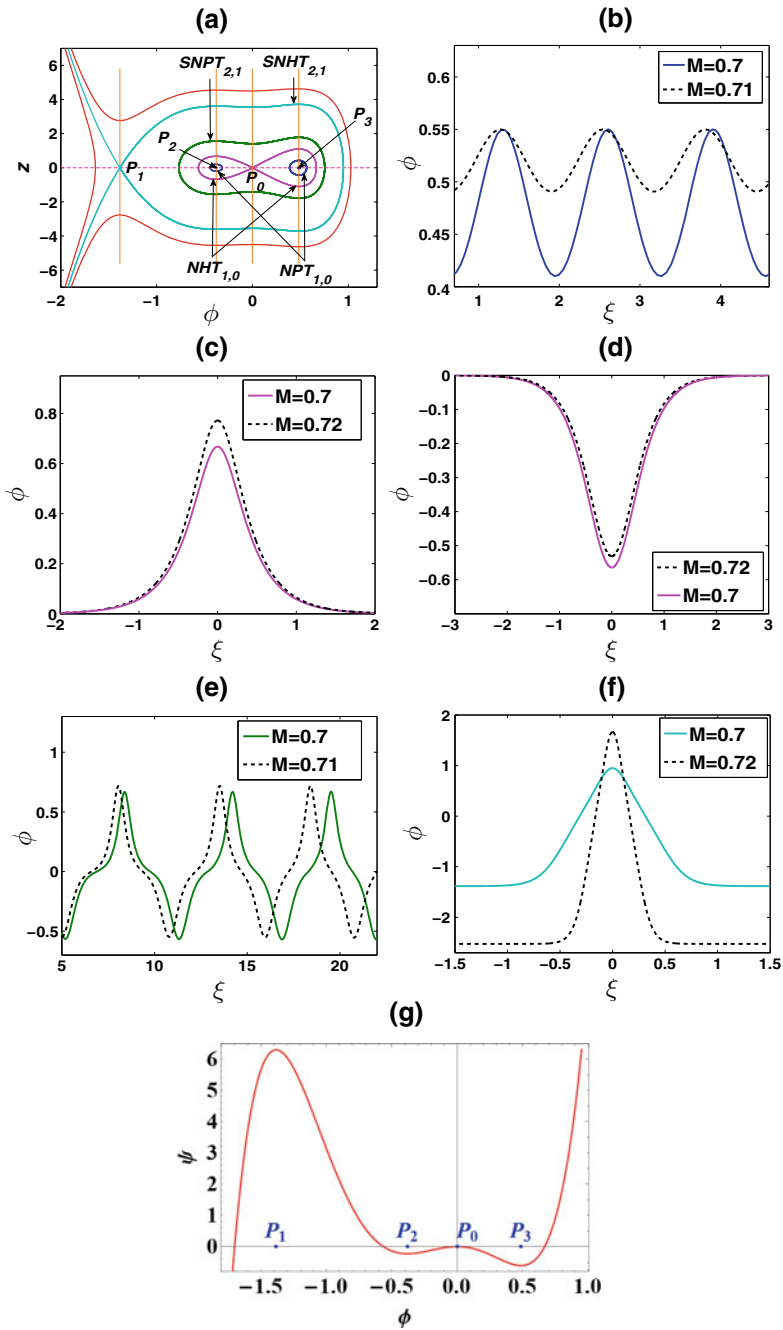


**Fig. 2** a Phase portrait of the PDS (9) for  $M = 0.7$ . Influence of  $M$  on NA b periodic, c compressive solitary, d rarefactive solitary, e superperiodic and f compressive supersolitary waves. g Sagdeev pseudopotential  $\psi$  versus  $\phi$  for  $M = 0.7$

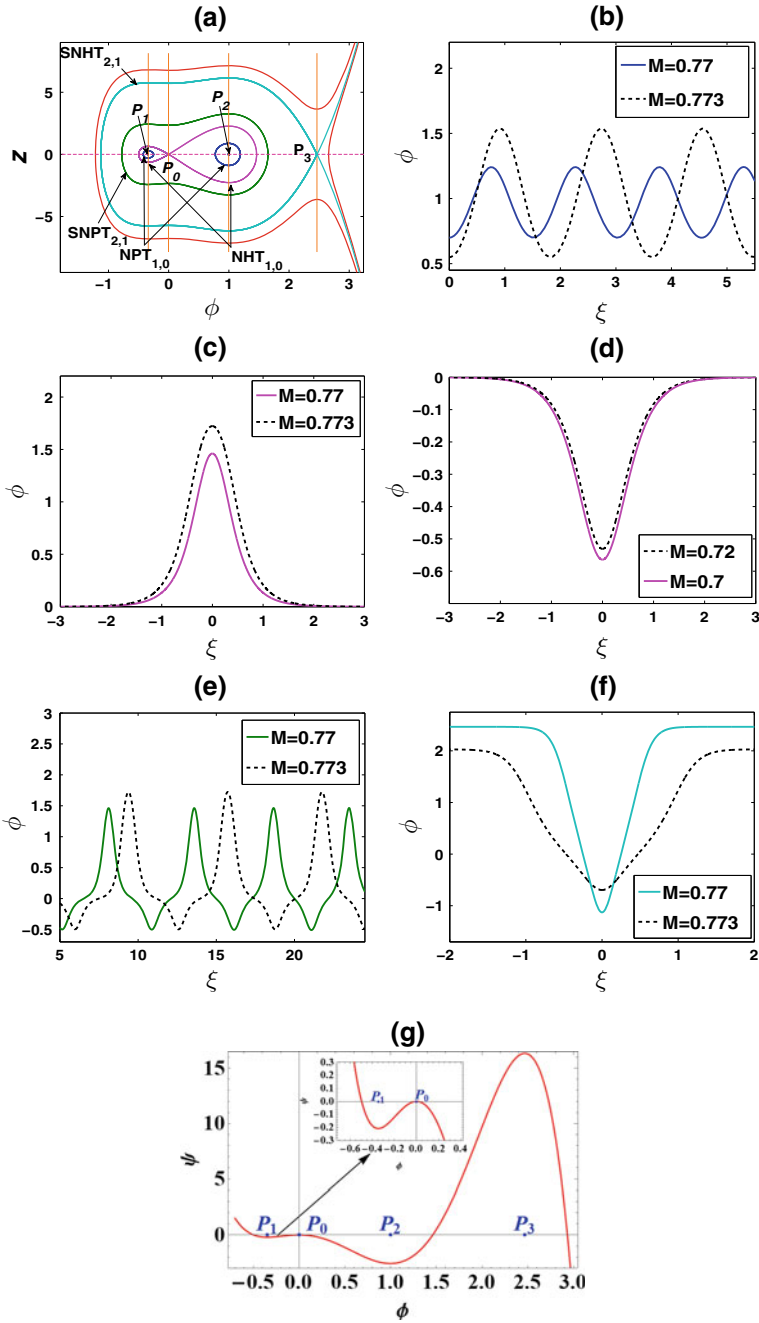


**Fig. 3** a Phase portrait of the PDS (9) for  $M = 0.77$ . Influence of  $M$  on NA b periodic, c compressive solitary, d rarefactive solitary e superperiodic and f rarefactive supersolitary waves. g Sagdeev pseudopotential  $\psi$  versus  $\phi$  for  $M = 0.77$

show influence of Mach number  $M$  on NA periodic, superperiodic, compressive solitary, rarefactive solitary and compressive supersolitary wave structures in Fig. 3b–f, respectively. Clearly, one can see that enhancement of  $M$  results in increase in heights of NA periodic, superperiodic and compressive solitary wave structures and decrease in heights of NA rarefactive solitary and rarefactive supersolitary wave structures. Simultaneously, enhancement of  $M$  brings about expansion in widths of periodic, superperiodic, compressive solitary and rarefactive supersolitary wave structures and a slight decrease in width of rarefactive solitary wave. In fact, compressive solitary wave is seen to flourish on enhancing  $M$ . It has been numerically observed that such type of phase plot (Fig. 3a) is possible if  $M$  varies from  $M = 0.748$  to  $M = 0.776$  (approximately). Corresponding Sagdeev’s pseudopotential is given in Fig. 3b, which presents two minima at  $P_1$  and  $P_2$  with a maxima at  $P_0$  in between.

Figure 4a displays phase portrait of PDS (9) for the sonic case, i.e.,  $M = 1$ . Clearly, there exist two critical points  $P_0$  and  $P_1$ . The origin  $P_0$  is a saddle while  $P_1$  is a center. A family of periodic trajectories surround  $P_1$  while a homoclinic trajectory begins and terminates at  $P_0$ . This plasma system has a family of periodic wave structures given by  $H(\phi, z) = h, h \in (h_2, 0)$  and a rarefactive solitary wave structure given by  $H(\phi, z) = 0$ . Impact of  $M$  on NA periodic wave solution is shown Fig. 4b. Vividly,

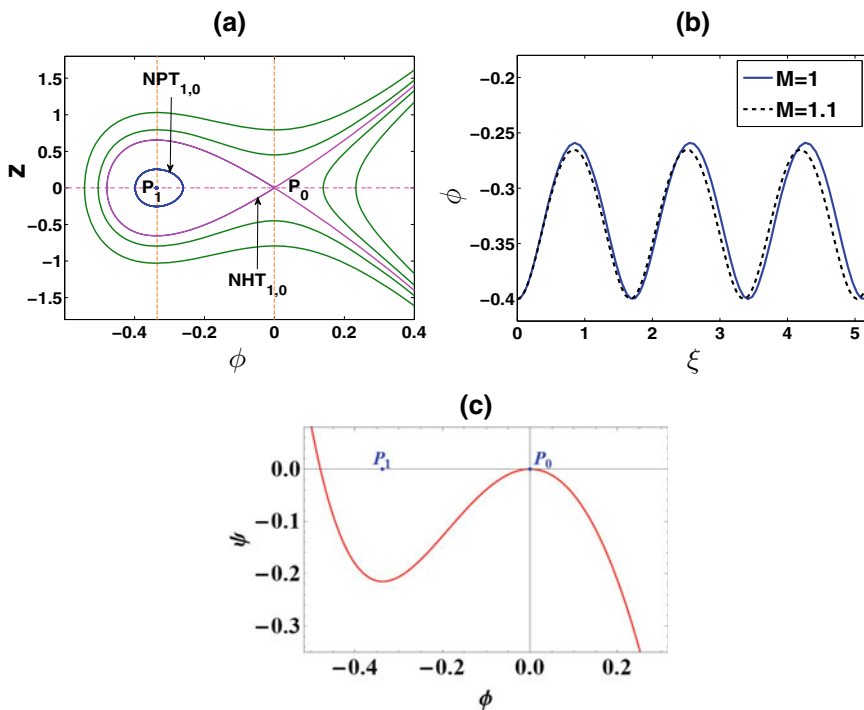


**Fig. 4** a Phase portrait of the PDS (9) for  $M = 1$ , b impact of  $M$  on NA periodic wave solution and c Sagdeev pseudopotential  $\psi$  versus  $\phi$  for  $M = 1$

one can notice that amplitude as well as width of NA periodic wave decrease on enhancing the value of  $M$ . Corresponding Sagdeev's pseudopotential is depicted in Fig. 4c. Similar phase portrait can be observed for the supersonic case, i.e.,  $M > 1$ .

## 5 Conclusion

We have shown the existence of arbitrary amplitude nucleus-acoustic superperiodic and supersolitary waves in a three component degenerate plasma system. Four qualitatively different phase plots of the system have been obtained for four distinct values of Mach number. Thus, we can say that bifurcation occurred and Mach number acted as a bifurcation parameter. For two different ranges of Mach number, two qualitatively different phase profiles distinguished by compressive and rarefactive type supernonlinear homoclinic trajectories have been obtained. It has been numerically observed that NA compressive supersoliton was possible if  $M$  varied from 0.666 to 0.747 (approximately) while NA rarefactive supersoliton was possible if  $M$  varied from 0.748 to 0.776 (approximately). In both the cases, pseudopotential curve formed a double well with two minima separated by a maxima satisfying the necessary condition for the existence of supernonlinear wave. Mach number  $M$  has significant influence on superperiodic and supersolitary wave solutions. An increase in  $M$  increased amplitudes of superperiodic and compressive supersolitary wave solutions and decreased amplitude of rarefactive supersolitary wave solution. The parameter values are taken in such a way that the results of this work find its application in examining NA supernonlinear waves in dense astrophysical objects.

**Acknowledgements** Barsha Pradhan is grateful to Sikkim Manipal University for providing TMA Pai Research Grant (Ref. Nos. 118/SMU/REG/UOO/104/2019).

## References

1. Shapiro, S.L., Teukolsky, S.A.: Black Holes, White Dwarfs, and Neutron Stars: The Physics of Compact Objects. Wiley, New York (1983)
2. Koester, D., Chanmugam, G.: Physics of white dwarf stars. Rep. Prog. Phys. **53**, 837 (1990)
3. Van Horn, H.M.: Dense astrophysical plasmas. Science **252**, 384 (1991)
4. Vanderburg, A., Johnson, J.A., Rappaport, S., Bieryla, A., Irwin, J., Lewis, J.A., Kipping, D., Brown, W.R., Dufour, P., Ciardi, D.R., Angus, R., Schaefer, L., Latham, D.W., Charbonneau, D., Beichman, C., Eastman, J., McCrady, N., Wittenmyer, R.A., Wright, J.T.: A disintegrating minor planet transiting a white dwarf. Nature **526**, 546 (2015)
5. Jannat, S., Mammun, A.A.: Nucleus-acoustic shock waves in white dwarfs. Pramana J. Phys. **90**, 51 (2018)
6. Chandrasekhar, S.: The density of white dwarf stars. Philos. Mag. Ser. **7**(11), 592 (1931)
7. Chandrasekhar, S.: The maximum mass of ideal white dwarfs. Astrophys. J. **74**, 81 (1931)
8. Sultana, S., Schlickeiser, R.: Arbitrary amplitude nucleus-acoustic solitons in multi-ion quantum plasmas with relativistically degenerate electrons. Phys. Plasmas **25**, 022110 (2018)



9. Mamun, A.A., Amina, M., Schlickeiser, R.: Nucleus-acoustic shock structures in a strongly coupled self-gravitating degenerate quantum plasma. *Phys. Plasmas* **23**, 094503 (2016)
10. Zaman, D.M.S., Amina, M., Dip, P.R., Mamun, A.A.: Planar and non-planar nucleus-acoustic shock structures in self-gravitating degenerate quantum plasma systems. *Eur. Phys. J. Plus* **132**, 457 (2017)
11. Zaman, D.M.S., Amina, M., Dip, P.R., Mamun, A.A.: Nucleus-acoustic solitary waves in self-gravitating degenerate quantum plasmas. *Chin. Phys. B* **27**, 040402 (2018)
12. Samanta, U.K., Saha, A., Chatterjee, P.: Bifurcations of dust-ion-acoustic travelling waves in a magnetized quantum dusty plasma. *Astrophys. Space Sci.* **347**, 293 (2013)
13. Sahu, B., Poria, S., Roychoudhury, R.: Solitonic, quasi-periodic and periodic pattern of electron acoustic waves in quantum plasma. *Astrophys. Space Sci.* **341**, 567 (2012)
14. El-Labany, S.K., El-Taibany, W.F., Atteya, A.: Bifurcation analysis for ion acoustic waves in a strongly coupled plasma including trapped electrons. *Phys. Lett. A* **382**, 412 (2018)
15. Saha, A., Pradhan, B., Banerjee, S.: Multistability and dynamical properties of ion-acoustic wave for the nonlinear Schrödinger equation in an electron-ion quantum plasma. *Phys. Scr.* **95**, 055602 (2020)
16. Dubinov, A.E., Kolotkov, D.Y.: Ion-acoustic supersolitons in plasma. *Plasma Phys. Rep.* **38**, 909 (2012)
17. Dubinov, A.E., Kolotkov, D.Y.: Ion-acoustic super solitary waves in dusty multispecies plasmas. *IEEE Trans. Plasma Sci.* **40**, 1429 (2012)
18. Verheest, F., Hellberg, M.A., Kourakis, I.: Dust-ion-acoustic supersolitons in dusty plasmas with nonthermal electrons. *Phys. Rev. E* **87**, 043107 (2013)
19. Saha, A., Tamang, J.: Effect of q-nonextensive hot electrons on bifurcations of nonlinear and supernonlinear ion-acoustic periodic waves. *Adv. Space Res.* **63**, 1596 (2019)
20. Tamang, J., Saha, A.: Dynamical behavior of supernonlinear positron-acoustic periodic waves and chaos in nonextensive electron-positron-ion plasmas. *Zeitschrift Für Naturforschung A* **74**, 6 (2019)
21. Taha, R.M., El-Taibany, W.F.: Bifurcation analysis of nonlinear and supernonlinear dust-acoustic waves in a dusty plasma using the generalized (r, q) distribution function for ions and electrons. *Contrib. Plasma Phys.* **2020**, e202000022 (2020)
22. Saha, A., Chatterjee, P., Banerjee, S.: An open problem on supernonlinear waves in a two-component Maxwellian plasma. *Eur. Phys. J. Plus* **135**, 801 (2020)
23. Guckenheimer, J., Holmes, P.J.: *Nonlinear Oscillations, Dynamical Systems and Bifurcations of Vector Fields*. Springer, New York (1983)

# Effect of $q$ Parameter and Critical Beam Radius on Propagation Dynamics of $q$ Gaussian Beam in Cold Quantum Plasma



P. T. Takale, K. Y. Khandale, V. S. Pawar, S. S. Patil, P. P. Nikam,  
T. U. Urunkar, S. D. Patil , and M. V. Takale 

**Abstract** The  $q$  Gaussian intensity distribution is very interesting as in the limit  $q \rightarrow \infty$ , it reduces to the Gaussian intensity profile. Naturally, the freedom of exploring the  $q$  exponent enables us to study a wide range of propagation dynamics. The quantum plasma offers wide possibilities of its existence right from astrophysical situations to laboratory plasmas. Keeping in mind the wide applicability domain of cold quantum plasma, we have theoretically investigated the propagation behavior of  $q$  Gaussian laser beam in cold quantum plasma. The ordinary nonlinear differential equation is set up by following Akhmanov's parabolic equation approach under WKB and paraxial approximations. The effect of the  $q$  parameter on the critical curve is explored graphically. The variation in the beam width parameter  $f$  over normalized distance  $\zeta$  due to variation in the  $q$ -parameter is graphically depicted and discussed at the end. It is observed that the supercritical region and self focusing length are affected by the  $q$  parameter significantly.

**Keywords**  $q$ -Gaussian · Cold quantum plasma · Critical beam radius · Self focusing

---

Supported by DST-SERB, New Delhi, the Special Assistance Program (SAP), Department of Physics, Shivaji University, Kolhapur.

---

P. T. Takale (✉) · K. Y. Khandale · T. U. Urunkar · M. V. Takale  
Department of Physics, Shivaji University, Kolhapur 416004, India  
e-mail: [mansingtakale@gmail.com](mailto:mansingtakale@gmail.com)

V. S. Pawar  
Department of Physics, Rajer Ramrao Mahavidyalay, Jath 416404, India

P. P. Nikam · S. D. Patil  
Department of Physics, Devchand College, Arjunnagar, Kolhapur 591237, India

S. S. Patil  
Department of Physics, Vivekanand College, Tarabai Park, Kolhapur 416003, India

© The Author(s), under exclusive license to Springer Nature Switzerland AG 2022  
S. Banerjee and A. Saha (eds.), *Nonlinear Dynamics and Applications*,  
Springer Proceedings in Complexity,  
[https://doi.org/10.1007/978-3-030-99792-2\\_5](https://doi.org/10.1007/978-3-030-99792-2_5)

## 1 Introduction

Interaction of intense laser beam with plasma has received great attention due to its various application such as laser induced fusion [1–3], particle accelerators [4–7], high harmonic generations [8], compact X-ray sources [9–11]. It necessitates studying propagation behaviour of the laser beams through plasma. In all the above applications, the requirement of propagation of laser beam over several Rayleigh lengths is very essential. However, it is impossible to self trap the given laser beam due to diffraction. Due to the nonlinear interaction of the laser and plasma, plasma behaves as a converging lens. Laser beam alters dielectric behaviour of plasma. Intensity pattern of beam along wavefront causes change in refractive index. Eventually beam gets focused.

Quantum plasma has promising applications in cosmological and astrophysical situations, fusion science, laser solid interaction, and nanotechnology. Various studies have been done on cold quantum plasma. Patil et al. [12] have reported the propagation behaviour of beam in quantal-medium. They have found that quantum effects plays important role in laser plasma interaction. Habibi et al. [13] have investigated time independent self focusing in cold quantum plasma using ramp density profile. They have studied the effect on behavior of oscillatory beam width parameter due to quantum effects and inhomogeneity of plasma such as upward ramp density profile. Apart from these few studies, dynamical aspects of propagation of elliptical laser beams, Hermite Cosine Gaussian laser beams, cosh Gaussian laser beams in cold quantum plasma are also studied [14–16].

The study of Valcan Petawatt laser proposes that the intensity distribution deviates from the Gaussian distribution [17]. Nakatsutsumi et al. [18] on further study suggests that intensity distribution is in q-Gaussian which in function form can be written as

$$I(r) = I_0(r) \left( 1 + \frac{r^2}{q^2 r_0^2} \right)^{-q} \quad (1)$$

Here real parameters  $q$  and  $r_0$  are based on experimental data. The  $q$  parameter represents the departure from the Gaussian beam's field distribution. Variation from the Gaussian beam may be due to unexpected inclusion in the gain medium or small obstacles. The investigation of this intensity distribution could be more practical. Sharma and Kourakis [19] have studied relativistic propagation of q Gaussian laser beam analytically and numerically. Using higher order corrections, Kaur et al. [20] have explored the propagation in relativistic anisotropic medium for our plasma. Using the variational technique, Wang et al. [21] have reported the propagation behavior of q-Gaussian laser beam in a systematized plasma channel. Valkunde et al. [22] have studied self focusing in inhomogeneous plasma of exponential profile for varied q values. Vhanmore et al. [23] have investigated the influence of q parameter on the propagation of beam considering relativistic nonlinearity. Kashyap et al. [24] have studied self focusing of q Gaussian laser beam in relativistic plasma considering the effect of light absorption. Gupta and Kumar [25] and Gupta et al. [26] have also

studied q Gaussian laser beam. We have explored the effect q and critical radius on propagation characteristics of laser beam in quantum medium by using parabolic equation. The dielectric function of cold quantum plasma and the intensity distribution of a q Gaussian laser beam are reported in Sect. 2. Second order nonlinear differential equation is obtained. Section 3 is dedicated to the result and discussion. Brief some important conclusions are given in Sect. 4.

## 2 Basic Formulation

Consider q-Gaussian laser beam propagating through relativistic cold quantum plasma along  $\hat{z}$  direction. The electric field of beam is given as

$$E(r, z) = A(r, z) \text{Exp}[i(kz - \omega t)] \quad (2)$$

where  $A(r, z)$  is complex amplitude of electric field.  $k = \frac{\omega\sqrt{\epsilon_0}}{c}$  is propagation constant and  $\omega$  is frequency of laser beam. A following  $z$  dependent intensity of q-Gaussian laser beam can be given as [18]

$$A^2 = \frac{E_0^2}{f} \left( 1 + \frac{r^2}{qr_0^2 f^2} \right)^{-q} \quad (3)$$

where  $E_0$  is the amplitude at  $r = z = 0$ ,  $r_0$  is the initial spot size and q parameter alters beam intensity profile from that of Gaussian profile. Intensity distribution which becomes Gaussian when  $q \rightarrow \infty$  i.e

$$\lim_{q \rightarrow \infty} EE^* = \frac{E_0^2}{f} \exp\left(-\frac{r^2}{r_0^2 f^2}\right) \quad (4)$$

Propagation of laser in plasma having effecting dielectric constant  $\epsilon$  is governed by following equation

$$\nabla^2 E + \frac{\omega^2}{c^2} \epsilon E = 0 \quad (5)$$

The effective dielectric constant in general is given as [12]

$$\epsilon = \epsilon_0 + \phi(EE^*) \quad (6)$$

where  $\epsilon_0$  and  $\phi(EE^*)$  are linear and nonlinear terms of dielectric constant. Here  $\epsilon_0 = 1 - \left(\frac{\omega_p}{\omega}\right)^2$  and  $\omega_p = \sqrt{\frac{4\pi n_0 e^2}{m}}$  where  $e$ ,  $m$ ,  $n_0$  are electrons charge, mass of electron and electron density respectively. In case of cold quantum plasma, intensity dependent dielectric constant is given as [12]

$$\phi(EE^*) = \left(\frac{\omega_p}{\omega}\right)^2 \left[1 - \frac{1}{\gamma} \left(1 - \frac{\delta}{\gamma}\right)^{-1}\right] \quad (7)$$

where  $\gamma = \sqrt{1 + \alpha EE^*}$ ,  $\delta = \frac{4\pi^4 h^2}{m_0^2 \omega^2 \lambda^4}$ ,  $h$  is Planck's constant,  $\lambda$  is wavelength of laser source.

Following Akhmanov's parabolic approach et al. [27] and its extension by Sodha et al. [28], differential equation of beam width parameter ( $f$ ) for q Gaussian beam in cold quantum plasma can be obtained as

$$\frac{\partial^2 f}{\partial \zeta^2} = \frac{4+q}{qf^3} - \frac{\alpha E_0^2 \sqrt{1 + \frac{\alpha E_0^2}{f} \left(\frac{r_0 \omega_p}{c}\right)^2}}{2 * \left(\delta - \sqrt{1 + \frac{\alpha E_0^2}{f}}\right)^2 f^2 (\alpha E_0^2 + f)} \quad (8)$$

where  $\zeta = \frac{z}{kr_0^2}$  is dimensionless distance of propagation. Using boundary conditions  $f = 1$ ,  $\frac{\partial f}{\partial \zeta} = 0$  corresponding to initial wave front at  $\zeta = 0$ , (8) is solved numerically.

### 3 Result and Discussion

Equation (8) is a non integrable that governs the propagation behavior of laser beam in plasma. It is observed that as  $q \rightarrow \infty$  (8) reduces to similar differential equation which is obtained earlier [12]. On right hand side in (8), the first term is responsible for diffraction divergence and the second term is responsible for the convergence of beam. Equation (8) is solved numerically using the following numerical parameters  $\omega = 1.77800 \times 10^{20} \frac{\text{rad}}{\text{s}}$ ,  $m_0 = 9.10938 \times 10^{-28} \text{ g}$ ,  $h = 6.62618 \times 10^{-27} \text{ erg}\cdot\text{sec}$ ,  $c = 2.99792 \times 10^{10} \text{ cm/sec}$ . Under critical conditions,  $\frac{\partial^2 f}{\partial \zeta^2} = 0$ ,  $\frac{\partial f}{\partial \zeta} = 0$ ,  $f = 1$ ,  $\alpha E_0^2 = p_0$ ,  $\frac{r_0 \omega_p}{c} = \rho_0$ , (8) reduces to

$$\rho_0 = \sqrt{\frac{(4+q) 2 (\delta - \sqrt{1+p_0})^2 (\sqrt{1+p_0})}{qp_0}} \quad (9)$$

It is noted that as  $q \rightarrow \infty$ , one can obtain the critical curve equation for Gaussian beam in quantum-medium. Figure 1 gives the critical curve for varied values of  $q$ . It is a graphical representation of the relation between critical beam radius ( $\rho_0$ ) and initial intensity parameter ( $p_0$ ). Critical curve divides the graph into self focusing and defocusing regions. In Fig. 1, arbitrary choice of point ( $p_0, \rho_0$ ) in a region above the critical curve (supercritical region) promises focusing of beam and point ( $p_0, \rho_0$ ) below the critical curve (subcritical region) leads to defocusing of beam. Any point on the critical curve leads to self trapping of the laser beam. In Fig. 1, it is observed that, initially  $\rho_0$  decreases rapidly within the short range of  $p_0$  and attains minimum value. Then  $\rho_0$  increases slowly with a further increase in  $p_0$ . It is observed that the

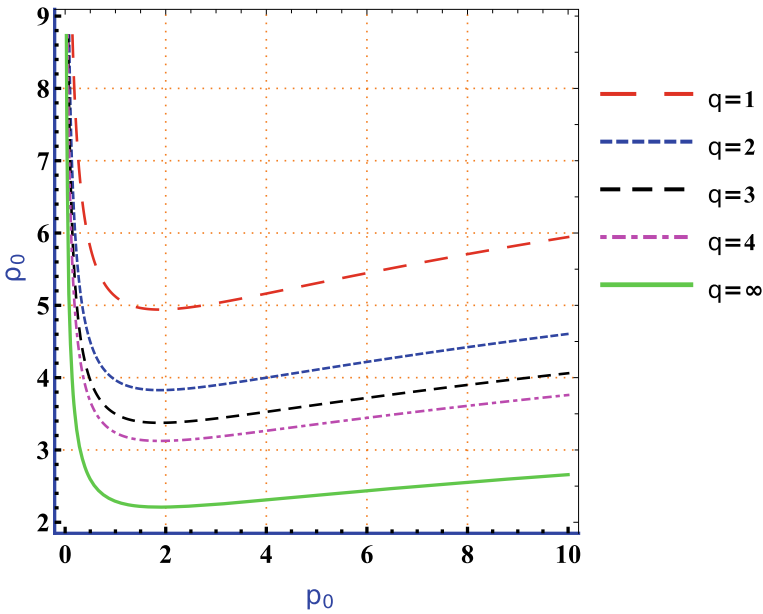


Fig. 1 Variations of  $\rho_0$  versus  $p_0$  (critical curves) for varied values of  $q$  i.e. ( $q = 1, 2, 3, 4, \infty$ )

critical curve shifts downward as  $q$  increases. For the Gaussian beam, the supercritical region is relatively the largest.

Figure 2, reveals propagation behavior of  $q$  Gaussian laser beam i.e. variation of  $f$  against  $\zeta$ . Self focusing of beam in oscillatory mode is observed for  $q = 1, 2, 3, 4, \infty$  (for  $p_0 = 2, \rho_0 = 6$  i.e. in supercritical region). Also in Fig. 2, it is observed that as the value of parameter  $q$  increases, the beam width parameter and self focusing length decrease which indicates enhanced self focusing. At  $q \rightarrow \infty$  i.e. Gaussian beam, self-focusing length is minimum. In Fig. 2, steady defocusing is observed (for  $p_0 = 2, \rho_0 = 1.5$  i.e. in subcritical region). Also, it is observed that the rate of defocusing of  $f$  decreases as  $q$  increases.

### 4 Conclusion

In present paper, the study of propagation behavior of  $q$ -Gaussian beam in cold quantum plasma has been done. Using Akhmanov’s approach et al. [27], nonlinear ordinary differential equation of beam width parameter has been obtained. Propaga-

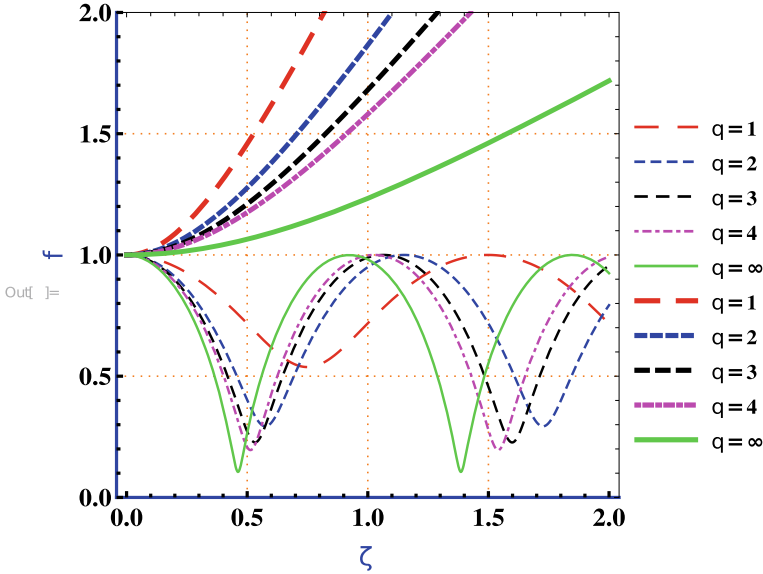


**Fig. 2** Variation of  $f$  along  $\zeta$  with  $p_0 = 2, \rho_0 = 6$  (thin lines) and  $p_0 = 2, \rho_0 = 1.5$  (thick lines) (Color Online)

tion behavior of  $q$  Gaussian laser beam can be effectively explored by varying the limits of  $q$  from extremely low value to infinity. The significant change in  $f$  and self focusing length takes place in the limit  $q \rightarrow \infty$  as compared to lower values of  $q$ .

## References

1. Deutsch, C., Furukawa, H., Mima, K., Murakami, M., Nishihara, K.: Interaction physics of the fast ignitor concept. *Phys. Rev. Lett.* **77**, 2483 (1996). <https://doi.org/10.1103/PhysRevLett.77.2483>
2. Tabak, M., Hammer, J., Glinsky, M.E., Kruer, W.L., Wilks, S.C., Woodworth, J., Campbell, E.M., Perry, M.D., Mason, R.J.: Ignition and high gain with ultrapowerful lasers. *Phys. Plasmas* **1**, 1626 (1994). <https://doi.org/10.1063/1.870664>
3. Regan, S.P., Bradley, D.K., Chirikikh, A.V., Craxton, R.S., Meyerhofer, D.D., Seka, W., Short, R.W., Simon, A., Town, R.P.J., Yaakobi, B.: Laser-plasma interactions in long-scale-length plasmas under direct-drive National Ignition Facility conditions. *Phys. Plasmas* **6**, 2072 (1999). <https://doi.org/10.1063/1.873716>
4. Malka, V.: Laser plasma accelerators. *Phys. Plasmas* **19**, 055501 (2012). <https://doi.org/10.1063/1.3695389>
5. Wiggins, S.M., Issac, R.C., Welsh, G.H., Brunetti, E., Shanks, R.P., Anania, M.P., Cipiccia, S., Manahan, G.G., Aniculaesei, C., Ersfeld, B., Islam, M.R., Burgess, R.T.L., Vieux, G., Gillespie, W.A., MacLeod, A.M., van der Geer, S.B., de Loos, M.J., Jaroszynski, D.A.: High quality electron beams from a laser wakefield accelerator. *Plasma Phys. Control. Fus.* **52**, 124032 (2010). <https://doi.org/10.1088/0741-3335/52/12/124032>

6. Fiuza, F., Stockem, A., Boella, E., Fonseca, R.A., Silva, L.O., Haberberger, D., Tochitsky, S., Gong, C., Mori, W.B., Joshi, C.: Laser-driven shock acceleration of monoenergetic ion beams. *Phys. Rev. Lett.* **109**, 215001 (2012). <https://doi.org/10.1103/PhysRevLett.109.215001>
7. Hooker, S.M.: Developments in laser-driven plasma accelerators. *Nat. Photonics* **7**, 775 (2013). <https://doi.org/10.1038/nphoton.2013.234>
8. Sprangle, P., Esarey, E., Ting, A.: Nonlinear theory of intense laser-plasma interactions. *Phys. Rev. Lett.* **64**, 2011 (1990). <https://doi.org/10.1103/PhysRevLett.64.2011>
9. Ferrari, H.E., Lifschitz, A.F., Maynard, G., Cros B.: Electron acceleration by laser wakefield and X-ray emission at moderate intensity and density in long plasmas. *Phys. Plasmas* **18**, 083108 (2011). <https://doi.org/10.1063/1.3624771>
10. Liu, Y., Dong, Q., Peng, X., Jin, Z., Zhang, J.: Soft X-ray emission, angular distribution of hot electrons, and absorption studies of argon clusters in intense laser pulses. *Phys. Plasmas* **16**, 043301 (2009). <https://doi.org/10.1063/1.3125308>
11. Bagchi, S., Kiran, P.P., Yang, K., Rao, A.M., Bhuyan, M.K., Krishnamurthy, M., Kumar, G.R.: Bright, low debris, ultrashort hard x-ray table top source using carbon nanotubes. *Phys. Plasmas* **18**, 014502 (2011). <https://doi.org/10.1063/1.3531685>
12. Patil, S.D., Takale, M.V., Navare, S.T., Dongare, M.B., Fulari, V.J.: Self-focusing of Gaussian laser beam in relativistic cold quantum plasma. *Optik* **124**, 180–183(2013). <https://doi.org/10.1016/j.ijleo.2011.11.061>
13. Habibi, M., Ghamari, F.: Stationary self-focusing of intense laser beam in cold quantum plasma using ramp density profile. *Phys. Plasmas* **19**, 103110 (2012). <https://doi.org/10.1063/1.4762848>
14. Walia, K., Tripathi, D.: Self-focusing of elliptical laser beam in cold quantum plasma. *Optik* **186**, 46–51(2019). <https://doi.org/10.1016/j.ijleo.2019.04.081>
15. Thakur, V., Kant, N.: Combined effect of chirp and exponential density ramp on relativistic self-focusing of Hermite-Cosine-Gaussian laser in collisionless cold quantum plasma. *Braz. J. Phys.* **49**, 113–118 (2019). <https://doi.org/10.1007/s13538-018-00624-7>
16. Habibi, M., Ghamari, F.: Improved focusing of a Cosh-Gaussian laser beam in quantum plasma: higher order paraxial theory. *IEEE Trans. Plasma Sci.* **43**, 2160–2165 (2015). <https://doi.org/10.1109/TPS.2015.2440319>
17. Patel, P.K., Key, M.H., MacKinnon, A.J., Berry, R., Borghesi, M., Chambers, D.M., Chen, H., Clarke, R., Damian, C., Eagleton, R., Freeman, R., Glenzer, S., Gregori, G., Heathcote, R., Hey, D., Izumi, N., Kar, S., King, J., Nikroo, A., Niles, A., Park, H.S., Pasley, J., Patel, N., Shepherd, R., Snavely, R.A., Steinman, D., Stoeckl, C., Storm, M., Theobald, W., Town, R., Van Maren, R., Wilks, S.C., Zhang, B.: Integrated laser-target interaction experiments on the RAL petawatt laser. *Plasma Phys. Control Fus.* **47**, B833–B840 (2005). <https://doi.org/10.1088/0741-3335/47/12B/S65>
18. Nakatsutsumi, M., Davies, J.R., Kodama, R.: Space and time resolved measurements of the heating of solids to ten million kelvin by a petawatt laser. *New J. Phys.* **10**, 043046 (2008). <https://doi.org/10.1088/1367-2630/10/4/043046>
19. Sharma, A., Kourakis, I.: Spatial evolution of a q-Gaussian laser beam in relativistic plasma. *Laser Part. Beams* **28**, 479–489 (2010). <https://doi.org/10.1017/S0263034610000479>
20. Kaur, R., Gill, T.S.: Relativistic effects on evolution of a q-Gaussian laser beam in magneto-plasma: application of higher order corrections. *Phys. Plasmas* **24**, 053105 (2017). <https://doi.org/10.1063/1.4983309>
21. Wang, L., Hong, X.-R., Sun, J.-A., Tang, R.-A., Yang, Y., Zhou, W.-J., Tian, J.-M., Duan, W.-S.: Effects of relativistic and channel focusing on q-Gaussian laser beam propagating in a preformed parabolic plasma channel. *Phys. Lett. A*, **381**, 2065–2071 (2017). <https://doi.org/10.1016/j.physleta.2017.04.033>
22. Valkunde, A.T., Vhanmore, B.D., Urunkar, T.U., Gavade, K.M., Patil, S.D., Takale, M.V.: Effect of exponential density transition on self-focusing of q-Gaussian laser beam in collisionless plasma. *AIP Conf. Proc.* **1953**, 140088 (2018). <https://doi.org/10.1063/1.5033263>
23. Vhanmore, B.D., Patil, S.D., Valkunde, A.T., Urunkar, T.U., Gavade, K.M., Takale, M.V., Gupta, D.N.: Effect of q-parameter on relativistic self focusing of q Gaussian laser beam in plasma. *Optik* **158**, 574–579 (2018). <https://doi.org/10.1016/j.ijleo.2017.12.182>



24. Kashyp, R., Aggrawal, M., Gill, T.S., Arora, N.S., Kumar, H., Moudhagill, D.: Self-focusing of q-Gaussian laser beam in relativistic plasma under the effect of light absorption. *Optik Int. J. Light Electron. Opt.* **182**, 1030–1038 (2019). <https://doi.org/10.1016/j.ijleo.2018.12.105>
25. Gupta, N., Kumar, S.: Generation of second harmonics of relativistically self-focused q-Gaussian laser beams in underdense plasma with axial density ramp. *Opt. Quant. Electron.* **53**, 193 (2021). <https://doi.org/10.1007/s11082-021-02827-w>
26. Gupta, N.: Second harmonic generation of q-Gaussian laser beam in plasma channel created by ignitor heater technique. *Laser Part. Beams* **37**, 184–196 (2019). <https://doi.org/10.1017/S0263034619000193>
27. Akhmanov, S.A., Sukhorukov, A.P., Khokhlov, R.V.: Self-focusing and diffraction of light in a nonlinear medium. *Sov. Phys. Uspekhi* **10**(5), 609–636 (1968). <https://doi.org/10.1070/PU1968v010n05ABEH005849>
28. Sodha, M.S., Ghatak, A.K., Tripathi, V.K.: Self focusing of laser beams in plasmas and semi-conductors. *Prog. Opt.* **13**, 169–265 (1976). [https://doi.org/10.1016/S0079-6638\(08\)70021-0](https://doi.org/10.1016/S0079-6638(08)70021-0)

# Study of Quantum-Electron Acoustic Solitary Structures in Fermi Plasma with Two Temperature Electrons



Shilpi, Sharry , Chinmay Das , and Swarniv Chandra 

**Abstract** One dimensional Quantum Hydrodynamic (QHD) model is used to study linear and non-linear effects of Quantum Electron Acoustic waves. We have derived the KdV equations using Reductive Perturbation Technique and obtained solitary wave solutions for Quantum Electron acoustic waves. The mutual interaction of such stationary formations and the breakdown mechanism are studied. We have used a newly designed code to study the time evolution of wave-wave interaction and the breakdown mechanism. In order to discover the stability regime and chaotic scenario in quantum electron-acoustic waves, bifurcation analysis and dynamical system research are used. A dynamical system is investigated further to determine the stability factors and the parametric range for such stability. The chaotic behaviour of the system is studied through Largest Lyapunov exponent. This work will find applications in polar capes, magnetospheres and stellar media.

**Keywords** Electron-acoustics wave · Linear dispersion relation · Quantum hydrodynamic model · Two-temperature electron

---

Shilpi · Sharry  
Physics Department, Guru Nanak Dev University, Amritsar 143001, India

C. Das  
Department of Mathematics, Govt. General Degree College at Kushmandi, Dakshin Dinajpur  
733121, India

S. Chandra (✉)  
Department of Physics, Govt. General Degree College at Kushmandi, Dakshin Dinajpur 733121,  
India  
e-mail: [swarniv147@gmail.com](mailto:swarniv147@gmail.com)

C. Das · S. Chandra  
Institute of Natural Sciences and Applied Technology, Kolkata 700032, India

© The Author(s), under exclusive license to Springer Nature Switzerland AG 2022  
S. Banerjee and A. Saha (eds.), *Nonlinear Dynamics and Applications*,  
Springer Proceedings in Complexity,  
[https://doi.org/10.1007/978-3-030-99792-2\\_6](https://doi.org/10.1007/978-3-030-99792-2_6)

## 1 Introduction

The fourth state of matter is Plasma which is a hot ionizing gas created from roughly equal numbers of charged ions and charged electrons. The charged particles in plasma travel at random. They interact with each other via their own electromotive force and also respond to exterior disturbances [1]. The perturbations forces can be pressure force, microwave, or laser injection. Due to the coherent motion of plasma particles various collective wave phenomena arise. Since plasma is strongly influenced by electric and magnetic fields hence a possibility of a wide range of longitudinal and transverse waves. plasma acoustic wave is a longitudinal wave that propagates due to compression and rarefaction of plasma particles.

Plasma waves can be in electron acoustic, ion-acoustic, or dust acoustic mode. The present paper will stick to the Electrostatic modes in plasma. Electrostatic modes rely on the mass of the electrons whereas ions are supposed to be infinitely heavy i.e. stationary. Electron acoustic waves (EAWs) is one of the longitudinal waves in plasma. EAWs are created by two groups of electrons with differing temperatures, called cold and hot electrons [2–11]. The distinction between two electron groups comes from their energy. The thermal energy of warm electrons is higher than cold electrons. The corresponding pressure perturbations from fast and slow particles are hugely different; cool electrons, as they are immobile, are in-charge of providing the inertial effects [12–19] whereas extremely heated electrons can move freely and their pressure provides restoring force. EAWs are high frequency (as compared to ion plasma frequency) modes of electrostatic waves. For frequencies greater than ion plasma frequencies as in the case of EAWs, ions do not take part in dynamics, they play the role of maintaining the charge neutrality. Plasma with two temperature electrons exist in space plasma [20–23] and also occur in laboratory plasma [24–34]. EAWs are thrust areas of research as various phenomenons are explained by them like wave emission in different regions of Earth's magnetosphere (region of space around the earth in which charged particles are affected by Earth's magnetic field), hiss in the polar cusp region (where the particles from the sun have direct access to Earth's atmosphere) and the source of broadband electrostatic noise. The research on the nonlinear evolution of EAWs has increased in recent years [12, 35–44]. Initially, the research was carried out using classical non-relativistic less dense plasma in which thermal de-Broglie wavelength was much less than inter-Fermion distance. But for high-density plasma, as in space plasma, where thermal de-Broglie wavelength becomes comparable to or more than the inter-Fermion distance, quantum effects become important [45–48]. So an additional quantum diffraction term or Bohm potential term is added in the momentum equations of hot and cold electrons. Since ions do not take part in dynamics, no such equations are defined for them. Theoretical research was done on linear and nonlinear propagation of various electrostatics modes in quantum plasmas using QHD [49–63]. The Quantum hydrodynamic QHD model is the most widely used formula for describing the behavior of plasma particles at quantum sizes. Studies show that quantum effects can considerably alter the linear and non-linear properties of plasma.

We have studied various mechanism for soliton breakdown [64, 65] and soliton-soliton interaction [66, 67]. Solitons are linear flaws that bend randomly at a finite temperature. This causes solitons to collide, changing the nature of the soliton-soliton interaction [68–72]. The solitons may be decelerated/accelerated through the interactions of soliton with background waves which may be utilized to study tsunami waves and fiber soliton communications [73]. Dynamical systems theory was used to report bifurcations of nonlinear travelling wave solutions in such plasmas [74]. Various solitonic and quasiperiodic wave characteristics for ion-acoustic waves have been investigated by reducing the nonlinear equation to a Hamiltonian system with electrostatic potential and applying the bifurcation theory of dynamical systems [75–79]. The paper is organized in the following way. In the Sect. 2, the basic equations and it's normalized forms are presented and in Sect. 3, Linear Dispersion Relation is derived. Further, the Derivation of KdV Equation is there in Sect. 4, in which soliton-soliton interaction and breakdown of solitons is discussed under Sects. 5.1 and 5.2. Then, the Dynamical study of Electron Acoustic KdV Solitons is carried out in Sect. 6.

## 2 Basic Equations

We consider the plasma consisting of of two separate groups of electrons namely cold electron fluid, hot electron fluid [13, 18, 80–91] and ions forming uniform neutralizing background, this allows the generation of quantum electron acoustic modes in plasma. To study the linear and non-linear behavior we obtain normalized (dimensionless) fluid continuity, momentum, and Poisson's equations through some appropriate transformations. The unnormalized equations are as following.

### 2.1 Continuity Equations for Hot and Cold Electrons

$$\frac{\partial n_h}{\partial t} + \frac{\partial (n_h u_h)}{\partial x} = 0 \quad (1)$$

where  $n_h$  is hot electron density in plasma and  $u_h$  is the velocity of hot electrons.

$$\frac{\partial n_c}{\partial t} + \frac{\partial (n_c u_c)}{\partial x} = 0 \quad (2)$$

where  $n_c$  is cold electron density in plasma and  $u_c$  is the velocity of cold electrons.

## 2.2 Momentum Equations

$$0 = e \frac{\partial \phi}{\partial x} - \frac{1}{n_h} \frac{\partial P_h}{\partial x} + \frac{\hbar^2}{2m_e} \frac{\partial}{\partial x} \left\{ \frac{1}{\sqrt{n_h}} \frac{\partial^2 \sqrt{n_h}}{\partial x^2} \right\} \quad (3)$$

This is the momentum equation of hot electrons where  $\phi$  is electrostatic wave potential,  $e$  is the electric charge, and  $p_h$  is the pressure of hot electrons which provides restoring force to the EAW's. The left-hand side of this equation i.e the inertial term is zero because of the very high mobility of hot electrons.

$$\left( \frac{\partial}{\partial t} + u_c \frac{\partial}{\partial x} \right) u_c = \frac{1}{m_e} \left[ e \frac{\partial \phi}{\partial x} + \frac{\hbar^2}{2m_e} \frac{\partial}{\partial x} \left\{ \frac{1}{\sqrt{n_c}} \frac{\partial^2 \sqrt{n_c}}{\partial x^2} \right\} \right] \quad (4)$$

This is the momentum equation for cold electrons. Here inertial term is non-zero because of the very low mobility of cold electrons. cool electrons are providing restoring force for electron acoustic oscillations.

## 2.3 Poisson's Equation

The Poisson's equation closes the system of equations as

$$\frac{\partial^2 \phi}{\partial x^2} = 4\pi e (n_c + n_h - Z_i n_i) \quad (5)$$

where  $\hbar$  is the reduced Planck's constant ( $\hbar/2\pi$ ) and  $Z_i e$  is the charge on ion.

## 2.4 The Pressure Law

Here we assume that plasma particles behave as 1-D Fermi gas and therefore taking the Fermi pressure  $P_j$  as [92–95]:

$$P_j = \frac{m_j c_{sj}^2}{3n_{j0}^2} n_j^3 \quad (6)$$

Normalized Fermi pressure term for hot electrons is given as:-

$$P_h = \frac{m_e c_{sh}^2}{3n_{h0}^2} n_h^3 n_{h0}^3 = \frac{m_e c_{sh}^2}{3} n_h^3 n_{h0} \quad (7)$$

Using the normalization scheme as  $x \rightarrow x\omega_j/c_{sj}$ ,  $t \rightarrow t\omega_j$ ,  $\phi \rightarrow e\phi/2k_B T_{Fj}$ ,  $u_j \rightarrow u_j/c_{sj}$ ,  $n_j \rightarrow n_j/n_{j0}$ ,  $\eta_c \rightarrow \eta_c\omega_j/m_e c_{sj}^2$ , Eqs. (1–5) can be written as:

$$\frac{\partial n_h}{\partial t} + \frac{\partial (n_h u_h)}{\partial x} = 0 \quad (8)$$

$$\frac{\partial n_c}{\partial t} + \frac{\partial (n_c u_c)}{\partial x} = 0 \quad (9)$$

$$0 = \frac{\partial \phi}{\partial x} - n_h \frac{\partial n_h}{\partial t} + \frac{H^2}{2} \frac{\partial}{\partial x} \left[ \frac{1}{\sqrt{n_h}} \frac{\partial^2 \sqrt{n_h}}{\partial x^2} \right] \quad (10)$$

$$\left( \frac{\partial}{\partial t} + u_c \frac{\partial}{\partial x} \right) u_c = \frac{\partial \phi}{\partial x} + \frac{H^2}{2} \frac{\partial}{\partial x} \left[ \frac{1}{\sqrt{n_h}} \frac{\partial^2 \sqrt{n_h}}{\partial x^2} \right] \quad (11)$$

$$\frac{\partial^2 \phi}{\partial x^2} = n_c + \frac{n_h}{\delta} - \frac{\delta_i}{\delta} n_i \quad (12)$$

where  $H = \hbar\omega_j/2k_B T_{Fj}$  is a non-dimensional quantum diffraction parameter,  $\delta = n_{c0}/n_{h0}$  and  $\delta_i = Zn_{i0}/n_{h0}$ .

### 3 Linear Dispersion Relation

To investigate the nonlinear behavior of electron acoustic waves, we consider the following perturbation expansion for the field quantities:

$$\begin{bmatrix} n_h \\ n_c \\ u_h \\ u_c \\ \phi \end{bmatrix} = \begin{bmatrix} 1 \\ 1 \\ u_0 \\ u_0 \\ \phi_0 \end{bmatrix} + \epsilon \begin{bmatrix} n_h^{(1)} \\ n_c^{(1)} \\ u_h^{(1)} \\ u_c^{(1)} \\ \phi^{(1)} \end{bmatrix} + \epsilon^2 \begin{bmatrix} n_h^{(2)} \\ n_c^{(2)} \\ u_h^{(2)} \\ u_c^{(2)} \\ \phi^{(2)} \end{bmatrix} + \dots \quad (13)$$

where  $j = h, c$  is the subscript which is for both hot and cold electrons,  $n_j$  is the number density of hot and cold electrons,  $u_j$  is the velocity of hot and cold electrons in plasma,  $\phi$  is electro-static wave potential and  $\epsilon$  is the smallness parameter, powers of  $\epsilon$  represents the order of perturbation. By assuming that all field quantities vary as  $e^{i(kx - \omega t)}$  such that eigenvalues of  $\frac{\partial}{\partial t}$  and  $\frac{\partial}{\partial x}$  are  $-i\omega$  and  $ik$  respectively. Now in order to obtain linear dispersion relation substituting perturbation expansion of field quantities in governing equations and keeping only first-order terms in  $\epsilon$  we get the following linear dispersion relation for normalized wave frequency ( $\omega$ ) and wavenumber ( $k$ ):

$$1 = \frac{1}{(\omega - ku_0)^2 - \frac{H^2k^4}{4}} - \frac{1}{\delta k^2 \left\{ 1 + \frac{H^2k^2}{4} \right\}} \quad (14)$$

Equation (14) represents the linear dispersion relation for EAW's in Fermi plasma, the form of wave frequency  $\omega$  is given as follows:

$$\omega = \left[ \frac{\delta k^2 \left( 1 + \frac{H^2k^2}{4} \right)}{1 + \delta k^2 \left( 1 + \frac{H^2k^2}{4} \right)} + \frac{H^2k^4}{4} \right]^{1/2} + ku_0 \quad (15)$$

## 4 Derivation of KDV Equation

To study the nonlinear behavior of electron acoustic waves we consider inertialess warm electrons, inertial cool electrons and stationary ions. The pressure effect is only due to hot electrons which provide restoring force. We explore the collision of two solitary waves using an expanded PLK perturbation approach. The following are the perturbed quantities:

$$Y = Y_0 + \sum_{r=1}^{\infty} \epsilon^{r+1} Y_r, \quad \Gamma = \sum_{r=1}^{\infty} \epsilon^{r+2} \Gamma_r \quad (16)$$

where  $Y = (n_d, u_{dz}, \psi)$ ,  $Y_0 = (1, 0, 0)$ , and  $\Gamma = (u_{dx}, u_{dy})$ . The scaling variables  $x$  and  $t$  are stretched by the new coordinate system  $\xi, \eta$  and  $\tau$  in many scale variables:

$$\xi = \epsilon (l_x x + l_y y + l_z z - V_0 t) + \epsilon^2 M_0(\eta, \tau) + \dots \quad (17)$$

$$\eta = \epsilon (l_x x + l_y y + l_z z + V_0 t) + \epsilon^2 N_0(\xi, \tau) + \dots \quad (18)$$

$$\tau = \epsilon^3 t \quad (19)$$

where  $\xi$  and  $\eta$  denote the opposite side trajectories of solitary waves and  $\epsilon$  is a parameter that determines the strength of nonlinearity.  $l_x, l_y$ , and  $l_z$  are direction cosines along the  $x, y$ , and  $z$  directions, and hence  $l_x^2 + l_y^2 + l_z^2 = 1$ . Using (17)–(19) into (8)–(12) and comparing lowest order  $\epsilon$  and taking direction cosines as  $(1, 0, 0)$  as wave propagation is along  $x$ -axes only, we get the normalized phase velocity for magnetized plasma as:

$$V_0 = \frac{\omega}{k} = \left[ \frac{\delta \left( 1 + \frac{H^2k^2}{4} \right)}{1 + \delta k^2 \left( 1 + \frac{H^2k^2}{4} \right)} + \frac{H^2k^2}{4} \right]^{1/2} + u_0 \quad (20)$$

Next taking higher order of  $\epsilon$ , we get the following equations:

$$\frac{\partial \phi^{(1)}}{\partial \tau} + A_1 \phi^{(1)} \frac{\partial \phi^{(1)}}{\partial \xi} + B_1 \frac{\partial^3 \phi^{(1)}}{\partial \xi^3} = 0 \quad (21)$$

$$\frac{\partial \phi^{(1)}}{\partial \tau} - A_2 \phi^{(1)} \frac{\partial \phi^{(1)}}{\partial \eta} - B_2 \frac{\partial^3 \phi^{(1)}}{\partial \eta^3} = 0 \quad (22)$$

where

$$A_1 = \frac{p_2^2 (V_0 - u_0)^2}{\delta} - p_1^2 - 2p_1 p_2 \quad (23)$$

$$A_2 = \frac{p_2^2 (V_0 - u_0)^2}{\delta} - p_1^2 - 2p_1 p_2 \quad (24)$$

$$B_1 = \frac{(V_o - u_o)^2 - \frac{H^2}{4} p_2 (V_o - u_o)^2}{p_1 + (V_o - u_o) p_2} \quad (25)$$

$$B_2 = \frac{(V_o - u_o)^2 - \frac{H^2}{4} p_2 (V_o - u_o)^2}{p_1 + (u_o - V_o) p_2} \quad (26)$$

Equations (21) and (22) are the KdV equations of two solitary waves move towards one another in the reference frame of  $\xi$  and  $\eta$ .

## 5 Simulation Results

Soliton-soliton collision and decomposition of stationary structures into the secondary formation are the two mechanisms which explains the result of this analytic study. We start with the KdV equation and use our choice of initial and boundary conditions which show many intermittent phenomena that are crucial in understanding of these mechanisms. The simulation carried out here had been designed by Chinmay Das and Swarniv Chandra in the summer of 2021 at the computational faculty of Institute of Natural Sciences and Applied Technology, Kolkata. It explains Fourier transform coupled with Runge Kutta technique. The code has been named as INSAT-FORK code and is referred to in literature [41].



### 5.1 Interaction of Solitary Structures

Here we would study the time evolution of the stationary structures when two of them collide with each other. The interacting solitons can either be of the same or opposite structures. Density structures can be either solitary wavelets or of opposite polarity (expressed as a hyperbolic secant function) depending upon whether the solitons have similar structures or different ones at the beginning. These structures will give us different mechanisms if we let them propagate in space. The mechanisms we get from these are that the propagations are dependent on the scaling scheme i.e the order of scheme which we want to study. Here the scale of interaction is normalization. From figures, we get the information of soliton-soliton collision and their evolution with time. Figure 1 shows that initially two Gaussian pulses are separated by some distance and they are moving towards each other. The perturbation caused by their interaction stays a bit longer even though the interaction is over. Perturbation stays after the interaction of two hyperbolic secant squared waves too, but in this case, perturbation caused is more frequent and of sharp and high altitudes (Fig. 2). The cause behind this can be the higher peaks and sharpness of both waves. The interaction of two sinusoidal waves in Fig. 3 causes equal and opposite disturbance in opposite polarity regions of the wave at time  $\tau = 3$ , which immediately disappears.

Figure 4 shows the interaction of two Gaussian pulses caused by an external force. Even in this interaction too, the disturbance remains even after the interaction has finished. Next, in Fig. 5, the interaction of secant hyperbolic squared pulses after the external force is applied. As can be seen, the peaks of perturbation caused at time  $\tau=4$  and 10 are higher than when no external force was applied. Even in the interaction of two sinusoidal waves (Fig. 6, the external force caused to have a little disturbance after the interaction, which was not there without external force.

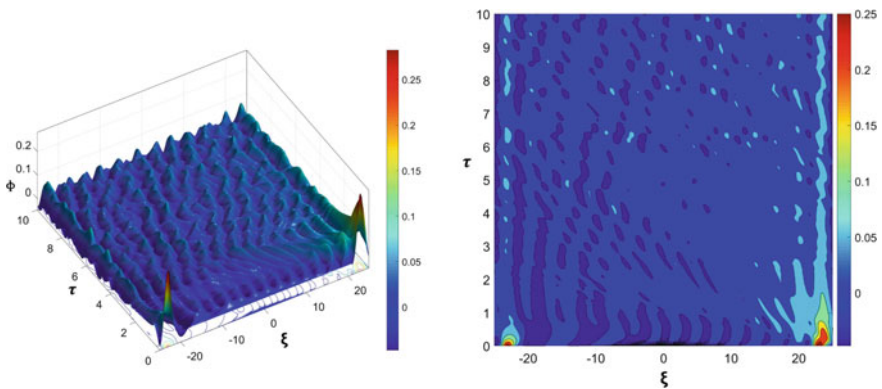


**Fig. 1** (i) Variation in soliton-soliton collisions for two Gaussian pulses. (ii) Counter plots of variation in soliton-soliton collisions for two Gaussian pulses

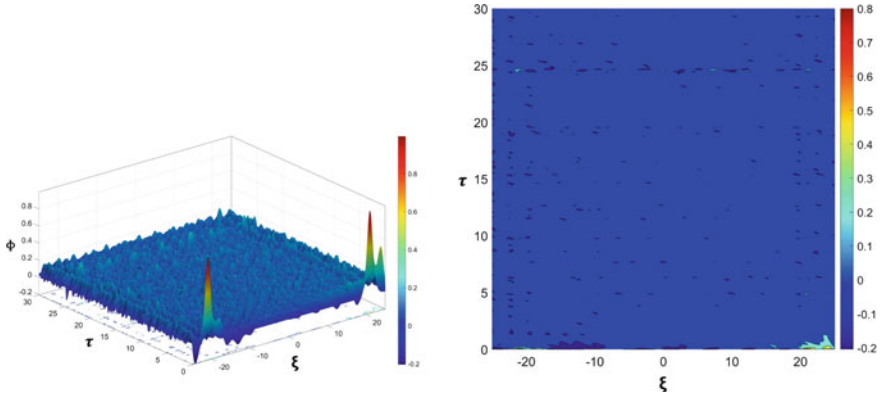


**Fig. 2** (i) Variation in soliton-soliton collisions for two hyperbolic secant squared type pulses. (ii) Counter plots of variation in soliton-soliton collisions for two hyperbolic secant squared type pulses

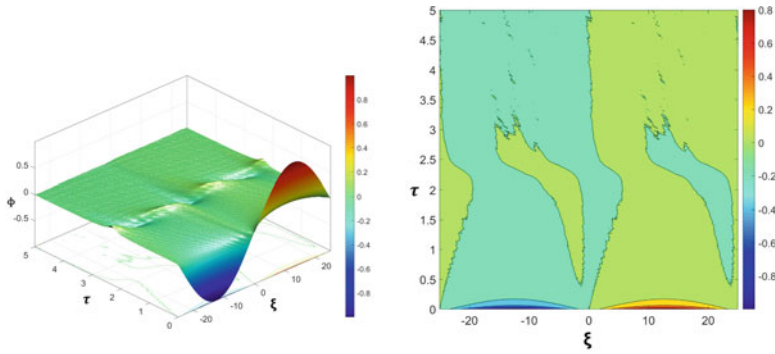


**Fig. 3** (i) Variation in soliton-soliton collisions for two sinusoidal propagating pulses. (ii) Counter plots of variation in soliton-soliton collisions for two sinusoidal propagating pulses

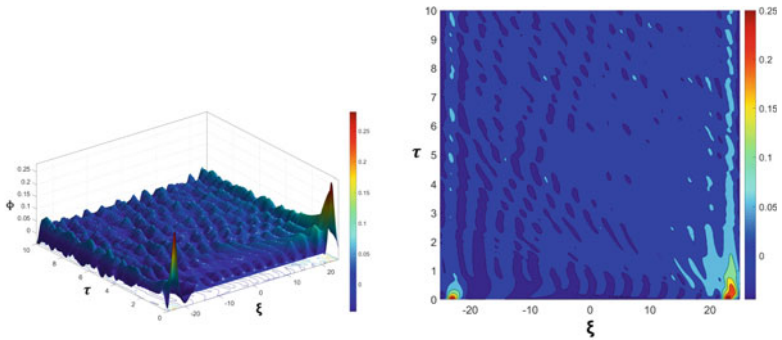


**Fig. 4** (i) Interaction of two Gaussian pulses from both extremities towards a single point under the action of an external force. (ii) Counter plots of two Gaussian pulses from both extremities towards a single point under the action of an external force

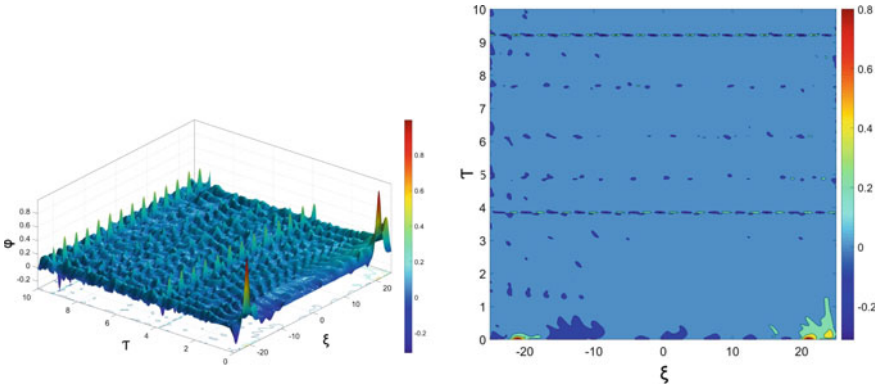


**Fig. 5** (i) Time evolution of the potential profile formed by the collision of two secant hyperbolic squared type pulses under the action of an external force. (ii) Counter plots of the time evolution of the potential profile formed by the collision of two secant hyperbolic squared type pulses under the action of an external force

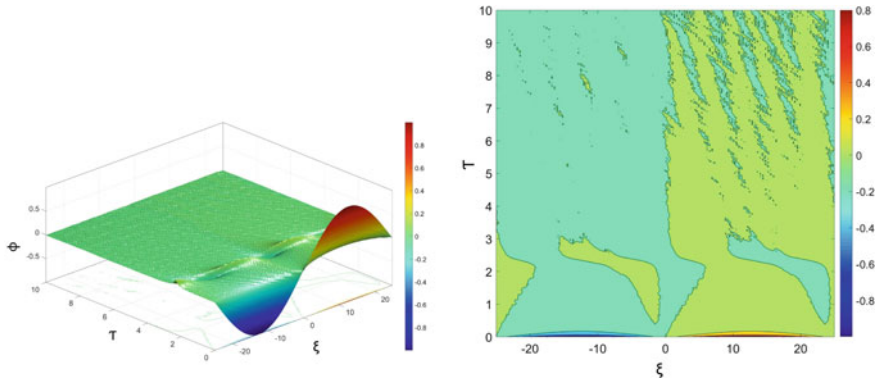


**Fig. 6** (i) Time evolution of the potential profile formed by the collision of two sinusoidal pulses under the action of an external force. (ii) Counter plots of the time evolution of the potential profile formed by the collision of two sinusoidal pulses under the action of an external force

### 5.2 Breakdown of Stationary Structures

Here, we would study the decomposition mechanism of stationary structures for different initial conditions. An initial Gaussian function is seen to break into multiple fluctuations of potential (Fig. 7), which eventually take on distinct values at the boundary. This mechanism can be explained as follows: dispersion forces tear down the Gaussian profile, whereas nonlinear forces seek to strengthen it. Similar is the case of hyperbolic secant squared pulse in Fig. 8 but the fluctuations, in this case, are of lower amplitude. The effect of a sinusoidal waveform is spatially extended but

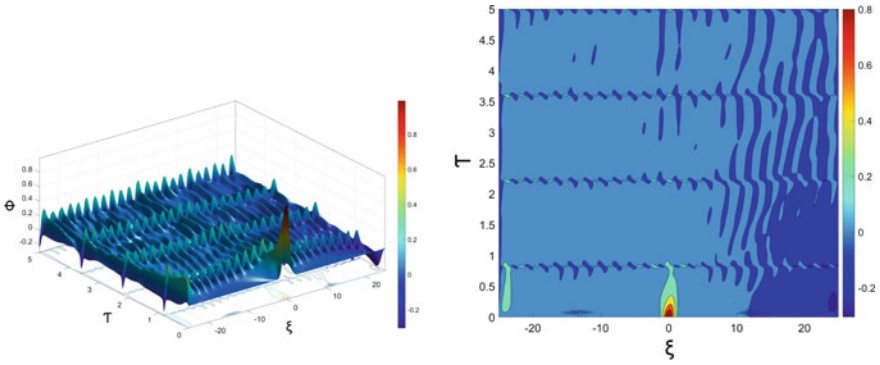


**Fig. 7** (i) Breakdown of initial Gaussian pulse. (ii) Counter plots of breakdown of Gaussian pulses

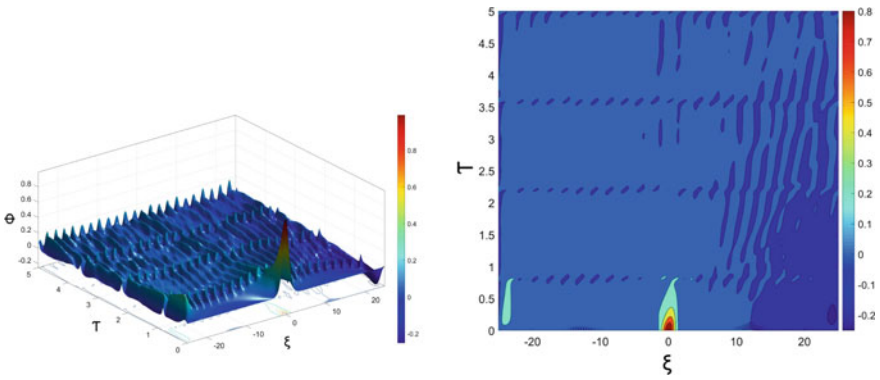


**Fig. 8** (i) Breakdown of Initial hyperbolic secant squared hyperbolic function. (ii) Counter plots of Breakdown of secant hyperbolic squared function

temporally localized, implying that when the energy of the disturbance dissipates, the sinusoidal profile is effective at exciting the entire medium into small scale short-lived perturbations that occupy otherwise homogenous media (Fig. 9).

## 6 Dynamical Study of Electron Acoustic KdV Solitons

In this part, we would determine how EAWs propagates and evolves, how it behaves when the small perturbation is given to the system, its stability and its chaotic behavior i.e. when very small changes are made in the initial conditions how the system would respond to them. Dynamics of both perturbed and unperturbed would be discussed.

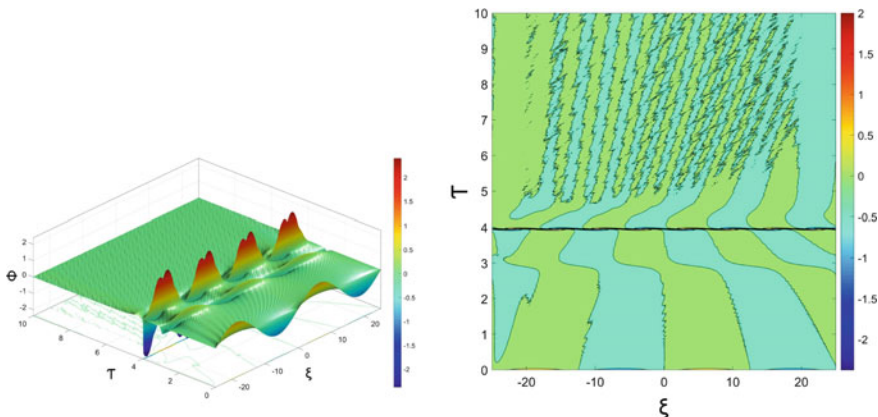


**Fig. 9** (i) Breakdown of sinusoidal propagating pulses. (ii) Counter plots of breakdown of initial sinusoidal propagating pulses

## 6.1 Unperturbed System

In order to investigate the dynamical systems (DS) behavior of the system which is not perturbed corresponding to the KdV-equation (21), a one-dimensional traveling wave transformation  $\eta = \xi - M\tau$  has been considered with boundary conditions  $\psi \rightarrow 0, \frac{\partial\psi}{\partial\xi} \rightarrow 0$  as  $\eta \rightarrow \pm\infty$ , where  $M$  is the velocity of the wave frame. By using this transformation in the KdV equation (21) and after integrating w.r.t  $\eta$ , we get

$$\frac{\partial^2\psi}{\partial\xi^2} = R\psi - T\psi^2 \quad (27)$$

where  $R = \frac{M}{Bl^3}, T = \frac{A}{2Bl^2}$

By assuming

$$\frac{\partial\psi}{\partial\eta} = z_1 \quad (28)$$

The equation (27) transformed into the dynamical system of the form

$$\frac{\partial z}{\partial\eta} = R\psi - T\psi^2 \quad (29)$$

The two nonlinear differential equations (27) and (28) represent the dynamics of the unperturbed KdV equation (21). The system will be conservative if the divergence of field is zero ( $\nabla \cdot \mathbf{F} = 0$ ) i.e the field is Solenoidal, where  $\mathbf{F}(z, R\psi^{(1)} - T\psi^{(1)^3})$ . Hence the Hamiltonian of the planar system is given by:

$$H(\psi, z) = \frac{z^2}{4} - \frac{R\psi^2}{2} + \frac{T\psi^4}{4} \tag{30}$$

The term Bifurcation is used for the mathematical investigation of dynamical systems. Bifurcation is the study of unforeseen changes in the qualitative or topological structure of a given family, such as the integral curves of a family of vector fields, and the solutions of a family of differential equations when a small smooth change is made to the bifurcation parameters [96–100]. Hence we also analyze the Bifurcation as the phase plots describe all equations of EAWs with different initial conditions.

### 6.2 Perturbed System

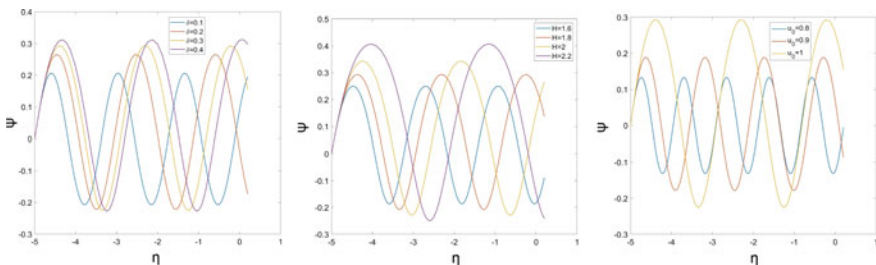
The system is said to be perturbed when there is some external source of disturbance and the effects of these small external disturbances/forces/perturbations on the system are of great importance. Different types of forces affect the system differently. For our case, the provided external force is  $f_0 \cos(\omega\eta)$ . Under such an external force the modeled equation will result in the forced KdV. Hence, we obtain

$$\frac{\partial \Psi}{\partial \eta} = z \tag{31}$$

$$\frac{\partial z}{\partial \eta} = R\psi^{(1)} - T\psi^2 + f_0 \cos(\omega\eta) \tag{32}$$

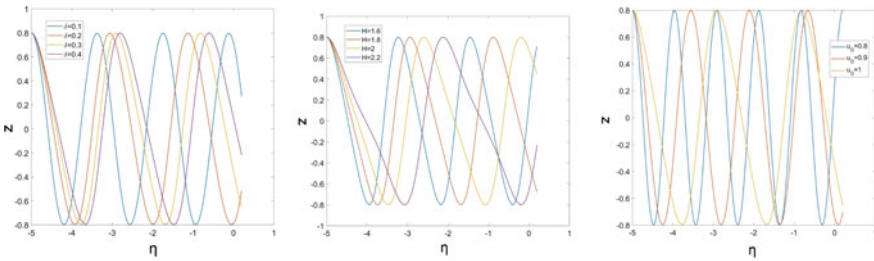
These two DS equations represent the dynamics of forced KdV. Here  $\eta$  is the external perturbation,  $f_0$  is the strength of the perturbation and  $\omega$  is the compound frequency.

Figure 10 shows super nonlinear wave solution with variation of  $\psi$  for different values of  $\delta$ , H and  $u_0$ . There is an increase in the amplitude and wavelength with every greater value of  $\delta$  and so is the case of increase in value of H and  $u_0$  but



**Fig. 10** Super nonlinear wave solution with variation of  $\psi$  corresponding to dynamical system for forced KdV equation with different values of (i)  $\delta = 0.1$  (Sky Blue), 0.2 (yellow), 0.3 (Brown), 0.4 (purple), (ii)  $H = 1.6$  (Sky Blue), 1.8 (yellow), 2 (Brown) 2.2 (Purple), (iii)  $u_0 = 0.8$  (Sky blue), 0.9 (Brown), 1 (Yellow)





**Fig. 11** Super nonlinear wave solution with variation of  $z$  corresponding to dynamical system for forced KdV equation with different values of (i)  $\delta = 0.1$  (Sky Blue),  $0.2$  (yellow),  $0.3$  (Brown),  $0.4$  (purple), (ii)  $H = 1.6$  (Sky Blue),  $1.8$  (yellow),  $2$  (Brown)  $2.2$  (Purple), (iii)  $u_0 = 0.8$  (Sky blue),  $0.9$  (Brown),  $1$  (Yellow)

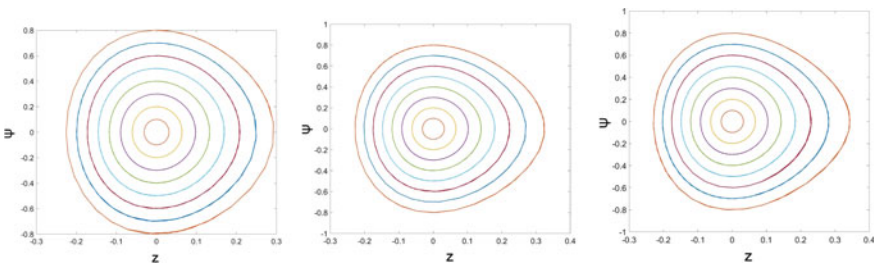


**Fig. 12** Phase portrait of forced KdV for different values of (i)  $\delta = 0.3$ , (ii)  $\delta = 0.5$ , (iii)  $\delta = 0.7$

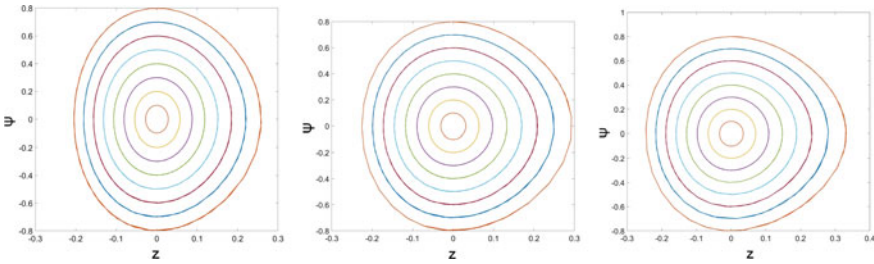


**Fig. 13** Phase portrait of forced KdV for different values of (i)  $H = 1.8$ , (ii)  $H = 2$ , (iii)  $H = 2.2$

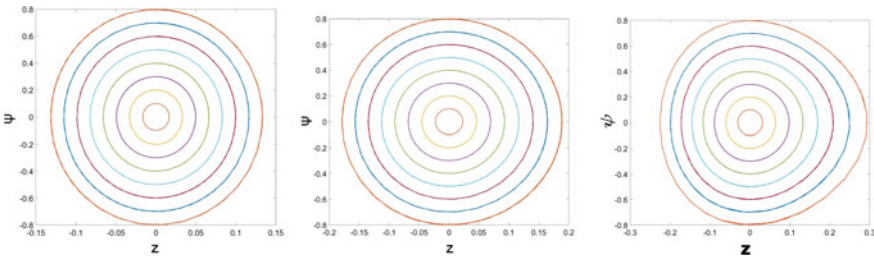


**Fig. 14** Phase portrait of forced KdV for different values of (i)  $u_0 = 0.8$ , (ii)  $u_0 = 0.9$ , (iii)  $u_0 = 1$

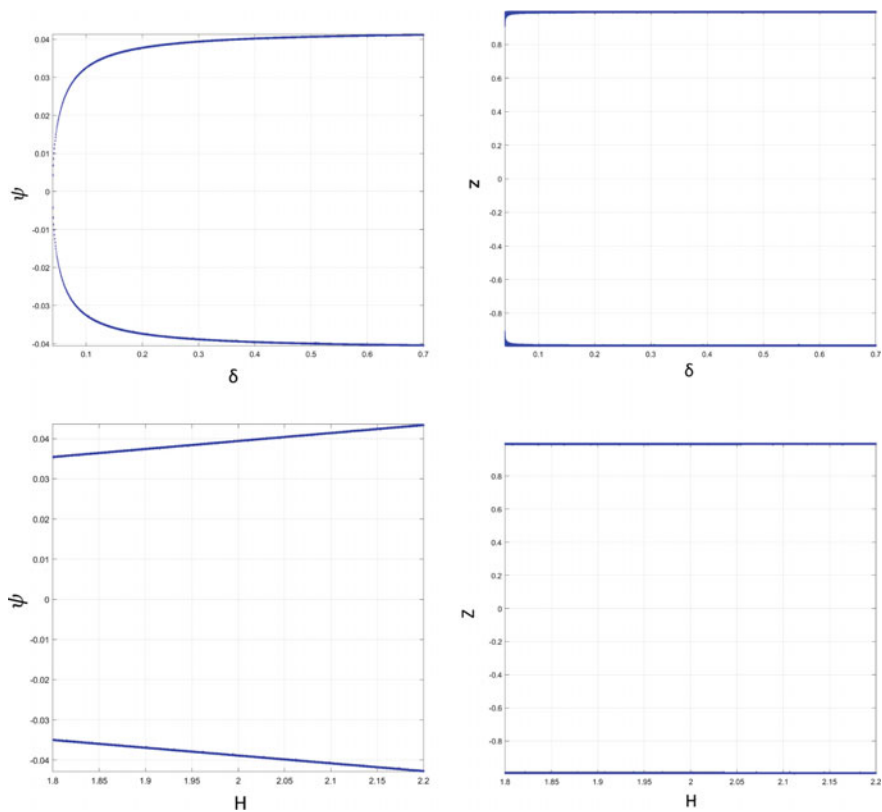


Fig. 15 Bifurcation plots for forced KdV

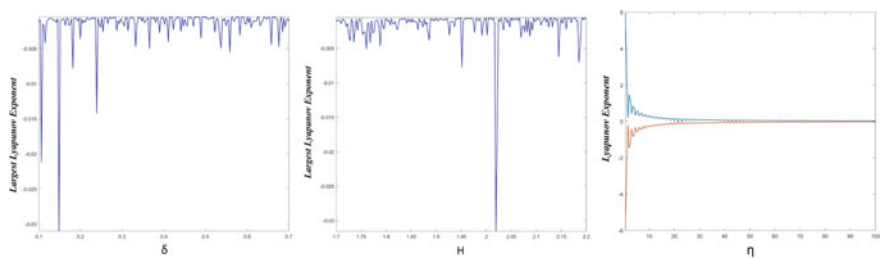


Fig. 16 Largest Lyapunov exponent for Forced KdV for variation of (i)  $\delta$ , (ii)  $H$  and (iii)  $\eta$



the increase in wavelength is much more dominating in case of higher value of  $H$  whereas in case of  $u_0$  it is the increase in amplitude that dominates.

In Fig. 11, super nonlinear wave solution with variation of  $z$  for different values of  $\delta$ ,  $H$  and  $u_0$  are shown. In all the three cases here, it is only the wavelength that increases with rise in any of the three parameters. The phase portrait plot, different initial conditions have closed loops. In Figs. 12 and 13, the loop is unsymmetrical along  $z$  and tend to elongate itself even more in the direction of  $z$  with rise in  $\delta$ . In Fig. 14, the loop is initially symmetrical but with rise in  $u_0$  becomes elongated and unsymmetrical.

Figure 15, the bifurcation plots for forced KdV are presented for different parameters. With variation in  $\delta$ , the position varies exponentially whereas there is no change in momentum. And further, as  $H$  varies, the position varies linearly but momentum has no effect of  $H$  also. As Lyapunov exponent represents chaos, Chaotic behaviour for different parameters is shown in Fig. 16. For  $\delta$ , the chaotic peaks lie between 0.1 and 0.3 and for  $H$  lies near 2. The chaotic behaviour is kind of perturbed and exponential in case of  $\eta$ .

## 7 Conclusion

We have studied two temperature plasma with Quantum-Hydrodynamic (QHD) Model, deriving its dispersion relation and further studied the decomposition of soliton and interaction of two solitons. The solution to the Forced-KdV equation demonstrates how the behaviour of these perturbed solitons is affected by the parameters used. The unperturbed plasma system is investigated first, followed by how the perturbation impacts the system.

The dynamical system is also investigated. The significance of researching Dynamical systems is demonstrated through phase pictures. The qualitative shift in this system's dynamics with changes in parameters is explained by bifurcation, which uses the Lyapunov exponent to characterise the rate of separation of infinitesimally close paths. The system's chaotic behaviour is investigated using the Largest Lyapunov exponent. This research can be used to a variety of astrophysical phenomena, such as stellar media, magnetospheres, and polar caps.

## References

1. Akter, T., Deeba, F., Kamal-Al-Hassan, Md.: Electron-acoustic solitary waves in a two-temperature plasma having electrons with kappa distribution. *IEEE Trans. Plasma Sci.* **44**(8), 1449–1459 (2016)
2. Sahu, B.: Electron acoustic solitary waves and double layers with superthermal hot electrons. *Phys. Plasmas* **17**(12), 122305 (2010)

3. Saha, A., Chatterjee, P.: Electron acoustic blow up solitary waves and periodic waves in an unmagnetized plasma with kappa distributed hot electrons. *Astrophys. Space Sci.* **353**(1), 163–168 (2014)
4. Chandra, S., Ghosh, B.: Modulational instability of electron-acoustic waves in relativistically degenerate quantum plasma. *Astrophys. Space Sci.* **342**(2), 417–424 (2012)
5. Chatterjee, M., Dasgupta, M., Das, S., Halder, M., Chandra, S.: Study of dynamical properties in shock & solitary structures and its evolutionary stages in a degenerate plasma. *African Rev. Phys.* **15**, 75 (2021)
6. Chandra, S., Goswami, J., Sarkar, J., Das, C.: Analytical and simulation studies of forced kdv solitary structures in a two-component plasma. *J. Korean Phys. Soc.* **76**(6), 469–478 (2020)
7. Chandra, S., Das, C., Sarkar, J.: Evolution of nonlinear stationary formations in a quantum plasma at finite temperature. *Zeitschrift für Naturforschung A* **76**(4), 329–347 (2021)
8. Ballav, S., Das, A., Pramanick, S., Chandra, S.: Plasma shock wave in gamma-ray bursts: nonlinear phenomena and radiative process. *IEEE Trans. Plasma Sci.* (2021)
9. Chandra, S., Goswami, J., Sarkar, J., Das, C., Ghosh, B., Nandi, D.: Formation of electron acoustic shock wave in inner magnetospheric plasma. *Indian J. Phys.* (2021). <https://doi.org/10.1007/s12648-021-02276-x>
10. Ballav, S., Kundu, S., Das, A., Chandra, S.: Non-linear behaviour of dust acoustic wave mode in a dynamic dusty plasma containing negative dust particles and positrons. *African Rev. Phys.* **15**, 54 (2021)
11. Chandra, S., Sarkar, J., Das, C., Ghosh, B.: Self-interacting stationary formations in plasmas under externally controlled fields. *Plasma Phys. Rep.* **47**, 306–317 (2021)
12. Sultana, S., Kourakis, I.: Electrostatic solitary waves in the presence of excess superthermal electrons: modulational instability and envelope soliton modes. *Plasma Phys. Control. Fusion* **53**(4), 045003 (2011)
13. Watanabe, K., Taniuti, T.: Electron-acoustic mode in a plasma of two-temperature electrons. *J. Phys. Soc. Jpn.* **43**(5), 1819–1820 (1977)
14. Yu, M.Y., Shukla, P.K.: Linear and nonlinear modified electron-acoustic waves. *J. Plasma Phys.* **29**(3), 409–413 (1983)
15. Tokar, R.L., Gary, S.P.: Electrostatic hiss and the beam driven electron acoustic instability in the dayside polar cusp. *Geophys. Res. Lett.* **11**(12), 1180–1183 (1984)
16. Mace, R.L., Hellberg, M.A.: Higher-order electron modes in a two-electron-temperature plasma. *J. Plasma Phys.* **43**(2), 239–255 (1990)
17. Stix, H.: *Waves in plasmas* American Institute of Physics, New York (1992). Borg, G.G., Harris, J.H., Miljak, D.G., et al.: Plasma columns as radiating elements. *IEEE Trans. Plasma Sci.* submitted, 29
18. Treumann, R.A., Baumjohann, W.: *Advanced Space Plasma Physics*, vol. 30. Imperial College Press, London (1997)
19. Gary, S.P., Tokar, R.L.: The electron-acoustic mode. *Phys. Fluids* **28**(8), 2439–2441 (1985)
20. Feldman, W.C., Asbridge, J.R., Bame, S.J., Montgomery, M.D., Gary, S.P.: Solar wind electrons. *J. Geophys. Res.* **80**(31), 4181–4196 (1975)
21. Feldman, W.C., Anderson, R.C., Bame, S.J., Gary, S.P., Gosling, J.T., McComas, D.J., Thomson, M.F., Paschmann, G., Hoppe, M.M.: Electron velocity distributions near the earth's bow shock. *J. Geophys. Res. Space Phys.* **88**(A1), 96–110 (1983)
22. Feldman, W.C., Anderson, R.C., Bame, S.J., Gosling, J.T., Zwickl, R.D., Smith, E.J.: Electron velocity distributions near interplanetary shocks. *J. Geophys. Res. Space Phys.* **88**(A12), 9949–9958 (1983)
23. Barnes, W.L., Dereux, A., Ebbesen, T.W.: Surface plasmon subwavelength optics. *Nature* **424**, 824 (2003)
24. Ditmire, T., Springate, E., Tisch, J.W.G., Shao, Y.L., Mason, M.B., Hay, N., Marangos, J.P., Hutchinson, M.H.R.: Explosion of atomic clusters heated by high-intensity femtosecond laser pulses. *Phys. Rev. A* **57**(1), 369 (1998)
25. Gudmundsson, J.T., Alami, J., Helmersson, U.: Spatial and temporal behavior of the plasma parameters in a pulsed magnetron discharge. *Surface Coat. Technol.* **161**(2–3), 249–256 (2002)

26. Kadomtsev, B.B., Pogutse, O.P.: Trapped particles in toroidal magnetic systems. *Nucl. Fus.* **11**(1), 67 (1971)
27. Henry, D., Trguier, J.P.: Propagation of electronic longitudinal modes in a non-maxwellian plasma. *J. Plasma Phys.* **8**(3), 311–319 (1972)
28. Saberian, E., Esfandyari-Kalejahi, A.: Kinetic theory of acoustic-like modes in nonextensive pair plasmas. *Astrophys. Space Sci.* **349**(2), 799–811 (2014)
29. Das, C., Chandra, S., Ghosh, B.: Amplitude modulation and soliton formation of an intense laser beam interacting with dense quantum plasma: symbolic simulation analysis. *Contrib. Plasma Phys.* 10–1002 (2020)
30. Das, C., Chandra, S., Ghosh, B.: Nonlinear interaction of intense laser beam with dense plasma. *Plasma Phys. Control. Fus.* **63**, 015011 (2020)
31. Das, C., Chandra, S., Ghosh, B.: Effects of exchange symmetry and quantum diffraction on amplitude modulated electrostatic waves in quantum magnetoplasma. *Pramana-J. Phys.* **95**(2) (2021)
32. Das, A., Ghosh, P., Chandra, S., Raj, V.: Electron acoustic peregrine breathers in a quantum plasma with 1-d temperature anisotropy. *IEEE Trans. Plasma Sci.* 1–12 (2021)
33. Dey, S., Maity, D., Ghosh, A., Samanta, P., De, A., Chandra, S.: Chaotic excitations of rogue waves in stable parametric region for highly-energetic pair plasmas. *African Rev. Phys.* **15**, 33 (2021)
34. Dey, A., Chandra, S., Das, C., Mandal, S., Das, T.: Rogue wave generation through non-linear self interaction of electrostatic waves in dense plasma. *IEEE Trans. Plasma Sci.* 10–1109 (2022)
35. Bains, A.S., Tribeche, M., Gill, T.S.: Modulational instability of ion-acoustic waves in a plasma with aq-nonextensive electron velocity distribution. *Phys. Plasmas* **18**(2), 022108 (2011)
36. Kourakis, I., Shukla, P.K.: Electron-acoustic plasma waves: oblique modulation and envelope solitons. *Phys. Rev. E* **69**(3), 036411 (2004)
37. Singh, S.V., Lakhina, G.S.: Generation of electron-acoustic waves in the magnetosphere. *Planet. Space Sci.* **49**(1), 107–114 (2001)
38. Ghosh, B., Chandra, S., Paul, S.N.: Relativistic effects on the modulational instability of electron plasma waves in quantum plasma. *Pramana* **78**(5), 779–790 (2012)
39. Ghosh, T., Pramanick, S., Sarkar, S., Dey, A., Chandra, S.: Chaotic scenario in three-component fermi plasma. *African Rev. Phys.* **15**, 45 (2021)
40. Ghosh, S., Saha, S., Chakraborty, T., Sadhukhan, K., Bhanja, R., Chandra, S.: Linear and non-linear properties of electron acoustic waves in a viscous plasma. *African Rev. Phys.* **15**, 90 (2021)
41. Ghosh, A., Goswami, J., Chandra, S., Das, C., Arya, Y., Chhibber, H.: Resonant interactions and chaotic excitation in nonlinear surface waves in dense plasma. *IEEE Trans. Plasma Sci.* (2021)
42. Goswami, J., Chandra, S., Ghosh, B.: Study of small amplitude ion-acoustic solitary wave structures and amplitude modulation in e-p-i plasma with streaming ions. *Laser Part. Beams* **36**(1), 136–143 (2018)
43. Goswami, J., Chandra, S., Ghosh, B.: Shock waves and the formation of solitary structures in electron acoustic wave in inner magnetosphere plasma with relativistically degenerate particles. *Astrophys. Space Sci.* **364**(4), 1–7 (2019)
44. Goswami, J., Chandra, S., Sarkar, J., Chaudhuri, S., Ghosh, B.: Collision-less shocks and solitons in dense laser-produced fermi plasma. *Laser Part. Beams* **38**(1), 25–38 (2020)
45. Sah, O.P., Manta, J.: Nonlinear electron-acoustic waves in quantum plasma. *Phys. Plasmas* **16**(3), 032304 (2009)
46. Manfredi, G., Haas, F.: Self-consistent fluid model for a quantum electron gas. *Phys. Rev. B* **64**(7), 075316 (2001)
47. Manfredi, G.: Fields inst. commun. In: *Proceedings of the Workshop on Kinetic Theory (The Fields Institute, Toronto, Canada, 29 March 2 April 2004)*, vol. 46, p. 263 (2005)
48. Santamato, E.: Geometric quantum mechanics. In: *Fundamental Aspects of Quantum Theory*, pp. 443–444. Springer (1986)

49. Gardner, C.L., Ringhofer, C.: Smooth quantum potential for the hydrodynamic model. *Phys. Rev. E* **53**(1), 157 (1996)
50. Shukla, P.K., Eliasson, B.: Formation and dynamics of dark solitons and vortices in quantum electron plasmas. *Phys. Rev. Lett.* **96**(24), 245001 (2006)
51. Sahu, B., Roychoudhury, R.: Electron acoustic solitons in a relativistic plasma with nonthermal electrons. *Phys. Plasmas* **13**(7), 072302 (2006)
52. Shukla, P.K., Ali, S.: Dust acoustic waves in quantum plasmas. *Phys. Plasmas* **12**(11), 114502 (2005)
53. Ali, S., Shukla, P.K.: Dust acoustic solitary waves in a quantum plasma. *Phys. Plasmas* **13**(2), 022313 (2006)
54. Ergun, R.E., Carlson, C.W., McFadden, J.P., Mozer, F.S., Muschietti, L., Roth, I., Strangeway, R.J.: Debye-scale plasma structures associated with magnetic-field-aligned electric fields. *Phys. Rev. Lett.* **81**(4), 826 (1998)
55. Ergun, R.E., Carlson, C.W., McFadden, J.P., Mozer, F.S., Delory, G.T., Peria, W., Chaston, C.C., Temerin, M., Roth, I., Muschietti, L., et al.: Fast satellite observations of large-amplitude solitary structures. *Geophys. Res. Lett.* **25**(12), 2041–2044 (1998)
56. Manfredi, G.: How to model quantum plasmas. *Fields Inst. Commun.* **46**, 263–287 (2005)
57. Haas, F., Garcia, L.G., Goedert, J., Manfredi, G.: Quantum ion-acoustic waves. *Phys. Plasmas* **10**(10), 3858–3866 (2003)
58. Mamun, A.A., Shukla, P.K.: Solitary waves in an ultrarelativistic degenerate dense plasma. *Phys. Plasmas* **17**(10), 104504 (2010)
59. Goswami, J., Chandra, S., Sarkar, J., Ghosh, B.: Electron acoustic solitary structures and shocks in dense inner magnetosphere finite temperature plasma. *Radiat. Effects Defects Solids* **175**(9–10), 961–973 (2020)
60. Goswami, J., Chandra, S., Sarkar, J., Ghosh, B.: Amplitude modulated electron acoustic waves with bipolar ions and kappa distributed positrons and warm electrons. *Pramana-J. Phys.* **95**, 54 (2021)
61. Goswami, J., Chandra, S., Das, C., Sarkar, J.: Nonlinear wave-wave interaction in semiconductor junction diode. *IEEE Trans. Plasma Sci.* (2021). <https://doi.org/10.1109/TPS.2021.3124454>
62. Goswami, J., Chandra, S., Sarkar, J., Ghosh, B.: Quantum two stream instability in a relativistically degenerate magnetised plasma. In: *AIP Conference Proceedings*, vol. 2319, pp. 030005. AIP Publishing LLC (2021)
63. Kapoor, S., Dutta, D., Ghosh, M., Chandra, S.: Magnetosonic shocks and solitons in fermi plasma with quasiperiodic perturbation. *IEEE Trans. Plasma Sci.* (2022)
64. Kockaert, P., Haelterman, M.: Stability and symmetry breaking of soliton bound states. *JOSA B* **16**(5), 732–740 (1999)
65. Ermakov, A., Stepanyants, Y.: Soliton interaction with external forcing within the korteweg-de vries equation. *Chaos Interdisc. J. Nonlinear Sci.* **29**(1), 013117 (2019)
66. Han, J.-N., Luo, J.-H., Li, S.-C., Liu, S.-W., Yang, Y., Duan, W.-S., Han, J.-F., Li, J.-X.: Composite nonlinear structure within the magnetosonic soliton interactions in a spin-1/2 degenerate quantum plasma. *Phys. Plasmas* **22**(6), 062101 (2015)
67. Howes, G.G.: Laboratory space physics: investigating the physics of space plasmas in the laboratory. *Phys. Plasmas* **25**(5), 055501 (2018)
68. Naumovets, A.G.: *Two-Dimensional Crystals*. Elsevier (2012)
69. Maiti, A., Chowdhury, S., Singha, P., Ray, S., Dasgupta, R., Chandra, S.: Study of small amplitude ion-acoustic bunched solitary waves in a plasma with streaming ions and thermal electrons. *African Rev. Phys.* **15**, 97 (2021)
70. Majumdar, A., Sen, A., Panda, B., Ghosal, R., Mallick, S., Chandra, S.: Study of shock fronts and solitary profile in a weakly relativistic plasma and its evolution into an amplitude modulated envelop soliton. *African Rev. Phys.* **15**, 18 (2021)
71. Mukhopadhyay, A., Bagui, D., Chandra, S.: Electrostatic shock fronts in two-component plasma and its evolution into rogue wave type solitary structures. *African Rev. Phys.* **15**, 25 (2021)

72. Paul, I., Chandra, S., Chattopadhyay, S., Paul, S.N.: W-type ion-acoustic solitary waves in plasma consisting of cold ions and nonthermal electrons. *Indian J. Phys.* **90**(10), 1195–1205 (2016)
73. Cheng, X.-P., Lou, S.Y., Chen, C.-L., Tang, X.-Y.: Interactions between solitons and other nonlinear schrödinger waves. *Phys. Rev. E* **89**(4), 043202 (2014)
74. Prasad, P.K., Gowrisankar, A., Saha, A., Banerjee, S.: Dynamical properties and fractal patterns of nonlinear waves in solar wind plasma. *Physica Scripta.* **95**(6), 065603 (2020)
75. Abdikian, A., Saha, A., Alimirzaei, S.: Bifurcation analysis of ion-acoustic waves in an adiabatic trapped electron and warm ion plasma. *J. Taibah Univ. Sci.* **14**(1), 1051–1058 (2020)
76. Roychowdhury, A., Banerjee, S., Chandra, S.: Stationary formation of dust-ion acoustic waves in degenerate dusty plasma at critical regime. *African Rev. Phys.* **15**, 102 (2021)
77. Sahoo, H., Chandra, S., Ghosh, B.: Dust acoustic solitary waves in magnetized dusty plasma with trapped ions and q-non-extensive electrons. *African Rev. Phys.* **10**(32), 235 (2015)
78. Sahoo, H., Das, C., Chandra, S., Ghosh, B., Mondal, K.K.: Quantum and relativistic effects on the kdv and envelope solitons in ion-plasma waves. *IEEE Trans. Plasma Sci.* (2021). <https://doi.org/10.1109/TPS.2021.3120077>
79. Samanta, P., De, A., Dey, S., Maity, D., Ghosh, A., Chandra, S.: Nonlinear excitations in dust-ion acoustic waves and the formation of rogue waves in stable parametric region in a 3-component degenerate plasma. *African Rev. Phys.* **15**, 10 (2021)
80. Mahmood, S., Masood, W.: Electron acoustic solitary waves in unmagnetized two electron population dense plasmas. *Phys. Plasmas* **15**(12), 122302 (2008)
81. ur Rehman, S. Linear and nonlinear quantum ion acoustic waves in a plasma with positive, negative ions and fermi electron gas. *Phys. Plasmas* **17**(6), 062303 (2010)
82. Lakhina, G.S., Kakad, A.P., Singh, S.V., Verheest, F.: Ion-and electron-acoustic solitons in two-electron temperature space plasmas. *Phys. Plasmas* **15**(6), 062903 (2008)
83. Jones, W.D., Lee, A., Gleman, S.M., Doucet, H.J.: Propagation of ion-acoustic waves in a two-electron-temperature plasma. *Phys. Rev. Lett.* **35**(20), 1349 (1975)
84. Ghosh, B., Chandra, S., Paul, S.N.: Amplitude modulation of electron plasma waves in a quantum plasma. *Phys. Plasmas* **18**(1), 012106 (2011)
85. Chandra, S., Paul, S.N., Ghosh, B.: Electron-acoustic solitary waves in a relativistically degenerate quantum plasma with two-temperature electrons. *Astrophys. Space Sci.* **343**(1), 213–219 (2013)
86. Sarkar, J., Goswami, J., Chandra, S., Ghosh, B.: Study of ion-acoustic solitary wave structures in multi-component plasma containing positive and negative ions and q-exponential distributed electron beam. *Laser Part. Beams* **35**(4), 641–647 (2017)
87. Sarkar, J., Chandra, S., Goswami, J., Ghosh, B.: Formation of solitary structures and envelope solitons in electron acoustic wave in inner magnetosphere plasma with suprathermal ions. *Contrib. Plasma Phys.* **60**(7), e201900202 (2020)
88. Sarkar, J., Chandra, S., Ghosh, B.: Resonant interactions between the fundamental and higher harmonic of positron acoustic waves in quantum plasma. *Zeitschrift für Naturforschung A* **75**(10), 819–824 (2020)
89. Sarkar, J., Chandra, S., Dey, A., Das, C., Marick, A., Chatterjee, P.: Forced kdv and envelope soliton in magnetoplasma with kappa distributed ions. *IEEE Trans. Plasma Sci.* 10–1109 (2021)
90. Sarkar, J., Chandra, S., Goswami, J., Das, C., Ghosh, B.: Growth of rt instability at the accreting magnetospheric boundary of neutron stars. In: *AIP Conference Proceedings*, vol. 2319, p. 030006. AIP Publishing LLC (2021)
91. Sarkar, S., Dey, A., Pramanick, S., Ghosh, T., Das, C., Chandra, S.: Homotopy study of spherical ion-acoustic waves in relativistic degenerate galactic plasma. *IEEE Trans. Plasma Sci.* 10–1109 (2022)
92. Ghosh, M., Sharry, K., Dutta, D., Chandra, S.: Propagation of rogue waves and cnoidal waves formations through low frequency plasma oscillations. *African Rev. Phys.* **15** (2021)
93. Singh, A.K., Chandra, S.: Electron acceleration by ponderomotive force in magnetized quantum plasma. *Laser Part. Beams* **35**(2), 252–258 (2017)

94. Singh, A.K., Chandra, S.: Second harmonic generation in high density plasma. *African Rev. Phys.* **12**(11), 84 (2018)
95. Thakur, S., Das, C., Chandra, S.: Stationary structures in a four component dense magneto-plasma with lateral perturbations. *IEEE Trans. Plasma Sci.* (2021)
96. Papavaritis, P., Pardo, W.B.: Numerical mode and boundary analysis of bifurcation phenomena in plasmas with stationary striations. In: *IEEE 1989 International Conference on Plasma Science*, p. 154. IEEE (1989)
97. Devaney, R.L.: *An Introduction to Chaotic Dynamical Systems*. CRC Press (2018)
98. Robinson, C.: *Dynamical systems: stability, symbolic dynamics, and chaos*. CRC Press (1998)
99. Arnold, V.I., Afrajmovic, V.S., Il'yasenkov, U.S., Shil'nikov, L.P.: *Bifurcation Theory and Catastrophe Theory*. Springer (1999)
100. Saha, A., Chatterjee, P.: Bifurcations of electron acoustic traveling waves in an unmagnetized quantum plasma with cold and hot electrons. *Astrophys. Space Sci.* **349**(1), 239–244 (2014)

# Motion of Adiabatic or Isothermal Flow Headed by a Magnetogasdynamic Cylindrical Shock Through Rotating Dusty Gas



P. K. Sahu 

**Abstract** Expansion of cylindrical shocks pushed out through a dynamic piston via rotating perfect dust-pervade gas in the presence of spatially diminishing magnetic field is inquired. The velocity and magnetic field are presumed to comply with power rules. The gas should be conducting electrically. The shock wave proceeds by mutable velocity as well as the total energy being non-stationary. Numerical calculations are accomplished to access the flow variable's profiles. It is also assessed as to how the magnetic field affects the behaviour of the flow parameters. Further, it's far exciting to word that in attendance of an azimuthal magnetic field the density and pressure evanesce at expansive region and therefore void is constituted at the symmetry's axis, that's in great accordance with laboratory situations to generate shock-wave.

**Keywords** Magnetic field · Perfect dust-pervade gas · Rotating medium · Adiabatic and isothermal flows · Mechanics of fluids

## 1 Introduction

“When the energy of the electric field is much smaller than that of the magnetic field, then all the electromagnetic quantities can be expressed in terms of the magnetic field, then only the interaction between gas-dynamic field and magnetic field can be considered. Such analysis is known as Magnetogasdynamics.” Prime persuasive for considering magnetogasdynamics is it has several implementations in the area of astrophysics, aerodynamics, as well as atmospheric sciences. The comprehensive investigation of magnetogasdynamics shock is offered by several researchers (see Hartmann [1], Balick and Frank [2], Nath [3], Nath and Sahu [4], Nath et al. [5, 6], Sahu [7–9] and the references cited therein). For evaluation of improvements

---

P. K. Sahu (✉)

Department of Mathematics, Government Shyama Prasad Mukharjee College, Sitapur 497111, Chhattisgarh, India

e-mail: [praveensahu173@gmail.com](mailto:praveensahu173@gmail.com)

© The Author(s), under exclusive license to Springer Nature Switzerland AG 2022

S. Banerjee and A. Saha (eds.), *Nonlinear Dynamics and Applications*,

Springer Proceedings in Complexity,

[https://doi.org/10.1007/978-3-030-99792-2\\_7](https://doi.org/10.1007/978-3-030-99792-2_7)

of the statistical approach in MHD (Magnetohydrodynamics) turbulence, refer to Verma [10].

The topic of magneto-gas-dynamic shock wave expansion in a rotating interstellar environment is of special relevance in the investigation of astronomical events. The external atmospheres of the planets spin as a result of the planets' spinning, according to experimental research and astrophysical observations. In an interstellar environment with spin, macroscopic motion at supersonic speeds occurs, and shock waves are created. Furthermore, because the intergalactic magnetic field is linked to the rotating sun, a wide-scale magnetic field may arise in quickly rotating stars. Thus, the spin of planets or stars has a substantial impact on the processes occurring in their outermost parts. As a result, topics concerning detonation in spinning gas atmospheres are of great astronomical importance. Many academics have researched these issues in recent years (see, Levin and Skopina [11], Nath [12], Nath et al. [13], Nath and Sahu [14–16], Sahu [17–19]).

Recently, the perusal of fluid flow in a dust-pervade gas is a topic of high involvement because it has extensive implementations in environmental as well as industrial fields like lunar-ash flowing, nozzle flowing, volcanic explosions, under-ground explosion, cosmic explosion, the formation of polluted crystals, formation of the stars, supersonic flights and various others real-life problems of engineering and science. Several research articles based on the screening of the shock waves expansion in a dust-pervade gas (see Refs. Pai et al. [20], Higashino [21], Miura and Glass [22], Popel and Gisko [23], Pai [24], Nath and Sahu [25, 26], Sahu [27, 28] as well as the sources listed throughout).

Notwithstanding, in a dust-pervade gas, similarity approaches have been mentioned very drastically within the literature, but they have hardly been investigated taking magnetic field into account. In this article, a system of non-linear PDEs that describes the cylindrically symmetric flow is considered through a perfect dust-pervade gas in the existence of a magnetic field for both isothermal and adiabatic flows. When radiative transfer effects are included, the isothermal flow hypothesis is physically plausible. This supposition about the flow's nature correlates to the start of a highly powerful explosion (for instance, subterranean, volcano, and cosmological blasts; or coal-mine bursts) when the temperature of the gas is exceptionally high (Sedov [29], Laumbach and Probstein [30]). The extant work is the enhancement of Vishwakarma and Pandey's [31] work by recognising the consequences of the rotating medium as well magnetic fields in cylindrical coordinate. The extant work is also the enhancement of Nath's [3, 12] works by recognising the consequences of dust particles or magnetic fields respectively in perfect dust-pervade gas.

## 2 Governing Equations—Adiabatic Flow

The executive equations describing 1D adiabatic, non-stationary, cylindrical, perfect dust-pervade rotating gas flow together with an azimuthal or axial magnetic field can be compiled like (c.f. Nath [3, 12], Sahu [7, 17], Levin and Skopina [11], Pai et al. [20])



$$\frac{D\rho}{Dt} + \rho \left( \frac{\partial u}{\partial r} + \frac{u}{r} \right) = 0, \quad (1)$$

$$\rho \frac{Du}{Dt} + \frac{\partial p}{\partial r} + \frac{\partial h}{\partial r} + \frac{2ih}{r} - \frac{\rho v^2}{r} = 0, \quad (2)$$

$$\frac{Dv}{Dt} + \frac{uv}{r} = 0, \quad (3)$$

$$\frac{Dw}{Dt} = 0, \quad (4)$$

$$\frac{Dh}{Dt} + 2h \left( \frac{\partial u}{\partial r} + \frac{u(1-i)}{r} \right) = 0, \quad (5)$$

$$\frac{DE_m}{Dt} + p \frac{D}{Dt} \left( \frac{1}{\rho} \right) = 0. \quad (6)$$

in which  $r$  and  $t$  are unattached space as well as time coordinates;  $u$ ,  $v$ ,  $w$  designate dust-pervade gas's velocity components;  $p$ ,  $\rho$ , and  $E_m$  designate dust-pervade gas's pressure, density, and internal energy;  $h = \frac{\mu H^2}{2}$  designates magnetic pressure,  $H$  designates the intensity of the magnetic field, it might be alternatively axial ( $i = 0$ ) or azimuthal ( $i = 1$ );  $\mu$  designates magnetic permeability.  $\frac{D}{Dt} = \left( \frac{\partial}{\partial t} \right) + u \left( \frac{\partial}{\partial r} \right)$  being material derivative.

The governing Eqs. (1–6) ought to be enclosed by an equation of state (see, Sahu [18], Nath and Sahu [25], Vishwakarma and Pandey [31]).

$$p = \frac{(1 - \chi_p)}{(1 - Z)} \rho R^* T, \quad E_m = \frac{p(1 - Z)}{(\Gamma - 1)\rho}. \quad (7)$$

We assumed that the medium rotated around a symmetry axis. For details of that readers are referred to see, Levin and Skopina [11], Sahu [17–19]. Flow factors forthwith preceding the shock are considered as (see, Sahu [7, 17])

$$H = H_1 = H_0 r_s^{-\delta}, \quad \rho = \rho_1 = \text{constant},$$

$$u = u_1 = 0, \quad v = v_1 = v_0 r_s^\alpha, \quad w = w_1 = w_0 r_s^\lambda,$$

$$p = p_1 = \left( \frac{i - \delta}{2\delta} \right) \mu H_0^2 r_s^{-2\delta} + \frac{\rho_1 v_0^2}{2\alpha} r_s^{2\alpha}, \quad \delta \neq 0, \quad \alpha \neq 0 \quad (8)$$

in which  $v_0$ ,  $w_0$ ,  $H_0$ ,  $\alpha$ ,  $\lambda$  and  $\delta$  designate dimensional constants;  $r_s$  designates shock-radius and relator 1 designates circumstances forthwith preceding shock.

The Rankine-Hugoniot stipulations are (c.f. Sahu [18], Vishwakarma and Pandey [31]) namely,

$$\begin{aligned} \rho_2 &= \rho_{r=r_s} = \frac{\rho_1}{\beta}, \quad u_2 = u_{r=r_s} = (1 - \beta)U_s, \quad v_2 = v_{r=r_s} = v_1 \\ p_2 &= p_{r=r_s} = \left[ (1 - \beta) + C_a \left( 1 - \frac{1}{\beta^2} \right) + \frac{1}{\gamma M^2} \right] \rho_1 U_s^2, \quad (9) \\ w_2 &= w_{r=r_s} = w_1, \quad h_2 = h_{r=r_s} = \frac{h_1}{\beta^2}, \quad Z_2 = \frac{Z_1}{\beta} \end{aligned}$$

Relator 2 designates situations forthwith back of the shock,  $U_s (= \frac{dr_s}{dt})$  designates shock front velocity,  $M (= \frac{\rho_1 U_s^2}{\gamma p_1})^{\frac{1}{2}}$  and  $C_a (= \frac{h_1}{\rho_1 U_s^2})$  designate shock-Mach and Cowling number. Following interrelation is used to specify the density ratio  $\beta$  throughout the shock (see, Sahu [17, 18])

$$\beta^3(\Gamma + 1) - \beta^2 \left[ \frac{2\Gamma}{\gamma M^2} + \Gamma(1 + 2C_a) + 2Z_1 - 1 \right] + 2\beta C_a(Z_1 + \Gamma - 2) + 2C_a Z_1 = 0. \quad (10)$$

### 3 Self-similarity Transformations

Behind the shock, the interior extent of flow is avowed to be an expansive region. Following Sedov [29], in the formation of self-similarity, the expansive region's velocity is putative to adhere to a power-law that reads (see, Sahu [9, 28], Steiner and Hirschler [32], Zel'Dovich and Raizer [33])

$$u_p = \frac{dr_p}{dt} = U_0 \left( \frac{t}{t_0} \right)^n, \quad (11)$$

where  $r_p$  designates expansive region's radius,  $t_0$  designates reference-time,  $n$  designates constant and  $U_0$  designates expansive region velocity at reference-time.

In terms of extent stipulation, similarity solution asserts that the shock velocity is proportional to expansive region velocity, as shown below

$$U_s = \frac{dr_s}{dt} = CU_0 \left( \frac{t}{t_0} \right)^n, \quad (12)$$

in which  $C$  designates dimensionless constant. Also,

$$\varpi(\text{self-similarity variable}) = \frac{r}{r_s} = \left[ \frac{(n+1)t_0^n}{CU_0} \right] \left( \frac{r}{t^{n+1}} \right). \quad (13)$$

Certainly, onto the shock  $\varpi = 1$  and  $\varpi = \varpi_p \left( = \frac{r_p}{r_s} \right)$  upon the expansive region.

The unknown variables are noted down in the under-mentioned form to obtain the similarity solutions, (Sahu [7, 9, 28], Steiner and Hirschler [32])

$$u = \frac{r}{t} V(\varpi), v = \frac{r}{t} \phi(\varpi), w = \frac{r}{t} \psi(\varpi), p = \rho_1 \frac{r^2}{t^2} P(\varpi),$$

$$\rho = \rho_1 D(\varpi), h = \rho_1 \frac{r^2}{t^2} B(\varpi), Z = Z_1 D(\varpi), \quad (14)$$

where  $V, \phi, \psi, P, D$  and  $B$  are functions of  $\varpi$  only.

Furthermore, the total energy of the shock is

$$E = 2\pi \int_{r_p}^{r_s} \rho \left[ E_m + \frac{1}{2} (u^2 + v^2 + w^2) + \frac{h}{\rho} \right] r dr. \quad (15)$$

Using (7) and (14), Eq. (15) becomes

$$E = 2\pi\rho_1 \left[ \frac{CU_0}{(n+1)t_0^n} \right]^{\frac{2}{n+1}} r_s^{\frac{4n+2}{n+1}} \int_{\varpi_p}^1 \left[ \frac{P(1-Z_1D)}{(\Gamma-1)} + \frac{D}{2} (U^2 + \psi^2 + \phi^2) + B \right] \varpi^3 d\varpi. \quad (16)$$

Therefore, the total energy of the shock wave is non-stationary and varies as  $r_s^{\frac{4n+2}{n+1}}$  (see, Freeman [34], Sahu [35–37]).

Given the similarity of the results, entities  $M$  and  $C_a$  are intended to be unchanging in this case

$$\alpha = -\delta = \frac{n}{n+1}. \quad (17)$$

We now obtain  $\alpha < 1$  (see, Levin and Skopina [11], Sahu [17–19]). As a result of Eq. (17), we obtain  $\frac{n}{n+1} < 1$ . Thus

$$M^2 = \frac{\delta}{\gamma C_a \left[ (i - \delta) - \frac{\rho_1 v_0^2}{\mu H_0^2} \right]}. \quad (18)$$

Equation (18) demonstrates that the solutions to the identified issue may be limited to the situation when the ambient media is non-rotating (i.e.  $v_0 = 0$  and  $w_0 = 0$ ).

Employing the Eq. (14), the governing apparatus of Eqs. (1)–(6) metamorphose into the consecutive apparatus of ODEs:

$$\frac{dD}{d\varpi} = \frac{1}{L} \left[ \{V - (n+1)\} 2VD - DV(V-1) - 2P - 2B(i+1) + \frac{2P(V-1) - 2B - (i-1)2BV}{\{V - (n+1)\}} + D\phi^2 \right], \quad (19)$$

$$\frac{dV}{d\varpi} = -\frac{[V - (n+1)]}{D} \frac{dD}{d\varpi} - \frac{2V}{\varpi}, \quad (20)$$

$$\frac{dP}{d\varpi} = \frac{\Gamma P}{D(1 - Z_1 D)} \frac{dD}{d\varpi} - \frac{2P(V-1)}{\varpi [V - (n+1)]}, \quad (21)$$

$$\frac{dB}{d\varpi} = \frac{2B + (i-1)2BV}{\varpi [V - (n+1)]} + \frac{2B}{D} \frac{dD}{d\varpi}, \quad (22)$$

$$\frac{d\phi}{d\varpi} = \frac{(1-2V)\phi}{\varpi [V - (n+1)]}, \quad (23)$$

$$\frac{d\psi}{d\varpi} = \frac{(1-V)\psi}{\varpi [V - (n+1)]}, \quad (24)$$

where

$$L = L(\varpi) = \frac{\varpi}{D(1 - Z_1 D)} \left[ \Gamma P + 2B(1 - Z_1 D) - (1 - Z_1 D) D \{V - (n+1)\}^2 \right]. \quad (25)$$

Employing Eq. (14), the transformed shock circumstances be

$$B(1) = \frac{C_a}{\beta^2} (n+1)^2 D(1) = \frac{1}{\beta}, \quad V(1) = (1 - \beta)(n+1),$$

$$P(1) = \left[ (1 - \beta) + C_a \left( 1 - \frac{1}{\beta^2} \right) + \frac{1}{\gamma M^2} \right] (n+1)^2. \quad (26)$$

$$\phi(1) = v_0 \left[ \frac{C U_0}{t_0^n (n+1)} \right]^{\frac{-1}{(n+1)}}, \quad \psi(1) = w_0 \left[ \frac{C U_0}{t_0^n (n+1)} \right]^{\frac{-1}{(n+1)}},$$

where  $\alpha = \lambda = -\delta$  was required to get the similarity solutions.

## 4 Isothermal Flow

In this part, we show the solution in respect of isothermal, cylindrically symmetric, perfect dust-pervade rotating gas flow having a magnetic field that might be alternatively axial or azimuthal. The issue's boundary circumstances are the shock circumstances (9), i.e. same as the scenario of adiabatic flow.

In respect of isothermal flow, Eq. (6) is rewritten as (see, Sahu [7, 17])

$$\frac{\partial T}{\partial r} = 0. \quad (27)$$

Equation (27), when combined using Eq. (14), yields

$$\frac{p}{p_2} = \frac{\rho(1 - Z_2)}{\rho_2(1 - Z)}. \quad (28)$$

Equation (27), when combined using Eqs. (14) and (26), presents a kind of a relationship connecting  $P$  and  $D$

$$P(\varpi) = \left[ (1 - \beta) + \frac{C_a(\beta^2 - 1)}{\beta^2} + \frac{1}{\gamma M^2} \right] \frac{(\beta - Z_1) D (n + 1)^2}{\varpi^2 [1 - Z_1] D}. \quad (29)$$

Employing the Eq. (14), the governing apparatus of equations and (27) metamorphose into the consecutive apparatus of ODE :

$$\frac{dD}{d\varpi} = \frac{1}{N} \left[ \{V - (n + 1)\} 2VD - DV(V - 1) - 2B(i + 1) - \frac{2B + (i - 1)2BV}{\{V - (n + 1)\}} + D\phi^2 \right], \quad (30)$$

where

$$N = N(\varpi) = \frac{\varpi}{D(1 - Z_1 D)} \left[ P + 2B(1 - Z_1 D) - (1 - Z_1 D) D \{V - (n + 1)\}^2 \right]. \quad (31)$$

For obtaining numerical results, it's suitable to compose variables  $u, v, w, p, \rho$  and  $h$  in the under-mentioned form (non-dimensional)

$$\begin{aligned} \frac{u}{u_2} &= \varpi \frac{V(\varpi)}{V(1)}, \quad \frac{v}{v_2} = \varpi \frac{\phi(\varpi)}{\phi(1)}, \quad \frac{w}{w_2} = \varpi \frac{\psi(\varpi)}{\psi(1)}, \\ \frac{p}{p_2} &= \varpi^2 \frac{P(\varpi)}{P(1)}, \quad \frac{\rho}{\rho_2} = \frac{Z}{Z_2} = \frac{D(\varpi)}{D(1)}, \quad \frac{h}{h_2} = \varpi^2 \frac{B(\varpi)}{B(1)}. \end{aligned} \quad (32)$$

Also, we have

$$V(\varpi_p) = n + 1. \quad (33)$$

## 5 Results and Discussion

The flow parameters distribution between  $\varpi = 1$  and  $\varpi = \varpi_p$  are decided by means of numerically integrating Eqs. (19)–(24) in respect of adiabatic flow as well as

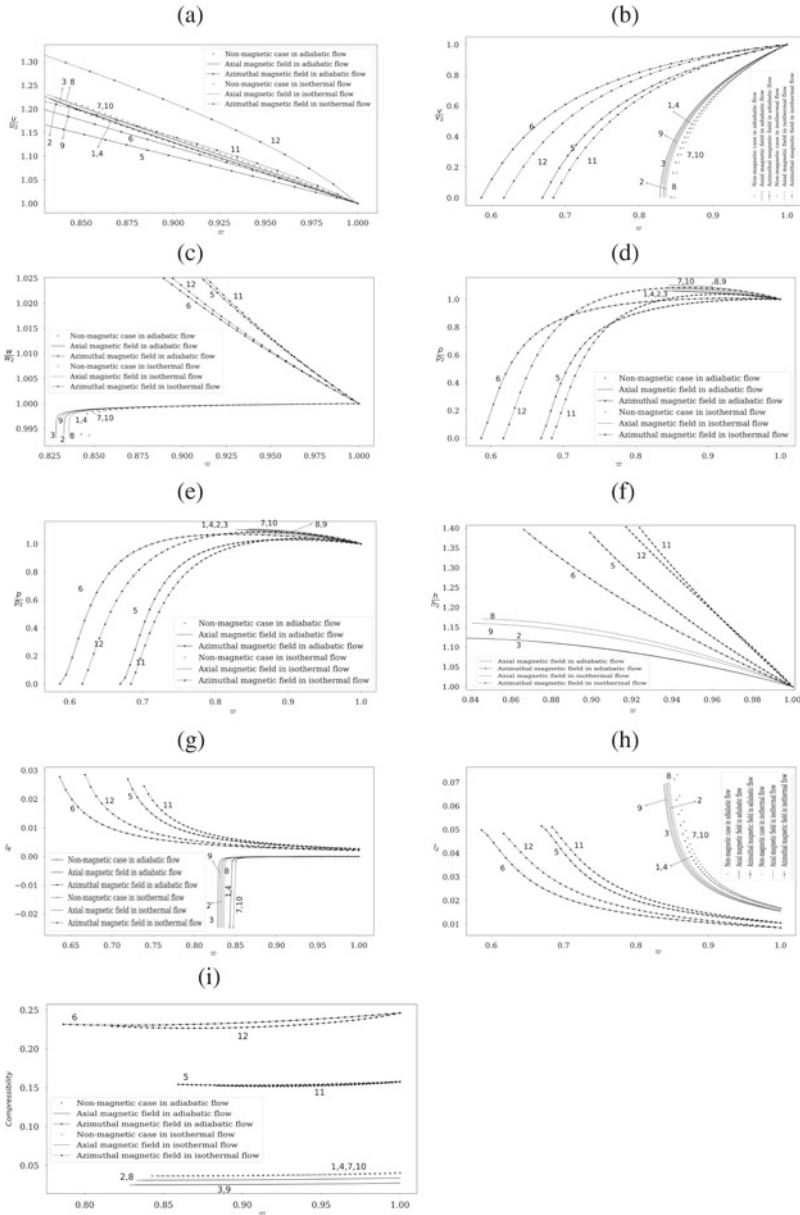


**Fig. 1** Variability of dust-pervade gas parameters at the back of the shock: **a** radial component of fluid velocity  $\frac{u}{u_2}$ , **b** azimuthal component of fluid velocity  $\frac{v}{v_2}$ , **c** axial component of fluid velocity  $\frac{w}{w_2}$ , **d** density  $\frac{\rho}{\rho_2}$ , **e** pressure  $\frac{p}{p_2}$ , **f** magnetic field  $\frac{h}{h_2}$ , **g** azimuthal component of vorticity vector  $l_\theta$ , **h** axial component of vorticity vector  $l_z$ , **i** compressibility : adiabatic ( $C_{adi}$ )  $p_1$ , and isothermal ( $\tau_{iso}$ )  $p_1$  (Reference Table 1 for further information on input variables)

**Table 1** Taking into account different aspects of  $i$  and  $C_a$  with  $\gamma = \frac{5}{3}$ ;  $\beta' = 1$ ;  $\chi_p = 0.1$ ;  $G_1 = 10$ ;  $n = -0.1$

$i$	$C_a$	$\beta$	$\varpi_p$	
			Adiabatic flow (Case No. in Fig. 1)	Isothermal flow (Case No. in Fig. 1)
0	0.0	0.300699	0.842824 (1)	0.847369 (7)
	0.01	0.309486	0.837828 (-)	0.841335 (-)
	0.02	0.317855	0.833051 (2)	0.835803 (8)
	0.03	0.325860	0.828462 (3)	0.830629 (9)
1	0.0	0.300699	0.842824 (4)	0.847369 (10)
	0.01	0.357026	0.755073 (-)	0.761960 (-)
	0.02	0.471998	0.669336 (5)	0.684021 (11)
	0.03	0.585440	0.586502 (6)	0.617276 (12)

by means of Eqs. (20), (22)–(24), (30) in respect of isothermal flow with (26, 33) using fourth-order Runge-Kutta method. The extant work is also the enhancement of Nath’s [3, 12] works recognising the consequences of dust particles or magnetic fields respectively in perfect dust-pervade gas. Figure 1 shows that the procured solution is in nice concurrence with the established solutions of Nath [3, 12].

### 5.1 Efficacy of the Existence of the Magnetic Field Is as Adhere

By enhancing the value of  $C_a$ ; the extent between expansive region and shock as well as  $\beta$  enhances (see Table 1). Physically it approaches that the gas at the back of the shock contracted lower, i.e. the shock strength reduces in the existence of both azimuthal or axial magnetic fields.  $\frac{u}{u_2}$  enhances while moving inside towards expansive region through shock, though, it reduces in the existence of axial magnetic field for an isothermal flow.  $\frac{v}{v_2}$  enhances, but to reduce  $\frac{h}{h_2}$  and  $l_{z^*}$  while moving inside towards expansive region through shock.  $\frac{w}{w_2}$  and  $l_\theta$  enhance, but to reduce  $\frac{\rho}{\rho_2}$ ,  $\frac{p}{p_2}$ ,  $(C_{adi}) p_1$ , and  $(\tau_{iso}) p_1$  in the existence of axial magnetic field; though, inverted conduct is executed in the existence of azimuthal magnetic field (see Fig. 1).

### 5.2 The Differences of Adiabatic and Isothermal Motions

It is obvious through Table 1 that  $\varpi_p$  in isothermal flow is bigger than  $\varpi_p$  in adiabatic flow. Physically, it indicates that the gas is condensed further in isothermal flow than

in adiabatic flow. As a result, the shock strength is greater for isothermal flow than in the adiabatic flow.

## 6 Conclusions

On the ground of the aforementioned work, the succeeding conclusions could be sketched:

- (i) Investigation of shock expansion in the existence of the magnetic field in an ideal dust-pervade gas through adiabatic and isothermal flows for cylindrical shock, has not been made previously.
- (ii) The supposition of a constant temperature difference eliminates the discontinuities that occur in the scenario of adiabatic flow.
- (iii) The azimuthal magnetic field contemplation produces outstanding distinction in the flow variables distribution.
- (iv) In the attendance of magnetic field the density and pressure evanesce at the expansive region and therefore void is constituted at the symmetry's centre.

**Acknowledgements** The author is thankful to **Prof. M. K. Verma**, Department of Physics, Indian Institute of Technology Kanpur, Kanpur–208016, India for fruitful discussions. This work was supported by the research grant no. **TAR/2018/000150** under **Teachers Associateship for Research Excellence (TARE)** scheme from the **Science and Engineering Research Board (SERB)**, India. The author gracefully acknowledges financial support from **SERB**.

## References

1. Hartmann, L.: *Accretion Processes in Star Formation*. Cambridge University Press, Cambridge (1998)
2. Balick, B., Frank, A.: Shapes and shaping of planetary nebulae. *Ann. Rev. Astron. Astrophys.* **40**(1), 439–486 (2002)
3. Nath, G.: Magnetogasdynamic shock wave generated by a moving piston in a rotational axisymmetric isothermal flow of perfect gas with variable density. *Adv. Space Res.* **47**(9), 1463–1471 (2011)
4. Nath, G., Sahu, P.K.: Flow behind an exponential shock wave in a rotational axisymmetric perfect gas with magnetic field and variable density. *SpringerPlus* **5**(1), 1–18 (2016)
5. Nath, G., Sahu, P.K., Chaurasia, S.: Modelling. *Measur. Control B* **87**(4), 236–243 (2018)
6. Nath, G., Sahu, P.K., Chaurasia, S.: Self-similar solution for the flow behind an exponential shock wave in a rotational axisymmetric non-ideal gas with magnetic field. *Chin. J. Phys.* **58**, 280–293 (2019)
7. Sahu, P.K.: Shock wave driven out by a piston in a mixture of a non-ideal gas and small solid particles under the influence of azimuthal or axial magnetic field. *Braz. J. Phys.* **50**(5), 548–565 (2020)
8. Sahu, P.K.: Magnetogasdynamic exponential shock wave in a self-gravitating, rotational axisymmetric non-ideal gas under the influence of heat-conduction and radiation heat-flux. *Ricerche di Matematica* 1–37 (2021)



9. Sahu, P.K.: The influence of magnetic and gravitational fields in a non-ideal dusty gas with heat conduction and radiation heat flux. *Indian J. Phys.* 1–15 (2022)
10. Verma, M.K.: Statistical theory of magnetohydrodynamic turbulence: recent results. *Phys. Rep.* **401**(5–6), 229–380 (2004)
11. Levin, V.A., Skopina, G.A.: Detonation wave propagation in rotational gas flows. *J. Appl. Mech. Tech. Phys.* **45**(4), 457–460 (2004)
12. Nath, G.: Self-similar solution of cylindrical shock wave propagation in a rotational axisymmetric mixture of a non-ideal gas and small solid particles. *Meccanica* **47**(7), 1797–1814 (2012)
13. Nath, G., Sahu, P.K., Dutta, M.: Magnetohydrodynamic cylindrical shock in a rotational axisymmetric non-ideal gas under the action of monochromatic radiation. *Proc. Eng.* **127**, 1126–1133 (2015)
14. Nath, G., Sahu, P.K.: Unsteady adiabatic flow behind a cylindrical shock in a rotational axisymmetric non-ideal gas under the action of monochromatic radiation. *Proc. Eng.* **144**, 1226–1233 (2016)
15. Nath, G., Sahu, P.K.: Flow behind an exponential shock wave in a rotational axisymmetric non-ideal gas with conduction and radiation heat flux. *Int. J. Appl. Comput. Math.* **3**(4), 2785–2801 (2017)
16. Nath, G., Sahu, P.K.: Similarity solution for the flow behind a cylindrical shock wave in a rotational axisymmetric gas with magnetic field and monochromatic radiation. *Ain Shams Eng. J.* **9**(4), 1151–1159 (2018)
17. Sahu, P.K.: Propagation of an exponential shock wave in a rotational axisymmetric isothermal or adiabatic flow of a self-gravitating non-ideal gas under the influence of axial or azimuthal magnetic field. *Chaos Solitons Fractals* **135**, 109739 (2020)
18. Sahu, P.K.: Shock wave propagation in perfectly conducting rotational axisymmetric two-phase medium with increasing energy under the action of heat conduction and radiation heat flux. *Chin. J. Phys.* **72**, 176–190 (2021)
19. Sahu, P.K.: Flow behind the magnetogasdynamic cylindrical shock wave in rotating non-ideal dusty gas with monochromatic radiation. *Plasma Res. Exp.* **3**(4), 045004 (2021)
20. Pai, S.I., Menon, S., Fan, Z.Q.: Similarity solutions of a strong shock wave propagation in a mixture of a gas and dusty particles. *Int. J. Eng. Sci.* **18**(12), 1365–1373 (1980)
21. Higashino, F., Suzuki, T.: The effect of particles on blast waves in a dusty gas. *Zeitschrift für Naturforschung A* **35**(12), 1330–1336 (1980)
22. Miura, H., Glass, I.I.: *Proc. R. Soc. Lond. A. Math. Phys. Sci.* **397**, 295–309 (1985)
23. Popel, S.I., Gisko, A.A.: *Nonlinear Process. Geophys.* **13**, 223–229 (2006)
24. Pai, S.I.: *Two-Phase Flows*, vol. 3. Springer (2013)
25. Nath, G., Sahu, P.K.: Self-similar solution of a cylindrical shock wave under the action of monochromatic radiation in a rotational axisymmetric dusty gas. *Commun. Theor. Phys.* **67**(3), 327 (2017)
26. Nath, G., Sahu, P.K.: Propagation of a cylindrical shock wave in a mixture of a non-ideal gas and small solid particles under the action of monochromatic radiation. *Combust. Explos. Shock Waves* **53**(3), 298–308 (2017)
27. Sahu, P.K.: Self-similar solution of spherical shock wave propagation in a mixture of a gas and small solid particles with increasing energy under the influence of gravitational field and monochromatic radiation. *Commun. Theor. Phys.* **70**(2), 197 (2018)
28. Sahu, P.K.: Analysis of magnetogasdynamic spherical shock wave in dusty real gas with gravitational field and monochromatic radiation. *Eur. Phys. J. Plus* **136**(4), 1–19 (2021)
29. Sedov, L.I.: *Similarity and dimensional methods in mechanics*. Academic Press, New York (1959)
30. Laumbach, D.D., Probstein, R.F.: Self-similar strong shocks with radiation in a decreasing exponential atmosphere. *Phys. Fluids* **13**(5), 1178–1183 (1970)
31. Vishwakarma, J.P., Pandey, S.N.: Propagation of strong spherical shock waves in a dusty gas. *Phys. Scripta* **68**(4), 259 (2003)
32. Steiner, H., Hirschler, T.: A self-similar solution of a shock propagation in a dusty gas. *Eur. J. Mech. B Fluids* **21**(3), 371–380 (2002)

33. Zel'Dovich, Y.B., Raizer, Y.P.: *Physics of shock waves and high-temperature hydrodynamic phenomena*. Courier Corporation (2002)
34. Freeman, R.A., Craggs, J.D.: Shock waves from spark discharges. *J. Phys. D Appl. Phys.* **2**(3), 421 (1969)
35. Sahu, P.K.: Similarity solution for a spherical shock wave in a non-ideal gas under the influence of gravitational field and monochromatic radiation with increasing energy. *Math. Methods Appl. Sci.* **42**(14), 4734–4746 (2019)
36. Sahu, P.K.: Similarity solution for the flow behind an exponential shock wave in a rotational axisymmetric non-ideal gas under the influence of gravitational field with conductive and radiative heat fluxes. In: *International Conference on Innovation in Modern Science and Technology*, pp. 1060-1070. Springer, Cham (2019)
37. Sahu, P.K.: Unsteady flow behind an MHD exponential shock wave in a rotational axisymmetric non-ideal gas with conductive and radiative heat fluxes. In: *International Conference on Innovation in Modern Science and Technology*, pp. 1049–1059. Springer, Cham (2019)

# Structural Variations of Ion-Acoustic Solitons



Hirak Jyoti Dehingia  and P. N. Deka 

**Abstract** In this paper, we have presented our investigation on the variation in the structure of ion-acoustic solitons due to variation of densities in the presence of isothermal electrons in the plasma. We have considered the standard ion density profile and its variations and studied the effects of density variation on solitons. We have considered the governing fluid equations of plasma and derived the modified Kadomtsev–Petviashvili (KP) equation using the reductive perturbation technique (RPT). The solution of the KP equation indicates the variation in soliton structures.

**Keywords** Ion-acoustic solitons · Inhomogeneous plasma · Isothermal electrons

## 1 Introduction

Solitons or solitary waves are special wave packets or self-reinforcing waves that maintain their shape during their propagation at a constant speed. Solitons are formed by canceling the nonlinear and dispersive effects in the respective medium. Washimi and Taniuti [1] started extensively exploring the Korteweg de-Vries equation (KdV) for describing ion-acoustic solitons. Then, Nishikawa and Kaw [2] considered the inhomogeneous plasmas for studying ion-acoustic soliton propagation for the first time. Kuehl [3] has investigated the reflection of ion-acoustic solitons theoretically. He concluded that there were some changes in the amplitudes of both reflected and incident solitons. Later, Kuehl and Imen [4] studied soliton propagations in inhomogeneous plasmas considering the set of fluid equations. Nejoh [5] has investigated the various effects of ion temperature on the characteristics of soliton propagation in collisionless, inhomogeneous relativistic plasmas. Singh and Dahiya [6] extended the theory of the KdV equation by using the Reductive Perturbation Technique (RPT) in inhomogeneous plasmas. A Large member of the plasma physics community has studied soliton and their other characteristics in various physical situations. Some of

---

H. J. Dehingia (✉) · P. N. Deka  
Department of Mathematics, Dibrugarh University, Dibrugarh 786004, Assam, India  
e-mail: [hirakjyotidehingia1@gmail.com](mailto:hirakjyotidehingia1@gmail.com)

© The Author(s), under exclusive license to Springer Nature Switzerland AG 2022  
S. Banerjee and A. Saha (eds.), *Nonlinear Dynamics and Applications*,  
Springer Proceedings in Complexity,  
[https://doi.org/10.1007/978-3-030-99792-2\\_8](https://doi.org/10.1007/978-3-030-99792-2_8)

the authors have studied soliton propagation in inhomogeneous plasma in the presence of finite ion temperature [7, 8], negative ions [9–12], dust effect [13], etc. Singh and Malik investigated the energy of solitons at both the critical and noncritical densities for negative ions under the influence of magnetized warm plasmas [14]. Hellberg and Verheest studied ion-acoustic solitary waves in inhomogeneous plasmas in the presence of two-temperature ions [15]. Baluku et al. studied dust ion-acoustic solitary waves in inhomogeneous plasmas under the influence of  $\kappa$ -distributed electrons [16]. Later, Kakad et al. [17] investigated experimentally the chain formation and validation of nonlinear fluid theory on ion-acoustic solitary waves in magnetized electron–ion plasmas. Gogoi and Deka [18] have studied the solitary waves for weakly inhomogeneous plasmas in the presence of nonthermal electrons. Mukherjee et al. [19] studied soliton bending for weak and slowly varying inhomogeneous unmagnetized plasmas. Again, Gogoi and Deka [20] studied the dust acoustic solitary wave’s propagation in inhomogeneous plasmas in the presence of dust charge fluctuations. Zhou and Hutchinson investigated the motion of slow electron holes associated with one-dimensional ion-acoustic solitary waves [21]. Wang et al. studied the numerical simulation of dark envelope solitary waves in electron–ion plasmas. They concluded that the plasma waves are not described in the linear superposition of modes. They are described in the mode of nonlinear dynamical waves [22]. Later, Shi et al. studied the nonlocal Kundu-nonlinear Schrödinger equation (Kundu-NLS) for investigating the dynamics of solitary wave solutions which is obtained from coupled Kundu-NLS system [23]. Song et al. studied the various recent progress of solitons or solitary waves in optical fiber lasers [24]. Rani and Yadav studied the nonlinear propagation of electron acoustic solitary waves in the presence of dense magnetized plasma under the effect of degenerate quantum electrons [25]. Chen et al. investigated the dynamics of solitary waves in quantum plasmas with nonlinear effects and higher-order dispersion [26]. Prayitno and Budi studied the energy solution of solitary waves numerically in the KdV equation [27]. Lu and Liu investigated some ion-acoustic solitary waves having small amplitude with regularized  $\kappa$ -distributed electrons [28]. Then by using the inverse scattering method, Wu studied Kadomtsev–Petviashvili (KP) perturbed multi-line solitons [29]. Recently, the dust ion-acoustic solitary waves and double layers were studied [30] in the presence of adiabatic positive dust grains, ion species, and Cairns-distributed electrons. Thus, understanding the present importance of soliton study in different astrophysical situations, we have considered our investigation on the structural variations of ion-acoustic solitons due to variation of densities in the presence of isothermal electrons plasmas.

## 2 Governing Equations and Derivations

Let us consider two-dimensional, unmagnetized, collisionless inhomogeneous plasma consisting of cold and hot isothermal electrons. The dimensionless ion continuity equation and momentum equation, along with Poisson’s equation and the equation for electron Boltzmann distribution, is taken as follows:

$$\left. \begin{aligned} \frac{\partial n}{\partial t} + \frac{\partial(nu_x)}{\partial x} + \frac{\partial(nu_y)}{\partial y} &= 0 \\ \frac{\partial u_x}{\partial t} + u_x \frac{\partial u_x}{\partial x} + u_y \frac{\partial u_x}{\partial y} + \frac{\partial \emptyset}{\partial x} &= 0 \\ \frac{\partial u_y}{\partial t} + u_x \frac{\partial u_y}{\partial x} + u_y \frac{\partial u_y}{\partial y} + \frac{\partial \emptyset}{\partial y} &= 0 \\ \frac{\partial^2 \emptyset}{\partial x^2} &= n_e - n \\ n_e &= e^{\emptyset} \end{aligned} \right\} \quad (1)$$

To study ion-acoustic solitary waves and their propagation in inhomogeneous plasmas, we have considered the following two dimensional stretched coordinates [19]:

$$\eta = \epsilon^{3/2}x, \lambda = \epsilon y, \xi = \epsilon^{1/2}(x - Vt) \quad (2)$$

where  $V$  is a constant or the phase velocity of the normalized wave, normalized by ion-acoustic speed  $C_s$ ,  $\epsilon$  is an expansion parameter.

We consider the plasma model [19] in which unperturbed number density for ions of the form  $\tilde{n}_0(\eta) = 1 + \delta f_0(\eta)$ , where  $\delta$  is a very small parameter. To use the Reductive Perturbation Technique (RPT) method for the small expansion parameter  $\epsilon$  we use some expanded variables are follows

$$\left. \begin{aligned} n &= 1 + \epsilon\{f_0(\eta) + n_1(\eta, \gamma, \xi)\} + \epsilon^2 n_2(\eta, \gamma, \xi) + \dots \\ \phi &= \epsilon\{f_0(\eta)2c_1^2 + \phi_1(\eta, \gamma, \xi)\} + \epsilon^2 \phi_2(\eta, \gamma, \xi) + \dots \\ u_x &= c_1 + \epsilon\{u_1(\eta, \gamma, \xi) - c_1 f_0(\eta)\} + \epsilon^2 u_2(\eta, \gamma, \xi) + \dots \\ u_y &= \epsilon^{3/2} v_1(\eta, \gamma, \xi) + \epsilon^{5/2} v_2(\eta, \gamma, \xi) + \dots \end{aligned} \right\} \quad (3)$$

After using the set of stretched coordinates referred by Eq. (2) and expanded variables referred by Eq. (3) in the governing Eq. (1) we get some sets of equations. Then the coefficients of various powers of  $\epsilon$  are compared. After evaluating and combining the new set of equations, will generate an equation is of the form

$$\frac{\partial}{\partial \xi} \left[ A \frac{\partial n_1}{\partial \eta} + 2n_1 \frac{\partial n_1}{\partial \xi} + \frac{\partial^3 n_1}{\partial \xi^3} \right] + \frac{\partial^2 n_1}{\partial \lambda^2} - 2c_1 f_0 \frac{\partial^2 n_1}{\partial \xi^2} = 0 \quad (4)$$

Here  $A$  is a constant,  $c_1 = \frac{1}{\sqrt{2}}$  and Eq. (4) is a modified KP equation. But the last extra term arises in Eq. (4) due to inhomogeneity.

Now, let us consider a new frame of reference  $X = \xi + p(\eta)$ ,  $Y = \lambda$ ,  $T = \eta$  where  $p(\eta) = \frac{1}{\sqrt{2+1}} \int f_0(\eta) d\eta$ . Using this new frame of reference Eq. to (4) we get the modified form of KP equation is

$$\frac{\partial}{\partial X} \left[ \frac{\partial S}{\partial \tau} + 6S + \frac{\partial S}{\partial X} + \frac{\partial^3 S}{\partial X^3} \right] + \frac{\partial^2 S}{\partial Y^2} = 0 \quad (5)$$

The solution of the above modified KP equation i.e., Eq. (5) will give the soliton solutions. In the new co-ordinate  $X$ , the structural variations of the soliton solutions can be seen due to the presence of  $p(\eta)$  which is related to  $f_0(\eta)$ .

### 3 Results

The one soliton solution of (5) is given by [31]

$$S = \frac{k_1^2}{2} \operatorname{sech}^2 \left[ \frac{1}{2} \left( k_1 X + m_1 Y - \frac{k_1^4 + m_1^2}{k_1} \right) \right]$$

$$\Rightarrow n_1 = \frac{3k_1^2}{2} \operatorname{sech}^2 \left[ \frac{1}{2} \left( k_1 \xi + k_1 p(\eta) + m_1 \lambda - \frac{k_1^4 + m_1^2}{k_1 \sqrt{2}(\sqrt{2} + 1)} \eta \right) \right] \quad (6)$$

where  $k_1$  and  $m_1$  are arbitrary constants.

Similarly, two soliton solution of Eq. (4) is given by [31]

$$S = 2 \frac{\partial^2}{\partial \xi^2} (\ln C)$$

$$\Rightarrow n_1 = 6 \frac{\partial^2}{\partial \xi^2} (\ln C) \quad (7)$$

where

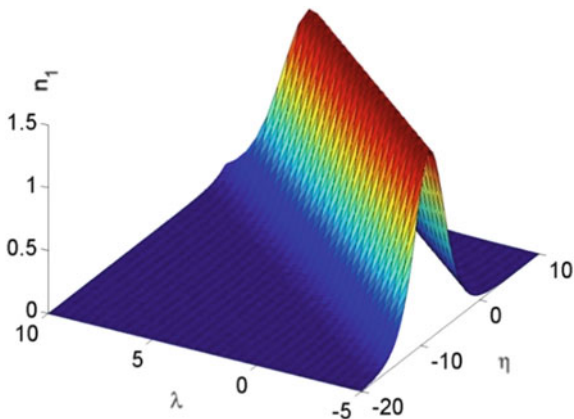
$$C = 1 + e^{\eta_1} + e^{\eta_2} + B e^{\eta_1 + \eta_2}, \quad B = \frac{(K_1 - K_2)^2 - (M_1 - M_2)^2}{(K_1 + K_2)^2 - (M_1 - M_2)^2}$$

$$\eta_1 = K_1 \left[ \xi + p(\eta) + \sqrt{3} M_1 \lambda - \frac{(K_1^2 + 3M_1^2)}{(2 + \sqrt{2})} \eta \right],$$

$$\eta_2 = K_2 \left[ \xi + p(\eta) + \sqrt{3} M_2 \lambda - \frac{(K_2^2 + 3M_2^2)}{(2 + \sqrt{2})} \eta \right]$$

where  $K_1, K_2, M_1,$  and  $M_2$  are arbitrary constants. The structural variations of a soliton will take place due to the presence of inhomogeneous ion number density and the term  $p(\eta)$ , which is related to  $f_0(\eta)$ . The inhomogeneities will be different based on the various choices of  $f_0(\eta)$ . So, for the trivial choice of  $f_0$ , i.e.,  $f_0 = 0$ , the inhomogeneous ion number density profile will reproduce the homogenous line

**Fig. 1** Picture of one soliton solution given by Eq. (6) at  $f_0 = 0$ , representing a homogeneous line soliton solution reproduced from the chosen Inhomogeneous plasmas or ion number density



soliton, shown in Fig. 1. Similarly, the structural variations of one soliton solution will also be seen based on the various choices of  $f_0(\eta)$ , which are shown in Fig. 2. The different structural variations for two soliton solutions can also be observed by considering  $f_0 = 0$  and based on the various choices of  $f_0(\eta)$ . Here, the graphical interpretations of the two soliton solutions are not presented in this work.

Now to investigate how many structural variations of a soliton will occur or what condition the structural variations will be seen.

In the case of one soliton solution given by Eq. (6), for the static case, i.e.,  $\xi = 0$ , the locus of maximum amplitude is of from

$$k_1 p(\eta) + m_1 \lambda - \frac{k_1^4 + m_1^2}{k_1 \sqrt{2}(\sqrt{2} + 1)} \eta = 0$$

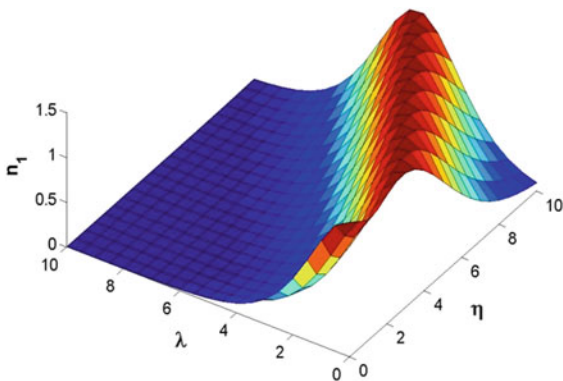
Then for some chosen  $k_1, m_1$ , we have

$$\frac{du}{d\eta} = \frac{df_0}{d\eta} \tag{8}$$

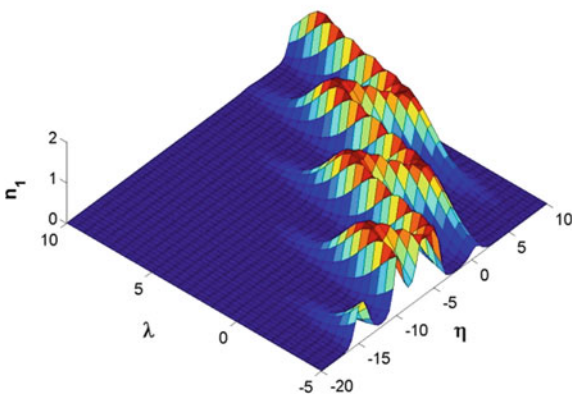
where  $u = \frac{d\lambda}{d\eta}$  is the slope for the locus of the maximum amplitude. The above Eq. (8) implies the larger variation of soliton structures in the larger rate of slope variation. Hence for the larger variation of soliton structures, RHS of Eq. (8) must be larger, i.e., the first-order derivative of  $f_0$  w.r.t.  $\eta$  also must be immense. So we can choose some functional forms of  $f_0$  to show the variations of various soliton structures.

In Fig. 2a, we have seen that if we increase the amplitude of  $f_0$ , then the structure of the soliton will be more deformed and will cause larger bending. Again, if we decrease the amplitude of  $f_0$ , then the structural variations of the solitons will be seen relatively less. Similarly, we can also observe similar things in Fig. 2b, where the sum of sine and cosine functions goes more rapidly. Also, based on the increasing/decreasing wave vector of  $f_0$ , the soliton will cause mores/less deformed. Thus based on both

**Fig. 2** For some chosen  $k_1, m_1, K_1, K_2$ , and  $\xi = 0$ , various functional forms of  $f_0(\eta)$  are considered above to show the structural variations of solitons by changing the phase of the solitary waves



(a) One soliton for  $f_0 = \tanh(\eta)$



(b) One soliton for  $f_0 = \sin\eta + \cos\eta$

amplitude and wave vector of  $f_0$ , the first-order derivative of  $f_0$  will increase/decrease and will case the structural variations of soliton in the more/less amount. Hence, some similar conclusions can also be given for various choices of  $f_0(\eta)$ .

Thus in this work, the structural variations of solitons are presented analytically. The structural variations are shown based on the dependency of  $f_0$ , is related to the ion number density for inhomogeneous plasmas. For the above investigations, here exactly the KP Eq. (5) is solved for the propagation of ion-acoustic soliton in two-dimensional inhomogeneous plasmas. As we have transformed the derived Eq. (4) into a standard, modified KP Eq. (6) with constant coefficient, we have seen that the phase modifications for each and every solution was controlled by the function  $f_0$ , which causes the structural modifications of the soliton solutions in the two-dimensional plane. Here the amplitude of the soliton solution is unchanged.



## 4 Conclusion

We have studied the ion-acoustic solitary waves in inhomogeneous unmagnetized plasmas in the presence of cold and hot isothermal electrons. During these investigations, we have solved the modified KP equation to understand the structural variations of soliton in the presence of the above-considered model. In solving the modified KP equation, we have seen the phase of the solitary wave solution gets modified by the function  $f_0(\eta)$ . Under the above considerations and constant amplitude, some structural variations of the soliton are seen accordingly. The study on the structural variation of soliton inhomogeneous plasmas is a very important feature like the other important features propagation, transmission, reflection, etc. In our future work, we wish to study the structural variations of soliton in inhomogeneous plasmas in the presence of magnetic field and dust effect.

## References

1. Washimi, H., Taniuti, T.: Propagation of ion-acoustic solitary waves of small amplitude. *Phys. Rev. Lett.* **17**, 996–998 (1966)
2. Nishikawa, N., Kaw, K.: Propagation of solitary ion-acoustic waves in inhomogeneous plasmas. *Phys. Lett.* **50**(A), 455–456 (1975)
3. Kuehl, H.H.: Reflection of an ion-acoustic soliton by plasma inhomogeneities. *Phys. Fluids* **26**(6), 1577–1583 (1983)
4. Kuehl, H.H., Imen, K.: Finite amplitude ion-acoustic solitons in weakly inhomogeneous plasmas. *Phys. Fluids* **28**, 2375–2381 (1985)
5. Nejoh, Y.: The effect of the ion temperature on the ion-acoustic solitary waves in a collisionless relativistic plasma. *J. Plasma Phys.* **37**(3), 487–495 (1987)
6. Singh, S., Dahiya, R.P.: Effect of ion temperature and plasma density on an ion-acoustic soliton in a collisionless relativistic plasma: an application to radiation belts. *Phys. Fluids B* **2**(5), 901–906 (1990)
7. Singh, S., Dahiya, R.P.: Effect of zeroth-order density inhomogeneity on ion-acoustic soliton reflection in a finite ion temperature plasma. *Phys. Fluids B* **3**(1), 255–258 (1991)
8. Singh, S., Dahiya, R.P.: Propagation characteristics and reflection of an ion-acoustic soliton in an inhomogeneous plasma having warm ions. *J. Plasma Phys.* **41**(1), 185–197 (1989)
9. Malik, H.K., Dahiya, R.P.: Ion acoustic solitons in finite ion temperature inhomogeneous plasmas having negative ions. *Phys. Plasmas* **1**(9), 2872–2875 (1994)
10. Singh, D.K., Malik, H.K.: Soliton reflection in a negative ion containing plasma: Effect of magnetic field and ion temperature. *Phys. Plasmas* **13**(8), 082104(1–10) (2006)
11. Chauhan, S.S., Malik, H.K., Dahiya, R.P.: Reflection of ion acoustic solitons in a plasma having negative ions. *Phys. Plasmas* **3**(11), 3932–3938 (1996)
12. Singh, D.K., Malik, H.K.: Modified Korteweg-de Vries soliton evolution at critical density of negative ions in an inhomogeneous magnetized cold plasma. *Phys. Plasmas* **14**(6), 062113 (2007)
13. Xiao, D., Ma, J. X., Li, Y., Xia, Y., Yu, M. Y.: Evolution of nonlinear dust-ion-acoustic waves in an inhomogeneous plasma. *Phys. Plasmas* **13**(5), 052308(1–7) (2006)
14. Singh, D.K., Malik, H.K.: Modified Korteweg-de Vries soliton evolution at critical density of negative ions in an inhomogeneous magnetized cold plasma. *Phys. Plasmas* **14**(6), 112103(1–8) (2007)

15. Hellberg, M.A., Verheest, F.: Dust acoustic solitons in plasmas with kappa-distributed electrons and/or ions. *Phys. Plasmas* **15**(12), 062307(1–11) (2008)
16. Baluku, T.K., Hellberg, M.A., Kourakis, I., Saini, N.S.: Dust ion acoustic solitons in a plasma with kappa-distributed electrons. *Phys. Plasmas* **17**(5), 053702(1–11) (2010)
17. Kakad, A., Omura, K., Kakad, B.: *Phys. Plasmas* **20**(6), 062103(1–13) (2013)
18. Gogoi, L.B., Deka, P.N.: Solitary waves in weakly inhomogeneous plasma with nonthermal electrons. *Int. J. Appl. Eng. Res.* **93**(1), 51–64 (2015)
19. Mukherjee, A., Janaki, M.S., Kundu, A.: Bending of solitons in weak and slowly varying inhomogeneous plasma. *Phys. Plasmas* **22**(12), 122114(1–7) (2015)
20. Gogoi, L.B., Deka, P.N.: Propagation of dust acoustic solitary waves in inhomogeneous plasma with dust charge fluctuations. *Phys. Plasmas* **24**(3), 033708(1–6) (2017)
21. Zhou, C., Hutchinson, I.H.: Dynamics of a slow electron hole coupled to an ion-acoustic soliton. *Phys. Plasmas* **25**(3), 0823039(1–13) (2018)
22. Wang, F.P., Zhang, J.F., Gao, D.N., Li, Z.Z., Duan, W. S., Zhang, H.: Numerical simulation of dark envelope soliton in plasma. *Phys. Plasmas* **25**(3), 032121(1–6) (2018)
23. Shi, X., Li, J., Wu, C.: Dynamics of soliton solutions of the nonlocal Kundu-nonlinear Schrödinger equation. *Chaos* **29**, 023120(1–12) (2019)
24. Song, Y., Shi, X., Wu, C., Zhang, H.: Recent progress of study on optical solitons in fiber lasers. *Appl. Phys. Rev.* **6**, 021313(1–20) (2019)
25. Rani, N., Yadav, M.: Propagation of nonlinear electron acoustic solitons in magnetized dense plasma with quantum effects of degenerate electrons. In: *AIP Conference Proceedings*, vol. 2352, pp. 030008(1–8). AIP Publishing (2020)
26. Chen, C., Pan, Y., Guo, J., Wang, Y., Gao, G., Wang, W.: Soliton dynamics for quantum systems with higher-order dispersion and nonlinear interaction. *AIP Adv.* **10**, 065313(1–4) (2020)
27. Prayitno, T.B., Budi, E.: Numerical calculation on energy of static soliton solution for KdV equation. In: *AIP Conference Proceedings 2021, 9th National Physics Seminar*, vol. 2320, pp. 050014(1–3). AIP Publishing, Jakarta (2021)
28. Lu, F.F., Liu, S.Q.: Small amplitude ion-acoustic solitons with regularized  $\kappa$ -distributed electrons. *AIP Adv.* **11**, 085223(1–5) (2021)
29. Wu, D.: The direct scattering problem for perturbed Kadomtsev–Petviashvili multi line solitons. *J. Math. Phys.* **62**, 091513(1–19) (2021)
30. Mushinzimana, X., Nsengiyumva, F., Yadav, L.L., Baluku, T.K.: Dust ion acoustic solitons and double layers in a dusty plasma with adiabatic positive dust, adiabatic positive ion species, and Cairns-distributed electrons. *AIP Adv.* **12**, 015208(1–10) (2022)
31. Wazwaz, A.M.: Multiple-soliton solutions for the KP equation by Hirota’s bilinear method and by the tanh–coth method. *Appl. Math. Comput.* **190**, 633 (2007)

# Effect of Kappa Parameters on the Modulational Instability in a Polarized Dusty Plasma



A. Abdikian 

**Abstract** In this paper, we have studied the propagation of dust-acoustic modulated waves in the polarized dusty plasmas. The distributions of electrons and ions are Boltzmann and Kappa, respectively. We have used the reductive perturbation method (RPM) to find out the nonlinear amplitude modulation of dust-acoustic waves in an unmagnetized collisionless polarized dusty plasma and a modified nonlinear Schrodinger equation governing the evolution of the dust-acoustic envelope waves has been derived. The effects of the Kappa parameter on the modulational instability (MI) was discussed by using the numerical values. It is found that increasing the value of  $\kappa$  causes to increase the value of the dispersion relation and the group velocity. It was shown that the MI maximum growth rate firstly increases and then decreases as the mentioned plasma parameter increases.

**Keywords** Polarized dusty plasmas · Modulational instability · Nonlinear Schrodinger equation

## 1 Introduction

Over the last decade, the study of dusty plasma was an important issue among researchers because of its applications in variety environments from interstellar space to laboratory plasma systems [1]. A dusty plasma defined as a common plasma with massive dust grains in it. The presence of these additional charged particles can remarkably change the characteristics and behaviors of a plasma [2, 3] and new low frequency dust mode so-called “dust-acoustic wave” (DAW) give rise. DAW would be due to the restoring force provided by the plasma thermal pressure while the inertia is due to the dust mass [4].

The polarization force is one of the important forces that change the linear and nonlinear dust dynamics and studies on it are increasing [5]. Physically, the polarization

---

A. Abdikian (✉)

Department of Physics, Malayer University, Malayer, 65719-95863, Iran  
e-mail: [abdykian@gmail.com](mailto:abdykian@gmail.com)

force comes from the deformation of the spherical Debye screening of the dusty grains and it is defined as [6, 7]

$$\mathbf{F}_p = -\frac{q_d^2}{2\lambda_D^2}\nabla\lambda_D, \quad (1)$$

where  $q_d$  is the grain charge and  $\lambda_D = \lambda_{Di}/\sqrt{1 + n_e T_i/n_i T_e}$  is the linearized Debye radius with the ion Debye radius  $\lambda_{Di} = \epsilon_0 k_B T_i/(e^2 n_i)$ , and  $T_{i(e)}$  is the ion (electron) temperature and  $n_{i(e)}$  is the ion (electron) number density. It has been shown that the linear dispersions and nonlinear peculiarities of the DAWs have been modified by polarization force [8, 9]. Khrapak et al. [8] found that the wave phase velocity would be decreased in the presence of the polarization effect. Recently, considering a system of dusty plasma including the negatively charged dust, Maxwellian and superthermally distributed for electrons and ions respectively, [10], Singh et al. have reported the impact of polarization force on dust-acoustic cnoidal waves. They found that an increase in superthermality index of ions leads to a decrease in polarization parameter. Very recently, the importance of the consideration of nonthermally polarization force on modulational instability (MI) of dust acoustic waves was investigated theoretically by Singh and Saini [11]. By supposing a dusty plasma system with negatively charged dust, Maxwellian and Cairns' nonthermal distributed for electrons and ions respectively, they have studied the evolution of DA breathers, namely rogue waves. The standard reductive perturbation method (RPM) is generally applied to obtain a nonlinear Schrodinger (NLS) equation. the Peregrine soliton is the analytical solution of the NLS equation [13]. The Peregrine solitary wave is a significant collective behavior in plasma, since it can be described as an rogue waves [14, 15]. The modulational instability (MI) of several plasma modes is amount of interest in studying because the wave propagation stability depend on its relevance [12, 16, 17]. The kappa distribution function, which represents superthermal particles, was first proposed by Vasyliunas [18]. This distribution function with spectral index  $\kappa$ , which determines the particle velocity distribution, is suitable for the behavior of particles in space and interplanetary environment and has attracted a lot of interest. This distribution function in the limit  $\kappa \rightarrow \infty$  includes the Maxwellian distribution function [19]. Since electrons have less inertia than ions their thermal energy is higher than ions. Hence, in this paper, we have considered the Maxwellian distribution for electrons and the kappa distribution has been suggested for the ion particles. Also, since the ratio masses of the electron and ion to the dust particles are so small, these particles can be considered as non- inertial particles [20]. The aims of the present paper using of the hydrodynamic (HD) model are to peruse the effects Kappa parameters on the dust-acoustic modulational instability and the propagation of pulse waves in a polarized dusty plasma. The paper is organized as follows. In Sect. 2, the model equations that include the effects of polarization force and the superthermal ions are presented, and then using the standard reductive perturbation method, the NLS

equation is derived. In Sect. 3, using the plasma parameter values, the numerical discussion is presented and the effects of the Kappa parameters on the modulational instability are also searched. Finally, in Sect. 4 the conclusion is reported.

## 2 Mathematical Formulation

Considering a dusty plasma media including electrons, ions and charged dust particles. The normalized dynamic of the DAWs is governed by the following equations including the polarization force [5, 21]

$$\frac{\partial n}{\partial t} + \frac{\partial (nu)}{\partial x} = 0, \quad (2)$$

$$\frac{\partial u}{\partial t} + u \frac{\partial u}{\partial x} = \chi \frac{\partial \Phi}{\partial x}, \quad (3)$$

$$\frac{\partial^2 \Phi}{\partial x^2} = \mu_e n_e - \mu_i n_i + n, \quad (4)$$

where  $\Phi$  is the electrostatic potential normalized by  $(k_B T_i / e)$ ,  $n_j$  is densities of  $j$ th species normalized by its unperturbed densities ( $n_{j0}$ ),  $u$  is dust fluid velocity normalized by DA speed  $C_d = \sqrt{Z_d k_B T_i / m_d}$ ,  $x$  normalized by the dust Debye length  $\lambda_{D0} = \epsilon_0 k_B T_i / Z_d^2 n_{d0}$ ,  $t$  normalized by  $\omega_{pd}^{-1} = \epsilon_0 m_d / e^2 Z_d^2 n_{d0}$ ,  $\mu_e = n_{e0} / Z_d n_{d0}$ ,  $\mu_i = n_{i0} / Z_d n_{d0}$ ,  $\chi = 1 - R$  and  $R \approx q_d e / 16 \pi \epsilon_0 \lambda_{D0} k_B T_i$  [5]. Here, we assume that the ions obey the Kappa distribution function given by

$$n_i = \left( 1 + \frac{\Phi}{\kappa - 3/2} \right)^{-\kappa + 1/2}, \quad (5)$$

while the electrons satisfy the Boltzmann relation routinely in the DAWs slow time regime,

$$n_e = \exp(\sigma_i \Phi), \quad (6)$$

where  $\sigma_i = T_i / T_e$ .

we have applied the standard reductive perturbation method (RPM) to obtain a nonlinear Schrodinger (NLS) equation and then to study the modulation of the DAWs in the mentioned media [4, 22, 23]. We employ the following stretching of independent variables

$$\xi = \varepsilon(x - v_g t), \tau = \varepsilon^2 t, \quad (7)$$

in which  $\varepsilon$  is the nonlinearity strength and also is a small value ( $0 < \varepsilon \ll 1$ ) and  $v_g$  is the group velocity of the wave propagating.

$$n = 1 + \sum_{m=1}^{\infty} \varepsilon^m \sum_{\ell=-m}^m n_{\ell}^{(m)}(\xi, \tau) \exp[i\ell(kx - \omega t)], \quad (8)$$

$$u = \sum_{m=1}^{\infty} \varepsilon^m \sum_{\ell=-m}^m u_{\ell}^{(m)}(\xi, \tau) \exp[i\ell(kx - \omega t)], \quad (9)$$

$$\Phi = \sum_{m=1}^{\infty} \varepsilon^m \sum_{\ell=-m}^m \Phi_{\ell}^{(m)}(\xi, \tau) \exp[i\ell(kx - \omega t)], \quad (10)$$

One can substitute the Expression (7) into the Eqs. (2)–(4) and then collect terms in the different powers of  $\varepsilon$ , by this method there are some  $m$ th-order equations. One can obtain the following equation for the first-order  $m = 1$  and  $\ell = 1$

$$\begin{pmatrix} n_1^{(1)} \\ u_1^{(1)} \end{pmatrix} = \begin{pmatrix} C_1 - k^2 \\ -k \chi/\omega \end{pmatrix} \Phi_1^{(1)}, \quad (11)$$

and the dispersion relation

$$\omega = \frac{k \sqrt{\chi}}{\sqrt{k^2 - C_1}}, \quad (12)$$

and group velocity

$$v_g = \frac{C_1 \omega^2}{\omega^2 - \chi} \equiv \frac{\partial \omega}{\partial k}, \quad (13)$$

And then one can get the following relations between second harmonic modes and terms of  $\Phi_1^{(1)}$ . For  $m = 2$  and  $\ell = 0$

$$\begin{pmatrix} n_0^{(2)} \\ u_0^{(2)} \\ \Phi_0^{(2)} \end{pmatrix} = \begin{pmatrix} -\frac{2\chi(C_1^2 k v_g \omega + C_2 \omega^2 - C_1 k^2 (\chi + k v_g \omega))}{(C_1 v_g^2 - \chi) \omega^2} \\ \frac{2\chi(C_1 k \chi (k v_g - \omega) + \omega(k^3 \chi - C_2 v_g \omega))}{(C_1 v_g^2 - \chi) \omega^2} \\ \frac{2(-k^2 \chi^2 + C_1 k v_g \chi \omega - k^3 v_g \chi \omega + C_2 v_g^2 \omega^2)}{(C_1 v_g^2 - \chi) \omega^2} \end{pmatrix} \left| \Phi_1^{(1)} \right|^2, \quad (14)$$

for  $m = 2$ ,  $\ell = 1$ , we have

$$\begin{pmatrix} n_1^{(2)} \\ u_1^{(2)} \end{pmatrix} = - \begin{pmatrix} C_1 + k^2 \\ (k^2 - C_1)k/\omega \end{pmatrix} \Phi_1^{(2)} + 2i(k^2 - C_1) \begin{pmatrix} 1/k\omega \\ 1/k^2 \end{pmatrix} (k v_g - \omega) \frac{\partial \Phi_1^{(1)}}{\partial \xi}, \quad (15)$$

and for  $m = 2$  and  $\ell = 2$ :

$$\begin{pmatrix} n_2^{(2)} \\ u_2^{(2)} \\ \Phi_2^{(2)} \end{pmatrix} = \begin{pmatrix} -\frac{k^2\chi(C_1k^2\chi+4k^4\chi-2C_1^2\omega^2-2C_2\omega^2-6C_1k^2\omega^2+8k^4\omega^2)}{2\omega^2(k^2\chi-C_1\omega^2-4k^2\omega^2)} \\ -\frac{k\chi(-C_1k^2\chi+6k^4\chi-2C_2\omega^2)}{2\omega(k^2\chi-C_1\omega^2-4k^2\omega^2)} \\ \frac{-k^4\chi^2+2C_1k^2\chi\omega^2-2k^4\chi\omega^2+2C_2\omega^4}{2\omega^2(-k^2\chi+C_1\omega^2+4k^2\omega^2)} \end{pmatrix} \left(\Phi_1^{(1)}\right)^2, \quad (16)$$

By continuing the same method for the third order and simultaneously considering the above equations, one can derive the NLS equation as follow

$$i \frac{\partial \Phi}{\partial \tau} + \frac{P}{2} \frac{\partial^2 \Phi}{\partial \xi^2} + Q |\Phi|^2 \Phi = 0, \quad (17)$$

where  $\Phi = \Phi_1^{(1)}$ . The dispersion coefficient relation ( $P$ ) is

$$P = \frac{3C_1\omega^5}{k^4\chi^2}, \quad (18)$$

while the nonlinear coefficient relation ( $Q$ ) defines as

$$Q = -\frac{\omega}{4(C_1 - k^2)(2C_1 + 3k^2)(2C_1^3 - 3C_1^2k^2 + 3C_1k^4 - k^6)} \left[ 18C_1^7 + 23C_1^6k^2 \right. \\ \left. + C_1^5(80C_2 - 274k^4) + 2k^6(2C_2^2 + 9C_3k^2 + 12C_2k^4) \right. \\ \left. - 3C_1^4(8C_3 + 64C_2k^2 - 177k^6) + C_1^3(-24C_2^2 + 84C_2k^4 - 449k^8) \right. \\ \left. - 3C_1k^4(4C_2^2 + 14C_3k^2 + 36C_2k^4 + 9k^8) \right. \\ \left. + 2C_1^2k^2(-6C_2^2 + 9C_3k^2 + 56C_2k^4 + 89k^8) \right], \quad (19)$$

### 3 Results and Discussion

In this section, we want to study the stability/instability of the modulated envelope waves on the basis of the NLS Eq. (14) of the DAWs in polarized dusty plasma. For this purpose, we have chosen the parameters in dusty plasmas in which the grain radius  $r_d = 1\mu\text{m}$ ,  $n_{i0} = 1.65 \times 10^8 \text{cm}^{-3}$ ,  $T_e = 3 \text{eV}$  and  $\sigma_i = 0.01$  are applied. It is proved that [24] the unstable of the modulated wave packets (bright solitary wave) occurs when the product  $PQ$  is positive and the stable of the modulated wave packets (dark envelope soliton) exists when the product  $PQ < 0$  in the modulation wave number region  $k^2 > 2Q|\Phi_0|^2/P$ , where  $\Phi_0$  is the amplitude of the carrier waves. Besides, one can choose the wavenumber as  $k = |\Phi_0|\sqrt{Q/P}$  and then attain the

maximum growth rate as  $Q |\Phi_0|^2$ . It is proposed the following breather solution in the unstable regions for the NLS Eq. (14) [15, 25]

$$\Phi = \sqrt{\frac{P}{Q}} \left[ -1 + \frac{4(1 + 2i P \tau)}{1 + 4\xi^2 + 4P^2\tau^2} \right] \exp(i P \tau), \quad (20)$$

We numerically investigate the effect of the polarization force on the nature and behavior of the solution by identification the sign of the product  $PQ$ . The critical wave number is defined as the value of  $k = k_c = |\Phi_0| \sqrt{Q/P}$  for the onset of the modulational instability. It should be noted that choosing  $Q=0$  leads to  $P/Q \rightarrow \pm\infty$ . Figure 1 depicts the dispersion relation ( $\omega$ ) and the group velocity ( $v_g$ ) versus wave number ( $k$ ) for the different values of the Kappa parameters ( $\kappa$ ). It is seen from Fig. 1a that although  $\omega$  boosts as the value of  $k$  enhances, it shifts towards lower values as  $\kappa$  increases. This means that the wave energy would be decrease when the value of the  $\kappa$  parameter increases. The schematic of the group velocity of the solitary wave for three values of the Kappa parameters ( $\kappa$ ) is illustrated in Figure 1b. For plotting, the Kappa parameters ( $\kappa$ ) are chosen as  $\kappa = 3, 5$  and  $10$  for blue, orange and green lines, respectively. The group velocity ( $v_g$ ) would be decreased when the values of the Kappa parameters ( $\kappa$ ) increase.

Figure 2 show the MI region as a blue area for relevant physical parameters. The stable modulational pulses are depicted by the white regions (where  $PQ < 0$ ) and the dark solitary waves can propagate. While the blue area corresponds to the unstable modulational pulses where the bright solitary waves can exist. It should be notified that the solid blue line in this figure represents the critical wave number  $k_c$ . The behavior of the value  $k_c$  is depending to the Kappa parameter and increasing the value of  $\kappa$  causes to a shift of  $k_c$  towards higher values.

Figure 3a, b demonstrate the absolute of the DA rogue pulse  $|\Phi|$  against  $\xi$  for several plasma values such as (a) the Kappa parameters ( $\kappa$ ), (b)  $\sigma_i$ , (c)  $\mu_e$  and  $R$ .

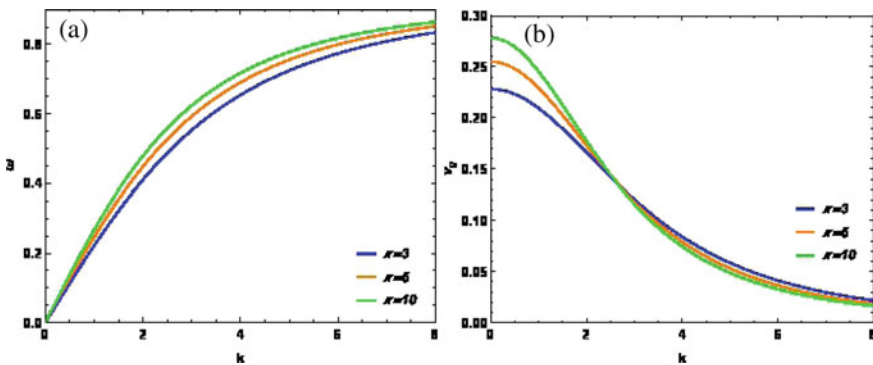


**Fig. 1** The carrier frequency  $\omega$  and the group velocity  $v_g$  are plotted against the wave number  $k$  for different values of  $\kappa$ . Here,  $\kappa = 3$  (blue line),  $\kappa = 5$  (orange line) and  $\kappa = 10$  (green line)



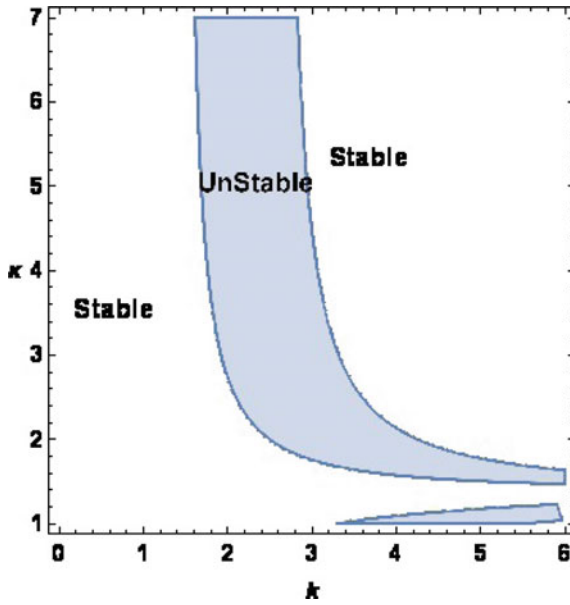


Fig. 2 The contour of  $PQ$  is plotted versus the wave number  $k$  and the  $\kappa$  parameter

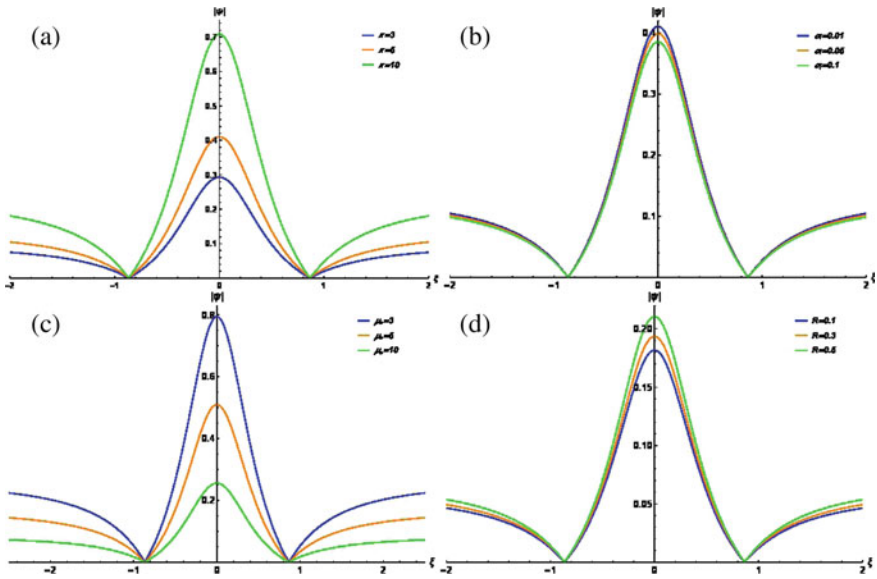


Fig. 3 a The absolute of the rogue wave against  $\xi$  for different plasma values a  $\kappa$  b  $\sigma_i$ , c  $\mu_e$  and  $R$

Although, as can be observed that from Fig. 3a, d that the amplitude of the DA rogue pulse would be increased when the values of the superthermal ions ( $\kappa$ ) and the magnitude of the polarization force ( $R$ ) enhanced, its amplitude decreased when the ratio of ion temperature  $\sigma_i$  and the density of electrons  $\mu_e$  increased.

## 4 Conclusion

In the present work, using a Boltzmann electrons and Kappa ion distributions, we have studied the nonlinear amplitude modulation of dust-acoustic waves in an unmagnetized collisionless dusty polarized plasma. Using the reductive perturbation method, a modified nonlinear Schrodinger equation governing the evolution of the dust-acoustic envelope waves has been derived. The effects of the  $\kappa$  parameter on the modulational instability (MI) were investigated by changing the numerical values. It is found that increasing the value of  $\kappa$  causes to increase the value of the dispersion relation and the group velocity. It was shown that by increasing the superthermal ions ( $\kappa$ ) and the magnitude of the polarization force ( $R$ ), the amplitude of DA rogue waves decreased while by enhancing the ratio of ion temperature  $\sigma_i$  and the density of electrons  $\mu_e$  caused to increased its amplitude.

## References

1. Shukla, P.K., Mamun, A.: Introduction to Dusty Plasma Physics. CRC Press (2015)
2. Abdikian, A.: Dust-ion-acoustic solitary waves in a magnetized dusty pair-ion plasma with Cairns-Gurevich electrons and opposite polarity dust particles. *Contrib. Plasma Phys.* **59**, 20 (2019)
3. El Awady, E., El Tantawy, S., Abdikian, A.: Dissipative cylindrical magnetosonic solitary waves in a magnetized quantum dusty plasma. *Rom. Rep. Phys.* **71**, 105 (2019)
4. Bouzit, O., Tribeche, M.: Dust-acoustic waves modulational instability and rogue waves in a polarized dusty plasma. *Phys. Plasmas* **22**, 103703 (2015)
5. Chen, H., Zhou, S., Luo, R., Liu, S.: Nonlinear dust acoustic waves with polarization force effects in Kappa distribution plasma. *Jpn. J. Appl. Phys.* **56**, 016101 (2016)
6. Hamaguchi, S., Farouki, R.: Phys. Rev. E Polarization force on a charged particulate in a nonuniform plasma. *Phys. Rev. E* **49**, 4430 (1994)
7. Hamaguchi, S., Farouki, R.: Plasma-particulate interactions in nonuniform plasmas with finite flows. *Phys. Plasmas* **1**, 2110 (1994)
8. Khrapak, S., Ivlev, A., Yaroshenko, V., Morfill, G.: Influence of a polarization force on dust acoustic waves. *Phys. Rev. Lett.* **102**, 245004 (2009)
9. Mamun, A., Ashrafi, K., Shukla, P.: Effects of polarization force and effective dust temperature on dust-acoustic solitary and shock waves in a strongly coupled dusty plasma. *Phys. Rev. E* **82**, 026405 (2010)
10. Singh, K., Ghai, Y., Kaur, N., Saini, N.S.: Effect of polarization force on dust-acoustic cnoidal waves in dusty plasma. *Eur. Phys. J. D* **72**, 1 (2018)
11. Singh, K., Saini, N.S.: Breather structures and peregine solitons in a polarized space dusty plasma. *Front. Phys.* **8**, 511 (2020)

12. Demiray, H., Abdikian, A.: Modulational instability of acoustic waves in a dusty plasma with nonthermal electrons and trapped ions. *Chaos Soliton Fract.* **121**, 50 (2019)
13. Peregrine, D.: Water waves, nonlinear Schrodinger equations and their solutions. *J. Aust. Math. Soc. B Appl. Math.* **25**, 16 (1983)
14. Draper, L.: "Freak" ocean waves. *Weather* **21**, 2 (1966)
15. Abdikian, A., Ismaeel, S.: Ion-acoustic rogue waves and breathers in relativistically degenerate electron-positron plasmas. *Eur. Phys. J. Plus* **132**, 368 (2017)
16. Bhowmik, C., Misra, A., Shukla, P.: Oblique modulation of electron-acoustic waves in a Fermi electron-ion plasma. *Phys. Plasmas* **14**, 122107 (2007)
17. Bains, A.S., Tribeche, M., Gill, T.S.: Modulational instability of electron-acoustic waves in a plasma with a q-nonextensive electron velocity distribution. *Phys. Lett. A* **375**, 2059 (2011)
18. Vasyliunas, V.M.: A survey of low-energy electrons in the evening sector of the magnetosphere with OGO 1 and OGO 3. *J. Geophys. Res.* **73**, 2839 (1968)
19. Hau, L.-N., Fu, W.-Z.: Mathematical and physical aspects of Kappa velocity distribution. *Phys. Plasmas* **14**, 110702 (2007)
20. Abdikian, A., Sultana, S.: Dust-acoustic solitary and cnoidal waves in a dense magnetized dusty plasma with temperature degenerate trapped electrons and nonthermal ions. *Phys. Scr.* **96**, 095602 (2021)
21. Mayout, S., Bentabet, K., Tribeche, M.: Effect of the polarization force on the dust-acoustic soliton energy. *Contrib. Plasma Phys.* **56**, 99 (2016)
22. Abdikian, A., Tamang, J., Saha, A.: Electron-acoustic supernonlinear waves and their multi-stability in the framework of the nonlinear Schrödinger equation. *Commun. Theor. Phys.* **72**, 075502 (2020)
23. Abdikian, A.: Modulational instability of ion-acoustic waves in magnetoplasma with pressure of relativistic electrons. *Phys. Plasmas* **24**, 052123 (2017)
24. Amin, M., Morfill, G., Shukla, P.: Modulational instability of dust-acoustic and dust-ion-acoustic waves. *Phys. Rev. E* **58**, 6517 (1998)
25. Pathak, P., Sharma, S., Nakamura, Y., Bailung, H.: Observation of second order ion acoustic Peregrine breather in multicomponent plasma with negative ions. *Phys. Plasmas* **23**, 022107 (2016)

# Nonlinear Wave Structures in Six-Component Cometary Ion-Pair Dusty Plasma



Punam Kumari Prasad , Jharna Tamang ,  
and Nur Aisyah Binti Abdul Fataf 

**Abstract** The dust-ion-acoustic waves (DIAWs) in a six-component plasma constituting of ion-pair, negatively charged fluid dusts, superthermal light hydrogen ion, solar electrons and cometary tail electrons are studied. Employing the technique of reductive perturbation, the Korteweg-de Vries (KdV) equation is formulated and the corresponding phase plane is analyzed. The analytical wave solutions and electric field under the effect of plasma parameters are examined. The findings of the present work can be useful to understand nonlinear wave features in the region of the cometary tail where plasma particles are superthermal in nature.

**Keywords** Superthermal plasma · Electric field · Solitary wave

## 1 Introduction

A study of nonlinear wave features in dusty plasma enables us to understand the behavior and physical processes that occur in various space and astrophysical surroundings like interplanetary space, interstellar medium, planetary rings, cometary tails, asteroid zones, astroclouds, etc. The embedded charged dust particles in an electron-ion plasma modify the collective behavior of a plasma and also lead to the excitation of wave modes such as dust-acoustic waves (DAWs) [1], dust ion-acoustic waves (DIAWs) [2], and dust lattice waves [3]. Very recently, authors [4],

---

P. K. Prasad (✉) · J. Tamang

Department of Mathematics, Sikkim Manipal Institute of Technology, Sikkim Manipal University, Majitar, Rangpo, East-Sikkim 737136, India  
e-mail: [psikkim@ymail.com](mailto:psikkim@ymail.com)

J. Tamang

Department of Mathematics, Sikkim Alpine University, Kamrang, Namchi, South Sikkim 737126, India

N. A. B. A. Fataf

Cyber Security Centre, National Defence University of Malaysia (NDUM), Kuala Lumpur, Malaysia

[5] investigated the existence of nonlinear arbitrary amplitude solitary waves in a six-component cometary dusty plasmas. Venugopal and Neethu [6] investigated the influence of variable dusts on dust acoustic shock waves in a six-component cometary dusty plasma with pair of oppositely charged heavy ions.

A vaporized gas of cloud at the tail region of comets formed due to the solar wind-comet interaction. In addition to the dust species, the plasma environment of a comet is essentially dominated by the newly generated multi-ion species that include water group ions ( $\text{OH}^+$ ,  $\text{H}_2\text{O}^+$  and  $\text{H}_3\text{O}^+$ ) with solar wind protons and electrons [7]. The dissociation of molecules of water group leads to the formation of positively charged oxygen ( $\text{O}^+$ ) and hydrogen ( $\text{H}^+$ ) ions with photo-electrons [8]. Along with these positive ions, the Giotto spacecraft also identified negative ions in the plasma environment of the comet with energies ranging from 0.03 to 3.0 keV. Among all ionic species, negatively charged ions ( $\text{O}^-$ ) are clearly identified [9].

The Rosetta spacecraft at comet 67P/Churyumov-Gerasimenko, has observed the signature of highly energetic superthermal electrons that deviate significantly from the Maxwellian distribution [10]. The source for the formation of energetic cometary plasma particles are the production of photo-electrons by photo-ionization of the cometary coma and inward movement of solar wind electrons into the coma region [11]. Thus, light hydrogen ions, solar and cometary electrons are characterized by superthermal  $\kappa$ -distributions having distinct temperatures and spectral indices ( $\kappa$ ). Low values of  $\kappa$  signify the distributions with relatively large components of superthermal particles than thermal particles [12]. Moreover, superthermal  $\kappa$ -distribution tends to Maxwellian distribution for higher values of  $\kappa$ . Recently, authors [13, 14] investigated the influence of  $\kappa$ -distributed particles on small-amplitude nonlinear waves in multi-component plasma system.

The phase plane analysis is an effective concept to investigate the dynamical features for any nonlinear system. Implementing this concept, Samanta et al. [15] studied bifurcation behavior of the nonlinear DIAWs in a magneto-dusty plasma. Selim et al. [16] explored bifurcations behavior of nonlinear waves in a magnetized multi-component plasma with superthermal electrons. Recently, Monier and Atteya [17] explored the properties of the KdVB equation in a dusty plasma. Rahim et al. [18] investigated the dynamical behaviors of DA solitary structures in Thomas Fermi dusty plasma. Tamang et al. [19] explored the existence of localized structures which are featured by the nontrivial topology of their phase portraits under the framework of higher order Korteweg-deVries (KdV) equations. Very recently, the method of phase plane analysis is adopted to analyze small-amplitude nonlinear waves in various three-component plasma systems [20, 21]. This paper investigates the propagation of small-amplitude nonlinear DIAWs in six-component plasma constituting of ion-pair, negatively charged fluid dusts, superthermal light hydrogen ion, solar electrons and cometary tail electrons.

The paper is organized as: in Sect. 2, the basic equations which describe the dynamics of DIAWs in cometary plasma system are considered. Section 3 deals with the derivation of the nonlinear KdV equation and phase plane analysis with the analytical wave solution corresponding to the KdV equation are done in Sect. 4. The concluding remarks are presented in Sect. 5.

## 2 Basic Equations

One can consider a six-component dusty plasma system consisting of ion pair (negatively and positively charged oxygen ions indicated, respectively, by subscripts ‘-’ and ‘+’), negatively charged dust particles (indicated by subscript ‘d’), kappa distributed light hydrogen ions (indicated by subscript ‘H’), hot solar electrons and cold cometary tail electrons (indicated respectively by subscripts ‘se and ‘ce’). The dynamics of DIAWs can be studied by considering the normalized fluid equations given as [4]:

$$\frac{\partial n_-}{\partial t} + \frac{\partial}{\partial x}(n_- v_-) = 0, \quad (1)$$

$$\frac{\partial v_-}{\partial t} + v_- \frac{\partial v_-}{\partial x} = \frac{z_- \alpha_-}{z_d} \frac{\partial \phi}{\partial x} - \frac{3\alpha_- \sigma_-}{z_d} n_- \frac{\partial n_-}{\partial x}, \quad (2)$$

$$\frac{\partial n_+}{\partial t} + \frac{\partial}{\partial x}(n_+ v_+) = 0, \quad (3)$$

$$\frac{\partial v_+}{\partial t} + v_+ \frac{\partial v_+}{\partial x} = -\frac{z_+ \alpha_+}{z_d} \frac{\partial \phi}{\partial x} - \frac{3\alpha_+ \sigma_+}{z_d} n_+ \frac{\partial n_+}{\partial x}, \quad (4)$$

$$\frac{\partial n_d}{\partial t} + \frac{\partial}{\partial x}(n_d v_d) = 0, \quad (5)$$

$$\frac{\partial v_d}{\partial t} + v_d \frac{\partial v_d}{\partial x} = \frac{\partial \phi}{\partial x}, \quad (6)$$

$$\frac{\partial^2 \phi}{\partial x^2} = n_d + \mu_- n_- - \mu_+ n_+ - \mu_H n_H + \mu_{se} n_{se} + \mu_{ce} n_{ce}, \quad (7)$$

where,  $\mu_- = \frac{z_- n_{-0}}{z_d n_{d0}}$ ,  $\mu_+ = \frac{z_+ n_{+0}}{z_d n_{d0}}$ ,  $\mu_H = \frac{n_{H0}}{z_d n_{d0}}$ ,  $\mu_{se} = \frac{n_{se0}}{z_d n_{d0}}$ ,  $\mu_{ce} = \frac{n_{ce0}}{z_d n_{d0}}$ ,  $\sigma_- = \frac{T_-}{T_d}$ ,  $\sigma_+ = \frac{T_+}{T_d}$ ,  $\alpha_- = \frac{m_d}{m_-}$  and  $\alpha_+ = \frac{m_d}{m_+}$ . Here,  $n_j$  is the number densities of  $j$ th plasma particles, where  $j = -, +, H, d, se,$  and  $ce$ , with ‘0’ denoting the unperturbed state of plasma particles.  $\phi$  denotes the electrostatic wave potential. Furthermore,  $v_{-,+,d}$ ,  $m_{-,+,d}$  and  $z_{-,+,d}$  represent velocity, mass and charge number of negative oxygen ions, positive oxygen ions, and negative dust particles, respectively. The normalized variables are as follows:  $v_j \rightarrow v_j/C_d$ ,  $n_j \rightarrow n_j/n_{j0}$  (where,  $j = -, +, H, d, se$  and  $ce$ ),  $\phi \rightarrow \phi e/k_B T_d$ ,  $t \rightarrow \omega_{pd} t$  and  $x \rightarrow x/\lambda_{Dd}$ , where the DA wave speed  $C_d = (z_{d0} k_B T_d / m_d)^{1/2}$ , dust frequency  $\omega_{pd}^{-1} = (m_d / 4\pi z_{d0}^2 e^2 n_{d0})^{1/2}$  and Debye length for the dust plasma  $\lambda_{Dd} = (k_B T_d / 4\pi z_{d0}^2 n_{d0} e^2)^{1/2}$ . Here  $k_B$  represents the Boltzmann constant,  $e$  denotes the electronic charge. The equation of state is  $p_{-,+,d} = cn_{-,+,d}^\nu$ , where  $\nu = (f + 2)/f$  with  $f$  as the degree of freedom. For one-dimensional adiabatic state,  $f = 1$  and hence  $\nu = 3$ .

The normalized number densities of light hydrogen ions ( $n_H$ ), hot solar electrons ( $n_{se}$ ) and cold cometary tail electrons ( $n_{ce}$ ) are given as follows:

$$n_H = \left(1 + \frac{\phi}{\sigma_H(\kappa_H - 3/2)}\right)^{-\kappa_H + 1/2}, \quad (8)$$

$$n_{se,ce} = \left(1 - \frac{\phi}{\sigma_{se,ce}(\kappa_{se,ce} - 3/2)}\right)^{-\kappa_{se,ce} + \frac{1}{2}}, \quad (9)$$

where,  $\sigma_H = \frac{T_H}{T_d}$ ,  $\sigma_{se} = \frac{T_{se}}{T_d}$ , and  $\sigma_{ce} = \frac{T_{ce}}{T_d}$ . The spectral indices  $\kappa_{H,se,ce}$  represents the superthermality of hydrogen ions, solar and cometary tail electrons, respectively. Evidently, one requires  $\kappa_{H,se,ce} > 3/2$  and if  $\kappa_{H,se,ce} \rightarrow \infty$  then distributions (8)–(9) reduce to Maxwell–Boltzmann distribution.

### 3 Formulation of Korteweg–DeVries (KdV) Equation

To study DIAWs in the considered cometary plasma system, one can employ the technique of reductive perturbation to formulate the KdV equation. For this purpose, dependent variables are expanded as:

$$\begin{aligned} n_j &= 1 + \varepsilon n_j^{(1)} + \varepsilon^2 n_j^{(2)} + \dots \\ v_j &= 0 + \varepsilon v_j^{(1)} + \varepsilon^2 v_j^{(2)} + \dots \\ \phi &= 0 + \varepsilon \phi^{(1)} + \varepsilon^2 \phi^{(2)} + \dots \end{aligned} \quad (10)$$

where,  $j = -, +, d$  and  $\varepsilon$  is an indicative of the magnitude of perturbation. Furthermore, stretching of the independent variables are introduced as:

$$\tau = \varepsilon^{3/2} t \quad \xi = \varepsilon^{1/2}(x - v_0 t), \quad (11)$$

where, the  $v_0$  denotes phase velocity of DIAWs.

Substituting expressions (10) and (11) in system of normalized Eqs. (1)–(7) and equating the coefficients of various powers of  $\varepsilon$  to zero, one can get

$$\left\{ \begin{aligned} n_-^{(1)} &= \frac{1}{v_0} v_-^{(1)} = \left( \frac{z - \alpha_-}{3\alpha_- \sigma_- - v_0^2 z_d} \right) \phi^{(1)}, \\ n_+^{(1)} &= \frac{1}{v_0} v_+^{(1)} = \left( \frac{z + \alpha_+}{v_0^2 z_d - 3\alpha_+ \sigma_+} \right) \phi^{(1)}, \\ n_d^{(1)} &= \frac{1}{v_0} v_d^{(1)} = -\frac{1}{v_0^2} \phi^{(1)}, \\ \frac{z - \alpha_- \mu_-}{3\alpha_- \sigma_- - v_0^2 z_d} + \frac{z + \alpha_+ \mu_+}{3\alpha_+ \sigma_+ - v_0^2 z_d} - \frac{1}{v_0^2} + T_1 &= 0, \end{aligned} \right. \quad (12)$$

$$\frac{\partial n_-^{(1)}}{\partial \tau} + \frac{\partial v_-^{(2)}}{\partial \xi} - v_0 \frac{\partial n_-^{(2)}}{\partial \xi} + \frac{\partial}{\partial \xi} (n_-^{(1)} v_-^{(1)}) = 0, \quad (13)$$

$$\frac{\partial n_+^{(1)}}{\partial \tau} + \frac{\partial v_+^{(2)}}{\partial \xi} - v_0 \frac{\partial n_+^{(2)}}{\partial \xi} + \frac{\partial}{\partial \xi} (n_+^{(1)} v_+^{(1)}) = 0, \quad (14)$$

$$\frac{\partial n_d^{(1)}}{\partial \tau} + \frac{\partial v_d^{(2)}}{\partial \xi} - v_0 \frac{\partial n_d^{(2)}}{\partial \xi} + \frac{\partial}{\partial \xi} (n_d^{(1)} v_d^{(1)}) = 0, \quad (15)$$

$$\frac{\partial v_-^{(1)}}{\partial \tau} - v_0 \frac{\partial v_-^{(2)}}{\partial \xi} + v_-^{(1)} \frac{\partial v_-^{(1)}}{\partial \xi} - \alpha_- \frac{z_-}{z_d} \frac{\partial \phi^{(2)}}{\partial \xi} + \frac{3\alpha_- \sigma_-}{z_d} n_-^{(1)} \frac{\partial n_-^{(1)}}{\partial \xi} + \frac{3\alpha_- \sigma_-}{z_d} \frac{\partial n_-^{(2)}}{\partial \xi} = 0, \quad (16)$$

$$\frac{\partial v_+^{(1)}}{\partial \tau} - v_0 \frac{\partial v_+^{(2)}}{\partial \xi} + v_+^{(1)} \frac{\partial v_+^{(1)}}{\partial \xi} + \alpha_+ \frac{z_+}{z_d} \frac{\partial \phi^{(2)}}{\partial \xi} + \frac{3\alpha_+ \sigma_+}{z_d} n_+^{(1)} \frac{\partial n_+^{(1)}}{\partial \xi} + \frac{3\alpha_+ \sigma_+}{z_d} \frac{\partial n_+^{(2)}}{\partial \xi} = 0, \quad (17)$$

$$\frac{\partial v_d^{(1)}}{\partial \tau} - v_0 \frac{\partial v_d^{(2)}}{\partial \xi} + v_d^{(1)} \frac{\partial v_d^{(1)}}{\partial \xi} - \frac{\partial \phi^{(2)}}{\partial \xi} = 0, \quad (18)$$

$$\frac{\partial^2 \phi^{(1)}}{\partial \xi^2} = n_d^{(2)} + \mu_- n_-^{(2)} - \mu_+ n_+^{(2)} + T_1 \phi^{(2)} + T_2 \left( \phi^{(1)} \right)^2, \quad (19)$$

where,  $T_1 = \mu_{ce} \frac{1}{\sigma_{ce}} \frac{2\kappa_{ce} - 1}{2\kappa_{ce} - 3} + \mu_{se} \frac{1}{\sigma_{se}} \frac{2\kappa_{se} - 1}{2\kappa_{se} - 3} + \mu_H \frac{1}{\sigma_H} \frac{2\kappa_H - 1}{2\kappa_H - 3}$ , and

$$T_2 = \frac{\mu_{ce}}{2\sigma_{ce}^2} \frac{4\kappa_{ce}^2 - 1}{(2\kappa_{ce} - 3)^2} + \frac{\mu_{se}}{2\sigma_{se}^2} \frac{4\kappa_{se}^2 - 1}{(2\kappa_{se} - 3)^2} - \frac{\mu_H}{2\sigma_H^2} \frac{4\kappa_H^2 - 1}{(2\kappa_H - 3)^2}.$$

Using above set of relations (12)–(19), one can formulate the following KdV equation

$$\frac{\partial \phi^{(1)}}{\partial \tau} + A \phi^{(1)} \frac{\partial \phi^{(1)}}{\partial \xi} + B \frac{\partial^3 \phi^{(1)}}{\partial \xi^3} = 0, \quad (20)$$

where,  $A = -N/D$ , and  $B = 1/D$  with  $N = \frac{3}{v_0^4} - \frac{3\mu_- \alpha_-^2 z_-^2 (v_0^2 z_d + \alpha_- \sigma_-)}{(3\alpha_- \sigma_- - v_0^2 z_d)^3} + \frac{3\mu_+ \alpha_+^2 z_+^2 (v_0^2 z_d + \alpha_+ \sigma_+)}{(3\alpha_+ \sigma_+ - v_0^2 z_d)^3} - 2T_2$ , and  $D = \frac{2}{v_0^3} + \frac{2v_0 z_d \mu_- \alpha_- z_-}{(3\alpha_- \sigma_- - v_0^2 z_d)^2} + \frac{2v_0 z_d \mu_+ \alpha_+ z_+}{(3\alpha_+ \sigma_+ - v_0^2 z_d)^2}$ .

## 4 Phase Plane Analysis

To analyze the phase plane of dynamical function corresponding to the KdV Eq. (20), one can take a traveling wave transformation  $\chi = \xi - V\tau$ , where  $V$  is DIAW velocity. Thus, the following dynamical systems is obtained on using transformation  $\chi$  into the Eq. (20):



$$\begin{cases} \frac{d\phi^{(1)}}{dX} = y, \\ \frac{dy}{dX} = \frac{V}{B}\phi^{(1)} - \frac{A}{2B}(\phi^{(1)})^2, \end{cases} \quad (21)$$

The above dynamical system depends on superthermal parameters ( $\kappa_{H,se,ce}$ ), charge numbers ( $z_{-,+,d}$ ), number densities ( $n_{-,+,H,d,se,ce}$ ), temperatures ( $T_{-,+,H,d,se,ce}$ ), mass ratios ( $\alpha_{-,+}$ ), and DIAW velocity ( $V$ ). To investigate the influence of equilibrium plasma parameters associated with cometary plasma system, one can consider the typical range of parameters observed in the surroundings of various comets. In this work, the following values of parameters relevant to comet Halley [5, 8, 22, 23] are considered: hydrogen ions with temperature  $T_H = 8 \times 10^4$  K and number density  $n_H = 4.95 \text{ cm}^{-3}$ , solar electron with temperature  $T_{se} = 2 \times 10^5$  K and number density same as that of hydrogen ions. Cometary electron with temperature  $T_{ce} = 2 \times 10^4$  K and the negatively charged dust particles with temperature  $T_d = 2 \times 10^3$  K, number density  $n_{d0} = 10^{-5} \text{ cm}^{-3}$ , and charge number  $Z_{d0} = 10^3$ . The temperatures of the negative and positive Oxygen ions are taken as  $T_- = T_+ = 1.16 \times 10^4$  K with number densities  $n_{-0} = 0.05 \text{ cm}^{-3}$ ,  $n_{+0} = 0.5 \text{ cm}^{-3}$  and charges  $z_- = 1$ , and  $z_+ = 2$ , respectively. The masses of dust particles, ion-pair of Oxygen are considered such that  $\alpha_- = \alpha_+ = 10^3$ .

The phase plane of any dynamical system determines the instantaneous behavior of its trajectories for a set of initial conditions. The stability or instability of the equilibrium points predicts the nature of nearby trajectories. Using the concept of phase plane analysis [24, 25], one can investigate the phase portraits of any nonlinear dynamical system which may vary consequentially on numbers of fixed points and separatrix layers [26]. To distinguish trajectories in the phase portrait, following representations are used:  $NPT_{m,n}$ , and  $NHT_{m,n}$  for nonlinear periodic, and homoclinic trajectories, respectively, where  $m$  indicates number of stable center points and  $n$  denotes number of separatrix layers. Every trajectory in phase portrait corresponds to a traveling wave solution for the considered plasma system. For example, periodic, and homoclinic trajectories of the dynamical system correspond to periodic and solitonic wave solutions of the plasma system, respectively. In addition to the trajectories, one can also check the conservative nature from phase plane of a dynamical system [27]. Figure 1 shows the plots of potential energy function, and phase plane corresponding to Eq. (20) for  $\kappa_{se} = \kappa_{ce} = \kappa_H = 2$ ,  $n_{-0} = 0.05 \text{ cm}^{-3}$ ,  $n_{+0} = 0.5 \text{ cm}^{-3}$ ,  $n_H = n_{se0} = 4.95$ ,  $n_{d0} = 10^{-5} \text{ cm}^{-3}$ ,  $T_- = T_+ = 1.16 \times 10^4$  K,  $T_H = 8 \times 10^4$  K,  $T_{se} = 2 \times 10^5$  K,  $T_{ce} = 2 \times 10^4$  K,  $T_d = 2 \times 10^3$  K,  $\alpha_- = \alpha_+ = 10^3$ ,  $z_- = 1$ ,  $z_+ = 2$ ,  $Z_{d0} = 10^3$ , and  $V = 0.1$ . Figure 1a illustrates the graph of potential function  $\psi$  against  $\phi^{(1)}$ . Here, local minima in potential plots signify the existence of solitary solutions and the potential dip at  $\phi^{(1)} > 0$  corresponds to a compressive solitonic solution whereas the potential dip at  $\phi^{(1)} < 0$  signify a rarefactive solitonic solution. Therefore, for the condition  $A > 0$ , one can obtain only compressive DIAW solution of Eq. (20). Figure 1b displays the phase portrait of the system (21) for the specified set of parameters and shows the existence of two fixed points, namely, saddle point at  $E_0(0, 0)$  and center at  $E_1(\frac{2V}{A}, 0)$ . There also exist two distinct types of phase trajectories, i.e., homoclinic trajectory ( $NHT_{1,0}$ ) and a family of nonlin-

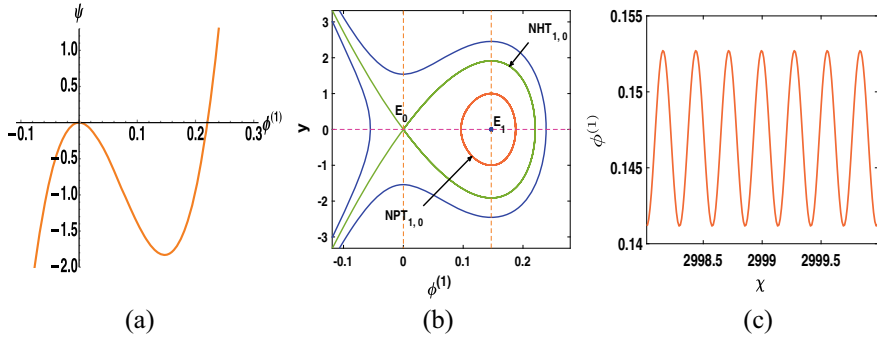


**Fig. 1** **a** Potential graph, **b** Phase portrait, and **c** Periodic wave solution of system (21) for  $\kappa_{se} = \kappa_{ce} = \kappa_H = 2$ ,  $n_{-0} = 0.05 \text{ cm}^{-3}$ ,  $n_{+0} = 0.5 \text{ cm}^{-3}$ ,  $n_H = n_{se0} = 4.95 \text{ cm}^{-3}$ ,  $n_{d0} = 10^{-5} \text{ cm}^{-3}$ ,  $T_- = T_+ = 1.16 \times 10^4 \text{ K}$ ,  $T_H = 8 \times 10^4 \text{ K}$ ,  $T_{se} = 2 \times 10^5 \text{ K}$ ,  $T_{ce} = 2 \times 10^4 \text{ K}$ ,  $T_d = 2 \times 10^3 \text{ K}$ ,  $\alpha_- = \alpha_+ = 10^3$ ,  $z_- = 1$ ,  $z_+ = 2$ ,  $Z_{d0} = 10^3$ , and  $V = 0.1$

ear periodic trajectories ( $NPT_{1,0}$ ). The periodic wave solution for initial condition (0.13, 0), corresponding to a periodic trajectory presented in Fig. 1b is displayed in Fig. 1c.

#### 4.1 Solitary Wave Solutions

Considering the transformation  $\chi = \xi - V\tau$  and using boundary conditions  $\phi^{(1)} \rightarrow 0$  and  $\frac{d\phi^{(1)}}{d\chi} \rightarrow 0$  as  $\chi \rightarrow \pm\infty$ , one can derive compressive solitonic wave solution of equation (20) analogous to the homoclinic trajectory at fixed point  $E_0$  and enclosing point  $E_1$  as

$$\phi^{(1)} = \frac{3V}{A} \text{sech}^2\left(\sqrt{\frac{V}{4B}}\chi\right), \quad (22)$$

with the electric field  $E = -\nabla\phi^{(1)}$ , i.e.,

$$E = \frac{3V}{A} \sqrt{\frac{V}{B}} \text{sech}^2\left(\sqrt{\frac{V}{4B}}\chi\right) \tanh\left(\sqrt{\frac{V}{4B}}\chi\right). \quad (23)$$

The effects of plasma parameters on the basic properties (amplitude and width) of compressive solitary wave solution of system (20) and its associated electric field are depicted in Figs. 2 and 3, respectively. Both the figures are obtained by varying the mentioned parameters and keeping the other parameter fixed as  $\kappa_{se} = \kappa_{ce} = \kappa_H = 2$ ,  $n_{-0} = 0.05 \text{ cm}^{-3}$ ,  $n_{+0} = 0.5 \text{ cm}^{-3}$ ,  $n_H = n_{se0} = 4.95$ ,  $n_{d0} = 10^{-5} \text{ cm}^{-3}$ ,  $T_- = T_+ = 1.16 \times 10^4 \text{ K}$ ,  $T_H = 8 \times 10^4 \text{ K}$ ,  $T_{se} = 2 \times 10^5 \text{ K}$ ,  $T_{ce} = 2 \times 10^4$

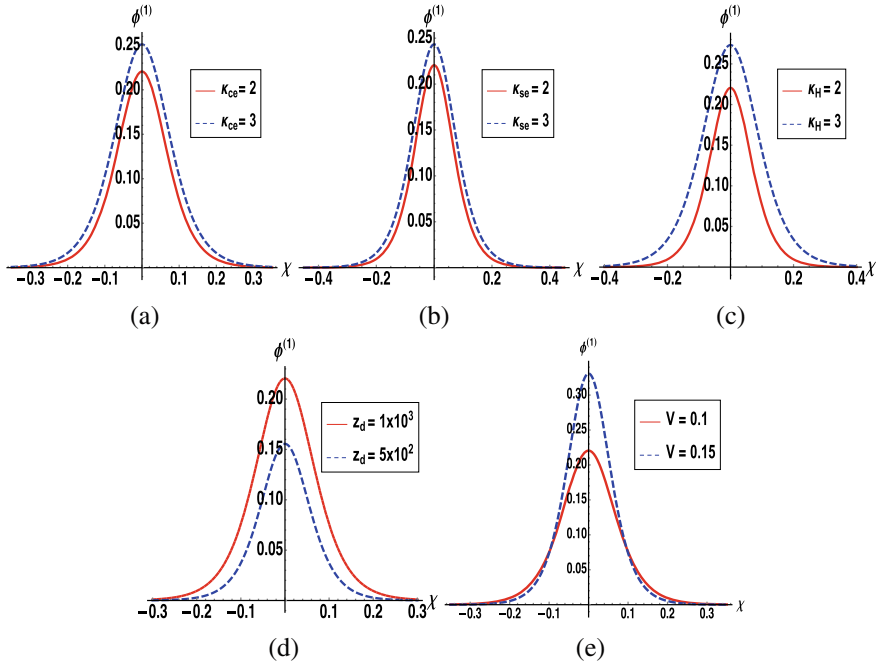


**Fig. 2** Dependency of DIA solitary wave solution of equation (3) on mentioned plasma parameters

$K$ ,  $T_d = 2 \times 10^3$  K,  $\alpha_- = \alpha_+ = 10^3$ ,  $z_- = 1$ ,  $z_+ = 2$ ,  $Z_{d0} = 10^3$ , and  $V = 0.1$ . It can be inferred from Fig. 2 that when superthermal plasma particles move far away from the Maxwellian then both amplitude and width of DIA compressive solitary wave also deplete. Now, growing value of dust charge number ( $z_d$ ) amplifies and broadens the solitary wave. Furthermore, the DIA solitary waves amplify and become narrow as the wave moves towards supersonic region. From Fig. 3, it can be noted that  $\kappa_{ce}$  influences electric field differently as compared to  $\kappa_{se}$  and  $\kappa_H$ . Both amplitude and width of electric field associated with solitary wave solution of the KdV equation (20) enhance with an increase in the value of  $\kappa_{ce}$  i.e., decrease in superthermality of cometary electrons whereas superthermality of solar electrons and hydrogen ions are responsible in the reduction of the amplitude of electric field. The influence of dust charge number and wave velocity ( $V$ ) is similar to that of the DIA compressive solitary wave.

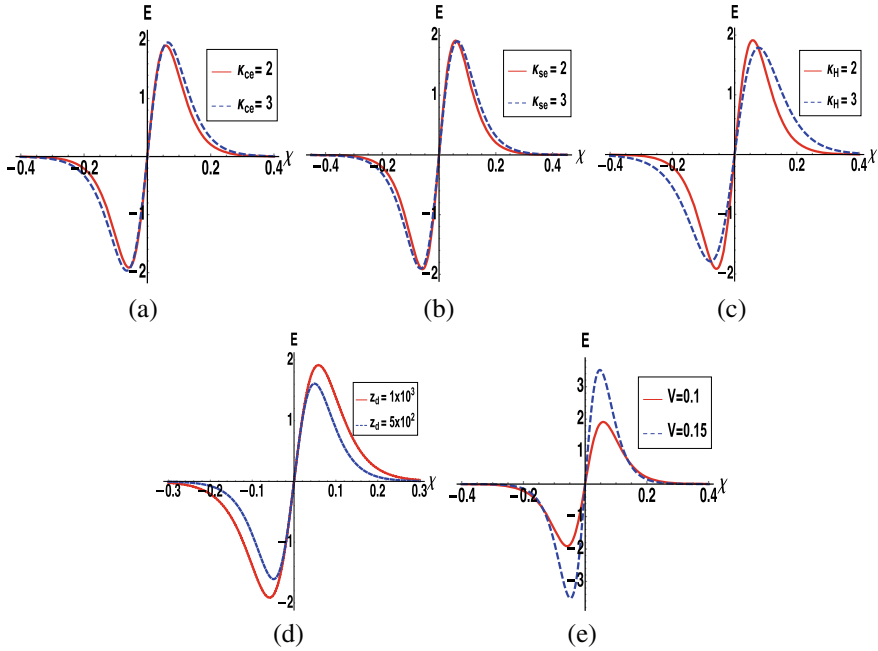


**Fig. 3** Effect of plasma parameters on electric field associated with compressive solitary wave solution of Eq. (3)

### 5 Conclusion

The DIAWs are studied in a six-component cometary tail plasma constituting Oxygen ion-pair, negatively charged dusts with superthermal light hydrogen ions, solar electrons, and cometary electrons. Phase plane analysis of DIAWs in the framework of the KdV equation is carried out. Typical set of plasma parameters observed in the tail region of comet Halley [5, 8, 22, 23] are considered for numerical simulation. The main results of our work are mentioned below:

1. Phase plane corresponding to KdV Eq. (20) only defines a homoclinic orbit on the positive phase of wave potential, which signifies the existence of a compressive solitary wave in the tail region of comet Halley.
2. On analysis of analytical wave solutions of Eq. (20), it is predicted that the DIA solitary wave amplifies when plasma particles tends towards the Maxwellian. On the contrary, electric field enhances with decrease in superthermality of cometary electrons whereas it grows with increase in superthermality of hydrogen ions and solar electrons.
3. The increasing values of dust charge number amplify the DIA solitary wave and its associated electric field. Also, the soliton and its associated electric field amplify and become narrow as the velocity of traveling wave increases.

**Acknowledgements** The first author is obliged to the Sikkim Manipal Institute of Technology and Sikkim Manipal University for providing research fellowship under TMA Pai University Research Fund (Ref. No. 118/SMU/REG/ UOO/104/2019).

## References

1. Rao, N.N., Shukla, P.K., Yu, M.Y.: Dust-acoustic waves in dusty plasmas. *Planet. Space Sci.* **38**, 543–546 (1990)
2. Shukla, P.K., Silin, V.P.: Dust ion-acoustic wave. *Phys. Scripta* **45**, 508 (1992)
3. Melandso, F.: Lattice waves in dust plasma crystals. *Phys. Plasmas* **3**, 3890–3901 (1996)
4. Abulwafa, E.M., AtallaElhanbaly, A.A.M., Bedeir, A.M.: Linear and nonlinear study of six-component dusty cometary plasma. In: *Proceedings of the 11th Conference on Nuclear and Particle Physics*, vol. 20, p. 23 (2019)
5. Bedeir, A.M., Abulwafa, E.M., Elhanbaly, A.M., Mahmoud, A.A.: A fully nonlinear solitary wave in six-component dusty cometary plasma. *Phys. Scripta* **96**(9), 095603 (2021)
6. Venugopal, C., Neethu, T.W.: Dust acoustic shock waves in a six component charge varying cometary plasma. *J. Phys. Adv. App.* **1**(1), 1–12 (2020)
7. Rubin, M., Hansen, K.C., Gombosi, T.I., Combi, M.R., Altwegg, K., Balsiger, H.: Ion composition and chemistry in the coma of Comet 1P/Halley-A comparison between Giotto's ion mass spectrometer and our ion-chemical network. *Icarus* **199**, 505–519 (2009)
8. Brinca, A.L., Tsurutani, B.T.: Unusual characteristics of electromagnetic waves excited by cometary newborn ions with large perpendicular energies. *Astron. Astrophys.* **187**, 311–319 (1987)
9. Chaizy, P., Reme, H., Sauvaud, J.A., d'Uston, C., Lin, R.P., Larson, D.E., Mitchell, D.L., Anderson, K.A., Carlson, C.W., Korth, A., Mendis, D.A.: Negative ions in the coma of comet Halley. *Nature* **349**, 393–396 (1991)
10. Madanian, H., Cravens, T.E., Rahmati, A., Goldstein, R., Burch, J.: Suprathermal electrons near the nucleus of comet 67P/Churyumov-Gerasimenko at 3 AU: model comparison with Rosetta data. *J. Geophys. Res. Space Phys.* **121**, 5815 (2016)
11. Willington, N.T., Varghese, A., Saritha, A.C., Philip, N.S., Venugopal, C.: Ion acoustic shock waves with drifting ions in a five component cometary plasma. *Adv. Space Res.* **68**, 4292–4302 (2021)
12. Saini, N.S., Kourakis, I., Hellberg, M.A.: Arbitrary amplitude ion-acoustic solitary excitations in the presence of excess superthermal electrons. *Phys. Plasmas* **16**, 62903 (2009)
13. Sarkar, J., Chandra, S., Goswami, J., Ghosh, B.: Formation of solitary structures and envelope solitons in electron acoustic wave in inner magnetosphere plasma with suprathermal ions. *Contrib. Plasma Phys.* **60**(7), e201900202 (2020)
14. Goswami, J., Sarkar, J., Chandra, S., Ghosh, B.: Amplitude-modulated electron-acoustic waves with bipolar ions and kappa-distributed positrons and warm electrons. *Pramana J. Phys.* **95**, 54 (2021)
15. Samanta, U.K., Saha, A., Chatterjee, P.: Bifurcations of dust ion acoustic travelling waves in a magnetized dusty plasma with a q-nonextensive electron velocity distribution. *Phys. Plasmas* **20**, 022111 (2013)
16. Selim, M.M., El-Depsy, A., El-Shamy, E.F.: Bifurcations of nonlinear ion-acoustic travelling waves in a multicomponent magnetoplasma with superthermal electrons. *Astrophys. Space Sci.* **360**, 66 (2015)
17. El-Monier, S.Y., Atteya, A.: Bifurcation analysis for dust-acoustic waves in a four-component plasma including warm ions. *IEEE Trans. Plasma Sci.* **46**, 815–824 (2018)
18. Rahim, Z., Adnan, M., Qamar, A., Saha, A.: Nonplanar dust-acoustic waves and chaotic motions in Thomas Fermi dusty plasmas. *Phys. Plasmas* **25**, 083706 (2018)

19. Tamang, J., Saha, A.: Bifurcations of small-amplitude supernonlinear waves of the mKdV and modified Gardner equations in a three-component electron-ion plasma. *Phys. Plasmas* **27**(1), 012105 (2020)
20. Prasad P.K., Saha A.: Dynamical behavior of ion-acoustic periodic and solitary structures in magnetized solar wind plasma. In: Giri, D., Buyya, R., Ponnusamy, S., De D., Adamatzky, A., Abawajy, J.H. (eds.) *Proceedings of the Sixth International Conference on Mathematics and Computing. Advances in Intelligent Systems and Computing*, vol. 1262, pp. 419–428. Springer, Singapore (2021). [https://doi.org/10.1007/978-981-15-8061-1\\_33](https://doi.org/10.1007/978-981-15-8061-1_33)
21. Atteya, A., El-Borie, M., Roston, G., El-Helbawy, A., Prasad, P., Saha, A.: Ion-acoustic stable oscillations, solitary, periodic and shock waves in a quantum magnetized electron-positron-ion plasma. *Zeitschrift für Naturforschung A* **76**(9), 757–768 (2021)
22. Michael, M., Willington, N.T., Jayakumar, N., Sebastian, S., Sreekala, G., Venugopal, C.: Korteweg-deVries-Burgers (KdVB) equation in a five component cometary plasma with kappa described electrons and ions. *J. Theor. Appl. Phys.* **10**, 289–296 (2016)
23. Neethu, T.W., Shilpa, S., Saritha, A.C., Philip, N.S., Venugopal, C.: Dust acoustic solitary waves in a five component cometary plasma with dust charge variation. *Radiat. Effects Defects Solids* **176**, 284–299 (2021)
24. Guckenheimer, J., Holmes, P.J.: *Nonlinear Oscillations Dynamical Systems and Bifurcations of Vector Fields*. Springer, New York (1983)
25. Chow, S.N., Hale, J.K.: *Methods of Bifurcation Theory*. Springer, New York (1981)
26. Dubinov, A.E., Kolotkov, D.Y., Sazonkin, M.A.: Nonlinear theory of ion-sound waves in a dusty electron-positron-ion plasma. *Tech. Phys.* **57**, 585–593 (2012)
27. Strogatz, S.H.: *Nonlinear dynamics and chaos: with applications to physics, biology, chemistry, and engineering*, 1st Indian edn. CRC Press (2007)

# Cylindrical and Spherical Ion-Acoustic Shock and Solitary Waves in a Nonplanar Hybrid $q$ -nonextensive Nonthermal Plasma



Subrata Roy , Santanu Raut , and Rishi Raj Kairi 

**Abstract** In this article we investigate the propagating properties of ion-acoustic wave (IAW) in a plasma comprising positively charged ions and electrons abiding by hybrid  $q$ -non-extensive non-thermal velocity distribution equation. The nonplanar KdV-Burger (NKDVB) equation is derived from the basic governing equation. Considering the impact from the ion streaming velocity, inter-particle collisions, and viscosity, a Burgers term is introduced in the present system and using Weighted Residual Method (WRM) and Simplified Hirota bilinear method (SHBM) progressive solitary wave solution and shock wave are derived. Finally, the effect of different physical parameters on solitary and shock wave on the propagation of IAW in the present plasma environment is noticed.

**Keywords** Ion-acoustic wave · Hybrid  $q$ -nonextensive non-thermal distribution · Nonplanar kdV-Burgers equation · Solitary and shock wave

## 1 Introduction

Investigation on plasma environment becomes an interesting topic in recent times as it is ubiquitously found in space environments as well as laboratory experiments. Sagdeev [1] observed theoretically these types of waves by considering a mechanical analogy whereas, Ikezi [2] in the year 1970 studied the same with an experimental set-up. Subsequently, several authors paid their attention to observe the various types of plasma models. Shukla and Silin [3] investigated theoretically dust ion acoustic wave (DIAW) in a dust plasma and Barkan et al. observe the same experimentally in [4]. Angelo [5] observed high-frequency and low-frequency acoustic waves in a

---

S. Roy (✉) · R. R. Kairi

Department of Mathematics, Cooch Behar Panchanan Barma University, Cooch Behar 736101, India

e-mail: [send2sroy94@gmail.com](mailto:send2sroy94@gmail.com)

S. Raut

Department of Mathematics, Mathabhanga College, Coochbehar 736146, India

© The Author(s), under exclusive license to Springer Nature Switzerland AG 2022

S. Banerjee and A. Saha (eds.), *Nonlinear Dynamics and Applications*,

Springer Proceedings in Complexity,

[https://doi.org/10.1007/978-3-030-99792-2\\_11](https://doi.org/10.1007/978-3-030-99792-2_11)

plasma environment in an experimental setup. Dubuloz et al. [6] observed the solitary IAW as well as DIAW in a plasma medium utilizing the KdV model as well as modified KdV model. It is unfortunate that most of the observation on IAW in plasma systems are considered in linear space only. But, in many cases, the reality in the laboratory, as well as the space environment, is totally different. Sometimes, the physical plasma environment becomes finite and the waves are confined to move in a bounded state. Such type of nonplanar geometrical space arises in Capsule implosions, Supernova explosions, Saturn's magnetosphere, etc. In the year 1974, Maxon and Viicelli [7] investigated the characteristic of IAW in nonplanar geometrical space and found that the nonplanar wave moves faster than the planar counterparts. Gao et al. [8] observed the propagating behaviors of nonplanar DIAW in unmagnetized dusty plasma through the KdV-Burgers model. Further, several authors performed various theoretical and experimental works to observe the behaviors of IAW in different nonplanar plasma systems [9, 10]. Recently, Demiray [11] observed the IAW propagating in a nonplanar plasma system comprising positively charged cold ions and electrons satisfying hybrid  $q$ -nonextensive nonthermal velocity distribution. Some experimental on plasma circumstances indicates that the characteristic of wave propagation in a dissipative system significantly depends on interparticle collisions and viscosity etc. [12]. To consider the impact from viscosity a Burgers term is added to Demiray's observation [11] which may produce solitary (in case of the negligible effect of dissipation) as well as shock (in case of strong dissipation) type wave features. The SHBM is employed to find an approximate analytical solution that produces a shock wave. In the present observation, we analyze the significant impact of different physical parameters as well as time parameter ( $\tau$ ) on shock and solitary IAW through the NKDVB framework. The work of this manuscript is formulated as follows: In Sect. 2, the governing equations for the system are stated and the NKDVB equation is derived employing RPM. In Sect. 3 NKDVB model is derived by using RPM. Sect. 4 presents an approximate analytical solitary wave solution for the said equation. In Sect. 5, a shock solution is generated by employing Hirota's bi-linear approach. In Sect. 6, analyzes the numerical structure of the solutions. Section 7 concludes the investigation.

## 2 Problem Formulation

We consider here a unmagnetized viscous plasma comprising positively charged cold ions along with  $q$ -nonextensive nonthermal velocity distributed electrons. The dynamics of the system is described by the normalized basic governing equations:

$$\frac{\partial n}{\partial t} + \nabla \cdot (n\mathbf{u}) = 0 \quad (1)$$

$$\frac{\partial \mathbf{u}}{\partial t} + (\mathbf{u} \cdot \nabla) \mathbf{u} = -\nabla \psi + \delta \nabla^2 \mathbf{u} \quad (2)$$

$$\nabla^2 \psi = n_e - n \quad (3)$$



where  $n$  and  $n_e$  denote normalized number densities of cold ion and electron,  $\mathbf{u}$  represents velocity of the ion fluid whereas, the electrostatic potential is noted by  $\psi$  and  $\delta$  is the viscosity coefficient. Density of normalized  $q$ -nonextensive nonthermal electron is given by

$$n_e = [1 + (q - 1)\psi]^{\frac{q+1}{2(q-1)}} (1 + L_1\psi + L_2\psi^2) \quad (4)$$

The coefficients  $L_1$  and  $L_2$  are as

$$L_1 = -\frac{16q\alpha}{(3 - 14q + 15q^2 + 12\alpha)}, \quad L_2 = -(2q - 1)L_1. \quad (5)$$

where the parameter  $\alpha$  determines nonthermal electrons numbers in the system. The parametric zones of  $(q, \alpha)$  and their validity for solitary wave solutions are described by Williams et al. [13]. In the extensive limiting case ( $q \rightarrow 1$ ) and  $\alpha = 0$ , reduces the distribution to the Maxwell-Boltzmann velocity distribution whereas, it reduces to Cairn distribution [14] for the case ( $q \rightarrow 1$ ) and  $\alpha \neq 0$ . We consider the field Eqs. (1)–(3) in the following form,

$$\frac{\partial n}{\partial t} + \frac{1}{R^\mu} \frac{\partial(R^\mu nu)}{\partial R} = 0, \quad (6a)$$

$$\frac{\partial u}{\partial t} + u \frac{\partial u}{\partial R} = -\frac{\partial \psi}{\partial R} + \delta \left[ \frac{1}{R^\mu} \frac{\partial}{\partial R} \left( R^\mu \frac{\partial u}{\partial R} \right) - \frac{\mu u}{R^2} \right], \quad (6b)$$

$$\frac{1}{R^\mu} \frac{\partial}{\partial R} \left( R^\mu \frac{\partial \psi}{\partial R} \right) = n_e + n \quad (6c)$$

Here the parameter  $\mu = 1, 2$  signify the motion of cylindrical and spherical IAWs whereas, the dynamics of planar IAW is represented by  $\mu = 0$ . For small values of  $\psi$ , the electron number density  $n_e$  expressed in Eq. (4) can be presented in a power series as,

$$n_e = 1 + p_1\psi + p_2\psi^2 + p_3\psi^3 + \dots \quad (7)$$

Here the coefficients  $p_1, p_2$  and  $p_3$ , are taken as

$$p_1 = L_1 + \frac{q+1}{2}, \quad p_2 = L_2 + L_1 \left( \frac{q+1}{2} \right) + \frac{(q+1)(3-q)}{2} \quad (8)$$

$$p_3 = \frac{(q+1)(3-q)(5-3q)}{48} + L_1 \frac{(q+1)(3-q)}{8} + L_2 \frac{(q+1)}{2} \quad (9)$$

### 3 Formation of Nonplaner KdV Burgers Equation

To derive the NKDVB equations the standard RPM [15] will be utilized. In order to derive the depending variables  $n$ ,  $u$ , and  $\psi$  are stretched in a series of  $\epsilon$  as [16],

$$\begin{aligned} n &= 1 + \epsilon n_1 + \epsilon^2 n_2 + \epsilon^3 n_3 + \dots \\ u &= 0 + \epsilon u_1 + \epsilon^2 u_2 + \epsilon^3 u_3 + \dots \\ \psi &= 0 + \epsilon \psi_1 + \epsilon^2 \psi_2 + \epsilon^3 \psi_3 + \dots \end{aligned} \quad (10)$$

Now, the new stretched coordinates are taken as,

$$\xi = \epsilon^{1/2}(R - v_p t), \quad \tau = \epsilon^{3/2}t. \quad (11)$$

We assume a weak damping in the viscous plasma and write

$$\delta \approx \epsilon^{1/2} \delta_0 \quad (12)$$

Substituting the expression in Eq. (10) along with the coordinates (11) into the (6a)–(6c) and equating the coefficients of different order of  $\epsilon$  we obtain,

$$n_1 v_p = u_1 \quad (13)$$

$$\frac{\partial n_1}{\partial \tau} - v_p \frac{\partial n_2}{\partial \xi} + \frac{\mu u_1}{v_p \tau} - \frac{\partial}{\partial \tau}(n_1 u_1 + u_2) = 0 \quad (14)$$

$$v_p u_1 = \psi_1 \quad (15)$$

$$\frac{\partial u_1}{\partial \tau} - v_p \frac{\partial u_2}{\partial \xi} - u_1 \frac{\partial u_1}{\partial \xi} + \frac{\partial \psi_1}{\partial \xi} - \delta_0 \frac{\partial^2 u_1}{\partial \xi^2} = 0 \quad (16)$$

$$n_1 = p_1 \psi_1 \quad (17)$$

$$\frac{\partial^2 \psi_1}{\partial \xi^2} - p_1 \psi_2 - p_2 \psi_1^2 - n_2 = 0 \quad (18)$$

Using the results (13), (15) and (17), we find  $v_p = \frac{1}{p_1^{1/2}}$  which signifies the phase velocity of the perturbation mode and the parameter  $\epsilon$  measures the weakness and the dispersion of the perturbation. Using the results (13)–(18) stated above and setting  $\psi_1 = \psi$  we obtain the NKDVB equation as

$$\frac{\partial \psi}{\partial \tau} + P \psi \frac{\partial \psi}{\partial \xi} + Q \frac{\partial^3 \psi}{\partial \xi^3} + R \frac{\partial^2 \psi}{\partial \xi^2} + S \psi = 0, \quad (19)$$

where  $P = \frac{3}{2}p_1^{1/2} - \frac{p_2}{p_1^{3/2}}$ ,  $Q = \frac{1}{2p_1^{3/2}}$ ,  $R = -\frac{\delta_0}{2}$ ,  $S = \mu/2\tau$ . Here, the nonlinear coefficient  $P$  is a function of the parameters  $\alpha$  and  $q$ . The solitary type wave becomes compressive when  $P > 0$ , whereas, it becomes rarefactive for  $P < 0$ .

### 4 Progressive Wave Solution for Nonplanar KdV-Burgers (NKDVB) Equation

Here, we apply the WRM to obtain an approximate analytical solution for the NKDVB equation. In order to employ WRM [10, 11] we utilize the solution of the standard KdV equation. In consideration of negligible small values of  $\delta_0$  and large time  $\tau$  the nonplanar KdV-Burgers Eq. (19) is written as

$$\frac{\partial \psi}{\partial \tau} + P\psi \frac{\partial \psi}{\partial \xi} + Q \frac{\partial^3 \psi}{\partial \xi^3} = 0 \tag{20}$$

which permits the solution

$$\psi = \lambda_0 \text{sech}^2 \eta_0, \quad \eta_0 = w(\xi - V_0\tau) \tag{21}$$

with

$$w^2 = \frac{P\lambda_0}{12Q}, \quad V_0 = \frac{P\lambda_0}{3} \tag{22}$$

Here  $\lambda_0$  presents the constant amplitude of the soliton. Now we assume that amplitude and width of the soliton will be time dependent due to the application of Burgers term and geometric term. Thus, the progressive wave solution of Eq. (21) is proposed as

$$\psi = \lambda(\tau) \text{sech}^2 \eta, \quad \eta = w(\xi - V(\tau)) \tag{23}$$

with

$$w^2(\tau) = \frac{P\lambda(\tau)}{12Q}, \quad V'(\tau) = \frac{P\lambda(\tau)}{3} \tag{24}$$

Here the prime stands for presenting differentiation of  $V(\tau)$  against  $\tau$ . Actually, the solution presented in (23) is the same as the solution appeared in (22) except the presence of  $\lambda(\tau)$  in (24). However,  $\lambda(\tau)$  is to be determined for the later. It is found that though the solution (23) satisfies the Eq. (19) rather a residue term  $\mathcal{R}(\eta, \tau)$  presents there as,

$$\mathcal{R}(\eta, \tau) = \left[ \lambda' + 4R\lambda Q^2 + S\lambda - \frac{2\lambda w' \eta}{w} \tanh \eta \right] \text{sech}^2 \eta - 6Rw^2 \lambda \text{sech}^4 \eta. \tag{25}$$

Here, the term  $\mathcal{R}(\eta, \tau)$  is an even function of  $\eta$ . To obtain a differential equation for finding  $\lambda(\tau)$ , a strong restriction on  $\lambda(\tau)$  is imposed by introducing a weighted function. Here, we choose  $\text{sech}^2\eta$  as a weighted function. We multiply Eq. (25) by  $\text{sech}^2\eta$ , and integrate it from  $\eta = -\infty$  to  $\eta = \infty$  and lastly put the result to zero,

$$\lambda' + S\lambda - \frac{w'\lambda}{2w} - \frac{4Rw^2\lambda}{5} = 0. \quad (26)$$

We eliminate  $w$  between the Eqs. (24) and (26) and get,

$$\lambda' + \frac{4}{3}S\lambda = \frac{4PR}{45Q}\lambda^2. \quad (27)$$

The solution of Eq. (27) becomes

$$\lambda(\tau) = \left( M\tau^{\frac{2\mu}{3}} + \frac{4PR\tau}{(\frac{2\mu}{3} - 1)45Q} \right)^{-1}, \quad (28)$$

where  $M$  is a simple integration constant and  $\lambda_0$  ( $\tau \rightarrow \tau_0$ ,  $\lambda(\tau) \rightarrow \lambda_0$ ) is the initial amplitude satisfying Eq. (22). Thus,  $\lambda(\tau)$  is written as

$$\lambda(\tau) = \lambda_0 \left( \frac{\tau_0}{\tau} \right)^{\frac{2\mu}{3}} \left( 1 + \frac{4PR\lambda_0\tau_0}{(\frac{2\mu}{3} - 1)45Q} \left[ \left( \frac{\tau_0}{\tau} \right)^{\frac{2\mu}{3} - 1} - 1 \right] \right)^{-1}. \quad (29)$$

Using (29) in the expression  $V'(\tau)$  and integrating we get

$$V(\tau) = \frac{P\lambda_0}{3} - \frac{45Q}{4R} \ln \left[ \left( \frac{\tau_0}{\tau} \right)^{\frac{2\mu}{3}} \left( \frac{\lambda_0}{\lambda} \right) \right], \quad (30)$$

Using the result (24) we find

$$w(\tau) = \sqrt{\frac{P\lambda_0}{12Q}} \left( \frac{\tau_0}{\tau} \right)^{\frac{\mu}{3}} \left( 1 + \frac{4PR\lambda_0\tau_0}{(\frac{2\mu}{3} - 1)45Q} \left[ \left( \frac{\tau_0}{\tau} \right)^{\frac{2\mu}{3} - 1} - 1 \right] \right)^{-\frac{1}{2}}. \quad (31)$$

Thus, the final solution of equation is

$$\psi(\xi, \tau) = \lambda(\tau)\text{sech}^2[w(\tau)(\xi - V(\tau))], \quad (32)$$

where the results (29)–(31) provide the values of  $\lambda(\tau)$ ,  $V(\tau)$  and  $w(\tau)$  respectively.

This analytical solution (32) can be reduced to the planar solution of Eq. (19) for  $\mu = 0$  whereas, the cylindrical and spherical wave solution are given by ( $\mu = 1$ ) and ( $\mu = 2$ ) respectively.

## 5 Shock Type Wave Solution for Nonplanar KdV-Burgers (NKDVB) Equation

The strong anomalous dissipation may cause to form shock type wave solution. Now, to explore shock type wave solution, we utilize SHBM [17] and rewrite Eq. (19) in the following form:

$$\frac{\partial \psi}{\partial \tau} + P(\tau)\psi \frac{\partial \psi}{\partial \xi} + Q(\tau) \frac{\partial^3 \psi}{\partial \xi^3} + R(\tau) \frac{\partial^2 \psi}{\partial \xi^2} + S(\tau)\psi = 0. \quad (33)$$

To find a single kink solution, We first use the transformation

$$\psi(\xi, \tau) = e^\theta, \quad \text{where } \theta = k\xi - \omega(\tau). \quad (34)$$

We derive the dispersion relation as

$$\omega(\tau) = \int_{\tau_0}^{\tau} (Q(\tau)k^3 + R(\tau)k^2 + S(\tau))d\tau, \quad (35)$$

The shock solution of Eq. (33) is taken as  $\psi = A(\ln(f))_\xi$  where  $f(\xi, \tau)$ , is determined as

$$f(\xi, \tau) = 1 + e^\theta = 1 + e^{k\xi - \omega(\tau)}, \quad (36)$$

Utilizing Eqs. (35) and (36) we find,

$$\psi = A \frac{ke^\theta}{1 + e^\theta}. \quad (37)$$

Substituting Eq. (37) into Eq. (33) we obtain a polynomial equation for  $e^{n\theta}$ . Putting the coefficient of  $e^{n\theta}$ , to zero, a system of algebraic equation is obtained. Solving these algebraic equation we get

$$A = \frac{2k^3 R(\tau) - S(\tau)}{P(\tau)k^2}. \quad (38)$$

Combining Eqs. (37) and (38) we find the singleton shock solution as,

$$\psi(\theta) = \frac{2k^3 R(\tau) - S(\tau)}{2P(\tau)k} \left( 1 + \tanh\left(\frac{\theta}{2}\right) \right) \quad (39)$$

where  $\theta = k\xi - \int_{\tau_0}^{\tau} (Q(\tau)k^3 + R(\tau)k^2 + S(\tau))d\tau$ .

Putting the expression as  $P(\tau) = P, Q(\tau) = Q, R(\tau) = R$ , and  $S(\tau) = \frac{\mu}{2\tau}$  in Eq. (33), we find the standard non planer KdV-Burgers equation and the shock solution of Eq. (19) can be written as,

$$\psi(\xi, \tau) = \frac{4k^3R - \frac{\mu}{\tau}}{4Pk} \left( 1 + \tanh\left(\frac{\theta}{2}\right) \right), \tag{40}$$

$$\text{where } \theta = k\xi - \left[ (Qk^3 + Rk^2)(\tau - \tau_0) + \frac{\mu}{2} \ln\left(\frac{\tau}{\tau_0}\right) \right].$$

### 6 Results and Discussion

To detect a suitable parametric domain, the variation of the nonlinear coefficient  $P$  and the dispersion coefficient  $Q$  due to the change in the parameter  $\alpha$  and  $q$  are shown in Figs. 1a–d. Figure 2a exhibits the variation of amplitude in planar and nonplanar wave profiles and it is found that the planar wave moves over the cylindrical wave and the spherical wave. Figures 2b, c show the evolution of cylindrical and spherical wave respectively for different time intervals. The significant impact of the Burgers term follows from Fig. 2d. Enhancing  $\delta_0$  causes for losing of potential energy of the system and naturally the soliton have negligible backward shifting with declining amplitude. The impacts of the nonextensive parameters  $q$  on wave propagation depicted in Fig. 2e. It is found that the wave gets steepened with enhancing  $\alpha$  and gets flattened due to the rise in nonthermal electron numbers (see Fig. 2f). For a clear vision of wave propagation, the three-dimensional profiles of the cylindrical and the spherical wave are drawn in Fig. 3a, b. The significant impact of Burgers term in diminishing amplitude is also understood from Fig. 3c. Figures 4a and 5a exhibit the evolution of kink type soliton for different times in cylindrical geometry. Figures 4b and 5b shows that the increasing  $\delta_0$  leads the soliton to move dipper. The significant effect of the nonextensive parameter  $q$  is shown in Figs. 4c and 5c. It is important to note

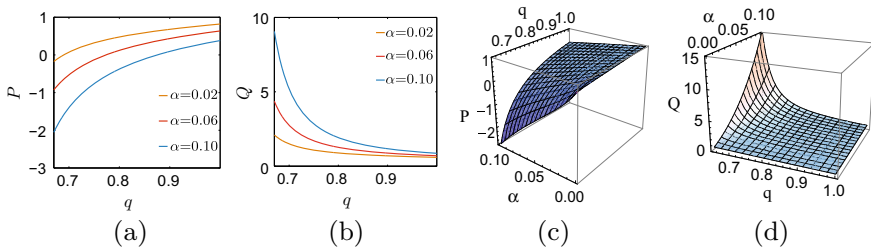


**Fig. 1** a Variation of nonlinearity coefficient  $P$  with  $q$  for various values of  $\alpha$ , b Variation of dispersion coefficient  $Q$  with  $q$  for various values of  $\alpha$ . c 3D Variation of nonlinearity coefficient  $P$  with  $q$  and  $\alpha$ , d 3D Variation of dispersion coefficient  $Q$  with  $q$  and  $\alpha$

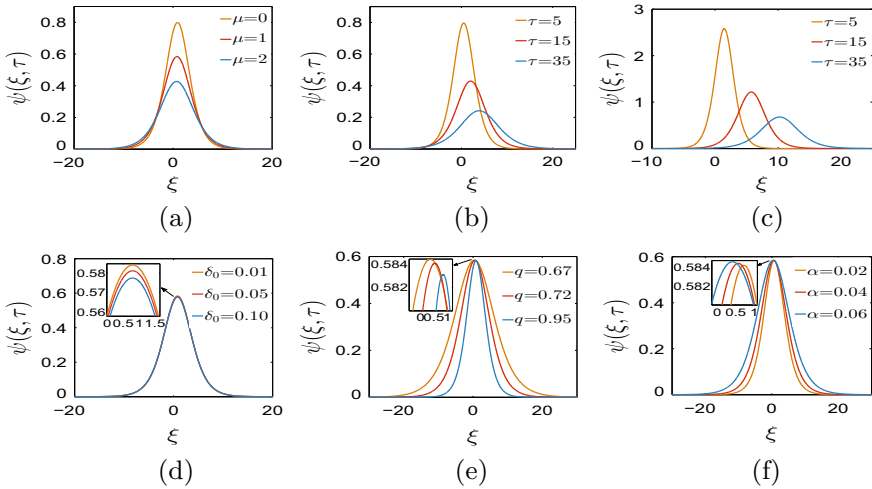


**Fig. 2** Profiles of  $\psi(\xi, \tau)$  versus  $\xi$  of Solution (32), **a** when  $q = 0.9, \alpha = 0.01, \tau_0 = 5, \delta_0 = 0.01, \tau = 8, \lambda_0 = 0.8$ , **b** when  $q = 0.95, \alpha = 0.01, \tau_0 = 5, \delta_0 = 0.02, \mu = 1, \lambda_0 = 0.9$ , **c** when  $q = 0.9, \mu = 1, \tau_0 = 5, \alpha = 0.01, \tau = 8, \lambda_0 = 0.8$ , **d** when  $q = 0.9, \alpha = 0.02, \tau_0 = 4, \delta_0 = 0.02, \mu = 1, \lambda_0 = 3$ , **e**  $\delta_0 = 0.02, \mu = 1, \tau_0 = 5, \alpha = 0.01, \tau = 8, \lambda_0 = 0.8$ , **f** when  $q = 0.9, \mu = 1, \tau_0 = 5, \delta_0 = 0.01, \tau = 8, \lambda_0 = 0.8$

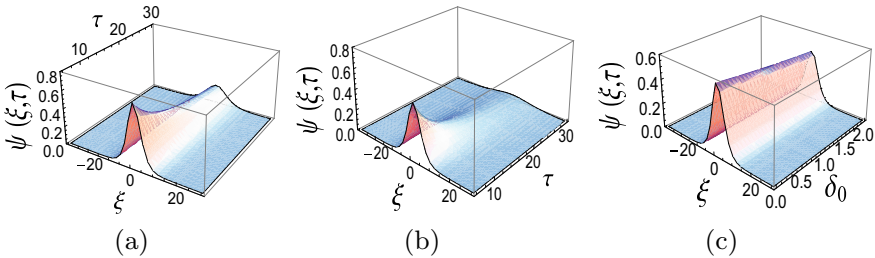


**Fig. 3** 3D Profiles of Solution (32), **a** when  $\mu = 1, q = 0.9, \alpha = 0.01, \tau_0 = 5, \delta_0 = 0.01, \tau = 8, \lambda_0 = 0.8$ , **b** when  $\mu = 2, q = 0.9, \alpha = 0.01, \tau_0 = 5, \delta_0 = 0.01, \tau = 8, \lambda_0 = 0.8$ , **c** when  $\mu = 1, q = 0.9, \alpha = 0.01, \tau_0 = 5, \tau = 8, \lambda_0 = 0.8$

that there is a critical point of the parameter  $q$  for which anti-kink type shocks are found below the values of critical point and oppositely kink type shocks exist for the higher values of  $q$ .

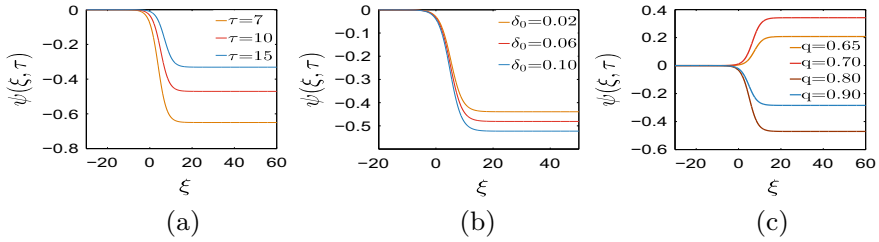


**Fig. 4** 2D Profiles of Solution (40), **a** when  $q = 0.8$ ,  $\alpha = 0.05$ ,  $\tau_0 = 5$ ,  $k = 0.5$ ,  $\delta_0 = 0.05$ ,  $\mu = 1$ , **b** when  $\alpha = 0.05$ ,  $\tau_0 = 5$ ,  $k = 0.5$ ,  $\mu = 1$ ,  $q = 0.8$ ,  $\tau = 10$ , **c** when  $q = 0.8$ ,  $\tau = 10$ ,  $\tau_0 = 5$ ,  $k = 0.5$ ,  $\delta_0 = 0.05$ ,  $\mu = 1$ , **d** when  $\alpha = 0.05$ ,  $\tau_0 = 5$ ,  $k = 0.5$ ,  $\mu = 1$ ,  $\delta_0 = 0.05$ ,  $\tau = 10$

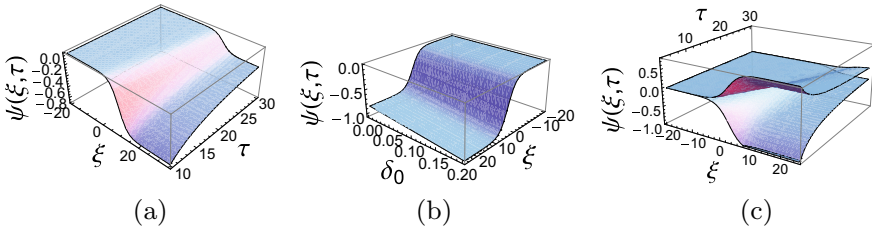


**Fig. 5** 3D Profiles of Solution (40), **a** when  $q = 0.8$ ,  $\alpha = 0.05$ ,  $\tau_0 = 4$ ,  $k = 0.5$ ,  $\delta_0 = 0.05$ ,  $\mu = 0$ , **b** when  $q = 0.8$ ,  $\alpha = 0.05$ ,  $\tau_0 = 4$ ,  $k = 0.5$ ,  $\mu = 1$ , **c** when  $q = 0.7, 0.8$ ,  $\alpha = 0.05$ ,  $\tau_0 = 4$ ,  $k = 0.5$ ,  $\delta_0 = 0.05$ ,  $\mu = 1$ ,

## 7 Conclusion

Using the basic governing equation the propagation of cylindrical and spherical IAW in unmagnetized plasma comprising positively charge cold ions and electrons describing hybrid  $q$ -nonextensive nonthermal velocity distribution are analyzed through the NKDVB model. The WRM and SHBM are employed to obtain a new class of the solitary and shock wave solution for the present system. The significant effects of different physical parameters such as  $\alpha$ ,  $q$ ,  $\delta_0$  and time parameter  $\tau$  are observed from a numerical standpoint. Finally, it can be concluded that the results of our investigation may be helpful to observe the propagating behavior of solitary and shock waves in laboratory plasma as well as space plasma environments.

## References

1. Sagdeev, R.Z.: Cooperative phenomena and shock waves in collisionless plasmas. *Rev. Plasma Phys.* **4**, 23 (1966)
2. Taylor, R.J., Baker, D.R., Ikezi, H.: Observation of collisionless electrostatic shocks. *Phys. Rev. Lett.* **24**(5), 206 (1970)
3. Shukla, P.K., Silin, V.P.: Dust ion-acoustic wave. *Phys. Scr.* **45**(5), 508 (1992)



4. Barkan, A., D'angelo, N., Merlino, R.L.: Experiments on ion-acoustic waves in dusty plasmas. *Planet. Space Sci.* **44**(3), 239–242 (1996)
5. D'Angelo, N.: Coulomb solids and low-frequency fluctuations in RF dusty plasmas. *J. Phys. D: Appl. Phys.* **28**(5), 1009 (1995)
6. Dubouloz, N., Pottelette, R., Malingre, M., Treumann, R.A.: Generation of broadband electrostatic noise by electron acoustic solitons. *Geophys. Res. Lett.* **18**(2), 155–158 (1991)
7. Maxon, S., Viecelli, J.: Cylindrical solitons. *Phys. Fluids* **17**(8), 1614–1616 (1974)
8. Gao, D.N., Zhang, Z.R., Wu, J.P., Luo, D., Duan, W.S., Li, Z.Z.: Cylindrical and Spherical Dust-Ion Acoustic Solitary Waves by Damped Korteweg-de Vries-Burgers Equation. *Braz. J. Phys.* **49**(5), 693–697 (2019)
9. Masood, W., Imtiaz, N., Siddiq, M.: Ion acoustic shock waves in dissipative electron-positron-ion plasmas with weak transverse perturbations. *Phys. Scr.* **80**(1), 015501 (2009)
10. Roy, S., Saha, S., Raut, S., Das, A.N.: Studies on the effect of kinematic viscosity on electron-acoustic cylindrical and spherical solitary waves in a plasma with trapped electrons. *J. Appl. Math. Comput. Mech.* **20**(2) (2021)
11. Demiray, H.: Analytical solution for nonplanar waves in a plasma with q-nonextensive nonthermal velocity distribution: weighted residual method. *Chaos, Solitons & Fractals* **130**, 109448 (2020)
12. Raut, S., Mondal, K.K., Chatterjee, P., Roy, A.: Propagation of dust-ion-acoustic solitary waves for damped modified Kadomtsev-Petviashvili-Burgers equation in dusty plasma with a q-nonextensive nonthermal electron velocity distribution. *SeMA J.* 1–23 (2021)
13. Williams, G., Kourakis, I., Verheest, F., Hellberg, M.A.: Re-examining the Cairns-Tsallis model for ion acoustic solitons. *Phys. Rev. E* **88**(2), 023103 (2013)
14. Cairns, R.A., Bingham, R., Dendy, R.O., Nairn, C.M.C., Shukla, P.K., Mamun, A.A.: Ion sound solitary waves with density depressions. *Le J. de Phys. IV* **5**(C6), C6-43, 072306 (1995)
15. Taniuti, T.: Reductive perturbation method and far fields of wave equations. *Prog. Theor. Phys. Suppl.* **55**, 1–35, 023103 (1974)
16. Mushtaq, A., Shah, H.A.: Nonlinear Zakharov-Kuznetsov equation for obliquely propagating two-dimensional ion-acoustic solitary waves in a relativistic, rotating magnetized electron-positron-ion plasma. *Phys. Plasmas* **12**(7), 072306 (2005)
17. Awawdeh, F., Jaradat, H.M., Al-Shara, S.: Applications of a simplified bilinear method to ion-acoustic solitary waves in plasma. *Eur. Phys. J. D* **66**(2), 1–8, 072306 (2012)

# Formation of Shocks in Ionospheric Plasma with Positron Beam



Sunidhi Singla , Manveet Kaur , and Nareshpal Singh Saini 

**Abstract** The nonlinear dynamics of ion acoustic shocks (IAShs) in electron-ion plasma has been studied in the presence of relativistic positron beam as a result of the vital importance in astrophysical environments mainly ionospheric region. The Korteweg-de Vries-Burgers (KdVB) equation and its oscillatory solution is derived by employing reductive perturbation method. From the solution of KdVB equation, existence of oscillatory IAShs and their characteristics are studied under the influence of various plasma parameters such as temperature of ions as well as positron, relativistic factor, viscosity of ions and different parameters of beam. The behaviour of IAShs propagating in a relativistic plasma model is strongly dependent on the ion and positron temperatures, the mass ratio and the relativistic effects. The kinematic viscosity and the equilibrium ion number density play very important roles in the basic features of the produced IAShs.

**Keywords** Shocks · Ion acoustic · Positron beam · Reductive perturbation

## 1 Introduction

During the past two decades, many authors have studied the electron-ion plasma in different space and laboratory environments. Electron-ion plasma evokes great interest for many researches due to its existence in pulsar environments, earth's ionosphere, polar regions of neutron stars, white dwarfs [1, 2], pulsar magnetosphere [3–5] etc. It is noteworthy that introduction of positron beam immensely affects the physical properties of plasma. Misra et al. [6] studied the nonlinear propagation and interaction of electron–positron plasma that shows distinctive behavior feature from the usual linear mode. With the increase in the superthermality of electrons and positron beam speed, amplitude and width of the solitons get modified significantly as reported by Shan et al. [7]. Numerous studies has confirmed the influence

---

S. Singla (✉) · M. Kaur · N. S. Saini  
Department of Physics, Guru Nanak Dev University, Amritsar 143005, India  
e-mail: [singla.sunidhi94@gmail.com](mailto:singla.sunidhi94@gmail.com)

and importance of interaction of ion/electron/positron beam in space and laboratory plasmas [8–11]. Sarma et al. studied the propagation properties of ion acoustic nonlinear structures (IANSs) in a relativistic plasma containing ion fluid, positron and relativistic electrons. It was reported that different plasma parameters have immense impact on the characteristics of IANSs [12].

For the formation of KdV-Burgers equation reductive perturbation approach was used, and the influence of various plasma physical parameters on IA shock waves was depicted. Many KdV-Burgers equations solutions were examined and in the presence of electron orbital motion excitation from KdV oscillations to the shock solution was described [13]. Very recently, Singh et al. [14] studied the effect of anisotropic term on electron-acoustic shocks by deriving the KdV-Burgers equation in superthermal plasma. To the best of our knowledge, study of oscillatory shocks in a electron-ion plasma in the presence of relativistic positron beam has not been reported yet. In this investigation, main focus of the study is to illustrate the influence of positron beam on ion acoustic shocks by deriving KdV-Burgers equation and its oscillatory solution. The manuscript is organized as follows: in Sect. 2, three fluids beam-plasma model is described. The derivation of KdV-Burgers equation are presented in Sect. 3. Oscillatory solution of KdV-Burgers equation is illustrated in Sect. 4. Parametric analysis is presented in Sect. 5 and conclusions are summarized in Sect. 6.

## 2 Three-Fluid Beam-Plasma Model

An unmagnetized plasma involving three components specifically cold inertial ions, hot inertial electrons with injection of relativistic positron beam is considered to study the characteristics of IA shock waves. The normalized equations for three fluids model (continuity, momentum, pressure and Poisson equations) are described as follows:

For ions:

$$\frac{\partial n_i}{\partial t} + \frac{\partial}{\partial x}(n_i v_i) = 0, \quad (1)$$

$$\frac{\partial v_i}{\partial t} + v_i \frac{\partial v_i}{\partial x} + \frac{\sigma}{n_i} \frac{\partial p_i}{\partial x} = -\frac{\partial \phi}{\partial x} + \eta_i \frac{\partial^2 v_i}{\partial x^2}, \quad (2)$$

$$\frac{\partial p_i}{\partial t} + v_i \frac{\partial p_i}{\partial x} + 3p_i \frac{\partial v_i}{\partial x} = 0, \quad (3)$$

For electrons:

$$\frac{\partial n_e}{\partial t} + \frac{\partial}{\partial x}(n_e v_e) = 0, \quad (4)$$

$$\beta_1 n_e \left( \frac{\partial v_e}{\partial t} + v_e \frac{\partial v_e}{\partial x} \right) + \frac{\partial p_e}{\partial x} = n_e \frac{\partial \phi}{\partial x} + \eta_e \frac{\partial^2 v_e}{\partial x^2}, \quad (5)$$

$$\frac{\partial p_e}{\partial t} + v_e \frac{\partial p_e}{\partial x} + 3p_e \frac{\partial v_e}{\partial x} = 0, \quad (6)$$

For positron beam:

$$\frac{\partial n_b}{\partial t} + \frac{\partial}{\partial x}(n_b v_b) = 0, \quad (7)$$

$$\beta_2 n_b \left( \frac{\partial v'_b}{\partial t} + v_b \frac{\partial v'_b}{\partial x} \right) + \alpha \frac{\partial p_b}{\partial x} = -n_b \frac{\partial \phi}{\partial x}, \quad (8)$$

$$\frac{\partial p_b}{\partial t} + v_b \frac{\partial p_b}{\partial x} + 3p_b \frac{\partial v'_b}{\partial x} = 0, \quad (9)$$

$$\frac{\partial^2 \phi}{\partial x^2} = n_e(1 + \mu_b) - n_b \mu_b - n_i. \quad (10)$$

where,  $l = i, e, b$ ,  $\sigma = \frac{T_l}{T_e}$ ,  $\beta_1 = \frac{m_e}{m_i}$ ,  $\mu_b = \frac{n_{bo}}{n_{io}}$ ,  $v'_b = v_b \left(1 + \frac{v_b^2}{2c_1^2}\right)$ ,  $\beta_2 = \frac{m_b}{m_i}$  and  $\alpha = \frac{T_b}{T_e}$ ,  $c_1 = \frac{c}{c_s}$ , Normalisation of the physical quantities are done as follows to make them dimensionless.  $t = T'/\omega_{pi}$ ,  $x = X'/\lambda_{Di}$ ,  $v_l = V'_l/c_s$ ,  $n_l = N'_l/N'_{l0}$ ,  $\phi = e\Phi'/k_B T_e$ ,  $p_l = P'_l/n_{l0} k_B T_l$  and the kinematic viscosity  $\eta_l$  is normalized by  $\lambda_{Di}^2 n_{l0} M_l \omega_{pl}$ , where  $\omega_{pi} = \sqrt{4\pi N_{io} e^2 / (k_B T_e)}$  is the ion-plasma oscillation frequency,  $c_s = \sqrt{k_B T_e / m_i}$  is the ion acoustic speed,  $\lambda_{Di}$  represents Debye length,  $N_{l0}$  is the unperturbed number density. The temperature of the  $l$ -th charged particle is  $T_l$ .

### 3 Derivation of KdV-Burgers Equation and Its Solution

To study the nonlinear propagation of ion acoustic shock waves in a plasma with relativistic positron beam, we introduce the following stretching coordinates [13]:

$$\zeta = \epsilon^{\frac{1}{2}}(x - v_p t), \quad \tau = \epsilon^{\frac{3}{2}} t. \quad (11)$$

where  $v_p$  denotes the phase velocity of the IASh. The weakness of the perturbation is measured by  $\epsilon$ , which is small in the range ( $0 < \epsilon < 1$ ). Expansions of the state variables in power series of  $\epsilon$  is illustrated as;

$$\begin{aligned} n_{i,e,b} &= 1 + \epsilon n_{i,e,b1} + \epsilon^2 n_{i,e,b2} + \epsilon^3 n_{i,e,b3} + \dots \\ p_{i,e,b} &= 1 + \epsilon p_{i,e,b1} + \epsilon^2 p_{i,e,b2} + \epsilon^3 p_{i,e,b3} + \dots \\ v_{i,e} &= \epsilon v_{i,e1} + \epsilon^2 v_{i,e2} + \epsilon^3 v_{i,e3} + \dots \\ v_b &= v_{bo} + \epsilon v_{b1} + \epsilon^2 v_{b2} + \epsilon^3 v_{b3} + \dots \\ \phi &= \epsilon \phi_1 + \epsilon^2 \phi_2 + \epsilon^3 \phi_3 + \dots \end{aligned}$$

We consider  $\eta_{e,i} = \epsilon^{\frac{1}{2}} \eta_{e0}(\eta_{i0})$ , where  $\eta_{e0}(\eta_{i0})$  is the equilibrium fluid viscosity of electron (ion). Also, scaling of  $\eta$  is taken into account in such a manner that only dissipative term is getting affected and not affecting other terms namely nonlinear and dispersive terms. After using stretching coordinates and expansion of state variable perturbation in Eqs. (1–10) and collecting the coefficients of lowest power of  $\epsilon$  we get:

$$n_{i1} = R\phi_1, \quad v_{i1} = Rv_p\phi_1, \quad p_{i1} = 3R\phi_1 \quad (12)$$

$$n_{e1} = S\phi_1, \quad v_{e1} = Sv_p\phi_1, \quad p_{e1} = 3S\phi_1 \quad (13)$$

$$n_{b1} = 2c_1^2 P Q \phi_1, \quad v_{b1} = 2c_1^2 P Q (v_p - v_{bo}) \phi_1, \quad p_{b1} = 3Q \phi_1 \quad (14)$$

$$\text{where } R = \frac{1}{(v_p^2 - 3\sigma)}, \quad S = \frac{1}{(3 - \beta_1 v_p^2)}, \quad P = \frac{1}{(1 + 3v_{bo}^2)}, \quad Q = \frac{1}{(\beta_2 (v_p - v_{bo})^2 - 3\alpha)};$$

and Poisson equation leads to the dispersion relation,

$$(1 + \mu_b)S - \mu_b 2c_1^2 P Q - R = 0 \quad (15)$$

The next higher order equations from the perturbation theory are as follows:

$$\frac{\partial n_{i1}}{\partial \tau} - v_p \frac{\partial n_{i2}}{\partial \zeta} + \frac{\partial v_{i2}}{\partial \zeta} + \frac{\partial}{\partial \zeta} (n_{i1} v_{i1}) = 0, \quad (16)$$

$$\begin{aligned} \frac{\partial v_{i1}}{\partial \tau} - v_p \frac{\partial v_{i2}}{\partial \zeta} + v_{i1} \frac{\partial v_{i1}}{\partial \zeta} + \sigma \frac{\partial p_{i2}}{\partial \zeta} - \sigma n_{i1} \frac{\partial p_{i1}}{\partial \zeta} \\ - \eta_i \frac{\partial^2 v_{i1}}{\partial \zeta^2} + \frac{\partial \phi_2}{\partial \zeta} = 0, \end{aligned} \quad (17)$$

$$\frac{\partial p_{i1}}{\partial \tau} - v_p \frac{\partial p_{i2}}{\partial \zeta} + v_{i1} \frac{\partial p_{i1}}{\partial \zeta} + 3 \frac{\partial v_{i2}}{\partial \zeta} + 3 p_{i1} \frac{\partial v_{i1}}{\partial \zeta} = 0, \quad (18)$$

$$\frac{\partial n_{e1}}{\partial \tau} - v_p \frac{\partial n_{e2}}{\partial \zeta} + \frac{\partial v_{e2}}{\partial \zeta} + \frac{\partial}{\partial \zeta} (n_{e1} v_{e1}) = 0, \quad (19)$$

$$\begin{aligned} \beta_1 \frac{\partial v_{e1}}{\partial \tau} - v_p \beta_1 \frac{\partial v_{e2}}{\partial \zeta} + \beta_1 v_{e1} \frac{\partial v_{e1}}{\partial \zeta} - \beta_1 v_p n_{e1} \frac{\partial v_{e1}}{\partial \zeta} \\ + \frac{\partial p_{e2}}{\partial \zeta} - \eta_e \frac{\partial^2 v_{e1}}{\partial \zeta^2} - n_{e1} \frac{\partial \phi_1}{\partial \zeta} = \frac{\partial \phi_2}{\partial \zeta}, \end{aligned} \quad (20)$$

$$\frac{\partial p_{e1}}{\partial \tau} - v_p \frac{\partial p_{e2}}{\partial \zeta} + v_{e1} \frac{\partial p_{e1}}{\partial \zeta} + 3 \frac{\partial v_{e2}}{\partial \zeta} + 3 p_{e1} \frac{\partial v_{e1}}{\partial \zeta} = 0, \quad (21)$$

$$\frac{\partial n_{b1}}{\partial \tau} - (v_p - v_{bo}) \frac{\partial n_{b2}}{\partial \zeta} + \frac{\partial v_{b2}}{\partial \zeta} + \frac{\partial}{\partial \zeta} (n_{b1} v_{b1}) = 0, \quad (22)$$

$$\begin{aligned} \frac{\beta_2}{2c_1^2} \left( (1 + 3v_{bo}^2) \frac{\partial v_{b1}}{\partial \tau} - (1 + 3v_{bo}^2)(v_p - v_{bo}) \frac{\partial v_{b2}}{\partial \zeta} + \frac{\partial v_{b1}}{\partial \zeta} \right. \\ \left. - 2v_{bo}(v_p - v_{bo})v_{b1} \right) - \frac{\beta_2}{2c_1^2} (v_p - v_{bo})(1 + 3v_{bo}^2)n_{b1} \frac{\partial v_{b1}}{\partial \zeta} \\ + \alpha \frac{\partial p_{b2}}{\partial \zeta} = - \frac{\partial \phi_2}{\partial \zeta} - n_{b1} \frac{\partial \phi_1}{\partial \zeta}, \end{aligned} \quad (23)$$

$$\frac{\partial p_{b1}}{\partial \tau} - (v_p - v_{bo}) \frac{\partial p_{b2}}{\partial \zeta} + v_{b1} \frac{\partial p_{b1}}{\partial \zeta} + \frac{3(1 + 3v_{bo}^2)}{2c_1^2} \quad (24)$$

$$\left( \frac{\partial v_{b2}}{\partial \zeta} + p_{b1} \frac{\partial v_{b1}}{\partial \zeta} \right) + \frac{6}{2c_1^2} v_{bo} v_{b1} \frac{\partial v_{b1}}{\partial \zeta} = 0,$$

$$(1 + \mu_b)n_{e2} - \mu_b n_{b2} - n_{i1} = 0. \quad (25)$$

By differentiating Eq. (25) w.r.t.  $\zeta$ , we have;

$$(1 + \mu_b) \frac{\partial n_{e2}}{\partial \zeta} - \mu_b \frac{\partial n_{b2}}{\partial \zeta} - \frac{\partial n_{i2}}{\partial \zeta} = 0 \quad (26)$$

Eliminating the second order perturbed quantities from Eqs. (16–25), we obtain the following KdV-Burgers Equation:

$$\frac{\partial \phi_1}{\partial \tau} + A \phi_1 \frac{\partial \phi_1}{\partial \zeta} + B \frac{\partial^3 \phi_1}{\partial \zeta^3} = C \frac{\partial^2 \phi_1}{\partial \zeta^2} \quad (27)$$

where, nonlinear coefficient,  $A = \frac{B'}{A'}$ ,

dispersion coefficient,  $B = \frac{1}{A'}$

and dissipation coefficient,  $C = \frac{C'}{A'}$

and

$$A' = -(1 + \mu_b)2\beta_1 v_p S^2 - \mu_b 2\beta_2 2c_1^2 (v_p - v_{bo}) P Q^2 - 2v_p R^2 \quad (28)$$

$$B' = -\mu_b 2c_1^2 P Q^2 (2c_1^2 P (1 - 2v_{bo}(v_p - v_{bo})P) + 9Q) - 3(1 + \mu_b)(4S - 1)S^2 - 3(1 + 4\sigma R)R^2 \quad (29)$$

$$C' = (1 + \mu_b)\eta_e v_p S^2 + \eta_i v_p R^2 \quad (30)$$

Solution of Eq. (27) represents the formation of shock waves with different coefficient A, B and C. In the limiting case, i.e. in the absence of dissipation term, ( $C = 0$ ) Eq. (27) transforms to KdV equation and it agrees with the results obtained in [12]. Furthermore, we have studied the formation of shocks whereas in authors in ref. [12] have studied the formation of solitons.

## 4 Solution of KdV-Burgers Equation

By introducing single variable transformation in Eq. (27), we have examined its analytical solution. The solution of Eq. (27) is determined by using the Tanh-method [14],

$$\phi_1(\xi, \tau) = \phi_{max} \left( 1 - \frac{1}{4} \left[ 1 + \tanh \left( \frac{\xi - u\tau}{W} \right) \right]^2 \right) \quad (31)$$

where,  $\phi_{max} = \frac{12C^2}{25AB}$ ,  $W = \nabla^{-1} = \frac{10B}{C}$  and  $u = \frac{6C^2}{25B}$

### 4.1 Oscillatory Shocks Solution

After dealing with different asymptotic boundary conditions, different type of solution for Eq. (27) is obtained. Using transformation  $\xi = \zeta - U\tau$  in the Eq. (27) and assuming  $\phi = \phi_0 + \Phi$  with  $\phi_0 = 2U/A$  and after linearising with respect to  $\phi$ , we obtain,

$$\frac{d^2\Phi}{d\xi^2} - \frac{C}{B} \frac{d\Phi}{d\xi} - \frac{U}{B}\Phi = 0. \quad (32)$$

The solution of above equation represents damped harmonic oscillator. Thus, the oscillatory shock wave solutions of Eq. (27) is given as [13]

$$\phi_{osc} = \frac{2U}{A} + \Theta \exp(-\Omega\xi) \cos(\varpi_1\xi) \quad (33)$$

where,  $\Theta$  is arbitrary constant,  $\Omega = -C/2B$  is the damping factor and  $\varpi_1 = \sqrt{\frac{U}{B}(1 - \frac{C^2}{4UB})}$ , also  $\frac{U}{B}$  represents the natural frequency of the plasma system.

### 5 Parametric Analysis

The propagation properties of ion acoustic shocks by changing the values of different physical parameters are analyzed numerically. We have considered positron beam density ( $\mu_b$ ) of the range 0.2–0.8, electron to ion temperature ratio( $\sigma$ ) of the range 0.1–0.5 and kinematic viscosity ranges from 0.2–0.8. The considered plasma parameters are from the Earth’s upper atmosphere (ionosphere region) [8]. It is numerically that with different plasma parameters, A shows negative value, which implies only negative potential IAShs.

The solution of oscillatory shock waves is plotted against  $\xi$  for different plasma parameters. Figure 1 represents the variation of oscillatory shocks with different values of positron beam density ratio ( $\mu_b$ ). It is seen that increase in the value of  $\mu_b$  leads to the decrease in amplitude of shocks. Thus, with the introduction of positron beam, shocks of smaller amplitude are formed and with increase in the value of  $\mu_b$  oscillatory behavior of the shocks tends to diminish. Figure 2 depicts the influence of electron to ion temperature ratio ( $\sigma$ ), it is remarked that the with increase in the value of  $\sigma$ , amplitude of shocks decreases. Figure 3 represents the variation of profile of oscillatory with viscosity of electrons ( $\eta_e$ ), it is depicted that the amplitude is decreased with change in the value of  $\eta_e$ . Furthermore, lesser viscous medium tends to have stronger oscillatory shock waves. Similar behavior is seen for kinematic viscosity of ions  $\eta_i$ . Finally, it is highlighted that the important findings may be useful in describing clearly the propagation properties of IAShs in multi-component plasma with positron beam which is found in Earth’s ionospheric region.

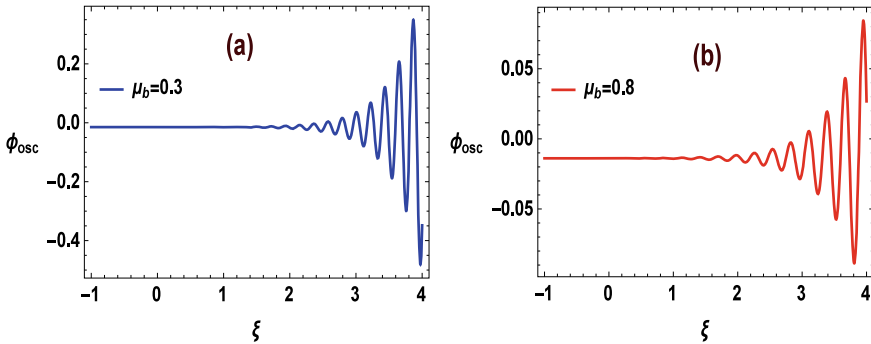


**Fig. 1** The variation of ion acoustic oscillatory shocks for different values of positron beam density ratio ( $\mu_b$ ) **a**  $\mu_b = 0.3$  **b**  $\mu_b = 0.8$ , with fixed values of  $\sigma = 0.1$  and  $\eta_e = 0.2$



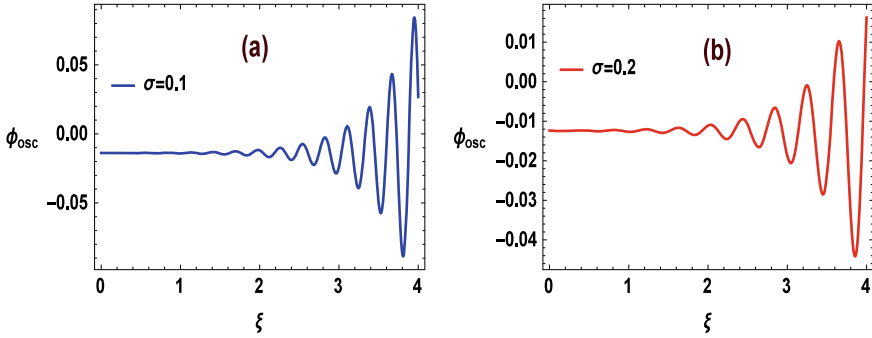


**Fig. 2** The variation of ion acoustic oscillatory shocks for different values of  $\sigma = 0.1$  and  $\sigma = 0.2$  respectively, where  $\mu_b = 0.5$  and  $\eta_e = 0.2$

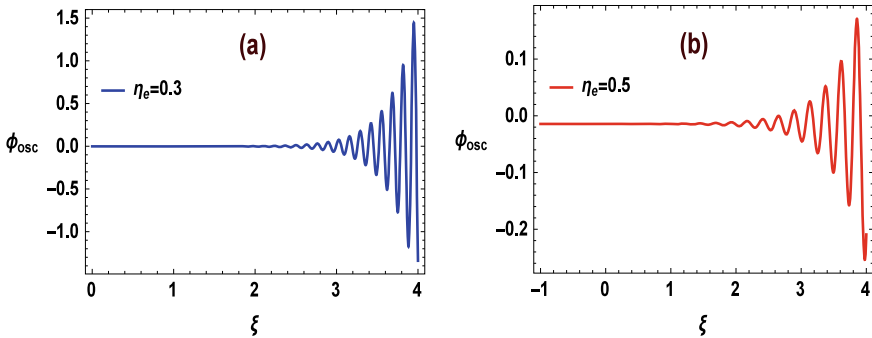


**Fig. 3** The variation of ion acoustic oscillatory shocks for different values of  $\eta_e = 0.2$  and  $\eta_e = 0.5$  respectively, where  $\sigma = 0.1$  and  $\mu_b = 0.5$

## 6 Conclusions

In this manuscript, the propagation properties of IAShs in a electron-ion plasma in the presence of beam of relativistic positrons. After the implication of reductive perturbation method, KdV-Burgers equation and its solution are derived. Only negative potential shocks are obtained. Positron beam and other physical parameters play an important role in the formation of different types of oscillatory shocks and their characteristics. The amplitude of oscillatory shocks decreases with the increase in  $\mu_b$  and  $\eta_e$ . This investigation may be useful to understand the nonlinear phenomena leading to the formation of ion acoustic shocks in astrophysical dense plasma environments, especially in Earth's ionospheric region [8, 12].

**Acknowledgements** Department of Science and Technology, Govt. of India, New Delhi under DST-SERB project No. CRG/2019/003988 is highly acknowledged to support this investigation.

## References

1. Lallement, R., Welsh, B.-Y., Barstow, M.-A., Casewell, S.-L.: High ions towards white dwarfs: circumstellar line shifts and stellar temperature. *Astrophys. Astron.* **533**(A140), 1–13 (2011)
2. Sabry, R., Moslem, W.-M., Shukla, P.-K.: Freak waves in white dwarfs and magnetars. *Phys. Plasmas* **19**(12), (122903 (1–7)) (2012)
3. Tribeche, M., Aoutou, K., Younsi, S., Amour, R.: Nonlinear positron acoustic solitary waves. *Phys. Plasmas* **16**(7), 072103(1–6) (2009)
4. Rahman, M.-M., Alam, M.-S., Mamun, A.-A.: Cylindrical and spherical positron-acoustic Gardner solitons in electron-positron-ion plasmas with nonthermal electrons and positrons. *Astrophys. Space Sci.* **352**, 193–200 (2014)
5. El-Shamy, E.-F.: Nonlinear propagation of positron-acoustic periodic travelling waves in a magnetoplasma with superthermal electrons and positrons. *Chin. Phys. Lett.* **34**(6), 065201(1–5) (2017)
6. Misra, A.-P., Roy Chowdhury, A.: Nonlinear interaction of electromagnetic pulses with an electron–positron plasma coupled NLS equation. *Chaos, Solitons Fractals* **15**(5), 1–10 (2003)
7. Shan, S.-A., El-Tantawy, S.-A., Moslem, W.-M.: On the fully nonlinear acoustic waves in a plasma with positrons beam impact and superthermal electrons. *Phys. Plasmas* **20**(8), 082104(1–7) (2013)
8. Gsponer, A.: The Physics of high-intensity high-energy Particle Beam Propagation in open Air and outer-space. *Plasmas*. <http://arxiv.org/abs/physics/0409157v3> [physics.plasm-ph] (2004)
9. Popel, S.-I., Vladimirov, S.-V., Shukla, P.-K.: Ion-acoustic solitons in electron-positron-ion plasmas. *Phys. Plasmas* **2**(716), 1–5 (1995)
10. Shan, S.-A., El-Tantawy, S.-A., Moslem, W.-M.: On the fully nonlinear acoustic waves in a plasma with positrons beam impact and superthermal electrons. *Phys. Plasmas*, **20**(8), 082104(1–7) (2013)
11. Singla, S., Saini, N.-S.: Head-on collision of ion-acoustic multi-solitons and study of rogue waves in electron-beam superthermal plasma. *Results Phys.* **22**(10), 103898( 1–11) (2021)
12. Sarma, R., Mishra, A.-P., Adhikary, N.-C.: Nonlinear ion–acoustic solitary waves in an electron–positron–ion plasma with relativistic positron beam. *Chin. Phys. B* **27**(10), 105207(1–6) (2018)
13. Atteya, A., Behery, E.-E., El-Taibany, W.-F.: Ion acoustic shock waves in a degenerate relativistic plasma with nuclei of heavy elements. *Eur. Phys. J. Plus* **132**(109), 1–8 (2017)
14. Singh, K., Saini, N.-S.: Effect of anisotropic pressure on electron acoustic oscillatory and monotonic shocks in superthermal magnetoplasma. *Radio Sci.* **54**(12), 1192–1203 (2019)

# Nonlinear Propagation of Gaussian Laser Beam in an Axially Magnetized Cold Quantum Plasma



P. P. Nikam, V. S. Pawar, S. D. Patil, and M. V. Takale

**Abstract** The evolution of self-focusing of Gaussian laser beam in underdense magnetized cold quantum plasma has been studied under parabolic equation approach. We have established beam-width parameter differential equation of Gaussian laser beam using WKB and paraxial approximations. This equation is solved numerically. The results are presented graphically by considering applied magnetic field along (forward) as well as opposite (reverse) to the axis of propagation of laser. It is seen that, the forward magnetization increase the self-focusing effect as compared to the reverse magnetization. In addition, quantum effects enhance the self-focusing behaviour of laser.

**Keywords** Gaussian beam · Self-focusing · Plasma · Magnetized · Quantum

## 1 Introduction

Many applications likes fusion by lasers [1], generation of higher order harmonics [2], laser having wavelength in the X-ray region [3] and other applications [4, 5] based on laser-plasma experiments. For such applications, laser should propagate more distance than the Rayleigh length. In plasmas, different nonlinear optical effects are present. Self-focusing (SF) of laser beam is one of them [6, 7]. SF in plasmas is mainly contributed due to three mechanisms such as; relativistic, ponderomotive and thermal. Recently, laser-matter (plasma) interaction in quantum regime has been investigated considerably [8]. Patil et al. [9] highlighted the SF of Gaussian beam in quantum plasma and extended the same to thermal quantum plasma [9]. Aggarwal

---

P. P. Nikam · S. D. Patil (✉)

Department of Physics, Devchand College, Arjunnagar 591 237, Maharashtra, India

e-mail: [sdpatilphy@gmail.com](mailto:sdpatilphy@gmail.com)

V. S. Pawar

Department of Physics, Raje Ramrao Mahavidyalaya, Jath 416 404, Maharashtra, India

M. V. Takale

Department of Physics, Shivaji University, Kolhapur 416 004, Maharashtra, India

© The Author(s), under exclusive license to Springer Nature Switzerland AG 2022

S. Banerjee and A. Saha (eds.), *Nonlinear Dynamics and Applications*,

Springer Proceedings in Complexity,

[https://doi.org/10.1007/978-3-030-99792-2\\_13](https://doi.org/10.1007/978-3-030-99792-2_13)

et al. [10] studied Gaussian beam propagation in density ramped magnetized cold plasma. Also, collective consequence of relativistic and ponderomotive mechanisms on SF of Gaussian beam was studied by Aggarwal et al. [11–13] in magnetized RCQP. Recently, Pawar et al. [14] explored effect of laser (aperture coefficient) and plasma (density) parameters on SF of finite AiG beams in RCQP.

In this present paper SF of Gaussian beams in underdense, magnetized RCQP is studied. An external magnetic field is parallel (forward) or antiparallel (reverse) to the propagation vector of beam. In Sect. 2, nonlinear ordinary second order beam-width parameter (BWP) differential equation has been achieved under WKB and paraxial approximations. Sections 3 and 4 contains graphical results and conclusions respectively.

## 2 Theoretical Formulation

Consider the wave vector of cylindrically distributed Gaussian beam propagating on the z-axis in magnetized RCQP. The total dielectric function  $\varepsilon$  of plasma is written as,

$$\varepsilon = \varepsilon_0 + \varepsilon_2(EE^*) \quad (1)$$

Here,  $\varepsilon_0$  and  $\varepsilon_2$  are intensity independent and dependent parts of  $\varepsilon$ . The  $\varepsilon_2$  has various forms under different physical conditions. The effective plasma electron density  $n_e$  for relativistic, magnetized plasma can be given as [12]

$$n_e = \frac{n_0}{\gamma(1 - (\omega_c/\gamma\omega))}$$

here,  $\omega_c$  and  $\omega$  are the electron cyclotron frequency and frequency of laser used,  $\gamma$  is the relativistic factor written as;

$$\gamma = \left[ 1 + A^2 + 2A^2(\sigma\Omega_c) \left( \frac{1}{\sqrt{1 + A^2}} \right) + 3A^2(\sigma\Omega_c)^2 \left( \frac{1}{1 + A^2} \right) \right]^{\frac{1}{2}}$$

where,  $A^2 = \frac{e^2|E_0|^2}{m^2c^2\omega^2}$  with  $c$  is velocity of light in free space,  $e$  and  $m$  are electronic charge and electrons rest mass respectively. For collisionless, magnetized cold quantum plasma  $\varepsilon_0$  and  $\varepsilon_2$  can be written as [12]

$$\varepsilon_0 = 1 - \frac{\Omega_p^2}{1 - \sigma\Omega_c} \quad (2)$$

$$\varepsilon_2(EE^*) = \Omega_p^2 \left( 1 - \frac{n_e}{n_0} \left( 1 - \frac{\beta}{\gamma} \right)^{-1} \right) \quad (3)$$

where,  $\Omega_p = \omega_p/\omega$ ,  $\Omega_c = \omega_c/\omega$ ,  $\beta = 4\pi^4 h^2/m^2 \omega^2 \lambda^4$ ,  $\omega_p = (4\pi n_0 e^2/m)^{1/2}$  and  $\omega_c = eB_0/mc$ . Here,  $\omega_p$  is frequency of plasma electron,  $h$  is Planck's constant,  $\lambda$  is the wavelength of laser beam,  $B_0$  is an external magnetic field,  $\sigma$  is magnetization parameter, which decides type of magnetization. For the case of forward (reverse) magnetization  $\sigma = +1$  ( $\sigma = -1$ ). The unmagnetized case of reference corresponds to  $\sigma = 0$ .

The wave equation for laser beam in plasmas with  $\varepsilon$  assumed to be as,

$$\nabla^2 E - \frac{\varepsilon}{c^2} \frac{\partial^2 E}{\partial t^2} + \nabla \left( \frac{E \cdot \nabla \varepsilon}{\varepsilon} \right) = 0 \quad (4)$$

By employing WKB approximation,  $(c^2/\omega^2)|(\frac{1}{\varepsilon})\nabla^2 \ln \varepsilon| \ll 1$ . Therefore,  $\nabla \left( \frac{E \cdot \nabla \varepsilon}{\varepsilon} \right)$  can be ignored. By assuming electric field  $E = A(x, y, z)e^{i(\omega t - kz)}$ , the evolution of  $E$  in magnetized plasma is governing by following nonlinear differential equation,

$$\frac{\partial^2 E}{\partial z^2} - 2ik \frac{\partial E}{\partial z} + \delta \left( \frac{\partial^2 E}{\partial r^2} + \frac{1}{r} \frac{\partial E}{\partial r} \right) + \frac{\omega^2}{c^2} (\varepsilon - \varepsilon_0) E = 0 \quad (5)$$

where,  $\delta = [1 + (\varepsilon_0/\varepsilon_{0zz})]/2$  with  $\varepsilon_{0zz} = 1 - \Omega_p^2$ . By substituting  $E = A_0 \exp(-ikS(r, z))$ , where  $k$  and  $S$  are the wave vector and eikonal of beam. One can write for initially Gaussian beam as,

$$A_0^2 = \frac{E_0^2}{f^2} \exp\left(-\frac{r^2}{r_0^2 f^2}\right) \quad (6)$$

$$S = \frac{r^2}{2f} \frac{df}{dz} + \varphi(z) \quad (7)$$

where,  $E_0$  is electric field at the central position  $r = z = 0$ ,  $r_0$  is initial beam radius and  $f$  is dimensionless BWP.

In subsequent stages, by succeeding proposal developed by Akhmanov et al. [6] and its modification lead by Sodha et al. [7]. An expression for  $f$  under paraxial approximation as

$$\frac{d^2 f}{d\xi^2} = \frac{4\delta^2}{f^3} - \frac{\rho^2 p \chi (-\psi + \delta \sigma \Omega_c) \delta}{f^3 (\beta - \sqrt{\psi})^2 \sqrt{\psi} (\sqrt{\psi} - \sigma \Omega_c)^2} \quad (8)$$

where,

$$\chi = 1 - \frac{p\sigma\Omega_c}{f^2\left(1+\frac{p}{f^2}\right)^{\frac{3}{2}}} + \frac{2\sigma\Omega_c}{\sqrt{1+\frac{p}{f^2}}} - \frac{3p\sigma^2\Omega_c^2}{f^2\left(1+\frac{p}{f^2}\right)^2} + \frac{3\sigma^2\Omega_c^2}{\left(1+\frac{p}{f^2}\right)} \text{ and } \psi = 1 + \frac{p}{f^2} + \frac{2p\sigma\Omega_c}{f^2\sqrt{1+\frac{p}{f^2}}} + \frac{3p\sigma^2\Omega_c^2}{f^2\left(1+\frac{p}{f^2}\right)}.$$

Here,  $\xi = z/kr_0^2$  is non-dimensional distance travelled by laser in plasma and  $p = \alpha E_0^2$  is initial intensity parameter of beam.

### 3 Results and Discussion

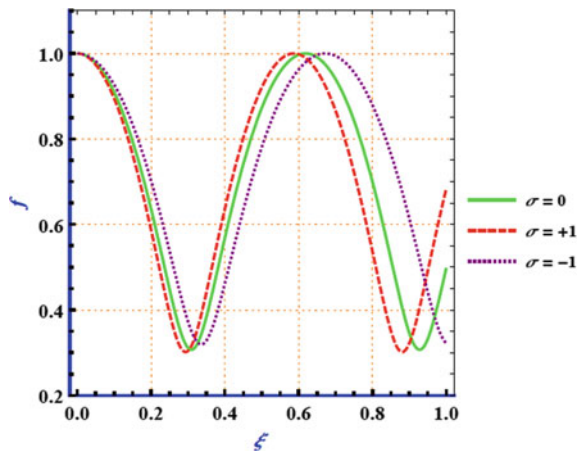
Equation (8) is an ordinary nonlinear beam width parameter differential equation in magnetized RCQP. The Eq. (8) is solved by considering following laser-plasma parameters as:  $\omega = 1.778 \times 10^{20}$  rad/s,  $r_0 = 20\mu\text{m}$ ,  $\Omega_p = 0.1$ ,  $\Omega_c = 0.2$ ,  $p = 1$  and  $\sigma = 0, \pm 1$ .

Figure 1 shows, the effect of  $\sigma$  on  $f(\xi)$ . The behaviour of  $f$  with  $\xi$  is accordance with density gradient which is further responsible for changes in  $\varepsilon$  of plasma. It is observed that, the SF is more (less) dominant in forward (reverse) magnetization in comparison with unmagnetized case of reference. Figure 2 shows effect of  $\sigma$  on  $\varepsilon(\xi)$ . From Fig. 2, it is observed that variation of  $\varepsilon$  is also oscillatory with  $\xi$ . The oscillatory peaks of  $\varepsilon$  in Fig. 2 matches to the oscillatory valleys of  $f$  in Fig. 1.

Figure 3, illustrates the effect of plasma density on  $f(\xi)$ . From this it is clear that, as density parameter  $\Omega_p$  increases, enhanced SF of beam occurs with decrease in SF length. However, oscillatory behaviour of  $f$  with  $\xi$  for different  $\sigma$  values is same as in Fig. 1. As usual, SF in plasma is enhanced by addition of quantum effects.

Effect of different values of  $\Omega_c$  on  $f(\xi)$  is plotted in Fig. 4. From this it is clear that, as magnetic field parameter  $\Omega_c$  increases, SF length decreases. The effect of  $\sigma$  on behavior of  $f$  with  $\xi$  is same as observed in Fig. 1.

Fig. 1 Effect of  $\sigma$  on  $f(\xi)$



**Fig. 2** Effect of  $\sigma$  on  $\varepsilon(\xi)$

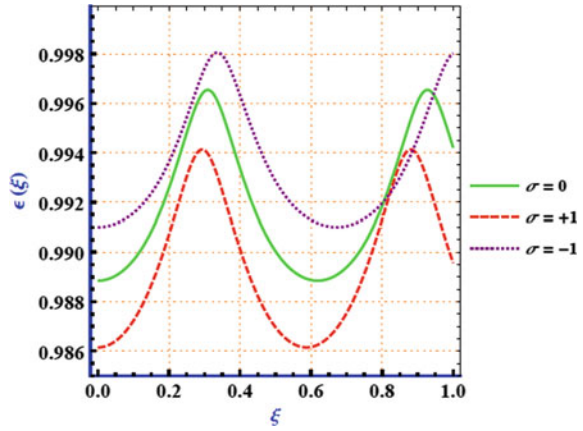


**Fig. 3** Effect of  $\Omega_p$  on  $f(\xi)$ . Solid curves ( $\sigma = 0$ ), Dashed curves  $\sigma = +1$ , Dotted curves  $\sigma = -1$

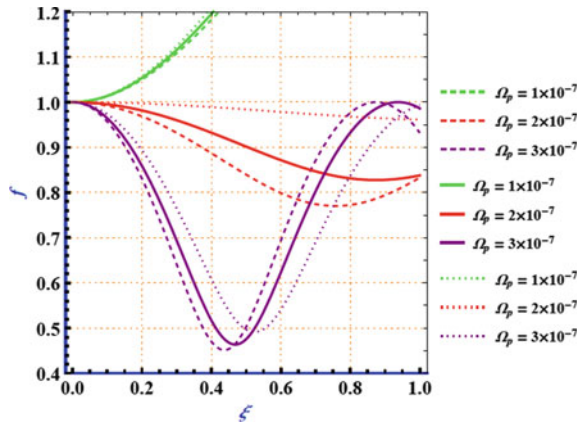
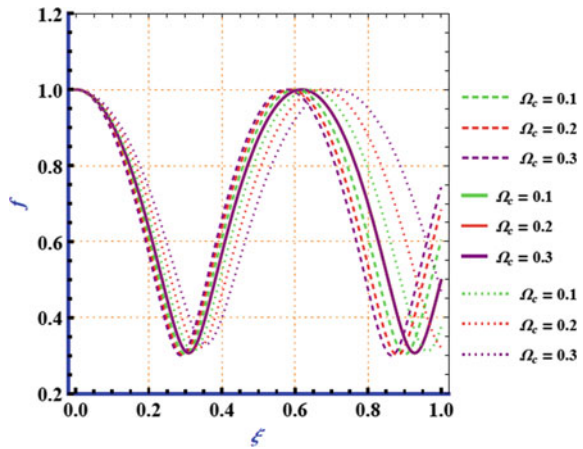


**Fig. 4** Effect of  $\Omega_c$  on  $f(\xi)$ . Solid curves ( $\sigma = 0$ ), Dashed curves  $\sigma = +1$ , Dotted curves  $\sigma = -1$



## 4 Conclusions

In this paper, second order nonlinear BWP differential equation of Gaussian beam in magnetized RCQP is obtained. It is found that, strength and direction of external magnetic field affects the SF of the Gaussian beam in plasma. In addition, quantum mechanical effects add the SF behaviour of laser in plasma.

## References

1. Lalouis, P., Foldes, I.B., Hora, H.: Ultrahigh acceleration of plasma by picosecond terawatt laser pulses for fast ignition of fusion. *Laser Part. Beams* **30**, 233–242 (2012)
2. Askari, H.R., Azish, Z.: Effect of a periodic magnetic field on phase matching condition in second harmonic generation at interactions of laser-plasma. *Optik* **122**, 1159 (2011)
3. Lemoff, B.E., Yin, G.Y., Gordon, C.L., Barthy, C.P.J., Harris, S.E.: Demonstration of a 10-Hz femtosecond-pulse-driven XUV laser at 41.8 nm in Xe IX. *Phys. Rev. Lett.* **74**, 1574 (1995)
4. Parashar, J., Pandey, H.D., Tripathi, V.K.: Two-dimensional effects in a tunnel ionized plasma, *Phys. Plasmas* **4**, 3040 (1997)
5. Liu, C.S., Tripathi, V.K.: Self-focusing and frequency broadening of an intense short-pulse laser in plasmas. *J. Opt. Soc. Am. A* **18**, 1714 (2001)
6. Akhmanov, S.A., Sukhorukov, A.P., Khokhlov, R.V.: Self-focusing and diffraction of light in a Nonlinear medium. *Sov. Phys. Usp.* **10**, 609–636 (1968)
7. Sodha, M.S., Ghatak, A.K., Tripathi, V.K.: Self-focusing of laser beams in plasmas and semiconductors. *Prog. Opt.* **13**, 169–265 (1976)
8. Marklund, M., Shukla, P.K.: Nonlinear collective effects in photon-photon and photon-plasma interactions. *Rev. Mod. Phys.* **78**, 591 (2006)
9. Patil, S.D., Takale, M.V.: Stationary self-focusing of Gaussian laser beam in relativistic thermal quantum plasma. *Phys. Plasmas* **20**, 072703 (2013)
10. Aggarwal, M., Kumar, H., Kant, N.: Propagation of Gaussian laser beam through magnetized cold plasma with increasing density ramp. *Optik* **127**, 2212–2216 (2016)
11. Aggarwal, M., Kumar, H., Richa., Gill, T.S.: Self-focusing of Gaussian laser beam in weakly relativistic and ponderomotive cold quantum plasma. *Phys. Plasmas* **24**, 013108 (2017)
12. Aggarwal, M., Goyal, V., Richa, Kumar, H., Gill, T.S.: Weakly relativistic self-focusing of Gaussian laser beam in magnetized cold quantum plasma. *Laser Part. Beams* **35**, 699–705 (2017).
13. Aggarwal, M., Goyal, V., Gill, T.S.: Relativistic-Ponderomotive Self-focusing of Gaussian laser beam propagating in magnetized cold quantum plasma. *Braz. J. Phys.* **51**, 1642–1650 (2021)
14. Pawar, V.S., Nikam, P.P., Kokare, S.R., Patil, S.D., Takale, M.V.: Relativistic self-focusing of finite Airy-Gaussian laser beams in cold quantum plasma. *J. Opt.* **50**, 403–409 (2021)



# Inelastic Soliton Collision in Multispecies Inhomogeneous Plasma



K. Raghavi, L. Kavitha, and C. Lavanya

**Abstract** In the present study, the multispecies in homogeneous dusty plasma with three constituents electrons, positrons and ions are observed. The Non linear Schrödinger Equation (NLSE) is obtained along the lines of commonly using reductive perturbation technique. We explore the collision of inelastic solitons upon employing the Hirota's bilinearization procedure. The results show that the properties of soliton collision are significantly influenced by the positron embedded in the three component plasma.

**Keywords** Inhomogeneous plasma · Reductive perturbation technique · Hirota bilinearization

## 1 Introduction

At present wave phenomena in dusty plasmas have much importance by reason of its part in the analysis of space and astrophysical background which includes tail of comets, ring of planets, interstellar space, asteroid zones etc. [1–3]. In a similar dusty plasma system, the grains of dust are immersed in the surrounding plasma and dispersion background. They interact with plasma particles owing to the charge associated with them. The dust, gain charge because of some conditions such as Collisional charging, Photo electric emission etc., and the state of unchanged charged dust grains modify the wave spectra whereas dynamics of dust supports the new eigen modes in dusty plasma [4–8]. In early stages, Zabusky and Kruskal observed

---

K. Raghavi · L. Kavitha (✉)  
Department of Physics, School of Basic and Applied Sciences,  
Central University of Tamil Nadu, Thiruvarur 610005, India  
e-mail: [lkavitha@cutn.ac.in](mailto:lkavitha@cutn.ac.in)

L. Kavitha  
The Abdus Salam International Centre for Theoretical Physics, Trieste, Italy

C. Lavanya  
Department of Physics, Periyar University, Salem 636 011, Tamil Nadu, India

© The Author(s), under exclusive license to Springer Nature Switzerland AG 2022  
S. Banerjee and A. Saha (eds.), *Nonlinear Dynamics and Applications*,  
Springer Proceedings in Complexity,  
[https://doi.org/10.1007/978-3-030-99792-2\\_14](https://doi.org/10.1007/978-3-030-99792-2_14)

the influence of solitons in the plasma system which is collisionless and found the recurrence of beginning states [9]. S. Gardner et al. derived a technique for solving the Korteweg-de Vries equation which can be applied to forecast exactly the solitary waves that emerges from random initial conditions [10]. The Ion waves in a massively charged dusty plasma was examined by Angelis et al. and they derived an equation explaining low-frequency electrostatic perturbations on a non homogeneous background. The model is used for interpreting noise enhancement in low frequency range in the regions of dust in Halley's comet [5]. T. E. Sheridan investigated the characteristics of large amplitude negative potential solitary wave in multi-component dusty plasma particularly consisting of three components [11]. T. S. Gill and H. Kaur used the Sagdeev Pseudopotential method to study the solitary waves in unmagnetised dusty plasma [12]. Xue investigated the collision between dust acoustic solitary waves in an unmagnetised dusty plasma and established the phase shift modification by varying dust charge [13]. One dimensionally solitary waves in plasma system was reported by many investigators. Sayed and Mamum investigated the solitary waves in dusty plasma system consisting of four components using the reductive perturbation method [14]. Lin and Duan studied DASWs using multi-component dusty plasma consisting of non thermal ions, electrons that obey Boltzmann distribution law and negatively charged dust fluid [15]. Dusty plasma consisting of positive dust grains were investigated by T. K. Baluku et al. and tracked down the results that the DIA solitons are restricted to the positive potential whereas in case of negative dust grains either positive or negative potential may exist [16]. Harvey et al. observed the interaction of two counterpropagating solitons of identical amplitude and found that during collision, the sum of the initial soliton amplitudes was greater than the overlapped soliton amplitude [17]. T. Suji and Oikawa investigated the influence of solitons in a two layer fluid two dimensionally and finally generated a new wave called stem [18]. The collisional properties of dust acoustic solitary waves is investigated by Ghosh et al. using Poincare Lighthill Kuo method [19]. Alfvén waves in space and astrophysical regions are studied by V. Jatenco-Pereira et al. and resulted that the existence of superthermal ions and dust modifies the dispersion of Alfvén waves [3]. S. K. Sharma et al. investigated the collision and propagation of DASW in a strongly coupled dusty plasma [20]. L. Kavitha et al. investigated the excitations of solitons in low frequency Alfvén waves in magnetized dusty plasmas [21]. Najah Kaban et al. recorded the DA multisoliton interactions using numerical simulations in the system of dusty plasma which is strongly coupled [22]. Krishan Kumar et al. reported the reflection aspects of DA solitary waves in dusty plasma in an experimental view [23]. The manuscript is organized as follows. Sect. 1 gives an introduction to the work with related literature. In Sect. 2 we establish the nonlinear equations for ion acoustic solitary waves. We use the reductive perturbation approach and arrive the nonlinear Schrödinger equation in Sect. 3 elucidate the collisional attributes of dust acoustic solitary waves. Sect. 4 contains a brief summary of our investigation.

## 2 Theoretical Model and Equation of Motion

An inhomogeneous plasma which exhibits less collision is considered. The constituents of such plasma are positrons, electrons and ions [24]. The dynamics of the ions are represented in normalized form by the below equations.

$$\frac{\partial n_i}{\partial t} + \frac{\partial(n_i v_i)}{\partial x} = 0, \quad (1)$$

$$\frac{\partial v_i}{\partial t} + v_i \frac{\partial v_i}{\partial x} = -\frac{\partial \phi}{\partial x}, \quad (2)$$

and

$$\frac{\partial^2 \phi}{\partial x^2} = (n_e - n_i - n_p). \quad (3)$$

The densities of positron, electron and ion are expressed in terms of  $n_p, n_e, n_i$  respectively. The velocity of ion fluid ( $v_i$ ) and electrostatic potential ( $\phi$ ) are the variables of the equation. The debye length  $\lambda_{Dd} = \sqrt{\frac{T_e}{4\pi e^2 n_0}}$ , normalizes the space coordinate and ion inverse plasma frequency  $\omega_{pi}^{-1} = \sqrt{\frac{m_i}{4\pi e^2 n_0}}$ , normalizes the time coordinates. Further, the electrostatic potential is normalized by  $\frac{T_e}{e}$  and velocity by  $c_{si} = \sqrt{\frac{T_e}{m_i}}$ .  $T_p$  and  $T_e$  represents the temperature of positron and electron respectively. Moreover,  $m_i$  is the ion mass and  $e$  designates the magnitude of the electron charge. The evolution equation we arrived is the Nonlinear Schrödinger equation, by involving the standard reductive perturbation technique [25, 26] and the nonlinear Schrödinger equation we obtained is:

$$i \frac{\partial \phi}{\partial \tau} + P \frac{\partial^2 \phi}{\partial \xi^2} + Q |\phi|^2 \phi = 0, \quad (4)$$

In Eq. (4),  $P$  is the nonlinearity coefficient and  $Q$  is the dispersion coefficient. They are given as

$$P = \frac{1}{k \left[ -k^2 - n_{e0} \left( \frac{e}{T_e} \right) - n_{p0} \left( \frac{e}{T_p} \right) \right]} \left[ -v_g k A_1 J + 2v_g k^2 + A_2 J k n_{i0} - 2k\omega \right. \\ \left. + 2k^2 v_{i0} - v_g A_1 + n_{i0} A_2 + v_{i0} A_1 + v_{i0} k A_1 J - 2v_{i0} k^2 \right],$$

$$Q = \frac{-1}{2n_{i0} T_e^2 T_p^2 \left[ -k^2 - n_{e0} \left( \frac{e}{T_e} \right) - n_{p0} \left( \frac{e}{T_p} \right) \right]} \left[ -6k A_1^2 A_2 T_e^2 T_p^2 + 8A_1 \omega B T_e^2 T_p^2 k^2 \right. \\ \left. + 2A_1 \omega B T_e T_p^2 n_{e0} e + 2A_1 \omega B T_e^2 T_p n_{e0} e + A_1 \omega n_{e0} e^2 T_p^2 - A_1 \omega n_{p0} e^2 T_e^2 - A_1 \omega \right. \\ \left. \times n_{p0} T_e^2 T_p^2 - 8A_1 k^3 v_{i0} B T_e^2 T_p^2 - 2A_1 k v_{i0} B T_e T_p^2 n_{e0} e - 2A_1 k v_{i0} B T_e^2 T_p n_{p0} e - 3 \right. \\ \left. \times A_1 k v_{i0} n_{e0} e^2 T_p^2 + 3A_1 k v_{i0} n_{p0} T_e^2 e^2 + A_1 k v_{i0} n_{p0} T_e^2 T_p^2 + 8k^3 A_2 n_{i0} B T_e^2 T_p^2 + 2k A_2 \right. \\ \left. \times n_{i0} B T_e T_p^2 n_{e0} e + 2k A_2 n_{i0} B T_e^2 T_p n_{p0} e + 3k A_2 n_{i0} n_{e0} B e^2 T_p^2 - 3k A_2 n_{i0} n_{p0} T_e^2 e^2 \right]$$

$$\begin{aligned}
 & -kA_2n_{i0}n_{p0}T_e^2T_p^2 - 2kA_1ev_{i0}CT_eT_p^2n_{e0} - 2kA_1ev_{i0}CT_e^2T_pn_{p0} + 2kA_1ev_gCT_e \\
 & \times T_p^2n_{p0} + 2kA_1ev_gCT_e^2T_pn_{p0} + 2kA_1v_gn_{e0}e^2T_p^2 - 2kA_1v_gn_{p0}T_e^2e^2 + 2A_2ken_{i0}C \\
 & \times T_eT_p^2n_{e0} + 2A_2ken_{i0}CT_e^2T_pn_{p0}],
 \end{aligned}$$

where

$$\begin{aligned}
 J &= \frac{1}{-kn_{i0}(A_2\omega - A_2kv_{i0} - k)} \left[ -2k\omega^2 + 4\omega k^2v_{i0} - \omega v_gA_1 + \omega n_{i0}A_2 + \omega v_{i0}A_1 \right. \\
 & \left. - 2k^3v_{i0}^2 + kv_{i0}v_gA_1 - kv_{i0}^2A_1 - v_gA_2kn_{i0} + kn_{i0} \right], \\
 B &= \frac{(-\omega + kv_{i0}) - 8ikn_{i0} \left[ (\omega - kv_{i0}) \left( \frac{n_{e0}e^2}{2T_e^2} - \frac{n_{p0}e^2}{2T_p^2} + \frac{1}{2} \right) - kA_1A_2 \right] - ikA_1A_2}{\frac{-\omega + kv_{i0}}{kn_{i0}} \left[ (4k^2 + \frac{n_{e0}e}{T_e} + \frac{n_{p0}e}{T_p}) \right] + 2ik}, \\
 C &= \frac{2A_1A_2 + \frac{(v_{i0} - v_g)^2}{n_{i0}} \left[ \frac{n_{e0}e^2}{T_e^2} - \frac{n_{p0}e^2}{T_p^2} \right] - A_2A_2}{\frac{-(v_{i0} - v_g)^2}{n_{i0}} \left[ \frac{n_{e0}e}{T_e} + \frac{n_{p0}e}{T_p} \right] + 1}, \\
 A_1 &= k^2 + n_{e0} \frac{n_{e0}e}{T_e} + \frac{n_{p0}e}{T_p},
 \end{aligned}$$

and

$$A_2 = \frac{i\omega k^2 + n_{e0} \frac{n_{e0}e}{T_e} + \frac{n_{p0}e}{T_p} - ikv_{i0}k^2 + n_{e0} \frac{n_{p0}e}{T_p}}{ikn_{i0}}.$$

### 3 Hirota Bilinearization and Plasmic Solitons

The solution for Nonlinear Wave Equations (NWEs) or Partial Differential Equations (PDEs) became a major challenge in solving NonLinear problems. Though many influential techniques like Inverse scattering transform, Bäcklund transformation, etc., exist, Hirota Direct method [27–31] is one of the capable technique for the construction of Multi-soliton solutions. The above technique not only helps in constructing the multi solitonic solution but also helps in obtaining the solutions of

integrable nonlinear evolution equations. We apply rational transformation, to find the solution for Eq. (4).

$$\phi = \frac{g(\xi, \tau)}{f(\xi, \tau)}. \tag{5}$$

Here  $g(\xi, \tau)$  and  $f(\xi, \tau)$  are complex and real function which is to be determined. Further, using Eq. (5) in place of Eq. (4), we gain the following Hirota's bilinear form

$$\begin{aligned} [i D_\tau + P D_\xi^2]g \cdot f &= 0 \\ P D_\xi^2(f \cdot f) - Q g g^* &= 0, \end{aligned} \tag{6}$$

where  $*$  is the symbol of asymmetricity and Bilinear operators introduced by Hirota,  $D_\xi$  and  $D_\tau$  are given by

$$D_\xi^m D_\tau^n (g \cdot f) = \left( \frac{\partial}{\partial \xi} - \frac{\partial}{\partial \xi'} \right)^m \left( \frac{\partial}{\partial \tau} - \frac{\partial}{\partial \tau'} \right)^n g(\xi, \tau) f(\xi', \tau') \Big|_{\xi'=\xi, \tau'=\tau}. \tag{7}$$

using a small expansion parameter  $\epsilon$ ,  $g$  and  $f$  are expanded, Then we obtain

$$\begin{aligned} g &= \epsilon g_1 + \epsilon^3 g_3 + \epsilon^5 g_5 + \dots, \\ f &= 1 + \epsilon^2 f_2 + \epsilon^4 f_4 + \epsilon^6 f_6 + \dots \end{aligned} \tag{8}$$

on substituting the above Eq. (8) into Eq. (6), and solving we get the recursion relations.

### 3.1 One Soliton Solution

For the construction of one soliton solution, we assume;

$$\begin{aligned} g &= \epsilon g_1, \\ f &= 1 + \epsilon^2 f_2. \end{aligned} \tag{9}$$

The one-soliton solution is obtained explicitly by substitution of Eq. (9) into Eq. (6) and finally solving the resulting equation. The solution is

$$\phi = \frac{e^{\eta}}{1 + f_2}, \tag{10}$$

where

$$\begin{aligned}
 f_2 &= \frac{Q}{2P(k_1 + k_1^*)^2} e^{\eta_1 + \eta_1^*}, \\
 \eta_1 &= k_1 \xi - \omega_1 \tau + \eta_{10}, \\
 \omega_1 &= -ik_1^2 P,
 \end{aligned}$$

Here,  $\omega_1$  and  $k_1$  are complex parameters whereas  $\eta_{10}$  is a constant.

### 3.2 Two-Soliton Solution

In order to find solutions of two-soliton, we introduce the following series:

$$\begin{aligned}
 g &= \epsilon g_1 + \epsilon^3 g_3, \\
 f &= 1 + \epsilon^2 f_2 + \epsilon^4 f_4.
 \end{aligned} \tag{11}$$

and replacing in Eq. (6) and working out the developed group of PDE, the definite two soliton solutions is arrived as follows:

$$\phi = \frac{\epsilon g_1 + \epsilon^3 g_3}{1 + \epsilon^2 f_2 + \epsilon^4 f_4}. \tag{12}$$

$$\begin{aligned}
 g_3 &= e^{a_1} e^{\eta_1 + \eta_1^* + \eta_2} + e^{b_1} e^{\eta_1 + \eta_2 + \eta_2^*}, \\
 f_2 &= \frac{Q}{2P} \left[ e^{R_1} e^{\eta_1 + \eta_1^*} + e^{R_2} e^{\eta_1 + \eta_2^*} + e^{R_3} e^{\eta_2 + \eta_1^*} + e^{R_4} e^{\eta_2 + \eta_2^*} \right], \\
 f_4 &= e^{\eta_1 + \eta_1^* + \eta_2 + \eta_2^* + \delta},
 \end{aligned}$$

where

$$\begin{aligned}
 e^{a_1} &= \frac{Q(k_1 - k_2)^2}{2P(k_2 + k_1^*)^2(k_1 + k_1^*)^2}, \\
 e^{b_1} &= \frac{Q(k_1 - k_2)^2}{2P(k_2 + k_2^*)^2(k_1 + k_2^*)^2}, \\
 e^{R_1} &= \frac{1}{(k_1 + k_1^*)^2},
 \end{aligned}$$

$$\begin{aligned}
e^{R_2} &= \frac{1}{(k_1 + k_2^*)^2}, \\
e^{R_3} &= \frac{1}{(k_2 + k_1^*)^2}, \\
e^{R_4} &= \frac{1}{(k_2 + k_2^*)^2}, \\
e^\delta &= \frac{Q^2}{2P} \left[ \frac{(k_1 - k_2)^2 (k_1^* - k_2^*)^2}{(k_1 + k_1^*)^2 (k_2 + k_2^*)^2 (k_1 + k_2)^2 (k_1^* - k_2^*)^2} \right].
\end{aligned}$$

## 4 Results and Discussion

We investigated the effects of positron concentration on the plasmic soliton collision in electron positron ion plasma. We discuss graphically the interactions of solitary waves through the solution Eq. (12). Figure 1 indicates the interaction between the two soliton solutions Eq. (12) for arbitrary choices of parameters  $n_{i0}$ ,  $T_e$ ,  $T_p$  and for different values of density of positron  $n_{p0}$ . When  $n_{p0} = 0.008$  units, the amplitude of soliton  $s_1$  and  $s_2$  is observed at 45 and 40 units respectively. Similarly by setting  $n_{p0} = 0.09$ , 0.21 and 3 units, the solitons  $s_1$  and  $s_2$  suffers a fall in amplitude as shown in Fig. 1. The Fig. 2 shows the cumulative intensity plot before collision ( $t = -10$ ) and after collision ( $t = 10$ ). The graphical representation of Fig. 2 clearly indicates that the two solitons  $s_1$  and  $s_2$  undergo a significant inelastic collision in which the amplitude of plasmic soliton decreases with the enhancement of positron density  $n_{p0}$ .

## 5 Conclusions

We have explored the collisional dynamics of solitary waves in an unmagnetized plasma consisting of positrons along with electrons and ions. The dynamics of such wave is described by the celebrated nonlinear Schrödinger equation. By applying the technique of Hirota bilinearization, the interaction between the two soliton solution is presented. It is observed that an increase in the positron density generates the inelastic soliton collision. The results manifested that the presence of positrons display a significant play role on the amplitude of the profile of the plasmic solitons.

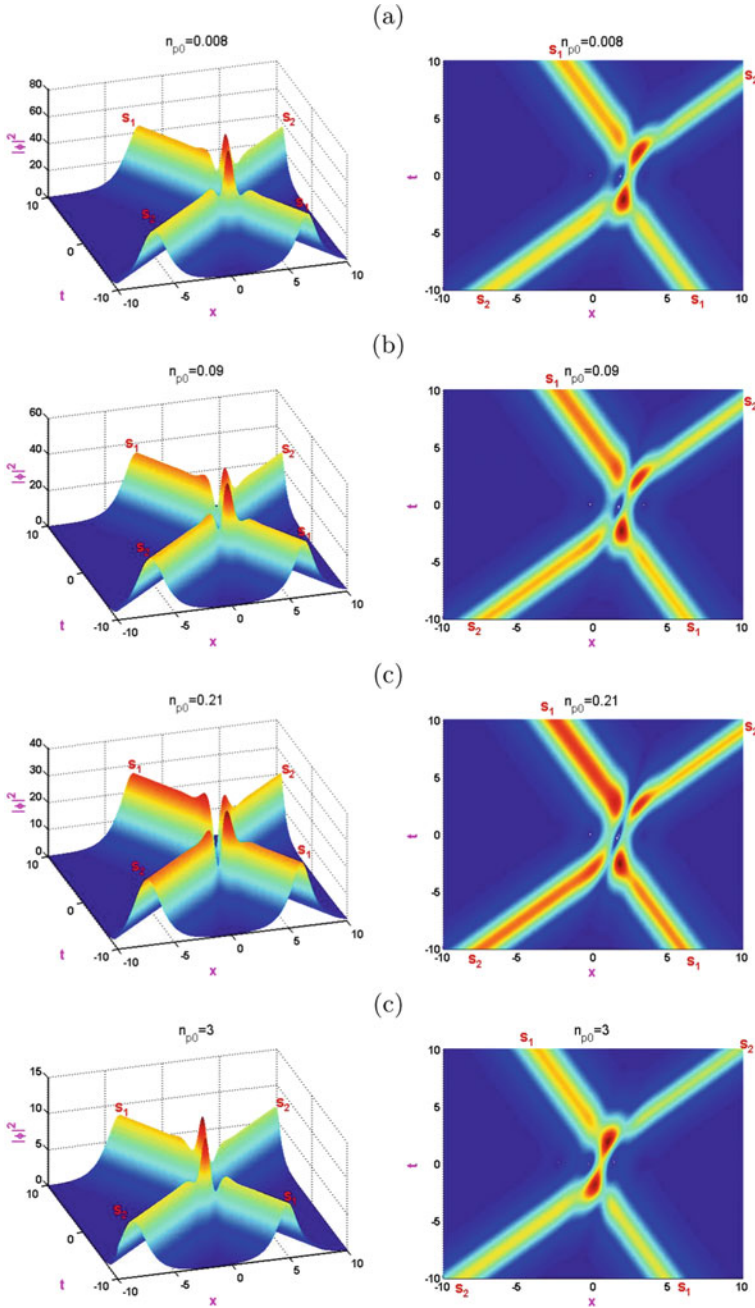


**Fig. 1** Snapshots of collision between two soliton to the solution 4.27 with the various choices of parameters  $T_e = 1.0$ ,  $n_{i0} = 6.7$ ,  $n_{e0} = 0.85$ ,  $e = -1.6 \times 10^{-19}C$ ,  $\omega = 9$ ,  $v_g = 0.79$ ,  $v_{i0} = 0.7$ ,  $k = 0.7$ ,  $T_p = 6.0eV$ , **a**  $n_{p0} = 0.008$ , **b**  $n_{p0} = 0.09$ , **c**  $n_{p0} = 0.21$  and **d**  $n_{p0} = 3$



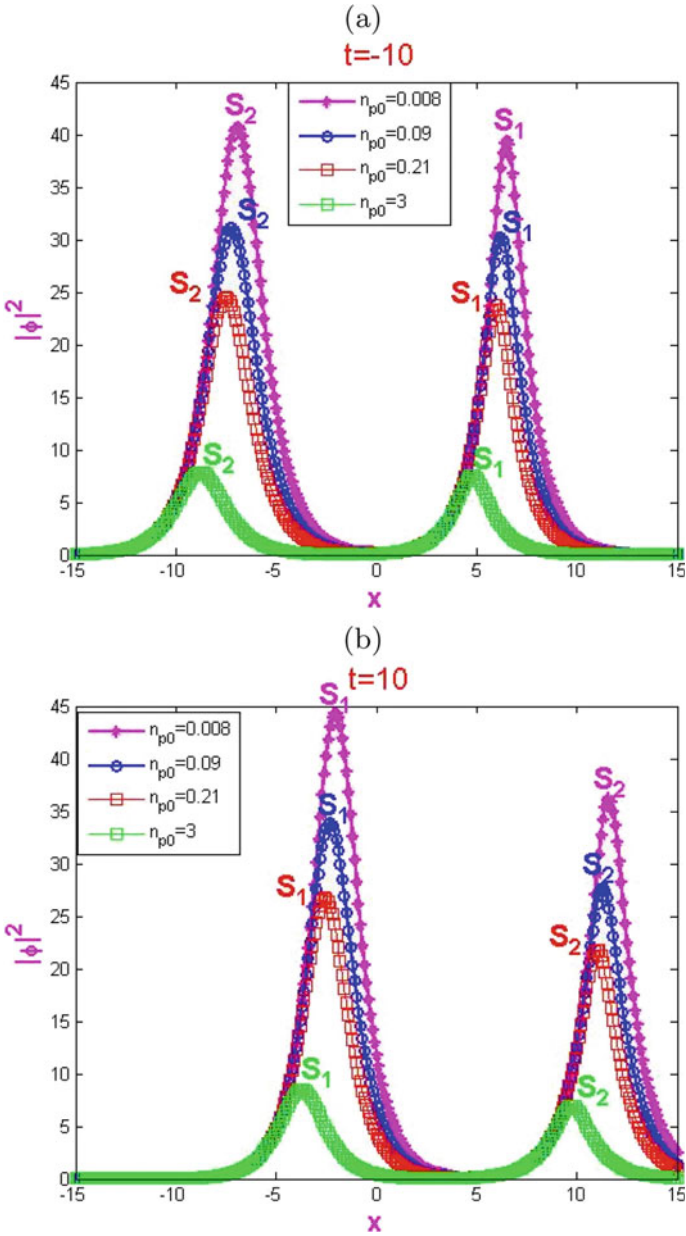


**Fig. 2** The cumulative plot showing the intensity profile of two soliton collision for various values of  $n_{p0}$  **a** before ( $t = -10$ ) and after **b** ( $t = 10$ ) collision

**Acknowledgements** K.R. acknowledges the financial support from Central University of Tamil Nadu in the form of URF. L.K. gratefully acknowledges the financial support in the form of Major Research Projects by CSIR (Ref.No.:03(1418)/17/EMR-II), India, UGC-DAE CSR (Ref. No.: CSR-KN/CRS-102/2018-19/1047), DST-SERB (Ref.No.:MTR/2017/000314/MS), India and ICTP, Italy in the form of a Regular Associateship.

## References

1. Horanyi, M., Mendis, D.A.: The effects of electrostatic charging on the dust distribution at Halley's Comet. *Astrophys. J.* **294**, 357–368 (1985)
2. Mendis, D.A., Rosenberg, M.: Some aspects of dust-plasma interactions in the cosmic environment. *IEEE Trans. Plasma Sci.* **20**, 6 (1992)
3. Jatenco-Pereira, V., Chian, A.C.L., Rubab, N.: Alfvén waves in space and astrophysical dusty plasmas. *Nonlin. Proces. Geophys.* **21**, 405–416 (2014)
4. Havens, O., Goertz, C.K., Morfill, G.E., Grun, E., Ip, W.: Confinement and structure of electrostatically coupled dust clouds in a direct current plasma-sheath. *J. Geophys. Res.* **92**, 2281–2287 (1987)
5. de Angelis, U., Formisano, V., Giordano, M.: Electromagnetic wave scattering in dusty plasmas. *J. Plasma Phys.* **40**, 399–406 (1988)
6. de Angelis, U., Bingham, R., Tsyтовich, V.N.: Electromagnetic wave scattering in dusty plasmas. *J. Plasma Phys.* **40**, 445–456 (1989)
7. de Angelis, U., Forlani, A., Bingham, R., Shukla, P.K., Ponomarev, A., Tsyтовich, V.N.: Damping and absorption of high-frequency waves in dusty plasmas. *Phys. Plasmas* **1**, 236 (1994)
8. Walch, B., Horanyi, M., Robertson, S.: Charging of dust grains in plasma with energetic electrons. *Phys. Rev. Lett.* **75**, 838–841 (1995)
9. Zabusky, N.J., Kruskal, M.D.: Interaction of “Solitons” in a collisionless plasma and the recurrence of initial states. *Phys. Rev. Lett.* **15**, 240–243 (1965)
10. Gardner, C.S., Greene, J.M., Kruskal, M.D., Miura, R.M.: Method for Solving the Korteweg-deVries equation. *Phys. Rev. Lett.* **19**, 1095–1097 (1967)
11. Sheridan, T.E.: On the origin of the ion acoustic soliton. *J. Plasma Phys.* **60**, 17–28 (1998)
12. Gill, T.S., Kaur, H.: Effect of nonthermal ion distribution and dust temperature on nonlinear dust acoustic solitary waves. *Pramana* **55**, 855–859 (2000)
13. Xue, J-K.: Head-on collision of dust-acoustic solitary waves. *Phys. Rev. E* **69**, 016403 (2004)
14. Sayed, F., Mamun, A.A.: Solitary potential in a four-component dusty plasma. *Phys. Plasmas*, **14**, 014501 (2007)
15. Lin, M., Duan, W.-S.: Envelope solitons in plasma with vortex-like electrons. *Chaos, Solitons Fractals* **33**, 1189–1196 (2007)
16. Baluku, T.K., Hellberg, M.A., Mace, R.L.: Dust acoustic solitons in plasmas with kappa-distributed electrons and/or ions. *Phys. Plasmas* **15**, 03701 (2008)
17. Harvey, P., Durniak, C., Samsonov, D., Morfill, G.: Soliton interaction in a complex plasma. *Phys. Rev. E* **81**, 057401 (2010)
18. Tsuji, H., Oikawa, M.: Two-dimensional interactions of solitons in a two-layer fluid of finite depth. *Fluid Dyn. Res.* **42**, 065506 (2010)
19. Ghosh, U.N.G., Roy, K., Chatterjee, P.: Head-on collision of dust acoustic solitary waves in a four-component dusty plasma with nonthermal ions. *Phys. Plasmas* **18**, 103703 (2011)
20. Sharma, S.K., Boruah, A., Bailung, H.: Head-on collision of dust-acoustic solitons in a strongly coupled dusty plasma. *Phys. Rev. E* **89**, 013110 (2014)
21. Kavitha, L., Lavanya, C., Senthil Kumar, V., Gopi, D., Pasqua, A.: Perturbed soliton excitations of Rao-dust Alfvén waves in magnetized dusty plasmas. *Phys. Plasmas*, **23**, 043702 (2016)
22. Kabalan, Najah, Ahmad, Mahmoud, Asad, Ali: Study of dust-acoustic multisoliton interactions in strongly coupled dusty plasmas. *Adv. Math. Phys.* **2020**, 1–9 (2020)

23. Kumar, K., Bandyopadhyay, P., Singh, S., Arora, G., Sen, A.: Reflection of a dust acoustic solitary wave in a dusty plasma. *Phys. Plasmas* **1**, 12959 (2021)
24. Kaur, H., Gill, T.S., Saini, N.S.: The Kadomstev-Petviashvili equation in dusty plasma with variable dust charge and two temperature ions. *Pramana* **66**, 1049–1056 (2006)
25. Tiwari, R.S., Mishra, M.K.: Ion-acoustic dressed solitons in a dusty plasma. *Phys. Plasmas* **13**, 062112 (2006)
26. Kavitha, L., Raghavi, K., Lavanya, C., Kailas, M., Gopi, D.: Propagation of electrostatic solitary waves in the four-component dusty plasma. *IEEE Trans. Plasma Sci.* **49**, 546 (2021)
27. Kavitha, L., Saravanan, M., Senthilkumar, V., Ravichandran, R., Gopi, D.: Collision of electromagnetic solitons in a weak ferromagnetic medium. *J. Mag. Magn. mater.* **355**, 37–50 (2014)
28. Kavitha, L., Srividhya, B., Dhamayanthi, S., Senthil Kumar, V., Gopi, D.: Collision and propagation of electromagnetic solitons in an antiferromagnetic spin ladder medium. *Appl. Math. Comput.* **251**, 643–668 (2015)
29. Kavitha, L., Venkatesh, M., Dhamayanthi, S., Gopi, D.: Nonlinear refractive index induced collision and propagation of nematicons. *J. Mol. Liq.* **192**, 142–151 (2014)
30. Kavitha, L., Muniyappan, A., Zdravkovic, S., Sataric, M.V., Marlewski, A., Dhamayanthi, S., Gopi, D.: Propagation of kink-antikink pair along microtubules as a control mechanism for polymerization and depolymerization processes. *Chin. Phys. B* **9**, 098703 (2014)
31. Lakshmanan, M., Rajasekar, S.: *Nonlinear Dynamics Integrability*. Springer, Chaos and Patterns (2003)

# Propagation of Rarefactive Dust Acoustic Solitary and Shock Waves in Unmagnetized Viscous Dusty Plasma Through the Damped Kadomtsev-Petviashvili Burgers Equation



Tanay Sarkar , Santanu Raut , and Prakash Chandra Mali 

**Abstract** The non-linear propagation of dust acoustic waves (DAWs) in collisional, unmagnetized, viscous dusty plasma systems containing two temperature ions, electrons, high negatively charged dust grains are investigated. By using the reductive perturbation method (RPM) the damped Kadomtsev-Petviashvili Burgers (dKPB) equation that governs the DAWs is derived. Generally, the impact of viscosity is ignored during the studies of wave dynamics in a plasma medium. In the present investigation, a Burgers term is introduced in order to express the dissipation effect in the viscous plasma circumstance. The strong dissipation due to the presence of Burgers term may cause for rising of a shock solution. However, in a very weak dissipative system, the solitary-like wave solution may arise due to the balance between the dispersion and nonlinearity. Assuming conservation law in the present system, solitary type wave solution is explored, and shock type wave solution is determined by means of Simplified Hirota bilinear method (SHBM). Finally, the effect of the kinematic viscosity, collisional frequency, etc. on wave propagation is demonstrated from numerical understanding.

**Keywords** Dust acoustic waves · Reductive Perturbation method · Damped KP-Burgers equation · Burgers term · Shock solution · Solitary like wave solution

## 1 Introduction

Dusty plasma plays a vital role in understanding different nonlinear phenomena appearing in space and astrophysical studies [1, 2]. Due to the presence of different kinds of dust particles of different sizes and masses, dusty plasma gave birth to

---

T. Sarkar (✉) · P. C. Mali  
Department of Mathematics, Jadavpur University, Kolkata 700032, India  
e-mail: [sarkartanay9@gmail.com](mailto:sarkartanay9@gmail.com)

S. Raut  
Department of Mathematics, Mathabhanga College, Coochbehar 736146, India

© The Author(s), under exclusive license to Springer Nature Switzerland AG 2022  
S. Banerjee and A. Saha (eds.), *Nonlinear Dynamics and Applications*,  
Springer Proceedings in Complexity,  
[https://doi.org/10.1007/978-3-030-99792-2\\_15](https://doi.org/10.1007/978-3-030-99792-2_15)

various wave modes such as dust acoustic mode [3], dust ion-acoustic mode [4], etc. Over the past few decades, DAW of dusty plasma has come up as a hot research topic and research on this topic is still ongoing. In 1990, Rao et al. [3] first theoretically brought the DAWs to everyone and after five years Barkan et al. [5] confirm the earlier prediction through laboratory experiments.

DAW is the most fundamental content of dusty plasma. DAWs are largely found in the rings of the various planets, mesosphere of the Earth, tails of comets, etc. [6]. A lot of research has been done on dust acoustic waves [7–10].

Among the various nonlinear structures of DAWs, dust acoustic solitary waves (DASWs) and dust acoustic shock waves (DASHWs) are the vastly growing area of research nowadays. Presently DASWs and DASHWs acquired a special place in space plasma research, laboratory plasma research, etc. Solitary waves are produced when there is a balance between nonlinearity and dispersive effects whereas the reason behind the production of shock waves is the dominance of dissipation over the dispersion in nonlinear media [11, 12]. Several researchers have worked for the development of DASWs [13, 14] and DASHWs [15]. Both DASW and DASHW structures may contain in a plasma system where both dispersion and dissipation are present [16].

In the present paper, we analyzed the propagation of DAWs in a collisional, unmagnetized, viscous dusty plasma system comprising of electrons, two temperature ions, and dust particles with a high negative charge. Applying reductive perturbation method, dKPB equation is derived, and using momentum conservation law solitary waves solutions are derived. Shock solution is also obtained for this equation by the SHBM technique. The remaining portion of this paper is arranged as follows: The basic governing equations are considered in Sect. 2. The damped KP-Burgers equation is originated by using RPM in Sect. 3. Solutions of the dKPB equation are given in Sect. 4. The parametric discussion of the solution with diagrams is delivered in Sect. 5 and the conclusions are given in Sect. 6.

## 2 Basic Model Equations

We consider here an unmagnetized viscous dusty plasma containing of high negatively charged dust grains, electrons and two different temperature ions. For the neutrality of net charge at equilibrium satisfies

$$N_{e0} + N_{d0}Z_{d0} - N_{i10} - N_{i20} = 0, \quad (1)$$

where  $N_{e0}$ ,  $N_{d0}$ ,  $N_{i10}$  and  $N_{i20}$  are the values of the number densities of electrons, dust, lower temperature ions and higher temperature ions at equilibrium respectively.  $Z_{d0}$  is the unperturbed number of charges on the dust particles. Then the dynamics of DAWs for variable dust charge can be described by the following continuity, motion for the dust and Poisson's equations as

$$\frac{\partial N_d}{\partial t} + \frac{\partial}{\partial x}(N_d U_d) + \frac{\partial}{\partial y}(N_d V_d) = 0, \tag{2}$$

$$\frac{\partial U_d}{\partial t} + U_d \frac{\partial U_d}{\partial x} + V_d \frac{\partial U_d}{\partial y} = Z_d \frac{\partial \phi}{\partial x} - \zeta \left( \frac{\partial^2}{\partial x^2} + \frac{\partial^2}{\partial y^2} \right) U_d - \mu_{id} U, \tag{3}$$

$$\frac{\partial V_d}{\partial t} + U_d \frac{\partial V_d}{\partial x} + V_d \frac{\partial V_d}{\partial y} = Z_d \frac{\partial \phi}{\partial y} - \zeta \left( \frac{\partial^2}{\partial x^2} + \frac{\partial^2}{\partial y^2} \right) V_d - \mu_{id} V, \tag{4}$$

$$\frac{\partial^2 \phi}{\partial x^2} + \frac{\partial^2 \phi}{\partial y^2} = Z_d N_d + N_e - N_{il} - N_{ih}, \tag{5}$$

where  $N_d$  denotes the dust number density,  $Z_d$  denotes the number of charges on dust particles. The effective temperature  $T_{eff}$  satisfies

$$T_{eff} = N_{d0} Z_{d0} \left( \frac{N_{e0}}{T_e} + \frac{N_{il0}}{T_{il}} + \frac{N_{ih0}}{T_{ih}} \right)^{-1}, \tag{6}$$

where  $T_e$ ,  $T_{ih}$  and  $T_{il}$  are temperature of electrons, higher temperature ions and lower temperature ions respectively.  $U_d$  and  $V_d$  are the velocities of the dust flow along the direction of x-axis and y-axis respectively and normalized by the dust acoustic speed  $c_d = \left( \frac{K_B T_{eff} Z_{d0}}{m_d} \right)^{\frac{1}{2}}$  in which  $K_B$  is the Boltzmann constant and  $m_d$  represents the dust particles mass. The electrostatic potential  $\phi$  is normalized as  $\phi = \frac{K_B T_{eff}}{e}$ . Space and time variables are scaled over the effective Debye length,  $\lambda_d = \left( \frac{K_B T_{eff}}{4\pi N_{d0} Z_{d0} e^2} \right)^{\frac{1}{2}}$  and the inverse of dust plasma frequency,  $\omega_{pd}^{-1} = \left( \frac{m_d}{4\pi N_{d0} Z_{d0}^2 e^2} \right)^{\frac{1}{2}}$ .  $\zeta = \frac{\zeta_0}{\omega_{pd} \lambda_d^2}$ , here  $\zeta_0$  denotes the kinematic viscosity of dust.  $\mu_{id}$  represents the collisional frequency.

$N_e$ ,  $N_{il}$  and  $N_{ih}$  are respectively the number densities for electrons, lower temperature ions, higher temperature ions and which are given by

$$N_e = \frac{N_{e0}}{N_{d0} Z_{d0}} \exp(\beta_2 s \phi), \tag{7}$$

$$N_{il} = \frac{N_{il0}}{N_{d0} Z_{d0}} \exp(-s \phi), \tag{8}$$

$$N_{ih} = \frac{N_{e0}}{N_{d0} Z_{d0}} \exp(-\beta_1 s \phi), \tag{9}$$

where  $\beta_1 = \frac{T_{il}}{T_{ih}}$ ,  $\beta_2 = \frac{T_{il}}{T_e}$ ,  $\beta_3 = \frac{T_{ih}}{T_e}$ ,  $s = \frac{T_{eff}}{T_{il}}$ ,  $\rho_1 = \frac{N_{il0}}{N_{e0}}$ ,  $\rho_2 = \frac{N_{ih0}}{N_{e0}}$ .  $\tag{10}$

From (1) and (10) it follows

$$\rho_1 + \rho_2 - 1 = 0, \tag{11}$$

$$s = \frac{\rho_1 + \rho_2 - 1}{\rho_1 + \rho_2\beta_1 + \beta_2}. \quad (12)$$

The variable  $Q_d$  of dust charge can be calculated from the equation [17]

$$\left( \frac{\partial}{\partial t} + \vec{\nabla} \cdot \vec{\nabla} \right) Q_d = J_e + J_{il} + J_{ih}, \quad (13)$$

where  $\vec{\nabla} = (U_d, V_d)$  and  $J_e$ ,  $J_{il}$  and  $J_{ih}$  are the electron, lower temperature ions and higher temperature ions currents respectively. We assume that the thermal velocities of electrons and ions are much greater than the streaming velocities, thus  $\frac{dQ_d}{dt} \ll J_e, J_{il}, J_{ih}$  and the equation (13) looks [1]

$$J_e + J_{il} + J_{ih} \approx 0. \quad (14)$$

The electron and ion currents are satisfied the relation [1]

$$J_e = -e\pi r^2 \left( \frac{8T_e}{\pi m_e} \right)^{\frac{1}{2}} N_e \exp\left( \frac{e\Phi}{T_e} \right), \quad (15)$$

$$J_{il} = e\pi r^2 \left( \frac{8T_{il}}{\pi m_i} \right)^{\frac{1}{2}} N_{il} \left( 1 - \frac{e\Phi}{T_{il}} \right), \quad (16)$$

$$J_{ih} = e\pi r^2 \left( \frac{8T_{ih}}{\pi m_i} \right)^{\frac{1}{2}} N_{ih} \left( 1 - \frac{e\Phi}{T_{ih}} \right), \quad (17)$$

where  $\Phi$  is the potential of dust particles surface related to the plasma potential  $\phi$ . We gain the dust charge  $Z_d$  in normal condition, from  $Z_d = \frac{\psi}{\psi_0}$ , where  $\psi = \frac{\exp\phi}{T_{eff}}$ , and  $\psi_0 = \psi(\phi = 0)$ . Expressing  $Z_d$  in terms of  $\phi$  we get [18]

$$Z_d = 1 + \gamma_1\phi + \gamma_2\phi^2 + \dots, \quad (18)$$

where  $\gamma_1 = \frac{1}{\psi_0} \left( \frac{d\psi(\phi)}{d\phi} \right)_{\phi=0}$  and  $\gamma_2 = \frac{1}{2\psi_0} \left( \frac{d^2\psi(\phi)}{d\phi^2} \right)_{\phi=0}$ .

### 3 Derivation of Damped KP-Burgers Equation

In this section we derive the damped KP-Burgers equation and for this purpose we have employed the RPM [19]. The stretching co-ordinates are given as

$$\xi = \epsilon(x - \lambda_p t), \quad \tau = \epsilon^3 t, \quad \eta = \epsilon^2 y, \quad (19)$$

where the small parameter  $\epsilon$  characterizes the strength of the non-linearity of the system and  $\lambda_p$  stands for presenting the phase velocity of the wave. To get the damped KP-Burgers equation, we expand the perturbation quantities  $N_d, U_d, V_d, Z_d$  and  $\phi$  in power series of  $\epsilon$  as

$$N_d = N_{d0} + \epsilon^2 N_{d1} + \epsilon^4 N_{d2} + \dots, \tag{20}$$

$$U_d = U_{d0} + \epsilon^2 U_{d1} + \epsilon^4 U_{d2} + \dots, \tag{21}$$

$$V_d = V_{d0} + \epsilon^3 V_{d1} + \epsilon^5 V_{d2} + \dots, \tag{22}$$

$$Z_d = Z_{d0} + \epsilon^2 Z_{d1} + \epsilon^4 Z_{d2} + \dots, \tag{23}$$

$$\phi = \phi_0 + \epsilon^2 \phi_1 + \epsilon^4 \phi_2 + \dots, \tag{24}$$

$$\zeta = \epsilon \zeta_0, \mu_{id} = \epsilon^3 \mu_{id0}. \tag{25}$$

By using the RPM from Eqs. (2)–(5) and using stretching coordinates (19) along with state variables from Eqs. (20)–(25), we gain a evolution equations set. Calculating and considering  $\phi_1 = \phi$ , we obtain the damped KP-Burgers equation as

$$\frac{\partial}{\partial \xi} \left( \frac{\partial \phi}{\partial \tau} + A \phi \frac{\partial \phi}{\partial \xi} + B \frac{\partial^3 \phi}{\partial \xi^3} + C \frac{\partial^2 \phi}{\partial \xi^2} + D \phi \right) + E \frac{\partial^2 \phi}{\partial \eta^2} = 0, \tag{26}$$

where  $A = \frac{\lambda_p^3}{2} \left[ (\rho_1 + \rho_2 \beta_1^2 - \beta_2^2) \frac{(\rho_1 + \rho_2 - 1)}{(\rho_1 + \rho_2 \beta_1 + \beta_2)^2} - 2\gamma_2 \right] + \frac{3}{2} \gamma_1 \lambda_p - \frac{3}{2\lambda_p}$ ,  $B = \frac{\lambda_p^3}{2}$ ,  $C = \frac{\zeta_0}{2}$ ,  $D = \frac{\mu_{id0}}{2}$ ,  $E = \frac{\lambda_p}{2}$ , and  $\lambda_p = (1 + \gamma_1)^{-\frac{1}{2}}$ .

## 4 Solution of Damped KP-Burgers Equation

### 4.1 Solitary Wave Solutions

In this part we will solve damped KP-Burgers equation (26) using momentum conservation law. Integrating (26) with respect to  $\xi$  we have

$$\frac{\partial \phi}{\partial \tau} + A \phi \frac{\partial \phi}{\partial \xi} + B \frac{\partial^3 \phi}{\partial \xi^3} + C \frac{\partial^2 \phi}{\partial \xi^2} + D \phi + E \int \frac{\partial^2 \phi}{\partial \eta^2} d\xi = 0. \tag{27}$$

Let  $z = \xi + \eta$ , then (27) reduces to

$$\frac{\partial \phi}{\partial \tau} + A \phi \frac{\partial \phi}{\partial z} + B \frac{\partial^3 \phi}{\partial z^3} + C \frac{\partial^2 \phi}{\partial z^2} + D \phi + E \frac{\partial \phi}{\partial z} = 0. \tag{28}$$



removing burgers and damping term from the above equation by putting  $C = 0$ ,  $D = 0$  then Eq. (28) changes to the equation

$$\frac{\partial \phi}{\partial \tau} + E \frac{\partial \phi}{\partial z} + A \phi \frac{\partial \phi}{\partial z} + B \frac{\partial^3 \phi}{\partial z^3} = 0, \quad (29)$$

which is the KdV type equation and solitary wave solution is of the form

$$\phi(z, \tau) = \phi_m \operatorname{sech}^2 \left( \frac{z - M\tau}{W} \right), \quad (30)$$

where  $\phi_m = \frac{3(M-E)}{A}$  indicates the amplitude,  $W = 2\sqrt{\frac{B}{M-E}}$  indicates the width and  $M$  indicates the speed of DASW. To find solitary wave solutions of dKPB Eq. (26) we use (30) as a seed solution and so for small values of  $C$  (Burgers coefficient) and  $D$  (damping coefficient), we assume that the DASW solutions of Eq. (26) with considering amplitude  $\phi_m$ , width  $W$  and velocity  $M$  are time  $\tau$  dependent as

$$\phi(z, \tau) = \phi_m(\tau) \operatorname{sech}^2 \left( \frac{z - M(\tau)\tau}{W(\tau)} \right). \quad (31)$$

Now conserved quantity for KdV type equation (29) is [20]

$$I = \int_{-\infty}^{\infty} \phi^2 dz, \quad (32)$$

gives

$$I = 24 \frac{\sqrt{B}}{A^2} (M(\tau) - E)^{\frac{3}{2}}. \quad (33)$$

Differentiating (32) w.r.to  $\tau$

$$\frac{dI}{d\tau} = -2DI + \frac{32}{15} C \frac{\phi_0^2(\tau)}{W(\tau)}. \quad (34)$$

Again differentiating (33) w.r.to  $\tau$

$$\frac{dI}{d\tau} = 36 \frac{\sqrt{B}}{A^2} (M(\tau) - E)^{\frac{1}{2}} \frac{dM(\tau)}{d\tau}. \quad (35)$$

From (34) and (35)

$$\frac{d}{d\tau} (M(\tau) - E) + \frac{4D}{3} (M(\tau) - E) = \frac{4C}{15B} (M(\tau) - E)^2. \quad (36)$$

Solving we get

$$M(\tau) = E + \frac{1}{\frac{C}{5BD} + \left(\frac{1}{M_0 - E} - \frac{C}{5BD}\right) e^{\frac{4}{3}D\tau}}, \tag{37}$$

where  $M_0$  represent the value of  $M(\tau)$  at  $\tau = 0$ . Thus the solution of dKPB equation is

$$\phi(\xi, \tau) = \phi_m(\tau) \operatorname{sech}^2 \left( \frac{\xi + \eta - M(\tau)\tau}{W(\tau)} \right), \tag{38}$$

where  $\phi_m(\tau) = \frac{3(M(\tau)-E)}{A}$ ,  $W(\tau) = 2\sqrt{\frac{B}{M(\tau)-E}}$  and (37) provides  $M(\tau)$ .

### 4.2 Shock Wave Solutions

Burger’s medium produces solitary wave solutions when there is weak dissipation. However, the powerful dissipation can result in shock waves. We have already derive solitary solution using conservation law. Now, to investigate shock wave solution, we operate SHBM [21] on dKPB equation

$$\frac{\partial \phi}{\partial \tau} + A\phi \frac{\partial \phi}{\partial \xi} + B \frac{\partial^3 \phi}{\partial \xi^3} + C \frac{\partial^2 \phi}{\partial \xi^2} + D\phi + E \int \frac{\partial^2 \phi}{\partial \eta^2} d\xi = 0. \tag{39}$$

Introducing the potential  $w$ , defined by

$$\phi = w_\xi, \tag{40}$$

we may write the Eq.(39) as

$$w_{\tau\xi} + Aw_{\xi\xi}^2 + Bw_{\xi\xi\xi\xi} + Cw_{\xi\xi\xi} + Du_\xi + +Ew_{\eta\eta} = 0. \tag{41}$$

Using the transformation below

$$w = e^\theta, \text{ where } \theta = k\xi + n\eta - \omega\tau. \tag{42}$$

We get the dispersion relation as

$$\omega = \frac{Bk^4 + Ck^3 + En^2 + Dk}{k}. \tag{43}$$

Assumed that the solution of Eq. (41) in the form of shock as

$$w = R(\ln(f)), \tag{44}$$

where the function  $f(\xi, \eta, \tau)$  is defined as

$$f(\xi, \eta, \tau) = 1 + e^\theta = 1 + e^{k\xi+n\eta-\omega\tau}, \tag{45}$$

Substituting Eqs. (44) and (45) into Eq. (41) we obtain a polynomial equation for  $e^{n\theta}$ . By setting the coefficient of  $e^{n\theta}$  to zero, we obtain a system of algebraic equation. Solving we get

$$R = \frac{2(Ck^2 - D)}{Ak^2}. \tag{46}$$

Combining Eqs. (40), (44) and (46) we find the shock solution of dKPB Eq. (39) as,

$$\phi(\xi, \eta, \tau) = \frac{(Ck^2 - D)}{Ak^2} \left( 1 + \tanh \left( \frac{k\xi + n\eta - \frac{Bk^4 + Ck^3 + En^2 + Dk}{k} \tau}{2} \right) \right). \tag{47}$$

### 5 Parametric Discussion

In this part, we will discuss the influence of various physical parameters on solitary and shock wave solutions of the dKPB equation. For the present study, the coefficient  $B$  of dispersion is always positive. Thus, the compressive soliton is found for positive values of the nonlinear coefficient  $A$ , whereas, the soliton remains rarefactive for negative nonlinear coefficient. From Fig. 1a and b it is obvious that  $A$  is negative and thus, only the rarefactive soliton exists in the present system.

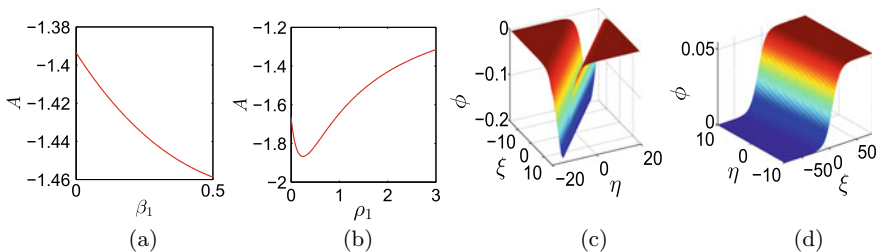


**Fig. 1** Variation  $A$  vs various parameter, **a** when  $\rho_2 = 0.6, \rho_1 = 2, \beta_2 = 0.4, \gamma_1 = 0.3, \gamma_2 = 0.3$ . **b** When  $\beta_2 = 0.4, \rho_2 = 0.6, \beta_1 = 0.2, \gamma_1 = 0.3, \gamma_2 = 0.3$ . **c** 3D profile of  $\phi(\tau)$  is plotted against  $\xi$  and  $\eta$  with the parameters  $\gamma_1 = 0.7, \gamma_2 = 0.2, \beta_1 = 0.4, \rho_2 = 4, \rho_1 = 3, \beta_2 = 0.4, \tau = 2, M_0 = 0.5, \tau = 2, \zeta_0 = 0.04$ . **d** 3D profile of  $\phi(\tau)$  is plotted against  $\xi$  and  $\eta$  with the parameters  $\gamma_1 = 0.7, \gamma_2 = 0.3, \beta_1 = 0.3, \rho_2 = 3, \mu_{id0} = 0.04, \beta_2 = 0.7, k = 0.15, n = 0.1, \zeta_0 = 0.04, \tau = 2$

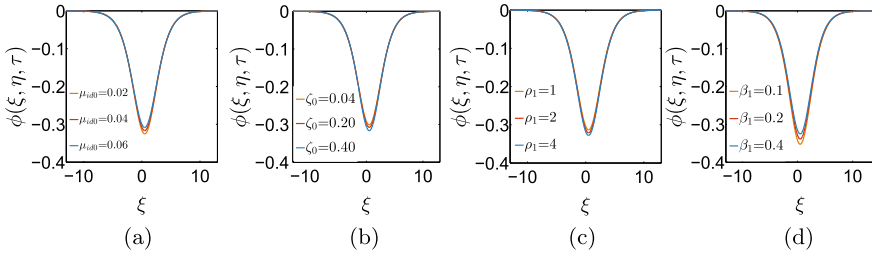


**Fig. 2** 2D profiles of  $\phi(\xi, \eta, \tau)$  for solution (38) is plotted against  $\xi$ , **a** when  $\gamma_1 = 0.7, \gamma_2 = 0.2, \zeta_0 = 0.04, \rho_2 = 4, \rho_1 = 3, \beta_1 = 0.4, \beta_2 = 0.4, \tau = 2, M_0 = 0.5, \eta = 0.5$ , **b** when  $\gamma_1 = 0.7, \gamma_2 = 0.2, \rho_1 = 3, \rho_2 = 4, \mu_{id0} = 0.02, \beta_1 = 0.4, \beta_2 = 0.4, \tau = 2, M_0 = 0.5, \eta = 0.5$ , **c** when  $\gamma_1 = 0.7, \gamma_2 = 0.2, \zeta_0 = 0.04, \rho_2 = 4, \mu_{id0} = 0.02, \beta_1 = 0.4, \beta_2 = 0.4, \tau = 2, M_0 = 0.5, \eta = 0.5$ , **d** when  $\gamma_1 = 0.7, \gamma_2 = 0.2, \zeta_0 = 0.04, \rho_2 = 4, \mu_{id0} = 0.02, \rho_1 = 3, \beta_2 = 0.4, \tau = 2, M_0 = 0.5, \eta = 0.5$

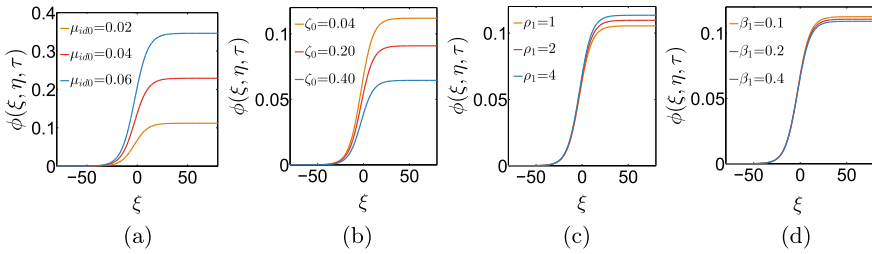


**Fig. 3** 2D profiles of  $\phi(\xi, \eta, \tau)$  for solution is plotted against  $\xi$ , **a** when  $\gamma_1 = 0.7, \gamma_2 = 0.3, \beta_1 = 0.3, \rho_2 = 3, \rho_1 = 3, \beta_2 = 0.7, k = 0.15, n = 0.1, \eta = 0.5, \zeta_0 = 0.04, \tau = 2$ , **b** when  $\gamma_1 = 0.7, \gamma_2 = 0.3, \beta_1 = 0.3, \rho_2 = 3, \rho_1 = 3, \beta_2 = 0.7, k = 0.15, n = 0.1, \eta = 0.5, \mu_{id0} = 0.04, \tau = 2$ , **c** when  $\gamma_1 = 0.7, \gamma_2 = 0.3, \beta_1 = 0.3, \rho_2 = 3, \mu_{id0} = 0.04, \beta_2 = 0.7, k = 0.15, n = 0.1, \eta = 0.5, \zeta_0 = 0.04, \tau = 2$ , **d** when  $\gamma_1 = 0.7, \gamma_2 = 0.3, \rho_1 = 3, \rho_2 = 3, \mu_{id0} = 0.04, \beta_2 = 0.7, k = 0.15, n = 0.1, \eta = 0.5, \zeta_0 = 0.04, \tau = 2$

The effect of the collision frequency ( $\mu_{id0}$ ) and kinematic viscosity ( $\zeta_0$ ) on the solitary wave solutions are displayed in respectively Fig. 2a, b. It is clear from Fig. 2a that the rarefactive soliton goes deeper for higher  $\mu_{id0}$ . The occurrence of this type of nonlinear phenomenon can be predicted as: As  $\mu_{id0}$  enhances the value of negative potential energy of the system decrease and naturally, the soliton rises. In respect to Fig. 2a, totally opposite result is seen in Fig. 2b where the rarefactive soliton goes deeper for increment of  $\zeta_0$ . It is expected because enhancing  $\zeta_0$  causes the increase of dissipation in a medium and the soliton becomes wider and deeper. The characteristic of shock waves under the variations of physical parameters  $\mu_{id0}$  and  $\zeta_0$  are depicted respectively in Fig. 3a and b. In Fig. 3a find enhances of  $\mu_{id0}$  causes rising of the amplitude of shock wave, where as the Fig. 3b demonstrates that the diminishing effect of the amplitude of shock wave due to the increase of  $\zeta_0$ . Figures 2c and d, 3c and d are depicted to exhibit the effect of the parameters  $\rho_1$  (the ratio of equilibrium values of the number densities of lower temperature ions to the unperturbed number of electrons) and  $\beta_1$  (ratio of two type of temperature ions) on solitary and shock

propagation. For a clear vision of wave propagation in the plasma medium, the three-dimensional profiles of the solitary and shock wave are depicted in Fig. 1a and c respectively.

## 6 Conclusion

This article demonstrates the propagating behaviors of DASWs and DASHWs in an unmagnetized collisional dusty plasma containing two temperature ion and Maxwellian electrons. The solitary and shock solution are explored employing conservation law and SHBM respectively. Further the solutions are studied from numerical understanding. It is found that the solitary wave rises above due to the enhance in damping coefficient  $\mu_{id0}$  as damping minimizes the system's negative potential energy. On the other hand, the depth of the shock enhances with the enhance in  $\mu_{id0}$ . During the evolution of solitary wave, it is also found that soliton goes dipper as viscosity enhances whereas, the shock declines for enhancing  $\zeta_0$ . Significant impacts from other physical parameters on wave propagation are observed.

## References

1. Pakzad, H.R.: Solitary waves of the Kadomtsev-Petviashvili equation in warm dusty plasma with variable dust charge, two temperature ion and nonthermal electron. *Chaos, Solitons Fractals* **42**(2), 874–879 (2009)
2. Raut, S., Mondal, K.K., Chatterjee, P., Roy, A.: Propagation of dust-ion-acoustic solitary waves for damped modified Kadomtsev-Petviashvili-Burgers equation in dusty plasma with a q-nonextensive nonthermal electron velocity distribution. *SeMA* **78**(4), 571–593 (2021)
3. Rao, N.N., Shukla, P.K., Yu, M.Y.: Dust-acoustic waves in dusty plasmas. *Planetary Space Sci.* **38**(4), 543–546 (1990)
4. Shukla, P.K., Silin, V.P.: Dust ion-acoustic wave. *Physica Scripta* **45**(5), 508 (1992)
5. Barkan, A., Merlino, R.L., D'angelo, D.: Laboratory observation of the dust-acoustic wave mode. *Phys. Plasma* **2**(10), 3563–3565 (1995)
6. Merlino, R.L.: 25 years of dust acoustic waves. *J. Plasma Phys.* **80**(06), 773–786 (2014)
7. Hartquist, T.W., Havnes, O.: Energy deposition due to the dissipation of dust-acoustic waves. *Astrophys. Space Sci.* **240**(2), 235–239 (1996)
8. Rosenberg, M., Kalman, G.: Dust acoustic waves in strongly coupled dusty plasmas. *Phys. Rev. E* **56**(6), 7166–7173 (1997)
9. Yaroshenko, V.V., Verheest, F., Morfill, G.E.: Dust-acoustic waves in collisional dusty plasmas of planetary rings. *Astron. Astrophys.* **461**(2), 385–391 (2006)
10. Shukla, P.K.: Twisted dust acoustic waves in dusty plasmas. *Phys. Plasmas* **19**(8) (2012)
11. Shukla, P.K., Mamun, A.A.: Introduction to Dusty Plasma Physics, 1st edn. IOP, London (2002)
12. Mondal, K.K., Roy, A., Chatterjee, P., Raut, S.: Propagation of dust-ion-acoustic solitary waves for damped forced Zakharov-Kuznetsov equation in a relativistic rotating magnetized electron-ion-plasma plasma. *Int. J. Appl. Comput. Math.* **6**(3), 1–17 (2020)
13. Bains, A.S., Saini, N.S., Gill, T.S.: Dust acoustic solitary structures in multidust fluids superthermal plasma. *Can. J. Phys.* **91**(7), 582–587 (2013)
14. Saha, A., Chatterjee, P.: Bifurcations of dust acoustic solitary waves and periodic waves in an unmagnetized plasma with nonextensive ions. *Astrophys. Space Sci.* **351**(2), 533–537 (2014)

15. Melandso, F., Shukla, P.K.: Theory of dust-acoustic shocks. *Planet. Space Sci.* **43**(5), 635–648 (1995)
16. Mamun, A.A., Shukla, P.K.: Electrostatic solitary and shock structures in dusty plasmas. *Phys. Scr.* **T98**, 107–114 (2002)
17. Melands, F., Aslaksen, T., Havnes, O.: A new damping effect for the dust-acoustic wave. *Planet. Space Sci.* **41**(4), 321–325 (1993)
18. Gill, T.S., Saini, N.S., Kaur, H.: The Kadomstev-Petviashvili equation in dusty plasma with variable dust charge and two temperature ions. *Chaos Solitons Fractals* **28**(4), 1106–1111 (2006)
19. Washimi, H., Taniuti, T.: Propagation of ion-acoustic solitary waves of small amplitude. *Phys. Rev. Lett.* **17**(19), 996–998 (1966)
20. Ali, A., Kalisch, H.: On the formulation of mass, momentum and energy conservation in the KdV equation. *Acta Applicandae Mathematicae* **133**(1), 113–131 (2014)
21. Awawdeh, F., Jaradat, H.M., Al-Shara, S.: Applications of a simplified bilinear method to ion-acoustic solitary waves in plasma. *Eur. Phys. J. D* **66**(2), 40 (2012)

# Stability of the Dust-Acoustic Solitons in the Thomas-Fermi Dense Magnetoplasma



A. Atteya 

**Abstract** An investigation is presented theoretically for the multi-dimensional instability of dust-acoustic solitary waves in the dense Thomas-Fermi magnetoplasma. The plasma system contains classical negatively charged dust grains with degenerate electrons and ions particles. Based on the reductive perturbation approach, the Zakharov-Kuznetsov (ZK) equation has been formulated. This nonlinear ZK equation is analyzed for its solitary wave solutions. Only rarefactive solitary waves are obtained, those are influenced by the parameters such as the dust temperature and number density, the electrons, and ions Fermi temperatures, and densities. The waves growth rate of the is computed. The previous parameters' effects on the instability are also discussed. The present results are beneficial in understanding the propagation and the instability of nonlinear aspects in dense plasma systems like white dwarfs and high-intensity laser-solid matter interaction experiments where the Thomas-Fermi dense magnetoplasma state may occur.

**Keywords** Quantum semiconductor plasma · Degenerate holes · Plasma waves · Exchange-correlation forces · Zakharov-Kuznetsov equation · Bright soliton · Dark soliton

## 1 Introduction

Quantum plasma physics is important for understanding the superdense astrophysical bodies performance [1] (such as, the white dwarfs, neutron stars, and Jupiter interior), ultrasmall electronic devices [2], microplasmas [3], and ultracold plasmas [4], laser-based plasma compression [5], etc. Manfredi investigated the quantum plasma through different approaches [6].

A quintessential plasma contains the electrons and ions, while dusty plasmas are extended by containing massive negative or positive dust grains. The dusty plasmas

---

A. Atteya (✉)

Department of Physics, Faculty of Science, Alexandria University, P.O. 21511, Alexandria, Egypt  
e-mail: [ahmedatteya@alexu.edu.eg](mailto:ahmedatteya@alexu.edu.eg)

have attracted significant interest in the recent past, and it is associated with industrial applications, and also in astrophysical environments [7–10]. As a result of the charge, size, and mass of the massive dust component, the dynamical profile which characterizes dusty plasmas is complex on comparing to electron-ion plasmas. Furthermore, the electrostatic waves phase speed is affected by the dust-modified charge balance in the case of dust-ion-acoustic (DIA) waves [11], as also confirmed experimentally [12, 13]. On the other side, the dust components take the dust-acoustic (DA) waves aspect, where they are low-frequency oscillations [14–16].

In opposite to classical plasmas, low temperature and the high number density of the particles characterize dense quantum plasmas, and the Wigner-Poisson or the Schrödinger-Poisson treatment are used to model it [6]. Due to quantum corrections, they host various nonlinear structures, and instabilities [6]. Accordingly, fluid transport models have been used in various frameworks of condensed matter physics, such as semiconductors [17], nanoparticles, superfluidity [18], and superconductivity [19]. Fluid transport models with no effects of the quantum diffraction are termed as Thomas-Fermi non-stationary models.

In the Maxwell-Boltzmann statistics, as the temperature and density increase, the ideal quasi-neutral classical gas pressure increases, thus confirm thermodynamical equilibrium at the high temperature case. However, for the very dense plasma, new laws are associated with the distribution of the Fermi-Dirac, at high Fermi temperature. At an absolute zero temperature, the pressure remains nonzero and becomes only a function of the density. The chemical potential  $\mu$  for such a completely degenerate plasma comes near to the value of the Fermi energy, so we can neglect the quantum diffraction effects. This is applicable only if number density of plasma particle is high degeneracy state, with slightly weak interactions. Hence, the density of plasma is important in the dynamics of collective modes in degenerate dusty plasma, comprising of mobile dust grains and degenerate inertialess ions and electrons [20–24]. Abdelsalam et al. investigated the properties of the dust excitations in the Thomas-Fermi plasma. Later, the extended study [25] derived the magnetized Korteweg-de Vries (KdV), KdV-Burger, Zakharov-Kuznetsov (ZK) and ZK-Burger equations and concluded that DA shock and solitary waves are changed due to the variation of temperatures, concentrations, and viscosity of the dust. The solitary and rogue DA waves formation and propagation are examined in a degenerate thermal Thomas-Fermi dusty plasma through the incorporation of transverse velocity perturbation effects [26]. The Thomas-Fermi density distribution is taken for ions and electrons, whereas the dust is considered as classical and dynamic. Obliquely propagating waves nonlinear properties are studied by Irfan et al. [27] in a dense degenerate cold Thomas-Fermi magnetoplasma, comprising of contains non-degenerate negatively-charged dust species. They derived and analyzed numerically the dust-cyclotron dispersion relation. They also formulated an equation of energy-balance by employing the Sagdeev pseudopotential theory. It was concluded that the soliton existence domain and the wave characteristics depend upon the system parameters. Unidirectional DA waves Overtaking collision in the Thomas-Fermi magnetoplasma has been analyzed [28].



The ZK equation has been derived when nonthermal ions are present in an external magnetic field to analyze the DA solitary waves characteristics [29]. The dispersion of linear DA waves in a dusty plasma have been examined [30, 31], where twisted DA vortex beam creation was reported. The instability of DA waves in a magneto-dusty plasma was checked by the small- $k$  expansion technique [32–36]. The instability of DA waves in a magnetized dusty plasma was checked by Mamun [32]. Unstable DA wave structures were found due to the presence of the external magnetic field. The finite-amplitude DA waves' instabilities in a magnetized three-component dusty plasma with nonthermal particles were also discussed by Mamun et al. [33]. They illustrated that the features of the produced DA waves is modified by temperature of dusts and the nonthermal ions, while the DA wave stability is not affected by the nonthermal parameter variation.

The DIA waves three-dimensional stability have been also studied in a magnetized multicomponent dusty plasma by El-Taibany et al. [34] through using the small- $k$  expansion technique. They showed that the higher growth rate associated with the larger wave amplitude and results in unstable solitary waves that are formed in the presence of negatively-charged ions. Akhter et al. [35] investigated the stability of DA waves in a magnetized dusty plasma. They found that the presence of an external magnetic field and the opposite polarity dust particles modified the DA wave instability-criterion. The obliquely propagating DA waves stability in a magnet0- multicomponent dusty plasma was derived by El-Labany et al. [36]. Saini et al. [37] derived the Zakharov-Kuznetsov (ZK) nonlinear equation for ion-acoustic solitary waves in a magnetized plasma. They also studied the stability analysis and checked the parametric range for the presence of stable and unstable solitons. The ZK equation was derived to study the DA solitary waves propagation in a magnetized dusty plasma containing massive, positive, and negative dust [38]. The wave's growth rate was derived and is affected by the polarization force. It is found also that, the instability is affected by the physical parameters. El-Taibany et al. [39] investigated the multi-dimensional instability in strongly coupled dusty plasma comprising ions and electrons in superthermal distribution. The produced waves growth rate is obtained, which is affected by the weakly and strongly coupling cases and the superthermal distribution of both the ions and electrons. The effects of polarization and trapping on multi-dimensional instability of ion-acoustic solitary waves in a multi-ion plasma system were theoretically investigated by Zedan et al. [40]. The instability and growth rate were found to be dependent on the density ratio between ions and dust, obliqueness, the dust cyclotron frequency, and other system parameters [41]. This manuscript is organized as follows. The governing equations and the derivation of the magnetized ZK equation is provided in Sect. 2. The solitary wave solution is in Sect. 3. The stability analysis for the DA waves is examined in Sect. 4. The numerical investigations and discussion are made in Sect. 5. At last, the conclusions are presented in Sect. 6.

## 2 Derivation of the ZK Equation

We consider quantum Thomas-Fermi dense magnetized plasma comprising of negatively-charged dust particles with degenerate ions and electrons obeying the Fermi-Dirac distributions. The external magnetic field  $\mathbf{B}_0$  confined the plasma system and it is in the z-direction, i.e.,  $\mathbf{B}_0 = \hat{z}B_0$  where  $B_0$  is the magnetic field strength and  $\hat{z}$  is the unit vector along z-axis. The quasineutrality condition is  $N_{e0} = N_{i0} - N_{d0}Z_{d0}$  at equilibrium, where  $Z_{d0}$  is the dust charge at equilibrium,  $N_{s0}$  is the  $s^{\text{th}}$  species equilibrium density ( $s = e, i$ , and  $d$  for electrons, ions, and negatively charged dust grains respectively). The propagation of the DA for the Thomas-Fermi magnetoplasma is governed by [28]

$$\left. \begin{aligned} \frac{\partial N_d}{\partial t} + \nabla \cdot (N_d U_d) &= 0, \\ \frac{\partial \mathbf{U}_d}{\partial t} + \mathbf{U}_d \cdot \nabla \mathbf{U}_d &= \nabla \psi - \Omega \mathbf{U}_d \times \hat{z} - \sigma_d N_d \nabla N_d, \\ \nabla^2 \psi &= \mu_e N_e - \mu_i N_i + N_d, \\ N_e &= (1 + \sigma_i \psi)^{3/2}, \\ N_i &= (1 - \psi)^{3/2}, \end{aligned} \right\} \quad (1)$$

where  $N_s$  is the normalized number density,  $U_d$  dust fluid velocity that normalized by the DA speed  $C_d = (2Z_{d0}k_B T_{Fi}/m_d)^{1/2}$ ,  $\psi$  is the wave potential that normalized by  $2k_B T_{Fi}/e$ .  $\Omega = \omega_{cd}/\omega_{pd}$  is the normalized dust gyro-frequency with  $\omega_{cd} = eZ_{d0}B/m_d$  and  $\omega_{pd} = (4\pi Z_{d0}^2 n_{d0} e^2/m_d)^{1/2}$ . Also,  $\sigma_d = T_d/T_{Fi} Z_{d0}$ ,  $\mu_i = n_{i0}/Z_d n_{d0}$ , and  $\mu_e = n_{e0}/Z_d n_{d0}$ , are the dust temperature-to-ion Fermi temperature ratio, the ion concentration, and electron concentration, divided by  $n_{d0} Z_{d0}$ , respectively, with  $e$  is the electronic charge,  $k_B$  is the Boltzmann constant.  $\sigma_i = T_{Fi}/T_{Fe}$  is the ion-to-electron Fermi temperature ratio. The charge-neutrality condition at equilibrium becomes  $\mu_i = \mu_{e+1}$ . The space variable is normalized by  $\lambda_0 = (2k_B T_{Fi}/4\pi Z_d n_{d0} e^2)^{1/2}$ , and the time variable  $t$  is normalized by  $\omega_{pd}^{-1}$ .

The ZK equation is formulated by employing the stretching of the independent variables  $x$ ,  $y$ , and  $t$  to be defined as [24]

$$X = \epsilon^{1/2} x, Y = \epsilon^{1/2} y, Z = \epsilon^{1/2} (z - v_0 t), T = \epsilon^{3/2} t, \quad (2)$$

where  $\epsilon$  is a formal small expansion parameter which indicates strength of the system nonlinearity,  $v_0$  is the phase velocity. The dependent variables can be considered as:

$$\left. \begin{aligned} N_d &= 1 + \epsilon N_d^{(1)} + \epsilon^2 N_d^{(2)} + \epsilon^3 N_d^{(3)} + \dots, \\ U_{dx,y} &= \epsilon^{3/2} U_{dx,y}^{(1)} + \epsilon^2 U_{dx,y}^{(2)} + \epsilon^{5/2} U_{dx,y}^{(3)} + \dots, \\ U_{dz} &= \epsilon U_{dz}^{(1)} + \epsilon^2 U_{dz}^{(2)} + \epsilon^3 U_{dz}^{(3)} + \dots, \\ \psi &= \epsilon \psi^{(1)} + \epsilon^2 \psi^{(2)} + \epsilon^3 \psi^{(3)} + \dots \end{aligned} \right\} \quad (3)$$

Putting Eqs. (2) and (3) into Eqs. (1), and the lowest orders perturbed quantities by collecting lowest order of  $\epsilon$ , we get

$$N_d^{(1)} = \frac{-\psi^{(1)}}{v_0^2 - \sigma_d}, U_{dz}^{(1)} = \frac{v_0 \psi^{(1)}}{v_0^2 - \sigma_d}. \quad (4)$$

The propagation phase velocity of the DA waves in the magnetized dusty plasma is

$$v_0 = \sqrt{\frac{2 + 3\mu_i \sigma_d + 3\mu_e \sigma_d \sigma_i}{3\mu_i + 3\mu_e \sigma_i}}. \quad (5)$$

Combining the next higher-orders contributions lead to

$$\left. \begin{aligned} U_{dx}^{(1)} &= \frac{-v_0^2}{\Omega(v_0^2 - \sigma_d)} \frac{\partial \psi^{(1)}}{\partial Y}, \\ U_{dy}^{(1)} &= \frac{v_0^2}{\Omega(v_0^2 - \sigma_d)} \frac{\partial \psi^{(1)}}{\partial X}, \\ U_{dx}^{(2)} &= \frac{-v_0^3}{\Omega(v_0^2 - \sigma_d)} \frac{\partial^2 \psi^{(1)}}{\partial X \partial Z}, \\ U_{dy}^{(2)} &= \frac{-v_0^3}{\Omega(v_0^2 - \sigma_d)} \frac{\partial^2 \psi^{(1)}}{\partial Y \partial Z}. \end{aligned} \right\} \quad (6)$$

Now, the next higher order of  $\epsilon$  gives

$$\left. \begin{aligned} \frac{\partial N_d^{(2)}}{\partial Z} &= -\frac{2v_0}{(v_0^2 - \sigma_d)^2} \frac{\partial \psi^{(1)}}{\partial T} + \frac{(3v_0^2 + \sigma_d)}{(v_0^2 - \sigma_d)^3} \psi^{(1)} \frac{\partial \psi^{(1)}}{\partial Z} - \frac{1}{(v_0^2 - \sigma_d)} \frac{\partial \psi^{(2)}}{\partial Z} \\ &\quad - \frac{v_0^4}{\Omega^2 (v_0^2 - \sigma_d)^2} \frac{\partial^3 \psi^{(1)}}{\partial Y^2 \partial Z} - \frac{v_0^4}{\Omega^2 (v_0^2 - \sigma_d)^2} \frac{\partial^3 \psi^{(1)}}{\partial X^2 \partial Z}. \end{aligned} \right\} \quad (7)$$

Substituting in the Poisson's equations, we derive the following equation

$$\frac{\partial \psi^{(1)}}{\partial T} + A \psi^{(1)} \frac{\partial \psi^{(1)}}{\partial Z} + B \frac{\partial^3 \psi^{(1)}}{\partial Z^3} + C \left( \frac{\partial^3 \psi^{(1)}}{\partial X^2 \partial Z} + \frac{\partial^3 \psi^{(1)}}{\partial Y^2 \partial Z} \right) = 0. \quad (8)$$

This equation is the ZK equation with the following nonlinearity coefficient  $A$ , and the dispersive terms  $B$ , and  $C$ :

$$\left. \begin{aligned} A &= \left( \frac{3v_0^2 + \sigma_d - \frac{3}{4}(v_0^2 - \sigma_d)^3 (\mu_i - \mu_e \sigma_i^2)}{2v_0 \sigma_d - 2v_0^3} \right), \\ B &= \frac{(v_0^2 - \sigma_d)^2}{2v_0}, \\ C &= \frac{1}{2v_0} \left( (v_0^2 - \sigma_d)^2 + \frac{v_0^4}{\Omega^2} \right). \end{aligned} \right\} \quad (9)$$

### 3 Solitary Wave Analysis

To obtain the solitary wave solution of Eq. (8), we shall follow the transformation of the independent variables [32, 42, 43] rotating by an angle  $\theta$  about the coordinate axes  $(X, Z)$  as

$$\left. \begin{aligned} \xi &= X \sin \theta + Z \cos \theta, \\ \zeta &= X \cos \theta - Z \sin \theta, \\ \eta &= Y, \text{ and } \tau = T. \end{aligned} \right\} \quad (10)$$

Using transformations (10) to the ZK Eq. (8), we get

$$\left. \begin{aligned} \frac{\partial \psi^{(1)}}{\partial \tau} + S_1 \psi^{(1)} \frac{\partial \psi^{(1)}}{\partial \xi} + S_2 \frac{\partial^3 \psi^{(1)}}{\partial \xi^3} + S_3 \psi^{(1)} \frac{\partial \psi^{(1)}}{\partial \zeta} + S_4 \frac{\partial^3 \psi^{(1)}}{\partial \zeta^3} \\ + S_5 \frac{\partial^3 \psi^{(1)}}{\partial \xi^2 \partial \zeta} + S_6 \frac{\partial^3 \psi^{(1)}}{\partial \xi \partial \zeta^2} + S_7 \frac{\partial^3 \psi^{(1)}}{\partial \xi \partial \eta^2} + S_8 \frac{\partial^3 \psi^{(1)}}{\partial \zeta \partial \eta^2} = 0, \end{aligned} \right\} \quad (11)$$

where

$$\left. \begin{aligned} S_1 &= A \cos \theta, S_2 = B \cos^3 \theta + C \sin^2 \theta \cos \theta, \\ S_3 &= -A \sin \theta, S_4 = -B \sin^3 \theta - C \cos^2 \theta \sin \theta, \\ S_5 &= 2C(\sin \theta \cos^2 \theta - \frac{1}{2} \sin^3 \theta) - 3B \cos^2 \theta \sin \theta, \\ S_6 &= -2C(\sin^2 \theta \cos \theta - \frac{1}{2} \cos^3 \theta) + 3B \sin^2 \theta \cos \theta, \\ S_7 &= C \cos \theta, S_8 = -C \sin \theta. \end{aligned} \right\} \quad (12)$$

The solution of ZK equation in the steady-state takes the form

$$\psi^{(1)} = \psi_0(\rho),$$

where  $\rho = \xi - M\tau$ , and Mach number ( $M$ ) is normalized by DA speed  $C_d$ . Thus, Eq. (11) can be written as [44]

$$-M \frac{d\psi_0}{d\rho} + S_1 \psi_0 \frac{d\psi_0}{d\rho} + S_2 \frac{d^3 \psi_0}{d\rho^3} = 0. \quad (13)$$

integrating and applying appropriate boundary conditions, we obtain the DA pulse solution as

$$\phi_0(\rho) = \phi_m \operatorname{sech}^2 \left( \frac{\rho}{W} \right), \quad (14)$$

where  $W$  and  $\phi_m$  are the width and amplitude of the solitary wave, respectively; these are expressed as

$$\phi_m = 3M/S_1 \text{ and } W = 2\sqrt{S_2/M}.$$

The associated electric field is obtained as

$$E_0(\rho) = -\nabla \phi_1 = \frac{2\phi_m}{W} \operatorname{sech}^2 \left( \frac{\rho}{W} \right) \tanh \left( \frac{\rho}{W} \right). \quad (15)$$

### 4 Stability Analysis

The small- $k$  expansion perturbation technique [42, 43] is adopted to examine the stability of the DA structures. We consider [32, 36]

$$\phi^{(1)} = \phi_0(\rho) + \Phi(\rho, \zeta, \eta, \tau), \tag{16}$$

where  $\Phi$  represents an obliquely propagating long-wavelength plane-wave that is given by

$$\Phi(\rho, \zeta, \eta, \tau) = \psi(\rho) \exp i[k(l_\xi \rho + l_\zeta \zeta + l_\eta \eta) - \gamma \tau], \tag{17}$$

in which  $l_\xi^2 + l_\zeta^2 + l_\eta^2 = 1$ ,  $\psi(\rho)$  and  $\gamma$  can be expanded by considering small values of  $k$  to the form

$$\left. \begin{aligned} \psi(\rho) &= \psi_o + k\psi_1 + k^2\psi_2 + \dots, \\ \gamma &= k\gamma_1 + k^2\gamma_2 + \dots \end{aligned} \right\} \tag{18}$$

Putting Eq. (16) into Eq. (11) to obtain the linearized ZK equation as

$$\left. \begin{aligned} &\frac{\partial \Phi}{\partial \tau} - M \frac{\partial \Phi}{\partial \rho} + S_1 \phi_0 \frac{\partial \Phi}{\partial \rho} + S_2 \frac{\partial^3 \Phi}{\partial \rho^3} \\ &+ S_3 \phi_0 \frac{\partial \Phi}{\partial \zeta} + S_4 \frac{\partial^3 \Phi}{\partial \zeta^3} + S_5 \frac{\partial^3 \Phi}{\partial \rho^2 \partial \zeta} + S_6 \frac{\partial^3 \Phi}{\partial \rho \partial \zeta^2} + S_7 \frac{\partial^3 \Phi}{\partial \rho \partial \eta^2} + S_8 \frac{\partial^3 \Phi}{\partial \zeta \partial \eta^2} = 0. \end{aligned} \right\} \tag{19}$$

Substituting Eqs. (17) and (18) into Eq. (19) and we get for the zeroth-order of  $k$

$$(-M + S_1 \phi_0)\psi_o + S_2 \frac{d^2 \psi_o}{d\rho^2} = C', \tag{20}$$

where  $C'$  is the integral constant. Two linearly independent solutions for the homogeneous part of Eq. (20), namely [32],

$$f = \frac{d\psi_0}{d\rho}, g = f \int^\rho \frac{d\rho}{f^2}. \tag{21}$$

Thus, the general solution can be given as

$$\psi_0 = C_1 f + C_2 g - C' f \int^\rho \frac{g}{S_2} d\rho + C' g \int^\rho \frac{f}{S_2} d\rho, \tag{22}$$

where  $C_1$  and  $C_2$  are the integral constants. The Wronskian ( $\hat{W}$ ) is defined by

$$\hat{W} = f(dg/d\rho) - g(df/d\rho).$$

The general solution of zeroth-order equation is simplified as

$$\psi_0 = C_1 f. \tag{23}$$

The first and second-order equation from Eqs. (17)–(19) can be obtained, where their solutions lead to the following dispersion relation:

$$\gamma_1 = \Delta - Ml_\xi + \sqrt{\Delta^2 - \Gamma}, \quad (24)$$

where

$$\left. \begin{aligned} \Delta &= \frac{2}{3}(\mu_1\phi_m - 2\mu_2/W^2), \\ \Gamma &= \frac{16}{45}(\mu_1^2\phi_m^2 - 3\mu_1\mu_2\phi_m/W^2 - 3\mu_2^2/W^4 + 12S_2\mu_3/W^4), \\ \mu_1 &= (S_1l_\xi + S_3l_\zeta), \mu_2 = (3S_2l_\xi + S_5l_\zeta), \\ \text{and } \mu_3 &= (3S_2l_\xi^2 + 2S_5l_\xi l_\zeta + S_6l_\zeta^2 + S_7l_\eta^2). \end{aligned} \right\} \quad (25)$$

Therefore, from Eq. (24), we observe that if the condition  $\Gamma - \Delta^2 > 0$  is satisfied then instability occurs. We obtain the instability growth rate,  $gr$ , to be represented as

$$gr = \sqrt{\Gamma - \Delta^2}. \quad (26)$$

This instability growth rate depends on the system parameters.

## 5 Numerical Investigations and Discussion

We have formulated the ZK equation by applying the reductive perturbation approach. The small- $k$  perturbation expansion technique examines the multi-dimensional instability of DAWs that is governed by this ZK equation [8, 40]. The results of this study can be summarized as follows:

The basic properties of the DA waves (polarity, amplitude, width, and speed) are found to be slightly modified by the dust temperature and density beside electron and ions densities and also their Fermi temperatures have a considerable effect.

The impact of slight fluctuation in dust temperature via  $\sigma_d$  on the phase speed  $v_0$  for distinct values of ion-to-electron Fermi temperature ratio,  $\sigma_i$  is presented in Fig. 1. The phase speed enhances with the increase of  $\sigma_d$ , while it shrinks with the increase of  $\sigma_i$ , i.e. the DA wave propagates faster if the dust temperature becomes higher or the ions Fermi temperature becomes lower. The wave steepening is determined by the nonlinear term  $A$ . This term determine also the polarity of the DA waves (Fig. 1). Figure 2a illustrates the dependence of the nonlinear coefficient of  $A$  on  $\sigma_i$  and  $\sigma_d$ . It is depicted that,  $A$  is negative for all values of  $\sigma_i$  and  $\sigma_d$  and its absolute value increases as  $\sigma_i$  and  $\sigma_d$  increase. The effects of  $\sigma_i$  and  $\sigma_d$  on the longitudinal,  $B$ , and the transverse,  $C$ , dispersion coefficients properties are manifested in Fig. 2b and c, respectively. Both coefficients are positive and decrease as  $\sigma_i$  increases, while  $B$  ( $C$ ) attains lower (higher) values with increasing  $\sigma_d$ . The soliton solution Eq. (14) occurs due to the balance between nonlinearity and dispersion effects, maintains its profile. The electrostatic solitary wave amplitude,  $\psi_m$  depends on parameters  $\sigma_i$ ,  $\sigma_d$ ,

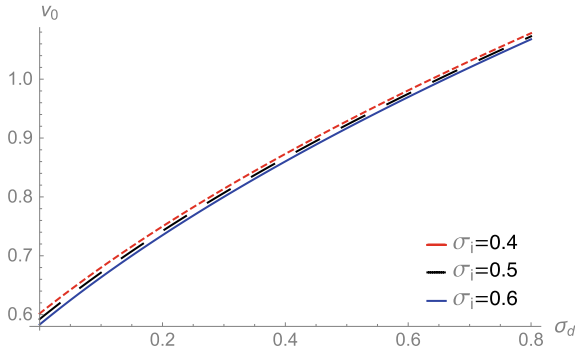


**Fig. 1** The phase speed  $v_0$  variation against  $\sigma_d$  at different values of  $\sigma_i$  at  $\mu_i=0.6$

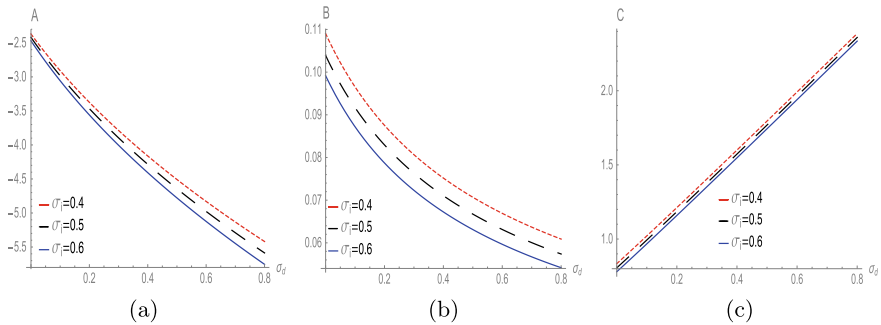


**Fig. 2** **a** The variation of the nonlinear term **A**, **b** the dispersive term **B**, **c** the dispersive term **C** represented by Eq. (9) against  $\sigma_d$  for distinct values of  $\sigma_i$  at  $\mu_i = 0.6$  and  $\Omega = 0.5$

the electron to dust equilibrium densities ratio via  $\mu_e$ , and obliquity angle  $\theta$  as shown in Fig. 3. Since the amplitude depends on the nonlinear term,  $A$ , the amplitude is negative for all parameters values as depicted in Fig. 2a. The amplitude (in absolute value) becomes larger for smaller values of dust temperature, ion Fermi temperature, and electron equilibrium density or larger values of electron Fermi temperature and obliquity angle. Moreover, width  $W$  of the wave is suppressed by increasing values of both  $\sigma_i$ , below a critical value of  $\sigma_d$  and the magnetic field through  $\Omega$ , as seen in Fig. 4. The angle  $\theta$  and  $\sigma_d$  larger than the critical value increase lead to increasing  $W$ . The results obtained from Figs. 3 and 4 are confirmed through the solitary wave profiles and associated electric field as shown in Figs. 5 and 6, respectively. The variation of the growth rate,  $gr$ , against  $\sigma_i$ ,  $\sigma_d$ ,  $\mu_e$ ,  $\Omega$ ,  $\theta$ , and frame velocity,  $M$  is depicted in Fig. 7, it is obvious that  $gr$  goes to zero as  $\sigma_d$ ,  $\mu_e$ , and  $\theta$  increase. The reduction of  $gr$  becomes sharp as  $\sigma_i$  and  $M$  increase or as  $\Omega$  decreases.

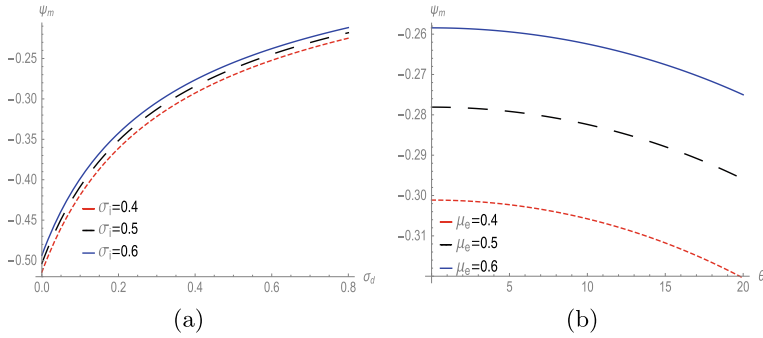


**Fig. 3** The effects on the rarefactive DA soliton amplitude  $\psi_m$  **a** against  $\sigma_d$  for distinct values of  $\sigma_i$  at  $\mu_e = 0.6$  with  $\theta = 10$ , **b** against  $\theta$  for different values of  $\mu_e$  with  $\sigma_d = 0.5$  and  $\sigma_i = 0.5$

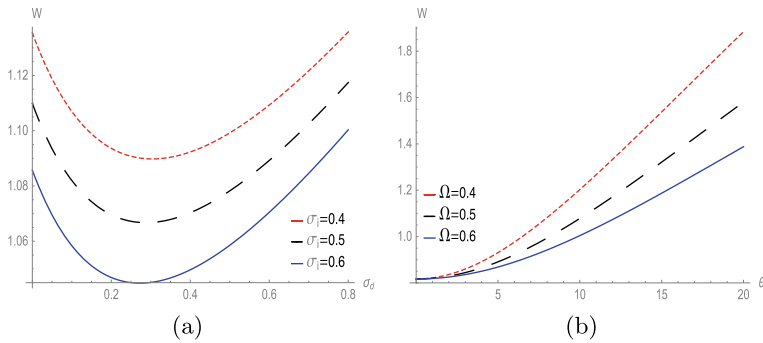


**Fig. 4** The effects on the rarefactive DA soliton width  $W$ , at  $\mu_e = 0.6$  **a** against  $\sigma_d$  for distinct values of  $\Omega$  with  $\theta = 10$ , **b** against  $\theta$  for distinct values of  $\Omega$  with  $\sigma_d = 0.5$  and  $\sigma_i = 0.5$

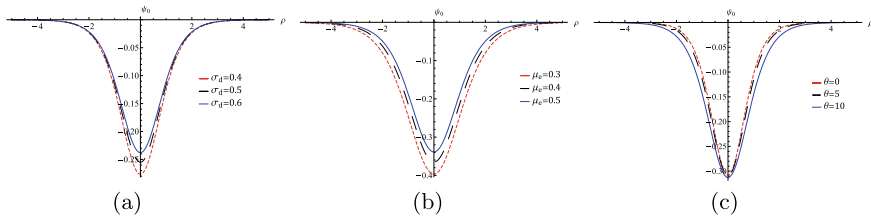


**Fig. 5** The evolution of  $\psi_0$  of DA waves that represented by equation (14) with  $\rho$  at  $\sigma_i = 0.5$   $M = 0.4$  and  $\Omega = 0.5$  for distinct values of **a**  $\sigma_d$  with  $\mu_e = 0.6$ , and  $\theta = 10$ , **b**  $\mu_e$  with  $\sigma_d = 0.3$ , and  $\theta = 13$ , and **c**  $\theta = 13$  with  $\sigma_d = 0.3$ , and  $\mu_e = 0.6$



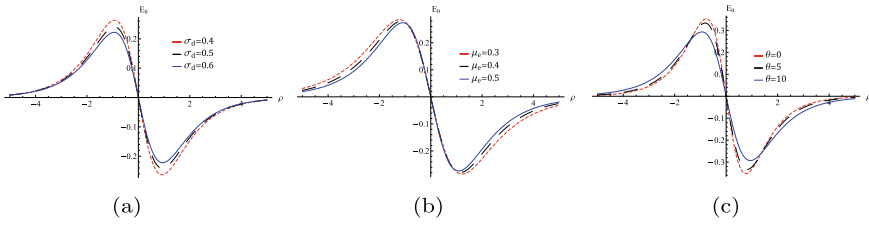


**Fig. 6** The evolution of the associated electric field,  $E_0$  of DA waves that represented by Eq. (5) with  $\rho$  for the potentials those represented by Fig. 5

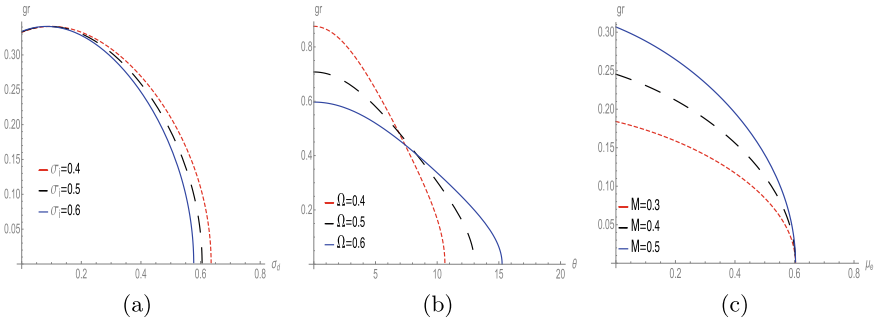


**Fig. 7** (Color online) The effects on the growth rate,  $gr$ , that represented by Eq. (26) at  $l_\xi = 0.7$ ,  $l_\eta = 0.4$  **a** against  $\sigma_d$  for distinct values of  $\sigma_i$  at  $\mu_e = 0.6$ ,  $\theta = 10$ ,  $M = 0.4$  and  $\Omega = 0.5$ , **b** against  $\theta$  for distinct values of  $\Omega$  at  $\mu = 0.6$ ,  $\sigma_d = 0.3$ ,  $\sigma_i = 0.5$  and  $M = 0.4$ , and **c** against  $\mu_e$  for distinct values of  $M$  at  $\theta = 13$ ,  $\sigma_d = 0.3$ ,  $\sigma_i = 0.5$  and  $\Omega = 0.5$

## 6 Conclusions

The hydrodynamic model has been employed to study a quantum Thomas-Fermi dense plasma consisting of negative dust particles with degenerate ions and electrons obeying the Fermi-Dirac distributions, embedded in a uniform magnetic field. The ZK equation has been formulated by employing the reductive perturbation approach. The solution of ZK equation has been used to explore the characteristics of the solitary wave. Interesting, the soliton amplitude is negative for all values of the ions and electrons densities and Fermi temperatures. This negative polarity structures may occur, depending on the negatively charged dust. The dependence of the soliton width on the electrons densities and Fermi temperatures, on the obliqueness, and the magnetic field (strength) was investigated.

The stability investigation and analysis of the solitary wave solution of ZK equation have been carried out. The influences of various physical parameters on the instability growth rate have been examined. It has been shown that an increase in the dust temperature, magnetic field strength and obliqueness can lessen the instability growth rate. The reduction of the growth rate also obtained by the decrease of the dust equilibrium density.

Our present results can be applied to discern the dynamics of nonlinear localized structures in laboratory and space manners where Thomas-Fermi dense magnetoplasma occurs, e.g. in the high-intensity laser-solid matter interaction experiments, and also in the white dwarfs [26, 27, 40, 45–48].

## References

1. Jung, Y.D.: Quantum-mechanical effects on electron-electron scattering in dense high-temperature plasmas. *Phys. Plasmas* **8**(8), 3842–3844 (2001)
2. Markowich, P.A., Ringhofer, C.A., Schmeiser, C.: *Semiconductor Equations*, 1st edn. Springer, New York (1990)
3. Becker, K., Koutsospyros, K., Yin, S.M., et al.: Environmental and biological applications of microplasmas. *Plasma Phys. Control. Fusion* **47**, B513–B523 (2005)
4. Killian, T.C.: Physics-cool vibes. *Nature (London)* **441**, 297–298 (2006)
5. Malkin, V.M., Fisch, N.J., Wurtele, J.S.: Compression of powerful x-ray pulses to attosecond durations by stimulated Raman backscattering in plasmas. *Phys. Rev. E* **75**, 026404 (2007)
6. Manfredi, G.: How to model quantum plasmas. *Fields Inst. Commun.* **46**, 263–287 (2005)
7. Shukla, P.K., Mamun, A.A.: *Introduction to Dusty Plasma Physics*, 1st edn. Institute of Physics, Bristol (2002)
8. Fortov, V.E., Ivlev, A.V., Khrapak, S.A., Morfill, G.E.: Complex (dusty) plasmas. *Phys. Rep.* **421**, 1–103 (2005)
9. Atteya, A., El-Borie, M.A., Roston, G.D., El-Helbawy, A.S., Prasad, P.K., Saha, A.: Ion-acoustic stable oscillations, solitary, periodic and shock waves in a quantum magnetize electron-positron-ion plasma. *Zeitschrift für Naturforschung A* **76**(9), 757–768 (2021)
10. El-Monier, S.Y., Atteya, A.: Dust-acoustic Gardner solitons in cryogenic plasma with the effect of polarization in the presence of a quantizing magnetic field. *Zeitschrift für Naturforschung A* **76**(2), 121–130 (2021)
11. Shukla, P.K., Silin, V.P.: Dust ion-acoustic wave. *Phys. Scr.* **45**(5), 508 (1992)
12. Barkan, A., D’Angelo, N., Merlino, R.L.: Experiments on ion-acoustic waves in dusty plasmas. *Planet. Space Sci.* **44**, 239–242 (1996)
13. Merlino, R.L., Barkan, A., Thompson, C., D’Angelo, N.: Laboratory studies of waves and instabilities in dusty plasmas. *Phys. Plasmas* **5**, 1607–1614 (1998)
14. Rao, N.N., Shukla, P.K., Yu, M.Y.: Dust-acoustic waves in dusty plasmas. *Planet. Space Sci.* **38**, 543–546 (1990)
15. Barkan, A., Merlino, R.L., D’Angelo, N.: Laboratory observation of the dust-acoustic wave mode. *Phys. Plasmas* **2**, 3563–3565 (1995); Pieper, J. B.: J. Goree, *Phys. Rev. Lett.* **77**, 3137 (1996)
16. Prabhakara, H.R., Tanna, V.L.: Trapping of dust and dust acoustic waves in laboratory plasmas. *Phys. Plasmas* **3**, 3176–3181 (1996)
17. Banerjee, A., Harbolaa, M.K.: Hydrodynamic approach to time-dependent density functional theory; Response properties of metal clusters. *J. Chem. Phys.* **113**, 5614–4623 (2000)
18. Doms, A., Reinhard, P.-G., Suraud, E.: Theoretical estimation of the importance of two-electron collisions for relaxation in metal clusters. *Phys. Rev. Lett.* **81**, 5524–5527 (1998)
19. Loffredo, M., Morato, L.: On the creation of quantized vortex lines in rotating He II. *Nuovo Cimento Soc. Ital. Fis., B* **108**, 205–215 (1993)
20. Feynman, R.: *Statistical Mechanics. A Set of Lectures*, 1st edn. Benjamin, Reading (1972)
21. Dubinov, A.E., Dubinova, A.A.: Nonlinear theory of ion-acoustic waves in an ideal plasma with degenerate electrons. *Plasma Phys. Rep.* **33**, 859–870 (2007)
22. Abdelsalam, U.M., Moslem, W.M., Shukla, P.K.: Localized electrostatic excitations in a Thomas-Fermi plasma containing degenerate electrons. *Phys. Plasmas* **15**, 052303 (2008)

23. Abdelsalam, U.M., Moslem, W.M., Shukla, P.K.: Ion-acoustic solitary waves in a dense pair-ion plasma containing degenerate electrons and positrons. *Phys. Lett. A* **372**, 4057–4061 (2008)
24. Atteya, A., El-Borie, M.A., Roston, G.D., El-Helbawy, A.S.: Nonlinear dust acoustic waves in an inhomogeneous magnetized quantum dusty plasma. *Waves Random Complex Media* 1–16 (2021). <https://doi.org/10.1080/17455030.2021.1880030>
25. Rahim, Z., Ali, S., Qamar, A.: Dust acoustic solitary and shock excitations in a Thomas-Fermi magnetoplasma. *Phys. Plasmas* **21**(7), 072305 (2014)
26. Irfan, M., Ali, S., Mirza, A.M.: Dust-acoustic solitary and rogue waves in a Thomas-Fermi degenerate dusty plasma. *Astrophys Space Sci.* **353**(2), 515–523 (2014)
27. Irfan, M., Ali, S., Ata-ur-Rahman, Mirza, A.M.: Arbitrary amplitude oblique electrostatic solitary waves in a degenerate cold dusty magnetoplasma. *IEEE Trans. Plasma Sci.* **47**(8), 4151–4158 (2019)
28. Abd-Elzaher, M., Atteya, A.: Obliquely overtaking collisions of electrostatic N-soliton in the Thomas-Fermi dense magnetoplasma. *Waves Random Complex Media* 1–21 (2021). <https://doi.org/10.1080/17455030.2021.1974121>
29. El-Taibany, W.F., Sabry, R.: Dust-acoustic solitary waves and double layers in a magnetized dusty plasma with nonthermal ions and dust charge variation. *Phys. Plasmas* **12**, 082302 (2005)
30. Shukla, P.K.: Twisted dust acoustic waves in dusty plasmas. *Phys. Plasmas* **19**, 083704 (2012)
31. Shukla, P.K.: Twisted electrostatic ion-cyclotron waves in dusty plasmas. *Phys. Rev. E* **87**, 015101 (2013)
32. Mamun, A.A.: Instability of obliquely propagating electrostatic solitary waves in a magnetized nonthermal dusty plasma. *Phys. Scr.* **58**, 505–509 (1998)
33. Mamun, A.A., Russell, S.M., Mendoza-Briceno, C.A., Alam, M.N., Datta, T.K., Das, A.K.: Multi-dimensional instability of electrostatic solitary structures in magnetized nonthermal dusty plasmas. *Planet. Space Sci.* **48**, 163–173 (2000)
34. El-Taibany, W.F., El-Bedwehy, N.A., El-Shamy, E.F.: Three-dimensional stability of dust-ion acoustic solitary waves in a magnetized multicomponent dusty plasma with negative ions. *Phys. Plasmas* **18**, 033703 (2011)
35. Akhter, T., Hossain, M.M., Mamun, A.A.: Multi-dimensional instability of dust-acoustic solitary waves in a magnetized plasma with opposite polarity dust. *Phys. Plasmas* **19**, 093707 (2012)
36. El-Labany, S.K., El-Taibany, W.F., Behery, E.E.: Stability of three-dimensional dust acoustic waves in a dusty plasma with two opposite polarity dust species including dust size distribution. *Phys. Rev. E* **88**, 023108 (2013)
37. Saini, N.S., Chahal, B.S., Bains, A.S., Bedi, C.: Zakharov-Kuznetsov equation in a magnetized plasma with two temperature superthermal electrons. *Phys. Plasmas* **21**, 022114 (2014)
38. El-Labany, S.K., El-Taibany, W.F., Behery, E.E., Zedan, N.A.: Stability of three-dimensional obliquely propagating dust acoustic waves in dusty plasma including the polarization force effect. *Eur. Phys. J. Plus* **130**, 250 (2015)
39. El-Taibany, W.F., Zedan, N.A., Atteya, A.: Stability of three-dimensional dust acoustic waves in a strongly coupled dusty plasma including kappa distributed superthermal ions and electrons. *Eur. Phys. J. Plus* **134**, 479 (2019)
40. Zedan, N.A., Atteya, El-Taibany, W.F., El-Labany, S.K.: Stability of ion-acoustic solitons in a multi-ion degenerate plasma with the effects of trapping and polarization under the influence of quantizing magnetic field. *Waves in Random and Complex Media* 1–15 (2020). <https://doi.org/10.1080/17455030.2020.1798560>
41. Gao, D.-N.: Multi-dimensional instability of dust acoustic waves in magnetized quantum plasmas with positive or negative dust. *Brazil. J. Phys.* **51**, 66–74 (2021)
42. Allen, M.A., Rowlands, G.: Determination of the growth rate for the linearized Zakharov-Kuznetsov equation. *J. Plasma Phys.* **50**, 413–424 (1993)
43. Allen, M.A., Rowlands, G.: Stability of obliquely propagating plane solitons of the Zakharov-Kuznetsov equation. *J. Plasma Phys.* **53**, 63–73 (1995)
44. Haider, M.M., Mamun, A.: Ion-acoustic solitary waves and their multi-dimensional instability in a magnetized degenerate plasma. *Phys. Plasmas* **19**, 102105 (2012)

45. Jehan, N., Salahuddin, M., Mahmood, S., Mizra, A.M.: Electrostatic solitary ion waves in dense electron-positron-ion magnetoplasma. *Phys. Plasmas* **16**, 042313 (2009)
46. Chatterjee, P., Saha, T., Muniandy, S.V., ap, S.L., Wong, C.S.: Solitary waves and double layers in dense magnetoplasma. *Phys. Plasmas* **16**, 072110 (2009)
47. Rahim, Z., Adnan, M., Qamar, A., Saha, A.: Nonplanar dust-acoustic waves and chaotic motions in Thomas Fermi dusty plasmas. *Phys. Plasmas* **25**, 083706 (2018)
48. Roy, D., Ghosh, N., Sahu, B.: Nonlinear modulation of quantum electron acoustic waves in a Thomas–Fermi plasma with effects of exchange-correlation. *Indian J Phys.* **95**(11), 2479–2490 (2020)

# Existence and Stability of Dust-Ion-Acoustic Double Layers Described by the Combined SKP-KP Equation



Sankirtan Sardar and Anup Bandyopadhyay

**Abstract** Sardar et al. [Phys Plasmas 24:063705 (2017)] have investigated dust-ion-acoustic (DIA) solitons of a combined Schamel's modified Kadomtsev Petviashvili-Kadomtsev Petviashvili (SKP-KP) equation in a dusty plasma consisting of nonthermal electrons which obeys vortex-like velocity distribution. In this paper, we have investigated the existence of double layer solutions and its stability by considering the same combined SKP-KP equation. We have seen that this double layer solution exists when  $L = 0$ , where  $L$  is a function of the parameters. We have analytically discussed the stability of the double layer solutions.

**Keywords** Stability · Double layers · Combined SKdV-KdV equation · Combined SKP-KP equation

## 1 Introduction

For the first time, Kadomtsev and Petviashvili [1] attempted to model a soliton in two dimensions known as KP equation. KP equation is generally used to discuss the stability of the Korteweg-de Vries (KdV) solitons. In an unmagnetized plasma, Kako and Rowlands [2] obtained KP equation to discuss the stability of ion acoustic (IA) solitons. Using this KP equation, Infeld et al. [3] investigated the stability of the KdV solitons. They have found that KdV solitons are stable with respect to the transverse perturbation. Employing small-k perturbation expansion method [4–7], Chakraborty and Das [8] derived a modified KP (MKP) equation to study the stability of IA soliton of the MKP equation. Employing multiple-scale perturbation expansion method [9, 10], Chakraborty and Das [11] also studied the higher stability of the same MKP equation in an another paper. Several authors [12–29] have derived the KP equation

---

S. Sardar (✉)

Department of Mathematics, Guru Ghasidas Vishwavidyalaya, Bilaspur 495009, India  
e-mail: [sankirtansardar@gmail.com](mailto:sankirtansardar@gmail.com)

A. Bandyopadhyay

Department of Mathematics, Jadavpur University, Kolkata 700032, India

© The Author(s), under exclusive license to Springer Nature Switzerland AG 2022  
S. Banerjee and A. Saha (eds.), *Nonlinear Dynamics and Applications*,  
Springer Proceedings in Complexity,  
[https://doi.org/10.1007/978-3-030-99792-2\\_17](https://doi.org/10.1007/978-3-030-99792-2_17)

193

or different modified KP (MKP) equations and used this KP equation to study the dynamics of IA/dust-acoustic (DA)/DIA waves in different plasmas.

Sardar et al. [30] have investigated dust-ion-acoustic (DIA) solitons of a combined SKP-KP equation in a dusty plasma consisting of warm adiabatic ions, isothermal positrons, immobile dust grains and nonthermal electrons. The electron species obeys vortex-like velocity distribution, where the background distribution is Cairns non-thermal distribution [31]. They have investigated that the alternative soliton of the combined SKP-KP equation exists if and only if  $L > 0$ , where  $L$  is a function of the parameters. They have observed that the alternative soliton cannot define the nonlinear dynamics of DIA waves for  $L = 0$  or  $L \approx O(\epsilon)$ , where  $\epsilon$  is a small parameter. In this situation, they have reported that further development is required.

In this paper, our aim is to investigate the existence of double layer solutions and its stability by considering the same combined SKP-KP equation. We have seen that this double layer solution exists when  $L = 0$ . We have analytically discussed the stability of the double layer solutions. Here we have extended previous work of Sardar et al. [30] by considering  $L = 0$ .

## 2 Evolution Equation

Considering continuity equation, motion equation, pressure equation for ions, Poisson equation, the equations for the velocity distribution functions for positrons and electrons, and the unperturbed charged neutrality condition, Sardar et al. [30] have derived the following equation:

$$\begin{aligned} \frac{\partial}{\partial \xi} \left[ \phi_{\tau}^{(1)} + AB\sqrt{\phi^{(1)}}\phi_{\xi}^{(1)} + AB_1\phi^{(1)}\phi_{\xi}^{(1)} + \frac{1}{2}AC\phi_{\xi\xi\xi}^{(1)} \right] \\ + \frac{1}{2}AD\left(\phi_{\eta\eta}^{(1)} + \phi_{\zeta\zeta}^{(1)}\right) = 0. \end{aligned} \quad (1)$$

This equation explains the dynamics of alternative DIA solitons in the present plasma system considered by Sardar et al. [30] when  $L > 0$ . Here  $\xi$ ,  $\eta$ ,  $\zeta$  are the stretched spatial coordinates and  $\tau$  is the stretched time coordinate. The equations of (28), (29), (30), (18) and (34) of Sardar et al. [30] give the expressions of  $A$ ,  $B$ ,  $D$ ,  $C$  and  $B_1$  respectively.

In this problem, using the same evolution Eq. (1), we have analyzed DL solution and its stability when  $L = 0$ .

### 3 DL Solutions of Combined SKP-KP Equation

For DL solutions of (1), we have considered the following transformations:

$$\eta' = \eta, \zeta' = \zeta, X = \xi - U\tau, \tau' = \tau. \tag{2}$$

Here,  $U$  is a constant normalized velocity. Under transformation (2), (1) reduces to the following equation:

$$\begin{aligned} \frac{\partial}{\partial X} \left[ -U\phi_X^{(1)} + \phi_\tau^{(1)} + AB\sqrt{\phi^{(1)}}\phi_X^{(1)} + AB_1\phi^{(1)}\phi_X^{(1)} + \frac{1}{2}AC\phi_{XXX}^{(1)} \right] \\ + \frac{1}{2}AD\left(\phi_{\eta\eta}^{(1)} + \phi_{\zeta\zeta}^{(1)}\right) = 0. \end{aligned} \tag{3}$$

We consider the following equation for travelling waves of (3):

$$\phi^{(1)} = \phi_0(X). \tag{4}$$

Employing (4) in (3), we obtain

$$\frac{d^2}{dX^2} \left[ -U\phi_0 + \frac{2}{3}AB(\phi_0)^{\frac{3}{2}} + \frac{1}{2}AB_1(\phi_0)^2 + \frac{1}{2}AC\frac{d^2\phi_0}{dX^2} \right] = 0. \tag{5}$$

Now, we use the following boundary condition

$$\phi_0, \frac{d^n \phi_0}{dX^n} \rightarrow 0 \text{ as } X \rightarrow \infty \text{ for all } n = 1, 2, 3, \dots \tag{6}$$

or

$$\phi_0, \frac{d^n \phi_0}{dX^n} \rightarrow 0 \text{ as } X \rightarrow -\infty \text{ for all } n = 1, 2, 3, \dots \tag{7}$$

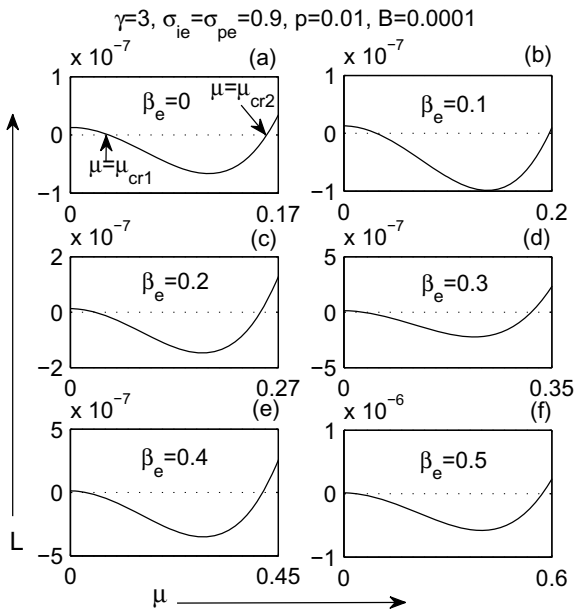
With the help of (6) or (7), the Eq. (5) can be written as follows:

$$-U\phi_0 + \frac{2}{3}AB(\phi_0)^{\frac{3}{2}} + \frac{1}{2}AB_1(\phi_0)^2 + \frac{1}{2}AC\frac{d^2\phi_0}{dX^2} = 0. \tag{8}$$

Following Das et al. [32], the DL solution of (8) is given as follows:

$$\phi_0 = a^2 \left( 1 - \lambda \tanh \frac{X}{W_1} \right)^2, \text{ where } a = -\frac{2B}{5B_1}, \tag{9}$$

**Fig. 1** For different values of  $\beta_e$ ,  $L$  is drawn with respect to  $\mu$  for  $\gamma = 3$ ,  $\sigma_{ie} = 0.9$ ,  $p = 0.01$ ,  $\sigma_{pe} = 0.9$  and  $B = 0.0001$



$$L = B^2 + \frac{75}{2} B_1 C p_1^2 = 0 \text{ with } p_1 = \frac{1}{W_1}. \tag{10}$$

Here  $\lambda = \pm 1$  and these two values of  $\lambda$  give two different DL solutions of (1) for the DIA waves corresponding to the boundary conditions (6) and (7) respectively. It is impossible to get alternative soliton of the combined SKP-KP equation by considering only one of the following two conditions:

$$\phi_0, \frac{d^n \phi_0}{dX^n} \rightarrow 0 \text{ as } X \rightarrow \infty \text{ for } n = 1, 2, 3, \dots \tag{11}$$

$$\phi_0, \frac{d^n \phi_0}{dX^n} \rightarrow 0 \text{ as } X \rightarrow -\infty \text{ for } n = 1, 2, 3, \dots \tag{12}$$

Specifically, using the condition (11), we get a Z-type DL solution whereas considering condition (12), we get a S-type DL solution. But both the conditions are necessary to get an alternative soliton of (1).

Now, we can consider  $B = 0.0001$  because  $B \neq 0$  but  $B \rightarrow 0$ . Figures 1(a)–1(f) show the variation of  $L$  against  $\mu$  for different values of  $\beta_e$  when values of  $p (= 0.01)$ ,  $\sigma_{pe} (= 0.9)$ ,  $\gamma$  and  $\sigma_{ie}$  are fixed. Each Fig. 1(a)–1(f) has two critical values of  $\mu$  where  $L = 0$ .

The solution (9) is the steady state DL solution of (1) along the  $x$ -axis. This solution is same as the DL solution of the Schamel’s modified Korteweg-de Vries-Korteweg-de Vries (SKdV-KdV) equation, i.e., the steady state DL solution of the equation



$$\phi_\tau^{(1)} + AB\sqrt{\phi^{(1)}}\phi_\xi^{(1)} + AB_1\phi^{(1)}\phi_\xi^{(1)} + \frac{1}{2}AC\phi_{\xi\xi\xi}^{(1)} = 0 \quad (13)$$

is exactly same as the Eq. (9). In the next section, we have considered the stability analysis of DL solution (9) of Eq. (1).

## 4 Stability Analysis

In the previous section, we have seen that the Eq. (9) gives two different DL solutions for  $\lambda = +1$  and  $\lambda = -1$ . Here, we have analyzed the stability of DL solutions (9) for  $\lambda = +1$ . Following the same procedure, one can easily analyse the stability of the DL solution (9) for  $\lambda = -1$ .

To use the multiple-scale perturbation expansion method of Allen and Rowlands [9, 10], we write

$$\phi^{(1)} = \phi_0(X) + q(X, \eta, \zeta, \tau). \quad (14)$$

Here  $\phi_0(X)$  is the DL solution (9) of the equation (3) and  $q(X, \eta, \zeta, \tau)$  is perturbed component of  $\phi^{(1)}$ . Substituting (14) into (3) and linearizing the equation, we obtain

$$q_{X\tau} + (Mq)_{XX} + \frac{1}{2}AD(q_{\eta\eta} + q_{\zeta\zeta}) = 0, \quad (15)$$

where

$$M = -U + AB\sqrt{\phi_0} + AB_1\phi_0 + \frac{1}{2}AC\frac{\partial^2}{\partial X^2}. \quad (16)$$

For long-wavelength plane-wave perturbation along a direction having direction cosines  $(l, m, n)$ , we consider

$$q(X, \eta, \zeta, \tau) = \bar{q}(X)e^{i\{k(lX+m\eta+n\zeta)-\omega\tau\}}. \quad (17)$$

Here  $k$  is small and direction cosines follow the relation  $l^2 + m^2 + n^2 = 1$ . Substituting (17) into (15), we get the following equation:

$$\begin{aligned} & (M\bar{q})_{XX} - i\omega\bar{q}_X + kl\left\{\omega\bar{q} + 2i(M\bar{q})_X + iAC\bar{q}_{XXX}\right\} \\ & - k^2l^2\left\{M\bar{q} + \frac{5}{2}AC\bar{q}_{XX} + AD\frac{m^2+n^2}{2l^2}\bar{q}\right\} \\ & - k^3l^3\left\{2iAC\bar{q}_X\right\} + k^4l^4\left\{\frac{1}{2}AC\bar{q}\right\} = 0, \end{aligned} \quad (18)$$

Following the multiple-scale perturbation expansion method [9, 10], we expand  $\bar{q}(X)$  and  $\omega$  as

$$\bar{q}(X) = \sum_{j=0}^{\infty} k^j q^{(j)}(X, X_1, X_2, X_3, \dots), \quad \omega = \sum_{j=0}^{\infty} k^j \omega^{(j)}, \quad (19)$$

where  $\omega^{(0)} = 0$ ,  $X_j = k^j X$ ,  $j = 0, 1, 2, \dots$ , and each  $q^{(j)} (= q^{(j)}(X, X_1, X_2, X_3, \dots))$  is a function of  $X, X_1, X_2, X_3, \dots$ . It is important to note that  $X_0 = X$ .

Finally, substituting first and second equation of (19) into (18) and comparing the coefficients of different powers of  $k$ , we obtain the following equations:

$$\frac{\partial}{\partial X}(Mq^{(j)}) = Q^{(j)}, \quad \text{where } Q^{(j)} = \int_{\infty}^X R^{(j)} dX, \quad (20)$$

and the expressions of  $R^{(0)}$  and  $R^{(1)}$  are given as follows:

$$R^{(0)} = 0 \quad (21)$$

$$R^{(1)} = i\omega^{(1)}q_0^{(0)} - iAClq_{000}^{(0)} - ACq_{0001}^{(0)} - 2il[Mq^{(0)}]_0 - 2[Mq^{(0)}]_{01}, \quad (22)$$

and we have used the notations:  $q_r^{(j)} = \frac{\partial q^{(j)}}{\partial X_r}$ ,  $q_{rs}^{(j)} = \frac{\partial^2 q^{(j)}}{\partial X_r \partial X_s}$ ,  $q_{rst}^{(j)} = \frac{\partial^3 q^{(j)}}{\partial X_r \partial X_s \partial X_t}$ ,  $q_{rsty}^{(j)} = \frac{\partial^4 q^{(j)}}{\partial X_r \partial X_s \partial X_t \partial X_y}$  and  $[Mq^{(j)}]_{rs} = \frac{\partial^2 (Mq^{(j)})}{\partial X_r \partial X_s}$ .

Considering that  $q^{(j)}$  and its first order, second order, and third order derivatives vanish as  $X \rightarrow \infty$  and from the Eq. (20), we obtain the following general solution:

$$q^{(j)} = A_1^{(j)} f + A_2^{(j)} f \int \frac{1}{f^2} dX + A_3^{(j)} f \int \frac{\phi_0}{f^2} dX + \frac{2}{AC} f \int \frac{\int (f \int \frac{Q^{(j)}}{f^2} dX) dX}{f^2} dX, \quad (23)$$

where  $f = \frac{d\phi_0}{dX}$ ,  $\phi_0$  is given by (9) for  $\lambda = 1$  and  $A_1^{(j)}, A_2^{(j)}, A_3^{(j)}$  are all arbitrary functions of  $X_1, X_2, X_3, \dots$ .

Using MATHEMATICA [33], the solution (23) for  $\lambda = +1$  can be written as follows:

$$\begin{aligned}
q^{(j)} = & A_1^{(j)} f + \frac{3W_1^2}{256a^4} (5A_2^{(j)} + 8a^2 A_3^{(j)}) f X - \frac{W_1^2}{128a^2} (5A_2^{(j)} + 8a^2 A_3^{(j)}) \\
& + \frac{3W_1^2}{128a^2} (5A_2^{(j)} + 8a^2 A_3^{(j)}) (1 - R) + \frac{W_1^2}{128a^2} (5A_2^{(j)} + 8a^2 A_3^{(j)}) e^{-\frac{2X}{W_1}} \\
& - \frac{W_1^2}{1024a^2} (85A_2^{(j)} + 192a^2 A_3^{(j)} + 35A_2^{(j)} R) S^2 - \frac{W_1^2}{16a^2} A_2^{(j)} \frac{1}{S^2} \\
& - \frac{W_1^2}{16a^2} A_2^{(j)} (1 - R) \frac{1}{S^4} + \frac{2}{AC} f \int \frac{\int (f \int \frac{Q^{(j)} dX}{f^2}) dX}{f^2} dX, \tag{24}
\end{aligned}$$

where  $S = \operatorname{sech} \frac{X}{W_1}$  and  $R = \tanh \frac{X}{W_1}$ .

#### 4.1 Zeroth Order Equation

For  $j = 0$ , using (21), one can write (24) as

$$\begin{aligned}
q^{(0)} = & A_1^{(0)} f + \frac{3W_1^2}{256a^4} (5A_2^{(0)} + 8a^2 A_3^{(0)}) f X - \frac{W_1^2}{128a^2} (5A_2^{(0)} + 8a^2 A_3^{(0)}) \\
& + \frac{3W_1^2}{128a^2} (5A_2^{(0)} + 8a^2 A_3^{(0)}) (1 - R) + \frac{W_1^2}{128a^2} (5A_2^{(0)} + 8a^2 A_3^{(0)}) e^{-\frac{2X}{W_1}} \\
& - \frac{W_1^2}{1024a^2} (85A_2^{(0)} + 192a^2 A_3^{(0)} + 35A_2^{(0)} R) S^2 - \frac{W_1^2}{16a^2} A_2^{(0)} \frac{1}{S^2} \\
& - \frac{W_1^2}{16a^2} A_2^{(0)} (1 - R) \frac{1}{S^4}, \tag{25}
\end{aligned}$$

To make  $q^{(0)}$  bounded and consistent at  $X = +\infty$ , we obtain the following two equations:

$$-\frac{W_1^2}{16a^2} A_2^{(0)} = 0 \text{ and } -\frac{W_1^2}{128a^2} (5A_2^{(0)} + 8a^2 A_3^{(0)}) = 0. \tag{26}$$

From the Eq. (26), we get  $A_2^{(0)} = A_3^{(0)} = 0$ . So the expression of  $q^{(0)}$  assumed as follows:

$$q^{(0)} = A_1^{(0)} f = A_1^{(0)} \frac{d\phi_0}{dX}. \tag{27}$$

## 4.2 First Order Equation

Using the Eqs. (22), (27) and MATHEMATICA [33], one can write (24) for  $j = 1$  as

$$\begin{aligned}
 q^{(1)} = & A_1^{(1)} f + \left\{ \frac{3W_1^2}{256a^4} (5A_2^{(1)} + 8a^2 A_3^{(1)}) + iA_1^{(0)} \frac{\omega^{(1)} - 2IU}{2U} - \frac{\partial A_1^{(0)}}{\partial X_1} \right\} fX \\
 & - \frac{W_1^2}{128a^2} (5A_2^{(1)} + 8a^2 A_3^{(1)}) - \left\{ \frac{3W_1^2}{128a^2} (5A_2^{(1)} + 8a^2 A_3^{(1)}) + iA_1^{(0)} \frac{a^2 \omega^{(1)}}{U} \right\} \\
 & \times (1 - R) - \left\{ \frac{W_1^2}{128a^2} (5A_2^{(1)} + 8a^2 A_3^{(1)}) + iA_1^{(0)} \frac{2a^2 \omega^{(1)}}{U} \right\} e^{-\frac{2X}{W_1}} \\
 & - \left\{ \frac{W_1^2}{1024a^2} (85A_2^{(1)} + 192a^2 A_3^{(1)} + 35A_2^{(1)} R) + iA_1^{(0)} \frac{a^2 \omega^{(1)}}{4U} (7 - 3R) \right\} S^2 \\
 & - \frac{W_1^2}{16a^2} A_2^{(1)} \frac{1}{S^2} - \frac{W_1^2}{16a^2} A_2^{(1)} (1 - R) \frac{1}{S^4}, \tag{28}
 \end{aligned}$$

To make  $q^{(1)}$  bounded and consistent at  $X = +\infty$ , we get  $A_2^{(1)} = A_3^{(1)} = 0$ . So the expression of  $q^{(1)}$  assumed as follows:

$$\begin{aligned}
 q^{(1)} = & A_1^{(1)} f + \left( iA_1^{(0)} \frac{\omega^{(1)} - 2IU}{2U} - \frac{\partial A_1^{(0)}}{\partial X_1} \right) fX + iA_1^{(0)} \frac{2a^2 \omega^{(1)}}{U} e^{-\frac{2X}{W_1}} \\
 & + iA_1^{(0)} \frac{a^2 \omega^{(1)}}{U} (1 - R) - iA_1^{(0)} \frac{a^2 \omega^{(1)}}{4U} (7 - 3R) S^2. \tag{29}
 \end{aligned}$$

Now, as the first term of  $q^{(1)}$  has already been included in  $q^{(0)}$ , one can remove this term from  $q^{(1)}$ . One can also remove the ghost secular term of  $q^{(1)}$  by choosing

$$\frac{\partial A_1^{(0)}}{\partial X_1} = iA_1^{(0)} \frac{\omega^{(1)} - 2IU}{2U}. \tag{30}$$

Therefore, from the Eq. (29), we obtain

$$q^{(1)} = iA_1^{(0)} \frac{2a^2 \omega^{(1)}}{U} e^{-\frac{2X}{W_1}} + iA_1^{(0)} \frac{a^2 \omega^{(1)}}{U} (1 - R) - iA_1^{(0)} \frac{a^2 \omega^{(1)}}{4U} (7 - 3R) S^2. \tag{31}$$

Now we see that second and third term of  $q^{(1)}$  is bounded at  $X = \pm\infty$  but the first term of  $q^{(1)}$  is not bounded at  $X = -\infty$  because of the presence of the term  $e^{-\frac{2X}{W_1}}$ . To make  $q^{(1)}$  bounded at  $X = -\infty$ , We must have  $iA_1^{(0)} \frac{2a^2 \omega^{(1)}}{U} = 0$  and consequently we get

$$\omega^{(1)} = 0. \tag{32}$$

From (32), we see that there is no imaginary part of  $\omega^{(1)}$  and consequently DL solution for  $\lambda = 1$  is stable at the lowest order of  $k$ . The same analysis is true for  $\lambda = -1$ .

## 5 Conclusions

In this paper, we have considered the DL solution and its stability described by the combined SKP-KP equation. The form of the DL solution as given by the Eq. (9) suggests that corresponding to a given set of values of the parameters there are two types of DL solutions for  $\lambda = +1$  and for  $\lambda = -1$ . Finally, we have found that DLs are stable at the lowest order of the wave number.

**Acknowledgements** The authors have used the constructive comments of the reviewer to prepare the manuscript of this paper.

## References

1. Kadomtsev, B.B., Petviashvili, V.I.: Sov. Phys. Dokl **15**, 539 (1970)
2. Kako, M., Rowlands, G.: Plasma Phys. **18**, 165 (1976)
3. Infeld, E., Hen, M., Rowlands, G.: Acta Phys. Polon. A **54**, 131 (1978)
4. Rowlands, G.: J. Plasma Phys. **3**, 567 (1969)
5. Infeld, E.: J. Plasma Phys. **8**, 105 (1972)
6. Infeld, E., Rowlands, G.: J. Plasma Phys. **10**, 293 (1973)
7. Zakharov, V.E., Rubenchik, A.M.: Sov. Phys. JETP **38**, 494 (1974)
8. Chakraborty, D., Das, K.P.: J. Plasma Phys. **60**, 151 (1998)
9. Allen, M.A., Rowlands, G.: J. Plasma Phys. **50**, 413 (1993)
10. Allen, M.A., Rowlands, G.: J. Plasma Phys. **53**, 63 (1995)
11. Chakraborty, D., Das, K.P.: J. Plasma Phys. **70**, 89 (2004)
12. Duan, W.S.: Chaos Solitons Fractals **14**, 1315 (2002)
13. Lin, M., Duan, W.S.: Chaos Solitons Fractals **23**, 929 (2005)
14. Pakzad, H.R., Javidan, K.: Chaos Solitons Fractals **42**, 2904 (2009)
15. Pakzad, H.R.: Pramana **74**, 605 (2010)
16. Dorrnian, D., Sabetkar, A.: Phys. Plasmas **19**, 013702 (2012)
17. Samanta, U.K., Saha, A., Chatterjee, P.: Phys. Plasmas **20**, 022111 (2013)
18. Samanta, U.K., Saha, A., Chatterjee, P.: Astrophys. Space Sci. **347**, 293 (2013)
19. Sahu, B., Ghosh, N.K.: Astrophys. Space Sci. **343**, 289 (2013)
20. Saha, A., Pal, N., Chatterjee, P.: Phys. Plasmas **21**, 102101 (2014)
21. Saha, A., Chatterjee, P.: Astrophys. Space Sci. **349**, 813 (2014)
22. Saha, A., Pal, N., Chatterjee, P.: Braz. J. Phys. **45**, 325 (2015)
23. Saini, N.S., Kaur, N., Gill, T.S.: Adv. Space Res. **55**, 2873 (2015)
24. Sardar, S., Bandyopadhyay, A., Das, K.P.: Phys. Plasmas **23**, 073703 (2016)
25. Sardar, S., Bandyopadhyay, A., Das, K.P.: Phys. Plasmas **23**, 123706 (2016)
26. Seadawy, A.R., El-Rashidy, K.: Results Phys. **8**, 1216 (2018)
27. Shahein, R.A., Seadawy, A.R.: Indian J. Phys. **93**, 941 (2019)
28. Varghese, A., Saritha, A.C., Willington, N.T., Michael, M., Sebastian, S., Sreekala, G., Venugopal, C.: J. Astrophys. Astr **41**, 1 (2020)
29. Prasad, P.K., Saha, A.: J. Astrophys. Astr **42**, 1 (2021)

30. Sardar, S., Bandyopadhyay, A., Das, K.P.: Phys. Plasmas **24**, 063705 (2017)
31. Cairns, R.A., Mamun, A.A., Bingham, R., Boström, R., Dendy, R.O., Nairn, C.M.C., Shukla, P.K.: Geophys. Res. Lett. **22**, 2709 (1995)
32. Das, J., Bandyopadhyay, A., Das, K.P.: J. Plasma Phys. **74**, 163 (2008)
33. Wolfram, S.: The MATHEMATICA® book, version 4. Cambridge university press (1999)

# Dust-ion Collisional and Periodic Forcing Effects on Solitary Wave in a Plasma with Cairns-Gurevich Electron Distribution



Anindya Paul , Niranjan Paul , Kajal Kumar Mondal ,  
and Prasanta Chatterjee 

**Abstract** In this work, our aim is to investigate the effects of dust-ion collision and external periodic force on the ion-acoustic solitary wave (IASW) in the framework of damped forced Korteweg de-Vries (KdV) like Schamel equation. Collisional dusty plasma with Cairns-Gurevich electron distribution has been taken into account to study the propagation of IASW. Reductive perturbation technique (RPT) is employed to derive the damped forced KdV like Schamel equation and its approximate analytical solitary wave solution is determined considering momentum conservation law of KdV like Schamel equation. It also has been shown that, how the other plasma parameters *viz.* non-thermal parameter and ratio of free and trapped electron temperature influence the solitary wave solution in presence of damping and external periodic force. The approximate analytical results of this manuscript may be helpful to understand the basic features of solitary structures in astrophysical plasma where non-thermal and trapped electron distributions are present.

**Keywords** Damped forced KdV like Schamel equation · Cairns-Gurevich electron distribution · Dust-ion collisional frequency · Non-thermal parameter · RPT · External periodic force

## 1 Introduction

Analysis of solitary wave structures has become very interesting topic of research to the physicists and mathematicians since last few decades for its versatile application in laboratory and astrophysical plasma [1–3]. Bernstein [4] introduced the idea of

---

A. Paul (✉) · K. K. Mondal  
Department of Mathematics, Cooch Behar Panchanan Barma University, Cooch Behar 736101,  
West Bengal, India  
e-mail: [paul.anindya20@gmail.com](mailto:paul.anindya20@gmail.com)

N. Paul · P. Chatterjee  
Department of Mathematics, Siksha Bhavana, Visva-Bharati, Santiniketan, Santiniketan 731235,  
West Bengal, India

trapped electrons which was observed in space and laboratory plasma. Plasma species are named as trapped when they move in a finite domain through closed path. Gurevich [5] introduced trapping as a microscopic process where electrons are trapped by potential wells. He showed the effect of trapped electrons in IASWs. To explain characteristic of non-linear electrostatic structures in upper ionosphere observed by Viking and Freja satellites, Cairns et al. [6] considered non-thermal electron distribution and showed that nature of ion-acoustic solitary wave changes significantly in presence of non-thermal electrons. Later Tang [7] and Mamun [18] also worked to show the effect of non-thermal electrons on the IASWs. Abdikian [9] explored dust-ion-acoustic solitary waves in dusty plasma with presence of non-thermal and trapped electrons considering modified Zarakov Kuznetsov equation. Annou et al. [10] investigated the combine effect of trapped and non-thermal electrons on solitons in plasma expansion into vacuum. El-Taibany et al. [11] studied modulated ion-acoustic wave in plasma with electrons obeying Cairns-Gurevich distribution.

Collisions among different plasma constituents occur continuously [12–15]. Due to collisional effects of plasma constituents, damping force is created in plasma medium which influences nonlinear structures in plasma [16–20]. Several works have been studied to investigate the effects of various types of external forces on IASWs. Mainly two kinds of forces have been taken into consideration viz. periodic type source and *sech*( $\xi$ ,  $\tau$ ) type [21, 22] source that arises from experimental condition or space debris. The results of [23–27] show that the presence of external periodic force brings behavioural changes in IASWs. In [25–27] the effect of frequency & strength of periodic force on solitary wave solution was studied in collisional plasma. The studies [23–27] were done taking external periodic force in the form of *cos*( $\xi$ ,  $\tau$ ). Chowdhury et al. [24] studied the forced KdV like Schamel equation in a super thermal plasma consisting trapped electron and Paul et al. [20] investigated damped KdV like Schamel equation in a collisional plasma where electrons follow Cairns-Gurevich distribution. To best of our knowledge no work till now has been reported that investigates both dust-ion collisional effect and external periodic forcing effects on solitary wave in plasma where electrons follow Cairns-Gurevich distribution.

The rest of this paper is organized as follows: in Sect. 2, the basic equations and electron which follows the Cairns-Gurevich distribution has been presented. The formation of damped forced KdV like Schamel equation and its time dependent approximate analytical solution has been determined in Sect. 3. In Sect. 4, the effects of different physical parameters on the nonlinear waves have been discussed in detail. Section 5 contains conclusions.



## 2 Basic Set of Equations and Cairns-Gurevich Electron Distribution

In this work, we consider an unmagnetized, collisional plasma consisting of cold fluid ions, static dust granules with negative charge, electrons following Cairns-Gurevich distribution. Normalized continuity equation, momentum equation and Poisson's equation are respectively given by,

$$\frac{\partial n_i}{\partial t} + \frac{\partial(n_i u)}{\partial x} = 0, \quad (1)$$

$$\frac{\partial u}{\partial t} + u \frac{\partial u}{\partial x} = -\frac{\partial \phi}{\partial x} - \nu_{id} u, \quad (2)$$

$$\frac{\partial^2 \phi}{\partial x^2} = n_e - n_i + S(x, t). \quad (3)$$

Here,  $n_i$  is the ion number density and it is normalized by the unperturbed equilibrium plasma density  $n_0$ .  $u$  is the ion velocity, normalized to the ion-acoustic speed  $C_s = (\frac{T_e}{m_i})^{1/2}$ .  $\phi$  is the electrostatic wave potential which is normalized to  $T_e/e$ . The time and space variables are in units of the ion plasma frequency  $(\omega_{pi})^{-1}$  and the electron Debye radius  $\lambda_D = (\frac{T_e}{4\pi n_0 e^2})^{1/2}$ .  $T_e$  is defined as the temperature of electron. The dust-ion collisional frequency is  $\nu_{id}$  and  $S(x, t)$  is a source term that arises from experimental conditions.

In small amplitude limit of  $\phi < 1$ , the normalized density of non-thermal electrons obeys the following Cairns-Gurevich distribution [11],

$$n_e = (1 - b\phi + 2b\phi^2) \left( 1 + \phi - \frac{4(1 - \beta)}{3\sqrt{\pi}} \phi^{3/2} + \frac{1}{2} \phi^2 \right), \quad (4)$$

where  $b$  is the non-thermal parameter which depends on  $\alpha$  and the relation between them is  $b = \frac{4\alpha}{1+3\alpha}$ . Here,  $\alpha$  represents the population of non-thermal electrons and  $\beta$ , the trapping parameter, is the ratio of free electron temperature ( $T_{fe}$ ) and trapped electron temperature ( $T_{et}$ ). If  $\beta = 0$  then the electron distribution (4) represents plateau like electron distribution and if  $\beta = 1$ , it becomes Maxwellian.

## 3 Derivation of Damped Forced KdV Like Schamel Equation and Its Time Dependent Approximate Analytical Solution

To derive the damped forced KdV like Schamel equation, we wish to use Reductive Perturbation Technique (RPT) in a collisional dusty plasma in presence of non-thermal and trapped electrons. The stretched coordinates are taken [20] as follows,

$$\begin{cases} \xi = \epsilon^{1/4}(x - v_0t), \\ \tau = \epsilon^{3/4}t, \end{cases} \tag{5}$$

where  $\epsilon$  and  $v_0$  are the strength of nonlinearity and phase velocity of IASW respectively. The expansion of the dependent variables [20, 24] are given by :

$$\begin{cases} n_i = 1 + \epsilon n_i^{(1)} + \epsilon^{3/2}n_i^{(2)} + \dots, \\ u = 0 + \epsilon u_1 + \epsilon^{3/2}u_2 + \dots, \\ \phi = 0 + \epsilon \phi_1 + \epsilon^{3/2}\phi_2 + \dots, \\ v_{id} \sim \epsilon^{3/4}v_{id0}, \\ S \sim \epsilon^{3/2}S_2. \end{cases} \tag{6}$$

Then, using chain rule, we have,

$$\begin{aligned} \frac{\partial}{\partial x} &\equiv \frac{\partial}{\partial \xi} \frac{\partial \xi}{\partial x} + \frac{\partial}{\partial \tau} \frac{\partial \tau}{\partial x} = \epsilon^{1/4} \frac{\partial}{\partial \xi}, \\ \frac{\partial^2}{\partial x^2} &\equiv \epsilon^{1/2} \frac{\partial^2}{\partial \xi^2}, \end{aligned}$$

and

$$\frac{\partial}{\partial t} \equiv \frac{\partial}{\partial \xi} \frac{\partial \xi}{\partial t} + \frac{\partial}{\partial \tau} \frac{\partial \tau}{\partial t} = -v_0\epsilon^{1/4} \frac{\partial}{\partial \xi} + \epsilon^{3/4} \frac{\partial}{\partial \tau}.$$

Using the expansion (6) and (5) into Eqs. (1)–(3) and taking the lowest order coefficient of  $\epsilon$ , we obtain the following three equations,

$$\epsilon^{5/4} : -v_0 \frac{\partial n_i^{(1)}}{\partial \xi} + \frac{\partial u_1}{\partial \xi} = 0, \tag{7}$$

$$\epsilon^{5/4} : -v_0 \frac{\partial u_1}{\partial \xi} + \frac{\partial \phi_1}{\partial \xi} = 0, \tag{8}$$

$$\epsilon^1 : -(1 - b)\phi_1 + n_i^{(1)} = 0. \tag{9}$$

Now, from the Eqs. (7), (8) and (9), we obtain the following dispersion relation,

$$v_0 = \frac{1}{\sqrt{1 - b}}. \tag{10}$$

Equating the next higher order coefficient of  $\epsilon$ , we get the following equations from (1), (2) and (3) respectively as,

$$\epsilon^{7/4} : \frac{\partial n_i^{(1)}}{\partial \tau} - v_0 \frac{\partial n_i^{(2)}}{\partial \xi} + \frac{\partial u_2}{\partial \xi} = 0, \tag{11}$$

$$\epsilon^{7/4} : \frac{\partial u_1}{\partial \tau} - v_0 \frac{\partial u_2}{\partial \xi} + \frac{\partial \phi_2}{\partial \xi} + v_{id0} u_1 = 0, \tag{12}$$

$$\epsilon^{3/2} : \frac{\partial^2 \phi_1}{\partial \xi^2} = (1 - b)\phi_2 - \frac{4(1 - \beta)}{3\sqrt{\pi}} \phi_1^{3/2} - n_i^{(2)} + S_2. \tag{13}$$

Differentiating Eq. (13) partially with respect to  $\xi$ , and eliminating the terms  $n_i^{(2)}$ ,  $u_2$  and  $\phi_2$  from the Eqs. (7)–(13) with the help of dispersion relation, the following nonlinear evolution equation is obtained,

$$\frac{\partial \phi_1}{\partial \tau} + A\sqrt{\phi_1} \frac{\partial \phi_1}{\partial \xi} + B \frac{\partial^3 \phi_1}{\partial \xi^3} + C\phi_1 = B \frac{\partial S_2}{\partial \xi}, \tag{14}$$

where  $A = \frac{v_0^3(1-\beta)}{\sqrt{\pi}}$ ,  $B = \frac{v_0^3}{2}$  and  $C = \frac{v_{id0}}{2}$ .

The external periodic force  $S_2$  can be taken as  $S_2 = f_0 \xi \cos(\omega \tau)$ , where  $f_0$  and  $\omega$  stands for the strength and frequency of the source respectively. Using the above source term in the Eq. (14) we get the following equation,

$$\frac{\partial \phi_1}{\partial \tau} + A\sqrt{\phi_1} \frac{\partial \phi_1}{\partial \xi} + B \frac{\partial^3 \phi_1}{\partial \xi^3} + C\phi_1 = B f_0 \cos(\omega \tau), \tag{15}$$

which is the desired damped forced KdV like Schamel equation.

If  $C = f_0 = 0$ , the Eq. (15) becomes the KdV like Schamel equation,

$$\frac{\partial \phi_1}{\partial \tau} + A\sqrt{\phi_1} \frac{\partial \phi_1}{\partial \xi} + B \frac{\partial^3 \phi_1}{\partial \xi^3} = 0, \tag{16}$$

and its solution is given by,

$$\phi_1 = \phi_m \operatorname{sech}^4 \left( \frac{\xi - U\tau}{W} \right), \tag{17}$$

where  $\phi_m = (\frac{15U}{8A})^2$  and  $W = \sqrt{\frac{16B}{U}}$ , represent amplitude and width of the solitary wave respectively. Here,  $U$  is the speed of the wave.

For small values of  $f_0$  and  $C$ , we assume the solution of damped forced KdV like Schamel equation (15) as,

$$\phi_1 = \phi_m(\tau) \operatorname{sech}^4 \left( \frac{\xi - U(\tau)\tau}{W(\tau)} \right), \tag{18}$$

where  $U(\tau)$  is an unknown function of  $\tau$ ,  $\phi_m(\tau) = (\frac{15U(\tau)}{8A})^2$  and  $W(\tau) = \sqrt{\frac{16B}{U(\tau)}}$ .

It is well known that

$$I = \int_{-\infty}^{\infty} \phi_1^2 d\xi, \tag{19}$$

is a conserved quantity for a KdV like Schamel equation [20]. Using the momentum conservation law (19) and with the help of [20] and [24], we get the following differential equation for the unknown function  $U(\tau)$ ,

$$U(\tau) \frac{dU(\tau)}{d\tau} + \frac{4}{7}CU(\tau)^2 = \frac{224}{995}A^2Bf_0\cos(\omega\tau). \tag{20}$$

Solving the differential equation (20) with an initial condition  $U(0) = U_0$ , we get,

$$U(\tau) = \sqrt{\frac{448 A^2 B f_0}{135(64 C^2 + 49 \omega^2)} (8 C \cos(\omega \tau) + 7 \omega \sin(\omega \tau)) + K e^{-\frac{8 C}{7} \tau}}, \tag{21}$$

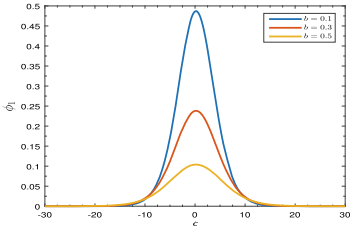
where  $K$  is given by

$$K = U_0^2 - \frac{3584 A A^2 B C f_0}{135(64 C^2 + 49 \omega^2)}. \tag{22}$$

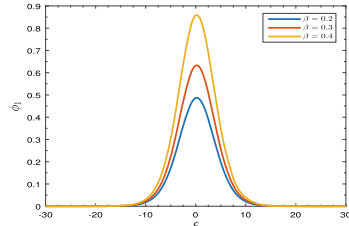
Using the value of  $U(\tau)$ , we subsequently deduce the values of  $W(\tau)$  and  $\phi_m(\tau)$ . Putting these values in Eq. (18), one can obtain the solution of damped forced KdV like Schamel equation (15).

### 4 Effects of Various Parameters

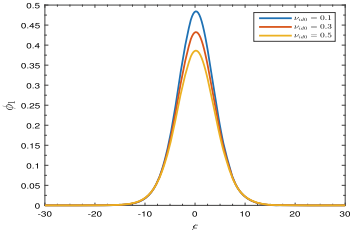
In this section, the effects of various parameters such as  $b$ ,  $\beta$ ,  $v_{id0}$ ,  $\omega$  and  $f_0$  on solution of Eq. (15) is demonstrated. Figure 1a represents the variation of amplitude in solitons for three distinct values of  $b = 0.1, 0.3, 0.5$  when the other parameters are  $U_0 = 0.2, \tau = 1, \beta = 0.2, v_{id0} = 0.09, f_0 = 0.01, \omega = 0.5$ . It is noticed that the amplitude of the solitary waves decreases as  $b$  increases and width of the solitary wave increases a little with the increment of  $b$ . Figure 1b shows the variation of solitons for different values of trapping parameter ( $\beta$ ). When  $b = 0.1$  and the other parameters are same as shown in the caption of Fig. 1a. As the value of trapping parameter increases, the amplitude of the solitary wave increase significantly. The width of the solitary waves also increases with the increment of  $\beta$ . In Fig. 1c, the value of  $v_{id0}$  is taken in the interval (0.01, 0.13) and the other parameters are same as in the caption of the figure. From this figure it is clearly observed that as  $v_{id0}$  increases the amplitude of solitary waves increases significantly whereas it is hard to draw conclusion about change in the width of waves from that same figure. Therefore,



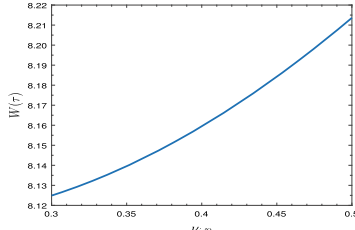
(a) Plots of  $\phi_1$  vs  $\xi$  for different values of  $b$  with  $U_0 = 0.2, \beta = 0.2, v_{id0} = 0.09, f_0 = 0.01, \omega = 0.5, \tau = 1$ .



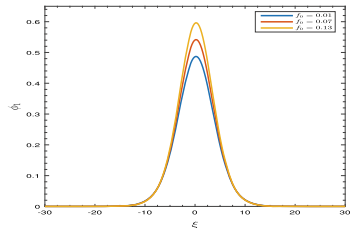
(b) Plots of  $\phi_1$  vs  $\xi$  for different values of  $\beta$  with  $U_0 = 0.2, b = 0.1, v_{id0} = 0.09, f_0 = 0.01, \omega = 0.5, \tau = 1$ .



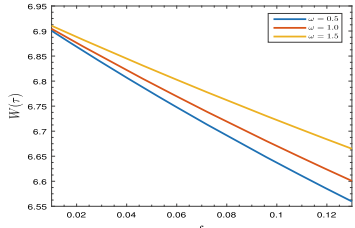
(c) Plots of  $\phi_1$  vs  $\xi$  for different values of  $v_{id0}$  with  $U_0 = 0.2, \beta = 0.2, b = 0.1, f_0 = 0.01, \omega = 0.5, \tau = 1$ .



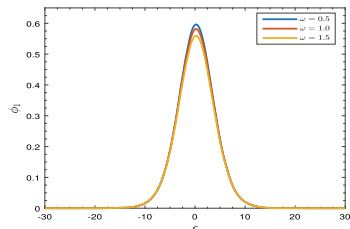
(d) Plot of  $W(\tau)$  vs  $v_{id0}$  with  $U_0 = 0.2, b = 0.1, \beta = 0.2, f_0 = 0.05, \omega = 0.5, \tau = 1$ .



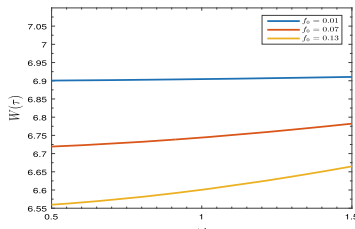
(e) Plots of  $\phi_1$  vs  $\xi$  for different values of  $f_0$  with  $U_0 = 0.2, \beta = 0.2, b = 0.1, v_{id0} = 0.09, \omega = 0.5, \tau = 1$ .



(f) Plots of  $W(\tau)$  vs  $f_0$  for different values of  $\omega$  with  $U_0 = 0.2, b = 0.1, \beta = 0.2, v_{id0} = 0.09, \tau = 1$ .



(g) Plots of  $\phi_1$  vs  $\xi$  for different values of  $\omega$  with  $U_0 = 0.2, \beta = 0.2, b = 0.1, v_{id0} = 0.09, f_0 = 0.01, \tau = 1$ .



(h) Plots of  $W(\tau)$  vs  $\omega$  for different values of  $f_0$  with  $U_0 = 0.2, \beta = 0.2, v_{id0} = 0.09, b = 0.1, \omega = 0.5, \tau = 1$ .

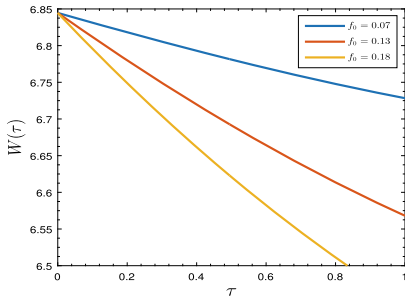
**Fig. 1** Graphical presentations of approximate analytical solitary wave solution with variation of amplitude and width w.r.t to different parameters

Fig. 1d is plotted between  $W(\tau)$  versus  $v_{id0}$  for different values of  $b$  to understand the variation of the width of solitary waves. It is clear from the graph that the width of the solitary wave increases as the dust-ion collisional frequency grows. Figure 1e represents the variation of solitary wave against  $\xi$  where other parameters are same as in the caption. It shows that solitary wave become more and more spiky as the strength of the periodic force  $f_0$  grows. From this figure, it is hard to draw conclusion on the variation of width. Thus, a graph of  $W(\tau)$  versus  $f_0$  is plotted in Fig. 1f for three distinct values of  $\omega = 0.5, 1.0, 1.5$  when the other parameters are  $U_0 = 0.2, \tau = 1, \beta = 0.2, v_{id0} = 0.09, f_0 = 0.01, b = 0.1$ . It shows that as the strength of the periodic force  $f_0$  increases the width of the solitary waves decrease. From Fig. 1f represents the profile for  $\phi_1$  against  $\xi$ , keeping all other parameters same as the caption. It is noticed that the height of the solitary wave decreases with the enhancement  $\omega$ . To understand the effect of the frequency of the force on the width of the solitary wave, a graph is plotted between  $W(\tau)$  versus  $\omega$  in Fig. 1h. a small increment in the width of the solitary wave is observed as  $\omega$  of the external periodic force grows.

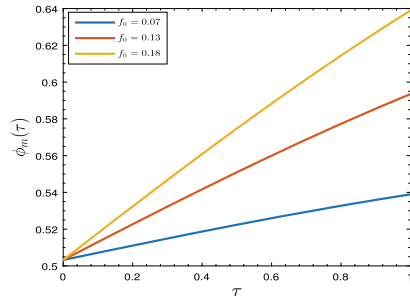
Figure 2a and b show the variance of width and amplitude of solitary wave respectively against  $\tau$  at different strength of the periodic force when other parameters are same as in the caption. Figure 2a interprets that width of solitary wave decreases as  $\tau$  increases. Figure 2b explicates that amplitude of solitary wave rises as  $\tau$  grows. Figure 2c is plotted for  $W(\tau)$  against  $\tau$  for three values of  $v_{id0} = 0.2, 0.3, 0.4$  when  $U_0 = 0.2, \beta = 0.2, b = 0.1, f_0 = 0.05, \omega = 0.5$ . The plot elucidates that width of the solitary wave surges as  $\tau$  enhances. Figure 2d depicts a graph between  $\phi_m(\tau)$  versus  $\tau$  at different values of  $v_{id0}$  when  $U_0 = 0.2, \beta = 0.2, b = 0.1, f_0 = 0.05$  &  $\omega = 0.5$ . The graph shows that the amplitude of the IASW reduces with the increment of  $\tau$ .

## 5 Conclusions

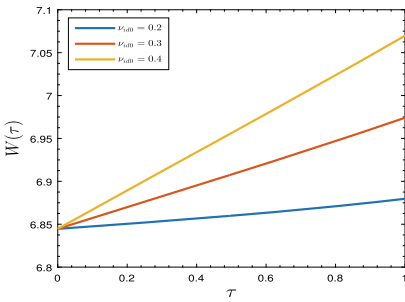
Using RPT, a damped forced KdV like Schamel equation is derived and the behaviour of its wave propagation has been discussed in a collisional plasma consisting dust granules, trapped and non-thermal electrons which follows Cairns-Gurevich distribution. The study shows that non-thermal parameter ( $b$ ), trapping parameter ( $\beta$ ) strength ( $f_0$ ) and frequency ( $\omega$ ) of external force, dust-ion collisional frequency ( $v_{id0}$ ) have significant effects on the amplitude and the width of solitary waves. It is seen that the amplitude of the solitary waves decreases as the non-thermal parameter ( $b$ ) increases. This is because, as the value of  $b$  increases, the external periodic force helps to decrease the positive potential energy in the solitary wave. It is observed that with the increment of trapping parameter ( $\beta$ ), the positive potential energy in the solitary wave increases that helps in the increment of both amplitude and width of the solitary wave. As the dust-ion collisional frequency parameter ( $v_{id0}$ ) increases, the collision between the dust granules and ions grows in a more narrow region of the plasma space that results in decay of the internal potential energy of the solitary



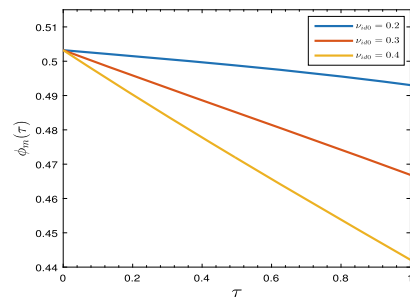
(a) Plots of  $W(\tau)$  vs  $\tau$  for different values of  $f_0$  with  $U_0 = 0.2, \beta = 0.2, b = 0.1, \nu_{id0} = 0.1, \omega = 0.5$ .



(b) Plots of  $\phi_m(\tau)$  vs  $\tau$  for different values of  $f_0$  with  $U_0 = 0.2, \beta = 0.2, b = 0.1, f_0 = 0.05, \omega = 0.5$ .



(c) Plots of  $W(\tau)$  vs  $\tau$  for different values of  $\omega$  with  $U_0 = 0.2, \beta = 0.2, b = 0.1, f_0 = 0.05, \omega = 0.5$ .



(d) Plots of  $\phi_m(\tau)$  vs  $\tau$  for different values of  $\omega$  with  $U_0 = 0.2, \beta = 0.2, b = 0.1, f_0 = 0.05, \omega = 0.5$ .

**Fig. 2** Variation of amplitude and width of approximate analytical solitary wave solution w.r.t different parameters

wave causing decrease in the amplitude with almost unaltered width. The increase in strength of the external force ( $f_0$ ) causes the rise in the positive potential energy of IASW. As a result the peak of the amplitude of the solitary wave increases significantly. The increase in frequency of the external periodic force ( $\omega$ ) causes the insignificant decrement in amplitude of the solitary waves. These results may help in further study of IASWs.

## References

1. Ikezi, H., Taylor, R., Baker, D.: Formation and interaction of ion-acoustic solitons. Phys. Rev. Lett. **25**, 11 (1970)
2. Washimi, H., Taniuti, T.: Propagation of ion acoustic waves of small amplitude. Phys. Rev. Lett **77**, 996 (1996)
3. Goertz, C.K.: Dusty plasmas in the solar system. Rev. Geophys. **27**, 271 (1989)

4. Bernstein, I.B., Greene, J.M., Kruskal, M.D.: Exact nonlinear plasma oscillations. *Phys. Rev.* **108**, 546 (1957)
5. Gurevich, A.V.: Distribution of captured particles in a potential well in the absence of collisions. *Sov. Phys. JETP* **26**, 575–580 (1968)
6. Cairns, R.A., Mamun, A.A., Bingham, R., Bostrom, R., Dendy, R.O., Nairn, C.M., Shukla, P.K.: Electrostatic solitary structures in nonthermal plasmas. *Geophys. Res. Lett.* **22**, 2709 (1995)
7. Tang, R.A., Xue, J.K.: Nonthermal electrons and warm ions effects on oblique modulation of ion-acoustic waves. *Phys. Plasmas* **11**, 3939–3944 (2004)
8. Mamun, A.: Effects of ion temperature on electrostatic solitary structures in nonthermal plasmas. *Phys. Rev. E* **55**, 1852–1857 (1997)
9. Abdikian, A.: Dust-ion-acoustic solitary waves in a magnetized dusty pair-ion plasma with Cairns-Gurevich electrons and opposite polarity dust particles. *Contrib. Plasma Phys.* **59**, 20 (2019)
10. Annou, K., Bara, D., Bennaceur-Doumaz, D.: Cairns-Gurevich equation for soliton in plasma expansion into vacuum. *J. Plasma Phys.* **81** (2015)
11. El-Taibany, W.F., Sabry, R.: Dust-acoustic solitary waves and double layers in a magnetized dusty plasma with nonthermal ions and dust charge variation. *Plasma Phys.* **12**, 082302 (2005)
12. Yang, X., Wang, C.L., Liu, C.B., Zhang, J.R., Shi, Y.R.: The collision effect between dust grain and ions to the dust ion acoustic waves in a dusty plasma. *Phys. Plasmas* **19**, 103705 (2012)
13. Popel, S.I., Golub', A.P., Losseva, T.V.: Weakly dissipative dust-ion-solitons. *Phys. Rev. E* **67**, 056402 (2003)
14. Nakamura, Y., Sarma, A.: Observation of ion-acoustic solitary waves in a dusty plasma. *Phys. Plasmas* **8**, 3921 (2001)
15. Losseva, T.V., Popel, S.I., Golub', A.P., Izvekova, Yu.N., Shukla, P.K.: Weakly dissipative dust-ion-acoustic solitons in a complex plasmas and the effect of electromagnetic radiation. *Phys. Plasmas* **19**, 013703 (2012)
16. Misra, A.P., Choudhury, A.R., Choudhury, K.R.: Effect of dust ion collision on dust ion acoustic solitary waves for nonextensive plasmas in the framework of damped Korteweg-de Vries-Burgers equation. *Phys. Lett. A* **323**, 110 (2004)
17. Maitra, S., Banerjee, G.: Dust ion acoustic solitary waves in a collisional dusty plasma with dust grains having Gaussian distribution. *Phys. Plasmas* **21**, 113707 (2014)
18. Das, T.K., Ali, R., Chatterjee, P.: Effect of dust ion collision on dust ion acoustic waves in the framework of damped Zakharov-Kuznetsov equation in presence of external periodic force. *Phys. Plasmas* **24**, 103703 (2017)
19. Paul, N., Mondal, K.K., Chatterjee, P.: Effect of dust ion collision on dust ion acoustic solitary waves for nonextensive plasmas in the framework of Damped Korteweg-de Vries-Burgers equation. *Zeitschrift für Naturforschung a* **74**(10), (2019)
20. Paul, N., Ali, R., Mondal, K.K., Chatterjee, P.: Ion-neutral collisional effect on solitary waves in weakly ionized plasma with Cairns-Gurevich distribution of electrons. *Int. J. Appl. Comput. Math.* **7**, 172 (2021)
21. Sen, A., Tiwari, S., Misra, S., Kaw, P.: Nonlinear wave excitations by orbiting charged space debris objects. *Adv. Space Res.* **56**, 429 (2015)
22. Bhowmick, S., Sahu, B.: Propagation of nonlinear excitations of dust acoustic waves by a moving charged object in superthermal plasmas. *Indian J. Phys.* (2021)
23. Ali, R., Saha, A., Chatterjee, P.: Analytical electron acoustic solitary wave solution for the forced KdV equation in superthermal plasma. *Phys. Plasmas* **24**, 122106 (2017)
24. Chowdhury, S., Mandi, L., Chatterjee, P.: Effect of externally applied periodic force on ion acoustic waves in superthermal plasmas. *Phys. Plasmas* **25**, 042112 (2018)
25. Chatterjee, P., Ali, R., Saha, A.: Analytical solitary wave solution of the dust ion acoustic waves for the damped forced Kortewegde Vries equation in superthermal plasmas. *Zeitschrift für Naturforschung A* **73**, 151 (2018)



26. Mandi, L., Mondal, K.K., Chatterjee, P.: Analytical solitary wave solution of the dust ion acoustic waves for the damped forced modified Korteweg-de Vries equation in q-nonextensive plasmas. *Eur. Phys. J. Spl. Topics* **228**, 2753 (2019)
27. Paul, N., Mondal, K.K., Ali, R., Chatterjee, P.: Analytical solitary wave solution of dust ion acoustic waves in nonextensive plasma in the framework of damped forced Korteweg-de Vries-Burgers equation. *Indian J. Phys.* **95**(12), 2855–2863 (2021)

# Electron-Acoustic Solitons in a Multicomponent Superthermal Magnetoplasma



Rajneet Kaur , Geetika Slathia , Kuldeep Singh ,  
and Nareshpal Singh Saini 

**Abstract** In this paper, electron-acoustic solitons (EASs) in magnetized multicomponent plasma having fluid of cold electrons, positrons, superthermal electrons, and positive ions are examined. The nonlinear Zakharov-Kuznetsov (ZK) equation is derived by applying the reductive perturbation method (RPM). The effect of various plasma parameters (concentration of electrons, superthermality of hot electrons/positrons and magnetic field strength) on the characteristic properties of EASs is analysed.

**Keywords** EA solitons · Superthermal distribution · Zakharov-Kuznetsov equation

## 1 Introduction

From the past many years, the study of electron-acoustic (EA) has become very fascinating among plasma physicists because of their pivotal role in different plasma environments e.g. astrophysical, laboratory and space plasmas [1]. These waves are evolved due to the existence of two temperature electrons. Due to two distinct temperatures, pressure of hot electrons provide the required restoring force and cold electrons become inertial. Further, due to large mass of ions as compared to that of electrons, ions are considered to form a stationary background. Numerous investigation have already been done to examine the propagation properties of linear and nonlinear EASs. Yu and Shukla [2] reported the characteristics of EASs in a magnetoplasma with multi-temperature electrons. Mace and Hellberg [3] studied the EASs in a fluid model composed of two temperature electrons with magnetized and unmagnetized fluid ions. They discussed the propagation properties of KdV-

---

R. Kaur (✉) · G. Slathia · K. Singh · N. S. Saini  
Department of Physics, Guru Nanak Dev University, Amritsar 143005, India  
e-mail: [rajneetkaur909@gmail.com](mailto:rajneetkaur909@gmail.com)

K. Singh  
Department of Mathematics, Khalifa University of Science and Technology, Abu Dhabi, UAE

ZK equation with plane and multidimensional solitary wave solutions. Danehkar et al. [4] developed a general plasma fluid model to describe the large amplitude EASs in superthermal plasma using pseudopotential method. They showed that only negative potential EASs are formed in a plasma. Devanandhan et al. [5] studied the EASs in a magnetized and plasma composed of hot ions and cold electrons obeying a kappa distribution. They observed that the magnetic field and other plasma parameters have strongly modified the characteristics of EASs. Various researchers have reported the properties of EASs in electron-positron-ion (e-p-i) plasmas. The characteristic properties of positron acoustic solitons in a multicomponent plasma have been examined by Alam et al. [6]. They studied the basic features of Double layer, Gardner solitons with solitary wave solution of mKdV equation. Adnan et al. [7] analysed the ion acoustic waves in a superthermal e-p-i plasma under the influence of magnetic field. They found that the effect of positron concentration and superthermality has modified the ion acoustic solitary waves. Ferdousi et al. [8] studied the ion acoustic solitons in a magnetized plasma composed of nonextensive positrons and electrons. It was observed that nonextensive parameter has altered the propagation properties of ion acoustic solitons. Saha and Tamang [9] analysed the behaviour of positron acoustic waves in a multicomponent plasma containing inertial positrons and Kaniadakis distributed positrons and hot electrons. They observed that the effect of different parameters have modified the nonlinear structures. Bansal et al. [10] examined the characteristic properties of EASs in a magnetoplasma composed of superthermal distributed two temperature electrons, positrons and uniform stationary background ions. The results showed that the nonplanar EASs are significantly modified due to the effect of positron densities as well as positron temperature and other components. The dissipative effects of ion acoustic solitons in a multicomponent collisional e-p-i plasma with non-thermal electrons and isothermal positrons were studied by Gul and Ahmed [11].

Electron-acoustic waves gain more importance when high energy particles in plasmas come into picture. The occurrence of these high energy particles are well explained by kappa distribution function. The superthermal distribution function was first well explained by Vasyliunas [12]. Various researchers have examined the role of high energy superthermal particles in nonlinear dynamics. The characteristic properties of ion acoustic waves with two fluid ions in superthermal plasma were studied by Shahmansouri and Tribeche [13]. The nonlinearity and dispersion properties of ion acoustic solitons are significantly enhanced with change in superthermality parameter. Singh and Sethi [14] studied the characteristic properties of mKdV equation in a collisionless plasma composed of negatively charged dust, two temperature kappa distributed electrons and hot ions. Singh and Saini [15] investigated the EA shock waves in a magnetized multicomponent plasma consists of cold electrons as a fluid, hot positrons and superthermal electrons. They analysed that the strength of EA shocks is increased with increase in superthermality of electrons. The aim of our present work is to study nonlinear dynamics of EASs in an e-p-i superthermal magnetoplasma. The paper is arranged as follows: Sect. 2 presents the basic fluid

model equations. The derivation of ZK equation and its solution are illustrated in Sect. 3. Numerical analysis is illustrated in Sect. 4. Conclusions are mentioned in the Sect. 5.

## 2 Basic Fluid Equations

The dimensionless expressions of densities of superthermal positrons and hot electrons are given as [15]

$$n_p = 1 - \gamma b_1 \phi + \gamma^2 b_2 \frac{\phi^2}{2} + \dots \quad (1)$$

$$n_h = 1 + a_1 \phi + a_2 \frac{\phi^2}{2} + \dots \quad (2)$$

Here,  $a_1 = \left( \frac{\kappa_e - \frac{1}{2}}{\kappa_e - \frac{3}{2}} \right)$ ,  $a_2 = \left( \frac{\kappa_e^2 - \frac{1}{4}}{(\kappa_e - \frac{3}{2})^2} \right)$ ,  $b_1 = \left( \frac{\kappa_p - \frac{1}{2}}{\kappa_p - \frac{3}{2}} \right)$ ,  $b_2 = \left( \frac{\kappa_p^2 - \frac{1}{4}}{(\kappa_p - \frac{3}{2})^2} \right)$ . Here,  $\kappa_{e,p}$  are the superthermality spectral indices of electrons and positrons. The Maxwellian case can be obtained as  $\kappa_{e,p} \rightarrow \infty$ .

At equilibrium  $n_{oh} + n_{oc} = n_{oi} + n_{op}$ , where  $n_{oj}$  (for  $j = c, p, i, h$ ) are undisturbed number density of cold electrons, hot positrons, stationary ions and hot electrons respectively. The wave is propagating in the  $x$ - $z$  plane. We consider the dimensionless equations as [15]:

$$\frac{\partial n_c}{\partial t} + \frac{\partial(n_c u_{cx})}{\partial x} + \frac{\partial(n_c u_{cz})}{\partial z} = 0, \quad (3)$$

$$\frac{\partial u_{cx}}{\partial t} + u_{cx} \frac{\partial u_{cx}}{\partial x} + u_{cz} \frac{\partial u_{cx}}{\partial z} = \frac{\partial \phi}{\partial x} - \Omega u_{cy}, \quad (4)$$

$$\frac{\partial u_{cy}}{\partial t} + u_{cx} \frac{\partial u_{cy}}{\partial x} + u_{cz} \frac{\partial u_{cy}}{\partial z} = \Omega u_{cx}, \quad (5)$$

$$\frac{\partial u_{cz}}{\partial t} + u_{cx} \frac{\partial u_{cz}}{\partial x} + u_{cz} \frac{\partial u_{cz}}{\partial z} = \frac{\partial \phi}{\partial z}, \quad (6)$$

$$\begin{aligned} \frac{\partial^2 \phi}{\partial x^2} + \frac{\partial^2 \phi}{\partial z^2} = & 1 - \alpha + n_c \sigma - \delta + \phi(a_1 + \alpha \gamma b_1) \\ & + \frac{\phi^2}{2}(a_2 - \alpha \gamma^2 b_2), \end{aligned} \quad (7)$$

The fluid velocity  $u_c$ , and electrostatic potential  $\phi$ , are normalized with respect to EA speed,  $C_e = \left( \frac{T_h}{m_e} \right)^{\frac{1}{2}}$ , and  $\frac{T_h}{e}$ , respectively. The space coordinate ( $x$ ) is normalized by

electron Debye length  $\lambda_D = (\frac{T_h}{4\pi n_{oh} e^2})^{\frac{1}{2}}$  and time coordinate ( $t$ ) is scaled by inverse of plasma frequency of electrons,  $\omega_{ph} = (\frac{4\pi n_{oh} e^2}{m_e})^{\frac{1}{2}}$ . The gyrofrequency of electron,  $\omega_c = \frac{eB}{m_e c}$  is scaled with respect to  $\omega_{ph}$ ,  $\Omega = \frac{\omega_c}{\omega_{ph}}$ .  $\alpha = \frac{n_{op}}{n_{oh}}$ ,  $\sigma = \frac{n_{oc}}{n_{oh}}$ ,  $\delta = \frac{n_{oi}}{n_{oh}}$  and  $\gamma = \frac{T_h}{T_p}$ .

### 3 Derivation of ZK Equation and Its Solution

To study the dynamics of EASs with weak dispersion and of weak nonlinearity, we assume  $\omega$  (or  $k$ )  $\ll 1$ . All physical quantities vary slowly in space and vary more slowly in time. We have used the RPM to find the ZK equation. The stretched coordinates are given as [16, 17]:

$$\xi = \epsilon^{\frac{1}{2}} (z - Vt), \quad \zeta = \epsilon^{\frac{1}{2}} x, \quad \text{and} \quad \phi = \frac{3}{2} t \quad (8)$$

The expansions used are given as:

$$n_c = 1 + \epsilon n_{c1} + \epsilon^2 n_{c2} + \epsilon^3 n_{c3} + \dots, \quad (9)$$

$$u_{cx} = \epsilon^{\frac{3}{2}} u_{cx1} + \epsilon^2 u_{cx2} + \epsilon^{\frac{5}{2}} u_{cx3} + \dots, \quad (10)$$

$$u_{cy} = \epsilon^{\frac{3}{2}} u_{cy1} + \epsilon^2 u_{cy2} + \epsilon^{\frac{5}{2}} u_{cy3} + \dots, \quad (11)$$

$$u_{cz} = \epsilon u_{cz1} + \epsilon^2 u_{cz2} + \epsilon^3 u_{cz3} + \dots, \quad (12)$$

$$\phi = \epsilon \phi_1 + \epsilon^2 \phi_2 + \epsilon^3 \phi_3 + \dots, \quad (13)$$

using Eqs. (8)–(13) in Eqs. (3)–(7) neutrality condition is obtained as:  $(\delta + \alpha) = (1 + \sigma)$ . After simplifying, we get the first order equations as:

$$n_{c1} = -\phi_1 Q, \quad (14)$$

$$u_{cy1} = \frac{1}{\sigma} \frac{\partial \phi_1}{\partial \zeta}, \quad (15)$$

$$u_{cz1} = -V \phi_1, \quad (16)$$

$$V = \frac{1}{\sqrt{Q}}, \quad (17)$$

where,  $V$  is the phase velocity of EASs and  $Q = \frac{(a_1 + \alpha \gamma b_1)}{\sigma}$ . By equating the quantities for higher orders of  $\epsilon$  and doing rigorous calculations, we have obtained the following

ZK equation as:

$$\frac{\partial \phi}{\partial \tau} + A\phi \frac{\partial \phi}{\partial \xi} + B \frac{\partial^3 \phi}{\partial \xi^3} + C \frac{\partial}{\partial \xi} \left( \frac{\partial^2 \phi}{\partial \zeta^2} \right) = 0, \quad (18)$$

where,  $\phi_1 = \phi$  and nonlinear coefficient  $A = B(-3\sigma Q^2 - (a_2 - \alpha\gamma^2 b_2))$ , dispersion coefficient  $B = \frac{1}{2VQ^2\sigma}$ , and transverse dispersion coefficient  $C = B(1 + \frac{\sigma}{\Omega^2})$ .

We consider a transformation  $Y = l_x \zeta + l_z \xi - \Lambda \tau$ , ( $l_x, l_z$  are the direction cosines), to evaluate the solution of Eq. (18).  $\Lambda$  denotes the velocity of solitons w.r.t. moving frame scaled with  $C_e$ . The solution of ZK equation is obtained as [18]:

$$\phi = \phi_0 \operatorname{sech}^2 \left( \frac{Y}{\Delta} \right), \quad (19)$$

where  $\phi_0 = \frac{3\Lambda}{Al_z}$  is maximum amplitude and  $\Delta = \left( \frac{4Fl_z}{\Lambda} \right)^{\frac{1}{2}}$  is the width of EASs.

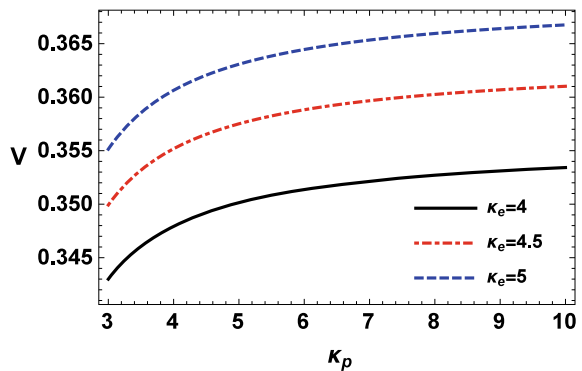
Here,  $F = Bl_z^2 + C(1 - l_z^2)$ .

## 4 Numerical Analysis

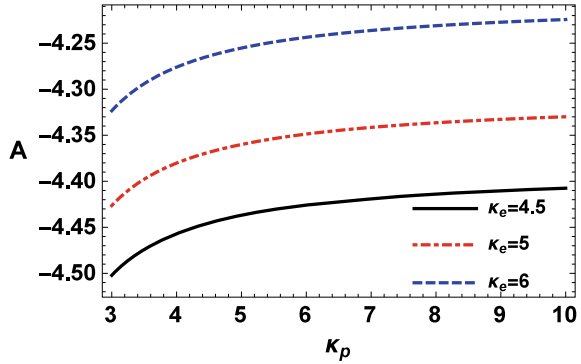
To carry out numerical analysis, the range of various physical parameters in laboratory and astrophysical/space plasmas [19] is chosen as:  $n_{op} \sim (1.5-3) \text{ cm}^{-3}$ ,  $n_{oc} \sim (0.1-0.4) \text{ cm}^{-3}$ ,  $T_h \sim (200-1,000) \text{ eV}$ ,  $n_{oh} \sim (1.5-3) \text{ cm}^{-3}$ , and  $T_p \sim (200-1,000) \text{ eV}$ . The propagation properties of EASs are strongly influenced by the change in the value of any parameter.

Figure 1, describes the behaviour of phase velocity ( $V$ ) with superthermality index of positrons (via  $\kappa_p$ ) and superthermality index of hot electrons (via  $\kappa_e$ ).

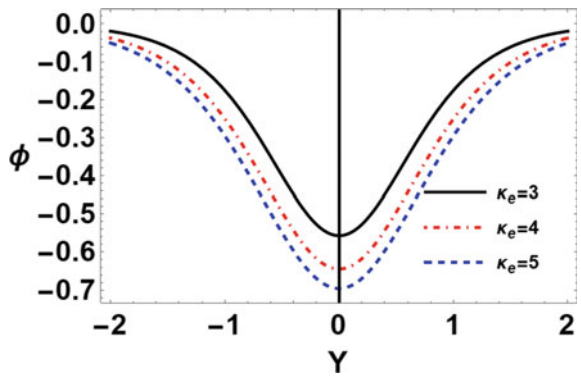
**Fig. 1** Plot for the phase velocity ( $V$ ) with superthermality of positrons ( $\kappa_p$ ) and with electrons ( $\kappa_e$ )



**Fig. 2** Plot for the nonlinear coefficient ( $A$ ) with superthermality index of positrons (via  $\kappa_p$ ) and with superthermality index of electrons ( $\kappa_e$ )



**Fig. 3** Plot for EASs profile ( $\phi$ ) with superthermality index of electrons ( $\kappa_e$ ), here  $\gamma = 4, \delta = 0.1, \kappa_p = 4, \sigma = 0.2, l_z = 0.6, \omega = 0.2, \Lambda = 0.3$



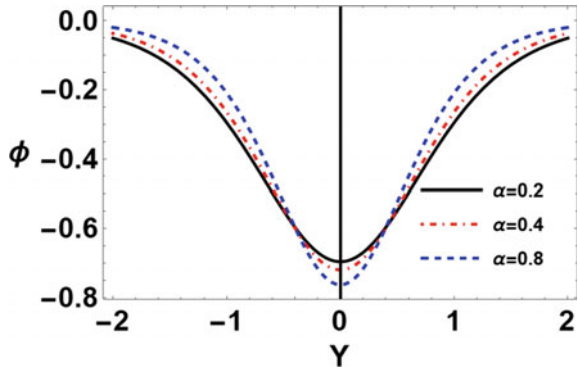
It is found that with increment in  $\kappa_p$  and  $\kappa_e$  (i.e., decrease in the superthermality of positrons/electrons), the phase velocity of EASs is enhanced. It is clear that superthermality effects have significantly modified the dispersion properties of EASs and makes the wave to propagate slowly in case of more superthermal charged particles.

Figure 2, describes the nature of coefficient ( $A$ ) with superthermality index of positrons( $\kappa_p$ ) and superthermal index of hot electrons (via  $\kappa_e$ ). It is seen that with increase in  $\kappa_p$  and  $\kappa_e$ , magnitude of  $A$  increases. It is found that  $A$  is negative, so only negative potential EASs are reported in the considered plasma model.

In Fig. 3, we have analysed the characteristics of EASs profile ( $\phi$ ) with superthermality of electrons (via  $\kappa_e$ ). It is noticed that with increase in the value of  $\kappa_e$ , the amplitude and width of EASs are increased along negative axis. This variation in the properties of EASs occurs due to the change in nonlinearity and dispersion effects.

In Fig. 4, depicts the nature of EASs profile ( $\phi$ ) with number density ratio of positron to hot electron  $\alpha(= n_{op}/n_{oh})$  and shows that amplitude(width) of EASs is increased (decreased) with increase in  $\alpha$ . It is noteworthy to mention that any change in number density ratios makes variation in the nonlinear coefficient  $A$  that further modifies the profile of solitons.

**Fig. 4** Plot for EASs profile ( $\phi$ ) with number density ratio  $\alpha(= n_{op}/n_{oh})$



**Fig. 5** Plot for EASs profile ( $\phi$ ) with magnetic field strength ( $\Omega$ )

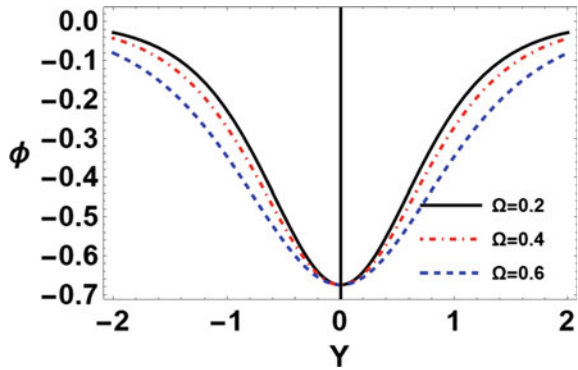


Figure 5, describes the profile of EASs ( $\phi$ ) with magnetic field strength (via  $\Omega$ ). The width of EASs increases with the increase in the value of magnetic field strength, whereas the amplitude remains same. It is clear that the dispersion effects are more pronounced with the variation of magnetic field strength.

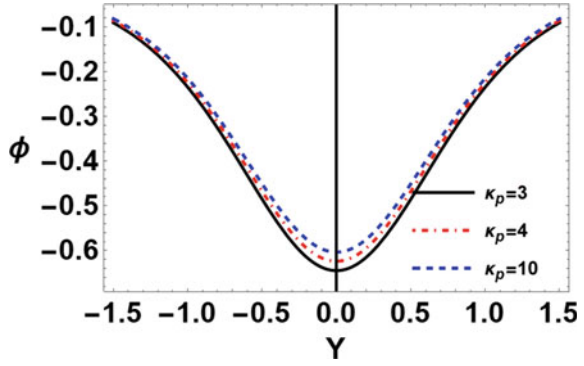
Figure 6, describes the variation of profile of EASs ( $\phi$ ) for multiple values of ( $\kappa_p$ ). It is analysed that with rise in superthermality index of positrons (via  $\kappa_p$ ), the magnitude of EASs decreases. This emphasizes that superthermality index has strongly influenced the properties of EASs with change in different nonlinear effects.

Figure 7, depicts the variation of EASs profile ( $\phi$ ) for multiple values of temperature ratio of hot electrons to positrons  $\gamma(= \frac{T_h}{T_p})$  and highlights that width and amplitude of EASs are decreased with increase in the value of  $\gamma(= \frac{T_h}{T_p})$ . This highly change in width and amplitude of EA solitons is noticed due to the effect of temperature ratio on the nonlinear coefficient  $A$ .

Figures 8 and 9, represent the 3D profiles of EASs with magnetic field strength ( $\Omega$ ) and superthermality of positrons ( $\kappa_p$ ) respectively. These figures further confirm the modification in the profile of EA solitons with the variation of different parameters simultaneously.



**Fig. 6** Plot for EASs profile ( $\phi$ ) with superthermality index of positrons ( $\kappa_p$ )



**Fig. 7** Plot for EASs profile ( $\phi$ ) with temperature ratio of hot electrons to positrons  $\gamma (= \frac{T_h}{T_p})$

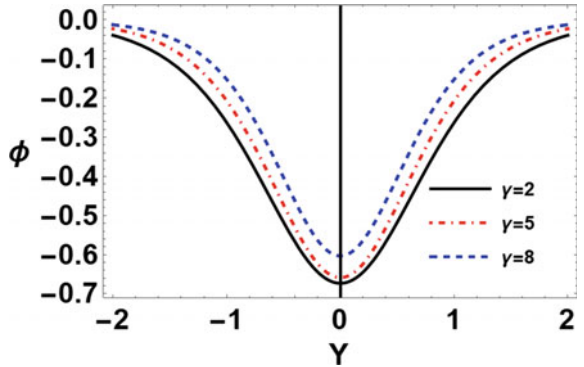


**Fig. 8** Plot for 3D EASs profile ( $\phi$ ) with magnetic field strength ( $\Omega$ )

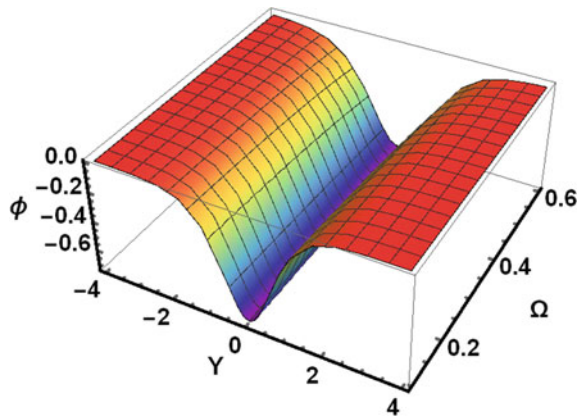
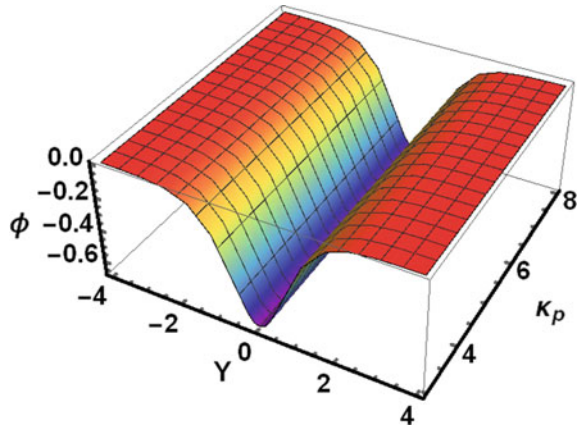


**Fig. 9** Plot for 3D EASs profile ( $\phi$ ) with superthermality index of positrons ( $\kappa_p$ )



## 5 Conclusion

We have studied the salient features of EASs in a magnetized multicomponent plasma having inertial cold electrons, inertialess ions and superthermal positrons as well as electrons. The RPM is adopted to develop the nonlinear ZK equation and its solution to describe the dynamics of EASs. Only EASs with negative polarity exist. The effects of various plasma parameters such as  $\kappa_p$ ,  $\kappa_e$ ,  $\alpha$ ,  $\gamma$  and  $\Omega$  have significantly influence the characteristic properties of EASs. The phase velocity of solitons is enhanced with increase in  $\kappa_p$  and  $\kappa_e$ . Nonlinear coefficient ( $A$ ) flourishes with increase in  $\kappa_p$  and  $\kappa_e$ . The width and amplitude of EASs are increased with increase in  $\kappa_e$  and  $\alpha$ . The width of EASs increases with increase in the value of strength of magnetic field ( $\Omega$ ). With the increase in the value of ratio of temperature of hot electrons to positrons  $\gamma (= \frac{T_h}{T_p})$ , the width and amplitude of EASs are decreased. Negative potential EASs are significantly influenced with the change in dispersion and nonlinearity effects.

The outcome of present study can be beneficial for the indepth understanding of EASs with superthermal positrons and electrons in Van Allen radiation belts, auroral zone, planetary magnetospheres [20–23].

## References

1. Mace, R.-L., Baboolal, S., Bharuthram, R., Hellberg, M.-A.: Arbitrary-amplitude electron-acoustic solitons in a two-electron-component plasma. *J. Plasma Phys.* **45**(1), 323–338 (1991)
2. Yu, M.-Y., Shukla, P.-K.: Linear and nonlinear modified electron-acoustic waves. *J. Plasma Phys.* **29**(3), 409–413 (1983)
3. Mace, R.-L., Hellberg, M.-A.: The Korteweg-de Vries-Zakharov-Kuznetsov equation for electron-acoustic waves. *Phys. Plasmas* **8**(6), 2649–2656 (2001)
4. Danehkar, A., Saini, N.-S., Hellberg, M.-A., Kourakis, I.: Electron-acoustic solitary waves in the presence of a suprathermal electron component. *Phys. Plasmas* **18**(7), 072902(1–10) (2011)

5. Devanandhan, S., Singh, S.-V., Lakhina, G.-S., Bharuthram, R.: Electron acoustic waves in a magnetized plasma with kappa distributed ions. *Phys. Plasmas* **19**(8), 082314(1–7) (2012)
6. Alam, M.-S., Uddin, M.-J., Masud, M.-M., Mamun, A.-A.: Roles of superthermal electrons and positrons on positron-acoustic solitary waves and double layers in electron-positron-ion plasmas. *Chaos* **24**(3), 033130(1–8) (2014)
7. Adnan, M., Mahmood, S., Qamar, A.: Coupled ion acoustic and drift waves in magnetized superthermal electron-positron-ion plasmas. *Phys. Plasmas* **21**(9), 092119(1–8) (2014)
8. Ferdousi, M., Sultana, S., Mamun, A.-A.: Oblique propagation of ion-acoustic solitary waves in a magnetized electron-positron-ion plasma. *Phys. Plasmas* **22**(3), 032117(1–7) (2015)
9. Sahaa, A., Tamang, J.: Qualitative analysis of the positron-acoustic waves in electron-positron-ion plasmas with  $\kappa$  deformed Kaniadakis distributed electrons and hot positrons. *Phys. Plasmas* **24**(7), 082101(1–10) (2017)
10. Bansal, S., Aggarwal, M., Gill, T.-S.: Planar and nonplanar electron-acoustic solitary waves in the presence of positrons. *Plasma Phys. Rep.* **46**(7), 715–723 (2020)
11. Gul, N., Ahmad, R.: Dissipative ion-acoustic solitons in electron-positron-ion plasma with non-thermal electrons and iso-thermal positrons. *Adv. Space Res.* **68**(1), 161–169 (2021)
12. Vasyliunas, V.-M.: A survey of low-energy electrons in the evening sector of the magnetosphere with OGO 1 and OGO 3. *J. Geophys. Res.* **73**(9), 2839–2884 (1968)
13. Shahmansouri, M., Tribeche, M.: Propagation properties of ion acoustic waves in a magnetized superthermal bi-ion plasma. *Astrophys. Space Sci.* **350**(2), 623–630 (2014)
14. Saini, N.-S., Sethi, P.: Dust ion-acoustic cnoidal waves in a plasma with two temperature superthermal electrons. *Phys. Plasmas* **23**(10), 103702(1–10) (2016)
15. Singh, K., Saini, N.-S.: Effect of anisotropic pressure on electron acoustic oscillatory and monotonic shocks in superthermal magnetoplasma. *Radio Sci. J.* **54**(12), 1192–1203 (2019)
16. Washimi, H., Taniuti, T.: Propagation of ion-acoustic solitary waves of small amplitude. *Phys. Rev. Lett.* **17**(19), 996–998 (1966)
17. Elwakil, S.-A., El-Shewy, E.-K., Abdelwahed, H.-G.: Solution of the perturbed Zakharov-Kuznetsov (ZK) equation describing electron-acoustic solitary waves in a magnetized plasma. *Chin. J. Phys.* **49**(3), 732–744 (2011)
18. Singh, K., Sethi, P., Saini, N.-S.: Nonlinear excitations in a degenerate relativistic magneto-rotating quantum plasma. *Phys. Plasma* **26**(9), 092104 (1–10) (2019)
19. Jilani, K., Mirza, A.-M., Khan, T.-A.: Electrostatic electron acoustic solitons in electron-positron-ion plasma with superthermal electrons and positrons. *Astrophys. Space Sci.* **349**(1), 255–263 (2015)
20. Voronov, S.-A., Galper, A.-M., Kirilov-Ugryumov, V.-G., Koldashov, S.-V., Popov, A.-V.: Charge composition of the high-energy electrons and positrons in the Van Allen radiation belts. *JETP Lett.* **43**, 306–307 (1986)
21. Galper, A.-M., Koldashov, S.-V., Mikhailov, V.-V., Voronov, S.-A.: Electrons with energy greater than 20 MeV in the inner radiation belt. *Radiat. Meas.* **26**(3), 375–378 (1996)
22. Pottelette, R., Ergun, R.-E., Treumann, R.-A., Berthomier, M., Carlson, C., McFadden, J.-P., Roth, I.: Modulated electron acoustic waves in auroral density cavities: FAST observations. *Geophys. Res. Lett.* **26**(16), 2629–2632 (1999)
23. Plyaskin, V.: Mapping Earth's radiation belts using data from STS91 mission of AMS. *Astropart. Phys.* **30**(1), 18–27 (2008)

# Non-linear Fluctuating Parts of the Particle Distribution Function in the Presence of Drift Wave Turbulence in Vlasov Plasma



Banashree Saikia  and P. N. Deka 

**Abstract** We have considered a Vlasov plasma with both the resonant and non-resonant mode waves. The non-resonant mode is considered as a perturbation to plasma where a turbulent field is present which is in resonant mode. The interaction of these waves is characterized by the Vlasov Maxwell set of equations. The evaluation process of the fluctuating parts of the distribution function owing to the presence of resonant mode wave, due to the modulation field, and the nonlinear fluctuating parts of distribution function due to the non-resonant wave is presented in this work.

**Keywords** Nonlinear wave-particle interaction · Density and temperature gradients · Drift wave turbulence

## 1 Introduction

In this paper, we have considered electromagnetic Ordinary (O) mode as high-frequency wave and ion cyclotron drift wave as the low-frequency resonant mode wave. In high beta plasmas, Davidson and Wu [1] first discussed the O-mode wave instability, which is exclusively increasing mode. A group of experts studied the formation of unstable ordinary mode waves in the Earth's magnetospheric Auroral region [2, 3]. Increased electromagnetic radiation in the top ionospheric regions has been thoroughly investigated, and this radiation has been labelled as Auroral Kilometric Radiation(AKR) [3]. The Auroral Kilometric Radiation is made up of X and O-mode radiations according to later research [3]. In a series of investigations, Ibscher and Schlickeiser [4–7] investigated the Ordinary mode instability expanding it to the small beta plasma region by using a counter-streaming bi-Maxwellian model [9]. On the other hand, the Ordinary mode instability has mostly been studied in terms of marginal instability criterion rather than numerical dispersion relation solution. In a magnetized non relativistic bi-Maxwellian plasma, [8] temperature anisotropic

---

B. Saikia (✉) · P. N. Deka  
Department of Mathematics, Dibrugarh University, Dibrugarh 786004, Assam, India  
e-mail: [spinkjht@gmail.com](mailto:spinkjht@gmail.com)

© The Author(s), under exclusive license to Springer Nature Switzerland AG 2022  
S. Banerjee and A. Saha (eds.), *Nonlinear Dynamics and Applications*,  
Springer Proceedings in Complexity,  
[https://doi.org/10.1007/978-3-030-99792-2\\_20](https://doi.org/10.1007/978-3-030-99792-2_20)

225

effects on O-mode and its instability were examined. Deka and Borgohain [3] investigated the amplification of O-mode in inhomogeneous plasma using plasma maser theory. In this study, they have investigated that the amplification of electromagnetic wave is achievable in space plasma at the expense of drift wave turbulence. The amplification process and wave energy exchange are also possible at some energy level since the plasma maser effect doesn't require a frequency matching condition. Deka and Deka [10] investigated the amplification of ion-acoustic waves in Burning plasma in presence of drift wave turbulence. Here, they have discussed ion acoustic instabilities while considering the ion distribution function that is consistent in burning plasma. Recently, Senapati and Deka [11] studied the instability of electron Bernstein mode in the presence of drift wave turbulence caused by density and temperature gradients. In their research, they have studied the growth rate of high frequency electron Bernstein mode in Tokamak plasmas as a function of density and temperature gradients. In this paper, we have investigated the formation of O-mode waves in non-uniform plasma media through non-linear wave particle interaction in the context of ion cyclotron drift wave turbulence.

## 2 Formulation of the Problem

In our problem, we have considered an inhomogeneous plasma which supports drift motion and turbulence. To describe this system, we consider a particle distribution function [12] which involve gradient parameters for temperature and density associated with external force. The density and temperature gradients are taken along the positive y-direction (Fig. 1).

$$f_j(T_j, y, \mathbf{v}) = \left( \frac{m}{2\pi T_{0j}} \right)^{3/2} \left[ 1 + \mu \left( y + \frac{v_x}{\Omega_j} \right) \right] \exp \left[ - \left( \frac{m\mathbf{v}^2}{2T_{0j}} - \frac{Fy}{T_{0j}} \right) \right] \quad (1)$$

where  $\Omega_j = \frac{eB_0}{mc}$  denotes the cyclotron frequency of the ion,  $\mu$  denotes the density and gradient smallness parameter which can be derived using equation (1) at  $y=0$  as

$$\mu = \left[ \left( \frac{\partial}{\partial T_j} \frac{dT_j}{dy} \right) + \left( \frac{1}{f_0} \frac{df_j}{dy} \right) \right]_{y=0} - \frac{F}{T_{0j}}$$

The particle drift motion owing to the pressure gradient is caused by the force field  $\mathbf{F}$  and the equation of the motion is given by:

$$m \frac{d\mathbf{v}}{dt} = \mathbf{F} - \frac{e}{c} \mathbf{v} \times \mathbf{B}_0$$

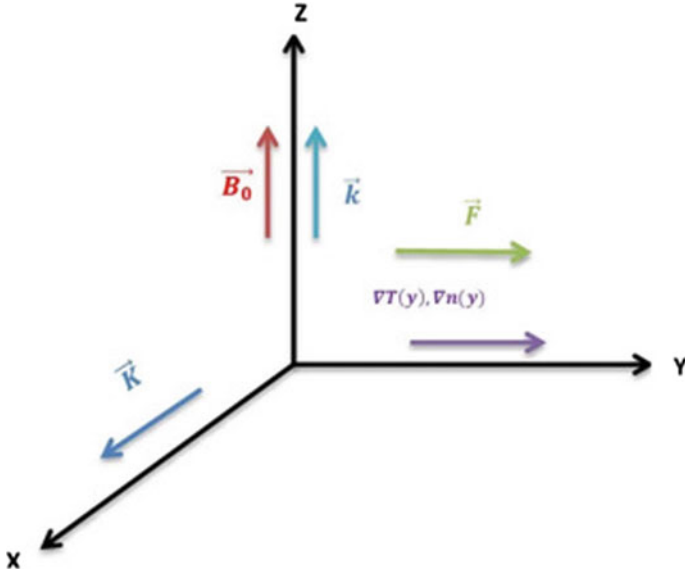


**Fig. 1** Geometry of the model:  $\mathbf{K} = (K_{\perp}, 0, 0)$  represents the propagation vector of the Ordinary mode wave  $\mathbf{k} = (0, 0, k_{\parallel})$  represents the propagation vector of the ion-cyclotron drift wave  $\mathbf{B}_0$  represents the magnetic field along the positive z-axes

$$\frac{d\mathbf{v}}{dt} = \frac{\mathbf{F}}{m} \hat{y} - \Omega_j(\mathbf{v} \times \hat{z})$$

The interaction of the high frequency Ordinary mode with ion-cyclotron drift wave is governed by Vlasov–Maxwell set of equations

$$\left[ \frac{\partial}{\partial t} + \mathbf{v} \cdot \frac{\partial}{\partial \mathbf{r}} - \left\{ \frac{e}{m} \left( \mathbf{E} + \frac{\mathbf{v} \times \mathbf{B}_0}{c} \right) - \frac{\mathbf{F}}{m} \right\} \cdot \frac{\partial}{\partial \mathbf{v}} \right] F_{0j}(\mathbf{r}, \mathbf{v}, t) = 0 \quad (2)$$

$$\nabla \times \mathbf{E} = -\frac{1}{c} \frac{\partial \mathbf{B}}{\partial t} \quad (3)$$

$$\nabla \times \mathbf{B} = \frac{1}{c} \frac{\partial \mathbf{E}}{\partial t} + \frac{4\pi}{c} \mathbf{J} \quad (4)$$

$$\mathbf{J} = -en_j \int \mathbf{v} f_{0j}(\mathbf{r}, \mathbf{v}, t) d\mathbf{v} \quad (5)$$

$$\nabla \cdot \mathbf{E} = -4en_j \pi \int f_j(\mathbf{r}, \mathbf{v}, t) d\mathbf{v} \quad (6)$$

The unperturbed particle distribution function and fields are described by the linear response theory [13] of a turbulent plasma.

$$F_{0j} = f_{0j} + \epsilon f_{1j} + \epsilon^2 f_{2j} \quad (7)$$

and

$$\mathbf{E}_{0l} = \epsilon \mathbf{E}_l + \epsilon^2 \mathbf{E}_2 \quad (8)$$

Here,  $\epsilon$  denotes a smallness parameter related to ion-cyclotron drift wave turbulent field  $\mathbf{E}_l = (0, 0, E_{l\parallel})$  having propagation vector  $\mathbf{k} = (0, 0, k_{\parallel})$ ,  $f_{0j}$  denotes the spatial and time averaged components of the distribution function,  $f_{1j}$  and  $f_{2j}$  denotes the fluctuating parts of the particle distribution function and  $\mathbf{E}_2$  denotes the electric field of second order.

To the order of  $\epsilon$ , from Eq. (2), we get:

$$\left[ \frac{\partial}{\partial t} + \mathbf{v} \cdot \frac{\partial}{\partial \mathbf{r}} - \left\{ \frac{e}{m} \left( \frac{\mathbf{v} \times \mathbf{B}_0}{c} \right) - \frac{\mathbf{F}}{m} \right\} \cdot \frac{\partial}{\partial \mathbf{v}} \right] f_{1j}(\mathbf{r}, \mathbf{v}, t) = \frac{e}{m} \left( \mathbf{E}_l \cdot \frac{\partial}{\partial \mathbf{v}} f_{0j} \right) \quad (9)$$

Now to obtain  $f_{1j}$ , we apply Fourier transform,

$$A(\mathbf{r}, \mathbf{v}, t) = \Sigma_{\mathbf{k}, \omega} A(\mathbf{k}, \omega, \mathbf{v}) \exp[i(\mathbf{k} \cdot \mathbf{r} - \omega t)] \quad (10)$$

The fluctuating parts  $f_{1j}$  of the low frequency turbulence field is determined from Eq. (9) by integrating along the unperturbed orbit.

$$f_{1j}(\mathbf{k}, \omega) = \frac{ie}{m} \frac{E_{l\parallel} \cdot \frac{\partial}{\partial v_{\parallel}} f_{0j}}{\omega - k_{\parallel} v_{\parallel} + i \cdot 0^+} \quad (11)$$

We next apply a perturbation  $\delta \mathbf{E}_h$  of a high frequency ordinary mode with an electric field  $\delta \mathbf{E}_h = (0, 0, \delta E_h)$  having propagation vector  $\mathbf{K} = (K_{\perp}, 0, 0)$ , a magnetic field  $\delta \mathbf{B}_h = (0, \delta B_h, 0)$ , and frequency  $\Omega$ .

We calculate the total perturbed electric field, the magnetic field and the particle distribution function as:

$$\begin{aligned} \delta \mathbf{E} &= \mu' \delta \mathbf{E}_h + \mu' \epsilon \delta \mathbf{E}_{lh} + \mu' \epsilon^2 \Delta \mathbf{E} \\ \delta \mathbf{B} &= \mu' \delta \mathbf{B}_h + \mu' \epsilon \delta \mathbf{B}_{lh} + \mu' \epsilon^2 \Delta \mathbf{B} \\ \delta f &= \mu' \delta f_h + \mu' \epsilon \delta f_{lh} + \mu' \epsilon^2 \Delta f \end{aligned}$$

where  $\delta \mathbf{E}_{lh}$ ,  $\Delta \mathbf{E}$ ,  $\delta \mathbf{B}_{lh}$ ,  $\Delta \mathbf{B}$  denotes the modulation fields,  $\delta f_h$  denotes the fluctuating part owing to a high frequency Ordinary mode,  $\delta f_{lh}$  and  $\Delta f$  denotes the particle distribution function corresponding to the modulation field and  $\mu' \ll \epsilon$  where  $\mu'$  denotes the smallness parameter for perturbed field. To the order of  $\mu$ ,  $\mu\epsilon$  and  $\mu\epsilon^2$ , we now have

$$P \delta f_h = \frac{e}{m} \left( \delta \mathbf{E}_h + \frac{\mathbf{v} \times \delta \mathbf{B}_h}{c} \right) \cdot \frac{\partial f_{0j}}{\partial \mathbf{v}} \quad (12)$$

$$P\delta f_{lh} = \frac{e}{m}\delta\mathbf{E}_h \cdot \frac{\partial}{\partial\mathbf{v}}f_{1j} + \frac{e}{m} \cdot \frac{\mathbf{v} \times \delta\mathbf{B}_h}{c} \cdot \frac{\partial}{\partial\mathbf{v}}f_{1j} + \frac{e}{m}\delta\mathbf{E}_{lh} \cdot \frac{\partial}{\partial\mathbf{v}}f_{0j} \\ + \frac{e}{m}\mathbf{E}_l \cdot \frac{\partial}{\partial\mathbf{v}}\delta f_h + \frac{e}{m} \cdot \frac{\mathbf{v} \times \delta\mathbf{B}_{lh}}{c} \cdot \frac{\partial}{\partial\mathbf{v}}f_{0j} \quad (13)$$

$$P\Delta f = \frac{e}{m} \left[ \delta\mathbf{E}_{lh} \cdot \frac{\partial f_{1j}}{\partial\mathbf{v}} + \frac{\mathbf{v} \times \delta\mathbf{B}_{lh}}{c} \cdot \frac{\partial f_{1j}}{\partial\mathbf{v}} + \mathbf{E}_l \cdot \frac{\partial}{\partial\mathbf{v}}\delta f_{lh} \right] \quad (14)$$

where  $P = \left[ \frac{\partial}{\partial t} + \mathbf{v} \cdot \frac{\partial}{\partial \mathbf{r}} - \left\{ \frac{e}{m} \left( \frac{\mathbf{v} \times \mathbf{B}_0}{c} \right) - \frac{\mathbf{F}}{m} \right\} \cdot \frac{\partial}{\partial \mathbf{v}} \right]$ .

### 3 Nonlinear Dispersion Relation of Electromagnetic O-Mode Wave

Considering the linear response theory of plasma turbulence, we obtain  $\delta f_h$ ,  $\delta f_{lh}$  and  $\Delta f$  by integrating along the unperturbed orbits, using cylindrical co-ordinate system to the velocity space [13, 14].

From equation (12), we have

$$\delta f_h = -\frac{ie}{m}\delta\mathbf{E}_h \left[ \left( 1 - \frac{K_{\perp}v_{\perp}}{\omega} \cos\theta \right) \frac{\partial f_{0j}}{\partial v_{\parallel}} S_{p,q} - f_{0j} \left\{ \frac{mv_{\parallel}}{\Omega T_{0j}} + \left( \frac{mv_{\parallel}}{T_{0j}} - \frac{\epsilon K_{\perp}v_{\parallel}}{\Omega \Omega_j} \right) S_{p,q} \right\} \right] \quad (15)$$

where  $S_{p,q} = \sum_{a,b} \frac{J_a(\alpha') J_b(\alpha') \exp[i(b-a)\theta]}{a\Omega_j - \Omega + K_{\perp}v_F}$ ,  $\alpha = \frac{K_{\perp}v_{\perp}}{\Omega_j}$

From equation (13), we have

$$\delta f_{lh} = I_{lh}^1 + I_{lh}^2 + I_{lh}^3 \quad (16)$$

where

$$I_{lh}^1 = \frac{e}{m} \int_{-\infty}^0 \left[ \mathbf{E}_l \cdot \frac{\partial}{\partial\mathbf{v}}\delta f_h \right] \exp \left[ i \left\{ (\mathbf{K} - \mathbf{k}) \cdot (\mathbf{r}' - \mathbf{r}) - (\Omega - \omega)\tau \right\} \right] d\tau \quad (17)$$

$$I_{lh}^2 = \frac{e}{m} \int_{-\infty}^0 \left[ \delta\mathbf{E}_h + \frac{\mathbf{v} \times \delta\mathbf{B}_h}{c} \cdot \frac{\partial f_{1e}}{\partial\mathbf{v}} \right] \exp \left[ i \left\{ (\mathbf{K} - \mathbf{k}) \cdot (\mathbf{r}' - \mathbf{r}) - (\Omega - \omega)\tau \right\} \right] d\tau \quad (18)$$

$$I_{lh}^3 = \frac{e}{m} \int_{-\infty}^0 \left[ \delta\mathbf{E}_{lh} + \frac{\mathbf{v} \times \delta\mathbf{B}_{lh}}{c} \cdot \frac{\partial f_{0e}}{\partial\mathbf{v}} \right] \exp \left[ i \left\{ (\mathbf{K} - \mathbf{k}) \cdot (\mathbf{r}' - \mathbf{r}) - (\Omega - \omega)\tau \right\} \right] d\tau \quad (19)$$

From equation (14), we have

$$\Delta f = \frac{e}{m} \int_{-\infty}^0 \left[ \delta\mathbf{E}_{lh} + \frac{\mathbf{v} \times \delta\mathbf{B}_{lh}}{c} \cdot \frac{\partial f_{1e}}{\partial\mathbf{v}} + \mathbf{E}_l \cdot \frac{\partial}{\partial\mathbf{v}}\delta f_{lh} \right] \exp \left[ i \left\{ \mathbf{K} \cdot (\mathbf{r}' - \mathbf{r}) - \Omega\tau \right\} \right] d\tau \quad (20)$$



The Maxwell's equation gives the modulated field as

$$\begin{aligned}\nabla \times \delta \mathbf{B}_{lh} &= \frac{1}{c} \frac{\partial}{\partial t} \delta \mathbf{E}_{lh} + \frac{4\pi}{c} \mathbf{J} \\ \mathbf{J} &= -en_e \int \mathbf{v} \delta f_{lh} d\mathbf{v} \\ \nabla \times \delta \mathbf{E}_{lh} &= -\frac{1}{c} \frac{\partial}{\partial t} \delta \mathbf{B}_{lh}\end{aligned}$$

Therefore, we have

$$\nabla \times \delta \mathbf{B}_{lh} = \frac{1}{c} \frac{\partial}{\partial t} \delta \mathbf{E}_{lh} - \frac{4\pi en_e}{c} \int \mathbf{v} \delta f_{lh} d\mathbf{v}$$

This can be written in the simplified form as:

$$\delta E_h = \frac{4\pi i en_e (\Omega - \omega)}{c^2 K_{\perp}^2 - \Omega^2} \int v_{\parallel} (\delta f_h + \Delta f) d\mathbf{v}$$

This equation may be expressed as follows after simplification:

$$\delta E_h \epsilon_h(\mathbf{K}, \Omega) = 0 \quad (21)$$

Here  $\epsilon_h(\mathbf{K}, \Omega)$  indicates the non-linear dispersion relation of O-mode wave which is described by

$$\epsilon_h(\mathbf{K}, \Omega) = \epsilon_0(\mathbf{K}, \Omega) + \epsilon_d(\mathbf{K}, \Omega) + \epsilon_p(\mathbf{K}, \Omega). \quad (22)$$

## 4 Discussions

In our present study, we have been calculating the nonlinear dispersion relation of electromagnetic Ordinary mode waves in context of ion cyclotron drift wave turbulence, that is a frequent characteristics in an inhomogeneous plasma. The fluctuating parts  $f_{1j}$ ,  $\delta f_h$ ,  $\delta f_{lh}$  and  $\Delta f$  which are provided in Eqs. (11), (15), (16) and (20) respectively have been obtained. Here,  $f_{1j}$  denotes the fluctuating part due to ion-cyclotron turbulent field which is linear in nature. Further,  $\delta f_h$  denotes the fluctuating part of particle distribution function due to perturbed electromagnetic ordinary mode whereas  $\delta f_{lh}$  and  $\Delta f$  denotes the nonlinear fluctuating parts of distribution function. We are focussing on nonlinear fluctuating part  $\Delta f$  for estimating growth rate of O-mode. The expressions of  $\Delta f$  contains polarisation coupling and direct coupling terms. The turbulent field parameters  $E_l$ ,  $k_{\perp 1}$ ,  $v_{\parallel}$  are involved besides the parameter associated with O-mode phenomena. Nonlinear dispersion relation will be given by

$$\epsilon_h(\mathbf{K}, \Omega) = \epsilon_0(\mathbf{K}, \Omega) + \epsilon_d(\mathbf{K}, \Omega) + \epsilon_p(\mathbf{K}, \Omega)$$

containing the linear part  $\epsilon_0(\mathbf{K}, \Omega)$ , the direct coupling part  $\epsilon_d(\mathbf{K}, \Omega)$  and the polarisation coupling part  $\epsilon_p(\mathbf{K}, \Omega)$ .

## 5 Conclusions

In previous research [3], Ordinary mode was examined in the context of drift wave turbulence in absence of external force causing particle drift. Only density gradient parameters were to emerge in the nonlinear dispersion relation in those circumstances. However, drift motion of particles owing to pressure gradient must exist in practical instances in space and tokamak plasmas, and is connected with  $\mathbf{F} \times \mathbf{B}$  drift. As a result, we've incorporated the external force  $\mathbf{F}$  in our current research, which ties drift motion to particles.

## References

1. Davidson, R.C., Wu, C.S.: Ordinary-mode electromagnetic instability in high-beta plasmas. *Phys. Fluids* **13**, 1407–1409 (1970)
2. Gurnett, D.A.: The earth as radio source: terrestrial kilometric radiation. *J. Geophys. Res.* **79**, 4227–4238 (1974)
3. Deka, P.N., Borgohain, A.: On unstable electromagnetic radiation through nonlinear wave-particle interactions in presence of drift wave turbulence. *J. Plasma Phys.* **78**(5), 515–524 (2012)
4. Ibscher, D., Lazar, M., Schlickeiser, R.: On the existence of Weibel instability in a magnetized plasma. II. Perpendicular wave propagation: the ordinary mode. *Phys. Plasmas* **19**, 072116-1–072116-10 (2012)
5. Ibscher, D., Lazar, M., Michno, M.J., Schlickeiser, R.: Towards a complete parametrization of the ordinary-mode electromagnetic instability in counterstreaming plasmas. I. Minimizing ion dynamics. *Phys. Plasmas* **20**, 012103-1–012103-9 (2013)
6. Ibscher, D., Schlickeiser, R.: Towards a complete parametrization of the ordinary-mode electromagnetic instability in counterstreaming plasmas. II. Ion effects. *Phys. Plasmas* **20**, 042121-1–042121-9 (2013)
7. Ibscher, D., Schlickeiser, R.: Solar wind kinetic instabilities at small plasma betas. *Phys. Plasmas* **21**, 022110-1–022110-4 (2014)
8. Bashir, M.F., Murtaza, G.: Effect of temperature anisotropy on various modes and instabilities for a magnetized non-relativistic Bi-Maxwellian plasma. *Braz. J. Phys.* **42**, 487–504 (2012)
9. Hadi, F., Bashir, M.F., Qamar, A., Yoon, P.H., Schlickeiser, R.: On the ordinary mode instability for low beta plasmas. *Phys. Plasmas* **21**, 052111-1–052111-5 (2014)
10. Deka, P.N., Deka, J.K.: On amplification of ion-acoustic mode in burning plasma in presence of drift wave turbulence. *J. Fusion Energy* **37**, 301–307 (2018)
11. Senapati, P., Deka, P.N.: Instability of electron Bernstein mode in presence of drift wave turbulence associated with density and temperature gradients. *J. Fusion Energy* **39**, 477–490 (2020)
12. Ichimaru, S.: Basic principles of plasma physics a statistical approach, vol. 1, 1st edn. Addison-Wesley, Boca Raton (1973)
13. Krall, N.A., Trivelpiece, A.W.: Principles of plasma physics, 2nd edn., pp. 403–407. McGraw-Hill, New York (1973)
14. Chen, F.: Introduction to plasma physics and controlled fusion, vol. 1, 2nd edn. Plenum Press, New York (1974)

# Effect of Superthermal Charge Fluctuation on Bifurcation of Dust-Ion-Acoustic Waves Under the Burgers Equation in a Magnetized Plasma



Jharna Tamang 

**Abstract** Bifurcation of dust-ion-acoustic waves (DIAWs) in dusty plasmas composed of fluid ions, immobile dust grains, and superthermal charge fluctuations of electrons and ions is examined. The study is done under the framework of the Burgers equation obtained through the reductive perturbation technique. The effect of charge fluctuations holds the responsibility for formation of the shock solution of the Burgers equation. The changes on periodic and shock wave solutions of the Burgers equation are shown varying system parameters. The results of this study, shock and periodic wave solutions of the Burgers equation in plasmas with dust charge fluctuation in magnetized plasmas, are shown for the first time implementing the notion of nonlinear dynamical systems.

**Keywords** Phase plane profile · Periodic wave · Kink and anti-kink waves · Dynamical system

## 1 Introduction

Dusty plasmas have wide applications in astrophysics, plasma, biophysics, fusion devices, space science [1, 2]. The charged dust grains produces wave modes, named as dust-ion-acoustic wave (DIAW) and dust-acoustic wave (DAW). Experimentally Barkan et al. [3] discovered DIAWs for the first time. Theoretically, Shukla and Silin [4] were the first to report a observation of low frequency DIAW in a dusty plasma. Many researchers [4–7] studied propagation of DIAW both theoretically and experimentally in various plasma systems while, some researchers [8–11] studied impacts of external magnetic force on the electrostatic waves. Under magnetic effect,

---

J. Tamang (✉)

Department of Mathematics, Sikkim Manipal Institute of Technology, Sikkim Manipal University, Majitar, East-Sikkim 737136, India  
e-mail: [jharnatamang.12@gmail.com](mailto:jharnatamang.12@gmail.com)

Department of Mathematics, Sikkim Alpine University, Kamrang, Namchi, South-Sikkim 737126, India

Anowar and Mamun [12] studied the same under the KdV equation in dusty plasmas. In magnetic dusty plasma, El-Labany et al. [13] investigated solitary DIAWs with isothermal electrons. Shalaby et al. [14] reported DIAW in magnetized dusty plasmas under the ZK equation. Very recently, Samanta et al. [15] discussed the formation of rogue waves and examined DIAWs in multicomponent degenerate plasmas.

Many particles of plasmas follow Maxwellian distributions. However, space plasma is usually noticed to follow non-Maxwellian distributions. These distributions can be structured by kappa distribution [16]. In magnetized plasmas, superthermal parameter affects the nature of electrostatic waves [17, 18]. Alinejad et al. [19] examined shock DIAWs in dusty plasmas with effect of superthermal electrons. Recently, Shahmansouri and Alinejad [10] reported the impacts of direction of propagation and superthermal electrons under magnetic field on large amplitude DIAW. The charge on dust grains in dusty plasmas is not definite because of ion and electron currents passing through the grain surface. While, the dissipation may occur due to charge fluctuations of dust in dusty plasmas [20, 21] and is responsible generation of shock structures.

The concept of dynamical systems [22–24] has discovered many characteristics of nonlinear waves in plasmas through phase portrait and time series analysis. Recently, many researchers [25–28] reported the propagation of nonlinear acoustic waves in plasmas. In 2018, Tamang et al. [5] studied DIAWs in collisional dusty plasma under the ionization effect implementing the notion of planar dynamical systems. Chatterjee et al. [29] reported solitary wave solution of DIAWs in superthermal plasmas. Very recently, Sharma et al. [30] studied dynamical features of DIAWs in nonextensive dusty plasma applying the same theory. Using this notion of dynamical systems, the dynamical feature of DIAWs based on the Burgers equation under the magnetic and charge fluctuation is not reported as yet.

The manuscript is organized as: in Sect. 2, the model equations are considered. In Sect. 3, we derive the Burgers equation. In Sect. 4, the dynamical system of the Burgers equation is formed. The potential energy function plot is also displayed. In Subsections of 4, analytical wave solutions are presented. Lastly, conclusions are given in Sect. 5.

## 2 Model Equations

The traveling of DIAWs in an electron-ion plasma system under magnetic field is represented by the following model equations [11]

$$\frac{\partial n}{\partial t} + \vec{\nabla} \cdot (n \vec{u}) = 0, \quad (1)$$

$$\frac{\partial \vec{u}}{\partial t} + (\vec{u} \cdot \vec{\nabla}) \vec{u} = -\vec{\nabla} \phi + \omega_{ci} \vec{u} \times \hat{z}, \quad (2)$$

$$\vec{\nabla}^2 \phi = \mu n_e - n + (1 - \mu) Z_d. \quad (3)$$

where  $n$  and  $n_e$  represent ion and electron number densities. Here, velocity component is given by  $\vec{B}_0 = B_0 \hat{z}$ ,  $\vec{u} = (u, v, w)$  and  $\nabla = (\partial x, \partial y, \partial z)$ . Electromagnetic wave potential is given by  $\phi$ . Temperature ratio is given by  $\sigma = \frac{T_i}{T_e}$ , where  $T_i$  ( $T_e$ ) is temperature of ions (electrons). Dust-acoustic speed is given by  $C_s = \sqrt{T_e/m_i}$  and ion-cyclotron frequency is given by  $\omega_{pi} = \sqrt{4\pi n_{i0} e^2/m_i}$ . The Debye length is given by  $\lambda_D = C_s/\omega_{pi}$ , where  $k_B$  refers to the Boltzmann constant and  $m_h$  is hot electron mass. Here,  $\mu = n_{e0}/n_{i0} = 1 - \frac{Z_{d0} n_{d0}}{n_{i0}}$ .

$$n_e = 1 + C_1 \phi + C_2 \phi^2, \quad (4)$$

$$\text{where } C_1 = -\frac{-\kappa - 1/2}{\kappa - 3/2} \text{ and } C_2 = \frac{1}{2} \frac{(-\kappa - 1/2)(-\kappa + 1/2)}{(\kappa - 3/2)^2}.$$

The electron and ion charging currents are considered as:

$$I_e = -e\pi r_d^2 n_{e0} \sqrt{\frac{8T_e}{\pi m_e}} \sqrt{\frac{\kappa - 3/2}{\kappa^4}} \frac{\kappa}{\kappa - 1} \frac{\Gamma(\kappa + 1)}{\Gamma(\kappa - 1/2)} \left(1 + \frac{\alpha Z_d - \phi}{\kappa - 3/2}\right)^{1-\kappa}, \quad (5)$$

$$I_i = e\pi r_d^2 n_{i0} \sqrt{\frac{8T_i}{\pi m_i}} \left(1 + \frac{\alpha Z_d}{\sigma}\right). \quad (6)$$

where  $r_d$  is the radius of dust,  $\sigma = \frac{T_i}{T_e}$  and  $\alpha = Z_{d0} e^2 / r_d T_e$ .

The normalized dust charging fluctuation is described by the succeeding equation

$$v \left( \frac{\partial Z_d}{\partial t} + u_d \frac{\partial Z_d}{\partial x} \right) = \gamma \left( 1 + \frac{\alpha Z_d - \phi}{\kappa - 3/2} \right)^{1-\kappa} - \chi n_i \left( 1 + \frac{\alpha Z_d}{\sigma} \right), \quad (7)$$

where  $v = \sqrt{\alpha m_e (1 - \mu) / 2 m_i}$ ,  $\chi = \left( \frac{r_d}{n_{d0}^{-1/2}} \right)^{3/2} \sqrt{m_e T_i / T_e m_i}$  and

$$\gamma = \mu \left( \frac{r_d}{n_{d0}^{-1/2}} \right)^{3/2} \sqrt{\kappa - 3/2} \Gamma(\kappa + 1) / \Gamma(\kappa - 1/2) \kappa (\kappa - 1).$$

The normalized dust charging frequency follows as:

$$\nu_{ch} = \frac{1}{e} \frac{\partial}{\partial Z_d} (I_e + I_i) |_{\phi=0, Z_d=1} = \sqrt{\frac{Z_{d0}^2 r_d^2}{2\pi\sigma} \frac{\omega_{pi}}{\lambda_D} \frac{(\alpha\kappa + \kappa - 3/2) + \sigma(\kappa - 1)}{\sigma + \kappa - 3/2}}. \quad (8)$$

### 3 Derivation of the Burgers Equation

We obtain the Burger equation using the stretching of independent variables as

$$\xi = \epsilon(l_x x + l_y y + l_z z - Vt), \quad \tau = \epsilon^2 t, \tag{9}$$

where  $\epsilon$  is small parameter ( $0 < \epsilon \ll 1$ ) and  $V$  is phase velocity of the wave. Next, the dependent variables expanded as,

$$\begin{cases} n = 1 + \epsilon n_1 + \epsilon^2 n_2 + \dots, \\ u = \epsilon u_1 + \epsilon^2 u_2 + \dots, \\ v = \epsilon v_1 + \epsilon^2 v_2 + \dots, \\ w = \epsilon w_1 + \epsilon^2 w_2 + \dots, \\ Z_d = 1 + \epsilon Z_{d1} + \epsilon^2 Z_{d2} + \dots, \\ \phi = \epsilon \phi_1 + \epsilon^2 \phi_2 + \dots. \end{cases} \tag{10}$$

By collecting terms of lowest order  $\epsilon^{\frac{3}{2}}$ , we get the following equations

$$\begin{cases} n_1 = \frac{l_z}{V} w_1, \\ u_1 = -\frac{l_y}{\omega_{ci}} \frac{\partial \phi_1}{\partial \xi}, \\ v_1 = \frac{l_x}{\omega_{ci}} \frac{\partial \phi_1}{\partial \xi}, \\ w_1 = \frac{l_z}{V} \phi_1, \\ \mu C_1 \phi_1 - n_1 + (1 - \mu) Z_{d1} = 0, \\ -Z_{d1} + d_1 \phi_1 - d_2 n_1 = 0, \end{cases} \tag{11}$$

where  $d_1 = v \frac{1 - \kappa}{\kappa - 3/2} \frac{1}{\gamma \alpha^{\frac{1-\kappa}{\kappa-3/2}} - \chi \frac{\alpha}{\sigma}}$  and  $d_2 = \frac{\chi(1 + \alpha/\sigma)}{\chi \frac{\alpha}{\sigma} - \gamma \alpha^{\frac{1-\kappa}{\kappa-3/2}}}$ .

Due to  $E \times B_0$  drift in magnetized plasma,  $u_1$  and  $v_1$  show up. We obtain the dispersion relation of the DIAW as follows

$$V = l_z \sqrt{\frac{1 + (1 - \mu)d_2}{\mu C_1 + (1 - \mu)d_1}}. \tag{12}$$

Collecting terms of the next higher order of  $\epsilon$ , we get

$$\begin{cases} \frac{\partial n_1}{\partial \tau} - V \frac{\partial n_2}{\partial \xi} + l_z \frac{\partial}{\partial \xi} (n_1 w_1) + l_x \frac{\partial u_1}{\partial \xi} + l_y \frac{\partial v_1}{\partial \xi} + l_z \frac{\partial w_2}{\partial \xi} = 0, \\ \frac{\partial w_1}{\partial \tau} - V \frac{\partial w_2}{\partial \xi} + l_z w_1 \frac{\partial w_1}{\partial \xi} = -l_z \frac{\partial \phi_2}{\partial \xi}, \\ \mu C_1 \phi_2 + \mu C_2 \phi_1^2 - n_2 + (1 - \mu) Z_{d2} = 0 \\ Z_{d2} = d_1 \phi_2 + d_4 \phi_1^2 - d_2 n_2 + d_3 \frac{\partial \phi_1}{\partial \xi}, \end{cases} \quad (13)$$

where  $d_3 = V \nu \left( \frac{-d_1 + d_2 \frac{l_z^2}{V^2}}{\gamma \alpha \frac{1-\kappa}{\kappa-3/2} - \chi \frac{\alpha}{\sigma}} \right)$  and  $d_4 = \frac{\chi \alpha l_z^2}{\sigma V^2} \left( \frac{d_1 - d_2 \frac{l_z^2}{V^2}}{\gamma \alpha \frac{1-\kappa}{\kappa-3/2} - \chi \frac{\alpha}{\sigma}} \right)$ .

The following relation is obtained by comparing the terms of order  $\epsilon^2$

$$\mu C_1 \phi_2 + \mu C_2 \phi_1^2 - n_2 + (1 - \mu) Z_{d2} = 0. \quad (14)$$

Differentiating equation (14) and eliminating higher order perturbed terms using equations (11)–(13), we finally acquire the Burgers equation as

$$\frac{\partial \phi_1}{\partial \tau} + A \phi_1 \frac{\partial \phi_1}{\partial \xi} = B \frac{\partial^2 \phi_1}{\partial \xi^2}, \quad (15)$$

where  $A$  and  $B$  are the nonlinear and dispersion coefficients given respectively as

$$A = \frac{l_z^2}{2V} + \frac{l_z}{V} - \frac{V[\mu C_2 + (1 - \mu)d_4]}{2[\mu C_1 + (1 - \mu)d_1]} \quad \text{and} \quad B = \frac{V(1 - \mu)d_3}{2[\mu C_1 + (1 - \mu)d_1]}.$$

## 4 Dynamical System

The Burgers equation (15) is converted into dynamical system (DS) using the transfiguration

$$\eta = \xi - U\tau, \quad (16)$$

with  $U$  as the wave speed. Thus, we obtain the following DS as

$$\begin{cases} \frac{d\phi_1}{d\eta} = y, \\ \frac{dy}{d\eta} = \frac{A^2}{2B^2} \phi_1 \left( \phi_1 - \frac{U}{A} \right) \left( \phi_1 - \frac{2U}{A} \right). \end{cases} \quad (17)$$

In Fig. 1, fixed points ( $P_0$  and  $P_2$ ) are connected by nonlinear heteroclinic trajectories (NHET<sub>1,0</sub>) enclosing center at fixed point ( $P_1$ ). A trajectory that starts from one fixed point and ends in another fixed point is said to form heteroclinic structure [24, 31, 32]. Such trajectories are associated with shock waves, such as kink and anti-kink waves. A trajectory that encloses one fixed point and has zero separa-

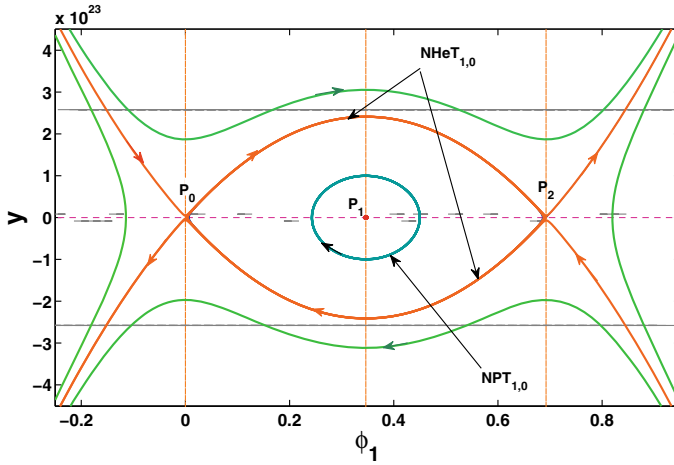


**Fig. 1** Phase portrait of equation (17) for  $\kappa = 2, l_z = 0.1, \sigma = 0.1, \mu = 0.3, \omega_{ci} = 0.5, r_d = 2 \mu\text{m}, Z_{d0} = 10^4, n_{d0} = 1 \text{ m}^{-3}$  and  $U = 0.2$

trix is said to form nonlinear periodic trajectory. Here, nonlinear periodic trajectory ( $NPT_{1,0}$ ) encloses one fixed point ( $P_1$ ) that corresponds to periodic wave solution [33]. The nonlinear wave trajectories portrayed in Fig. 1 describe nonlinear wave solutions of the Burgers equation through phase plane plots. The nonlinear periodic wave solution shown here are different from supernonlinear periodic waves as supernonlinear periodic waves are characterized by nontrivial topology of their phase portraits. Supernonlinear periodic trajectory encloses more than one fixed points and are separated by at least one separatrix layer [33].

Next, we analyze the occurrence of wave forms by examining potential energy function. Let  $\psi$  be the potential energy function such that

$$\frac{d^2\phi_1}{d\eta^2} = -\frac{d\psi}{d\phi_1}, \tag{18}$$

which gives

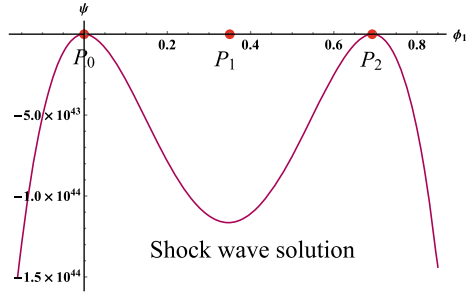
$$\psi = -\frac{A^2}{2B^2} \left( \frac{1}{4}\phi_1^4 - \frac{U}{A}\phi_1^3 + \frac{U^2}{A^2}\phi_1^2 \right). \tag{19}$$

Now, we plot the curve of the potential energy function corresponding to Fig. 1.

From Fig. 2 it is evident that there exist one maximum point and two local minima in the potential energy function graph. The region enclosed by the trajectory from fixed points ( $P_0$  and  $P_2$ ) are region of the shock wave solution while, the region about maximum point at  $P_1$  describes the periodic wave solution. In Fig. 2, potential dip at  $P_1$  denotes stable fixed point and maxima at points  $P_0$  and  $P_2$  represent unstable points [24]. Stable fixed point indicates periodic trajectory and from the other two



**Fig. 2** Potential energy function of equation (19) for same parametric values as Fig. 1



fixed points ( $P_0$  and  $P_2$ ) the shock wave feature is interpreted from the potential profile that represents dissipation. Here, dissipation leads to the formation of shock structures [20].

### 4.1 Periodic Wave Solution

The analytical periodic solution of the Burgers equation (15) can be obtained from equation (17) considering the Hamiltonian function  $H(\phi_1, y)$  as

$$H(\phi_1, y) = \frac{y^2}{2} - \frac{A^2}{B^2} \left( \frac{\phi_1^4}{4} - \frac{U\phi_1^3}{A} + \frac{U^2\phi_1^2}{A^2} \right) = h, \tag{20}$$

from which one can obtain

$$\frac{dy}{d\eta} = \frac{A}{2B} \sqrt{(r_1 - \psi)(\psi - r_2)(\psi - r_3)(\psi - r_4)}, \tag{21}$$

where  $r_1, r_2, r_3$  and  $r_4$  are roots of  $h_i + \frac{A^2}{4B^2} \left( \phi_1^4 - \frac{4U\phi_1^3}{A} + \frac{4U^2\phi_1^2}{A^2} \right) = 0$ . Substituting Eq. (21) in Eq. (20), one can obtain the nonlinear periodic dust-ion-acoustic wave (NPDIAW) solution given by

$$\phi_1 = \frac{r_1 + r_4 \left\{ \frac{r_1 - r_2}{r_2 - r_4} sn^2 \left( \frac{A}{2Bg} \eta, z \right) \right\}}{1 + \frac{r_1 - r_2}{r_2 - r_4} sn^2 \left( \frac{A}{2Bg} \eta, z \right)}, \tag{22}$$

with  $sn$  being the Jacobi elliptic function,  $g = \frac{2}{\sqrt{(r_1 - r_3)(r_2 - r_4)}}$  and

$$z = \sqrt{\frac{(r_1 - r_2)(r_3 - r_4)}{(r_1 - r_3)(r_2 - r_4)}}.$$

In Fig. 3, we show the variation of nonlinear periodic dust-ion-acoustic wave (NPDIAW) solution varying parameters  $\kappa$ ,  $l_z$  and  $\mu$ . It is clear from the Fig. 3 that NPDIAW becomes spiky as the values of parameter  $\kappa$  rise, while the NPDIAW becomes smooth for higher values of  $l_z$  and  $\mu$  as the height of NPDIAW diminishes. It is also observed from Fig. 3 that the width of NPDIAW narrows down as parameters  $\kappa$ ,  $l_z$  and  $\mu$  are increased.

### 4.2 Dust-Ion-Acoustic Kink Wave (DIAKW) and Dust-Ion-Acoustic Anti-kink Wave (DIAAKW)

In order to acquire DIAKW and DIAAKW solutions analytically, we introduce a new variable  $\zeta$  as

$$\zeta = c(\xi - \lambda\tau), \tag{23}$$

with wave speed given by  $\lambda$  and  $c > 0$ .

Solving with  $\tanh$  method, the DIAKW and DIAAKW solutions of equation (15) are obtained as

$$\phi_1(\xi, \tau) = \pm \frac{\lambda}{A} \left[ 1 - \tanh \left\{ \frac{\lambda}{2B} (\xi - \lambda\tau) \right\} \right]. \tag{24}$$

With the help of numerical simulations, the DIAKW and DIAAKW solutions are presented in Fig. 4 varying  $\kappa$ ,  $l_z$  and  $\mu$  by keeping  $\tau = 1$  with other physical parameters same as Fig. 1. It is noticed that as we increase the values of superthermal

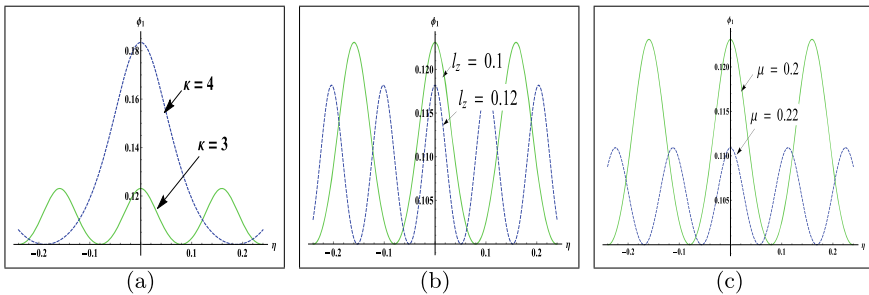


**Fig. 3** NPDIAW variations changing parameters  $\kappa$ ,  $l_z$  and  $\mu$  with other parameters are same as in Fig. 1

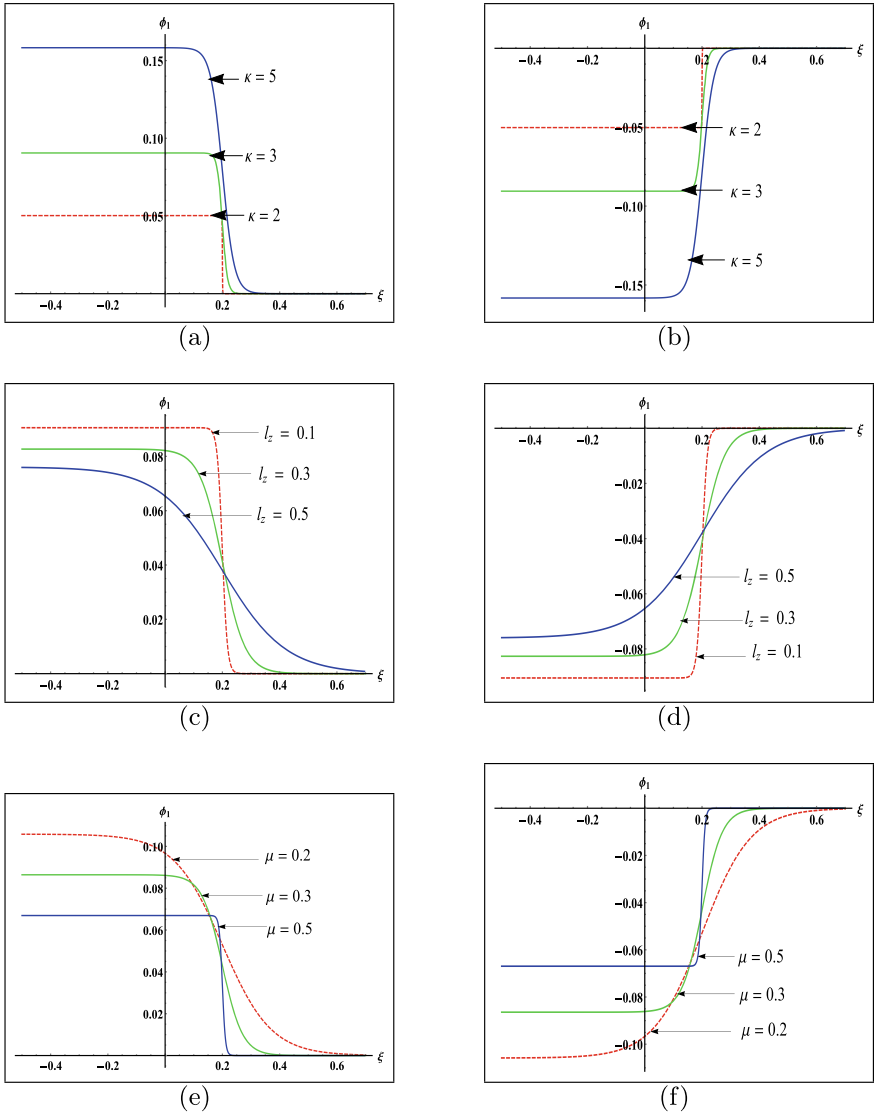


**Fig. 4** DIAKW and DIAKW variations changing parameters  $\kappa$ ,  $l_z$  and  $\mu$  with other parameters same as in Fig. 1

parameter ( $\kappa$ ), the height of the wave increases. Whereas, the height diminishes while the smoothness of DIAKW and DIAKW increases when the values of direction cosine ( $l_z$ ) and number density ratio of electrons and ions ( $\mu$ ).

## 5 Conclusions

The DIAWs in a superthermal dust charge fluctuation plasma system under the Burgers equation are studied. Using the traveling wave transformations, the Burgers equation is converted into dynamical systems. Through phase plane plot and potential energy function, the shock wave and periodic wave solutions are made evident. Analytical wave solutions of DIAWs are derived using Hamiltonian function. Effects of superthermal charge fluctuation parameters on shock wave and periodic wave solutions of DIAWs are shown. Superthermal parameter ( $\kappa$ ), number density ratio ( $\mu$ ) and direction cosine ( $l_z$ ) have huge impacts on DIAWs. The existence of shock and periodic wave solutions of the Burgers equation for DIAW is shown for the first time in superthermal charge fluctuation in magnetized plasma systems employing the notion of planar dynamical systems. Dusty plasmas are observed in astrophysical environments, namely solar and planetary nebulae and usually with an involvement of magnetic fields [34–36]. Our study may be helpful to understand behaviors of DIAWs existing in magnetized plasma systems where superthermal charge fluctuation occurs, such as in solar wind, mercury, Saturn and Earth's magnetosphere [31].

## References

1. Shukla, P.K., Mamun, A.A.: Introduction to Dusty Plasma Physics. Institute of Physics, Bristol (2002)
2. Verheest, F.: Waves in Dusty Space Plasmas, vol. 35. Kluwer Academic, Dordrecht (2000)
3. Barkan, A., D'Angelo, N., Merlino, R.L.: Experiments on ion-acoustic waves in dusty plasmas. *Planet. Space Sci.* **44**, 239 (1996)
4. Shukla, P.K., Silin, V.P.: Dust-ion-acoustic wave. *Phys. Scr.* **45**, 508 (1992)
5. Tamang, J., Sarkar, K., Saha, A.: Solitary wave solution and dynamic transition of dust ion acoustic waves in a collisional nonextensive dusty plasma with ionization effect. *Phys. A Stat. Mech. Appl.* **505**, 18–34 (2018)
6. Nakamura, Y., Bailung, H., Shukla, P.K.: Observation of ion-acoustic shocks in a dusty plasma. *Phys. Rev. Lett.* **83**, 1602 (1999)
7. El-Taibany, W.F., El-Bedwely, N.A., El-Shamy, E.F.: Three-dimensional stability of dust-ion-acoustic solitary waves in a magnetized multicomponent dusty plasma with negative ions. *Phys. Plasmas* **18**, 033703 (2011)
8. Ghosh, S., Sarkar, S., Khan, M.: Low frequency wave propagation in a cold magnetized dusty plasma. *Planet. Space Sci.* **47**, 273 (1998)
9. Ghosh, S., Sarkar, S., Khan, M., Gupta, M.R.: Small amplitude nonlinear dust ion acoustic waves in a magnetized dusty plasma with charge fluctuation. *Phys. Scr.* **63**, 395, 033703 (2001)
10. Shahmansouri, M., Alinejad, H.: Arbitrary amplitude dust ion acoustic solitary waves in a magnetized suprathermal dusty plasma. *Phys. Plasmas* **19**, 123701 (2012)

11. Shahmansouri, M.: Dynamics of dust-ion acoustic shock waves in a magnetized charge variable superthermal complex plasma. *Phys. Scr.* **89**, 075604 (2014)
12. Anowar, M.G.M., Mamun, A.A.: Dust ion-acoustic solitary waves in a hot adiabatic magnetized dusty plasma. *Phys. Lett. A* **372**, 5896, 075604 (2008)
13. El-Labany, S.K., Shalaby, M., El-Shamy, E.F., El-Sherif, L.S.: Effects of two-temperature electrons, external oblique magnetic field, concentration of charged dust grains and higher-order nonlinearity on dust ion-acoustic solitary waves in Saturn's E-ring. *Planet. Space Sci.* **57**, 1246, 075604 (2009)
14. Shalaby, M., El-Labany, S.K., El-Shamy, E.F., El-Taibany, W.F., Khaled, M.A.: On the stability of obliquely propagating dust ion-acoustic solitary waves in hot adiabatic magnetized dusty plasmas. *Phys. Plasmas* **16**, 123706 (2009)
15. Samanta, P., De, A., Dey, S., Maity, D., Ghosh, A., Chandra, S.: Nonlinear excitations in dust-ion acoustic waves and the formation of Rogue waves in stable parametric region in a 3-component degenerate plasma. *Afr. Rev. Phys.* **15**, 10, 123706 (2021)
16. Goswami, J., Sarkar, J., Chandra, S., et al.: Amplitude-modulated electron-acoustic waves with bipolar ions and kappa-distributed positrons and warm electrons. *Pramana-J. Phys.* **95**, 54, 123706 (2021)
17. Alinejad, H., Mamun, A.A.: Oblique propagation of electrostatic waves in a magnetized electron-positron-ion plasma with superthermal electrons. *Phys. Plasmas* **18**, 112103 (2011)
18. Sultana, S., Kourakis, I., Hellberg, M.A.: Oblique propagation of arbitrary amplitude electron acoustic solitary waves in magnetized kappa-distributed plasmas. *Plasma Phys. Control Fusion* **54**, 105016 (2012)
19. Alinejad, H., Tribeche, M., Mohammadi, M.A.: Dust ion-acoustic shock waves due to dust charge fluctuation in a superthermal dusty plasma. *Phys. Lett. A* **375**, 4183, 105016 (2011)
20. Ghosh, S., Chaudhury, T.K., Sarkar, S., Khan, M., Gupta, M.R.: Collisionless damping of nonlinear dust ion acoustic wave due to dust charge fluctuation. *Phys. Rev. E* **65**, 037401 (2002)
21. Mamun, A.A., Shukla, P.K.: Electrostatic solitary and shock structures in dusty plasmas. *Phys. Scr.* **T98**, 107, 037401 (2002)
22. Strogatz, S.H.: *Nonlinear Dynamics and Chaos*. Levant, Kolkata (2007)
23. Chow, S.N., Hale, J.K.: *Methods of Bifurcation Theory*, 1st edn. Springer, New York (1982)
24. Saha, A., Banerjee, S.: *Dynamical Systems and Nonlinear Waves in Plasmas*, 1st edn. CRC Press, Boca Raton (2021)
25. Samanta, U.K., Saha, A., Chatterjee, P.: Bifurcations of dust-ion-acoustic travelling waves in a magnetized dusty plasma with a  $q$ -nonextensive electron velocity distribution. *Phys. Plasma* **20**, 022111 (2013)
26. Selim, M.M., El-Depsy, A., El-Shamy, E.F.: Bifurcations of nonlinear ion-acoustic travelling waves in a multicomponent magnetoplasma with superthermal electrons. *Astrophys. Space Sci.* **360**, 66, 022111 (2015)
27. El-Monier, S.Y., Atteya, A.: Bifurcation analysis for dust-acoustic waves in a four-component plasma including warm ions. *IEEE Trans. Plasma Sci.* **46**, 815–824, 022111 (2018)
28. El Ghani, O., Driouch, I., Chatei, H.: Effects of non-extensive electrons on the sheath of dusty plasmas with variable dust charge. *Contrib. Plasma Phys* **59**, e201900030 (2019)
29. Chatterjee, P., Ali, R., Saha, A.: Analytical solitary wave solution of the dust ion acoustic waves for the damped forced Korteweg-de Vries equation in superthermal plasmas. *Zeitschrift für Naturforschung A* **73**, 151–159, e201900030 (2018)
30. Sharma, P., Das, A., Tamang, J., Saha, A.: Dynamical properties of dust-ion-acoustic wave solutions in a nonextensive collisional dusty plasma. *J. Taibah Univ. Sci.* **15**, 710–720, e201900030 (2021)
31. Saha, A., Chatterjee, P.: Dust ion acoustic travelling waves in the framework of a modified Kadomtsev-Petviashvili equation in a magnetized dusty plasma with superthermal electrons. *Astrophys. Space Sci.* **349**, 813–820, e201900030 (2014)
32. Tamang, J., Saha, A.: Dynamical properties of nonlinear ion-acoustic waves based on the nonlinear Schrödinger equation in a multi-pair nonextensive plasma. *Zeitschrift für Naturforschung A* **75**, 687–697, e201900030 (2020)

33. Saha, A., Tamang, J.: Effect of q-nonextensive hot electrons on bifurcations of nonlinear and supernonlinear ion-acoustic periodic waves. *Adv. Space Res.* **63**, 1596–1606 (2019)
34. Melzer, A., Krüger, H., Maier, D., et al.: Physics of magnetized dusty plasmas. *Rev. Mod. Plasma Phys.* **5**, 11, e201900030 (2021)
35. Reissl, S., Stutz, A.M., Klessen, R.S., Seifried, D., Walch, S.: Magnetic fields in star-forming systems ii: examining dust polarization, the Zeeman effect, and the faraday rotation measure as magnetic field tracers. *Mon. Not. R. Astron. Soc.* **500**(1), 153, e201900030 (2020)
36. Li, H.B.: Magnetic fields in molecular clouds-observation and interpretation. *Galaxies* **9**(2), 41, e201900030 (2021)

# Dynamical Aspects of Ion-Acoustic Solitary Waves in a Magnetically Confined Plasma in the Presence of Nonthermal Components



Jintu Ozah  and P. N. Deka 

**Abstract** The characteristics of three-dimensional ion-acoustic solitary waves (IASWs) have been investigated in a magnetized plasma including ions, nonthermally dispersed electrons and positrons. The reductive perturbation technique (RPT) is used to develop the Zakharov–Kuznetsov (ZK) equation for observing ion-acoustic wave structure, and a soliton solution is obtained by using the tangent hyperbolic (*tanh*) method. The influence of various parameters on the soliton profile, such as nonthermal parameters for electrons and positrons, density ratios of positron–electron and ion–electron, and temperature ratio of electron–positron, is presented graphically.

**Keywords** Solitary waves · Reductive perturbation technique · Magnetized plasma · Nonthermal electrons · Positrons

## 1 Introduction

Investigation of ion-acoustic solitary waves is an interesting research problem in the field of plasma physics that has been extensively studied by numerous authors [1–4]. For the first time, Washimi and Taniuti [5] observed the distinctive behaviour of ion-acoustic solitary waves in plasma, which can be investigated using the Korteweg–de Vries (K–dV) equation. After that, ion-acoustic solitary waves in both magnetized and unmagnetized plasmas have been studied by a large number of researchers in different theoretical and experimental circumstances during the past few decades. There has been a lot of interest in the investigation of different types of nonlinear solitary waves in plasmas, like magneto-acoustic solitary waves, spherical and cylindrical-acoustic solitary waves, and lower-hybrid solitary waves [6–9]. A study of ion-acoustic solitary waves in magnetized negative ion plasma consisting of nonthermal electrons was carried out by Labany et al. [10]. They observed that the solitary waves are substantially influenced by the positive-to-negative ion mass ratio, the corresponding negative-to-positive ion density ratio, and the parameters of nonthermal electrons.

---

J. Ozah (✉) · P. N. Deka  
Dibrugarh University, Dibrugarh, Assam 786004, India  
e-mail: [jintuozah@gmail.com](mailto:jintuozah@gmail.com)

© The Author(s), under exclusive license to Springer Nature Switzerland AG 2022  
S. Banerjee and A. Saha (eds.), *Nonlinear Dynamics and Applications*,  
Springer Proceedings in Complexity,  
[https://doi.org/10.1007/978-3-030-99792-2\\_22](https://doi.org/10.1007/978-3-030-99792-2_22)

245

For analysing ion-acoustic waves in a magnetized plasma, Zakharov and Kuznetsov developed the nonlinear equation known as the ZK equation. This ZK equation may be found in many branches of physics, such as fluid mechanics, astrophysics, solid state physics, and so on [11, 12]. It is most apparent in the subject of plasma physics. Using the extended *tanh* approach and the direct assumption method, Li et al. derived the ZK equation and got an exact travelling wave solution [13]. Taibany et al. [14] developed the ZK equation to investigate the IASWs in a magnetized multicomponent dusty plasma with negative ions. Recently, many researchers have been showing an interest in studying the impact of nonextensive electron distribution on IASWs in magnetized plasma. Mandi et al. [15] have investigated the effect of the  $q$ -nonextensivity of electrons on the characteristics of IASWs. Furthermore, the propagation of solitons in nonthermal plasma has generated much interest among researchers. Because of their practical significance, they continue to pique people's curiosity. Many studies in plasma physics, as well as complex plasma, have focused on ion-acoustic solitary waves and their properties in the field of nonthermal plasma. Pakzad [16] studied the behaviour of soliton structures in a three-component unmagnetized plasma containing cold ions, nonthermal electrons, and positrons. Dev et al. [17] studied the dust IASWs in a magnetized plasma in the presence of nonthermal electrons, positrons and relativistic thermal ions. They discovered that in the absence of nonthermal electron and positron populations, the plasma system behaves in the least nonlinear manner, but the system behaves in the most nonlinear manner when the populations of nonthermal electrons and positrons have the maximal value. In their investigation into three-dimensional ion-acoustic soliton structures, including warm ions, positrons, and nonthermal electrons, Chawla et al. [18] reveal that the presence of nonthermal electrons considerably impacts the amplitude and width of soliton pulses.

In this paper, the effects of nonthermal electrons, nonthermal positrons, and the influence of magnetic fields on the structure of three-dimensional nonlinear IASWs are investigated. We anticipate that the presence of nonthermal electrons and positrons will alter the characteristics of solitons as well as their existence regime.

## 2 Basic Model Equations

We consider a plasma model with constituent ions, nonthermal electrons and nonthermal positrons, where the magnetic field  $B_0$  is along the  $z$ -axis. The following normalized sets of ion continuity equations, momentum equations, and Poisson equations serve as the governing equations for the current plasma model:

$$\frac{\partial n_i}{\partial t} + \frac{\partial(n_i u)}{\partial x} + \frac{\partial(n_i v)}{\partial y} + \frac{\partial(n_i w)}{\partial z} = 0 \quad (1)$$

$$\frac{\partial u}{\partial t} + u \frac{\partial u}{\partial x} + v \frac{\partial u}{\partial y} + w \frac{\partial u}{\partial z} = -\frac{\partial \phi}{\partial x} + \frac{\Omega_i}{\omega_{pi}} v \quad (2)$$



$$\frac{\partial v}{\partial t} + u \frac{\partial v}{\partial x} + v \frac{\partial v}{\partial y} + w \frac{\partial v}{\partial z} = -\frac{\partial \phi}{\partial y} - \frac{\Omega_i}{\omega_{pi}} u \quad (3)$$

$$\frac{\partial w}{\partial t} + u \frac{\partial w}{\partial x} + v \frac{\partial w}{\partial y} + w \frac{\partial w}{\partial z} = -\frac{\partial \phi}{\partial z} \quad (4)$$

$$\frac{\partial^2 \phi}{\partial x^2} + \frac{\partial^2 \phi}{\partial y^2} + \frac{\partial^2 \phi}{\partial z^2} = n_e - \mu_p n_p - \mu_i n_i \quad (5)$$

The Boltzmann distributions [17] for nonthermal electrons and positrons are defined as

$$n_e = (1 - \beta_e \phi + \beta_e \phi^2) \exp(\phi) \quad (6)$$

$$n_p = (1 + \sigma_{pe} \beta_p \phi + \sigma_{pe}^2 \beta_p \phi^2) \exp(-\sigma_{pe} \phi) \quad (7)$$

In the above expressions.

Also  $\mu_p = \frac{n_{p0}}{n_{e0}}$ ,  $\mu_i = \frac{n_{i0}}{n_{e0}}$  and  $\sigma_{pe} = \frac{T_e}{T_p}$ .

$$\beta_e = \frac{4\alpha_e}{1 + 3\alpha_e}, \beta_p = \frac{4\alpha_p}{1 + 3\alpha_p}$$

here,  $\alpha_e$  is the nonthermal parameter for electrons and  $\alpha_p$  is the nonthermal parameter for positrons, which represent the population of energetic nonthermal electrons and positrons, respectively.  $T_e$  and  $T_p$  are the temperatures of electrons and positrons. In the above equations, the ion number densities  $n_i$  are normalized by  $n_{i0}$  and velocities ( $u, v, w$ ) by the ion-acoustic speed  $C_s = (T_e/m_i)^{1/2}$ , where  $m_i$  is the ion mass. Space coordinates ( $x, y, z$ ) and time  $t$  are normalized in terms of Debye length  $\lambda_D = (\varepsilon_0 T_e / n_i^0 e^2)^{1/2}$  and the inverse of plasma frequency  $\omega_{pi} = (4\pi e^2 n_i^0 / m_i)^{1/2}$  respectively. The electric potential  $\phi$  is normalized by  $T_e/e$ , where  $e$  is the electronic charge.  $\Omega_i$  and  $\omega_{pi}$  are the ion-cyclotron frequency and plasma frequency.

### 3 Reductive Perturbation Method

To derive the ZK equation from the above basic set of equations, we used the reductive perturbation technique. The stretching coordinates [10, 19] are assume as

$$\xi = \varepsilon^{1/2} x, \eta = \varepsilon^{1/2} y, \zeta = \varepsilon^{1/2} (z - \lambda_0 t) \text{ and } \tau = \varepsilon^{3/2} t \quad (8)$$

where the symbol  $\varepsilon$  is the expansion parameter that measures the strength of nonlinearity and  $\lambda_0$  is the phase velocity of IASWs. We express the physical parameters in

the power series expansion of  $\varepsilon$  in the following way:

$$\left. \begin{aligned} n_i &= 1 + \varepsilon^1 n^1 + \varepsilon^2 n^2 + \varepsilon^3 n^3 + \dots \\ u &= \varepsilon^{3/2} u^1 + \varepsilon^2 u^2 + \varepsilon^{5/2} u^3 + \dots \\ v &= \varepsilon^{3/2} v^1 + \varepsilon^2 v^2 + \varepsilon^{5/2} v^3 + \dots \\ w &= 0 + \varepsilon^1 w^1 + \varepsilon^2 w^2 + \varepsilon^3 w^3 + \dots \\ \phi &= 0 + \varepsilon^1 \phi^1 + \varepsilon^2 \phi^2 + \varepsilon^3 \phi^3 + \dots \end{aligned} \right\} \tag{9}$$

We transform  $x$  and  $t$  by using the stretch coordinates as

$$\left. \begin{aligned} \frac{\partial}{\partial x} &\equiv \varepsilon^{1/2} \frac{\partial}{\partial \xi}, \quad \frac{\partial}{\partial y} \equiv \varepsilon^{1/2} \frac{\partial}{\partial \eta}, \quad \frac{\partial}{\partial z} \equiv \varepsilon^{1/2} \frac{\partial}{\partial \zeta}, \quad \frac{\partial}{\partial t} \equiv -\lambda_0 \varepsilon^{1/2} \frac{\partial}{\partial \zeta} + \varepsilon^{3/2} \frac{\partial}{\partial \tau} \\ \frac{\partial^2}{\partial x^2} &\equiv \varepsilon \frac{\partial^2}{\partial \xi^2}, \quad \frac{\partial^2}{\partial y^2} \equiv \varepsilon \frac{\partial^2}{\partial \eta^2}, \quad \frac{\partial^2}{\partial z^2} \equiv \varepsilon \frac{\partial^2}{\partial \zeta^2} \end{aligned} \right\} \tag{10}$$

Using (10), the transformation equations of (1)–(5) may be obtained as

$$-\lambda_0 \varepsilon^{1/2} \frac{\partial n_i}{\partial \zeta} + \varepsilon^{3/2} \frac{\partial n_i}{\partial \tau} + \varepsilon^{1/2} \frac{\partial(n_i u)}{\partial \xi} + \varepsilon^{1/2} \frac{\partial(n_i v)}{\partial \eta} + \varepsilon^{1/2} \frac{\partial(n_i w)}{\partial \zeta} = 0 \tag{11}$$

$$-\lambda_o \varepsilon^{1/2} \frac{\partial u}{\partial \zeta} + \varepsilon^{3/2} \frac{\partial u}{\partial \tau} + u \varepsilon^{1/2} \frac{\partial u}{\partial \xi} + v \varepsilon^{1/2} \frac{\partial u}{\partial \eta} + w \varepsilon^{1/2} \frac{\partial u}{\partial \zeta} = -\varepsilon^{1/2} \frac{\partial \phi}{\partial \xi} + \frac{\Omega_i}{\omega_{pi}} v \tag{12}$$

$$-\lambda_o \varepsilon^{1/2} \frac{\partial v}{\partial \zeta} + \varepsilon^{3/2} \frac{\partial v}{\partial \tau} + u \varepsilon^{1/2} \frac{\partial v}{\partial \xi} + v \varepsilon^{1/2} \frac{\partial v}{\partial \eta} + w \varepsilon^{1/2} \frac{\partial v}{\partial \zeta} = -\varepsilon^{1/2} \frac{\partial \phi}{\partial \eta} + \frac{\Omega_i}{\omega_{pi}} u \tag{13}$$

$$-\lambda_o \varepsilon^{1/2} \frac{\partial w}{\partial \zeta} + \varepsilon^{3/2} \frac{\partial w}{\partial \tau} + u \varepsilon^{1/2} \frac{\partial w}{\partial \xi} + v \varepsilon^{1/2} \frac{\partial w}{\partial \eta} + w \varepsilon^{1/2} \frac{\partial w}{\partial \zeta} = -\varepsilon^{1/2} \frac{\partial \phi}{\partial \zeta} \tag{14}$$

$$\varepsilon \frac{\partial^2 \phi}{\partial \xi^2} + \varepsilon \frac{\partial^2 \phi}{\partial \eta^2} + \varepsilon \frac{\partial^2 \phi}{\partial \zeta^2} = n_e - \mu_p n_p - \mu_i n_i \tag{15}$$

Now using (9) in the above equations and then collecting the lowest order terms. in  $\varepsilon$ , we get

$$\left. \begin{aligned} n^1 &= \frac{w^1}{\lambda_0}, & w^1 &= \frac{\phi^1}{\lambda_0}, \\ u^1 &= -\frac{\omega_{pi}}{\Omega_i} \frac{\partial \phi^1}{\partial \eta}, & \phi^1 &= \frac{\mu_i n^1}{(1 - \beta_e + \mu_p \sigma_{pe} - \beta_p \mu_p \sigma_{pe})} \\ v^1 &= \frac{\omega_{pi}}{\Omega_i} \frac{\partial \phi^1}{\partial \xi}, \end{aligned} \right\} \tag{16}$$

After solving for the first order perturbation terms, the dispersion relation of nonlinear IASWs is obtained as

$$\lambda_0 = \sqrt{\frac{\mu_i}{1 - \beta_e + \mu_p \sigma_{pe} - \beta_p \mu_p \sigma_{pe}}} \tag{17}$$

Equation (17) represents the phase velocity of nonlinear IASWs. The next higher order of  $\varepsilon$  gives

$$u^2 = \frac{\omega_{pi} \lambda_0}{\Omega_i} \frac{\partial v^1}{\partial \zeta}, \tag{18}$$

$$v^2 = -\frac{\omega_{pi} \lambda_0}{\Omega_i} \frac{\partial u^1}{\partial \zeta}, \tag{19}$$

$$\frac{\partial n_i^1}{\partial \tau} - \lambda_0 \frac{\partial n_i^2}{\partial \zeta} + \frac{\partial u^2}{\partial \xi} + \frac{\partial v^2}{\partial \eta} + \frac{\partial w^2}{\partial \zeta} + \frac{\partial(n_i^1 w^1)}{\partial \zeta} = 0, \tag{20}$$

$$\frac{\partial w^1}{\partial \tau} - \lambda_0 \frac{\partial w^2}{\partial \zeta} + w^1 \frac{\partial w^1}{\partial \zeta} + \frac{\partial \phi^2}{\partial \zeta} = 0, \tag{21}$$

$$\begin{aligned} &\frac{\partial^2 \phi^1}{\partial \xi^2} + \frac{\partial^2 \phi^1}{\partial \eta^2} + \frac{\partial^2 \phi^1}{\partial \zeta^2} - (1 - \beta_e + \mu_p \sigma_{pe} - \beta_p \mu_p \sigma_{pe}) \phi^2 \\ &- \frac{1}{2} (1 - \sigma_{pe}^2 \mu_p) (\phi^1)^2 + \mu_i n^2 = 0, \end{aligned} \tag{22}$$

Now, differentiating equation (22) w.r.t  $\zeta$ , we get

$$\begin{aligned} &\frac{\partial}{\partial \zeta} \left( \frac{\partial^2 \phi^1}{\partial \xi^2} + \frac{\partial^2 \phi^1}{\partial \eta^2} \right) + \frac{\partial^3 \phi^1}{\partial \zeta^3} - (1 - \beta_e + \mu_p \sigma_{pe} - \beta_p \mu_p \sigma_{pe}) \frac{\partial \phi^2}{\partial \zeta} \\ &- (1 - \sigma_{pe}^2 \mu_p) \phi^1 \frac{\partial \phi^1}{\partial \zeta} + \mu_i \frac{\partial n^2}{\partial \zeta} = 0. \end{aligned} \tag{23}$$

Now, using the lowest order terms, the Eq. (23) can be written as

$$\frac{\partial}{\partial \zeta} \left( \frac{\partial^2 \phi^1}{\partial \xi^2} + \frac{\partial^2 \phi^1}{\partial \eta^2} \right) + \frac{\partial^3 \phi^1}{\partial \zeta^3} - \frac{\mu_i}{\lambda_0^2} \frac{\partial \phi^2}{\partial \zeta} - (1 - \sigma_{pe}^2 \mu_p) \phi^1 \frac{\partial \phi^1}{\partial \zeta} + \mu_i \frac{\partial n^2}{\partial \zeta} = 0. \tag{24}$$

Now, eliminating the second order quantities from (20), (21) and (24), we obtain the ZK equation in terms of  $\phi^1$  as

$$\frac{\partial \phi^1}{\partial \tau} + A \phi^1 \frac{\partial \phi^1}{\partial \zeta} + B \frac{\partial^3 \phi^1}{\partial \zeta^3} + C \frac{\partial}{\partial \zeta} \left( \frac{\partial^2 \phi^1}{\partial \xi^2} + \frac{\partial^2 \phi^1}{\partial \eta^2} \right) = 0, \tag{25}$$

where the non-linear coefficient  $A$  is given by

$$A = \frac{2}{\lambda_0} - \frac{\lambda_0^3}{2\mu_i} (1 - \sigma_{pe}^2 \mu_p).$$

$B$  and  $C$  are the dispersive and higher order coefficients, expressed as

$$B = \frac{\lambda_0^3}{2\mu_i}, \text{ and } C = \frac{\lambda_0^3}{2\mu_i} + \frac{\lambda_0^3}{2} \frac{\omega_{pi}^2}{\Omega_i^2}.$$

### 4 Solution of ZK Equation

To analyse the Eq. (25), we use the *tanh* method. We consider the transformation  $\chi = \gamma(l\xi + m\eta + n\zeta - U\tau)$ , where  $\phi(\xi, \eta, \zeta, \tau) = \psi(\chi)$ , we can use the following changes:

$$\begin{aligned} \frac{\partial}{\partial \tau} &\equiv -U\gamma \frac{d}{d\chi}, \quad \frac{\partial}{\partial \xi} \equiv l\gamma \frac{d}{d\chi}, \quad \frac{\partial}{\partial \eta} \equiv \gamma m \frac{d}{d\chi}, \quad \frac{\partial}{\partial \zeta} \equiv \gamma n \frac{d}{d\chi}, \\ \frac{\partial^2}{\partial \xi^2} &\equiv \gamma^2 l^2 \frac{d^2}{d\chi^2}, \quad \frac{\partial^2}{\partial \eta^2} \equiv \gamma^2 m^2 \frac{d^2}{d\chi^2}, \quad \frac{\partial^3}{\partial \zeta^3} \equiv \gamma^3 n^3 \frac{d^3}{d\chi^3} \end{aligned}$$

Now the Eq. (25) becomes a reduced ordinary differential equation as

$$-U\gamma \frac{d\psi}{d\chi} + \frac{A\gamma n}{2} \frac{d\psi^2}{d\chi} + B\gamma^3 n^3 \frac{d^3\psi}{d\chi^3} + C\gamma n \frac{d}{d\chi} \left[ \gamma^2 (l^2 + m^2) \frac{d^2\psi}{d\chi^2} \right] = 0. \tag{26}$$

Integrating the above equation, we get

$$-U\psi + \frac{1}{2} An\psi^2 + \gamma^2 n [Bn^2 + C(l^2 + m^2)] \frac{d^2\psi}{d\chi^2} = 0 \tag{27}$$

To solve the above equation, we use the *tanh* method. Consider a new independent variable as:

$$z = \tan(\chi), \text{ where } \psi(\chi) = w(z).$$

and we get.

$$\frac{d^2}{d\chi^2} = (1 - z^2)^2 \frac{d^2}{dz^2} - 2z(1 - z^2) \frac{d}{dz}.$$

Now the Eq. (27) becomes

$$-Uw + \frac{1}{2} Anw^2 + \gamma^2 n (Bn^2 + C(l^2 + m^2)) (1 - z^2)^2 \frac{d^2w}{dz^2}$$

$$-2\gamma^2 n(Bn^2 + C(l^2 + m^2))z(1 - z^2) \frac{dw}{dz} = 0. \tag{28}$$

In the *tanh* method the series solution of the Eq. (28) can be written as:

$$w(z) = \sum_{i=1}^m a_i z^i \tag{29}$$

In Eq. (29), the value of  $m$  can be obtained by balancing the highest order linear term with the nonlinear terms. On substitution of Eq. (29) into Eq. (28), we get  $m = 2$ .

As a result, the solution  $w(z) = \sum_{i=1}^m a_i z^i$  is of the form

$$w(z) = a_0 + a_1 z + a_2 z^2. \tag{30}$$

Now substituting  $w, \frac{dw}{dz}, \frac{d^2w}{dz^2}$  from (30) into (28), then equating different coefficient of  $z$ , we get.

$$a_0 = -a_2 \text{ and } a_1 = 0.$$

Hence Eq. (30) reduce as

$$w(z) = a_0(1 - z^2). \tag{31}$$

Using (31) into (28) and equating the coefficients of  $z^2$ , we get

$$a_0 = \frac{12\gamma^2 [Bn^2 + C(l^2 + m^2)]}{A}.$$

And hence  $\gamma = \sqrt{\frac{U}{4n(Bn^2 + C(l^2 + m^2))}}$ .

Using the values of the parameters, Eq. (31) provides a solution as

$$\phi = \phi_m \operatorname{sech}^2\left(\frac{X}{W}\right). \tag{32}$$

Here, (32) represents the solution of the Eq. (25), where  $\phi_m$  and  $W$  are the amplitude and width of the soliton.

$$\text{Where } \phi_m = \frac{3U}{An} \tag{33}$$

and

$$W = \sqrt{\frac{U}{4n(Bn^2 + C(l^2 + m^2))}}. \tag{34}$$

### 5 Results and Discussion

For the study of soliton structures due to the existence of nonthermal components of electrons and positrons, we have plotted the variation of nonlinear coefficient  $A$  with electron-to-positron temperature ratio ( $\sigma_{pe}$ ), positron-to-electron density ratio ( $\mu_p$ ) and ion-to-electron density ratio ( $\mu_i$ ) for different parameters of nonthermal electrons and positrons. The polarity (positive or negative) of the soliton structure completely depends on the sign of the nonlinear coefficient  $A$ . The positive polarity (compressive soliton) structure exists for the positive value of the nonlinear coefficient and the negative polarity (rarefactive soliton) structure exists for the negative value of the nonlinear coefficient. Figure 1 shows that the nonlinearity of plasma increases with the electron-to-positron temperature ratio ( $\sigma_{pe}$ ). The same result has been observed in Fig. 2, where the nonlinearity changes with the positron-to-electron density ratio ( $\mu_p$ ). The variation of nonlinearity with ion-to-electron density ratio ( $\mu_i$ ) in Fig. 3 shows the existence of rarefactive soliton structures. It can be seen from this graph that the sign of nonlinearity becomes negative after a certain value of  $\mu_i$ . Therefore, the parameter  $\mu_i$  is very crucial to obtaining rarefactive soliton structures. The range of the parameter  $\mu_i$  for the existence of negative polarity can be obtained from Fig. 3b. Further, it is observed that, in all cases, the nonlinearity of plasma decreases as the parameters of nonthermal electrons and positrons are increased.

Figure 4 shows the change of the compressive soliton structure with  $\chi$  for different values of nonthermal parameters of electrons ( $\alpha_e$ ) and positrons ( $\alpha_p$ ). As in equation (34), it shows that the amplitude is the inverse of the nonlinear coefficient  $A$ . As a result, as nonthermal parameters are increased, plasma nonlinearity decreases, and hence the amplitude of the soliton structure rises.

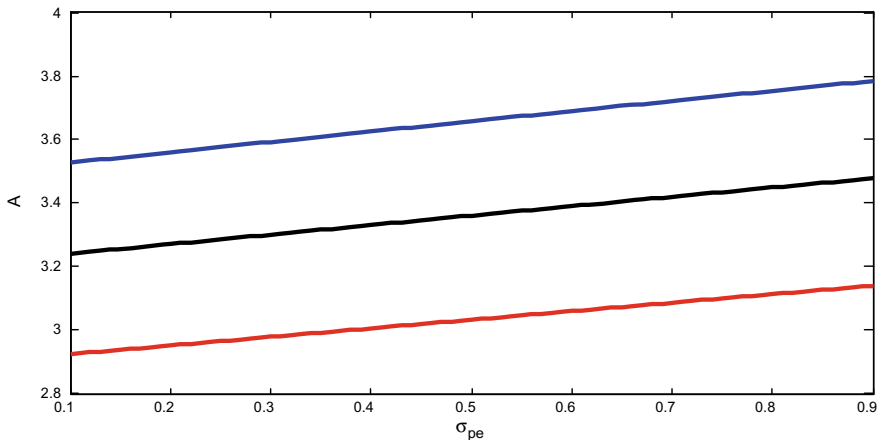


**Fig. 1** Variation of nonlinear coefficient against electron-to-positron temperature ratio ( $\sigma_{pe}$ ) with  $\mu_i = 0.3$  and  $\mu_p = 0.2$ . Blue line corresponds to  $\alpha_e = 0.01, \alpha_p = 0.02$ ; black line corresponds to  $\alpha_e = 0.03, \alpha_p = 0.04$ ; red line corresponds to  $\alpha_e = 0.05, \alpha_p = 0.06$

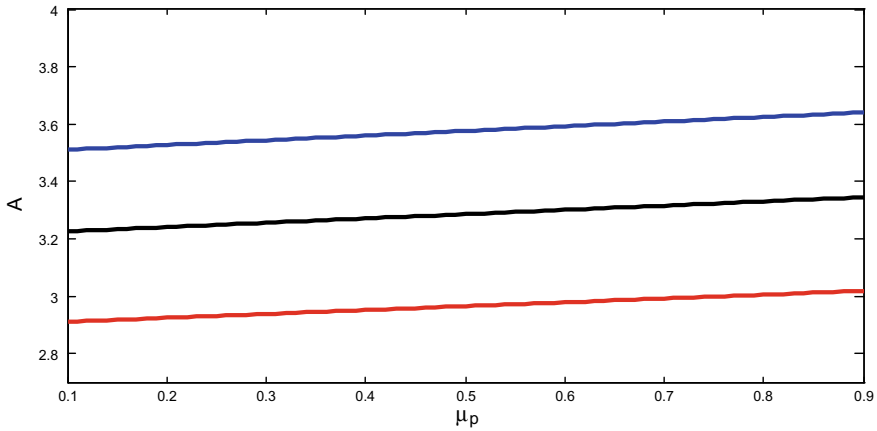


**Fig. 2** Variation of nonlinear coefficient against positron-to-electron density ratio ( $\mu_p$ ) with  $\sigma_{pe} = 0.1$  and  $\mu_i = 0.3$ . Blue line corresponds to  $\alpha_e = 0.01, \alpha_p = 0.02$ ; black line corresponds to  $\alpha_e = 0.03, \alpha_p = 0.04$ ; red line corresponds to  $\alpha_e = 0.05, \alpha_p = 0.06$

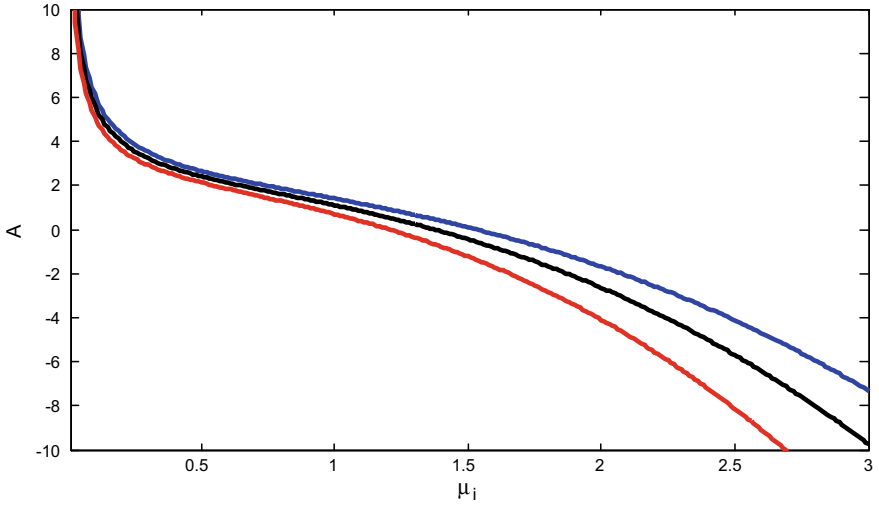
We have also shown the rarefactive soliton structure in Fig. 5 for different values of nonthermal parameters while keeping all other parameters fixed. The amplitude (width) of the solitons decreases (increases) with an increase in the values of  $\alpha_e$  and  $\alpha_p$ .

A similar kind of variation in the soliton structure is observed in Fig. 6, when we change the positron-to-electron density ratio ( $\mu_p$ ). This observation also provides an information about the change in amplitude and width when the value of ( $\mu_p$ ) changes. Increase in the density ratio, enhances the amplitude of the soliton.

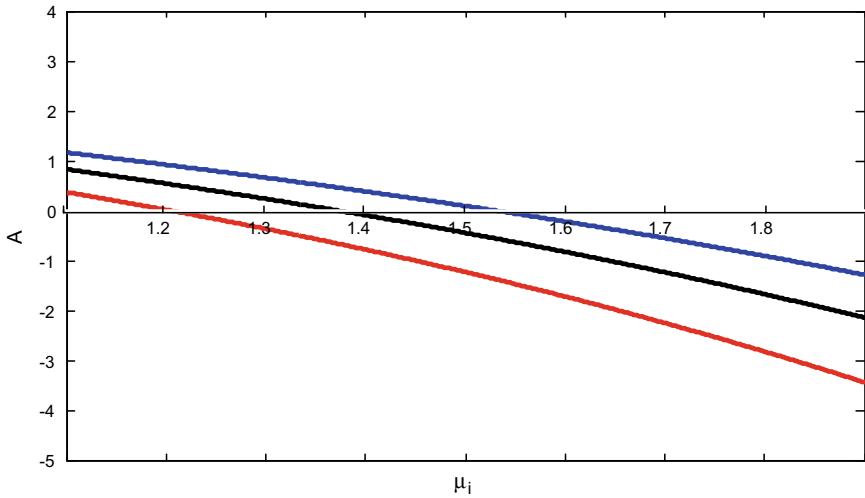
## 6 Conclusion

In the present work, we have studied the characteristics (amplitude and width) of nonlinear ion-acoustic solitary waves in a **magnetically confined plasma** under the influence of nonthermal electrons and positrons. We have determined the range of the parameters for the existence of both the positive and negative polarity soliton. We have noticed the following main results in our present study:

1. In our investigation, both the positive and negative polarity of soliton exist, whereas in the earlier study, this aspect was not covered by Chawla et al. [18].
2. The parameter ion-to-electron density ratio ( $\mu_i$ ) is very crucial to getting two kinds of soliton structure. A very small change in this parameter, changes the polarity of the soliton structure.
3. We can obtain the parameter range for the existence of a negative polarity soliton from Fig. 3b.



(a)



(b)

**Fig. 3** Variation of nonlinear coefficient against ion-to-electron density ratio ( $\mu_i$ ) with  $\sigma_{pe} = 0.1$  and  $\mu_p = 0.2$ . Blue line corresponds to  $\alpha_e = 0.01, \alpha_p = 0.02$ ; black line corresponds to  $\alpha_e = 0.03, \alpha_p = 0.04$ ; red line corresponds to  $\alpha_e = 0.05, \alpha_p = 0.06$



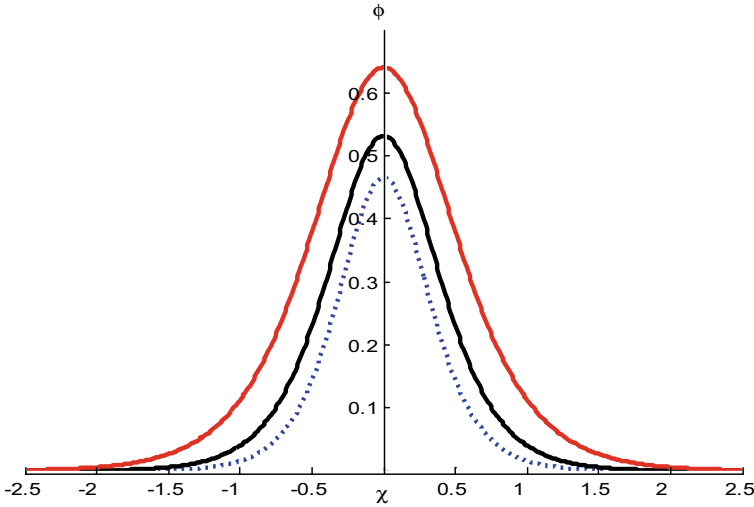


**Fig. 4** Variation of compressive soliton wave structure for different values of  $\alpha_e$  and  $\alpha_p$ , with  $\mu_i = 0.3$ ,  $\sigma_{pe} = 0.1$ ,  $\mu_p = 0.2$ ,  $n = 0.6$ ,  $U = 0.9$ ,  $\Omega_i = 0.5$  and  $\omega_{pi} = 1.4$ . Blue (dotted) curve corresponds to  $\alpha_e = 0.01$  and  $\alpha_p = 0.03$ ; black (solid) curve corresponds to  $\alpha_e = 0.04$  and  $\alpha_p = 0.06$ ; red (solid) curve corresponds to  $\alpha_e = 0.07$  and  $\alpha_p = 0.09$

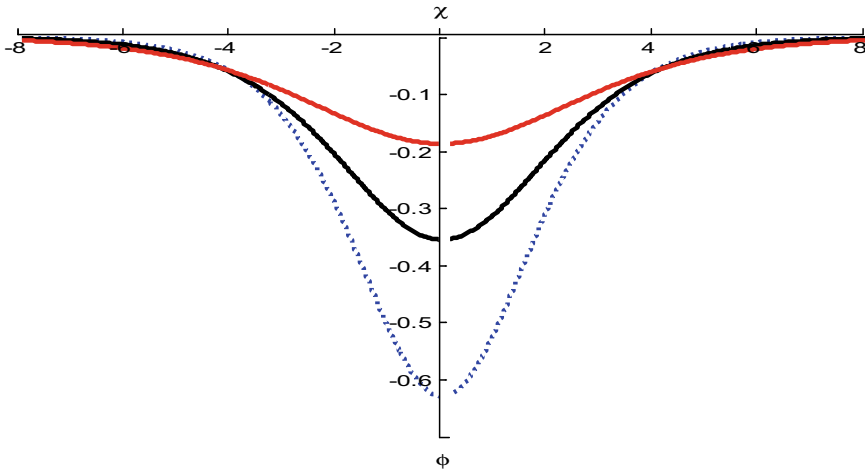


**Fig. 5** Variation of rarefactive soliton structure for different values of  $\alpha_e$  and  $\alpha_p$ , with  $\mu_i = 1.8$ ,  $\mu_p = 0.2$ ,  $\sigma_{pe} = 0.1$ ,  $n = 0.6$ ,  $U = 0.9$ ,  $\Omega_i = 0.5$  and  $\omega_{pi} = 1.4$ . Blue (dotted) curve corresponds to  $\alpha_e = 0.01$  and  $\alpha_p = 0.03$ ; black (solid) curve corresponds to  $\alpha_e = 0.04$  and  $\alpha_p = 0.06$ ; red (solid) curve corresponds to  $\alpha_e = 0.07$  and  $\alpha_p = 0.09$

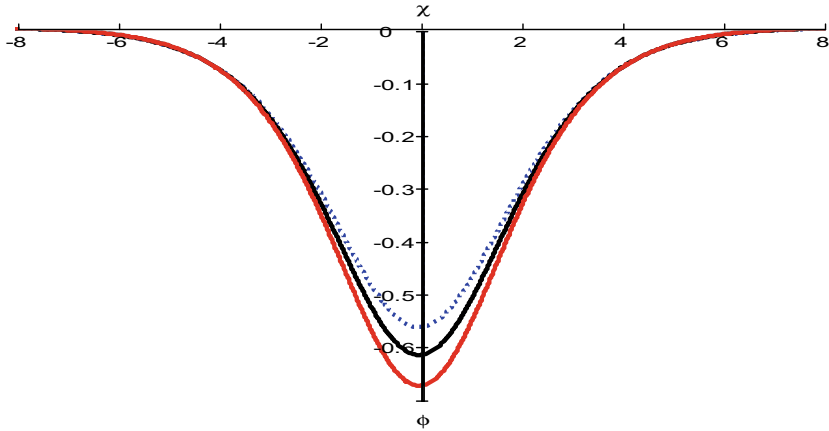


**Fig. 6** Variation of rarefactive soliton structure for different values of  $\mu_p$ , with  $\mu_i = 1.8$ ,  $\sigma_{pe} = 0.1$ ,  $n = 0.6$ ,  $U = 0.9$ ,  $\Omega_i = 0.5$  and  $\omega_{pi} = 1.4$ ,  $\alpha_e = 0.05$  and  $\alpha_p = 0.06$ . Blue (dotted) curve corresponds to  $\mu_p = 0.1$ ; black (solid) curve corresponds to  $\mu_p = 0.5$  and; red (solid) curve corresponds to  $\mu_p = 0.9$

We hope these results will be incredibly helpful in both space and laboratory plasmas, where solitary wave propagation is quite useful.

## References

1. Kamalam, T., Ghosh, S.S.: Ion acoustic super solitary waves in a magnetized plasma. *Phys. Plasmas* **25**, 122302 (2018)
2. Salmanpoor, H., Sharifian, M., Gholipour, S., Zarandi, M.B., Shokri, B.: Oblique propagation of solitary waves in weakly relativistic magnetized plasma with kappa distributed electrons in the presence of negative ions. *Phys. Plasmas* **25**, 032102 (2018)
3. Sultana, S., Islam, S., Mamun, A.A., Schlickeiser, R.: Oblique propagation of ion-acoustic solitary waves in a magnetized plasma with electrons following a generalized distribution function. *Phys. Plasmas* **26**, 012107 (2019)
4. Debnath, D., Bandyopadhyay, A., Das, K.P.: Ion acoustic solitary structures in a magnetized nonthermal dusty plasma. *Phys. Plasmas* **25**, 033704 (2018)
5. Washimi, H., Taniuti, T.: Propagation of ion-acoustic solitary waves of small amplitude. *Phys. Rev. Lett.* **17**, 996 (1996)
6. Obregon, M.A., Stepanyants, Y.A.: Oblique magneto-acoustic solitons in a rotating plasma. *Phys. Lett. A* **249**, 315–323 (1998)
7. Mamun, A.A., Shukla, P.K.: Spherical and cylindrical dust acoustic solitary waves. *Phys. Lett. A* **290**, 173–175 (2001)
8. Huang, G., Velarde, M.G.: Head-on collision of two concentric cylindrical ion acoustic solitary waves. *Phys. Rev. E* **53**, 2988–2991 (1996)
9. Schuck, P.W., Bonnell, J.W., Pincon, J.-L.: Properties of lower hybrid solitary structures: a comparison between space observations, a laboratory experiment, and the cold homogeneous plasma dispersion relation. *J. Geophys. Res.* **109**, A01310 (2004)

10. El-Labany, S.K., Sabry, R., El-Taibany, W.F., Elghmaz, E.A.: Propagation of three-dimensional ion-acoustic solitary waves in magnetized negative ion plasmas with nonthermal electrons. *Phys. Plasmas* **17**, 042301 (2010)
11. Seadawy, A.R.: Three-dimensional nonlinear modified Zakharov-Kuznetsov equation of ion-acoustic waves in a magnetized plasma. *Comput. Math. Appl.* **71**, 201–212 (2016)
12. Biswas, A., Zerrad, E.: Solitary wave solution of the Zakharov-Kuznetsov equation in plasmas with power law nonlinearity. *Nonlinear Anal. RWA* **11**, 3272–3274 (2010)
13. Li, B., Chen, Y., Zhang, H.: Exact travelling wave solutions for a generalized Zakharov-Kuznetsov equation. *Appl. Math. Comput.* **146**, 653–666 (2003)
14. El-Taibany, W.F., El-Bedwehy, N.A., El-Shamy, E.F.: Three-dimensional stability of dust-ion acoustic solitary waves in a magnetized multicomponent dusty plasma with negative ions. *Phys. Plasmas* **18**, 033703 (2011)
15. Mandi, L., Mondal, K.K., Chatterjee, P.: Analytical solitary wave solution of the dust ion acoustic waves for the damped forced modified Korteweg-de Vries equation in  $q$ -nonextensive plasmas. *Eur. Phys. J. Special Topics* **228**, 2753–2768 (2019)
16. Pakzad, H.R.: Ion acoustic solitary waves in plasma with nonthermal electron and positron. *Phys. Lett. A* **373**, 847–850 (2009)
17. Dev, A.N., Deka, M.K., Kalita, R.K., Sarma, J.: Effect of non-thermal electron and positron on the dust ion acoustic solitary wave in the presence of relativistic thermal magnetized ions. *Eur. Phys. J. Plus* **135**, 843 (2020)
18. Chawla, J.K., Singhadiya, P.C., Tiwari, R.S.: Ion-acoustic waves in magnetised plasma with nonthermal electrons and positrons. *Pramana J. Phys.* **94**, 13 (2020)
19. Seadawy, A.R., Lu, D.: Ion acoustic solitary wave solutions of three-dimensional nonlinear extended Zakharov-Kuznetsov dynamical equation in a magnetized two-ion-temperature dusty plasma. *Results Phys.* **6**, 590–593 (2016)

# Maxwellian Multicomponent Dusty-Plasma with Fluctuating Dust Charges



Ridip Sarma 

**Abstract** By employing a method known as  $\left(\frac{G'}{G}\right)$  expansion method, we rekindle our study on the existences of soliton propagation in a complex plasma consisting of Maxwellian electrons, negative ions, positive ions and positrons, in the presence of dust charge fluctuation. The study involves the augmentation of KdV Equation and then Burger Equation derivable by usual reductive perturbation technique. In this paper we expect to evaluate some important observations which could be of interest in the scientific community. We have investigated our observations in the context of Auroral region, radial spokes of Saturn's ring system and Solar F Corona region.

**Keywords** Maxwellian multicomponent plasma · Dust charge variation · Nonlinear waves · Soliton and shock dynamics ·  $G'/G$  method · Space plasmas

## 1 Introduction

The presence of negative ions in a plasma has been studied in a number of papers. We mention here some of these papers. Tagare and Reddy [1] investigated the ionic temperature effect on ion-acoustic solitons in a warm plasma consisting of positive ions and negative ions and non-isothermal electrons on the basis of a modified KdV equation derived by using the reductive perturbation method. Nakamura et al. [2] experimentally investigated Ion–Acoustic waves in a multicomponent plasma with negative ions. Earlier D'Angelo et al. [3] studied theoretically ion-acoustic waves in a multicomponent plasma with negative ions.

Mamun and Shukla [4] studied the role of negative ions on the charging of dust grains. They have considered two models for negative ions: streaming negative ions and Boltzmannian negative ion distribution. They have found that the effects of negative ion number density, negative ion charge and negative ion streaming speed,

---

R. Sarma (✉)

Department of Mathematics, Assam Don Bosco University, Tapesia, Sonapur, Assam 782402, India

e-mail: [ridip.sarma@dbuniversity.ac.in](mailto:ridip.sarma@dbuniversity.ac.in)

significantly impact the dust grain charge. Oohura and Hatakeyama [5] have experimentally studied in the laboratory certain aspects of pair-ion ( $C_{60}^+$  and  $C_{60}^-$ ) plasma. Adhikary et al. [6] experimentally studied in a dusty plasma, the propagation characteristics of rarefactive ion-acoustic solitary waves containing negative ions. They compared their experimental results with the theoretical results of KdV-Burgers equation. In a later paper, Adhikary [7] studied a dusty plasma composed of Boltzmannian distributed singly charged positive ions, singly charged negative ions, electrons, positrons and cold static negatively charged dust particles. He took into account viscous effect and found that viscosity plays an important role in dissipation of the Dust Ion Acoustic (DIA) shock wave propagating through it. In another paper, Adhikary et al. [8] presented an investigation of the properties of Dust Acoustic (DA) solitary wave propagation under the effect of non-thermal ions and trapped electrons in an adiabatic dusty plasma. The plasma is composed of electrons, singly charged positive and negative ions and charged dust particles. They derived a modified KdV equation and obtained a stationary analytical solution. From the study of the solution they observed that both the ions in the dusty plasma play a key role for the formation of both rarefactive and compressive DA solitary waves and that the ion concentration impacts the transformation of negative to positive potentials of the waves. Haider and Nahar [9] studied the nonlinear dynamics of Dust Ion Acoustic (DIA) solitary and shock waves in a plasma composed of positive and negative ions, oppositely charged stationary dust particles and superthermal electrons. There are many researchers [10–12], who studied four component dusty plasma.

We consider in this work a four-component plasma model with negatively charged dust. The constituents are negatively charged dust particles under the influence of Maxwellian distributed positive and negative ions, electrons and positrons. The manuscript is ordered as follows: Sect. 2 illustrates the basic equations governing the plasma dynamics. Sect. 3 describes the derivation of nonlinear equations. To study the existence and propagation of solitons and shocks, a  $\left(\frac{G'}{G}\right)$  method [13] has been used. The speciality of the method is it is concise and straightforward and can be used to solve evolutionary equations directly without any requirement for initial/boundary conditions or initial trial function at the outset. Graphical representation includes specific choice of typical parameters of various astrophysical regions playing a vital role in different domains of cosmic dust-laden plasmas. Results and Discussions are in Sect. 4 analysing a comparative study of the different waves in various plasma spaces, followed by Conclusions in Sect. 5.

## 2 Basic Model Equations Governing Plasma Dynamics

The basic equations governing our plasma dynamics are written as [13, 14]

### Equation of continuity

$$\frac{\partial n_d}{\partial t} + \nabla \cdot (n_d u_d) = 0 \quad (1)$$

### Equation of motion

$$\frac{\partial n_d}{\partial t} + \nabla \cdot (n_d u_d) = 0 \quad (2)$$

along with the Poisson equation

$$\nabla^2 \varphi = -4\pi \sum q_\beta n_\beta z_\beta \quad (3)$$

where  $\beta = i, n, e, p, d$  represents positive ions, negative ions, electrons, positrons and dust particles respectively.  $q_\beta$  represents  $+e$  for positive ion, positron and  $-e$  for an electron, negative ion and a dust particle. Here, dust particle's mass is represented by  $m_d$ , velocity by  $u_d$  and the charge density by  $n_d$ . Here,  $u_d$  is normalised by  $c_i = (\frac{k_B T_{e0}}{m_i})^{\frac{1}{2}}$  ( $k_B$  represents Boltzmannian constant) and  $n_\beta$  represents the density of charge number, normalized with the equilibrium value  $n_{\beta 0}$ , where the equilibrium state is represented by suffix 0. The positive ion, negative ion, positron and the dust charge numbers are represented as  $z_{i,n,p,d}$ , where  $z_d$  is the number of electrons residing on a dust particle.  $\varphi$  is the electrostatic potential normalised by  $(\frac{k_B T_{e0}}{4\pi e^2 n_{i0}})$ . The time variable  $t$  and space variable  $x$  are normalised respectively by  $\omega_{pi}^{-1} = (\frac{m_i}{4\pi e^2 n_{i0}})$  and  $D = (\frac{k_B T_{e0}}{4\pi e^2 n_{i0}})^{\frac{1}{2}}$ , known as inverse of plasma frequency and Debye length respectively.

We perturb the parameters as  $f_\beta = f_{\beta 0} + \tilde{f}_\beta$  ( $f = u, n, z$ ), where the corresponding equilibrium value is  $f_{\beta 0}$  and the perturbed value is  $\tilde{f}_\beta$ . We assume that electrons and ions are Maxwellian, and therefore we can write the Eq. (3) as

$$\nabla^2 \varphi = \alpha \varphi + \alpha' \varphi^2 + 4\pi e (z_{d0} \tilde{n}_d + \tilde{z}_d n_{d0} + \tilde{z}_d \tilde{n}_d) \quad (4)$$

where

$$\alpha = \frac{4\pi e^2}{K_B} \left( \frac{n_{e0}}{T_e} + \frac{n_{i0} z_i^2}{T_i} + \frac{n_{p0}}{T_p} + \frac{n_{n0} z_n^2}{T_n} \right) = (1/\lambda_D^2)$$

$$\text{and } \alpha' = \frac{2\pi e^3}{K_B^2} \left( \frac{n_{e0}}{T_e^2} - \frac{n_{i0} z_i^3}{T_i^2} + \frac{n_{n0} z_n^3}{T_n^2} - \frac{n_{p0}}{T_p^2} \right)$$

where  $T_{i,e,n,p}$  represents the temperatures of positive ions, electrons, negative ions and positrons respectively.

When we immerse the dust particles in a plasma, the basic charging equation is written as

$$\frac{dQ_d}{dt} = \sum I_\gamma, \gamma = i, e, n, p \quad (5)$$

where  $I_\gamma$  is the current [15–17] generated on the dust grains by charged particle  $\gamma$  given by

$$I_i = \pi a^2 e \sqrt{\frac{8T_i}{\pi m_i}} n_i \left(1 - \frac{eq_d}{aT_i}\right)$$

$$I_n = -\pi a^2 e \sqrt{\frac{8T_n}{\pi m_n}} n_n \left(1 + \frac{eq_d}{aT_n}\right)$$

$$I_e = -\pi a^2 e \sqrt{\frac{8T_e}{\pi m_e}} n_e \exp\left(\frac{eq_d}{aT_e}\right)$$

and

$$I_p = \pi a^2 e \sqrt{\frac{8T_p}{\pi m_p}} n_p \exp\left(-\frac{eq_d}{aT_p}\right)$$

Now following Jana et al. [15], and applying on our current model, we obtain

$$\frac{dQ_d}{dt} + \tilde{Q}_d = |I_{e0}| \left( \frac{\tilde{n}_i}{n_{i0}} + \frac{\tilde{n}_p}{n_{p0}} - \frac{\tilde{n}_n}{n_{n0}} - \frac{\tilde{n}_e}{n_{e0}} \right) \quad (6)$$

where

$$Q_d = Q_{d0} + \tilde{Q}_d \quad (7)$$

with  $Q_{d0}$  and  $\tilde{Q}_d$  considered at equilibrium to be the dust charges and perturbed states respectively. Also, we have.

$$\eta = \left( |eI_{e0}|/C \right) \left( \frac{1}{k_B T_e} + \frac{1}{k_B T_p} + \frac{1}{\omega_{i0}} + \frac{1}{\omega_{n0}} \right), \quad (8)$$

where  $C$  is the capacitance of the dust grains,  $\omega_{i0} = k_B T_i - e\varphi_{f0}$  and  $\omega_{p0} = k_B T_p - e\varphi_{f0}$  where  $\varphi_{f0}$  is the floating potential.

Substituting in Eq. (6) the values of Eqs. (7) and (8), we get

$$\frac{\partial \tilde{z}_d}{\partial t} + \tilde{z}_d = P_1 \varphi + P_2 \varphi^2 \quad (9)$$

with

$$P_1 = |I_{e0}|/k_B \left( \frac{z_i}{T_i} + \frac{z_n}{T_n} + \frac{1}{T_e} + \frac{1}{T_p} \right) \tag{10}$$

$$P_2 = |I_{e0}|e/k_B^2 \left( \frac{1}{T_e^2} + \frac{z_n^2}{T_n^2} - \frac{1}{T_p^2} - \frac{z_i^2}{T_i^2} \right) \tag{11}$$

### 3 Nonlinear Wave Equations: Derivation and Solution

#### 3.1 Korteweg De Vries Equation

Following Washimi and Tanuiti [18], we apply the reductive perturbation method to the basic equations for studying soliton dynamics. The stretching coordinates of the model are:

$$\zeta = \sqrt{\epsilon}(x - v_0t), \tau = \sqrt[3]{\epsilon} t \tag{12}$$

where,  $\epsilon$  measures the small expansion parameter.

We use the perturbed expansion:

$$(S = ud, nd, \varphi) = \sum_{N=0}^{\infty} \epsilon^N S^{(N)}, \tag{13}$$

having  $S^{(0)} = 0$  for  $\varphi$  and  $u_d$ .

For the first order in  $\epsilon$ , we use reductive perturbation scheme and stretching coordinates in the basic equations to get the following relations.

$$u_{d,x}^{(1)} = -\frac{(ez_{d0})}{(m_d v_0)} \varphi^{(1)}, \tag{14}$$

$$n_d^{(1)} = -\frac{\left(\alpha + \frac{P}{\eta}\right)}{4\pi e z_{d0}} \varphi^{(1)}, \tag{15}$$

$$z_d^{(1)} = \frac{P_1}{-1} \varphi^{(1)} \tag{16}$$

Now, the result for phase velocity comes out to be

$$v_0^2 = \omega_{pd}^2 \left( \alpha + \frac{P}{\eta} \right)^{-1} \tag{17}$$



where  $\omega_{pd}$  is the dust charge frequency defined as

$$\omega_{pd} = (4\pi e^2 z_{d0}^2 n_{d0} / m_d)^{\frac{1}{2}} \quad (18)$$

$$P = 4\pi e n_{d0} P_1 \quad (19)$$

The subsequent higher order term in  $\epsilon$  gives the following equations

$$\frac{\partial n_d^{(1)}}{\partial \tau} - v_0 \frac{\partial n_d^{(2)}}{\partial \zeta} + n_{d0} \frac{\partial u_{d,x}^{(2)}}{\partial \zeta} + \frac{\partial (n_d^{(1)} u_{d,x}^{(1)})}{\partial \zeta} = 0 \quad (20)$$

$$\frac{\partial \vec{u}_d^{(1)}}{\partial \tau} - v_0 \frac{\partial \vec{u}_d^{(2)}}{\partial \zeta} + u_{d,x}^{(1)} \frac{\partial \vec{u}_{d,x}^{(1)}}{\partial \zeta} = \frac{e}{m_d} (z_{d0} \frac{\partial \varphi^{(2)}}{\partial \zeta} \hat{x} + z_d^{(1)} \frac{\partial \varphi^{(1)}}{\partial \zeta} \hat{x}) \quad (21)$$

where along x-direction, the unit vector is  $\hat{x}$ .

$$\frac{\partial^2 \varphi^{(1)}}{\partial \zeta^2} = \alpha \varphi^{(2)} + \alpha' (1) 2 + 4\pi e (z_{d0} n_d^{(2)} + z_d^{(2)} n_{d0} + z_d^{(1)} n_d^{(1)}) \quad (22)$$

$$z_d^{(2)} = \frac{P_1}{-} \varphi^{(2)} + \frac{P_2}{-} (\varphi^{(1)})^2 \quad (23)$$

Applying the results of the order  $\epsilon$  from Eqs. (14) to (17) in Eqs. (20) to (23) along with some mathematical simplifications, the K-dV equation is obtained as

$$\frac{\partial \varphi^{(1)}}{\partial \tau} + A \varphi^{(1)} \frac{\partial \varphi^{(1)}}{\partial \zeta} + B \frac{\partial^3 \varphi^{(1)}}{\partial \zeta^3} = 0 \quad (24)$$

where the coefficients A and B are

$$A = \frac{3v_0}{8\pi e z_{d0} n_{d0}} \frac{P}{-} - \left( \alpha' + \frac{P'}{-} \right) \frac{v_0^3}{\omega_{pd}^2} - \frac{3e z_{d0}}{2m_d v_0} \quad (25)$$

$$B = \frac{v_0^3}{2\omega_{pd}^2} \quad (26)$$

where

$$P' = 4\pi e n_{d0} P_2$$

Applying the  $(\frac{G'}{G})$  method, and the transformation  $\varphi^{(1)}(\zeta, \tau) = \psi(\xi)$ , with  $\xi = \zeta - V\tau$  where the frame is moving with the velocity  $V$  having boundary conditions

$$(i) \varphi^{(1)} \rightarrow 0, (ii) \frac{d\varphi^{(1)}}{d\xi} \rightarrow 0, (iii) \frac{d^2\varphi^{(1)}}{d\xi^2} \rightarrow 0 \text{ as } |\xi| \rightarrow \infty \quad (27)$$

enabling us to obtain the solution of the KdV equation as.

$$\psi(\xi) = \frac{3V}{A} \operatorname{sech}^2\left(\frac{\sqrt{V}}{2\sqrt{B}}\xi\right), \text{ where } \xi = \zeta - V\tau$$

$$\text{Or } \psi(\xi) = \psi_m \operatorname{sech}^2\left(\frac{\xi}{\psi_w}\right), \text{ where } \psi_m = \frac{3V}{A} \text{ and } \psi_w = 2\sqrt{\frac{B}{V}} \quad (28)$$

We leave out two other solutions yielded by the  $(\frac{G'}{G})$  method as they are not relevant to the soliton character.

The coefficients A and B of the solution (Eq. 28) are functions of plasma parameters. Now to study the nature of the soliton, we consider some values of plasma parameters [19] as reported in Auroral region, Saturn's radial spokes and Solar F Corona astrophysical region.

It has to be noted that the following expressions are considered while writing the relation Eq. (25):

$$\begin{aligned} \frac{P}{-} &= 4\pi r_d n_{d0} \left[ \frac{(T_i + T_e + T_n + T_p) T_{eff}}{(T_i + T_n)(T_e + T_p + T_{eff})} \right] \\ \frac{P'}{k_B} &= \frac{4\pi r_d n_{d0}}{k_B} \left[ \frac{T_{eff}((T_i + T_n)^2 - (T_e + T_p)^2)}{(T_e + T_p)(T_i + T_n)^2((T_e + T_p) + T_{eff})} \right] \\ T_{eff} &= (T_i + T_n) - \frac{e^2 Z_d}{K_B r_d} \end{aligned}$$

where the values of  $v_0$ ,  $\alpha$  &  $\alpha'$  have been used.

### 3.2 Burgers Equation

To study the propagation of shock waves, we take the help of pair of stretching coordinates,  $\zeta = \epsilon(x - v_0 t)$  and  $\tau = \epsilon^2 t$ , to the same set of governing Eqs. (1) to (3) and equating first order in  $\epsilon$ , we obtain:

$$u_{d,x}^{(1)} = -\frac{(e z_{d0})}{(m_d v_0)} \varphi^{(1)}, \quad (29)$$

$$n_d^{(1)} = -\frac{\left(\alpha + \frac{e}{\eta}\right)}{4\pi e z_{d0}} \varphi^{(1)}, \quad (30)$$

$$z_d^{(1)} = \frac{P_1}{\omega_{pd}^2} \varphi^{(1)} \tag{31}$$

Now, the result for phase velocity comes out to be

$$v_0^2 = \omega_{pd}^2 \left( \alpha + \frac{P}{\omega_{pd}^2} \right)^{-1} \tag{32}$$

with the dust plasma frequency defined as

$$\omega_{pd} = (4\pi e^2 z_{d0}^2 n_{d0} / m_d)^{\frac{1}{2}} \tag{33}$$

and

$$P = 4\pi e n_{d0} P_1 \tag{34}$$

However, for the next higher order of  $\epsilon$ , we get-

$$\frac{\partial n_d^{(1)}}{\partial \tau} - v_0 \frac{\partial n_d^{(2)}}{\partial \zeta} + n_{d0} \frac{\partial u_{d,x}^{(2)}}{\partial \zeta} + \frac{\partial (n_d^{(1)} u_{d,x}^{(1)})}{\partial \zeta} = 0 \tag{35}$$

$$\frac{\partial \vec{u}_d^{(1)}}{\partial \tau} - v_0 \frac{\partial \vec{u}_d^{(2)}}{\partial \zeta} + u_{d,x}^{(1)} \frac{\partial \vec{u}_d^{(1)}}{\partial \zeta} = \frac{e}{m_d} \left( z_{d0} \frac{\partial \varphi^{(2)}}{\partial \zeta} \hat{x} + z_d^{(1)} \frac{\partial \varphi^{(1)}}{\partial \zeta} \hat{x} \right) \tag{36}$$

where along x-direction,  $\hat{x}$  is the unit vector.

$$\frac{\partial^2 \varphi^{(1)}}{\partial \zeta^2} = \alpha \varphi^{(2)} + \alpha' (\varphi^{(1)})^2 + 4\pi e (z_{d0} n_d^{(2)} + z_d^{(2)} n_{d0} + z_d^{(1)} n_d^{(1)}) \tag{37}$$

$$z_d^{(2)} = \frac{P_1}{\omega_{pd}^2} \varphi^{(2)} + \frac{P_2}{\omega_{pd}^2} (\varphi^{(1)})^2 + \frac{v_0}{\omega_{pd}^2} \frac{\partial z_d^{(1)}}{\partial \zeta} \tag{38}$$

Applying the perturbed relations, with some mathematical simplifications, we derive the Burgers equation

$$\frac{\partial \varphi^{(1)}}{\partial \tau} + A \varphi^{(1)} \frac{\partial \varphi^{(1)}}{\partial \zeta} - C \frac{\partial^2 \varphi^{(1)}}{\partial \zeta^2} = 0 \tag{39}$$

where

$$A = \frac{3v_0}{8\pi e z_{d0} n_{d0}} \frac{P}{\omega_{pd}^2} - \left( \alpha' + \frac{P'}{\omega_{pd}^2} \right) \frac{v_0^3}{\omega_{pd}^2} - \frac{3e z_{d0}}{2m_d v_0} \tag{40}$$

$$C = \frac{v_0^4}{2w_{pd}^2} \frac{P}{2} \tag{41}$$

where  $P' = 4\pi en_{d0} P_2$ .

Considering the transformation  $\varphi(\zeta, \tau) = \varphi(\xi)$ , where  $\xi = \zeta - V\tau$  and applying the  $\left(\frac{G'}{G}\right)$  method, we obtain the shock wave solution

$$\varphi(\xi) = -\varphi_m \left(1 - \tanh\left(\frac{\xi}{\varphi_w}\right)\right) \tag{42}$$

Here,  $\varphi_m = \frac{V}{A}$ ,  $\varphi_w = \frac{2C}{V}$  represents the amplitude and width of the shock structure respectively.

Now to study the nature of the soliton, we consider some values of plasma parameters [19] as reported in Auroral region, Saturn’s radial spokes and Solar F Corona astrophysical region.

We use the following expressions to write the Eq. (40),

$$\begin{aligned} \frac{P}{-} &= 4\pi r_d n_{d0} \left[ \frac{(T_i + T_e + T_n + T_p) T_{eff}}{(T_i + T_n)(T_e + T_p + T_{eff})} \right] \\ \frac{P'}{-} &= \frac{4\pi r_d n_{d0}}{k_B} \left[ \frac{T_{eff} \left( (T_i + T_n)^2 - (T_e + T_p)^2 \right)}{(T_e + T_p)(T_i + T_n)^2 \left( (T_e + T_p) + T_{eff} \right)} \right] \end{aligned}$$

$T_{eff} = (T_i + T_n) - \frac{e^2 Z_d}{K_B r_d}$  have been used.

## 4 Results and Discussions

Figure 1 exhibits plotting of the Auroral region of Ionosphere where the ion (positive and negative) temperature is taken as (I)  $T_{i,n} = 2 \times 10^3 K$ , (II)  $T_{i,n} = 4 \times 10^3 K$  and (III)  $T_{i,n} = 5 \times 10^3 K$ . We consider the temperature of electron and positron to be fixed at  $T_{e,p} = 10^4 K$ . Figure 1a exhibits nonlinear coefficient A with varying dust density  $n_{d0}$ . We find that at lower density  $n_{d0}$ , there is fast increase in A, then at higher density slows down. Secondly, the rate of slowing down of curve (III) is more than curves (I) and (II) so that curve (III) intersects curve (II) at P and gradually comes closer to curve (I) and may intersect it at a very high density. Thirdly, the rarefactive and compressive regions show up at all the temperatures.

Figure 1b exhibits shock waves, showing that nonlinear term A drops fastly at lower density and then at higher density slows down. However, the curve (I) goes farthest down intersecting the curve (II) at Q and the curve (III) at R. Secondly, the curve (II) slows down more than the curve (III) and meets it. Thirdly, in the density

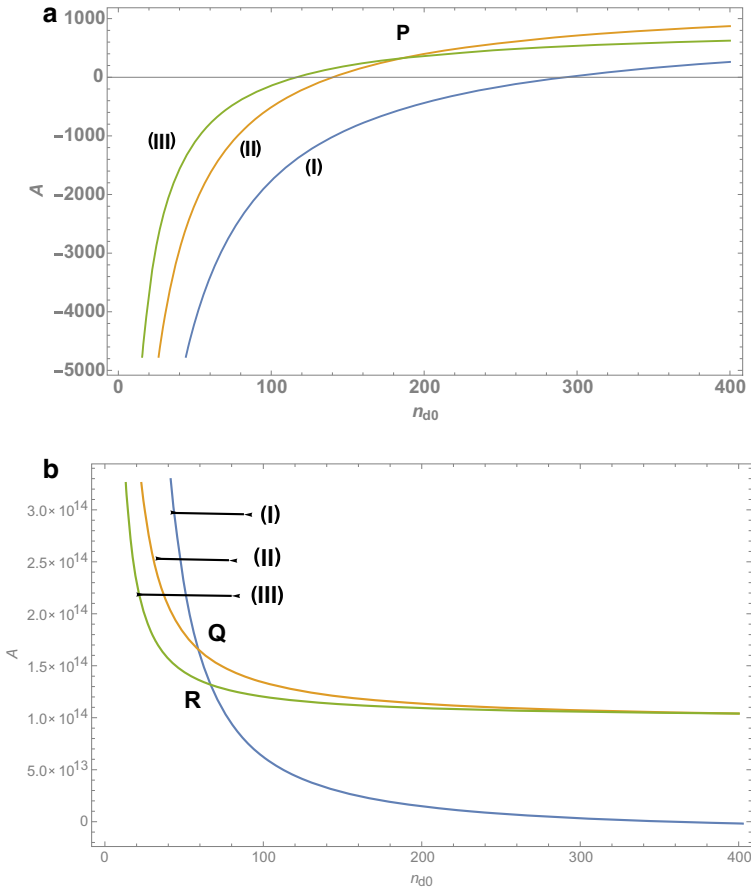


**Fig. 1** **a** Plotting of coefficient of nonlinearity  $A$  with varying density of dust  $n_{d0}$  for solitons found in the Auroral region of Ionosphere where the positive and negative ions temperature is taken as (I)  $T_{i,n} = 3 \times 10^3 K$ , (II)  $T_{i,n} = 5 \times 10^3 K$  and (III)  $T_{i,n} = 7 \times 10^3 K$ . We have considered  $T_{e,p} = 10^4 K$  as the value for electron and positron temperature. **b** Plotting of coefficient of nonlinearity  $A$  with varying density of dust  $n_{d0}$  for shocks found in the Auroral region of Ionosphere where the positive and negative ions temperature is taken as (I)  $T_{i,n} = 3 \times 10^3 K$ , (II)  $T_{i,n} = 5 \times 10^3 K$  and (III)  $T_{i,n} = 7 \times 10^3 K$ . We have considered  $T_{e,p} = 10^4 K$  as the value for electron and positron temperature.

range under consideration, remembering the comment after Eq. (42), (II) and (III) are in the rarefactive region but (I) is mostly in the rarefactive region but just dips into the compressive region at the higher density end.

If we compare Fig. 1a, b we first observe that with increase in  $n_{d0}$ ,  $A$  rises for solitons and on the other hand  $A$  drops with  $n_{d0}$  in case of shock waves. We also observe that there is some similar character like at lower density value,  $A$  varies fast but at higher values of density, slows down. In Fig. 1a, all the curves are partly in

the compressive region and partly in the rarefactive region, in Fig. 1b, according to the comment after Eq. (42), the curve (II) and curve (III) are in the rarefactive region but the curve (I) is mostly in the rarefactive region and just dips in the compressive region at the higher density end. Finally, intersections of curves occur for both types of waves.

Figure 2 exhibits the Saturn’s radial spokes where the pair of ion (positive and negative) temperature is taken as (I)  $T_{i,n} = 1 \times 10^3 K$ , (II)  $T_{i,n} = 2 \times 10^3 K$ , and

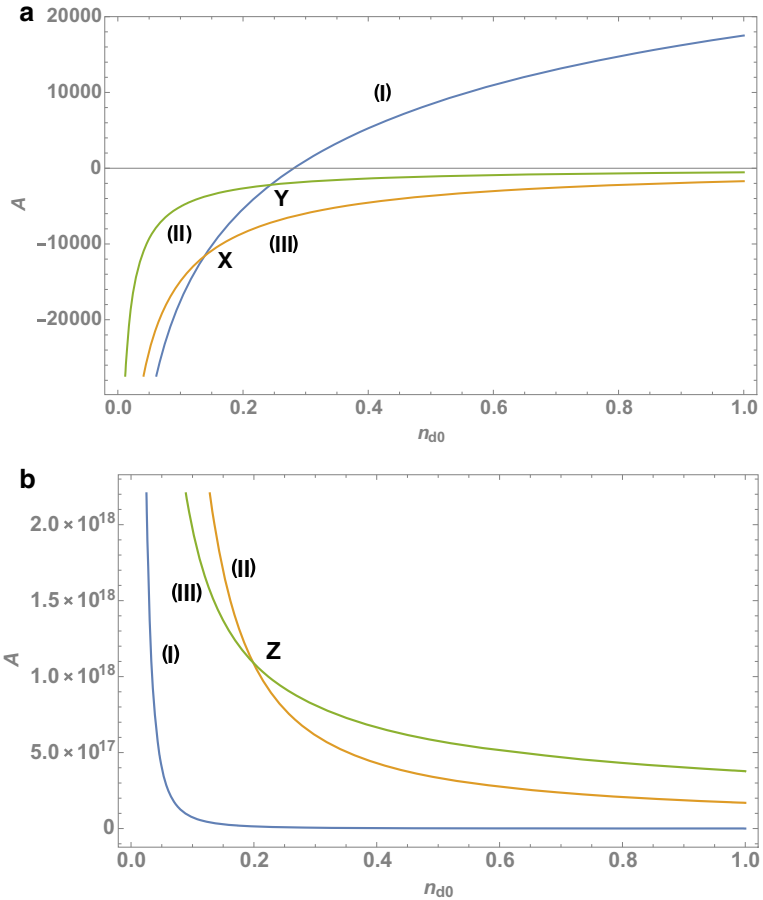


**Fig. 2 a** Plotting of coefficient of nonlinearity  $A$  with varying density of dust  $n_{d0}$  for solitons found in the Saturn’s radial spokes where the positive and negative ions temperature is taken as (I)  $T_{i,n} = 1 \times 10^3 K$ , (II)  $T_{i,n} = 2 \times 10^3 K$  and (III)  $T_{i,n} = 4 \times 10^3 K$ . We have considered  $T_{e,p} = 2 \times 10^4 K$  as the value for electron and positron temperature. **b** Plotting of coefficient of nonlinearity  $A$  with varying density of dust  $n_{d0}$  for shocks found in the Saturn’s radial spokes where the positive and negative ions temperature is taken as (I)  $T_{i,n} = 1 \times 10^3 K$ , (II)  $T_{i,n} = 2 \times 10^3 K$  and (III)  $T_{i,n} = 4 \times 10^3 K$ . We have considered  $T_{e,p} = 2 \times 10^4 K$  as the value for electron and positron temperature.

(III)  $T_{i,n} = 4 \times 10^3 K$ . We have considered  $2 \times 10^4 K$  as fixed electron and positron temperature. We can observe for Fig. 2a that for lower density A rise fast and and slows down at higher values of density. However, the curve (I) rises higher than the curve (II) and curve (III) so that the curve (I) intersects the curve (II) at X and the curve (III) at Y. Secondly, the curve (I) has both rarefactive and compressive regions. But the curve (II) and curve (III) have only the rarefactive region.

In Fig. 2b for shock waves, at lower density A falls fast and at higher density slows down. However, the curve (I) falls faster than the curve (II) and curve (III) and then curve (I) remains unchanged with change of density. Secondly, the curve (II) falls faster than curve (III) so that curve (II) intersects curve (III) at Z. Thirdly, as per the comment after Eq. (42), the curve (II) and curve (III) have only the rarefactive region but the curve (I) lies first in the rarefactive region and then in the borderline between compressiveness and rarefactivity.

If we compare Fig. 2a, b we first observe that with increase in  $n_{d0}$ , A rises for solitons and on the other hand A drops with  $n_{d0}$  in case of shock waves. We also observe that there is some similar character like at lower density value, A varies fast but at higher values of density, slows down. Both the curve (II) and (III) are in the rarefactive region (vide comment after Eq. (42)) in both figures. But whereas the curve (I) has both compressive and rarefactive regions in Fig. 2a. the curve (I) is in the rarefactive region at lower density and then lies at the borderline between the rarefactivity and compressiveness.

In Fig. 3a, we choose the Solar F Corona region having the ion (positive and negative) temperature as (I)  $T_{i,n} = 2 \times 10^4 K$ , (II)  $T_{i,n} = 4 \times 10^4 K$ , (III)  $T_{i,n} = 8 \times 10^4 K$ . We consider the electron temperature and positron temperature to be fixed at  $T_{e,p} = 8 \times 10^5 K$ . For solitons all the curves (I), (II) and (III) slowly and steadily rise with no tendency to intersect. Secondly, corresponding to any dust density, (I) < (II) < (III). Thirdly, all the curves are in the rarefactive region.

Figure 3b exhibits shock waveform in the Solar F Corona region, the positive and negative ions temperature is taken as (I)  $T_{i,n} = 2 \times 10^4 K$ , (II)  $T_{i,n} = 4 \times 10^4 K$ , (III)  $T_{i,n} = 8 \times 10^4 K$ . We have fixed the electron and positron temperature as  $T_{e,p} = 8 \times 10^5 K$ . For shock waves, we note first that all the curves for (I), (II), and (III) at lower density falls fast and then at higher density slows down. Secondly, at higher density they show a tendency to come closer to one another and may intersect one another at still higher density. Thirdly, at any density, (II) > (I) > (III). Finally, according to the comment after Eq. (42), all the curves are in the rarefactive region.

We conclude with a comment on the points of intersection P, Q, R, X, Y, and Z in Figs. 1a, b and 2a, b. At such a point, say at P, corresponding to the same dust density which we call a “critical dust density”, we have (II) = (III) corresponding to two different temperatures. In other words, at this dust density, the electrostatic potential is the same. This seems to be an interesting role played by the charged dust density!

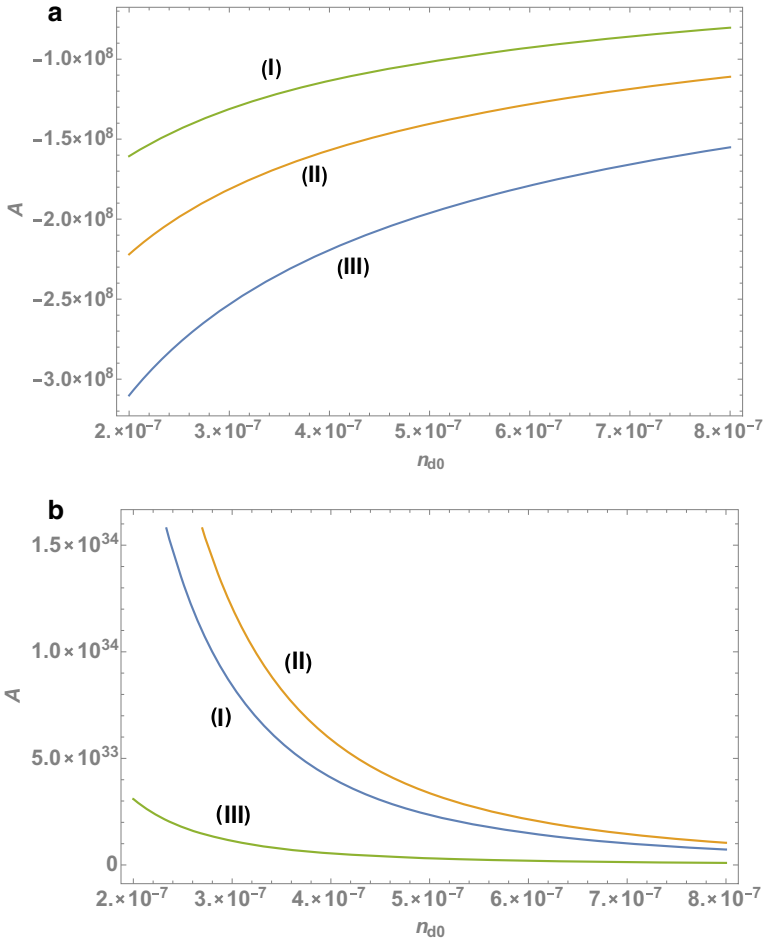


**Fig. 3** **a** Plotting of coefficient of nonlinearity  $A$  with varying density of dust  $n_{d0}$  for solitons found in the Solar Corona where the positive and negative ions temperature is taken as (I)  $T_{i,n} = 2 \times 10^4 K$ , (II)  $T_{i,n} = 4 \times 10^4 K$  and (III)  $T_{i,n} = 8 \times 10^4 K$ . We have considered  $T_{e,p} = 8 \times 10^5 K$  as the value for electron and positron temperature. **b** Plotting of coefficient of nonlinearity  $A$  with varying density of dust  $n_{d0}$  for shocks found in the Solar Corona where the positive and negative ions temperature is taken as (I)  $T_{i,n} = 2 \times 10^4 K$ , (II)  $T_{i,n} = 4 \times 10^4 K$  and (III)  $T_{i,n} = 8 \times 10^4 K$ . We have considered  $T_{e,p} = 8 \times 10^5 K$  as the value for electron and positron temperature.

## 5 Conclusion

In the present paper, we have conducted a systematic study of the effects of nonlinear wave dynamics and dust density in multicomponent plasma on the formation of solitons and shockwaves along with consideration of dusty plasma in different regions



and Boltzmann distributed electrons and ions. It is seen that compared to earlier observations, the presence of Maxwellian charges presents different natures of soliton. The present literature exhibited a plasma model to know the effect of Maxwellian force on nonlinear waves with the expectation of new findings. Here, in this paper, by employing reductive perturbation method and the unified method of  $\left(\frac{G'}{G}\right)$  expansion method we have derived the salient features of solitons and shockwaves. It is shown that for any dusty plasma model, there exists a critical dust density,  $n_{dc}$  at which it is not possible to obtain soliton like structures and at which the nonlinear coefficient becomes zero. It has been observed that at the neighbourhood of the critical dust density both compressive and rarefactive solitons grow in amplitude under the action of Maxwellian force exhibiting generation of high energy which in turn finds the phenomena of soliton radiation.

## References

1. Tagare, S.G., Reddy, R.V.: Effect of ionic temperature on ion-acoustic solitons in a two-ion warm plasma consisting of negative ions and non-isothermal electrons. *Plasma Phys. Control. Fus.* **29**(5), 671–676 (1987)
2. Nakamura, Y., Odagiri, T., Tsukabayashi, I.: Ion acoustic waves in a multicomponent plasma with negative ions. *Plasma Phys. Control. Fus.* **39**, 105–115 (1997)
3. D'Angelo, N.D., Goeler, S.V., Ohe, T.: Propagation and damping of ion waves in a plasma with negative ions. *Phys. Fluids* **9**, 1605–1606 (1966)
4. Mamun, A.A., Shukla, P.K.: Solitary potentials in cometary dusty plasmas. *Geophys. Res. Letts.* **29**(18), 1870–1873 (2002)
5. Oohura, W., Hatakeyama, R.: Basic studies of the generation and collective motion of pair-ion plasmas. *Phys. Plasmas* **14**, 055704–055710 (2007)
6. Adhikary, N.C., Deka, M.K., Bailung, H.: Observation of rarefactive ion acoustic solitary waves in dusty plasma containing negative ions. *Phys. Plasmas* **16**, 063701–063707 (2009)
7. Adhikary, N.C.: Effect of viscosity on dust-ion acoustic shock wave in dusty plasma with negative ions. *Phys. Lett. A* **376**, 1460–1464 (2012)
8. Sarma, R., Misra, A.P., Adhikary, N.C.: Nonlinear ion acoustic solitary waves in an electron positron ion plasma with relativistic positron beam. *Chin. Phys. B* **27**(10), 105207–105212 (2018)
9. Haider, M.M., Nahar, A.: Dust-ion-acoustic solitary and shock structures in multi-ion plasmas with nonthermal electrons, *Z. Naturforsch.* **72**(7), 627–635 (2017)
10. Ahmad, M., Ahmad, Z., Farooq, M., Gul, A.: Kinetic treatment of acoustic waves in a four component dusty plasma. *Cont. Plasma Phys.* **59**(3), 367–380 (2019)
11. Jahan, S., Mannan, A., Chowdhury, N.A., Mamun, A.A.: Kinetic treatment of acoustic waves in a four component dusty plasma. *Plasma Phys. Reports* **46**, 90 (2020)
12. Raghavi, K., Kavitha L.: Modulational instability analysis of four component dusty plasma system. *IEEE Trans. Plasma Sci.* <https://doi.org/10.1109/TPS.2021.3122447>
13. Das, G.C., Sarma, R.: New method for rekindling the nonlinear solitary waves in Maxwellian complex space plasma. *Phys. Plasmas* **25**, 043703–043711 (2018)
14. Sarma, R., Das, G.C., Das, R., Adhikary, N.C.: On the nonlinear solitary and shock waves in Maxwellian multicomponent space plasma. *Phys. Plasmas* **25**, 073704–073710 (2018)
15. Jana, M.R., Sen, A., Kaw, P.K.: Collective effects due to charge fluctuation dynamics in a dusty plasma. *Phys. Rev. E* **48**, 3930–3933 (1993)
16. Bhatt, J.R., Pandey, B.P.: Self consistent charge dynamics and collective modes in a dusty plasma. *Phys. Rev. E* **50**, 3980–3983 (1994)

17. Shukla, P.K., Mamun, A.A.: Introduction to dusty plasma physics. IOP, Bristol (2002)
18. Washimi, H., Tanuiti, T.: Propagation of ion acoustic solitary waves of small amplitude. *Phys. Rev. Lett.* **17**, 996–998 (1966)
19. Mendis, D.A.: Progress in the study of dusty plasmas. *Plasma Sources Sci. Tech.* **11A**, 219–228 (2002)

# Effect of Polarization Force on Dust-Acoustic Solitary and Rogue Waves in $(r, q)$ Distributed Plasma



Manveet Kaur , Sunidhi Singla , and Nareshpal Singh Saini 

**Abstract** In this investigation, dust-acoustic solitary and rogue waves are analysed by including the role of polarization force in a dusty plasma in the presence of ions obeying  $(r, q)$  distribution velocity. The  $(r, q)$  distributed ions lead to change in the expression of polarization force which subsequently modifies the nonlinear structures. Using reductive perturbation technique, the Kadomstev–Petviashvili equation and nonlinear Schrödinger equation (NLSE) are formulated. From the solution of KP equation, we have studied the characteristics of small amplitude dust-acoustic structures under transverse perturbations. We have also presented the stability of the solitary wave solutions of KP equation. Further, from the rational solutions of NLSE, we have analysed the characteristics of dust-acoustic rogue waves by varying different plasma parameters. It is emphasized that all different physical parameters have great influence on the characteristics of dust-acoustic solitary waves and different order rogue waves.

**Keywords** KP equation · NLSE · Polarization force ·  $(r, q)$  distribution

## 1 Introduction

Over the last five decades, researchers have focused on the study of various nonlinear structures (such as solitons, rogue, shocks waves, double layers, and so on) and instabilities in various types of plasmas utilising Maxwellian and non-Maxwellian velocity distributions. Numerous nonlinear equations and energy balance equations have been constructed in the framework of perturbative and non-perturbative methodologies respectively to explore such nonlinear structures (with small or high amplitudes) in space/astrophysical plasmas. These nonlinear equations' solutions have been utilised to explain nonlinear solitary formations in 1-D, 2-D, and 3-D under the influence of different plasma parameters. The Kadomstev–Petviashvili (KP) [1]

---

M. Kaur (✉) · S. Singla · N. S. Saini  
Department of Physics, Guru Nanak Dev University, Amritsar 143005, India  
e-mail: [manveetsandhu7@gmail.com](mailto:manveetsandhu7@gmail.com)

© The Author(s), under exclusive license to Springer Nature Switzerland AG 2022  
S. Banerjee and A. Saha (eds.), *Nonlinear Dynamics and Applications*,  
Springer Proceedings in Complexity,  
[https://doi.org/10.1007/978-3-030-99792-2\\_24](https://doi.org/10.1007/978-3-030-99792-2_24)

275

equation is one of the nonlinear equations used to describe nonlinear systems in two dimensions. It is an extension of the Korteweg-de Vries (KdV) equation. Numerous researchers have studied the characteristics of nonlinear structures by employing KP equation in different type of plasma environments [2–9].

Numerous research articles published over the last three decades have reported the various physical aspects that due to their existence in dusty plasma, the nonlinear structures viz., dust-acoustic waves (DAWs) and dust-ion acoustic waves (DIAWs) are modified. In an unmagnetized plasma, one of such aspect is the forces on charged particles such as electrostatic force, ion drag force, the net plasma pressure force and most importantly polarization force [10]. Although the polarization force is small in comparison to other forces of system but its effects are prominent for low frequency DAWs and incur in a dusty plasma due to deformation of Debye sheath around the particles. It is directed opposite to electric field, direction in which Debye length increases and alters with variation in dust size but independent of charge on the dust particles [11]. Several authors have investigated the role of polarization force on various nonlinear solitary structures utilising different distributions (Maxwellian and non-Maxwellian) in the context of the reductive perturbation methodology and the Sagdeev method [12–22]. In a highly coupled dusty plasma, the influence of polarization force and temperature of dust on DA solitary and shock waves was studied by Mamun and Ashrafi [12]. They observed that the properties of nonlinear structures are highly modified. In an inhomogeneous unmagnetized dusty plasma, Asaduzzaman and Mamun [14] analysed the effect of polarization force owing to dust density inhomogeneity on linear DA waves and reported that the dust grain charge inhomogeneity and grain size distribution along with density inhomogeneity altered the propagation properties of linear and nonlinear waves. Ashrafi et al. [15] investigated the polarization force for non-thermal and trapped ions, adiabaticity of electrons and ions. They explored that magnitude of the polarization force is significantly influenced in different dusty plasma situations. The effect of the polarization force on the dust-acoustic soliton energy was examined by Mayout et al. [16]. They explored that when net force acting on the grains decreases then DA soliton energy shows depletion.

The effect of polarization force and Cairns distributed ions on different DA nonlinear structures was illustrated by Singh and Saini [20]. They reported the influence of polarization parameter for existence domain of such kind of nonlinear structures. Further, the influence of nonextensively modified polarization force on interaction of DA shock waves in a magnetized dusty plasma was illustrated by Saini et al. [22]. They observed that change in values of parameters influence significantly the propagation properties of DA shocks and phase shifts evolved because of interaction of DA shocks.

Satellite data has revealed that particle distributions in different regions of space diverge significantly from Maxwellian distributions. The well-known nonthermal property of space plasmas reveals the presence of superthermal tails and flat tops at low energies. According to observation and theory, some space plasmas can be more successfully described by a generalized  $(r, q)$  distribution function. The major aspect of the  $(r, q)$  distribution function in space plasmas is that it depicts distributions

ranging from flat-topped to kappa distributions in the limiting situation [23]. In general,  $(r, q)$  distribution function is written as follows [23, 24]:

$$f_{r,q}(v) = \frac{a_1}{\pi b_1^{3/2} v_{th}^{3/2}} \left[ 1 + \frac{1}{q-1} \left( \frac{v^2 - 2e\phi/m_e}{b_1(2T_e/m_e)^{r+1}} \right) \right]^{-q}, \quad (1)$$

$$\text{where } a_1 = \frac{3\Gamma[q](q-1)^{3/(2+2r)}}{4\Gamma[q - \frac{3}{2+2r}]\Gamma[1 + \frac{3}{2+2r}]},$$

$$\text{and } b_1 = \frac{3(q-1)^{\frac{-1}{(1+r)}}\Gamma[q - \frac{3}{2+2r}]\Gamma[\frac{3}{2+2r}]}{\Gamma[q - \frac{5}{2+2r}]\Gamma[\frac{5}{2+2r}]},$$

where the electrostatic potential is represented by  $\phi$ , the electron temperature and mass are denoted as  $T_e$  and  $m_e$  respectively. The distribution contains two spectral indices,  $r$  and  $q$ , which regulate the flatness at lower energies and the tail at higher energies [23]. It must establish the  $q > 1$  and  $(r+1) > 5/2$  as requirement [23]. The distribution reduces to a Maxwellian distribution when  $r = 0$  and  $q \rightarrow (\kappa + 1)$ , and this becomes a generalized Lorentzian distribution, when  $r = 0$  and  $q \rightarrow (\kappa + 1)$  [23]. The generalized  $(r, q)$  distribution is suggested by Qureshi et al. [24], which has been studied extensively for various types of plasmas [23–26]. Shah et al. [23] explained the density depletions reported by the Freja and Viking satellites with a generalized  $(r, q)$  distribution, formerly illustrated with Cairns distribution function. Ali et al. [25] determined theoretically the potential on the surface of spherical dust in a multi-ion  $(r, q)$  distributed dusty plasma. Nasir et al. [26] studied the instability of currentless ion acoustic waves using Boltzmann-Vlasov kinetic model with generalized  $(r, q)$  distribution in electrons and ions plasma.

Due to importance of polarization force in dusty plasma and the concept of generalized  $(r, q)$  distribution, we have investigated the solitary and rogue waves under the effect of polarization force in a dusty plasma composed of Boltzmann distributed electrons and generalized  $(r, q)$  distributed ions. The manuscript is described as follows: The fluid model is presented in Sect. 2. The derivation of Kadomstev–Petviashvili (KP) equation and its solution has been described in Sect. 2.1. The derivation of NLSE and its solution are presented in Sect. 2.2. Parametric analysis is described in Sect. 2.3. Section 2.4 illustrates conclusions.

## 2 Fluid Model

We have considered a plasma having Maxwell Boltzmann distributed electrons,  $(r, q)$  distributed ions, polarization force and negatively charged dust particles as fluid. The

expression for polarization force is [20]

$$F_p = -Z_d e F_R C_{r0} \left[ 1 - C_{r1} \left( \frac{e\phi}{K_B T_i} \right) + C_{r2} \left( \frac{e\phi}{K_B T_i} \right)^2 \right]^{\frac{1}{2}} \tag{2}$$

where  $F_R = \frac{Z_d e^2}{4K_B T_i \lambda_{Di0}}$ ,  $\lambda_{Di0} = (\epsilon K_B T_i / n_i e^2 C_{r1})^{\frac{1}{2}}$ ,  $C_{r0} = (C_{r1} - 2C_{r2}\phi)$ ,

$$C_{r1} = \frac{(q - 1)^{\frac{-1}{(r+1)}} \Gamma \left[ \frac{1}{2(r+1)} \right] \Gamma \left[ q - \frac{1}{2(r+1)} \right]}{2b_1 \Gamma \left[ \frac{3}{2(r+1)} \right] \Gamma \left[ q - \frac{3}{2(r+1)} \right]},$$

$$C_{r2} = \frac{-(q - 1)^{\frac{-2}{1+r}} (1 + 4r) \Gamma \left[ \frac{-1}{2(1+r)} \right] \Gamma \left[ q + \frac{1}{2(r+1)} \right]}{8b_1^2 \Gamma \left[ \frac{3}{2(r+1)} \right] \Gamma \left[ q - \frac{3}{2(r+1)} \right]},$$

Equation (2) illustrates that polarization force expression is dependent upon  $(r, q)$  distributed ions and independent of role of electrons. It approaches to Maxwellian limit when  $r = 0$  and  $q \rightarrow \infty$  and if  $r = 0, q \rightarrow (\kappa + 1)$ , then the  $(r, q)$  distribution becomes kappa distribution. The normalized fluid equations are written as [20]:

$$\frac{\partial n_{d'}}{\partial t} + \frac{\partial(n_{d'}u_{d'})}{\partial x} + \frac{\partial(n_{d'}v_{d'})}{\partial y} = 0 \tag{3}$$

$$\frac{\partial u_{d'}}{\partial t} + u_{d'} \frac{\partial u_{d'}}{\partial x} + v_{d'} \frac{\partial u_{d'}}{\partial y} = F_p \frac{\partial \phi'}{\partial x} \tag{4}$$

$$\frac{\partial v_{d'}}{\partial t} + u_{d'} \frac{\partial v_{d'}}{\partial x} + v_{d'} \frac{\partial v_{d'}}{\partial y} = F_p \frac{\partial \phi'}{\partial y} \tag{5}$$

$$\frac{\partial^2 \phi'}{\partial x^2} + \frac{\partial^2 \phi'}{\partial y^2} = n_{d'} + n_{e'} - n_i' \tag{6}$$

The expressions for number density of  $(r, q)$  distributed ions and Maxwellian electrons in dimensionless form are written as [20, 23]:

$$n_i' = \mu_i (1 - C_{r1}\phi' + C_{r2}\phi'^2 - C_{r3}\phi'^3 + \dots), \tag{7}$$

$$n_{e'} = \mu_e \left( 1 + \theta_{ie}\phi' + \frac{\theta_{ie}^2 \phi'^2}{2} + \frac{\theta_{ie}^3 \phi'^3}{6} \right). \tag{8}$$

Also  $F_p$  in governing equations is expressed as

$$F_p = \left[ 1 - F_R(C_{r1} - 2C_{r2}\phi' + \frac{1}{2}C_{r1}^2\phi' - \dots) \right] \tag{9}$$

where  $F_R$  is the polarization force parameter that describes the impact of negatively charged dust particles on  $(r, q)$  distributed ions. The number density of ions  $n_i'$ , electrons  $n_e'$  and electric potential  $\phi'$  are normalized as  $n_e' = n_e/(Z_{d0}n_{d0})$ ,  $n_i' = n_i/(Z_{d0}n_{d0})$  and  $\phi' = (e\phi)/(K_B T_i)$ . By applying these normalized values and using  $\theta_{ie} = T_i/T_e$ ,  $\mu_e = n_{e0}'/(Z_{d0}n_{d0}') = 1/(\mu_{ie}-1)$ ,  $\mu_i = n_{i0}'/(Z_{d0}n_{d0}') = \mu_{ie}/(\mu_{ie}-1)$  and  $\mu_{ie} = n_{i0}'/n_{e0}'$  is the ratio of number density of ions to electrons in equilibrium such that  $\mu_e - \mu_i = -1$ . After substituting the values of ion and electron number density in equation (6), Poisson equation become as a function of potential,

$$\frac{\partial^2 \phi'}{\partial x^2} + \frac{\partial^2 \phi'}{\partial y^2} = n_d' - \mu_i \left[ 1 - C_{r1}\phi' + C_{r2}\phi'^2 - C_{r3}\phi'^3 + \dots \right] + \mu_e \left[ 1 + \theta_{ie}\phi' + \frac{\theta_{ie}^2\phi'^2}{2} + \frac{\theta_{ie}^3\phi'^3}{6} + \dots \right], \tag{10}$$

For further analysis, we have dropped prime sign from the variables and other quantities for mathematical simplicity.

### 2.1 Derivation of Kadomstev Petviashvili (KP) Equation

For present fluid model having nonthermal ions under polarization force effect, we have used following stretching co-ordinates [7]:

$$\xi = \epsilon(x - Vt), \quad \tau = \epsilon^3 t \quad \text{and} \quad \eta = \epsilon^2 y \tag{11}$$

to derive KP equation, where  $\epsilon$  is dimensionless quantity which describes role of weak nonlinearity,  $V$  represents the phase velocity of solitons. In this investigation, waves having weak dispersion as well as nonlinearity are considered with  $\omega$  (or  $k$ )  $\ll 1$ . Different physical quantities are varying slowly in space and very slowly in time. The stretching coordinates defined in Eq. 11 are essential components of reductive perturbation method for deriving KP equation. The expansion for depended variables is written as:

$$S = S_{d0} + \sum_{j=1}^{\infty} \epsilon^{2j} S_{dj}, \quad v_d = \sum_{j=1}^{\infty} \epsilon^{2j+1} v_{dj}. \tag{12}$$

The system variables  $n_d$ ,  $u_d$  and  $\phi$  are represented by  $S$  at a given position and time. The small deviation of these variables from equilibrium state is represented by  $S_{d0}$ , the values of system of variables  $n_{d0}$ ,  $u_{d0}$  and  $\phi_0$  are 1, 0 and 0 respectively. Thus, applying these stretching co-ordinates and expansions in the set of modified dust model equations (3–5) and (10), yields different kinds of equations. Then, by collecting the lower order quantities of  $\epsilon$ , we obtain the following:

$$n_{d1} = -\frac{1 - F_R C_{r1}}{V^2} \phi_1, u_{d1} = -\frac{1 - F_R C_{r1}}{V} \phi_1, \quad (13)$$

$$\frac{\partial v_{d1}}{\partial \xi} = \frac{1 - F_R C_{r1}}{V} \frac{\partial \phi_1}{\partial \eta} \quad \text{and} \quad V = \sqrt{\frac{1 - F_R C_{r1}}{C_3}}.$$

where  $C_3 = \mu_i C_{r1} + \mu_e \theta_{ie}$ . Similarly by collecting coefficients of higher power of  $\epsilon$ , we obtain

$$\frac{\partial n_{d1}}{\partial \tau} - V \frac{\partial n_{d2}}{\partial \xi} + \frac{\partial(n_{d1} u_{d1})}{\partial \xi} + \frac{\partial u_{d2}}{\partial \xi} + \frac{\partial v_{d1}}{\partial \eta} = 0, \quad (14)$$

$$\begin{aligned} \frac{\partial u_{d1}}{\partial \tau} - V \frac{\partial u_{d2}}{\partial \xi} + u_{d1} \frac{\partial u_{d1}}{\partial \xi} &= 2F_R C_{r2} \phi_1 \frac{\partial \phi_1}{\partial \xi} - \frac{F_R C_{r1}^2}{2} \phi_1 \frac{\partial \phi_1}{\partial \xi} \\ &+ \frac{3F_R}{2} C_{r1} C_{r2} \phi_1^2 \frac{\partial \phi_1}{\partial \xi} + (1 - F_R C_{r1}) \frac{\partial \phi_2}{\partial \xi}, \end{aligned} \quad (15)$$

$$\begin{aligned} \frac{\partial v_{d1}}{\partial \tau} - V \frac{\partial v_{d2}}{\partial \xi} + u_{d1} \frac{\partial v_{d1}}{\partial \xi} &= 2F_R C_{r2} \phi_1 \frac{\partial \phi_1}{\partial \eta} - \frac{F_R C_{r1}^2}{2} \phi_1 \frac{\partial \phi_1}{\partial \eta} \\ &+ \frac{3F_R}{2} C_{r1} C_{r2} \phi_1^2 \frac{\partial \phi_1}{\partial \eta} + (1 - F_R C_{r1}) \frac{\partial \phi_2}{\partial \eta}, \end{aligned} \quad (16)$$

$$\frac{\partial^2 \phi_1}{\partial \xi^2} = n_{d2} + \mu_i C_{r1} \phi_2 - \mu_i C_{r2} \phi_1^2 + \mu_e \theta_{ie} \phi_2 + \frac{\mu_e \theta_{ie}^2}{2} \phi_1^2 \quad (17)$$

After long mathematical calculations in above different equations, we have obtained the KP equation as [7]

$$\frac{\partial}{\partial \xi} \left[ \frac{\partial \phi}{\partial \tau} + A \phi \frac{\partial \phi}{\partial \xi} + B \frac{\partial^3 \phi}{\partial \xi^3} \right] + C \frac{\partial^2 \phi}{\partial \eta^2} = 0 \quad (18)$$

where

$$A = \frac{-V^3}{2(1 - F_R C_{r1})} \left[ \frac{3(1 - F_R C_{r1})^2}{V^4} - \frac{2F_R C_2}{V^2} + \frac{F_R C_{r1}^2}{2V^2} + 3C_4 \right], \quad (19)$$

$$B = \frac{V^3}{2(1 - F_R C_{r1})}, C = \frac{V}{2} \quad \text{and} \quad C_4 = -\mu_i C_{r2} + \mu_e \frac{\theta_{ie}^2}{2} \quad (20)$$

The nonlinear coefficient is represented by  $A$ ,  $B$  represents the dispersion coefficient and  $C$  is higher order coefficient.



To find the steady solution of KP equation (18), we have transformed this equation with  $\Lambda = \xi - \eta - u\tau$  as an appropriate transformation, where  $u$  represents the velocity of frame. By substituting this single variable transformation, we get KP equation in ordinary differential form. Thus, by integration with proper boundary conditions ( $\phi(\Lambda), \phi'(\Lambda) \rightarrow 0$  as  $|\Lambda| \rightarrow \infty$ ), we obtain

$$\phi = \phi_m \operatorname{sech}^2\left(\frac{\Lambda}{w}\right), \tag{21}$$

where  $\phi_m = 3\left(\frac{u-C}{A}\right)$  represents peak amplitude and  $w = 2\sqrt{\frac{B}{u-C}}$  is width of the KP solitons.

### 2.2 The Derivation of NLSE and Its Solution

To explore the characteristics of dust-acoustic waves in the  $(r, q)$  distributed plasma under the impact of polarization force, we find the solutions of Eq. (18) by incorporating the following new variables as  $\phi(\xi, \eta, \tau) = \phi(\varrho, \tau)$  and  $\varrho = F\xi + G\eta - m\tau$ . Here,  $F$  and  $G$  are direction cosines, so that  $F^2 + G^2 = 1$ .  $m$  is a which may be considered like the Mach number. Now, by substituting new variable in (18), we get:

$$\frac{\partial}{\partial \tau} \phi(\varrho, \tau) + FA\phi(\varrho, \tau) \frac{\partial}{\partial \varrho} \phi(\varrho, \tau) + F^3 B \frac{\partial^3}{\partial \varrho^3} \phi(\varrho, \tau) = 0, \tag{22}$$

$m = \frac{G^2 C}{F} = \frac{(1-F^2)C}{F}$ . The solution of this equation is assumed as [27, 28]:

$$\phi(\varrho, \tau) = \sum_{n=1}^{\infty} \epsilon^n \sum_{l=-\infty}^{\infty} \phi_l^n(\varrho, \tau) \exp [il(k\varrho - \omega\tau)], \tag{23}$$

we consider  $\xi = \epsilon(\varrho - u_g \tau)$  and  $t = \epsilon^2 \tau$  as stretching coordinates, where  $u_g$  denotes the group velocity.

Now, consider that all perturbed states rely solely upon rapid scales (through the phase  $(k\varrho - \omega\tau)$ ). Whereas, the prolonged scale  $(\xi, t)$  enter the argument of the  $l$ th harmonic amplitude  $\phi_l^n$ . If the condition  $\phi_{-l}^n = \phi_l^{n*}$  (\* defines complex conjugate) is satisfied only then  $\phi(\varrho, \tau)$  will be real. The derivative operator are written as [27, 28]:

$$\frac{\partial}{\partial \varrho} \equiv \frac{\partial}{\partial \varrho} + \epsilon \frac{\partial}{\partial \xi}, \tag{24}$$

$$\frac{\partial}{\partial \tau} \equiv \frac{\partial}{\partial \tau} - u_g \epsilon \frac{\partial}{\partial \xi} + \epsilon^2 \frac{\partial}{\partial t}. \tag{25}$$

For  $l = 1, n = 1$ , the different expressions yields as  $\omega = -F^3k^3B$ , and from  $l = 1, n = 2$ , we find the group velocity is  $u_g = -3F^3k^2B$ . The zeroth harmonic with  $l = 0, n = 2$  gives

$$\phi_2^{(0)} = \left(\frac{A}{u_g}\right) |\phi_1^{(1)}|^2. \tag{26}$$

From second harmonic, we get

$$\phi_2^{(2)} = \left(\frac{A}{6F^2k^2B}\right) |\phi_1^{(1)}|^2. \tag{27}$$

From  $n = 3, l = 1$ , and doing rigorous analytical calculations, we get the NLSE as [29]

$$i \frac{\partial \phi}{\partial t} + \frac{\mathcal{P}}{2} \frac{\partial^2 \phi}{\partial \xi^2} + \mathcal{Q} |\phi|^2 \phi = 0, \tag{28}$$

for simplicity  $\phi_1^{(1)} = \phi$ .  $\mathcal{Q} = \frac{A^2F^2}{\mathcal{P}}$  represents nonlinear coefficient and  $\mathcal{P} = 6F^3Bk$  denoted as dispersion coefficient. The different solutions of Eq. (28) are determined respectively as [30]

$$|\phi_1(\xi, t)| = \left(\frac{4(1 + 2it)}{1 + 4t^2 + 4\frac{\xi^2}{\mathcal{P}}} - 1\right) \frac{e^{it}}{\sqrt{\mathcal{Q}}}, \tag{29}$$

$$|\phi_2(\xi, t)| = \sqrt{\frac{\mathcal{P}}{\mathcal{Q}}} \left(1 + \frac{m_1 + im_2}{m_3}\right) e^{(i\mathcal{P}t)}, \tag{30}$$

where,  $m_1 = \left[\frac{3}{8} - \frac{\xi^4}{2} - \frac{3\xi^2}{2} - 6(\mathcal{P}\xi t)^2 - 10(\mathcal{P}t)^4 - 9(\mathcal{P}t)^2\right]$ ,  
 $m_2 = -\mathcal{P}t \left(-\frac{15}{4} + \xi^4 - 3\xi^2 + 4(\mathcal{P}\xi t)^2 + 4(\mathcal{P}t)^4 + 2(\mathcal{P}t)^2\right)$  and  
 $m_3 = \frac{3}{32} + \frac{\xi^6}{12} + \frac{\xi^4}{8} + \frac{1}{2}\xi^4(\mathcal{P}t)^2 + \frac{9\xi^2}{16} + \xi^2(\mathcal{P}t)^4 - \frac{3(\mathcal{P}\xi t)^2}{2} + \frac{2(\mathcal{P}t)^6}{3} + \frac{9(\mathcal{P}t)^4}{2} + \frac{33(\mathcal{P}t)^2}{8}$ .

$|\phi_1(\xi, t)|$  ( $|\phi_2(\xi, t)|$ ) describes the characteristics of first (second) order rogue waves.

### 2.3 Parametric Analysis

The role of variety of physical parameters such as polarization parameter (via  $F_R$ ), ratio of number density of ions to electrons (via  $\mu_{ie}$ ), ratio of temperature of ions to electrons (via  $\theta_{ie}$ ), spectral indices  $r$ , and  $q$  on properties of DA solitary and rogue waves. For numerical analysis, we have considered the data from the planetary rings [31]. The parametric ranges are  $n_{e0} = 4 \times 10^7, n_d = 10^7, n_{i0} = 5 \times 10^7, Z_d = 3 \times 10^3, F_R = 0 - 0.14$ .

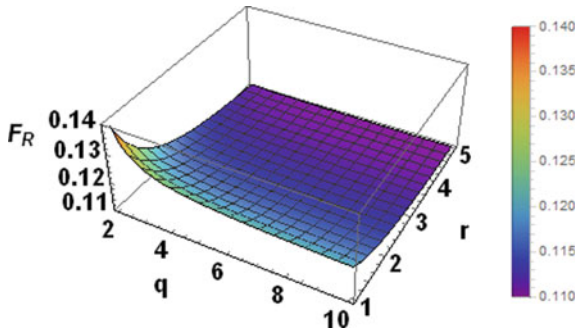


Fig. 1 The polarization force parameter ( $F_R$ ) versus spectral indices (a)  $r$ ; (b)  $q$

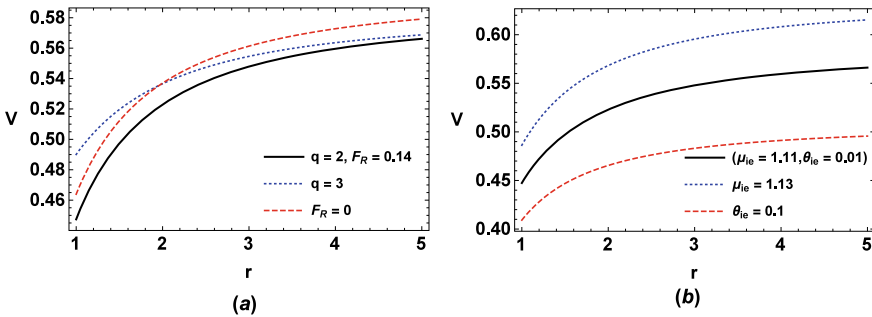
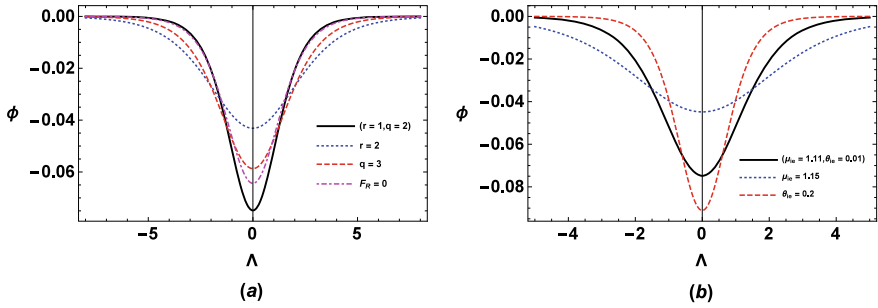


Fig. 2 The phase velocity ( $V$ ) versus index  $r$  for different values of (a) index  $q$ , polarization force parameter ( $F_R$ ); (b) ratio of number density of ions to electrons ( $\mu_{ie}$ ) and ratio of temperature of ions to electrons ( $\theta_{ie}$ )

The Fig. 1 shows the polarization force parameter ( $F_R$ ) versus indices  $r$  and  $q$ . It is shown that when the values of  $r$  and  $q$  are increased,  $F_R$  decreases. In other words, when the indices  $r$  and  $q$  decrease, the polarization parameter increases. This means that indices  $r$  and  $q$  have a big influence on the polarization parameter.

The variation of phase velocity ( $V$ ) with index  $r$  for different values of index  $q$ , polarization force parameter ( $F_R$ ), ratio of number density of ions to electrons ( $\mu_{ie}$ ) and ratio of temperature of ions to electrons ( $\theta_{ie}$ ) is portrayed in Fig. 2. It is depicted that with increase in  $r$ ,  $q$ , ratio of number density of ions to electrons and without polarization force parameter ( $F_R$ ), the phase velocity is increased and it is reduced with enhancement in ratio of temperature of ions to electrons. This implies that polarization force suppresses the phase velocity of solitary waves.

Figure 3a, b elucidate the solitary profile ( $\phi$ ) with  $\Lambda$  for the change in values of  $r$  and  $q$ , polarization force parameter ( $F_R$ ), ratio of number density of ions to electrons ( $\mu_{ie}$ ) and ratio of temperature of ions to electrons ( $\theta_{ie}$ ). It is described that with increase in  $r$ ,  $q$  indices, ratio of number density of ions to electrons and without polarization force parameter ( $F_R$ ), the nonlinearity effect decreases and dispersion effect increases, so the amplitude of solitary waves is decreased on negative axis and



**Fig. 3** The soliton profile ( $\phi$ ) for different values of (a)  $r, q$  indices, polarization force parameter ( $F_R$ ); (b) ratio of number density of ions to electrons ( $\mu_{ie}$ ) and ratio of temperature of ions to electrons ( $\theta_{ie}$ )

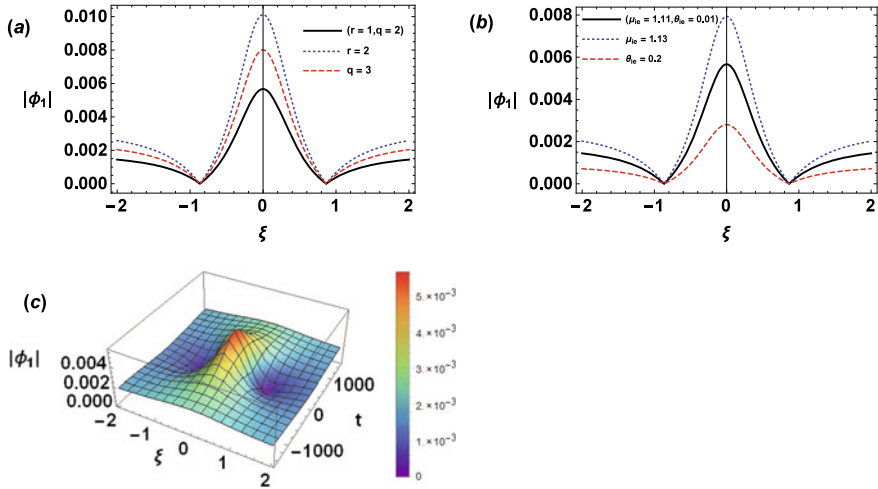


**Fig. 4** The variation of first order rogue wave profile with (a)  $r, q$  indices; (b) ratio of number density of ions to electrons ( $\mu_{ie}$ ) and ratio of temperature of ions to electrons ( $\theta_{ie}$ ); (c) 3-D representation

width is increased. The amplitude of solitary wave is enhanced and width is reduced with change in the value of ratio of temperature of ions to electrons, this occurs due to increase in nonlinearity and decrease in dispersion effects. This also implies that contribution of polarization force enhances, the amplitude of solitary waves along negative axis.

The variation of first order profile ( $|\phi_1|$ ) and second order profile ( $|\phi_2|$ ) of rogue waves with  $\xi$  for change in  $r, q$  indices,  $\mu_{ie}$  and  $\theta_{ie}$  is presented in Figs. 4 and 5. It is noticed that with increase in  $r, q$  indices and  $\mu_{ie}$  (i.e., ratio of number density of ions to electrons) the nonlinearity increases so the amplitude of both orders rogue waves is increased. The amplitude is reduced with increase in  $\theta_{ie}$  (i.e., ratio of temperature

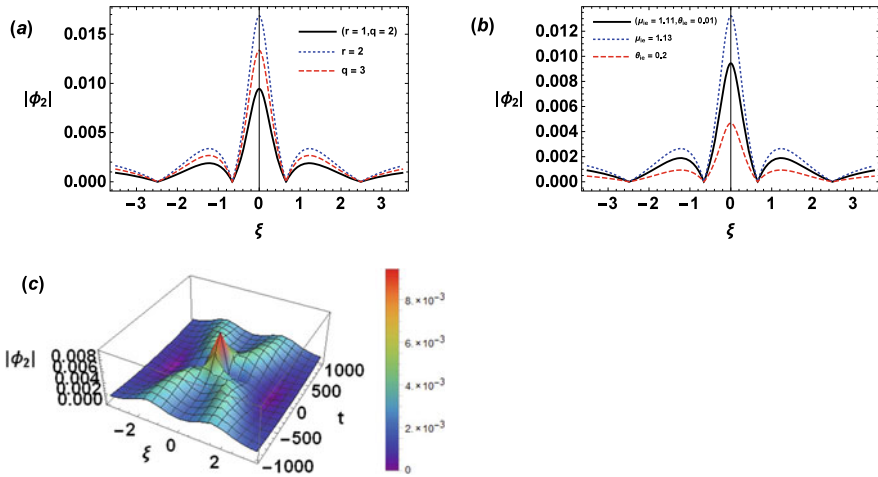


**Fig. 5** The second order rogue wave profile with (a)  $r, q$  indices; (b) ratio of number density of ions to electrons ( $\mu_{ie}$ ) and ratio of temperature of ions to electrons ( $\theta_{ie}$ ); (c) 3-D representation

of ions to electrons) due to decrease in nonlinearity. Its 3-dimensional presentation is described in Figs.4c and 5c.

From the whole numerical analysis we can conclude that all physical parameters such as  $r, q$  indices, polarization force parameter ( $F_R$ ), ratio of number density of ions to electrons ( $\mu_{ie}$ ) and ratio of temperature of ions to electrons ( $\theta_{ie}$ ) have great influence on propagation properties of dust-acoustic solitary and rogue waves.

### 2.4 Conclusion

The influence of polarization force on characteristics of dust-acoustic (DA) solitary and rogue waves in negatively charged dusty plasma containing Maxwellian electrons and ions with generalized ( $r, q$ ) distribution is studied. The KP and NLS equations have been derived. From their respective solutions characteristics of solitary and rogue waves have also been examined. We observe negative polarity DA KP solitons. The polarization parameter ( $F_R$ ) is suppressed with increase  $r, q$  indices. The propagation properties of DA solitary and rogue waves are highly affected by variation in  $r, q$  indices, ratio of number density of ions to electrons, ratio of temperature of ions to electrons, and with polarization force parameter. It is emphasized that the implication of this work may be of great importance to analyse the nonlinear phenomena from physics point of view in planetary rings [31].

## References

1. Kadomtsev, B.-B., Petviashvili, V.-I.: On stability of solitary waves in weakly dispersive media. *Sov. Phys. Doklady* **15**(4), 753–756 (1970)
2. Mushtaq, A., Khan, S.-A.: Ion acoustic solitary wave with weakly transverse perturbations in quantum electron-positron-ion plasma. *Phys. Plasmas* **14**(5), 052307(1–6) (2007)
3. Pakzad, H.-R.: The Kadomtsev–Petviashvili (KP) equation ion acoustic waves in weakly relativistic plasma with nonthermal electron, positron and warm ion. *J. Phys.: Conf. Series* **96**, 012146(1–6) (2008)
4. Jian-Hong, C.: Effects of dust size distribution on nonlinear waves in a dusty plasma. *Chinese Phys. B* **18**(6), 2121–2128 (2009)
5. Dorrnian, D., Sabetkar, A.: Dust acoustic solitary waves in a dusty plasma with two kinds of nonthermal ions at different temperatures. *Phys. Plasmas* **19**(1), 013702–6 (2012)
6. Elwakil, S.-A., El-hanbaly, A.-M., El-Shewy, E.-K., El-Kamash, I.-S.: Electron acoustic soliton energy of the Kadomtsev–Petviashvili equation in the Earth’s magnetotail region at critical ion density. *Astrophys. Space Sci.* **349**(1), 197–203 (2014)
7. Saini, N.-S., Kaur, N., Gill, T.-S.: Dust acoustic solitary waves of Kadomtsev–Petviashvili (KP) equation in superthermal dusty plasma. *Adv. Space Res.* **55**(12), 2873–2882 (2015)
8. Kohli, R., Kaur, N., Singh, M., Saini, N.-S.: Effect of ion beam on dust-acoustic waves under transverse perturbations in dusty plasma. *IEEE Trans. Plasma Sci.* **46**(4), 782–789 (2018)
9. Ruderman, M.-S.: Kadomtsev–Petviashvili equation for magnetosonic waves in Hall plasmas and soliton stability. *Phys. Scripta* **95**(9), 095601(1–9) (2020)
10. Hamaguchi, S., Farouki, R.-T.: Plasma-particulate interactions in nonuniform plasmas with finite flows. *Phys. Plasmas* **1**(7), 2110–2118 (1994)
11. Khrapak, S.-A., Ivlev, A.-V., Yaroshenko, V.-V., Morfill, G.-E.: Influence of a polarization force on dust acoustic waves. *Phys. Rev. Lett.* **102**(24), 245004-3 (2009)
12. Mamun, A.-A., Ashrafi, K.-S., Shukla, P.-K.: Effects of polarization force and effective dust temperature on dust-acoustic solitary and shock waves in a strongly coupled dusty plasma. *Phys. Rev. E* **82**(2), 026405–6 (2010)
13. Shukla, N., Shukla, P.-K.: Polarization-force-induced dust grain acceleration and intrinsic magnetization of dusty plasmas. *J. Plasma Phys.* **76**(5), 677–680 (2010)
14. Asaduzzaman, M., Mamun, A.-A.: Roles of polarization force and nonthermal electron on dust-acoustic waves in an inhomogeneous dusty plasma with positively charged dust. *Phys. Plasmas* **19**(9), 093704–6 (2012)
15. Ashrafi, K.-S., Mamun, A.-A., Shukla, P.-K.: Polarization force for different dusty plasma situations. *J. Plasma Phys.* **80**(1), 1–7 (2014)
16. Mayout, S., Bentabet, K., Tribeche, M.: Effect of the polarization force on the dust-acoustic soliton energy. *Contribut. Plasma Phys.* **56**(2), 99–103 (2016)
17. Bentabet, K., Tribeche, M.: Dust-acoustic solitons in a polarized dusty plasma with nonthermal ions. *IEEE Trans. Plasma Sci.* **45**(4), 736–741 (2017)
18. Abbasi, A., Vaziri, M.-R.: Effect of polarization force on the Jeans instability in collisional dusty plasmas. *Plasma Sci. Technol.* **20**(3), 035301(1–4) (2018)
19. Singh, K., Ghai, Y., Kaur, N., Saini, N.-S.: Effect of polarization force on dust-acoustic cnoidal waves in dusty plasma. *European Phys. J. D* **72**(9), 160(1–8) (2018)
20. Singh, K., Saini, N.-S.: Breather structures and peregrine solitons in a polarized space dusty plasma. *Front. Phys.* **8**, 602229(1–12) (2020)
21. Dolai, B., Prajapati, R.-P.: Effects of dust-charge gradient and polarization forces on the waves and Jeans instability in strongly coupled dusty plasma. *Phys. Lett. A* **384**(25), 126462(1–7) (2020)
22. Saini, N.-S., Singh, K., Sethi, P.: Interaction of dust-acoustic shock waves in a magnetized dusty plasma under the influence of polarization force. *Laser Particle Beams* **2021**, 6679085(1–8) (2021)
23. Shah, K.-H., Qureshi, M.-N.-S., Masood, W., Shah, H.-A.: An alternative explanation for the density depletions observed by Freja and Viking satellites. *AIP Adv.* **8**(8), 085010–12 (2018)

24. Qureshi, M.-N.-S., Shah, H.-A., Murtaza, G., Schwartz, S.-J., Mahmood, F.: Parallel propagating electromagnetic modes with the generalized  $(r, q)$  distribution function. *Phys. Plasmas* **11**(8), 3819–3829 (2004)
25. Ali, S., Abid, A.-A., Du, J., Mamun, A.-A.: Dust surface potential in a generalized  $(r, q)$ -distributed multi-ion dusty plasma. *Contribut. Plasma Phys.* **58**(10), 976–984 (2018)
26. Nasir, W., Ehsan, Z., Qureshi, M.-N.-S., Shah, H.-A.: Solar wind driven electrostatic instabilities with generalized  $(r, q)$  distribution function. *Contribut. Plasma Phys.* **59**(9), e201800159(1–8) (2019)
27. El-Labany, S.-K., Moslem, W.-M., El-Bedwehy, N.-A., Abd El-Razek, H.-N.: Rogue wave in Titan's atmosphere. *Astrophys. Space Sci.* **338**(1), 3–8 (2012)
28. El-Shewy, E.-K., Abdelwahed, H.-G., Abdo, N.-F., Shahein, R.-A.: Rogue waves for Kadomstev–Petviashvili solutions in a warm dusty plasma with opposite polarity. *Chem. Phys. Phys. Kinet. Plasma Phys.* **71**, 284–291 (2016)
29. Saini, N.-S., Singh, M., Bains, A.-S.: Dust kinetic Alfvén solitary and rogue waves in a superthermal dusty plasma. *Phys. Plasmas* **22**(11), 113702–10 (2015)
30. Peregrine, D.-H.: Water waves, nonlinear Schrödinger equations and their solutions. *J. Australian Math. Soc. Series B-Appl. Math.* **25**, 16–43 (1983)
31. Goertz, C.-K., Linhua-Shan, S., Havnes, O.: Electrostatic forces in planetary rings. *Geophys. Res. Lett.* **15**(1), 84–87 (1988)

# Dust-Ion-Acoustic Multisoliton Interactions in the Presence of Superthermal Particles



Dharitree Dutta  and K. S. Goswami

**Abstract** The propagation and interaction of dust-ion-acoustic solitons in the plasma composed of superthermal electrons and positrons, positively charged inertial ion, and static dust particles is examined in this work. The reductive perturbation method for small amplitude is adopted to derive the KdV equation. Hirota's bilinear method has been employed to calculate the multisoliton solutions of the KdV equation. The role of various plasma parameters on the soliton has been studied. It has been observed that the superthermality of the electrons and positrons and their concentration can alter the nature of the solitons. The presence of dust particles also influence the solitary structures. These results can be used to understand the nonlinear structures in different space and atmospheric environment, e.g. in the Van Allen radiation belt.

**Keywords** DIA soliton · Reductive perturbation method · Hirota's bilinear method

## 1 Introduction

In recent years, there is plenty of research [1–8] in the fascinating field of nonlinear structures because of their occurrence in different space and atmospheric environment. Soliton is one of those nonlinear structures which receive a huge amount of interests from the researcher worked in different fields of plasma physics. The distinguishing feature of a soliton is that it can maintain the size and shape even after its interaction with another soliton or solitons. These nonlinear structures are generated because of the balance between nonlinearity and dispersion. Initially it was stud-

---

D. Dutta (✉)

Department of Physics, Anandaram Dhekial Phookan College, Nagaon, Assam 782002, India  
e-mail: [dutta3dharitree@gmail.com](mailto:dutta3dharitree@gmail.com)

K. S. Goswami

Centre of Plasma Physics—Institute for Plasma Research, Nazirakhat, Sonapur, Kamrup(M), Assam 782402, India



ied in electron-ion plasma. However, dust being omnipresent at different space and ionospheric plasma, it has been later observed that the presence of dust particles in a plasma introduces various low frequency waves and nonlinear structures [9]. Dust-ion-acoustic wave is one of the distinct normal modes observed in unmagnetized dusty plasma. Shukla and Silin had introduced this dust-ion-acoustic wave through their theoretical work, later which was proved experimentally by Barkan et al. [9]. Since then, this nonlinear structure has attained considerable amount of interests from the researchers.

Recently, the plasma physicists have proclaimed the presence of electron-positron-ion plasma in various space and atmospheric environment. In addition, in some other environment e.g., the interior region of accretion disks near neutron stars and magnetars, in the Milky Way, in the Saturn's and Jupiter's magnetosphere, the electron-positron-ion-dust (e-p-i-d) plasma have been observed [10]. The presence of positron in the e-i-d plasma brings significant changes in the nature of the nonlinear waves. This is because the intrinsic symmetry between the electron ( $e^-$ ) and positron ( $e^+$ ) within the plasma brings a dynamical change from that of an electron-ion-dust plasma. The symmetry in the mass of the electron and positron originates different fluid and kinetic instabilities in the plasma, and controls the possibility of the generation of nonlinear acoustic waves [11]. In view of the vital role of electron-positron-ion-dust plasma in space and atmospheric plasma environment, in this work, the formation of a DIA soliton in an unmagnetized dusty plasma comprise of superthermal electrons and positrons, cold fluid ions and static dust grains have been studied. The KdV equation is derived using the reductive perturbation method. Another salient feature of this work is to incorporate the soliton interactions. Different space-based observations proved the existence of a series of solitons and double layers in different space and atmospheric environment. NASA's Van Allen Probe spacecraft had shown recently the existence of a series of low frequency electrostatic solitons in the Earth's magnetosphere [12, 13]. The interaction of multiple solitons can be studied with the help of Hirota's bilinear method [14]. This method was first published in 1971 by Hirota. The multi soliton solutions of the KdV equation have been derived using this method. The effect of different plasma parameters on the soliton interactions have also been discussed. The manuscript is organized as: the Sect. 2 contains theoretical formulation. In Sect. 3, the Hirota's bilinear method has been employed. In Sect. 4, the results have been discussed. Finally it has been concluded with a brief summery in Sect. 5.

## 2 Theoretical Formulation

A homogeneous, collisionless, unmagnetized plasma comprise of superthermal electrons and positrons, cold fluid ions along with stationary dust particles in the background have been considered here. The set of normalized equations [15] describing the plasma model have been given bellow.

$$\frac{\partial N_i}{\partial t} + \frac{\partial(N_i U_i)}{\partial x}, \quad (1)$$

$$\frac{\partial U_i}{\partial t} + U_i \frac{\partial U_i}{\partial x} + 3\sigma N_i \frac{\partial N_i}{\partial x} = -\frac{\partial \phi}{\partial x}, \quad (2)$$

$$\frac{\partial^2 \phi}{\partial x^2} = \mu_e N_e + \mu_d - \mu_p N_p - N_i. \quad (3)$$

Here,  $N_i$  and  $U_i$  are the number densities and velocities of ions normalized by equilibrium ion density ( $n_{i0}$ ) and ion-acoustic velocity ( $c_i = \sqrt{k_B T_e / m_i}$ ), respectively, where  $T_e$  is the electron temperature and  $m_i$  is the ion mass.  $\phi$  is the normalized potential (normalized by  $k_B T_e / e$ ,  $e$  being the electric charge).  $\sigma$  is the ratio of ion and electron mass.  $\mu_e$ ,  $\mu_d$ , and  $\mu_p$  are the normalized equilibrium densities of electrons, dust, and positrons, respectively, i.e.,  $\mu_e = n_{e0} / n_{i0}$ ,  $\mu_d = Z_d n_{d0} / n_{i0}$ , and  $\mu_p = n_{p0} / n_{i0}$ . The equilibrium condition states:  $\mu_e = 1 - \mu_d + \mu_p$ . The time variable is normalized by the inverse of ion plasma frequency ( $\omega_i = \sqrt{4\pi n_{i0} e^2 / m_i}$ ), whereas the space variable is normalized by the ion Debye length ( $\lambda_{Di} = \sqrt{k_B T_e / 4\pi n_{i0} e^2}$ ). The superthermal electrons and positrons can be described with the  $\kappa$ -distribution and the expression for their respective normalized number densities are,

$$N_e = \left(1 - \frac{\phi}{\kappa_e - 3/2}\right)^{-\kappa_e + 1/2}, \quad N_p = \left(1 + \frac{\phi}{\beta(\kappa_p - 3/2)}\right)^{-\kappa_p + 1/2}. \quad (4)$$

Here,  $\kappa_e$  and  $\kappa_p$  are superthermality index of electrons and positrons respectively.  $\beta$  is the positron to electron temperature ratio ( $\beta = T_p / T_e$ ).

The KdV equation is derived using equations 1–4 and the stretched coordinates [16] used here are  $\xi = \epsilon^{1/2}(x - Mt)$ , and  $\tau = \epsilon^{3/2}t$ , where  $\epsilon$  is the smallness parameter that measures the weakness of the amplitude and  $M$  is the Mach number. The variable  $N_i$ ,  $U_i$  and  $\phi$  can be expanded about the unperturbed states in the power series of  $\epsilon$  as,

$$\begin{aligned} N_i &= N_i^{(0)} + \epsilon N_i^{(1)} + \epsilon^2 N_i^{(2)} + \epsilon^3 N_i^{(3)} + \dots \\ U_i &= \epsilon U_i^{(1)} + \epsilon^2 U_i^{(2)} + \epsilon^3 U_i^{(3)} + \dots \\ \phi &= \epsilon \phi^{(1)} + \epsilon^2 \phi^{(2)} + \epsilon^3 \phi^{(3)} + \dots \end{aligned} \quad (5)$$

After following the reductive perturbation method, and solving the set of equations of first order perturbed quantities the dispersion relation for linear dust-ion-acoustic waves has been calculated.

$$M = \left[ \frac{1 + 3\sigma(\mu_e P_1 + \mu_p Q_1)}{\mu_e P_1 + \mu_p Q_1} \right]^{1/2}. \quad (6)$$

Here,  $P_1 = (2\kappa_e - 1)/(2\kappa_e - 3)$ , and  $Q_1 = (2\kappa_p - 1)/\beta(2\kappa_p - 3)$ . Further manipulation of the the second order perturbed quantities finally results the KdV equation,

$$\frac{\partial \psi}{\partial \tau} + A \psi \frac{\partial \psi}{\partial \xi} + B \frac{\partial^3 \psi}{\partial \xi^3} = 0, \tag{7}$$

where,  $\psi = \phi^{(1)}$ . A, and B represents the nonlinearity and dispersion coefficients, and their expression are,

$$A = \frac{(\mu_p Q_2 - \mu_e P_2)(M^2 - 3\sigma)^2}{M} + \frac{3(M^2 + \sigma)}{2M(M^2 - 3\sigma)}, B = \frac{(M^2 - 3\sigma)^2}{2M}. \tag{8}$$

Here,  $P_2 = (4\kappa_e^2 - 1) / 2(2\kappa_e - 3)^2$ , and  $Q_2 = (4\kappa_p^2 - 1) / 2\beta^2(2\kappa_p - 3)^2$ .

### 3 Multisoliton Solution of the KdV Equation

To employ Hirota’s bilinear method, the dependent variable  $\psi$  of the KdV equation has been transformed to a new form which is a logarithmic transformation of an auxiliary function  $f(\xi, \tau)$  [14],

$$\psi(\xi, \tau) = \frac{12B}{A} \frac{\partial^2 [\ln f(\xi, \tau)]}{\partial \xi^2}. \tag{9}$$

Substituting this transformation for Eq. 7 and integrating once with respect to  $\xi$ ,

$$\left( \frac{f_{\xi, \tau}}{f} - f_{\xi} f_{\tau} \right) + 3B \left( \frac{f_{\xi, \xi}}{f} \right)^2 - 4B \frac{f_{\xi} f_{\xi, \xi, \xi}}{f^2} + B \frac{f_{\xi, \xi, \xi, \xi}}{f} = 0. \tag{10}$$

Multiplying Eq. 10 with  $f^2$  results in the bilinear form as,

$$f f_{\xi, \tau} - f f_{\xi} f_{\tau} + 3B (f_{\xi, \xi})^2 - 4B f_{\xi} f_{\xi, \xi, \xi} + B f f_{\xi, \xi, \xi, \xi} = 0. \tag{11}$$

From Eq. 11, it has been observed that the transformation leads to the disappearance of the nonlinearity coefficient (A) from the bilinear form of the KdV equation. The bilinear equation can be simplified and converted to an ODE in terms of Hirota derivative as

$$D_{\xi} (D_{\tau} + B D_{\xi}^3) (f(\xi, \tau) \cdot f(\xi, \tau)) = 0. \tag{12}$$

Here,  $D_{\xi}$ ,  $D_{\tau}$  are binary operators and on a paired function it can be expressed as,

$$D_{\xi}^m D_{\tau}^n (f \cdot f) = \left( \frac{\partial}{\partial \xi} - \frac{\partial}{\partial \xi'} \right)^m \left( \frac{\partial}{\partial \tau} - \frac{\partial}{\partial \tau'} \right)^n (f(\xi, \tau) \cdot f(\xi', \tau'))|_{\xi=\xi', \tau=\tau'} \tag{13}$$

The function  $f(\xi, \tau)$  can be expanded in the power series of  $\iota$  as

$$f(\xi, \tau) = 1 + \iota f_1 + \iota^2 f_2 + \iota^3 f_3 + \dots \tag{14}$$

If the original equation (KdV equation in this case) admits a N-soliton solution, then Eq. 14 will truncate at the  $n = N$  term provided  $f$  is the sum of precisely N simple exponential terms.

### 3.1 One and Two Soliton Solutions

For the one soliton solution of Eq. 7, it has been considered that  $f_1 = e^\eta$ , where  $\eta = k\xi + \omega\tau$ . For  $i = 1$ ,

$$f(\xi, \tau) = 1 + e^\eta \tag{15}$$

Substituting Eqs. 13–15 the dispersion relation for the DIA wave can be derived and is,  $\omega = -Bk^3$ .

Therefore, the known form of a single soliton has been recovered as,

$$\psi(\xi, \tau) = \frac{12B}{A} \frac{\partial^2 [\ln(1 - \exp(k\xi - Bk^3\tau))]}{\partial \xi^2} = \frac{3B}{A} k^2 \operatorname{sech}^2 \left( \frac{k\xi - Bk^3\tau}{2} \right). \tag{16}$$

Here,  $k$  is the propagation vector, and  $3Bk^2/A$  represents the amplitude of the soliton.

For two soliton solutions of Eq. 7, the function  $f(\xi, \tau)$  can be expressed as,

$$f(\xi, \tau) = 1 + e^{\eta_1} + e^{\eta_2} + a_{12}e^{\eta_1+\eta_2}, \tag{17}$$

where  $\eta_i = k_i\xi + \omega_i\tau + \gamma_i$ ,  $k_i$  are the propagation vectors,  $\gamma_i$  are the phase shifts,  $\omega_i = -Bk_i^3$  and  $i = 1, 2$  for the first and second soliton respectively.  $a_{12}$  is an interaction parameter of the two solitons and it depends upon the propagation vectors  $k_1$ , and  $k_2$  and can be expressed as,  $a_{12} = (k_1 - k_2/k_1 + k_2)^2$ .

The two soliton solution can be derived using the transformation (9) to the function  $f(\xi, \tau)$ .

$$\psi(\xi, \tau) = \frac{12B}{A} \frac{k_1^2 e^{\eta_1} (1 + a_{12} e^{2\eta_2}) + k_2^2 e^{\eta_2} (1 + a_{12} e^{2\eta_1}) + 2(k_1 - k_2)^2 e^{\eta_1 + \eta_2}}{(1 + e^{\eta_1} + e^{\eta_2} + a_{12} e^{\eta_1 + \eta_2})^2}. \tag{18}$$

Equation 18 represents the two solitons solution which indicates the interaction of two solitons. If initially  $\tau \rightarrow -\infty$ , the larger soliton is behind the smaller one, then the phase shifts [17] after interaction of the two solitons are

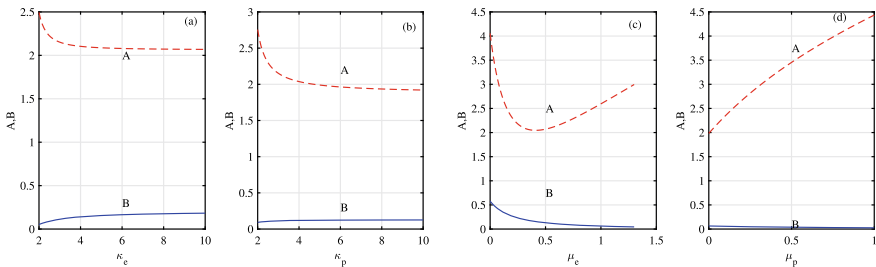
$$\gamma_1 = \frac{2B^{1/3}}{k_1} \ln \frac{k_1 + k_2}{k_1 - k_2}, \gamma_2 = -\frac{2B^{1/3}}{k_2} \ln \frac{k_1 + k_2}{k_1 - k_2}, \tag{19}$$

for larger and smaller solitons respectively. The phenomenon can easily be understood from Fig. 3, and is explained in the next section.

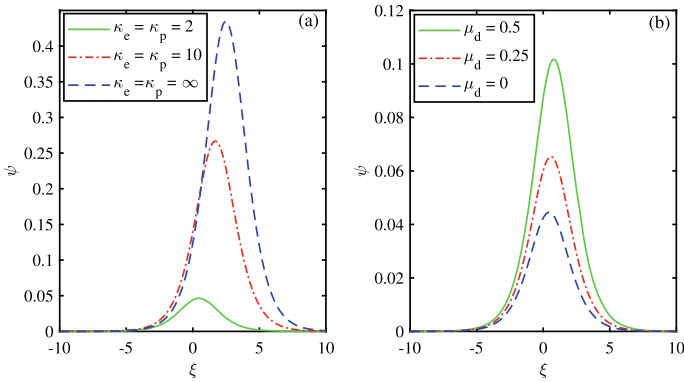
### 4 Results and Discussions

Figure 1 shows how the plasma parameters alter the nonlinearity and dispersion of the solitary wave. In Fig. 1a, b, the variation of ‘A’, and ‘B’ with the superthermality of the electrons and positrons have been shown. From the figure, it has been observed that both the nonlinearity and dispersion of the soliton are strongly influenced by the superthermality of the electrons and positrons. The nonlinearity coefficients are higher for higher superthermality (i.e. lower values of  $\kappa_e$ , and  $\kappa_p$ ), whereas the dispersion coefficients are lower for higher superthermality. The electron and positron densities also have impact on the nonlinearity and dispersion of the soliton. The nonlinearity decrease with increasing electron density and after reaching the minimum value, it increases with increasing electron density, as shown in Fig. 1c. On the other hand, the nonlinearity increases with increasing positron density (Fig. 1d). However, the dispersion is higher for lower electron and positron densities. From Fig. 1, it has been observed that for all values of  $\kappa_e$ ,  $\kappa_p$ ,  $\mu_e$ , and  $\mu_p$  only compressive soliton will generate.

The change in the potential of the single compressive soliton at  $\tau = 0$  for different values of the plasma parameters have been shown in Fig. 2. The potential of the soliton is maximum for Maxwellian electrons and positrons ( $\kappa_e = \kappa_p \rightarrow \infty$ ), and is minimum for highly superthermal electrons and positrons ( $\kappa_e = \kappa_p = 2$ ), as shown in Fig. 2a. This result can be elucidated as the increasing spectral indices cause increase in the electron and positron pressure. The increased pressure enhance the restoring force, due to which the potential of the soliton is higher for larger values of  $\kappa_e$  and  $\kappa_p$ . The potential of the soliton also depends upon the densities of the component. In Fig. 2b, the amplitude of the soliton for different dust densities has been shown. It is observed that the amplitude of the soliton is minimum for ion-acoustic mode ( $\mu_d = 0$ ) and it increases on increase of the dust density ( $\mu_d$ ). The increase in dust density indicates a decrease in electron density, which leads to the increase of the



**Fig. 1** The nonlinear (A) and dispersion coefficient (B) of the KdV equation for the variation of (a) the superthermal index of electron ( $\kappa_e$ ) with  $\kappa_p = 2$ ,  $\sigma = 0.01$ ,  $\mu_e = 1.27$ ,  $\mu_p = 0.3$ ,  $\beta = 1$ , (b) the superthermal index of positron ( $\kappa_p$ ) with  $\kappa_e = 2$ ,  $\sigma = 0.01$ ,  $\mu_e = 1.27$ ,  $\mu_p = 0.3$ ,  $\beta = 1$ , (c) the electron density ( $\mu_e$ ) with  $\kappa_p = \kappa_e = 2$ ,  $\sigma = 0.01$ ,  $\mu_p = 0.3$ ,  $\beta = 1$ , and (d) the positron density ( $\mu_p$ ) with  $\kappa_p = \kappa_e = 3$ ,  $\sigma = 0.01$ ,  $\mu_e = 1.27$ ,  $\beta = 1$



**Fig. 2** Variation of  $\psi$  versus  $\xi$  with (a)  $\sigma = 0.01, k = 1, \mu_e = 1.27, \mu_p = 0.3, \beta = 1$ , and (b)  $\sigma = 0.01, k = 1, \mu_p = 0.3, \kappa_e = \kappa_p = 2$ , and  $\beta = 1$

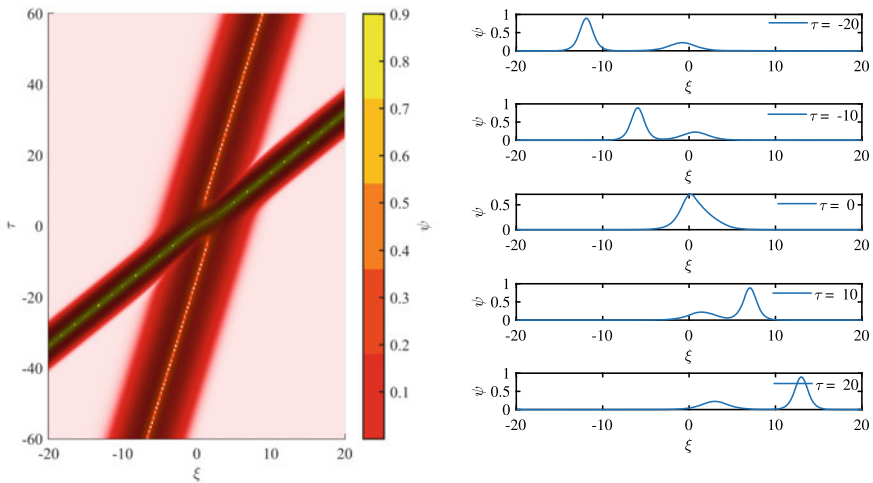


**Fig. 3** (LHS) Surface plot of the electrostatic potential ( $\psi$ ) of two interacting solitary waves with  $\sigma = 0.01, k_1 = 1, k_2 = 2, \mu_e = 1.27, \mu_p = 0.3, \kappa_e = \kappa_p = 2$ , and  $\beta = 1$ , (RHS) Variation of the electrostatic potential ( $\psi$ ) of two interacting solitary waves versus  $\xi$

dispersion as well as nonlinearity of the solitary waves. Therefore, the width and amplitude of the soliton increase with increased dust density.

The time evolution of the compressive DIA soliton in the plasma has been shown in Fig. 3. Two compressive DIA solitons, one with larger amplitude and narrower width than the second one, travelling in the same direction, undergone an interaction. At the interaction region, a single soliton is formed whose amplitude and width lie within the intermediate range of their respective amplitudes and widths. Then the single soliton breaks into two solitary structures and return to their initial amplitudes and widths to

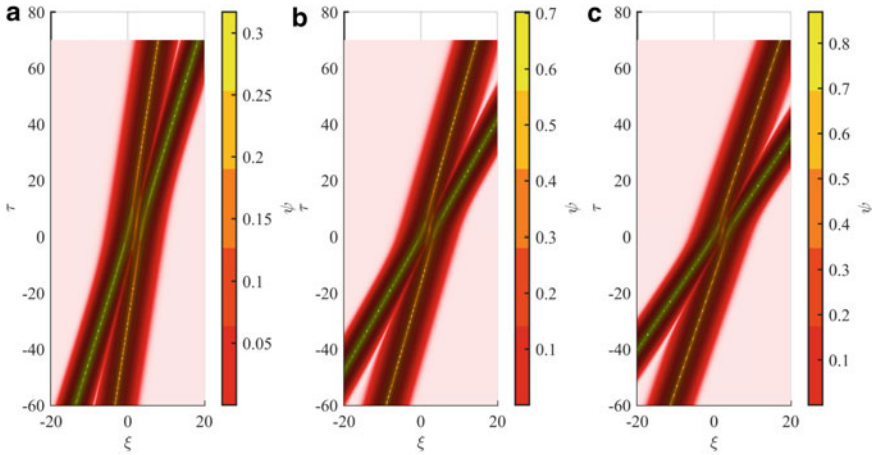


**Fig. 4** Surface plot of the electrostatic potential ( $\psi$ ) of two interacting solitary waves with  $\sigma = 0.01$ ,  $k_1 = 1$ ,  $k_2 = 2$ ,  $\mu_e = 1.27$ ,  $\mu_p = 0.3$ ,  $\beta = 1$  for three different set of values of  $\kappa_e$  and  $\kappa_p$ : **a**  $\kappa_e = \kappa_p = 2$  (highly suprathermal electrons and positrons), **b**  $\kappa_e = \kappa_p = 10$  (moderately suprathermal electrons and positrons), and **c**  $\kappa_e = \kappa_p \rightarrow \infty$  (Maxwellian electrons and positrons)

regain their shape at a later time. The surface plot for the interaction of two solitons has been shown in Fig. 3a. The trajectories of the solitons and the phase shifts induced in the trajectories of the solitons after collision can be observed from the figure. The propagation of the solitons at different time ( $\tau$ ), and their interaction has been shown in Fig. 3b. The parameters used are  $\sigma = 0.01$ ,  $k_1 = 1$ ,  $k_2 = 2$ ,  $\mu_e = 1.27$ ,  $\mu_p = 0.3$ ,  $\kappa_e = \kappa_p = 2$ , and  $\beta = 1$ . From the figure, it has been observed that at  $\tau = -20$ , the soliton with large amplitude is behind the one with smaller amplitude. At  $\tau = -10$ , the larger one starts to interact with the smaller one and become a single soliton at  $\tau = 0$ . At  $\tau = 10$ , the single soliton decompose to two solitons and the larger soliton overtake the smaller one. Finally at  $\tau = 20$ , each soliton appears as separate soliton acquiring their initial size and shape. The phase shifts of the two solitons can also be clearly observable from the figure (RHS). Both of the solitons have positive phase shifts. However, the larger soliton has a higher phase shift than the smaller soliton.

Figure 4 depicts the surface plots of the interacting DIA solitons for three cases of superthermality ( $\kappa$ ): (a) highly superthermal electrons and positrons ( $\kappa_e = \kappa_p = 2$ ), (b) moderately superthermal electrons and positrons ( $\kappa_e = \kappa_p = 10$ ), and (c) Maxwellian electrons and positrons ( $\kappa_e = \kappa_p \rightarrow \infty$ ). The figure shows that the amplitude of the two solitons increase with the increased values of spectral indices. The influence of the superthermal particles on the phase shift of the solitons after collision can be observed from the figure. The phase shift, i.e., the temporal change of the position of the two solitons is minimum for highly superthermal electrons and positrons, and is maximum for Maxwellian electrons and positrons. It can be explained with the help of the results shown in Fig. 3. From that figure we have observed that the larger soliton moves with a faster speed. Moreover, the increase

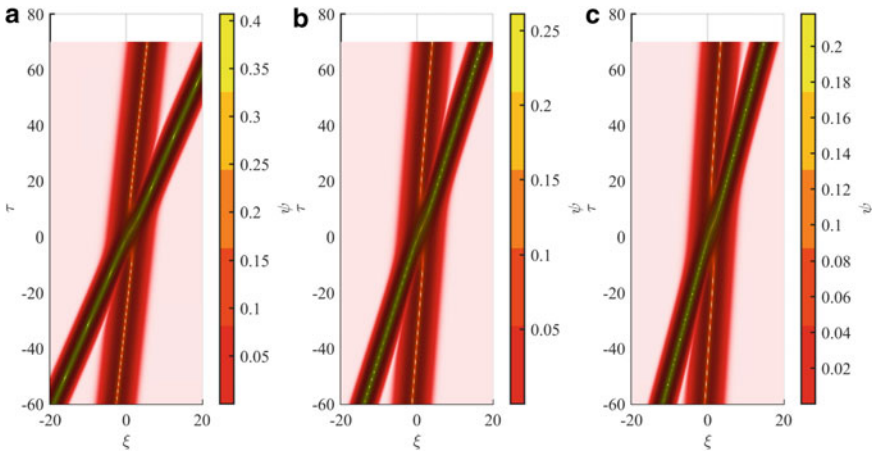


**Fig. 5** Surface plot of the electrostatic potential ( $\psi$ ) of two interacting solitary waves with  $\sigma = 0.01$ ,  $k_1 = 1$ ,  $k_2 = 2$ ,  $\mu_p = 0.3$ ,  $\beta = 1$ ,  $\kappa_e = \kappa_p = 2$  for three different set of values of  $\mu_d$ : **a**  $\mu_d = 0.5$ , **b**  $\mu_d = 0.25$ , and **c**  $\mu_d = 0$

in spectral index leads to the soliton with higher amplitude. So, on increase of the spectral index, the speeds of the solitons increase. This cause a faster change in the position of the two solitons and hence an increased phase shift. On the other hand, with a decrease in the superthermality, the temporal scale of interaction is reduced. This is because the solitary waves with Maxwellian particles have higher amplitudes as compared to superthermal particles. The larger amplitude solitons move with higher speed than the smaller amplitude solitons and, therefore, interact in a less time interval. The interaction of the solitons in presence of different dust concentrations have been shown in Fig. 5. In Fig. 5a, b the normalized dust densities are 0.5, and 0.25 respectively. In the absence of dust (i.e.  $\mu_d = 0$ ), the interaction of the ion-acoustic solitons are shown in Fig. 5c. From the figure, it has been observed that the increased dust density enhances the phase shift. Similarly, the time of interaction of the solitons is reduced with reduced dust density.

## 5 Conclusion

Here the generation and interaction of two DIA solitons in the plasma containing superthermal electrons and positrons, inertial positive ions and negatively charged static dust have been studied. It has been observed that the superthermal particles play a vital role on the nature of the solitons. The superthermality of electrons and positrons, and dust concentrations also play a crucial role on the nature of DIA solitons, and on the interaction of two dust-ion-acoustic solitons. The outcome of this work would helped to understand the collision of solitons in different laboratory and



space plasma such as, Earth's magnetosphere, Van Allen radiation belt etc., where a large number of low frequency electrostatic solitary waves have been detected.

## References

1. Rao, N.N., Shukla, P.K., Yu, M.Y.: Dust acoustic waves in dusty plasmas. *Planet. Space Sci.* **38**, 543–546 (1990). [https://doi.org/10.1016/0032-0633\(90\)90147-1](https://doi.org/10.1016/0032-0633(90)90147-1)
2. Baluku, T.K., Hellberg, M.A., Mace, R.L.: Electron acoustic waves in double-kappa plasmas: application to Saturn's magnetosphere. *J. Geophys. Res.* **116**, A04227 (2011). <https://doi.org/10.1029/2010JA016112>
3. Ghorui, M.K., Samanta, U.K., Maji, T.K., Chatterjee, P.: Head-on collisions of two type of dust-acoustic solitons in a magnetized plasma. *Astrophys. Space Sci.* **352**, 159–169 (2014). <https://doi.org/10.1007/s10509-014-1812-3>
4. Dutta, D., Goswami, K.S.: Dust ion acoustic double layer in the presence of superthermal electrons. *Indian J. Phys.* **93**, 257–265 (2019). <https://doi.org/10.1007/s12648-018-1279-0>
5. Dutta, D., Goswami, K.S.: Electron acoustic double layers in a magnetized plasma in the presence of superthermal particles. *J. Plasma Phys.* **85**, 905850308 (2019). <https://doi.org/10.1017/S0022377819000424>
6. Dutta, D., Adhikari, S., Moulick, R., Goswami, K.S.: Evolution of dust ion acoustic soliton in the presence of superthermal electrons. *Phys. Scr.* **94**, 125210 (2019). <https://doi.org/10.1088/1402-4896/ab3a5b>
7. Sahu, B., Roychoudhury, R.: Two-soliton solution of ion acoustic solitary waves in nonplanar geometry. *Astrophys. Space Sci.* **345**, 91–98 (2013). <https://doi.org/10.1007/s10509-013-1378-5>
8. Jahangir, R., Masood, W.: Interaction of electron acoustic waves in the presence of superthermal electrons in terrestrial magnetosphere. *Phys. Plasmas* **27**, 042105 (2020). <https://doi.org/10.1063/1.5143400>
9. Shukla, P.K., Mamun, A.A.: *Introduction to dusty plasma physics*, 1st edn. IOP, Bristol (2002)
10. Banerjee, G., Maitra, S.: Arbitrary amplitude dust ion acoustic solitons and double layers in the presence of nonthermal positrons and electrons. *Phys. Plasmas* **23**, 123701 (2016). <https://doi.org/10.1063/1.4971223>
11. Sarri, G., et al.: Generation of neutral and high-density electron-positron pair plasmas in the laboratory. *Nat. Commun.* **6**, 6747 (2015). <https://doi.org/10.1038/ncomms7747>
12. Mozer, F.S., Bale, S.D., Bonnell, J.W., Chaston, C.C., Roth, I., Wygant, J.: Megavolt parallel potentials arising from double-layer streams in the earth's outer radiationbelt. *Phys. Rev. Lett.* **111**, 1–5 (2013). <https://doi.org/10.1103/PhysRevLett.111.235002>
13. Dillard, C.S., Vasko, I.Y., Mozer, F.S., Agapitov, O.V., Bonnell, J.W.: Electron-acoustic solitary waves in the Earth's inner magnetosphere. *Phys. Plasmas* **25**, 022905 (2018). <https://doi.org/10.1063/1.5007907>
14. Hirota, R.: Exact solution of the Korteweg-de Vries equation for multiple collisions of solitons. *Phys. Rev. Lett.* **27**, 1192 (1971). <https://doi.org/10.1103/PhysRevLett.27.1192>
15. Saini, N.S., Singh, K.: Head-on collision of two dust ion acoustic solitary waves in a weakly relativistic multicomponent superthermal plasma. *Phys. Plasmas* **23**, 103701 (2016). <https://doi.org/10.1063/1.4963774>
16. Taniuti, T., Wei, C.C.: Reductive perturbation method in nonlinear wave propagation. *J. Phys. Soc. Jpn.* **24**, 941–946 (1968). <https://doi.org/10.1143/JPSJ.24.941>
17. Marchant, T.R., Smyth, N.F.: Soliton interaction for the extended Korteweg-de Vries equation. *IMA J. Appl. Math.* **56**, 157–176 (1996). <https://doi.org/10.1093/imamat/56.2.157>

# **Fluid Dynamics and Nonlinear Flows**

# Numerical Study of Shear Flow Past Two Flat Inclined Plates at Reynolds Numbers 100, 200 Using Higher Order Compact Scheme



Rajendra K. Ray and Ashwani

**Abstract** In this study, an incompressible two-dimensional flow across two flat inclined plates is investigated numerically using a Higher-order compact (HOC) finite difference scheme. The shear parameter values  $P = 0.0, 0.1$  are used to simulate simulations for two Reynolds numbers ( $Re$ ), 100 and 200. Each plate is of length “ $d$ ” and the shortest distance between the plates is exactly half of the plate’s length (i.e.,  $0.5d$ ). Plate-1 and Plate-2 are inclined with angles of attack (i.e., with x-axis),  $\alpha = (\pi - 45^\circ)$  and  $-\alpha$ , respectively. The impact of the Reynolds numbers and shear rate on the process of vortex shedding is investigated from the perspective of stream function, vorticity contours, center-line velocity fluctuation, and phase diagrams. The numerical findings show not only the influence of vortex shedding from two flat inclined plates in shear flow but also several important flow generating properties with  $P$  and  $Re$ . This is the first time, to our knowledge, a numerical investigation has been performed to study the vortex shedding phenomena for two flat inclined plates with angles of attacks,  $\alpha = (\pi - 45^\circ)$  and  $-\alpha$  respectively.

**Keywords** Shear flow · Flat inclined plates · HOC Scheme · Streamlines · Vorticity contours · Phase diagram

## 1 Introduction

The flow around bluff bodies has attracted much interest for for well over a century because of its engineering utility as well as its scientific significance in fluid dynamics. Flow through offshore platforms, heat exchangers and around bridge piers are just a few examples of mechanical, civil, and marine engineering applications. As a result, over the preceding century, a number of successful numerical, experimental,

---

R. K. Ray · Ashwani (✉)

School of Basic Sciences, Indian Institute of Technology Mandi, Mandi, Himachal Pradesh 175005, India

e-mail: [mr.punia11@gmail.com](mailto:mr.punia11@gmail.com)

URL: <https://www.iitmandi.ac.in/>

© The Author(s), under exclusive license to Springer Nature Switzerland AG 2022

301

S. Banerjee and A. Saha (eds.), *Nonlinear Dynamics and Applications*,

Springer Proceedings in Complexity,

[https://doi.org/10.1007/978-3-030-99792-2\\_26](https://doi.org/10.1007/978-3-030-99792-2_26)

and analytical research were carried out. In a uniform flow, the majority of study on flow through flat plates, square and circular cylinders has already been published in the literature [1–11]. At a Reynolds number of 250, Najjar and Balachandar [19] conducted a 3D numerical study of the flow behind a standard flat plate. It was noticed that the wake had small unsteadiness, which affected the flow field while also global integral characteristics like the drag coefficient and Strouhal number. Fage and Johansen [20] demonstrated that the Strouhal number had an almost constant value of 0.148 at angles of attack  $\alpha$  ranging from  $30^\circ$  to  $90^\circ$  in their early experiments using a plate at 18 distinct angles of incidence. Vortex shedding takes place at the two corners of a plate that is slanted, resulting in uneven mean velocity profile in the recirculation region's very nearby wake. According to Lam [21], The wake is regulated by a sequence of counterclockwise vortices shed from the top edge of the plate at an impact angle of  $30^\circ$ . Breuer and Jovicic [22] and Breuer et al. [23] studied the flow across an inclined plate at an angle of  $18^\circ$  with a Reynolds number of 20000, and their large-eddy simulation (LES) findings clearly revealed that the trailing edge vortices were significantly dominated by the wake. There's also no frequent vortex shedding right at the front edge, according to them. Turki [24] presented a numerical analysis of the control of vortex shedding behind a square cylinder in a laminar channel flow with a plate in the  $110 \leq Re \leq 200$  range. At the plate with a critical length ( $L_C$ ), the author presented that the vortex shedding completely stopped. When the inlet flow is sheared instead than uniform, wake exhibits a different flow behavior, as demonstrated from both numerical and experimental analysis by Ayukawa et al. [15], Kiya et al. [13], Hayashi and Yoshino [27], Adachi and Kato [12], Cheng et al. [17], Kwon et al. [14], Cao et al. [16], Kumar and Ray [18].

Kalita et al. [25] worked on higher-order compact schemes (HOC) for the unsteady 2D convection-diffusion equation with variable convection coefficients in 2002 and they demonstrated that in an area with a greater level of complexity, HOC scheme can produce extremely precise results with a small selection of grid points. The HOC approach for incompressible viscous flows in the polar coordinate system ( $r, \theta$ ) was further developed by Ray and Kalita [26] in 2009. As a result, the Higher Order Compact (HOC) finite difference methods for the calculation of incompressible viscous flows have been slowly gaining traction in recent years because of their excellent precision and advantages over compact difference stencils.

The flow behaviour of laminar shear flow over two flat inclined plates is investigated in this work. The angle positions of the flat plate with respect to the  $x$ -axis are  $\alpha = (\pi - 45^\circ)$  and  $-\alpha$ . The problem is solved numerically by using the higher-order compact (HOC) finite difference technique. In time variable, it's second-order accurate, while in space variables, it's fourth-order accurate. Figure 1 shows a graphic representation of the problem.

The rest of the work is structured in the following manner. The mathematical description of the physical problem as well as the discretization technique of governing equations is described in Sect. 2. Section 3 i.e Results and Discussion section deals with numerical investigation of the flow through two flat inclined plates. Finally, we explain our findings in Sect. 4 (conclusion section), which is followed by references.

## 2 Mathematical Modelling

An incompressible, unsteady shear flow past two flat inclined plates is considered here. The length of both plates is exactly  $d$  and the shortest distance between two plates is exactly half of the length of the plate as depicted in the problem's schematic diagram Fig. 1. The incompressible, two-dimensional (2D) Navier–Stokes equations govern the flow. In Cartesian coordinate  $(x, y)$ , the stream-function vorticity ( $F - \vartheta$ ) formulation of the 2D, incompressible Navier–Stokes equation in non-dimensional form is as follows:

$$\frac{\partial^2 \vartheta}{\partial x^2} + \frac{\partial^2 \vartheta}{\partial y^2} = Re \left( \frac{\partial \vartheta}{\partial t} + u \frac{\partial \vartheta}{\partial x} + v \frac{\partial \vartheta}{\partial y} \right) \tag{1}$$

$$\frac{\partial^2 F}{\partial y^2} + \frac{\partial^2 F}{\partial x^2} = -\vartheta \tag{2}$$

where vorticity and stream-function are represented by  $\vartheta$  and  $F$ , respectively.

$v$  = component of velocity in the  $y$ -direction,  $u$  = component of velocity in the  $x$ -direction

In terms of stream function ( $F$ ), the velocity component  $u, v$  may be represented as follows:

$$v = -\frac{\partial F}{\partial x}, u = \frac{\partial F}{\partial y} \tag{3}$$

so vorticity,

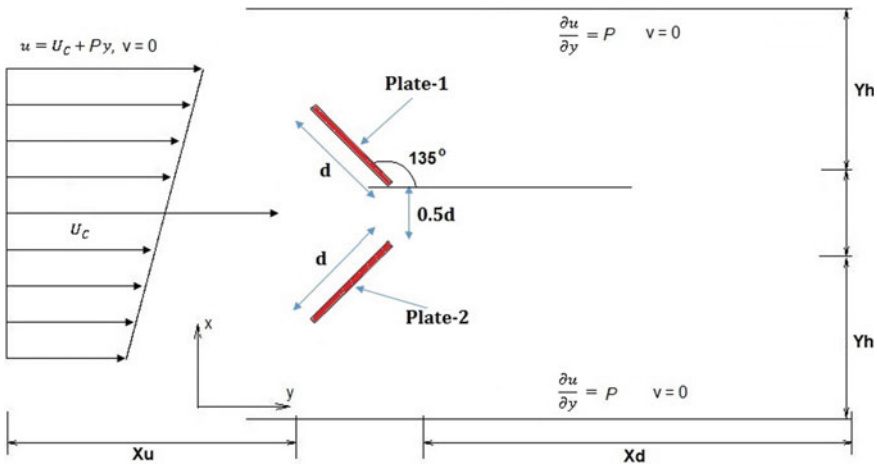


Fig. 1 Schematic Diagram of flow across two flat inclined plates

$$\vartheta = \frac{\partial v}{\partial x} - \frac{\partial u}{\partial y} \quad (4)$$

Although the physical domain is infinite, we consider a finite domain for computational purposes, where downstream boundaries, as well as the boundaries at top and bottom of the domain, are maintained far enough away from the plates so that the near wake instability should not be influenced by these boundaries of the computational domain. At the top and bottom boundaries, we use slip boundary conditions, and at the downstream border, we use convective boundary conditions [9, 18, 18]. On the surface of the flat inclined plate, the no-slip boundary condition is utilized. The linear shear flow is considered at the inlet boundary, i.e.,

$$u = U_c + Py, \quad v = 0 \quad (5)$$

where,  $U_c$  = Inflow velocity at the center-line,  $P$  = Shear rate

## 2.1 Numerical Discretization

Higher order compact (HOC) finite difference technique on uniform Cartesian grid [9, 18, 25] is used to discretize the governing equations. HOC scheme has already shown the ability to reproduce complex flow phenomena very efficiently and very accurately [9, 18, 26, 28, 29]. The governing equations (1) are discretized using HOC scheme at the  $(i, j)^{th}$  node as follows:

$$\begin{aligned} & [Re + P_{ij}\delta_x^2 + Q_{ij}\delta_y^2 + R_{ij}\delta_x + S_{ij}\delta_y + T_{ij}\delta_x\delta_y + \\ & \quad U_{ij}\delta_x\delta_y^2 + V_{ij}\delta_x^2\delta_y + W_{ij}\delta_x^2\delta_y^2]\vartheta_{ij}^{n+1} \\ = & [Re + P_{ij}\delta_x^2 + Q_{ij}\delta_y^2 + R_{ij}\delta_x + S_{ij}\delta_y + T_{ij}\delta_x\delta_y + \\ & \quad U_{ij}\delta_x\delta_y^2 + V_{ij}\delta_x^2\delta_y + W_{ij}\delta_x^2\delta_y^2]\vartheta_{ij}^n \end{aligned} \quad (6)$$

Likewise, (2) has the following HOC discretization:

$$[\delta_x^2 + \delta_y^2 - (K1 + L1)\delta_x^2\delta_y^2]F_{i,j} = [-1 + K1\delta_x^2 + L1\delta_y^2]\vartheta_{i,j} \quad (7)$$

where,

$$\begin{aligned} P_{i,j} &= -M2Re - 0.5\Delta t X1_{i,j} \\ Q_{i,j} &= -N2Re - 0.5\Delta t X2_{i,j} \\ R_{i,j} &= -M1Re - H12u_{i,j}(Re)^2 - 0.5\Delta t X3_{i,j} \\ S_{i,j} &= -N1Re - K12v_{i,j}(Re)^2 - 0.5\Delta t X4_{i,j} \\ T_{i,j} &= -0.5\Delta t X5_{i,j} \\ U_{i,j} &= -0.5\Delta t X6_{i,j} \\ V_{i,j} &= -0.5\Delta t X7_{i,j} \\ W_{i,j} &= -0.5\Delta t X8_{i,j} \end{aligned}$$

and,

$$X1_{i,j} = 1 + M1Reu_{i,j} + M2(Re)^2u_{i,j}^2 + 2M2Re(u_x)_{i,j}$$

$$X2_{i,j} = 1 + N1Rev_{i,j} + N2(Re)^2v_{i,j}^2 + 2N2Re(v_y)_{i,j}$$

$$X3_{i,j} = -Reu_{i,j} + M1Re(u_x)_{i,j} + N1Re(u_y)_{i,j} + M2Re^2u_{i,j}(u_x)_{i,j} \\ + M2Re(u_{xx})_{i,j} + N2Re(u_{yy})_{i,j} + N2Re^2v_{i,j}(u_y)_{i,j}$$

$$X4_{i,j} = -Rev_{i,j} + M1Re(v_x)_{i,j} + N1Re(v_y)_{i,j} + M2Re^2u_{i,j}(v_x)_{i,j} \\ + M2Re(v_{xx})_{i,j} + N2Re(v_{yy})_{i,j} + N2Re^2v_{i,j}(v_y)_{i,j}$$

$$X5_{i,j} = M1Rev_{i,j} + N1Reu_{i,j} + M2Re^2u_{i,j}v_{i,j} + 2M2Re(v_x)_{i,j} + 2N2Re(u_y)_{i,j} + \\ N2Re^2u_{i,j}v_{i,j}$$

$$X6_{i,j} = -M1 - M2Reu_{i,j} + N2Reu_{i,j}$$

$$X7_{i,j} = -N1 + M2Rev_{i,j} - N2Rev_{i,j}$$

$$X8_{i,j} = -M2 - N2$$

$$K1 = -h^2/12, \quad L1 = -H^2/12,$$

$$M1 = N1 = Reu_{i,j}h^2/6,$$

$$M2 = N2 = -h^2/12,$$

Where, The grid spacings in space variables and time variables are  $h$  and  $k$ , respectively.  $\delta_x$  and  $\delta_y$  are the first order central difference operators and  $\delta_x^2$  and  $\delta_y^2$  are the second order central difference operators in  $x$  and  $y$  direction, respectively. More information on the HOC discretization may be found in [9, 25].

### 3 Results and Discussion

#### 3.1 Grid and Time Independence Test

Uniform grids are used to discretize the computing domain. For three distinct grid sizes ( $400 \times 137$ ), ( $800 \times 275$ ) and ( $1600 \times 550$ ), a grid independence test was performed with a constant time increment of 0.01, and the results are presented in Table 1 for a representative point (0.8, -0.5). Table 1 indicates that a grid size of ( $800 \times 275$ ) is sufficient to generate acceptable results. For the grid sizes ( $800 \times 275$ ) and ( $1600 \times 550$ ), the relative error is only 0.394%. Table 2 presents the time independence test at a representative location (0.80, -0.50) behind the two inclined plates for 3 time increments 0.002, 0.006, and 0.01 values, on a grid of size ( $800 \times 275$ ). One can easily see that the variable's values are not changing much. So, the grid ( $800 \times 275$ ) with a time increment of 0.01 is adequate to depict the flow phenomena properly, based on the previous findings. We used a grid of size ( $800 \times 275$ ) and  $\Delta t = 0.01$  in our computations.

**Table 1** Velocities, Stream function, vorticity readings at (0.80, -0.5) behind the two inclined plates with  $\Delta t = 0.01$  at  $P = 0.1$ ,  $Re = 100$  at various grid sizes

$t$	$(L \times B)$	$u$	$v$	$F$	$\vartheta$	Max. relative error (%)
12.0	(400 × 137)	-0.20132	0.03171	-051582	-1.83485	8.433%
	(800 × 275)	-0.27180	0.08238	-0.61532	-2.00384	0.394%
	(1600 × 550)	-0.27150	0.08218	-0.61588	-2.01175	–

**Table 2** The influence of time increment on the outputs for  $Re = 100$ ,  $P = 0.1$ ,  $t = 5.0$  at point (0.80, -0.5)

$\Delta t$	$u$	$v$	$F$	$\vartheta$
0.002	-0.41745	0.05158	-0.56567	0.13175
0.006	-0.41723	0.05234	-0.56602	0.12851
0.01	-0.41710	0.05268	-0.56622	0.13413

### 3.2 Numerical Study

The influence of shear rate ( $P$ ) on the vortex shedding phenomena of flow across two flat inclined plates is investigated here for Reynolds numbers  $Re = 100, 200$  and shear parameters  $P = 0.0, 0.1$ . Figure 2a and b plot the streamline pattern for  $P = 0.0$  and  $P = 0.1$  respectively at Reynold number ( $Re$ ) = 100 for fully developed flow. The uniform flow is represented by  $P = 0.0$ . Fluid particles have distinct relative velocities on both the upper and lower surface of the Plates for positive  $P$  values.

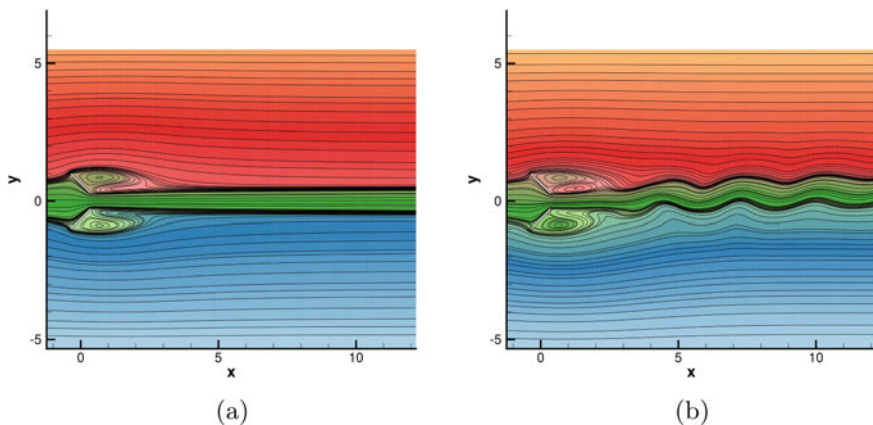


**Fig. 2** Streamline flow at  $Re = 100$ , **a**  $P = 0.0$ , **b**  $P = 0.1$



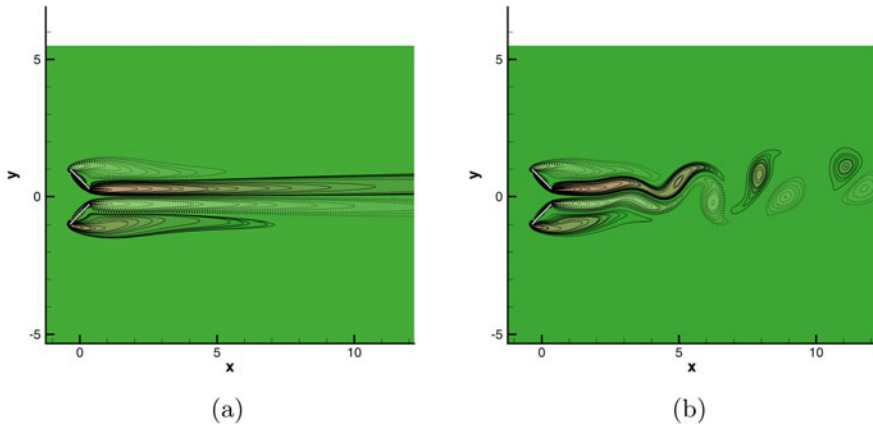


**Fig. 3** Contours of vorticity for  $Re = 100$ : **a**  $P = 0.0$ , **b**  $P = 0.1$

This causes an asymmetric shear gradient at the plate’s surface in the boundary layer. Asymmetrical vortices are created from the plate surface because the initial vortex is always generated from the surface with the greater relative velocity. The strengths of these asymmetrical vortices vary, resulting in uneven transverse and longitudinal vortex spacing. As a result, shear flows passing between two inclined plates display more intricate vortex shedding than uniform flows. For  $P = 0.0$ , the flow behind the two plates ultimately becomes fully steady, while for  $P = 0.1$ , the flow becomes unsteady from the start. The wake is symmetric along the centerline when  $P = 0.0$  and does not change with time. Figure 3a and b show the shear influence on vortex shedding more clearly for  $Re = 100$ . It is clear from Fig. 3a that flow has stabilised for  $P = 0.0$ . Because of the asymmetry in the entering freestream, the vortex shedding phenomena behind the two plates is different when  $P = 0.1$  than when  $P = 0.0$ . The Kármán vortex street is maintained by the periodic vortex shedding occurrence, although the positive and negative vortices are varied in size and intensity for  $P = 0.1$ . The vortices that emerge from the lower side of the top plate are larger than those that emerge from the top side of the lower plate.

The flow phenomena are next investigated for  $Re = 200$  with  $P = 0.0$  and  $0.1$ . The streamlines contours for  $P = 0.0$  and  $0.1$  are plotted in Figs. 4a and b, respectively. The streamline pattern for the uniform flow ( $P = 0.0$ ) is different from the preceding ( $Re = 100$ ). The flow behind the two plates does not become stable at  $Re = 200$  for uniform flow. As demonstrated in Fig. 4a, the flow pattern behind the plates is symmetric. Because of the shear impact, the streamlines pattern differs from  $P = 0.0$  to  $P = 0.1$  (Fig. 4b). Figure 5a and b shows the vorticity contours for  $P = 0.0$  and  $P = 0.1$  for  $Re = 200$ . Our findings in Fig. 4a and b are confirmed in these graphs. For  $Re = 200$ , the vortex shedding phenomenon is observed to be different for  $Re = 100$  and  $P = 0.0$ . Here, The flow-pattern is symmetric and periodic behind the two plates. The periodic vortex shedding phenomena still exists for  $P = 0.1$ , but the positive and negative vortices are distinct in size, shape, and inten-

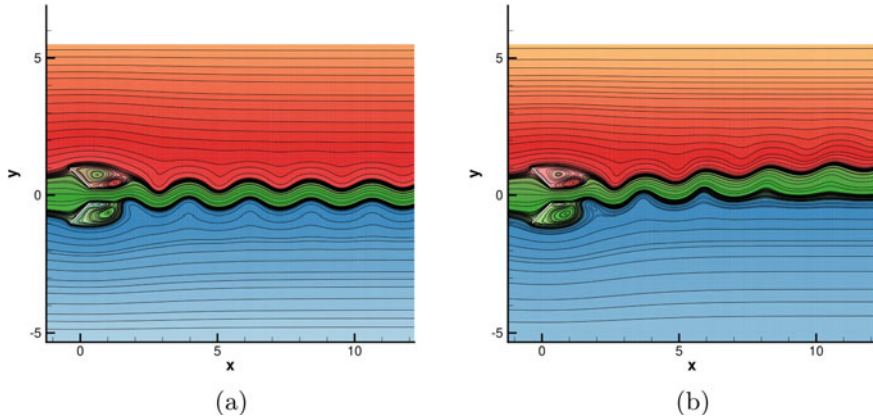


**Fig. 4** Streamline flow at  $Re = 200$ , **a**  $P = 0.0$ , **b**  $P = 0.1$

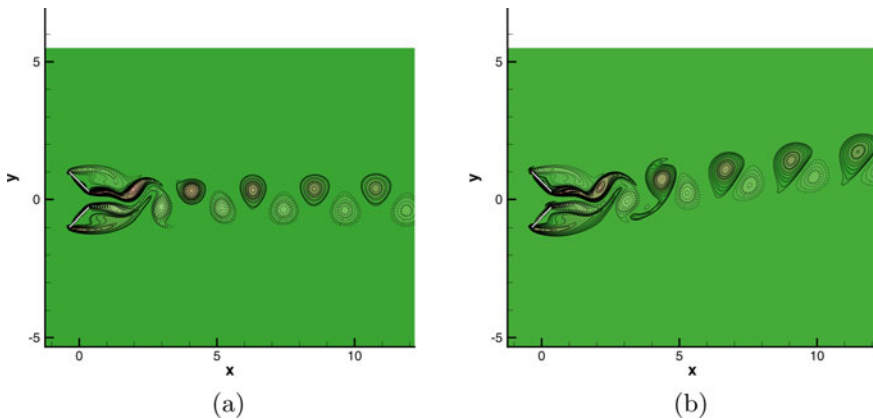


**Fig. 5** Contours of vorticity for  $Re = 200$ : **a**  $P = 0.0$ , **b**  $P = 0.1$

sity. The vortices on the bottom side of the Plate-1 are larger than the vortices on the top side of the Plate-2 ( $P = 0.1$ ). The frequency of vortex shedding is significantly greater for  $Re = 200$  and  $P = 0.1$ , but the vortex size and intensity are lower than for  $Re = 100$  and  $P = 0.1$ .

We plot the axial velocity profiles of  $v$  versus  $x$  at  $y = 0$  in Fig. 6a and  $u$  over  $y$  at  $x = 0$  in Fig. 6b for  $Re = 100$  after the flow has fully developed into its periodic condition. These figures show that there is no fluctuation in  $v$  velocity for  $P = 0.0$  as the flow accelerates equally from both surface of the two inclined plates and  $v$  velocity decrease along the  $x$ -axis for  $P = 0.1$ . whereas the amount of  $v$  variation is greater in the nearby wake region for  $P = 0.1$ . Figure 6a shows that as  $P$  rises,  $u$  rises in the upper part of the plates while falling in the lower part. Central-line velocity fluctuation also plotted for different values of  $P$  at  $Re = 200$  as shown in Fig. 7a

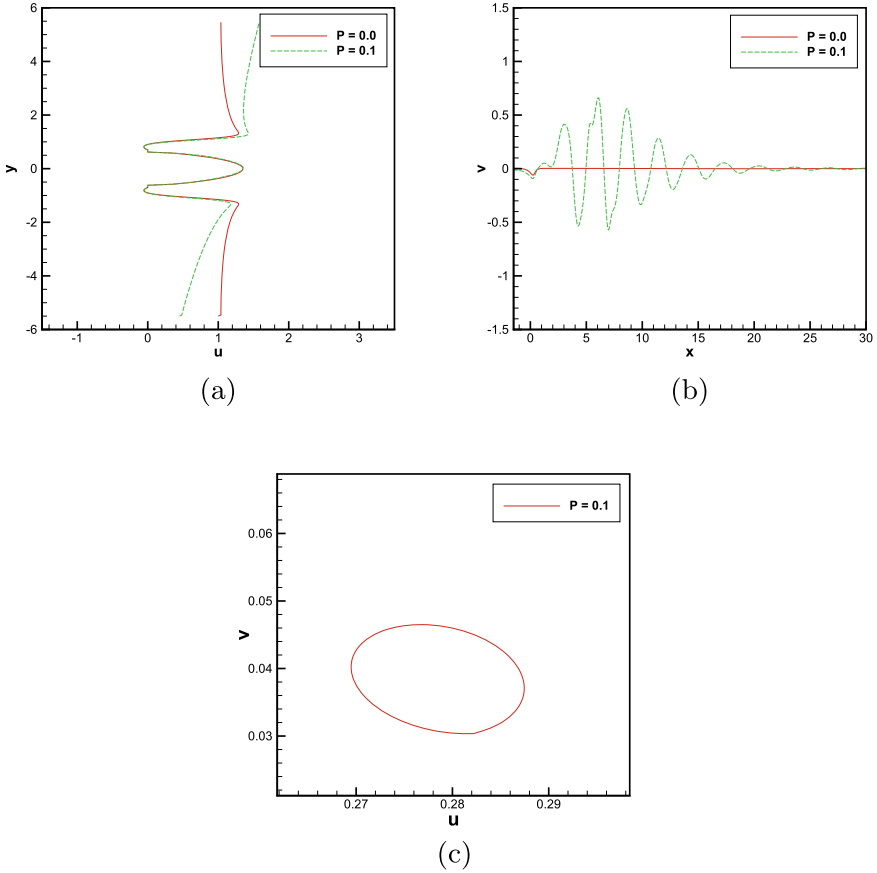


**Fig. 6** Centerline velocity variation at  $Re = 100$  and various  $P$  values: **a**  $u$  along the  $y$ -axis, **b**  $v$  along the  $x$ -axis, **c** ( $u$ - $v$ ) phase diagram

and b. We can observe that the  $u$  velocity profile behaves similarly to the previous  $Re = 100$  value, but  $v$ -velocity varies with the increased height of oscillations along the  $x$ -axis only in the near wake. When the flow has reached a stable periodic condition phase diagram (Figs. 6c, 7c) are also drawn between  $u$  versus  $v$  at a measuring point  $(0.80, -0.5)$  behind the both flat inclined plates for  $Re = 100, 200$  at various values of  $P$ . A periodic solution is depicted from these graphs.

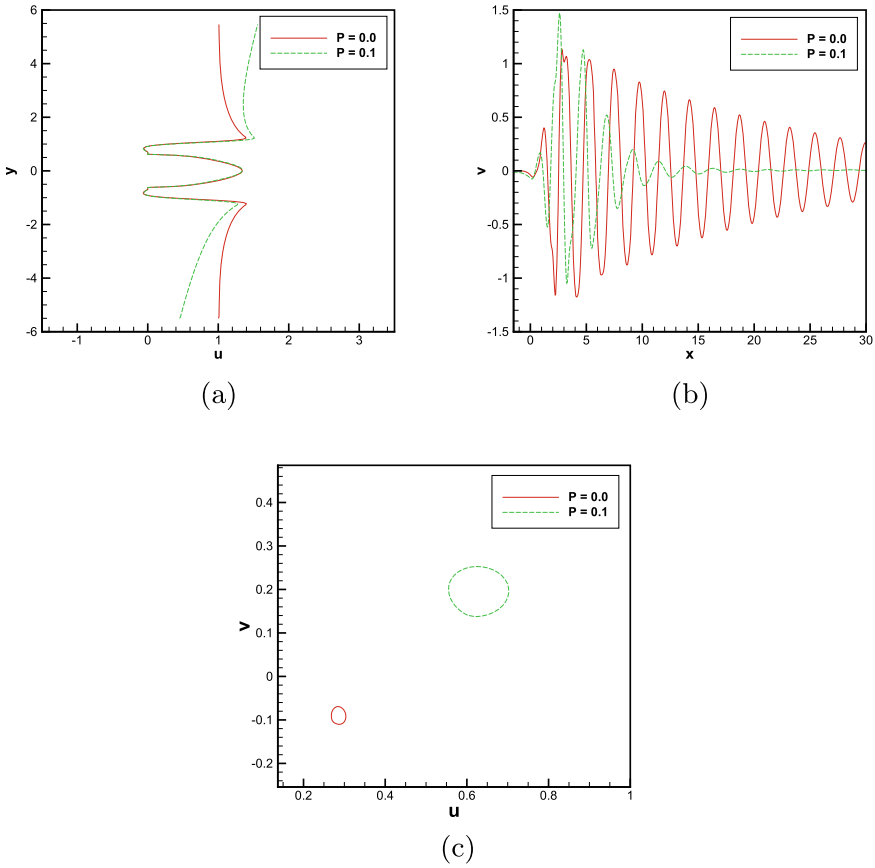


**Fig. 7** Centerline velocity variation at  $Re = 200$  and various  $P$  values: **a**  $u$  along the  $y$ -axis, **b**  $v$  along the  $x$ -axis, **c**  $(u-v)$  phase diagram

### 4 Conclusion

The HOC finite difference simulation of incompressible, linear shear flow across two flat inclined plates at  $Re = 100, 200$  and various  $P$  values is presented in this paper. The current simulation yields some new and useful details on flow near the two flat inclined plates at various shear parameter values ( $P = 0.0, P = 0.1$ ). The development of the wake behind inclined plates and the vortex shedding phenomena are substantially influenced by shear rate and Reynolds number, according to our findings. For all parameter values examined here, the flow that is completely developed is investigated in terms of streamline flow, vorticity contours, centerline velocity fluctuation, and phase diagrams. For different Reynolds numbers, certain intriguing flow phenomena have been observed. At  $Re = 200$ , the vorticity contours are symmetric about  $y = 0$  for uniform flow ( $P = 0.0$ ), whereas at  $Re = 100$ , the flow becomes

almost steady-state for uniform flow ( $P = 0.0$ ). The variations in the size and intensity of the alternatively shedding vortices become much more noticeable with shear flow. The frequency of vortex shedding is significantly greater for  $Re = 200$  and  $P = 0.1$ , but the vortex size and intensity are lower than for  $Re = 100$  and  $P = 0.1$ . Although the positive vortices have a narrow form and Over the positive vortices, the negative vortices are rounded for both  $Re = 100$  and  $Re = 200$  at  $P = 0.1$ . We can observe that for  $Re = 200$ , u-velocity behaves similarly to the preceding  $Re$ . But, On the other hand, the v-velocity profile has a periodic characteristic. For both  $P$  values, the amplitudes are bigger than those of  $Re = 100$ .

## References

1. Yang, D., Pettersen, B., Andersson, H., Narasimhamurthy, V.: Vortex shedding in flow past an inclined flat plate at high incidence. *Phys. Fluids* **24**, 084103 (2012)
2. Xu, L., Nitsche, M.: Start-up vortex flow past an accelerated flat plate. *Phys. Fluids* **27**, 033602 (2015)
3. Xu, L., Nitsche, M., Krasny, R.: Computation of the Starting Vortex Flow Past a Flat Plate. *Procedia IUTAM* **20**, 136–143 (2017)
4. Sohankar, A., Norberg, C., Davidson, L.: Simulation of three-dimensional flow around a square cylinder at moderate Reynolds numbers. *Phys. Fluids* **11**, 288–306 (1999)
5. Ranjan, R., Dalal, A., Biswas, G.: A numerical study of fluid flow and heat transfer around a square cylinder at incidence using unstructured grids. *Numer. Heat Transf. Part A: Appl.* **54**, 890–913 (2008)
6. A transformation-free HOC scheme for incompressible viscous flow past a rotating and translating circular cylinder. *J. Sci. Comput.* **46**, 265–293 (2010)
7. Kalita, J., Sen, S.: Triggering asymmetry for flow past circular cylinder at low Reynolds numbers. *Comput. Fluids* **59**, 44–60 (2012)
8. Mushyam, A., Bergada, J.: A numerical investigation of wake and mixing layer interactions of flow past a square cylinder. *Meccanica* **52**, 107–123 (2016)
9. Ray, R., Kumar, A.: Numerical study of shear rate effect on unsteady flow separation from the surface of the square cylinder using structural bifurcation analysis. *Phys. Fluids* **29**, 083604 (2017)
10. Kalita, J., Sen, S.: Unsteady separation leading to secondary and tertiary vortex dynamics: the sub- and sub-phenomena. *J. Fluid Mech.* **730**, 19–51 (2013)
11. Shademan, M., Naghib-Lahouti, A.: Effects of aspect ratio and inclination angle on aerodynamic loads of a flat plate. *Adv. Aerodyn.* **2** (2020)
12. Yoshioka, N., Adachi, K., Nakamura, A., Ishimura, H.: An experimental investigation of viscoplastic flow past a circular cylinder at high Reynolds numbers. *Rheol. Acta* **14**, 993–1000 (1975)
13. Kiya, M., Tamura, H., Arie, M.: Vortex shedding from a circular cylinder in moderate-Reynolds-number shear flow. *J. Fluid Mech.* **101**, 721–735 (1980)
14. Kwon, T., Sung, H., Hyun, J.: Experimental investigation of uniform-shear flow past a circular cylinder. *J. Fluids Eng.* **114**, 457–460 (1992)
15. Ayukawa, K., Ochi, J., Kawahara, G., Hirao, T.: Effects of shear rate on the flow around a square cylinder in a uniform shear flow. *J. Wind Eng. Ind. Aerodyn.* **50**, 97–106 (1993)
16. Cao, S., Hirano, K., Ozono, S., Wakasugi, Y.: On the vortex shedding from a circular cylinder in a linear shear flow. *J. Wind Eng.* **25**, 53–62 (2000)
17. Cheng, M., Tan, S., Hung, K.: Linear shear flow over a square cylinder at low Reynolds number. *Phys. Fluids* **17**, 078103 (2005)

18. Kumar, A., Ray, R.: Numerical study of shear flow past a square cylinder at Reynolds numbers 100, 200. *Proc. Eng.* **127**, 102–109 (2015)
19. Najjar, F., Balachandar, S.: Low-frequency unsteadiness in the wake of a normal flat plate. *J. Fluid Mech.* **370**, 101–147 (1998)
20. Fage, A., Johansen, F.: *On the Flow of Air Behind an Inclined Flat Plate of Infinite Span.* HMSO, London (1927)
21. Lam, K.: Phaselocked eduction of vortex shedding in flow past an inclined flat plate. *Phys. Fluids* **8**, 1159–1168 (1996)
22. Breuer, M., Jovicic, N.: Separated flow around a flat plate at high incidence: An LES investigation. *J. Turbul.* **2**, N18 (2001)
23. Breuer, M., Jovicic, N., Mazaev, K.: Comparison of DES, RANS and LES for the separated flow around a flat plate at high incidence. *Int. J. Numer. Meth. Fluids* **41**, 357–388 (2003)
24. Turki, S.: Numerical simulation of passive control on vortex shedding behind square cylinder using splitter plate. *Eng. Appl. Comput. Fluid Mech.* **2**, 514–524 (2008)
25. Kalita, J., Dalal, D., Dass, A.: A class of higher order compact schemes for the unsteady two-dimensional convection-diffusion equation with variable convection coefficients. *Int. J. Numer. Meth. Fluids* **38**, 1111–1131 (2002)
26. Kalita, J., Ray, R.: A transformation-free HOC scheme for incompressible viscous flows past an impulsively started circular cylinder. *J. Comput. Phys.* **228**, 5207–5236 (2009)
27. Hayashi, T., Yoshino, F.: On the evaluation of the aerodynamic forces acting on a circular cylinder in a uniform shear flow. *Trans. Jpn. Soc. Mech. Eng. Ser. B* **56**, 289–294 (1990)
28. Mittal, H., Al-Mdallal, Q., Ray, R.: Locked-on vortex shedding modes from a rotationally oscillating circular cylinder. *Ocean Eng.* **146**, 324–338 (2017)
29. Ray, R.: A transformation-free HOC scheme for incompressible viscous flow past a rotating and translating circular cylinder. *J. Sci. Comput.* **46**, 265–293 (2010)

# On Transport Phenomena of Solute Through a Channel with an Inclined Magnetic Field



Susmita Das  and Kajal Kumar Mondal 

**Abstract** Under the effect of an angled magnetic field and the constant gradient of pressure, the present study investigates the solute dispersion in a Magneto-Hydrodynamics (MHD) flow between two infinite parallel plates, with the upper plate moving at a constant speed while the lower plate remains stationary. The unsteady advection-diffusion equation is solved by Aris's moments method with aid of a finite-difference scheme. It is shown that with the enhancement of absorption parameter, inclination angle of magnetic field and Hartmann number, the dispersion of the solute decreases. It is observed that after a certain critical time, the coefficient of dispersion asymptotically comes to a stationary circumstance for all cases. The present result may be applied for separation of matter from the fluids. The reaction parameter ( $\beta$ ), inclination of an angle of the magnetic field ( $\alpha$ ), the Hartmann number ( $M$ ), and the dispersion time ( $t$ ) all have a significant impact on the solute's mean concentration profiles.

**Keywords** Inclined magnetic field · Dispersion · Method of moments · Channel · Absorption · Dispersion · Distribution of mean Concentration

## 1 Introduction

The study of the behavior of electrically conducting fluids and their magnetic properties is known as magneto-hydrodynamics. Due to its several applications in a variety of fields, including MHD power generation, oil reservoir engineering, separation of matter from fluids, aerodynamics, astrophysics and environmental mechanics, the study of dispersion phenomena in MHD fluids flows is highly important. Taylor [1] first studied the basic mechanism of dispersion of tracers in a laminar Poiseuille

---

Supported by Science and Technology and Biotechnology Department, Government of West Bengal, India.

---

S. Das (✉) · K. K. Mondal  
Cooch Behar Panchanan Barma University, Cooch Behar 736101, India  
e-mail: [rimidas2105@gmail.com](mailto:rimidas2105@gmail.com)

© The Author(s), under exclusive license to Springer Nature Switzerland AG 2022  
S. Banerjee and A. Saha (eds.), *Nonlinear Dynamics and Applications*,  
Springer Proceedings in Complexity,  
[https://doi.org/10.1007/978-3-030-99792-2\\_27](https://doi.org/10.1007/978-3-030-99792-2_27)

flow through a pipe. Aris [2] developed Taylor's work by removing some restrictions using his method of moments.

Gupta and Chatterjee [3] explained the solute transport in a MHD flow which is flowing through a channel with the aid of a transverse magnetic field analytically. They revealed that the coefficient of dispersion reduces as the magnetic field enhances. Annapurna and Gupta [4] extended the work and showed that the fluctuations in the dispersion coefficient reduces with enhancement of the Hartmann number. Many researchers [5–9] explore this area successfully.

Mazumder and Das [10] investigated that the first order boundary absorption on the dispersion process when the fluid is moving through a tube. They showed that the coefficient of dispersion reaches to its stationary circumstance after a certain critical time. Using a semi analytical approach, Sebastian and Nagarani [11] analyzed the dispersion of the contaminant through an annulus with an reaction parameter at the outer wall.

The dispersion of solute has been studied by many researchers over the last two decades in different flow geometry. But till now, no work has been discussed to study the mass transport phenomena of solute through a channel with absorption boundary consisting of an inclined magnetic field. The primary objective of the present research work is to present the effects of Hartmann number, the angle of inclination of the magnetic field and absorption parameter on the dispersion process of tracers through a channel of electrically conducting fluid. The inclined magnetic field is a magnetic field with nonzero inclination and it is the angle between the direction of the vector  $\vec{B}$  with the perpendicular to the flow direction. Since, it significantly effects the velocity profile and consequently, on the dispersion process of the solute, the recent study is highly important for investigation of the basic mechanism of the tracers in a MHD flow. The time-dependent advection-diffusion equation with recommended initial and boundary conditions is solved using Aris' method of moments followed by a finite difference implicit scheme. The coefficient of dispersion and the distribution of the mean concentration of the contaminant are presented for all time period.

## 2 Formulation of the Problem

Consider a steady, laminar, fully developed, incompressible, viscous, two dimensional electrically conducting fluid, flowing through a infinite parallel plates caused by a constant gradient of pressure along the  $x^*$ -direction and  $y^*$ -axis is taken perpendicular to the direction of the channel flow. The stationary lower plate is situated at  $y^* = -h$ . The upper plate is at  $y^* = h$  and it moves at a constant speed  $U$  (Fig. 1). A magnetic field  $\vec{B}$  is applied at an angle  $\alpha$  with the vertical  $y^*$ -direction. The interaction between magnetic and velocity fields give rise to an electric field  $\vec{E}$  and it satisfies the relation  $\vec{E} = \vec{V} \times \vec{B}$ . In this research, the flow is considered along the  $x^*$ -direction only and consequently, the velocity and magnetic flux profiles are given by  $\vec{V} = (u, 0, 0)$  and  $\vec{B} = (0, B \sin \alpha, 0)$ . It is also assumed no electric



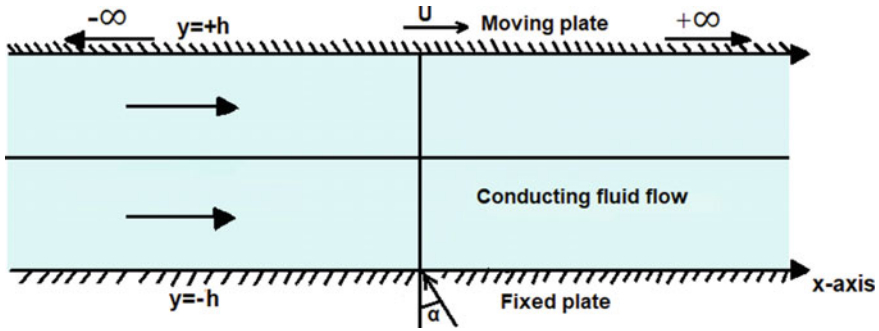


Fig. 1 MHD flow through a infinite parallel plates in presence of an inclined magnetic field

field is applied in the above mentioned flow. In this flow situation, the dimensional  $\vec{x}$  -momentum equation is

$$0 = -\frac{1}{\rho} \frac{\partial p^*}{\partial x^*} + \frac{\mu}{\rho} \left( \frac{\partial^2 u^*}{\partial x^{*2}} \right) + \frac{\sigma B^2 \sin^2 \alpha}{\rho} u^* \tag{1}$$

and consequently, the dimensionless form of the Eq. (1) can be expressed as

$$\frac{d^2 u}{dy^2} - M^2 \sin^2 \alpha u = -P \tag{2}$$

where  $P (= -\frac{dp}{dx})$  is the pressure gradient which is constant, in the longitudinal  $x$ -direction,  $\alpha$  is an inclination of angle of the magnetic field and  $M = Bh\sqrt{\frac{\sigma}{\rho\nu}}$  is the Hartmann number which is directly proportional to the the Magnetic field  $B$ . Also,  $M$  represents the relative significance between the magnetic force and the viscous force. Solving (1) with respect to the non-dimensional boundary conditions  $u = 0$  at  $y = -1$  and  $u = 1$  at  $y = 1$ , the dimensionless velocity distribution is given by

$$u(y) = \frac{1}{\sinh(2M \sin \alpha)} \left[ \sinh(M \sin(y + 1)) - \frac{P}{M^2 \sin^2 \alpha} \sinh(M \sin \alpha) \times \cosh(M \sin \alpha)y \right] + \frac{P}{M^2 \sin^2 \alpha} \tag{3}$$

Figure 2a and b represent the velocity distribution for different values of Hartmann number ( $M$ ) and inclination of an angle ( $\alpha$ ) of the magnetic field respectively. From the figures, it is seen that velocity significantly decreases with the increment of  $M$  and  $\alpha$ . This is because, the applied magnetic field produces a Lorentz force which acts against the flow. In a similar manner, the inclination of an angle of the magnetic field resists the flow.

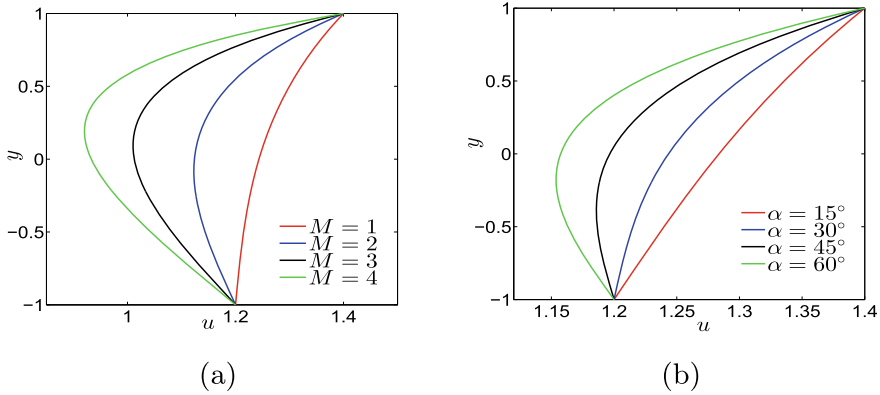


**Fig. 2** Velocity distribution for various values of **a**  $M$  when  $\alpha = 30^\circ$ , **b**  $\alpha$  when  $M = 1$

When a passive solute with an invariable molecular diffusivity  $D$  is introduced in the above mentioned flow in existence of a first-order reaction at the inner and outer walls of the channel, the mean concentration  $C(x, y, t)$  of the tracers satisfies the following dimensionless advection-diffusion equation,

$$\frac{\partial C}{\partial t} + S_c u(y) \frac{\partial C}{\partial x} = \frac{\partial^2 C}{\partial x^2} + \frac{\partial^2 C}{\partial y^2}, \tag{4}$$

Here, the dimensionless parameters are  $t = \frac{D t^*}{h^2}$ ,  $x = \frac{x^*}{h}$ ,  $y = \frac{y^*}{h}$ ,  $u = \frac{u^* h}{\nu}$  where  $\nu = \frac{\mu}{\rho}$  and  $S_c = \frac{\nu}{D}$  is the Schmidt number expressed as the ratio of momentum diffusivity (kinematic viscosity) and mass diffusivity. The Schmidt number is used to characterize the fluid flow in which momentum and mass diffusion processes occur simultaneously. The corresponding initial and boundary conditions are considered as,

$$C(x, y, 0) = \delta(y) \tag{5a}$$

$$\left[ \frac{\partial C}{\partial y} + \beta C \right]_{y=1} = 0 \quad \text{at } y = 1 \tag{5b}$$

$$\left[ \frac{\partial C}{\partial y} - \beta C \right]_{y=-1} = 0 \quad \text{at } y = -1 \tag{5c}$$

Also, it is assumed that at all points, the value of  $C$  is finite,

$$\frac{1}{2} \int_{-1}^1 \int_{-\infty}^{\infty} C(x, y, 0) dx dy = 1 \tag{6}$$

where  $\beta = (\beta^* h)$  defines the first-order reaction rate or reaction parameter corresponding to the catalytic reaction at both walls. If  $\beta = 0$  then one can suggest the

dispersion process of solute is chemically inert or neutrally buoyant. From Aris's moment method, the  $k$ th integral moment of the mean concentration distribution is as follows,

$$C_k(y, t) = \int_{-\infty}^{\infty} x^k C(x, y, t) dx \tag{7}$$

The concentration of the solute is distributed along the channel's cross section as follows,

$$M_k(t) = \bar{C}_k = \frac{\int_{-1}^1 C_k(y, t) dy}{2} \tag{8}$$

Using (7), the diffusion Eq. (4) with initial and boundary conditions become

$$\frac{\partial C_k}{\partial t} - \frac{\partial^2 C_k}{\partial y^2} = ku(y)S_c C_{k-1} + k(k-1)C_{k-2} \tag{9}$$

with

$$C_k(y, 0) = \delta(y) \tag{10}$$

where

$$C_k(y, 0) = 1 \quad \text{for } k = 0 \tag{11}$$

$$C_k(y, 0) = 0 \quad \text{for } k > 0 \tag{12}$$

$$\left[ \frac{\partial C_k}{\partial y} + \beta C_k \right]_{y=1} = 0 \tag{13a}$$

$$\left[ \frac{\partial C_k}{\partial y} - \beta C_k \right]_{y=-1} = 0 \tag{13b}$$

and

$$\frac{dM_k}{dt} = kS_c \overline{u(y)C_{k-1}} + k(k-1)\bar{c}_{k-2} - \frac{1}{2}\beta[C_k(-1, t) + C_k(+1, t)] \tag{14}$$

Where

$$M_k(0) = 1 \quad \text{for } k = 0 \tag{15}$$

$$M_k(0) = 0 \quad \text{for } k > 0 \tag{16}$$

The cross-sectional mean concentration of the tracers is indicated by the over-bar. For a concentration distribution, the  $k$ th integral moment about the mean is given by

$$v_k(t) = \frac{1}{2M_0} \int_{-1}^1 \int_{-\infty}^{\infty} (x - x_g) C dx dy \tag{17}$$

where

$$x_g = \frac{1}{2M_0} \int_{-1}^1 \int_{-\infty}^{\infty} x C dx dy = \frac{M_1}{M_0} \tag{18}$$

$x_g$  represents the first moment or the centroid of the solute which defines the initial location of the slug’s centre of gravity with mean fluid velocity and  $M_0$  is the total mass of the contaminant. The variance, skewness, and kurtosis of a contaminant’s distribution are designated as  $v_2, v_3$  and  $v_4$  respectively. The non-zero values of skewness suggest the deviation from the Gaussianity of the concentration distribution and when the kurtosis is greater than 3, the peak of the mean concentration of the contaminant becomes sharper.

### 3 Numerical Procedure

when  $k \geq 1$  and  $\beta \neq 0$ , a finite difference implicit scheme is used for solving the Eq. (9), with above initial (10) and boundary [(13a)–(13b)] conditions, due to the analytical complexity. Here, the mesh point  $(p, q)$  indicates a point where  $t_p = (p - 1) \times \Delta t$  and  $y_q = -1 + (q - 1) \times \Delta y$ . The increments along the time  $t$  direction and the space  $y$  directions are represented by  $\Delta t = t_{p+1} - t_p$  and  $\Delta y = y_{p+1} - y_p$  respectively. Using forward difference for  $\frac{\partial C_k}{\partial t}$  and three-point averaged central difference for  $\frac{\partial^2 C_k}{\partial y^2}$ , the resulting system of linear algebraic equation is given by,

$$E_q \Omega_k(p + 1, q + 1) + F_q \Omega_k(p + 1, q) + G_q \Omega_k(p + 1, q - 1) = H_q \tag{19}$$

where  $E_q, F_q, G_q$  and  $H_q$  are the matrix elements. The finite difference schemes for the initial and boundary conditions are

$$C_k(1, q) = \begin{cases} 1 & \text{for } k = 0, \\ 0 & \text{for } k \geq 1 \end{cases} \tag{20}$$

and for  $k \geq 0$

$$C_k(p + 1, 0) = C_k(p + 1, 2) - 2\beta \Delta y C_k(p + 1, 1) \quad \text{at } y = -1 \tag{21a}$$

$$C_k(p + 1, M + 1) = C_k(p + 1, M - 1) - 2\beta \Delta y C_k(p + 1, M) \quad \text{at } y = 1 \tag{21b}$$

In this work,  $M(=31)$  is the value of the index  $q$  at the outer wall of the channel. The index  $p$  which represents the dispersion time is lies between 1 and  $N$  where  $N_{\max}$

is taken as 12000. The Thomas algorithm [12] is employed to solve the resultant tri-diagonal coefficient matrix. Simpson's one-third rule is used to compute the values of  $M_k$  using the known values of  $u(y)$  and  $C_k$ .

Since the diffusion of the contaminant along the longitudinal direction is negligibly small in compare to that of in the lateral direction, the effective longitudinal dispersion coefficient is taken as [13]

$$D_a = \frac{1}{2P_e^2} \frac{dv_2}{dt} \quad (22)$$

Also, the coefficients of skewness and kurtosis of the tracer distribution are represented as,

$$\beta_2 = \frac{v_3}{v_2^{\frac{3}{2}}} \quad (23a)$$

$$\beta_3 = \frac{v_4}{v_2^2} - 3 \quad (23b)$$

To find the distribution of the mean concentration  $C_m(x, t)$  along the longitudinal direction, the Hermite polynomial expression [14] and the central moments  $v_2$ ,  $\beta_2$ ,  $\beta_3$  are used. The Hermite polynomial expression for the distribution of the mean concentration is of the form,

$$C_m(t, x) = M_0(t)e^{-X^2} \sum_{r=0}^{\infty} a_r(t)H_r(x) \quad (24)$$

where  $X = \frac{x-x_g}{\sqrt{2v_2}}$ ,  $x_g = \frac{M_1}{M_0}$  and the Hermite polynomials  $H_r(x)$  that satisfy the recurrence relation [14]

$$H_{r+1}(x) = 2xH_r(x) - 2rH_{r-1}(x), \quad r = 1, 2, 3, \dots \quad (25)$$

with  $H_0(x) = 1$ . The coefficients  $a_r$  are found [14] from Eq. (24),

$$a_0 = \frac{1}{\sqrt{2\pi v_2}}, \quad a_1 = a_2 = 0, \quad a_3 = \frac{\sqrt{2}a_0\beta_2}{24}, \quad a_4 = \frac{a_0\beta_3}{96}.$$

## 4 Results and Discussions

In this section, the different flow characteristic such as dispersion coefficient and mean concentration distribution of the solute are studied with respect to the various flow parameters namely, Hartmann number ( $M$ ), absorption parameter ( $\beta$ ) and inclination of an angle ( $\alpha$ ) of the magnetic field. Figure 3a, b and c represent the

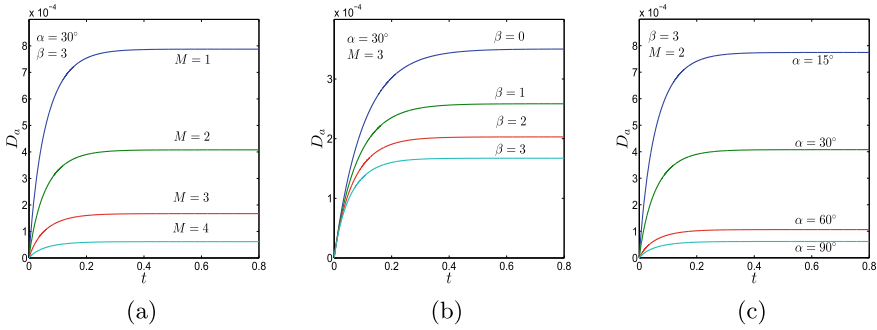


**Fig. 3** Coefficient of Dispersion  $D_a$  for  $S_c = 1000$  and different values of **a**  $M$  when:  $\beta = 3$  and  $\alpha = 30^\circ$ . **b**  $\beta$  when:  $\alpha = 30^\circ$  and  $M = 3$ . **c**  $\alpha$  when:  $\beta = 3$  and  $M = 2$

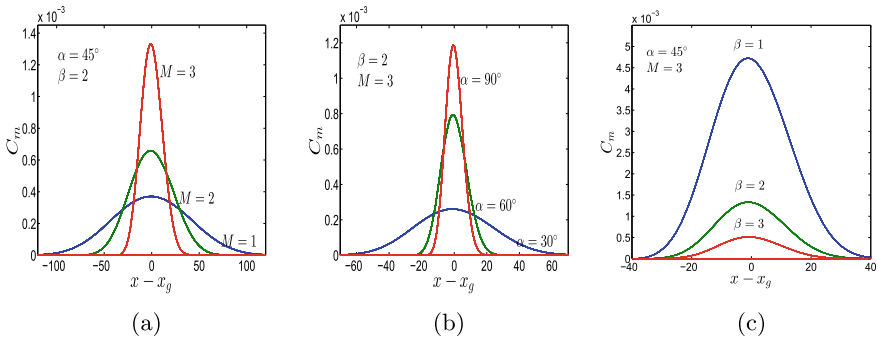


**Fig. 4** Distribution of Mean concentration  $C_m(t, x)$  for  $S_c = 1000$  at time  $t = 1.1$  for various values of **a**  $M$  when  $\alpha = 45^\circ$  and  $\beta = 2$  **b**  $\alpha$  when  $M = 3$  and  $\beta = 2$  **c**  $\beta$  when  $\alpha = 45^\circ$  and  $M = 3$

variations of the dispersion coefficient for different values of  $M$ ,  $\beta$  and  $\alpha$  against the dispersion time  $t$ , where the other flow parameter are described in the caption of the figure. Figure 3a shows that the coefficient of dispersion  $D_a$  of the solute reduces if the Hartmann number enhances. The cause behind this, as  $M$  increases, the resisting Lorentz force enhances and consequently, there is a drop in  $D_a$ . The reduction in the coefficient of dispersion is also observed with the enhancement of both  $\beta$  and  $\alpha$  [see Fig. 3b and c]. It is seen that for all cases the  $D_a$  reaches to a stationary circumstance after certain dispersion time. It is also observed from the Fig. 3b that in absence of reaction parameter at the walls, the  $D_a$  reaches to its steady state after a longer instant of time in compare to that of the dispersion coefficient when  $\beta$  is present.

Figure 4a exhibits the variation of the distribution of mean concentration  $C_m(t, x)$  at a particular time ( $t = 1.1$ ) against the axial distance  $x - x_g$  for different  $M$  when  $\alpha = 45^\circ$ ,  $\beta = 2$  and  $S_c = 1000$ . It is shown that the enhancement of  $M$  leads to increment of the peak of the distribution of the mean concentration of the tracer molecules but the axial expansion of the distributions diminishes. The reason behind this, as  $M$  increases the flow velocity as well the dispersion coefficient reduces along

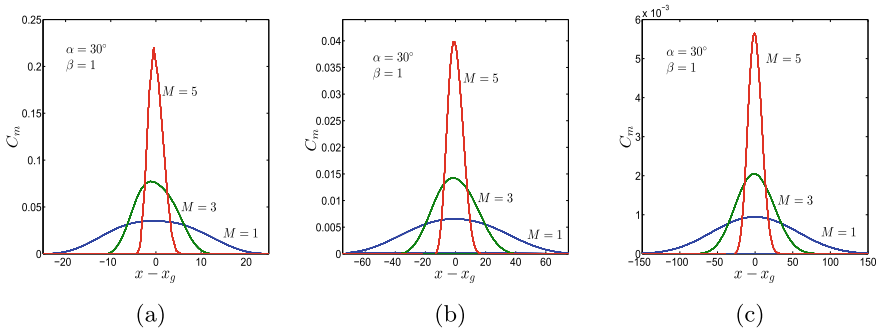


**Fig. 5** Distribution of Mean concentration  $C_m(t, x)$  for  $S_c = 1000$ ,  $\beta = 1$  and  $\alpha = 30^\circ$  for various  $M$  at time **a**  $t = 0.08$  **b**  $t = 0.4$  **c**  $t = 1.2$

the axial direction and hence there is an increment in the amplitude of the mean concentration. The similar behavior is observed for the variation of  $\alpha$  in the mean concentration distribution [see Fig. 4b]. Figure 4c illustrates the mean concentration distribution for various values of  $\beta$  where the other parameters are  $\alpha = 45^\circ$ ,  $M = 3$  and  $S_c = 1000$ . An opposite phenomena is found in the distribution of the mean concentration of the traces in compared to that of the Fig. 4a and b, as  $\beta$  increases. As  $\beta$  increases, the tracer molecules are attracted by the reaction parameter and it is depleted along the walls. Thus, the distribution of the concentration mean becomes flatter.

Figure 5a–c represent the mean concentration distribution  $C_m(t, x)$  for different values of Hartmann number with the dispersion times  $t = 0.08, 0.4, 1.2$  respectively, where the fixed parameter are  $\alpha = 30^\circ$ ,  $\beta = 1$  and  $S_c = 1000$ . It is observed for all cases that, as the Hartmann number enhances, the amplitude of the mean concentration profiles enhances. But, the strength of the concentration of the solute decreases prominently as time proceeds. It is significantly note that the mean concentration distribution of the tracers shows asymmetry when the dispersion time is small (see Fig. 5a) and it tends to become symmetric when  $t$  is large (see Fig. 5c).

## 5 Conclusions

The present investigation addresses an analysis on the solute dispersion through an incompressible magneto-hydrodynamics flow governed by an unsteady advection-diffusion equations, by employing Aris’s method of moments with aid of a finite difference implicit method. The effects of Hartmann number  $M$ , angle of inclination of magnetic field  $\alpha$  and reaction parameter  $\beta$  on the coefficient of dispersion and profiles of the solute’s mean concentration are investigated. It is shows that the coefficient of Dispersion  $D_a$  reduces with the enhancement of  $\beta$ ,  $M$  and  $\alpha$ . When the absorption parameter  $\beta$  enhances at the both boundary, an enhances the number of

molecules of the solute undergoes in the absorption and hence there is a reduction in  $D_a$ . Again, when  $M$  and  $\alpha$  increases, the resisting Lorentz force enhances and thus  $D_a$  decreases. It is seen that the peak of the mean concentration profiles increase with the increment of both  $M$  and  $\alpha$ . This is because, with the increment of  $M$  and  $\alpha$ , the flow velocity reduces and consequently, the mixing of the molecules with the flow decreases. Thus, the amplitude of distribution of the mean concentration enhances. But, the opposite phenomena is observed for the reaction parameter  $\beta$ . The reason behind this, the total amount of the tracers reduces in the channel flow due to the absorption effect of  $\beta$  at the walls. It is remarkable to note that as time proceeds the strength of distribution of the mean concentration decreases significantly, as the rate of the mixing of the solute material is large in compare to that of in smaller times. It is seen that the profiles of distribution of the mean concentration contain an asymmetric behavior for small dispersion time and it becomes symmetric when the dispersion time reaches in a Taylor regime.

**Acknowledgements** The work is financially supported by **Science & Technology and Biotechnology Department, Government of West Bengal, India** under the project grant number 342 (Sanc.)—ST/P/S & T/16G-27/2018.

## References

1. Taylor, G.I.: Dispersion of soluble matter in solvent flowing slowly through a tube. Proc. R. Soc. A **219**, 186–203 (1953)
2. Aris, R.: On the dispersion of a solute in a fluid flowing through a tube. Proc. R. Soc. A **235**, 67–77 (1956)
3. Gupta, A.S., Chatterjee, A.S.: Dispersion of soluble matter in the hydro-magnetic laminar flow between two parallel plates. Math. Proc. Camb. Phil. Soc. **64**(4), 1209 (1968)
4. Annapurna, N., Gupta, A.S.: Exact analysis of unsteady m.h.d convective diffusion. Proc. R. Soc. A **367**, 281–289 (1979)
5. Mondal, K.K., Mazumder, B.S.: On solute dispersion in pulsatile flow through a channel with absorbing walls. Int. J. Non-Linear Mech. **40**(1), 69–81 (2004)
6. Roy, A.K., Saha, A.K.: Mathematical model on magneto-hydrodynamic dispersion in a porous medium under the influence of bulk chemical reaction. Korea-Aust. Rheol. J. **32**(4), 287–299 (2020)
7. Gupta, P.S.: Effect of conducting walls on the dispersion of soluble matter in MHD channel flow. Chem. Eng. Commun. **7**(4–5), 301–307 (1980)
8. Mondal, K.K., Dhar, S., Mazumder, B.S.: On dispersion of solute in steady flow through a channel with absorption boundary: an application to sewage dispersion. Theor. Comput. Fluid Dyn **34**, 643–658 (2020)
9. Dhar, S., Poddar, N., Mondal, K.K., Mazumder, B.S.: On Dispersion of solute in a hydro-magnetic flow between two parallel plates with boundary absorption. Phys. Fluids **33**, 083609 (2021)
10. Mazumder, B.S., Das, S.K.: Effect of boundary reaction on solute dispersion in pulsatile flow through a tube. J. Fluid Mech **239**, 523 (1992)
11. Sebastian, B.T., Nagarani, P.: Convection-diffusion in unsteady non-Newtonian fluid flow in an annulus with wall absorption. Korea-Aust. Rheol. J. **30**(4), 261–271 (2018)
12. Anderson, D.A., Tanehill, J.C., Pletcher, R.H.: Computational Fluid Mechanics and Heat Transfer, 599 (1984)



13. Mondal, K.K., Mazumder, B.S.: On the solute dispersion in a pipe of annular cross-section with absorption boundary. *ZAMM. Z. Angew. Math. Mech.* **85**, 422–430 (2005)
14. Mehta, R.V., Merson, R.L., Mccoy, B.J.: Hermite Polynomial representation of chromatography elution curves. *J. Chromatogr.* **88**, 1 (1974)

# Unsteady MHD Hybrid Nanoparticle (Au-Al<sub>2</sub>O<sub>3</sub>/Blood) Mediated Blood Flow Through a Vertical Irregular Stenosed Artery: Drug Delivery Applications



Rishu Gandhi  and Bhupendra K. Sharma 

**Abstract** The current study investigates the influence of hybrid nanoparticles (Au & Al<sub>2</sub>O<sub>3</sub>) on blood flow through a vertical artery with irregular stenosis with two-dimensional pulsatile blood flow, an inclined external magnetic field, viscous dissipation, and Joule heating. The blood flow is assumed to be unsteady, laminar, viscous, and incompressible, and the artery walls are considered permeable. The Reynolds temperature-dependent viscosity model is used to determine the variable viscosity effects. The governing momentum and energy equations are solved using Crank–Nicolson finite difference method by employing an appropriate coordinate transformation to build an accurate mesh using rectangular mesh units. Outcomes of the work are represented graphically for non-dimensional velocity, wall shear stress, flow rate, and non-dimensional temperature, respectively. The recent findings could be useful to biological researchers looking into the therapy of different cardiovascular disorders.

**Keywords** Irregular-shaped stenosis · Heat transfer · Joule heating · Temperature-dependent viscosity · Hybrid nanoparticles

## 1 Introduction

Cardiovascular diseases (CVDs) have become a significant global public health issue, with the highest morbidity and mortality rates among all conditions. A growing body of evidence in the scientific literature indicates vascular fluid dynamics plays a vital role in the onset and progression of arterial disorders. Stenosis is a term used to describe narrowing an artery segment's lumen. This is caused by the deposition of numerous chemicals on the endothelium of the artery wall, such as cholesterol. Many researchers have studied blood circulation dynamics via stenosed arteries, both

---

R. Gandhi (✉) · B. K. Sharma  
Department of Mathematics, Birla Institute of Technology and Science, Pilani, Rajasthan, India  
e-mail: [rishugandhi155@gmail.com](mailto:rishugandhi155@gmail.com)  
URL: <https://www.bits-pilani.ac.in>

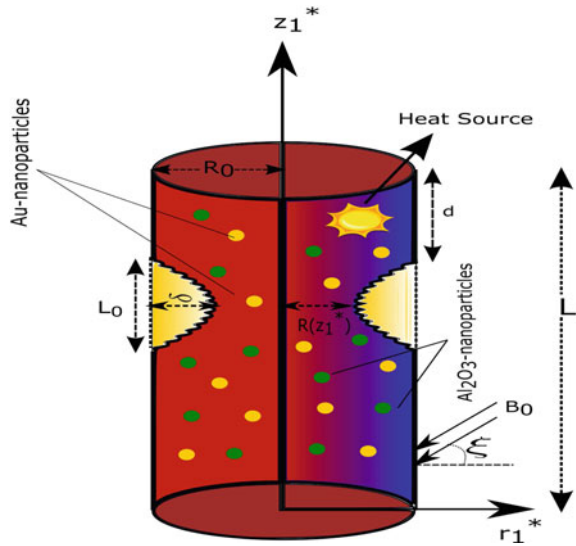
© The Author(s), under exclusive license to Springer Nature Switzerland AG 2022  
S. Banerjee and A. Saha (eds.), *Nonlinear Dynamics and Applications*,  
Springer Proceedings in Complexity,  
[https://doi.org/10.1007/978-3-030-99792-2\\_28](https://doi.org/10.1007/978-3-030-99792-2_28)

325

theoretically and experimentally. Ponalagusamy et al. [12] investigated blood flow through an artery with tapered stenosis considering an unsteady two-fluid model of blood. Basri et al. [2] employed Fluid-Structure Interaction to perform a transient study of three pulse cycles to examine hemodynamic parameters in normal and single stenosed renal arteries. Chandgar et al. [4] considered an inclined multiple stenosed artery and analyzed drug transport utilizing spherical gold nanoparticles by employing a single-phase model as well as a discrete-phase model. Mensah et al. [10] highlighted the 15 most prevalent causes of death from cardiovascular disorders and the 13 risk factors associated with them. Ponalagusamy [11] depicted a four-layered mathematical model of blood flow through a mildly stenosed artery. To determine how varying core viscosity influences blood flow control, they compared the outcomes for variable core viscosity with constant core viscosity. By considering blood as a biomagnetic fluid, Sharma et al. [15] explored Soret and Dufour's effects in an artery with tapering effects. Chen et al. [5] examined the influence of coexisting cardiovascular disease on the severity of COVID-19 and discovered that COVID-19 could have a significant effect on heart function and lead to myocardial damage. Majee et al. [9] conducted a comprehensive study on targeted drug delivery with magnetic nanoparticles with the goal of better understanding the blood flow in an atherosclerotic artery. Shahzadi et al. [13] addressed the importance of permeability in hybrid nanofluid blood flow through a bifurcated stenosed artery. She discovered that permeability effects are more efficient at reducing hemodynamic effects in atherosclerotic arteries with bifurcation effects. Tripathi et al. [17] investigated the impact of heat and mass transmission through a stenosed artery considering the variable magnetic field and varying viscosity. Kumawat et al. [8] investigated two-phase blood flow in a curved artery with time-variant stenosis, taking into account variable viscosity in the core and plasma region, respectively. Sharma et al. [14] investigated heat transmission and entropy generation in a multi-stenosed artery with tapering effects, viscous dissipation, radiation, and Joule heating using hybrid nanoparticles (gold and alumina).

Nanotechnology's application in biomedicine is a rapidly growing field with promising prospects for improving human illness diagnosis and therapy. The capacity to incorporate medications into a functionalized nanoparticle marks a new beginning in which drugs can be delivered to tissues or cells selectively. Consistent drug delivery to a target produces a more substantial therapeutic effect with lower drug levels than conventional dosing approaches. This research work is also motivated by the benefits of the nanoparticle drug delivery system. Having surveyed the literature, it is visualized that the inclined external magnetic field effects on hybrid nanoparticles (Au & Al<sub>2</sub>O<sub>3</sub>) via a vertical artery with irregular stenosis having permeable walls is not investigated yet. Most studies have overlooked the effects of Joule heating, viscous dissipation, and variable viscosity in blood flow problems. In this work, the Reynolds model for temperature-dependent viscosity is employed. The form of the stenosis or the fatty buildup of particles on the artery wall cannot be precisely described so, we've considered an irregular geometry of stenosis. The study's objective is to explore inclined magnetic field effects through an irregular stenosed artery consider-

**Fig. 1** The geometrical representation of an artery with irregular stenosis



ing permeable wall conditions in the presence of Joule heating, viscous dissipation, and variable viscosity.

## 2 Mathematical Modeling

The cylindrical coordinate system  $(r_1^*, \tilde{\theta}, z_1^*)$  is considered to analyze the blood flow behavior through a vertical artery with irregular stenosis by assuming blood as a Newtonian fluid. The flow is in the radial (i.e.,  $r_1^*$ -axis) and axial ( $z_1^*$ -axis) directions respectively. The mild stenotic assumption reduces the bi-directional flow to uni-directional flow. The impact of an inclined external magnetic field, Joule heating, pulsatile blood flow, and viscous dissipation is the subject of this study. The induced magnetic field is considered meager compared to the applied magnetic field. Figure 1 represents the geometry of the artery with suspended nanoparticles.

The geometry of the stenosis (irregular-shaped) [18] is assumed as

$$R(z_1^*) = \begin{cases} R_0 - 2\delta \left[ \cos\left(\frac{2\pi}{L_0}\left(\frac{z_1^* - d}{2} - \frac{L_0}{4}\right)\right) - \frac{7}{100} \cos\left(\frac{32\pi}{L_0}\left(z_1^* - d - \frac{L_0}{2}\right)\right) \right] & d \leq z_1^* \leq d + L_0, \\ R_0 & \text{otherwise.} \end{cases} \quad (1)$$

where  $R(z_1^*)$  represents the radius of the artery's stenosed portion,  $d$  indicates the stenosis location,  $R_0$  represents the radius of the artery in the non-stenotic area,  $\delta$  represents the critical stenosis height, and  $L_0$  represents the length of the stenosis.

### 2.1 Governing Equations

The velocity and temperature fields for the present study are defined as follows in the case of unsteady and axisymmetric hybrid nanoparticle-doped blood flow:

$$\tilde{V}^* = \tilde{V}^*[u_1^*(r_1^*, z_1^*, t_1^*), 0, w_1^*(r_1^*, z_1^*, t_1^*)], \quad \tilde{T}^* = \tilde{T}^*(r_1^*, z_1^*, t_1^*)$$

where  $u_1^*$  represents the radial component and  $w_1^*$  represents the axial component respectively.

The governing equations of the flow are represented as:

$$\frac{\partial u_1^*}{\partial r_1^*} + \frac{u_1^*}{r_1^*} + \frac{\partial w_1^*}{\partial z_1^*} = 0 \tag{2}$$

$$\begin{aligned} \rho_{hnf} \left[ \frac{\partial u_1^*}{\partial t_1^*} + u_1^* \frac{\partial u_1^*}{\partial r_1^*} + w_1^* \frac{\partial u_1^*}{\partial z_1^*} \right] &= -\frac{\partial p_1^*}{\partial r_1^*} + \frac{1}{r_1^*} \frac{\partial}{\partial r_1^*} \left[ \mu_{hnf}(\tilde{T}^*) \frac{\partial u_1^*}{\partial r_1^*} \right] \\ &+ \frac{\partial}{\partial z_1^*} \left[ \mu_{hnf}(\tilde{T}^*) \left( \frac{\partial u_1^*}{\partial z_1^*} + \frac{\partial w_1^*}{\partial r_1^*} \right) \right] \\ &- 2\mu_{hnf}(\tilde{T}^*) \frac{u_1^*}{r_1^{*2}} - \sigma_{hnf} B_0^2 \cos^2 \xi w_1^* \end{aligned} \tag{3}$$

$$\begin{aligned} \rho_{hnf} \left[ \frac{\partial w_1^*}{\partial t_1^*} + u_1^* \frac{\partial w_1^*}{\partial r_1^*} + w_1^* \frac{\partial w_1^*}{\partial z_1^*} \right] &= -\frac{\partial p_1^*}{\partial z_1^*} + \frac{1}{r_1^*} \frac{\partial}{\partial r_1^*} \left[ r_1^* \mu_{hnf}(\tilde{T}^*) \left( \frac{\partial u_1^*}{\partial z_1^*} + \frac{\partial w_1^*}{\partial r_1^*} \right) \right] \\ &+ \frac{\partial}{\partial z_1^*} \left[ 2\mu_{hnf}(\tilde{T}^*) \frac{\partial w_1^*}{\partial z_1^*} \right] \\ &+ (\rho\gamma)_{hnf} g(\tilde{T}^* - \tilde{T}_1^*) - \sigma_{hnf} B_0^2 \sin^2 \xi w_1^* \end{aligned} \tag{4}$$

$$\begin{aligned} (\rho C_p)_{hnf} \left[ \frac{\partial \tilde{T}^*}{\partial t_1^*} + u_1^* \frac{\partial \tilde{T}^*}{\partial r_1^*} + w_1^* \frac{\partial \tilde{T}^*}{\partial z_1^*} \right] &= k_{hnf} \left[ \frac{\partial^2 \tilde{T}^*}{\partial r_1^{*2}} + \frac{1}{r_1^*} \frac{\partial \tilde{T}^*}{\partial r_1^*} + \frac{\partial^2 \tilde{T}^*}{\partial z_1^{*2}} \right] \\ &+ \sigma_{hnf} B_0^2 \sin^2 \xi w_1^{*2} + \phi^* \end{aligned} \tag{5}$$

where

$$\phi^* = 2\mu_{hnf} \left[ \left( \frac{\partial u_1^*}{\partial r_1^*} \right)^2 + \left( \frac{u_1^*}{r_1^*} \right)^2 + \left( \frac{\partial w_1^*}{\partial z_1^*} \right)^2 + \frac{1}{2} \left( \frac{\partial u_1^*}{\partial z_1^*} + \frac{\partial w_1^*}{\partial r_1^*} \right)^2 \right] \tag{6}$$

The boundary conditions for the flow are:

Thermophysical Properties of Hybrid Nanofluid	
Viscosity	$\mu_{hnf} = \frac{\mu_f}{(1 - \phi_1)^{2.5}(1 - \phi_2)^{2.5}}$
Density	$\rho_{hnf} = [(1 - \phi_2)\{(1 - \phi_1)\rho_f + \phi_1\rho_{s_1}\}] + \phi_2\rho_{s_2}$
Heat Capacity	$(\rho C_p)_{hnf} = [(1 - \phi_2)\{(1 - \phi_1)(\rho C_p)_f + \phi_1(\rho C_p)_{s_1}\}] + \phi_2(\rho C_p)_{s_2}$
Thermal Conductivity	$k_{hnf} = \frac{k_{s_2} + (n - 1)k_{bf} - (n - 1)\phi_2(k_{bf} - k_{s_2})}{k_{bf} = \frac{k_{s_2} + (n - 1)k_{bf} + \phi_2(k_{bf} - k_{s_2})}{k_f = \frac{k_{s_1} + 2k_f - (n - 1)\phi_1(k_f - k_{s_1})}{k_{s_1} + (n - 1)k_f + \phi_1(k_f - k_{s_1})}}$ where $\frac{k_{bf}}{k_f} = \frac{k_{s_1} + 2k_f - (n - 1)\phi_1(k_f - k_{s_1})}{k_{s_1} + (n - 1)k_f + \phi_1(k_f - k_{s_1})}$
Electrical Conductivity	$\sigma_{hnf} = \frac{\sigma_{s_2} + (n - 1)\sigma_{bf} - (n - 1)\phi_2(\sigma_{bf} - \sigma_{s_2})}{\sigma_{bf} = \frac{\sigma_{s_2} + (n - 1)\sigma_{bf} + \phi_2(\sigma_{bf} - \sigma_{s_2})}{\sigma_{bf} = \frac{\sigma_{s_1} + (n - 1)\sigma_f - (n - 1)\phi_1(\sigma_f - \sigma_{s_1})}{\sigma_{s_1} + (n - 1)\sigma_f + \phi_1(\sigma_f - \sigma_{s_1})}}$ where $\frac{\sigma_{bf}}{\sigma_f} = \frac{\sigma_{s_1} + (n - 1)\sigma_f - (n - 1)\phi_1(\sigma_f - \sigma_{s_1})}{\sigma_{s_1} + (n - 1)\sigma_f + \phi_1(\sigma_f - \sigma_{s_1})}$
Thermal Expansion Coefficient	$\gamma_{hnf} = [(1 - \phi_2)\{(1 - \phi_1)\gamma_f + \phi_1\gamma_{s_1}\}] + \phi_2\gamma_{s_2}$

(a)

Thermophysical Properties	Blood	Gold (Au)	Alumina (Al <sub>2</sub> O <sub>3</sub> )
Density [ $\rho$ (kg/m <sup>3</sup> )]	1063	19320	3970
Thermal Conductivity [(W/mK)]	0.492	314	40
Thermal Expansion Coefficient [ $\gamma \times 10^{-5}$ (K <sup>-1</sup> )]	0.18	1.4	0.85
Heat Capacitance [ $C_p$ (J/kgK)]	3594	129	765
Electrical Conductivity [ $\sigma$ (S/m)]	$6.67 \times 10^{-1}$	$4.52 \times 10^7$	$3.5 \times 10^7$

(b)

**Fig. 2 a** Thermophysical parameters of hybrid nanofluid [6], **b** Thermophysical properties of blood and nanoparticles

$$\frac{\partial w_1^*}{\partial r_1^*} = 0, \quad \frac{\partial \tilde{T}^*}{\partial r_1^*} = 0 \quad \text{at } r_1^* = 0; \tag{7}$$

$$w = w_s, \quad \frac{\partial w_1^*}{\partial r_1^*} = \frac{\alpha}{\sqrt{k_1^*}}(w_s - w_{porous}), \quad \tilde{T}^* = \tilde{T}_w^* \quad \text{at } r_1^* = R, \tag{8}$$

where  $w_{porous}$  is the velocity in the permeable boundary,  $w_s$  is the slip velocity, Da is the Darcy number,  $\alpha$  (called the slip parameter) is a dimensionless quantity depending on the material parameters which characterize the structure of the permeable material within the boundary region.

The initial conditions are assumed as:

$$w_1^* = 0, \quad \tilde{T}^* = 0 \quad \text{at } t_1^* = 0 \tag{9}$$

Figure 2a depicts the thermophysical parameters of hybrid nanofluid whereas Fig. 2b shows the thermophysical properties of blood and nanoparticles.

Blood flows through the cardiovascular system due to the heart’s pumping motion, causing a pressure gradient across the vascular network. The pressure gradient is separated into two parts: non-fluctuating (continuous) and fluctuating (pulsatile) [3]:

$$-\frac{\partial p_1^*}{\partial z_1^*} = A_0 + A_1 \cos(w_p t_1^*), t_1^* > 0 \tag{10}$$

where  $w_p = 2\pi f_p$ ,  $f_p$  denotes the heart pulse frequency,  $A_0$  signifies the amplitudes of the steady-state component, and  $A_1$  represents the pulsatile components of the pressure gradient, respectively.

The preceding governing equations (2)–(5) are non-dimensionalized to achieve a numerical solution by introducing the following transformation variables:

$$\begin{aligned} \bar{r}_1^* &= \frac{r_1^*}{R_0}, \bar{w}_1^* = \frac{w_1^*}{U_0}, \bar{u}_1^* = \frac{L_0 u_1^*}{\delta^* U_0}, \bar{t}_1^* = \frac{U_0 t_1^*}{R_0}, \bar{z}_1^* = \frac{z_1^*}{L_0}, \bar{p}_1^* = \frac{R_0^2 p_1^*}{U_0 L_0 \mu_0}, \bar{\theta} = \frac{\tilde{T}^* - \tilde{T}_1^*}{\tilde{T}_w^* - \tilde{T}_1^*}, \\ \bar{R} &= \frac{R}{R_0}, \bar{d} = \frac{d}{L_0}, \bar{w}_s = \frac{w_s}{U_0}, \bar{w}_{porous} = \frac{w_{porous}}{U_0}, \bar{Q} = \frac{Q_0 R_0^2}{(\tilde{T}_w^* - \tilde{T}_1^*) k_f}, Re = \frac{U_0 \rho_f R_0}{\mu_f}, \\ Gr &= \frac{\rho_f R_0^2 g \gamma_f (\tilde{T}_w^* - \tilde{T}_1^*)}{\mu_f U_0}, M^2 = \frac{\sigma_f B_0^2 R_0^2}{\mu_f}, Ec = \frac{U_0^2}{C_p (\tilde{T}_w^* - \tilde{T}_1^*)}, Pr = \frac{\mu_f C_p}{k_f}, \\ Da &= \frac{k_1^*}{R_0^2}, Br = Ec Pr = \frac{\mu_f U_0^2}{k_f (\tilde{T}_w^* - \tilde{T}_1^*)}. \end{aligned} \tag{11}$$

After inserting the non-dimensionalized variables, the normalized form of the pressure gradient is:

$$-\frac{\partial p_1^*}{\partial z_1^*} = B_1 [1 + e \cos(c_1 t_1^*)] \tag{12}$$

where

$$e = \frac{A_1}{A_0}, B_1 = \frac{A_0 R_0^2}{\mu_0 U_0}, c_1 = \frac{2\pi R_0 f_p}{U_0} \tag{13}$$

With the substitution of variables given in (11), ignoring the bars, assuming that in comparison to the radius of the artery, the maximal height of stenosis is lesser, i.e.,  $\delta (= \delta^*/R_0) \ll 1$  and the radius of the artery and the length of the stenotic area have comparable magnitudes, i.e.,  $\epsilon (= R_0/L_0) = O(1)$ , and further utilizing the radial coordinate transformation given by  $\left(x_1^* = \frac{r_1^*}{R(z_1^*)}\right)$ , the governing (2)–(5) become:

$$\begin{aligned} Re \frac{\rho_{hnf}}{\rho_f} \frac{\partial w_1^*}{\partial t_1^*} &= B_1 [1 + e \cos(c_1 t_1^*)] + \left(\frac{\mu_{hnf}(\tilde{\theta})}{\mu_0}\right) \left(\frac{1}{R^2}\right) \left[\frac{\partial^2 w_1^*}{\partial x_1^{*2}} + \frac{1}{x_1^*} \frac{\partial w_1^*}{\partial x_1^*}\right] \\ &+ \frac{(\rho\gamma)_{hnf}}{(\rho\gamma)_f} Gr \tilde{\theta} - \frac{\sigma_{hnf}}{\sigma_f} M^2 w_1^* \end{aligned} \tag{14}$$

**Table 1** The values of emerging parameters

Parameters	$\phi_1$	$\phi_2$	$d$	$B_1$	$c_1$	$e$	$\delta$	$\beta_0$	$w_s$	$\alpha$	$\xi$	$M$	$Gr$	$Da$	$Re$	$Pr$	$Ec$
Value	0.03	0.03	0.56	1.41	1	0.2	0.1	0.5	0.1	0.1	$\pi/4$	$\sqrt{3}$	0.5	0.1	2	21	0.1

$$\begin{aligned}
 \frac{(\rho C_p)_{hnf}}{(\rho C_p)_f} \frac{\partial \tilde{\theta}}{\partial t_1^*} &= \frac{1}{RePr} \frac{k_{hnf}}{k_f} \left( \frac{1}{R^2} \right) \left[ \frac{\partial^2 \tilde{\theta}}{\partial x_1^{*2}} + \frac{1}{x_1^*} \frac{\partial \tilde{\theta}}{\partial x_1^*} \right] + \frac{\sigma_{hnf}}{\sigma_f} \frac{EcM^2}{Re} w_1^{*2} \\
 &+ \frac{\mu_{hnf}(\tilde{\theta})}{\mu_0} \frac{Ec}{Re} \left( \frac{1}{R^2} \right) \left( \frac{\partial w_1^*}{\partial x_1^*} \right)^2
 \end{aligned}
 \tag{15}$$

Here, Reynolds viscosity model [7] is considered for the temperature-dependent viscosity, which is as follows:

$$\mu_f(\tilde{\theta}) = \mu_0 e^{-\beta_0 \tilde{\theta}} = \mu_0 [1 - \beta_0 \tilde{\theta}] \text{ where } \beta_0 \ll 1
 \tag{16}$$

The associated boundary conditions (7), (8) and the initial conditions (9) becomes:

$$\left. \frac{\partial w_1^*}{\partial x_1^*} \right|_{x_1^*=0} = 0, \left. \frac{\partial w_1^*}{\partial x_1^*} \right|_{x_1^*=1} = \frac{\alpha}{\sqrt{Da}} (w_s - w_{porous}), w_1^*|_{x_1^*=1} = w_s, \left. \frac{\partial \tilde{\theta}}{\partial x_1^*} \right|_{x_1^*=0} = 0, \tilde{\theta}|_{x_1^*=1} = 1
 \tag{17}$$

$$w_1^*|_{t_1^*=0} = 0, \tilde{\theta}|_{t_1^*=0} = 0
 \tag{18}$$

The wall shear stress (WSS) and the flow rate are expressed as:

$$\tau_w = -\frac{1}{R} \left( \frac{\partial w_1^*}{\partial x_1^*} \right)_{x_1^*=1}
 \tag{19}$$

$$Q_1 = 2\pi R^2 \int_0^1 w_1^* x_1^* dx_1^*
 \tag{20}$$

The equations given by (14) and (15) are coupled partial differential equations, and numerical schemes are often used to solve these equations as finding an exact solution is a tedious work. The Crank–Nicolson scheme is based on the implicit finite difference method. The fact that this method is unconditionally stable is one of the key reasons for its use [16]. Furthermore, the order of convergence is two in time and space. The step size in the spatial direction is  $x = 1/N+1$ , discretizing the spatial variable in  $N+1$  grid points. The value of  $t^k$  given as  $t^k = (k - 1)dt$ , determines the time instant, and  $dt$  signifies a small increment in time. The method being implicit is stable for any value of  $dt$  and  $dx$ , we have chosen the values very precisely as  $dt = 0.0001$  and  $dx = 0.0001$ . Also, no further change is noticed in the results with a decrement in these values. The reduced system of Eqs. (14) and (15) are solved



using the Tri-diagonal Matrix Algorithm (TDMA) [1] as they form a tri-diagonal system of equations.

### 3 Results and Graphical Analysis

The goal of this study is to investigate the hemodynamic features under the effect of pulsatile blood flow via an artery with irregular stenosis, an inclined external magnetic field, viscous dissipation, and Joule heating incorporating hybrid nanoparticles. The validation of the work done is depicted by Fig. 3. Streamline contours for different flow parameters are depicted in Figs. 4 and 5. The results for velocity, wall shear stress, volumetric flow rate, and temperature are illustrated graphically in Figs. 6, 7, 8 and 9. The computational work has been carried out by using the data illustrated in the Table 1.

#### 3.1 Validation of the Numerical Results

The results obtained are compared with previously published work to authenticate the results obtained in the present study. Figure 3a, b are used for validating velocity and temperature profiles of the present work with previous study done by Tripathi et al. [18]. The results are compared for Au-nanoparticles, which is common in both the research work and the effect of the Darcy number (Da), velocity slip ( $\alpha$ ), and Eckert number (Ec) has been ignored. Tripathi et al. [18] used the FTCS scheme to solve the dimensionless governing equations. Therefore, in this comparison, the FTCS scheme is employed for [18] work, and the Crank–Nicolson scheme is used in the current study. These figures show a good agreement between our study for velocity and temperature with the previous research [18].

The velocity contours depict the actual blood flow patterns as these correctly illustrate the research efforts. Figures 4 and 5 represent these contours for different influential parameters. The impact of  $w_s$  is depicted in Fig. 4. The number of trapped boluses and their size increases with increasing  $w_s$  values implying that the velocity profile elevates with an increase in  $w_s$ . The slip effect amplifies the acceleration in the axial flow, which is the reason for elevation in velocity profiles with increasing  $w_s$  values. The velocity contours for different Re values are illustrated in Fig. 5. With increasing Re values, the trapped boluses become fewer and eventually vanish, suggesting a drop in velocity values. The regime becomes viscous-dominated at low Re values. As a result, a drop in velocity is correlated with a rise in Re values.

The velocity profiles for Darcy number (Da), wall slip velocity ( $w_s$ ), inclination parameter ( $\xi$ ), and varying concentrations of Au & Al<sub>2</sub>O<sub>3</sub> nanoparticles ( $\phi_1, \phi_2$ ) are illustrated in Fig. 6. Figure 6a shows the influence of Da on non-dimensional velocity profiles in the presence and absence of a magnetic field. The medium's permeability increases as the value of Da rises, resulting in a declination of the velocity profile.

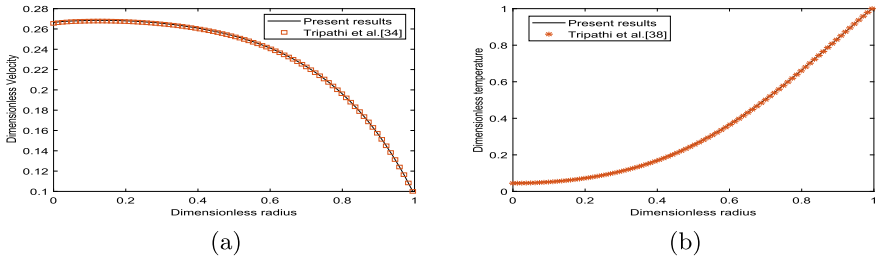


**Fig. 3** **a** Comparison of velocity profile for  $M^2 = \sqrt{3}$ , **b** Comparison of temperature profile for  $Pr = 21$

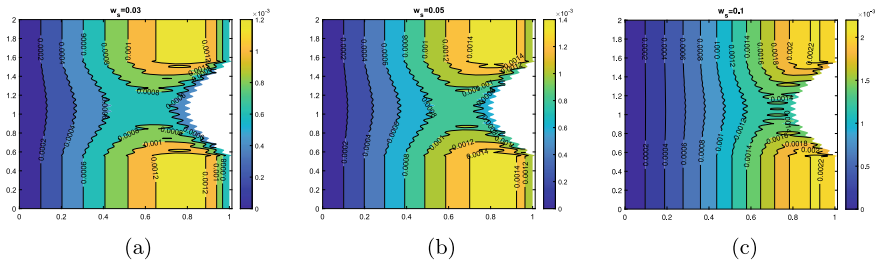


**Fig. 4** Velocity contours for wall slip velocity **a**  $w_s = 0.03$ , **b**  $w_s = 0.05$ , **c**  $w_s = 0.1$

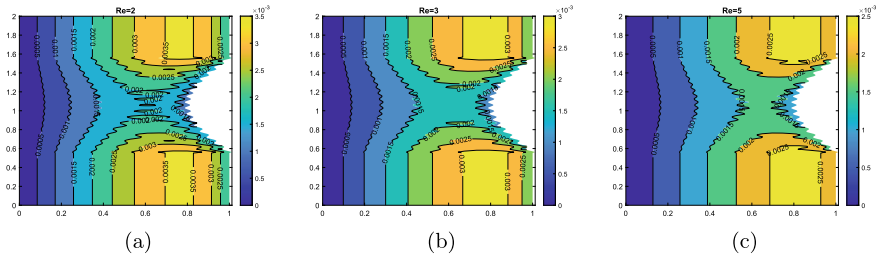


**Fig. 5** Velocity contours for Reynolds number **a**  $Re = 2$ , **b**  $Re = 3$ , **c**  $Re = 5$

It's also worth noting that when  $M^2$  rises, the velocity profile declines slightly. This demonstrates that using a magnetic field to reduce blood velocity is advantageous. The velocity profiles for different values of  $w_s$  is represented by Fig. 6b. The hydrodynamic wall slip effect causes the axial flow to accelerate as the wall slip velocity increases. The inclusion of slip results in a momentum increases at the application zone, which improves the velocity profile. The Au-Al<sub>2</sub>O<sub>3</sub>/blood hybrid nanofluid consistently reaches lower magnitudes than the Au/blood nanofluid, showing the presence of Al<sub>2</sub>O<sub>3</sub> nanoparticles decelerates the blood flow. Figure 6c highlights the influence of  $\xi$  on the dimensionless velocity profile. With increasing values of  $\xi$ , a decreasing trend in velocity profiles is observed. This is because as the angle of inclination increases, the influence of the magnetic field on fluid particles increases. Thus,

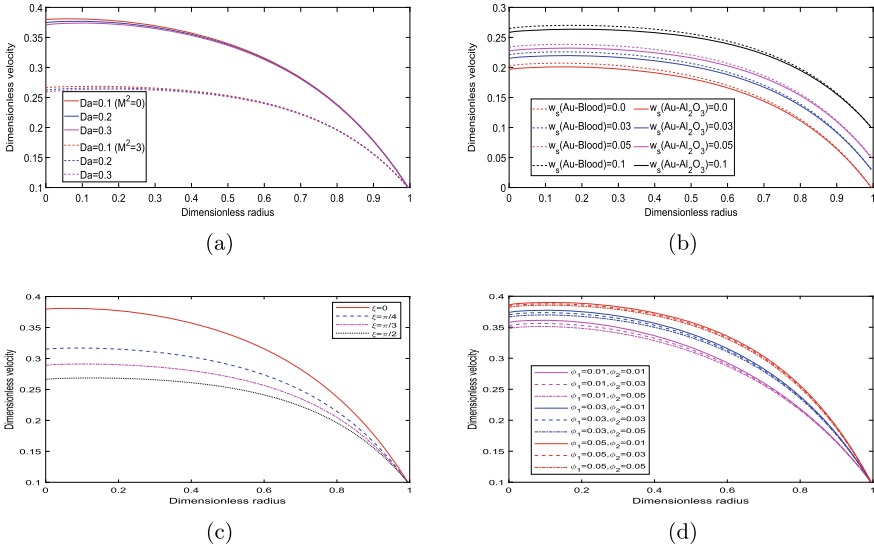


**Fig. 6** Effect of **a** Darcy number (*Da*), **b** wall slip velocity ( $w_s$ ), **c** inclination parameter ( $\xi$ ), and **d** varying concentrations of Au & Al<sub>2</sub>O<sub>3</sub> nanoparticles ( $\phi_1, \phi_2$ ) on velocity at  $z_1^* = 1.06$  and  $t_1^* = 1.2$

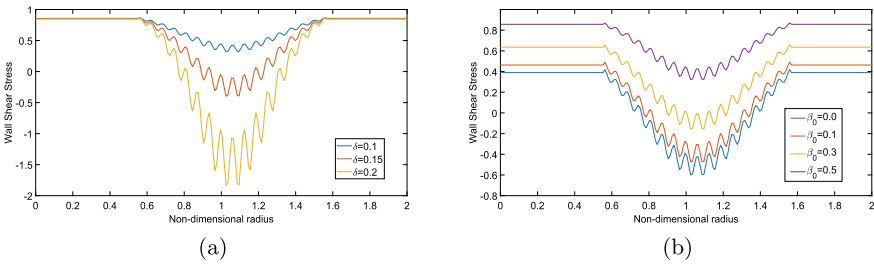


**Fig. 7** Influence of **a** stenotic depth ( $\delta$ ), **b** viscosity parameter ( $\beta_0$ ), on wall shear stress at  $t_1^* = 1.2$

the Lorentz force enhances, which causes a reduction in velocity values. The influence of varying concentrations of Au & Al<sub>2</sub>O<sub>3</sub> nanoparticles ( $\phi_1, \phi_2$ ) on velocity profile is shown in Fig. 6d. The value  $\phi_1 = 0.01, \phi_2 = 0.05$  shows minimal velocity, whereas the maximum velocity is shown for  $\phi_1 = 0.05, \phi_2 = 0.01$ . This demonstrates that Au & Al<sub>2</sub>O<sub>3</sub> nanoparticles show opposite effects on velocity. The velocity profiles show an enhancement with an increase in the concentration of Au-nanoparticles, whereas a decrement in velocity profile is analyzed with an increase in Al<sub>2</sub>O<sub>3</sub>-nanoparticles. This benefits bringing blood velocity under control and allowing surgeons to make adjustments as needed.

The profiles corresponding to wall shear stress are demonstrated in Fig. 7 for stenotic depth ( $\delta$ ) and viscosity parameter ( $\beta_0$ ). The wall shear stress profiles highlighting the impact of  $\delta$  are represented by Fig. 7a. As shown by the profiles, the

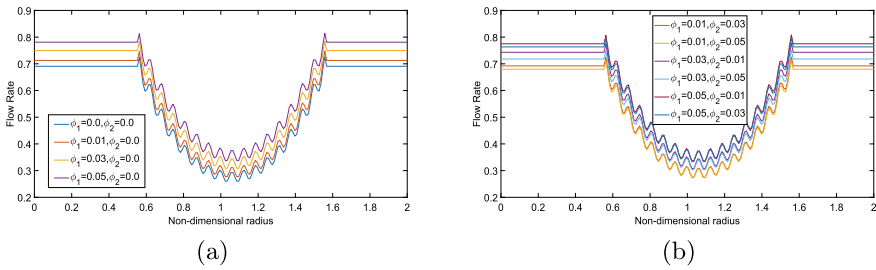


**Fig. 8** Effect of **a** different concentrations of Au-nanoparticles ( $\phi_1$ ), **b** varying concentrations of Au & Al<sub>2</sub>O<sub>3</sub> nanoparticles ( $\phi_1, \phi_2$ ) on Flow rate at  $t_1^* = 1.2$

values of wall shear stress show a decrement with increasing  $\delta$  values. This implies that there are lower shear stress values with an increment in the stenotic depth. These lower values are more dangerous, as suggested by Zhang et al. [19] in their study. Figure 7b signifies the wall shear stress profiles for different values of  $\beta_0$ . With an increase in the  $\beta_0$  values corresponding increase in the wall shear stress values is observed. The increment in wall shear stress denotes that the particles' internal resistance has decreased as the magnitude of the viscosity parameter has increased.

The volumetric flow rate is the amount of fluid(blood) that flows in a given amount of time. The flow rate profiles for varying concentrations of Au-nanoparticles ( $\phi_1$ ) and varying concentrations of Au & Al<sub>2</sub>O<sub>3</sub> nanoparticles ( $\phi_1, \phi_2$ ) are depicted in Fig. 8. Figure 8a represents the influence of Au-nanoparticles concentration on volumetric flow rate. According to the findings, the flow rate profiles demonstrate an increasing trend with increasing concentration of Au-nanoparticles. The flow rate profiles for the influence of varying concentrations of Au & Al<sub>2</sub>O<sub>3</sub> nanoparticles is shown in Fig. 8b. It can be interpreted that there is a declination in flow rate on increasing the concentration of Al<sub>2</sub>O<sub>3</sub> nanoparticles, whereas it enhances with increment in Au-nanoparticles. So, it can be concluded from Fig. 8a and b that the Al<sub>2</sub>O<sub>3</sub> nanoparticles reduce the flow rate.

The non-dimensional temperature profiles for Eckert number (Ec) and Prandtl number (Pr) are illustrated by Fig. 9. Figure 9a depicts the impact of Ec on the non-dimensional temperature profile. The Ec describes how work against viscous fluid stress converts kinetic energy into internal energy. The heat energy develops in the fluid due to this conversion which causes the fluid's (blood) temperature to rise. As a result, a rise in Ec denotes a higher temperature distribution. Figure 9b portrays the non-dimensional temperature profiles for different values of Pr. With increasing Pr, the temperature profiles show a decreasing trend. The Pr is a dimensionless quantity that correlates viscosity to thermal conductivity in a fluid. As a result, it determines the link between the motion of a fluid and its heat transfer capacity. The thickness of the thermal boundary layer reduces, which means the transfer of heat from the artery decreases with increasing Pr values leading to a declination of arterial temperature.

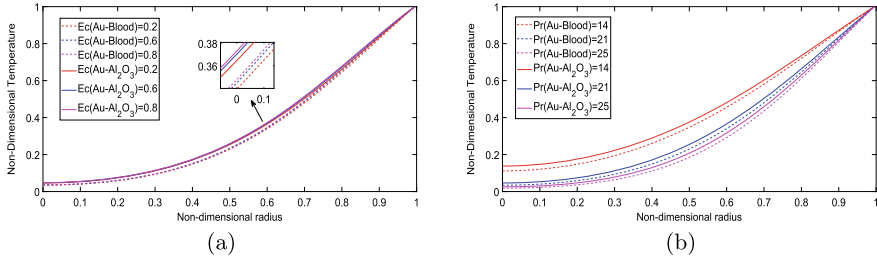


**Fig. 9** The non-dimensional temperature profiles for **a** Eckert number (Ec), **b** Prandtl number (Pr) at  $z_1^* = 1.06$  and  $t_1^* = 1.2$

### 4 Conclusions

This study focuses on the influence of hybrid nanoparticles on blood flow through an artery with mild irregular stenosis. This model aims to improve nanoparticle drug delivery to a desired location in the human body. The partial differential equations are solved using an implicit finite difference scheme, i.e., the Crank–Nicolson scheme. The effects of a wide range of physical parameters have been evaluated on axial blood velocity, temperature profile, volumetric flow rate, and artery wall shear stress (WSS). The following are some of the study’s key findings: The streamline contours illustrate that as  $w_s$  increases, so does the velocity. The velocity profile diminishes as Da and  $\xi$  are increased. The profiles for wall shear stress show an enhancement with increasing  $\beta_0$  values, whereas an increase in  $\delta$  leads to lower profiles. The flow rate increases as  $\phi_1$  increases but decreases as  $\phi_2$  increases. The temperature profiles increase as the Ec values rise but decrease as the Pr values rise.

### References

1. Anderson, J.D., Wendt, J.: Computational fluid dynamics, vol. 206. Springer, Berlin (1995)
2. Basri, A.A., Khader, S.M.A., Johny, C., Pai, R., Zuber, M., Ahmad, K.A., Ahmad, Z.: Numerical study of haemodynamics behaviour in normal and single stenosed renal artery using fluid-structure interaction. *J. Adv. Res. Fluid Mech. Therm. Sci.* **51**(1), 91–98 (2018)
3. Burton, A.C.: Physiology and biophysics of the circulation. *Acad. Med.* **40**(8), xxx–xxxvi (1965)
4. Changdar, S., De, S.: Investigation of nanoparticle as a drug carrier suspended in a blood flowing through an inclined multiple stenosed artery. *Bionanoscience* **8**(1), 166–178 (2018)
5. Chen, C., Yan, J., Zhou, N., Zhao, J., Wang, D.: Analysis of myocardial injury in patients with covid-19 and association between concomitant cardiovascular diseases and severity of covid-19. *Zhonghua xin xue guan bing za zhi*, pp. 567–571 (2020)
6. Devi, S.A., Devi, S.S.U.: Numerical investigation of hydromagnetic hybrid cu-al2o3/water nanofluid flow over a permeable stretching sheet with suction. *Int. J. Nonlinear Sci. Numer. Simul.* **17**(5), 249–257 (2016)

7. Ellahi, R., Raza, M., Vafai, K.: Series solutions of non-newtonian nanofluids with reynolds' model and vogel's model by means of the homotopy analysis method. *Math. Comput. Modell.* **55**(7–8), 1876–1891 (2012)
8. Kumawat, C., Sharma, B., Mekheimer, K.: Mathematical analysis of two-phase blood flow through a stenosed curved artery with hematocrit and temperature dependent viscosity. *Phys. Scripta* **96**(12), 125277 (2021)
9. Majee, S., Shit, G.: Modeling and simulation of blood flow with magnetic nanoparticles as carrier for targeted drug delivery in the stenosed artery. *Europ. J. Mech.-B/Fluids* **83**, 42–57 (2020)
10. Mensah, G.A., Roth, G.A., Fuster, V.: The global burden of cardiovascular diseases and risk factors: 2020 and beyond (2019)
11. Ponalagusamy, R., Manchi, R.: A four-layered model for flow of non-newtonian fluid in an artery with mild stenosis. *Sādhanā* **44**(7), 1–14 (2019)
12. Ponalagusamy, R., Priyadarshini, S.: Numerical investigation on two-fluid model (micropolar-newtonian) for pulsatile flow of blood in a tapered arterial stenosis with radially variable magnetic field and core fluid viscosity. *Comput. Appl. Math.* **37**(1), 719–743 (2018)
13. Shahzadi, I., Bilal, S.: A significant role of permeability on blood flow for hybrid nanofluid through bifurcated stenosed artery: drug delivery application. *Comput. Methods Programs Biomed.* **187**, 105248 (2020)
14. Sharma, B., Gandhi, R., Bhatti, M.: Entropy analysis of thermally radiating mhd slip flow of hybrid nanoparticles (au-al<sub>2</sub>o<sub>3</sub>/blood) through a tapered multi-stenosed artery. *Chem. Phys. Lett.* 139348 (2022)
15. Sharma, M., Sharma, B.K., Gaur, R., Tripathi, B.: Soret and dufour effects in biomagnetic fluid of blood flow through a tapered porous stenosed artery. *J. Nanofluids* **8**(2), 327–336 (2019)
16. Smith, G.D., Smith, G.D., Smith, G.D.S.: Numerical solution of partial differential equations: finite difference methods. Oxford University Press, Oxford (1985)
17. Tripathi, B., Sharma, B.K.: Influence of heat and mass transfer on two-phase blood flow with joule heating and variable viscosity in the presence of variable magnetic field. *Int. J. Comput. Methods* **17**(03), 1850139 (2020)
18. Tripathi, J., Vasu, B., Bégh, O.A., Gorla, R.S.R.: Unsteady hybrid nanoparticle-mediated magneto-hemodynamics and heat transfer through an overlapped stenotic artery: Biomedical drug delivery simulation. *Proc. Inst. Mech. Eng. Part H: J. Eng. Med.* 095441192111026095 (2021)
19. Zhang, B., Gu, J., Qian, M., Niu, L., Zhou, H., Ghista, D.: Correlation between quantitative analysis of wall shear stress and intima-media thickness in atherosclerosis development in carotid arteries. *Biomed. Eng. Online* **16**(1), 1–17 (2017)

# An Analytical Approach to Study the Environmental Transport of Fine Settling Particles in a Wetland Flow



Subham Dhar , Nanda Poddar , and Kajal Kumar Mondal 

**Abstract** The present research deals with an analytical solution of convection-diffusion equation which represents the water phase based superficial concentration in a vegetated wetland. Gill's series expansion method is used to obtain the dispersion coefficient and mean concentration distribution of the settling particles. For the limiting case of vegetation factor, tortuosity and settling velocity, the dispersivity is compared with the earlier research work and an excellent agreement is achieved with them. Effects of settling velocity, tortuosity and vegetation factor, on the dispersion coefficient and mean concentration are observed. A physical application is performed to predict the critical length of the concentration cloud beyond the ecological safe level. It is seen that with the increment of settling velocity, the duration for safe level increases. Moreover, the study provides two important criteria for wastewater treatment namely critical length and duration of solute cloud in the wetland. The work may also be applicable to investigate the sedimentation process and flood damage control.

**Keywords** Vegetated wetland · Gill's series expansion method · Dispersion · Settling velocity · Critical length

## 1 Introduction

The study of solute dispersion phenomena was initially introduced by Taylor [1]. Following his work, Aris [2] employed the method of moments and removed some restrictions of Taylor's theory. Later, Gill and Sankarasubramanian [3, 4] used the series expansion method to find the solution of the convection-diffusion equation. Several researchers [5–7] investigated the free surface effect on the dispersion of

---

Supported by CSIR India and UGC India.

---

S. Dhar (✉) · N. Poddar · K. K. Mondal  
Cooch Behar Panchanan Barma University, Cooch Behar 736101, India  
e-mail: [dharsuvam94@gmail.com](mailto:dharsuvam94@gmail.com)

© The Author(s), under exclusive license to Springer Nature Switzerland AG 2022  
S. Banerjee and A. Saha (eds.), *Nonlinear Dynamics and Applications*,  
Springer Proceedings in Complexity,  
[https://doi.org/10.1007/978-3-030-99792-2\\_29](https://doi.org/10.1007/978-3-030-99792-2_29)

339

tracer in a wetland flow. The influences of bed absorption and bulk degradation on mass transfer phenomena are studied by numerous researchers [8, 9]. Various analytical methods such as multi-scale analysis [5, 10–12], method of moments [13, 14], Taylor's classical technique [15] were used to investigate the environmental dispersivity and mean concentration distribution. Hammer [16] and Zhou et al. [17] showed how the constructed wetland is useful for wastewater treatment. Wu et al. [18] observed the tidal effect on environmental dispersion coefficient for a depth dominated wetland flow. Recently, Dhar et al. [19] and Poddar et al. [20] explored the dispersion of settling particles in a wetland flow using finite difference technique and the method of moments respectively.

The current research presents an analytical approach to investigate the environmental transport of fine particles with settling velocity in a depth dominated wetland flow. The influences of linear and nonlinear boundary reactions on the solute dispersion was studied by many researchers but the transport of fine sediment particles in a wetland flow paid low attention though it has a wide range of applications in the direction of environmental engineering. Gill's series expansion method is used to explore the environmental dispersivity and mean concentration in this study. Moreover, the critical length and the duration of the concentration cloud are obtained with the help of the mean concentration profile of the tracers. It is seen that, the solute concentration is conglomerated near the source when the fall velocity of the particles in the wetland flow increase significantly. The maximum critical length and corresponding duration of the cloud of settling particles are obtained for 5 day Biochemical Oxygen Demand ( $BOD_5$ ), Total Phosphorus (TP) and Total Nitrogen (TN) which relates the wastewater treatment in the wetland.

## 2 Mathematical Formulation

### 2.1 Velocity Distribution

Consider the dispersion of settling particles in a fully developed and unidirectional flow with constant porosity ( $\phi$ ), vegetation force ( $F$ ), tortuosity ( $\kappa$ ), momentum dispersivity ( $L$ ) and mass dispersivity  $K$  in a depth dominated wetland channel of depth  $H$ . A Cartesian coordinate system is used where  $x^*$ -axis is along the longitudinal direction,  $y^*$ -axis along the vertical direction and the origin is situated at the bed surface. For a depth dominated wetland channel, effects of width are considered negligible as the first approximation, and so related terms are taken as width-averaged (see Fig. 1). For a constant pressure gradient, the momentum equation reduces as [15],



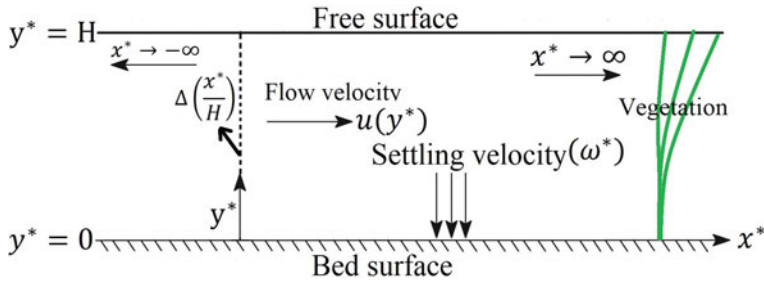


Fig. 1 Sketch of the present model

$$\kappa(\mu + L_{yy}) \frac{d^2u}{dy^{*2}} = \mu Fu + \frac{dp}{dx^*} \tag{1}$$

with stationary conditions,  $u(y^*)|_{y^*=0} = u'(y^*)|_{y^*=H} = 0$  (2)

Considering the characteristic velocity  $u_c = -\frac{dp}{dx^*} \cdot \frac{H^2}{\mu + L_{yy}}$  and the dimensionless parameter  $y = \frac{y^*}{H}$ , Eq. (1) can be rewritten as,

$$\kappa \frac{d^2u}{dy^2} - \alpha^2 u = -u_c, \tag{3}$$

where,  $\alpha = \sqrt{\frac{\mu FH^2}{\mu + L_{yy}}}$  is the vegetation factor which depends on vegetation force ( $F$ ), fluid viscosity ( $\mu$ ) and vertical momentum dispersivity ( $L_{yy}$ ). The corresponding stationary condition is given by,

$$u(y)|_{y=0} = u'(y)|_{y=1} = 0. \tag{4}$$

Solving (3) and (4), the normalized velocity profile is found as,

$$\psi = \frac{u}{u_c} = \frac{1}{\alpha^2} \left( 1 - \frac{\cosh(\frac{\alpha}{\sqrt{\kappa}}(y - 1))}{\cosh(\frac{\alpha}{\sqrt{\kappa}})} \right). \tag{5}$$

It is amusing to observe that, without vegetation factor and tortuosity (i.e.,  $\alpha \rightarrow 0, \kappa = 1$ ), the velocity profile becomes an open channel flow as

$$\lim_{\alpha \rightarrow 0, \kappa \rightarrow 1} \psi = \frac{y(2 - y)}{2} \tag{6}$$

The effects of vegetation factor and tortuosity on the velocity profile are shown in Fig. 2. It is observe that, when the amount of vegetation in wetland increases, the flow velocity significantly decreases as the vegetation factor resists the flow. On the

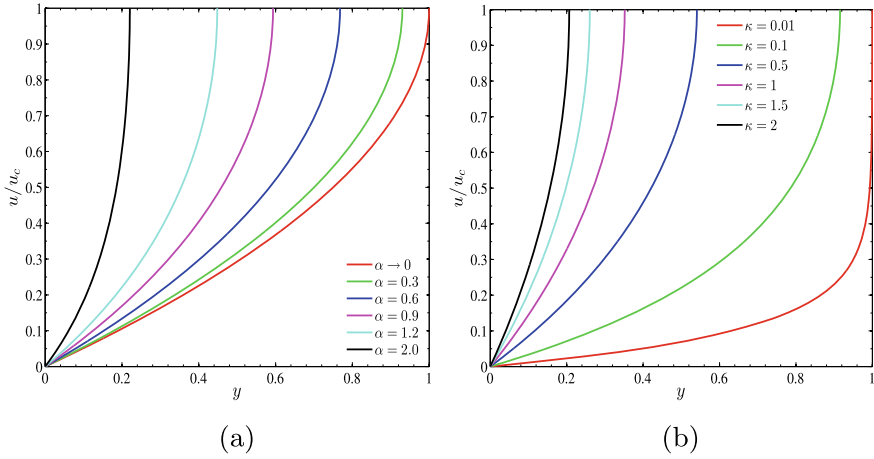


**Fig. 2** Variation of velocity profile  $u(y)/u_c$ : **a**  $\alpha \rightarrow 0, \alpha = 0.3, 0.6, 0.9, 1.2, 2$  with  $\kappa = 0.5$  and **b**  $\kappa = 0.01, 0.1, 0.5, 1, 1.5, 2$  with  $\alpha = 1$

other hand, as tortuosity increases the flow becomes tortuous and consequently speed of the flow decreases.

### 2.2 Mass Transport Equation

When the fine particles of settling velocity  $\omega^*$  with mass diffusivity  $\lambda$  is injected into the above mentioned vegetated wetland flow, the water phase based concentration  $C^*$  satisfies the following mass transfer equation

$$\frac{\partial C^*}{\partial t^*} + \frac{u}{\varphi} \frac{\partial C^*}{\partial x^*} - \omega^* \frac{\partial C^*}{\partial y^*} = \kappa \left( \lambda + \frac{K}{\varphi} \right) \left( \frac{\partial^2 C^*}{\partial x^{*2}} + \frac{\partial^2 C^*}{\partial y^{*2}} \right). \tag{7}$$

with the corresponding initial and boundary conditions

$$C^*(x^*, y^*, t^*)|_{t^*=0} = \Delta \left( \frac{x^*}{H} \right) \tag{8a}$$

$$\left[ \kappa \left( \lambda + \frac{K}{\varphi} \right) \frac{\partial C^*}{\partial y^*} + \omega^* C^* \right]_{y^*=0, H} = 0 \tag{8b}$$

$$C^*(x^*, y^*, t^*)|_{x^* \rightarrow \pm \infty} = 0. \tag{8c}$$

Introducing the non-dimensional parameters  $t = \frac{\kappa(\lambda + \frac{\kappa}{\varphi})t^*}{H^2}$ ,  $y = \frac{y^*}{H}$ ,  $C = \frac{C^*}{Q/H^2}$ ,  $x = \frac{\kappa(\lambda + \frac{\kappa}{\varphi})}{H^2\bar{u}}(x^* - \bar{u}t^*)$ ,  $\Psi = \frac{u}{\bar{u}}$ ,  $\omega = \frac{\omega^*H}{\kappa(\lambda + \frac{\kappa}{\varphi})}$ , the Eq. (7) becomes

$$\frac{\partial C}{\partial t} + (\Psi - 1)\frac{\partial C}{\partial x} - \omega\frac{\partial C}{\partial y} = \frac{1}{P_e^2}\frac{\partial^2 C}{\partial x^2} + \frac{\partial^2 C}{\partial y^2} \tag{9}$$

where  $P_e = \frac{\bar{u}H}{\kappa(\lambda + \frac{\kappa}{\varphi})\varphi}$  is the Péclet number which measures the ratio of the convection rate to diffusion rate. Also, the respective non-dimensional initial and boundary conditions are given by

$$C(x, y, t)|_{t=0} = \Delta(x) \tag{10a}$$

$$\left[ \frac{\partial C}{\partial y} + \omega C \right]_{y=0,1} = 0 \tag{10b}$$

$$C(x, y, t)|_{x \rightarrow \pm\infty} = 0 \tag{10c}$$

### 3 Mean Concentration Expansion

The solution of Eq. (9) can be formulated using Gill's series expansion method as [4],

$$C = \bar{C} + \sum_{k=1}^{\infty} f_k(t, y) \frac{\partial^k \bar{C}}{\partial x^k} \tag{11}$$

where  $\bar{C} = \int_0^1 C dy$ . Putting (11) in Eq. (9), one can get

$$\begin{aligned} \frac{\partial \bar{C}}{\partial t} + (\Psi - 1)\frac{\partial \bar{C}}{\partial x} - \frac{1}{P_e^2}\frac{\partial^2 \bar{C}}{\partial x^2} + \sum_{k=1}^{\infty} \left[ \left( \frac{\partial f_k}{\partial t} - \frac{\partial^2 f_k}{\partial y^k} - \omega \frac{\partial f_k}{\partial y} \right) \frac{\partial^k \bar{C}}{\partial x^k} \right. \\ \left. + (\Psi - 1)f_k \frac{\partial^{k+1} \bar{C}}{\partial x^{k+1}} - \frac{1}{P_e^2} \frac{\partial^{k+2} \bar{C}}{\partial x^{k+2}} + f_k \frac{\partial^{k+1} \bar{C}}{\partial x^k \partial t} \right]. \end{aligned} \tag{12}$$

To obtain the time dependent dispersion coefficient, the dispersion model can be expressed as

$$\frac{\partial \bar{C}}{\partial t} = \sum_{i=1}^{\infty} K_i(t) \frac{\partial^i \bar{C}}{\partial x^i}, \tag{13}$$

and consequently one can have

$$\frac{\partial^{k+1}\bar{C}}{\partial x^k \partial t} = \sum_{i=1}^{\infty} K_i(t) \frac{\partial^{i+k}\bar{C}}{\partial x^{i+k}}. \tag{14}$$

Using (13) and (14) in (12), we get

$$\left( K_1(t) + \Psi - 1 + \frac{\partial f_1}{\partial t} - \frac{\partial^2 f_1}{\partial y^2} - \omega \frac{\partial f_1}{\partial y} \right) \frac{\partial \bar{C}}{\partial x} + \left( K_2(t) - \frac{1}{P_e^2} + (\Psi - 1)f_1 + f_1 K_1 + \frac{\partial f_2}{\partial t} - \frac{\partial^2 f_2}{\partial y^2} - \omega \frac{\partial f_2}{\partial y} \right) \frac{\partial^2 \bar{C}}{\partial x^2} + \dots = 0. \tag{15}$$

On comparing the terms associated with  $\frac{\partial \bar{C}}{\partial x}$  and  $\frac{\partial^2 \bar{C}}{\partial x^2}$ , we have,

$$K_1(t) + \Psi - 1 + \frac{\partial f_1}{\partial t} - \frac{\partial^2 f_1}{\partial y^2} - \omega \frac{\partial f_1}{\partial y} = 0, \tag{16}$$

$$K_2(t) - \frac{1}{P_e^2} + (\Psi - 1)f_1 + f_1 K_1 + \frac{\partial f_2}{\partial t} - \frac{\partial^2 f_2}{\partial y^2} - \omega \frac{\partial f_2}{\partial y} = 0. \tag{17}$$

Similarly, putting Eq.(11) in (10b), we get

$$\left[ \frac{\partial f_k}{\partial y} + \omega f_k = 0 \right]_{y=0,1} \quad \text{for } k = 1, 2, \dots \tag{18}$$

Taking average operation on Eqs.(16) and (17), it is found that

$$K_1(t) = 0, \tag{19}$$

$$K_2(t) = \frac{1}{P_e^2} - \int_0^1 \Psi f_1 dy. \tag{20}$$

Since, mean concentration satisfies the one dimensional diffusion like equation, one can neglect other terms of Eq. (13) and it becomes

$$\frac{\partial \bar{C}}{\partial t} = K_2(t) \frac{\partial^2 \bar{C}}{\partial x^2}. \tag{21}$$

Now, solving Eq.(16) with the help of (18),  $f_1$  can be found as

$$f_1 = \frac{\tanh K_a}{K_a - \tanh K_a} \left( \frac{1 + \omega - \omega y}{\omega^2} \right) + \left( \frac{K_a \cosh(K_a(y - 1)) - \omega \sinh(K_a(y - 1))}{(K_a - \tanh K_a)(K_a^2 - \omega^2) \cosh K_a} \right) + A e^{-\omega y} + e^{-\frac{\omega y}{2}} \sum_{n=1}^{\infty} \frac{1 - \cos(n\pi)}{n\pi} e^{-(n^2\pi^2 + \frac{\omega^2}{4})t} \left( \cos(n\pi y) - \frac{\omega}{2n\pi} \sin(n\pi y) \right). \tag{22}$$

where  $A = \frac{\omega}{e^{-\omega}-1} \left[ \frac{(\omega+2) \tanh K_a}{2\omega^2(K_a-\tanh K_a)} + \frac{K_a \sinh K_a + \omega(\cosh K_a - 1)}{K_a(K_a^2 - \omega^2)(K_a - \tanh K_a) \cosh K_a} \right]$  and  $K_a = \frac{\alpha}{\sqrt{\kappa}}$ . Now, using (22) in (20), one can get  $K_2(t)$  as

$$K_2(t) = \frac{1}{P_e^2} + \frac{K_a}{K_a \cosh K_a - \sinh K_a} \left[ \frac{(1 + \omega) \tanh K_a \sinh K_a}{\omega^2 K_a (K_a - \tanh K_a)} - \frac{\tanh K_a (\cosh K_a - 1)}{\omega K_a^2 (K_a - \tanh K_a)} \right] + \frac{1}{(K_a - \tanh K_a)(K_a^2 - \omega^2) \cosh K_a} \left[ \frac{\sinh 2K_a}{4} + \frac{K_a}{2} + \frac{\omega \sinh^2 K_a}{2K_a(K_a^2 - \omega^2)} \right] - A \left( \frac{\omega(\cosh K_a - e^{-\omega}) - K_a \sinh K_a}{K_a^2 - \omega^2} \right) + \sum_{n=1}^{\infty} B_n e^{-(n^2\pi^2 + \frac{\omega^2}{4})t}, \tag{23}$$

where  $B_n = \frac{1 - \cos(n\pi)}{n\pi} \left[ \left(1 - \frac{\omega}{2n\pi}\right) B_{n1} + \left(1 + \frac{\omega}{2n\pi}\right) B_{n2} \right]$ ,  $B_{n1} = \frac{2K_a - \omega}{(2K_a - \omega)^2 + 4n^2\pi^2} (e^{-\omega/2} \cos n\pi - e^{-K_a})$  and  $B_{n2} = \frac{2K_a + \omega}{(2K_a + \omega)^2 + 4n^2\pi^2} (-e^{-\omega/2} \cos n\pi + e^{-K_a})$ . Thus, the dispersion coefficient becomes  $D_T = P_e^2 K_2(t)$ . Now, for large time evolution, without vegetation, tortuosity and settling velocity (i.e.,  $t \rightarrow \infty, \alpha \rightarrow 0, \kappa = 1, \omega \rightarrow 0$ ), the dispersion coefficient becomes

$$\lim_{t \rightarrow \infty} \lim_{\alpha \rightarrow 0} \lim_{\omega \rightarrow 0} D_T = 1 + \frac{2}{945} P_e^2 \tag{24}$$

which is exactly equal with the steady dispersion coefficient of Bandyopadhyay and Mazumder [24], and it validates the present solution. Taking the average operation on the initial condition (10a), the solution of the Eq. (13) becomes longitudinal Gaussian distribution as

$$\bar{C} = \frac{1}{\sqrt{4\pi K_2(t)}} \exp\left(-\frac{x^2}{4K_2(t)}\right). \tag{25}$$

Now, let us consider a free surface wetland with porosity  $\phi = 0.9$ , mean stem diameter  $d = 10^{-2}$  m and  $H = 1$  m as in [21]. From the Bruggemann equation [22], one can obtain the tortuosity as  $\kappa = \sqrt{\phi}$ . The vegetated shear force  $F$  can be obtained from the Ergun equation [23] as  $F = \frac{150(1-\phi^2)}{d^2\phi^3}$ . One can take the ambient properties of water such as density  $\rho = 10^3 \text{ kgm}^{-3}$ , viscosity  $\mu = 10^{-3} \text{ kgm}^{-1}\text{s}^{-1}$ , and diffusivity  $\lambda = 10^{-5} \text{ m}^2 \text{ s}^{-1}$  as in [22]. Also, the mass diffusivity and momentum dispersivity can be taken as  $K = 2.86 \times 10^{-3} \text{ m}^2 \text{ s}^{-1}$  and  $L_{yy} = 1.28 \text{ kgm}^{-1}\text{s}^{-1}$  respectively [21]. In case of wastewater emission into the wetland, a sediment cloud would appear in the flow and the mean concentration decays under the combined action of fall velocity and hydraulic transport. For an environmental or ecological risk assessment, related with the solute cloud moving downwards with the mean flow, an influenced region where the involved concentration is beyond the standard level can be obtained. From Eq. (25), the critical length of the influenced region can be found as

$$S(t) = 4\sqrt{-K_2 \log\left(\frac{C_0\phi H^2 \sqrt{4\pi K_2}}{Q}\right)}. \tag{26}$$

For an instantaneous emanation of unit quantity per unit width is taken as  $Q = 1 \text{ kgm}^{-1}$  in this work. The basic limited values of  $C_0$  for BOD<sub>5</sub>, TN and TP are taken as  $4 \times 10^{-3} \text{ kgm}^{-3}$ ,  $1 \times 10^{-3} \text{ kgm}^{-3}$  and  $2 \times 10^{-4} \text{ kgm}^{-3}$  respectively [22].

### 4 Discussion of Results

In this section, the effects of Péclet number, vegetation factor, tortuosity and settling velocity on the dispersion coefficient and on the mean concentration distribution are described. Also, a physical application of the current work is shown. From Fig. 3a, it is seen that the dispersion coefficient of the tracers increases with the increment of Péclet number because it increases the convection rate. Enhancement in vegetation results the flow resistance in the wetland and thus the dispersion coefficient decreases gradually (see Fig. 3b). From Fig. 3c, it is observed that, if tortuosity  $\kappa \leq 0.1$ , a boundary layer is created near the bed surface and consequently, the dispersion coefficient enhances with the enhancement of it. On the other hand, if  $\kappa > 0.1$ , the flow becomes tortuous and thus dispersivity reduces significantly. The concentration of the fine particles conglomerated near the bed surface as the settling velocity increases and consequently, dispersion of the contaminants decreases prominently and it is presented in Fig. 3d.

Figure 4a shows the temporal evolution of the dispersion coefficient of the solute. It is seen from the figure that, as time progresses dispersion increases for small dispersion times and it reaches its stationary state after a certain critical time. Since, the vegetation factor and tortuosity resists the flow, it is seen from Fig. 4b, c that with the increment of vegetation factor and tortuosity, the concentration agglomerated near the source and hence the peak of the mean concentration profile increases. Figure 4d depicts the mean concentration of the tracers for different values of settling velocity. It is seen that as the settling velocity increases, the peak of the mean concentration distribution enhances. This is because, the deposition of the settling particles

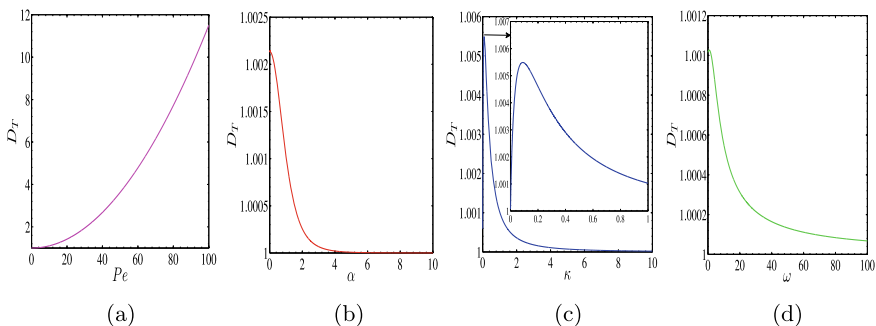


**Fig. 3** Variation of dispersion coefficient with **a** Peclet number  $P_e$ , **b** vegetation factor  $\alpha$ , **c** tortuosity  $\kappa$ , **d** settling velocity  $\omega$

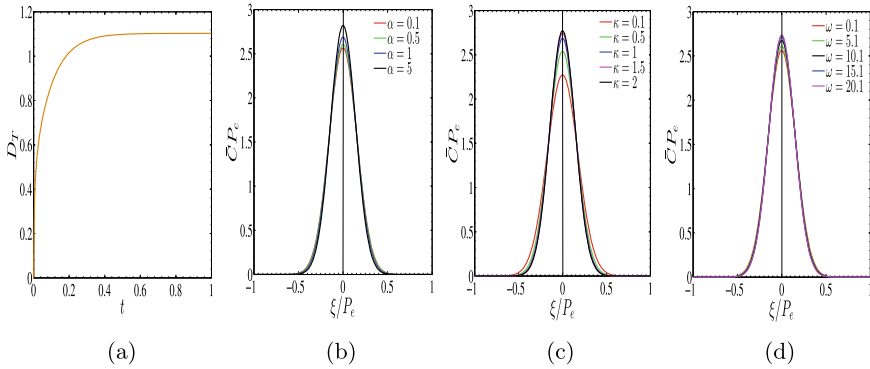


**Fig. 4** **a** Temporal evolution of dispersion coefficient; Variation of mean concentration with **b** vegetation factor ( $\alpha$ ), **c** tortuosity ( $\kappa$ ), **d** settling velocity ( $\omega$ )

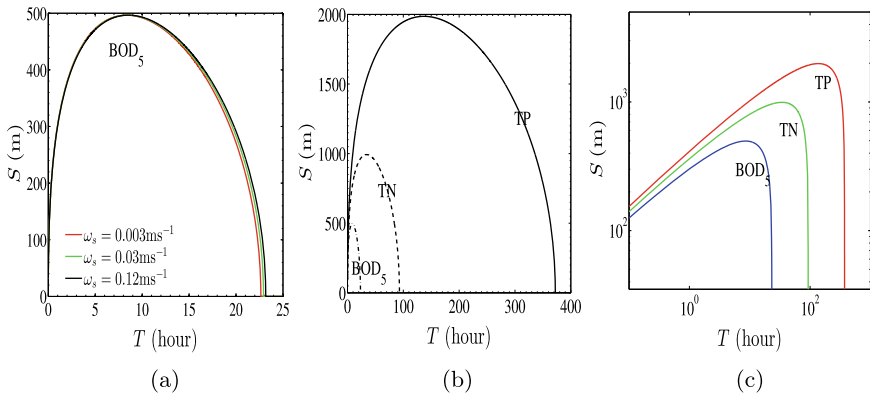


**Fig. 5** **a** Variation of influenced region ( $S$ ) with settling velocity; **b** influenced region for  $BOD_5$ , TN, TP; **c** influenced region for  $BOD_5$ , TN, TP (log-log)

increases with the increasing values of settling velocity and thus the distribution of mean concentration enhances.

From Fig. 5a, it is observed that the length of the influenced region increases as time proceeds and after a certain time it reaches its maximum and finally it decreases to zero. The maximum critical length for 5 day Biochemical Oxygen Demand ( $BOD_5$ ), Total Nitrogen (TN) and Total Phosphorus (TP) are 500 m, 1000 m and 2000 m corresponding to the duration 8.6 h, 30 h and 135 h respectively. It is interesting to observe that, the duration of the influenced region of  $BOD_5$  increases with the increment of the settling velocity of the fine particles although the maximum length remains unchanged. This is because, the fine particles settle at the bed of the wetland and consequently the solute particles stay in the wetland for longer time (see Fig. 5a). The removal of  $BOD_5$  also depends on the settling velocity of the particles. It is seen that the duration of the particle cloud enhances though the maximum length

remains unaltered with the enhance of settling velocity. It is seen from Fig. 5b and c that, when the releasing quantity is unaltered, BOD<sub>5</sub> has the weakest and TP has the strongest detrimental effect, because the metabolism due to suspended or vegetation supported bacteria may accelerate the removal of soluble organism. Again, since the removal of TP is mainly depends on the decomposition of chemical molecule, it has much stronger damage compare to other constituents.

## 5 Conclusions

In the present study, Gill's series expansion method is employed to study the transport of fine particles having settling velocity in a wetland flow. Moreover, analytical expressions for Taylor dispersivity and the mean concentration profile of tracer particles are obtained. The present research shows that the dispersion of settling particles decreases with the enhancement of vegetation factor, tortuosity and settling velocity in the wetland flow. It is seen that the concentration of settling particles agglomerated near the source when the settling velocity of particles, tortuosity of the flow and vegetation of the wetland increases. It is also observed that the duration of the settling particles for 5 day Biochemical Oxygen demand (BOD<sub>5</sub>) increases with the enhancement of settling velocity. The results may play a significant role to study the wastewater treatment and sedimentation process.

## References

1. Taylor, G.I.: Dispersion of soluble matter in solvent flowing slowly through a tube. *Proc. R. Soc. Lond. A* **219**, 186–203 (1953). <https://doi.org/10.1098/rspa.1953.0139>
2. Aris R.: On the dispersion of a solute in a fluid flowing through a tube. *Proc. R. Soc. Lond. A* **235**, 67–77 (1956). <https://doi.org/10.1098/rspa.1956.0065>
3. Gill, W.N.: A Note on the Solution of Transient Dispersion Problems. *Proc. R. Soc. A: Math. Phys. Eng. Sci.* **298**(1454), 335–339 (1967). <https://doi.org/10.1098/rspa.1967.0107>
4. Gill, W.N., Sankarasubramanian, R.: Exact analysis of unsteady convective diffusion. *Proc. R. Soc. Lond. A* **316**, 341–350 (1970). <https://doi.org/10.1098/rspa.1970.0083>
5. Wu, Z., Li, Z., Zeng, L., Shao, L., Tang, H., Yang, Q., Chen, G.: Environmental dispersivity in free-water-surface-effect dominated wetland: multi-scale analysis. *Front. Environ. Sci. & Eng. China* **5**(4), 597–603 (2011). <https://doi.org/10.1007/s11783-011-0311-9>
6. Zeng, L., Wu, Y.H., Ji, P., Chen, B., Zhao, Y.J., Chen, G.Q., Wu, Z.: Effect of wind on contaminant dispersion in a wetland flow dominated by free-surface effect. *Ecol. Model.* **237–238**, 101–108 (2012). <https://doi.org/10.1016/j.ecolmodel.2012.04.020>
7. Wang, P., Wu, Z., Chen, G.Q., Cui, B.S.: Environmental dispersion in a three-layer wetland flow with free-surface. *Commun. Nonlinear Sci. Numer. Simul.* **18**(12), 3382–3406 (2013). <https://doi.org/10.1016/j.cnsns.2013.04.027>
8. Zeng, L., Chen, G.Q.: Ecological degradation and hydraulic dispersion of contaminant in wetland. *Ecol. Modell.* **222**, 293–300 (2011). <https://doi.org/10.1016/j.ecolmodel.2009.10.024>
9. Wang, H., Zhu, Z., Li, S., Huai, W.: Solute dispersion in wetland flows with bed absorption. *J. Hydrol.* **579**, 124149 (2019). <https://doi.org/10.1016/j.jhydrol.2019.124149>



10. Wu, Z., Li, Z., Chen, G.Q.: Multi-scale analysis for environmental dispersion in wetland flow. *Commun. Nonlinear Sci. Numer. Simul.* **16**, 3168–3178 (2011). <https://doi.org/10.1016/j.cnsns.2010.12.002>
11. Zhi, L., Ping, W., Tao, S., Yiran, A., Xodong, W.: Critical length of contaminant cloud in a three-layer wetland: multi-scale analysis for environmental dispersivity. *Wetlands* **36**, 193–203 (2016). <https://doi.org/10.1007/s13157-015-0663-1>
12. Wu, Z., Zeng, L., Chen, G.Q.: Analytical modeling for environmental dispersion in Wetland. *Ecolog. Modell. Eng. Lakes Wetl.* **26**, 251–274 (2014). <https://doi.org/10.1016/b978-0-444-63249-4.00011-7>
13. Wu, Z., Chen, G.Q., Zeng, L.: Environmental dispersion in a two-zone wetland. *Ecol. Model.* **222**(3), 456–474 (2011). <https://doi.org/10.1016/j.ecolmodel.2010.10.026>
14. Wang, H., Huai, W.: Analysis of environmental dispersion in a wetland flow under the effect of wind: extended solution. *J. Hydrol.* **557**, 83–96 (2018). <https://doi.org/10.1016/j.jhydrol.2017.12.029>
15. Zeng, L., Chen, G.Q., Tang, H.S., Wu, Z.: Environmental dispersion in wetland flow. *Commun. Nonlinear Sci. Numer. Simul.* **16**(1), 206–215 (2011). <https://doi.org/10.1016/j.cnsns.2010.02.019>
16. Hammer, D.A.: *Constructed wetlands for Wastewater Treatment: Municipal, Industrial, and Agricultural*. Lewis Publishers, Chelsea, MI, USA (1989). <https://doi.org/10.1201/9781003069850>
17. Zhou, J.B., Jiang, M.M., Chen, B., Chen, G.Q.: Emergy evaluations for constructed wetland and conventional wastewater treatments. *Commun. Nonlinear Sci. Numer. Simul.* **14**(4), 1781–1789 (2009). <https://doi.org/10.1016/j.cnsns.2007.08.010>
18. Wu, Z., Zeng, L., Chen, G.Q., Li, Z., Shao, L., Wang, P., Jiang, Z.: Environmental dispersion in a tidal flow through a depth-dominated wetland. *Commun. Nonlinear Sci. Numer. Simul.* **17**(12), 5007–5025 (2012). <https://doi.org/10.1016/j.cnsns.2012.04.006>
19. Dhar, S., Poddar, N., Kairi, R.R., Mazumder, B.S., Mondal, K.K.: Numerical study on dispersion of fine settling particles in a depth dominated wetland flow. *Commun. Nonlinear Sci. Numer. Simulat.* **96**, 105707 (2021). <https://doi.org/10.1016/j.cnsns.2021.105707>
20. Poddar, N., Das, S., Dhar, S., Mondal, K.K.: Semi-analytical study on environmental dispersion of settling particles in a width-independent wetland flow. *Environ. Fluid Mech.* **21**(4), 1–22 (2021). <https://doi.org/10.1007/s10652-021-09809-2>
21. CPCB, Annual Water Quality Statistics of India, from 2019. Central Pollution Control Board, Government of India (2019). [http://www.cpcbenviis.nic.in/waterpollution/2019/Water\\_Quality\\_Canals\\_Sea\\_Water\\_Drains\\_STPs\\_2019.pdf](http://www.cpcbenviis.nic.in/waterpollution/2019/Water_Quality_Canals_Sea_Water_Drains_STPs_2019.pdf)
22. Liu, S., Masliyah, J.H.: Dispersion in porous media. In: Vafai, K. (ed.) *Handbook of Porous Media*. CRC Press, Boca Raton, FL, USA, pp. 81–140 (2005), <https://www.routledge.com/Handbook-of-Porous-Media/Vafai/p/book/9781439885543>
23. Ergun, S.: Fluid flow through packed columns. *Chem. Eng. Prog.* **48**, 89–94 (1952). <http://dns2.asia.edu.tw>
24. Bandyopadhyay, S., Mazumder, B.S.: Unsteady convective diffusion in a pulsatile flow through a channel. *Acta Mech.* **134**, 1–16 (1999). <https://doi.org/10.1007/BF01170300>

# Effects of Radiation and Chemical Reaction on MHD Mixed Convection Flow over a Permeable Vertical Plate



C. Sowmiya and B. Rushi Kumar

**Abstract** In this paper, we investigate the mixed convective flow of a viscous fluid in a vertical plate fixed in a porous medium under radiation, Dufour effect. Consider an incompressible, two-dimensional steady-state fluid subjected to flow over a semi-infinite plate influence of viscous dissipation, magnetic field. The non-linear PDEs convert into non-linear ODEs by using non-dimensionalization. The problem solved analytically by employing perturbation method. A study of the effects of velocity, temperature, concentration is significantly determined by existence of viscous dissipation, chemical reaction, radiation, Dufour effect are obtained. In addition, the effects of skin friction, the rate of energy, mass transfer are determined. It is notice, radiation parameter increases with temperature declines, Diffusion mass decreases with chemical reaction constraints.

**Keywords** Vertical plate · Slip condition · Buoyancy effect · Heat and mass transfer

## 1 Introduction

Several fields of science and engineering contain significant applications of hydro-magnetic incompressible viscous flow as it involves heat, mass transfer under chemical reaction regions. Observing a field, we realize its influence, mixed convection arising flow from heated vertical plate is a significant problem from a theoretical and practical perspective. It is one of the most common topics of interest recently, it has become a separate focus of intensive research since heat and mass are constantly being transferred through porous media, which occur as part of a variety of technological processes. Heat and mass transfer have made considerable progress in magnetohydrodynamic flows over the past few years the MHD power generators and

---

C. Sowmiya · B. R. Kumar (✉)

Department of Mathematics, SAS, Vellore Institution of Technology, Vellore 632014,

Tamil Nadu, India

e-mail: [rushikumar@vit.ac.in](mailto:rushikumar@vit.ac.in)

© The Author(s), under exclusive license to Springer Nature Switzerland AG 2022

351

S. Banerjee and A. Saha (eds.), *Nonlinear Dynamics and Applications*,

Springer Proceedings in Complexity,

[https://doi.org/10.1007/978-3-030-99792-2\\_30](https://doi.org/10.1007/978-3-030-99792-2_30)

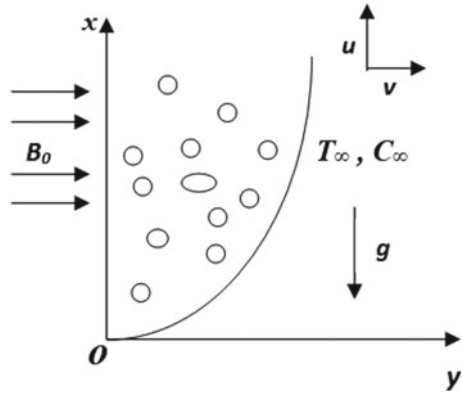
Hall accelerators are a few examples of their use. Mixed convection proceeding from fluid flow through a upright plate under the impact of magnetic field was studied by Yih [1], Barletle [2], Chin [3], Chamkha [4]. Micropolar fluids move convectively past vertical porous plates when they heated or absorbed by heat to which magnetic field applied was investigated by Rahman et al. [5]. Motsa [6] studied based on magneto-hydrodynamic of thermal and mass transfer by convection under radiation and chemical effect, through a vertical permeable plate. The hydromagnetic flow of a heat-generating or absorbing vertical surfaces, effects of chemical and hall current had examined by Patil et al. [7]. Makinde et al. [8] examined a diagonal magnetic field, radiation, and heat transfer from variable viscosity fluid observed without accounting for chemical reactions. Impact of buoyancy, radiation on mass transfer across semi-infinite surfaces explored by Shateyi [9]. Mansour et al. [10] described the MHD convection flow and chemical reaction. Palani et al. [11] discussed about heat transfer which lies between vertical plates convective MHD flow effects. Talukdar et al. [12] investigated boundary layer slip condition with thermal radiation, chemical reaction is characterized by mass and energy transfer across a vertical permeable plate. Pal et al. [13] analyzed thermodynamics of mixed convection heat transfer in porous media. Makinde et al. [14] studied dufour and soret effects of a convective boundary layer through a porous medium. Chemical reactions, heat sources have attracted attention in the flow of electrically conductive fluid in various design was evaluated by Bisht et al. [15]. Olanrewaju et al. [17] analysed flat plate subjected to an thermal boundary layer produced by exponentially declining internal heat generation, convective boundary conditions. Makinde et al. [16] analyzed the interaction between MHD mixed convection, radiation, higher order chemical reactions. The boundary layer of an incompressible fluid travels past a semi-infinite vertical plate investigated by Rushi kumar et al. [18]. Sheea Juliet et al. [19] Studied flow over a porous medium over a surface subject to exponential stretching under free convection. Nalivela Nagi Reddy et al. [20] determined effect of mass movement, chemical transmission on the natural movement of mass through endless perpendicular plates, dissipative and radiative liquids glide in convection.

Motivated by the aforementioned literature review, we investigate the effects on steady convection boundary layer through a permeable vertical plate influence of viscous dissipation, buoyancy, heat source, radiation, Dufour effect, chemical reaction, nonlinear PDEs transform into nonlinear ODEs by using non-dimensionalization. The problem solved analytically by employing perturbation method, impact of pertinent parameters on the flow rate of temperature, concentration is graphically depicted.

## 2 Formulation of the Problem

We consider an incompressible two-dimensional steady flow, viscous, heat-source fluid past a vertical permeable plate with slip flow. There exists a first-order chemical reaction with a fixed rate.  $B_0$  is a magnetic field applied in the existence of radiation and buoyancy effects. The  $x$ -axis is taken to the vertical direction along the pla-

**Fig. 1** Sketch of flow geometry



nar surface,  $y$ -axis taken surface normal to plate. According to the principle of the immeasurable plane surface, the fluid flow variables are the functions of  $y, t$  only (Fig. 1).

Governing equations of fluid flow as follows:

$$\frac{\partial u}{\partial x} + \frac{\partial v}{\partial y} = 0, \tag{1}$$

$$\left( u \frac{\partial u}{\partial x} + v \frac{\partial u}{\partial y} \right) = \nu \left( \frac{\partial^2 u}{\partial x^2} + \frac{\partial^2 u}{\partial y^2} \right) - \frac{\sigma B_0^2}{\rho} u + g\beta_T(T - T_\infty) + g\beta_c(C - C_\infty) - \frac{\nu}{k} u, \tag{2}$$

$$\begin{aligned} \left( u \frac{\partial T}{\partial x} + v \frac{\partial T}{\partial y} \right) &= \frac{k}{\rho C_p} \left( \frac{\partial^2 T}{\partial x^2} + \frac{\partial^2 T}{\partial y^2} \right) + \frac{\nu}{\rho C_p} \left( \frac{\partial u}{\partial x} + \frac{\partial u}{\partial y} \right)^2 - \frac{Q(T - T_\infty)}{\rho C_p} \\ &\quad - \frac{1}{\rho C_p} \frac{\partial q_r}{\partial y} + \frac{D_m k_T}{C_s C_p} \frac{\partial^2 C}{\partial y^2}, \end{aligned} \tag{3}$$

$$\left( u \frac{\partial C}{\partial x} + v \frac{\partial C}{\partial y} \right) = D \left( \frac{\partial^2 C}{\partial x^2} + \frac{\partial^2 C}{\partial y^2} \right) + k_r(C - C_\infty). \tag{4}$$

Where  $(u, v)$  be the velocity components of  $(x, y)$ ,  $C$ -mass concentration,  $T$ -temperature,  $\nu$ -kinematic viscosity,  $g$ -gravity acceleration,  $\sigma$ -conductivity of fluid,  $\beta_T$ -thermal expansion coefficient,  $k_T$ -thermal conductivity,  $C_\infty$ -ambient concentration,  $T_\infty$ -ambient temperature,  $C_p$ -specific heat.

The boundary conditions are:

$$\begin{aligned} u &= U_{slip}, \quad T = T_w, \quad C = C_w \quad \text{at } y = 0; \\ u &\rightarrow u_\infty = 0, \quad T_w \rightarrow T_\infty, \quad C_w \rightarrow C_\infty \quad \text{as } y \rightarrow \infty. \end{aligned} \tag{5}$$

A two-dimensional motion and an adequate length of the plate produce a situation, the x-axis is independent of all physical variables,

$$\frac{\partial u}{\partial x} = 0, \tag{6}$$

From equation of continuity, the suction velocity is either a function of  $t$  or constant. Hence integrate (1), we get the following form,

$$v = -V_0, \tag{7}$$

where  $V_0$  is velocity for scale of suction which has positive constant other than zero. Energy flux due to radiation is follows,

$$\frac{\partial q_r}{\partial y} = -4a\sigma(T_\infty^4 - T^4), \tag{8}$$

In the fluid flow region, the temperature difference is small enough, so if Taylor series are expanded around  $T_\infty$ ,  $T^4$  can be obtained by omitting the coefficients of higher order,

$$T^4 = 4T_\infty^3 T - 3T_\infty^4,$$

Non-dimensional transformation are described below:

$$U = \frac{u}{U_0}, \quad V = \frac{v}{V_0}, \quad Y = \frac{V_0 y}{\nu}, \quad \theta = \frac{T - T_\infty}{T_w - T_\infty}, \quad \phi = \frac{C - C_\infty}{C_w - C_\infty}. \tag{9}$$

In non-dimensional form, the above transformation (2) to (4) obtain as follows,

$$-\frac{\partial U}{\partial Y} = \frac{\partial^2 U}{\partial Y^2} + Gr\theta + Gc\phi - \left(M^2 + \frac{1}{\lambda}\right)U, \tag{10}$$

$$-\frac{\partial \theta}{\partial Y} = \frac{1}{Pr} \frac{\partial^2 \theta}{\partial Y^2} + E \left(\frac{\partial U}{\partial Y}\right)^2 + N \frac{\partial^2 \theta}{\partial Y^2} + Du \frac{\partial^2 \phi}{\partial Y^2} - \alpha\theta, \tag{11}$$

$$-\frac{\partial \phi}{\partial Y} = \frac{1}{Sc} \frac{\partial^2 \phi}{\partial Y^2} + K\phi. \tag{12}$$

Combined boundary conditions are;

$$\begin{aligned} U &= U_{slip}, & \theta &= 1, & \phi &= 1 \quad \text{at } Y = 0, \\ U &\rightarrow 0, & \theta &\rightarrow 0, & \phi &\rightarrow 0 \quad \text{at } Y \rightarrow \infty. \end{aligned} \tag{13}$$

Since the flow will be super imposed on main flow due to joules dissipation, the Eckart number is always less than 1 ( $E \ll 1$ ). where  $Gr = \frac{\gamma g \beta_r (T_w - T_\infty)}{V_0^2 U_0}$  is the thermal Grashof number,  $Gc = \frac{g \beta_c \gamma (C_w - C_\infty)}{V_0^2 U_0}$  is the solutal Grashof number,

$M = \frac{\gamma\sigma B_0^2}{\rho V_0^2}$ , -magnetic field,  $Pr = \frac{C_p \mu}{k}$ -Prandtl number,  $N = \frac{16\sigma T_\infty \gamma}{V_0^2 \rho C_p 3k}$ -radiation heat-flux,  $Du = \frac{(C_w - C_\infty) D_m k_T}{(T_w - T_\infty) \gamma C_p}$  is the Dufour number,  $Sc = \frac{\nu}{D}$  is the schmidt number,  $K = \frac{k_r \gamma}{V_0^2}$  is the chemical reaction,  $E = \frac{U_0^2}{\rho C_p (T_w - T_\infty)}$ ,  $\lambda = \frac{V_0^2 K}{\gamma^2}$ -porous permeability,  $\alpha = \frac{Q}{\rho C_p V_0^2}$ -heat absorption.

### 3 Method of Solution

A closed form solution cannot be found for this set of partial differential equation (10)–(13). In an analytical form, it is possible to solve the problems by using ordinary differential equations, we can solve these equations in which velocity, energy, and mass can be represented as dimensionless form,

$$U(y) = U_0(y) + EU_1(y) + O(E^2), \tag{14}$$

$$\theta(y) = \theta_0(y) + E\theta_1(y) + O(E^2), \tag{15}$$

$$\phi(y) = \phi_0(y) + E\phi_1(y) + O(E^2). \tag{16}$$

Applying (14) to (16) in (10) to (13), and comparing the balanced and unbalanced terms, ignoring higher power of  $O(E^2)$ , we obtained,

$$U_0'' + U_0' - \left(M^2 + \frac{1}{\lambda}\right) U_0 = -Gr\theta_0 - Gc\phi_0, \tag{17}$$

$$U_1'' + U_1' - \left(M^2 + \frac{1}{\lambda}\right) U_1 = -Gr\theta_1 - Gc\phi_1, \tag{18}$$

$$\theta_0''(1 + PrN) + \theta_0' Pr - \alpha\theta_0 Pr = -Du Pr \phi_0'', \tag{19}$$

$$\theta_1''(1 + PrN) + \theta_1' Pr - \alpha\theta_1 Pr = -Du Pr \phi_1'' - U_0'^2 Pr, \tag{20}$$

$$\phi_0'' + Sc\phi_0' + KSc\phi_0 = 0, \tag{21}$$

$$\phi_1'' + Sc\phi_1' + KSc\phi_1 = 0. \tag{22}$$

Boundary condition are transformed by,

$$\begin{aligned} U_0 = \gamma U_0', \quad U_1 = \gamma U_1', \quad \theta_0 = 1, \quad \theta_1 = 1, \quad \phi_0 = 1 \quad \phi_1 = 1 \quad \text{as } y = 0, \\ U_0 = 0, \quad U_1 = 0, \quad \theta_0 \rightarrow 0, \quad \theta_1 \rightarrow 0, \quad \phi_0 \rightarrow 0 \quad \phi_1 \rightarrow 0 \quad \text{as } y \rightarrow \infty. \end{aligned} \tag{23}$$

Solving the (17)–(22) along with (23) we get,

$$U_0 = A_2e^{-m_1y} + A_3e^{-m_2y} + A_4e^{-m_3y} \tag{24}$$

$$U_1 = A_{13}e^{-m_1y} + A_{14}e^{-m_2y} + A_{21}e^{-m_3y} + A_{15}e^{-2m_1y} + A_{16}e^{-2m_2y} + A_{17}e^{-2m_3y} + A_{18}e^{-(m_1+m_2)y} + A_{19}e^{-(m_1+m_3)y} + A_{20}e^{-(m_3+m_2)y}, \tag{25}$$

$$\theta_0 = (1 - A_1)e^{-m_2y} + A_1e^{-m_1y}, \tag{26}$$

$$\theta_1 = A_5e^{-m_1y} + A_{12}e^{-m_2y} + A_6e^{-2m_1y} + A_7e^{-2m_2y} + A_8e^{-2m_3y} + A_9e^{-(m_1+m_2)y} + A_{10}e^{-(m_3+m_2)y} + A_{11}e^{-(m_1+m_3)y}, \tag{27}$$

$$\phi_0 = e^{-m_1y}, \tag{28}$$

$$\phi_1 = e^{-m_1y}. \tag{29}$$

The density, temperature, and concentration distributions were determined by substituting (24)–(29) in (14) to (16)

$$U(Y, t) = [A_2e^{-m_1y} + A_3e^{-m_2y} + A_4e^{-m_3y}] + E[A_{13}e^{-m_1y} + A_{14}e^{-m_2y} + A_{21}e^{-m_3y} + A_{15}e^{-2m_1y} + A_{16}e^{-2m_2y} + A_{17}e^{-2m_3y} + A_{18}e^{-(m_1+m_2)y} + A_{19}e^{-(m_1+m_3)y} + A_{20}e^{-(m_3+m_2)y}], \tag{30}$$

$$\theta(Y, t) = [(1 - A_1)e^{-m_2y} + A_1e^{-m_1y}] + E[A_5e^{-m_1y} + A_{12}e^{-m_2y} + A_6e^{-2m_1y} + A_7e^{-2m_2y} + A_8e^{-2m_3y} + A_9e^{-(m_1+m_2)y} + A_{10}e^{-(m_3+m_2)y} + A_{11}e^{-(m_1+m_3)y}], \tag{31}$$

$$\phi(Y, t) = e^{-m_1y}[1 + E]. \tag{32}$$

The physical parameter of wall shear stress  $\tau_w$  is given by,

$$\tau_w = \mu \left( \frac{\partial u}{\partial y} \right)_{y=0} = \frac{U_0 V_0}{\rho} \left( \frac{\partial U}{\partial Y} \right)_{Y=0},$$

Local skin friction coefficient  $\tau$  is given by,

$$\tau = \frac{\tau_w \rho}{U_0 V_0}, \tag{33}$$

$$\tau = U'(0) = - (A_2m_1 + A_3m_2 + A_4m_3) - E(A_{13}m_1 + A_{14}m_2 + A_{21}m_3 + 2A_{15}m_1 + 2A_{16}m_2 + 2A_{17}m_3 + A_{18}(m_1 + m_2) + A_{19}(m_3 + m_2) + A_{20}(m_1 + m_3)), \tag{34}$$

Local surface heat flux is given by,

$$q_w = -K \frac{\partial T}{\partial y} = \frac{-K (T_w - T_\infty) V_0}{\gamma} \left( \frac{\partial \theta}{\partial Y} \right)_{Y=0},$$

$$\begin{aligned}
 Nu = \frac{Nu_x}{Re_x} = \theta'(0) = & ((1 - A_1)m_3 + A_1m_1) \\
 & - \epsilon e^{nt} (A_5m_2 + A_{12}m_5 + 2A_6m_1 + 2A_7m_3 \\
 & + 2A_8m_4 + A_9(m_1 + m_3) + A_{10}(m_3 + m_4) + A_{11}(m_1 + m_4)), \quad (35)
 \end{aligned}$$

$K$ —effective heat conductivity.

Local surface mass flux is given by,

$$Sh = \frac{Sh_x}{Re_x} = \phi'(0) = -m_1(1 + E). \quad (36)$$

Here,  $Re_x = \frac{V_0 K}{\nu}$  is Reynolds Number.

### 4 Results and Discussion

The problem consider a two-dimensional steady convective fluid over a vertical plate submerged in a porous medium. It include radiation, chemical reaction, Dufour effect in the occurrence of suction. The numerical values of various parameters  $Gr, Gc, M, \lambda, \alpha, Pr, Sc, N, K, Du$ . have been computed with boundary condition. The results are depicted as graphs in Figs. 2, 3, 4, 5, 6, 7, 8, 9, 10, 11, 12, 13, 14 and 15.

The most important fluids are atmospheric in air,  $H_2O$ , results are limited for Prandtl's number ( $Pr = 0.71, 7.0$ ) representing air,  $H_2O$  at  $20^\circ C$ , were chosen Schmidt numbers of ( $Sc = 0.21, 0.62, 0.78, 2.62$ ) representing chemical species of  $H_2, O_2, CO_2, C_9H_{12}$  diffusing in the air. In the velocity boundary layer, thermal Grashof number is equal to the relation of buoyant to viscous forces acting on a fluid. For the following graphs we have used  $Gr = 1, Gc = 1, E = 0.2, \alpha = 0.1, \lambda = 2, M = 2, N = 1, \gamma = 1, K = 1, Du = 0.5, Sc = 0.6$ .

The velocity distribution in Fig. 2 shows that velocity decreases as the values of  $M$  increase because of the existence of magnetic field sets in Lorentz force which induces the retarding force on velocity field. Figure 3 depicts velocity rising with an rise the values  $\lambda$  since porosity reduce the drag force help fluid to go fast. The effects of thermal, solutal Grashof number depicted in Figs. 4, 5, from these figures shown the velocity increases with raise the values of  $Gr$  and  $Gc$  it is due to the presence of thermal buoyancy boost the velocity distribution.

In Fig. 6 temperature distribution diminishes as the value of heat absorption increases, that has a tendency to lower thermal buoyancy effects.  $Pr$  increased then fluid temperature distribution is decreases displayed in Fig. 7. By increasing  $Pr$ , thermal conductivities will decreases, which leads to faster diffusion of heat apart from heated plate. Figure 8 shown Dufour number rises temperature distribution falls. Radiation heat-flux  $N$  causes the fluid temperature distribution to increase as displayed in Fig. 9. When  $N$  increases thickness of boundary layer, heat transfer rate also increase. Figure 10 presented the mass distribution is decreasing while increas-



**Fig. 2** Effect of  $M$  on velocity distribution

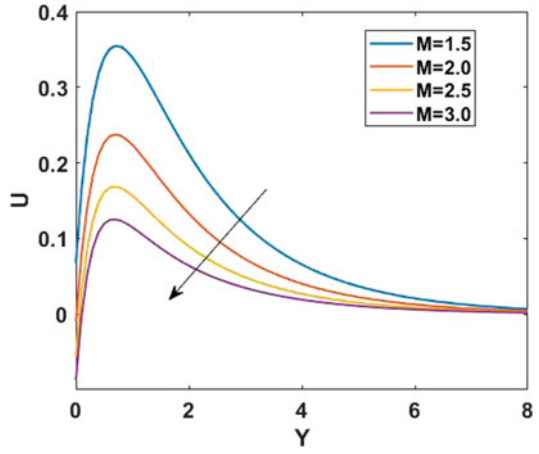


**Fig. 3** Effect of  $\lambda$  on velocity distribution

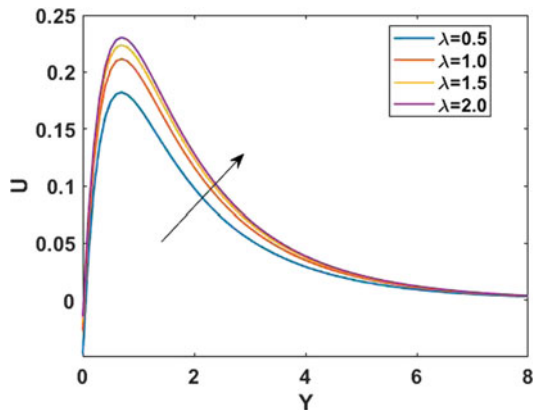


**Fig. 4** Effect of  $Gc$  on velocity distribution

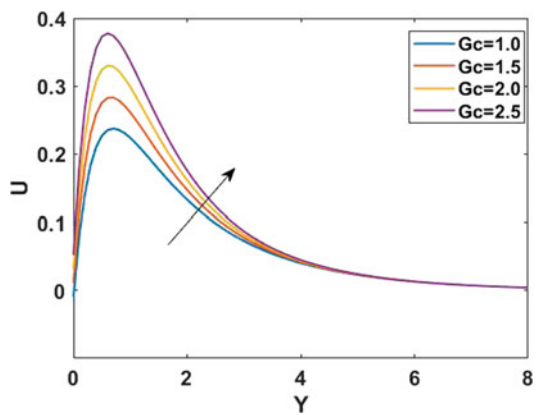


**Fig. 5** Effect of  $Gr$  on velocity distribution

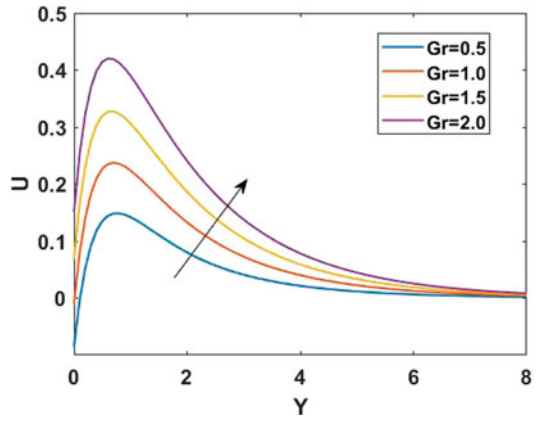


**Fig. 6** Effect of  $\alpha$  on temperature distribution

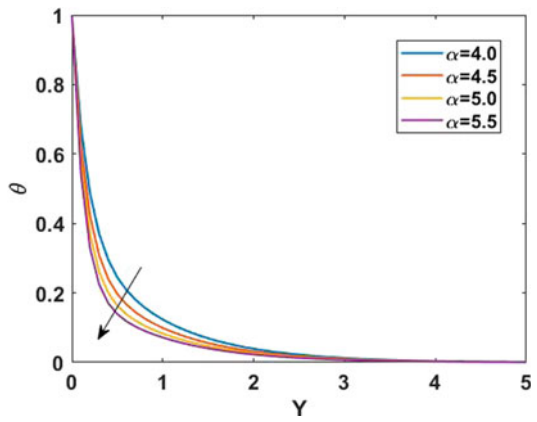


**Fig. 7** Effect of  $Pr$  on temperature distribution

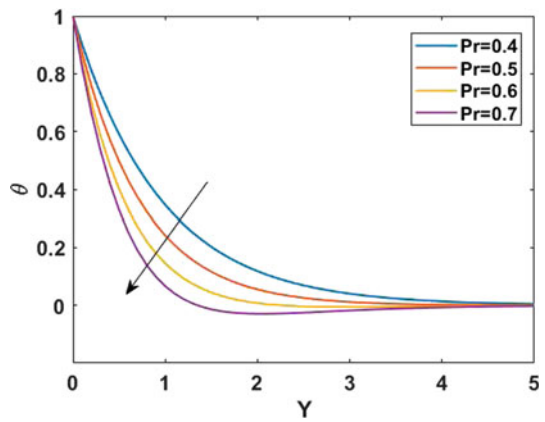


**Fig. 8** Effect of  $Du$  on temperature distribution

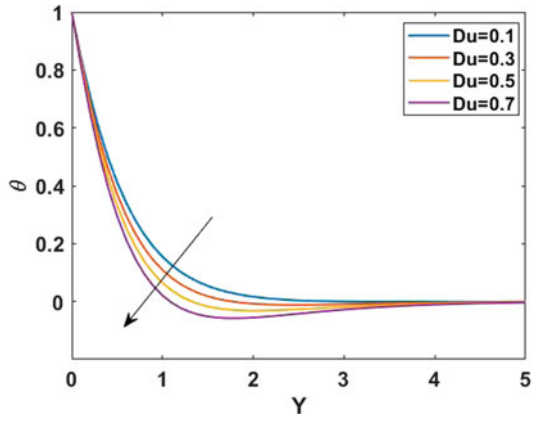


**Fig. 9** Effect of radiation on temperature distribution

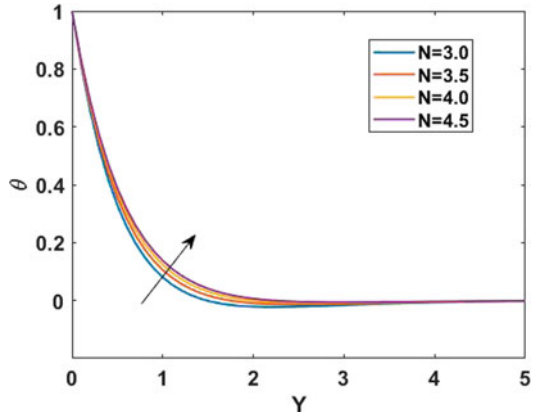


**Fig. 10** Effect of  $Sc$  on concentration distribution

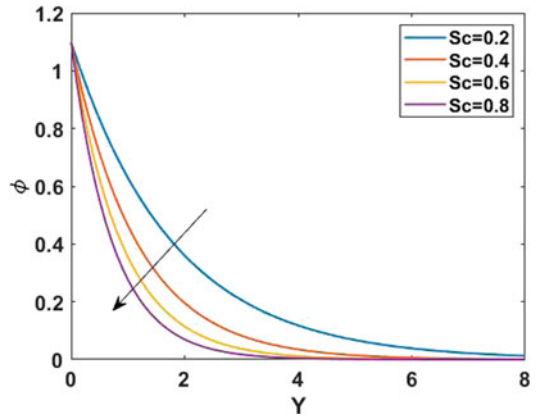


**Fig. 11** Effect of  $K$  on concentration distribution

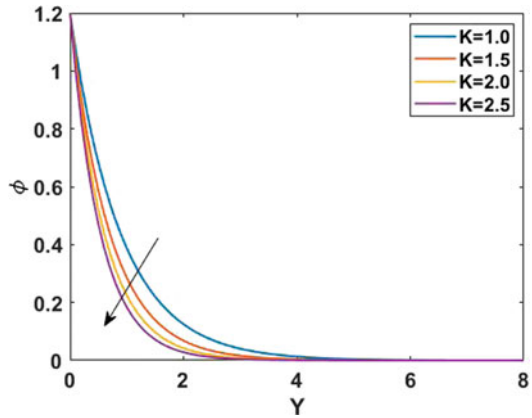
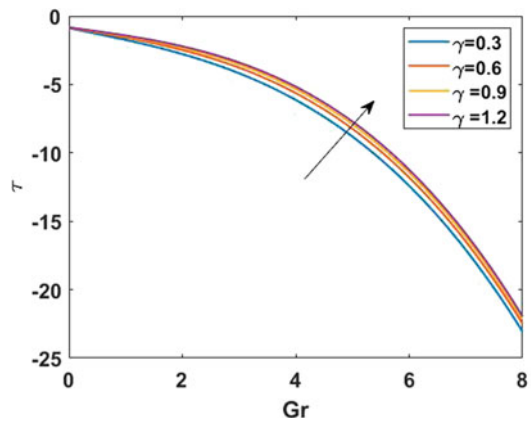


**Fig. 12** Effect of  $\gamma$  on skin friction distribution



ing the values of  $Sc$ , because  $Sc$  is small, it leads to smaller diffusivity which results fall in mass. By increasing chemical reaction values  $K$ , the concentration decreases as shown in Fig. 11. The reverse trend is noticed due to appearance of chemical reaction at constant rate. When  $\gamma$  increases, the skin friction also increase and increase the value  $Gc$ , skin friction decreases as shown in Fig. 13.  $Nu$  against  $M$ , various values of  $Pr$  is increases in heat transfer monotonically, which is shown in Fig. 14.  $Sh$  against the  $M$  for various values  $K$ , resulting in mass transfer being reduced as represented in Fig. 15.

**Fig. 13** Effect of  $Gc$  on skin distribution

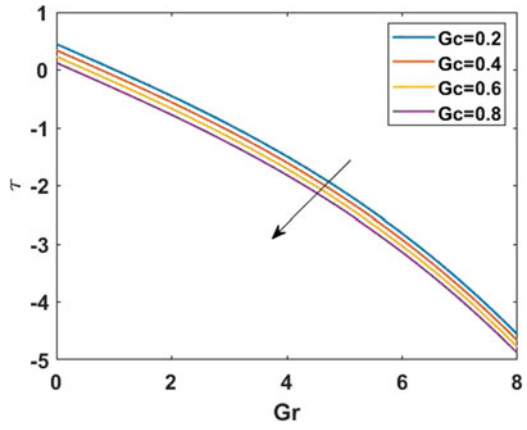


**Fig. 14** Effect of  $Du$  on Nusselt number distribution

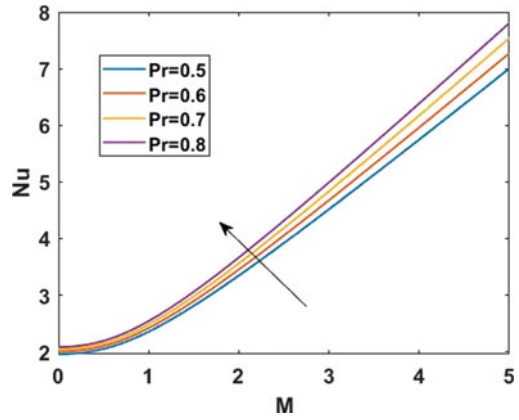
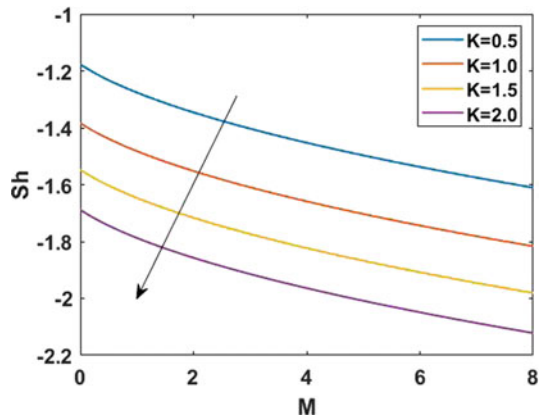


**Fig. 15** Effect of  $K$  on Sherwood number distribution



### 5 Conclusion

We have investigate steady state mixed convectional heat, mass transfer in a permeable vertical plates with Dufour and chemical reaction. By using perturbation method, we have obtain an analytical solution to this problem and numerical results are depicted as graphs. Several important parameters are analyzed in this study. Following are some highlights.

- If magnetic field is increases, velocity distribution is decreases.
- If  $\lambda$ ,  $Gc$ ,  $Gr$  increases, there is an enhancement in velocity profile.
- An temperature distribution is diminished by increasing heat absorption, Prandtl number, Dufour effects.
- Raising radiation parameter 'N', increases temperature distribution.
- Concentration distribution decreases while  $Sc$ ,  $K$  are increases.

### Appendix

$$\begin{aligned}
 m_1 &= \frac{Sc + \sqrt{Sc^2 - 4KSc}}{2}, \quad m_2 = \frac{-pr}{1 + PrN}, \quad m_3 = \frac{1 + \sqrt{1 + 4N}}{2}, \\
 A_1 &= \frac{-Du.Pr.m_1^2}{(1 + PrN)m_1^2 - m_1pr - \alpha pr}, \quad A_2 = \frac{-(GrA_1 + Gc)}{m_1^2 - m_1 - N}, \quad A_3 = \frac{Gr(1 - A_1)}{m_3^2 - m_3 - N}, \\
 A_4 &= \frac{-A_2[1 + \gamma m_1] - A_3[1 + \gamma m_2]}{1 + \gamma m_3}, \quad A_5 = \frac{-pr.Du.m_1^2}{m_1^2(1 + Npr) - m_1Pr - \alpha pr}, \\
 A_6 &= \frac{-pr.A_2^2m_1^2}{4m_1^2(1 + Npr) - 2m_1Pr - \alpha pr}, \quad A_7 = \frac{-pr.A_3^2m_2^2}{4m_2^2(1 + Npr) - 2m_2Pr - \alpha pr}, \\
 A_8 &= \frac{-pr.A_4^2m_3^2}{4m_3^2(1 + Npr) - 2m_3Pr - \alpha pr}, \quad A_9 = \frac{-2pr.A_2A_3m_1m_2}{(m_1 + m_2)(1 + Npr) - (m_1 + m_2)Pr - \alpha pr}, \\
 A_{10} &= \frac{-2pr.A_4A_3m_2m_3}{(m_2 + m_3)(1 + Npr) - (m_2 + m_3)Pr - \alpha pr}, \\
 A_{11} &= \frac{-2pr.A_2A_4m_1m_3}{(m_1 + m_3)(1 + Npr) - (m_1 + m_3)Pr - \alpha pr}, \quad A_{12} = -A_5 - \dots - A_{11}, \\
 A_{13} &= \frac{GrA_5 + Gc}{m_1^2 - m_1 - N_1}, \quad A_{14} = \frac{GrA_{12}}{m_2^2 - m_2 - N_1}, \quad A_{15} = \frac{GrA_6}{4m_1^2 - 2m_1 - N_1}, \\
 A_{16} &= \frac{GrA_7}{4m_2^2 - 2m_2 - N_1}, \quad A_{17} = \frac{GrA_8}{4m_3^2 - 2m_3 - N_1}, \quad A_{18} = \frac{GrA_9}{(m_1 + m_2)^2 - (m_1 + m_2) - N_1}, \\
 A_{19} &= \frac{GrA_{10}}{(m_2 + m_3)^2 - (m_2 + m_3) - N_1}, \quad A_{20} = \frac{GrA_{11}}{(m_1 + m_3)^2 - (m_1 + m_3) - N_1}, \\
 A_{21} &= -(A_{13}[1 + \gamma m_1] + A_{14}[1 + \gamma m_2] + A_{15}[1 + \gamma 2m_1] + A_{16}[1 + \gamma 2m_2] \\
 &+ A_{17}[1 + \gamma 2m_3] + A_{18}[1 + \gamma(m_1 + m_2)] + A_{19}[1 + \gamma(m_2 + m_3)] \\
 &+ A_{20}[1 + \gamma(m_1 + m_3)])/(1 - \gamma m_3).
 \end{aligned}$$

## References

1. Yih, K.A.: The effect of transpiration on coupled heat and mass transfer in mixed convection over a vertical plate embedded in a saturated porous medium. *Int. Commun. Heat Mass Trans.* **24**, 265–275 (1997)
2. Barletle, A.: Combined forced and free convection with viscous dissipation in a vertical duct. *Int. J. Heat Mass Transfer* **42**, 2243–2253 (1999)
3. Chin, K.E., Nazar, R., Arifin, N.M., Pop, I.: Effect of variable viscosity on mixed convection boundary layer flow over a vertical surface embedded in a porous medium. *Int. Commun. Heat Mass Trans.* **34**, 464–473 (2007)
4. Chamkha, A.J.: Hydromagnetic three-dimensional free convection on a vertical stretching surface with heat generation or absorption. *Int. J. Heat Fluid Flow* **20**(1), 84–92 (1999)
5. Rahman, M.M., Sattar, M.A.: Magnetohydrodynamic convective flow of a micropolar fluid past a continuously moving vertical porous plate in the presence of heat generation/absorption. *J. Heat Trans.* **128**(2), 142–152 (2006)
6. Motsa, S.S.: The effects of thermal radiation, hall currents, sores, and dufour on MHD flow by mixed convection over a vertical surface in porous media. *SAMSA J. Pure Appl. Math.* **3**, 58–65 (2008)
7. Patil, P.M., Kulkarni, P.S.: Effects of chemical reaction on free convective flow of a polar fluid through a porous medium in the presence of internal heat generation. *Int. J. Therm. Sci.* **47**(8), 1043–1054 (2008)
8. Makinde, O.D., Ogulu, A.: The effect of thermal radiation on the heat and mass transfer flow of a variable viscosity fluid past a vertical porous plate permeated by a transverse magnetic field. *Chem. Eng. Commun.* **195**(12), 1575–1584 (2008)
9. Shateyi, S.: Thermal radiation and buoyancy effects on heat and mass transfer over a semi-infinite stretching surface with suction and blowing. *J. Appl. Math.* Article ID 414830 (2008)
10. Mansour, M.A., El-Anssary, N.F., Aly, A.M.: Effect of chemical reaction and viscous dissipation on MHD natural convection flows saturated in porous media with suction or injection. *Int. J. Appl. Math. Mech.* **4**(2), 60–70 (2008)
11. Palani, G., Srikanth, U.: MHD flow past a semi-infinite vertical plate with mass transfer. *Nonlinear Anal.: Modell. Control* **14**(3), 345–356 (2009)
12. Pal, D., Talukdar, B.: Perturbation analysis of unsteady magnetohydrodynamic convective heat and mass transfer in a boundary layer slip flow past a vertical permeable plate with thermal radiation and chemical reaction. *Commun. Nonlinear Sci. Numer. Simul.* **15**, 1813–1830 (2010)
13. Pal, D., Talukdar, B.: Buoyancy and chemical reaction effects on MHD mixed convection heat and mass transfer in a porous medium with thermal radiation and Ohmic heating. *Commun. Nonlinear Sci. Numer. Simul.* **15**, 2878–2893 (2010)
14. Makinde, O.D.: On MHD heat and mass transfer over a moving vertical plate with a convective surface boundary condition. *Can. J. Chem. Eng.* **88**(6), 983–990 (2010)
15. Bisht, V., Kumar, M., Uddin, Z.: Effect of variable thermal conductivity and chemical reaction on steady mixed convection boundary layer flow with heat and mass transfer inside a cone due to a point. *J. Appl. Fluid Mech.* **4**(4), 59–63 (2011)
16. Makinde, O.D.: MHD mixed-convection interaction with thermal radiation and nth order chemical reaction past a vertical porous plate embedded in a porous medium. *Chem. Eng. Commun.* **198**(4), 590–608 (2011)
17. Olanrewaju, P.O., Arulogun, O.T., Adebimpe, K.: Internal heat generation effect on thermal boundary layer with a convective surface boundary condition. *Amer. J. Fluid Dyn.* **2**(1), 1–4 (2012)
18. Kumar, B.R., Sivaraj, R.: MHD mixed convection flow over a permeable vertical plate with Buoyancy and Soret effects. *Int. J. Appl. Mech. Eng.* **17**, 51–76 (2012). <https://doi.org/10.12725/mjs.22.3> <https://doi.org/10.12725/mjs.22.3>
19. Juilet, S.S., Vidhya, M., Govindarajan, A.: Effect of mass transfer with chemical reactions on MHD free convective flow of dissipative and radiative fluid past an infinite vertical plate. *AIP Conf. Proc.* **2277**, 030017 (2020)

20. Reddy, N.N., Rao, V.S., Ravindra Reddy, B.: Chemical reaction impact on MHD natural convection flow through porous medium past an exponentially stretching sheet in presence of heat source/sink and viscous dissipation. *Case studies Thermal Engineering*, vol. 25 (2021)



# Note on the Circular Rayleigh Problem



G. Chandrashekhar  and A. Venkatalaxmi 

**Abstract** We consider stability of axial flows of an incompressible, inviscid homogeneous fluid to axisymmetric disturbances known as circular Rayleigh problem of hydrodynamic stability. For circular Rayleigh problem, we derived instability region for a class of flows and which intersect with Batchelor and Gill semicircle under some conditions. Also, we derived a necessary condition for stability.

**Keywords** Inviscid fluid · Axial flows · Incompressible · Axisymmetric disturbances

## 1 Introduction

The study of linear stability of axial flows of an inviscid, incompressible, homogeneous fluid to axisymmetric disturbances is an important part of fluid dynamics and geophysical fluid dynamics (cf. [1, 3]). Circular Rayleigh problem is a inviscid case of Orr-Sommerfeld problem (cf. [2]) which deals with incompressible inviscid homogeneous axial flows to axisymmetric disturbances. Many analytical results have been proved for this problem. Reference [1] derived a necessary condition for instability which states that  $r \left( \frac{w}{r} \right)'$  should changes its sign at least once. Also, he proved that

---

Supported by Organization X

---

G. Chandrashekhar (✉) · A. Venkatalaxmi  
Department of Mathematics, Osmania University, Hyderabad, TG, India  
e-mail: [chandu.724@gmail.com](mailto:chandu.724@gmail.com)

A. Venkatalaxmi  
e-mail: [akavaramv1r@gmail.com](mailto:akavaramv1r@gmail.com)

$K(r) = \frac{-\psi(r)}{r(W-W_s)} > 0$ , where  $\psi(r) = r \left(\frac{W'}{r}\right)'$ . For instability [4] derived a necessary condition which is  $r \left(\frac{W'}{r}\right)' (W - W_s) < 0$  at least once. They also proved a semi-circle known as Batchelor & Gill semi-circle which gives the location of eigen values. Reference [5] proved Howard's conjecture namely growth rate  $k c_i$  approaches to zero as wave number  $k$  approaches to infinity. Reference [7] derived a sufficient condition for stability and short-wave stability. Reference [6] derived a parabolic instability regions which intersects with Batchelor and Gills semi-circle [4] by following the approach of [9]. The parabolic instability region derived by [6] depends on  $\phi(r) > 0$  or  $\psi(r) < 0$ .

In this present work, we derived parabolic instability regions for a class of flows and which intersects with Bachelor and Gill semicircle under some condition. Also, we derived a necessary condition for stability, namely  $k^2 > k_c^2$  where  $k_c$  is the critical value of the wave number then the flow is stable. This has been illustrated with an example.

## 2 Circular Rayleigh Problem

The circular Rayleigh Problem (cf. p. 361 of [1]) is given by

$$(W - c) [DD_* - k^2] u - rD \left[ \frac{DW}{r} \right] u = 0, \tag{1}$$

with boundary conditions

$$u(R_1) = 0 = u(R_2). \tag{2}$$

Where  $D_* = D + \frac{1}{r}$ ,  $D = \frac{d}{dr}$ ,  $W$  is the velocity function,  $c = c_r + i c_i$  (Complex eigen value),  $u$  is the eigen function and  $k$  is the wave number .

Apply the transformation  $u = (W - c)^{\frac{1}{2}} G$ , we get

$$D [(W - c) D_* G] - \frac{1}{2} r D \left[ \frac{DW}{r} \right] G - \frac{(W')^2}{4(W - c)} G - k^2 (W - c) G = 0, \tag{3}$$

$$\text{With boundary conditions } G(R_1) = 0 = G(R_2). \tag{4}$$

### 3 Instability Region

**Theorem 1** *If  $W_{\min} > 0$ ,  $c_i > 0$ , then  $c_i^2 \leq \lambda [c_r - (W_{\max} - W_{\min})]$ , where,  $\lambda = \frac{(W')^2_{\max}}{4 W_{\min} \left[ \frac{R_1 \pi^2}{R_2 (R_2 - R_1)^2} + k^2 R_1 \right]}$ .*

**Proof** Multiplying (3) by  $r G^*$ , integrating, using (4), we get

$$\int_{R_1}^{R_2} (W - c) [|D_* G|^2 + k^2 |G|^2] r dr + \int_{R_1}^{R_2} \frac{1}{2} r \left( \frac{W'}{r} \right)' r |G|^2 dr + \int_{R_1}^{R_2} \left( \frac{\frac{(W')^2}{4}}{(W - c)} \right) r |G|^2 dr = 0. \tag{5}$$

Equating real and imaginary parts, we have

$$\int_{R_1}^{R_2} (W - c_r) [|D_* G|^2 + k^2 |G|^2] r dr + \frac{1}{2} \int_{R_1}^{R_2} r \left( \frac{W'}{r} \right)' r |G|^2 dr + \int_{R_1}^{R_2} \left( \frac{\frac{(W')^2}{4} (W - c_r)}{|W - c|^2} \right) r |G|^2 dr = 0. \tag{6}$$

Since  $c_i > 0$ , we have

$$\int_{R_1}^{R_2} [|D_* G|^2 + k^2 |G|^2] r dr - \int_{R_1}^{R_2} \left( \frac{\frac{(W')^2}{4}}{|W - c|^2} \right) r |G|^2 dr = 0. \tag{7}$$

Multiplying (7) by  $[W_{\min} - W_{\max}]$  and adding with (6), we get

$$\int_{R_1}^{R_2} (W - c_r + W_{\min} - W_{\max}) [|D_* G|^2 + k^2 |G|^2] r dr + \frac{1}{2} \int_{R_1}^{R_2} r \left( \frac{W'}{r} \right)' r |G|^2 dr + \int_{R_1}^{R_2} \left( \frac{\frac{(W')^2}{4} (W - c_r - W_{\min} + W_{\max})}{|W - c|^2} \right) r |G|^2 dr = 0. \tag{8}$$

Since  $W_{\min} < c_r < W_{\max}$  this implies that  $(W - c_r + W_{\min} - W_{\max})$  is negative hence dropping the first integral term in the above equation, we get

$$\frac{1}{2} \int_{R_1}^{R_2} r \left( \frac{W'}{r} \right)' r |G|^2 dr \geq \int_{R_1}^{R_2} \left( \frac{\frac{(W')^2}{4} (W_{\min} - W_{\max} + c_r - W)}{|W - c|^2} \right) r |G|^2 dr . \tag{9}$$

Multiplying (7) by  $c_r$  and adding with (6), we get

$$\begin{aligned} &\int_{R_1}^{R_2} W [D_*G|^2 + k^2 |G|^2] r dr + \frac{1}{2} \int_{R_1}^{R_2} r \left( \frac{W'}{r} \right)' r |G|^2 dr \\ &+ \int_{R_1}^{R_2} \left( \frac{\frac{(W')^2}{4} (W - 2c_r)}{|W - c|^2} \right) r |G|^2 dr = 0 . \end{aligned} \tag{10}$$

Substituting (9) in (10), we have

$$\int_{R_1}^{R_2} W [D_*G|^2 + k^2 |G|^2] r dr \leq \int_{R_1}^{R_2} \left( \frac{\frac{(W')^2}{4} (c_r - W_{\min} + W_{\max})}{|W - c|^2} \right) r |G|^2 dr .$$

Using Rayleigh Ritz inequality and  $\frac{1}{|W-c|^2} \leq \frac{1}{c_i^2}$ , we have

$$c_i^2 \leq \lambda [c_r - W_{\min} + W_{\max}] , \tag{11}$$

where  $\lambda = \frac{\frac{(W')^2_{\max}}{4}}{W_{\min} \left[ \frac{R_1 \pi^2}{R_2 (R_2 - R_1)^2} + R_1 k^2 \right]}$ .

**Theorem 2** *If  $\lambda < \lambda_c$ , where critical value  $\lambda_c = 3 W_{\max} - W_{\min} - 2 \sqrt{W_{\max} (2 W_{\max} - W_{\min})}$ , then the parabola  $c_i^2 \leq \lambda [c_r - W_{\min} + W_{\max}]$  intersect with Batchelor and Gill semicircle.*

**Proof** Batchelor and Gill semicircle (cf. [4]) is given by

$$\left[ c_r - \frac{W_{\min} + W_{\max}}{2} \right]^2 + c_i^2 \leq \left[ \frac{W_{\max} - W_{\min}}{2} \right]^2 . \tag{12}$$

Substituting (11) in (12), we get

$$c_r^2 + [\lambda - (W_{\min} + W_{\max})] c_r + [W_{\min} W_{\max} + \lambda (W_{\max} - W_{\min})] \leq 0 .$$

Above equation is a quadratic equation in  $c_r$ , for real roots, its discriminant part should be greater than or equal to zero, we have

$$\lambda^2 - 2 [3 W_{\max} - W_{\min}] + [W_{\max} - W_{\min}]^2 \geq 0 .$$

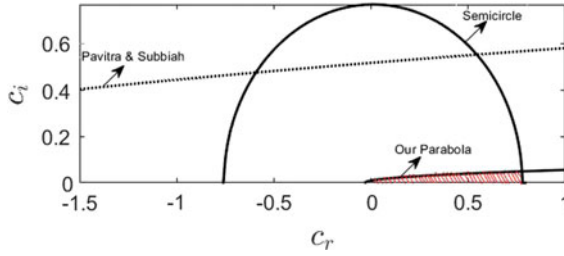


Fig. 1  $c_r$  vs  $c_i$  (The instability region is the shaded region)

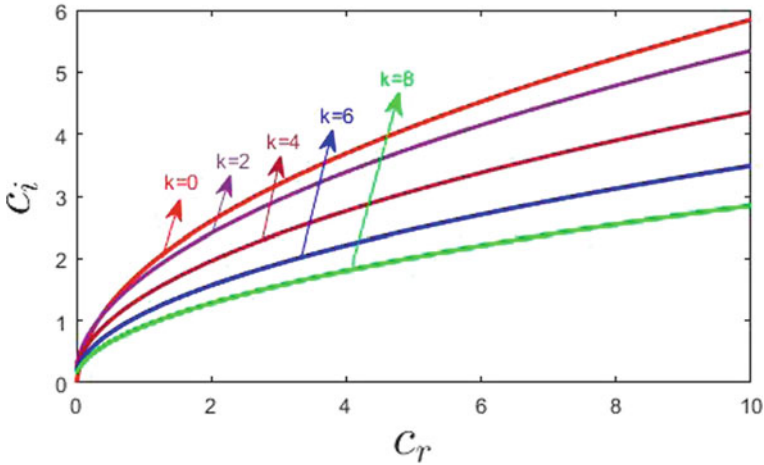


Fig. 2  $c_r$  vs  $c_i$  (Parabolic instability region)

Solving the above equation, we get  $\lambda = 3 W_{max} - W_{min} \pm 2\sqrt{W_{max}(2 W_{max} - W_{min})}$ .  $\lambda = 3 W_{max} - W_{min} + 2\sqrt{W_{max}(2 W_{max} - W_{min})}$  will lead to  $c_r < W_{min}$  and hence

$$\lambda_c = (3 W_{max} - W_{min}) - 2\sqrt{W_{max}(2 W_{max} - W_{min})},$$

then the parabola (11) intersect with Batchelor and Gill semicircle (12).

**Example 1** Let us consider example  $W(r) = \sin(r^2)$ ,  $R_1 = 1, R_2 = 2$ .  $W_{min} = 0.03925 > 0, W_{max} = 0.069756$  and  $\lambda = 0.003, \lambda_c = 0.00308$ . so,  $\lambda < \lambda_c$  which implies that the parabola intersects the semi circle (Fig. 1).

Figure 2 illustrate the reduction of parabolic instability region for different values of  $k$ , as wave number  $k$  increases, the instability region reduces.

**Example 2** Let us consider example  $W(r) = 1 + (r - \frac{1}{2})$ ,  $R_1 = 1, R_2 = 2$ .  $W_{min} = 1.5 > 0, W_{max} = 2.5$  and  $\lambda = 0.03376, \lambda_c = 0.0839$ . so,  $\lambda < \lambda_c$  which implies that the parabola intersects the semi circle.

**Theorem 3** If  $c_i > 0$  and  $(\frac{W'}{r})'_{min} > 0$  then  $c_i^2 \leq \lambda' [c_r - 2 W_{min} + W_{max}]$ , where  $\lambda' = \frac{(W')^2_{max}}{2(\frac{W'}{r})'_{min} \cdot R_1}$ .

**Proof** Multiplying (7) by  $(W_{max} - W_{min})$  and adding with (6) and since  $W_{min} < c_r < W_{max}$ , this implies that  $(W - c_r + W_{max} - W_{min})$  is positive and hence dropping the first integral term, we get

$$\frac{1}{2} \int_{R_1}^{R_2} r \left(\frac{W'}{r}\right)' r |G|^2 dr + \int_{R_1}^{R_2} \left(\frac{(W')^2}{4} \frac{(W - c_r - W_{max} + W_{min})}{|W - c|^2}\right) r |G|^2 dr \leq 0.$$

Since  $\frac{1}{|W - c|^2} \leq \frac{1}{c_i^2}$ , we have

$$R_1 \left(\frac{W'}{r}\right)'_{min} \int_{R_1}^{R_2} r |G|^2 dr \leq \frac{1}{2} \left(\frac{(W')^2_{max} (c_r - W_{min} + W_{max} - W_{min})}{c_i^2}\right) \int_{R_1}^{R_2} r |G|^2 dr.$$

$$i.e., c_i^2 \leq \lambda' [c_r - 2 W_{min} + W_{max}], \tag{13}$$

where  $\lambda' = \frac{(W')^2_{max}}{2(\frac{W'}{r})'_{min} \cdot R_1}$ .

**Theorem 4** If  $\lambda' < \lambda'_c$ , where  $\lambda'_c = (3 - 2\sqrt{2})(W_{max} - W_{min})$ , then the parabola  $c_i^2 \leq \lambda' [c_r - 2W_{min} + W_{max}]$  intersect with Batchelor and Gill semicircle.

**Proof** Proceeding in the same way as in Theorem 3.2, we get the proof.

### 4 Short Wave Stability

**Theorem 5** For an unstable mode ( $c_i > 0$ ), it is necessary that  $k^2 < k_c^2$ , where

$$k_c^2 = \frac{-\left[r\left(\frac{W'}{r}\right)'\right]^2}{2r\left(\frac{W'}{r}\right)'(W - W_s)}$$

**Proof** Multiplying (1) by  $r \left[ \frac{(r u^*)'}{r} \right]'$ , integrating and applying (2), we get

$$\int_{R_1}^{R_2} \left| \left[ \frac{(r u)'}{r} \right]' \right|^2 r dr - \int_{R_1}^{R_2} \left[ k^2 + \frac{r \left( \frac{W'}{r} \right)'}{W - c} \right] u r \left( \frac{(r u^*)'}{r} \right)' dr = 0. \tag{14}$$

From (1), taking complex conjugate, we have

$$\left( \frac{(r u^*)'}{r} \right)' = \left[ k^2 + \frac{r \left( \frac{W'}{r} \right)'}{W - c^*} \right] u^*. \tag{15}$$

Substituting (15) in (14), we have

$$\begin{aligned} &\int_{R_1}^{R_2} \left| \left[ \frac{(r u)'}{r} \right]' \right|^2 r dr - k^4 \int_{R_1}^{R_2} |u|^2 r dr - k^2 \int_{R_1}^{R_2} \left[ \frac{r \left( \frac{W'}{r} \right)'}{W - c} \right] \\ &|u|^2 r dr - k^2 \int_{R_1}^{R_2} \left[ \frac{r \left( \frac{W'}{r} \right)'}{W - c^*} \right] |u|^2 r dr - \int_{R_1}^{R_2} \frac{\left[ r \left( \frac{W'}{r} \right)'\right]^2}{|W - c|^2} |u|^2 r dr = 0. \end{aligned}$$

Equating real parts, we get

$$\begin{aligned} &\int_{R_1}^{R_2} \left| \left[ \frac{(r u)'}{r} \right]' \right|^2 r dr - k^4 \int_{R_1}^{R_2} |u|^2 r dr - 2k^2 \int_{R_1}^{R_2} \left[ \frac{r \left( \frac{W'}{r} \right)' (W - c_r)}{|W - c|^2} \right] |u|^2 r dr \\ &- \int_{R_1}^{R_2} \frac{\left[ r \left( \frac{W'}{r} \right)'\right]^2}{|W - c|^2} |u|^2 r dr = 0. \end{aligned} \tag{16}$$

Multiplying (1) by  $r u^*$ , integrating, applying (2) and equating imaginary part, we get

$$- c_i \int_{R_1}^{R_2} \left[ \frac{r \left( \frac{W'}{r} \right)'}{|W - c|^2} \right] r |u|^2 dr = 0. \tag{17}$$

Multiplying (17) by  $2k^2 \left( \frac{c_r - W_s}{c_i} \right)$  and adding with (16), we get

$$\int_{R_1}^{R_2} \left| \left[ \frac{(ru)'}{r} \right]' \right|^2 r dr - k^4 \int_{R_1}^{R_2} |u|^2 r dr - \int_{R_1}^{R_2} \left[ \frac{2k^2 r \left( \frac{W'}{r} \right)' (W - W_s) + \left[ r \left( \frac{W'}{r} \right)' \right]^2}{|W - c|^2} \right] |u|^2 r dr = 0 .$$

From the above equation, we have

$$2k^2 r \left( \frac{W'}{r} \right)' (W - W_s) + \left[ r \left( \frac{W'}{r} \right)' \right]^2 > 0 .$$

Which implies that,  $k^2 < \left[ \frac{\left[ r \left( \frac{W'}{r} \right)' \right]^2}{-2r \left( \frac{W'}{r} \right)' (W - W_s)} \right]_{r=r_p}$ .

Hence  $k^2 < k_c^2$ , where

$$k_c^2 = \frac{\left[ r \left( \frac{W'}{r} \right)' \right]^2}{-2r \left( \frac{W'}{r} \right)' (W - W_s)} . \tag{18}$$

**Theorem 6** If  $k^2 > k_c^2$ , where  $k_c^2 = \frac{\left[ r \left( \frac{W'}{r} \right)' \right]^2}{-2r \left( \frac{W'}{r} \right)' (W - W_s)}$  then the flow is stable.

**Proof** Follows from (18).

**Example 3** Let us consider example  $W(r) = \sin(r^2)$ ,  $R_1 = 1$ ,  $R_2 = 2$ .  $r \left( \frac{W'}{r} \right)' = -4r^2 \sin(r^2)$  and  $r \left( \frac{W'}{r} \right)'$  changes its sign at  $r_s = \sqrt{\pi}$ , hence the value of  $W_s$  is zero. Which implies  $k_c^2 = 8$ . Therefore If  $k > 2.828$  then the flow is stable (Fig. 3).



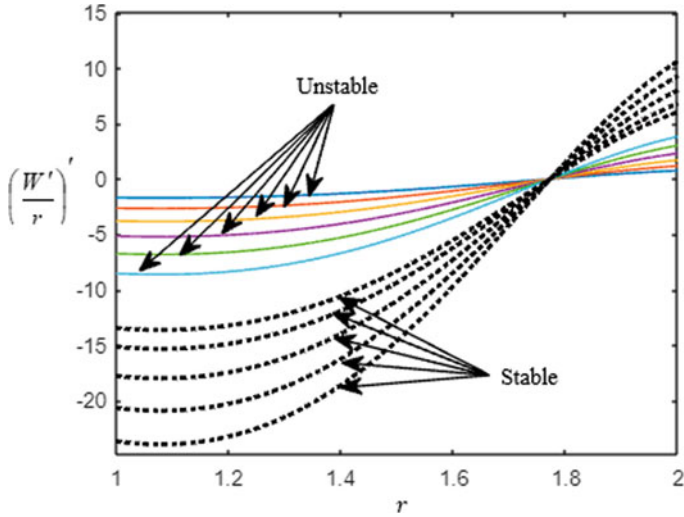


Fig. 3  $r$  vs  $\left(\frac{W'}{r}\right)'$  (The Stable and Unstable modes for different values of  $k_c$ )

### 5 Concluding Remarks

In this paper, we consider linear stability of axial flows of an inviscid, incompressible, homogeneous fluid to axisymmetric disturbances. For this problem, we derived parabolic instability region for a class of flows, and which intersect with Batchelor and Gill semicircle under some conditions. Also, we derived a necessary condition for stability, namely if the wave number  $k$  is greater than or equal to critical wave number  $k_c$  then the flow is stable.

**Acknowledgements** We are thankful to the reviewer for his suggestions in improving the presentation of our paper.

### References

1. Chandrasekhar, S.: Hydrodynamic and Hydromagnetic Instability. Clarendon Press, Oxford (1961)
2. Walton, A.G.: Stability of circular Poiseuille-couette flow to axisymmetric disturbances. *J. Fluid. Mech.* **500**, 169–210 (2004)
3. Drazin, P.G., Reid, W.H.: hydrodynamic Stability. Cambridge University Press, Cambridge (2004)
4. Batchelor, G.K., Gill, A.E.: On the hydrodynamic and hydromagnetic stability of swirling flows. *J. Fluid. Mech.* **14**, 529–551 (1962)
5. Iype, M.S.A., Subbiah, M.: On the hydrodynamic and hydromagnetic stability of inviscid flows between coaxial cylinders. *Inter. J. Fluid. Mech. Res.* **37**, 1–15 (2010)

6. Pavithra, P., Subbiah, M.: Note on instability regions in the circular Raleigh problem of hydrodynamic stability. *Proc. Natl. Aca. Sci., Sect. A: Phys. Sci.* **91**, 49–54 (2021)
7. Pavithra, P., Subbiah, M.: On sufficient conditions for stability in the circular Rayleigh problem of hydrodynamic stability. *J. Anal.* **27**, 781–795 (2019)
8. Banerjee, M.B., Gupta, J.R., Subbiah, M.: on reducing Howard's semicircle for homogeneous shear flows. *J. Math. Anal. Appl.* **130**, 398–402 (1988)
9. Gupta, J.R., Shandil, R.G., Rana, S.D.: On the limitations of the complex wave velocity in the instability problem of heterogeneous shear flows. *J. Math. Anal. Appl.* **144**, 367–376 (1989)
10. Howard, L.N.: Note on a paper of J W Miles. *J Fluid Meh.* **10**, 509–512 (1961)

# Soret and Chemical Reaction Effects on Heat and Mass Transfer in MHD Flow of a Kuvshinski Fluid Through Porous Medium with Aligned Magnetic Field and Radiation



Raghunath Kodi  and Mohana Ramana Ravuri 

**Abstract** This article explores the free convective outflow of radiative kuvshinski fluid through an inclined upward permeable platter implanted in the porous object in the proximity of Radiation absorption, thermal-diffusion (Soret) and aligned magnetic field. When a crosswise magnetic domain exists, it is known that the base is immersed in an identical permeable medium and travels at a fixed velocity in the movement regulation. The nonlinear systems of partial differential equations are changed to the ordinarily differential equalities by utilizing similarities transformations. The changed systems of equations were then solved making use of the perturbation methodology. The graphical representations of velocity, temperature, and concentration distributions obtained from mathematical solutions. Additionally, examine the effect of several specifications of the skin interference, the rate of warmth transference in the frame of the Nusselt number, and the mass transference rate at the surface as measured by the Sherwood number. It was observed that progressing the buoyancy and Soret specifications increased the velocity distribution while diminishes magnetic field specification. Temperature declined when the Prandtl number and Radiation absorption has raised, whereas concentration diminished when the Schmidt number and chemical reaction specification were progressed.

**Keywords** Radiation absorption · Chemical reaction · Soret effect

---

R. Kodi (✉)

Department of Humanities and Sciences (Mathematics), Bheema Institute of Technology and Science, Adoni, AP 518301, India  
e-mail: [kraghunath25@gmail.com](mailto:kraghunath25@gmail.com)

M. R. Ravuri

Department of Basic Science and Humanities (Mathematics), Narasaraopeta Engineering College, Narasaraopeta, AP 522601, India

## 1 Introduction

The flows of the non-Newtonian fluids are increasing considerably owing to plentiful practical submissions in manufactures as well as industrially procedures. Examples of non Newtonian fluids are molten plastic, blood, ketchups, grease, artificially fiber, paints, and certain oily liquids, in addition to numerous others. These fluids violate Newton's law of viscosity. Those liquids were extremely glutinous those did expose their important property of elasticity. Those models of liquids are important in compositely process, polymers depolarization, bubbles absorptions, as well as boiling points, etc. The second-grade fluid exhibited the effects of the natural stress as well as cannot predict the shear thin in addition to shear thicken phenomenon. But a model of the third ordered liquids can predicts together the natural stresses as well as the shear thin as well as the shear thicken phenomenon evenly the constitutive governing equations had more complexity. The resolutions of the specialized third graded liquid toward the stagnation points of the unstable absorbent stretched and/or shrinking surfaces are obtained by Naganthran et al. [1]. The phenomenon's of increment of the thermally conductance of the liquid through scattering nano-particles were studied by Masuda et al. [2]. Buongiorno [3] found that the Brownians movement as well as thermophoresis impacts of nanofluids gave an outstanding increment in fluids thermally conductivities. The computational resolution of nanofluids over the stretched sheets utilizing Buongiorno's modeling as well as analyzing the Brownians movement as well as the thermophoresis impacts on the temperature transportation rates at the surface are obtained through Khan as well as Pop [4]. Khan et al. [5] considered the effects of non-linearly radiating on a MHD flows of the Carreau's liquids over the non-linearly stretched surfaces by the convection frontier conditions.

The term "non-Newtonian" is most commonly used to describe fluids that can be used in such diverse areas as chemical, mechanical, and biotechnological systems. Two teams of physicists, mathematicians, and engineers (and several other individuals in various locations) had differing viewpoints on the primary concept of the Kuvshinski fluid flow was examined due to a multitude of factors. Given the plethora of factors to be considered in magnetic flow, the authors Seth and Bhattacharya [6] recently addressed the new Statistical Simulation of hydromagnetic Convection in Porous Media with higher Order Chemical reactions and Newtonian warming. As Newtonian flow is combined with additional diffusion in non-expanding porous media, as hypothesized by Seth et al. [7], they found a new system double-diffusive MHD flow in the pore fluids. Seth et al. [8] decentralized the Flow warmth and magnitude variations are crucial in designing vertical-screw turbines that rotate against fluid or natural convection. Seth et al. [9] study a consequence of Hall movement on MHD Natural Convection in a revolving Fluid/Solid Coupling System on Study of Past-slip non-mode of Viscoelastic Flow past. Seth et al. [10] have tackled the concept of diffusion-controlled convection, which has imperfectly approximated the motion of viscous fluid on rough interfaces and discovered time-dependent hydromagnetic unsteady flow with the Hall Effect and ocean stream expands and contracts with a

fast turning mechanism. Hari and Patel [11] have done warmth and expanse variation tests in MHD capillary-coupled capillary tube movement beyond a revolving upright platter within a penetrable object wall at ramped temperature differences. Akhil and Harshad [12] have recently discovered the significance of MHD on mixed convection, a breakthrough in understanding it. Krishna et al. [13] expressed MHD Convection outpour of Kuvshinski liquid movement an indefinite Upright permeable Platter with thermic dispersal and radiation impacts. Krishna et al. [14] conferred the radiating and absorbing on the MHD convection flows of nanoliquids over a vertically travels porous plate.

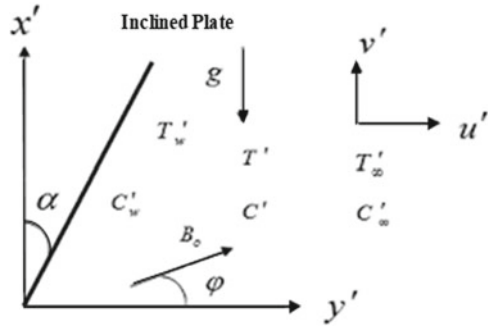
The attending work is affected by the aligned magnetic domain, Soret consequence, Radiation and Kuvshinski liquid specification on MHD convective warmth and mass transfer outpour of an unstable, incompressible electrically manipulating fluid beyond a semi-unbounded inclined upright permeable platter in the existence of chemical response and Radiation absorption. The governing equations of movement are translated analytically by utilizing the perturbation approach. In this deconstruction, we have generalized the outcome done by Raghunath et al. [15] by evaluating Radiation absorption and Kuvshinski liquid specification. This contemplation may be generous in several industrial applications, such as polymer exhibition, ceramics or glassware edibles processing, and so forth.

## 2 Mathematical Formulation

Regard an unstable bi-dimensional outpour of a laminar, dense, isentropic, eclectically functioning, emitting, and chemically responding Kuvshinski liquid via a permeable object beyond a semi-unbounded abrupt moving platter. In accord with the coordinate approach, \* x-axis is carried along the upright permeable platter in the upward directive and \* y-axis expected to it. The liquid is supposed to be a gray, immersing emitting but non dispersion object. The radiative warmth instability in the \* x-supervision is regarded inconsequential analogized to that in the \* y-supervision. An invariant magnetic specialization is spread perpendicular to the liquid gush approach and presumed that an influenced magnetic area is ignored. Viscous and Darcy antagonism spans are carried into account. The liquid belongings are presumed to be invariant, excluding thickness deviation with temperature and concentration in the body significance stint. The level of foreign mass is assumed to be low So that the Dufour effect is neglected. Also, believe that the overindulgence consequences are overlooked. The physical structure of the problem followed by Obulesu et al. [16]. Beneath the above speculations and gathering the Boussinesq expression, the border coating equations controlling the warmth and mass transmission of a viscoelastic liquid can be composed as (Fig. 1).

$$\frac{\partial v^*}{\partial y^*} = 0 \rightarrow v^* = -v_0(v_0 > 0) \quad (1)$$

**Fig. 1** Physical structure of the problem



$$\left(1 + \lambda \frac{\partial}{\partial t^*}\right) \frac{\partial u^*}{\partial t^*} + v^* \frac{\partial u^*}{\partial y^*} = -\frac{1}{\rho} \frac{\partial p^*}{\partial x^*} + \nu \frac{\partial^2 u^*}{\partial y^{*2}} + g\beta_T(T^* - T_\infty^*) \cos\alpha + g\beta_C(C^* - C_\infty^*) \cos\alpha - \frac{\sigma B_0^2}{\rho} \sin^2\gamma u^* - \frac{\nu u^*}{k^*} \tag{2}$$

$$\frac{\partial T^*}{\partial t^*} + v^* \frac{\partial T^*}{\partial y^*} = \frac{K}{\rho C_p} \frac{\partial^2 T^*}{\partial y^{*2}} - \frac{1}{\rho C_p} \frac{\partial q_r^*}{\partial y^*} + \frac{Q^*}{\rho C_p} (C^* - C_\infty^*) \tag{3}$$

$$\frac{\partial C^*}{\partial t^*} + v^* \frac{\partial C^*}{\partial y^*} = D \frac{\partial^2 C^*}{\partial y^{*2}} - K^*(C^* - C_\infty^*) + D_1 \frac{\partial^2 T^*}{\partial y^{*2}} \tag{4}$$

With the connected primary along with border stipulations were,

$$u^* = u_p^*, T^* = T_w^* + \varepsilon(T_w^* - T_\infty^*)e^{n^*t^*}, C^* = C_w^* + \varepsilon(C_w^* - C_\infty^*)e^{nt} \text{ at } y^* = 0$$

$$u^* \rightarrow u_\infty^* = U_0(1 + se^{n^*t^*}), T^* \rightarrow T_\infty^* \quad C^* \rightarrow C_\infty^* \text{ as } y^* \rightarrow \infty \tag{5}$$

The continuity equation renders that  $V^*$  is either an invariant or some position of time, hence supposing that.

$$v^* = -V_0(1 + A\varepsilon e^{n^*t^*}) \tag{6}$$

where  $A$  is a real optimistic invariant,  $\varepsilon$  and  $A\varepsilon$  are smallish than unity,  $V_0$  is the scale of the suction velocity, which has a non-zero optimistic invariant.

Beyond the border layer, Eq. (2) gives

$$-\frac{1}{\rho} \frac{\partial p^*}{\partial x^*} = \frac{\partial U_\infty^*}{\partial t^*} + \frac{v}{k^*} U_\infty^* + \frac{\sigma B_0^2}{\rho} U_\infty^* \sin^2\gamma \tag{7}$$

We assess an arithmetical prototype for an optically delicate limit gray gas near equaliser in the layout presented by Cramer and Pai [17]. Later Grief et al. [18]

$$\frac{\partial q_r^*}{\partial y^*} = 4(T^* - T_w^*) I \tag{8}$$

where  $I = \int_0^\infty K_{\lambda\omega} \left( \frac{\partial eb\lambda}{\partial T} \right)_\omega d\lambda$ ,  $K_{\lambda\omega}$  the absorption specification at the wall and  $eb\lambda$  is Planck's specification.

To formalize the arithmetical embodiment of the physical concern, familiarise the subsequent non-dimensional amounts and specifications

$$u = \frac{u^*}{U_0}, y = \frac{U_0 y^*}{\vartheta}, T = \frac{T^* - T_\infty^*}{T_w^* - T_\infty^*}, C = \frac{C^* - C_\infty^*}{C_w^* - C_\infty^*}, Pr = \frac{\mu\rho C_p}{k_T}, Sc = \frac{\vartheta}{D}, M = \frac{\sigma B_0^2 \vartheta}{\rho U_0^2},$$

$$Gr = \frac{\vartheta g \beta (T_w^* - T_\infty^*)}{U_0^3}, Gm = \frac{\vartheta g \beta^* (C_w^* - C_\infty^*)}{U_0^3}, K = \frac{U_0^2 K_0^*}{\vartheta^2}, t = \frac{t^* U_0^2}{\vartheta},$$

$$K_r = \frac{\vartheta K_C^*}{U_0^2}, R = \frac{16a^* v^2 \sigma T_\infty^{*3}}{k U_0^2}, Q = \frac{Q_1 v}{U_0^2}, S_0 = \frac{D_1 (T_w^* - T_\infty^*)}{\vartheta (C_w^* - C_\infty^*)}, R = \frac{4\vartheta n^*}{U_0^2} \tag{9}$$

The non-dimensional form of the equalizations (2), (3) and (4) are

$$\left( 1 + \lambda \frac{\partial}{\partial t} \right) \frac{\partial u}{\partial t} - \frac{\partial u}{\partial y} = \frac{\partial^2 u}{\partial y^2} + Gr \theta \cos\alpha + Gm \phi \cos\alpha - \left( 1 + \lambda \frac{\partial}{\partial t} \right) \xi u \tag{10}$$

$$\frac{\partial \theta}{\partial t} - \frac{\partial \theta}{\partial y} = \frac{1}{Pr} \frac{\partial^2 \theta}{\partial y^2} + Q\phi - R\theta \tag{11}$$

where  $\xi = \left( \frac{1}{k} + M u \sin^2 \gamma \right)$

$$\frac{\partial \phi}{\partial t} - \frac{\partial \phi}{\partial y} = \frac{1}{Sc} \frac{\partial^2 \phi}{\partial y^2} + S_0 \frac{\partial^2 \phi}{\partial y^2} - K_r \phi \tag{12}$$

The connected border circumstances are given by

$$u = U_p \quad \theta = 1 + \varepsilon e^{nt} \quad \phi = 1 + \varepsilon e^{nt}, \quad \text{at } y = 0$$

$$U \rightarrow U_\infty = 1 + \varepsilon e^{nt}, \quad \theta \rightarrow 0, \quad \phi \rightarrow 0 \quad \text{as } y \rightarrow \infty \tag{13}$$

### 3 Method of Solution

The equalizations (11)–(13) are the partial differential arrangement that can't be decrypted in sealed conditions. Regardless, these can be decoded by consolidating them into regular differential equations utilizing the subsequent perturbation approach. Now describe the velocity, temperature, and concentration disbandments in stints of harmonic and non-harmonic processes as

$$\begin{aligned}
 U(y, t) &= u_0(y) + \varepsilon u_1(y)e^{nt} + O(\varepsilon^2) \\
 T(y, t) &= \theta_0(y) + \varepsilon \theta_1(y)e^{nt} + O(\varepsilon^2) \\
 C(y, t) &= \phi_0(y) + \varepsilon \phi_1(y)e^{nt} + O(\varepsilon^2)
 \end{aligned}
 \tag{14}$$

Covering Equalization (15) into equalizations (11)–(13), and correlating the harmonic and non-harmonic stints, and overlooking the more elevated mandate stints of  $\varepsilon$ , acquire the subsequent teams of equations of ordering zero and one.

#### 3.1 Zero Order Terms

$$u''_0 + u'_0 - \xi u_0 = -Gr \cos\alpha \theta_0 - Gm \cos\alpha \phi_0 \tag{15}$$

$$\theta''_0 + Pr \theta'_0 + Pr Q \phi_0 - R Pr \theta_0 = 0 \tag{16}$$

$$\phi''_0 + Sc \phi'_0 - Sc K \phi_0 = -Sc Sr \theta_0 \tag{17}$$

#### 3.2 First Order Terms

$$u''_1 + u'_1 - (\xi + n) u_1 = -Gr \cos\alpha \theta_1 - Gm \cos\alpha \phi_1 \tag{18}$$

$$\theta''_1 + Pr \theta'_1 - n Pr \theta_1 - Pr Q \phi_1 + Pr R \theta_1 = -Pr A \theta'_0 \tag{19}$$

$$\phi''_1 + Sc \phi'_1 - Sc (K + n) \phi_1 = -A Sc \phi'_0 - Sc Sr \theta_1 \tag{20}$$

The corresponding boundary conditions are

$$\begin{aligned}
 u_0 &= U_p, u_1 = 0, \theta_0 = 1, \theta_1 = 1, C_0 = 1, C_1 = 1 \text{ at } y = 0 \\
 u_0 &= 1, u_1 = 1, \theta_0 \rightarrow 0, \theta_1 \rightarrow 0, C_0 \rightarrow 0, C_1 \rightarrow 0 \text{ as } y \rightarrow \infty
 \end{aligned}
 \tag{21}$$



Solving Eqs. (15)–(20) under the boundary conditions (21), the following solutions are obtained

$$\phi_0 = A_3 \exp(-m_1 y) + A_4 \exp(-m_3 y) \quad (22)$$

$$\theta_0 = \exp(-m_1 y) \quad (23)$$

$$u_0 = 1 + A_9 \exp(-m_5 y) + A_{10} \exp(-m_3 y) + A_{11} \exp(-m_5 y) \quad (24)$$

$$\phi_1 = A_5 \exp(-m_1 y) + A_6 \exp(-m_2 y) + A_7 \exp(-m_3 y) + A_8 \exp(-m_4 y) \quad (25)$$

$$\theta_1 = A_1 \exp(-m_1 y) + A_2 \exp(-m_2 y) \quad (26)$$

$$u_1 = 1 + A_{12} \exp(-m_1 y) + A_{13} \exp(-m_2 y) + A_{14} \exp(-m_3 y) + A_{15} \exp(-m_4 y) \\ + A_{16} \exp(-m_3 y) + A_{17} \exp(-m_6 y) \quad (27)$$

Substituting Eqs. (22)–(27) in Eq. (14), obtain the velocity, temperature and concentration distribution in the boundary layer as follows

$$u = (1 + A_9 \exp(-m_1 y) + A_{10} \exp(-m_3 y) + A_{11} \exp(-m_5 y)) + \varepsilon e^{nt} (1 + A_{12} \exp(-m_1 y) + \\ A_{13} \exp(-m_2 y) + A_{14} \exp(-m_3 y) + A_{15} \exp(-m_4 y) + A_{16} \exp(-m_5 y) + A_{17} \exp(-m_6 y)) \quad (28)$$

$$\theta = \exp(-m_1 y) + \varepsilon e^{nt} (A_1 \exp(-m_1 y) + A_2 \exp(-m_2 y)) \quad (29)$$

$$\phi = A_3 \exp(-m_1 y) + A_4 \exp(-m_3 y) + \varepsilon e^{nt} (A_5 \exp(-m_2 y) + \\ A_6 \exp(-m_2 y) + A_7 \exp(-m_3 y) + A_8 \exp(-m_4 y)) \quad (30)$$

### 3.3 Skin Friction

$$\tau = -(m_1 A_9 + m_3 A_{10} + m_5 A_{11}) \\ - \varepsilon e^{nt} (m_1 A_{12} + m_2 A_{13} + m_3 A_{14} + m_4 A_{15} + m_5 A_{16} + m_6 A_{17}) \quad (31)$$

### 3.4 Nusselt Number

$$Nu = -\left(\frac{\partial \theta}{\partial y}\right)_{y=0} = -m_1 - \varepsilon e^{nt} (m_1 A_1 + m_2 A_2) \quad (32)$$

### 3.5 Sherwood Number

$$Sh = m_1A_3 + m_3A_4 + \varepsilon e^{nt}(m_1A_5 + m_2A_6 + m_4A_7 + m_5A_8) \quad (33)$$

## 4 Results and Discussion

The consequence of the Grashof numeral on the velocity silhouettes is caught in Fig. 2. A proliferation in Gr contributes to an upsurge in velocity when all different specifications in the velocity domain are held unchanging. Also, it is detected that as we push away from the platter, the consequence of Gr is not that influential. The adjusted Grash of numeral Gm on the velocity silhouettes is memorialized in Fig. 3. A proliferation in Gm is seen to exploit the velocity to rise. Also, it is noticed that as we push far away from the platter, it is caught that the outcome of Gm is discovered to be not that influential.

The consequences of the magnetic domain specification on the velocity dispersal silhouettes across the border coating are exemplified in Fig. 4. The outcome of

**Fig. 2** The consequence of thermal Grash of number (Gr) specification on velocity

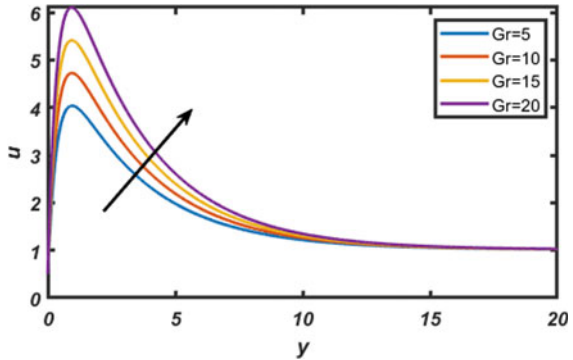


**Fig. 3** The consequence of Mass Grash of number (Gm) specification on velocity

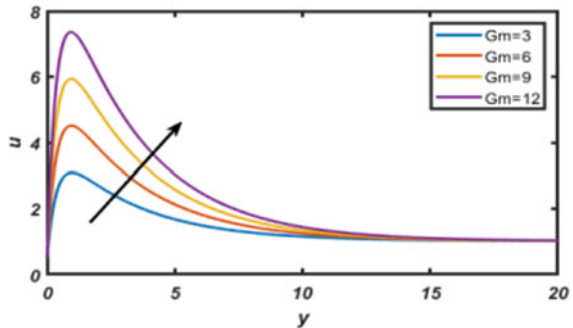
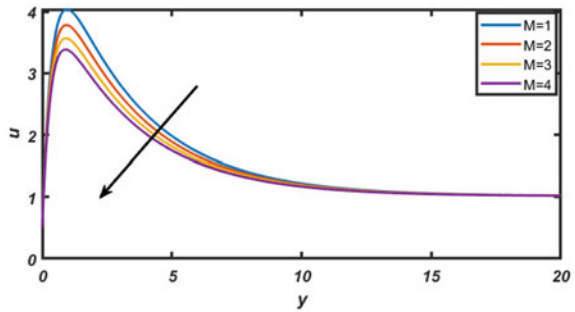


**Fig. 4** The consequence of Magnetic field (M) specification on velocity



raising magnetic domain specification  $M$  diminishes the velocity issuance across the bordering coat. This is because the intro of a transverse magnetic domain standard to the outpour movement compels the trend to create a drag squad due to Lorentz power, retarding the velocity silhouettes. It can be glimpsed in Fig. 5 that gradient of inclination ( $\alpha$ ) diminishes the consequence of the buoyancy power due to thermal disbandment. Hence, the enterprising significance to the liquid diminishes as a outcome velocity of the liquid declines. The impact of the aligned magnetic domain specification in the velocity silhouette is portrayed in Fig. 6. It is regarded that the velocity lessens with an enlargement aligned magnetic domain ( $\gamma$ ) specification. Figure 7 depicts the consequence of the permeability specification ( $k$ ) on the velocity disbandment silhouettes from which it evolves transparent that as the permeability specification ( $k$ ) raises, the velocity gains along with the border layer consistency, which is anticipated since when the hollows of the permeable medium evolve more expansive, the resistivity of the medium may be overlooked. Figure 8 exhibits the consequences of Soret numeral ( $Sr$ ) on the velocity domain; it is encountered that the velocity expands with an expansion in  $Sr$ .

Figure 9 exemplifies the radiation absorption specification consequence on the border layer's temperature silhouettes. As the radiation absorption specification

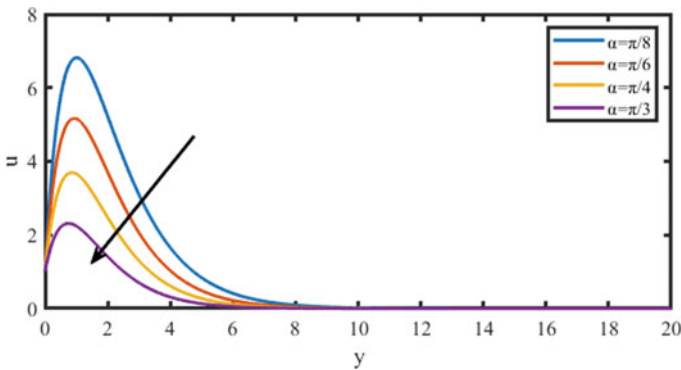


**Fig. 5** The consequence of inclined angle ( $\alpha$ ) specification on velocity

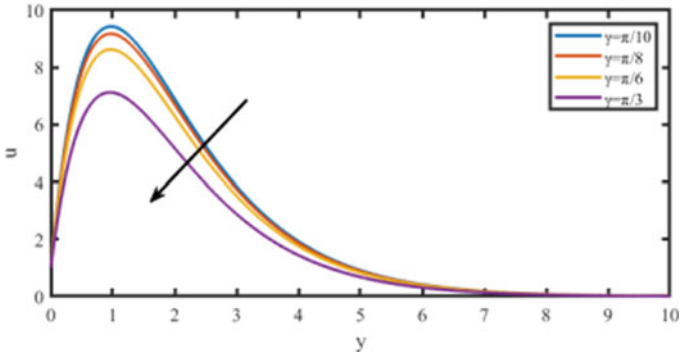


**Fig. 6** The consequence of Aligned magnetic field ( $\gamma$ ) specification on velocity outlines

**Fig. 7** The consequence of Permeability of porous media ( $k$ ) on velocity outlines

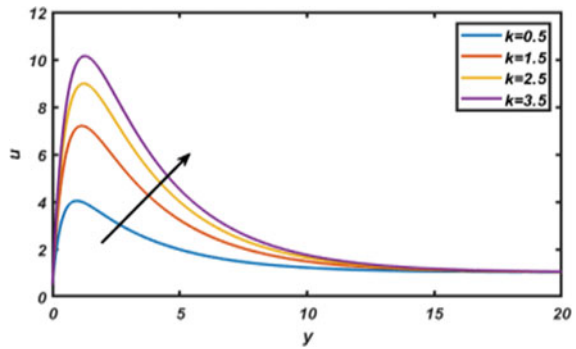
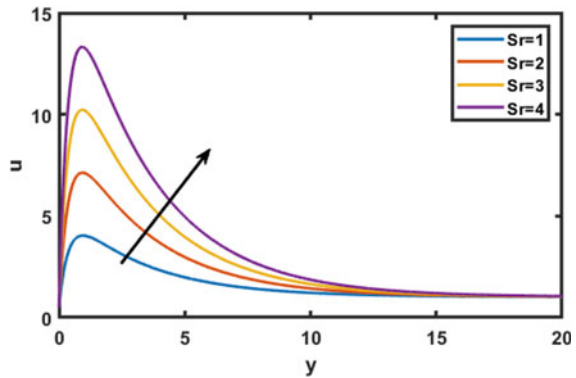


**Fig. 8** The consequence of Permeability Soret ( $Sr$ ) specification on velocity outlines



expansions, temperature dispersals rise when the additional physical specifications are designated. Figure 10 portrays the consequence of Prandtl numeral ( $Pr$ ) on temperature silhouettes in existence of some established fluids such as Hydrogen ( $Pr = 0.68$ ), Air ( $Pr = 0.71$ ), Carbon dioxide ( $Pr = 0.76$ ) and Electrolytic solution

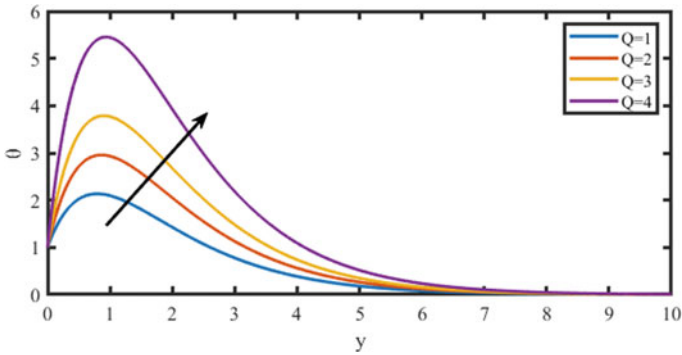
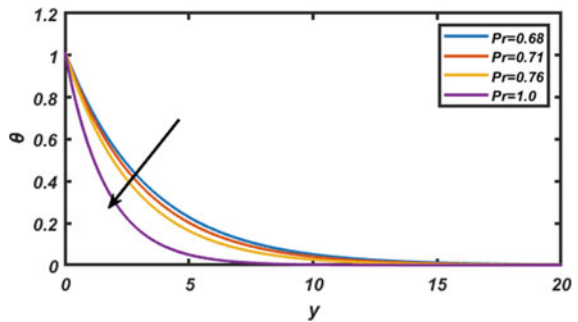


Fig. 9 The consequence of radiation absorption (Q) specification on temperature outlines

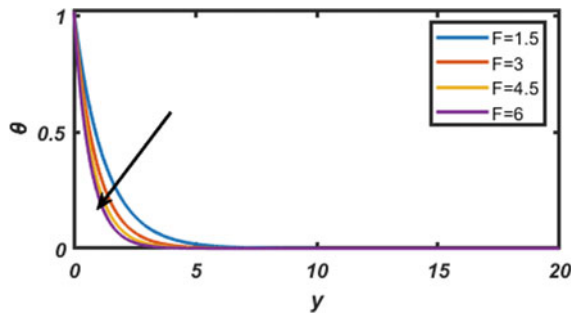
Fig. 10 The consequence of Prandtl number (Pr) specification on temperature



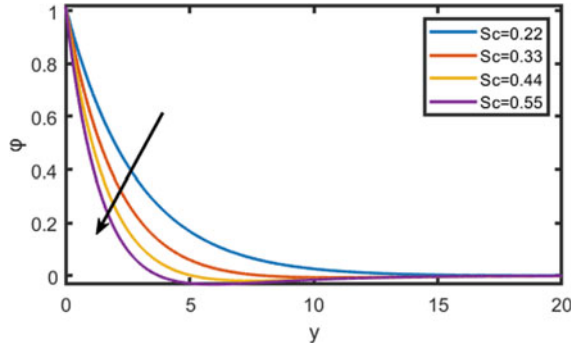
( $Pr = 1$ ). This sculpture regarded that enlargement in the Prandtl numeral lessens the temperature of the outpour domain at all matters. Due to the proportion of swiftness diffusivity to thermic diffusivity. Figure 11 depicts the temperature disbandment on the radiation specification (F). This sculpture exhibits that the temperature lessens with an accumulation in the Radiation Specification.

Figure 12 depicts Concentration silhouette for distinct significances of Schmidt

Fig. 11 The consequence of radiation parameter (F) specification on temperature



**Fig. 12** The consequence of Schmidt number ( $Sc$ ) specification on concentration



numeral  $Sc$ , delivers that growth in  $Sc$  declines the concentration silhouette. Physically, this is accurate because the wetness hazes can possess a definitive concentration area, whereas hydrogen can be utilized to preserve an adequate concentration area. Figure 13 exemplifies the concentration silhouettes for distinct matters of Soret numeral  $Sr$ . As witnessed from this chart, the concentration of species declines with the importance of the accumulation of the Soret number. Figure 14 depicts the

**Fig. 13** The consequence of Soret number ( $Sr$ ) specification on concentration

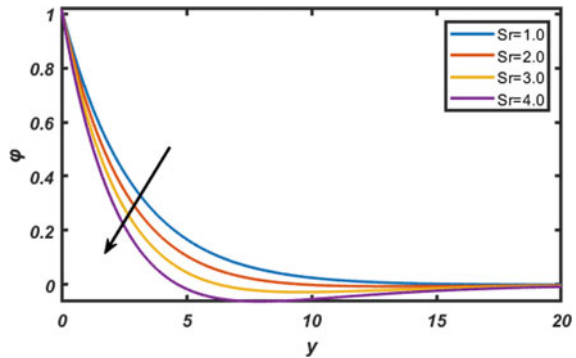
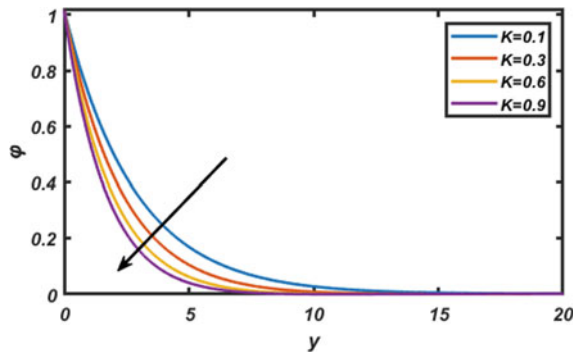


**Fig. 14** The consequence of Chemical reaction ( $K$ ) specification on concentration outlines



convincing of the chemical response influence on concentration. This mannequin viewer’s concentration declines with an accumulation in the significances of the chemical retort specification.

The interpretation in skin-friction specification, the rate of warmth transmission in the physique of Nusselt numeral, and the rate of mass transmission in the physique of Sherwood numeral for miscellaneous specification are dissected via Tables 1, 2, 3. For

**Table 1** Skin friction

M	$\gamma$	Gr	Gm	Q	Kr	$\tau$ (previous) Obulesu et al. [16]	$\tau$ (previous) Ragunath et al. [15]	$\tau$
1	$\pi/6$	5	5	0.5	0.8	0.0985	0.0927	0.0827
1.5						0.1745	0.1680	0.1370
2						0.1985	0.1851	0.1881
	$\pi/4$					0.1247	0.1254	0.1881
	$\pi/3$					0.2876	0.2897	0.2819
		7.5				1.2479	1.2654	1.2862
		10				2.5478	2.4785	2.4898
			7.5			-1.7854	-1.6754	-1.6192
			10			-3.4578	-3.3324	-3.3212
						-0.6478	-0.6782	-0.6470
						0.0457	0.0467	0.0827
				0.2		-0.3547	-0.3457	-0.3673
				0.4		-2.4785	-2.4578	-2.4396
					1.0	0.2478	0.2547	0.1968
					1.5	0.3245	0.3245	0.2660
						16.1475	16.1547	16.5628
						20.4789	20.4578	20.5053
						24.4521	24.4577	24.1451

**Table 2** Nusselt number

Q	Pr	R	Nu (previous) Obulesu et al. [16]	Nu (previous) Ragunath et al. [15]	Nu (present)
0.2	0.71	2	-1.7575	-1.6765	-1.6897
0.4	0.71	2	-1.6785	-1.6093	-1.6797
0.6	0.71	2	-1.5782	-1.5381	-1.5370
0.1	0.25	2	-0.2478	-0.2512	-0.2896
0.1	0.71	2	-1.7210	-1.7088	-1.7820
0.1	7.0	2	-9.3547	-9.3225	-9.4271
0.1	0.71	1	-1.3478	-1.3372	-1.3823
0.1	0.71	3	-1.9874	-1.9969	-1.9856
0.1	0.71	5	-2.4007	-2.4559	-2.5880

**Table 3** Sherwood Number

Q	Kr	Sr	Sh (previous) Obulesu et al. [16]	Sh (previous) Raghunath et al. [15]	Sh (present)
0.2	0.5	2	0.4785	0.5868	0.5457
0.4	0.5	2	0.5478	0.5586	0.4577
0.6	0.5	2	0.5367	0.5286	0.5247
0.1	2	2	-0.0874	-0.0722	-0.0687
0.1	4	2	0.6712	0.6003	0.6154
0.1	6	2	3.6874	3.6683	3.7857
0.1	05	1	0.2101	0.2501	0.2155
0.1	0.5	3	0.9875	0.9504	0.9851
0.1	0.5	5	1.6780	1.6507	1.7514

the reality of our work, to analogize our consequences with the existent consequences of Raghunath et al. [15] in the scarcity of permeable object and heat conception. Our result arises to be in exceptional arrangement with the present consequences.

## 5 Conclusion

From the current examination, the subsequent findings can be illustrated:

1. The liquid velocity supplements when the Grashof numeral (Gr), altered Grashof numeral (Gm), the Soret numeral (Sr), the permeable media (k) proliferation.
2. The liquid velocity diminishes with an accumulation aligned magnetic domain specification ( $\gamma$ ), chemical reaction specification (K), and the angle of inclination specification ( $\alpha$ ).
3. The liquid temperature diminishes with the consequence of the Prandtl numeral (Pr), radiation specification (R), and enhanced when increases of radiation absorption specification (Q).
4. The concentration declines with enhancing of Soret numeral (Sr) chemical reaction specification (Kr) and the Schmidt number (Sc).

## References

1. Naganthran, K., Nazar, R., Pop, I.: Unsteady stagnation-point flow and heat transfer of a special third-grade fluid past a permeable stretching/shrinking sheet. *Sci. Rep.* **6**, 1–13 (2016)
2. Masuda, H., Teramae, A.E.K., Hishinuma, N.: Alteration of thermal conductivity and viscosity of liquid by dispersing ultrane particles. *NetsuBussei* **7**, 227–233 (1993)
3. Buongiorno, J.: Convective transport in nanofluids. *ASME J. Heat Transf.* **128**, 240–250 (2006)
4. Khan, W.A., Pop, I.: Boundary-layer flow of a nanofluid past a stretching sheet. *Int. J. Heat Mass Transf.* **53**, 2477–2483 (2010)



5. Khan, M., Hashim, M., Hussain, M., Azam, M.: Magneto hydrodynamic flow of Carreau fluid over a convectively heated surface in the presence of non-linear radiation. *J. Magn. Mater.* **412**, 63–68 (2016)
6. Seth, G.S., Bhattacharyya, A., Kumar, R., Mishra, M.K.: Modelling and numerical simulation of hydromagnetic natural convection Casson fluid flow with  $n$ th-order chemical reaction and Newtonian heating in porous medium. *J. Porous Media* **22**(9), 1141–1157 (2019)
7. Seth, G.S., Kumar, R., Tripathi, R., Bhattacharyya, A.: Double diffusive MHD Casson fluid flow in a non-Darcy porous medium with Newtonian heating and thermo-diffusion effects. *Int. J. Heat Technol.* **36**(4), 1517–1527 (2019). <https://doi.org/10.18280/ijht.360446>
8. Seth, G.S., Bhattacharyya, A., Tripathi, R.: Effect of hall current on MHD natural convection heat and mass transfer flow of rotating fluid past a vertical plate with ramped wall temperature. *Front. Heat Mass Transf. (FHMT)* **9**, 21 (2017). <https://doi.org/10.5098/hmt.9.21>
9. Seth, G.S., Bhattacharyya, A., Mishra, M.K.: Study of partial slip mechanism on free convection flow of viscoelastic fluid past a nonlinearly stretching surface. *Comput. Therm. Sci.: Int. J.* 105–117 (2019). <https://doi.org/10.1615/ComputThermalSci.2018024728>
10. Seth, G.S., Mahto, N., Tripathi, R., Bhattacharyya, A.: Unsteady hydromagnetic flow formation with hall effect due to time-dependent free stream in a rotating medium. *J. Nat. Sci. Sustain. Technol.* **11**(3), 197–211 (2018)
11. Hari, R.K., Harshad, P.R.: Heat and mass transfer in magnetohydrodynamic (MHD) Casson fluid flow past over an oscillating vertical plate embedded in porous medium with ramped wall temperature. *Propuls. Power Res.* **7**(3), 257–267 (2018)
12. Akhil, S., Harshad, P.R.: Influence of thermophoresis and Brownian motion on mixed convection two dimensional MHD Casson fluid flow with non-linear radiation and heat generation. *Phys. A* **537**, 122710 (2020). <https://doi.org/10.1016/j.physa.2019.122710>
13. Krishna, R.V., Reddy, G.V., Kiran Kumar, R.V.M.S.S., Varma, S.V.K.: MHD convection flow of kuvshinski fluid past an infinite vertical porous plate with thermal diffusion and radiation effects. *Chem. Mater. Res.* **8**(2), 18–31 (2016)
14. Krishna, M.V., Ahamad, N.A., Chamkha, A.J.: Radiation absorption on MHD convective flow of nanofluids through vertically travelling absorbent plate. *Ain Shams Eng. J.* **11**, 1–14 (2021). <https://doi.org/10.1016/j.asej.2020.10.028>
15. Raghunath, K., Gulle, N., Vaddemani, R.R., Mopuri, O.: Unsteady MHD fluid flow past an inclined vertical porous plate in the presence of chemical reaction with aligned magnetic field, radiation, and Soret effects. *Heat Trans.* **51**, 1–19 (2022). <https://doi.org/10.1002/hjt.22423>
16. Mopuri, O., Kodi, R., Ganteda, C., Srikakulapu, R., Lorenzini, G.: MHD heat and mass transfer steady flow of a convective fluid through a porous plate in the presence of diffusion thermo and aligned magnetic field. *J. Adv. Res. Fluid Mech. Therm. Sci.* **89**(1), 62–76 (2022). <https://doi.org/10.37934/arfm.89.1.6276>
17. Cramer, K.P., Pai, S.I.: *Magneto Fluid Dynamics for Engineers and Applied Physics*. McGraw-Hill Book Co, New York (1973)
18. Grief, G., Habib, I.S., Lin, L.C.: Laminar convection of a radiating gas in a vertical channel. *J. Fluid Mech.* **45**, 513–520 (1971)

# Effect of Reversible Reaction on Concentration Distribution of Solute in a Couette Flow



Nanda Poddar , Subham Dhar , and Kajal Kumar Mondal 

**Abstract** A multiple-scale homogenization technique is employed in the current research to show the dispersion phenomena in a Couette flow where the solute may undergoes a reversible phase exchange between the immobile phase (stationary boundary bed phase) and mobile phase (fluid phase). Analytical solutions are obtained to view the influences of retardation factor and phase exchange kinetics on transport coefficient as well as in the two-dimensional longitudinal and transverse concentration distributions. Effects of several transversal position and dispersion time on longitudinal real concentration and the impact of different downstream stations on transverse concentration distributions are also determined. It is seen that with the increment of Damkohlar number the effective dispersivity reduces.

**Keywords** Homogenization technique · Dispersion · Couette flow · Reversible reaction · Phase exchange kinetics

## 1 Introduction

The dispersion of solute affected by reversible reaction is motivated for its huge applications in the fields of biological, environmental and chemical engineering. Due to its practical importance, the researchers has paid attention to study the influence of reversible reaction on the transport of tracer in flows in recent days. Sir Taylor [1] presented solute dispersion process through a tube in his pioneer work. He introduced an approximate solution which was valid for large dispersion time under some certain limiting conditions. Then after, Aris [2] dispelled those restrictions employing the method of moments for the solution of advection-diffusion equation. Later, Chatwin [3] accquired an asymptotic series solution of advection-diffusion equation

---

Supported by UGC India and CSIR India

---

N. Poddar (✉) · S. Dhar · K. K. Mondal  
Cooch Behar Panchanan Barma University, Cooch Behar, WB 736101, India  
e-mail: [nandapoddarc7@gmail.com](mailto:nandapoddarc7@gmail.com)

© The Author(s), under exclusive license to Springer Nature Switzerland AG 2022  
S. Banerjee and A. Saha (eds.), *Nonlinear Dynamics and Applications*,  
Springer Proceedings in Complexity,  
[https://doi.org/10.1007/978-3-030-99792-2\\_33](https://doi.org/10.1007/978-3-030-99792-2_33)

393

for a pipe. Mei et al. [4] introduced a multi-scale asymptotic homogenization method to determine the dispersion coefficient which is also valid for longer dispersion time in compare to diffusion time. By applying this technique, to investigate the solute transport phenomena, it is observed that longitudinal real concentration, transverse concentration and mean concentration distributions can be found simultaneously. Bandyopadhyay and Mazumder [5] analyzed the scalar transport phenomena in generalized Couette flow by the method of moments. Afterwards, Ng and Yip [6] and Ng and Bai [7], Mazumder and Paul [13], Barik and Dalal [14] studied the effect of reversible sorptive exchange in open channel flow and oscillatory Couette flow respectively. In recent time, several researchers such as Wu and Chen [8], Barik and Dalal [9], Poddar et al. [10], Dhar et al. [11] and Das et al. [12] applied multiple-scale homogenization theory for study the dispersion phenomena of solute through various flow geometry to show the impacts of different flow parameters.

The study of dispersion process of tracers with reversible reaction in steady Couette flow is investigated using homogenization technique for the first time. The main purpose of the present research is to view the effect of reversible phase exchange kinetics between the fluid phase and the stationary boundary bed in a simple Couette flow by employing the multi-scale homogenization technique. In view of the previous literature survey, it is found that, this is the first time in which the study on dispersion of solute is performed for a simple Couette flow for finding the dispersion coefficient, longitudinal real concentration and transverse concentration together. The analytical expressions for dispersion coefficient and real concentration distribution are obtained to inspect the impacts of reversible phase exchange kinetics, retardation factor, time of dispersion and other flow parameters on them. The current analytical result is compared with the results of Bandyopadhyay and Mazumder [5] and Ng and Bai [7] for confirmation of validation. It is seen that, in absence of the retardation factor, the present result of dispersion coefficient of the solute is exactly equal with those of [5, 7].

## 2 Formulation of the Problem

### 2.1 Velocity Profile

For the current research problem an one-dimensional laminar, viscous, incompressible Couette flow is considered between two infinite parallel plates. The plates are separated by a distance  $h$ . The  $\bar{x}$  axis and  $\bar{y}$  axis are taken along the longitudinal and transversal directions respectively in a Cartesian coordinate system. It is assumed that the lower plate is situated at  $\bar{y} = 0$  and it is at rest, however the upper plate oscillates with a constant characteristic velocity  $U$  in its own plane. Neglecting the pressure gradients, momentum equation reduces to

$$\frac{d^2 \bar{u}}{d\bar{y}^2} = 0, \tag{1}$$

with boundary conditions

$$\bar{u}(\bar{y})|_{\bar{y}=0} = 0 \quad \text{and} \quad \bar{u}(\bar{y})|_{\bar{y}=h} = U. \tag{2}$$

The analytical solution for velocity distribution in Couette flow is

$$\bar{u} = U \frac{\bar{y}}{h}, \tag{3}$$

### 2.2 Governing Equation and Boundary Conditions

Consider the dispersion of reactive species through the above mentioned flow (see Fig. 1). It is assumed that the tracer material is fully mixable in the flow of fluid. A portion of tracer concentration is flows with the fluid and the rest stay at the the boundary during the flow. The mobile phase or fluid phase is the phase where concentration moves with the flowing fluid and the immobile phase is that in which the tracer retains at the boundary.

The dispersion problem of concentration of the solute, when it released into the above mentioned Couette flow, is given by:

$$\frac{\partial C}{\partial \bar{t}} + \bar{u} \frac{\partial C}{\partial \bar{x}} = D \left( \frac{\partial^2 C}{\partial \bar{x}^2} + \frac{\partial^2 C}{\partial \bar{y}^2} \right), \quad 0 < \bar{y} < h, \tag{4}$$

where,  $C(\bar{x}, \bar{y}, \bar{t})$  is the solute concentration (mass of reactive contaminant dissolved per bulk volume of the fluid) of the fluid phase  $\bar{t}$  is the time and  $D$  is the molecular diffusivity.

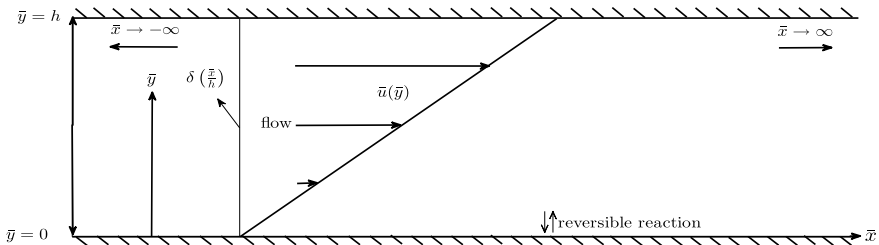


Fig. 1 Systematic diagram of Couette flow

Consider a uniform and instantaneous release of solute with mass  $Q$  at the cross-section of  $\bar{x} = 0$  at time  $\bar{t} = 0$ , the initial condition can be taken as

$$C(\bar{x}, \bar{y}, 0) = \frac{Q}{h} \delta\left(\frac{\bar{x}}{h}\right) \quad (5)$$

where,  $\delta(\bar{x})$  is the Dirac delta function.

The boundary conditions respectively given as

$$D \frac{\partial C}{\partial \bar{y}} = 0, \quad \text{at } \bar{y} = h \quad (6)$$

$$D \frac{\partial C}{\partial \bar{y}} = \frac{\partial C_s}{\partial \bar{t}} = \gamma(\bar{\theta}C - C_s), \quad \text{at } \bar{y} = 0 \quad (7)$$

where,  $C_s$  is the immobile phase concentration (mass of reactive contaminant retained per unit area of channel bed surface),  $\gamma$  is the reversible reaction rate and  $\bar{\theta}$  is the retention factor or partition coefficient that relates the concentrations of mobile and immobile phases.

Since, the tracer material can not move at infinity, the upstream and downstream conditions are given by

$$C(\bar{x}, \bar{y}, \bar{t})|_{\bar{x} \rightarrow \pm\infty} = 0 \quad (8)$$

### 3 Multi-scale Method of Homogenization

#### 3.1 Scales Selection

In order to find the solution of convection diffusion equation three different time scales are taken as Mei's multi-scale homogenization technique, related with two scales of length  $h$  (the channel width) and  $L$  (relative length of the tracer cloud). These are  $T_0$ ,  $T_1$  and  $T_2$ , where,  $T_0 = h^2/D$  as the diffusion time across the channel width,  $T_1 = L/U$  as the convection time across the characteristic length and  $T_2 = L^2/D$  is the diffusion time along longitudinal direction. The general expression of the ratio of three distinct time scales is given by

$$T_0 : T_1 : T_2 = 1 : \frac{1}{\epsilon} : \frac{1}{\epsilon^2} \quad (9)$$

where  $\epsilon = \frac{h}{L} (\ll 1)$  can be taken as perturbation parameter.

### 3.2 Dimensionless Governing Equation and Velocity Profile

On introduction of the dimensionless parameters

$$x = \frac{\bar{x}}{L}, y = \frac{\bar{y}}{h}, u = \frac{\bar{u}}{U}, t = \frac{D\bar{t}}{h^2}, Pe = \frac{Uh}{D}, Da = \frac{\gamma h^2}{D}, \theta = \frac{\bar{\theta}}{h}, \quad (10)$$

where  $Pe, Da, \theta$  are the Peclet number, Damkohler number and dimensionless retention parameter respectively.

Then the concentration transport equation and the associate stationary conditions is reduces to

$$\frac{\partial C}{\partial t} + \epsilon Pe u \frac{\partial C}{\partial x} = \epsilon^2 \frac{\partial^2 C}{\partial x^2} + \frac{\partial^2 C}{\partial y^2}, \quad 0 < y < 1, \quad (11)$$

$$\frac{\partial C}{\partial y} = 0, \quad \text{at } y = 1, \quad (12)$$

$$\frac{\partial C}{\partial y} = \frac{\partial C_s}{\partial t} = Da(\theta C - C_s), \quad \text{at } y = 0. \quad (13)$$

The dimensionless velocity is defined as

$$u = y. \quad (14)$$

### 3.3 Homogenization

Mei's homogenization technique [4] is employed for the asymptotic analysis. The expansion of mobile and immobile concentration into multi-scale are

$$C = C^{(0)} + \epsilon C^{(1)} + \epsilon^2 C^{(2)} + O(\epsilon^3), \quad (15)$$

and

$$C_s = C_s^{(0)} + \epsilon C_s^{(1)} + \epsilon^2 C_s^{(2)} + O(\epsilon^3), \quad (16)$$

On the basis of discussion of Sect. 3.1 the fast, medium and slow time variables are taken as

$$t_0 = t, t_1 = \epsilon t, t_2 = \epsilon^2 t. \quad (17)$$

The original time derivative becomes, according to the chain rule

$$\frac{\partial}{\partial t} \equiv \frac{\partial}{\partial t_0} + \epsilon \frac{\partial}{\partial t_1} + \epsilon^2 \frac{\partial}{\partial t_2} \quad (18)$$

Substitution of Eqs. (15) and (18) into Eqs. (11)–(13) results in

$$\left(\frac{\partial C^{(0)}}{\partial t_0} - \frac{\partial^2 C^{(0)}}{\partial y^2}\right) + \epsilon \left(\frac{\partial C^{(0)}}{\partial t_1} + \frac{\partial C^{(1)}}{\partial t_0} + uP_e \frac{\partial C^{(0)}}{\partial x} - \frac{\partial^2 C^{(1)}}{\partial y^2}\right) + \epsilon^2 \left(\frac{\partial C^{(0)}}{\partial t_2} + \frac{\partial C^{(1)}}{\partial t_1} + \frac{\partial C^{(2)}}{\partial t_0} + uP_e \frac{\partial C^{(1)}}{\partial x} - \frac{\partial^2 C^{(0)}}{\partial x^2} - \frac{\partial^2 C^{(2)}}{\partial y^2}\right) + O(\epsilon^3) = 0, \quad 0 < y < 1, \tag{19}$$

$$\frac{\partial C^{(0)}}{\partial y} + \epsilon \frac{\partial C^{(1)}}{\partial y} + \epsilon^2 \frac{\partial C^{(2)}}{\partial y} + O(\epsilon^3) = 0 \text{ at } y = 1, \tag{20}$$

and

$$\begin{aligned} \frac{\partial C^{(0)}}{\partial y} + \epsilon \frac{\partial C^{(1)}}{\partial y} + \epsilon^2 \frac{\partial C^{(2)}}{\partial y} + O(\epsilon^3) &= \frac{\partial C_s^{(0)}}{\partial t_0} + \epsilon \left(\frac{\partial C_s^{(0)}}{\partial t_1} + \frac{\partial C_s^{(1)}}{\partial t_0}\right) \\ &+ \epsilon^2 \left(\frac{\partial C_s^{(0)}}{\partial t_2} + \frac{\partial C_s^{(1)}}{\partial t_1} + \frac{\partial C_s^{(2)}}{\partial t_0}\right) + O(\epsilon^3) = Da (\theta C^{(0)} - C_s^{(0)}) \\ &+ \epsilon (Da (\theta C^{(1)} - C_s^{(1)})) + \epsilon^2 (Da (\theta C^{(2)} - C_s^{(2)})) + O(\epsilon^3) \text{ at } y = 0. \end{aligned} \tag{21}$$

Using this perturbation analysis, for leading order ( $O(1)$ ) the general solution of  $C^{(0)}$  is given by

$$C^{(0)} = C_0^{(0)}(x, t_1, t_2) + \sum_{n=1}^{\infty} \text{Re} [C_n^{(0)}(x, t_1, t_2) e^{in\pi y}] e^{-n^2\pi^2 t_0}. \tag{22}$$

The solution can be considered

$$C^{(0)} = C_0^{(0)}(x, t_1, t_2) \tag{23}$$

On omitting the reliance of  $C^{(0)}$  on  $y$ , the stationary condition from (21) (leading order ( $O(1)$ )) gives

$$C_s^{(0)} = \theta C_0^{(0)} \tag{24}$$

Since, the time scale  $t_0$  is larger than the another time scale  $t_1$ , the derivative with respect to  $t_0$  is negligible, for first order ( $O(\epsilon)$ ) the perturbation problem becomes

$$\frac{\partial C^{(0)}}{\partial t_1} + uP_e \frac{\partial C^{(0)}}{\partial x} = \frac{\partial^2 C^{(1)}}{\partial y^2}, \quad 0 < y < 1, \tag{25}$$

we define section average function  $\langle f \rangle$  of a function  $f$  with respect to  $y$  as

$$\langle f \rangle = \int_0^1 f dy \tag{26}$$

Now taking this section average of Eqs. (25) subject to the condition from perturbation analysis, we get

$$\frac{\partial C^{(0)}}{\partial t_1} + P_e \frac{\langle u \rangle}{R} \frac{\partial C^{(0)}}{\partial x} = 0, \tag{27}$$

here  $R = 1 + \theta$  is the retardation parameter.

Subtracting (27) from (26), which suggest the following substitutions

$$C^{(1)} = P_e A(y) \frac{\partial C_0}{\partial x} \tag{28}$$

$$C_s^{(1)} = P_e A_s \frac{\partial C_0}{\partial x} \tag{29}$$

On comparing terms related with  $\frac{\partial C^{(0)}}{\partial x}$ , the function  $A(y)$  is found to be governed by

$$\frac{d^2 A}{dy^2} = u - \frac{\langle u \rangle}{R}, \quad 0 < y < 1, \tag{30}$$

with the stationary conditions

$$\frac{dA}{dy} = 0, \quad \text{at } y = 1, \tag{31}$$

$$\frac{dA}{dy} = \frac{\theta \langle u \rangle}{R} = Da(\theta A - A_s), \quad \text{at } y = 0, \tag{32}$$

and

$$\langle A \rangle = 0. \tag{33}$$

Solving the above equations, we get

$$A = \frac{y^3}{6} - \frac{y^2}{4R} - \frac{1}{2} \left( 1 - \frac{1}{R} \right) y + \frac{5}{24} - \frac{1}{6R} \tag{34}$$

$$A_s = \frac{5R}{24} - \frac{3}{8} - \frac{1}{6R} + \frac{1}{2Da} \left( 1 - \frac{1}{R} \right) \tag{35}$$

From second order ( $O(\epsilon^2)$ ) perturbation analysis the effective transport equation is given by

$$\frac{\partial C^{(0)}}{\partial t} + \epsilon P_e \frac{\langle u \rangle}{R} \frac{\partial C^{(0)}}{\partial x} = \epsilon^2 \left( \frac{1}{R} - P_e^2 \frac{\langle uA \rangle}{R} + P_e^2 \frac{\langle u \rangle A_s}{R^2} \right) \frac{\partial^2 C^{(0)}}{\partial x^2}, \tag{36}$$

using (14) and (34) one can easily get



$$\langle uA \rangle = \frac{1}{30} - \frac{1}{16R} - \frac{1}{6} \left( 1 - \frac{1}{R} \right) + \frac{1}{2} \left( \frac{5}{24} - \frac{1}{6R} \right). \tag{37}$$

In terms of new variables  $\tau = T, \xi = \frac{\bar{x}}{h} - P_e \frac{\langle u \rangle R}{T}$  with the help of initial and boundary conditions, the solution of (36) is given by

$$C^{(0)} = \frac{1}{\sqrt{4\pi D_T T}} \exp \left( -\frac{\xi^2}{4D_T T} \right), \tag{38}$$

where

$$D_T = \frac{1}{R} - P_e^2 \frac{\langle uA \rangle}{R} + P_e^2 \frac{\langle u \rangle A_s}{R^2} \tag{39}$$

is the dispersion coefficient.

The explicit form of the dispersion coefficient is

$$D_T = \frac{1}{R} - \frac{P_e^2}{R} \left( \frac{-7}{240} + \frac{1}{48R} \right) + \frac{P_e^2}{2R^2} \left( \frac{5R}{24} - \frac{3}{8} + \frac{1}{6R} \right) + \frac{1}{2Da} \left( 1 - \frac{1}{R} \right) \tag{40}$$

In the similar manner of (28) and (29) one can easily find

$$C^{(2)} = P_e^2 B(y) \frac{\partial^2 C^{(0)}}{\partial x^2}, \tag{41}$$

$$C_s^{(2)} = P_e^2 B_s \frac{\partial^2 C^{(0)}}{\partial x^2}. \tag{42}$$

On comparing the terms related with  $\frac{\partial^2 C^{(0)}}{\partial x^2}$ , we have

$$\frac{d^2 B}{dy^2} = \left( u - \frac{\langle u \rangle}{R} \right) A - \frac{\langle uA \rangle}{R} + \frac{\langle u \rangle A_s}{R^2}, \quad 0 < y < 1, \tag{43}$$

with the boundary conditions

$$\frac{dB}{dy} = 0, \quad \text{at } y = 1, \tag{44}$$

$$\frac{dB}{dy} = \frac{\theta \langle uA \rangle}{R} - \frac{\langle u \rangle A_s}{R^2} = Da(\theta A - A_s), \quad \text{at } y = 0, \tag{45}$$

and

$$\langle B \rangle = 0. \tag{46}$$

Solving the above equations, we get

$$\begin{aligned}
 B = \frac{y^6}{30} - \frac{y^5}{60R} - \frac{1}{24} \left( 1 - \frac{1}{R} - \frac{1}{4R^2} \right) y^4 + \frac{1}{24} \left( \frac{5}{6} + \frac{1}{3R} - \frac{1}{R^2} \right) y^3 \\
 + \left( \frac{7}{240} - \frac{1}{8R} + \frac{1}{12R^2} \right) y - \frac{691}{20160} - \frac{177}{1440R} \quad (47)
 \end{aligned}$$

$$B_s = -\frac{691R}{20160} + \frac{1769}{20160} - \frac{25}{288R} + \frac{1}{30R^2} - \frac{1}{Da} \left( \frac{7}{240} - \frac{1}{8R} - \frac{1}{12R^2} \right) \quad (48)$$

when  $P_e > 100$  the longitudinal diffusion is usually disregarded. Therefore the the dispersion coefficient becomes

$$D_T \approx D_{Ta} \quad (49)$$

where

$$D_{Ta} = \frac{\langle uA \rangle}{R} + \frac{\langle u \rangle A_s}{R^2} \quad (50)$$

is called the apparent dispersion coefficient, which is depending on  $\theta$  and  $Da$ . Also the real concentration distribution is obtained in new  $P_e$  independent system  $\{\eta/P_e, CP_e\}$ .

For validation the result, the limiting case ( $\theta = 0$  or  $R = 1$ ) of apparent dispersion coefficient is compared with the previous result of Ng & Bai and Bandyopadhyay & Mazumder.

In the case of  $\theta = 0$  or  $R = 1$  the dispersion coefficient becomes

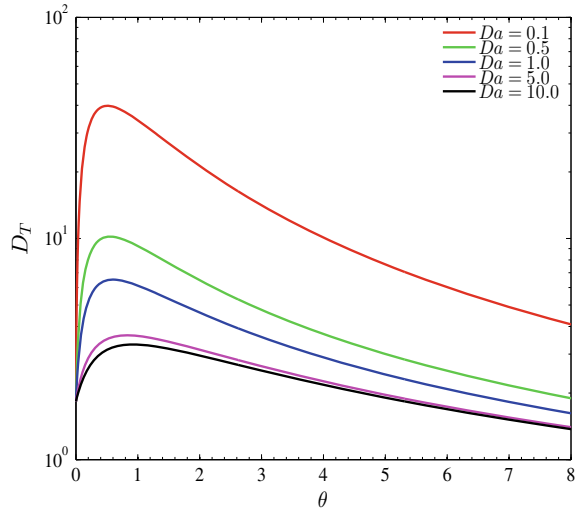
$$D_{Ta} = \frac{1}{120}, \quad (51)$$

which is Taylor dispersion coefficient for simple Couette flow. It is exactly same result as of limiting case of dispersion coefficient as Bandyopadhyay and Mazumder [5] and Ng and Bai [7].

## 4 Results and Discussion

How the dispersion coefficient changes with the sorptive partition coefficient ( $\theta$ ) and kinetics (depending on  $Da$ ) are sketched in Fig.2. It is observed that lower kinetics of sorptive exchange i.e. when  $Da$  is larger, dispersion coefficient is smaller. It is remarkable to note that if the phase exchange kinetics is mild i.e.  $Da \ll 1$ , the dispersion coefficients are large in comparison to that of the phase exchange kinetics is fast i.e.  $Da > 1$ . The reason behind this as the phase exchange kinetics is slow that is rate of reversible reaction is less so the solute restrained with the flow as a result dispersion coefficient is large, on the other way when the phase exchange kinetics is large, the rate of reversible reaction is high which absorbs the solute more so the dispersion coefficient is small. It is also clearly seen that with

**Fig. 2** Evolution of effective dispersivity with retention factor  $\theta$  for different values of Damkohler number  $Da$



the increases of retardation factor  $\theta$  the dispersion coefficient initially increases and after a certain value of  $\theta$  it decreases. The dispersion coefficient attains their highest values when the values of  $\theta$  in between 0.2–0.4. After a critical value of  $\theta$ , with the enhancement of  $\theta$  transport coefficient decreases due to the larger retardation parameter, which reduces the tracer spreading with the flow. In the Fig. 3a longitudinal real concentration distribution is sketched for different transversal position with  $\theta = 1$ ,  $Da = 1$ ,  $T = 1$ . It is observed that as transversal width increases from the lower plate the concentration distribution move away through the longitudinal direction. The cause behind this with the increases of transversal width from the lower plate the velocity is increases as a result convection also increases. Effect of several dispersion time on real concentration distribution are depicted in Fig. 3b with  $\theta = 1$ ,  $Da = 1$ ,  $y = 0.5$ . It is clearly obtained that as dispersion time progresses the peak of the real concentration distribution decreases and becomes more flatter. This is because as time proceeds the dispersion in the longitudinal direction increases prominently due to the combined effect of convection, diffusion of the solute. Variations of real concentration distribution for different Damkohlar number with  $\theta = 1$ ,  $T = 1$ ,  $y = 0.5$  are shown in Fig. 3c. With the enhancement of  $Da$  the peak of the real concentration distribution increases. It occurs when the diffusion rate is much slower than the reversible reaction rate i.e.  $Da \gg 1$ . As a result from the immobile phase (i.e. the lower plate) the solute moves quickly to the flow and the tracer concentration enhances in the mobile phase. The opposite phenomena happens when molecular diffusion rules the rate of reversible reaction i.e.  $Da \ll 1$  and it makes the real concentration distribution more flatter also blunt. Longitudinal real concentration distribution for several values of  $\theta$  are observed in Fig. 3d with  $Da = 1$ ,  $T = 1$ ,  $y = 0.5$ . It is interesting to note that the peak of the real concentration distribution of the solute decreases with the increase of  $\theta$  and after a certain value it also increases.

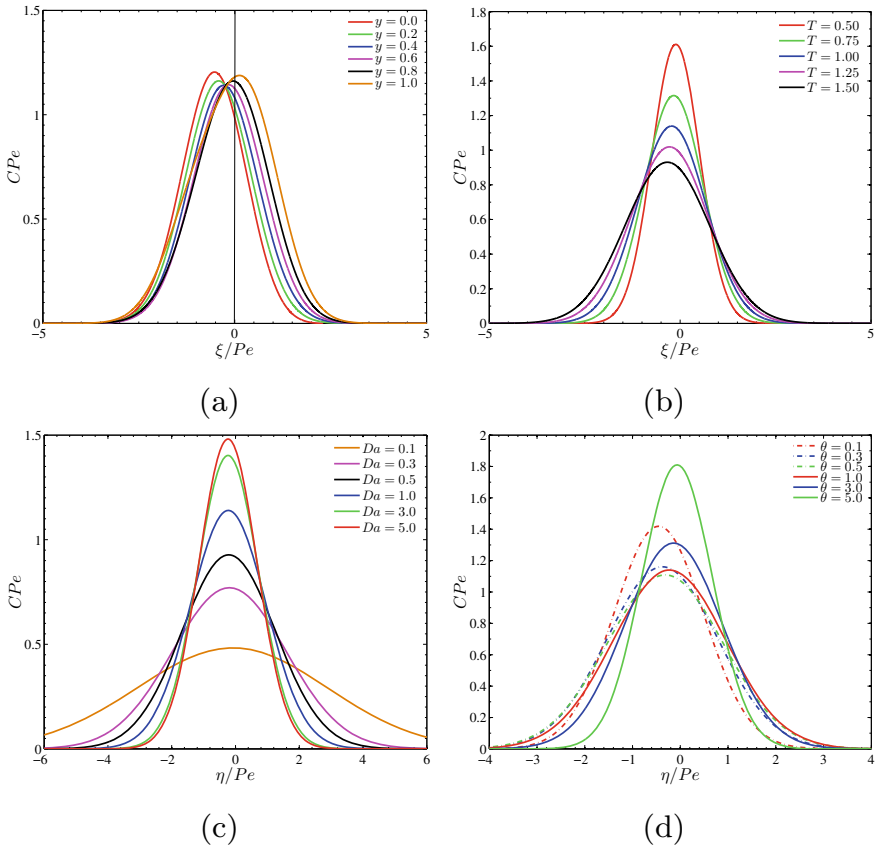


**Fig. 3** Longitudinal real concentration distribution for different **a** transversal position  $y$ , **b** dispersion time  $T$ , **c** different Damkohlar number  $Da$ , **d** different retardation factor  $\theta$

Transverse concentration distribution for various values of retardation factor is plotted in Fig. 4a. It is seen that initially with the enhancement of retardation factor the transverse concentration decreases and after a certain value as of real concentration distribution it also enhances. Figure 4b shows the transverse concentration of the solute at different downstream locations. It is seen that the concentration of the solute decreases significantly as it is moving towards the downstream directions. For all the downstream stations, the concentration of the tracer is maximum at  $y = 1$  and it becomes minimum at the lower plate. The reason behind it, the flow velocity is maximum at  $y = 1$  and minimum at  $y = 0$ .

Effect of reversible reaction on solute transport in Couette flow is sketched in Fig. 5. It is clearly observed that in mobile phase as the Damkohlar number  $Da$  increases the concentration of the solute agglomerated near the source. The reason may be the faster rate of exchange between the lower plate of the channel and fluid phase enhances the contaminant concentration in the phase of fluid. Also, the

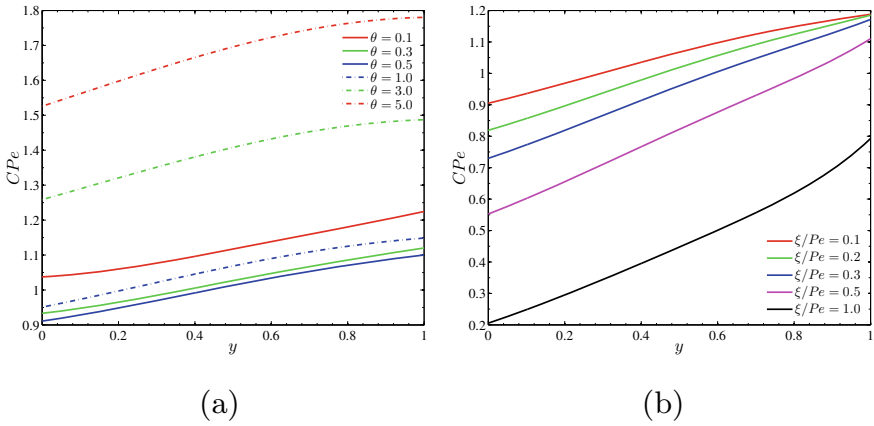


**Fig. 4** Transverse variation of concentration profile for different values of **a** retardation factor, **b** downstream stations

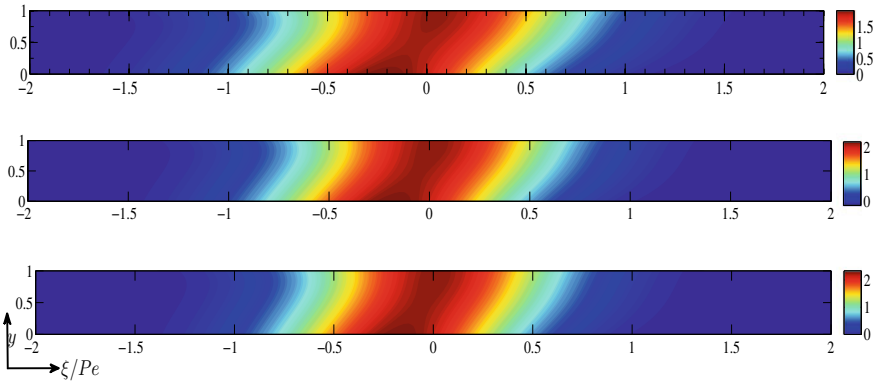


**Fig. 5** Mobile phase concentration contours for different  $Da = 0.5, 2, 10$

Damkohlar number disproportionate with the diffusivity i.e. with the increment of reversible phase exchange kinetics (Damkohlar number), diffusion decreases, as a result concentration of the solute conglomerated near the source.

### 5 Conclusion

The solute transport phenomena in simple Couette flow with reversible reaction which relate the phase exchange between the mobile phase and immobile phase is investigated analytically by multi-scale homogenization method. The limiting case of the result is compared with the established analytical result and achieved an excellent agreement. The results shows the effect of Damkohlar number (phase exchange

kinetics), retention factor, dispersion time on dispersion coefficient, transverse and longitudinal real concentration distributions. Some major outcomes are as follows:

(I) with the enhancement of  $Da$  the dispersion coefficient decreases.

(II) With the increment of  $\theta$  the dispersion coefficient increases and after a certain value it is decreases.

(III) When  $Da \gg 1$  i.e. the diffusion rate is much slower than the reversible reaction rate, the real concentration distribution of the solute increases. Opposite phenomena occurs for  $Da \ll 1$ , also peak of the real concentration become blunt.

(IV) As dispersion time progresses the peak of the concentration decreases and become flatter.

## References

1. Taylor, G.I.: Dispersion of soluble matter in solvent flowing slowly through a tube. Proc. R. Soc. Lond. A **219**(1137), 186–203 (1953). <https://doi.org/10.1098/rspa.1953.0139>
2. Aris, R.: On the dispersion of a solute in a fluid flowing through a tube. Proc. Royal Soc. Lond. A. **235**(1200), 67–77 (1956). <https://doi.org/10.1098/rspa.1956.0065>
3. Chatwin, P.C.: The approach to normality of the concentration distribution of a solute in a solvent flowing along a straight pipe. J. Fluid Mech. **43**(02), 321 (1970). <https://doi.org/10.1017/s0022112070002409>
4. Mei, C.C., Auriault, J.L., Ng, C.O.: Some applications of the homogenization theory. Adv. Appl. Mech. **32**, 277–348 (1996). [https://doi.org/10.1016/s0065-2156\(08\)70078-4](https://doi.org/10.1016/s0065-2156(08)70078-4)
5. Bandyopadhyay, S., Mazumder, B.S.: On contaminant dispersion in unsteady generalised Couette flow. Int. J. Eng. Sci. **37**(11), 1407–1423 (1999). [https://doi.org/10.1016/s0020-7225\(98\)00132-3](https://doi.org/10.1016/s0020-7225(98)00132-3)
6. Ng, C.O., Yip, T.L.: Effects of kinetic sorptive exchange on solute transport in open-channel flow. J. Fluid Mech. **446**, 321–345 (2001). <https://doi.org/10.1017/S0022112001005791>
7. Ng, C.O., Bai, Y.C.: Dispersion in oscillatory Couette flow with sorptive boundaries. Acta Mech. **178**(1–2), 65–84 (2005). <https://doi.org/10.1007/s00707-005-0230-6>
8. Wu, Z., Chen, G.Q.: Approach to transverse uniformity of concentration distribution of a solute in a solvent flowing along a straight pipe. J. Fluid Mech. **740**, 196–213 (2014). <https://doi.org/10.1017/jfm.2013.648>
9. Barik, S., Dalal, D.C.: Multi-scale analysis for concentration distribution in an oscillatory Couette flow. Proc. R. Soc. Lond. A **475**(2221), 20180483 (2018). <https://doi.org/10.1098/rspa.2018.0483>
10. Poddar, N., Dhar, S., Mazumder, B.S., Mondal, K.K.: An exact analysis of scalar transport in hydromagnetic flow between two parallel plates: a multi-scale approach. Proc. R. Soc. Lond. A **477**(2248), 20200830 (2021). <https://doi.org/10.1098/rspa.2020.0830>
11. Dhar, S., Poddar, N., Mondal, K.K., Mazumder, B.S.: On dispersion of solute in a hydro-magnetic flow between two parallel plates with boundary absorption. Phys. Fluids **33**, 083609 (2021). <https://doi.org/10.1063/5.0060404>
12. Das, D., Poddar, N., Dhar S., Kairi, R.R., Mondal, K. K.: Multi-scale approach to analyze the dispersion of solute under the influence of homogeneous and inhomogeneous reactions through a channel. Int. Commun. Heat Mass Transf. **129**, 105709 (2021). <https://doi.org/10.1016/j.icheatmasstransfer.2021.105709>
13. Mazumder, B.S., Paul, S.: Dispersion of reactive species with reversible and irreversible wall reactions. Heat Mass Transf. **48**(6), 933–944 (2011). <https://doi.org/10.1007/s00231-011-0920-7>

14. Barik, S., Dalal, D. C.: Analytical solution for concentration distribution in an open channel flow with phase exchange kinetics. *Acta Mech. Sin.* **1** (2021). <http://ams.cstam.org.cn/EN/abstract/abstract157644.shtml>

# Mathematical Analysis of Hybrid Nanoparticles ( $Au - Al_2O_3$ ) on MHD Blood Flow Through a Curved Artery with Stenosis and Aneurysm Using Hematocrit-Dependent Viscosity



Poonam and Bhupendra K. Sharma

**Abstract** The current study deals with hybrid nanoparticles ( $Au - Al_2O_3/blood$ ) to explore the impact of hemodynamic parameters (such as wall shear stress and resistive impedance) on unsteady MHD blood flow via a curved artery in the presence of stenosis and aneurysm. The governing momentum equation is solved using the Crank-Nicolson method. Velocity contours for numerous parameters have been provided to study the overall behavior of flow patterns. Comprehensive solutions for gold and gold-aluminum oxide hybrid blood flow are presented using medically relevant hemodynamic data. The investigation shows that hybrid nanoparticles ( $Au - Al_2O_3$ ) have lower hemodynamic characteristics such as WSS (wall shear stress) and resistive impedance. The findings could aid in identifying and treating cancer, plaque rupture, the clearance of blood clots, infections, and brain aneurysms.

**Keywords** Curved artery · Hematocrit-dependent viscosity · Hybrid nanoparticles · Aneurysm · Stenosis

## 1 Introduction

The addition of nanoparticles to blood flow in a curved stenotic artery significantly impacts hemodynamical variables (such as WSS and impedance). Because of the low cytotoxicity of gold nanoparticles and their inert nature, localized SPR, and distinctive optical properties, these nanoparticles are frequently utilized as precise cancer killers. Hybrid nanoparticles are gaining popularity due to innovations in the treatment of numerous cardiovascular problems. Hybrid nanoparticles possess a range of uses in biosciences, including angioplasty, cancer therapy, angiography, and bio-nanopolymer coatings of surgical equipment. Zaman et al. [1] investigated the effect of silver-alumina hybrid nanoparticles on blood flow through an artery with stenosis and an aneurysm. Das et al. [2] looked into the hemodynamic and rhe-

---

Poonam (✉) · B. K. Sharma

Department of Mathematics, BITS Pilani, Pilani Campus, Pilani 333031, Rajasthan, India  
e-mail: [aggarwalpurnima123@gmail.com](mailto:aggarwalpurnima123@gmail.com)

© The Author(s), under exclusive license to Springer Nature Switzerland AG 2022  
S. Banerjee and A. Saha (eds.), *Nonlinear Dynamics and Applications*,  
Springer Proceedings in Complexity,  
[https://doi.org/10.1007/978-3-030-99792-2\\_34](https://doi.org/10.1007/978-3-030-99792-2_34)

407



logical changes generated by blood-mediated hybrid nanoparticles  $Cu - Al_2O_3$ . Jayanti Tripathi et al. performed simulation studies with hybrid nano blood (Au-Ag/blood) via irregular stenosis [3]. Cardiovascular disorders are the leading cause of death worldwide, accounting for approximately 30% of all deaths. According to the literature, the effects of stenosis on the hemodynamics of blood going beyond and through the tapered arterial section have been studied in many theoretical and experimental studies. These researches can contribute to the detection and treatment of a wide range of cardiovascular disorders. The post-stenotic blood flow is induced as the stenosis advances due to the increased wall shear stress caused by the stenosis. This post-stenotic flow contributes to arterial wall weakening and post-stenotic dilation (aneurysm). When compared to a single segment (with stenosis only), the combined impact of various anomalies necessarily raises the chances of rupturing these stenotic segments. Arterial curvature also affects the growth of the abnormal segment of the atherosclerotic artery. As a result, it is a crucial geometrical parameter to research. With this objective in mind, Zaman et al. [4, 5] developed several mathematical models to study the unsteady flow of blood via a curved artery with associated stenosis and aneurysm. The majority of prior studies assumed constant viscosity; however, viscosity is influenced by several factors, including hematocrit, temperature, and shear rate. The hematocrit has a considerable impact on whole blood viscosity. Several mathematical models have been used to investigate the effects of altering viscosity on blood flow hemodynamics. The study mentioned above did not include hematocrit-dependent viscosity and curved arterial flow.

Nomenclature			
$x$	Axial direction	$B_1$	Pressure gradient parameter
$r$	Radial direction	Re	Reynold's Number
$t$	Time	$B$	Uniform Magnetic Field
$R^*$	Radius of the curved channel	$R_c$	dimensionless radius of curvature of the artery
$u$	Radial Velocity component	$v$	Axial velocity component
$M^2$	Magnetic Number	$Q$	volumetric flow Rate
$u_0$	Reference velocity	$P$	Pressure
$e$	Systolic to diastolic pressure ratio	$R_0$	Radius of normal artery
$A_1$	Amplitude of pulsatile component	<b>Abbreviation</b>	
$A_0$	Amplitude of pressure gradient	WSS	Wall Shear Stress
Greek Letters			
$\tau_w$	Shear stress at the wall	$\delta$	Stenosis depth
$\sigma$	Electrical conductivity	$\rho_{hnf}$	Density of hybrid nano-fluid
$\mu_0$	Reference viscosity	$\phi_1, \phi_2$	Nanoparticles Concentration
$\mu_f$	Blood's viscosity	$\lambda$	Impedance, $\omega_p$ Circular frequency

Based on our literature study, no attempt has been made to investigate the effects of magnetic field and body acceleration on the flow of a hybrid nanofluid ( $Au - Al_2O_3/blood$ ) via a curved channel with stenosis and aneurysm using hematocrit-dependent viscosity. We developed a mathematical model to examine curvature effects,  $Au - Al_2O_3$  hybrid nanoparticles, body acceleration, hematocrit-dependent viscosity, external magnetic field on pulsatile blood flow through a curved artery with stenosis and aneurysm. The objective of this research is to learn more about how to cure atherosclerosis without surgery to save money on health expenses.

## 2 Model Formulation

### 2.1 Geometry of the Model

Consider blood as an unsteady, Newtonian, laminar, viscous, incompressible fluid moving through a stenosed curved artery with aneurysm. The uniform magnetic field  $B$  is applied perpendicular to the axial direction. The diseased segment's geometry (Fig. 1) can be mathematically characterized as follows [5]:

$$R(x) = \begin{cases} (\alpha_i^* x + R_0) \left( 1 - \left( \frac{\delta_i^*}{2R_0} \left( 1 + \cos \frac{2\pi}{\lambda_i} \left( x - \sigma_i^* - \frac{\lambda_i}{2} \right) \right) \right) \right), & \sigma_i^* \leq x \leq \sigma_i^* + \lambda_i, i = 1, 2 \\ (\alpha_i^* x + R_0) & \text{Otherwise,} \end{cases} \tag{1}$$

$$-R(x) = \begin{cases} (\alpha_i^* x - R_0) \left( 1 - \left( \frac{\delta_i^*}{2R_0} \left( 1 + \cos \frac{2\pi}{\lambda_i} \left( x - \sigma_i^* - \frac{\lambda_i}{2} \right) \right) \right) \right), & \sigma_i^* \leq x \leq \sigma_i^* + \lambda_i, i = 1, 2 \\ (\alpha_i^* x - R_0) & \text{Otherwise,} \end{cases} \tag{2}$$

where  $R(x)$  denotes the upper wall geometry of a curved artery and  $-R(x)$  denotes the lower wall geometry.  $L$  is the length of the arterial channel,  $\alpha = \tan \psi$  represents the constriction of the diseased artery,  $\psi$  represents the tapering angle,  $\lambda_i$  denotes the length of the diseased segment, and  $\sigma_i^*$  is the length of the  $i$ th abnormal section from the origin and  $\delta_i^*$  stands for the critical height of the  $i$ th diseased section occurring at two explicit locations given by:

$x = \sigma_1^* + \lambda_1/2$ , and  $x = \sigma_2^* + \lambda_2/2$ , where the value of  $\delta_i^*$  takes a positive value for stenosis and a negative value for an aneurysm.

### 2.2 Governing Equations

The current flow model is illustrated by two-dimensional orthogonal curvilinear coordinates  $(r, x)$ . The flow velocity vector is defined as  $V = (u(r, x, t), v(r, x, t))$ , with  $u$  and  $v$  representing the radial and axial velocity components, respectively. Figure 1 shows the geometry of a curved artery with stenosis and aneurysm.

The equations for continuity, momentum, and energy are written as:

#### Continuity equation

$$\frac{\partial u}{\partial r} + \frac{u}{R^* + r} + \frac{R^*}{R^* + r} \frac{\partial v}{\partial x} = 0. \tag{3}$$

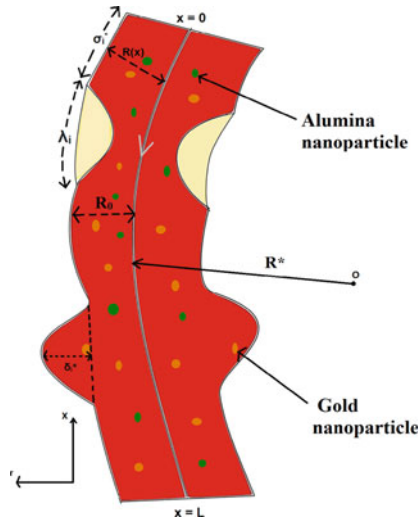


Fig. 1 Geometrical representation of diseased artery

**Momentum equations  
r- direction**

$$\rho_{hnf} \left[ \frac{\partial u}{\partial t} + u \frac{\partial u}{\partial r} + \frac{R^*v}{R^*+r} \frac{\partial v}{\partial x} - \frac{v^2}{R^*+r} \right] = -\frac{\partial P}{\partial r} + \mu_{hnf} \left[ \frac{\partial^2 u}{\partial r^2} + \frac{1}{R^*+r} \frac{\partial u}{\partial r} + \left( \frac{R^*}{R^*+r} \right)^2 \frac{\partial^2 u}{\partial x^2} - \frac{u}{(R^*+r)^2} - \frac{2R^*}{(R^*+r)^2} \frac{\partial v}{\partial x} \right] + \left( \frac{4}{3} \frac{\partial u}{\partial r} - \frac{2}{3} \left( \frac{R^*}{R^*+r} \frac{\partial v}{\partial x} + \frac{u}{R^*+r} \right) \right) \frac{\partial \mu_{hnf}}{\partial r},$$

**x-direction**

$$\rho_{hnf} \left[ \frac{\partial v}{\partial t} + u \frac{\partial v}{\partial r} + \frac{R^*v}{R^*+r} \frac{\partial v}{\partial x} + \frac{uv}{R^*+r} \right] = -\frac{R^*}{R^*+r} \frac{\partial P}{\partial x} + G(t) + \mu_{hnf} \left[ \frac{\partial^2 v}{\partial r^2} + \frac{1}{R^*+r} \frac{\partial v}{\partial r} + \left( \frac{R^*}{R^*+r} \right)^2 \frac{\partial^2 v}{\partial x^2} - \frac{v}{(R^*+r)^2} + \frac{2R^*}{(R^*+r)^2} \frac{\partial u}{\partial x} \right] + \left( \frac{R^*}{R^*+r} \frac{\partial u}{\partial x} + \frac{\partial v}{\partial r} - \frac{v}{R^*+r} \right) \frac{\partial \mu_{hnf}}{\partial r} - \sigma_{hnf} B^2 v. \tag{4}$$

The following is the equation for the axial pressure gradient:

$$-\frac{\partial \bar{P}}{\partial \bar{x}} = A_0 + A_1 \cos(2\pi \omega_p t), \quad t > 0,$$

where,  $A_1$  = Amplitude of the pulsatile component,  $A_0$  = Mean pressure gradient,  $\omega_p = 2\pi f_p$ .

The initial and boundary conditions that the flow is subjected to are as follows:

$$\begin{cases} v = 0 & \text{at } t = 0, \\ v = 0, & \text{at } r = R \text{ and } r = -R. \end{cases} \tag{5}$$

Here, hematocrit-dependent viscosity is considered which is illustrated as:

$$\mu_f = \mu_0[1 + \beta_1 h(r)], \tag{6}$$

where,  $h(r) = h_m \left[ 1 - \left( \frac{r}{R_0} \right)^m \right]$ ,  $h_m$  = maximum hematocrit at the center of the artery.

$\beta_1 = 2.5$ ,  $m$  = exact shape of velocity profile,  $m \geq 2$ .

### 2.3 Non-dimensionalization of Governing Equations

The previous flow Eqs.(3)–(4) is non-dimensionalized using the non-dimensional parameters listed below to evaluate numerical solutions:

$$\begin{aligned} \bar{r} &= \frac{r}{R_0}, \quad \bar{x} = \frac{x}{\lambda_i}, \quad \bar{u} = \frac{\lambda_i u}{\delta^* u_0}, \quad \bar{v} = \frac{v}{u_0}, \quad \bar{t} = \frac{u_0 t}{R_0}, \\ R_c &= \frac{R^*}{R_0}, \quad \epsilon = \frac{R_0}{\lambda_i}, \quad Re = \frac{\rho_f u_0 R_0}{\mu_0}, \quad \delta = \frac{\delta^*}{R_0}, \\ \bar{P} &= \frac{R_0^2 P}{\mu_0 u_0 \lambda_i}, \quad M^2 = \frac{\sigma_f B^2 R_0^2}{\mu_0}. \end{aligned}$$

After using non-dimensional parameter and mild stenotic condition, i.e.,  $\delta (= \frac{\delta^*}{R_0}) \ll 1$ ,  $\epsilon (= \frac{R_0}{\lambda_i}) = O(1)$ , Eqs.(3)–(4) will be reduced as:

#### Non-dimensional equations

$$\frac{\partial \bar{P}}{\partial \bar{r}} = 0, \tag{7}$$

$$\begin{aligned} \frac{\rho_{hnf}}{\rho_f} Re \frac{\partial \bar{v}}{\partial \bar{t}} &= -\frac{R_c}{R_c + \bar{r}} \frac{\partial \bar{P}}{\partial \bar{x}} + \frac{\mu_{hnf}}{\mu_0} \left[ \frac{\partial^2 \bar{v}}{\partial \bar{r}^2} + \frac{1}{R_c + \bar{r}} \frac{\partial \bar{v}}{\partial \bar{r}} - \frac{\bar{v}}{(R_c + \bar{r})^2} \right] \\ &- \left( \frac{\partial \bar{v}}{\partial \bar{r}} + \frac{\bar{v}}{R_c + \bar{r}} \right) \frac{m \beta_1 h_m \bar{r}^{m-1}}{(1 - \phi_1)^{2.5} (1 - \phi_2)^{2.5}} - \frac{\sigma_{hnf}}{\sigma_f} M^2 \bar{v}, \end{aligned} \tag{8}$$

Pressure gradient and body acceleration are obtained as follows after non-dimensionalization:

$$\frac{\partial \bar{P}}{\partial \bar{x}} = B_1(1 + e \cos(c_1 \bar{t})),$$

where  $B_1 = \frac{A_0 R_0^2}{\mu_0 u_0}$ ,  $e = \frac{A_1}{A_0}$ ,  $c_1 = \frac{2\pi R_0 w_p}{u_0}$ .

Non-dimensionalized form of associated initial and boundary conditions subjected to the flow are rewritten as:

$$\begin{cases} \bar{v} = 0 & \text{at } t = 0, \\ \bar{v} = 0 & \text{at } r = R \text{ and } r = -R. \end{cases} \tag{9}$$

Now, the non-dimensionalized form of geometry of curved arterial channel with stenosis and aneurysm is obtained as:

$$R(x) = \begin{cases} (1 + \alpha x) \left( 1 - \left( \frac{\delta}{2} \left( 1 + \cos 2\pi \left( x - \sigma_i - \frac{1}{2} \right) \right) \right) \right), & \sigma_i \leq x \leq \sigma_i + 1, i = 1, 2 \\ (1 + \alpha x) & \text{Otherwise,} \end{cases} \tag{10}$$

with  $\sigma_i = \frac{\sigma_i^*}{\lambda_i}$ ;  $\alpha = \frac{\alpha^* \lambda_i}{R_0}$ .

In Eq. (10), the tapering parameter is  $\alpha = \tan(\psi)$ , and the associated taper angle is  $\psi$ . The following are the mathematical formulae for hemodynamical factors such as wall shear stress, volumetric flow rate, and resistive impedance:

$$\tau_w = \left( \frac{\partial \bar{v}}{\partial \bar{r}} \right)_{\bar{r}=R}, \quad Q = \int_{-R}^R \bar{v} \bar{r} d\bar{r}, \quad \lambda = \frac{L \left( \frac{\partial \bar{P}}{\partial \bar{x}} \right)}{Q}. \tag{11}$$

**Hybrid nano fluid equation**

$$\mu_{hnf} = \frac{\mu_f}{(1 - \phi_1)^{2.5} (1 - \phi_2)^{2.5}},$$

$$\rho_{hnf} = (1 - \phi_2)[(1 - \phi_1)\rho_f + \phi_1\rho_{s1}] + \phi_2\rho_{s2},$$

$$\sigma_{hnf} = \sigma_{bf} \left[ \frac{\sigma_{s2}(1 + 2\phi_2) + 2\sigma_f(1 - \phi_2)}{\sigma_{s2}(1 - \phi_2) + \sigma_f(2 + \phi_2)} \right],$$

where

$$\sigma_{bf} = \sigma_f \left[ \frac{\sigma_{s1}(1 + 2\phi_1) + 2\sigma_f(1 - \phi_1)}{\sigma_{s1}(1 - \phi_1) + \sigma_f(2 + \phi_1)} \right].$$

### 3 Solution Process

Since the governing equations (8) is a non-linear partial difference equation, so a robust numerical method is used to solve the resulting dimensionless boundary value problem. An implicit Crank-Nicolson (an unconditionally stable) scheme based on a finite difference approach is used for the current blood flow problem. Furthermore, in both space and time, this technique is second-order convergent. The partial spatial and temporal derivatives used in this method are stated as:

$$\frac{\partial \bar{v}}{\partial \bar{r}} = \frac{\bar{v}_{i+1}^k - \bar{v}_{i-1}^k}{2\Delta \bar{r}}, \quad \frac{\partial^2 \bar{v}}{\partial \bar{x}^2} = \frac{\bar{v}_{i+1}^k - 2\bar{v}_i^k + \bar{v}_{i-1}^k}{(\Delta \bar{x})^2}, \quad \frac{\partial \bar{v}}{\partial \bar{t}} = \frac{\bar{v}_i^{k+1} - \bar{v}_i^k}{\Delta \bar{t}}. \quad (12)$$

#### 3.1 Discretization of Governing Equations

By using the partial derivatives as given in Eq. (12), we discretize the governing equations (8).

The following are the discretized boundary and initial conditions related with the governing equations:

$$\bar{v}_1^{k+1} = 0, \quad \bar{v}_{N+1}^{k+1} = 0, \quad \bar{v}_i^1 = 0. \quad (13)$$

The spatial variable is now uniformly discretized into  $N + 1$  discrete grid points  $x_i$ , ( $i = 1, 2, \dots, N + 1$ ), with  $\Delta x = 1/(N + 1)$  as the step size.  $t^k = (k - 1)\Delta t$  indicates the time levels, with  $\Delta t$  representing a small increment in time. Despite the fact that this approach is unconditionally stable for all values of  $\Delta t$  and  $\Delta x$ , we have chosen  $\Delta t = 10^{-4}$  and  $\Delta x = 10^{-4}$  as the choices for step sizes. As previously stated, the Crank-Nicolson approach is an implicit one, hence the governing equation (8) is reduced to Eq. (14). It form a tri-diagonal system of equations that can be simplified using the Tri-diagonal Matrix Algorithm.

Equation (8) corresponds to a tri-diagonal system, which can be calculated as follows:

$$S_i^k \bar{v}_{i-1}^{k+1} + T_i^k \bar{v}_i^{k+1} + U_i^k \bar{v}_{i+1}^{k+1} = S_i'^k \bar{v}_{i-1}^k + T_i'^k \bar{v}_i^k + U_i'^k \bar{v}_{i+1}^k + F_i^k, \quad (14)$$

where  $S_i^k, T_i^k, U_i^k, S_i'^k, T_i'^k, U_i'^k, F_i^k$  are the corresponding coefficient matrices.

## 4 Results and Graphical Analysis

This mathematical investigation aims to see how hematocrit-dependent viscosity and nanofluid hemodynamics affect blood flow via a curved artery with two aberrant segments (stenosis and aneurysm). As hybrid nanoparticles,  $Au$  and  $Al_2O_3$  nanoparticles are combined. The effect of emergent characteristics such as hematocrit-dependent viscosity ( $h_m$ ), magnetic field ( $M^2$ ), on WSS and impedance profiles of hybrid blood ( $\phi_1 = 0.01, \phi_2 = 0.01$ ) is investigated. The Crank-Nicolson method has been used to simplify dimensionless governing equations. The wall shear stress and impedance profiles are computed using MATLAB algorithms for the C-N approach. The flow patterns for different values of  $R_c$  and volume fraction of nanoparticles are studied using velocity contours.

The computational work has been done by utilizing the default values of parameters as illustrated in (Table 1b).

**Table 1** Thermophysical properties and Physical parameters’s values table

(a) Thermophysical properties of blood,  $Au$  and  $Al_2O_3$  nanoparticles

Thermophysical properties	Gold	Alumina	Blood
Thermal Conductivity [ $K (W/mK)$ ]	314	40	0.492
Electrical Conductivity [ $\sigma (S/m)$ ]	$4.10 \times 10^7$	$3.5 \times 10^7$	0.667
Density [ $\rho (kg/m^3)$ ]	19320	3970	1063
Thermal Expansion Coefficient [ $\beta \times 10^{-5} (K^{-1})$ ]	1.4	0.85	0.18
Heat Capacitance [ $C_p (J/kgK)$ ]	129	765	3594

(b) Physical parameters’s values with their sources

Parameters	Ranges	Sources
Magnetic Number	0–4	[6]
Maximum Hematocrit	0–2	[7]
Thermal Grashof number	0–6	[8]

### 4.1 Validation of the Numerical Results

The validation of our study is consummated with published work Zaman [5] for the curved artery with stenosis and aneurysm, which is common in both the study. The graphs (Fig. 2a, b) for dimensionless velocity profiles have been plotted for authentication using the following set of emergent parameters:  $Pr = 14, Gr = 0.8, Re = 0.5, Nr = 0, h_m = 0, M^2 = 0, s = 0, R_c = 3$ , slip parameter ( $\alpha = 0$ ), thermal slip parameter ( $\gamma = 0$ ), heat source or sink parameter ( $\beta = 0$ ),  $B_2 = 0, B_1 = 1.41$ ,

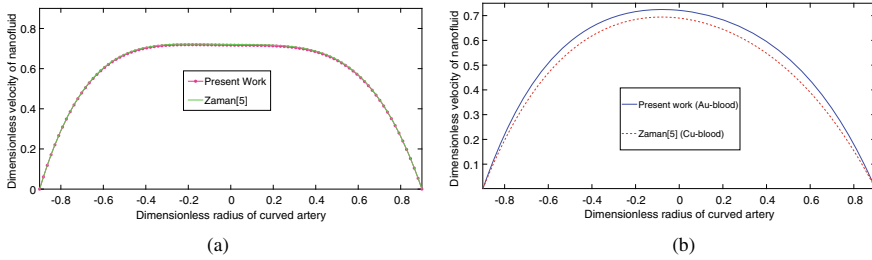


**Fig. 2** Variation of velocity profile patterns for **a** Cu-blood, **b** Cu and Au-blood at  $t = 0.86$  and  $x = 0.7$

$\psi = 0, \phi_1 = 0.05, \phi_2 = 0$ . The published work Zaman [5] for the curved artery with stenosis and aneurysm (which is prevalent in both studies), completes the confirmation of our research. The Cu-blood velocity profiles in both studies are shown in Fig. 2a. The current paper’s velocity profile matches the published paper [5] quite well.

The velocity profiles of Au-blood (present work) and Cu-blood [5] are compared in Fig. 2b. There is a great match between the velocity trend in our study and the velocity profile trend in Ref. [5]. There is a little difference in velocity profiles due to the use of gold nanoparticles instead of copper nanoparticles since Au-blood velocity is greater than Cu-blood velocity [9].

### 4.2 Velocity Contours

The varied blood flow patterns in terms of velocity contours are incorporated the research efforts more correctly. The influence of the curved artery’s non - dimensional radius ( $R_c$ ) on the flow patterns are shown in Fig. 3a–c, which shows that the pattern of streamlines and circulating bolus shrinks to symmetric form as the value of  $R_c$  increases.

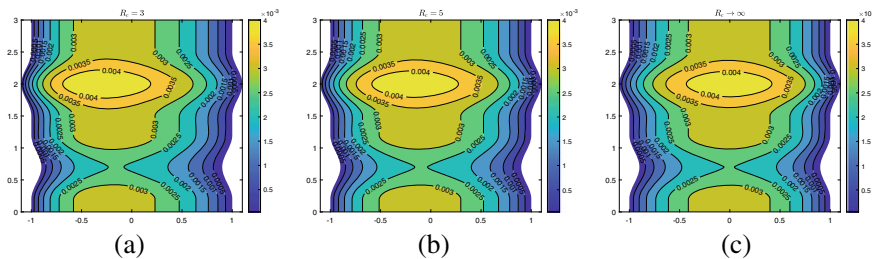


**Fig. 3** Variation in blood flow patterns for different values of dimensionless radius of curved channel, **a**  $R_c = 3$ , **b**  $R_c = 5$ , **c**  $R_c \rightarrow \infty$



### 4.3 Resistance Impedance

The ratio of pressure drop to the flow rate is known as resistive impedance. The study of variation in resistive impedance is quite helpful in controlling blood flow during surgery. Figure 4a shows the variation of resistive impedance in the axial direction for different values of the hematocrit parameter ( $h_m$ ). It can be observed from the figure that flow impedance increases as the hematocrit parameter increases. Blood viscosity increases as  $h_m$  increases, blocking blood flow. The impedance variation at the stenotic neck is greater than at the aneurysm neck for varied  $h_m$  values. Figure 4b shows the temporal variation of resistive impedance for different values of dimensionless radius of curvature of the artery. It can be noted from the figure that impedance varies periodically as time passes. The resistive impedance decreases as  $R_c$  grows, illustrating that the resistance to the flow in a curved artery is greater than in a straight arterial channel. In addition, when  $R_c$  increases, the impedance profiles become close.

The relationship between frictional resistance and maximal stenosis height for varying lengths of the curved artery is shown in Fig. 4c. As the artery lengthens, the resistive impedance rises. This indicates that resistive impedance in the large arteries is higher than in the smaller arteries figure also depicts that the frictional resistance increases (almost linearly) as the stenotic depth grows (owing to increased flow obstruction, which raises flow resistance). It should also be noted that frictional resistance is insignificant in the absence of stenosis, i.e., for ( $\delta = 0$ ). The impedance variation ( $\lambda$ ) with axial direction for different values of magnetic number is shown

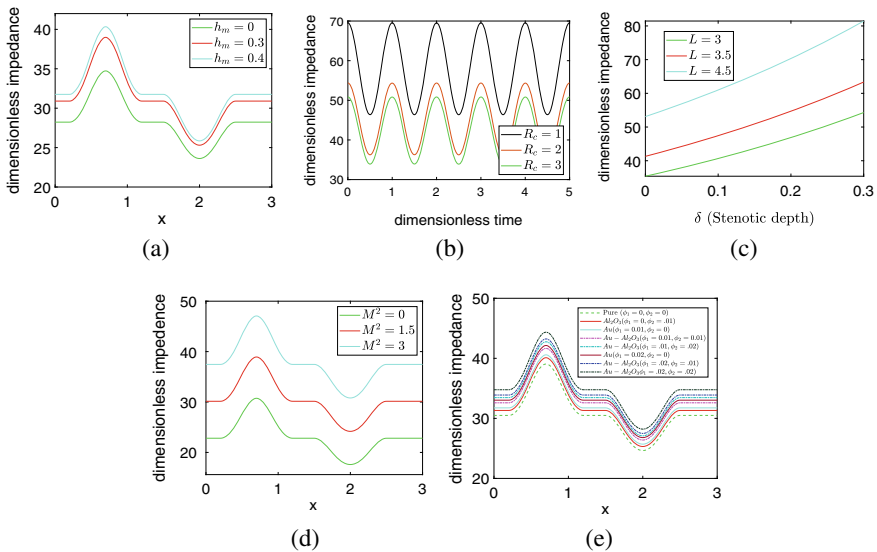


**Fig. 4** Variation in impedance profile for, **a**  $h_m$ , **b** time and  $R_c$ , **c**  $L$  with  $\delta$ , **d**  $M^2$ , **e**  $\phi_1, \phi_2$

in Fig. 4d. The figures show that when the magnetic number increases, flow resistance increases. When the magnetic field intensity increases, the Lorentz force is generated, slowing the flow and increasing the flow impedance. The influence of the nanoparticle's volume fraction on the flow resistance for  $Au - Al_2O_3/blood$  in the axial direction is depicted in Fig. 4e. The resistive impedance increases as the volume fraction of gold and alumina nanoparticles increases. This is very helpful the controlling the flow rate during surgical processes.

#### 4.4 Wall Shear Stress

Wall shear stress in arterial blood flow is described as the force per unit area applied to the blood by the artery's walls parallel to the local tangent plane. As we know, arterial sections with low wall shear stress or significantly oscillating WSS are the most susceptible to atherogenesis disorders. The atherogenic process is influenced by pulsatile blood flow in the arterial system. WSS values can be determined using velocity patterns along the artery's walls. In Fig. 5a, the variation of WSS in the axial direction for different values of magnetic number is illustrated. In the absence of an applied magnetic field, i.e.,  $M^2 = 0$ , the wall shear stress is greatest, and when  $M^2$  increases, a fall in wall shear stress can be observed. For a given value of  $M^2$ , WSS in the aneurysm region is higher than WSS in the stenotic region because WSS changes with stenotic depth. The variation in wall shear stress with the depth of the stenosis for various values of magnetic number is depicted in Fig. 5b. The flow is subjected to an opposing Lorentz force as  $M^2$  increases, reducing velocity and wall shear stress. It is also noted that when maximum stenotic depth rises, WSS also reduces. WSS decreases when blood lipids increase, which is consistent with Zhang's experimental findings [10]. Figure 5c shows WSS time series plots in stenotic and aneurysm sites for various values of  $R_c$ . The radius of curvature has a significant impact on the WSS profile towards the artery's outer wall. It is revealed that if the channel has a small radius of curvature or a high curvature, the WSS drops, which is consistent with the findings of the [11]. The curved artery's shape is reduced to a straight channel ( $R_c = \infty$  or curvature of channel = 0) when the value  $R_c$  grows, meaning that the straight artery's WSS remains higher than the curved artery ( $R_c < \infty$ ). Figure 5d depicts the effect of volume fraction of nanoparticles on the axial variation of WSS profile for  $Au - Al_2O_3/blood$ . The WSS decreases as the volume fraction of gold and alumina nanoparticles increases indicating that the effects of both nanoparticles on WSS are the same.

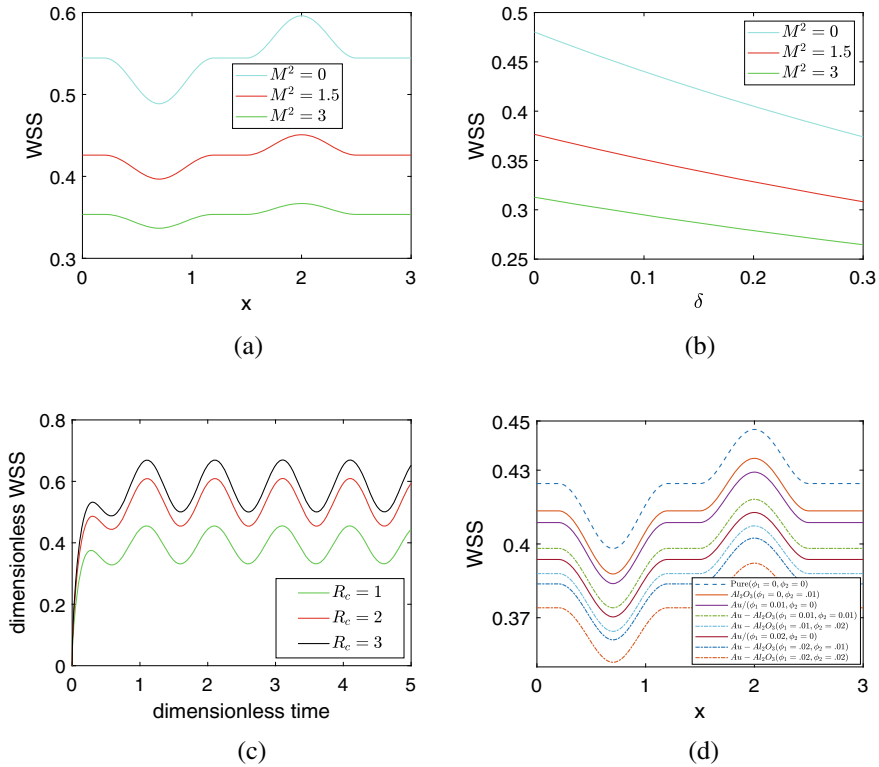


Fig. 5 Variation in WSS for, **a**  $M^2$  with  $x$ , **b**  $M^2$  with  $\delta$ , **c**  $R_c$  with time, **d**  $\phi_1, \phi_2$

### 5 Conclusion

The current study examined the effects of addition of nanoparticle on blood flow through a curved artery with minor stenosis and aneurysm circumstances having variable viscosity. This model aims to increase the delivery of medicine in a confined curved artery using nanoparticles. The results shows that Impedance to the flow decreases with increment in  $R_c$ , which signifies that resistive impedance is greater for curved artery than for straight channel. WSS decreases when the concentration of gold and alumina nanoparticles increases. Impedance increases when the concentration of gold and alumina nanoparticles increases. It is found that the high curvature or small radius of curvature of the channel leads to a decrease in the WSS.

## References

1. Zaman, A., Ali, N., Khan, A.A.: Computational biomedical simulations of hybrid nanoparticles on unsteady blood hemodynamics in a stenotic artery. *Math. Comput. Simul.* **169**, 117–132 (2020)
2. Das, S., Pal, T., Jana, R.: Outlining impact of hybrid composition of nanoparticles suspended in blood flowing in an inclined stenosed artery under magnetic field orientation. *BioNanoScience* **11**(1), 99–115 (2021)
3. Tripathi, J., Vasu, B., Bég, O.A.: Computational simulations of hybrid mediated nano-hemodynamics (Ag-Au/Blood) through an irregular symmetric stenosis. *Comput. Biol. Med.* **130**, 104213 (2021)
4. Zaman, A., Ali, N., Sajjad, M.: Effects of nanoparticles (Cu, TiO<sub>2</sub>, Al<sub>2</sub>O<sub>3</sub>) on unsteady blood flow through a curved overlapping stenosed channel. *Math. Comput. Simul.* **156**, 279–293 (2019)
5. Zaman, A., Ali, N., Ali, I.: Effects of nanoparticles (Cu (Copper), Silver (Ag)) and slip on unsteady blood flow through a curved stenosed channel with aneurysm. *Therm. Sci. Eng. Prog.* **5**, 482–491 (2018)
6. Abdel-wahed, M.S.: Magnetohydrodynamic Ferro-Nano fluid flow in a semi-porous curved tube under the effect of hall current and nonlinear thermal radiative. *J. Magn. Magn. Mater.* **474**, 347–354 (2019)
7. Tripathi, B., Sharma, B.K.: Influence of heat and mass transfer on two-phase blood flow with joule heating and variable viscosity in the presence of variable magnetic field. *Int. J. Comput. Methods* **17**(03), 1850139 (2017)
8. Tripathi, B., Sharma, B.K., Sharma, M.: MHD pulsatile two-phase blood flow through a stenosed artery with heat and mass transfer **474** (2017). [arXiv:1705.09794](https://arxiv.org/abs/1705.09794)
9. Elnaqeeb, T., Shah, N.A., Mekheimer, K.S.: Hemodynamic characteristics of gold nanoparticle blood flow through a tapered stenosed vessel with variable nanofluid viscosity. *BioNanoScience* **9**(2), 245–255 (2019)
10. Zhang, B., Gu, J., Qian, M., Niu, L., Zhou, H., Ghista, D.: Correlation between quantitative analysis of wall shear stress and intima-media thickness in atherosclerosis development in carotid arteries. *Biomed. Eng. Online* **16**(1), 1–17 (2017)
11. Shahzadi, I., Nadee, S.: Analysis of Ag/blood-mediated transport in curved annulus with exclusive nature of convective boundary. *Physica Scripta* **94**(11), 115011 (2019)

# Response Behavior of a Coaxial Thermal Probe Towards Dynamic Thermal Loading



Anil Kumar Rout, Niranjana Sahoo, Pankaj Kalita, and Vinayak Kulkarni

**Abstract** An in-house fabricated fast responsive coaxial thermal probe has been utilized to capture the transient temperature response in the exhaust of an internal combustion (IC) engine. The high temperature coaxial thermal probe (ht-CTP) is fabricated from chromel and constantan in the laboratory scale. A constantan wire (of 0.91 mm diameter and 15 mm length) is placed inside the chromel wire (of 3.25 mm diameter and 10 mm length) and clubbed together with an epoxy which also acts as an insulator separating the two. The junction between them is prepared at the surface using abrasion method. The sensor is flush mounted at the exhaust pipe of an IC engine at a distance of 20 mm from the exhaust manifold. In a 4 stroke engine, there is only one exhaust stroke in a complete cycle; therefore, the valve at the exhaust also allows gases one time in a cycle. Therefore, the heat load (contained in the exhaust gas) is also imparted on the sensor in a periodic manner. Hence, by measuring the consecutive temperature response, the cycle time duration has been measured and the engine RPM has been calculated. The RPM is compared with the recorded RPM by the RPM sensor. Along with this, the initial temperature signal is processed for heat flux estimation through analytical method which provides an estimate about the magnitude of transient heat flux imparted on the sensor by the exhaust gas of the engine.

**Keywords** Thermocouple · Transient temperature · Coaxial thermal probe · IC engine · Cycle time · Transient heat flux

---

A. K. Rout (✉) · N. Sahoo · P. Kalita · V. Kulkarni  
School of Energy Science and Engineering, Indian Institute of Technology Guwahati, Guwahati,  
India  
e-mail: [anil.rout@iitg.ac.in](mailto:anil.rout@iitg.ac.in)

© The Author(s), under exclusive license to Springer Nature Switzerland AG 2022  
S. Banerjee and A. Saha (eds.), *Nonlinear Dynamics and Applications*,  
Springer Proceedings in Complexity,  
[https://doi.org/10.1007/978-3-030-99792-2\\_35](https://doi.org/10.1007/978-3-030-99792-2_35)

421

## 1 Introduction

The information about transient thermal parameters such as “Transient temperature” and “Transient heat flux” are required for the efficient design and modeling of many engineering systems and sub-systems. Very limited sensors are used to capture instantaneous temperatures. One prominent sensor amongst them is coaxial thermal probe (CTP). Due to fast response, CTP is capable to record instantaneous events in tough conditions like shock tubes, shock tunnels, Gas turbines etc. [1]. Here, the capability of the sensor has been evaluated in other tough conditions like the exhaust flow of internal combustion engine. Nevertheless, the temperature information in combustion chamber of IC engines, the temperature at the exhaust is the vital parameter necessary for upgrading the IC engines.

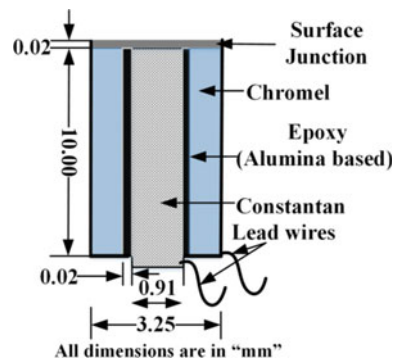
The information about the temperature in combustion chamber of IC engines is very important which was commonly measured by using sound waves. A transient sound pulse was the main medium for the measurement. The transient sound pulse was applied inside the test chamber and the difference in time between the generated pulsed signal and transmitted pulse was calculated [2]. Another method was preferred for the measurement of average gas temperature where, a steady temperature state was allowed to establish between a thin metallic wire and the gas temperature [3, 4]. Fast response thermocouples were employed for the measurement of transient temperature as well as heat flux through different types of thermocouples [5–10]. The information about both the input and output helps in proper thermodynamic analysis of the engine. Hence, the temperature information at the outlet of engine is also an important aspect in the learning of IC engine features [7, 8 and 11]. Some information about the engine phenomena can be obtained from the exhaust gas analysis and also from the exhaust gas temperature [9]. The unsteadiness of the temperature signal can imply some information about the combustion phenomena taking place inside the combustion chamber [10, 12]. It is also observed that the surface temperature and heat flux obey similar pattern as observed inside the cylinder but, the trend varied when it is measured away from the exhaust [13].

The exhaust valve of an internal combustion engine opens periodically after a certain interval of time corresponding to the engine speed. These CTPs (if mounted at any place in the exhaust line of the engine) can respond to the exhaust hot gas that goes outside through the exhaust manifold after the completion of combustion process inside the engine cylinder. The time difference between the successive responses can be measured and the cycle time corresponding to the engine RPM can be calculated. Therefore, the present work focus on in-house fabrication of a high temperature thermal probe (ht-CTP) for engine and its application in the engine exhaust to capture transient temperature. Subsequently, the information of cycle time is obtained from the temperature response and compared with the cycle time calculated using the value from RPM sensor of the engine. The heat flux imparted on the sensor by the exhaust gas is also estimated using the analytical modeling of the sensor.

## 2 Fabrication and Calibration of the Thermal Probe

A coaxial probe (ht-CTP) has been fabricated in-house using chromel and constantan as primary elements. For the present case, a (chromel-constantan) thermocouple (CTP) is used due to its high sensitivity, called as “thermo-power” sensor. Constantan wire (0.91 mm diameter, 15 mm length) and chromel wire (3.25 mm diameter, 10 mm length) are considered for fabrication of E-type CTP probe. The inner element (constantan wire) is put into the outer element (chromel) concentrically and symmetrically along with a minimal insulation thickness ( $\sim 20 \mu$ ) in between them. An adequate thickness of epoxy is maintained for its whole length leaving the sensing surface unaffected. The epoxy acts as both electrical insulator as well as binder for both the thermo-elements providing strength to the sensor. Proper care has been taken to make sure that the inner element is straight, co-axial and there is no linkage between the thermo-elements throughout the length to avoid any possibility of multiple connections. A suitable length (10 mm) of the probe is chosen for proper operation and experimentation. An alumina based adhesive is used as insulating material which can sustain a temperature of  $1500 \text{ }^\circ\text{C}$ . The expected temperature at the exhaust of the IC engine for the present experimental condition is nearly  $400 \text{ }^\circ\text{C}$  and an E-type probe can record a temperature up to  $700 \text{ }^\circ\text{C}$ . Therefore, these probes can be used to capture the response confidently. The linkage amongst the two elements is prepared at the measuring surface using scratching technique. Same wires (Chromel and constantan) are spot welded for further instrumentation purpose. The schematic of the fabricated probe is mentioned in Fig. 1. The output from the probe is in the form of electromotive force (EMF) which is generated in response to the change in temperature obeying Seebeck effect. Therefore, to convert voltage into temperature, a correlation is required which is commonly known as the sensitivity of the probe. A furnace based set up is used to calibrate the probe where the probe is placed along with a reference temperature probe in a heating environment and both the temperature and EMF are noted for the change in temperature. The slope of the EMF and Temperature plot provides the sensitivity value which for the present case found to be  $59 \mu\text{V}/^\circ\text{C}$  [1].

**Fig. 1** Schematic of the high temperature probe



### 3 Experimental Engine Set Up

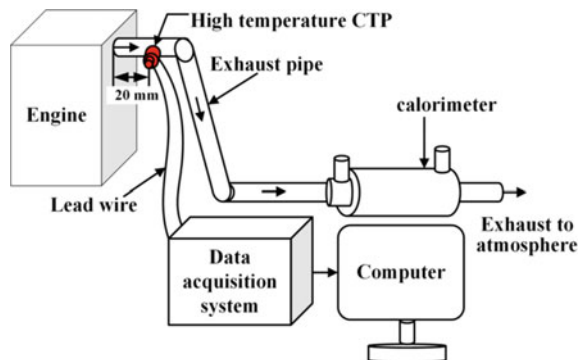
The sensor is mounted at the exhaust of a four stroke research engine running with petrol. The engine is equipped with eddy current type water cooled dynamometer attached to a loading unit. Piezo type pressure transducer is attached for pressure measurement and Pt-100 RTD for temperature measurement. All the outputs from the sensors equipped with the engine are directly linked to DAS (Make: NI USB-6210, 16-bit). It is a water cooled Research Engine setup-single cylinder, four stroke, Multi-fuel VCR engine with bore and stroke dimensions of 87.5 mm \* 110 mm. the capacity is 661 cc and connecting rod length as 234 mm. It has a compression ratio which can be adjusted in between 6–10. The engine has a power rating of 4.5 KW at 1800 rpm, Range of speed: 1200–1800 rpm. Along with the mentioned characteristics, the engine test bench was equipped with many general purpose attachments.

- Fuel tank with a capacity of 15 lit. attached to a measuring tube
- Orifice meter and mano-meter attached air box.
- Rotameters for water flow measurement
- Load sensor indicator
- Calorimeter and its attachments

#### 3.1 Experimental Procedure

The in-house fabricated CTP is exposed to the hot engine by product (hot air) at the exhaust of the engine. The CTP is mounted at 20 mm distance from the exhaust manifold (Fig. 2). The sensor is flush mounted so that the flow is not disturbed by the presence of the sensor and the sensing surface is nicely exposed to the heat load. The sensor is linked to a DAS (Make: NI, Model: NI-9223/ cDAQ-9178) to record high frequency voltage signal at a rate of 100,000 samples per second. The compression ratio is set to 10 which is almost one end for petrol engine. The engine is run for

**Fig. 2** Schematic highlighting the sensor location





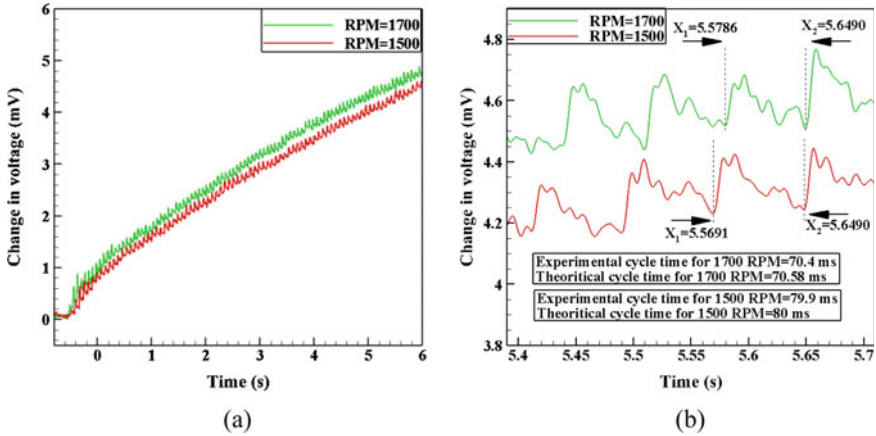


Fig. 3 Temperature response from the probe; a voltage signal; b Cycle time calculation

two different RPMs (1500 & 1700) with full throttle condition and responses are captured (Fig. 3).

### 4 Results and Discussion

The voltage signals are recorded using a NI based data acquisition system with the help of lab view interface. The signal is filtered with low pass filter and the results are plotted for 1500 and 1700 RPM in Fig. 3a. The sensor indicates a sharp rise at the arrival of the hot gases and then the subsequent cooling phase. This cycle repeats itself as the exhaust valve of the engine opens after a certain interval of time corresponding to the RPM of the engine. According to the speed of the crank shaft, the time required for 4 stroke cycles can be evaluated using Eq. 1. The experimental cycle time is calculated using the time span between two sharp rise in signal and is compared with the theoretical cycle time (Fig. 3b). The experimental and theoretical cycle time is tabulated in Table 1. A deviation of 0.12 and 0.25% are observed in 1500 RPM and 1700 RPM, respectively.

$$Cycletime, t (ms) = \frac{2 \times 60}{RPM} \times 1000 \tag{1}$$

Table 1 Comparison of experimental and theoretical cycle time

RPM	Experimental cycle time (ms)	Theoretical cycle time (ms)	Deviation (%)
1500	79.9	80	0.12
1700	70.4	70.58	0.25

### 4.1 Transient Heat Flux Calculation Using Analytical Approach

Owing to the unavailability of any straight relation for the transient heat-flux calculation for short duration experiments, it is calculated through appropriate modeling of the sensor. The time-varying temperature obtained from the experiment is employed for the estimation of heat-flux. The process is carried out by considering one-dimensional heat conduction in a semi-infinite substrate. With appropriate assumptions, and boundary conditions, the heat conduction equations take a shape as mention in Eq. 2.

$$\dot{q}_s(t) = \frac{\beta}{\sqrt{\pi}} \int_0^t \frac{1}{\sqrt{t-\tau}} \frac{d\{T_s(\tau)\}}{d\tau} d\tau ; \beta = \sqrt{\rho c k} \tag{2}$$

The form presented in Eq. (2) need to be discretized for the temperature. Here, a cubic spline of third order is used to discretize the temperature signal as explained below [6, 7]:

$$[T_s(\tau)]_{CS} = C_{1,i} + C_{2,i}(\tau - \tau_i) + \frac{1}{2}C_{3,i}(\tau - \tau_i)^2 + \frac{1}{6}C_{4,i}(\tau - \tau_i)^3; \tag{3}$$

$$\tau_i \leq \tau \leq \tau_{i-1}, i = 1, 2, \dots M$$

T where,  $\tau = S_t t$  is the scaled time and  $S_t$  is the scaling factor that is considered as unity in this case. The coefficients are given by Eq. 4.

$$C_{n,i} = \frac{dT_s^{n-1}(\tau_i)}{d\tau} \tag{4}$$

Finally, the surface heat flux is estimated using Eq. 5.

$$\dot{q}_s(\tau_{M+1}) = \left\{ 2 \frac{\beta}{\sqrt{\pi}} \sum_{i=1}^{M-1} V_i \left( P_i^{\frac{1}{2}} - R_i^{\frac{1}{2}} \right) - \frac{W_i}{3} \left( P_i^{\frac{3}{2}} - R_i^{\frac{3}{2}} \right) + \frac{C_{4,i}}{10} \left( P_i^{\frac{5}{2}} - R_i^{\frac{5}{2}} \right) \right\} \tag{5}$$

$$+ 2 \sqrt{\frac{\rho c k}{\pi}} \left( V_M P_M^{\frac{1}{2}} - \frac{W_M}{3} P_M^{\frac{3}{2}} + \frac{C_{4,M}}{10} P_M^{\frac{5}{2}} \right)$$

$\sqrt{S_t}$ ;  $M = 1, 2, \dots J - 1$  where,  $P_i = \tau_{M-1} - \tau_i$ ;  $R_i = \tau_{M+1} - \tau_{i+1}$ ;  $F_i = C_{1,i} + C_{2,i} P_i$   
 $+ \frac{C_{3,i}}{2} P_i^2 + \frac{C_{4,i}}{6} P_i^3$ ;  $V_i = \frac{dF_i}{d\tau_{M+1}}$ ;  $W_i = \frac{d^2 F_i}{d\tau_{M+1}^2}$

The heat flux signals for all the inputs are acquired from the discretized temperature signals using Eq. (5). More information regarding discretization can be obtained from the reference [14]. Referring to Eq. 2; the magnitude of thermal product ( $\beta$ ) for a sensor is required for the calculation of the heat-flux. Researchers adopted various magnitudes for the thermal product. It is tough to access the actual percentage from

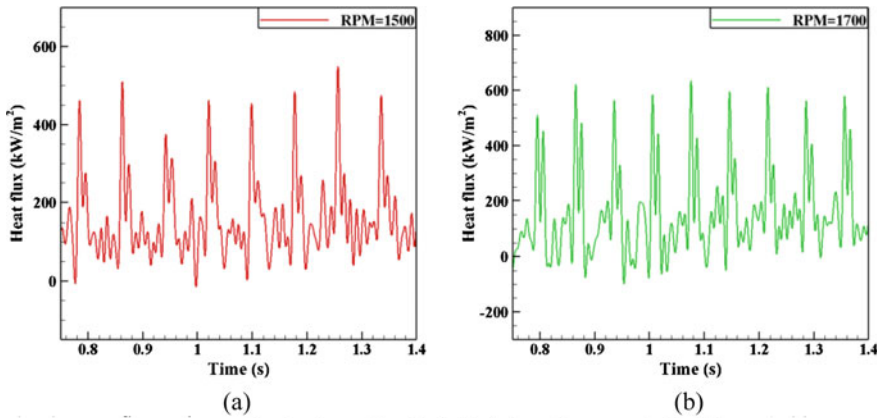


**Fig. 4** Heat flux estimation for 0.5 s after the initial rise; **a** RPM = 1500; **b** RPM = 1700

individual thermo-element in the preparation of the junction. Hence, here the thermal product magnitude is considered with 50% stake from individual component and the magnitude calculated is  $8650.2 \text{ Jm}^{-2} \text{ K}^{-1} \text{ s}^{-0.5}$  [15]. The heat-flux signals are drawn in Fig. 4. Considering the restrictions in the validity of one dimensional heat conduction and semi-infinite substrate assumption, the signal is considered for 0.5 s after from the initial rise of the temperature for the heat flux estimation. As inferred from Fig. 4, the peak magnitude of heat flux is in the range of  $500 \pm 50 \text{ kW/m}^2$  for 1500 RPM and  $550 \pm 50 \text{ kW/m}^2$  for 1700 RPM. The exhaust valve opens once in a cycle (4 strokes) and the sensor receives an instantaneous heat load. Therefore, the peak heat flux of nearly similar magnitude indicates the nearly equivalent combustion process.

## 5 Conclusion

The coaxial probe is exposed to the exhaust gas coming out from the engine exhaust manifold. The cyclic nature of heat load is well captured by the probe. From the experiment it is clear that the sensor is able to capture cycle time correctly. The transient temperature data is used to estimate the heat content getting lost as by product in terms of heat flux. As expected, the peak magnitude of cyclic heat flux are nearly equal and are in the range of  $500 \pm 50 \text{ kW/m}^2$  for 1500 RPM and  $550 \pm 50 \text{ kW/m}^2$  for 1700 RPM. The aim of the study can be extended to engines in moving vehicles where a sensor can be mounted somewhere in the line of exhaust and some amount of exhaust air may be blown over it. From the response, the driver can get the on time engine health monitoring.

## References

1. Rout, A.K., Sahoo, N., Kalita, P.: Effectiveness of coaxial surface junction thermal probe for transient measurements through laser based heat flux assessment. *Heat Mass Transf.* **56**(4), 1141–1152 (2020)
2. Livengood, J.C., Rona, T.P., Baruch, J.J.: Ultrasonic temperature measurement in internal combustion engine chamber. *J. Acoust. Soc. Am.* **26**(5), 824–830 (1954)
3. Nagao, et al.: Measurement of cylinder gas temperature of internal combustion engines. *Bull. JSME* **13**(64), 1240–1246 (1970)
4. Touloukian, Y.S.: Specific heat metallic elements and alloys. In: Touloukian, Y.S. (ed.) *Thermo-Physical Properties of Matter*; TPRC Data Series, vol. 4. IFI/Plenum Press, New York (1970).
5. Assanis, D.N., Badillo, E.: On heat transfer measurements in diesel engines using fast-response coaxial thermocouples. *J. Eng. Gas Turbines Power, Trans. ASME* **111**, 458–465 (1989)
6. Rakopoulos, C.D., Mavropoulos, G.C.: Experimental instantaneous heat fluxes in the cylinder head and exhaust manifold of an air-cooled diesel engine. *Energy Convers. Manage.* **41**, 1265–1281 (2000)
7. Kar, et al.: Instantaneous exhaust temperature measurements using thermocouple compensation techniques. SAE Technical Paper Series 2004-01-1418 (2004)
8. Kee, et al.: Fast response exhaust gas temperature measurement in IC engines. SAE Technical Paper Series 2006-01-1319 (2006)
9. Wang, X., Stone, C.R.: A study of combustion, instantaneous heat transfer, and emissions in a spark ignition during warm-up. *J. Automob. Eng., IMechE, Part-D* **222**, 607–618 (2008)
10. Hotta, S.K., Sahoo, N., Mohanty, K., Kulkarni, V.: Ignition timing and compression ratio as effective means for the improvement in the operating characteristics of a biogas fueled spark ignition engine. *Renew. Energy* **150**, 854–867 (2020)
11. Sujith, R.I., Unni, V.R.: Dynamical systems and complex systems theory to study unsteady combustion. *Proc. Combust. Inst.* **38**(3), 3445–3462 (2021)
12. Marr, et al.: A fast response thermocouple for internal combustion engine surface temperature measurements. *Exp. Therm. Fluid Sci.* **34**, 183–189 (2010)
13. Mavropoulos, G.C.: Unsteady heat conduction phenomena in internal combustion engine chamber and exhaust manifold surfaces. *Heat Transf.-Eng. Appl.* 283–308 (2011)
14. Taler, J.: Theory of transient experimental techniques for surface heat transfer. *Int. J. Heat Mass Transf.* **39**(17), 3733–3748 (1996)
15. Agarwal, S., Sahoo, N., Singh, R.K.: Experimental techniques for thermal product determination of coaxial surface junction thermocouples during short duration transient measurements. *Int. J. Heat Mass Transf.* **103**, 327335 (2016)

# Soret and Dufour Effects on Thin Film Micropolar Fluid Flow Through Permeable Media



G. Gomathy and B. Rushi Kumar

**Abstract** In this study, thin films of micropolar fluid flowing through porous media are analysed over a stretching sheet with heat effect subjected to thermophoresis. We assume that micropolar fluid is the base fluid and that the plate moves linearly and is subjected to reference temperature and concentration variations. An analysis of fluid flow over a steady stretching sheet utilizes the Soret and Dufour effects has been conducted in this study. Through the use of similarity variables, basic fluid flow equations are transformed to a nonlinear set of coupled equations with boundary conditions. MATLAB bvp4c solver is used to solve the problem. Graphs are used to illustrate the impact of physical parameters on the flow profiles that demonstrate the velocity, concentration, and temperature of thin fluid films. A series of tables illustrate the effects of dimensionless parameters on skin friction coefficients, Nusselt and Sherwood numbers. It is observed that increasing permeability parameter results in the decline of the velocity profile. With increasing Dufour and Soret number, temperature and concentration profiles are observed to increase, respectively.

**Keywords** Micropolar fluid · Dufour-Soret effect · Thin film · Thermophoresis

## 1 Introduction

In recent decades, micropolar fluids have gained significant attention within the engineering community due to the limitations of Newtonian fluids. Particles in suspension prevent Newtonian fluids from describing fluid flow. In contrast, micropolar fluids can simulate fluid in the presence of dust particles. Micropolar fluids are present in animal blood, dumbbell-shaped molecules, liquid suspensions, and polymer fluids. The subject of thin film flow has recently become prominent in research. In chemical techniques, thin film fluids are used to make heat exchangers, requiring

---

G. Gomathy · B. Rushi Kumar (✉)  
Department of Mathematics, School of Advanced Sciences, Vellore Institute of Technology,  
Vellore, Tamilnadu, India  
e-mail: [rushikumar@vit.ac.in](mailto:rushikumar@vit.ac.in)

© The Author(s), under exclusive license to Springer Nature Switzerland AG 2022  
S. Banerjee and A. Saha (eds.), *Nonlinear Dynamics and Applications*,  
Springer Proceedings in Complexity,  
[https://doi.org/10.1007/978-3-030-99792-2\\_36](https://doi.org/10.1007/978-3-030-99792-2_36)

429

in-depth expertise in motion. Coating of wires and fibres, polymer preparation are possible applications. Tiny particles moved from a hot surface onto a cold one during the extrusion process, is called thermophoresis. As dust particles move along the temperature gradient in gases, they exert thermophoretic force, and the acceleration achieved is referred to as thermophoretic velocity.

Eringen's [4] theory of micropolar fluids took into consideration the microscopic influence caused by the local structure and micro-rotation of fluid particles and believed to have a mathematical model explaining non-Newtonian fluid behaviour. Thermophoresis involves transfer of small particles to cold surfaces, while hot surfaces resist particle transfer; thus, a layer of free particles occurs around hot surface, as determined by Goldsmith and May [7]. Kim and Lee [10] analytically studied a semi-infinite vertical rotating porous plate with electrically conducting viscous incompressible micropolar fluid. They looked at the effect of different thermophysical and flow parameters and how they affected the temperature and flow fields in the boundary layer. A thermophoresis effect is observed in the free convective flow of boundary layer over a permeable barriers was reported by Chamka et al. [5, 9]. The aim of Rashidi et al. [15] was to develop a complete and accurate method to predict thermal transfer of micropolar fluid across a porous media with radiations based on Homotopy analysis. Several investigations regarding micropolar fluids with different physical structures and thermal radiations were discussed in [1, 3, 6, 8, 16].

Omowaye et al. [13] developed an analytical method to flow of an incompressible viscous fluid that flows past a semi-infinite plate that is embedded in porous media. They presumed fluid properties would remain unchanged except for the viscosity of a fluid, which is inversely related to temperature. Shah et al. [17] conducted a study over an unsteady stretched surface that included flow of thin film with effects of Dufour and Soret, which is reported to be the first to incorporate such effects in flow of thin film fluid. Tripathy et al. [18] numerically studied the interaction of a chemical reaction on the convective flow, mass transfer and heat capacity of a micropolar fluid over a stretched sheet embedded in porous media in the presence of a volumetric non-uniform heat source. Palwasha et al. [14] investigated thin film flow of fluid in three dimensions with different thermophysical properties of boundary layers. Vakkar Ali et al. [2] examined the flow of a thin film of micropolar fluid through porous layers subjected to thermophoresis and heat effect past a stretching plate under the assumption that the micropolar fluid itself is the base fluid. Usman et al. [19] investigated variations in Brownian motion, Hall current, thermophoresis and couple stress within the steady convection MHD flow of micropolar nanofluid to understand non-isothermal heat transfer from non-linear walls. Megahed et al. [11] addressed the laminar boundary layer flow, heat transfer problem for MHD fluid caused by a stretched sheets which is unsteady with prolonged heat flux. Naseem et al. [12] computed Soret and Dufour effects applied on radiated material on a porous stretched surface with thermal conductivity that depends on temperature.

To the author's knowledge, there are no studies in the literature that analyze the combined effects of Soret and Dufour of micropolar fluid in porous media over a stretching sheet in the presence of thermal radiation and thermophoresis along with magnetic field. Thus in the current work, we have considered thin films of micropolar

fluid flowing through a porous media over a stretching sheet with combined effects of Soret and Dufour in the presence of thermal radiation and thermophoresis along with magnetic field. Once the boundary layer PDE are transformed into ODE, they are solved numerically using shooting technique along with RK4 method. Graphs are made to illustrate the impact of physical parameters like permeability, inertia coefficient, microrotation, thermophoretic, radiation, and dimensionless numbers such as Prandtl, Dufour and Soret on the flow profiles that demonstrate velocity, concentration and temperature of thin fluid flow.

## 2 Mathematical Formulation

Let us consider the flow of thin micropolar fluids on a stretched plate, stretched at a linear velocity  $U_w = ax$ . The constant  $a > 0$  indicates the stretching rate, while  $x$  represents the flow direction. The film is chosen to have a uniform thickness  $\delta$ , while the nature of the medium is porous, as indicated by Fig. 1. During stretching, the temperature of the stretching plate is set at  $T_w$  and the concentration at  $C_w$ . On the surface,  $T_w = T_0 - T_{ref} \left(\frac{U_w x}{2v}\right)$  and  $C_w = C_0 - C_{ref} \left(\frac{U_w x}{2v}\right)$  are presume to differ with distance  $x$  relative to the plate. In addition to the temperature  $T_0$  and concentration  $C_0$  at the plate, there are constant reference temperature  $T_{ref}$  ( $0 \leq T_{ref} \leq T_0$ ) and concentration  $C_{ref}$  ( $0 \leq C_{ref} \leq C_0$ ) as well. Moreover, it is speculated that the liquid film grips and releases radiation. On the  $x$ -axis the radiative flux is taken into account, while the  $y$ -axis is ignored.

Our suggested model's basic flow equations are:

$$\frac{\partial u}{\partial x} + \frac{\partial v}{\partial y} = 0, \tag{1}$$

$$u \frac{\partial u}{\partial x} + v \frac{\partial u}{\partial y} = v \frac{\partial^2 u}{\partial y^2} + k_c \frac{\partial \sigma}{\partial y} + \frac{v\varphi}{K}(U_w - u) + Cr\varphi(U_w^2 - u^2), \tag{2}$$

$$G_1 \frac{\partial^2 \sigma}{\partial y^2} - 2\sigma \frac{\partial u}{\partial y} = 0, \tag{3}$$

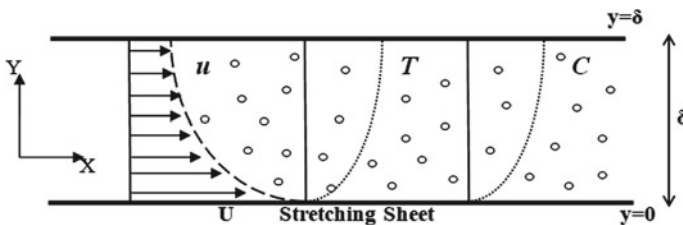


Fig. 1 A schematic diagram of the physical system

$$u \frac{\partial T}{\partial x} + v \frac{\partial T}{\partial y} = \frac{k}{\rho c_p} \frac{\partial^2 T}{\partial y^2} - \frac{1}{\rho c_p} \frac{\partial q_r}{\partial y} + \frac{D_m k_T}{c_s c_p} \frac{\partial^2 C}{\partial y^2}, \tag{4}$$

$$u \frac{\partial C}{\partial x} + v \frac{\partial C}{\partial y} = D_m \frac{\partial^2 C}{\partial y^2} + \frac{D_m k_T}{T_m} \frac{\partial^2 T}{\partial y^2} - \frac{\partial(V_T C)}{\partial y}. \tag{5}$$

For the two-dimensional flow of a liquid film, these are the boundary conditions:

$$u = U_w = ax, v = 0, \sigma = 0, T = T_w, C = C_w \text{ at } y = 0$$

$$\frac{\partial u}{\partial y} = 0, \frac{\partial T}{\partial y} = 0, \frac{\partial \sigma}{\partial y} = 0, \frac{\partial C}{\partial y} = 0, v = \delta x \text{ at } y = \delta \tag{6}$$

where thermophoretic velocity  $V_T$  can be taken as  $V_T = -\frac{k_1 \nu}{T_{ref}} \frac{\partial T}{\partial y}$ ,  $k_1$  represents thermophoretic coefficient.

As defined by Rosseland, the Rosseland approximation is:

$$q_r = -\frac{4\sigma^*}{3k^*} \frac{\partial T^4}{\partial y} \tag{7}$$

As a result of Taylor’s series,  $T^4$  can be rewritten as follows:

$$T^4 = 4T_1^3 T - 3T_1^4 \tag{8}$$

Equation (4) can be reduced using Eqs. (7) and (8) as follows:

$$u \frac{\partial T}{\partial x} + v \frac{\partial T}{\partial y} = \frac{k}{\rho c_p} \frac{\partial^2 T}{\partial y^2} + \frac{16\sigma^* T_1^3}{3\rho c_p k^*} \frac{\partial^2 T}{\partial y^2} \tag{9}$$

Incorporating transformations for the non-dimensional variables  $f, g, \theta, \phi$  and the similarity variable ' $\eta$ ' as,

$$u = U_w f'(\eta), \quad v = -\left(\frac{\nu U_w}{2x}\right)^{\frac{1}{2}} f(\eta), \quad \sigma = \left(\frac{U_w}{2\nu x}\right)^{\frac{1}{2}} U_w g(\eta), \quad \eta = \left(\frac{a}{2\nu}\right)^{\frac{1}{2}} y \tag{10}$$

$$T = T_0 - T_{ref} \left(\frac{U_w x}{2\nu}\right) \theta(\eta), \quad C = C_0 - C_{ref} \left(\frac{U_w x}{2\nu}\right) \phi(\eta) \tag{11}$$

When Eq. (10) and (11) are substituted into Eqs. (1)–(6), the basic governing equations with boundary conditions can be written as follows:

$$f''' + ff'' - 2f'^2 + \Delta g' + \frac{1}{Mr}(1 - f') + Nr(1 - f'^2) = 0, \tag{12}$$



$$Gr g'' - 2(2g + f'') = 0, \tag{13}$$

$$\theta''(1 + \frac{4}{3}R) - Pr(2f'\theta - f\theta') + 2Pr Du \phi'' = 0, \tag{14}$$

$$\phi'' + Sc(Sr - \tau\phi)\theta'' + Sr(f - \tau\theta')\phi' - 2Sc\phi f' = 0. \tag{15}$$

$$\begin{aligned} f(0) = 0, g(0) = 0, f'(0) = 1, \theta(0) = 1, \phi(0) = 1, \\ f''(1) = 0, f(1) = 0, g'(1) = 0, \theta'(1) = 0, \phi'(1) = 0. \end{aligned} \tag{16}$$

here  $f, g, \theta$ , and  $\phi$  represents dimensionless velocity, micro-rotation angular velocity, temperature and concentration function respectively.  $\beta$  represents fluid film non-dimensional thickness. Also  $\Delta, Mr, Nr, Gr, R, \tau$  represents parameter of vortex-viscosity, permeability, inertia coefficient micro-rotation, radiation, thermophoretic respectively, and  $Pr, Du, Sc, Sr$ , represents Prandtl, Dufour, Schmidt, and Soret number.

From a mathematical perspective, these parameters can be expressed as follows:

$$\begin{aligned} \Delta = \frac{k_c}{\nu}; \quad Mr = \frac{Ka}{2\phi\nu}; \quad Nr = \frac{2\phi C_r U_w}{a}; \quad Gr = \frac{G_1 a}{\nu}; \quad R = \frac{4\sigma^* T_1^3}{kk^*} \\ Du = \frac{D_m k_T}{c_s c_p \nu} \frac{C_w - C_0}{T_w - T_0}; \quad Sc = \frac{\nu}{D_m}; \quad Sr = \frac{D_m k_T}{\nu T_m} \frac{T_w - T_0}{C_w - C_0}; \quad \tau = \frac{k_1 U_w^2}{2\nu a} \end{aligned}$$

Skin friction coefficient, Nusselt number and Sherwood number are defined as follows

$$C_f = \frac{\mu \left(\frac{\partial u}{\partial y}\right)_{y=0}}{\frac{1}{2} \rho U_w^2}, \quad Nu = \frac{-kx \left(\frac{\partial T}{\partial y}\right)_{y=0}}{k(T_w - T_0)}, \quad Sh = \frac{-D_m x \left(\frac{\partial C}{\partial y}\right)_{y=0}}{D_m(C_w - C_0)}$$

with variables in Eq. (10), we can determine expressions for non-dimensional skin friction, Nusselt number and Sherwood number as follows:

$$C_f \left(\frac{Re}{2}\right)^{\frac{1}{2}} = f''(0), \quad Nu \left(\frac{Re}{2}\right)^{-\frac{1}{2}} = -\theta'(0), \quad Sh \left(\frac{Re}{2}\right)^{-\frac{1}{2}} = -\phi'(0) \tag{17}$$

$Re = \frac{U_w x}{\nu}$  stands for Reynold's number based on stretching velocity.

### 3 Solution Approach

A finite-difference algorithm in MATLAB, which is called the `bvp4c` solver, is used to solve boundary value problems (12)–(15), using boundary conditions (16). As an adaptive mesh solver, this solver utilizes residual control to select the mesh and control the error. Using this solver, we can create differential equations by using the `odefun` function, boundary conditions by using the `bcfun` function, and initial guesses by using the `solinit` function. By converting the boundary value problem (BVP) to an initial value problem (IVP) and reducing the higher order ODE's to first order ODE's, this code could be applied to the boundary value problem (BVP). First order ODE's are transformed as follows:

$$f = f(1); \quad f' = f(2); \quad f'' = f(3);$$

$$f''' = -f(1)f(3) + 2(f(2))^2 - \Delta f(5) - \frac{1}{Mr}(1 - f(2)) - Nr(1 - (f(2))^2);$$

$$g = f(4); \quad g' = f(5);$$

$$g'' = \frac{1}{Gr}[2(2f(4) + f(3))];$$

$$\theta = f(6); \quad \theta' = f(7);$$

$$\theta'' = \frac{1}{(1 + \frac{4}{3}R) - 2PrDuSc(Sr - \tau f(8))} [Pr(2f(2)f(6)) + 2PrDuSr(f(1) - \tau f(7))f(9) - 4PrDuScf(2)];$$

$$\phi = f(8); \quad \phi' = f(9);$$

$$\phi'' = \frac{1}{2PrDuSc(Sr - \tau f(8)) - (1 + \frac{4}{3}R)} [PrSc(Sr - \tau f(8))(2f(2)f(6) - f(1)f(7) + (1 + \frac{4}{3}R)Sr(f(1) - \tau f(7))f(9) - 2Sc(1 + \frac{4}{3}R)f(2)f(8))]$$

### 4 Results and Discussion

An investigation has been conducted on the thin film motion of a micropolar fluid through porous media. It includes the effects of energy radiation and thermophoresis, as well as Dufour-Soret effect through a stretching plate. Numerical computations are performed for  $Mr = Nr = Gr = R = Sr = Du = Sc = \Delta = \tau = 1$ ,  $Pr = 0.71$ .

**Table 1** Values of  $f''(0)$  with  $Mr$ ,  $Nr$  and  $\Delta$  variation

$Mr$	$Nr$	$\Delta$	$f''(0)$
0.8	0.3	0.3	2.302991
0.9	0.3	0.3	2.330854
1.0	0.3	0.3	2.353966
0.8	0.3	0.3	2.353966
0.8	0.4	0.3	2.317195
0.8	0.5	0.3	2.282024
0.8	0.3	0.3	2.282024
0.8	0.3	0.4	2.265702
0.8	0.3	0.5	2.249314

**Table 2** Values of  $\theta'(0)$  with  $R$ ,  $Pr$  and  $Du$  variation

$R$	$Pr$	$Du$	$-\theta'(0)$
0.3	0.3	0.3	1.562135
0.4	0.3	0.3	1.221797
0.5	0.3	0.3	1.003682
0.3	0.3	0.3	1.003682
0.3	0.4	0.3	1.292026
0.3	0.5	0.3	1.561992
0.3	0.3	0.3	1.561992
0.3	0.3	0.4	1.471936
0.3	0.3	0.5	1.381899

Tables 1, 2 and 3, shows the computed value of skin friction coefficient, local Nusselt number, and Sherwood number. Figures 2, 3, 4, 5, 6, 7, 8, 9 and 10 illustrates velocity, temperature, and concentration profiles of flow of thin film with variation over physical parameters.

Based on different values of permeability, Fig. 2 displays the variation in velocity distribution. The presence of a porous medium causes higher fluid flow restriction, which subsequently causes deceleration of fluid. Thus, increasing permeability decreases fluid velocity due to fluid motion resistance. According to Fig. 3, higher values of the inertia coefficient lead to increased fluid velocity, as it is directly related to fluid motion. Figure 4 depicts the inertia parameter varies on the profile of micro-rotation, which is dimensionless. A decrease in the microrotation profile is observed when the inertia parameter increases. From Fig. 5, the microrotation profile of fluid film decreases with increasing its parameter due to the inverse relationship between the microrotation and viscosity parameter is depicted. Thus, as Gr increases, the viscosity of the fluid decreases.

**Table 3** Values of  $\phi'(0)$  with  $Sc$ ,  $Sr$  and  $\tau$  variation

$Sc$	$Sr$	$\tau$	$-\phi'(0)$
0.3	0.3	0.3	1.267877
0.4	0.3	0.3	1.624919
0.5	0.3	0.3	1.957370
0.3	0.3	0.3	1.957370
0.3	0.4	0.3	1.896043
0.3	0.5	0.3	1.835538
0.3	0.3	0.3	1.197621
0.3	0.3	0.4	1.178786
0.3	0.3	0.5	1.160595

**Fig. 2** Velocity profile with  $Mr$  variation

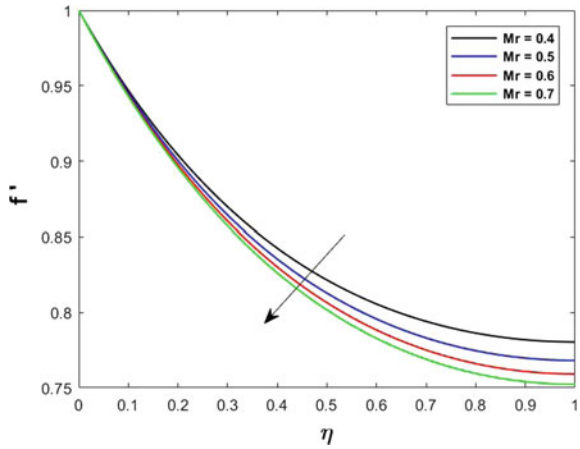


**Fig. 3** Velocity profile with  $Nr$  variation

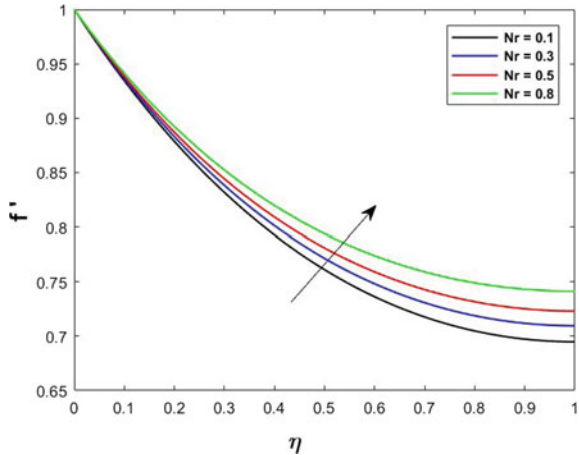


**Fig. 4** Microrotation profile with  $Nr$  variation

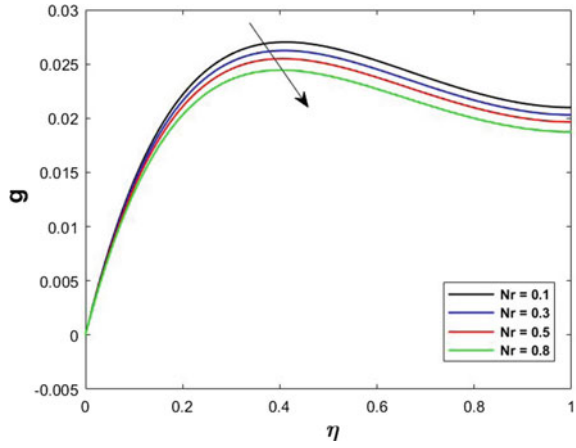


**Fig. 5** Microrotation profile with  $Gr$  variation

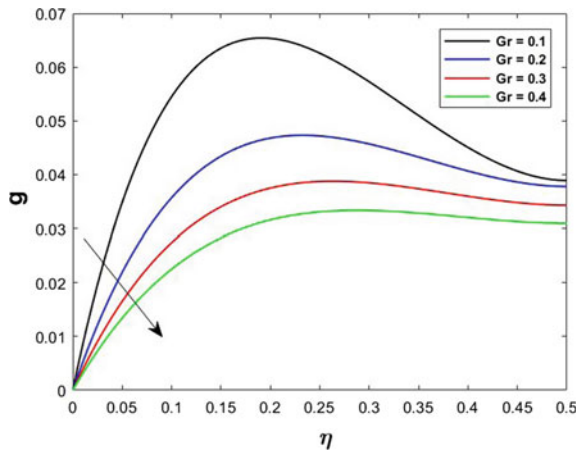


**Fig. 6** Temperature profile with  $R$  variation

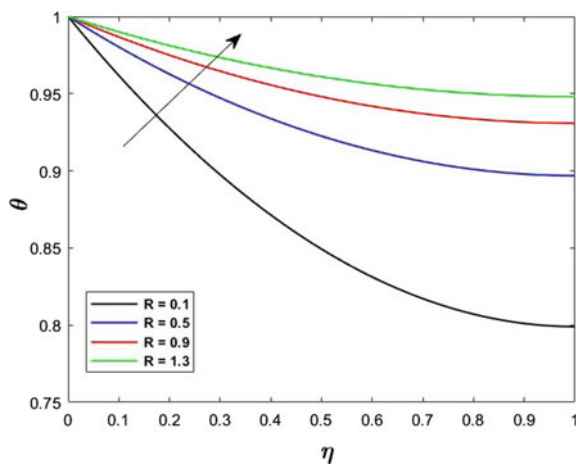


**Fig. 7** Temperature profile with  $Du$  variation

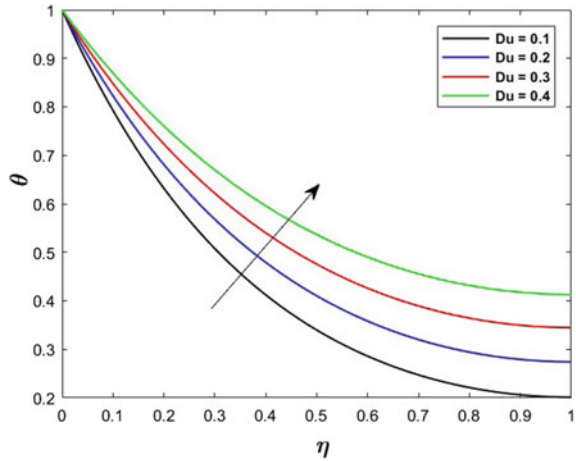
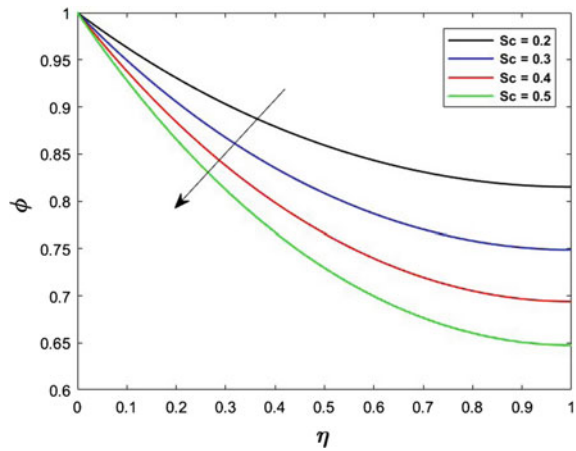


**Fig. 8** Concentration profile with  $Sc$  variation



Radiation from thermal sources is always included as a special case in the energy equation. Temperature rise with higher thermal radiation parameter is illustrated in Fig. 6. Physically, a rise in temperature can be attributed to the rate at which energy is transported in the fluid. As shown in Fig. 7, the Dufour number is influenced by the temperature profile. Dufour number refers to how much thermal energy is transferred in a flow due to concentration gradients. Consequently, concentration gradients become larger at higher Dufour number. Therefore, mass diffusion takes place faster, and energy is transferred from one particle to another at a higher rate. This causes the temperature profile to rise.

In Fig. 8, Schmidt number is weighed against concentration. Due to the inverse relationship between  $Sc$  and molecular diffusivity, increasing Schmidt numbers decrease the concentration field. Schmidt numbers characterize the flow of fluids where momentum dissipation is concurrent with mass dissipation. Figure 9 illus-

**Fig. 9** Concentration profile with  $Sr$  variation

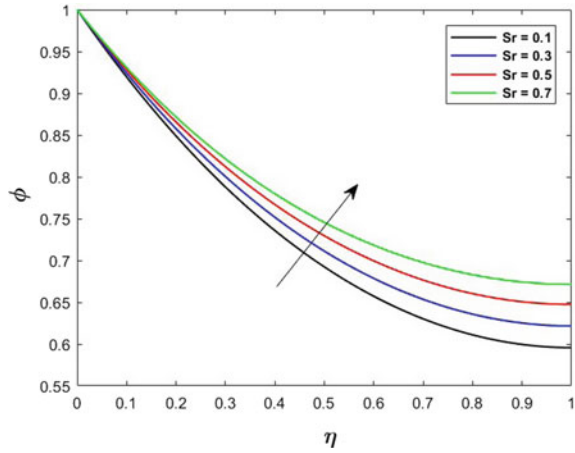
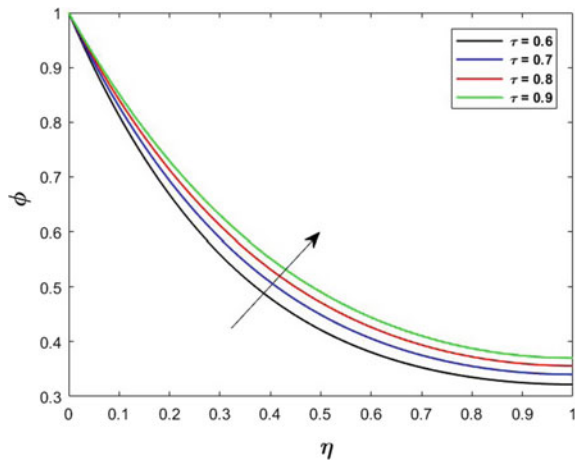


**Fig. 10** Concentration profile with  $\tau$  variation



trates the effect of the Soret number on  $\phi$ . A higher Soret number causes the viscosity to increase, and  $\phi$  to accelerate. Due to the increase in Soret number, the difference in temperature between hot and the surrounding fluids increases, so the temperature rises, which results in a higher concentration. Figure 10 illustrates the relation between concentration and thermophoretic parameter. As the thermophoretic parameter increases, the nondimensional concentration profile also increases.

## 5 Conclusion

In this study, the flow of thin films past a stretched sheet through a permeable medium is investigated. A micropolar fluid served as base fluid, influenced by thermal radiation and thermophoresis. Bvp4c solver is used to solve coupled nonlinear differential equations modelled in this study. We have displayed and discussed how the physical parameters affect the profile of velocity, concentration, and temperature. Accordingly the problem outcomes are:

- Increase in permeability causes a decrease in fluid velocity due to fluid motion resistance.
- Higher values of the inertia coefficient lead to increased fluid velocity.
- A decrease in the microrotation profile is observed when the inertia parameter increases.
- Due to the growth of energy and transport, the temperature field increases as the thermal radiation parameter increases. This elevates the temperature profile.
- It was found that temperature field enhancement occurs when Dufour number increases.
- It has been found that, as Schmidt number increases, the mass diffusivity decreases, which decreases the concentration.
- Observations shows that an increase in Soret number boosts concentration field.

The subject of thin film flow has recently become prominent in research. In chemical techniques, thin film fluids are used to make heat exchangers, which necessitate an in-depth expertise in motion. This study has possible applications in coating of wires, fibres, and polymer preparation industries.

## References

1. Abo-Eldahab, E.M., Ghonaim, A.F.: Radiation effect on heat transfer of a micropolar fluid through a porous medium. *Appl. Math. Comput.* **169**(1), 500–510 (2005)
2. Ali, V., Gul, T., Afridi, S., Ali, F., Alharbi, S.O., Khan, I.: Thin film flow of micropolar fluid in a permeable medium. *Coatings* **9**(2) (2019)
3. Bhattacharyya, K., Mukhopadhyay, S., Layek, G., Pop, I.: Effects of thermal radiation on micropolar fluid flow and heat transfer over a porous shrinking sheet. *Int. J. Heat Mass Transf.* **55**, 2945–2952 (2012)
4. C., E.A.: Theory of micropolar fluids. *J. Math. Mech.* **16**, 1–18 (1966)
5. Chamkha, A.J., Al-Mudhaf, A.F., Pop, I.: Effect of heat generation or absorption on thermophoretic free convection boundary layer from a vertical flat plate embedded in a porous medium. *Int. Commun. Heat Mass Transf.* **33**(9), 1096–1102 (2006)
6. Das, K.: Effect of chemical reaction and thermal radiation on heat and mass transfer flow of mhd micropolar fluid in a rotating frame of reference. *Int. J. Heat Mass Transf.* **54**(15), 3505–3513 (2011)
7. Goldsmith, P., May, F.G.: Diffusiophoresis and Thermophoresis in Water Vapour Systems, pp. 163–194. *Aerosol Science*, Academic Press, London (1966)



8. Heydari, M., Loghmani, G., Hosseini, S.M.: Exponential bernstein functions: an effective tool for the solution of heat transfer of a micropolar fluid through a porous medium with radiation. *Comput. Appl. Math.* **36**, 647–675 (2015)
9. Chamkha, J.A., Pop, I.: Effect of thermophoresis particle deposition in free convection boundary layer from a vertical flat plate embedded in a porous medium. *Int. Commun. Heat Mass Transf.* **31**(3), 421–430 (2004)
10. Kim, Y.J., Lee, J.C.: Analytical studies on mhd oscillatory flow of a micropolar fluid over a vertical porous plate. *Surf. Coat. Technol.* **171**(1), 187–193 (2003)
11. Megahed, A.M., Reddy, M.G., Abbas, W.: Modeling of MHD fluid flow over an unsteady stretching sheet with thermal radiation, variable fluid properties and heat flux. *Math. Comput. Simul. (MATCOM)* **185**(C), 583–593 (2021)
12. Naseem, T., Nazir, U., El-Zahar, E.R., Algelany, A.M., Sohail, M.: Numerical computation of dufour and soret effects on radiated material on a porous stretching surface with temperature-dependent thermal conductivity. *Fluids* **6**(6), 2311–5521 (2021)
13. Omowaye, A., Fagbade, A., Ajayi, A.: Dufour and soret effects on steady mhd convective flow of a fluid in a porous medium with temperature dependent viscosity: Homotopy analysis approach. *J. Niger. Math. Soc.* **34**(3), 343–360 (2015)
14. Palwasha, Z., Khan, N.S., Shah, Z., Islam, S., Bonyah, E.: Study of two-dimensional boundary layer thin film fluid flow with variable thermo-physical properties in three dimensions space. *AIP Adv.* **8**(10), 105318 (2018)
15. Rashidi, M., Mohimanian Pour, S.: A novel analytical solution of heat transfer of a micropolar fluid through a porous medium with radiation by dtm-padé. *Heat Transf.-Asian Res.* **39**(8), 575–589 (2010)
16. Rashidi, M., Mohimanian pour, S., Abbasbandy, S.: Analytic approximate solutions for heat transfer of a micropolar fluid through a porous medium with radiation. *Commun. Nonlinear Sci. Numer. Simul.* **16**(4), 1874–1889 (2011)
17. Shah, Q., Gul, T., Mamat, M.B., Khan, W., Tofany, N.: Soret and dufour effect on the thin film flow over an unsteady stretching surface. *AIP Conf. Proc.* **1775**(1), 030088 (2016)
18. Tripathy, R., Dash, G., Mishra, S., Hoque, M.M.: Numerical analysis of hydromagnetic micropolar fluid along a stretching sheet embedded in porous medium with non-uniform heat source and chemical reaction. *Eng. Sci. Technol. Int. J.* **19**(3), 1573–1581 (2016)
19. Usman, A.H., Shah, Z., Humphries, U.W., Kumam, P., Thounthong, P.: Soret, dufour, and activation energy effects on double diffusive convective couple stress micropolar nanofluid flow in a hall mhd generator system. *AIP Adv.* **10**(7), 075010 (2020)

# Effects of Slip Velocity and Bed Absorption on Transport Coefficient in a Wetland Flow



Debabrata Das , Subham Dhar , Nanda Poddar , Rishi Raj Kairi ,  
and Kajal Kumar Mondal 

**Abstract** In this research work, an investigation on solute transport in a width independent wetland flow with the appearance of the vegetation, bed absorption and slip velocity is explored. The equations of moment are formed from the governing convection-diffusion equation with the help of method of moments. A finite difference implicit technique is imposed to find the solution of the resultant moment equations. The behavior of the dispersion coefficient and skewness is analyzed graphically for the various values of slip parameter, inhomogeneous reaction at the bed surface and for vegetation parameter in the wetland. It is found that the slip velocity reduces the dispersion of the tracers in the wetland flow. The uplifted values of slip parameter, inhomogeneous reaction rate and vegetation factor shorten the critical time to reach the stationary state of the transport coefficient. The slip effect reduces the asymmetry of solute distribution, while the enlarged absorption introduces asymmetry in the tracer distribution.

**Keywords** Wetland flow · Slip velocity · Bed absorption · Moment method · Dispensivity

## 1 Introduction

Wetland caused by the flood of the water permanently or seasonally got remarkable attention in last two decades for its huge application in different ecosystems. Wetlands are benefiting human society in different ways, such as through irrigation, flood control, water purification, ecological restoration and biodiversity conservation etc. Also, its play a vital role for the supply of water, climate regulation as well as for contaminant degradation. Aris [1] was the first who introduce the method of moments to

---

Supported by CSIR INDIA and UGC INDIA.

---

D. Das (✉) · S. Dhar · N. Poddar · R. R. Kairi · K. K. Mondal  
Cooch Behar Panchanan Barma University, Cooch Behar 736101, India  
e-mail: [debabratadas359548@gmail.com](mailto:debabratadas359548@gmail.com)

© The Author(s), under exclusive license to Springer Nature Switzerland AG 2022  
S. Banerjee and A. Saha (eds.), *Nonlinear Dynamics and Applications*,  
Springer Proceedings in Complexity,  
[https://doi.org/10.1007/978-3-030-99792-2\\_37](https://doi.org/10.1007/978-3-030-99792-2_37)

observed the dispersion of the substance in fluid flowing through a tube. The erosion of average mean concentration due to the environmental dispersion was obtained by Zeng et al. [2] with the help of Aris's moment method. Later, to observe the variation of solute concentration in a width dominated flow, Wu et al. [3] applied the multi-scale technique. Zeng et al. [4] discussed a theoretical analysis for the degeneration of depth-averaged concentration with the combined effect of hydraulic dispersion and ecological degradation. To examine the behavior of the vertical distribution of solute concentration in a wetland flow, Wu et al. [5] used mean concentration expansion technique. In this direction, the transport of contaminant in a width independent wetland flow with the presence of absorption and bulk degradation was analyzed by Wang and Chen [6]. They showed that solute cloud becomes more shrunk and reformed with the enhancement of damping factor in presence of the bed absorption. The homogenization method was employed by Wang et al. [7] to find the solution for spatial concentration distributions of solute and reported that non-uniformity occurs in vertical concentration profiles for vegetation shear. In recent time, Dhar et al. [8] investigated environmental dispersion of settling particles numerically and revealed the effects of some important parameters on sediment transport. Further, Poddar et al. [9] introduced integral moment method to notice the dispersion phenomena in a time independent wetland flow and employed Hermite polynomial representation to determine the mean concentration distribution. Ng [10] showed the influence of wall slippage on hydrodynamic dispersion in a parallel-plate channel and observed that keeping slip length constant in the channel, the mixing of a contaminant cloud reduces with the boundary slip. Munoz et al. [11] employed homogenization technique to study the slippage effect on hydrodynamic dispersion of a passive tracers in a oscillatory electro-osmotic flow.

In the present investigation, the main focus is to explore the effect of slip velocity in a width independent wetland flow. A finite difference technique is employed to find the solution of the moment equations. Further, the behavior on dispersion coefficient and skewness for the values of slip parameter, inhomogeneous reaction and vegetation parameter are analyzed. The novelty of the present research is to observe the slip effect on environmental dispersion which has a wide range of application.

## 2 Mathematical Formulation

In general, near the phase average scale, the basic momentum equation for a wetland flow can be considered as

$$\rho \left( \frac{\partial \mathbf{U}}{\partial \tau} + \nabla \cdot \frac{\mathbf{U}\mathbf{U}}{\phi} \right) = -\nabla p - \mu F \mathbf{U} + \kappa \mu \nabla^2 \mathbf{U} + \kappa \nabla \cdot (\mathbf{L} \cdot \nabla \mathbf{U}), \quad (1)$$

where  $U$ ,  $\rho$ ,  $\phi$ ,  $\mu$ ,  $\tau$ ,  $p$ ,  $\kappa$ ,  $F$  are the velocity, density, porosity, dynamic viscosity, time, pressure, tortuosity, shear factor respectively and  $L$  is taken as momentum dispersivity. For the shallow wetland flow, the momentum equation is expressed

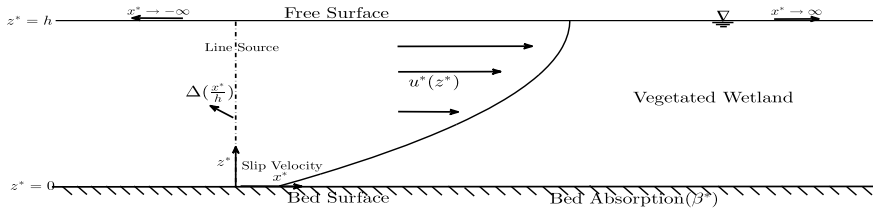


Fig. 1 Schematic diagram for the present model

with the combination of Navier-Stokes equation (single-phase flow), Darcy’s law (porous media) and a second order derivative term for the momentum dispersion.

Here, the contaminant transport phenomena is considered in a fully exhibited unidirectional flow, where  $\phi$ ,  $\kappa$ ,  $F$ , and  $L$  are constants in the wetland flow of height  $h$ . In the above discussed flow, with the help of Cartesian coordinate system,  $x^*$ -axis and  $z^*$ -axis are taken along the longitudinal and transversal direction of the flow, respectively. Where the origin is considered at one of the channel banks (See Fig. 1). For a width independent wetland flow, width effects are not significant and the concerned quantities are assumed as width-averaged. Equation 1 is transformed due to the pressure gradient as

$$\kappa(\mu + L_z) \frac{d^2 u^*}{dz^{*2}} - \mu F u^* = \frac{dp}{dx^*}, \tag{2}$$

where  $\rho$  is the fluid density. For the wetland flow, the slip condition at bed surface ( $z^* = 0$ ) with slip length  $L_s$  and the no flux boundary condition at the free surface ( $z^* = h$ ) are respectively as,

$$\left[ L_s \frac{du^*(z^*)}{dz^*} - u^*(z^*) \right]_{z^*=0} = \left[ \frac{du^*(z^*)}{dz^*} \right]_{z^*=h} = 0. \tag{3}$$

The characteristic velocity is defined as  $u_c = -\frac{dp}{dx} \frac{W^2}{\mu + L_z}$ . Introducing the dimensionless parameters  $\zeta = \frac{z^*}{h}$ ,  $l_s = \frac{L_s}{h}$ ,  $u = \frac{u^*}{u_c}$ , the general solution of Eq. (2) with the help of boundary conditions (3) becomes,

$$u(z) = \frac{1}{\alpha^2} \left( 1 - \frac{\cosh\{\alpha(z - 1)\}}{l\alpha \sinh \alpha + \cosh \alpha} \right), \tag{4}$$

where  $\alpha \left( = \sqrt{\frac{\mu F h^2}{\kappa(\mu + L_z)}} \right)$  is the vegetation parameter which illustrates the amalgamated action of the depth of the channel wetland, fluid viscosity, effective vegetation force, tortuosity of the flow and the momentum dispersivity towards the vertical direction. The space variables  $x^*$  and dispersion time  $t^*$  is normalized as follows,

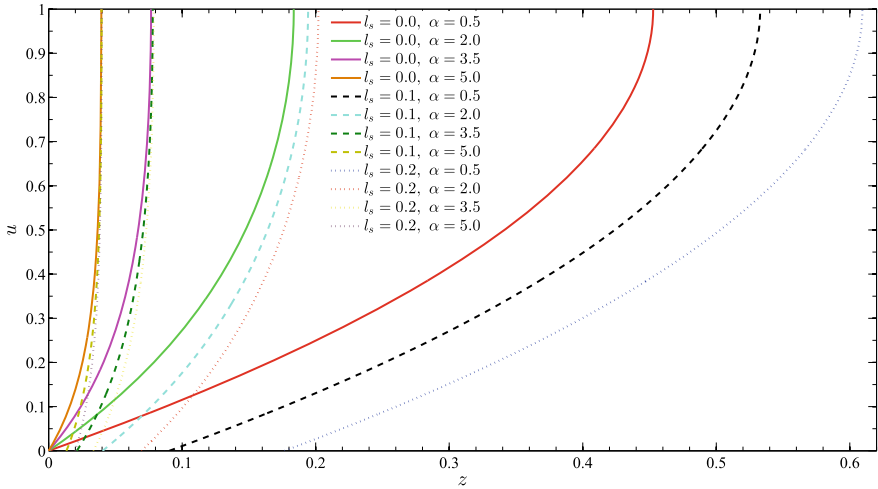


**Fig. 2** Velocity profile for different values of vegetation and slip parameters

$$x = \frac{x^*}{h}, \quad t = \frac{t^* h^2}{\kappa(\lambda + K_z/\phi)}.$$

The velocity distribution in a wetland flow due to different values of vegetation parameter and slip length is shown in Fig. 2. It is noticed that with the increment of vegetation  $\alpha$ , velocity decreases and for high vegetation, velocity profiles behave like a log-law profile. Moreover, when slip velocity is present in the flow, it is seen that, near the bed surface, velocity profile slips from the initial point towards the longitudinal direction. It is fascinating to note that as vegetation increases in the wetland, the slip effect diminishes. Whereas for high vegetation, the effects of slip velocity is negligible near the free surface.

When a solute with mass concentration diffusivity  $\lambda$  is injected in the above mentioned flow, the concentration  $C^*(x^*, z^*, t^*)$  satisfies the following advection-diffusion equation,

$$\frac{\partial C^*}{\partial t^*} + \frac{u^*}{\phi} \frac{\partial C^*}{\partial x^*} = \kappa \left( \lambda + \frac{K_x}{\phi} \right) \frac{\partial^2 C^*}{\partial x^{*2}} + \kappa \left( \lambda + \frac{K_z}{\phi} \right) \frac{\partial^2 C^*}{\partial z^{*2}}, \tag{5}$$

where  $K_x$  and  $K_z$  are the constant value known as longitudinal and transversal mass dispersivity. The non-dimensional concentration is  $C = \frac{C^*}{Q_m/\phi h}$ , where  $Q_m$  is the amount of instantaneous released mass at the cross section of  $x^* = 0$  and time  $t = 0$ . The governing Eq. (5) becomes

$$\frac{\partial C}{\partial t} + Peu \frac{\partial C}{\partial x} = R \frac{\partial^2 C}{\partial x^2} + \frac{\partial^2 C}{\partial z^2}, \tag{6}$$

where  $Pe = \frac{u_c h}{\kappa(\lambda\phi + K_z)}$  and  $R = \frac{\phi\lambda + K_x}{\phi\lambda + K_z}$ . Here, Peclet number,  $Pe$  is the ratio of the characteristic time for diffusion process  $\left(\frac{\phi h^2}{\kappa(\phi\lambda + K_z)}\right)$  to the time of the convection process  $\left(\frac{h}{u_c}\right)$ , and  $R$  describes the ratio of total mass dispersivity and diffusivity along the longitudinal and transversal direction. The boundary conditions are given by

$$\left[ \kappa \left( \lambda + \frac{K_z}{\phi} \right) \frac{\partial C}{\partial z^*} - \beta^* C^* \right]_{z^*=0} = \left[ \kappa \left( \lambda + \frac{K_z}{\phi} \right) \frac{\partial C}{\partial z^*} \right]_{z^*=h} = 0, \tag{7}$$

and their dimensionless forms are,

$$\left[ \frac{\partial C}{\partial z} - \beta C \right]_{z=0} = \left[ \frac{\partial C}{\partial z} \right]_{z=1} = 0, \tag{8}$$

The corresponding dimensionless initial input condition is

$$C(x, z, t)|_{t=0} = \delta(x), \tag{9}$$

where  $\delta$  is the Dirac delta function. Since, the concentration of the solute particles cannot move at infinity, the normalized additional condition can be taken as

$$C(x, z, t)|_{x \rightarrow \pm\infty} = 0. \tag{10}$$

Using  $p$ -th order integral moment of  $C(x, z, t)$  with respect to  $x$  according to the method of moments (Aris [1]), we have

$$C_p(z, t) = \int_{-\infty}^{\infty} x^p C(x, z, t) dx. \tag{11}$$

Taking depth average of  $C_p(z, t)$ , one can obtain

$$M_p(t) = \bar{C}_p = \int_0^1 C_p(z, t) dz. \tag{12}$$

Using (11)–(12) in Eq. (6), with the initial condition (10) and boundary conditions (8), one can get

$$\frac{\partial C_p}{\partial t} = puPeC_{p-1} + Rp(p-1)C_{p-2} + \frac{\partial^2 C_p}{\partial z^2}, \tag{13}$$

with

$$C_p(z, 0) = \begin{cases} 1 & \text{for } p = 0 \\ 0 & \text{for } p > 0 \end{cases}, \tag{14}$$

and

$$\left[ \frac{\partial C_p}{\partial z} - \beta C_p \right]_{z=0} = \left[ \frac{\partial C_p}{\partial z} \right]_{z=1} = 0, \tag{15a}$$

and therefore,

$$\frac{dM_p}{dt} = pPeu\overline{C}_{p-1} + p(p-1)R\overline{C}_{p-2} - \beta C_p(0, t), \tag{16}$$

with

$$M_p(0) = \begin{cases} 1 & \text{if } p = 0 \\ 0 & \text{if } p > 0 \end{cases}, \tag{17}$$

for  $p = 0$ , it is found that

$$M_0(t) = 1 - \beta \int C_p(0, t) dt. \tag{18}$$

### 3 Description of Statistical Components

The  $p$ -th order integral moment about the distribution of mean concentration is as follows

$$\nu_p(t) = \frac{1}{M_0} \int_0^1 \int_{-\infty}^{\infty} (x - x_g)^p C dx dz, \tag{19}$$

where

$$x_g = \frac{1}{M_0} \int_0^1 \int_{-\infty}^{\infty} x C dx dz. \tag{20}$$

Here,  $M_0$  defines the total amount of mass of the solute in the whole volume of the wetland.  $x_g$  is the centroid of the tracers, it determines the location of the center of gravity of the movement of concentration cloud with the mean velocity of the fluid. Also, variance ( $\nu_2$ ), skewness ( $\nu_3$ ) and kurtosis ( $\nu_4$ ) are represented by the second, third and fourth moments of contaminant distribution, respectively.

Taylor’s approximation for the diffusion coefficient  $D_a = Pe/192 + 1/Pe$  is developed by Aris [1], where the dispersion time is characterized asymptotically large. In compare to the vertical diffusion, longitudinal diffusion is insignificant and so, the effective transport coefficient may be express as

$$D_a = \frac{1}{2Pe^2} \frac{d\nu_2}{dt}, \tag{21}$$

$D_a$  describes the relation between diffusion and convection process. For a wetland flow,  $D_a$  depends on the absorption parameter  $\beta$ , vegetation parameter  $\alpha$  and dispersion time  $t$ .

To determine the sharpness and symmetry of the concentration distribution of the solute, the coefficients of skewness and kurtosis are the important criteria. The skewness and kurtosis are given respectively as

$$\beta_2 = \frac{\nu_3}{\nu_2^{\frac{3}{2}}}, \tag{22a}$$

$$\beta_3 = \frac{\nu_4}{\nu_2^2} - 3. \tag{22b}$$

When  $\beta_2 = \beta_3 = 0$ , the concentration distribution of solute is normal and their nonzero values indicate the deviations from the Gaussianity.

### 4 Numerical Computation

When  $p > 1$ , the analytical solution of moment equations with concerned initial and boundary conditions is quite complicated. Thus, using a finite difference implicit scheme based on Crank-Nicholson approach is employed to study the transport of solute particles in the wetland. The grid point  $(m, n)$  indicates a point where  $z_m = (m - 1) \times \Delta z$  and  $t_n = (n - 1) \times \Delta t$ . The enhancements of  $z$  and  $t$  are  $\Delta z = z_{m+1} - z_m$  and  $\Delta t = t_{n+1} - t_n$  respectively. All the elements are determined at the grid point  $(m, n + 1)$ , where  $m = 1$  relates the bottom of the wetland  $z = 0$  and  $n = 1$  relates the dispersion time  $t = 0$ . The two point forward difference technique is adopted for  $\frac{\partial C_p}{\partial t}$  at the  $(n + 1)$ -th mesh point

$$\frac{\partial C_p}{\partial t} \Big|_{(m,n+1)} = \frac{C_p(m, n + 1) - C_p(m, n)}{\Delta t}. \tag{23}$$

To discretize  $\frac{\partial C_p}{\partial z}$ , two point averaged central difference technique is used and it is given by

$$\frac{\partial C_p}{\partial z} \Big|_{(m,n+1)} = \frac{C_p(m + 1, n + 1) - C_p(m - 1, n + 1) + C_p(m + 1, n) - C_p(m - 1, n)}{4\Delta z}. \tag{24}$$

The discretization for  $\frac{\partial^2 C_p}{\partial z^2}$  is taken as three-point averaged central difference scheme and it is written as



$$\frac{\partial^2 C_p}{\partial z^2} \Big|_{(m,n+1)} = \frac{1}{2\Delta z^2} [C_p(m+1, n+1) - 2C_p(m, n+1) + C_p(m-1, n+1) + C_p(m+1, n) - 2C_p(m, n) + C_p(m-1, n)]. \tag{25}$$

For the term  $uC_{p-1}$ , the discretization is as follows,

$$uC_{p-1}|_{(m,n+1)} = u(m, n+1)C_{p-1}(m, n+1). \tag{26}$$

The finite difference schemes for the initial condition is

$$C_p(m, 1) = \begin{cases} 1 & \text{for } p = 0, \\ 0 & \text{for } p \geq 1 \end{cases}, \tag{27}$$

and the boundary condition are

$$C_p(0, n+1) = C_p(2, n+1) - 2\beta\Delta z C_p(1, n+1), \quad \text{at the bed surface} \tag{28a}$$

$$C_p(M+1, n+1) = C_p(M-1, n+1). \quad \text{at the free surface} \tag{28b}$$

A tri-diagonal matrix is obtained by using the the above mentioned discretization and it is given by

$$P_m C_p(m+1, n+1) + Q_m C_p(m, n+1) + R_m C_p(m-1, n+1) = S_m, \tag{29}$$

where  $P_m, Q_m, R_m$  and  $S_m$  are the matrix elements and they are describes as follow

$$\left. \begin{aligned} P_m &= -\frac{\Delta t}{2\Delta z^2}, \\ Q_m &= \left[ 1 + \frac{\Delta t}{\Delta z^2} \right], \\ R_m &= -\frac{\Delta t}{2\Delta z^2}, \\ S_m &= \left[ \frac{\Delta t}{2\Delta z^2} \right] C_p(m+1, n) + \left[ 1 - \frac{\Delta t}{\Delta z^2} \right] C_p(m, n) + \left[ 2\frac{\Delta t}{\Delta z^2} \right] C_p(m-1, n) \\ &\quad + [puPeC_{p-1}(m, n+1) + p(p-1)RC_{p-2}(m, n+1)] \Delta t. \end{aligned} \right\} \tag{30}$$

The index  $m$  relates the wetland space whose range is from the value 1 to  $M$ . At the wetland free surface, the value of  $m$  is considered as  $M$ . To obtain an optimal result, in a steady flow through a wetland, the time grid and the space grid size are taken as  $\Delta t = 0.0001$  and  $\Delta z = 0.02$ . The mesh size for steady flow is taken as  $\Delta t = 0.0001$ . The index related to the time is  $n$  and it is expanded from 1 to  $N$ . The tri-diagonal coefficient matrix is constructed and solved with the help of initial and boundary condition applying the Thomas algorithm. Simpson's one-third formula is used to compute the values of  $M_p$  with the known values of  $u(z)$  and  $C_p$  at the corresponding mesh points.

## 5 Discussion of Results

In this section, the temporal variations of dispersion and skewness are illustrated for various values of slip parameter ( $l_s$ ), absorption parameter ( $\beta$ ), vegetation factor ( $\alpha$ ) and  $R$ . From Fig. 3a, it is seen that the increment in the slip length minimizes the dispersion in the flow. Slip on the bed surface reduces the velocity gradient along the transverse direction of the flow and therefore, it abates the dispersion process of the solute. Figure 3b is described that the presence of bed absorption declines the solute dispersion. Further, dispersion coefficient prominently reduces with enlarge values of the bed absorption strength, because enhanced value of  $\beta$ , increases the depletion rate of the solute material at the bed surface. Also, due to the increase of vegetation force in the wetland, reduction in the dispersion coefficient is found (Fig. 3c). This is because of the resisting force in the flow, imposed by the vegetation in the wetland. Moreover, it is interesting to observe from the Fig. 3a–c that the critical time for reaching to the stationary state decreases with the rise in the values of  $l_s$ ,  $\beta$ ,  $\alpha$ . However, the opposite phenomena is noticed in Fig. 3d i.e., the coefficient of dispersion of the solute enhances with the increment of  $R$ . The reason behind this, the longitudinal diffusion increases as  $R$  enlarges.

The influence of different crucial flow parameters on skewness is depicted in Fig. 4. The variation of skewness of the distribution of solute material is shown in Fig. 4a for different slip length. The increment in slip parameters result skewness coefficient to move towards zero i.e. it reduces the asymmetry of the solute distribution and moves towards the Gaussianity. Whereas, the reverse phenomena is found in Fig. 4b for various values of the reaction parameter  $\beta$ . It illustrates that enhanced value of absorption parameter introduces asymmetry in the tracer distribution. From Fig. 4c, it is observed that the enhancement of  $\alpha$ , the distribution of tracers gradually becomes symmetric. Moreover, when  $\alpha \rightarrow 2$ , the skewness of the concentration vanishes and it follows Gaussian distribution. It is remarkable to note that the effect of  $R$  is similar to the slip parameter  $l_s$  (See Fig. 4d).

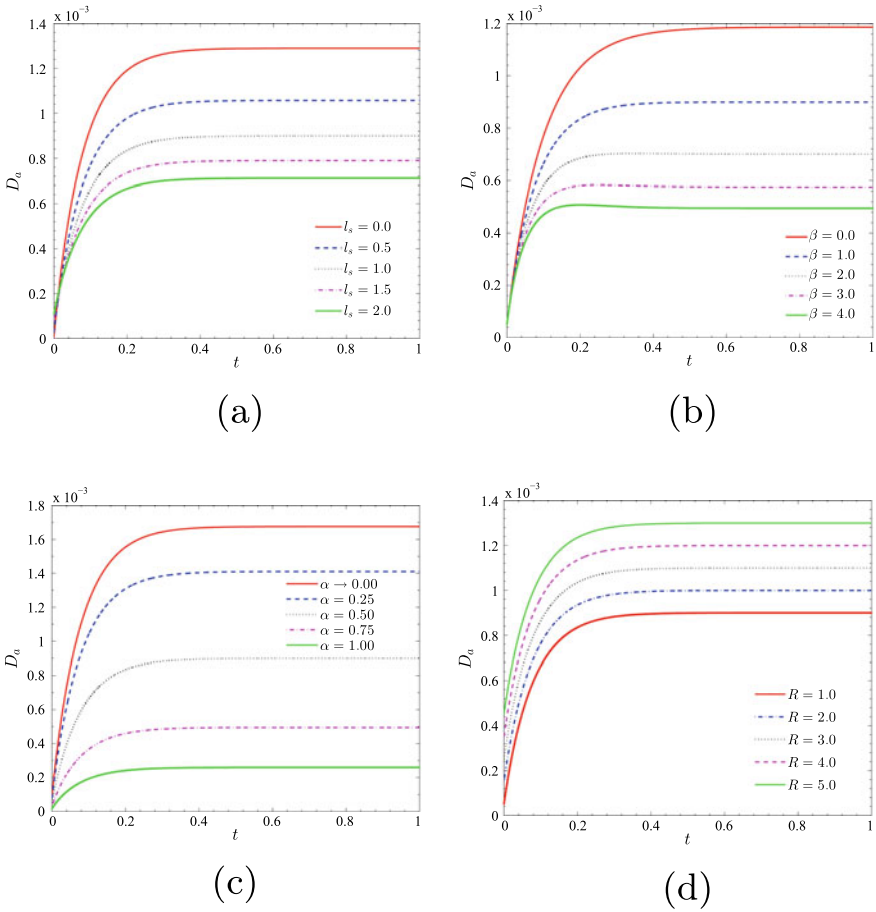


**Fig. 3** Dispersivity  $D_a$  with time for different values of **a** slip parameter  $l_s$ , **b** bed absorption  $\beta$ , **c** vegetation factor  $\alpha$  **d**  $R$ ; when  $\alpha = 0.5$ ,  $l_s = 1$ ,  $\beta = 1$ ,  $P_e = 100$  and  $R = 1$

The variation of the kurtosis is delineated in Fig. 5. The kurtosis of the tracer distribution is presented in Fig. 5a for various values of slip length. Due to the enhancement in slip parameter, the kurtosis of the tracer distribution moves toward zero for large dispersion time. The similar behaviour is observed in the kurtosis for various values of  $\beta$  and  $R$  (See Fig. 5b, d). From the figures, it is concluded that for small dispersion time ( $t < 0.2$ ), the distribution of the tracer material deviates from the Gaussianity and for large dispersion time with large  $l_s$ ,  $\beta$ , and  $R$ , the distribution tends to reach the normal distribution. From Fig. 5c, it is seen that, when  $\alpha \rightarrow 0$ , the distribution approaches towards Gaussian distribution. Moreover, when  $\alpha$  increases in the wetland, the flow of the tracer decreases, which increases the peak of the concentration.

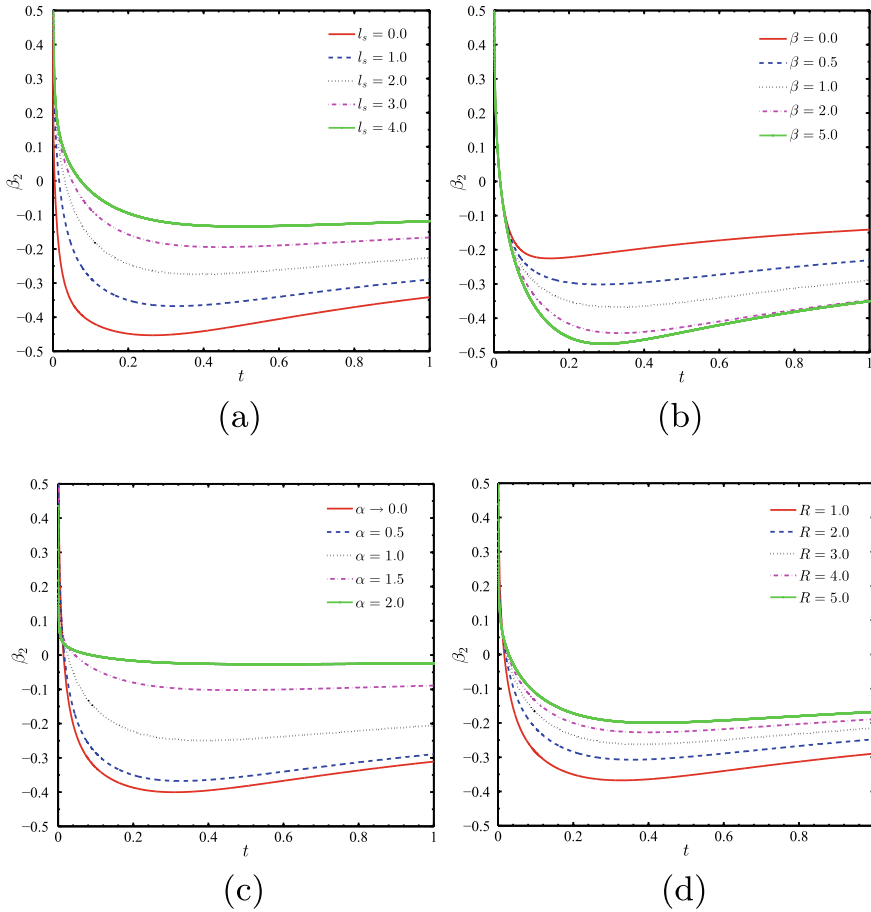


**Fig. 4** Skewness  $\beta_2$  of solute distribution with time for different values of **a** slip parameter  $l_s$ , **b** bed absorption  $\beta$ , **c** vegetation factor  $\alpha$  **d**  $R$ ; when  $\alpha = 0.5, l_s = 1, \beta = 1, P_e = 100$  and  $R = 1$

## 6 Conclusion

An investigation on solute transport in a width independent vegetated wetland channel flow is presented with the appearance of slip condition and absorption at the bed surface. A finite difference implicit method is used to find the solution of the moment equations. Some crucial observations are noticed in this work:

- (a) The Enhancement of slip parameter reduces the dispersion coefficient in the flow.
- (b) The uplifted values of slip parameter, inhomogeneous reaction rate and vegetation factor shorten the critical time to reach the stationary state of the transport coefficient.

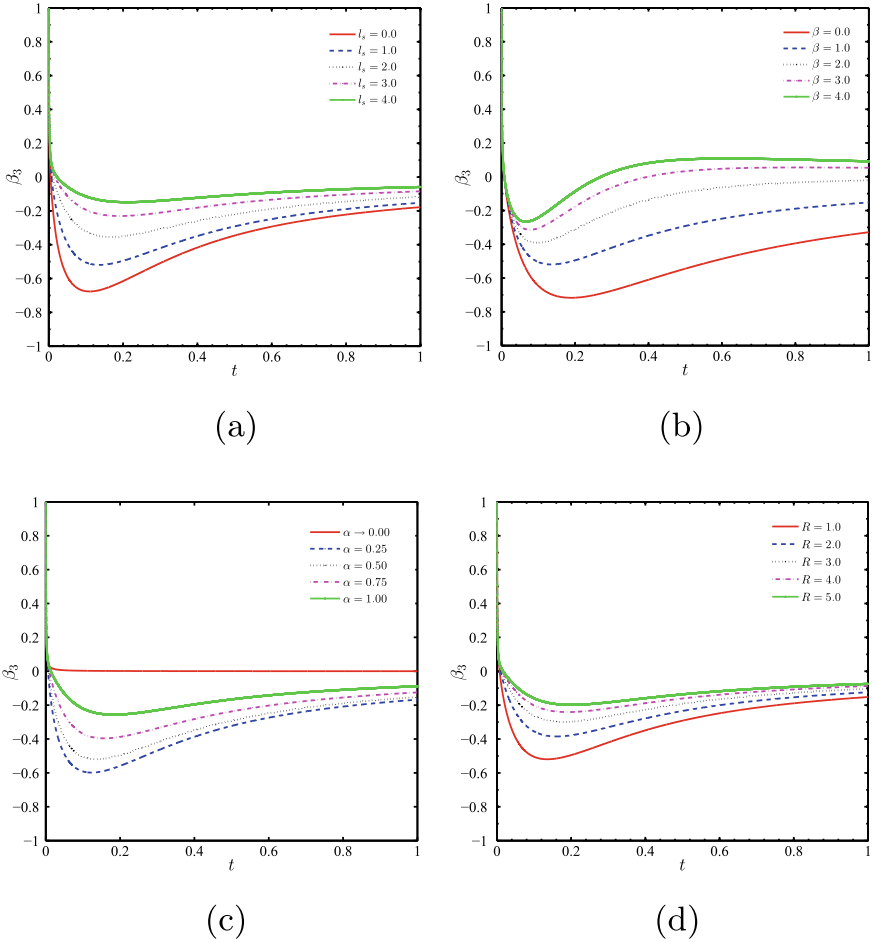


**Fig. 5** Kurtosis  $\beta_3$  of solute distribution with time for different values of **a** slip parameter  $l_s$ , **b** bed absorption  $\beta$ , **c** vegetation factor  $\alpha$  **d**  $R$ ; when  $\alpha = 0.5$ ,  $l_s = 1$ ,  $\beta = 1$ ,  $P_e = 100$  and  $R = 1$

- (c) The slip effect reduces the asymmetry of solute distribution, while the enlarged absorption introduces asymmetry in the tracer distribution.
- (d) At small dispersion time, the distribution of tracer deviates from Gaussianity. However, for large dispersion time with large  $l_s$ ,  $\beta$ , and  $R$ , the distribution tends to reach the normal distribution.

## References

1. Aris, R.: On the dispersion of a solute in a fluid flowing through a tube. *Proc. R. Soc. Lond.* **235**, 67–77 (1956)
2. Zeng, L., Chen, G.Q., Tang, H.S., Wu, Z.: Environmental dispersion in wetland flow. *Commun. Nonlinear Sci. Numer. Simulat.* **16**, 206–215 (2010)
3. Wu, Z., Li, Z., Chen, G.Q.: Multi-scale analysis for environmental dispersion in wetland flow. *Commun. Nonlinear Sci. Numer. Simulat.* **16**(8), 3168–3178 (2011)
4. Zeng, L., Chen, G.Q.: Ecological degradation and hydraulic dispersion of contaminant in wetland. *Ecol. Modell.* **222**, 293–300 (2011)
5. Wu, Z., Fu, X., Wang, G.: Concentration distribution of contaminant transport in wetland flows. *J. Hydrol.* **525**, 335–344 (2015)
6. Wang, P., Chen, G.Q.: Contaminant transport in wetland flows with bulk degradation and bed absorption. *J. Hydrol.* **552**, 674–683 (2017)
7. Wang, H., Zhu, Z., Li, S., Huai, W.: Solute dispersion in wetland flows with bed absorption. *J. Hydrol.*, pp. 124–149 (2019)
8. Dhar, S., Poddar, N., Kairi, R.R., Mazumder, B.S., Mondal, K.K.: Numerical study on dispersion of fine settling particles in a depth dominated wetland flow. *Commun. Nonlinear Sci. Numer. Simulat.* **96**, 105707 (2021)
9. Poddar, N., Das, S., Dhar, S., Mondal, K.K.: Semi-analytical study on environmental dispersion of settling particles in a width-independent wetland flow. *Environ. Fluid Mech.* **21**(4), 1–22 (2021)
10. Ng, C.O.: How does wall slippage affect hydrodynamic dispersion? *Microfluidics Nanofluidics* **10**(1), 47–57 (2010)
11. Munoz, J., Arcos, J., Bautista, O., Mendez, F.: Slippage effect on the dispersion coefficient of a passive solute in a pulsatile electro-osmotic flow in a microcapillary. *Phys. Rev. Fluids* **3**(8) (2018)

# Entropy Analysis for MHD Flow Subject to Temperature-Dependent Viscosity and Thermal Conductivity



Umesh Khanduri  and Bhupendra K. Sharma 

**Abstract** This research aimed to figure out how to optimise the entropy of MHD flow past a continuously stretching surface. The effect of temperature-dependent variables viscosity and electric conductivity has been taken into account. The fluid region is subjected to a uniform magnetic field. By using similarity analysis, the governing coupled partial differential equations (PDEs) that describe the model are turned into non-linear ordinary differential equations and then computed by employing “BVP4C” in MATLAB software. The effect of various pertinent parameters like Magnetic field parameter  $M$ , radiation parameter  $R$ , Grashof number  $Gr$ , Brinkman number  $Br$ , Reynold number  $Re$ , and a variation of variables viscosity  $\epsilon_1$  and electric conductivity  $\epsilon_2$  is analysed and presented graphically on velocity, temperature, entropy, and concentration profile. The comparison is based on previously published studies, and there is a considerable deal of agreement.

**Keywords** Entropy · Variable viscosity · Stretching sheet · MHD · Viscous dissipation

## 1 Introduction

Numerous researchers and analysts studied the effect of MHD flow across the stretching sheet due to its wide applications in industrial fields such as machine design, magnetic drug targeting, glass blowing, electronic chips and astrophysics sensors. Hayat et al. [1] demonstrated the influence of magnetic field and porous media on the flow velocity and heat transfer profile under the exponential stretching sheet condition.

---

The first author’s work is supported by CSIR, India, which provides the Ph.D. fellowship and CSIR file No. is 09/719(0105)/2019-EMR-I.

---

U. Khanduri (✉) · B. K. Sharma  
Department of Mathematics, Birla Institute of Technology and Science, Pilani, Rajasthan, India  
e-mail: [umeshkhanduri09@gmail.com](mailto:umeshkhanduri09@gmail.com)  
URL: <https://www.bits-pilani.ac.in>

© The Author(s), under exclusive license to Springer Nature Switzerland AG 2022  
S. Banerjee and A. Saha (eds.), *Nonlinear Dynamics and Applications*,  
Springer Proceedings in Complexity,  
[https://doi.org/10.1007/978-3-030-99792-2\\_38](https://doi.org/10.1007/978-3-030-99792-2_38)

457

This study also considered the velocity and thermal slip conditions and performed it by adopting the “Homotopy analysis method”. Further, motivated by the applications of boundary layer flow, Sandeep et al. [2] extended the above study on the thin stretching surface. Reddy et al. [3] considered the non-flat sheet and studied the impact of Williamson nanofluid with variable thermal conductivity. In this investigation, they considered the flow viscosity as temperature-dependent instead of constant. They observed that non-dimensional heat and mass transfer profiles rise significantly due to temperature-dependent viscosity inflow. The impact of heat source, radiation and chemical reaction under the convective boundary conditions has been studied by Ram et al. [4] and state that the magnitude of heat and mass transfer rates at the wall improves with the positive add in thermal and solute Biot numbers. Recently, Sharma et al. [5] studied a mathematical model of blood flow to identify the effects of Ohmic heating on the stretched arterial surface, claiming that heat transfer at the surface diminishes as the Ohmic heating parameter increases. Reddy et al. [6] studied the effect of different parameters on the blood flow inside the permeable wall with heat source and viscous dissipation. Tripathi et al. [7] employed the “Homotopy perturbation method” to study the arterial blood flow using the variable viscosity. They considered mild stenosis and hematocrit-dependent viscosity to analyze the blood flow behaviour. Further, they [8] examined the temperature-dependent viscosity and two-layer fluid model in blood flow with elliptical shaped stenosis.

Entropy generation is one of the fundamental phenomena associated with a level of irreversibility that occurs in any thermal process. Several researchers have examined the effect of entropy generation in MHD flow due to its application in many engineering systems. In order to reduce the irreversibility process, one can employ the second law of thermodynamic for designing better thermal equipment. Bejan [9] first introduced this concept by introducing the Bejan number, which signifies the thermal irreversibility to the total heat loss due to fluid frictions. Bhatti et al. [10] discussed the entropy generation on MHD Casson fluid with radiation and the effect of nanoparticles over the porous surface. Mandal et al. [11] studied the properties of nanoparticles by considering Buongiorno’s model and delineated the radiation and viscous dissipation effect on unsteady MHD flow. By considering viscous dissipation and the magnetic field effect, Afridi et al. [12] explored entropy generation in boundary layer flows. They perceived irreversible conduction as the principal source of entropy generation far beyond the boundary. Several other researchers [13, 14] have investigated the effect of Entropy generation on MHD flow.

In the present study, we have studied the effect of temperature-dependent variable viscosity and thermal conductivity on the stretching sheet, including entropy generation. The governing equations are converted into ordinary differential equations and then solved using MATLAB software by implementing “BVP4C”. The effect of various pertinent parameters had been analyzed and presented graphically on different profile like velocity, temperature, entropy, and concentration.



## 2 Mathematical Formulation

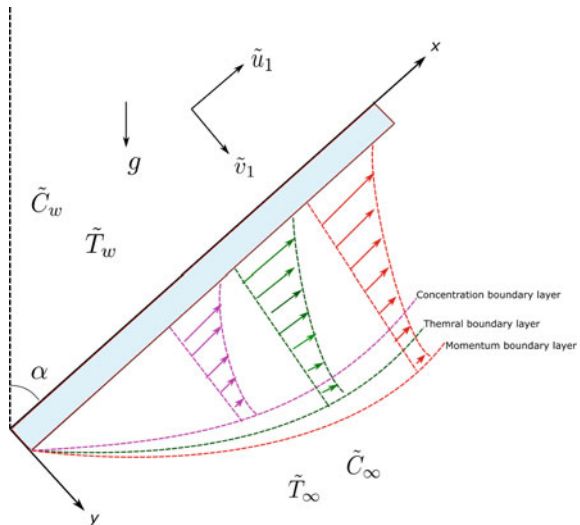
An unsteady, incompressible, two-dimensional MHD flow over a time-dependent stretching sheet in the X-Y plane is considered as depicted in Fig. 1. The sheet is aligned at an angle  $\alpha$  with the vertical and uniform inclined magnetic field  $B(t)$  is applied at an angle  $\xi$  to the sheet. At time  $t = 0$ , the sheet is stretched along the x-axis with velocity  $\tilde{U}_w(x, t) = \frac{dx}{(1-\chi t)}$ . Here,  $d$  and  $\chi$  are constant with conditions  $d > 0$ ,  $\chi \geq 0$  and  $\chi t < 1$ . The velocity components  $\tilde{u}_1$  and  $\tilde{v}_1$  are taken along x and y axis. Here,  $\tilde{T}$  and  $\tilde{T}_\infty$  denotes the temperature and ambient temperature of the fluid,  $\sigma$  is the electric conductivity,  $\beta$  is coefficient of temperature expansion,  $C_p^*$  is the specific heat,  $\tilde{\beta}^*$  is coefficient of concentration expansion,  $\tilde{C}$  and  $\tilde{C}_\infty$  denotes the concentration and ambient concentration of the fluid,  $D_B^*$  is mass diffusion coefficient, and  $g$  represent acceleration due to gravity. Temperature-dependent viscosity  $\mu(\tilde{T})$  is assumed to change linearly with temperature as follows:

$$\mu(\tilde{T}) = \mu_\infty \left[ 1 + \frac{\epsilon_1}{\Delta\tilde{T}} (\tilde{T}_w - \tilde{T}) \right] \tag{1}$$

Here  $\Delta\tilde{T} = \tilde{T}_w - \tilde{T}$ ,  $\epsilon_1$  is the temperature difference and viscosity variation parameter respectively. And, temperature-dependent thermal conductivity is given as:

$$K(\tilde{T}) = \kappa_\infty \left[ 1 - \frac{\epsilon_2}{\Delta\tilde{T}} (\tilde{T} - \tilde{T}_\infty) \right] \tag{2}$$

**Fig. 1** Pictorial representation of the problem



Here  $\epsilon_2$  denotes the thermal conductivity variation parameter. The magnetic Reynold number is assumed to be less than unity, so the induced magnetic field effect is negligible. The fluid properties are considered to be constant. Based on the order of magnitude along with Boussinesq approximation and using the above assumption, the governing equations are:

**Continuity:**

$$\frac{\partial \tilde{u}_1}{\partial x} + \frac{\partial \tilde{v}_1}{\partial y} = 0, \tag{3}$$

**Momentum:**

$$\begin{aligned} \frac{\partial \tilde{u}_1}{\partial t} + \tilde{u}_1 \frac{\partial \tilde{u}_1}{\partial x} + \tilde{v}_1 \frac{\partial \tilde{u}_1}{\partial y} = g\beta(\tilde{T} - \tilde{T}_\infty) \cos \alpha + g\tilde{\beta}^*(\tilde{C} - \tilde{C}_\infty) \cos \alpha + \frac{1}{\rho} \frac{\partial}{\partial y} \left( \mu(\tilde{T}) \frac{\partial \tilde{u}_1}{\partial y} \right) \\ - \frac{\sigma B^2(t)}{\rho} \sin^2 \xi \tilde{u}_1 - \frac{\mu(\tilde{T})}{\rho l_1(t)} \tilde{u}_1, \end{aligned} \tag{4}$$

**Energy:**

$$\frac{\partial \tilde{T}}{\partial t} + \tilde{u}_1 \frac{\partial \tilde{T}}{\partial x} + \tilde{v}_1 \frac{\partial \tilde{T}}{\partial y} = \frac{1}{\rho C_p^*} \frac{\partial}{\partial y} \left( K(\tilde{T}) \frac{\partial \tilde{u}_1}{\partial y} \right) - \frac{1}{\rho C_p^*} \frac{\partial q_r}{\partial y} + \frac{\mu(\tilde{T})}{\rho C_p^*} \left( \frac{\partial \tilde{u}_1}{\partial y} \right)^2 + \frac{\sigma B^2(t)}{\rho C_p^*} \sin^2 \xi \tilde{u}_1^2, \tag{5}$$

**Concentration:**

$$\frac{\partial \tilde{C}}{\partial t} + \tilde{u}_1 \frac{\partial \tilde{C}}{\partial x} + \tilde{v}_1 \frac{\partial \tilde{C}}{\partial y} = D_B^* \frac{\partial^2 \tilde{C}}{\partial y^2} - \Gamma(t)(\tilde{C} - \tilde{C}_\infty), \tag{6}$$

The associate boundary conditions are:

$$\begin{cases} \tilde{u}_1 = \tilde{U}_w + H\mu \frac{\partial \tilde{u}_1}{\partial y}, \quad \tilde{C} = \tilde{C}_w + J \frac{\partial \tilde{C}}{\partial y}, \quad \tilde{v}_1 = \tilde{V}_w, \quad \tilde{T} = \tilde{T}_w + P \frac{\partial \tilde{T}}{\partial y}, & \text{at } y = 0 \\ \tilde{u}_1 \rightarrow 0, \quad \tilde{C} \rightarrow \tilde{C}_\infty, \quad \tilde{T} \rightarrow \tilde{T}_\infty & \text{as } y \rightarrow \infty. \end{cases} \tag{7}$$

Where,  $H = H_0(1 - \chi t)^{\frac{1}{2}}$  represent the velocity slip factor,  $P = P_0(1 - \chi t)^{\frac{1}{2}}$  represent the thermal slip factor,  $J = J_0(1 - \chi t)^{\frac{1}{2}}$  represent the concentration slip factor. The surface temperature  $\tilde{T}_w(x, t)$ , stretching velocity  $\tilde{U}_w(x, t)$ , and the concentration  $\tilde{C}_w(x, t)$  are given as:

$$\tilde{T}_w = \tilde{T}_\infty + \frac{cx}{1 - \chi t}, \quad \tilde{U}_w = \frac{dx}{1 - \chi t}, \quad \tilde{C}_w = \tilde{C}_\infty + \frac{ex}{1 - \chi t}.$$

Here,  $c$  and  $e$  are constant and satisfies the condition  $c, e \geq 0$  and  $\chi t < 1$ . In Eq. (7),  $\tilde{V}_w$  represent the injection/suction velocity:

$$\tilde{V}_w = -\sqrt{\frac{\tilde{U}_w}{x}} f(0). \tag{8}$$

The mass transfer at the wall is represented by Eq. (7) with velocity  $\tilde{V}_w > 0$  in which  $\tilde{V}_w > 0$  represents injection and  $\tilde{V}_w < 0$  represents the suction case. The expression  $l_1(t)$  used in the Eq. (4) represents the time-dependent permeability and it satisfies the equation  $l_1(t) = l_2(1 - \chi t)$ . Let us now consider the magnetic field  $B(t) = B_0(1 - \chi t)^{-\frac{1}{2}}$  and chemical reaction parameter as  $\Gamma(t) = \Gamma_0(1 - \chi t)^{-1}$ . Here  $B_0$  represent the magnetic field at initial time, and  $\Gamma_0$  as constant. In Eq. (5), the radiative heat flux [6] is approximate by Rosseland mean approximation and it is simplified as:

$$q_r = -\frac{4\sigma^*}{3k^*} \frac{\partial \tilde{T}^4}{\partial y} . \tag{9}$$

Here  $k^*$  and  $\sigma^*$  are the mean absorption coefficient and the Stefan-Boltzman constant, respectively. We linearize the term  $\tilde{T}^4$  using a Taylor series about the free steam function  $\tilde{T}_\infty$ , ignoring higher order terms by assuming small temperature differences.

$$\tilde{T}^4 \cong 4\tilde{T} \tilde{T}_\infty^3 - 3\tilde{T}_\infty^4 . \tag{10}$$

Now, similarity transformations are defined as:

$$\begin{cases} \eta = d^{\frac{1}{2}} v^{-\frac{1}{2}} (1 - \chi t)^{-\frac{1}{2}} y, \\ \psi = d^{\frac{1}{2}} x v^{\frac{1}{2}} (1 - \chi t)^{-\frac{1}{2}} f(\eta), \\ \theta(\eta) = \left( \frac{\tilde{T} - \tilde{T}_\infty}{\tilde{T}_w - \tilde{T}_\infty} \right), \\ \phi(\eta) = \left( \frac{\tilde{C} - \tilde{C}_\infty}{\tilde{C}_w - \tilde{C}_\infty} \right). \end{cases} \tag{11}$$

Here,  $\eta$  represent the independent similarity variable,  $\psi$  denotes the stream function and it is defined as  $\tilde{u}_1 = \frac{\partial \psi}{\partial y}$ ,  $\tilde{v}_1 = -\frac{\partial \psi}{\partial x}$ , which automatically satisfies Eq. (3). Now, substitute Eqs. (10) and (11) into Eqs. (4)–(6), to get differential equations as:

$$(1 + e_1(1 - \theta))f''' + ff'' - A \left( f' + \frac{1}{2}\eta f'' \right) - (f')^2 + Gr\theta \cos \alpha + Gc\phi \cos \alpha - e_1\theta' f'' - M^2 f' \sin^2 \xi - (1 + e_1(1 - \theta))\frac{f'}{K} = 0 , \tag{12}$$

$$\frac{(1 + R + e_2\theta)}{Pr} \theta'' - A \left( \theta + \frac{1}{2}\eta\theta' \right) + f\theta' - f'\theta + Ec(1 + e_1(1 - \theta))(f'')^2 + Ec * M^2 (f')^2 \sin^2 \xi + e_2 \frac{(\theta')^2}{Pr} = 0, \tag{13}$$

$$\frac{1}{Sc} \phi'' + f\phi' - f'\phi - A \left( \phi + \frac{1}{2}\eta\phi' \right) - \gamma\phi = 0 , \tag{14}$$

The associated boundary conditions are:

**Table 1** Various dimensionless parameters involved in Eqs. (12)–(14)

$M = B_0 \sqrt{\frac{\sigma}{\rho d}}$	$Gr = \frac{g\beta x(\tilde{T}_w - \tilde{T}_\infty)}{\tilde{U}_w^2}$	$A = \frac{\chi}{d}$	$Ec = \frac{\tilde{U}_w^2}{C_p^*(\tilde{T}_w^* - \tilde{T}_\infty)}$
$Gc = \frac{g\beta^* x(\tilde{C}_w - \tilde{C}_\infty)}{\tilde{U}_w^2}$	$Sc = \frac{\nu}{D_B^*}$	$Pr = \frac{\mu_\infty C_p^*}{\kappa_\infty}$	$\gamma = \frac{\Gamma_0}{d}$
$R = \frac{16\sigma^* \tilde{T}_\infty^3}{3\kappa_\infty k^*}$	$\Omega = \frac{\tilde{T}_w - \tilde{T}_\infty}{\tilde{T}_\infty}$	$K = \frac{dl_2}{\nu}$	$Re = \frac{U_w x}{\nu}$
$Br = \frac{\mu_\infty U_w^2}{\kappa_\infty \Delta T}$	$\nu = \frac{\mu_\infty}{\rho}$	$\Lambda = \frac{RD\tilde{C}_\infty}{\kappa}$	$\Psi = \frac{\tilde{C}_w - \tilde{C}_\infty}{\tilde{C}_\infty}$

$$\begin{cases} f = S, & f' = 1 + S_f f''(0), & \theta = 1 + S_t \theta'(0), & \phi = 1 + S_c \phi'(0) & \text{at } \eta = 0, \\ f' \rightarrow 0, & \theta \rightarrow 0, & \phi \rightarrow 0, & & \text{as } \eta \rightarrow \infty. \end{cases} \tag{15}$$

The non-dimensional thermal slip  $S_t$ , velocity slip  $S_f$ , and solutal slip  $S_c$  parameters are defined as:

$$S_t = P_0 \sqrt{\frac{d}{\nu}}, \quad S_f = H_0 \rho \sqrt{d\nu}, \quad S_c = J_0 \sqrt{\frac{d}{\nu}}.$$

Here, prime denotes the differentiation with respect to  $\eta$ . In Eqs. (12)–(14), if  $A = 0$ , it will correspondence that the problem reduce to the steady state flow. Also, in Eq. (15), if  $S > 0$ , it indicates suction,  $S < 0$  indicates injection. The dimensionless numbers and parameter used in Eqs. (12)–(14) are specified in Table 1.

### 2.1 Quantities of Physical Interest

The quantities like heat transfer rate, skin friction coefficient, and mass transfer are defined as:

$$Nu_x = \frac{xq_w}{K(\tilde{T})(\tilde{T}_w - \tilde{T}_\infty)}, \quad C_f = \frac{\tau_w}{\rho \tilde{U}_w^2}, \quad Sh_x = \frac{m_w x}{D_B^* \rho (\tilde{C}_w - \tilde{C}_\infty)}. \tag{16}$$

Where the surface heat flux, wall shear stress, and mass flux are given by:

$$\begin{cases} q_w = -K(\tilde{T}) \left( \frac{\partial \tilde{T}}{\partial y} \right)_{y=0}, \\ \tau_w = \mu(\tilde{T}) \left( \frac{\partial \tilde{u}_1}{\partial y} \right)_{y=0}, \\ m_w = -\rho D_B^* \left( \frac{\partial \tilde{C}}{\partial y} \right)_{y=0}. \end{cases} \tag{17}$$

Use Eq. (17), to rewrite quantity (16) as:

$$Nu_x = -Re_x^{\frac{1}{2}}\theta'(0), \quad C_f = 2(1 + \epsilon_1(1 - \theta))Re_x^{-\frac{1}{2}}f''(0), \quad Sh_x = -Re_x^{\frac{1}{2}}\phi'(0). \tag{18}$$

The quantity like Nusselt number  $Nu_x$ , skin-friction coefficient  $C_f$ , and Sherwood number  $Sh_x$  are dependent on the variation of the factors  $-\theta'(0)$ ,  $f''(0)$ , and  $-\phi'(0)$  respectively.

### 3 Entropy

Expression for entropy generation is defined as:

$$S'''_G = \frac{K(\tilde{T})}{\tilde{T}_\infty^2} \left\{ \left( \frac{\partial \tilde{T}}{\partial y} \right)^2 + \frac{16\sigma^* \tilde{T}_\infty^3}{3k^*k} \left( \frac{\partial \tilde{T}}{\partial y} \right)^2 \right\} + \frac{\mu(\tilde{T})}{\tilde{T}_\infty} \left( \frac{\partial \tilde{u}_1}{\partial y} \right)^2 + \frac{\sigma}{\tilde{T}_\infty} (\tilde{u}_1^2 B^2) + \frac{\mu(\tilde{T})}{\tilde{T}_\infty K_1} \tilde{u}_1^2 + \frac{RD}{\tilde{T}_\infty} \frac{\partial \tilde{T}}{\partial y} \frac{\partial \tilde{C}}{\partial y} \tag{19}$$

Characteristic entropy rate is defined as:

$$S'''_0 = \frac{K(\tilde{T})(\Delta \tilde{T})^2}{x^2 \tilde{T}_\infty^2} \tag{20}$$

Dimensionless entropy generation is defined as:

$$N_G = \frac{S'''_G}{S'''_0} \tag{21}$$

Use Eqs. (20)–(21) to write the entropy generation number  $N_G$  as:

$$N_G = Re_x \left( 1 + \frac{R}{1 + \epsilon_2 \theta} \right) (\theta')^2 + \frac{ReBr}{\Omega} \left( 1 + \frac{1}{K} \right) \left( \frac{1 + \epsilon_1(1 - \theta)}{1 + \epsilon_2 \theta} \right) + \frac{ReBrM}{\Omega(1 + \epsilon_2 \theta)} (f')^2 + Re\Psi \frac{\Lambda}{\Omega} \theta' \phi'. \tag{22}$$

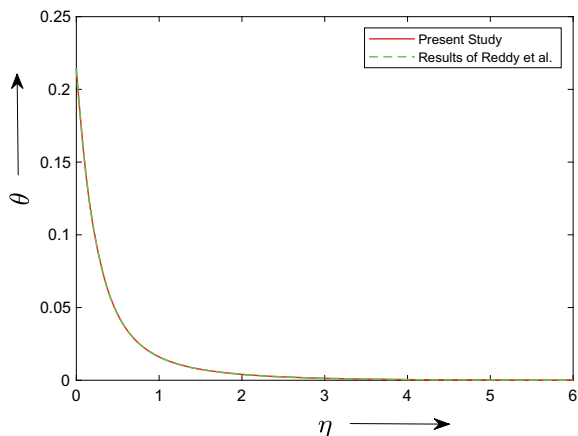
Here,  $Re$ ,  $Br$ , and  $\Omega$  are Reynolds number, Brinkmann number, and temperature difference parameters respectively.

### 4 Result and Discussion

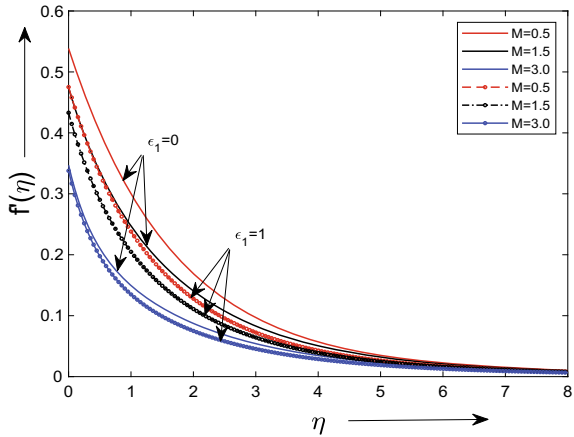
This section deals with the characteristic behaviours of different relevant parameters on velocity, temperature, entropy, and concentration profile. For numerical results, the values of pertinent parameters are given as:  $M = 0.4, K = 0.5, Gr = 2, Pr = 0.71, \epsilon_1 = 0.1, A = 0.5, Gc = 2, \xi = \pi/4, \alpha = \pi/4, \epsilon_2 = 0.1, Sc = 0.6, Br=0.5, Re = 0.5, S_f = 1.5, S_t = 1, S = 0.5, S_p = 0.5$ . Moreover, the values of specific parameters are kept constant throughout the study unless mentioned in the appropriate graphs. Figure 2 depicts the validation of the previous published work for temperature profile at  $R = 1.5$  with current work. Reddy et al. [6] used the shooting technique to solve the dimensionless governing equations. And, in the current work, we used BVP4C technique that works on the collocation method.

Figure 3 shows the decreasing nature with both parameters  $M$  and  $\epsilon_1$ . As the magnetic field parameter  $M$  increases from 0.5 to 3, the velocity profile  $f'(\eta)$  decreases; this has happened due to an enhancement of Lorentz force that decreases the fluid velocity. It depicts the significant phenomena used in the medical field to regulate human blood by varying magnetic field. Figure 4 depicts the velocity profile with varying parameter  $Gr$  and  $\epsilon_1$ . From the figure, it can be interpreted that the velocity profile  $f'(\eta)$  will increase if the parameter  $Gr$  increases while the reverse trend is observed with  $\epsilon_1$ . The velocity profile is shown in Fig. 5 for various values of the inclination angle  $\alpha$  and viscosity parameter  $\epsilon_1$ . The velocity profile  $f'(\eta)$  decreases with an increase in both the parameters  $\alpha$  and viscosity parameter  $\epsilon_1$ . At an angle  $\alpha = 0$ , there is a 17.80% decrement in the velocity profile for a change in viscosity parameter  $\epsilon_1$  from 0 to 1. The decrement in velocity profile with varying  $\alpha$  can be explained by the fact that changing the inclination angle ( $\alpha = 0, \pi/4, \pi/3$ ) results in a reduction of the term  $\cos \alpha$  in the momentum equation, which lowers the buoyancy force due to thermal diffusion. The temperature profile increases with an increase in the parameter  $R$  and thermal conductivity  $\epsilon_2$ . An increment in thermal conductivity

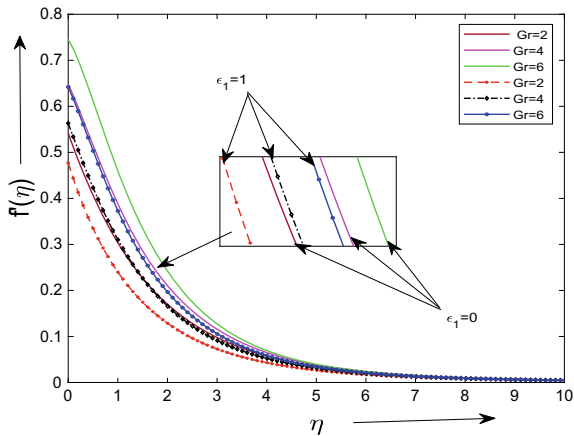
**Fig. 2** Comparison on Temperature profile for  $R = 1.5$



**Fig. 3** Velocity profile  $f'(\eta)$  by varying  $M$



**Fig. 4** Non-dimensional Velocity profile by varying  $Gr$



signifies the faster rate at which the heat will be transferred in the fluid. It can be noted from the Fig. 6 that the temperature profile enhances as the radiation parameter varies from  $R = 0$  to  $R = 1.5$ .

In Fig. 7, we analyzed the change in temperature profile by varying parameters  $\epsilon_2$  and  $Ec$ . Here,  $Ec$  (0.5, 1.5, 3) is positive, which signifies that the heat is transferred from the stretching sheet to the fluid. Eckert number can be characterised as the self-heating of the fluid because dissipation effect enhances the thermal boundary layer. Increasing both parameters  $\epsilon_2$  and  $Ec$  will raise the temperature profile. As Prandtl number  $Pr$  varies from 2 to 6, the fluid's thermal conductivity decreases, reducing the thermal boundary layer. Similarly, the temperature profile increases with an increase in thermal conductivity parameter,  $\epsilon_2$  from 0 to 1. Higher thermal conductivity means that the fluid will dissipate heat more rapidly. It signifies that the temperature profile decreases with an increase in the parameter  $Pr$  while the reverse trend is observed for thermal conductivity parameter  $\epsilon_2$  as depicted in Fig. 8. It is noted from Fig. 9

**Fig. 5** Non-dimensional Velocity profile by varying  $\alpha$

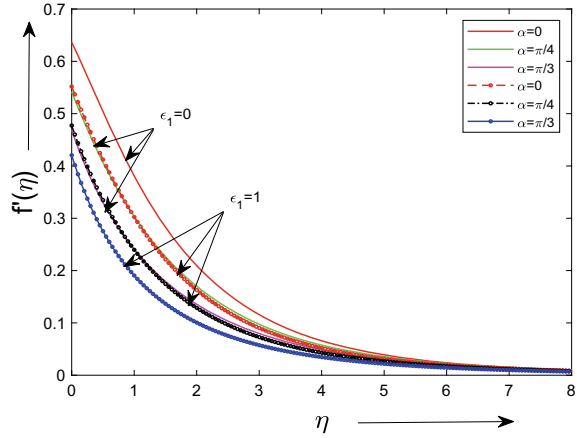


**Fig. 6** Variation in temperature profile by varying  $R$

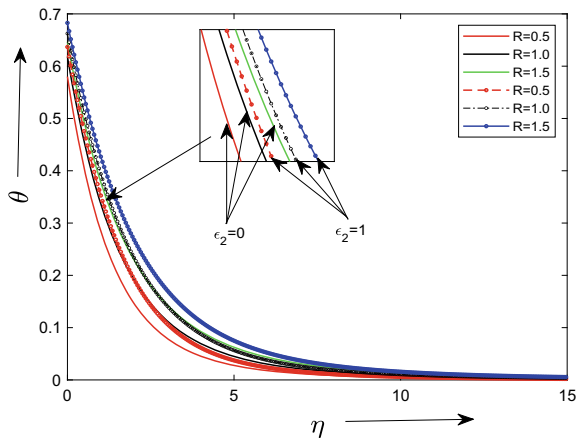


**Fig. 7** Variation in temperature profile by varying  $Ec$

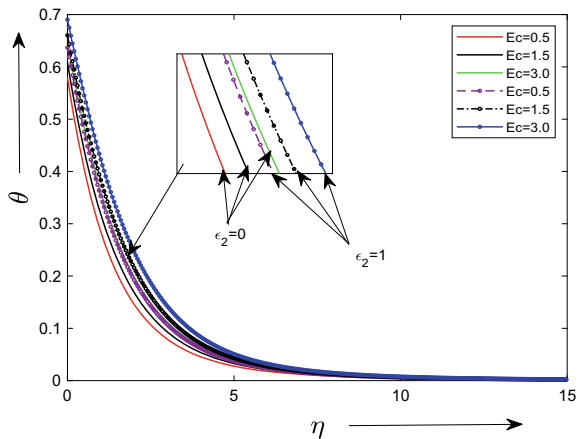




**Fig. 8** Variation in temperature profile by varying  $Pr$

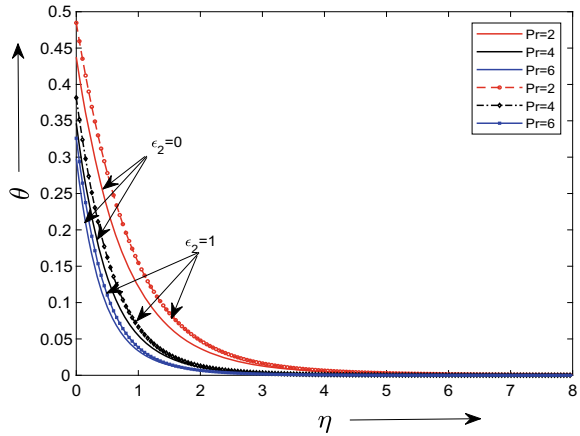
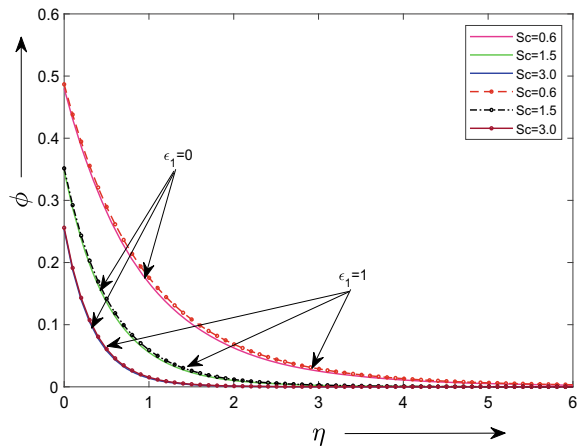


**Fig. 9** Variation in concentration profile by varying  $Sc$



that the concentration profile decreases with an increase in parameter  $Sc$ . Although, little variation is observed with a change in viscosity parameter  $\epsilon_1$  from 0 to 1. As the Schmidt number is inversely proportional to the diffusion coefficient, it declines the solutal boundary layer. Figures 10, 11, 12 and 13 illustrate the effect of different parameters on entropy number  $N_G$ .

Entropy determines the possible ways of energy distribution in a system of molecules. In other words, the measurable physical quantity that is associated with the disordered movement of particles. The knowledge of entropy optimization helps in enhancing the mechanical device's performance. Therefore, it is essential to know the effect of different parameters associated with entropy change. Figure 10 shows the variation of entropy number  $N_G$  with variation of  $Br$  and  $\eta$ . Entropy increases with an increase in parameter  $Br$  but decreases asymptotically for  $\eta$ . Brinkman number is one parameter that correlates with the system's convective heat transfer in laminar and transient flow. Its application can be seen in the microchannels flow, such as

**Fig. 10** Surface plot of  $N_G$  with axial direction  $\eta$  and  $Br$

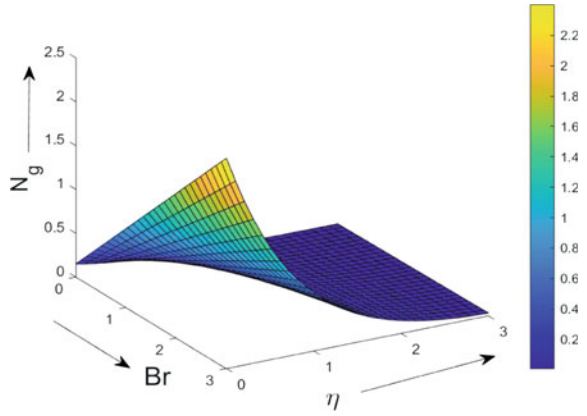


**Fig. 11** Surface plot of  $N_G$  with axial direction  $\eta$  and  $R$

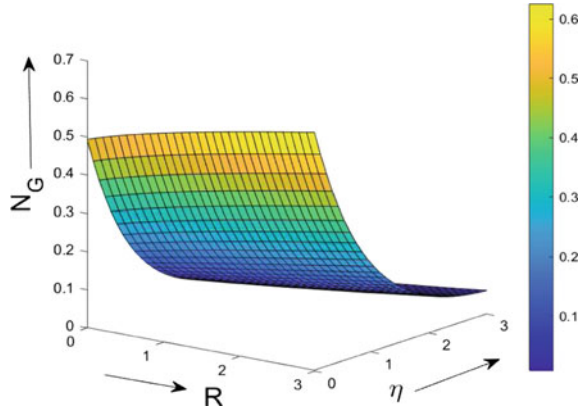


**Fig. 12** Surface plot of  $N_G$  with axial direction  $\eta$  and  $Re$

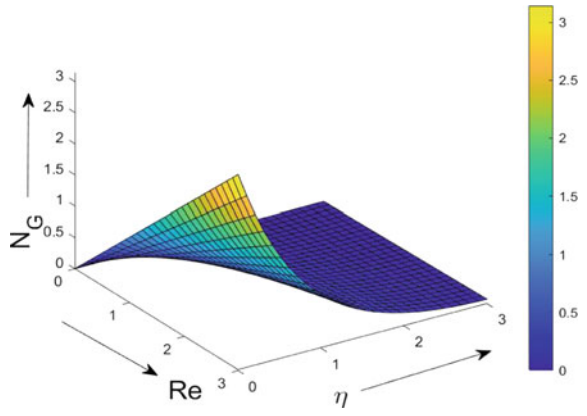
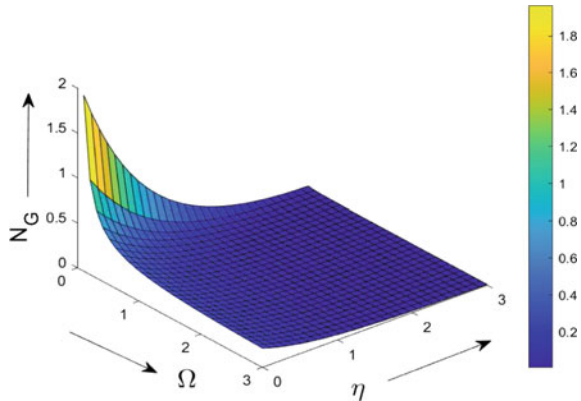


**Fig. 13** Surface plot of  $N_G$  with axial direction  $\eta$  and  $\Omega$



cooling integrated circuit (IC) chips. The boost in entropy number due to an increase in Brinkman  $Br$  can be explained by the fact that the Brinkman number signifies the heat source in the fluid region and, together with the heat generated from the wall, enhances the entropy rate.

Increasing the radiation parameter will increase more heat in the system, resulting in the uplifting of the entropy rate. It is noted from the Fig. 12 that the entropy rate  $N_G$  increases as the Reynolds number  $Re$  increases and decreases asymptotically with  $\eta$ . As the value of the Reynolds number increases, the frictional resistance increases, resulting in more frictional irreversibility. This causes an increase in entropy. In contrast, the entropy decreases with an increase in the axial direction. The initial temperature difference is an essential criterion for the critical design of thermal equipment. Figure 13 display the surface plot of entropy with parameters  $\Omega$  and  $\eta$ . It shows the decreasing trend of entropy with an increase in both the parameters  $\Omega$  and  $\eta$ . For a small value of temperature difference, the system’s entropy will be low due to the dominant effect of viscous friction. At  $\eta = 0$  and with the change in magnitude of  $\Omega$  from 0.103 to 3, there is a decrease of 89.22% in the entropy rate. Similarly, there is a 95.86% decrease in entropy rate with parameter  $\eta$  from 0 to 3.

## 5 Conclusion

In this study, we addressed the entropy generation on MHD fluid over a stretching sheet with variable viscosity  $\mu(\tilde{T})$  and thermal conductivity  $K(\tilde{T})$  by altering the parameter  $\epsilon_1$  and  $\epsilon_2$ . The governing coupled PDEs that characterise the model are transformed into non-linear ODEs using similarity analysis and then solved using MATLAB software by implementing the “BVP4C” technique. The current study can aid scientists in comprehending their findings and using this approach to mechanical and industrial operations, including material processing, fuel cells, gas turbines, ventilation and renewable energy. From the above discussion, we concluded that

the velocity profile declines with increased viscosity parameter  $\epsilon_1$  and magnetic field parameter  $M$ . Positive growth in an Eckert number  $Ec$  and viscosity variation parameters are responsible for enhancing the temperature profile. Increasing parameters  $Br$  and  $R$  will increase the Entropy generation  $N_G$  profile, while the reverse trend is observed with temperature difference parameter  $\Omega$ .

## References

- Hayat, T., Shafiq, A., Alsaedi, A., Shahzad, S.A.: Unsteady MHD flow over exponentially stretching sheet with slip conditions. *Appl. Math. Mech.* **37**(2), 193–208 (2016). <https://doi.org/10.1007/s10483-016-2024-8>
- Babu, M.J., Sandeep, N., Ali, M.E., Nuhait, A.O.: Magnetohydrodynamic dissipative flow across the slendering stretching sheet with temperature dependent variable viscosity. *Results Phys.* **7**, 1801–1807 (2017). <https://doi.org/10.1016/j.rinp.2017.05.018>
- Reddy, S., Naikoti, K., Mehdi Rashidi, M.: MHD flow and heat transfer characteristics of Williamson nanofluid over a stretching sheet with variable thickness and variable thermal conductivity. *Trans. A. Razmadze Math. Inst.* **171**(2), 195–211 (2017). <https://doi.org/10.1016/j.tmi.2017.02.004>
- Sharma, R.P., Ibrahim, S.M., Mishra, S.R., Tinker, S.: Impact of dissipative heat and radiative heat on MHD viscous flow through a slendering stretching sheet with temperature-dependent variable viscosity. *Heat Transf.* **50**(8), 7568–7587 (2021). <https://doi.org/10.1002/htj.22243>
- Sharma, Bhupendra K., Kumawat, Chandan: Impact of temperature dependent viscosity and thermal conductivity on MHD blood flow through a stretching surface with ohmic effect and chemical reaction. *Nonlinear Eng.* **10**(1), 255–271 (2021). <https://doi.org/10.1515/nleng-2021-0020>
- Reddy, A., Bala, P., Reddy, S.R.R., Suneetha, S.: magnetohydro dynamic flow of blood in a permeable inclined stretching surface with viscous dissipation, non-uniform heat source/sink and chemical reaction. *Front. Heat Mass Transf. (FHMT)* **10**, 22 (2018). <https://doi.org/10.5098/hmt.10.22>
- Tripathi, B., Sharma, B.K.: Effect of variable viscosity on MHD inclined arterial blood flow with chemical reaction. *Int. J. Appl. Mech. Eng.* **23**(3) (2018). <https://doi.org/10.2478/ijame-2018-0042>
- Tripathi, B., Kumar Sharma, B., Sharma, M.: Modeling and analysis of MHD two-phase blood flow through a stenosed artery having temperature-dependent viscosity. *Eur. Phys. J. Plus* **134**(9), 466 (2019) . <https://doi.org/10.1140/epjp/i2019-12813-9>
- Bejan, Adrian: A study of entropy generation in fundamental convective heat transfer. *J. Heat Transf.* **101**(4), 718–725 (1979). <https://doi.org/10.1115/1.3451063>
- Qing, J., Mubashir Bhatti, M., Ali Abbas, M., Mehdi Rashidi, M., El-Sayed Ali, M.: Entropy generation on MHD Casson nanofluid flow over a porous stretching/shrinking surface. *Entropy* **18**(4), 123 (2016). <https://doi.org/10.3390/e18040123>
- Shit, G.C., Mandal, S.: Entropy analysis on unsteady MHD flow of Casson nanofluid over a stretching vertical plate with thermal radiation effect. *Int. J. Appl. Comput. Math.* **6**(1), 1–22 (2020). <https://doi.org/10.1007/s40819-019-0754-4>
- Afridi, M.I., Qasim, M., Khan, I., Shafie, S., Saleh Alshomrani, A.: Entropy generation in magnetohydrodynamic mixed convection flow over an inclined stretching sheet. *Entropy* **19**(1), 10 (2017). <https://doi.org/10.3390/e19010010>
- Shah, Zahir, Kumam, Poom, Deebani, Wejdan: Radiative MHD Casson nanofluid flow with activation energy and chemical reaction over past nonlinearly stretching surface through Entropy generation. *Sci. Reports* **10**(1), 1–14 (2020). <https://doi.org/10.1038/s41598-020-61125-9>

14. Megahed, A.M., Gnanaswara Reddy, M., Abbas, W.: Modeling of MHD fluid flow over an unsteady stretching sheet with thermal radiation, variable fluid properties and heat flux. *Math. Comput. Simul.* **185**, 583–593 (2021). <https://doi.org/10.1016/j.matcom.2021.01.011>

# A Numerical Investigation on Transport Phenomena in a Nanofluid Under the Transverse Magnetic Field Over a Stretching Plate Associated with Solar Radiation



Shiva Rao  and P. N. Deka 

**Abstract** This numerical investigation considers the solar radiation effect on a nanofluid over a stretching plate acted upon by a transverse magnetic field focusing on the stagnation points. Here, linear Rosseland approximation is applied for solar radiation. The physical flow problem is modeled using the sets of partial differential equations, which are then transformed into a set of non-linear ordinary differential equations by using the appropriate similarity transformation. We have a new `bvp4c` solver in the MATLAB platform to solve the equations numerically to investigate the solar radiation effect on various flow parameters associated with MHD nanofluids such as Brownian motion, velocity, temperature and concentration. A comparative analysis is performed for the results with previous studies in some limiting cases to prove the efficiency of the numerical approach. The results have been presented graphically as well as in tabular form to intricate the flow pattern.

**Keywords** MHD flow · Solar radiation · Stretching plate · Rosseland approximation · Stagnation point · Brownian motion

## 1 Introduction

Growing energy demand and associated energy crises coupled with environmental issues are now considered with priority across the globe. Attention towards renewable energy has increased as these can replace fossil fuels and reduce the ejection of Green House Gases. Out of different renewable energies like hydro-power from water, geothermal energy, wind energy, biomass from plants, solar energy is one of the cleanest renewables that comes directly from the sun and can be transformed into electricity directly by photoelectric effect and into heat by photo-thermal conversion. Hence, the implementation of solar energy has gained mass attention recently.

Voltaic cells and solar thermal plants are the main gateways to use solar energy and its efficiency can be increased by improving solar energy absorption. The dependence

---

S. Rao (✉) · P. N. Deka  
Dibrugarh University, Dibrugarh, Assam 786004, India  
e-mail: [shivarao374@gmail.com](mailto:shivarao374@gmail.com)

© The Author(s), under exclusive license to Springer Nature Switzerland AG 2022  
S. Banerjee and A. Saha (eds.), *Nonlinear Dynamics and Applications*,  
Springer Proceedings in Complexity,  
[https://doi.org/10.1007/978-3-030-99792-2\\_39](https://doi.org/10.1007/978-3-030-99792-2_39)

on fossil fuel can be reduced by using renewable energy which mainly relies on the absorption of solar energy and conversion into thermal energy. However, there is a significant loss of energy in the absorption of sunlight by collecting panels. The weak thermo-physical properties of convectional fluids make it non-viable to construct heat exchangers with greater efficiency [1]. The water-dispersed nano-particles are found to improve the absorption of sunlight [27]. To increase the absorption efficiency different researchers have tested different nano-particles. In recent decades, nanofluids are extensively used in collectors as they elevate greater heat elimination due to their superiority in thermo-physical properties in comparison to traditional fluid [20].

Nowadays, industrial fluids are studied by researchers very intensively. Recently, there has been a great discussion about the parameters behind the heat transfer in nanofluid, despite many studies done already [33]. Nanofluids are made by the suspension of nanoparticles in the base fluid. Choi [5] was the first researcher to discover that the suspended nanoparticles in the base fluid could enhance the thermal conductivity. Lee et al. [19] measured the thermal conductivity of different metal oxides and revealed that both shape and size played an important role in enhancing thermal conductivity of the nanofluid. Nanoparticles not only increase thermal conductivity but also increase the heat transfer capacity by convection [25]. Eastman et al. [7] by their study conclude that the addition of copper nanoparticles with volume fraction less than 1% in ethylene glycol could increase the thermal conductivity up to 40%. Buonigiorno [4] attempted to explain the increase in the thermal conductivity of the nanofluid by pointing out two slip mechanism i.e., Brownian motion and thermophoresis for effective enhancement of thermal conductivity of the base fluid. MHD nanofluid has a great significance in engineering. Buonigiorno's model [4] of viscous and incompressible nanofluid flow between a vertical flat plate and a porous medium was investigated by Nield and Kuznetsov [18]. Khan and Pop [16] were the first to investigate the evolution of heat transfer and nanoparticle volume fraction in a nanofluid across a stretching sheet. Rana and Bhargava [28] used the FEM approach to solve Khan and Pop's problem for the nonlinearly stretching sheet. Makinde and Aziz [23] investigated the heat transfer properties in nanofluid flow utilising convective boundary conditions. The convectional flow in a square duct in the presence of a high transverse magnetic field was investigated by Chutia and Deka [6]. Some recent work on MHD nanofluid are presented in Refs. [12, 13, 15, 30].

Thermal radiation on natural convection has become a great importance due to its wide range application in physics and engineering especially in the design of components and equipment, space technology and gas turbine, etc. Unlike conduction and convection, thermal radiation does not need any medium to transmit the heat. These properties make thermal radiation much significant in heat transfer of MHD nanofluid as it reduces the loss of heat. England and Emery [8] investigated the effect of thermal radiation on the natural convective boundary layer flow along vertical plate for absorbing and non-absorbing gases. Kumar et al. [17] presented an idea of the impact of thermal radiation on nanofluid model for flow and heat transfer over an infinite vertical plate under magnetic field and viscous dissipation.

Ali et al. [2] studied the impact on thermal radiation and non-uniform heat flux of the MHD hybrid nanofluid over the stretching cylinder. The effect of hall current which chemical reaction and thermal radiation of a nanofluid flow in a rotating channel was numerically investigated by Lv et al. [22].

Improvement in Solar collector model is one of the major priority for the use of solar energy. Nanofluid is used as a main operating fluid in most of the solar collector nowadays. Javadi et al. [14] have studied the working principle of nanofluid on solar collector in details. Yousefi et al. [35] used  $Al_2O_3$ -water nanofluids as an operating fluid in solar collector and draw a very interesting conclusion that the nanofluid based model increases the efficiency of solar collector by 28.3%. Faizal et al. [9] claim the possibility to make a smaller solar collector, using different nanofluid which produces the same output as the larger one. The action of  $CuO$ -water and water in a solar collector was compared by Liu et al. [21]. Sarkar and Kundu [31] studied an unsteady MHD nanofluid near a spinning sphere in the presence of solar radiation. Mushtaq et al. [24] studied the radiation effect of the MHD nanofluid flow in the two-dimensional form through the Runge–Kutta method with an appropriate shooting technique. Ghasemi et al. [10, 11] used the Keller box and Differential quadrature method (DQM) to conduct a numerical analysis of Mushtaq's work under the effects of radiation.

In this study, an investigation is done numerically with the following highlights:

- PDE's are reduced to the sets of ODE's by using similarity transformation.
- MATLAB build-in solver `bvp4c` is used to solve the ODE's to investigate the non-linear radiative transport phenomena in nanofluid flow under the action of transverse magnetic field under solar radiation.
- This study presents a nanofluid model for a solar collector by considering some thermal effects which can increase its efficiency to much extend.
- The study presents the velocity, temperature and concentration profiles to investigate the effect of solar radiation along with the other MHD flow parameters.
- The validity of the current results is verified by Mushtaq et al. [24]'s previous study.
- Graphical results are discussed in details with physical reasoning to clarify findings.
- The Nusselt number and Sherwood number for various parameters are thoroughly explored.

## 2 Mathematical Formulation

In the present study, we consider a steady two dimensional flow of a nanofluid under transverse magnetic field over a stretching sheet under the Solar radiation. As shown in Fig. 1 the stretching sheet is placed at  $y = 0$  and the fluid start flowing towards  $x$ -axis when the sheet is stretched (force applied) along the same axis. The magnetic field  $B_o$  acts perpendicular to the direction of the flow. The stretching velocity along the  $x$ -axis is  $u_w = ax$  and velocity outside the boundary layer is  $u_\infty = bx$ .



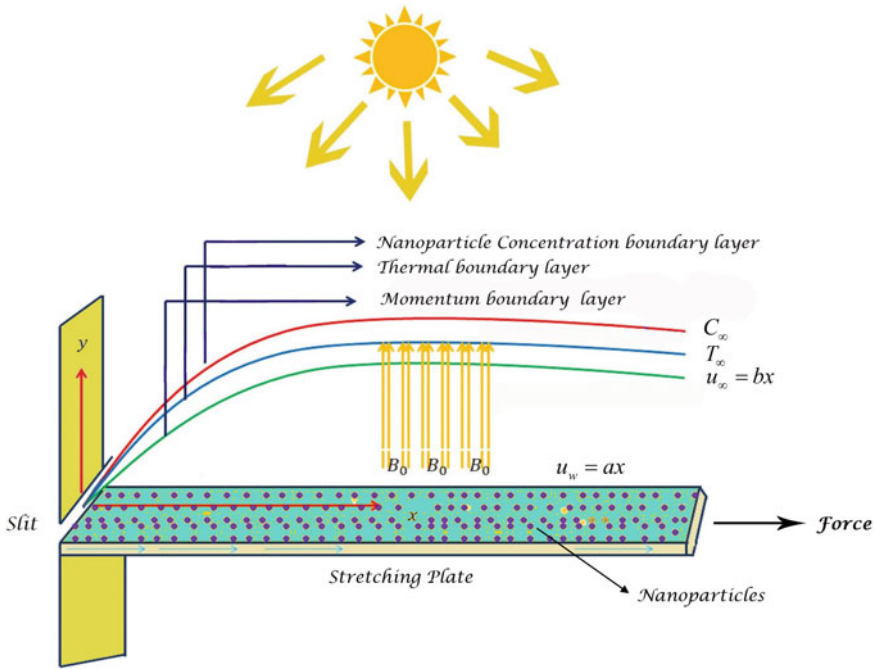


Fig. 1 Schematic diagram of the problem

The system of governing equations (see Refs. [18, 26, 32]) of the flow is given as follows:

$$\frac{\partial u}{\partial x} + \frac{\partial v}{\partial y} = 0 \tag{1}$$

$$u \frac{\partial u}{\partial x} + v \frac{\partial u}{\partial y} = u_\infty \frac{\partial u_\infty}{\partial x} + \nu_f \frac{\partial^2 u}{\partial y^2} - \frac{\sigma_e B_o^2}{\rho_f} (u - u_\infty) \tag{2}$$

$$u \frac{\partial T}{\partial x} + v \frac{\partial T}{\partial y} = \alpha \frac{\partial^2 T}{\partial y^2} + \frac{\nu_f}{C_f} \left( \frac{\partial u}{\partial y} \right)^2 - \frac{1}{(\rho C)_f} \left( \frac{\partial q_r}{\partial y} \right) + \frac{\sigma_e B_o^2}{(\rho C)_f} (u - u_\infty)^2 + \tau \left[ D_B \frac{\partial T}{\partial y} \frac{\partial C}{\partial y} + \frac{D_T}{T_\infty} \left( \frac{\partial T}{\partial y} \right)^2 \right] + \frac{Q_o}{\rho_f C_p} (T - T_\infty) \tag{3}$$

$$u \frac{\partial C}{\partial x} + v \frac{\partial C}{\partial y} = D_B \frac{\partial^2 C}{\partial y^2} + \frac{D_t}{T_\infty} \frac{\partial^2 T}{\partial y^2} \tag{4}$$

where  $u$  and  $v$  are velocity component along the direction of  $x$ -axis and  $y$ -axis respectively,  $T$  is the temperature and  $C$  is the nanoparticle concentration,  $\nu_f = \frac{\mu_f}{\rho}$  is the kinematic viscosity,  $\sigma_e$  is the electrical conductivity,  $\alpha = \frac{\kappa}{(\rho C)_f}$  is the thermal

diffusivity,  $q_r$  is the radiation parameter,  $Q_o$  is the internal heat generation/absorption coefficient,  $D_B$  and  $D_\tau$  are coefficients of Brownian and thermophoretic diffusion parameter respectively. In this case, we consider the Rosseland approximation for radiation heat flux, which is mathematically expressed as (see Refs. [3, 29, 34]):

$$q_r = -\frac{4\sigma^*}{3k^*} \frac{\partial^4 T}{\partial y^4} \tag{5}$$

where  $\sigma^*$  and  $k^*$  are Stefan-Boltzmann and mean absorption coefficient respectively. Expanding the Taylor series and neglecting the higher order, we get

$$T^4 = 4 T_\infty^3 T - 3 T_\infty^4$$

Hence Eqs. (5) becomes-

$$\frac{\partial q_r}{\partial y} = -\frac{16\sigma^*}{3k^*} T_\infty^3 \frac{\partial^2 T}{\partial y^2} \tag{6}$$

The boundary conditions (see Ref. [16]) for the considered problem are:

$$\begin{aligned} u = u_w(x) = ax, v = 0, \\ -k \frac{\partial T}{\partial y} = h(T - T_f), C = C_w \text{ at } y = 0. \\ u \rightarrow u_\infty(x) = bx, T \rightarrow T_\infty, C \rightarrow C_\infty \text{ as } y \rightarrow \infty \end{aligned} \tag{7}$$

The similarity transformation used to make Eqs. (1) to (4) dimensionless are as follows (see Ref. [18]):

$$\begin{aligned} \eta = \sqrt{\frac{a}{v_f}} y, u = ax f'(\eta), v = -\sqrt{av_f} f(\eta), \\ \theta = \frac{T - T_\infty}{T_f - T_\infty}, \phi = \frac{C - C_\infty}{C_w - C_\infty} \end{aligned} \tag{8}$$

The set of PDE's (2) to (4) are transformed by using the set of transformation Eq. (7) to obtain:

$$f'''(\eta) + f(\eta)f''(\eta) - (f'(\eta))^2 + \lambda^2 + M(\lambda - f'(\eta)) = 0 \tag{9}$$

$$\begin{aligned} \frac{1}{Pr} [1 + (Rd(1 + (\theta_w - 1)\theta(\eta))^3)] \theta''(\eta) + f(\eta)\theta'(\eta) + A\theta + N_b\theta'(\eta)\phi'(\eta) + \\ N_t(\theta'(\eta))^2 + E_c(f''(\eta))^2 + ME_c(\lambda - f'(\eta))^2 = 0 \end{aligned} \tag{10}$$

$$\phi''(\eta) + Lef(\eta)\phi(\eta) + \frac{N_t}{N_b}\theta''(\eta) = 0 \tag{11}$$

where  $M = \frac{\sigma B_0^2}{\rho_f a}$  is the parameter associated with magnetic field strength,  $\lambda = \frac{b}{a}$  is the ratio of rates of free stream velocity to the velocity of the stretching sheet,  $Pr = \frac{\nu_f}{\alpha}$  is the Prandtl number,  $R_d = \frac{16\sigma^* T_\infty^3}{3kk^*}$  is the Radiation parameter,  $\theta_w = \frac{T_f}{T_\infty}$  is the Temperature parameter,  $N_b = \frac{\tau D_B (C_w - C_\infty)}{\nu_f}$  is the Brownian motion parameter,  $N_t = \frac{\tau D_t (T_w - T_\infty)}{T_\infty \nu_f}$  is the Thermophoresis parameter,  $A = \frac{Q_0}{a\rho_f c_p}$  is the heat source and heat sink parameter for  $A > 0$  and  $A < 0$  respectively,  $E_c = \frac{u_w}{C_p(T_w - T_\infty)}$  is the Eckert number and  $Le = \frac{\nu_f}{D_B}$  is the Lewis number.

The boundary condition (7) in the dimensionless form are as follows:

$$f(0) = 0, f'(0) = 1, \theta'(0) = -\gamma[1 - \theta(0)], \phi(0) = 1$$

$$f'(+\infty) \rightarrow \lambda, \theta(+\infty) \rightarrow 0, \phi(+\infty) \rightarrow 0 \tag{12}$$

where  $\gamma = \frac{h}{k\sqrt{\nu_f/a}}$  is the Biot number.

The surface heat flux and mass flux in dimensionless form can be represented as follows:

$$\frac{Nu_x}{\sqrt{Re_x}} = -[1 + Rd\theta_w^2]\theta'(0) = Nur \tag{13}$$

$$\frac{Sh}{\sqrt{Re_x}} = -\phi'(0) = Shr \tag{14}$$

### 3 Method of Solutions

The dimensionless ordinary differential Eqs. (9) to (11) along with dimensionless boundary conditions (12) are solved using a MATLAB built-in solver bvp4c package. The equations are converted into the set of first order differential equations as follows:

$$f = y_1, f' = y_1' = y_2, f'' = y_2' = y_3, \theta = y_4,$$

$$\theta' = y_4' = y_5, \phi = y_6, \phi' = y_6' = y_7$$

$$f''' = y_3' = y_2^2 - y_1 y_3 + \lambda^2 + M(\lambda - y_2) \tag{15}$$

$$\theta'' = y_5' = \frac{-Pr[y_1 y_5 + A y_4 + N_b y_5 y_7 + N_t y_7^2 + E_c y_3^2 + M E_c (\lambda - y_2)^2]}{1 + Rd(1 - (\theta_w - 1)y_4)^3} \tag{16}$$

$$\phi'' = y_7' = -Le y_1 y_7 - \frac{N_t}{Nb} y_5 \tag{17}$$

The boundary conditions are given by:

$$y_1(0) = 0, y_2(0) = 1, y_5(0) = -\gamma[1 - y_4(0)], y_6(0) = 1, \tag{18}$$

$$y_2(+\infty) = \lambda, y_4(+\infty) = 0, y_6(+\infty) = 0$$

### 4 Results and Discussions

Influence of non-dimensional parameter such as Radiation parameter  $R_d$ , along with Brownian motion parameter  $N_b$ , Thermophoresis parameter  $N_t$ , Magnetic field parameter  $M$ , Lewis number  $Le$ , Biot number  $\gamma$ , Prandtl number  $Pr$  and Eckert number  $E_c$  on Temperature profile  $\theta(\eta)$ , Nanoparticle concentration  $\phi(\eta)$ , reduced Nusselt number and reduced Sherwood number graphically and numerically.

The obtained numerical solutions are compared with those of prior published Mushtaq et al. [24] to justify the correctness of the employed approach. Table 1 illustrates the numerical value of heat and mass transfer, as well as the results reported by [24] in the presence and absence of radiation, which demonstrates great agreement with the results achieved in this investigation.

Table 2 shows the effect of radiation, together with other parameters, on heat and mass transfer as numerical values of  $-\theta'(0)$  and  $-\phi'(0)$ .

Figures 2 and 3 depict the effect of  $N_t$  along with  $R_d$  on the temperature profile and Nanoparticle concentration profile respectively and it can be observed that the

**Table 1** Comparison of values of  $-\theta'(0)$  and  $-\phi'(0)$  for the various value of  $N_b$  with Mushtaq et al. [24]

$N_b$	$R_d$	Mushtaq et al. [24]		Present study	
		$-\theta'(0)$	$-\phi'(0)$	$-\theta'(0)$	$-\phi'(0)$
0.1	0	0.078993	2.44780	0.0785	2.4478
	1	0.081387	2.40369	0.0815	2.4061
0.2	0	0.070373	2.43727	0.0704	2.4373
	1	0.078183	2.39810	0.0779	2.4001
0.3	0	0.058202	2.44012	0.0582	2.4401
	1	0.074496	2.39670	0.0735	2.3991
0.4	0	0.040852	2.44673	0.0409	2.4467
	1	0.070375	2.39623	0.0681	2.3970
0.5	0	0.018834	2.45314	0.0189	2.4531
	1	0.065911	2.39605	0.0615	2.3961

**Table 2** Value of  $Nur$  and  $Shr$  for different parameters along with radiation

$R_d$	$N_t$	$N_b$	$M$	$Pr$	$Le$	$\gamma$	$E_c$	$-\theta'(0)$	$-\phi'(0)$
0	0.1	0.1	0.5	5.0	1.0	0.1	0.1	0.0880	0.6586
	0.2							0.0879	0.6211
	0.3							0.0878	0.5847
1	0.1	0.1	0.5	5.0	1.0	0.1	0.1	0.0871	0.6589
	0.2							0.0870	0.6213
	0.3							0.0869	0.5846
0	0.1	0.1	0.5	5.0	1.0	0.1	0.1	0.0880	0.6586
		0.2						0.0650	0.6812
		0.3						0.0847	0.6891
1	0.1	0.1	0.5	5.0	1.0	0.1	0.1	0.0871	0.6589
		0.2						0.0860	0.6801
		0.3						0.0848	0.6874
0	0.1	0.1	0.5	5.0	1.0	0.1	0.1	0.0880	0.6586
			1.0					0.0866	0.6599
			1.5					0.0853	0.6616
1	0.1	0.1	0.5	5.0	1.0	0.1	0.1	0.0871	0.6587
			1.0					0.0860	0.6580
			1.5					0.0850	0.6577
0	0.1	0.1	0.5	5.0	1.0	0.1	0.1	0.0880	0.6586
				7.0				0.0881	0.6602
				9.0				0.0880	0.6622
1	0.1	0.1	0.5	5.0	1.0	0.1	0.1	0.0871	0.6589
				7.0				0.0877	0.6581
				9.0				0.0880	0.6583
0	0.1	0.1	0.5	5.0	1.0	0.1	0.1	0.0880	0.6586
					4.0			0.0870	1.4480
					7.0			0.0865	1.9696
1	0.1	0.1	0.5	5.0	1.0	0.1	0.1	0.0871	0.6589
					4.0			0.0865	1.4408
					7.0			0.0863	1.9586
0	0.1	0.1	0.5	5.0	1.0	0.1	0.1	0.0880	0.6586
						0.2		0.1651	0.6061
						0.3		0.2329	0.5601
1	0.1	0.1	0.5	5.0	1.0	0.1	0.1	0.0871	0.6589
						0.2		0.1598	0.6147
						0.3		0.2213	0.5776

(continued)

**Table 2** (continued)

$R_d$	$N_t$	$N_b$	$M$	$Pr$	$Le$	$\gamma$	$E_c$	$-\theta'(0)$	$-\phi'(0)$
0	0.1	0.1	0.5	5.0	1.0	0.1	0.1	0.0880	0.6586
							0.2	0.0826	0.6844
							0.3	0.0771	0.7103
1	0.1	0.1	0.5	5.0	1.0	0.1	0.1	0.0871	0.6589
							0.2	0.0830	0.6764
							0.3	0.0790	0.6940

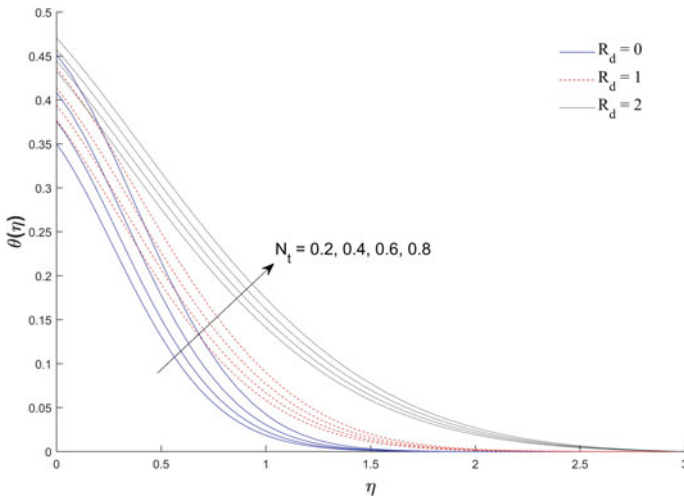


**Fig. 2** Effect of  $N_t$  along with  $R_d$  on  $\theta(\eta)$

temperature increases with the increase of both  $N_t$  and  $R_d$  whereas the nanoparticle concentration increases with  $N_t$  but decreases with an increase in radiation. Figure 4 describes the effect of  $N_t$  and  $R_d$  on the temperature derivative profile ( $-\theta'(\eta)$ ) and it is clear that it increases with the increase of  $N_t$  and  $R_d$ . The results are important for calculating the Nusselt number since they have a direct relationship to its value when  $\eta = 0$ . The reason behind the fact is that the increase in  $N_t$  results the enhancement of thermophoresis forces which has the tendency to fast flow the nanoparticles from hot surface to cold surface away from stretching. This results in an increase of heat and mass transfer in the boundary layer region for nanoparticles.

Figures 5 and 6 illustrate how  $N_b$  affects the temperature and nanoparticle concentration profiles in conjunction with the specified radiation. The study elucidates that the temperature increases with the increment  $N_b$  but decreases with  $R_d$  whereas the concentration decreases with the increase in both  $N_b$  and  $R_d$ . The impact of  $N_b$  along with  $R_d$  on  $-\theta'(\eta)$  is depicted in Fig. 7 and an increase is observed with the increase in  $N_b$  but an opposite trend is seen with  $R_d$ . It is well known that as  $N_b$  increases, so

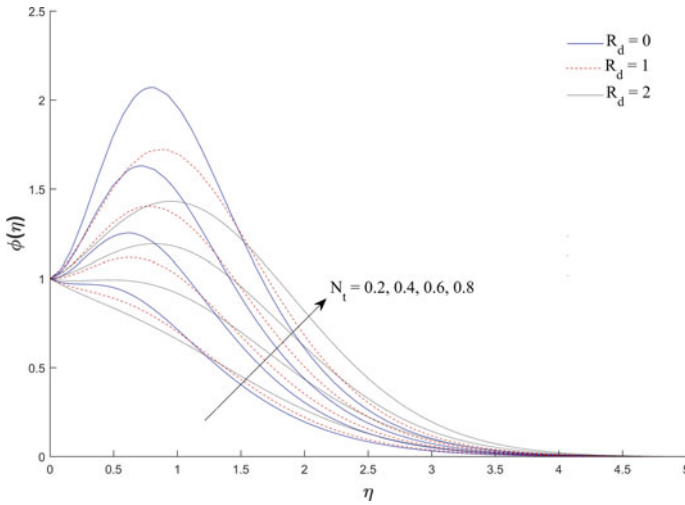


Fig. 3 Effect of  $N_t$  along with  $R_d$  on  $\phi(\eta)$

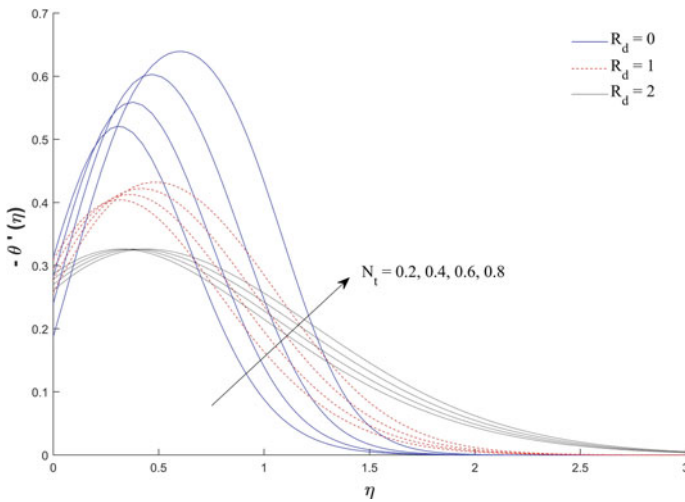


Fig. 4 Effect  $N_t$  of along with  $R_d$  on  $-\theta'(\eta)$

does the random motion of nanoparticles, resulting in an increase in collisions with other nanoparticles. As a result, the kinetic energy is transformed into heat energy, and the temperature rises. But the rate of mass transfer decreases because of the tendency of the particle to get close to each other as  $N_b$  increases.

Figures 8 and 9 show the effect of Biot number  $\gamma$  on both temperature and nanoparticle concentration and it is observed that both increases with the increase in  $\gamma$ . The main reason behind the fact is that, increase in biot number means increase

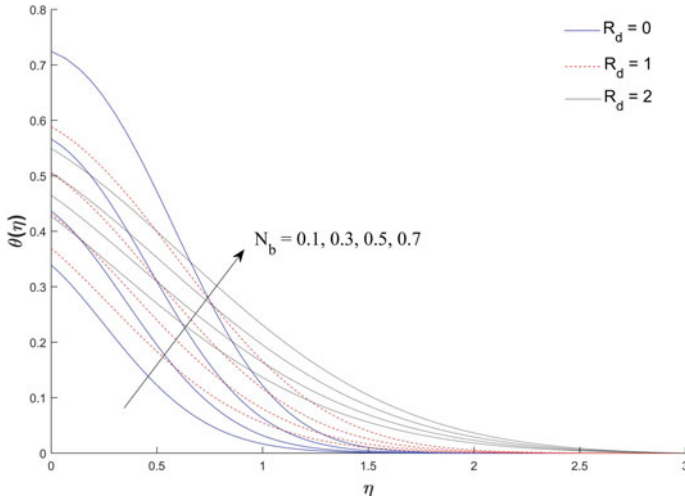


Fig. 5 Effect of  $N_b$  along with  $R_d$  on  $\theta(\eta)$

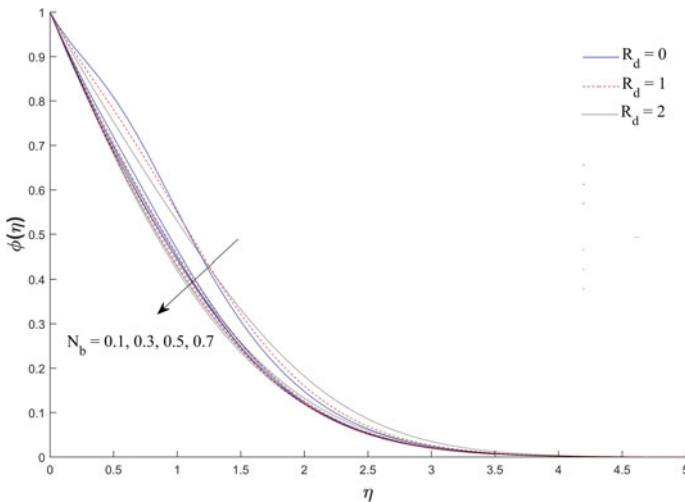


Fig. 6 Effect of  $N_b$  along with  $R_d$  on  $\phi(\eta)$

in convective heat exchange at the surface which results in the increase in thermal boundary layer thickness and which in turn increases the nanoparticle concentration. Figures 10 shows that the temperature decreases with the increase of Prandtl number  $Pr$  whereas Fig. 11 shows that the nanoparticle concentration profile increases with  $Pr$ . The main reason behind the fact that with the higher value in  $Pr$  the heat diffuses



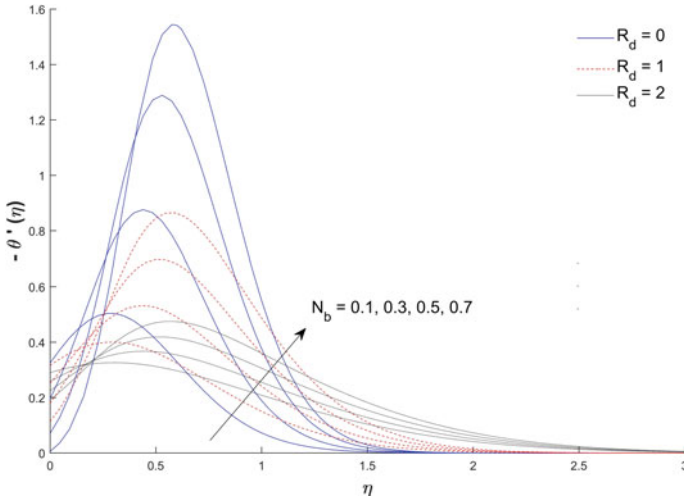


Fig. 7 Effect of  $N_b$  along with  $R_d$  on  $-\theta'(\eta)$

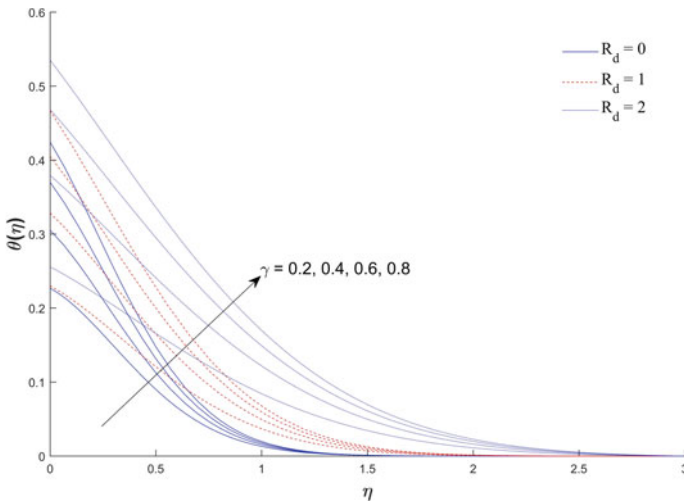


Fig. 8 Effect of  $\gamma$  along with  $R_d$  on  $\theta(\eta)$

more rapidly than the momentum. It is also observed that at large  $Pr$  the temperature falls more drastically due to the fact that the large values of  $Pr$  leads to the low thermal conductivity.

Figure 12 depicts the impact of  $E_c$  on the temperature profile. We know that Eckert number expresses a direct relationship of flow's kinetic energy to the boundary layer enthalpy differences. This leads to the fact that the increases in  $E_c$  enhance the kinetic energy. Whereas it is well known that the temperature is an average kinetic energy.

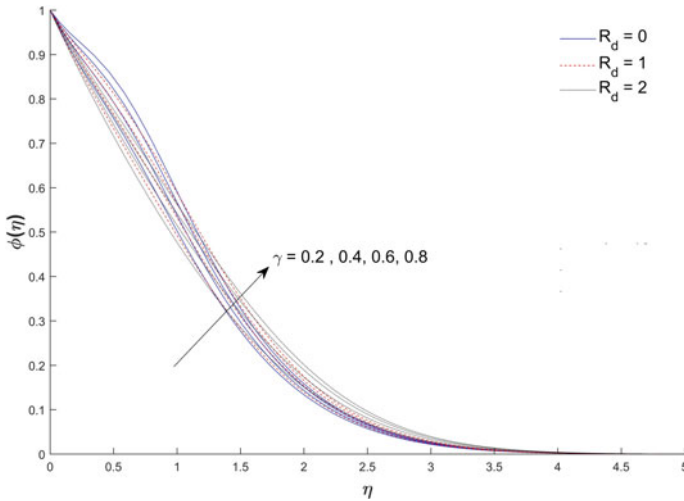


Fig. 9 Effect of  $\gamma$  along with  $R_d$  on  $\phi(\eta)$

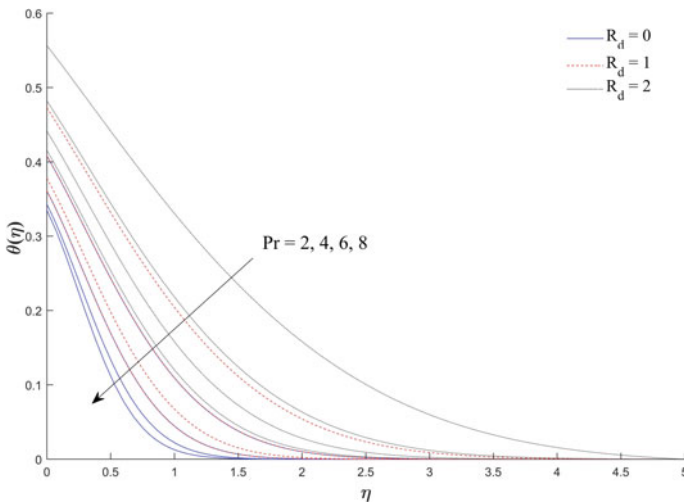


Fig. 10 Effect of  $Pr$  along with  $R_d$  on  $\theta(\eta)$

Hence alternatively we can say that temperature rises with the increase in Eckert number and which can be clearly seen in the figure.

Figures 13, 14 and 15 show the effect of magnetic parameters on velocity, temperature, and nanoparticle concentration respectively. It is noticed from the velocity profile that the velocity decreases with the increase in magnetic parameter. An exact opposite behavior is seen in the case of temperature profile where the temperature

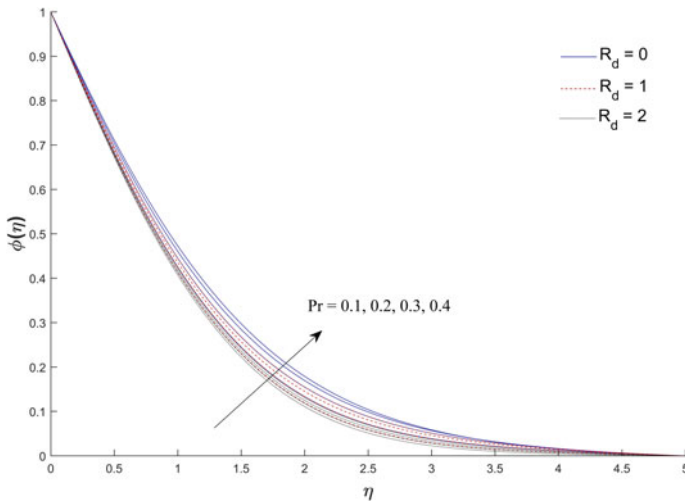


Fig. 11 Effect of  $Pr$  along with  $R_d$  on  $\phi(\eta)$

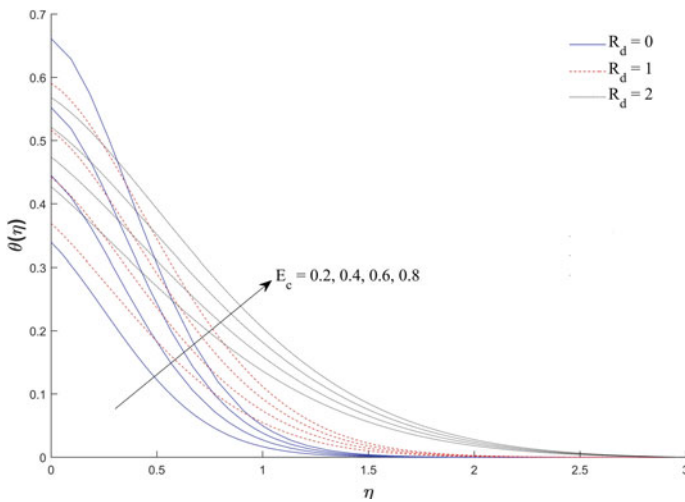
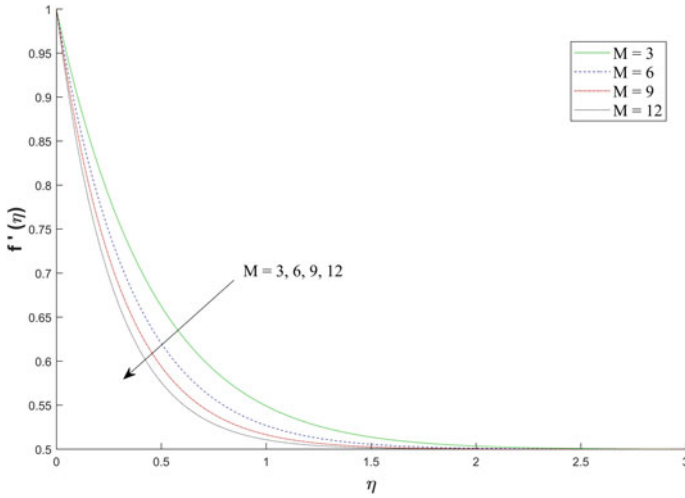
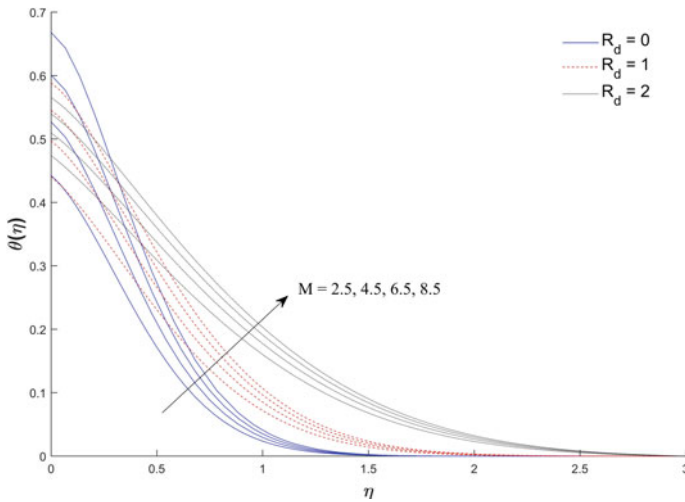


Fig. 12 Effect of  $E_c$  along with  $R_d$  on  $\theta(\eta)$

increases with the increase in  $M$  and radiation  $R_d$ . In the case of nanoparticle concentration, it is clear from the graph that the concentration increases with the increasing magnetic parameter but decreases with stronger radiation. As the magnetic field parameter increases, a resistive force called a Lorentz force is produced which retards in the form magnetic pressure drop on the velocity, as a result the motion gets slowed down. Therefore the velocity decreases with the increasing value of  $M$ . Again due to the Lorentz force a resistance is offered to the flow which results in warming up



**Fig. 13** Effect of  $M$  along with  $R_d$  on  $f'(\eta)$



**Fig. 14** Effect of  $M$  along with  $R_d$  on  $\theta(\eta)$

the boundary layer region. Hence the temperature increases as the values of  $M$  gets increase.

The influence of Lewis number on temperature and nanoparticle concentration can be depicted in Figs. 16 and 17 respectively. It is noted that a growing behavior is found for temperature profile with the increment in  $Le$  and  $R_d$  whereas the concentration decreases with the increase in  $Le$ . It is observed that a smaller increase in  $Le$  results in larger differences in temperature and a thinner concentration boundary layer due to

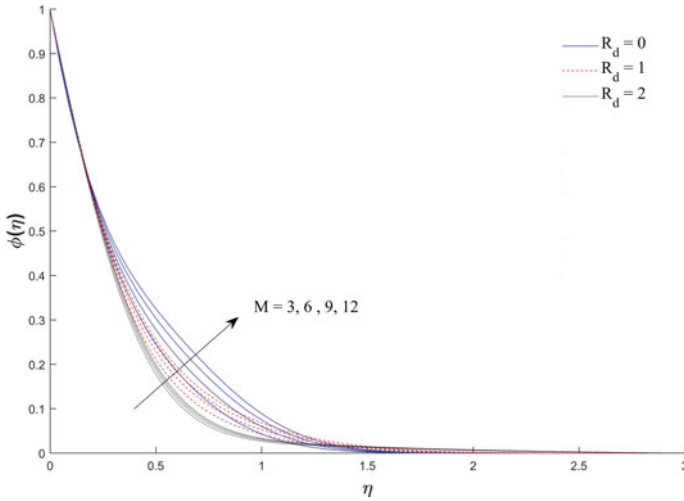


Fig. 15 Effect of  $M$  along with  $R_d$  on  $\phi(\eta)$

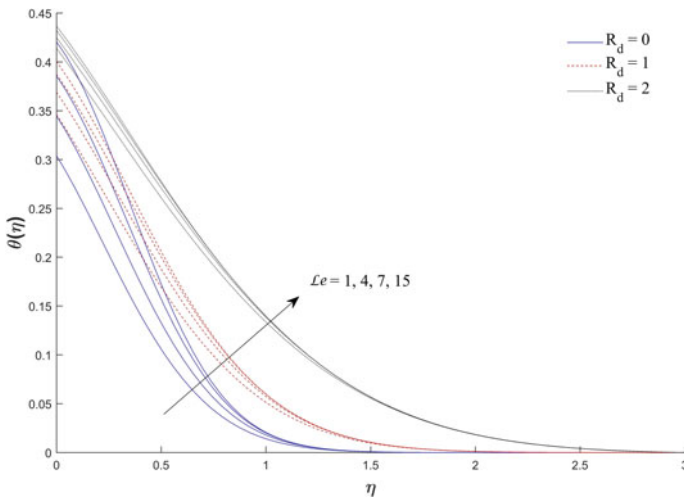


Fig. 16 Effect of  $Le$  along with  $R_d$  on  $\theta(\eta)$

a weak molecular diffusivity. Figures 18 and 19 depicts the behavior of temperature profile for heat source parameter ( $A > 0$ ) and heat sink parameter ( $A < 0$ ) respectively. It is observed that the temperature of the thermal boundary layer increases with the increase in  $A$  (heat source parameter) and decreases with the decrease in  $A$  (heat sink parameter) under constant thermal radiation.

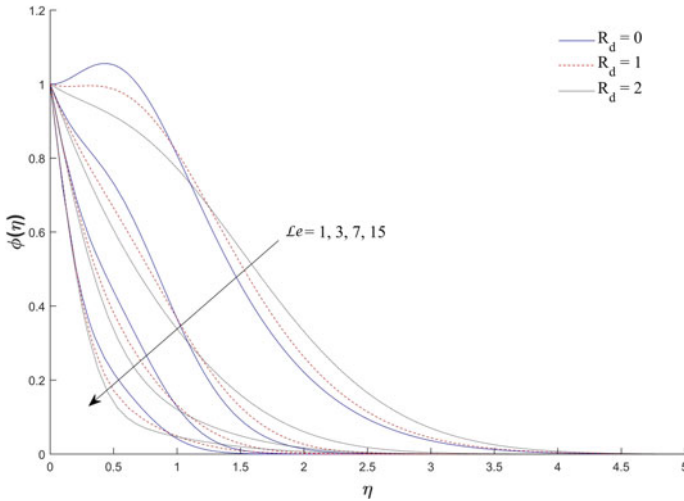


Fig. 17 Effect of  $Le$  along with  $R_d$  on  $\phi(\eta)$

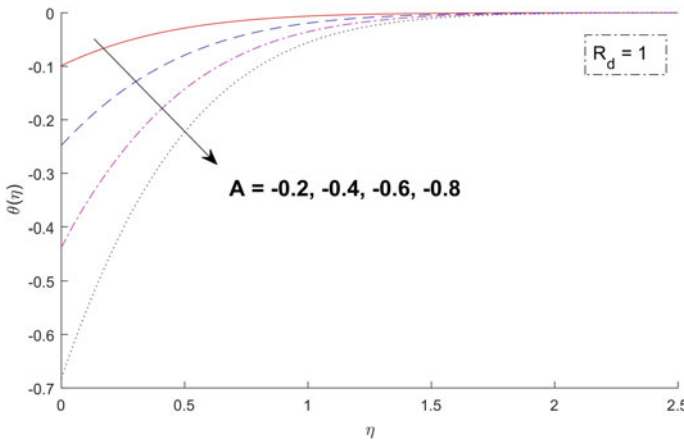
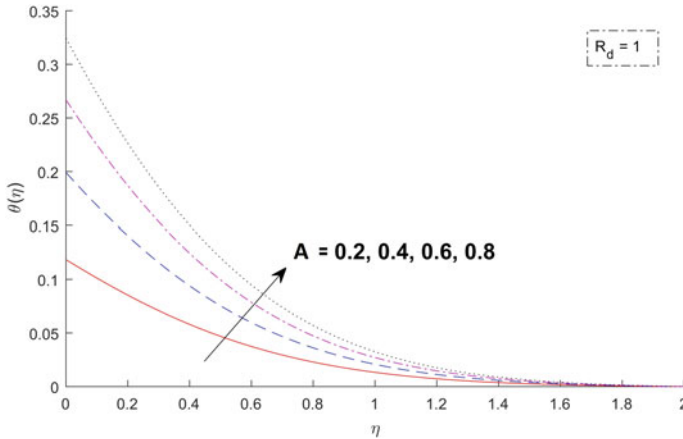


Fig. 18 Effect of  $A < 0$  on  $\theta(\eta)$

## 5 Conclusions

The influence of solar radiation on a constant two-dimensional MHD flow across a stretched plate is examined for various parameters in this study. The findings acquired in this investigation using the MATLAB programme `bvp4c` and the results obtained in the previous study utilizing the Runge Kutta Fourth Order Scheme showed great consistency. The impact of various parameters in our present investigation are as follows:



**Fig. 19** Effect of  $A > 0$  on  $\theta(\eta)$

- The increasing value of Magnetic field parameter can decrease the nanoparticle velocity.
- The temperature distribution in the boundary layer region can be enhanced with the increment of Magnetic field parameter, Biot number Thermophoresis parameter, Brownian motion parameter, Heat source parameter, Lewis number and Eckert number.
- The temperature distribution diminishes with the increasing value of Prandtl number and Heat sink parameter.
- Nanoparticle volume fraction in the boundary layer region can be enriched by increasing the value of Thermophoresis parameter, Biot number, Magnetic field parameter, Lewis number and Prandtl number while it can decrease with the increase in Brownian motion parameter.
- The increasing value of Radiation parameter increases the Temperature profile and decreases the Nanoparticle volume fraction profile.
- The value of reduced Nusselt number is increased with the increase in Biot number and the Prandtl number and decreases with magnetic field parameter, Lewis number, Thermophoresis parameter and Brownian motion parameter.
- The value of reduced Sherwood number is increased with the increase in Brownian motion parameter, Magnetic field parameter, Prandtl number, Lewis number and Eckert number but decreases with Thermophoresis parameter and Biot number.
- It is very interesting to note that increase in Radiation parameter lead to the decrease in Reduced Nusselt number and increase in Reduced Sherwood number.
- The applicability of MATLAB's software bvp4c (Boundary layer problem of fourth-order) is ensured by verifying the findings as compared to the previously published results.
- The present study finds an application in efficient Solar collector, Cooling problems in industry, etc.

## References

1. Akilu, S., Sharma, K. v., Baheta, A. T., & Mamat, R.: A review of thermophysical properties of water based composite nanofluids. In: *Renewable and Sustainable Energy Reviews*, vol. 66, pp. 654–678. Elsevier Ltd. (2016)
2. Bansal, J.L.: *Magnetofluidynamics of Viscous Fluids*. Jaipur Publishing House, Jaipur India (1994)
3. Brewster, M.Q.: *Thermal Radiative Transfer Properties*. John Wiley and Sons, New York (1972)
4. Buongiorno, J.: Convective transport in nanofluids. *J. Heat Transf.* **128**(3), 240–250 (2006)
5. Choi, S.U.S.: Enhancing thermal conductivity of fluids with nanoparticles. *ASME Int. Mech. Eng. Cong. Expo.* **66**, 99–105 (1995)
6. Chutia, M., Deka, P.N.: Numerical study on MHD mixed convection flow in a vertical insulated square duct with strong transverse magnetic field. *J. Appl. Fluid Mech.* **8**(3), 473–481 (2015)
7. Eastman, J.A., Choi, S.U.S., Li, S., Yu, W., Thompson, L.J.: Anomalous increased effective thermal conductivities of ethylene glycol-based nanofluids containing copper nanoparticles. *Appl. Phys. Lett.* **78**(6), 718–720 (2001)
8. England, W.G., Emery, A.F.: Thermal radiation effects on the laminar free convection boundary layer of an absorbing gas. *ASME J. Heat Transfer.* **91**(1), 37–44 (1969)
9. Faizal, M., Saidur, R., Mekhilef, S., Alim, M.A.: Energy, economic and environmental analysis of metal oxides nanofluid for flat-plate solar collector. *Energy Convers. Manage.* **76**, 162–168 (2013)
10. Ghasemi, S.E., Hatami, M.: Solar radiation effects on MHD stagnation point flow and heat transfer of a nanofluid over a stretching sheet. *Case Stud. Thermal Eng.* **25** (2021)
11. Ghasemi, S.E., Hatami, M., Jing, D., Ganji, D.D.: Nanoparticles effects on MHD fluid flow over a stretching sheet with solar radiation: a numerical study. *J. Mol. Liq.* **219**, 890–896 (2016)
12. Gireesha, B.J., Mahanthesh, B., Shivakumara, I.S., Eshwarappa, K.M.: Melting heat transfer in boundary layer stagnation-point flow of nanofluid toward a stretching sheet with induced magnetic field. *Eng. Sci. Technol. Int. J.* **19**(1), 313–321 (2016)
13. Hayat, T., Imtiaz, M., Alsaedi, A., Kutbi, M.A.: MHD three-dimensional flow of nanofluid with velocity slip and nonlinear thermal radiation. *J. Magn. Magn. Mater.* **396**, 31–37 (2015)
14. Javadi, F. S., Saidur, R., Kamalifarvestani, M.: Investigating performance improvement of solar collectors by using nanofluids. In: *Renewable and Sustainable Energy Reviews*, vol. 28, pp. 232–245 (2013)
15. Khan, W.A., Makinde, O.D.: MHD nanofluid bioconvection due to gyrotactic microorganisms over a convectively heat stretching sheet. *Int. J. Therm. Sci.* **81**(1), 118–124 (2014)
16. Khan, W.A., Pop, I.: Boundary-layer flow of a nanofluid past a stretching sheet. *Int. J. Heat Mass Transf.* **53**(11–12), 2477–2483 (2010)
17. Kumar, M.A., Reddy, Y.D., Rao, V.S., Goud, B.S.: Thermal radiation impact on MHD heat transfer natural convective nano fluid flow over an impulsively started vertical plate. *Case Stud. Thermal Eng.* **24**, 100826 (2021)
18. Kuznetsov, A.V., Nield, D.A.: Natural convective boundary-layer flow of a nanofluid past a vertical plate. *Int. J. Thermal Sci.* **49**(2), 243–247 (2010)
19. Lee, S., Choi, S., Li, S., Eastman, J.A.: *Measuring Thermal Conductivity of Fluids Containing Oxide Nanoparticles* (1999). <http://heattransfer.asmedigitalcollection.asme.org/>
20. Lenert, A., Nam, Y., Wang, N.E.: Heat transfer fluids. *Ann. Rev. Heat Trans.* **15**(2), 45 (2012)
21. Liu, Z.H., Hu, R.L., Lu, L., Zhao, F., Xiao, H.S.: Thermal performance of an open thermosyphon using nanofluid for evacuated tubular high temperature air solar collector. *Energy Convers. Manage.* **73**, 135–143 (2013)
22. Lv, Y.P., Shaheen, N., Ramzan, M., Mursaleen, M., Nisar, K.S., Malik, M.Y.: Chemical reaction and thermal radiation impact on a nanofluid flow in a rotating channel with Hall current. *Sci. Rep.* **11**(1) (2021)
23. Makinde, O.D., Aziz, A.: Boundary layer flow of a nanofluid past a stretching sheet with a convective boundary condition. *Int. J. Therm. Sci.* **50**(7), 1326–1332 (2011)



24. Mushtaq, A., Mustafa, M., Hayat, T., Alsaedi, A.: Nonlinear radiative heat transfer in the flow of nanofluid due to solar energy: a numerical study. *J. Taiwan Inst. Chem. Eng.* **45**(4), 1176–1183 (2014)
25. Otanicar, T.P., Phelan, P.E., Prasher, R.S., Rosengarten, G., Taylor, R.A.: Nanofluid-based direct absorption solar collector. *J. Renew. Sustain. Energy* **2**(3) (2010)
26. Pai, S.I.: *Viscous Flow Theory: I Laminar Flow*. D. VanNostrand Co., New York, USA (1956)
27. Patel, H.E., Sundararajan, T., Das, S.K.: An experimental investigation into the thermal conductivity enhancement in oxide and metallic nanofluids. *J. Nanopart. Res.* **12**(3), 1015–1031 (2010)
28. Rana, P., Bhargava, R.: Flow and heat transfer of a nanofluid over a nonlinearly stretching sheet: a numerical study. *Commun. Nonlinear Sci. Numer. Simul.* **17**(1), 212–226 (2012)
29. Raptis, A.: Radiation and free convection flow through a porous medium. *Int. Commun. Heat Mass Transf.* **25**, 289–295 (1998)
30. Rashidi, M.M., Vishnu Ganesh, N., Abdul Hakeem, A.K., Ganga, B.: Buoyancy effect on MHD flow of nanofluid over a stretching sheet in the presence of thermal radiation. *J. Mol. Liq.* **198**, 234–238 (2014)
31. Sarkar, A., Kundu, P.K.: Framing the upshot of Hall current on MHD unsteady nanofluid flow from a rotating spherical body in presence of solar radiation. *Int. J. Ambient Energy* (2021)
32. Schlichting H.: *Boundary Layer Theory*, vol. 6. McGraw-Hill, New York (1964)
33. Shdaifat, M.Y.A., Zulkifli, R., Sopian, K., Salih, A. A.: Thermal and hydraulic performance of CuO/water nanofluids: a review. In: *Micromachines*, vol. 11, Issue 4 (2020)
34. Sparrow, E.M., Cess, R.D.: *Radiation Heat Transfer*. Hemisphere, Washington (1978)
35. Yousefi, T., Veysi, F., Shojaeizadeh, E., Zinadini, S.: An experimental investigation on the effect of  $\text{Al}_2\text{O}_3\text{-H}_2\text{O}$  nanofluid on the efficiency of flat-plate solar collectors. *Renew. Energy* **39**(1), 293–298 (2012)

# Analysis of Solute Dispersion Through an Open Channel Under the Influence of Suction or Injection



Gourab Saha , Nanda Poddar , Subham Dhar ,  
and Kajal Kumar Mondal 

**Abstract** In presence of suction or injection, the process of dispersion of solute in an open channel flow is investigated through this work. The dispersion coefficient is analytically determined by using Mei's multi-scale analysis approach up to second order. The effect of suction or injection on dispersion coefficient are displayed graphically and discussed. The novelty of the present research is to find the effect of suction/injection Reynolds number on the dispersion coefficient and concentration distribution of the solute. It is found that the mass dispersivity decreases with the increment of suction/injection Reynolds number. The present study may play a significant role in the process of wastewater treatment. It is observed that, as dispersion time progresses, the amplitude of the concentration curves along longitudinal direction becomes flat. It is observed that the iso-concentration contour spreads along the longitudinal direction with the enhancement of injection Reynolds number.

**Keywords** Open channel · Multi-scale approach · Suction · Injection · Dispersivity

## 1 Introduction

The study of dispersion phenomena of solute through various flow situation has a great importance because the results of this study may be applied in diverse fields, namely, biology, chemical engineering, chromatography, environment fluid mechanics etc. For controlling the air or water pollution, to create a design of chemical reaction, for targeting drug delivery etc., the investigation of the mass transport of the solute is highly important. Several researchers studied the Newtonian fluid flows in different flow geometry. Suction/injection in the fluid flow can be a powerful

---

Supported by DST, India, UGC, India and CSIR, India.

---

G. Saha (✉) · N. Poddar · S. Dhar · K. K. Mondal  
Cooch Behar Panchanan Barma University, Cooch Behar 736101, India  
e-mail: [gourabsaha2019@gmail.com](mailto:gourabsaha2019@gmail.com)

© The Author(s), under exclusive license to Springer Nature Switzerland AG 2022  
S. Banerjee and A. Saha (eds.), *Nonlinear Dynamics and Applications*,  
Springer Proceedings in Complexity,  
[https://doi.org/10.1007/978-3-030-99792-2\\_40](https://doi.org/10.1007/978-3-030-99792-2_40)

mechanism for the flow management. This technique has an important potential in bio-medical engineering, rocket technology and food processing. In medical engineering, it plays a significant role for artificial qualitative analysis.

In an incompressible fluid flow, the longitudinal dispersion of solute through a circular tube was first studied by Taylor [1]. There were some limitations in Taylor's research work, by removing those restrictions, Aris [2] introduced a method of moment to analyze the dispersion phenomena of the tracers. Gill [3] obtained a series solution for the dispersion of solute in a laminar flow through a tube using mean concentration expansion technique. Mondal et al. [4] explored the dispersion process of settling particles in a turbulent open channel flow from an elevated continuous source. Mei [5] proposed a multiple scale analysis to investigate the dispersion of solute through various flow geometries. In this process, one can analyze the dispersion phenomena for different time scales. Later, Wu et al. [6] used the multi-scale analysis to observe the environmental dispersion in wetland flow.

Several researchers [7–10] used the boundary layer theory to analyze the impact of suction or injection in various flow field. To control fluid flow on the surface of subsonic aircraft suction/injection was imposed by Shojaefard et al. [7]. Suction/injection of a fluid has a great importance in heat transfer cooling [8]. Finite difference implicit Keller-box method applied by Ishak et al. [9] to show that how suction or injection can significantly change the flow field and it affects the rate of heat transfer from the plate. An analytical solution for energy and momentum equations in presence of suction or injection was obtained by Jha et al. [10]. Recently, Sasikumar et al. [11] investigated the effect of suction and injection on an unsteady oscillating flow of an incompressible viscous electrically conducting fluid through an asymmetric channel filled with perforated medium and oscillating wall temperature. In presence of extending surface effect with suction/injection, MHD Casson nanofluid flow over nonlinearly heated porous medium was studied by Abo-Dahab et al. [12] and they determined the wall drag, thermal and mass fluxes in the said model.

The main purpose of the present study is to investigate the effect of suction/injection Reynolds number on dispersion phenomena of solute in a laminar flow through an open channel. The analytical results are derived with the help of multi-scale homogenization process. The impact of suction/injection parameter on the dispersion coefficient, transverse concentration and longitudinal concentration distributions are discussed.

## 2 Mathematical Formulation

For this work, a two dimensional laminar flow of a viscous incompressible fluid through an open channel is considered. We introduce  $x'$ -axis along the direction of flow and  $y'$ -axis perpendicular to the flow. It is assumed that the depth of the channel is very small compared to the length of the channel. The velocity distribution

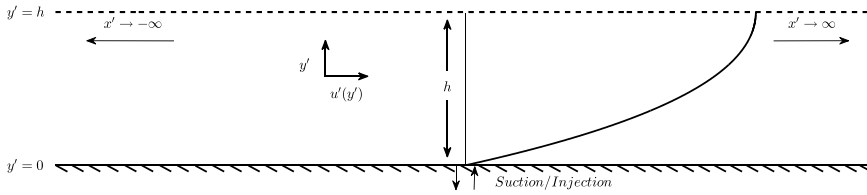


**Fig. 1** Schematic diagram of the above flow

$u'(y')$  parallel to the  $x'$ -axis of the above mentioned flow satisfies the Navier-Stokes equation

$$v \frac{d^2 u'}{dy'^2} - V_0 \frac{du'}{dy'} = \frac{1}{\rho} \frac{\partial p}{\partial x'}, \tag{1}$$

where  $v$  is the kinematic viscosity of the fluid. The boundary conditions of the flow field are taken as  $u'(y') = 0$  at  $y' = 0$  and  $\frac{du'}{dy'} = 0$  at  $y' = h$  (See Fig. 1).

Introducing the following dimensionless quantities

$$x = \frac{x'}{L}, y = \frac{y'}{h}, t = \frac{t'}{h^2/\nu}, u = \frac{u'}{u_c}, Sc = \frac{\nu}{D}. \tag{2}$$

The Eq. (1) takes the form

$$\frac{d^2 u}{dy^2} - \gamma \frac{du}{dy} = -1, \tag{3}$$

where  $u_c = -\frac{h^2}{\rho\nu} \frac{\partial p}{\partial x'}$  and  $\gamma (= \frac{V_0 h}{\nu})$  is the suction Reynolds number ( $-\gamma$  stands for injection Reynolds number). The respective non dimensional boundary conditions are

$$u(y) = 0 \quad \text{at} \quad y = 0, \quad \frac{du}{dy} = 0 \quad \text{at} \quad y = 1. \tag{4}$$

Solving Eq. (3) with the help of boundary condition Eq. (4), one can obtain

$$u(y) = \frac{e^{-\gamma}}{\gamma^2} [1 - e^{\gamma y}] + \frac{y}{\gamma}. \tag{5}$$

Figure 2 shows the velocity profile through the considered open channel for various values of suction/injection Reynolds number. It is observed that the velocity increases with the increment of injection parameter and if positive value of  $\gamma$  i.e. if suction increases, the velocity reduces in the flow field. In the limiting case of suction/injection Reynolds number i.e. when  $\gamma \rightarrow 0$ , the velocity of the fluid is exactly similar to that of an open channel flow and its mathematical form is given below

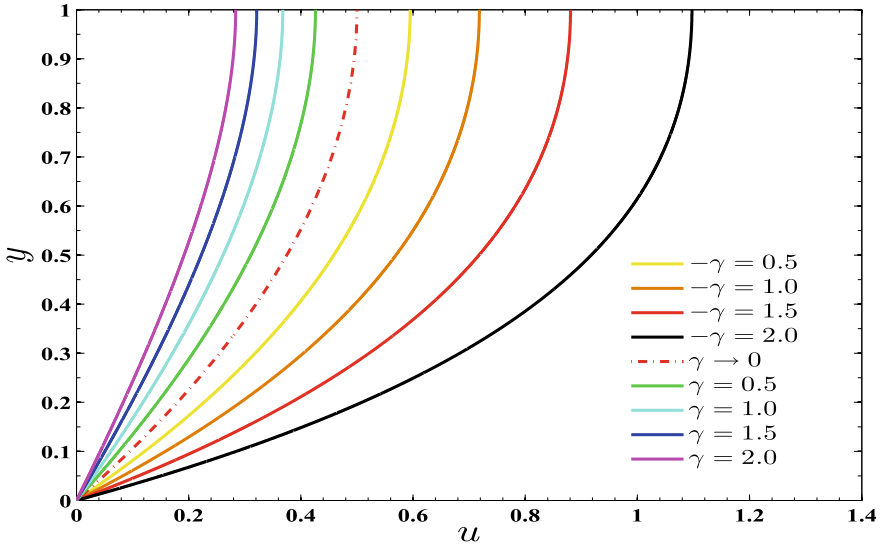


Fig. 2 Velocity profiles for different values of suction ( $\gamma$ ) and injection ( $-\gamma$ ) Reynolds number

$$\lim_{\gamma \rightarrow 0} u(y, \gamma) = y - \frac{y^2}{2}. \tag{6}$$

If we add the solute with constant diffusivity  $D$  in the above mentioned flow, the concentration  $C(x', y', t')$  of the tracers molecules satisfies the convective-diffusion equation

$$\frac{\partial C}{\partial t'} + u' \frac{\partial C}{\partial x'} - V_0 \frac{\partial C}{\partial y'} = D \left( \frac{\partial^2 C}{\partial x'^2} + \frac{\partial^2 C}{\partial y'^2} \right), \quad \text{for } 0 < y' < h \tag{7}$$

with the following conditions

$$C(x', y', t')|_{t'=0} = \delta\left(\frac{x'}{h}\right), \tag{8a}$$

$$D \frac{\partial C}{\partial y'} \Big|_{y'=0} = 0, \tag{8b}$$

$$D \frac{\partial C}{\partial y'} \Big|_{y'=h} = 0, \tag{8c}$$

$$C(x', y', t')|_{x' \rightarrow \pm\infty} = 0, \tag{8d}$$

where  $\delta(\cdot)$  is the Dirac delta function.

### 2.1 Different Time-Scales

Mei [5] first introduced multi-scale analysis to study the dispersion related problems. For the present work, three different time scales and two length scales are used. The length scales are taken as the channel depth ( $h$ ) and the characteristic length of the concentration cloud ( $L$ ). The timescales are defined as  $T_0$  (i.e. the diffusion time along the depth of the channel),  $T_1$  (i.e. the convection time along characteristic length) and  $T_2$  (i.e. the diffusion time along the characteristic length), where

$$T_0 = h^2/D, \quad T_1 = L/U, \quad T_2 = L^2/D.$$

So, the ratio of the different time scales are

$$T_0 : T_1 : T_2 = 1 : \frac{1}{\epsilon} : \frac{1}{\epsilon^2},$$

where  $\epsilon = \frac{h}{L} (\ll 1)$  is the perturbation parameter.

### 2.2 Dimensionless Concentration Equation

Using Eqs. (2) into (7) and (8), the dimensionless concentration equation and the respective initial and boundary conditions becomes

$$\frac{\partial C}{\partial t} + \epsilon u P_e \frac{\partial C}{\partial x} - \epsilon \gamma^* S_c \frac{\partial C}{\partial y} = \epsilon^2 \frac{\partial^2 C}{\partial x^2} + \frac{\partial^2 C}{\partial y^2}, \quad \text{for } 0 < y < 1 \quad (9)$$

$$C(x, y, t)|_{t=0} = \delta\left(\frac{x}{\epsilon}\right), \quad (10a)$$

$$\frac{\partial C}{\partial y} \Big|_{y=0} = 0, \quad (10b)$$

$$\frac{\partial C}{\partial y} \Big|_{y=1} = 0, \quad (10c)$$

$$C(x, y, t)|_{x \rightarrow \pm\infty} = 0, \quad (10d)$$

where  $P_e = \frac{u_c h}{D}$  is the Péclet number which is the ratio of convection rate  $\left(\frac{1}{h/u_c}\right)$  and diffusion rate  $\left(\frac{1}{h^2/D}\right)$ . Also, the suction/injection Reynolds number is defined as  $\gamma = \frac{V_0 h}{\nu} = \frac{V_0 L}{\nu} \frac{h}{L} = \epsilon \gamma^*$ .

### 2.3 Homogenization

In the present work, Mei’s homogenization method is used for asymptotic analysis and we define the following time variables (fast, medium and slow) as

$$t_0 = t, \quad t_1 = \epsilon t, \quad t_2 = \epsilon^2 t. \tag{11}$$

Using chain rule, one can get

$$\frac{\partial}{\partial t} \equiv \frac{\partial}{\partial t_0} + \epsilon \frac{\partial}{\partial t_1} + \epsilon^2 \frac{\partial}{\partial t_2}. \tag{12}$$

The asymptotic expression for concentration  $C$  can be expanded into multi-scale as

$$C(x, y, t) = C_0(x, y, t_0, t_1, t_2) + \epsilon C_1(x, y, t_0, t_1, t_2) + \epsilon^2 C_2(x, y, t_0, t_1, t_2) + O(\epsilon^3). \tag{13}$$

Substituting Eqs. (12) and (13) into (9), (10b) and (10c), one can obtain

$$\begin{aligned} & \left[ \frac{\partial C_0}{\partial t_0} - \frac{\partial^2 C_0}{\partial y^2} \right] + \epsilon \left[ \frac{\partial C_0}{\partial t_1} + \frac{\partial C_1}{\partial t_0} + u P_e \frac{\partial C_1}{\partial x} - \gamma^* S_c \frac{\partial C_0}{\partial y} - \frac{\partial^2 C_1}{\partial y^2} \right] \\ & + \epsilon^2 \left[ \frac{\partial C_0}{\partial t_2} + \frac{\partial C_1}{\partial t_1} + \frac{\partial C_2}{\partial t_0} + u P_e \frac{\partial C_0}{\partial x} - \gamma^* S_c \frac{\partial C_1}{\partial y} - \frac{\partial^2 C_0}{\partial x^2} - \frac{\partial^2 C_2}{\partial y^2} \right] + O(\epsilon^3) = 0, \end{aligned}$$

*for*  $0 < y < 1$  (14)

and

$$\frac{\partial C_0}{\partial y} + \epsilon \frac{\partial C_1}{\partial y} + \epsilon^2 \frac{\partial C_2}{\partial y} + O(\epsilon^3) = 0 \text{ at } y = 0, 1. \tag{15}$$

For the zeroth order ( $O(\epsilon^0)$ ) perturbation, Eq. (14) and (15) gives

$$\frac{\partial C_0}{\partial t_0} = \frac{\partial^2 C_0}{\partial y^2}, \quad \text{for } 0 < y < 1 \tag{16}$$

and

$$\left. \frac{\partial C_0}{\partial y} \right|_{y=0,1} = 0. \tag{17}$$

The general solution of Eq. (16) with boundary condition (17) is

$$C_0 = C_0^{(0)}(x, t_1, t_2) + \sum_{n=1}^{\infty} \operatorname{Re} \left[ C_0^{(n)}(x, t_1, t_2) e^{in\pi y} \right] e^{-n^2\pi^2 t_0}. \quad (18)$$

For large time evolution, one can consider only the first term of the expression and take the solution (18) as

$$C_0 = C_0(x, t_1, t_2). \quad (19)$$

Also, for the first order ( $O(\epsilon)$ ) perturbation, comparing the coefficients of  $\epsilon$  from Eqs. (14) to (15), we have

$$\frac{\partial C_0}{\partial t_1} + \frac{\partial C_1}{\partial t_0} + u P_e \frac{\partial C_0}{\partial x} - \gamma^* S_c \frac{\partial C_0}{\partial y} - \frac{\partial^2 C_1}{\partial y^2} = 0, \quad (20)$$

$$\left. \frac{\partial C_1}{\partial y} \right|_{y=0,1} = 0. \quad (21)$$

As  $C_0$  is independent of  $y$ ,  $\frac{\partial C_0}{\partial y} = 0$ . Thus, Eq. (20) reduces to

$$\frac{\partial C_0}{\partial t_1} + \frac{\partial C_1}{\partial t_0} + u P_e \frac{\partial C_0}{\partial x} - \frac{\partial^2 C_1}{\partial y^2} = 0. \quad (22)$$

Since  $t_0$  is very large, Eq. (22) becomes

$$\frac{\partial C_0}{\partial t_1} + u P_e \frac{\partial C_0}{\partial x} - \frac{\partial^2 C_1}{\partial y^2} = 0. \quad (23)$$

Consider the depth averaged function  $\langle g \rangle$  of a function  $g$  with respect to  $y$  as

$$\langle g \rangle = \int_0^1 g dy. \quad (24)$$

Now, taking depth average of Eq. (23) and applying the conditions Eqs. (21), (23) takes the form

$$\frac{\partial C_0}{\partial t_1} + \langle u \rangle P_e \frac{\partial C_0}{\partial x} = 0. \quad (25)$$

Subtracting Eq. (25) from Eq. (22), we get

$$\frac{\partial C_1}{\partial t_0} + P_e (u - \langle u \rangle) \frac{\partial C_0}{\partial x} = \frac{\partial^2 C_1}{\partial y^2}. \quad (26)$$

Considering the following substitution,

$$C_1 = P_e F(y) \frac{\partial C_0}{\partial x} \quad (27)$$



in Eq. (26) and comparing the coefficients of  $\frac{\partial C_0}{\partial x}$  from both sides, one can get

$$\frac{d^2 F}{dy^2} = u - \langle u \rangle \tag{28}$$

and

$$\left. \frac{dF}{dy} \right|_{y=0,1} = 0, \tag{29a}$$

$$\langle F \rangle = 0. \tag{29b}$$

For second order  $o(\epsilon^2)$  perturbation, Eqs. (14) and (15) gives

$$\frac{\partial C_0}{\partial t_2} + \frac{\partial C_1}{\partial t_1} + \frac{\partial C_2}{\partial t_0} + P_e u \frac{\partial C_1}{\partial x} - \gamma^* S_c \frac{\partial C_1}{\partial y} - \frac{\partial^2 C_0}{\partial x^2} - \frac{\partial^2 C_2}{\partial y^2} = 0, \tag{30}$$

$$\left. \frac{\partial C_2}{\partial y} \right|_{y=0,1} = 0. \tag{31}$$

Again, since  $t_0$  is very large, Eq. (30) reduces to

$$\frac{\partial C_0}{\partial t_2} + \frac{\partial C_1}{\partial t_1} + P_e u \frac{\partial C_1}{\partial x} = \gamma^* S_c \frac{\partial C_1}{\partial y} + \frac{\partial^2 C_0}{\partial x^2} + \frac{\partial^2 C_2}{\partial y^2} \tag{32}$$

Taking depth average on Eq. (32) and applying the conditions (31) & using Eq. (27), the Eq. (32) becomes

$$\begin{aligned} \frac{\partial C_0}{\partial t_2} + \frac{\partial \langle C_1 \rangle}{\partial t_1} + P_e \langle u \frac{\partial C_1}{\partial x} \rangle &= \gamma^* S_c P_e [F(1) - F(0)] \frac{\partial C_0}{\partial x} + \frac{\partial^2 C_0}{\partial x^2} \\ \implies \frac{\partial C_0}{\partial t_2} + P_e \langle u \frac{\partial C_1}{\partial x} \rangle &= \gamma^* S_c P_e [F(1) - F(0)] \frac{\partial C_0}{\partial x} + \frac{\partial^2 C_0}{\partial x^2}. \end{aligned} \tag{33}$$

Subtracting Eqs.(33) from Eq. (30), on can get

$$\begin{aligned} \frac{\partial C_1}{\partial t_1} + \frac{\partial C_2}{\partial t_0} + P_e \left( u \frac{\partial C_1}{\partial x} - \langle u \frac{\partial C_1}{\partial x} \rangle \right) &= \gamma^* S_c \frac{\partial C_1}{\partial y} + \frac{\partial^2 C_2}{\partial y^2} \\ &\quad - \gamma^* S_c P_e [F(1) - F(0)] \frac{\partial C_0}{\partial x}. \end{aligned} \tag{34}$$

Also, from Eq. (27), we have

$$\frac{\partial C_1}{\partial x} = P_e F \frac{\partial^2 C_0}{\partial x^2} \tag{35}$$

and

$$u \frac{\partial C_1}{\partial x} = P_e u F \frac{\partial^2 C_0}{\partial x^2}. \tag{36}$$

Again, taking depth average of Eq. (36), we get

$$\langle u \frac{\partial C_1}{\partial x} \rangle = P_e \langle u F \rangle \frac{\partial^2 C_0}{\partial x^2}. \tag{37}$$

Substituting Eqs. (37) in (33), it becomes

$$\frac{\partial C_0}{\partial t_2} = [1 - P_e^2 \langle u F \rangle] \frac{\partial^2 C_0}{\partial x^2} + \gamma^* S_c P_e [F(1) - F(0)] \frac{\partial C_0}{\partial x}. \tag{38}$$

Multiplying Eq. (25) by  $\epsilon$  and Eq. (38) by  $\epsilon^2$  and adding them, the result gives

$$\frac{\partial C_0}{\partial t_0} + \epsilon \frac{\partial C_0}{\partial t_1} + \epsilon^2 \frac{\partial C_0}{\partial t_2} + \epsilon P_e [\langle u \rangle - \gamma S_c \{F(1) - F(0)\}] \frac{\partial C_0}{\partial x} = \epsilon^2 [1 - P_e^2 \langle u F \rangle] \frac{\partial^2 C_0}{\partial x^2}. \tag{39}$$

Since  $C_0$  is independent of  $t_0$ ,  $\frac{\partial C_0}{\partial t_0} = 0$ . Using the identity (12), Eq. (39) reduces to

$$\frac{\partial C_0}{\partial t} + \epsilon P_e [\langle u \rangle - \gamma S_c \{F(1) - F(0)\}] \frac{\partial C_0}{\partial x} = \epsilon^2 [1 - P_e^2 \langle u F \rangle] \frac{\partial^2 C_0}{\partial x^2}. \tag{40}$$

Introducing the following new dimensionless variables in the above equation

$$\tau = t, \quad \xi = \frac{x}{\epsilon} - P_e [\langle u \rangle - \gamma S_c \{F(1) - F(0)\}] \tau, \tag{41}$$

the Eq. (40) takes the following form

$$\frac{\partial C_0}{\partial \tau} = D_T \frac{\partial^2 C_0}{\partial \xi^2}, \tag{42}$$

where

$$D_T = 1 - P_e^2 \langle u F \rangle. \tag{43}$$

After solving Eq. (42) with the help of Eq. (10), one can get

$$C_0 = \frac{1}{\sqrt{4\pi D_T \tau}} \exp\left(\frac{-\xi^2}{4D_T \tau}\right). \tag{44}$$

Using Eq. (27), (36) and (37) in Eq. (34), we have

$$\frac{\partial C_2}{\partial t_0} + P_e^2 [uF - \langle u \rangle F - \langle uF \rangle] \frac{\partial^2 C_0}{\partial x^2} = \gamma^* S_c P_e \left[ \frac{dF}{dy} - \{F(1) - F(0)\} \right] \frac{\partial C_0}{\partial x} + \frac{\partial^2 C_2}{\partial y^2}, \tag{45}$$

where  $\frac{\partial C_1}{\partial t_1} = -P_e^2 \langle u \rangle F \frac{\partial^2 C_0}{\partial x^2}$ . On considering the following substitution in Eq. (45)

$$C_2 = P_e^2 G(y) \frac{\partial^2 C_0}{\partial x^2} + \gamma^* P_e S_c H(y) \frac{\partial C_0}{\partial x}, \tag{46}$$

and comparing the coefficients of  $\frac{\partial^2 C_0}{\partial x^2}$  and  $\frac{\partial C_0}{\partial x}$  from the both sides of Eq. (45), one can get

$$\frac{d^2 G}{dy^2} = uF - \langle u \rangle F - \langle uF \rangle, \tag{47}$$

along with the conditions

$$\left. \frac{dG}{dy} \right|_{y=0,1} = 0, \tag{48a}$$

$$\langle G \rangle = 0 \tag{48b}$$

and

$$\frac{d^2 H}{dy^2} = - \left[ \frac{dF}{dy} - \{F(1) - F(0)\} \right], \tag{49}$$

with

$$\left. \frac{dH}{dy} \right|_{y=0,1} = 0, \tag{50a}$$

$$\langle H \rangle = 0. \tag{50b}$$

Solving Eqs. (28), (47) and (49) with respective boundary conditions, the solutions are given below

$$F = \frac{e^{-\gamma}}{\gamma^3} \left[ (e^\gamma - 1) \left( \frac{y^2}{2} + \frac{1}{\gamma^2} - \frac{1}{6} \right) - \frac{e^{\gamma y}}{\gamma} + y - \frac{1}{2} \right] + \frac{1}{\gamma} \left( \frac{y^3}{6} - \frac{y^2}{4} + \frac{1}{24} \right), \tag{51}$$

$$\begin{aligned}
 G = & a_1 \left( \frac{y^2}{2} - \frac{1}{6} \right) + a_2 \left( \frac{y^3}{6} - \frac{1}{24} \right) + a_3 \left( \frac{y^4}{12} - \frac{1}{60} \right) + a_4 \left( \frac{y^5}{20} - \frac{1}{120} \right) \\
 & + a_5 \left( \frac{y^6}{30} - \frac{1}{210} \right) + a_6 \left( \frac{e^{\gamma y}}{2} - \frac{y}{\gamma} - \frac{e^{\gamma}}{\gamma^3} + \frac{1}{2\gamma} + \frac{1}{\gamma^3} + \right) \\
 & + a_7 \left( \frac{ye^{\gamma y}}{\gamma^2} - \frac{2e^{\gamma y}}{\gamma^3} + \frac{y}{\gamma^2} - \frac{e^{\gamma}}{\gamma^3} + \frac{3e^{\gamma}}{\gamma} - \frac{1}{2\gamma^2} - \frac{3}{\gamma^4} \right) \\
 & + a_8 \left( \frac{y^2 e^{\gamma y}}{\gamma^2} - \frac{4ye^{\gamma y}}{\gamma^3} + \frac{6e^{\gamma y}}{\gamma^4} - \frac{2y}{\gamma^3} - \frac{e^{\gamma}}{\gamma^3} + \frac{6e^{\gamma}}{\gamma^4} - \frac{12e^{\gamma}}{\gamma^5} + \frac{1}{\gamma^3} + \frac{12}{\gamma^5} \right) \\
 & + a_9 \left( \frac{y^3 e^{\gamma y}}{\gamma^2} - \frac{6y^2 e^{\gamma y}}{\gamma^3} + \frac{18ye^{\gamma y}}{\gamma^4} - \frac{24e^{\gamma y}}{\gamma^5} + \frac{6y}{\gamma^4} - \frac{e^{\gamma}}{\gamma^3} + \frac{9e^{\gamma}}{\gamma^4} - \frac{36e^{\gamma}}{\gamma^4} - \frac{36e^{\gamma}}{\gamma^5} \right. \\
 & \left. + \frac{60e^{\gamma}}{\gamma^6} - \frac{3}{\gamma^4} - \frac{60}{\gamma^6} \right) + a_{10} \left( \frac{e^{2\gamma y}}{4\gamma^2} - \frac{y}{2\gamma} - \frac{e^{2\gamma}}{8\gamma^3} + \frac{1}{4\gamma} + \frac{1}{8\gamma^3} \right), \tag{52}
 \end{aligned}$$

where

$$\begin{aligned}
 a_1 = & \left[ \frac{e^{-\gamma}}{\gamma^3} (e^{\gamma} - 1) \left( \frac{1}{\gamma^2} - \frac{1}{6} \right) - \frac{e^{-\gamma}}{2\gamma^3} + \frac{1}{24\gamma} \right] \left[ \frac{e^{-\gamma} (e^{\gamma} - 1)}{\gamma^3} - \frac{1}{2\gamma} \right] - \langle uF \rangle, \\
 a_2 = & \frac{1}{\gamma} \left[ \frac{e^{-\gamma}}{\gamma^3} (e^{\gamma} - 1) \left( \frac{1}{\gamma^2} - \frac{1}{6} \right) - \frac{e^{-\gamma}}{2\gamma^3} + \frac{1}{24\gamma} \right] + \frac{e^{-\gamma}}{\gamma^3} \left[ \frac{e^{-\gamma} (e^{\gamma} - 1)}{\gamma^3} - \frac{1}{2\gamma} \right], \\
 a_3 = & \frac{e^{-\gamma}}{\gamma^4} + \left[ \frac{e^{-\gamma} (e^{\gamma} - 1)}{2\gamma^3} - \frac{1}{4\gamma} \right] \left[ \frac{e^{-\gamma} (e^{\gamma} - 1)}{\gamma^3} - \frac{1}{2\gamma} \right], \\
 a_4 = & \frac{1}{\gamma} \left[ \frac{e^{-\gamma} (e^{\gamma} - 1)}{2\gamma^3} - \frac{1}{4\gamma} \right] + \frac{1}{6\gamma} \left[ \frac{e^{-\gamma} (e^{\gamma} - 1)}{\gamma^3} - \frac{1}{2\gamma} \right], \quad a_5 = \frac{1}{6\gamma^2}, \\
 a_6 = & -\frac{e^{-\gamma}}{\gamma^2} \left[ \frac{e^{-\gamma}}{\gamma^3} (e^{\gamma} - 1) \left( \frac{1}{\gamma^2} - \frac{1}{6} \right) - \frac{e^{-\gamma}}{2\gamma^3} + \frac{1}{24\gamma} \right] - \frac{e^{-\gamma}}{\gamma^4} \left[ \frac{e^{-\gamma} (e^{\gamma} - 1)}{\gamma^3} - \frac{1}{2\gamma} \right], \\
 a_7 = & -\frac{e^{-2\gamma}}{\gamma^5} - \frac{e^{-\gamma}}{\gamma^5}, \quad a_8 = -\frac{e^{-\gamma}}{\gamma^2} \left[ \frac{e^{-\gamma} (e^{\gamma} - 1)}{2\gamma^3} - \frac{1}{4\gamma} \right], \\
 a_9 = & -\frac{e^{-\gamma}}{6\gamma^3}, \quad a_{10} = \frac{e^{-2\gamma}}{\gamma^6},
 \end{aligned}$$

$$\begin{aligned}
 H = & -\frac{e^{-\gamma}}{\gamma^3} \left[ (e^{\gamma} - 1) \left( \frac{y^3}{6} - \frac{1}{24} \right) + \left( \frac{y^2}{2} - \frac{1}{6} \right) - \frac{e^{\gamma y}}{\gamma^2} + \frac{y}{\gamma} + \frac{e^{\gamma}}{\gamma^3} - \frac{1}{2\gamma} - \frac{1}{\gamma^3} \right] \\
 & - \frac{1}{\gamma} \left( \frac{y^4}{24} - \frac{y^3}{12} + \frac{1}{80} \right) + [F(1) - F(0)] \left( \frac{y^2}{2} - \frac{1}{6} \right). \tag{53}
 \end{aligned}$$

### 3 Result and Discussions

This section deals with a discussion of mean concentration distribution and Taylor dispersivity under the influence of suction/injection Reynolds number ( $\gamma$ ).

The transverse concentration distribution and mean concentration distribution are given as follows

$$C = C_0 + \varepsilon C_1 + \varepsilon^2 C_2, \quad (54)$$

$$\langle C \rangle = C_0 + \varepsilon \langle C_1 \rangle + \varepsilon^2 \langle C_2 \rangle. \quad (55)$$

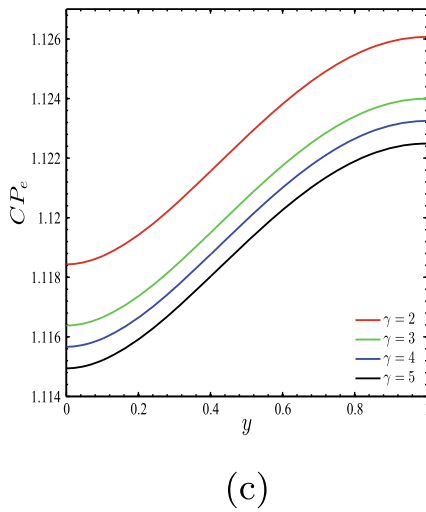
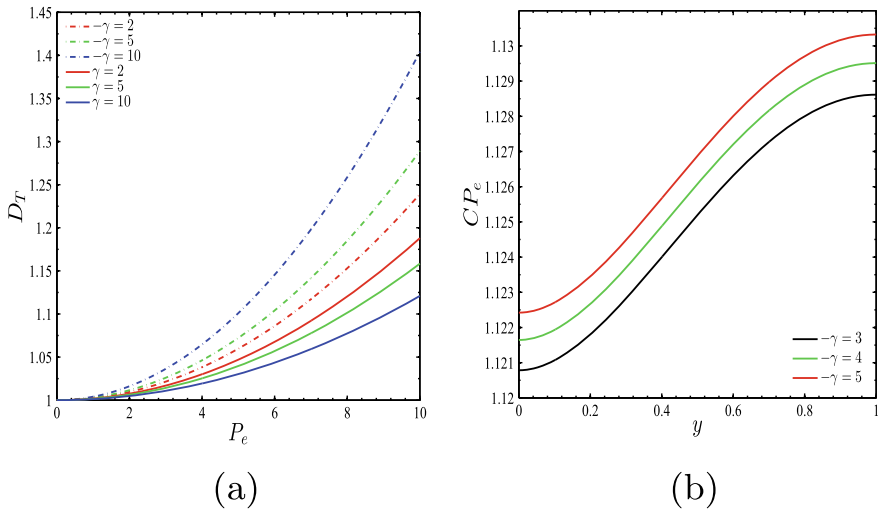
The Taylor dispersion coefficient is given by

$$D_T = 1 - P_e^2 \langle uF \rangle. \quad (56)$$

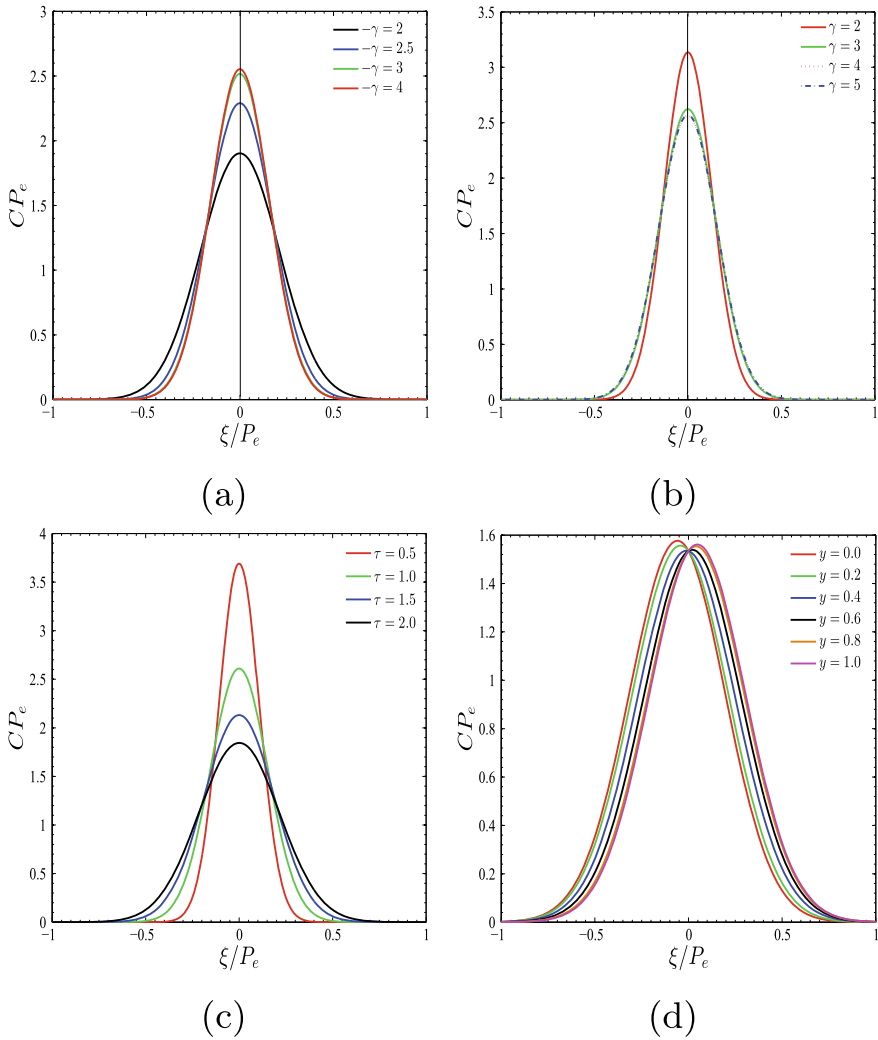
Figure 3 describes the dispersion coefficient of solute for various values of  $\gamma$ . It is seen from Fig. 3a that the dispersivity increases significantly for large values of injection parameter ( $-\gamma$ ). On the other hand, the opposite situation arises when the suction parameter ( $\gamma$ ) increases. In case of injection, the dispersion coefficient is large in compare to that of the case in suction parameter. Also, it is observe that, for all cases, the dispersion coefficient increases as the Péclet number enhances. Figure 3b depicts the Taylor dispersivity of the solute material for different values of injection parameter with respect to the channel height  $y$ . It is seen that as the injection Reynolds number increases, the dispersivity increases throughout the whole channel height. It is also visible from the Fig. 3b that near the bed ( $y = 0$ ), the dispersivity is very low and as, height of the channel rises, the dispersivity also increases. It is observed that at the free surface of the open channel ( $y = 1$ ), the Taylor dispersivity gains it's maximum value. The Taylor dispersivity is presented for various values of suction Reynolds number in Fig. 3c. The opposite phenomena on the dispersion coefficient is observed in compare to that of in Fig. 3b.

Figure 4 displays the longitudinal real concentration for different values of  $\gamma$ ,  $\tau$  and  $y$ . It is seen from Fig. 4a that with the enhancement of injection parameter, the amplitude of the concentration distribution increases. It is noted that when  $-\gamma \geq 3$ , the effect of injection on concentration along longitudinal direction is negligible. Influence of suction on distribution of concentration is shown in Fig. 4b and it is observed that the peak of the concentration curve reduces as suction Reynolds number increases. It is noticed from Fig. 4c that the amplitude of the longitudinal real concentration reduces significantly with the increment of dispersion time. It is interesting to note that the concentration distribution moves towards the downstream direction when transverse position raises from the bed surface (see Fig. 4d).

Iso-concentration contours are depicted in Fig. 5 for different values of injection parameter. When  $-\gamma = 3$  the concentration stay at the bed surface. The concentration starts to move away longitudinally for  $-\gamma = 5$ , the reason behind this, the introduction of injection in the flow, the flow velocity increases, as a result convec-



**Fig. 3** a Dispersion coefficient for different values of injection ( $-\gamma$ ) and suction ( $\gamma$ ) Reynolds number, b Transverse concentration for various values of injection Reynolds number ( $-\gamma$ ), c Transverse concentration for different values of suction Reynolds number ( $\gamma$ )



**Fig. 4** Longitudinal real concentration distribution for various values of: **a** injection Reynolds number ( $-\gamma$ ), **b** suction Reynolds number ( $\gamma$ ), **c** dispersion time, **d** height of the channel

tion takes places in the flow. Also for  $-\gamma = 10$  the rate of convection is large as compared to the previous values of injection Reynolds number.

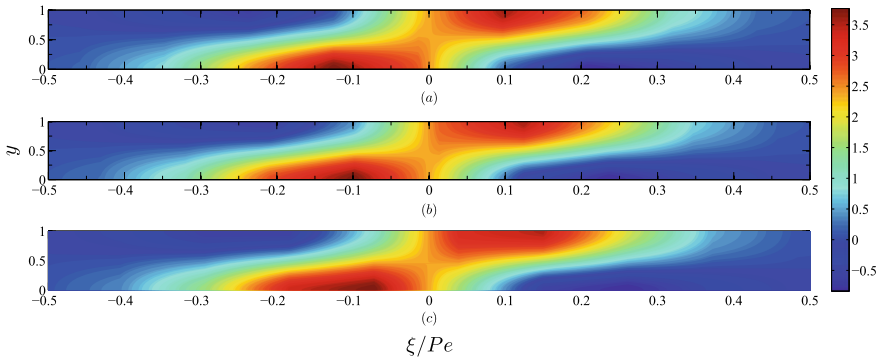


**Fig. 5** Iso-concentration contour for: **a**  $-\gamma = 3$ , **b**  $-\gamma = 5$ , **c**  $-\gamma = 10$

## 4 Conclusion

In the present study, solute transport in an open channel flow is analyzed by using multi-scale analysis technique. The real concentration distribution and Taylor dispersivity of the solute is evaluated analytically. It is observed that Taylor dispersivity decreases with the increment of suction Reynolds number and it increases with the enhancement of injection Reynolds number. The reason behind this, when  $\gamma$  increases, the flow decreases, as a result rate of dispersion reduces and consequently, the peak of the amplitude of the longitudinal concentration distribution decreases. The opposite scenario arises when  $-\gamma$  increases, i.e. when injection Reynolds number increases. With the enhancement of  $-\gamma$ , the flow velocity increases which helps to increase the rate of dispersion. Therefore, one can observe the increment in the amplitude of the real concentration along the longitudinal direction. As dispersion time progresses, the amplitude of the concentration curves along longitudinal direction becomes flat. This is because, with the increment of time, the mixing of the solute increases. It is observed that the iso-concentration contour spreads along the longitudinal direction with the enhancement of injection Reynolds number ( $-\gamma$ ), because the rate of convection becomes large for higher values of the injection Reynolds number ( $-\gamma$ ).

## References

1. Taylor, G.I.: Dispersion of soluble matter in solvent flowing slowly through a tube. Proc. R. Soc. Lond. A **219**, 186–203(1953). <https://doi.org/10.1098/rspa.1953.0139>
2. Aris, R.: On the dispersion of a solute in a fluid flowing through a tube. Proc. R. Soc. Lond. A **235**, 67–77 (1956). <https://doi.org/10.1098/rspa.1956.0065>
3. Gill, W.N.: A note on the solution of transient dispersion problems. In: Proc. R. Soc. Lond. Ser. A **298**(1454), 335–339 (1967). <https://doi.org/10.1098/rspa.1967.0107>



4. Mondal, K.K.: On dispersion of settling particles from an elevated sources in an open channel flow. *J. Comput. Appl. Math.* **193**(1), 22–37 (2006). <https://doi.org/10.1016/j.cam.2005.04.068>
5. Mei, C.C., Vernescu, B.: Homogeniyation methods for multiscale mechanics. In: World scientific (2010). [http://refhub.elsevier.com/S1007-5704\(18\)30135-7/sbref0045](http://refhub.elsevier.com/S1007-5704(18)30135-7/sbref0045)
6. Wu, Z., Li, Y., Chen, G.Q.: Multi-scale analysis for environmental dispersion in wetland flow. *Commun. Nonlinear Sci. Numer. Simul.* **16**, 3168–3178 (2011). <https://doi.org/10.1016/j.cnsns.2010.12.002>
7. Shojaefard, M.H., Noorpoor, A.R., Avanesians, A. Ghaffapour, M.: Numerical investigation of flow control by suction and injection on a subsonic airfoil. *Am. J. Appl. Sci.* **2**(10), 1474–1480 (2005). <https://thescipub.com/abstract/10.3844/ajassp.2005.1474.1480>
8. Barnwell, R.W., Hussaini, M.Y.: Natural laminar flow and laminar flow control. Springer, New York (1992). <https://doi.org/10.1007/978-1-4612-2872-1>
9. Ishak, A.J., Merkin, H., Nazar, R., Pop, I.: Mixed convection boundary layer flow over a permeable vertical surface with prescribed wall heat flux. In: *ZAMP: Zeitschrift für angewandte Mathematik und Physik*, vol. 59(1), pp. 100–123 (2008). <https://doi.org/10.1155/2010/659023>
10. Jha, B.K., Aina, B.: Role of suction/injection on steady fully developed mixed convection flow in a vertical parallel plate microchannel. *Ain Shams Eng. J.* **9**(4), 747–755(2018). <https://doi.org/10.1016/j.asej.2016.05.001>
11. Sasikumar J, Bhati, D., Bhaskar, V.: Effect of heat and mass transfer on MHD oscillatory flow through asymmetric wavy channel in a porous medium with suction and injection. In: *AIP Conference Proceedings*, vol. 2277, p. 030009 (2020). <https://doi.org/10.1063/5.0025530>
12. Abo-Dahab, S.M., Abdelhafez, M.A., Mebarek-Oudina, F., Bilal, S.M.: MHD Casson nanofluid flow over nonlinearly heated porous medium in presence of extending surface effect with suction/injection. *Indian J. Phys.* **95**, 2703–2717 (2021). <https://doi.org/10.1007/s12648-020-01923-z>

# Mathematical Modelling of Magnetized Nanofluid Flow Over an Elongating Cylinder with Erratic Thermal Conductivity



Debasish Dey, Rupjyoti Borah, and Joydeep Borah

**Abstract** An attempt has been made to analyze the flow behaviours of magnetized nanofluid due to an elongating cylinder with the contemporary effects of both heat and mass transference. The flow governing equations are re-modeled into a solvable form by considering a suitable similarity transformation. The MATLAB fourth-order Runge-Kutta shooting technique is implemented to work out the problem. The numerical findings are assembled on a system of tables and diagrams. These results show nanofluid properties for a wide range of circulations such as motion, thermal and mass fractions including physical dimensionless numbers. The major result of this study is that the thermal fraction of the nanofluid is an escalating function of the flow parameters namely the magnetic, Brownian motion, thermophoresis, temperature ratio and the curvature parameters.

**Keywords** Nanofluid · Heat transfer · Mass transfer · Extending cylinder · Variable thermal conductivity

## 1 Introduction

The flow of different fluid models caused due to an extending or contracting geometries have lots of applications in engineering sciences, industrial processes and medical sciences etc. Crane [1] was the first author who has discussed the fluid's flow caused due to stretching/shrinking surfaces in 1970. Again, the relevance of magnetic field on the fluid's flow caused due to different surfaces has plentiful applications in diverse fields. In the last five years, many researchers Gangadhar et al. [2], Das et al. [3], Dey et al. [4], Dey and Borah [5], Dey et al. [6, 7] etc. have

---

D. Dey (✉) · R. Borah  
Department of Mathematics, Dibrugarh University, Dibrugarh 786004, AS, India  
e-mail: [debasish41092@gmail.com](mailto:debasish41092@gmail.com)

J. Borah  
Department of Mathematics, D. D. R. College, Chabua 786184, AS, India

© The Author(s), under exclusive license to Springer Nature Switzerland AG 2022  
S. Banerjee and A. Saha (eds.), *Nonlinear Dynamics and Applications*,  
Springer Proceedings in Complexity,  
[https://doi.org/10.1007/978-3-030-99792-2\\_41](https://doi.org/10.1007/978-3-030-99792-2_41)

509

discussed the effects of magnetic field on the different fluids flow by considering stretching/shrinking surfaces.

The simultaneous effects of both thermal and mass transmission on fluid flows have multifarious applications. The effect of heat transfer has drawn many researchers due to its applications in different fields such as industrial processes, medical sciences and biological systems. The mass transfer phenomenon draws an imperative function in realizing industrial processes such as reverse osmosis, membrane separation, dissemination of chemical impurities and distillation of water etc. Manjunatha et al. [8] and Divya et al. [9] have discussed the simultaneous effects of both heat and mass transfers in the peristaltic mechanism of the Jeffrey fluid flow model. In recent time, Prasad et al. [10], Dey and Borah [11] and Vaidya et al. [12] etc. have discussed the flow behaviours with the influenced of both heat and mass transfers due to a stretching/shrinking geometries respectively. Abel et al. [13] and Jahan et al. [14] have explored the nature of flow by considering variable fluid properties.

The nanofluid signifies a crucial function in the modern time because it can enhance the thermal transmission that is important in industrial processes. It is one kind of fluid that contains solid particles with dimension less than 100 nm. Suspension of nanoparticles in fluid is one of the most appropriate techniques for enhancing heat transmission coefficients. It is a smart fluid where we can reduce or enhance the heat transfer phenomenon as requirement. The nanofluid has lots of applications such as industrial processes, nuclear reactors, transportation, electronics, extraction of geothermal power, biomedicine and food processing etc. In 1995, Choi [15] has developed the term 'Nanofluid'. Many researchers have influenced the various applications of nanofluid in modern times and put their ideas to rich the research level on nanofluids. Das et al. [16], Ghosh and Mukhopadhyay [17] and Molli and Naikoti [18] etc. have investigated the behaviour of nanofluid flow and their importance in different physical fields. Prasad et al. [10], Li et al. [19] and Narender et al. [20] have examined the flow nature of nanofluid with the effects of both heat and mass transfers. Khashi'ie et al. [21] have given the mathematical model of hybrid nanofluid flow due to a shrinking cylinder which is situated in porous medium.

The intention of this model is catalogued below:

- i. Time-independent flow of magnetized nanofluid due to an extending cylinder with the effects of both thermal and concentration diffusions is considered.
- ii. The governing equations viz., equation of motion, energy and species of the nanofluid are transformed into solvable form by adopting appropriate similarity transformation and hence decipher with the support of MATLAB fourth-order Runge- Kutta Shooting method.
- iii. Flow behaviours of nanofluid with temperature and mass fractions are presented pictorially for assorted amount of novel flow parameters.
- iv. The physical measures of curiosity such as drag force, local Nusselt number and mass diffusion rate of the fluid at the vicinity of the system are tabulated.
- v. A comparison table is made to validate our results for the limiting case with the pioneer works of Jahan et al. [14].

We believed that this work carries lots of novelty such as idea of nanofluid, variable fluid properties and elongating cylinder etc. and may be applied in various industrial processes, scientific fields and medical sciences etc. In future, researchers may extend this work by considering different geometries by assisting different approaches.

## 2 Problem Construction

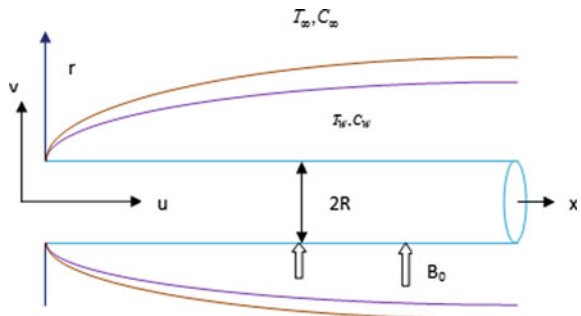
To form the mathematical model of this problem, the following suppositions are made.

- (i) The steady, 2D, incompressible and viscous nanofluid flow over an extending cylinder with the synchronized influences of both heat and mass transference.
- (ii) The flow is governed by (a) inertia force, (b) viscous force and (c) pressure gradient.
- (iii) The cylinder of diameter  $2R$  is immersed horizontally in the nanofluid with the ambient fluid's velocity is  $U_e = bx$  where  $b \geq 0$ .
- (iv) A constant magnetic field of strength ( $B_0$ ) is considered in the vertical direction of the flow.
- (v) The surface of the geometry is characterized by the velocity  $U_w(x) = ax$ , where  $a$  is the constant such that  $a > 0$  signifies elongate at the surface with the prescribed wall temperature and concentration are  $T_w(x) - T_\infty = x$  &  $C_w(x) - C_\infty = x$  respectively, where  $T_\infty$  and  $C_\infty$  are the ambient temperature and concentration respectively.
- (vi)  $k(T)$  is supposed to fluctuate with temperature in linear manner.

The schematic illustration of this problem is drawn in Fig. 1. Following Jahan et al. [14], the leading equations are:

$$\frac{\partial}{\partial x}(ru) + \frac{\partial}{\partial r}(rv) = 0, \tag{1}$$

Fig. 1 Flow diagram



$$u \frac{\partial u}{\partial x} + v \frac{\partial u}{\partial r} = v \left( \frac{\partial^2 u}{\partial r^2} + \frac{1}{r} \frac{\partial u}{\partial r} \right) + \frac{\sigma B_0^2}{\rho} (u - U_e), \tag{2}$$

$$u \frac{\partial T}{\partial x} + v \frac{\partial T}{\partial r} = \frac{1}{\rho c_p} \frac{1}{r} \frac{\partial}{\partial r} \left[ k(T)r \frac{\partial T}{\partial r} \right] + \tau \left[ D_B \frac{\partial C}{\partial r} \frac{\partial T}{\partial r} + \frac{D_T}{T_\infty} \left( \frac{\partial T}{\partial r} \right)^2 \right] + \frac{\sigma B_0^2}{\rho c_p} u^2, \tag{3}$$

$$u \frac{\partial C}{\partial x} + v \frac{\partial C}{\partial r} = D_B \left[ \frac{\partial^2 C}{\partial r^2} + \frac{1}{r} \frac{\partial C}{\partial r} \right] + \frac{D_T}{T_\infty} \left[ \frac{\partial^2 T}{\partial r^2} + \frac{1}{r} \frac{\partial T}{\partial r} \right]. \tag{4}$$

The relevant boundary conditions are

$$\begin{aligned} u = U_w = ax, v = 0, T = T_w, C = C_w \text{ at } r = R, \\ u \rightarrow U_e = bx, T \rightarrow T_\infty, C \rightarrow C_\infty \text{ as } r \rightarrow \infty, \end{aligned} \tag{5}$$

To transform the Eqs. (1)–(4) into solvable form, the following new quantities are launched (following Jahan et al. [14]):

$$\begin{aligned} \eta = \sqrt{\frac{a}{2\nu}} \left( \frac{r^2 - R^2}{R} \right), \psi = \sqrt{\frac{\nu a}{2}} R x f(\eta), T - T_\infty = (T_w - T_\infty) \theta(\eta), \\ C - C_\infty = (C_w - C_\infty) \phi(\eta), u = \frac{1}{r} \frac{\partial \psi}{\partial r}, v = -\frac{1}{r} \frac{\partial \psi}{\partial x}. \end{aligned} \tag{6}$$

For liquid metal,  $k$  revolutionize with temperature in linear way from  $0^\circ F - 400^\circ F$  approximately (Keys [22]). Following Abels et al. [13], we define  $k(T) = k_\infty(1 + \varepsilon\theta)$ , where  $\varepsilon = \frac{k_w - k_\infty}{k_\infty}$  is the small temperature parameter.

The Eq. (1) is satisfied by the Eq. (6) which represents the validation of the similarity transformation. Applying Eq. (6) into the Eqs. (2)–(4) and (5) we have achieved the following solvable equations along with boundary condition.

$$(2 + 2K\eta) f''' + f f'' - (f')^2 + 2K f'' - M^2 (f' - A) + A^2 = 0, \tag{7}$$

$$\begin{aligned} (1 + \varepsilon\theta)(2 + 2K\eta) \theta'' + \varepsilon(2 + 2K\eta) (\theta')^2 + (1 + \varepsilon\theta) K \theta' + \text{Pr} (f \theta' + M^2 E c f'^2) \\ + 2 \text{Pr} N_b (2 + 2K\eta) \theta' \phi' + \text{Pr} N_T (2 + 2K\eta) \theta'^2 = 0, \end{aligned} \tag{8}$$

$$(2 + 2K\eta) \phi'' + K \phi' + \frac{N_t}{N_b} (2 + 2K\eta) \theta'' + \frac{N_t}{N_b} K \theta' + L e (f \phi' - f' \phi) = 0. \tag{9}$$

The surface restrictions are:

$$\begin{aligned} f(0) = 0, f'(0) = 1, \theta(0) = 1, \phi(0) = 1; \\ f'(\infty) \rightarrow A, \theta(\infty) \rightarrow 0, \phi(\infty) \rightarrow 0. \end{aligned} \tag{10}$$

where, the parameters are defined in the following way:

$$K = \frac{1}{R} \sqrt{\frac{2\nu}{a}}, \text{Pr} = \frac{\mu c_p}{k_\infty}, M^2 = \frac{\sigma B_0^2}{\rho a}, Ec = \frac{U_w^2}{c_p(T_w - T_\infty)},$$

$$A = \frac{b}{a}, N_b = \frac{\tau D_B(C_w - C_\infty)}{\nu}, N_t = \frac{\tau D_T(T_w - T_\infty)}{\nu T_\infty} \& Le = \frac{\nu}{D_B}.$$

The dimensionless numbers such as drag force of the fluid at surface, local Nusselt number and mass accumulation rate (determined by Sherwood number) are observed in this study. These quantities play a vital role in significant real life areas. These quantities are defined in the following way:

$$C_f = \frac{1}{\rho U_w^2} \mu \left( \frac{\partial u}{\partial r} \right)_{r=R}, Nu_x = - \frac{x}{(T_w - T_\infty)} \left( \frac{\partial T}{\partial r} \right)_{r=R}$$

$$Sh_x = - \frac{x}{(C_w - C_\infty)} \left( \frac{\partial C}{\partial r} \right)_{r=R}. \tag{11}$$

The Eq. (6) is implemented on this Eq. (11), we have got the following form:

$$\frac{1}{\sqrt{2}} C_f Re_x^{1/2} = f''(0), \frac{1}{\sqrt{2}} Nu_x Re_x^{-1/2} = -\theta'(0), \frac{1}{\sqrt{2}} Sh_x Re_x^{-1/2} = -\phi'(0). \tag{12}$$

### 3 Methodology

Following Hazarika [23] and Hazarika et al. [24], the MATLAB fourth-order Runge–Kutta shooting scheme is adopted to solve the Eqs. (7)–(9) along with the surface restriction (10). Shooting technique is a suitable scheme for solving a boundary value problem of fluid dynamics. It is a sophisticated computer oriented numerical method. This method can be used for solving both systems of linear and non linear equations, highly coupled boundary value problems of ordinary differential equations. This method does not need linearization of the equations, has been effectively applied to this class of problems.

In case of boundary value problems of second order differential equations, one condition is prescribed at either of the end points. Hence, at the initial point of integration, one condition is always missing. Shooting method estimates the missing initial condition in such a way that the estimation satisfies the condition prescribed at the boundary too, to some desired accuracy. At the beginning, the missing value is guessed and refined by using an iterative technique until the desired accuracy is obtained.

### 4 Results and Discussion

The above mentioned numerical technique is adopted to obtain the effects of flow parameters on the nanofluid flow in terms of velocity, temperature and mass fraction. A special emphasis is given on the effects of the magnetic ( $M$ ), curvature ( $K$ ), small temperature ( $\epsilon$ ), Brownian motion ( $N_b$ ) and thermophoresis ( $N_t$ ) parameters in the flow. We have fixed the value of the Lewis number ( $Le$ ) (ratio of the Schmith number and Prandtl number) is 2 throughout the study. The greater value of  $Le$  than 1 represents that the heat will neutralize more hurriedly than species.

Influence of  $M$  on the velocity and temperature fields of the nanofluid flow are shown in Figs. 2 and 3. Application of magnetic field on the fluid decelerates the motion during the flow region which is in consistency with the reality that the Lorentz force plays as a hindering force and, subsequently, it shrinks the thickness of the boundary-layer of the motion. But, temperature of the nanofluid is an amplifying function of  $M$ . This ensues due to the strength of the applied magnetic field enhances in an electrically conducting fluid, it develops the resistive type force called ‘Lorentz force’. This force decelerates the motion of the fluid. Again, the thermal force as the supplementary work done involved to defy the nanofluid against the exploit of  $M$ . It warms up the conducting nanofluid and raises the temperature field. Figures 4, 5 and 6 are depicted to demonstrate the persuade of  $K$  on the flow. To control the fluid’s velocity and mass fraction, the curvature parameter is very important. That is the fluid’s velocity dwindles when the curvature of the cylinder enlarges (see Fig. 4). But, the fluid’s temperature is an increasing function of  $K$  (see Fig. 5) whereas, the mass fraction of the nanofluid drop downs with  $K$  (see Fig. 6). It can be accomplished that the curvature of the cylinder is a controlling parameter of fluid’s velocity and mass fraction. Moreover, the larger boundary layer thickness of the momentum and concentration of the flow are obtained with lower values of  $K$ . The Brownian motion

**Fig. 2** Velocity outline against  $\eta$  for incremental amount of  $M$

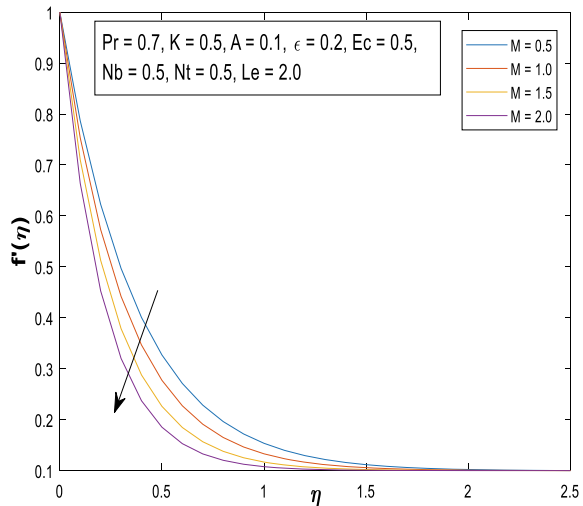


**Fig. 3** Temperature field against  $\eta$  for incremental amount of  $M$

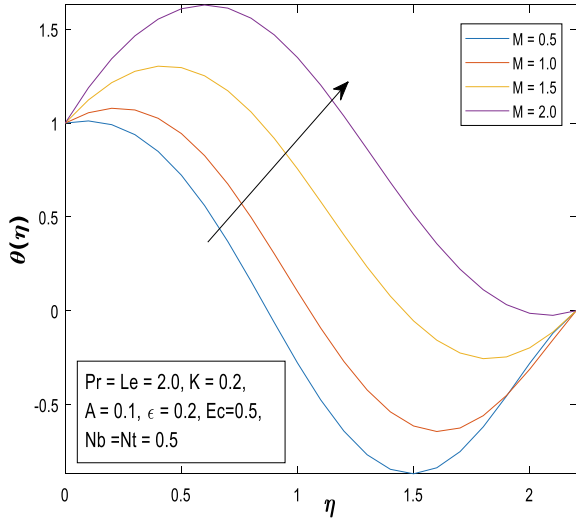
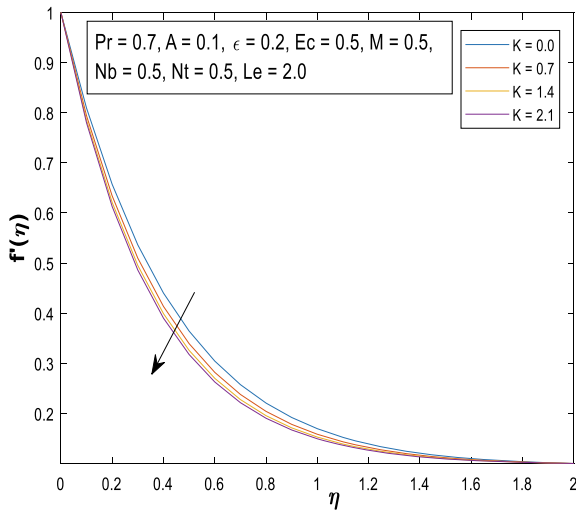


**Fig. 4** Velocity outline against  $\eta$  for different amount of  $K$



(represents the random motion of nano-particles) effects on the temperature and mass fraction of the nanofluid are shown pictorially in Figs. 7 and 8. From these figures, it is perceived that the fluid's temperature and mass fraction are increasing function of  $N_b$ . The reason behind this phenomenon is that the augmented values of  $N_b$  enhances the thickness of the thermal and concentration boundary layers, which eventually boost ups the fluid's temperature and concentration. Influence of  $N_t$  on the thermal and mass fraction of the fluid are elaborated in Figs. 9 and 10. The thermophoresis parameter helps to enhance the thermal transmission of the nanofluid (see Fig. 9). From this figure, it is noticed that the thermal boundary layer thickness enhances and



**Fig. 5** Temperature field against  $\eta$  for different amount of  $K$

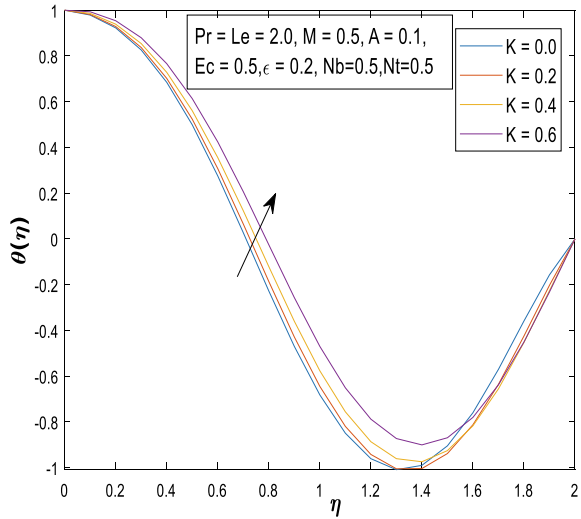
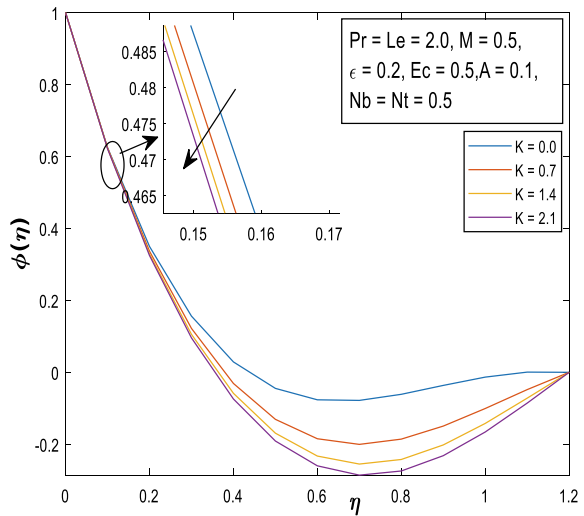


**Fig. 6** Mass Fraction against  $\eta$  for different amount of  $K$



tends asymptotically to zero as the distance rises from the surface of the cylinder. It can be endorsed that the escalating amount of  $Nt$  improves the liquid temperature which is happened due to development in nanoparticles percentage with  $Nt$ . But, the mass fraction of the nanoparticles lessens with the improving values of  $Nt$  (see Fig. 10). The Fig. 11 is depicted to show the influence of small temperature parameter ( $\epsilon$ ) which is responsible for variable thermal conductivity. The thermal transmission rate enhances for improving values of  $\epsilon$ . The physics behind this characteristics is that on growing values of  $\epsilon$  increases the thermal conductivity of the fluid which allows for a faster rate of heat transfer. The Fig. 12 shows the effect of Lewis number ( $Le$ ) on the

**Fig. 7** Temperature field against  $\eta$  for different amount of  $Nb$

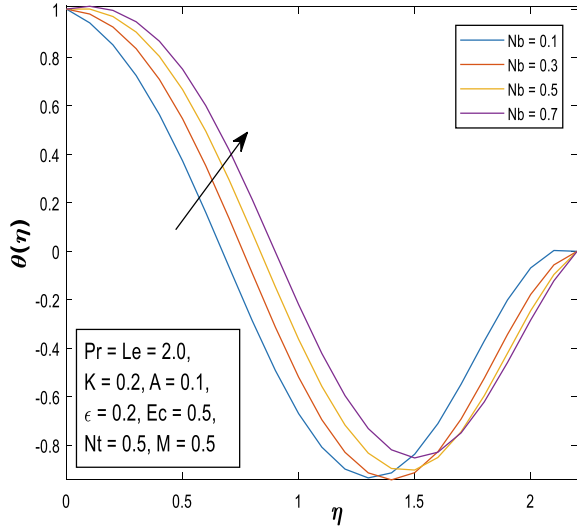
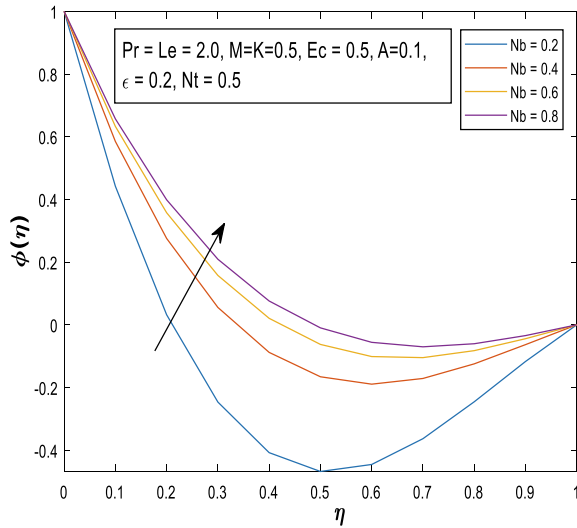


**Fig. 8** Mass fraction against  $\eta$  for different amount of  $Nb$



volume fraction of the nano-particles suspended in the fluid. It is discerned that the escalating values of  $Le$  significantly drops down the mass fraction of the nanofluid. Increasing values of  $Le$  signifies the larger thermal boundary film width at the outflow of dropping the width of the concentration boundary film and, consequently, the mass fraction of the nanfluid drops down.

In the nonappearance of nanofluid and concentration effects, the governing Eqs. (1)–(3) along with their boundary restrictions are fit with Jahan et al. [13] works. They have studied the boundary layer fluid’s flow due to a stretching cylinder

**Fig. 9** Temperature field against  $\eta$  for different amount of  $Nt$

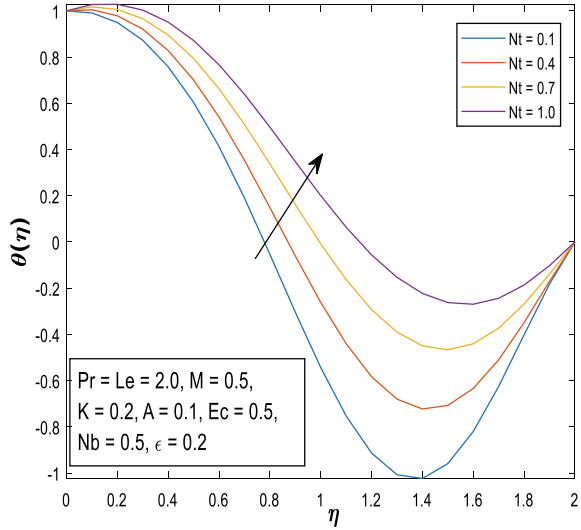
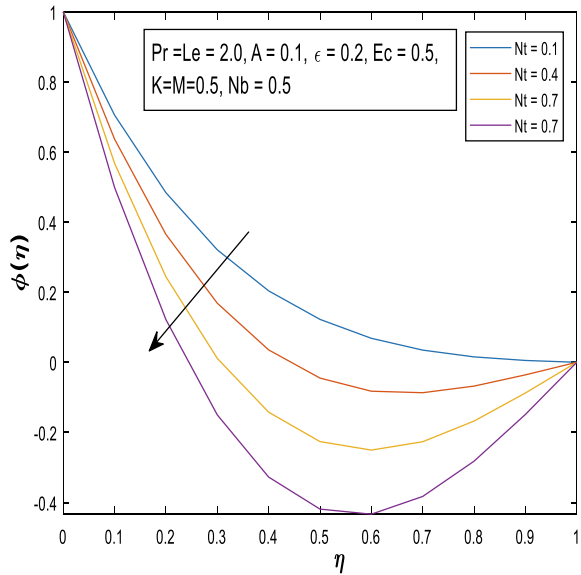


**Fig. 10** Mass fraction against  $\eta$  for different amount of  $Nt$



with variable thermal conductivity. We have matched up to our numerical values (bvp4c and shooting method solutions) of drag force at the surface of the cylinder with the results of Jahan et al. [13] (see Table 1).

From this Table 1, a good reasonable conformity is observed of our solutions with the work of Jahan et al. [14]. The bvp4c solution of the drag force is comparatively matched with Jahan et al. [14] works than the shooting method solution.

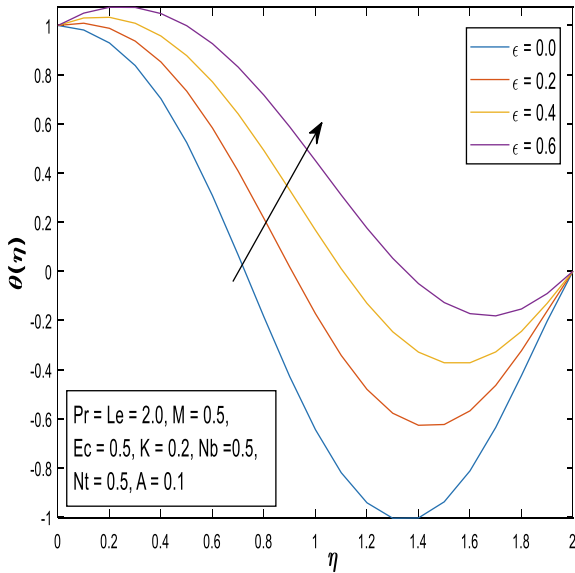


Fig. 11 Temperature field against  $\eta$  for different amount of  $\epsilon$

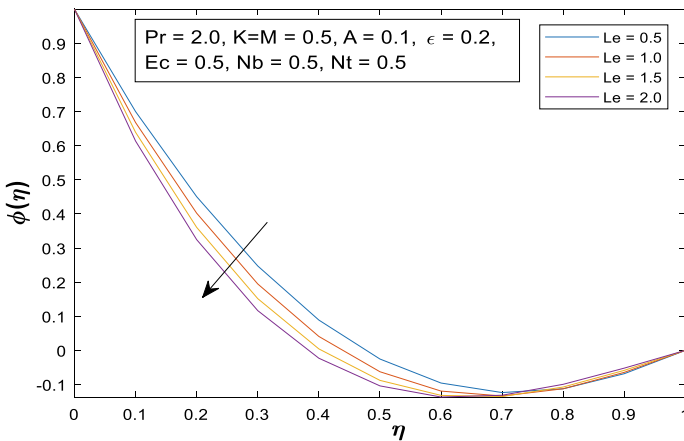


Fig. 12 Mass fraction against  $\eta$  for different amount of  $Le$

The Table 2 demonstrates the outcome of the dimensionless parameter  $M$ ,  $K$  &  $A$  on the skin friction coefficient of the nanofluid. From this table, it is perceived that the skin friction coefficient is a decreasing function of  $M$  &  $K$ . Therefore, we can reduce the effects of drag force ( $f''(0)$ ) of the nanofluid flow caused due to stretching cylinder by applying magnetic field. But, the drag force of the fluid increases with  $A$ . It is also seen that the numerical values of skin friction coefficient obtained by shooting method is higher than the bvp4c solver solutions. The numerical values of

**Table 1** Drag force at the surface for the flow parameters  $Pr = 1, \varepsilon = 0.2, Ec = 0.5, Le = Nt = Nb = 0$

K	M	A	Skin friction coefficient		
			Jahan et al. [14] works	Present results	
				Bvp4c solution	Shooting method solution
0.0	0.2	0.1	- 0.68667	- 0.6829	- 0.7098
0.2			- 0.72698	- 0.7293	- 0.7326
0.3	0.5		- 0.81618	- 0.8122	- 0.7948
	0.2	0.2	- 0.7136	- 0.7136	- 0.7123
		0.5	- 0.5111	- 0.5011	- 0.5395

**Table 2** Skin friction coefficient for the flow parameters  $M, K \& A$  when  $Pr = Le = 2.0, Nt = Nb = 0.5, \varepsilon = 0.2 \& Ec = 0.5$

M	K	A	Skin friction coefficient ( $f''(0)$ )	
			Bvp4c solver	Shooting method
0.2	0.2	0.1	- 0.8217	- 0.7326
0.5			- 0.8962	- 0.7873
0.5	0.2		- 0.8962	- 0.7873
	0.4		- 0.9751	- 0.8016
	0.2	0.3	- 0.7538	- 0.6711
		0.5	- 0.5756	- 0.5171

Nusselt number with different values of flow parameters are tabulated in Table 3. From this table, it is perceived that the Nusselt number reduces for the increasing values of the  $M, Nt \& Nb$ , whereas, the flow parameters  $K \& \varepsilon$  enhance the heat transfer rate in the vicinity of the surface. Again, the Shooting method solutions of Nusselt number is smaller than the Bvp4c solver solutions. The Brownian motion ( $Nb$ ), thermophoresis ( $Nt$ ) and Lewis number ( $Le$ ) parameters enhance the mass accumulation rate of the nanofluid at the surface of the cylinder (see Table 4). The Bvp4c solver solutions of the Sherwood number are comparatively smaller than the Shooting method solutions.

### 5 Conclusions

From this investigation, the following conclusions are established:

- Effects of  $M \& K$  reduce the motion of the nanofluid, whereas, they enhance the temperature of the fluid.
- The temperature of the nanofluid enhances due to the presence of  $Nb, Nt \& \varepsilon$ .

**Table 3** Nusselt number for the flow parameters  $M, K, Nt, Nb$  &  $\varepsilon$  when  $Pr = Le = 2.0$  &  $Ec = 0.5$

$M$	$K$	$Nt$	$Nb$	$\varepsilon$	Nusselt number ( $-\theta'(0)$ )	
					Bvp4c solver	Shooting method
0.2	0.2	0.5	0.5	0.2	0.1564	0.1057
0.5					0.1344	0.0748
0.5	0.2	0.5	0.5	0.2	0.1344	0.0748
	0.4				0.1492	0.1293
0.5	0.2	0.4	0.5	0.2	0.1406	0.0679
		0.7			0.1224	0.0528
	0.5	0.5	0.5	0.2	0.1007	0.0748
					0.8	0.0354
	0.5	0.5	0.5	0.2	0.1007	0.0748
				0.4	0.1095	0.1335

**Table 4** Sherwood number for the flow parameters  $Pr = Le = 2.0, Ec = 0.5, M = 0.5, K = 0.2$  &  $\varepsilon = 0.2$

$Nb$	$Nt$	$Le$	Sherwood number ( $-\phi'(0)$ )	
			Bvp4c solution	Shooting method solution
0.2	0.5	2.0	1.0181	1.2550
0.5			1.1227	1.4238
0.5	0.4	2.0	1.1028	1.3345
	0.7		1.1665	1.6028
0.5	0.5	1.0	0.7873	1.1846
		2.0	1.1227	1.4238

- The volume fraction of the nanofluid boosts up due to the effects of  $Nb$ . But, influence of  $Nt$  &  $Le$  lessen the nanofluid’s volume fraction.
- By applying magnetic field, we can reduce the effects of drag force of the nanofluid at the surface of the cylinder.
- From the comparative study, we have achieved that the MATLAB built-in bvp4c solver scheme gives nearest exact solution than the Shooting technique.

**Nomenclature:**

$\rho$ -density,  $\nu$ -kinematic viscosity,  $c_p$ -specific heat,  $\sigma$ -electric charge density  $u$ -velocity along  $x$ -axis,  $v$ -velocity along  $r$ -direction,  $D_B$ -the Brownian diffusion coefficient,  $D_T$ -thermophoretic coefficient,  $R$ -radius of the cylinder,  $a, b$ -constants,  $\psi$ -dimensionless stream function,  $K$ -curvature parameter,  $Pr$ -Prandtl number,  $M$ -Magnetic field,  $Ec$ -Eckert number,  $A$ -velocity ratio parameter,  $N_b$ -Brownian

motion parameter,  $N_f$ -thermophoresis parameter,  $\varepsilon$ -small temperature parameter,  $Le$ -Lewis number,  $\theta(\eta)$ -dimensionless temperature,  $\phi(\eta)$ -dimensionless concentration,  $Re_x$ -local Reynolds number,  $\tau = \frac{(\rho C)_p}{(\rho C)_f}$ -the ratio of effective heat capacity of the nanoparticle and base”.

## References

1. Crane, L.J.: Flow past a stretching plate. *Zeitschrift für Angew. Math. und Phys. ZAMP* **21**(4), 645–647 (1970)
2. Gangadhar, K., Ramana, K.V., Makinde, O.D., Kumar, B.R.: MHD flow of a Carreau fluid past a stretching cylinder with Cattaneo-Christov heat flux using spectral relaxation method. *Defect Diffus. Forum.* **387**, 91–105 (2018)
3. Das, S., Chakraborty, S., Makinde, O.D., Jana, R.N.: Entropy analysis of MHD variable thermal conductivity fluid flow past a convectively heated stretching cylinder. *Defect Diffus. Forum.* **387**, 244–259 (2018)
4. Dey, D., Borah, R., Mahanta, B.: Boundary layer flow and its dual solutions over a stretching cylinder: stability analysis. In: *Emerging Technologies in Data Mining and Information Security. Advances in Intelligent Systems and Computing*, pp. 27–38 (2021)
5. Dey, D., Borah, R.: Stability analysis on dual solutions of second-grade fluid flow with heat and mass transfers over a stretching sheet. *Int. J. Thermofluid Sci. Technol.* **8**(2) (2021)
6. Dey, D., Borah, R., Khound, A.S.: Stability analysis on dual solutions of MHD Casson fluid flow with thermal and chemical reaction over a permeable elongating sheet. *Heat Transf.* 1–17 (2022)
7. Dey, D., Hazarika, M., Borah, R.: Entropy generation analysis of magnetized micropolar fluid streaming above an exponentially extending plane. *Lat. Am. Appl. Res.* **51**(4), 255–260 (2021)
8. Manjunatha, G., Rajashekhar, C., Vaidya, H., Prasad, K.V., Vajravelu, K.: Impact of heat and mass transfer on the peristaltic mechanism of Jeffrey fluid in a non-uniform porous channel with variable viscosity and thermal conductivity. *J. Therm. Anal. Calorim.* **139**(2), 1213–1228 (2020)
9. Divya, B.B., Manjunatha, C., Rajashekhar, G., Vaidya, H., Prasad, K.V.: The hemodynamics of variable liquid properties on the MHD peristaltic mechanism of Jeffrey fluid with heat and mass transfer. *Alexandria Eng. J.* **59**(2), 693–706 (2020)
10. Durga Prasad, P., Kiran Kumar, R.V.M.S.S., Varma, S.V.K.: Heat and mass transfer analysis for the MHD flow of nanofluid with radiation absorption. *Ain Shams Eng. J.* **9**(4), 801–813 (2018)
11. Dey, D., Borah, R.: Dual solutions of boundary layer flow with heat and mass transfers over an exponentially shrinking cylinder: stability analysis. *Lat. Am. Appl. Res.* **50**(4), 247–253 (2020)
12. Vaidya, H., Rajashekhar, C., Manjunatha, G., Prasad, K.V., Makinde, O.D., Vajravelu, K.: Heat and mass transfer analysis of MHD peristaltic flow through a compliant porous channel with variable thermal conductivity. *Phys. Scr.* **95**(4) (2020)
13. Abel, M.S., Datti, P.S., Mahesha, N.: Flow and heat transfer in a power-law fluid over a stretching sheet with variable thermal conductivity and non-uniform heat source. *Int. J. Heat Mass Transf.* **52**(11–12), 2902–2913 (2009)
14. Jahan, S., Sakidin, H., Nazar, R.M.: MHD stagnation point flow over a stretching cylinder with variable thermal conductivity and joule heating. *AIP Conf. Proc.* **1787** (2016)
15. Choi, S.U.S.: Enhancing thermal conductivity of fluids with nanoparticles. In: *Proceedings of the 1995 ASME International Mechanical Engineering Congress and Exposition, San Francisco, USA, ASME FED 231/MD, 1995*, pp. 99–105 (1995)

16. Das, K., Acharya, N., Kundu, P.K.: Influence of variable fluid properties on nanofluid flow over a wedge with surface slip. *Arab. J. Sci. Eng.* **43**(5), 2119–2131 (2018)
17. Ghosh, S., Mukhopadhyay, S.: Flow and heat transfer of nanofluid over an exponentially shrinking porous sheet with heat and mass fluxes. *Propuls. Power Res.* **7**(3), 268–275 (2018)
18. Molli, S., Naikoti, K.: MHD natural convective flow of Cu-Water nanofluid over a past infinite vertical plate with the presence of time dependent boundary condition. *Int. J. Thermofluid Sci. Technol.* **7**(4), 1–15 (2020)
19. Li, X., Khan, A.U., Khan, M.R., Nadeem, S., Khan, S.U.: Oblique stagnation point flow of nanofluids over stretching/shrinking sheet with Cattaneo-Christov heat flux model: existence of dual solution. *Symmetry (Basel)* **11**(9) (2019)
20. Narender, G., Govardhan, K., Sarma, G.S.: J. Heat Mass Trans. Res. Heat Mass Trans. Nanofluid Over Linear Stretching Surf. Viscous Dissipation Effect **6**, 117–124 (2019)
21. Khashi'ie, N.S., Arifin, N.M., Pop, I., Wahid, N.S.: Flow and heat transfer of hybrid nanofluid over a permeable shrinking cylinder with Joule heating: a comparative analysis. *Alexandria Eng. J.* **59**(3), 1787–1798 (2020)
22. Keys, W.M.: *Convective Heat and Mass Transfer*. McGraw-Hill, New York (1966)
23. Hazarika, G.C.: *Shooting Method to Some Problems of Fluid Mechanics*. LAP Lambert Academic Publishing (2012)
24. Hazarika, G.C., Borah, J., Konch, J.: Effects of variable viscosity and thermal conductivity on free convective MHD fluid flow over a stretching sheet. *Math. Forum* **27**, 2015–2019



# **Graphs, Networks and Communication**

# Structure of Protein Interaction Network Associated With Alzheimer's Disease Using Graphlet Based Techniques



Ahamed Khasim , Venkatesh Subramanian , K. M. Ajith ,  
and T. K. Shajahan 

**Abstract** The crucial step in analyzing a real-world network is to choose an acceptable network model. We try to select an appropriate network model for the protein-protein interaction (PPI) network of Alzheimer's disease (AD) using Graphlet-based metrics. The Relative Graphlet Frequency (RGF) count in the AD-PPI network is similar to that of the corresponding Scale-Free network. However, based on Graphlet Degree Distribution (GDD), the AD-PPI network has a good match with Geometric random graphs. The graphlet correlation statistics of the AD network show that it has a core-periphery topology.

**Keywords** Alzheimer's disease · Protein-protein interaction networks · Graphlets · Graphlet Correlation Matrix

## 1 Introduction

Alzheimer's Disease (AD) is a complex disease whose genetic architecture is believed to be polygenic [4]. Hence its genotype can be modeled with a biological network depicting the interaction between causal agents. In this paper, we model it with a Protein-Protein Interaction (PPI) network. In the case of general datasets, it is commonplace to establish their theoretical model before proceeding to analyze them. For instance, one makes statements like, '*this dataset has a normal distribution*', before proceeding to the analysis. We would like to do the same, but for network datasets. Specifically, we study the large-scale structure of AD linked network. In the case of networks, some examples of theoretical models are Erdős-Rényi random graph (ER) [3], Scale-Free graph (SF) [1], Geometric random graph (GEO) [9], etc. In this paper we assess which of these theoretical models are a good fit for the AD-associated PPI network.

---

A. Khasim · V. Subramanian · K. M. Ajith · T. K. Shajahan (✉)  
National Institute of Technology Karnataka, Surathkal, Mangaluru, India  
e-mail: [shajahan@nitk.edu.in](mailto:shajahan@nitk.edu.in)

© The Author(s), under exclusive license to Springer Nature Switzerland AG 2022  
S. Banerjee and A. Saha (eds.), *Nonlinear Dynamics and Applications*,  
Springer Proceedings in Complexity,  
[https://doi.org/10.1007/978-3-030-99792-2\\_42](https://doi.org/10.1007/978-3-030-99792-2_42)

527

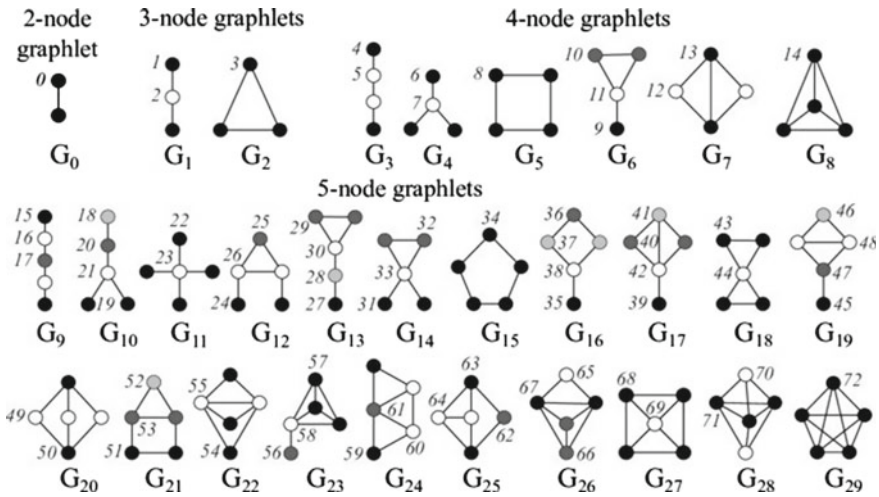


**Fig. 1**  $G_0$  to  $G_{29}$  graphlets of 2–5 nodes. The orbits are labeled from 0 to 72. In a particular graphlet, the similar types of nodes (automorphism orbits) are colored the same. [17]

We adopted a bottom-up method to investigate the network’s local structural features and to provide a theoretical model. The degree distribution of several disease PPI networks is a power-law distribution, implying that they belong to Scale-free networks. A more general method had been implemented using graphlets by N. Pržulj et al. [13, 14]. The graphlets are small non-isomorphic subgraphs that exist in a network (see Fig. 1). The graphlet degree distribution is one of the metrics to check the similarity between two networks. In a network, the distribution of a 2-node graphlet is the standard degree distribution, which is just one among the 30 graphlet distributions. Thus, the graphlet-based method is more general and provides a more in-depth examination of the network.

In this study, we collected AD-associated proteins from several databases and their physical interacting partners present in the human PPI network. Three graphlet-based metrics are used to analyze the network: Relative Graphlet Frequency Distance (RGFD), Graphlet Degree Distribution Agreement (GDDA), and Graphlet Correlation Matrix (GCM-11). We recognize that the constructed AD network has a core-periphery structure with features of SF, ER-DD, and GEO network models.

## 2 Methodology

### 2.1 Collection of AD-Related Genes

Genes related to Alzheimer's disease are retrieved from several databases using the methods described in the article of A Podder et al. [12]. 105 AD-associated genes are collected from NeuroDNet [16]. NeuroDNet has experimentally verified genetic information associated with neurodegenerative diseases sourced from the research literature. A set of 183 AD-associated genes extracted through text mining and genome-wide association studies (GWAS) are collected from DISEASE database [11]. AD-related genes appeared in the PubMed literature repository with more than two pieces of literature evidence (Number of PubMed IDs  $\geq 2$ ) are collected from DisGeNet and GLAD4U databases. 853 genes are collected from DisGeNet [10] and 54 genes are collected from GLAD4U [5]. AD-associated genes reported in genome-wide association studies (GWAS) are collected from two databases; GWAS Catalog [8] and GWASdb2 [7]. 98 genes are collected from GWA studies.

All of the datasets discussed above generated a total of 1293 genes associated with Alzheimer's disease. Since all databases do not use the same symbol format to represent genes, we converted all gene symbols to HUGO nomenclature committee (HGNC) approved symbol format [2].

### 2.2 Construction of AD-Associated Network

Direct physical interaction partners of AD-associated genes are retrieved from the Human Interactome project portal of the Center for Cancer Systems Biology (CCSB) database [15]. CCSB database has six independent datasets of binary interaction data of human proteins. Out of 1293 AD-associated genes collected from different sources, only 904 genes were listed in the CCSB database. The interacting partners of 904 genes are collected and constructed an AD-associated protein interaction network. The AD-related network has 4253 nodes and 7429 interactions. The largest connected component of the constructed network is considered for further topological analysis which comprises 4073 nodes and 7150 interactions after removing self-loops and multiple edges.

### 2.3 Network Topology Using Graphlet Analysis

We employed graphlet-based analysis to learn about the large-scale structure of the network. Graphlets are small connected non-isomorphic subgraphs in a large network. 30 graphlet structures of 2 to 5 nodes are shown in Fig. 1.

Relative graphlet frequency (RGF) can be used to check similarity between two networks [14]. The relative graphlet frequency of a network  $G$  is

$$F_i(G) = \frac{N_i(G)}{T(G)} \tag{1}$$

where  $N_i(G)$  is the number of graphlets of type  $i \in (0, 1, 2, \dots, 29)$  and  $T(G)$  is the total number of graphlets in the large network. The similarity between two networks  $G$  and  $H$  is measured using relative graphlet frequency distance and is defined as [14]

$$RGFD(G, H) = \sum_{i=0}^{29} \left| \log \frac{N_i(G)}{T(G)} - \log \frac{N_i(H)}{T(H)} \right| \tag{2}$$

The lower the RGFD value, the greater the similarity between two networks.

Each of the graphlets has certain symmetries and hence automorphic orbits are defined for each of them. This results in a total of 73 orbits in the 30 graphlets. In a large network, the number of nodes that touches  $j$ th orbit  $k$  times is denoted as  $d_G^j(k)$ . Hence the  $j$ th orbit degree distribution [13] is defined as

$$S_G^j(k) = \frac{d_G^j(k)}{k} \tag{3}$$

along with a scaling factor of  $\frac{1}{k}$ . We use the scaled degree distribution so that the orbits with a higher degree do not dominate the metric. We can normalize the scaled graphlet degree distribution [13] as,

$$N_G^j(k) = \frac{S_G^j(k)}{T_G^j} \tag{4}$$

where  $T^j(G) = \sum_{k=1}^{\infty} S_G^j(k)$

The similarity between two networks can be measured using the graphlet degree distribution distance [13] and is defined as

$$D^j(G, H) = \left( \sum_{k=1}^{\infty} [N_G^j(k) - N_H^j(k)]^2 \right)^{\frac{1}{2}} \tag{5}$$

The GDD agreement of  $j$ th orbit between two networks [13]

$$A^j(G, H) = 1 - D^j(G, H) \tag{6}$$

Considering all orbits  $j \in \{0, 1, 2, \dots, 72\}$  from 30 graphlets; the GDD agreement [13]

$$GDDA(G, H) = \frac{1}{73} \sum_{j=0}^{72} A^j(G, H) \quad (7)$$

We compared the RGFD and GDDA values of the created AD network to those of several model networks. Model networks include (1) Erdős-Rényi random graphs (ER) with the same number of nodes and edges as AD networks, (2) Erdős-Rényi random graphs with the same degree distribution as AD networks (we denote as ER-DD), (3) Scale-Free networks with the same number of nodes (SF), (4) 2-dimensional geometric random graph (GEO 2D), and (5) 3-dimensional geometric random graph (GEO 3D). From each type, 20 model networks have been constructed. To assess the similarity of model networks, the RGFD and GDDA of the AD network and 100 model networks are computed using the Graphcrunch software [6].

In a large network, each node may be represented as a 73-dimensional vector, with each dimension corresponding to the number of connected orbits in contact with the node. This vector is termed as Graphlet Degree Vector (GDV). GDV of  $i^{th}$  node is  $GDV_i = (C_0, C_1, C_2, \dots, C_{72})$  where  $C_0$  is the number of orbit-0 in contact with node  $i$  and similarly for other orbits also. By considering only 11 non-redundant orbits of 2- to 4-node graphlets, the graphlet degree vector may be reduced to 11 dimensions [18]. A metric is defined to characterize a network based on the correlations between the 11 non-redundant orbits ( $j=\{0,1,2,4,5,6,7,8,9,10,11\}$ ) of 2- to 4-node graphlets [18]. 11 dimensional GDV of each node is calculated and are arranged in an  $n \times 11$  matrix with each row corresponds to a node. Now, Spearman correlation coefficient ( $r_s$ ) is calculated for every possible pair of columns. Then a  $11 \times 11$  matrix is made, called the Graphlet Correlation Matrix (GCM), with the  $r_s$  values [18]. That is, one computes  $r_s$  for columns 1 and 2 of the  $n \times 11$  matrix and sets it as  $GCM_{12}$ , then computes  $r_s$  for columns 1 and 3 and sets it as  $GCM_{13}$ , and so on. Thus, regardless of the number of nodes in the network, one ends up with an  $11 \times 11$  matrix.

### 3 Results and Discussion

#### 3.1 RGFD Between AD-Network and Model Networks

We calculated the relative graphlet frequency of the AD-associated network and compared it with the model networks. The similarity between the AD network and model network is quantified using RGFD value (see Table 1). Based on the RGFD value, the AD network is far from ER but close to ER-DD and SF model networks. A similar kind of analysis using graphlet frequency count (of 3–5 nodes graphlets) had been done by N. Pržulj et al. [14] on 4 PPI network data sets of fruit fly and yeast. All those PPI had a better fit with GEO, except for one network data set of fruit fly, which had more noise. But in our network, the edge density is 0.086%, hence the chance of noise is low. In our analysis, in addition to 3–5 node graphlets, we accounted for

**Table 1** The RGFD and GDDA value between AD-PPI network and different model networks. The RGFD and GDDA between AD-PPI and 20 model networks from each type were calculated, and their average is tabulated here

Model Networks	RGFD	GDDA
ER	8.6027	0.6823
ER-DD	3.6045	0.7925
SF	3.6971	0.7668
GEO 2D	6.1738	0.8100
GEO 3D	5.7149	0.8214

the frequency of 2 nodes graphlet ( $G_0$ ) also. Based on the RGFD metric we say that AD-associated PPI has more fit with SF and ER-DD networks.

### 3.2 Graphlet degree distribution agreement

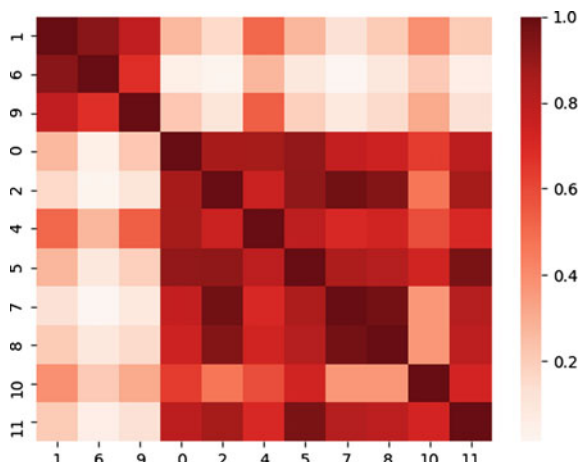
The graphlet degree distribution of 73 orbits present in the AD network and the corresponding 100 model networks are calculated. GDDA between AD network and 20 model networks of each type (ER, ER-DD, SF, GEO 2D, and GEO 3D) are calculated and their average is given in Table 1. The AD network has more than 60% agreement with all model networks. The agreement is highest for GEO 3D graphs (GDDA = 0.8214) compared to ER, ER-DD, SF, and GEO 2D. The agreement of GEO 3D with PPI networks had been reported in [13]. Since all model networks show an agreement of more than 60%, we cannot claim that the AD-associated PPI is strictly geometric random graphs.

### 3.3 Graphlet correlation matrix of AD-related PPI network

The graphlet correlation matrix (Fig. 2) of the AD network is constructed for 11 non-redundant orbits. The GCM-11 have two separated correlated clusters; correlation cluster of orbits {1, 6, 9} and orbits {0, 2, 4, 5, 7, 8, 10, 11}. Orbits 1 and 6 are single degree nodes in graphlets  $G_1$  and  $G_4$  respectively. Hence, the correlation of orbits 1 and 6 can be characterized as the existence of degree-1 nodes in the networks.

Orbits 7 and 8 exhibit a significant correlation in GCM-11's second correlation cluster (nearly equal to 1). Orbit 7 and 8 are mediator nodes in  $G_4$  and  $G_5$ . This correlation indicates the existence of mediator nodes in the network. Similarly, the high correlations of orbits 7 with 2, 5 with 11, and 8 with 2 are observed in GCM-11. Orbits {11} corresponds to higher degree mediator nodes while {2,5,7,8} corresponds to just broker type nodes (act as a link between two nodes) in the networks. In short,

**Fig. 2 GCM-11 of the AD-related PPI network.** Non-redundant orbits from 0 to 11 are labeled on the horizontal and vertical axes. Each cell's color gradient represents Spearman's correlation value between corresponding orbits. The strongly correlated orbits are brought together in the illustration



the correlation between the orbits in the second cluster indicates that the network comprises mediator nodes that are either highly connected or just brokers.

A similar correlation pattern was identified in GCM-11 of world trade network (WTN) [18]. Countries that participate in global markets are either on the periphery or at the center of WTN. Similarly, in the AD-associated PPI network, the proteins are either sparsely distributed on the network's outer shell or located in the network's inner core as mediators or hubs.

## 4 Conclusion

Graphlet-based metrics were used in this study to assess the resemblance of the protein protein interaction network (PPI) associated with Alzheimer's Disease (AD) to several theoretical network models. The Relative Graphlet Frequency Distance (RGFD) and Graphlet Degree Distribution Agreement (GDDA) are used to calculate the resemblance of created AD-network to theoretical model networks. According to the RGFD value, the network is more similar to the Erdős-Rényi random graph with degree distribution same as that of AD network (ER-DD) and Scale-Free (SF) networks. Our results contradict the prior conclusion, in which PPI was near to 3 Dimensional Geometric random graph (GEO 3D) [14]. Using GDDA data, our AD-associated PPI outperforms other model networks in terms of agreement with GEO 3D. The resemblance with other model networks is likewise noteworthy (greater than 60% agreement). Based on the RGFD and GDDA metrics, AD network shows features of all three models: i.e., Geometric random, Scale-Free, or Erdős-Rényi random. We can also see from the graphlet correlation matrix of the AD-related network that the proteins are either on the network's periphery or at its center. That is, the network has a core-periphery structure.



## References

1. Barabási, A.L., Albert, R.: Emergence of scaling in random networks. *Science* **286**(5439), 509–512 (1999)
2. Braschi, B., Denny, P., Gray, K., Jones, T., Seal, R., Tweedie, S., Yates, B., Bruford, E.: Gene-names.org: the HGNC and VGNC resources in 2019. *Nucl. Acids Res.* **47**(D1), D786–D792 (2019)
3. Erdős, P., Rényi, A., et al.: On the evolution of random graphs. *Publ. Math. Inst. Hung. Acad. Sci* **5**(1), 17–60 (1960)
4. Ertekin-Taner, N.: Genetics of Alzheimer disease in the pre-and post-GWAS era. *Alzheimer's Res. Therapy* **2**(1), 1–12 (2010)
5. Jourquin, J., Duncan, D., Shi, Z., Zhang, B.: Glad4u: deriving and prioritizing gene lists from Pubmed literature. *BMC Genomics* **13**(8), 1–12 (2012)
6. Kuchaiev, O., Stevanović, A., Hayes, W., Pržulj, N.: Graphcrunch 2: software tool for network modeling, alignment and clustering. *BMC Bioinf.* **12**(1), 1–13 (2011)
7. Li, M.J., Liu, Z., Wang, P., Wong, M.P., Nelson, M.R., Kocher, J.P.A., Yeager, M., Sham, P.C., Chanock, S.J., Xia, Z., et al.: Gwasdb v2: an update database for human genetic variants identified by genome-wide association studies. *Nucl. Acids Res.* **44**(D1), D869–D876 (2016)
8. Morales, J., Welter, D., Bowler, E.H., Cerezo, M., Harris, L.W., McMahon, A.C., Hall, P., Junkins, H.A., Milano, A., Hastings, E., et al.: A standardized framework for representation of ancestry data in genomics studies, with application to the nhgri-ebi gwas catalog. *Genome Biol.* **19**(1), 1–10 (2018)
9. Penrose, M.: *Random Geometric Graphs*, vol. 5. OUP Oxford (2003)
10. Piñero, J., Queralt-Rosinach, N., Bravo, A., Deu-Pons, J., Bauer-Mehren, A., Baron, M., Sanz, F., Furlong, L.I.: Disgenet: a discovery platform for the dynamical exploration of human diseases and their genes. *Database* **2015** (2015)
11. Pletscher-Frankild, S., Pallejà, A., Tsafou, K., Binder, J.X., Jensen, L.J.: Diseases: text mining and data integration of disease-gene associations. *Methods* **74**, 83–89 (2015)
12. Podder, A., Pandit, M., Narayanan, L.: Drug target prioritization for alzheimer's disease using protein interaction network analysis. *OMICS: A J. Integr. Biol.* **22**(10), 665–677 (2018)
13. Pržulj, N.: Biological network comparison using graphlet degree distribution. *Bioinformatics* **23**(2), e177–e183 (2007)
14. Pržulj, N., Corneil, D.G., Jurisica, I.: Modeling interactome: scale-free or geometric? *Bioinformatics* **20**(18), 3508–3515 (2004)
15. Rolland, T., Taşan, M., Charlotheaux, B., Pevzner, S.J., Zhong, Q., Sahni, N., Yi, S., Lemmens, I., Fontanillo, C., Mosca, R., et al.: A proteome-scale map of the human interactome network. *Cell* **159**(5), 1212–1226 (2014)
16. Vasaikar, S.V., Padhi, A.K., Jayaram, B., Gomes, J.: Neurodnet-an open source platform for constructing and analyzing neurodegenerative disease networks. *BMC Neurosci.* **14**(1), 1–13 (2013)
17. Yaveroglu, O.N.: Graphlet correlations for network comparison and modelling: World Trade Network example. Ph.D. thesis, Imperial College London, UK (2013)
18. Yaveroglu, Ö.N., Malod-Dognin, N., Davis, D., Levnajic, Z., Janjic, V., Karapandza, R., Stojmirovic, A., Pržulj, N.: Revealing the hidden language of complex networks. *Sci. Rep.* **4**(1), 1–9 (2014)

# On Divisor Function Even(Odd) Sum Graphs



S. Shanmugavelan and C. Natarajan

**Abstract** The theory of numbers has numerous applications in cryptography and information security. Number theoretic graphs are a novel and hybrid branch of number theory and graph theory. In this paper, we introduce a new structure of graphs called divisor function even sum graphs and divisor function odd sum graphs, which are analogous to divisor function graphs, and investigate some of their properties. In addition, we present a MATLAB code for generating the graph in  $O(n)$  time.

**Keywords** Number theoretic graphs · Divisor function even sum graph · Divisor function odd sum graph

## 1 Introduction

For each natural number  $n$ , Number Theory is compounded with a variety of functions such as the Euler function  $\phi(n)$ , sigma function  $\sigma(n)$ , divisor function  $D(n)$ , Möbius function  $\mu(n)$  and so on. These functions are used to construct number theoretic graphs, a developing field that has captivated researcher's interest ([9, 13]). In the last decade, various research studies about such graphs have been conducted ([2, 7, 14, 15, 17]). In spectral graph theory, a number theoretic graph known as Ramanujan networks is employed to solve optimization problems in communication network theory ([4, 18]) and is also used in cryptography [1]. Engineering and communication networks make advantage of the cycle structure of arithmetic Cayley graphs ([10, 11]), which are number theoretic graphs. For notations and terminologies in graph theory and number theory that are not defined here, we generally follow ([3, 5]).

---

S. Shanmugavelan (✉) · C. Natarajan  
Department of Mathematics, Srinivasa Ramanujan Centre, SASTRA Deemed University,  
Kumbakonam 612001, India  
e-mail: [shanmugavelan@src.sastra.edu](mailto:shanmugavelan@src.sastra.edu)

C. Natarajan  
e-mail: [natarajan\\_c@maths.sastra.edu](mailto:natarajan_c@maths.sastra.edu)

© The Author(s), under exclusive license to Springer Nature Switzerland AG 2022  
S. Banerjee and A. Saha (eds.), *Nonlinear Dynamics and Applications*,  
Springer Proceedings in Complexity,  
[https://doi.org/10.1007/978-3-030-99792-2\\_43](https://doi.org/10.1007/978-3-030-99792-2_43)

535

Throughout our discussion, the set of all factors for each natural number  $n$  is denoted as Divisor function  $D(n)$ , and whose cardinality is known as the tau function  $\tau(n)$ , which will be computed from the prime factorization of  $n = p_1^{r_1} \times p_2^{r_2} \times \dots \times p_n^{r_n}$ , where  $p_i$ 's are distinct primes and  $r_i$ 's are positive integers.

In 2015, Kannan et al. [8] introduced the divisor function graph  $G_{D(n)}$ . In addition, they proved that  $G_{D(n)}$  is always connected and complete graph if and only if no two proper divisors in  $D(n)$  are relatively prime. Also, for perfect square numbers, the chromatic number for  $G_{D(n)}$  is at least 3 and it is Eulerian. For further studies on divisor function graph, we may refer ([12, 16]). Chalapathi and Kiran Kumar [6] presented Euler even graphs  $\varepsilon_n$  and Euler odd graphs  $O_n$  for  $2n$  and  $2n + 1$  in 2016, examined connectedness and completeness, and established that the graph  $\varepsilon_{2n+1}$  is isomorphic to disjoint union of two complete graphs. They also proved that the graph  $O_{2n+1}$  is Eulerian if and only if  $\phi(2n + 1)$  is a multiple of 4. Motivated by this, we introduce divisor function even (odd) sum graphs and study their properties. We also write a MATLAB code to get graphical representation, order and size, which will be used to study numerous graph theory concepts.

## 2 Divisor Function Even Sum Graph

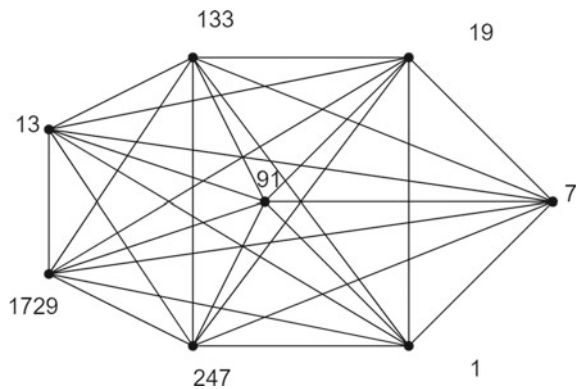
In this section, we introduce the Divisor function even sum graph and study its basic properties.

**Definition 1** For any natural number  $n$ , the Divisor function even sum graph is a simple graph  $(V, E)$  where  $V = \{d_i : d_i \mid n, n \text{ is any positive integer}\}$  is the vertex set and the edge set  $E = \{d_i d_j : d_i + d_j = \text{an even number}\}$ . We denote it by  $G_{eD(n)}$ .

**Example 1** The Divisor function even sum graph of Ramanujan number 1729 which has all its divisors as odd is shown in Fig. 1.

**Theorem 1**  $G_{eD(n)}$  is complete iff it has only odd divisors.

**Fig. 1** Divisor function even sum graph  $G_{eD(1729)}$



**Proof Necessity:** Assume that  $G_{eD(n)}$  is complete. Clearly, the sum of an edge's endpoints is even. Suppose that one of the divisors is an even number. Because 1 is a divisor for any integer, the sum of such end vertices with 1 leads to an odd sum, implying that there are no edges in this case, which is impossible.

**Sufficiency:** Assume that  $n$  has only odd divisors for every number  $n$ . The sum of two odd divisors, on the other hand, is always even. As a result, every distinct pair of vertices has an edge, and the graph is complete.

**Corollary 1**  $G_{eD(2n+1)}$  is complete.

**Corollary 2**  $G_{eD(p^n)}$  is complete,  $p \neq 2$ .

**Proof** Since all the divisors of prime powers are  $\{1, p, p^2, \dots, p^{n-1}, p^n\}$  which are clearly odd. By Theorem 1, the proof follows.

**Theorem 2**  $G_{eD(n)}$  is not a bipartite graph.

**Proof** Suppose that  $G_{eD(n)}$  is bipartite.

**Case 1:  $n$  is an Odd Integer**

In this case, one of the partitions, say  $X$ , only has one vertex 1. The second partition,  $Y$ , is comprised of all the remaining vertices, and because odd numbers only have odd divisors, the sum of 1 and the other odd divisor is even. The sum of two odd divisors in  $Y$ , on the other hand, is even, which is not possible.

**Case 2:  $n$  is an Even Number**

One of the partitions say  $X$ , consists of improper divisors of  $n$  only. Note that even numbers may have both odd and even divisors.

**Case 2a: Odd Proper Divisors**

It is not possible to have odd proper divisors in  $X$ , since the sum of 1 with such odd proper divisors would result in an even sum. Then, by Case 1, all such divisors must be placed in  $Y$ , which is impossible.

**Case 2b: Even Proper Divisors**

Here, it is not possible to have even proper divisors in  $X$ , since the sum of  $n$  with such even proper divisors will result in an even sum. Then all such divisors must be placed in  $Y$ , which is impossible in this instance as well because the sum of any two even proper divisors is also even.

**Theorem 3** For an odd composite number  $n$ ,  $G_{eD(n)}$  is an Euler graph iff and it has odd number of divisors.

**Proof Necessity:** Assume that  $G_{eD(n)}$  is an Euler graph. We claim that  $n$  has an odd number of divisors. If  $n$  has an even number of odd divisors, then all of the vertices will have an odd degree, since the sum of any two odd divisors in  $G_{eD(n)}$  is even, contradicting our hypothesis.

**Sufficiency:** Assume that  $n$  is odd composite and has odd number of divisors. Clearly, the graph's vertices should then be adjacent to each other. Because the number of divisors is odd, every vertex should receive an even degree, and so  $G_{eD(n)}$  is Eulerian.

**Theorem 4** Any regular non-complete  $G_{eD(2n)}$  can be decomposed into disjoint union of  $2K_{\frac{\tau(2n)}{2}}$ ,  $n \geq 2$ .

**Proof** Let the prime factorisation of  $2n = 2^a \times p_1^{r_1} \times p_2^{r_2} \times \dots \times p_k^{r_k}$ , where  $p_i$ 's are odd. Hence,  $\tau(2n) = |V(G_{eD(n)})| = (a + 1)(r_1 + 1) \dots (r_k + 1)$ . Let the total number of odd divisors of  $2n = (r_1 + 1) \times \dots \times (r_k + 1) = \mathcal{O}$  (say).

**Claim:**  $\mathcal{O} = \frac{\tau(2n)}{2}$ .

Clearly,  $\mathcal{O} \leq \frac{\tau(2n)}{2}$ .

Suppose that  $\tau(2n) < 2\mathcal{O}$ .

(i.e.)  $(a + 1) \times (r_1 + 1) \times \dots \times (r_k + 1) < 2\mathcal{O}$ .

Then,  $(a + 1) \times (r_1 + 1) \times \dots \times (r_k + 1) < 2(r_1 + 1) \times \dots \times (r_k + 1)$  which makes  $a < 1$  and so  $a$  is either 0 or negative integer. Since  $n \geq 2$ ,  $a$  cannot be negative. Therefore, the only probability is  $a = 0$  (i.e.)  $\tau(2n) = p_1^{r_1} \times \dots \times p_k^{r_k}$ , which is a factorization as product of odd primes only, which is a contradiction and hence,  $\frac{\tau(2n)}{2} \geq \mathcal{O}$ .

Let us label the vertices of odd factors of  $2n$  as  $o_1, o_2 \dots o_{\tau(2n)/2}$  whose induced subgraph is isomorphic to  $K_{\tau(2n)/2}$ . Now, the total number of even divisors (say) ( $\mathcal{E}$ ). Now,

$$\begin{aligned} \mathcal{E} &= \tau(2n) - \mathcal{O} \\ &= (a + 1) \times (r_1 + 1) \times \dots \times (r_k + 1) - (r_1 + 1) \times \dots \times (r_k + 1) \\ &= [a + 1 - 1](r_1 + 1) \dots (r_k + 1) \\ &= a \times [(r_1 + 1) \dots (r_k + 1)]. \end{aligned}$$

Let us label the vertices of even divisors of  $2n$  as  $e_1, e_2 \dots e_\xi$  whose induced sub graph is a complete of order  $\xi$ . Also note that there is no edge connecting the vertices of  $\mathcal{O}_i$ 's to  $\mathcal{E}_j$ 's,  $i = 1, 2 \dots \frac{\tau(2n)}{2}$ ,  $j = 1, 2 \dots \xi$ . Now it is enough to prove  $\xi = \tau(2n)/2$ .

Suppose that  $2\xi > \tau(2n)$ . This implies,  $2 \times a \times (r_1 + 1) \times \dots \times (r_k + 1) < (a + 1) \times (r_1 + 1) \times \dots \times (r_k + 1)$ , a similar contradiction is arrived. Hence the proof.

The following MATLAB Code is used to get a graph of divisor even sum graph with its order and size.

**Input:** Any natural number  $n > 1$ .

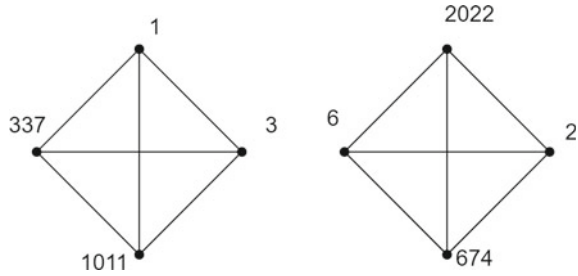
**Output:** A graph of Divisor even sum graph with its order and size.

```

1     function Divisorfunction_evensum_graph(n)
2     n=input('Enter any natural number>1');
3     sum=0;
4     j=0;
5     for i=1:n
6     if mod(n,i)==0
7     j=j+1;
8     a(j)=i;
9     end
10    end
11    disp('The Vertices of Divisor Even sum ...
        graph are');
12    disp(a);
13    disp(' ');
14    x=1;y=1;
15    disp('The Divisor Even sum graph Edges are');
16    for i=1:j-1
17    for k=i+1:j
18    sum=a(i)+a(k);
19    if mod(sum,2)==0
20    fprintf('%d,%d',a(i),a(k));
21        disp(' ');
22        s(x)=a(i);
23        t(y)=a(k);
24        x=x+1;y=y+1;
25    end
26    end
27    end
28    G=graph(s,t);
29    o=0;
30    for q=1:n
31    if(q≠a)
32    o=o+1;
33    m(o)=q;
34    end
35    end
36    GE=rmnode(G,[m]);
37    PO=plot(GE);
38    PO.NodeColor='k';
39    PO.EdgeColor='k';
40    PO.NodeLabel=[a];
41    title('Divisor Even Sum Graph of ',n);
42    m=numnodes(GE);
43    disp('The Order of Divisor Even Sum ...
        Graph is');
44    disp(m);
45    ne=numedges(GE);
46    disp('The size of Divisor Even Sum ...
        Graph is');
47    disp(ne);
48    end

```

**Fig. 2** Divisor Even sum graph of 2022



**Example 2** The sample output of divisor even sum graph of  $n = 2022$  (satisfies the hypothesis of Theorem 4 which is isomorphic to union of two complete graphs  $K_4$  is shown in Fig. 2.

### 3 Divisor Function Odd Sum Graph

Let us define a Divisor function odd sum graph:

**Definition 2** For any natural number  $n$ , Divisor function odd sum graph is a simple  $(V, E)$  graph such that  $V = \{d_i : d_i \mid n, n \text{ is any positive integer}\}$  and the edge set  $E = \{d_i d_j : d_i + d_j = \text{an odd number}\}$ . We denote it by  $G_{oD(n)}$ .

**Example 3** The Divisor function odd sum graph for  $n = 1234$  is shown in Fig. 3.

**Theorem 5**  $G_{oD(2^n)}$  is always a star for any positive integer  $n$ .

**Proof** Clearly, there is no edge between  $2^i$  and  $2^j$ ,  $1 \leq i, j \leq n$ . But,  $1 \in V[G_{oD}(2^n)]$ , the sum of 1 with remaining  $n$  vertices leads to odd sum only. As a result, a star graph is formed by keeping all even powers in one partition and 1 in another.

**Theorem 6**  $LG_{oD(2^n)}$  is complete for any positive integer  $n$ .

**Fig. 3** Divisor function odd sum graph  $G_{oD(1234)}$

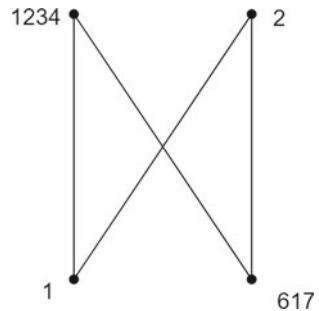
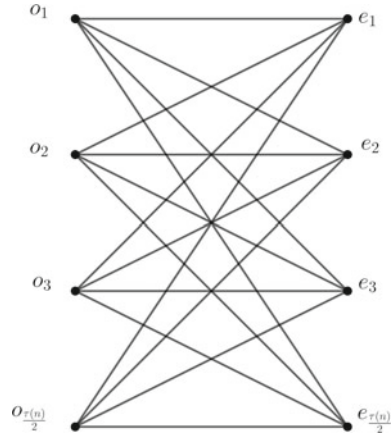


**Fig. 4**  $k$ -Regular even  $G_{oD(n)}$



**Proof** Clearly,  $V(G_{oD(2^n)}) = \{2^0, 2^1 \dots 2^k\}$  and  $G_{oD(2^k)} \simeq K_{1,k}$  because 1 is the only odd divisor of  $2^n$  and remaining  $n$  divisors are even, all of those can be kept in same partition. Moreover, it is obvious that the line graph of a star graph is always complete, the proof follows.

**Theorem 7** For a  $k$ -Regular even  $G_{oD(n)}$ ,  $\alpha = \beta = \frac{\tau(n)}{2}$ .

**Proof** Assume that  $G_{oD(n)}$  be a  $k$ -Regular graph of even order  $p$ . Clearly,  $D(n)$  contains a set of all even(odd) divisors (say)  $E(O)$  respectively. Since  $G_{oD(n)}$  is  $k$ -regular, it follows that  $|O| = |E| = \frac{\tau(n)}{2}$ . Let the odd divisors be  $o_1, o_2, \dots, o_{\frac{\tau(n)}{2}}$  and the even divisors be  $e_1, e_2, \dots, e_{\frac{\tau(n)}{2}}$ . Note that there exists an edge from  $o_i$  to  $e_i$ ,  $i = 1, 2 \dots \tau(n)$  and there is no edge from  $o_i$  to  $o_j$  and  $e_i$  to  $e_j$ ,  $i \neq j$ .

Clearly,  $G_{oD(n)} \simeq K_{\frac{\tau(n)}{2}, \frac{\tau(n)}{2}}$  (refer Fig. 4) and hence any minimum vertex cover must include vertices only from  $O$  or only from  $E$ . Henceforth,

$$\begin{aligned}
 |O| &= \beta = \frac{\tau(n)}{2} \\
 \text{Now, } \alpha &= p - \beta \\
 &= p - \frac{\tau(n)}{2} = \frac{\tau(n)}{2}.
 \end{aligned}$$

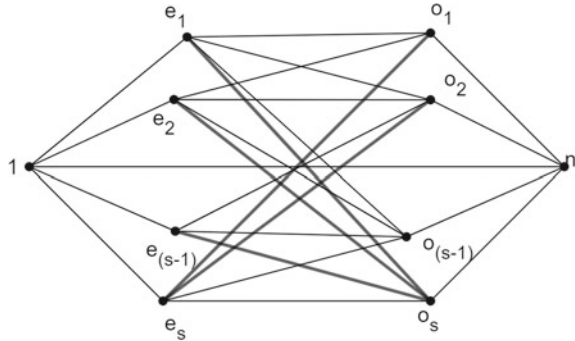
**Theorem 8** If  $n$  is factorised as an equal number of odd and even proper divisors, then  $G_{oD(n)}$  is Hamiltonian.

**Proof** Without loss of generality, let us assume  $n$  be an even integer, which may have both odd and even divisors. Let  $O$  denotes a set of all odd proper divisors and label the vertices of  $O$  as  $\{o_1, o_2 \dots o_s\}$  and  $E$  denotes a set of all even proper divisors which are labelled as  $\{e_1, e_2 \dots e_s\}$ .

Let us prove the theorem by induction on  $s$ . For  $s = 1$ , the resulting graph is  $C_4$  which has a spanning cycle with vertices  $\{1, o_1, e_1, n\}$ . Assume that the result is true



Fig. 5 Hamiltonian  $G_{oD(n)}$



for all integer  $n$  which has at most  $(s - 1)$  odd proper divisors. Consider the case in which  $n$  has  $s$  odd proper divisors. Note that the induced subgraphs  $G[\{1\} \cup V(E)]$  and  $G[\{n\} \cup V(O)]$  forms a star.

The vertex 1 is not adjacent any odd proper divisor  $o_i$ 's , the vertex  $n$  is not adjacent to any even proper  $e_j$ 's and there exists an edge between every  $o_i$ 's and  $e_j$ 's,  $1 \leq i \leq (s - 1)$ ,  $1 \leq j \leq (s - 1)$  (Refer Fig. 5). By hypothesis, we have a spanning cycle  $C$  for any arbitrary vertex (say)  $e_i$ ,  $1 \leq i \leq (s - 1)$  which comprises of a walk  $W : \{e_i o_i, o_i e_{i+1}, e_{i+1} o_{i+1} \dots e_{(s-1)} o_{(s-1)}\}$  followed by edges  $\{o_{(s-1)} n, n 1, 1 e_i\}$  such that the length of  $C$  is  $2(s - 1) + 3 = 2s - 1$ . Now, consider a subgraph  $C' = C - \{e_{(s-1)} o_{(s-1)}, o_{(s-1)} n\}$  adding the edges  $\{e_{s-1} o_s, o_s e_s, e_s o_{s-1}\}$  to  $C'$  again forms spanning cycle which includes all  $2s + 2$  vertices.

### 4 Conclusion

In this article, we introduced a new class of number theoretic graph structures termed divisor even sum (odd sum) graphs. We also studied several properties of these graphs, such as covering number, completeness, etc. In addition, we created a MATLAB method to draw these graphs, which will allow us to explore various other properties of these graphs. This research work has possible applications in communication networks and will be studied further in the future.

**Acknowledgements** The authors would like to thank the referees for their valuable comments. Also, the authors thank the Department of Science and Technology, Government of India for the financial support to the Department of Mathematics, SASTRA Deemed to be University under FIST Programme -Grant No. : SR/FST/MSI-107/2015(c).

## References

1. Costache, A., Feigon, B., Lauter, K., Massierer, M., Puskas, A.: Ramanujan graphs in cryptography. *J. Cryptol. Res.* 1–33 (2018). <https://eprint.iacr.org/2018/593.pdf>
2. Aravinth, R.H., Vignesh, R.: Mobius Function Graph  $M_n(G)$ . *International Journal of Innovative Technology and Exploring Engineering.* **8**(10), 1481–1484 (2019)
3. Bondy, J.A.: *USR Murty: Graph Theory with Application*. Springer, New York (2017)
4. Bien, F.: Construction of telephone networks by group representations. *Not. Am. Math. Soc.* **36**(1), 5–22 (1989)
5. Burton, D.M.: *Elementary Number Theory*. 7th edn. The McGraw-Hill Companies (2010)
6. Chalapathi, T., Kumar, K.: Graph structures of Euler totient numbers. *DIU J. Sci. Technol.* **11**(2), 19–29 (2016)
7. Saliha, H.F.M., Badal Ibrahim, N.: Generalized the divisor sum  $T_k$  – function of graph. *General Lett. Math.* **8**(2), 67–74 (2020)
8. Kannan, K., Narasimhan, D., Shanmugavelan, S.: The graph of divisor function  $D(n)$ . *Int. J. Pure Appl. Math.* **102**(3), 483–494 (2015)
9. Somer, L., Krizek, M.: On a connection of number theory with graph theory. *Czechoslovak Math. J.* **54**(129), 465–485 (2004)
10. Madhavi, L., Maheswari, B.: Enumeration of triangles and Hamilton cycles in quadratic residue Cayley graphs. *Chamchuri J. Math.* **1**, 95–103 (2009)
11. Madhavi, L., Maheswari, B.: Enumeration of Hamilton cycles and triangles in Euler totient Cayley graphs. *Graph Theory Notes of New York* **LIX**, 28–31 (2010)
12. Narasimhan, D., Elamparithi, A., Vignesh, R.: Connectivity, independency and colorability of divisor function graph  $G_{D(n)}$ . *Int. J. Eng. Adv. Technol.* **8**(2S), 209–213 (2018)
13. Alan, N., Erdos, P.: An application of graph theory to additive number theory. *Eur. J. Combin.* **6**(3), 201–203 (1985)
14. Jose, R., Susha, D.:  $\mu$  – graph of a finite group. *Int. J. Math. Trends Technol.* **67**(1), 129–135 (2021)
15. Shanmugavelan, S.: The Euler function graph  $G(\phi(n))$ . *Int. J. Pure Appl. Math.* **116**(1), 45–48 (2018)
16. Shanmugavelan, S., Thanga Rajeswari, K., Natarajan, C.: A note on indices of primepower and semiprime divisor function graph. *TWMS J. Appl. Eng. Math.* **11**(special issue), 51–62 (2021)
17. V M S S Kiran Kumar, R., Chalapathi, T.: Difference divisor graph of the finite group. *Int. J. Res. Ind. Eng.* **7**(2), 235–242 (2018)
18. Chow, Y.-T., Shi, W., Wu, T., Yin, W.: Expander Graph and Communication-Efficient Decentralized Optimization (2016). <https://arxiv.org/abs/1810.01053v1>

# A Visible Watermarking Approach Likely to Steganography Using Nonlinear Approach



Sabyasachi Samanta

**Abstract** Digital watermarking is the course of action of set in information into digital content. Authenticity or integrity is one of the key features of watermarking. Perceptibility or existence of information on cover signal depends on nature of watermarking process. In this effort, a massive amount of message may embed in cooperation with nonlinear pixel and bit positions of image. Without embedding any specific position, data embedded to entire image stating from an arbitrary position chosen by the secret key. The number of effected pixels of carrier image is proportionally got higher with the level of message. Choice of pixel position entirely depends on the size of message. At decryption era, without inspect all of the pixels of cover image, data bits are composed from that special pixel and bit positions. With embedding of large amount of information, sometimes it produces some visible scrap to the carrier. Though it's visible to us but it's still secure to us, as it's embedded through some key to some nonlinear pixel positions. This approach is highly convinced the visible watermarking approach as well as the steganography approach also.

**Keywords** Information Security · Payload · Nonlinear Pixel Position (NPP) · Steganography · Visible Watermarking

## 1 Introduction

Digital Watermarking is the development of embedding a message on a host signal. A watermark can either be visible or invisible [16]. In visible watermarking the information comes to be visible on the image or video or picture [2, 4]. That is typically used for logos or text. Invisible digital watermarking is a type of steganography that aims to secrete information through medium to substantiate ownership, truthfulness or deliver additional information [9–12]. Steganography hides the visibility through the carrier like invisible watermarking [13–15]. Here I have proposed the Nonlinear Pixel Position-4 bit (NPP-4 bit) method, which is based on nonlinear pixel position

---

S. Samanta (✉)

Department of Information Technology, Haldia Institute of Technology, Haldia, WB, India  
e-mail: [sabyasachi.smnt@gmail.com](mailto:sabyasachi.smnt@gmail.com)

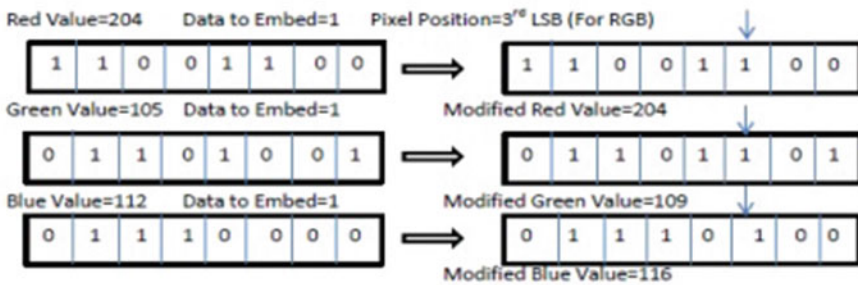
© The Author(s), under exclusive license to Springer Nature Switzerland AG 2022  
S. Banerjee and A. Saha (eds.), *Nonlinear Dynamics and Applications*,  
Springer Proceedings in Complexity,  
[https://doi.org/10.1007/978-3-030-99792-2\\_44](https://doi.org/10.1007/978-3-030-99792-2_44)

545

selection through the image. The pixel positions are selected depending on the size of the message. Six digits key value is taken as a private key. Using the key value the initial and total pixel positions are selected. Then the pixel positions are calculated by doing the exponential function with the height and width of the image. In this proposed technique, the embedding process is made by the exponential values started from nonlinear pixel position of the carrier image. The bit position is calculated from the exponential values. Depending on the magnitude of the message the next pixel positions are selected by the combination of key. In this process the primary pixel position is not unique to all, i.e. it's varied from process to process and entirely depends on key. Also depending on payload and size of the image, the pixel positions varied from one to other. All over the data bits are being embedded to the entire carrier image. Figure 1 describes the 4 bits embedding process to the different bit positions for color images.

Section 2 represents the related works related with the watermarking and steganography technique. Section 3 represents an implementation of the technique of visible watermarking approach. Section 4 demonstrates the evidence of experimental result. Section 5 is with the performance analysis of NPP-4 bit methodology. Section 6 draws the conclusion of the work.

*Case 1:*



*Case 2:*

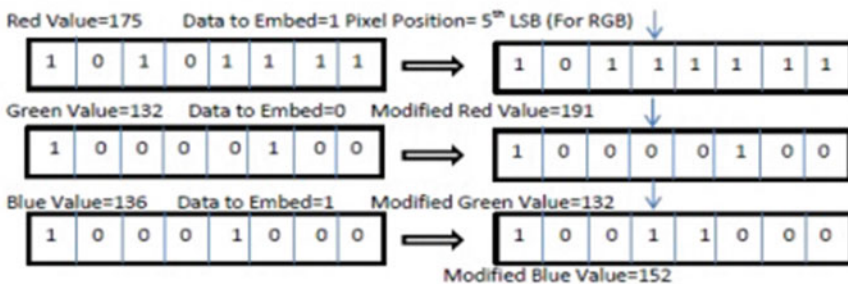


Fig. 1 Working principle of NPP-4 bit for color image

## 2 Related Works

Jiasheng Qu et al. [1] proposed a visible image watermarking scheme based on gradient-weighted class activation mapping. They have proposed the region of interest selection strategy to locate the secluded body of images for watermark embedding. They have used the similar technique for gray scale and each component of colour image.

Kamaldeep Joshi et al. [3] planned an image steganography using 7th bit of a pixel as indicator by introducing the successive temporary pixel in the gray scale image. One bit is hidden at the selected pixel position and the second bit is hidden to the next pixel position. On the basis of the seventh bit of the pixels of an image, a mathematical function is applied to that bit position of the pixels.

Hide in Picture (HIP) [5] was created by Davi Tassinari de Figueiredo. HIP technique uses only for bitmap images. If payload is high, it's necessary to modify more than one bit from each byte of the image. This process uses password protection to hide files and only those who know the password, are able to retrieve the data.

QuickStego [6]: QuickStego modify the pixels of the image. It encodes the secret text by adding small deviation in color to the image. In practice these small differences does not appear to the human eye. This technique does not encrypt the secret text message by any encoding scheme.

Mansoor Fateh et al. [7] proposed an improved version of the LSB matching. They proposed the scheme which contains two phases including embedding and extracting the message. Here a pair of bits of the secret message is hidden in a pair of pixels with only one change.

Wenfa Qi et al. [8] proposed an adaptive embedding method for visible watermarking. Here they have embedded watermark image the host image Just Noticeable Difference coefficient. Mukherjee et al. [17] proposed the mid position value technique to embed data bits within the tangled cover image. Also they applied the inverse Arnold transformation on stego image.

## 3 The Scheme

This section represents the algorithm for visible watermarking approach. Section A explains the total encryption process and section B depicts the decryption of plain text from the stego image.

### A. Algorithm for data embedding in cover image.

Step I: Take message input, compute the length and create an array.

Step II: Select the initial pixel position using the key.

- (i) Calculate the number of required pixel positions.
- (ii) Calculate the exponential of function using key (or key set).

- (iii) Take the digits up to “e”. Accumulate first three digits to  $A[x]$ , next three digits to  $A[y]$  and last digit to  $A[z]$ .

Step III: Replace of data bits with R, G & B values of pixels.

- (i) Calculate the width and height of the image as  $(M \times N)$ .
- (ii) Select the pixel position and set the value of  $x$  and  $y$  with the value of  $M$  and  $N$   $((0, 0)$  to  $(M-1, N-1)$ ).

If  $(x > (M-1))$  or  $(y > (N-1))$  then Set  $P(x, y) = P(0 + (x \% (M-1)), (0 + (y \% (N))))$  else set  $P(x, y) = (x, y)$ .

- (iii) To select the bit position, set  $z = A[z]$  of a pixel.
- (iv) The four data bits are replaced in analogous bit position of each RGB elements and pixels are reformed.

Step IV: Repeat Step II to Step IV.

Step V: Stop.

### **B. Algorithm for data extraction from stego image.**

Step I: To search out the pixel and bit position in R, G & B of selected pixels follow Step II and step III of Algorithm A.

Step II: Retrieve the embedded data bits from the selected bit positions of selected pixels and accumulate it to data array.

Step III: Initially find out the length of the message from the encrypted array.

Step IV: Find out the embedded data bits from the stego image and bring together the delivered message.

Step V: Stop.

## **4 Implementation of Process and Experimental Result**

Figure 2 stands for the cover and stego image of LENA and MONALISHA after embedding 1000 characters. Figure 3 shows the histogram of LENA image  $(512 \times 512)$  as cover and stego image. Figure 4 shows the histogram comparison using PoV for Red, Green, for Blue using LENA Image.

## **5 Performance Analysis of NPP-4 Methodology**

Invisible digital watermarking is called a kind of steganography. Embedding of 500 more characters using NPP-4 bit method creates visible dissimilarities at the output image. Sometimes NPP-1 bits may also create tiny spots in stego image. As a result

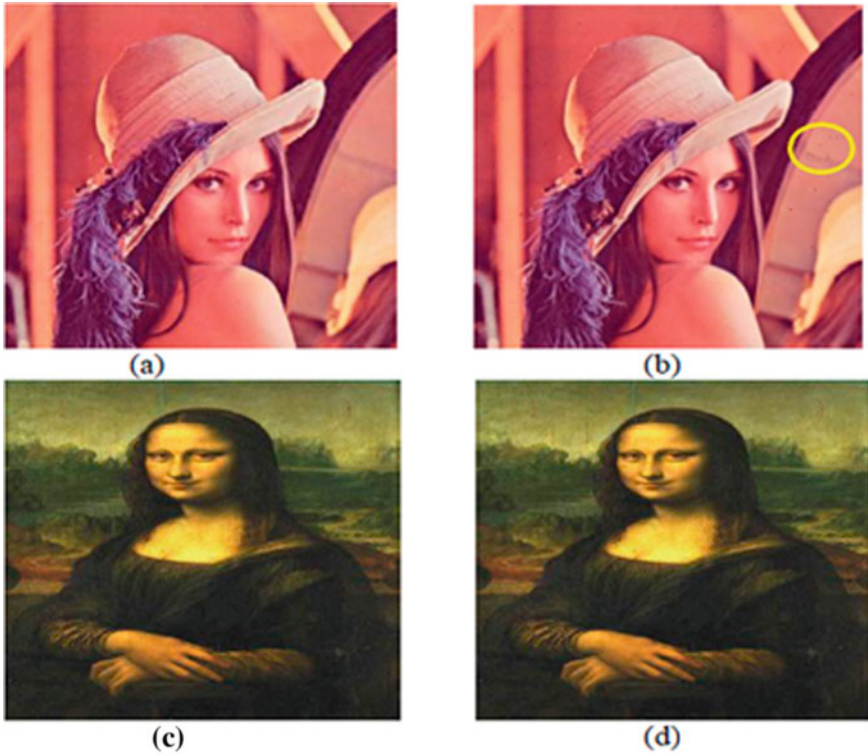


Fig. 2 (a, c) Cover and (b, d) Stego image of LENA and MONALISA after embedding 1000 characters using NPP-4 bit

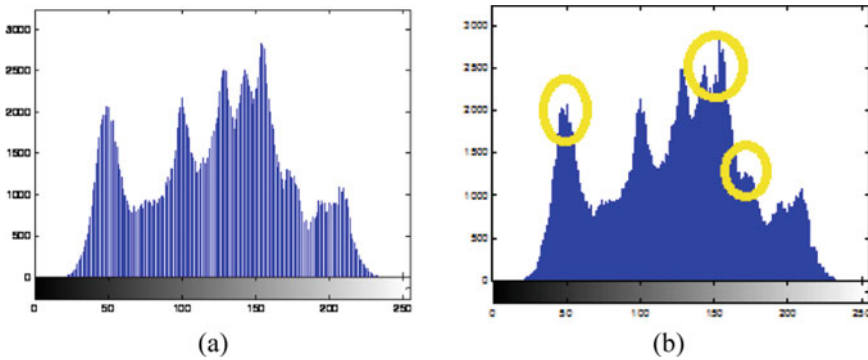


Fig. 3 Histogram of LENA as (a) Cover and (b) Stego image after embedding 1000 characters using NPP-4 bit



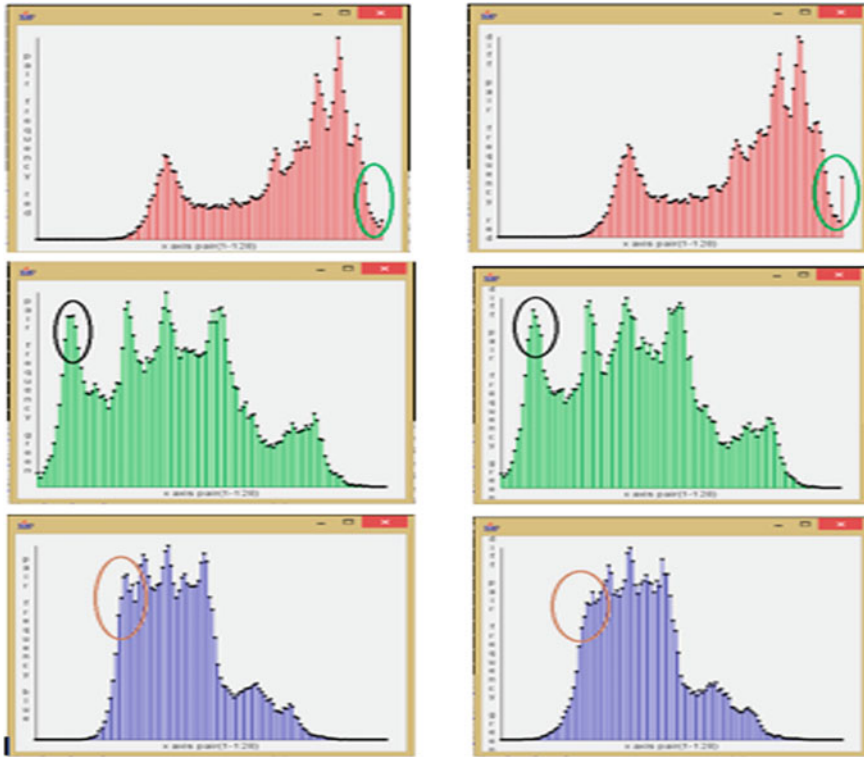
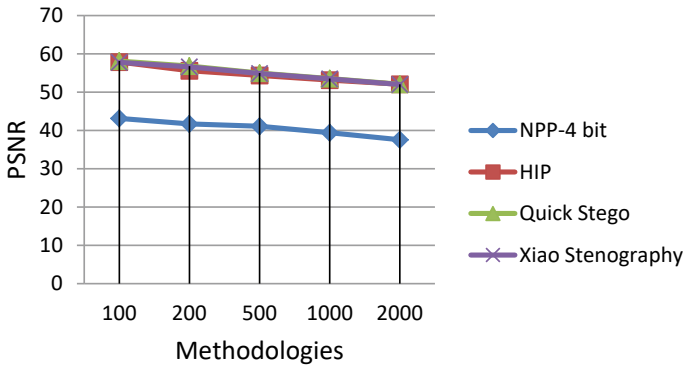


Fig. 4 Histogram comparison using PoV for Red, Green, and Blue using LENA image

its do not support the benchmarks of invisible digital watermarking. The visible variations or patches on cover image do not break any principles of information security or confidentiality. As the data bits have embedded to arbitrary pixel and bit positions of entire image. Without applying the embedding algorithm or key value, the extraction of original message from noticeable zones of stego image is quite impossible to attackers. In steganography, the embedding algorithm produces the image output as the attacker does not minds the presence of message. Also invisible digital watermarking produces similar like output. To measure the qualitative performance of developed NPP-4bit approach, HIP (Hide In Picture) [18], QuickStego [19] and Xiao Steganohraphy [20] tools have choosen.

The x-y direction of the following figures represents the methodologies and different performance metrics respectively. The x-direction of following igures represent the NPP-4 bit and other well known existing methodologies like HIP, QuickStego and Xiao Steganohraphy. Figures 5 and 6 represent the comparison for PSNR between NPP-4 bit and other well known approaches for color and gray scale image using LENA (128 × 128) as a cover respectively. Figures 7 and 8 subsequently signify the superiority of SSIM between NPP 4bit and other well known approaches for color and gray scale image as same cover image. As I have explained the embedding of





**Fig. 5** PSNR comparison of different NPP approaches with other methodologies using LENA/(Color, 128 × 128) Images

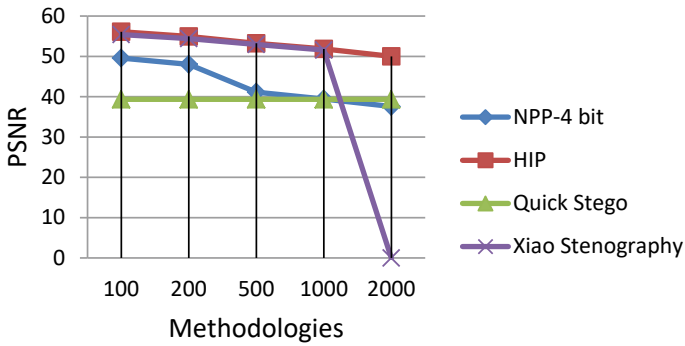


**Fig. 6** PSNR comparison of different NPP approaches with other methodologies using LENA/(Gray Scale, 128 × 128) Images

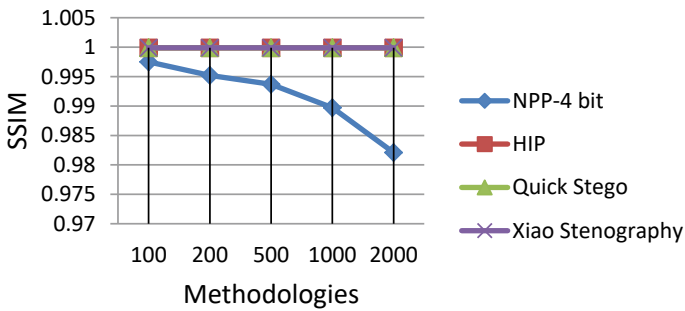


**Fig. 7** SSIM comparison of different NPP approaches with other methodologies using LENA/(Color, 128 × 128) Images

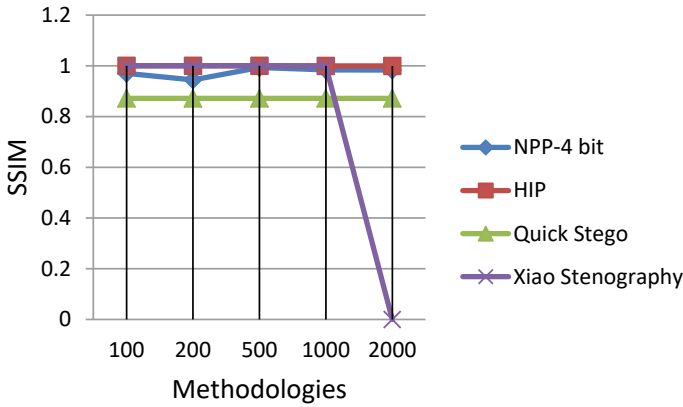


**Fig. 8** SSIM comparison of different NPP approaches with other methodologies using LENA/(Gray Scale, 128 × 128) Images

four bits i.e. NPP-4 bit generate the tiny spot on image. So for the PSNR for both color and gray scale stego image sometimes generates lower result for the newly developed methodology. The SSIM measure for color images produces the likewise result for NPP-1 bit and NPP-2 bit techniques. The SSIM measure for both the color and gray scale images generates similar graph for newly developed methodology.

## 6 Conclusion

Here I have proposed a visible watermarking approach likely to steganography using nonlinear approach and private key cryptographic technique. In this approach, four data bits have placed in every selected pixel element with random pixel positions about the image. Moreover for fewer number of content, sometimes it produces the similar images in naked eye. But for more it produces nonlinear tiny spots throughout the image. So for this approach I have named as a visible watermarking approach likely to steganography. Though the tiny spots are visible to us as effected location, but it's quite impossible to retrieve the embedded message from stego image. Only using the key and proper set of pixel and bit positions embedded message can retrieve from the watermarked image. So it's the visible watermarking approach through NPP but the methodology hold up the unadulterated steganography approaches.

## References

1. Jiasheng, Q., Wei, S., Xiangchun, L., Lizhi Zhao, and Xiaobing Zhao: A Novel Improved Reversible Visible Image Watermarking Algorithm Based on Grad-CAM and JND. Secur.

- Commun. Netw. Article ID 6652897, 1–17 (2021). <https://doi.org/10.1155/2021/6652897>
2. Mahbuba, B., Mohammad, S.U.: Analysis of digital image watermarking techniques through hybrid methods. *Adv. Multimed.* Article ID 7912690, 1–12 (2020). <https://doi.org/10.1155/2020/7912690>
  3. Kamaldeep, J., Swati, G., Rajkumar, Y.: A new method of image steganography using 7th bit of a pixel as indicator by introducing the successive temporary pixel in the gray scale image. *J. Comput. Netw. Commun.* Article ID 9475142, 1–11 (2018). <https://doi.org/10.1155/2018/9475142>
  4. Nandhini, S., Somaya, A.-M., Ahmed, B.: Image steganography. A Review of the Recent Advances. *IEEE Access*, vol. 9, pp. 1–15. Digital Object Identifier (2021). <https://doi.org/10.1109/ACCESS.2021.3053998>
  5. Pedram, H., Vidyasagar, P., Elizabeth, C.: A Survey of Steganographic and Steganalytic Tools for the Digital Forensic Investigator, pp. 1–12. [http://www.pedramhayati.com/images/docs/survey\\_of\\_steganography\\_and\\_steganalytic\\_tools.pdf](http://www.pedramhayati.com/images/docs/survey_of_steganography_and_steganalytic_tools.pdf)
  6. Naveen Brahma Teja, K., Madhumati, G.L., Rama Koteswara Rao, K.: Data hiding using EDGE based steganography. *Int. J. Emerging Technol. Adv. Eng.* 2(11), 354–360(2012). ISSN 2250–2459
  7. Mansoor, F., Mohsen, R., Yasser, I.: A new method of coding for steganography based on LSB matching revisited. *Secur. Commun. Netw.* Article ID 6610678, pp 1–15(2021). <https://doi.org/10.1155/2021/6610678>
  8. Wenfa, Q., Yuxin, L., Sirui, G., Xiang, W., Zongming, G.: An adaptive visible watermark embedding method based on region selection. *Secur. Commun. Netw.* Article ID 6693343, pp 1–15 (2021). <https://doi.org/10.1155/2021/6693343>
  9. Robert, L., Shanmugapriya, T.: A study on digital watermarking techniques. *Int. J. Recent Trends Eng.* 1(2), 223–225 (2009)
  10. Janu, N., Kumar, A., Dadheech, P., Sharma, G., Kumar, A., Raja, L.: Multiple watermarking scheme for video & image for authentication & copyright protection, IOP conference series. *Mater. Sci. Eng.* (2021). <https://doi.org/10.1088/1757-899X/1131/1/012020>, pp.1-12, ICETCE 2021
  11. Shweta, W., Deepa, K., Ankit, R., Aruna, J., Vishal, J.: A comprehensive review on digital image watermarking. Workshop on Computer Networks & Communications, Chennai, India, May 01, 2021, pp. 126–143 (2021)
  12. Fu, Z., Li, E., Cheng, X., Huang, Y., Hu, Y.: Recent advances in image steganography based on deep learning. *J. Comput. Res. Dev.* 58(3), 548–568 (2021)
  13. Dinu, C.: Low distortion transform for reversible watermarking. *IEEE Transactions on Image Processing*, Jan. 2012, vol. 21, no. 1, pp. 412–417 (2012).
  14. Caldelli, R., Macaluso, G., Bartolini, F., Barni, M.: Near Lossless Image authentication Transparent to near Lossless Coding. *Security, Steganography, and Watermarking of Multimedia Contents, VI*, SPIE, vol. 5306, pp. 737–747(2004).
  15. Afroja, A., Muhammad A.U.: Digital watermarking with a new algorithm. *IJRET: Int. J. Res. Eng. Technol.* 03(03), 212–217(2014). eISSN: 2319–1163, pISSN: 2321–7308
  16. Supriadi, R., De Rosal, I.M.S., Abdul, S., Pulung, N.A.: Inverted LSB image steganography using adaptive pattern to improve imperceptibility. *J. King Saud Univ.—Comput. Inf. Sci.* 1–10 (2021). <https://doi.org/10.1016/j.jksuci.2020.12.017>
  17. Mukherjee, S., Roy, S., Sanyal, G.: Image Steganography using mid position value Technique. In: *International Conference on Computational Intelligence and Data Science (ICCIDS 2018)*, Procedia Computer Science, vol. 132, pp. 461–46 (2018)
  18. Image Steganography tool: <http://www.softpedia.com/get/Security/Security-Related/Hide-In-Picture.shtml>
  19. Image Steganography tool: [http://download.cnet.com/QuickStego/3000-2092\\_4-75593140.html](http://download.cnet.com/QuickStego/3000-2092_4-75593140.html)
  20. Image Steganography tool: [http://download.cnet.com/Xiao-Steganography/3000-2092\\_4-10541494.html](http://download.cnet.com/Xiao-Steganography/3000-2092_4-10541494.html)

# A New Public Key Encryption Using Dickson Polynomials Over Finite Field with $2^m$



Kamakhya Paul , Madan Mohan Singh , and Pinkimani Goswami 

**Abstract** The Dickson polynomials are widely used in different context. Because of the permutation behaviors and semi-group property under composition, its application can also be noticed in cryptography. In this paper, we propose a new public key encryption scheme based on Dickson polynomial of first kind over a finite field with  $2^m$ , where  $m$  is the product of two large primes  $p$  and  $q$ , with primes  $2^p - 1$  and  $2^q - 1$ . The security of the proposed scheme is equally dependent on the Integer Factorization Problem (IFP) and the Discrete Dickson Problem (DDP). We also compared the encryption-decryption performance of the proposed scheme with some other existing schemes and found that the performance of the proposed scheme is better compared to them.

**Keywords** Dickson polynomial · Integer Factorization Problem · Discrete Dickson Problem · Discrete Logarithm Problem · Encryption scheme

## 1 Introduction

Public key cryptography, also known as asymmetric cryptography, where transmission of messages takes place over an open network, was first introduced by Diffie and Hellman [1] in 1976. Here separate keys are used for encryption and decryption,

---

K. Paul (✉)  
North Eastern Hill University, Shillong 793022, ML, India  
e-mail: [kamakhyapaul4@gmail.com](mailto:kamakhyapaul4@gmail.com)

M. M. Singh  
Department of Basic Sciences & Social Sciences, North Eastern Hill University, Shillong 793022, ML, India  
e-mail: [mmsingh2004@gmail.com](mailto:mmsingh2004@gmail.com)

P. Goswami  
Department of Mathematics, University of Science and Technology Meghalaya, Ri-Bhoi 793101, ML, India  
e-mail: [pinkimanigoswami@yahoo.com](mailto:pinkimanigoswami@yahoo.com)

and hence the insecurity of transmitting the secret key over an insecure channel was overcome. This is observed in symmetric cryptosystems.

Dickson [2] first introduced a type of polynomial, which was later labeled by Schur [3] as Dickson polynomial. With the proposition by Dickson [2], extensive research and looking into the properties of the polynomial had started and hence followed by application of Dickson polynomial in cryptography [4–7]. Lidl [7], also surveyed the algebraic properties of the Dickson polynomial over  $\mathbb{F}_q$  and over the integers  $\mathbb{Z}_n$ .

Most of the cryptographic schemes are being developed based on the hard problems that can be solved both ways only if prior knowledge of the related problem is known. Initially, the hard problems that were being used includes discrete logarithm and factoring of a large composite number in terms of primes, taken only one hard problem at a time. McCurley [8] in 1988 was the first to use two different number theoretic assumptions in the development of a single key distribution protocol. Many more cryptosystems were later proposed [9–12, 14–16, 24, 25], which were based on the merging of two hard problems such as Discrete Logarithm and Factoring of a large composite number, Elliptic Curve Discrete Logarithm, Knapsack problem, and many more. Which prompted us to use two hard problem in Dickson polynomial to propose a public key encryption scheme.

In this paper, we have operated Discrete Logarithm and Integer Factorization in the Discrete Dickson Problem (DDP) over the finite field with cardinality  $2^m$  and proposed a cryptosystem whose security is based on the hardness of solving IFP and DDP.

## 2 Dickson Polynomial

A type of polynomial was introduced by Dickson [2] in 1896 in the form of

$$x^k + k \sum_{i=1}^{(k-1)/2} \frac{(k-i-1)\dots(k-2i+1)}{2.3\dots i} a^i x^{k-2i}, \quad k \text{ is odd}, \tag{1}$$

over the finite field  $F_q$ , which later came to be known as the Dickson polynomial.

### 2.1 Definition (Dickson Polynomial of First Kind)

Assume  $n$  be a positive integer and  $a \in \mathbb{F}_q$ , then the Dickson polynomial  $D_n(x, a)$  of the first kind over any finite field  $\mathbb{F}_q$  is defined by

$$D_n(x, a) = \sum_{i=0}^{\lfloor \frac{n}{2} \rfloor} \frac{n}{n-i} \binom{n-i}{i} (-a)^i x^{n-2i} \tag{2}$$

where  $\lfloor \frac{n}{2} \rfloor$  is the largest integer less than or equal to  $\frac{n}{2}$ .

The Dickson polynomial satisfy the recurrence relation:  $D_n(x, a) = xD_{n-1}(x, a) - aD_{n-2}(x, a)$ ,  $n \geq 2$ , under the initial condition  $D_0(x, a) = 2$  and  $D_1(x, a) = x$  and a few initial polynomials are given below:

$$\begin{aligned} D_2(x, a) &= x^2 - 2a \\ D_3(x, a) &= x^3 - 3ax \\ D_4(x, a) &= x^4 - 4ax^2 + 2a^2 \\ D_5(x, a) &= x^5 - 5ax^3 + 5a^2x \end{aligned}$$

Commutativity under composition is of considerable importance and is satisfied by the Dickson polynomial for  $a = 0$  or  $1$  [18], and hence it satisfies the semi-group property under composition:

$$D_{mn}(x, 1) = D_m(D_n(x, 1), 1) = D_m(x, 1) \circ D_n(x, 1) = D_n(x, 1) \circ D_m(x, 1) = D_n(D_m(x, 1), 1) = D_{nm}(x, 1).$$

### 2.2 Definition (Modified Dickson Polynomial)

Let us define a map,  $D_p : \mathbb{Z}_n \rightarrow \mathbb{Z}_n$ , which is defined as  $y = D_p(x) \pmod n$ , with  $x$  and  $n$  being integers. Here, we call  $y = D_p(x) \pmod n$  as the modified Dickson polynomial. Below are a few properties satisfied by modified Dickson polynomial.

1. The modified Dickson polynomial is commutative under composition, that is  $D_p(D_q(x) \pmod n) = D_{pq}(x) \pmod n = D_q(D_p(x) \pmod n)$
2. Let  $q$  be an odd prime and let  $x \in \mathbb{Z}$  such that  $0 \leq x < q$ . Then the period of the sequence  $D_n(x) \pmod q$  for  $n = 0, 1, 2, 3, 4, \dots$  is a divisor of  $q^2 - 1$ .

The first key exchange cryptosystem which was based on Dickson polynomial was introduced by Müller and Nöbauer [18] in 1981, where the power functions of the RSA system, introduced by Rivest et al. [17] in 1978, was replaced by Dickson polynomials  $D_n(x, a)$  with parameter  $a = -1, 0, 1$ . It was also observed that the RSA cryptosystem was equivalent to the Dickson system for parameter  $a = 0$  [18]. In 2011, Wei [13] introduced in his paper that the Dickson polynomial  $D_n(x, 1)$  over a finite field  $2^m$  is a permutation polynomial if and only if  $n$  is odd and proved that solving a Discrete Dickson Problem (DDP) is as difficult as solving Discrete Logarithmic Problem (DLP). Note that the hardness of DLP was also observed by McCurley [20]. It is also observed that computable groups where DLP is hard to solve [21–23] are of great importance in cryptography.

### 2.3 Definition (Discrete Dickson Problem)

Let  $R$  be a commutative ring with unity, for any  $n \in \mathbb{Z}^+$ , and given  $y$  and  $x$ , the problem of calculating the value of  $n$  such that  $y = D_n(x, 1)$  is called the Discrete Dickson Problem(DDP).

It is observed throughout the paper that we have used for  $a = 1$ ,  $D_n(x, 1) = D_n(x)$ .

## 3 Our Proposed Public Key Encryption Scheme

Here we propose our scheme, which consists of three parts, that includes, Key generation, encryption, and decryption.

### Key Generation

The generation of the key includes the below given steps:

1. Choose two random large primes,  $p$  and  $q$ , of the same size, such that  $2^p - 1$  and  $2^q - 1$  are prime.
2. Using the above  $p$  and  $q$ , compute  $n = 2^m$ , where  $m = p \times q$ .
3. For the value of  $n$ , find  $\phi(n)$ , where  $\phi(n) = (2^{2p} - 2^{p+1}) \times (2^{2q} - 2^{q+1})$ .
4. Choose  $e$ , such that  $1 < e < \phi(n)$  and  $\gcd(e, \phi(n)) = 1$ .
5. Find  $d$ , such that  $ed \equiv 1 \pmod{\phi(n)}$ , where  $d$  is the modular inverse of  $e$ .
6. Choose  $a$ , such that  $0 \leq a \leq \phi(n) - 1$ .
7. Choose a random  $\alpha \in \mathbb{Z}_n^*$  and compute  $x = \frac{1}{2}D_a(2\alpha) \pmod{n}$ .

– **PUBLIC KEY:**  $(n, e, x, \alpha)$

– **PRIVATE KEY:**  $(p, q, a, d)$

### Encryption

Here the process of encrypting the simple plain text into cipher text is performed, so that an intruder doesn't get to read the message. For the message  $M \in \mathbb{Z}_n$ ,

1. Select a random  $r \in \mathbb{Z}_n^*$  and for the selected  $r$ , compute  $k_1 = \frac{1}{2}D_e(2r) \pmod{n}$ .
2. Similarly select  $c \in \mathbb{Z}_n^*$  and for the selected  $c$ , compute  $k_2 = \frac{1}{2}D_c(2\alpha) \pmod{n}$ .
3. Now finally compute  $k_3$  using selected  $r$  and the given  $x$ , where  $k_3 = \frac{M}{4}D_c(2x)D_e(2r) \pmod{n}$ .

For the plain text message “ $M$ ”, the encrypted ciphertext is  $(k_1, k_2, k_3)$ , which will be received by the decoder to generate the message.

**Decryption**

On receiving the encrypted message  $(k_1, k_2, k_3)$ , the receiver performs the below given steps:

1. Firstly, he/she deals with obtaining the value of  $r$ , by computing  $\frac{1}{2}D_d(2k_1) \pmod n$ .
2. Followed by computing  $Y$ , where  $Y = k_1^{-1} \pmod n$ .
3. Compute  $W$ , where  $W = k_3Y \pmod n$ .
4. Then compute  $Z$ , where  $Z = \frac{1}{2}D_{a^{\phi(n)+1}}(2k_2) \pmod n = \frac{1}{2}D_c(2x) \pmod n$ .
5. Finally obtain the plain-text message  $M = WZ^{-1} \pmod n$ .

**Verification**

First verification is dealing with obtaining the value  $r$  in the decryption.

$$\begin{aligned} & \frac{1}{2}D_d(2k_1) \pmod n \\ &= \frac{1}{2}D_d(2\frac{1}{2}D_e(2r)) \pmod n \\ &= \frac{1}{2}D_d(D_e(2r)) \pmod n \\ &= \frac{1}{2}D_{de}(2r) \pmod n \\ &= \frac{1}{2}2r \\ &= r \end{aligned}$$

As Dickson polynomial is commutative under composition, we have  $D_d(D_e(\alpha)) \pmod n = D_{(de)}(\alpha) \pmod n = D_e(D_d(\alpha) \pmod n) = D_1(\alpha) \pmod n = \alpha$ , also

$$\begin{aligned} & Z \\ &= \frac{1}{2}D_{a^{\phi(n)+1}}(2k_2) \pmod n \\ &= \frac{1}{2}D_a(2\frac{1}{2}D_c(2\alpha)) \pmod n \\ &= \frac{1}{2}D_c(D_a(2\alpha)) \pmod n \\ &= \frac{1}{2}D_c(2x) \pmod n \end{aligned}$$

And the verification of the message to be generated is

$$\begin{aligned} & WZ^{-1} \pmod n \\ &= k_3YZ^{-1} \pmod n \\ &= k_3k_1^{-1}(\frac{1}{2}D_c(2x))^{-1} \pmod n \\ &= \frac{M}{4}D_c(2x)D_e(2r)(\frac{1}{2}D_e(2r))^{-1}(\frac{1}{2}D_c(2x))^{-1} \pmod n \\ &= \frac{M}{4}D_c(2x)D_e(2r)2D_e^{-1}(2r)2D_c^{-1}(2r) \pmod n \\ &= M \end{aligned}$$



## 4 Explanation with a Simple Example Using Wolfram Mathematica

### Key Generation

1. Let  $p = 3$  and  $q = 5$ , so  $2^3 - 1$  and  $2^5 - 1$  is prime.
  2. So  $n = 2^{15}$ , where  $m = 3 * 5$ .
  3. For  $n = 32768$ ,  $\phi(n) = 46080$ .
  4.  $e = 11$  and  $\gcd(e, \phi(n)) = 1$ .
  5.  $d = 41891$ , for  $ed \equiv 1 \pmod{n}$ .
  6. Choose  $a = 122$ .
  7. For  $\alpha = 177$ ,  $x = \frac{1}{2}D_{122}(2 \times 177) \pmod{32768} = 15041$ .
- **PUBLIC KEY:** (32768, 11, 15041, 177)
  - **PRIVATE KEY:** (3, 5, 122, 41891)

### Encryption

For message  $M = 4433$ .

1. Taking  $r = 223$ ,  $k_1 = \frac{1}{2}D_{11}(2 \times 223) \pmod{32768} = 6623$ .
2. Taking  $c = 19$ ,  $k_2 = \frac{1}{2}D_{19}(2 \times 177) \pmod{32768} = 29745$ .
3.  $k_3 = \frac{4433}{4}D_{19}(2 \times 15041)D_{11}(2 \times 223) \pmod{32768} = 20943$ .

**Encrypted message** (6623, 29745, 20943).

### Decryption

1.  $\frac{1}{2}D_{41891}(2 \times 6623) \pmod{32768} = 223$ .
2.  $Y = 6623^{-1} \pmod{32768} = 25119$ .
3.  $W = 20943 \times 25119 \pmod{32768} = 9745$ .
4.  $Z = \frac{1}{2}D_{122\phi(32768)+1}(2 \times 29745) \pmod{32768} = \frac{1}{2}D_{19}(2 \times 15041) \pmod{32768} = 6337$ .
5.  $6337^{-1} \pmod{32768} = 30529$ .
6. Finally  $9745 \times 30529 \pmod{32768} = 4433 = M$ .

And hence the original message is generated.

## 5 Security

In the proposed cryptosystem, the security is found to be completely built upon the Integer Factorization Problem (IFP) and the Discrete Dickson Problem (DDP). Here

we have observed a few cases of common attacks where the proposed cryptosystem was well secured.

As the encrypted message can be assessed by an intruder, he/she can have an assess to  $(k_1, k_2, k_3)$ . Now, for him/her to generate the message  $M$ , he/she has to obtain the value of  $p$  and  $q$  of  $m$  and so the value of  $d$ , followed by finding  $a$  from  $\frac{1}{2}D_a(2\alpha) \pmod n$ . And this can only be achieved if both the Integer Factorization Problem and Discrete Dickson Problem can be solved. The value of  $p$  and  $q$  is chosen in such a way that the size of  $m$  is 1024-bit or above, so no known algorithm can be used to factor  $m$ . And also to find  $a$  from  $\frac{1}{2}D_a(2\alpha) \pmod n$ , the intruder have to solve DDP. Also, the value of  $\alpha$  and  $r$  should be large enough to prevent exhaustive search attack. It should be kept in mind that to encrypt different messages different values of  $r$  and  $c$  should be used. Because if a sender uses same parameters for the encryption of two different messages  $M_1$  and  $M_2$ , then the intruder can obtain  $k_3 = \frac{M_1}{4}D_c(2x)D_e(2r) \pmod n$  and  $k'_3 = \frac{M_2}{4}D_c(2x)D_e(2r) \pmod n$ . And hence from the relation  $M_2 = k'_3k_3^{-1}M_1$ , the intruder can have the message  $M_2$  on knowing  $M_1$ . So on choosing different values of  $r$  and  $c$ , the message  $M_2$  cannot be known even on knowing  $M_1$ .

Suppose the intruder somehow manages to find the values of  $p$  and  $q$  and then computes  $r = \frac{1}{2}D_d(2k_1) \pmod n$  and  $W = k_3Y \pmod n = k_3k_1^{-1} \pmod n = \frac{M}{2}D_c(2x) \pmod n$ . To find the message  $M$  from above, one has to know  $c$ , which is a computationally impossible assumption of the Discrete Dickson Problem which is equivalent to solving Discrete Logarithm Problem (DLP).

## 6 Performance Analysis

Here we have observed the performance of our proposed cryptosystem.

Let  $T_{ddp}$ ,  $T_{mul}$ ,  $T_{exp}$ ,  $T_{ch}$ , and  $T_{inv}$  represents the time for execution of Discrete Dickson Problem, time for modular multiplication, time for modular exponential operation, time for Chebyshev map and time for modular inverse computation respectively. And the time for computation is  $1T_{ddp} = 0.172$  s,  $1T_{mul} = 0.00207$  s,  $1T_{exp} = 5.37$  s,  $1T_{ch} = 0.172$  s and  $1T_{inv} = 0.0207$  s. Hence in our cryptosystem, the total computational complexity required is  $6T_{ddp} + 8T_{mul} + 2T_{inv}$  and the total time is equivalent to 1.09012 s, which is comparatively a smaller amount of time taken for computation.

Below we have compared the computational complexity of the proposed scheme with few other existing schemes (Table 1).

**Table 1** Comparison Table

Scheme	Encryption	Decryption	Time encryption (s)	Time decryption(s)	Total time(s)
Gowsami et al. [9]	$6T_{exp} + 3T_{mul}$	$4T_{exp} + 3T_{mul} + 3T_{inv}$	32.22621	21.54831	53.77452
Poulakis [10]	$6T_{exp} + 4T_{mul}$	$3T_{exp} + 2T_{mul} + 2T_{inv}$	32.22828	16.15554	48.38302
Goswami et al. [25]	$4T_{exp} + 2T_{mul}$	$3T_{exp} + 2T_{mul} + 2T_{inv}$	21.48414	16.15554	37.63968
Tahat et al. [24]	$6T_{ch} + 3T_{mul}$	$4T_{ch} + 3T_{mul} + 3T_{inv}$	1.03821	0.75631	1.79452
Proposed Scheme	$4T_{ddp} + 4T_{mul}$	$2T_{ddp} + 4T_{mul} + 2T_{inv}$	0.69628	0.39384	1.09012

## 7 Conclusion

In this paper, we have proposed a public key cryptosystem based on IFP and DDP. The use of IF and DDP has highly enhanced the security of the proposed cryptosystem and it is also observed that the computational complexity is quite low compared to that of other schemes.

## References

1. Diffie, W., Hellman, M.: New directions in cryptography. *IEEE Trans. Inf. Theory* **22**(6), 644–654 (1976)
2. Dickson, L.E.: The analytic representation of substitutions on a power of a prime number of letters with a discussion of the linear group. *Ann. Math.* **11**(1), 65–120 (1896/1897)
3. Schur, I.: Arithmetisches über die Tschbyscheffschen Polynome. *Gesammelte Abhandlungen* **3**, 422–453 (1973)
4. Lidl, R., Müller, W.B.: Permutation polynomials in RSA-cryptosystems, In: Chaum, D. (eds.), *Advances in Cryptology*, pp. 293–301. Springer, Boston, MA (1984). <https://doi.org/10.1007/978-1-4684-4730-923>
5. Lidl, R., Müller, W.B.: A note on polynomials and functions in algebraic cryptography. *Ars Combinatoria* **17**, 223–229 (1984)
6. Lidl, R., Müller, W.B.: On commutative semigroups of polynomials with respect to composition. *Monatshefte für Mathematik* **102**(2), 139–153 (1986)
7. Lidl, R.: Theory and applications of Dickson polynomials. *Top. Polynomials One Sev. Var. Their Appl. Vol. Dedic. Mem. PL Chebyshev* **1821–1894**, 371–395 (1993)
8. McCurley, K.S.: A key distribution system equivalent to factoring. *J. Cryptol.* **1**(2), 95–105 (1988)
9. Goswami, P., Singh, M.M., Bhuyan, B.: A new public key scheme based on integer factorization and discrete logarithm. *Palest. J. Math.* **6**(2), 580–584 (2017)
10. Poulakis, D.: A public key encryption scheme based on factoring and discrete logarithm. *J. Disc. Math. Sci. Cryptograp.* **12**(6), 745–752 (2009)

11. Guo, R., Wen, Q., Jin, Z., Zhang, H.: Pairing based elliptic curve encryption scheme with hybrid problems in smart house. In: 2013 Fourth International Conference on Intelligent Control and Information Processing (ICICIP), pp. 64–68. Institute of Electrical and Electronics Engineers (IEEE), Beijing, China (2013)
12. Shao, Z.: Signature schemes based on factoring and discrete logarithms. *IEE Proc.-Comput. Digit. Tech.* **145**(1), 33–36 (1998)
13. Wei, P., Liao, X., Wong, K.W.: Key exchange based on Dickson Polynomials over finite field with  $2^m$ . *J. Comput.* **6**(12), 2546–2551 (2011)
14. Ismail, E.S., Hijazi, M.S.N.: A new cryptosystem based on factoring and discrete logarithm problems. *J. Math. Stat.* **7**(3), 165–168 (2011)
15. Mohamad, M.S.A., Ismail, E.S.: Threshold cryptosystem based on factoring and discrete logarithm problems. In: AIP Conference Proceedings, pp. 1020–1023. American Institute of Physics, Selangor, Malaysia (2013)
16. Baocang, W., Yupu, H.: Public key cryptosystem based on two cryptographic assumptions. In: IEE Proceedings—Communications, vol. 152(6), pp. 861–865 (2005). <https://doi.org/10.1049/ip-com:20045278>
17. Rivest, R., Shamir, A., Adleman, L.: A method for obtaining digital signatures and public key cryptosystems. *Commun. ACM* **21**(2), 120–126 (1978)
18. Müller, W.B., Nöbauer, R.: Some remarks on public key cryptography. *Studia Scientiarum Mathematicarum, Hungarica* **16**, 71–76 (1981)
19. Mullen, G.L., Panario, D.: Handbook of Finite Fields (Discrete Mathematics and Its Applications), 1st edn. CRC Press, Boca Raton (2013)
20. McCurley, K.S.: The discrete logarithm problem. In: Proceedings of Symposia in Applied Mathematics, Cryptology and Computational Number Theory, vol. 42, pp. 49–74. American Mathematical Society, Boulder Colorado (1990)
21. Menezes, A.J., Van Oorschot, P.C., Vanstone, S.A.: Hand Book of Applied Cryptography. CRC Press, Bacon Raton (2018)
22. Álvarez, R., Tortosa, L., Vicent, J.F., Zamora, A.: Analysis and design of a secure key exchange scheme. *Inf. Sci.* **179**(12), 2014–2021 (2009)
23. Coppersmith, D., Odlyzko, A.M., Schroepfel, R.: Discrete logarithms in  $GF(p)$ . *Algorithmica* **1**(1), 1–15 (1986)
24. Tahat, N., Tahat, A.A., Abu-Dalu, M., Albadarneh, R.B., Abdallah, A.E., Al-Hazaimeh, O.M.: A new public key encryption scheme with chaotic maps. *Int. J. Electr. Comput. Eng.* **10**(2), 1430–1437 (2020)
25. Goswami, P., Singh, M.M., Bhuyan, B.: A new public key scheme based on DRSA and generalized GDLP. *Disc. Math. Algorithms Appl.* **8**(4), 1650057 (2016)

# Strongly $k$ -Regular Dominating Graphs



Anjan Gautam  and Biswajit Deb 

**Abstract** A dominating set  $D$  of  $V(G)$  is defined to be a  $k$ -regular dominating set if the subgraph of  $G$  induced by  $D$  is  $k$ -regular. We define a graph to be a *strongly  $k$ -regular dominating graph* if each dominating set of it is  $k$ -regular. Some classes of graphs that are strongly 0-regular and 1-regular are characterized. In particular, all trees  $T$  with  $\text{diam}(T) \leq 7$  for which trees are strongly 0-regular dominating are characterized.

**Keywords** Tree · Domination number ·  $k$ -regular dominating set · Triangular Snake graph

## 1 Introduction

A graph  $G$  is a pair  $(V(G), E(G))$ , where  $V(G)$  is a finite nonempty set and  $E(G)$  is a set of unordered pairs of distinct elements of  $V(G)$ . The degree of a vertex  $v \in V(G)$  is the number of edges incident to it in  $G$  and it is denoted by  $\text{deg}(v)$ . If all the vertices of  $G$  have the same degree  $k$ , then  $G$  is  $k$ -regular, or simply regular.

The eccentricity  $\epsilon(v)$  of a vertex  $v$  is the greatest distance between  $v$  and any other vertex, that is

$$\epsilon(v) = \max_{u \in V} d(v, u).$$

The center of a graph is the set of all vertices with minimum eccentricity. The diameter of a graph is the maximum eccentricity of any vertex in the graph. A graph  $H$  is said to be a subgraph of  $G$  if  $V(H) \subseteq V(G)$  and  $E(H) \subseteq E(G)$ . The induced subgraph  $\langle S \rangle$  is the graph whose vertex set is  $S \subseteq V$  and whose edge set consists of all of the edges in  $E$  that have both endpoints in  $S$ .

The open neighborhood  $N(v)$  of  $v \in V(G)$  is defined as

---

A. Gautam (✉) · B. Deb

Department of Mathematics, Sikkim Manipal Institute of Technology, Sikkim Manipal University, Majitar, Rangpo, East-Sikkim 737136, India  
e-mail: [anjangautam12@gmail.com](mailto:anjangautam12@gmail.com)

$$N(v) = \{u \in V : uv \in E\}$$

and the closed neighborhood  $N[v]$  of  $v$  is defined as

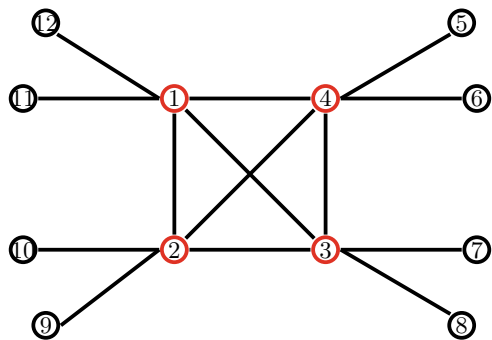
$$N[v] = \{u \in V : uv \in E\} \cup \{v\}.$$

A vertex of degree one is called a pendant vertex, its neighbor a support vertex, and its incident edge a pendant edge or leaves. If a vertex  $v$  is adjacent to two or more leaves,  $v$  is said to be a strong support vertex. For standard terminology in graphs, we refer the book by Harary [2].

The set  $S$  is called a dominating set of  $G$  if every vertex in  $V \setminus S$  has a neighbor in  $S$ . The domination number  $\gamma(G)$  is the cardinality of a minimum dominating set of  $G$ . A set  $D \subseteq V(G)$  is a totally dominating set of a graph  $G$  if every vertex  $v$  in  $V(G)$  is adjacent to some vertex in  $D$ . The total domination number  $\gamma_t(G)$  is the cardinality of the minimum totally dominating set. For concepts related to domination we refer [7]. Recently in 2019, a new lower bound on the domination number of a graph is observed [10]. A dominating set  $D$  of  $V(G)$  is defined to be a  $k$ -regular dominating set if  $\langle D \rangle$  is  $k$ -regular. We define a graph to be a strongly  $k$ -regular dominating graph if each minimum dominating set of it is  $k$ -regular (For example see Fig. 1). The concept of the domination number in a graph was defined by Berge [1] as, “coefficient of external stability”. Later in 1962, Ore [3] used the name “domination number” for the same. The connected domination number was studied by Sampathkumar and Walikar [4]. In 1994 Sampathkumar and Latha studied set domination in graphs [5]. The concept of regular set domination number was introduced by Kulli and Janakiram [6] in 2009. For a survey on domination in graphs, we refer book “Topics in Domination in Graphs” [8].

Consider a region that is suffering from a pandemic situation like COVID-19. Suppose that regular testing has to be done of the entire population and to achieve this new test centers are to be established. With limited resources, test center with medical facilities are to be placed with back up in strategic locations. The problem is to decide about the locations where such testing center needs back up. Let vertices represent different localities of the region and an edge connects two localities that

**Fig. 1** Strongly 3-regular dominating graph with dominating set  $D = \{1, 2, 3, 4\}$



share boundary. A locality (or vertex) and all of the regions that are adjacent to it we can refer as the neighborhood of that locality. A testing center in a location can serve the people in the localities in its neighborhood. Here the domination problem is to choose localities at which place these service facility to be located such that each neighborhood contains at least one and if required their must be a backup testing center in its neighborhood. An optimal solution for this problem can be achieved by obtaining a  $k$ -regular dominating set for  $k \geq 1$  with minimum number of vertices. It is to be noted that a connected dominating set may not be a good idea to solve the above problem due to the scarcity of the resources and high demand of the test centers.

## 2 Results

### 2.1 Strongly 0-Regular Dominating Graph

**Theorem 1** *Let  $P_n$  be a path with  $n$  vertices. Then  $P_n$  is strongly 0-regular dominating graph if and only if  $n \equiv 0$  or  $2 \pmod{3}$ .*

**Proof** The domination number of a path with  $n$  vertices is  $\gamma(P_n) = \lceil \frac{n}{3} \rceil$ . Let  $P_n = v_1 v_2 \dots v_n$  be strongly 0-regular dominating graph. If possible let  $n \equiv 1 \pmod{3}$ . Consider the partition  $A_0, A_1, \dots, A_{m-1}, m = \lceil \frac{n}{3} \rceil$ , where  $A_i = \{v_{3i+1}, v_{3i+2}, v_{3i+3}\}$  for  $i = 0, 1, \dots, m - 2$  and  $A_{m-1} = \{v_{3(m-1)+1}\}$ . The vertex  $v_{3i+2}$ , covers  $A_i$ , for  $i = 0, 1, \dots, m - 2$ , and vertex  $v_{3(m-1)+1}$  is covered by  $v_{3(m-2)+3}$  or itself. If we consider a dominating set  $D = \{v_2, v_5, \dots, v_{3(m-2)+2}, v_{3(m-2)+3}\}$  of size  $m = \lceil \frac{n}{3} \rceil$ , then  $v_{3(m-1)+2}$  and  $v_{3(m-1)+3}$  are adjacent as shown in Fig. 2 so,  $\langle D \rangle$  is not 0-regular, a contradiction. Thus  $n \equiv 0$  or  $2 \pmod{3}$ .

Conversely, let  $n \equiv 0$  or  $2 \pmod{3}$ .

Case 1:  $n \equiv 0 \pmod{3}$ .

The set  $S = \{v_2, v_5, \dots, v_{3(m-1)+2}\}$  is the only dominating set of size  $m = \lceil \frac{n}{3} \rceil$ . If possible let, there exist a dominating set  $T = \{u_1, u_2, \dots, u_m\}$  of size  $m$  other than  $S$ . As  $n \equiv 0 \pmod{3}$  each vertex  $u_i, i = 1, 2, \dots, m$  must cover 2 other vertices. If  $u_1 = v_1$  then  $u_1$  will cover just one vertex  $v_2$  and if  $u_1 = v_3$  then  $u_1$  will cover  $v_2$  and  $v_4$ , which makes  $v_1$  uncovered. Thus, we can say  $u_1 = v_2$ . Similarly  $u_2 = v_5, u_3 = v_8, \dots, u_m = v_{3(m-1)+2}$ . As  $\langle S \rangle$  is 0-regular which implies  $P_n$  is strongly 0-regular dominating graph.

Case 2:  $n \equiv 2 \pmod{3}$ .

In this case there are only two dominating set of size  $m$ .

Let  $D = \{v_2, v_5, \dots, v_{3(m-2)+2}, v_{3(m-1)+1}\}$

and  $S = \{v_2, v_5, \dots, v_{3(m-2)+2}, v_{3(m-1)+1}\}$  be dominating set of size  $m$ .

One can similarly show as Case 1, that any other dominating set  $T$  of size  $m$  is either  $D$  or  $S$ . As  $\langle D \rangle$  and  $\langle S \rangle$  are both 0-regular, thus  $P_n$  is strongly 0-regular dominating graph.

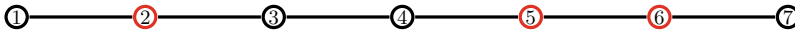


Fig. 2 A Path  $P_7$  with dominating set  $D = \{2, 5, 6\}$

**Theorem 2** Let  $C_n$  be a cycle with  $n$  vertices. Then  $C_n$  is strongly 0-regular dominating graph if and only if  $n \equiv 0$  or  $2 \pmod{3}$ .

We can write the proof of Theorem 2 on the same line as Theorem 1.

**Lemma 1** A strongly 0-regular dominating graph  $G$  cannot have a pair of pendant vertices at distance 3 apart.

**Proof** Let  $G$  be a graph with a path of length 3 between any two pendent vertices  $u, v$ . Let the path be  $\{u, u_1, v_1, v\}$  and  $D$  be a minimum dominating set of  $G$ . As  $u$  and  $v$  are pendent vertices, we may consider  $u$  and  $v$  to be in  $D$  but alternately, we can also consider  $u_1, v_1 \in D$  to cover  $u$  and  $v$ . As  $\{u_1, v_1\}$  is an edge so  $G$  is not strongly 0-regular dominating graph.

**Remark 1** If a tree has no pendant vertices at distance 3, then no two support vertices in  $T$  are adjacent.

**Theorem 3** A tree  $T$  with  $diam(T) \leq 5$  is strongly 0-regular dominating graph if and only if no two pendant vertices are at distance 3.

**Proof** Let a tree  $T$  with  $diam(T) \leq 5$  is 0-regular dominating graph. If possible let two pendant vertices are at distance 3 then by Lemma 1 graph  $T$  is not strongly 0-regular dominating graph, a contradiction.

Conversely, let  $T$  has no pendant vertices at distance 3. Let  $D$  be a minimum dominating set. For a tree  $T$  with  $diam(T) = 1, 2$ , the result holds as dominating set consists of one vertex. Tree which holds the condition with  $diam(T) = 3$  does not exist.

Consider a tree  $T$  with  $diam(T) = 4$  and  $u_1u_2u_3u_4u_5$  be its diametric path. Any minimum dominating set  $D$  consists of either support vertex or pendant vertex. By Remark 1  $D$  is 0-regular, thus  $T$  with  $diam(T) = 4$  is strongly 0-regular dominating graph.

Consider  $diam(T) = 5$  and  $u_1u_2 \dots u_6$  be a diametric path. Diametric path and pendant vertices of  $u_2, u_5$  will be covered by  $u_2$  and  $u_5$ . If  $u_3$  has a tail  $u_3v_1v_2$ , then  $v_1$  or  $v_2$  will cover its tail. Thus any minimum dominating set  $D$  comprises of strong support vertices, and support vertices or pendent vertices. As two support vertices are not adjacent thus  $D$  is 0-regular dominating set.

**Theorem 4** A tree  $T$  with  $diam(T) = 6$  is strongly 0-regular dominating graph if and only if

- (i) no two pendant vertices are at distance 3, and
- (ii) center of  $T$  contains a pendant vertex or a tail of length 2.



**Proof** Let  $T$  be a strongly 0-regular dominating tree with  $diam(T) = 6$  and  $u_1u_2 \dots u_7$  be a diametric path in it. By Lemma 1  $G$  cannot have a pendant vertices at distance 3 apart. If possible let  $center(T)$  does not contains a pendant vertex or a tail of length 2. Let  $D$  be a minimum dominating set containing all the support vertices. A set aggregating only of all support vertices will not dominates  $center(T) = u_4$ , as  $v_3$  or  $v_5$  has no pendant vertices. Thus  $D$  consisting of support vertices along with  $v_3$  or  $v_5$  is not 0-regular dominating set, a contradiction. Hence, center of  $T$  contains a pendant vertex or a tail of length 2.

Conversely, assume that (i) and (ii) holds for a tree  $T$ . Let  $D$  be any minimum dominating set of  $T$ .

Case 1: Center of  $T$  contains a pendant vertex.

As (i) implies  $u_3$  and  $u_5$  are not support vertices, so  $u_3, u_5 \notin D$ . For, if  $u_3 \in D$ , then  $u_3$  covers  $u_2, u_4$  and the support vertex  $w_1$  of any tail  $u_3w_1w_2$  at  $u_3$ , if there is any. To cover the pendant vertices at  $u_2, u_4$  and  $w_1$  we need 3 more vertices other than  $u_3$  in  $D$ . But all these vertices may be covered by  $\{u_2, u_4, w_1\}$ , contradicting our assumption that  $D$  is minimum. Similarly we can argue that  $u_5 \notin D$ . Therefore,  $u_4 \in D$  and  $u_3, u_5 \notin D$ . Any other vertex in  $D$  will be a support vertex or a pendant vertex. By (i) no two support vertices are adjacent, so  $\langle D \rangle$  is 0-regular.

Case 2: Center of  $T$  contains a tail of length 2.

Let  $u_4v_1v_2$  be a tail of length 2 at  $u_4$ . We claim that,  $u_3, u_4, u_5 \notin D$ . For if  $u_4 \in D$ , then either  $v_1$  or  $v_2 \in D$ .

If  $v_1 \in D$ , then  $u_4$  must cover either  $u_3$  or  $u_5$ . Suppose  $u_4$  covers  $u_3$ . Then either  $deg(u_3) = 2$  or there is a tail at  $u_3$  other than  $u_3u_2u_1$ , whose pendant vertex is in  $D$ . Also either  $u_1$  or  $u_2 \in D$ . Contradicting the minimality of  $D$ .

If  $v_2 \in D$ , then  $u_4$  is either covering itself or  $u_3$  or  $u_5$ . If  $u_4$  covering  $u_3$  or  $u_5$ , then arguing in the same way as above, we can show that  $D$  is not minimum. If  $u_4$  covering itself, than dropping  $u_4$  and  $v_2$  from  $D$  and including  $v_1$  we can get a dominating set smaller than  $D$ , contradiction to the minimality of  $D$ . Therefore,  $u_4 \notin D$  and  $v_1 \in D$ .

For if  $u_3 \in D$ , then  $u_3$  is either covering itself or  $u_2$  or  $w_1$  of any tail  $u_3w_1w_2$  at  $u_3$ . But  $u_3$  does not cover  $u_2$  or  $w_1$  as it is covered by its pendant vertex. If  $u_3$  covers itself then removing  $u_3$  and  $u_1$  from  $D$  and adding  $u_2$  we can get dominating set smaller than  $D$ , a contradiction. Therefore,  $u_3 \notin D$ , similarly  $u_5 \notin D$ . Thus, any vertex in  $D$  is either support vertex or a pendant vertex, so  $\langle D \rangle$  is 0-regular.

As every minimum dominating set  $D$  of  $T$  is 0-regular, so  $T$  is a strongly 0-regular dominating graph.

**Definition:** For any two vertices  $u_1, u_2 \in V(G)$ , by saying that  $(u_1, u_2)$  has a tail of length  $(a_1, a_2)$  we mean that there is a tail at  $u_i$  of length  $a_i$ , for  $i = 1, 2$ .

**Theorem 5** Let  $T$  be a tree with  $diam(T) = 7$  and center  $\{u_4, u_5\}$ . Then  $T$  is strongly 0-regular dominating graph if and only if

- (i) no two pendant vertices in  $T$  are at distance 3, and
- (ii)  $(u_4, u_5)$  does not have a tail of length  $(2, 0)$  and  $(2, 3)$ .

**Proof** Consider a tree  $T$  with  $\text{diam}(T) = 7$  and center  $\{u_4, u_5\}$  that is strongly 0-regular dominating graph, and  $u_1u_2 \dots u_8$  be a diametric path. Let  $D$  be a minimum dominating set of  $T$ . By Lemma 1  $T$  cannot have pendant vertices at distance 3 apart. If possible let there exist a tail at  $(u_4, u_5)$  of length  $(2, 0)$  or  $(2, 3)$ . Let  $u_4v_1v_2$  be a tail at  $u_4$  and  $u_5w_1w_2w_3$  at  $u_5$ .

Case 1:  $(u_4, u_5)$  has a tail of length  $(2, 0)$ .

As  $u_6, u_4$  has no pendant vertex,  $D$  consisting of  $u_2, u_7, v_1$ , support vertices of tails at  $u_3$  or  $u_6$  if any, along with  $u_4$  or  $u_6$  or  $u_5$  will cover  $T$ . Considering  $u_4 \in D$ ,  $u_4v_1$  will be an edge in  $\langle D \rangle$ , therefore it is not 0-regular, a contradiction.

Case 2:  $(u_4, u_5)$  has a tail of length  $(2, 3)$ .

Similarly as above,  $D$  consisting of  $u_2, u_7, v_1$ , support vertices of tails at  $u_3$  or  $u_6$  along with  $u_4$  or  $u_6$  or  $u_5$  or  $w_1$  will cover  $T$ . Considering  $u_4$  or  $u_6$  or  $w_1 \in D$ ,  $\langle D \rangle$  will not be 0-regular, a contradiction.

Thus, if  $T$  is strongly 0-regular dominating graph then (i), (ii) holds.

Conversely, let (i), (ii) holds and  $D$  be any minimum dominating set of  $T$ . We consider the following cases.

Case 1:  $u_4, u_5 \notin$  closed neighbor of any support vertex.

In this case  $(u_4, u_5)$  may have tail of length  $(3, 3)$  or  $(0, 3)$  or  $(3, 0)$  or they may have no tail. In any case  $D$  consist of support vertex or pendant vertex together with  $u_4$  or  $u_5$ , so  $\langle D \rangle$  is 0-regular. Hence  $T$  is strongly 0-regular dominating graph.

Case 2: Either  $u_4$  or  $u_5 \in$  closed neighbor of any support vertex.

If  $u_4 \in$  closed neighbor of any support vertex, then  $(u_4, u_5)$  may have tail of length  $(1, 0)$  or  $(1, 2)$  or  $(1, 3)$  or  $(2, 2)$ . If  $(u_4, u_5)$  have tail of length  $(1, 0)$  or  $(1, 3)$ , then  $u_4$  must be in  $D$  to cover  $u_5$  and pendant vertex of  $u_4$ . If  $u_4 \notin D$  then we need two more vertex in  $D$ , contradicting the minimality of  $D$ . Therefore,  $D$  comprise of support vertex or pendant vertex together with  $u_4$ , thus  $\langle D \rangle$  is 0-regular.

If  $(u_4, u_5)$  have tail of length  $(1, 2)$ , then  $u_5 \notin D$ . For if  $u_5 \in D$  we will need two more vertex in  $D$  to cover pendant vertex at  $u_4$  and pendant vertex of a tail of length 2 at  $u_5$ . But if we just consider  $u_4$  and support vertex of a tail at  $u_5$ , then they will cover same number of vertices as,  $u_6$  can be covered by  $u_7$ . In this case any  $D$  will consist of support vertices or pendant vertices, Thus  $\langle D \rangle$  is 0-regular.

If  $(u_4, u_5)$  have tail of length  $(2, 2)$ , then support vertices of tails from  $u_4$  and  $u_5$  will cover them respectively. Arguing as above  $\langle D \rangle$  will be 0-regular. For if  $u_4$  and  $u_5$  have more than one tail of different lengths then we can argue similarly as above that, any  $D$  will consist of support vertices or pendant vertices. Thus, in any case  $\langle D \rangle$  is 0-regular. Hence  $T$  is strongly 0-regular dominating graph.

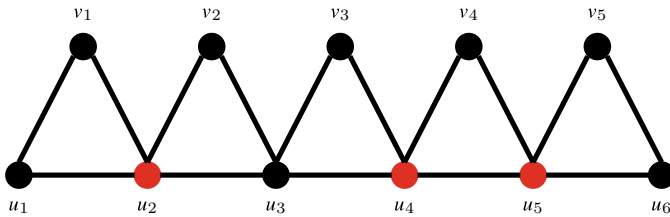


**Fig. 3** A Triangular Snake  $T_6$  with dominating set  $D = \{u_2, u_4, u_5\}$

**Definition:** A Triangular Snake graph  $T_n$  is obtained from a path  $u_1, \dots, u_n$  by joining  $u_i$  and  $u_{i+1}$  to a new vertex  $v_i$  for  $1 \leq i \leq n - 1$ . That is, every edge of a path is replaced by a triangle.

**Theorem 6** A Triangular Snake  $T_n$  is strongly 0-regular dominating graph if and only if  $n \equiv 1 \pmod{2}$ .

**Proof** Let a Triangular Snake  $T_n$  be strongly 0-regular dominating graph. Domination number of Triangular Snake  $T_n = \lfloor \frac{n}{2} \rfloor$ . If possible let  $n \equiv 0 \pmod{2}$ .

Consider the partition  $A_0, A_1, \dots, A_{m-1}$ ,  $m = \lfloor \frac{n}{2} \rfloor$ , where  $A_0 = \{u_1, u_2, u_3, v_1, v_2\}$ ,  $A_i = \{u_{2(i+1)}, u_{2(i+1)+1}, v_{2i+1}, v_{2(i+1)}\}$ , for  $1 \leq i \leq m - 2$  and  $A_{m-1} = \{u_n, v_{n-1}\}$ . The vertex  $u_2$  dominates  $A_0$  and  $u_{2(i+1)}$  dominates  $A_i$  for  $1 \leq i \leq m - 2$ .  $A_{m-1}$  is dominated by  $u_n$  or by  $u_{n-1}$ . Let us consider the dominating set of size  $\lfloor \frac{n}{2} \rfloor$ ,  $D = \{u_2, u_4, \dots, u_{n-2}, u_{n-1}\}$ , as shown in Fig. 3 (for  $n = 6$ ). As  $\langle D \rangle$  contains an edge  $u_{n-2}u_{n-1}$  so  $T_n$  is not strongly 0-regular dominating graph, a contradiction.

Conversely, let  $n \equiv 1 \pmod{2}$ . Then the set  $D = \{u_2, u_4, \dots, u_{n-1}\}$  is the only dominating set of size  $\lfloor \frac{n}{2} \rfloor$ . If possible let  $S = \{w_1, w_2, \dots, w_m\}$ , be a another dominating set of size  $m = \lfloor \frac{n}{2} \rfloor$ . If  $w_1 = u_1$  then  $u_3$  and  $v_2$  is not covered and if  $w_1 = u_3$  then  $u_1$  and  $v_1$  is not covered. Thus  $w_1 = u_2$  will cover all the vertices of partition  $A_0$ . Similarly we can show  $w_2 = u_4, \dots, w_m = u_{n-1}$ . As  $\langle D \rangle$  is 0-regular, therefore  $T_n$  is strongly 0-regular dominating graph.

**Remark 2** For  $k \geq 2$  a tree  $T$  is not strongly  $k$ -regular dominating graph.

### 2.2 Strongly 1-Regular Dominating Graphs

**Double star:** Double star  $S_{m,n}$  is the graph obtained by joining the center of two stars  $K_{1,n}$  and  $K_{1,m}$  with an edge.

**Remark 3** Double star  $S_{m,n}$  is strongly 1-regular dominating graph for  $m, n \geq 2$ .

**Book Graph:** The  $m$ -book graph is defined as the graph Cartesian product  $B_m = K_{m,1} \square P_2$ , where  $K_{m,1}$  is a star graph and  $P_2$  is the path graph on two vertices.



**Fig. 4** A Path  $P_4$  with dominating set  $D = \{2, 4\}$  or  $\{2, 3\}$  or  $\{1, 4\}$  or  $\{1, 3\}$  and total dominating set  $S = \{2, 3\}$

**Theorem 7** Book graph  $B_m$  is strongly 1-regular dominating graph for  $m \geq 2$ .

*Proof* Consider a book graph  $B_m = K_{m,1} \square P_2$ , where  $K_{m,1}$  is a star graph and  $P_2$  is the path graph on two vertices. Let  $V(K_{m,1}) = 1, 2, \dots, m + 1$ , where the center is 1, and  $V(P_2) = a, b$ . Now,  $V(B_m) = (1, a), (1, b), (2, a), (2, b), \dots, (m + 1, a), (m + 1, b)$ . From the definition of Cartesian product the set  $D = \{(1, a), (1, b)\}$  is sufficient to cover all the vertices of  $B_m$ , for all  $m$ . For  $m \geq 2$ , every dominating set  $D = \{(1, a), (1, b)\}$ , thus  $\langle D \rangle$  is 0-regular, and  $B_m$  is strongly 1-regular dominating graph.

**Lemma 2** A strongly 1-regular dominating graph cannot have a path of length 3, with degree sequence of its vertices as  $1, a, 2, 1$ , for  $a \geq 2$ .

*Proof* Let  $G$  be a graph with a path of length 3 and degree sequence of vertices of path  $\{u_1, u_2, u_3, u_4\}$  is  $1, a, 2, 1, a \geq 2$ . Let  $D$  be a minimum dominating set of  $G$ . We can consider  $u_2, u_3 \in D$  or  $u_2, u_4 \in D$  to dominate vertices of path. As we have  $u_2, u_4 \in D$  so,  $G$  is not strongly 1-regular dominating graph.

**Theorem 8** If a graph is strongly 1-regular dominating graph, then every minimum dominating set of  $G$  is equal to its minimum total dominating set.

*Proof* Let a graph  $G$  be strongly 1-regular dominating graph and  $D$  be any minimum dominating set. As every vertex of  $V(G)$  has a neighbor in  $D$ , thus  $D$  is a total dominating set.

**Remark 4** The converse of Theorem 8 is not true. For example, see Fig. 4, here domination number is equal to total domination number, but induced subgraph of every dominating set is not 1-regular.

### 2.3 Construction of Strongly $k$ -Regular Dominating Graph

Given a graph  $G$  we can construct strongly  $k$ -regular dominating graph.

- Take a complete graph  $K_{k+1}$ .
- Put at least two pendant vertices to each vertex of  $K_{k+1}$ .
- Now select two vertices  $u, v$  of  $K_{k+1}$  and add one more vertex to both of them (those vertices has degree at least  $k + 3$ ).
- Take an edge  $xy \in E(G)$  and replace  $x$  and  $y$  with any one of the pendant vertices of  $u$  and  $v$ .

- Take  $|E(G)|$  copies of  $K_{k+1}$  with pendant vertices.
- Repeat the above step with each edge of  $G$ .
- Dominating set  $\gamma(G)$  contains all the vertices of  $K_{k+1}$  which is  $k$ -regular.

### 3 Conclusion

In this study, the concept of a strongly  $k$ -regular dominating graph is introduced and some classes of strongly 0-regular and 1-regular dominating graphs are characterized. Specifically, all 0-regular dominating trees  $T$  with  $diam(T) \leq 7$  are characterized. Application of domination number is discussed in various field such as Computer Communication Networks, Radio Stations, Facility Location Problems, Coding Theory etc. [9].

### References

1. Berge, C.: Theory of Graphs and Its Applications. Dunod Paris (1958)
2. Harary, F.: Graph Theory. Wiley Online Library (1969)
3. Ore, O.: Theory of Graphs. American Mathematical Society Colloquium Publications, vol. 38, pp. 206–212 (1962)
4. Sampathkumar, E., Walikar, H.B.: The connected domination number of a graph. J. Math. Phys **13**, 607–613 (1979)
5. Sampathkumar, E., Latha, L.P.: Set domination in graphs. J. Graph Theory **18**, 489–495 (1994)
6. Kulli, V.R., Janakiram, B.: Regular set domination in graphs. Natl. Acad. Sci. Lett. (India) **32**, 351–355 (1981)
7. Haynes, T.W., Hedetniemi, S., Slater, P.: Fundamentals of Domination in Graphs. CRC press 1 (2013)
8. Haynes, T.W., Hedetniemi, S.T., Henning, M.A.: Topics in Domination in Graphs. Springer, 64 (2020)
9. Gupta, Preeti: Domination in graph with application. Indian J. Res. **2**, 115–117 (2013)
10. Hajian, M., Henning, M.A., Rad, N.J.: A new lower bound on the domination number of a graph. J. Comb. Optim. **38**, 721–738 (2019)

# Chaotic Based Image Steganography Using Polygonal Method



Dipankar Dey, Solanki Pattanayak, and Sabyasachi Samanta

**Abstract** Information security is the most concerning factor in the time of tremendous innovative headway. Immense specialized information cleared a way for the development of information taking methods. Steganographic methods help to veil the mysterious data with some other media that goes about as a spread to the data. This strategy makes it hard for programmers to see the data since it shows up as a media instead of as data itself. Image steganography assists with concealing mystery data in any dimension and worth of images. These pictures can be traded without looking for any consideration of programmers to the mystery data inside it. Here the information is encoded into the image through an arbitrary rectangular region, to make it more secure. Using chaotic map we have generated random number series through which data embedded in rectangular region with uneven interval. This can be unscrambled at the beneficiary side with the best possible calculation alongside the secret key. We have scrambling the data and concealing it in the image utilizing the chaotic map. Removing the data and unscrambling it is done at the beneficiary. Embedding capacity of the proposed methodology is also comparable with other well known existing methodologies. Performance analysis is also measured and the proposed methodology generates enhanced result than the others.

**Keywords** Steganography · Chaotic map · Rectangular region · Encryption · Decryption · Cover image

---

D. Dey

Department of Computer Science and Technology, Global Institute of Science and Technology, Haldia, WB, India

e-mail: [dey\\_dipankar@rediffmail.com](mailto:dey_dipankar@rediffmail.com)

S. Pattanayak

Department of Computer Science, Haldia Institute of Management, Haldia, WB, India

e-mail: [solankipattanayak16@gmail.com](mailto:solankipattanayak16@gmail.com)

S. Samanta (✉)

Department of Information Technology, Haldia Institute of Technology, Haldia, WB, India

e-mail: [sabyasachi.smnt@gmail.com](mailto:sabyasachi.smnt@gmail.com)

© The Author(s), under exclusive license to Springer Nature Switzerland AG 2022

S. Banerjee and A. Saha (eds.), *Nonlinear Dynamics and Applications*,

Springer Proceedings in Complexity,

[https://doi.org/10.1007/978-3-030-99792-2\\_47](https://doi.org/10.1007/978-3-030-99792-2_47)

## 1 Introduction

Various strategies such as encryption and steganography are used to protect the data on the Internet. Encryption is the study of transforming a mysterious message into another structure, and the ultimate goal is not universally understandable. Steganography is a strategy for making sure about data by concealing it in some other medium, with the end goal that the presence of data is disguised to everybody aside from the planned sender and collector. Steganography suggest to the craftsmanship and study of concealing mystery data from other media [7, 8]. The data that is hidden is called a mystery message, and the medium in which the data is hidden is called a distribution report. A distributed dataset containing implied messages is called a stego report. A calculation used to obfuscate a message on the sender's propagating media and remove the obfuscated message from the saver's stego archive called stego framework [9–12]. Here in this study introduces image steganography technology the contributions of this work is very inventive. Initially we have inserted a gray scale image with size of  $M \times N$  and chosen a rectangular region to hide the text inside the image using chaotic map to generate the random number. We have used the mathematical functions which give the better output collect to other existing techniques and unauthorized users can not access our information.

Section 2 gives an overview of some existing related systems. The proposed system is presented and the analysis of the proposed system is evaluated in Sect. 3. Section 4 explains the performance of the proposed system with the relevant existing system. Finally, the conclusion of this work is in Sect. 5.

## 2 Literature Review

Information covering by using LSB [1] is one of the most basic and habitual strategies so far. This methodology works by concealing information at all noteworthy bits of the pixels (LSB). Huge however it's yet at the same time a few changes in the picture may disable the implanted information. The Pixel Value Differencing (PVD) [2], recommended by Wu and Tsai is one of the convincing cryptographic approach. It structures pixel hinders from the spread and adjusts the pixel contrast in each pair of squares for information inclusion. More prominent the distinction more is the adjustment made. In light of PVD, another technique for tri method of pixel esteem differencing is proposed by Chang et al. [3]. This new strategy has shown better performance in terms of payload [4, 18] and PSNR. Gray Level Correction (GLM) [5] proposed by Potder Et al. is another strategy for mapping information by reforming the dark level estimates of the pixels present in the image. The gray level estimates for the selected pixels are distinguished based on the secret information bits. Several strategies have also been proposed to combine PVD and GLM techniques with the goal of increasing payload. One such technology is Safarpour Et al. is taught by [6]. When inspected, the image is screened and split at the correct pixels using

bit substitution. These pixels are randomly selected rather than in order. Chen Et al. adopted the strategy used when using the side match technique [13]. Using particle swarm optimization and chaos theory, authors propose a steganography technique that finds the optimal pixel position in the cover image and hides confidential data while preserving the quality of the resulting stego image. To increase the embedded capacity, the host and secret images are divided into blocks, each block containing the appropriate amount of secret bits. In [14], Hsiao Et al. suggested a method of data hiding based on a  $16 \times 16$  Sudoku matrix by taking a  $16 \times 16$  Sudoku matrix and extending it to a two-layer magic square. Low-cost data embedding methods are also being considered to improve PSNR and maintain good image quality with the same embedding capacity. Here Manikandan et al. [15] proposes a method to validate the receiver by incorporating the E-mail and OTP verification to get the encrypted image. Mansoor Fateh et al. [16] proposed an improved version of the LSB matching, which works with two phases including embedding and extracting the message. In this method two bits of the secret message are hidden in two pixels with only one change. Wenfa Qi et al. [17] proposed an adaptive embedding method for visible watermarking where they embedded watermark image in the host image.

### 3 Proposed Work and Algorithms

#### 3.1 Process of the Proposed Work

The following is an overview of a new plan using the chaos system with the goal of being able to change the intensity values for all pixels. To hide the secret data in the proposed plot, (a) we make a square shape district of dimension  $512 \times 512$  of a unique picture (dimension of the gray scale picture is  $512 \times 512$ ); (b) input different payload type text as 1024 bytes text and store in  $s1$  variable (c) Chaotic maps are used to generate private keys. (d) A bitwise XOR operation is applied between the target pixel and the private key to get the final encrypted image. Figure 1 shows a block diagram of the proposed method.

#### 3.2 Algorithm for Encoding Process

Step 1: Input gray scale image of size  $512 \times 512$  and a text (size of text vary with respect to programming).

Step 2: Initialize the variable  $q = 0.9898$  (the value of  $q$  is determined from chaotic map) and  $s = 5$ ,  $xc = \frac{row}{2}$ ,  $yc = \frac{col}{2}$ , where row and col is the size of the image. Choose the value of  $n$  (secret key) as in following order of varying text file( $n, s1$ ). Here  $s1$  is the size of text file. The text file is stored in  $p_k$  in one dimensional array.



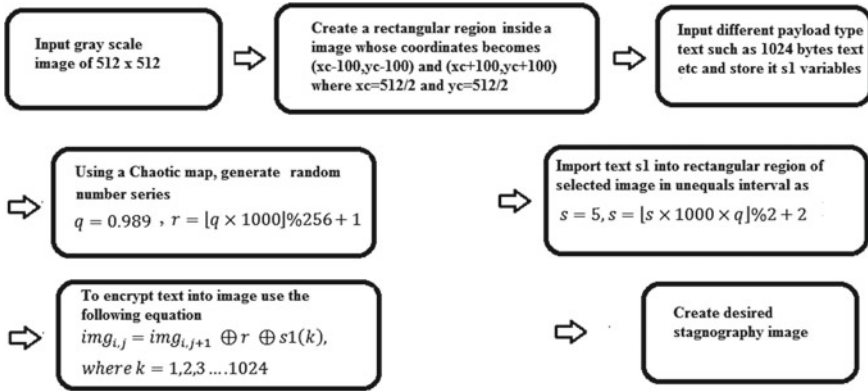


Fig. 1 Block diagram of the proposed method

{(4, 100), (8, 500), (12, 1000), (17, 2000), (22, 3000), (26, 5000), (30, 10000), (33, 20000) and (36, X)}, here X is the remaining text file size. Store the value of n into image location which will be used in decryption process for extract the original text file. The value of n is stored in image location as  $img(\frac{row}{2} + 10, \frac{col}{2} + 10) = n$ . Here image location is also a secret key.

Step 3: Initialize  $i = xc - n, j = yc - n$ .

Step 4: If  $(i \leq xc + n \text{ and } j \leq yc + n)$

Step 5: Then

$$r = [q \times 1000] \% 125, \quad q = 3.5 \times q \times (1 - q),$$

$$img_{i,j} = img_{i,j+1} \oplus r \oplus p_k, \text{ where } k \text{ is the size of text file,}$$

$$s = [s \times 1000 \times q] \% 2 + 2,$$

Iterate uneven gap which is s times.

Step 6: Repeat Step 4 until condition is false.

Step 7: Create the desired steganography image.

Step 8: Stop.

### 3.3 Flow Chart of Encoding Process

### 3.4 Algorithm for Decoding Process

Step 1: Input gray scale image (steganography img) of size  $512 \times 512$  and a text (cover text may differ from process to process).

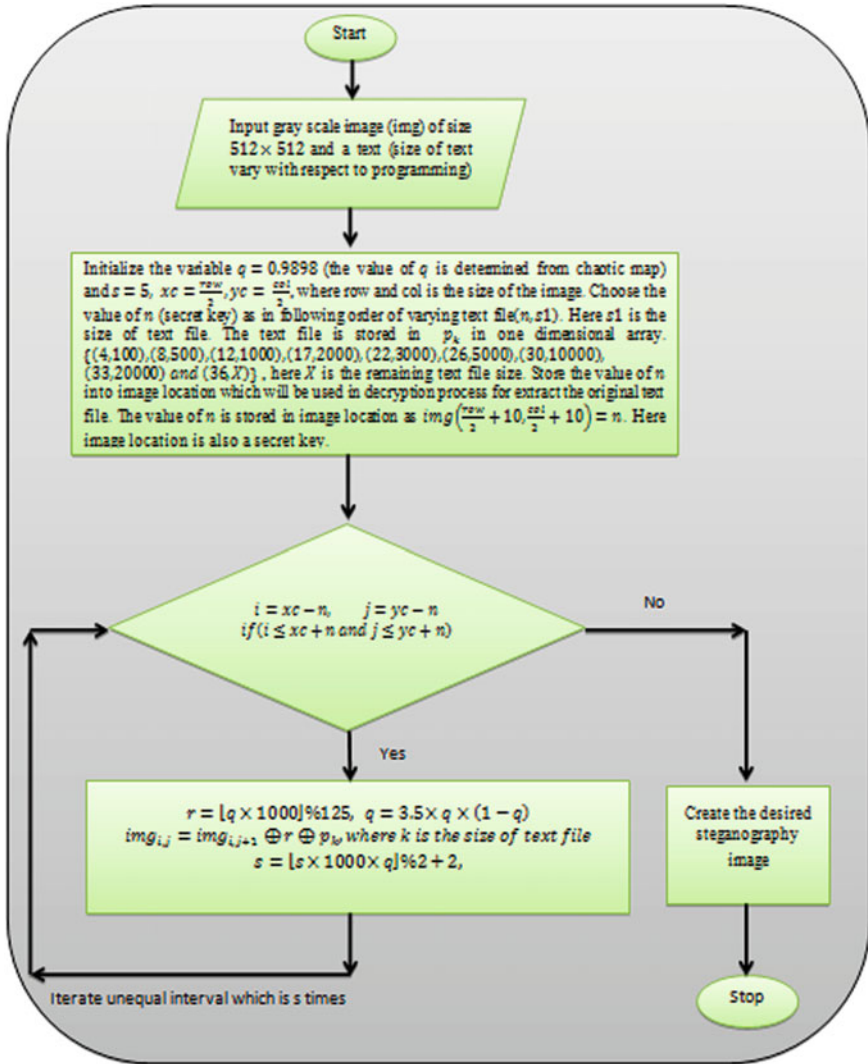


Fig. 2 Encoding flow chart

Step 2: Initialize the variable  $q = 0.9898$  (the value of  $q$  is determined from chaotic map) and  $s = 5$ ,  $xc = \frac{row}{2}$ ,  $yc = \frac{col}{2}$ , where row and column is the measurement of the picture.

The merit of  $n$  is accepted via image location as  $n = img(\frac{row}{2} + 10, \frac{col}{2} + 10)$ . Here image location is defined during encryption process.

Step 3: Initialize as  $i = xc - n$ ,  $j = yc - n$ .

Step 4: If  $(i \leq xc + n \text{ and } j \leq yc + n)$

Step 5: Then

$$r = \lfloor q \times 1000 \rfloor \% 125, q = 3.5 \times q \times (1 - q),$$

$$p_k = img_{i,j+1} \oplus r \oplus img_{i,j}, \text{ where } k \text{ is the size of text file,}$$

$$s = \lfloor s \times 1000 \times q \rfloor \% 2 + 2,$$

Repeat for  $s$  times.

Step 6: Repeat Step 4 until condition is false.

Step 7: Extract the desired text file.

Step 8: Stop.

### 3.5 Flow Chart of Decoding Technique

## 4 Performance Analysis

Here we have considered the performance metrics as Structural Similarity Index Measure, Peak Signal Noise Ratio, Mean Square Error, Root Mean Square Error, Average Difference (AD), Normalized Cross—Correlation (NK), Maximum Difference, Laplacian Mean Square Error, Normalized Absolute Error and Entropy. Some trial results are acquainted with exhibit the visual quality and implanting the payload of the proposed strategy is in Table 1. Table 2 describes the performance matrix of the different statistical parameters. The different capacity of information has been concealed inside the image like “LENA” and “PEPPER”. If we could able to preserve the quality of the secret information which is embedded inside the image, the hiding process is very successful. In our proposed method, each single bit of the secret image is embedded into the cover image and also we can extract all the embedded bits without any distortion. So the quality of the image is conserved as the cover image was.

Figure 4 shows the cover and stego image of PEPPER after embedding message. Figures 5, 6 and 7 show the comparison of the different methods of related to different images [18–21]. Various text capacities embedded in the image. Figure 5 describes the graphical representation of information inside the image and results is compare with the other existing scheme with our proposed scheme. Here, the comparison result shows that our proposed scheme is extremely secure in the scheme of information hiding through image. Figure 6 shows the comparison of PSNR value with the other existing scheme with our proposed scheme. Our chaotic method’s based algorithm has been found the optimized value of PSNR and the value of this statisticle parameter is better which has been compare with other scheme.

Figure 7 illustrates the Similarity Measure for Chaotic Method over other Existing Technique. The SSIM result of our proposed scheme describe that the quality of information has been preserved 100% that is there are no difference between information (before embedding and after extraction) which has been hidden inside the images.

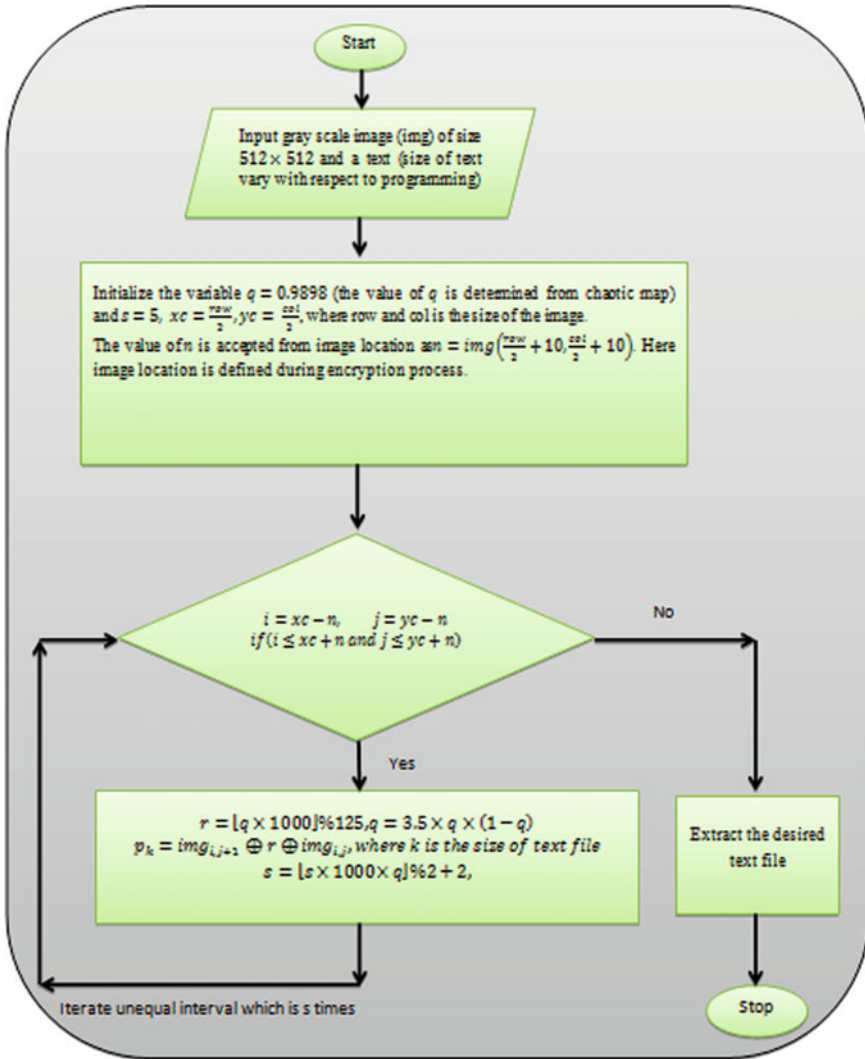


Fig. 3 Decoding flow chart

### 5 Conclusion

Steganography is incredible and powerful for the correspondence of mystery information. For image steganography, different techniques have been utilized. Here, we have proposed an approach that hides the mystery messages in the image utilizing a chaotic map. Image steganography strategies can be utilized to spare significant passwords and keys without recognizable to the outside world. It can likewise be utilized by the advanced craftsmanship creators to secure the copyrights of their

**Table 1** Embedding capacity through different methodology

Comparison of embedding capacity							
Image	Image size	PVD	GLM	Ahmad T et al	Safarpour et al	MPV	Proposed scheme
LENA	128 × 128	**	2048	2493	3906	4096	5000
	256 × 256	**	8192	10,007	15,500	16,384	20,000
	512 × 512	50,960	32,768	40,017	58,861	65,536	60,000
PEPPER	128 × 128	**	2048	2493	3906	4096	5000
	256 × 256	**	8192	9767	15,500	16,384	20,000
	512 × 512	50,685	32,768	39,034	58,861	65,536	60,000

(\*\* For PVD method, all the images that were used, are of size 512 × 512)

computerized expressions by implanting their subtleties into the work. It is to give greater security to mystery interchanges. In this manner, the proposed strategy also limits obfuscation methods for hiding secret message. The security features split through the proposed chaotic method is quite not viable as data embedded through the key. Moreover the proposed methodology is one of the novel secure techniques in the field of image steganography. Also it gives better result both in payload and in performance measure though performance metrics.





Fig. 4 (a) Cover and (b) Stego image of PEPPER after embedding 20,000 characters

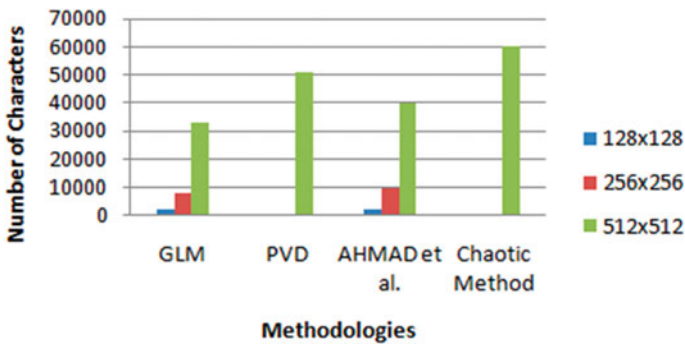


Fig. 5 Graphical representation of embedding capacity for chaotic method over other existing

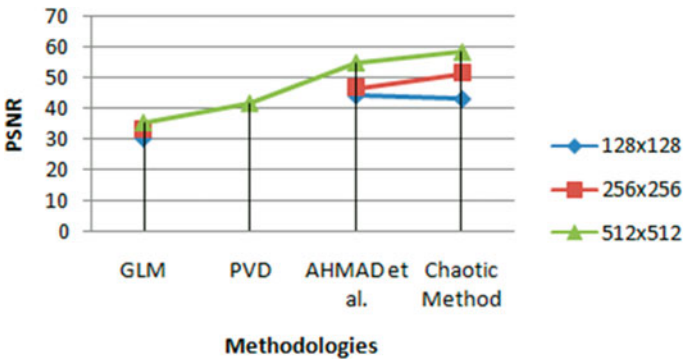


Fig. 6 Comparison of PSNR for chaotic method over other existing techniques

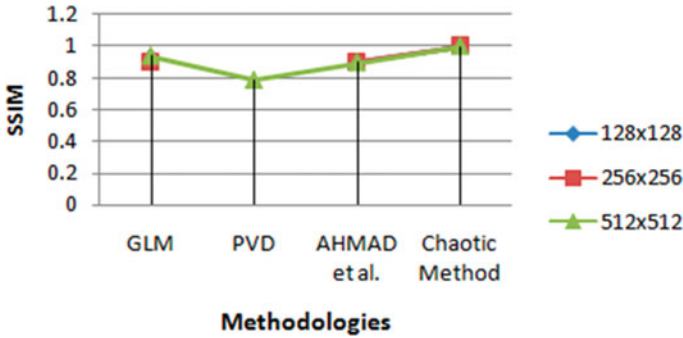


Fig. 7 Comparison of SSIM for chaotic method over other existing techniques

### References

- Rustad, S., Syukur, A., Andono, P.N.: Inverted LSB image steganography using adaptive pattern to improve imperceptibility. *J. King Saud Univ. – Comput. Inf. Sci.* 1–10 (2021). <https://doi.org/10.1016/j.jksuci.2020.12.017>
- Sancheti, A.: Pixel value differencing image steganography using secret key. *Int. J. Innov. Technol. Explor. Eng.* **2**(1), 68–72 (2012). ISSN: 2278-3075
- Huang, P., Chang, K.C., Chang, C.P., Tu, T.M.: A novel image steganography method using tri-way pixel value differencing. *J. Multimed.* (2008). <https://doi.org/10.4304/jmm.3.2.37-44>, pp. 37-44
- Lan, T., Mansour, M., Tewfik, A.: Robust high capacity data embedding. In: *International Conference on Image Processing—Vancouver, BC, Canada, Proceedings 2000*, pp. 581–584 (2000). <https://doi.org/10.1109/icip.2000.901025>
- Potdar, V., Chang, E.: Gray level modification steganography for secret communication. In: *IEEE International Conference on Industrial Informatics, Berlin, Germany*, pp. 355–368 (2004)
- Safarpour, M., Charmi, M.: Capacity enlargement of the PVD steganography method using the GLM technique, pp. 1–6 (2016). <https://www.researchgate.net/publication/289406922>
- Al-Taani, A.T., AL-Issa, A.M.: A novel steganographic method for gray-level images. *Int. J. Comput., Inf., Syst. Sci., Eng.* **3**(3), 574–579 (2009). <https://www.researchgate.net/publication/238749025>
- Kanan, H., Nazeri, B.: A novel image steganography scheme with high embedding capacity and tunable visual image quality based on a genetic algorithm. *Expert Syst. Appl.* **41**(14), 6123–6130 (2014)
- Mukherjee, S., Sanyal, G.: Enhanced position power first mapping (PPFM) based Image Steganography. *Int. J. Comput. Appl. (IJCA)*, Taylor and Francis **39**, 59–68 (2017)
- Almohammad, A., Ghinea, G.: Stego-image quality and the reliability of PSNR. In: *Image Processing Theory, Tools and Applications. IEEE, Paris, France* (2010). <https://doi.org/10.1109/IPTA.2010.5586786>
- Ash, S., Mukherjee, S., Sanyal, G.: A DWT based steganographic method using prime first mapping (PFM). In: *Advances in Computing and Communicational Engineering, ICACCE*, pp. 471–476 (2015)
- Mukherjee, S., Roy, S., Sanyal, G.: Image steganography using mid position value technique. In: *International Conference on Computational Intelligence and Data Science (ICCIDS 2018)*, *Procedia Computer Science* vol. 132, pp. 461–46 (2018)
- B’ohme, R., Westfeld, A.: Breaking cauchy model-based JPEG steganography with first order statistics. In: *9th European Symposium on Research Computer Security*, vol. 3193, pp. 125–140 (2009)



14. Hsiao, T., Liu, D., Chen, T., Chen, C.: Research on image steganography based on sudoku matrix. *symmetry* **13**(3), 387, 1–11 (2021). <https://doi.org/10.3390/sym13030387>
15. Manikandan, T., Muruganandham, A., Babuji, R., Nandalal, V., Mazher, Iqbal, J.I.: Secure E-health using images steganography. *J. Phys., Conf. Ser.* **1917**(012016), 1–7 (2021). <https://doi.org/10.1088/1742-6596/1917/1/012016>
16. Fateh, M., Rezvani, M., Irani, Y.: A new method of coding for steganography based on LSB matching revisited. *Secur. Commun. Netw.* **2021**(6610678), 1–15 (2021) <https://doi.org/10.1155/2021/6610678>
17. Qi, W., Liu, Y., Guo, S., Wang, X., Guo, Z.: An adaptive visible watermark embedding method based on region selection. *Secur. Commun. Netw.* **2021**(6693343), 1–11 (2021). <https://doi.org/10.1155/2021/6693343>
18. Sun, W., Zhou, J., Li, Y., Cheung, M., She, J.: Robust high-capacity watermarking over online social network shared images. *IEEE Trans. Circuits Syst. Video Technol.* 1–14 (2020). <https://doi.org/10.1109/TCSVT.2020.2998476>
19. Image Steganography tool.: <http://www.softpedia.com/get/Security/Security-Related/Hide-In-Picture.shtml>
20. Image Steganography tool.: [http://download.cnet.com/QuickStego/3000-2092\\_4-75593140.html](http://download.cnet.com/QuickStego/3000-2092_4-75593140.html)
21. Image Steganography tool.: [http://download.cnet.com/Xiao-Steganography/3000-2092\\_4-10541494.html](http://download.cnet.com/Xiao-Steganography/3000-2092_4-10541494.html)

# On the Construction Structures of $3 \times 3$ Involutory MDS Matrices over $\mathbb{F}_{2^m}$



Meltem Kurt Pehlivanoglu , Mehmet Ali Demir ,  
Fatma Büyüksaraçoğlu Sakallı , Sedat Akleylek ,  
and Muharrem Tolga Sakallı 

**Abstract** In this paper, we propose new construction structures, in other words, transposition-permutation path patterns for  $3 \times 3$  involutory and MDS permutation-equivalent matrices over  $\mathbb{F}_{2^3}$  and  $\mathbb{F}_{2^4}$ . We generate  $3 \times 3$  involutory and MDS matrices over  $\mathbb{F}_{2^3}$  and  $\mathbb{F}_{2^4}$  by using the matrix form given in [1], and then all these matrices are analyzed by finding all their permutation-equivalent matrices. After that, we extract whether there are any special permutation patterns, especially for this size of the matrix. As a result, we find new 28,088 different transposition-permutation path patterns to directly construct  $3 \times 3$  involutory and MDS matrices from any  $3 \times 3$  involutory and MDS representative matrix over  $\mathbb{F}_{2^3}$  and  $\mathbb{F}_{2^4}$ . The 35 patterns are in common with these finite fields. By using these new transposition-permutation path patterns, new  $3 \times 3$  involutory and MDS matrices can be generated especially for different finite fields such as  $\mathbb{F}_{2^8}$  (is still an open problem because of the large search space). Additionally, the idea of finding the transposition-permutation path patterns can be applicable to larger dimensions such as  $8 \times 8$ ,  $16 \times 16$ , and  $32 \times 32$ . To the best of our knowledge, the idea given in this paper to find the common and unique transposition-permutation path patterns over different finite fields is the first work in the literature.

---

M. Kurt Pehlivanoglu (✉) · M. Ali Demir  
Kocaeli University, Kocaeli 41001, Turkey  
e-mail: [meltem.kurt@kocaeli.edu.tr](mailto:meltem.kurt@kocaeli.edu.tr)

M. Ali Demir  
e-mail: [215112045@kocaeli.edu.tr](mailto:215112045@kocaeli.edu.tr)

F. Büyüksaraçoğlu Sakallı · M. Tolga Sakallı  
Trakya University, Edirne 22030, Turkey  
e-mail: [fbuyuksaracoglu@trakya.edu.tr](mailto:fbuyuksaracoglu@trakya.edu.tr)

M. Tolga Sakallı  
e-mail: [tolga@trakya.edu.tr](mailto:tolga@trakya.edu.tr)

S. Akleylek  
Ondokuz Mayıs University, Samsun 55200, Turkey  
e-mail: [sedat.akleylek@omu.edu.tr](mailto:sedat.akleylek@omu.edu.tr)

**Keywords** MDS matrix · Lightweight cryptography · Diffusion matrices · Permutation-equivalent matrices

## 1 Introduction

Substitution-Permutation Networks (SPNs) are one of the main structures used in designing a block cipher. SPNs include three components: key scheduling, non-linear layer (e.g., Substitution boxes (S-boxes)), and linear layer (or diffusion layer).

Maximum Distance Separable (MDS) matrices have the maximum branch number that ensures the maximum diffusion [2]. Recently, studies based on designing efficient MDS diffusion layers aim to minimize the circuit depth and reduce the required number of logical gates (especially Exclusive-OR (XOR) gates). XOR count metric defines the hardware implementation cost of a diffusion layer. To design circuit implementation of a diffusion layer with the lowest circuit depth ensures low latency.

Basically, the construction methods for MDS matrices are divided into three methods: direct construction methods, search-based methods, and hybrid methods. Cauchy matrices [4], companion matrices [5], Vandermonde matrices [6], and the  $3 \times 3$  matrix form given in [1] are direct construction methods. Because of their algebraic structures, an MDS matrix can be generated directly (without searching) by using these structures. In search-based methods, the special matrix forms such as circulant matrices, Hadamard matrices, Toeplitz matrices are used to generate MDS matrices. Hybrid construction methods combine direct construction method and search-based method. Generalized Hadamard (GHadamard) [7] matrix form is a hybrid construction method and generates directly new (involutory) MDS matrices by using an (involutory and MDS) Hadamard matrix of which MDS property can be confirmed by search. But, all these construction methods are evaluated as local optimization technique that focuses on the diffusion matrix coefficients with minimum XOR count. They do not guarantee to find the best circuits. Recent studies have been focused on optimizing the diffusion matrix circuits globally [3, 11–13].

In this paper, efficient construction structures of involutory and MDS matrices are evaluated. In [8], the authors proved the existence of special matrix types (patterns) for constructing involutory Hadamard MDS matrices. In [9], the authors generated lightweight involutory and MDS matrices by using elementary block matrices. They also focused on the properties of block matrices and gave some construction methods. In [10], the authors defined new constructions based on the idea of the subfield construction method to identify involutory MDS matrices. In [11], the authors extracted special construction methods. They used permutation-equivalent classes to search for involutory MDS matrices.

In this paper, we focus on using the permutation-equivalent classes for finding whether there are any special transposition-permutation path patterns, especially for  $3 \times 3$  involutory and MDS matrices over  $\mathbb{F}_{2^3}$  and  $\mathbb{F}_{2^4}$  defined by the irreducible polynomials  $x^3 + x + 1$  (the hexadecimal notation  $0xb$  corresponds to this polynomial notation),  $x^3 + x^2 + 1$  ( $0xd$ ),  $x^4 + x + 1$  ( $0x13$ ) and  $x^4 + x^3 + 1$  ( $0x19$ ),

respectively. The  $3 \times 3$  matrix form given in [1] is used to generate all involutory and MDS matrices over these finite fields. Then, we find the representative matrices which can represent a class of all permutation-equivalent matrices. After that, we extract all the transposition-permutation paths where  $P_c$ ,  $P_r$  and  $T$  express column permutation, row permutation, and matrix transposition, respectively. To find new transposition-permutation path patterns, column permutation ( $P_c$ ), row permutation ( $P_r$ ) and matrix transposition ( $T$ ) steps are applied repetitively on each representative matrix. There are 1,176 and 37,800  $3 \times 3$  involutory and MDS matrices over  $\mathbb{F}_{2^3}$  and  $\mathbb{F}_{2^4}$  (See Proposition 1. [1]). So, we analyze 2,352 and 75,600  $3 \times 3$  involutory and MDS matrices in total over  $\mathbb{F}_{2^3}$  and  $\mathbb{F}_{2^4}$ , respectively.

## 1.1 Motivation and Contribution

To design an efficient involutory and MDS matrix is a challenging open problem [2]. Recent studies have focused on the global optimization of the lightweight involutory and MDS matrices to extract the lightest circuits. In [3], it has also remained as future work to focus on the integration of local and global optimization techniques to increase the potential of all these techniques. Especially, it is important to construct involutory and MDS matrices with lightweight coefficients in the local optimization. But first, it is important to know that how one can directly construct an involutory and MDS matrix in an efficient way. Then the local optimization and global optimization techniques are used to reduce the hardware cost. The contributions of this paper can be summarized as follows:

- To the best of our knowledge, the idea based on finding the common and unique transposition-permutation path patterns over different finite fields is the first work in the literature.
- We give all found transposition-permutation path patterns results publicly available at <https://github.com/mkurtpehlivanoglu/transposition-permutation-path-patterns.git>.
- We give new transposition-permutation path patterns especially for  $3 \times 3$  involutory and MDS matrices over  $\mathbb{F}_{2^3}$  and  $\mathbb{F}_{2^4}$ . For all generated  $3 \times 3$  involutory and MDS matrices over these finite fields, permutation-equivalent matrices are grouped together, in other words, permutation-equivalent classes are found. Then, we extract all the transposition-permutation paths. Finally, we find 28,088 different transposition-permutation path patterns that construct all the permutation-equivalent classes. The 35 patterns are in common with these finite fields.
- These patterns could be applied to any involutory and MDS matrix, then its permutation-equivalent matrices could be constructed directly without any searching cost. Additionally, by using these new transposition-permutation path patterns, new  $3 \times 3$  involutory and MDS matrices can be generated especially for different finite fields which have large search space such as  $\mathbb{F}_{2^8}$ . Moreover, the idea of

finding the transposition-permutation path patterns can be applied not only  $3 \times 3$  dimension but also to different larger dimensions.

### 1.2 Organization

This paper is organized as follows, the preliminaries on the involutory and MDS matrices and the special matrix form used in generating all  $3 \times 3$  involutory and MDS matrices are given in Sect. 2. In Sect. 3, we show that how to find new transposition-permutation path patterns and we give these structures. The conclusion is given in the last section.

## 2 Preliminaries

In this paper, we use the  $\mathbb{F}_{2^m}/p(x)$  notation to express the finite field  $\mathbb{F}_{2^m}$  defined by the irreducible polynomial  $p(x)$ . The hexadecimal notation of the irreducible polynomial  $p(x)$  can be used instead of the polynomial notation, e.g. the hexadecimal notation  $0xb$  corresponds to polynomial notation of the irreducible polynomial  $x^3 + x + 1$  in  $\mathbb{F}_{2^3}$ , and it can be represented by  $\mathbb{F}_{2^3}/0xb$ . In Definition 1, we recall the MDS matrix definition.

**Definition 1** Let  $L$  be an  $n \times n$  matrix in  $M_n(\mathbb{F}_{2^m})$ ,  $L$  is an MDS matrix if and only if it's all square sub-matrices are non-singular [11].

**Theorem 1** Let  $A$  and  $B$  be two  $n \times n$  matrices in  $M_n(\mathbb{F}_{2^m})$ . If  $A$  is an MDS matrix, and  $A$  and  $B$  are permutation-equivalent matrices, if and only if  $B$  is an MDS matrix [11].

From Theorem 1, if we permute the rows and columns of an MDS matrix, the MDS property will be preserved.

**Corollary 1** Let  $A$  and  $B$  be two  $n \times n$  matrices in  $M_n(\mathbb{F}_{2^m})$ . If  $A$  and  $B$  are permutation-equivalent matrices, then  $A$  and  $B$  have the same implementation cost (XOR count) [11].

**Definition 2** Let  $A = \begin{bmatrix} a_{11} & a_{12} & a_{13} \\ a_{21} & a_{22} & a_{23} \\ a_{31} & a_{32} & a_{33} \end{bmatrix}$  be a  $3 \times 3$  over  $\mathbb{F}_{2^m}$  for  $a_{12} = (a_{11} + 1)b_0, a_{13} = (a_{11} + 1)b_1, a_{21} = (a_{22} + 1)b_0^{-1}, a_{23} = (a_{22} + 1)b_0^{-1}b_1, a_{31} = (a_{11} + a_{22})b_1^{-1}, a_{32} = (a_{11} + a_{22})b_1^{-1}b_0, a_{33} = a_{11} + a_{22} + 1$ , where  $a_{11} \neq a_{22} \neq a_{33}$  and  $b_0, b_1 \in \mathbb{F}_{2^m} - \{0\}$  [1].

The  $3 \times 3$  matrix form  $IM$  can be represented as follows:

$$IM = \begin{bmatrix} a_{11} & (a_{11} + 1)b_0 & (a_{11} + 1)b_1 \\ (a_{22} + 1)b_0^{-1} & a_{22} & (a_{22} + 1)b_0^{-1}b_1 \\ (a_{11} + a_{22})b_1^{-1} & (a_{11} + a_{22})b_1^{-1}b_0 & a_{11} + a_{22} + 1 \end{bmatrix} \tag{1}$$

By using Eq. 1, all  $3 \times 3$  involutory and MDS matrices over the  $\mathbb{F}_{2^m}$  (See proof [1]) can be generated. Moreover, the number of all  $3 \times 3$  involutory and MDS matrices over  $\mathbb{F}_{2^m}$  is  $(2^m - 1)^2 \cdot (2^m - 2) \cdot (2^m - 4)$ , where  $m > 2$  [1].

In this paper, we use the matrix form given in Eq. 1, then we generate all  $3 \times 3$  involutory and MDS matrices over the  $\mathbb{F}_{2^3}/0 \times b$ ,  $\mathbb{F}_{2^3}/0 \times d$ ,  $\mathbb{F}_{2^4}/0 \times 13$  and  $\mathbb{F}_{2^4}/0 \times 19$ .

The number of  $3 \times 3$  involutory and MDS matrices over  $\mathbb{F}_{2^3}$  is  $(2^3 - 1)^2 \cdot (2^3 - 2) \cdot (2^3 - 4) = 1,176$ , and the number of  $3 \times 3$  involutory and MDS matrices over  $\mathbb{F}_{2^4}$  is  $(2^4 - 1)^2 \cdot (2^4 - 2) \cdot (2^4 - 4) = 37,800$  for each irreducible polynomial.

### 3 Findings on New Transposition-Permutation Path Patterns

Totally 77,952  $3 \times 3$  involutory and MDS matrices are generated over  $\mathbb{F}_{2^3}$  and  $\mathbb{F}_{2^4}$ . We search all the permutation-equivalent matrices and grouped them together, i.e. permutation-equivalent classes are found. Then, one representative matrix is picked from each class. As a result, we find 100 different  $3 \times 3$  involutory and MDS representative matrices over  $\mathbb{F}_{2^3}/0 \times b$  and  $\mathbb{F}_{2^3}/0 \times d$  finite fields, and also find 3,132 and 3,119 different  $3 \times 3$  involutory and MDS representative matrices over  $\mathbb{F}_{2^4}/0 \times 13$  and  $\mathbb{F}_{2^4}/0 \times 19$ , respectively. After that,  $P_c$ ,  $P_r$  and  $T$  steps are applied repetitively on each representative matrix to find its own permutation-equivalent matrices, and all these transposition-permutation paths are recorded. We find a total of 28,088 different transposition-permutation path patterns which give the possible transposition-permutation steps to construct whole permutation-equivalent matrices from one representative matrix. In Table 1, we give 35 common path patterns which are found over  $\mathbb{F}_{2^3}$  and  $\mathbb{F}_{2^4}$ . In Table 2, we give most commonly used 50 path patterns over  $\mathbb{F}_2^4$ . The  $P_{c_{i,j}}$ ,  $P_{r_{i,j}}$  and  $T$ , notations given in the tables represent changing (permutation) the  $i$ th column with the  $j$ th column, changing the  $i$ th row with the  $j$ th row, and transposition of the given matrix, respectively, where  $0 \leq i, j \leq 2$ . The path numbers (the first column) which are given in bold in the tables indicate the common paths over two finite fields. All the common transposition-permutation path patterns for  $\mathbb{F}_{2^3}$  and  $\mathbb{F}_{2^4}$  finite fields are given in bold in Tables 1 and 2.

In Table 1, we give a total of 35 common transposition-permutation path patterns. Normally, we find totally 537 different path patterns over these fields. The second column of the table represents which steps have to be applied to the representative matrix, and the third column represents how many  $3 \times 3$  involutory and MDS representative matrix uses the related pattern to construct its permutation-equivalent matrices. For example, for the third path pattern " $P_{c_{1,0}}, P_{r_{1,0}}$ " indicates two steps:

**Table 1** Generated common transposition-permutation path patterns for  $\mathbb{F}_{2^3}$  and  $\mathbb{F}_{2^4}$ .

No	Transposition-permutation path patterns	Number of matrices			
		$\mathbb{F}_{2^3}/0 \times b$	$\mathbb{F}_{2^3}/0 \times d$	$\mathbb{F}_{2^4}/0 \times 13$	$\mathbb{F}_{2^4}/0 \times 19$
1	$P_{c_{1,2}}, P_{r_{1,2}}, T$	13	12	415	399
2	$P_{c_{0,1}}, P_{r_{0,1}}, T$	12	24	424	412
3	$P_{c_{1,0}}, P_{r_{0,1}}$	6	13	422	411
4	$P_{c_{2,0}}, P_{r_{0,2}}$	35	15	434	398
5	$P_{c_{2,1}}, P_{r_{1,2}}, T$	4	17	446	402
6	$P_{c_{1,2}}, P_{r_{2,1}}$	4	14	415	415
7	$P_{c_{1,0}}, P_{r_{1,0}}, T$	19	13	374	421
8	$P_{c_{0,1}}, P_{r_{0,1}}$	9	29	411	418
9	$P_{c_{0,2}}, P_{r_{0,2}}$	12	12	381	404
10	$P_{c_{1,2}}, P_{r_{1,2}}$	11	15	418	399
11	$P_{c_{2,0}}, P_{r_{0,2}}, T$	28	14	373	418
12	$P_{c_{2,1}}, P_{r_{2,1}}$	19	2	421	380
13	$P_{c_{2,0}}, P_{r_{2,0}}$	9	6	411	416
14	$P_{c_{0,1}}, P_{r_{1,0}}, T$	18	11	414	398
15	$P_{c_{2,0}}, P_{r_{2,0}}, T$	10	5	427	444
16	$P_{c_{1,2}}, P_{r_{2,1}}, T$	8	14	385	379
17	$P_{c_{1,0}}, P_{r_{0,1}}, T$	2	5	425	370
18	$P_{c_{2,1}}, P_{r_{1,2}}$	12	18	383	430
19	$P_{c_{1,0}}, P_{r_{1,0}}$	27	6	438	399
20	$P_{c_{1,2}}, P_{r_{2,1}}, T - P_{c_{0,2}}, P_{r_{2,0}}$	1	1	9	16
21	$P_{c_{2,1}}, P_{r_{2,1}}, T$	24	2	408	392
22	$P_{c_{0,2}}, P_{r_{2,0}}$	14	15	404	455
23	$P_{c_{0,2}}, P_{r_{2,0}}, T$	17	19	408	395
24	$P_{c_{0,2}}, P_{r_{0,2}}, T$	8	9	405	413
25	$P_{c_{1,2}}, P_{r_{2,1}}, T - P_{c_{0,2}}, P_{r_{2,0}}, T$	1	4	9	11
26	$P_{c_{0,1}}, P_{r_{1,0}}$	14	16	415	406
27	$P_{c_{0,2}}, P_{r_{2,1}}, T - P_{c_{1,0}}, P_{r_{2,1}}, T$	6	1	12	11
28	$P_{c_{0,1}}, P_{r_{2,0}}, T - P_{c_{1,2}}, P_{r_{0,2}}$	5	2	12	10
29	$P_{c_{1,0}}, P_{r_{1,2}}, T - P_{c_{2,0}}, P_{r_{1,2}}$	7	5	6	16
30	$P_{c_{2,0}}, P_{r_{0,1}}, T - P_{c_{0,1}}, P_{r_{2,0}}$	6	8	9	15
31	$P_{c_{2,0}}, P_{r_{1,0}}, T - P_{c_{0,2}}, P_{r_{2,1}}, T$	7	2	19	19
32	$P_{c_{1,0}}, P_{r_{1,2}}, T - P_{c_{2,0}}, P_{r_{1,2}}, T$	4	4	12	11
33	$P_{c_{2,1}}, P_{r_{2,0}}, T - P_{c_{2,1}}, P_{r_{1,0}}, T$	2	1	10	14
34	$P_{c_{1,0}}, P_{r_{1,2}}, T - P_{c_{2,0}}, P_{r_{2,1}}$	2	4	10	15
35	$P_{c_{2,0}}, P_{r_{2,0}}, T - P_{c_{0,1}}, P_{r_{0,1}}$	1	3	9	14

firstly replace the second column of this matrix with first column, and then replace the second row of the matrix with first row. In total 25 and 814 representative matrices use this patterns over  $\mathbb{F}_{2^3}$  and  $\mathbb{F}_{2^4}$ , respectively.

**Table 2** Most commonly used 50 transposition-permutation path patterns for  $\mathbb{F}_{2^4}$ .

No	Transposition-permutation path patterns	Number of matrices	
		$\mathbb{F}_{2^4}/0 \times 13$	$\mathbb{F}_{2^4}/0 \times 19$
1	$P_{c_{2,1}}, P_{r_{1,2}}, T$	446	402
2	$P_{c_{1,0}}, P_{r_{1,0}}$	438	399
3	$P_{c_{2,0}}, P_{r_{0,2}}$	434	398
4	$P_{c_{2,0}}, P_{r_{2,0}}, T$	427	444
5	$P_{c_{1,0}}, P_{r_{0,1}}, T$	425	370
6	$P_{c_{0,1}}, P_{r_{0,1}}, T$	424	412
7	$P_{c_{1,0}}, P_{r_{0,1}}$	422	411
8	$P_{c_{2,1}}, P_{r_{2,1}}$	421	380
9	$P_{c_{1,2}}, P_{r_{1,2}}$	418	399
10	$P_{c_{1,2}}, P_{r_{2,1}}$	415	415
11	$P_{c_{0,1}}, P_{r_{1,0}}$	415	406
12	$P_{c_{1,2}}, P_{r_{1,2}}, T$	415	399
13	$P_{c_{0,1}}, P_{r_{1,0}}, T$	414	398
14	$P_{c_{0,1}}, P_{r_{0,1}}$	411	418
15	$P_{c_{2,0}}, P_{r_{2,0}}$	411	416
16	$P_{c_{0,2}}, P_{r_{2,0}}, T$	408	395
17	$P_{c_{2,1}}, P_{r_{2,1}}, T$	408	392
18	$P_{c_{0,2}}, P_{r_{0,2}}, T$	405	413
19	$P_{c_{0,2}}, P_{r_{2,0}}$	404	455
20	$P_{c_{1,2}}, P_{r_{2,1}}, T$	385	379
21	$P_{c_{2,1}}, P_{r_{1,2}}$	383	430
22	$P_{c_{0,2}}, P_{r_{0,2}}$	381	404
23	$P_{c_{1,0}}, P_{r_{1,0}}, T$	374	421
24	$P_{c_{2,0}}, P_{r_{0,2}}, T$	373	418
25	$P_{c_{2,1}}, P_{r_{0,1}}, TP_{c_{2,1}}, P_{r_{2,0}}, T$	27	14
26	$P_{c_{2,0}}, P_{r_{1,2}}, TP_{c_{0,2}}, P_{r_{1,0}}$	24	15
27	$P_{c_{1,0}}, P_{r_{0,1}}, TP_{c_{0,1}}, P_{r_{1,0}}$	24	15
28	$P_{c_{0,2}}, P_{r_{2,1}}, TP_{c_{0,1}}, P_{r_{2,1}}, T$	24	13
29	$P_{c_{2,0}}, P_{r_{1,2}}, TP_{c_{2,1}}, P_{r_{0,2}}$	22	11
30	$P_{c_{2,1}}, P_{r_{1,0}}, TP_{c_{2,1}}, P_{r_{2,0}}$	21	15
31	$P_{c_{0,2}}, P_{r_{2,0}}, TP_{c_{1,0}}, P_{r_{1,0}}$	21	8
32	$P_{c_{1,2}}, P_{r_{1,2}}, TP_{c_{0,1}}, P_{r_{1,0}}$	20	17
33	$P_{c_{2,1}}, P_{r_{0,1}}, TP_{c_{2,0}}, P_{r_{0,1}}, T$	20	12
34	$P_{c_{0,2}}, P_{r_{0,2}}, TP_{c_{0,1}}, P_{r_{1,0}}, T$	20	11
35	$P_{c_{0,2}}, P_{r_{1,0}}, TP_{c_{2,0}}, P_{r_{1,2}}$	20	7
36	$P_{c_{2,0}}, P_{r_{1,0}}, TP_{c_{0,2}}, P_{r_{2,1}}, T$	19	19

(continued)



**Table 2** (continued)

No	Transposition-permutation path patterns	Number of matrices	
		$\mathbb{F}_{2^4}/0 \times 13$	$\mathbb{F}_{2^4}/0 \times 19$
37	$P_{c_{0,2}}, P_{r_{2,1}}, TP_{c_{1,2}}, P_{r_{2,0}}$	19	14
38	$P_{c_{2,1}}, P_{r_{0,1}}, TP_{c_{2,1}}, P_{r_{2,0}}$	19	12
39	$P_{c_{2,1}}, P_{r_{1,2}}, TP_{c_{1,2}}, P_{r_{1,2}}$	19	12
40	$P_{c_{1,0}}, P_{r_{2,0}}, TP_{c_{0,1}}, P_{r_{1,2}}, T$	19	10
41	$P_{c_{2,0}}, P_{r_{1,2}}, TP_{c_{0,1}}, P_{r_{1,2}}$	19	9
42	$P_{c_{1,2}}, P_{r_{1,0}}, TP_{c_{0,2}}, P_{r_{1,0}}$	18	16
43	$P_{c_{0,2}}, P_{r_{1,2}}, TP_{c_{2,0}}, P_{r_{1,0}}, T$	18	16
44	$P_{c_{1,0}}, P_{r_{1,2}}, TP_{c_{1,2}}, P_{r_{0,1}}$	18	16
45	$P_{c_{0,2}}, P_{r_{2,1}}, TP_{c_{1,0}}, P_{r_{2,1}}$	18	16
46	$P_{c_{1,0}}, P_{r_{1,2}}, TP_{c_{1,2}}, P_{r_{1,0}}$	18	15
47	$P_{c_{0,1}}, P_{r_{0,1}}, TP_{c_{1,2}}, P_{r_{2,1}}, T$	18	14
48	$P_{c_{0,1}}, P_{r_{0,2}}, TP_{c_{1,0}}, P_{r_{1,2}}, T$	18	14
49	$P_{c_{2,1}}, P_{r_{2,1}}, TP_{c_{1,0}}, P_{r_{1,0}}, T$	18	13
50	$P_{c_{2,0}}, P_{r_{1,0}}, TP_{c_{2,1}}, P_{r_{0,1}}$	18	13

In Table 2, we give the most commonly used 50 transposition-permutation path patterns over  $\mathbb{F}_{2^4}$ . Normally, we find 27,551 different path patterns over  $\mathbb{F}_{2^4}/0 \times 13$  and  $\mathbb{F}_{2^4}/0 \times 19$  and 2,722 of these paths are common.

By using these new transposition-permutation path patterns, new  $3 \times 3$  involutory and MDS matrices can be generated especially for different finite fields such as  $\mathbb{F}_{2^8}$ . Finding lightweight involutory MDS matrices over  $\mathbb{F}_{2^8}$  is a challenging problem because there are  $\approx 2^{31.95} 3 \times 3$  involutory and MDS matrices over these fields. Instead of searching involutory and MDS matrices, finding direct construction structures is crucial. Finding new transposition-permutation path patterns for different finite fields will ensure the extraction of many common paths. Moreover, the idea given in this paper can be extended to larger dimensions. Firstly, some representative matrices for these large dimensions can be found, then new transposition-permutation path patterns given in this paper can be used to generate new involutory MDS matrices. That will be more efficient because it does not require any search cost.

## 4 Conclusion and Future Works

Designing of involutory and MDS matrices is a challenging problem. In this paper, we focus on finding new transposition-permutation path patterns from  $3 \times 3$  representative matrices over the finite fields  $\mathbb{F}_{2^3}$  and  $\mathbb{F}_{2^4}$ . We generate 28,088 different and 35 common transposition-permutation path patterns for these finite fields. It is remarkable that all the common path patterns over  $\mathbb{F}_{2^3}/0 \times b$  and  $\mathbb{F}_{2^3}/0 \times d$  are also

take place over  $\mathbb{F}_{2^4}/0 \times 13$  and  $\mathbb{F}_{2^4}/0 \times 19$ . It is clear that all the patterns could be applied to any involutory and MDS matrix, then permutation-equivalent matrices could be computed directly without any search cost.

As a future work, it would be interesting to focus on finding new transposition-permutation path patterns for  $3 \times 3$  involutory and MDS matrices over different finite fields. Then, all these path patterns would be compared to extract the common paths. Thus, these common paths would ensure a direct construction method for finding permutation-equivalent matrices of any representative involutory and MDS matrix. Moreover, the idea given in this paper for  $3 \times 3$  involutory and MDS matrices could be applied to larger dimensions such as  $8 \times 8$ ,  $16 \times 16$ , and  $32 \times 32$ .

## References

1. Guzel, G.G., Sakalli, M.T., Akleylek, S., Rijmen, V., Cengellenmis, Y.: A new matrix form to generate all  $3 \times 3$  involutory MDS matrices over  $\mathbb{F}_{2^m}$ . *Inf. Process. Lett.* **147**, 61–68 (2019)
2. Duval, S., Leurent, G.: MDS matrices with lightweight circuits. *IACR Trans. Sym. Crypt.* **2**, 48–78 (2018)
3. Tan, Q.Q., Peyrin, T.: Improved heuristics for short linear programs. *IACR Trans. Cryptogr. Hardw. Embed. Syst.* **2020**(1), 203–230 (2020)
4. Youssef A.M., Mister S., Tavares S.E. On the design of linear transformation for substitution permutation encryption networks. In: *Selected Areas in Cryptography (SAC)*, pp. 40–48, Ottawa Ontario, Canada, (1997)
5. Guo, J., Peyrin, T., Poschmann, A.: The PHOTON family of lightweight hash functions. In: Rogaway, P. (eds.) *Advances in Cryptology - CRYPTO 2011*. CRYPTO 2011. LNCS, vol 6841. pp. 222–239. Springer, Heidelberg (2011). [https://doi.org/10.1007/978-3-642-22792-9\\_13](https://doi.org/10.1007/978-3-642-22792-9_13)
6. Gupta, K.C., Ray, I.G.: On Constructions of circulant MDS matrices for lightweight cryptography. In: Huang X., Zhou J. (eds) *Information Security Practice and Experience. ISPEC 2014*. LNCS, vol. 8128, pp. 29–43. Springer, Cham (2013). [https://doi.org/10.1007/978-3-319-06320-1\\_41](https://doi.org/10.1007/978-3-319-06320-1_41)
7. Pehlivanoglu, M.K., Sakalli, M.T., Akleylek, S., Duru, N., Rijmen, V.: Generalisation of Hadamard matrix to generate involutory MDS matrices for lightweight cryptography. *IET Inf. Secur.* **12**(4), 348–355 (2018)
8. Zhou, L., Wang, L., Sun, Y.: On efficient constructions of lightweight MDS matrices. *IACR Trans. Symmetric Cryptol.* **2018**(1), 180–200 (2018)
9. Wang, S., Li, Y., Tian, S., Zeng, X.: Four by four MDS matrices with the fewest XOR gates based on words. *Adv. Math. Commun.* 1–28 (2021)
10. Li, S., Sun, S., Li, C., Wei, Z., Hu, L.: Constructing low-latency involutory MDS matrices with lightweight circuits. *IACR Trans. Symmetric Cryptol.* **2019**(1), 84–117 (2019)
11. Yang, Y., Zeng, X., Wang, S.: Construction of lightweight involutory MDS matrices. *Des. Codes Cryptogr.* **89**, 1453–1483 (2021)
12. Maximov, A., Ekdahl, P.: New circuit minimization techniques for smaller and faster AES Sboxes. *IACR Trans. Cryptogr. Hardw. Embed. Syst.* **2019**(4), 91–125 (2019)
13. Xiang, Z., Zeng, X., Lin, D., Bao, Z., Zhang, S.: Optimizing implementations of linear layers. *IACR Trans. Symmetric Cryptol.* **2020**(2), 120–145 (2020)

# **Fractional System and Applications**

# A Novel Generalized Method for Evolution Equation and its Application in Plasma



Santanu Raut, Subrata Roy, and Ashim Roy

**Abstract** This article presents a new class of the kink soliton, anti-kink soliton solution for the Zakharov-Kuznetsov-Burgers (ZKB) equation. To establish the existence of such type of model in a real physical situation, an unmagnetized viscous plasma containing cold ions and the electrons obeying Cairns-Tallis distribution is considered, and employing reductive perturbation method (RPM) classical ZKB equation is derived. The Generalised Kudryashov method (GKM) is employed to explore the solution of the aforesaid equation and the symbolic software package Maple is adopted in carrying out the complicated algebraic computation. Finally, the physical significance of different parameters on wave propagation is demonstrated through numerical understanding.

**Keywords** Zakharov-Kuznetsov-Burgers equation · Cairns-Tallis distribution · Reductive perturbation method · Generalised Kudryashov method

## 1 Introduction

During the last few decades, nonlinear evolution equations (NLEEs) have gained a lot of attention from the authors, due to their vast applications in different branches of nonlinear sciences. For example, NLEEs have been utilized to formulate various problems associated with protein chemistry, chemical kinetics, quantum mechanics, plasma physics, the propagation of shallow-water waves, etc. The classical KdV equation is an example of NLEE which is extensively utilized to model weakly non-

---

S. Raut (✉)

Department of Mathematics, Mathabhanga College, Coochbehar 736146, India  
e-mail: [raut\\_santanu@yahoo.com](mailto:raut_santanu@yahoo.com)

S. Roy

Department of Mathematics, Cooch Behar Panchanan Barma University, Cooch Behar 736101, India

A. Roy

Department of Mathematics, Alipurduar Univeristy, Alipurduar 736121, India

linear long waves. In many works [1, 2], the investigations done were restricted to the only one-dimensional flow of the ions and the electrons. However, in many situations, the classical KdV equation becomes inappropriate when one encounters a situation where the higher dimensional coordinate system is included. The Kadomtsev-Petviashvili (KP) equation and the Zakharov-Kuznetsov (ZK) equation [3] are adopted to investigate the properties of solitary waves in various nonlinear systems with higher dimensional systems. To determine characteristics of IAW wave, as well as DAW, is determined in different plasma mediums the ZK model is utilized in many situations [4]. For the first time, Munro and Parkes [5] found that the governing equation ZK turns into a modified form (mentioned as modified ZK equation) in a plasma environment when the non-isothermal type electrons are considered. Further, it was also found that choosing a suitable form of electron number density in a particular form of plasma environment suggested by Schamel [6], causes to form modified form of ZK equation through RPT [7]. It is found that in most of the observations for finding propagating characteristics of IAW in a plasma environment the impact of viscosity, collisions, ion streaming velocity is neglected. But, a large number of experimental studies has been carried out in different plasma states and it has been observed that the evolution of solitary wave in a dissipative system significantly depends on inter-particle collisions and viscosity, etc. [8–10]. Recently, some authors observed IAW in the ZK model along with the consideration of Burgers term. For instance, Moselem et al. [11] report some analytical solutions of the ZKB equation to investigate IAW propagating in a magnetized dusty plasma containing isothermal electron and cold positive ions. Bedwehy and Moslem [12] again applied the ZK model to observe the characteristic of the shock waves in three-component plasma. Yin et al. [13] find some solitary wave solution of  $(2 + 1)$ -dimensional ZKB equation in order to find the generalized beta effect in the system. Seadawy in the year 2015, find some nonlinear wave solutions for the  $(3 + 1)$ -dimensional ZKB equation in [14] and discuss the stability of the solutions briefly. In the year 2016, Yang et al. [15] reports some three-dimensional Rossby solitary waves solutions for the ZKB model. Abdullah et al. [16] employed a modified extended mapping method in order to obtain a solitary wave solution for  $(3 + 1)$ -dimensional ZKB equation. To solve different kinds of NLEEs, several researchers have proposed and applied various analytical, as well as numerical techniques, such as the modified trial equation method (MTEM), the modified Kudryashov method,  $(G'/G)$ -expansion method, the functional variable method, and many other symbolic techniques involving tedious computations, [17–19]. Recently, The generalized Kudryashov method (GKM) is employed to construct traveling wave solutions of different evolution equations. Compared with other nonlinear techniques, the GKM is more efficient to construct directly the exact solutions of high order nonlinear partial differential equations [19]. To acquire the traveling wave solutions of the ZKB equation the GKM is applied in the present investigation.

We observe the weakly nonlinear IAW in collisionless, unmagnetized, plasma system containing nonextensive electrons and cold ions. To aim this, we first derive the  $(2+1)$ -dimensional ZKB equation and apply GMK various types of solution such as kink and anti-kink soliton have been derived. In the present investigation, we

consider Cairns-Tallis distribution because such a two-parameter mixed distribution function may describe effectively various nonlinear phenomena in a nonthermal plasma environment. For the first time, Tribeche et al. [20] proposed this distribution and addressed the effectivity of the distribution when nonthermal and non-extensivity may act simultaneously. Model equation and Definition of Corresponding Parameters and derivation of the ZK-Burgers equation are describe in Sect. 2. An outline for the proposed nonlinear method and a set of the new solution are derived using GKM in Sect. 3. Section 4 briefly discusses the numerical structure of the solutions. Finally, concluding remarks are given in Sect. 5.

## 2 Model Equation and Definition of Corresponding Parameters

To verify the reliability of our results, a magnetized three-component plasma system with cold ions, electrons obeying  $q$  nonextensive nonthermal distribution and immobile negatively charged dust grains is considered. The external magnetic field is directed along  $x - axis$ , i.e.  $\mathbf{B} = B_0 \hat{x}$ . At equilibrium, the charge neutrality condition can be written as  $n_{i0} = n_{e0} + Z_d n_{d0}$  where  $n_{j0}$  represent the equilibrium densities of  $j$ th species ( $j = e, i, d$  stands for electron, ion and dust grains respectively) and  $Z_d$  denotes the charge number of dust grains. Assuming the existence of such a plasma environment, the dynamics of IAWs is governed by

$$\frac{\partial n_i}{\partial t} + \nabla \cdot (n_i \mathbf{u}_i) = 0 \tag{1a}$$

$$\frac{\partial \mathbf{u}_i}{\partial t} + (\mathbf{u}_i \cdot \nabla) \mathbf{u}_i = -\nabla \phi + \Omega (\mathbf{u}_i \times \hat{x}) + \nu_i \nabla^2 \mathbf{u}_i \tag{1b}$$

$$\nabla^2 \phi = n_e - n_i + \delta \tag{1c}$$

where  $\delta = \frac{Z_d n_{d0}}{n_{i0}}$  and  $n_j$  is the density of the  $j$ th species ( $j = e, i, d$  stands for electron, ion and dust grains respectively).  $\mathbf{u}_i$  is the ion fluid velocity and  $\phi$  is chosen an electrostatic potential. Here  $n_j$  is normalized by the unperturbed ion density  $n_{i0}$ .  $u_i$  is normalized by the ion-acoustic speed  $C_{si} = \sqrt{\frac{T_e}{m_i}}$ .  $\phi$ , the electrostatic wave potential is normalized by  $\frac{T_e}{e}$ . The space and time variables are in units of the ion Debye length  $\lambda_{di} = \sqrt{\frac{T_e}{4\pi n_{i0} e^2}}$  and the ion plasma period  $\omega_{pi}^{-1} = \sqrt{\frac{m_i}{4\pi n_{i0} e^2}}$ . Also  $\Omega = \frac{\omega_{ci}}{\omega_{pi}}$  where the ion gyrofrequency  $\omega_{ci}$  is defined as  $\omega_{ci} = \frac{e B_0}{m_i c}$  and  $c$  is the velocity of light.  $\nu_i = \frac{\nu_0}{\omega_{pi} \lambda_{di}^2}$  represent the normalized ion kinematic viscosity where  $\nu_0$  is the unnormalized kinematic viscosity.  $e$  is the magnitude of electron charge,  $m_i$  is mass of ion.

The electron density is given by

$$n_e(\phi) = n_{e0} \left\{ 1 + (q - 1) \frac{e\phi}{T_e} \right\}^{\frac{q+1}{2(q-1)}} \left\{ 1 + L_1 \left( \frac{e\phi}{T_e} \right) + L_2 \left( \frac{e\phi}{T_e} \right)^2 \right\} \tag{2}$$

where

$$L_1 = -\frac{16q\alpha}{3 - 14q + 15q^2 + 12\alpha}$$

$$L_2 = \frac{16q\alpha(2q - 1)}{3 - 14q + 15q^2 + 12\alpha}$$

Here,  $\alpha$  stands to present the spectral index and the density ( $n_e$ ) of nonextensive nonisothermal electrons can be written as

$$n_e = \mu \{ 1 + (q - 1) \phi \}^{\frac{q+1}{2(q-1)}} \{ 1 + L_1 \phi + L_2 \phi^2 \} \tag{3}$$

which implies

$$n_e = \mu \left\{ 1 + \frac{1+q}{2} \phi + \frac{(1+q)(3-q)}{8} \phi^2 + \frac{(1+q)(3-q)(5-3q)}{48} \phi^3 \right\} \times$$

$$\{ 1 + L_1 \phi + L_2 \phi^2 \}$$

$$= \mu \{ 1 + \beta_1 \phi + \beta_2 \phi^2 + \beta_3 \phi^3 + \dots \} \tag{4}$$

where

$$\mu = \frac{n_{e0}}{n_{i0}}$$

$$\beta_1 = L_1 + \frac{1+q}{2}$$

$$\beta_2 = L_2 + L_1 \frac{1+q}{2} + \frac{(1+q)(3-q)}{8}$$

$$\beta_3 = L_2 \frac{1+q}{2} + L_1 \frac{(1+q)(3-q)}{8} + \frac{(1+q)(3-q)(5-3q)}{48}$$

Here  $\mu$  denotes the unpertubated density ratios of electrons to ions ( $= \frac{n_{e0}}{n_{i0}}$ ). We express Eqs. (1a)–(1c) as follows

$$\frac{\partial n_i}{\partial t} + \frac{\partial (n_i u_{ix})}{\partial x} + \frac{\partial (n_i u_{iy})}{\partial y} = 0 \tag{5a}$$

$$\frac{\partial u_{ix}}{\partial t} + \left( u_{ix} \frac{\partial}{\partial x} + u_{iy} \frac{\partial}{\partial y} \right) u_{ix} = -\frac{\partial \phi}{\partial x} - \nu_i \left( \frac{\partial^2}{\partial x^2} + \frac{\partial^2}{\partial y^2} \right) u_{ix} \tag{5b}$$

$$\frac{\partial u_{iy}}{\partial t} + \left( u_{ix} \frac{\partial}{\partial x} + u_{iy} \frac{\partial}{\partial y} \right) u_{iy} = \frac{\partial \phi}{\partial y} - \nu_i \left( \frac{\partial^2}{\partial x^2} + \frac{\partial^2}{\partial y^2} \right) u_{iy} + \Omega u_{iz} \tag{5c}$$

$$\frac{\partial u_{iz}}{\partial t} + (u_{ix} \frac{\partial}{\partial x} + u_{iy} \frac{\partial}{\partial y})u_{iz} = \frac{\partial \phi}{\partial y} - \nu_i \left( \frac{\partial^2}{\partial x^2} + \frac{\partial^2}{\partial y^2} \right) u_{iz} + \Omega u_{iy} \tag{5d}$$

$$\left( \frac{\partial^2}{\partial x^2} + \frac{\partial^2}{\partial y^2} \right) \phi = n_e - n_i + \delta \tag{5e}$$

Independent variables are stretched as

$$\xi = \epsilon^{\frac{1}{2}}(x - v_p t), \eta = \epsilon^{\frac{1}{2}}y, \tau = \epsilon^{\frac{3}{2}}t \tag{6}$$

Actually to derive ZKB equation, the dependent variables are expanded as [21]

$$n_i = 1 + \epsilon n_{i1} + \epsilon^2 n_{i2} + \dots \tag{7a}$$

$$u_{ix} = \epsilon u_{ix1} + \epsilon^2 u_{ix2} + \dots \tag{7b}$$

$$u_{iy} = \epsilon^2 u_{iy1} + \epsilon^3 u_{iy2} + \dots \tag{7c}$$

$$u_{iz} = \epsilon^{3/2} u_{iz1} + \epsilon^{5/2} u_{iz2} + \dots \tag{7d}$$

$$\phi = \epsilon \phi_1 + \epsilon^2 \phi_2 + \dots \tag{7e}$$

$$\nu_i \approx \epsilon^{1/2} \nu_{i0} \tag{7f}$$

Here  $v_p = \sqrt{\frac{1}{\mu\beta_1}}$  is phase velocity. Using RPT method [7] and after setting  $\phi_1 = \Phi$ , we finally get a relation that can be claimed as the (2+1)-dimensional ZKB equation

$$\frac{\partial \Phi}{\partial \tau} + A \Phi \frac{\partial \Phi}{\partial \xi} + B \frac{\partial^3 \Phi}{\partial \xi^3} + C \frac{\partial^3 \Phi}{\partial \xi \partial \eta^2} + D \left( \frac{\partial^2}{\partial \xi^2} + \frac{\partial^2}{\partial \eta^2} \right) \Phi = 0 \tag{8}$$

where

$$A = \frac{3}{2v_p} - \mu\beta_2 v_p^3, \quad B = \frac{v_p^3}{2}, \quad C = \frac{v_p^3}{2}(1 + \Omega^{-2}), \quad D = -\frac{\nu_{i0}}{2}.$$

### 3 Solution of (2+1)-Dimensional ZKB Equation

#### 3.1 Description of the Generalized Kudryashov Method

In the present section, a generalized structure of the GKM is described in brief. We consider the fractional differential equation as,

$$u_\tau = \mathcal{N}(u_\xi, u_{\xi\xi}, u_{\tau\xi}, u_{\xi\xi\xi}, u_{\xi\xi\xi\dots}) \tag{9}$$



where  $u = u(\xi, \eta, \tau)$ . The main steps of GKM are stated below as,

**Step 1.** We introduce a new variable  $\theta$  to substitute the variables  $\xi, \eta$  and  $\tau$ . Now, we write

$$u(\xi, \eta, \tau) = V(\theta), \quad \theta = k\xi + n\eta - \omega\tau \tag{10}$$

where  $k, n$  and  $\omega$ , are the constants to be determined later. Then, the Eq. (9) is converted into a nonlinear ordinary differential equation (NODE) as,

$$\omega V' = \mathcal{Q}(V, V', V'', V''', \dots) \tag{11}$$

for  $V = V(\theta)$  where  $\mathcal{Q}$  presents a polynomial of  $V$  along with its derivatives (the superscripts stands for presenting the differential w.r.t.  $\theta$ ).

**Step 2.** Now, we choose the solution of Eq. (11) in the particular form presented below as,

$$V(z) = \frac{\sum_{i=0}^r a_i Y^i(\theta)}{\sum_{j=0}^p a_j Y^j(\theta)} = \frac{a_0 + a_1 Y(\theta) + a_2 Y^2(\theta) + \dots + a_r Y^r(\theta)}{b_0 + b_1 Y(\theta) + b_2 Y^2(\theta) + \dots + b_p Y^p(\theta)}. \tag{12}$$

where  $Y = Y(\theta)$  obeys the NODE,

$$Y' = Y^2 - Y, \tag{13}$$

Combining Eqs. (12) and (11) we find the polynomial equation  $Y$ . Using the homogeneous balance principle the relation between  $p$  and  $r$  is determined.

**Step 3.** Equating the coefficients of the term  $Y^m$  a system of algebraic equation is determined. Utilizing the symbolic system package Maple this system is solved. Finally, the values of  $a_i, i = 0, 1, 2, 3, \dots, r$  and  $b_j, j = 0, 1, 2, \dots, p$  are determined.

**Step 4.** Substituting the parametric values  $a_i$  and  $b_j$ , and setting the general solution of Eq. (13)  $Y = 1/(1 \pm e^\theta)$  in Eq. (12), the solutions of Eq. (9) are obtained.

### 3.2 Application of the Generalized Kudryashov Method on ZKB Equation

In this sub-section generalized kudryashov method is employed to construct a set of exact analytic solution of ZK-Burgers equation. To get traveling wave solution of Eq. (8), we consider the transformation

$$\Phi(\xi, \eta, \tau) = V(\theta), \quad \theta = k\xi + n\eta - \omega\tau. \tag{14}$$

Substituting Eq. (14) into Eq. (8), we have obtained the following nonlinear differential equation:

$$-\omega V' + AkVV' + Bk^3V''' + Ckn^2V''' + Dk^2V'' + Dn^2V'' = 0 \tag{15}$$

Integrating we get

$$-\omega V + \frac{AkV^2}{2} + Bk^3V'' + Ckn^2V'' + Dk^2V' + Dn^2V' = 0 \tag{16}$$

Applying homogeneous balance principle between  $V''$  and  $V^2$ , we find a relationship for  $r, p$  as,

$$r = p + 2$$

Taking  $p = 1$ , gives  $r = 3$ . We choose a trial solution of Eq. (16) as

$$V = \frac{a_0 + a_1Y + a_2Y^2 + a_3Y^3}{b_0 + b_1Y} \tag{17}$$

Putting Eq. (17) into Eq. (16) a system of algebraic equations is obtained and by solving this system with the help of symbolic computation software Maple, we find the values of the involved coefficients. These are determined as,

**Set 1.**

$$a_2 = -\frac{12Db_0(k^2 + n^2)}{5Ak}, B = -\frac{5Cn^2 - Dk^2 - Dn^2}{5k^2}, \omega = -\frac{6D(k^2 + n^2)}{5},$$

$$a_0 = 0, a_1 = 0, a_2 = a_2, a_3 = 0, b_0 = b_0, b_1 = 0 \tag{18}$$

By using Eq. (18), the solution can be written as

$$\Phi_{2a} = -\frac{3D(k^2 + n^2)}{5Ak} \left( 1 - \tanh\left(\frac{\theta}{2}\right) \right)^2 \tag{19}$$

where  $\theta = k\xi + n\eta + \frac{6D(k^2+n^2)\tau}{5}$ .

**Set 2.**

$$B = -\frac{Cn^2}{k^2}, \omega = -D(k^2 + n^2), a_0 = 0, a_1 = -\frac{2Db_0(k^2 + n^2)}{kA}, a_2 = 0,$$

$$a_3 = 0, b_0 = b_0, b_1 = 0. \tag{20}$$

By using Eq. (20), the soliton solution can be written as

$$\Phi_{1a} = -\frac{D(k^2 + n^2)}{kA} \left( 1 - \tanh\left(\frac{\theta}{2}\right) \right) \quad (21)$$

where  $\theta = k\xi + n\eta + D(k^2 + n^2)\tau$ .

**Set 3.**

$$B = -\frac{5Cn^2 - Dk^2 - Dn^2}{5k^2}, \quad \omega = \frac{6D(k^2 + n^2)}{5}, \quad a_0 = -a_2, \quad a_1 = 0, \quad a_2 = a_2, \\ a_2 = \frac{-12Db_0(k^2 + n^2)}{5kA}, \quad a_3 = 0, \quad b_0 = b_0, \quad b_1 = 0 \quad (22)$$

By using Eq. (22), the soliton solution can be termed as

$$\Phi_{3a} = \frac{3D(k^2 + n^2)}{5kA} \left( 1 - \left( 1 - \tanh\left(\frac{\theta}{2}\right) \right)^2 \right) \quad (23)$$

where  $\theta = k\xi + n\eta - \frac{6D(k^2+n^2)\tau}{5}$ .

## 4 Results and Discussion

This work presents a new class of effective solutions for ZK-Burgers model. In fact, we choose some particular numerical values for the coefficients (depending on various parameters) of the equation and plot some 2D and 3D graphs accordingly. Figure 1a is drawn to exhibit the effect of Burgers term in shock profile. Figure 1a clearly shows that the amplitude of the wave substantially depends on dust kinematic viscosity. Increasing  $\nu_{i0}$  leads for rising dissipation in a system and naturally the amplitudes of the shock rises. The effect of the variation of unperturbed density ratio of electrons to that of ions ( $\mu$ ) in wave profile is demonstrated in Fig. 1(b) where enhancing  $\mu$  causes for rising of the amplitude of the shocks. In order to show the effect of variation of the parameters spectral index ( $\alpha$ ) and nonextensive parameter  $q$  Fig. 1c, d are plotted, where enhancing of both the parameters causes for diminishing of the amplitude of the shocks. Utilizing the symbolic computation system Mathematica, two three dimensional graphs of the obtained solutions of ZKB medium are drawn in Fig. 2. Figure 2a clearly shows the propagation of shock in space zone whereas the significant effect of the viscosity parameter  $\nu_{i0}$  is shown in Fig. 2b.

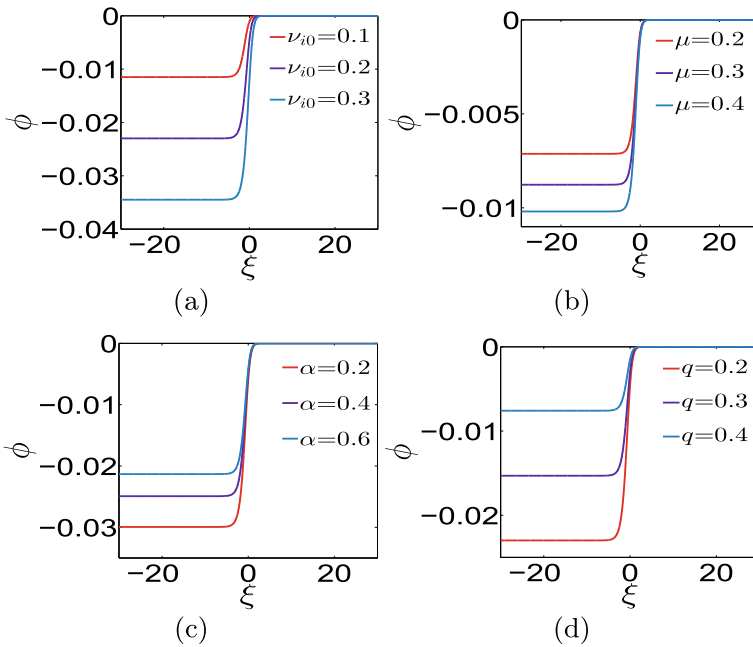


**Fig. 1** **a** The 2D Profiles of Solution (19) for  $\alpha = 0.5, q = 0.2, \tau = 1, n = \frac{1}{\sqrt{2}}, k = \frac{1}{\sqrt{2}}, \eta = 1, \mu = 0.5, \omega = 0.5$ , **b** when  $\alpha = 0.5, q = 0.2, \tau = 1, n = \frac{1}{\sqrt{2}}, k = \frac{1}{\sqrt{2}}, \eta = 1, \nu_{i0} = 0.1, \omega = 0.5$  **c** when  $\nu_{i0} = 0.1, q = 0.2, \tau = 1, n = \frac{1}{\sqrt{2}}, k = \frac{1}{\sqrt{2}}, \eta = 1, \mu = 0.5, \omega = 0.5$ , **d** when  $\alpha = 0.5, \nu_{i0} = 0.1, \tau = 1, n = \frac{1}{\sqrt{2}}, k = \frac{1}{\sqrt{2}}, \eta = 1, \mu = 0.5, \omega = 0.5$

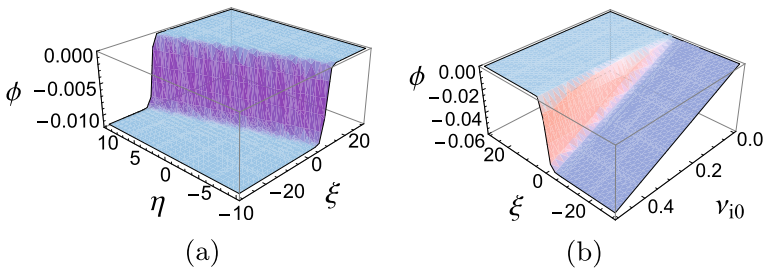


**Fig. 2** **a** The 3D Profiles of Solution (19) for  $\alpha = 0.5, q = 0.2, \tau = 1, n = \frac{1}{\sqrt{2}}, k = \frac{1}{\sqrt{2}}, \mu = 0.5, \omega = 0.5, \nu_{i0} = 0.1$ , **b** for  $\alpha = 0.5, q = 0.2, \tau = 1, n = \frac{1}{\sqrt{2}}, k = \frac{1}{\sqrt{2}}, \eta = 1, \mu = 0.5, \omega = 0.5$

## 5 Conclusion

We have utilized the ZKB model to observe IAW propagating in a non-extensive plasma medium, this example has been provided basically to establish the existence of such types of models in different physical situations. Actually, in the light of our observation, emphasis is imposed on deriving the model solutions. The GKM method, a newly developed novel nonlinear technique, is employed to ZKB equation and a new class of effective solutions such as kink soliton, anti-kink soliton, are derived which may be useful in the various dynamic systems of physical situations like the water wave phenomena, the elastic media, the quantum mechanics, the dynamics of adiabatic parameters, problems on the industrial phenomena, etc. Some complicated algebraic calculations have been solved with the help of the symbolic computations package Maple. Finally, some 2D and 3D figures are also drawn to show the impact of different parameters on wave structures.

## References

1. Das, G.C., Paul, S.N.: Ionacoustic solitary waves in relativistic plasmas. *Phys. fluids* **28**(3), 823–825 (1985)
2. Roychoudhury, R.K., Bhattacharyya, S.: Effect of ion temperature on ion-acoustic solitary waves: a pseudopotential approach. *Can. J. Phys.* **65**(7), 699–702 (1987)
3. Zakharov, V.E., Kuznetsov, E.A.: On threedimensional solitons. *Zhurnal Eksp. Teoret. Fiz* **66**, 594–597 (1974)
4. Mondal, K.K., Roy, A., Chatterjee, P., Raut, S.: Propagation of ion-acoustic solitary waves for damped forced Zakharov Kuznetsov equation in a relativistic rotating magnetized electron-positron-ion plasma. *Int. J. Appl. Comput. Math.* **6**(3), 1–17 (2020)
5. Munro, S., Parkes, E.J.: The stability of obliquely-propagating solitary-wave solutions to a modified Zakharov-Kuznetsov equation. *J. Plasma Phys.* **70**(5), 543–552 (2004)
6. Schamel, H.: A modified Korteweg-de Vries equation for ion acoustic waves due to resonant electrons. *J. Plasma Phys.* **9**(3), 377–387 (1973)
7. Kakutani, T., Ono, H., Taniuti, T., Wei, C.C.: Reductive perturbation method in nonlinear wave propagation II. Application to hydromagnetic waves in cold plasma. *J. Phys. Soc. Jpn.* **24**(5), 1159–1166 (1968)
8. El-Bedwehy, N.A., Moslem, W.M.: Zakharov-Kuznetsov-Burgers equation in super thermal electron-positron-ion plasma. *Astrophys. Space Sci.* **335**(2), 435–442 (2011)
9. Raut, S., Mondal, K.K., Chatterjee, P., Roy, A.: Two-dimensional ion-acoustic solitary waves obliquely propagating in a relativistic rotating magnetised electron-positron-ion plasma in the presence of external periodic force. *Pramana* **95**(2), 1–13 (2021)
10. Raut, S., Mondal, K.K., Chatterjee, P., Roy, A.: Propagation of dust-ion-acoustic solitary waves for damped modified Kadomtsev-Petviashvili-Burgers equation in dusty plasma with a q-non extensive nonthermal electron velocity distribution. *SeMA J.* 1–23 (2021)
11. Moslem, W.M., Sabry, R.: Zakharov-Kuznetsov-Burgers equation for dust ion acoustic waves. *Chaos Solitons Fractals* **36**(3), 628–634 (2008)
12. El-Bedwehy, N.A., Moslem, W.M.: Zakharov-Kuznetsov-Burgers equation in super thermal electron-positron-ion plasma. *Astrophys. Space Sci.* **335**(2), 435–442 (2011)
13. Yin, X., Yang, L., Liu, Q., Wu, G.: (2+ 1)-dimensional ZK-Burgers equation with the generalized beta effect and its exact solitary solution. *Comput. Math. Appl.* **77**(1), 302–310 (2019)

14. Seadawy, A.R.: Nonlinear wave solutions of the three-dimensional Zakharov-Kuznetsov-Burgers equation in dusty plasma. *Physica A: Stat. Mech. Appl.* **439**, 124–131 (2015)
15. Yang, H.W., Xu, Z.H., Feng, X.R., Yin, B.S., Dong, H.H.: ZK-Burgers equation for three-dimensional Rossby solitary waves and its solutions as well as chirp effect. *Adv. Differ. Equ.* **2016**(1), 1–22 (2016)
16. Seadawy, A.R., Jun, W.: Mathematical methods and solitary wave solutions of three-dimensional Zakharov-Kuznetsov-Burgers equation in dusty plasma and its applications. *Results in Phys.* **7**, 4269–4277 (2017)
17. Yel, G., Sulaiman, T.A., Baskonus, H.M.: On the complex solutions to the (3+ 1)-dimensional conformable fractional modified KdV-Zakharov-Kuznetsov equation. *Mod. Phys. Lett. B* **34**(05), 2050069 (2020)
18. Islam, M.H., Khan, K., Akbar, M.A., Salam, M.A.: Exact traveling wave solutions of modified KdV-Zakharov-Kuznetsov equation and viscous Burgers equation. *SpringerPlus* **3**(1), 1–9 (2014)
19. Ryabov, P.N., Sinelshchikov, D.I., Kochanov, M.B.: Application of the Kudryashov method for finding exact solutions of the high order nonlinear evolution equations. *Appl. Math. Comput.* **218**(7), 3965–3972 (2011)
20. Tribeche, M., Amour, R., Shukla, P.K.: Ion acoustic solitary waves in a plasma with nonthermal electrons featuring Tsallis distribution. *Phys. Rev. E* **85**, 037401 (2012)
21. Mushtaq, A., Shah, H.A.: Nonlinear Zakharov-Kuznetsov equation for obliquely propagating two-dimensional ion-acoustic solitary waves in a relativistic, rotating magnetized electron-positron-ion plasma. *Phys. Plasmas* **12**(7), 072306 (2005)

# Impact of Fear and Strong Allee Effects on the Dynamics of a Fractional-Order Rosenzweig-MacArthur Model



Hasan S. Panigoro and Emli Rahmi

**Abstract** This paper discusses the impact of fear and strong Allee on the dynamical behaviors of the prey and predator relationship following the Rosenzweig-MacArthur model using fractional-order derivative as the operator. As results, four equilibrium points are identified namely the origin point, a pair of axial points, and the interior point. The origin is always locally asymptotically stable while others are conditionally asymptotically stable. The occurrence of transcritical bifurcation around the axial and Hopf bifurcation in the interior are also successfully investigated. The numerical simulations are conducted to support analytical findings. Some interesting dynamics such as forward bifurcation and bistability condition are also provided numerically.

**Keywords** Fractional-order · Rosenzweig-MacArthur · Allee effect · Fear effect

## 1 Introduction

Food chain schemes are always found in nature. Every organism may become a predator to others due to its need for food. As a result, each organism has a chance to go extinct as an impact of this ecological mechanism. Therefore, studying the existence of organisms that have prey and predator relationship always be a crucial issue for researchers. One of the much-publicized ways is using mathematical modeling.

In 1963, a mathematical model is developed by Rosenzweig and MacArthur based on the Lotka-Volterra predator-prey model which assumes that the population of prey grows logistically and its hunting by the predator for foods following Holling type-II as the predator functional response [1]. Nowadays, the Rosenzweig-MacArthur model becomes an attractive reference to establish a novel predator-prey model by

---

H. S. Panigoro (✉) · E. Rahmi

Department of Mathematics, State University of Gorontalo, Bone Bolango 96119, Indonesia  
e-mail: [hspanigoro@ung.ac.id](mailto:hspanigoro@ung.ac.id)

E. Rahmi

e-mail: [emlirahmi@ung.ac.id](mailto:emlirahmi@ung.ac.id)

**Table 1** The biological interpretation of variables and parameters

Variables and parameters	Biological interpretation
$x$	The density of prey
$y$	Density of predator
$r$	Intrinsic growth rate of prey
$k$	Level of fear
$K$	Environmental carrying capacity of prey
$b$	Allee threshold
$m$	Predation rate
$a$	Half saturation constant of predation
$n$	Predator growth rate which converted from the predation process
$d$	Predator death rate

involving some ecological components associated with real phenomena in nature. For example, see [2, 3] and references therein.

In this paper, we assume that the growth rate of prey is influenced by the indirect impact of the predator through the fear effect [4]. We also assume that this intrinsic growth rate could also decrease by the intraspecific competition and difficulty in finding mates is known as the Allee effect [5]. Thus, we have the following model.

$$\begin{aligned} \frac{dx}{dt} &= \frac{rx}{1+ky} \left(1 - \frac{x}{K}\right) (x - b) - \frac{mxy}{a+x}, \\ \frac{dy}{dt} &= \frac{nxy}{a+x} - dy. \end{aligned} \tag{1}$$

See Table 1 for the biological interpretation of variables and parameters. The term  $(x - b)$  represents the Allee effect where for  $b \leq 0$  called weak Allee effect and  $b > 0$  called strong Allee effect. In our work, we assume that the intrinsic growth rate of prey affected by strong Allee effect. Due to biological purpose, other parameters also positive constant and both  $x(t)$  and  $y(t)$  satisfy  $(x, y) \in \mathbb{R}_+^2$  where  $\mathbb{R}_+^2 := \{(x, y) \mid x \geq 0, y \geq 0, x \in \mathbb{R}, y \in \mathbb{R}\}$ .

Since the current state of both prey and predator depends on all of their previous conditions, using fractional-order derivative is considered more appropriate in expressing the model better than classical integer-order derivative [3, 6, 7]. Following a similar way with [3, 7] such as replacing the first-order with fractional-order derivative and scaling the time dimension, we obtain the new model as follows.

$$\begin{aligned} {}^C\mathcal{D}_t^\alpha x &= \frac{rx}{1+ky} \left(1 - \frac{x}{K}\right) (x - b) - \frac{mxy}{a+x}, \\ {}^C\mathcal{D}_t^\alpha y &= \frac{nxy}{a+x} - dy, \end{aligned} \tag{2}$$



where  ${}^c\mathcal{D}_t^\alpha$  is Caputo fractional-order derivative defined by

$${}^c\mathcal{D}_t^\alpha f(t) = \frac{1}{\Gamma(1-\alpha)} \int_a^t \frac{f'(\tau)}{(t-\tau)^\alpha} d\tau,$$

$\alpha \in (0, 1]$  is the order of the derivative and  $\Gamma(\cdot)$  is Euler Gamma function [8].

In Sasmal [9], the predator-prey model involving fear and Allee effects has been studied. Sasmal’s model is quite similar to ours both in assumptions and the deterministic model. The big difference which becomes the novelty of our works lies in the predator functional response and the operator of the model. In our works, the Michaelis-Menten type is used as the predator functional response which is considered more realistic than bilinear ones. The fractional-order derivative is also used to replace the first-order derivative as the operator to cover the memory effect.

The rest of the paper is arranged as follows. In Sect. 2, the feasibility and local stability of equilibrium points are verified. Furthermore, the existence of transcritical and Hopf bifurcations are examined in Sect. 3. Several numerical simulations are explored in Sect. 4 not only to support the analytical findings but also to show other dynamical behaviors such as the occurrence of forward bifurcation and bistability conditions. We finally end our work by giving a conclusion in Sect. 5.

## 2 Feasibility and Stability of Equilibrium Points

The feasible equilibrium points of model (2) are acquired by finding the the positive solution of the following equations.

$$\begin{aligned} \left[ \frac{r(x-b)}{1+ky} \left( 1 - \frac{x}{K} \right) - \frac{my}{a+x} \right] x &= 0, \\ \left[ \frac{nx}{a+x} - d \right] y &= 0. \end{aligned}$$

Therefore, four equilibrium points are identified as follows.

- (i) The origin  $E_0 = (0, 0)$  which represents the extinction of both populations.
- (ii) A pair of axial points  $E_1 = (b, 0)$  and  $E_2 = (K, 0)$  which represent the existence of prey and the extinction of predator.
- (iii) The interior point  $E_3 = (\hat{x}, \hat{y})$  which represents the existence of both populations where  $\hat{x} = \frac{ad}{n-d}$  and  $\hat{y}$  is the positive solution respect to  $y$  of the following equation.

$$y^2 + \frac{y}{k} + \frac{\hat{m}}{4k^2m} = 0, \tag{3}$$

where  $3\hat{m} = \frac{4(\hat{x}-K)(\hat{x}-b)(\hat{x}+a)kr}{K}$ . Since  $E_i \in \mathbb{R}_+^2 \forall i = 0, 1, 2$ , then they always exist. Furthermore, the existence condition of  $E_3$  is given by the following theorem.

**Theorem 1** *If  $n > d$  and (i)  $m \leq \hat{m}$  then the interior point does not exist; (ii)  $m > \hat{m}$  then there exists an interior point.*

**Proof** Since  $n > d$  then  $\hat{x}$  is always positive. Thus, the existence of  $E_3$  depends on the positive solution of quadratic equation (3). If  $m < \hat{m}$  then the solution of equation (3) is a pair of complex conjugate numbers and hence the interior point does not exist. When  $m = \hat{m}$ , we have  $\hat{y} = -\frac{1}{2k} < 0$ , and hence  $E_3$  also does not exist. For  $m > \hat{m}$ , the only positive solution of equation (3) is given by  $\hat{y} = -\frac{1}{2k} \left( 1 - \sqrt{1 - \frac{\hat{m}}{m}} \right)$ . This completes the proof.  $\square$

Now, we discuss the local stability for each equilibrium point. The following theorems are presented.

**Theorem 2** *The origin  $E_0 = (0, 0)$  is always locally asymptotically stable.*

**Proof** The linearization around  $E_0$  gives the Jacobian matrix as follows.

$$\mathcal{J}(x, y)|_{E_0} = \begin{bmatrix} -br & 0 \\ 0 & -d \end{bmatrix}.$$

The eigenvalues of  $\mathcal{J}(x, y)|_{E_0}$  are  $\lambda_1 = -br$  and  $\lambda_2 = -d$  which give  $|\arg(\lambda_i)| = \pi > \alpha\pi/2 \forall i = 1, 2$ . According to the Matignon condition [10],  $E_0$  is always locally asymptotically stable.  $\square$

**Theorem 3** *The axial point  $E_1 = (b, 0)$  is locally asymptotically stable if  $b > K$  and  $n < \frac{(a+b)d}{b}$ .*

**Proof** For the axial point  $E_1$ , we have the Jacobian matrix

$$\mathcal{J}(x, y)|_{E_1} = \begin{bmatrix} -\frac{(b-K)br}{K} & -\frac{bm}{a+b} \\ 0 & \frac{bn}{a+b} - d \end{bmatrix}, \tag{4}$$

which give eigenvalues  $\lambda_1 = -\frac{(b-K)br}{K}$  and  $\lambda_2 = \frac{bn}{a+b} - d$ . Based on Matignon condition [10], the local asymptotic stability condition are satisfied when  $\lambda_i < 0, i = 1, 2$  which are given by  $b > K$  and  $n < \frac{(a+b)d}{b}$ .  $\square$

**Theorem 4** *The axial point  $E_2 = (K, 0)$  is locally asymptotically stable if  $b < K$  and  $n < \frac{(a+K)d}{K}$ .*

**Proof** The Jacobian matrix evaluated at  $E_2$  is given by

$$\mathcal{J}(x, y)|_{E_2} = \begin{bmatrix} (b-K)r & -\frac{mK}{a+K} \\ 0 & \frac{nK}{a+K} - d \end{bmatrix}, \tag{5}$$

where the eigenvalues are  $\lambda_1 = (b-K)r$  and  $\lambda_2 = \frac{nK}{a+K} - d$ . If  $b < K$  and  $n < \frac{(a+K)d}{K}$  then  $|\arg(\lambda_i)| = \pi > \alpha\pi/2, i = 1, 2$  that obeys the Matignon condition [10].  $\square$

**Theorem 5** *The interior point  $E_3 = (\hat{x}, \hat{y})$  is locally asymptotically stable if (i)  $\xi_1 < 0$ , or (ii)  $\xi_1 > 0$ ,  $\xi_1^2 < 4\xi_2$ , and  $\alpha < \hat{\alpha}$ , where  $\xi_1 = -\frac{(3\hat{x}^2 - 2(b+K)\hat{x} + bK)r}{(1+k\hat{y})K} - \frac{am\hat{y}}{(a+\hat{x})^2}$ ,  $\xi_2 = \frac{(1+2k\hat{y})ad^3m\hat{y}}{(1+k\hat{y})n^2\hat{x}^2}$ , and  $\hat{\alpha} = \frac{2}{\pi} \tan^{-1} \left( \frac{\sqrt{4\xi_2 - \xi_1^2}}{\xi_1} \right)$ .*

**Proof** At  $E_3$ , we have

$$\mathcal{J}(x, y)|_{E_3} = \begin{bmatrix} \xi_1 & -\frac{n\xi_2\hat{x}^2}{ad^2\hat{y}} \\ \frac{ad^2\hat{y}}{n\hat{x}^2} & 0 \end{bmatrix}. \tag{6}$$

Therefore, the polynomial characteristic is obtained as follows.

$$\lambda^2 - \xi_1\lambda + \xi_2 = 0. \tag{7}$$

Since  $\xi_2 > 0$ , by obeying Proposition 1 in [11], the stability conditions given in Theorem 5 are proven.  $\square$

### 3 Bifurcation Analysis

In this section, we give two types of bifurcations phenomena namely transcritical and Hopf bifurcations by following theorems.

**Theorem 6** *Suppose that  $n < \min \left\{ \frac{(a+b)d}{b}, \frac{(a+K)d}{K} \right\}$ . Two axial points  $E_1$  and  $E_2$  exchange their stability via transcritical bifurcation when  $b$  crosses  $K$ .*

**Proof** Since  $n < \min \left\{ \frac{(a+b)d}{b}, \frac{(a+K)d}{K} \right\}$ , we have  $|\arg(\lambda_2)| = \pi > \alpha\pi/2$  for each Jacobian matrix (4) and (5). Therefore, the stability of  $E_1$  and  $E_2$  depend on the sign of  $\lambda_1$ . When  $b < K$ ,  $|\arg(\lambda_1)| = \pi > \alpha\pi/2$  for Jacobian matrix (5) and  $|\arg(\lambda_1)| = 0 < \alpha\pi/2$  for Jacobian matrix (4). Hence,  $E_1$  is a saddle point while  $E_2$  is locally asymptotically stable. When  $b = K$ ,  $E_1 = E_2$  and  $|\arg(\lambda_1)| = \alpha\pi/2$  which represents a non-hyperbolic equilibrium point. For  $b > K$  the sign of  $|\arg(\lambda_1)|$  for Jacobian matrices (4) and (5) are switched which indicates the stability of  $E_1$  and  $E_2$  changes. According to those circumstances, the transcritical bifurcation occurs driven by the Allee threshold ( $b$ ).  $\square$

**Theorem 7** *Let  $\xi_1 > 0$  and  $\xi_1^2 < 4\xi_2$ . A Hopf bifurcation occurs around the interior point  $E_3 = (\hat{x}, \hat{y})$  when  $\alpha$  passes through  $\hat{\alpha}$ .*

**Proof** From (7), the appropriated eigenvalues are given by

$$\lambda_{1,2} = \frac{1}{2} \left( \xi_1 \pm \sqrt{\xi_1^2 - 4\xi_2} \right). \tag{8}$$

Since  $\xi_1 > 0$  and  $\xi_1^2 < 4\xi_2$ , the eigenvalues (8) are a pair of complex conjugate numbers with positive real parts. It is also valid that  $m(\hat{\alpha}) = \hat{\alpha}\pi/2 - \min_{1 \leq i \leq 2} |\arg(\lambda_i)| = 0$  and  $\left. \frac{dm(\alpha)}{d\alpha} \right|_{\alpha=\hat{\alpha}} \neq 0$ . According to Theorem 4.6 in [12], Hopf bifurcation occurs around  $E_3$  driven by  $\alpha$  with  $\hat{\alpha}$  is the critical point. □

## 4 Numerical Simulation

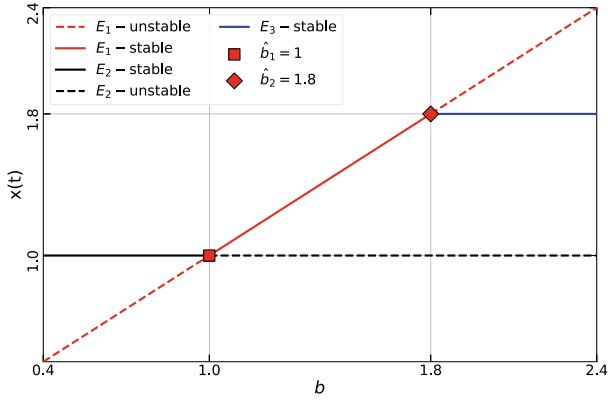
Some numerical simulations are demonstrated using a generalized predictor-corrector scheme given by Diethelm et al. [13]. This scheme is applied to numerical software called *Python-3* to produce some figures such as bifurcation diagrams and time series. In this paper, we study numerically the influence of the Allee threshold ( $b$ ) and the order of the derivative ( $\alpha$ ) to the dynamical behaviors of model (2). Since the model does not discuss a specific case, all parameter values are chosen hypothetically by considering the previous analytical results. We first set the parameter as in Table 2 and varying the Allee threshold ( $b$ ) in interval  $[0.4, 2.4]$ , see Fig. 1.

From the bifurcation diagram given by Fig. 1a, when  $b$  is varied in the interval  $[0.4, 2.4]$ , the dynamical behaviors change two times. For  $0.4 \leq b < 1$ , we have a locally asymptotically stable equilibrium point  $E_2$  and an unstable point  $E_1$ . The stability of both  $E_1$  and  $E_2$  change sign when  $b$  crosses  $\hat{b}_1 = 1$  which confirm the existence of transcritical bifurcation given by Theorem 6. This dynamical behaviors are maintained for  $\hat{b}_1 < b < \hat{b}_2 = 1.8$ . Denote that the interior point  $E_3$  does not exist for interval  $0.4 \leq b < \hat{b}_2$ . When  $b$  passes  $\hat{b}_2$ , the axial point  $E_1$  again losses its stability, and a locally asymptotically stable point  $E_3$  emerges which indicates the existence of forward bifurcation. This conditions are preserved for  $\hat{b}_2 < b \leq 2.4$ . Remember that  $E_0$  is always locally asymptotically stable and hence the bistability condition always occurs for each case when the dynamical behaviors change. We perform the phase portraits by picking the values of  $b = 0.5, 1.5, 2.3$ , which presents the dynamical behavior for each interval. See Fig. 1b, c, d. The stability shifts from  $E_2$  to  $E_1$  and finally to  $E_3$  while  $E_0$  always locally asymptotically stable. This means, the bistability condition always exists for  $[0.4, 2.4]$  except in every bifurcation point. This means that the existence of populations depends on the initial values. From those phase portraits, we show that for the given two close initial values, the solutions tend to distinct equilibrium points. Both populations could be extinct or only the existence of prey is preserved.

The next simulation aims to show the influence of the order of the derivative ( $\alpha$ ) to the dynamical behaviors of model (2). The parameter values are chosen as

**Table 2** Parameter values for numerical simulations given in Fig. 2

Parameters	$r$	$k$	$K$	$m$	$a$	$n$	$d$	$\alpha$
Values	0.4	0.8	1	0.3	0.9	0.15	0.1	0.9



(a) Bifurcation diagram driven by the Allee threshold  $b$

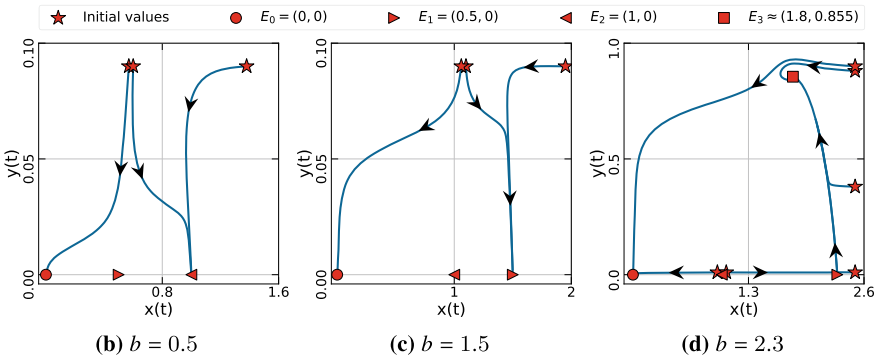


**Fig. 1** Bifurcation diagram and phase portraits of model (2) with parameter values as in Table 2

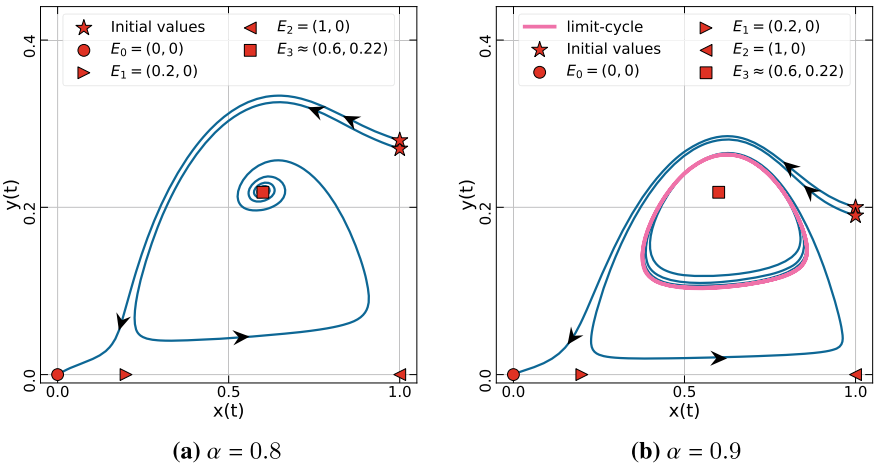


**Fig. 2** Phase portraits of model (2) with parameter values as in Table 3

**Table 3** Parameter values for numerical simulations given in Fig. 2

Parameters	r	k	K	b	m	a	n	d
Values	0.4	0.8	1	0.2	0.3	0.6	0.2	0.1

in Table 2. Based on Theorem 5, The Jacobian matrix (6) has a pair of complex conjugate eigenvalues with positive real parts. Thus, from Theorem 7, the interior point  $E_3$  undergoes a Hopf bifurcation when  $\alpha$  passes through the critical point  $\hat{b}$ . By using these parameter values, we confirm that the critical point is  $\hat{\alpha} \approx 0.84304$ . To show this condition, we pick  $\alpha = 0.8$  and  $\alpha = 0.9$  and the numerical results given by the phase portraits in Fig. 2. When  $\alpha = 0.8$ , two locally asymptotically stable equilibrium points occur i.e.  $E_0 = (0, 0)$  and  $E_3 \approx (0.6, 0.22)$ . As the impact, the model (2) leads to bistability condition. For two close initial values, the solutions convergent to different equilibrium points namely  $E_0$  and  $E_3$ . When  $\alpha$  is increased to 0.9,  $E_3$  losses its stability and nearby solution convergent to a periodic signal namely limit-cycle. Although the interior point is unstable, both populations are still preserved periodically around the interior point. This ends our numerical simulations.

## 5 Conclusion

The dynamical behaviors of a fractional-order Rosenzweig-MacArthur model involving fear and strong Allee effects have been studied. The model has four equilibrium points namely the origin, a pair in axial, and a unique interior point. Those two equilibrium points in the axial may exchange their stability via transcritical bifurcation. For the interior point, the stability may change via Hopf bifurcation driven by the order of the derivative. To support the analytical findings, numerical simulations are provided including a bifurcation diagram and phase portraits. We have found numerically that the model undergoes transcritical bifurcation, forward bifurcation, Hopf bifurcation, and bistability conditions. From the biological viewpoint, these circumstances mean that the existence of both prey and predator are threatened due to predation mechanism, fear, and allee effects.

## References

1. Rosenzweig, M.L., MacArthur, R.H.: Graphical representation and stability conditions of predator-prey interactions. *Am. Nat.* **97**, 209–223 (1963). <https://doi.org/10.1086/282272>
2. Moustafa, M., Mohd, M.H., Ismail, A.I., Abdullah, F.A.: Stage structure and refuge effects in the dynamical analysis of a fractional order Rosenzweig-MacArthur prey-predator model. *Prog. Fract. Differ. Appl.* **5**, 49–64 (2019). <https://doi.org/10.18576/pfda/050106>
3. Panigoro, H.S., Suryanto, A., Kusumawinahyu, W.M., Darti, I.: A Rosenzweig-MacArthur model with continuous threshold harvesting in predator involving fractional derivatives

- with power law and mittag-leffler kernel. *Axioms* **9**, 122 (2020). <https://doi.org/10.3390/axioms9040122>
4. Barman, D., Roy, J., Alrabaiah, H., Panja, P., Mondal, S.P., Alam, S.: Impact of predator incited fear and prey refuge in a fractional order prey predator model. *Chaos Solitons Fractals* **142**, 110420 (2021). <https://doi.org/10.1016/j.chaos.2020.110420>
  5. Allee, W.C.: *Animal Aggregations, A Study in General Sociology*. The University of Chicago Press, Chicago (1931)
  6. Panigoro, H.S., Suryanto, A., Kusumawinahyu, W.M., Darti, I.: Global stability of a fractional-order Gause-type predator-prey model with threshold harvesting policy in predator. *Commun. Math. Biol. Neurosci.* **2021**, 63 (2021). <https://doi.org/10.28919/cmbn/6118>
  7. Rahmi, E., Darti, I., Suryanto, A.: Trisilowati: a modified Leslie-Gower model incorporating Beddington-DeAngelis functional response, double Allee effect and memory effect. *Fractal Fract.* **5**, 84 (2021). <https://doi.org/10.3390/fractalfract5030084>
  8. Petras, I.: *Fractional-Order Nonlinear Systems: Modeling, Analysis and Simulation*. Springer, London, Beijing (2011)
  9. Sasmal, S.K.: Population dynamics with multiple Allee effects induced by fear factors - A mathematical study on prey-predator interactions. *Appl. Math. Model.* **64**, 1–14 (2018). <https://doi.org/10.1016/j.apm.2018.07.021>
  10. Matignon, D.: Stability results for fractional differential equations with applications to control processing. *Comput. Eng. Syst. Appl.* , 963–968 (1996). <https://doi.org/10.1.1.40.4859>
  11. Ahmed, E., El-Sayed, A.M.A., El-Saka, H.A.A.: On some Routh-Hurwitz conditions for fractional order differential equations and their applications in Lorenz, Rössler, Chua and Chen systems. *Phys. Lett. A.* **358**, 1–4 (2006). <https://doi.org/10.1016/j.physleta.2006.04.087>
  12. Baisad, K., Moonchai, S.: Analysis of stability and Hopf bifurcation in a fractional Gauss-type predator-prey model with Allee effect and Holling type-III functional response. *Adv. Differ. Equ.* **2018**, 82 (2018). <https://doi.org/10.1186/s13662-018-1535-9>
  13. Diethelm, K., Ford, N.J., Freed, A.D.: A predictor-corrector approach for the numerical solution of fractional differential equations. *Nonlinear Dyn.* **29**, 3–22 (2002). <https://doi.org/10.1023/A:1016592219341>

# Stabilization of Fractional Order Uncertain Lü System



Manoj Kumar Shukla

**Abstract** This paper presents a stabilization strategy for fractional order chaotic systems (FOCS) with unknown parameters. Control of FOCS is a less explored area and very limited approaches have been put forward in the literature. Here, an effort has been made to propose an improved stabilizing controller for a particular class of systems. The control structure is obtained by using a systematic adaptive backstepping procedure which is based on fractional order extension of Lyapunov stability results. The designed controller also avoids the singularity problem common in the traditional backstepping procedure. Parameter update laws achieved while applying adaptive backstepping strategy give estimates of the uncertain parameters of the system. The numerical simulation results given at the end validate the control strategy proposed for the stabilization of uncertain Lü system.

**Keywords** Fractional calculus · Chaotic system · Adaptive backstepping · Lü system

## 1 Introduction

Fractional derivative and integration have found wide applications in the past two decades. Control system has become one of the areas of application of fractional calculus. Nonlinear systems especially chaotic systems find applicability in almost every area of engineering and science. The fractional order version of the chaotic systems also called as fractional order chaotic systems (FOCS) have become the point of discussion in the past 15 years and various researchers have put forward the analysis and control of different FOCS [1, 2].

Several techniques that have been employed for control of integer order chaotic systems (IOCS) [3, 4], have been extended for FOCS also [5, 6].

One of the main advantages of going for fractional order chaotic systems is that such systems display chaos for a range of values of fractional order and hence can

---

M. K. Shukla (✉)

Lovely Professional University, Phagwara, Punjab, India  
e-mail: [manoj.22223@lpu.co.in](mailto:manoj.22223@lpu.co.in)

© The Author(s), under exclusive license to Springer Nature Switzerland AG 2022  
S. Banerjee and A. Saha (eds.), *Nonlinear Dynamics and Applications*,  
Springer Proceedings in Complexity,  
[https://doi.org/10.1007/978-3-030-99792-2\\_51](https://doi.org/10.1007/978-3-030-99792-2_51)

621



be used for different applications. Fractional order version of various IOCS has been studied in the literature. Some prominent contributions can be found in [7, 8], etc. The backstepping control technique developed by Kristic et al. [9] is widely used for the control of IOCS with known or unknown parameters. It is based on the Lyapunov stability technique and ensures the global stability of systems. Podlubny et al. [10] extended Lyapunov theory to fractional order nonlinear systems which is further based on Mittag-Leffler stability concept and both of these combined with backstepping approach have been utilized in the present manuscript.

The main contribution of the work is to propose a stabilizing controller for a class of FOCS. The technique is further implemented for control of fractional order Lü System. Various approaches have been proposed in the literature for designing feedback controller for this system but these techniques have some drawbacks and also most of these cannot handle the case of unknown parameters. In [11, 12], the system stability is analyzed via traditional Lyapunov stability, whereas in the present work, Lyapunov method is extended for FOCS on the basis of Mittag-Leffler stability which proves to give better performance in comparison to traditional methods. Multiple controllers are to be designed in the techniques presented in [13, 14]. On the other hand, only one controller needs to be designed in the strategy presented in the present manuscript.

Further, Sect. 2 gives the basic idea of fractional calculus and the stability of FOCS. The controller design approach is given in Sect. 3. Section 4 gives numerical simulations results. Section 5 concludes the contributions made here.

## 2 Basic Preliminaries of Fractional Calculus

The fractional order derivative and integral can be defined as

$${}_a D_t^q = \begin{cases} \frac{d^q}{dt^q} & q > 0 \\ 1 & q = 0 \\ \int_a^t (d\tau)^{-q} & q < 0 \end{cases} \quad (1)$$

The major definitions are expressed as

*Grunwald–Letnikov Definition*

$$D_t^q f(t) = \lim_{h \rightarrow 0} \frac{1}{h^q} \sum_{j=0}^{\infty} (-1)^j \binom{q}{j} f(t - jh) \quad (2)$$

*Riemann–Liouville Definition*

$$\mathcal{I}^q f(t) \triangleq \frac{1}{\Gamma(q)} \int_0^t (t - \tau)^{q-1} f(\tau) d\tau \tag{3}$$

*Caputo Definition (Derivative)*

$$\mathcal{D}^q f(t) \triangleq \mathcal{I}^{m-q} \mathcal{D}^m f(t) = \frac{1}{\Gamma(m - q)} \int_0^t \frac{f(\tau)^m}{(t - \tau)^{q-m+1}} f(\tau) d\tau \tag{4}$$

The solution of nonlinear fractional order differential equation (FODEs) can be derived from Grunwald–Letnikov definition [1, 15, 16]. The following expression gives the numerical solution of the nonlinear FODE of form  ${}_a D_t^q y(t) = f(y(t), t)$

$$y(t_k) = f(y(t_k), t_k) h^q - \sum_{j=1}^k c_j^{(q)} y(t_{k-j}) \tag{5}$$

### 3 Stabilization Strategy

The approach for obtaining the stabilizing controller by using adaptive version of backstepping control for the systems of a particular class. The system parameters are taken to be unknown. The general form of the class of the systems is given below:

$$\begin{aligned} D_t^{q_1} x_1(t) &= \theta_1(x_2(t) - x_1(t)) \\ D_t^{q_2} x_2(t) &= -x_1(t)x_3(t) + \theta_2 x_1(t) + \theta_3 x_2(t) \\ D_t^{q_3} x_3(t) &= x_1(t)x_2(t) - \theta_4 x_3(t) + u \end{aligned} \tag{6}$$

where,  $\theta_1, \theta_2, \theta_3$  and  $\theta_4$  are unknown constant parameters  $u$  is the controller. Table 1 gives a list of these types of systems.

The backstepping technique is modified to tackle the singularity problem. The result can be written in form of the following theorem:

**Theorem 1** *The system in (6), can be controlled by the controller which is expressed as*

$$u = -kz_1^2 + \hat{\theta}_4 \alpha_2 + D^q \alpha_2 \tag{7}$$

**Table 1** FOCS represented by the class of systems given in (6)

Name of System	Dynamics
Liu system	$D_t^{q_1} x_1(t) = a(x_2(t) - x_1(t))$ $D_t^{q_2} x_2(t) = -kx_1(t)x_3(t) + bx_1(t)$ $D_t^{q_3} x_3(t) = x_1(t)x_2(t) - bx_3(t)$
Lü system	$D_t^{q_1} x_1(t) = a(x_2(t) - x_1(t))$ $D_t^{q_2} x_2(t) = -x_1(t)x_3(t) + cx_2(t)$ $D_t^{q_3} x_3(t) = x_1(t)x_2(t) - bx_3(t)$
Chen system	$D_t^{q_1} x_1(t) = a(x_2(t) - x_1(t))$ $D_t^{q_2} x_2(t) = -x_1(t)x_3(t) + dx_1(t) + cx_2(t)$ $D_t^{q_3} x_3(t) = x_1(t)x_2(t) - bx_3(t)$

The controller guarantees the asymptotic stabilization of the system, provided,  $\frac{\theta_3}{\theta_1} < k < 1$  with an assumption  $\theta_1 > 0$ , where  $k$  is the design parameter. The variable  $z_1 = x_1$ ,  $\alpha_2$  is the virtual controller given as  $\alpha_2 = \hat{\theta}_1 + \hat{\theta}_2 + k\hat{\theta}_3 - k^2\hat{\theta}_1 + k\hat{\theta}_1$ , where,  $\hat{\theta}_i; i = 1, 2, 3, 4$ ; are the estimates of unknow system parameters which can be expressed as:

$$\begin{aligned}
 D^q \hat{\theta}_1 &= \gamma z_1 z_2 (1 - k^2 + k); \\
 D^q \hat{\theta}_2 &= \gamma z_1 z_2; \\
 D^q \hat{\theta}_3 &= \gamma k z_1 z_2; \\
 D^q \hat{\theta}_4 &= -\gamma z_3 \alpha_2
 \end{aligned}$$

**Proof** By choosing  $q_1 = q_2 = q_3 = q$ , let  $z_1 = x_1$  and  $z_2 = x_2 - \alpha_1$ , where  $\alpha_1$  is the virtual controller. It gives,

$$D^q z_1 = \theta_1(x_2 - x_1) = \theta_1 z_2 + \theta_1 \alpha_1 - \theta_1 x_1 \tag{8}$$

One can chose the as  $V_1 = \frac{1}{2}z_1^2$ . One can differentiate  $V_1$  w.r.t. time while taking a fractional order  $q$ ,

$$D^q V_1 \leq z_1 D^q z_1 \Rightarrow D^q V_1 \leq z_1(\theta_1 z_2 + \theta_1 \alpha_1 - \theta_1 x_1)$$

The dynamics gets modified to,

$$D^q z_1 = \theta_1 z_2 + \theta_1(kz_1 - z_1) = \theta_1 z_2 - \theta_1(1 - k)z_1 \tag{9}$$

where,  $\alpha_1 = kz_1$ . Also, the fractional derivative of  $V_1$  now satisfies the following condition:

$$D^q V_1 \leq -\theta_1(1 - k)z_1^2 + \theta_1 z_1 z_2$$

In a similar fashion, with the help of equations in (6) the second transformation variable will be represented as:

$$D^q z_2 = -z_1 x_3 + \theta_2 x_1 + \theta_3 x_2 - k(D^q z_1)$$

$$\Rightarrow D^q z_2 = -z_1(z_3 + \alpha_2) + \theta_2 z_1 + \theta_3 z_2 + \theta_3 k z_1 - k\theta_1 z_2 + k(1 - k)\theta_1 z_1 \quad (10)$$

where,  $z_3 = x_3 - \alpha_2$ . The Lyapunov function for the overall system up to this stage shall be expressed as:

$$V_2 = V_1 + \frac{1}{2}z_2^2 + \frac{1}{2}\gamma^{-1}(\theta_1 - \hat{\theta}_1)^2 + \frac{1}{2}\gamma^{-1}(\theta_2 - \hat{\theta}_2)^2 + \frac{1}{2}\gamma^{-1}(\theta_3 - \hat{\theta}_3)^2$$

which further can be written as,

$$\begin{aligned} D^q V_2 &\leq -\theta_1(1 - k)z_1^2 + \theta_1 z_1 z_2 + z_2 D^q z_2 - \gamma^{-1}(\theta_1 - \hat{\theta}_1)(D^q \hat{\theta}_1) \\ &\quad - \gamma^{-1}(\theta_2 - \hat{\theta}_2)(D^q \hat{\theta}_2) - \gamma^{-1}(\theta_3 - \hat{\theta}_3)(D^q \hat{\theta}_3) \\ \Rightarrow D^q V_2 &\leq -\theta_1(1 - k)z_1^2 - (\theta_1 k - \theta_3)z_2^2 \\ &\quad - z_1 z_2 z_3 + z_1 z_2 \{ \theta_1 + \theta_2 + \theta_3 k + \theta_1 k - \theta_1 k^2 - \alpha_2 \} \\ &\quad - \gamma^{-1}(\theta_1 - \hat{\theta}_1)(D^q \hat{\theta}_1) - \gamma^{-1}(\theta_2 - \hat{\theta}_2)(D^q \hat{\theta}_2) \\ &\quad - \gamma^{-1}(\theta_3 - \hat{\theta}_3)(D^q \hat{\theta}_3) \end{aligned}$$

Here,  $\hat{\theta}_1$ ,  $\hat{\theta}_2$  and  $\hat{\theta}_3$  estimates of system parameters  $\theta_1$ ,  $\theta_2$  and  $\theta_3$ , respectively. Also,  $\gamma$  is a parameter that controls the convergence of the estimates of the parameters. For stabilizing the system and to satisfy the stability criterion  $\alpha_2$  may be selected as:

$$\alpha_2 = \hat{\theta}_1 + \hat{\theta}_2 + k\hat{\theta}_3 - k^2\hat{\theta}_1 + k\hat{\theta}_1 \quad (11)$$

The following expressions give the parameter update laws as,

$$D^q \hat{\theta}_1 = \gamma z_1 z_2 (1 - k^2 + k); \quad D^q \hat{\theta}_2 = \gamma z_1 z_2; \quad D^q \hat{\theta}_3 = \gamma k z_1 z_2 \quad (12)$$

The update laws and the controller led to the following expression:

$$D^q V_2 \leq -\theta_1(1 - k)z_1^2 - (\theta_1 k - \theta_3)z_2^2 - z_1 z_2 z_3$$

With the assumption,  $\theta_1 > 0$ , one has to ensure that,  $\frac{\theta_3}{\theta_1} < k < 1$ , so that stability can be ensured. Further, from the 3rd expression in (6), one can have,

$$D^q z_3 = x_1 x_2 - \theta_4 x_3 + u - D^q \alpha_2 = z_1 z_2 + k z_1^2 - \theta_4 z_3 - \theta_4 \alpha_2 + u - D^q \alpha_2 \quad (13)$$

Finally, the overall Lyapunov function for the transformed system dynamics in (8), (10) and (13), can be chosen as:

$$V_3 = V_2 + \frac{1}{2} z_3^2 + \frac{1}{2} \gamma^{-1} (\theta_4 - \hat{\theta}_4)^2$$

which further leads to the following expression:

$$\begin{aligned} D^q V_3 \leq & -\theta_1 (1 - k) z_1^2 - (\theta_1 k - \theta_3) z_2^2 - z_1 z_2 z_3 \\ & + z_3 (z_1 z_2 + k z_1^2 - \theta_4 z_3 - \theta_4 \alpha_2 + u - D^q \alpha_2) \end{aligned}$$

The final control law and the expressions for parameter update for stabilization of the whole system are given below:

$$u = -k z_1^2 + \alpha_2 \hat{\theta}_4 + z_3 \hat{\theta}_4 + D^q \alpha_2 \quad (14)$$

$$\& \quad D^q \hat{\theta}_4 = -\gamma z_3 \alpha_2 \quad (15)$$

The above selection of the controller and update law, leads to the following stability condition:

$$D^q V_3 \leq -\theta_1 (1 - k) z_1^2 - (\theta_1 k - \theta_3) z_2^2 - \theta_4 z_3^2 \quad (16)$$

The results in (14), (15) and (16) confirm the finite time convergence of transformation variables  $z_1$ ,  $z_2$  and  $z_3$  to zero, which further ensures stabilization of the system states  $x_1$ ,  $x_2$  and  $x_3$ . The controller obtained here avoids the singularity problem.

## 4 Simulation Results for Fractional Order Lü System

The controller design approach is illustrated in this section with the help of an example system. Fractional order Lü system which belongs to the category of systems given in Table 1, can be described as:

$$D_t^q x_1(t) = \theta_1 (x_2(t) - x_1(t))$$

$$D_t^q x_2(t) = -x_1(t)x_3(t) + \theta_2 x_2(t) \quad (17)$$

$$D_t^q x_3(t) = x_1(t)x_2(t) - \theta_3 x_3(t) + u$$

Here, parameters  $\theta_1$ ,  $\theta_2$  and  $\theta_3$  are considered to be uncertain. For  $q_1 = q_2 = q_3 = q$ , the final controller structure using the approach mentioned in Sect. 3, is described as follows:

$$u = \hat{\theta}_3 \alpha_2 + D^q \alpha_2 - k z_1^2 \quad (18)$$

and the updating laws for parameter estimates are given as,

$$\begin{aligned} D^q \hat{\theta}_1 &= \gamma x_1 (x_2 - k x_1) (1 - k^2 + k) \\ D^q \hat{\theta}_2 &= \gamma x_1 (x_2 - k x_1) (1 + k) \end{aligned} \quad (19)$$

$$D^q \hat{\theta}_3 = \gamma (x_3 - \alpha_2) \alpha_2$$

where,  $z_1 = x_1$ ,  $z_2 = x_2 - \alpha_1$  and  $z_3 = x_3 - \alpha_2$ . Here,  $\theta_1 > 0$ , and also,  $\frac{\theta_2}{\theta_1} < k < 1$ . With controller  $u$  in action, on the basis of the same arguments given in the previous section, the stability of the system can be ensured.

The system parameters are chosen as  $(\theta_1, \theta_2, \theta_3) = (36, 3, 20)$  and the design constant  $k$  is taken as:  $k = 0.7$ . The initial values of the system states have been chosen as:  $(x_1(0), x_2(0), x_3(0)) = (-0.1, 0.5, 0.2)$  and the order of derivative is taken as,  $q = 0.95$ . The convergence parameter is selected as  $\gamma = 1.5$ . The simulation time is taken as 10 s with a step size of  $h = 0.005$  s. Figure 1 depicts the convergence of the  $x_1$  and  $x_2$  converge to zero in finite time, whereas, state  $x_3$  can be seen to be bounded as time tends towards infinity. Therefore, one can conclude that the proposed control strategy leads the systems towards stability in finite time, even when the system parameters are uncertain.

The controller for the particular system has been derived by using the backstepping strategy which is further based on the Lyapunov stability criterion. While applying the backstepping technique, in each step Lyapunov function has to be framed and its derivative is calculated which should be proven to be negative definite for a particular choice of controller. After the subsequent steps, the final controller is obtained while ensuring that the time derivative of the overall Lyapunov function is negative definite. this ensures the stability of the whole system, whatever be the dynamics.

With the right choice of the controller and ensuring the stability of the whole system, it can be concluded that the states of the systems are converging which is evident from the simulation results.

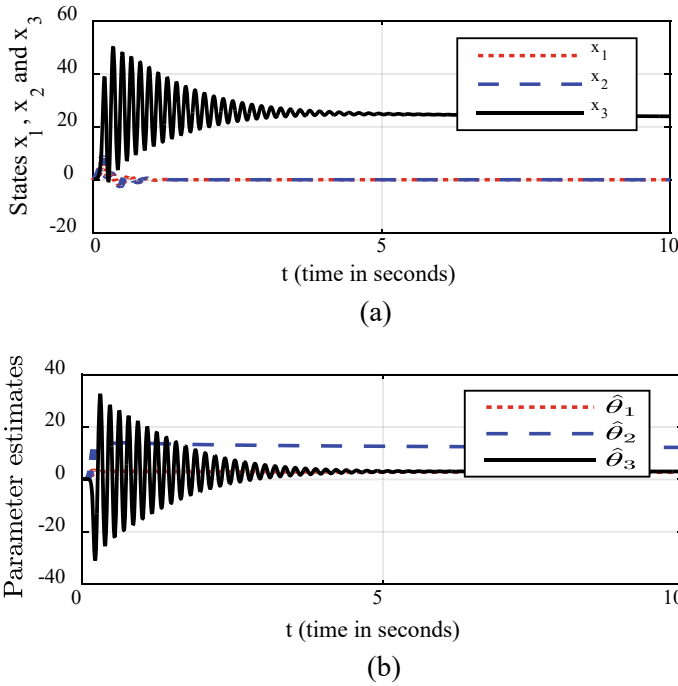


**Fig. 1** a Convergence of system states b Estimates of the unknown parameters

## 5 Conclusion

The paper presents a novel method for the stabilization of uncertain FOCS of a particular class. The backstepping method used here is systematic and ensures asymptotic stability. The proposed controller has been employed for the stabilization of uncertain fractional order Lü system. The simulation results validate the efficacy of the same. The controllers presented here can be extended for synchronization of the chaotic systems which further can be used for different practical applications like secure communication etc.

## References

1. Petras, I.: Fractional-Order Nonlinear Systems: Modeling, Analysis, and Simulation. Springer Science & Business Media (2008)
2. Shukla, M.K., Sharma, B.B.: Control and synchronization of a class of uncertain fractional order chaotic systems via adaptive Backstepping control. *Asian J Control* **20**, 707–720 (2018). <https://doi.org/10.1002/asjc.1593>
3. Yassen, M.T.: Chaos synchronization between two different chaotic systems using active control. *Chaos Solitons Fractals* **23**, 131–140 (2005)

4. Astakhov, V.V., Anishchenko, V.S., Kapitaniak, T., Shabunin, A.V.: Synchronization of chaotic oscillators by periodic parametric perturbations. *Phys. D Nonlinear Phenom.* **109**, 11–16 (1997)
5. Sharma, B.B., Kar, I.N.: Contraction theory based adaptive synchronization of chaotic systems. *Chaos Solitons Fractals* **41**, 2437–2447 (2009)
6. Sharma, B.B., Kar, I.N.: Stabilization and tracking controller for a class of nonlinear discrete-time systems. *Chaos Solitons Fractals* **44**, 902–913 (2011). <https://doi.org/10.1016/j.chaos.2011.07.009>
7. Hartley, T.T., Lorenzo, C.F., Qammer, H.K.: Chaos in a fractional order Chua's system. *IEEE Trans. Circuits Syst. I Fundam. Theory Appl.* **42**, 485–490 (1995)
8. Lu, J.G.: Chaotic dynamics of the fractional-order Lü system and its synchronization. *Phys. Lett. A* **354**, 305–311 (2006)
9. Krstic, M., Kanellakopoulos, I., Kokotovic, P.V.: *Nonlinear and Adaptive Control Design*. Wiley (1995)
10. Li, Y., Chen, Y., Podlubny, I.: Stability of fractional-order nonlinear dynamic systems: Lyapunov direct method and generalized Mittag—Leffler stability. *Comput. Math. with Appl.* **59**, 1810–1821 (2010). <https://doi.org/10.1016/j.camwa.2009.08.019>
11. Chen, D., Liu, Y., Ma, X., Zhang, R.: Control of a class of fractional-order chaotic systems via sliding mode. *Nonlinear Dyn.* **67**, 893–901 (2012)
12. Aghababa, M.P.: Robust stabilization and synchronization of a class of fractional-order chaotic systems via a novel fractional sliding mode controller. *Commun. Nonlinear Sci. Numer. Simul.* **17**, 2670–2681 (2012). <https://doi.org/10.1016/j.cnsns.2011.10.028>
13. Odibat, Z.M.: Adaptive feedback control and synchronization of non-identical chaotic fractional order systems. *Nonlinear Dyn.* **60**, 479–487 (2010). <https://doi.org/10.1007/s11071-009-9609-6>
14. Radwan, G., Moaddy, K., Salama, K.N., et al.: Control and switching synchronization of fractional order chaotic systems using active control technique. *J. Adv. Res.* **5**, 125–132 (2014). <https://doi.org/10.1016/j.jare.2013.01.003>
15. Vinagre, B.M., Chen, Y.Q., Petráš, I.: Two direct Tustin discretization methods for fractional-order differentiator/integrator. *J. Franklin Inst.* **340**, 349–362 (2003)
16. Dorcak, L.: Numerical models for the simulation of the fractional-order control systems. *Slovak Acad. Sci.* (1994)



# **Artificial Intelligence, Internet of Things and Smart Learning**

# The Transfer Trajectory onto the Asteroid for Mining Purposes Using LPG-Algorithm



Vijil Kumar  and Badam Singh Kushvah

**Abstract** In this research, a new methodology named as LPG-Algorithm is designed to determine the transfer trajectory between two celestial bodies or any two locales in space. It is constructed by combining Lambert's problem with the genetic algorithm (GA). In this algorithm, the initial state of the transfer trajectory has been optimized with the help of GA, which is already attained by solving Lambert's problem. We have successfully applied this algorithm to obtain the transfer trajectory of a spacecraft from the Low Earth orbit (LEO) to some desired asteroid within a time frame. For this purpose, 8 Near-Earth Asteroids (NEAs) have been selected. These are likely assets to help space industrialization, as they have the earmarks of being the least affordable source of certain required crude materials like valuable metals and semiconducting elements. The convergence of the genetic algorithm to the optimal initial state of the transfer trajectory is also shown in this research.

**Keywords** Asteroid mining · Genetic algorithm · Lambert's problem · Orbital mechanics · Transfer trajectory trajectory

## 1 Introduction

The asteroids are also a part of our solar system like all planets. All asteroids were formed at the beginning of the solar system. On January 1, 1801, the first asteroid *1Ceres* was discovered by G. Piazzi from the Palermo astronomical observatory. About 100 years later the first Near Earth Asteroid *433Eros* was discovered by G. Witt. The astronomers are constantly searching for asteroids in our solar system and have so far identified about 600,000 asteroids. Nearly 10,000 asteroids of total asteroids, passes close to Earth's orbit, and orbiting around the Sun, are called

---

V. Kumar (✉) · B. S. Kushvah  
Department of Mathematics and Computing, Indian Institute of Technology (ISM),  
Dhanbad 826004, Jharkhand, India  
e-mail: [vijilchoudhary@gmail.com](mailto:vijilchoudhary@gmail.com)

© The Author(s), under exclusive license to Springer Nature Switzerland AG 2022  
S. Banerjee and A. Saha (eds.), *Nonlinear Dynamics and Applications*,  
Springer Proceedings in Complexity,  
[https://doi.org/10.1007/978-3-030-99792-2\\_52](https://doi.org/10.1007/978-3-030-99792-2_52)

633

Near-Earth Asteroids (NEAs) [22]. The NEAs are some of the most accessible real estate in the solar system. Onto the 17% NEAs, is much easier to reach than a soft landing on the Earth's moon.

Only in one Platinum Group Metals (PGMs) rich asteroid of diameter 50-m, may contain 174 times the monthly world output of PGMs [7]. The most useful PGMs are platinum, iridium, osmium, palladium, rhodium and ruthenium. Some asteroids may found metallic elements like iron, nickel and copper sometimes in incredible quantities [17, 26]. In addition, asteroids may contain water and other gases, like  $CO_2$ ,  $CO$ , nitrogen and methane. Some semiconductors non-metallic & metallic also found in asteroids. The semiconductors like tellurium, antimony, indium, cadmium, selenium, arsenic, germanium, gallium and phosphorus are used in micro electronic manufacturing. These are the key to supporting life in the present timespan [2, 6].

On the other hand, the two-point boundary value problem (TPBVP) in the two-body dynamical environment is known as Lambert's problem. To solve this problem, we required the positions of any two celestial bodies respectively and also the transfer time between them. The solution of the Lambert's problem gives the initial and final velocity of the transfer trajectory. A brief knowledge about Lambert's problem is given by Blanchard [5]. They discuss all the various cases of Lambert's theorem in to a single form, which especially suitable for numerical work. The determination of an orbit having a specified flight time and connecting two position vectors, frequently referred to as Lambert's problem. A variety of methods of dealing with this problem has been discussed over the years by many writers. There are many solutions of this problem that may be found in the literature. Most of the earlier methods have been characterized by a particular formulation of the time of flight equation and a particular independent variable to be used in a Newton-Raphson style of iteration [21]. Finding low energy transfer of satellite, minimum transfer time, optimal burnout angle of transfer and so on, they are just a few examples of the trajectory design problem in astrophysics [20]. Levine showed that the true anomaly of the point in an orbit where the velocity vector is parallel to the line of sight from an initial point to the terminal point is independent of the orbit [15]. In his research, they developed a new corollary to the famous Lambert's problem and apply a new property of two body boundary value problem [24]. The elementary form of Kepler's equation provides the analytic description of the time of flight [3, 13].

Thenceforth, the convergence is remarkable rapid and almost uniform as well as being essentially independent of the initial guess [4]. In a research, the author finds the new conic direction that interfaces two points of a gravity field in a given time, which is represented by a set of transcendental equations due to Lagrange. The Lagrange equation for the orbital transfer time can be expressed as a series expansion for all cases. Lambert's theorem is one of the most useful tool for interplanetary transfer trajectory design. The interplanetary transfer trajectory has three phases. The first phase is the powered phase. In which spacecraft gets an impulse to jump from parking orbit of departure planet to transfer orbit. The second phase is called the free-flight phase, in which the spacecraft freely move towards the destination point with the help of center gravitational force. The final phase is re-entry phase. In this phase the spacecraft enter the parking orbit of destination planet with the help of

backward impulse [14, 28]. The backward impulse is used to decrease the velocity of a spacecraft. Besides, the accuracy of interplanetary transfer trajectory depends significantly on the free flight phase.

However, The purpose of issue here is that the free flight phase is the biggest dynamic factor in the transfer trajectory. It will take 90% to 98% time of whole transfer time and also has the least control. This implies that the accuracy of the free flight phase depends on the accuracy of the powered and re-entry phase. So, these must be selected with as greater precision as possible. We calculate the synodic period of every asteroid to know the next encounter with the Earth. The synodic period is calculated to dividing the product of two orbital periods by their differences, i.e. when the two orbital periods are nearly equal then the synodic period is quite long. We are getting the close encounter epoch of the asteroid and the Earth from the [JPL Small-Body Database Browser](#). The collision point of an asteroids with the Earth is determined. The important figuring is done to counteract the collision, for example, the diversion in the trajectory of the asteroid by hitting the Earth. In this way, with the assistance of spacecraft, the asteroid could be pushed far away from the Earth's impact point.

On the other hand, the genetic algorithm has been included in LPG-Algorithm for optimizing the investigation of the interplanetary trajectory. The genetic algorithm has been effectively applied to a few streamlining undertakings, going in size from 2-variable to the 7-variable problem [8, 31]. In every case, its performs significantly better than the grid search technique that is commonly used [9, 19]. Most of the basic and advanced properties of the genetic algorithm are given by the author Mitsuo gen in his research. They described detail of the use of the genetic algorithm in the area of optimization research like advanced planning and scheduling model, real time task scheduling models, reliability optimization models, communication network model, interplanetary transfer trajectory design, multi-objective rendezvous model and many more [11]. A classical multi-objective technique requires a prior problem information. Since the GA uses population points, they might have the option to numerous Pareto-optimal arrangements at the same time [18]. The results of recent research suggests that the non-dominated sorting GA can be effectively used to discover various Pareto-optimal solution, the information on which could be helpful to the best optimal launch date and optimal initial velocity for trajectory design [27, 29]. Many of the methods like differential correction methods have been used to improve the initial state. Because the solution of the transfer trajectory is very sensitive for the initial state of the transfer trajectory [16, 30].

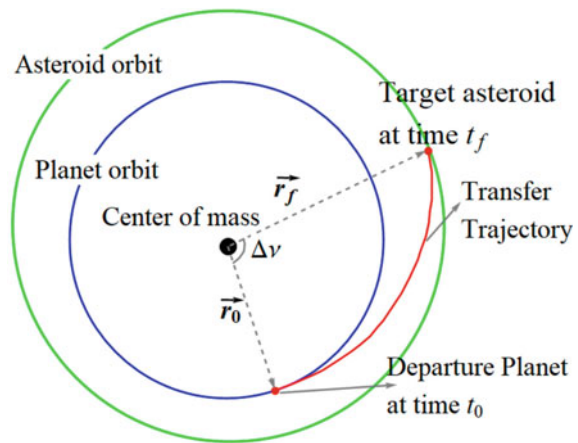
We introduced a new algorithm to obtain a suitable initial state of the transfer trajectory. i.e., LPG-Algorithm. The results indicate the promising performance of the proposed method in providing an appropriate initial state for reaching the spacecraft to the asteroid. LPG-Algorithm is specially made for interplanetary transfer trajectory. In this research, this technique have used to transfer a spacecraft on the near Earth asteroids. It is guaranteed to impact the spacecraft to the asteroid even if the solution of Lambert's problem is not optimal. The solution of the Lambert's problem gives us the initial velocity vector. If we have a non-optimal solution then it is required more fuel and also longer maneuver time. Then the genetic algorithm is

applied on it. Thus, the fittest part of the last generation of the LPG-Algorithm will be the optimal initial state of the transfer trajectory. And the spacecraft will precisely land on the pre-selected asteroid with the least error in position.

## 2 LPG-Algorithm

A new algorithm has been developed for transfer trajectory from one celestial body onto another celestial body. It's named **LPG-Algorithm**. We combine Lambert's problem with the Genetic Algorithm (GA) in this methodology. And it has used to solve the most famous astrophysics problem with high accuracy. The Lambert's problem is an approach to fathom for the direction interfacing two position vectors with a given time of transfer. Figure 1 demonstrates that  $\mathbf{r}_0$  is the initial position vector at the time  $t_0$  and  $\mathbf{r}_f$  is the final position vector at the time  $t_f$ .  $\Delta t = t_f - t_0$  is the transfer time of the spacecraft between the two positions and  $\Delta v$  is the transfer angle between the two positions. The transfer trajectory is depicted in Fig. 1 by the red color arc. The Earth's orbit and the asteroid's orbit is portrayed by blue and green color, respectively. The departure and arrival position is portrayed by the red dot. Lambert's problem is the well known problem in astrophysics. So, we are not going in details to the solution of the Lambert's problem. Any interested reader may go through the references papers [5, 24] for more explanation. Further, the genetic algorithm is a population based stochastic process. A single variable, which the genetic algorithm will optimize, is called genes. The collocation of all genes is called the chromosomes. And the number of chromosomes used in a single iteration is denoted as population, which is depicted in Fig. 2. It generates randomly and then reaches the best optimal value by the genetic algorithm process. The three leading operators are used in it, namely; Selection, Crossover and Mutation. There are many

**Fig. 1** Transfer trajectory using solution of Lambert problem without scale



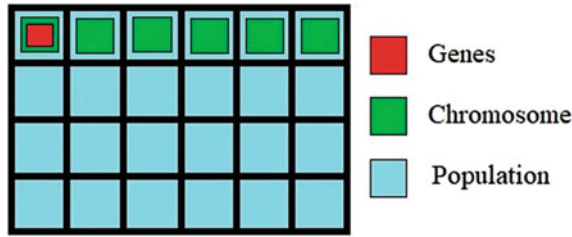


Fig. 2 Distribution of population for the genetic algorithm

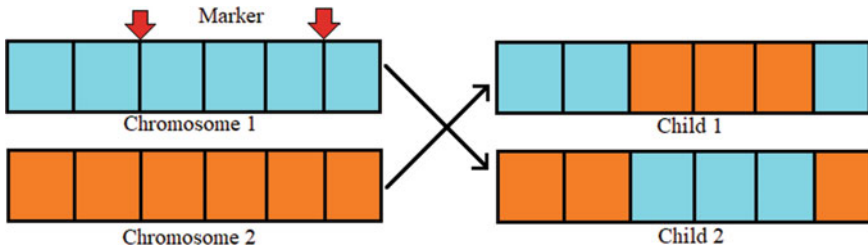
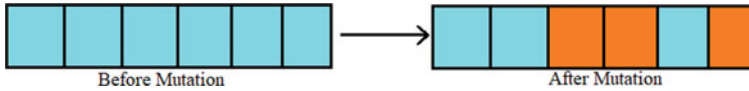


Fig. 3 Crossover process

methods that were found in literature for the selection process. We are using one of the most common method that are the roulette wheel selection process [23].

In the crossover process, we select two parents chromosomes and create randomly two markers on the chromosomes. Then interchange the genes between the markers and generate two new child chromosomes. it is also showing in Fig. 3. We can see that the three genes of parent 1 (orange) are replaced by parent 2 (cyan) and generate two new child chromosomes. After creating the child chromosomes, we select the better one between the parent and the child chromosomes.

The mutation operators are for the most part used to give investigation. The crossover operators is generally used to lead the population to converge on one good solution found up until now. Thus, while crossover tries to converge to a particular point in the scene, the mutation forth a valiant effort to stay away from assembly and investigate more regions. We like to investigate substantially more toward the start of the pursuit procedure. Then again, we lean toward more exploitation toward the finish of the inquiry procedure to guarantee the convergence of the population to the global optimum [10]. There is only an exemption; when population joins to a nearby optimum, we should expand the population assorted variety to investigate different regions. As indicated by the above actualities, too high mutation rate builds the likelihood of looking through more regions in search space, however, it prevents the population to converge to an optimum solution. On the other hand, too small mutation rates may result in falling to local optima instead of the global optimum i.e., too high mutation rate reduces the search ability of the genetic algorithm to a



**Fig. 4** Mutation process

simple random walk while a too small mutation rate almost always falls to a local optimum. So, in our computation we are using 35% mutation factor (Fig. 4).

### 3 Problem Statment and Solution Process

It is demonstrated by an pseudo code and given below:

---

#### Algorithm 1 Problem formulation and LPG-Algorithm process

---

**procedure** LPG- ALGORITHMMM PROCEDURE

**Step 1:** We assume the equation of motion of two body problem [20] under the central gravitational force as the Sun.

**Step 2:** To solve the Lambert problem for the velocity of spacecraft  $[v_a, v_b]$  at the low Earth orbit and the pre-selected asteroid respectively.

**Step 3 (goal):** Next, we formulate an objective function for genetic algorithm, that minimize the distance between the spacecraft position  $[X, Y, Z]$  and the target position  $[R_x, R_y, R_z]$ .

**Step 4:** Now, we update the initial state  $[r_0, v_a]$  of the transfer trajectory using genetic algorithm.

**Step 5 (output):** Finally, we get the optimized initial state  $[r_0, v_a]$  and described the needed data in the tables and figures.

---

#### 3.1 Advantage and Limitations

The merits and demerits of the proposed methodology are as follows: This concept is easy to understand. It searches from a population of points, not a single point, which means it calculates the value of the objective function and chooses the minimum of them. LPG-Algorithm is robust concerning the optimum local value of the objective function. It is stochastic and can be operated on many representations.

However, this requires less information about the problem, but designing an objective function and the representation and operators can be difficult. It is a computationally expensive algorithm i.e., it is time-consuming.

### 4 Apply on the Equation of Motion

Let us suppose two celestial bodies that are rotating about their center of mass.  $r_0$  &  $v_0$  are the position & velocity vectors of the first celestial body at the departure time  $t_0$ .  $r_f$  &  $v_f$  are the position & velocity vectors of the second celestial body at the arrival time  $t_f$  and is defined as:

$$r_0 = [r_{0x}, r_{0y}, r_{0z}], \tag{1}$$

$$v_0 = [v_{0x}, v_{0y}, v_{0z}], \tag{2}$$

$$r_f = [r_{fx}, r_{fy}, r_{fz}], \tag{3}$$

$$v_f = [v_{fx}, v_{fy}, v_{fz}] \tag{4}$$

where the subscript “ $f$ ” and “ $0$ ” denote the arrival and departure states respectively. The subscript “ $x$ ”, “ $y$ ” and “ $z$ ” denote the unit vectors along with the  $x$ -axis,  $y$ -axis &  $z$ -axis respectively. Now find the solution of Lambert’s problem using  $r_0$ ,  $r_f$  and the transfer time  $\Delta t = t_f - t_0$ . The solution comes in the form of velocity vectors of the transfer trajectory at the departure and arrival position. Suppose that velocity vectors are:

$$v_a = [v_{ax}, v_{ay}, v_{az}], \tag{5}$$

$$v_b = [v_{bx}, v_{by}, v_{bz}] \tag{6}$$

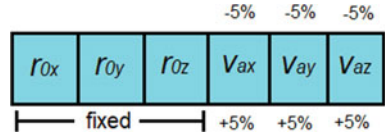
The initial state for the transfer trajectory from  $r_0$  onto  $r_f$  is given:

$$\text{initial state} = [r_{0x}, r_{0y}, r_{0z}, v_{ax}, v_{ay}, v_{az}] \tag{7}$$

where, the first three quantity  $[r_{0x}, r_{0y}, r_{0z}]$  are the departure position of spacecraft in 3-D coordinate respectively. And last three quantity  $[v_{ax}, v_{ay}, v_{az}]$  are the velocity of the spacecraft in  $x, y, z$  direction respectively. The velocity vectors  $v_a = [v_{ax}, v_{ay}, v_{az}]$  are obtained from the solution of Lambert’s problem. This initial state is non optimal because, the spacecraft fails to reach the desired position using this initial state. We apply the Genetic algorithm to optimize it. For the Genetic algorithm, we generate the random chromosomes as follows: We generate the number of chromosomes is equal to the number of population size. Here, the position vectors is fixed, because the departure position of spacecraft does not change. Further, calculate the fitness value of every chromosomes using two-body simulation as the solution of Keplerian orbit [12]. The central gravitational force in two-body simulation and Lambert’s solution are the same. The gravitational force of the Sun is  $1.3271 \times 10^{11} \text{ km}^3 \text{ s}^{-2}$ . A new optimization function is introduced which is defined below (Fig. 5):



**Fig. 5** Non-optimal initial state of transfer trajectory



$$F_{opt} = \{\|X - r_{fx}\| + \|Y - r_{fy}\| + \|Z - r_{fz}\|\} \tag{8}$$

subject to:

$$\sqrt{(R_x - r_{fx})^2 + (R_y - r_{fy})^2 + (R_z - r_{fz})^2} = R_{park} \tag{9}$$

where,  $\|\cdot\|$  is denotes the modulus value,  $[X, Y, Z]$  is the position vector of the spacecraft. We obtain this from the solution of two-body problem. The position vector  $[r_{fx}, r_{fy}, r_{fz}]$  of target celestial body and is defined in Eq. 3 and  $R_{park}$  is a user-defined quantity, which may be varies for the different planets or asteroids. It denotes the radius of parking orbit around the target celestial body. The Eq. 9 gives the constrained condition of the objective function (8). We can understand the LPG-Algorithm in a better way from the short python program, which is given in Fig. 6. Where the python function *TwoBody()* contains the equations of motion of the two-body problem. The python function *RKF45()* is defined for integration, which is based on Runge-Kutta-Fehlberg Method. It has a methodology to decide whether the proper step size  $h$  is being utilized. At each progression, two unique approximations for the solution are made and compared. In the event that the two answers are in close understanding, the estimate is accepted. On the off chance that the two answers don't consent to a predefined tolerance, the step size is diminished. And also if the answer consent to more significant digits than required, the step size is expanded. The input required for the function is a mathematical model (here *TwoBody()*), the initial state of the mathematical model (given in equation-7), the initial and final time for integration time (here  $[t_0, t_f]$ ) and a initial step size (here  $h$ ). We set the relative tolerance as  $1.0 e^{-10}$ . The python function *CalculateF()* is made to calculate the fitness value for every generated chromosomes. The inputs required for this function are the position vectors of the target celestial body (here  $r_f$ ), the spacecraft (here  $[X, Y, Z]$ ) and the radius of parking orbit around the target celestial body (here  $R_{park}$ ).

The function *GeneticAlgorithm()* is the main optimization process function. It takes input a mathematical model function *TwoBody()*, a integration method *RKF45()*, a function to calculate the fitness value *CalculateF()* and the initial state of the model to integrate it. With in this function, we take the population size is equal to 100. It generates randomly chromosomes equal to the population size as the initial state of the mathematical model. Further, integrates the mathematical model for every chromosomes using given integrating function and also calculate the fitness value using the fitness function (8). Then the function *GeneticAlgorithm()*, picks up a most optimal chromosome refers to the optimal initial state. For future investigation,

---

```

i, MaxIteration, ClosePoint = 0, 10000, 1.0e-3
while(Fopt <= ClosePoint):
    vanew = GeneticAlgorithm(TwoBody, RKF45, CalculateF, [r0, vaold])
    this function takes 100 chromosomes at once and select
    most appropriate velocity vector & returns it
    ...
    solution = RKF45(TwoBody, [r0, vanew], [t0, tf], h, tol=e-10)
    ...
    this returns float array of 6 element in which first
    3 is position and last 3 is velocity of the spacecraft
    ...
    X, Y, Z = solution[0], solution[1], solution[2]
    Fopt = CalculateF(tf, [X, Y, Z], Rpark)
    ...
    CalculateF function is calculate the value of Fopt using
    optimize function (defined in equation -7) & returns it
    ...
    # store the numerical data of every iteration in a file
    file = open('TransferData.txt', 'a')
    file.write(i, X, Y, Z, Fopt)
    file.close()
    i=i+1 # update number of iteration
    vaold = vanew # change velocity vector for next iteration
    if (i == MaxIteration):
        break

```

---

Fig. 6 A python program to demonstrate the basic of LPG-Algorithm

we make a separate data text file to store the numerical data of every iteration. We repeat this process either till they complete the *MaxIteration* or satisfies the optimal condition  $F_{opt} \leq 1 \cdot e^{-9}$ .

## 5 Numerical Simulation

We are introducing here a new methodology for the interplanetary transfer trajectory design. A genuine interplanetary transfer trajectory experiences different gravitational forces consistently such as radiation pressure, magnetic forces, atmospheric drag, sun oriented radiation, etc. The interplanetary transfer trajectory design problem can be expressed as an optimization issue. Where one of the essential objectives is to minimize fuel requirements. Some other optimization problems are intermediate planetary flybys, type of arrival, mission duration and velocity constraints, etc. The primary thought of the proposed methodology comprises of focusing on an asteroid that might be a good source of extraterrestrial Platinum Group Metals (PGMs). The asteroids are chosen from the close Earth class with the fly-by distance from the Earth smaller than  $2.647e^{-2} AU$ . From the past few decades, these types of asteroids have attracted the attention of researchers for their spacious storage of precious metals. An asteroid must be selected before starting the asteroid mining mission. The selection of asteroids for mining purposes, and mission design follows the following these steps.

**Table 1** Name of selected asteroid with their properties and the close encounter epoch to the Earth

Asteroid name	Diameter ( <i>m.</i> )	Mass( <i>kg.</i> )	Close encounter epoch (MJD)	Close encounter distance (AU)
1996 GT	670	$5.44 \times e^{11}$	59856.40833	$7.123 \times e^{-2}$
1999 RA32	170	$9.37 \times e^9$	60756.32569	$9.184 \times e^{-2}$
1998 SF36	380	$1.04 \times e^{11}$	63679.66319	$8.529 \times e^{-2}$
1999 JU3	380	$1.01 \times e^{11}$	63952.24513	$4.744 \times e^{-2}$
1986 EB	1800	$1.11 \times e^{13}$	64408.32569	$2.647 \times e^{-1}$
2011 UW158	280	$3.94 \times e^{10}$	69293.18402	$4.315 \times e^{-2}$
1996 FG3	550	$3.13 \times e^{11}$	70134.60347	$5.646 \times e^{-2}$
1999 RQ36	180	$9.91 \times e^9$	73725.02500	$5.007 \times e^{-3}$

- In the first step, the required minerals for mining must be determined.
- Then, the asteroids with the probable of being endowed in the target minerals must be found.
- Before examining the subtleties of these two stages, it is important to talk about the conceivable objective bodies and minerals that can be found in the core of the Near-Earth Asteroid (NEAs).

In Table 1, we listed some selected asteroids who will pass near the Earth in the upcoming four decades. The name of the selected asteroids are given in the first column. The diameter of the asteroids is shown in the second column. The mass of the asteroids is shows in the next column. The fourth column shows the close encounter epoch of the asteroid in Modified Julian Date(MJD) format, which referred from [JPL HORIZONS Web-Interface](#). And the last column denote the close encounter distance between the Earth and the asteroid. The spacecraft follows the following steps to reach on the surface of the asteroid.

1. Start of spacecraft from Low Earth Orbit (LEO) to asteroid along transfer trajectory using a solution of Lambert's problem.
2. The Lambert solution fails to get optimal initial state to reach onto the desired asteroid.
3. Next, we update the initial state of the spacecraft using the LPG-Algorithm.
4. Finally, we get an optimal initial state of the spacecraft with good accuracy.

The significant errand of the mission design everywhere comprises of the picked of all factor free parameters. The first step is to choose an launch date few hours before the close encounter epoch of the asteroid. Now we execute the mission from solving Lambert's problem, which allows transferring the zero mass object from one space point to another along Keplerian orbit in given transfer time. The coordinates of the Earth and the asteroid are taken from JPL small body database. The gravitational field is supposed to the center of the Sun. It should be mentioned that on the phase of calculation of asteroid motion. Then find the transfer time between these two position

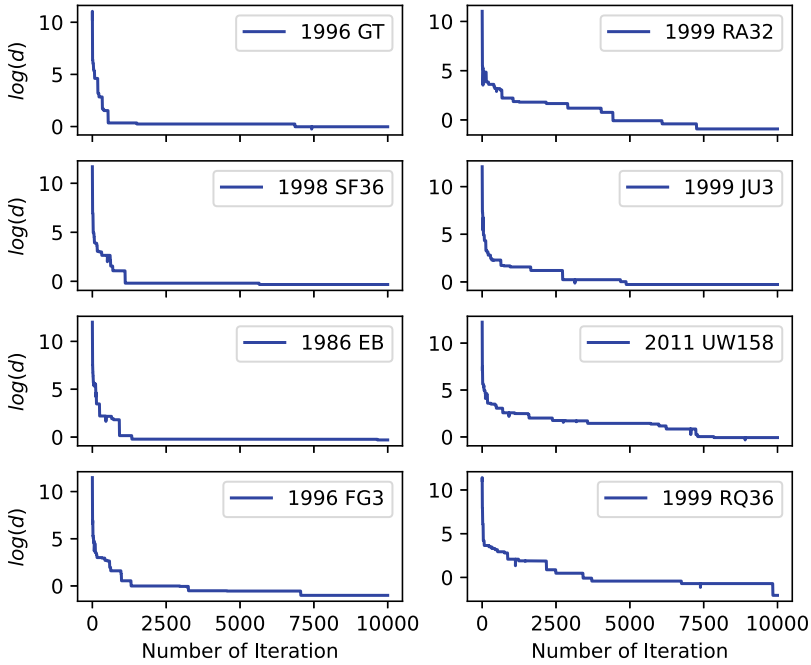


**Fig. 7** Iteration of all asteroids versus logarithmic function of distance

vectors  $\Delta t = t_f - t_0$ . We have three parameters here i.e., departure position vector, arrival position vector and the transfer time. Now we apply the LPG-Algorithm successfully. It gives the optimal initial state, allowing the spacecraft to reach as close to the prearranged target asteroid as possible. Here the value of  $R_{park}$  is set equal to radius of the target asteroid, because our goal is to reach onto the asteroid.

We use python interpreted language for the computational purpose. For the numerical calculation of the LPG-Algorithm, we run it up to 10 thousand iterations and save the data of each iteration in a separate text file. Figure 7 portrays a graphs between the number of iterations and the distance between the spacecraft & the asteroids. We see that when the iteration of the genetic algorithm is increased up to 10000, the distance is going to decrease continuously up to  $1e^{-3} Km$  from the asteroid. In first, 10% iterations, the distance is decreased rapidly and in the remaining iterations it is approximately constant (decreasing slowly). In the first 10% iterations, the distance reduces from 0.15 million kilometers to 10km, which is hard to show in a single plot because of a huge difference along with the iterations. So, here we have changed the scale of the distance to the logarithmic function with base “e”. i.e., 0.15 million kilometers on y-axis denoted by 11.91839057 and 10km on y-axis denoted by 2.30258509. It is an easy way to show a large distance and a small distance in a graph. All the sub-plot of Fig. 7 are shown the number of iteration of the genetic algorithm and logarithmic function of distance( $d$ ) with base “e” of all pre-selected asteroids.

**Table 2** All necessary calculated data of transfer trajectory to the asteroids

Asteroid Name	Departure (Earth)	Arrival (Asteroid)	Transfer time (Hours)	$\Delta V_1$ ( $\frac{Km.}{sec}$ )	$\Delta V_2$ ( $\frac{Km.}{sec}$ )	Computational time (Minutes)
1996 GT	59839.20000	59856.40833	413	3.49857	4.07962	10.2356
1999 RA32	60732.15902	60756.32569	579	4.16823	5.39587	12.8542
1998 SF36	63659.99652	63679.66319	482	4.57381	3.76428	13.5168
1999 JU3	63932.99513	63952.24513	473	5.07286	3.10864	9.4687
1986 EB	64371.40208	64408.32569	571	5.78610	6.37561	10.2584
2011 UW158	69273.64236	69293.18402	469	2.50942	3.82617	8.0962
1996 FG3	70114.06180	70134.60347	493	5.68423	4.11682	10.5962
1999 RQ36	73709.23333	73725.02500	379	3.18354	6.74251	9.5316

Our computer has intel *i7*, 7th generation, 16 GB RAM, 3.5 GHz processor and Windows 10. And we use this computer for all numerical simulations. The necessary computation of the transfer trajectory is shown in Table 2. All the pre-selected asteroids names are given in the first column of the Table 2, which is also given in Table 1. The second and third column describes departure and arrival epoch of the spacecraft in MJD format respectively. In the fourth column, the transfer time is given in hours. We chose the arrival time few hours before the close encounter epoch. The fifth column represents the minimum required impulse ( $\Delta V_1$ ), when the spacecraft is going to leave Low Earth Orbit (LEO). The required second impulse ( $\Delta V_2$ ) is given in the next column. The spacecraft enter in the parking orbit of the asteroid after applying the second impulse. The total computational time of the respective asteroid is given in the last column.

Figure 8 has portrayed the graph of the transfer trajectory from Low Earth Orbit to the asteroids. These asteroids are selected randomly from the list of pre-selected asteroids. In left side sub-figure Fig. 8a, c, e are the asteroid **1996 GT**, **1999 RA32** and **1999 RQ36** respectively. These sub-figures demonstrates:

1. Earth orbit with a blue line and Earth position on departure time with a blue dot.
2. Asteroid orbit with a green line and the asteroid position on an arrival time with a green dot.
3. The yellow dotted line shows the keplerian orbit of the transfer trajectory by using Lambert’s problem.
4. The red line shows the keplerian orbit of the transfer trajectory by using LPG-Algorithm.

We portray the transfer trajectory in these left side graph but it is not visible because of too close. It can not be seen without zoom in. So, we have added extra sub-figure in the right side. These all sub-figures Fig. 8b, d, f show a particular part (vicinity of the asteroid) of the left side sub-figures Fig. 8a, c, e respectively. Here, in the right side sub-figures shows:

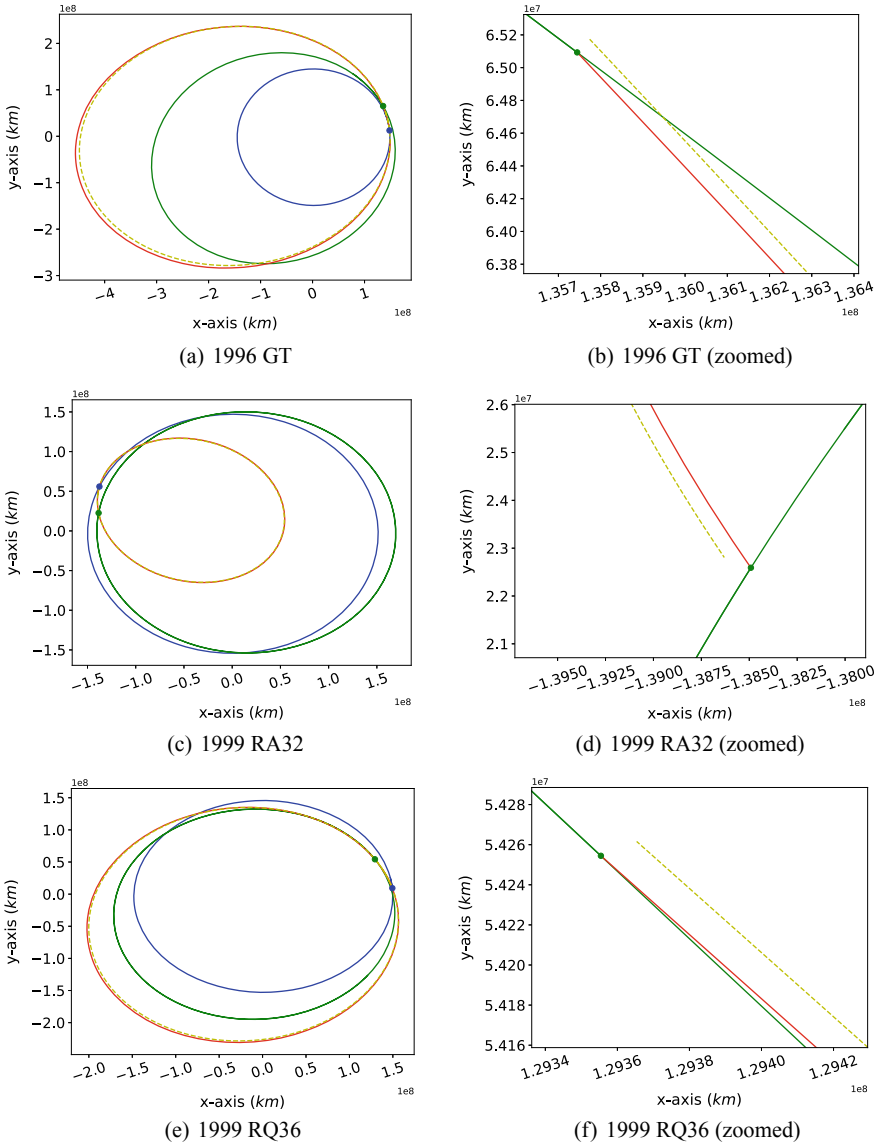


Fig. 8 The difference in the transfer trajectory using Lambert's problem and the LPG-Algorithm

1. The green dot shows the arrival position of the asteroid.
2. The blue and green lines shows the Earth's orbit and the asteroid's orbit respectively.
3. The yellow dotted line shows the transfer trajectory by using Lambert's problem.
4. The red line shows the transfer trajectory by applying LPG-Algorithm.

We observe that from the figures and calculations, the transfer trajectory by using Lambert's problem and by using LPG-Algorithm are approximately same in periods. Only difference is in accuracy of results. We find that the error in target position is approximately  $1e^{-3}$  by the Lambert solution. And by the LPG-Algorithm this error can be reduced to less than  $1e^{-9}$ . The LPG-Algorithm gives more accurate optimal initial state of the transfer trajectory. And LPG-Algorithm is effective and transfers the spacecraft exactly to the desired asteroid even if the solution of the Lambert's problem is far from the global optimum. Only three variable i.e., velocity component of the initial state is needed for a interplanetary transfer trajectory from Low Earth Orbit to the asteroid [1, 25]. It must renovates the possibility to reach the desired asteroid.

## 6 Conclusions

In this article, we present the LPG-Algorithm, a new substantial methodology for solving the Lambert problem using a genetic algorithm. It has also been demonstrated that, because of its low complexity, it has numerous advantages in terms of generality and performance. It has been implemented to find the transfer trajectory from the Low Earth Orbit to the 8 selected asteroids. The asteroids, which may have perilous metals. All these asteroids are in Near-Earth Asteroid (NEA) group and they also close fly-by to the Earth. The results show that two small impulses on the spacecraft can transfer it to the asteroid. The numerical simulation data and figure show the clear difference between the solution of Lambert's problem and the LPG-Algorithm. In both cases, the transfer time is the same. The LPG-Algorithm is very useful for interplanetary transfer trajectory design and gives more accurate results. This algorithm can be implemented in an interplanetary transfer trajectory design and a ballistic missile trajectory.

**Acknowledgements** All the required data has downloaded through the following:

1. <https://ssd.jpl.nasa.gov/sbdb.cgi>
2. <https://ssd.jpl.nasa.gov/horizons.cgi>
3. <http://www.asterank.com/>.

## References

1. Abdelkhalik, O., Mortari, D.: N-impulse orbit transfer using genetic algorithms. *J. Spacecraft Rockets* **44**(2), 456–460 (2007)
2. Andrews, D.G., Bonner, K., Butterworth, A., Calvert, H., Dagang, B., Dimond, K., Eckenroth, L., Erickson, J., Gilbertson, B., Gompertz, N., et al.: Defining a successful commercial asteroid mining program. *Acta Astronautica* **108**, 106–118 (2015)
3. Battin, R.H., Fill, T.J., Shepperd, S.W.: A new transformation invariant in the orbital boundary-value problem. *J. Guidance Control* **1**(1), 50–55 (1978)
4. Battin, R.H., Vaughan, R.M.: An elegant lambert algorithm. *J. Guidance Control Dyn.* **7**(6), 662–670 (1984)
5. Blanchard, R., Devaney, R., Lancaster, E.: A note on lambert's theorem. *J. Spacecraft Rockets* **3**(9), 1436–1438 (1966)
6. Brophy, J.R., Friedman, L., Culick, F.: Asteroid retrieval feasibility. In: 2012 IEEE Aerospace Conference, pp. 1–16. IEEE (2012)
7. Busch, M.: Profitable asteroid mining. *JBIS* **57**, 301–305 (2004)
8. Cage, P., Kroo, I., Braun, R.: Interplanetary trajectory optimization using a genetic algorithm. In: *Astrodynamics Conference*, p. 3773 (1994)
9. Coit, D.W., Smith, A.E.: Reliability optimization of series-parallel systems using a genetic algorithm. *IEEE Trans. Reliab.* **45**(2), 254–260 (1996)
10. Dos Santos, D.P., Prado, A.F.: Minimum fuel multi-impulsive orbital maneuvers using genetic algorithms. *Adv. Astron. Sci.* **145**, 1137–1150 (2012)
11. Gen, M., Lin, L.: Genetic algorithms. *Wiley Encyclopedia of Computer Science and Engineering*, pp. 1–15 (2007)
12. Hinckley, D.W., Hitt, D.L.: Evolutionary approach to lambert's problem for non-keplerian spacecraft trajectories. *Aerospace* **4**(3), 47 (2017)
13. Ivashkin, V., Lan, A.: Construction of the optimal trajectories for the earth-asteroid-earth mission under high-thrust flight. *Cosmic Res.* **58**, 111–121 (2020)
14. Ivashkin, V., Lang, A.: Optimum trajectories for an earth–asteroid–earth mission with a high thrust flight. In: *Reports of the Academy of Sciences*, vol. 484, pp. 161–166 (2019)
15. Izzo, D.: Revisiting lambert's problem. *Celestial Mech. Dyn. Astron.* **121**(1), 1–15 (2015)
16. Jiang, R., Chao, T., Wang, S., Yang, M.: Adaptive genetic algorithm in rendezvous orbit design. In: 2016 35th Chinese Control Conference (CCC), pp. 5677–5682. IEEE (2016)
17. Kargel, J.S.: Metalliferous asteroids as potential sources of precious metals. *J. Geophys. Res. Planets* **99**(E10), 21129–21141 (1994)
18. Kim, Y.H., Spencer, D.B.: Optimal spacecraft rendezvous using genetic algorithms. *J. Spacecraft Rockets* **39**(6), 859–865 (2002)
19. Kumar, V., Kushvah, B.: Computation of periodic orbits around 1 1 and 1 2 using pso technique. *Astron. Reports* **64**(1), 82–93 (2020)
20. Lawden, D.: Minimal rocket trajectories. *J. Amer. Rocket Soc.* **23**(6), 360–367 (1953)
21. Lei, H., Xu, B.: Families of impulsive transfers between libration points in the restricted three-body problem. *Monthly Notices Royal Astron. Soc.* **461**(2), 1786–1803 (2016)
22. Lewicki, C., Diamandis, P., Anderson, E., Voorhees, C., Mycroft, F.: Planetary resources-the asteroid mining company. *New Space* **1**(2), 105–108 (2013)
23. Lipowski, A., Lipowska, D.: Roulette-wheel selection via stochastic acceptance. *Phys. A: Stat. Mech. Appl.* **391**(6), 2193–2196 (2012)
24. Nelson, S.L., Zarchan, P.: Alternative approach to the solution of lambert's problem. *J. Guidance Control Dyn.* **15**(4), 1003–1009 (1992)
25. Rauwolf, G.A., Coverstone-Carroll, V.L.: Near-optimal low-thrust orbit transfers generated by a genetic algorithm. *J. Spacecraft Rockets* **33**(6), 859–862 (1996)
26. Sonter, M.J.: The technical and economic feasibility of mining the near-earth asteroids. *Acta Astronautica* **41**(4–10), 637–647 (1997)
27. Srinivas, N., Deb, K.: Multiobjective optimization using nondominated sorting in genetic algorithms. *Evolut. Comput.* **2**(3), 221–248 (1994)



28. Wheelon, A.D.: Free flight of a ballistic missile. *ARS J.* **29**(12), 915–926 (1959)
29. Wu, G.q., Tan, L.G., Li, X., Song, S.M.: Multi-objective optimization for time-open lambert rendezvous between non-coplanar orbits. *Int. J. Aeronaut. Space Sci.*, 1–16 (2019)
30. Yokoyama, N., Suzuki, S.: Modified genetic algorithm for constrained trajectory optimization. *J. Guidance Control Dyn.* **28**(1), 139–144 (2005)
31. Zhang, D., Song, S., Duan, G.: Fuel and time optimal transfer of spacecrafts rendezvous using lambert's theorem and improved genetic algorithm. In: 2008 2nd International Symposium on Systems and Control in Aerospace and Astronautics, pp. 1–6. IEEE (2008)

# Prediction of Chaotic Attractors in Quasiperiodically Forced Logistic Map Using Deep Learning



J. Meiyazhagan and M. Senthilvelan 

**Abstract** We forecast two different chaotic dynamics of the quasiperiodically forced logistic map using the well-known deep learning framework Long Short-Term Memory. We generate two data sets and use one in the training process and the other in the testing process. The predicted values are evaluated using the metric called Root Mean Square Error and visualized using the scatter plots. The robustness of the Long Short-Term Memory model is evaluated using the number of units in the layers of the model. We also make multi-step forecasting of the considered system. We show that the considered Long Short-Term Memory model performs well in predicting chaotic attractors upto three steps.

**Keywords** Logistic map · Chaos · Prediction · Deep learning · Long short-term memory

## 1 Introduction

Recently, Machine Learning (ML) and Deep Learning (DL) models have been used in various fields of physics [1–3]. In the study of dynamics of nonlinear systems, ML and DL algorithms are extensively used for the prediction and discovery of the behaviour of the chaotic and complex systems. For example, they have been used to identify chimera states [4, 5], in the replication of chaotic attractors [6], using symbolic time series for network classification [7], separating chaotic signals [8], learning dynamical systems in noise [9] and in the prediction of extreme events [10–15]. Very recently, the authors of Ref. [16] have considered Hénon map and used a ML algorithm, namely Artificial Neural Network (ANN), to study the extreme events in it. The authors have focussed on binary classification and classified the data points as extreme and non-extreme [16].

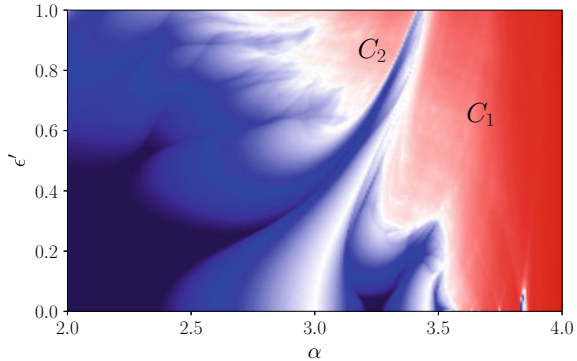
---

J. Meiyazhagan · M. Senthilvelan (✉)  
Department of Nonlinear Dynamics, Bharathidasan University,  
Tiruchirappalli 620024, Tamil Nadu, India  
e-mail: [senthilvelan.m@bdu.ac.in](mailto:senthilvelan.m@bdu.ac.in)

© The Author(s), under exclusive license to Springer Nature Switzerland AG 2022  
S. Banerjee and A. Saha (eds.), *Nonlinear Dynamics and Applications*,  
Springer Proceedings in Complexity,  
[https://doi.org/10.1007/978-3-030-99792-2\\_53](https://doi.org/10.1007/978-3-030-99792-2_53)

649

**Fig. 1** Schematic phase diagram of the quasiperiodically forced logistic map.  $C_1$  and  $C_2$  are two different chaotic regimes



In our studies, we consider logistic map with quasiperiodic forcing and predict the time series of the system which is not continuous. The system exhibits chaos in two different regimes. We predict both the chaotic attractors of this system with the help of the DL framework, namely Long Short-Term Memory (LSTM). The logistic map with quasiperiodic forcing is described by the following equations, namely [17, 18]

$$x_{n+1} = \alpha[1 + \epsilon \cos(2\pi\phi_n)]x_n(1 - x_n), \tag{1a}$$

$$\phi_{n+1} = \phi_n + \omega \pmod{1}, \tag{1b}$$

where  $\epsilon$  and  $\omega = (\sqrt{5} - 1)/2$  are the forcing amplitude and irrational driving frequency respectively. The authors in Ref. [17] redefined the driving parameter as  $\epsilon' = \epsilon/(4/\alpha - 1)$  to study the dynamics of the system in the regimes of  $0 \leq x \leq 1$ ,  $0 \leq \phi \leq 1$  and  $0 \leq \epsilon \leq 1$ . The schematic phase diagram [17] of the system is given in Fig. 1. The system shows various dynamic behaviours, namely periodic, strange non-chaotic and chaotic attractors which can be characterized by the nonzero Lyapunov exponent  $\Lambda$  [17], where

$$\Lambda = \lim_{N \rightarrow \infty} \frac{1}{N} \sum_{i=1}^N \ln |\alpha[1 + \epsilon \cos(2\pi\phi_i)](1 - 2x_i)|. \tag{2}$$

From Fig. 1, we can notice the interesting behaviour of the considered system which has two chaotic regimes, namely  $C_1$  and  $C_2$ . The  $C_1$  regime is the continuation of the chaotic regime in the logistic map for  $\epsilon = 0$  at the end of the period-doubling cascade, at  $\alpha = 3.5699\dots$ . The chaos in  $C_2$  regime is due to low nonlinearity and large amplitude forcing [17]. Our aim is to predict chaotic attractors in both the regime using LSTM model since it is capable of forecasting the data which is in the form of a sequence.

We organize our work as follows. In Sect. 2, we discuss the generation of training and testing data. In Sect. 3, we consider a DL framework called LSTM and train it using training set data and predict the test set data. The performance of the LSTM model is discussed in Sect. 4. We present the conclusion in Sect. 5.

## 2 Data Preparation

Generating data is the foremost task in prediction because prediction is done only by learning the relationship between the given data. We calculate the value of  $x$  for  $10^5$  iterations using Eqs. (1a, 1b) in both the regimes  $C_1$  and  $C_2$ . This discrete space data is then converted into supervised learning data by taking  $x_n$  as input and  $x_{n+1}$  as output. The chaotic attractors in the both regimes  $C_1$  and  $C_2$  are shown in Fig. 2. The Fig. 2a, b corresponding to the regime  $C_1$  and Fig. 2c, d correspond to the  $C_2$  regime.

The values of the parameters are taken as (a)  $\alpha = 3.6, \epsilon' = 0.5$ , (b)  $\alpha = 3.9, \epsilon' = 1.0$ , (c)  $\alpha = 3.0, \epsilon' = 1.0$  and (d)  $\alpha = 3.1, \epsilon' = 0.8$ . We divide the data into two parts: (i) training set and (ii) test set. Training set data are used during the training process of the DL model and test set data are used for the evaluation of the ability of the DL model. In Fig. 2, the blue dots are the data used for training purpose and the

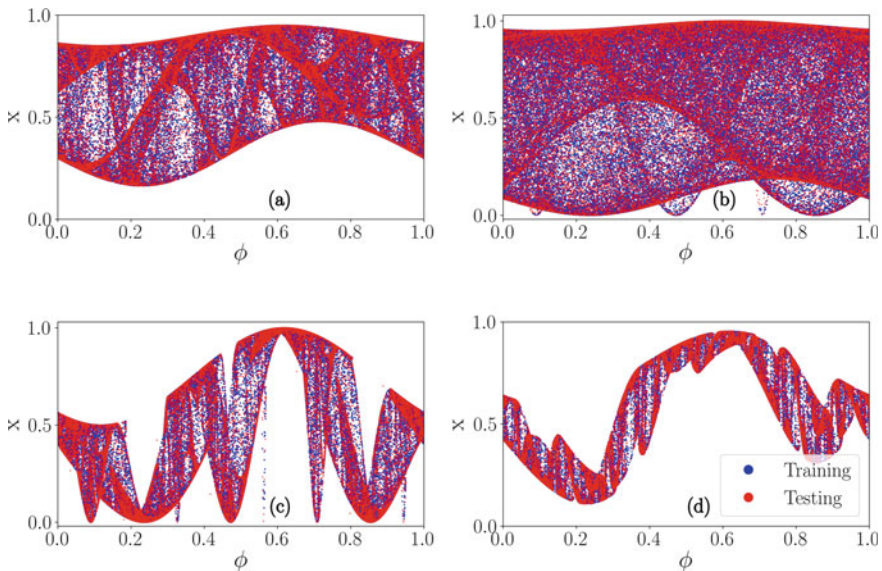


**Fig. 2** Chaotic attractors in two different regimes  $C_1$  and  $C_2$ . **a**  $\alpha = 3.6, \epsilon' = 0.5$  and **b**  $\alpha = 3.9, \epsilon' = 1.0$  correspond to  $C_1$ . **c**  $\alpha = 3.0, \epsilon' = 1.0$  and **d**  $\alpha = 3.1, \epsilon' = 0.8$  correspond to  $C_2$ . The points in blue (colour online) denoting the training set data and red (colour online) denoting the test set data

red coloured data are used for testing. We use  $6 \times 10^4$  data as training set data and  $4 \times 10^4$  data as test set data.

These two sets of data are rescaled using min-max normalization which is given by the formula [19],

$$x_i^{rescaled} = a + \frac{(x_i - x_{min})(b - a)}{x_{max} - x_{min}}, \quad i = 1, 2, 3, \dots, n, \quad (3)$$

where  $x_{min}$  and  $x_{max}$  are the minimum and maximum value of the data set respectively. We fix  $a = -1$  and  $b = +1$  in order to scale the data between  $-1$  and  $+1$ . During the testing phase, this preprocessing scaling step is reversed after obtaining the output from the DL model in order to compare the results with the actual data.

### 3 Deep Learning Framework: Long Short-Term Memory

When the data is in a sequential form one can make use of the Recurrent Neural Networks (RNN) [20] which is a type of ANN. For the present study we consider a DL framework known as LSTM [21] which is a special kind of RNNs. In recent years, LSTM framework has proven to be capable of forecasting time series of the chaotic systems even when there are extreme events in the time series [10, 13, 14]. The main feature that differentiates LSTM from the other RNNs is that the latter has only one activation function for the neurons that is tanh but in the case of the former, a sigmoid function is used for recurrent activations and tanh is used for the activation of neurons. The sigmoid activation function is defined by [22],

$$\sigma(z) = \frac{1}{1 + e^{-z}}. \quad (4)$$

We construct the LSTM model in the following way. We consider two LSTM layers each having 16 units in it and followed by a layer which has one neuron for output. During the training, we give both the input and the corresponding output to the model, that is we give  $x_n$  as the input and  $x_{n+1}$  as the output. By doing this, the model will learn the nonlinear relations between the given data. After training, the learned model is used to forecast the data steps. During the testing phase, we feed only the input data and ask the model for the corresponding output. The predicted values at the output given by the LSTM model are compared with actual values to determine the efficiency of the model in forecasting the chaotic attractors of the considered system.

### 4 Results and Discussion

To visualize the performance of the considered DL model, predicted data are plotted over the actual data in Fig. 3. Black dots (colour online) denote the actual value and green dots (colour online) denote the predicted value. The data in Fig. 3a, b correspond to  $C_1$  regime and Fig. 3c, d correspond to  $C_2$  regime. From the plots, we can see that relatively all predicted data coincide with the actual data. To have a clear understanding of the efficiency of the model we calculate the Root Mean Square Error (RMSE) value using the formula,

$$RMSE = \sqrt{\frac{\sum_{i=1}^{N_{Test}} (\hat{Y}_i^{Test} - Y_i^{Test})^2}{N_{Test}}}, \tag{5}$$

where  $\hat{Y}_i^{Test}$ ,  $Y_i^{Test}$  and  $N_{Test}$  denote the predicted values, actual values and total number of data in the test set respectively. We make use of the scatter plots which are plotted by taking actual values in the  $x$ -axis and predicted values in the  $y$ -axis (see Fig. 4). From Fig. 4a, b we can see that the RMSE values for the regime  $C_1$  are 0.015 and 0.012 respectively for the parameter values  $\alpha = 3.6, \epsilon' = 0.5$  and  $\alpha = 3.9, \epsilon' = 1.0$ . The outcome of the scatter plots almost fit in straight line, thereby indicating that the difference between predicted and actual values are very low. From Fig. 4c, d

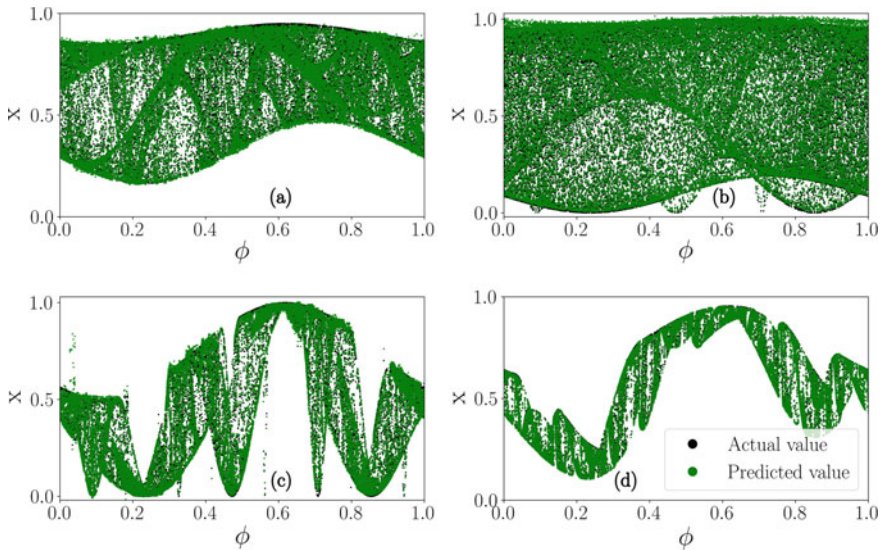


**Fig. 3** Plots of forecasted values over the actual values for four different sets of  $\alpha$  and  $\epsilon$  values as mentioned in Fig. 2. The Figures a, b correspond to  $C_1$  regime and c, d correspond to  $C_2$  regime. Black dots denote the actual value and green dots denote the predicted value

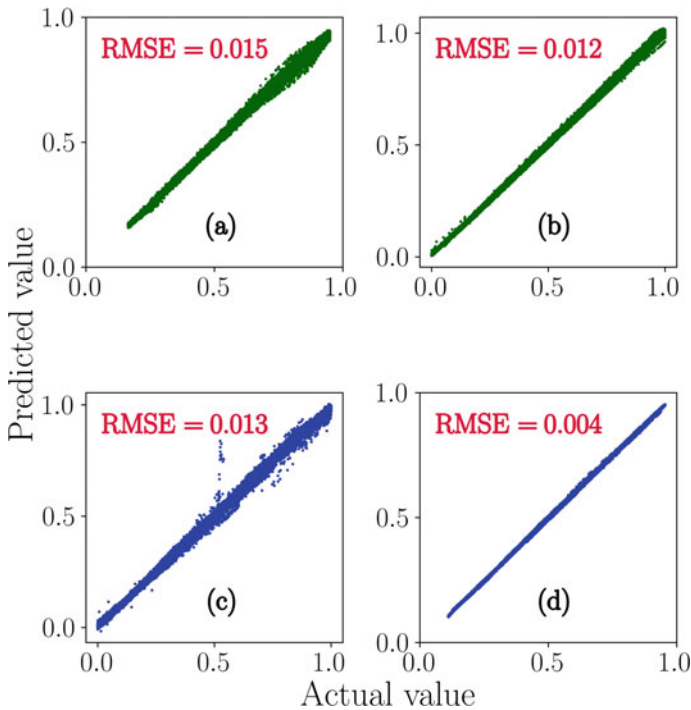


**Fig. 4** Scatter plots and RMSE values of the four different cases. The green colour plots correspond to the regime  $C_1$  and blue colour corresponds to  $C_2$

we can see that the results of the second regime  $C_2$  are calculated as 0.013 and 0.004 respectively for the parameter values  $\alpha = 3.0$ ,  $\epsilon' = 1.0$  and  $\alpha = 3.1$ ,  $\epsilon' = 0.8$ . The scatter plots for the test set data of regime  $C_2$  also show very little scatter points, thereby indicating the best fit of predicted data with the actual data.

#### 4.1 Effect of Model Architecture

To study the effect of model architecture on the performance of the considered model we vary the number of units and analyse the performance based on the RMSE values. For this purpose, we change the units in both LSTM layers and train the model. Then each trained model is evaluated using the test set data. The outcome is shown in Fig. 5. For the  $C_1$  regime, we evaluate the model with the data corresponding to  $\alpha = 3.6$ ,  $\epsilon' = 0.5$  and plot the results in Fig. 5a. For the  $C_2$  regime, we evaluate the model with the data corresponding to  $\alpha = 3.0$ ,  $\epsilon' = 1.0$  and plot the results in Fig. 5b. The RMSE value changes while varying the number of units in the LSTM layers.

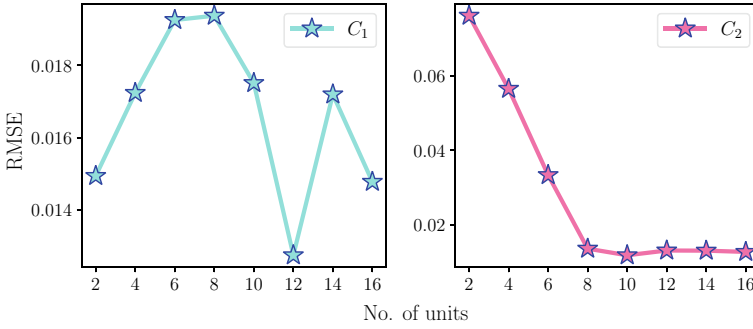


**Fig. 5** RMSE values for various number of units in LSTM layers. **a, b** corresponds to the regimes  $C_1$ ,  $\alpha = 3.6$ ,  $\epsilon' = 0.5$  and  $C_2$ ,  $\alpha = 3.0$ ,  $\epsilon' = 1.0$  respectively

### 4.2 Multi-step Forecasting

Now, we consider the task of multi-step forecasting. To do this, while preparing the supervised learning data, instead of having only one future step value, we take more than one value at the output. For this we consider the data in both the regimes  $C_1$  ( $\alpha = 3.6$ ,  $\epsilon' = 0.5$ ) and  $C_2$  ( $\alpha = 3.0$ ,  $\epsilon' = 1.0$ ). The results of multi-step forecasting are shown in Fig. 6.

From this figure we can infer that in the forecasting of multi-steps two and three, the considered model outperformed our expectations in the prediction task, the plots have fewer scatter points and the RMSE values are in admissible range. But for steps

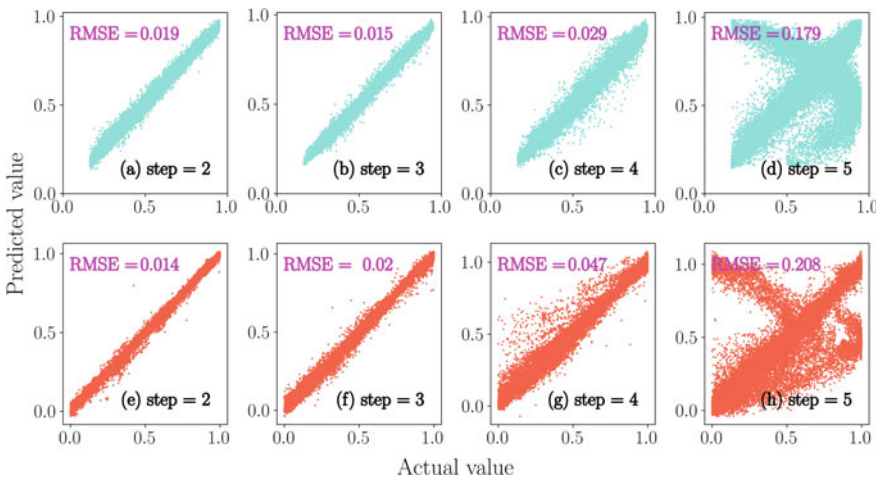


**Fig. 6** Scatter plots with RMSE values for the multi-step forecasting. **a–d** correspond to  $C_1$  regime  $\alpha = 3.6$ ,  $\epsilon' = 0.5$  and **e–f** correspond to  $C_2$  regime  $\alpha = 3.0$ ,  $\epsilon' = 1.0$



four and five, the model failed to give accurate values in both the regimes. It can be seen from Fig. 6c, d, g, h, the points are scattered much when making forecasting with fourth and fifth steps.

## 5 Conclusion

In this work, we have considered the logistic map with quasiperiodic forcing. The system exhibits chaos in two different regimes. We employed a DL framework LSTM, for the prediction of two different chaos. For this, we have generated  $10^5$  data totally and used  $6 \times 10^4$  data for training and the remaining  $4 \times 10^4$  data for the purpose of testing. We forecast the chaos corresponding to the two regimes  $C_1$  and  $C_2$ . The outcome of the experiments are evaluated using the performance metric RMSE value and they are analyzed through the scatter plots which have been plotted between the predicted value and actual value. Further, we have checked the effect of the number of units of the LSTM layers on the performance of the model. In this connection, we have done multi-step forecasting in order to predict more than one future value of the considered map. From the obtained results, we conclude that the developed LSTM framework can be used for forecasting the chaotic dynamics of the discrete system, namely quasiperiodically forced logistic map described by Eqs. (1a, 1b).

**Acknowledgements** JM thanks RUSA 2.0 project for providing a fellowship to carry out this work. MS acknowledges RUSA 2.0 project for providing financial support in procuring a high-performance GPU server which highly assisted this work.

## References

1. Carleo, G., Cirac, I., Cranmer, K., Daudet, L., Schuld, M., Tishby, N., Vogt-Maranto, L., Zdeborová, L.: Machine learning and the physical sciences. *Rev. Mod. Phys.* **91**, 045002 (2019)
2. Choudhary, A., Lindner, J.F., Holliday, E.G., Miller, S.T., Sinha, S., Ditto, W.L.: Physics-enhanced neural networks learn order and chaos. *Phys. Rev. E* **101**, 062207 (2020)
3. Miller, S.T., Lindner, J.F., Choudhary, A., Sinha, S., Ditto, W.L.: The scaling of physics-informed machine learning with data and dimensions. *Chaos Solitons Fractals: X* **5**, 100046 (2020)
4. Barmparis, G.D., Neofotistos, G., Mattheakis, M., Hizanidis, J., Tsironis, G.P., Kaxiras, E.: Robust prediction of complex spatiotemporal states through machine learning with sparse sensing. *Phys. Lett. A* **384**(15), 126300 (2020)
5. Ganaie, M.A., Ghosh, S., Mendola, N., Tanveer, M., Jalan, S.: Identification of chimera using machine learning. *Chaos* **30**(6), 063128 (2020)
6. Pathak, J., Zhixin, L., Hunt, B.R., Girvan, M., Ott, E.: Using machine learning to replicate chaotic attractors and calculate lyapunov exponents from data. *Chaos* **27**(12), 121102 (2017)
7. Panday, A., Lee, W.S., Dutta, S., Jalan, S.: Machine learning assisted network classification from symbolic time-series. *Chaos* **31**(3), 031106 (2021)
8. Krishnagopal, S., Girvan, M., Ott, E., Hunt, B.R.: Separation of chaotic signals by reservoir computing. *Chaos* **30**(2), 023123 (2020)

9. Mukhopadhyay, S., Banerjee, S.: Learning dynamical systems in noise using convolutional neural networks. *Chaos* **30**(10), 103125 (2020)
10. Meiyazhagan, J., Sudharsan, S., Senthilvelan, M.: Model-free prediction of emergence of extreme events in a parametrically driven nonlinear dynamical system by deep learning. *Europ. Phys. J. B* **94**(8), 1–13, 100046 (2021)
11. Meiyazhagan, J., Sudharsan, S., Venkatasen, A., Senthilvelan, M.: Prediction of occurrence of extreme events using machine learning. *Eur. Phys. J. Plus* **137**, 1–20 (2022)
12. Pyragas, V., Pyragas, K.: Using reservoir computer to predict and prevent extreme events. *Phys. Lett. A* **384**(24), 126591 (2020)
13. Ray, A., Chakraborty, T., Ghosh, D.: Optimized ensemble deep learning framework for scalable forecasting of dynamics containing extreme events. *Chaos* **31**(11), 111105 (2021)
14. Nag Chowdhury, S., Ray, A., Mishra, A., Ghosh, D.: Extreme events in globally coupled chaotic maps. *J. Phys. Complex.* **2**(3), 035021 (2021)
15. Asch, A., Brady, E., Gallardo, H., Hood, J., Chu, B., Farazmand, M.: Model-assisted deep learning of rare extreme events from partial observations. [arXiv:2111.04857](https://arxiv.org/abs/2111.04857) (2021)
16. Lellep, M., Prexl, J., Linkmann, M., Eckhardt, B.: Using machine learning to predict extreme events in the h enon map. *Chaos* **30**(1), 013113 (2020)
17. Prasad, A., Mehra, V., Ramaswamy, R.: Strange nonchaotic attractors in the quasiperiodically forced logistic map. *Phys. Rev. E* **57**(2), 1576 (1998)
18. Heagy, J.F., Hammel, S.M.: The birth of strange nonchaotic attractors. *Physica D: Nonl. Phenomena* **70**(1–2), 140–153, 100046 (1994)
19. Al Shalabi, L., Shaaban, Z., Kasasbeh, B.: Data mining: a preprocessing engine. *J. Comput. Sci.* **2**(9), 735–739 (2006)
20. Rumelhart, D.E., Hinton, G.E., Williams, R.J.: Learning representations by back-propagating errors. *Nature* **323**(6088), 533–536 (1986)
21. Hochreiter, S., Schmidhuber, J.: Long short-term memory. *Neural Comput.* **9**(8), 1735–1780, 100046 (1997)
22. Goodfellow, I., Bengio, Y., Courville, A.: *Deep Learning*. MIT Press (2016)

# Dynamic Calibration of a Stress-Wave Force Balance Using Hybrid Soft Computing Approach



Sima Nayak and Niranjan Sahoo

**Abstract** Aerodynamic vehicles come across the influence of impulsive forces and these are the major concerns associated with high-speed atmospheric vehicles. These shock wave induced impulsive forces impart hazardous effects on the surface of the vehicle. So, the magnitude of these forces is required for the design and modification of aerospace vehicles. Due to practical constraints, the real-time experiment is very difficult. Therefore, the ground-based test facilities are carried out using an aerodynamic model in shock tubes and shock tunnels. These models are required to be calibrated properly before carrying out the actual experiments. In the present study, a bi-cone model with a stress-wave force balance is used to perform the calibration task. The balance is mounted inside the model with strain gauge which records strain signal related to the applied force acting on the nose of bi-cone model. The strain signals of impulsive forces are captured for different magnitude and these signals are used for training and recovery of forces. Two different methods have been adopted for the recovery of the forces; one through classical de-convolution technique and another using the hybrid soft-computing approach, Adaptive neuro-fuzzy inference system (ANFIS). The forces recovered through both the techniques are compared with the known forces and also with each other. This provided an insight about the feasibility and applicability of the soft computing approach towards the inverse recovery of unknown forces for short duration experiments.

**Keywords** ANFIS · De-convolution · Short duration force recovery · Soft computing · Strain gauge

## 1 Introduction

In aerodynamic industry impulsive forces are the key concerns allied with hypersonic space vehicles like missiles, aircrafts, space shuttle, etc. The impulsive forces are resulted due to the shock waves generated in high-speed flow conditions. The impact

---

S. Nayak (✉) · N. Sahoo

Department of Mechanical Engineering, Indian Institute of Technology Guwahati, Guwahati, India  
e-mail: [n.sima@iitg.ac.in](mailto:n.sima@iitg.ac.in)

© The Author(s), under exclusive license to Springer Nature Switzerland AG 2022  
S. Banerjee and A. Saha (eds.), *Nonlinear Dynamics and Applications*,  
Springer Proceedings in Complexity,  
[https://doi.org/10.1007/978-3-030-99792-2\\_54](https://doi.org/10.1007/978-3-030-99792-2_54)

659

of such forces on the aerodynamic bodies causes serious damages to the structures causing huge losses to the aerospace programs. Pre-determination of the magnitude of such forces helps in the modification of the existing aero structural designs and also in the development of new designs. Nevertheless, such forces are highly transient and impulsive in nature that exists for a very small duration of time. Owing to the constraints associated with actual aerodynamic experiments, ground-based test facilities like shock tubes and shock tunnels are often employed to create such an impulsive environment where similar aero models are tested for impulsive forces [1, 2]. As a common practice, the aero models are tested in the test section of the shock tubes or shock tunnels where the high-speed flows having Mach numbers in the range of supersonic flow are imparted on the model surface. For the measurement purpose, the sensors are placed on any attachment mounted on the aero models where the effect of the forces can be felt by the attached structure [3]. These mounting structures are popularly known as stress-wave force balance which is judiciously designed to capture the appropriate response from the sensors [4, 5]. Two types of force balances are mostly used for calibration purposes; one is inertia-dominated and another is stiffness-based. The shock wave imparts an impulsive force on the body of the model where the magnitude in general is higher at the nose of the model. It may be noted here that, due to the short duration of action, direct measurement of the steady-state value of the force is difficult. Therefore, it is inversely predicted from strain gauge or accelerometer responses.

The response from the strain gauge or accelerometer is required to be post-processed to get the imparted force through inverse calculation. The convolution-deconvolution approach is popularly used for the recovery of such impulsive forces. For a single-component, linear system, with an applied load  $u(t)$  and a single-output signal  $y(t)$ , a convolution integral relates between input forces and output responses through an impulse response function  $g(t)$  as presented by Eq. (1).

$$y(t) = \int_0^t g(t - \tau) u(\tau) d\tau \quad (1)$$

The solution of this equation is obtained in the time domain by discretizing the signals with a time step  $\Delta t$  and Eq. (1) is represented in the following form in which  $g(t)$  is obtained via calibration tests.

The researchers make use of different calibration strategies in order to evaluate  $g(t)$  for which the mathematical formulation relies on a linear relationship between the input and output responses. Therefore, this process is mathematically complex and cumbersome. However, with the advancement of the soft-computing approach, a simplified model can be adopted for the recovery of such forces. In fact, the soft computing approach is mathematically less intensive and can also provide accurate prediction results [6]. The soft computing approach is very popular among researchers nowadays due to its simplicity and versatility. Therefore, its use is found in various fields of engineering such as image recognition, control theory, power sectors, etc. [7, 8]. The most popular soft computing approaches are the neural network, fuzzy logic, genetic algorithms, etc. However, the hybrid method proved

to be better in recent times. One such hybrid approach is the “adaptive neuro-fuzzy inference system” (ANFIS) which is a combination of fuzzy logic and artificial neural network (ANN). It is an assembly of Takagi–Sugeno type fuzzy inference system embedded in the network of ANN. Moreover, it is a data-driven approach driven by the ANN with a fuzzy system acting as a front-end pre-processor for the input–output task [9, 10].

Most of the researchers have adopted the de-convolution approach for the inverse prediction of impulsive forces whereas, a very limited use of the ANFIS technique is observed in the open literature. Therefore, the objective of the present work is to implement and test the usage of the ANFIS technique for the recovery of impulsive forces in the case of short-duration aerodynamic experiments. To accomplish the objective one aero model (blunt bi-cone model) has been fabricated (DASA CTV) in-house and a calibration task has been performed using an impulse hammer and strain gauges. A suitable stiffness-based force balance has been fabricated and the location of maximum strain has been identified through numerical simulation using the finite element method (ANSYS Workbench 18.0). The strain gauge is mounted at the location of maximum strain corresponding to the axial force. The strain data is recorded for known impulsive forces (applied using the impulse hammer) of different magnitude. These “time-strain-force” signals are used to train the ANFIS system and the force is predicted for time-strain input using the trained ANFIS system and compared with the known forces as well as with the forces recovered through deconvolution technique. The detailed working procedure has been elaborated in the Fig. 1.

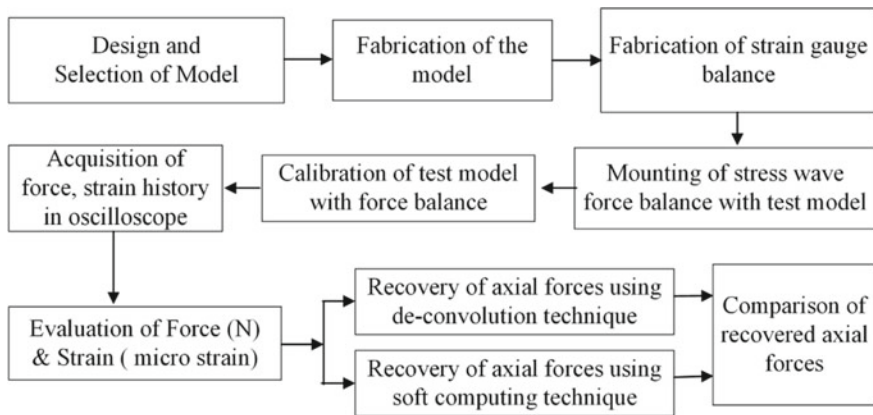


Fig. 1 Layout of the proposed work

## 2 Calibration Experiment

To check the effectiveness of the ANFIS system for the prediction of impulsive forces during short duration experiments is the aim of the present work. To train the ANFIS system there is a requirement of strain and force signals. Therefore, a calibration task has been planned by mounting stiffness-based force balance on the fabricated model [11]. Typically, force measurement using any force balance (Fig. 2) includes various considerations such as; the design of force balance for specific sensors, their mounting structure, choice of sensing location, balance calibration and force recovery [12–15]. Stiffness dominated force balance is generally used for measurement of forces through the measurement of strain signal using semiconductor strain gauges. In this category of force balance, model is assumed to behave as a rigid body. When the model is subjected to an impulsive force (using impulse hammer), it imparts a strain signal corresponding to the applied force where, the response is captured using a strain gauge module and data acquisition system. The strain gauge is mounted at the specified axial location (Fig. 2) on the force balance and connected to a Wheatstone bridge circuit. The balance is mounted on a fixed support using a bench vice. The strain signal is captured by an Oscilloscope (Model: MDO3024, Tektronix, USA, 2.5GS/s) corresponding to the impulsive force applied by the impulse hammer. These known forces along with their corresponding strain signals are used to establish a relation between the strain and force so that the unknown forces can be inversely estimated using the strain signal. In the present studies, the calibration has been done at the nose of the test model with the help of the impulse hammer.

The direction of the impulse hit should be normal to the hitting surface of the test model. Strain signals are recorded in the oscilloscope during calibration experiments for different impulsive forces. Typical signals of the impulsive force and strain responses for the axial direction are shown in Fig. 3. The initial strain values show the values in the negative direction indicating a compression strain. This is expected

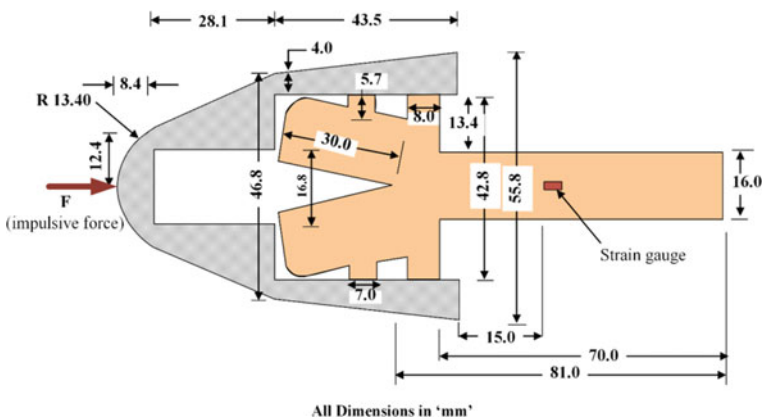
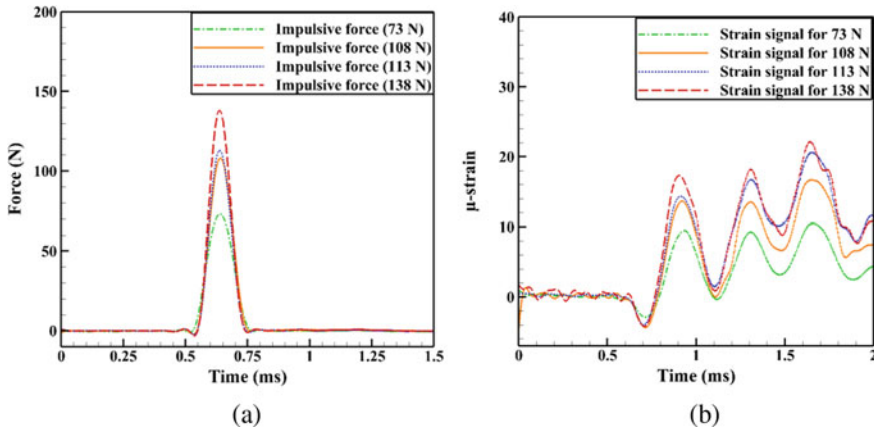


Fig. 2 Sectional view of the test model integrated with force balance



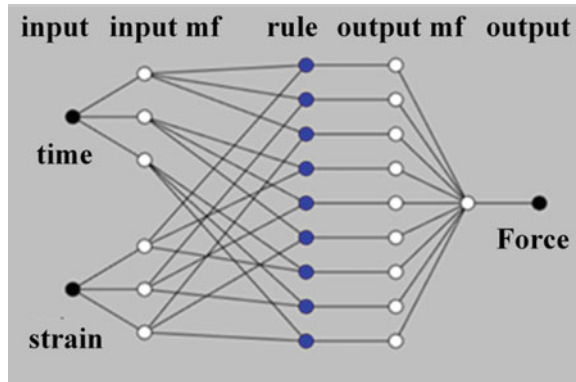
**Fig. 3** Force and strain signals from the calibration **a** Impulsive force from the impulse hammer **b** Strain responses from the strain gauge

as the balance is mounted on support. The known set (4 sets) of “time-strain-force” signals are used to train the ANFIS system and the other forces are recovered and compared with the known data. Similarly, the strain signals are used to predict the forces through de-convolution technique.

### 3 Recovery of Forces Using ANFIS Method

The recovery of impulsive forces using the soft computing-based ANFIS approach is the central theme of the present work. The strain signals obtained from the calibration experiment corresponding to four different (73 N, 108 N, 113 N, and 138 N) impulsive loads are used for the training and recovery of force through the ANFIS method. As inferred from the literature, the prediction through ANFIS technique is better when the recovered datasets are within the training range. Therefore, for the present case, 108 N and 113 N forces are recovered individually, after training the other three data sets. As mentioned previously, the ANFIS is a data-driven method dealing with input–output mapping. It is a multi-input single-output system (MISO) consisting of one input layer, four hidden layers and one output layer [16]. The ANFIS architecture is shown in Fig. 4. One of the standard modules of MATLAB is equipped with ANFIS architecture is used for the training and testing purpose. It works with hybrid and steepest descent algorithm providing a better output. As mentioned previously ANFIS is a combination of neural network and fuzzy logic; their combined effect help in better training and recovery of the impulsive force [17]. Therefore, the “time-strain-force” combinations for all four sets are used for this purpose. The system is trained with three sets of data excluding the set of data to be recovered. Successful implementation of ANFIS for the present exercise needs a proper understanding of

**Fig. 4** ANFIS architecture for optimized combinations



the process and algorithm to be followed. All such steps require different user inputs to achieve proper training and recovery [18].

The ANFIS training system starts with the fuzzification of the training data sets. The fuzzy logic part of the hybrid approach helps in the fuzzification of the data sets. The parametric variations for fuzzification depend on the type of membership functions (MFs) to normalize the input training data set [19]. The available options for these functions are from the broad categories as piecewise linear functions, Gaussian functions, bell-shaped functions, and sigmoid functions. Therefore, the standard input MFs used are triangular MFs, trapezoidal MFs, bell-shaped MFs, sigmoid MFs, Gauss MFs, singleton MF, pi MF, etc. Similarly, there are two types of output MFs viz. “linear” and “constant”. Out of the different MFs, the selection of a suitable one depends on the type of data and the user experience. With the help of MFs, the fuzzy system can be tuned by adopting an optimization technique out of the available ones as “backpropagation method” and “hybrid method” such that the input–output modelling can be carried out. The backpropagation method adopts the steepest descent algorithm for modifying all parameters during training whereas, the hybrid model uses the least square method for parameters linked to the output MFs and backpropagation for the parameters linked to the input MFs [20]. Since various options are available and the best one needs to be selected, parametric studies are performed to find out the input requirements of ANFIS, and its capability is judged for the force recovery. According to the evidence from literature, the grid partition type of clustering technique is suitable for problem definitions having a smaller number of input variables (less than 6). After few iterations with the available parameters, it is observed that a combination of “three linguistics variables”, “gauss-gauss2 IMF combinations”, constant output MF, and hybrid optimization technique yields a better recovery of the data set due to less root mean square error (RMSE). Therefore, all the results are obtained using these optimized parameters which are discussed in the next section.



### 4 Recovery of Forces Using De-convolution Technique

As mentioned previously, the classical way of inverse prediction of the forces is using the convolution-deconvolution approach. Here, the time domain is converted to the frequency domain and the response function is generated which acts as the linkage parameter and remains nearly constant. For the present case, two intermediate forces are recovered to compare with the ANFIS. The 108 N and 113 N forces are recovered by using the time strain signal corresponding to the other three forces individually. A Mat Lab based programming is used to recover the unknown forces and compared with the known value. All these results are compared with the ANFIS results.

### 5 Results and Discussion

The accuracy of the force prediction on applying impulse loads in axial directions on nose of model is analyzed using ANFIS method as well as Deconvolution method. The impulsive forces in axial direction of the model along with the corresponding strain signals are filtered using a low pass filter of 12.5 kHz to remove the noise. The system is trained with three sets of data leaving the one to be recovered. Out of four different magnitudes of forces (73 N, 108 N, 113 N, and 138 N), 108 N force is recovered after training the ANFIS with 73 N, 113 N and 138 N force. Similarly, 113 N force is recovered after training the ANFIS with 73 N, 108 N and 138 N force.

The peak magnitudes of these forces have been compared with the original signals and the percentage of deviation is calculated for all the cases. The ANFIS is able to predict the unknown forces with a certain degree of accuracy for the different data sets. An error of 2.87% and 3.54% are obtained for 108 N and 113 N force, respectively when compared with the actual signal (Table.1). Similarly, the intermediate forces (108 N and 113 N) are recovered individually, through deconvolution technique by

**Table 1** Error calculation between the recovered and the input value

Categories of forces: Actual Value = 108 N	Force (N)	Error (%) $\left  \frac{F_{\text{Actual}} - F_{\text{recovered}}}{F_{\text{Actual}}} \right  \times 100$	Categories of forces: Actual value = 113 N	Force (N)	Error (%) $\left  \frac{F_{\text{Actual}} - F_{\text{recovered}}}{F_{\text{Actual}}} \right  \times 100$
Deconvolution (DC-1)	111.9	3.6	Deconvolution (DC-4)	108.4	4.77
Deconvolution (DC-2)	112.6	4.25	Deconvolution (DC-5)	120.7	6.81
Deconvolution (DC-3)	114.0	5.55	Deconvolution (DC-6)	122.6	8.49
ANFIS recovered	104.9	2.87	ANFIS recovered	109.0	3.54

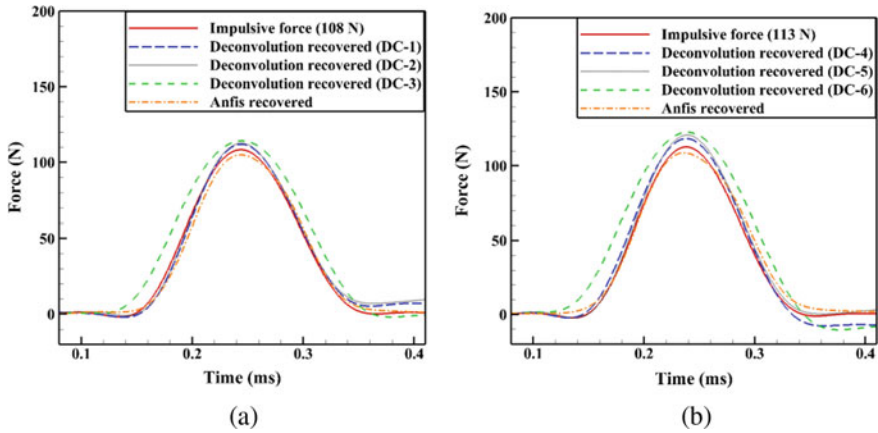


Fig. 5 Recovered signals using ANFIS and Deconvolution technique; (a) 108 N; (b)113 N

obtaining the response function from other three forces. The 108 N is recovered with the help of 113 N (DC-1), 138 N (DC-2) and 73 N (DC-3). Similarly, 113 N is recovered with the help of 108 N (DC-4), 138 N (DC-5) and 73 N (DC-6).

All the results obtained for 108 N and 113 N are compared with the original signal as well as with the ANFIS and deconvolution recovered results (Fig. 5). For 108 N recovery, a deviation of 2.87% is observed amongst ANFIS predicted results as compared with the original results and a maximum deviation of 5.55% with the results obtained through deconvolution technique. Similarly, for 113 N recovery, a deviation of 3.54% is observed amongst ANFIS predicted results as compared with the original result and a maximum deviation of 8.49% with the results obtained through deconvolution technique. The recovery signal trend is matching well with the original results. Therefore, the results obtained through ANFIS recovery matches well within the uncertainty band.

## 6 Conclusion

The stress wave force balance and bi-cone model have been successfully fabricated and by using a semiconductor strain gauge module, the calibration experiment has been performed. The strain signals corresponding to four sets of impulsive forces (applied with the help of an impulse hammer) is recorded with the help of an oscilloscope and the results are filtered using a low pass filter at a frequency of 12.5 kHz. These “time-strain-force” signals are used to train and recover the forces through an ANFIS based soft computing approach. The system is trained with three sets of data leaving the data to be recovered. All the known data sets are recovered and their peak magnitudes are compared with the actual ones. It is observed that the ANFIS is able to predict the forces within a certain range of accuracy. Similarly, the forces

are also recovered using deconvolution technique and the results are compared with the ANFIS recovered results as well with the original ones. The ANFIS results are found obeying the signal trend pretty well. Compared to the original value, the least error of peak magnitude value is less in case of ANFIS recovered results (2.87%) as compared to the de-convolution results (3.6%). However, the maximum error of 3.54% is observed in case of ANFIS as compared to 8.49% in deconvolution results. Therefore, the ANFIS method can be used for short duration force recovery well within the training range where the prediction can fall in the acceptable error range.

## References

1. Mee, D.J.: Dynamic calibration of force balances for impulse hypersonic facilities. *Shock Waves* **12**(6), 443–455 (2003)
2. Sahoo, N., Reddy, K.P.J.: Force measurement techniques for hypersonic flows in shock tunnels. *Int. J. Hypersonics* **1**(1), 31–58 (2010)
3. Naumann, K.W., Ende, H., Mathieu, G.: Technique for aerodynamic force measurement within milliseconds in shock tunnel. *Shock Waves* **1**(3), 223–232 (1991)
4. Abdel-Jawad, M.M., Mee, D.J., Morgan, R.G.: New calibration technique for multiple-component stress wave force balances. *Rev. Sci. Instrum.* **78**(6) (2007)
5. Tuttle, S.L., Mee, D.J., Simmons, J.M.: Drag measurements at Mach 5 using a stress wave force balance. *Exp. Fluids* **19**(5), 336–341 (1995)
6. Nanda, S.R., Kulkarni, V., Sahoo, N., Menezes, V.: An innovative approach for prediction of aerodynamic coefficients in shock tunnel testing with soft computing techniques. *Meas. J. Int. Meas. Confed.* **134**, 773–780 (2019)
7. Rout, A.K., Nanda, S.R., Sahoo, N., Kalita, P., Kulkarni, V.: Soft computing—a way ahead to recover heat flux for short duration experiments. *J. Therm. Sci. Eng. Appl.* **14**(3), 1–11 (2022)
8. Zhu, F., Wu, Y.: A rapid structural damage detection method using integrated ANFIS and interval modeling technique. *Appl. Soft Comput.* **25**, 473–484 (2014)
9. Azari, A., Poursina, M., Poursina, D.: Radial forging force prediction through MR, ANN, and ANFIS models. *Neural Comput. Appl.* **25**(3–4), 849–858 (2014)
10. Kumar Rout, A., Ranjan Nanda, S., Sahoo, N., Kalita, P., Kulkarni, V.: Implementation of soft computing technique for recovery of impulsive heat loads. *J. Thermophys. Heat Transf.* **1**, 1–10 (2021)
11. Abdel-Jawad, M.M., Mee, D.J., Morgan, R.G.: New calibration technique for multiple-component stress wave force balances. *Rev. Sci. Instrum.* **78**(6), 1–7 (2007)
12. Deka, S., Kamal, A., Pallekonda, R.B., Rahang, M., Kulkarni, V.: Measurement technique for ideal selection of sensors and accurate force recovery on aerodynamic models. *Exp. Tech.* (2021)
13. Nanda, S.R., Kulkarni, V., Sahoo, N., Menezes, V.: A comparison of accelerometer and piezofilm-based force balances for hypersonic shock tunnels. *Proc. Inst. Mech. Eng. Part G J. Aerosp. Eng.* **233**(14), 5310–5320 (2019)
14. Wang, Y., Liu, Y., Luo, C., Jiang, Z.: Force measurement using strain-gauge balance in a shock tunnel with long test duration. *Rev. Sci. Instrum.* **87**(5) (2016)
15. Deka, S., Pallekonda, R.B., Rahang, M.: Comparative assessment of modified deconvolution and neuro-fuzzy technique for force prediction using an accelerometer balance system. *Meas. J. Int. Meas. Confed.* **171** (2019)
16. Jang, J.S.R.: ANFIS: adaptive-network-based fuzzy inference system. *IEEE Trans. Syst. Man Cybern.* **23**(3), 665–685 (1993)

17. Ramesh, P., Nanda, S.R., Kulkarni, V., Dwivedy, S.K.: Application of neural-networks and neuro-fuzzy systems for the prediction of short-duration forces acting on the blunt bodies. *Soft Comput.* **23**(14), 5725–5738 (2019)
18. Nanda, S.R., Kulkarni, V., Sahoo, N., Menezes, V.: Sensitivity studies of ANFIS based force recovery technique towards prediction of aerodynamic load. *Flow Meas. Instrum.* **80**, 101969 (2021)
19. Nanda, S.R., Kulkarni, V., Sahoo, N.: Design of artificial neuro-fuzzy based methodology for six component force balance. *Procedia Eng.* **144**, 528–536 (2016)
20. Pratihari, D.K.: *Soft computing: fundamentals and applications*. Alpha Sci. Int. Ltd (2013)

# Environment-Friendly Smart City Solution with IoT Application



Ayush Kumar, Saket Kumar Jha, and Jitendra Singh Tamang

**Abstract** In the proposed system, a whole city will be spectated and observed. Since a Smart City is considered, it is likely to be a metropolitan city so that basic necessities like transportation, internet, telecommunication, etc. are presumed to be available. The proposed system will be equally expensive for both brownfield and Greenfield projects of Smart Cities. With the advancing times, IoT technology is getting familiar to every section of society and by the virtue of advent of the 5G system, the IoT appears to be the primus inter pares for its application in the futuristic scenario. The sensor arrays and input/output devices are being used in different sections of the devices to perform the required operation. The introduction of solar powered independent systems proved to be an autonomous robust technology. The low latency communication between node clusters can be a significant factor for the development and transformation of smart cities in a modern fashion that is the root basis for the introduction of futuristic models.

**Keywords** IoT · 5G · Sensor array · Solar powered · Low latency · Node clusters · Smart city · Futuristic model

## 1 Introduction

In 1998 the term smart city erupted [1] and has gained its popularity in recent years. This new generation holds youth of technical era; every sector of society is shifting from the product centric pattern to the service-oriented pattern to follow up with latest trends of Internet of Things. Now, Societies ponder Smart cities as an ecosystem of infrastructure and services due to its all-rounder essence with context of its reasonable facilities [2]. In attempt to provide these services globally, one must have a holistic view of every smart city problem and its comprehensive solution. The IoT and 5G combination enable a unified ecosystem for wide range of

---

A. Kumar · S. Kumar Jha (✉) · J. Singh Tamang  
Department of Electronics and Communication Engineering, Sikkim Manipal Institute of Technology, Sikkim Manipal University, Majitar 737136, Sikkim, India  
e-mail: [saketjha55288@gmail.com](mailto:saketjha55288@gmail.com)

© The Author(s), under exclusive license to Springer Nature Switzerland AG 2022  
S. Banerjee and A. Saha (eds.), *Nonlinear Dynamics and Applications*,  
Springer Proceedings in Complexity,  
[https://doi.org/10.1007/978-3-030-99792-2\\_56](https://doi.org/10.1007/978-3-030-99792-2_56)

669

applications in metropolitan vicinity, with the benefit that authorities can operate the e-administration and services for the means to produce inexpensive and resilient smart city infrastructure. In addition, for a holistic smart city development, a centralized approach for the processing of large amounts of data flow in the same network infrastructure is needed for data processing that can be further used for providing the instruction to the actuators using edge computing paradigm, [3] which pushes computation and data processing away from the core datacenters to the outer edge of networks that are closer to the data sources. The main benefit of this work is it makes the process faster in computation, processing of data and increases the ability as well as scalability. The IoT era means a whole new world of applications and services. This includes the Smart City surveillance and evaluation where a set of smart sensors and IoT devices monitors everyday smart city activities and helps in forecasting, reducing energy consumption, keeping the administration updated about big and small incidents of vicinity with centralized management server. It is a robust technology for the futuristic management which just not only insures real-time service delivery potential but simultaneously prevents the global warming and facilitates the residents with latest infrastructure. Perfect mixtures of small and big technologies are preferable so that innovation possibilities could cope up with future advancements. Currently, widely used platforms that are addressing up with our needs are Radiofrequency identification (RFID), Bluetooth Low-Energy (BLE), Near Field Communication (NFC) and Fourth Generation of cellular systems (4G) and for the long range of applications, the Low Power Wide Area (LPWA) has its superset LoRa WAN protocol and the future cellular IoT [4]. Smart City applications potentially benefit from IoT technologies; particularly they take advantage of the diversified and reactive character of IoT infrastructure. Others have addressed smart city applications like typical grid computing, using cloud services as a measure to work around the scope and complexity. This has led to extreme utilization of multiple parallel processing methodologies such as general data transmission or data sharing that have been long used to develop Distributed Systems applications, [5] where it was observed as a primitive coordination model and illustrates a more advanced version of the dataflow model. Data management is a component in the IoT for enabling the smart cities infrastructure which consists of data acquisition, processing and dissemination [6]. Data standards, quality, and utilization are the different aspects of data acquisition. When 5G is used in conjunction with its advanced characteristics, it enables an increase in the number of peripherals, acquires optimum bandwidth for uplink and downlink, ultra—low latency and supports energy-efficient data transmission [7]. Smart cities are built on the experiences and success of decades [8] which resembles a nation's innovation capabilities and success approaching determination [9]. There is no doubt that future of administration lies in the lap of IoT and corresponding steps by the administration is necessary to deal the future [10].

Conflict arises when existing IoTs are being compared with futuristic 5G IoT system. However, 5G beats the existing technology in all manners except for capital. These 5G antennas have very narrow coverage length and hence require huge physical infrastructure investment for its successful implementation. Moreover, it is found out

to be a one-time investment as it balances the chart with its efficient and worthwhile returns in account of futuristic demands.

In this paper we will talk about our approach of designing a networking system in smart city and will be talking about different layers of our model in detail. The model will explain about methodology of fetching the data from physical layer to processing and managing the data in the servers and its utilization. This system will be managing environmental parameters primarily, fetched from different parts of region along with some other data sets and will transmit details to the centers. This will not only help in getting to know about the real-time local conditions but will also help administration to identify the relatively polluted regions and work as needed. The data acquitted can be used for various statistical purposes in future.

## 2 Smart City Solution (Model Approach)

The concept entails splitting the city into 3–4 specified regions, each with its own Base Station. A Central Hub must be created in the heart of the city for cohesive strategic planning and as a location for preserving maintenance data. The base must be separated into distinct network stations in order to have practical non-erroneous data analysis capabilities that can handle ground reports and maintain the databases up to date with real-time environment parameter reports. Such characteristics are to be harvested from node clusters generated by taking into account certain nodes from specified locations.

The nodes will be having 5G connectivity from which the communication with peer nodes and network stations are to be established. From Fig. 1, the sensed data are being recorded by nodal database and then transmitted using 5G protocol.

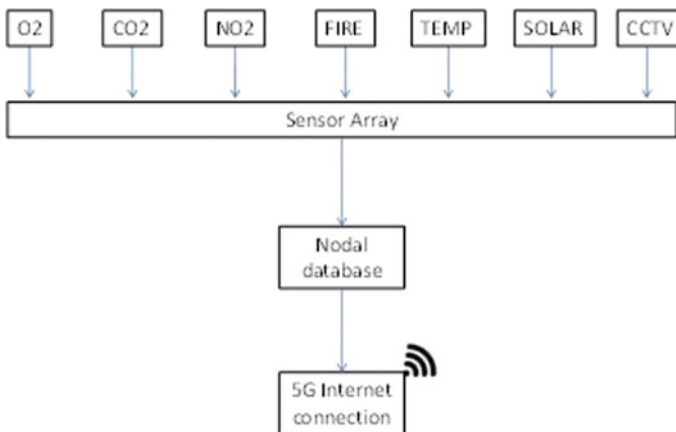
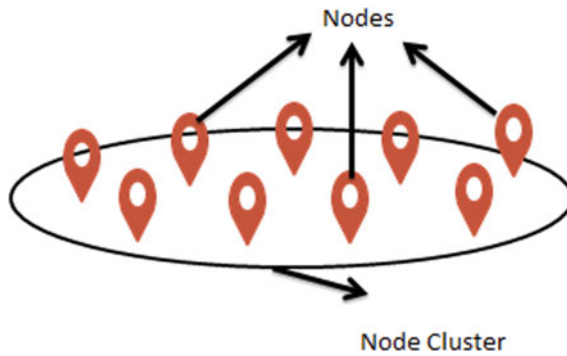


Fig. 1 Basic structure of a node



**Fig. 2** A node cluster

A cluster of nodes will consist of 8–10 nodes in a region and will be required for certain locations in order to centralize infrastructure that can be used as unified eco-space for better and more efficient human surveillance in a confined region. This is necessary to avoid machine malfunctions and to ensure that the installed infrastructure is properly maintained. The node cluster is seen in Fig. 2. Clusters are described as communication between peer nodes in defined areas, despite the fact that no specific node is necessary to bind nodes to create a cluster. The importance of constructing a cluster is that network stations can observe an average and accurate information about a region's climatic component. However for very local and root level details of small area data obtained from nodes are best suited.

The Network Stations will have access to the data collected by the nodes. The Network Stations will keep an eye on various nodes and may be regarded a place where actual human beings are sitting and observing data. Any unexpected findings from the node clusters must first be validated by a person before being sent to the Base Station who oversees the numerous network stations. The Base Station will continue to supervise the Network Stations' appropriate operation and administration. Network Stations authority would be able to make critical decisions at the local level to avert public disruption and improve service performance. If Network Stations detect a fire or a water leak through sensors, police may check the situation using a CCTV camera and then quickly make remedial arrangements for the risky situation. Furthermore, Network Stations may connect with local police stations to take required steps in emergency situations, such as evacuation of regions, etc.

The Node Clusters, Network Stations, Base Stations, and Central Hub are aligned hieratically in Fig. 3 to build a systematic smart city model, with the Central Hub having to serve as the top authority with administration, execution, and crucial decision-making powers. Multiple base stations will be linked to the central hub. Base Stations are subservient to the Central Hub, which monitors Network Station activities, supervises their coordination, and double-checks the smooth functioning and decision-making. It also maintains the link between the Central Hub and the Network Stations. Network stations on the other hand are to be seen as local



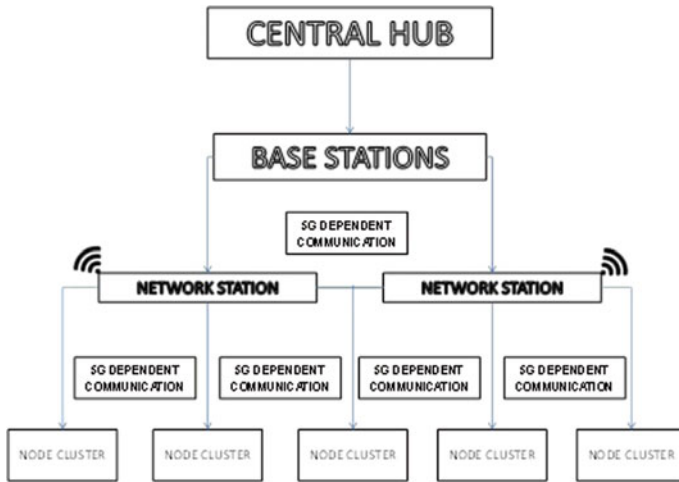


Fig. 3 5G Structured communication model

level smart city authority which will be monitoring all the Node Clusters under its boundaries and will be keeping a watch on instances being observed by the nodes. In case of non-urgent but important decision needed, it should be relayed to the Central Hub via Base Stations so that it can be carried out correctly and methodically.

### 3 Future Scope and Conclusion

The optimum use of 5G technology occurs when it is combined with Internet of Things. It is very remarkable to witness data being delivered in real-time. Environmental characteristics from a confined area under observation are being acquired using sensors placed at each node having 5G connectivity. The benefit of adopting 5G communications technology is the ability to communicate with peer nodes and Network Stations with minimal latency. One may speculate that the sensors employed can only perceive a restricted area, but this goes in hand with 5G technology, which offers more bandwidth while communicating in a limited area since bandwidth and distance of a channel are inversely related to each other. As a result, bringing nodes closer together would result in perfect synchronization with 5G low-latency communication and viable surveillance. Each node will have its own local data acquisition system, allowing data to be retained locally for future reference.

Henceforth 5G technology when combined with IoT for noble purpose like Environment monitoring as a pollution control measure can prove to be a boon for society. This will not just keep us updated about our environment parameter real-time but can also help government to take steps in maintaining pollution levels on different parts of city. Also, this will enable us to get information of our very local environment

parameters as well important and urgent activities on our fingertips through mobile phone. Thus, this paper gives a structural overview to a method for working and maintenance of a noble purpose like Smart city environment monitoring.

## References

1. Van Bastelaer, B.: Digital cities and transferability of results. In: 4th EDC Conference on Digital Cities, Salzburg, pp. 61–70 (1998)
2. Bruneo, D., Distefano, S., Giacobbe, M., Minnolo, A.L., Longo, F., Merlino, G., Mulfari, D., et al.: An IoT service ecosystem for smart cities: The# smartme project. *Internet Things* **5**, 12–33 (2019)
3. Cicirelli, F., Guerrieri, A., Spezzano, G., Vinci, A.: An edge-based platform for dynamic smart city applications. *Future Gener. Comput. Syst.* **76**, 106–118 (2017)
4. Goudos, S.K., Dallas, P.I., Chatziefthymiou, S., Kyriazakos, S.: A survey of IoT key enabling and future technologies: 5G, mobile IoT, semantic web and applications. *Wirel. Pers. Commun.* **97**(2), 1645–1675 (2017)
5. Giang, N.K., Lea, R., Blackstock, M., Leung, V.C.: On building smart city IoT applications: a coordination-based perspective. In: *Proceedings of the 2nd International Workshop on Smart*, pp. 1–6 (2016)
6. Gharaibeh, A., Salahuddin, M.A., Hussini, S.J., Khreishah, A., Khalil, I., Guizani, M., Al-Fuqaha, A.: Smart cities: a survey on data management, security, and enabling technologies. *IEEE Commun. Surv. Tutor.* **19**(4), 2456–2501 (2017)
7. Rao, S.K., Prasad, R.: Impact of 5G technologies on smart city implementation. *Wirel. Pers. Commun.* **100**(1), 161–176 (2018)
8. Repko, J., DeBroux, S.: Smart cities literature review and analysis. *IMT 598 Spring 2012 Emerg. Trends Inf. Technol.* (2012)
9. Nam, T., Pardo, T.A.: Smart city as urban innovation: focusing on management, policy, and context. In: *Proceedings of the 5th International Conference on Theory and Practice of Electronic Governance*, pp. 185–194 (2011)
10. Kumar, S., Tiwari, P., Zymbler, M.: Internet of Things is a revolutionary approach for future technology enhancement: a review. *J. Big Data* **6**, 111 (2019)

# Parametric Optimization of WEDM Process on Nanostructured Hard Facing Alloy Applying Metaheuristic Algorithm



Abhijit Saha , Pritam Pain , and Goutam Kumar Bose 

**Abstract** Wire Electric Discharge Machining (WEDM) is broadly utilized for manufacturing geometrically intricate and hard material parts. Taguchi orthogonal array using L25 is applied as design of experiment for the five input process parameters. Artificial Neural Network is utilized for testing and validation of the experimental data. This is trailed by employing a multi-objective optimization through Genetic Algorithm (GA) approach. As the outcomes got through GA infer a set of possible solutions. Grey Relation Analysis (GRA) is applied theory to find out the best parametric amalgamation among the arrangement of practical other options. In this case the weights are considered through Fuzzy set. Lastly the optimized results are obtained with regards to discharge pulse time (0.5  $\mu$ s), discharge stop time (12  $\mu$ s), servo voltage (36 V), wire tension (501gm), wire feed rate (8 m/min) correspondingly.

**Keywords** Artificial Neural Network (ANN) · Multi objective Genetic Algorithm (M-GA) · Grey relational analysis · Wire Electric Discharge Machining (WEDM) · Orthogonal array

## 1 Introduction

The capability to fabricate coatings is significant to manufacturing blueprint. Numerous segments need utilization of extra layers to enhance the mechanical properties and secure against hazardous environments. Nanostructured hard facing alloy are extensively used in various die and tool making industries. Machining of these materials is rather challenging if higher machined quality is warranted. Wire electric discharge machining (WEDM) process has evolved as a promising cutting strategy for cutting such hard to cut conductive materials.

---

A. Saha (✉) · P. Pain · G. Kumar Bose  
Department of Mechanical Engineering, Haldia Institute of Technology, Haldia 721657,  
West Bengal, India  
e-mail: [saha.abhijit1798@gmail.com](mailto:saha.abhijit1798@gmail.com)

© The Author(s), under exclusive license to Springer Nature Switzerland AG 2022  
S. Banerjee and A. Saha (eds.), *Nonlinear Dynamics and Applications*,  
Springer Proceedings in Complexity,  
[https://doi.org/10.1007/978-3-030-99792-2\\_57](https://doi.org/10.1007/978-3-030-99792-2_57)

675

In WEDM process, the workpiece material is taken out by a progression of series of distinct electrical spark between the anode workpiece and cathode wire. Due to the presence of dielectric fluid those sparks are extremely focused and due to this the temperature of that local area increases rapidly. That temperature is high enough to melt and instantly vaporize the workpiece material.

Based on the past research work by several researchers a brief literature review is presented here. Somashekhar et al. [1] employed ANN for modeling and optimize the input process parameters in micro-electric discharge machining. Ming et al. [2] also used ANN to predict cutting parameters in WEDM.

Genetic algorithms depend on procedure of natural selection and natural heredity qualities, which are supplementary strong and bound to find the universal best possible combinations. A few uses of GA-based method in nontraditional process optimization issues have been accounted in the literature. Kuriakose and Shunmugam [3] developed multiple regression models to represent association among WEDM input parameters and output responses. GA was used to obtain a most favorable amalgamation of process parameters. Mahapatra and Patnaik [4] employed genetic algorithm technique to optimize the WEDM process parameters. Prasad and Krishna [5] used GA to optimize the cutting speed and surface roughness in WEDM process. Pasam et al. [6] also evaluated the control parameters of WEDM titanium alloy (Ti6Al4V) using GA.

Moreover, Kuruville and Ravindra [7] applied Taguchi's technique and a genetic algorithm to resolve parametric influence and optimal process parameters in WEDM process. Kumar and Agarwal [8] also used a GA to optimize the machining setting in WEDM. Zhang et al. [9] proposed hybrid method of RSM and GA for multi-criteria optimization of WEDM process parameters. Padhi et al. [10] also employed non dominating sorting GA technique to optimize the multiple responses of WEDM process. Sharma et al. [11] developed mathematical model using RSM and optimization has been carried using GA. Varun and Venkaiah [12] applied grey relational analysis coupled with GA based hybrid technique to simultaneously optimize the process responses in WEDM. Nair et al. [13] used GRA and GA to optimize the multi-performance characteristics in WEDM of Inconel 617. Shandilya et al. [14] applied various techniques viz. teaching-learning-based optimization, grey relational analysis and genetic algorithm for parametric optimization of WEDM process parameters. Various specialists have concentrated on the impacts of ideal machining boundaries on exhibitions in WEDM process utilizing a variety of optimization techniques [15–17].

Additionally, it is found however, from the machining literature that a not many researchers [18–20] assessed the best amalgamation of different input process parameters on finishing attributes in WEDM for machining nanostructured hardfacing material. Very little investigation has been accessible on optimization of WEDM condition for nanostructured hard facing alloy using multi-objective GA. It is essential to explore the quality characteristics of any finished component in order to illustrate its performance. In order to find out the best parametric blend of GA results a Multi-Criteria Decision Making (MCDM) technique which is commonly known as GRA method has been employed.

## 2 Experimental Setup

The current experiments were done on 5 axes CNC Wire Electric Discharge Machining. The figure of the machining system is shown in the Fig. 1.

To reduce the experiments machining were carried out following  $L_{25}$  Orthogonal Array taking five important input parameters like discharge pulse time ( $T_{on}$ ), discharge stop time ( $T_{off}$ ), servo voltage (SV), wire tension (WT) and wire feed rate (WF) [16]. The factors and their levels as considered for testing is shown in the Table 1.

After the experiments average surface roughness (Ra) of all machined surface were measured by using Taylor Hobson’s Talysurf. The MRR is calculated by measuring the area of the work surface removed by time. The machining time is calculated by using stopwatch.

Fig. 1 WEDM machine



Table 1 Machining inputs with their ranges [16]

Machining parameter	Unit	Range
$T_{on}$	$\mu s$	0.3–0.5
$T_{off}$	$\mu s$	8–12
SV	V	35–47
WT	gm	500–900
WF	m/min	5–9

### 3 Results and Discussions

Artificial Neural Network (ANN) has been applied for identifying and learning the link between the input statistics and corresponding responses. The outcomes can be predicted once the training, validation and testing of the trial data is over by applying ANN. Figure 2 shows the simulink model for ANN.

#### 3.1 ANN Analysis

For training 80% of the data have been considered, 10% of the data have been considered for validation and for testing 10% of data are considered during ANN analysis of MRR. MSE achieved after 6 iterations and it was ended. Figures 3 and 4 show regression and performance plot of the MRR.

Here in Fig. 2 shows, training  $R = 0.99854$ , validation  $R = 0.90286$  and testing  $R = 0.96343$ . Thus overall value of the  $R$  is  $0.91931$ . Hence, the training data suggests a noble fit because the validation and test results showing the values of  $R$  is greater than  $0.9$ . Similarly Fig. 5a and 5b illustrate the final performance plot for machining time and Ra respectively.

#### 3.2 Multi-objective Optimization of Responses

In this current examination, an effort has been made to choose the ideal estimations of input process parameters to get the main quality outputs inside the boundaries ranges. A practical advancement system, GA is created to deal with the streamlining issue for this assessment. In GA the numerical condition is outlined to give as the input parameter. As the outcomes acquired through GA suggest a domain of solutions, for that reason where the weight of the control parameters are calculated via Fuzzy

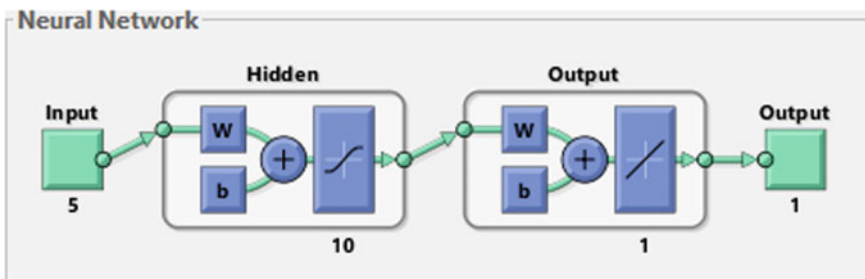


Fig. 2 Simulink diagram

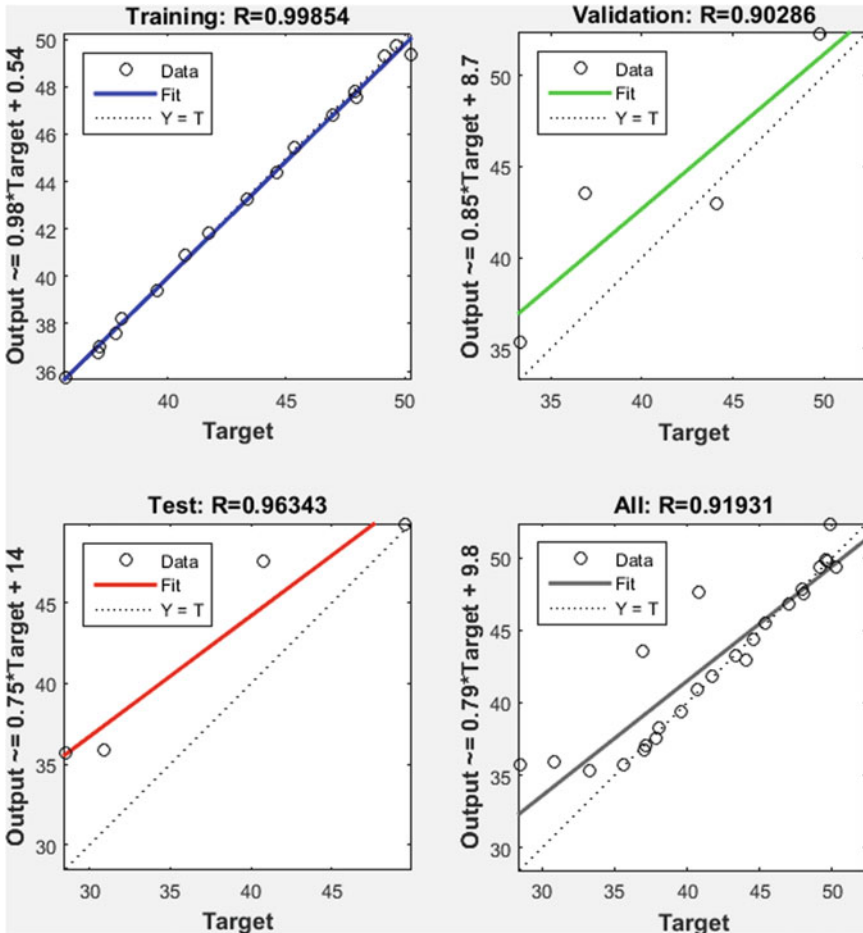


Fig. 3 Regression plot [MRR]

set hypothesis, there GRA can be applied. This can calculate the best parametric alternatives from the solution region (Fig. 6).

The specified weights of MRR, machining time and Ra are 33%, 26% and 41% respectively as determined by using Fuzzy set theory. Table 2 exhibits the results of grade and their ranks. It has been found that experiment number 3 has the maximum grey relational grade point. Consequently, the experimental run of 3 which has parametric combination  $T_{on}$  0.5  $\mu$ Sec,  $T_{off}$  12  $\mu$ Sec, SV 36 V, WT 501 g and WF 8 m/min is the finest amongst other experimental trail for having high MRR and lower machining time and Ra.

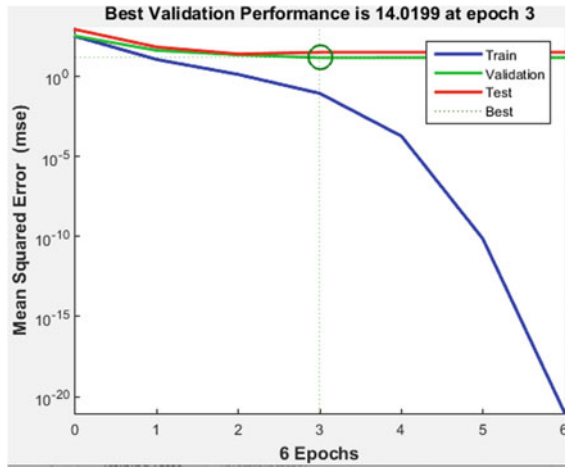


Fig. 4 Performance plot [MRR]

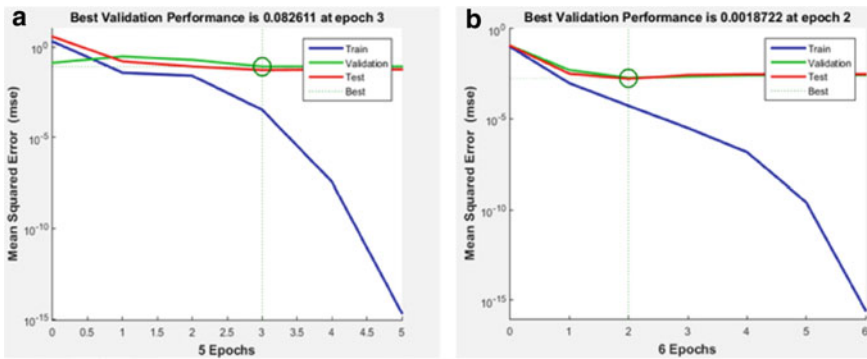


Fig. 5 Performance plot **a** Machining time **b** Surface roughness

### 3.3 Confirmation Experiments

Confirmation tests were performed in order to validate the optimization results by setting input parameters ( $T_{on} = 0.5$ ,  $T_{off} = 12$ ,  $SV = 36$ ,  $WT = 501$  and  $WF = 8$ ). The corresponding responses (MRR, machining time and  $R_a$ ) were measured. Predicted error lies within the limit of 5% and hence, can be considered as significant for acceptance (Table 3).



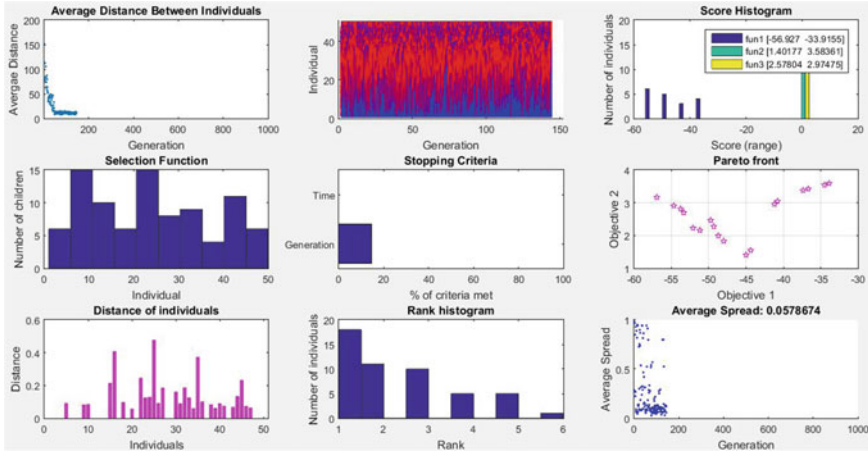


Fig. 6 Plot functions for GA

Table 2 Optimization results

Exp. no	Control parameters					Responses			Grey grade	Rank
	T <sub>on</sub>	T <sub>off</sub>	SV	WT	WF	MRR	Machining	R <sub>a</sub>		
1	0.3	12	44	523	5	33.915	3.58	2.58	0.485	7
2	0.4	12	42	510	5	41.236	2.96	2.61	0.481	10
<b>3</b>	<b>0.5</b>	<b>12</b>	<b>36</b>	<b>501</b>	<b>8</b>	<b>44.987</b>	<b>1.40</b>	<b>2.72</b>	<b>0.640</b>	<b>1</b>
4	0.3	12	44	523	5	34.527	3.54	2.58	0.484	8
5	0.3	12	44	522	5	36.658	3.42	2.58	0.492	6
6	0.5	8	36	508	7	52.081	2.24	2.97	0.436	15
7	0.5	9	44	506	7	54.722	2.92	2.91	0.460	13
8	0.5	8	46	506	7	56.927	3.16	2.93	0.519	3
9	0.5	9	42	507	8	53.387	2.70	2.88	0.445	14
10	0.4	12	44	522	5	37.349	3.37	2.58	0.492	5
11	0.5	10	41	506	7	49.769	2.47	2.81	0.423	18
12	0.4	12	43	522	5	40.734	3.05	2.60	0.483	9
13	0.5	10	36	506	8	48.690	2.00	2.89	0.435	16
14	0.5	12	36	510	7	44.412	1.55	2.69	0.588	2
15	0.5	8	36	512	8	51.147	2.16	2.97	0.429	17
16	0.5	10	36	506	8	47.943	1.82	2.83	0.474	11
17	0.5	12	41	502	7	49.284	2.27	2.67	0.512	4
18	0.5	10	44	506	7	53.768	2.80	2.84	0.460	12

**Table 3** Confirmation of optimization results

Comparison	MRR	Machining time	R <sub>a</sub>
Experimental	44.987	1.40	2.72
Predicted	45.811	1.37	2.63
% Error	1.83	2.14	3.3

## 4 Conclusions

Metaheuristic methods have verified their effectiveness in solving difficult optimization problems. It can adequately uphold the leaders to decide the ideal interaction boundary setting for any industrialized practice. The incorporated methodology might be utilized for a determination issue including quite a few choice standards.

Lastly the optimized results are obtained with regards to  $T_{on} = 0.5$ ,  $T_{off} = 12$ ,  $SV = 36$ ,  $WT = 501$  and  $WF = 8$  respectively. This examination work might be broadened further by considering some other exhibition qualities, for example, kerf, form factor as well as relevant input process parameters such as peak current, wire diameter in WEDM.

## References

1. Somashekhar, K.P., Ramachandran, N., Mathew, J.: Optimization of material removal rate in micro-EDM using Artificial Neural Network and Genetic Algorithms. *Mater. Manuf. Process.* **25**(6), 467–475 (2010). <https://doi.org/10.1080/10426910903365760>
2. Ming, W., Hou, J., Zhang, Z., Huang, H., Xu, Z., Zhang, G., Huang, Y.: Integrated ANN- LWPA for cutting parameter optimization in WEDM. *Int. J. Adv. Manuf. Technol.* 1–18 (2015)
3. Kuriakose, S., Shunmugam, M.S.: Multi-objective optimization of wire-electro discharge machining process by non-dominated Sorting Genetic Algorithm. *J. Mater. Process. Technol.* **170**, 133–141 (2005)
4. Mahapatra, S.S., Patnaik, A.: Optimization of wire electrical discharge machining (WEDM) process parameters using Taguchi method. *Int. J. Adv. Manuf. Technol.* **34**(9–10), 911–925 (2007)
5. Prasad, D.V.S.S.V., Krishna, A.G.: Empirical modeling and optimization of wire electrical discharge machining. *Int. J. Adv. Manuf. Technol.* **43**, 914–925 (2009)
6. Pasam, V.K., Battula, S.B., Valli, P.M., Swapna, M.: Optimizing surface finish in WEDM using the taguchi parameter design method. *J. Braz. Soc. Mech. Sci. Eng.* **32**(2), 107–113 (2010)
7. Kuruvila, N., Ravindra, H.V.: Parametric influence and optimization of wire EDM of hot die steel. *Mach. Sci. Technol.* **15**(1), 47–75 (2011)
8. Kumar, K., Agarwal, S.: Multi-objective parametric optimization on machining with wire electric discharge machining. *Int. J. Adv. Manuf. Technol.* **62**, 617–633 (2012)
9. Zhang, G., Zhang, Z., Ming, W., Guo, J., Huang, Y., Shao, X.: The multi-objective optimization of medium-speed WEDM process parameters for machining SKD11 steel by the hybrid method of RSM and NSGA-II. *Int. J. Adv. Manuf. Technol.* **70**, 2097–2109 (2014)
10. Padhi, P.C., Mahapatra, S.S., Yadav, S.N., Tripathy, D.K.: Multi-objective optimisation of machining parameters in wire electrical discharge machine using non-dominating sorting genetic algorithm. *Int. J. Prod. Qual. Manag.* **14**, 107–129 (2014)
11. Sharma, N., Khanna, R., Gupta, R.D.: WEDM process variables investigation for HSLA by response surface methodology and genetic algorithm. *Eng. Sci. Technol.* **18**, 171–177 (2015)

12. Varun, A., Venkaiah, N.: Simultaneous optimization of WEDM responses using grey relational analysis coupled with genetic algorithm while machining EN 353. *Int. J. Adv. Manuf. Technol.* **76**, 675–690 (2015)
13. Nair, A., Kumanan, S., Shanavas, K.P.: Multi-performance optimization in wire EDM of Inconel 617 using GRA and genetic algorithm. *Mater. Today: Proc.* (2021). ISSN: 2214-7853. <https://doi.org/10.1016/j.matpr.2021.08.279>
14. Shandilya, P., Rouniyar, A.K., Saikiran, D.: Multi-objective parametric optimization on machining of Inconel-825 using wire electrical discharge machining. *Proc. Inst. Mech. Eng. C J. Mech. Eng. Sci.* **234**(20), 4056–4068 (2020). <https://doi.org/10.1177/0954406220917706>
15. Majumder, H., Paul, T.R., Dey, V., Dutta, P., Saha, A.: Use of PCA-grey analysis and RSM to model cutting time and surface finish of Inconel 800 during wire electro discharge cutting. *Measurement* **107**, 19–30 (2017). ISSN: 0263-2241 (Elsevier)
16. Paul, T.R., Saha, A., Majumder, H., Dey, V., Dutta, P.: Multi-objective optimization of some correlated process parameters in EDM of inconel 800 using a hybrid approach. *Int. J. Braz. Soc. Mech. Sci. Eng.* (2019). <https://doi.org/10.1007/s40430-019-1805-9>. (Springer (Accepted, SCI))
17. Saha, A., Mondal, S.C.: Optimization of wire electric discharge machining process: a review and reflection. *Int. J. Prod. Qual. Manag.* **22**(3), 340–362 (2017)
18. Saha, A., Mondal, S.C.: Statistical analysis and optimization of process parameters in wire cut machining of welded nano-structured hardfacing material. *Silicon* (2018). <https://doi.org/10.1007/s12633-018-9924-y>. (Springer (Accepted, SCI))
19. Saha, A., Mondal, S.C.: Experimental investigation and modelling of WEDM process for machining nano-structured hardfacing material. *J Braz. Soc. Mech. Sci. Eng.* **39**, 3439–3455 (2016)
20. Saha, A., Mondal, S.C.: Multi-objective optimization in WEDM process of nanostructured hardfacing materials through hybrid techniques. *Measurement* **94**, 46–59 (2017)

# Object Detection: A Comparative Study to Find Suitable Sensor in Smart Farming



Mohit Kumar Mishra  and Deepa Sonal 

**Abstract** Crop-loss is one of the major factors that led the farmers to ruin their lives and everything they possess. Internet of Things (IoT) is an advanced technology that is effectively benefitting various fields nowadays. We have tried to use this technology to save the lives of farmers by saving their crops from being ruined. For this, we have proposed a model that is going to be used in the agricultural fields to prevent wildlife attacks that is one of the major factors of crop loss. As we know that Animal hunting is one of the punishable offences in many countries. We want the animals to run away from the field without any physical harm. In this paper, we have tried to do a comparative study of sensors that would be most preferable for our proposed model. We want to find out which sensor is most suitable for the detection of wild animals in the agriculture field. For finding that we have done some experiments and observed the results to justify our sensor selection. As we want to choose the most suitable sensors for our crop protection model.

**Keywords** IoT · Sensors · Crop protection · IR sensor · Ultrasonic sensor · Attack detection · Comparative study · Another keyword

## 1 Introduction

There is no doubt that a significant amount of research has been done in the realm of software and hardware applications in Internet of Things (IoT). One of them is the suggested research project. In most cases, a typical pest repeller will emit a consistent frequency. This consistent frequency will only deter the pest for a short time and is ineffective [1]. It is because strong and unusual sounds, such as ultrasonic sounds that rats can hear, frequently scare them and cause transient aversion lasting anywhere

---

M. Kumar Mishra  
Department of Electronics and Communication Engineering, Manipal University, Jaipur, India

D. Sonal (✉)  
Department of Computer Science, V.K.S. University, Arrah 802301, India  
e-mail: [deepsonapwc@gmail.com](mailto:deepsonapwc@gmail.com)

from a few minutes to a few weeks. In this research, we have tried to find out the most suitable sensors used for detecting the animals or pests in this animal repelling system [2]. One important commitment, we are going to make here is we don't want to physically harm any animal or pest for repulsion [3]. We want only to scare them and ran them away from the agricultural field as they enter the field [4]. An IoT based system is implemented to detect the Animal and produce repelling sound and repelling frequency to scare them away from the crop field [5].

We have two options for animal detection sensors. First one is ultrasonic sensor and second one is IR sensor. Both the sensors can be used to detect any object comes in the way. Let us first know about both the sensors individually. Some of the recent studies done in this field is given in [6] where the author has described that ultrasonic sensor can work well with sponge, wood, Tile and plastic whereas IR sensor can work only with Paper sheet typen of products.

### 1.1 IR Sensor

Infrared Sensor or IR Sensor is an equipment used to detect the objects present in surrounding by sending infrared waves which is usually has frequency in range of 300GHz to 400 THz. This sensor works on the theory of reflected light waves. Reflected infrared light or light emitted from an infrared remote or beacon. Distance and vicinity are also determined via infrared sensors [7]. After detecting the reflected light, a range calculation between the sensor and the target is computed [8]. The Fig. 1 given below shows the diagram of IR sensor.

### 1.2 Ultrasonic Sensor

An ultrasonic sensor is also used to detect the obstacle in the way and determine the distance of the object. It works on the principle of reflecting sound waves [9, 10]. The ultrasonic sensor emits sound waves, which are reflected if an obstacle is before it. Ultrasound is a type of sound that is inaudible to the individual ear since its lowest working frequency is still higher than the human hearing threshold of roughly 20 kHz. Ultrasound spans a wide range of frequencies, from 40 kHz for

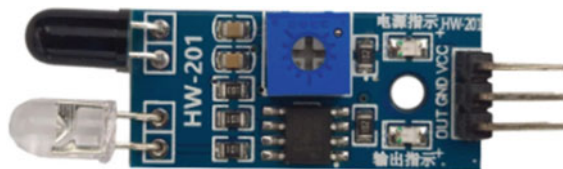


Fig. 1 IR sensor



**Fig. 2** Ultrasonic sensor

proximity sensors to 1 MHz and above for diagnostic imaging. The range finding by an ultrasonic sensor can be seen in the Fig. 2 given.

So, objective of this research paper is to find out the most suitable sensor for animal detection so that Animal repeller system can work efficiently. In first section of this paper, we have given the introduction about the system and sensors. In second section, we have described the methodology for showing difference in the sensors theoretically and experimentally. In third section, we have done analysis on data observed in experiment and in fourth section we have given the conclusion of this research.

## 2 Methodology

Choosing a sensor for particular application might be difficult in either project. The dependability of the sensor and other application equipment has a big impact on the effectiveness of the machine. There are a few factors to contemplate when choosing a sensor for your applications. Accuracy refers to how accurate the measurement is in relation to the genuine distance. The minimal reading or variation in readings that can be recorded is called resolution.

Precision refers to the tiniest measurement that can be taken frequently and dependably.

To compare and study the behavior of both the above sensors, it is very important to list out the features of IR and ultrasonic sensor theoretically. Then we have done some experiments on both the sensors by attaching it to Arduino board one by one and checking out its performance through observations. And finally checking out the observation results through data analysis whether the experiment result is significant or not.

### 2.1 Theoretical Differences in Features of Both the Sensors

The main distinction among the two types of sensors is that IR sensors sense electromagnetic radiation, whereas ultrasonic sensors sense mechanical or auditory energy. Hard things (e.g. walls, doors), fog, dust, mist, sunlight, and other factors alter infrared frequencies. As a result, it cannot pass through walls or doors. It works on line of sight (LoS), so point-to-point communication is done.

Infrared sensors have a number of drawbacks, including the inability to utilize them in direct sunlight due to interference. It can make it difficult to use outdoor applications or dismal indoor applications. Ultrasonic sensors identify obstructions through sound waves and are unaffected by a variety of circumstances. Ultrasonic sensors are more efficient than infrared sensors if reliability is a priority in the sensor choices.

### 2.2 Experimental Observations for Both the Sensors

We have done experiments also to take observations for checking efficiency of both the sensors one by one. We have collected data readings through serial monitor, some during day time and some at night time. Various parameters for both the sensors can be seen in the given dataset table Table 1.

First we have taken the readings for ultrasonic sensor in day time and night time for object detection. Figure 3 here shows the reading taken on experimental setup of

**Table 1** Various parameters for experimental setup

Parameters	IR Sensor	Ultrasonic sensor
Range	10–80 cm	2–10 cm
Beam-width	75°	30°
Beam Pattern	Narrow (Line)	Canonical
Frequency	353 THz	40 kHz
Unit cost	~750 INR	~130 INR



**Fig. 3** Ultrasonic sensor data displayed on serial monitor of arduino IDE

ultrasonic sensor with Arduino UNO microcontroller. Figure 4 is showing the circuit diagram of experimental setup.

The circuit diagram in Fig. 4 has been designed using tinkercad.com online app. Experimental setup of given circuit design has been done which is shown in Fig. 5. The same experiment we have done with IR sensor and taken the observations to check its efficiency in day time and night time.

The Fig. 6 shows the observation taken during the daytime in sunlight using both the sensors one-by-one. It shows the efficiency of both the sensors of sensing the

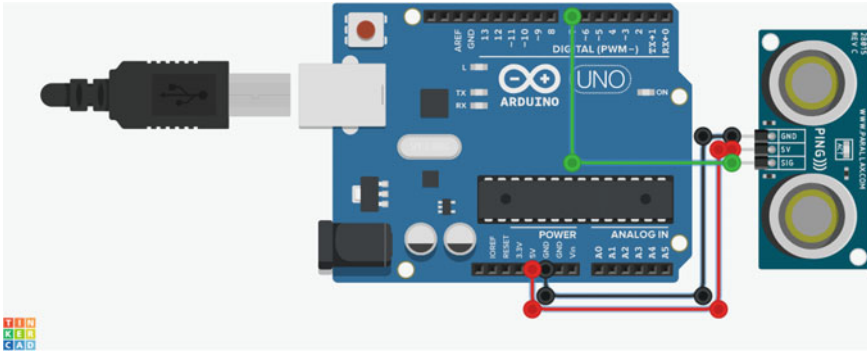


Fig. 4 Circuit design of ultrasonic sensor with arduino UNO

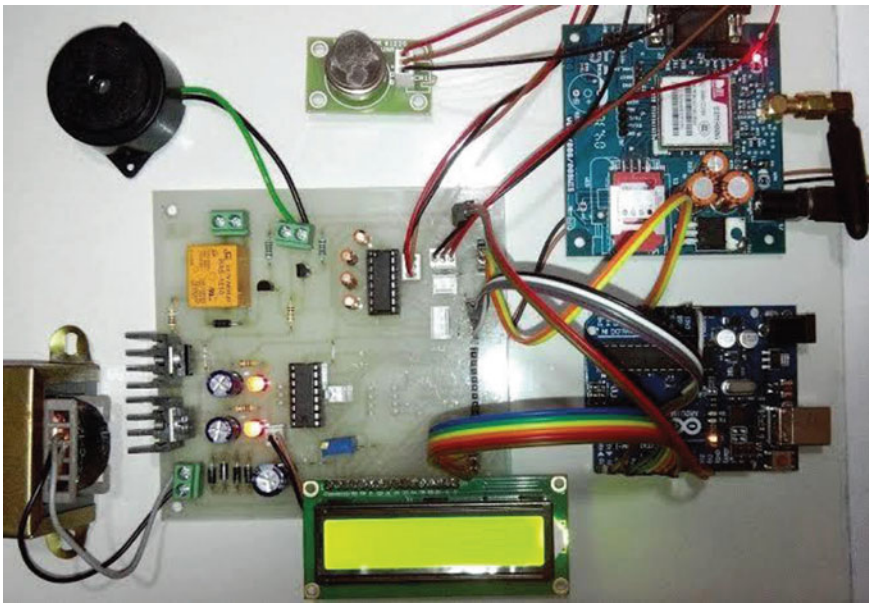


Fig. 5 Experimental setup with LCD display to show distance



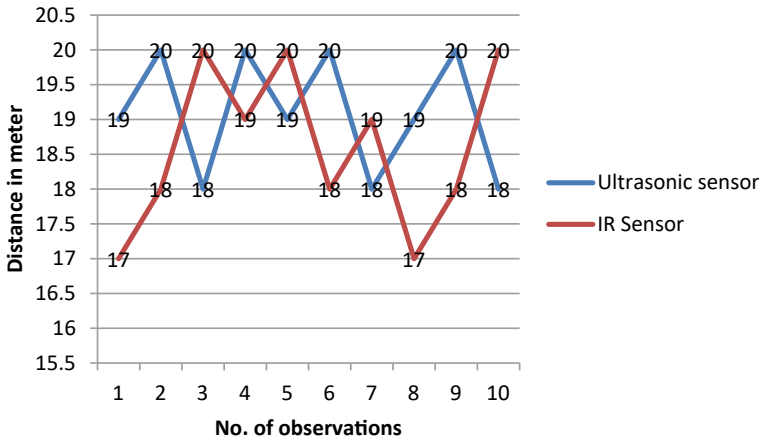


Fig. 6 Detection of an object coming toward both sensors in the daytime

object coming towards them. It is visible from the above chart that the IR sensor is also working efficiently during day-time in Sunlight. IR sensor is able to detect the object as efficiently as ultrasonic sensor can detect.

- (a) Then we perform the same experiment at night and dark environment to check the efficiency of both the sensors using the same experimental setup. And based on the readings of the experiment for both the sensors, Fig. 7 has been plotted as given.

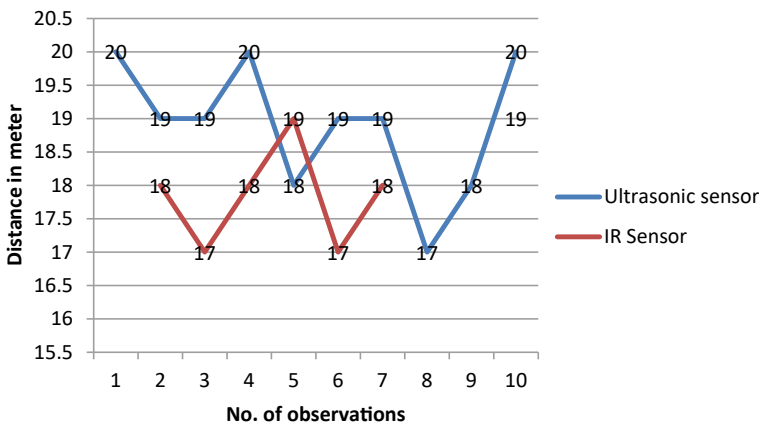


Fig. 7 Detection of an object coming toward both sensors in the night time

We can see the difference in working efficiency of both the sensors at night/dark. It is very much clear from the above plotted graph that IR sensor was unable to detect the coming object three times. It shows that IR sensor is not that much reliable during night.

### 3 Results and Discussion

From these experimental observations, we can discuss that IR sensor can be used efficiently in day time and for indoor experiments, while for outdoor experiments that needs to be done at night or in darkness; ultrasonic sensor is much more efficient than the IR sensor. For strongly supporting our experiment, we have done data analysis also that can show the significance of our experiment being carried out.

Both the experiments are analyzed and we have tried to find out the significance of experiment conducted during day and night time respectively (as shown in Tables 2 and 3). In Table 3, total no. of observations is 7 whereas actually total 10 observations

**Table 2** Data analysis showing significance of experiment during daytime

<i>SUMMARY</i>						
Groups	Count	Sum	Average	Variance		
Column 1	10	191	19.1	0.766667		
Column 2	10	186	18.6	1.377778		
<i>ANOVA</i>						
Source of variation	SS	df	MS	F	P-value	F crit
Between groups	1.25	1	4.25	4.165803	0.294521	4.413873
Within groups	19.3	18	1.072222			
Total	20.55	19				

**Table 3** Data analysis at night/dark

<i>SUMMARY</i>						
Groups	Count	Sum	Average	Variance		
Column 1	10	189	18.9	0.988889		
Column 2	7	126	18	0.666667		
<i>ANOVA</i>						
Source of variation	SS	df	MS	F	P-value	F crit
Between groups	3.335294	1	3.335294	3.878249	0.067672	4.543077
Within groups	12.9	15	0.86			
Total	16.23529	16				

were taken. IR sensor was not able to sense object 3 times in night/dark. The F-tabulated and F-calculated values are also very closed in observational analysis during day time. It shows the significance of observation and experiment. It implies that IR sensor is not reliable for object detection in fields. As we have to make guarding system especially for nights when Farmers are either sleeping or not in the agricultural fields. In fact in day time if there is a cloudy day, then also it will not work effectively because of lack of light. So it is most efficient to work with ultrasonic sensor than IR sensor where  $24 \times 7$  guarding is required.

## 4 Conclusion

We can conclude that we should go for ultrasonic sensor instead of infrared sensor in our Animal repeller proposed model. We have to design and develop a final cropland guarding system that can help out farmers not only in daytime but especially during night [11]. So we should use the best components in our animal repeller system. Before repelling the wild animals, it is very much essential to detect the animals at right time and quickly [3]. So that crop harm can be minimized or removed. Thus we have concluded to use ultrasonic sensor for our animal detection system.

## References

1. Louis, L.: Working principle of arduino and using it as a tool for study and research. *Int. J. Control. Autom. Commun. Syst.* **1**(2), 21–29 (2016). <https://doi.org/10.5121/ijcacs.2016.1203>
2. Ragavi, B., Pavithra, L., Sandhiyadevi, P., Mohanapriya, G.K., Harikirubha, S.: Smart sgriculture with AI sensor by using agrobot. In: 2020 Fourth International Conference on Computing Methodologies and Communication (ICCMC), pp. 1–4 (2020)
3. Haque, M.A., Sonal, D., Haque, S., Nezami, M.M., Kumar, K: An IoT-based model for defending against the novel coronavirus (COVID-19) outbreak. *Solid State Technol.* 592–600 (2020)
4. Kumar, S.: *Artificial Intelligence in Indian Irrigation* (2019)
5. Samarasinghe, M.G.P.M.: Use of IoT for Smart Security Management in Agriculture, vol. 978, pp. 65–73 (2019)
6. Adarsh, S., Kaleemuddin, S.M., Bose, D., Ramachandran, K.I.: Performance comparison of Infrared and Ultrasonic sensors for obstacles of different materials in vehicle/ robot navigation applications. *IOP Conf. Ser. Mater. Sci. Eng.*, **149**(1), (2016). <https://doi.org/10.1088/1757-899X/149/1/012141>
7. David, S., Anand, R.S., Sagayam, M.: Enhancing AI based evaluation for smart cultivation and crop testing using agro-datasets. *J. Artif. Intell. Syst.* **2**(1), 149–167 (2020)
8. Divya, R., Chinnaiyan, R.: Reliable AI-based smart sensors for managing irrigation resources in agriculture—a review. In: *International Conference on Computer Networks and Communication Technologies*, pp. 263–274 (2019)
9. Smart Agriculture Sensors|Mouser. <https://www.mouser.in/applications/smart-agriculture-sensors/>. Last accessed 30 Apr 2021

10. Baranwal, T.: "Nitika and PK Pateriya" Development of IoT based smart security and monitoring devices for agriculture. In: Proceeding of the 2016 6th International Conference-Cloud System Big Data Engineering Confluence 2016, no. November 2020, pp. 597–602 (2016). <https://doi.org/10.1109/CONFLUENCE.2016.7508189>
11. Parashar, M.: Candidate Declaration "IoT Based Smart Agriculture Monitoring System," vol. 151042

# Robust Adaptive Controller for a Class of Uncertain Nonlinear Systems with Disturbances



Ngo Tri Nam Cuong, Le Van Chuong, and Mai The Anh

**Abstract** This paper presents a method to synthesize the controller for uncertain nonlinear systems based on a combination of sliding mode control, adaptive control, and radial basis function (RBF) neural network. We propose an adaptive control law based on the RBF neural network to identify and compensate for variable parameter components, nonlinear function vectors, and external disturbance. The main linear component is built based on a sliding control. The designed controller has the advantage of being resistant to the elements of uncertainty and has a high control quality.

**Keywords** Nonlinear systems · Adaptive control · System identification

## 1 Introduction

In practice, the uncertain nonlinear systems are affected by external disturbances which are very common. The existence of uncertain parameters adversely affects the performance of the system. Control design for such a class of objects has attracted the attention of many researchers in past decades. A combination of the adaptive control method and the neural network has been shown in the researches [1–4], in which nonlinear components and external disturbance are identified using the neural network to generate a compensation control signal for the uncertain components. Some researches on adaptive control have been implemented for such variable nonlinear systems, where variable parameters are identified and adjusted by adaptive control law [5–7]. In [8], a control law is built based on sliding mode control in which uncertain components are considered for control design, and thus the designed system is stability. The control design using backstepping and fuzzy techniques is

---

N. T. N. Cuong  
Systemtec JSC, Hanoi, Vietnam

L. V. Chuong (✉) · M. T. Anh  
Vinh University, Vinh city, Nghean, Vietnam  
e-mail: lvchuong85@gmail.com; chuonglv@vinhuni.edu.vn

© The Author(s), under exclusive license to Springer Nature Switzerland AG 2022  
S. Banerjee and A. Saha (eds.), *Nonlinear Dynamics and Applications*,  
Springer Proceedings in Complexity,  
[https://doi.org/10.1007/978-3-030-99792-2\\_59](https://doi.org/10.1007/978-3-030-99792-2_59)

695

implemented in [9], where the external disturbance is identified and compensated by fuzzy logic, the variable parameters are determined based on the backstepping technique. In the papers [10, 11], identifying and correcting uncertain parameters are also implemented based on the backstepping control. Thus, there are many different methods to synthesize control systems for the class of nonlinear objects under the affection of variable parameters and external disturbance. Many results have been shown advantages of different methods, however enhancing performance of the designed system is still problems of interest to many researches. This paper presents a method of synthesizing a stable adaptive controller based on combining adaptive control, sliding control, and RBF neural network.

## 2 Problem Formulation

A multi-input multi-output (MIMO) nonlinear system will be considered in the paper:

$$\dot{\mathbf{x}} = \mathbf{A}\mathbf{x} + [\mathbf{B} + \Delta\mathbf{B}]\mathbf{u} + \mathbf{f}(\mathbf{x}) + \mathbf{d}(t), \quad (1)$$

where  $\mathbf{x} = [x_1, x_2, \dots, x_n]^T$  is state vector;  $\mathbf{u} = [u_1, u_2, \dots, u_m]^T$  is control vector;  $\mathbf{A} \in \mathbb{R}^{n \times n}$  is Hurwitz matrix with fixed elements;  $\mathbf{B} \in \mathbb{R}^{n \times m}$  is matrix with fixed elements;  $\Delta\mathbf{B} \in \mathbb{R}^{n \times m}$  matrix matched uncertainty;  $\mathbf{f}(\mathbf{x}) = [f_1(\mathbf{x}), f_2(\mathbf{x}), \dots, f_n(\mathbf{x})]^T$  is smooth nonlinear vector, matched uncertainty;  $\mathbf{d}(t) = [d_1(t), d_2(t), \dots, d_n(t)]^T$  is external disturbance vector with slow variable elements, matched uncertainty  $|d_i(t)| \leq d_M$ .

The block diagram of the designed system using identification structure with compensation of uncertain component and external disturbance is shown in Fig. 1. MODEL is the identification model; IDENT is the identification block; COMP is the compensation block of uncertain components and external disturbance; SMC is the sliding mode controller.

The control signal can be considered as follow:

$$\mathbf{u} = \mathbf{u}_{smc} + \mathbf{u}_c, \quad (2)$$

where  $\mathbf{u}_{smc}$  is control signal vector of SMC;  $\mathbf{u}_c$  is control signal vector for compensation of uncertain component and external disturbance.

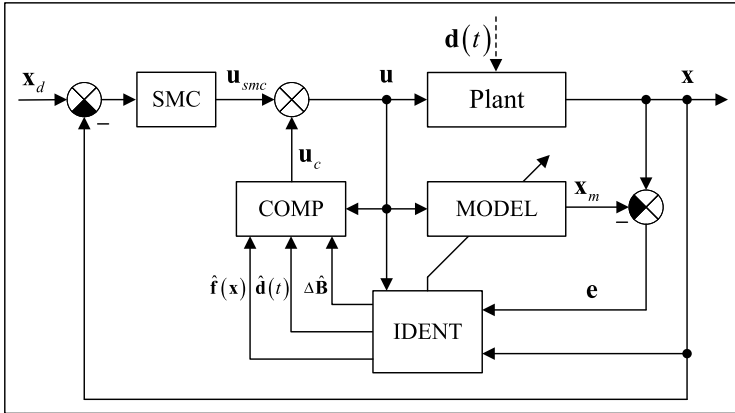


Fig. 1 Block diagram of the designed system

### 3 Algorithm for Identification and Compensation of Uncertain Parameters

Uncertain components  $\Delta\mathbf{B}$ ,  $\mathbf{f}(\mathbf{x})$ ,  $\mathbf{d}(t)$  in (1) need to be identified and adjusted for compensation. The identification model for uncertain parameters in (1) can be written:

$$\dot{\mathbf{x}}_m = \mathbf{A}\mathbf{x}_m + [\mathbf{B} + \Delta\hat{\mathbf{B}}]\mathbf{u} + \hat{\mathbf{f}}(\mathbf{x}) + \hat{\mathbf{d}}(t), \tag{3}$$

where  $\mathbf{x}_m = [x_{m1}, x_{m2} \dots x_{mn}]^T$  is state vector of the model;  $\Delta\hat{\mathbf{B}}$  is the estimated matrix of  $\Delta\mathbf{B}$  which is defined by elements  $\Delta b_{ij}$ ;  $\hat{\mathbf{f}}(\mathbf{x}) = [\hat{f}_1(\mathbf{x}), \hat{f}_2(\mathbf{x}), \dots, \hat{f}_n(\mathbf{x})]^T$  is the estimated vector of  $\mathbf{f}(\mathbf{x})$ ;  $\hat{\mathbf{d}}(t) = [\hat{d}_1(t), \hat{d}_2(t), \dots, \hat{d}_n(t)]^T$  is the estimated vector of  $\mathbf{d}(t)$ .

From (1) and (3), we have:

$$\dot{\mathbf{e}} = \mathbf{A}\mathbf{e} + \Delta\tilde{\mathbf{B}}\mathbf{u} + \tilde{\mathbf{f}}(\mathbf{x}) + \tilde{\mathbf{d}}(t), \tag{4}$$

where  $\mathbf{e} = \mathbf{x} - \mathbf{x}_m$ ;  $\Delta\tilde{\mathbf{B}} = \Delta\mathbf{B} - \Delta\hat{\mathbf{B}}$ ;  $\tilde{\mathbf{f}}(\mathbf{x}) = \mathbf{f}(\mathbf{x}) - \hat{\mathbf{f}}(\mathbf{x})$ ;  $\tilde{\mathbf{d}}(t) = \mathbf{d}(t) - \hat{\mathbf{d}}(t)$ . Identification progress will be converging when  $\Delta\tilde{\mathbf{B}} \rightarrow 0$ ,  $\tilde{\mathbf{f}}(\mathbf{x}) \rightarrow 0$ ,  $\tilde{\mathbf{d}}(t) \rightarrow 0$ . Because  $\mathbf{A}$  is defined by a Hurwitz matrix, so  $\mathbf{e} \rightarrow 0$ , and (4) is stability.

With  $\mathbf{f}(\mathbf{x})$  is a smooth function vector, by using a RBF neural network for the approximation. The elements of  $\mathbf{f}(\mathbf{x})$  can be written:

$$f_i(\mathbf{x}) = \sum_{j=1}^L w_{ij}^* \phi_{ij}(\mathbf{x}) + \varepsilon_i, \tag{5}$$

$\forall i = \overline{1, n}; j = \overline{1, L}$ , where  $L$  is number of basis function with a large enough number to guarantee the error  $|\varepsilon_i| < \varepsilon_i^m$ ,  $w_{ij}^* = const$  is the ideal weights. The basis functions are selected by the following form:

$$\phi_{ij}(\mathbf{x}) = \exp\left(-\frac{\|\mathbf{x} - \mathbf{c}_{ij}\|^2}{2\sigma_{ij}^2}\right), \tag{6}$$

where  $\mathbf{c}_{ij}$  are the position of the center of the basis functions  $\phi_{ij}(\mathbf{x})$ , and  $\sigma_{ij}$  are the standard deviation of the basis functions. The evaluation vector  $\hat{\mathbf{f}}(\mathbf{x})$  is defined by (6) with adjusted weights  $\hat{w}_{ij}$ :

$$\hat{f}_i(\mathbf{x}) = \sum_{j=1}^L \hat{w}_{ij} \phi_{ij}(\mathbf{x}), i = \overline{1, n}. \tag{7}$$

Training of the RBF neural network is implemented by adjustment of the weights  $\hat{w}_{ij}$  in comparison with the ideal weights  $w_{ij}^*$ :

$$\tilde{w}_{ij} = w_{ij}^* - \hat{w}_{ij}, \tag{8}$$

from (5), (7) and (8), we have:

$$f_i(\mathbf{x}) = \hat{f}_i(\mathbf{x}) + \varepsilon_i \rightarrow \tilde{f}(\mathbf{x}) = \sum_{j=1}^L \tilde{w}_{ij} \phi_{ij}(\mathbf{x}) + \varepsilon_i, \tag{9}$$

$\varepsilon_i$  is the approximate error with a sufficiently small value.

**Theorem 1** Equation (4) are stable when the following conditions are satisfied:

$$\|\mathbf{e}\| > \frac{2 \sum_{i=1}^n \varepsilon_i \|\bar{\mathbf{P}}_i\|}{r_{\min}(\mathbf{Q})}; \tag{10}$$

$$\mathbf{u}^T \mathbf{\Delta} \tilde{\mathbf{B}}^T \mathbf{P} \mathbf{e} + \sum_{i=1}^n \sum_{j=1}^m \Delta \dot{\tilde{b}}_{ij} \Delta \tilde{b}_{ij} = 0; \tag{11}$$

$$\mathbf{e}^T \mathbf{P} \begin{bmatrix} \sum_{j=1}^L \tilde{w}_{1j} \phi_{1j}(\mathbf{x}) \\ \vdots \\ \sum_{j=1}^L \tilde{w}_{nj} \phi_{nj}(\mathbf{x}) \end{bmatrix} + \sum_{i=1}^n \sum_{j=1}^L \dot{\tilde{w}}_{ij} \tilde{w}_{ij} = 0; \tag{12}$$



$$\mathbf{e}^T \mathbf{P} \tilde{\mathbf{d}}(t) + \sum_{i=1}^n \dot{\tilde{d}}_i \tilde{d}_i = 0. \quad (13)$$

$\mathbf{P}$  is a positive definite symmetric matrix □

**Proof.** For Eq. (4), the Lyapunov function is selected as follows::

$$V = \mathbf{e}^T \mathbf{P} \mathbf{e} + \sum_{i=1}^n \sum_{j=1}^m \Delta \tilde{b}_{ij}^2 + \sum_{i=1}^n \sum_{j=1}^L \tilde{w}_{ij}^2 + \sum_{i=1}^n \tilde{d}_i^2. \quad (14)$$

The Eq. (4) will be stable if the derivative (14)  $\dot{V} < 0$ . From (14), we have:

$$\dot{V} = \mathbf{e}^T \dot{\mathbf{P}} \mathbf{e} + \mathbf{e}^T \mathbf{P} \dot{\mathbf{e}} + 2 \sum_{i=1}^n \sum_{j=1}^m \Delta \dot{\tilde{b}}_{ij} \Delta \tilde{b}_{ij} + 2 \sum_{i=1}^n \sum_{j=1}^L \dot{\tilde{w}}_{ij} \tilde{w}_{ij} + 2 \sum_{i=1}^n \dot{\tilde{d}}_i \tilde{d}_i. \quad (15)$$

Substitute (4) into (15):

$$\begin{aligned} \dot{V} = & \mathbf{e}^T (\mathbf{A}^T \mathbf{P} + \mathbf{P} \mathbf{A}) \mathbf{e} + 2 \mathbf{u}^T \Delta \tilde{\mathbf{B}}^T \mathbf{P} \mathbf{e} + 2 \mathbf{e}^T \mathbf{P} \tilde{\mathbf{f}}(\mathbf{x}) + 2 \mathbf{e}^T \mathbf{P} \tilde{\mathbf{d}}(t) + \\ & + 2 \sum_{i=1}^n \sum_{j=1}^m \Delta \dot{\tilde{b}}_{ij} \Delta \tilde{b}_{ij} + 2 \sum_{i=1}^n \sum_{j=1}^L \dot{\tilde{w}}_{ij} \tilde{w}_{ij} + 2 \sum_{i=1}^n \dot{\tilde{d}}_i \tilde{d}_i. \end{aligned} \quad (16)$$

From (16) and (9), we have:

$$\begin{aligned} \dot{V} = & \mathbf{e}^T (\mathbf{A}^T \mathbf{P} + \mathbf{P} \mathbf{A}) \mathbf{e} + 2 \mathbf{e}^T \mathbf{P} \boldsymbol{\varepsilon} + 2 (\mathbf{u}^T \Delta \tilde{\mathbf{B}}^T \mathbf{P} \mathbf{e} + \sum_{i=1}^n \sum_{j=1}^m \Delta \dot{\tilde{b}}_{ij} \Delta \tilde{b}_{ij}) + \\ & + 2 (\mathbf{e}^T \mathbf{P} \begin{bmatrix} \sum_{j=1}^L \tilde{w}_{1j} \phi_{ij}(\mathbf{x}) \\ \vdots \\ \sum_{j=1}^L \tilde{w}_{nj} \phi_{ij}(\mathbf{x}) \end{bmatrix} + \sum_{i=1}^n \sum_{j=1}^L \dot{\tilde{w}}_{ij} \tilde{w}_{ij}) + 2 (\mathbf{e}^T \mathbf{P} \tilde{\mathbf{d}}(t) + 2 \sum_{i=1}^n \dot{\tilde{d}}_i \tilde{d}_i). \end{aligned} \quad (17)$$

Substitute (11), (12), and (13) into (17):

$$\dot{V} = \mathbf{e}^T (\mathbf{A}^T \mathbf{P} + \mathbf{P} \mathbf{A}) \mathbf{e} + 2 \mathbf{e}^T \mathbf{P} \boldsymbol{\varepsilon}. \quad (18)$$

The Eq. (18) can be written:

$$\dot{V} = -\mathbf{e}^T \mathbf{Q} \mathbf{e} + 2 \sum_{i=1}^n \varepsilon_i \bar{\mathbf{P}}_i \mathbf{e}, \quad (19)$$

$\mathbf{Q} = -(\mathbf{A}^T \mathbf{P} + \mathbf{P} \mathbf{A})$ ,  $\bar{\mathbf{P}}_i$  is the  $i$ -th row of the matrix  $\mathbf{P}$ .

Using inequality transformations [12], the Eq. (19) can be written:

$$\dot{V} = -\mathbf{e}^T \mathbf{Q} \mathbf{e} + 2 \sum_{i=1}^n \varepsilon_i \bar{\mathbf{P}}_i \mathbf{e} < -r_{\min}(\mathbf{Q}) \|\mathbf{e}\|^2 + 2 \sum_{i=1}^n \varepsilon_i \|\bar{\mathbf{P}}_i\| \|\mathbf{e}\|. \quad (20)$$

Substitute (10) into (20), we have  $\dot{V} < 0$ , the Eq. (4) is stable. □

The expressions (11), (12), and (13) of the Theorem 1 contain identification algorithms  $\Delta \mathbf{B}$ ,  $\mathbf{f}(\mathbf{x})$ , and  $\mathbf{d}(t)$ .

The Eq. (11) contains slowly variable elements, i.e.  $\Delta \hat{b}_{ij} \approx 0$ . The matrix  $\Delta \mathbf{B}$  with uncertain parameters is identified by the matrix  $\Delta \hat{\mathbf{B}}$  using the update law:

$$\Delta \hat{b}_{ij} = u_j \bar{\mathbf{P}}_i \mathbf{e}. \quad (21)$$

From (7) and (12), because of  $w_{ij}^* = const$ , we have  $\dot{w}_{ij}^* = 0$ . The vector  $\hat{\mathbf{f}}(\mathbf{x})$  for identification of the nonlinear function  $\mathbf{f}(\mathbf{x})$  can be written:

$$\hat{f}_i(\mathbf{x}) = \sum_{j=1}^L \hat{w}_{ij} \phi_{ij}(\mathbf{x}), i = \overline{1, n}. \quad (22)$$

The update weights can be defined:

$$\dot{\hat{w}}_{ij} = \bar{\mathbf{P}}_i \mathbf{e} \phi_{ij}(\mathbf{x}). \quad (23)$$

From (13), because of slow-varying external disturbance  $\dot{d}(t) \approx 0$ . The vector  $\hat{\mathbf{d}}(t)$  for identification of  $\mathbf{d}(t)$  can be written:

$$\dot{\hat{d}}_i(t) = \bar{\mathbf{P}}_i \mathbf{e}. \quad (24)$$

The received results from (21), (22), (23), and (24) are used to synthesis the compensation control law  $\mathbf{u}_c$ .

The Eq. (1) can be again written as follows:

$$\dot{\mathbf{x}} = \mathbf{A} \mathbf{x} + \mathbf{B} \mathbf{u} + \mathbf{I} \mathbf{f}_{\Sigma}(t), \quad (25)$$

where  $\mathbf{f}_{\Sigma}(t) = \Delta \mathbf{B} \mathbf{u} + \mathbf{f}(\mathbf{x}) + \mathbf{d}(t)$ ,  $\mathbf{f}_{\Sigma}(t) = [f_1^{\Sigma}, f_2^{\Sigma}, \dots, f_n^{\Sigma}]^T$ ;  $\mathbf{I}^{n \times n}$  has main diagonal elements  $I_{ij} = 1, i = j = \overline{1, n}$  are rows which corresponds to the vector  $\mathbf{f}_{\Sigma}(t)$  in the case  $|f_i^{\Sigma}| \neq 0$ ; other elements  $I_{ij} = 0$  in the case  $i \neq j$  and  $|f_i^{\Sigma}| = 0$ .

Substitute (2) into (25):

$$\dot{\mathbf{x}} = \mathbf{A} \mathbf{x} + \mathbf{B} \mathbf{u}_{smc} + \mathbf{B} \mathbf{u}_c + \mathbf{I} \mathbf{f}_{\Sigma}(t). \quad (26)$$

The vector  $\mathbf{u}_c$  can be selected:

$$\mathbf{u}_c = -\mathbf{H} \hat{\mathbf{f}}_{\Sigma}(t), \quad (27)$$

$$\hat{\mathbf{f}}_{\Sigma}(t) = \Delta \mathbf{B} \mathbf{u} + \hat{\mathbf{f}}(\mathbf{x}) + \hat{\mathbf{d}}(t); \quad (28)$$

$\Delta \hat{\mathbf{B}}$ ,  $\hat{\mathbf{f}}(\mathbf{x})$ , and  $\hat{\mathbf{d}}(t)$  are presented in (21), (22), (23), and (24).

Substitute (27) into (26):

$$\dot{\mathbf{x}} = \mathbf{A} \mathbf{x} + \mathbf{B} \mathbf{u}_{smc} - \mathbf{B} \mathbf{H} \hat{\mathbf{f}}_{\Sigma}(t) + \mathbf{I} \mathbf{f}_{\Sigma}(t). \quad (29)$$

From (29) we can see that uncertain elements will be compensated with the condition:

$$- \mathbf{B} \mathbf{H} \hat{\mathbf{f}}_{\Sigma}(t) + \mathbf{I} \mathbf{f}_{\Sigma}(t) = 0. \quad (30)$$

The Eq. (30) will be satisfied with the following condition:

$$\mathbf{B} \mathbf{H} = \mathbf{I}. \quad (31)$$

The Eq. (31) will be satisfied with:

$$\mathbf{H} = \mathbf{B}^+. \quad (32)$$

where  $\mathbf{B}^+$  is the pseudo-inverse matrix of  $\mathbf{B}$ .

Thus, the article has synthesized the compensation control law  $\mathbf{u}_c$  (27) with identification vectors  $\hat{\mathbf{f}}_{\Sigma}(t)$  (28),  $\mathbf{H}$  (32).

Using the compensation control law (27), the Eq. (29) can be written:

$$\dot{\mathbf{x}} = \mathbf{A} \mathbf{x} + \mathbf{B} \mathbf{u}_{smc}. \quad (33)$$

Thus, in this section, the identification and compensation control law  $\mathbf{u}_c$  (27) for the uncertain components of (1) have been presented, and then (1) is rewritten to (33). For (33), the control law is synthesized based on the sliding mode control.

## 4 Synthesis of the Sliding Mode Control Law

The error vector between the state vector  $\mathbf{x}$  and the desired state vector  $\mathbf{x}_d$ :

$$\tilde{\mathbf{x}} = \mathbf{x} - \mathbf{x}_d \rightarrow \mathbf{x} = \tilde{\mathbf{x}} + \mathbf{x}_d. \quad (34)$$

Substitute (34) into (33), we have:

$$\dot{\tilde{\mathbf{x}}} = \mathbf{A} \tilde{\mathbf{x}} + \mathbf{B} \mathbf{u}_{smc} + \mathbf{A} \mathbf{x}_d - \dot{\mathbf{x}}_d. \quad (35)$$

For (35), the hyper sliding surface is chosen as follows [13]:

$$\mathbf{s} = \mathbf{C} \tilde{\mathbf{x}}, \quad (36)$$

where  $\mathbf{C}$  is the parameter matrix of hyper sliding surface,  $\mathbf{s} = [s_1, s_2, \dots, s_n]^T$ .

The next problem is to define the control law  $\mathbf{u}_{smc}$  which ensures movement of the system (35) towards the hyper sliding surface (36) and keep it there.

The control signal  $\mathbf{u}_{smc}$  can be written by:

$$\mathbf{u}_{smc} = \begin{cases} \mathbf{u}_s & \text{if } \mathbf{s} \neq 0 \\ \mathbf{u}_{eq} & \text{if } \mathbf{s} = 0 \end{cases}, \quad (37)$$

$\mathbf{u}_s$  is the control signal that moves the system (35) towards the hyper sliding surface (36);  $\mathbf{u}_{eq}$  is the equivalent control signal that keeps the system (35) on the hyper sliding surface (36).

The Eq. (37) can be rewritten as:

$$\mathbf{u}_{smc} = \mathbf{u}_{eq} + \mathbf{u}_s, \quad (38)$$

$\mathbf{u}_{eq}$  is defined in [13]:

$$\dot{\mathbf{s}} = \mathbf{C}\dot{\tilde{\mathbf{x}}} = 0. \quad (39)$$

From (35) and (39), we have:

$$\mathbf{C}(\mathbf{A}\tilde{\mathbf{x}} + \mathbf{B}\mathbf{u}_{eq} + \mathbf{A}\mathbf{x}_d - \dot{\mathbf{x}}_d) = 0. \quad (40)$$

From (40), the equivalent control signal can be defined as follows:

$$\mathbf{u}_{eq} = -[\mathbf{CB}]^{-1} [\mathbf{CA}\tilde{\mathbf{x}} + \mathbf{CA}\mathbf{x}_d - \mathbf{C}\dot{\mathbf{x}}_d]. \quad (41)$$

Next, we define the control signal  $\mathbf{u}_s$  that moves the system (35) towards the hyper sliding surface (36).

For the hyper sliding surface (36), the Lyapunov function can be selected by:

$$V = \frac{1}{2} \mathbf{s}^T \mathbf{s}. \quad (42)$$

Condition for the existence of slip mode can be written:

$$\dot{V} = \mathbf{s}^T \dot{\mathbf{s}} < 0. \quad (43)$$

Substitute (35) and (38) into (43), with attention to (39), (40) we have:

$$\dot{V} = \mathbf{s}^T [\mathbf{C}(\mathbf{A}\tilde{\mathbf{x}} + \mathbf{B}\mathbf{u}_{eq} + \mathbf{A}\mathbf{x}_d - \dot{\mathbf{x}}_d) + \mathbf{CB}\mathbf{u}_s] < 0. \quad (44)$$

Inequality (43) can be written as:

$$\mathbf{s}^T [\mathbf{CB}\mathbf{u}_s] < 0. \quad (45)$$

So to satisfy the condition (43), the control signal from (45) can be defined as follows:

$$\mathbf{u}_s = -[\mathbf{CB}]^{-1}[\delta \text{sgn}(s_1), \delta \text{sgn}(s_2), \dots, \delta \text{sgn}(s_n)]^T, \tag{46}$$

$\delta$  is a positive coefficient. Substituting (41) and (46) into (37), the control signal can be defined by  $\mathbf{u}_{smc}$  as follows:

$$\mathbf{u}_{smc} = \begin{cases} -[\mathbf{CB}]^{-1}[\delta \text{sgn}(s_1), \delta \text{sgn}(s_2), \dots, \delta \text{sgn}(s_n)]^T & \text{if } \mathbf{s} \neq 0 \\ -[\mathbf{CB}]^{-1}[\mathbf{CA}\tilde{\mathbf{x}} + \mathbf{CA}\mathbf{x}_d - \mathbf{C}\dot{\mathbf{x}}_d] & \text{if } \mathbf{s} = 0 \end{cases}. \tag{47}$$

Finally, the control signals (27) and (47) are used for (2), and the control laws of (1) have been synthesized successfully.

### 5 Results and Discussion

Simulations are implemented on the Matlab environment for the controller (2) where parameter matrix, nonlinear function vectors, disturbance vectors of the system (1) are defined as follows:

$$\begin{aligned} \mathbf{A} &= \begin{bmatrix} -3.7376 & 0.0779 \\ 2.3515 & -4.1702 \end{bmatrix}; \mathbf{B} = \begin{bmatrix} 0.7014 & 0.5629 \\ 0.7248 & 0.4541 \end{bmatrix}; \Delta\mathbf{B} = \begin{bmatrix} 0.2104 & 0.1689 \\ 0.2174 & 0.1362 \end{bmatrix}; \\ \mathbf{f}(\mathbf{x}) &= \begin{bmatrix} 0.02 \sin(x_1) \sin(x_2) \\ 0.02x_1^2 \end{bmatrix}; \mathbf{d}(t) = \begin{bmatrix} 0.2 \sin(0.5t) \\ 0.2 \cos(0.7t + 2) \end{bmatrix}. \end{aligned} \tag{48}$$

With the desired signal  $\mathbf{x}_d = [1.5, 1.0]^T$ . The simulation results are shown in Figs. 2, 3 and 4.

The results of the identification of variable parameter components, nonlinear function vectors, and external disturbance are shown in Fig. 2. The results after using the compensation signal from the identification rule for uncertain components are presented in Fig. 3. From Figs. 2 and 3, we can see that the uncertain components are identified and compensated with an asymptotic error of zero. Figure 4 depicts responses of the system which present the result of tracking the state vectors of the system with the desired signal vector. These simulation results once again prove the correctness and effectiveness of the proposed control law.

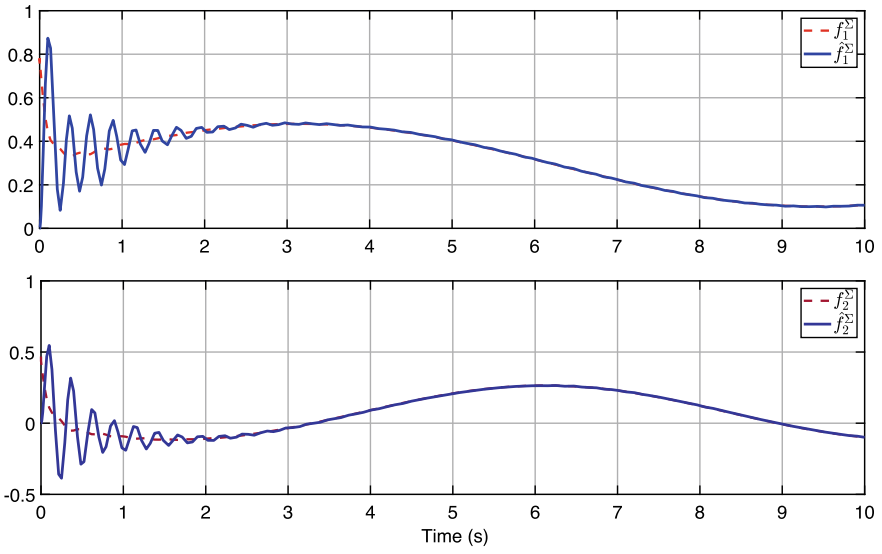


**Fig. 2** The identification vectors  $\hat{f}_\Sigma$  (28)

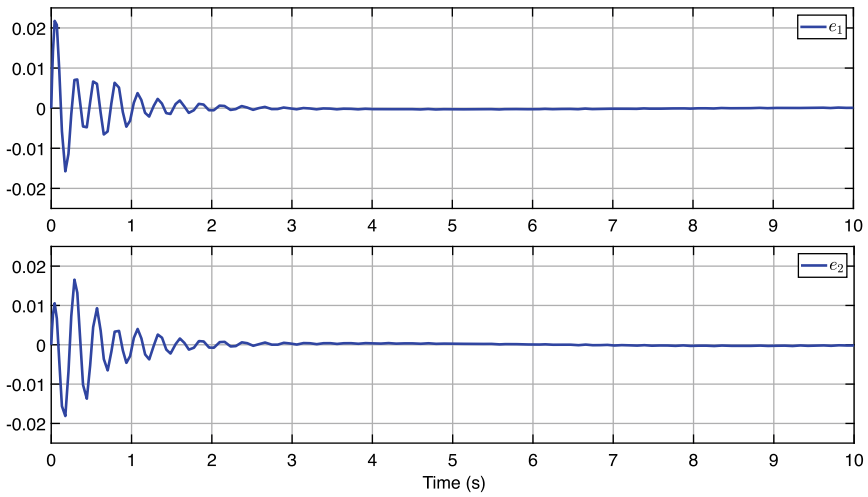


**Fig. 3** The error between (1) and linear model (33) with compensation for uncertain components

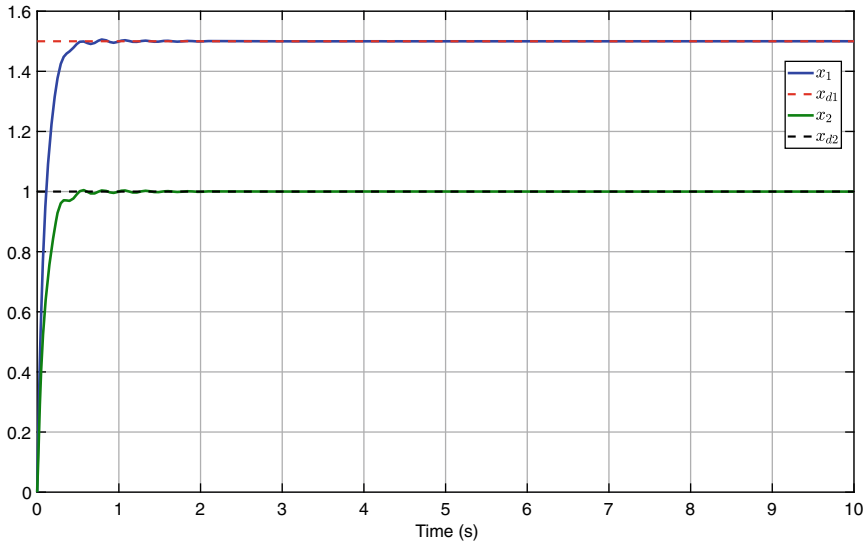


**Fig. 4** Responses of the system for the desired signals  $x_d$

## 6 Conclusion

The article has synthesized the controller for a class of nonlinear objects. Lyapunov stability theory is used to design the adaptive update law which allows identifying uncertain parameter components, nonlinear function vectors, and external disturbance. The identification results are used to generate adaptive control rules that compensate for the uncertain components. And then, the linear part of the control law is synthesized based on sliding mode control. The simulation results show that the variable parameter components, nonlinear function vectors, and external disturbance are identified and compensated according to the algorithm proposed by the article; the output vector of the system tracks to the desired set signal vector with high controllability.

## References

1. Huang, S.N., Tan, K.K., Lee, T.H.: A combined PID/adaptive controller for a class of nonlinear systems. *Automatica* **37**(4), 611–618 (2001). [https://doi.org/10.1016/S0005-1098\(00\)00195-3](https://doi.org/10.1016/S0005-1098(00)00195-3)
2. Arefi, M., Jahed-Motlagh, M., Karimi, H.: Adaptive neural stabilizing controller for a class of mismatched uncertain nonlinear systems by state and output feedback. *IEEE Trans. Cybern.* **45**(8), 1587–1596 (2015). <https://doi.org/10.1109/TCYB.2014.2356414>
3. Oveisi, A., Jeronimo, M., Nestorović, T.: Nonlinear observer-based recurrent wavelet neuro-controller in disturbance rejection control of flexible structures. *Eng. Appl. Artif. Intell.* **69**,

- 50–64 (2018). <https://doi.org/10.1016/j.engappai.2017.12.009>
4. Zhang, Y., Qin, S.: Adaptive actuator fault compensation for linear systems with matching and mismatching uncertainties. *J. Process. Control.* **19**(6), 985–990 (2009). <https://doi.org/10.1016/j.jprocont.2008.12.008>
  5. Tao, G., Chen, S., Joshi, S.: An adaptive actuator failure compensation controller using output feedback. *IEEE Trans. Autom. Control.* **47**(3), 506–511 (2002). <https://doi.org/10.1109/9.989150>
  6. Tang, X., Tao, G., Wang, L., Stankovic, J.: Robust and adaptive actuator failure compensation designs for a rocket fairing structural-acoustic model. *IEEE Trans. Aerosp. Electron. Syst.* **40**(4), 1359–1366 (2004). <https://doi.org/10.1109/TAES.2004.1386887>
  7. Maity, A., Höcht, L., Holzapfel, F.: Time-varying parameter model reference adaptive control and its application to aircraft. *Eur. J. Control.* **50**, 161–175 (2019). <https://doi.org/10.1016/j.ejcon.2019.04.007>
  8. Zhang B., Liu L., Ding K.: Optimal integral sliding mode control with feedforward compensation for nonlinear systems and its applications. In: 34th Chinese Control Conference (CCC), 2015-September, pp. 3367–3372 (2015). <https://doi.org/10.1109/ChiCC.2015.7260159>
  9. Huang, Y., Wang, T., Wang, J., Ma, K., Zhang, C., Huang, X.: Extended fuzzy adaptive event-triggered compensation control for uncertain nonlinear systems with input hysteresis. *IEEE Access* **7**, 89658–89666 (2019). <https://doi.org/10.1109/ACCESS.2019.2926280>
  10. Quang L., Putov V., Sheludko V., Kuznetsov A., Chernyshev M.: Adaptive robust control of an uncertain multi-degree-of-freedom elastically deformable electromechanical plant with adaptive compensation for an unknown disturbance. In: 10th Mediterranean Conference on Embedded Computing (MECO), pp 1–6 (2021). <https://doi.org/10.1109/MECO52532.2021.9460305>
  11. Xu, Z., Li, L., Yao, J., Hu, X., Liu, Q., Xie, N.: State constraint control for uncertain nonlinear systems with disturbance compensation. *IEEE Access* **7**, 155251–155261 (2019). <https://doi.org/10.1109/ACCESS.2019.2947629>
  12. Ortega J.: *Matrix Theory*. Springer US (1987). <https://doi.org/10.1007/978-1-4899-0471-3>
  13. Utkin, V.: *Sliding Modes in Control and Optimization*. Springer, Berlin (1992). <https://doi.org/10.1007/978-3-642-84379-2>



# **Mathematical Modeling: Trends and Applications**

# Role of Additional Food in a Delayed Eco-Epidemiological Model with the Fear-Effect



Chandan Jana , Dilip Kumar Maiti , and Atasi Patra Maiti 

**Abstract** This paper proposes an eco-epidemiological system with saturated incidence kinetics and a generalised Holling type-response function. Logistically growing prey species are partitioned into susceptible and infected prey. Predator-induced fear among prey populations suppresses the logistic growth rate and incidence rate. Additional food is supplied to predators to support them. Time-delay is incorporated to transform susceptible prey into infected prey. We derive the conditions for the existence, permanence, stability of all feasible equilibrium and the occurrence of Hopf bifurcation. Optimal control strategies are used for disease controlling by supplying additional food. Numerically, we verify analytical results and exhibit the system's dynamicity. Predator-induced fear lowers their size and switches an unstable system into a stable one. Also, an appropriate additional food supply to predators protects them from extinction and controls prey's infection.

**Keywords** Eco-epidemic · Fear · Additional food · Delay · Disease control · Chaos

## 1 Introduction

Eco-epidemiology is the intermixing of two biological fields: ecology which studies about population dynamics, and epidemiology which studies about infectious diseases in biological communities. In an epidemiological system, disease transmits from infected populations to susceptible ones due to their mutual coexistence and interaction. There are several disease transmission functions (incidence rate): the

---

C. Jana · D. Kumar Maiti (✉)

Department of Applied Mathematics with Oceanology and Computer Programming, Vidyasagar University, Midnapore 721102, West Bengal, India

e-mail: [d\\_iitkgp@yahoo.com](mailto:d_iitkgp@yahoo.com)

A. Patra Maiti

Directorate of Distance Education, Vidyasagar University, Midnapore 721102, West Bengal, India

law of mass action ( $\beta SI$ ) [2], saturated incidence  $\left(\frac{\beta SI}{1+\alpha I}\right)$  [9], and standard incidence  $\left(\frac{\beta SI}{S+I}\right)$  [6], etc. In ecology the prey-predator correlation is described by the term ‘functional responses’ which is the intake rate of a predator in unit time as a function of food density. Over the last decades, researchers have studied various ‘functional response’, like Holling type-II [7], Holling type-III [1], Crowley-Martin [5] to demonstrate prey-predator interaction.

Some recent studies [10, 11] established that due to fear of predation, prey individuals enhance their vigilance, give up their favourite food zone and habitation, migrate to a relatively low-risk region for foraging, and control their reproductive strategies accordingly. These survival strategies lower their birth rate, mutual contact and consequently decrease the infection rate. Samaddar et al. [10] explored the influence of predator-imposed fear in the prey-predator system associated with additional food to predators. They investigated that the fear together with additional food play an essential role in persisting a stable coexistence ecosystem.

Through literature reviews, to best of our knowledge, an eco-epidemiological system with (i) saturated incidence rate, (ii) Holling type-II functional response, (iii) predator-imposed fear among preys, (iv) incidence delay and (v) additional food supply to predators has not been studied yet. The main objectives of the present work are:

- To investigate how does the force of infection drive the population dynamicity?
- To illuminate the contribution of fear-effects to species survival and improvement of ecosystem stability?
- To observe whether additional food supply to predators can sustain their existence and control the disease of prey species?

This paper is arranged as follows: In Sect. 2, we formulate both non-delayed and delayed models. The well-posedness of the model is verified in Sect. 3. We analyse local stability and Hopf-bifurcation in Sect. 4. An attempt is made to control the disease in Sect. 5. In Sect. 6, we validate analytical results and investigate the system’s dynamicity through numerical simulation. At last, the conclusion and significance of the work are presented in Sect. 7.

## 2 Mathematical Model Formulation

Some basic assumptions are taken into account to formulate the model.

- The model consists three subpopulations: susceptible prey ( $S(t)$ ), infected prey ( $I(t)$ ) and predator ( $P(t)$ ) at any time  $t$ .
- Disease transmits from infected preys to susceptible individuals due to their coexistence by saturated incidence rate  $\frac{\beta SI}{1+\alpha I}$  where  $\beta$  represents the infection force and  $\alpha$  is the effect of inhibition.
- Prey-predator interaction is governed by a generalised Holling type II functional response.

**Table 1** Units and description of the used symbols

Parameters	Biological meaning	Unit
$r$	Birth rate of prey population	Time <sup>-1</sup>
$k$	Environmental carrying capacity for total prey	Biomass
$k_1, k_2$	Cost of fear	Biomass <sup>-1</sup>
$\alpha$	Inhibition effect	Time <sup>-1</sup>
$\beta$	Force of infection	Time <sup>-1</sup>
$m_1$	Rate of predation of susceptible prey	Time <sup>-1</sup>
$m_2$	Rate of predation of infected prey	Time <sup>-1</sup>
$a_1, a_2$	Handling time	Time <sup>-1</sup>
$e_1, e_2$ and $e_3$	Conversion efficiency of $P$ on $S, I$ and $\Lambda$ , respectively	Constant
$\Lambda$	Additional food	Constant
$\varphi$	Quality of additional food	Constant
$n$	Quantity of additional food	Biomass
$d_1$	Death rate of infected prey	Time <sup>-1</sup>
$d_2$	Death rate of predator	Time <sup>-1</sup>

- Due to fear of predation, fear among prey populations suppresses the logistic growth rate and incidence rate.
- The non-reproducing additional food, proportionate to the density of predators, is provided to predators at constant rate to survive them from their extinction.

Considering all these biological factors, proposed model is expressed as follows:

$$\frac{dS}{dt} = \frac{rS}{1 + k_1P} \left( 1 - \frac{S + I}{k} \right) - \frac{\beta SI}{(1 + \alpha I)(1 + k_2P)} - \frac{m_1 SP}{1 + a_1S + a_2I + \varphi n \Lambda} = \bar{f}_1(S, I, P), \tag{1}$$

$$\frac{dI}{dt} = \frac{\beta SI}{(1 + \alpha I)(1 + k_2P)} - \frac{m_2 IP}{1 + a_1S + a_2I + \varphi n \Lambda} - d_1 I = \bar{f}_2(S, I, P), \tag{2}$$

$$\frac{dP}{dt} = \frac{(e_1 m_1 S + e_2 m_2 I + e_3 n \Lambda) P}{1 + a_1 S + a_2 I + \varphi n \Lambda} - d_2 P = \bar{f}_3(S, I, P) \tag{3}$$

where  $r, k, n, a_1, a_2, d_1, d_2, e_1, e_2, e_3, k_1, k_2, m_1, m_2, \alpha, \beta, \varphi$  and  $\Lambda$  are positive constants (ref. Table 1) and  $S(0) = s_0 > 0, I(0) = i_0 > 0, P(0) = p_0 > 0$ . A schematic representation of interaction among  $S, I$  and  $P$  is presented in Fig. 1.

Let,  $\tau$  be the time lag to transform the susceptible individual into an infected one until the disease spreads to his body up to a certain level. Then, the delayed system is governed by the following equations:

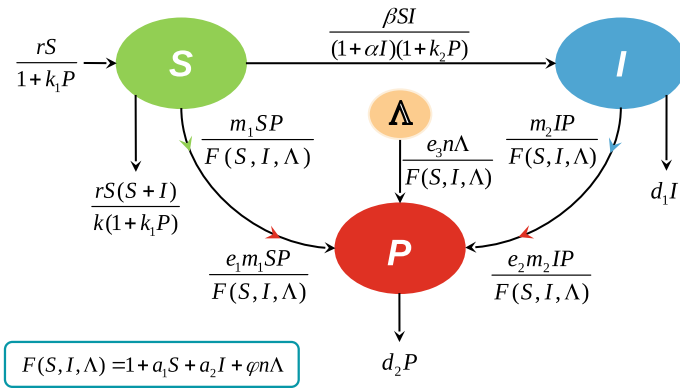


**Fig. 1** Schematic view of the dynamical interactions of  $S, I$  and  $P$  in the propose model

$$\frac{dS}{dt} = \frac{rS}{1+k_1P} \left(1 - \frac{S+I}{k}\right) - \frac{\beta SI(t-\tau)}{\{1+\alpha I(t-\tau)\}(1+k_2P)} - \frac{m_1SP}{1+a_1S+a_2I+\varphi n\Lambda} = f_1(S, I, P), \tag{4}$$

$$\frac{dI}{dt} = \frac{\beta SI(t-\tau)}{\{1+\alpha I(t-\tau)\}(1+k_2P)} - \frac{m_2IP}{1+a_1S+a_2I+\varphi n\Lambda} - d_1I = f_2(S, I, P), \tag{5}$$

$$\frac{dP}{dt} = \frac{(e_1m_1S + e_2m_2I + e_3n\Lambda)P}{1+a_1S+a_2I+\varphi n\Lambda} - d_2P = f_3(S, I, P) \tag{6}$$

where  $S(0) = \vartheta_1(\xi) > 0, I(0) = \vartheta_2(\xi) > 0, P(0) = \vartheta_3(\xi) > 0, \xi \in [-\tau, 0]$  and  $\vartheta_j \in C([-\tau, 0] \rightarrow \mathbb{R}^+)$  for  $j=1, 2, 3$ .

### 3 Basic Mathematical Results

**Theorem 1** *The system (Eqs. 1–3) is invariant in the positive octant of  $\mathbb{R}_3$  (i.e.,  $\mathbb{R}_3^+$ ).*

**Theorem 2** *All the solutions  $(S, I, P)$  of the system (Eqs. 1–3), starting from  $\mathbb{R}_3^+$ , are uniformly bounded in the area  $\Delta = \{(S, I, P) \in \mathbb{R}_3^+ : 0 < S + I \leq k, 0 < P \leq \frac{\phi}{\eta} - k\}$ , where  $\phi = \frac{rk}{4} \left(1 + \frac{\eta}{r}\right)^2$  and  $0 < \eta \leq \min \left\{d_1, d_2 - \frac{e_3}{\varphi}\right\} > 0$ , provided  $d_2 > \frac{e_3}{\varphi}$ .*

## 4 Equilibrium Points and Stability Analysis

### 4.1 Equilibrium Points

The stagnant state ( $\bar{f}_i(S, I, P) = 0$  for  $i = 1, 2, 3$ ) of the system (Eqs. 1–3) yield the following ecologically meaningful equilibria:

- (i) Trivial equilibria  $E_0(0, 0, 0)$  which always exists.
- (ii) Disease-free and predator-free equilibrium  $E_1(k, 0, 0)$  exists if  $\beta \leq d_1$  and  $\frac{e_1 m_1 k}{1 + a_1 k + \varphi n \Lambda} \leq d_2$ .
- (iii) Disease-free equilibria  $E_2(\hat{S}, 0, \hat{P})$  where  $\hat{S} = \frac{d_2(1+n\varphi\Lambda) - e_3 n \Lambda}{e_1 m_1 - a_1 d_2}$  (provided  $e_1 m_1 > a_1 d_2$  and  $d_2(1 + n\varphi\Lambda) > e_3 n \Lambda$ ) and  $\hat{P}$  is the positive root of the following equation:  $kk_1 m_1 P^2 + km_1 P - (k - \hat{S})(1 + a_1 \hat{S} + n\varphi\Lambda) = 0$ . Since  $k > \hat{S}$ , using Descartes' rule of signs, this equation must have unique positive root of  $P$ , say,  $\hat{P}$ .
- (iv) Predator-free equilibria  $E_3(S', I', 0)$  where  $S' = \frac{d_1(1+\alpha I')}{\beta}$  and  $I'$  is obtained from the following equation:  $(d_1\alpha + \beta)r\alpha I^2 + \{r(d_1\alpha + \beta) + \beta^2 k - \alpha r(\beta k - d_1)\}I - (\beta k - d_1) = 0$ . For the existence of  $E_3$ , we must have  $\beta k > d_1$ . Using Descartes' rule of signs, it is deduced that this equation possesses unique positive root of  $I$ , say,  $I'$ .
- (v) Coexistence equilibria  $E_4(S^*, I^*, P^*)$ :  $(I^*, P^*)$  is the intersection point of null-clines:  $\Phi_1(I, P) = \frac{r}{1+k_1 P} \left(1 - \frac{f(I)+I}{k}\right) - \frac{m_1 P}{1+a_1 f(I)+a_2 I+\varphi n \Lambda} - \frac{\beta I}{(1+\alpha I)(1+k_2 P)}$  and  $\Phi_2(I, P) = \frac{\beta f(I)}{(1+\alpha I)(1+k_2 P)} - \frac{m_2 P}{1+a_1 f(I)+a_2 I+\varphi n \Lambda} - d_1$ . Here,  $S = \frac{(a_2 d_2 - e_2 m_2) I}{e_1 m_1 - a_1 d_2} + \frac{d_2 + (d_2 \varphi - e_3) n \Lambda}{e_1 m_1 - a_1 d_2} = f(I)$ , and consequently one can compute  $S^*$  using the value of  $I^*$ .

### 4.2 Stability Analysis

The characteristic of the delayed system (Eqs. (4–6)) at  $E_4$  is

$$\lambda^3 + M_1 \lambda^2 + M_2 \lambda + M_3 + e^{-\lambda \tau} (N_1 \lambda^2 + N_2 \lambda + N_3) = 0 \tag{7}$$

where  $M_1 = -(m_{11} + m_{22})$ ,  $M_2 = m_{11} m_{22} - m_{12} m_{21} - m_{13} m_{31} - m_{23} m_{32}$ ,  $M_3 = m_{11} m_{23} m_{32} - m_{13} m_{21} m_{32} + m_{13} m_{22} m_{31} - m_{12} m_{23} m_{31}$ ,  $N_1 = -n_{22}$ ,  $N_2 = m_{11} n_{22} - m_{21} n_{12}$  and  $N_3 = m_{31}(m_{13} n_{22} - m_{23} n_{12})$ .

**Non-delay system** ( $\tau = 0$ ): The characteristic Eq. (7) becomes  $\lambda^3 + L_1 \lambda^2 + L_2 \lambda + L_3 = 0$  where  $L_i = M_i + N_i$  ( $i = 1, 2, 3$ ). By applying Routh Hurwitz stability criterion, we provide the stability condition at  $E_4$  in the Theorem 3.

**Theorem 3** *The interior equilibria  $E_4$  locally asymptotically stable (LAS) if the conditions are fulfilled: (i)  $L_1 > 0$ ,  $L_3 > 0$  and (ii)  $L_1 L_2 - L_3 > 0$ .*

**Lemma 1** *Trivial equilibrium  $E_0$  is always saddle.*

**Lemma 2** *Axial equilibria  $E_1$  and predator-free equilibria  $E_3$  are always locally asymptotic stable.*

**Lemma 3** *Disease-free equilibria  $E_2(\hat{S}, 0, \hat{P})$  is LAS if  $r\hat{S}(1 + a_1\hat{S} + \varphi n\Lambda) > a_1m_1k\hat{S}\hat{P}(1 + k_1\hat{P})$ .*

**Delayed system**( $\tau > 0$ ): Here, we derive the critical value of delay parameter ( $\tau$ ) at which delayed system (Eqs. (4–6)) switch its dynamical behaviour.

**Theorem 4** *The delayed system is asymptotically stable around  $E_4$  for  $\tau < \tau_c$  and undergoes through Hopf bifurcation at  $\tau = \tau_c$  which is given by*

$$\tau_c = \frac{1}{\hat{\omega}} \arccos\left(\frac{L_4L_6 + L_5L_7}{L_4^2 + L_5^2}\right) + \frac{2j\pi}{\hat{\omega}}, \quad j = 0, 1, 2, \dots \tag{8}$$

where  $L_4 = N_1\hat{\omega}^2 - N_3$ ,  $L_5 = -N_2\hat{\omega}$ ,  $L_6 = M_3 - M_1\hat{\omega}^2$  and  $L_7 = M_2\hat{\omega} - \hat{\omega}^3$ .

### 4.3 Hopf Bifurcation

**Theorem 5** *Taking the force of infection ( $\beta$ ) as bifurcation parameter, non-delay system undergoes through Hopf bifurcation under the following conditions:*

- (i)  $L_1 > 0$  and  $L_3 > 0$  at  $\beta = \beta_c$ ,
- (ii)  $L_1L_2 - L_3 = 0$  at  $\beta = \beta_c$  (for pair of purely imaginary eigenvalues),
- (iii)  $[L_1(\beta_c)L_2(\beta_c)]' \neq L_3'(\beta_c)$ ,

where  $L_i$ 's ( $i = 1, 2, 3$ ) are mentioned formerly.

## 5 Implementation of Optimal Control to Disease

We apply control on the quality ( $\varphi$ ) and quantity ( $n$ ) of additional food to minimize the infection and finally to eradicate diseases from system. Due to seasonal variation of contact rate, we consider  $\varphi$  and  $n$  as time dependent. Let us consider objective functional  $J$  as

$$J = \min_{\varphi, n} \int_{t_0}^{t_f} \{I + \Upsilon_1\varphi^2(t) + \Upsilon_2n^2(t)\}dt \tag{9}$$

subject to the Eqs. (1–3) and the parameters  $t_0$  and  $t_f$  are beginning and end time, respectively. We have to optimize  $J$ . Here,  $\Upsilon_1$  and  $\Upsilon_2$  are weights related with controls  $\varphi$  and  $n$ , respectively. For the optimal control  $(\varphi^*, n^*)$ , we have  $J(\varphi^*, n^*) = \min_{\varphi, n \in \Delta} J(\varphi, n)$  where  $\Delta = \{(\varphi, n) : 0 \leq \varphi(t) \leq M_\varphi, 0 \leq n(t) \leq M_n, t \in [t_0, t_f]\}$

is the measurable set.  $M_\varphi$  and  $M_n$  represent the respective upper bound of controls  $\varphi$  and  $n$ , respectively.

To solve the optimal control problem (Eq. (9)), let us consider the Lagrangian  $L = I + \Upsilon_1\varphi^2 + \Upsilon_2n^2$  which is to be minimized. Then, the Hamiltonian of the system is  $H = L + \gamma_1 \frac{dS}{dt} + \gamma_2 \frac{dI}{dt} + \gamma_3 \frac{dP}{dt}$  where the adjoint variables  $\gamma_i$  ( $i = 1, 2, 3$ ) can be computed by solving the system of Eq. (10):

$$\dot{\gamma}_1 = -\frac{\partial H}{\partial S}, \quad \dot{\gamma}_2 = -\frac{\partial H}{\partial I} \quad \text{and} \quad \dot{\gamma}_3 = -\frac{\partial H}{\partial P} \tag{10}$$

satisfying transversality conditions:  $\gamma_i(t_f) = 0$  for  $i = 1, 2, 3$ . Let  $\bar{\gamma}_1, \bar{\gamma}_2, \bar{\gamma}_3$  be the solutions of the system (Eq. 10) and  $(\bar{S}, \bar{I}, \bar{P})$  as optimum value of  $(S, I, P)$ .

**Theorem 6** [3, 4] *There is an optimal control  $(\varphi^*, n^*)$  such that  $J(I(t), \varphi^*(t), n^*(t)) = \min_{\varphi, n} J(I(t), \varphi(t), n(t))$  subject to the Eqs. (1–3).*

We use Pontryagin’s Maximum Principle [8, 9] to prove the Theorem 6.

**Theorem 7** *Over the region  $\Delta$ , values of optimal control pair  $(\varphi^*, n^*)$  which minimizes  $J$  is given by  $\varphi^* = \max\{0, \min(\hat{\varphi}, M_\varphi)\}$  and  $n^* = \max\{0, \min(\hat{n}, M_n)\}$  where  $\hat{\varphi}$  and  $\hat{n}$  are provided later.*

**Proof** According to the optimality condition, we have  $\frac{\partial H}{\partial \varphi} = 0$  when  $n$  is fixed and  $\frac{\partial H}{\partial n} = 0$  when  $\varphi$  is fixed. These equations yield least positive real roots, say,  $\hat{\varphi}$  and  $\hat{n}$ . Again,  $0 \leq \varphi(t) \leq M_\varphi$  and  $0 \leq n(t) \leq M_n$  for  $t \in [t_0, t_f]$ . So, we have  $\varphi^* = \max\{0, \min(\hat{\varphi}, M_\varphi)\}$  and  $n^* = \max\{0, \min(\hat{n}, M_n)\}$ , and consequently the optimized  $J$ .

## 6 Numerical Simulation

We perform numerical simulation to validate the analytical results and observe dynamical behaviour of the system. A set of parameters’ values are considered, based on idea related to the sensitivity of parameters, as  $Z = \{r = 1, k = 5, a_1 = 1, a_2 = 0.9, d_1 = 0.15, d_2 = 0.1, e_1 = 0.5, e_2 = 0.4, e_3 = 0.15, k_1 = 0.15, k_2 = 0.02, m_1 = 0.4, m_2 = 0.5, \alpha = 0.6, \beta = 2, \varphi = 1, n = 0.65, L = 1\}$ .

### 6.1 Non-delay System

Evidently, for the set  $Z$  two nullclines  $\Phi_1(I, P) = 0$  and  $\Phi_2(I, P) = 0$  intersect uniquely at (0.4517, 0.5754) in the  $IP$ -plane (ref. Fig. 2a). Then, we have  $S^* = 0.1788$ , i.e. the coexistence equilibria  $E_4(0.1788, 0.4517, 0.5754)$  exists (ref. Fig. 2b). At  $E_4$ , we have the eigenvalues as  $-0.0297 + 0.4295i, -0.0297 - 0.4295i,$



−0.0029, i.e., real part of all the eigenvalues are negative. Moreover, all the quantities  $L_1 = 0.0560$ ,  $L_2 = 0.0008$  and  $L_1L_2 - L_3 = 0.0112$  are positive at  $E_4$  (i.e., all the criterias of Theorem 3 are fulfilled). Therefore,  $E_4$  is asymptotically stable for non-delay system which is illuminated in Fig. 2d.

In Fig. 3, an attempt is made to illuminate system behaviour with the variation of force of infection  $\beta$  considering three cases: (a–c) absence of fear ( $k_1 = 0, k_2 = 0$ ) and additional food ( $\Lambda = 0$ ), (d–f) absence of fear ( $k_1 = 0, k_2 = 0$ ) and the presence of additional food ( $\Lambda = 1$ ), and (g–i) presence of fear ( $k_1 = 0.15, k_2 = 0.02$ ) and additional food ( $\Lambda = 1$ ). For these three situations, corresponding Hopf-points are  $\beta_c = 1.35, 2.1$  and  $1.7$ , respectively, i.e., at those points system’s stability switches from unstable to stable one. It is seen that in the absence of fear ( $k_1 = 0, k_2 = 0$ ) and additional food ( $\Lambda = 0$ ), predator extinct beyond  $\beta = 1.55$ . But, in the presence of additional food (ref. Fig. 3f), predators extinct beyond  $\beta = 2.4$ . Biologically speaking, an additional food supply to predators can survive themselves from its extinction

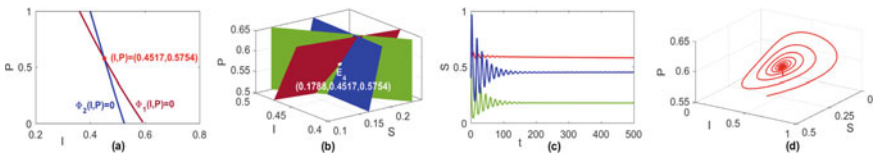


**Fig. 2** **a** Existence of the intersection point of the nulllines  $\Phi_1(I, P) = 0$  and  $\Phi_2(I, P) = 0$ ; **b** existence of unique  $E_4(0.1788, 0.4517, 0.5754)$ ; **c** time histories of populations; **d** stable focus for the parameter set  $Z$  of system (Eqs. 1–3)

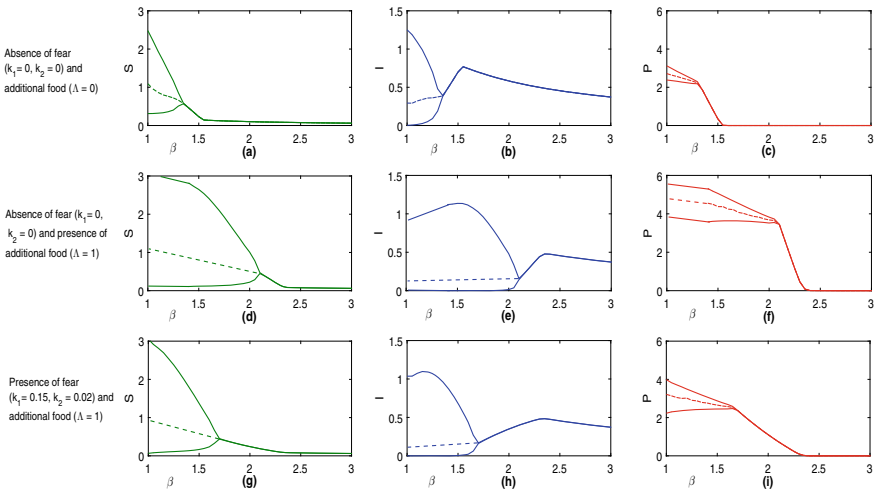


**Fig. 3** Bifurcation diagram against force of infection  $\beta$  for the parameter set  $Z$ . **a–c** in the absence of fear ( $k_1 = 0, k_2 = 0$ ) and additional food ( $\Lambda = 0$ ), **d–f** in the absence of fear ( $k_1 = 0, k_2 = 0$ ) and the presence of additional food ( $\Lambda = 1$ ), and **g–i** in the presence of fear ( $k_1 = 0.15, k_2 = 0.02$ ) and additional food ( $\Lambda = 1$ )

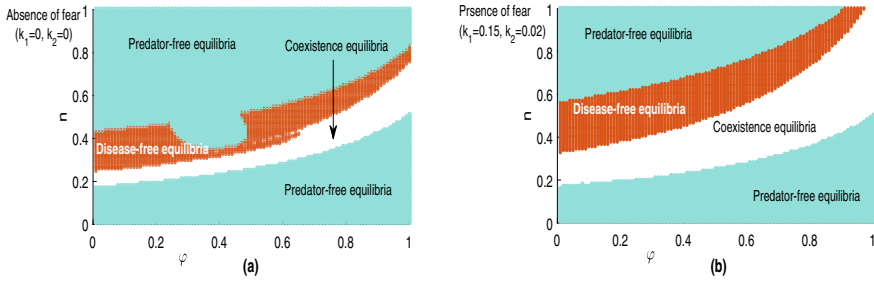


**Fig. 4** Existence of various equilibria in  $\varphi n$ -plane

on a large scale of  $\beta$ , relatively. Further, incorporating fear-effect (ref. Fig. 3g–i), it can be seen that system becomes stable on a relatively large scale of  $\beta$ . Hence, fear-effect is efficient to make a sustainable stable ecosystem. It may be mentioned that a certain level of fear is fruitful to survive all the populations. But, a level of fear may eradicate predators from the system. Evidently, infected populations increase up to a certain level of increasing  $\beta$ . After that, all the populations decrease noticeably with a further increase in  $\beta$ . This is biologically reasonable because the density of the  $I$ -population attains a maximum value at a threshold  $\beta$ . Thereafter, the system declines to increase the density of infected population as  $S$ -populations decrease with increasing  $\beta$ .

In Fig. 4, we present various equilibria in  $\varphi n$ -plane in the presence or absence of fear. One may observe that both quality ( $\varphi$ ) and quantity ( $n$ ) of additional food must be a reasonable amount for the existence of all the populations; otherwise, predators may become extinct from the system. Also, by supplying suitable quality ( $\varphi$ ) and quantity ( $n$ ) of additional food, we make a system disease-free as seen in Fig. 4. We use Pontryagin’s Maximum Principle to find the optimum value of  $(\varphi, n)$  for disease controlling by supplying additional food. Moreover, the presence of the fear-effect increase the region of existence of interior equilibria.

### 6.2 Delayed System

Taking  $\tau$  as a bifurcation parameter, the dynamical behaviour of the delayed system is explored in Fig. 5 with the help of the bifurcation diagram. The delayed system is stable for  $\tau < 0.72$ . For  $\tau > 0.72$ , the delayed system’s exhibits complex dynamics, discussed in Fig. 5. It is seen that when  $\tau$  crosses the critical values, steady-state values separated into maximum and minimum of the periodic oscillatory solution, and coexistence steady-state becomes unstable, i.e., Hopf bifurcation occurs at point of separation. For a fixed  $\tau$ , the occurrence of too many local maxima/ minima indicates that the system performs chaotic behaviour. However, during the chaotic situation, populations take successive values randomly occupying a fixed range of correspond-

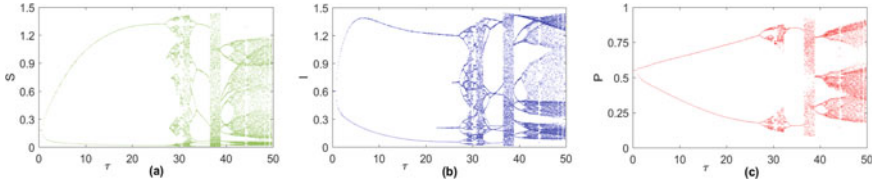


**Fig. 5** Bifurcation diagram against delay parameter  $\tau$  for the parameter set  $Z$

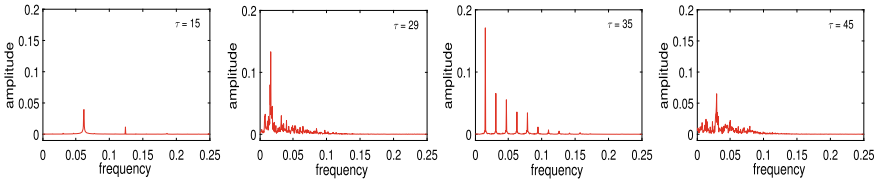


**Fig. 6** Spectra of instantaneous  $S$ -population for several fixed  $\tau$  for the parameter set  $Z$

ing populations, similar to a situation of  $\sin(\frac{1}{x})$  as  $x$  gets closer to zero. It is seen that the system is periodic for  $\tau \in [0.72, 27.04] \cup [33.57, 36.75] \cup [39.25, 40.53]$ , otherwise chaotic. This complexity in the system’s dynamics can be verified from Fig. 6. A finite number of the spectral peak corresponds to periodic behaviour, while no definite spectral peak exposes system’s chaotic behaviour.

## 7 Conclusion

Here, we have proposed and analysed an eco-epidemiological system with infection among prey species, and additional food is provided to predators. Fear-effect is incorporated as a reducing factor in logistic growth of prey species and the disease transmission function. Also, we consider incidence delay to make the system biologically more realistic.

The numerical analyses is executed extensively to investigate the potentiality that cost of fears and additional supplied food can play a pivotal role in the system. It has been observed that a suitable choice of additional food may eradicate the disease from the system and help the predators to survive. Also, an adequate level of fear transforms an unstable system into a stable one. The system exhibits rich dynamics in the presence of incidence delay. Hence, a reasonable amount of fear-effect and additional food is essential to survive all the populations and to make a sustainable stable ecosystem. Our studies reveal a non-chemical approach to control disease in an eco-epidemiological system.

**Acknowledgements** Author Dilip K. Maiti acknowledges supports given by the DST-FIST, INDIA (Sanction Order No.: SR/FST/MS-1/2018/21(C) dated-13/12/2019) for upgradation of research facility at the departmental level.

## References

1. Banerjee, R., Das, P., Mukherjee, D.: Global dynamics of a holling type-iii two prey-one predator discrete model with optimal harvest strategy. *Nonlinear Dyn.* **99**(4), 3285–3300 (2020)
2. Greenhalgh, D., Khan, Q.J., Al-Kharousi, F.A.: Eco-epidemiological model with fatal disease in the prey. *Nonlinear Anal. Real World Appl.* **53**, 103072 (2020)
3. Kar, T., Ghorai, A., Jana, S.: Dynamics of pest and its predator model with disease in the pest and optimal use of pesticide. *J. Theoret. Biol.* **310**, 187–198, 103072 (2012)
4. Lukes, D.L.: *Differential Equations: Classical to Controlled* (1982)
5. Maiti, A.P., Jana, C., Maiti, D.K.: A delayed eco-epidemiological model with nonlinear incidence rate and crowley-martin functional response for infected prey and predator. *Nonlinear Dyn.* **98**(2), 1137–1167, 103072 (2019)
6. Maji, C., Kesh, D., Mukherjee, D.: The effect of predator density dependent transmission rate in an eco-epidemic model. *Differ. Equ. Dyn. Syst.* **28**(2), 479–493, 103072 (2020)
7. Panday, P., Samanta, S., Pal, N., Chattopadhyay, J.: Delay induced multiple stability switch and chaos in a predator-prey model with fear effect. *Math. Comput. Simul.* **172**, 134–158, 103072 (2020)
8. Pontryagin, L.S.: *Mathematical Theory of Optimal Processes*. CRC Press (1987)
9. Sahoo, B.: Role of additional food in eco-epidemiological system with disease in the prey. *Appl. Math. Comput.* **259**, 61–79, 103072 (2015)
10. Samaddar, S., Dhar, M., Bhattacharya, P.: Effect of fear on prey–predator dynamics: exploring the role of prey refuge and additional food. *Chaos Interdiscip. J. Nonlinear Sci.* **30**(6), 063129 (2020)
11. Sha, A., Samanta, S., Martcheva, M., Chattopadhyay, J.: Backward bifurcation, oscillations and chaos in an eco-epidemiological model with fear effect. *J. Biolog. Dyn.* **13**(1), 301–327, 103072 (2019)

# Impact of Predator Induced Fear in a Toxic Marine Environment Considering Toxin Dependent Mortality Rate



Dipesh Barman, Jyotirmoy Roy, and Shariful Alam

**Abstract** The concentration of harmful toxins in the marine ecosystem coming from different external sources is increasing day by day and becomes a serious threat to living organisms. On the other hand, in the field of predator-prey interactions, one main aspect which has been neglected for decades is predator-induced fear to prey species that affects reproduction rate of prey individuals. Keeping in mind both the factors, a mathematical model has been proposed by incorporating predator-induced fear in that toxic ecosystem. It has been observed that the system undergoes Hopf-bifurcation with respect to both the parameters associated with fear factor and toxicity. Also, there is a complex relationship between these two parameters and fear factor plays a significant role in predator extinction. All the analytical findings have been verified through numerical simulations by considering appropriate hypothetical parameter sets.

**Keywords** Fear effect · Toxicity · Hopf-bifurcation · Population density

## 1 Introduction

Till decades one of the most ignoring fact in predator-prey interactions is to avoid the indirect effect of predator induced fear to prey species. Most of the researchers formulated predator-prey model by taking into consideration the direct predation of prey species and accordingly analyze the system dynamics. But, in 2011, Zanette et al. [16] made an experiment to song sparrow by supplying their predator's vocal cues to some of the song sparrow population while the remaining others do not experience any vocal cues of their predators. However, it is observed that, all the song sparrow populations who suffered from predator cues have shown a lessen activity in reproduction by 40% as compared to the population who did not receive

---

D. Barman (✉) · J. Roy · S. Alam  
Indian Institute of Engineering Science and Technology, Shibpur, Howrah 711103, West Bengal,  
India  
e-mail: [dipeshrs2018@gmail.com](mailto:dipeshrs2018@gmail.com)

© The Author(s), under exclusive license to Springer Nature Switzerland AG 2022  
S. Banerjee and A. Saha (eds.), *Nonlinear Dynamics and Applications*,  
Springer Proceedings in Complexity,  
[https://doi.org/10.1007/978-3-030-99792-2\\_61](https://doi.org/10.1007/978-3-030-99792-2_61)

721

any disturbance of predator's sound. Influencing by this phenomenon, Wang et al. [14] formulated a mathematical model and observed that predator induced fear has an immense impact on system dynamics. Later on many researchers [1–3, 13, 15, 17] modified predator-prey model by considering this fear effect and analyzes them accordingly (for more interest one may read the references therein).

Marine pollution happens due to the entry of harmful chemicals, metals, etc., from different point and non point sources into the sea water. The vast majority of marine contamination comes from land. Air contamination is likewise a contributing component via carting away iron, sulfur, nitrogen, silicon, carbonic acid, pesticides or residue particles into the ocean [5]. The point source pollution includes entry of harmful particles from a easily identified source while non point source contamination describes pollutants coming from agricultural activities, wind-blown debris, and dust. At the point when pesticides are joined into the marine environment, they immediately become consumed into marine food webs and as a consequence various types of illness such as disease, mutation, tissue related problems, decrease in reproduction, etc., begin to occur in marine life [7, 9, 11, 12]. So, due to toxicity many marine species suffered from increasing mortality rate. Not only this toxin harms marine species, it also has an immense impact on the higher tropic level in food web including sea birds and human being who consume this species [6].

In recent days, a lot of attention by researchers was paid to address the impact of toxicants in environment. In this regard, Hallam and Clark [8] studied the first order kinetics of a population in the presence of toxicity. After that, Hallam and De Luna [9] investigated a model considering toxins from both the environmental and food chain pathways. Later on, Chattopadhyay [4] performed a study on two species competing with each other and observed that all the populations persist with the help of toxicants. Again, Huang et al. [10] demonstrated through a research study of a prey-predator model with the influence of environmental toxicants where both prey and predator are exposed to the toxicants simultaneously. However, in this study, we have made an attempt to realize the effect of toxic substance in marine environment in the presence of predator induced fear. Here, we have made an attempt in exploring the role of predator exerted fear on prey population where both the species suffer from an increased mortality rate due to toxicity of water in marine ecosystem. The motivation of this study includes to explore the role of fear effect and toxicity in system dynamics in the presence of external toxin sources. Not only this thing, how toxicity and fear level are related to each other in system dynamics is also an interest of this study. This article has been organized in several sections such as: Sect.2 describes about the formation of model system (1); Sect.3 verifies the well-posedness of system (1) while Sect.4 manages to analyse local stability around different equilibrium points. The findings of this system have been obtained in Sect. 5 with the help of MATLAB & MATCONT. Finally, this article ends with Sect. 6 as conclusion.

## 2 Model Formulation

Here, we have formulated a predator-prey model in (1) by considering predator induced fear to prey population in a toxic marine ecosystem as follows:

$$\begin{cases} \frac{dx}{dt} = \frac{rx}{1+fy} - d_1x - mx^2 - \frac{\alpha xy}{1+bx} - \frac{e\gamma T}{1+e\gamma T}x, \\ \frac{dy}{dt} = \frac{\beta xy}{1+bx} - d_2y - \frac{e\gamma T}{1+e\gamma T}y, \\ \frac{dT}{dt} = A - aT - \gamma(x+y)T, \end{cases} \tag{1}$$

with initial conditions

$$x(0) > 0, y(0) > 0, T(0) > 0, \tag{2}$$

where  $x$ ,  $y$  and  $T$  respectively denote the density of prey population, predator population and harmful toxin concentration at any time  $t$ . The above model (1) has been constructed based on some assumptions such as

- (i) In the absence of predator population, prey individuals grow logistically with growth rate  $r$  and natural mortality rate  $d_1$ . Furthermore, prey individuals engage into a clash among themselves at a rate  $m$  for food resources.
- (ii) Predator population consumes prey individuals according to Holling type -II functional response at a rate  $\alpha$  and predator species get benefited by reproducing new offsprings at a rate  $\beta$  from this food consumption. They die naturally at a rate  $d_2$ .
- (iii) The birth rate of prey species reduces due to the fear exerted from predator species according to a function  $\phi(f, y) = \frac{1}{1+fy}$  as proposed by Wang et al. [14]. One can read the detailed biological assumptions for constructing this fear function described in [14].
- (iv) The harmful toxins for both species are coming from various types of man made external sources like industries, households, pesticides used in agriculture, etc. at a constant rate  $A$ . It is assumed that toxin declines naturally or toxic materials in marine system have been removed at a rate  $a$  due to different types of government initiatives or awareness. Furthermore, it is assumed that toxin concentration reduces due to the interaction between toxin and both the species at a rate  $\gamma$ .
- (v) It is further assumed that due to the interaction with toxin, both the species die out from the system and this death rate depends on the concentration of toxin and strength in toxin, i.e., toxicity  $e$ . We have proposed that both the

species die according to the function  $\Psi(e, T) = \frac{e\gamma T}{1 + e\gamma T}$ . Clearly, it is to be noted that, both species do not die in the absence of toxin as  $\Psi(e, T) = 0$ ; level of toxin, i.e., toxicity may influence the death rate because for  $e = 0$ ,  $\Psi(e, T)$  becomes zero. Interestingly,  $\frac{\partial \Psi}{\partial e} > 0$  and  $\frac{\partial \Psi}{\partial T} > 0$  indicates that both population suffers a higher death rate with the increase of both the toxicity level  $e$  and toxin concentration  $T$ .

### 3 Well-posedness

#### 3.1 Positivity

**Theorem 1** *Every solution of system (1) starting from IC (2) remains positive for any time  $t > 0$ .*

**Proof** The proof is very much straight forward and hence omitted.

#### 3.2 Boundedness

**Theorem 2** *Every solution of system (1) starting from IC (2) is always bounded.*

**Proof** The proof is very much straight forward and hence omitted.

### 4 Stability Analysis

#### 4.1 Fixed Points with Their Existence Conditions

Model system (1) has three fixed or equilibrium points, namely

- (i) Axial equilibrium point  $E_1 \left( 0, 0, \frac{A}{a} \right)$  always exists;
- (ii) Planar equilibrium point  $E_2 \left( \bar{x}, 0, \frac{A}{a + \gamma \bar{x}} \right)$  exists for  $Ae\gamma < (r - d_1)(a + Ae\gamma)$  and  $\bar{x}$  has to be extracted from the underlying equation

$$m\gamma x^2 + \{m(a + Ae\gamma) - \gamma(r - d_1)x\} + Ae\gamma - (r - d_1)(a + Ae\gamma) = 0.$$

- (iii) Interior equilibrium point  $E^* (x^*, y^*, T^*)$  where



$$x^* = \frac{e\gamma T^* + d_2(1 + e\gamma T^*)}{(1 + e\gamma T^*)(\beta - bd_2) - be\gamma T^*}$$

exists for  $\beta - bd_2 > \frac{Abe\gamma}{Ae\gamma + a + \gamma(x^* + y^*)}$ ,

$$T^* = \frac{A}{a + \gamma(x^* + y^*)},$$

and  $y^*$  has to be calculated from

$$\alpha f y^2 - \{f(d_2 - d_1 - mx^*)(1 + bx^*) - \alpha - \beta f x^*\}y + \beta x^* - r - (d_2 - d_1 - mx^*)(1 + bx^*) = 0,$$

under the restriction  $\beta x^* + (mx^* + d_1 - d_2)(1 + bx^*) < r$ .

### 4.2 Local Stability Analysis (LAS)

In this subsection, our main interest is to explore the restrictions under which system (1) remains close enough to the corresponding fixed points under a slight given perturbation and this job has been performed with the help of the following theorems.

**Theorem 3** System (1) exhibits LAS behavior around axial equilibrium point  $E_1 \left(0, 0, \frac{A}{a}\right)$  for  $r < d_1 + \frac{Ae\gamma}{a + Ae\gamma}$ .

**Proof** Eigenvalues of Jacobian matrix computed at axial equilibrium point  $E_1 \left(0, 0, \frac{A}{a}\right)$  are

$$\lambda_1 = r - d_1 - \frac{Ae\gamma}{a + Ae\gamma} < 0 \text{ for } r < d_1 + \frac{Ae\gamma}{a + Ae\gamma}, \lambda_2 = -d_2 - \frac{Ae\gamma}{a + Ae\gamma} < 0, \lambda_3 = -a < 0.$$

Hence the result.

**Theorem 4** System (1) exhibits LAS behavior around planar equilibrium point  $E_2 \left(\bar{x}, 0, \frac{A}{a + \gamma\bar{x}}\right)$  for

- (i)  $\frac{\beta\bar{x}}{1 + b\bar{x}} < d_2 + \frac{e\gamma\bar{T}}{1 + e\gamma\bar{T}}$ ,
- (ii)  $r < a + (\gamma + 2m)\bar{x} + d_1 + \frac{e\gamma\bar{T}}{1 + e\gamma\bar{T}}$ ,
- (iii)  $(a + \gamma\bar{x}) \left(r - d_1 - 2m\bar{x} - \frac{e\gamma\bar{T}}{1 + e\gamma\bar{T}}\right) + \frac{e\gamma^2\bar{x}\bar{T}}{(1 + e\gamma\bar{T})^2} < 0$ .

**Proof** One eigenvalue of Jacobian matrix computed at planar equilibrium point  $E_2 \left(\bar{x}, 0, \frac{A}{a + \gamma\bar{x}}\right)$  is

$$\lambda_1 = \frac{\beta\bar{x}}{1 + b\bar{x}} - d_2 - \frac{e\gamma\bar{T}}{1 + e\gamma\bar{T}} < 0 \text{ for } \frac{\beta\bar{x}}{1 + b\bar{x}} < d_2 + \frac{e\gamma\bar{T}}{1 + e\gamma\bar{T}},$$

and other two eigenvalues has to be obtained from

$$\lambda^2 - \left( r - d_1 - 2m\bar{x} - \frac{e\gamma\bar{T}}{1 + e\gamma\bar{T}} - a - \gamma\bar{x} \right) \lambda - \frac{e\gamma^2\bar{x}\bar{T}}{(1 + e\gamma\bar{T})^2} - (a + \gamma\bar{x}) \left( r - d_1 - 2m\bar{x} - \frac{e\gamma\bar{T}}{1 + e\gamma\bar{T}} \right) = 0.$$

The above equation will have two negative real roots for conditions (ii) and (iii). Hence the result.

**Theorem 5** System (1) displays LAS behavior close to interior equilibrium point  $E^*(x^*, y^*, T^*)$  if  $\xi_1 > 0$ ,  $\xi_3 > 0$  and  $\xi_1\xi_2 > \xi_3$  hold.

**Proof** Characteristic equation of the Jacobian matrix computed at interior equilibrium point  $E^*(x^*, y^*, T^*)$  is given by

$$\lambda^3 + \xi_1\lambda^2 + \xi_2\lambda + \xi_3 = 0, \tag{3}$$

where

$$\begin{aligned} \xi_1 &= -J_{11}^* - J_{22}^* - J_{33}^*, \\ \xi_2 &= J_{11}^*J_{22}^* + J_{11}^*J_{33}^* + J_{22}^*J_{33}^* - J_{23}^*J_{32}^* - J_{12}^*J_{21}^* + J_{13}^*J_{21}^*, \\ \xi_3 &= J_{12}^*J_{21}^*J_{33}^* - J_{12}^*J_{31}^*J_{23}^* - J_{13}^*J_{21}^*J_{33}^* + J_{13}^*J_{23}^*J_{31}^* - J_{11}^*J_{22}^*J_{33}^* + J_{11}^*J_{23}^*J_{32}^* \end{aligned}$$

and

$$\begin{aligned} J_{11}^* &= \frac{r}{1 + fy^*} - d_1 - 2mx^* - \frac{\alpha y^*}{(1 + bx^*)^2} - \frac{e\gamma T^*}{1 + e\gamma T^*}, \quad J_{12}^* = -\frac{rfx^*}{(1 + fy^*)^2} - \frac{\alpha x^*}{1 + bx^*}, \\ J_{13}^* &= -\frac{e\gamma x^*}{(1 + e\gamma T^*)^2}, \quad J_{21}^* = \frac{\beta y^*}{(1 + bx^*)^2}, \quad J_{22}^* = \frac{\beta x^*}{1 + bx^*} - d_2 - \frac{e\gamma T^*}{1 + e\gamma T^*}, \quad J_{23}^* = -\frac{e\gamma y^*}{(1 + e\gamma T^*)^2}, \\ J_{31}^* &= -\gamma T^*, \quad J_{32}^* = -\gamma T^*, \quad J_{33}^* = -a - \gamma(x^* + y^*). \end{aligned}$$

From Routh Hurwitz criteria, equation (3) have negative root or roots having negative real part if  $\xi_1 > 0$ ,  $\xi_3 > 0$  and  $\xi_1\xi_2 > \xi_3$  hold. Hence the theorem.

### 4.3 Existence of Hopf-bifurcation

Here, we are going to explore the Hopf-bifurcation existence conditions of the model system (1) around the interior equilibrium point  $E^*(x^*, y^*, T^*)$  w.r.t the fear effect  $f$ .

**Theorem 6** The system (1) undergoes Hopf-bifurcation around the interior equilibrium point  $E^*(x^*, y^*, T^*)$  w.r.t the fear effect  $f$  if  $f$  exceeds the threshold value

$f = f^*$ . The necessary and sufficient conditions for occurring Hopf-bifurcation at  $f = f^*$  of the model system (1) are

- (i)  $\eta_1(f^*)\eta_2(f^*) - \eta_3(f^*) = 0$ ,
- (ii) The transversality condition  $\frac{d}{df}[Re(\lambda(f))]_{f=f^*} \neq 0$ .

**Proof** The characteristic equation (3) at  $f = f^*$  becomes

$$(\lambda^2 + \eta_2)(\lambda + \eta_1) = 0, \tag{4}$$

i.e.,  $\lambda_1 = i\sqrt{\eta_2}$ ,  $\lambda_2 = -i\sqrt{\eta_2}$  and  $\lambda_3 = -\eta_1$ .

For  $f \in (f^* - \mu, f^* + \mu)$ , where  $\mu$  is a sufficiently small positive quantity and the general root can be taken as follows

$$\begin{aligned} \lambda_1(f) &= \theta_1(f) + i\theta_2(f), \\ \lambda_2(f) &= \theta_1(f) - i\theta_2(f), \\ \lambda_3(f) &= -\eta_1. \end{aligned}$$

Now, let us try to figure out the restrictions for which the transversality condition is satisfied.

Substituting  $\lambda_1(f) = \theta_1(f) + i\theta_2(f)$  into (4) and taking the derivative w.r.t  $f$ , we get

$$\begin{aligned} E(f)\theta'_1(f) - F(f)\theta'_2(f) + G(f) &= 0, \\ F(f)\theta'_1(f) + E(f)\theta'_2(f) + H(f) &= 0, \end{aligned}$$

where

$$\begin{aligned} E(f) &= 3\theta_1^2(f) + 2\eta_1(f)\theta_1(f) + \eta_2(f) - 3\theta_2^2(f), \\ F(f) &= 6\theta_1(f)\theta_2(f) + 2\eta_1(f)\theta_2(f), \\ G(f) &= \theta_1^2(f)\eta'_1(f) + \eta'_2(f)\theta_1(f) + \eta'_3(f) - \eta'_1(f)\theta_2^2(f), \\ H(f) &= 2\theta_1(f)\theta_2(f)\eta'_1(f) + \eta'_2(f)\theta_2(f). \end{aligned}$$

Since  $\theta_1(f^*) = 0$ ,  $\theta_2(f^*) = \sqrt{\eta_2(f^*)}$ , so

$$\begin{aligned} E(f^*) &= -2\eta_2(f^*), \\ F(f^*) &= 2\eta_1(f^*)\sqrt{\eta_2(f^*)}, \\ G(f^*) &= \eta'_3(f^*) - \eta'_1(f^*)\eta_2(f^*), \\ H(f^*) &= \eta'_2(f^*)\sqrt{\eta_2(f^*)}. \end{aligned}$$

Therefore,

$$\begin{aligned}
 & \frac{d}{df} [Re(\lambda(f))]_{f=f^*} \\
 &= - \frac{F(f^*)H(f^*) + E(f^*)G(f^*)}{E^2(f^*) + F^2(f^*)} \\
 &= - \frac{2\eta_1(f^*)\sqrt{\eta_2(f^*)}\eta'_2(f^*)\sqrt{\eta_2(f^*)} + (-2\eta_2(f^*))\{\eta'_3(f^*) - \eta'_1(f^*)\eta_2(f^*)\}}{(-2\eta_2(f^*))^2 + \{(2\eta_1(f^*)\sqrt{\eta_2(f^*)}\}^2} \\
 &= - \frac{\eta_1(f^*)\eta'_2(f^*) - \eta'_3(f^*) + \eta'_1(f^*)\eta_2(f^*)}{2\{\eta_2(f^*) + \eta_1(f^*)\}^2} \\
 &\neq 0, \quad \text{if } \eta'_3(f^*) \neq \eta_1(f^*)\eta'_2(f^*) + \eta'_1(f^*)\eta_2(f^*) \text{ and } \lambda_3(f^*) = -\eta_1(f^*) \neq 0.
 \end{aligned}$$

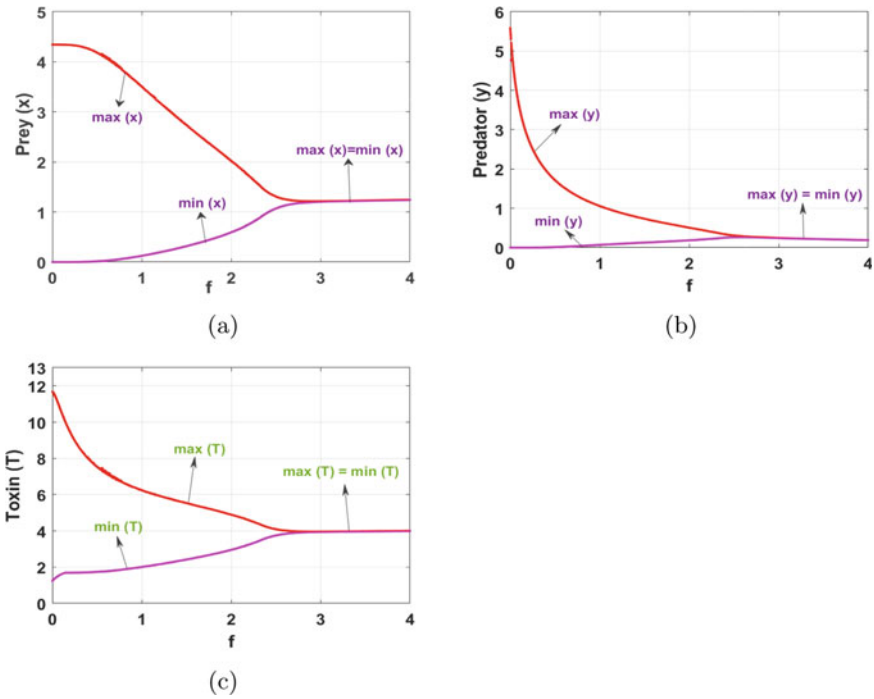
Hence the theorem.

### 5 Numerical Simulation

In this section, we are going to verify all the analytical findings as discussed before by using the softwares MATLAB and MATCONT. So, at first, we have to choose the parameter set as follows:

$$r = 0.5, \quad f = 0.01, \quad m = 0.1, \quad \alpha = 0.5, \quad \beta = 0.4, \quad b = 2, \quad e = 1.16, \quad A = 0.6, \quad a = 0.05, \quad \gamma = 0.07, \quad d_1 = 0.01, \quad d_2 = 0.02. \tag{5}$$

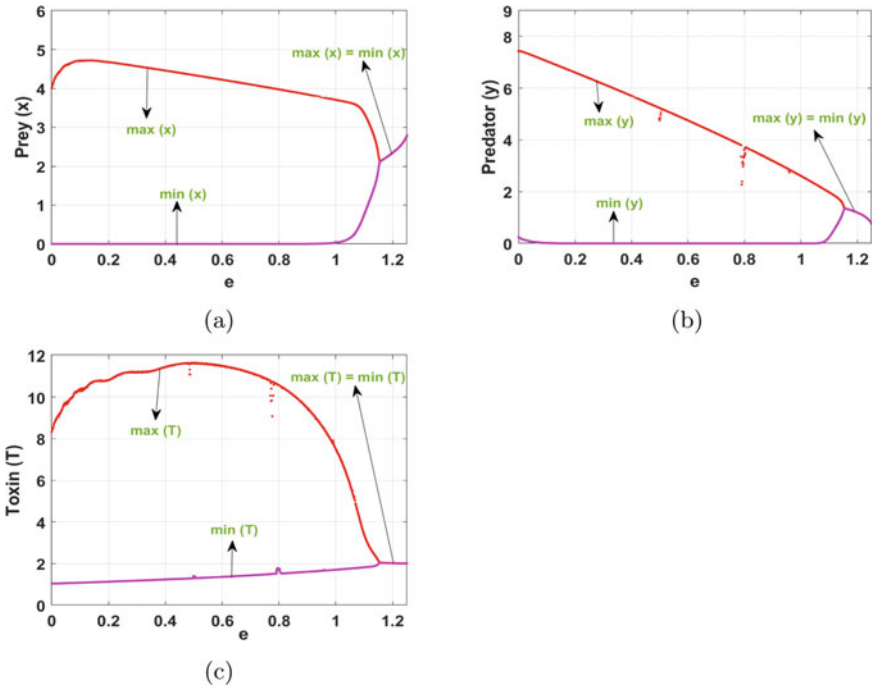
To check the influence of predator generated fear in system dynamics, we have considered periodic behavior of system dynamics by choosing  $e = 0.5$  and varied fear level in different ranges. We have observed that fear level  $f$  plays a contributory role in the context of stability through a super-critical Hopf-bifurcation (as the first lyapunov co-efficient is a negative quantity). It is observed that system remains in periodic mode until  $f$  passes away its threshold value  $f = f^* = 2.8$  as shown in Fig. 1. Ecologically, it signifies that with the increase in fear level, predator’s food resources decrease which consequently makes a balance in system dynamics to exhibit stable behavior. Now, we want to explore the impact of toxin in system dynamics through the parameter strength in toxin  $e$ . Similarly, here also we have noticed that  $e$  has a huge impact in system dynamics in terms of stability. The system exhibits unstable behavior for lower level of toxicity ( $e \leq 1.16$ ) and becomes stable for higher level of toxicity ( $e > 1.16$ ) as displayed in Fig. 2. It is to be noted that with increasing value of  $e$ , both prey and predator population suffer from higher mortality rate and hence both population density decline which somehow makes a balance in the system to exhibit stable behavior. Now, we have plotted population biomass with respect to  $f$  to check its impact in population density in Fig. 3. From Fig. 3, we observed that both prey density and toxin concentration initially increases and then saturates as  $f$  increases. The prey population saturates after increasing its



**Fig. 1** Bifurcation diagram w.r.t. predator induced fear  $f$  in  $[0, 4]$  by considering  $e = 0.5$  and rest other parameters are kept as fixed. All the three figures jointly describe that the system (1) remains in periodic manner as long as  $f$  does not exceed  $f = f^* = 2.8$ . But, as soon as  $f$  crosses the threshold value  $f = f^* = 2.8$ , the system instantly becomes stable by removing the periodic oscillations of the solution trajectory

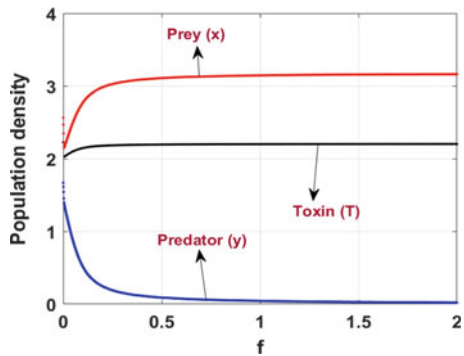
density because of controlled population growth rate. But, strangely, as  $f$  increases, predator population goes to extinction. The reason behind it may be interpreted as the reduction in food sources for predator species due to the decline in prey's growth rate caused by increasing level of fear.

However, one question comes to our mind that, is there any relation between fear level  $f$  and toxicity  $e$ ? To answer this question we have plotted a two parametric bifurcation diagram (see Fig. 4) around the co-existence steady state and observed that both  $f$  and  $e$  are inversely related with each other. The reason behind such observation may be interpreted as prey species are less frightened from predation due to the illness of predator species caused from consuming more toxic foods. From Fig. 4, it is noticed that low level of fear  $f$  is required to obtain the Hopf-bifurcation curve with the increasing level of toxicity  $e$ . It explains that prey species is less sensitive in perceiving the predation risk with increasing toxicity  $e$  in that ecosystem.



**Fig. 2** Bifurcation diagram w.r.t. strength of toxin  $e$  in  $[0, 1.25]$  by considering  $f = 0.01$  and rest other parameters are kept as fixed of system (1). All the three figures jointly describe that the system remains in periodic manner as long as  $e$  does not surpass  $e = e^* = 1.16$ . But, as soon as  $e$  passes the threshold value  $e = e^* = 1.16$ , the system quickly becomes stable by eliminating the periodic oscillations of the solution trajectory

**Fig. 3** Plot of population density under the variation of predator incited fear  $f$  by choosing  $e = 1.16$ . It is noticed that both prey density and toxin concentration initially saturates and then increases as  $f$  increases. But, interestingly, as  $f$  increases, predator population goes to extinction



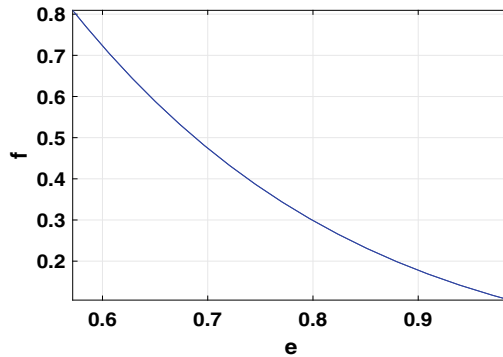


**Fig. 4** Two dimensional projection of Hopf-bifurcation curve in  $f$  vs  $e$  parametric plane revealing that the existence of inverse linear relationship between  $f$  and  $e$ . It is clear that need of higher level of predator induced fear is necessary to obtain the critical line of Hopf-bifurcation curve for decaying level in strength of toxin  $e$

## 6 Conclusion

In this article, a predator-prey model has been proposed and analysed in a toxic marine environment by considering predator induced fear to prey's birth rate and toxin dependent death rate for both species. The well-posedness of model system (1) along with stability analysis has been performed analytically. It is noticed that both fear factor and toxicity play a crucial role in controlling the system dynamics in a complex way. Model system (1) undergoes Hopf-bifurcation w.r.t. both these parameters. Predator produced fear has a stable impact on system dynamics for increasing level of fear in the presence of toxin. Strangely, for lower level of toxicity the system exhibits periodic solution whereas for higher level of toxicity it shows stable behavior by eliminating the periodic oscillations. The lower the toxicity level, the higher the periodic oscillations which is quite interesting. Apart from controlling the stability of system dynamics w.r.t. fear factor, it has an immense impact on population density. Although, fear factor does not influence prey biomass and toxin concentration significantly, it horribly forces the predator species in extinction due to lack of nourishing food resources. This model can be further extended by taking into consideration various toxin related factors which can be left as future work to the interested audience.

## References

1. Barman, D., Roy, J., Alam, S.: Trade-off between fear level induced by predator and infection rate among prey species. *J. Appl. Math. Comput.* **64**(1), 635–663 (2020)
2. Barman, D., Roy, J., Alam, S.: Dynamical behaviour of an infected predator-prey model with fear effect. *Iranian J. Sci. Technol. Trans. A: Sci.* **45**(1), 309–325 (2021)

3. Barman, D., Roy, J., Alrabaiah, H., Panja, P., Mondal, S.P., Alam, S.: Impact of predator incited fear and prey refuge in a fractional order prey predator model. *Chaos Solitons Fractals* **142**, 110420 (2021)
4. Chattopadhyay, J.: Effect of toxic substances on a two-species competitive system. *Ecological Model* **84**(1–3), 287–289, 110420 (1996)
5. Duce, R.A., Galloway, J.N., Liss, P.S., et al.: The impacts of atmospheric deposition to the ocean on marine ecosystems and climate. *World Meteorol. Organ. (WMO) Bull.* **58**(1), 61 (2009)
6. Espinoza, R.: Chemical waste that impact on aquatic life or water quality. <https://blog.idrenvironmental.com/chemical-waste-that-impact-on-aquatic-life-or-water-quality>. Accessed: 18 July 2021
7. Griffitht, R.J., Luo, J., Gao, J., Bonzongo, J.C., Barber, D.S.: Effects of particle composition and species on toxicity of metallic nanomaterials in aquatic organisms. *Environ. Toxicol. Chem. An Int. J.* **27**(9), 1972–1978, 110420 (2008)
8. Hallam, T., Clark, C., Lassiter, R.: Effects of toxicants on populations: a qualitative approach i. equilibrium environmental exposure. *Ecological Model.* **18**(3–4), 291–304 (1983)
9. Hallam, T., De Luna, J.: Effects of toxicants on populations: a qualitative: approach iii. environmental and food chain pathways. *J. Theoret. Biol.* **109**(3), 411–429 (1984)
10. Huang, Q., Wang, H., Lewis, M.A.: The impact of environmental toxins on predator-prey dynamics. *J. Theoret. Biol.* **378**, 12–30, 110420 (2015)
11. Kahru, A., Savolainen, K.: Potential hazard of nanoparticles: from properties to biological and environmental effects. *Toxicology* **2**(269), 89–91 (2010)
12. Rana, S., Samanta, S., Bhattacharya, S., Al-Khaled, K., Goswami, A., Chattopadhyay, J.: The effect of nanoparticles on plankton dynamics: a mathematical model. *Biosystems* **127**, 28–41, 110420 (2015)
13. Roy, J., Barman, D., Alam, S.: Role of fear in a predator-prey system with ratio-dependent functional response in deterministic and stochastic environment. *Biosystems* **197**, 104176 (2020)
14. Wang, X., Zanette, L., Zou, X.: Modelling the fear effect in predator-prey interactions. *J. Math. Biol.* **73**(5), 1179–1204, 110420 (2016)
15. Wang, X., Zou, X.: Modeling the fear effect in predator-prey interactions with adaptive avoidance of predators. *Bull. Math. Biol.* **79**(6), 1325–1359, 110420 (2017)
16. Zanette, L.Y., White, A.F., Allen, M.C., Clinchy, M.: Perceived predation risk reduces the number of offspring songbirds produce per year. *Science* **334**(6061), 1398–1401 (2011)
17. Zhang, H., Cai, Y., Fu, S., Wang, W.: Impact of the fear effect in a prey-predator model incorporating a prey refuge. *Appl. Math. Comput.* **356**, 328–337, 110420 (2019)



# Stability Analysis of the Leslie-Gower Model with the Effects of Harvesting and Prey Herd Behaviour



Md. Golam Mortuja, Mithilesh Kumar Chaube, and Santosh Kumar

**Abstract** Prey herd behaviour has been studied using a modified Leslie-Gower model, including harvesting in both populations. Three separate fixed points can be seen in the model. Local stability theory has been used to investigate the fixed point's stability. The stability of the interior fixed point under a parametric condition is investigated. Few numerical simulations are run to verify the results.

**Keywords** Predator-prey system · Prey group defense · Fixed points · Local stability · Environmental sustainability

## 1 Introduction

Since the classical Lotka-Volterra model [1, 2], which was developed by Lotka and Volterra, many researchers have become interested in such concerns [3–5], and they have approached the topic from several perspectives yielding numerous important conclusions [6–8]. Such as the authors in [9] analyzed the bifurcations of a Leslie type predator-prey model with Holling type-III functional response. Lin et al. discussed the multitype bi-stability using the population model in [10]. In [11] the authors analyzed the model using Allee effect. Specifically, the authors in [12] looked at the Leslie-Gower predator-prey model, which is given by:

$$\begin{cases} \frac{dX}{dt} = rX \left(1 - \frac{X}{P}\right) - \frac{\alpha_1 XY}{N_1 + X}, \\ \frac{dY}{dt} = SY \left(1 - \frac{\alpha_2 XY}{N_2 + X}\right) \end{cases} \quad (1)$$

where  $X$  is the density of prey, and  $Y$  is the density of predators. The authors have studied the above model, and by using the Lyapunov function, they analyzed the

---

Md. G. Mortuja (✉) · M. K. Chaube · S. Kumar  
Dr. SPM IIT Naya Raipur, C.G., Raipur, India  
e-mail: [mdgolam@iitnr.edu.in](mailto:mdgolam@iitnr.edu.in)

© The Author(s), under exclusive license to Springer Nature Switzerland AG 2022  
S. Banerjee and A. Saha (eds.), *Nonlinear Dynamics and Applications*,  
Springer Proceedings in Complexity,  
[https://doi.org/10.1007/978-3-030-99792-2\\_62](https://doi.org/10.1007/978-3-030-99792-2_62)

733

stability of the fixed points. In [13] the authors examined the global stability of Leslie-Gower model with feedback controls.

Harvesting is an excellent strategy for people [14, 15] to keep predator and prey populations in balance so that the population can continue to grow appropriately and offer economic benefits [16, 17]. In research, prey harvesting is generally seen merely to control population numbers. The Leslie-Gower predator-prey systems with constant prey harvesting were examined by the authors in [18]. Later, the Leslie-Gower predator-prey model with nonlinear prey harvesting was explored by the authors in [19]. In a Leslie-Gower model, Xie et al. [20] investigated the impact of harvesting and looked at the super-critical Hopf bifurcation that leads to a stable limit cycle. In a discrete modified LG model, Anuraj et al. [21] investigated many co-dimension 1 and 2 bifurcations. A diffusive LG model with Allee effects and mutual predator interface was developed and analyzed by Tiwari & Raw [22]. The dynamics of a stochastic modified LG model with time delay and prey harvest were investigated in [23]. We must consider the harvesting in the prey population and the predator for ecological balance and good economic development. In the present paper, proportional harvesting is regarded in both populations.

Some prey populations show herd behavior, in which predator and prey interact around the perimeter of the prey species, resulting in the predator's hunting rate of prey that varies from that predicted by conventional models. In the ocean, a fish's rate of collecting zooplankton is more significant than a fish's rate of capturing phytoplankton. In this case, the phytoplankton is acting in a herd-like way. That kind of interaction cannot be fully described by Holling-type functional responses. To comprehend the prey population's herd behavior, Ajraldi et al. [24] utilized the square root of the prey density, such that there is an interaction between both species in the prey herd behavior. The paper's main objective is to analyze the dynamics of the Leslie-Gower model with harvesting in both populations considering prey herd behaviour.

## 1.1 Mathematical Modeling

The modified Leslie-Gower model [12] with harvesting in both population considering prey herd is as follows (after scaling the parameter and variables):

$$\begin{cases} \frac{dX}{dt} = X(1 - X) - \frac{\alpha\sqrt{XY}}{m+\sqrt{X}} - \gamma X, \\ \frac{dY}{dt} = kY\left(1 - \frac{dY}{m+\sqrt{X}}\right) - \delta Y \end{cases} \quad (2)$$

The Jacobian matrix of the above system at origin is undefined. For that the transformation  $X = x^2$ ,  $Y = y$  has been applied on the above system:

$$\begin{cases} \frac{dx}{dt} = \frac{1}{2} \left[ x(1 - x^2) - \frac{\alpha y}{m+x} - \gamma x \right], \\ \frac{dy}{dt} = ky \left( 1 - \frac{dy}{m+x} \right) - \delta y \end{cases} \tag{3}$$

## 2 Fixed Points and Their Stability

In this section, the existence and stability of the fixed point of the system have been studied. For the background of biology it is considered that the fixed points all are non negative.

### 2.1 Existence of Fixed Points

To find the fixed points of the system need to solve the following equations:

$$\begin{cases} x(1 - x^2) - \gamma x - \frac{\alpha y}{1+mx} = 0, \\ ky(1 - \frac{dy}{m+x}) - \delta y = 0, \end{cases} \tag{4}$$

The following theorem is about the fixed points of the system and their existence.

**Theorem 1** *The system have three fixed points which are:*

- (i)  $E_0 = (0, 0)$ , the population free fixed point.
- (ii)  $E_1 = (x_1, 0)$ , the predator fixed point, if  $\gamma < 1$ .
- (iii)  $E_2 = (x_2, y_2)$ , the interior fixed point.

**Proof** By solving the equations it is easy to see that  $(0, 0)$  is a fixed point of the system. Now if  $y = 0$  then  $1 - x^2 - \gamma = 0$ . As we considered that the fixed point are non negative, the predator free fixed point will be  $(\sqrt{1 - \gamma}, 0)$  if  $\gamma < 1$  from  $1 - x^2 - \gamma = 0$ . Now, the interior fixed point  $E_2$  is exists satisfying the equations:

$$\begin{cases} x_2(1 - x_2^2) - \gamma x_2 = \frac{\alpha}{d} (1 - \frac{k}{\delta}), \\ y_2 = \frac{1}{d} (m + x_2) (1 - \frac{k}{\delta}), \end{cases} \tag{5}$$

### 2.2 Stability of the Fixed Points

The stability of the fixed point has been analyzed in this subsection. The Jacobian matrix of the system at  $(x, y)$ :

$$J(x, y) = \begin{pmatrix} \frac{1}{2} \left[ 1 - 3x^2 + \frac{\alpha y}{(m+x)^2} - \gamma \right] & -\frac{1}{2} \left( \frac{\alpha}{m+x} \right) \\ \frac{dky^2}{(m+x)^2} & k - \frac{2dy}{m+x} - \delta \end{pmatrix}.$$

**Theorem 2** *The fixed point  $E_0$  is:*

- (i) *unstable if  $1 > \gamma, k > \delta$ ,*
- (ii) *stable if  $1 < \gamma, k < \delta$ ,*
- (iii) *saddle if  $1 > \gamma, k < \delta$  or  $1 < \gamma, k > \delta$ ,*
- (iv) *non-hyperbolic if either  $1 = \gamma$  or  $k = \delta$ .*

**Proof** The real eigenvalues of the Jacobian matrix  $J(x, y)$  at  $E_0$  are  $\frac{1}{2}(1 - \gamma), k - \delta$ . It is easy to see that if  $1 > \gamma, k > \delta$  then the eigenvalues are positive implies  $E_0$  is unstable node. If  $1 < \gamma, k < \delta$  then the eigenvalues are negative implies  $E_0$  is stable node. If  $1 > \gamma, k < \delta$  or  $1 < \gamma, k > \delta$ , then the eigenvalues are opposite in sign implies  $E_0$  is saddle. If either  $1 = \gamma$  or  $k = \delta$  then one of the eigenvalues is zero implies  $E_0$  is non-hyperbolic.

**Theorem 3** *The fixed point  $E_1$  is:*

- (i) *stable if  $k < \delta$ ,*
- (ii) *saddle if  $k > \delta$ ,*
- (iv) *non-hyperbolic if  $k = \delta$ .*

**Proof** The real eigenvalues of the Jacobian matrix  $J(x, y)$  at  $E_1$  are  $-x_1^2, k - \delta$ . First eigenvalue is always positive as  $x_1 = \sqrt{1 - \gamma} > 0$  since  $\gamma < 1$ . It is easy to see that if  $k < \delta$  then the eigenvalues are negative implies  $E_1$  is stable node. If  $k > \delta$ , then the eigenvalues are opposite in sign implies  $E_1$  is saddle. If  $k = \delta$  then the second eigenvalue is zero implies  $E_1$  is non-hyperbolic.

**Theorem 4** *The fixed point  $E_2$  is stable if  $T < 0, D > 0$ .*

**Proof** The characteristic equation of the Jacobian matrix  $J$  at  $(x_2, y_2)$  is given by  $\mu^2 - T\mu + D = 0$ , where

$$\begin{cases} T = \frac{1}{2} \left[ 1 - 3x_2^2 + \frac{\alpha y}{(m + x_2)^2} - \gamma \right] + \frac{dy_2}{m + x_2}, \\ D = \frac{1}{2} \left[ 1 - 3x_2^2 + \frac{\alpha y}{(m + x_2)^2} - \gamma \right] \left( \frac{dy_2}{m + x_2} \right) + -\frac{1}{2} \left( \frac{\alpha}{m + x} \right) \left( \frac{dky^2}{(m + x)^2} \right). \end{cases} \tag{6}$$

Now if  $T < 0, D > 0$  then the Jacobian matrix  $J$  has two eigenvalues having negative real parts. Hence the theorem.

### 3 Discussion with Numerical Examples

By introducing the parameter values the following results have been identified:

For  $\gamma = 0.5337, \alpha = 0.005, d = 0.14, m = 0.8, \delta = 0.5$ , if  $k = 0.8 > \delta$  then the axial fixed point  $E_1$  is saddle (Fig. 1b) and if  $k = 0.45 < \delta$  then the axial fixed point  $E_1$  is stable (Fig. 1a). For  $\alpha = 0.005, d = 0.14, m = 0.8, \delta = 0.5, k = 0.8$ , if  $\gamma = 0.15$  then the interior fixed point  $E_2$  is stable (Fig. 1c). For  $\gamma = 0.1, \alpha = 0.05, d = 0.14, m = 0.6, \delta = 0.5$  we plot the time series with respect to prey and predator by changing the parameter value  $k = 0.8 > \delta$  and  $k = 0.45 < \delta$ . There are three equilibrium states, as we can see. The first is  $E_0(0, 0)$ , which means there are no members of either species present. The second is  $E_1(x_1, 0), x_1 = \sqrt{1 - \gamma}$ , in which the predators are not present and the preys are at their maximum sustainable number  $x_1$ . Both populations are present in the third state. Using the above mentioned parameters values, we see from the eigenvalues that  $E_1$  is a strictly stable node for  $k < \delta$ , and is a saddle and therefore unstable for any  $k > \delta$ . At this point we have a rather complete picture of the equilibria of the system and the stability. For  $k < \delta$ , the only stable equilibrium state is the all prey populations state at the maximum sustainable population  $x_1 = \sqrt{1 - \gamma}$  (Fig. 2).

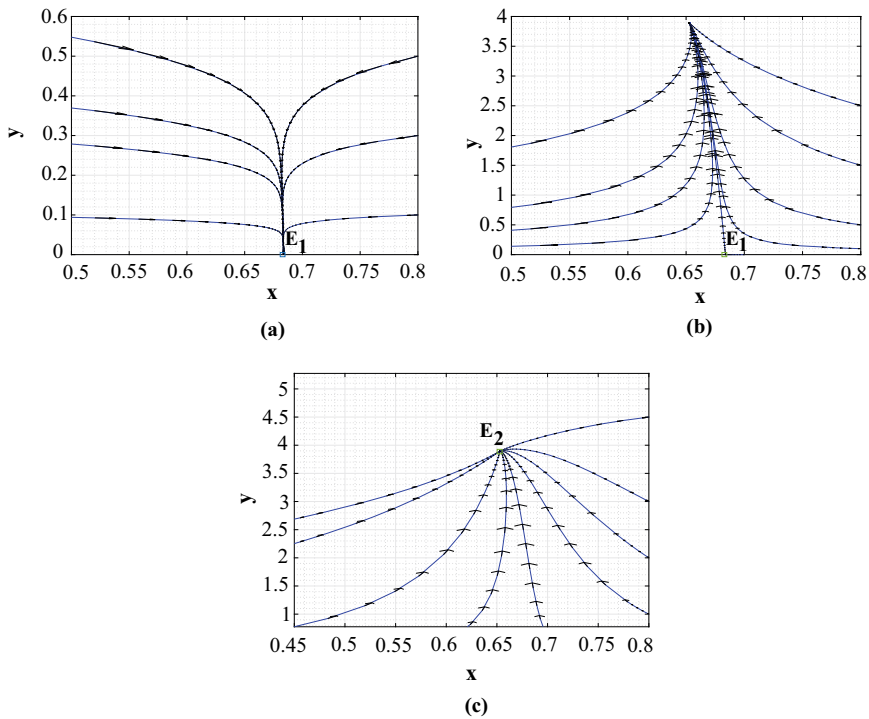
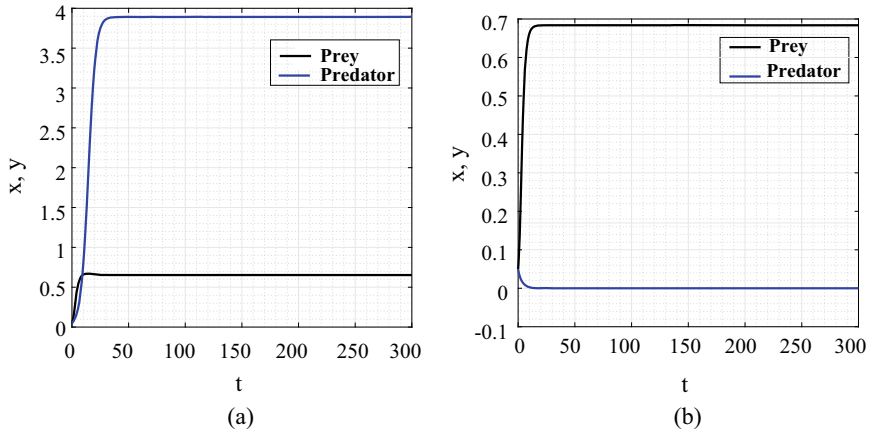


Fig. 1 a  $E_1$  is stable, b  $E_1$  is saddle, c  $E_2$  is stable



**Fig. 2** Time series **a**  $k > \delta$ , **b**  $k < \delta$

## 4 Conclusion

A modified Leslie-Gower model with harvesting in both populations has been developed considering prey herd behaviour. The model exhibits three different fixed points population-free, predator-free and interior fixed point. The stability of the fixed point has been analyzed by local stability theory. If  $1 < \gamma$ ,  $k < \delta$ , the origin is stable, otherwise unstable, or non-hyperbolic. Predator-free fixed point is stable if  $1 < \gamma$ ,  $k < \delta$ . It is examined that the interior fixed point is stable under a parametric condition. We also include some numerical simulations to support our analytical findings and conclusions. As a result, our research could help to ensure long-term environmental sustainability. In a pond or natural ocean system, huge fishes eat small fish as their main source of nutrition. To defend their predator, certain fish gather. As a result, the findings of the article could be useful in fisheries management. Management will be informed of the rate at which little fish species (preys) must be taken to maintain ecological balance based on the findings of this study.

## References

1. Lotka, A.J.: Elements of Physical Biology. Williams & Wilkins (1925)
2. Volterra, V.: Principes de biologie mathématique. Acta biotheoretica **3**(1), 1–36 (1937)
3. Britton, N.F.: Essential Mathematical Biology. Springer, Berlin, Germany (2013)
4. Murray, J.D.: Mathematical Biology I: An Introduction. Springer, Berlin, Germany (2002)
5. Murray, J.D.: Mathematical Biology: Spatial Models and Biomedical Applications. Springer, Berlin, Germany (2002)
6. Brauer, F., Castillo-Chavez, C.: Mathematical Models in Population Biology and Epidemiology. Springer, Berlin, Germany (2011)

7. Yang, W., Li, Y.: Dynamics of a diffusive predator-prey model with modified Leslie-Gower and Holling-type III schemes. *Comput. Math. Appl.* **65**(11), 1727–1737 (2013)
8. Wu, F. Jiao, Y.: Stability and Hopf bifurcation of a predator-prey model. *Boundary Value Problems* (2019)
9. Huang, J., Ruan, S., Song, J.: Bifurcations in a predator prey system of Leslie type with generalized Holling type III functional response. *J. Differ. Equ.* **257**(6), 1721–1752 (2014)
10. Lin, G., Ji, J., Wang, L., Yu, J.: Multitype bistability and long transients in a delayed spruce budworm population model. *J. Differ. Equ.* **283**, 263–289 (2021)
11. Mart-Jeraldo, N., Aguirre, P.: Allee effect acting on the prey species in a Leslie-Gower predation model. *Nonlinear Anal. Real World Appl.* **45**, 895–917 (2019)
12. Aziz-Aloui, M., Daher Okiye, M.: Boundedness and global stability for a predator-prey model with modified Leslie-Gower and holling-type II schemes. *Appl. Math. Lett.* **16**, 1069–1075 (2003)
13. Chen, L., Chen, F.: Global stability of a Leslie-Gower predator-prey model with feedback controls. *Appl. Math. Lett.* **22**(9), 1330–1334 (2009)
14. Huang, J., Gong, Y., Gong, Y., Ruan, S.: Bifurcation analysis in a predator-prey model with constant-yield predator harvesting. *Discrete Contin. Dyn. Syst. B* **18**(8), 2101–2121 (2013)
15. Chakraborty, S., Pal, S., Bairagi, N.: Predator-prey interaction with harvesting: mathematical study with biological ramifications. *Appl. Math. Model.* **36**(9), 4044–4059 (2012)
16. Lenzini, P., Rebaza, J.: Nonconstant predator harvesting on ratio-dependent predator-prey models. *Appl. Math. Sci.* **4**, 791–803 (2010)
17. Ali, J., Shivaji, R., Wampler, K.: Population models with diffusion, strong Allee effect and constant yield harvesting. *J. Math. Anal. Appl.* **352**(2), 907–913 (2009)
18. Zhu, C., Lan, K.: Phase portraits. Hopf bifurcations and limit cycles of Leslie-Gower predator-prey systems with harvesting rates. *Discrete Contin. Dyn. Syst. Ser. B* **14**, 289–306 (2010)
19. Gupta, R.P., Chandra, P.: Bifurcation analysis of modified Leslie-Gower predator-prey model with Michaelis-Menten type prey harvesting. *J. Math. Anal. Appl.* **398**(1), 278–295 (2013)
20. Xie, J., Liu, H., Luo, D.: The effects of harvesting on the dynamics of a Leslie-Gower model. *Discrete Dyn. Nature Soc.* (2021)
21. Singh, A., Malik, P.: Bifurcations in a modified Leslie-Gower predator-prey discrete model with Michaelis-Menten prey harvesting. *J. Appl. Math. Comput.*, 1–32 (2021)
22. Tiwari, B., Raw, S.N.: Dynamics of Leslie-Gower model with double Allee effect on prey and mutual interference among predators. *Nonlinear Dyn.* **103**(1), 1229–1257 (2021)
23. Liu, Y., Liu, M., Xu, X.: Dynamics analysis of stochastic modified Leslie-Gower model with time-delay and Michaelis-Menten type prey harvest. *J. Appl. Math. Comput.*, 1–28 (2021)
24. Ajraldi, V., Pittavino, M., Venturino, E.: Modeling herd behavior in population systems. *Nonlinear Anal. Real World Appl.* **12**(4), 2319–2338 (2011)

# Modeling the Symbiotic Interactions Between *Wolbachia* and Insect Species



Davide Donnarumma, Claudia Pio Ferreira, and Ezio Venturino

**Abstract** A sex-structured mathematical model is proposed to address the interactions among *Wolbachia* and *Aedes* mosquitoes. Several features associated with the infection that impacts mosquito phenotype like the cytoplasmic incompatibility, sex ratio biased to females, and maternal inheritance are considered. The analysis of the model shows the presence of three equilibria: the infection-free point, which is attainable only for a narrow range of initial conditions, the point where all individuals are infected, which however arises only in a very particular situation, namely the full vertical transmission of the bacterium, and the endemic equilibrium. Thresholds for the stability of the coexistence equilibrium are obtained, and they involve a relation among parameters and the initial prevalence of the infected mosquito in the population. As expected, increasing the sex ratio biased to females promotes the fixation of the infection on the population at high values.

**Keywords** Ordinary differential equations · Stability analysis · Thresholds

## 1 Introduction

*Wolbachia* is a common type of Gram-negative bacteria that infects about 60% of all arthropods, but is harmless for animals and humans. These obligated intracellular parasites are harbored mainly in the reproductive organs of the insects [20], but also in the legs and guts [6]. It is known that *Wolbachia* infection of the common mosquito *Culex pipiens* alters its reproduction in diverse ways that favor its invasion

---

D. Donnarumma · E. Venturino (✉)  
Università di Torino, 120123 Torino, Italy  
e-mail: [ezio.venturino@unito.it](mailto:ezio.venturino@unito.it)

D. Donnarumma  
e-mail: [davide.donnarumma@edu.unito.it](mailto:davide.donnarumma@edu.unito.it)

C. Pio Ferreira  
São Paulo State University (UNESP), Botucatu 18618-970, Brazil  
e-mail: [claudia.pio@unesp.br](mailto:claudia.pio@unesp.br)

© The Author(s), under exclusive license to Springer Nature Switzerland AG 2022  
S. Banerjee and A. Saha (eds.), *Nonlinear Dynamics and Applications*,  
Springer Proceedings in Complexity,  
[https://doi.org/10.1007/978-3-030-99792-2\\_63](https://doi.org/10.1007/978-3-030-99792-2_63)

741



of wild non-infected populations. For example, infected males cannot reproduce with uninfected females because of cytoplasmic incompatibility (CI). Female-biased sex ratio can burst the size of the infected population and can be achieved by killing part of the males at the larval stage, or by the feminization of males (males develop as sterile females), or by parthenogenesis (infected females generate offsprings without mating with males) [9]. Fitness cost associated with carrying the bacteria (like an increase in the mortality rate) can be overcome by the CI and maternal inheritance (infected females can transmit vertically the *Wolbachia* bacteria to their offsprings) [14].

Two types of mosquitoes have attained the limelight in recent years, being particularly harmful. They are currently spreading northwards (and southwards) from tropical regions, carrying with them the viruses of formerly unknown diseases at temperate latitudes, such as Chikungunya, Dengue, Zika [20]. They are the *Aedes albopictus* and the *Aedes aegypti* mosquitoes. Ways of controlling their spread vary from larvicide and insecticide spraying, through mosquito surveillance, and population education programs with focusing attention on their living surroundings, for example, by removing standing water which may serve as a breeding site for the mosquito [22].

A different way of fighting mosquitoes, that does not involve genetically modified insects, is based on the observation that *Aedes aegypti* does not harbor the *Wolbachia* bacteria. This fact has been exploited to devise a biological control program, for which *Aedes aegypti* are inoculated with *Wolbachia*. Thus, males infected in the laboratory are subsequently released into the environment, and their mating with wild females is unsuccessful, producing eggs that do not hatch, reducing the size of the next generation population. The release however should be monitored and repeated in time, as *Wolbachia* dies with the host insect [21].

Results on the effectiveness of these programs have been reported in several countries. Besides the reduction of the mosquito population, the presence of *Wolbachia* interferes with arboviruses by reducing its infection into mosquitoes [17]. Therefore, geographic areas where the presence of the infected mosquito is high are expected to report less prevalence of arboviruses on the human population. For instance, in Indonesia, the release of *Aedes aegypti* inoculated by the wMel strain of *Wolbachia* in several randomly-selected geographical locations were proven to offer protection efficacy (by reducing the incidence of dengue disease) against the four serotypes of dengue in 77.1% of the people taking part in the experiment [19]. As a consequence of the bacterium introgression in the mosquito population, the need for hospital treatment was reduced for the virologically-confirmed dengue patients living in the areas subject to the treatment. The symptomatic cases as well as the hospitalizations were significantly lower than in other areas where *Wolbachia* release had not been implemented.

In Brazil, deployments of the wMel strain of *Wolbachia* in selected geographic areas were monitored by keeping track of the monthly reported human cases of Dengue, Chikungunya, and Zika, against the data coming from an untreated region. The bacterium release was associated with a 69% reduction in Dengue incidence, in a little more than a half reduction of the incidence for Chikungunya and a little more than a third of the Zika cases. Thus, a significant benefit can result for the

health system by the presence of bacterium-affected mosquitoes in urban areas, independently of the possible spatial heterogeneity [13].

In Italy, a similar technique is being used against *Aedes albopictus* [4]. These mosquitoes have been inoculated with the *Wolbachia* naturally present in *Culex pipiens*, and then reared in the laboratory to produce males that are incompatible with the wild *Aedes albopictus* females. Again, these males are subsequently released into the environment, leading to mating that produce infertile eggs.

From the mathematical point of view, several models have been proposed to study aspects of this new symbiotic interaction. For instance, [1] showed that the cytoplasmic incompatibility does not guarantee establishment of the *Wolbachia*-infected mosquitoes if the imperfect maternal transmission is considered. For this, the optimal *Wolbachia* release problem was studied in different scenarios, where the decision makers either aim for replacement or co-existence of both populations. As in other works [5, 16], the viability of the technique relies on the number of infected mosquito released, and on and periodicity of the releasing. In [2, 8] a delay differential model was derived with the aim of studying the colonization and persistence of the *Wolbachia*-transinfected *Aedes aegypti* mosquito. The conditions of existence for each equilibrium of the model were obtained analytically. The persistence of both infected and wild populations was explored in the context of mosquito's fitness, host-symbiont interaction, and temperature change. It was shown that the increase of the delay, which represents the development time, can promote, through Hopf bifurcation, stability switch towards instability for the nonzero equilibria. A two-sex mosquito model, that accounts for multiple pregnant states and the aquatic-life stage, is used to compare the effectiveness of different integrated mitigation strategies to establish the *Wolbachia* infection on the population [15]. The proposed model presents a subcritical bifurcation indicating that even when  $R_0 < 1$ , there can still exist a stable endemic equilibrium. Also, it argues that mitigation strategies to reduce the population of wild uninfected mosquitoes before releasing numerous *Wolbachia*-infected mosquitoes could improve the establishment of the infection in the population. Coupling mosquito population with human population, other works assessed the reduction of dengue transmission by the fact that a *Wolbachia* infection is established in the mosquito population [7, 10, 23]. In this case, the susceptibility of *Wolbachia*-carrying mosquito to dengue infection is explored under different scenarios that take in consideration variation in mosquito fitness, maternal inheritance, and cytoplasmic incompatibility inherent to each *Wolbachia* strain.

In this paper, we develop a model to study the introduction and persistence of the *Wolbachia* bacteria into the mosquito population, partitioning the mosquito population among sexes and infection status. Only adult mosquitoes were considered. The paper is organized as follows. In the next section, we formulate the model. Trajectories are shown to be bounded in Sect. 3, the equilibria are studied in Sect. 4, and the simulations for the endemic case are reported in Sect. 4.3. A thorough investigation of the equilibria in terms of the model parameter variations concludes the paper.

## 2 Model Setup

Let  $F$  represent the susceptible female mosquitoes, i.e. those not infected with the *Wolbachia* bacterium,  $I$  the *Wolbachia*-infected female mosquitoes,  $M$  the susceptible male mosquitoes and  $U$  the *Wolbachia*-infected male mosquitoes. Now, reproduction success is determined by the presence of the *Wolbachia*, in the sense that reproduction after mating of an infected male with any female occurs at a much lower rate than for a couple of healthy individuals, and furthermore an infected female that mates a healthy male has very, very low chances of success, if at all. In other words, the outcomes are schematically represented in Table 1.

The ordinary differential system is given by

$$\begin{aligned}
 \frac{dF}{dt} &= \frac{1}{2}r \frac{M}{M+U}F + pr_1(1-\rho)I + pkr \frac{U}{U+M}F - mF - aF(F+M+I+U), \\
 \frac{dI}{dt} &= pr_1\rho I - \mu I - bI(F+M+I+U), \\
 \frac{dM}{dt} &= \frac{1}{2}r \frac{M}{M+U}F + qr_1(1-\rho)I + qkr \frac{U}{U+M}F - mM - cM(F+M+I+U), \\
 \frac{dU}{dt} &= qr_1\rho I - \mu U - gU(F+M+I+U).
 \end{aligned}
 \tag{1}$$

Note that in order to make sense both mathematically and biologically, in this model we assume

$$U + M \neq 0. \tag{2}$$

The other parameters of the model are as follows. In all (susceptible) compartments, the natural mortality  $m$  explicitly appears. Also, in the last terms of all the equations, we allow for possible intraspecific competition among the four classes, at rate  $a$  for the susceptible females,  $b$  for the infected ones,  $c$  for susceptible males and  $g$  for the infected ones.

The first equation describes the evolution of susceptible female mosquitoes. They are born by mating with a susceptible male, first term with reproduction (oviposition) rate  $r$ , assuming that the offsprings split evenly among the two sexes with the same ratio (1/2). A similar term is indeed found in the susceptible male’s equation. The

**Table 1** Reproduction rates given by all possible mating combinations. The wild populations are denoted by  $F$  and  $M$ , and the *Wolbachia*-infected one by  $I$  and  $U$ . Here  $r_1 < r$  and  $k \ll 1$ , possibly  $k = 0$

Male	Female	
	$F$	$I$
$M$	$r$	$r_1$
$U$	$kr$	$r_1$

second term accounts for the mating of an infected female, which may occur with a healthy male, with probability  $M(M + U)^{-1}$ , or with an infected one, with probability  $U(M + U)^{-1}$ . The resulting reproduction however has a lower rate  $r_1 < r$  than for a healthy-healthy mating, and furthermore we allow for possible vertical transmission of the *Wolbachia*. Thus, if  $\rho < 1$  represents the vertical transmission of the infection, a portion  $1 - \rho$  of the offspring are born healthy. In case of infection, we also account for the possibility of *Wolbachia* presence altering the sex ratio of the offspring:  $p$  is the fraction of female offspring, while  $q = 1 - p$  represents the male fraction [3]. To sum up, the second term represents the healthy females generated by mating infected females with a male. The third term models the mating of a susceptible female with an infected male at a rate  $r$ , which has a probability of success  $k \ll 1$ , if not  $k = 0$ . The offspring have an altered sex ratio so that we find  $p$  healthy females.

The second equation for the infected females contains the recruitment term coming from the mating of infected females at a reduced rate  $r_1$  with any kind of male. The sex ratio is altered,  $p$  for the female offspring, and the bacteria are vertically transmitted with probability  $\rho$  which generates infected individuals. The second term contains the natural plus infection-induced mortality  $\mu > m$ .

Susceptible males dynamics is represented in the third equation, with reproduction and mortality terms that are identical to those of the healthy females. However, here, the offsprings coming from infected females have the sex ratio altered by the fraction  $q$ .

The infected males, fourth equation, again are recruited from infected females with reduced reproduction rate  $r_1$  and with a fraction  $q$  of sex ratio and probability of vertical bacteria transmission  $\rho$ . They are subject to natural plus infection-related mortality  $\mu$ , the very same as for the females.

The Jacobian of (1), needed for the stability analysis, turns out to be:

$$J = \begin{pmatrix} J_{1,1} & pr_1(1 - \rho) - aF & r \frac{FU(\frac{1}{2} - pk)}{(M+U)^2} - aF & -r \frac{FM(\frac{1}{2} - pk)}{(M+U)^2} - aF \\ -bI & J_{2,2} & -bI & -bI \\ r \frac{\frac{1}{2}M + qkU}{M+U} - cM & qr_1(1 - \rho) - cM & J_{3,3} & -r \frac{MF(\frac{1}{2} - qk)}{(M+U)^2} - cM \\ -gU & qr_1\rho - gU & -gU & J_{4,4} \end{pmatrix}, \tag{3}$$

with

$$\begin{aligned} J_{1,1} &= \frac{1}{2}r \frac{M}{M + U} + pkr \frac{U}{U + M} - m - a(F + M + I + U) - aF, \\ J_{2,2} &= pr_1\rho - \mu - b(F + M + I + U) - bI, \\ J_{3,3} &= \frac{1}{2}r \frac{U}{(M + U)^2} F - qkr \frac{U}{(M + U)^2} F - m - c(F + M + I + U) - cM, \\ J_{4,4} &= -\mu - g(F + M + I + U) - gU. \end{aligned}$$

### 3 Boundedness

First, note that

$$p + q = 1. \tag{4}$$

Let  $Z = F + I + M + U$  denote the total mosquito population. Summing the equations in (1), for  $\eta > 0$ , recalling (4) we obtain

$$\begin{aligned} \frac{dZ}{dt} + \eta Z &= r \frac{M + kU}{M + U} F + r_1 (1 - \rho) I - m(F + M) - \mu(U + I) + r_1 \rho I \\ &\quad - (aF + bI + cM + gU)Z + \eta Z \\ &\leq (r + \eta)F + (r_1 + \eta)I - aF^2 - bI^2 - cM^2 - gU^2 \\ &\leq (r + \eta)F + (r_1 + \eta)I - aF^2 - bI^2 \\ &\leq F_* + I_* = Z_*, \quad \text{with } F_* = \frac{(r + \eta)^2}{4a}, \quad \text{and } I_* = \frac{(r_1 + \eta)^2}{4b}. \end{aligned}$$

From the resulting differential inequality for  $Z$ ,

$$\frac{dZ}{dt} + \eta Z \leq Z_*,$$

we get

$$Z(t) \leq e^{-\eta t} \left[ Z(0) - \frac{Z_*}{\eta} \right] \frac{Z_*}{\eta} \leq \max \left\{ Z(0), \frac{Z_*}{\eta} \right\} = Z_+.$$

In view of the fact that all populations are nonnegative, we finally find

$$F(t), I(t), M(t), U(t) \leq Z_+$$

i.e. the solution trajectories of (1) are bounded.

### 4 Equilibria

Here, we are looking for points  $(\bar{F}, \bar{I}, \bar{M}, \bar{U})$  that solve the equilibrium equations of the system (1).

### 4.1 The Infection-Free Case

In this case we have  $\bar{I} = 0, \bar{U} = 0$  and the admissible equilibrium turns out to be

$$E_1 = \left( \frac{2arm - 4am^2 + 4cm^2 - 4cmr + cr^2}{2a(2ma + ar - 2cm + cr)}, 0, \frac{r(r - 2m)}{2(2ma + ar - 2cm + cr)}, 0 \right).$$

To achieve feasibility, we need to ensure that the following inequalities hold true:

$$\bar{F} = \frac{cr^2 - 2mr(2c - a) - 4m^2(a - c)}{2a[r(a + c) - 2m(c - a)]} > 0, \quad \bar{M} = \frac{r(r - 2m)}{2a[r(a + c) - 2m(c - a)]} > 0.$$

Now, the denominator of both fractions is nonnegative for

$$r > 2m \frac{c - a}{c + a}. \tag{5}$$

Note that the above condition holds unconditionally in case  $c < a$ . To have the numerator of  $\bar{F}$  nonnegative we need either one of the following inequalities to be satisfied

$$r < 2m \frac{c - a}{c}, \quad r > 2m, \tag{6}$$

with the proviso that for  $c < a$  the former is not satisfied, since all model's parameters are positive. Now, to have the numerator of  $\bar{M}$  nonnegative we need

$$r > 2m, \tag{7}$$

and combining (5), (6) and (7),  $E_1$  is feasible for

$$r > 2m. \tag{8}$$

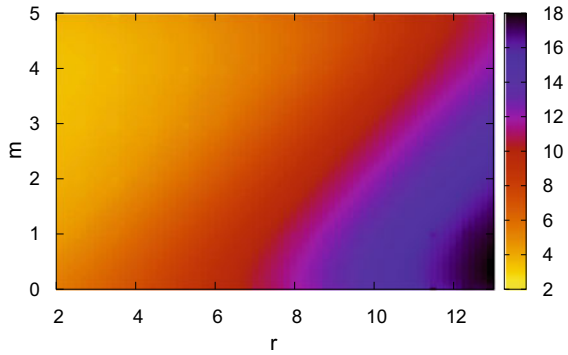
Thus, this equilibrium feasibility depends only on the birth and death rates. Following the same argument it is easy to see that if

$$r < 2m \frac{c - a}{c + a}$$

we cannot have both  $\bar{F}$  and  $\bar{M}$  nonnegative.

Figure 1 shows the total population at equilibrium  $E_1$  as a function of  $m$  and  $r$  for  $a = c = 1$ . The initial conditions are the following:  $M_0 = F_0 = 1, U_0 = I_0 = 0$ . The other parameters are arbitrary, since the equilibrium does not depend on them. Assuming that the condition  $r > 2m$  is satisfied, either the increase of  $r$  or decrease of  $m$  or both promote the increase of  $\bar{Z} = \bar{F} + \bar{M}$ .

**Fig. 1** The figure shows the total healthy population  $\bar{Z} = \bar{F} + \bar{M}$  (here  $\bar{I} = \bar{U} = 0$ ) at the infection-free equilibrium  $E_1$  as function of  $r$  and  $m$  for  $a = 1, c = 1$



Stability of this equilibrium can be assessed in view of the fact that the characteristic equation factorizes into the product of the two minors of the following matrices:

$$A = \begin{pmatrix} \frac{r}{2} - m - a(\bar{F} + \bar{M}) - a\bar{F} & -a\bar{F} \\ \frac{r}{2} - c\bar{M} & -m - c(\bar{F} + \bar{M}) - c\bar{M} \end{pmatrix},$$

$$B = \begin{pmatrix} \frac{\rho r_1}{2} - \mu - b(\bar{F} + \bar{M}) & 0 \\ \frac{\rho r_1}{2} & -\mu - g(\bar{F} + \bar{M}) \end{pmatrix}.$$

The Routh-Hurwitz conditions for  $A$  give

$$\text{tr}(A) = \frac{r}{2} - m - a(\bar{F} + \bar{M}) - a\bar{F} - m - c(\bar{F} + \bar{M}) - c\bar{M} < 0$$

which explicitly becomes

$$\frac{r^2(c^2 + 3ac) - r(c^2 + ac - a^2) - 4m^2(ac - c^2)}{2a(r(c + a) - 2m(c - a))} > 0. \tag{9}$$

The numerator is positive for  $r < r_-$  or  $r > r_+$ , with

$$r_{\pm} = 2m \frac{-a^2 + ac + c^2 \pm \sqrt{a^4 - 2a^3c + 2a^2c^2}}{c(3a + c)}.$$

The denominator is positive for  $r > r_3$ , with

$$r_3 = 2m \frac{c - a}{c + a}.$$

Note that  $r_{\pm}, r_3 < 2m$ . Therefore, (9) holds if the following condition is satisfied,

$$r > \max\{r_{\pm}, r_3\}.$$

The second Routh-Hurwitz condition for  $A$  is

$$\det(A) = \left[ \frac{r}{2} - m - a(\bar{F} + \bar{M}) - a\bar{F} \right] [-m - c(\bar{F} + \bar{M}) - c\bar{M}] + a\bar{F} \left[ \frac{r}{2} - c\bar{M} \right]$$

and explicitly it yields

$$\frac{4am^2 - 2amr - 4cm^2 + 4cmr - cr^2}{4a} < 0$$

which is satisfied for  $r < 2m(c - a)c^{-1}$  or for  $r > 2m$ .

Combining these result with (8), these stability conditions for  $E_1$  coming from  $A$  hold unconditionally whenever the equilibrium is feasible.

For the minor  $B$  we have

$$\text{tr}(B) = \frac{\rho r_1}{2} - \mu - b(\bar{F} + \bar{M}) - \mu - g(\bar{F} + \bar{M}) < 0$$

which explicitly gives the first stability condition

$$(\rho r_1 - 4\mu)a + (b + g)(2m - r) < 0. \tag{10}$$

Further,

$$\det(B) = \left[ \frac{\rho r_1}{2} - \mu - b(\bar{F} + \bar{M}) \right] [\mu + g(\bar{F} + \bar{M})] < 0.$$

from which we obtain the second stability condition

$$b(r - 2m) > a(\rho r_1 - 2\mu). \tag{11}$$

In conclusion,  $E_1$  is stable if both (10) and (11) hold.

Figure 2c shows the total mosquito population  $\bar{Z} = \bar{F} + \bar{M}$  at equilibrium  $E_1$  as a function of the parameters  $a$  and  $c$ . The influence of the latter is scant, while the population size grows fast for very small values of  $a$ , the intraspecific competition rate affecting the healthy females. Figure 2a shows the decrease in the different populations when  $a$  increases. The females disappear faster than the males, as it should be expected, since  $a$  influences directly their population. Figure 2b shows the populations behavior when  $c$  increases. The females grow, males drop, while the total population remains constant. For  $c < a$  males exceed the females. In all sets of parameters, the initial condition is the same one used in Fig. 1; recall that the other parameters are chosen arbitrarily.

In conclusion, feasibility for  $E_1$  requires the oviposition rate for healthy mosquitoes to be at least twice as much as their mortality rate. Stability hinges on (10) and (11); in particular  $E_1$  can be destabilized by the suitable introduction of bacteriological infection, as these conditions contain parameters related to the *Wolbachia* action.



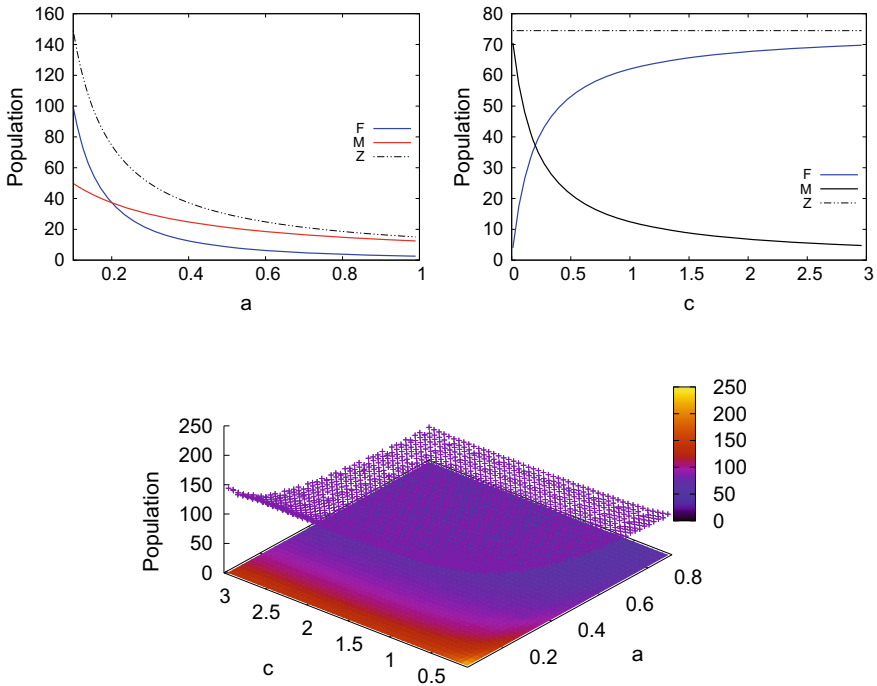


**Fig. 2** In **a** top right, Female  $F$ , males  $M$ , and the total population  $Z = F + M$  at the disease-free equilibrium  $E_1$  as function of the females intraspecific competition rate  $a$  with  $c = 0.2$ , and in **b** top left,  $F$ ,  $M$ , and  $Z$  populations at the disease-free equilibrium  $E_1$  as function of the males intraspecific competition rate  $c$ , with  $a = 0.2$ , and in **c** bottom, the total healthy population  $Z$  at the disease-free equilibrium  $E_1$  as function of the intraspecific competition rates  $a$  for females and  $c$  for males, with  $r = 30$ ,  $m = 0.1$ . In both **(a)** and **(b)** the parameters  $r$  and  $m$  are fixed as in **(c)**

### 4.2 Persistence of the Wolbachia-Infected Population and Extinction of the Wild Population

Here we consider the equilibrium with  $\bar{F} = \bar{M} = 0$ , but this situation could arise only in the full vertical transmission case  $\rho = 1$ . The corresponding equilibrium is

$$E_2 = \left( 0, \frac{2br_1\mu - 4b\mu^2 + 4g\mu^2 - 4g\mu r_1 + gr_1^2}{2b(2\mu b + br_1 - 2g\mu + gr_1)}, 0, \frac{r_1(r_1 - 2\mu)}{2(2\mu b + br_1 - 2g\mu + gr_1)} \right).$$

The analysis follows very closely the one of  $E_1$ , so that we just mention the final results. Feasibility holds in case

$$r_1 > 2\mu, \tag{12}$$

which concerns only reproduction rate and mortality of the infected mosquitoes and is independent of their intraspecific competition rates  $b$  and  $g$ . For stability, the Jacobian again factorizes and ultimately  $E_2$  is stable whenever feasible.

Similarly, the dependence of the population values on  $b$  and  $g$  indicates that increasing the intraspecific competition  $b$  among infected females implies a sharp reduction in the total (infected) population  $\bar{Z} = \bar{I} + \bar{U}$  (as here  $\bar{F} = \bar{M} = 0$ ), while the latter is scantily affected by changes in  $g$ , although the male to female ratio is much reduced.

In summary, this equilibrium would be beneficial, because all the insects would be *Wolbachia*-affected. Thus, in case of a bacterium with perfect vertical transmission rate, it would always be possible to attain a stable endemic state at which all individuals are infected and the population is lower, using considerations already seen for equilibrium  $E_1$ , due to the bacteria-induced reduced reproductive capacity and higher mortality.

### 4.3 Coexistence with Endemic Infection

This equilibrium is investigated numerically. To this end, we use information obtained from the literature [12], such as the vertical bacterial transmission that is taken to be almost perfect,  $\rho \simeq 99\%$ .

The reduction of adult longevity is about  $p \simeq 21\%$ , thus from

$$\mu = m \frac{p}{100 - p},$$

we find

$$\mu \simeq 1.27 m. \tag{13}$$

Egg survival is about  $\simeq 83 - 96\%$ , which combined with their reduction due to the action of the bacterium, estimated to be about  $\simeq 15\%$  [8], implies that the reduced reproduction rate is

$$0.7055 r < r_1 < 0.8160 r. \tag{14}$$

Finally, following [18], we assume that *Wolbachia* prevents the successful mating of an infected male with a susceptible female, thereby setting

$$k \simeq 0. \tag{15}$$

For the remaining parameters, we fix the following hypothetical values

$$\begin{aligned} r &= 150, & r_1 &= 120, & m &= 20, & \mu &= 25.4, & \rho &= 0.99, \\ k &= 0.01, & a &= 1, & b &= 1, & c &= 1, & g &= 1, & p &= q = 0.5. \end{aligned} \tag{16}$$

The initial conditions are

$$F_0 = I_0 = M_0 = U_0 = 1. \tag{17}$$

Solving numerically system (1), three cases of interest arise:

(i) bacteria-free equilibrium (the equilibrium  $E_1$  which was already discussed in Sect. 4.1), with  $\bar{F}_1 = 27.5, \bar{M}_1 = 27.5$  and of course  $\bar{I}_1 = \bar{U}_1 = 0$  (observe that the condition  $r > 2m$  is satisfied for this chosen parameter set). The Jacobian eigenvalues are all negative,  $-55.0, -75.0, -80.4$  and  $-21.0$ , so it is asymptotically stable.

(ii) two coexistence points:

(a)  $E_3 = (\bar{F}_3, \bar{I}_3, \bar{M}_3, \bar{U}_3)$  with

$$\bar{F}_3 = 0.2, \quad \bar{I}_3 = 16.8, \quad \bar{M}_3 = 0.2, \quad \bar{U}_3 = 16.8.$$

The eigenvalues of the Jacobian matrix are all negative,  $-34.0, -51.6, -54.0, -59.4$ . Thus, this point is asymptotically stable; and

(b)  $E_4 = (\bar{F}_4, \bar{I}_4, \bar{M}_4, \bar{U}_4)$  where

$$\bar{F}_4 = 12.1, \quad \bar{I}_4 = 4.9, \quad \bar{M}_4 = 12.1, \quad \bar{U}_4 = 4.9.$$

The eigenvalues of the Jacobian matrix in this case are:  $-34.0, -54.0, -59.4$  and  $14.9$ . Because the last one is positive, this equilibrium is unstable.

Note that the total mosquitoes populations are  $\bar{Z} = \bar{F} + \bar{M} = 55$  at  $E_1$  and  $\bar{Z} = \bar{F} + \bar{I} + \bar{M} + \bar{U} = 34$  at  $E_4$ , with almost all (99%) mosquitoes infected. Thus, in addition to render the insects infected, *Wolbachia* reduces also their population size, in agreement with the field studies [4, 6, 13, 19].

The unstable equilibrium  $E_4$  gives us tips about the invasion threshold; it says that the initial prevalence of the infection must exceed 0.285, i.e.,

$$I_0 + U_0 > 0.285 (F_0 + I_0 + M_0 + U_0). \tag{18}$$

In Figure 3 we show the bistability situation that arises in case (ii). We plot the system trajectories in the projection of the phase space onto the plane that contains the infected populations  $I + U$  versus the healthy ones  $F + M$ . The initial points are in red, in blue the equilibria. The one near the vertical axis represents the endemic case  $E_3$ , while the one over the horizontal axis is the disease-free point  $E_1$ . In the former, as stated above, the healthy population is scant, and the level of the infected population at the endemic equilibrium  $\bar{I} + \bar{U}$ , and consequently the resulting total population at this point, is much lower than the total (healthy) population  $\bar{Z} = \bar{F} + \bar{M}$  at the disease-free equilibrium  $E_1$ . We also report both healthy and infected populations of females against males, in Fig. 4. Because these are projections of the trajectories of a four dimensional system onto planes, there are some apparent intersections, not

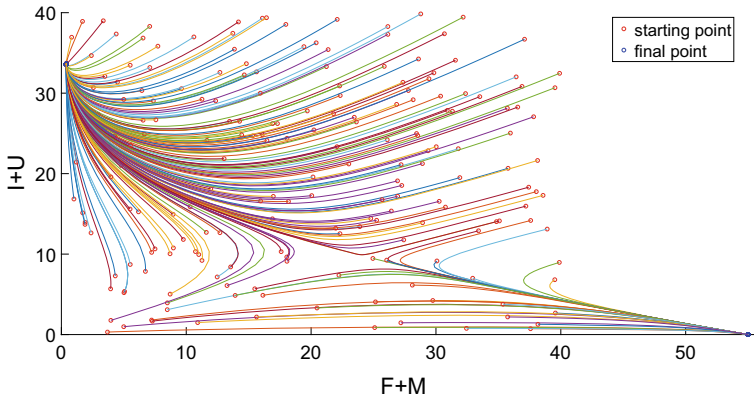


**Fig. 3** Projections of the system trajectories on the infected  $I + U$  versus healthy  $F + M$  total populations, with randomly generated initial conditions (red circles). The trajectories tend to either one of the equilibria (blue circles), the endemic point near the vertical axis and the disease-free over the horizontal axis. Here, the initial conditions are always chosen so that  $I_0 = U_0$  and  $M_0 = F_0$

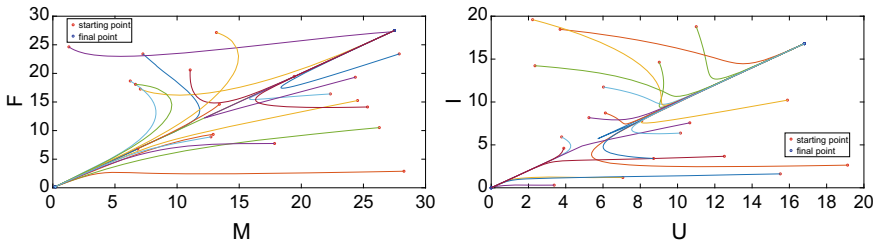


**Fig. 4** The same simulations of Fig. 3, with the same parameters and with randomly generated initial conditions for all the populations, with trajectories projected onto the healthy plane  $M - F$ , left, and onto the infected plane  $U - I$ , right. In these simulations, conditions  $I_0 = U_0$  and  $M_0 = F_0$  do not hold

occurring in the four dimensional phase space. Note also that in these simulations taking  $p = q = 0.5$ , as well as  $a = c$  and  $b = g$ , implies that the equilibria are found on the bisectrix, as the size of male and female populations are the same. Figure 3 suggests the presence of a separatrix in the four dimensional population space. Its position and shape depends on the choice of the parameters, here (16). Note that in particular, condition (17) has been set so that the bacterium can settle endemically in the population.

## 5 Numerical Simulations

In this section, we will focus on the case of persistence of both populations of mosquitoes, the infected and uninfected ones. Therefore, all simulations were done using the baseline parameters. Also, the initial subpopulation values are set to 1, so that  $I_0 + U_0 = 2$ ,  $F_0 + I_0 + M_0 + U_0 = 4$ , and their ratio is  $0.5 > 0.285$ , ensuring the endemicity of the bacterium. This sets up a proxy for the study of the coexistence equilibrium as a function of some parameters.

### 5.1 Oviposition

Figure 5a shows the total mosquito population  $Z = F + I + M + U$  as function of the reproduction parameters  $r$  and  $r_1$ . For low values of both oviposition rates, the population is much reduced. For higher values of  $r$  and low  $r_1$  the population grows linearly, with the healthy portion prevailing on the infected one, as can be seen in Fig. 5a and b. When instead  $r_1$  grows and  $r$  is small in comparison, the bacterium establishes endemically in the mosquito population. In such case, the total population (on the right of Fig. 5a) grows in a slower way and attains lower values than those found for the healthy one, on the left of the Fig. 5a. This is in agreement with the fact that the introduction of *Wolbachia*-carrying mosquitoes, when successful, can decrease the total mosquitoes population. The sharp jump that separates the two surfaces represents the reduction of mosquitoes due to the *Wolbachia* presence. Its position clearly depends on the model parameters.

### 5.2 Mortality

For high values of the mortality rates ( $2m > r$ ,  $2\mu > r_1$ ) the population dies out, which is apparent in the front part of the Fig. 6a, which is rotated, with the origin in the back. For values of  $m$  and  $\mu$  becoming lower, the population increases linearly, as expected. Again, on the left of Fig. 6a we find the bacteria-free case, as the *Wolbachia*-

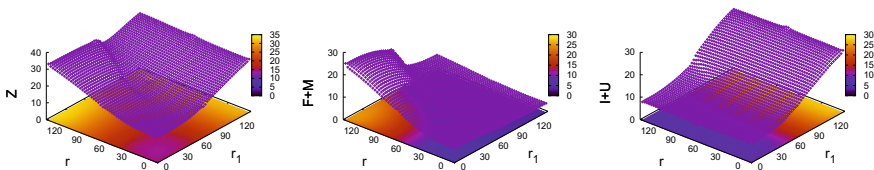


**Fig. 5** Mosquito populations at equilibrium as a function of the oviposition rates  $r$  and  $r_1$ . In **a** left, the total mosquito population  $Z = F + I + M + U$ , in **b** center, the healthy mosquito population  $F + M$ , and in **c** right, the infected mosquito population  $I + U$

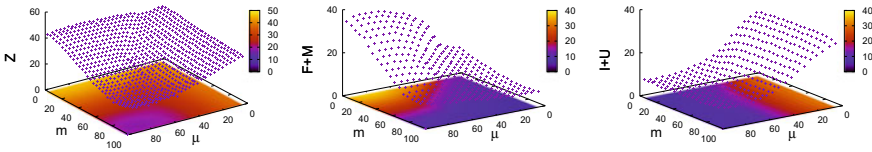


**Fig. 6** Mosquito population at equilibrium in terms of the mortality rates  $m$  and  $\mu$ . In **a** left, the total mosquito population  $Z = F + I + M + U$ ; note that this frame is rotated with respect to most of the other ones, the origin being located at the far end of the frame, in **b** center, the healthy mosquito population  $F + M$ , and in **c** right, the infected mosquito population  $I + U$

induced mortality  $\mu$  is much higher than the natural mortality  $m$ ; on the right of Fig. 6a instead the system settles to the endemic situation, because here the bacterium has a reduced impact on the single individual. This situation corresponds to the phenomenon observed in various natural situations, where diseases with high killing rates are of course lethal for the individual, but in this way they have fewer chances to spread in the whole community, with a thereby resulting smaller impact for the population as a whole. For better understanding of these remarks, see Fig. 6b and c for the total healthy and infected subpopulations.

### 5.3 Vertical Transmission

Figure 7 shows the healthy, infected and total mosquito populations as function of the *Wolbachia* vertical transmission rate  $\rho$ , in the meaningful range  $\rho \in [0.7, 1]$ , because for lower values the equilibrium becomes bacterium-free. The infected population is clearly seen to rise with higher values of the transmission coefficient. Therefore, it is important to choose a strain of *Wolbachia* that optimizes the transmission of the bacteria from mother to its offspring.

### 5.4 Mating Prevention

The role of *Wolbachia* as preventing agent for mating reproduction success among an infected male and a healthy female transpires from Fig. 8. In view of the field findings, [18], only very small values of  $k \ll 1$  are meaningful, and in such case the healthy population settles at very low levels, as it should be expected. Comparing Figs. 8 and 7 we observe that the coexistence equilibrium is more sensitive to the parameter  $\rho$  that is related to bacteria inheritance than to  $k$  that accounts for the cytoplasmic incompatibility.

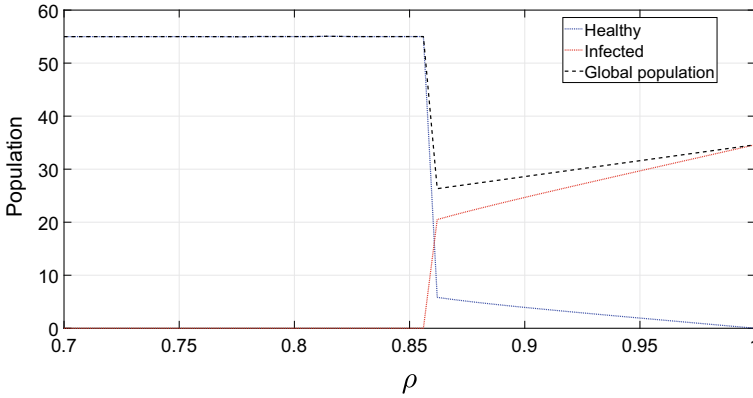


**Fig. 7** Mosquito populations at equilibrium in terms of the vertical transmission rate  $\rho$ . Blue line: the total healthy population  $F + M$ ; red line: the total infected population  $I + U$ ; black line: the total mosquito population  $Z = F + I + M + U$

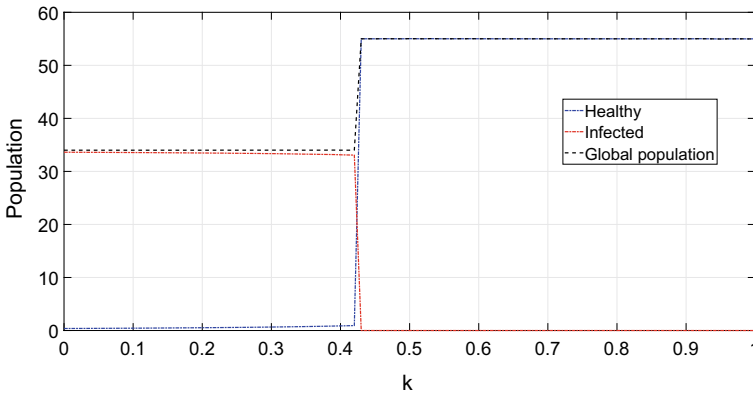


**Fig. 8** Mosquito populations at equilibrium in terms of the bacterium-induced mating prevention action  $k$ . Blue line: the total healthy population  $F + M$ ; red line: the total infected population  $I + U$ ; black line: the total mosquito population  $Z = F + I + M + U$

### 5.5 Intraspecific Competition

In Fig. 9a, where again the origin is at the far end, for decreasing and low values of  $b$ , the intraspecific competition experienced by the infected females entails a large increase in the mosquito level, independently of the intraspecific competition experienced by the healthy females  $a$ . The increase is due to *Wolbachia* endemic presence in the population, see Fig. 9b and c. Large values of  $b$  coupled with low values of  $a$  determine also a sharp population increase, in this case, being due to the bacterium eradication.

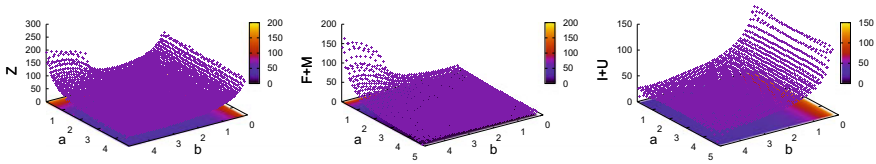


**Fig. 9** Equilibrium in terms of the healthy and infected females intraspecific competitions  $a$  and  $b$ . In **a** left, the total mosquito population  $Z = F + I + M + U$ , in **b** center, the healthy mosquito population  $F + M$ , and in **c** right, the infected mosquito population  $I + U$

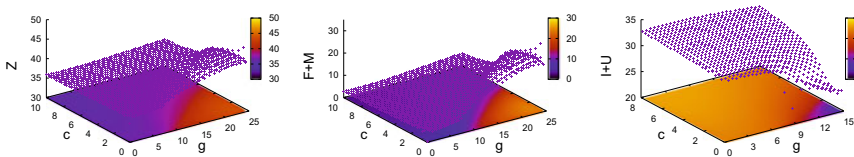


**Fig. 10** Equilibrium in terms of the healthy and infected males intraspecific competitions  $c$  and  $g$ . In **a** left, the total mosquito population  $Z = F + I + M + U$ , in **b** center, the healthy mosquito population  $F + M$ , and in **c** right, the infected mosquito population  $I + U$

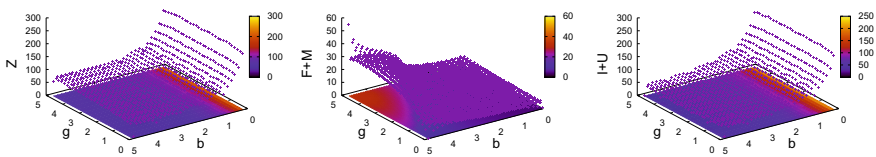


**Fig. 11** Equilibrium in terms of the infected females and males intraspecific competitions  $b$  and  $g$ . In **a** left, the total mosquito population  $Z = F + I + M + U$ ; note that the figure is rotated and the origin is located in the right corner; in **b** center, the healthy mosquito population  $F + M$ ; and in **c** right, the infected mosquito population  $I + U$

A sharp increase in the mosquito population level is found in the right corner of Fig. 10a, i.e. for low values of healthy males intraspecific competition  $c$  and large ones for their infected counterparts,  $g$ . Again, the sudden surge is due to the disappearance of the bacterium from the population, compare Fig. 10b and c.

As it has been discovered in the left frame of Fig. 9, also in case of changes in the infected subpopulations intraspecific coefficients  $b$  and  $g$  a jump is observed, Fig. 11, when large values of both coefficients produce higher equilibrium value, where the infection is eradicated. On the other hand, small values of the female competition  $b$  induce the endemic equilibrium, independently of the value that  $a$  attains, see the central and right frames in Fig. 11.

Finally, the healthy female and male intraspecific parameters  $a$  and  $c$  do not alter the coexistence equilibrium. And, in order to increase its presence in the mosquito population, the bacteria must increase male's mortality.



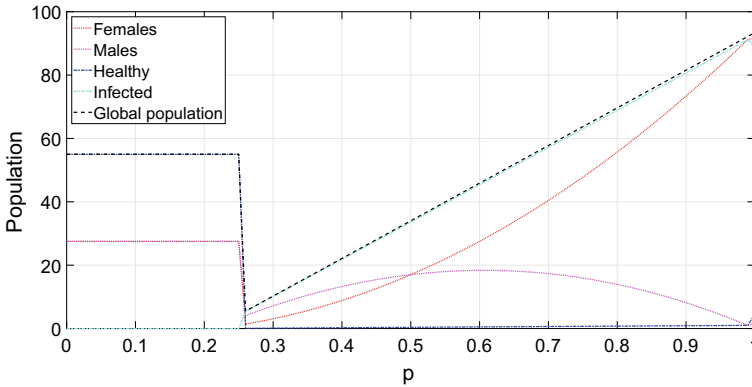


**Fig. 12** Mosquito populations at equilibrium in terms of the sex ratio parameter  $p$ . Red line: the total female population  $F + I$ ; magenta line: the total male population  $M + U$ ; black line: the total mosquito population  $Z = F + I + M + U$ ; cyan line: the total infected population  $I + U$  blue line: the total healthy population  $F + M$

### 5.6 Sex Ratio

Here it is seen that a low value of the female offsprings newborns  $p$ , induced by the *Wolbachia* action, entails a low female to male subpopulations’ ratio, as it should be expected, Fig. 12. At a critical value of  $p \simeq 0.25$  the females suddenly disappear, to rebound to higher values for increasing values of  $p$ , up to 90% when  $p = 1$ . A corresponding linear increase of the total population is also observed. The males instead in the interval of  $p \in [0.25, 1]$  experience an increase to the peak at  $p \simeq 0.6$ , to decline afterwards up to a tenth of the total population when  $p = 1$ . If we consider the infected population, it is absent for  $p < 0.25$ , and correspondingly the total population is healthy. For  $p > 0.25$  the infected population starts to increase, with increasing  $p$ , attaining 90% of the population for  $p = 1$ , and a corresponding decrease of the healthy individuals occurs. Thus, as it is expected, sex relation bias to female ( $p > 0.5$ ) increases the probability of the *Wolbachia* infection’s fixation in the population, especially when the bacteria vertical transmission rate is high.

## 6 Conclusion

The introduction of *Wolbachia*-infected mosquito into uninfected wild populations of *Aedes* mosquito can reduce or halt the transmission of some arboviruses. This occurs because disease transmission depends on the ratio between vector and human populations, and the *Wolbachia*-carrying mosquitoes have reduced vectorial capacity when challenged with dengue virus. The establishment of a *Wolbachia*-carrying population in an area where a *Wolbachia*-free population is endemic depends on several param-

eters like mosquitoes fitness, maternal inheritance and cytoplasmic incompatibility. Therefore, using a sex-structured epidemiological model, we discussed populations competition and persistence under several scenarios. The proposed model has four equilibria: (i) extinction of mosquito population, (ii) extinction of infected population and persistence of uninfected one, (iii) extinction of uninfected population and persistence of infected one, and (iv) coexistence of both populations. First, the persistence of the population (infected or uninfected one) occurs only for  $r > 2m$  or,  $r_1 > 2\mu$  which means that reproduction rates overcome mortality rates. Besides, case (iii) is possible only when maternal inheritance is perfect. Moreover, coexistence is achieved given that the initial infection prevalence is above a threshold value (given by Eq. 18) which depends on model parameters. Finally, female-biased sex ratio (see Fig. 12), or high maternal inheritance (see Fig. 7), or high cytoplasmic incompatibility (see Fig. 8) promote the fixation of the *Wolbachia*-infection on the mosquito population. Overall, the results obtained here are in agreement with the ones described in the literature.

## References

1. Adekunle, A.I., Meehan, M.T., McBryde, E.S.: Mathematical analysis of a *Wolbachia* invasive model with imperfect maternal transmission and loss of *Wolbachia* infection. *Infect. Dis. Model.* **4**, 265–285 (2019)
2. Benedito, A.S., Ferreira, C.P., Adimy, M.: Modeling the dynamics of *Wolbachia*-infected and uninfected *Aedes aegypti* populations by delay differential equations. *Math. Model. Nat. Phenom.* **15**, 76 (2020)
3. Biedler, J.K., Tu, Z.: Sex determination in mosquitoes. *Adv. Insect Physiol.* **51**, 37–66 (2016)
4. Calvitti, M.: Studio della simbiosi tra *Aedes Albopictus* e *Wolbachia Pipientis* in rapporto allo sviluppo di tecniche di lotta basate sulla incompatibilità citoplasmatica. (Symbiosis study between *Aedes Albopictus* and *Wolbachia Pipientis* in relationship with fighting techniques development based on cytoplasmatic incompatibility) Università degli Studi della Tuscia di Viterbo (2008). <https://dspace.unitus.it/handle/2067/1966?mode=full&locale=it>
5. Campo-Duarte, D.E., Vasilieva, O., Cardona-Salgado, D., Svinin, M.: Optimal control approach for establishing wMelPop *Wolbachia* infection among wild *Aedes aegypti* populations. *J. Math. Biol.* **76**(7), 1907–1950 (2018)
6. Ding, H., Yeo, H., Puniamoorthy, N.: *Wolbachia* infection in wild mosquitoes (Diptera: Culicidae): implications for transmission modes and host-endosymbiont associations in Singapore. *Parasites Vectors* **13**, 612 (2020). <https://doi.org/10.1186/s13071-020-04466-8>
7. Dorigatti, I., McCormack, C., Nedjati-Gilani, G., Ferguson, N.M.: Using *Wolbachia* for dengue control: insights from modelling. *Trends Parasitol.* **34**(2), 102–113 (2018)
8. Ferreira, C.P.: *Aedes aegypti* and *Wolbachia* interaction: population persistence in an environment changing. *Theor. Ecol.* **13**, 137–148 (2020). <https://doi.org/10.1007/s12080-019-00435-9>
9. Fallon, A.M.: Growth and maintenance of *Wolbachia* in insect cell lines. *Insects* **12**(8), 706 (2021)
10. King, J.G., Souto-Maior, C., Sartori, L.M., Maciel-de-Freitas, R., Gomes, M.G.M.: Variation in *Wolbachia* effects on *Aedes* mosquitoes as a determinant of invasiveness and vectorial capacity. *Nat. Commun.* **9**(1), 1–8 (2018)
11. Medici, A.: Ricerche di campo per lo sviluppo della tecnologia del maschio sterile nella lotta ad *Aedes Albopictus*. (Field research for the development of sterile males in the fight against *Aedes Albopictus*) Università di Bologna (2013). <http://amsdottorato.unibo.it/5386/>

12. Moretti, R., Yen, P.S., Houé, V., Lampazzi, E., Desiderio, A., Failloux, A.B., Calvitti, M.: Combining *Wolbachia*-induced sterility and virus protection to fight *Aedes albopictus*-borne viruses. PLOS Negl. Trop. Dis. (2018). <https://doi.org/10.1371/journal.pntd.0006626>
13. Pinto, S.B., Riback, T.I.S., Sylvestre, G., Costa, G., Peixoto, J., Dias, F.B.S., Tanamas, S.K., Simmons, C.P., Dufault, S.M., Ryan, P.A., O'Neil, S.L., Muzzi, F.C., Kutcher, S., Montgomery, J., Green, B.R., Smithyman, R., Eppinghaus, A., Saraceni, V., Durovni, B., Anders, K.L., Moreira, L.A.: Effectiveness of *Wolbachia*-infected mosquito deployments in reducing the incidence of dengue and other *Aedes*-borne diseases in Niterói, Brazil: A quasi-experimental study. PLOS Negl. Tropic. Dis. (2021). <https://doi.org/10.1371/journal.pntd.0009556>
14. Pocquet, N., et al.: Assessment of fitness and vector competence of a New Caledonia w Mel *Aedes aegypti* strain before field-release. PLoS Negl. Trop. Dis. **15**(9), e0009752 (2021)
15. Qu, Z., Xue, L., Hyman, J.M.: Modeling the transmission of *Wolbachia* in mosquitoes for controlling mosquito-borne diseases. SIAM J. Appl. Math. **78**(2), 826–852 (2018)
16. Rafikov, M., Meza, M.E.M., Ferruzzo Correa, D.P., Wyse, A.P.: Controlling *Aedes aegypti* populations by limited *Wolbachia*-based strategies in a seasonal environment. Math. Methods Appl. Sci. **42**(17), 5736–5745 (2019)
17. Reyes, J.I., Suzuki, Y., Carvajal, T., Muñoz, M.N., Watanabe, K.: Intracellular interactions between arboviruses and *Wolbachia* in *Aedes aegypti*. Front. Cell. Infect. Microbiol. **11**, 690087 (2021). <https://doi.org/10.3389/fcimb.2021.690087>
18. Ross, P.A., Wiwatanaratnabutr, I., Axford, J.K., White, V.L., Endersby-Harshman, N.M., Hoffman, A.A.: *Wolbachia* infections in *Aedes aegypti* differ markedly in their response to cyclical heat stress. PLoS Pathog **13**(1), e1006006 (2017). <https://doi.org/10.1371/journal.ppat.1006006>. <https://journals.plos.org/plospathogens/article?id=10.1371/journal.ppat.1006006>
19. Utarini, A., Indriani, C., Ahmad, R.A., Tantowijoyo, W., Arguni, E., Ansari, R., Supriyati, E., Wardana, D.S., Meitika, Y., Ernesia, I., Nurhayati, I., Prabowo, E., Andari, B., Green, B.R., Hodgson, L., Cutcher, Z., Rancès, E., Ryan, P.A., O'Neil, S.L., Dufault, S.M., Tanamas, S.K., Jewell, N.P., Anders, K.L., Simmons, C.P.: Efficacy of *Wolbachia*-infected mosquito deployments for the control of dengue. New Engl. J. Med. (2021) <https://www.nejm.org/doi/10.1056/NEJMoa2030243>
20. Centers for Disease Control and Prevention. <https://www.cdc.gov/mosquitoes/mosquito-control/community/sit/wolbachia.html>
21. World Mosquito Program. <https://www.worldmosquitoprogram.org/en/work/wolbachia-method/how-it-works>
22. Yang, H.M., Ferreira, C.P.: Assessing the effects of vector control on dengue transmission. Appl. Math. Comput. **198**(1), 401–413 (2008)
23. Zhang, H., Lui, R.: Releasing *Wolbachia*-infected *Aedes aegypti* to prevent the spread of dengue virus: A mathematical study. Infect. Dis. Model. **5**, 142–160 (2020)

# Effect of Nonlinear Harvesting on a Fractional-Order Predator-Prey Model



Kshirod Sarkar and Biswajit Mondal

**Abstract** In this paper, we have introduced nonlinear harvesting to study a fractional-order predator-prey model with Holling-II response. Existence of multiple equilibrium points of the model and their stability under different conditions are analyzed. Global stability analysis of the co-existence equilibrium point has examined by considering suitable Lyapunov function. we have observed that fractional-order model is more viable for the memory-based system than integer-order model. Our model exhibits Hopf bifurcation with respect to fractional-order of the derivative. Furthermore, we have investigated period of doubling bifurcation with respect to some other parameters. Numerical simulations have performed to verify the theoretical results using Adams-Bashforth-Moulton type scheme.

**Keywords** Fractional-order · Nonlinear harvesting · Stability analysis · Hopf bifurcation

## 1 Introduction

For the basic needs, harvesting of biological resources are rigorously practiced for fishing and management of wildlife etc. The study of dynamical systems with harvesting is another important research topic in population dynamics. It is observed that the nonlinear harvesting is more reasonable when the number of harvesting of species is very large. Furthermore, It is quite realistic to implement linear harvesting when prey population is low. In linear harvesting, the harvesting function  $h(x) = qEx$ , increases proportionally as harvesting species  $x$  increases, which is unrealistic in the

---

K. Sarkar (✉) · B. Mondal  
Raja N.L. Khan Women's College (Autonomous), Vidysagar University Road, Midnapore  
721102, West Bengal, India  
e-mail: [kshirodsarkar8@gmail.com](mailto:kshirodsarkar8@gmail.com); [ks\\_mathematics@mlkwc.ac.in](mailto:ks_mathematics@mlkwc.ac.in)

B. Mondal  
e-mail: [bm-mathematics@mlkwc.ac.in](mailto:bm-mathematics@mlkwc.ac.in)

© The Author(s), under exclusive license to Springer Nature Switzerland AG 2022  
S. Banerjee and A. Saha (eds.), *Nonlinear Dynamics and Applications*,  
Springer Proceedings in Complexity,  
[https://doi.org/10.1007/978-3-030-99792-2\\_64](https://doi.org/10.1007/978-3-030-99792-2_64)

761

biological sense. But these unreasonable features can be fixed by applying nonlinear type harvesting.

Many researchers have considered nonlinear harvesting in their models. Hu and Cao [7] has incorporated a nonlinear type prey harvesting in Leslie-Gower model and have discussed different types of bifurcation analysis. A bioeconomic predator-prey model is studied by [9] and they consider nonlinear harvesting for prey only. Also [6] have discussed the predator-prey model with nonlinear harvesting in predator population and established that nonlinear harvesting is more realistic for large population. Stability and bifurcation analysis in a prey-predator model with group defence as well as nonlinear harvesting are studied by [8]. Effect of nonlinear harvesting in a prey-predator model with square root functional response are discussed by [14]. Furthermore, a notable research considering nonlinear type harvesting have examined by [5]. Stability and bifurcation analysis of a prey-predator model with Holling-IV functional response and nonlinear harvesting are examined by [16]. Recently, [11] have examined the dynamical effects of nonlinear harvesting in prey species with Holling-II predation in their model and have considered the harvesting function  $h(x) = \frac{hu}{h+u}$  where  $h$  is positive constants. But the form of this type nonlinear harvesting function is a particular case rather than the general case. The general form of nonlinear harvesting function is  $f(u) = \frac{qEu}{m_1E+m_2u}$ . Here,  $q$  denotes the harvesting coefficient,  $E$  denotes the harvesting effort and  $m_1, m_2$  are positive constants. We have incorporated nonlinear harvesting function  $\frac{qEu}{m_1E+m_2u}$  in our model

$$\begin{aligned} \frac{du}{d\tau} &= ru \left(1 - \frac{u}{k}\right) - \frac{buv}{c+u} - \frac{qEu}{m_1E+m_2u} \\ \frac{dv}{d\tau} &= \frac{evu}{c+u} - dv, \end{aligned} \tag{1}$$

where  $u(0) > 0, v(0) > 0$ . Here  $r$  and  $k$  are intrinsic growth rate and carrying capacity of prey species respectively. Parameter  $b$  is the consumption rate per unit time,  $c$  is the half saturation constant,  $e$  is the conversion factor per unit time by per predator and  $d$  is the death rate of predator species. To reduce free and floating parameters, we have applied non-dimensional scheme. Thus we take some set of transformation as follows:  $x = \frac{u}{k}, y = \frac{bv}{k}, t = r\tau, \beta = \frac{1}{r}, \alpha = \frac{c}{k}, h = \frac{qE}{m_2rk}, m = \frac{m_1E}{m_2k}, \beta_1 = \frac{e}{r}$  and  $\delta = \frac{d}{r}$ . Then we have obtained a dynamical model:

$$\begin{aligned} \frac{dx}{dt} &= x(1-x) - \frac{\beta xy}{\alpha+x} - \frac{hx}{m+x} \\ \frac{dy}{dt} &= \frac{\beta_1 xy}{\alpha+x} - \delta y, \end{aligned} \tag{2}$$

Fractional order differential equations manifests greater degrees of freedom and some realistic results in complex dynamical model. Fractional order differential equation is more appropriate to analyze biological system as it contains the memory kernel. In recent years, many researches have been done in fractional-order model due to

its ability to execute a better approximation of nonlinear dynamics. Now consider  $n - 1 < \mu < n$  and  $n \in \mathbb{N}$ , then the Caputo type fractional derivative of order  $\mu > 0$  is defined as [2]:

$$D_t^\mu f(t) = \frac{1}{\Gamma(n - \mu)} \int_{t_0}^t \frac{f^n(s)}{(t - s)^{\mu+1-n}} ds,$$

where  $f(t)$  is a function of order  $\mu$  and  $f(t) \in C^n([t_0, \infty), \mathbb{R})$ . There are very few articles which have discussed fractional-order prey-predator model with nonlinear harvesting. Fractional order Leslie-Gower model with nonlinear harvesting is studied by [4]. Further, authors [12] have considered a fractional-order Leslie-Gower model with nonlinear harvesting and discussed the optimal control strategies. Here we consider the model 2 with fractional order differential equation as follows:

$$\begin{aligned} \frac{d^\mu x}{dt^\mu} &= x(1 - x) - \frac{\beta xy}{\alpha + x} - \frac{hx}{m + x} \\ \frac{d^\mu y}{dt^\mu} &= \frac{\beta_1 xy}{\alpha + x} - \delta y, \end{aligned} \tag{3}$$

where  $x(0) > 0, y(0) > 0$  and  $0 < \mu \leq 1$ .

The arrangement of remaining portion of the paper is given as follows: existence of different equilibrium points and their local stability are examined in Sect. 2. The global stability and Hopf bifurcation are discussed in Sects. 3 and 4 respectively. Numerical simulations have been organized in Sect. 5 and finally, conclusions have discussed in Sect. 6.

## 2 Equilibrium Points and Local Stability

The trivial equilibrium point  $E_0 = (0, 0)$  is always exist. This model has at most two predator free equilibrium(PFE) points, namely it is  $E_L = (x_L, 0)$  and  $E_R = (x_R, 0)$  and it depends on the equation  $g(x) = 1 - x - \frac{h}{m+x} = 0$ . Then roots of the equation are  $x_L$  and  $x_R$ , where  $x_L = \frac{1}{2} \left( 1 - m - \sqrt{(1 - m)^2 - 4(h - m)} \right)$  and  $x_R = \frac{1}{2} \left( 1 - m + \sqrt{(1 - m)^2 - 4(h - m)} \right)$ . Conditions for the existence of two PFE points is  $m < h < m_0 = \left(\frac{1+m}{2}\right)^2$ , where  $m < 1$ . In this case obviously,  $g'(x_L) > 0$  and  $g'(x_R) < 0$ . Only axial PFE point  $E_R = (x_R, 0)$  exist for  $h \leq m$ . If  $h = m_0$ , these two PFE points collides each other at the point  $\left(\frac{1-m}{2}, 0\right)$  and then  $g'\left(\frac{1-m}{2}\right) = 0$ . No axial equilibrium point exist for  $h > m_0$ . Co-existing equilibrium point is obtained at  $E_* = \left(x^*, y^* = \left(\frac{\alpha+x^*}{\beta}\right) g(x^*)\right)$ , where  $x^* = \frac{\delta\alpha}{\beta_1 - \delta}$ , which is meaningful only when  $\beta_1 > \delta$ . Hence from the above studies, we have the following results:

(i) If  $m < h < m_0$ , system has two PFE points  $E_R$  and  $E_L$ . Interior equilibrium point  $E_*$  exists if  $x_L < x^* < x_R$ .

(ii) If  $m \geq h$ , system has one PFE point  $E_R$ . Interior equilibrium point  $E_*$  exist if  $0 < x^* < x_R$ .

(iii) If  $h = m_0$ , two PFE points  $E_R$  and  $E_R$  collide with each other. No interior equilibrium point exists when  $h \geq m_0$ .

The Jacobian matrix at any point  $(x, y)$  of the system 3 is

$$J(x, y) = \begin{pmatrix} 1 - 2x - \frac{\beta\alpha y}{(\alpha+x)^2} - \frac{hm}{(m+x)^2} & -\frac{\beta x}{\alpha+x} \\ \frac{\beta_1\alpha y}{(\alpha+x)^2} & \frac{\beta_1 x}{\alpha+x} - \delta \end{pmatrix}. \tag{4}$$

### 2.1 $m < h < m_0$

**Theorem 1** (a) *The trivial equilibrium point  $E_0$  is locally asymptotically stable (LAS).*

(b) *Both the equilibrium points  $E_L$  and  $E_R$  are saddle point if  $x_L < x^* < x_R$ .*

(c) *The equilibrium point  $E_L$  is unstable, while equilibrium point  $E_R$  is a saddle point if  $0 < x^* < x_L$ .*

(d) *The equilibrium point  $E_L$  is saddle point, while equilibrium point  $E_R$  is LAS if  $x_R < x^*$ .*

(e) *If  $T(J(E_*)) \leq 0$ , then the equilibrium point  $E_*$  of the system 3 is LAS.*

(f) *If  $T(J(E_*)) > 0$  and  $T^2(J(E_*)) < 4D(J(E_*))$ , then the equilibrium point  $E_*$  is LAS for  $\mu$  if  $\sqrt{|T^2(J(E_*)) - 4D(J(E_*))|} > T(J(E_*))\tan\left(\frac{\mu\pi}{2}\right)$ .*

**Proof** We have analysed the local stability of the different equilibrium points according to the results of [13, 15]. (a) We have obtained the eigen values of the matrix  $J(E_0)$ . It is observed that the eigenvalues of  $\lambda_1 < 0$  if  $h > m$  and  $\lambda_2 < 0$ , consequently we get  $|\arg(\lambda_1)| = \pi > \frac{\mu\pi}{2}$ . Hence according to Matignon’s condition,  $E_0$  is LAS when  $h > m$ .

(b) From Eq. 4, we have obtained the eigenvalues of the Jacobian matrix  $J(E_L)$  as  $\lambda_1 = x_L g'(x_L)$  and  $\lambda_2 = \frac{\beta_1 x_L}{\alpha+x_L} - \delta$ . For  $x_L < x^* < x_R$  it gives  $g'(x_L) > 0$  and  $\frac{\beta_1 x_L}{\alpha+x_L} < \delta$ , consequently we have  $\lambda_1 > 0$  and  $\lambda_2 < 0$ . Thus  $E_L$  is saddle point. The eigenvalues of the matrix  $J(E_R)$  are obtained as  $\lambda_1 = x_R g'(x_R)$  and  $\lambda_2 = \frac{\beta_1 x_R}{\alpha+x_R} - \delta$ . But in this case we have  $\lambda_1 < 0$  and  $\lambda_2 > 0$ , as  $g'(x_R) < 0$  and  $\frac{\beta_1 x_R}{\alpha+x_R} > \delta$ . Hence  $E_R$  is also a saddle point.

(c) For the case  $0 < x^* < x_L$ , it is obvious that eigenvalue  $\lambda_1 > 0$  of  $J(E_L)$  as  $g'(x_L) > 0$  and eigenvalue  $\lambda_2 > 0$  as  $\frac{\beta_1 x_L}{\alpha+x_L} - \delta > 0$ . So the condition  $|\arg(\lambda_i)| > \frac{\mu\pi}{2}$ , for  $i = 1, 2$  does not satisfy.

Hence in this case  $E_L$  is unstable. Now eigenvalue of the matrix  $J(E_R)$  are such that  $\lambda_1 = x_R g'(x_R)$  and  $\lambda_2 = \frac{\beta_1 x_R}{\alpha+x_R} - \delta$ . Similarly in this case we obtained as  $\lambda_1 < 0$  and  $\lambda_2 > 0$ . Therefore  $E_R$  is a saddle point.

(d) If  $x_R < x^*$ , then eigenvalues of  $J(E_L)$  is such that  $\lambda_1 > 0$  and  $\lambda_2 < 0$ . Hence  $E_L$  is saddle point. Now eigenvalues of  $J(E_R)$  is such that  $\lambda_1 < 0$  and  $\lambda_2 < 0$ . Therefore, using Matignon’s condition of stability we have  $E_R$  is LAS.

(e) In this case coexistence equilibrium point  $E_*$  exist when  $x_L < x^* < x_R$ . The characteristic equation of  $J(E_*)$  is given by  $\lambda^2 - T(J(E_*))\lambda + D(J(E_*)) = 0$ . Then it gives  $T(J(E_*)) = 1 - 2x^* - \frac{\beta\alpha y^*}{(\alpha+x^*)^2} - \frac{hm}{(m+x^*)^2}$  and  $D(J(E_*)) = \frac{\beta\alpha\beta_1 x^* y^*}{(\alpha+x^*)^3} > 0$ . Now if  $T(J(E_*)) = 0$ , then  $J(E_*)$  has two purely imaginary complex conjugate eigenvalues  $\lambda_1$  and  $\lambda_2$  such that  $|\arg(\lambda_{1,2})| = \frac{\pi}{2}$ . Hence the equilibrium point  $E_*$  is stable. If  $T(J(E_*)) < 0$ , then also the eigenvalues of  $J(E_*)$  are satisfied the Matignon’s condition and hence  $E_*$  is LAS.

(f) If  $T(J(E_*)) > 0$  and  $T^2(J(E_*)) < 4D(J(E_*))$ , then  $J(E_*)$  has a pair of complex conjugate eigenvalues  $\lambda_1$  and  $\lambda_2$  with positive real parts. From the given condition it is obvious that  $Im(\lambda_1) > Re(\lambda_1) \tan(\frac{\mu\pi}{2})$  and  $-Im(\lambda_2) > Re(\lambda_2) \tan(\frac{\mu\pi}{2})$ . After some calculation it implies that  $|\arg(\lambda_i)| > \frac{\mu\pi}{2}$ , for  $i = 1, 2$ . Hence  $E_*$  is LAS for  $\mu \in (0, \mu^*]$ , where the critical value  $\mu^*$  is given by  $\mu^* = \frac{2}{\pi} \tan^{-1} \left( \sqrt{|T^2(J(E_*)) - 4D(J(E_*))|} / T(J(E_*)) \right)$ .

### 2.2 $h \leq m$

**Theorem 2** (a) *The trivial equilibrium point  $E_0$  is saddle point when  $h < m$  and stable when  $h = m$ .*

(b) *Only PFE point  $E_R$  is saddle point if  $0 < x^* < x_R$  and LAS if  $x_R < x^*$ .*

(c) *Interior equilibrium point  $E_*$  of the system 3 is LAS if  $T(J(E_*)) \leq 0$ .*

(d) *If  $T(J(E_*)) > 0$  and  $T^2(J(E_*)) < 4D(J(E_*))$ , then the equilibrium point  $E_*$  is LAS for  $\mu$  if  $\sqrt{|T^2(J(E_*)) - 4D(J(E_*))|} > T(J(E_*)) \tan \left( \frac{\mu\pi}{2} \right)$ .*

**Proof** (a) The eigenvalues of  $J(E_0)$  are  $\lambda_1 = 1 - \frac{h}{m}$  and  $\lambda_2 = -\delta < 0$ . Now for  $h < m$ , we have  $\lambda_1 > 0$  and hence  $E_0$  is saddle point for the case  $h < m$ .

(b) In this case only one PFE point  $E_R$  exist. Now we obtain the eigenvalues of  $J(E_R)$  as  $\lambda_1 = x_R g'(x_R)$  and  $\lambda_2 = \frac{\beta_1 x_R}{\alpha + x_R} - \delta$ . For  $0 < x^* < x_R$ , it gives  $g'(x_R) < 0$  and  $\frac{\beta_1 x_R}{\alpha + x_R} > \delta$ . Consequently we have  $\lambda_1 < 0$  and  $\lambda_2 > 0$ . Thus  $E_R$  is saddle point. But when  $x_R < x^*$ , we have  $\lambda_1 < 0$  and  $\lambda_2 < 0$ . Hence in this case  $E_R$  is LAS, since it satisfies the Matignon’s condition. In this case coexistence equilibrium point  $E_*$  exist when  $0 < x^* < x_R$ . Local stability analysis around  $E_*$  of the Theorem 2c and d are same as the Theorem 1e and f respectively.

### 2.3 $h \geq m_0$

It is clear that when  $g'(x_L) = 0$ , then  $E_L$  coincide with  $E_R$ . Thus in this case saddle-node bifurcation occurs at  $h = m_0$ , when  $m \neq 1$ . the only equilibrium point  $E_0$  exists when  $h \geq m_0$ . Eigen values of  $J(E_0)$  are  $\lambda_1 = 1 - \frac{h}{m} < 0$  and  $\lambda_2 = -\delta < 0$  and hence  $E_0$  is LAS when  $h \geq m_0$ .



### 3 Global Stability

**Theorem 3** *The co-existence equilibrium point  $E_*$  of the dynamical model 3 is globally asymptotically stable if it is locally asymptotically stable.*

**Proof** For  $E_* = (x^*, y^*)$ , we have  $1 - x^* - \frac{\beta y^*}{\alpha + x^*} - \frac{h}{m + x^*} = 0$  and  $\frac{\beta_1 x^*}{\alpha + x^*} - \delta = 0$ . Consider a function  $L_1(x, y) = (x - x^* - x^* \log \frac{x}{x^*}) + a_1 \left( y - y^* - y^* \log \frac{y}{y^*} \right)$ . where  $a_1 > 0$  is a constant. Now applying  $\mu$  fractional order derivative of  $L_1(x, y)$  and apply the Lemma 3.1 of [17]. After some calculations it follows that  $\frac{d^\mu L_1}{dt^\mu} \leq \left( \frac{\beta y^*}{(\alpha + x)(\alpha + x^*)} + \frac{h}{(m + x)(m + x^*)} - 1 \right) (x - x^*)^2 + (a_1 \alpha \beta_1 - \beta x^* - \beta \alpha) \frac{(x - x^*)(y - y^*)}{(\alpha + x)(\alpha + x^*)}$ .

Now choosing the constant  $a_1 = \frac{\beta(\alpha + x^*)}{\alpha \beta_1}$  and after some calculations it has  $\frac{d^\mu L_1}{dt^\mu} \leq \left( \frac{\beta y^*}{\alpha(\alpha + x^*)} + \frac{h}{m(m + x^*)} - 1 \right) (x - x^*)^2$ . Now consider the two functions  $L_2(x, y) = \frac{1}{2} [(x - x^*) + \frac{\beta}{\beta_1} (y - y^*)]^2$  and  $L_3(x, y) = [(x - x^*) + \frac{\beta}{\beta_1} (y - y^*)]$ .

Then take  $\mu$  fractional-order derivative of  $L_3(x, y)$  and using linearity property we get that  $\frac{d^\mu L_3}{dt^\mu} = -x(x - x^*) + \frac{hx(x - x^*)}{(m + x)(m + x^*)} + \frac{\beta y^*(x - x^*)}{\alpha + x^*} - \frac{\beta x^*(y - y^*)}{\alpha + x^*}$ . Again applying  $\mu$  fractional-order derivative in  $L_2(x, y)$  we have

$$\begin{aligned} \frac{d^\mu L_2}{dt^\mu} < & \left( \frac{h}{m + x^*} + \frac{\beta y^*}{\alpha + x^*} + \frac{\beta y^*}{\beta_1} \right) (x - x^*)^2 - \frac{\beta^2 x^*(y - y^*)^2}{\beta_1(\alpha + x^*)} + \\ & \left( \frac{\beta h}{\beta_1(m + x^*)} + \frac{\beta^2 y^*}{\beta_1(\alpha + x^*)} - \frac{\beta x^*}{\beta_1} - \frac{\beta x^*}{\alpha + x^*} \right) (x - x^*)(y - y^*). \end{aligned} \tag{5}$$

It is noted that  $\left( \frac{\beta h}{\beta_1(m + x^*)} + \frac{\beta^2 y^*}{\beta_1(\alpha + x^*)} - \frac{\beta x^*}{\beta_1} - \frac{\beta x^*}{\alpha + x^*} \right) (x - x^*)(y - y^*) \leq P(x - x^*)^2 + \frac{\beta^2 x^*(y - y^*)^2}{2\beta_1(\alpha + x^*)}$ , where  $P = \frac{\left( \frac{\beta h}{\beta_1(m + x^*)} + \frac{\beta^2 y^*}{\beta_1(\alpha + x^*)} - \frac{\beta x^*}{\alpha + x^*} - \frac{\beta x^*}{\beta_1} \right)^2}{2\beta^2 x^*/\beta_1(\alpha + x^*)}$ . Thus from Eq. 5 we have

$$\frac{d^\mu L_2}{dt^\mu} \leq \left( \frac{h}{m + x^*} + \frac{\beta y^*}{\alpha + x^*} + \frac{\beta y^*}{\beta_1} + P \right) (x - x^*)^2 - \frac{\beta^2 x^*(y - y^*)^2}{2\beta_1(\alpha + x^*)}$$

Now consider the Lyapunov function  $L(x, y) = L_1(x, y) + a_2 L_2(x, y)$ , where  $a_2 > 0$  is a positive constant. Therefore taking  $\mu$  order derivative of  $L(x, y)$  and after simplification it has

$$\begin{aligned} \frac{d^\mu L}{dt^\mu} \leq & - \left( \left( 1 - \frac{\beta y^*}{\alpha(\alpha + x^*)} - \frac{h}{m(m + x^*)} \right) - a_2 \left( \frac{\beta y^*}{\alpha + x^*} + \frac{h}{m + x^*} + \frac{\beta y^*}{\beta_1} + P \right) \right) \\ & \times (x - x^*)^2 - \frac{a_2 \beta^2 x^*(y - y^*)^2}{2\beta_1(\alpha + x^*)}. \end{aligned}$$

Now we can choose constant  $a_2$  in a suitable way such that  $\left( 1 - \frac{\beta y^*}{\alpha(\alpha + x^*)} - \frac{h}{m(m + x^*)} \right) - a_2 \left( \frac{\beta y^*}{\alpha + x^*} + \frac{h}{m + x^*} + \frac{\beta y^*}{\beta_1} + P \right) = \frac{1}{2} \left( 1 - \frac{\beta y^*}{\alpha(\alpha + x^*)} - \frac{h}{m(m + x^*)} \right)$ . Thus it gives us  $\left( 1 - \frac{\beta y^*}{\alpha(\alpha + x^*)} - \frac{h}{m(m + x^*)} \right) = 2a_2 \left( \frac{\beta y^*}{\alpha + x^*} + \frac{h}{m + x^*} + \frac{\beta y^*}{\beta_1} + P \right) > 0$ . Then we get that  $\frac{d^\mu L}{dt^\mu} \leq -\frac{1}{2} \left( 1 - \frac{\beta y^*}{\alpha(\alpha + x^*)} - \frac{h}{m(m + x^*)} \right) (x - x^*)^2 - \frac{a_2 \beta^2 x^*(y - y^*)^2}{2\beta_1(\alpha + x^*)}$ . Therefore we have

$\frac{d^\mu L}{dt^\mu} < 0$ , for  $(x, y) \neq (x^*, y^*)$  and  $\frac{d^\mu L}{dt^\mu} = 0$  for  $(x, y) = (x^*, y^*)$ . Hence  $E_*$  of the system 3 is GAS.

### 4 Hopf Bifurcation

**Theorem 4** *The necessary and sufficient conditions for the dynamical system 3 exhibits Hopf bifurcation through  $E_*$  if the parameter  $\mu$  crosses the critical value  $\mu^* = \frac{2}{\pi} \tan^{-1} \left( \frac{\sqrt{|T^2(J(E_*)) - 4D(J(E_*))|}}{T(J(E_*))} \right)$ , where  $T(J(E_*)) > 0$  and  $T^2(J(E_*)) < 4D(J(E_*))$ .*

**Proof** From the given conditions it is clear that the eigenvalues of the Jacobian matrix  $J(E_*)$  are  $\lambda_{1,2} = \phi \pm i\omega$  where we have  $\phi = \frac{1}{2}T(J(E_*)) > 0$  and also  $\omega = \frac{1}{2}\sqrt{|T^2(J(E_*)) - 4D(J(E_*))|}$ . Now it has  $G_{1,2}(\mu^*) = \frac{\mu^*\pi}{2} - |arg(\lambda_i)| = \frac{\mu^*\pi}{2} - \tan^{-1} |\omega/\phi| = \tan^{-1} |\omega/\phi| - \tan^{-1} |\omega/\phi| = 0$  and obviously  $\frac{\partial G_{1,2}}{\partial \mu} |_{\mu=\mu^*} = \frac{\pi}{2} \neq 0$ . Therefore, according to Sect.(2.2) of [1] Hopf bifurcation occurs if the bifurcation parameter  $\mu$  crosses the value  $\mu = \mu^*$ .

### 5 Numerical Simulation

Here we have performed some numerical computations to check the feasibility of our model. In this fractional-order model, a generalized Adams-Bashforth-Moulton type scheme is used accordingly by [3, 10]. We have observed that the parameters  $h$  and  $m$  have a major biological impact on the model. In Fig. 1, we have drawn

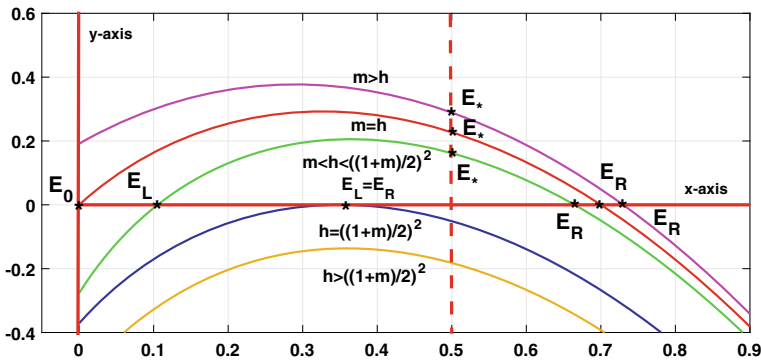


**Fig. 1** The existence of various PFE equilibrium points depends on the parameters  $h$  and  $m$ . X-nullcline and y-nullcline for different values of parameters that are fixed except  $h$  and  $m$  are obtained

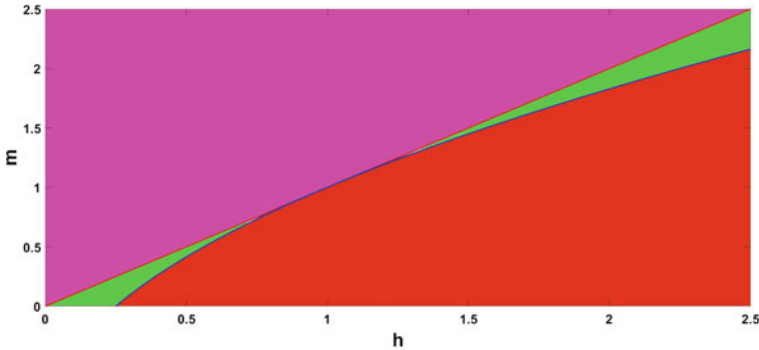


**Fig. 2** No interior, as well as PFE point exists in the red shaded region. The interior equilibrium point and two PFE points exist in the green shaded region. Whereas interior equilibrium point and one PFE point exist in the cyan region

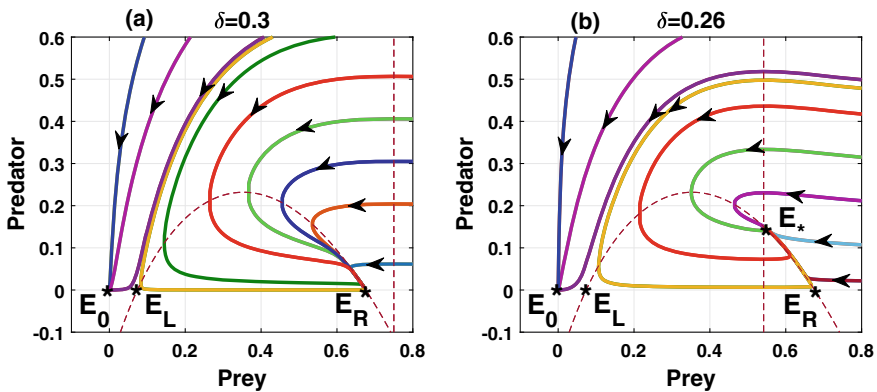


**Fig. 3** Phase portraits are obtained for  $\mu = 0.99, \alpha = 0.5, \beta = 0.55, \beta_1 = 0.5, h = 0.3, m = 0.25$ . **a** no interior equilibrium exist,  $E_R$  is LAS,  $E_L$  is saddle point and  $E_0$  is LAS. **b** Interior equilibrium point  $E_*$  is nodal sink,  $E_R$  and  $E_L$  are saddle point and  $E_0$  is LAS

$x$ -nullcline and  $y$ -nullcline where we consider different values of  $h, m$  along with  $\beta = 0.55, \beta_1 = 0.5, \alpha = 0.5, \delta = 0.25$ .

The Existence of the interior equilibrium and PFE points depends on two parameters  $h$  and  $m$ , which are shown in Fig. 2. First we check the case  $m < h < m_0$  and consider the parameters  $\beta = 0.55, \beta_1 = 0.5, \alpha = 0.5, h = 0.3, m = 0.25$  and  $\delta = 0.3$ . In this case two PFE points  $E_R = (0.67604, 0)$  and  $E_L = (0.07396, 0)$  are exist and no interior equilibrium exist as the condition  $x_L < x^* < x_R$  does not follows. It is observed that  $E_0$  is LAS as  $h > m, E_R$  is a nodal sink and  $E_L$  is a saddle point as  $x^* > x_R$  and drawn in Fig. 3a. Now consider  $\delta = 0.26$  and other parameters are the same. Then the system has two PFE points and interior equilibrium points at  $E_* = (0.54167, 0.15035)$  which is a nodal sink as  $T(J(E_*)) = -0.2411 < 0$  and depicted in Fig. 3b.

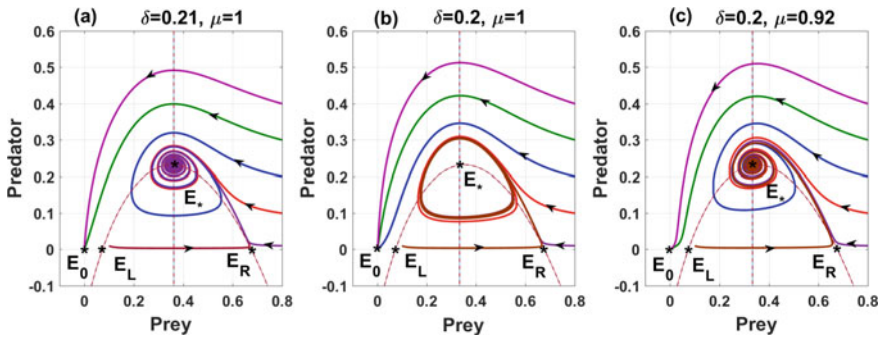


Fig. 4 Phase planes are drawn at  $\beta = 0.55, \beta_1 = 0.5, \alpha = 0.5, h = 0.3$  and  $m = 0.25$

Consider  $\delta = 0.21$  and other parameters are same. Then the Phase portraits given by Fig. 4a shows that system 3 has interior equilibrium at  $E_* = (0.36207, 0.23165)$ . We found that  $E_*$  is a spiral sink and  $E_0$  is LAS. Here  $E_L$  and  $E_R$  are saddle points. Now take  $\delta = 0.2$  with the other parameters are same. We have seen that from Fig. 4b, coexistence equilibrium point  $E_* = (0.34746, 0.23176)$  is unstable as  $T(J(E_*)) = 0.0062 > 0$ . But if we consider  $\mu = 0.92$ , system 3 becomes LAS around the  $E_*$  and displayed in Fig. 4c. Now consider  $\delta = 0.1$  and other parameters are fixed. Then  $E_* = (0.125, 0.085227)$  is unstable and two PFE points are saddle points, which is shown in Fig. 5a. When  $\delta = 0.05$ , no interior equilibrium exists. We examine that  $E_L$  is a nodal source and  $E_R$  is a saddle point because  $0 < x^* < x_L$  and depicted in Fig. 5b.

To check the dynamics for the case  $h < m$ , we have considered  $\beta = 0.55, \beta_1 = 0.5, \alpha = 0.5, h = 0.3, m = 0.35$  and  $\delta = 0.3$ . Here, no coexistence equilibrium exist as  $x^* > x_R$ , one PFE point  $E_R$  exist and it is LAS and trivial equilibrium  $E_0$  is a saddle point as  $h < m$  and shown in Fig. 6a. Now consider  $\delta = 0.25$  along with the same parameters value. It has examined that  $E_*$  exist as  $x^* > x_R$  and it is

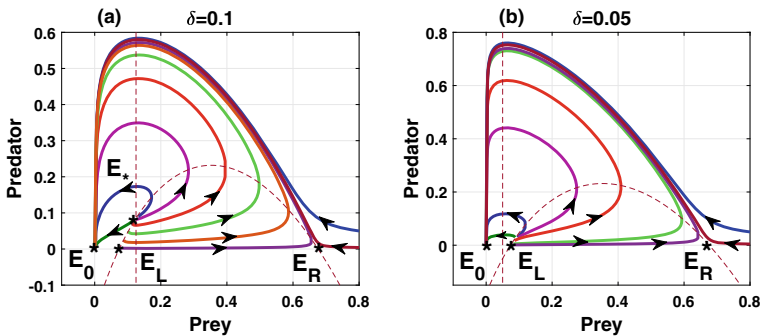


Fig. 5 Phase planes are drawn at  $\mu = 0.99, \beta = 0.55, \alpha = 0.5, \beta_1 = 0.5, h = 0.3$  and  $m = 0.25$

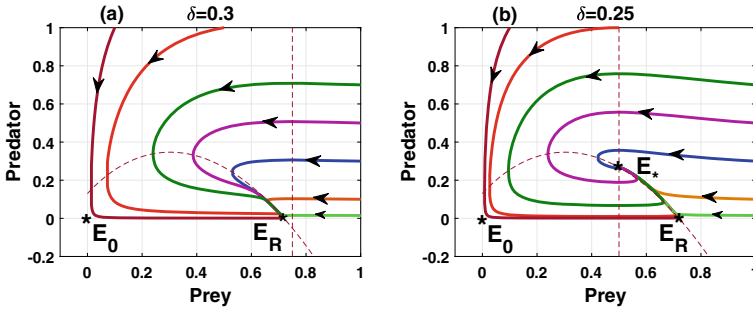


Fig. 6 Phase planes are drawn with the values of  $\mu = 1, \beta = 0.55, \alpha = 0.5, \beta_1 = 0.5, h = 0.3$  and  $m = 0.35$

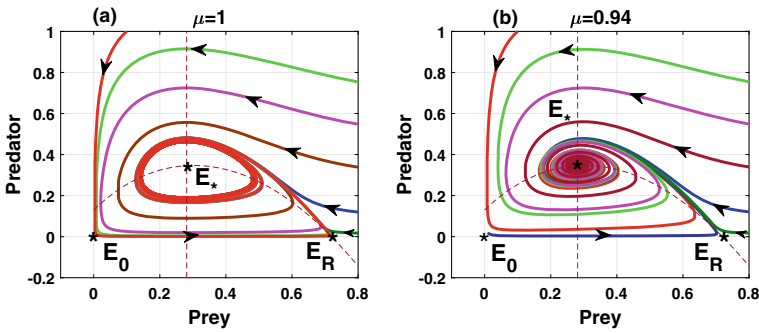
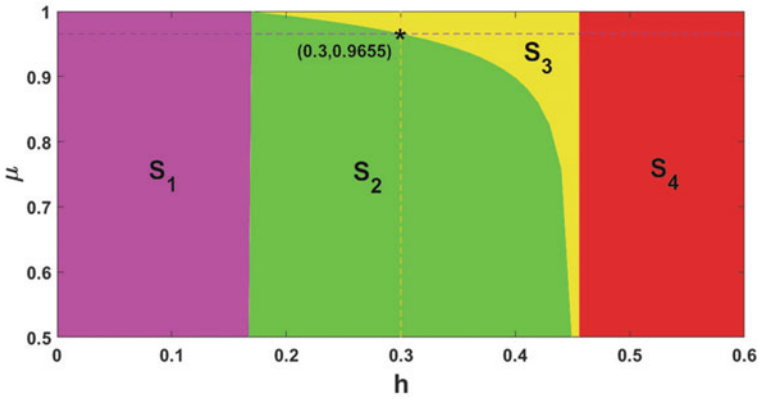


Fig. 7 Phase planes are drawn at  $\beta = 0.55, \alpha = 0.5, \beta_1 = 0.5, h = 0.3, m = 0.35$  and  $\delta = 0.18$

spiral sink. Beside these,  $E_0$  and  $E_R$  are saddle point. Now consider  $\delta = 0.18$  along with the same parameters value. We have obtained for integer-order system that the coexistence equilibrium  $E_*$  is a unstable and  $E_0, E_R$  are saddle points. But the system 3 with  $\mu = 0.94$  becomes LAS around  $E_*$  as  $\mu < \mu^* = 0.9655$ , obtained from the Theorem 4 and shown in Fig. 7.

With the same parameters value we have obtained a figure with various regions of influence in  $(h, \mu)$ -plane in Fig. 8. For  $h = 0.3$ , we have obtained  $\mu^* = 0.9655$  and which is again verified in this figure. To check the effect  $\delta$  and  $h$  in the system 3, we have obtained some bifurcation diagrams and have displayed in Figs. 9 and 10. We have observed that for  $\mu = 1$  model 3 exhibits Hopf bifurcation around  $E_*$  at  $\delta = 0.2331$ . It is observed from Fig. 9 that predator species can be extinct if  $\delta > 0.4985$ . The bifurcation diagram given by the Fig. 10 shows that extinction of both species can happen if  $h > 0.81$ .



**Fig. 8** We have obtained various regions in  $(h, \mu)$ -plane for the parameters value  $\beta = 0.55, \alpha = 0.5, m = 0.35, \beta_1 = 0.5$  and  $\delta = 0.18$ . Equilibrium point  $E_*$  is LAS in  $S_1$  for integer-order as well as fractional-order system, LAS only for fractional-order system in  $S_2$ , unstable in  $S_3$  and no co-existence equilibrium point exists in  $S_4$

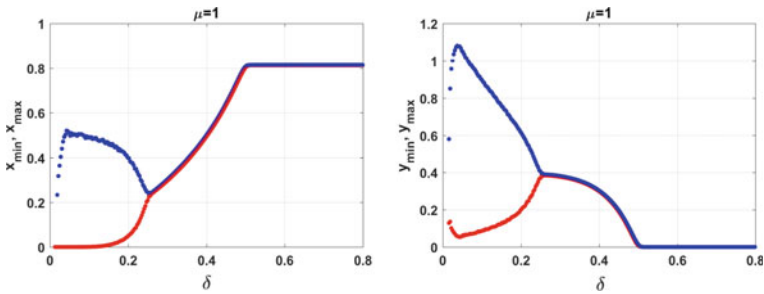


**Fig. 9** Double period bifurcation occurs for  $\delta$  when  $\beta = 0.9, \alpha = 0.5, h = 0.3, m = 0.8$  and  $\beta_1 = 0.8$ . Hopf bifurcation occurs at the critical value  $\delta = 0.2331$ . When  $\mu = 1$ , model 3 becomes unstable around  $E_*$  when  $0 \leq \delta < 0.2331$ , LAS when  $0.2331 < \delta < 0.5$  and extinction of predator species can happen for  $\delta > 0.5$

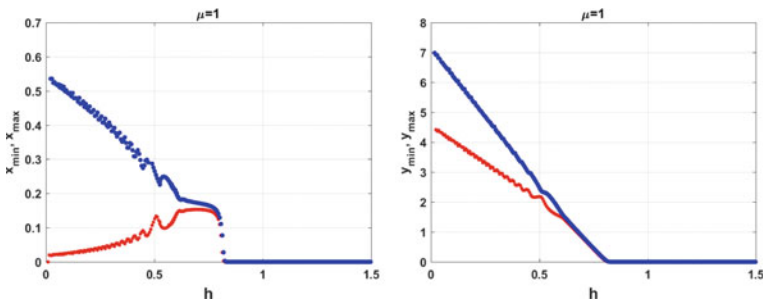


**Fig. 10** Double period bifurcation when  $\mu = 1$  and other parameters are considered as  $\beta = 0.9, \alpha = 0.5, m = 0.8, \beta_1 = 0.8$  and  $\delta = 0.2$

## 6 Conclusions

It is observed that predator-prey model with nonlinear harvesting possesses multiple predator free equilibrium points under the different conditions of the harvesting parameters  $h$  and  $m$ . It is observed theoretically that both prey and predator species can be extinct if  $h > m_0$  and validates this result by Figs. 8 and 10. Coexistence equilibrium point  $E_* = (x^*, y^*)$  exist only when the prey equilibrium value  $x^*$  is less than the value  $x_R$ . Stability analysis of the fractional-order model 3 has been studied according to Matignon's conditions. Global stability analysis has been demonstrated successfully by constructing a suitable Lyapunov function and have verified it that  $E_*$  is globally asymptotically stable. We have discussed the occurrence of Hopf bifurcation for the fractional-order  $\mu$  and have examined it theoretically and numerically. Also we have studied that Hopf bifurcation of the system 3 when  $\mu = 1$  for the parameters  $\delta$  and  $h$  occurs around the coexistence equilibrium point and have discussed in numerical simulation. It is shown that a larger death rate of predators can be extinct predator species. We have examined the influence of the fractional-order  $\mu$  on the fractional-order system and it is shown that an unstable integer order system becomes stable in fractional-order system which obeys the theoretical results.

## References

1. Abdelouahab, M.S., Hamri, N.E., Wang, J.: Hopf bifurcation and chaos in fractional-order modified hybrid optical system. *Nonlinear Dyn.* **69**(1), 275–284 (2012)
2. Diethelm, K., Ford, N.J.: Analysis of fractional differential equations. *J. Math. Anal. Appl.* **265**(2), 229–248 (2002)
3. Diethelm, K., Ford, N.J., Freed, A.D.: A predictor-corrector approach for the numerical solution of fractional differential equations. *Nonlinear Dyn.* **29**(1), 3–22 (2002)
4. Ghaziani, R.K., Alidousti, J., Eshkaftaki, A.B.: Stability and dynamics of a fractional order Leslie-Gower prey-predator model. *Appl. Math. Model.* **40**, 2075–2086 (2016)
5. Gupta, R., Banerjee, M., Chandra, P.: Period doubling cascades of prey- predator model with nonlinear harvesting and control of over exploitation through taxation. *Commun. Nonlinear Sci. Numer. Simul.* **19**(7), 2382–2405 (2014)
6. Gupta, R., Chandra, P., Banerjee, M.: Dynamical complexity of a prey- predator model with nonlinear predator harvesting. *Discret. Contin. Dyn. Syst. B* **20**(2), 423–443 (2015)
7. Hu, D., Cao, H.: Stability and bifurcation analysis in a predator-prey system with michaelis-menten type predator harvesting. *Nonlinear Anal. Real World Appl.* **33**, 58–82 (2017)
8. Kumar, S., Kharbanda, H.: Chaotic behavior of predator-prey model with group defense and non-linear harvesting in prey. *Chaos Solitons Fractals* **119**, 19–28 (2019)
9. Li, M., Chen, B., Ye, H.: A bioeconomic differential algebraic predator-prey model with non-linear prey harvesting. *Appl. Math. Model.* **42**, 17–28 (2017)
10. Li, C., Tao, C.: On the fractional adams method. *Comput. Math. Appl.* **58**(8), 1573–1588 (2009)
11. Lv, Y., Pei, Y., Wang, Y.: Bifurcations and simulations of two predator-prey models with nonlinear harvesting. *Chaos Solitons Fractals* **120**, 158–170 (2019)
12. Ma, L., Liu, B.: Dynamic analysis and optimal control of a fractional order singular Leslie-Gower prey-predator model. *Acta Math. Sci.* **40**, 1525–1552 (2020)
13. Matignon, D.: Stability results for fractional differential equations with applications to control processing. In: *Computational Engineering in Systems Applications*, vol. 120, pp 963–968. Citeseer (1996)

14. Mortuja, M.G., Chaube, M.K., Kumar, S.: Dynamic analysis of a predator-prey system with nonlinear prey harvesting and square root functional response. *Chaos Solitons Fractals* **148**, 111071 (2021)
15. Petráš, I.: *Fractional-order nonlinear systems: modeling, analysis and simulation*. Springer Science & Business Media (2011)
16. Shang, Z., Qiao, Y., Duan, L., Miao, J.: Stability and bifurcation analysis in a nonlinear harvested predator-prey model with simplified holling type IV functional response. *Int. J. Bifurc. Chaos* **30**, 2050205 (2020)
17. Vargas-De-León, C.: Volterra-type Lyapunov functions for fractional-order epidemic systems. *Commun. Nonlinear Sci. Numer. Simul.* **24**(1–3), 75–85 (2015)



# A Numerical Application of Collocation Method for Solving KdV-Lax Equation



Seydi Battal Gazi Karakoc  and Derya Yildirim Sucu 

**Abstract** In this paper, a mathematical model representing the numerical solutions of Lax equation which is version of generalized fifth-order nonlinear KdV equation (fKdV) is studied. Collocation method with septic B-splines has been used for the model problem. Using a powerful Fourier series analysis of the linearized scheme, the numerical results have been shown to be unconditionally stable.  $L_2$  and  $L_\infty$  error norms are calculated for single solutions to show practicality and robustness of proposed scheme. The obtained numerical results are shown in the table. Also, all simulations are shown to illustrate the numerical behavior of a single soliton. Present results show that the method provides highly accurate solutions. Therefore, the current scheme will be useful for other nonlinear scientific problems.

**Keywords** Lax equation · Finite element method · Collocation

## 1 Introduction

Fifth-order KdV-type equation in its general form is given by

$$u_t + \alpha u^2 u_x + \beta u_x u_{xx} + \gamma u u_{xxx} + u_{xxxx} = 0. \quad (1)$$

Here  $\alpha$ ,  $\beta$  and  $\gamma$  are arbitrary positive parameters. These parameters strongly change the properties of the equation. This type of fifth-order Eq. (1) is the universal model for the study of shallow water waves with surface tension and has many physical applications a wide range of areas. Many versions of fKdV equation can be generated using different values of these parameters. For example, the following KdV-Lax equation

---

S. B. G. Karakoc · D. Y. Sucu (✉)

Faculty of Science and Art, Department of Mathematics, Nevsehir Haci Bektas Veli University, Nevsehir 50300, Turkey

e-mail: [deryasucu@aksaray.edu.tr](mailto:deryasucu@aksaray.edu.tr)

S. B. G. Karakoc

e-mail: [sbgkarakoc@nevsehir.edu.tr](mailto:sbgkarakoc@nevsehir.edu.tr)

$$u_t + 30u^2u_x + 30u_xu_{xx} + 10uu_{xxx} + u_{xxxxx} = 0, \tag{2}$$

with  $\alpha = 30, \beta = 30,$  and  $\gamma = 10.$

In this study, Lax equation, which is one of the fKdV equation, will be discussed. Many applications of various methods for the all forms of the fKdV equation can be found in the literature, but our scheme has not been implemented before. Because of the great importance of fKdV equation in nonlinear equations, many scientists obtained analytical and numerical solutions. In the literature, one can find out that the equation was solved with several methods, among others; Adomian [1], extended tanh [2], Haar wavelet sorting [3], Hirota’s bilinear [4], auto-Bäcklund and Hirota transform [5], inverse scattering transform [6].

In addition, Inan and Ugurlu applied exp-function method for fifth-order KdV equation [7]. Bilige et al. [8] proposed an extended simplest equation method to search for full traveling wave solutions for various forms of the fifth-order KdV equation. The existence and stability of traveling waves of the fifth order KdV equation are investigated for a general class of nonlinearity satisfying power-like scaling relationships at [9]. A numerical approach based on the Homotopy perturbation transform method (HPTM) was applied to obtain exact and approximate solutions of nonlinear fifth-order KdV equations to study magneto-acoustic waves in the plasma at [10]. Travelling wave solutions were found for the generalized nonlinear fifth-order Korteweg-de Vries (KdV) equations using the direct algebraic method at [11]. Seventh order Lax equation is analyzed by Darvishi et al. with pseudospectral method [12].

The main form of our study can be briefly stated as follows: In Sect. 2, the septic B-spline approach is shown and the solution of the KdV-Lax equation by the finite element method is proposed. The stability analysis of the method is discussed in Sect. 3. In Sect. 4, numerical applications and their results are shown in table and graphs. In the final, a brief conclusion is given on the method presented in Sect. 5.

## 2 Septic B-Spline Approximation

In this study, we are interested in the numerical solutions of the KdV-Lax equation, whose bidirectional generalisation is given below:

$$u_t + 30u^2u_x + 30u_xu_{xx} + 10uu_{xxx} + u_{xxxxx} = 0, \tag{3}$$

with initial and boundary conditions

$$u(x, 0) = f(x), \quad a \leq x \leq b, \tag{4}$$

$$u(a, t) = 0, \quad u_x(a, t) = 0, \tag{5}$$

$$u(b, t) = 0, \quad u_x(b, t) = 0, \quad t > 0. \tag{6}$$

KdV-Lax equation is searched into the boundary conditions  $u \rightarrow 0$  while  $x \rightarrow \pm\infty$ ,  $x$  and  $t$  which generally denote time and space, respectively. The equation is a member of the completely integrable hierarchy of higher-order KdV equations [13]. To start the procedure, our first task to solve the initial-boundary value problem given in Eqs.(3)–(6) numerically is to separate the solution domain. The septic B-spline functions  $\{\phi_{-3}(x), \phi_{-2}(x), \dots, \phi_{N+3}(x)\}$ , at the nodes  $x_m$  are described on the solution zone  $[a, b]$  in [14].

Now, we continue the numerical treatment, which we will apply using the septic B-spline collocation finite element method, by generating an approximate solution for the equation system. We find the numerical approximation solution  $u_N(x, t)$  in the following form,

$$u_N(x, t) = \sum_{m=-3}^{N+3} \phi_m(x)\sigma_m(t). \tag{7}$$

Applying the following transformation

$$h\xi = x - x_m, \quad 0 \leq \xi \leq 1 \tag{8}$$

to the specific finite region  $[x_m, x_{m+1}]$  is planned to more easily practicable region  $[0, 1]$  [15]. Thus, septic B-splines depending on variable  $\xi$  over the finite element  $[0, 1]$  are described as:

$$\begin{aligned} \phi_{m-3} &= 1 - 7\xi + 21\xi^2 - 35\xi^3 + 35\xi^4 - 21\xi^5 + 7\xi^6 - \xi^7, \\ \phi_{m-2} &= 120 - 392\xi + 504\xi^2 - 280\xi^3 + 84\xi^5 - 42\xi^6 + 7\xi^7, \\ \phi_{m-1} &= 1191 - 1715\xi + 315\xi^2 + 665\xi^3 - 315\xi^4 - 105\xi^5 + 105\xi^6 - 21\xi^7, \\ \phi_m &= 2416 - 1680\xi + 560\xi^4 - 140\xi^6 + 35\xi^7, \\ \phi_{m+1} &= 1191 + 1715\xi + 315\xi^2 - 665\xi^3 - 315\xi^4 + 105\xi^5 + 105\xi^6 - 35\xi^7, \\ \phi_{m+2} &= 120 + 392\xi + 504\xi^2 + 280\xi^3 - 84\xi^5 - 42\xi^6 + 21\xi^7, \\ \phi_{m+3} &= 1 + 7\xi + 21\xi^2 + 35\xi^3 + 35\xi^4 + 21\xi^5 + 7\xi^6 - \xi^7, \\ \phi_{m+4} &= \xi^7. \end{aligned} \tag{9}$$

The values of  $u_m$ , and its derivatives at the knots are calculated from using Eq. (7) and septic B-splines (9) in terms of element parameters  $\sigma_m$  in following form

$$\begin{aligned} u_N(x_m, t) &= \sigma_{m-3} + 120\sigma_{m-2} + 1191\sigma_{m-1} + 2416\sigma_m + 1191\sigma_{m+1} + 120\sigma_{m+2} + \sigma_{m+3}, \\ u'_m &= \frac{7}{h}(-\sigma_{m-3} - 56\sigma_{m-2} - 245\sigma_{m-1} + 245\sigma_{m+1} + 56\sigma_{m+2} + \sigma_{m+3}), \\ u''_m &= \frac{42}{h^2}(\sigma_{m-3} + 24\sigma_{m-2} + 15\sigma_{m-1} - 80\sigma_m + 15\sigma_{m+1} + 24\sigma_{m+2} + \sigma_{m+3}), \\ u'''_m &= \frac{210}{h^3}(-\sigma_{m-3} - 8\sigma_{m-2} + 19\sigma_{m-1} - 19\sigma_{m+1} + 8\sigma_{m+2} + \sigma_{m+3}), \\ u^{iv}_m &= \frac{840}{h^4}(\sigma_{m-3} - 9\sigma_{m-1} + 16\sigma_m - 9\sigma_{m+1} + \sigma_{m+3}), \\ u^v_m &= \frac{2520}{h^5}(-\sigma_{m-3} + 4\sigma_{m-2} - 5\sigma_{m-1} + 5\sigma_{m+1} - 4\sigma_{m+2} + \sigma_{m+3}). \end{aligned} \tag{10}$$

Now, using the (7) and (10) into Eq. (2), following general form equation is reached for the linearization technique:

$$\begin{aligned} &\dot{\sigma}_{m-3} + 120\dot{\sigma}_{m-2} + 1191\dot{\sigma}_{m-1} + 2416\dot{\sigma}_m + 1191\dot{\sigma}_{m+1} + 120\dot{\sigma}_{m+2} + \dot{\sigma}_{m+3} \\ &+ (30Z_{m1} + 20Z_{m2})\frac{7}{h}(-\sigma_{m-3} - 56\sigma_{m-2} - 245\sigma_{m-1} + 245\sigma_{m+1} + 56\sigma_{m+2} + \sigma_{m+3}) \\ &+ 10Z_{m3}\frac{210}{h^3}(-\sigma_{m-3} - 8\sigma_{m-2} + 19\sigma_{m-1} - 19\sigma_{m+1} + 8\sigma_{m+2} + \sigma_{m+3}) \\ &+ \frac{2520}{h^5}(-\sigma_{m-3} + 4\sigma_{m-2} - 5\sigma_{m-1} + 5\sigma_{m+1} - 4\sigma_{m+2} + \sigma_{m+3}) = 0, \end{aligned} \tag{11}$$

where  $\dot{\sigma} = \frac{d\sigma}{dt}$  and

$$\begin{aligned} Z_{m1} &= u^2 = (\sigma_{m-3} + 120\sigma_{m-2} + 1191\sigma_{m-1} + 2416\sigma_m + 1191\sigma_{m+1} + 120\sigma_{m+2} + \sigma_{m+3})^2, \\ Z_{m2} &= u_{xx} = \frac{42}{h^2}(\sigma_{m-3} + 24\sigma_{m-2} + 15\sigma_{m-1} - 80\sigma_m + 15\sigma_{m+1} + 24\sigma_{m+2} + \sigma_{m+3}), \\ Z_{m3} &= u = \sigma_{m-3} + 120\sigma_{m-2} + 1191\sigma_{m-1} + 2416\sigma_m + 1191\sigma_{m+1} + 120\sigma_{m+2} + \sigma_{m+3}. \end{aligned}$$

Let's discretize for time parameters  $\sigma_i$ 's according to the Crank-Nicolson formula and it is separated using forward finite difference approximation for its spatial variables and their derivatives  $\dot{\sigma}$ 's in the following form in Eq. (11):

$$\sigma_i = \frac{\sigma_i^{n+1} + \sigma_i^n}{2}, \dot{\sigma}_i = \frac{\sigma_i^{n+1} - \sigma_i^n}{\Delta t}. \tag{12}$$

Thus, the above operation allows us to derive a recursion relationship between two time levels based on the parameters  $\delta_i^{n+1}$  and  $\delta_i^n$  for as:

$$\begin{aligned} &\lambda_1\sigma_{m-3}^{n+1} + \lambda_2\sigma_{m-2}^{n+1} + \lambda_3\sigma_{m-1}^{n+1} + \lambda_4\sigma_m^{n+1} + \lambda_5\sigma_{m+1}^{n+1} + \lambda_6\sigma_{m+2}^{n+1} + \lambda_7\sigma_{m+3}^{n+1} \\ &= \lambda_7\sigma_{m-3}^n + \lambda_6\sigma_{m-2}^n + \lambda_5\sigma_{m-1}^n + \lambda_4\sigma_m^n + \lambda_3\sigma_{m+1}^n + \lambda_2\sigma_{m+2}^n + \lambda_1\sigma_{m+3}^n, \end{aligned} \tag{13}$$

where

$$\begin{aligned} \lambda_1 &= [1 - E - T - M], \\ \lambda_2 &= [120 - 56E - 8T + 4M], \\ \lambda_3 &= [1191 - 245E + 19T - 5M], \\ \lambda_4 &= [2416], \\ \lambda_5 &= [1191 + 245E - 19T + 5M], \\ \lambda_6 &= [120 + 56E + 8T - 4M], \\ \lambda_7 &= [1 + E + T + M], \\ E &= \frac{a}{2}\Delta t, \quad T = \frac{b}{2}\Delta t, \quad M = \frac{2520}{2h^5}\Delta t, \\ a &= [30Z_{m1} + 20Z_{m2}], \\ b &= [\frac{2100}{h^3}Z_{m3}]. \end{aligned} \tag{14}$$

If we take a look at the algebraic system (13) we obtained above, the number of linear equations are less than the number of unknown coefficients, that is, the system involves of  $(N + 1)$  equation  $(N + 7)$  unknown time dependent parameters [16]. The simplest way to find a unique solution is to remove six unknowns  $\sigma_{-3}, \sigma_{-2}, \sigma_{-1}, \dots, \sigma_{N+1}, \sigma_{N+2}$ , and  $\sigma_{N+3}$  from the system. This procedure is applied using the boundary conditions with the values of  $u$  and after eliminating unknowns, a matrix system of  $(N + 1)$  linear equations with  $(N + 1)$  unknown parameters  $d^n = (\sigma_0, \sigma_1, \dots, \sigma_N)^T$  are obtained in the form of the following matrix-vector system:

$$Rd^{n+1} = Sd^n. \tag{15}$$

### 3 Stability Analysis

In this part, we explain through the Von-Neumann theory to demonstrate stability of the linearized numerical algorithm. To show the stability analysis, the fKdV equation was linearized by supposing that the quantities  $u^2$ ,  $u_{xx}$  and  $u$  in the nonlinear terms  $u^2u_x$ ,  $u_xu_{xx}$  and  $uu_{xxx}$  are locally constant, respectively. Growth factor  $\xi$  of a characteristic Fourier mode is identified as:

$$\sigma_m^n = \xi^n e^{imkh}, \tag{16}$$

here  $i = \sqrt{-1}$ ,  $h$  is the element greatness and  $k$  is the mode number, is obtained from the linear stability analysis of the algorithm. Putting the equality (16) into the iterative system (13), which gives the growth factor

$$\xi = \frac{\rho_1 - i\rho_2}{\rho_1 + i\rho_2}, \tag{17}$$

where

$$\begin{aligned} \rho_1 &= 2 \cos(3kh) + 240 \cos(2kh) + 2382 \cos(kh) + 2416, \\ \rho_2 &= (2M + 2T + 2E) \sin(3kh). \end{aligned} \tag{18}$$

$|\xi| = 1$  is obtained when we take the modulus of Eq. (17). In this way, we demonstrate that scheme (13) is unconditionally stable under the present conditions.

### 4 Numerical Applications and Discussions

In this section, we exemplify our method improved in Sect. 2 to the KdV-Lax equation for different parameters of the time and space division. To check the sensibility and reliability of the presented method, the following  $L_2$  and  $L_\infty$  error norms will be used respectively:

$$L_2 = \|u^{exact} - u_N\|_2 \simeq \sqrt{h \sum_{j=1}^N |u_j^{exact} - (u_N)_j|^2}, \tag{19}$$

$$L_\infty = \|u^{exact} - u_N\|_\infty \simeq \max_j |u_j^{exact} - (u_N)_j|, \quad j = 1, 2, \dots, N. \tag{20}$$

Lax equation has an exact solution of the form

$$u(x, t) = 2k^2 (2 - 3 \tanh^2 [k(x - 56k^4t - x_0)]), \tag{21}$$

where  $k$  and  $x_0$  are arbitrary real numbers. We will consider the Lax equation with the boundary-initial condition which is

**Table 1** Error norms for  $k = 0.01$ ,  $\Delta t = 0.0004$  and various values of  $h$

$t$	$\Delta t = 0.0004, h = 0.5$		$\Delta t = 0.0001, h = 0.05$	
	$L_2$	$L_\infty$	$L_2$	$L_\infty$
0.1	0.0007476185	0.0003786723	0.0006605026	0.0003870472
0.2	0.0008112957	0.0003797258	0.0006965400	0.0004162210
0.3	0.0008167458	0.0003793303	0.0007209887	0.0003999905
0.4	0.0008542324	0.0003784037	0.0007876002	0.0004253867
0.5	0.0008354053	0.0003899616	0.0008298723	0.0005542919
0.6	0.0008850945	0.0003787136	0.0009135698	0.0009698522
0.7	0.0008491875	0.0003800426	0.0011118805	0.0022608287
0.8	0.0008693723	0.0003949290	0.0019634349	0.0059890208
0.9	0.0009128289	0.0003794148	0.0048874414	0.0170258202
1.0	0.0008974475	0.0003791528	0.0140005587	0.0499546306

$$u(x, 0) = 2k^2 \tanh^2 [k(x - x_0)], \tag{22}$$

where  $u \rightarrow 0$  as  $x \rightarrow \pm\infty$ . We let  $x_0 = 0$  and  $k = 0.01$  over the interval  $x \in [-20, 20]$ , to present numerical solutions.

The algorithm has been performed in the calculation range  $[-20, 20]$  and up to time  $t = 1$ . It was recorded that the solitary wave has amplitude  $A = 0.0002$  at  $x = 0$  and at the initial moment of  $t = 0$ . In simulation calculations, typical values we use are  $\Delta t = 0.0004; 0.0001$  with  $h = 0.5$  and  $0.05$ . Values of the  $L_2$  and  $L_\infty$  error norms are displayed in Table 1. It has been observed that the calculated values of the error norms are found to be adequately small. It is evident that the minimum  $L_\infty$  error norm  $3.786723 \times 10^{-4}$  with the parameters  $\Delta t = 0.0004$  and  $h = 0.5$ . These errors do not change much over time. In addition, it can be seen that the real solutions and the numerical solutions are in good agreement and the method is efficient when the values of the error norms are seen from the table. If the Fig. 1 is examined, we can clearly see that the three dimensional states of the bell shaped solitary wave solutions produced from  $t = 0$  to  $t = 1$ . It can be said that amplitude and shape are preserved as time passes. On the other hand, numerical error distribution is also plotted at time  $t = 1$  for different values of  $h$  and  $\Delta t$  in Fig. 1.

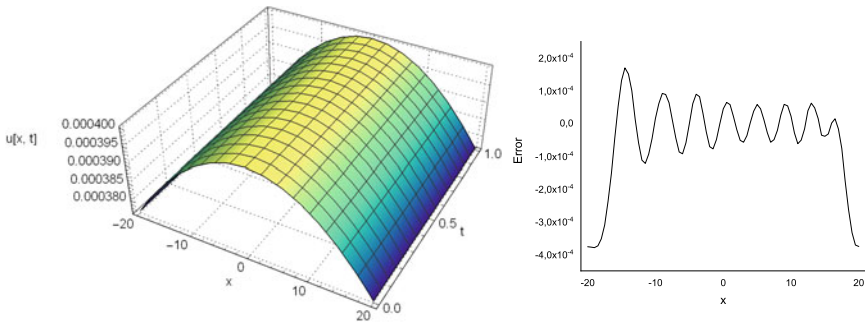


**Fig. 1** Motion of single solitary wave and the error distributions at  $t = 1$  for the parameters  $\Delta t = 0.0004$  and  $h = 0.5$

### 5 Conclusion

In this study, numerical solutions of Lax equation, which is a fifth-order KdV equation, are investigated by considering some fixed selection initial and boundary conditions. In this trajectory, a combination of the collocation method on the finite element approach is used to construct the numerical scheme of the equation. Septic B-splines have been chosen as the interpolation functions of this application. We have shown that our linearized scheme is unconditionally stable. In order to perform numerical experiments, the algorithm is studied with a single solitary wave motion whose analytical solution is known. The performance and validity of the numerical scheme was measured by calculating both  $L_2$  and  $L_\infty$  error norms. All experiments were supported by figures and table. The sampled results confirm that our error norms are good enough as required. It may be concluded that the method used here is powerful, efficient and confidential technique for solving a wide class of nonlinear evolution equations.

### References

1. Kaya, D.: An explicit and numerical solutions of some fifth-order KdV equation by decomposition method. *Appl. Math. Comput.* **144**, 353–363 (2003)
2. Wazwaz, A.M.: The extended tanh method for new solitons solutions for many forms of the fifth-order KdV equations. *Appl. Math. Comput.* **184**(2), 1002–1014 (2007)
3. Saleem, S., Hussain, M.Z.: Numerical solution of nonlinear fifth-order KdV-type partial differential equations via Haar wavelet. *Int. J. Appl. Comput. Math.* **6**(6), 1–16 (2020)
4. Wazwaz, A.M.: N-soliton solutions for the combined KdV-CDG equation and the KdV-Lax equation. *Appl. Math. Comput.* **203**(1), 402–407 (2008)
5. Lei, Y., Fajiang, Z., Yinghai, W.: The homogeneous balance method, Lax pair, Hirota transformation and a general fifth-order KdV equation. *Chaos Solitons Fractals* **13**(2), 337–340 (2002)

6. Ablowitz, M.J., Ablowitz, M.A., Clarkson, P.A., Clarkson, P.A.: *Solitons, Nonlinear Evolution Equations and Inverse Scattering*. Cambridge University Press (1991)
7. Inan, I.E., Ugurlu, Y.: Exp-function method for the exact solutions of fifth order KdV equation and modified Burgers equation. *Appl. Math. Comput.* **217**(4), 1294–1299 (2010)
8. Bilige, S., Chaolu, T.: An extended simplest equation method and its application to several forms of the fifth-order KdV equation. *Appl. Math. Comput.* **216**(11), 3146–3153 (2010)
9. Esfahani, A., Levandosky, S.: Existence and stability of traveling waves of the fifth-order KdV equation. *Phys. D* **421**, 132872 (2021)
10. Goswami, A., Singh, J., Kumar, D.: Numerical simulation of fifth order KdV equations occurring in magneto-acoustic waves. *Ain Shams Eng. J.* **9**(4), 2265–2273 (2018)
11. Seadawy, A.R., Lu, D., Yue, C.: Travelling wave solutions of the generalized nonlinear fifth-order KdV water wave equations and its stability. *J. Taibah Univ. Sci.* **11**(4), 623–633 (2017)
12. Darvishi, M.T., Khani, F., Kheybari, S.: A numerical solution of the Lax's 7th-order KdV equation by Pseudospectral method and Darvishi's preconditioning. *Int. J. Contemp. Math. Sci* **2**(22), 1097–1106 (2007)
13. Lax, P.D.: Integrals of nonlinear equations of evolution and solitary waves. *Commun. Pure Appl. Math.* **21**(5), 467–490 (1968)
14. Prenter, P.M.: *Splines and Variational Methods*. Wiley, New York (1975)
15. Karakoc, S.B.G., Saha, A., Sucu, D.: A novel implementation of Petrov-Galerkin method to shallow water solitary wave pattern and superperiodic traveling wave and its multistability: Generalized Korteweg-de Vries equation. *Chin. J. Phys.* **68**, 605–617 (2020)
16. Karakoc, S.B.G., Omrani, K., Sucu, D.: Numerical investigations of shallow water waves via generalized equal width (GEW) equation. *Appl. Numer. Math.* **162**, 249–264 (2020)



# Influence of Suspension Lock on the Four-Station Military Recovery Vehicle with Trailing Arm Suspension During Crane Operation



M. Devesh, R. Manigandan, and Saayan Banerjee

**Abstract** The present work is focused on the development of a non-linear dynamic mathematical model of a four-station military recovery vehicle with trailing arm hydro-gas suspension (HSU) during crane operations over flat terrain. The influence of the crane payload non-linear motion on the trailing arm dynamic behavior is brought out in the dynamic model. The model additionally contains non-linearities due to the penalty contact phenomenon, which are associated with the HSU rebound/bump-stoppers, suspension locks or between the dummy masses and ground. Second-order coupled governing non-linear differential equations of motion are formulated for 13 degrees of freedom of the vehicle, namely, sprung mass bounce, pitch and roll, angular motions of the 4 unsprung masses, crane payload angular motions in the longitudinal and lateral directions as well as bounce motion of the 4 dummy masses. The equations of motion are coded and solved in MATLAB. The maximum pay-load lifting capacity could be determined by modeling the dynamic influence of the suspension locks on the recovery vehicle static equilibrium configuration, which is an essential pre-requisite before deciding upon the vehicle moving speed with the crane payload. This model is novel, generic and would provide deep insight into the development of a recovery vehicle simulator.

**Keywords** Military recovery vehicle · Suspension lock · Trailing arm · Hydro-gas suspension · Non-linear dynamics

---

M. Devesh · R. Manigandan  
School of Mechanical Engineering, Vellore Institute of Technology, Chennai, India  
e-mail: [m.devesh2016@vitstudent.ac.in](mailto:m.devesh2016@vitstudent.ac.in)

R. Manigandan  
e-mail: [manigandan.r2016@vitstudent.ac.in](mailto:manigandan.r2016@vitstudent.ac.in)

S. Banerjee (✉)  
Centre for Engineering Analysis and Design, Combat Vehicles R&D Establishment, DRDO,  
New Delhi, India  
e-mail: [saayanbanerjee.cvrde@gov.in](mailto:saayanbanerjee.cvrde@gov.in)

## 1 Introduction

Military recovery vehicle cranes are typically used to lift and carry required payloads from the battlefield to the nearest base workshop. The payload inertias can directly influence the vehicle stability, which necessitates a detailed study to determine the maximum payload capacity with the trailing arm hydro-gas suspension configuration. The comparative dynamic analysis of a military recovery vehicle during crane operations with linear suspension over flat terrain was discussed by Nikhil [1]. However, in Nikhil [1], linear vertical spring-mass system was considered to determine the maximum crane payload which would yield definite differences in sprung mass responses when compared to that with trailing arm suspension. The effects of the integrated ride and cornering dynamics of a military vehicle on the weapon responses were brought out by Banerjee et al. [2]. A non-linear mathematical model of a single station with hydro-gas trailing arm suspension was developed by Banerjee et al. [3]. However, in Banerjee et al. [2] and Banerjee et al. [3], the dynamic effects from sprung mass large pitch and roll angular motions were not considered in the governing equations. Moreover, in Banerjee et al. [2] and Banerjee et al. [3], contact algorithms were not incorporated into the governing equations to simulate the stoppers or loss of ground contact. The meshed gear profile penalty contact formulation is established accurately by Xiufeng and Yabin [4]. A sprung mass non-linear pitch dynamics mathematical model with a trailing arm torsion bar suspension system was developed by Devesh et al. [5]. However, in Devesh et al. [5], an in-plane dynamic model with two degrees of freedom is only considered to determine the sprung mass dynamic responses.

It is noteworthy that extensive research has been undertaken in the field of military vehicle dynamics. However, the present study brings out the integrated dynamic influence of crane payload inertias and suspension locks with their associated penalty contact formulation on the military recovery vehicle static settlement configuration through a detailed non-linear dynamic mathematical model, which has not been reported in the literature to date. The road-holding phenomenon of the unsprung masses under such integrated dynamic influence is additionally simulated through penalty contact formulation in the governing equations, which has also not been brought out in literature to date. The dynamic effects of sprung mass large pitch and roll angular motions are additionally considered in the present mathematical model. This dynamic model is very novel and generic. It would establish a stepping stone towards deciding upon the vehicle moving speed along with the crane payload and development of a recovery vehicle simulator.

## 2 Description of the Four-Station Military Recovery Vehicle Dynamic Model

The second-order coupled governing differential equations of motion consists of 13 degrees of freedom, namely, sprung mass bounce, pitch, roll about its CG, left ( $LH_i$ ) and right ( $RH_i$ ) unsprung mass angular motions from the rebound ( $i = 1$  to  $2$ ), crane payload angular motions in the longitudinal and lateral directions with respect to the vertical axis and as well as left ( $LH_i$ ) and right ( $RH_i$ ) dummy mass bounce motions ( $i = 1$  to  $2$ ). The hydro-gas suspension rebound, bump-stoppers and suspension locks are modelled by using penalty contact formulation with high magnitudes of torsional stiffness and damping. The loss of wheel-to-ground contact under high pay-load magnitudes is also simulated through the penalty contact formulation by the introduction of suitable dummy masses. Figure 1 represents the coordinates for different degrees of freedom and other vehicle parameters. Figure 2 describes the associated free body diagram with a detailed representation of forces and moments

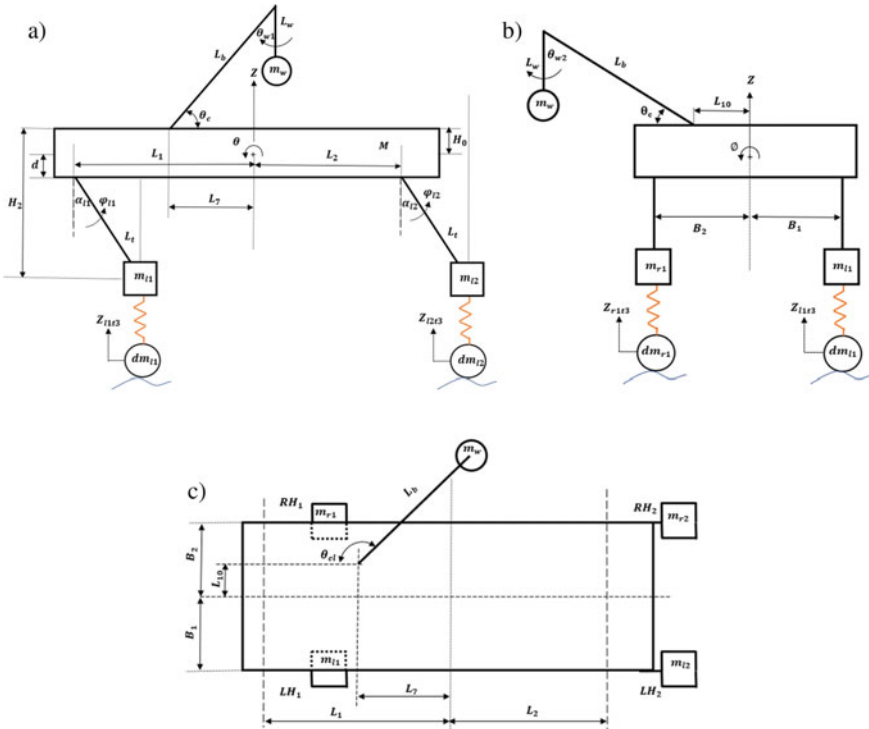


**Fig. 1** Vibration model of the military recovery vehicle with crane payload- **a** Side View of the vehicle, **b** Front View of the vehicle, **c**. Top View of the vehicle

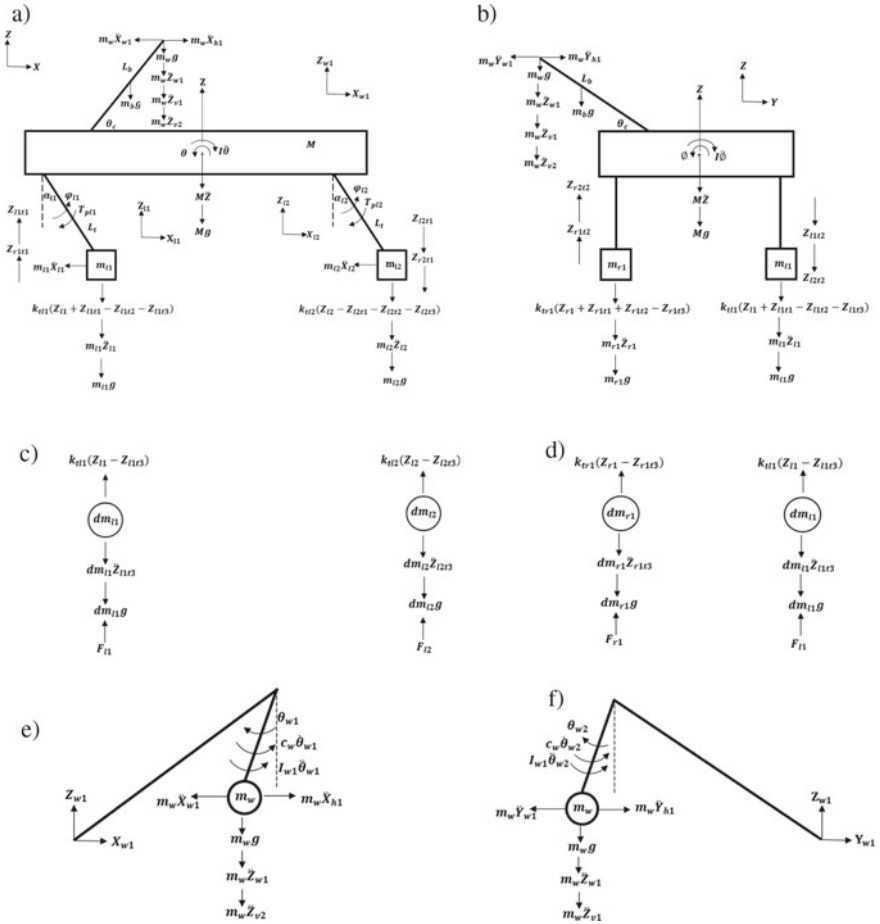


**Fig. 2** Free body diagram of four-station military recovery vehicle with crane payload- **a** Sprung mass bounce & pitch angular motion and angular motion of unsprung masses, **b** Sprung mass roll motion, **c** Bounce motion of the dummy masses from side view, **d** Bounce motion of the dummy masses from front view, **e** Crane payload angular motion in the longitudinal direction, **f** Crane payload angular motion in the lateral direction

on the crane, sprung and unsprung masses. The description of different variables which are used in the free body diagram and their corresponding magnitudes are highlighted in Table 1.

**Table 1** Description and magnitudes of the variables

Variable	Definition	Magnitude
$M$	Sprung mass	20,000 kg
$I$	Pitch moment inertia of sprung mass about the CG	170,000 kgm <sup>2</sup>
$J$	Roll moment inertia of sprung mass about the CG	17,000 kgm <sup>2</sup>
$m_{li}, m_{ri}$	LH <sub>i</sub> & RH <sub>i</sub> ( $i = 1, 2$ ) unsprung masses	500 kg
$k_{lli}, k_{lri}$	LH <sub>i</sub> & RH <sub>i</sub> ( $i = 1, 2$ ) road-wheel & track pad vertical stiffness	8000 kN/m
$c$	Viscous damping coefficient along the direction of actuator piston motion	400 kNs/m
$L_1$	Longitudinal dist. from sprung mass CG to front suspension pivotal points	3.3 m
$L_2$	Longitudinal dist. from sprung mass CG to rear suspension pivotal points	2.7 m
$B_1$	Lateral dist. from sprung mass CG to left suspension stations	1.45 m
$B_2$	Lateral dist. from sprung mass CG to right suspension stations	1.55 m
$L_7$	Longitudinal dist. from sprung mass CG to crane boom mounting location	2.8 m
$L_{10}$	Lateral dist. from sprung mass CG to crane boom mounting location	1 m
$L_t$	Axle arm length	0.5 m
$H_2$	Vertical dist. from unsprung mass CG to crane boom mounting location	2 m
$H_0$	Vertical dist. from sprung mass CG to crane boom mounting location	1 m
$d$	Vertical dist. from sprung mass CG to the suspension pivotal points	0.25 m
$\alpha_{li}, \alpha_{ri}$	LH <sub>i</sub> & RH <sub>i</sub> ( $i = 1, 2$ ) suspension axle arm rebound angles	42 <sup>0</sup>
$m_b$	Mass of the crane boom	1100 kg
$c_w$	Torsional viscous damping coefficient about the payload hinge point	100 kNm/s/rad
$L_b$	Length of the crane boom	5.4 m
$L_w$	Length of the payload string	3 m
$\theta_c$	Crane boom inclination with respect to longitudinal axis (in XZ plane)	67 <sup>0</sup>
$\theta_{cl}$	Crane boom inclination with respect to longitudinal axis (in XY plane)	135 <sup>0</sup>
$dm_{li}, dm_{ri}$	LH <sub>i</sub> & RH <sub>i</sub> ( $i = 1, 2$ ) dummy masses	1 kg
$k_{sli}, k_{sri}$	Contact stiffness between the dummy masses and ground	10 <sup>5</sup> kN/m
$c_{sli}, c_{sri}$	Contact damping between dummy masses and ground	1 kNs/m
$k_{ub}$	Contact stiffness of the bump stopper	10 <sup>5</sup> kNm/rad
$k_{rb}$	Contact stiffness of the rebound stopper	10 <sup>5</sup> kNm/rad

(continued)

**Table 1** (continued)

Variable	Definition	Magnitude
$c_{ub}$	Contact damping coefficient of the bump stopper	1 kNms/rad
$c_{rb}$	Contact damping coefficient of the rebound stopper	1 kNms/rad
$m_w$	Crane payload mass including the mass of the string and hook (Variable magnitude)	
$\varphi_s$	Bump stopper/Suspension lock angle with respect to rebound position (Variable magnitude)	

### 3 Equations of Motion of the Four-Station Military Vehicle

The second order coupled governing non-linear differential equations of motion are derived by referring to the free body diagram in Fig. 2. The non-linear bounce equation of the sprung mass, which is measured at its CG, is written as

$$M\ddot{Z} + P_{l1} + P_{l2} + P_{r1} + P_{r2} + k_{tl1}Z_{tl1} + k_{tl2}Z_{tl2} + k_{tr1}Z_{tr1} + k_{tr2}Z_{tr2} + M_1g + m_w\ddot{Z}_{w1} + m_w\ddot{Z}_{v1} + m_w\ddot{Z}_{v2} = 0 \tag{1}$$

where  $M\ddot{Z}$  is the sprung mass vertical inertia,  $P_{li}$  &  $P_{ri}$  are the vertical inertias of the LH<sub>*i*</sub> & RH<sub>*i*</sub> (*i* = 1 to 2) unsprung masses, respectively,  $k_{tli}Z_{tli}$  &  $k_{tri}Z_{tri}$  are restoring forces from the road wheel springs of the LH<sub>*i*</sub> and RH<sub>*i*</sub> (*i* = 1 to 2) stations, respectively,  $M_1g$  is the force due to self-weight of the sprung and unsprung masses as well as crane boom and payload,  $m_w\ddot{Z}_{w1}$ ,  $m_w\ddot{Z}_{v1}$  and  $m_w\ddot{Z}_{v2}$  are the crane payload vertical inertias due to sprung mass bounce, pitch and roll motions as well as due to its own angular motion in the longitudinal and lateral directions, respectively. The effects of sprung mass large pitch and roll angular motions along with its inertia coupling with the unsprung mass and crane payload angular motion, are highlighted in the subsequent equations.

In Eq. (1),  $P_{li} = m_{li}\ddot{Z}_{li}$ ,  $P_{ri} = m_{ri}\ddot{Z}_{ri}$ , where

$$Z_{li} = Z + L_i \cos\alpha_{li} - L_i \cos(\alpha_{li} + \varphi_{li} + \theta) + d - d\cos\theta + pL_i \sin\theta + B_1 \sin\varnothing \tag{2}$$

$$Z_{ri} = Z + L_i \cos\alpha_{ri} - L_i \cos(\alpha_{ri} + \varphi_{ri} + \theta) + d - d\cos\theta + pL_i \sin\theta - B_2 \sin\varnothing \tag{3}$$

( $p = -1$  for  $i = 1$  and  $p = +1$  for  $i = 2$ ).

The LH<sub>*i*</sub> and RH<sub>*i*</sub> road-wheel spring vertical displacements  $Z_{tli}$  and  $Z_{tri}$  (*i* = 1 to 2), respectively, which are obtained by accounting for the load transfer effects due to crane payload inertias in both longitudinal and lateral directions, are described by

$$Z_{tli} = (Z_{li} + pZ_{lit1} - Z_{lit2} - Z_{lit3}) \tag{4}$$

( $p = +1$  for  $i = 1$  and  $p = -1$  for  $i = 2$ )

$$Z_{iri} = (Z_{ri} + pZ_{rit1} + Z_{rit2} - Z_{rit3}) \tag{5}$$

( $p = +1$  or  $i = 1$  and  $p = -1$  for  $i = 2$ )

where  $Z_{lit1}$  &  $Z_{rit1}$  ( $i = 1$  to  $2$ ) are components of the  $LH_i$  &  $RH_i$  ( $i = 1$  to  $2$ ) road-wheel spring vertical displacements, respectively, due to load transfer effects from the crane payload longitudinal inertias and  $Z_{lit2}$  &  $Z_{rit2}$  ( $i = 1$  to  $2$ ) are components of the  $LH_i$  &  $RH_i$  ( $i = 1$  to  $2$ ) road-wheel spring vertical displacements, respectively, due to load transfer effects from the crane payload lateral inertias.

$$Z_{jit1} = \frac{(L_{ji} B_q)(m_w \ddot{X}_{h1} - m_w \ddot{X}_{w1})\{(H_2 - H_0)\cos\theta + Z\}}{(B_1 + B_2)(k_{tj1} L_{j1}^2 + k_{tj2} L_{j2}^2)} \tag{6}$$

( $j = l$  or  $r$ ;  $q = 2$  for  $j = l$ ;  $q = 1$  for  $j = r$ )

$$Z_{jit2} = \frac{B_q(m_w \ddot{Y}_{h1} - m_w \ddot{Y}_{w1})\{(H_2 - H_0)\cos\theta + Z\}}{2(k_{tl1} B_1^2 \cos\varnothing + k_{tr1} B_2^2 \cos\varnothing)} \tag{7}$$

( $j = l$  or  $r$ ;  $q = 1$  for  $j = l$ ;  $q = 2$  for  $j = r$ )

In Eqs. (1), (6) and (7),

$$L_{j1} = L_1 \cos\theta - L_t \sin(\alpha_{j1} + \varphi_{j1} + \theta) - d \sin\theta \tag{8}$$

$$L_{j2} = L_2 \cos\theta + L_t \sin(\alpha_{j2} + \varphi_{j2} + \theta) + d \sin\theta \tag{9}$$

where  $j = l$  or  $r$

$$M_1 = (M + m_{l1} + m_{l2} + m_{r1} + m_{r2} + m_b + m_w) \tag{10}$$

$$Z_{w1} = Z - L_7 \sin\theta - L_{10} \sin\varnothing \tag{11}$$

$$Z_{v1} = L_w - L_w \cos\theta_{w1} \tag{12}$$

$$Z_{v2} = L_w - L_w \cos\theta_{w2} \tag{13}$$

The sprung mass non-linear pitch equation of motion about its CG, is written as

$$I\ddot{\theta} - P_{l1}L_{l1} + P_{l2}L_{l2} - P_{r1}L_{r1} + P_{r2}L_{r2} + H_{l1}L_{l3} + H_{l2}L_{l4} + H_{r1}L_{r3} + H_{r2}L_{r4} - k_{tl1}Z_{tl1}L_{l1} + k_{tl2}Z_{tl2}L_{l2} - k_{tr1}Z_{tr1}L_{r1} + k_{tr2}Z_{tr2}L_{r2} - m_{l1}gL_{l1} + m_{l2}gL_{l2} - m_{r1}gL_{r1} + m_{r2}gL_{r2} - (m_w g + m_w \ddot{Z}_{w1} + m_w \ddot{Z}_{v1} + m_w \ddot{Z}_{v2})$$

$$U_{c1} + (m_w \ddot{X}_{h1} - m_w \ddot{X}_{w1})V_c - m_b g U_{c2} = 0 \tag{14}$$

In Eq. (14),  $H_{li} = m_{li} \ddot{X}_{li}, H_{ri} = m_{ri} \ddot{X}_{ri}$ , where

$$X_{li} = -pL_i - L_i \sin \alpha_{li} + pL_i \cos \theta + d \sin \theta + L_i \sin(\alpha_{li} + \varphi_{li} + \theta) \tag{15}$$

$$X_{ri} = -pL_i - L_i \sin \alpha_{ri} + pL_i \cos \theta + d \sin \theta + L_i \sin(\alpha_{ri} + \varphi_{ri} + \theta) \tag{16}$$

( $p = -1$  for  $i = 1$  and  $p = +1$  for  $i = 2$ )

$$X_{h1} = L_w \sin \theta_{w1} \tag{17}$$

$$X_{w1} = L_7 - L_7 \cos \theta \tag{18}$$

$$L_{j3} = L_t \cos(\alpha_{j1} + \varphi_{j1} + \theta) + d \cos \theta + L_1 \sin \theta \tag{19}$$

$$L_{j4} = L_t \cos(\alpha_{j2} + \varphi_{j2} + \theta) + d \cos \theta - L_2 \sin \theta \quad (j = l \text{ or } r) \tag{20}$$

$$U_{c1} = L_b \cos(\theta_c - \theta - \varnothing) \cos \theta_{cl} + L_7 \cos \theta + H_0 \sin \theta \tag{21}$$

$$V_c = L_b \sin(\theta_c - \theta - \varnothing) - L_7 \sin \theta + H_0 \cos \theta \tag{22}$$

$$U_{c2} = (L_b/2) \cos(\theta_c - \theta - \varnothing) \cos \theta_{cl} + L_7 \cos \theta + H_0 \sin \theta \tag{23}$$

The second order non-linear roll equation of the sprung mass with reference to the CG of the vehicle is written as

$$\begin{aligned} & J \ddot{\varnothing} + P_{l1} B_1 \cos \varnothing + P_{l2} B_1 \cos \varnothing - P_{r1} B_2 \cos \varnothing - P_{r2} B_2 \cos \varnothing + k_{tl1} Z_{tl1} B_1 \cos \varnothing \\ & + k_{tl2} Z_{tl2} B_1 \cos \varnothing - k_{tr1} Z_{tr1} B_2 \cos \varnothing - k_{tr2} Z_{tr2} B_2 \cos \varnothing + m_{l1} g B_1 \cos \varnothing + m_{l2} g B_1 \cos \varnothing \\ & - m_{r1} g B_2 \cos \varnothing - m_{r2} g B_2 \cos \varnothing - (m_w \ddot{Z}_{w1} + m_w \ddot{Z}_{v1} + m_w \ddot{Z}_{v2} + m_w g) U_{d1} \\ & + (M_w \ddot{Y}_{h1} - M_w \ddot{Y}_{w1}) V_d - m_b g U_{d2} = 0 \end{aligned} \tag{24}$$

where  $J \ddot{\varnothing}$  is the sprung mass roll moment of inertia about its CG,  $m_w \ddot{Y}_{h1}$  &  $m_w \ddot{Y}_{w1}$  are the crane payload inertias in the lateral direction due its own angular motion as well as due to coupling with the sprung mass large roll angular motion, respectively.

In Eq. (24),  $Y_{w1} = L_{10} - L_{10} \cos \varnothing, Y_{h1} = L_w \sin \theta_{w2}$

$$U_{d1} = L_b \cos(\theta_c - \theta - \varnothing) \sin \theta_{cl} + L_{10} \cos \varnothing + H_0 \sin \varnothing \tag{25}$$



$$V_d = L_b \sin(\theta_c - \theta - \varnothing) + L_{10} \sin \varnothing + H_0 \cos \varnothing \tag{26}$$

$$U_{d2} = (L_b/2) \cos(\theta_c - \theta - \varnothing) \sin \theta_{cl} + L_{10} \cos \varnothing + H_0 \sin \varnothing \tag{27}$$

The governing non-linear equations of motion, which represent the angular motions of LH<sub>*i*</sub> & RH<sub>*i*</sub> (*i* = 1 to 2) unsprung masses about their respective pivotal points, are written as.

$$P_{li} L_t \sin(\alpha_{li} + \varphi_{li} + \theta) + H_{li} L_t \cos(\alpha_{li} + \varphi_{li} + \theta) + m_{li} g L_t \sin(\alpha_{li} + \varphi_{li} + \theta) + k_{tli} Z_{tli} \sin(\alpha_{li} + \varphi_{li} + \theta) + T_{pli} = 0 \tag{28}$$

$$P_{ri} L_t \sin(\alpha_{ri} + \varphi_{ri} + \theta) + H_{ri} L_t \cos(\alpha_{ri} + \varphi_{ri} + \theta) + m_{ri} g L_t \sin(\alpha_{ri} + \varphi_{ri} + \theta) + k_{tri} Z_{tri} L_t \sin(\alpha_{ri} + \varphi_{ri} + \theta) + T_{pri} = 0 \tag{29}$$

where  $T_{pli}$  &  $T_{pri}$  are the sum of moments about pivotal points of the LH<sub>*i*</sub> & RH<sub>*i*</sub> (*i* = 1 to 2) unsprung masses due to the gas restoring force & damping force on the actuator piston as well as due to bump-stopper/rebound stopper contact forces. It may be noted that the bump-stopper or rebound stopper contact forces would act only if contact is established with the suspension axle arm during its angular motion. The hydro-gas suspension kinematics, stiffness & damping properties are arrived at by referring to [3].

$$T_{pji} = \begin{cases} T_{ji} \{ \varphi_{ji} \} + c \dot{x}_{ji} \{ \varphi_{ji} \} L_0; 0 \leq \varphi_{ji} \leq \varphi_s, j = l \text{ or } r, \\ (T_{ji} \{ 0 \} - k_{rb} (\varphi_{ji})^2) + (c \dot{x}_{ji} \{ 0 \} L_0 + c_{rb} (\dot{\varphi}_{ji})); \varphi_{ji} < 0, \\ (T_{ji} \{ \varphi_s \} + k_{ub} (\varphi_{ji} - \varphi_s)^2) + (c \dot{x}_{ji} \{ \varphi_s \} L_0 + c_{ub} (\dot{\varphi}_{ji})); \varphi_{ji} > \varphi_s \end{cases} \tag{30}$$

The governing second order non-linear equations, which represent vertical motion of the LH<sub>*i*</sub> & RH<sub>*i*</sub> (*i* = 1 to 2) dummy masses, are written as

$$dm_{li} \ddot{Z}_{lit3} - k_{tli} (Z_{li} - Z_{lit3}) + dm_{li} g - F_{li} = 0 \tag{31}$$

$$dm_{ri} \ddot{Z}_{rit3} - k_{tri} (Z_{ri} - Z_{rit3}) + dm_{ri} g - F_{ri} = 0 \tag{32}$$

where  $dm_{li} \ddot{Z}_{lit3}$  &  $dm_{ri} \ddot{Z}_{rit3}$  are the LH<sub>*i*</sub> & RH<sub>*i*</sub> (*i* = 1 to 2) dummy mass vertical inertia forces,  $k_{tli} (Z_{li} - Z_{lit3})$  &  $k_{tri} (Z_{ri} - Z_{rit3})$  are the LH<sub>*i*</sub> & RH<sub>*i*</sub> (*i* = 1 to 2) road-wheel spring restoring forces,  $dm_{li} g$  &  $dm_{ri} g$  represent self-weight of the LH<sub>*i*</sub> & RH<sub>*i*</sub> (*i* = 1 to 2) dummy masses,  $F_{li}$  &  $F_{ri}$  are the ground contact forces on the LH<sub>*i*</sub> & RH<sub>*i*</sub> (*i* = 1 to 2) dummy masses such that

$$F_{ji} = \begin{cases} k_{sji}(Z_{jit3})^2 - c_{sji}(\dot{Z}_{jit3}); & Z_{jit3} \leq 0, j = lorr, \\ 0; & Z_{jit3} > 0 \end{cases} \quad (33)$$

The crane pay-load angular motion about its hinge point in the longitudinal and lateral directions are written as

$$I_{w1}\ddot{\theta}_{w1} + m_w g L_w \sin\theta_{w1} - m_w \ddot{X}_{w1} L_w \cos\theta_{w1} + c_w \dot{\theta}_{w1} + m_w \ddot{Z}_{w1} L_w \sin\theta_{w1} + m_w \ddot{Z}_{v2} L_w \sin\theta_{w1} = 0 \quad (34)$$

$$I_{w1}\ddot{\theta}_{w2} + m_w g L_w \sin\theta_{w2} - m_w \ddot{Y}_{w1} L_w \cos\theta_{w2} + c_w \dot{\theta}_{w2} + m_w \ddot{Z}_{w1} L_w \sin\theta_{w2} + m_w \ddot{Z}_{v1} L_w \sin\theta_{w2} = 0 \quad (35)$$

where  $I_{w1}\ddot{\theta}_{w1}$  &  $I_{w1}\ddot{\theta}_{w2}$  are the crane payload rotational inertia about its hinge point in the longitudinal and lateral directions, respectively,  $c_w \dot{\theta}_{w1}$  &  $c_w \dot{\theta}_{w2}$  are the viscous torsional damping moments about the crane payload hinge point in the longitudinal and lateral directions, respectively,  $m_w \ddot{X}_{w1} L_w \cos\theta_{w1}$  &  $m_w \ddot{Y}_{w1} L_w \cos\theta_{w2}$  are the moments about the hinge point due to the payload horizontal inertia by virtue of its coupling with the sprung mass large pitch & roll motions, respectively,  $m_w \ddot{Z}_{w1} L_w \sin\theta_{w1}$  &  $m_w \ddot{Z}_{v1} L_w \sin\theta_{w2}$  are the moments about the hinge point due to the payload vertical inertia by virtue of its coupling with the sprung mass degrees of freedom.

#### 4 Static Equilibrium Response Comparison with and Without Suspension Lock Over Flat Terrain

Equations (1) to (35) are coded in MATLAB and solved by using similar technique as that described in [3]. The magnitudes of various fixed parameters are described in Table 1. The four-station military vehicle is considered to have bump-stopper ( $\varphi_s = 60^\circ$ ) at every suspension station with which the dynamic effects of variation in the crane payload ( $m_w$ ) from 4.5 t, 8.5 t, 12.5 t & 14.5 t on the sprung mass roll angle and RH<sub>1</sub> & LH<sub>2</sub> wheel reactions are observed initially. Thereafter, suspension locks, which are similar in functionality to the usual bump-stoppers, were added to each station in order to limit the wheel travel and sprung mass roll as well as to reduce the suspension loads. In this regard, the suspension lock angle  $\varphi_s$  is reduced to  $35^\circ$  from  $60^\circ$ . It may be noted that since the crane payload acts on the vehicle right side and that too on one corner, RH<sub>1</sub> & LH<sub>2</sub> wheel stations encounter the extreme loading conditions. Therefore, the transient dynamic and subsequent static equilibrium response comparison (in terms of sprung mass roll angle and LH<sub>2</sub> & RH<sub>1</sub> vertical wheel reactions) with the suspension lock and usual bump-stopper over flat terrain under different crane-payload conditions, is brought out from the non-linear dynamic mathematical model of the military vehicle.

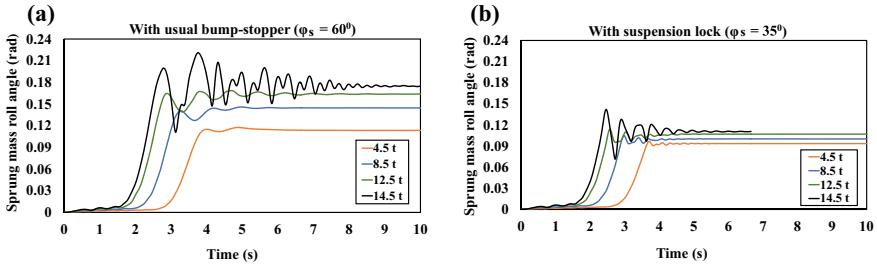


**Fig. 3** **a** Sprung mass roll under different payloads when  $\varphi_s = 60^\circ$ , **b** Sprung mass roll under different payloads when  $\varphi_s = 35^\circ$

The HSU rebound gas charging pressure is considered to be 95 bar in all the stations for all the load cases. Figure 3a and b highlight the time dependent sprung mass roll angular displacement variation with usual bump-stopper at  $60^\circ$  and suspension lock at  $35^\circ$ , respectively. Figure 4a and b represent the vertical reaction load variation on the RH<sub>1</sub> suspension station and Fig. 5a and b highlight the vertical reaction load variation on the LH<sub>2</sub> suspension station with usual bump-stopper at  $60^\circ$  and suspension lock at  $35^\circ$ , respectively. Table 2 indicates the comparative final static

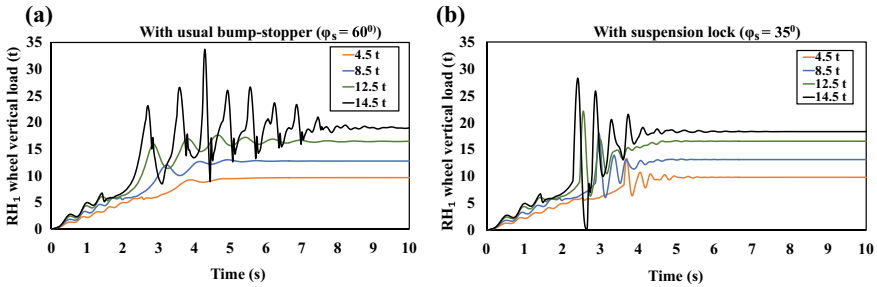


**Fig. 4** **a** RH<sub>1</sub> wheel vertical load under different payloads when  $\varphi_s = 60^\circ$ , **b** RH<sub>1</sub> wheel vertical load under different payloads when  $\varphi_s = 35^\circ$

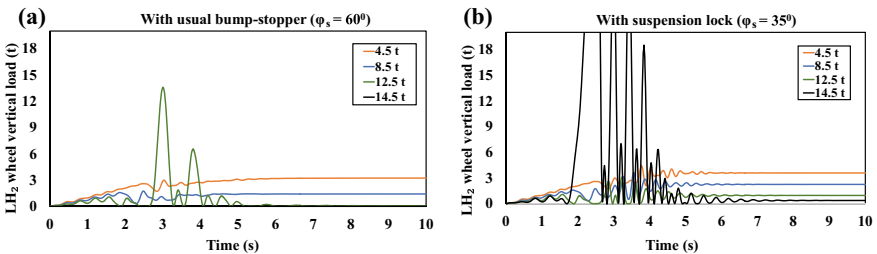


**Fig. 5** **a** LH<sub>2</sub> wheel vertical load under different payloads when  $\varphi_s = 60^\circ$ , **b** LH<sub>2</sub> wheel vertical load under different payloads when  $\varphi_s = 35^\circ$

**Table 2** Final static equilibrium configuration of the four-station military vehicle with the crane payload

Crane payload (t)	Sprung mass roll (rad)		RH <sub>1</sub> wheel vertical reaction (t)		LH <sub>2</sub> wheel vertical reaction (t)	
	$\varphi_s = 60^\circ$	$\varphi_s = 35^\circ$	$\varphi_s = 60^\circ$	$\varphi_s = 35^\circ$	$\varphi_s = 60^\circ$	$\varphi_s = 35^\circ$
4.5	0.114	0.093	9.65	9.84	3.23	3.59
8.5	0.144	0.1	12.76	13.13	1.42	2.25
12.5	0.164	0.106	16.47	16.57	0.06	0.96
14.5	0.174	0.11	18.34	18.99	0	0.37

equilibrium response in terms of the sprung mass roll, RH<sub>1</sub> & LH<sub>2</sub> vertical wheel reaction loads. It is observed from Fig. 3a and b and Table 2 that the sprung mass roll angular displacement reduces further with the suspension lock when compared to that with the usual bump-stopper under all the loading conditions. Therefore, as the sprung mass roll is reduced, the wheel travel also gets limited. Moreover, as the crane payload increases, there is more reduction in the sprung mass roll displacement. Therefore, it clearly reveals the advantage of implementing the suspension lock at a lesser angle by reducing the roll over tendency under given payloads. This is evident from the LH<sub>2</sub> wheel vertical reaction load which tends to become zero (i.e., tends to lose ground contact) without the suspension lock. It is observed from Figs. 4a and b, 5a and b and from Table 2 that there is a marginal increase in the RH<sub>1</sub> and LH<sub>2</sub> wheel vertical reaction loads with implementation of the suspension lock. However, it may be noted that with addition of the suspension lock at a lesser angle, the vertical reaction load is shared by both the lock and HSU. This reduces the overall suspension loads with addition of the lock. It is estimated from Table 2 that the safe crane payload for the given vehicle & suspension configuration is 12.5 t by considering a load factor of 1.5.

## 5 Conclusion

The non-linear mathematical model of the four-station military vehicle with trailing arm HSU and crane hanging payload is developed to simulate the dynamic influence of suspension lock on the vehicle dynamic behavior and final static equilibrium configuration. The trailing arm dynamic behavior, inertia coupling effects between the sprung & unsprung masses as well as hanging payload, rebound/bump-stopper and ground contact phenomenon is brought out in the mathematical model. The safe crane payload can also be estimated from the model. With the suspension lock at a relatively lesser angle, sprung mass roll and overall suspension load reduction are observed. Therefore, the implementation of suspension lock ascertains vehicle stability. The model is a prerequisite for deciding upon the allowable vehicle speed

during movement with the crane payload. The model is very novel & generic and provides deep insight into the development of the recovery vehicle simulator.

**Acknowledgements** The authors would like to thank Shri Balamurugan V, Director, CVRDE & Shri Murugesan R, Addl. Director (CEAD) for extending all required facilities to carry out the research work, Shri S. Pazhanikumar, Sc 'G' & Shri Arun Kumar Deokar, Sc 'C' from SV group and Shri N.S. Sekar, Sc 'F' (Retd.) from RG group. The authors express their gratitude to Dr. V. Balamurugan, Addl. Director (AP) & Prof. R. Krishna Kumar, IIT (M). The authors would also like to thank Shri Abu Bakr Azam, Research Scholar, Nanyang Technological University for his noteworthy assistance.

## References

1. Mankar, N.A.: Comparative dynamic analysis of a military recovery vehicle during crane operations with linear suspension. M. Tech Thesis, DIAT (Pune), India (2019)
2. Banerjee, S., Balamurugan, V., Krishna, KR.: Effect of integrated ride and cornering dynamics of a military vehicle on the weapon responses. In: Proceedings of The Institution of Mechanical Engineers, Part K: Journal of Multi-body Dynamics, 232.4 pp. 536–554 (2018)
3. Banerjee, S., Balamurugan, V., Krishna, KR.: Ride dynamics mathematical model for a single station representation of tracked vehicle. *J. Terramech.* **53**, 47–58 (2014)
4. Li, X., Wang, Y.: Analysis of mixed model in gear transmission based on ADAMS. *Chin. J. Mech. Eng.* **25**(5), 968–973 (2012)
5. Devesh, M., Manigandan, R., Banerjee, S., Mailan, L.B.: Development of sprung mass non-linear mathematical model of pitch dynamics with trailing arm suspension. *Vibroeng Proc* **37**, 1–6 (2021)

# One-Dimensional Steady State Heat Conduction Equation with and Without Source Term by FVM



Neelam Patidar  and Akshara Makrariya 

**Abstract** A One-dimensional (1D) steady-state heat conduction equation with and without source term is presented in this paper. The temperature distribution in a body is determined by the model of the heat equation based on some physical assumptions. The heat equation is solved by finite volume method (FVM). By using the Matlab software, a numerical simulation of the raised examples was investigated. The results of the heat equation with and without source term are well compared and it is found that the temperature distribution of 1D steady-state heat equation with source term is parabolic whereas the temperature distribution without source term is linear. The results concluded that the numerical solutions perfectly matched the exact solutions as expected.

**Keywords** Heat equation · Heat conduction equation · Source term · Finite volume method (FVM) · Partial differential equation (PDE) · One-dimensional (1D)

## 1 Introduction

The heat equation is a crucial PDE that defines how heat (or temperature variation) is distributed in a particular location over time. Mathematical analysis, numerical computations, and experiments are all made easier by the heat equation. It's also extremely practical: engineers must ensure that engines do not melt and computer chips do not overheat [1]. We must examine the concepts in depth because of these and

---

VIT Bhopal University

---

N. Patidar (✉) · A. Makrariya  
School of Advanced Science-Mathematics, VIT Bhopal University, Bhopal, Madhya Pradesh,  
India  
e-mail: [neelampatidar1994@gmail.com](mailto:neelampatidar1994@gmail.com)

A. Makrariya  
e-mail: [akshara.makrariya@vitbhopal.ac.in](mailto:akshara.makrariya@vitbhopal.ac.in)

© The Author(s), under exclusive license to Springer Nature Switzerland AG 2022  
S. Banerjee and A. Saha (eds.), *Nonlinear Dynamics and Applications*,  
Springer Proceedings in Complexity,  
[https://doi.org/10.1007/978-3-030-99792-2\\_67](https://doi.org/10.1007/978-3-030-99792-2_67)

797

many other real-world applications of the heat equation [2, 3]. The control volume approach has become a prominent fluid flow solution procedure over the last two decades.

Chai et al. [4] presented a finite volume method (FVM) to capture collimated beam. To demonstrate the FVM's capabilities, it has been used in two- and three-dimensional enclosures with transparent, emitting, absorbing and anisotropically scattering media. All The obtained results have been compared with other published results. And, it was conclude that the FVM is accurate and efficient.

Li et al. [5] proposed a new FVM for cylindrical heat conduction issues. The problem was taken based on a local analytical solution. The novel approach's computation results are compared to those of the traditional second-order FVM. The developed method for cylindrical heat conduction issues is more accurate than previous methods. The obtained results reveal that the novel method takes much less computation effort than traditional methods to achieve the same degree of accuracy.

Belghazi et al. [6] presented an analytical approach of unsteady-state heat conduction. The study has done for two-layered material based on moving Gaussian laser. The homogeneous part of the heat equation was solved by the separation of variables method. This model can also be used to calculate the thermal contact resistance between layers.

A method for the solution of heat conduction problems with phase-changing and movable boundary conditions has been developed by Juan [7]. The problem has been solved by the element-free Galerkin method [8, 9]. According to the results of this approach, it can effectively deal with the marked nonlinearity of fusion latent heat release in heat transfer problems with phase change. Numerical results are obtained accurate and stable by its straightforward implementation.

A numerical simulation of non-Fourier heat conduction in fins under periodic boundary conditions has been done by Liu et al. [10]. To evaluate the non-fourier heat conduction, the Lattice Boltzmann approach was used [11]. The study analyzed the effect of frequency, shape and relaxation time of the base temperature oscillations on heat transfer efficiency [12].

We have looked at 1D heat conduction in a steady state. Steady means the temperatures do not change with time and hence, the heat flow does not change over time. 1D means that the temperature is determined by a single dimension [13].

**Heat Conduction:** The thermal conductivity is defined by Fourier's law. According to Fourier's law, the area at right angles to the gradient through which the heat flows is proportional to the negative gradient of temperature and the time rate of heat transfer. Fourier's law is also known as the law of heat conduction [14]. The aim of this study is to derive a 1D heat equation with and without source term, and its solution using the FVM along with its numerical analysis using MATLAB.

**Finite volume method:** The FVM is a numerical method that converts PDEs into discrete algebraic equations. The PDEs express conservation laws across differential volumes. Discrete algebraic equations can be solved over finite volumes [15, 16]. To obtain the values of the dependent variables for each element, the system of these

equations was solved. The resulting system of equations usually includes fluxes that enter the finite volume faces, hence flux calculations are crucial in FVM [17, 18]. Interpolation and gradient methods are also used in this process [19].

## 2 Solution of 1D Steady-State Heat Conduction Equation by FVM

The 1D steady-state heat conduction equation with the source term that we are using in this study is created using the given formula

$$\frac{d}{dx} \left( k \frac{dT}{dx} \right) + S = 0$$

where ‘T’ is the rod’s temperature. The temperature boundary of values at A and B are specified. Thermal diffusivity is denoted by the letter k and the source term is S.

### 2.1 Grid Generation

The discretization of the domain into discrete control volumes is the first stage in the finite control volume, as shown in Fig. 1.

In this figure, the number of nodal points is placed between A and B. Here are three nodal points. We are calculating the equation at node P. The finite control volume is represented by the highlighted area. P is the center of control volume and W and E are the neighboring nodes of the node P to its west and east respectively. The w represents the interface between W-P and e represents the interface between P-E. Grid size is denoted by  $\delta x$ . For this problem, we have assumed a uniform grid [15, 20].

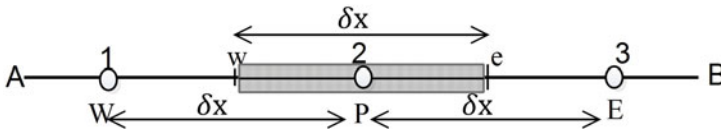


Fig. 1 discretization of the domain



## 2.2 Discretization

Over the control volume, integrate the governing equation as follows:

$$\int_{\Delta V} \frac{d}{dx} \left( \alpha \frac{dT}{dx} \right) dV + \int_{\Delta V} S dV = 0$$

The cross-sectional area of the control volume is  $A$ .  $\Delta V$  is the control volume. The average value of the source  $S$  over the control volume is  $S$ . Hence,  $dV = A dx$  and  $\Delta V = A \delta x$ . since the heat generation rate is uniform, So the equation becomes

$$\int_w^e \frac{d}{dx} \left( \alpha A \frac{dT}{dx} \right) dx + S \int_{\Delta V} dV = 0$$

$$\left[ \left( \alpha A \frac{dT}{dx} \right)_e - \left( \alpha A \frac{dT}{dx} \right)_w \right] + S \Delta V = 0$$

The above equation states that the generation of temperature is equal to the diffusive flux of temperature leaving the east face of the control volume minus the diffusive flux of temperature entering the west face. As we can observed that, the flow is conserved within the control volume [21]. To derive useful forms of the discretized equation, the interface diffusion coefficient and temperature gradient at east and west face are required. Linear approximations seem to be the obvious and this is the easiest method of computing interface values and gradients. This practice is called a central differencing scheme [22].

$$\alpha_w = \frac{\alpha_W + \alpha_P}{2}, \quad \alpha_e = \frac{\alpha_E + \alpha_P}{2}$$

And the diffusive flux terms are calculated as follows:

$$\left( \alpha A \frac{dT}{dx} \right)_e = \alpha_e A_e \left( \frac{T_E - T_P}{\delta x_{PE}} \right)$$

$$\left( \alpha A \frac{dT}{dx} \right)_w = \alpha_w A_w \frac{T_P - T_W}{\delta x_{WP}}$$

The finite volume method approximates the source term as

$$S \Delta V = S_u + S_p T_P$$

The final equation can be rearranged as

$$\left( \alpha_e A_e \cdot \frac{T_E - T_P}{\delta x_{PE}} \right) - \left( \alpha_w A_w \cdot \frac{T_P - T_W}{\delta x_{WP}} \right) + (S_u + S_p T_P) = 0$$

This can be arranged as

$$\left( \frac{\alpha_e A_e}{\delta x_{PE}} + \frac{\alpha_w A_w}{\delta x_{WP}} - S_p \right) T_P = \left( \frac{\alpha_w A_w}{\delta x_{WP}} \right) T_W + \left( \frac{\alpha_e A_e}{\delta x_{PE}} \right) T_E + S_u$$

Identifying the coefficient of  $T_P, T_W, T_E$  as  $a_w, a_P, a_E$  and rearranging the equation as under

$$a_P T_P = a_W T_W + a_E T_E + S_u$$

where

$$a_W = \frac{\alpha_w A_w}{\delta x_{WP}}, \quad a_P = \frac{\alpha_e A_e}{\delta x_{PE}}, \quad a_E = a_W + a_P - S_p$$

### 3 Numerical Solution

A textbook exam is taken “An Introduction to Computational Fluid Dynamics” by Versteeg and Malasekara [15]: Consider the problem of heat conduction with and without source term in an insulated rod whose ends are kept at a constant temperature of 100 °C and 500 °C respectively. Calculate the temperature distribution in a rod at a steady state. The cross-sectional area  $A$  is  $10 \times 10^{-3} \text{ m}^2$  and the thermal conductivity is 1000 W/m/K.

#### 3.1 The Heat Conduction Equation with Source Term

Under uniform heat generation  $S = 1000\text{K}$ , the equation for the governing process is

$$\frac{d}{dx} \left( K * \frac{dT}{dx} \right) + S = 0$$

Integrating above the control volume  $dV$  and discretization of the above equation will yield

$$K \cdot A \cdot \left( \frac{T_E - T_P}{dx} \right) - K \cdot A \cdot \left( \frac{T_P - T_W}{dx} \right) = S \Delta x \frac{2K \cdot A}{dx} \cdot T_P = \frac{K \cdot A}{dx} \cdot T_E + \frac{K \cdot A}{dx} \cdot T_W + S \Delta x$$

The above equation represents the solution of temperature at the inner nodes. The boundary conditions for this domain are  $T_1 = 100 \text{ °C}$  (left end) and  $T_2 = 500 \text{ °C}$  (right end). At the left control volume, the node associated with the left boundary is

$$\frac{2KA}{dx} \cdot T_P = \frac{KA}{dx} \cdot T_A + \frac{KA}{dx} \cdot T_E + S \Delta x$$

And, the node associated with the right boundary is

$$\frac{2KA}{dx} \cdot T_P = \frac{KA}{dx} \cdot T_B + \frac{KA}{dx} \cdot T_W + SA dx$$

### 3.2 The Heat Conduction Equation Without Source Term

$$\frac{d}{dx} \left( K * \frac{dT}{dx} \right) = 0$$

Integrating above control volume  $dV$  and discretization of the above equation will yield

$$KA \cdot \left( \frac{T_E - T_P}{dx} \right) - KA \cdot \left( \frac{T_P - T_W}{dx} \right) = 0$$

$$\frac{2KA}{dx} \cdot T_P = \frac{KA}{dx} \cdot T_E + \frac{KA}{dx} \cdot T_W$$

The above equation represents the solution of temperature at the inner nodes. The node associated with the left boundary

$$\frac{2KA}{dx} \cdot T_P = \frac{KA}{dx} \cdot T_A + \frac{KA}{dx} \cdot T_E$$

The node associated with the right boundary

$$\frac{2KA}{dx} \cdot T_P = \frac{KA}{dx} \cdot T_B + \frac{KA}{dx} \cdot T_W$$

To verify the accuracy, the final equation is performed in MATLAB on 5, 10, and 25 nodes. The numerical solution is compared to the exact solution. The exact solution is contained in the textbook [15].

## 4 Results and Discussion

The temperature distributions were analyzed at 5, 10 and 25 nodes to validate the results. From the results, it was found that numerical accuracy increases as we increase the number of nodes. The following outputs were obtained from the study.

The temperature distribution of the rod is shown in Fig. 2. In this figure, the straight line shows the temperature distribution of a rod obtained by numerical method and the dotted line represents the exact temperature distribution. The temperature of a

**Fig. 2** Temperature distribution of rod

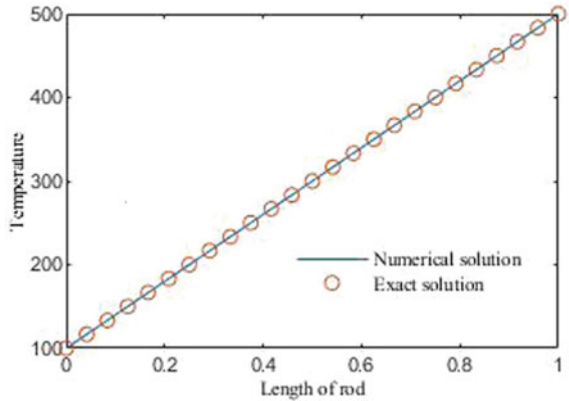
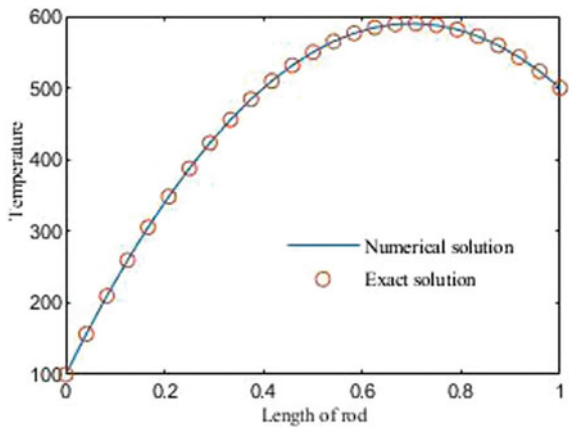


**Fig. 3** Temperature distribution of rod on adding external source

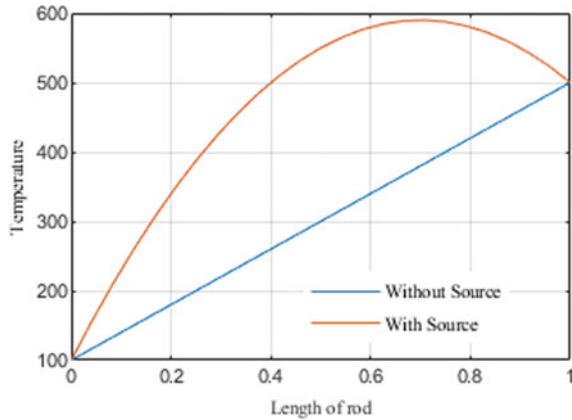


rod increases with increasing the length of rod. The temperature start increasing from 100 °C then reached at 500 °C. The temperature increases linearly.

Figure 3 shows the distribution of temperature of the rod on adding an external heat source. In this figure, the straight line shows the temperature distribution of a rod obtained by FVM and the dotted line represents the exact temperature distribution. The temperature of a rod increases as increasing the length of the rod. The temperature starts increasing from 100 °C and reached at 590 °C then again starts decreasing and reached at 500 °C. The temperature distribution was obtained parabolically.

Figure 4 shows the comparison between one-dimensional heat conduction equations with and without source term. It was obtained that the temperature distribution of a rod without an external heat source is linear. On adding the external heat source in a rod, the temperature distribution gets changed and becomes parabolic. From all these results it was observed that the external source affects the temperature distribution of a rod.

**Fig. 4** Comparison between heat equations with and without source term



## 5 Conclusion

A one-dimensional heat equation can be used to represent many physical phenomena that are connected to temperature distribution, as demonstrated in this study. Analytical solutions are sometimes insufficient for understanding the behavior of solutions. Due to this, we may rely on numerical solutions to find out more about the inherent problems. In this study, we have seen how to obtain and solve a 1D steady-state heat equation with and without a source term. It was observed that the temperature distribution of 1D steady-state heat equation with source term is parabolic whereas the temperature distribution without source term is linear. The numerical solutions were found to be similar to the exact solutions, as expected. Furthermore, by using MATLAB programming, we have provided a real comprehension of the example mentioned in the study.



## References

1. Tipler, P.A., Mosca, G.: *Physics for Scientists and Engineers*. Macmillan (2007)
2. Asmar, N.H.: *Partial Differential Equations with Fourier Series and Boundary Value Problems*. Courier Dover Publications (2016)
3. Abdisa, L.T.: *One Dimensional Heat Equation and its Solution by the Methods of Separation of Variables, Fourier Series and Fourier Transform* (2021)
4. Chai, J.C., Lee, H.S., Patankar, S.V.: Finite volume method for radiation heat transfer. *J. Thermophys. Heat Transf.* **8**(3), 419–425 (1994)
5. Li, W., Yu, B., Wang, X., Wang, P., Sun, S.: A finite volume method for cylindrical heat conduction problems based on local analytical solution. *Int. J. Heat Mass Transf.* **55**(21–22), 5570–5582 (2012)
6. Belghazi, H., El Ganaoui, M., Labbe, J.-C.: Analytical solution of unsteady heat conduction in a two-layered material in imperfect contact subjected to a moving heat source. *Int. J. Thermal Sci.* **49**(2), 311–318 (2010)

7. Álvarez-Hostos, J.C., Gutierrez-Zambrano, E.A., Salazar-Bove, J.C., Puchi-Cabrera, E.S., Bencomo, A.D.: Solving heat conduction problems with phase-change under the heat source term approach and the element-free Galerkin formulation. *Int. Commun. Heat Mass Transf.* **108**, 104321 (2019)
8. Hostos, J.C., Fachinotti, V.D., Piña, A.J., Bencomo, A.D., Cabrera, E.S.: Implementation of standard penalty procedures for the solution of incompressible Navier-Stokes equations, employing the element-free Galerkin method. *Eng. Anal. Boundary Elem.* **96**, 36–54 (2018)
9. Ling, J., Yang, D.S., Zhai, B.W., Zhao, Z.H., Chen, T.Y., Xu, Z.X., Gong, H.: Solving the single-domain transient heat conduction with heat source problem by virtual boundary meshfree Galerkin method. *Int. J. Heat Mass Transf.* **1**(115), 361–7 (2017)
10. Liu, Y., Li, L., Zhang, Y.: Numerical simulation of non-Fourier heat conduction in fins by lattice Boltzmann method. *Appl. Therm. Eng.* **166**, 114670 (2020)
11. Bamdad, K., Ashorynejad, H.R.: Inverse analysis of a rectangular fin using the lattice Boltzmann method. *Energy Convers. Manage.* **97**, 290–7 (2015)
12. Wankhade, P.A., Kundu, B., Das, R.: Establishment of non-Fourier heat conduction model for an accurate transient thermal response in wet fins. *Int. J. Heat Mass Transf.* **126**, 911–23 (2018)
13. Date, A.W.: *Introduction to Computational Fluid Dynamics*. Cambridge University Press, Cambridge (2005)
14. Wang, L.: Generalized Fourier law. *Int. J. Heat Mass Transfer* **37**(17), 2627–2634 (1994)
15. Versteeg, H.K., Malalasekera, W.: *An Introduction to Computational Fluid Dynamics: The Finite Volume Method [OpenFOAM]*, vol. M (2015)
16. Moukalled, F., Mangani, L., Darwish, M.: *The Finite Volume Method in Computational Fluid Dynamics*, vol. 113. Springer, Berlin (2016)
17. Akhtar, F.: Introduction and application of finite volume method (FVM) for 1-D linear heat conduction equation. *Heat Equ* 1–17 (2021)
18. Banerjee, S.: *Mathematical Modeling- Models*. CRC Press, Analysis and Applications (2014)
19. *An Introduction to Computational Fluid Dynamics: The Finite Volume Method. [OpenFOAM]* (2015)
20. Zienkiewicz, O.C., Taylor, R.L., Nithiarasu, P., Zhu, J.Z.: *The Finite Element Method*, vol. 3. McGraw-Hill, London (1977)
21. Barth, T., Ohlberger, M.: Finite volume methods: foundation and analysis. *Encyclop. Comput. Mech.* **1**(15), 1–57 (2004)
22. Akhtar, F.: Solving 1-D steady state heat conduction equation using finite volume method (FVM) M, 1–15 (2021)
23. Makrariya, A., Adlakha, N.: Two-dimensional finite element model to study temperature distribution in peripheral regions of extended spherical human organs involving uniformly perfused tumors. *Int. J. Biomath.* **8**(06), 1550074 (2015)
24. Makrariya, A., Pardasani, K.R.: Finite element method to study the thermal effect of cyst and malignant tumor in women's breast during menstrual cycle under cold environment. *Adv. Appl. Math. Sci.* **18**(1), 29–43 (2018)

# Travelling and Solitary Wave Solutions of (2+1)-Dimensional Nonlinear Evolution Equations by Using Khater Method



Ram Mehar Singh , S. B. Bhardwaj , Anand Malik, Vinod Kumar, and Fakir Chand

**Abstract** The most of the physical systems are nonlinear by nature which can be represented by various nonlinear partial differential equations. Here, we present a simple technique say Khater method to find the Travelling and Solitary Wave solutions of (2+1)-dimensional nonlinear evolution equations. This method is a very powerful tool for obtaining the exact solutions of various nonlinear differential equations. In this study, modified Korteweg- de Vries-Zakharov-Kuznetsov (mKdV-ZK) equation is taken as an example of nonlinear evolution equation which is used in astrophysics to study various space phenomena, dynamics of plasma etc.

**Keywords** mKdV-ZK equation · Khater method · Traveling wave solutions · Solitary wave solutions

## 1 Introduction

The concept of solitary wave was introduced by Zabusky and Kruskal in 1965 in their well known experiment on KdV- equation . It gain interest of researchers working in areas of nonlinear dynamics. Various phenomena such as prolongation structures, space curves , gauge-equivalence, Lie-algebraic properties , singularity structures are related to the concept of solitons and can be described by different nonlinear evolution equations(NLEEs) [1–3]. The investigation of travelling and solitary wave solutions of these equations is a major component of the

---

R. M. Singh (✉) · V. Kumar

Department of Physics, Chaudhary Devi Lal University, Sirsa 125055, India  
e-mail: [dixit\\_rammehar@yahoo.co.in](mailto:dixit_rammehar@yahoo.co.in); [dixitrammehar@cdu.ac.in](mailto:dixitrammehar@cdu.ac.in)

S. B. Bhardwaj

Department of Physics, SUS Govt. College Matak-Majri, Karnal 132041, India

A. Malik

Department of Physics, Chaudhary Ranbir Singh University, Jind 126102, India

F. Chand

Department of Physics, Kurukshetra University, Kurukshetra 136119, India

research that play a significant role in the description of various nonlinear systems. The exact solutions of such equations yield lot of information about the system concerned [4, 5] which can be obtained by reducing the nonlinear partial differential equations(NLPDEs) to associated ordinary differential equations by using the ansatz  $g(x, y, t) = g(\xi), \quad \xi = x + y - ct$  . In past, several efforts have been made by mathematicians and physicists to find the exact solutions of the nonlinear partial differential equations by employing various methods like extended modified auxiliary equation mapping method, exp-function method, ansatz method, trial equation method, extended direct algebraic method, auxiliary equation method,  $e^{(-i\phi\xi)}$ -expansion method, extended tanh-function method, Kudryashov and modified Kudryashov methods, improved  $\tan(\frac{\phi}{2})$ -expansion method,  $(\frac{G'}{G})$ -expansion method , novel  $(\frac{G'}{G})$ -expansion method, improved  $(\frac{G'}{G})$ -expansion method etc. [6–12].

Now, we introduce a new method for solving various NLEEs i.e. Khater method which is one of the few general methods available for solving various NLEEs. There are lot of NLEEs to describe various nonlinear systems but in the present study, we have computed the travelling and solitary wave solutions of (2+1)-dimensional mKdV-ZK equation [13–15]which is an important class of NLEEs arising in fluid dynamics, plasma physics,Bose-Einstein condensate, shallow water waves, nonlinear optics astrophysics, quantum optic, hydrodynamic and mathematical physics to study nonlinear physical phenomena.The organization of the paper is as follow : The basic formulation of the Khater method is discussed in Sect. 2. Under the elegance of Khater method, exact solitonic solutions of (2+1)-dimensional mKdV-ZK equation and their graphical representations are given in Sect. 3. Finally concluding remarks are addressed in Sect. 4.

## 2 Khater Method

Consider the nonlinear evolution equation as :

$$P(u, D_x^\eta q, D_y^\eta q, D_z^\eta q, D_t^\eta q, D_x^\eta D_y^\eta q, D_x^\eta D_t^\eta q, D_y^\eta D_t^\eta q, \dots) = 0, \tag{1}$$

where P is a polynomial in  $q(x,y,t)$  and its partial derivatives .

**Step 1.** Consider the transformation

$$g(x, y, t) = g(\xi), \quad \xi = x + y - c_1 t, \tag{2}$$

where  $c_1$  is the constant, then Eq.(2) transformed in the following ODE:

$$Q(q, q', q'', q''', \dots) = 0 \tag{3}$$

where Q is a polynomial in  $q(\xi)$  and its various derivatives.



**Step 2.** Consider solution of Eq. (3) as

$$q(\xi) = \sum_{i=0}^N a_i a^{ig(\xi)}, \tag{4}$$

where  $a, a_i$ , are constants to be calculated, such that  $a_N \neq 0$  and  $g(\xi)$  satisfies the following differential equation :

$$g'(\xi) = \frac{1}{\ln(a)} \left( \eta a^{-g(\xi)} + \rho + \delta a^{g(\xi)} \right) \tag{5}$$

**Step 3.** Determine the positive integer  $N$  in Eq. (5) by balancing the highest order derivatives and the nonlinear terms.

**Step 4.** Inserting Eq. (4) along Eq. (5) into Eq. (3) and rationalization of the resultant expression, we met a set of algebraic equations, which can be solved by symbolic computation to get the values of  $a_i$  and  $(\eta, \rho, \delta)$ .

The solutions of Eq. (5):

**When**  $(\rho^2 - \eta\delta < 0 \ \& \ \sigma = 0)$ .

$$a^{f(\xi)} = \left[ \frac{-\rho}{\delta} + \frac{\sqrt{-(\rho^2 - \eta\delta)}}{\delta} \tan \left( \frac{\sqrt{-(\rho^2 - \eta\delta)}}{2} \xi \right) \right] \tag{6}$$

or

$$a^{f(\xi)} = \left[ \frac{-\rho}{\delta} + \frac{\sqrt{-(\rho^2 - \eta\delta)}}{\delta} \cot \left( \frac{\sqrt{-(\rho^2 - \eta\delta)}}{2} \xi \right) \right] \tag{7}$$

**When**  $(\rho^2 + \eta\delta > 0 \ \& \ \delta \neq 0)$ .

$$a^{f(\xi)} = \left[ \frac{-\rho}{\delta} - \frac{\sqrt{(\rho^2 - \eta\delta)}}{\delta} \tanh \left( \frac{\sqrt{(\rho^2 - \eta\delta)}}{2} \xi \right) \right] \tag{8}$$

or

$$a^{f(\xi)} = \left[ \frac{-\rho}{\delta} - \frac{\sqrt{-(\rho^2 - \eta\delta)}}{\delta} \coth \left( \frac{\sqrt{(\rho^2 - \eta\delta)}}{2} \xi \right) \right] \tag{9}$$

**When**  $(\rho^2 + \eta^2 > 0 \ \& \ \delta \neq 0 \ \& \ \delta = -\eta)$ .

$$a^{f(\xi)} = \left[ \frac{\rho}{\eta} + \frac{\sqrt{(\rho^2 + \eta^2)}}{\eta} \tanh \left( \frac{\sqrt{(\rho^2 + \eta^2)}}{2} \xi \right) \right], \tag{10}$$

or

$$a^{f(\xi)} = \left[ \frac{\rho}{\eta} + \frac{\sqrt{(\rho^2 + \eta^2)}}{\eta} \coth \left( \frac{\sqrt{(\rho^2 + \eta^2)}}{2} \xi \right) \right]. \tag{11}$$

**When**  $(\rho^2 + \eta^2 < 0 \ \& \ \delta \neq 0 \ \& \ \delta = -\eta)$ .

$$a^{f(\xi)} = \left[ \frac{\rho}{\eta} + \frac{\sqrt{-(\rho^2 + \eta^2)}}{\eta} \tan\left(\frac{\sqrt{-(\rho^2 + \eta^2)}}{2} \xi\right) \right], \quad (12)$$

or

$$a^{f(\xi)} = \left[ \frac{\rho}{\eta} + \frac{\sqrt{-(\rho^2 + \eta^2)}}{\eta} \cot\left(\frac{\sqrt{-(\rho^2 + \eta^2)}}{2} \xi\right) \right]. \quad (13)$$

**When**  $(\rho^2 - \eta^2 < 0 \ \& \ \delta = \eta)$ .

$$a^{f(\xi)} = \left[ \frac{-\rho}{\eta} + \frac{\sqrt{-(\rho^2 - \eta^2)}}{\eta} \tan\left(\frac{\sqrt{-(\rho^2 - \eta^2)}}{2} \xi\right) \right], \quad (14)$$

$$a^{f(\xi)} = \left[ \frac{-\rho}{\eta} + \frac{\sqrt{-(\rho^2 - \eta^2)}}{\eta} \cot\left(\frac{\sqrt{-(\rho^2 - \eta^2)}}{2} \xi\right) \right]. \quad (15)$$

**When**  $(\rho^2 - \eta^2 > 0 \ \& \ \delta = \eta)$ .

$$a^{f(\xi)} = \left[ \frac{-\rho}{\eta} + \frac{\sqrt{(\rho^2 + \eta^2)}}{\eta} \tanh\left(\frac{\sqrt{(\rho^2 + \eta^2)}}{2} \xi\right) \right], \quad (16)$$

$$a^{f(\xi)} = \left[ \frac{-\rho}{\eta} + \frac{\sqrt{(\rho^2 + \eta^2)}}{\eta} \coth\left(\frac{\sqrt{(\rho^2 + \eta^2)}}{2} \xi\right) \right]. \quad (17)$$

**When**  $(\eta = \delta = 0)$ .

$$a^{f(\xi)} = \left[ \frac{-(1 + e^{2\rho\xi}) \pm \sqrt{2(e^{4\rho\xi} + 1)}}{e^{2\rho\xi} - 1} \right] \quad (18)$$

or

$$a^{f(\xi)} = \left[ \frac{-(1 + e^{2\rho\xi}) \pm \sqrt{e^{4\rho\xi} + 6e^{2\rho\xi} + 1}}{2e^{2\rho\xi}} \right] \quad (19)$$

**When**  $(\rho^2 = \eta\delta)$ .

$$a^{f(\xi)} = \left[ \frac{-\eta(\rho\xi + 2)}{\rho^2\xi} \right] \quad (20)$$

**When**  $(\rho = k, \eta = 2k, \delta = 0)$ .

$$a^{f(\xi)} = \left[ e^{k\xi} - 1 \right]. \quad (21)$$

**When**  $(\rho = \mathbf{k}, \delta = 2\mathbf{k}, \eta = \mathbf{0})$ .

$$a^{f(\xi)} = \left[ \frac{e^{k\xi}}{1 - e^{k\xi}} \right]. \quad (22)$$

**When**  $(2\rho = \eta + \delta)$ .

$$q(x, y, t) = -(c_1 + \eta + \delta) - 4\delta \left[ \frac{1 - \eta e^{\frac{1}{2}(\eta - \delta)(x + y - c_1 t)}}{1 - \delta e^{\frac{1}{2}(\eta - \delta)(x + y - c_1 t)}} \right], \quad (23)$$

or

$$q(x, y, t) = -(c_1 + \eta + \delta) - 4\delta \left[ \frac{1 + \eta e^{\frac{1}{2}(\eta - \delta)(x + y - c_1 t)}}{-1 - \delta e^{\frac{1}{2}(\eta - \delta)(x + y - c_1 t)}} \right]. \quad (24)$$

**When**  $(-2\rho = \eta + \delta)$ .

$$a^{f(\xi)} = \left[ \frac{\eta e^{1/2(\eta - \delta)\xi} + \eta}{\delta e^{1/2(\eta - \delta)\xi} + \delta} \right]. \quad (25)$$

**When**  $(\eta = \mathbf{0})$ .

$$a^{f(\xi)} = \left[ \frac{\rho e^{\rho\xi}}{1 + \frac{\delta}{2} e^{\rho\xi}} \right] \quad (26)$$

**When**  $(\rho = \eta = \delta \neq \mathbf{0})$ .

$$a^{f(\xi)} = \left[ \frac{-(\eta\xi + 2)}{\eta\xi} \right]. \quad (27)$$

**When**  $(\rho = \eta = \mathbf{0})$ .

$$a^{f(\xi)} = \left[ \frac{-2}{\delta\xi} \right]. \quad (28)$$

**When**  $(\beta = \mathbf{0}, \eta = \delta)$ .

$$a^{f(\xi)} = \left[ \tan\left(\frac{\eta\xi + C}{2}\right) \right]. \quad (29)$$

**When**  $(\delta = \mathbf{0})$ .

$$a^{f(\xi)} = \left[ e^{\beta\xi} - \frac{\eta}{2\rho} \right]. \quad (30)$$

where C is arbitrary constant.

**Step 5.** Implying these values and the solutions of Eq. (5) into Eq. (4), one obtains the exact solutions of Eq. (1).

### 3 Example

In this section, we employ Khater method to obtain travelling and solitary wave solutions of the (2+1)-dimensional mKdV-ZK equation [13–15] given by

$$q_t + \alpha q^2 q_x + (q_{xx} + q_{yy})_x = 0, \tag{31}$$

Using the transformation(2) in Eq. (31), we get

$$6q'' + \alpha q^3 - c_1 q = 0, \tag{32}$$

by using the principle of homogeneity, we have  $N = 1$  then Eq. (4) becomes

$$q(\xi) = a_0 + a_1 a^{g(\xi)}, \tag{33}$$

Inserting Eq. (33) and its derivative into Eq. (32) and then after rationalization, one obtain a system of algebraic equations on solving by symbolic computation

$$a^{0g} : 6a_1 \eta \rho + \alpha a_0^3 - ca_0 = 0, \tag{34}$$

$$a^{1g} : 6a_1(\rho^2 + 2\eta\rho) + 3\alpha a_0^2 a_1 - ca_1 = 0 \tag{35}$$

$$a^{2g} : 18a_1 \delta \rho + 3\alpha a_0 a_1^2 = 0 \tag{36}$$

$$a^{3g} : 12a_1 \delta^2 + \alpha a_1^3 = 0 \tag{37}$$

After solving these equations, we get

$$a_1 = 2\delta \sqrt{\frac{-3}{\alpha}} = 2\delta m, \quad a_0 = -\frac{-3\rho}{\alpha m} = \sqrt{\frac{c_1 - 12\eta\delta}{\alpha}}. \tag{38}$$

So that, the exact traveling wave solution of equation (31) be in the form:

$$q(x, y, t) = \sqrt{\frac{c_1 - 12\eta\delta}{\alpha}} + 2\delta m a^{g(\xi)}. \tag{39}$$

Thus, solitary wave solutions for different parametric conditions are When  $(\rho^2 - \eta\delta < 0 \ \& \ \delta \neq 0)$ .

$$q(x, y, t) = -\sqrt{\frac{c_1 - 12\eta\delta}{\alpha}} + 2\sqrt{\frac{3(\rho^2 - \eta\delta)}{\alpha}} \tan\left(\frac{\sqrt{-(\rho^2 - \eta\delta)}}{2}(x + y - c_1 t)\right), \tag{40}$$

or

$$q(x, y, t) = -\sqrt{\frac{c_1 - 12\eta\delta}{\alpha}} + 2\sqrt{\frac{3(\rho^2 - \eta\delta)}{\alpha}} \cot\left(\frac{\sqrt{-(\rho^2 - \eta\delta)}}{2}(x + y - c_1t)\right), \tag{41}$$

When  $(\rho^2 + \eta\delta > 0 \ \& \ \delta \neq 0)$ .

$$q(x, y, t) = -\sqrt{\frac{c_1 - 12\eta\delta}{\alpha}} + 2\sqrt{\frac{-3(\rho^2 - \eta\delta)}{\alpha}} \tan\left(\frac{\sqrt{(\rho^2 - \eta\delta)}}{2}(x + y - c_1t)\right), \tag{42}$$

or

$$q(x, y, t) = -\sqrt{\frac{c_1 - 12\eta\delta}{\alpha}} + 2\sqrt{\frac{-3(\rho^2 - \eta\delta)}{\alpha}} \cot\left(\frac{\sqrt{(\rho^2 - \eta\delta)}}{2}(x + y - c_1t)\right), \tag{43}$$

When  $(\rho^2 + \eta^2 > 0 \ \& \ \delta \neq 0 \ \& \ \delta = -\eta)$ .

$$q(x, y, t) = -\sqrt{\frac{c_1 - 12\eta\delta}{\alpha}} - 2\sqrt{\frac{-3(\rho^2 + \eta^2)}{\alpha}} \tan\left(\frac{\sqrt{(\rho^2 + \eta^2)}}{2}(x + y - c_1t)\right), \tag{44}$$

or

$$q(x, y, t) = -\sqrt{\frac{c_1 - 12\eta\delta}{\alpha}} - 2\sqrt{\frac{-3(\rho^2 + \eta^2)}{\alpha}} \cot\left(\frac{\sqrt{(\rho^2 + \eta^2)}}{2}(x + y - c_1t)\right), \tag{45}$$

When  $(\rho^2 + \eta^2 < 0 \ \& \ \delta \neq 0 \ \& \ \delta = -\eta)$ .

$$q(x, y, t) = -\sqrt{\frac{c_1 - 12\eta\delta}{\alpha}} - 2\sqrt{\frac{3(\rho^2 + \eta^2)}{\alpha}} \tan\left(\frac{\sqrt{-(\rho^2 + \eta^2)}}{2}(x + y - c_1t)\right), \tag{46}$$

or

$$q(x, y, t) = -\sqrt{\frac{c_1 - 12\eta\delta}{\alpha}} - 2\sqrt{\frac{3(\rho^2 + \eta^2)}{\alpha}} \cot\left(\frac{\sqrt{-(\rho^2 + \eta^2)}}{2}(x + y - c_1t)\right), \tag{47}$$

When  $(\rho^2 - \eta^2 < 0 \ \& \ \delta = \eta)$ .

$$q(x, y, t) = \sqrt{\frac{c_1 - 12\eta\delta}{\alpha}} + 2\sqrt{\frac{3(\rho^2 - \eta^2)}{\alpha}} \tan\left(\frac{\sqrt{-(\rho^2 - \eta^2)}}{2}(x + y - c_1t)\right), \tag{48}$$

or

$$q(x, y, t) = \sqrt{\frac{c_1 - 12\eta\delta}{\alpha}} + 2\sqrt{\frac{3(\rho^2 - \eta^2)}{\alpha}} \cot\left(\frac{\sqrt{-(\rho^2 - \eta^2)}}{2}(x + y - c_1t)\right), \tag{49}$$

When  $(\rho^2 - \eta^2 > 0 \ \& \ \delta = \eta)$ .

$$q(x, y, t) = \sqrt{\frac{c_1 - 12\eta\delta}{\alpha}} + 2\sqrt{\frac{-3(\rho^2 - \eta^2)}{\alpha}} \tanh\left(\frac{\sqrt{(\rho^2 - \eta^2)}}{2}(x + y - c_1t)\right), \quad (50)$$

or

$$q(x, y, t) = \sqrt{\frac{c_1 - 12\eta\delta}{\alpha}} + 2\sqrt{\frac{-3(\rho^2 - \eta^2)}{\alpha}} \coth\left(\frac{\sqrt{(\rho^2 - \eta^2)}}{2}(x + y - c_1t)\right), \quad (51)$$

When  $(\rho^2 = \eta\delta)$ .

$$q(x, y, t) = \sqrt{\frac{c_1 - 12\rho^2}{\alpha}} - \left[ \frac{2\sqrt{-3}(\rho(x + y - c_1t) + 2)}{\sqrt{\alpha}(x + y - c_1t)} \right] \quad (52)$$

When  $(\rho = k, \delta = 2k, \eta = 0)$ .

$$q(x, y, t) = \sqrt{\frac{c_1}{\alpha}} + 4k\sqrt{\frac{-3}{\alpha}} \left[ \frac{e^{k(x+y-c_1t)}}{1 - e^{k(x+y-c_1t)}} \right]. \quad (53)$$

When  $(2\rho = \eta + \delta)$ .

$$q(x, y, t) = \sqrt{\frac{c_1 - 12\eta\delta}{\alpha}} + 2\delta\sqrt{\frac{-3}{\alpha}} \left[ \frac{1 - \eta e^{\frac{1}{2}(\eta-\delta)(x+y-c_1t)}}{1 - \delta e^{\frac{1}{2}(\eta-\delta)(x+y-c_1t)}} \right], \quad (54)$$

or

$$q(x, y, t) = \sqrt{\frac{c_1 - 12\eta\delta}{\alpha}} + 2\delta\sqrt{\frac{-3}{\alpha}} \left[ \frac{1 + \eta e^{\frac{1}{2}(\eta-\delta)(x+y-c_1t)}}{-1 - \delta e^{\frac{1}{2}(\eta-\delta)(x+y-c_1t)}} \right]. \quad (55)$$

When  $(-2\rho = \eta + \delta)$ .

$$q(x, y, t) = \sqrt{\frac{c_1 - 12\eta\delta}{\alpha}} + 2\delta\sqrt{\frac{-3}{\alpha}} \left[ \frac{\eta + e^{\frac{1}{2}(\eta-\delta)(x+y-c_1t)}}{\delta + e^{\frac{1}{2}(\eta-\delta)(x+y-c_1t)}} \right], \quad (56)$$

When  $(\eta = 0)$

$$q(x, y, t) = \sqrt{\frac{c_1}{\alpha}} + 2\delta\sqrt{\frac{-3}{\alpha}} \left[ \frac{\rho e^{\rho(x+y-c_1t)}}{1 + \frac{\delta}{2}e^{\rho(x+y-c_1t)}} \right] \quad (57)$$

When  $(\rho = \eta = \delta \neq 0)$ .

$$q(x, y, z, t) = \sqrt{\frac{c_1 - 12\eta^2}{\alpha}} + 2\eta\sqrt{\frac{-3}{\alpha}} \left[ \frac{-(\eta(x + y - c_1t) + 2)}{\eta(x + y - c_1t)} \right]. \quad (58)$$

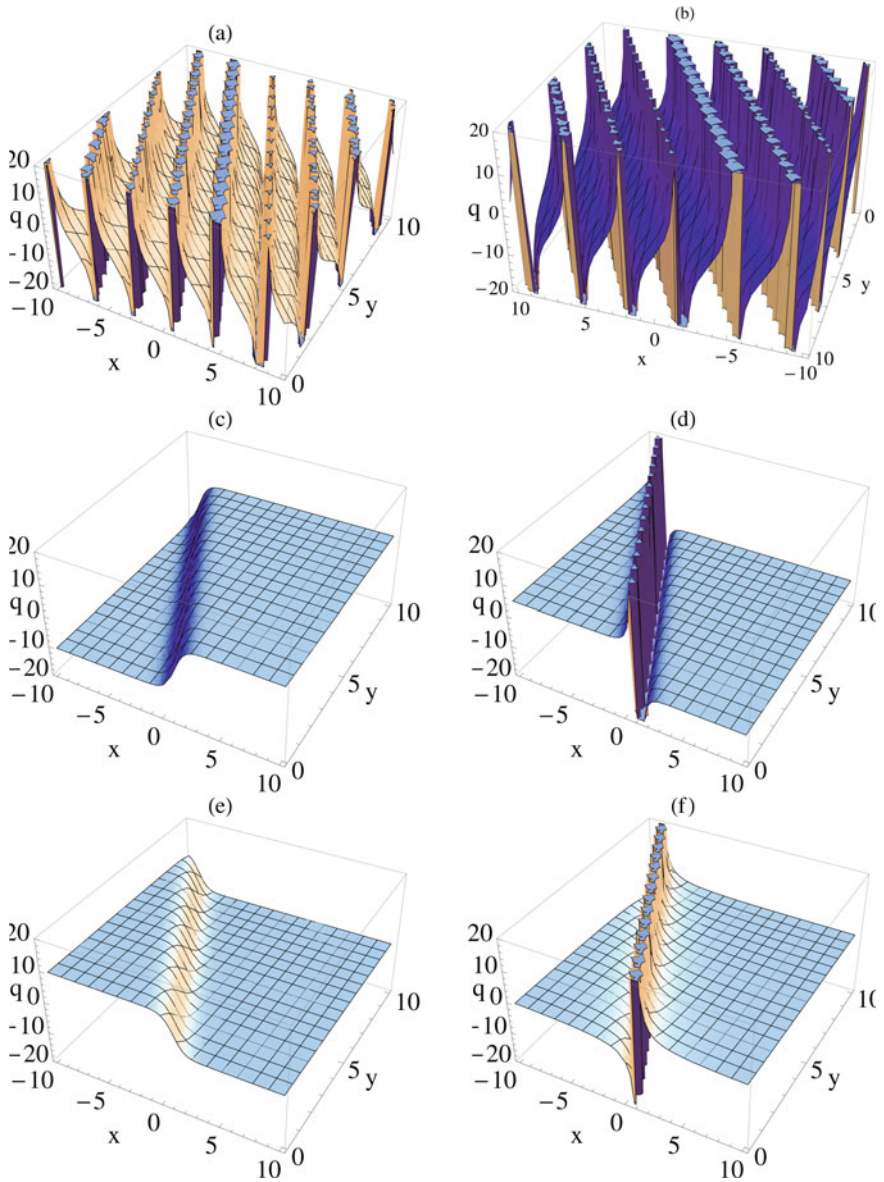


**Fig. 1** Solitary wave solution of Eqs. (41, 44–46, 50, 56) with  $\alpha = -1, \delta = \eta = t = c_1 = 1$  &  $\rho = 2$

When  $(\rho = \eta = 0)$ .

$$q(x, y, z, t) = -\frac{4\sqrt{-3}}{\sqrt{\alpha}(x + y - c_1t)}. \quad (59)$$

When  $(\rho = 0, \eta = \delta)$ .

$$q(x, y, t) = 2\eta\sqrt{\frac{-3}{\alpha}}\tan\left(\frac{\eta(x + y + z - c_1t) + C}{2}\right). \quad (60)$$

**Graphical representation of solutions:** We have obtained the travelling and solitary wave solutions of mKdV-ZK equation for various cases in terms of unknown parameters. The solitary wave solutions can be derived from the travelling wave solutions for the specific value of parameters. Some plots of solitary waves for suitable values of unknown parameters are shown in Fig. 1. For  $\alpha = -1, \delta = \eta = t = c_1 = 1$  &  $\rho = 2$ . Equations (41), (44), (45), (46), (50) and (56) represent the periodic waves, Kink wave, dark and bright solitons, soliton-like travelling wave and bright solitons etc.

## 4 Conclusions

In this paper, we have obtained the solitary and travelling wave solutions of the (2+1)-dimensional mKdV-ZK equation by the Khater method using symbolic computation. Various higher-order polynomials arising in mathematical physics, high energy physics, fluid dynamics, geochemistry and chemical kinematics can be solved by this method. It is seen that the Khater method provides an effective and powerful technique for solving various nonlinear evaluation equations used in the area of science and engineering. The solitary wave solutions computed in this study are hyperbolic, trigonometric and exponential forms, which are discussed graphically as shown in Fig. 1. The computed solutions play a significant role in various disciplines of sciences and engineering and are useful for the physical interpretation of a nonlinear system also [13].

## References

1. Wazwaz, A.-M.: The tanh method for traveling wave solutions of nonlinear equations. *Appl. Math. Comput.* **154**(3), 713–723 (2004)
2. Xu, G.: An elliptic equation method and its applications in nonlinear evolution equations. *Chaos, Solitons Fractals* **29**(4), 942–947 (2006)
3. Seadawy, A.R.: Travelling-wave solutions of a weakly nonlinear two-dimensional higher-order Kadomtsev-Petviashvili dynamical equation for dispersive shallow-water waves. *Eur. Phys. J. Plus* **29**, 132 (2017)
4. Seadawy, A.R., Lu, D.: Bright and dark solitary wave soliton solutions for the generalized higher 4 order nonlinear Schrödinger equation and its stability. *Results Phys.* **6**(590), 3 (2016)



5. Kim, H., Sakthivel, R.: New exact traveling wave solutions of some nonlinear higher dimensional physical models. *Rep. Math. Phys.* **70**(1), 39–50 (2012)
6. Selima, E.S., Seadawy, A.R., Yao, X.: The nonlinear dispersive Davey-Stewartson system for surface waves propagation in shallow water and its stability. *Eur. Phys. J. Plus* **131**(425), (2016)
7. Islam, M.T., Akbar, M.A., Azad, M., et al.: A Rational (G/G)-expansion method and its application to the modified KdV-Burgers equation and the (2+1)-dimensional Boussinesq equation. *Nonlinear Study* **6**(4), 1–11 (2015)
8. Khater, M.M., Seadawy, A.R.: D. Lu Elliptic and solitary wave solutions for Bogoyavlenskii equations system, couple Boiti-Leon-Pempinelli equations system and Time-fractional Cahn-Allen equation, *Results in physics* **7**, 2325–2333 (2017)
9. Alam, M.N., Akbar, M.A., Hoque, M.F.: Exact travelling wave solutions of the (3+1)-dimensional mKdV-ZK equation and the (1+1)-dimensional compound KdVB equation using the new approach of generalized (G/GG/G)-expansion method. *Pramana* **83**(3), 317–329 (2014)
10. Biswas, A., Triki, H., Hayat, T., Aldossary, O.M.: 1-Soliton solution of the generalized Burgers equation with generalized evolution. *Appl. Math. Comput.* **217**(24), 10289–10294 (2011)
11. Kuo, C.-K.: The new exact solitary and multi-soliton solutions for the (2+1)-dimensional Zakharov-Kuznetsov equation. *Comput. Math. Appl.* **75**(8), 2851–2857 (2018)
12. Bekir, A., Cevikel, A.C., Güner, Ö., San, S.: Bright and dark soliton solutions of the (2 + 1)-dimensional evolution equations. *Math. Model. Anal.* **19**(1), 118–126 (2014)
13. Alam, M.N., Hafez, M., Akbar, M.A., et al.: Exact traveling wave solutions to the (3 + 1)-dimensional mKdV-ZK and the (2+ 1)-dimensional Burgers equations via exp (-  $\Phi(\eta)$ )-expansion method. *Alex. Eng. J.* **54**(3), 635–644 (2015)
14. Aslan, İ: Generalized solitary and periodic wave solutions to a (2 + 1)-dimensional Zakharov-Kuznetsov equation. *Appl. Math. Comput.* **217**(4), 1421–1429 (2010)
15. Wang, G., Kara, A.: A (2+ 1)-dimensional KdV equation and mKdV equation: symmetries, group invariant solutions and conservation laws. *Phys. Lett. A* **383**(8), 728–731 (2019)

# Cosmological Models for Bianchi Type-I Space-Time in Lyra Geometry



Pratik V. Lapse and Binaya K. Bishi

**Abstract** The main purpose of this manuscript is to investigate the Bianchi type-I dark energy cosmological models in the framework of Lyra geometry. The modified Einstein's field equations is derived for Lyra geometry and obtained the exact solutions. In order to obtained the exact solutions volumetric expansion law is used. As per the Exponential and Power-law expansion, we have discussed the two cosmological models. Several physical parameters are obtained for both the models and discuss its physical importance following the observational data.

**Keywords** Bianchi type-I · Cosmological constant · Lyra geometry

## 1 Introduction

The concept of dark energy should be explored for the better understanding of the universe. The cosmologist, scientist and astronomers believed that dark energy is a kind of a repulsive force which acts as an antigravity and responsible for accelerated expansion of the universe, is termed as dark energy. The experiments, particularly WMAP (Wilkinson Microwave Anisotropic Probe) and satellite experiment [1] concludes that, our universe consists of three major components namely dark energy nearly 73%, dark matter 23% and usual matter is about 4% [1–3]. The supernova project and HIGH-Z Supernova team reveals that the universe is expanding with acceleration. For closed universe, Hubble parameter  $H$ , the matter energy density parameter  $\Omega_M$  and the dark energy density parameter  $\Omega_\Lambda$ , predicted by Tegmark [4] are near about  $H \approx 0.32$ ,  $\Omega_m \approx 0.23$  and  $\Omega_\Lambda \approx 1.17$ . For flat cosmological model,

---

P. V. Lapse (✉) · B. K. Bishi

Department of Mathematics, Lovely Professional University, Jalandhar, Phagwara 144401, Panjab, India

e-mail: [pratiklapse124@gmail.com](mailto:pratiklapse124@gmail.com)

B. K. Bishi

Department of Mathematical Sciences, University of Zululand, Kwa-Dlangezwa 3886, South Africa

the cosmological observation [5, 6] suggested the existence of a positive cosmological term- $\Lambda$  with magnitude  $\Lambda \approx 10^{-123}$  and with  $\Omega_m = 0.3, \Omega_\Lambda = 0.7$  in the accelerating universe.

The dark energy is characterised through the equation of state (EoS) parameter  $p = \omega\rho$  in the universe. Here  $\omega$  may be a constant or a function of cosmic time. The cosmic time dependent  $\omega(t)$  is revive from experimental data. The analysis is performed on the experimental data in ordered to determine  $\omega(t)$  [11, 12]. This parameter  $\omega(t)$  have been calculated with some reasoning leading to simple parameterization of the dependence character of  $\omega$  by many authors [13–16]. In view of galaxy clustering statistics [4] and SNe Ia data with CMBR,  $\omega$  is approximated as  $\omega \approx -0.977$ . The above discussed results are consistent with both time dependent and time independent equation of state parameter  $\omega$ . The different values of  $\omega$  corresponds to the different type of universe. The universe is classified with the different value of  $\omega$  as [17, 18]

$$\omega = \begin{cases} -1 : & \text{Vacuum fluid universe} \\ 0 : & \text{Dust fluid univesrse} \\ \frac{1}{3} : & \text{Radiation fluid universe} \\ 1 : & \text{Stiff fluid universe} \end{cases}$$

The variable  $\omega$  as  $\omega(t)$  or  $\omega(z)$ ,  $z$  denotes redshift is investigated by Jimenez [19] and Das et al. [20]. The quintessence models,  $\omega > -1$  and phantom model,  $\omega < -1$  give rise to dependent  $\omega(t)$  [21–24]. Several forms of  $\omega(t)$  can be found in the literature, which are involved in investigating dark energy [25–28].

After the formulation of General Relativity, Einstein devoted his entire life in the search of the theory that takes into account both gravitation and electromagnetism. He was not happy with the field equations  $R_{ij} - \frac{1}{2}Rg_{ij} = -kT_{ij}$  of General Relativity. Since the right hand side is not geometrical in nature although the left hand side is. Further, the solution of the field equations are not free from singularities. A total field theory should not give rise to singularities. There have been various attempts to unify the gravitation and electromagnetism either by considering non-Riemannian geometry of four dimensions or by considering Riemannian spaces of higher dimensions.

Lyra [29] adduced Riemannian geometry by incorporating a gauge function in to the manifold, which is in fact structure less. In such case the geometry naturally gives rise to cosmological constant. This bears the remarkable resemblance to Wely’s geometry. The Einstein’s field equations (EFEs) based on Lyra’s manifold in normal gauge is expressed as (Take  $c = 1$  and  $8\pi G = 1$ )

$$R_{ij} - \frac{1}{2}Rg_{ij} + \frac{3}{2}\phi_i\phi_k - \frac{3}{4}g_{ik}\phi_m\phi^m = -kT_{ij}. \tag{1}$$

In which  $\phi_i$  is the displacement vector defined through the gauge function  $\beta$ . The displacement vector field is considered as

$$\phi_i = (0, 0, 0, \beta(t)). \quad (2)$$

In this paper, we have studied the exponential-law expansion model and power-law expansion model in Bianchi type-I universe in view of Lyra geometry. We distributed our work in section wise like in Sect. 2. Bianchi type-I metric is presented and field equations for Lyra's manifold are derived. In Sect. 3 the solution of the Bianchi type-I cosmological model is constructed under exponential and power-law expansion. Conclusive remarks of the work is described in Sect. 4.

## 2 Field Equations for Bianchi Type-I Line Element

let us consider the Bianchi type-I line element of the form

$$ds^2 = -dt^2 + A^2 dx^2 + B^2 dy^2 + c^2 dz^2. \quad (3)$$

Here  $A$ ,  $B$  and  $C$  are function of  $t$  only. The energy momentum tensor  $T_i^j$  is considered as

$$T_j^i = (\rho + p)v_i v^j + p g_i^j \quad (4)$$

Here  $\rho$  and  $p$  represents the proper energy density and pressure respectively. The quantity  $\theta$  is the scalar of expansion which is given by,

$$\theta = v_{|i}^i \quad (5)$$

and  $v^j$  satisfies the relation

$$g_{ij} v^i v^j = -1. \quad (6)$$

we assume that coordinates to be co-moving, so that

$$v^1 = v^2 = v^3 = 0, v^4 = 1. \quad (7)$$

Equation (4) yield

$$\begin{aligned} T_1^1 &= p_x = \omega_x \rho = \omega \rho, \\ T_2^2 &= p_y = \omega_y \rho = (\omega + \gamma) \rho, \\ T_3^3 &= p_z = \omega_z \rho = (\omega + \delta) \rho, \\ T_4^4 &= p_x = -\rho. \end{aligned} \quad (8)$$

where  $p_x$ ,  $p_y$ ,  $p_z$  and  $\omega_x$ ,  $\omega_y$ ,  $\omega_z$  indicates the directional pressure and equation of state (EoS) parameters along  $x$ ,  $y$  and  $z$  axes respectively. The EoS parameter of the fluid, which is deviation free is denoted by  $\omega$ . We have parameterized the deviation

from isotropy by setting  $\omega_x = \omega$  and then introducing skewness parameter  $\gamma$  and  $\delta$  that are the deviation from  $\omega$  along  $y$  and  $z$  axes, which are  $\omega_y = (\omega + \gamma)$  and  $\omega_z = (\omega + \delta)$  respectively.

The field Eq. (1) in Lyra's geometry, for the metric (2), using Eqs. (2) and (4) takes the form

$$\frac{B_{44}}{B} + \frac{C_{44}}{C} + \frac{B_4 C_4}{BC} + \frac{3}{4} \beta^2 = -\omega \rho \tag{9}$$

$$\frac{A_{44}}{A} + \frac{B_{44}}{B} + \frac{A_4 B_4}{AB} + \frac{3}{4} \beta^2 = -(\omega + \gamma) \rho \tag{10}$$

$$\frac{A_{44}}{A} + \frac{C_{44}}{C} + \frac{A_4 C_4}{Ac} + \frac{3}{4} \beta^2 = -(\omega + \delta) \rho \tag{11}$$

$$\frac{A_4 B_4}{AB} + \frac{B_4 C_4}{BC} + \frac{A_4 C_4}{AC} - \frac{3}{4} \beta^2 = \rho \tag{12}$$

where  $A_4 = \frac{dA}{dt}$ ,  $A_{44} = \frac{d^2 A}{dt^2}$ .

The energy conservation  $T_{i,j}^j = 0$  leads to

$$\frac{3}{2} \beta \beta_4 + \frac{3}{2} \beta^2 \left( \frac{A_4}{A} + \frac{B_4}{B} + \frac{C_4}{C} \right) = 0 \tag{13}$$

The spatial volume  $V$  for model and the average scale factor are defined as

$$V = a^3 = ABC \tag{14}$$

In terms of scale factor or metric potentials, the Hubble parameter may be define as

$$H = \frac{a_4}{a} = \frac{1}{3} \left( \frac{A_4}{A} + \frac{B_4}{B} + \frac{C_4}{C} \right) \tag{15}$$

The deceleration parameter,  $q$  is expressed as

$$q = -\frac{aa_{44}}{a_4^2} \tag{16}$$

The following physical parameters are defined as

$$\text{Scalar expansion} = \theta = \frac{A_4}{A} + \frac{B_4}{B} + \frac{C_4}{C} \tag{17}$$

$$\text{Shear scalar} = \sigma^2 = \frac{1}{2} \sum_{i=1}^3 \left( H_i^2 - \frac{1}{3} \theta^2 \right) \tag{18}$$

$$\text{Average anisotropy parameter} = A_m = \frac{1}{3} \sum_{i=1}^3 \left( \frac{\Delta H_i}{H} \right)^2 \tag{19}$$

where  $\Delta H_i = H_i - H$ ,  $i = 1, 2, 3$ .  $H_i$  represents the directional Hubble parameter  $H$  along  $x$ ,  $y$  and  $z$  axes respectively.

### 3 Solutions of Field Equation

The field Eqs. (9) to (12) are the four differential equations with eight unknown parameters  $A, B, C, \beta, \rho, \omega, \delta$  and  $\gamma$ . To make the system complete, we need the additional four conditions. Special law of variation for generalized Hubble’s parameter is used as the first condition, which provides a constant value of deceleration parameter. The mean Hubble parameter  $H$  and the average scale factor are related through the expression as

$$H = la^{-n} \tag{20}$$

From which we write (using Eq. (15))

$$a_4 = la^{-n+1} \tag{21}$$

$$a_{44} = -l^2(n - 1)a^{-2n+1} \tag{22}$$

Using Eqs. (21) and (22) in the Eq. (16) we have

$$q = n - 1 \tag{23}$$

The inflation of a model is determined by the sign of  $q$ .  $q$  has positive sign for  $n > 1$  corresponding to “standard” decelerating model whereas it has negative sign for  $0 \leq n < 1$  indicating accelerating model [30]. Integration of Eq. (21), leads to

$$a = \begin{cases} (nlt + \alpha_1)^{\frac{1}{n}}, & \text{for } n \neq 0 \\ \alpha_2 e^{lt}, & \text{for } n = 0 \end{cases} \tag{24}$$

where  $\alpha_1$  and  $\alpha_2$  are constants and which come out from the integration. Thus, the law (20) generate volumetric expansion in the form of power-law (PL) and exponential-law (EL)(One can see from Eq. (24)). We assume the second condition as  $\sigma_1^1 \propto \theta$ , which leads

$$A = (BC)^m \tag{25}$$

where  $m > 0$ . As a third assumption, we take  $\gamma = \delta$  that means the deviation from  $\omega$  along  $y$  and  $z$  axes are equal. From the differential Eqs. (10) and (11), we deduced

$$\frac{B}{C} = \alpha_3 \exp \left[ \alpha_4 \int (ABC)^{-1} dt \right] \tag{26}$$

where  $\alpha_3$  and  $\alpha_4$  are integration constants. In view of the parameter  $n$ , for  $n = 0$  and  $n > 0$  corresponds to the exponential-law (EL) and power-law (PL) respectively.

### 3.1 Model in Exponential-Law expansion

In this case, lengthy but straight forward calculation leads to the metric potentials in the following forms:

$$\begin{aligned} A(t) &= \alpha_2^{\frac{3m}{m+1}} \exp \left( \frac{3ml}{m+1} t \right) \\ B(t) &= \sqrt{\alpha_3 \alpha_2^{\frac{3}{2(m+1)}}} \exp \left[ \frac{3lt}{2(m+1)} - \frac{\alpha_4}{6l\alpha_2^3} e^{-3lt} \right] \\ C(t) &= \frac{\alpha_2^{\frac{3}{2(m+1)}}}{\sqrt{\alpha_3}} \exp \left[ \frac{3lt}{2(m+1)} + \frac{\alpha_4}{6l\alpha_2^3} e^{-3lt} \right] \end{aligned} \tag{27}$$

Thus in EL expansion (24), the required metric is

$$\begin{aligned} ds^2 &= -dt^2 + \alpha_2^{\frac{6m}{m+1}} \exp \left( \frac{6ml}{m+1} \right) dx^2 + \alpha_3 \alpha_2^{\frac{3}{(m+1)}} \exp \left[ \frac{3lt}{(m+1)} - \frac{\alpha_4}{3l\alpha_2^3} e^{-3lt} \right] dy^2 \\ &+ \frac{\alpha_2^{\frac{3}{(m+1)}}}{\alpha_3} \exp \left( \frac{3lt}{m+1} + \frac{\alpha_4}{3l\alpha_2^3} e^{-3lt} \right) dz^2 \end{aligned} \tag{28}$$

At early time, the scale factor is constant but it increases with time and reaches infinity at the late epoch of time. It shows that at first, the universe starts with a constant volume and expands exponentially to infinity. Let us calculate all physical quantities  $\beta(t)$ ,  $H_1$ ,  $H_2$ ,  $H_3$ ,  $\theta$ ,  $\sigma$ ,  $A_m$ ,  $\rho$ ,  $\omega$ ,  $\gamma$  and  $\delta$  for exponential law. When Eq. (15) is applied to Eq. (13), the gauge function  $\beta(t)$  takes the form

$$\beta(t) = \frac{N}{\alpha_2^3 e^{3lt}}, \tag{29}$$

where  $N$  is constant of integration. At initial stage of time, gauge function  $\beta(t)$  return constant value and it is decreasing exponentially with increasing in time at later time. So that gauge function  $\beta(t)$  of the model is goes over to the model of general relativity (Pradhan et al. [35]). The directional Hubble parameter  $H$  along  $x$ ,  $y$  and  $z$  axes are given by

$$H_1 = \frac{A_4}{A} = \frac{3ml}{m + 1} \tag{30}$$

$$H_2 = \frac{B_4}{B} = \frac{3l}{2(m + 1)} + \frac{\alpha_4}{2\alpha_2^3} e^{-3lt} = \frac{3l}{2(m + 1)} + \frac{\alpha_4}{2} \left( \frac{\beta}{N} \right) \tag{31}$$

$$H_3 = \frac{C_4}{C} = \frac{3l}{2(m + 1)} - \frac{\alpha_4}{2\alpha_2^3} e^{-3lt} = \frac{3l}{2(m + 1)} - \frac{\alpha_4}{2} \left( \frac{\beta}{N} \right) \tag{32}$$

It is noticed from the above equations that,  $H_i$  ( $i = 2, 3$ ) depends upon gauge function  $\beta(t)$ . When  $\beta(t) = 0$ , this shows the nature of directional Hubble parameter and they are constant at early stage as well as lateral stage of time  $t$ . The following physical parameters for the model (28) are deduced as

$$\theta = 3H = 3l \tag{33}$$

$$\sigma^2 = \frac{3l^2(2m - 1)^2}{4(m + 1)^2} + \frac{\alpha_4^2}{4\alpha_2^6} e^{-6lt} = \frac{3l^2(2m - 1)^2}{4(m + 1)^2} + \frac{\alpha_4^2}{4N^2} \beta^2 \tag{34}$$

$$A_m = \frac{(2m - 1)^2}{2(m + 1)^2} + \frac{\alpha_4^2}{6l^2\alpha_2^6} e^{-6lt} = \frac{(2m - 1)^2}{2(m + 1)^2} + \frac{\alpha_4^2}{6l^2N^2} \beta^2 \tag{35}$$

The expansion scalar  $\theta$  exhibit constant value for whole range of time  $t$ . This show uniform exponential expansion of the model. The shear of the model is depending upon gauge function  $\beta(t)$ . Initially it has constant value and goes on decreasing with increasing time  $t$ . When  $t \rightarrow \infty$ ,  $\sigma^2 \rightarrow \frac{(2m-1)^2}{2(m+1)^2}$  and  $A_m \rightarrow \frac{(2m-1)^2}{2(m+1)^2}$ . Further, it is noticed that at late time shear and average anisotropy parameter vanishes for  $m = \frac{1}{2}$ . Using the Eqs. (27) and (29), in differential Eq. (12), we obtained  $\rho$  as

$$\begin{aligned} \rho &= \frac{9l^2(4m + 1)}{4(m + 1)^2} - \frac{3N^2}{4\alpha_4^4} e^{-4lt} - \frac{\alpha_4^2}{4\alpha_2^6} e^{-6lt} \\ &= \frac{9l^2(4m + 1)}{4(m + 1)^2} - \frac{3}{4} \beta^2 - \frac{\alpha_4^2}{4N^2} \beta^2 \end{aligned} \tag{36}$$

The energy density depends upon the gauge function  $\beta(t)$ . At initial time, the energy density has a constant value  $9(4m + 1)\alpha_2^6 l^2 - (m + 1)^2(\alpha_4^2 + 3\alpha_2^2 N^2)$ . The positivity of energy density leads to the constraint on  $m$  such that  $\frac{4m+1}{(m+1)^2} > \frac{(\alpha_4^2 + 3\alpha_2^2 N^2)}{9\alpha_2^6 l^2}$ . When  $t \rightarrow \infty$ , the energy density  $\rho \rightarrow \frac{9l^2(4m+1)}{4(m+1)^2}$ . With the help of Eqs. (9) and (12), the EoS parameter  $\omega$  has been calculated as



$$\begin{aligned} \omega &= \frac{(27l^2\alpha_2^6e^{6lt} + \alpha_4^2(m+1)^2)e^{4lt} + 3N^2\alpha_2^2e^{6lt}(m+1)^2}{(-9\alpha_2^6(4m+1)l^2e^{6lt} + \alpha_4^2(m+1)^2)e^{4lt} + 3N^2\alpha_2^2e^{6lt}(m+1)^2} \\ &= \frac{-27N^2l^2 - 3N^3(m+1)^2\beta^2 - \alpha_4^2(m+1)^2\beta^2}{9(4m+1)l^2N^2 - 3N^3(m+1)^2\beta^2 - \alpha_4^2(m+1)^2\beta^2} \end{aligned} \tag{37}$$

In this exponential-law of expansion, the EoS parameter  $\omega$  depends upon gauge function  $\beta(t)$ . In early time of the universe, the  $\omega$  takes a constant value equal to  $\frac{27\alpha_2^6l^2+(m+1)^2(3N^2\alpha_2^2+\alpha_4^2)}{(m+1)^2(3N^2\alpha_2^2+\alpha_4^2)-9(4m+1)\alpha_2^6l^2}$ . In late time, it approaches  $-\frac{3}{4m+1}$ . We write the values of the skewness parameter  $\gamma$  and  $\delta$ , using the Eqs. (9), (10), (29) and (36) as follows:

$$\begin{aligned} \gamma = \delta &= \frac{18(m+1)e^{4lt}(2m-1)e^{6lt}\alpha_2^6l^2}{3\alpha_2^2(-3\alpha_4^2l^2(4m+1)e^{4lt} + N^2(m+1)^2)e^{6lt} + (m+1)^2e^{4lt}\alpha_4^2} \\ &= \frac{18(m+1)N^2(2m-1)l^2}{\alpha_4^2(m+1)^2\beta^2 + 3N^2(m+1)^2\beta^2 - 9(4m+1)l^2N^2} \end{aligned} \tag{38}$$

For the value of time  $t = \tau_0$  given by

$$\tau_0 = \frac{1}{2l} \log \left[ \frac{2\alpha_4^2(m+1)^2\Sigma_0}{\alpha_2^2(\Sigma_0^2 - 2N^2(m+1)^2\Sigma_0 + 4N^4(m+1)^4)} \right], \tag{39}$$

which leads to equation of state parameter  $\omega = 0$ . So that dusty universe at time  $t = \tau_0$  given by Eq. (39). Again, it is to be noted that when time  $t$  lies in open interval  $\tau_1 < t < \tau_2$  with

$$\tau_1 = \frac{1}{2l} \ln \left[ \frac{178(m+1)^2\alpha_4^2\Sigma_1}{\alpha_2^2(\Sigma_1^2 - 178(m+1)^2N^2\Sigma_1 + 31684(m+1)^4N^4)} \right] \tag{40}$$

$$\tau_2 = \frac{1}{2l} \log \left[ \frac{6(m+1)^2\alpha_4^2\Sigma_2}{\alpha_2^2(\Sigma_2^2 + 6N^2(m+1)^2\Sigma_2 + 36(m+1)^4N^4)} \right] \tag{41}$$

the equation of state parameter  $\omega$  lies in the range  $-1.67 < \omega < -0.62$ , which consistent and in good agreement with the limiting observational results [31]. Where

$$\begin{aligned} \Sigma_0 &= \sqrt[3]{-8 \left( -\frac{3\sqrt{3}\alpha_4^2l}{2} \sqrt{4N^6(m+1)^2 + 27\alpha_4^4l^2} + N^6(m+1)^2 + \frac{27\alpha_4^4l^2}{2} \right) (m+1)^4} \\ \Sigma_1 &= \sqrt[3]{-\left\{ -\frac{2l\alpha_4^2}{89} \sqrt{-\left( 44589(m+1)^2N^6 - 251001\alpha_4^4l^2 \left( m - \frac{133}{668} \right) \right) \left( m - \frac{133}{668} \right)} \right.} \\ &\quad \left. - \frac{1002\alpha_4^4l^2}{89} \left( m - \frac{133}{668} \right) + (m+1)^2N^6 \right\} 5639752(m+1)^4} \end{aligned}$$

$$\Sigma_2 = \sqrt[3]{\begin{aligned} & -216(m+1)^4 \left\{ -\frac{2\alpha_4^2 l}{3} \sqrt{-\left(31(m+1)^2 N^6 - \frac{961 \alpha_4^4 l^2}{9} \left(m - \frac{119}{124}\right)\right) \left(m - \frac{119}{124}\right)} \right. \\ & \left. + N^6 m^2 + \left(2N^6 - \frac{62 \alpha_4^4 l^2}{9}\right) m + N^6 + \frac{119 \alpha_4^4 l^2}{18} \right\} \end{aligned}}$$

Further for the value of time  $t = \tau$ , given by

$$\tau = \frac{1}{2l} \ln \left[ \frac{2\alpha_4^2(m+1)^2 \Sigma}{\alpha_2^2(\Sigma^2 - 2N^2(m+1)^2 \Sigma + 4N^4(m+1)^4)} \right] \tag{42}$$

where

$$\Sigma = \sqrt[3]{\begin{aligned} & -8(m+1)^4 \left\{ -\frac{3\alpha_4^2 l}{2} \sqrt{(9(2m-1)\alpha_4^4 l^2 - 4N^6(m+1)^2)(2m-1)} \right. \\ & \left. + N^6(m+1)^2 - 9l^2 \left(m - \frac{1}{2}\right) \alpha_4^4 \right\} \end{aligned}}$$

The values of  $\omega$  comes out to be  $-1$ . For flat model, the matter energy density  $\Omega_M$  and dark energy  $\Omega_\Lambda$ , satisfies

$$\Omega_M + \Omega_\Lambda = 1 \tag{43}$$

where

$$\Omega_M = \frac{\rho}{3H^2} \quad \text{and} \quad \Omega_\Lambda = \frac{\Lambda}{3H^2} \tag{44}$$

Thus, Eqs. (43) and (44) gives

$$\rho + \Lambda = 3H^2$$

and then using Eqs. (33) and (36), we write the expressions of  $\Lambda$  as

$$\begin{aligned} \Lambda &= 3l^2 + \frac{3N^2}{4\alpha_4^4} e^{-4lt} + \frac{\alpha_4^2}{4\alpha_2^6} e^{-6lt} - \frac{9l^2(4m+1)}{4(m+1)^2} \\ &= 3l^2 + \frac{3}{4}\beta^2 + \frac{\alpha_4^2}{4N^2}\beta^2 - \frac{9l^2(4m+1)}{4(m+1)^2} \end{aligned} \tag{45}$$

From Eq. (45), one can noticed that cosmological constant  $\Lambda$  takes a positive constant value  $\frac{3l^2(2m-1)^2\alpha_2^6+(m+1)^2(3N^2\alpha_4^2+\alpha_4^2)}{4\alpha_2^6(m+1)^2}$  at early stage of the universe and approaches to a positive value  $3l^2 \left[ 1 - \frac{3(4m+1)}{4(m+1)^2} \right]$  at late time for all values of  $m$  and  $l$ . From Eqs. (33), (36) and (45), we have

$$\begin{aligned} \Omega_M &= \frac{3(4m + 1)}{4(m + 1)^2} - \frac{N^2}{4l^2\alpha_2^4}e^{-4lt} - \frac{\alpha_4^2}{12l^2\alpha_2^6}e^{-6lt} \\ &= \frac{3(4m + 1)}{4(m + 1)^2} - \frac{1}{4l^2}\beta^2 - \frac{\alpha_4^2}{12l^2N^2}\beta^2 \end{aligned} \tag{46}$$

$$\begin{aligned} \Omega_\Lambda &= \frac{N^2}{4l^2\alpha_2^4}e^{-4lt} + \frac{\alpha_4^2}{12l^2\alpha_2^6}e^{-6lt} - \frac{3(4m + 1)}{4(m + 1)^2} + 1 \\ &= \frac{1}{4l^2}\beta^2 + \frac{\alpha_4^2}{12l^2N^2}\beta^2 - \frac{3(4m + 1)}{4(m + 1)^2} + 1 \end{aligned} \tag{47}$$

From Eq. (46), we have observed that the matter energy density  $\Omega_m$  takes the value  $\frac{3(4m+1)}{4(m+1)^2} - \left[ \frac{N^2}{4l^2\alpha_2^4} + \frac{\alpha_4^2}{12l^2\alpha_2^6} \right]$  at initial time. At late time,  $\Omega_m$  is positive valued with the value  $\frac{3(4m+1)}{4(m+1)^2}$ . Further Eq. (47) indicates that, the dark energy  $\Omega_\Lambda$  is positive valued at initial and late time for all the values of parameters involved in the expression.  $\Omega_\Lambda$  is a decreasing function of cosmic time and approaches to  $1 - \frac{3(4m+1)}{4(m+1)^2}$  when  $t \rightarrow \infty$ .

### 3.2 Model in Power-Law Expansion

We solved the differential Eqs. (9), (10), by using the power-law expansion ( $n \neq 0$ ) (24) and Eqs. (25) and (26), we arrived at

$$\begin{aligned} A(t) &= (nlt + \alpha_1)^{\frac{3m}{n(m+1)}} \\ B(t) &= \sqrt{\alpha_3}(nlt + \alpha_1)^{\frac{3}{2n(m+1)}} \exp \left[ \frac{\alpha_4}{2l(n-3)}(nlt + \alpha_1)^{\frac{n-3}{n}} \right] \\ C(t) &= \frac{1}{\sqrt{\alpha_3}}(nlt + \alpha_1)^{\frac{3}{2n(n-3)}} \exp \left[ -\frac{\alpha_4}{2l(m+1)}(nlt + \alpha_1)^{\frac{n-3}{n}} \right] \end{aligned} \tag{48}$$

Thus the metric (3) reduced to (*for*  $n \neq 0$ ), for power law expansion

$$\begin{aligned} ds^2 &= -dt^2 + (nlt + \alpha_1)^{\frac{6m}{n(m+1)}} dx^2 + \alpha_3(nlt + \alpha_1)^{\frac{3}{n(m+1)}} \exp \left[ \frac{\alpha_4}{2l(n-3)}(nlt + \alpha_1)^{\frac{n-3}{n}} \right] dy^2 \\ &+ \frac{1}{\alpha_3}(nlt + \alpha_1)^{\frac{3}{n(m+1)}} \exp \left[ -\frac{\alpha_4}{2l(n-3)}(nlt + \alpha_1)^{\frac{n-3}{n}} \right] dz^2 \end{aligned} \tag{49}$$

At early time, the scale factor is constant but it increases with time and reaches infinity at the late epoch of time. It shows that at first, the universe starts with a constant volume and expands rapidly to infinity. Let us calculate all physical quantities  $\beta(t)$ ,  $H_1$ ,  $H_2$ ,  $H_3$ ,  $\theta$ ,  $\sigma$ ,  $A_m$ ,  $\rho$ ,  $\omega$ ,  $\gamma$  and  $\delta$  for power law. When Eq. (15) is applied to Eq. (13), the gauge function  $\beta(t)$  takes the form for  $n \neq 0$  as,

$$\beta(t) = N(nlt + \alpha_1)^{-\frac{3}{n}} \tag{50}$$

where  $N$  is constant of integration. At initial stage of time, gauge function  $\beta(t)$  return constant value and it is decreasing with evolution of time. The directional Hubble parameters  $H_i$  along  $x, y$  and  $z$  axes are given by

$$H_1 = \frac{A_4}{A} = \frac{3ml}{m + 1} \frac{1}{(nlt + \alpha_1)} \tag{51}$$

$$H_2 = \frac{B_4}{B} = \frac{1}{2} \left[ \frac{3l}{(1 + m)(\alpha_1 + nlt)} + \alpha_4(\alpha_1 + nlt)^{-\frac{3}{n}} \right] \tag{52}$$

$$H_3 = \frac{C_4}{C} = \frac{1}{2} \left[ \frac{3l}{(1 + m)(\alpha_1 + nlt)} - \alpha_4(\alpha_1 + nlt)^{-\frac{3}{n}} \right] \tag{53}$$

The physical parameters for the model (49) are deduced as

$$\theta = 3H = 3l(nlt + \alpha_1)^{-1} \tag{54}$$

$$\begin{aligned} \sigma^2 &= \frac{1}{4} \left[ \frac{3l^2(1 - 2m)^2}{(1 + m)^2(\alpha_1 + nlt)^2} + \alpha_4^2\beta(t)^2N^{-2} \right] \\ &= \frac{1}{4} \left[ \frac{3l^2(1 - 2m)^2}{(1 + m)^2(\alpha_1 + nlt)^2} + \alpha_4^2(\alpha_1 + nlt)^{-\frac{6}{n}} \right] \end{aligned} \tag{55}$$

$$\begin{aligned} A_M &= \frac{1}{6} \left[ \frac{3(1 - 2m)^2}{(1 + m)^2} + \frac{\alpha_4^2\beta(t)^2N^{-2}(\alpha_1 + nlt)^2}{l^2} \right] \\ &= \frac{1}{6} \left[ \frac{3(1 - 2m)^2}{(1 + m)^2} + \frac{\alpha_4^2(\alpha_1 + nlt)^{\frac{2n-6}{n}}}{l^2} \right] \end{aligned} \tag{56}$$

The expansion scalar  $\theta$  is a decreasing function of cosmic time  $t$ . It exhibit a constant value initially and approaching to zero with the evolution of cosmic time. The shear and average anisotropy parameters of the model is depending upon the gauge function  $\beta(t)$ . Both the parameters are decreasing function of cosmic time  $t$ . Initially  $\sigma^2$  has constant value and approaching towards zero at late time. The anisotropy parameter  $A_M$  has constant value initially and  $A_M \rightarrow \infty$  and  $A_M \rightarrow \frac{(1-2m)^2}{2(1+m)^2}$  for  $n > 3$  and  $0 < n < 3$  respectively. Using the Eqs. (48) and (50), in differential Eq. (12), we obtained  $\rho$  as

$$\begin{aligned} \rho &= \frac{1}{4} \left[ \frac{9l^2(1 + 4m)}{(1 + m)^2(\alpha_1 + nlt)^2} - \alpha_4^2\beta(t)^2N^{-2} - 3\beta(t)^2 \right] \\ &= \frac{1}{4} \left[ \frac{9l^2(1 + 4m)}{(1 + m)^2(\alpha_1 + nlt)^2} - (\alpha_1 + nlt)^{-\frac{6}{n}}(\alpha_4^2 + 3N^2(\alpha_1 + nlt)^{\frac{2}{n}}) \right] \end{aligned} \tag{57}$$

The energy density depends upon the gauge function  $\beta(t)$ . At initial time, the energy density has a constant value  $\frac{1}{4} \left[ \frac{9l^2(1+4m)}{\alpha_1^2(1+m)^2} - \alpha_1 \frac{-6}{n} (\alpha_4^2 + 3N^2\alpha_1 \frac{2}{n}) \right]$ . The positivity of energy density leads to the constraint on  $m$  such that  $\frac{4m+1}{(m+1)^2} > 4\alpha_1 \frac{2n-6}{9l^2} (\alpha_4^2 + 3N^2\alpha_1 \frac{2}{n})$ . When  $t \rightarrow \infty$ , the energy density  $\rho \rightarrow \frac{9l^2(4m+1)}{\alpha_1^2(m+1)^2}$ . Using the Eqs. (48) and (57) in Eq. (9), the EoS parameter  $\omega$  have been calculated as

$$\begin{aligned} \omega &= \frac{\frac{3l^2(4(1+m)n-9)}{(1+m)^2(\alpha_1+nl)^2} - \alpha_4^2\beta(t)^2N^{-2} - 3\beta(t)^2}{\frac{9l^2(1+4m)}{(1+m)^2(\alpha_1+nl)^2} - \alpha_4^2\beta(t)^2N^{-2} - 3\beta(t)^2} \\ &= \frac{\frac{3l^2(4(1+m)n-9)}{(1+m)^2(\alpha_1+nl)^2} - (\alpha_1 + nlt) \frac{-6}{n} (\alpha_4^2 + 3N^2(\alpha_1 + nlt) \frac{2}{n})}{\frac{9l^2(1+4m)}{(1+m)^2(\alpha_1+nl)^2} - (\alpha_1 + nlt) \frac{-6}{n} (\alpha_4^2 + 3N^2(\alpha_1 + nlt) \frac{2}{n})} \end{aligned} \tag{58}$$

In this power-law of expansion, the EoS parameter  $\omega$  depends upon gauge function  $\beta(t)$  from (50). In early time of the universe, the  $\omega$  takes a constant value equal to  $\frac{3l^2(-9+4(1+m)n)}{\alpha_1^2(1+m)^2} - \alpha_1 \frac{-6}{n} (\alpha_4^2 + 3\alpha_1 \frac{2}{n} N^2)$ . In late time, it approaches  $\frac{4n(1+m)-3}{1+4m}$  for  $0 < n < 2$ . We write the values of the skewness parameter  $\gamma$  and  $\delta$ , using the Eqs. (50), (57) and (58) in (10) as follows

$$\begin{aligned} \gamma = \delta &= \frac{4 \left[ \frac{9l^2(1+4m)}{4(1+m)^2(\alpha_1+nl)^2} + \frac{3l^2(3+2m(3-2m(n-3)-3n)-2n)}{4(1+m)^2(\alpha_1+nl)^2} + \frac{3l^2(4(1+m)n-9) - \alpha_4^2\beta(t)^2N^{-2} - 3\beta(t)^2}{(1+m)^2(\alpha_1+nl)^2} \right]}{\frac{9l^2(1+4m)}{(1+m)^2(\alpha_1+nl)^2} - \alpha_4^2\beta(t)^2N^{-2} - 3\beta(t)^2} \\ &= \frac{4 \left[ \frac{9l^2(1+4m)}{4(1+m)^2(\alpha_1+nl)^2} + \frac{3l^2(3+2m(3-2m(n-3)-3n)-2n)}{4(1+m)^2(\alpha_1+nl)^2} \right. \\ &\quad \left. + \frac{3l^2(4(1+m)n-9) - (\alpha_1+nlt) \frac{-6}{n} (\alpha_4^2 + 3N^2(\alpha_1+nlt) \frac{2}{n})}{(1+m)^2(\alpha_1+nl)^2} \right]}{\frac{9l^2(1+4m)}{(1+m)^2(\alpha_1+nl)^2} - (\alpha_1 + nlt) \frac{-6}{n} (\alpha_4^2 + 3N^2(\alpha_1 + nlt) \frac{2}{n})} \end{aligned} \tag{59}$$

For the value of time  $t = \tau_0$  given by

$$\tau_0 = \frac{1}{nl} \left[ \frac{l}{m+1} \sqrt{\frac{3[4n(m+1)-9]}{\alpha_4^2 + 3N^2(\alpha_1 + nlt) \frac{2}{n}}} \right]^{\frac{n}{n-3}} - \frac{\alpha_1}{nl} \tag{60}$$

the equation of state parameter  $\omega = 0$ . So that we have dusty universe at time  $t = \tau_0$  given by Eq. (60). It is to be noted that when time  $t$  lies in open interval  $\tau_1 < t < \tau_2$ , where

$$\tau_1 = \frac{1}{nl} \left[ \frac{1.06l}{m+1} \sqrt{\frac{[4n(m+1) + 4(5m-1)]}{\alpha_4^2 + 3N^2(\alpha_1 + nlt)^{\frac{2}{n}}}} \right]^{\frac{n}{n-3}} - \frac{\alpha_1}{nl} \tag{61}$$

$$\tau_2 = \frac{1}{nl} \left[ \frac{1.36l}{m+1} \sqrt{\frac{[4n(m+1) + 7.44m - 7.1]}{\alpha_4^2 + 3N^2(\alpha_1 + nlt)^{\frac{2}{n}}}} \right]^{\frac{n}{n-3}} - \frac{\alpha_1}{nl} \tag{62}$$

then the equation of state parameter  $\omega$  lies in the range  $-1.67 < \omega < -0.62$ , which consistent and in good agreement with the limiting observational results [31]. When the domain of time  $t$  is  $\tau_3 < t < \tau_4$ , in which

$$\tau_3 = \frac{1}{nl} \left[ \frac{1.13l}{m+1} \sqrt{\frac{[4n(m+1) + 15.96m - 5.01]}{\alpha_4^2 + 3N^2(\alpha_1 + nlt)^{\frac{2}{n}}}} \right]^{\frac{n}{n-3}} - \frac{\alpha_1}{nl} \tag{63}$$

$$\tau_4 = \frac{1}{nl} \left[ \frac{1.29l}{m+1} \sqrt{\frac{[4n(m+1)9.48m - 6.63]}{\alpha_4^2 + 3N^2(\alpha_1 + nlt)^{\frac{2}{n}}}} \right]^{\frac{n}{n-3}} - \frac{\alpha_1}{nl} \tag{64}$$

then we observed the values of  $\omega$  as  $-1.33 < \omega < -0.79$  which coincides with the values obtained from observational results [32]. Also it is noticed that when  $t$  lies in the open interval  $\tau_5 < t < \tau_6$  where

$$\tau_5 = \frac{1}{nl} \left[ \frac{1.10l}{m+1} \sqrt{\frac{[4n(m+1) + 17.28m - 4.68]}{\alpha_4^2 + 3N^2(\alpha_1 + nlt)^{\frac{2}{n}}}} \right]^{\frac{n}{n-3}} - \frac{\alpha_1}{nl} \tag{65}$$

$$\tau_6 = \frac{1}{nl} \left[ \frac{1.25l}{m+1} \sqrt{\frac{[4n(m+1) + 11.04m - 6.24]}{\alpha_4^2 + 3N^2(\alpha_1 + nlt)^{\frac{2}{n}}}} \right]^{\frac{n}{n-3}} - \frac{\alpha_1}{nl} \tag{66}$$

then the values of  $\omega$  are found to be  $-1.44 < \omega < -0.92$  which are very much consistent with the values of  $\omega$  of latest observational results in 2009 [33, 34]. Further for the value of time  $t = \tau$ , given by

$$\tau = \frac{1}{nl} \left[ \frac{1.22l}{m+1} \sqrt{\frac{[4n(m+1) + 12m - 6]}{\alpha_4^2 + 3N^2(\alpha_1 + nlt)^{\frac{2}{n}}}} \right]^{\frac{n}{n-3}} - \frac{\alpha_1}{nl}, \tag{67}$$

the values of  $\omega$  comes out to be  $-1$ . The geometrical and physical behaviour of the dark energy model is to be discussed on the values of EoS parameter and the gauge function  $\beta(t)$ . The gauge function  $\beta(t)$  is appeared in all physical quantity like  $H, \sigma, A_M, \rho, \omega, \delta, \gamma$ . If the constant of integration  $N = 0$  then  $\beta(t) = 0$  from Eq. (50). Thus for  $N = 0$ , the physical quantity  $\rho, \omega$  and time  $t$  in our model goes over to the result of Pradhan et al. [35]. If  $N \neq 0$ , then the gauge function  $\beta(t)$  play a role in our models. Thus in this note, an attempt has been made to generalize the

model of Pradhan et al. [35], in Lyra’s geometry. For flat model (in the absence of curvature), the matter energy density  $\Omega_M$  and dark energy  $\Omega_\Lambda$ , satisfies the relation

$$\Omega_M + \Omega_\Lambda = 1 \tag{68}$$

where

$$\begin{aligned} \Omega_M &= \frac{\rho}{3H^2} \\ \Omega_\Lambda &= \frac{\Lambda}{3H^2}. \end{aligned} \tag{69}$$

Thus, Eqs. (68) and (69) gives

$$\rho + \Lambda = 3H^2$$

and then using Eqs. (54) and (57), we write the values of  $\Lambda$  as

$$\begin{aligned} \Lambda &= \frac{1}{4} \left[ \frac{3l^2(3 + 4m + 4m^2)}{(1 + m)^2(\alpha_1 + nlt)^2} + \alpha_4^2\beta(t)^2N^{-2} + 3\beta(t)^2 \right] \\ &= \frac{1}{4} \left[ \frac{3l^2(3 + 4m + 4m^2)}{(1 + m)^2(\alpha_1 + nlt)^2} + (\alpha_1 + nlt)^{-\frac{6}{n}}(\alpha_4^2 + 3N^2(\alpha_1 + nlt)^{\frac{2}{n}}) \right] \end{aligned} \tag{70}$$

From Eq. (70), one can noticed that cosmological constant  $\Lambda$  takes a positive constant value  $\frac{1}{4} \left[ \frac{3l^2(3+4m+4m^2)}{(1+m)^2\alpha_1^2} + \alpha_1^{-\frac{6}{n}}(\alpha_4^2 + 3N^2\alpha_1^{\frac{2}{n}}) \right]$  at early stage of the universe and approaches to zero at late time for all the parameters involved in the expression (70). The cosmological term  $\Lambda$  is a decreasing function of cosmic time  $t$ . From Eqs. (54), (57) and (70), we write the values of the matter energy density  $\Omega_M = \frac{\rho}{3H^2}$  and dark energy  $\Omega_\Lambda = \frac{\Lambda}{3H^2}$  as,

$$\Omega_M = \frac{3(4m + 1)}{4(m + 1)^2} - \frac{(\alpha_1 + nlt)^{2-\frac{6}{n}}(\alpha_4^2 + 3N^2(\alpha_1 + nlt)^{\frac{2}{n}})}{12l^2} \tag{71}$$

$$\Omega_\Lambda = \frac{1}{4} \frac{(4m^2 - 4m + 1)}{(m + 1)^2} + \frac{(\alpha_1 + nlt)^{2-\frac{6}{n}}(\alpha_4^2 + 3N^2(\alpha_1 + nlt)^{\frac{2}{n}})}{12l^2} \tag{72}$$

Here we noticed that both the matter energy density  $\Omega_M$  and dark energy  $\Omega_\Lambda$  start evolve with a constant value. Further,  $\Omega_M \rightarrow \frac{3}{4} \frac{(4m+1)}{(m+1)^2}$  and  $\Omega_\Lambda \rightarrow \frac{1}{4} \frac{(4m^2-4m+1)}{(m+1)^2}$  when  $t \rightarrow \infty$  for  $0 < n < 2$ . The  $\Omega_\Lambda$  is a decreasing function of cosmic time  $t$ .

## 4 Concluding Remarks

In this manuscript, we have studied the dark energy cosmological models for Bianchi type-I universe in view of Lyra geometry. We have analysed two cosmological models namely PL model and EL model. The outcomes obtained from these two models are presented below:

- In both the models, the energy density  $\rho$  starts with a constant value initially and approaches to same value  $\frac{9l^2(4m+1)}{4(m+1)^2}$  at late time for  $\alpha_1 = \pm 2$ .
- The cosmological constant  $\Lambda$  is depending on the gauge function and in terms of cosmic time, the qualitative behaviour of  $\Lambda$  is decreasing in nature for both the discussed models. In case of exponential model and power law model, cosmological constant  $\Lambda$  approaches to  $3l^2 \left[ 1 - \frac{3(4m+1)}{4(m+1)^2} \right]$  and zero at late time respectively.
- In both the models, the dark energy  $\Omega_\Lambda$  is a decreasing function of cosmic time  $t$ . In PL ( $n = 0$ ) and EL ( $0 < n < 2$ ) models  $\Omega_\Lambda \rightarrow 1 - \frac{3(4m+1)}{4(m+1)^2}$  and  $\Omega_\Lambda \rightarrow \frac{(2m-1)^2}{4(m+1)^2}$  respectively at late time.
- The results discussed in Lyra's geometry reduces to the results of general relativity for  $N = 0$ .

## References

1. Bennett, C.L., Halpern, M., Hinshaw, G.: First-year wilkinson microwave anisotropy probe (WMAP) observations: preliminary maps and basic results. *Astrophys. J. Suppl. Ser. ED-148*, 1–7 (2003)
2. Spergel, D.N., Verde, L., Peiris, H.V., Komatsu, E., Nolta, M.R., Bennett, C.L., Halpern, M., Hinshaw, G., Jarosik, N., Kogut, A., Limon, M.: First-year Wilkinson microwave anisotropy probe (WMAP) observations: determination of cosmological parameters. *Astrophys. J. Suppl. Ser. ED-148(1)*, 175–179 (2003)
3. Tegmark, M., Strauss, M.A., Blanton, M.R., Abazajian, K., Dodelson, S., Sandvik, H., Wang, X., Weinberg, D.H., Zehavi, I., Bahcall, N.A., Hoyle, F.: Cosmological parameters from SDSS and WMAP. *Phys. Rev. D ED-69(10)*, 103501 (2004)
4. Tegmark, M., Strauss, M.A., Blanton, M.R., Abazajian, K., Sandvik, H., Wang, X., Weinberg, D.H., Zehavi, I., Bahcall, N.A., Hoyle, F.: Cosmological parameters from SDSS and WMAP. *Phys. Rev. D ED-69(10)*, 103501 (2004)
5. Garnavich, P.M., Kirshner, R.P., Challis, P., Tonry, J., Gilliland, R.L., Smith, R.C., Clocchiatti, A., Diercks, A., Filippenko, A.V., Hamuy, M., Hogan, C.J.: Constraints on cosmological models from Hubble Space Telescope observations of high- $z$  supernovae. *Astrophys. J. Lett. ED-493(2)*, L53 (1998)
6. Garnavich, P.M., Jha, S., Challis, P., Clocchiatti, A., Diercks, A., Filippenko, A.V., Gilliland, R.L., Hogan, C.J., Kirshner, R.P., Leibundgut, B., Phillips, M.M.: Supernova limits on the cosmic equation of state. *Astrophys. J. ED-509(1)*, 74 (1998)
7. Perlmutter, S., Gabi, S., Goldhaber, G., Goobar, A., Groom, D.E., Hook, I.M., Kim, A.G., Kim, M.Y., Lee, J.C., Pain, R., Pennypacker, C.R.: Measurements of the cosmological parameters  $\Omega$  and  $\Lambda$  from the first seven supernovae at  $z \geq 0.35$ . *Astrophys. J. ED-483(2)*, 565 (1997)
8. Perlmutter, S., Aldering, G., Della Valle, M., Deustua, S., Ellis, R.S., Fabbro, S., Fruchter, A., Goldhaber, G., Groom, D.E., Hook, I.M., Kim, A.G.: Discovery of a supernova explosion at half the age of the Universe. *Nature ED-391(6662)*, 51 (1998)



9. Perlmutter, S., Aldering, G., Goldhaber, G., Knop, R.A., Nugent, P., Castro, P.G., Deustua, S., Fabbro, S., Goobar, A., Groom, D.E., Hook, I.M.: Measurements of  $\Omega$  and  $\Lambda$  from 42 high-redshift supernovae. *Astrophys. J.* ED-517(2), 565 (1999)
10. Sahni, V., Starobinsky, A.: Reconstructing dark energy. *Int. J. Modern Phys. D* ED- 15(12), 2105–2132 (2006)
11. Sahni, V., Shafieloo, A., Starobinsky, A.A.: Two new diagnostics of dark energy. *Phys. Rev. D* ED-78(10), 103502 (2008)
12. Huterer, D., Turner, M.S.: Probing dark energy: Methods and strategies. *Phys. Rev. D* ED-64(12), 123527 (2001)
13. Weller, J., Albrecht, A.: Future supernovae observations as a probe of dark energy. *Phys. Rev. D* ED-65(10), 103512 (2002)
14. Linden, S., Virey, J.M.: Test of the Chevallier-Polarski-Linder parametrization for rapid dark energy equation of state transitions. *Phys. Rev. D* ED-78(2), 023526 (2008)
15. Krauss, L.M., Jones-Smith and Huterer, D.K.: Dark energy, a cosmological constant, and type Ia supernovae. *New J. Phys.* ED-9(5), 141 (2007)
16. Usmani, A.A., Ghosh, P.P., Mukhopadhyay, U., Ray, P.C., Ray, S.: The dark energy equation of state. *Monthly Notices Royal Astronom. Soc. Lett.* ED- 386(1), L92-L95 (2008)
17. Kujat, J., Linn, A.M., Scherrer, R.J., Weinberg, D.H.: Prospects for determining the equation of state of the dark energy: what can be learned from multiple observables? *Astrophys. J.* ED-572(1), 1 (2002)
18. Bartelmann, M., Dolag, K., Perrotta, F., Baccigalupi, C., Moscardini, L., Meneghetti, M., Tormen, G.: Evolution of dark-matter haloes in a variety of dark-energy cosmologies. *New Astron. Rev.* ED- 49(2–6), 199-203, (2005)
19. Jimenez, R.: The value of the equation of state of dark energy. *New Astron. Rev.* ED-47(8–10), 761–767 (2003)
20. Das, A., Gupta, S., Saini, T.D., Kar, S.: Cosmology with decaying tachyon matter. *Phys. Rev. D* ED-72(4), 043528 (2005)
21. Turner, M.S., White, M.: CDM models with a smooth component. *Phys. Rev. D* ED- 56(8), R4439 (1997)
22. Caldwell, R.R., Dave, R., Steinhardt, P.J.: Cosmological imprint of an energy component with general equation of state. *Phys. Rev. Lett.* ED-80(8), 1582 (1998)
23. Liddle, A.R., Scherrer, R.J.: Classification of scalar field potentials with cosmological scaling solutions. *Phys. Rev. D* ED-59(2), 023509 (1998)
24. Steinhardt, P.J., Wang, L., Zlatev, I.: Cosmological tracking solutions. *Phys. Rev. D* ED-59(12), 123504 (1999)
25. Rahaman, F., Bhui, B.C., Bhui, B.: Cosmological model with a viscous fluid in a Kaluza-Klein metric. *Astrophys. Space Sci.* ED-301(1–4), 47–49 (2006)
26. Mukhopadhyay, U., Ray, S., DChoudhury, S.:  $\Lambda$ -CDM universe: a phenomenological approach with many possibilities. *Int. J. Modern Phys. D* ED- 17(02), 301–309 (2008)
27. Ray, S., Rahaman, F., Mukhopadhyay, U., Sarkar, R.: Variable equation of state for generalized dark energy model. *Int. J. Theoret. Phys.* ED-50(9), 2687–2696 (2011)
28. Akarsu, Ö, Kılınc, C.B.: Bianchi type III models with anisotropic dark energy. *General Relat. Gravit.* ED-42(4), 763–775 (2010)
29. Lyra, G.: Ubereine Modifikation der Riemannschen Geometrie, *Math.Z.* ED-54(1), 52–54 (1957)
30. Vishwakarma, V.: A study of angular size-redshift relation for models in which  $\Lambda$  decays as the energy density. *Classical Quant. Grav.* ED- 17(18), 3833 (2000)
31. Knop, R.A., Aldering, G., Amanullah, R., Astier, P., Blanc, G., Burns, M.S. Conley, A., Deustua, S.E., Doi, M., Ellis, R., Fabbro, S.: New constraints on  $\Omega_M$ ,  $\Omega_\Lambda$ , and  $\omega$  from an independent set of 11 high-redshift supernovae observed with the Hubble Space Telescope. *Astrophys. J.* ED-598(1), 102 (2003)
32. Tegmark, M., Blanton, M.R. Strauss, M.A., Hoyle, F. Schlegel, D. Scoccamarro, R., Vogeley, M.S., Weinberg, D.H., Zehavi, I., Berlind, A., Budavari, T.: The three-dimensional power spectrum of galaxies from the sloan digital sky survey. *Astrophys. J.* ED-606(2), 702 (2004)

33. Hinshaw, G., Weiland, J.L., Hill, R.S., Odegard, N., Larson, D., Bennett, C.L., Dunkley, J., Gold, B., Greason, M.R., Jarosik, N., Komatsu, E.: Five-year wilkinson microwave anisotropy probe observations: data processing, sky maps, and basic results. *Astrophys. J. Suppl. Ser. ED-180(2)*, 225 (2009)
34. Komatsu, E., Dunkley, J., Nolta, M.R., Bennett, C.L., Gold, B., Hinshaw, G., Osik, J.N., Larson, D., Limon, M., Page, L., Spergel, D.N.: Five-year wilkinson microwave anisotropy probe observations: cosmological interpretation. *Astrophys. J. Suppl. Ser. ED-180(2)*, 330 (2009)
35. Pradhan, A., Amirhashchi, H., Saha, B.: Bianchi type-I anisotropic dark energy model with constant deceleration parameter. *Int. J. Theoret. Phys. ED-50(9)*, 2923–2938 (2011)

# A Non-linear Model of a Fishery Resource for Analyzing the Effects of Toxic Substances



Sudipta Sarkar, Tanushree Murmu, Ashis Kumar Sarkar,  
and Kripasindhu Chaudhuri

**Abstract** The goal of the proposed model is to investigate and analyze the qualitative behaviour of predator-prey fishery resource in an aquatic ecosystem by a non-linear mathematical model in which prey and predator species are contaminated by the toxic substances released by each of the species. In this model the species are subjected to bio-economic combined harvesting and obey the logistic growth rate function. Bio-economic harvesting of prey-predator species in presence of harmful toxic substances released by them is analyzed here by using modified catch rate function. Boundedness of the proposed model is examined here. Biological and bionomic steady states of the proposed model are derived. The conditions for local behaviour, instability and global behaviour of the steady states are exhibited in this paper. Optimal harvesting policy with the help of Pontryagin's maximal principle and finally, numerical examples are illustrated to verify theoretical observations obtained from proposed model.

**Keywords** Fishery resource · Bioeconomic combined harvesting · Stability · Steady state · Optimal equilibrium · Toxicity · Net revenue

## 1 Introduction

Sustainable resources fishery, forestry, wild life etc. are vital origins of food and other necessary commodities in human life. These resources play a salient role for existence and advancement of biological populations. For these renewable resources management, our aim is to maximize the current value of advantages obtained from

---

Supported by organization x.

---

S. Sarkar (✉)

Department of Mathematics, Heritage Institute of Technology, Anandapur, Kolkata 700107,  
West Bengal, India

e-mail: [sudipta.jumath@gmail.com](mailto:sudipta.jumath@gmail.com)

T. Murmu · A. Kumar Sarkar · K. Chaudhuri

Department of Mathematics, Jadavpur University, Kolkata 700032, India

© The Author(s), under exclusive license to Springer Nature Switzerland AG 2022

837

S. Banerjee and A. Saha (eds.), *Nonlinear Dynamics and Applications*,

Springer Proceedings in Complexity,

[https://doi.org/10.1007/978-3-030-99792-2\\_70](https://doi.org/10.1007/978-3-030-99792-2_70)

these sustainable resources and their proper preservation so that the extinction of these resources can be preserved. One of the most vital problems in an aquatic ecological system is the consequence of toxic elements. The growth of the fish and other aquatic organisms is highly influenced by these toxic substances. During the last few decades, so many researchers have carried out their investigations regarding fishery resource management. Clark [2, 3], Meserton-Gibbons [10, 11] have pursued their valuable analysis based on mathematical modeling of harvesting of fishery. Excessive and unregulated harvesting is not only the cause of depletion of fish species but also the consequence of toxic substances, the competitiveness of inter and intra species among predator-prey resources etc. are reasons. Chattopadhyay [1], Kar and Chaudhuri [7], Kar et al. [8], Dubey and Hussain [4] and Mukhopadhyay et al. [12] have conducted their mathematical analysis based on non-linear mathematical modeling of predator-prey fishery resource keeping the salient focus in toxicity. Our main focus is to find out the optimal control so that maximal value of the benefits obtained from this predator-prey fishery resource in presence of toxic substances by using a modified catch rate function preserving the extinction of both species. Further, the concept of Maynard [9] for competing fishery model subjected to commercially exploitation and toxicity was developed by Kar and Chaudhuri [7]. Ghosh et al. [5] developed a non-linear model to show the consequences of toxic elements on predator-prey fishery resource. Haque and Sarwardi [6], Pal et al. [13] developed a non-linear model to exhibit the effects of toxic elements for an aquatic system. A non-linear model was introduced by Sarkar et al. [15] using a modified catch rate function.

Our current model is arranged in the following manner: In Sect. 2: problem construction, Sect. 3: equilibria of the proposed dynamical system are exhibited. In Sect. 4: qualitative behaviour of the proposed model are analyzed. Finally, optimal harvesting policy with the help of Pontryagin's maximal principle, numerical results as well as interpretations of our proposed model have been shown in the consecutive sections.

## 2 Model Formulation

After incorporation of toxic affects, the dynamical system of prey-predator competing fishery resource model is as follows:

$$\begin{aligned}\frac{dx}{dt} &= rx \left(1 - \frac{x}{K}\right) - \alpha xy - \gamma_1 x^3 y - \frac{q_1 E x}{b_1 + E}, \\ \frac{dy}{dt} &= sy \left(1 - \frac{y}{L}\right) - \beta xy - \gamma_2 x y^2 - \frac{q_2 E y}{b_2 + E}.\end{aligned}\tag{1}$$

Here,  $x = x(t)$ ,  $y = y(t)$  denote prey and predator population density at time  $t$  respectively.  $r$ ,  $s$ ,  $\alpha$ ,  $\beta$ ,  $K$ ,  $L$  denote maximum growth rate of prey and predator fish species, coefficients of competition and environmental carrying capacities of prey and predator fish species respectively.

Here,  $\gamma_1, \gamma_2$  represent the toxicity co-efficient of prey and predator fish populations. The parameters assumed in this paper are all positive constants. The term  $\gamma_1 x^3$  is treated as one kind of response function of the predator fish to the prey population and it originates from the toxic substances by the predator species to put off the prey population from sharing the common resources. Here, the terms  $\frac{d(\gamma_1 x^3)}{dx} = 3\gamma_1 x^2 > 0$  and  $\frac{d^2(\gamma_1 x^3)}{dx^2} = 6\gamma_1 x > 0$  are positive. So, increasing growth rate of the toxic elements is observed as the biomass of prey-predator populations  $s$  are increased. Here,  $q_1, q_2$  denote the coefficients of catchability of both fish species respectively and  $b_1, b_2$  are all positive constants.

In the beginning of fishery resource models, the catch rate function is usually taken in the form  $h = qEx$  based on the CPUE (catch-per-unit-effort) hypothesis [2]. Later on, it is revised in the form as  $h = \frac{qEx}{bE+Ix}$ .

It is assumed that the fisherman search randomly in a given area effectively which is a function of the effort level to harvest the fish resource by the fisherman. We rename this concept as a searching efficiency for the area of discovery. The capture rate of fish resource dependent on how effectively (efficiently) the effort level is used in presence of other fisherman. On the basis of the above hypothesis accordingly, we modify the catch rate function as a function of the fish resource population being captured for different effort levels in the form  $h = \frac{qEx}{b+E}$ , where  $E, q, b$  denote the harvesting effort, the catchability coefficient and a positive constant respectively.

### 3 The Equilibria and Their Feasibility

There are four equilibria of the dynamical system of Eqs. (1) which are  $E_0(0, 0), E_1(x_1, 0), E_2(0, y_2) \& E^*(x^*, y^*)$ , where  $x_1 = \frac{K}{r} \left( r - \frac{q_1 E}{b_1 + E} \right), y_2 = \frac{L}{s} \left( s - \frac{q_2 E}{b_2 + E} \right), y^* = \frac{L(s - \beta x^* - \frac{q_2 E}{b_2 + E})}{s + L\gamma_2 x^*}$  and we get the value of  $x^*$  from the following cubic equation

$$A_1 x_1^{*3} + A_2 x_1^{*2} + A_3 x_1^* + A_4 = 0, \tag{2}$$

where  $A_1 = \gamma_1 L\beta, A_2 = \frac{-r}{K} L\gamma_2 - \gamma_1 Ls + \frac{L\gamma_1 q_2 E}{b_2 + E}, A_3 = \frac{-rs}{K} + rL\gamma_2 + \alpha L\beta - \frac{q_1 EL\gamma_2}{b_1 + E}$  and  $A_4 = rs - \alpha Ls + \frac{q_2 E\alpha L}{b_2 + E} - \frac{q_1 Es}{b_1 + E}$ .

It is observed that the steady state  $E_0$  is always feasible,  $E_1$  is feasible if  $r > \frac{q_1 E}{b_1 + E}$  and  $E_2$  exists if  $s > \frac{q_2 E}{b_2 + E}$ .

If  $D < 0$ , then there exists at least one positive root say  $x^*$  of the Eq. (3). So, the existence condition of  $E^*(x^*, y^*)$  is  $s - \beta x^* - \frac{q_2 E}{b_2 + E} > 0$  and  $s >$

$$\frac{\alpha L q_2 E}{\alpha L(b_2 + E) - r(b_2 + E) + \frac{q_1 E(b_2 + E)}{(b_1 + E)}}.$$

## 4 Qualitative Analysis

### 4.1 Boundedness

In the system (1), the solutions are uniformly bounded.

#### Proof

To prove the boundedness of the system let us choose a function  $\omega = x + y$ .

$$\begin{aligned} \frac{d\omega}{dt} + \zeta\omega &= rx \left(1 - \frac{x}{K}\right) + sy \left(1 - \frac{y}{L}\right) - (\alpha + \beta)xy - xy(\gamma_1x^2 + \gamma_2y)r \\ &\quad - E \left( \frac{q_1x}{b_1 + E} + \frac{q_2y}{b_2 + E} \right) + \zeta(x + y) \\ &< \frac{K}{4r} \left( r + \zeta - \frac{Eq_1}{b_1 + E} \right)^2 + \frac{L}{4s} \left( s + \zeta - \frac{Eq_2}{b_2 + E} \right)^2 = \eta. \end{aligned}$$

Thus, we get  $0 < \omega(x, y) < \frac{\eta}{\zeta}(1 - \exp^{-\zeta t}) + \omega(0) \exp^{-\zeta t} < \max \left\{ \frac{\eta}{\zeta}, \omega(0) \right\}$ .

Therefore, the solutions are uniformly bounded in

$$\mathbf{R}_{xy} = \left\{ (x, y) \in \mathfrak{R}_+^2 : \omega(x, y) \leq \frac{\eta}{\zeta} + \varepsilon \text{ for any } \varepsilon > 0 \right\}.$$

### 4.2 Local Behaviour of the Equilibria

Let  $J_n$  be the variational matrix of the steady states  $E_n$  where  $n = 0, 1, 2$ . The eigenvalues of  $J_0$  are  $r - \frac{q_1E}{b_1 + E}$  and  $s - \frac{q_2E}{b_2 + E}$ . So,  $E_0(0, 0)$  is stable node if  $E >$

$\max \left( \frac{b_1r}{q_1 - r}, \frac{b_2s}{q_2 - s} \right)$  and unstable if  $E < \min \left( \frac{b_1r}{q_1 - r}, \frac{b_2s}{q_2 - s} \right)$ .

The eigen values of  $J_1$  are  $\lambda_1 = \frac{-rx_1}{K}$  and  $\lambda_2 = s - \beta x_1 - \frac{q_2E}{b_2 + E}$ . Obviously,  $\lambda_1 < 0$  and hence  $E_1(x_1, 0)$  is a stable node if  $\lambda_2 < 0$  which imply that  $E > \frac{b_2(s - \beta x_1)}{q_2 - s + \beta x_1}$ . It can be shown that  $E_1(x_1, 0)$  is saddle if  $E < \frac{b_2(s - \beta x_1)}{q_2 - s + \beta x_1}$ .

The eigen values of  $J_2$  are  $\lambda_1 = r - \alpha y_2 - \frac{q_1E}{b_1 + E}$  and  $\lambda_2 = \frac{-sy_2}{L}$ . It is observed that  $\lambda_2 < 0$ . Hence  $E_2(0, y_2)$  is a stable node when  $\lambda_1 < 0$  i.e., if  $E > \frac{b_1(r - \alpha y_2)}{q_1 - r + \alpha y_2}$  and saddle point if  $E < \frac{b_1(r - \alpha y_2)}{q_1 - r + \alpha y_2}$ .

The variational matrix of (1) around  $E^*$  is as follows:

$$J^* = \begin{pmatrix} \frac{-r_1x^*}{K} - 2\gamma_1x^{*2}y^* & -\alpha x^* - \gamma_1x^{*3} \\ -\beta y^* - \gamma_2y^{*2} & \frac{-sy^*}{L} - \gamma_2x^*y^* \end{pmatrix}$$

Here,  $trace(J^*) < 0$ . So, for the local stability of the system of Eq. (1) around  $E^*$ , we have to show that  $det(J^*)$  is strictly positive.

$$det(J^*) = x^*y^* \left[ \frac{rs}{KL} - \alpha\beta + \gamma_2 \left( \frac{q_1E}{b_1+E} - r \right) - \beta\gamma_1x^{*2} + 2x^* \left( \gamma_1\gamma_2x^*y^* + \frac{s\gamma_1y^*}{L} + \frac{r\gamma_2}{K} \right) \right]. \tag{3}$$

So,  $det(J^*) > 0$  if  $x^{*2} < \frac{1}{\beta\gamma_1} \left[ \frac{rs}{KL} + \gamma_2 \left( \frac{q_1E}{b_1+E} - r \right) - \alpha\beta \right]$ .

### 4.3 Non-existence of Periodic Solution

The system of Eq. (1) can be written in the form  $\dot{Y} = G(Y)$ , where  $Y = (x, y)$  and  $G = (G_1, G_2)$ . Here,  $G_1, G_2 \in C^\infty(\mathbf{R})$ ,  $G_1 = rx \left( 1 - \frac{x}{K} \right) - \alpha xy - \gamma_1x^3y - \frac{q_1Ex}{b_1+E}$  and  $G_2 = y \left( 1 - \frac{y}{L} \right) - \beta xy - \gamma_2xy^2 - \frac{q_2Ey}{b_2+E}$ . Let us consider a function  $F(x, y) = \frac{1}{xy}$ . Then  $F(x, y) > 0$  for  $(x, y) \in \mathbf{R}_{xy}$ .

$$\nabla \cdot (FG) = - \left[ \frac{r}{Ky} + 2\gamma_1x + \frac{s}{Lx} + \frac{\gamma_2y}{x} \right] < 0 \quad \forall (x, y) \in \mathbf{R}_{xy}. \tag{4}$$

It follows that  $\nabla \cdot (FG) < 0$  always. So, by Bendixson-Dulac’s criterion, there does not exist any periodic orbit for the proposed model.

### 4.4 Global Stability Analysis

For global stability analysis of the dynamical system (1), a Lyapunov function is constructed as follows:

$$V(x, y) = \left[ \left( x - x^* \log \frac{x}{x^*} \right) + \left( y - y^* \log \frac{y}{y^*} \right) \right]. \tag{5}$$

Here,  $V$  is positive definite  $\forall (x, y) \in \mathfrak{R}_+^2$ . Now,

$$\frac{dV}{dt} = - \left[ P(x - x^*)^2 + R(x - x^*)(y - y^*) + Q(y - y^*)^2 \right], \tag{6}$$

where  $P = \frac{r}{K} + \gamma_1y(x + x^*) > 0$ ,  $Q = \frac{s}{L} + \gamma_2x > 0$ ,  $R = \alpha + \beta + \gamma_1x^{*2} + \gamma_2y^* > 0$ .

Now,  $4PQ - R^2 = 4 \left\{ \frac{r}{K} + \gamma_1 y(x + x^*) \right\} \left\{ \frac{s}{L} + \gamma_2 x \right\} - \left\{ \alpha + \beta + \gamma_1 x^{*2} + \gamma_2 y^* \right\}^2 > 0$ , if  $4rs > KL \{ \alpha + \beta + \gamma_1 x^* + \gamma_2 \}^2$ .

So,  $\frac{dV}{dt} = 0$  at  $E^*(x^*, y^*)$  and  $\frac{dV}{dt} < 0$  at all the points other than  $E^*(x^*, y^*)$ . Using Lyapunov- LaSalle's invariance principle, we have shown that  $E^*(x^*, y^*)$  is globally asymptotically stable under certain conditions.

### 4.5 Bionomic Steady States

When the total revenue (TR) achieved by selling the harvested biomass is equal to the total cost (TC) for the harvesting, then the bionomic equilibrium is obtained. Then the net revenue at any time is as follows:

$$\pi(x, y, E, t) = \left( \frac{p_1 q_1 x}{b_1 + E} + \frac{p_2 q_2 y}{b_2 + E} - C \right) E, \tag{7}$$

where  $C$ =constant cost for fishing per unit effort,  $p_1$ =constant price per unit prey biomass,  $p_2$ = constant price per unit predator biomass. To make our calculation simple, the cost of harvesting per unit effort is considered as constant.

Now, from equation  $\dot{x} = 0$ , we get  $E = \frac{\alpha y b_1 + \gamma_1 x^2 y b_1 - r(1 - \frac{x}{K}) b_1}{r(1 - \frac{x}{K}) - \alpha y - \gamma_1 x^2 y - q_1}$ .

Thus,  $E$  is positive, when  $\alpha y + \gamma_1 x^2 y < r(1 - \frac{x}{K}) < \alpha y + \gamma_1 x^2 y + q_1$ .

Similarly, from the equation  $\dot{y} = 0$  we get  $E = \frac{\beta b_2 x + \gamma_2 x y b_2 - s(1 - \frac{y}{L}) b_2}{s(1 - \frac{y}{L}) - \beta x - \gamma_2 x y - q_2}$ .

So,  $E$  is positive when  $\beta x + \gamma_2 x y < s(1 - \frac{y}{L}) < \beta x + \gamma_2 x y + q_2$ . Therefore, the interior equilibrium point exists on the curve

$$\frac{\alpha y b_1 + \gamma_1 x^2 y b_1 - r(1 - \frac{x}{K}) b_1}{r(1 - \frac{x}{K}) - \alpha y - \gamma_1 x^2 y - q_1} = \frac{\beta b_2 x + \gamma_2 x y - s(1 - \frac{y}{L}) b_2}{s(1 - \frac{y}{L}) - \beta x - \gamma_2 x y - q_2}, \tag{8}$$

where  $0 \leq x \leq K$  and  $0 \leq y \leq L$ .

We can find the bionomic steady states of the open access fishery model using Eq. (8) and condition  $\pi = TR - TC = 0$ , which gives the result  $\left( \frac{p_1 q_1 x}{b_1 + E} + \frac{p_2 q_2 y}{b_2 + E} - C \right) = 0$ .

## 5 Optimal Harvesting Policy

Our salient task is to fix the optimal adjustment between the current and future harvests values. The current value  $I$  of revenues is as follows:

$$I = \int_0^\infty \pi(x, y, E, t) e^{-\delta t} dt. \tag{9}$$



Here,  $\pi(x, y, E, t) = \frac{p_1q_1xE}{b_1+E} + \frac{p_2q_2yE}{b_2+E} - CE$  and  $\delta$  denotes the instant annual discount rate,  $C$  is the fishing cost per unit effort,  $p_1, p_2$  are prices per unit prey and predator biomass respectively. Our main focus is to maximize  $I$  along with the Eq. (1) with the help of Pontryagin’s Maximum Principle [14]. Here,  $0 \leq E(t) \leq E_{max}$  and control set  $V_t = [0, E_{max}]$  where  $E_{max}$  is the possible maximum value of the effort of harvesting.

For our problem, the Hamiltonian is given by:

$$H = \left( \frac{p_1q_1x}{b_1+E} + \frac{p_2q_2y}{b_2+E} - C \right) E e^{-\delta t} + \lambda_1 \left[ rx \left( 1 - \frac{x}{K} \right) - \alpha xy - \gamma_1 x^3 y - \frac{q_1 E x}{b_1+E} \right] + \lambda_2 \left[ sy \left( 1 - \frac{y}{L} \right) - \beta xy - \gamma_2 xy^2 - \frac{q_2 E y}{b_2+E} \right]. \tag{10}$$

Here,  $\lambda_1, \lambda_2$  are adjoint variables. For finding an optimal solution, we are taking

$$E = \frac{\alpha y b_1 + \gamma_1 x^2 y b_1 - r \left( 1 - \frac{x}{K} \right) b_1}{r \left( 1 - \frac{x}{K} \right) - \alpha y - \gamma_1 x^2 y - q_1} = \frac{\beta b_2 x + \gamma_2 x y b_2 - s \left( 1 - \frac{y}{L} \right) b_2}{s \left( 1 - \frac{y}{L} \right) - \beta x - \gamma_2 x y - q_2}. \tag{11}$$

Now, from the two adjoint equations ( $\frac{d\lambda_1}{dt} = -\frac{\partial H}{\partial x}$  and  $\frac{d\lambda_2}{dt} = -\frac{\partial H}{\partial y}$ ), we get

$$\frac{d^2\lambda_1}{dt^2} - \left( \frac{rx}{K} + 2\gamma_1 x^2 y + \frac{sy}{L} + xy\gamma_2 \right) \frac{d\lambda_1}{dt} + \left[ \left( \frac{rx}{K} + 2\gamma_1 x^2 y \right) \left( \frac{sy}{L} + xy\gamma_2 \right) - \left( \beta y + \gamma_2 y^2 \right) \left( \alpha x + \gamma_1 x^3 \right) \right] \lambda_1 = M_1 e^{-\delta t}, \tag{12}$$

where  $M_1 = \left( \frac{p_1q_1E\delta}{b_1+E} \right) + \left( \frac{sy}{L} + xy\gamma_2 \right) \frac{p_1q_1E}{b_1+E} - \left( \beta y + \gamma_2 y^2 \right) \frac{p_2q_2E}{b_2+E}$ .

The auxiliary equation for the Eq. (12) is as follows:

$$\mu^2 - \left( \frac{rx}{K} + 2\gamma_1 x^2 y + \frac{sy}{L} + xy\gamma_2 \right) \mu + \left[ \left( \frac{rx}{K} + 2\gamma_1 x^2 y \right) \left( \frac{sy}{L} + xy\gamma_2 \right) - \left( \beta y + \gamma_2 y^2 \right) \left( \alpha x + \gamma_1 x^3 \right) \right] = 0. \tag{13}$$

Then, complete solution of the Eq. (13) is as follows:

$$\lambda_1(t) = A_1 e^{\mu_1(t)} + A_2 e^{\mu_2(t)} + \left( \frac{M_1}{N_1} \right) e^{-\delta t}. \tag{14}$$

Here,  $N_1 = \left[ \delta^2 - \delta \left( \frac{rx}{k} + 2\gamma_1 x^2 y + \frac{sy}{L} + xy\gamma_2 \right) + \left( \frac{rx}{k} + 2\gamma_1 x^2 y \right) \left( \frac{sy}{L} + xy\gamma_2 \right) - \left( \beta y + \gamma_2 y^2 \right) \left( \alpha x + \gamma_1 x^3 \right) \right] \neq 0$ . It is true that  $\lambda_1$  is bounded if  $A_1 = A_2 = 0$ .

So, we have  $\lambda_1(t) = \left( \frac{M_1}{N_1} \right) e^{-\delta t}$  and  $\lambda_2(t) = \left( \frac{M_2}{N_1} \right) e^{-\delta t}$ , where  $M_2 = \frac{p_2 q_2 E \delta}{b_2 + E} + \left( \frac{rx}{k} + 2\gamma_1 x^2 y \right) \frac{p_2 q_2 E}{b_2 + E} - \left( \alpha x + \gamma_1 x^3 \right) \frac{p_1 q_1 E}{b_1 + E}$ .

At  $t \rightarrow \infty$ ,  $\lambda_i(t)e^{\delta t}$ ,  $i = 1, 2$  become constant if they satisfy the transversality condition.

Now, the equation  $\frac{\partial H}{\partial E} = 0$  along with  $\lambda_1(t)$  and  $\lambda_2(t)$  gives the following:

$$\left( p_1 - \frac{M_1}{N_1} \right) \frac{q_1 b_1 x}{(b_1 + E)^2} + \left( p_2 - \frac{M_2}{N_1} \right) \frac{q_2 b_2 y}{(b_2 + E)^2} = C. \tag{15}$$

Using the Eqs. (11) and (15), we get the optimal equilibrium of the populations i.e.,  $x = x_\delta, y = y_\delta$ .

At  $\delta \rightarrow \infty$ , Eq. (15) gives the result  $\frac{p_1 q_1 b_1 x}{(b_1 + E)^2} + \frac{p_2 q_2 b_2 y}{(b_2 + E)^2} = C$  which implies  $\frac{\partial \pi}{\partial E} = 0$ .

Thus, the economic rent is totally vanished. Then, from the Eqs. (11) and (15), we get the following:

$$\frac{\partial \pi}{\partial E} = \frac{M_1}{N_1} \frac{q_1 b_1 x}{(b_1 + E)^2} + \frac{M_2}{N_1} \frac{q_2 b_2 y}{(b_2 + E)^2}. \tag{16}$$

Since  $M_1$  and  $M_2$  are  $o(\delta)$  where  $N_1$  is  $o(\delta^2)$ , it is found that  $\frac{\partial \pi}{\partial E}$  is  $o(\delta^{-1})$ . So,  $\frac{\partial \pi}{\partial E}$  is gradually decreasing function with  $\delta (\geq 0)$ .

Therefore, it is concluded that  $\frac{\partial \pi}{\partial E}$  attains it's maximum value at  $\delta = 0$ .

## 6 Numerical Simulations

Here, we verify the analytical findings numerically using MATLAB-2016a and Maple-18. For this purpose, a set of parameter values have been taken as follows:  $r=3.5, k=300, \alpha = 0.02, q_1 = 0.9, E = 10, b_1 = 0.5, \gamma_1 = 0.0002, s = 1.1, l = 100, \beta = 0.001, \gamma_2 = 0.0001, q_2 = 0.7, b_2 = 0.3$ . For the same set of parameter values, it is shown that: (i)  $E_0(0, 0)$  is unstable, (ii)  $E_1(226.53, 0)$  is stable node, (iii)  $E_2(0, 38.22)$  is stable node, (iv)  $E^*(16.8679, 31.8064)$  is both locally and globally asymptotically stable node.

From Figs. 1 and 2, it is seen that the system possesses an interior equilibrium point  $E^* = (16.8679, 31.8064)$  and around that point, the system (1) is globally asymptotically stable.

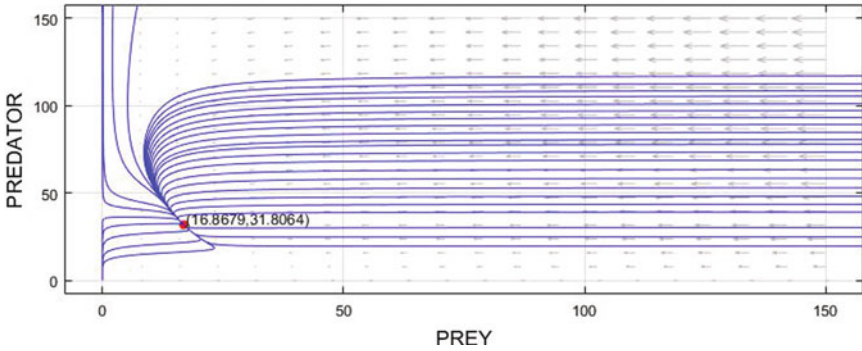


**Fig. 1** Globally stable steady state of the fishery resource model with various initial values

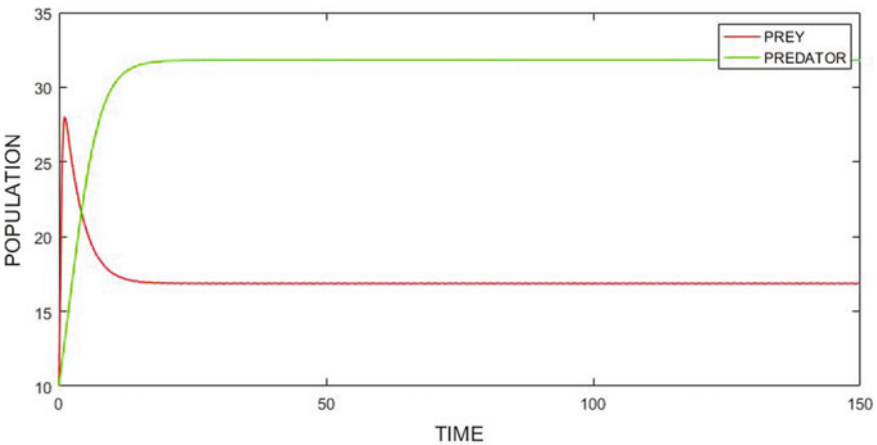


**Fig. 2** Globally stable steady state of the fishery resource model with various initial values

It is found that the bionomic equilibrium i.e.,  $(x_\infty, y_\infty) = (16.5346, 33.2731)$  (Fig. 3) occurs for the same parameter values  $p_1 = 10, p_2 = 10, C = 50$  and  $E = \frac{\alpha y b_1 + \gamma_1 x^2 y b_1 - r(1 - \frac{x}{k}) b_1}{r(1 - \frac{x}{k}) - \alpha y - \gamma_1 x^2 y - q_1}$ .

Without the effect of toxicity i.e.,  $(\gamma_1 = \gamma_2 = 0)$ , we found  $(x_\infty, y_\infty) = (190.84, 21.24)$  (Fig. 4).

From the figures, it is concluded that the population density of prey ( $x_\infty = 190.84$ ) at which the bionomic equilibrium occurs without toxicity is greater than the biomass density of prey ( $x_\infty = 16.5346$ ) with toxicity. On the other hand, the population density of predator ( $y_\infty = 21.24$ ) at which the bionomic equilibrium occurs without toxicity is lower than the population density of predator ( $y_\infty = 33.2731$ ) with toxicity.

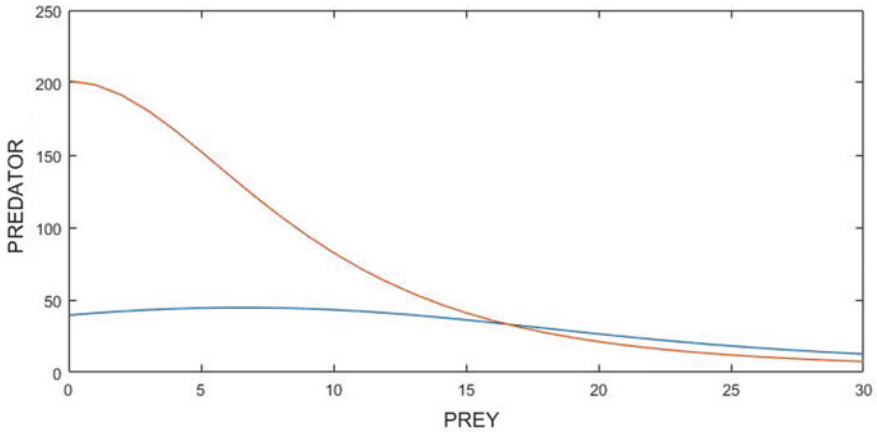


Fig. 3 Bionomic equilibrium of the fishery model when toxicity  $\neq 0$

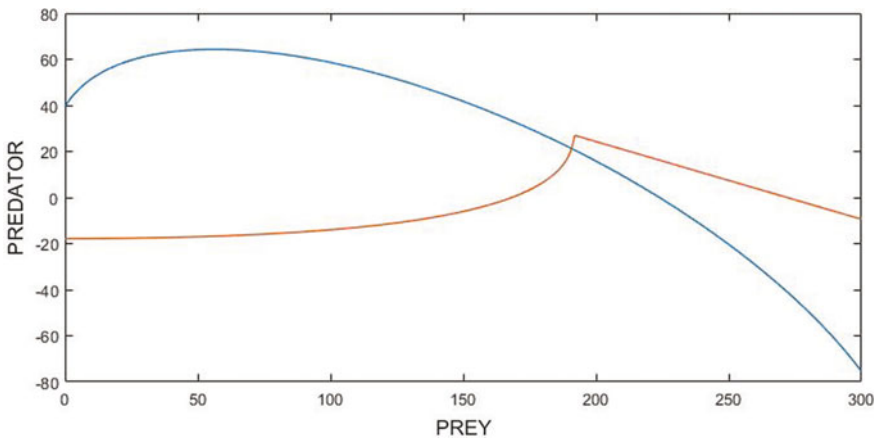


Fig. 4 Bionomic equilibrium of the fishery model when toxicity  $= 0$

### 7 Conclusions

On a note to conclude, it can be prudently placed that this paper, has attempted to discuss the consequences of toxic elements released by both species in a competing predator-prey fishery model, where both the species are subjected to harvesting with a modified catch rate function. An effort has been taken to examine both the local and global stabilities. An endeavour, in this article has also been taken to delineate the existence of bionomic equilibrium in presence of toxicity along with the task of portrayal of the state of the bionomic equilibrium in absence of toxicity. The numerical examples adopted for the present purpose, suggest that the severity of releasing toxins by predator-prey species may change the qualitative nature of the proposed model,

explicating the fact that toxicity may cause extinction of any one of the species. It has been observed that if the toxicity is considered, the population level of the bionomic equilibria steady states for the first species quickly decreases, whereas in the second species, it slowly increases. Thus, to put this in a nutshell, it can be said that the moderate increase of toxic substances come from both the predator-prey species, have severe impact on both and would finally lead to annihilation. The optimal harvesting policy, has also been discussed, as another key component of the paper. The policy, which has been employed, applying the Pontryagin maximum principle, has revealed the maximization of net revenue . The investigation has also ascertained that the shadow price remains constant with respect to time, as the transversality condition is satisfied by the optimal equations at infinity. The model has led us to derive the fact that the maximization of net revenue is led by the zero-discounting rate while the completion dissipation of net revenues is led by the infinite discounting rate.

## References

1. Chattopadhyay, J.: Effect of toxic substances on a two species competitive system. *Ecol. Model* **84**, 287–289 (1997)
2. Clark, C.W.: *Mathematical Bioeconomics: the Optimal Management of Renewable Resources*. Wiley, New York (1976)
3. Clark, C.W.: *Bioeconomic Modeling and Fisheries Management*. Wiley, New York (1985)
4. Dubey, B., Hussain, J.: A model for the allelopathic effect on two competing fish species. *Ecol. Model* **129**, 195–207 (2000)
5. Ghosh, M., Chandra, P., Sinha, P.: A mathematical model to study the effects of toxic chemicals on a prey-predator type fishery. *J. Biol. Syst.* **10**(2), 97–105 (2002)
6. Haque, M.: Sarwadi: effect of toxicity on a harvested fishery model. *Model. Earth Syst. Environ.* **2**, 122 (2016)
7. Kar, T.K., Chaudhuri, K.S.: On non-selective harvesting of two competing fish species in the presence of toxicity. *Ecol. Model.* **161**, 125–137 (2003)
8. Kar, T.K., Pahari, U.K., Chaudhuri, K.S.: Management of a prey -predator fishery based on continuous fishinf effort. *J. Biol. Syst.* **12**(3), 301–313 (2004)
9. Maynard, J.M.: *Models in Ecology*. xii, 146. University Press, New York (1974)
10. Meserton-Gibbons, M.: On the optimal policy for the combined harvesting of predator and prey. *Nat. Res. Model* **3**, 63–90 (1988)
11. Meserton-Gibbons, M.: A technique for finding optimal two species harvesting policies. *Ecol. Model* **92**, 235–244 (1996)
12. Mukhopadhyay, A., Chattopadhyay, J., Tapaswi, P.K.: A delay differential equations model of plankton alleopathy. *Maths. Biosci.* **149**, 167–189 (1998)
13. Pal, D., Mahapatra, G.S., Mahato, S.K., Samanta, G.P.: A mathematical model of a prey-predator type fishery in the presence of toxicity with fuzzy optimal harvesting with fuzzy optimal harvesting. *J. Appl. Math. Inf.* **38**, 13–36 (2020)
14. Pontryagin, L.S., Boltyanskii, V.S., Gamkrelidze, R.V., Mishchenko, E.F.: *The Mathematical Theory of Optimal Processes*. Wiley, New York (1962)
15. Sarkar, S., Sarkar, A., Chaudhuri, K.S.: Modeling of single species fishery resource harvesting with modified catch rate function. *Bull. Cal. Math. Soc.* **112**(6), 512–524 (2020)

# Analysis for the Impact of HIV Transmission Dynamics in Heterosexuality and Homosexuality



Regan Murugesan , Suresh Rasappan , and Nagadevi Bala Nagaram 

**Abstract** The purpose of this paper is to examine the aspects of the mathematical analysis of HIV transmission through homo and heterosexual. A system of differential equations is designed for the transmission for homo and heterosexual. Equilibrium and interior equilibrium points are identified. Bifurcation analysis forms an important tool in this study. The asymptotic mean square stability criterion is derived for non-deterministic situations. The non-deterministic analysis has been performed around the interior equilibrium point. Numerical simulation is carried out and it supports the theoretical result. Derivation of a mathematical model is the outcome of this study.

**Keywords** HIV transmission · Homosexual · Heterosexual · Bifurcation

## 1 Introduction

Mathematical modeling comes in handy to describe and analyze a real life situation. The Human Immunodeficiency Virus (HIV) turned into diagnosable in 1980s [1]. It is a type of lentivirus. It continues to be a noteworthy worldwide medical problem [2]. According to 2017 statistics, 36.9 million individuals live with HIV and most strikingly around 25% of them do not know that they have the virus [3]. 940,000

---

Supported by Vel Tech University, Avadi, Chennai, Tamil Nadu, India.

---

R. Murugesan (✉) · N. B. Nagaram  
Vel Tech Rangarajan Dr. Sagunthala R & D Institute of Science and Technology, # 42 Avadi- Vel Tech Road, Avadi, Chennai 600062, Tamil Nadu, India  
e-mail: [mreganprof@gmail.com](mailto:mreganprof@gmail.com)

S. Rasappan  
University of Technology and Applied Sciences- Ibri, Sultanate of Oman, Ibri, Oman

© The Author(s), under exclusive license to Springer Nature Switzerland AG 2022  
S. Banerjee and A. Saha (eds.), *Nonlinear Dynamics and Applications*,  
Springer Proceedings in Complexity,  
[https://doi.org/10.1007/978-3-030-99792-2\\_71](https://doi.org/10.1007/978-3-030-99792-2_71)

people have died due to AIDS related illnesses. The homosexual and heterosexual form the major root cause for the transmission of HIV. In India, 2.1 million people live with HIV and especially 86% of people are affected by HIV through sexual transmission. It has been the third biggest HIV epidemic around the world [3].

The majority among HIV people are located in low- and middle-income countries [3]. Sex laborers, men who have intercourse with men (MSM), individuals who infuse drugs (PWID), Hijiras/transgender individuals, migrant workers and truck drivers are the major key affected HIV population in India. There is no solution to cure the diseases till now but controlling the diseases is possible. Controlling the HIV transmission in the external i.e., person to person through sex, needles etc., is more important than the internal of the human body i.e., after presence of HIV in human body cells. Prevention and public awareness are the major instruments to control the HIV infection.

NACO [3] is in charge of defining policy and executing programs for the hindrance and control of the HIV prevalence in India. The main motive of the NACO is to reduce the annual new HIV infections through HIV treatment, education, care and support for those at high risk of HIV.

AIDS is one of the universal menaces to humanity, so most of the mathematicians have been evincing interest to take a look at the transmission of HIV/AIDS and its dynamics by using the mathematical model. Sex structured models are bringing out the better understanding the associated nuances of the disease. Many mathematicians have developed various models without considering the sex structure wherein they have mainly focused on the dynamics of the disease by considering suitable systems of nonlinear differential equations. However, inclusion of sex structure in a mathematical model would make it more realistic.

It would be worthwhile to refer to some of the related works of the previous researchers. Abu and Emeje analyzed the strategies to control HIV/AIDS with mathematical models [4]. The objective of their research is the identification of the effect of condom use and antiretroviral therapy separately and the combination of both as control strategies. Miao et al proposed an SIR model for a stochastic system and investigated the transmission vertically i.e., mother to child and vaccination [5]. The threshold dynamics conditions are explored. They have incorporated less noise and large noise in their model. Their model helps to control the epidemic of infective disease. Bushnaq et al built a biological model to examine the existence and stability of HIV/AIDS infection employing fractional order derivative [6].

The present study focuses attention on the prevention of HIV affected people by undertaking mathematical analysis. Its main focus is on HIV education and counselling support. Due to continuous monitoring (feedback from HIV prevention programmes) of key affected people, the annual threshold level may be stabilized. Our results may also support development in the direction of 90-90-90 objectives in India.

## 2 System Description

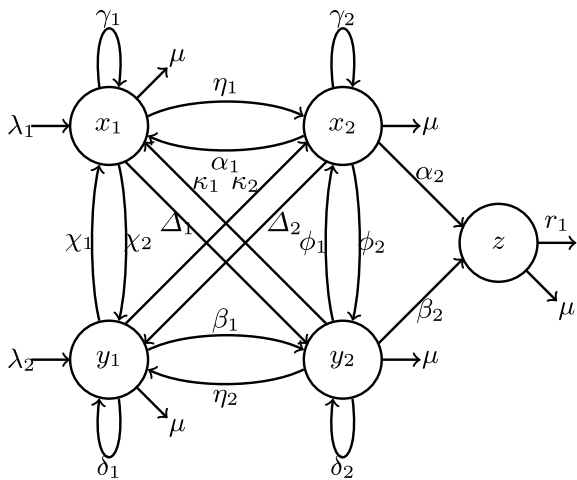
A mathematical model is one way of describing the system using mathematical concept or any mathematical tools. HIV/AIDS is a challenging illness in medical sector. Sex laborers, men who have intercourse with men (MSM), individuals who infuse drugs (PWID), Hijras/transgender individuals, migrant workers and truck drivers are identified as key transmitters. A system of differential equation was designed for HIV transmission [7, 8] under the category homo and heterosexuality. In the present study, a mathematical model is developed based on the following general assumptions:

The sexually active population is divided into five sectors respectively as susceptible female, infected female, susceptible male, infected male and AIDS affected individuals. The population sizes of the genders are initially assumed respectively as  $\lambda_1$  and  $\lambda_2$ . The direct transmission from female-to-female phenomenon is considered. The age factor is ignored. The natural mortality rate  $\mu$  is considered to be equal in all the sectors. All possibilities of HIV transmission through the factors are considered.

The following Fig. 1 represents the flow diagram of HIV transmission. The Mathematical model for the HIV transmission is developed as

$$\begin{aligned}
 \dot{x}_1 &= (\lambda_1 + \gamma_1 - \mu - \alpha_1 - \psi_2 - \Delta_1)x_1 + \eta_1x_2 + y_1 + \kappa_1y_2 \\
 \dot{x}_2 &= \alpha_1x_1 + (\gamma_2 - \eta_1 - \kappa_2 - \mu - \alpha_2 - \phi_1)x_2 + \Delta_2y_1 + \phi_2y_2 \\
 \dot{y}_1 &= \psi_2x_1 + \kappa_2x_2 + (\lambda_2 + \delta_1 - \psi_1 - \Delta_2 - \beta_1 - \mu)y_1 + \eta_2y_2 \\
 \dot{y}_2 &= \Delta_1x_1 + \phi_1x_2 + \beta_1y_1 + (\delta_2 - \eta_2 - \kappa_1 - \phi_2 - \beta_2 - \mu)y_2 \\
 \dot{z} &= \alpha_2x_2 + \beta_2y_2 - (\mu + r_1)z
 \end{aligned} \tag{1}$$

**Fig. 1** Flow diagram of HIV transmission





The modified Mathematical model is

$$\begin{aligned}
 \dot{x}_1 &= \xi_1 x_1 + \eta_1 x_2 + \psi_1 y_1 + \kappa_1 y_2 \\
 \dot{x}_2 &= \alpha_1 x_1 + \xi_2 x_2 + \Delta_2 y_1 + \phi_2 y_2 \\
 \dot{y}_1 &= \psi_2 x_1 + \kappa_2 x_2 + \xi_3 y_1 + \eta_2 y_2 \\
 \dot{y}_2 &= \Delta_1 x_1 + \phi_1 x_2 + \beta_1 y_1 + \xi_4 y_2 \\
 \dot{z} &= \alpha_2 x_2 + \beta_2 y_2 - \xi_5 z
 \end{aligned}
 \tag{2}$$

where  $x_1$  identifies the population suppressed under susceptible females,  $x_2$  represents the individual population of infected females,  $y_1$  identifies the individual population suppressed under susceptible males,  $y_2$  represents the individual population of infected males,  $z$  represents the AIDS affected population,  $\eta_1$  and  $\alpha_1$  are the rates of transmission from  $x_1$  to  $x_2$  and  $x_2$  to  $x_1$ ,  $\beta_1$  and  $\eta_2$  are the rates of transmission from  $y_1$  to  $y_2$  and  $y_2$  to  $y_1$ ,  $\chi_1$  and  $\chi_2$  are the rates of transmission from  $y_1$  to  $x_1$  and  $x_1$  to  $y_1$ ,  $\phi_1$  and  $\phi_2$  are the rates of transmission from  $y_2$  to  $x_2$  and  $x_2$  to  $y_2$ ,  $\Delta_1$  and  $\kappa_1$  are the rates of transmission from  $x_1$  to  $y_2$  and  $y_2$  to  $x_1$ ,  $\Delta_2$  and  $\kappa_2$  are the rates of transmission from  $x_2$  to  $y_1$  and  $y_1$  to  $x_2$ ,  $\gamma_1$  and  $\gamma_2$  are the rates of transmission from  $x_1$  to  $x_1$  and  $x_2$  to  $x_2$ ,  $\delta_1$  and  $\delta_2$  are the rates of transmission from  $y_1$  to  $y_1$  and  $y_2$  to  $y_2$ ,  $\alpha_2$  and  $\beta_2$  are the rates of transmission from  $x_2$  to  $z$  and  $y_2$  to  $z$ ,  $\mu$  and  $r_1$  are the natural death rate at all states and death rate due to AIDS concerning  $z$ , respectively.

### 3 HIV Impact, Equilibrioception and Stability

#### 3.1 Equilibrioception Points

The equilibrioception points arising from the HIV impact are obtained with the fulfillment of the condition  $\dot{x}_1 = \dot{x}_2 = \dot{y}_1 = \dot{y}_2 = \dot{z} = 0$ . The equilibrioception is estimated at individual sectors of the system which is carried out in five cases.

**Case 1:** The HIV transmission rate from susceptible female is assumed to be zero, i.e.,  $\dot{x}_1 = 0$ . After computation, the possible equilibrioception points of the susceptible females are obtained as  $(-\frac{(\kappa_1 y_2 + \psi_1 y_1)}{\xi_1}, 0, 0, 0, 0)$ ,  $(-\frac{(\eta_1 x_2 + \psi_1 y_1)}{\xi_1}, 0, 0, 0, 0)$ ,  $(-\frac{(\eta_1 x_2 + \kappa_1 y_2)}{\xi_1}, 0, 0, 0, 0)$ . These are called as equilibrioception points of susceptible females.

**Case 2:** Consider the case of the transmission rate from infected females taking the value zero i.e.,  $\dot{x}_2 = 0$ . The possible equilibrioception points of the infected females are obtained as  $(0, -\frac{(\Delta_2 y_1 + \phi_2 y_2)}{\xi_2}, 0, 0, 0)$ ,  $(0, -\frac{(\alpha_1 x_1 + \phi_2 y_2)}{\xi_2}, 0, 0, 0)$ ,  $(0, -\frac{(\alpha_1 x_1 + \Delta_2 y_1)}{\xi_2}, 0, 0, 0)$ . They are called infected female equilibrioception points.

**Case 3:** The rate of transmission from susceptible males is taken as zero, i.e.,  $\dot{y}_1 = 0$ . The equilibrioception points in this case are obtained as  $(0, 0, -\frac{(\kappa_2 x_2 + \eta_2 y_2)}{\xi_3}, 0, 0)$ ,  $(0, 0, -\frac{(\psi_2 x_1 + \eta_2 y_2)}{\xi_3}, 0, 0)$  and  $(0, 0, -\frac{(\psi_2 x_1 + \kappa_2 x_2)}{\xi_3}, 0, 0)$ . They are called susceptible male equilibrioception.

**Case 4:** The infected male equilibriocation points are determined when  $\dot{y}_2 = 0$ . They are  $(0, 0, 0, -\frac{(\Delta_1 x_1 + \phi_1 x_2)}{\xi_4}, 0)$ ,  $(0, 0, 0, -\frac{(\beta_1 y_1 + \Delta_1 x_1)}{\xi_4}, 0)$ ,  $(0, 0, 0, -\frac{(\beta_1 y_1 + \phi_1 x_2)}{\xi_4}, 0)$

**Case 5:** Finally, when the transmission rate of AIDS affected people is considered as zero, i.e.,  $\dot{z}_h = 0$ , the equilibriocation points are derived as  $(0, 0, 0, 0, -\frac{\beta_2 y_2}{\xi_5})$  and  $(0, 0, 0, 0, -\frac{\beta_2 x_2}{\xi_5})$ .

### 3.2 Endemic Equilibriocation

The endemic equilibrium point is got as  $E^*(x_1^*, x_2^*, y_1^*, y_2^*, x_1^*, z^*)$  where  $x_1^* = -(\eta_1 x_2 + \kappa_1 y_2 + \psi_1 y_1) / \xi_1$ ,  $x_2^* = -(\alpha_1 x_1 + \Delta_2 y_1 + \phi_2 y_2) / \xi_2$ ,  $y_1^* = -(\psi_2 x_1 + \kappa_2 x_2 + \eta_2 y_2) / \xi_3$ ,  $y_2^* = -(\beta_1 y_1 + \Delta_1 x_1 + \phi_1 x_2) / \xi_4$  and  $z^* = (\alpha_2 x_2 + \beta_2 y_2) / x_{i5}$ . It is seen that HIV transmission persists or exists.

## 4 The Stability of the HIV Impaction

**Theorem 1** *The endemic equilibriocation point  $E^*$  is asymptotically stable globally, if  $(x_1^* - x_1) = \xi_1 + (\eta_1 x_2 + \kappa_1 y_2 + \psi_1 y_1) / x_1$ ,  $(x_2^* - x_2) = \xi_2 + (\alpha_1 x_1 + \Delta_2 y_1 + \phi_2 y_2) / x_2$ ,  $(y_1^* - y_1) = \xi_3 + (\psi_2 x_1 + \kappa_2 x_2 + \eta_2 y_2) / y_1$ ,  $(y_2^* - y_2) = \xi_4 + (\beta_1 y_1 + \Delta_1 x_1 + \phi_1 x_2) / y_2$  and  $(z^* - z) = (\alpha_2 x_2 + \beta_2 y_2) / z - \xi_5$ .*

**Proof** The stability of HIV impaction of the model is obtained by Lyapunov function. It is HIV transmitting function.  $x_1^* - x_1$ ,  $x_2^* - x_2$ ,  $y_1^* - y_1$ ,  $y_2^* - y_2$  and  $z^* - z$  are acting as HIV disease spreading reducers. The stability of the model is depending on the disease reducers. These reducers are considered around the endemic equilibriocation.

Consider the Lyapunov function

$$\begin{aligned}
 V &= (x_1 - x_1^* - x_1^* \log(x_1 / x_1^*)) + (x_2 - x_2^* - x_2^* \log(x_2 / x_2^*)) \\
 &\quad + (y_1 - y_1^* - y_1^* \log(y_1 / y_1^*)) \\
 &\quad + (y_2 - y_2^* - y_2^* \log(y_2 / y_2^*)) + (z - z^* - z^* \log(z / z^*)) \\
 \dot{V} &= (x_1 - x_1^*) \dot{x}_1 / x_1 + (x_2 - x_2^*) \dot{x}_2 / x_2 + (y_1 - y_1^*) \dot{y}_1 / y_1 \\
 &\quad + (y_2 - y_2^*) \dot{y}_2 / y_2 + (z - z^*) \dot{z} / z.
 \end{aligned}$$

By applying endemic equilibrioception point, we obtain

$$\begin{aligned} \dot{V} &= (x_1-x_1^*)(\xi_1 + (\eta_1x_2 + \kappa_1y_2 + \psi_1y_1)/x_1) \\ &\quad + (x_2-x_2^*)(\xi_2 + (\alpha_1x_1 + 2y_1 + \phi_2y_2)/x_2) \\ &\quad + (y_1-y_1^*)(\xi_3 + (\psi_2x_1 + \kappa_2x_2 + \eta_2y_2)/y_1) \\ &\quad + (y_2-y_2^*)(\xi_4 + (\beta_1y_1 + 1x_1 + \phi_1x_2)/y_2) \\ &\quad + (z-z^*)((\alpha_2x_2 + \beta_2y_2)/z-\xi_5) \\ \dot{V} &= -(x_1-x_1^*)^2-(x_2-x_2^*)^2-(y_1-y_1^*)^2-(y_2-y_2^*)^2-(z-z^*)^2 \\ \dot{V} &< 0 \end{aligned}$$

which is negative definite. Hence by LaSalle’s invariance principle, the HIV transmission dynamic (1) is globally asymptotically stable at endemic equilibrioception.

### 5 The Non-deterministic Model

The non-deterministic model is considered for the homo and heterosexual population in a HIV transmission. In this model, the perturbations are permitted into the factors  $x_1, x_2, y_1, y_2$  and  $z$  around the endemic equilibrioception  $E^*$  for the situation when it is feasible and regionally asymptotically steady. Local steadiness of  $E^*$  is implied via the existence conditions of  $E^*$ . So in the model (1), it is assumed that the stochastic disturbances of the factors around their values at  $E^*$  are of white noise type, which are relative to the distances of  $x_1, x_2, y_1, y_2$  and  $z$  from the values of  $x_1^*, x_2^*, y_1^*, y_2^*$  and  $z^*$ . The Stochastic differential equation of the HIV is

$$\begin{aligned} dx_1 &= [\xi_1x_1 + \eta_1x_2 + \psi_1y_1 + \kappa_1y_2]dt + \sigma_1[x_1-x_1^*]dw_1(t) \\ dx_2 &= [\alpha_1x_1 + \xi_2x_2 + 2y_1 + \phi_2y_2]dt + \sigma_2[x_2-x_2^*]dw_2(t) \\ dy_1 &= [\psi_2x_1 + \kappa_2x_2 + \xi_3y_1 + \eta_2y_2]dt + \sigma_3[y_1-y_1^*]dw_3(t) \\ dy_2 &= [1x_1 + \phi_1x_2 + \beta_1y_1 + \xi_4y_2]dt + \sigma_4[y_2-y_2^*]dw_4(t) \\ dz &= [\alpha_2x_2 + \beta_2y_2-\xi_5z]dt + \sigma_4[z-z^*]dw_5(t) \end{aligned} \tag{3}$$

where  $\sigma_i, i = 1, 2, 3, 4, 5$  are real constants and  $w_i(t), i = 1, 2, 3, 4, 5$  are independent from each other by standard Wiener processes [9].

### 6 Stability of the Non-deterministic Model

The non-deterministic model (3) can be centered at its endemic equilibrioception  $E^*$  positively by the change of variables  $u_1 = (x_1-x_1^*), u_2 = (x_2-x_2^*), u_3 = (y_1-y_1^*), u_4 = (y_2-y_2^*), u_5 = (z-z^*)$ . The non-deterministic differential equations around the endemic equilibrioception  $E^*$  are linearized and taken in the form

$$du(t) = f(u(t))dt + g(u(t))dw(t) \tag{4}$$

where  $u(t) = [u_1(t)u_2(t)u_3(t)u_4(t)u_5(t)]^T$

$$f(u(t)) = \begin{bmatrix} \xi_1 & 0 & 0 & 0 & 0 \\ 0 & \xi_2 & 0 & 0 & 0 \\ 0 & 0 & \xi_3 & 0 & 0 \\ 0 & 0 & 0 & \xi_4 & 0 \\ 0 & 0 & 0 & 0 & \xi_5 \end{bmatrix} u(t) \tag{5}$$

$$g(u(t)) = \begin{bmatrix} \sigma_1 u_1 & 0 & 0 & 0 & 0 \\ 0 & \sigma_2 u_2 & 0 & 0 & 0 \\ 0 & 0 & \sigma_3 u_3 & 0 & 0 \\ 0 & 0 & 0 & \sigma_4 u_4 & 0 \\ 0 & 0 & 0 & 0 & \sigma_5 u_5 \end{bmatrix} \tag{6}$$

In (4) the positive interior equilibrium  $E^*$  corresponds to the trivial solution  $u(t) = 0$ . Let  $U$  be the set  $U = \{(t \geq t_0) \times R^n, t_0 \in R^+\}$ .

Thus,  $V \in C_2^0(U)$  is two times constantly differentiable function with respect to  $u$  and a continuous function with respect to  $t$ . With reference to Afanasev et al. [10], the Eq. (4) implies the following Itô differential equation

$$LV(t, u) = \frac{\partial V(t, u)}{\partial t} + f^T(u) \frac{\partial V(t, u)}{\partial t} \frac{1}{2} \text{trace} \left[ g^T(u) \frac{\partial^2 V(t, u)}{\partial u^2} g(u) \right]$$

where  $\frac{\partial V}{\partial u} = Col \left( \frac{\partial V}{\partial u_1}, \frac{\partial V}{\partial u_2}, \frac{\partial V}{\partial u_3}, \frac{\partial V}{\partial u_4}, \frac{\partial V}{\partial u_5} \right)$  and  $\frac{\partial^2 V(t, u)}{\partial u^2} = \frac{\partial^2 V}{\partial u_j \partial u_i}, i, j = 1, 2, 3, 4$ .

### Remarks

Suppose the function  $V \in C_2^0(U)$  exists as above. Then if the inequalities

$$M_1|u|^q \leq V(t, u) \leq M_2|u|^q, \tag{7}$$

$$LV(t, u) \leq -M_3|u|^q, M_i > 0, q > 0 \tag{8}$$

hold, then the trivial solution of (4) is exponentially  $q$ -stable for  $t \geq 0$ . When  $q = 2$  the trivial solution due to (7) and (8) is globally asymptotically steady in probability.

**Theorem 2** *If  $\sigma_1^2 = -4\xi_1, \sigma_2^2 = -4\xi_2, \sigma_3^2 = -4\xi_3, \sigma_4^2 = -4\xi_4$  and  $\sigma_5^2 = -4\xi_5$ , then the solution with the zero of (4) is asymptotically mean square steady.*

**Proof** Let us assume the Lyapunov function

$$V(u) = \frac{1}{2}[w_1u_1^2 + w_2u_2 + w_3u_3^2 + w_4u_4^2 + w_5u_5^2]$$

where  $w_i, i = 1, 2, 3, 4, 5$  are real positive constants to be chosen. It is straightforward to check that the inequalities (7) and (8) hold with  $q = 2$ . Now the Itô Process gives

$$V(u) = w_1(\xi_1u_1)u_1 + w_2(\xi_2u_2)u_2 + w_3(\xi_3u_3)u_3 + w_4(\xi_4u_4)u_4 + w_5(\xi_5u_5)u_5 + \frac{1}{2}\text{trace} \left[ g^T(u) \frac{\partial^2 V(t, u)}{\partial u^2} g(u) \right]$$

$$V(u) = w_1(\xi_1u_1)u_1 + w_2(\xi_2u_2)u_2 + w_3(\xi_3u_3)u_3 + w_4(\xi_4u_4)u_4 + w_5(\xi_5u_5)u_5 + \frac{1}{2}[\sigma_1^2w_1u_1^2 + \sigma_2^2w_2u_2^2 + \sigma_3^2w_3u_3^2 + \sigma_4^2w_4u_4^2 + \sigma_5^2w_5u_5^2] = w_1(\xi_1 + \sigma_1^2)u_1^2 + w_2(\xi_2 + \sigma_2^2)u_2^2 + w_3(\xi_3 + \sigma_3^2)u_3^2 + w_4(\xi_4 + \sigma_4^2)u_4^2 + w_5(\xi_5 + \sigma_5^2)u_5^2$$

$$V(u) = -\xi_1w_1u_1^2 - \xi_2w_2u_2^2 - \xi_3w_3u_3^2 - \xi_4w_4u_4^2 - \xi_5w_5u_5^2$$

Hence the system is asymptotically mean square stable.

## 7 Numerical Simulation for Deterministic Model

A simulation was carried out by taking the initial conditions  $x_1 = 5.013, y_1 = 4.218, z = 1.298, x_2 = 4.558, y_2 = 9.383$ . and the parametric values

$$\xi_1 = 0.2345, \eta_1 = 0.3837, \psi_1 = 0.2312, \varphi_1 = 0.2345, \xi_2 = 0.4834, \eta_2 = 0.7845, \psi_2 = 0.7543, \varphi_2 = 0.4567, \xi_3 = 0.1987, \alpha_1 = 0.1976, \beta_1 = 0.9109, 1 = 0.1209, \xi_4 = 0.2987, \alpha_2 = 0.7652, \beta_2 = 0.2109, 2 = 0.5768, \xi_5 = 0.2345, \kappa_1 = 0.9872, \kappa_2 = 0.6092$$

As a result of this simulation process between the five states, it is observed that the dissemination of HIV in a homo and heterosexual affected populace is stabilized at the origin. The result is depicted in Fig. 2.

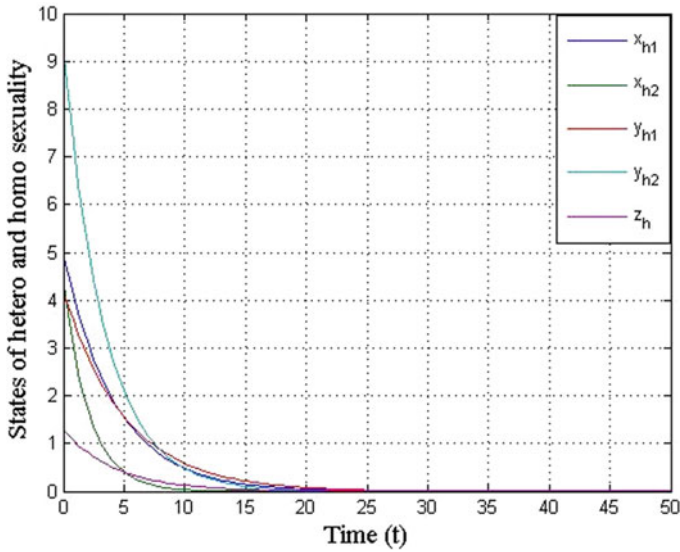


**Fig. 2** Analysis of deterministic system for dissemination of HIV among homosexual and heterosexual affected population

### 8 Numerical Example for Non-deterministic Model

A simulation was carried out by taking the initial conditions  $x_1 = 15.013$ ,  $y_1 = 17.218$ ,  $z = 5.298$ ,  $x_2 = 18.558$ ,  $y_2 = 15.383$  and the parametric values  $\xi_1 = 0.5645$ ,  $\eta_1 = 0.7247$ ,  $\psi_1 = 0.6542$ ,  $\varphi_1 = 0.7250$ ,  $\xi_2 = 0.5234$ ,  $\eta_2 = 0.6845$ ,  $\psi_2 = 0.3543$ ,  $\varphi_2 = 0.6567$ ,  $\xi_3 = 0.7987$ ,  $\alpha_1 = 0.2376$ ,  $\beta_1 = 0.7609$ ,  $\gamma_1 = 0.6209$ ,  $\xi_4 = 0.1257$ ,  $\alpha_2 = 0.7651$ ,  $\beta_2 = 0.8654$ ,  $\gamma_2 = 0.2768$ ,  $\xi_5 = 0.8765$ ,  $\kappa_1 = 0.1872$ ,  $\kappa_2 = 0.1092$ .

The noise band in Wiener process is taken as the closed interval  $[0, 1]$ . With the above values, the following observations are made.

When the value of  $\sigma$  is in the range between 0.1 and 0.49, susceptible males and infected females are affected more by HIV. When the value of  $\sigma$  is in the range between 0.5 and 1, the persons in all the five categories namely susceptible female, infected female, susceptible male, infected male and AIDS affected people are impacted by the HIV transmission of homo and heterosexual population. The simulation result for the non-deterministic model is furnished in Fig. 3.

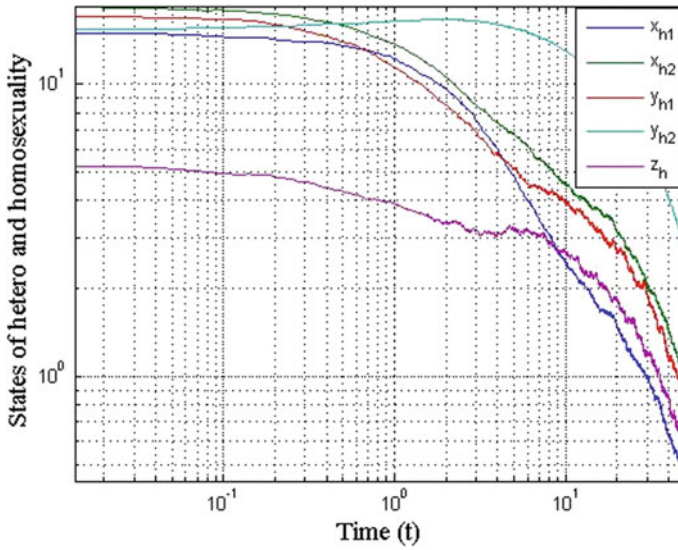


Fig. 3 Non-deterministic nature of homosexual and heterosexual affected population

## 9 Hyperbolic Equilibria and Bifurcation Analysis

### 9.1 Hyperbolic Equilibria

The Jacobian matrix of the model (1) is

$$J = \begin{bmatrix} \xi_1 & \eta_1 & \psi_1 & \kappa_1 & 0 \\ \alpha_1 & \xi_2 & \Delta_2 & \phi_2 & 0 \\ \psi_2 & \kappa_2 & \xi_3 & \eta_2 & 0 \\ \Delta_1 & \phi_1 & \beta_1 & \xi_4 & 0 \\ 0 & \alpha_2 & 0 & \beta_2 & -\xi_5 \end{bmatrix} \tag{9}$$

The characteristic equation of the Jacobian matrix  $J$  is

$$\lambda^5 - a\lambda^4 - b\lambda^3 - c\lambda^2 - d\lambda - E = 0 \tag{10}$$

In this analysis, If  $E \neq 0$ , then there exists a hyperbolic equilibrium point for the system. This equilibrium point is robust. Therefore the system of equations is structurally stable and when  $E = 0$ , there exists a non-hyperbolic equilibrium point.

## 9.2 Bifurcation

If  $\eta_1, \psi_1, \kappa_1, \alpha_2, \beta_1$  and  $\beta_2$  are negative, or  $\eta_1, \psi_1, \kappa_1, \beta_1 = 0$  or negative,  $\alpha_2 = 0$  and  $\beta_2 = 0$ , then  $J$  has a pair of imaginary eigen values. Consequently, the stability of the system may change or disappear or split into many equilibrium points. This indicates the existence of bifurcation. If  $\xi_1 = \xi_4 = \xi_5 = 0$ , then  $J$  has zero eigenvalue and a pair of imaginary eigen values. In this case also, bifurcation exists.

## 10 Conclusion

The mathematical analysis of the problem of HIV transmission through homo and heterosexual investigated by designing a new mathematical model. A non-deterministic model is investigated and its qualitative properties are analyzed. Hyperbolic equilibrium points and bifurcation analysis strengthen the qualitative properties of the proposed model. The hyperbolic equilibrium points give the robustness of the proposed model. Numerical computations concerning the stability analysis of the proposed model using the MATLAB software are presented. From the bifurcation analysis, it is observed that the disease-free equilibrium condition is not possible if the individual can suppress AIDS and the mortality rate or mortality span may undergo change due to continuous prevention and treatment. As a result of this study it is seen that, due to the severity of the HIV transmission, the endemic equilibrium may change, disappear or split into many endemic equilibrium.

**Acknowledgements** The authors are thankful to the Reviewer for the comments and suggestions towards the improvement of the paper.

## References

1. Dietz, K.: On the transmission dynamics of HIV. *Math. Biosci.* **90**(1–2), 397–414 (1988)
2. Kremer, M., Morcom, C.: The effect of changing sexual activity on HIV prevalence. *Math. Biosci.* **151**(1), 99–122 (1998)
3. Global information and education on HIV and AIDS. <https://www.avert.org/global-HIV-and-AIDS-statistics> (2019)
4. Abu, O., Emeje, M.A.: Comparative analysis of HIV/AIDS control strategies with mathematical models. *J. Scient. Eng. Res.* **3**, 442–448 (2016)
5. Miao, A., Zhang, J., Zhang, T., Pradeep, B.G.: Threshold dynamics of a stochastic model with vertical transmission and vaccination. *Comput. Math. Methods Med.*, 1–10 (2017)
6. Bushnaq, S., Khan, S.A., Shah, K., Zaman, G.: Mathematical analysis of HIV/AIDS infection model with Caputo-Fabrizio fractional derivative. *Cogent Math. Stat.* **5**(1), 1432521 (2018)
7. May, R.M., Anderson, R.M., McLean, A.R.: Possible demographic consequences of HIV/AIDS epidemics II. Assuming HIV infection does not necessarily lead to AIDS. In: *Mathematical Approaches to Problems in Resource Management and Epidemiology* (Ithaca, NY, 1987), Lecture Notes in Biomathematics, Springer, Berlin, 81, 220–248 (1989)



8. Sani, A., Kroese, D.P., Pollett, P.K.: Stochastic models for the spread of HIV in a mobile heterosexual population. *Math. Biosci.* **208**(1), 98–124 (2007)
9. Mukherjee, D.: Stability analysis of a stochastic model for prey-predator system with disease in the prey. *Nonlinear Anal. Model. Control* **8**(2), 83–92 (2003)
10. Afanas'ev, V.N., Kolmanowski, V.B., Nosov, V.R.: *Mathematical Theory of Global Systems Design*. Kluwer Academic, Dordrecht (1996)

# Exact Traveling Wave Solutions to General FitzHugh-Nagumo Equation



Subin P. Joseph

**Abstract** A general FitzHugh–Nagumo equation is considered in this paper and new traveling wave exact solutions for this nonlinear partial differential equation are derived. This nonlinear reaction-diffusion equation models several evolution equations such as the transmission of nerve impulses and the evolutionary rescue in the case of spatial invasions. Since the equation is highly nonlinear, the exact solutions are computed using certain ansatz forms and using a computer algebra system.

**Keywords** FitzHugh–Nagumo equation · Nonlinear evolution equation · Exact solutions

## 1 Introduction

In this paper we consider the cubic nonlinear evolutionary equation

$$\frac{\partial u}{\partial t} - \eta \frac{\partial^2 u}{\partial x^2} = \alpha_1 u + \alpha_2 u^2 + \alpha_3 u^3 \quad (1)$$

where  $u = u(x, t)$  and  $\eta, \alpha_1, \alpha_2$  and  $\alpha_3$  are real parameters. This equation is the generalization of FitzHugh–Nagumo equation [11, 12] given by

$$\frac{\partial u}{\partial t} - \frac{\partial^2 u}{\partial x^2} = u(1 - u)(u - \rho), \quad (2)$$

with  $\alpha_1 = -\rho, \alpha_2 = (1 + \rho), \alpha_3 = -1, \eta = 1$  and  $0 < \rho < 1$ . Equation (2) has many applications in the fields of astrophysics, fluid mechanics, exciting electronic circuit theory, population genetics, heart electrical waves, chemical chemistry, trans-

---

Supported by TEQIP-II Four Funds, Government Engineering College, Wayanad.

---

S. P. Joseph (✉)  
Government Engineering College, Wayanad, Thalapuzha, Kerala, India  
e-mail: [subinpj@gecwyd.ac.in](mailto:subinpj@gecwyd.ac.in)

© The Author(s), under exclusive license to Springer Nature Switzerland AG 2022  
S. Banerjee and A. Saha (eds.), *Nonlinear Dynamics and Applications*,  
Springer Proceedings in Complexity,  
[https://doi.org/10.1007/978-3-030-99792-2\\_72](https://doi.org/10.1007/978-3-030-99792-2_72)

mission of nerve impulses and the evolutionary rescue in the case of spatial invasions etc. [1, 2, 4–7, 10, 13–15, 17–19].

The theory which investigate evolutionary rescue in the case of well-mixed populations that are declining due to an environmental shift and spatial invasions are presented in [19]. The prevention of population extinction by adaptation is termed as evolutionary rescue [3, 8]. If  $u(x, t)$  is the relative invader frequency, then its rate of change is

$$\frac{\partial u}{\partial t} - \eta \frac{\partial^2 u}{\partial x^2} = \omega u(1 - u), \quad (3)$$

where  $\eta$  and  $\omega$  are the species diffusion constant and the frequency independent fitness advantage for the invader respectively. Similarly, when the fitness of the resident is linearly decreasing with respect to the frequency of the invader, then

$$\frac{\partial u}{\partial t} - \eta \frac{\partial^2 u}{\partial x^2} = \omega u^2(1 - u). \quad (4)$$

The Eqs. (3) and (4) are special cases of the general Eq. (1). Putting  $\alpha_1 = \omega$ ,  $\alpha_2 = -\omega$ ,  $\alpha_3 = 0$  and putting  $\alpha_1 = 0$ ,  $\alpha_2 = \omega$ ,  $\alpha_3 = -\omega$  in Eq. (1), we can recover these equations respectively.

Since the evolutionary equations given above are having many applications in different fields such as natural computations, exact solutions are necessary for the better analysis of the situation in hand as well as checking the accuracy of approximate solutions. But the available exact solutions are rare for these nonlinear evolutionary equations [5–7]. Nonlinear partial differential equations are very difficult to solve in general to find exact solutions. Several methods are developed to find exact solutions for nonlinear equations that appear in mathematical physics. But the efficient and widely used method to solve these equations are various ansatz methods, such as tanh method, sech method, sinh-cosh method, Exp-function method, the Jacobi elliptic function expansion method and (G'/G)-expansion method and several variants of these methods [9, 16, 20, 21]. In this paper also we apply ansatz method to find new traveling wave exact solutions to the general evolution Eq. (1). Since the computations are much involved, we need to depend on any of the powerful computer algebra system in performing the required computations. In the next section we explain the algorithm used to compute the solutions. Several new exact solutions for the general evolution equation are derived in the third section. The paper is concluded in the last section with a discussion.

## 2 Method

We need to find the traveling wave solutions to the evolution Eq. (1). First of all, the traveling wave transformation  $u(x, t) = v(\xi)$  is used to convert this equation in to an ordinary differential equation, where  $\xi = dx + ct$  and  $d$  and  $c$  are traveling wave parameters. The resulting ordinary differential equation is then given by

$$d^2\eta v''(\xi) - cv'(\xi) + \alpha_1 v(\xi) + \alpha_2 v(\xi)^2 + \alpha_3 v(\xi)^3 = 0. \tag{5}$$

Now, to derive the exact solutions, we assume that the solutions to the above ordinary differential equation exist in the form

$$v(\xi) = a_0 + \frac{a_1 + a_2 g_1(\xi) + a_3 h_1(\xi)}{b_1 + b_2 g_2(\xi) + b_3 h_2(\xi)} \tag{6}$$

where the functions  $g_1, g_2, h_1$  and  $h_2$  and the parameters  $a_i$ 's and  $b_i$ 's are to be determined later. Then,  $v(\xi)$  given by Eq. (6) is substituted in to the ordinary differential Eq. (5). Then we obtain a system of nonlinear algebraic equations corresponding to this differential equation by using any of the computational algebra system. This system of equations is then solved to determine the value of the parameters. Using these parametric values we can determine the exact solutions to Eq. (1). We use different trial functions to derive new exact solutions in the following section.

### 3 Exact Solutions

To obtain the first family of solutions, we select the trial function  $g_1(\xi) = \operatorname{sech}^2(\xi), g_2(\xi) = \operatorname{csch}^2(\xi), h_1(\xi) = \tanh(\xi)$  and  $h_2(\xi) = \operatorname{coth}(\xi)$ . Then Eq. (6) becomes

$$v(\xi) = a_0 + \frac{a_1 + a_2 \operatorname{sech}^2(\xi) + a_3 \operatorname{csch}^2(\xi)}{b_1 + b_2 \tanh(\xi) + b_3 \operatorname{coth}(\xi)}. \tag{7}$$

Substituting this value of  $v(\xi)$  in Eq. (5), we get a system of thirteen nonlinear algebraic equations given in appendix. Solving this system of algebraic equations, the following sets of different solutions are obtained.

SET-I:

$$c = \pm \frac{\alpha_2 \sqrt{\alpha_2^2 - 4\alpha_1\alpha_3}}{4\alpha_3}, \quad d = -\frac{\sqrt{4\alpha_1\alpha_3 - \alpha_2^2}}{2\sqrt{2}\sqrt{\alpha_3}\sqrt{\eta}}, \quad b_1 = -\frac{a_1\alpha_2}{2\alpha_1}, \quad a_0 = 0$$

$$b_2 = \mp \frac{a_1\sqrt{\alpha_2^2 - 4\alpha_1\alpha_3}}{2\alpha_1}, \quad b_3 = 0, \quad a_2 = \frac{1}{4}a_1 \left( \frac{\alpha_2^2}{\alpha_1\alpha_3} - 4 \right), \quad a_3 = 0. \tag{8}$$

SET-II:

$$c = \pm \frac{\alpha_2 \sqrt{\alpha_2^2 - 4\alpha_1\alpha_3}}{4\alpha_3}, \quad d = -\frac{\sqrt{4\alpha_1\alpha_3 - \alpha_2^2}}{2\sqrt{2}\sqrt{\alpha_3}\sqrt{\eta}}, \quad b_1 = -\frac{a_1\alpha_2}{2\alpha_1}, \quad a_0 = 0$$

$$b_2 = 0, \quad b_3 = \mp \frac{a_1\sqrt{\alpha_2^2 - 4\alpha_1\alpha_3}}{2\alpha_1}, \quad a_2 = 0, \quad a_3 = a_1 \left( 1 - \frac{\alpha_2^2}{4\alpha_1\alpha_3} \right). \tag{9}$$

SET-III:

$$\begin{aligned}
 c &= \pm \frac{\alpha_2 \sqrt{\alpha_2^2 - 4\alpha_1\alpha_3}}{8\alpha_3}, & d &= -\frac{\sqrt{4\alpha_1\alpha_3 - \alpha_2^2}}{4\sqrt{2}\sqrt{\alpha_3}\sqrt{\eta}}, & b_1 &= -\frac{a_1\alpha_2}{2\alpha_1}, & a_0 &= 0 \\
 b_2 &= \mp \frac{a_1\sqrt{\alpha_2^2 - 4\alpha_1\alpha_3}}{4\alpha_1}, & b_3 &= \mp \frac{a_1\sqrt{\alpha_2^2 - 4\alpha_1\alpha_3}}{4\alpha_1}, \\
 a_2 &= \frac{1}{16}a_1 \left( \frac{\alpha_2^2}{\alpha_1\alpha_3} - 4 \right), & a_3 &= \frac{1}{16}a_1 \left( 4 - \frac{\alpha_2^2}{\alpha_1\alpha_3} \right).
 \end{aligned}
 \tag{10}$$

SET-IV:

$$\begin{aligned}
 c &= \pm \frac{\alpha_2 \sqrt{\alpha_2^2 - 4\alpha_1\alpha_3}}{8\alpha_3}, & d &= -\frac{\sqrt{4\alpha_1\alpha_3 - \alpha_2^2}}{4\sqrt{2}\sqrt{\alpha_3}\sqrt{\eta}}, & b_1 &= -\frac{a_1\alpha_2}{2\alpha_1}, & a_0 &= 0 \\
 b_2 &= \mp \frac{a_1\sqrt{\alpha_2^2 - 4\alpha_1\alpha_3}}{4\alpha_1}, & b_3 &= \mp \frac{a_1\sqrt{\alpha_2^2 - 4\alpha_1\alpha_3}}{4\alpha_1}, & a_2 &= 0, & a_3 &= 0.
 \end{aligned}
 \tag{11}$$

SET-V:

$$\begin{aligned}
 c &= \pm \frac{\alpha_2 \sqrt{\alpha_2^2 - 4\alpha_1\alpha_3}}{4\alpha_3}, & d &= \frac{\sqrt{4\alpha_1\alpha_3 - \alpha_2^2}}{2\sqrt{2}\sqrt{\alpha_3}\sqrt{\eta}}, & b_1 &= -\frac{a_1\alpha_2}{2\alpha_1}, & a_0 &= 0 \\
 b_2 &= 0, & b_3 &= \mp \frac{a_1\sqrt{\alpha_2^2 - 4\alpha_1\alpha_3}}{2\alpha_1}, & a_2 &= 0, & a_3 &= 0.
 \end{aligned}
 \tag{12}$$

SET-VI:

$$\begin{aligned}
 c &= \pm \frac{\alpha_2 \sqrt{\alpha_2^2 - 4\alpha_1\alpha_3}}{4\alpha_3}, & d &= \frac{\sqrt{4\alpha_1\alpha_3 - \alpha_2^2}}{2\sqrt{2}\sqrt{\alpha_3}\sqrt{\eta}}, & b_1 &= -\frac{a_1\alpha_2}{2\alpha_1}, & a_0 &= 0 \\
 b_2 &= \mp \frac{a_1\sqrt{\alpha_2^2 - 4\alpha_1\alpha_3}}{2\alpha_1}, & b_3 &= 0, & a_2 &= 0, & a_3 &= 0.
 \end{aligned}
 \tag{13}$$

Corresponding to each set of above solutions, the exact solutions for the FitzHugh–Nagumo equation are given below respectively.

$$v_{1,2}(x, t) = -\frac{\operatorname{sech}^2(ct + dx) (\alpha_2^2 + 4\alpha_1\alpha_3 \sinh^2(ct + dx))}{2\alpha_3 \left( \alpha_2 \pm \sqrt{\alpha_2^2 - 4\alpha_1\alpha_3} \tanh(ct + dx) \right)}, \tag{14}$$

$$v_{3,4}(x, t) = \frac{\alpha_2^2 \operatorname{csch}^2(ct + dx) - 4\alpha_1\alpha_3 \operatorname{coth}^2(ct + dx)}{2\alpha_3 \left( \alpha_2 \pm \sqrt{\alpha_2^2 - 4\alpha_1\alpha_3} \operatorname{coth}(ct + dx) \right)}, \tag{15}$$

$$v_{5,6}(x, t) = \frac{\operatorname{csch}(ct + dx)\operatorname{sech}(ct + dx) (\alpha_2^2 - 4\alpha_1\alpha_3 \cosh^2(2(ct + dx)))}{4\alpha_3 \left( \alpha_2 \sinh(2(ct + dx)) \pm \sqrt{\alpha_2^2 - 4\alpha_1\alpha_3 \cosh(2(ct + dx))} \right)}, \quad (16)$$

$$v_{7,8}(x, t) = -\frac{2\alpha_1 \sinh(2(ct + dx))}{\alpha_2 \sinh(2(ct + dx)) \pm \sqrt{\alpha_2^2 - 4\alpha_1\alpha_3 \cosh(2(ct + dx))}}, \quad (17)$$

$$v_{9,10}(x, t) = -\frac{2\alpha_1}{\alpha_2 \pm \sqrt{\alpha_2^2 - 4\alpha_1\alpha_3} \coth(ct + dx)}, \quad (18)$$

$$v_{11,12}(x, t) = -\frac{2\alpha_1}{\alpha_2 \pm \sqrt{\alpha_2^2 - 4\alpha_1\alpha_3} \tanh(ct + dx)}, \quad (19)$$

where the values of  $c$  and  $d$  are given by Eqs. (8)–(13). Graphical representation of the first solution  $u_1(x, t)$  is given in Fig. 1.

Now, we will derive second family of solutions by letting  $g_1(\xi) = \coth(\xi)$ ,  $g_2(\xi) = 0$ ,  $h_1(\xi) = \coth^2(\xi)$  and  $h_2(\xi) = 0$ . Then Eq. (6) becomes

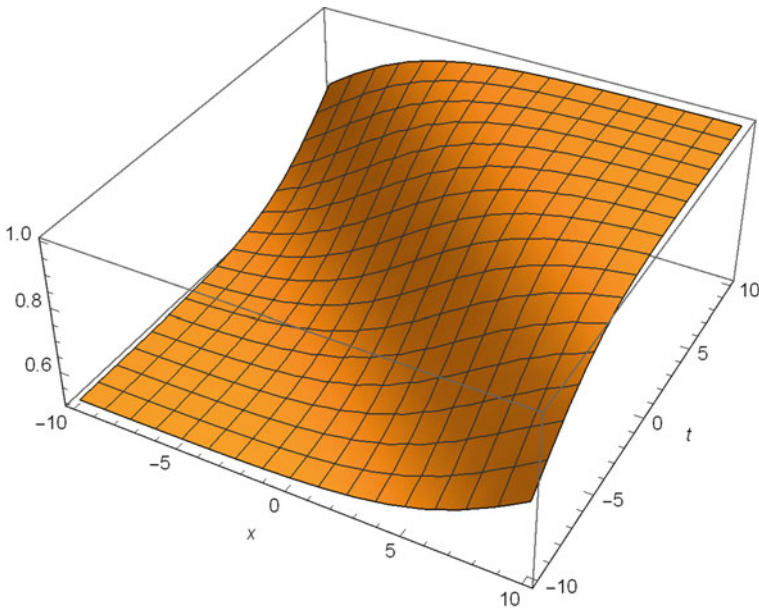


**Fig. 1** Graphical representation of the exact solution  $v_1(x, t)$  given by Eq. (14) of the FitzHugh–Nagumo equation, where  $\eta = 1$ ,  $\alpha_1 = -\frac{1}{2}$ ,  $\alpha_2 = \frac{3}{2}$ ,  $\alpha_3 = -1$

$$v(\xi) = a_0 + \frac{a_1 + a_2 \coth(\xi)}{b_1 + b_2 \coth^2(\xi)}. \tag{20}$$

Substituting this value of  $v(\xi)$  in Eq. (5), we get another system of nonlinear algebraic equations given by

$$\begin{aligned} a_2 b_1^2 c &= \alpha_3 a_1^3 + a_1^2 b_1 (3a_0 \alpha_3 + \alpha_2) + a_0 b_1^3 (a_0 (a_0 \alpha_3 + \alpha_2) + \alpha_1) \\ &\quad + a_1 b_1 (b_1 (3\alpha_3 a_0^2 + 2\alpha_2 a_0 + \alpha_1) - 2b_2 d^2 \eta), \\ 2a_1 (b_1 - b_2) b_2 c &= \alpha_3 a_2^3 + 2a_2 (b_2 b_1 (2a_0 \alpha_2 + 3a_0^2 \alpha_3 + \alpha_1 + 6d^2 \eta) \\ &\quad + b_2 (a_1 (3a_0 \alpha_3 + \alpha_2) + b_2 d^2 \eta) + b_1^2 d^2 \eta), \\ b_2 (a_0 b_2 (a_0 (a_0 \alpha_3 + \alpha_2) + \alpha_1) - a_2 c + 2a_1 d^2 \eta) &= 0, \\ b_2 (2a_1 b_2 c + a_2 (b_2 (-2a_0 \alpha_2 - 3a_0^2 \alpha_3 - \alpha_1 + 2d^2 \eta) + 6b_1 d^2 \eta)) &= 0, \\ b_2 (a_2^2 (3a_0 \alpha_3 + \alpha_2) + 3a_0 b_1 b_2 (a_0 (a_0 \alpha_3 + \alpha_2) + \alpha_1) \\ &\quad + a_2 b_2 c + a_1 (b_2 (2a_0 \alpha_2 + 3a_0^2 \alpha_3 + \alpha_1 - 8d^2 \eta) - 6b_1 d^2 \eta)) = 0, \\ 2a_1 b_1 b_2 c + a_2 (3\alpha_3 a_1^2 + b_1^2 (2a_0 \alpha_2 + 3a_0^2 \alpha_3 + \alpha_1 - 2d^2 \eta) \\ &\quad + b_1 (2a_1 (3a_0 \alpha_3 + \alpha_2) - 6b_2 d^2 \eta)) a_2^2 (3a_1 \alpha_3 + b_1 (3a_0 \alpha_3 + \alpha_2)) \\ &\quad + a_2 b_1^2 c + b_2 (a_1^2 (3a_0 \alpha_3 + \alpha_2) + 3a_0 b_1^2 (a_0 (a_0 \alpha_3 + \alpha_2) + \alpha_1) \\ &\quad + 2a_1 (b_1 (2a_0 \alpha_2 + 3a_0^2 \alpha_3 + \alpha_1 + 4d^2 \eta) + 3b_2 d^2 \eta)) = 0. \end{aligned} \tag{21}$$

Solving this system of algebraic equations, the following sets of different solutions are obtained.

SET-I:

$$\begin{aligned} c &= \pm \frac{\alpha_2 \sqrt{\alpha_2^2 - 4\alpha_1 \alpha_3}}{4\alpha_3}, d = -\frac{\sqrt{4\alpha_1 \alpha_3 - \alpha_2^2}}{2\sqrt{2}\sqrt{\alpha_3}\sqrt{\eta}}, \\ a_2 &= \mp \frac{a_1 \sqrt{\alpha_2^2 - 4\alpha_1 \alpha_3}}{\alpha_2}, b_1 = -\frac{a_1 \alpha_2}{2\alpha_1}, b_2 = a_1 \left( \frac{\alpha_2}{2\alpha_1} - \frac{2\alpha_3}{\alpha_2} \right). \end{aligned} \tag{22}$$

SET-II:

$$\begin{aligned} c &= \pm \frac{\alpha_2 \sqrt{\alpha_2^2 - 4\alpha_1 \alpha_3}}{4\alpha_3}, d = \frac{\sqrt{4\alpha_1 \alpha_3 - \alpha_2^2}}{2\sqrt{2}\sqrt{\alpha_3}\sqrt{\eta}}, \\ a_2 &= \mp \frac{a_1 \sqrt{\alpha_2^2 - 4\alpha_1 \alpha_3}}{\alpha_2}, b_1 = -\frac{a_1 \alpha_2}{2\alpha_1}, b_2 = a_1 \left( \frac{\alpha_2}{2\alpha_1} - \frac{2\alpha_3}{\alpha_2} \right). \end{aligned} \tag{23}$$

Corresponding to the above sets of solutions, the only exact solutions for the FitzHugh–Nagumo equation are given by .

$$v_{13,14}(x, t) = -\frac{2\alpha_1 \left( \alpha_2 \pm \sqrt{\alpha_2^2 - 4\alpha_1\alpha_3} \coth(ct + dx) \right)}{4\alpha_1\alpha_3 \coth^2(ct + dx) - \alpha_2^2 \operatorname{csch}^2(ct + dx)}. \tag{24}$$

where the values of  $c$  and  $d$  are given by Eqs. (22) and (23).

Finally, we derive a third family of solutions by letting  $g_1(\xi) = \tanh(\xi)$ ,  $g_2(\xi) = 0$ ,  $h_1(\xi) = \operatorname{sech}^2(\xi)$  and  $h_2(\xi) = 0$ . Then Eq. (6) becomes

$$v(\xi) = a_0 + \frac{a_1 + a_2 \tanh(\xi)}{b_1 + b_2 \operatorname{sech}^2(\xi)}. \tag{25}$$

Substituting this value of  $v(\xi)$  in the Eq. (5), we get a system of nonlinear algebraic equations given by

$$\begin{aligned} & a_2 (b_1 + b_2)^2 c = \alpha_3 a_1^3 + a_1^2 (b_1 + b_2) (3a_0\alpha_3 + \alpha_2) + a_0 (b_1 + b_2)^3 (a_0 (a_0\alpha_3 + \alpha_2) + \alpha_1) \\ & + a_1 (b_1 + b_2) (b_1 (a_0 (3a_0\alpha_3 + 2\alpha_2) + \alpha_1) + b_2 (2a_0\alpha_2 + 3a_0^2\alpha_3 + \alpha_1 + 2d^2\eta)), \\ & b_2 (a_0 b_2 (a_0 (a_0\alpha_3 + \alpha_2) + \alpha_1) + a_2 c - 2a_1 d^2 \eta) = 0, \\ & b_2 (a_2^2 (- (3a_0\alpha_3 + \alpha_2)) + 3a_0 b_2 (b_1 + b_2) (a_0 (a_0\alpha_3 + \alpha_2) \\ & + \alpha_1) + a_2 b_2 c + a_1 (b_2 (2a_0\alpha_2 + 3a_0^2\alpha_3 + \alpha_1 - 2d^2\eta) + 6b_1 d^2 \eta)) = 0, \\ & b_2 (a_1^2 (3a_0\alpha_3 + \alpha_2) + 3a_0 (b_1 + b_2)^2 (a_0 (a_0\alpha_3 + \alpha_2) + \alpha_1) \\ & + 2a_1 (b_2 (2a_0\alpha_2 + 3a_0^2\alpha_3 + \alpha_1 + d^2\eta) + b_1 (2a_0\alpha_2 + 3a_0^2\alpha_3 + \alpha_1 + 4d^2\eta))) \\ & = a_2 (a_2 (3a_1\alpha_3 + b_1 (3a_0\alpha_3 + \alpha_2)) + b_2 (3a_0\alpha_3 + \alpha_2)) + (b_1 + b_2)^2 c, \end{aligned} \tag{26}$$

$$\begin{aligned} & b_2 (a_2 (b_2 (2a_0\alpha_2 + 3a_0^2\alpha_3 + \alpha_1 + 4d^2\eta) + 6b_1 d^2 \eta) - 2a_1 b_2 c) = 0, \\ & a_2 (b_2 b_1 (2a_0\alpha_2 + 3a_0^2\alpha_3 + \alpha_1 + 4d^2\eta) + b_2 (a_1 (3a_0\alpha_3 + \alpha_2) \\ & + b_2 (2a_0\alpha_2 + 3a_0^2\alpha_3 + \alpha_1 + 4d^2\eta)) + b_1^2 (-d^2) \eta) = \alpha_3 a_2^3 + 2ca_1 b_2 (b_1 + 2b_2), \\ & 2a_1 b_2 (b_1 + b_2) c + a_2 (-3\alpha_3 a_1^2 - 2a_1 b_2 (3a_0\alpha_3 + \alpha_2) \\ & - b_2^2 (2a_0\alpha_2 + 3a_0^2\alpha_3 + \alpha_1 + 4d^2\eta) + b_1^2 (-2a_0\alpha_2 - 3a_0^2\alpha_3 - \alpha_1 + 2d^2\eta) \\ & - 2b_1 (a_1 (3a_0\alpha_3 + \alpha_2) + b_2 (2a_0\alpha_2 + 3a_0^2\alpha_3 + \alpha_1 + d^2\eta))) = 0. \end{aligned} \tag{27}$$

Solving this system of algebraic equations, the following sets of different solutions are obtained.

SET-I:

$$\begin{aligned} c &= \pm \frac{\alpha_2 \sqrt{\alpha_2^2 - 4\alpha_1\alpha_3}}{4\alpha_3}, d = -\frac{\sqrt{4\alpha_1\alpha_3 - \alpha_2^2}}{2\sqrt{2}\sqrt{\alpha_3}\sqrt{\eta}}, \\ a_1 &= -\frac{\alpha_2 b_1}{2\alpha_3}, a_2 = \mp \frac{\sqrt{\alpha_2^2 - 4\alpha_1\alpha_3} b_1}{2\alpha_3}, b_2 = \frac{1}{4} \left( \frac{\alpha_2^2}{\alpha_1\alpha_3} - 4 \right) b_1. \end{aligned} \tag{28}$$



SET-II:

$$c = \pm -\frac{\alpha_2\sqrt{\alpha_2^2 - 4\alpha_1\alpha_3}}{4\alpha_3}, d = \frac{\sqrt{4\alpha_1\alpha_3 - \alpha_2^2}}{2\sqrt{2}\sqrt{\alpha_3}\sqrt{\eta}}, \tag{29}$$

$$a_1 = -\frac{\alpha_2 b_1}{2\alpha_3}, a_2 = \mp \frac{\sqrt{\alpha_2^2 - 4\alpha_1\alpha_3} b_1}{2\alpha_3}, b_2 = \frac{1}{4} \left( \frac{\alpha_2^2}{\alpha_1\alpha_3} - 4 \right) b_1.$$

Corresponding to the above sets of solutions, the only exact solutions for the FitzHugh–Nagumo equation are given by .

$$v_{15,16}(x, t) = -\frac{2\alpha_1 \cosh^2(ct + dx) \left( \alpha_2 \pm \sqrt{\alpha_2^2 - 4\alpha_1\alpha_3} \tanh(ct + dx) \right)}{4\alpha_1\alpha_3 \sinh^2(ct + dx) + \alpha_2^2}. \tag{30}$$

where the values of  $c$  and  $d$  are given by Eqs. (28) and (29). Graphical representation of the first solution  $u_{15}(x, t)$  is given in Fig. 2.

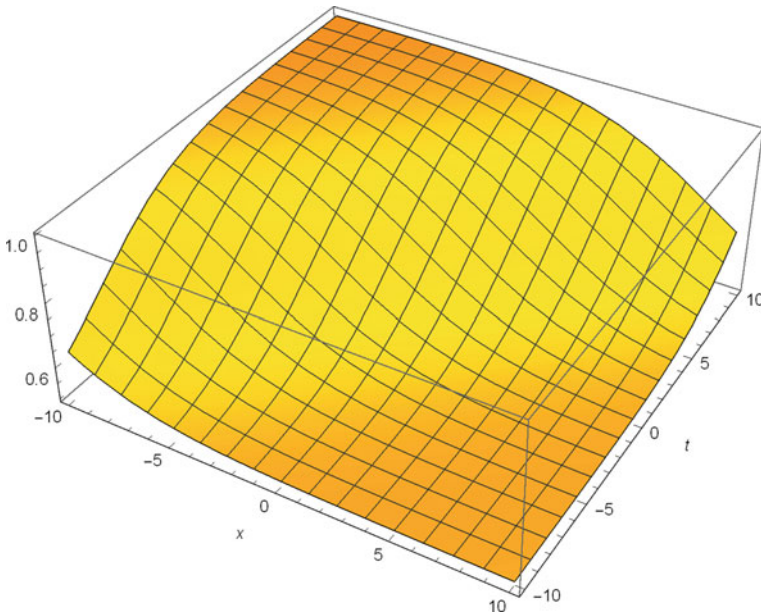


**Fig. 2** Graphical representation of the exact solution  $v_{15}(x, t)$  given by Eq. (30) of the FitzHugh–Nagumo equation, where  $\eta = 1, \alpha_1 = -\frac{1}{2}, \alpha_2 = \frac{3}{2}, \alpha_3 = -1$

### 4 Discussion

Three families of new exact solutions to the nonlinear evolution Eq. (1) are derived in this paper. This equation represents several physical and biological processes such as transmission of nerve impulses and the evolutionary rescue from biological invasion. The number of existing exact solutions for this equation are very rare. But, exact solutions for such equations are required for a better understanding of the physical problem and for checking accuracy of any numerical algorithm developed for solving the real problems. Since it is difficult to derive the exact solutions using any analytical methods, we employ ansatz method to derive the exact solutions. But, when using this method, a large nonlinear system of equations are obtained corresponding to each ansatz form. It is needed to find out the nontrivial solutions that simultaneously satisfy this system of algebraic equations. This is can be done by using any of the computational algebra system. Other exact solutions for FitzHugh–Nagumo equation can also be derived by assuming similar ansatz forms for exact solutions.

### Appendix

Substituting this value of  $v(\xi)$  in Eq. (5), we get a system of nonlinear algebraic equations given by

$$\begin{aligned}
 &\alpha_3 a_2^3 + 2a_2 b_2^2 d^2 \eta = 0, \quad \alpha_3 a_3^3 + 2a_3 b_3^2 d^2 \eta = 0, \\
 &a_2 b_2 (-a_2 (3a_0 \alpha_3 + \alpha_2) + b_2 c + 6b_1 d^2 \eta) = 0, \\
 &a_2 (-3a_2 (a_1 + a_2 - a_3) \alpha_3 + b_1 (3b_2 c - a_2 (3a_0 \alpha_3 + \alpha_2)) \\
 &\quad + b_2^2 (2a_0 \alpha_2 + 3a_0^2 \alpha_3 + \alpha_1 - 2d^2 \eta) + 6b_1^2 d^2 \eta + 6b_2 b_3 d^2 \eta) = 0, \\
 &a_2 (-a_2 b_3 (3a_0 \alpha_3 + \alpha_2) + 2b_2 ((a_1 + a_2 - a_3) (3a_0 \alpha_3 + \alpha_2) \\
 &\quad + 2b_3 c) + b_1 (b_2 (4a_0 \alpha_2 + 6a_0^2 \alpha_3 + 2\alpha_1 - 4d^2 \eta) + 16b_3 d^2 \eta) + 2b_1^2 c) \\
 &= b_2 (a_0 b_2^2 (a_0 (a_0 \alpha_3 + \alpha_2) + \alpha_1) - a_1 (b_2 c + 2b_1 d^2 \eta) + a_3 (b_2 c + 2b_1 d^2 \eta)), \\
 &a_3 b_3 (a_3 (3a_0 \alpha_3 + \alpha_2) + b_3 c + 6b_1 d^2 \eta) = 0, \\
 &3\alpha_3 a_2^3 + a_2^2 (3 (2a_1 - 3a_3) \alpha_3 + 2b_1 (3a_0 \alpha_3 + \alpha_2)) + a_2 (b_1 (2 (a_1 - a_3) (3a_0 \alpha_3 + \alpha_2) - 2b_2 c + 5b_3 c) \\
 &\quad + b_1^2 (2a_0 \alpha_2 + 3a_0^2 \alpha_3 + \alpha_1 - 8d^2 \eta) + 2b_2 b_3 (2a_0 \alpha_2 + 3a_0^2 \alpha_3 + \alpha_1 + d^2 \eta) + 3 (\alpha_3 (a_1 - a_3)^2 + 4b_3^2 d^2 \eta) \\
 &\quad + b_2^2 (-2a_0 \alpha_2 - 3a_0^2 \alpha_3 - \alpha_1 + 2d^2 \eta)) + b_2 (-3a_0 b_1 b_2 (a_0 (a_0 \alpha_3 + \alpha_2) + \alpha_1) \\
 &\quad + a_3 (b_2 (2a_0 \alpha_2 + 3a_0^2 \alpha_3 + \alpha_1 - 8d^2 \eta) - b_1 c - 6b_3 d^2 \eta) \\
 &\quad + a_1 (b_2 (-2a_0 \alpha_2 - 3a_0^2 \alpha_3 - \alpha_1 + 2d^2 \eta) + b_1 c + 6b_3 d^2 \eta)) = 0, \\
 &a_2^2 (b_2 - 2b_3) (3a_0 \alpha_3 + \alpha_2) + a_2 (2b_2 ((a_1 - 2a_3) (3a_0 \alpha_3 + \alpha_2) + 2b_3 c) \\
 &\quad + b_3 (-2 (a_1 - a_3) (3a_0 \alpha_3 + \alpha_2) - 3b_3 c)
 \end{aligned}$$

$$\begin{aligned}
& +2b_1 (b_2 (2a_0\alpha_2 + 3a_0^2\alpha_3 + \alpha_1 + d^2\eta) + b_3 (-2a_0\alpha_2 - 3a_0^2\alpha_3 - \alpha_1 + 11d^2\eta)) \\
& +2b_1^2c + b_2^2c) + b_2 (a_1^2 (3a_0\alpha_3 + \alpha_2) + a_3^2 (3a_0\alpha_3 + \alpha_2) \\
& +3a_0 (b_1^2 + b_2b_3) (a_0 (a_0\alpha_3 + \alpha_2) + \alpha_1) \\
& +a_1 (-2a_3 (3a_0\alpha_3 + \alpha_2) + 2b_1 (2a_0\alpha_2 + 3a_0^2\alpha_3 + \alpha_1 + d^2\eta) + b_2c) \\
& -2a_3 (b_1 (2a_0\alpha_2 + 3a_0^2\alpha_3 + \alpha_1 - 2d^2\eta) + 2b_2c)) = 0, \\
& \alpha_3a_3^3 + 9a_2^2\alpha_3a_3 + a_3 (3\alpha_3a_1^2 + b_1 (2a_1 (3a_0\alpha_3 + \alpha_2) + 6b_2c + b_3c) \\
& +b_1^2 (2a_0\alpha_2 + 3a_0^2\alpha_3 + \alpha_1 - 2d^2\eta) + 2b_2b_3 (2a_0\alpha_2 + 3a_0^2\alpha_3 + \alpha_1 + 7d^2\eta) \\
& +b_2^2 (-2a_0\alpha_2 - 3a_0^2\alpha_3 - \alpha_1 + 20d^2\eta) + 2b_3^2d^2\eta) \\
& + a_2 (-3\alpha_3d_1^2 + 12a_3\alpha_3a_1 - 9a_3^2\alpha_3 + 2a_0\alpha_2b_3^2 + 3a_0^2\alpha_3b_3^2 \\
& -b_1 (2(a_1 - 2a_3) (3a_0\alpha_3 + \alpha_2) + b_2c + 6b_3c) - 2b_2b_3 (2a_0\alpha_2 + 3a_0^2\alpha_3 + \alpha_1 + 7d^2\eta) \\
& +b_1^2 (-2a_0\alpha_2 - 3a_0^2\alpha_3 - \alpha_1 + 2d^2\eta) + \alpha_1b_3^2 - 2b_2^2d^2\eta - 20b_3^2d^2\eta) \\
& = a_1^3\alpha_3 + a_2^3\alpha_3 + \alpha_3a_3^3b_1 (b_1^2 + 6b_2b_3) + a_2a_0^2b_1 (b_1^2 + 6b_2b_3) \\
& + a_0b_1 (3 (a_2^2 + a_3^2) \alpha_3 + \alpha_1b_1^2 + 6\alpha_1b_2b_3) + a_2^2\alpha_2b_1 + a_3^2\alpha_2b_1 \\
& + a_1^2b_1 (3a_0\alpha_3 + \alpha_2) + a_1 (3\alpha_3a_2^2 + 3a_3^2\alpha_3 \\
& +b_1^2 (a_0 (3a_0\alpha_3 + 2\alpha_2) + \alpha_1) + 2b_2b_3 (2a_0\alpha_2 + 3a_0^2\alpha_3 + \alpha_1 + 6d^2\eta) \\
& +b_1 (b_2 + b_3) c + 2b_2^2d^2\eta + 2b_3^2d^2\eta) , \\
& a_3 (3a_3^2\alpha_3 - 3a_1a_3\alpha_3 - 3a_2a_3\alpha_3 - 2a_0\alpha_2b_3^2 - 3a_0^2\alpha_3b_3^2 \\
& -b_1 (a_3 (3a_0\alpha_3 + \alpha_2) + 3b_3c) - \alpha_1b_3^2 - 6b_1^2d^2\eta + 2b_3^2d^2\eta - 6b_2b_3d^2\eta) = 0, \\
& 3\alpha_3a_3^3 + a_3 (3\alpha_3a_1^2 + 6a_2\alpha_3a_1 + 3a_2^2\alpha_3 - 2a_0\alpha_2b_3^2 - 3a_0^2\alpha_3b_3^2 \\
& +b_1 (2 (a_1 + a_2) (3a_0\alpha_3 + \alpha_2) + 5b_2c - 2b_3c) \\
& +b_1^2 (2a_0\alpha_2 + 3a_0^2\alpha_3 + \alpha_1 - 8d^2\eta) \\
& +2b_2b_3 (2a_0\alpha_2 + 3a_0^2\alpha_3 + \alpha_1 + d^2\eta) - \alpha_1b_3^2 + 12b_2^2d^2\eta + 2b_3^2d^2\eta) \\
& + b_3 (3a_0b_1b_3 (a_0 (a_0\alpha_3 + \alpha_2) + \alpha_1) + a_2 (b_3 (2a_0\alpha_2 + 3a_0^2\alpha_3 \\
& + \alpha_1 - 8d^2\eta) - b_1c - 6b_2d^2\eta) + a_1 (b_3 (2a_0\alpha_2 + 3a_0^2\alpha_3 + \alpha_1 - 2d^2\eta) \\
& -b_1c - 6b_2d^2\eta)) = a_3^2 (3 (2a_1 + 3a_2) \alpha_3 + 2b_1 (3a_0\alpha_3 + \alpha_2)) , \\
& a_3 (b_3 ((2a_1 + 4a_2 - a_3) (3a_0\alpha_3 + \alpha_2) + b_3c) + 2b_2 (2b_3c - (a_1 + a_2 - a_3) \\
& (3a_0\alpha_3 + \alpha_2)) + 2b_1 (b_3 (2a_0\alpha_2 + 3a_0^2\alpha_3 + \alpha_1 + d^2\eta) \\
& +b_2 (-2a_0\alpha_2 - 3a_0^2\alpha_3 - \alpha_1 + 11d^2\eta)) + 2b_1^2c - 3b_2^2c) \\
& = b_3 (a_1^2 (3a_0\alpha_3 + \alpha_2) + a_2^2 (3a_0\alpha_3 + \alpha_2) \\
& +3a_0 (b_1^2 + b_2b_3) (a_0 (a_0\alpha_3 + \alpha_2) + \alpha_1) \\
& +a_1 (2a_2 (3a_0\alpha_3 + \alpha_2) + 2b_1 (2a_0\alpha_2 + 3a_0^2\alpha_3 + \alpha_1 + d^2\eta) + b_3c) \\
& +a_2 (b_1 (4a_0\alpha_2 + 6a_0^2\alpha_3 + 2\alpha_1 - 4d^2\eta) + 4b_3c)) , \\
& b_3 (-a_0b_3^2 (a_0 (a_0\alpha_3 + \alpha_2) + \alpha_1) + a_1 (b_3c + 2b_1d^2\eta) + a_2 (b_3c + 2b_1d^2\eta)) \\
& = a_3 (2 (a_1 + a_2 - a_3) b_3 (3a_0\alpha_3 + \alpha_2) + b_2 (a_3 (3a_0\alpha_3 + \alpha_2) + 4b_3c) \\
& +2b_1 (b_3 (2a_0\alpha_2 + 3a_0^2\alpha_3 + \alpha_1 - 2d^2\eta) + 8b_2d^2\eta) + 2b_1^2c) .
\end{aligned}$$

## References

1. Banasiak, J., Mokhtar-Kharroubi, M. (Eds), *Evolutionary Equations with Applications in Natural Sciences*. Springer (2014)
2. Bell, G.: Evolutionary rescue. *Annu. Rev. Ecol. Evolut. Syst.* **48**, 605–27 (2017)
3. Carlson, S.M., Cunningham, C.J., Westley, P.A.H.: Evolutionary rescue in a changing world. *Trends Ecol. Evolut.* **29**, 521–530 (2014)
4. FitzHugh, R.: *Mathematical Models of Excitation and Propagation in Nerve*, Biological Engineering. In: Schwann H. (ed.), pp. 1–85. McGraw-Hill, New York (1969)
5. Foroutan, M., Manafian, J., Taghipour-Farshi, H.: Exact solutions for FitzHugh-Nagumo model of nerve excitation via Kudryashov method. *Opt Quant. Electron.* **49**, 352 (2017)
6. Gawlik, A., Vladimirov, V., Skurativskiy, S.: Solitary wave dynamics governed by the modified fitzhugh-nagumo equation. *J. Comput. Nonlinear Dynam.* **15**(6), 061003 (2020)
7. Gawlik, A., Vladimirov, V., Skurativskiy, S.: Existence of the solitary wave solutions supported by the modified FitzHugh-Nagumo system. *Nonlinear Anal. Model. Control* **25**(3), 482–501 (2020)
8. Gonzalez, A., Ronce, O., Ferriere, R., Hochberg, M.E.: Evolutionary rescue: an emerging focus at the intersection between ecology and evolution. *Philos. Trans. Royal Soc. B*, 20120404 (2013)
9. Hafez, M.G.: New travelling wave solutions of the (1+1)-dimensional cubic nonlinear Scrodinger equation using novel (G/G)-expansion method. *Beni-Suef Univ. J. Basic Appl. Sci.* **5**(2), 5109–118 (2016)
10. Khan, Y.: A variational approach for novel solitary solutions of FitzHugh-Nagumo equation arising in the nonlinear reaction-diffusion equation. *Int. J. Numer. Methods Heat Fluid Flow* (2020). <https://doi.org/10.1108/HFF-05-2020-0299>
11. McKean, H., Jr.: Nagumo's equation. *Adv. Math.* **4**(3), 209–223 (1970)
12. Nagumo, J., Arimoto, S., Yoshizawa, S.: An active impulse transmission line simulating Nerve Axon. *Proc. IRE* **50**(10), 2061–2070 (1962)
13. Nucci, M.C., Clarkson, P.A.: The nonclassical method is more general than the direct method for symmetry reductions: an example of the Fitzhugh-Nagumo equation. *Phys. Lett. A* **164**(1), 49–56 (1992)
14. Orr, H.A., Unckless, R.L.: The population genetics of evolutionary rescue. *PLoS Genetics* **10**, e1004551 (2014)
15. Samani, P., Bell, G.: The ghosts of selection past reduces the probability of plastic rescue but increases the likelihood of evolutionary rescue to novel stressors in experimental populations of wild yeast. *Ecol. Lett.* **19**, 289–298, e1004551 (2016)
16. Liu, S., Fu, Z., Liu, S., Zhao, Q.: Jacobi elliptic function expansion method and periodic wave solutions of nonlinear wave equations **289**(1–2), 69–749 (2001)
17. Shen, Y., He, J.-H.: Variational principle for a generalized KdV equation in a fractal space. *Fractals* **28**(4), 2050069 (2020). <https://doi.org/10.1142/S0218348X20500693>
18. Tanaka, H., Stone, A., Nelson, D.R.: Spatial gene drives and pushed genetic waves, *PNAS* **114**(32) 8452–8457 (2017)
19. Van Dyken, J.D.: Evolutionary rescue from a wave of biological invasion. *Amer. Naturalist* **195**(1) (2020) <https://doi.org/10.1086/706181>
20. Wazwaz, A.M.: A sine-cosine method for handling nonlinear wave equations. *Math. Comput. Model* **40**, 499–508 (2004)
21. Zayed, E.M.E., Abdelaziz, M.A.M.: Exact solutions of the nonlinear Schrodinger equation with variable coefficients using the generalized extended tanh-function method, the sin-cosine and the exp-function methods. *Appl. Math. Comput.* **218**, 2259–2268, e1004551 (2011)

# A Multi-criteria Model of Selection of Students for Project Work Based on the Analysis of Their Performance



Sukarna Dey Mondal , Dipendra Nath Ghosh ,  
and Pabitra Kumar Dey 

**Abstract** Project work does not always imply extensive knowledge, but it does imply the application of such information. Through this project work, students are exposed to educational ideas as well as technical ideas. Therefore, the selection and evaluation of students are crucial parts of any project for any education organization concerning excellence. So, an attempt has been made to draw a mathematical model with the help of several MCDM techniques and Statistics from which it will be very easy to evaluate and select a suitable student for the project. First of all, a payoff matrix has been created with the AHP method. Entropy is used to calculate the total weight. Then utility based, distance based, and out-ranking based MCDM techniques are applied to get several ranking structures. Ultimately, through a voting method, the study offers a ranking of 5 students under student excellence.

**Keywords** AHP · Entropy · TOPSIS · VIKOR · COPRAS · PROMETHEE-2 · WSM · Voting system

## 1 Introduction

In recent times, project work is gradually becoming compulsory in schools and colleges. A properly decorated project can carry extra marks in an interview or an exam. Project work is essential to escalating the volume of conception. Thus, command of the project matter, technical skill, ability to communicate, discipline & behavior, experience, leadership and managing power, and stress tolerance are

---

S. Dey Mondal (✉)

Department of Mathematics, Dr. B.C. Roy Engineering College, MAKAUT, Kolkata,  
West Bengal, India

e-mail: [sukarnadey@gmail.com](mailto:sukarnadey@gmail.com)

D. Nath Ghosh

Controller of Examinations, Kazi Nazrul University, Asansol, West Bengal, India

P. Kumar Dey

Department of Computer Applications, Dr. B.C. Roy Engineering College, MAKAUT, Durgapur,  
West Bengal, India

© The Author(s), under exclusive license to Springer Nature Switzerland AG 2022

873

S. Banerjee and A. Saha (eds.), *Nonlinear Dynamics and Applications*,

Springer Proceedings in Complexity,

[https://doi.org/10.1007/978-3-030-99792-2\\_73](https://doi.org/10.1007/978-3-030-99792-2_73)

important requirements towards performance analysis of students. MCDM approach delivers upgraded knowledge to scrutinize the potential of a student in an education organization for ranking a project. Project work means that not only good students are eligible, but also all types of students have to do project work. In many cases due to their lack of technical intelligence, very good students did not get a place in that project. So, finding a skilled student for a project is an important part of the research. A mathematical model has been created by looking into everything from which it will be very easy to rank all these skilled students.

A scientific model related to students' project work has already been created where AHP, PROMETHEE-2, and TOPSIS were used. With the previous model in mind, another new scientific model has been developed and several MCDM approaches like Entropy, VIKOR, COPRAS, and WSM have been applied. Whereas early model only one ranking was found as two MCDM methods were used but now there are several rankings for using several MCDM methods. For this model, the opinions of several project guides have been taken to the performance of the students concerning some pre-assigned criteria. Ultimately, an experiment has been made to explicate in particular how the voting system has been transported from several ranking structures to the single ranking structure to take the final decision.

## 2 Literature Review

The pair-wise comparison method and the hierarchical model were developed in 1980 by Saaty in the context of the Analytical Hierarchy Process (AHP) [1, 2]. A pis and nis based method (TOPSIS) is sketched [3]. To inspect the quality of performance assessment, a study has been developed on performance management [4]. "The Effects of the Performance Evaluation Process on Academic employees in Higher Education Institutions" is an important research work in today's scenario with the help of the performance estimation [5]. Research work has been carried out with the help of different multi-criteria-decision-making like AHP, Fuzzy-AHP, COPRAS, TOPSIS, Cooperative Game Theory, Compromise Programming, and Group Decision to analyse the performance of a teacher [6]. To examine the performance of supporting staff, a mathematical model is designed using multi-criteria decision making by eight methodologies containing AHP, COPRAS, SAW, TOPSIS, Fuzzy-TOPSIS, PROMETHEE-II, Compromise Programming, Normalized-Weighted-Average and Group Decision-Making method [7]. Another research work is done on how Employee Management can be effectively managed in the future by using performance management, performance appraisal [8]. In recent situations, educational organizations have grown day by day. However, the quality and effective performance among them has not increased proportionally. Already an innovative statistical model has been initiated to explore the NAAC rating of a well-known Engineering College using Multi-Criteria Decision-Making Methods, Statistics, and Group Decision Making [9]. Another research work has been carried out to select the best engineering college by using AHP, TOPSIS, and Fuzzy AHP [10]. College placement

is a procedure in which professionals assess each candidate's performance against a set of pre-determined criteria. So, using TOPSIS and AHP in an Interval Types 1 and 2 fuzzy environment (IT1F, IT2F), a mathematical model has been developed to analyse specific criteria [11]. A preference function approach (PROMETHEE-2) is introduced [12]. It is one of the versions, out of 5 of PROMETHEE, i.e., 1–5 [13, 14]. The scholars of V.G.T. University, (Zavadskas et al. 1996) initiated the COPRAS method (Complex Proportional Assessment), applicable for max. and min. criteria values. In 2007, the substitute MCDM method VIKOR was approached by Opricovic et al. [15]. Another method used as a benchmark solution in the situations (Entropy Method) approximates the weights of the criteria. Hwang and Yoon [16] the Entropy Method simplifies disparities between sets of data. Weighted Average Method is a software-kind MCDM approach. Here objective functions are transformed by defining as weighed sums of various objects [17, 18].

### 3 Proposed Methodology

In the beginning, a literature inspection was conducted. Five different categories of students were observed and arbitrarily nominated for the current study w.r.to 5 scale rating.

It is considered as

Two students are below average, one is normal, and two are above average.

The sample of five different categories must be preserved separately, according to NBA (National Board of Accreditation) or NAAC (National Assessment and Accreditation Council) rules. In the same way, 5 students have been given importance in this matter.

An additional survey was arranged between Experts (E1, E2), for adding/removing criteria. They furnished their valuable judgment w.r.to the following criteria (Fig. 1 and Table 1).

- C1—command of the project matter
- C2—technical skill
- C3—ability to communicate clearly
- C4—discipline & behavior
- C5—past experience
- C6—leadership and managing power
- C7—stress tolerance

#### 3.1 Proposed Flowchart

See Fig. 2.

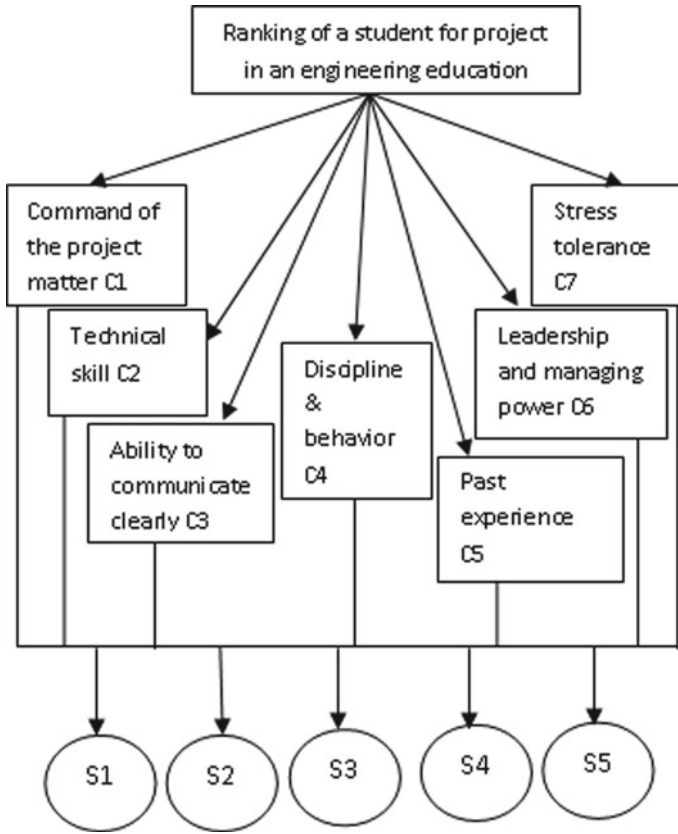


**Fig. 1** Hierarchy of ranking students based on the below mentioned criteria

**Table 1** Experts' opinion against each student with respect to each criteria

Students/Experts	Criteria													
	C1		C2		C3		C4		C5		C6		C7	
	E1	E2	E1	E2	E1	E2	E1	E2	E1	E2	E1	E2	E1	E2
S1	VG	E	E	VG	E	G	G	G	E	G	B	G	G	G
S2	G	G	G	G	B	A	VG	E	E	G	VG	G	VG	A
S3	E	E	VG	G	E	E	VG	VG	G	E	B	G	B	G
S4	G	VG	B	G	E	VG	G	B	VG	VG	VG	G	G	VG
S5	VG	VG	G	E	G	A	G	VG	VG	VG	G	B	A	B



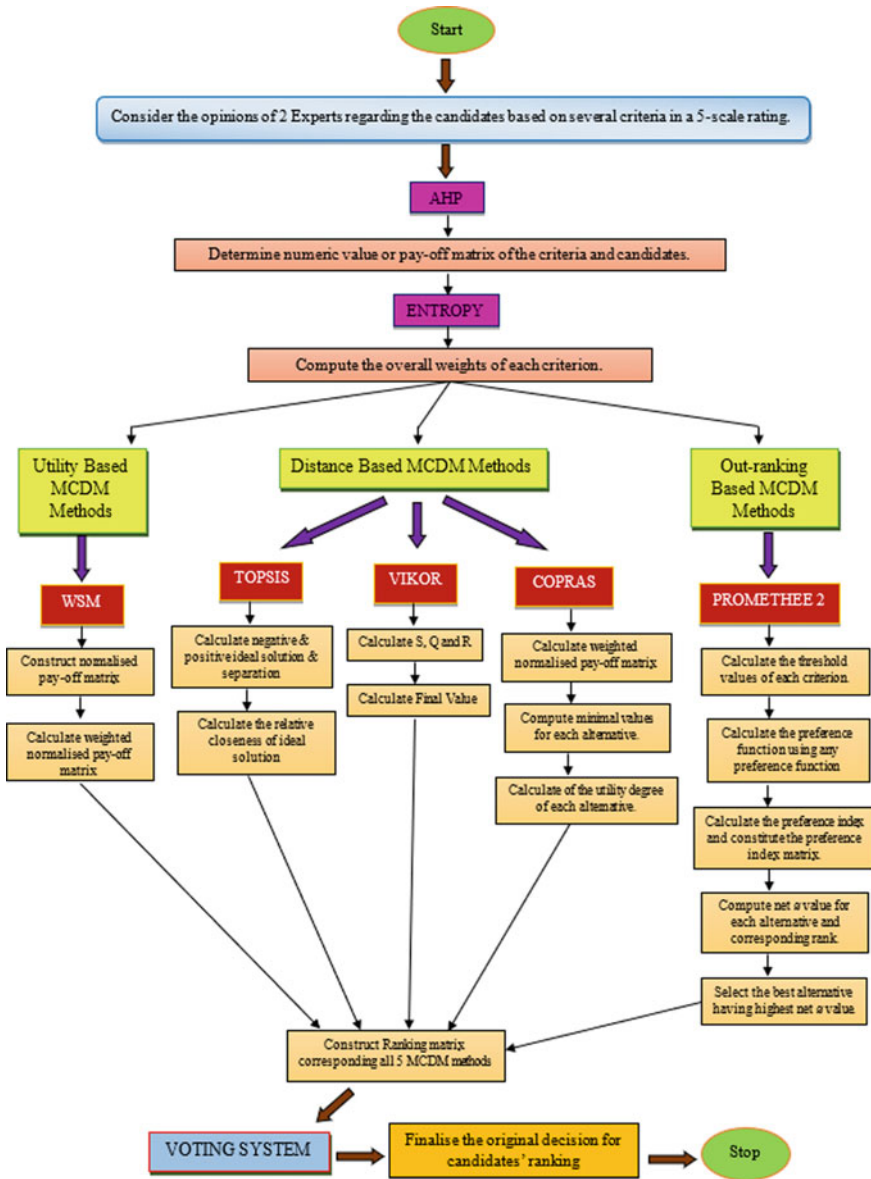


Fig. 2 Proposed flowchart for selection of students for project work

### 3.2 Proposed Algorithm

See Table 2.

## 4 Analysis and Discussion

After using the opinions which are collected from the experts, prepare a pay-off matrix and, using the Entropy technique (see Table 4), determine the weight of the criteria. The Entropy method is emphasized here due to the important aspect of entropy, where the result of entropy will change with the change of data. For this characteristic, Entropy is different from the rest of the methods for estimating weights (Table 3).

With the help of the pay-off matrix, five MCDM methods have been applied consecutively. Then from there the rankings of students in different methods were found. It is noticed that the students' rankings in TOPSIS and COPRAS are identical. On the other hand, again the ranking of students in VIKOR, PROMETHEE-2, and WSM are identical. The complete ranking of students in numerous MCDM methods is expressed in Table 5.

Earlier a mathematical model for students' projects was created using three MCDM approaches where the rankings of students from different MCDMs were more or less the same. And the biggest advantage was that there was only one student who got the same first position in all three MCDM methods. So, it has been possible to find the best student for the project very easily from that mathematical model but the rest are not so easy. This work has been extended where frequent MCDM methods have been applied. Along with this model, another mathematical model has been created in this current study whereas previous work has been extended with some more MCDM approaches.

Finally, a system has been applied to the rankings of students obtained from Table 5. The name of the system is Voting System. It is a majority system. "Majority decision wins the match". This fact has been used here. Therefore, it has been possible to get a single ranking structure of students through the voting system based on the majority ranking obtained from the MCDM methods from Table 6. It is very easy to find the best student as well as the ranking of other students for the project from this single ranking structure. This way any educational organization can effortlessly find the best team of students for their project through this mathematical model. In such a manner, the validity of the voting system has been maintained here (Table 6).

**Table 2** Proposed algorithm for selection of students for project work

Step 1	Consider the opinions of 2 Experts regarding the candidates
Step 2	Apply pairwise comparison method AHP to find the numeric value or pay-off matrix of the criteria and candidates
Step 3	Using the Entropy approach, measure the weight of each condition
<i>MCDM Approaches</i>	
<b>Utility/Priority-Based MCDM Methods</b>	<b>WSM</b>
Step 4.1.1	Normalize the pay-off matrix obtained from AHP
Step 4.1.2	Calculate weighted normalized matrix
Step 4.1.3	Rank the candidates in descending order
<b>Distance-Based MCDM Methods</b>	<b>TOPSIS</b>
Step 5.1.1	Compute the pis and nis as for each criterion: $A^* = \{v_1^*, v_2^*, \dots, v_n^*\}$ where $v_n^*$ gives the maximum value of nth criteria $A^- = \{v_1^-, v_2^-, \dots, v_n^-\}$ where $v_n^-$ gives the minimum value of nth criteria
Step 5.1.2	Calculate the distance of individual alternatives from PIS and NIS, as well as their relative proximity to the optimal answer, where there are J alternatives and n criteria $CC_i = \frac{d_i^-}{d_i^* + d_i^-}$ $i = 1, 2, 3, \dots, J$
Step 5.1.3	Rank the candidates in descending order
	<b>VIKOR</b>
Step 5.2.1	Calculate R, S, and Q $Q_i = \vartheta \left[ \frac{S_i - S^*}{S^- - S^*} \right] + (1 - \vartheta) \left[ \frac{R_i - R^*}{R^- - R^*} \right]$ where $Q_i$ signifies the $i$ -th VIKOR value, $i = 1, 2, 3 \dots m$ ; $S^* = \text{Min}(S_i)$ ; $S^- = \text{Max}(S_i)$ ; $R^* = \text{Min}(R_i)$ ; $R^- = \text{Max}(R_i)$ and $\vartheta$ is the utmost group utility's value (usually it is to be set to 0.5)
Step 5.2.2	The choice with the lowest VIKOR value is considered to be the right approach
Step 5.2.3	Rank the candidates in descending order
	<b>COPRAS</b>
Step 5.3.1	Calculate weighted normalized decision matrix

(continued)

**Table 2** (continued)

Step 1	Consider the opinions of 2 Experts regarding the candidates
Step 5.3.2	Obtain the sums of the threshold values for each choice (bigger values are preferred) (optimization direction is maximization)
Step 5.3.3	Obtain the sums of the threshold values for each choice (smaller values are preferred) (optimization direction is minimization)
Step 5.3.4	Determine the minimal value
Step 5.3.5	Calculate the utility degree of each alternative
Step 5.3.6	Rank the candidates in descending order
<b>Outranking-Based MCDM Methods</b>	<b>PROMETHEE-2</b>
Step 6.1.1	Normalize all the values w.r.to any normalization method
Step 6.1.2	Calculate the threshold values of each criterion
Step 6.1.3	Calculate the preference function using any preference function; here Gaussian function is used as a preference function
Step 6.1.4	Construct the preferences factor matrices by estimating the preference score
Step 6.1.5	Analyze net $\phi$ value of each option and the associated rank
Step 6.1.6	Choose the best option that has the biggest $\phi$ value
Step 6.1.7	Rank the candidates in descending order
	<b>VOTING SYSTEM</b>
Step 7.1.1	Construct Ranking Matrix corresponding to all 5 MCDM methods
Step 7.1.2	Apply voting system to finalize the original decision

**Table 3** Saaty's 9-point of pairwise comparison

Scale	Compare factor of i and j
1	Equally important
3	Weakly important
5	Strongly important
7	Very strongly important
9	Extremely important
2,4,6,8	Intermediate value between adjacent scales

**Table 4** Weights of criteria by Entropy method

Criteria	Weights
C1	0.1438
C2	0.1407
C3	0.1477
C4	0.1442
C5	0.1386
C6	0.1426
C7	0.1425

**Table 5** Ranking of students in different MCDM methods

Students	MCDM methods				
	TOPSIS	VIKOR	COPRAS	PROMETHEE-2	WSM
S1	2	3	2	3	3
S2	4	4	4	4	4
S3	1	1	1	1	1
S4	3	2	5	2	2
S5	5	5	3	5	5

**Table 6** Final ranking of students based on the Voting System

Students	MCDM methods					Voting system
	TOPSIS	VIKOR	COPRAS	PROMETHEE-2	WSM	
S1	2	3	2	3	3	3
S2	4	4	4	4	4	4
S3	1	1	1	1	1	1
S4	3	2	5	2	2	2
S5	5	5	3	5	5	5

## 5 Conclusion

Student selection and evaluation for the project are significant parts of any educational organization. Improving the teaching–learning in school or college mostly depends on the student’s project. Through this project, various educational organizations have often received different funds. Therefore, appropriate students are very much desirable to accomplish the projects. So, this study establishes an innovative MCDM model that amalgamates AHP, Entropy, TOPSIS, VIKOR, COPRAS, PROMRTHEE-2, and WSM to keep up with students’ performance ranking decisions. Finally, an experiment was conducted to demonstrate how the voting system is transformed from many ranking structures to a single ranking structure to get the conclusion. So, with

the help of this model not only the educational organization will benefit but will also work in the same way where performance is evaluated with judgment on different criteria.

## References

1. Saaty, T.L.: *The Analytic Hierarchy Process*. McGraw-Hill, New York (1980)
2. Saaty, T.L.: Priority setting in complex problems. *IEEE Trans. Eng. Manage.* **30**(3), 140–155 (1983)
3. Hwang, C.L., Yoon, K.: *Multiple Attribute Decision Making Methods and Applications*. Springer, Berlin Heidelberg (1981)
4. Lohman, L.: Evaluation of university teaching as sound performance appraisal, Elsevier. <https://doi.org/10.1016/j.stueduc.2021.101008>
5. Dasanayaka, C.H., Abeykoon, C., Ranaweera, R.A.A.S., Koswatte, I.: The Impact of the Performance Appraisal Process on Job Satisfaction of the Academic Staff in Higher Educational Institutions. <https://doi.org/10.3390/educsci1100623> (2021)
6. Dey, S., Ghosh, D.N.: An integrated approach of multi-criteria group decision making techniques to evaluate the overall performance of teachers. *Int. J. Adv. Res. Comput. Sci.* **7**(5) (2016)
7. Dey, S., Ghosh, D.N.: Non-teaching staff performance analysis using multi-criteria group decision making approach. *Int. J. Educ. Learn.* **4**(2), 35–50 (2015)
8. Brown, T.C., O’Kane, P., Mazumdar, B., McCracken, M.: Performance management: a scoping review of the literature and an agenda for future research **18**(1), 47–82 (2019)
9. Dey, S., Ghosh, D.N., Dey, P. K.: Prediction of NAAC grades for affiliated institute with the help of statistical multi criteria decision analysis: national conference on recent trends in IOT. *Mach. Learn. Artif. Intell. Appl.* **1**(2), 116–126 (2021)
10. Rana, S., Dey, P.K., Ghosh, D.N.: Best engineering college selection through fuzzy multi-criteria decision making approach: a case study: universal journal of applied computer science and technology **2**(2), 246–256 (2012)
11. Dey, S., Ghosh, D.N.: Comparative evaluation of students’ performance in campus recruitment of a technical institution through Fuzzy-MCDM techniques. *Int. J. Comput. Sci. Eng.* **7**(Special issue), 1
12. Brans, J.P., Vincke, Ph., Mareschal, B.: How to select and how to rank projects: the Promethee method. *Europ. J. Oper. Res.* **24**, 228–238 (1986)
13. Taleb, M.F.A., Mareschal, B.: Water resources planning in the middle east: application of the Promethee v Multicriteria method. *Eur. J. Oper. Res.* **81**, 500–511 (1995)
14. Pomerol, J.Ch., Romero, S.B.: *Multi-criterion Decision in Management: Principles and Practice*, Kluwer Academic, Netherlands (2000)
15. Opricovic, S., Treng, G.H.: Compromise solution by MCDM methods: a comparative analysis of VIKOR and TOPSIS. *Eur. J. Oper. Res.* **156**, 445–455 (2004)
16. Hwang, C., Yoon, K.: *Multiple Attribute Decision-Making*. Springer-Verlag, Methods and Application. A State-of-the-Art Survey (1981)
17. Loucks, D.P., Stedinger, J.R., Haith, D.A.: *Water Resources Systems Planning and Analysis*. Prentice-Hall, Englewood Cliffs, New Jersey (1981)
18. Vedula, S., Mujumdar, P.P.: *Water Resources Systems, Modelling Techniques, and Analysis*. Tata McGraw-Hill Publishing Company Limited, New Delhi (2005)

# Mathematical Modeling of Thermal Error Using Machine Learning



Rohit Ananthan and N. Rino Nelson

**Abstract** On many types of machine tools, thermal effects produce the most of machining defects, with linear expansion and deformation of structural parts creating undesired movement between the tool and the workpiece. Thermal flaws are difficult to control without some type of compensation because heat inputs that produce temperature rise and gradients occur from a variety of sources both within and outside the machine tool. Moreover, heat generation also cannot be prevented. As a result, the goal of this research is to focus on thermal error modelling and evaluate the various machine learning algorithms to discover the most effective solution.

**Keywords** CNC machine · Multiple regression · Thermal expansion · Linear regression

## 1 Introduction

Because of the expanding need in the contemporary industry, thermal compensation has been thoroughly explored. These complex machines generate a lot of heat, which causes the machine tools and the work piece to distort, which is the main source of inaccuracy [1]. According to Bryan's research published in 1990, the thermal error accounts for 40–70% of the total error [2]. In general, there are two kinds of heat sources in machine tools, namely internal and external heat sources, bringing about the temperature rising and thermal errors [3].

- Internal heat sources: heat generated from cutting process; heat generated from frictions in ball screws, spindle, gear box, guides, etc.; heat generated in motor; heating or cooling influences provided by the various cooling systems.
- External heat sources: environmental temperature variation; solar and personal radiations.

---

R. Ananthan · N. Rino Nelson (✉)  
Mechanical Engineering, Indian Institute of Information Technology, Design and Manufacturing,  
Kancheepuram, Chennai 600127, India  
e-mail: [rino@iiitdm.ac.in](mailto:rino@iiitdm.ac.in)

As the core component in machine tool, the spindle would generate large amounts of heat when it is running at a high speed. Among the heat sources listed above, the spindle is considered as an important one [4].

In order to minimize the spindle thermal error, there are namely three methods:

1. Thermal error avoidance
2. Thermal error control
3. Thermal error compensation

Here we have taken up thermal error compensation as our topic of research. Compared with other two types of methods, thermal error compensation is more convenient and cost-efficient [5]. The most obvious method for reducing the implications of thermal error in machine tool is to compensate for the changes. The simplest and most widely used way is to record temperature and thermal displacement, which may then be used to create a model. The measured temperatures will be input to the developed mode for predicting the thermal displacement of the spindle which will be compensated using a controller. Error compensation approaches try to create an artificial error in order to compensate for the real one [6]. The foundation of accurate thermal error identification is advanced detection technology. A laser interferometer or other measuring instruments can easily measure the geometric error as well as thermally induced errors. Yang suggested a new spindle thermal error monitoring method based on a ball bar system rather than a capacitance sensor system.

Thermal errors on CNC machine tools can be well predicted by splitting the machine tool into its constituent elements and modelling just those portions exhibiting the highest thermal movement. They also demonstrated that machine tool structural elements may be accurately simulated using rectangle-based prisms. White shown that in order to predict the two-dimensional deformation of a machine tool structural element over a wide range of machine operating conditions, it was necessary to know both the magnitude and position of temperature gradients.

## 2 Creation of a Thermal Model

The created thermal model is used to compensate for thermal errors. Temperature and displacement sensors are measured from key spots on the machine tool, as well as other potential locations (Fig. 1).

Heat emanates from a variety of places in precision machine tools.

- The heat generated during the cutting process. The work piece, the chips, and the coolant [7] all exposed to the heat. The bulk of heat is taken away by chips (60–80%) and finally passed to the coolant.
- Heat was generated as a result of mechanical, electrical, and hydraulic losses [7]. Motion (spindle bearing) losses are used to indicate mechanical losses. The heat generated in motors and drives represents the electrical losses. Fluid dynamic



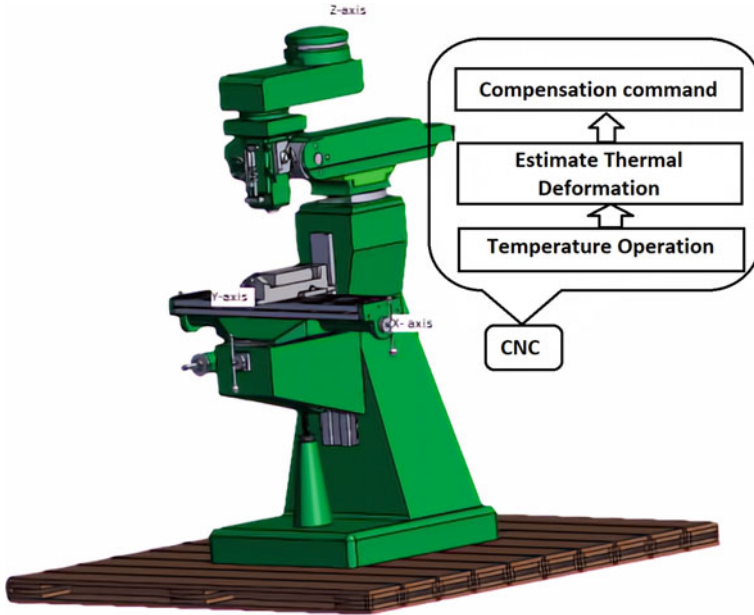


Fig. 1 Concept diagram of thermal compensation system

friction energy losses in the collet closer, hydraulic, and coolant pump constitute hydraulic losses [7].

- Changes in the ambient environment’s thermal influence.

Thermal deformation of machine tool components can be caused by both internal and external heat sources, resulting in poor geometric precision in work parts after machining. Temperature and thermal deformation issues account for approximately 40–70% of total machining errors. As a result, developing solutions for reducing and eliminating thermal deformation faults is crucial and attracts a lot of attention in high-precision machining [8]. Temperature-sensitive points, also known as key temperature measurement sites on a machine tool, are locations where temperature changes have a strong relationship with thermal displacement.

### 3 Thermal Modelling

One of the most important tasks in successful thermal error modelling and correction is to identify the source of the error. The temperature of the primary locations on the machine, as well as other available factors, can be used to determine deformations or displacement changes at specific places of machine tools owing to thermal inaccuracy [9]. This approach makes use of temperature factors, which show a strong

link between thermal deformation and critical components. This effective approach has now been adopted for a variety of machine equipment. Thermal error compensation includes recording thermal deformation measurement, create an error model and then compensate it.

### ***3.1 Sensor Placement***

This research [10] established a measuring and compensating control system for machine tool spindle thermal expansion. The tool setting probe MP4 and the low-cost yet precise thermal sensor of AD 590 IC were designed for temperature and spindle expansion measurements, respectively [10]. The error model is developed from the cutting state rather than the non-cutting condition. Using accessible temperature data points at any given moment, a linear error model may be developed.

### ***3.2 Estimating Thermal Deformation of Main Spindle***

The primary spindle rotation causes the greatest amount of thermal deformation due to internal heating. The spindle speed affects this property of thermal deformation. As a result, precisely estimating thermal deformation proved challenging. To overcome this challenge, we used experimental formulations based on spindle speed parameters to characterize these deformation characteristics, and we added the formula for compensating in a continuously transient condition into the computation for predicting thermal deformation. This has made it possible to precisely predict thermal deformation at all rotation speeds.

### ***3.3 Linear Regression Analysis***

Linear-regression models are relatively simple and provide an easy-to-interpret mathematical formula that can generate predictions. The relationship between predictor and responder variables is explicitly described in a data model. Linear regression is used to fit a data model with linear coefficients. A least-squares fit is the most frequent sort of linear regression, and it can fit both lines and polynomials, among other linear models. Linear regression is an extensively used method to compare the correlation between two variables using a linear line. The dependent variable can be predicted using the independent variable as well [11] (Table 1).

$$Y = \beta_0 + \beta_1 * x_1 + \beta_2 * x_2 + \beta_3 * x_3 + \epsilon \quad (1)$$

**Table 1** Linear regression results

<i>Training results</i>	
RMSE (Validation)	8.6107
R-Squared (Validation)	1
MSE (Validation)	74.144
MAE (Validation)	6.5657
Prediction speed	13,000 obs/sec
Training time	1.2053s
<i>Test results</i>	
RMSE (Test)	8.3586
R-Squared (Test)	1
MSE (Test)	69.866
MAE (Test)	6.359

$$\varepsilon = \sum_{i=1} (y_i - \hat{y}_i)^2 \tag{2}$$

- $x$  is the independent variable
- $Y$  is the dependent variable
- $\beta_0$  is the constant term
- $\beta_1$  is the coefficient of  $x_I$
- $\epsilon$  is the total error of the actual and predicted value
- $y_i$  is the  $i$  th input value
- $\hat{y}_i$  is the  $i$  th predicted value

As shown in the above Fig. 2, the linear graph has been presented with DIA (diameter) versus Temperature recorded in the spindle housing bed using MATLAB regression analyzer.

### 3.4 ANN (Artificial Neural Networks)

The neural network is a complicated algorithm used for predictive analysis that is physiologically inspired by the structure of the human brain. Time series data may be predicted using neural networks. A neural network may be programmed to recognize patterns in incoming data and provide noise-free output.

Even when the data contains a substantial quantity of noise, neural networks have a high degree of accuracy. This is a significant benefit; if the hidden layer can still uncover correlations in the data despite noise, you may be able to use otherwise worthless data. Multiple variables are employed as input and output in the neural network model, as shown in Fig. 3. In a traditional NN model, there are

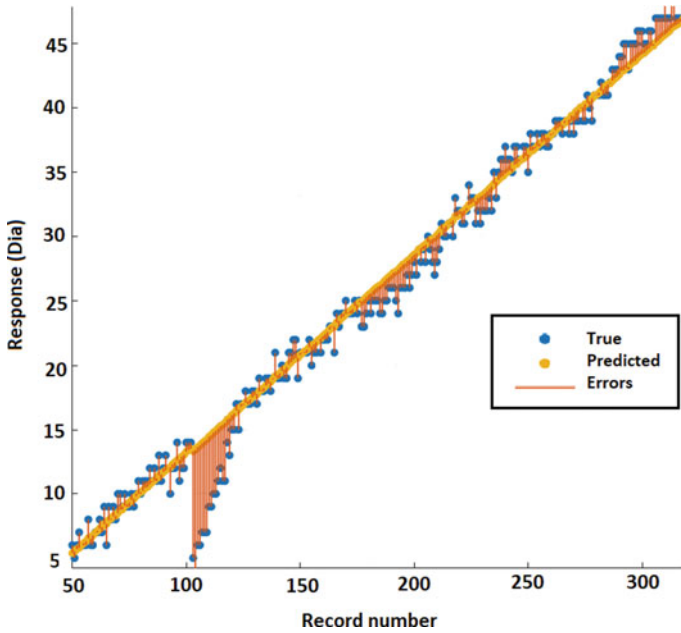


Fig. 2 Linear regression plot

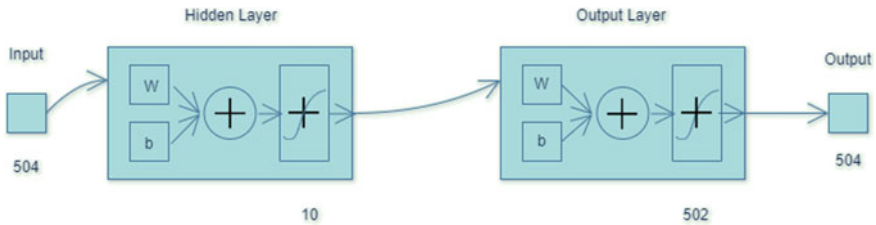


Fig. 3 ANN

three layers (input, output, and hidden). Figure 3 shows how the input layer, hidden layer and output layer minimizes the error during the training phase due to the input being continuously being optimized while moving towards the output layer. External signals and data are accepted by the input layer. The hidden layer is a unit that resides between the input and output layers and cannot be seen from the outside of the system, and it realizes the output of the system processing results.

In the NN training procedure, the Sum-Square Error (SSE) is the object function of the network optimization under the same training epoch (the number of iterations). A high number of training epochs may result in a small training error (SSE), but it does not necessarily lead to a better network. An error goal that is too small will also lead to an over-training problem similar to a surplus of neurones in the hidden layer.

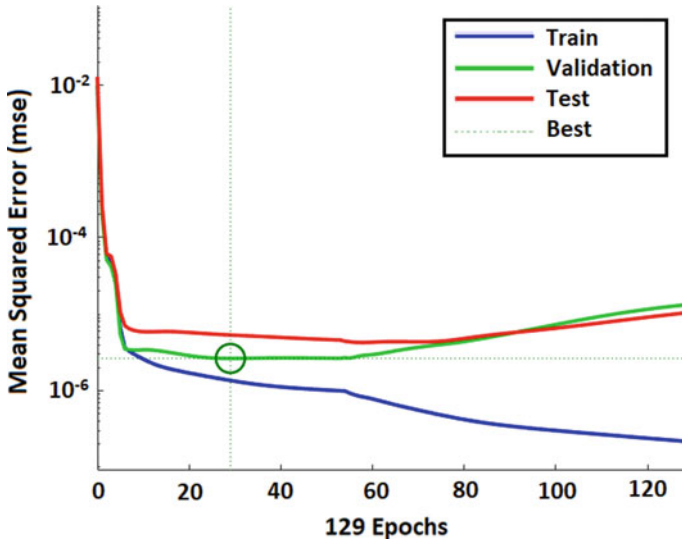


Fig. 4 ANN validation epoch plot

It involves,

1. Processing the dataset
2. Making the artificial neural network
3. Training the ANN
4. Testing the ANN

The following results were acquired after analyzing the input and output layers with MATLAB’s neural network toolbox, which were both analyzed and then lowered to smaller values to reduce error. Figure 4 demonstrate how the RMSE value changed over time and at which epoch the performance was at its best, which is  $2.6471e-06$  at epoch 29.

### 3.5 SVM

SVM is a pattern recognition classifier derived from the generalized portrait technique. For the leaderway-V450 machining center, Miao et al. developed spindle thermal error models based on SVM and multiple regression in 2013. It was determined that the SVM model employed for thermal error correction not only had high accuracy, but also good robustness, by examining the accuracy of the cross-quarter experimental data [12]. One of the most important aspects of machine learning is data classification. The aim behind a support vector machine is to establish a hyper plane between data sets to show which class they belong to. The goal is to teach the machine to recognize structure in data and map it to the appropriate class label. The

hyper plane has the greatest distance to the nearest training data points of any class, resulting in the best outcome.

In kernel SVM, you map your data points onto a Hilbert space H with potentially infinite dimensions. The normal vector to the separating hyperplane (which completely characterizes the decision boundary) turns out to have the form

$$w = \sum_{i=1}^n \alpha_i y_i \phi(x_i) \tag{3}$$

We classify a point x via

$$\text{sgn}(b + \langle w, x \rangle) = \text{sgn}\left(b + \sum_{i=1}^n \alpha_i y_i K(x_i, x)\right) \tag{4}$$

where K is the kernel function. For K,

$$K(x, x') = \exp\left(-\gamma \|x - x'\|^2\right) \tag{5}$$

We have,

$$\|x - x'\|^2 = \|x\|^2 + \|x'\|^2 - 2x^T x' \tag{6}$$

Each test point's squared norm is computed by X1, while each training point's squared norm is computed by X2. Then compute the total of these minus two times the data points' inner products, which is the (or at least a) vectorized approach to do all pairwise calculations (Table 2).

$$\|x - x'\|^2 \tag{7}$$

**Table 2** SVM results

<i>Training results</i>	
RMSE (Validation)	10.193
R-Squared (Validation)	1.00
MSE (Validation)	103.9
MAE (Validation)	8.3483
Prediction speed	24,000 Obs/s
Training time	3.1051
<i>Test results</i>	
RMSE (Test)	10.023
R-Squared (Test)	1.00
MSE (Test)	100.46
MAE (Test)	8.3321

### 3.6 Bagged Trees

The primary idea behind bagged trees is that instead of relying on a single decision tree, you rely on a large number of them, allowing you to combine the insights of multiple models. The problem is that any small change in the data might cause significant changes in the model and future forecasts. The rationale for this is that one of the advantages of bagged trees is that it reduces variation while maintaining bias consistency.

Given a set of independent observations,

$$Z_1, \dots, Z_n$$

Each with variance

$$\sigma^2$$

The variance of  $Z'$  is

$$(\sigma^2)/n$$

Calculation using  $N$  separate training sets

$$\widehat{f}^1(x), \widehat{f}^2(x), \dots, \widehat{f}^N(x)$$

And obtain a low variance statistical learning model using

$$\widehat{f}_{ave}(x) = \frac{1}{N} \sum_{n=1}^N \widehat{f}^n(x) \tag{8}$$

$N$  distinct bootstrapped training data sets are constructed from repeated samples from the taken data set. In order to get

$$\widehat{f}^{*n}(x)$$

The  $n$ th bootstrapped training set is trained.

Finally

$$\widehat{f}_{bag}(x) = \frac{1}{N} \sum_{n=1}^N \widehat{f}^{*n}(x) \tag{9}$$

is calculated by averaging all of the forecasts.

Regression trees are not trimmed and have a deep root system. As a result, each tree has a high variation but a low bias. As a result, by averaging these  $B$  trees, the

**Table 3** Bagged trees results

<i>Training results</i>	
RMSE (Validation)	3.977
R-Squared (Validation)	1.00
MSE (Validation)	15.817
MAE (Validation)	2.4622
Prediction speed	5400 obs/s
Training time	3.5372
<i>Test results</i>	
RMSE (Test)	2.333
R-Squared (Test)	1.00
MSE (Test)	5.443
MAE (Test)	1.4669

variance is reduced. By grouping hundreds or even thousands of trees into a single method, bagging has been shown to provide significant gains in accuracy (Table 3).

## 4 Conclusion

This work aims to improve the efficiency of compensation system in CNC machine. The location of the sensor is observed to play a significant influence in building a robust thermal model. A total of four key sensing stations were chosen after testing many temperature fields. The following conclusions are derived,

1. The thermal errors are unpredictably variable, resulting in a distinct thermal model each time. The use of linear regression revealed that it is one of the simplest and most straightforward methods.
2. In ANN, the nonlinearity won't be captured if there aren't enough neurons in the hidden layer. In contrast, if we include too many neurons, the ANN suffers from overfitting, resulting in a lack of generalizability. The RMSE value is lower than all other approaches and is beneficial in prediction when a large number of data points are involved.
3. A fully formed decision tree, has a large variance and a low bias. Bagging forest aggregates these high variance models in order to minimize variance and hence improve prediction accuracy. This leads in reduced RMSE values for the bagged trees approach, which has been demonstrated to be more efficient than linear regression.



## References

1. Li, Y., Zhao, W., Lan, S., Ni, J., Wu, W., Lu, B.: A review on spindle thermal error compensation in machine tools. *Int. J. Mach. Tools Manuf.* **95**, 20–38 (2015)
2. Bryan, J.: International status of thermal error research. *CIRP Ann.* **39**(2), 645–656 (1990)
3. Ramesh, R., Mannan, M., Poo, A.: Error compensation in machine tools—a review: Part ii: thermal errors. *Int. J. Mach. Tools Manuf* **40**(9), 1257–1284 (2000)
4. Haitao, Z., Jianguo, Y., Jinhua, S.: Simulation of thermal behavior of a cnc machine tool spindle. *Int. J. Mach. Tools Manuf* **47**(6), 1003–1010 (2007)
5. Aguirre, G., Nanclares, A., Urreta, H.: Thermal error compensation for large heavy-duty milling-boring machines. Proceedings of the 29th Annual Meeting of the American Society for Precision Engineering, pp. 57–62. Zurich, Switzerland (2014)
6. Han, Z.Y., Jin, H.Y., Liu, Y.L., Fu, H.Y.: A review of geometric error modeling and error detection for cnc machine tool. *Appl. Mech. Mater.* **303**, 627–631 (2013)
7. Kushnir, E.: Thermal compensation algorithm for machine tool. *Amer. Soc. Mech. Eng.* **493**, 51–60 (2005). New York, N.Y
8. Tsai, P.C., Cheng, C.C., Chen, W.J., Su, S.J.: Sensor placement methodology for spindle thermal compensation of machine tools. *Int. J. Adv. Manuf. Technol.* **106**(11), 5429–5440 (2020)
9. Chen, T.C., Chang, C.J., Hung, J.P., Lee, R.M., Wang, C.C.: Real-time compensation for thermal errors of the milling machine. *Appl. Sci.* **6**(4), 4–8 (2016)
10. Fan, K.C.: An intelligent thermal error compensation system for cnc machining centers. *J. Chinese Soc. Mech. Eng.* **28**(1), 81–90 (2007)
11. Lin, C.J., Su, X.Y., Hu, C.H., Jian, B.L., Wu, L.W., Yau, H.T.: A linear regression thermal displacement lathe spindle model. *Energies* **13**(4), 1–12 (2020)
12. Gong, Y.Y., Miao, E.M., Chen, H.D., Cheng, T.J.: Application of support vector regression machine to thermal error modelling of machine tools. *Opt. Precis. Eng.* **4** (2013)

# Establishing the Planting Calendar for Onions (*Allium cepa L*) Using Localized Data on Temperature and Rainfall



Jubert B. Oligo and Julius S. Valderama

**Abstract** The study aimed to determine a planting calendar for a red variety of onion (*Allium cepa L*) in Aritao, Nueva Vizcaya utilizing the temperature and rainfall data of the locality and matched with the temperature and water requirements of the onion plant. Onion has 9 stages starting from the sowing stage to the fall-down stage that lasted for an average of 126 days. Onions require cooler weather during the early stages of growth while a dry atmosphere with moderately high temperature is necessary for bulb development up to maturation until the harvesting period. Water requirements of the onion plant also vary from every stage; lack of water, as well as excessive water, could be disadvantageous to the plant growth and development. Ten years of data on rainfall and temperature of the locality were sourced-out in the NVSU Agromet station. These data were used to forecast 12 months of data on temperature and rainfall using three forecasting methods of the SPSS, NCSS, and MS Excel. The forecasted rainfall and temperature data on weekly basis were matched to the 9 stages of onions to its temperature and water requirements starting from the sowing stage to the fall-down stage. The study was able to determine the best timing for the plant; it is on the second week of February up to the third week of June. Onions planted at this time interval have a high forecasted percentage of survival as the temperature and water requirements of the plant in its stages were all sustained.

**Keywords** Climate adaptation · Planting calendar · Time-series analysis

---

J. B. Oligo

College of Teacher Education, Nueva Vizcaya State University, Bayombong, Philippines

J. S. Valderama (✉)

College of Arts and Sciences, Nueva Vizcaya State University, Bayombong, Philippines

e-mail: [valderamajulius@gmail.com](mailto:valderamajulius@gmail.com)

© The Author(s), under exclusive license to Springer Nature Switzerland AG 2022

S. Banerjee and A. Saha (eds.), *Nonlinear Dynamics and Applications*,

Springer Proceedings in Complexity,

[https://doi.org/10.1007/978-3-030-99792-2\\_75](https://doi.org/10.1007/978-3-030-99792-2_75)

895

## 1 Introduction

Climate change presents significant risks and opportunities for agriculture [1]. Chmielewski et al. [2], Kalbarczyk [3] confirmed that rapid changes in air temperature in the rest of the world and it is associated to the so-called climate change. According to Altieri et al. [4], climate change impact potentially significant to small farm production is loss of soil organic matter due to soil warming. Higher air temperatures are likely to speed the natural decomposition of organic matter and to increase the rates of other soil processes that affect fertility. Climate changes remote from production areas may also be critical. Irrigated agricultural land comprises less than one-fifth of all cropped area but produces between 40 and 45% of the world's food and water for irrigation is often extracted from rivers that depend upon distant climatic conditions [5]. Climate change produces a basic sense of ethical and existential violation that creates new norms, laws, markets, technologies, understandings of the nation and the state, urban forms, and international cooperation [6].

Air temperature is one of the most important meteorological elements, deciding the rate of a plant's growth and development. The examined onion phenophases were most correlated at  $P < 0.01$ , with the mean air temperature from the period of 6–9 weeks before the earliest date of their occurrence [3]. Hatfield and Prueger [7] states that changes in short-term temperature extremes can be critical, especially if they coincide with key stages of development. Only a few days of extreme temperature (greater than 32 °C) at the flowering stage of many crops can drastically reduce yield.

The same is true with precipitation—gross production value in agriculture would decrease by 0.24 for every 1 mm increase in precipitation but more number of rain days would increase gross production value by 1.24. An increase in Diurnal range temperature as measured by the difference between the daily maximum and minimum temperature would decrease gross production value by 5.74 [8]. Daymond et al. [9] revealed that Measurements of the ratio of the maximum diameter of the bulb to the minimum diameter of the neck for onions showed that there was little or no influence of CO<sub>2</sub>, whereas the effect of temperature was substantial. Bulbing was accelerated by high temperature and was greatly delayed at low temperature.

Onion farmers aimed to produce quality onions. The quantity of their harvest is dependent on the available land area for cultivation, capital for the expenditures, manpower, and some resources which limits the capacity of the farmer to produce a larger quantity. In onion production and on its business side, the quality and quantity of the harvest are two inseparable ideas. Some researchers like Al-jamal et al. [10] have worked on optimizing the yields in onion productions but maintaining the farm inputs practices to produce quality onions. They focused on improving the yield but not sacrificing the quality of the onions. On the other hand, some researchers like Boyhan et al. [11] ventured on producing quality onions, but not sacrificing the yield produced. Moreover, researchers like Piri and Naserin [12], de Santa et al. [13], Zheng et al. [14], Channagoudra et al. [15] who have worked on how to improve the quality of onions produced and the same time the quantity produced.

As a tropical country, the Philippines is acknowledged as an onion-growing state. Because the versatile high-value crop could be grown all over the archipelago, many rice farmers have shifted to onion farming as they tried and proven that they earn more from cultivating the red bulb better known to Filipinos as “sibuyas”. In Aritao, Nueva Vizcaya, farmers shifted to growing onions in large-scale production. Onion has become the town’s One Town, One Product. The production surplus of onions in the province is also seen as a bright opportunity among farmers as an alternative source of income and to boost the local economy [16]. The study was limited to the red variety of onions as this variety of onions is commonly planted by the farmers in the locality.

Onion farmers used to plant onions (*Allium cepa* L) from December to April when rain is not expected to occur. However, because of climate change, even during these said months, rains already occur. Making the time to plant onions becomes unpredictable and risky, thus resulting in a poor harvest of farmers. It is for this reason that this research was conducted to determine the right timing for farmers to plant onions to obtain a bountiful harvest. In this study, the objectives were: (1) to determine the trend of temperature and rainfall from January, 2008 to March, 2018, (2) to determine the water and temperature requirements of onions, (3) to predict the rainfall and temperature for the next planting seasons of onions, and (4) to establish the planting calendar for onions.

## 2 Methods

Descriptive—exploratory type of research was used in this study. The descriptive type was used to describe the onion’s water and temperature requirements, as well as the trends of the climatic data using 10 years of previous data on temperature and rainfall. The exploratory part of the design was used in the generation of mathematical models for forecasting one-year data for rainfall and temperature. Exploration was also used in establishing the planting calendar.

Physiological characteristics of the red onions, particularly its need requirements for water and temperature was established through literature reviews, guidebooks in onion productions, fact sheets, and internet resources. These onions’ characteristics were then presented to experts for their validation and further enhancement or recommendation. Experts in Onion cropping and production, as well as the farmers, were identified with the assistance of the Department of Agriculture—Aritao.

The study was conducted mid-year of 2019, however, the available data on rainfall and temperature used for the analysis includes from January 2008 to March 2019. Temperature and Rainfall data from January 2008 to March 2019 was collected from the Agromet Station of Nueva Vizcaya State University Bayombong (NVSU-PAGASA). The study was conducted at Aritao, Nueva Vizcaya since red-onion production is more abundant in the said municipality.

The growth and production of onions are influenced by several factors like soil moisture and nutrients [17], soil quality or types [18], farm irrigation [19], and others.

Since the study was conducted purposely for Aritao, other parameters were no longer considered as all the red-onion farms in the locality were all paddy, not irrigated, and with soil pH ranging from <4.50 to >6.80.

The data was transformed into weekly temperature and rainfall data by getting the average of the 7 consecutive days. The data was used to determine the climatic condition of Nueva Vizcaya Province. In addition, this was also used to predict the climate condition for the next 48 weeks (1 year) using the three different forecasting models namely SPSS forecast, MS Excel, and NCSS. The average of the obtained weekly forecasted data was then utilized to analyze whether or not possible to plant onion in the week/month of the year 2020 considering the water and temperature requirements of the onions.

### 3 Results and Discussion

#### 3.1 The Water and Temperature Requirements of Onions

Table 1 reflects the stages of onions starting from sowing to harvesting. The average number of weeks in every stage was also included in the table. Onions cropping is ideal if the plot has provisions for irrigation, however, onions are dependent on rainfall as rainfall could cause excessive water in the plot and later cause the plant to wilt and die.

Land preparation is done one month (4 weeks) prior to transplanting. Transplant seedlings 4–6 weeks after sowing. First side-dressing will be done ten days after transplanting 4,6,8 weeks after transplanting. Depending on soil types, irrigation varies between 4 to 7 days. Stop irrigation 2–3 weeks before harvest. Harvest when the tops begin to fold over. Ambient temperature requires the Seedling growth 20–22 °C, before bulbing 15–24 °C and for bulb development 15–24 °C. Bulb Onions grow well in an easily crumbled and well-drained loam soil with good water holding

**Table 1** Stages of planting onions

Stages	Allowable Time (in weeks)
Land preparation (Basal)/sowing transplanting and fertilization	4 week
Transplanting	4–6 weeks after sowing
Fertilization (side dress)	4–8 weeks after transplanting
Irrigation	1 week <i>Note: stop irrigation 2-3 weeks before harvest</i>
Pest & Disease management	As the need arises
Harvesting	Harvest when the tops begin to fold over

**Table 2** Water and temperature requirements of onion on its stages

Growth stage	Average water use rate (mm/day)	Total water use during stage	No. of days
Seed in soil after sowing	33.0	33.0	1.0
Loop stage	4.9	98.0	20.0
First leaf 'flag' stage	3.4	41.0	12.0
Cotyledon senescence	3.6	36.0	10.0
Fourth leaf 'leek' stage	3.6	51.0	14.0
Fall of the first leaf	3.7	52.0	14.0
Start of bulbing	3.6	51.0	14.0
Bulb swelling	2.8	75.0	27.0
Fall-down or soft neck	3.6	50.0	14.0
Total		487.0	126.0

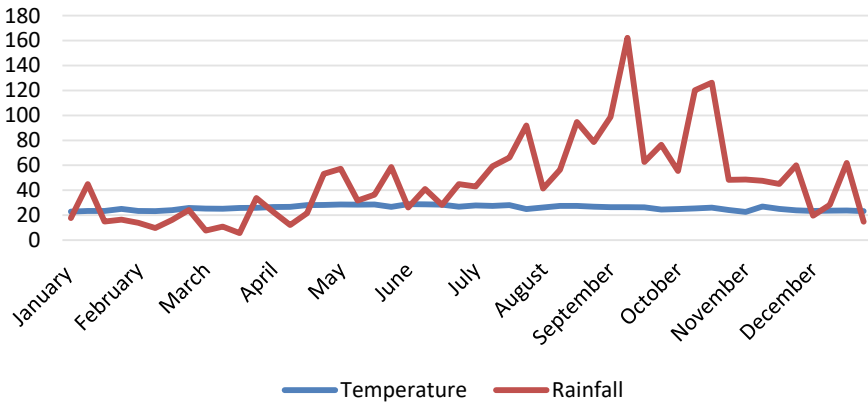
capacity and pH between 6 and 7. The result was supported by Netafim. The Best Management Practices (BMPs) determined the additional proven research becomes available wherein the optimum ambient temperatures for onion are: Seedling growth 20–25 °C, vegetative growth 13–24 °C, before bulbing 15–21 °C and for bulb development 20–25 °C. The soil suitability must be fertile, light, deep friable well-drained fine sandy, loamy and alluvial and the optimum soil pH is 5.8 to 6.5 [20–24].

Table 2 reflects the water and temperature requirements of Onions in all the stages. On average, one-onion cropping lasted for 126 days starting from sowing up to fall-downstage. Included in the table are the data on the average water use rate (mm/day) of the onions, and the total water use for the entire specific growth stage.

The data in Table 2 was supported by the study of Pejic [25] the effect of different irrigation schedules on yield and water use of onion (*Allium cepa L.*), the values of evapotranspiration of 450–500 mm could be used as a good platform for onion growers in the region in terms of maximum yield and optimum utilization of irrigation water. The average daily water needs of onion during irrigation season grown in a semi-arid climate with a mean temperature of 20 °C needs approximately 6.5 mm of water per day and the indicative values of crop water needs are 350–550 mm. Harvesting starts at 95 DAT or 125 DAS.

### 3.2 The Monthly Average of the Rainfall and Temperature

Figure 1 reveals the average monthly rainfall for 10 years from January 2008–May 2019 of Nueva Vizcaya particularly. On average, water precipitation from January to April was at the minimum or scarce level, little precipitation occurred from May to July, high volume of water precipitation was down-pour from August to December. These rainfall patterns coincide with the weather seasons of the Philippines.



**Fig. 1** Average rainfall and temperature from 2008–2019

On the other hand, seemingly there was small variation as to temperature reading from January to December. The coldest months were from December to February, and the hottest months were from March to May.

These patterns or trends of temperature and rainfall occurred repeatedly every year following the weather cycle of the Philippines. Water precipitation increases in the months of June and begins to decrease in the months of November. Temperature also follows a trend.

### 3.3 Forecasted One-Year Data of Rainfall and Temperature

Table 3 is the weekly forecasted rainfall and temperature of Aritao, Nueva Vizcaya. Model 1 corresponds for time series analysis using SPSS, Model 2 for NCSS, Model 3 for MS Excell, and Ave Model for the average of the values.

Table 3 shows the forecasted weekly rainfall and temperature for January 2020 to March 2021 through the use of SPSS time series (Model 1), NCSS forecasting (Model 2), and MS Excel forecast function (Model 3). The averages of these data were used to determine the planting season onions (*Allium cepa L*) in Aritao to be able to have an effective yield. On the other hand, the average slightest rainfall forecasted is the third week of January 2019 to the second week of April 2019 which is ranging from 10–32 mm while the average forecasted temperature for the whole year round is ranging from 22 °C–28 °C.

**Table 3** Forecasted temperature and forecasted rainfall for the January 2020–March 2021

Month/wk	Forecasted temperature				Forecasted rainfall			
	Model 1	Model 2	Model 3	Model Tmp	Model 1	Model 2	Model 3	Model Rnf
<i>January</i>								
w1–w2	23.5	23	24	23.5	84.5	17	34	45.5
w3–w4	24.5	23	25	24.5	31.5	14	17	20.5
<i>February</i>								
w1–w2	25	23.5	24	24	26	11	13	16.5
w3–w4	27	25.5	26	26	25	16	22	21
<i>March</i>								
w1–w2	26.5	23.5	26	25.5	24.5	6	10	13.5
w3–w4	27	23.5	27	25.5	26.5	15.5	21.5	21
<i>April</i>								
w1–w2	29	24	28	27	23	14.5	19	18.5
w3–w4	29.5	24	29	27.5	61	25.5	41	42.5
<i>May</i>								
w1–w2	30	24	30	28	82	24.5	49	52
w3–w4	29.5	24	29	27.5	59.5	32.5	52.5	48
<i>June</i>								
w1–w2	30	24	30	28	66.5	20.5	37	41
w3–w4	29.5	24	29	27.5	56.5	25.5	40	40.5
<i>July</i>								
w1–w2	29	23	28.5	27	93	32	56	60.5
w3–w4	28.5	23	27.5	26	110	49	87	82
<i>August</i>								
w1–w2	28.5	23	27.5	26	66	35.5	54	52
w3–w4	28	22	28.5	26	78	71.5	96	81.5
<i>September</i>								
w1–w2	28.5	22.5	27.5	26	65	107	144	105.5
w3–w4	27	22	26.5	25.5	82	49	77	69.5
<i>October</i>								
w1–w2	25.5	21.5	26	24	49.5	73	97	73
w3–w4	26	21.5	26	24.5	55	71.5	96.5	74
<i>November</i>								
w1–w2	24.5	21	26	24	56	38	53.5	49
w3–w4	24.5	20	25.5	23.5	60	40.5	58	52.5

(continued)



**Table 3** (continued)

Month/wk	Forecasted temperature				Forecasted rainfall			
	Model 1	Model 2	Model 3	Model Tmp	Model 1	Model 2	Model 3	Model Rnf
<i>December</i>								
w1–w2	23.5	20	24.5	22.5	18	20	26.5	21.5
w3–w4	23	19	24.5	22	21	38.5	42.5	34
<i>January</i>								
w1–w2	23.5	18.5	24	22	85	13	35	44.5
w3–w4	25	19	25	23	32.5	12.5	17.5	20.5
<i>February</i>								
w1–w2	25	19	24	23	27	10.5	13	16.5
w3–w4	27	19.5	26	24	26	15	22.5	21
<i>March</i>								
w1–w2	27	18.5	26	24	25	5.5	10	14
w3–w4	27	18.5	27	24	27	15	22	21

### 3.4 The Planting Calendar for Onions

The predicted rainfall data and temperature data in Table 3 were matched to established water and temperature requirements as presented in Table 1. The forecasted rainfall and temperature; and the onion's water and temperature requirements were analyzed to come up with a planting schedule that can sustain the growth and yield production of the plant. This was determined using the identified water and temperature requirements of the plant and matched to the value of the Model average for rainfall and temperature.

$$\text{Wkly prob} = \begin{cases} 1 & \text{if computed Model ave is lower than the plant requirement} \\ 0 & \text{if computed Model ave is higher than the plant requirement} \end{cases}$$

In every stage of the plant, if it is denoted by 1, it means to say that the onion's requirements, both temperature, and rainfall were satisfied. Thus, the plant life can be sustained in that week. On the contrary, if it is denoted by 0, it means that either or both the onion's requirements on water or temperature were not sustained. Thus, the plant life is at risk on that week.

The rate of survival indicates the percentage of the number of weeks the plant sustained over the total number of weeks. Thus, 100% implies that plant life will be sustained throughout the cropping; and 90% could be sustained with 10% risk.

There are six identified planting schedules for onion. These six schedules have a high probability of supporting the water and temperature requirement of onion for 18 weeks from planting up to harvesting. As presented in Table 4, these were the following schedules (planting—harvesting):

**Table 4** Schedule of Planting Onions

Month/wk	Forecasted temperature				Forecasted rainfall			
	Model 1	Model 2	Model 3	Model Tmp	Model 1	Model 2	Model 3	Model Rnf
<i>January</i>								
w1-w2	23.5	23	24	23.5	84.5	17	34	45.5
w3-w4	24.5	23	25	24.5	31.5	14	17	20.5
<i>February</i>								
w1-w2	25	23.5	24	24	26	11	13	16.5
w3-w4	27	25.5	26	26	25	16	22	21
<i>March</i>								
w1-w2	26.5	23.5	26	25.5	24.5	6	10	13.5
w3-w4	27	23.5	27	25.5	26.5	15.5	21.5	21
<i>April</i>								
w1-w2	29	24	28	27	23	14.5	19	18.5
w3-w4	29.5	24	29	27.5	61	25.5	41	42.5
<i>May</i>								
w1-w2	30	24	30	28	82	24.5	49	52
w3-w4	29.5	24	29	27.5	59.5	32.5	52.5	48
<i>June</i>								
w1-w2	30	24	30	28	66.5	20.5	37	41
w3-w4	29.5	24	29	27.5	56.5	25.5	40	40.5
<i>July</i>								
w1-w2	29	23	28.5	27	93	32	56	60.5
w3-w4	28.5	23	27.5	26	110	49	87	82
<i>August</i>								
w1-w2	28.5	23	27.5	26	66	35.5	54	52
w3-w4	28	22	28.5	26	78	71.5	96	81.5
<i>September</i>								
w1-w2	28.5	22.5	27.5	26	65	107	144	105.5
w3-w4	27	22	26.5	25.5	82	49	77	69.5
<i>October</i>								
w1-w2	25.5	21.5	26	24	49.5	73	97	73
w3-w4	26	21.5	26	24.5	55	71.5	96.5	74
<i>November</i>								
w1-w2	24.5	21	26	24	56	38	53.5	49
w3-w4	24.5	20	25.5	23.5	60	40.5	58	52.5

(continued)

**Table 4** (continued)

Month/wk	Forecasted temperature				Forecasted rainfall			
	Model 1	Model 2	Model 3	Model Tmp	Model 1	Model 2	Model 3	Model Rnf
<i>December</i>								
w1–w2	23.5	20	24.5	22.5	18	20	26.5	21.5
w3–w4	23	19	24.5	22	21	38.5	42.5	34
<i>January</i>								
w1–w2	23.5	18.5	24	22	85	13	35	44.5
w3–w4	25	19	25	23	32.5	12.5	17.5	20.5
<i>February</i>								
w1–w2	25	19	24	23	27	10.5	13	16.5
w3–w4	27	19.5	26	24	26	15	22.5	21
<i>March</i>								
w1–w2	27	18.5	26	24	25	5.5	10	14
w3–w4	27	18.5	27	24	27	15	22	21

1—water and temperature requirements can be sustained

0—water and temperature requirements cannot be sustained

x, y—planting time, harvesting time

Table 4 shows the schedule of planting Onions (*Allium cepa L*) for C.Y. 2020. The requirements for planting Onions as shown in the table using the codes 0 and 1; whereas code 0 means the plant will not survive on that specific stage as the temperature requirement or rainfall requirement or both requirements were not sustained. Code 1 means that both temperature and rainfall were sustained in that specific week. X marks reefer to planting time, and Y represents the harvesting time. The probability of 100% survival indicates that the plant requirement for rainfall and temperature were all sustained.

In the table, the highest probability rate of survival falls under schedule 6 which is the 2nd week of February 2020 to the 3rd week of June 2020 with a probability rate of 94% while the lowest probability rate is schedule 1 which is the 1st week of January 2020 to 2nd week of May 2020 with a probability rate of 72%. For best growth and bulb quality, onion requires cooler weather during the early stages of growth and a dry atmosphere with moderately high temperature for bulb development & maturation until the harvesting period.

## 4 Conclusions and Recommendations

The study has shown the seasonality of rainfall and temperature of Bayombong Nueva Vizcaya for 10 years. The dry season's starts in the months of January 2020 up to

April 2020 while the wet season starts with the months of May 2020 to November 2020, then another cycle of the dry season in the months of January 2021 up to April 2021. The study suggested the planting seasons of onions for CY 2021 could be scientifically determined using combinations of time-series analysis. Based on the established planting calendar of onions, the highest probability rate of survival is if the plant will be planted on the 2nd week of February 2020 to the 1st week of March 2020 and expected to be harvested on the 3rd week of June to 2nd week of July. The forecasting procedure of the study could be repeated for the year 2022 or in the future years to determine the planting calendar of the red onion, white onion, and yellow onion.

## References

1. Cradock-Henry, N.A. et al.: Climate adaptation pathways for agriculture: insights from a participatory process. *Environ. Sci. Policy* **107**, 66–79 (2020)
2. Chmielewski, F.-M., Rötzer, T.: Annual and spatial variability of the beginning of growing season in Europe in relation to air temperature changes. *Climate Res.* **19**(3), 257–264 (2002)
3. Kalbarczyk, R.: The effect of climate change in Poland on the phenological phases of onion (*Allium cepa* L.) between 1966 and 2005. *Agric. Conspec. Sci.* **74**(4), 297–304 (2009)
4. Altieri, M.A., Koohafkan, P.: Enduring farms: climate change, smallholders and traditional farming communities (2008)
5. Siebert, S., Döll, P.: 2.4 Irrigation water use—a global perspective. *Central Asia* **14**, 10–2 (2007)
6. Beck, U.: How climate change might save the world. *Develop. Soc.* **43**(2), 169–183 (2014)
7. Hatfield, J.L., Prueger, J.H.: Temperature extremes: Effect on plant growth and development. *Weather Climate Extremes* **10**, 4–10 (2015)
8. Dait, J.M.: Effect of climate change on Philippine agriculture. *Int. J. Sci. Res.* **4**, 1922–1924 (2013)
9. Daymond, A.J., et al.: The growth, development and yield of onion (*Allium cepa* L.) in response to temperature and CO<sub>2</sub>. *J. Horticult. Sci.* **72**(1), 135–145 (1997)
10. Al-Jamal, M.S., et al.: Computing the crop water production function for onion. *Agric. Water Manag.* **46**(1), 29–41 (2000)
11. Boyhan, G.E. et al.: Evaluation of poultry litter and organic fertilizer rate and source for production of organic short-day onions. *HortTechnology* **20**(2), 304–307 (2010)
12. Piri, H., Naserin, A.: Effect of different levels of water, applied nitrogen and irrigation methods on yield, yield components and IWUE of onion. *Sci. Hortic.* **268**, 109361 (2020)
13. de Santa Olalla, F.M., Dominguez-Padilla, A., Lopez, R.: Production and quality of the onion crop (*Allium cepa* L.) cultivated under controlled deficit irrigation conditions in a semi-arid climate. *Agric. Water Manag.* **68**(1), 77–89 (2004)
14. Zheng, J., et al.: Effects of water deficits on growth, yield and water productivity of drip-irrigated onion (*Allium cepa* L.) in an arid region of Northwest China. *Irrigation Science* **31**(5), 995–1008 (2013)
15. Channagoudra, R.F., Prabhudeva, A., Kamble, A.S.: Response of onion (*Allium cepa* L.) to different levels of irrigation and sulphur in alfisols of northern transitional tract of Karnataka. *Asian J. Horticult.* **4**(1), 152–155 (2009)
16. Perante, Leonardo II. East-West Seed PHL projects sustainable onion industry nationwide. <https://businessmirror.com.ph/2018/05/05/east-west-seed-phl-projects-sustainable-onion-industry-nationwide/>
17. Kumar, S., Imtiyaz, M., Kumar, A.: Effect of differential soil moisture and nutrient regimes on postharvest attributes of onion (*Allium cepa* L.). *Scientia Horticult.* **112**(2), 121–129 (2007)

18. Shock, C.C., Wang, F.-X.: Soil water tension, a powerful measurement for productivity and stewardship. *HortScience* **46**(2), 178–185 (2011)
19. Mermoud, A., Tamini, T.D., Yacouba, H.: Impacts of different irrigation schedules on the water balance components of an onion crop in a semi-arid zone. *Agric. Water Manag.* **77**(1–3), 282–295 (2005)
20. López-Urrea, R., et al.: Single and dual crop coefficients and water requirements for onion (*Allium cepa* L.) under semiarid conditions. *Agric. Water Manag.* **96**(6), 1031–1036 (2009)
21. De Lis, B.R., et al.: Studies of water requirements of horticultural crops: II. Influence of drought at different growth stages of onion 1. *Agron. J.* **59**(6), 573–576 (1967)
22. Bekele, S., Tilahun, K.: Regulated deficit irrigation scheduling of onion in a semiarid region of Ethiopia. *Agric. Water Manag.* **89**(1–2), 148–152 (2007)
23. Ortola, M.P., Knox, J.W.: Water relations and irrigation requirements of onion (*Allium cepa* L.): a review of yield and quality impacts. *Exp. Agric.* **51**(2), 210–231 (2015)
24. El Balla, M.M.A.D., Hamid, A.A., Abdelmageed, A.H.A.: Effects of time of water stress on flowering, seed yield and seed quality of common onion (*Allium cepa* L.) under the arid tropical conditions of Sudan. *Agric. Water Manag.* **121**, 149–157 (2013)
25. Pejić, B. et al.: Effect of irrigation schedules on yield and water use of onion (*Allium cepa* L.). *African J. Biotechnol.* **10**(14), 2644–2652 (2011)

# Growth of Single Species Population: A Novel Approach



Suvankar Majee, Soovoojeet Jana, Anupam Khatua, and T. K. Kar

**Abstract** In this paper, we have proposed a new growth model for a single species population that captures certain features of logistic growth. We have constructed the growth model for a single species population on the basis of the assumptions that the individual reproduction rate is proportional with the available resources and a portion of the population species have no reproduction power. We have shown that this model would give better realistic phenomena than the other existing models, and also, it is capable of making new useful models.

**Keywords** Ecological problems · Birth-death process · Growth rate · Environmental carrying capacity · Reproduction rate

## 1 Introduction

In mathematical ecology, the growth rate of a population species is one of the most important aspects. Several growth models have been developed considering different biological organisms. In most cases, the population dynamics are modeled continuously. In their books, Kot [1] and Britton [2] described different growth rates for living creatures. The very basic model to describe the growth of species without

---

S. Majee (✉) · A. Khatua · T. K. Kar  
Department of Mathematics, Indian Institute of Engineering Science and Technology, Shibpur,  
Howrah 711103, India  
e-mail: [suvankarmajee2@gmail.com](mailto:suvankarmajee2@gmail.com)

S. Jana  
Department of Mathematics, Ramsaday College, Amta, Howrah 711401, India

© The Author(s), under exclusive license to Springer Nature Switzerland AG 2022  
S. Banerjee and A. Saha (eds.), *Nonlinear Dynamics and Applications*,  
Springer Proceedings in Complexity,  
[https://doi.org/10.1007/978-3-030-99792-2\\_76](https://doi.org/10.1007/978-3-030-99792-2_76)

constraint is exponential growth. In this model, the equation for the single species population whose biomass density is  $x$  can be written as follows:

$$\frac{dx}{dt} = rx, \quad x(0) = x_0 \quad (1)$$

Where the single population species has an average birth rate, say,  $b$  and, has an average death rate, say,  $d$  and then the intrinsic growth rate is defined as  $r = b - d$ . This type of growth is known as the Malthusian growth. The main drawback of the exponential growth is  $x \rightarrow \infty$  as  $t \rightarrow \infty$  if  $r > 0$ , i.e., the population biomass would go at infinite level along with time. If there are some limitations, the growth must be checked, and then the population would not grow following geometric ratio or exponential ratio. As there are some limitations (like limitations in available food, place for living, etc.) regarding the growth of any population species, therefore the Malthusian growth is modified. The simplest modifications have been done by the logistic type growth where it is considered that environmental carrying capacity is fixed and the growth of the population depends on that capacity. In this model, the growth of a single species population is described by the following equation:

$$\frac{dx}{dt} = rx \left(1 - \frac{x}{K}\right), \quad x(0) = x_0 \quad (2)$$

where the environmental carrying capacity is taken as  $K > 0$ .

Later on, many researchers have generalized the growth model and also proposed new types of growth functions. Different types of growth functions are available in the literature, for example, generalized logistic growth Nelder [11], Von Bertalanffy's growth [8], Richards's growth [9], Gompertz growth [10], Weibull function (Rwalings et al. [12]), Allee type growth function (Courchamp et al. [16]), etc. Some other growth functions and the estimation of the system parameters can be found in Tsoularis and Wallace [3], Bhowmick and Bhattacharya [4], Bhowmick et al. [4], Koya and Goshu [7], Crescenzo and Spina [6], Misra and Chaturvedi [13], Misra and Babu [14] and Kumar et al. [15]. The proper growth model is extremely important in studying the biological growth problems.

In the logistic type of growth, we have to consider a non-linear term of the state variable limiting the growth of the population species. This article proposes a new type of growth curve of a single species population. In this model, we consider the growth equation as the Malthusian type, although the intrinsic growth rate varies from time to time, and the intrinsic growth rate depends on the available environmental resource.

### 1.1 The Growth Model

Obviously, for each species, there are some individuals, who may be identified and differ from others, have no reproduction power. Besides the juvenile and the old individuals, there is a certain number of other individuals who have no reproduction power, and their reproduction power has been destroyed due to some disease or by means of some natural reason. For example, in species like bee, most portions of the individuals have no reproduction power, and thus considering an average per capita birth for each individual is not logical at all. Therefore, to overcome these inconveniences, we can propose two separate ways to consider the birth rate of a species. In the first assumption, we can assume that a certain portion of the species, say,  $\rho(0 \leq \rho \leq 1)$  has no reproduction power, and the rest portion  $(1 - \rho)$  has that power. On the other hand, the species like bees, etc., we can assume constant biomass, say,  $m$  has reproduction power, and the rest of individual biomass  $(x - m)$  are not capable of reproducing. However, in both cases, the birth rate of those individuals who have no reproduction power should be zero. In contrast, for the parameter death rate, we don't claim that any particular individual has zero death rates, although it is quite true that some individual has some less death rates and the other has some more death rate. Therefore, without loss of generality, we can assume that the death rate of the single species individual follows a distribution such that the weighted mean of this distribution exists and say it is  $d$ , i.e., the per capita death rate of each individual is  $d$ . In the rest of the paper, by the phrase 'birth rate' we would mean that the per capita birth rate of those individuals which have reproduction power.

Now we assume that the portion  $\rho(0 \leq \rho \leq 1)$  has no reproduction power whether the others are capable of reproducing. We also consider the per capita birth rate is  $b$  and the per capita death rate is  $d$ . Therefore, the governing equation regarding the change of the biomass of the single species population  $x(t)$  with time is given by:

$$\frac{dx}{dt} = (1 - \rho)bx - dx, \text{ with } x(0) = x_0. \tag{3}$$

The system (3) can be written in the following form:

$$\frac{dx}{dt} = (b - d - b\rho)x, \text{ with } x(0) = x_0. \tag{4}$$

From system (4), it may be concluded that,  $x(t) \rightarrow \infty$  if  $\rho < \frac{b-d}{b}$  whereas if  $\rho > \frac{b-d}{b}$  then the population species go to extinct and lastly for  $\rho = \frac{b-d}{b}$  we have  $x(t) = x_0$  for all time  $t$  (here we assume that  $b > d$ ). Thus, it can be concluded that if  $\rho > \frac{b-d}{b}$ , i.e., if the portion of the individual has no reproduction power is greater than some threshold, then the population species may go extinct. Hence for any population species, if the biomass of old age individuals is on the higher side continuously, then that species either goes extinct, or its biomass would be very low. Our present model can draw an extensive light on these types of natural phenomena.



Both the exponential growth and logistic growth models (as presented in Eqs. (1) and (2)), the intrinsic growth rate ( $r$ ) is considered as an independent model parameter. But according to our explanations,  $r$  cannot be an independent parameter, rather, it should depend on mainly three parameters, namely (i) the portion of the population ( $\rho$ ) which have no reproduction power, (ii) the birth rate ( $b$ ), and (iii) the per capita death rate ( $d$ ). Thus we can define the intrinsic growth rate as follows:

$$r = b - d, \text{ for those portions which are capable of reproducing offspring,}$$

$$= -d, \text{ for those portions which are unable to reproducing offspring.}$$

Therefore, we can define the intrinsic growth rate  $r$  as follows

$$r = (1 - \rho)b - d, \quad 0 \leq \rho \leq 1 \tag{5}$$

where  $\rho, b, d$  are defined earlier. Here  $\rho = \rho(K, t)$  is a function of available resource (i.e., the carrying capacity of the individual  $K$ ), and it varies with time. Now obviously,  $\rho$  will be inversely related to environmental carrying capacity  $K$ . Depending upon the numeric value of  $\rho$ , the intrinsic growth rate  $r$  may be positive or negative. The parameter  $\rho$  can be treated as a control parameter, and this parameter has a huge and important role, not only to evaluate the exact value of  $r$  but also to determine the exact population biomass level at any time.

With the help of the above definition of  $r$ , the growth of the single species population whose biomass is  $x(t)$  can be defined as follows:

$$\frac{dx}{dt} = rx, \quad x(0) = x_0 \tag{6}$$

where  $r$  may be positive or negative or zero. This type of growth is also one type of exponential growth, but the main difference of this type of growth is that here  $r$  is not always positive.

## 2 Explanations of the Model

Now suppose that initially  $r > 0$ , then after some time, say after  $t = t_1$ , the biomass of the population will be  $x_0 \exp(rt_1)$ . Now the growth, birth, and death of the population depend on the quantity as well as the quality of the available resource. If the available resource can sufficient to fulfill the requirement of  $x = x_1$  number of individuals, then as soon as the population goes beyond the level of  $x_1$ , then there will be a competition among them for the resource and due to this competition, some of them unable to avail any resource or a negligible amount of resource. When the population biomass goes beyond this level  $x_1$ , then due to the competition, some less amount of biomass than the level  $x_1$  would able to use the resource, and they remain stronger, and the rest portion (which is greater than the  $(x - x_1)$  when  $x > x_1$ ) becomes weaker. Now at

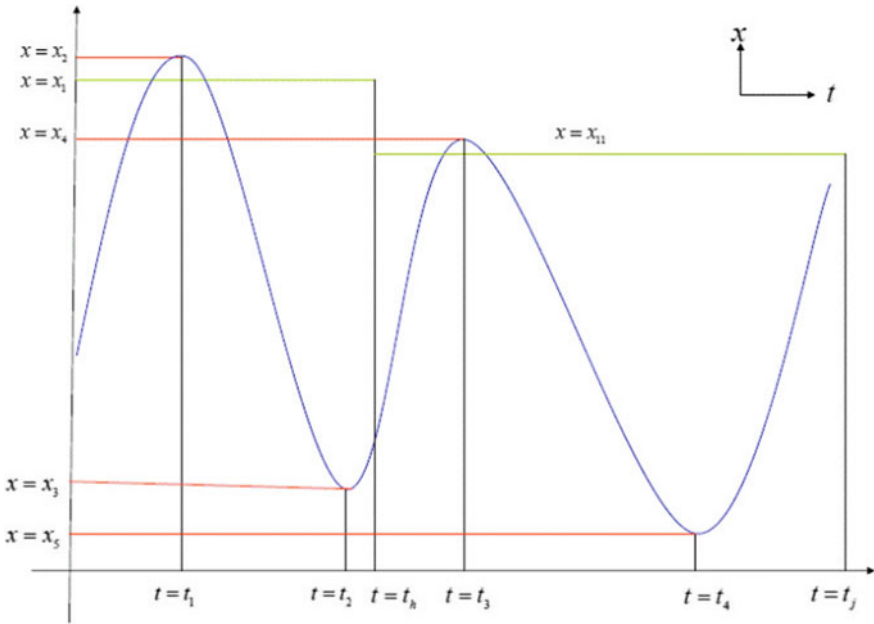


**Fig. 1** Growth of population species

$x = x_2$ , level, say the individual of biomass  $(x_2 - x_1 - \eta x)$ ,  $0 \leq \eta < 1$  don't get any resource to live. Thus we may consider that the individual of biomass  $(x_2 - x_1 - \eta x)$  have no birth rate although they have death rate  $d$ . Now recalling the definition of  $r$ , we can conclude that the intrinsic growth rate  $r$  of that portion will be  $-d$ . Therefore, after a certain amount of time, say,  $t_1$ ,  $r$  will be negative, and then the biomass of the species will decrease instantaneously. Again let after  $t = t_2$ , the population biomass reaches at  $x_3$ , far below the maximum available resource  $x_1$  and then again  $r$  changes its sign and  $r$  becomes positive, until the population biomass  $x$  reaches some  $x_{11}$ , (which may be different from  $x_1$  because the available resource may vary time to time) and after that  $r$  will again change its sign and will be negative. This process will continue, and if the population follows this type of growth, then the population will remain between some  $\underline{x} (\geq 0)$  to some  $\bar{x} (< \infty)$  level as the environmental carrying capacity is always finite, however large it may be (Figs. 1 and 2). This type of growth can define the extinction of a population species also. For example, for some time period,  $r$  will be less than zero and the available resource also reduces with time and eventually becomes so less that it will make tough to live for individuals of the species, then  $r$  will never be positive since the birth rate entirely depends on the resource. In this situation  $x(t) \rightarrow 0$  after  $t > t_1$  and it remains stable there.

The main difference of considering this type growth rate and the logistic type and the classical exponential growth rate are as follows:

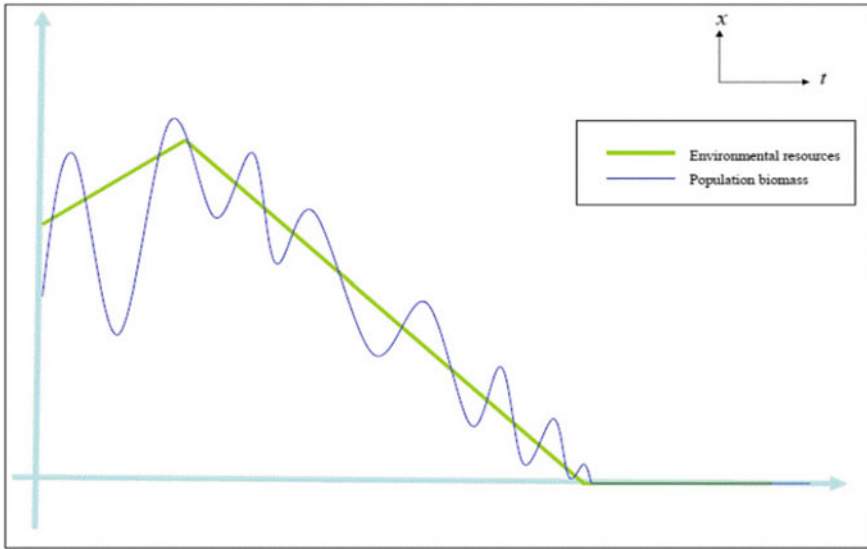


**Fig. 2** Extinction of a population species due to unavailability of resource. Here green line represents the carrying capacity of the environment for that population species and deep blue line represents the level of population biomass

- (1) Here, we need not consider any intraspecific competition term in the differential equation of the population, i.e., in (6) there is no carrying capacity term. The available resource depends on the growth rate
- (2) The carrying capacity is taken as a fixed quantity in logistic type growth model, although in reality, it changes time to time.
- (3) The logistic growth model is unable to produce a sufficient explanation of the extinction of a species in a single species model (since for logistic growth, the trivial equilibrium  $x(t) = 0$  is an unstable equilibrium).
- (4) The logistic type growth explains that  $x(t) \rightarrow K$  as  $t \rightarrow \infty$  but here we explain that through our model,  $x(t)$  will oscillate within some region unless it goes to extinct, and this phenomenon is a quite more realistic one.
- (5) Our model is quite simple than the logistic type growth model (since here (the model (6)) right-hand side is the simple linear function of the single variable  $x$  and there is no quadratic term in it) and can describe more broad dynamics. Through our described model (6) can describe the dynamics of any population species.
- (6) Through this model (6), we can define the local asymptotic stability of the single species population at its environmental carrying capacity level provided the available resource to live always remains constant, say some  $k_1$ . In this situation we have,  $\underline{x} = k_1 - \epsilon$  and  $\bar{x} = k_1 + \epsilon$  for  $\epsilon > 0$  and then the population always remains within  $(k_1 - \epsilon, k_1 + \epsilon)$  and hence it can be concluded that if the available resource is sufficient for  $k_1$  amount of population biomass, and  $k_1$  will

always remain constant then the population will asymptotically stable at  $x = k_1$  (Fig. 3). Thus we can derive the result of the logistic growth model through our model (6).

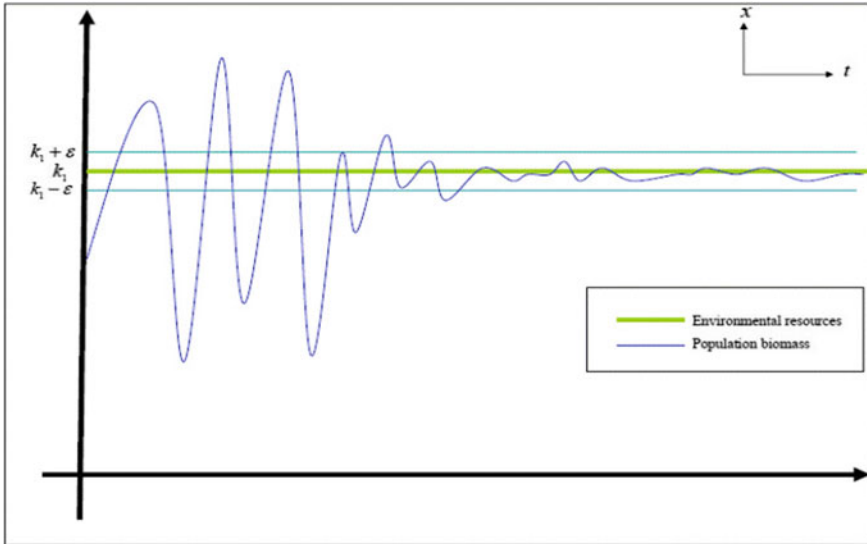


**Fig. 3** Asymptotic stability of population biomass near where is the upper limit of the population biomass such that the population can live healthy with the help of available resource which always remains same

### 3 An Application in Ecology

Our present analysis can be used to solve different ecological problems concerning the growth of population species. For example, when we are concerned about the pest control problem or vector disease problem, to keep our society free from pests or vectors, we have to reduce their corresponding resources. If a living creature can be used to eat same food as those of the larvae of mosquitoes, then the resource for mosquitoes' larvae would be reduced. Thus, the growth of mosquitoes can be checked.

## 4 Conclusions

This paper introduces a new ordinary differential equation-based mathematical model for a single species model in order to study the dynamics of a single-dimensional population species, where a significant number of individuals have no reproduction power. Our present assumption and the model of type (6) would be very helpful in studying the growth of single species, and it is very close to reality. In spite of being the model the first-order ODE, it is capable of capturing the dynamics of non-linear ODE-based growth like logistic growth. The present study draws light on a possible cause of the extinction of species. In order to control the agricultural pest, notorious vectors which cause diseases, if it is possible to make non-reproductive individuals greater than some threshold for a continuous time period, then those pests and the vector populations can be controlled significantly. On the other hand, if the alive member of a species is very low and the species is threatening to go to extinct, then one significant way to keep that species exist is to increase the birth rate.

**Acknowledgements** Research work of Suvankar Majee is financially supported by Council of Scientific and Industrial Research (CSIR), India (File No. 08/003(0142)/2020-EMR-I, dated: 18th March 2020). Moreover, the authors are very much thankful to the anonymous reviewers for their constructive comments and helpful suggestions to improve both the quality and presentation of the manuscript significantly.

## References

1. Kot, M.: *Elements of Mathematical Ecology*. Cambridge University Press (2001)
2. Britton, N.F.: *Essential Mathematical Biology*. Springer (2003)
3. Tsoularis, A., Wallace, J.: Analysis of logistic growth models. *Math. Biosci.* **179**(1), 21–55 (2002)
4. Bhowmick, A.R., Chattopadhyay, G., Bhattacharya, S.: Simultaneous identification of growth law and estimation of its rate parameter for biological growth data: a new approach. *J. Biol. Phys.* **40**(1), 71–95 (2014)
5. Bhowmick, A.R., Bhattacharya, S.: A new growth curve model for biological growth: some inferential studies on the growth of *Cirrhinus mrigala*. *Math. Biosci.* **254**, 28–41 (2014)
6. Di Crescenzo, A., Spina, S.: Analysis of a growth model inspired by Gompertz and Korf laws, and an analogous birth-death process. *Math. Biosci.* **282**, 121–134 (2016)
7. Koya, P.R., Goshu, A.T.: Generalized mathematical model for biological growths. *Open J. Modell. Simul.* (2013)
8. Von Bertalanffy, L.: A quantitative theory of organic growth (inquiries on growth laws. II). *Human Biol.* **10**(2), 181–213 (1938)
9. Richards, F.J.: A flexible growth function for empirical use. *J. Exper. Botany* **10**(2), 290–301 (1959)
10. Gompertz, B.: On the nature of the function expressive of the law of human mortality, and on a new mode of determining the value of life contingencies. *Philos. Trans. R. Soc. Lond.* **155**, 513–583 (1825)
11. Nelder, J.A.: The fitting of a generalization of the logistic curve. *Biometrics* **17**(1), 89–110 (1961)
12. Rawlings, J.O., Pantula, S.G., Dickey, D.A.: *Applied Regression Analysis: A Research Tool*. Springer Science & Business Media (2001)

13. Misra, O.P., Chaturvedi, D.: Fate of dissolved oxygen and survival of fish population in aquatic ecosystem with nutrient loading: a model. *Model. Earth Syst. Environ.* **2**(3), 1–14 (2016)
14. Misra, O.P., Babu, A.R.: Mathematical study of a Leslie-Gower-type tritrophic population model in a polluted environment. *Model. Earth Syst. Environ.* **2**(1), 29 (2016)
15. Kumar, A., Agrawal, A.K., Hasan, A., Misra, A.K.: Modeling the effect of toxicant on the deformity in a subclass of a biological species. *Model. Earth Syst. Environ.* **2**(1), 40 (2016)
16. Couchamp, F., Berec, L., Gascoigne, J.: *Allee Effects in Ecology and Conservation*. OUP Oxford (2008)

# A Numerical Approximation of the KdV-Kawahara Equation via the Collocation Method



Seydi Battal Gazi Karakoc and Derya Yıldırım Sucu

**Abstract** This paper presents a finite element scheme for numerical solution of the Korteweg-de Vries-Kawahara (KdV-K) equation using septic B-spline functions as approximate functions.  $L_2$  and  $L_\infty$  error norms are calculated for single solutions to show the practicality and robustness of the proposed scheme. Applying von-Neumann theory, we demonstrate that the scheme is marginally stable. Obtained numerical results have been illustrated with tables and graphics for easy visualization of properties of the problem modelled. Numerical experiment supports the correctness and reliability of the method.

**Keywords** KdV-Kawahara equation · Finite element method · Collocation

## 1 Introduction

Almost all physical processes encountered in nature are defined by various types of non-linear partial differential equations (NLPDEs). Understanding the structure of these NLPDEs and seeking their solutions is of prime importance for scientists, as their solutions illuminate the way to understand the behavior of systems and help to predict the development of the process in nature [1]. However, usually it is difficult to find their solutions analytically and sometimes it is almost impossible. Therefore many researchers have been working on to obtain efficient and high accurate numerical algorithms to overcome such problems [2].

In 1895, Dutch mathematician Korteweg and de-Vries defined a PDE (KdV) equation

---

S. B. G. Karakoc (✉) · D. Y. Sucu  
Department of Mathematics, Faculty of Science and Art, Nevsehir Haci Bektas Veli University,  
Nevsehir 50300, Turkey  
e-mail: [sbgk44@gmail.com](mailto:sbgk44@gmail.com)

© The Author(s), under exclusive license to Springer Nature Switzerland AG 2022  
S. Banerjee and A. Saha (eds.), *Nonlinear Dynamics and Applications*,  
Springer Proceedings in Complexity,  
[https://doi.org/10.1007/978-3-030-99792-2\\_77](https://doi.org/10.1007/978-3-030-99792-2_77)

917

$$u_t + uu_x + u_{xxx} = 0, \tag{1}$$

which models the propagation of wide waves in shallow water waves to model Russell’s soliton phenomenon. They observed that these solitons treat as particles [3]. Kawahara equation which is known as a fifth-order KdV type equation has the following form

$$u_t + \kappa uu_x + qu_{xxx} - ru_{xxxxx} = 0, \tag{2}$$

where  $\kappa, q, r$  are constants [4, 5]. Another form of the Kawahara equation is following modified Kawahara equation [6, 7]:

$$u_t + \kappa u^2 u_x + qu_{xxx} - ru_{xxxxx} = 0. \tag{3}$$

By coupling the KdV equation and the modified Kawahara equation, one can obtain the following generalized Korteweg-de Vries-Kawahara (GKdV-K) equation [8, 9]

$$u_t + \alpha u_x + \kappa u^p u_x + qu_{xxx} - ru_{xxxxx} = 0, \tag{4}$$

where  $p \geq 1$  is a positive integer,  $\alpha \geq 0, \kappa > 0, q > 0$  and  $r > 0$  [10]. In recent years, many authors have been interested in the solution of the equation [11–16].

The main form of the paper can be outlined in brief as follows: In Sect. 2, septic B-spline approximation is introduced and finite element solution of KdV-K ( for  $p = 1$ ) equation is proposed. Stability analysis of method has been done in Sect. 4. Sect. 4.1 exhibited numerical application and it’s results with table and graphs to see the performance and accuracy of the method. Finally, in Sect. 5, a brief conclusion about the presented method is given.

## 2 Application of the Numerical Method

In this section, our goal is to find numerical solution of the KdV-K Eq.(4) with following initial and homogeneous boundary conditions below:

$$\begin{aligned} u(x, 0) &= f(x), & a \leq x \leq b, \\ u(a, t) &= 0, & u(b, t) = 0, \\ u_x(a, t) &= 0, & u_x(b, t) = 0, \\ u_{xx}(a, t) &= 0, & u_{xx}(b, t) = 0, \end{aligned} \tag{5}$$

where  $f(x)$  is a detected function. To obtain the solution on the interval  $a \leq x \leq b$  division  $a = x_0 < x_1 < \dots < x_N = b$  of the space domain is imagined scattered uniformly with  $h = \frac{b-a}{N} = (x_{m+1} - x_m)$  for  $m = 1(1)N$ . The septic B-spline functions at the nodes  $x_m$  are described on the solution region  $[a, b]$  by Prenter [17]:



$$\phi_m(x) = \frac{1}{h^7} \begin{cases} l, & [x_{m-4}, x_{m-3}], \\ l - 8m, & [x_{m-3}, x_{m-2}], \\ l - 8m + 28n, & [x_{m-2}, x_{m-1}], \\ l - 8m + 28n - 56p, & [x_{m-1}, x_m], \\ r - 8s + 28y - 56z, & [x_m, x_{m+1}], \\ r - 8s + 28y, & [x_{m+1}, x_{m+2}], \\ r - 8s, & [x_{m+2}, x_{m+3}], \\ r, & [x_{m+3}, x_{m+4}], \\ 0, & otherwise \end{cases} \tag{6}$$

where  $l = (x - x_{m-4})^7$ ,  $m = (x - x_{m-3})^7$ ,  $n = (x - x_{m-2})^7$ ,  $p = (x - x_{m-1})^7$ ,  $r = (x_{m+4} - x)^7$ ,  $s = (x_{m+3} - x)^7$ ,  $y = (x_{m+2} - x)^7$ ,  $z = (x_{m+1} - x)^7$ . Now, we continue the numerical treatment, which we will apply using the septic B-spline collocation finite element method, by generating an approximate solution for the equation. Approximate solution  $u_N(x, t)$  for analytical solution  $u(x, t)$  are sought in the following equality,

$$u_N(x, t) = \sum_{m=-3}^{N+3} \phi_m(x) \sigma_m(t) \tag{7}$$

where  $\sigma_m(t)$  are time dependent unknown coefficients specified from the boundary conditions [18]. In each element, when we use the following equality,

$$h\sigma = x - x_m, \quad 0 \leq \xi \leq 1 \tag{8}$$

Equation (6) is defined in terms of  $\sigma$  on interval  $[0, 1]$  as [19]:

$$\begin{aligned} \phi_{m-3} &= 1 - 7\sigma + 21\sigma^2 - 35\sigma^3 + 35\sigma^4 - 21\sigma^5 + 7\sigma^6 - \sigma^7, \\ \phi_{m-2} &= 120 - 392\sigma + 504\sigma^2 - 280\sigma^3 + 84\sigma^5 - 42\sigma^6 + 7\sigma^7, \\ \phi_{m-1} &= 1191 - 1715\sigma + 315\sigma^2 + 665\sigma^3 - 315\sigma^4 - 105\sigma^5 + 105\sigma^6 - 21\sigma^7, \\ \phi_m &= 2416 - 1680\sigma + 560\sigma^4 - 140\sigma^6 + 35\sigma^7, \\ \phi_{m+1} &= 1191 + 1715\sigma + 315\sigma^2 - 665\sigma^3 - 315\sigma^4 + 105\sigma^5 + 105\sigma^6 - 35\sigma^7, \\ \phi_{m+2} &= 120 + 392\sigma + 504\sigma^2 + 280\sigma^3 - 84\sigma^5 - 42\sigma^6 + 21\sigma^7, \\ \phi_{m+3} &= 1 + 7\sigma + 21\sigma^2 + 35\sigma^3 + 35\sigma^4 + 21\sigma^5 + 7\sigma^6 - \sigma^7, \\ \phi_{m+4} &= \sigma^7. \end{aligned} \tag{9}$$

The values of  $u_m$  and its derivatives at the knots are calculated as:

$$\begin{aligned}
 u_N(x_m, t) &= \sigma_{m-3} + 120\sigma_{m-2} + 1191\sigma_{m-1} + 2416\sigma_m + 1191\sigma_{m+1} + 120\sigma_{m+2} + \sigma_{m+3}, \\
 u'_m &= \frac{7}{h}(-\sigma_{m-3} - 56\sigma_{m-2} - 245\sigma_{m-1} + 245\sigma_{m+1} + 56\sigma_{m+2} + \sigma_{m+3}), \\
 u''_m &= \frac{42}{h^2}(\sigma_{m-3} + 24\sigma_{m-2} + 15\sigma_{m-1} - 80\sigma_m + 15\sigma_{m+1} + 24\sigma_{m+2} + \sigma_{m+3}), \\
 u'''_m &= \frac{210}{h^3}(-\sigma_{m-3} - 8\sigma_{m-2} + 19\sigma_{m-1} - 19\sigma_{m+1} + 8\sigma_{m+2} + \sigma_{m+3}), \\
 u_m^{iv} &= \frac{840}{h^4}(\sigma_{m-3} - 9\sigma_{m-1} + 16\sigma_m - 9\sigma_{m+1} + \sigma_{m+3}), \\
 u_m^v &= \frac{2520}{h^5}(-\sigma_{m-3} + 4\sigma_{m-2} - 5\sigma_{m-1} + 5\sigma_{m+1} - 4\sigma_{m+2} + \sigma_{m+3}).
 \end{aligned}
 \tag{10}$$

Now, using (7) and (10) into Eq. (4), the following general form of equation is reached:

$$\begin{aligned}
 &\dot{\sigma}_{m-3} + 120\dot{\sigma}_{m-2} + 1191\dot{\sigma}_{m-1} + 2416\dot{\sigma}_m + 1191\dot{\sigma}_{m+1} + 120\dot{\sigma}_{m+2} + \dot{\sigma}_{m+3} \\
 &+ (\alpha + \kappa Z_m) \frac{7}{h}(-\sigma_{m-3} - 56\sigma_{m-2} - 245\sigma_{m-1} + 245\sigma_{m+1} + 56\sigma_{m+2} + \sigma_{m+3}) \\
 &+ q \frac{210}{h^3}(-\sigma_{m-3} - 8\sigma_{m-2} + 19\sigma_{m-1} - 19\sigma_{m+1} + 8\sigma_{m+2} + \sigma_{m+3}) \\
 &- r \frac{2520}{h^5}(-\sigma_{m-3} + 4\sigma_{m-2} - 5\sigma_{m-1} + 5\sigma_{m+1} - 4\sigma_{m+2} + \sigma_{m+3}) = 0,
 \end{aligned}
 \tag{11}$$

where  $\dot{\sigma} = \frac{d\sigma}{dt}$  and

$$Z_m = u = (\sigma_{m-3} + 120\sigma_{m-2} + 1191\sigma_{m-1} + 2416\sigma_m + 1191\sigma_{m+1} + 120\sigma_{m+2} + \sigma_{m+3}).$$

Both the finite difference approach and the Crank-Nicolson diagrams described below can be applied to the Eq. (11):

$$\sigma_i = \frac{\sigma_i^{n+1} + \sigma_i^n}{2}, \dot{\sigma}_i = \frac{\sigma_i^{n+1} - \sigma_i^n}{\Delta t}.$$
(12)

So, the above operation allows us to derive a recursion relationship between two time levels based on the parameters  $\sigma_i^{n+1}$  and  $\sigma_i^n$  as:

$$\begin{aligned}
 &\lambda_1\sigma_{m-3}^{n+1} + \lambda_2\sigma_{m-2}^{n+1} + \lambda_3\sigma_{m-1}^{n+1} + \lambda_4\sigma_m^{n+1} + \lambda_5\sigma_{m+1}^{n+1} + \lambda_6\sigma_{m+2}^{n+1} + \lambda_7\sigma_{m+3}^{n+1} \\
 &= \lambda_7\sigma_{m-3}^n + \lambda_6\sigma_{m-2}^n + \lambda_5\sigma_{m-1}^n + \lambda_4\sigma_m^n + \lambda_3\sigma_{m+1}^n + \lambda_2\sigma_{m+2}^n + \lambda_1\sigma_{m+3}^n,
 \end{aligned}
 \tag{13}$$

where

$$\begin{aligned}
 \lambda_1 &= [1 - EZ_m - M + K], & \lambda_2 &= [120 - 56EZ_m - 8M - 4K], \\
 \lambda_3 &= [1191 - 245EZ_m + 19M + 5K], & \lambda_4 &= [2416], \\
 \lambda_5 &= [1191 + 245EZ_m - 19M - 5K], & \lambda_6 &= [120 + 56EZ_m + 8M + 4K], \\
 \lambda_7 &= [1 + EZ_m + M - K], \\
 E &= \frac{7}{2h}\omega\Delta t, \quad M = \frac{105}{h^3}q\Delta t, \quad K = \frac{2520}{h^5}r\Delta t, \quad \omega = (\alpha + \kappa Z_m).
 \end{aligned}
 \tag{14}$$

In this algebraic system (13), the number of linear equations are less than the number of unknown coefficients, that is, the system contains the  $(N + 1)$  equation and  $(N + 7)$  unknown time-dependent parameters [20]. The best way to obtain a unique solution is to remove the six unknowns  $\sigma_{-3}, \sigma_{-2}, \sigma_{-1}, \dots, \sigma_{N+1}, \sigma_{N+2}$ , and  $\sigma_{N+3}$  from the system. This procedure is implemented using the boundary conditions with the values of  $u$  and after removing the unknowns, using a matrix system consisting of linear equations  $(N + 1)$  unknown parameters  $d^n = (\sigma_0, \sigma_1, \dots, \sigma_N)^T$  is obtained the following matrix vector form:

$$Rd^{n+1} = Sd^n. \tag{15}$$

### 3 Stability Analysis

In this section, Von-Neumann theory was used for the stability of the algorithm. To display stability analysis, KdV-Kawahara equation was linearized by supposing that quantities  $u^p$  in nonlinear term  $u^p u_x$  is locally constant. Growth factor  $\xi$  of a characteristic Fourier mode is identified as:

$$\sigma_m^n = \xi^n e^{imkh}, \tag{16}$$

here  $i = \sqrt{-1}$ . Putting the equality (16) into the iterative systems (13), gives the following growth factor

$$\xi = \frac{\rho_1 - i\rho_2}{\rho_1 + i\rho_2}, \tag{17}$$

where

$$\begin{aligned} \rho_1 &= 2 \cos(3kh) + 240 \cos(2kh) + 2382 \cos(kh) + 2416, \\ \rho_2 &= (2M + 2T + 2E) \sin(3kh). \end{aligned} \tag{18}$$

$|\xi| = 1$  is obtained when we take the modulus of Eq. (17). In this way, we demonstrate that scheme (13) is unconditionally stable under the present conditions.

### 4 Numerical Experiment and Discussion

In this part, we illustrate our method, improved in Sect. 2, to the KdV-K equation for single solitary wave. Effectiveness of the suggested method will be checked with the  $L_2$  and  $L_\infty$  error norms given as [21]

$$L_2 = \|u^{exact} - u_N\|_2 \simeq \sqrt{h \sum_{j=1}^N |u_j^{exact} - (u_N)_j|^2}, \tag{19}$$

and

$$L_\infty = \|u^{exact} - u_N\|_\infty \simeq \max_j |u_j^{exact} - (u_N)_j|, \quad j = 1, 2, \dots, N. \quad (20)$$

KdV-K equation (4) possesses three conservation constants given by

$$\begin{aligned} I_1 &= \int_a^b U dx \simeq h \sum_{j=1}^N U_j^n, \\ I_2 &= \int_a^b U^2 dx \simeq h \sum_{j=1}^N (U_j^n)^2, \\ I_3 &= \int_{-\infty}^\infty U^{p+2}(x, t) dx. \end{aligned} \quad (21)$$

which correspond to conversation of mass, momentum and energy, respectively.

### 4.1 Case 1

KdV-K equation has the following exact solution:

$$u(x, t) = \frac{105}{169} sech^4 \left[ \frac{1}{2\sqrt{13}} \left( x - \frac{205}{169} t - x_0 \right) \right], \quad (22)$$

$x_0$  is the center of the solitary wave. For the equation following initial condition is chosen

$$u(x, 0) = \frac{105}{169} sech^4 \left[ \frac{1}{2\sqrt{13}} (x - x_0) \right]. \quad (23)$$

To illustrate the validity of our numerical scheme, the algorithm was run up to time  $t = 30$ . The solitary wave has amplitude  $A = 0.62130$  at  $x = 0$ . In simulation calculations, typical values  $\Delta t = 0.01$  with  $h = 0.1$  were used. In Table 1, the conserved quantities and error norms  $L_2$  and  $L_\infty$  for different time levels and different step sizes were presented. The table shows that the three conserved amounts remained nearly constant over time and the changes in the amounts are in good agreement with their analytical values. Thus, the effects of the amount of sorting points on the numerical method can be seen more easily. The calculated  $L_2$  and  $L_\infty$  errors were found to be satisfactorily small. These errors hardly change as time progresses. If we examine Fig. 1, two and three dimensional state of the bell shaped solitary wave solutions produced from  $t = 0$  to  $t = 30$  can be clearly seen. From the figures, it can be noticed that studied method executes the propagation movement of a single wave, it conserves the amplitude and shape.

**Table 1** Invariants and error norms for single solitary wave

Time	$I_1$	$I_2$	$I_3$	$L_2$	$L_\infty$
0	5.9734098	1.2724981	0.6839459	0.00000000	0.00000000
5	5.9734128	1.2724980	0.6839449	0.00012014	0.00014431
10	5.9733848	1.2724980	0.6839444	0.00012188	0.00015202
15	5.9733818	1.2724980	0.6839422	0.00012665	0.00015689
20	5.9733887	1.2724980	0.6839417	0.00013701	0.00016202
25	5.9733943	1.2724980	0.6839418	0.00015282	0.00016746
30	5.9733890	1.2724980	0.6839406	0.00017237	0.00017310

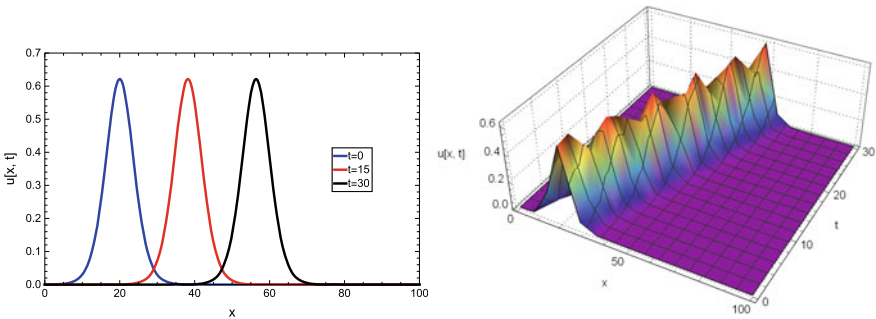


**Fig. 1** Numerical solutions of KdV-K equation at different time stages with  $\Delta t = 0.01$  and  $h = 0.1$

### 5 Conclusion

In this paper, numerical solution of KdV-K equation has been investigated by considering some fixed selection initial and boundary conditions. Our numerical algorithm is shown to be unconditionally stable. The algorithm has been tested for single solitary wave in which the exact solution is known.  $L_2$  and  $L_\infty$  error norms and the invariants are calculated to show the reliability and accuracy of the method. From these calculations, we can say that the proposed method yield good enough results. For our method, we portray some graphical illustrations of the obtained solutions of the equation. It may be concluded that the method used here is a powerful, efficient and powerful technique for solving a wide class of nonlinear evolution equations.

### References

1. Sari, M., Gurarslan, M.: A sixth-order compact nite difference scheme to the numerical solutions of Burgers' equation. *Appl. Math. Comput.* **208**, 475–483 (2009)
2. Saleem, S., Hussain, M.Z.: Numerical solution of nonlinear fifth-order KdV-type partial differential equations via Haar Wavelet. *Int. J. Appl. Comput. Math.* **6**(164), 1–16 (2020)

3. Goswami, A., Singh, J., Kumar, D.: Numerical simulation of fifth order KdV equations occurring in magneto-acoustic waves. *Ain Shams Eng. J.* **9**, 2265–2273 (2018)
4. Chen, M.: Internal controllability of the Kawahara equation on a bounded domain. *Nonlinear Anal.* **185**, 356–373 (2019)
5. Kawahara, T.: Oscillatory solitary waves in dispersive media. *J. Phys. Soc. Japan* **33**, 260–264 (1972)
6. Biswas, A.: Solitary wave solution for the generalized Kawahara equation. *Appl. Math. Lett.* **22**, 208–210 (2009)
7. Ak, T., Karakoc, S.B.G.: A numerical technique based on collocation method for solving modified Kawahara equation. *J. Ocean Eng. Sci.* **3**, 67–75 (2018)
8. Ceballos, J.C., Sepúlveda, J.C., Villagrán, O.P.V.: The Korteweg-de Vries-Kawahara equation in a bounded domain and some numerical results. *Appl. Math. Comput.* **190**, 912–936 (2007)
9. Sepúlveda, M., Villagrán, O.P.V.: Numerical method for a transport equation perturbed by dispersive terms of 3rd and 5th order. *Sci. Ser. A Math. Sci.* **13**, 13–21 (2006)
10. Wang, X., Cheng, H.: Solitary wave solution and a linear mass-conservative difference scheme for the generalized Korteweg-de Vries-Kawahara equation. *Comput. Appl. Math.* **40**(273), 1–26 (2021)
11. Assas, L.M.B.: New exact solutions for the Kawahara equation using Exp-function method. *J. Comput. Appl. Math.* **233**, 97–102 (2009)
12. Ye, Y.H., Mo, L.F.: He's variational method for the Benjamin-Bona-Mahony equation and the Kawahara equation. *Comput. Math. Appl.* **58**, 2420–2422 (2009)
13. Wazwaz, A.M.: New solitary wave solutions to the modified Kawahara equation. *Phys. Lett. A* **360**, 588–592 (2007)
14. Kaya, D.: An explicit and numerical solutions of some fifth-order KdV equation by decomposition method. *Appl. Math. Comput.* **144**, 353–363 (2003)
15. He, D.: Exact solitary solution and a three-level linearly implicit conservative finite difference method for the generalized Rosenau-Kawahara-RLW equation with generalized Novikov type perturbation. *Nonlinear Dyn.* **85**, 479–498 (2016)
16. Nanta, S., Yimnet, S., Poochinapan, K., Wongsajjai, B.: On the identification of nonlinear terms in the generalized Camassa-Holm equation involving dual-power law nonlinearities. *Appl. Numer. Math.* **160**, 386–421 (2021)
17. Prenter, P.M.: *Splines and Variational Methods*. Wiley, New York (1975)
18. Karakoc, S.B.G., Zeybek, H.: A septic B spline collocation method for solving the generalized equal width wave equation. *Kuwait J. Sci.* **43**, 20–31 (2016)
19. Karakoc, S.B.G., Saha, A., Sucu, D.: A novel implementation of Petrov-Galerkin method to shallow water solitary wave pattern and super periodic traveling wave and its multistability: Generalized Korteweg-de Vries equation. *Chinese J. Phys.* **68**, 605–617 (2020)
20. Karakoc, S.B.G., Zeybek, H.: Solitary wave solutions of the GRLW equation using septic B spline collocation method. *Appl. Math. Comput.* **289**, 159–171 (2016)
21. Karakoc, S.B.G.: A new numerical application of the generalized Rosenau-RLW equation. *Scientia Iranica B* **27**(2), 772–783 (2020)

# Approximate Solutions to Pseudo-Parabolic Equation with Initial and Boundary Conditions



Nishi Gupta and Md. Maqbul

**Abstract** This manuscript concerned with the pseudo-parabolic equation along with initial and boundary conditions. We prove the existence and uniqueness of a solution with the aid of Rothe's time-discretization technique. We have exemplified the main result.

**Keywords** Pseudo-parabolic equation · Semidiscretization method · Boundary conditions · Strong solution

## 1 Introduction

Rothe's time-discretization method has been opted by many researcher for solving differential equations. In this paper, approximate solutions, as well as the existence of unique strong solution, are established by applying Rothe's method for the following pseudo-parabolic equation

$$\frac{\partial g}{\partial t} - \mu \frac{\partial^3 g}{\partial t \partial y^2} - \mu \frac{\partial^2 g}{\partial y^2} = p(t, g(t, y)), \quad t \in (0, \top], y \in (0, 1) \quad (1)$$

subject to the following initial and the boundary conditions

$$g(0, y) = G_0(y) \quad \text{and} \quad \frac{\partial^2 g}{\partial y^2}(0, y) = G_1(y) \quad \text{for all } y \in (0, 1), \quad (2)$$

$$g(t, 0) = g(t, 1) \quad \text{for all } t \in [0, \top], \quad (3)$$

where,  $\top > 0$ ,  $\mu > 0$ , and  $p$ ,  $G_0$ , and  $G_1$  are some given suitable functions.

---

N. Gupta (✉) · Md. Maqbul  
National Institute of Technology Silchar, Silchar, Assam 788010, India  
e-mail: [nishigupta4792@gmail.com](mailto:nishigupta4792@gmail.com)

Type (1) equations have various applications in many physical situations, namely, in the study of homogeneous fluid seepage in fissured rocks [1], heat conduction and newtonian fluids theory [2, 3]. Maqbul and Raheem [5] established unique solution to semilinear pseudo parabolic equation with integral conditions by using Rothe’s method.

## 2 Abstract Formulation and Preliminaries

Defining  $s(t, y)$  as

$$s(t, y) = g(t, y) - \mu \frac{\partial^2 g}{\partial y^2}. \tag{4}$$

Then, (1)–(3) becomes

$$\frac{\partial s}{\partial t} + s(t, y) = g(t, y) + p(t, g(t, y)), \tag{5}$$

$$g(0, y) = G_0(y) \quad \text{and} \quad s(0, y) = S_0(y), \tag{6}$$

$$g(t, 0) = g(t, 1), \tag{7}$$

where,  $S_0(y) = G_0(y) - \mu G_1(y)$ .

Let  $L^2(0, 1) = \mathcal{H}$  be the Hilbert space. Defining two functions  $g : [0, \top] \rightarrow \mathcal{H}$ ,  $s : [0, \top] \rightarrow \mathcal{H}$ , and the nonlinear map  $p : [0, \top] \times \mathcal{H} \rightarrow \mathcal{H}$  as

$$g(t)(y) = g(t, y), \quad s(t)(y) = s(t, y), \quad p(t, g(t))(y) = p(t, g(t, y)),$$

respectively. Consider the following presumptions:

(C1)  $\top$  and  $\mu$  are positive real numbers.

(C2)  $G_0, G_1 \in \mathcal{H}$ .

(C3)  $p : [0, \top] \times \mathcal{H} \rightarrow \mathcal{H}$  holds the Lipschitz inequality that  $\exists \zeta > 0$  as

$$\|p(t, g) - p(\delta, s)\| \leq \zeta(|t - \delta| + \|g - s\|) \quad \text{for all } t, \delta \in [0, \top], \quad \text{for all } g, s \in \mathcal{H}.$$

$\mathcal{D}(\cdot)$  and  $\mathcal{R}(\cdot)$ , domain and range of an operator respectively. Consider the linear operator  $\mathcal{A}$  defined as

$$\mathcal{D}(\mathcal{A}) := \left\{ \ell \in \mathcal{H} : \ell'' \in \mathcal{H}, \ell(0) = \ell(1) \right\}, \quad \mathcal{A}\ell = -\ell''.$$

Then,  $-\mathcal{A}$  is an infinitesimal generator of  $C_0$ -semigroups of contractions in Hilbert space. Therefore, (4)–(7) become



$$g(t) + \mu \mathcal{A}g(t) = s(t), \tag{8}$$

$$\frac{ds}{dt} + s(t) = g(t) + p(t, g(t)), \tag{9}$$

$$g(0) = G_0, \quad s(0) = S_0. \tag{10}$$

Hence, both (1)–(3) and (8)–(10) represent the same problem.

### 3 Discretization Scheme and a Priori Estimates

Assume that (C1) – (C3) are true for the rest of this article. Dividing  $[0, T]$  into  $m$  subintervals  $[t_{k-1}^m, t_k^m]$  with  $\bar{h}_m = \frac{T}{m}$  for each  $m \in \mathbb{N}$ , where  $t_k^m = k\bar{h}_m$ , for  $k = 1, 2, \dots, m$ . Let  $g_0^m = G_0$  and  $s_0^m = S_0$  for all  $m \in \mathbb{N}$ . Successively,  $\{g_k^m\}$  and  $\{s_k^m\}$  are unique solution of the equations.

$$g_k^m + \mu \mathcal{A}g_k^m = s_k^m \tag{11}$$

and

$$\frac{s_k^m - s_{k-1}^m}{\bar{h}_m} + s_k^m = g_{k-1}^m + p(t_k^m, g_{k-1}^m). \tag{12}$$

**Lemma 1** *There exists  $\kappa > 0$  such that*

$$\|g_k^m\| + \|s_k^m\| \leq \kappa, \quad k = 1, 2, \dots, m, \quad m \geq 1. \tag{13}$$

**Proof** In view of (11) and Theorem 1.4.3 of [6]

$$\|g_k^m\| \leq \|s_k^m\|. \tag{14}$$

By (12),

$$\left\langle \frac{1}{\bar{h}_m} s_k^m, s_k^m \right\rangle + \langle s_k^m, s_k^m \rangle = \left\langle \frac{1}{\bar{h}_m} s_{k-1}^m + g_{k-1}^m + p(t_k^m, g_{k-1}^m), s_k^m \right\rangle. \tag{15}$$

Therefore,

$$\|s_k^m\| \leq \|s_{k-1}^m\| + \bar{h}_m \|g_{k-1}^m\| + \bar{h}_m \|p(t_k^m, g_{k-1}^m)\|. \tag{16}$$

Thus,

$$\begin{aligned} \|s_k^m\| &\leq \|s_0^m\| + \hbar_m \sum_{i=1}^k (\|g_{i-1}^m\| + \|p(t_i^m, g_{i-1}^m)\|) \\ &\leq \|S_0\| + (\zeta + 1)\hbar_m \sum_{i=1}^k \|s_{i-1}^m\| + \zeta\Upsilon^2 + \Upsilon\|p(0, 0)\|. \end{aligned} \tag{17}$$

Therefore,

$$\|s_k^m\| \leq \alpha_1 + \beta_1 \hbar_m \sum_{i=1}^k \|s_i^m\|, \tag{18}$$

where,  $\alpha_1 = (\zeta\Upsilon + \Upsilon + 1)\|S_0\| + \zeta\Upsilon^2 + \Upsilon\|p(0, 0)\|$  and  $\beta_1 = \zeta + 1$ .  
By Gronwall's inequality,

$$\|s_k^m\| \leq \frac{\alpha_1}{1 - \beta_1 \hbar_m} \exp\left(\frac{\beta_1(j-1)\hbar_m}{1 - \beta_1 \hbar_m}\right) \leq \frac{\alpha_1}{1 - \beta_1 \hbar_m} \exp\left(\frac{\Upsilon\beta_1}{1 - \beta_1 \hbar_m}\right).$$

Therefore,

$$\|s_k^m\| \leq \kappa, \text{ where } \kappa = \sup_{m \in \mathbb{N}} \left[ \frac{\alpha_1}{1 - \beta_1 \hbar_m} \exp\left(\frac{\Upsilon\beta_1}{1 - \beta_1 \hbar_m}\right) \right].$$

By (14),  $\|g_k^m\| \leq \kappa$ .

**Lemma 2** *There exists  $\kappa > 0$  such that*

$$\|g_k^m - g_{k-1}^m\| + \|s_k^m - s_{k-1}^m\| \leq \hbar_m \kappa, \quad k = 1, 2, \dots, m, \quad m \geq 1. \tag{19}$$

**Proof** In the view of (11), for  $k = 2, 3 \dots, m$ , and Theorem 1.4.3 of [6]

$$\|g_k^m - g_{k-1}^m\| \leq \|s_k^m - s_{k-1}^m\|. \tag{20}$$

By (12), for  $k = 2, 3 \dots, m$ ,

$$\frac{1}{\hbar_m} \|s_k^m - s_{k-1}^m\| \leq \|g_{k-1}^m - g_{k-2}^m\| + \|p(t_k^m, g_{k-1}^m) - p(t_{k-1}^m, g_{k-2}^m)\|. \tag{21}$$

Therefore, for  $k = 2, 3 \dots, m$ ,

$$\begin{aligned} \frac{1}{\hbar_m} \|s_k^m - s_{k-1}^m\| &\leq \sum_{i=2}^k \left( \|g_{i-1}^m - g_{i-2}^m\| + \|p(t_i^m, g_{i-1}^m) - p(t_{i-1}^m, g_{i-2}^m)\| \right) \\ &\leq \zeta(k-1)\hbar_m + (\zeta + 1) \sum_{i=2}^k \|g_{i-1}^m - g_{i-2}^m\| \end{aligned} \tag{22}$$

Thus,

$$\frac{1}{\hbar_m} \|s_k^m - s_{k-1}^m\| \leq \alpha_2 + \beta_2 \sum_{i=1}^k \|s_i^m - s_{i-1}^m\|, \tag{23}$$

where,  $\alpha_2 = \top\zeta$  and  $\beta_2 = \zeta + 1$ .

By Gronwall's inequality,

$$\frac{1}{\hbar_m} \|s_k^m - s_{k-1}^m\| \leq \frac{\alpha_2}{1 - \beta_2 \hbar_m} \exp\left(\frac{\beta_2(k-1)\hbar_m}{1 - \beta_2 \hbar_m}\right) \leq \frac{\alpha_2}{1 - \beta_2 \hbar_m} \exp\left(\frac{\top\beta_2}{1 - \beta_2 \hbar_m}\right).$$

Therefore,

$$\frac{1}{\hbar_m} \|s_k^m - s_{k-1}^m\| \leq \kappa, \text{ where } \kappa = \sup_{m \in \mathbb{N}} \left[ \frac{\alpha_2}{1 - \beta_2 \hbar_m} \exp\left(\frac{\top\beta_2}{1 - \beta_2 \hbar_m}\right) \right].$$

By (20),  $\frac{1}{\hbar_m} \|g_k^m - g_{k-1}^m\| \leq \kappa$ .

### 4 Convergence

Let  $m \in \mathbb{N}$ . Defining  $\mathcal{U}^m(t)$ ,  $\mathcal{W}^m(t)$ ,  $\mathcal{X}^m(t)$  and  $\mathcal{Y}^m(t)$  as

$$\mathcal{U}^m(t) = \begin{cases} g_0^m & \text{if } t = t_0^m, \\ g_k^m & \text{if } t \in (t_{k-1}^m, t_k^m], \end{cases} \tag{24}$$

$$\mathcal{W}^m(t) = \begin{cases} s_0^m & \text{if } t = t_0^m, \\ s_k^m & \text{if } t \in (t_{k-1}^m, t_k^m], \end{cases} \tag{25}$$

$$\mathcal{X}^m(t) = \begin{cases} g_0^m & \text{if } t = t_0^m, \\ g_{k-1}^m + (t - t_{k-1}^m)g_k^m & \text{if } t \in (t_{k-1}^m, t_k^m], \end{cases} \tag{26}$$

and

$$\mathcal{Y}^m(t) = \begin{cases} s_0^m & \text{if } t = t_0^m, \\ s_{k-1}^m + \frac{1}{\hbar_m}(t - t_{k-1}^m)(s_k^m - s_{k-1}^m) & \text{if } t \in (t_{k-1}^m, t_k^m], \end{cases} \tag{27}$$

where,  $k = 1, 2, \dots, m$ . For  $t \in (t_{k-1}^m, t_k^m]$ ,  $1 \leq k \leq m$ , define  $\mathcal{P}^m(t)$  by

$$\mathcal{P}^m(t) = g_{k-1}^m + p(t_k^m, g_{k-1}^m), \tag{28}$$

then (11) and (12) comes out to be

$$\frac{d^- \mathcal{X}^m}{dt}(t) + \mu \mathcal{A} \mathcal{U}^m(t) = \mathcal{W}^m(t), \quad t \in (0, \top], \tag{29}$$

$$\frac{d^- \mathcal{Y}^m}{dt}(t) + \mathcal{W}^m(t) = \mathcal{P}^m(t), \quad t \in (0, \top], \tag{30}$$

Integrating (30),

$$\mathcal{Y}^m(t) + \int_0^t \mathcal{W}^m(\delta)d\delta = S_0 + \int_0^t \mathcal{P}^m(\delta)d\delta. \tag{31}$$

**Lemma 3** *There exists  $g, s \in C([0, \top]; L^2(0, 1))$  such as  $\mathcal{X}^m(t) \rightarrow g(t)$  and  $\mathcal{Y}^m(t) \rightarrow s(t)$  uniformly on  $[0, \top]$ .  $g(t)$  and  $s(t)$  are differentiable a.e. on  $[0, \top]$  as well.*

**Proof** Consider  $t \in (t_{k-1}^m, t_k^m]$  and  $t \in (t_{l-1}^q, t_l^q]$ ,  $t_k^m \leq t_l^q$ ,  $1 \leq k \leq m$ ,  $1 \leq l \leq q$ . Then, by (29) and Theorem 1.4.3 of [6],

$$\frac{1}{2} \frac{d}{dt} \|\mathcal{X}^m(t) - \mathcal{X}^q(t)\|^2 \leq \|\mathcal{W}^m(t) - \mathcal{W}^q(t)\| \|\mathcal{X}^m(t) - \mathcal{X}^q(t)\|. \tag{32}$$

By (30),

$$\begin{aligned} & \left\langle \frac{d^-}{dt} (\mathcal{Y}^m(t) - \mathcal{Y}^q(t)), \mathcal{Y}^m(t) - \mathcal{Y}^q(t) \right\rangle + \langle \mathcal{W}^m(t) - \mathcal{W}^q(t), \mathcal{Y}^m(t) - \mathcal{Y}^q(t) \rangle \\ & = \langle \mathcal{P}^m(t) - \mathcal{P}^q(t), \mathcal{Y}^m(t) - \mathcal{Y}^q(t) \rangle. \end{aligned} \tag{33}$$

By (33) and using Lemmas 1 and 2,

$$\frac{1}{2} \frac{d}{dt} \|\mathcal{Y}^m(t) - \mathcal{Y}^q(t)\|^2 \leq 4\kappa^2(\hbar_m + \hbar_q) + \|\mathcal{P}^m(t) - \mathcal{P}^q(t)\| \|\mathcal{Y}^m(t) - \mathcal{Y}^q(t)\|. \tag{34}$$

Consider,

$$\|\mathcal{W}^m(t) - \mathcal{W}^q(t)\| \leq 2\kappa(\hbar_m + \hbar_q) + \|\mathcal{Y}^m(t) - \mathcal{Y}^q(t)\|,$$

and

$$\|\mathcal{P}^m(t) - \mathcal{P}^q(t)\| \leq (\zeta + 2\kappa + 2\zeta\kappa)(\hbar_m + \hbar_q) + (\zeta + 1)\|\mathcal{X}^m(t) - \mathcal{X}^q(t)\|.$$

Combining (32) and (34),

$$\begin{aligned} & \frac{1}{2} \frac{d}{dt} \left( \|\mathcal{X}^m(t) - \mathcal{X}^q(t)\|^2 + \|\mathcal{Y}^m(t) - \mathcal{Y}^q(t)\|^2 \right) \\ & \leq \kappa(\hbar_m + \hbar_q)[2\zeta + 10\kappa + 4\zeta\kappa + (\zeta + 3\kappa + 2\zeta\kappa)(\hbar_m + \hbar_q)] \\ & \quad + \left(1 + \frac{\zeta}{2}\right) (\|\mathcal{X}^m(t) - \mathcal{X}^q(t)\|^2 + \|\mathcal{Y}^m(t) - \mathcal{Y}^q(t)\|^2). \end{aligned}$$

Therefore,

$$\begin{aligned} & \frac{d}{dt} \left( \|\mathcal{X}^m(t) - \mathcal{X}^q(t)\|^2 + \|\mathcal{Y}^m(t) - \mathcal{Y}^q(t)\|^2 \right) \\ & \leq \varrho_{mq} + (\zeta + 2)(\|\mathcal{X}^m(t) - \mathcal{X}^q(t)\|^2 + \|\mathcal{Y}^m(t) - \mathcal{Y}^q(t)\|^2), \end{aligned}$$

where,

$$\varrho_{mq} = 2\kappa(\hbar_m + \hbar_q)[2\zeta + 10\kappa + 4\zeta\kappa + (\zeta + 3\kappa + 2\zeta\kappa)(\hbar_m + \hbar_q)].$$

Since  $\mathcal{X}^m(0) = G_0$  and  $\mathcal{Y}^m(0) = S_0$  for all  $m \in \mathbb{N}$ , for  $t \in [0, \top]$ ,

$$\begin{aligned} & \|\mathcal{X}^m(t) - \mathcal{X}^q(t)\|^2 + \|\mathcal{Y}^m(t) - \mathcal{Y}^q(t)\|^2 \\ & \leq \top \varrho_{mq} + (\zeta + 2) \int_0^t (\|\mathcal{X}^m(\delta) - \mathcal{X}^q(\delta)\|^2 + \|\mathcal{Y}^m(\delta) - \mathcal{Y}^q(\delta)\|^2) d\delta. \end{aligned}$$

Applying Gronwall’s inequality,

$$\|\mathcal{X}^m(t) - \mathcal{X}^q(t)\|^2 + \|\mathcal{Y}^m(t) - \mathcal{Y}^q(t)\|^2 \leq \top \varrho_{mq} e^{(\zeta+2)t} \leq \top \varrho_{mq} e^{(\zeta+2)\top} \quad \forall t \in [0, \top]. \tag{35}$$

Thus,  $\{\mathcal{X}^m(t)\}$  and  $\{\mathcal{Y}^m(t)\}$  are Cauchy sequences in  $C([0, \top]; L^2(0, 1))$ . Therefore we get  $g, s \in C([0, \top]; L^2(0, 1))$  such that  $\mathcal{X}^m(t) \rightarrow g(t)$  and  $\mathcal{Y}^m(t) \rightarrow s(t)$  uniformly on  $[0, \top]$ . As  $\|\mathcal{X}^m(t) - \mathcal{X}^m(\delta)\| \leq \kappa|t - \delta|$  and  $\|\mathcal{Y}^m(t) - \mathcal{Y}^m(\delta)\| \leq \kappa|t - \delta|$  hence  $g(t)$  and  $s(t)$  are Lipschitz continuous on  $[0, \top]$ . Therefore,  $\frac{dg}{dt}, \frac{ds}{dt} \in L^\infty([0, \top]; L^2(0, 1))$ .

## 5 Main Results

**Theorem 1** *If the presumptions (C1)–(C3) hold good, then (8)–(10) has a unique strong solution  $(g(t), s(t))$  on  $[0, \top]$ . Furthermore, the inequality  $\|g(t)\| \leq \|s(t)\|$  holds for all  $t \in (0, \top]$ .*

**Proof** Let  $g(t)$  and  $s(t)$  functions obtained from Lemma 3 and  $t \in (t_{k-1}^m, t_k^m]$ ,  $k = 1, 2, \dots, m$ ,  $m \in \mathbb{N}$ . Since,

$$\|\mathcal{U}^m(t) - g(t)\| \leq \kappa \hbar_m + \|\mathcal{X}^m(t) - g(t)\|,$$

and

$$\|\mathcal{W}^m(t) - s(t)\| \leq 2\kappa \hbar_m + \|\mathcal{Y}^m(t) - s(t)\|,$$

hence,  $\mathcal{U}^m(t) \rightarrow g(t)$  and  $\mathcal{W}^m(t) \rightarrow s(t)$  uniformly on  $[0, \top]$ . Therefore,  $\|\mathcal{U}^m(t)\|$  and  $\|\mathcal{W}^m(t)\|$  are bounded uniformly on  $[0, \top]$ .

Consider,

$$\begin{aligned} \|\mathcal{P}^m(t) - g(t) - p(t, g(t))\| &\leq \zeta \hbar_m + (\zeta + 1)(\|g_{k-1}^m - \mathcal{X}^m(t)\| + \|\mathcal{X}^m(t) - g(t)\|) \\ &\leq (\zeta + \kappa + \zeta\kappa)\hbar_m + (\zeta + 1)\|\mathcal{X}^m(t) - g(t)\|. \end{aligned}$$

Therefore,  $\mathcal{P}^m(t) \rightarrow g(t) + p(t, g(t))$  uniformly on  $[0, \top]$ . Thus,  $\|\mathcal{P}^m(t)\|$  is bounded uniformly on  $[0, \top]$ . By Lemmas 1 and 2,  $\|\frac{d\mathcal{X}^m}{dt}\|$  and  $\|\frac{d\mathcal{Y}^m}{dt}\|$  are bounded uniformly on  $[0, \top]$ . Hence,  $\|\mathcal{A}\mathcal{U}^m(t)\|$  is bounded uniformly on  $[0, \top]$ . From Lemma 2.5 of [4],  $\mathcal{A}\mathcal{U}^m(t) \rightarrow \mathcal{A}g(t)$  on  $[0, \top]$ . Clearly, (11) becomes

$$\mathcal{U}^m(t) + \mu\mathcal{A}\mathcal{U}^m(t) = \mathcal{W}^m(t), \quad t \in (0, \top]. \tag{36}$$

Therefore,  $\mathcal{A}\mathcal{U}^m(t) = \frac{1}{\mu}(\mathcal{W}^m(t) - \mathcal{U}^m(t)) \rightarrow \frac{1}{\mu}(s(t) - g(t))$  uniformly on  $[0, \top]$ . Hence,  $\mathcal{A}\mathcal{U}^m(t) \rightarrow \mathcal{A}y(t)$  uniformly on  $[0, \frac{\mu}{\top}]$ . Therefore,

$$g(t) + \mu\mathcal{A}g(t) = s(t), \quad t \in (0, \top]. \tag{37}$$

Since  $\mathcal{X}^m(t_0^m) = \mathcal{X}^m(0) = g_0^m = G_0$  for all  $m \in \mathbb{N}$ ,  $g(0) = G_0$ . By (31), for every  $\hbar \in \mathcal{H}$ ,

$$\int_0^t \langle \mathcal{W}^m(\delta), \hbar \rangle d\delta = \langle S_0, \hbar \rangle - \langle \mathcal{Y}^m(t), \hbar \rangle + \int_0^t \langle \mathcal{P}^m(\delta), \hbar \rangle d\delta.$$

By the bounded convergence theorem,

$$\int_0^t \langle s(\delta), \hbar \rangle d\delta = \langle S_0, \hbar \rangle - \langle s(t), \hbar \rangle + \int_0^t \langle g(\delta) + p(\delta, g(\delta)), \hbar \rangle d\delta. \tag{38}$$

Since  $s(t)$  is Bochner integrable function on  $[0, \top]$ , by (38),

$$\begin{cases} \frac{ds}{dt} + s(t) = g(t) + p(t, g(t)) \text{ a.e. } t \in [0, \top], \\ s(0) = S_0. \end{cases} \tag{39}$$

Thus, by (37) and (39), doublet of functions  $g$  and  $s$  is a strong solution of (8)–(10) on  $[0, \top]$ . By (37) and by Theorem 1.4.3 of [6],  $\|g(t)\| \leq \|s(t)\|$  holds for all  $t \in (0, \top]$ .

Suppose that  $(g_1, s_1)$  and  $(g_2, s_2)$  are two strong solutions of (8)–(10). Let  $g = g_1 - g_2$  and  $s = s_1 - s_2$ . Then,

$$\begin{aligned}
 g(t) + \mu Ag(t) &= s(t), \\
 \frac{ds}{dt} + s(t) &= g(t) + p(t, g_1(t)) - p(t, g_2(t)), \\
 g(0) = s(0) &= 0.
 \end{aligned}$$

Applying Theorem 1.4.3 of [6],

$$\|g(t)\| \leq \|s(t)\|, \tag{40}$$

and

$$\begin{aligned}
 \frac{d}{dt}(\|s(t)\|^2) &\leq 2\|g(t) + p(t, g_1(t)) - p(t, g_2(t))\|\|s(t)\| \\
 &\leq 2(\zeta + 1)\|g(t)\|\|s(t)\| \leq 2(\zeta + 1)\|s(t)\|^2.
 \end{aligned}$$

By Gronwall’s inequality,  $\|s(t)\|^2 = 0 \forall t \in [0, \top]$ . By (40),  $\|g(t)\| = 0$  for all  $t \in [0, \top]$ . Thus,  $g_1(t) = g_2(t)$  and  $s_1(t) = s_2(t) \forall t \in [0, \top]$ .

## 6 Applications

**Example 1** Consider the following pseudo-parabolic equation

$$\frac{\partial l}{\partial t} - \frac{\partial^3 l}{\partial t \partial y^2} - \frac{\partial^2 l}{\partial y^2} = \cos t + \varrho_1 l(t, y), \quad t \in (0, \top], \quad y \in (0, 1) \tag{41}$$

with initial conditions

$$l(0, y) = \sin y \quad \text{and} \quad \frac{\partial^2 l}{\partial y^2}(0, y) = \cos y \quad \text{for all } y \in (0, 1), \tag{42}$$

and boundary condition (3), where  $\top > 0$  and  $\varrho_1 > 0$ , and the unknown function  $l : [0, \top] \rightarrow L^2(0, 1)$ . Here,  $\mu = 1$ ,  $L_0(y) = \sin y$ ,  $L_1 = \cos y$ , and  $p(t, l(t, y)) = \cos t + \varrho_1 l(t, y)$ . Clearly, both functions  $L_0$  and  $L_1$  belong to  $L^2(0, 1)$ . Then, we have

$$\|p(t, l) - p(\delta, s)\| \leq \zeta(|t - \delta| + \|l - s\|),$$

where  $\zeta^2 = 2 \max\{1, \varrho_1^2\}$ . Therefore, from Theorem 1, the problem (41)–(42) with the boundary condition (3) has a unique strong solution  $l(t, y)$ .

## 7 Conclusions

Here, we considered a pseudo-parabolic equation (1) that is subjected to initial conditions (2) and a boundary condition (3). First, the problem (1)–(3) is reduced in the form of coupled Eqs. (8)–(10). To prove the existence and uniqueness of the solution of (1)–(3), Rothe's time-discretization technique is adopted. A pair of sequence of function is fabricated, and then established their uniform convergence to the unique pair of strong solutions. Eventually, we provided an example in support of the results.

## References

1. Barenblatt, G., Zheltov, I.P., Kochina, I.N.: Basic concepts in the theory of seepage of homogeneous liquids in fissured rocks. *J. Appl. Math. Mech.* **24**, 1286–1303 (1960)
2. Chen, P.J., Gurtin, M.E.: On a theory of heat conduction involving two temperatures. *Z. Angew. Math. Phys.* **19**, 614–627 (1968)
3. Coleman, B.D., Noll, W.: An approximation theorem for functionals, with applications in continuum mechanics. *Arch. Rational Mech. Anal.* **6**, 355–370 (1960)
4. Kato, T.: Nonlinear semigroup and evolution equations. *Math. Soc. Jpn.* **19**, 508–520 (1967)
5. Maqbul, Md., Raheem, A.: Time-discretization schema for a semilinear pseudo-parabolic equation with integral conditions. *Appl. Num. Math.* **148**, 18–27 (2020)
6. Pazy, A.: *Semigroup of Linear Operators and Application to Partial Differential Equations*. Springer-Verlag, New York (1983)



# Mathematical Model for Tumor-Immune Interaction in Imprecise Environment with Stability Analysis



Subrata Paul, Animesh Mahata, Supriya Mukherjee,  
Prakash Chandra Mali, and Banamali Roy

**Abstract** We introduce a tumor model with a tri-trophic level of prey, intermediate predator and top predator in an imprecise environment. The model consists of tumor cells, hunting predator cells, and resting predator cells in a three-dimensional predictable system. We investigated the non-negativity and boundedness of the system's solutions and identified all equilibrium points of the model along with their existence conditions. In the imprecise environment, stability analysis was performed and presented at all of the model system's equilibrium points. We also explain the global simulation study of such equilibrium position using an appropriate Lyapunov function. Detailed numerical simulations to investigate the dynamical behavior of the model are performed.

**Keywords** Tumor model · Stability analysis · Numerical simulation

## 1 Introduction

Over the last three decades, mathematical modeling has focused mostly on tumor development and immune system dynamics. Tumors are cancerous growths of aberrant cells that can infect tissues and cause death. Cancer cells can spread throughout

---

S. Paul (✉)

Department of Mathematics, Arambagh Govt. Polytechnic, Arambagh, West Bengal, India

e-mail: [paulsubrata564@gmail.com](mailto:paulsubrata564@gmail.com)

A. Mahata

Mahadevnagar High School, Maheshtala, Kolkata, West Bengal 700141, India

S. Mukherjee

Department of Mathematics, Gurudas College, Kolkata, West Bengal 700054, India

P. C. Mali

Department of Mathematics, Jadavpur University, Kolkata 700032, India

e-mail: [pcmali@math.jdvu.ac.in](mailto:pcmali@math.jdvu.ac.in)

B. Roy

Department of Mathematics, Bangabasi Evening College, Kolkata, West Bengal 700009, India

© The Author(s), under exclusive license to Springer Nature Switzerland AG 2022

935

S. Banerjee and A. Saha (eds.), *Nonlinear Dynamics and Applications*,

Springer Proceedings in Complexity,

[https://doi.org/10.1007/978-3-030-99792-2\\_79](https://doi.org/10.1007/978-3-030-99792-2_79)

the body via the bloodstream and lymphatic system. A tumor is a mass or lumps of tissue generated by an accumulation of aberrant cells, and it is the most serious sickness in medical science [1–3]. Evidence is accumulating in recent years demonstrating that the immune system may detect and eradicate malignant tumors. Before a tumor grows to the point that it kills the patient or permanently impairs their quality of life, it goes through numerous phases. Cancer is a group of illnesses distinguished by uncontrolled cell proliferation. Tumors can develop and cause problems with the digestive, neurological, and circulatory systems, as well as releasing hormones that cause changes in bodily processes. Our immune response serves a critical role in preventing the spread of malignant cells. Chemotherapy, immunotherapy, radiation therapy, surgery, and other treatments are available to patients with cancer. The type of treatment depends on the position and severity of the tumor, the phase of the disease, the patients' medical condition, and their age. The objective of treatment is to completely remove the cancer without causing harm to the rest of the body. However, the majority of cancer therapies have a harmful effect on normal bodily cells. The natural control techniques that exist for tumors must be considered while studying the growth and regulation of cancer. The use of mathematical models in the theoretical research of cancer is a particularly important strategy for shaping our understanding of tumor resistance dynamics [4–7]. Mathematical tools have been used in a range of studies in this field [8–10].

There are several studies of mathematical models of tumor development and interactions between the tumor and the immune system. The early research on tumor formation was aimed at figuring out how "normal" cells may transform become cancer cells. Cancer research, with a focus on theoretically and experimentally immunotherapy, receives a significant amount of human and financial resources, with both successful and unsuccessful outcomes. Despite the fact that cancer is one of the world's leading causes of death, it is common in the medical field for patients to present with advanced cancer that cannot be cured. This awe-inspiring phenomenon of unexpected cancer remission lives on in medical history, completely unexplainable but genuine. A significant amount of effort has gone into developing dynamical models that may be used to explain and predict tumor progression during the last few decades. There are a few more studies on tumor-immune interactions [11–15].

Researchers make various assumptions in mathematical modeling in order to replicate facts in a truncated but adequately meaningful way. Interaction between biotic and abiotic entities has been represented throughout the field of mathematical biology and ecology by many functions including many parameters, with the greatest of these values being regarded constant. However, due to incorporation of various human and ecological elements, it is widely accepted that uncertainty and imprecision about these characteristics cannot be disregarded. Despite the fact that a lot of work has previously been done in this topic involving uncertainty theory [16–18], there is still a lot of opportunities to improve and expand this area. The parameters of a tumor model with a tri-trophic level of prey-predator system are represented as fuzzy interval numbers in this paper. The findings have confirmed the imprecise solution's viewpoint, which has been visually and quantitatively connected.

## 2 Preliminaries

**Definition 1** The interval  $I = [\alpha, \beta]$  can be represented as  $f(\mu) = (\alpha)^{\mu-1}(\beta)^\mu$  for  $\mu \in [0, 1]$ , where  $f(\mu)$  : interval valued function.

## 3 Model Formulation

To formulate the model framework, the following assumption is made:

- $x(t)$  the number of tumor cells present,
- $y(t)$  the number of intermediate (hunting) predator cells present,
- $z(t)$  the number of top (resting) predator cells present,
- $r$  the development rate of tumor cells,
- $q$  the conversion of normal cells to malignant ones (fixed input),
- $k_1$  the maximum carrying or packing capacity of tumor cells,
- $k_2$  the maximum carrying capacity of resting cells (also,  $k_1 > k_2$ ),
- $a$  rate of predation of tumor cells by the hunting cells,
- $b$  resting cell to hunting cell conversion rate,
- $c$  natural death rate of hunting cell,
- $d$  development rate of resting predator cell,
- $e$  natural death rate of resting cell.

$$\begin{aligned}
 \frac{dx}{dt} &= q + rx \left( 1 - \frac{x}{k_1} \right) - axy \\
 \frac{dy}{dt} &= byz - cy \\
 \frac{dz}{dt} &= dz \left( 1 - \frac{z}{k_2} \right) - byz - ez
 \end{aligned}
 \tag{1}$$

In the imprecise environment where all the coefficients are interval numbers, the above-mentioned tumor model (1) can be altered as follows:

$$\begin{aligned}
 \frac{dx}{dt} &= q + \tilde{r}x \left( 1 - \frac{x}{k_1} \right) - \tilde{a}xy \\
 \frac{dy}{dt} &= \tilde{b}yz - \tilde{c}y \\
 \frac{dz}{dt} &= \tilde{d}z \left( 1 - \frac{z}{k_2} \right) - \tilde{b}yz - \tilde{e}z
 \end{aligned}
 \tag{2}$$

where,  $\tilde{r} = [r_m, r_n]$ ,  $\tilde{a} = [a_m, a_n]$ ,  $\tilde{b} = [b_m, b_n]$ ,  $\tilde{c} = [c_m, c_n]$ ,  $\tilde{d} = [d_m, d_n]$ ,  $\tilde{e} = [e_m, e_n]$  and  $r_m, r_n, a_m, a_n, b_m, b_n, c_m, c_n, d_m, d_n, e_m, e_n$  all are positive.

Using Definition 1, the system (2) can be written as

$$\begin{aligned} \frac{dx}{dt} &= q + r_m^{1-p} r_n^p x \left(1 - \frac{x}{k_1}\right) - a_n^{1-p} a_m^p x y \\ \frac{dy}{dt} &= b_m^{1-p} b_n^p y z - c_n^{1-p} c_m^p y \\ \frac{dz}{dt} &= d_m^{1-p} d_n^p z \left(1 - \frac{z}{k_2}\right) - b_n^{1-p} b_m^p y z - e_n^{1-p} e_m^p z \end{aligned} \tag{3}$$

where  $p \in [0, 1]$ .

### 3.1 Non-negativity and Boundedness

The non-negativity and boundedness of solutions of the system will be discussed in this section.

**Theorem 1** All the solutions of the system (3) are positive.

**Proof** From the system (3) we have.

$$\frac{dx}{dt} = q + r_m^{1-p} r_n^p x \left(1 - \frac{x}{k_1}\right) - a_n^{1-p} a_m^p x y.$$

Now, integrating in  $[0, t]$  we get,

$$x(t) = x(0) e^{\int_0^t \Psi(x,y,z) dt} \geq 0, \forall t$$

$$x(t) = x(0) e^{\int_0^t \Psi(x,y,z) dt} \geq 0, \forall t \text{ as, } x(0) \geq 0 \text{ where } \Psi(x, y, z) = \frac{q}{x} + r_m^{1-p} r_n^p \left(1 - \frac{x}{k_1}\right) - a_n^p a_m^{1-p} y.$$

Again, from second equation we have

$$\frac{dy}{dt} = b_m^{1-p} b_n^p y z - c_n^{1-p} c_m^p y$$

Integrating the above equation we get,  $y(t) = y(0) e^{\int_0^t \mu(x,y,z) dt} \geq 0 \forall t$  as,  $y(0) \geq 0$  where  $\mu(x, yz) = b_m^{1-p} b_n^p z - c_n^{1-p} c_m^p \cdot \frac{dz}{dt} = d_m^{1-p} d_n^p z \left(1 - \frac{z}{k_2}\right) - b_n^{1-p} b_m^p y z - e_n^{1-p} e_m^p z$

At last, integrating the above equation, we get,  $z(t) = z(0)e^{\int_0^t \omega(x,y,z)dt} \geq 0, \forall t$  as,  $z(0) \geq 0$  where  $\omega(x, y, z) = d_m^{1-p} d_n^p \left(1 - \frac{z}{k_2}\right) - b_n^{1-p} b_m^p y - e_n^{1-p} e_m^p$ .

Thus, all solutions of the system (3) are non-negative.

### 4 Stability Analysis

All the equilibrium points of system (3) as well as their existence requirements are presented in this section.

#### 4.1 Equilibrium Points and Existence Criteria

The equilibrium points of the system (3) are as follows:

- (i) Boundary equilibrium point  $E_1(x_1, 0, 0)$

where  $x_1 = \frac{k_1}{2} \left(1 + \sqrt{1 + \frac{4q}{k_1 r_m^{1-p} r_n^p}}\right)$ .

- (ii) Planar equilibrium point  $E_2(x_2, 0, y_2)$

where  $x_2 = \frac{k_1}{2} \left(1 + \sqrt{1 + \frac{4q}{k_1 r_m^{1-p} r_n^p}}\right)$  and  $y_2 = k_2 \left(1 - \frac{e_n^{1-p} e_m^p}{d_m^{1-p} d_n^p}\right)$ .

The existence of the planar equilibrium point depends on the criteria:

$$\frac{e_n^{1-p} e_m^p}{d_m^{1-p} d_n^p} < 1.$$

- (iii) Interior equilibrium point  $E_3(x^*, y^*, z^*)$

where,  $x^*$  is the solution of the equation,

$$\frac{r_m^{1-p} r_n^p}{k_1} x^{*2} + \left[ \frac{a_n^{1-p} a_m^p d_m^{1-p} d_n^p}{b_n^{1-p} b_m^p} \left(1 - \frac{c_n^{1-p} c_m^p}{k_2 b_m^{1-p} b_n^p}\right) - \frac{a_n^{1-p} a_m^p e_n^{1-p} e_m^p}{b_n^{1-p} b_m^p} - r_m^{1-p} r_n^p \right] x^* - q = 0,$$

$y^* = \frac{d_m^{1-p} d_n^p}{b_m^{1-p} b_n^p} \left(1 - \frac{c_n^{1-p} c_m^p}{k_2 b_m^{1-p} b_n^p}\right) - \frac{e_n^{1-p} e_m^p}{b_n^{1-p} b_m^p}$  and  $z^* = \frac{c_n^{1-p} c_m^p}{b_m^{1-p} b_n^p}$ .  $E_3(x^*, y^*, z^*)$  will exist if  $b_m^{1-p} b_n^p k_2 (d_m^{(1-p)} d_n^p - e_n^{(1-p)} e_m^p) > c_n^{(1-p)} c_m^p d_m^{(1-p)} d_n^p$ .

### 4.2 Local Stability Analysis

The Jacobian matrix at  $(x, y, z)$  of the system (3) can be written as

$$J(x, y, z) = \begin{pmatrix} r_m^{1-p} r_n^p \left(1 - \frac{2x}{k_1}\right) - a_n^{1-p} a_m^p y & -a_n^{1-p} a_m^p x & 0 \\ 0 & b_m^{1-p} b_n^p z - c_n^{1-p} c_m^p & b_m^{1-p} b_n^p y \\ 0 & -b_n^{1-p} b_m^p z & d_m^{1-p} d_n^p \left(1 - \frac{2z}{k_1}\right) - b_n^{1-p} b_m^p y - e_n^{1-p} e_m^p \end{pmatrix}$$

**Theorem 2** The system (3) displays unstable behavior at the boundary equilibrium point  $E_1(x_1, 0, 0)$ .

**Proof** The Jacobian matrix at the boundary equilibrium point  $E_1(x_1, 0, 0)$  is.

$$\begin{pmatrix} -r_m^{1-p} r_n^p \sqrt{1 + \frac{4q}{k_1 r_m^{1-p} r_n^p}} - \frac{a_n^{1-p} a_m^p k_1}{2} \left(1 + \sqrt{1 + \frac{4q}{k_1 r_m^{1-p} r_n^p}}\right) & 0 \\ 0 & -c_n^{1-p} c_m^p & 0 \\ 0 & 0 & d_m^{1-p} d_n^p - e_n^{1-p} e_m^p \end{pmatrix}$$

The eigen values of this matrix are  $\lambda_1 = -r_m^{1-p} r_n^p \sqrt{1 + \frac{4q}{k_1 r_m^{1-p} r_n^p}} < 0$ ,  $\lambda_2 = -c_n^{1-p} c_m^p < 0$  and  $\lambda_3 = d_m^{1-p} d_n^p - e_n^{1-p} e_m^p > 0$  (if the planar equilibrium point  $E_2$  exist, then  $\lambda_3 > 0$ ).

Therefore, the system is saddle at the boundary equilibrium point and we can say that, it is unstable at this point.

**Theorem 3** The model (3) is unstable at  $E_2(x_2, 0, y_2)$ .

**Proof** Now the Jacobian matrix at the planer equilibrium point  $E_2(x_2, 0, y_2)$  is.

$$\begin{pmatrix} -r_m^{1-p} r_n^p \sqrt{1 + \frac{4q}{k_1 r_m^{1-p} r_n^p}} - \frac{a_n^{1-p} a_m^p k_1}{2} \left(1 + \sqrt{1 + \frac{4q}{k_1 r_m^{1-p} r_n^p}}\right) & 0 \\ 0 & b_m^{1-p} b_n^p k_2 \left(1 - \frac{e_n^{1-p} e_m^p}{d_m^{1-p} d_n^p}\right) - c_n^{1-p} c_m^p & 0 \\ 0 & -b_n^{1-p} b_m^p k_2 \left(1 - \frac{e_n^{1-p} e_m^p}{d_m^{1-p} d_n^p}\right) & -(d_m^{1-p} d_n^p - e_n^{1-p} e_m^p) \end{pmatrix}$$

The eigen values of this Jacobian matrix are  $\lambda_1' = -r_m^{1-p} r_n^p \sqrt{1 + \frac{4q}{k_1 r_m^{1-p} r_n^p}} < 0$ ,  $\lambda_2' = b_m^{1-p} b_n^p k_2 \left(1 - \frac{e_n^{1-p} e_m^p}{d_m^{1-p} d_n^p}\right) - c_n^{1-p} c_m^p > 0$  (from the existence criteria of  $E_3$ ) and  $\lambda_3' = -(d_m^{1-p} d_n^p - e_n^{1-p} e_m^p) < 0$ . Hence the model (3) is unstable at  $E_2(x_2, 0, y_2)$  if  $E_3$  exist.

**Theorem 4** The model (3) is asymptotically stable at  $E_3(x^*, y^*, z^*)$ .

**Proof** Finally, the Jacobian matrix at the interior equilibrium point  $E_3$  is.

$$\begin{pmatrix} M - a_n^{1-p} a_m^p x^* & 0 \\ 0 & 0 \\ 0 & -\frac{b_n^{1-p} b_m^p c_n^{1-p} c_m^p}{b_m^{1-p} b_n^p} \end{pmatrix} b_m^{1-p} b_n^p \begin{bmatrix} \frac{d_m^{1-p} d_n^p}{b_n^{1-p} b_m^p} \left( 1 - \frac{c_n^{1-p} c_m^p}{k_2 b_m^{1-p} b_n^p} \right) - \frac{e_n^{1-p} e_m^p}{b_n^{1-p} b_m^p} \\ \frac{d_m^{1-p} d_n^p}{b_n^{1-p} b_m^p} \left( 1 - \frac{c_n^{1-p} c_m^p}{k_2 b_m^{1-p} b_n^p} \right) - \frac{e_n^{1-p} e_m^p}{b_n^{1-p} b_m^p} \end{bmatrix}$$

where,

$$M = -\sqrt{\left[ \frac{a_n^{1-p} a_m^p d_m^{1-p} d_n^p}{b_n^{1-p} b_m^p} \left( 1 - \frac{c_n^{1-p} c_m^p}{k_2 b_m^{1-p} b_n^p} \right) - \frac{a_n^{1-p} a_m^p e_n^{1-p} e_m^p}{b_n^{1-p} b_m^p} - r_m^{1-p} r_n^p \right]^2 + \frac{4r_m^{1-p} r_n^p q}{k_1}}$$

The eigen values of the Jacobian matrix are

$$\lambda_1^* = -\sqrt{\left[ \frac{a_n^{1-p} a_m^p d_m^{1-p} d_n^p}{b_n^{1-p} b_m^p} \left( 1 - \frac{c_n^{1-p} c_m^p}{k_2 b_m^{1-p} b_n^p} \right) - \frac{a_n^{1-p} a_m^p e_n^{1-p} e_m^p}{b_n^{1-p} b_m^p} - r_m^{1-p} r_n^p \right]^2 + \frac{4r_m^{1-p} r_n^p q}{k_1}},$$

$$\lambda_2^* = \frac{-h + \sqrt{h^2 - 4g}}{2} \text{ and } \lambda_3^* = \frac{-h - \sqrt{h^2 - 4g}}{2}$$

where,

$$h = \left[ \frac{2d_m^{1-p} d_n^p c_n^{1-p} c_m^p}{k_2 b_m^{1-p} b_n^p} - \frac{b_n^{1-p} b_m^p d_m^{1-p} d_n^p c_n^{1-p} c_m^p}{k_2 b_m^{1-p} b_n^p} \right] > 0,$$

$$g = d_m^{1-p} d_n^p c_n^{1-p} c_m^p \left( 1 - \frac{c_n^{1-p} c_m^p}{k_2 b_m^{1-p} b_n^p} \right) - c_n^{1-p} c_m^p e_n^{1-p} e_m^p > 0$$

(from the existence condition of  $E_3$ ).

Since,  $\lambda_1^* < 0$  and  $\lambda_2^*, \lambda_3^*$  have negative real part. Thus, the system is asymptotically stable around  $E_3$ .

### 4.3 Global Stability Analysis

The coexistence critical point's global stability indicates that all solution trajectories connected with the system (3) approach the point's trajectories.

**Theorem 5** The system (3) is globally asymptotically stable at  $E_3(x^*, y^*, z^*)$  in the region  $D = \left\{ (x, y, z) \in \mathbb{R}^3 : 0 < \frac{x}{x^*} = \frac{y}{y^*} = \frac{z}{z^*} < 1 \right\}$ .

**Proof** Taking the appropriate Lyapunov function into consideration.

$$L = A \left[ (x - x^*) - x^* \log \left( \frac{x}{x^*} \right) \right] + B \left[ (y - y^*) - y^* \log \left( \frac{y}{y^*} \right) \right] + C \left[ (z - z^*) - z^* \log \left( \frac{z}{z^*} \right) \right]$$

Taking time derivative, we get

$$\begin{aligned} \frac{dL(t)}{dt} &= A \frac{x - x^*}{x} \frac{dx(t)}{dt} + B \frac{y - y^*}{y} \frac{dy(t)}{dt} + C \frac{z - z^*}{z} \frac{dz(t)}{dt} \\ &= A \frac{x - x^*}{x} \left[ q + r_m^{1-p} r_n^p x \left( 1 - \frac{x}{k_1} \right) - a_n^{1-p} a_m^p xy \right] + B \frac{y - y^*}{y} \left[ b_m^{1-p} b_n^p yz - c_n^{1-p} c_m^p y \right] \\ &\quad + C \frac{z - z^*}{z} \left[ d_m^{1-p} d_n^p z \left( 1 - \frac{z}{k_2} \right) - b_n^{1-p} b_m^p yz - e_n^{1-p} e_m^p z \right] \\ &= A(x - x^*) \left[ \frac{q}{x} + r_m^{1-p} r_n^p \left( 1 - \frac{x}{k_1} \right) - a_n^{1-p} a_m^p y - \frac{q}{x^*} - r_m^{1-p} r_n^p \left( 1 - \frac{x^*}{k_1} \right) + a_n^{1-p} a_m^p y^* \right] \\ &\quad + B(y - y^*) \left[ b_m^{1-p} b_n^p z - c_n^{1-p} c_m^p - b_m^{1-p} b_n^p z^* + c_n^{1-p} c_m^p \right] \\ &\quad + C(z - z^*) \left[ d_m^{1-p} d_n^p \left( 1 - \frac{z}{k_2} \right) - b_n^{1-p} b_m^p y - e_n^{1-p} e_m^p - d_m^{1-p} d_n^p \left( 1 - \frac{z^*}{k_2} \right) + b_n^{1-p} b_m^p y^* + e_n^{1-p} e_m^p \right] \\ &= A \frac{q(x - x^*)^2}{(xx^*)} - A \left( \frac{r_m^{1-p} r_n^p}{k_1} \right) (x - x^*)^2 - C \frac{d_m^{1-p} d_n^p}{k_2} (z - z^*)^2 - a_n^{1-p} a_m^p (x - x^*)(y - y^*) \\ &\quad - B b_m^{1-p} b_n^p (y - y^*) \frac{(x^* z^* y - xzy^*)}{yy^*} - C b_m^{1-p} b_n^p (y - y^*)(z - z^*). \end{aligned}$$

So  $\frac{dL(t)}{dt} < 0$ , since  $D = \left\{ (x, y, z) \in \mathbb{R}^3 : 0 < \frac{x}{x^*} = \frac{y}{y^*} = \frac{z}{z^*} < 1 \right\}$ .

Hence the system (3) is globally asymptotically stable at  $E_3(x^*, y^*, z^*)$ .

## 5 Numerical Simulation

We use rigorous numerical study to assess and confirm the analytical conclusions of our model system in this section. To graphically forecast the model’s solution, we utilize MATLAB (2018).

In this scenario, we simulate the system (3) using the model parameter values provided in Table 1 and pick the value of parameter ‘p’ into three levels that satisfy the requirement specified in Theorem 4. At this equilibrium position, we ran the model system and computed the eigen values of the Jacobi matrix. Table 2 displays the eigen values. As a result all the eigen values of Jacobi matrix are negative, we may deduce that the interior equilibrium point  $E_3(x^*, y^*, z^*)$  is stable in nature when model parameters satisfy the criteria given in Theorem 4 (Figs. 1 and 2).



**Table 1** Parametric values for interior equilibrium point

Parameters	Values (for interior)
$\tilde{r}$	[0.9, 0.95]
$\tilde{a}$	[0.3, 0.35]
$\tilde{b}$	[0.1, 0.2]
$\tilde{c}$	[0.02, 0.03]
$\tilde{d}$	[0.8, 0.9]
$\tilde{e}$	[0.03, 0.04]
$k_1$	0.85
$k_2$	0.7
$q$	12

**Table 2** Eigen values and nature of equilibrium point  $E_3(x^*, y^*, z^*)$  for different levels of  $p$

$p$	Equilibrium point	Eigen value	Nature
0	(3.524, 1.638, 0.2912)	(-7.293, -0.63, -0.02)	Stable
0.5	(3.354, 2.628, 0.1813)	(-7.26, -0.048, -0.314)	Stable
1	(3.198, 3.768, 0.112)	(-7.33, -0.0305, -0.1705)	Stable

## 6 Conclusion

We have presented a tumor model for a tri-trophic level with prey, intermediate predator, and top predator in an imprecise environment. We have formulated the model system in an imprecise situation and realized all its stable state points. The feasibility criteria of the system equilibrium points in the supporting environment are studied along with their stability analysis. To justify and confirm the model's analytical conclusions, careful numerical simulations were performed. In nature, foraging behavior is frequent, and the best foraging technique plays an essential role in prey-predator engagements. The tumor growth mathematical models help us comprehend the nature of tumor-immune interactions. The major objective of health administrators, policymakers, and researchers is to create diverse cancer medications and identify the most effective therapy against tumor cell spread. Our model research is a little step in the right direction.

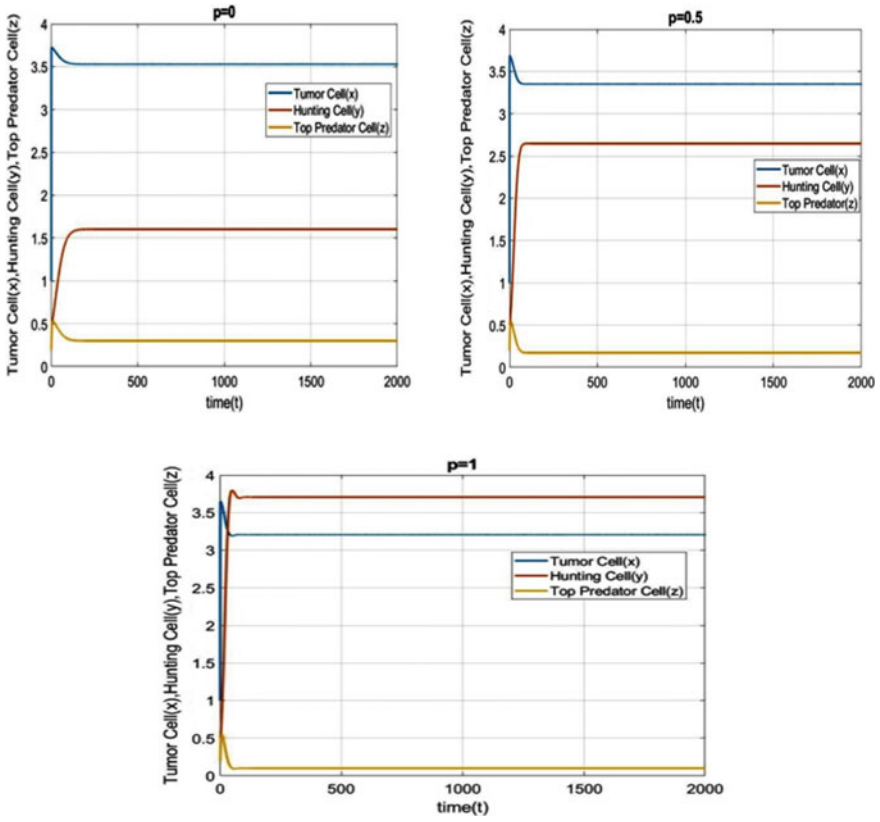


**Fig. 1** Time series plot of system (3) in  $[0, 2000]$  for various values of parameter ‘ $p$ ’. This figure shows that the interior equilibrium point  $E_3(x^*, y^*, z^*)$  is stable

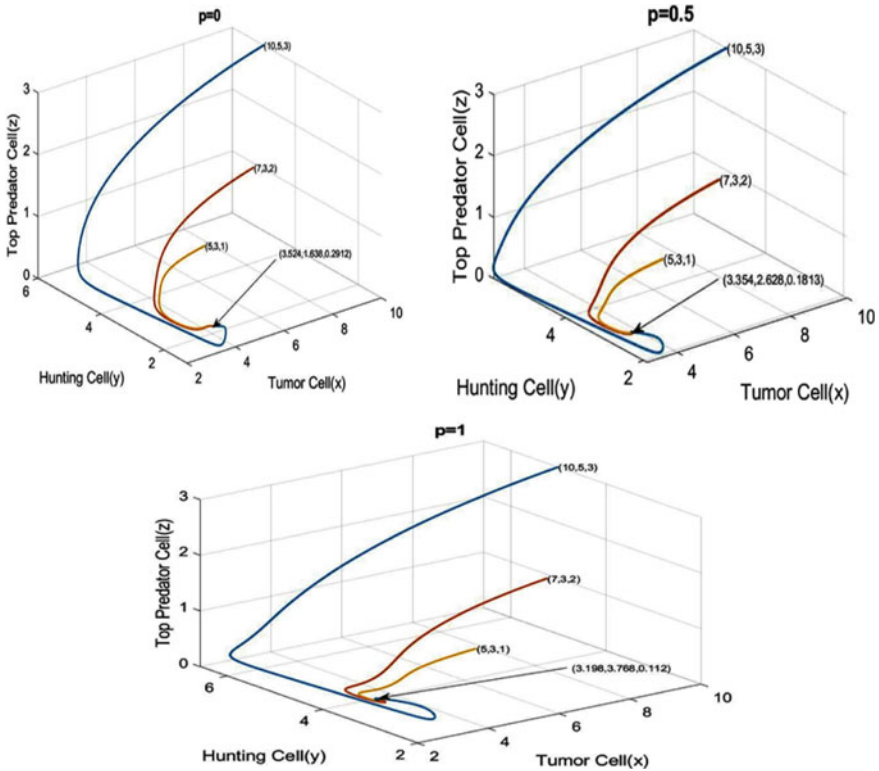


**Fig. 2** When numerical simulation is started from different beginning points under the option of model parameter values as indicated in Table 1, the system (3) approaches a stable interior equilibrium point  $E_3(x^*, y^*, z^*)$  for different values of the parameter  $p$

**References**

1. Sarkar, R.R., Chattopadhyay, J.: Occurrence of planktonic blooms under environmental fluctuations and its possible control mechanism—mathematical models and experimental observations. *J. Theor. Biol.* **224**, 501 (2003)
2. Rockne, R.C., Scott, J.G.: Introduction to mathematical oncology. *JCO Clin. Cancer Inform.* 1–4 (2019).
3. Jackson, T., Komarova, N., Swanson, K.: Mathematical oncology: using mathematics to enable cancer discoveries. *Amer. Math. Monthly* **121**, 840–856 (2014)
4. Abernathy, K., Abernathy, Z., Baxter, A., Stevens, M.: Global dynamics of a breast cancer competition model. *Differ. Equ. Dyn. Syst.* (2017)
5. Sarkar, R.R., Chattopadhyay, J.: The role of environmental stochasticity in a toxic phytoplankton—non-toxic phytoplankton—zooplankton system. *Environmetrics* **14**, 775 (2003)
6. Sharma, S., Samanta, G.P.: Dynamical behaviour of a tumor-immune system with chemotherapy and optimal control. *J. Nonlinear Dyn.* **608598**, 13 (2013)
7. Crespi, B., Summers, K.: Evolutionary biology of cancer. *Trends Ecol. Evol.* **20**(10), 545–552 (2005)
8. Pacheco, J.M., Santos, F.C., Dingli, D.: The ecology of cancer from an evolutionary game theory perspective. *Interface Focus* **4**(4), 20140019 (2014)

9. Xu, S., Feng, Z.: Analysis of a mathematical model for tumor growth under indirect effect of inhibitors with time delay in proliferation. *J. Math. Anal. Appl.* **374**, 178–186 (2011)
10. Li, F., Liu, B.: Bifurcation for a free boundary problem modeling the growth of tumors with a drug induced nonlinear proliferation rate. *J. Differ. Equ.* **263**, 7627–7646 (2017)
11. Fouad, Y.A., Aanei, C.: Revisiting the hallmarks of cancer. *Am. J. Cancer Res.* **7**(5), 1016 (2017)
12. Basanta, D., Anderson, A.R.: Exploiting ecological principles to better understand cancer progression and treatment. *Interface Focus* **3**(4), 20130020 (2013)
13. Escher, J., Matioc, A.V.: Radially symmetric growth of nonnecrotic tumors. *Nonlinear Differ. Equ. Appl.* **17**, 1–20 (2010)
14. Xu, S., Zhou, Q., Bai, M.: Qualitative analysis of a time-delayed free boundary problem for tumor growth under the action of external inhibitors. *Math. Methods Appl. Sci.* **38**, 4187–4198 (2015)
15. Pan, H., Xing, R.: Bifurcation for a free boundary problem modeling tumor growth with ECM and MDE interactions. *Nonlinear Anal. RWA* **43**, 362–377 (2018)
16. Salahshour, S., Ahmadian, A., Mahata, A., Mondal, S.P., Alam, S.: The behavior of logistic equation with alley effect in fuzzy environment: fuzzy differential equation approach. *Int. J. Appl. Comput. Math.* **4**(2), 1–20 (2018)
17. Obajemu, O., Mahfouf, M., Catto, J.W.: A new fuzzy modeling framework for integrated risk prognosis and therapy of bladder cancer patients. *IEEE Trans. Fuzzy Syst.* **26**(3), 1565–1577 (2017)
18. Tudu, S., Alam, S.: Tumour model with different imprecise coefficients. *Int. J. Hybrid Intell.* **2**(1), 15–25 (2021)

# Dromion Lattice Structure for Coupled Nonlinear Maccari's Equation



J. Thilakavathy , K. Subramanian , R. Amrutha ,  
and M. S. Mani Rajan 

**Abstract** In this article, we are interested to obtain analytic solutions of coupled nonlinear Maccari's equation. We employ Truncated Painlevé Approach to construct dromion lattice structure. The solution of the Maccari's equation is expressed in the form of arbitrary functions. Further, we have constructed dromion lattice structure graphically by considering suitable arbitrary functions. It is seen that the amplitude of the dromion lattice is stable and does not move during the time evolution. The coupled nonlinear Maccari's equation have wide applications in ocean wave theory.

**Keywords** Coupled nonlinear Maccari's equation · Truncated Painlevé approach · Dromion lattice

## 1 Introduction

Dromions [1–3] are the localized solutions that travel with a constant speed without dispersion or dissipation. Dromions have their origin at the intersection of two line-solitons. They have exponentially decaying tails in all the directions and in contrast to lumps that decay only algebraically. Earlier, dromion solution was constructed for

---

J. Thilakavathy (✉)

Department of Science and Humanities, Jerusalem College of Engineering, Chennai, India

e-mail: [cthilakay@gmail.com](mailto:cthilakay@gmail.com)

K. Subramanian

Department of Physics, SRM Institute of Science and Technology, Ramapuram Campus, Chennai, India

e-mail: [subramak2@srmist.edu.in](mailto:subramak2@srmist.edu.in)

R. Amrutha

Department of Physics, KCG College of Technology, Chennai, India

e-mail: [amrutha@kcgcollege.com](mailto:amrutha@kcgcollege.com)

M. S. Mani Rajan

Department of Physics, University College of Engineering, Anna University, Ramanathapuram, India

© The Author(s), under exclusive license to Springer Nature Switzerland AG 2022

S. Banerjee and A. Saha (eds.), *Nonlinear Dynamics and Applications*,

Springer Proceedings in Complexity,

[https://doi.org/10.1007/978-3-030-99792-2\\_80](https://doi.org/10.1007/978-3-030-99792-2_80)

the Davey–Stewartson I equation [4, 5] which is a  $(2 + 1)$  dimensional generalization of the nonlinear Schrödinger equation [6].

In this work, Truncated Painlevé Approach [7–9] is applied to obtain the localized solution such as dromion lattice structure [17] for the coupled nonlinear Maccari’s equation [10–12]. The Maccari’s equation was derived by Maccari from the Kadomtsev–Petviashvili equation, by means of a reduction method based on Fourier decomposition and space–time rescaling. Noteworthy developments have been established for examining the closed form solutions of Maccari’s equation in recent years. Plentiful effective tools have been utilized to handle Maccari’s equation, such as, Exp-function method [13], generalized Riccati relation [14], extended Fan sub-equation method [15], bilinear method [16] etc. and closed form solutions with arbitrary parameters are successfully obtained.

This paper is systematized as follows: In Sect. 2, the solution of coupled nonlinear Maccari’s equation has shown by using the tool Truncated Painlevé Approach. The Sect. 3 is devoted for the discussion on the dromion lattice structure. Finally, we have concluded with notes and comments.

## 2 Solution of Coupled Nonlinear Maccari’s Equation by Truncated Painlevé Approach

We consider the Maccari’s equation

$$iS_t + S_{xx} + LS = 0, \tag{1}$$

$$iK_t + K_{xx} + LK = 0, \tag{2}$$

$$L_y = (SS^* + KK^*)_x. \tag{3}$$

By considering,  $S = \alpha$ ,  $S^* = \beta$ ,  $K = \gamma$ ,  $K^* = \delta$ , then Eqs. (1)–(3) can be given as

$$i\alpha_t + \alpha_{xx} + L\alpha = 0, \tag{4}$$

$$-i\beta_t + \beta_{xx} + L\beta = 0, \tag{5}$$

$$i\gamma_t + \gamma_{xx} + L\gamma = 0, \tag{6}$$

$$-i\delta_t + \delta_{xx} + L\delta = 0, \tag{7}$$

$$L_y = (\alpha\beta)_x + (\gamma\delta)_x. \tag{8}$$

The truncated Laurent series of the solutions of Eqs. (4)–(8) results the following Bäcklund transformation

$$\alpha = \frac{\alpha_0}{\phi} + \alpha_1, \quad \beta = \frac{\beta_0}{\phi} + \beta_1, \quad \gamma = \frac{\gamma_0}{\phi} + \gamma_1, \quad \delta = \frac{\delta_0}{\phi} + \delta_1 \quad \text{and} \quad L = \frac{L_0}{\phi^2} + \frac{L_1}{\phi} + L_2. \quad (9)$$

We assume the vacuum solutions as  $\alpha_1 = \beta_1 = \gamma_1 = \delta_1 = 0$  and

$$L_2 = L_2(x, t). \quad (10)$$

By substituting Eq. (9) with the above vacuum solutions into Eqs. (4)–(8) and equate the like coefficients of  $\phi^{-3}$  to zero, one gets

$$2\alpha_0\phi_x^2 + L_0\alpha_0 = 0, \quad (11)$$

$$2\beta_0\phi_x^2 + L_0\beta_0 = 0, \quad (12)$$

$$2\gamma_0\phi_x^2 + L_0\gamma_0 = 0, \quad (13)$$

$$2\delta_0\phi_x^2 + L_0\delta_0 = 0, \quad (14)$$

$$2(\alpha_0\beta_0\phi_x + \gamma_0\delta_0\phi_x - L_0\phi_y) = 0. \quad (15)$$

From Eqs. (11)–(14), the value of  $L_0$  is determined by

$$L_0 = -2\phi_x^2 \quad (16)$$

and

$$\alpha_0\beta_0 + \gamma_0\delta_0 = -2\phi_x\phi_y. \quad (17)$$

Equating the like coefficients of  $\phi^{-2}$  to zero yields

$$-i\alpha_0\phi_t - 2\alpha_{0x}\phi_x - \alpha_0\phi_{xx} + L_1\alpha_0 = 0, \quad (18)$$

$$i\beta_0\phi_t - 2\beta_{0x}\phi_x - \beta_0\phi_{xx} + L_1\beta_0 = 0, \quad (19)$$

$$-i\gamma_0\phi_t - 2\gamma_{0x}\phi_x - \gamma_0\phi_{xx} + L_1\gamma_0 = 0, \quad (20)$$

$$i\delta_0\phi_t - 2\delta_{0x}\phi_x - \delta_0\phi_{xx} + L_1\delta_0 = 0, \quad (21)$$

$$L_{0y} - L_1\phi_y = (\alpha_0\beta_0 + \gamma_0\delta_0)_x. \quad (22)$$

Using Eqs. (16) and (17) in Eq. (22), we get

$$L_1 = 2 \frac{(\phi_{xx}\phi_y - \phi_{xy}\phi_x)}{\phi_y}. \tag{23}$$

By substituting Eq. (23) into Eqs. (18)–(21), the field variables  $\alpha_0, \beta_0, \gamma_0$  and  $\delta_0$  can be determined as

$$\alpha_0 = U(y) \exp \left[ \frac{1}{2} \int \frac{-i\phi_t + \phi_{xx} - \frac{2\phi_x\phi_{xy}}{\phi_y}}{\phi_x} dx \right], \tag{24}$$

$$\beta_0 = U(y) \exp \left[ \frac{1}{2} \int \frac{i\phi_t + \phi_{xx} - \frac{2\phi_x\phi_{xy}}{\phi_y}}{\phi_x} dx \right], \tag{25}$$

$$\gamma_0 = V(y) \exp \left[ \frac{1}{2} \int \frac{-i\phi_t + \phi_{xx} - \frac{2\phi_x\phi_{xy}}{\phi_y}}{\phi_x} dx \right], \tag{26}$$

$$\delta_0 = V(y) \exp \left[ \frac{1}{2} \int \frac{i\phi_t + \phi_{xx} - \frac{2\phi_x\phi_{xy}}{\phi_y}}{\phi_x} dx \right], \tag{27}$$

where  $U(y)$  and  $V(y)$  are arbitrary functions.

When the like coefficients of  $\phi^{-1}$  is equated to zero, it gives

$$i\alpha_{0t} + \alpha_{0xx} + L_2\alpha_0 = 0, \tag{28}$$

$$-i\beta_{0t} + \beta_{0xx} + L_2\beta_0 = 0, \tag{29}$$

$$i\gamma_{0t} + \gamma_{0xx} + L_2\gamma_0 = 0, \tag{30}$$

$$-i\delta_{0t} + \delta_{0xx} + L_2\delta_0 = 0, \tag{31}$$

$$L_{1y} = 0. \tag{32}$$

The Eq. (32) can be expressed as

$$\phi_{xxy}\phi_y^2 + \phi_x\phi_{xy}\phi_{yy} - \phi_{xy}^2\phi_y - \phi_x\phi_{xyy}\phi_y = 0. \tag{33}$$

The Eq. (33) can be solved as

$$\phi = \phi_1(x) + \phi_2(t), \tag{34}$$

where  $\phi_1(x)$  and  $\phi_2(t)$  are arbitrary functions.



When Eqs. (24)–(27) and (34) are plugged into Eq. (17), one obtains

$$V(y) = iU(y). \tag{35}$$

When the like coefficients of  $\phi^0$  is equated to zero, it gives

$$L_{2y} = 0. \tag{36}$$

The Eq. (36) is solved into

$$L_2 = \frac{1}{2} \int \frac{-\phi_{2tt}}{\phi_{1x}} dx - \frac{\phi_{1xxx}}{2\phi_{1x}} + \frac{\phi_{2t}^2 + \phi_{1xx}^2}{4\phi_{1x}^2}. \tag{37}$$

With the help of Eqs. (16), (23), (24)–(27), (34), (35) and (37) into Eq. (9), the solution of Eqs. (1)–(3) is obtained as

$$S = \frac{U(y) \exp \left[ \frac{1}{2} \int \frac{-i\phi_{2t} + \phi_{1xx}}{\phi_{1x}} dx \right]}{\phi_1(x) + \phi_2(t)}, \tag{38}$$

$$K = \frac{iU(y) \exp \left[ \frac{1}{2} \int \frac{-i\phi_{2t} + \phi_{1xx}}{\phi_{1x}} dx \right]}{\phi_1(x) + \phi_2(t)}, \tag{39}$$

$$L = \frac{-2\phi_{1x}^2}{(\phi_1(x) + \phi_2(t))^2} + \frac{2\phi_{1xx}}{(\phi_1(x) + \phi_2(t))} - \frac{1}{2} \int \frac{\phi_{2tt}}{\phi_{1x}} dx - \frac{\phi_{1xxx}}{2\phi_{1x}} + \frac{\phi_{2t}^2 + \phi_{1xx}^2}{4\phi_{1x}^2}. \tag{40}$$

The magnitudes of Eqs. (38) and (39) are represented as

$$|S|^2 = \frac{U^2(y)\phi_{1x}}{(\phi_1(x) + \phi_2(t))^2}, \tag{41}$$

$$|K|^2 = \frac{-U^2(y)\phi_{1x}}{(\phi_1(x) + \phi_2(t))^2}. \tag{42}$$

### 3 Dromion Lattice Solution

The dromion lattice solution is constructed by setting the  $\phi_1(x) = \exp(d_1x)$ ;  $\phi_2(t) = 1 + \exp(d_2t)$ ;  $F_1(y) = \exp(\cos(y) - d_3)$ . The snapshot of dromion lattice structure is shown in Fig. 1. It is noted that the peaks of dromion lattice is constant and it does not move during the time evolution.

*Notes and Comments.* In this paper, the solution of coupled integrable Maccari’s equation is obtained by the tool Truncated Painlevé Approach. The solution contains

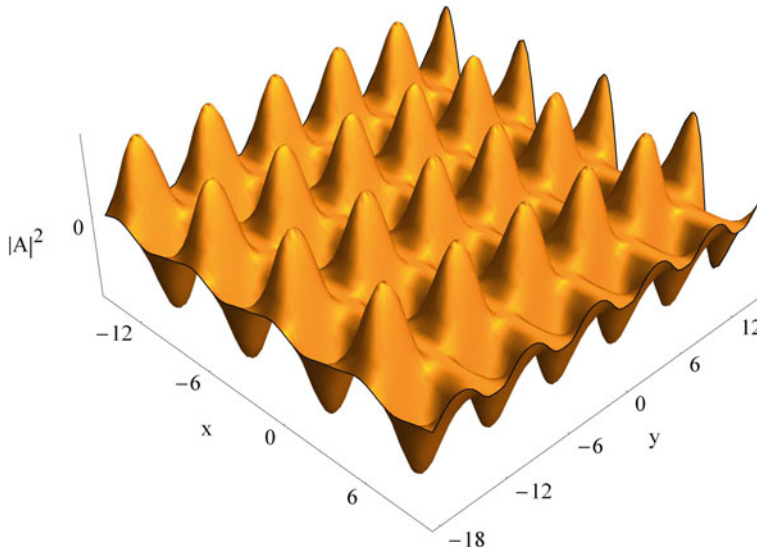


**Fig. 1** Dromion lattice pattern for arbitrary constants  $d_1 = 1$ ;  $d_2 = 1$ ;  $d_3 = 1$ ; at  $t = -10$

three arbitrary functions of space and time. By setting suitable arbitrary functions, the localized solution for dromion lattice has constructed. It is noted that the arbitrary manifold is independent of only one space variable  $y$ . To understand the physical behavior of the dromion lattice structure, it is also illustrated graphically. It would be interesting to note that the amplitude of dromion lattice is constant and the wave pattern is static during the time evolution. This eccentric nature occurs due the complete separation of arbitrary functions in space  $(x, y)$  and time  $(t)$ .

## References

1. Subramanian, K., Senthil Kumar, C., Radha, R., Alagesan, T.: Elusive noninteracting localized solutions of (2+1) dimensional Maccari equation. *Romanian. Rep. Phys.* **69**, 1–16 (2017)
2. Thilakavathy, R., Amrutha, K., Subramanian, M., Mani Rajan, S.: Different wave patterns for (2+1) dimensional Maccari's equation. *Nonlinear Dyn.* **107** (2022)
3. Boiti, M., Leon, J.J.P., Martina, L., Pempinelli, F.: Scattering of localized solitons in the plane. *Phys. Lett. A.* **32**, 432–439 (1988)
4. Fokas, A.S., Santini, P.M.: Dromions and a boundary value problem for the Davey-Stewartson I equation. *Physica D.* **44**, 99–130 (1990)
5. Radha, R., Vijayalakshmi, S., Lakshmanan, M.: Explode-decay dromions in the non-isospectral Davey-Stewartson (DSI) equation. *J. Nonlinear Math. Phys.* **6** (1999)
6. Radha, R., Vijayalakshmi, S., Lakshmanan, M.: Explode-decay dromions in the non-isospectral Davey-Stewartson (DSI) equation. *J. Nonlinear Math. Phys.* **6** (1996)
7. Radha, R., Lakshmanan, M.: A new class of induced localized coherent structures in the (2+1) dimensional nonlinear Schrodinger equation. *J. Phys. A: Math. Gen.* **30** (1997)

8. Radha, R., Tang, X.Y., Lou, S.Y.: Truncated Painlevé Expansion—A unified approach to exact solutions and dromion interactions of (2+1)-dimensional nonlinear systems. *Z. Naturforsch.* **62a**, 107–116 (2007)
9. Radha, R., Senthil Kumar, C., Subramanian, K.: Drone like dynamics of dromion pairs in the (2+1) AKNS equation. *Comput. Math. Appl.* **75**, 2356–2364 (2018)
10. Maccari, A.: Universal and integrable nonlinear evolution systems of equations in 2+1 dimensions. *J. Math. Phys.* **38**, 4151–4164 (1997)
11. Maccari, A.: The Kadomtsev-Petviashvili equation as a source of integrable model equations. *J. Math. Phys.* **37**, 6207–6212 (1996)
12. Yuan, F., Rao, J., Porsezian, K., Mihalache, D., He, J.: Various exact rational solutions of the two-dimensional Maccari's system. *Rom. Journ. Phys.* **61**, 378–399 (2016)
13. Zhang, S.: Exp-function method for solving Maccari system. *Phys. Lett. A.* **371**, 65–71 (2007)
14. Ting, P.J., Xun, G.L.: Exact solutions to Maccari system. *Commun. Theor. Phys.* **48**, 12–23 (2007)
15. Chema, N., Younis, M.: New and more exact traveling wave solutions to integrable (2+1)-dimensional Maccari system. *Nonlinear Dyn.* **83**, 1395 (2016)
16. Hua, W.G., Hong, W.L., Guang, R.J., Song, H.J.: New patterns of the two-dimensional rogue waves: (2 + 1)-dimensional Maccari system. *Commun. Theor. Phys.* **67** (2017)
17. Lai, D.W.C., Chow, K.W.: Coalescence of riplons, breathers, dromions and dark solitons. *J. Phys. Soc. Jpn.* **70**, 666–677 (2001)

# Solving Non-linear Partial Differential Equations Using Homotopy Analysis Method (HAM)



Ajay Kumar and Ramakanta Meher 

**Abstract** In this research paper, a semi-analytical method, i.e., homotopy analysis method, is implemented for finding the solution of non-linear partial differential equations. Homotopy analysis method is very effective, and easy to evaluate as compared to other numerical methods. The results through HAM on illustrative examples are compared with two well-known methods, namely, Variational Iteration Method (VIM) and Adomian Decomposition Method (ADM). The comparisons of obtained solutions results in the high accuracy through HAM when compared to the other competing methods. Hence, the solution obtained using HAM has much faster convergence to the exact solution.

**Keywords** Non-linear partial differential equation · Numerical results · Homotopy analysis method

## 1 Introduction

Solving a partial differential equation (PDE) involves lot of computations and when the PDE is non-linear it become really tough for solving and getting solutions. For solving non-linear PDE we have many numerical methods which provide numerical solutions. Also we solve non-linear PDE using analytic methods. The main difference between analytical and numerical approach is that numerical solution provides solution at discrete points while analytical technique provides continuous graph for the solution. Non-linear equations are not easy to solve, it needs better computational software and systems.

Homotopy analytical technique was firstly proposed by Liao [1–3] in 1992. Homotopy analytical method is based on the concept of homotopy of topology. The method has been widely implemented for solving several nonlinear problems in physical sci-

---

A. Kumar (✉) · R. Meher  
Department of Mathematics and Humanities, Sardar Vallabhbhai National Institute  
of Technology, Surat 395007, Gujarat, India  
e-mail: [ajaykhat123@gmail.com](mailto:ajaykhat123@gmail.com)

© The Author(s), under exclusive license to Springer Nature Switzerland AG 2022  
S. Banerjee and A. Saha (eds.), *Nonlinear Dynamics and Applications*,  
Springer Proceedings in Complexity,  
[https://doi.org/10.1007/978-3-030-99792-2\\_81](https://doi.org/10.1007/978-3-030-99792-2_81)

955

ence & engineering [4–12], after Liao published a book[13] in 2004. For solving non-linear problems, HAM [14–17] is a powerful mathematical tool. Adjusting and controlling the convergence region and rate of convergence of the series solution with the help of certain auxiliary parameter  $h$  is the main advantage of HAM.

The objective of the current paper is to solve initial value problems of non-linear partial differential equations by HAM and to make comparison of obtained approximate solutions by HAM with that already obtained by Variational Iteration Method [18–20] and Adomian Decomposition Method [21–23].

## 2 Analysis of Homotopy Analysis Method

Let’s consider a non-linear differential equation, for the better understanding of the method,

$$N[f(\zeta, \eta)] = 0, \tag{1}$$

where  $N$  is representing as operator for non-linearity,  $\zeta$  denotes spatial variables,  $\eta$  stands for time-related independent variables, &  $f(\zeta, \eta)$  is taken as an unknown function.

For quick understanding and simplification, each initial conditions and boundary conditions are intentionally ignored, which can be explained with similar way. According to the concept of homotopy, the so called 0th-order deformation equation can be constructed as follow,

$$(1 - q)\mathcal{L}[\psi(\zeta, \eta; q) - f_0(\zeta, \eta)] = hqH(\zeta, \eta)\mathcal{N}[\psi(\zeta, \eta; q)], \tag{2}$$

where  $q$  ( $0 \leq q \leq 1$ ) is known as embedding parameter,  $h$  is known as a non-zero auxiliary parameter,  $H(\zeta, \eta)$  is known as a non-zero auxiliary function,  $\mathcal{L}$  is known as an auxiliary operator for linearity,  $f_0(\zeta, \eta)$  is an initial assumption of the solution  $f(\zeta, \eta)$ , and  $\psi(\zeta, \eta; q)$  is an unspecified function. It must be noted that there is no restriction in choosing the initial assumption,  $\mathcal{L}$  the auxiliary operator for linearity,  $h$  the auxiliary parameter, and  $H(\zeta, \eta)$  the auxiliary function.

For  $q = 0$  &  $q = 1$ ,  $\psi(\zeta, \eta; q)$  can be expressed as follows

$$\psi(\zeta, \eta; 0) = f_0(\zeta, \eta), \quad \psi(\zeta, \eta; 1) = f(\zeta, \eta) \tag{3}$$

So,  $\psi(\zeta, \eta; q)$  reaches from the initial assumption  $f_0(\zeta, \eta)$  to  $f(\zeta, \eta)$  as a solution, when the value of  $q$  increases from 0 to 1. Expansion of  $\psi(\zeta, \eta; q)$  in the Taylor series concerning the parameter  $q$ , we obtain

$$\psi(\zeta, \eta; q) = f_0(\zeta, \eta) + \sum_{n=1}^{\infty} f_n(\zeta, \eta)q^n, \tag{4}$$

Here  $f_n(\zeta, \eta)$  stands for

$$f_n(\zeta, \eta) = \frac{1}{n!} \frac{\partial^n \psi(\zeta, \eta; q)}{\partial q^n} \Big|_{q=0} \tag{5}$$

At  $q = 1$ , the choice of auxiliary operator for linearity  $\mathcal{L}$ , the initial assumption  $f_0(\zeta, \eta)$ , the auxiliary parameter  $h$  and the auxiliary function  $H(\zeta, \eta)$  is proper then above series converges, and we obtain

$$f(\zeta, \eta) = f_0(\zeta, \eta) + \sum_{k=1}^{\infty} f_k(\zeta, \eta), \tag{6}$$

Equation (6) is original nonlinear equation's one of the solution. As shown in Eq. (6), the controlling equation can be obtained from 0th-order deformation equation. Define vector,

$$\bar{f}(\zeta, \eta) = \{f_0(\zeta, \eta), f_1(\zeta, \eta), f_2(\zeta, \eta), \dots, f_n(\zeta, \eta)\} \tag{7}$$

Taking n-times differentiation of 0th-order deformation equation concerning embedding parameter  $q$ , putting  $q = 0$  and after dividing with  $n!$ , the deformation equation of nth-order can be presented as follows

$$\mathcal{L}[f_n(\zeta, \eta) - \chi_n f_{n-1}(\zeta, \eta)] = hH(\zeta, \eta)R_n(\bar{f}_{n-1}) \tag{8}$$

where  $R_n(\bar{f}_{n-1})$  stands for

$$R_n(\bar{f}_{n-1}) = \frac{1}{(n-1)!} \frac{\partial^{n-1} \mathcal{N}[\psi(\zeta, \eta; q)]}{\partial q^{n-1}} \Big|_{q=0} \tag{9}$$

and

$$\chi_n = \begin{cases} 0, & n \leq 1 \\ 1, & n > 1. \end{cases} \tag{10}$$

Here, It is surely noted that when  $n \geq 1$ ,  $f_n(\zeta, \eta)$  is controlled by the linear deformation equation of nth-order .

### 3 Numerical Application

**Example 1** Consider the 1st-order quasi-linear homogeneous partial differential equation[24]

$$\frac{\partial u(\zeta, \eta)}{\partial \eta} + (1 + u(\zeta, \eta)) \frac{\partial u(\zeta, \eta)}{\partial \zeta} = 0, \quad 0 \leq \eta \tag{11}$$

with the initial condition

$$u(\zeta, 0) = \frac{\zeta - 1}{2}, \tag{12}$$

Equation (11) can be simply expressed as

$$\frac{\partial u}{\partial \eta} + \left(\frac{\partial u}{\partial \zeta}\right) + u\left(\frac{\partial u}{\partial \zeta}\right) = 0 \tag{13}$$

Exact solution for this problem is  $u(\zeta, \eta) = \frac{\zeta - \eta - 1}{\eta + 2}$ , which can also be verified.

For solving problem in Eq.(11) using HAM we need to consider initial approximation, letting the initial approximation to be

$$u_0(\zeta, \eta) = \frac{\zeta - 1}{2} \tag{14}$$

Here, nonlinear operator for Eq. (11) can be defined as

$$\mathcal{N}[\psi(\zeta, \eta; q)] = \frac{\partial \psi(\zeta, \eta; q)}{\partial \eta} - \left(\frac{\partial \psi(\zeta, \eta; q)}{\partial \zeta}\right) - \psi(\zeta, \eta; q)\left(\frac{\partial \psi(\zeta, \eta; q)}{\partial \zeta}\right) \tag{15}$$

Now, we have to construct the 0th-order deformation equation as

$$(1 - q)\mathcal{L}[\psi(\zeta, \eta; q) - u_0(\zeta, \eta)] = hq\mathcal{N}[\psi(\zeta, \eta; q)]. \tag{16}$$

where an auxiliary linear operator  $\mathcal{L}$  is expressed as

$$\mathcal{L}[\psi(\zeta, \eta; q)] = \frac{\partial \psi(\zeta, \eta; q)}{\partial \eta} \tag{17}$$

Also, at  $q = 0$  &  $1$ , we have  $\psi(\zeta, \eta; q)$  as

$$\psi(\zeta, \eta; 0) = u_0(\zeta, 0), \quad \psi(\zeta, \eta; 1) = u(\zeta, \eta). \tag{18}$$

Here,  $\psi(\zeta, \eta; q)$  varies from initial guess  $u_0(\zeta, \eta) = \frac{\zeta - 1}{2}$  to the solution  $u(\zeta, \eta)$ , as  $q$  varies from 0 to 1.

Now, we will have the nth-order deformation equation as

$$(1 - q)\mathcal{L}[u_n - \chi_n u_{n-1}] = h\mathcal{R}_n(\vec{u}_{n-1}), \tag{19}$$

where

$$\mathcal{R}_n(\vec{u}_{n-1}) = \frac{\partial u_{n-1}}{\partial \eta} - \frac{\partial u_{n-1}}{\partial \zeta} - \left(\sum_{i=0}^{n-1} u_i \frac{\partial u_{n-1-i}}{\partial \zeta}\right) \tag{20}$$

Therefore,

$$u_n = \chi_n u_{n-1} + h\mathcal{L}^{-1}[\mathcal{R}_n(\vec{u}_{n-1})], \tag{21}$$

where

$$\mathcal{L}^{-1} = \int (\cdot) d\eta \tag{22}$$

So, Eq. (19) becomes

$$u_n = \chi_n u_{n-1} + h \int \mathcal{R}_n(\vec{u}_{n-1}) d\eta, \tag{23}$$

The first few terms of the solution, with the help of  $u_0(\zeta, \eta)$  from Eq. (14) can be expressed as follows:

$$\begin{aligned} u_1(\zeta, \eta) &= h \left( \frac{\eta}{4} + \frac{1}{4} \zeta \eta \right) \\ u_2(\zeta, \eta) &= \frac{1}{4} h\eta + \frac{1}{4} h\zeta\eta + \frac{1}{8} \eta^2 h^2 + \frac{1}{8} \eta^2 h^2 \zeta + \frac{1}{4} h^2 \eta + \frac{1}{4} h^2 \zeta \eta \\ u_3(\zeta, \eta) &= \frac{1}{4} h\eta + \frac{1}{4} h\zeta\eta + \frac{1}{4} \eta^2 h^2 + \frac{1}{4} \eta^2 h^2 \zeta + \frac{1}{2} h^2 \eta + \frac{1}{2} h^2 \zeta \eta + \frac{1}{16} \eta^3 h^3 \\ &\quad + \frac{1}{16} \eta^3 h^3 \zeta + \frac{1}{4} \eta^2 h^3 + \frac{1}{4} \eta^2 h^3 \zeta + \frac{1}{4} h^3 \eta + \frac{1}{4} h^3 \zeta \eta \end{aligned}$$

Thus, the approximated series solution

$$\begin{aligned} u(\zeta, \eta) &= u_0(\zeta, \eta) + u_1(\zeta, \eta) + u_2(\zeta, \eta) + u_3(\zeta, \eta) + \dots \\ &= \frac{\zeta - 1}{2} + h \left( \frac{\eta}{4} + \frac{1}{4} \zeta \eta \right) + \frac{1}{4} h\eta + \frac{1}{4} h\zeta\eta + \frac{1}{8} \eta^2 h^2 + \frac{1}{8} \eta^2 h^2 \zeta + \frac{1}{4} h^2 \eta \\ &\quad + \frac{1}{4} h^2 \zeta \eta + \frac{1}{4} h\eta + \frac{1}{4} h\zeta\eta + \frac{1}{4} \eta^2 h^2 + \frac{1}{4} \eta^2 h^2 \zeta + \frac{1}{2} h^2 \eta \\ &\quad + \frac{1}{2} h^2 \zeta \eta + \frac{1}{16} \eta^3 h^3 + \frac{1}{16} \eta^3 h^3 \zeta + \frac{1}{4} \eta^2 h^3 + \frac{1}{4} \eta^2 h^3 \zeta + \frac{1}{4} h^3 \eta + \frac{1}{4} h^3 \zeta \eta + \dots \end{aligned}$$

**Example 2** Consider the second order nonlinear hyperbolic equation [25]

$$\frac{\partial^2 u(\zeta, \eta)}{\partial \eta^2} = \frac{\partial}{\partial \zeta} \left( u(\zeta, \eta) \frac{\partial u(\zeta, \eta)}{\partial \zeta} \right), \quad 0 \leq \eta \tag{24}$$

with the initial conditions

$$u(\zeta, 0) = \zeta^2, \quad u_\eta(\zeta, 0) = -2\zeta^2 \tag{25}$$



Equation (24) can be simply expressed as

$$\frac{\partial^2 u}{\partial \eta^2} = \left(\frac{\partial u}{\partial \zeta}\right)^2 + u\left(\frac{\partial^2 u}{\partial \zeta^2}\right) \tag{26}$$

Exact solution for this problem Eq. (24) is  $u(\zeta, \eta) = \left(\frac{\zeta}{1+\eta}\right)^2$ , which can be verified also.

For solving Eq. (24) using HAM, let the initial approximation be

$$u_0(\zeta, \eta) = \zeta^2 (1 - 2 \eta) \tag{27}$$

Here, nonlinear operator for Eq. (24) can be defined as

$$\mathcal{N}[\psi(\zeta, \eta; q)] = \frac{\partial^2 \psi(\zeta, \eta; q)}{\partial \eta^2} - \left(\frac{\partial \psi(\zeta, \eta; q)}{\partial \zeta}\right)^2 - \psi(\zeta, \eta; q)\left(\frac{\partial^2 \psi(\zeta, \eta; q)}{\partial \zeta^2}\right) \tag{28}$$

Now, we have to construct the 0th-order deformation equation as

$$(1 - q)\mathcal{L}[\psi(\zeta, \eta; q) - u_0(\zeta, \eta)] = hq\mathcal{N}[\psi(\zeta, \eta; q)]. \tag{29}$$

where an auxiliary linear operator  $\mathcal{L}$  is expressed as

$$\mathcal{L}[\psi(\zeta, \eta; q)] = \frac{\partial^2 \psi(\zeta, \eta; q)}{\partial \eta^2} \tag{30}$$

Also, at  $q = 0$  &  $1$ , we have  $\psi(\zeta, \eta; q)$  as

$$\psi(\zeta, \eta; 0) = u_0(\zeta, 0), \quad \psi(\zeta, \eta; 1) = u(\zeta, \eta). \tag{31}$$

Here,  $\psi(\zeta, \eta; q)$  varies from initial guess  $u_0(\zeta, \eta) = \zeta^2 (1 - 2 \eta)$  to the solution  $u(\zeta, \eta)$ , as  $q$  varies from 0 to 1.

Now, we will have the nth-order deformation equation as

$$(1 - q)\mathcal{L}[u_n - \chi_n u_{n-1}] = h\mathcal{R}_n(\vec{u}_{n-1}), \tag{32}$$

where

$$\mathcal{R}_n(\vec{u}_{n-1}) = \frac{\partial^2 u_{n-1}}{\partial \eta^2} - \left(\sum_{i=0}^{n-1} \frac{\partial u_i}{\partial \zeta} \frac{\partial u_{n-1-i}}{\partial \zeta}\right) - \left(\sum_{i=0}^{n-1} u_i \frac{\partial^2 u_{n-1-i}}{\partial \zeta^2}\right) \tag{33}$$

Therefore,

$$u_n = \chi_n u_{n-1} + h\mathcal{L}^{-1}[\mathcal{R}_n(\vec{u}_{n-1})], \tag{34}$$

where

$$\mathcal{L}^{-1} = \int \int (\cdot) d\eta d\eta \tag{35}$$

So, Eq. (32) becomes

$$u_n = \chi_n u_{n-1} + h \int \int \mathcal{R}_n(\vec{u}_{n-1}) d\eta d\eta, \tag{36}$$

The first few terms of the solution, with the help of  $u_0(\zeta, \eta)$  from Eq. (27) can be expressed as follows :

$$\begin{aligned} u_1(\zeta, \eta) &= h \left( -2\eta^4\zeta^2 + 4\eta^3\zeta^2 - 3\eta^2\zeta^2 \right) \\ u_2(\zeta, \eta) &= -2\eta^4\zeta^2h + 4\eta^3\zeta^2h - 3\eta^2\zeta^2h - \frac{4\eta^7h^2\zeta^3}{21} - \frac{8\eta^7h^2\zeta^2}{7} + \frac{2}{3}\eta^6\zeta^3h^2 \\ &\quad + 4\eta^6\zeta^2h^2 - \eta^5h^2\zeta^3 - 6\eta^5h^2\zeta^2 + 1/2\eta^4\zeta^3h^2 + \eta^4\zeta^2h^2 + 4\eta^3\zeta^2h^2 - 3\eta^2\zeta^2h^2 \\ u_3(\zeta, \eta) &= \frac{20\eta^9\zeta^2h^3}{7} - 12\eta^5h^2\zeta^2 - 3\eta^2\zeta^2h^3 - 6\eta^2\zeta^2h^2 - 3\eta^2\zeta^2h \\ &\quad + 4\eta^4\zeta^2h^3 + \frac{32\eta^7h^3\zeta^2}{7} - \eta^5h^3\zeta^3 - 2\eta^4\zeta^2h + \frac{80\eta^9\zeta^3h^3}{189} \\ &\quad + 2\eta^4\zeta^2h^2 + \frac{16\eta^7h^3\zeta^3}{21} - \frac{16\eta^{10}\zeta^3h^3}{189} + \frac{1}{3}\eta^6\zeta^3h^3 \\ &\quad + \frac{2}{3}\eta^6\zeta^3h^2 + 4\eta^3\zeta^2h^3 - 4/7\eta^{10}\zeta^2h^3 + 5\eta^6\zeta^2h^3 + 4\eta^3\zeta^2h + 8\eta^3\zeta^2h^2 \\ &\quad - 12\eta^5h^3\zeta^2 + \frac{1}{2}\eta^4\zeta^3h^2 - \frac{4\eta^7h^2\zeta^3}{21} - \frac{20\eta^8\zeta^3h^3}{21} \\ &\quad - \frac{16\eta^7h^2\zeta^2}{7} - \frac{45\eta^8\zeta^2h^3}{7} + \frac{1}{2}\eta^4\zeta^3h^3 + 8\eta^6\zeta^2h^2 - \eta^5h^2\zeta^3 \end{aligned}$$

Thus, the approximated series solution

$$u(\zeta, \eta) = u_0(\zeta, \eta) + u_1(\zeta, \eta) + u_2(\zeta, \eta) + u_3(\zeta, \eta) + \dots \tag{37}$$

From calculated  $u_i(\zeta, \eta)$ 's,  $i = 0, 1, \dots$  the above series solution when  $h = -1$  becomes

$$\begin{aligned} u(\zeta, \eta) &= -8\eta^7\zeta^2 - 6\eta^5\zeta^2 + 1/2\eta^4\zeta^3 + 7\eta^6\zeta^2 - 2\zeta^2\eta + \zeta^2 - \frac{8\eta^7\zeta^3}{7} + \eta^6\zeta^3 - \eta^5\zeta^3 \\ &\quad - \frac{20\eta^9\zeta^2}{7} + \frac{20\eta^8\zeta^3}{21} + 4/7\eta^{10}\zeta^2 - \frac{80\eta^9\zeta^3}{189} + \frac{45\eta^8\zeta^2}{7} + \frac{16\eta^{10}\zeta^3}{189} + 5\eta^4\zeta^2 \\ &\quad - 4\eta^3\zeta^2 + 3\eta^2\zeta^2 + \dots \end{aligned}$$

### 4 Results and Discussion

This section discusses the numerical values of the solution of some non-linear partial differential equations that has been solved using HAM. Table 1, shows the error of solution obtained by HAM that is compared with the errors of ADM [24] and VIM [24]. Table 2 discusses the error of solution obtained by HAM and is compared with the errors of ADM [25]. It is apparent from the tables that the error is lower with Homotopy Analysis Method as compared to Adomian Decomposition Method and Variational Iteration Method.

**Table 1** Comparison of the error in Example 1 of the solutions by  $u_{ADM}$ [24],  $u_{VIM}$ [24] and  $u_{HAM}$  ( $h = -0.77$ )

$\zeta$	$\eta$	$ u_{Exact} - u_{ADM} $	$ u_{Exact} - u_{VIM} $	$ u_{Exact} - u_{HAM} $
-1	0	0	0	0
-0.8	0.1	$6 \times 10^{-7}$	$7.7 \times 10^{-6}$	$3.3 \times 10^{-5}$
-0.6	0.2	$1.8 \times 10^{-5}$	$1.2 \times 10^{-4}$	$6.5 \times 10^{-5}$
-0.4	0.3	$1.3 \times 10^{-4}$	$5.4 \times 10^{-4}$	$5.8 \times 10^{-5}$
-0.2	0.4	$5.3 \times 10^{-4}$	$1.6 \times 10^{-4}$	$2.9 \times 10^{-5}$
0	0.5	$1.6 \times 10^{-3}$	$3.6 \times 10^{-3}$	$5.2 \times 10^{-6}$
0.2	0.6	$3.7 \times 10^{-3}$	$7.1 \times 10^{-3}$	$1 \times 10^{-10}$
0.4	0.7	$7.8 \times 10^{-3}$	$1.2 \times 10^{-2}$	$1.1 \times 10^{-5}$
0.6	0.8	$1.5 \times 10^{-2}$	$2 \times 10^{-2}$	$1.0 \times 10^{-4}$
0.8	0.9	$2.5 \times 10^{-2}$	$2.9 \times 10^{-2}$	$4.4 \times 10^{-6}$
1	1	$4.2 \times 10^{-2}$	$4.2 \times 10^{-2}$	$1.2 \times 10^{-3}$

**Table 2** Comparison of the error in Example 2 of the solutions by  $u_{ADM}$ [25] and  $u_{HAM}$  ( $h = -1$ )

$\zeta$	$\eta$	$ u_{Exact} - u_{ADM} $	$ u_{Exact} - u_{HAM} $
0	0	0	0
0.1	0.1	$5.4 \times 10^{-7}$	$4.0 \times 10^{-8}$
0.2	0.2	$6.2 \times 10^{-5}$	$4.1 \times 10^{-6}$
0.3	0.3	$9.7 \times 10^{-4}$	$5.1 \times 10^{-5}$
0.4	0.4	$6.7 \times 10^{-3}$	$2.5 \times 10^{-4}$
0.5	0.5	$3.0 \times 10^{-2}$	$5.8 \times 10^{-4}$
0.6	0.6	$9.8 \times 10^{-2}$	$1.6 \times 10^{-4}$
0.7	0.7	$2.7 \times 10^{-1}$	$4.3 \times 10^{-3}$
0.8	0.8	$6.5 \times 10^{-1}$	$2.0 \times 10^{-2}$
0.9	0.9	$1.4 \times 10^{-0}$	$5.9 \times 10^{-2}$
1	1	$2.8 \times 10^{-0}$	$1.3 \times 10^{-1}$

## 5 Conclusion

In this paper, two PDEs' analytical and approximate solutions are obtained using HAM. It is found that the obtained solutions using the HAM approach are very close to exact solutions as compared to the solutions of other available methods, as mentioned in the section. It can be seen from the comparison results that HAM is efficient and robust in finding analytical solutions for a broader class of problems. Furthermore, HAM gives us a free hand on adjusting and controlling the series solution's convergence by taking appropriate values of homotopy & auxiliary parameters accordingly. In conclusion, our method HAM also provides exact solutions accurately for various problems.

## References

1. Liao, S.J.: The proposed homotopy analysis techniques for the solution of nonlinear problems. Ph.D. dissertation, Shanghai Jiao Tong University, Shanghai (1992)
2. Liao, S.J.: A kind of linear invariance under homotopy and some simple applications of it in mechanics, Bericht Nr. 520. Institute fuer Schiffbau der Universitaet Hamburg (1992)
3. Liao, S.J.: Notes on the homotopy analysis method: some definitions and theorems. *Commun. Nonlinear Sci. Numer. Simul.* **14**(4), 983–997 (2009)
4. Kumar, S., Kumar, A., Odibat, Z.: A nonlinear fractional model to describe the population dynamics of two interacting species. *Math. Methods Appl. Sci.* **40** (11), 4134–4148 (2017)
5. Massa, F., Lallemand, B., Tison, T.: Multi-level homotopy perturbation and projection techniques for the reanalysis of quadratic eigenvalue problems: the application of stability analysis. *Mech. Syst. Signal Process.* **52**, 88–104 (2015)
6. Kumar, S., Singh, J., Kumar, D., Kapoor, S.: New homotopy analysis transform algorithm to solve Volterra integral equation. *Ain Shams Eng. J.* **5**(1), 243–246 (2014)
7. Martin, O.: On the homotopy analysis method for solving a particle transport equation. *Appl. Math. Model.* **37**(6), 3959–3967 (2013)
8. Nave, O., Gol'dshtein, V., Ajadi, S.: Singularly perturbed homotopy analysis method applied to the pressure driven flame in porous media. *Combust. Flame* **162**(3), 864–873 (2015)
9. Sardanyés, J., Rodrigues, C., Januário, C., Martins, N., Gil-Gómez, G., Duarte, J.: Activation of effector immune cells promotes tumor stochastic extinction: a homotopy analysis approach. *Appl. Math. Comput.* **252**(1), 484–495 (2015)
10. Molabahrami, A., Khani, F.: The homotopy analysis method to solve the Burgers-Huxley equation. *Nonlinear Anal. Real World Appl.* **10**(2), 589–600 (2009)
11. Shivanian, E., Abbasbandy, S.: Predictor homotopy analysis method: two points second order boundary value problems. *Nonlinear Anal. Real World Appl.* **15**, 89–99 (2014)
12. Yang, Z., Liao, S.: A HAM-based wavelet approach for nonlinear partial differential equations: two dimensional Bratu problem as an application. *Commun. Nonlinear Sci. Numer. Simul.* **53**, 249–262 (2017)
13. Liao, S.J.: *Beyond Perturbation: Introduction to Homotopy Analysis Method*. Chapman & Hall/CRC (2004)
14. Liao, S.J.: Homotopy analysis method and its applications in mathematics. *J. Basic Sci. Eng.* **5**(2), 111–125 (1997)
15. Gohil, V.P., Meher, R.: Effect of viscous fluid on the counter-current imbibition phenomenon in two-phase fluid flow through heterogeneous porous media with magnetic field. *Iran. J. Sci. Technol. Trans. A Sci.* **43**(4), 1799–810 (2019)

16. Kesarwani, J., Meher, R.: Modeling of an imbibition phenomenon in a heterogeneous cracked porous medium on small inclination. *Spec. Top. I Rev. Porous Media Int. J.* **12**(1) (2021)
17. Gohil, V.P., Meher, R.: Homotopy analysis method for solving counter current imbibition phenomena of the time positive fractional type arising in heterogeneous porous media. *Int. J. Math. I Comput.* **28**(2), 77–85 (2017)
18. Momani, S., Abuasad, S.: Application of He's variational iteration method to Helmholtz equation. *Chaos, Solitons Fractals* **27**(5), 1119–1123 (2006)
19. He, J.H.: Variational iteration method for delay differential equations. *Commun. Nonlinear Sci. Numer. Simul.* **2**(4), 235–236 (1997)
20. He, J.H.: Variational principle for some nonlinear partial differential equations with variable coefficients. *Chaos, Solitons Fractals* **19**(4), 847–851 (2004)
21. Adomian, G.: A review of the decomposition method in applied mathematics. *J. Math. Anal. Appl.* **135**, 501–544 (1988)
22. Wazwaz, A., El-Sayed, S.: A new modification of the Adomian decomposition method for linear and nonlinear operators. *Appl. Math. Comput.* **122**, 393–405 (2001)
23. Ray, S.S., Bera, R.K.: Solution of an extraordinary differential equation by adomian decomposition method. *J. Appl. Math.* **4**, 331–338 (2004)
24. Bildik, N., Konuralp, A.: Two-dimensional differential transform method, Adomian decomposition method and variational iteration method for partial differential equations. *Int. J. Comput. Math.* **83**, 973–987 (2006)
25. Odibat, Z., Momani, S.: Numerical methods for nonlinear partial differential equations of fractional order. *Appl. Math. Model.* **32**, 28–39 (2008)

# Nonlinear Modelling and Analysis of Longitudinal Dynamics of Hybrid Airship



Abhishek Kumar  and Om Prakash 

**Abstract** The objective of the paper is to develop a Nonlinear mathematical model for analyzing the longitudinal dynamics of a hybrid small sized airship that includes wings and elevators as a control surface. In this model will propose a single body longitudinal dynamics model for the hybrid airship and two body dynamics model for the hybrid airship with tethered suspended payload. Apparent mass matrix is taken care in the modelling of hybrid airship. Analysis of the system is done on MATLAB with simulated results.

**Keywords** Hybrid airship · Nonlinear longitudinal dynamics · Multi body dynamics

## 1 Introduction

This paper deals with the area of dynamics and modelling of lighter than air vehicles. More specifically modelling of hybrid airship is dealt. Modelling is usually done using some subset of the inputs and outputs, taken from flight data according to the objective. Due to huge cost, these plants are rarely accessible to do experiment design on it. Modelling work is carried out with the help of flight data, geometry data and aerodynamic data by understanding the mathematics and physics of the proposed model. Airships are being proposed for heavy freight aerial transport and also for surveillance tasks. The Hybrid airship system consists of semi rigid airship hull mass (including apparent mass and included air mass) and rigid wing attached below the hull and a payload is attached through number of riser lines. The suspension lines

---

A. Kumar (✉)

Department of Electrical Engineering, Manipal University Jaipur, Jaipur 303007, Rajasthan, India  
e-mail: [abhishekkumr@gmail.com](mailto:abhishekkumr@gmail.com)

A. Kumar · O. Prakash

Department of Aerospace Engineering, University of Petroleum and Energy Studies, Dehradun 248007, India  
e-mail: [omprakash@ddn.upes.ac.in](mailto:omprakash@ddn.upes.ac.in)

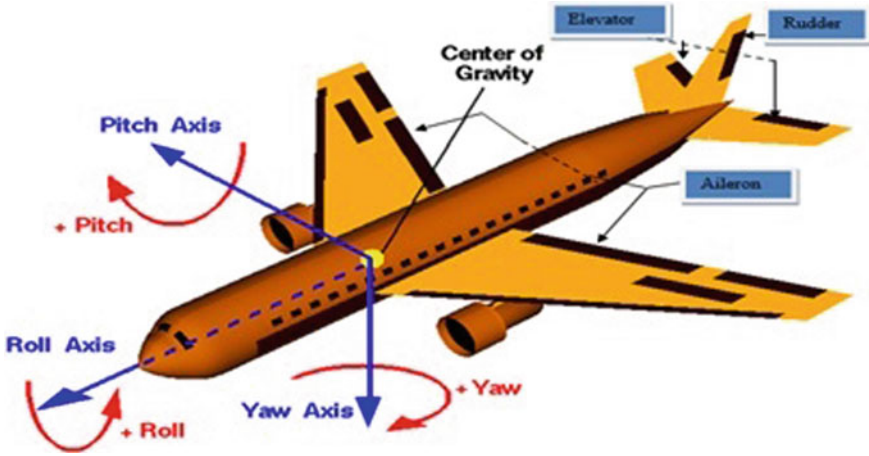


**Fig. 1** Body axes system of an aircraft with primary control surfaces

coming down from the hull are attached to the payload riser through a connection point allowing independent rotational motion of hull and payload.

The idea of the hybrid airship model has been taken from [1, 2] and Autonomous parafoil payload delivery systems. Here in Fig. 1, the positions of the three primary control surfaces (i.e. aileron  $\delta_a$  or  $\xi$ , elevator  $\delta_e$  or  $\eta$  and rudder  $\delta_r$  or  $\tau$ ) are shown properly. Centre of gravity is shown as a yellow dot near the join position of two wings and is also known as the origin of the body axes system. X-axis is in the forward direction of the pilot also known as Roll axis, Y-axis is towards the direction of right wing known as Pitch axis and Z-axis is in downward direction towards the gravity known as Yaw axis. Angular velocities or applied moments about the x, y and z body axes are described with the adjectives roll, pitch and yaw respectively. These moments are positive if they follow the directions as shown in the Fig. 1. The rigging angle is a critical design parameter as we have the provision to control the roll moment and pitch moment with deflecting the control lines attached to airship as shown in the Fig. 5. Improper choice of rigging angle can lead to adverse dynamics during deployment. The type of uncertainty expected for the trajectory tracking is primarily due to the inability to accurately predict the aerodynamics and control coefficients for the hybrid airship.

However, controller designed for airship must guarantee stability for the system and provide a satisfied control performance. The final control objective based on obtained design parameter such as rigging angle for two body dynamics is the robustness of stability and tracking performance to the presence of modelling uncertainty. Moreover, a control strategy is desired for which stability and robustness to uncertainty, collision avoidance and trajectory tracking can be guaranteed, and a solution can be obtained in real time. The parafoil/payload system described in reference [3] can be utilised for safe guided delivery of payload to a specific target region or to numerous targets from a single launch. In reference [2–4], a full 9 DOF or 4 DOF

two-body dynamic model for parafoil payload delivery system is used to capture these distinct motions along with pendulum stability effect and the hybrid airship 4 DOF model has been proposed with this concept. Unlike an aeroplane, where the wings are the most deformable, an airship's hull is the most flexible component. The hull shape of both semi-rigid and non-rigid airships is maintained by a pressure level greater than the surrounding air pressure. apparent mass matrix is taken care in modelling of hybrid airship. Mathematical modelling of hybrid airship with payload is more complicated compared with either Aircraft or with Parafoil delivery system.

## 2 Aircraft Dynamics and Parameter Definition

Flight test data is required for aerodynamic parameter estimation of a postulated mathematical model of an aircraft. The mathematical model consists of both the aircraft equations of motion and the equations for aerodynamic forces and moments, known as the aerodynamic model equations. State variables and control inputs of an aircraft are defined as shown in Fig. 2. An inertial coordinate system is fixed by earth's surface. The origin of the body-fixed coordinate system coincides with the centre of mass of the aircraft.

- Here some description of the notations used in Fig. 2. and they are as follows:
- $u, v, w$  = body-axis components of aircraft velocity relative to Earth axes.
- $p, q, r$  = body-axis components of aircraft angular velocity.
- $X_b, Y_b, Z_b$  = body-axis components of aerodynamic force acting on the aircraft.
- $L, M, N$  = body-axis components of aerodynamic moment acting on the aircraft.

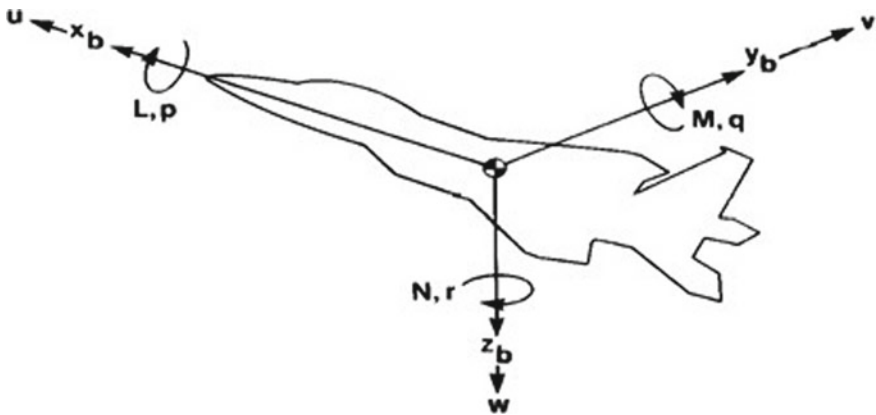


Fig. 2 Airplane notation and sign convention



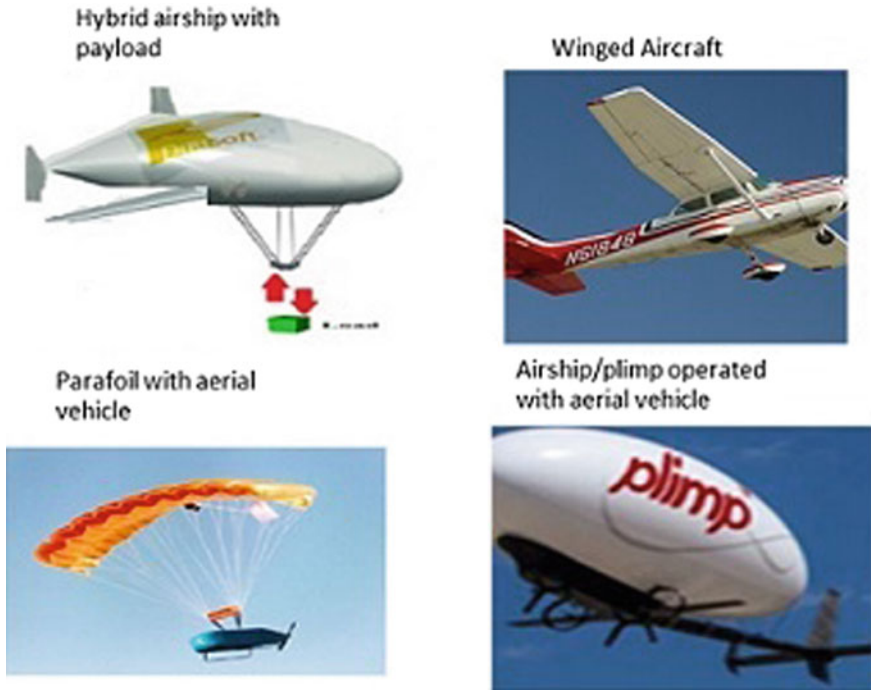


Fig. 3 Pictorial Idea for winged hybrid airship flight vehicle with suspended payload

### 3 Modelling of Hybrid Airship

As shown in Fig. 3, the proposed model named as “winged hybrid airship flight vehicle with suspended payload”, located at 1st row 1st column, having developed with combining the modelling features of winged aircraft, airship with aircraft feature known as ‘plimp’ and parafoil payload delivery flight system. The hybrid airship geometric, apparent mass and Inertia, aerodynamics data and payload data are taken from A.F.A. Gaffar [1] for dynamic simulation of Hybrid-Airship with payload system. The Hybrid Airship is assumed to carry attached payload (Tables 1 and 2).

### 4 Mathematical Modelling of Hybrid Airship

#### 4.1 Single Body Dynamics for Hybrid Airship

The complexity in mathematical derivation of hybrid airship is because of the centre of mass or centre of gravity and centre of volume is positioned at two distinct locations

**Table 1** Hull geometry

Hull Parameter	Value
Hull mass $m_k$	10 kg
Overall length, $L$	3.75 m
Maximum Diameter, $D$	1.6 m
Volume, $V$	$5.6 \text{ m}^3$
Hull Reference Area, $S_k$	$3.16 \text{ m}^2$
Hull Reference length, $c$	1.78 m
Ellipsoid semi-minor axis, $b$	0.8 m
Wing span $b$	3.06 m
Wing area, $S_t$	$1.72 \text{ m}^2$
tail span $b_t$	3.06 m
tail area, $S_t$	$0.916 \text{ m}^2$
$Rck$	0.8 m

**Table 2** Payload geometry

Payload Parameter	Value
mb	2 kg
Sb	$0.1 \times 0.2 \text{ m}^2$
Rcb	0.25 m
$C_D^B$	1.05

as shown in the Fig. 4. Moment equation and force equation is obtained easily on centre of mass or centre of gravity. In Hybrid airship, the centre of volume is almost

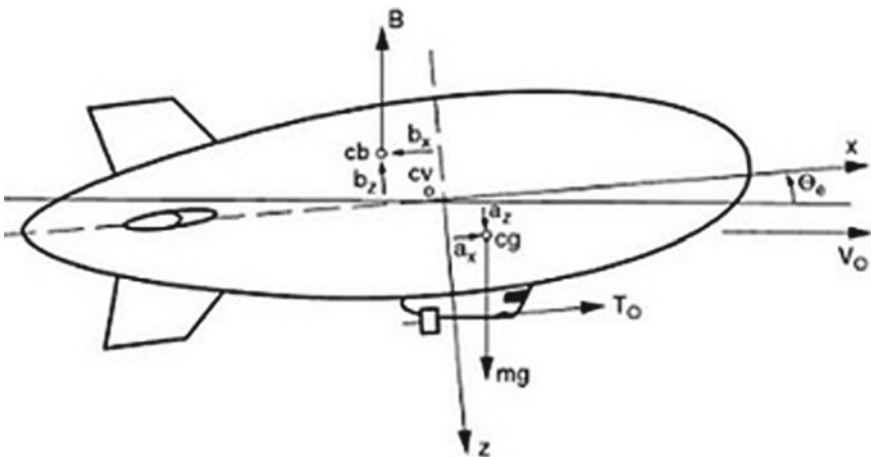


**Fig. 4** Coordinate location of CG and CV

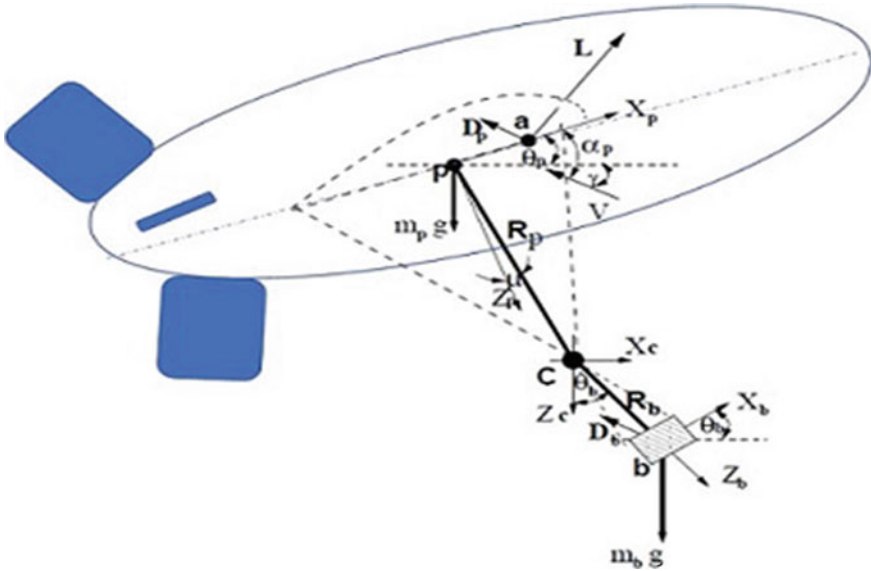


Fig. 5 4 DOF Longitudinal Two body dynamics for Hybrid Airship-payload system

located at the centre position of HULL that is filled with Helium or Hydrogen gas. Centre of mass or centre of gravity in hybrid airship is located near gondola where payload is attached, its mass is larger compared to HULL mass. Airship and hybrid airship is lighter than air vehicle, so we must take care of apparent mass of the system in the mathematical derivation which is not required in the final equation of motion of the aircraft as shown in Eq. (3).

For calculating the lift in airship design, Archimedes principle required volume for hydrostatic lift

$$L_{hst} = vol(\rho_a - \rho_g) \tag{1}$$

where  $\rho_a$  and  $\rho_g$  are densities of air and lifting gas.

$$w_{net} = (m_{GTW} \times g - L_{hst}) \tag{2}$$

Net weight  $w_{net}$  is gross take-off weight minus the weight balanced by the hydrostatic lift.

Hybrid airship 6 DOF Non-linear equation of motion:

$$\begin{bmatrix} ml_3 + M' & -mr_G^x \\ mr_G^x & I_0 + I'_0 \end{bmatrix} \begin{bmatrix} \dot{V}_0 \\ \dot{\omega}_0 \end{bmatrix} + \begin{bmatrix} m(\omega_0 \times V_0 + \omega_0 \times (\omega_0 \times r_G)) \\ \omega_0 \times (I_0 \omega_0) + mr_G^x \times (\omega_0 \times V_0) \end{bmatrix} = \begin{bmatrix} F \\ \zeta \end{bmatrix} \tag{3}$$

$$r_G^X = \begin{bmatrix} 0 & -a_z & a_y \\ a_z & 0 & -a_x \\ -a_y & a_x & 0 \end{bmatrix} \tag{4}$$

$$(r_G^X)^T = -(r_G^X) \tag{5}$$

Aircraft 6 DOF Non-linear equation of motion:

$$\begin{bmatrix} mI_3 & 0 \\ 0 & I_0 \end{bmatrix} \begin{bmatrix} \dot{V}_0 \\ \dot{\omega}_0 \end{bmatrix} + \begin{bmatrix} m(\omega_0 \times V_0) \\ \omega_0 \times (I_0\omega_0) \end{bmatrix} = \begin{bmatrix} F \\ \zeta \end{bmatrix} \tag{6}$$

Airship and hybrid airship is lighter than air vehicle, so we have to take of apparent mass of the system in the mathematical derivation which is not required in the final equation of motion of the aircraft as shown in Eq. (3) and (6).

The simplified version of the equation for propulsion system of hybrid airship is given in Eq. (7).

$$M_P = M_T = T d_z \tag{7}$$

where  $M_T$  is the moment due to propulsion system or thrust, T is total thrust generated by the engine and  $d_z$  is the distance of propulsion system from CV. For simplifying the complexity in the 6DOF non-linear dynamic equations of motion for hybrid airship (3), the dynamics can be analysed in two parts as longitudinal dynamics consists of 3DOF equation of motion and lateral dynamics consists of another 3DOF equation of motion. This can be done because, the shape of the hybrid airship is also symmetrical along x-axis just as an aircraft. The longitudinal dynamics consists of axial force equation ( $\dot{U}$ ), normal force equation ( $\dot{W}$ ), pitching moment equation ( $\dot{q}$ ) and kinematic equation ( $\dot{\theta}$ ). All the 6 DOF non-linear equation of motion is given in body axis frame of reference. The longitudinal 3 DOF non-linear equation of motion for single body dynamics of hybrid airship by considering the associated terms used for longitudinal dynamics and dropping out the remaining terms in the given 6 DOF nonlinear equation of motion for airship is proposed here. The simulation is done in wind axis coordinate system, so the terms used for simulation is  $\dot{V}$  (resultant of U and W velocity in wind axis),  $\dot{\gamma}$  (*gamma*),  $\dot{q}$  and  $\dot{\theta}$  for longitudinal dynamics of the system.

$$\dot{v} = \frac{1}{mx} \times (T \times \cos(\alpha) + \bar{q} \times s \times (-1) \times C_d - (m \times g - B) \times \sin(\gamma)) \tag{8}$$

$$\dot{\gamma} = \frac{1}{(mz \times v)} \times (T \times \sin(\alpha) + FAY - (m \times g - B) \times \cos(\gamma)) \tag{9}$$

$$\dot{q} = \frac{(((M_q - m \times a_x \times v \times \cos(\alpha) - m \times a_z \times v \times \sin(\alpha)) \times q) + M_a + M_s + M_T)}{I_H} \tag{10}$$

$$\dot{\theta} = q \tag{11}$$

$$FAY = \bar{q} \times s \times C_l + (-1) \times 0.5 \times \rho \times \frac{v}{2} \times S \times MAC \times c_{l_q} \times 0.5 \tag{12}$$

$$Mq = (\rho X v) X S X MAC^2 X Cmq \tag{13}$$

### 4.2 Two Body Dynamics for Hybrid Airship with Suspended Payload

Mathematical model of the hybrid airship for getting the desired objective is developed by applying physical laws which describes aerodynamics and non-linear dynamics of the hybrid airship. In reference [3], The aerodynamic forces and moments acting at parafoil canopy mass center are modelled in terms of aerodynamic force and moment coefficients as:

$$C_L = C_L(\alpha_p, \delta_s) + c_{L\delta_a} \delta_a \tag{14}$$

$$C_D^P = C_D^P(\alpha_p, \delta_s) + C_{D\delta_a} \delta_a + c_{L\delta_e} \delta_e \tag{15}$$

$$C_Y = C_Y \beta + C_{Y_r} r_p \frac{b}{2V_p} + c_{Y\delta_a} \delta_a \tag{16}$$

In terms of hybrid airship-fixed axis coefficients:

$$C_X = (-C_D^P u_p + C_L w_p) / V_p \tag{17}$$

$$C_Y = C_Y \tag{18}$$

$$C_z = (-C_D^P w_p - C_L u_p) / V_p \tag{19}$$

$$C_l = C_{l_\beta} + C_{l_p} P_p \frac{b}{2V_p} + C_{l\delta_a} \delta_a \tag{20}$$

$$C_m = \{C_{m_{c/4}}(\alpha_p, \delta_s) + x_{pa} C_z\} + C_{mq} q_p \frac{c}{2V_p} + C_{m\delta_a} \delta_a + c_{L\delta_e} \delta_e \tag{21}$$

$$C_n = C_{n\beta}\beta + C_{n_P}P_P \frac{b}{2V_P} + C_{n_{\delta_a}}\delta_a \quad (22)$$

$$M_s = -(mga_z + Bb_z) \sin \theta - (mga_x + Bb_x) \cos \phi \cos \theta \quad (23)$$

where symmetric brake deflection  $\delta_s$  corresponds both right and left brakes equally down, while asymmetric brake deflection  $\delta_a$  is defined as  $\delta_a = l/c$ , where  $l$  is length of control lines pulled down. Positive  $\delta_a$  represents right brake down and negative  $\delta_a$  represents left brake down. Positive  $\delta_e$  is considered in downward deflection. As shown in Fig. 5, the rigging angle  $\mu$  is the angle between the line joining mid-baseline point of the hull to joint C and the line parallel to Zh axis passing through the mid-baseline point. Therefore,

$$z_{c_p} = R_{ch} \cos \mu \quad (24)$$

$$x_{c_p} = R_{ch} \sin \mu \quad (25)$$

$$y_{c_p} = 0 \quad (26)$$

The 4DOF model of hybrid airship with suspended payload has been proposed as shown in Fig. 5 by combing the 3DOF longitudinal dynamics of hybrid airship with wing and the 3DOF equation of motions of suspended payload. The idea to develop the 4 DOF model of hybrid airship come from 9 DOF model of hybrid airship [2], the 9DOF and 4DOF model of parafoil payload system [4, 5]. 4-DOF model of winged hybrid airship flight vehicle -payload system is formed with B vector in Eq. (27a to f) and A system matrix in Eq. (28) and by deriving dynamic equations for winged hybrid airship flight vehicle. The 4DOF model of hybrid airship will consist of a Submodel of winged hybrid airship flight vehicle canopy, airship wing link and joint C and payload submodel consisting of payload, payload link and joint C, by separating the winged hybrid airship flight vehicle -payload system at the link joint C and considering components of internal joint forces  $F_x$ ,  $F_z$ , and their moment about airship CG and payload CG respectively. It is expected that the outcome of hybrid airship with wing and suspended payload is a combined effect of the dynamics of parafoil payload delivery system and dynamics of aircraft. For Level Flight Thrust is equal to drag force for airship dynamic model with velocity assumed to be constant at 20 m/s. In the moment equation the effect of elevator at wing and moment at fin is also considered. Apparent mass is also taken care in the modelling.

$$b_1 = -m_b g \sin \theta_b - Q_b S_b C_{D_b} \cos \alpha_b \quad (27a)$$

$$b_2 = m_b g \cos \theta_b - Q_b S_b C_{D_b} \sin \alpha_b + m_b R_b q_b^2 \quad (27b)$$

$$b_3 = 0 \tag{27c}$$

$$b_4 = -m_p g \sin \theta_p + Q_p S_p C_x + m_{pc} R_p \sin \mu q_p^2 - (C - A)(u_C \sin \theta_p + w_C \cos \theta_p) q_p \tag{27d}$$

$$b_5 = m_p g \cos \theta_p + Q_p S_p C_z + m_{pA} R_p \cos^{\mu} q_p^2 - (C - A)(U_C \cos \theta_p - w_C \sin \theta_p) q_p \tag{27e}$$

$$b_6 = -x_{pa} Q_p S_p C_z + Q_p S_{PC} C_M \tag{27f}$$

The two body dynamic model as 4DOF is developed for Parafoil payload delivery system and wing payload delivery system. For hybrid airship with payload delivery system, the two body dynamic 4DOF model has been proposed here and simulated on MATLAB and verified the result with single body 3DOF result and the result of Ghaffar [1].

$$\begin{bmatrix} m_b \cos \theta_b & -m_b \sin \theta_b & m_b R_b & 0 & \cos \theta_b & -\sin \theta_b \\ m_b \sin \theta_b & m_b \cos \theta_b & 0 & 0 & \sin \theta_b & \cos \theta_b \\ 0 & 0 & I_b & 0 & -R_b \cos \theta_b & R_b \sin \theta_b \\ m_{pA} \cos \theta_p & -m_{pA} \sin \theta_p & 0 & m_{pA} R_p \cos \mu & -\cos \theta_p & \sin \theta_p \\ m_{pC} \sin \theta_p & m_{pC} \cos \theta_p & 0 & -m_{pC} R_p \sin \mu & -\sin \theta_p & -\cos \theta_p \\ 0 & 0 & 0 & I_{pF} & z_{cp} & -x_{cP} \end{bmatrix} \begin{bmatrix} \dot{u}_C \\ \dot{w}_C \\ \dot{q}_b \\ \dot{q}_p \\ F_x \\ F_z \end{bmatrix} = \begin{bmatrix} b_1 \\ b_2 \\ b_3 \\ b_4 \\ b_5 \\ b_6 \end{bmatrix} \tag{28}$$

### 5 Simulation Result

As in Fig. 6, By changing the rigging angle  $\mu$ , the payload attached with airship moves backward and forward. If the payload movement is in backward side, then the airship noses up and vice-versa. So from changing the rigging angle also we

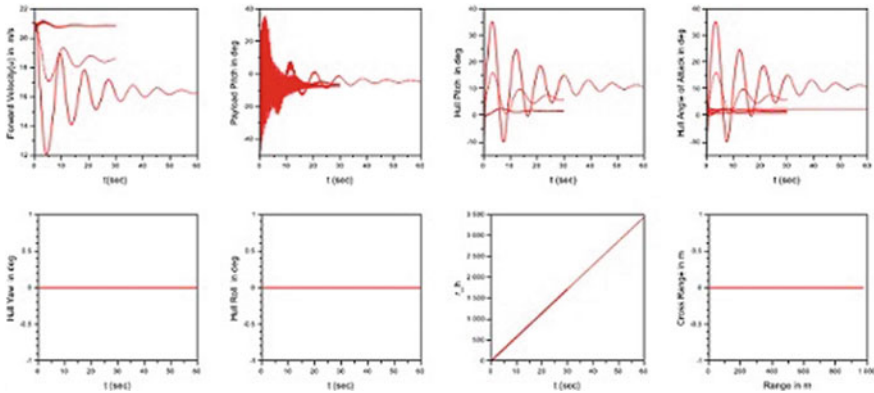
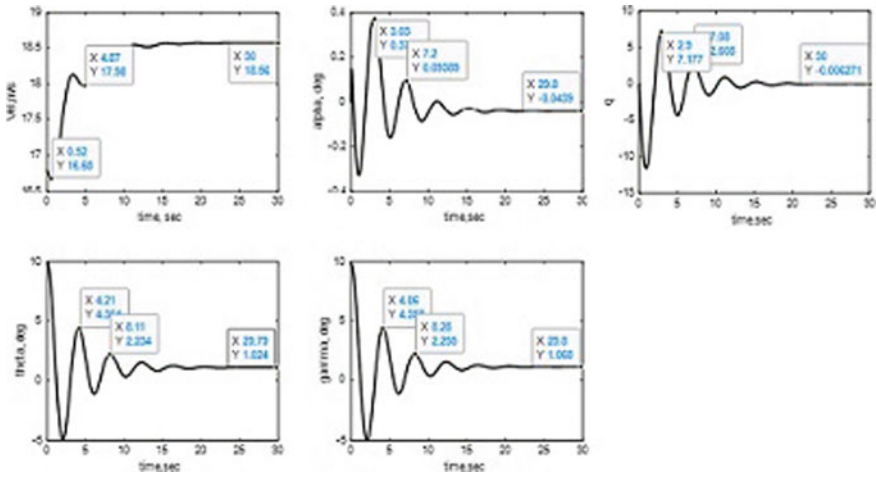
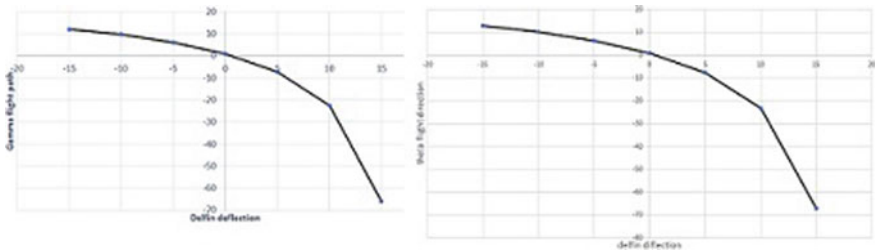


Fig. 6 Simulation result of 4DOF longitudinal dynamics of hybrid airship with suspended payload



**Fig. 7** Simulation result of 3DOF longitudinal dynamics of hybrid airship at delfin 0 degree deflection

can control the pitching moment of the airship. In Fig. 7, the values of alpha, q, theta and gamma trim at almost 0 degree which match with trim values of A.F.A. Gaffar [1]. The velocity trims at 18.5 m/s with initial value provided with 16.8 m/s. All the output settles the trim condition within 20 s. For q, time period is 4.1 s and oscillation frequency as 1.5 rad/sec. Time period of theta is 3.9 s with angular frequency as 1.6 rad/sec. The system is stable as it settles within 20 s. By deflecting the delfin also the trim value of the longitudinal dynamics of hybrid airship is noted down and it also settles down within 20 s. The trajectory variation is observed in longitudinal dynamics by looking the trajectory of flight path angle and theta angle, when a deflection happens in delfin control surface as shown in Fig. 8.



**Fig. 8** Flight path trajectory with delfin deflection



## 6 Conclusion

The 3DOF nonlinear longitudinal dynamic model for hybrid airship is developed and the simulation result is verified with trim values of A.F.A. Gaffar [1] obtained for linearized longitudinal model for the same. The 4 DOF nonlinear longitudinal dynamic model for hybrid airship with suspended payload has been developed and the simulated result is almost behaving like the result obtained from single body 3 DOF longitudinal model. The new thing in the 3 DOF hybrid model is included and that is fin deflection control maneuvers and in 4DOF, the new finding is by changing the rigging angle also pitch control of airship can be done. More accurate result will come if wind tunnel data for the system is available.

## References

1. Ghaffar, A.F.A.: The development of a mathematical model of a hybrid airship. Master of Science Thesis Aerospace Engineering, University of Southern California (2012)
2. Prakash, O., Purohit, S.: Multibody dynamics of winged hybrid airship payload delivery system. AIAA Aviation 2020 Forum (2020). <https://doi.org/10.2514/6.2020-3200>
3. Prakash, O., Ananthkrishnan, N.: NDI based generic heading tracking control law for parafoil/payload system. AIAA Aviation 2020 Forum (2020). <https://doi.org/10.2514/6.2020-3195>
4. Prakash, O., Ananthkrishnan, N.: Modeling and simulation of 9-DOF parafoil-payload system flight dynamics. In: AIAA Atmospheric Flight Mechanics Conference and Exhibit, AIAA, Keystone, Colorado USA (2006). <https://doi.org/10.2514/6.2006-6130>
5. Prakash, O., Daftary, A., Ananthkrishnan, N.: Bifurcation analysis of parafoil-payload system flight dynamics. In: AIAA Atmospheric flight mechanics conference and exhibit, AIAA, San Francisco, California, USA (2005). <https://doi.org/10.2514/6.2005-5806>
6. Tiwari, A., Vora, A., Sinha, N.K.: Airship trim and stability analysis using bifurcation techniques. In: 7th International Conference on Mechanical and Aerospace Engineering, IEEE Xplore (2016). 978-1-4673-8829-0/16

# A New Two-Parameter Odds Generalized Lindley-Exponential Model



Sukanta Pramanik 

**Abstract** A new two-parameter lifetime model, called Odds Generalized Lindley-Exponential distribution (OGLED), is proposed for modelling life time data. A detailed structural and reliability properties of the new distribution is derived. The mle method has been derived for estimating the model parameters. A real life time data set has been analysed to illustrates as application.

**Keywords** T-X family of distributions · Exponential distribution · Lindley distribution

## 1 Introduction

Fitting real-life dataset with a new probability distribution and synthesising information becomes a more challenging work for researchers. Classical probability distributions e.g. binomial, gamma, exponential, hypergeometric, Poisson, normal are insufficient to get information properly from the dataset. In nature now a day it is very complex to generate data from the day-to-day work environment. Statistical distributions are very important for parametric inferences and the applications to fit real-world phenomena. Various methods have been developed to generate statistical distributions in the literature to fit and analyse complex data. Some methods were developed prior to 1980s s like the Pearsonian system by Pearson [11], Johnson [6], and Tukey [14]. Azzalini [3], McDonald [10], Marshall and Olkin [9] are also developed since 1980s. In this current century, Eugene et al. [5] developed the beta generated family of distributions, Jones [7] and Cordeiro and de Castro [4] developed the beta generated family of distributions by using Kumaraswamy distribution in the place of beta distribution.

---

S. Pramanik (✉)

Department of Statistics, Siliguri College, North Bengal University,  
Siliguri 734 001, West Bengal, India  
e-mail: [skantapramanik@gmail.com](mailto:skantapramanik@gmail.com)  
URL: <http://siliguricollege.org.in/>

© The Author(s), under exclusive license to Springer Nature Switzerland AG 2022  
S. Banerjee and A. Saha (eds.), *Nonlinear Dynamics and Applications*,  
Springer Proceedings in Complexity,  
[https://doi.org/10.1007/978-3-030-99792-2\\_83](https://doi.org/10.1007/978-3-030-99792-2_83)

977

Alzaatreh et al. [2] has proposed a new generalized T-X (Transformed-Transformer) family of distributions. Using the T-X family of distributions, I have defined positive support of a generalized class of any distribution. Taking, the odds function  $W(F_\theta(x)) = \frac{F_\theta(x)}{1-F_\theta(x)}$ , the cdf of my proposed distribution is given by

$$F(x; \lambda, \theta) = \int_0^{\frac{F_\theta(x)}{1-F_\theta(x)}} f_\lambda(t)dt. \tag{1}$$

Here,  $\frac{F_\theta(x)}{1-F_\theta(x)} = \frac{F_\theta(x)}{\bar{F}_\theta(x)} = \infty$  as  $x \rightarrow \infty$  (assuming  $\frac{1}{0} = \infty$ ). The resulting distribution is not only generalized but also added with some parameter(s) to this base distribution. I called this kind of class of distributions as Odds Generalized family of distributions (OGFD).

In this present article, I choose the Lindley distribution as base distribution with pdf  $f_\lambda(x) = \frac{\lambda^2(1+x)}{1+\lambda} e^{-\lambda x}$  and the transformer distribution is exponential distribution in (1) i.e.  $F_\theta(x) = 1 - e^{-\theta x}$ . So, I call this distribution as a new two-parameter odds generalized Lindley-exponential distribution (OGLED).

In this article in Sect. 2, I developed the new modelling of the distribution. The mathematical, structural and reliability properties of the new model is derived in Sect. 3. In Sect. 4, I estimate the parameters. In Sect. 5, the applicability i.e. the application of the distribution is provided. At last in Sect. 6 conclusions.

## 2 The Pdf and Cdf of the OGLED

The c.d.f of the OGLED is given by

$$F(x; \lambda, \theta) = \int_0^{\frac{F(x)}{1-F(x)}} f_\lambda(x)dx = 1 - \frac{1 + \lambda e^{\theta x}}{1 + \lambda} e^{-\lambda(e^{\theta x} - 1)} \tag{2}$$

Also the p.d.f of the OGLED is given by

$$f(x; \lambda, \theta) = \frac{\lambda^2 \theta e^{2\theta x}}{(1 + \lambda)} e^{-\lambda(e^{\theta x} - 1)} \tag{3}$$

with range(0, ∞). Figure 1 is the pdf plot for  $\lambda = 2$  and 3 with different values of  $\theta$ . Figure 2 is the pdf plot for fixed  $\theta$  with different values of  $\lambda$ .

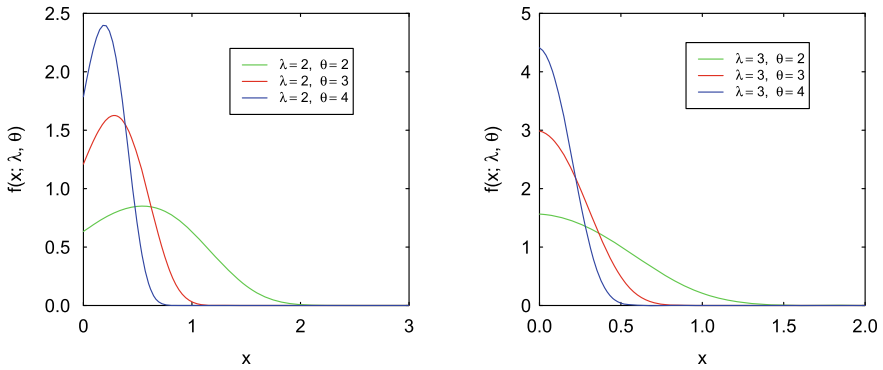


Fig. 1 The pdf of the OGLED

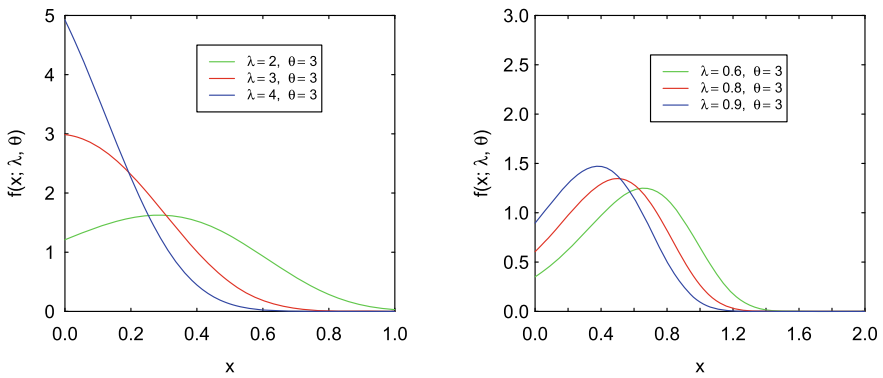


Fig. 2 The pdf of the OGLED

### 3 Properties of the Distribution

#### 3.1 The Limits of the Distribution

Since the cdf of this distribution is  $F(x; \lambda, \theta) = 1 - \frac{1+\lambda e^{\theta x}}{1+\lambda} e^{-\lambda(e^{\theta x}-1)}$

so,  $\lim_{x \rightarrow 0} F(x; \lambda, \theta) = \lim_{x \rightarrow 0} (1 - \frac{1+\lambda e^{\theta x}}{1+\lambda} e^{-\lambda(e^{\theta x}-1)}) = 0$

i.e.  $F(0) = 0$

Now  $\lim_{x \rightarrow \infty} F(x; \lambda, \theta) = \lim_{x \rightarrow \infty} (1 - \frac{1+\lambda e^{\theta x}}{1+\lambda} e^{-\lambda(e^{\theta x}-1)}) = 1$  i.e.  $F(\infty) = 1$ .

Figure 3 is the plot of the cdf for different values of  $\lambda$  and  $\theta$ .

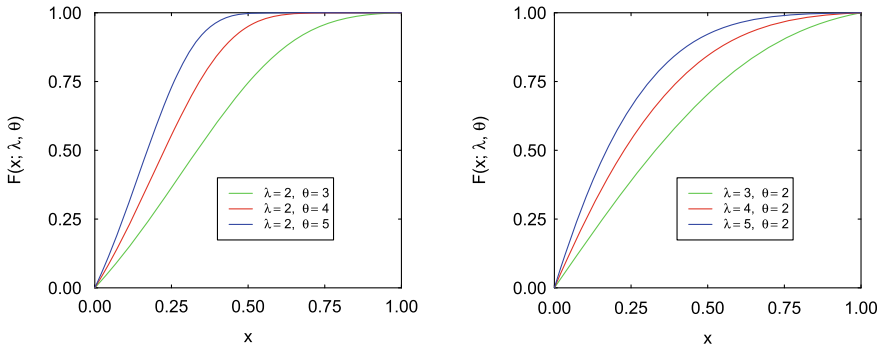


**Fig. 3** The cdf of the OGLED

### 3.2 Structural Properties of the OGLED

The **mean** value of this OGLED is:

$$\mu'_1 = \frac{e^\lambda}{(1 + \lambda)\theta} [\Gamma^{(1)}(2, \lambda) - \ln \lambda \cdot \Gamma(2, \lambda)]$$

The **median** value of our distribution is solving the following equation using numerical method

$$1 - \frac{1 + \lambda e^{\theta M}}{1 + \lambda} e^{-\lambda(e^{\theta M} - 1)} = \frac{1}{2}$$

The **mode** value of our distribution: mode= arg max(f(x))

So that  $\log f_{l.e}(x) = 2 \log \lambda + \log \theta + 2\theta x - \log(1 + \lambda) - \lambda(e^{\theta x} - 1)$

Now  $\frac{d}{dx} \log f_{l.e}(x) = 2\theta - \lambda\theta e^{\theta x} = 0$ , i.e.  $x = \frac{1}{\theta} \log\left(\frac{2}{\lambda}\right)$ ,

Thus the mode is  $\frac{1}{\theta} \log\left(\frac{2}{\lambda}\right)$ .

The rth raw moment of the OGLED is as follows:

$$E(X^r) = \frac{e^\lambda}{(1 + \lambda)\theta^r} \sum_{j=0}^r (-1)^{(r-j)} \binom{r}{j} (\ln \lambda)^{-(j-r)} \Gamma^{(j)}(2, \lambda) \tag{4}$$

Now putting suitable values of r in the above equation, I can have the Variance ( $\mu_2$ ), Skewness ( $\gamma_1$ ), and Kurtosis ( $\gamma_2$ ) of the OGLED.

**Moment Generating Function(MGF):**

$$M_X(t) = \sum_{r=0}^{\infty} \sum_{j=0}^r \frac{t^r}{r!} \frac{e^\lambda}{(1 + \lambda)\theta^r} (-1)^{-(j-r)} \binom{r}{j} (\ln \lambda)^{-(j-r)} \Gamma^{(j)}(2, \lambda) \tag{5}$$

**Characteristic Function(CF):**

$$\Psi_X(t) = \sum_{r=0}^{\infty} \frac{(it)^r}{r!} \frac{e^\lambda}{(1 + \lambda)\theta^r} \sum_{j=0}^r (-1)^{-(j-r)} \binom{r}{j} (\ln \lambda)^{-(j-r)} \Gamma^{(j)}(2, \lambda) \quad (6)$$

**Cumulant Generating Function(CGF):**

$$K_X(t) = \ln_e \left[ \sum_{r=0}^{\infty} \frac{t^r}{r!} \frac{e^\lambda}{(1 + \lambda)\theta^r} \sum_{j=0}^r (-1)^{-(j-r)} \binom{r}{j} (\ln \lambda)^{-(j-r)} \Gamma^{(j)}(2, \lambda) \right] \quad (7)$$

**Mean Deviation:**

The mean deviation about the mean is

$$MD_\mu = \frac{2e^\lambda}{(1 + \lambda)} \left[ \frac{1}{\theta} \{ \Gamma^{(1)}(2, \lambda e^{\theta\mu}) - \ln \lambda \cdot \Gamma(2, \lambda e^{\theta\mu}) \} - \mu(1 + \lambda e^{\theta\mu})e^{-\lambda e^{\theta\mu}} \right] \quad (8)$$

also mean deviation about the median is

$$MD_M = -\mu + \frac{2e^\lambda}{(1 + \lambda)\theta} [ \Gamma^{(1)}(2, \lambda e^{\theta M}) - \ln \lambda \cdot \Gamma(2, \lambda e^{\theta M}) ] \quad (9)$$

respectively, where  $\mu = E(X)$  and  $M = Median(X)$ .

**Conditional Moments:** The  $r$ th raw moment of the residual life is

$$m_r(t) = \frac{\sum_{j=0}^r \sum_{k=0}^j \frac{(-1)^j}{\theta^j} \binom{r}{j} t^{r-j} (-1)^{(j-k)} \binom{j}{k} (\ln \lambda)^{(j-k)} \Gamma^{(k)}(2, \lambda e^{\theta t})}{(1 + \lambda e^{\theta t})e^{-\lambda e^{\theta t}}}$$

The  $r$ th raw moment of the reversed residual life is

$$\bar{m}_r(t) = \frac{e^\lambda \sum_{j=0}^r \sum_{k=0}^j \frac{(-1)^j}{\theta^j} \binom{r}{j} t^{r-j} \binom{j}{k} (-\ln \lambda)^{j-k} [ \gamma^{(k)}(2, \lambda e^{\theta t}) - \gamma^{(k)}(2, \lambda) ]}{\{ 1 + \lambda - (1 + \lambda e^{\theta x})e^{-\lambda(e^{\theta x} - 1)} \}}$$

**Quantile function(Q(p)):** Let  $X$  denote a r.v. with the pdf in (3).

$$1 - \frac{1 + \lambda e^{\theta(Q(p))}}{1 + \lambda} e^{-\lambda[e^{\theta(Q(p))} - 1]} = p, \quad (10)$$

where,  $F(Q(p)) = p$

### 3.3 Incomplete Moment, Bonferroni and Lorenz Curves

The  $r$ th order incomplete moment of the OGLED is

$$m_r^I(t) = \frac{e^\lambda \lambda^2}{\theta^r (1 + \lambda)} [\Gamma^{(r)}(2, \lambda) - \Gamma^{(2)}(2, \lambda e^{\theta t})] \tag{11}$$

The Bonferroni and Lorenz curves are defined by

$$B(p) = \frac{m_1^I(x_p)}{p\mu} \tag{12}$$

and

$$L(p) = \frac{m_1^I(x_p)}{\mu} \tag{13}$$

respectively, where,  $\mu = E(X)$  and  $x_p = F^{-1}(p)$  which is to be calculated numerically using (10) for given  $p$ .

### 3.4 Entropies

The Rényi entropy for a new two-parameter model is

$$H_R(\beta) = -\log \theta + \frac{\lambda\beta}{1-\beta} - \frac{\beta}{1-\beta} \log(1 + \lambda) - \frac{2\beta}{1-\beta} \log \beta + \frac{\log \Gamma(2\beta, \lambda\beta)}{1-\beta}$$

Shannon measure of entropy for a new two parameter model is

$$H(f) = E[-\log f(X)] = -2 \log \lambda - \log \theta - \lambda + \log(1 + \lambda) + \frac{e^\lambda}{1 + \lambda} \Gamma(3, \lambda) - \frac{2e^\lambda}{(1 + \lambda)} [\Gamma^{(1)}(2, \lambda) - \log \lambda \cdot \Gamma(2, \lambda)]$$

### 3.5 Reliability Properties

The survival or reliability function is given by

$$R(x) = \frac{1 + \lambda e^{\theta x}}{1 + \lambda} e^{-\lambda(e^{\theta x} - 1)} \tag{14}$$

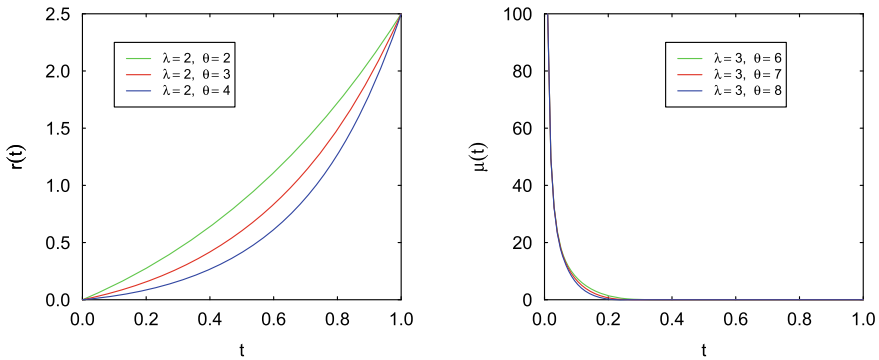


Fig. 4 Hazard rate and Reversed Hazard Rate of the OGLED

also the hazard rate function is given by

$$r(t) = \frac{\lambda^2 \theta e^{2\theta t}}{1 + \lambda e^{\theta t}} \tag{15}$$

Now,  $\log f(x) = 2 \log \lambda + \log \theta + \lambda - \log(1 + \lambda) + 2\theta x - \lambda e^{\theta x}$   
 So,  $\frac{d}{dx} \log f(x) = 2\theta - \lambda \theta e^{\theta x}$  and  $\frac{d^2}{dx^2} \log f(x) = -\lambda \theta^2 e^{\theta x}$   
 Since  $\lambda > 0, \theta > 0$  and  $x > 0$ ,  $\frac{d^2}{dx^2} \log f(x) < 0$ . Thus, the it is log-concave distribution. So, the distribution possesses an Increasing failure rate (IFR) and Decreasing Mean Residual Life (DMRL) property. Figure 4 is the Hazard rate and Reversed Hazard Rate of the OGLED plot for  $\lambda = 1.1$  and  $2.1$  with different values of  $\theta$ .

The expression of **mean residual life (MRL)** function is

$$m_1(t) = \frac{e^{\lambda e^{\theta t}}}{1 + \lambda e^{\theta t}} \left[ \frac{1}{\theta} \Gamma^{(1)}(2, \lambda e^{\theta t}) - \left( t + \frac{\ln \lambda}{\theta} \right) \Gamma(2, \lambda e^{\theta t}) \right]. \tag{16}$$

**Reversed Hazard rate:**

$$\mu(x) = \frac{f(x)}{F(x)} = \frac{\frac{\lambda^2 \theta e^{2\theta x}}{(1+\lambda)} e^{-\lambda(e^{\theta x}-1)}}{1 - \frac{1+\lambda e^{\theta x}}{1+\lambda} e^{-\lambda(e^{\theta x}-1)}} \tag{17}$$

The expression of **mean reversed residual life (MRRL)** function is

$$\bar{m}_1(t) = \frac{e^{\lambda} \left[ \left( t + \frac{\ln \lambda}{\theta} \right) \{ \gamma(2, \lambda) - \gamma(3, \lambda e^{\theta t}) \} - \frac{1}{\theta} \{ \gamma^{(2)}(2, \lambda) - \gamma^{(2)}(3, \lambda e^{\theta t}) \} \right]}{1 - (1 + \lambda e^{\theta t}) e^{-\lambda(e^{\theta t}-1)} + \lambda}$$

Figure 5 is the MRL and MRRL of the OGLED plot.



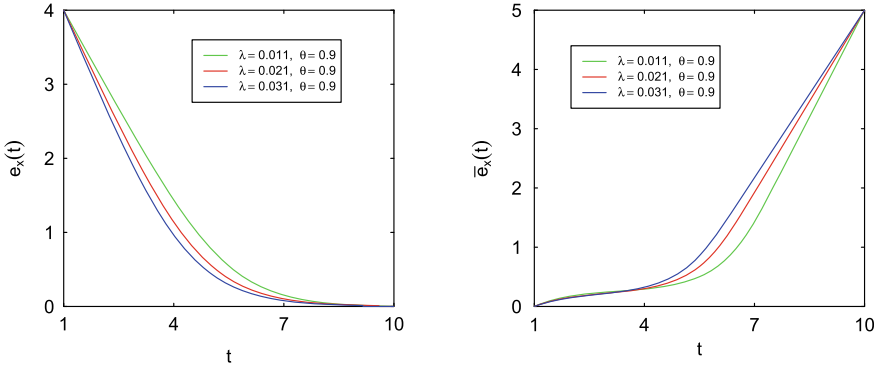


Fig. 5 Plots of the MRL and MRRL of the OGLED

### 3.6 Stress-Strength Reliability

The Stress-Strength reliability model describes the probability of surviving the life of a component with a random strength(X) subjected to a random stress(Y). Let  $X \sim OGLED(\lambda_1, \theta_1)$  and  $Y \sim OGLED(\lambda_2, \theta_2)$  be iid's. Thus,

$$R = P(X > Y) = 1 - \frac{e^{\lambda_1 + \lambda_2} \lambda_1^2 \theta_1}{(1 + \lambda_1)(1 + \lambda_2)} \int_0^\infty [1 + \lambda_2 e^{\theta_2 x}] e^{2\theta_1 x} e^{-\lambda_1 e^{\theta_1 x} - \lambda_2 e^{\theta_2 x}} dx$$

When both  $\theta_1$  and  $\theta_2$  are equal to  $\theta$ , then

$$R = 1 - \frac{\lambda_1^2}{(1 + \lambda_1)(1 + \lambda_2)} \left[ \frac{(1 + \lambda_2)}{(\lambda_1 + \lambda_2)} + \frac{(1 + 2\lambda_2)}{(\lambda_1 + \lambda_2)^2} + \frac{2\lambda_2}{(\lambda_1 + \lambda_2)^3} \right]$$

## 4 Estimation of the Parameters

Here, I estimate the parameters of the OGLED by using the method of Maximum Likelihood Estimation (MLE).

The MLEs of  $\lambda$  and  $\theta$  are the roots of

$$\frac{\partial \ln L(x; \lambda, \theta)}{\partial \lambda} = 0 \text{ and } \frac{\partial \ln L(x; \lambda, \theta)}{\partial \theta} = 0$$

Here using numerical methods, the two parameters  $\lambda$  and  $\theta$  are to be estimated.

**Table 1** Summarized table for fitting the data set

Distributions	Estimate of the parameter	AIC
Gamma-Half Normal	$\hat{\theta} = 0.3934, \hat{\alpha} = 2.8794, \hat{\beta} = 3.1725$	105.3572
OGLED	$\hat{\lambda} = 0.2202, \hat{\theta} = 1.3773$	102.3232

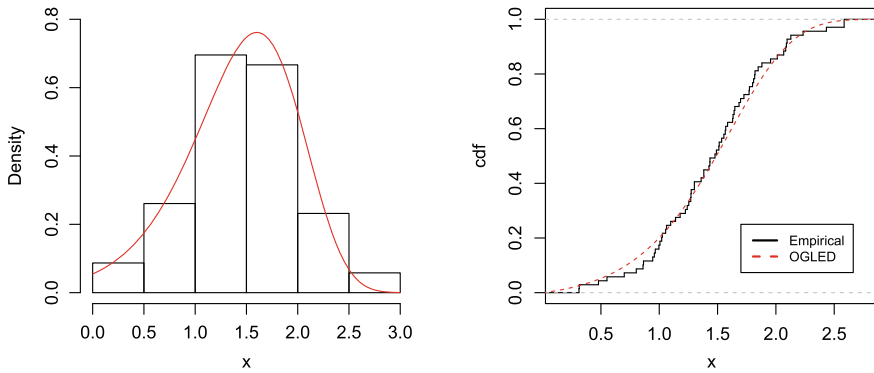


**Fig. 6** Plot of the OGLED model(pdf and cdf) for the above data set

## 5 Application

Here, I fit the new two-parameter OGLED model to a real data set which was obtained from Raqab et al. [12] in this section and the data set is the tensile strength, measured in GPa for single carbon fibers which were tested at 20mm. Gamma-Half Normal distribution has been fitted by Alzaatreh and Knight [1].  $\hat{\lambda} = 0.2202$  and  $\hat{\theta} = 1.3773$  are the estimated parameter values of the of OGLED and  $AIC = 102.3232$ . In the OGLED fitting, only two parameters are estimated to minimize estimation error (Table 1 and Fig. 6).

## 6 Conclusion

The above article, studied a new two-parameter Odds generalized Lindley-exponential distribution. The distribution is a particular form of the Transformed-Transformer (or T-X) family of distributions. The different properties like structural and reliability properties have been studied. The parameters are estimated by the maximum likelihood method of estimation. The appropriateness of fitting the new two-parameter Odds generalized Lindley-exponential model has been established by fitting a real-life data set.

**Acknowledgements** The author thank the anonymous referee for constructive suggestions, which immensely helped to improve the paper.

## References

1. Alzaatreh, A., Knight, K.: On the gamma-half normal distribution and its applications. *J. Mod. Appl. Stat. Methods* **12**(1), 103–119 (2013)
2. Alzaatreh, A., Lee, C., Famoye, F.: A new method for generating families of continuous distributions. *Metron* **71**, 63–79 (2013)
3. Azzalini, A.: A class of distributions which includes the normal ones. *Scand. J. Stat.* **12**, 171–178 (1985)
4. Cordeiro, G.M., de Castro, M.: A new family of generalized distributions. *J. Stat. Comput. Simul.* **81**(7), 883–898 (2011)
5. Eugene, N., Lee, C., Famoye, F.: Beta-normal distribution and its applications. *Comm. Statist. Theory Methods* **31**(4), 497–512 (2002)
6. Johnson, N.L.: Systems of frequency curves generated by methods of translation. *Biometrika* **36**, 149–176 (1949)
7. Jones, M.C.: Kumaraswamy's distribution: a beta-type distribution with tractability advantages. *Stat. Methodol* **6**, 70–81 (2009)
8. Lindley, D.V.: Fiducial distributions and Bayes' theorem. *J. Roy. Stat. Soc. B* **20**, 102–107 (1958)
9. Marshall, A.W., Olkin, I.: A new method for adding a parameter to a family of distributions with applications to the exponential and weibull families. *Biometrika* **84**, 641–652 (1997)
10. McDonald, J.B.: Some generalized functions for the size distribution of income. *Econometrica* **52**, 647–663 (1984)
11. Pearson, K.: Contributions to the mathematical theory of evolution to skew variation in homogeneous material. *Philos. Trans. R. Soc. Lond. A* **186**, 343–414 (1895)
12. Raqab, M., Madi, M., Kundu, D.: Estimation of  $P(Y < X)$  for the 3-parameter generalized exponential distribution. *Commun. Stat. Theory Methods* **37**(18), 2854–2864 (2008)
13. Rényi, A.: On measures of entropy and information, In: *Proceedings of the Fourth Berkeley Symposium on Mathematical Statistics and Probability I*, pp. 547–561. University of California Press, Berkeley, CA (1961)
14. Tukey, J.W.: *The Practical Relationship between the Common Transformations of Percentages of Counts and Amounts*, Technical Report 36, Princeton. Princeton University, Statistical Techniques Research Group, NJ (1960)

# Stability Switching in a Cooperative Prey-Predator Model with Transcritical and Hopf-bifurcations



Sajan , Ankit Kumar , and Balram Dubey 

**Abstract** In nature organisms attempt to adopt new techniques to diminish the possibilities of being falling prey. Interspecies cooperation is one of these approaches which two different types of prey can use against a common predator. Inspired by this, we purpose a prey-predator model having two prey who cooperate with each other while interacting with a predator. For making the model more general and realistic, the interactions between prey and predator are handled through general Holling type-IV and Crowley-Martin functional responses. For well-posedness of the proposed model, firstly, its boundedness is investigated which is followed by the vigorous proofs for the existence of equilibrium points, their stability analysis, evaluation of conditions for occurrence of transcritical and Hopf-bifurcations. Numerically, we observe that as the inverse measure of predator's immunity from first prey and coefficient of cooperation from first prey to second prey crosses some respective critical values, there is occurrence of Hopf-bifurcation. Transcritical bifurcation is also depicted numerically for the intrinsic growth rate of first prey and the death rate of predator species. Several phase portraits, bifurcation diagrams are drawn to support our analytical findings. We also endorse the attribute of bistability, and basins of attraction for both stable equilibrium points are also drawn.

**Keywords** Prey-predator · Cooperation · Bifurcation · Bistability

---

Sajan acknowledges the Ph.D. fellowship [File No. 09/719(0104)/2019-EMR-I] received from the Council of Scientific & Industrial Research, New Delhi, India.

---

Sajan (✉) · A. Kumar · B. Dubey  
Department of Mathematics, BITS Pilani, Pilani Campus, Pilani 333031, Rajasthan, India  
e-mail: [sajanmaths7@gmail.com](mailto:sajanmaths7@gmail.com)

A. Kumar  
e-mail: [ankitmaths2738@gmail.com](mailto:ankitmaths2738@gmail.com)

B. Dubey  
e-mail: [bdubey@pilani.bits-pilani.ac.in](mailto:bdubey@pilani.bits-pilani.ac.in)

© The Author(s), under exclusive license to Springer Nature Switzerland AG 2022  
S. Banerjee and A. Saha (eds.), *Nonlinear Dynamics and Applications*,  
Springer Proceedings in Complexity,  
[https://doi.org/10.1007/978-3-030-99792-2\\_84](https://doi.org/10.1007/978-3-030-99792-2_84)

987

## 1 Introduction

The study of prey-predator interrelationships is the foundation for research in the field of ecology. Exploring this relationship helps us to disclose various phenomena happening in ecology. Prey can use various techniques to reduce their predation like; camouflage, imitation of some dangerous breed, escape instead of direct encounter, use of harmful chemicals in the form of chemical defence, changing body color, formation of a team, etc. [1] There can be a reasonable possibility of cooperation among two types of prey to fight against a predator in an ecological sector. A nice introduction about teaming technique can be seen in [2]. Tripathi et al. [3] examined a three-dimensional model with two prey who help each other against a predator, although these two prey are competing internally. They discussed the persistence, permanence, and global stability of the model about an interior stationary point. Mishra and Raw [4] studied a prey-predator system having two prey and a predator involving teaming of prey. They used modified Holling type-IV and Holling type-II functional response to study the interaction against the predator.

Recently, Mondal and Samanta [5] worked on a three species population model having two prey and a predator. They assumed that prey help each other by forming team against the predator, and neglected the inter-species competition between these two types of prey. They used functional response of Holling type II, I and a single discrete delay in the model. Alsakaji et al. [6] extended the cooperation model by Tripathi et al. [3], by replacing the linear functional responses by Monod-Haldane functional responses with inclusion of two gestation delays in each response. They evaluated the critical values of delays for occurrence of Hopf-bifurcation. Ferrara et al. [7] extended the work of Mishra and Raw [4] with incorporation of two discrete delays. They did the Hopf-bifurcation and local stability analysis of the proposed model.

To the best knowledge of authors, a tri-trophic model with two prey and one predator model with cooperation between prey, where first prey is consumed by general Holling type-IV response while the interaction of predator with second one is dealt by Crowley-Martin functional response has not been studied yet.

## 2 Construction of Mathematical Model

Tripathi et al. [8] again investigated a two-prey one predator competitive system with help. But this time, they assumed that the predator consumes both the prey species via Beddington-DeAngelis response (model (1)). In this, the terms  $a_4xyz$  and  $b_4xyz$  correspond to the help provided by both prey species  $x$  and  $y$  to each other against the predator  $z$ , whereas the terms  $a_3xy$  and  $b_3xy$  signify the interspecies competition among both the prey species. The rest of the parameters in model (1) have their conventional meanings.

$$\begin{aligned}
 \frac{dx}{dt} &= a_1x \left(1 - \frac{x}{k_1}\right) - \frac{a_2xz}{m + m_1x + m_2z} - a_3xy + a_4xyz, \\
 \frac{dy}{dt} &= b_1y \left(1 - \frac{y}{k_1}\right) - \frac{b_2yz}{n + n_1y + n_2z} - b_3xy + b_4xyz, \\
 \frac{dz}{dt} &= -c_1z - c_2z^2 + \frac{c_3xz}{m + m_1x + m_2z} + \frac{c_4xz}{n + n_1x + n_2z}.
 \end{aligned}
 \tag{1}$$

Inspired from studies [3, 4, 8], we aim to study a 3-dimensional autonomous system of ordinary differential equations reflecting an interaction between a predator and a team of two prey species, in which these two prey species help each other against the predator to save themselves. A realistic example for this can be seen in forest when Antelope and Zebras cooperate in fighting against the predator like cheetah, lion, etc. Let  $x_1(t)$  and  $x_2(t)$  are the densities of two prey species where  $y(t)$  is the density of predator population. The purposed model can be written in the form of a system of three non-linear differential equations and which is based upon the following assumptions:

1. Both the prey,  $x_1$  and  $x_2$  grows logistically in the absence of predator  $y$ , which is reflected by the terms  $r_1x_1 \left(1 - \frac{x_1}{K_1}\right)$  and  $r_2x_2 \left(1 - \frac{x_2}{K_2}\right)$ , respectively. Here,  $r_i$  is the intrinsic growth rate and  $K_i$  is the carrying capacity of habitat, for prey  $x_i$ ,  $i = 1, 2$ .
  2. Prey  $x_1$  is assumed to show the characteristic of group defence, hence the interaction between  $x_1$  and  $y$  is addressed by generalised Holling type-IV functional response. This is given by the function  $f(x_1) = \frac{x_1}{ax_1^2 + bx_1 + c}$ , where  $a$  is the inverse measure of predator's immunity from prey,  $b$  is the handling time for each prey and  $c$  is the half saturation constant.
  3. Prey  $x_2$  is assumed to be consumed by Crowley-Martin response, given by function,  $g(x_2, y) = \frac{x_2}{(1 + \alpha x_2)(1 + \beta y)}$ . In this,  $\alpha$  is the handling time for each prey and  $\beta$  is coefficient of interference among predator species for this prey population.
  4. The terms  $\sigma_1x_1x_2y$  and  $\sigma_2x_1x_2y$  represent cooperation among both the prey species against the predator  $y$ . Here,  $\sigma_i$  is the coefficient of cooperation when  $x_j$  helps  $x_i$ ,  $i \neq j = 1, 2$ .
  5. Predator  $y$  is assumed to be a specific predator that is dependent only upon  $x_1$  and  $x_2$ . Hence, in the absence of these prey species it dies, which is shown by the term  $\delta_0y$  and the intraspecific competition among predator species is indicated by the term  $\delta_1y^2$ . The remaining parameters have their standard meanings.
- With all above assumptions, the purposed model is:

$$\begin{aligned} \frac{dx_1}{dt} &= r_1x_1\left(1 - \frac{x_1}{K_1}\right) - \frac{m_1x_1y}{ax_1^2 + bx_1 + c} + \sigma_1x_1x_2y = F_1(x_1, x_2, y), \\ \frac{dx_2}{dt} &= r_2x_2\left(1 - \frac{x_2}{K_2}\right) - \frac{m_2x_2y}{(1 + \alpha x_2)(1 + \beta y)} + \sigma_2x_1x_2y = F_2(x_1, x_2, y), \quad (2) \\ \frac{dy}{dt} &= \frac{c_1m_1x_1y}{ax_1^2 + bx_1 + c} + \frac{c_2m_2x_2y}{(1 + \alpha x_2)(1 + \beta y)} - \delta_0y - \delta_1y^2 = F_3(x_1, x_2, y), \end{aligned}$$

where  $r_i, K_i, m_i, a, b, c, \alpha, \beta, \sigma_i, c_i, \delta_0, \delta_1 \in (0, \infty)$  for  $i = 1, 2$ . The relevant biological initial condition for model (2) are  $x_1(0) \geq 0, x_2(0) \geq 0, y(0) \geq 0$ .

### 3 Kinetics of the Model

In this section, firstly we show that the solution of our system is bounded, which restricts the population explosion in finite time. Then we find all the possible equilibrium points and check their local and global behavior.

#### 3.1 Boundedness

**Theorem 1** *The set  $\Omega = \left\{ (x_1, x_2, y) : 0 \leq x_1 \leq K_1, 0 \leq x_2 \leq K_2, 0 \leq c_1x_1 + c_2x_2 + y \leq \frac{K}{\delta^*} \right\}$ , is a positive invariant set for all the solutions starting inside of the positive octant, where  $K = 2c_1r_1K_1 + 2c_2r_2K_2 + \frac{c_1^2\sigma_1^2K_1^2K_2^2}{2\delta_1} + \frac{c_2^2\sigma_2^2K_1^2K_2^2}{2\delta_1}$  and  $\delta^* = \min\{r_1, r_2, \delta_0\}$ .*

**Proof** From the first and second equation of model (2), it is easy to get

$$\limsup_{t \rightarrow \infty} x_1(t) \leq K_1 \text{ and } \limsup_{t \rightarrow \infty} x_2(t) \leq K_2.$$

Now, let  $M = c_1x_1 + c_2x_2 + y$ , which implies  $\frac{dM}{dt} = c_1\frac{dx_1}{dt} + c_2\frac{dx_2}{dt} + \frac{dy}{dt}$ , as mentioned in [3, 8], to avoid population explosion in upcoming time, we also assume that the cooperation terms in model (2) are dominated by the prey-predator interaction terms, thus using this fact we get

$$\begin{aligned} \frac{dM}{dt} &\leq c_1r_1\left(1 - \frac{x_1}{K_1}\right) + c_1\sigma_1x_1x_2y + c_2r_2\left(1 - \frac{x_2}{K_2}\right) + c_2\sigma_2x_1x_2y - \delta_0y - \delta_1y^2 \\ &\leq 2c_1r_1K_1 + 2c_2r_2K_2 - \frac{\delta_1}{2}\left(y - \frac{c_1\sigma_1K_2x_1}{\delta_1}\right)^2 + \frac{c_1^2\sigma_1^2K_2^2x_1^2}{2\delta_1} - \frac{\delta_1}{2}\left(y - \frac{c_2\sigma_2K_1x_2}{\delta_1}\right)^2 + \\ &\frac{c_2^2\sigma_2^2K_1^2x_2^2}{2\delta_1} - c_1r_1x_1 - c_2r_2x_2 - \delta_0y \end{aligned}$$

$$\leq 2c_1r_1K_1 + 2c_2r_2K_2 + \frac{c_1^2\sigma_1^2K_2^2x_1^2}{2\delta_1} + \frac{c_2^2\sigma_2^2K_1^2x_2^2}{2\delta_1} - c_1r_1x_1 - c_2r_2x_2 - \delta_0y.$$

So,  $\frac{dM}{dt} = K - \delta^*(c_1x_1 + c_2x_2 + y).$

Thus  $\limsup_{t \rightarrow \infty} M(t) \leq \frac{K}{\delta^*}$ , where  $K = 2c_1r_1K_1 + 2c_2r_2K_2 + \frac{c_1^2\sigma_1^2K_1^2K_2^2}{2\delta_1} + \frac{c_2^2\sigma_2^2K_1^2K_2^2}{2\delta_1}$  and  $\delta^* = \min\{r_1, r_2, \delta_0\}.$

Thereby, the solutions of the proposed model are bounded.

### 3.2 Existence of Biomass Stationary Points

Model (2) has seven equilibrium points, namely,  $E_0(0, 0, 0)$ ,  $E_1(K_1, 0, 0)$ ,  $E_2(0, K_2, 0)$ ,  $E_3(K_1, K_2, 0)$ ,  $E_4(0, \bar{x}_2, \bar{y})$ ,  $E_5(\bar{x}_1, 0, \bar{y})$  and  $E^*(x_1^*, x_2^*, y^*)$ . The equilibrium points  $E_0(0, 0, 0)$ ,  $E_1(K_1, 0, 0)$ ,  $E_2(0, K_2, 0)$  and  $E_3(K_1, K_2, 0)$  exist trivially. Now we drive the conditions under which remaining equilibrium points exist.

– Existence of  $E_4(0, \bar{x}_2, \bar{y})$  :  $x_2 = \bar{x}_2$ ,  $y = \bar{y}$  are the positive solutions of a system of equations given as

$$r_2\left(1 - \frac{\bar{x}_2}{K_2}\right) = \frac{m_2\bar{y}}{(1 + \alpha\bar{x}_2)(1 + \beta\bar{y})} = 0, \quad \frac{c_2m_2\bar{x}_2}{(1 + \alpha\bar{x}_2)(1 + \beta\bar{y})} - \delta_0 - \delta_1\bar{y} = 0. \tag{3}$$

Solving above both the equations, we obtain a 5-degree algebraic polynomial in terms of  $\bar{x}_2$ , given as:

$$A_5\bar{x}_2^5 + A_4\bar{x}_2^4 + A_3\bar{x}_2^3 + A_2\bar{x}_2^2 + A_1\bar{x}_2 + A_0 = 0, \tag{4}$$

where,  $A_5 = \left(\frac{c_2r_2^3\beta^2\alpha^2}{K_2^2}\right)$ ,  $A_4 = \left(-\frac{2c_2r_2^2\beta^2\alpha^2}{K_2} + \frac{2c_2r_2^2\beta^2\alpha}{K_2^2}\right)$ ,  $A_3 = \left(-\frac{4c_2r_2^2\beta^2\alpha}{K_2} + c_2r_2^2\beta^2\alpha^2 + \frac{c_2r_2^2\beta^2}{K_2^2} + \frac{2c_2m_2r_2\beta\alpha}{K_2} - \frac{\delta_0r_2\beta\alpha^2}{K_2} + \frac{\delta_1r_2\alpha^2}{K_2}\right)$ ,  $A_2 = \left(2c_2r_2^2\beta^2\alpha - \frac{2c_2r_2^2\beta^2}{K_2} - 2c_2m_2r_2\beta\alpha + \frac{2c_2m_2r_2\beta}{K_2} + \delta_0\alpha^2r_2\beta - \frac{2\delta_0r_2\beta\alpha}{K_2} - \delta_1r_2\alpha^2 + \frac{2\delta_1r_2\alpha}{K_2}\right)$ ,  $A_1 = \left(c_2r_2^2\beta^2 - 2c_2m_2\beta r_2 + \delta_0r_2\beta\left(2\alpha - \frac{1}{K_2}\right) - \delta_1r_2\left(2\alpha - \frac{1}{K_2}\right) + c_2m_2^2 - \delta_0m_2\alpha\right)$ ,  $A_0 = -\delta_0(m_2 - r_2\beta) - \delta_1r_2.$

By using Descarte’s rule of sign, (4) has at least one positive  $\bar{x}_2$  if

$$m_2 > r_2\beta.$$



Using this  $\bar{x}_2$  in first equation of (3), we get  $y = \frac{r_2(1+\alpha\bar{x}_2)\left(1-\frac{\bar{x}_2}{K_2}\right)}{m_2-r_2\beta(1+\alpha\bar{x}_2)\left(1-\frac{\bar{x}_2}{K_2}\right)}$ , which is positive under the condition  $m_2 > r_2\beta(1 + \alpha\bar{x}_2)\left(1 - \frac{\bar{x}_2}{K_2}\right)$ .

Therefore,  $E_4(0, \bar{x}_2, \bar{y})$  exists if

$$m_2 > \max \left\{ 1, (1 + \alpha\bar{x}_2)\left(1 - \frac{\bar{x}_2}{K_2}\right) \right\}.$$

- Existence of  $E_5(\tilde{x}_1, 0, \tilde{y})$  :  $x_1 = \tilde{x}_1, y = \tilde{y}$  are the positive solutions of a system of equations given by

$$r_1\left(1 - \frac{\tilde{x}_1}{K_1}\right) = \frac{m_1\tilde{y}}{a\tilde{x}_1^2 + b\tilde{x}_1 + c}, \quad \frac{c_1m_1\tilde{x}_1}{a\tilde{x}_1^2 + b\tilde{x}_1 + c} - \delta_0 - \delta_1\tilde{y} = 0. \tag{5}$$

By solving above both equations, again we get a 5-degree polynomial as in the previous one, and it is in terms of  $\tilde{x}_1$ , given as

$$B_5\tilde{x}_1^5 + B_4\tilde{x}_1^4 + B_3\tilde{x}_1^3 + B_2\tilde{x}_1^2 + B_1\tilde{x}_1 + B_0 = 0, \tag{6}$$

where,  $B_5 = \left(\frac{a^2\delta_1r_1}{m_1K_1}\right), B_4 = \left(-\frac{\delta_1r_1a^2}{m_1} + \frac{2ab\delta_1r_1}{m_1K_1}\right), B_3 = \left(-\frac{2ab\delta_1r_1}{m_1} + \frac{2ac\delta_1r_1}{m_1K_1} + \frac{\delta_1r_1b^2}{m_1K_1}\right), B_2 = \left(-\frac{\delta_1r_1b^2}{m_1} - \frac{2ac\delta_1r_1}{m_1} + \frac{2bc\delta_1r_1}{K_1m_1} - \delta_0a\right), B_1 = \left(-\frac{2\delta_1r_1bc}{m_1} + \frac{c^2\delta_1r_1}{m_1K_1} - \delta_0b + c_1m_1\right), B_0 = -\frac{\delta_1r_1c^2}{m_1} - \delta_0c$ . Again from Descarte’s rule of sign, (6) has at least one positive root  $\tilde{x}_1$  and using this in first equation of (5) we get

$$\tilde{y} = \frac{r_1}{m_1}\left(1 - \frac{\tilde{x}_1}{K_1}\right)(a\tilde{x}_1^2 + b\tilde{x}_1 + c),$$

and hence we obtain  $E_5(\tilde{x}_1, 0, \tilde{y})$ .

- Existence of  $E^*(x_1^*, x_2^*, y^*)$ :  
Interior equilibrium  $E^*$  is the positive solution of the system of equations given as:

$$r_1\left(1 - \frac{x_1^*}{K_1}\right) - \frac{m_1y^*}{ax_1^{*2} + bx_1^* + c} + \sigma_1x_2^*y^* = 0, \tag{7}$$

$$r_2\left(1 - \frac{x_2^*}{K_2}\right) - \frac{m_2y^*}{(1 + \alpha x_2^*)(1 + \beta y^*)} + \sigma_2x_1^*y^* = 0, \tag{8}$$

$$\frac{c_1m_1x_1^*}{ax_1^* + bx_1^* + c} + \frac{c_2m_2x_2^*}{(1 + \alpha x_2^*)(1 + \beta y^*)} - \delta_0 - \delta_1y^* = 0. \tag{9}$$

Since Eqs. (7–9) are complex, and hence it is not easy to prove the existence of interior equilibrium analytically. Thus we will show its existence numerically.

### 3.3 Stability Analysis

For local stability analysis of model (2), we have following findings:

- It is easy to see that the equilibrium point  $E_0(0, 0, 0)$  is a saddle point with unstable manifold along the  $x_1x_2$  plane and stable manifold along the  $y$ -axis.
- $E_1(K_1, 0, 0)$  is a saddle point with one dimensional stable manifold and two dimensional unstable manifold if  $\frac{c_1m_1K_1}{aK_1^2+bK_1+c} > \delta_0$  or with two dimensional stable manifold and one dimensional unstable manifold if  $\frac{c_1m_1K_1}{aK_1^2+bK_1+c} < \delta_0$ .
- $E_2(0, K_2, 0)$  is a saddle point with similar interpretation as of  $E_1$ .
- $E_3(K_1, K_2, 0)$  is locally asymptotically stable point, provided  $\frac{c_1m_1K_1}{aK_1^2+bK_1+c} + \frac{c_2m_2K_2}{(1+\alpha K_2)} < \delta_0$ , otherwise a saddle point.
- One of the eigenvalue of variational matrix for  $E_4(0, \bar{x}_2, \bar{y})$  is  $r_1 - \frac{m_1\bar{y}}{c} + \sigma_1\bar{x}_2\bar{y}$  and rest two of eigenvalues are given by the roots of equation given below.

$$\xi^2 + C_1\xi + C_2 = 0, \tag{10}$$

where,  $C_1 = \left(\frac{r_2\bar{x}_2}{K_2} - \frac{m_2\alpha\bar{x}_2\bar{y}}{(1+\alpha\bar{x}_2)^2(1+\beta\bar{y})} + \frac{c_2m_2\beta\bar{x}_2\bar{y}}{(1+\alpha\bar{x}_2)(1+\beta\bar{y})^2} + \delta_1\bar{y}\right)$  and  $C_2 = \left(\frac{r_2\bar{x}_2}{K_2} - \frac{m_2\alpha\bar{x}_2\bar{y}}{(1+\alpha\bar{x}_2)^2(1+\beta\bar{y})}\right) \left(\frac{c_2m_2\beta\bar{x}_2\bar{y}}{(1+\alpha\bar{x}_2)(1+\beta\bar{y})^2} + \delta_1\bar{y}\right) + \left(\frac{m_2\bar{x}_2}{(1+\alpha\bar{x}_2)(1+\beta\bar{y})}\right)\left(\frac{c_2m_2\bar{y}}{(1+\alpha\bar{x}_2)^2(1+\beta\bar{y})}\right)$ . From Routh–Hurwitz criteria the real part of all roots of (10) are negative iff  $C_1 > 0$  and  $C_2 > 0$ . Thus we can state the following theorem

**Theorem 2** *Model (2) is asymptotically stable in neighbourhood of stationary point  $E_4$  with three dimensional stable manifold, if  $r_1 < \frac{m_1\bar{y}}{c} - \sigma_1\bar{x}_2\bar{y}$  and  $r_2 > \frac{m_2K_2\alpha\bar{y}}{(1+\alpha\bar{x}_2)^2(1+\beta\bar{y})}$ .*

- Similarly one of the eigenvalue of Jacobian matrix corresponding to  $E_5(\tilde{x}_1, 0, \tilde{y})$  is  $r_2 - \frac{m_2\tilde{y}}{1+\beta\tilde{y}} + \sigma_2\tilde{x}_1\tilde{y}$  and rest of two eigenvalues are the roots of equation given by

$$\Pi^2 + D_1\Pi + D_2 = 0, \tag{11}$$

where,  $D_1 = \left(\frac{r_1\tilde{x}_1}{K_1} - \frac{m_1\tilde{y}(2a\tilde{x}_1^2+b\tilde{x}_1)}{(a\tilde{x}_1^2+b\tilde{x}_1+c)^2} + \delta\tilde{y}\right)$  and  $D_2 = \left(\frac{r_1\tilde{x}_1}{K_1} - \frac{m_1\tilde{y}(2a\tilde{x}_1^2+b\tilde{x}_1)}{(a\tilde{x}_1^2+b\tilde{x}_1+c)^2}\right)\delta\tilde{y} + \left(\frac{m_1\tilde{x}_1}{a\tilde{x}_1^2+b\tilde{x}_1+c}\right)\left(\frac{c_1m_1\tilde{y}(-a\tilde{x}_1^2+c)}{(a\tilde{x}_1^2+b\tilde{x}_1+c)^2}\right)$ . Again from Routh–Hurwitz criteria, we have the following theorem.

**Theorem 3** *The system (2) is asymptotically stable around the equilibrium  $E_5$  if  $r_2 < \frac{m_2\tilde{y}}{1+\beta\tilde{y}} - \sigma_2\tilde{x}_1\tilde{y}$  and  $r_1 > \frac{m_1K_1\tilde{y}(2a\tilde{x}_1^2+b\tilde{x}_1)}{\tilde{x}_1(a\tilde{x}_1^2+b\tilde{x}_1+c)^2}$ .*

– The variational matrix about  $E^*(x_1^*, x_2^*, y^*)$  is

$$J|_{E^*} = \begin{bmatrix} -\frac{r_1 x_1^*}{K_1} + \frac{m_1 y^* (2\alpha x_1^{*2} + b x_1^*)}{(\alpha x_1^{*2} + b x_1^* + c)^2} & \sigma_1 x_1^* y^* & -\frac{m_1 x_1^*}{\alpha x_1^{*2} + b x_1^* + c} + \sigma_1 x_1^* x_2^* \\ \sigma_2 x_2^* y^* & -\frac{r_2 x_2^*}{K_2} + \frac{m_2 \alpha x_2^* y^*}{(1 + \alpha x_2^*)^2 (1 + \beta y^*)} & -\frac{m_2 x_2^*}{(1 + \alpha x_2^*)(1 + \beta y^*)^2} + \sigma_2 x_1^* x_2^* \\ \frac{c_1 m_1 y^* (-\alpha x_1^{*2} + c)}{(\alpha x_1^{*2} + b x_1^* + c)^2} & \frac{c_2 m_2 y^*}{(1 + \alpha x_2^*)^2 (1 + \beta y^*)} & -\frac{c_2 m_2 \beta x_2^* y^*}{(1 + \alpha x_2^*)(1 + \beta y^*)^2} - \delta_1 y^* \end{bmatrix}$$

Characteristic equation corresponding to above variational matrix is

$$\lambda^3 + E_1 \lambda^2 + E_2 \lambda + E_3 = 0. \tag{12}$$

In equation (12), the multipliers  $E_1$ ,  $E_2$  and  $E_3$  are given as

$E_1 = -(k_{11} + k_{22} + k_{33})$ ,  $E_2 = (k_{22}k_{33} - k_{23}k_{32}) + (k_{11}k_{33} - k_{13}k_{31}) + (k_{11}k_{22} - k_{12}k_{21})$ , and  $E_3 = -(k_{11}(k_{22}k_{33} - k_{23}k_{32}) - k_{12}(k_{21}k_{33} - k_{23}k_{31}) + k_{13}(k_{21}k_{32} - k_{22}k_{31}))$ , where,  $k_{mn}$  for  $m, n = 1, 2, 3$  represent an entry in  $J|_{E^*}$ , in  $m^{th}$  row and  $n^{th}$  column. Again all eigenvalues of  $J|_{E^*}$  have negative real part iff  $E_1 > 0$ ,  $E_3 > 0$  and  $E_1 E_2 > E_3$ . Thus, we can state the following theorem.

**Theorem 4** *The interior equilibrium  $E^*(x_1^*, x_2^*, y^*)$  is asymptotically stable iff  $E_1 > 0$ ,  $E_3 > 0$  and  $E_1 E_2 - E_3 > 0$ .*

**Theorem 5** *The system (2) is globally asymptotically stable about the interior equilibrium  $E^*$  under the following conditions:  $\frac{r_1}{K_1} > \frac{m_1 y^* (a(K_1 + x_1^*) + b_1)}{(\alpha x_1^{*2} + b x_1^* + c)}$ ,  $\frac{r_2}{K_2} > \frac{\alpha m_2 y^*}{(1 + \alpha x_2^*)(1 + \beta y^*)}$ ,  $(\sigma_1 + \sigma_2 l_1)^2 y_M^2 < \left(\frac{r_1}{K_1} - \frac{m_1 y^* (a(K_1 + x_1^*) + b_1)}{(\alpha x_1^{*2} + b x_1^* + c)}\right) \left(\frac{r_2}{K_2} - \frac{\alpha m_2 y^*}{(1 + \alpha x_2^*)(1 + \beta y^*)}\right)$ ,  $\sigma_2^2 l_1^2 x_1^{*2} < \left(\frac{r_2}{K_2} - \frac{\alpha m_2 y^*}{(1 + \alpha x_2^*)(1 + \beta y^*)}\right) \left(\delta_1 + \frac{c_2 m_2 x_2^* \beta}{(1 + \beta y_M)(1 + \alpha x_2)(1 + \beta y^*)}\right)$ ,  $\left(\sigma_1 x_2^* + \frac{l_2 c_1 m_1 a K_1 x_1^*}{(\alpha x_1^{*2} + b x_1^* + c)}\right)^2 < \left(\frac{r_1}{K_1} - \frac{m_1 y^* (a(K_1 + x_1^*) + b_1)}{(\alpha x_1^{*2} + b x_1^* + c)}\right) \left(\delta_1 + \frac{c_2 m_2 x_2^* \beta}{(1 + \beta y_M)(1 + \alpha x_2)(1 + \beta y^*)}\right)$ .*

**Proof** Consider a positive definite function  $V$  as an appropriate Lyapunov function around  $E^*$  given as

$$V(x_1, x_2, y) = (x_1 - x_1^* - x_1^* \ln \frac{x_1}{x_1^*}) + l_1 (x_2 - x_2^* - x_2^* \ln \frac{x_2}{x_2^*}) + l_2 (y - y^* - y^* \ln \frac{y}{y^*}),$$

where  $l_1 = \frac{l_2 c_2 (1 + \beta y^*)}{(1 + \alpha x_2^*)}$  and  $l_2 = \frac{(\alpha x_1^{*2} + b x_1^* + c)}{c_1 c}$ . Now, after differentiating  $V$  with respect to time along with solution of (2) and with some algebraic manipulations, we get  $\frac{dV}{dt} = -\frac{1}{2} A_{11} (x_1 - x_1^*)^2 + A_{12} (x_1 - x_1^*) (x_2 - x_2^*) - \frac{1}{2} A_{22} (x_2 - x_2^*)^2 - \frac{1}{2} A_{22} (x_2 - x_2^*)^2 + A_{23} (x_2 - x_2^*) (y - y^*) - \frac{1}{2} A_{33} (y - y^*)^2 - \frac{1}{2} A_{11} (x_1 - x_1^*)^2 + A_{13} (x_1 - x_1^*) (y - y^*) - \frac{1}{2} A_{33} (y - y^*)^2$ ,

where,  $A_{11} = \frac{r_1}{K_1} - \frac{m_1 y^* (a(x_1 + x_1^*) + b_1)}{(\alpha x_1^{*2} + b x_1^* + c)(\alpha x_1^2 + b x_1 + c)}$ ,  $A_{22} = \frac{r_2}{K_2} - \frac{\alpha m_2 y^*}{(1 + \alpha x_2)(1 + \alpha x_2^*)(1 + \beta y^*)}$ ,  $A_{33} = \delta_1 + \frac{c_2 m_2 x_2^* \beta}{(1 + \beta y)(1 + \alpha x_2^*)(1 + \beta y^*)}$ ,  $A_{12} = \sigma_1 y + \sigma_2 l_1 y$ ,  $A_{13} = \sigma_1 x_2^* - \frac{l_2 c_1 m_1 a x_1 x_1^*}{(\alpha x_1^{*2} + b x_1^* + c)(\alpha x_1^2 + b x_1 + c)}$ ,  $A_{23} = \sigma_2 l_1 x_1^*$ .

So, using Sylvester’s criterion,  $\frac{dV}{dt}$  is negative definite under the hypothesis given in statement of the theorem. Therefore,  $E^*$  is globally asymptotically stable with the assumed conditions.

### 3.4 Bifurcation Assessment

**Theorem 6** *Coexistence equilibrium  $E^*$  is bifurcated from the planner equilibrium  $E_4$ , through a transcritical bifurcation, when parameter  $r_1$ , crosses its transcritical threshold value  $r_1 = r_1^{tc} = \frac{m_1 \bar{y}}{c} - \sigma_1 \bar{x}_2 \bar{y}$ .*

**Proof** To prove this theorem, we have to satisfy the conditions given in Sotomayor Theorem [9]. Consider,  $V = (v_1, v_2, v_3)^T$ ,  $W = (w_1, w_2, w_3)^T$  as the eigenvectors corresponding to zero eigenvalue of  $J|_{E_4}$  and  $J^T|_{E_4}$ , respectively. Here,  $v_1 = \frac{a_{22}a_{33} - a_{23}a_{32}}{a_{32}a_{21} - a_{22}a_{31}}$ ,  $v_2 = \frac{a_{23}a_{31} - a_{33}a_{21}}{a_{32}a_{21} - a_{22}a_{31}}$  and  $v_3 = 1$ , where  $a_{ij}$ , for  $i, j = 1, 2, 3$  is an entry in  $J|_{E_4}$  in  $i^{th}$  row and  $j^{th}$  column. Also  $W = (w_1, w_2, w_3)^T = (1, 0, 0)^T$ . Define,  $U(x_1, x_2, y) = (F_1, F_2, F_3)^T$ . Therefore,  $U_{r_1} = \left[ \frac{\partial F_1}{\partial r_1}, \frac{\partial F_2}{\partial r_1}, \frac{\partial F_3}{\partial r_1} \right]^T = \left[ x_1 \left( 1 - \frac{x_1}{K_1} \right), 0, 0 \right]^T$ . One can easily verify the transversality conditions:  $W^T U_{r_1}(E_4, r_1^{tc}) = 0$ ,  $W^T [DU_{r_1}(E_4, r_1^{tc})]V = v_1 \neq 0$ ,  $W^T [D^2U(E_4, r_1^{tc})(V, V)] = \left( -\frac{2r_1^{tc}}{K_1} + \frac{2m_1 b \bar{y}}{c^2} \right) v_1 v_1 + 2\sigma_1 \bar{y} v_1 v_2 - 2 \left( \frac{2m_1 b}{c^2} + \sigma_1 \bar{x}_2 \right) v_1 v_3$ . Hence, if  $\left( -\frac{2r_1^{tc}}{K_1} + \frac{2m_1 b \bar{y}}{c^2} \right) v_1 v_1 + 2\sigma_1 \bar{y} v_1 v_2 - 2 \left( \frac{2m_1 b}{c^2} + \sigma_1 \bar{x}_2 \right) v_1 v_3 \neq 0$  then can say that at  $r_1 = r_1^{tc}$ ,  $E^*$  is bifurcated from  $E_4$  by the transcritical bifurcation.

**Note:** A similar result can be established for transcritical bifurcation involving interior equilibrium  $E^*$  and predator free equilibrium  $E_3$  (depicted in numerical simulation). We also provide conditions under which our 3D-model (2) undergoes Hopf-bifurcation around the positive equilibrium  $E^*$  when the parameter  $\alpha$  passes its some critical value  $\alpha^{hf}$ .

**Theorem 7** *The necessary and sufficient prerequisites for occurrence of Hopf-bifurcation of system (2) around  $E^*$  at  $\alpha = \alpha^{hf}$  are*

1.  $E_1 > 0, E_3 > 0$ .
2.  $E_1 E_2 - E_3 = 0$ .
3.  $\frac{d}{d\alpha} (Re(\lambda))_{\alpha=\alpha^{hf}} \neq 0$ . This condition holds iff  $\frac{dR}{d\alpha} \neq 0$ , where  $R = E_1 E_2 - E_3$ .

**Proof** Proof of this theorem readily follows as in [8].

## 4 Numerical Simulation

$$\begin{aligned}
 r_1 = 7, K_1 = 10, m_1 = 0.45, a = 0.025, b = 0.1, c = 7, \sigma_1 = 0.001, r_2 = 5, K_2 = 15, m_2 = 0.1, \\
 \alpha = 0.07, \beta = 0.0025, \sigma_2 = 0.004, c_1 = 0.2222, c_2 = 0.7, \delta_0 = 0.01, \delta_1 = 0.001.
 \end{aligned}
 \tag{13}$$

For the set of parameters give in (13),  $E_0(0, 0, 0)$ ,  $E_1(10, 0, 0)$ ,  $E_2(0, 15, 0)$ ,  $E_3(10, 15, 0)$ ,  $E_4(0, 1.183603, 56.973631)$ ,  $E_5(5.600137, 0, 57.108613)$  are saddle points whereas  $E^*(3.982544, 0.573808, 73.695332)$  is a stable focus with  $(-0.033869 \pm$

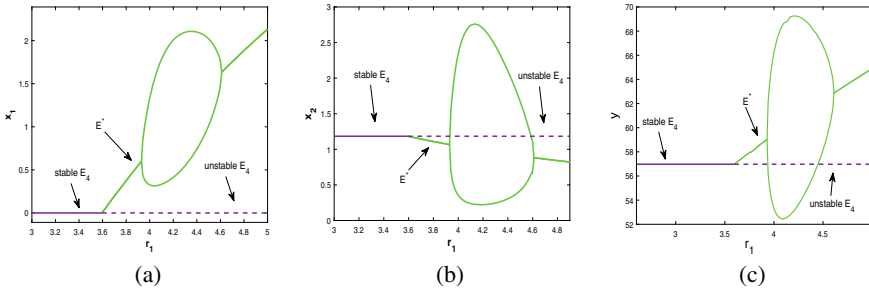


**Fig. 1**  $E_4$  is going for transcritical bifurcation with losing its stability which leads to generation of  $E^*$  and  $E^*$  changes its stability twice via Hopf-bifurcation on further increase of  $r_1$  with parameters same as in (13)

0.436450i, -2.108830) as eigenvalues. The system goes through transcritical as well as Hopf-bifurcation for the parameter  $r_1$  (Fig. 1). As long as  $r_1$  lies in the interval  $[0.1, r_1^{tc})$ ,  $E_4$  is a stable focus and in this interval  $E^*$  is not biologically feasible. At  $r_1 = r_1^{tc} = 3.595156$ ,  $E_4$  undergoes transcritical bifurcation to become unstable with  $\dim(W^u(E_4)) = 1$  and  $\dim(W^s(E_4)) = 2$ . The stable and unstable branches of  $E_4$  are shown by solid and dashed curves in purple colour, respectively. At this critical value,  $r_1^{tc}$ ,  $E^*$  is generated as a spiral sink. From Fig. 1, we can observe that, on further increase of  $r_1$ ,  $E^*$  passes through Hopf-bifurcation at  $r_1 = r_1^{hf1} = 3.930962$ , and on keep increasing  $r_1$ ,  $E^*$  again endures Hopf-bifurcation at  $r_1 = r_1^{hf2} = 4.599987$  to become stable and it maintains this behavior on further increment of  $r_1$ . So, we observed that  $E^*$  is bifurcated from  $E_4$  via a transcritical bifurcation and  $E^*$  switches its stability two times by means of Hopf-bifurcation with respect to parameter  $r_1$ . In this figure,  $E^*$  is indicated by the green colour.

Now, Keeping all the parameters fixed given in (13), when we use inverse measure of predator’s immunity  $a$ , as a control parameter then system (2) experiences Hopf-bifurcation in the vicinity of  $E^*$ . For  $a < a^{hf} = 0.072198$ ,  $E^*$  remains stable and at  $a = a^{hf}$ ,  $E^*$  becomes non-hyperbolic and then turn into a spiral source on continue increment of  $a$ . For an example, concerning with  $a$  as a bifurcation parameter, we simulate model (2) for  $a = 0.04 < a^{hf}$  and  $a = 0.08 > a^{hf}$ , showing the stable and unstable nature of the system, respectively. From Fig. 2(a), we can see that as long as  $a < a^{hf}$ , system remains stable. As  $a$  crosses its critical value  $a^{hf}$ , system go through Hopf-bifurcation to become unstable. The unstable nature of  $E^*$  is depicted in Fig. 2(b).

Now, we talk about the coefficient of help  $\sigma_2$ . When help provided by  $x_1$  to  $x_2$  is less than a threshold value, system remains stable but as it becomes  $\sigma_2 = \sigma_2^{hf} = 0.005389$ ,  $E^*$  suffers Hopf-bifurcation. So, the model (2) turns to be an unstable system. We have presented two illustrations of 3D-phase portraits for this case in Fig. 3. Firstly for  $\sigma_2 = 0.0045$  (Fig. 3(a)), we see that,  $E^*$  remains continue to be a stable focus until  $\sigma_2$  reaches its critical value. Secondly from  $\sigma_2 = 0.0065$ , (Fig. 3(b)), it is clear that system becomes unstable for  $\sigma_2 > \sigma_2^{hf}$ . So, the excess amount of help

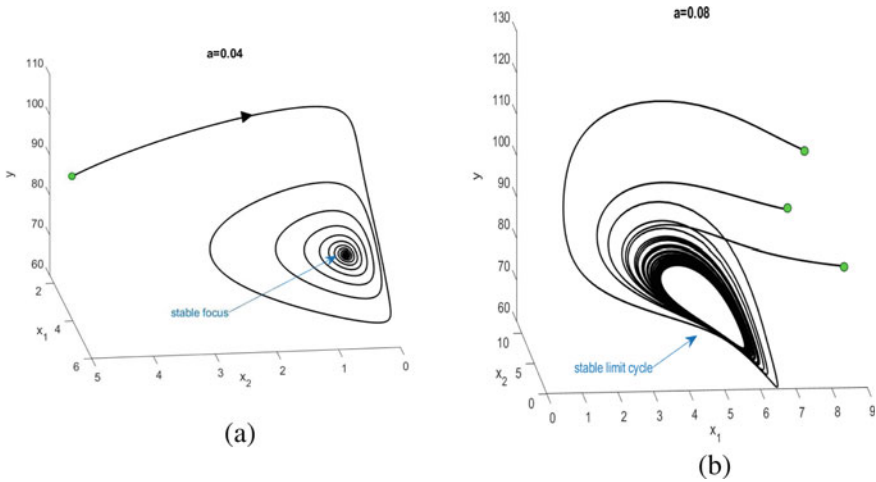


**Fig. 2** Stable nature of system for  $a = 0.04 < a^{hf}$  (Fig. a) and unstable nature for  $a = 0.08 > a^{hf}$  (Fig. b) with all parameters same as in (13)

from  $x_1$  to  $x_2$  makes the system unstable.

For  $\delta_0$ , the system experiences the change of stability twice by Hopf-bifurcation and then a transcritical bifurcation on its further increment. This involves the predator free equilibrium  $E_3$  and the coexistence equilibrium  $E^*$ . For  $\delta_0 < \delta_0^{hf1} = 0.049805$ ,  $E^*$  remains a stable focus and at  $\delta_0^{hf1}$ , the system suffers Hopf-bifurcation around  $E^*$ . Then it again become stable around  $E^*$  via Hopf-bifurcation at  $\delta_0^{hf2} = 0.102547$ . The interval  $(\delta_0^{hf1}, \delta_0^{hf2})$  corresponds to a stable limit cycle. For  $\delta_0 < \delta_0^{tc} = 0.607423$ ,  $E_3$  continue to be a proper unstable node. At  $\delta_0^{tc}$ ,  $E_3$  becomes a stable node, and  $E^*$  disappears through the transcritical bifurcation. These two bifurcations are shown simultaneously in Fig. 4 through three corresponding bifurcation diagrams. In this figure,  $E^*$  is indicated with green colour where unstable and stable components of  $E_3$  are shown by dashed and solid curves in purple colour, respectively.

Moreover, we have drawn Fig. 5 to depict the distribution of regions according to the feasibility of  $E_3$ ,  $E_4$  and  $E^*$  in the  $r_1\delta_0$ -plane. In region  $R_1$ ,  $E_3$  and  $E_4$  are the feasible equilibria. Region  $R_1$  and  $R_2$  are separated by the transcritical curve marked with red colour. When we moves from  $R_1$  to  $R_2$ , the interior equilibrium  $E^*$  is generated via transcritical bifurcation. Region  $R_2$  and  $R_3$  are separated by a blue coloured line  $\delta_0 = 0.512195$ . When  $\delta_0$  becomes greater than 0.512195,  $y$  component of  $E_4$  remains negative with all values of  $r_1$ , so  $E_4$  becomes non-feasible in  $R_3$ . Next, when  $\delta_0 > 0.607423$ ,  $E^*$  disappears beyond the transcritical curve  $\delta_0 = 0.607423$  marked with pink colour. So in region  $R_4$ ,  $E_3$  is the only feasible equilibrium point.

To show the bistability phenomenon in the system, we choose the following set of parameters:

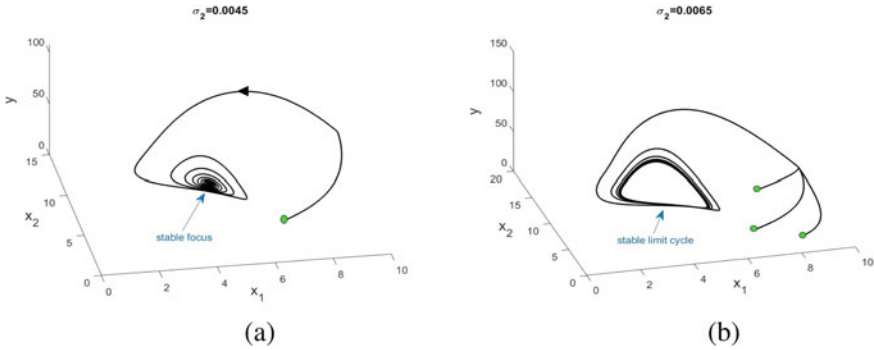


**Fig. 3** Using  $\sigma_2$  as the control parameter, phase portrait (Fig. a) shows the stable focus for  $\sigma_2 = 0.0045$  and (Fig. b) exhibits a stable limit cycle for  $\sigma_2 = 0.0065$  with parameters fixed in (13)

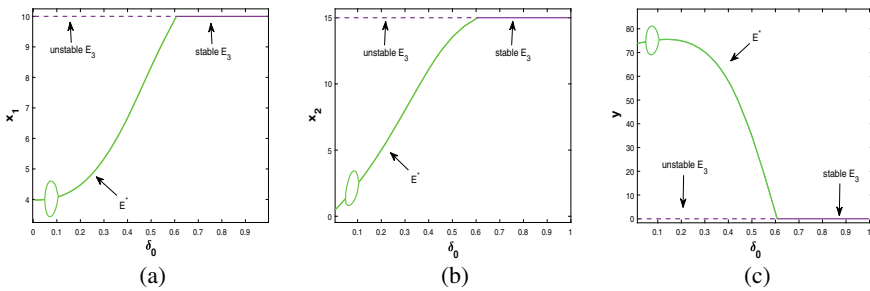


**Fig. 4**  $E^*$  changes its stability twice by Hopf-bifurcation and on further increase of  $\delta_0$ ,  $E^*$  disappears and  $E_3$  becomes stable via transcritical bifurcation, with parameters fixed in (13)

$$\begin{aligned}
 r_1 = 3, K_1 = 10, m_1 = 0.4, a = 0.1, b = 0.08, c = 0.11, \sigma_1 = 0.01, r_2 = 4, K_2 = 7, m_2 = 0.62, \\
 \alpha = 0.01, \beta = 0.03, \sigma_2 = 0.02, c_1 = 0.4, c_2 = 0.63, \delta_0 = 0.1, \delta_1 = 0.02.
 \end{aligned}
 \tag{14}$$

For set of parameters (14), we have two locally asymptotically stable equilibrium points; one is coexistence equilibrium  $E^*(7.792154, 0.593490, 12.534084)$ , and the other one is planner equilibrium  $E_4(0, 0.751129, 7.025585)$ . We have illustrated this characteristic of the system through a phase portrait diagram given in Fig. 6(a) in which two solutions started from two different initial conditions converge to these two different equilibrium points. We have also plotted their basin of attraction in Fig. 6(b).

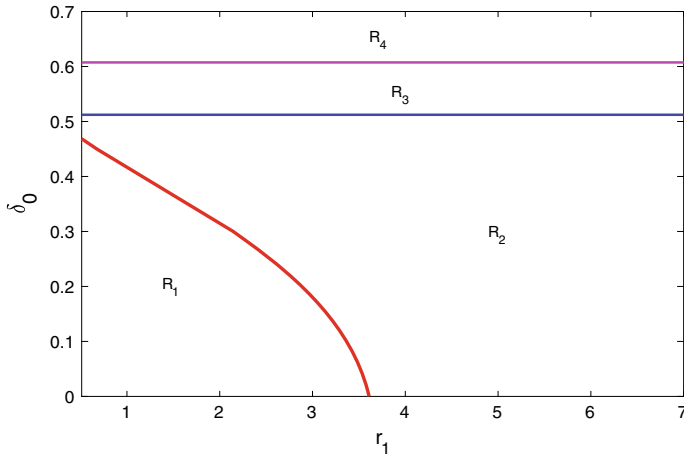


**Fig. 5** Distribution of regions for existence of  $E_3$ ,  $E_4$  and  $E^*$  in  $r_1\delta_0$ -plane with parameters same as in (13)

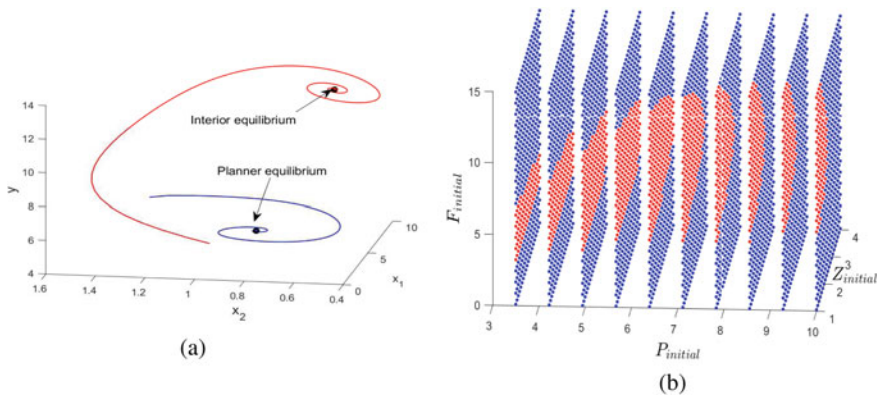


**Fig. 6** In Fig. (a) solutions in red and blue color are tending to  $E^*$  and  $E_4$ , respectively. Figure (b) represent the basin of attractions (red dots for interior and blue dots for planner equilibrium point) where  $P(0) \in [3.5, 10]$ ,  $Z(0) \in [1, 4]$  and  $F(0) \in [0.1, 15]$ , with parameters fixed in (14)

### 5 Conclusion

In the present work, we have formulated a prey-predator model with cooperation between two types of prey against a predator. Both the prey species are assumed to grow logistically whereas predator consume the one prey via Holling type-IV type response and another prey via Crowley–Martin type response. Firstly, we have proved that the model is biologically well-posed having the quality of being bounded in a compact domain  $\Omega$  of  $R_+^3$ . In the dynamics of the system, we study the existence of seven equilibrium points. During the stability analysis, we notice that  $E_0$ ,  $E_1$  and



$E_2$  always behave like saddle points, while  $E_3$ ,  $E_4$  and  $E_5$  are stable under some conditions. We also studied the global stability of  $E^*$  by picking an appropriate Lyapunov function. Further, we have analyzed the transcritical as well as Hopf-bifurcations for the system involving  $E_4$ ,  $E^*$  and  $E_3$ ,  $E^*$ . From the bifurcation diagrams for  $r_1$ , it can be noticed that on increase of  $r_1$ ,  $x_1$  increases which increase the efficiency of their group defence and so predator shifts its attention to prey  $x_2$  which decreases the density of  $x_2$  population. When we use  $a$  as the bifurcation parameter,  $x_1$  increases with a partial decrement in  $x_2$ . Now, as when we increase  $a$  more than a threshold value  $a = a^{hf}$ , there is a rise of periodic oscillations due to Hopf-bifurcation. Most importantly, when the help ( $\sigma_2$ ) provided by  $x_1$  to  $x_2$  is increased, there is a growth in the population density of  $x_2$  but this increased help imparts a negative effect on  $x_1$  population due to its sacrifice in helping  $x_2$ . Raising this help against a certain limit becomes a cause of instability in the system. The system also shows the property of bistability. From numerical simulation, we can see that our system shows much more rich dynamical behavior than the existing studies. Thus we hope that our work can be a useful source for ecologists to explore different segments of experimental and theoretical ecology in a better way.

## References

1. Barnard, C.J.: Animal Behaviour: Ecology and Evolution. Springer Science & Business Media (2012)
2. Dugatkin, L.A.: Cooperation among Animals: An Evolutionary Perspective. Oxford University Press on Demand (1997)
3. Tripathi, J.P., Abbas, S., Thakur, M.: Local and global stability analysis of a two prey one predator model with help. Commun. Nonlinear Sci. Numer. Simul. **19**(9), 3284–3297 (2014)
4. Mishra, P., Raw, S.N.: Dynamical complexities in a predator-prey system involving teams of two prey and one predator. J. Appl. Math. Comput. **61**(1–2), 1–24 (2019)
5. Mondal, S., Samanta, G.P.: Dynamical behaviour of a two-prey and one-predator system with help and time delay. Energy Ecology Environ. **5**(1), 12–33 (2020)
6. Alsakaji, H.J., Kundu, S., Rihan, F.A.: Delay differential model of one-predator two-prey system with Monod-Haldane and Holling type II functional responses. Appl. Math. Comput. **397**, 125919 (2021)
7. Ferrara, M., Gangemi, M., Pansera, B.A.: Dynamics of a delayed mathematical model for one predator sharing teams of two preys. Appl. Sci. **23**, 52–61 (2021)
8. Tripathi, J.P., Jana, D., Tiwari, V.: A Beddington-DeAngelis type one-predator two-prey competitive system with help. Nonlinear Dyn. **94**(1), 553–573 (2018)
9. Perko, L.: Differential Equations and Dynamical Systems, vol. 7. Springer Science & Business Media (2013)

# Mathematical Model of Solute Transport in a Permeable Tube with Variable Viscosity



M. Varunkumar 

**Abstract** The purpose of this paper is to investigate the influence of variable viscosity on solute transfer in fluid flow through a permeable tube with possible applications to the blood flow in glomerular capillaries. The difference in transcapillary hydrostatic pressure and the equivalent difference in colloid osmotic pressure regulates solute transport through the glomerular capillary wall (Starling's law). Fluid flow in a capillary is assumed to be viscous, incompressible, and Newtonian with variable viscosity. The nonlinear and coupled equations regulating fluid flow and solute transport are solved analytically and numerically. Graphs have been used to discuss the impacts of varying viscosity and flow parameters on hydrostatic and osmotic pressures, and solute concentrations using a set of physiological data. It is observed that increasing the viscosity coefficient raises the hydrostatic pressure while decreasing the osmotic pressure at the capillary's end. As the viscosity coefficient increases, the solute concentration at the exit falls and the solute clearance increases through the capillary wall.

**Keywords** Starling's law · Ultrafiltration · Variable viscosity · Permeable wall · Finite difference method

## 1 Introduction

The kidneys have two primary functions. They perform two functions: first, they excrete the large majority of waste products produced during metabolism, and second, they regulate the concentrations of the vast majority of body fluids. Insight into the mechanisms of glomerular ultrafiltration and blood waste removal, which

---

M. Varunkumar (✉)

Department of Basic Sciences and Humanities, GMR Institute of Technology, Rajam 532127, Andhra Pradesh, India  
e-mail: [varun.nitw@gmail.com](mailto:varun.nitw@gmail.com)

Department of Mathematics, School of Advanced Sciences, VIT-AP University, Amaravati 522237, Andhra Pradesh, India

© The Author(s), under exclusive license to Springer Nature Switzerland AG 2022  
S. Banerjee and A. Saha (eds.), *Nonlinear Dynamics and Applications*,  
Springer Proceedings in Complexity,  
[https://doi.org/10.1007/978-3-030-99792-2\\_85](https://doi.org/10.1007/978-3-030-99792-2_85)

1001

create urine. Normally, the capillaries walls pass roughly one-fifth to one-third of the amount of blood plasma entering each glomerulus. This fluid's composition is close to that of an ideal ultrafiltrate, with solute concentrations similar to plasma water. The development of this ultrafiltrate is controlled by the driving factors that dictate fluid flow through the capillaries, specifically the imbalance between transcapillary hydrostatic and colloid osmotic pressures. Ultrafiltrate plasma travels into Bowman's Space as a result of these pushing factors. Several theoretical and mathematical models developed to describe the dynamics of ultrafiltration assumed that the glomerulus's local driving factors for fluid transfer were evenly distributed throughout the entire glomerular capillary network [1–4].

A study by Brenner et al. [5, 6] focused on glomerular pressure measurements at the afferent and efferent ends of the glomerulus, as well as the glomerular filtering rate of single kidney nephrons, in addition to extravascular pressures in Bowman's space, solute concentrations, and colloid osmotic pressure. Deen et al. [7] examined the relationship between ultrafiltration and the rise in plasma protein concentration caused by ultrafiltration, and their findings led them to the conclusion that the overall filtration rate rises as blood volume flow rises. The models for glomerular ultrafiltration proposed by Marshal and Trowbridge [8] and Huss et al. [9] eliminated the assumption of a constant axial pressure gradient and regarded the intraluminal pressure gradient to be dependent on the axial distance. As seen in Papenfuss and Gross [10], a model developed by them examined the effects of intraluminal pressure drop and wall permeability on glomerular ultrafiltration. Papenfuss and Gross [11] and Salathe [12] investigated fluid exchange and solute transport in capillary tissue under the assumption that concentrations were identical at each cross-section. Axially, the concentration profiles were determined by assuming the capillary wall as impermeable and applying a constant hydrostatic pressure to the solute transfer in capillary, as done by Deen et al. [13].

Ross [14] proposed a mathematical model for mass transfer in fluid flow through a capillary membrane with a tiny radial fluid flux (ultrafiltration) assumed to be zero by zero osmotic pressure. In addition, it should be mentioned that the ultrafiltration process is regulated by hydrostatic and oncotic pressure differences (Starling's theory) as well as the solute transported across the permeable wall by diffusion and convection as investigated by Chaturani and Ranganatha [15]. In a porous tube with varying permeability, Varun and Muthu [16] obtained a solution for the transport of solutes.

The relationship between fluid viscosity and solute concentration is significant in the filtering process. The viscosity is treated as a constant in the previous research, but in reality, it is dependent on a wide range of fluid characteristics ([17, 18]). A steady-state boundary layer with changing diffusivity and viscosity, as explored by Davis and Leight [20], was considered by Davis and Sherwood [19]. For concentration-dependent viscosity and diffusion coefficient, Bowen and Williams [21] introduced cross flow ultrafiltration. As a result of this inspiration, the impact of varying viscosity is examined in this article.

## 2 Mathematical Model

Consider a fluid flow through a rigid cylindrical permeable tube with a radius  $R$  and a length  $L$  (refer Fig. 1). The set-up is considered to be axisymmetric, with axial and radial directions  $z$  and  $r$ , and corresponding velocity components  $v(r, z)$ (radial) and  $u(r, z)$ (axial). The following are the equations that govern viscous, incompressible Newtonian fluid flow and solute transport ([15, 16]):

$$\frac{\partial u}{\partial z} + \frac{\partial v}{\partial r} + \frac{v}{r} = 0 \tag{1}$$

$$u \frac{\partial u}{\partial z} + v \frac{\partial u}{\partial r} + \frac{1}{\rho} \frac{\partial P}{\partial z} - 2\mu(r) \frac{\partial^2 u}{\partial z^2} - \frac{1}{\rho r} \frac{\partial}{\partial r} \left( r\mu(r) \left( \frac{\partial v}{\partial z} + \frac{\partial u}{\partial r} \right) \right) = 0 \tag{2}$$

$$u \frac{\partial v}{\partial z} + v \frac{\partial v}{\partial r} + \frac{1}{\rho} \frac{\partial P}{\partial r} - 2 \frac{\partial}{\partial r} \left( \mu(r) \frac{\partial v}{\partial r} \right) - \frac{2}{r} \mu(r) \left( \frac{\partial v}{\partial r} - \frac{v}{r} \right) - \frac{\partial}{\partial z} \left( \mu(r) \left( \frac{\partial v}{\partial z} + \frac{\partial u}{\partial r} \right) \right) = 0 \tag{3}$$

$$v \frac{\partial c}{\partial r} + u \frac{\partial c}{\partial z} - D \left( \frac{\partial^2 c}{\partial r^2} + \frac{\partial^2 c}{\partial z^2} + \frac{1}{r} \frac{\partial c}{\partial r} \right) = 0 \tag{4}$$

where  $P$ ,  $\mu(r)$  and  $\rho$  are the fluid’s pressure, variable viscosity, and density, respectively. The solute concentration is denoted by  $c$ , while the diffusion coefficient is denoted by  $D$ .

The boundary conditions are expressed as follows ([15, 22, 23]):

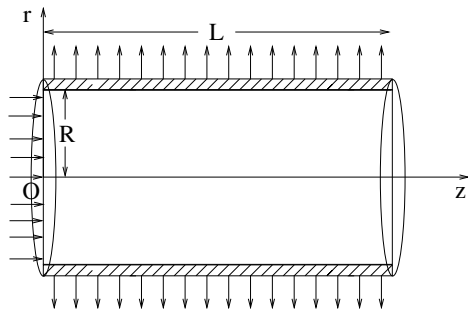
At  $z = 0$ ,

$$c = c_0, \quad \Delta P = \Delta P_a, \quad \int_0^R 2\pi r u(r, 0) dr = Q_0 \tag{5}$$

At  $r = 0$ ,

$$v = 0, \quad \frac{\partial u}{\partial r} = 0, \quad \frac{\partial c}{\partial r} = 0 \tag{6}$$

**Fig. 1** Geometric model of the glomerular capillary



At  $r = R$ ,

$$v = k(\Delta P - \sigma \Delta \pi) = V_R(z), u = 0, -D \frac{\partial c}{\partial r} = (T_R - 1)V_R \Phi + h(c - c_T) \quad (7)$$

The second boundary condition in (7) is stated according to Starling's hypothesis, which states that the flow velocity through the capillary wall is proportional to the difference between the hydrostatic and osmotic pressure differences. According to the third boundary condition in (7), the solute flow through membrane equals the solute flux via the interface. The product of solute permeability ( $h$ ) and concentration difference ( $c(r = R) - c_T$ ) gives the solute transported by ordinary diffusion via the membrane interface.  $((T_R - 1)V_R)$  is the solute flux through membrane pores.  $\Phi = \begin{cases} c; & V_R > 0 \\ c_T; & V_R < 0 \end{cases}$ ,  $\Delta P = P - P_T$ ,  $\Delta \pi = \pi - \pi_T$ , the hydrostatic pressures within and outside the capillary wall are  $P$  and  $P_T$ , respectively, while the corresponding osmotic pressures are  $\pi$  and  $\pi_T$ . The volume flow rate and hydrostatic pressure at channel's entry are  $Q_0$  and  $P_a$ . The wall's hydraulic permeability is  $k$ , and the reflection coefficient is  $\sigma$  ([24]).  $P_T$  and  $\pi_T$  are assumed to be constants. Here,  $c_0$  and  $c_T$  are represent the solute concentration at the tube's entry, and concentration outside the channel, respectively.  $h$  and  $T_R$  are represent the solute permeability at the wall, and transmittance coefficient, respectively.

In the present study, we considered the connection between osmotic pressure  $\pi$  and solute concentration  $c(r, z)$  as:

$$\pi(c) = 0.009 c^3 + 0.16 c^2 + 2.1 c \quad (8)$$

## 2.1 Non-dimensionalization

The non-dimensional quantities listed below are introduced in Eqs. (1)–(8):  $\hat{z} = z/R$ ,  $\hat{r} = r/R$ ,  $\hat{u} = u/U_0$ ,  $\hat{v} = v/U_0$ ,  $\hat{V}_R = V_R/U_0$ ,  $\hat{c} = c/c_0$ ,  $\hat{c}_T = c_T/c_0$ ,  $\Delta \hat{\pi} = \Delta \pi / \Delta P_a$ ,  $\Delta \hat{P} = \Delta P / \Delta P_a$ ,  $\hat{b}_1 = b_1 / (\Delta P_a / c_0)$ ,  $\hat{b}_2 = b_2 / (\Delta P_a / c_0^2)$ ,  $\hat{b}_3 = b_3 / (\Delta P_a / c_0^3)$ ,  $\hat{J}_S = J_S / (c_0 D / R)$ ,  $\hat{J}_C = J_C / Q_0 c_0$ ,  $\hat{\mu} = \mu / \mu_0$ ,  $\hat{Q} = Q / Q_0$ ,  $Q_0 = \pi R^2 U_0$ . In glomerular capillaries, axial diffusion is modest in comparison to radial diffusion [7]. There are no end effects since the tube length to radius ratio is expected to be so enormous. In addition, net radial flow is likewise minimal in comparison to average axial flow and inertial effects can be ignored (The Reynolds number is of  $10^{-3}$ ). The governing equations (1)–(8), which are based on non-dimensional quantities and assumptions, become (after dropping caps)

$$\frac{\partial u}{\partial z} + \frac{1}{r} \frac{\partial}{\partial r} (rv) = 0 \quad (9)$$

$$\frac{\partial(\Delta P)}{\partial z} = \frac{1}{R_p} \frac{1}{r} \left[ \frac{\partial}{\partial r} \left( r \mu(r) \frac{\partial u}{\partial r} \right) \right] \tag{10}$$

$$\frac{\partial(\Delta P)}{\partial r} = 0 \tag{11}$$

$$v \frac{\partial c}{\partial r} + u \frac{\partial c}{\partial z} = \frac{1}{Pe} \left[ \frac{\partial^2 c}{\partial r^2} + \frac{1}{r} \frac{\partial c}{\partial r} \right] \tag{12}$$

The non-dimensional boundary conditions leading to,

At  $z = 0$ ,

$$c = 1, \quad \Delta P = 1, \quad \int_0^1 2ru(r, 0)dr = 1 \tag{13}$$

At  $r = 0$ ,

$$v = 0, \quad \frac{\partial u}{\partial r} = 0, \quad \frac{\partial c}{\partial r} = 0 \tag{14}$$

At  $r = 1$ ,

$$v = \epsilon R_p (\Delta P - \sigma \Delta \pi) = V_R(z), \quad u = 0, \quad \frac{\partial c}{\partial r} = Pe(1 - T_R) V_R \Phi + Sh(c_T - c) \tag{15}$$

where,  $Pe = U_0 R / D$ ,  $Sh = h R / D$ ,  $R_p = (R \Delta P_a) / (\mu_0 U_0)$ , and  $\epsilon = k \mu_0 / R$  denote the Peclet number, the Sherwood number, the non-dimensional parameter and the filtration coefficient, respectively.

### 3 Method of Solution

The axial and radial velocities are calculated by solving Eqs. (9) and (10) using the conditions (14) and (15) as follows:

$$u(r, z) = -\frac{R_p}{2} \frac{d(\Delta P)}{dz} \int_r^1 \frac{r}{\mu(r)} dr \tag{16}$$

$$v(r, z) = \frac{R_p}{4} \frac{d^2(\Delta P)}{dz^2} \left( r \int_r^1 \frac{r}{\mu(r)} dr + \frac{1}{r} \int_0^r \frac{r^3}{\mu(r)} dr \right). \tag{17}$$

Equation (17) and the second boundary condition of (15) produce the equation for hydrostatic pressure,

$$\frac{d^2(\Delta P)}{dz^2} + \frac{4\epsilon}{I_1}(\sigma \Delta \pi - \Delta P) = 0. \quad (18)$$

The second and third conditions of (13) are written in the following form,

$$\Delta P = 1, \quad \frac{d\Delta P}{dz} = -\frac{1}{R_p I_2} \quad \text{at } z = 0 \quad (19)$$

$$\Delta \pi = 0.009[c^3 - c_T^3] + 0.16[c^2 - c_T^2] + 2.1[c - c_T], \quad (20)$$

$$I_1 = \int_0^1 \frac{r^3}{\mu(r)} dr, \quad I_2 = \int_0^1 r \left( \int_r^1 \frac{r}{\mu(r)} dr \right) dr \quad (21)$$

The viscosity affects the integrations in Eqs. (16)–(19). This study used the exponential viscosity model, which is provided as [17].

$$\mu(r) = e^{-\alpha r} \quad (22)$$

where  $\alpha$  denotes viscosity. The exponential type of viscosity was used in all of the calculations. Due to their dependency, the solutions of Eqs. (12) and (18), hydrostatic pressure ( $\Delta P$ ), and solute concentration ( $c$ ) are difficult to derive analytically in a closed form expression. Using the relevant boundary conditions of (13), (14) and (15), get numerical solutions for (12) and (18) correspondingly. For solute concentration, Eq. (12) is solved, which is linked with Eqs. (18), (16), (17) and (20), along with  $u$ ,  $v$  and  $\Delta P$  quantities. The solution technique was explained in detail by Varun and Muthu [16].

## 4 Results and Discussions

To understand the influence of variable viscosity during filtering, a mathematical model of solute transfer through a permeable tube was developed. Computations were performed utilizing physiological data from rat glomerular capillaries (Chaturani and Ranganatha [15]). The observed findings for  $\alpha = 0$  (zero viscosity) are in excellent accord with earlier research [15, 16]. The viscosity is modelled as an exponentially decreasing function of radial distance, with decreasing fluid viscosity as the viscosity parameter is increased. Viscosity parameter ( $\alpha$ ) and emerging parameters have substantial influence on flow quantities such as hydrostatic and osmotic pressures, and solute concentration investigated.

**Hydrostatic Pressure and Osmotic Pressure:** Figures 2 and 3 illustrate the distribution of hydrostatic pressure ( $\Delta P$ ) and osmotic pressure ( $\Delta \pi$ ) profiles for distinct values of viscosity parameter  $\alpha$  and other emerging parameters with regard to axial distance  $z$ . In accordance with the experimental results, the hydrostatic and

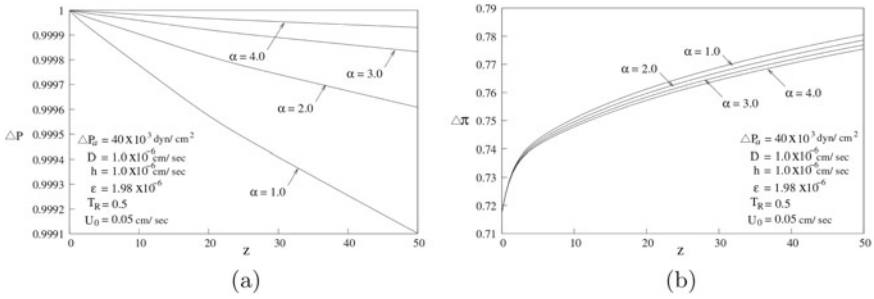


**Fig. 2** Effect of viscosity parameter ( $\alpha$ ) on hydrostatic and osmotic pressure distributions

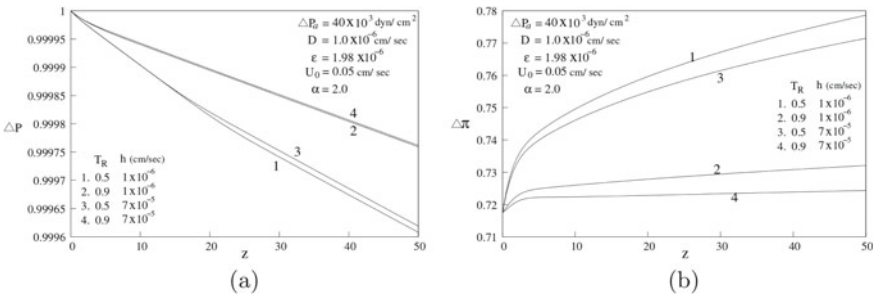


**Fig. 3** Effects of  $T_R$  and  $h$  on hydrostatic and osmotic pressure distributions

osmotic pressure curves may be seen in [23]. Osmotic pressure  $\Delta\pi$  rises nonlinearly as the axial length of the capillary decreases because of the linear reduction in  $\Delta P$ .

Figure 2 shows the effect of the viscosity parameter ( $\alpha$ ) on hydrostatic pressure and osmotic pressure. It is noticed that as the parameter  $\alpha$  is increased,  $\Delta P$  increases along the axial length. This indicates that driving fluids with greater viscosities requires a higher pressure (Fig. 2a). When predicted, the osmotic pressure ( $\Delta\pi$ ) values drop as the viscosity parameter ( $\alpha$ ) is increased in the  $z$ – direction (Fig. 2b). Figure 3 shows that solute wall permeability  $h$  and transmittance coefficient  $T_R$  have only a little impact on the  $\Delta P$  profiles. The osmotic pressure falls throughout the axial length as  $T_R$  and  $h$  rise, indicating that the solute has crossed the channel wall. The increase in  $T_R$  values indicates greater solute transfer across the capillary wall and as a result,  $\Delta\pi$  falls in the axial direction.

**Concentration Profiles  $c$ :** Figure 4 depicts the impact of the viscosity parameter ( $\alpha$ ) on concentration patterns at two distinct positions. The concentration at the centerline grows insignificantly while the concentration near the wall drops as ( $\alpha$ ) increases. The solute concentration falls as you get closer to the wall and reaches its maximum on the wall, as seen in this diagram. For various  $T_R$  and  $h$ , Fig. 5 depicts the distribution of solute concentration at two distinct positions along the tube’s length. Because of the delicate balance between convective protein transport and diffuse protein transport, at any given axial location the concentration of solutes at wall is



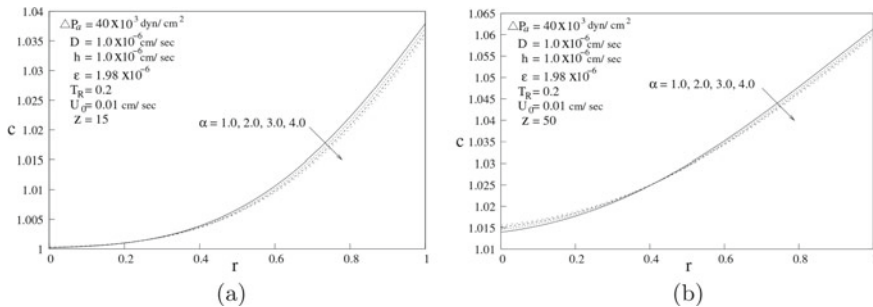


**Fig. 4** Effect of viscosity parameter ( $\alpha$ ) on concentration ( $c$ ) with  $r$  at different locations **a**  $z = 15$  and **b**  $z = 50$

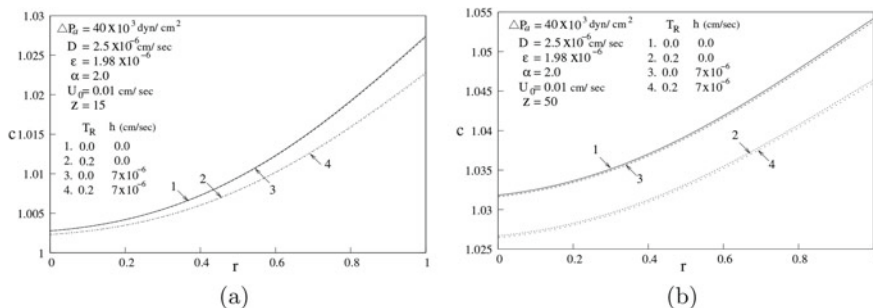


**Fig. 5** Effects of  $T_R$  and  $h$  on solute concentration ( $c$ ) with  $r$  at  $z = 15$  and  $z = 50$

larger than at centerline. The solute concentration increases with radial distance at any constant cross-sectional tube because solute particles remove via ultrafiltration.

The effect of  $\epsilon$  and  $D$  on concentration distribution is seen in Fig. 6. The concentration of solute increases as  $\epsilon$  increases, indicating that the solute volume per unit volume at the wall has risen. With a rise in  $D$ , the solute concentration decreases along the axis. It is true that in the situation of  $\epsilon = 0$ (zero ultrafiltration), it is a fact that no solute is transferred through the wall. That is, from the initial constant value ( $c_0 = 1$ ) to zero at cross-section  $z = 15$ , the radial concentration profile falls considerably.

**Concentration at the wall  $c_w$**  : The impact of the viscosity parameter ( $\alpha$ ) on wall concentration is seen in Fig. 7, along axial direction. It is noted that variation in the concentration exists only near the permeable wall. It is also worth noting that as ( $\alpha$ ), the concentration near the wall drops. The wall concentration with axial distance for two cases  $\Delta\pi \neq 0$  and  $\Delta\pi = 0$  with various values of the ultrafiltration parameter  $\epsilon$  are shown in Fig. 8. To enforce the scenario where there is no osmotic pressure across the permeable border explicitly,  $\Delta\pi = 0$  is used in Eq. (18). In both situations of  $\Delta\pi$ , as  $\epsilon$  rises, the wall concentration rises. In the case of  $\Delta\pi = 0$ , the numerical value of the wall concentration is higher than in the case of  $\Delta\pi \neq 0$ .

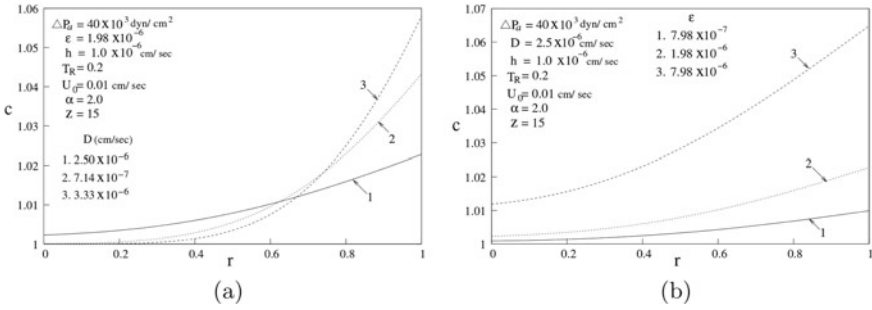


Fig. 6 Effects of  $D$  and  $\epsilon$  on concentration of solute ( $c$ ) with  $r$

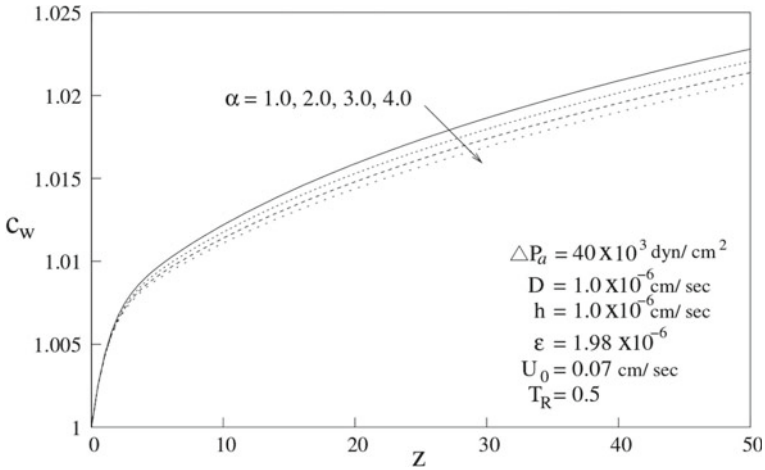


Fig. 7 Effect of viscosity parameter ( $\alpha$ ) on wall solute concentration ( $c_w$ )

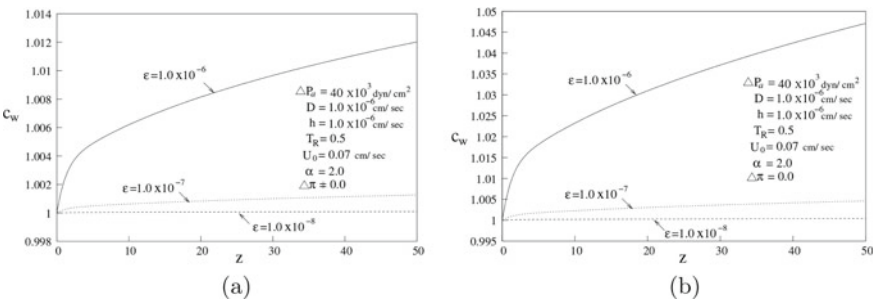


Fig. 8 Effects of  $\epsilon$  on wall concentration  $c_w$  for  $\Delta \pi = 0$  and  $\Delta \pi \neq 0$

## 5 Conclusions

This study concentrated on the quantitative evaluation of fluid and solute transfer in a tube with a permeable wall under the influence of varying viscosity. The controlling fluid flow and solute transport equations have been solved analytically and numerically. It is noteworthy to note that the hydrostatic pressure loss is quite minimal in the current results, whereas it is considered constant in some of the earlier models. The consideration of solute transport via the permeable tube in conjunction with exponentially varying viscosity, specifically in the flow through glomerular capillaries, is one of the study's unique aspects. The results are obtained for hydrostatic and osmotic pressures and, concentration profiles, demonstrating the impact of various viscosity parameter values and other factors. The following are the study's key findings:

- (i) The hydrostatic pressure drops linearly throughout the capillary's length. The  $\Delta P$  decreases as the viscosity parameter ( $\alpha$ ) rises. The osmotic pressure rises in a nonlinear fashion throughout the capillary's length. As ( $\alpha$ ) increase, the  $\Delta\pi$  lowers.
- (ii) As the viscosity parameter ( $\alpha$ ) is increased, the concentration increases along the axis and drops along the wall.
- (iii) As the viscosity parameter decreases, so does the concentration near the wall. For small values of  $\varepsilon$ , the findings for two specific instances  $\Delta\pi = 0$  and  $\Delta\pi \neq 0$  are close to each other. The discrepancy between the two outcomes increases as  $\varepsilon$  rises.

## References

1. Berman, A.S.: Laminar flow in channels with porous walls. *J. Appl. Phys.* **24**, 1232–1235 (1953)
2. Berman, A.S.: Laminar flow in an annulus with porous walls. *J. Appl. Phys.* **29**, 71–75 (1958)
3. Apelblat, A., Katchasky, A.K., Silberberg, A.: A mathematical analysis of capillary tissue fluid exchange. *Biorheology* **11**, 1–49 (1974)
4. Guyton, A.C.: Text Book of Medical Physiology, 7th edn. W. B, Saunders Company (1986)
5. Brenner, B.M., Troy, J.L., Daugharty, T.M., Deen, W.M.: Dynamics of glomerular ultrafiltration in the rat II plasma flow dependence of GFR. *Am. J. Physiol.* **223**, 1184–1190 (1972)
6. Brenner, B.M., Baylis, C., Deen, W.M.: Transport of molecules across renal glomerular capillaries. *Physiol. Rev.* **56**, 502–534 (1978)
7. Deen, W.M., Robertson, C.R., Brenner, B.M.: A model of glomerular ultrafiltration in the rat. *Am. J. Physiol.* **223**, 1178–1183 (1972)
8. Marshall, E.A., Trowbridge, E.A.: A mathematical model of the ultrafiltration process in a single glomerular capillary. *J. Theor. Biol.* **48**, 389–412 (1974)
9. Huss, R.E., Marsh, D.J., Kalaba, R.E.: Two models of glomerular filtration rate and renal blood flow in the rat. *Ann. Biomed. Eng.* **3**, 72–99 (1975)
10. Papenfuss, H.D., Gross, J.F.: Analytical study of the influence of capillary pressure drop and permeability on glomerular ultrafiltration. *Microvasc. Res.* **16**, 59–72 (1978)
11. Papenfuss, H.D., Gross, J.F.: Transcapillary exchange of fluid and plasma proteins. *Biorheology* **24**, 319–335 (1987)
12. Salathe, E.P.: Mathematical studies of capillary tissue exchange. *Bull. Math. Biol.* **50–3**, 289–311 (1988)

13. Deen, W.M., Robertson, C.R., Brenner, B.M.: Concentration polarization in an ultrafiltering capillary. *BioPhys. J.* **14**, 412–431 (1974)
14. Ross, M.S.: A mathematical model of mass transport in a long permeable tube with radial convection. *J. Fluid Mech.* **63**, 157–175 (1974)
15. Chaturani, P., Ranganatha, T.R.: Solute transfer in fluid in permeable tubes with application to flow in glomerular capillaries. *Acta Mechanica* **96**, 139–154 (1993)
16. Varunkumar, M., Muthu, P.: Fluid flow and solute transfer in a tube with variable wall permeability. *Zeitschrift für Naturforschung A—A J. Phys. Sci.* **74–12**, 1057–1067 (2019)
17. Umavathi, J.C.: Combined effect of variable viscosity and variable thermal conductivity on double-diffusive convection flow of a permeable fluid in a vertical channel. *Transp. Porous. Med.* **108**, 659–678 (2015)
18. Herterich, J.G., Griffiths, I.M., Vella, D., Field, R.W.: The effect of a concentration-dependent viscosity on particle transport in a channel flow with porous walls. *AIChE J* **60**, 1891–1904 (2014)
19. Davis, R.H., Sherwood, J.D.: A similarity solution for steady-state crossflow microfiltration. *Chem. Eng. Sci.* **45**, 3203–3209 (1990)
20. Davis, R.H., Leighton, D.T.: Shear-induced transport of a particle layer along a porous wall. *Chem. Eng. Sci.* **42**, 275–281 (1987)
21. Bowen, W.R., Williams, P.M.: Prediction of the rate of cross-flow ultrafiltration of colloids with concentration-dependent diffusion coefficient and viscosity-theory and experiment. *Chem. Eng. Sci.* **56**, 3083–3099 (2001)
22. Moustafa, E.: Blood flow in capillary under starling hypothesis. *Appl. Math. Comput.* **149**, 431–439 (2004)
23. Pollak, M.R., Susan, E.Q., Melanie, P.H., Lance, D.D.: The glomerulus: the sphere of influence. *Clin. J. Am. Soc. Nephrol.* **9**, 1461–1469 (2014)
24. Regirer, S.A.: Quasi one dimensional model of transcapillary filtration. *J. Fluid Dyn.* **10**, 442–446 (1975)

# **Dynamical Systems: Chaos, Complexity and Fractals**

# Impact of Cooperative Hunting and Fear-Induced in a Prey-Predator System with Crowley-Martin Functional Response



Anshu, Sourav Kumar Sasmal, and Balram Dubey

**Abstract** Cooperative hunting among predators and the fear-induced growth rate reduction in prey populations is an ecologically significant phenomenon. Many researchers have studied the effects of hunting cooperation and fear independently, but there has not been much research on the combined effect. This study analyzed a classical predator-prey system incorporating hunting cooperation and fear effect with Crowley-Martin functional response. We have done the basic analysis, including positivity, boundedness of solutions, existence and stability analysis of equilibria, Hopf-bifurcation, saddle-node bifurcation. We analyzed that incorporating cooperative hunting among predators may destabilize the system dynamics by producing limit cycles via Hopf-bifurcation. Furthermore, we noticed that the system shows bi-stability behavior between predator-free equilibrium and the coexistence equilibrium. Also, analysis shows that the system becomes unstable for a fixed hunting cooperation parameter on increasing the strength of fear. To validate the analytical conclusions, numerical simulations are conducted.

**Keywords** Prey-predator dynamics · Fear effect · Hunting cooperation · Stability analysis · Bifurcation.

## 1 Introduction

For many species, social interactions between individuals constitute an important aspect of their life histories. Cooperative behavior among animals is a common and essential phenomenon from a biological perspective. Cosner et al. [3] derived

---

Anshu (✉) · S. K. Sasmal · B. Dubey  
Department of Mathematics, BITS Pilani, Pilani Campus, Pilani 333031, Rajasthan, India  
e-mail: [anshumor028@gmail.com](mailto:anshumor028@gmail.com)

S. K. Sasmal  
e-mail: [sourav.kumar@pilani.bits-pilani.ac.in](mailto:sourav.kumar@pilani.bits-pilani.ac.in)

B. Dubey  
e-mail: [bdubey@pilani.bits-pilani.ac.in](mailto:bdubey@pilani.bits-pilani.ac.in)

© The Author(s), under exclusive license to Springer Nature Switzerland AG 2022  
S. Banerjee and A. Saha (eds.), *Nonlinear Dynamics and Applications*,  
Springer Proceedings in Complexity,  
[https://doi.org/10.1007/978-3-030-99792-2\\_86](https://doi.org/10.1007/978-3-030-99792-2_86)

1015

a functional response depending on the spatial distribution of predators when the predators aggregate for capturing prey. Berec [2] studied a prey-predator model and discovered that hunting cooperation destabilizes the system by affecting the encounter rate between prey and predator. Alves and Hilker [1] discovered that cooperative hunting might benefit the predator population by increasing the encounter rate, but it may also lead to a sudden collapse of the predator population.

Due to predation fear, preys exhibit a wide range of anti-predator behaviors, including habitat change, reduced foraging activities, reducing prey's per capita growth rate. Zanette et al. [11] conducted an experiment on song sparrows and discovered that only predation fear could reduce the reproduction rate of song sparrows by 40%. Wang et al. [10] studied the dynamics of a predator-prey model incorporating the fear effect and analyzed that relatively high values of the fear parameter may stabilize the system by excluding the existence of limit cycles. Sasmal and Takeuchi [9] investigated the effects of fear in a predator-prey model and analyzed that fear can greatly affect the system dynamics. In literature, many researchers have studied the effects of cooperative hunting and fear on the dynamics of the prey-predator system, but not much work has been done on the combined effects. Pal et al. [7] studied the dynamics of a prey-predator model incorporating hunting cooperation and fear and discovered that fear-induced due to cooperative hunting might destabilize the system by producing periodic oscillations.

Crowley-Martin type functional response shows that higher predator density reduces predator feeding rate due to interference among themselves for a limited resource [4]. This assumption makes the functional response more pragmatic from the ecological point of view. Kumar and Dubey [5] studied a predator-prey model with Crowley-Martin functional response and analyzed that preserving the prey population below a certain threshold level is beneficial to both the species. Maiti et al. [6] studied the dynamics of a stage-structured predator-prey system with Crowley-Martin type functional response. To the best of the authors' knowledge, the combined effect of hunting cooperation and fear induced by a predator on prey in a predator-prey system with Crowley-Martin type functional response has not been studied. Thus, we propose a mathematical model to study the dynamics of the prey-predator system incorporating the above aspects.

## 2 Mathematical Model

We consider a habitat in which prey of density  $x(t)$  and specialist predator of density  $y(t)$  live together at any time  $t$ . We assume that the prey species is growing logistically with intrinsic growth rate  $r$  and carrying capacity  $k$ , thus its dynamics leads to the following ODE:

$$\frac{dx}{dt} = rx \left( 1 - \frac{x}{k} \right). \quad (1)$$

Since the predator population may decline at high predator density due to interference among them for common limited resources, hence to capture this aspect Crowley-Martin [4–6] type functional response is more realistic. This functional response is given by

$$f(x, y) = \frac{\beta x}{(1 + ax)(1 + by)},$$

where  $\beta$  is attack rate,  $a$  is handling time required per prey and  $b$  is the magnitude of interference among predator individuals. It may be pointed out here that when  $a > 0$  and  $b = 0$ , then  $f(x, y)$  becomes Holling type-II functional response; when  $a = 0$  and  $b > 0$ , then  $f(x, y)$  describes a saturation response with respect to predator; when  $a = 0$  and  $b = 0$ ,  $f(x, y)$  denotes linear mass-action response.

Now, we assume that predators cooperate among themselves to encounter a strong prey, and in such a case the attack rate  $\beta$  is given by  $\beta = \alpha_0 + \alpha y$ , where  $\alpha_0$  is the capture rate without considering the cooperative hunting among predators and  $\alpha$  is hunting cooperation parameter among predators. These predators induce fear among prey which causes a decrease in the growth rate of prey. This fear function is described by [5, 9, 10]

$$g(e, \alpha, y) = \frac{1}{1 + e\alpha y},$$

where  $e$  is the cost of fear. Keeping all the above aspects in view, the dynamics of our proposed system can be governed by the following system of ODEs:

$$\begin{aligned} \frac{dx}{dt} &= \frac{rx}{(1 + e\alpha y)} \left(1 - \frac{x}{k}\right) - \frac{(\alpha_0 + \alpha y)}{(1 + ax)(1 + by)} xy, \\ \frac{dy}{dt} &= \frac{c(\alpha_0 + \alpha y)}{(1 + ax)(1 + by)} xy - \delta_0 y - \delta_1 y^2, \end{aligned} \tag{2}$$

$$x(0) \geq 0, \quad y(0) \geq 0.$$

In the above model,  $c(0 < c < 1)$  is the conversion rate from prey to predator density,  $\delta_0$  is the predators’ natural mortality rate, and  $\delta_1$  is the intraspecific interference coefficient among predators. It may be pointed out here that in case of strong prey,  $\alpha$  may be large and  $b$  negligible; and in case of weak prey  $\alpha$  may be negligible and  $b$  large.

### 3 Mathematical Analysis

Now, we will do the basic mathematical analysis of the model (2). All the parameters involved in our model are positive.



### 3.1 Basic Analysis

The proofs of the following two theorems are similar to [5] and hence, omitted.

**Theorem 1** All the solutions  $\phi(t) = (x(t), y(t))$  with initial conditions  $\phi_0(t) = (x_0, y_0) \in \mathbb{R}_+^2$  remains positive in the first quadrant.

**Theorem 2**  $\Omega_1 = \{(x, y) : 0 \leq x \leq k, 0 \leq x + \frac{1}{c}y \leq \frac{2rk}{\delta_{min}}\}$  is a positively invariant set for all the solutions originating from the first quadrant, where  $\delta_{min} = \min\{r, \delta_0\}$ .

### 3.2 Equilibria Analysis

The system (2) can have the following non-negative equilibria:

The trivial equilibrium  $E_0 = (0, 0)$ , and the predator-free equilibrium  $E_1 = (k, 0)$  always exist. We can find the interior equilibrium by solving the following set of equations:

$$\begin{aligned} \frac{r}{1 + e\alpha y} \left(1 - \frac{x}{k}\right) - \frac{(\alpha_0 + \alpha y)y}{(1 + ax)(1 + by)} &=: f(x, y) \\ \frac{c(\alpha_0 + \alpha y)x}{(1 + ax)(1 + by)} - \delta_0 - \delta_1 y &=: g(x, y) \end{aligned} \tag{3}$$

From  $f(x, y) = 0$ , it follows that:

When  $y = 0$ , then  $x_* = k$ . When  $x = 0$ , we get a cubic equation in  $y$  i.e.  $e\alpha^2 y^3 + \alpha(1 + e\alpha_0)y^2 + (\alpha_0 - rb)y - r = 0$  which has a positive root (using Descarte’s rule of sign). Now

$$\frac{dy}{dx} = - \frac{\left(\frac{r}{k(1 + e\alpha y)} - \frac{ay(\alpha_0 + \alpha y)}{(1 + ax)^2(1 + by)}\right)}{\left(\frac{re\alpha}{(1 + e\alpha y)^2} \left(1 - \frac{x}{k}\right) + \frac{(\alpha_0 + 2\alpha y + b\alpha y^2)}{(1 + ax)(1 + by)^2}\right)}$$

From above analysis, we notice that  $f(x, y) = 0$  passes through the points  $(k, 0)$  and  $(0, y_1)$  and it may increase or decrease depending upon the sign of  $\frac{dy}{dx}$ .

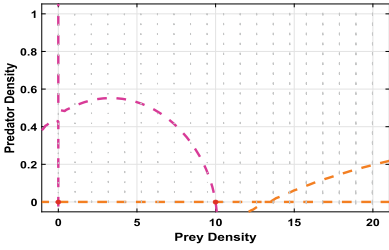
From  $g(x, y) = 0$ , it follows that:

When  $y = 0$ , then  $x_1 = \frac{\delta_0}{c\alpha_0 - a\delta_0}$ . When  $x = 0$ , then  $y_2 = -\frac{\delta_0}{\delta_1}$ .

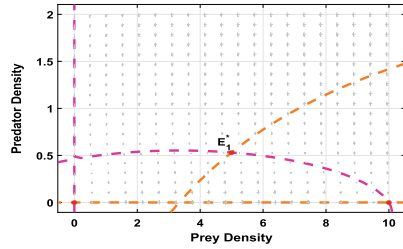
$$\frac{dy}{dx} = \frac{c(\alpha_0 + \alpha y)}{(1 + ax)^2(1 + by) \left(\frac{c(b\alpha_0 - \alpha)x}{(1 + ax)(1 + by)^2} + \delta_1\right)}$$

Therefore, the above analysis shows that  $g(x, y) = 0$  passes through  $(x_1, 0)$  and  $(0, y_2)$  and it may increase or decrease depending on the sign of  $\frac{dy}{dx}$ .

Now, based on the above analysis, we state the following theorems.

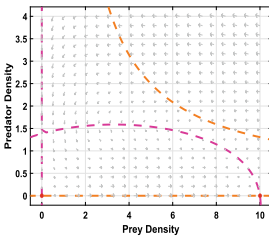


(a) No interior equilibrium point for  $\delta_0 = 0.8$ .

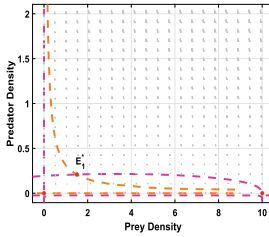


(b) Unique interior equilibrium point for  $\delta_0 = 0.5$ .

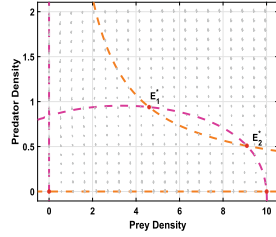
**Fig. 1** Existence of equilibria for model (2) with varying  $\delta_0$ . Remaining parameters are fixed as  $r = 4, k = 10, e = 10, c = 0.1, \alpha_0 = 3, \alpha = 0.5, a = 0.3, b = 0.5$  and  $\delta_1 = 0.03$ . Here, the slope of predator isocline is positive



(a) No interior equilibrium point for  $\alpha = 0.2$ .



(b) Unique interior equilibrium point for  $\alpha = 6$ .



(c) Two interior equilibrium points for  $\alpha = 0.5$ .

**Fig. 2** Existence of equilibrium points for the model (2) with varying  $\alpha$ . Remaining parameters are fixed as  $r = 4, k = 10, e = 10, c = 0.5, \alpha_0 = 0.5, a = 0.3, b = 0.01, \delta_0 = 0.9$  and  $\delta_1 = 0.03$ . Here, the slope of predator isocline is negative

**Theorem 3** The system will have at most one interior equilibrium if  $\left(\frac{c(b\alpha_0 - \alpha)x}{(1+ax)(1+by)^2} + \delta_1\right) > 0$  and  $k(c\alpha_0 - a\delta_0) > \delta_0$  hold (see Fig. 1).

**Theorem 4** The system will have at most two interior equilibrium if  $\left(\frac{c(b\alpha_0 - \alpha)x}{(1+ax)(1+by)^2} + \delta_1\right) < 0$  holds (see Fig. 2).

Now we have the following theorems for the stability analysis of different equilibria corresponding to system (2).

**Theorem 5** The trivial equilibrium  $E_0$  is always a saddle point.

**Proof** The eigenvalues of the Jacobian matrix at the trivial equilibrium  $E_0$  are given by  $\lambda_1 = r (> 0)$  and  $\lambda_2 = -\delta_0 (< 0)$ .

**Theorem 6** *The axial equilibrium  $E_1 = (k, 0)$  always exists and is locally asymptotically stable if  $ck\alpha_0 < \delta_0(1 + ak)$ .*

**Proof** The eigenvalues of the Jacobian matrix at the predator-free equilibrium  $E_1$  are given by  $\lambda_1 = -r (< 0)$  and  $\lambda_2 = \frac{ck\alpha_0}{1+ak} - \delta_0$ . Thus,  $E_1$  is locally asymptotically stable if  $ck\alpha_0 < \delta_0(1 + ak)$ .

**Theorem 7** *The interior equilibrium  $E^* = (x^*, y^*)$  is locally asymptotically stable if  $tr(J_{E^*}) < 0$  and  $det(J_{E^*}) > 0$ , where  $J_{E^*}$  is the Jacobian matrix evaluated at  $E^*$ .*

**Proof** The Jacobian matrix  $J_{E^*}$  at the interior equilibrium  $E^* = (x^*, y^*)$  is given by:

$$J_{E^*} = \begin{bmatrix} -\frac{rx^*}{k(1+e\alpha y^*)} + \frac{a(\alpha_0 + \alpha y^*)x^*y^*}{(1+ax^*)(1+by^*)} & \frac{-e\alpha rx^*}{(1+e\alpha y^*)^2} \left(1 - \frac{x^*}{k}\right) - \frac{(\alpha_0 + 2\alpha y^* + b\alpha(y^*)^2)x^*}{(1+ax^*)(1+by^*)^2} \\ \frac{c(\alpha_0 + \alpha y^*)y^*}{(1+ax^*)^2(1+by^*)} & -\left(\frac{c(b\alpha_0 - \alpha)x^*y^*}{(1+ax^*)(1+by^*)^2} + \delta_1 y^*\right) \end{bmatrix}.$$

From above matrix, we have the characteristic equation as:

$$\begin{aligned} & \lambda^2 - tr(J_{E^*})\lambda + det(J_{E^*}) = 0, \\ \lambda^2 + & \left[ \frac{rx^*}{k(1+e\alpha y^*)} - \frac{a(\alpha_0 + \alpha y^*)x^*y^*}{(1+ax^*)(1+by^*)} + \left(\frac{c(b\alpha_0 - \alpha)x^*y^*}{(1+ax^*)(1+by^*)^2} + \delta_1 y^*\right) \right] \lambda + \\ & \left[ \left(\frac{rx^*}{k(1+e\alpha y^*)} - \frac{a(\alpha_0 + \alpha y^*)x^*y^*}{(1+ax^*)(1+by^*)}\right) \left(\frac{c(b\alpha_0 - \alpha)x^*y^*}{(1+ax^*)(1+by^*)^2} + \delta_1 y^*\right) \right] + \\ & \left[ \left(\frac{e\alpha rx^*}{(1+e\alpha y^*)^2} \left(1 - \frac{x^*}{k}\right) + \frac{(\alpha_0 + 2\alpha y^* + b\alpha(y^*)^2)x^*}{(1+ax^*)(1+by^*)^2}\right) \left(\frac{c(\alpha_0 + \alpha y^*)y^*}{(1+ax^*)^2(1+by^*)}\right) \right] = 0 \end{aligned} \tag{4}$$

Thus,  $E^* = (x^*, y^*)$  is locally asymptotically stable if  $tr(J_{E^*}) < 0$  and  $det(J_{E^*}) > 0$  (using Routh-Hurwitz criterion).

**Remark:** It may be noted that if:

$$\frac{r}{k(1 + e\alpha y^*)} > \frac{a(\alpha_0 + \alpha y^*)y^*}{(1 + ax^*)(1 + by^*)}$$

holds, then  $tr(J_{E^*}) < 0$  and  $det(J_{E^*}) > 0$ , and hence  $E^* = (x^*, y^*)$  is locally asymptotically stable.

### 4 Bifurcation Analysis

Next, we investigate the possibility of existence of limit cycle via Hopf-bifurcation near the interior equilibrium  $E_1^*$  with respect to the parameter  $\alpha$ .

The characteristic equation evaluated from the Jacobian matrix at  $E_1^*$  is:

$$\lambda^2 - tr(J_{E_1^*})\lambda + det(J_{E_1^*}) = 0.$$

For the Hopf-bifurcation to occur, we need  $tr(J_{E_1^*}) = 0$ , and  $det(J_{E_1^*}) > 0$ . From the above two conditions, we calculate the critical value  $\alpha = \alpha_*$  of hunting cooperation parameter.

Then we check the transversality condition:

$$\frac{\partial}{\partial \alpha} |tr(J_{E_1^*})|_{\alpha=\alpha_*} = - \left[ \frac{rex^*y^*}{k(1+e\alpha y^*)^2} + \frac{ax^*(y^*)^2}{(1+ax^*)(1+by^*)} + \frac{cx^*y^*}{(1+ax^*)(1+by^*)} \right] \neq 0$$

Hence, the system experiences Hopf-bifurcation at the equilibrium point  $E_1^*$  when  $\alpha = \alpha_*$ .

**Theorem 8** *The system (2) goes through a saddle-node bifurcation around the equilibrium point  $E(\bar{x}, \bar{y})$  as the cooperation parameter  $\alpha$  crosses the bifurcation value  $\alpha = \alpha_c$  if and only if*

$$\begin{aligned} & - \left( \frac{-re\bar{x}\bar{y}}{(1+e\alpha_c\bar{y})^2} \left( 1 - \frac{\bar{x}}{k} \right) - \frac{\bar{x}\bar{y}^2}{(1+a\bar{x})(1+b\bar{y})} - \frac{f_{\bar{x}}}{g_{\bar{x}}(1+a\bar{x})(1+b\bar{y})} \right) \neq 0, \\ & \left[ \left( f_{\bar{x}\bar{x}} - \frac{f_{\bar{x}}}{f_{\bar{y}}} (f_{\bar{x}\bar{y}} + f_{\bar{y}\bar{x}}) + \frac{f_{\bar{x}}^2}{f_{\bar{y}}^2} f_{\bar{y}\bar{y}} \right) - \frac{f_{\bar{x}}}{g_{\bar{x}}} \left( g_{\bar{x}\bar{x}} - \frac{f_{\bar{x}}}{f_{\bar{y}}} (g_{\bar{x}\bar{y}} + g_{\bar{y}\bar{x}}) + \frac{f_{\bar{x}}^2}{f_{\bar{y}}^2} g_{\bar{y}\bar{y}} \right) \right] \neq 0, \end{aligned}$$

where

$$\begin{aligned} f_{\bar{x}} &= - \frac{r_1\bar{x}}{k(1+e\alpha_c\bar{y})} + \frac{a(\alpha_0 + \alpha_c\bar{y})\bar{x}\bar{y}}{(1+a\bar{x})(1+b\bar{y})}, \\ f_{\bar{y}} &= \frac{-e\alpha_c r x^*}{(1+e\alpha_c y^*)^2} \left( 1 - \frac{\bar{x}}{k} \right) - \frac{(\alpha_0 + 2\alpha_c\bar{y} + b\alpha_c(\bar{y})^2)\bar{x}}{(1+a\bar{x})(1+b\bar{y})^2}, \\ g_{\bar{x}} &= \frac{c(\alpha_0 + \alpha_c\bar{y})\bar{y}}{(1+a\bar{x})^2(1+b\bar{y})}, \\ g_{\bar{y}} &= - \left( \frac{c(b\alpha_0 - \alpha_c)\bar{x}\bar{y}}{(1+a\bar{x})(1+b\bar{y})^2} + \delta_1\bar{y} \right). \end{aligned}$$

**Proof** The Jacobian matrix calculated at the interior equilibrium  $E(\bar{x}, \bar{y})$  is :

$$J_{E(\bar{x}, \bar{y})} = \begin{bmatrix} - \frac{r\bar{x}}{k(1+e\alpha\bar{y})} + \frac{a(\alpha_0+\alpha\bar{y})\bar{x}\bar{y}}{(1+a\bar{x})(1+b\bar{y})} & \frac{-e\alpha r\bar{x}}{(1+e\alpha\bar{y})^2} \left( 1 - \frac{\bar{x}}{k} \right) - \frac{(\alpha_0+2\alpha\bar{y}+b\alpha(\bar{y})^2)\bar{x}}{(1+a\bar{x})(1+b\bar{y})^2} \\ \frac{c(\alpha_0+\alpha\bar{y})\bar{y}}{(1+a\bar{x})^2(1+b\bar{y})} & - \left( \frac{c(b\alpha_0-\alpha)\bar{x}\bar{y}}{(1+a\bar{x})(1+b\bar{y})^2} + \delta_1\bar{y} \right) \end{bmatrix}.$$

Now differentiating the given system w.r.t.  $\alpha$ , we get

$$F_{\alpha}(\bar{x}\bar{y}) = \begin{bmatrix} \frac{-re\bar{x}\bar{y}}{(1+e\alpha y)^2} \left( 1 - \frac{\bar{x}}{k} \right) - \frac{\bar{x}\bar{y}^2}{(1+a\bar{x})(1+b\bar{y})} \\ \frac{c\bar{x}\bar{y}^2}{(1+a\bar{x})(1+b\bar{y})} \end{bmatrix}$$

$$B = Df(E(\bar{x}, \bar{y}), \alpha_c) = \begin{bmatrix} f_x & f_y \\ g_x & g_y \end{bmatrix}$$

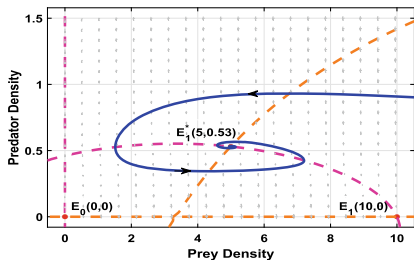
One can see that the eigenvector corresponding to zero eigenvalue of matrix  $B = Df(E(\bar{x}, \bar{y}), \alpha_c)$  is  $v' = \left[ 1 \quad \frac{-f_x}{f_y} \right]^T$ , and the eigenvector corresponding to zero eigenvalue of matrix  $B^T = [Df(E(\bar{x}, \bar{y}), \alpha_c)]^T$  is:  $w' = \left[ 1 \quad \frac{-f_x}{g_x} \right]^T$ . Using Sotomayor theorem [8] for saddle-node bifurcation, we get the conditions for saddle-node bifurcation by doing simple calculations.

### 5 Numerical Simulations

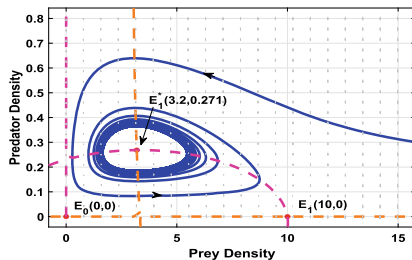
In this section, we perform some numerical simulations to show the population insights from our analytical findings.

In Fig. 3, we fixed the parameters as  $r = 4, k = 10, e = 10, c = 0.1, \alpha_0 = 3, \delta_0 = 0.5, a = 0.3, b = 0.5$  and  $\delta_1 = 0.03$ . For  $\alpha = 0.2$ , the system (2) has a stable unique interior equilibrium point i.e.  $E_1^*(5, 0.53)$  as a spiral sink (Fig. 3a) and for  $\alpha = 2$ , the system (2) has a stable limit cycle around the interior equilibrium point  $E_1^*(3.2, 0.271)$  i.e.  $E_1^*$  is a spiral source (Fig. 3b).

In Fig. 4, we fixed the parameters values as  $r = 4, k = 10, e = 10, c = 0.5, \alpha_0 = 0.5, \delta_0 = 0.8, a = 0.3, b = 0.01$  and  $\delta_1 = 0.03$  and here, the system has two interior equilibrium points  $E_1^*$  and  $E_2^*$ . For  $\alpha = 0.2$ , the system (2) has two possible attractors  $E_1(10, 0)$  and  $E_1^*(6.25, 1.45)$  (Fig. 4a). Moreover for  $\alpha = 0.25$ , the system (2) has a stable equilibrium point  $E_1(10, 0)$  and also, a spiral source equilibrium  $E_1^*(5.2, 1.3)$  (4b). In Fig. 4a, we notice that the system exhibits bi-stability between the interior equilibrium  $E_1^*(6.25, 1.45)$  and the axial equilibrium  $E_1(10, 0)$ . Moreover, in Fig. 5,

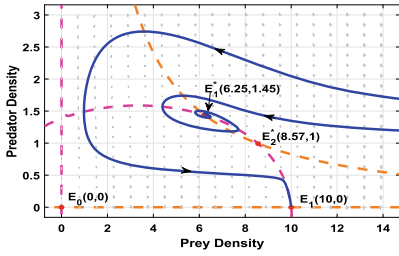


(a)  $\alpha = 0.2$ , the unique interior equilibrium  $E_1^* = (5, 0.53)$  is locally asymptotically stable.

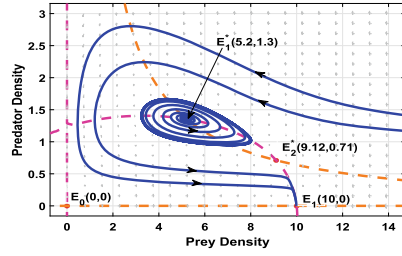


(b)  $\alpha = 2, E_1^* = (3.2, 0.271)$  is a spiral source.

**Fig. 3** All other parameters are fixed as  $r = 4, k = 10, e = 10, c = 0.1, \alpha_0 = 3, \delta_0 = 0.5, a = 0.3, b = 0.5$  and  $\delta_1 = 0.03$ . Here,  $E_0(0, 0)$  and  $E_1(10, 0)$  are always saddle points



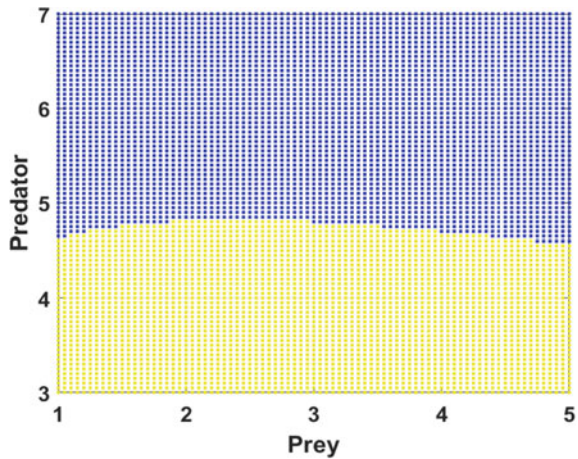
(a)  $\alpha = 0.2$ ,  $E_1(10,0)$  and  $E_1^*(6.25, 1.45)$  are locally asymptotically stable.



(b)  $\alpha = 0.25$ ,  $E_1(10,0)$  is locally asymptotically stable and  $E_1^*(5.2, 1.3)$  is a spiral source.

**Fig. 4** All other parameters are fixed as  $r = 4, k = 10, e = 10, c = 0.5, \alpha_0 = 0.5, \delta_0 = 0.8, a = 0.3, b = 0.01$  and  $\delta_1 = 0.03$ . Here,  $E_0$  and  $E_2^*$  are always saddle points

**Fig. 5** Basin of attraction for the prey-only equilibrium  $E_1(10, 0)$  and the interior equilibrium point  $E_1^*$ . Here, all the other parameters are fixed as  $r = 4, k = 10, e = 10, c = 0.5, \alpha_0 = 0.5, \alpha = 0.22, a = 0.3, b = 0.01, \delta_0 = 0.8$  and  $\delta_1 = 0.03$ . Blue and yellow represents the convergence region of  $E_1$  and  $E_1^*$ , respectively

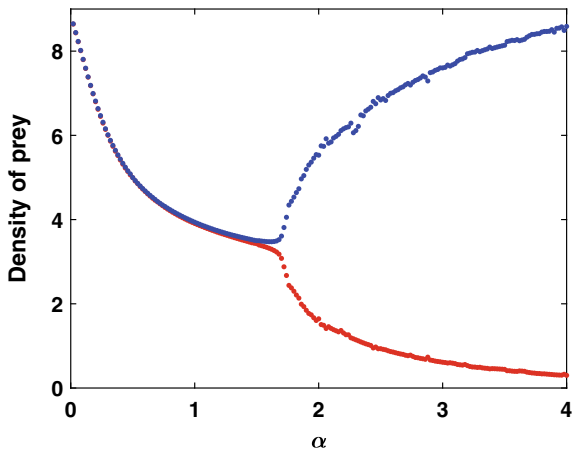


we show the basin of attraction for the predator-free equilibrium and the interior equilibrium. Basin of attraction for an equilibrium point is a set of initial points for which the solutions will converge to the same equilibrium point.

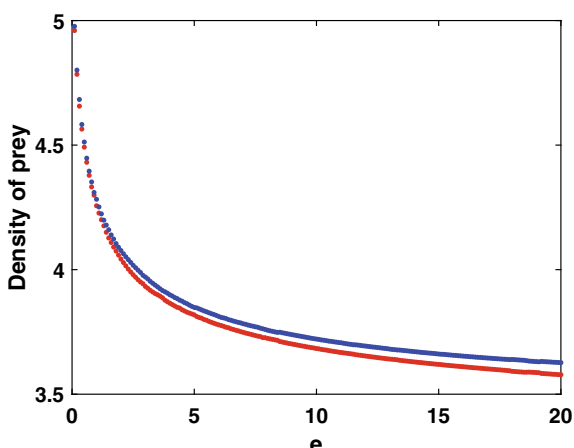
Next, we plot the bifurcation diagram of prey with respect to  $\alpha$  in Fig. 6. We notice that for relatively small cooperation parameter  $\alpha$  values, both prey and predator species have stable coexistence. As the cooperation parameter  $\alpha$  increases, Hopf-bifurcation occurs, and the stable coexistence equilibrium loses its stability and produces periodic oscillations. In Fig. 7, we show the bifurcation plot of prey with respect to the fear parameter  $e$ . We also observe that for a fixed value of cooperation parameter  $\alpha$ , the system tends to become unstable with an increase in the fear parameter  $e$ . Here, we have only shown bifurcation plot for prey population because prey and predator has the same bifurcation behavior.

Figure 8 depicts saddle-node bifurcation with respect to the parameter  $\alpha$ . We have fixed all the parameters as  $r = 4, k = 10, e = 10, c = 0.5, \alpha_0 = 0.5, a = 0.3,$

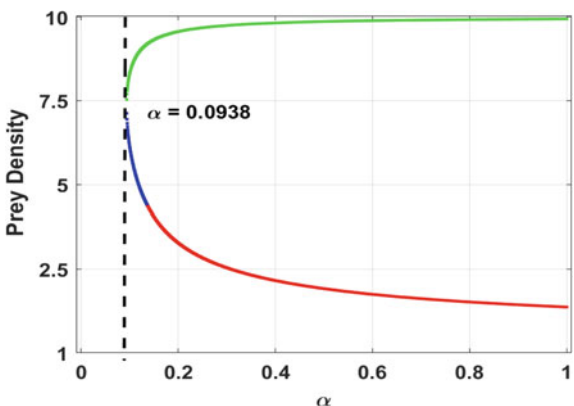
**Fig. 6** Bifurcation plot of prey for the model (2) with varying hunting cooperation parameter  $\alpha$ . Here, all the other parameters are fixed as  $r = 4, k = 10, e = 10, c = 0.1, \alpha_0 = 3, a = 0.3, b = 0.5, \delta_0 = 0.5$  and,  $\delta_1 = 0.03$



**Fig. 7** Bifurcation plot of prey for the model (2) with varying fear parameter  $e$ . Here, all the other parameters are fixed as  $r = 4, k = 10, c = 0.1, \alpha_0 = 3, \alpha = 1.2, a = 0.3, b = 0.5, \delta_0 = 0.5$  and,  $\delta_1 = 0.03$



**Fig. 8** Plot of saddle-node bifurcation with respect to the parameter  $\alpha$ . Remaining parameters are fixed as  $r = 4, k = 10, e = 10, c = 0.5, \alpha_0 = 0.5, a = 0.3, b = 0.01, \delta_0 = 0.8$  and  $\delta_1 = 0.03$ . Here, blue colour indicates stable equilibrium point; red colour indicates source; green colour indicates saddle point



$b = 0.01$ ,  $\delta_0 = 0.8$  and  $\delta_1 = 0.03$ . Here, we observe that the system goes through saddle node bifurcation at  $\alpha = 0.0938$  and the set of parameters satisfy the analytical conditions.

## 6 Discussion and Concluding Remarks

Social interactions within a population are a common and essential phenomenon from an ecological perspective. In particular, predators cooperate during hunting to increase the success rate of catching prey. Due to predation fear, prey shows a variety of anti-predator behavior, decreasing prey's per capita growth rate. The present manuscript considered a model incorporating both hunting cooperation and fear effect with Crowley-Martin functional response. First, we observed that incorporating hunting cooperation may produce limit cycles via Hopf-bifurcation and, hence, destabilizing the system. Also, the system undergoes saddle-node bifurcation with respect to the parameter  $\alpha$  under certain conditions. In addition, we noticed that the system shows bi-stability behavior in which the solution tends to prey-only equilibrium or coexisting equilibrium state. Furthermore, we have seen that for a fixed value of hunting cooperation parameter, increasing the strength of fear makes the system unstable. Hence, hunting cooperation and fear effect is of great significance from an ecological aspect.

**Acknowledgements** The authors are grateful to the anonymous referees for the critical review and suggestions that improved the quality of the paper. The first author, Anshu, acknowledges the Junior Research Fellowship received from UGC, New Delhi, India.

## References

1. Alves, M.T., Hilker, F.M.: Hunting cooperation and allee effects in predators. *J. Theor. Biol.* **419**, 13–22 (2017)
2. Berec, L.: Impacts of foraging facilitation among predators on predator-prey dynamics. *Bull. Mathem. Biol.* **72**(1), 94–121 (2010)
3. Cosner, C., DeAngelis, D.L., Ault, J.S., Olson, D.B.: Effects of spatial grouping on the functional response of predators. *Theor. Popul. Biol.* **56**(1), 65–75 (1999)
4. Crowley, P.H., Martin, E.K.: Functional responses and interference within and between year classes of a dragonfly population. *J. North Am. Benthol. Soc.* **8**(3), 211–221 (1989)
5. Kumar, A., Dubey, B.: Modeling the effect of fear in a prey-predator system with prey refuge and gestation delay. *Int. J. Bifurc. Chaos* **29**(14), 1950195 (2019)
6. Maiti, A.P., Dubey, B., Chakraborty, A.: Global analysis of a delayed stage structure prey-predator model with crowley-martin type functional response. *Mathem. Comput. Simul.* **162**, 58–84 (2019)
7. Pal, S., Pal, N., Chattopadhyay, J.: Hunting cooperation in a discrete-time predator-prey system. *Int. J. Bifurc. Chaos* **28**(07), 1850083 (2018)



8. Perko, L.: Differential equations and dynamical systems. Springer-Verlag New York **5** (2001)
9. Sasmal, S.K., Takeuchi, Y.: Dynamics of a predator-prey system with fear and group defense. *J. Mathem. Anal. Appl.* **481**(1), 123471 (2020)
10. Wang, X., Zanette, L., Zou, X.: Modelling the fear effect in predator-prey interactions. *J. Mathem. Biol.* **73**(5), 1179–1204 (2016)
11. Zanette, L.Y., White, A.F., Allen, M.C., Clinchy, M.: Perceived predation risk reduces the number of offspring songbirds produce per year. *Science* **334**(6061), 1398–1401 (2011)

# Chaotic Dynamics of Third Order Wien Bridge Oscillator with Memristor Under External Generalized Sinusoidal Stimulus



Aniruddha Palit 

**Abstract** The qualitative behaviour of the signals generated by a third order Wien bridge oscillator with memristor under external generalized sinusoidal stimulus is studied. The bifurcation of the nature of the solution for different range of the parameters of the system reveal that the external stimulus generates an added layer of security which can be used to build a secure communication channel using the synchronization of chaos. Some specific regimes of the parameters of the external stimulus are identified over which such secure channel can be established. The 0-1 test of chaos has been employed to verify the chaotic nature of the output signal.

**Keywords** Wien bridge oscillator · Memristor · Bifurcation · Chaos

## 1 Introduction

The study of dynamical behaviour of the signals in the circuit theory has always been a topic of interest because of the complex dynamics and noise arising in the output and the analysis of their characteristic properties is a matter of great importance in the transmission of signals to make a consistent communication system. In the year 1971 Leon Chua [4] first observed that four fundamental variables, namely charge ( $q$ ), current ( $i$ ), flux ( $\phi$ ) and voltage ( $v$ ) arise in mathematical formulation of a circuit. Determination of these four variables require four relations involving them out of which three relations can be generated by the axioms of classical two terminal circuit elements, namely inductor (relation involving  $i$  and  $\phi$ ), resistor (relation involving  $i$  and  $v$ ) and capacitor (relation involving  $v$  and  $q$ ). However, one relation between  $\phi$  and  $q$  remains undefined. Chua postulated this missing element, named as memristor which was realized recently [20] by Stan Williams group of HP Labs in 2008. The character of memristor is nonlinear and unique in the sense that no combination of nonlinear resistive, capacitive and inductive components can duplicate its excellent

---

A. Palit (✉)

Department of Mathematics, Surya Sen Mahavidyalaya, Siliguri 734004, India  
e-mail: [mail2apalit@gmail.com](mailto:mail2apalit@gmail.com)

© The Author(s), under exclusive license to Springer Nature Switzerland AG 2022  
S. Banerjee and A. Saha (eds.), *Nonlinear Dynamics and Applications*,  
Springer Proceedings in Complexity,  
[https://doi.org/10.1007/978-3-030-99792-2\\_87](https://doi.org/10.1007/978-3-030-99792-2_87)

1027

feature of memory and neuromorphic property. As a consequence the application of memristor has drawn the attention of many researchers in the construction of non-volatile memory [16], neural network [12], nonlinear circuits [23] and various other fields.

In the circuit theory Wien bridge oscillator is used to generate sinusoidal signals and is composed of resistors and capacitors. Recently memristors are used in such circuit exhibiting complex dynamic phenomena such as chaotic [22], hyperchaotic [25] behaviours as well as periodic and quasiperiodic behaviours for different regimes of the parameters present in the system. Wu et al. [22] designed a fourth order chaotic oscillator by the construction of a generalized memristor. Ye et al. [25] manufactured a fifth-order Wien-bridge hyperchaotic circuit. However, these higher order circuits are difficult to analyze due to their complex dynamics. Bao et al. [1] presented a third-order RLCM-four-elements-based autonomous memristive chaotic circuit by an active oscillator and a memristor. Rajagopal et al. [17] studied a third order Wien bridge oscillator (WBO) with fractional order memristor. Xu et al. [24] introduced external sinusoidal voltage stimulus in WBO and studied different complex behaviour. This kind of systems possessing complex dynamic behaviour can be used in information engineering such as generation of pseudorandom sequences in various information encryption, chaotic communication systems and synchronization etc.

Various electrical circuits such as Chua circuit, WBO etc. produce chaotic output which are categorized into self-excited and hidden attractors. The basin of attraction of a self-excited attractor is connected with neighbourhoods of unstable equilibrium point. Therefore, such attractors can be identified numerically following standard computational procedures in which starting from a sufficiently small neighbourhood of an unstable equilibrium point and after a transient process a trajectory is attracted to a state of oscillation and then traces it. On the other hand the basin of a hidden attractor is not connected with equilibria and hence it is very much challenging to visualize. Leonov et al. [11] classified hidden and self-excited attractors which captured the attention of the scientific community. Burkin and Khien [2] introduced an analytical-numerical method for localization of hidden attractors. Dynamics of self-excited and hidden attractors have been studied by Chen et al. [3], Stankevich et al. [19] and many more. Synchronization of such attractors in Chua circuit have been investigated by Kiseleva et al. [10]. Therefore, identification of chaotic attractors and realization of its nature is a challenging and active research of interest and is expected to contribute significantly in the transmission of confidential information through a secure communication channel.

Secure communication with chaos is an important field in engineering. A continuously changing chaotic signal is used as a carrier signal in the chaotic communication in contrast to a fixed carrier signal as used in classical communication. As a result it becomes very much difficult to predict the signal transmitted through chaotic communication thereby increases the security level and consequently it has very important place in secure communication system. Oppenheim et al. [14] first made the study of chaotic communication in 1992 and this field has been further explored by different researchers studying 5D hyperchaotic systems [26], chaotic systems with no

equilibrium [27] or hidden attractor [15]. Even chaotic system of fractional order [15], jerk chaotic system using sliding mode control [6] and several other interesting studies have been reported in literature. Therefore, identification of the regimes of the parameters of an WBO has significant applications in chaotic communication. One must apply proper verification method to identify the chaotic nature of a signal, without which definite decisions cannot be made. The computation of the maximal Lyapunov exponent is one such technique to determine chaos for quite a long time in the literature. However, we have used another method proposed by Gottwald and Melbourne [8] for detecting chaotic dynamics, known as 0-1 Test, which is based on time series data and has shown its potential in the determination of chaotic as well as non-chaotic nature of a signal in the recent past. The test can be applied in higher order systems without any practical difficulties.

In this article we have proposed a model of WBO under externally driven generalized sinusoidal voltage stimulus and studied the nature of the output signal. The objective of this paper is to check the potential of the driven stimulus on the output and to identify regimes of the parameters of these external forces for which chaotic signals can be generated by this kind of circuits. Such external stimulus enables us to make extra layer of security over the system parameters making the transmission of the signals in chaotic communication system more unpredictable and the system becomes more reliable.

The article is arranged as follows. A stability analysis of the equilibrium points of the WBO is presented in Sect. 2. The bifurcation of the output signals of driven WBO have been studied in Sect. 3 and the subsection therein and regimes of the parameters of the external stimulus are identified for which chaotic output is produced. A specimen of the parameter values are chosen and the 0-1 test is employed on the corresponding output signal to ensure its chaotic nature in Sect. 4. Conclusions and future aspects of this model are discussed in Sect. 5.

## 2 Stability Analysis of Wien Bridge Oscillator

The idea of memristor was first introduced by Chua [4] and its mathematical model was first proposed in [5]. A third order Wien bridge oscillator can be written in dimensionless form [17] as

$$\dot{x} = x(a - 1 - cz^2) - by \quad (1a)$$

$$\dot{y} = ax - by \quad (1b)$$

$$\dot{z} = -x - z(d - x^2) \quad (1c)$$

where  $a, b, c$  and  $d$  are parameters of the oscillator. In an electrical circuit the resistors and capacitors are responsible for the loss of electrical energy and so the external stimulus should be introduced in the circuit to restore this loss in order to execute the operation of the circuit for a long time. The external stimulus produces elec-

tromotive force (EMF) which is responsible to maintain voltage difference between the nodes of a circuit. Various external energy sources such as battery, generators etc. can be introduced at different nodes to boost the voltage differences in order to produce chaotic output of the circuit making it difficult to predict in advance unless one precisely knows the values of the parameters involved in the system and such output can be made to build a secure chaotic communication system. In order to enhance the security of the chaotic communication system more than one sources for production of EMF can be introduced in the above circuit having various magnitude, phase and frequency. We consider three different external sinusoidal stimulus having different magnitudes in the above system and check if the parameters of these external stimuli make any additional layer of security over the system parameters by producing chaotic output signal. Since, an autonomous system representation of a differential system is not unique, for the sake of simplicity, we can study the effect of these external stimuli separately in each of the above equations so that it can be written in generalized form as

$$\dot{x} = x(a - 1 - cz^2) - by + f_1 \cos(\omega t) \quad (2a)$$

$$\dot{y} = ax - by + f_2 \cos(\omega t) \quad (2b)$$

$$\dot{z} = -x - z(d - x^2) + f_3 \cos(\omega t) \quad (2c)$$

and study its qualitative behaviour under the influence of the parameters of these external stimuli.

The unperturbed system (1) has the fixed points at

$$P_0 = (0, 0, 0), \quad P_1 = \left( x_{P_1}, \frac{a}{b}x_{P_1}, \frac{x_{P_1}}{(x_{P_1})^2 - d} \right), \quad P_2 = \left( x_{P_2}, \frac{a}{b}x_{P_2}, \frac{x_{P_2}}{(x_{P_2})^2 - d} \right)$$

$$P_3 = \left( -x_{P_1}, -\frac{a}{b}x_{P_1}, -\frac{x_{P_1}}{(x_{P_1})^2 - d} \right) \text{ and } P_4 = \left( -x_{P_2}, -\frac{a}{b}x_{P_2}, -\frac{x_{P_2}}{(x_{P_2})^2 - d} \right)$$

where,

$$x_{P_1} = \frac{\sqrt{-c + \sqrt{c}\sqrt{c - 4d} + 2d}}{\sqrt{2}}, \quad x_{P_2} = -\frac{\sqrt{-c - \sqrt{c}\sqrt{c - 4d} + 2d}}{\sqrt{2}}.$$

It is notable that  $x_{P_1}$  and  $x_{P_2}$  are not real for any real value of  $c$  and  $d$  so that the only effective real fixed point of the system (1) is the point  $P_0$ . By linearizing the system near the point  $P_0$  the Jacobian Matrix can be expressed as

$$J = \begin{bmatrix} -1 + a & -b & 0 \\ a & -b & 0 \\ -1 & 0 & -d \end{bmatrix}$$

the characteristic equation of which is

$$\lambda^3 - (-1 + a - b - d)\lambda^2 - (-b - d + ad - bd)\lambda + bd = 0.$$

The eigen values of  $J$  at the fixed point  $P_0$  are the roots of the above characteristic equation given by

$$\lambda_1 = -d, \lambda_{2,3} = \frac{1}{2} \left( -1 + a - b \pm \sqrt{-4b + (1 - a + b)^2} \right).$$

It is clear that the eigen values  $\lambda_2$  and  $\lambda_3$  will be complex conjugates when the discriminant is negative i.e., if

$$-4b + (1 - a + b)^2 < 0 \text{ i.e. if } 1 - 2\sqrt{b} + b \leq a \leq 1 + 2\sqrt{b} + b.$$

In this interval if particularly  $a < b + 1$  along with  $d > 0$ , the real parts of  $\lambda_2$  and  $\lambda_3$  will be negative and in that case the equilibrium point will be asymptotically stable. However, if  $a > b + 1$  with  $d > 0$ , we have  $\lambda_1 < 0, \text{Re}(\lambda_2) > 0$  and  $\text{Re}(\lambda_3) > 0$  so that the points  $P_0$  becomes an unstable equilibrium point.

The oscillator (1) is generally known to generate sinusoidal waves in a large range of frequencies. However, we observe that the system has chaotic solution for different values of the parameters. Rajagopal et al. [17] studied the Wien Bridge Oscillator with fractional order memristor considering the values

$$b = 1, c = 0.5, d = 2 \tag{3}$$

as the parameter  $a$  increases. In this section we highlight similar nature of the solution of the system (1) for the above mentioned set of values of the parameters. The solution orbit for some discrete values of  $a$  are shown in Fig. 1.

We may observe different kind of orbits in these figures. Notably, a small change in  $a$  from 5.96 in the Fig. 1c to 5.97 in the Fig. 1d produces a bifurcation from an irregular orbit to a perfectly periodic orbit. The nature of the irregularity cannot be explicitly identified unless we perform certain test for confirmation of chaotic behaviour. One

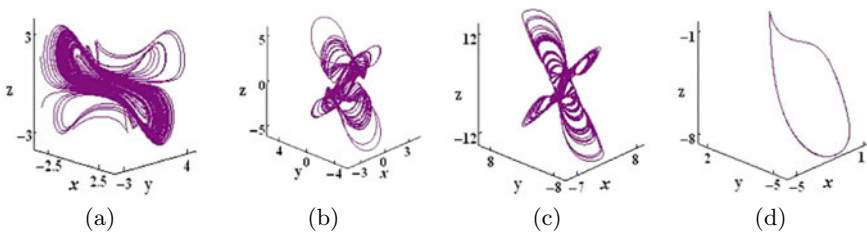


**Fig. 1** Solution orbit of the WBO system (1) with parameter values given by (3) for  $a = 2.55, 3, 5.96, 5.97$  respectively in the subfigures (a) – (d)

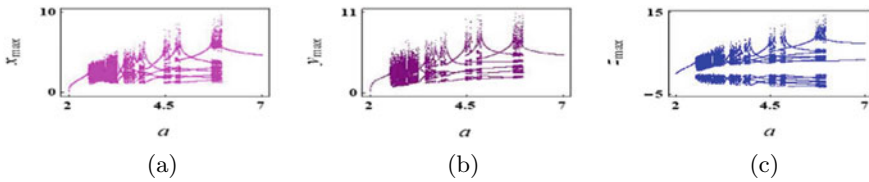


**Fig. 2** Bifurcation diagram of  $x_{\max}$ ,  $y_{\max}$  and  $z_{\max}$  of the solution orbit of the WBO system (1) for  $700 \leq t \leq 1000$  against the parameter  $a$  when  $b = 1$ ,  $c = 0.5$ ,  $d = 2$

can only state that the parameters present in the system have significant effect not only on the nature of the equilibrium point  $P_0$ , but also on the stability of the periodic solution. In order to have a proper idea regarding the effect of the parameter  $a$  on the periodic or chaotic nature of the solution orbit we draw the bifurcation diagram of  $x_{\max}$ ,  $y_{\max}$  and  $z_{\max}$  for  $700 \leq t \leq 1000$  against  $a$  as shown in Fig. 2.

It is clear from these figures that the system (1) exhibits sensitive dependence on the values the parameter  $a$ . The periodic and chaotic regimes occur alternately in the spectrum of the parameter  $a$ . Extensive study has been performed [1, 17, 25] for this classical third order WBO. A transmitter made by WBO generates sinusoidal waves which can be easily captured by a receiver thereby making a consistent communication system. However, such periodic transmission can be captured by any receiver synchronizing the parameter values without facing much difficulties, which makes the communication system open to all. Confidential information cannot be transmitted through such a system. A confidential information requires the data to be encrypted in such a manner that cannot be decrypted by anyone without the detailed specification of the communication system. Such a secure communication channel can be established by the synchronization of chaos, through which information can be transmitted and received and finally decrypted only when the chaotic data can be generated identically in the receiver end. Sensitive dependence of the system on more than one parameters like  $a$  may produce an additional layer of security and in order to introduce such extra layer we apply external generalized sinusoidal stimuli to the system (1) and construct the generalized forced system (2) and check if the externally excited system produce chaotic output signal controlled by the parameters  $f_1$ ,  $f_2$ ,  $f_3$  and  $\omega$ .

### 3 Qualitative Behaviour of Forced Wien Bridge Oscillator

The dynamic behaviour of nonautonomous memristor oscillator circuits have been investigated by several authors [24] showing complex dynamics induced by variations of the amplitude and frequency of the external stimulus and system parameters. Several experimental, simulative and theoretical aspects of the memristor have been studied by many authors [1, 17, 22, 25] in the last decade exhibiting different higher

and lower order complex dynamics. Such complex dynamical behaviour of the system are very much useful in the construction of chaotic communication system and remarkable results have been achieved by many researchers [6, 15, 26, 27]. The characters of chaotic signals, such as nonlinearity, unstability, aperiodicity etc. have made it attractive for the use in the chaotic communication to enhance the level of security of the transmission of the encrypted data. In this section we shall investigate how the external periodic forces applied on the traditional wien bridge oscillator impact on the generation of chaotic solution and construct an enhanced layer of security over the system parameters.

### 3.1 Effect of Amplitude of the Driven Forces

We first study the forced Wien bridge oscillator (FWBO) given by (2) for  $a = 2$ ,  $b = 1$ ,  $c = 0.5$ ,  $d = 2$  and check the behaviour of its solution for the special case when  $f_1 = f_2 = f_3 = f$  (say) and  $f$  increases in the range  $0 \leq f \leq 4$ , where we have chosen  $\omega = 1$ . We present the bifurcation diagram of the  $x, y$  coordinates of the points on the Poincare section of the solution by the half plane  $z = 0, x \geq 0$  along with the distance  $r = \sqrt{x^2 + y^2}$  from the fixed point  $P_0(0, 0, 0)$  in Fig. 3a-c as  $f$  increases in the range  $0 \leq f \leq 4$ . We observe that the deformation of the periodic orbit starts at  $f = 3.54$  and finally lead to chaotic orbit as  $f$  increases. We choose a specimen value  $f = 3.65$  from the chaotic regime and draw the solution orbit as shown in the Fig. 3d. The Poincare section of this orbit by the half plane  $z = 0, x \geq 0$  is presented in the Fig. 3e. The corresponding plots of  $x(t), y(t), z(t)$  are shown in Fig. 3f for  $700 \leq t \leq 1000$ .

The bifurcation diagrams shown in Fig. 3a-c clearly show that the FWBO produces periodic oscillation for a wide range of values of  $f$ . However, this periodic nature of the solution breaks and it deforms into unstable orbit which ultimately produces chaotic behaviour for little increase in the value of the amplitude  $f$ . In order to get a clear idea the solution orbit for  $f = 3.65$  is displayed in Fig. 3d which evidently shows that the orbit is not periodic at all for  $700 \leq t \leq 1000$ . It is clear that the orbit is chaotic in nature and becomes evident from its Poincare section in Fig. 3e, though some decisive tests such as 0-1 test is required to be performed as discussed in Sect. 4. The solutions  $x, y, z$  plotted against  $t$  in the Fig. 3f do not have any periodic nature. If the value of the parameter  $f$  is increased further the chaotic solution again deforms to period one. We clearly obtain periodic orbit when  $f$  increases beyond 3.765. Thus, we identify a small window of  $f$  for which the FWBO produces chaotic solution. Identification of such small window is necessary for the enhancement of the security of the chaotic communication system.



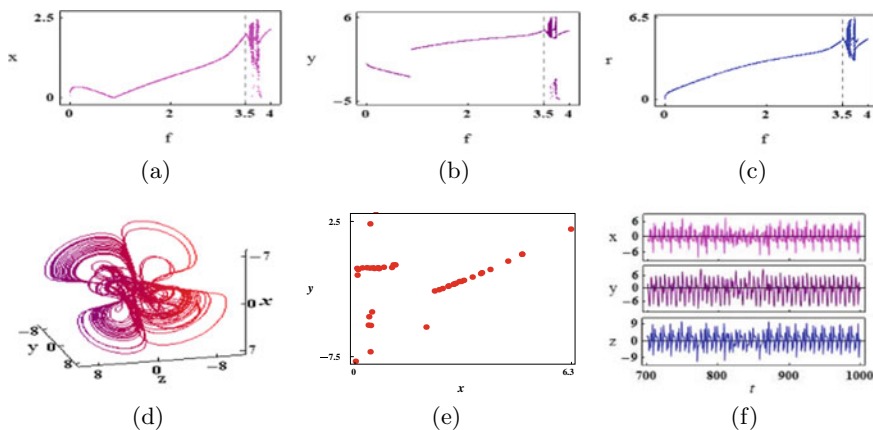


**Fig. 3** Bifurcation diagram of **a** the  $x$  coordinate, **b** the  $y$  coordinate, **c** the distance  $r = \sqrt{x^2 + y^2}$  from  $P_0(0, 0, 0)$  for the points of the Poincare section of the solution of the FWBO system (2) by the half plane  $z = 0, x \geq 0$  against the parameter  $f$ . **d** The solution orbit of the system (2) for  $f = 3.65$ , **e** corresponding Poincare section by the half plane  $z = 0, x \geq 0$  and **f** plots of  $x(t), y(t), z(t)$  for  $700 \leq t \leq 1000$ . Here,  $a = 2, b = 1, c = 0.5, d = 2, \omega = 1$  and  $f_1 = f_2 = f_3 = f$  in all the subfigures

### 3.2 Effect of Frequency of the Driven Forces

We next study the effect of the parameter  $\omega$  on the system (2). The vertical gridlines in Fig. 3a-c at  $f = 3.5$  show that the solution of this system is periodic for  $\omega = 1$ . We now see how the behaviour of the solution changes when the frequency  $\omega$  of the externally applied force vary. In order to study elaborately we may inspect the bifurcation diagram of the  $x, y$  coordinates of the points on the Poincare section of the solution along with the distance  $r = \sqrt{x^2 + y^2}$  when  $700 \leq t \leq 1000$  in Fig. 4a-c as  $\omega$  increases from 0.95 to 1. We find that as  $\omega$  decreases, the nature of the solution of the system deforms from periodic to chaotic through the route of periodic doubling bifurcation, starting from  $\omega = 0.9872$ . The chaotic orbit is observed when  $\omega$  decreases further and becomes less than 0.9829. Similar bifurcation diagrams are also plotted in Fig. 4d-f when  $\omega$  increases from 1.3 to 1.44. One may observe bifurcation of the periodic solution starting from  $\omega = 1.379$  and generates chaotic solution, but in this case it does not follow the route of periodic doubling. Thus, we identify two ranges of  $\omega$ , viz.  $0.95 \leq \omega \leq 0.9829$  and  $1.379 \leq \omega \leq 1.44$  in which the system (2) exhibits chaotic behaviour. Therefore, signals generated by FWBO in this kind of unusual windows of the frequency  $\omega$  may be securely transmitted exploiting its chaotic nature.

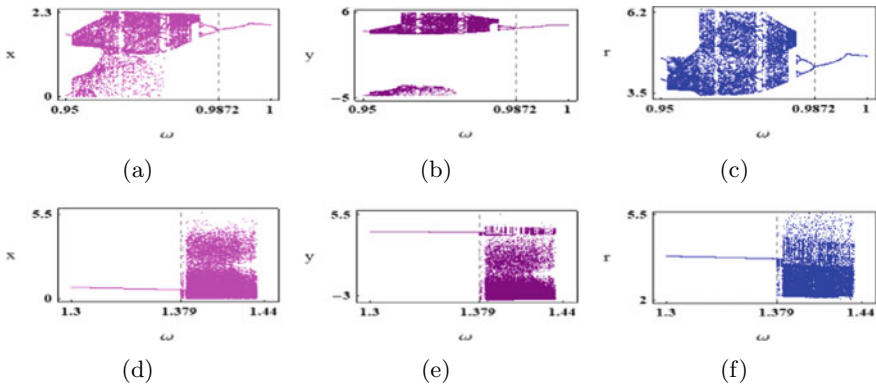


**Fig. 4** Bifurcation diagram of **a** the  $x$  coordinate, **b** the  $y$  coordinate, **c** the distance  $r = \sqrt{x^2 + y^2}$  from  $P_0(0, 0, 0)$  for the points of the Poincare section of the solution of the FWBO system (2) by the half plane  $z = 0, x \geq 0$  against the parameter  $\omega$  when  $0.95 \leq \omega \leq 1$ . Similar bifurcation diagram of **d** the  $x$  coordinate, **e** the  $y$  coordinate, **f** the distance  $r = \sqrt{x^2 + y^2}$  against the parameter  $\omega$  when  $1.3 \leq \omega \leq 1.44$ . Here,  $a = 2, b = 1, c = 0.5, d = 2$  and  $f_1 = f_2 = f_3 = f = 3.5$  in all the subfigures

### 3.3 Effect of Variable Amplitude of the Driven Forces

We have observed the effect of the external forces on the FWBO and identified some ranges of the amplitude  $f$  and frequency  $\omega$  in which the solution of the system has chaotic behaviour. So far we have imposed the restriction that  $f_1 = f_2 = f_3 = f$  (say). Here, we investigate the system under little general criteria assuming  $f_3 \neq f = f_1 = f_2$ . Similar to the Fig. 3d we fix  $f_3 = 3.65$ , but decrease the value of  $f$  and investigate the behaviour of the system. The Fig. 5 show the bifurcation of the  $x, y$  coordinates of the points on the Poincare section of the solution along with the distance  $r = \sqrt{x^2 + y^2}$  by the half plane  $z = 0, x \geq 0$  for the interval  $700 \leq t \leq 1000$ . It is interesting to see that the solution does not intersect the half plane for  $1.82725 \leq f \leq 2.16375$ . We, therefore, check the section of the solution orbit by the half plane  $z = -2, x \geq 0$  and find that it is periodic in this range and so no such diagram is presented here. Thus, we find that the system produces chaotic oscillation for quite a large value of the amplitude  $f$  of the driven forces.

## 4 The 0-1 Test for Chaos Applied on the FWBO

One standard technique for determination of the chaotic nature of a solution is to compute the maximal Lyapunov exponent [9]. Recently Gottwald and Melbourne proposed a new method [8] for detecting chaotic dynamics, known as 0-1 Test, which can be applied to ordinary and partial differential equations as well as on

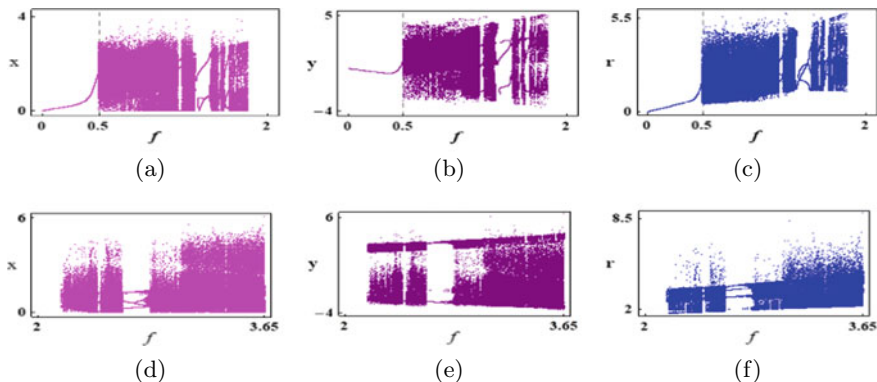


**Fig. 5** Bifurcation diagram of **a** the  $x$  coordinate, **b** the  $y$  coordinate, **c** the distance  $r = \sqrt{x^2 + y^2}$  from  $P_0(0, 0, 0)$  for the points of the Poincare section of the solution of the FWBO system (2) by the half plane  $z = 0, x \geq 0$  against the parameter  $f$  when  $0 \leq f \leq 2$ . Similar bifurcation diagram of **d** the  $x$  coordinate, **e** the  $y$  coordinate, **f** the distance  $r = \sqrt{x^2 + y^2}$  against the parameter  $f$  when  $2 \leq f \leq 3.65$ . Here,  $a = 2, b = 1, c = 0.5, d = 2, f_3 = 3.65$  and  $f_1 = f_2 = f$  in all the subfigures

maps. Even if the deterministic time series data is provided, one can bypass the phase space reconstruction technique using this 0-1 test and determine whether a solution is chaotic or non-chaotic. The simplicity of the technique has drawn the attention of many researchers in the recent past [7, 13, 18]. The main advantages of this test are (i) it is binary i.e., the output of this test can be 0 or 1, (ii) the nature of the vector field and the dimension of the system do not impose any practical limitations, (iii) the difficulty of the phase space reconstruction process can be avoided for time series data. In this section we apply the 0-1 test on FWBO for specific values of the parameters, as a specimen, to check if the signal so generated is chaotic in nature. We choose the parameter values given by (3) and

$$a = 2, f_1 = f_2 = 1, f_3 = 3.65, \omega = 1.4 \tag{4}$$

and verify whether the corresponding solutions  $x(t), y(t)$  and  $z(t)$  of FWBO are chaotic.

We briefly review this test in the context of the solution  $x(t)$ . The test has undergone through different equivalent modifications [8]. We are following the version, known as correlation method, discussed in [21] where a pseudo code is provided to determine the output  $K$  of the test. The values of  $x(t)$  are discretized to  $x_j = x(t_j)$  for  $j = 1, 2, \dots, N$  and generate the translation variables

$$p_n(c) = \sum_{j=1}^n x_j \cos(jc), q_n(c) = \sum_{j=1}^n x_j \sin(jc) \tag{5}$$

for  $n = 1, 2, \dots, N$ , where  $c \in (0, \pi)$ , with little abuse of notation of the parameter  $c$  in the FWBO (2). One important property of the test is that the method is independent of the discrete values of the solution and almost any choice of  $x_j$  will serve the requirement. The only precaution one should take is that discrete values must be chosen after sufficient long time so that the trajectories lie on the attractor or remain close to the attractor. Keeping this in mind we choose  $t_j$  in the domain  $[700, 10000]$  by considering  $t_1 = 700$  and choosing the subsequent values of  $t$  at a distance  $\Delta t = 2$  so that  $t_j = t_1 + (j - 1) \Delta t$ . The second important necessary requirement for the scheme is that the time series should be long enough to allow for asymptotic behaviour of  $p_n(c)$  and  $q_n(c)$ , which means that the value of  $N$  should be taken sufficiently large.

It is notable that the output of the test is independent of the choice of the parameter  $c$ . It can be rigorously shown that  $p_n(c)$  and  $q_n(c)$  are bounded if the underlying dynamics is periodic or quasiperiodic, whereas they behave like Brownian motion for large class of chaotic dynamical systems. These behaviours can be investigated by analyzing the mean square displacement defined by

$$M_n(c) = \lim_{n \rightarrow \infty} \frac{1}{N} \sum_{j=1}^N [p_{n+j}(c) - p_j(c)]^2 + [q_{n+j}(c) - q_j(c)]^2 \tag{6}$$

for  $n = 1, 2, \dots, N_c \ll N$ . In practice we have the approximate formula

$$M_n(c) \simeq \frac{1}{N} \sum_{j=1}^N [p_{n+j}(c) - p_j(c)]^2 + [q_{n+j}(c) - q_j(c)]^2 \tag{7}$$

where  $N$  is taken as a sufficiently large positive integer. The mean square displacement is a bounded function if the underlying signal is periodic or quasiperiodic, whereas it becomes unbounded for chaotic data. The asymptotic growth rate  $K(c)$  is defined by

$$K(c) = \lim_{n \rightarrow \infty} \rho(\mathbf{t}_n, \mathbf{M}_n(c)) \tag{8}$$

where  $\mathbf{t}_n = (t_1, t_2, \dots, t_n)$  and  $\mathbf{M}_n(c) = (M_1(c), M_2(c), \dots, M_n(c))$  and  $\rho$  designates the correlation coefficient between  $\mathbf{t}_n$  and  $\mathbf{M}_n(c)$ . This  $K(c)$  is practically computed by the approximation  $K_n(c) = \rho(\mathbf{t}_n, \mathbf{M}_n(c))$  for  $n = N_c$ . The process involves different approximations of  $M_n(c)$  and  $K(c)$  which may produce little variation in the asymptotic growth rate. The value of  $K(c)$  will be 1 for chaotic signal and 0 for periodic or quasiperiodic signal. However, the approximation process involved in the computation scheme will produce the value of  $K(c)$  close to either 1 or 0. In our computation we have taken  $N = 3200$ ,  $N_c = 400$ ,  $c = 1$  and the plot of  $p_n$  versus  $q_n$  is shown in Fig. 6a along with the graph of  $M_n(c)$  in Fig. 6b. The graph of  $K_n(c)$  is plotted in Fig. 6c for  $n \leq N_c$  showing that  $K_n(c) \simeq 1$  at  $n = N_c$ . Although the quantity  $K(c)$  is expected to produce a value which does not depend on  $c$ , the approximation process involved in this scheme may produce unexpected variation

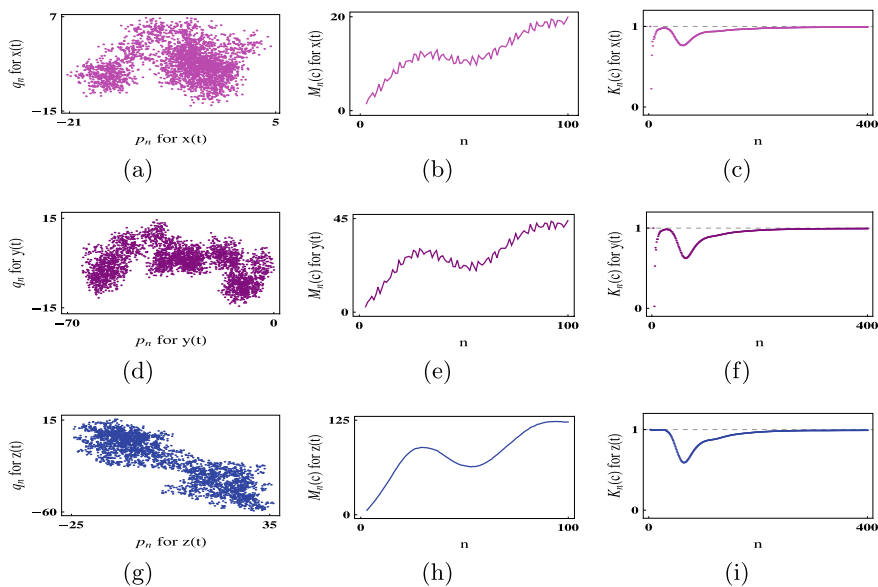


**Fig. 6** **a** The  $p_n$  versus  $q_n$  plot, **b** the graphs of  $M_n$ , **c** the graph of  $K_n$  computed for the solution  $x(t)$  of the FWBO system (2). Analogously, **d** The  $p_n$  versus  $q_n$  plot, **e** the graphs of  $M_n$ , **f** the graph of  $K_n$  computed for the solution  $y(t)$  of the system (2). Finally, **g** The  $p_n$  versus  $q_n$  plot, **h** the graphs of  $M_n$ , **i** the graph of  $K_n$  computed for the solution  $z(t)$  of the system (2). Here, the values of the parameters are given by (3) and (4) in all the subfigures

in the approximation of  $K(c)$  for some isolated value of  $c$ , such as resonant points. This problem is treated by considering  $K = \text{median} \{K(c_1), K(c_2), \dots, K(c_m)\}$ , where  $c_1, c_2, \dots, c_m$  are chosen randomly from the domain  $(0, \pi)$ . The median is taken in place of mean because of the fact that median is robust and less sensitive against outliers associated to resonances. We have restricted, for simplicity, the domain of  $c$  to  $[0.5, 1.5]$  and taken equidistant values of  $c$  as

$$c_1 = 0.5, c_2 = 0.75, c_3 = 1, c_4 = 1.25, c_5 = 1.5$$

and found the approximations  $K(c_1) = 0.990825, K(c_2) = 0.988733, K(c_3) = 0.994847, K(c_4) = 0.995746, K(c_5) = 0.995214$  and get  $K = 0.994847 \simeq 1$  showing that the solution  $x(t)$  is chaotic.

Analogous computations are performed for  $y(t)$  and  $z(t)$ . The  $p_n$  versus  $q_n$  plot, the graphs of  $M_n(c)$  and  $K_n(c)$  are shown in the Fig. 6d-f with  $c = 1$  for  $y(t)$ . Similar plots for  $z(t)$  are shown in Fig. 6g-i. The signals represented by  $y(t)$  produce the approximations  $K(c_1) = 0.997263, K(c_2) = 0.991210, K(c_3) = 0.995412, K(c_4) = 0.997774, K(c_5) = 0.978373$  so that  $K = 0.995412 \simeq 1$ . The signals represented by  $z(t)$  produce the approximations  $K(c_1) = 0.998093,$

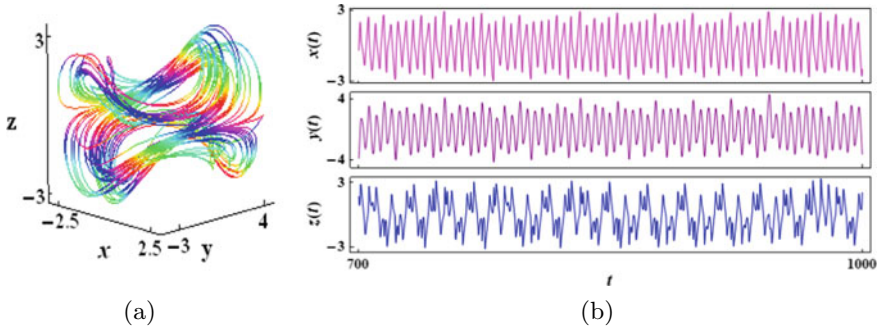


**Fig. 7** **a** The solution orbit of the FWBO system (2) and **b** the corresponding  $x(t)$ ,  $y(t)$ ,  $z(t)$ . Here, the values of the parameters are given by (3) and (4) in all the subfigures

$K(c_2) = 0.995041$ ,  $K(c_3) = 0.991666$ ,  $K(c_4) = 0.995254$ ,  $K(c_5) = 0.994567$  so that  $K = 0.995041 \simeq 1$ . Thus, we observe that the solutions  $y(t)$  and  $z(t)$  produce chaotic signals which can be used in the chaotic transmission. Therefore, the 0-1 test confirms the chaotic nature of the output signals generated by the FWBO where the parameter values of the system are given by (3) and (4). The solution orbit of this system is displayed in the Fig. 7a and the corresponding  $x(t)$ ,  $y(t)$ ,  $z(t)$  are presented in Fig. 7b.

## 5 Conclusion

A model of Wien bridge oscillator driven by external sinusoidal stimulus have been studied and regimes of the parameters of these external forces have been identified over which the signal so generated becomes very much unpredictable enhancing the security in chaotic communication system. A theoretical analysis of the system dynamics has been performed using phase portraits, bifurcation diagrams. It is found that the external periodic stimuli are responsible to generate chaotic carrier signals. The signals generated by the circuit have been tested by 0-1 test confirming its chaotic nature. The behaviour of the output generated under other kind of external stimulus such as digital, trapezoidal, triangular, sawtooth signals remains an open problem and will be studied elsewhere.

## References

1. Bao, B., Wu, P., Bao, H., Wu, H., Zhang, X., Chen, M.: Symmetric periodic bursting behavior and bifurcation mechanism in a third-order memristive diode bridge-based oscillator. *Chaos, Solit. Fract.* **109**, 146–153 (2018)
2. Burkin, I., Khien, N.N.: Analytical-numerical methods of finding hidden oscillations in multidimensional dynamical systems. *Diff. Equ.* **50**(13), 1695–1717 (2014)
3. Chen, M., Li, M., Yu, Q., Bao, B., Xu, Q., Wang, J.: Dynamics of self-excited attractors and hidden attractors in generalized memristor-based chua's circuit. *Nonl. Dyn.* **81**(1), 215–226 (2015)
4. Chua, L.: Memristor-the missing circuit element. *IEEE Transactions on circuit theory* **18**(5), 507–519 (1971), publisher: IEEE
5. Chua, L.O., Kang, S.M.: Memristive devices and systems. *Proceedings of the IEEE* **64**(2), 209–223 (1976), publisher: IEEE
6. Çiçek, S., Kocamaz, U.E., Uyaroğlu, Y.: Secure chaotic communication with jerk chaotic system using sliding mode control method and its real circuit implementation. *Iranian J. Sci. Technol. Trans. Elect. Eng.* **43**(3), 687–698 (2019)
7. Dawes, J., Freeland, M.: The '0–1 test for chaos' and strange nonchaotic attractors. preprint (2008)
8. Gottwald, G.A., Melbourne, I.: On the implementation of the 0–1 test for chaos. *SIAM J. Appl. Dyn. Syst.* **8**(1), 129–145 (2009)
9. Kantz, H., Schreiber, T.: *Nonlinear time series analysis*, vol. 7. Cambridge university press (2004)
10. Kiseleva, M., Kudryashova, E.V., Kuznetsov, N.V., Kuznetsova, O.A., Leonov, G.A., Yuldashev, M.V., Yuldashev, R.V.: Hidden and self-excited attractors in chua circuit: synchronization and spice simulation. *Int. J. Paral. Em. Distr. Syst.* **33**(5), 513–523 (2018)
11. Leonov, G., Kuznetsov, N.: Localization of hidden oscillations in dynamical systems (plenary lecture). In: 4th International Scientific Conference on Physics and Control (2009)
12. Lv, M., Ma, J.: Multiple modes of electrical activities in a new neuron model under electromagnetic radiation. *Neurocomputing* **205**, 375–381 (2016)
13. Martinsen-Burrell, N., Julien, K., Petersen, M.R., Weiss, J.B.: Merger and alignment in a reduced model for three-dimensional quasigeostrophic ellipsoidal vortices. *Phys. Fluids* **18**(5), 057101 (2006)
14. Oppenheim, A.V., Wornell, G.W., Isabelle, S.H., Cuomo, K.M.: Signal processing in the context of chaotic signals. In: *icassp*. vol. 4, pp. 117–120 (1992)
15. Pham, V.T., Volos, C., Jafari, S., Vaidyanathan, S., Kapitaniak, T., Wang, X.: A chaotic system with different families of hidden attractors. *Int. J. Bifurc. Chaos* **26**(08), 1650139 (2016)
16. Rabbani, P., Dehghani, R., Shahpari, N.: A multilevel memristor-cmos memory cell as a reram. *Microelect. J.* **46**(12), 1283–1290 (2015)
17. Rajagopal, K., Li, C., Nazarimehr, F., Karthikeyan, A., Duraisamy, P., Jafari, S.: Chaotic dynamics of modified wien bridge oscillator with fractional order memristor. *Radioengineering* **28**(1), 165–174 (2019)
18. Skokos, C., Antonopoulos, C., Bountis, T., Vrahatis, M.: Detecting order and chaos in hamiltonian systems by the sali method. *J. Phy. A: Mathem. General* **37**(24), 6269 (2004)
19. Stankevich, N.V., Kuznetsov, N.V., Leonov, G.A., Chua, L.O.: Scenario of the birth of hidden attractors in the chua circuit. *Int. J. Bifurc. Chaos* **27**(12), 1730038 (2017)
20. Strukov, D.B., Snider, G.S., Stewart, D.R., Williams, R.S.: The missing memristor found. *Nature* **453**(7191), 80–83 (2008)
21. Tosin, M., Issa, M.V., Matos, D., Do Nascimento, A., Cunha Jr, A.: Employing 0-1 test for chaos to characterize the chaotic dynamics of a generalized gauss iterated map. In: *XIV Conferência Brasileira de Dinâmica, Controle e Aplicações (DINCON 2019)* (2019)
22. Wu, H., Bao, B., Liu, Z., Xu, Q., Jiang, P.: Chaotic and periodic bursting phenomena in a memristive wien-bridge oscillator. *Nonl. Dyn.* **83**(1), 893–903 (2016)

23. Xia, X., Zeng, Y., Li, Z.: Coexisting multiscroll hyperchaotic attractors generated from a novel memristive jerk system. *Pramana* **91**(6), 1–14 (2018)
24. Xu, Q., Zhang, Q., Jiang, T., Bao, B., Chen, M.: Chaos in a second-order non-autonomous wien-bridge oscillator without extra nonlinearity. *Circuit world* (2018)
25. Ye, X., Mou, J., Luo, C., Wang, Z.: Dynamics analysis of wien-bridge hyperchaotic memristive circuit system. *Nonl. Dyn.* **92**(3), 923–933 (2018)
26. Zarei, A.: Complex dynamics in a 5-d hyper-chaotic attractor with four-wing, one equilibrium and multiple chaotic attractors. *Nonl. dyn.* **81**(1), 585–605 (2015)
27. Zhao, Q., Wang, C., Zhang, X.: A universal emulator for memristor, memcapacitor, and meminductor and its chaotic circuit. *Chaos: An Interdisciplinary Journal of Nonlinear Science* **29**(1), 013141 (2019)



# The Electrodynamic Origin of the Wave-Particle Duality



Álvaro García López 

**Abstract** A derivation of pilot waves from electrodynamic self-interactions is presented. For this purpose, we abandon the current paradigm that describes electrodynamic bodies as point masses. Beginning with the Liénard-Wiechert potentials, and assuming that inertia has an electromagnetic origin, the equation of motion of a nonlinear time-delayed oscillator is obtained. We analyze the response of the uniform motion of the electromagnetic charged extended particle to small perturbations, showing that very violent oscillations are unleashed as a result. The frequency of these oscillations is intimately related to the *zitterbewegung* frequency appearing in Dirac's relativistic wave equation. Finally, we compute the self-energy of the particle. Apart from the rest and the kinetic energy, we uncover a new contribution presenting the same fundamental physical constants that appear in the quantum potential.

**Keywords** Nonlinear dynamics · Chaos · Delay differential equations · Electrostatics · Retarded potentials · Pilot waves · Quantum mechanics

## 1 Introduction

Recently developed models of silicon droplets have shown deep connections between quantum mechanical systems and classic hydrodynamics, allowing nonlinear dynamists to grasp how the complex motion of a quantum particle can be [1, 2]. More specifically, these macroscopic systems describe the unpredictable dynamics of walking droplets as the result of a feedback interaction between the bouncing particle and the waves that it produces when it strikes the surface of a fluctuating medium underneath, close to and even beyond the Faraday threshold. Fortunately, and contrary to quantum mechanical models, these hydrodynamic analogs are investigated in terms of understandable and firmly established principles of chaos theory and nonlinear dynamical systems.

---

Á. García López (✉)

Universidad Rey Juan Carlos, Móstoles s/n 28933, Madrid, Spain  
e-mail: [alvaro.lopez@urjc.es](mailto:alvaro.lopez@urjc.es)

© The Author(s), under exclusive license to Springer Nature Switzerland AG 2022  
S. Banerjee and A. Saha (eds.), *Nonlinear Dynamics and Applications*,  
Springer Proceedings in Complexity,  
[https://doi.org/10.1007/978-3-030-99792-2\\_88](https://doi.org/10.1007/978-3-030-99792-2_88)

1043

Although the pilot wave dynamics of silicon droplets has been proposed as a candidate to comparatively investigate quantum systems, a specific homologous mechanism that can give rise to the wave-particle duality in the microscopic realm has not been rigorously developed until very recently [3]. In the present paper we provide strong evidence suggesting that the wave-particle duality has its basis in the theory of classical electromagnetism. For this purpose, we show that extended charged bodies can self-interact when they are accelerated. A certain region of the particle can emit radiation, which later on affects a different region of the same particle. This phenomenon introduces a time-delay in the self-force of the extended body.

Consequently, the description of the dynamics of charged bodies must be posed by means of retarded differential equations. As it is well-known, the solutions to these differential equations frequently present limit cycle behaviour as a consequence of the Andronov-Hopf bifurcation [4, 5]. The feedback interaction of radiative and Coulombian fields among different charged parts of the particle can trigger a fast oscillation, destabilizing its uniform motion. These fields produce dissipation and antidamping as a consequence of radiation reaction. In the thermodynamic context of open systems, such a periodic motion has been recently referred as a self-oscillation [6]. In this manner, we show that the wave-particle duality is just an immediate consequence of the self-oscillation of extended electrodynamic bodies, which can be regarded as dissipative structures.

## 2 Electrodynamics of an Extended Body

We model the electrodynamics of an extended charged body by using the Lagrangian density of Maxwell's theory of electrodynamics with sources. This density is written as

$$\mathcal{L} = -\frac{1}{4\mu_0} F_{\mu\nu} F^{\mu\nu} - A_\mu J^\mu, \quad (1)$$

where  $J^\mu$  denotes the four-current density representing the sources, and  $F^{\mu\nu}$  is the Faraday tensor. Then, Maxwell's equations can be derived in covariant form from the previous action by differentiation, yielding

$$\partial_\mu F^{\mu\nu} = \mu_0 J^\nu. \quad (2)$$

To describe the dynamics of the source of charge, we express the four-density as  $J^\mu = \rho_0 U^\mu$ , where the density of charge  $\rho_0$  in the proper frame and the four-velocity  $U^\mu$  have been introduced. The charge density  $\rho$  in some inertial reference frame can be related to the density in the proper frame by using the Lorentz factor  $\gamma$ , through the relation  $\rho = \gamma\rho_0$ . Then, the four-current is simply written as  $J^\mu = (\rho c, J)$ , with  $J = \rho v_s$  the euclidean current density. Here we are considering a rigid distribution of charge. This assumption allows us to write the charge density at time  $t$  as  $\rho(x, t) = \rho(x - x_s(t))$ , where the vector  $x_s(t)$  represents the position of the particle's centre

of mass at time  $t$ . Under these assumptions, Maxwell's equations can be solved in terms of retarded potentials, which allow to generally derive the fields by means of Jefimenko's equations. Using the fact that  $F_{\mu\nu} = \partial_\mu A_\nu - \partial_\nu A_\mu$ , the four-potential in the Lorenz gauge can then be written as

$$A^\mu(x, t) = \frac{1}{4\pi\epsilon_0 c^2} \int \frac{J^\mu(x, t_r)}{|x - x'|} d^3x', \quad (3)$$

where we have introduced the retarded time  $t_r = t - |x - x'|/c$ . The analysis presented ahead considers a very simple rigid charged distribution comprised of two point particles at a fixed distance. Therefore, in order to compute the self-force, we can simply use the *Liénard-Wiechert potential*. This potential is the solution to a charged point particle, whose charge density can be represented by means of the Dirac delta distribution, in the form  $\rho(x, t) = q\delta(x - x_s(t))$ . In the Lorenz gauge we have the solution

$$A^\mu(x, t) = \frac{q}{4\pi\epsilon_0 c} \left( \frac{v^\mu}{(1 - n_s \cdot \beta_s)|x - x_s|} \right)_{t=t_r}, \quad (4)$$

where the relative speed of the source  $\beta_s(t) = v_s(t)/c$  has been defined, together with the time-like four-vector  $v_s^\mu = (c, v_s(t))$ . Finally, the unit vector  $n_s(x, t) = (x - x_s(t))/|x - x_s(t)|$  has also been introduced. It points to the spatial point  $x$ , where we want to compute the value of the fields. Its application point is located at the position  $x_s(t)$ , where the charge was placed at the retarded time  $t = t_r$ .

## 2.1 A Model of an Electron

In the preset work we consider the charge density  $\rho(x, t) = -(e/2)\delta(x - x_s(t))\delta(z)(\delta(y + d/2) + \delta(y - d/2))$ . It is the most simple model of an electron, represented as an "extended" electrodynamic body, as shown in Fig. 1. This charge density represents a body formed by two points with charge  $-e/2$  placed at a fixed distance  $d$  in the  $y$ -axis, which moves along the  $x$ -axis. We restrict the motion to transversal displacements to simplify our study, since the non-conservative character of electrodynamics with sources makes the computations very entangled, due to the fact that the Liénard-Wiechert potential is retarded in time. By restricting ourselves to a one-dimensional translational motion, we avoid the more complicated three-dimensional problem, including self-torques. This fundamental model has been designed in previous works to underpin the use of the *Abraham-Lorentz* force and also to study the contribution of electromagnetic mass to inertia [7]. We use this elementary model hereafter, which suffices to explain the physical mechanism leading to the wave-particle duality.

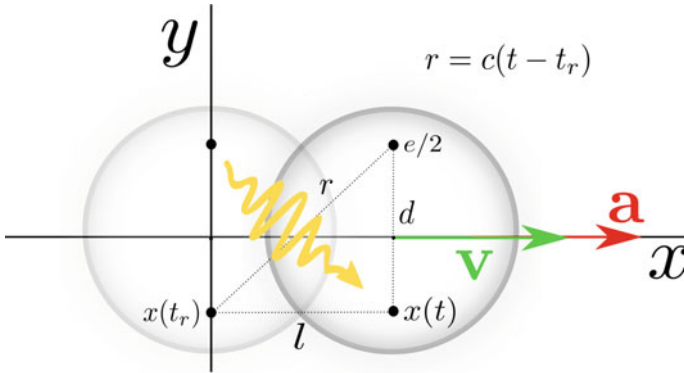


**Fig. 1** An electron is shown at the retarded time  $t_r$  and at the present time  $t$ . It consists of two point charges placed along the  $y$ -axis at a constant distance  $d$ . From  $t_r$  to  $t$ , the particle accelerates and advances a distance  $l$  along the  $x$ -axis. A field perturbation is shown emerging from the upper point at the retarded time (yellow photon). Later on, this perturbation exerts a force on the second point at the lower side of the body. In this manner, an extended corpuscle can feel itself in the past. The speed  $v$  and the acceleration  $a$  of the particle are represented in green and red, for clearness

## 2.2 The Self-Interaction

As shown in Fig. 1, an extended electrodynamic body can interact with itself. This kind of interaction is frequently called a *self-interaction* [7]. The upper charged point exerts an electromagnetic force on the lower point a short time later. The self-force appears because electromagnetic waves can travel between the two points of the electrodynamic body. Apart from a force of inertia, a term of damping and a restoring elastic force, it can induce the self-excited motion of the particle due to a radiation reaction force. We now compute the electric field produced by the upper point at the lower point of the body. If we utilize the Liénard-Wiechert potential of a point particle, we obtain

$$E = \frac{q}{8\pi\epsilon_0} \frac{r}{(\mathbf{r} \cdot \mathbf{u})^3} \left( \mathbf{u}(1 - \beta^2) + \frac{1}{c^2} \mathbf{r} \times (\mathbf{u} \times \mathbf{a}) \right), \quad (5)$$

where the relative position between the two points at different times is  $\mathbf{r}(t_r)$ , the normalized velocity is  $\boldsymbol{\beta}(t_r) = \mathbf{v}(t_r)/c$ , the acceleration  $\mathbf{a}(t_r)$  and the vector  $\mathbf{u} = \hat{\mathbf{r}} - \boldsymbol{\beta}$  has been introduced. We highlight that these kinematic variables depend on the retarded time  $t_r = t - r/c$ . This time-delay appears because electromagnetic field perturbations travel with limited velocity in spacetime, according to the principle of *causality*. This limitation puts a constraint  $r = c(t - t_r)$  on the self-interaction, assigning a specific event in the past light cone from which the signals coming from one point of the particle can affect the remaining point.

According to Fig. 1, we can write the position as  $\mathbf{r} = l\hat{\mathbf{x}} + d\hat{\mathbf{y}}$ , the velocity as  $\boldsymbol{\beta} = v/c\hat{\mathbf{x}}$  and the acceleration vector as  $\mathbf{a} = a\hat{\mathbf{x}}$ . These relations allow to compute the vector  $\mathbf{u}$  as  $\mathbf{u} = (l - r\beta)/r\hat{\mathbf{x}} + d/r\hat{\mathbf{y}}$ . Then, making use of the identity  $r^2 = (x(t) - x(t_r))^2 + d^2$ , the following inner product  $\mathbf{r} \cdot \mathbf{u} = r - l\beta$  results. Regarding the radiative component of the field, we need to expand the double cross-product in the form  $\mathbf{r} \times (\mathbf{r}\mathbf{u} \times \mathbf{a}) = -d^2a\hat{\mathbf{x}} + dal\hat{\mathbf{y}}$ . The total self-force on the center of mass of the particle can be written as  $\mathbf{F}_{\text{self}} = -e\mathbf{E}$ , where the symmetry of the arrangement has been taken into consideration. Because of the rigidity of the charge density, we recall that the the magnetic attractive forces and the electric repulsive forces all cancel each other along the y-axis. The resulting force that the particle exerts on itself is

$$\mathbf{F}_{\text{self}} = \frac{e^2}{8\pi\epsilon_0} \frac{1}{(r - l\beta)^3} \left( (l - r\beta)(1 - \beta^2) - \frac{d^2}{c^2}a \right) \hat{\mathbf{x}}. \quad (6)$$

### 2.3 Time-Delayed Equation of Motion

Following the tradition, we could now invoke Newton's second law of mechanics. For a non-relativistic particle it is written as  $\mathbf{F}_{\text{self}} = m\mathbf{a}$ , with  $m$  the electron's bare mechanical mass. However, it has been shown in recent works that the self-force can be expanded by using a Taylor series of the time-delay  $r/c$  [3]. Among the infinite linear and nonlinear terms that contribute to the self-force, the most well-known are the Lorentz-Abraham force, which consists of a linear term proportional to the jerk ( $\dot{a}$ ) of the particle, and the term of inertia, which is proportional to the acceleration. This term dominates over all other terms in the limit of very small  $d/c$ , what allows to approximate the self-force as  $\mathbf{F}_{\text{self}} = -m_e\mathbf{a}$  for non-relativistic velocities. To this end, we simply define the electromagnetic mass as  $m_e c^2 = e^2/16\pi\epsilon_0 d$ , where Einstein's mass-energy relation has been obviously used.

In the present work we are assuming that the rest mass of the electron comes entirely from its electrostatic energy, so that its bare mass can be made equal to zero. For if mass is not a fundamental property of particles, but just energy, all the mass in our model must come from the electrostatic energy of the two point charges. Then, if we use Sommerfeld's relation for the fine structure constant, the rest mass of the electron is

$$m_e = \frac{\hbar\alpha}{4dc}. \quad (7)$$

Using this relation, we can approximate a electron radius of  $r_e = d/2 = 0.35$  fm. Naturally, this value is closely related to the the electron's classical radius.

Therefore, this approach does not artificially introduce bare mechanical inertia in the theory of classical electromagnetism. Instead, we use the *principle of D'Alembert* that, in the approximation of macroscopic objects, leads to Newton's second law. Thus classical mechanics should be considered an emergent theory resulting from

averaging magnitudes over large numbers of electrodynamic bodies. As a corollary, we predict that the gravitational force between two particles have an electrodynamic origin as well. Consequently, we propose to replace Newton's second law by the static problem

$$\mathbf{F}_{\text{ext}} + \mathbf{F}_{\text{self}} = 0. \quad (8)$$

As long as we can approximate  $\mathbf{F}_{\text{self}} = -m_e \mathbf{a}$  in the macroscopic limit, we see that Newton's second law naturally arises from Maxwell's dynamical theory of the electromagnetic field. The force of inertia reveals in this way as an electromagnetic force of *self-induction*, coming from the interior of the body as a consequence of Faraday's law. This statement opposes to Mach's principle, which tries to justify the origin of inertial forces on external distant masses.

To study the "free" particle, we can settle the external forces to zero, thus we have the simple law of motion  $\mathbf{F}_{\text{self}} = 0$ . Its solution describes the geodesic motion of the electrodynamic body in the same way as in the theory of general relativity, for example. The differential equation of motion is

$$\frac{d^2}{c^2} a(t_r) + \frac{r}{c} \left( 1 - \frac{v^2(t_r)}{c^2} \right) v(t_r) + \left( 1 - \frac{v^2(t_r)}{c^2} \right) (x(t_r) - x(t)) = 0. \quad (9)$$

The difficulty with this state-dependent *delayed differential equation* [8] is that most kinematic variables are specified at the retarded time  $t_r = t - r/c$ . If we translate them to the present time  $t \rightarrow t + r/c$ , we obtain

$$a(t) + \frac{r}{d} \frac{c}{d} \left( 1 - \frac{v^2(t)}{c^2} \right) v(t) + \left( \frac{c}{d} \right)^2 \left( 1 - \frac{v^2(t)}{c^2} \right) (x(t) - x(t + \frac{r}{c})) = 0. \quad (10)$$

This differential equation clearly evokes a nonlinear oscillator [6]. We can identify a term of Newtonian inertia and a typical linear oscillating term representing an elastic restoring force. But we can see two more nonlinear contributions, as well. Firstly, the contribution appearing in the second term acts as a nonlinear damping force, producing the system's dissipation. Secondly, the advanced potential produces a non-conservative force of antidamping.

The frequency of oscillation can be approximated as  $\omega_0 = c/d$ , what yields a value of the period  $T_0 = 4\pi r_e/c = 1.18 \times 10^{-22}$  s, if we use the electron's classical radius. Thus the electron oscillates very fast describing a deterministic motion. However, this motion resembles a stochastic motion at large enough time scales. This jittery dynamics and the specific value of its period are very familiar to quantum mechanical theorists. They are closely related to the trembling motion appearing in Dirac's wave equation equation for relativistic particles, commonly known as *zitterbewegung*.

Importantly, we notice that the time-delay and the damping term involve an *arrow of time*. Irreversibility is inherent to non-conservative dynamical systems presenting limit cycle behavior. It is also conventional in time-delayed systems, whose trajectories are not specified by some initial conditions, but rely on the complete knowledge of functions describing part of their previous history. Of course, this non-conservative

dynamics only appears when we try to describe the motion of the particle solely, without reference to the dynamical fields.

In summary, fundamental particles can be considered as open dissipative structures. They are locally active and operate far from equilibrium by taking and releasing electromagnetic energy to their surroundings. The dissipative nature of classical electrodynamics with sources becomes manifest by the fact that a Lagrangian density for the motion of the particle cannot be written by using the traditional minimal coupling, as it is frequently done in quantum particle physics.

### 3 Stability Analysis

Now we prove that transversal motion at constant speed is not stable. Consequently, self-oscillatory motion is the only possibility, irrespective of the periodicity of this nonlinear oscillation. For this purpose, we consider the differential Eq. (10) and pose it in the phase space canonical variables. We obtain

$$\begin{aligned} \dot{x} &= v, \\ \dot{v} &= -\frac{c}{d} \frac{r}{d} \left(1 - \frac{v^2}{c^2}\right) v - \left(\frac{c}{d}\right)^2 \left(1 - \frac{v^2}{c^2}\right) (x - x_\tau). \end{aligned} \tag{11}$$

The variable  $x_\tau$  has been introduced. It represents the electron’s position evaluated at time  $t + \tau$ , where we recall that  $\tau = r/c$ . Consider that motion at constant speed  $\beta c$  is feasible. Since  $x(t) = vt$ , we also have  $x(t + r/c) = vt + vr/c$ , what yields  $x - x_\tau = -vr/c$ . If we now substitute in Eq. (11) we get

$$\begin{aligned} \dot{x} &= v, \\ \dot{v} &= -\frac{c}{d} \frac{r}{d} \left(1 - \frac{v^2}{c^2}\right) v + \frac{c}{d} \frac{r}{d} \left(1 - \frac{v^2}{c^2}\right) v = 0. \end{aligned} \tag{12}$$

Therefore, every uniform motion is an invariant solution of our delayed dynamical system. We now prove that these solutions are unstable as well. For this purpose, we compute the variational equations

$$\begin{aligned} \delta\dot{x} &= \delta v, \\ \delta\dot{v} &= -\frac{c}{d} \frac{\delta r}{d} \left(1 - \frac{v^2}{c^2}\right) v - \frac{c}{d} \frac{r}{d} \left(1 - \frac{v^2}{c^2}\right) \delta v + \frac{c}{d} \frac{r}{d} \frac{2v^2}{c^2} \delta v - \\ &\quad - \frac{c}{d} \frac{r}{d} \frac{2v^2}{c^2} \delta v - \left(\frac{c}{d}\right)^2 \left(1 - \frac{v^2}{c^2}\right) (\delta x - \delta x_\tau). \end{aligned} \tag{13}$$

We follow by computing  $\delta r$  when  $\dot{v} = 0$ , with  $v = \beta c$ . For this purpose, we use the relation  $r^2 = (x(t) - x(t_r))^2 + d^2$  and Eq. (9). If we combine these two equations

we can derive polynomial of degree two in  $r$ . If we also introduce the Lorentz factor  $\gamma = (1 - \beta^2)^{-1/2}$ , the solution to this polynomial yields

$$r = \gamma d \sqrt{1 + \gamma^6 \dot{\beta}^2 \left(\frac{d}{c}\right)^2} + \gamma^4 c \beta \dot{\beta} \left(\frac{d}{c}\right)^2. \quad (14)$$

Recall, the speed and the acceleration appearing in Eq. 14 are evaluated at time  $t_r$ . Interestingly, the *time-delay* becomes a function of the kinematic variables. When the particle increases its speed, the self-force is originated at an earlier past time, because the light cone of the particle evolves with its motion. Evaluating the Eq. (14) at time  $t$ , the computation of the variations of  $r$  can be done immediately, yielding

$$\delta r(t) = \gamma^4 \beta \left(\frac{d}{c}\right)^2 \delta \dot{v}(t) + d \delta \gamma(t). \quad (15)$$

Grouping terms and using the equation  $r = \gamma d$  for  $\dot{v} = 0$ , we obtain the variational equation

$$\begin{aligned} \delta \dot{x} &= \delta v, \\ \delta \dot{v} \gamma^2 &= -\frac{c}{d} \gamma \delta v - \left(\frac{c}{d}\right)^2 (1 - \beta^2) (\delta x - \delta x_r). \end{aligned} \quad (16)$$

If we consider exponential solutions  $\delta x = A e^{\lambda t}$ , the characteristic equation of the dynamical system (16) can be found. It reads

$$\mu^2 + \mu + (1 - \beta^2)(1 - e^\mu) = 0, \quad (17)$$

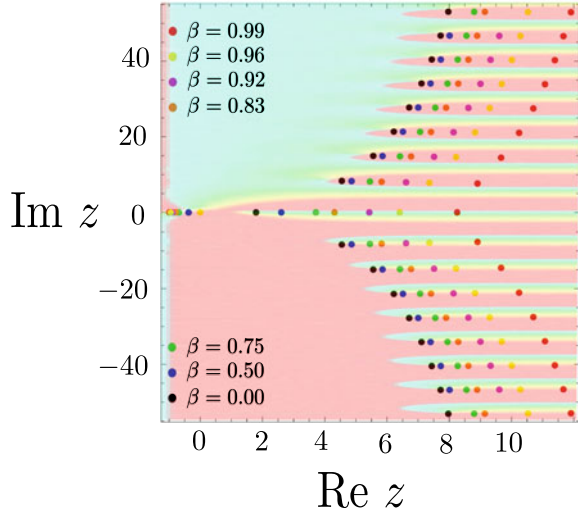
where the variable  $\mu = \lambda \gamma d / c$  has been defined. With the exception of one eigenvalue, the solutions to this equation always present a positive real part, what guarantees their instability for all values of  $\beta$ . As depicted in Fig. 2, this analytical statement is confirmed by numerical simulation. An infinite spectrum of *eigenvalues* of the frequency is obtained, with the following quantization rule

$$\omega_n = \eta_n \frac{c}{\gamma d}. \quad (18)$$

The appearance of the  $\gamma$  factor is due to the Lorentz boost, which produces a time dilation. The form factor  $\eta_n$  is characteristic of the geometry of the body. In summary, we have proved mathematically the existence of oscillatory motion in our dynamical system for any value of the relative velocity  $\beta$ . Importantly, we would like to mention



**Fig. 2** The complex function  $f(z) = z^2 + z + (1 - \beta^2)(1 - e^z)$  and its roots are computed for seven different values of the velocity, with the aid of Newton-Raphson method. Since  $z = \gamma d/c$ , we get the spectrum of eigenfrequencies of the self-oscillation, which can be approximated as  $\omega_n \propto nc/\gamma d$ . The background corresponds to a representation of the function for  $\beta = 0$ , using a domain coloring technique



that this instability depends on the shape of the particle. If the geometry of the electrodynamic body is switched from oblate to prolate, a Hopf bifurcation occurs [5].

### 4 The Quantum Potential

We conclude the present paper by deriving the relativistic kinetic energy and the quantum potential from the Liénard-Wiechert potential. The insertion of Eq. (14) into the equation  $r^2 = l^2 + d^2$  allows to exactly obtain  $l$  as a function of the relative speed  $\beta$  and the relative acceleration  $\dot{\beta}$ . The result yields the equation

$$l = \sqrt{\gamma^2 c^2 \beta^2 \left(\frac{d}{c}\right)^2 + \gamma^8 c^2 \dot{\beta}^2 (1 + \beta^2) \left(\frac{d}{c}\right)^4 + 2c^2 \gamma^5 \beta \dot{\beta} \left(\frac{d}{c}\right)^3 \sqrt{1 + \gamma^6 \dot{\beta}^2 \left(\frac{d}{c}\right)^2}} \tag{19}$$

Now we denote the self-energy of the particle as  $E$ , which we define as the energy of non-dissipative origin needed to build the charge and achieve its particular dynamical state of motion. As it is well-known, the magnetic fields perform no work, and because dissipated energy is being disregarded, we focus on the curl-free part of the electric field. Bearing in mind these considerations, the potential energy  $E$  of the electrodynamic particle can be defined by means of the Liénard-Wiechert potential as  $E = -ecA^0/2$ , what yields

$$E = \frac{e^2}{16\pi\epsilon_0} \frac{1}{\mathbf{r} \cdot \mathbf{u}}. \quad (20)$$

Using previous relations, this equation is written as

$$E = \frac{\hbar\alpha c}{4(r - l\beta)}. \quad (21)$$

If we replace the Eqs. (14) and (19) and expand the resulting self-potential in powers of  $d/c$ , we obtain the following Taylor series expansion

$$E = \gamma \frac{\hbar\alpha c}{4d} - \gamma^7 \frac{a^2}{2c^2} \frac{\hbar\alpha}{4} \left(\frac{d}{c}\right) + \gamma^{13} \frac{3a^4}{8c^4} \frac{\hbar\alpha}{4} \left(\frac{d}{c}\right)^3 - \gamma^{19} \frac{5a^6}{16c^6} \frac{\hbar\alpha}{4} \left(\frac{d}{c}\right)^5 + \dots \quad (22)$$

Again, we assume the idea that mass and inertia have a total electromagnetic origin. Therefore, the size of the particle can be written using Eq. (7) as  $d = \hbar\alpha/4m_e c$ . Noticeably, mass  $m_e$  is proportional to  $\hbar$ . This relation implies that any kind of energy or canonical momentum can be written as proportional to Planck's constant. Furthermore, if the speed of the particle is related to the group velocity of the pilot wave, then it seems reasonable to consider that the relation  $p = \hbar k$  holds. This introduces De Broglie's relation connecting the velocity of the particle and the wavelength of the electromagnetic pilot wave. Substitution of Eq. (7) in Eq. (22) yields

$$E = \gamma m_e c^2 + Q, \quad (23)$$

where we have introduced the potential

$$Q = \frac{\hbar^2}{2m_e} \frac{\alpha^2}{8d^2} \gamma \sum_{n=1}^{\infty} \frac{(-1)^n (2n-1)!!}{2^n n!} \gamma^{6n} \frac{a^{2n}}{c^{2n}} \left(\frac{d}{c}\right)^{2n}. \quad (24)$$

We detect two well differentiated terms in Eq. (23). The former corresponds to the famous relativistic equation representing the energy of a particle in the theory of special relativity. It contains the rest energy of the particle together with its kinetic energy. Importantly, we stress that these two magnitudes are not fundamental and correspond to plain electrodynamic energy. Additionally, apart from the rest mass and the kinetic energy, the new potential energy  $Q$  has appeared. By using a quadrature related to the coefficients in Eq. (24), the series can be computed and one last integration yields [3] the expression

$$Q = -\frac{\hbar^2}{2m_e} \frac{\alpha^2}{8d^2} \gamma \left(1 - 1/\sqrt{1 + \gamma^6 \beta^2 (d/c)^2}\right). \quad (25)$$

This new contribution vanishes for uniform motion. The Lorentz factor prevents the particle from traveling at velocities equal or above the speed of light. The constant

term  $\hbar^2/2m_e$  preceding this potential is identical to the quantum potential appearing in Bohmian mechanics [9], which can be written as  $Q = -(\hbar^2/2m_e)\nabla^2 R/R$ . This potential can not be derived from a Hamiltonian including an external source of potential, and involves a self-organising process produced by the internal electromagnetic field [3]. The quantum potential entails an interpretation of classical electrodynamic phenomena in terms of an emergent hydrodynamic theory [10, 11], which overcomes the representation of complicated internal self-interactions by using the concept of quantum pressure.

In theory, once the dynamical system approaches its asymptotic limit set, a functional relation between the position of the particle in the configuration space and its acceleration can be provided. This relation can be replaced in  $Q(x, t)$ , allowing to compute the function  $R(x, t)$ . Then, we can pose the Hamilton-Jacobi equation. If the particle is also subjected to the influence of a newtonian external potential  $V(x, t)$  and its average velocity is not relativistic, such an equation reads

$$\frac{\partial S}{\partial t} + \frac{1}{2m_e}(\nabla S)^2 + Q + V = 0. \quad (26)$$

After solving the previous equations, and making use of the information about the particle's trajectory, the wave function can be built using the polar expression  $\psi(x, t) = R(x, t) \exp(iS(x, t)/\hbar)$ . Importantly, we deduce from these relations that the wave function is not an ordinary probabilistic entity, but a *real* physical field [9] related to external and internal electrodynamic fields. These fields describe the pilot wave of the particle, which can produce well-known physical phenomena, as for example interference and diffraction.

A conservative approximation of the quantum potential has been derived in recent works, connecting it to typical potentials that break fundamental symmetries [3]. In particular, it has been claimed that the quantum potential can produce the symmetry breaking of the Lorentz group. Importantly, we recall that *symmetry breaking* is an essential feature in the study of nonlinear dynamics [12].

## 5 Conclusions and Discussion

The dynamics of an extended electrodynamic body has major similarities with the motion of silicon droplets found in many experiments during the past decade. In the present model, quantum waves have their origin in the self-oscillation of the electron, produced by the feedback interaction of the particle with its own electromagnetic field. This self-interaction enforces a pilot wave travelling with the corpuscle. Therefore, the wave-particle duality is immediately explained, since quantum waves appear naturally as perturbations of the dynamic electromagnetic fields. These self-interactions and their concomitant forces of recoil, perhaps together with external *zero-point fluctuations* [13], can prevent the collapse of the hydrogen atom [14].

The fact that electromagnetic mass allows to derive the exact relativistic kinetic energy analytically from the electrodynamic potentials strongly suggests that inertial mass is not a fundamental concept in physics, but an emergent one. This conclusion points towards the fact that gravitational mass is also a redundant idea in fundamental physics, and that the force of gravity has an electromagnetic origin as well. In this perspective, an electrodynamic theory of the gravitational force would also explain in simple terms the principle of equivalence. The equality of gravitational mass and inertial mass would then be explained because of their common origin in the electromagnetic force. Importantly, our finding that Newton's second law can be deduced from classical electrodynamics shows that classical mechanics is an emergent theory based on classical electromagnetism. Just in the same way as thermodynamics laws result from averaging mechanical properties over large number of ensembles. Consequently, equations in which the concept of mass appears as an elementary parameter, as it occurs with the Schrödinger or the Dirac equations, should not be considered fundamental in physics.

Finally, the model presented in this work is not very realistic because it considers a rigid charge density, which is structurally unstable. More reasonably, it is expected that fundamental particles can arise from self-confined fields as a consequence of the rotation of the fields and their electromagnetic stress, stabilizing the electron. This idea suggests that particles are *electromagnetic solitons* [15, 16], perhaps arising in the context of the Einstein-Maxwell equations. Then, *zitterbewegung* could be regarded from the point of view of a field theory as a quasi-breather solution.

Theories including more complex lagrangian densities with other general relativistic invariants or even nonlinear electrodynamic fields [17] might also allow to understand fundamental particles as compact field configurations. Then, the electric charge could be explained as the *topological charge* of the solitary wave, and not as a fundamental parameter. Anyway, no theory of elementary particles can be considered a fundamental theory as long as it does not conform to the principle of general covariance. Only this principle allows adopting any reference frame to describe the motion of dynamical fields, dispensing with the metaphysical concept of absolute spacetime.

## References

1. Protière, S., Boudaoud, A., Couder, Y.: Particle-wave association on a fluid interface. *J. Fluid Mech.* **544**, 85–108 (2006)
2. Fort, E., Eddi, A., Boudaoud, A., Moukhtar, J., Couder, Y.: Path-memory induced quantization of classical orbits. *Proc. Natl. Acad. Sci.* **107**, 17515–17520 (2010)
3. López, A.G.: On an electrodynamic origin of quantum fluctuations. *Nonl. Dyn.* **102**, 621–634 (2020)
4. Ghaffari, A., Tomizuka, M., Soltan, R.A.: The stability of limit cycles in nonlinear systems. *Nonl. Dyn.* **56**, 269–275 (2009)
5. López, A.G.: Stability analysis of the uniform motion of electrodynamic bodies. *Phys. Scr.* **96**, 015506 (2021)
6. Jenkins, A.: Self-oscillation. *Phys. Rep.* **525**, 167–222 (2013)

7. Griffiths, D.J.: Introduction to Electrodynamics. Prentice Hall, New Jersey (1989)
8. Keane, A., Krauskopf, B., Dijkstra, H.A.: The effect of state dependence in a delay differential equation model for the El Niño Southern Oscillation. *Phil. Trans. R. Soc. A* **377**, 20180121 (2019)
9. Bohm, D.: A suggested interpretation of the quantum theory in terms of "hidden" variables. I. *Phys. Rev.* **85**, 166–179 (1952)
10. Schönberg, M.: On the hydrodynamical model of the quantum mechanics. *Il Nuovo Cimento.* **12**, 103–133 (1954)
11. López, A.G., Ali, R., Mandi, L., Chatterjee, P.: Average conservative chaos in quantum dusty plasmas. *Chaos* **31**, 013104 (2021)
12. López, A.G., Benito, F., Sabuco, J., Delgado-Bonal, A.: The thermodynamic efficiency of the Lorenz system. Available at [arXiv:2202.07653](https://arxiv.org/abs/2202.07653) [cond-mat.stat-mech] (2022)
13. de la Peña, L., Cetto, A.M., Valdés-Hernandes, A.: The zero-point field and the emergence of the quantum. *Int. J. Mod. Phys. E* **23**, 1450049 (2014)
14. Raju, C.K.: The electrodynamic 2-body problem and the origin of quantum mechanics. *Found. Phys.* **34**, 937–963 (2004)
15. Faber, M.: Particles as stable topological solitons. In *Journal of Physics: Conference Series* **361**, 012022. IOP Publishing (2012)
16. Rañada, A.F., Trueba, J.: Electromagnetic knots. *Phys. Lett. A* **202**, 337–342 (1995)
17. Gullu, I., Mazharimousavi, S.H.: Black holes in double-Logarithmic nonlinear electrodynamic. *Phys. Scr.* **96**, 095213 (2021)

# Randomness and Fractal Functions on the Sierpinski Triangle



A. Gowrisankar and M. K. Hassan

**Abstract** The notion of fractal and its inherent characters are, in general, explained through the classical examples Cantor set and Sierpinski triangle. This article incorporates the probability and randomness on the dyadic Sierpinski triangle as follows. The construction process of dyadic Sierpinski triangle starts with an equilateral triangle as an initiator. Then, the generator divides the initiator into four equal triangles, by connecting the midpoints of three sides and removing the middle interior triangle with probability  $(1 - p)$ , here the probability gears the randomness. Further, the homogeneous relation between the fractal dimension of the dyadic Sierpinski triangle and its randomness is investigated. Finally, the fractal interpolation function with variable scaling is implemented on the Sierpinski triangle by defining its Laplacian.

## 1 Introduction

Fractal analysis is introduced to describe the irregular objects which are traditionally observed as too complex to describe using classical Euclidean geometry. Although the phenomena of a fractal does have a long history in mathematics, it is precisely defined as a particular class of processes called iterated function systems in which the so-called selfsimilar or fractal sets can be produced as follows. Let  $(X, d)$  be a complete metric space and  $(\mathcal{H}(X), H_d)$  denotes the corresponding hyperspace of nonempty compact subsets of  $X$  where  $H_d$  is Hausdorff metric. For  $n \in \mathbb{N}$ , let  $\mathbb{N}_n := \{1, 2, \dots, n\}$ . A complete metric space  $X$  consisting of a finite family of contractions  $f_k$  with the ratios  $\alpha_k$ , for  $k \in \mathbb{N}_n$ , constitutes an iterated function system (IFS) and it is symbolized by  $\{X; f_k : k \in \mathbb{N}_n\}$ . Define a self map  $\mathcal{F}$  on the complete metric space  $\mathcal{H}(X)$  by

---

A. Gowrisankar (✉)

Department of Mathematics, School of Advanced Sciences, Vellore Institute of Technology,  
Vellore 632 014, Tamil Nadu, India  
e-mail: [gowrisankargri@gmail.com](mailto:gowrisankargri@gmail.com)

M. K. Hassan

Department of Physics, University of Dhaka, Dhaka 1000, Bangladesh

$$\mathcal{F}(B) = \bigcup_{k \in \mathbb{N}_n} f_k(B) \tag{1}$$

which is a contraction with the ratio  $\alpha = \max\{\alpha_k : k \in \mathbb{N}_n\}$ , and thus it has a unique invariant point  $B^*$  in  $\mathcal{H}(X)$ . This invariant point  $B^*$  is referred as a deterministic fractal constructed by the IFS  $\{X; f_1, f_2, \dots, f_n\}$ . The fixed point  $B^*$  satisfies the Eq. (1), thus  $B^*$  can be written as the finite copies of itself. The fractal  $B^*$  generated by the above process obviously have exact self-similarity and hence  $B^*$  is called the deterministic fractal generated by the finite family of contraction mappings. For a detailed exposition of the iterated function system reader may refer to [1–4]. The powerful method to construct the deterministic fractals is iterated function system [2]. With the help of iterated function system, Barnsley [2] constructed the fractal interpolation function (FIF) as follows which is development over the interpolation techniques. A data set  $\{(x_k, y_k) \in \mathbb{R}^2 : k \in \mathbb{N}_n\}$  with  $x_1 < x_2 < \dots < x_n$  is given and  $x_i$ 's are not necessarily equidistant. Let  $I$  and  $I_k$  denote the closed intervals  $[x_1, x_n]$  and  $[x_k, x_{k+1}]$ , respectively, for  $k \in \mathbb{N}_{n-1}$  and  $L_k : I \rightarrow I_k, k \in \mathbb{N}_{n-1}$  be  $(n - 1)$  contraction homeomorphisms such that

$$L_k(x_1) = x_k, L_k(x_n) = x_{k+1}. \tag{2}$$

For  $r_k \in [0, 1), k \in \mathbb{N}_{n-1}$  and  $X := I \times \mathbb{R}$ . Set  $R_k : I \times \mathbb{R} \rightarrow \mathbb{R}$  be the  $n - 1$  continuous mappings satisfying

$$\begin{aligned} R_k(x_1, y_1) &= y_k, R_k(x_n, y_n) = y_{k+1} \\ |R_k(x, y_1) - R_k(x, y_2)| &\leq r_k |y_1 - y_2|, x \in I, y, y^* \in \mathbb{R}. \end{aligned} \tag{3}$$

That is,  $R_k$  is contraction mapping with respect to second variable. Define functions  $f_k : X \rightarrow I_k \times \mathbb{R}$  by  $f_k(x, y) = (L_k(x), R_k(x, y))$ , for  $k \in \mathbb{N}_{n-1}$ . Associated with the IFS  $\{X; f_k : k \in \mathbb{N}_{n-1}\}$ , a set valued mapping  $F$  is defined on  $\mathcal{K}(X)$  by

$$F(A) = \bigcup_{k \in \mathbb{N}_{n-1}} f_k(A),$$

for any  $A \in \mathcal{K}(X)$ .  $\mathcal{K}(X)$  together with the Hausdorff metric  $h$  is a complete metric space, since  $X$  is complete. Moreover, by the theory of IFS the contraction mapping  $F$  on  $\mathcal{K}(X)$  has a unique invariant set  $G$  such that  $G = F(G)$  and  $G$  is the graph of a continuous function  $g : I \rightarrow \mathbb{R}$  satisfying  $g(x_k) = y_k$  for  $k \in \mathbb{N}_n$ . For the data set  $\{(x_k, y_k) \in \mathbb{R}^2 : k \in \mathbb{N}_n\}$ , the function  $g$  whose graph is the attractor of an IFS  $\{X; f_k : k \in \mathbb{N}_{n-1}\}$  is called a fractal interpolation function.

Let a set of interpolation data  $\{(x_k, y_k) \in [x_1, x_k] \times \mathbb{R} : k \in \mathbb{N}_n\}$  be given. Then, the following process explains the construction of an iterated function system in  $\mathbb{R}^2$  such that its attractor is the graph of the interpolation function of given data. The interpolation function  $f^*$  is generated as the fixed point of the self mapping  $T : \mathbb{G} \rightarrow \mathbb{G}$  defined by

$$(Tf)(u) = R_k(L_k^{-1}(u), f \circ L_k^{-1}(u)), u \in I_k, k \in \mathbb{N}_{n-1},$$

where  $\mathbb{G} = \{h : I \rightarrow \mathbb{R} | h \text{ is continuous on } I, h(x_1) = y_1, h(x_n) = y_n\}$  is a complete metric space equipped with the uniform metric  $\delta(f, g) = \max\{|f(u) - g(u)| : u \in I\}$ . Then  $T$  is a contraction map on  $(\mathbb{G}, \delta)$  with contractivity factor  $r = \max\{r_k : k \in \mathbb{N}_{n-1}\} < 1$ . The invariant point  $f^*$  of  $T$  is the fractal interpolation function obeying the fixed point equation

$$f^*(u) = R_k(L_k^{-1}(u), f^* \circ L_k^{-1}(u)), u \in I_k, k \in \mathbb{N}_{n-1}. \tag{4}$$

As widened applications of FIF for approximating the naturally occurring functions, there have been sequel studies reported in the literature [10–20]. Mostly, the FIFs are generated from the IFS of the form

$$L_k(x) = a_kx + b_k, R_k(x, y) = \alpha_k(x)y + q_k(x), k \in \mathbb{N}_{n-1}, \tag{5}$$

where  $\{\alpha_k : \alpha_k \in (-1, 1), k \in \mathbb{N}_{n-1}\}$  is a family of parameters named as vertical scaling factors. The shape and fractal dimension of the fractal interpolation function are heavily influenced by the set of vertical scaling factors. The FIF generated by the constant vertical scaling parameter have self-similar character which could lead to loss of flexibility and may cause approximation error. Since, the natural functions are not necessarily self-similar and nature always like to enjoy the freedom of choice not determinism. To overcome this problem, a class of FIF with variable scaling parameter is introduced and analyzed based on the affine iterated function system by considering  $R_k(x, y) = \alpha_k(x)y + q_k(x), k \in \mathbb{N}_{n-1}$ , where  $\alpha_k \in C(I)$  satisfying  $\|\alpha_k\|_\infty = \sup\{|\alpha_k| : x \in I\} < 1$  (for more details, refer [7]). The fractal interpolation functions (FIFs) on the Sierpinski gasket is defined in [8] and some basic properties like finite energy, min-max property of uniform fractal interpolation functions explored in [9]. These study motivates to investigate the FIF with variable scaling parameter on the Sierpinski triangle by defining its Laplacian. Further, this paper explores the analogous facts about randomness on the Sierpinski triangle and generalized Cantor set, which should be regarded as the classical examples of a fractal supporting a concept of random fractals.

This paper is organized in the following manner. Section 2 starts with the construction of deterministic Sierpinski triangle and its fractal dimension is discussed through the scaling law. Additionally, the fractal dimension is estimated by defining the  $q^{th}$  moment of the remaining smaller equilateral triangle as sum of  $q^{th}$  power of its size. The dyadic Sierpinski triangle is explored by introducing the probability in the process of removing its middle part and its fractal dimension is measured through the moments. Further, the generalized Cantor set is presented in term of the partition value of the closed interval  $[0, 1]$  and the effect of partition value in the fractal dimension is investigated in Sect. 2. In Section 3, a new family of FIF with variable scaling parameter is described on the Sierpinski triangle which gives the degrees of freedom in the choice of vertical scaling of the fractal function.



## 2 Randomness on the Sierpinski Triangle

The pedagogical importance and impact of the Sierpinski triangle (ST) motivated us to investigate interesting variants of the Sierpinski triangle in which both probability and randomness are included in a logical progression in this section.

### 2.1 Sierpinski Triangle

Generalization of the Cantor set into higher dimension is Sierpinski triangle in this case the initiator is an equilateral triangle  $S_0$  and the generator divides it into four equal triangles, by connecting the midpoints of the sides and remove the interior triangle whose vertices are the midpoints of each side of the initiator leaving the boundary of the triangle. The resultant is  $S_1 \subseteq S_0$ . Next each of the remaining three triangles are split up into four smaller triangles with side length  $1/4$ , and three middle triangles are taken away. The resultant is  $S_2 \subseteq S_1$ . The generator is then applied over and over again to all the available triangles, this process gives sequence  $S_n$  of sets such that  $S_0 \supseteq S_1 \supseteq S_2 \supseteq \dots$ . The limit of  $S_n$  is called the Sierpinski triangle, thus  $S = \bigcap_{n \in \mathbb{N}} S_n$ .

It is easy to find out that at the  $n$ th step, there are  $N = 3^n$  triangles of side  $\delta = 2^{-n}$ . So the total area of  $S_n$  is  $3^n \cdot (1/2^n)^2 \cdot \sqrt{3}/4$ . As  $n \rightarrow \infty$ ,  $S_n$  approaches to 0. The total area of the Sierpinski triangle is 0. Further, all the subsequent approximations  $S_n, n \geq k$  will have the line segments that constitute the boundary of one of the triangles of  $S_n$ . Hence, the set  $S$  includes at least all boundaries. In  $S_n$ , there are  $3^n$  triangles, individually having 3 edges of length  $2^{-n}$ . Therefore, the length of entire  $S$  is at least  $3^n \cdot 3 \cdot 2^{-n}$ . This approaches  $\infty$  as  $n \rightarrow \infty$ . It gives that the total length of Sierpinski triangle is infinite. Moreover, eliminating  $n$  from the scaling law  $N(\delta) \sim \delta^{-d_f}$ , here  $N(\delta)$  is the number of boxes with size  $\delta$  required to cover the given object  $X$  and  $d_f$  is the fractal dimension of  $X$ . That is,  $3^n \sim (1/2)^{-nd_f}$  provides  $d_f = \frac{\ln 3}{\ln 2}$  which is the fractal dimension of the Sierpinski triangle.

Suppose  $x_1, x_2, \dots, x_N$  are size of each equilateral triangle. Define the  $q^{th}$  moment  $M_q$  of the remaining equilateral triangle by

$$M_q = \sum_i^N x_i^q, \tag{6}$$

where  $x_1 = x_2 = \dots = x_N = 2^{-n}$  and  $N = 3^n$  at the  $n^{th}$  step of the construction process. Observe,  $M_0, M_1$  are increasing quantity with  $n$  whereas  $M_2$  is decreasing quantity with  $n$ . Hence, there exists  $q \in (1, 2)$  such that  $M_q = \sum_i^N x_i^q = 1$ ,

$$M_q = e^{n \ln 3 - qn \ln 2}. \tag{7}$$

If  $q = \frac{\ln 3}{\ln 2}$ , then

$$M_{\frac{\ln 3}{\ln 2}} = \sum_{i=1}^{3^n} \left( \frac{1}{2^n} \right)^{\frac{\ln 3}{\ln 2}} = 1, \tag{8}$$

independent of  $n$  and  $d_f = \frac{\ln 3}{\ln 2}$  moment equal to size of  $S_0$ . At the  $n$ th step there are  $N = 3^n$  triangles of side  $\delta = 2^{-n}$ . Eliminating  $n$  in favor of  $\delta$  yields  $N \sim \delta^{-\frac{\ln 3}{\ln 2}}$ . One can also show that  $M \sim L^{\frac{\ln 3}{\ln 2}}$  and  $M_{-\frac{\ln 3}{\ln 2}} = 1$ . The conservation law

$$M_{-\frac{\ln 3}{\ln 2}} = 1 \tag{9}$$

is obeyed here as well regardless of  $n$  when the object is Sierpinski triangle.

### 2.2 Dyadic Sierpinski Triangle

Starts with a equilateral triangle as an initiator. The generator divides the initiator into four equal triangles, by connecting the midpoints of three sides and removing the middle interior triangle with probability  $(1 - p)$ . Now system have  $(3 + p)$  average number of smaller triangle each of size  $1/2$  because after step one the middle interior triangle is present with probability  $p$  and it has probability  $(1 - p)$  for absent. In second step, the generator is employed to each of the leftover  $(3 + p)$  smaller triangles to separate them into four equal parts. Thus, each of 3 smaller triangles in step one will have 3 triangles with absolute certainty and one triangle with probability  $p$ . Then, the middle interior triangle in step one will have 3 triangles with probability  $p$  and one triangle with probability  $p^2$ . Thus, after step two system will have  $(3 + p)^2$  average number of smaller triangles of size  $\frac{1}{2^2}$  and  $(1 - p)(3 + p)$  average number of smaller triangles are removed. First and second iteration are showed in Fig. 1. Continue this process recursively to all the remaining smaller triangles at each step, then the resultant system is dyadic Sierpinski triangle provided number of iteration approaches to infinity.

In  $n$ th step of the construction process of dyadic Sierpinski triangle there are  $(3 + p)^n$  average number of triangles with size  $\frac{1}{2^n}$ . By Eq. (6)

$$\begin{aligned} M_q &= \sum_{i=1}^{(3+p)^n} \left( \frac{1}{2^n} \right)^q \\ &= e^{n \ln(3+p) - nq \ln 2}, \end{aligned} \tag{10}$$

for all  $p \in (0, 1)$ . Thus,  $d_f = \frac{\ln(3+p)}{\ln 2}$  provides

$$M_{d_f} = \sum_{i=1}^{(3+p)^n} 2^{-nd_f} = 1. \tag{11}$$

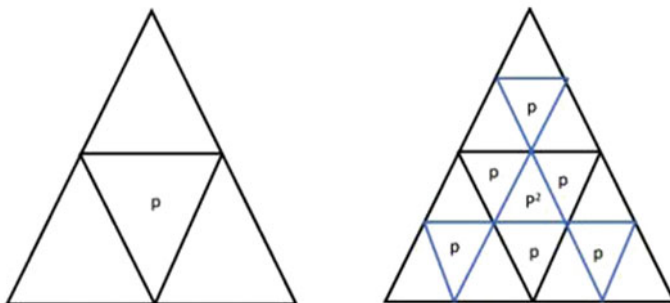


Fig. 1 First and second iteration of the dyadic Sierpinski triangle

It is independent of  $n$ . Therefore,  $d_f^{th}$  moment  $M_{d_f}$  of the  $(3 + p)^n$  average number of remaining triangles of size  $1/2^n$  is a conserved quantity. Meantime, adding all removed triangles at each step gives followings. After step 1 there are 3 triangles each of area  $1/4$ . One has area  $1/4$  with probability  $p$ . The one which is thrown out has area  $1/4$  with probability  $1 - p$ . If we sum them all we get

$$\frac{3}{4} + \frac{p}{4} + \frac{1 - p}{4} = 1, \tag{12}$$

which is the area of the initiator. After step 2, there are 9 triangles each of area  $1/4^2$ , 6 of them have area  $1/4^2$  with probability  $p$ , one of them have area  $1/4^2$  with probability  $p^2$ . The ones are thrown are as follows. Three of them have area  $1/4^2$  with probability  $(1 - p)$  and one of them have area  $1/4^2$  with probability  $p(1 - p)$ . If we now sum all the surviving triangles and the ones in the bin we get

$$\frac{9}{4^2} + \frac{6p}{4^2} + \frac{p^2}{4^2} + \frac{3(1 - p)}{4^2} + \frac{p(1 - p)}{4^2} + \frac{1 - p}{4} = 1, \tag{13}$$

the size of the initiator. Observe that the last term on the L.H.S. is the size of the thrown out quantity in the bin.

We thus see that the amount which is thrown in the bin at step 1 is  $(1 - p)/4$ . In step 2 we throw

$$\frac{3(1 - p)}{4^2} + \frac{p(1 - p)}{4^2} = \frac{1 - p}{4} \frac{(3 + p)}{4}. \tag{14}$$

Similarly, we can find that after step 3 the amount we throw to the bin is  $\frac{1 - p}{4 \left(\frac{3 + p}{4}\right)^2}$ .

We can now add all the quantities in the bin and find the following series

$$\frac{1 - p}{4} \left[ 1 + \frac{(3 + p)}{4} + \left(\frac{(3 + p)}{4}\right)^2 + \left(\frac{(3 + p)}{4}\right)^3 + \dots + \dots \right] = \frac{1 - p}{4} \frac{1}{1 - \frac{(3 + p)}{4}} = 1. \tag{15}$$

However, the  $d_f^h$  moment equals the size of the initiator providing that there are infinitely many smaller triangles in the resultant set.

**Example 1** Let  $X$  be an equilateral triangle with the vertices  $v_1 = (0, 0)$ ,  $v_2 = (1, 0)$  and  $v_3 = (1/2, \sqrt{3}/2)$  and consider the IFS on  $X$  consists of the following three contractions,  $f_1(u, v) = (\frac{1}{2}u, \frac{1}{2}v)$ ;  $f_2(u, v) = (\frac{1}{2}u + \frac{1}{2}, \frac{1}{2}v)$ ;  $f_3(u, v) = (\frac{1}{2}u + \frac{1}{4}, \frac{1}{2}v + \frac{\sqrt{3}}{4})$ . All these three contractions have contraction factor  $1/2$ . The resulting fractal is called Sierpinski triangle. If the contraction factor is chosen as an arbitrary number in  $(0, 1)$ , say  $\alpha$ , then it provides different fractal as function of  $\alpha$ . Thus,  $G : (0, 1) \rightarrow \mathcal{H}(X)$  defined by  $G(\alpha) = A_\alpha^*$ , where  $A_\alpha^*$  is a fixed point of the IFS including three contractions

$$\begin{aligned} f_1(u, v) &= (\alpha u, \alpha v); \\ f_2(u, v) &= (\alpha(u + 1), \alpha v); \\ f_3(u, v) &= \left(\alpha\left(u + \frac{1}{2}\right), \alpha\left(v + \frac{\sqrt{3}}{2}\right)\right). \end{aligned}$$

### 2.3 Generalized Triadic Cantor Set

The generalized triadic Cantor set is constructed as follows. Consider the unit length line segment as closed interval  $C_0 = [0, 1]$  which is called as an initiator. Initially to generate the set, divide the initiator into  $k(3 \leq k < \infty)$  equal pieces and remove the centre piece among  $k$  subintervals. It remains two closed intervals  $[0, \frac{1}{k}]$  and  $[\frac{k-1}{k}, 1]$  in step 1 each of length  $\frac{1}{k}$ . Thus,  $C_1 = [0, \frac{1}{k}] \cup [\frac{k-1}{k}, 1]$ . Now remove the middle parts from the leftover intervals thus, obtaining four equal pieces of closed interval of length  $\frac{1}{k^2}$  and they are  $[0, \frac{1}{k^2}]$ ,  $[\frac{k-1}{k^2}, \frac{1}{k}]$ ,  $[\frac{k-1}{k}, \frac{k^2-k-1}{k^2}]$ ,  $[\frac{k^2-1}{k^2}, 1]$ . This gives

$$C_2 = [0, \frac{1}{k^2}] \cup [\frac{k-1}{k^2}, \frac{1}{k}] \cup [\frac{k-1}{k}, \frac{k^2-k-1}{k^2}] \cup [\frac{k^2-1}{k^2}, 1].$$

Now remove the middle parts from each of the remaining four intervals to create eight smaller closed intervals. This continuous process gives the generalized triadic Cantor set as a limit  $C$  of the decreasing sequence  $(C_n)_{n \in \mathbb{N}}$  of sets. Hence, the limit is the intersection of the sets,  $C = \bigcap_{n \in \mathbb{N}} C_n$ . If one can continue the above construction process through infinitely many steps then the following questions naturally arise : (i) What is the cardinality of  $C$ ? (ii) How much of the initiator removed in  $[0, 1]$ ?

Start to generate the set by splitting the initiator into  $k$  equal parts and hence there are  $k$  number of smaller intervals which has size  $1/k$ . Removing the middle parts from the  $k$  subintervals means  $k - 2$  of them are removed in step one so that two closed intervals  $[0, 1/k]$  and  $[\frac{k-1}{k}, 1]$  is remained in the system. The sum of the sizes of all the intervals removed at this stage is  $\frac{k-2}{k}$ . In step two, each of the two subsets is divided into  $k$  intervals and remove the middle  $k - 2$  number of smaller intervals so

there will be four intervals  $[0, 1/k^2]$  and  $[k - 1/k^2, 1/k]$ . The size of the intervals being removed are  $\frac{k-2}{k}, \frac{2(k-2)}{k^2}, \frac{4(k-2)}{k^3}$  etc. If we sum them up, we get

$$\frac{k-2}{k} \sum_n \left(\frac{2}{k}\right)^n = \frac{k-2}{k} \frac{1}{1-2/k} = 1.$$

Moreover, the set  $C_n$  contains  $2^n$  disjoint closed intervals, each of length  $(\frac{1}{k})^n$  in step  $n$ . So the total length of  $C_n$ , (i.e.) the sum of the lengths, is  $(2/k)^n$  and its limit is  $\lim_{n \rightarrow \infty} (\frac{2}{k})^n = 0$ . Therefore, the total length of the Cantor set is zero.  $k = 3$  gives the total length of all the thrown intervals is equal to the size of the initiator and length of  $C$  is zero. If  $k$  approaches to infinity, then the total length of all intervals begin thrown away is zero as well as length of  $C$  is zero. This is quite surprising as it implies that there is hardly anything left in the Cantor set. However, there are infinite number of points in the Cantor set. Since construction of Cantor set started with the initiator  $[0, 1]$  and the endpoints 0 and 1 belong to all of the succeeding sets  $C_{n_0}, n_0 \geq n$ , and hence belong to the intersection  $C$ . Thus,  $C$  is nonempty and taking every endpoints of all the intervals in every approximations  $C_n$  provides an infinite number of endpoints which are belonging to  $C$ .

Define the  $q$ th moment  $M_q$  of the leftover intervals at the  $n$ th step of the construction process as

$$M_q = \sum_i^{2^n} x_i^q. \tag{16}$$

Note that each of the leftover intervals at the  $n$ th step are of equal size  $x_i = k^{-n}$  and hence can write

$$M_q = e^{n \ln 2 - qn \ln k}. \tag{17}$$

It means that if  $q = \frac{\ln 2}{\ln k}$  then

$$M_{\frac{\ln 2}{\ln k}} = 1, \tag{18}$$

independent of  $n$ . That is, this result is true even in the limit  $n \rightarrow \infty$ . Thus, it concludes that the set is nonempty which is another surprising fact of the Cantor set. In the construction process of Cantor set, the  $n$ th step starts with deleting the middle parts from each of the leftover  $2^{n-1}$  intervals in the  $(n - 1)^{th}$  step to produce  $2^n$  closed intervals of size  $1/k^n$  for each  $n$ . If one can take yardstick as  $\delta = k^{-n}$  then the number of yardsticks  $N(\delta)$  required to cover the set  $C$  is equal to  $N = 2^n$ . Removing  $n$  from  $N = 2^n$  with the help of  $\delta$  provides  $N(\delta)$  is direct proportion to  $\delta^{-d_f}$  that is  $N(\delta) \sim \delta^{-d_f}$  where  $d_f = \frac{\ln 2}{\ln k}$  is the box-counting or fractal dimension of the Cantor set.

**Remark 1** The fractal dimension of generalized Cantor set is  $d_f = \frac{\ln 2}{\ln k}$  which is decreasing quantity whenever  $k$  is increasing. Thus, if the partition of the initiator increased then it will give the more irregular Cantor type set.

If the partition of the initiator  $k = 3$ , then the generalized triadic Cantor set is known as the classical Cantor set and its fractal dimension  $d_f$  is  $\frac{\ln 2}{\ln 3}$ . Further, by applying probability on the construction of the Cantor set, one can get the dyadic Cantor set as follows: The generator divides the initiator  $[0, 1]$  into two equal parts. In which delete one subinterval with probability  $(1 - p)$ , remains another subinterval with probability  $p$ . Now, the system will have an average  $(1 + p)$  number of sub-intervals each of size  $1/2$ . By continuing the process over and over again on all the available intervals at each step recursively, the dyadic Cantor set is obtained. This result is investigated in [5]. If we find the  $d_f$ th moment  $M_{d_f}$  of the  $(1 + p)^n$  available intervals of size  $2^{-n}$  by using the Eq. (6), then it provides that  $M_{d_f}$  is conserved quantity. Hence, by changing the partition value  $k$  and applying above procedure one can get different types of the Cantor set with fractal dimension  $d_f = \frac{\ln 2}{\ln k}$ .

**Example 2** Let  $X = [0, 1]$  and consider the IFS on  $X$  with the following two mappings,  $f_1(x) = \frac{x}{3}$ ,  $f_2(x) = \frac{(x+2)}{3}$ . The self mappings  $f_1, f_2$  are contractions with contraction factor  $1/3$  and the resulting fractal of the IFS  $\{X; f_1, f_2\}$  is Cantor set. If the contraction factor  $\alpha$  is chosen as an arbitrary number in  $(0, 1)$ , then one can get different fractal as function of  $\alpha$ . Thus,  $G : (0, 1) \rightarrow \mathcal{H}(X)$  defined by  $G(\alpha) = A_\alpha^*$ , where  $A_\alpha^*$  is a fixed point of the IFS including two contractions  $f_1(x) = \alpha x$ ,  $f_2(x) = \alpha(x + 2)$ . As per the remark 1, if  $\alpha_1 \leq \alpha_2$ , then  $d_f(A_{\alpha_1}^*) \leq d_f(A_{\alpha_2}^*)$ . The relation between the contraction factor  $\alpha$  and the number of partition  $k$  in the construction of generalized Cantor set is  $\alpha = 1/k$ .

The influence of contraction factor in the shape of the resultant fractals is explained in Example 1 and Example 2.

### 3 Fractal Function on the Sierpinski Triangle

This section demonstrates the fractal interpolation function with variable scaling on the Sierpinski triangle by defining the Laplacian on the Sierpinski triangle (ST). That is the class of FIF with vertical scaling parameters  $\alpha_{w_k} : ST \rightarrow (-1, 1)$ , here  $\alpha_{w_k}$  is continuous and satisfies  $\|\alpha_{w_k}\|_\infty = \sup\{|\alpha_{w_k}| : \forall x \in ST\} < 1$ , are considered in this study.

#### 3.1 Laplacian on the Sierpinski Triangle

Let  $V_0 = \{p_1, p_2, p_3\}$  be a set of vertices of an equilateral triangle, say  $X$ , in  $\mathbb{R}^2$ . Define  $f_k(x) = \frac{1}{2}(x + p_k)$  on  $X$ . Then, the attractor of the iterated function system  $\{X; f_k : k = 1, 2, 3\}$  is a Sierpinski triangle. Define a sequence of finite sets  $(V_m)_{m \geq 0}$  by  $V_{m+1} = \cup_{k=1}^3 f_k(V_m)$ . We write  $f_w = f_{w_1} \circ f_{w_2} \circ \dots \circ f_{w_m}$  for any finite sequence  $w = (w_1, w_2, \dots, w_m)$  of length  $|w| = m, k \in \{1, 2, 3\}$  i.e.  $w \in \{1, 2, 3\}^m$ .

The union of the image of  $V_0$  under the iteration of  $f_w$  constitutes the set of  $m$  vertices  $V_m$ . For any  $p \in V_m$ , let  $N_{m,p}$  be the collection of the direct neighborhood of  $p$  in  $V_m$ .

Observe that, the cardinality of  $N_{m,p}$  is

$$|N_{m,p}| = \begin{cases} 4 & \text{if } p \notin V_0 \\ 2 & \text{if } p \in V_0. \end{cases}$$

Let  $C(V_m) = \{h : h \text{ is continuous on } V_m \text{ to } \mathbb{R}\}$  and define the linear operator  $\Delta_m : C(V_m) \rightarrow C(V_m)$  by

$$5^m(\Delta_m h)(p) = \sum_{q \in N_{m,p}} (h(q) - h(p))$$

for all  $h \in C(V_m)$  and all  $p \in V_m$ . Then the Laplacian on the Sierpinski triangle is defined by

$$(\Delta_m h)(p) \rightarrow (\Delta h)(p)$$

as  $m \rightarrow \infty$ . A function  $f \in C(V_m)$  is called as harmonic on  $V_m$  if  $(\Delta_m f)(p) = 0$  for all  $p \in V_m/V_0$ . A continuous function  $f : ST \rightarrow \mathbb{R}$  is said to be harmonic, if its restriction to  $V_m$  is harmonic for all  $m$ .

In [8], the first degree polynomials are constructed as classical harmonic functions on an interval and by substituting them on the Sierpinski triangle using the standard Laplacian on SG of fractal analysis, the theorem of interpolation for ST is obtained. Whereas, this study extends the class of FIF by considering vertical scaling parameters as  $\alpha_{w_k} : ST \rightarrow (-1, 1)$ , here  $\alpha_{w_k}$  is continuous and satisfies  $\|\alpha_{w_k}\|_\infty = \sup\{|\alpha_{w_k}| : \forall x \in ST\} < 1$  in place of constant scaling factors  $\alpha_{w_k} \in (-1, 1)$ , for all  $k \in \{1, 2, 3\}$ , in [6, 7]. Note that  $\alpha_w = \alpha_{w_1} \circ \alpha_{w_2} \circ \dots \circ \alpha_{w_m}$ .

**Theorem 1** *Let  $h \in C(V_m)$  be given and any  $\alpha_w(x)$  for  $w \in \{1, 2, 3\}^m$  with  $\|\alpha_w\| < 1$ . Then there is a unique continuous function  $g : ST \rightarrow \mathbb{R}$  satisfying  $g|_{V_m} = h$  and*

$$g(f_w(x)) = \alpha_w(x)g(x) + q_w(x)$$

where  $q_w$  is harmonic function on ST for all  $w \in \{1, 2, 3\}^m$ .

Let  $\mathcal{T} = \{t : ST \rightarrow \mathbb{R} \text{ continuous function with } t(p_k) = h(p_k), k = 1, 2, 3\}$ . Then  $\mathcal{T}$  is complete with respect to uniform metric. Define  $T : \mathcal{T} \rightarrow \mathcal{T}$  by

$$(Tt)(x) = \alpha_w(x)t(f_w^{-1}(x)) + q_w(f_w^{-1}(x))$$

where  $q_w$  is the harmonic function on ST with  $q_w(p_k) = h(f_w(p_k)) - \alpha_w(x)h(p_k)$  for  $k = 1, 2, 3$ . It is observed that,  $T$  is well defined, contractive with ratio  $\|\alpha_w\|$  and  $(Tt)(p_k) = h(p_k)$ . Then, the unique fixed point of  $T$  obeys

$$g(x) = \alpha_w(x)g(f_w^{-1}(x)) + q_w(f_w^{-1}(x))$$

for  $x \in f_w(ST)$  and  $w \in \{1, 2, 3\}^m$ ,

$$g(f_w(x)) = \alpha_w(x)g(x) + q_w(x).$$

**Remark 2** If  $\alpha_{wk}(x) = \alpha_{wk}$ , then Theorem 1 provides the results in [8] and [9]. In [8, 9], authors have considered the scaling factors  $\alpha_{wk}$  as constant value in between 1 and  $-1$  whereas in this paper scaling factors are considered as a function scaling.

## 4 Conclusion

In the present study, the dyadic Sierpinski triangle is introduced which is a classical example of the fractal supporting a concept of random fractal. Further, the fractal dimension of the dyadic Sierpinski triangle estimated by moments of available triangle in each iteration narrates that there is a conservative law on it since  $M_{-\frac{\ln 3}{\ln 2}} = 1$  which is independent of its iteration  $n$ . Consequently, the generalized Cantor set presented in term of the partition value of the closed interval in  $[0, 1]$  and the influence of partition value in the fractal dimension is investigated which generalizes the dyadic Cantor set considered in [5, 6]. Finally, a new set of fractal functions with variable scaling parameter on Sierpinski triangle is demonstrated which gives the more flexibilities and degrees of freedom in the choice of vertical scaling of the fractal function.

## References

1. Barnsley, M.F.: *Fractals Everywhere*. Academic Press, Dublin (1988)
2. Barnsley, M.F.: *Fractal functions and interpolation*. *Constr. Approx.* **2**(1), 303–329 (1986)
3. Santo Banerjee, Hassan, M.K., Sayan Mukherjee, Gowrisankar, A.: *Fractal patterns in nonlinear dynamics and applications*. CRC Press, Baco Raton (2019)
4. Santo Banerjee, Easwaramoorthy, D., Gowrisankar, A.: *Fractal Functions, Dimensions and Signal Analysis*. 1st ed. Springer, Cham (2021)
5. Hassan, M.K., Pavel, N.I., Pandit, R.K., Kurths, J.: Dyadic Cantor set and its kinetic and stochastic counterpart. *Chaos Solit. Fract.* **60**, 31–39 (2014)
6. Hassan, M.K.: Is there always a conservation law behind the emergence of fractal and multi-fractal? *Eur. Phys. J.: Spec. Top.* **228**(1), 209–232 (2019)
7. Wang, H.Y., Yu, J.S.: Fractal interpolation functions with variable parameters and their analytical properties. *J. Approx. Theory* **175**, 1–8 (2013)
8. Celik, D., Kocak, S., Ozdemir, Y.: Fractal interpolation on the Sierpinski gasket. *J. Math. Anal. Appl.* **337**, 343–347 (2008)
9. Ri, Song-Gyong., Ruan, Huo-Jun.: Some properties of fractal interpolation functions on Sierpinski gasket. *J. Math. Anal. Appl.* **380**, 313–322 (2011)



10. Barnsley, M.F., Elton, J., Hardin, D., Massopust, P.: Hidden variable fractal interpolation functions. *SIAM J. Math. Anal.* **20**(5), 1218–1242 (1989)
11. Navascués, M. A.: Fractal polynomial interpolation. *Z. Anal. Anwend.* **25**(2), 401–418 (2005)
12. Gowrisankar, A., Uthayakumar, R.: Fractional calculus on fractal interpolation function for a sequence of data with countable iterated function system. *Mediterr. J. Math.* **13**(6), 3887–3906 (2016)
13. Secelean, N.A.: The existence of the attractor of countable iterated function systems. *Mediterr. J. Math.* **9**, 61–79 (2012)
14. Priyanka, T.M.C., Gowrisankar, A.: Riemann-Liouville fractional integral of non-affine fractal interpolation function and its fractional operator. *Eur. Phys. J.: Spec. Top.* **230**, 3789–3805 (2021)
15. Priyanka, T.M.C., Gowrisankar, A.: Analysis on Weyl-Marchaud fractional derivative for types of fractal interpolation function with fractal dimension. *Fractals* **29**(7), 2150215 (2021)
16. Chand, A.K.B., Katiyar, S.K., Viswanathan, P.: Approximation using hidden variable fractal interpolation functions. *J. Fractal Geom.* **2**(1), 81–114 (2015)
17. Fataf, N.A.A., Gowrisankar, A.: Santo Banerjee: in search of self-similar chaotic attractors based on fractal function with variable scaling. *Phys. Scr.* **95**, 075206 (2020)
18. Min, Wu.: The Hausdorff measure of some Sierpinski carpets. *Chaos Solit. Fract.* **24**(3), 717–731 (2005)
19. Rani, M., Goel, S.: Categorization of new fractal carpets. *Chaos Solit. Fract.* **41**, 1020–1026 (2009)
20. Aslan, N., Saltan, M., Demir, B.: The intrinsic metric formula and a chaotic dynamical system on the code set of the Sierpinski tetrahedron. *Chaos Solit. Fract.* **123**, 422–428 (2019)

# Bifurcation Analysis of a Leslie-Gower Prey-Predator Model with Fear and Cooperative Hunting



Ashvini Gupta and Balram Dubey

**Abstract** The current work examines the dynamical features of a Leslie-Gower prey-predator model. The effects of fear and group defense among prey with the mechanism of cooperative hunting by predators are incorporated. The existence and uniqueness of the interior equilibrium are explained. We obtained sufficient conditions for the local and global stability behavior. With regard to the fear parameter and cooperation strength parameter, the proposed system undergoes Hopf-bifurcation, transcritical bifurcation, and saddle-node bifurcation. Moreover, the system exhibits the property of bi-stability between two interior equilibrium points. The basin of attraction of these points is also plotted. All theoretical results are verified numerically by MATLAB R2021a.

**Keywords** Prey-predator · Fear · Cooperative hunting · Bifurcation

## 1 Introduction

Understanding of prey-predator interactions via differential equations is a classical application of mathematics in ecology. The dynamics of such systems are often altered due to various ecological factors. Employing these factors makes the system more consistent with the real world. Introducing fear may cause the interacting populations to oscillate or stabilize about their steady-state [12]. These oscillations are most commonly due to the occurrence of Hopf-bifurcation [4]. In population dynamics, group defense is a common concept that describes an instance in which

---

The author (Ashvini Gupta) is grateful to the University Grants Commission, New Delhi, India, for the Junior Research Fellowship.

---

A. Gupta (✉) · B. Dubey

Department of Mathematics, BITS Pilani, Pilani Campus, Pilani 333031, Rajasthan, India  
e-mail: [aashvini28@gmail.com](mailto:aashvini28@gmail.com)

B. Dubey

e-mail: [bdubey@pilani.bits-pilani.ac.in](mailto:bdubey@pilani.bits-pilani.ac.in)

prey form groups to defend against the predator, which can cut off the predation rate. Considering Holling type IV or Monod-Haldane type functional response is the most frequent and accessible technique to implement group defense [6, 11]. It is evident from the research that dominance of defense could lead to predator’s extinction [5]. The cooperation among predators to hunt down the target significantly increase the chances of their survival [1]. Saha and Samanta [10] extensively studied a 3-D prey-predator model involving cooperative hunting strategy and group defense mechanism. They observed transcritical bifurcation, saddle-node bifurcation, Hopf-bifurcation, and many other type of bifurcations. Pal et al. [8] studied the combined effect of fear and cooperative hunting and they observed various bifurcations and bi-stability in their model. The predator often switches to a different food to prevent extinction and becomes a generalist. The standard way to incorporate this feature is to use the modified Leslie-Gower scheme. Many authors [2, 3, 7] remarked the persistence of species in the modified Leslie-Gower prey-predator model. As per our knowledge, there is no work done comprising fear, group hunting, and group defense in a Leslie-Gower prey-predator model. Hence our main purpose is to study the effects of group defense in prey, group hunting in predator and fear induced by predator in prey on the dynamical behavior of prey-predator system.

## 2 The Mathematical Model

The survival of species is one of the most fundamental and significant issues in ecology. The modified Leslie-Gower prey-predator model formulation is an interesting approach in species conservation. According to this scheme, the predator acts as a generalist, which increases their chances of survival. Inspiring from aforementioned facts and pioneering literature as cited in the introduction, we consider an ecosystem where prey-predator species are interacting with each other through modified Leslie-Gower scheme. Prey species defend themselves against predators for their survival. Predator species hunt prey in groups and induce fear in the prey. With all these assumptions, we propose the following model:

$$\begin{aligned}
 \frac{dx}{dt} &= \frac{rx}{1 + Ky} - r_0x - r_1x^2 - \frac{(\alpha + \lambda y)xy}{a + x^2} := f(x, y), \\
 \frac{dy}{dt} &= sy - \frac{\omega y^2}{b + x} := g(x, y), \\
 x(0) &\geq 0, \quad y(0) \geq 0.
 \end{aligned}
 \tag{1}$$

The variables and parameters involved in the model are listed in Table 1 with their biological meaning and dimensions.

**Table 1** Biological explanation and dimension of variables/parameters employed in model (1)

Variables/Parameters	Biological explanation	Dimensions
$x$	Prey density	Biomass
$y$	Predator density	Biomass
$r$	Birth rate of prey	Time <sup>-1</sup>
$K$	Cost of fear	Biomass <sup>-1</sup>
$r_0$	Prey mortality rate	Time <sup>-1</sup>
$r_1$	Death rate of prey due to competition among them	Biomass <sup>-1</sup> Time <sup>-1</sup>
$\alpha$	Predation rate	Biomass Time <sup>-1</sup>
$\lambda$	Cooperation strength of predators	Time <sup>-1</sup>
$a$	Half saturation constant of prey	Biomass <sup>2</sup>
$b$	Half saturation constant of predator	Biomass
$s$	Intrinsic growth rate of predator	Time <sup>-1</sup>
$\omega$	The highest rate of predator eradication per capita	Time <sup>-1</sup>

### 3 Dynamics of the System

The model (1) can be re-written as

$$\frac{dx}{dt} = x\phi_1(x, y), \quad \frac{dy}{dt} = y\phi_2(x, y),$$

where

$$\phi_1(x, y) = \frac{r}{1 + Ky} - r_0 - r_1x - \frac{(\alpha + \lambda y)y}{a + x^2}, \quad \phi_2(x, y) = s - \frac{\omega y}{b + x}.$$

It follows that

$$x(t) = x(0)e^{\int_0^t \phi_1(x(\theta), y(\theta))d\theta} \geq 0, \quad y(t) = y(0)e^{\int_0^t \phi_2(x(\theta), y(\theta))d\theta} \geq 0.$$

Hence, in  $R^2_+$ , all  $(x(t), y(t))$  solutions with the positive starting point stay positive.

Nature does not enable any species to spread rapidly due to a lack of resources. As a result, it is critical to ensure that the defined model is bounded.

**Theorem 1** *All solutions initiating in  $R^2_+$  are contained in the domain  $\Omega = \{(x, y) \in R^2_+ : 0 \leq x \leq K_1, 0 \leq y \leq \frac{s(b+K_1)}{\omega}\}$ , where  $K_1 = \frac{r-r_0}{r_1}$ .*

**Proof** We may write the first equation of the model as

$$\dot{x} \leq rx - r_0x - r_1x^2.$$

This implies

$$\limsup_{t \rightarrow \infty} x(t) \leq \frac{r - r_0}{r_1} := K_1.$$

To show the boundedness of  $y(t)$ , we can write

$$\dot{y} \leq sy - \frac{\omega y^2}{b + K_1}.$$

This entails

$$\limsup_{t \rightarrow \infty} y(t) \leq \frac{(b + K_1)s}{\omega} := K_2,$$

which completes the proof.

### 3.1 Equilibrium Points

The proposed system has four feasible equilibrium points: extinction equilibrium;  $E_0(0, 0)$ , predator-free equilibrium;  $E_1(K_1, 0)$ , prey-free equilibrium;  $E_2(0, \frac{bs}{\omega})$  and interior equilibrium;  $E^*(x^*, y^*)$ . Here  $x^*$  is a positive root of the following quartic equation:

$$A_1x^4 + A_2x^3 + A_3x^2 + A_4x + A_5 = 0, \tag{2}$$

where  $A_1 = r_1\omega^2sK$ ,  $A_2 = \omega^2(r_0Ks + r_1\omega + r_1Ksb) + s^3\lambda K$ ,  $A_3 = \omega^2Ks(r_0b + r_1a) + 3b\lambda Ks^3 + s^2\omega(\lambda + \alpha K) - (r - r_0)\omega^3$ ,  $A_4 = (r_0Ksa + r_1a(\omega + Ksb))\omega^2 + 3\lambda Kb^2s^3 + s\alpha\omega^2 + 2bs^2\omega(\lambda + \alpha K)$ ,  $A_5 = \lambda Kb^3s^3 + b^2s^2\omega(\lambda + \alpha K) + b\omega^2s(\alpha + r_0aK) - (r - r_0)a\omega^3$ .

Since  $A_1, A_2$  and  $A_4$  are positive. Therefore, according to the Descartes' rule of signs, Eq. (2) will have unique, two, three or no positive root based on the sign of  $A_3$  and  $A_5$  (refer to Table 2 and Fig. 1). It is worthy to note here that when  $A_3 > 0$  and

**Table 2** Existence of positive root of (2)

$A_3$	$A_5$	Number of positive roots	Color
-	+	2 or 0	yellow
-	-	3 or 1	red
+	-	1	green
+	+	0	blue

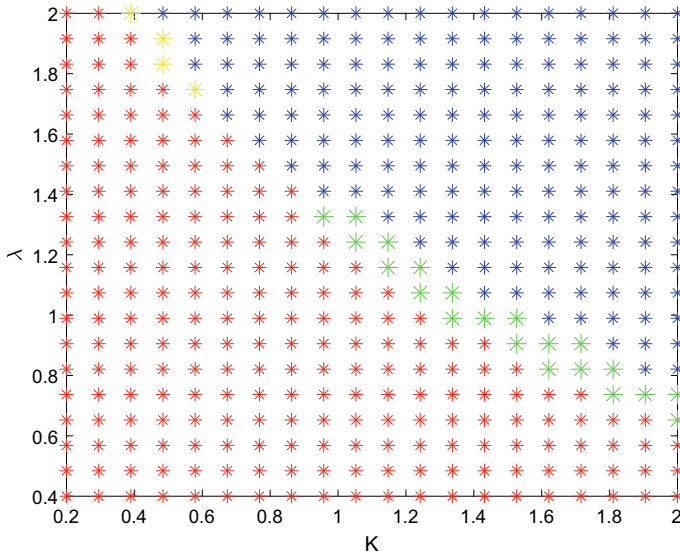


**Fig. 1** Different colors showing all cases of Table 2 in  $K\lambda$ -plane, where  $r = 0.6$ ,  $a = 1$ ,  $\alpha = 0.4$ ,  $\omega = 1$ ,  $b = 1$ ,  $s = 0.4$ ,  $r_0 = 0.05$ ,  $r_1 = 0.05$

$A_5 < 0$ , Eq. (2) has a unique positive solution  $x^*$ . On obtaining  $x^*$  from Eq. (2), we can easily determine  $y^*$  from the relation

$$y^* = \frac{s(b + \omega)}{x^*}.$$

### 3.2 Stability Analysis

The local stability feature of any equilibrium can be established using eigenvalue theory. The boundary equilibria with their local stability feature are described in Table 3.

**Table 3** The local stability characteristics of system (1)'s boundary equilibria

Equilibrium points	Stability characteristics
$E_0(0, 0)$	Unconditionally unstable
$E_1(K_1, 0)$	Always saddle point
$E_2(0, \frac{bs}{\omega})$	Asymptotically stable if $r < (1 + \frac{bKs}{\omega})(r_0 + \frac{(\alpha\omega + \lambda bs)bs}{a\omega^2})$ ; saddle if $r > (1 + \frac{bKs}{\omega})(r_0 + \frac{(\alpha\omega + \lambda bs)bs}{a\omega^2})$

**Biological significance:** As per the concept of the modified Leslie-Gower prey-predator model, the predator can switch to other food when prey is absent. Moreover, predator performs cooperative hunting and induce fear in prey. Due to all these factors, predators may not become extinct. Therefore, when the prey’s birth rate is less than a critical value, they might become extinct, nevertheless, predator always persists due to their generalist nature. Hence the prey-free equilibrium  $E_2(0, \frac{bs}{\omega})$  can be stable, but the extinction state  $E_0(0, 0)$  and predator-free state  $E_1(K_1, 0)$  can never be stable.

**Theorem 2**  $E^*(x^*, y^*)$  is locally asymptotically stable if and only if  $B_1 > 0$  and  $B_2 > 0$ , where  $B_1$  and  $B_2$  are stated in the proof.

**Proof** The Jacobian matrix, computed at positive equilibrium  $E^*(x^*, y^*)$  is given by

$$J|_{E^*} = \begin{pmatrix} -r_1x^* + \frac{2(\alpha+\lambda y^*)x^{*2}y^*}{(a+x^{*2})^2} & -\frac{rKx^*}{(1+Ky^*)^2} - \frac{(\alpha+2\lambda y^*)x^*}{a+x^{*2}} \\ \frac{\omega y^{*2}}{(b+x^*)^2} & -\frac{\omega y^*}{b+x^*} \end{pmatrix}.$$

The characteristic equation for the aforementioned matrix is as follows:

$$\xi^2 + B_1\xi + B_2 = 0, \tag{3}$$

where  $B_1 = -tr(J|_{E^*})$  and  $B_2 = det(J|_{E^*})$ .

As per the Routh-Hurwitz criterion, the interior equilibrium  $E^*(x^*, y^*)$  is locally asymptotically stable if and only if  $B_1 > 0$  and  $B_2 > 0$ .

**Remark.** If  $r_1 > \frac{2(\alpha+\lambda y^*)x^*y^*}{(a+x^{*2})^2}$ , then  $E^*(x^*, y^*)$  is locally asymptotically stable.

In a two-dimensional system, the possible attractors inside the positive invariant set could be equilibrium points and periodic solutions. If we are able to show that no periodic solution exists, and all boundary equilibrium points are unstable, then, in that case, all trajectories starting in the positive invariant region will eventually converge to the interior equilibrium  $E^*$  if it exists uniquely.

**Theorem 3** Let the positive equilibrium  $E^*$  exists uniquely. Then it is globally asymptotically stable under the following conditions:

- (i)  $r > (1 + \frac{bK_s}{\omega})(r_0 + \frac{(\alpha\omega + \lambda bs)bs}{a\omega^2})$ ,
- (ii)  $\frac{3\sqrt{3}(\alpha + \lambda K_2)}{8a\sqrt{a}} < \frac{r_1}{K_2} + \frac{\omega}{K_1(b + K_1)}$ .

**Proof** If (i) holds, it directly implies  $E_2(0, \frac{bs}{\omega})$  is a saddle point. Now, to show the non-existence of periodic solution, consider a function that is continuously differentiable in  $R^2_+$ ,  $H = \frac{1}{xy}$  and we define

$$\nabla = \frac{\partial}{\partial x}(fH) + \frac{\partial}{\partial y}(gH).$$

Simple calculation yields

$$\nabla = -\frac{r_1}{y} + \frac{2x(\alpha + \lambda y)}{(a + x^2)^2} - \frac{\omega}{x(b + x)}.$$

$\nabla$  remains negative if  $\frac{3\sqrt{3}(\alpha + \lambda K_2)}{8a\sqrt{a}} < \frac{r_1}{K_2} + \frac{\omega}{K_1(b + K_1)}$ .

Hence, system (1) cannot have a closed trajectory in the interior of the positive  $xy$ -plane, according to the Bendixson-Dulac criteria. In such a case, all solutions starting in  $\Omega$  will converge to the interior equilibrium  $E^*$ , if it exists uniquely.

### 3.3 Bifurcation Analysis

**Theorem 4** System (1) experiences a transcritical bifurcation between the axial equilibrium  $E_2(0, \frac{bs}{\omega})$  and interior equilibrium  $E^*(x^*, y^*)$  with respect to the parameter  $K$  at  $K^{[tc]} = \frac{\omega}{bs} \left( \frac{(r-r_0)a\omega^2 - (\alpha\omega + \lambda bs)bs}{r_0a\omega^2 + (\alpha\omega + \lambda bs)bs} \right)$  if  $(r - r_0)a\omega^2 > (\alpha\omega + \lambda bs)bs$  and  $\delta_3 \neq 0$ , where  $\delta_3$  is defined in the proof.

**Proof** At  $K = K^{[tc]}$ ,

$$A = J|_{E_2} = \begin{pmatrix} 0 & 0 \\ \frac{s^2}{\omega} & -s \end{pmatrix}.$$

$v = (1, \frac{s}{\omega})$  and  $w = (1, 0)$  are the eigenvectors of matrix  $A$  and  $A^T$  for the zero eigenvalue, respectively. Let  $F = (f, g)^T$ , where  $f$  and  $g$  are the RHS functions of model (1). Now, we define

$\delta_1 = w^T F_K(E_2, K^{[tc]})$ ,  $\delta_2 = w^T [DF_K(E_2, K^{[tc]})v]$ , and  $\delta_3 = w^T [D^2F(E_2, K^{[tc]})(v, v)]$ .

Simple computation yields

$$\delta_1 = 0, \delta_2 = -\frac{rbs\omega}{(\omega + bKs)^2} < 0$$

and

$$\delta_3 = -2r_1 - \frac{2}{ra^2\omega^4b}(r_0a\omega^2 + (\alpha\omega + \lambda bs)bs)((r - r_0)a\omega^2 - (\alpha\omega + \lambda bs)bs).$$

If  $\delta_3 \neq 0$ , then all the conditions of the Sotomayor’s Theorem [9] are satisfied. Hence, the system experiences a transcritical bifurcation at  $K = K^{[tc]} = \frac{\omega}{bs} \left( \frac{(r-r_0)a\omega^2 - (\alpha\omega + \lambda bs)bs}{r_0a\omega^2 + (\alpha\omega + \lambda bs)bs} \right)$  between prey-free equilibrium  $E_2$  and coexistence equilibrium  $E^*$ .

**Theorem 5** Let us assume that  $B_2$  is positive. Then system (1) experiences a Hopf-bifurcation with respect to the cooperation strength  $\lambda$  at  $\lambda = \lambda^{[hf]}$  around the coexistence equilibrium  $E^*$ .



**Proof** It can be noted that

- (i) When  $B_1 > 0$  and  $B_2 > 0$ ,  $E^*$  is locally asymptotically stable for  $\lambda < \lambda^{[hf]}$ .
- (ii) When  $B_1 < 0$  and  $B_2 > 0$ ,  $E^*$  is unstable for  $\lambda > \lambda^{[hf]}$ .

Here  $B_1$  and  $B_2$  are defined in Eq. (3). This indicates that there is a switching of stability when cooperative strength  $\lambda$  crosses the critical value  $\lambda = \lambda^{[hf]}$ . At this point,  $B_1 = 0$  and  $B_2 > 0$ , which implies that the eigenvalues are purely imaginary. Furthermore, we check the transversality condition *viz.*,

$$\left. \frac{dB_1}{d\lambda} \right|_{\lambda=\lambda^{[hf]}} = -\frac{2x^{*2}y^{*2}}{(a+x^{*2})^2} < 0.$$

Therefore, by the Andronov-Hopf bifurcation theorem, the system undergoes Hopf-bifurcation at  $\lambda = \lambda^{[hf]}$  near the equilibrium point  $E^*$ .

### 4 Numerical Simulation

We use MATLAB R2021a to run numerical simulations to validate our analytical results of the model. The dataset we have picked is as follows:

$$\begin{aligned} r &= 0.6, \lambda = 0.7, K = 0.1, a = 1, \alpha = 0.0005, \omega = 1, b = 1, s = 0.4, r_0 = 0.05, \\ r_1 &= 0.05 \end{aligned} \tag{4}$$

For  $\lambda = 0.005$  and other parameters from (4), the predator-only state (0, 0.4) is a saddle-point. As per the Theorem 3, we obtain  $\frac{3\sqrt{3}(\alpha+\lambda K_2)}{8a\sqrt{a}} - \frac{r_1}{K_2} + \frac{\omega}{K_1(b+K_1)} = -0.002$ , implying that the system cannot have a closed trajectory in  $R_+^2$ . The interior equilibrium  $E^*(7.8437, 3.5374)$  exists uniquely, and is a globally stable focus with eigenvalues  $-0.395 \pm 0.2044i$ . This phenomenon can be seen in Fig. 2.

In the model, fear parameter  $K$  plays a vital role. As per Theorem 4, we obtain  $K^{[tc]} = 6.7478$  and  $\delta_3 = -0.3367 \neq 0$ . All conditions of the theorem are satisfied, hence the system undergoes a transcritical bifurcation at  $K = K^{[tc]}$ . The phenomenon of transcritical bifurcation is easy to understand with the help of a bifurcation diagram. It can be depicted from Fig. 3,  $E^*$  is stable and  $E_2$  is unstable when  $K < K^{[tc]}$ . In this range, the value of  $\nabla$  remains negative. Therefore,  $E^*$  is globally stable. After crossing the threshold value of the fear parameter, the stability of  $E^*$  is transferred to  $E_2$  via a transcritical bifurcation.

The traits of the system (1) are not limited to transcritical bifurcation. It has been observed that there are three positive equilibrium points, out of which two are stable, and the other is a saddle-point for the parameters given in (4) with  $\alpha = 0.7$ . The stable point  $E^{*(1)}$  and saddle-point  $E^{*(2)}$  approach towards each other with the variation in cooperation strength. At  $\lambda = \lambda^{[sn]}$ , they annihilate one another by means of a saddle-node bifurcation (see Fig. 4).

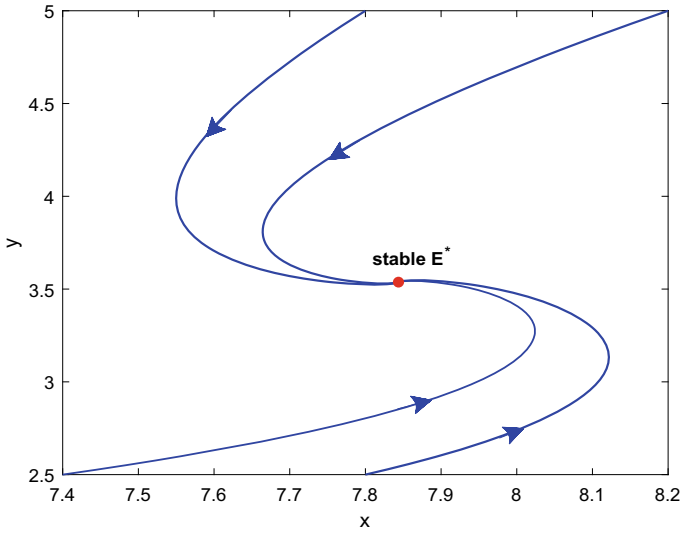


**Fig. 2** Phase portrait showing global stable node  $E^*$

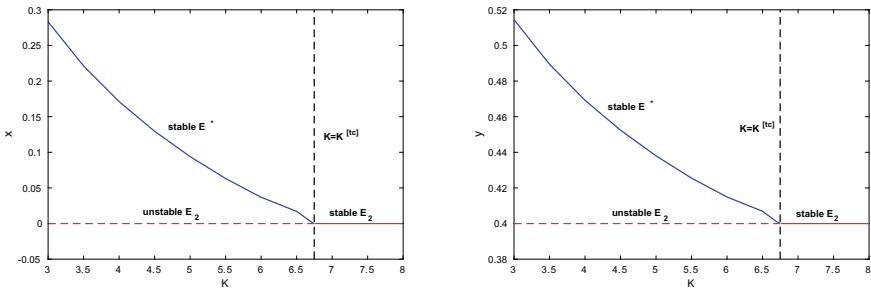


**Fig. 3** Transcritical bifurcation diagram with respect to fear parameter  $K$ . The other parameters are from (4)

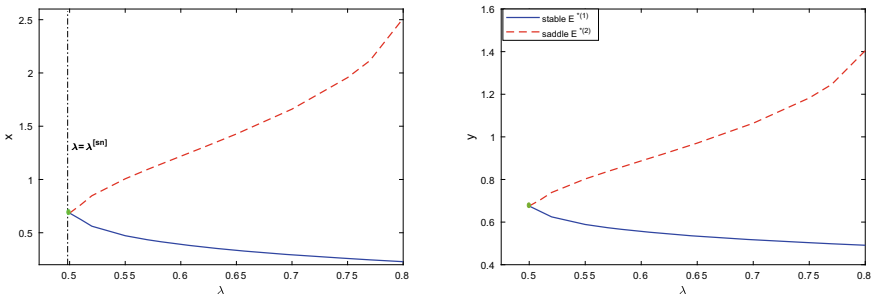


**Fig. 4** Saddle-node bifurcation diagram with respect to cooperation strength  $\lambda$ , where  $\alpha = 0.7$  and other parameters are same as in (4)

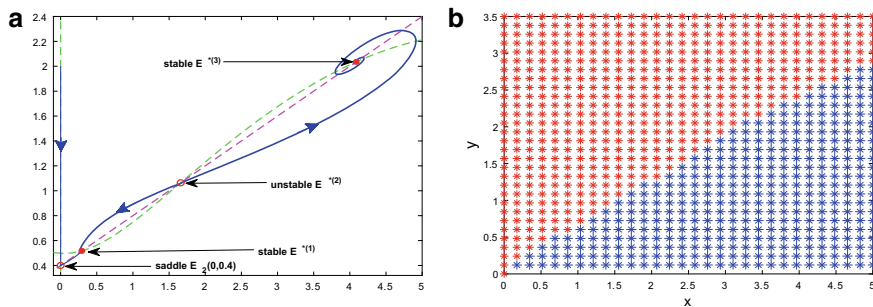


**Fig. 5** **a** Bi-stability between two interior equilibrium points at  $\alpha = 0.7$  and other parameters are from (4). Here green and magenta color dashed curves represent the prey and predator nullclines, respectively. **b** The basin of attraction for two stable points is shown by blue color for  $E^{*(3)}(4.088, 2.0352)$  and red color for  $E^{*(1)}(0.2929, 0.5171)$

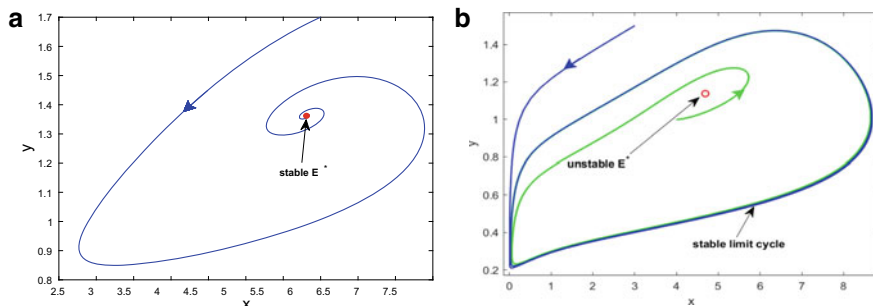


**Fig. 6** **a** Phase portrait showing  $E^*$  as stable focus at  $\lambda = 3$ . **b** After  $\lambda > \lambda^{[h_{f}]}$ , stable limit cycle surrounding unstable  $E^*$  at  $\lambda = 3.9$

The phase portrait diagram illustrating bi-stability between two interior equilibrium points ( $E^{*(1)}$ ,  $E^{*(3)}$ ) along with one saddle interior equilibrium  $E^{*(2)}$  and saddle prey-free equilibrium  $E_2$  is shown in Fig. 5a. In such a case, the initial condition of the solution decides its convergence. Here, the solutions from red color \* will eventually go to the attractor  $E^{*(1)}(0.2929, 0.5171)$ . On the other hand, if the solution begins from blue color \*, it will approach  $E^{*(3)}(4.088, 2.0352)$  in the future (refer to Fig. 5b).

For  $s = 0.2$ ,  $\alpha = 0.7$  and keeping other parameters same as in (4), we compute the value of Hopf-bifurcation point  $\lambda^{[h_{f}]}$  by equating  $B_1$  to zero, and we obtained  $\lambda^{[h_{f}]} = 3.6567$ . At this value,  $B_2 = 0.0424 > 0$ , and  $\left. \frac{dB_1}{d\lambda} \right|_{\lambda=\lambda^{[h_{f}]}} = -0.1064 < 0$ . Hence, according to the above theorem, the system experiences Hopf-bifurcation at  $\lambda^{[h_{f}]} = 3.6567$  around  $E^*(5.0208, 1.2041)$ .

For the lower value of cooperation strength  $\lambda$ , both species fluctuate for a finite time around their steady-state. They eventually reach the positive equilibrium  $E^*$  (see the phase portrait in Fig 6a at  $\lambda = 3 < \lambda^{[h_{f}]}$ ). When the value of  $\lambda$  is increased,  $E^*$

loses its stability with the formation of a stable limit cycle through Hopf-bifurcation at  $\lambda = \lambda^{[hfl]} = 3.6567$ . The phase portrait after Hopf-bifurcation is depicted in Fig. 6b at  $\lambda = 3.9 > \lambda^{[hfl]}$ .

## 5 Conclusion

In the present manuscript, we proposed a modified Leslie-Gower predator-prey model employing ordinary differential equations. While formulation, we considered that the birth rate of the prey population is reduced due to the fear induced by predators. Therefore we multiply the birth rate of the prey population with the decreasing function of the predator population size,  $\phi(K, y) = \frac{1}{1+Ky}$ . Moreover, we assumed that predators cooperate for hunting a common target. This mechanism affects the predation rate significantly. Therefore, the group hunting term  $\alpha + \lambda y$  is incorporated in the predation term. Prey species perform group defense for their survival in this situation, which is shown in the model through simplified Holling type IV functional response.

To ensure the biological validity of the system, we proved that all solutions are positive and bounded in  $R_+^2$ . We determined all feasible equilibrium points and analyzed their stability. The extinction state  $E_0(0, 0)$  and predator-free state  $E_1(K_1, 0)$  are always unstable. When the prey's birth rate is less than a critical value, the prey-free equilibrium  $E_2(0, \frac{bs}{\omega})$  is stable. All cases of the existence of positive equilibrium  $E^*$  are discussed. We obtained sufficient conditions for the local and global stability of  $E^*$ .

It is noticed that the fear parameter  $K$  and the cooperation strength parameter  $\lambda$  play a crucial role in the system's dynamics. The system experiences transcritical bifurcation for the fear parameter. Moreover, we remarked that a high level of fear might cause the prey species to be extinct. The system shows a feature of bi-stability between two interior points, and it undergoes a saddle-node bifurcation with respect to  $\lambda$ . We noticed that both species start to fluctuate about their co-existence state when the cooperation strength  $\lambda$  is more than a critical value  $\lambda^{[hfl]}$ . This change in dynamics is due to the Hopf-bifurcation at  $\lambda = \lambda^{[hfl]}$ .

## References

1. Mickaël Teixeira Alves, Frank M Hilker.: Hunting cooperation and Allee effects in predators. *J. Theor. Biol.* **419**:13–22 (2017)
2. Aziz-Alaoui, M.A., Daher Okiye, M.: Boundedness and global stability for a predator-prey model with modified Leslie-Gower and Holling-type II schemes. *Appl. Mathem. Lett.* **16**(7):1069–1075 (2003)
3. Chen, Fengde, Chen, Liujuan, Xie, Xiangdong: On a Leslie-Gower predator-prey model incorporating a prey refuge. *Nonl. Anal. Real World Appl.* **10**(5), 2905–2908 (2009)

4. Dubey, B., Sajan Sajan, Ankit Kumar.: Stability switching and chaos in a multiple delayed prey-predator model with fear effect and anti-predator behavior. *Mathem. Comput. Simul.* **188**:164–192 (2021)
5. Freedman, H.I., Wolkowicz, G.S.K.: Predator-prey systems with group defence: The paradox of enrichment revisited. *Bull. Mathem. Biol.* **48**, 493–508 (1986)
6. Gupta, Ashvini, Dubey, Balram: Bifurcations and multi-stability in an eco-epidemic model with additional food. *European Phys. J. Plus* **137**(118), 1–20 (2022)
7. Nindjin, A.F., Aziz-Alaoui, M.A.: Persistence and global stability in a delayed Leslie-Gower type three species food chain. *J. Mathem. Anal. Applic.* **340**(1), 340–357 (2008)
8. Pal, Saheb, Pal, Nikhil, Samanta, Sudip, Chattopadhyay, Joydev: Effect of hunting cooperation and fear in a predator-prey model. *Ecolog. Compl.* **39**, 100770 (2019)
9. Lawrence Perko.: *Differential Equations and Dynamical Systems*, vol. **7** (2000)
10. Sangeeta Saha, Samanta, G.P.: A prey–predator system with disease in prey and cooperative hunting strategy in predator. *J. Phy. A: Mathem. Theor.* **53**(48):485601 (2020)
11. Shang, Zuchong, Qiao, Yuanhua: Bifurcation analysis of a Leslie-type predator-prey system with simplified Holling type IV functional response and strong Allee effect on prey. *Nonl. Anal. Real World Appl.* **64**, 103453 (2022)
12. Wang, Xiaoying, Zanette, Liana, Zou, Xingfu: Modelling the fear effect in predator-prey interactions. *J. Mathem. Biol.* **73**(5), 1179–1204 (2016)

# Chaotic Behavior in a Novel Fractional Order System with No Equilibria



Santanu Biswas, Humaira Aslam, Satyajit Das, and Aditya Ghosh

**Abstract** This article takes into consideration a novel chaotic system of four dimensional fractional order having no equilibria. We cannot use mathematical methods such as Melnikov's and Shilnikov's method to prove that the given system is chaotic. We shall analyse the dynamical features of the fractional order system by using predictor-corrector algorithm. This method reports chaotic dynamics. We shall apply the basic ideas of non linear dynamical analysis such as bifurcation diagrams and Lyapunov exponents to recognise the chaotic behavior for the given system. One interesting phenomena for the system is that it has cascade of period doubling bifurcations and chaotic attractors without having any equilibrium points.

**Keywords** Fractional calculus · Lyapunov exponents · Chaotic dynamics · Predictor-corrector algorithm · No equilibrium point

## 1 Introduction

Fractional calculus is an ongoing topic which is being used since the last 300 years, however its implementation has been inflated in recent years. The mathematical phenomenon describe real objects more precisely than the classical integer methods. The concept of fractional calculus for example has been implemented for modelling circuit theory [1], control systems [13] etc. Li et al. [10] fractional order Chua's circuit, [22] fractional order Rossler system, [16], which describes that fractional order systems can also behave chaotically. Moreover all these fractional order systems deal with either one or maybe more than one equilibrium points; except for only few systems that have already been discovered exhibiting chaos without any equilibrium points until now.

---

S. Biswas (✉) · H. Aslam · S. Das · A. Ghosh  
Department of Mathematics, Adamas University, Kolkata 700126, India  
e-mail: [santanubiswas1988@gmail.com](mailto:santanubiswas1988@gmail.com)

S. Biswas  
Department of Mathematics, Jadavpur University, Kolkata 700032, India

© The Author(s), under exclusive license to Springer Nature Switzerland AG 2022  
S. Banerjee and A. Saha (eds.), *Nonlinear Dynamics and Applications*,  
Springer Proceedings in Complexity,  
[https://doi.org/10.1007/978-3-030-99792-2\\_91](https://doi.org/10.1007/978-3-030-99792-2_91)

1081

Sprott [14] found 19 chaotic models with five terms and six terms, including linear and quadratic terms by exhaustive computer searching with no more than three equilibrium points. Inspired by his pioneering work, the chaotic dynamics in an integer order model has been examined in [2, 9, 18, 20]. References [17, 19] introduced and analyzed new chaotic systems having no equilibrium points. The presence of chaos cannot be verified by Shilnikov method as, they can not have homoclinic or heteroclinic orbits. Referring to the fractional order system, as far as our knowledge goes only two systems [3, 11, 12] describe a system having chaotic dynamics without any equilibria.

In this article, we have described a novel 4D fractional jerk system with hidden attractors. The dynamics of the non commensurate order fractional model & the commensurate order fractional model, has been explained individually. The article can be helpful to solve the problem of sudden chaotic oscillation caused by hidden attractors, thus providing a good reference and inspiration for solving similar engineering oscillation problems.

Based on the given chaotic attractors it is exciting to develop the chaos theory in order to create new systems. From this point of view a novel fractional order system with chaotic dynamics is described in the given article. The presence of chaos is illustrated by using various bifurcation diagrams and maximum Lyapunov exponents. Using Adams–Bashforth Moulton algorithm we have solved the given fractional order system. One interesting phenomena for the above said system is that it has cascade of period doubling bifurcations and chaotic attractors without having any equilibrium points.

The remaining article is organized in the following manner: Sect. 2 focuses on the development of the integer order model with its basic dynamics; In Sect. 3, we deal with the fractional order model having no equilibrium. Elaborate discussion of the dynamical analysis of the fractional model is done in Sect. 4. The predictor corrector algorithm is described in Sect. 4 as well. We conclude the article with a discussion.

## 2 Proposed System

In the search for chaotic flows, we were inspired by [14] case K system,

$$\begin{aligned}\frac{dx}{dt} &= xy - z \\ \frac{dy}{dt} &= x - y \\ \frac{dz}{dt} &= x + 0.3z.\end{aligned}\tag{1}$$

Equation 1 has two equilibria.

We performed a search for additional chaotic system with no equilibria. We added a constant to each of the derivatives in Eq. 1 with the simplest four dimensional extension of the system using linear feedback control. We consider a general parametric form as

$$\begin{aligned}
 \frac{dx}{dt} &= ay^2 + \gamma_1xy + \gamma_2x^2 + \gamma_3z^2 + \gamma_4xz + \gamma_5yz - z + a_1 \\
 \frac{dy}{dt} &= bx - y + a_2 \\
 \frac{dz}{dt} &= cx + dz + a_3 + k_1w \\
 \frac{dw}{dt} &= -k_2z
 \end{aligned}
 \tag{2}$$

We search for the cases where we can show algebraically that the equilibrium points are imaginary. An extensive search for the chaotic system with no equilibrium points found the example

$$\begin{aligned}
 \frac{dx}{dt} &= ay^2 - z + a_1 \\
 \frac{dy}{dt} &= bx - y \\
 \frac{dz}{dt} &= cx + dz + k_1w \\
 \frac{dw}{dt} &= -k_2z
 \end{aligned}
 \tag{3}$$

where  $x, y, z, w$  are state variables and  $a, a_1, b, c, d, k_1, k_2$  are real constant parameters. Eq. 3 is dissipative if  $d < 1$ .

The system (3) can not have chaotic solution in few cases. So, we proved the following Theorem.

**Theorem 1** *Suppose that the following conditions hold:*

1.  $k_1 = 0, c = 0, a > 0$  and  $a_1 > 0$
2.  $k_1 = 0, c = 0, a < 0$  and  $a_1 < 0$

*then system (3) does not have bounded chaotic attractors.*

**Proof** From system (3) we get,

$$\ddot{y} - aby^2 + (1 + d)\dot{y} + \bar{d}y = \int_0^t [bd(ay^2 + a_1) - bk_1w - bcx]dy + C. \tag{4}$$

Under the above said assumptions Eq. 4 has a monotone left hand side. Arguing as [8] we can say that the system can not be chaotic.

### 2.1 Dynamics of the System (3)

The model (3) has no point of equilibria for  $a_1 > 0$ . Phase plot for the system (3) is drawn in Fig. 1 with parameter values as  $a = a_1 = 0.1; b = 0.1; c = 0.4; k_1 = k_2 = 0.01; d = 0.25$  and the initial value was assumed as  $[1, 1, 0, 1]$ . Figure 1 depicted chaotic dynamics for the system (3). Due to the chaotic behaviour of the system, the trajectories diverges from  $[1, 0.1, 0, 40]$  to the higher values. Small changes in the initial value may results dramatically different trajectories.

The divergence and convergence exponential rates of the trajectories close by in the phase plane of the given chaotic system is measured by the Lyapunov exponents.



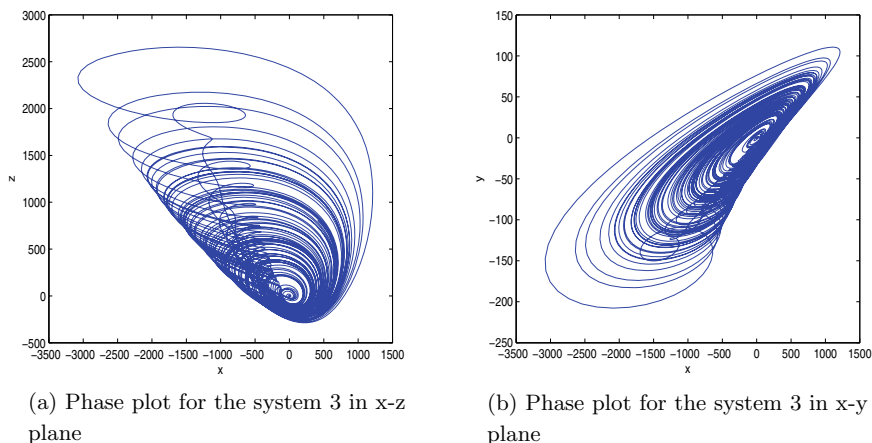


**Fig. 1** Phase plot for the system equation 3 in x-z plane and x-y plane

Hence we have constructed these Lyapunov exponents for the given system (3) by making use of the algorithm in [21] to verify that the given system is chaotic or not. We calculated the Lyapunov exponents and plot in the Fig. 2b for the system (3). We see that the two Lyapunov exponents is negative (cyan, red), one is zero (green) and another is positive (blue).

We define the Lyapunov dimension by

$$D_{ky} = j + \frac{1}{L_{j+1}} \sum_{i=1}^j L_i,$$

where  $j$  is the largest integer satisfying  $\sum_{i=1}^j L_i \geq 0$  and  $\sum_{i=1}^{j+1} L_i < 0$ . For the system equation 3,  $D_{ky} = 3.1456 > 3$ . Hence it is an indication of a strange attractor.

The bifurcation diagram for the given system (3) is depicted in Fig. 2a with reference to the parameter  $d$  in the range of  $d \in [-0.02, 0.25]$ . The values of the given parameters are fixed as  $a = a_1 = 0.1$ ;  $b = 0.1$ ;  $c = 0.4$ ;  $k_1 = k_2 = 0.01$ . Although the system (3) has no equilibrium but still the system (3) has period doubling bifurcation route to chaos. After  $d$  crosses the critical value 0, the system equation 3 losses it's stability and undergoes a period-doubling bifurcation. Gradual increase of  $d$  makes the system chaotic. We can observe that the bifurcation diagram and the Lyapunov exponents spectrum very well coincide.

### 3 Fractional Order Model

By fractional-order systems, we refer to dynamical systems which can be modeled using a fractional differential equation along with a non-integral derivative. Fractional

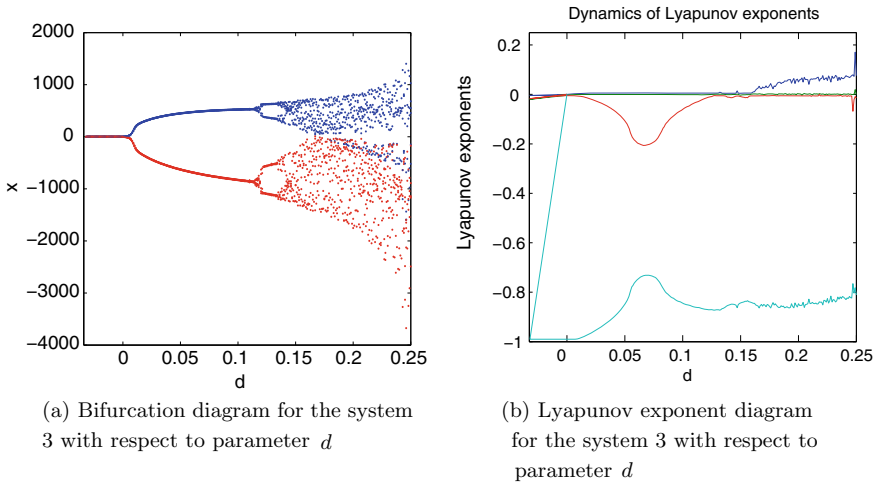


**Fig. 2** Chaotic dynamics for the system equation 3 with respect to parameter  $d$

order systems are quite useful in understanding the characteristics of the dynamical system in various fields of electrochemistry, biology, physics, and chaotic systems. Recently fractional-order systems have captured a lot of interest and recognition because of their usefulness in providing an exact description of various nonlinear phenomena. Control theory has a lot of applications in fractional-order systems since several physical systems cannot be effectively modeled using differential equations of integer order, hence fractional-order systems have an important role to play here. The presence of non-integral derivatives is the primary reason for selecting fractional-order systems in mathematical modeling problems. The fractional-order controller gives comparatively more adjustable time and frequency response for any given control system. Being a modified form of the integer order systems fractional order systems adjust the controllers more accurately according to the system requirements. Hence fractional-order systems are preferred over integer order systems for modeling various dynamical systems.

In this section we consider the fractional-order system denoted as Eq. 5. The standard derivative is replaced by a fractional derivative as follows:

$$\begin{aligned}
 D^{q_1} x &= ay^2 - z + a_1 \\
 D^{q_2} y &= bx - y \\
 D^{q_3} z &= cx + dz + k_1 w \\
 D^{q_4} w &= -k_2 z
 \end{aligned}
 \tag{5}$$

where  $0 < q_1, q_2, q_3, q_4 \leq 1$ ;  $D^{q_i}$  denote the Caputo fractional operator with initial time  $t_0 = 0$ . When  $q_1 = q_2 = q_3 = q_4 = 1$ , the above system becomes Eq. 3.

Next, we consider two methods to solve the system (5). We discuss the methods in next two sections.

### 4 Adams–Bashforth–Moulton Method

Diethelm and Ford [6] already discussed about converting to Volterra integral equations from fractional differential equations with initial conditions. Now, by applying the predictor-corrector algorithm [7], the solution of the system (5) can be written as:

$$\begin{aligned}
 x_{n+1} &= x_0 + \frac{h_1^q}{\Gamma(q_1+2)} \{ay_{n+1}^p y_{n+1}^p - z_{n+1}^p + a_1 + \sum_{j=0}^n a_{1,j,n+1} (ay_j^2 - z_j + a_1)\} \\
 y_{n+1} &= y_0 + \frac{h_2^q}{\Gamma(q_2+2)} \{bx_{n+1}^p - y_{n+1}^p + \sum_{j=0}^n a_{2,j,n+1} (bx_j - y_j)\} \\
 z_{n+1} &= z_0 + \frac{h_3^q}{\Gamma(q_3+2)} \{cx_{n+1}^p + dz_{n+1}^p + k_1 w_{n+1}^p + \sum_{j=0}^n a_{3,j,n+1} (cx_j + dz_j + k_1 w_j)\} \\
 w_{n+1} &= w_0 + \frac{h_4^q}{\Gamma(q_4+2)} \{-k_2 z_{n+1}^p + \sum_{j=0}^n a_{4,j,n+1} (-k_2 z_j)\}
 \end{aligned}
 \tag{6}$$

in which

$$\begin{aligned}
 x_{n+1}^p &= x_0 + \frac{1}{\Gamma(q_1)} \{ \sum_{j=0}^n b_{1,j,n+1} (ay_j^2 - z_j + a_1) \} \\
 y_{n+1}^p &= y_0 + \frac{1}{\Gamma(q_2)} \{ \sum_{j=0}^n b_{2,j,n+1} (bx_j - y_j) \} \\
 z_{n+1}^p &= z_0 + \frac{1}{\Gamma(q_3)} \{ \sum_{j=0}^n b_{3,j,n+1} (cx_j + dz_j + k_1 w_j) \} \\
 w_{n+1}^p &= w_0 + \frac{1}{\Gamma(q_4)} \{ \sum_{j=0}^n b_{4,j,n+1} (-k_2 z_j) \}
 \end{aligned}
 \tag{7}$$

#### 4.1 Chaos and Bifurcations with $q = q_1 = q_2 = q_3 = q_4$ for the System (5)

Assuming the parameter values as  $a = 0.1$ ;  $b = 0.1$ ;  $c = 0.4$ ;  $k_1 = k_2 = 0.01$ ;  $a_1 = .001$ ;  $d = 0.245$ ;  $q = q_1 = q_2 = q_3 = q_4 = 0.98$  and initial conditions as  $(1, 0.1, 0, 40)$  we get the following phase space trajectory in Fig. 3. The chaotic motion which was identified in Fig. 3 is confirmed by the maximum Lyapunov exponents following by [15] and plotted in Fig. 4.

In order to make it direct, a bifurcation diagram shall be drawn with respect to  $q = q_1 = q_2 = q_3 = q_4$  for  $0.86 \leq q \leq 0.99$  and the rest of the parameter values are fixed like in Fig. 3. The bifurcation diagram with respect to  $q$  plotted in Fig. 5, depicts the complex dynamical features in our presented model equation 5 from the limit cycle to chaos and on gradually increasing  $q$  we observe that the system switches its stability such that from being stable focus to limit cycle oscillation it becomes limit cycle oscillation to chaotic oscillation. We can observe that in Fig. 5

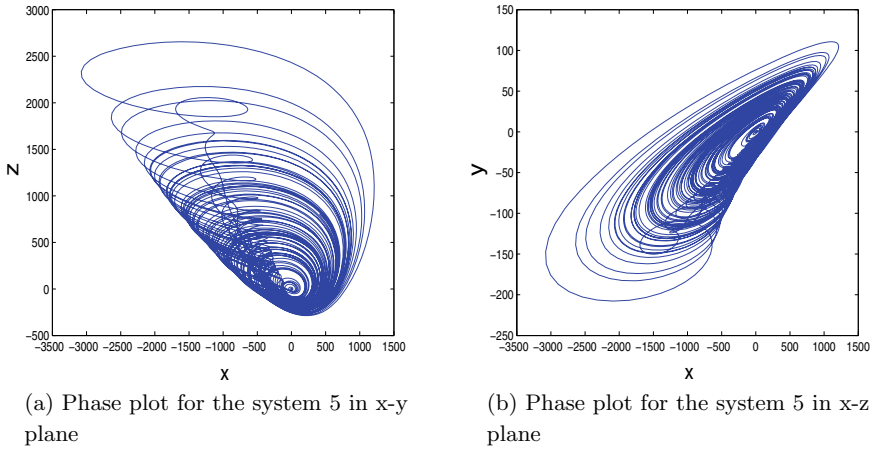


Fig. 3 Phase plot for the system (5) with commensurate fractional order

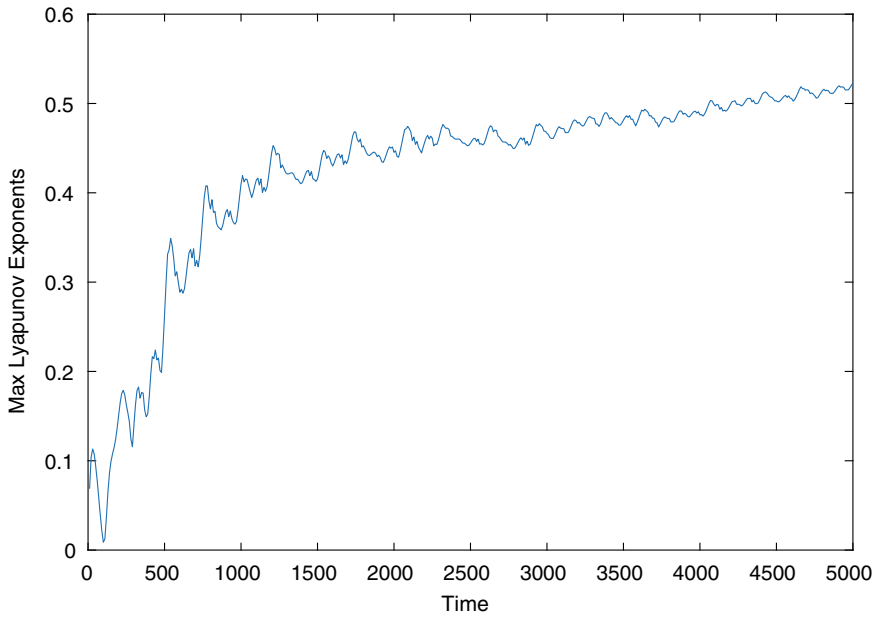
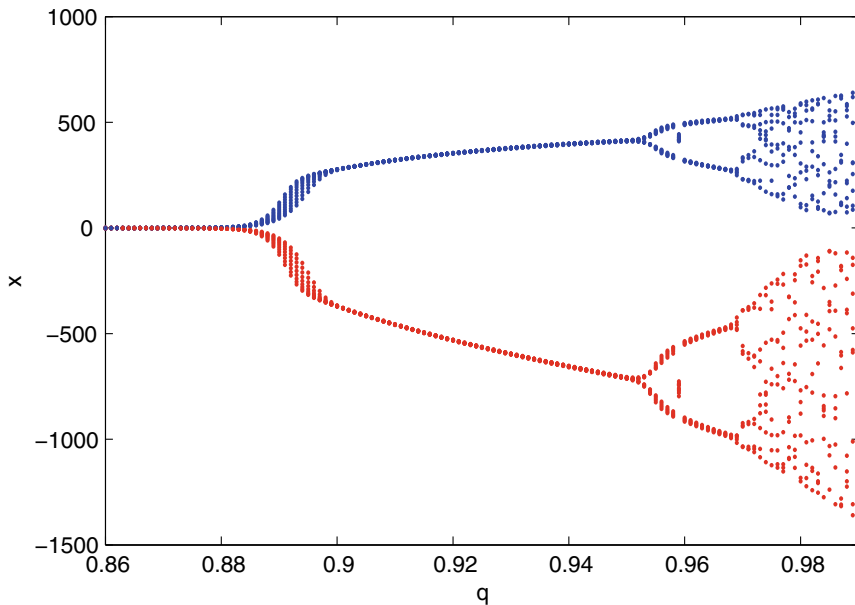


Fig. 4 Maximum Lyapunov exponents for the system (5)



**Fig. 5** Bifurcation diagram for the system (5) with respect to the parameter  $q$

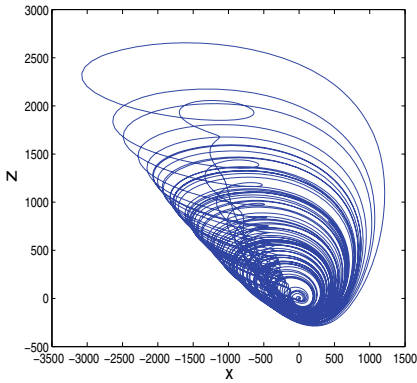
for  $q \in [0.86, 0.885)$  the system is stable, for  $q \in [0.885, 0.968)$  it exhibits limit cycle oscillations and for  $q \in [0.968, 0.99]$  it shows a comparatively higher periodic as well as chaotic oscillations.

#### **4.2 Chaos and Bifurcations with Different $q_i$ for the System (5)**

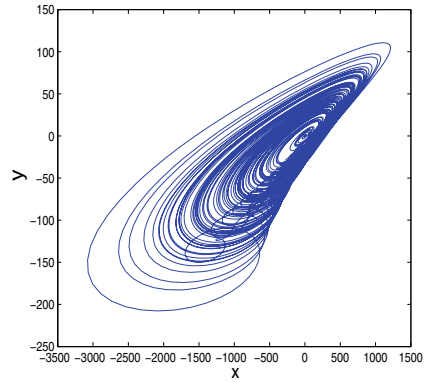
For the incommensurate order case we find dynamics present in the system (5) for  $q_1 = 0.98$ ;  $q_2 = 0.85$ ;  $q_3 = 0.98$ ;  $q_4 = 0.4$  as well. The corresponding phase plots and maximum Lyapunov exponents [4, 5] for the system equation 5 has been drawn in Fig. 6 and Fig. 7 respectively. We did not try to find the lowest order chaos for the incommensurate order case.

In order to understand the dynamics of the given system (5) with different  $q_i$  We shall consider the following three cases:

1. First with respect to  $q_1$  for  $0.7 < q_1 \leq 0.99$ , we shall draw a bifurcation diagram where the remaining parameters are fixed as in Fig. 3. The bifurcation diagram with reference to  $q_1$  shown in Fig. 8a, identifies the complex dynamical behaviour in the model (5) from the limit cycle to chaos. As we increase the values of  $q_1$  the system (5) converts from a stable focus to limit cycle oscillation and then limit cycle oscillation to chaotic oscillation. Figure 8a depicts that for  $q_1 \in (0.7, 0.78)$



(a) Phase plot for the system 5 in x-y plane



(b) Phase plot for the system 5 in x-z plane

**Fig. 6** Phase plot for the system (5) with non-commensurate fractional order

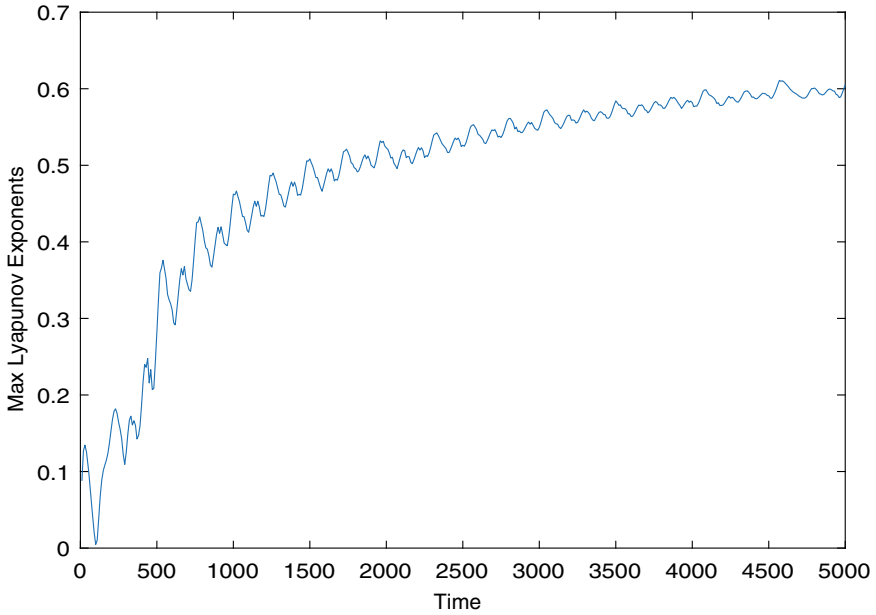


**Fig. 7** Maximum Lyapunov exponents for the system (5)

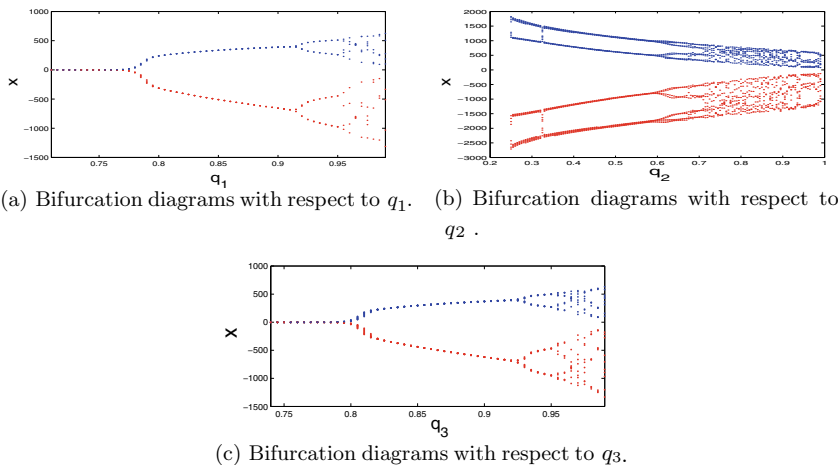


**Fig. 8** Bifurcation diagrams with respect to different  $q_i$  for the system (5)

the system equation 5 is stable, for  $q_1 \in [0.78, 0.95]$  it exhibits limit cycle oscillations, and for  $q_1 \in [0.95, 0.99]$  it shows a higher periodic as well as chaotic oscillation.

2. In the next step we shall draw the bifurcation diagram with reference to the parameter  $q_2$  for  $q_2 \in [0.25, 0.99]$  where  $q_1$  is kept constant at 0.98 and  $q_3 = q_4 = 0.98$ . From the Fig. 8b the complex dynamical behaviour of the system (5) with reference to  $q_2$  including chaos is clearly evident. We can also notice that for  $q_2 \in [0.25, 0.60)$  the system exhibits 4 - periodic solution, a 8 - periodic solution can be seen for  $0.60 < q_2 < 0.70$  and for  $q_2 \in [0.70, 0.99]$  the system exhibits higher periodic and chaotic oscillations.
3. On gradually increasing the parameter  $q_3$  the system equation 5 exhibits chaotic dynamics. Figure 8c shows that  $q_3$  behaves exactly in the same way as  $q_1$ . We omit the details. Here, all other parameters are fixed as in Fig. 3.

### 4.3 Chaos and Bifurcations with Different $d$ for the System (5)

Let us take the parameter values as  $a = 0.1$ ;  $b = 0.1$ ;  $c = 0.4$ ;  $k_1 = k_2 = 0.01$ ;  $a_1 = 0.001$ ;  $q_1 = q_2 = q_3 = q_4 = 0.98$  and vary  $d$  from  $-0.02$  to  $0.25$  with the initial condition  $(1, 0.1, 0, 40)$ . The bifurcation diagram is shown in Fig. 9. On comparing the fractional order system (5) with the integer order system (3) we see that they both have the same kind of tendency with the parameter  $d$ . For  $d \in [-0.02, 0.06)$  the system shows stable behaviour, for  $d \in [0.06, 0.18)$  the system exhibits limit cycle behaviour and higher periodic, chaotic oscillations can be seen for  $d \in [-0.18, 0.25]$ .

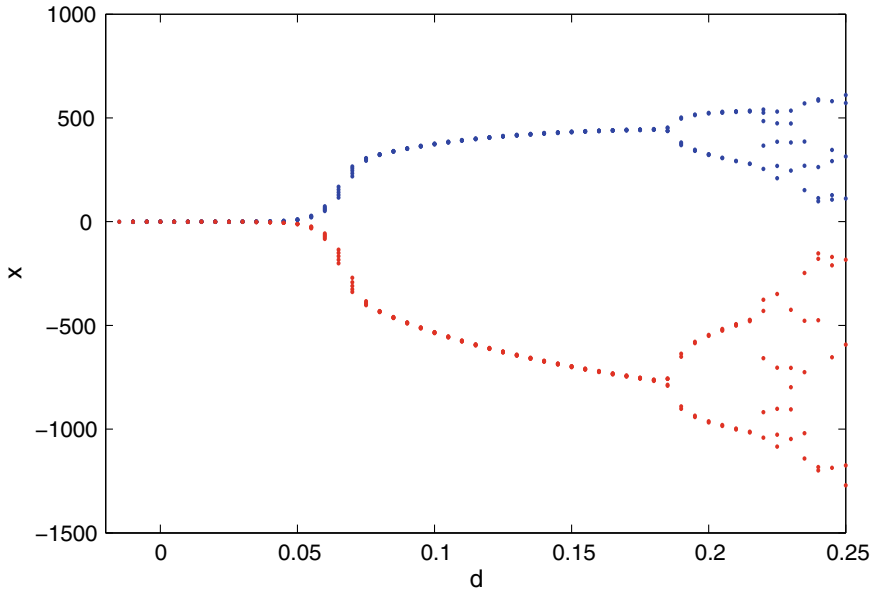


Fig. 9 Bifurcation diagram for the system (5) with respect to the parameter  $d$

### 5 Conclusion

The dynamics for the proposed system Eqs. 3 (integer order) and 5 (fractional order) has been studied in this article. We solve the system (5) using Adams-Bashforth-Moulton method. The method describes chaotic dynamics in the system (5) though the system has no equilibria. Several bifurcation diagrams and maximum Lyapunov exponents are drawn to establish our results by taking different values of the parameter  $d$  and the fractional order  $q_i$ . The existence of the attractors of the same kind in the integer order system and fractional order system both are a new field to explore, also it represents a new exciting phenomenon, which may serve helpful in the forthcoming research regarding the relations between integer order system and fractional order system. We leave synchronization control to the considered fractional model for future work.



**Acknowledgements** Research of Santanu Biswas is supported by Dr. D. S. Kothari Postdoctoral Fellowship under University Grants Commission scheme (Ref. No. F.4-2/2006 (BSR)/MA/19-20/0057). Special thanks to Prof. Sudeshna Banerjee for her valuable suggestions to improve the quality of the article.

## References

1. Arena, P., Caponetto, R., Fortuna, L., Porto, D.: *Nonlinear Non Integer Order Circuits and Systems-an Introduction*. World Scientific, Singapore (2000)
2. Bayani, A., Rajagopal, K., Khalaf, A., Jafari, S., Leutcho, G., Kengne, J.: Dynamical analysis of a new multistable chaotic system with hidden attractor: antimonotonicity, coexisting multiple attractors, and offset boosting. *Phys. Lett. A* **383**(13), 1450–1456 (2019)
3. Cafagna, D., Grassi, G.: Chaos in a fractional-order Rossler system. *Commun. Nonlinear Sci. Numer. Simul.* **19**, 2919–2927 (2014)
4. Danca, M.: Matlab code for Lyapunov exponents of fractional-order systems, part ii: the non-commensurate case. *Int. J. Bifurc. Chaos* **31**(12), 2150187 (2021)
5. Danca, M., Kuznetsov, N.: Matlab code for Lyapunov exponents of fractional-order systems. *Int. J. Bifurc. Chaos* **28**(05), 1850067 (2018)
6. Diethelm, K., Ford, N.: Analysis of fractional differential equations. *J. Math. Anal. Appl.* **265**, 229–248 (2002)
7. Diethelm, K., Ford, N., Freed, A.: A predictor-corrector approach for the numerical solution of fractional differential equations. *Nonlinear Dyn.* **29**, 3–22 (2002)
8. Fu, Z., heidel, J.: Non chaotic behaviour in three-dimensional quadratic systems. *Nonlinearity* 1289–1303 (1997)
9. Jafari, S., Sprott, J., Hashemi Golpayegani, S.: Elementary quadratic chaotic flows with no equilibria. *Phys. Lett. A* **377**, 699–702 (2013)
10. Li, C., Deng, W., Xu, D.: Chaos synchronization of the Chua system with a fractional order. *Phys. Lett. A* **360**, 171–85 (2006)
11. Li, H., Liao, X., Luo, M.: A novel non-equilibrium fractional-order chaotic system and its complete synchronization by circuit implementation. *Nonlinear Dyn.* **68**, 137–49 (2012)
12. Liu, T., Yan, H., Banerjee, S., Mou, J.: A fractional-order chaotic system with hidden attractor and self-excited attractor and its DSP implementation. *Chaos Solitons & Fractals* **145**, 110791 (2021)
13. Podlubny, I.: *Fractional Differential Equations*. Academic, New York (1999)
14. Sprott, J.: Some simple chaotic flows. *Phys. Rev. E* **50**(2) (1994)
15. Sprott, J.: *Chaos and Time Series Analysis* (Chap. 5). Oxford University Press, Oxford (2003)
16. Sun, K., Wang, X., Sprott, J.: Bifurcations and chaos in fractional-order simplified Lorentz system. *Int. J. Bifurc. Chaos* **20**(4), 1209–1219 (2010)
17. Tahir, F.R., Jafari, S., Pham, V., Volos, C., Wang, X.: A novel no-equilibrium chaotic system with multiwing butterfly attractors. *Int. J. Bifurc. Chaos* **25**(4), 1550056 (2015)
18. Tian, H., Wang, Z., Zhang, P., Chen, M., Wang, Y.: Dynamic analysis and robust control of a chaotic system with hidden attractor. *Complexity* (2021)
19. Wang, Z., Cang, S., Ochola, E., Sun, Y.: A hyperchaotic system without equilibrium. *Nonlinear Dyn.* **69**, 531–7 (2012)
20. Wei, Z.: Dynamical behaviors of a chaotic system with no equilibria. *Phys. Lett. A* **376**, 102–8 (2011)
21. Wolf, A., Swift, J., Swinney, H., Vastano, J.: Determining Lyapunov exponents from a time series. *Phys. D* **16**, 285–317 (1985)
22. Zhang, W., Zhao, S., Li, H., Zhu, H.: Chaos in a fractional-order Rossler system. *Chaos Solitons Fractals* **42**, 1684–1691 (2009)

# Soliton Dynamics in a Weak Helimagnet



Geo Sunny, L. Kavitha, and A. Prabhu

**Abstract** We considered a Helimagnetic nanowire, with an antisymmetric spin interaction known as the Dzyaloshinskii-Moriya (DM) interaction in analogy with Cholesteric Liquid Crystal (CLC) model. We derive the nonlinear dynamical equation after boronizing the nanowire with the Holstein–Primakoff (HP) transformation aided with Glauber’s coherent-state representation. The governing equation of motion is the celebrated Discrete Non-Linear Schrodinger (DNLS) equation for the Helimagnetic nanowire. We attempt to solve the DNLS equation, using Jacobian elliptical function (JEF) technique, and analyzed the competency of the helicity and the weak DM interaction on the dynamics of helimagnetic nanowire.

**Keywords** Soliton · Helimagnet · Dzyaloshinskii–Moriya (DM) interaction

## 1 Introduction

Recently, helimagnetic systems have been gaining lots of attention due to its contribution in the field of data storage technology [1, 2] as it can be easily fabricated into different structures like arrays of wires, dots, rings and sheets which have varied possibilities in the development of magnetic storage devices. Amid this, helimagnetic nanowire exhibits uniqueness due to its tunable magnetization properties which arises from its inherent shape anisotropy [3]. The current research in the field of helimagnetic nano-wire is the development of ultra-high density magnetic recordings incorporating the DM interaction. The DM interaction plays a crucial role in the for-

---

G. Sunny · L. Kavitha (✉)

Department of Physics, School of Basic and Applied Sciences, Central University of Tamil Nadu, Thiruvavur 610005, India  
e-mail: [lkavitha@cutn.ac.in](mailto:lkavitha@cutn.ac.in)

L. Kavitha

The Abdus Salam International Centre for Theoretical Physics, Trieste, Italy

A. Prabhu

Department of Physics, Periyar University, Salem 636011, India

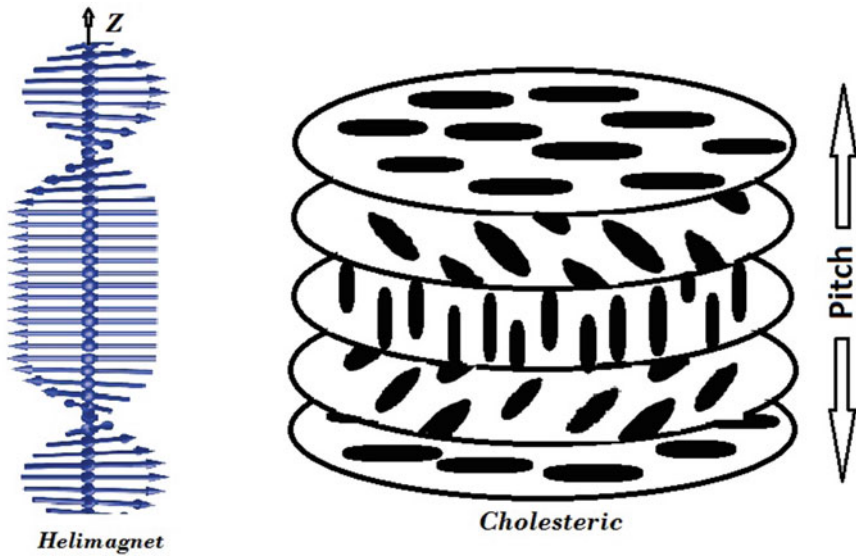


**Fig. 1** Schematic representation of a helimagnet

mation of chiral spin texture. It is generated by the strong spin-orbit coupling (SOC) between the atomic spins due to the chiral interaction between them. Recent study by Sampaio et al. demonstrated the influence of DM interaction in the magnetic memory cell performance [4]. Various experimental researches are also being conducted in this field, these provide validation to some of the theoretical works [5–7].

Various models have been proposed to investigate the dynamics of helimagnetic systems [8]. Chandra et al. showed that the large quantum fluctuations induce an anisotropy in the helimagnet [9]. Beula et al. investigated the influence of constant magnetic field on the dynamics of an anisotropic helimagnet and found that the spin configurations are unstable when the applied field is normal to the anisotropic axis [10]. Martin et al. studied the ground state of MnGe cubic alloy and observed proliferation in the long wavelength with gapless spin fluctuations which is associated with evolution of the helical correlation length [11]. Daniel et al. considered a Helimagnetic model in analogous to cholesteric liquid crystal and found that the soliton excitations govern the nonlinear dynamics of the helimagnet. They found that the helicity does not alter the nature of the soliton during propagation, however it suffers with some fluctuations in the localized region [12] (Fig. 1). The dynamics of Discrete Breather (DB) in an antiferromagnetic system under the influence of DM interaction has already been explored [13, 14]. The discrete Breathers are spatially localized nonlinear excitations which appear in classical discrete lattice systems [13, 15–17].

It has been a concern for the scientists to find an exact solution for the nonlinear dynamic equation. These solutions may provide more insight towards physical phenomenons happening in biology, chemistry, physics and various other fields. To obtain an exact solution to these dynamical equations various methods have been implemented such as the inverse scattering method, the tangent hyperbolic function method, the Jacobi elliptical function method, the sine-cosine function method, the trail function method, the nonlinear transformation method and so on. In this paper, we attempt to derive an exact solution for the helimagnetic system under the influence of DM interaction using jacobi elliptical method.

## 2 Governing Dynamical Model and Equation

We consider an one dimensional ferromagnetic system in analogous to the CLC model in order to incorporate the helicity. As the play role of the anisotropy is much significant for the intrinsic localisation of nonlinear spin waves, we consider an anisotropic weak ferromagnetic spin chain with appreciable helicity as represented by the Hamiltonian,

$$\tilde{H} = - \sum_n [J(\vec{S}_n \cdot \vec{S}_{n+1}) + \vec{D} \cdot (\vec{S}_n \times \vec{S}_{n+1}) + \tau \{[\hat{k} \cdot (\vec{S}_n \times \vec{S}_{n+1})]^2 - q_1^2\}] - A(S_n^z)^2 - A'(S_n^z)^4 \quad (1)$$

where  $\vec{S}_n = (S_n^x, S_n^y, S_n^z)$  represents the local spin vector at the lattice site 'n'.  $J > 0$  characterize the nearest-neighbor exchange interaction, which is a short ranged strong spin-spin exchange coupling. The second term designates the presence of DM interaction, and lead to the canting of spins which depends on the direction of the monoaxial vector  $\vec{D} = D\hat{e}_z$ , restricted to  $z$  axis. The cross product  $\vec{D}_n \cdot (\vec{S}_n \times \vec{S}_{n+1})$  characterize the spin-flop hopping arises due to the presence of DM interaction which occurs in the systems lacking inversion symmetry. The term represents the helical spin interaction similar to that of the molecular interaction in a CLC. We adopt a similar kind of helical twisting designated as  $\{[\hat{k} \cdot (S_n \times S_{n+1})]^2 - q_1^2\}^2$ , where  $k = (0, 0, 1)$ ,  $q_1$  is the helical pitch which controls the long-range ordering of spins. The last two terms designate the lower and higher order anisotropy mainly arised due to the combined effect of crystal field effect and spin-orbit interaction.  $A$  and  $A'$  respectively are the lower and higher order single-ion unizxial anisotropy parameters, when  $A(> 0)$ , we assume that all spins align along the  $z$  axis, being the easy axis of magnetization in the ground state. We map the spin operators of our one dimensional helimagnetic systems of spin- $s$  moments on a discrete lattice to bosonic creation  $a_i^\dagger$  and annihilation operator  $a_i$  using the Holstein–Primakoff (H–P) representation [18]

$$\hat{S}_i^+ = (2S)^{1/2} \left[ 1 - \frac{a_i^\dagger a_i}{2S} \right]^{1/2} a_i,$$

$$\hat{S}_i^- = (2S)^{1/2} a_i^\dagger \left[ 1 - \frac{a_i^\dagger a_i}{2S} \right]^{1/2},$$

$$\hat{S}_i^z = \left[ S - a_i^\dagger a_i \right].$$

where  $a_i^\dagger(a_i)$  is a bosonic creation(annihilation) operator at site ' $i$ ' satisfies the bosonic commutation relations in the second quantisation formulation of the helimagnetic spin lattice as  $[a_j, a_i^\dagger] = \delta_{ij}$ ,  $[a_j, a_i] = [a_j^\dagger, a_i^\dagger] = 0$ . and  $n_i = a_i^\dagger a_i$  represents the number operator. In this mapping, each Holstein–Primakoff bosonic operator represents a spin-1 moment in the  $-z$  direction and the vacuum state of the bosons, i.e.  $|n = 0\rangle$  has a spin of  $+S$  in the  $z$  direction. In this mapping, the vacuum state is not always the ground state, thereby representing a perturbation from the classical ferromagnetic ground state. Conceived by this physical picture, it is manifested that the factor  $\sqrt{2S - n_i}$ , limits the number of HP bosons to  $2S$  on a given site  $i$ , since the  $z$ -projection of the spin moment at a given site ' $i$ ' must be between  $-S$  and  $+S$ . Since low temperatures, the number of perturbations about the classical ground state is very small  $n_i \ll S$ , we invoke power series expansion of the HP transformation for the spin operators as,

$$\hat{S}_n^+ = \sqrt{2} \left[ 1 - \frac{\epsilon^2}{4} a_n^\dagger a_n - \frac{\epsilon^4}{32} a_n^\dagger a_n a_n^\dagger a_n - O\epsilon^6 \right] \epsilon a_n,$$

$$\hat{S}_n^- = \sqrt{2} \epsilon a_n^\dagger \left[ 1 - \frac{\epsilon^2}{4} a_n^\dagger a_n - \frac{\epsilon^4}{32} a_n^\dagger a_n a_n^\dagger a_n - O\epsilon^6 \right],$$

$$\hat{S}_n^z = [1 - \epsilon^2 a_n^\dagger a_n]. \tag{2}$$

where  $\epsilon = 1/\sqrt{S}$

$$i\hbar \frac{\partial a_n}{\partial t} = [a_n, H] = F(a_n^\dagger, a_n, a_{n+1}^\dagger, a_{n+1}).$$

We then introduce the Glauber’s coherent—state representation [19] defined by the product of the multimode coherent states  $|u\rangle = \prod_n |u_n\rangle$  with  $\langle u|u\rangle = 1$ . Here  $|u(n)\rangle$  is an eigenstate vector of the annihilation operator  $a_n$  i.e.,  $a_n|u\rangle = u_n|u\rangle$ , and  $u_n$  is the coherent amplitude. The  $p$ -representation of nonlinear equation leads,

$$\begin{aligned}
i \frac{du_n}{dt} = \epsilon^2 & \left[ 2(\tau - A - 2A')u_n - J(u_{n-1} + u_{n+1}) - iD^z(u_{n+1} - u_{n-1}) \right] \\
& + \frac{\epsilon^4}{4} \left[ J[|u_n|^2(u_{n+1} + u_{n-1}) + u_n^2(u_{n+1}^* + u_{n-1}^*) + |u_{n+1}|^2 u_{n+1} + |u_{n-1}|^2 u_{n-1}] \right. \\
& - 4(J + 2\tau)[|u_{n+1}|^2 + |u_{n-1}|^2]u_n + 8\tau[u_{n+1}^2 + u_{n-1}^2]u_n^* + 8(A + A')|u_n|^2 u_n \\
& \left. + iD^z[2(u_{n+1} - u_{n-1})|u_n|^2 - (u_{n+1}^* - u_{n-1}^*)u_n^2 + |u_{n+1}|^2 u_{n+1} - |u_{n-1}|^2 u_{n-1}] \right] \\
& + iD^z \frac{\epsilon^5}{32} \left[ 3|u_n|^4(u_{n+1} - u_{n-1}) - 2|u_n|^2 u_n^2(u_{n+1}^* - u_{n-1}^*) + |u_{n+1}|^4 u_{n+1} - |u_{n-1}|^4 u_{n-1} \right] \\
& + \frac{\epsilon^6}{32} \left[ J \left( 2u_n^2(|u_{n+1}|^2 u_{n+1}^* + |u_{n-1}|^2 u_{n-1}^*) + 4|u_n|^2(|u_{n+1}|^2 u_{n+1} + |u_{n-1}|^2 u_{n-1}) \right. \right. \\
& - 3|u_n|^4(u_{n+1} + u_{n-1}) - 2|u_n|^2 u_n^2(u_{n+1}^* + u_{n-1}^*) - (|u_{n+1}|^4 u_{n+1} - |u_{n-1}|^4 u_{n-1}) \left. \right) \\
& + 16\tau \left( 2u_n^*(|u_{n+1}|^2 u_{n+1}^* + |u_{n-1}|^2 u_{n-1}^*) + 3|u_n|^2 u_n^*(u_{n+1}^2 + u_{n-1}^2) - 2(|u_{n+1}|^4 + |u_{n-1}|^4)u_n \right. \\
& - 4|u_n|^2(|u_{n+1}|^2 + |u_{n-1}|^2)u_n + u_n^3(u_{n+1}^2 + u_{n-1}^2) \left. \right) + 384A'|u_n|^4 u_n \\
& \left. - iD^z \left( 2|u_n|^2(|u_{n+1}|^2 u_{n+1} - |u_{n-1}|^2 u_{n-1}) - u_n^2(|u_{n+1}|^2 u_{n+1}^* + |u_{n-1}|^2 u_{n-1}^*) \right) \right]. \tag{3}
\end{aligned}$$

Equation (3) represents the spin dynamics of an anisotropic weak helimagnet. This discrete equation leads to several nonlinear excitations. The combination of nonlinearity and discreteness gives rise to new types of nonlinear excitations which are not present in the continuum models. These complexities make it difficult to solve the equation directly.

### 3 Kink Solitonic Profile

The exact solution to the Eq. (3) can be obtained by the use of Jacobi elliptic function method [20]. We introduce the transformations [21]

$$u_n = e^{i\theta_n} \phi_n(\xi_n), \tag{4}$$

where,

$$\theta_n = pn + \omega t + \theta_0, \quad \xi_n = kn + ct + \chi_0,$$

using the trigonometric relation  $e^{\pm i p} = \cos(p) \pm i \sin(p)$ , separate the real and imaginary parts, we obtain following set of equations:

$$\begin{aligned}
 &\omega\phi_n + \epsilon^2[2(J - A - 2A')\phi_n - J(\phi_{n+1} + \phi_{n-1})(\cos p + D^z \sin(p))] + \\
 &(1/4)\epsilon^4 \left[ J \left[ (3\phi_n^2(\phi_{n+1} + \phi_{n-1}) \cos(p)) + (\phi_{n+1}^3 + \phi_{n-1}^3) \cos(p) \right] - 4(J + 2\tau) \right. \\
 &(\phi_{n+1}^2 + \phi_{n-1}^2)\phi_n + 8\tau\phi_n(\phi_{n+1}^2 + \phi_{n-1}^2) \cos(2p) + 8(A + 6A')\phi_n^3 + D^z \sin(p) \\
 &(2\phi_n^2(\phi_{n+1} - \phi_{n-1}) - \phi_{n+1} + \phi_{n-1} + \phi_{n+1}^3 - \phi_{n-1}^3) - (D^z \epsilon^5 \sin(p)/32)(5\phi_n^4 \\
 &(\phi_{n+1} + \phi_{n-1}) + \phi_{n+1}^5 + \phi_{n-1}^5) - (\epsilon^6/32)(J \cos(p)(\phi_n^2(\phi_{n+1}^3 + \phi_{n-1}^3)) - 5\phi_n^4 \\
 &(\phi_{n+1} + \phi_{n-1}) - \phi_{n+1}^5 - \phi_{n-1}^5) + 16\tau(\phi_n(\cos(2p) - 1)2(\phi_{n+1}^4 + \phi_{n-1}^4) + 4 \\
 &(\cos(2p) - 1) \times \phi_n^3(\phi_{n+1}^2 + \phi_{n-1}^2)) + 384A'\phi_n^5 + 3D^z \sin(p)\phi_n^2(\phi_{n+1}^3 + \phi_{n-1}^3) = 0, \quad (5) \\
 &-c\phi_n' - \epsilon^2(J(\phi_{n+1} - \phi_{n-1}) \sin(p) + D^z \cos(p)(\phi_{n+1} - \phi_{n-1})) + (1/4)\epsilon^4(J \\
 &(\phi_{n+1}^3 + \phi_{n-1}^3) \sin(p) + 8\tau\phi_n(\phi_{n-1}^2 - \phi_{n+1}^2) \sin(2p) + D^z \cos(p)(\phi_n^2(\phi_{n+1} \\
 &-\phi_{n-1}) + \phi_{n+1}^3 - \phi_{n-1}^3)) + (1/32)D^z \epsilon^5 \cos(p) \times (\phi_n^4(\phi_{n+1} - \phi_{n-1}) + \phi_{n+1}^5 \\
 &-\phi_{n-1}^5) - (1/32)\epsilon^6(J \sin(p) \times (2\phi_n^2(\phi_{n+1}^3 - \phi_{n-1}^3) - \phi_n^4(\phi_{n+1} - \phi_{n-1}) \\
 &-\phi_{n+1}^5 + \phi_{n-1}^5) + 32\tau \sin(2p)(\phi_n(\phi_{n+1}^4 - \phi_{n-1}^4) + \phi_n^3(\phi_{n+1}^2 - \phi_{n-1}^2)) \\
 &-D^z \cos(p)\phi_n^2(\phi_{n+1}^3 - \phi_{n-1}^3)) = 0. \quad (6)
 \end{aligned}$$

We use the following series of expression [22] as a solution:

$$\begin{aligned}
 \phi_n(\xi_n) &= a_0 + a_1 sn(\xi_n), \\
 \phi_{n+1}(\xi_n) &= a_0 + a_1 \frac{sn(\xi_n)cn(k, m)dn(k, m) + sn(k, m)cn(\xi_n)dn(\xi_n)}{1 - m^2 sn^2(\xi_n)sn^2(k)}, \\
 \phi_{n-1}(\xi_n) &= a_0 + a_1 \frac{sn(\xi_n)cn(k, m)dn(k, m) - sn(k, m)cn(\xi_n)dn(\xi_n)}{1 - m^2 sn^2(\xi_n)sn^2(k)}. \quad (7)
 \end{aligned}$$

Further substituting Eq. (7) into Eqs. (5) and (6) and after equating the coefficients of all power to zero, we get a series of algebraic equations. After solving these equations using symbolic computation, we obtain the following solution

$$\phi_n(\xi_n) = a_0 + \left[ \frac{2D^Z \sin(p) - 15360\epsilon\tau a_0 A' + 3\epsilon J \cos(p)a_0}{-3072\epsilon A'} \right] \tanh(kn + ct + \chi_0), \quad (8)$$

Upon substituting Eq. (8) in Eq. (4), we write the exact travelling solitary solution as,

$$u(n, t) = \left[ a_0 + \left[ \frac{2D^Z \sin(p) - 15360\epsilon\tau a_0 A' + 3\epsilon J \cos(p)a_0}{-3072\epsilon A'} \right] \tanh(kn + ct + \chi_0) \right] e^{i(pn + \omega t + \theta_0)} \quad (9)$$

The solution of Eq. (9) is plotted with set of parameters ( $a_0 = 0.2, J = 0.2$  and  $A' = 0.1$ ) and the Fig. 3 shows that the magnetic soliton assumes Kink soliton profile and propagates along the chain.

### 4 Results and Discussion

We have investigated the soliton profile of the Helimagnetic nanowire by varying the strength of helicity and DM interaction. It can be observed from the Fig.2 that there is a significant change in the soliton profile when the value of helicity ( $\tau$ ) is changed. When the value of  $\tau$  is increased from 0.1 to 0.9, nature of soliton profile

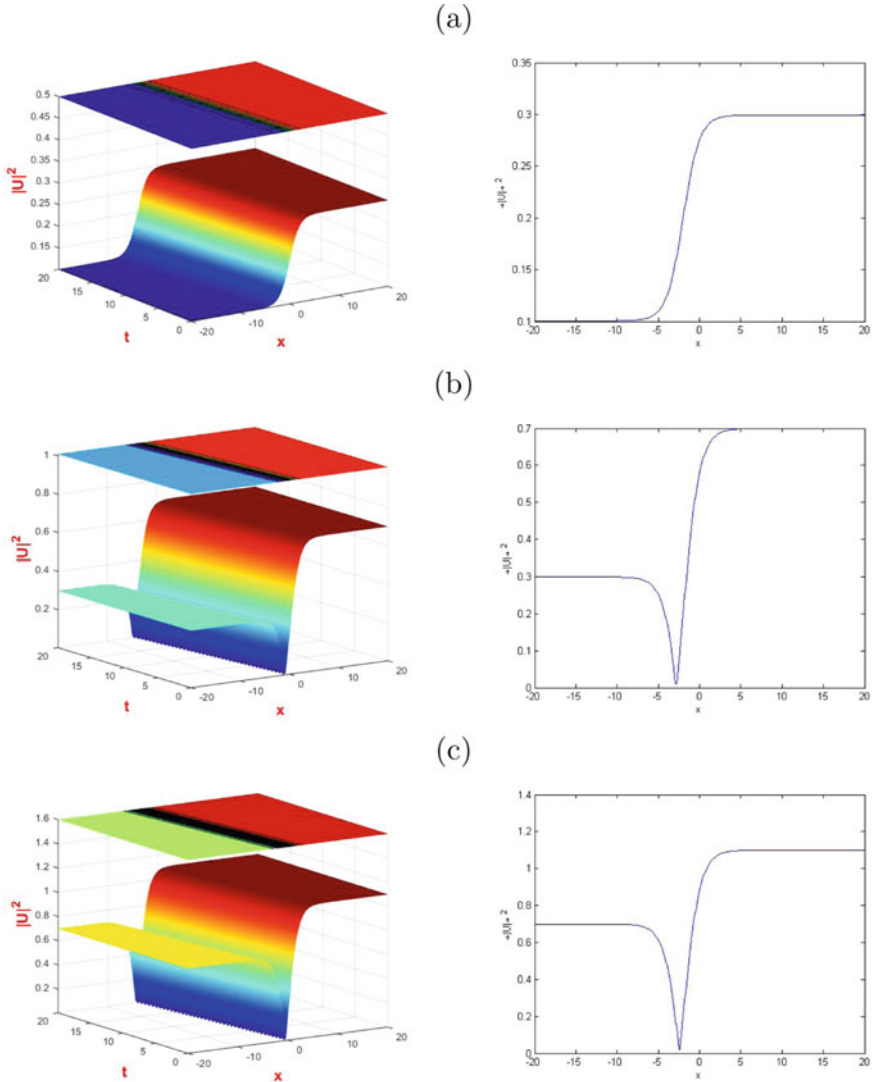


**Fig.2** Soliton profile for  $D^z = 0.1, a_0 = 0.2, J = 0.2, A' = 0.1$  and **a**  $\tau = 0.1$  **b**  $\tau = 0.5$  **c**  $\tau = 0.9$



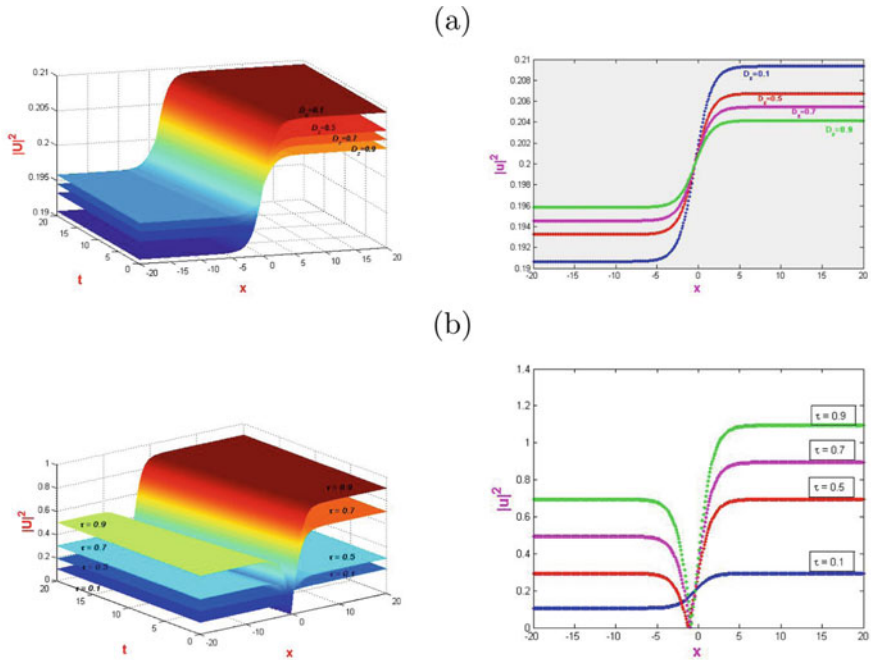


**Fig. 3** Cumulative plots for the soliton profile for values  $a_0 = 0.2, J = 0.2, A' = 0.1$  and **a**  $D^z = 0.1, D^z = 0.3, D^z = 0.5$  and  $D^z = 0.9$  **b**  $\tau = 0.1, \tau = 0.3, \tau = 0.5, \tau = 0.9$

changes from kink to antisoliton and there is also an increase in the amplitude of the profile. When  $\tau$  is 0.1, the kink soliton has an amplitude of 0.3 and for  $\tau = 0.9$ , the antisoliton has an amplitude of 1.1. So as  $\tau$  is increased from 0.1 to 0.9, the amplitude has increased at the blistering speed and grows exponentially. We can see that the difference between the height of the two maxima's is also very less for  $\tau = 0.1$  and is significantly larger when  $\tau$  reaches 0.9. So it can be inferred that the structure of helimagnet in analogy with CLC stabilizes the soliton and settle in a more robust and coherent profile fashion. In Fig. 3 we have plotted the cumulative plots for various values of  $\tau$  and  $D_z$ . On the left side, cumulative plot in 3D is displayed and the 2D plot for the same is displayed on the right side. It is evident from Fig. 3a that, there is a decrease in the amplitude of the soliton profile when there is an increase in the DM interaction. When  $D_z$  is 0.1, amplitude is 0.209 and when  $D_z$  is increased to 0.5, amplitude decreases to 0.207. Further increase in the  $D_z$  value to 0.9 decreases the amplitude to 0.204. Hence, the amplitude of the soliton is inversely proportional to the strength of the DM interaction in the Helimagnetic nanowire. Additionally, a marginal difference between the heights of the two maxima's can be seen, when the strength of the DM interaction is increased. It can be noted that there is no significant changes in the nature of soliton profile.

## 5 Conclusions

In this paper, we have investigated the effect of DM interaction along with the influence of helicity on a weak Helimagnetic nanowire. We have obtained a DNLS evolution equation using the HP transformation aided with the Glauber's coherent-state representation. The DNLS equation thus obtained is solved for exact solution using the JEF approach. Analyzing the soliton profile obtained, it is observed that the value of helicity plays a major role in the profile of the antisoliton. Even though the changes in the Kink soliton profile due to the varying DM interaction is significantly low, amplitude is influenced by the strength of the DM interaction. These results emphasize the significance of helicity and DM interaction in materials used for the memory storage devices.

**Acknowledgements** G.S gratefully acknowledges DST, India for the INSPIRE fellowship (IF160862). L.K acknowledges the financial support from UGC-DAE (Ref.No:CSR-KN/CRS-102/2019–20), India, CSIR (Ref.No:03(1414)/17/EMR-II), India and DST-SERB (Ref.No.:MTR/2017/000314/MS), India in the form of a major research project and ICTP, Italy in the form of a Regular Associateship.

## References

1. Beg, M., Carey, R., Wang, W., Cortés-Ortuño, D., Vousden, M., Bisotti, M.-A., Albert, M., Chernyshenko, D., Hovorka, O., Stamps, R.L., et al.: Ground state search, hysteretic behaviour and reversal mechanism of skyrmionic textures in confined helimagnetic nanostructures. *Sci. Rep.* **5**(1), 1–14 (2015)
2. Rybakov, F.N., Borisov, A.B., Blügel, S., Kiselev, N.S.: New type of stable particlelike states in chiral magnets. *Phys. Rev. Lett.* **115**(11), 117201 (2015)
3. Chui, C., Ma, F., Zhou, Y.: Geometrical and physical conditions for skyrmion stability in a nanowire. *AIP Adv.* **5**(4), 047141 (2015)
4. Sampaio, J., Khvalkovskiy, A., Kuteifan, M., Cubukcu, M., Apalkov, D., Lomakin, V., Cros, V., Reyren, N.: Disruptive effect of Dzyaloshinskii-Moriya interaction on the magnetic memory cell performance. *Appl. Phys. Lett.* **108**(11), 112403 (2016)
5. Osorio, S., Laliena, V., Campo, J., Bustingorry, S.: Creation of single chiral soliton states in monoaxial helimagnets. *Appl. Phys. Lett.* **119**(22), 222405 (2021)
6. Laliena, V., Bustingorry, S., Campo, J.: Dynamics of chiral solitons driven by polarized currents in monoaxial helimagnets. *Sci. Rep.* **10**(1), 1–10 (2020)
7. Saravanan, M.: Electromagnetic soliton propagation in an anisotropic Heisenberg helimagnet. *Phys. Lett. A* **378**(41), 3021–3027 (2014)
8. Sunny, G., Kavitha, L.: Modulational instability induced generation of solitary wave profile of an anisotropic-ferromagnetic nanowire with asymmetric Dzyaloshinskii-Moriya interaction. *Mater. Today: Proc.* (2020)
9. Chandra, P., Coleman, P., Larkin, A.: A quantum fluids approach to frustrated Heisenberg models. *J. Phys.: Condens. Matter* **2**(39), 7933 (1990)
10. Beula, J., Daniel, M.: Nonlinear spin excitations in a classical Heisenberg anisotropic helimagnet. *Phys. D* **239**(8), 397–406 (2010)
11. Martin, N., Mirebeau, I., Franz, C., Chaboussant, G., Fomicheva, L., Tsvyashchenko, A.: Partial ordering and phase elasticity in the MnGe short-period helimagnet. *Phys. Rev. B* **99**(10), 100402 (2019)

12. Daniel, M., Beula, J.: Soliton spin excitations in a Heisenberg helimagnet. *Chaos Solitons & Fractals* **41**(4), 1842–1848 (2009)
13. Kavitha, L., Parasuraman, E., Gopi, D., Prabhu, A., Vicencio, R.A.: Nonlinear nano-scale localized breather modes in a discrete weak ferromagnetic spin lattice. *J. Magn. Magn. Mater.* **401**, 394–405 (2016)
14. Kavitha, L., Sathishkumar, P., Saravanan, M., Gopi, D.: Soliton switching in an anisotropic Heisenberg ferromagnetic spin chain with octupole-dipole interaction. *Phys. Scr.* **83**(5), 055701 (2011)
15. Kavitha, L., Srividya, B., Dhamayanthi, S., Kumar, V.S., Gopi, D.: Collision and propagation of electromagnetic solitons in an antiferromagnetic spin ladder medium. *Appl. Math. Comput.* **251**, 643–668 (2015)
16. Kavitha, L., Mohamadou, A., Parasuraman, E., Gopi, D., Akila, N., Prabhu, A.: Modulational instability and nano-scale energy localization in ferromagnetic spin chain with higher order dispersive interactions. *J. Magn. Magn. Mater.* **404**, 91–118 (2016)
17. Darvishi, M., Louis, K., Najafi, M., Senthil Kumar, V.: Elastic collision of mobile solitons of a  $(3 + 1)$ -dimensional soliton equation. *Nonlinear Dyn.* **86** (2016). <https://doi.org/10.1007/s11071-016-2920-0>
18. Holstein, T., Primakoff, H.: Field dependence of the intrinsic domain magnetization of a ferromagnet. *Phys. Rev.* **58**(12), 1098 (1940)
19. Glauber, R.J.: Coherent and incoherent states of the radiation field. *Phys. Rev.* **131**(6), 2766 (1963)
20. Jacobi, C.: *New foundations of the theory of elliptic functions*. Königsberg, Borntraeger 1829 (2012)
21. Kovacic, I., Cveticanin, L., Zukovic, M., Rakaric, Z.: Jacobi elliptic functions: a review of nonlinear oscillatory application problems. *J. Sound Vib.* **380**, 1–36 (2016)
22. Wazwaz, A.-M.: A sine-cosine method for handling nonlinear wave equations. *Math. Comput. Model.* **40**(5–6), 499–508 (2004)

# Delay-Resilient Dynamics of a Landslide Mechanical Model



Srdan Kostić  and Nebojša Vasović 

**Abstract** In present paper we analyze dynamics of a simple landslide mechanical model induced by the co-action of included time delay between the motion of the neighboring blocks and their coupling strength. Analyzed mechanical model represents an idealized interaction between accumulation and feeder slope at the accumulation coast. Dynamics of the proposed dynamical system is examined by applying standard bifurcation analysis: we derive explicit relations between time delay, spring stiffness and control parameters, while bifurcation curves are derived numerically. The results of the presented research indicate the onset of Hopf bifurcation, i.e. occurrence of instability for rather high values of the assumed time delay and spring stiffness, which indicates that slope instability occurs only in case when feeder and accumulation slope are observed as strongly coupled, but with a significant delay in interaction. Moreover, we showed that the increase of friction force along the sliding surface suppresses the effect of time delay, indicating that sliding surfaces with low friction parameters are prone to onset of instability.

**Keywords** Landslide · Time delay · Spring stiffness · Friction · Bifurcation

## 1 Introduction

Mechanical models are commonly used to successfully simulate dynamics of many natural phenomena, since their dynamics could be reliably described by a set of ordinary/partial differential equations, whose solutions for different initial conditions and values of control parameters could also be confirmed by real physical simulation of the process under study. The most remarkable example of this approach is certainly Burridge–Knopoff model of the earthquake nucleation process, composed of series

---

S. Kostić (✉)

Geology Department, Jaroslav Černi Water Institute, Jaroslava Černog 80, 11226 Belgrade, Serbia  
e-mail: [srdjan.kostic@jcerni.rs](mailto:srdjan.kostic@jcerni.rs)

N. Vasović

Department of Applied Mathematics and Informatics, Faculty of Mining and Geology, University of Belgrade, Đušina 7, 11000 Belgrade, Serbia

© The Author(s), under exclusive license to Springer Nature Switzerland AG 2022

1103

S. Banerjee and A. Saha (eds.), *Nonlinear Dynamics and Applications*,

Springer Proceedings in Complexity,

[https://doi.org/10.1007/978-3-030-99792-2\\_93](https://doi.org/10.1007/978-3-030-99792-2_93)

of blocks, interconnected only to neighboring blocks, while sliding over the rough surface [1]. In their original paper, Burridge and Knopoff showed that sudden triggering events (“spikes”) which occur during the sliding of the blocks, follow macroseismological Gutenberg–Richter and Omori–Utsu laws. This original model has been in succeeding years used as a common model of seismogenic fault movement, whose dynamics has been described by different equations capturing different effect of controlling parameter and interactions among the blocks, including the variable friction laws [2–5]. Apart from the use of this model for description of earthquake nucleation process, it was also used for description of other processes, such as landslide dynamics. In a dynamical sense, both earthquakes and landslides act similarly: a period of no movement or with only small displacements is followed by the period of sudden large displacements, when accumulated energy is being dissipated. The first attempt of using spring-block model for simulation of landslide dynamics was made by Davis [6], who formulated simple mechanical model of two interconnected blocks (accumulation and feeder slope) sliding along the accumulation coast. In his paper, Davis recorded a certain time delay between the movement of the feeder and accumulation slope, which was not included in further analysis, but certainly have effect on the landslide dynamics. This model of Davis [6] was further examined by Morales et al. [7], who studied effect of different friction laws on the landslide dynamics.

In present paper, we start from the model proposed by Davis [6] and Morales et al. [7], but also explicitly include time delay effect between the feeder and accumulation slope, in order to analyze its effect on the onset of instability. Influence of time delay is examined in co-action with coupling strength between the neighboring blocks and frictional parameters along the sliding surface.

## 2 Description of the Proposed Model

We start from the model proposed by Davis [6]:

$$\begin{aligned}
 m_1 \dot{V}_1 &= W_1 \sin \beta_1 - S_1 - F \\
 m_2 \dot{V}_2 &= W_2 \sin \beta_2 - S_2 + F \\
 \dot{F} &= k(V_1 - V_2) + c(\dot{V}_1 - \dot{V}_2)
 \end{aligned} \tag{1}$$

where the superposed dot denotes differentiation with respect to time, and:  $W = m_i g$ —block weight,  $g$ —acceleration of gravity;  $S_i$ —sliding resistance on failure surface along each block,  $F$ —combined elastic and viscous forces,  $k$ —spring constant,  $c$ —dash pot constant, and  $\beta_i =$  slope angle. Sliding resistance along the failure surface is defined using conventional effective stress model for frictional

strength:  $S_i = W_i(1 - \alpha_i)\cos\beta_i f(V_i)$ , where  $\alpha$  represents the effect of piezometric elevation on the effective stress which acts on the failure surface:  $\alpha_i = \gamma_w h_{wi} / \gamma h_i$ , where  $\gamma$  and  $\gamma_w$  are the unit weights of the slide material and the pore water respectively, and  $h_i$  and  $h_{wi}$  are layer thickness and groundwater depth within the layer. The function  $f(V_i)$  represents the mobilized strength on the failure surface:

$$f(V_i) \begin{cases} = \tan\varphi & \text{for } V_i > 0 \\ \leq \tan\varphi & \text{for } V_i = 0 \end{cases} \tag{2}$$

where  $\varphi$  represents the effective stress friction angle appropriate to the slide material.

In contrast to Davis [6] and model (1), we consider the following:

- two blocks (upper feeder and accumulation slide) on an inclined plane are only connected by elastic springs (Fig. 1a), without the dash pot, which also reduces the effect of  $F$  only to elastic force;
- sliding resistance on failure surface is assumed to have the following general form:

$$S = aV_i^3 + bV_i^2 + cV_i \tag{3}$$

which is the nonmonotonic friction law according to Morales et al. [7], and it describes a smooth spinodal friction law similar to the one introduced in Cartwright et al. [3], see Fig. 1b.

- values of frictional parameters  $a$ ,  $b$ , and  $c$  are chosen according to Morales et al. [7], where cubic friction force is given for  $a = 1$ , where  $a$  is the location of the local minimum, i.e. the transition point from the velocity weakening ( $b < v < a$ ) to the velocity strengthening regime ( $v > a$ ).

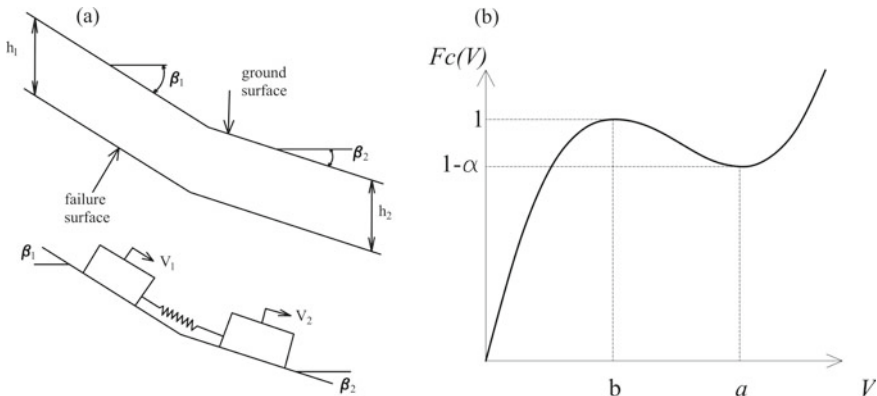


**Fig. 1** a (top) Typical accumulation slide profile; (bottom) idealized model for accumulation slide. b Assumed friction law along the sliding surface

Given this, we propose the model for landslide dynamics in the following general form:

$$\begin{aligned} \frac{dU_n}{dt} &= V_n \\ m \frac{dV_n}{dt} &= k(U_{n+1} - 2U_n + U_{n-1}) - F(V_0 + V_n) + G \end{aligned} \quad (4)$$

where  $G$  is the tangential component of the gravity force, and  $F(V)$  is a velocity-dependent friction force. A steady state of (4) exists when the block achieves a constant velocity motion  $dU/dt = V_0$ , and then  $F(V_0) = G$ , so Eq. (4) represents a dynamical system moving at velocity  $V_0$ . Hence, equilibrium state of the examined model is considered as a creep regime, with initial conditions set to  $(U_i, V_i) = (0.01, 0.02)$ . Such setup of the examined model corresponds to the old existing landslide where creep along the sliding surface is permanently observed and considered as equilibrium state, e.g. landslide “Plavinac” in Smederevo (Serbia).

Model (4) actually represents an infinite chain of identical blocks linearly coupled through Hookean springs of stiffness  $k$  that slips at the constant velocity  $V_0$  over an inclined surface.

For two coupled blocks, model (4) becomes:

$$\begin{aligned} \frac{dU_1}{dt} &= V_1 \\ m_1 \frac{dV_1}{dt} &= k(U_2 - U_1) - F(V_0 + V_1) + F(V_0) \\ \frac{dU_2}{dt} &= V_2 \\ m_2 \frac{dV_2}{dt} &= k(U_1 - U_2) - F(V_0 + V_2) + F(V_0) \end{aligned} \quad (5)$$

Model (5) with the included delayed interaction becomes:

$$\begin{aligned} \frac{dU_1(t)}{dt} &= V_1(t) \\ \frac{dV_1(t)}{dt} &= \frac{1}{m} [k(U_2(t - \tau) - U_1(t)) - F(V_0 + V_1(t)) + F(V_0)] \\ \frac{dU_2(t)}{dt} &= V_2(t) \\ \frac{dV_2(t)}{dt} &= [k(U_1(t - \tau) - U_2(t)) - F(V_0 + V_2(t)) + F(V_0)] \end{aligned} \quad (6)$$

### 3 Results

Linearization of the system (6) and substitution  $U_1 = A_1 e^{\lambda t}$ ,  $U_2 = A_2 e^{\lambda t}$ ,  $U_1(t - \tau) = A_1 e^{\lambda(t - \tau)}$ ,  $U_2(t - \tau) = A_2 e^{\lambda(t - \tau)}$ ,  $V_1 = B_1 e^{\lambda t}$  and  $V_2 = B_2 e^{\lambda t}$  results in a system of algebraic equations for the constants  $A_1$ ,  $A_2$ ,  $B_1$  and  $B_2$ . This system has a nontrivial solution if the following is satisfied:

$$\left[ \lambda \left( \lambda + \frac{1}{m} \frac{dF(V_0 + v)}{dv} \Big|_{v \equiv 0} \right) + \frac{k}{m} \right]^2 - \left[ \frac{k}{m} e^{-\lambda \tau} \right]^2 = 0 \tag{7}$$

Equation (7) is the characteristic equation of the system (6). Infinite dimensionality of the system (6) is reflected in the transcendental character of (7). By substituting  $\lambda = i\omega$  in Eq. (7) we obtain:

$$\left[ \frac{1}{m} \frac{dF(V_0 + v)}{dv} \Big|_{v \equiv 0} \right] \bullet \omega = \pm \frac{k}{m} \sin \omega \tau \tag{8}$$

In this way, one obtains parametric representations of the relations between  $\tau$  and the parameters, which correspond to the bifurcation values  $\lambda = i\omega$ . The general form of such relations is illustrated by the following formula for  $k$  as a function of  $\omega$ :

$$k = \frac{m}{2} \omega^2 + \frac{1}{2m} \left( \frac{dF(V_0 + v)}{dv} \Big|_{v \equiv 0} \right)^2 \tag{9}$$

and for  $\tau$  as a function of  $\omega$ :

$$\tau = \frac{1}{\omega} \arctan \left( \frac{\frac{1}{m} \frac{dF(V_0 + v)}{dv} \Big|_{v \equiv 0}}{\omega^2 - \frac{k}{m}} \right) + (2n + 1)\pi, n = 0, 1, 2, \dots \tag{10}$$

One should know that although the solution of characteristic equation is indicative of Hopf bifurcations, proof of this claim is rather lengthy to convey [8]. Instead, it could be numerically shown that the above parametric equations for  $k$  and  $\tau$  coincide with the Hopf bifurcation curve illustrated in Fig. 2, which shows the transition from constant slow creep of the landslide (which we consider as equilibrium state) to oscillatory periodic motion (which we consider as instable region).

As one can see a supercritical Hopf bifurcation occurs for rather strong spring stiffness  $k$  ( $>6$ ) and high values of time delay  $\tau$  ( $>1$ ). In present paper, we consider that onset of regular periodic oscillations indicates instability along the slope. Onset of instability for high spring stiffness indicates that system under study (conditionally stable slope) needs to be observed as a system of strongly coupled accumulation and feeder slope, in order to exhibit the instability. On the other hand, occurrence of instability for high values of time delay shows the high resilience of the conditionally



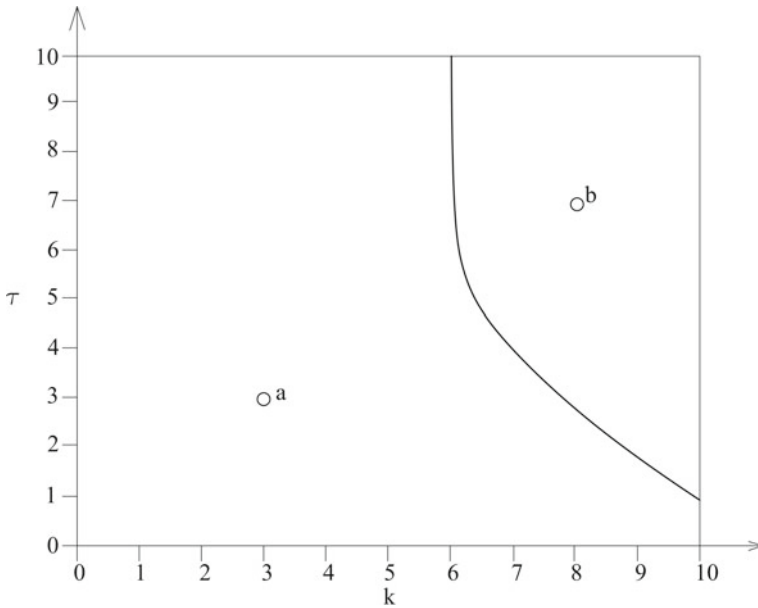


**Fig. 2** Hopf bifurcation curve  $k(\tau)$ , for the fixed values of parameters  $V_0 = 0.1$ ,  $a = 3.2$ ,  $b = -7.2$  and  $c = 4.8$ . Initial conditions are set to  $(U_i, V_i) = (0.01, 0.02)$ . The appropriate time series which correspond to points **a** and **b** are shown in Fig. 3

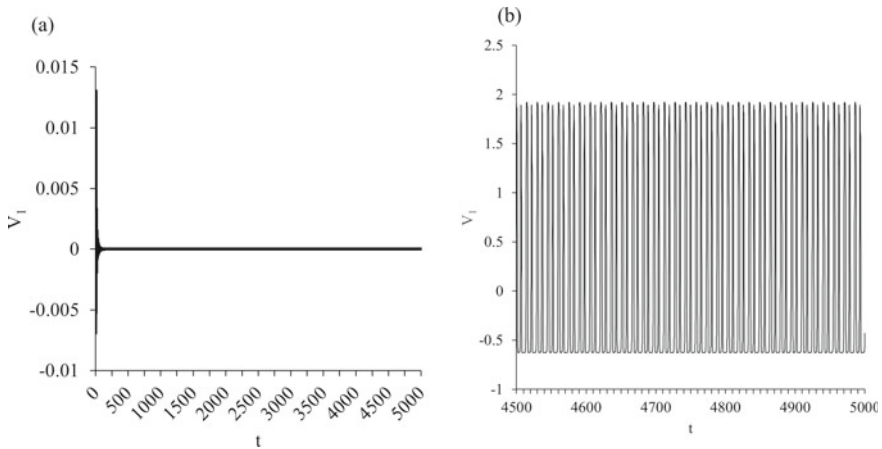


**Fig. 3** Temporal evolution of variable  $V_1$  for **a**  $\tau = 3$ ,  $k = 3$ , **b**  $\tau = 7$ ,  $k = 8$ . Time series are constructed for the fixed values of parameters  $V_0 = 0.1$ ,  $a = 3.2$ ,  $b = -7.2$  and  $c = 4.8$

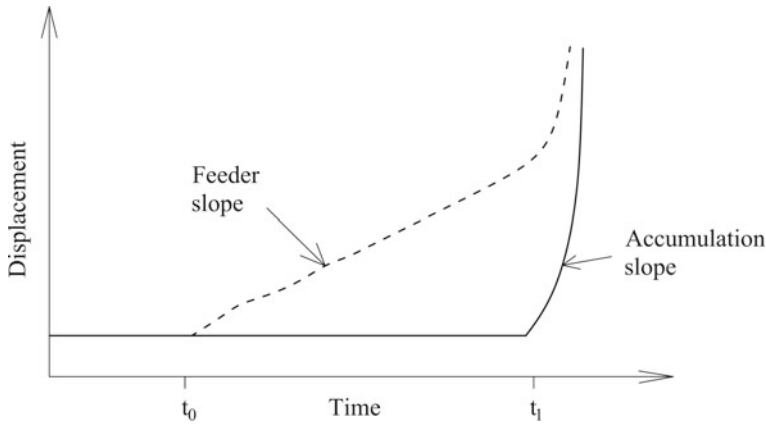


**Fig. 4** Time delay between the onset of feeder and accumulation slope, as suggested by Davis [6]

stable slope to occurrence of time delay between the motion of feeder and accumulation slope. This may indicate that the time delay indicated originally by Davis [6], as shown in Fig. 4, maybe does not have significant influence on the system dynamics, for the chosen values of friction parameters.

If we want further to examine the effect of time delay, let us analyze the influence of the frictional parameters on the effect of  $\tau$ . If one holds value of time delay and spring constant above the bifurcation curve, increase of parameters  $a$ ,  $b$  and  $c$  suppress the effect of the introduced time delay (Fig. 5). In particular, for lower values of parameter  $a$  (Fig. 5a),  $b$  (Fig. 5b) and  $c$  (Fig. 5c), observed dynamical system is in unstable regime (periodic motion), while further increase of the friction effect induces the transition to equilibrium state. This indicates that sliding surfaces with low friction parameters are more susceptible to the onset of instability.

## 4 Conclusions

In present paper we analyze the sensitivity of the landslide mechanical model to the effect of time delay between the displacement of the accumulation and feeder slope. The research was performed using standard bifurcation analysis, while bifurcation curves were constructed numerically. Assumed friction law along the existing sliding surface is assumed to have cubic expression. The case analyzed represents the case of the landslides with slow permanent displacement. Results obtained indicate that for the analyzed friction parameter values, instability occurs for high values of time delay and coupling strength, which indicates high resilience of the model under study to the effect of delayed interaction between the accumulation and feeder slope. Moreover, we showed that sliding surface with low frictional parameters is more prone to the onset of instability.

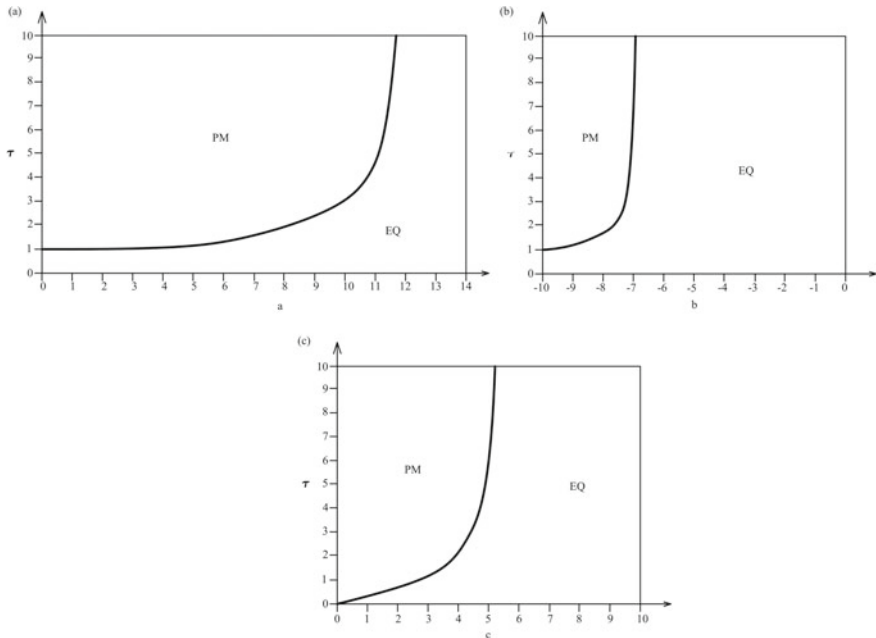


**Fig. 5** Bifurcation diagrams regarding the effect of frictional parameters on the onset of instability: **a**  $\tau = f(a)$ , **b**  $\tau = f(b)$ , **c**,  $\tau = f(c)$ , for fixed parameters values:  $V_0 = 0.1$ ,  $K = 7$ ,  $a = 3.2$ ,  $b = -7.2$  and  $c = 4.8$ . EQ stands for the equilibrium state, while PM denote periodic (oscillatory) regime

Further research on this topic should include additional inquiries on the types of instabilities which are formed with the increase of time delay, with the emphasis of irregular or stick–slip regime, which could be treated as an adequate representative of the real landslide motion. Moreover, one could analyze the effect of the choice of various friction laws on the onset of instability.

## References

1. Burridge, R., Knopoff, L.: Model and theoretical seismicity. *Bull. Seismol. Soc. Am.* **57**, 341–371 (1967)
2. Carlson, J.M., Langer, J.S.: Mechanical model of an earthquake fault. *Phys. Rev. A* **40**(11), 6470–6484 (1989)
3. Cartwright, J.H.E., Hernández-García, E., Piro, O.: Burridge-Knopoff models as elastic excitable media. *Phys. Rev. Lett.* **79**(3), 527–530 (1997)
4. Clancy, I., Corcoran, D.: State-variable friction for the Burridge-Knopoff model. *Phys. Rev. E Stat. Nonlinear Soft Matter Phys.* **80**(1), 016113 (2009)

5. Nkomom, T.N., Ndzana, F.I., Okaly, J.B., Mvogo, A.: Dynamics of nonlinear waves in a Burridge and Knopoff model for earthquake with long-range interactions, velocity-dependent and hydrodynamics friction forces. *Chaos Solitons Fractals* **150**, 111196 (2021)
6. Davis, R.O.: Modelling stability and surging in accumulation slides. *Eng. Geol.* **33**, 1–9 (1992)
7. Morales, J.E.M., James, G., Tonnelier, A.: Travelling waves in a spring-block chain sliding down a slope. *Phys. Rev. E* **96**, 012227 (2017)
8. Belair, J., Campbell, S.A.: Stability and bifurcations of equilibria in a multiple delayed differential equation. *SIAM Appl. Math.* **54**, 1402–1424 (1994)

# The Fifth Order Caudrey–Dodd–Gibbon Equation for Exact Traveling Wave Solutions Using the $(G'/G, 1/G)$ -Expansion Method



M. Mamun Miah

**Abstract** In this investigation, I am trying to extract abundant exact traveling wave solutions for the nonlinear partial fifth order Caudrey–Dodd–Gibbon (CDG) differential equation via the  $(G'/G, 1/G)$ -expansion method. Here I accomplish varieties types of wave solutions as like, trigonometric, hyperbolic, and rational function solution. Since new solutions provided us new physical explanation of the mathematical model for engineering applications and nonlinear sciences. So this article is very effective to extract abundant new analytic traveling wave solitons. Graphical representations of the obtained solutions are also portrayed and the shapes of the new solutions are bright soliton, dark soliton, periodic soliton etc. This eminent method is more applicable and easier to analysis nonlinear partial differential models.

**Keywords** Nonlinear partial differential equation · The fifth order Caudrey–Dodd–Gibbon equation · Traveling wave solutions · The  $(G'/G, 1/G)$ -expansion method

## 1 Introduction

Most of the physical conditions exist in all branches of engineering applications and scientific fields such as plasma physics, optical fibers, fluid mechanics, elastic media, solid state physics etc. may be expressed as in terms of mathematical models i.e. nonlinear partial differential equations (NLPDEs). So the studies of NLPDEs are most interesting topics in modern researcher. For the consequences of modern researcher there are many methods invented to investigate the nonlinear system, such as the homogeneous balance method [1, 2], the Jacobi elliptic function method [3], the tanh-coth method [4], the first integral method [5], the Kudryashov method [6, 7], the  $(G'/G)$ -expansion method [8], the unified method [9] etc. Recently a new technique is discovered for investigating nonlinear evolution equations (NLEEs) and the name

---

M. Mamun Miah (✉)

Department of Mathematics, Khulna University of Engineering & Technology, Khulna, Bangladesh

e-mail: [mamun0954@math.kuet.ac.bd](mailto:mamun0954@math.kuet.ac.bd)

of this method is the  $(G'/G, 1/G)$ -expansion method [10–12]. Many researcher are used this method and get outstanding performance for studying NLEEs. At first Li et al. [13] invented this eminent method and investigated the Zakharov equations for extracting abundant new traveling wave solutions. Recently, Chowdhury et al. [14] investigated the integro-differential equations make use of this eminent method. Very recently, Iqbal et al. [15] applied this method on Date–Jimbo–Kashiwara–Miwa equation with conformable derivative and obtained abundant exact traveling wave solutions. I have seen that, by using this renowned method there extract huge closed form wave solutions. Since no one scrutinized the fifth order CDG equation by means of the indicated method, so I used this method.

Our article is scheduled as following instruction: In Sect. 2, the applied method explanation. In Sect. 3, exact solutions of the fifth order CDG equation is scrutinized. In Sect. 4, graphical representations are delivered and finally, Sect. 5, the conclusions are given.

## 2 Explanation of the $(G'/G, 1/G)$ -Expansion Method

Here, I designate the brief explanation of the applied method for extracting wave solutions of denoted NLEE. At first I suppose that the auxiliary equation as,

$$G''(\xi) + \lambda G(\xi) = \mu \quad (1)$$

where both two of  $\mu$  and  $\lambda$  arbitrary constants and setup the expression as follows,

$$\varphi = G'/G, \quad \psi = 1/G \quad (2)$$

Thus,

$$\varphi' = -\varphi^2 + \mu\psi - \lambda, \quad \psi' = -\varphi\psi \quad (3)$$

Depends on  $\lambda$ , I have discussed three cases:

**Case 1:** For  $\lambda < 0$ , the general exact solution of Eq. (1),

$$G(\xi) = A_2 \cos(\sqrt{-\lambda} \xi) + A_1 \sinh(\sqrt{-\lambda} \xi) + \frac{\mu}{\lambda}, \quad (4)$$

where above two constants  $A_1$  and  $A_2$  are arbitrary. Consequently,

$$\psi^2 = \frac{-\lambda(\varphi^2 - 2\mu\psi + \lambda)}{\lambda^2\sigma + \mu^2}, \quad (5)$$

wherein,  $\sigma = A_1^2 - A_2^2$ .

**Case 2:** For  $\lambda > 0$ ,

$$G(\xi) = A_2 \cos(\sqrt{\lambda} \xi) + A_1 \sin(\sqrt{\lambda} \xi) + \frac{\mu}{\lambda}, \tag{6}$$

and hence

$$\psi^2 = \frac{\lambda(\varphi^2 - 2\mu\psi + \lambda)}{\lambda^2\rho - \mu^2}, \tag{7}$$

wherein  $\rho = A_1^2 + A_2^2$ .

**Case 3:** For  $\lambda = 0$ ,

$$G(\xi) = \frac{\mu}{2}\xi^2 + A_1 \xi + A_2, \tag{8}$$

and I obtain,

$$\psi^2 = \frac{(\varphi^2 - 2\mu\psi)}{A_1^2 - 2\mu A_2}. \tag{9}$$

Assume the following NLEE is in two variables  $x$  and  $t$  which are independent,

$$T(u, u_x, u_{xt}, u_t, u_{tt}, u_{xx}, u_{xxt} \dots) = 0, \tag{10}$$

here  $T$  is a function of nonlinear polynomial of  $u$  and its derivatives partially. Now to apply our desired method I consider the following steps:

**Step 1:** For transferring to ordinary from partial differential equation, I consider the wave variable as,

$$u(x, t) = u(\xi) \text{ and } \xi = x - v t \tag{11}$$

where  $v$  is a constant which takes arbitrary values.

From Eqs. (11) to (10),

$$M(u, u', -vu', v^2u'', u'' \dots) = 0, \tag{12}$$

wherein  $M$  is a function of nonlinear polynomial of  $u$  and its derivatives ordinary.

**Step 2:** Let us consider the solution of Eq. (12),

$$u(\xi) = \sum_{i=0}^N a_i \varphi(\xi)^i + \sum_{i=1}^N b_i \varphi(\xi)^{i-1} \psi(\xi), \tag{13}$$

where above two constants  $a_i$  and  $b_i$  are arbitrary and for both  $i = 1, 2, 3, 4 \dots$

**Step 3:** By the use of balance principal, the value of  $N$  and after setting the value of  $N$  into Eq. (13) and inserting this modified Eqs. (13) into (12), using (3) and (5) (for case 1), after this performances the left-hand side of Eq. (12) moves into a polynomial of  $\varphi$  and  $\psi$ , in which the degree of  $\varphi$  and  $\psi$  are zero to any positive integer and less than one respectively. Equating coefficient of the same powers to zero, gives a set of equations in arbitrary constants and solving these system yield the values of required arbitrary constants for  $\lambda < 0$ .

**Step 4:** Utilizing these obtained arbitrary values in step 3 and back substituting in Eqs. (10), (11) and (12), I obtain our desired wave solutions of the NLEEs.

**Step 5:** Again applying step 3 and step 4, back substituting Eqs. (13), (12), (3) and (7) for  $\lambda > 0$  (or from Eqs. (3) to (9) for  $\lambda = 0$ ), the exact solutions of Eq. (12) i.e. Eq. (10) demonstrated by trigonometric function solutions (or by the rational function solutions) respectively. The details of our applied method are given in Ref. [10–15].

### 3 Exact Solutions of the CDG Equation

First I introduce the fifth order CDG equation [16, 17],

$$u_t + u_{xxxxx} + 30 u u_{xxx} + 30 u_x u_{xx} + 180 u^2 u_x = 0. \tag{14}$$

Equation (14) moves to ordinary differential equation by applying the wave transformation Eq. (11) as,

$$-v u' + u^{(5)} + 30 u u' + 30 u' u'' + 180 u^2 u' = 0. \tag{15}$$

Integrating Eq. (15) and using  $c$  as integrating constant,

$$c - v u + u^{(4)} + 30 u u'' + 60 u^3 = 0. \tag{16}$$

Now applying the idea of homogeneous balance number between  $u^{(4)}$  and  $u^3$ , assume the solution of Eq. (16),

$$u(\xi) = a_0 + a_1 \varphi(\xi) + a_2 \varphi(\xi)^2 + b_1 \psi(\xi) + b_2 \varphi(\xi) \psi(\xi), \tag{17}$$

where  $b_1, b_2, a_0, a_1$  and  $a_2$  all are arbitrary constant which are determine below. Here I discuss three cases for solving the NLEE Eq. (14).



**Case 1.** When  $\lambda < 0$ , the final exact solution in terms of hyperbolic function are given as,

$$\begin{aligned}
 u(\xi) = & -\frac{5\lambda}{6} + \frac{\lambda\{A_2 \sinh(\sqrt{-\lambda}\xi) + A_1 \cosh(\sqrt{-\lambda}\xi)\}^2}{\{A_2 \cosh(\sqrt{-\lambda}\xi) + A_1 \sinh(\sqrt{-\lambda}\xi) + \frac{\mu}{\lambda}\}^2} \\
 & + \frac{\mu}{A_2 \cosh(\sqrt{-\lambda}\xi) + A_1 \sinh(\sqrt{-\lambda}\xi) + \frac{\mu}{\lambda}} \\
 & \pm \frac{\sqrt{\mu^2 + \lambda^2\sigma}\{A_2 \sinh(\sqrt{-\lambda}\xi) + A_1 \cosh(\sqrt{-\lambda}\xi)\}}{\{A_2 \cosh(\sqrt{-\lambda}\xi) + A_1 \sinh(\sqrt{-\lambda}\xi) + \frac{\mu}{\lambda}\}^2},
 \end{aligned}
 \tag{18}$$

wherein  $\xi = x + \frac{\lambda^3}{9}t$ ,  $v = \lambda^2$ ,  $\sigma = A_1^2 - A_2^2$ . For special case if  $A_2 = 0$ ,  $A_1 \neq 0$  and  $\mu = 0$  in Eq. (18), the traveling exact wave solution set as,

$$\begin{aligned}
 u(x, t) = & -\frac{5\lambda}{6} + \lambda \coth^2\left(\sqrt{-\lambda}\left(x + \frac{\lambda^3}{9}t\right)\right) \\
 & \pm \lambda \coth\left(\sqrt{-\lambda}\left(x + \frac{\lambda^3}{9}t\right)\right) \operatorname{cosech}\left(\sqrt{-\lambda}\left(x + \frac{\lambda^3}{9}t\right)\right)
 \end{aligned}
 \tag{19}$$

**Case 2.** When  $\lambda > 0$ , the exact solution in terms of trigonometric function are given as follows,

$$\begin{aligned}
 u(\xi) = & -\frac{5\lambda}{6} - \frac{\lambda\{-A_2 \sin(\sqrt{\lambda}\xi) + A_1 \cos(\sqrt{\lambda}\xi)\}^2}{\{A_2 \cos(\sqrt{\lambda}\xi) + A_1 \sin(\sqrt{\lambda}\xi) + \frac{\mu}{\lambda}\}^2} \\
 & + \frac{\mu}{A_2 \cos(\sqrt{\lambda}\xi) + A_1 \sin(\sqrt{\lambda}\xi) + \frac{\mu}{\lambda}} \\
 & \pm \frac{\sqrt{\lambda^2\rho - \mu^2}\{-A_2 \sin(\sqrt{\lambda}\xi) + A_1 \cos(\sqrt{\lambda}\xi)\}}{\{A_2 \cos(\sqrt{\lambda}\xi) + A_1 \sin(\sqrt{\lambda}\xi) + \frac{\mu}{\lambda}\}^2},
 \end{aligned}
 \tag{20}$$

wherein  $\xi = x + \frac{\lambda^3}{9}t$ ,  $v = \lambda^2$ ,  $\rho = A_2^2 + A_1^2$ . Again I consider  $A_1 = 0$ ,  $A_2 \neq 0$ ,  $\mu = 0$  in (20),

$$\begin{aligned}
 u(x, t) = & -\frac{5\lambda}{6} - \lambda \tan^2\left(\sqrt{\lambda}\left(x + \frac{\lambda^3}{9}t\right)\right) \\
 & \pm \lambda \tan\left(\sqrt{\lambda}\left(x + \frac{\lambda^3}{9}t\right)\right) \sec\left(\sqrt{\lambda}\left(x + \frac{\lambda^3}{9}t\right)\right)
 \end{aligned}
 \tag{21}$$

For  $A_2 = 0$ ,  $A_1 \neq 0$  and  $\mu = 0$  in (20),

$$\begin{aligned}
 u(x, t) = & -\frac{5\lambda}{6} - \lambda \cot^2\left(\sqrt{\lambda}\left(x + \frac{\lambda^3}{9}t\right)\right) \\
 & \pm \lambda \cot\left(\sqrt{\lambda}\left(x + \frac{\lambda^3}{9}t\right)\right) \operatorname{cosec}\left(\sqrt{\lambda}\left(x + \frac{\lambda^3}{9}t\right)\right). \tag{22}
 \end{aligned}$$

**Case 3.** When  $\lambda = 0$ , the exact solution in terms of rational function solution are given as follows,

$$\begin{aligned}
 u(\xi) = & a_0 - \frac{(\mu\xi + A_1)^2}{2\left(\frac{\mu}{2}\xi^2 + A_1\xi + A_2\right)^2} + \frac{\mu}{2\left(\frac{\mu}{2}\xi^2 + A_1\xi + A_2\right)} \\
 & \pm \frac{\sqrt{A_1^2 - 2\mu A_2(\mu\xi + A_1)}}{2\left(\frac{\mu}{2}\xi^2 + A_1\xi + A_2\right)^2}. \tag{23}
 \end{aligned}$$

where  $\xi = x + 120a_0^3t$ ,  $v = 180a_0^2$ ,  $a_0$ ,  $A_1$  and  $A_2$  are arbitrary constants. If I choose arbitrary constants to zero, further traveling exact wave solutions to the fifth order CDG equation can be extracted, but limitation of the article pages have not been sketched. The above solutions of Eq. (14) gives in our article are correct and new other than the solutions remaining in the research fields.

### 4 Graphical and Physical Explanation

In this section, I discussed about the graphical representation and physical explanation of some soliton solutions. The extracted solutions of our desire equation are different kind such as rational, hyperbolic and trigonometric function. Here, I plotted and discussed about three types of solutions. Figures 1 and 2 shows that the bright solitary wave of solution Eq. (18) for 3D plot and contour plot for the values of,  $\lambda = -2$ ,  $\mu = 1$ ,  $A_1 = 2$ ,  $A_2 = 1$  within  $x \in [-5, 5]$  and  $t \in [-5, 5]$ . Figures 3 and 4 shows the periodic solitary wave of solution Eq. (20) for 3D plot and contour plot for the values of,  $\lambda = 2$ ,  $\mu = 1$ ,  $A_1 = 1$ ,  $A_2 = 1$  within  $x \in [-5, 5]$  and  $t \in [-5, 5]$ . Figures 5 and 6 shows the dark solitary wave of solution Eq. (23) for 3D and contour plot for the values of,  $a_0 = 1$ ,  $\mu = 2$ ,  $A_1 = 3$ ,  $A_2 = 1$  within  $x \in [-5, 5]$  and  $t \in [-5, 5]$ . If I plotted the solution in Eq. (19), it's give same figure of Eq. (18) and similarly same shaped are obtained for the Eqs. (20) and (21). The following obtained figures have been plotted with the help of computation package program like Maple.

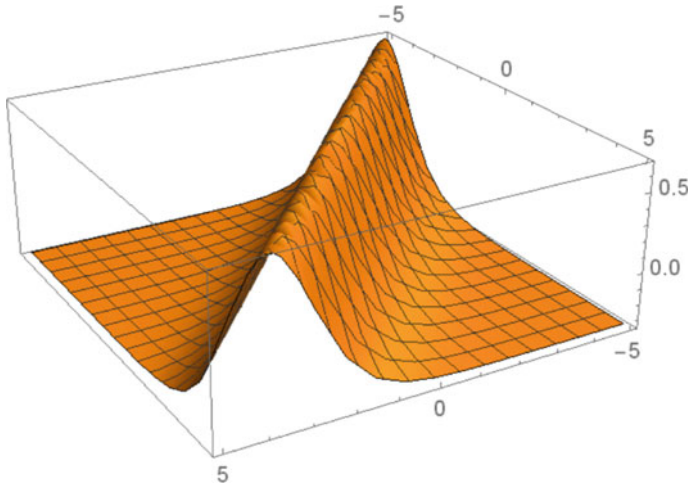


**Fig. 1** Bright solitary wave of solution Eq. (18), figure is 3D plot and right one is Contour Plot for the values  $\lambda = -2, \mu = 1, A_1 = 2$  and  $A_2 = 1$

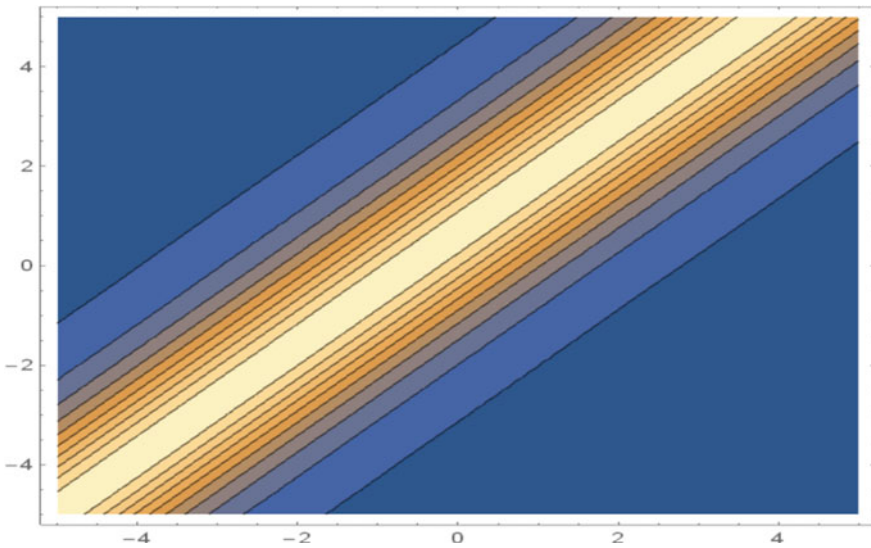


**Fig. 2** Bright solitary wave of solution Eq. (18), the figure is Contour Plot for the values,  $\lambda = -2, \mu = 1, A_1 = 2$  and  $A_2 = 1$

### 5 Conclusion

In our article, I extract numerous new exact solutions for the fifth order CDG equation and trace out the graphical representations of these results. There are special types of solutions are founded such as, bright soliton, dark soliton, periodic soliton etc.

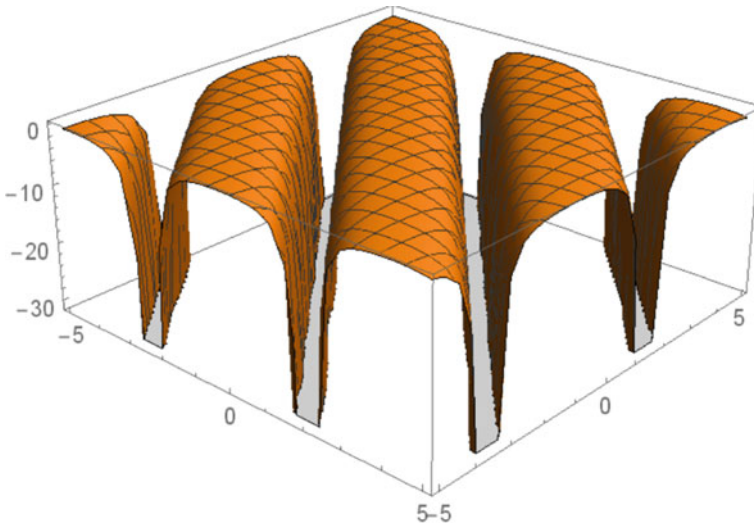


**Fig. 3** Periodic solitary wave of solution Eq. (20), the figure is 3D plot and right one is Contour Plot for the values  $\lambda = 2, \mu = 1, A_1 = 1$  and  $A_2 = 1$

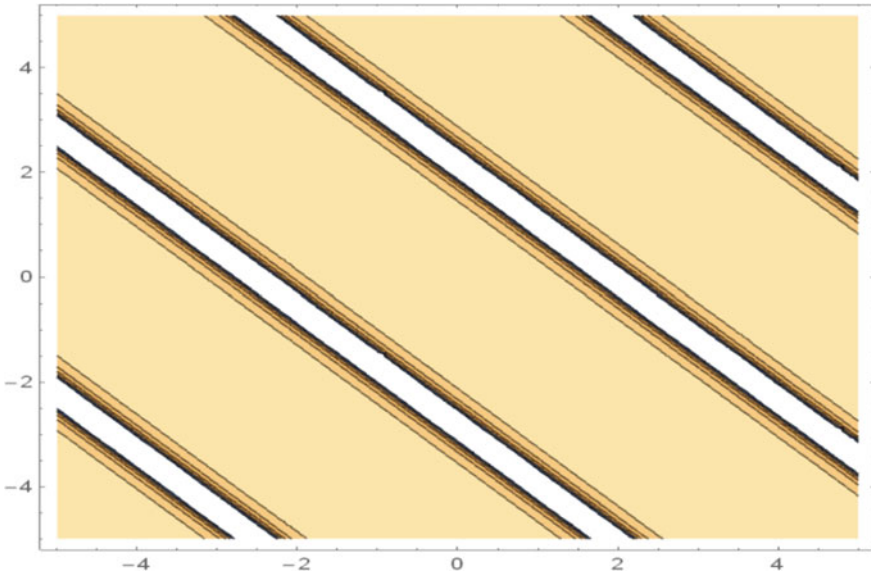


**Fig. 4** Periodic solitary wave of solution Eq. (20), the figure is Contour Plot for the values,  $\lambda = 2, \mu = 1, A_1 = 1$  and  $A_2 = 1$

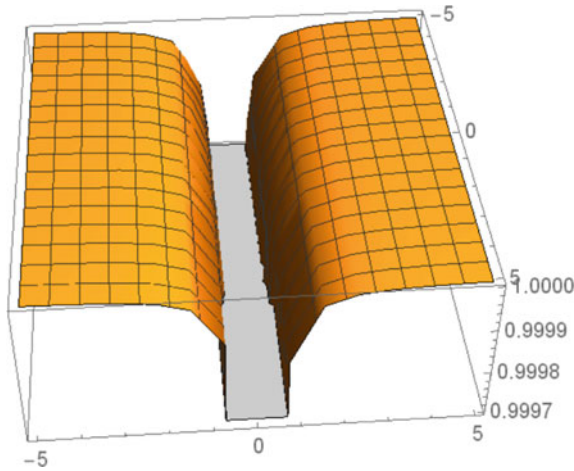


**Fig. 5** Dark solitary wave of solution (23), the figure is 3D plot for the values of  $a_0 = 1$ ,  $\mu = 2, A_1 = 3$  and  $A_2 = 1$

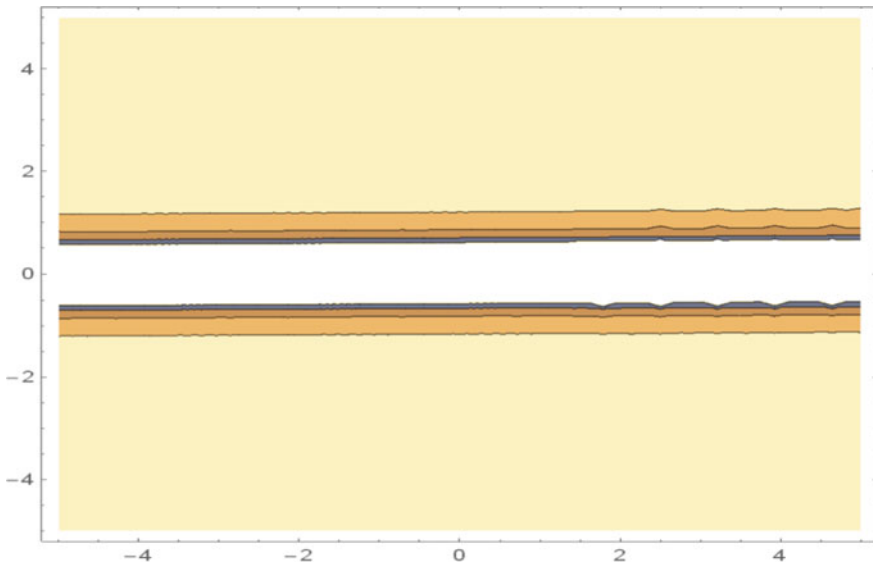


**Fig. 6** Dark solitary wave of solution Eq. (23), the figure is Contour Plot for the values of  $a_0 = 1$ ,  $\mu = 2, A_1 = 3$  and  $A_2 = 1$

and such solution pattern are important in nonlinear sciences. The obtained traveling wave solutions might have significant impact for further investigation of the fifth order CDG equation. For the performance of the  $(G'/G, 1/G)$ -expansion method, I conclude that the method is easier and faster compare to other method by means of

computational package program like Mathematica or Maple. Finally I conclude that, our investigation can be extended to other NLPDEs which arise in nonlinear physics, applied mathematics and other branches of engineering and nonlinear science.

## References

1. Wang, M.: Solitary wave solutions for variant Boussinesq equations. *Phys. Lett. A* **199**, 169–172 (1995)
2. Zayed, E.M.E., Zedan, H.A., Gepreel, K.A.: On the solitary wave solutions for nonlinear Hirota-Satsuma coupled KdV equations. *Chaos Solitons Fractals* **22**, 285–303 (2004)
3. Liu, G.T., Fan, T.Y.: New applications of developed Jacobi elliptic function expansion methods. *Phys. Lett. A* **345**, 161–166 (2005)
4. Wazwas, A.M.: The tanh-coth method for solitons and kink solutions for nonlinear parabolic equations. *Appl. Math. Comput.* **188**, 1467–1475 (2007)
5. Bekir, A., Unsal, O.: Periodic and solitary wave solutions of coupled nonlinear wave equations using the first integral method. *Phys. Scr.* **85**, 065003 (2012)
6. Eslami, M.: Exact traveling wave solutions to the fractional coupled nonlinear Schrodinger equations. *Appl. Math. Comput.* **285**, 141–148 (2016)
7. Ali, H.M.S., Habib, M.A., Miah, M.M., Akbar, M.A.: A modification of the generalized Kudryshov method for the system of some nonlinear evolution equations. *J. Mech. Cont. & Math. Sci.* **14**(1), 91–109 (2019)
8. Mirzazadeh, M., Eslami, M., Biswas, A.: 1-Soliton solution of KdV6 equation. *Nonlinear Dyn.* **80**(1–2), 387–396 (2015)
9. Osman, M.S.: New analytical study of water waves described by coupled fractional variant Boussinesq equation in fluid dynamics. *Pramana J. Phys.* **93**(2), 26 (2019)
10. Inc, M., Mamun Miah, M., Chowdhury, A., Shahadat Ali, H.M., Rezazadeh, H., Ali Akinlar, M., Ming Chu, Y.: New exact solutions for Kaup-Kupershmidt equation. *AIMS Math.* **5**, 6726–6738 (2020)
11. Zayed, E.M.E., Alurrfi, K.A.E.: The  $(G'/G, 1/G)$ -expansion method and its applications to two nonlinear Schrodinger equations describing the propagation of femtosecond pulses in nonlinear optical fibers. *Optik* **127**(4), 1581–1589 (2016)
12. Miah, M.M., Ali, H.M.S., Akbar, M.A., Seadawy, A.R.: New applications of the two variable  $(G'/G, 1/G)$ -expansion method for closed form traveling wave solutions of integro-differential equations. *J. Ocean Eng. Sci.* **4**(2), 132–143 (2019)
13. Li, L.X., Li, E.Q., Wang, M.L.: The  $(G'/G, 1/G)$ -expansion method and its application to traveling wave solutions of the Zakharov equations. *Appl. Math. J. Chin. Univ.* **25**(4), 454–462 (2010)
14. Chowdhury, M.A., Miah, M.M., Ali, H.M.S., Chu, Y.-M., Osman, M.S.: An investigation to the nonlinear  $(2+1)$ -dimensional soliton equation for discovering explicit and periodic wave solutions. *Res. Phys.* **23**, 10401 (2021)
15. Iqbal, M.A., Wang, Y., Miah, M.M., Osman, M.S.: Study on Date-Jimbo-Kashiwara-Miwa equation with conformable derivative dependent on time parameter to find the exact dynamical wave solutions. *Fractal Fract.* **6**(4) (2022)
16. Xu, Y.G., Zhou, X.W., Yao, L.: Solving the fifth order Caudrey-Dodd-Gibbon (CDG) equation using the exp-function method. *Appl. Math. Comput.* **206**(1), 70–73 (2008)
17. Jaradat, H.M., Syam, M., Jaradat, M., Mustafa, Z., Momani, S.: New solitary wave and multiple soliton solutions for fifth order nonlinear evolution equation with time variable coefficients. *Res. Phys.* **8**, 977–980 (2018)

# Results on Fractal Dimensions for a Multivariate Function



T. M. C. Priyanka and A. Gowrisankar

**Abstract** In the present work the fractal dimensions for the fractional integral on the multivariate function is explored. In particular, the upper bound of box dimension and Hausdorff dimension for the mixed Riemann–Liouville fractional integral of a multivariate function, which belongs to the class of Hölder continuous functions, is investigated. Further, if the multivariate function satisfies Lipschitz condition, the box dimension and the Hausdorff dimension of its mixed Riemann–Liouville fractional integral are estimated.

**Keywords** Multivariate function · Fractional integral · Hausdorff dimension · Box dimension

## 1 Introduction

Fractal dimension is the fundamental feature which distinguishes the naturally occurring functions into smooth and coarse functions. The most surprising aspect of fractal dimension is that it is not always an integer but can also be a fractional number. Box dimension and Hausdorff dimension are the widely discussed quantifiers in the fractal approximation theory. For the basic definitions of fractal dimension and fractal functions, the reader is encouraged to refer the textbooks [1–3].

The interesting connection between the fractal geometry and fractional calculus is the evaluation of fractal dimension for the graphs of fractional derivatives (integrals) of various types of fractal curves. Fractional calculus for different types of fractal functions has been discussed in [4–6]. Many elegant and simple results have been proved concerning the fractal dimension of univariate and bivariate continuous functions. For the Riemann–Liouville (RL) fractional integral of 1D continuous function of bounded variation, the box dimension is proved to be 1, in [7]. Liang has

---

T. M. C. Priyanka · A. Gowrisankar (✉)  
Department of Mathematics, School of Advanced Sciences, Vellore Institute of Technology,  
Vellore 632014, Tamil Nadu, India  
e-mail: [gowrisankargri@gmail.com](mailto:gowrisankargri@gmail.com)

© The Author(s), under exclusive license to Springer Nature Switzerland AG 2022  
S. Banerjee and A. Saha (eds.), *Nonlinear Dynamics and Applications*,  
Springer Proceedings in Complexity,  
[https://doi.org/10.1007/978-3-030-99792-2\\_95](https://doi.org/10.1007/978-3-030-99792-2_95)

1123

investigated the box dimension of 1D continuous functions of unbounded variation in [8] and its RL fractional integral in [9]. Fractal dimension of bivariate continuous functions of bounded variation and its fractional integral has been explored in [10]. Subhash and Syed have examined the box dimension of Katugampola fractional integral of 2D continuous functions in [11]. For more details on fractional calculus and fractal dimension, refer [13–16]. Several researchers have also discussed the fractal dimension of fractal functions, see for instance [17–19]. Recently, the bounds of Hausdorff dimension and box dimension of mixed RL fractional integral of bivariate continuous function is estimated in [12]. The aforementioned result stimulates an important question of whether an analogous result exists for a multivariate function. This paper estimates the bounds of Hausdorff dimension and box dimension of mixed RL fractional integral for a multivariate continuous function.

The rest of the paper is structured as follows: Preliminaries such as definition of mixed RL fractional integral of a multivariate function, box dimension, Hausdorff dimension and other basic terminologies are presented in Sect. 2. Estimation of bounds for the fractal dimensions of the mixed RL fractional integral of a multivariate function, which belongs to the class of Holder continuous functions, is discussed in Sect. 3. Conclusion of the paper is presented in Sect. 4.

## 2 Preliminaries

The basic terminologies that are necessary for the current study are precisely overviewed in this section.

**Definition 1** Suppose the function  $f$  is defined on  $[a_1, b_1] \times [a_2, b_2] \times \dots \times [a_n, b_n]$  with  $a_1, a_2, \dots, a_n \geq 0$ , then its mixed RL integral is given by

$$\mathcal{I}^\delta f(z_1, z_2, \dots, z_n) = \frac{1}{\Gamma(\delta_1)\Gamma(\delta_2)\dots\Gamma(\delta_n)} \int_{a_1}^{z_1} \int_{a_2}^{z_2} \dots \int_{a_n}^{z_n} (z_1 - w_1)^{\delta_1-1} (z_2 - w_2)^{\delta_2-1} \dots (z_n - w_n)^{\delta_n-1} f(w_1, w_2, \dots, w_n) dw_1 dw_2 \dots dw_n,$$

where  $\delta = (\delta_1, \delta_2, \dots, \delta_n)$  with  $\delta_1, \delta_2, \dots, \delta_n > 0$ .

**Definition 2** Consider a non-empty subset  $V$  of  $\mathbb{R}^n$ , the diameter of  $V$  is given by

$$|V| = \sup\{|u - t|; u, t \in V\}.$$

Consider the countable collection of sets  $\{V_k\}$  of diameter at most  $\epsilon$  which can cover  $A$ . That is,

$$A \subset \bigcup_{k=1}^{\infty} V_k, \quad 0 < |V_k| \leq \epsilon,$$

here  $\{V_k\}$  is a  $\epsilon$ -cover of  $A$  for each  $k$ . If  $A$  is a subset of  $\mathbb{R}^n$  and for any  $\epsilon > 0$ , define



$$\mathcal{H}_\epsilon^d(A) = \inf \left\{ \sum_{k=1}^\infty |V_k|^d : \{V_k\} \text{ is a } \epsilon\text{-cover of } A \right\}$$

where  $d$  is any non-negative real number. Then, for the set  $A$ , the  $d$ -dimensional Hausdorff measure is given by

$$\mathcal{H}^d(A) = \lim_{\epsilon \rightarrow 0} \mathcal{H}_\epsilon^d(A).$$

**Definition 3** For the subset  $A$  of  $\mathbb{R}^n$  and  $d > 0$ ,

$$\begin{aligned} \dim_{\mathcal{H}}(A) &= \sup\{d : \mathcal{H}^d(A) = \infty\} \\ &= \inf\{d : \mathcal{H}^d(A) = 0\} \end{aligned}$$

is known as the Hausdorff dimension of  $A$ . Suppose  $d = \dim_{\mathcal{H}}(A)$ ,  $\mathcal{H}^d(A)$  may be 0 or  $\infty$ , or may obey

$$0 < \mathcal{H}^d(A) < \infty \tag{1}$$

If a Borel set obeys (1), it is referred as a  $d$ -set.

**Definition 4** Consider a non-empty bounded subset  $A$  of  $\mathbb{R}^n$ . The least number of sets required to cover  $A$  is denoted by  $N_\epsilon(A)$  with diameter at most  $\epsilon$ . Then, the lower and upper box dimensions are, respectively, given by

$$\begin{aligned} \underline{\dim}_B(A) &= \lim_{\epsilon \rightarrow 0} \frac{\log N_\epsilon(A)}{-\log \epsilon}, \\ \overline{\dim}_B(A) &= \lim_{\epsilon \rightarrow 0} \frac{\log N_\epsilon(A)}{-\log \epsilon}. \end{aligned}$$

If  $\underline{\dim}_B(A) = \overline{\dim}_B(A)$ , the common value is termed as the box dimension for  $A$ . (i.e.,)

$$\dim_B(A) = \lim_{\epsilon \rightarrow 0} \frac{\log N_\epsilon(A)}{-\log \epsilon}.$$

Let  $Gr(f, J_1 \times J_2 \times \dots \times J_n)$  denote the graph of the function  $f$  defined on  $J_1 \times J_2 \times \dots \times J_n$  where  $J_i \subset \mathbb{R}$ , for  $i = 1, 2, \dots, n$  and  $\dim_{\mathcal{H}} Gr(f, J_1 \times J_2 \times \dots \times J_n), \dim_B Gr(f, J_1 \times J_2 \times \dots \times J_n)$  and  $\overline{\dim}_B Gr(f, J_1 \times J_2 \times \dots \times J_n)$  represent the Hausdorff dimension, box dimension and upper box dimension of  $f$  defined on  $J_1 \times J_2 \times \dots \times J_n$ , respectively, in this entire paper.

**Lemma 1** ([11]) *If  $f \in \mathcal{C}(J_1 \times J_2 \times \dots \times J_n)$  and for some  $C > 0, 0 \leq v \leq 1,$*

$$|f(p_1, p_2, \dots, p_n) - f(q_1, q_2, \dots, q_n)| \leq C \|(p_1, p_2, \dots, p_n) - (q_1, q_2, \dots, q_n)\|_2^v, \quad (2)$$

$\forall (p_1, p_2, \dots, p_n), (q_1, q_2, \dots, q_n) \in J_1 \times J_2 \times \dots \times J_n.$  *Then the inequality*

$$n \leq \dim_{\mathcal{H}} Gr(f, J_1 \times J_2 \times \dots \times J_n) \leq \overline{\dim}_B Gr(f, J_1 \times J_2 \times \dots \times J_n) \leq n + 1 - v$$

*remains true if (2) holds with  $\|(p_1, p_2, \dots, p_n) - (q_1, q_2, \dots, q_n)\|_2 < \epsilon$  for some  $\epsilon > 0.$  Suppose  $v = 1,$  the function  $f$  becomes Lipschitz continuous.*

**Lemma 2** [11] *Let*

$$H^v(J_1 \times J_2 \times \dots \times J_n) = \{f(z_1, z_2, \dots, z_n) : |f(z_1 + l_1, \dots, z_n + l_n) - f(z_1, \dots, z_n)| \leq C \|(l_1, l_2, \dots, l_n)\|_2^v\},$$

$\forall (z_1 + l_1, \dots, z_n + l_n), (z_1, \dots, z_n) \in J_1 \times J_2 \times \dots \times J_n,$  *be the set of all Hölder continuous functions with holder exponent  $v.$  If  $f \in H^v(J_1 \times J_2 \times \dots \times J_n),$  then*

$$n \leq \dim_{\mathcal{H}} Gr(f, J_1 \times J_2 \times \dots \times J_n) \leq \overline{\dim}_B Gr(f, J_1 \times J_2 \times \dots \times J_n) \leq n + 1 - v.$$

### 3 Fractal Dimensions of the Mixed RL Fractional Integral on Multivariate Function

This section establishes the relation between the two fractal dimensions namely box dimension and Hausdorff dimension of mixed RL fractional integral of a Hölder continuous multivariate function.

**Theorem 1** *Let  $f(z_1, z_2, \dots, z_n) \in H^v(J_1 \times J_2 \times \dots \times J_n)$  on  $[a_1, b_1] \times [a_2, b_2] \times \dots \times [a_n, b_n]$  such that  $f(0, 0, \dots, 0) = (0, 0, \dots, 0)$  and suppose its mixed RL type integral exists, then*

$$\dim_{\mathcal{H}} Gr(\mathcal{I}^\delta f, J_1 \times J_2 \times \dots \times J_n) \leq \overline{\dim}_B Gr(\mathcal{I}^\delta f, J_1 \times J_2 \times \dots \times J_n) \leq n + 1 - v,$$

$$0 < \delta_1, \delta_2, \dots, \delta_n < 1.$$

**Proof** Let  $0 < \delta_1, \delta_2, \dots, \delta_n < 1$  and  $0 \leq a_1 \leq z_1 \leq z_1 + l_1 \leq b_1, 0 \leq a_2 \leq z_2 \leq z_2 + l_2 \leq b_2, \dots, 0 \leq a_n \leq z_n \leq z_n + l_n \leq b_n.$  Then

$$\begin{aligned}
& (\mathcal{I}^\delta f)(z_1 + l_1, z_2 + l_2, \dots, z_n + l_n) - (\mathcal{I}^\delta f)(z_1, z_2, \dots, z_n) \\
&= \frac{1}{\Gamma(\delta_1)\Gamma(\delta_2)\dots\Gamma(\delta_n)} \int_{a_1}^{z_1+l_1} \int_{a_2}^{z_2+l_2} \dots \int_{a_n}^{z_n+l_n} (z_1 + l_1 - w_1)^{\delta_1-1} \\
& \quad (z_2 + l_2 - w_2)^{\delta_2-1} \dots (z_n + l_n - w_n)^{\delta_n-1} f(w_1, w_2, \dots, w_n) dw_1 dw_2 \dots dw_n \\
& \quad - \frac{1}{\Gamma(\delta_1)\Gamma(\delta_2)\dots\Gamma(\delta_n)} \int_{a_1}^{z_1} \int_{a_2}^{z_2} \dots \int_{a_n}^{z_n} (z_1 - w_1)^{\delta_1-1} \\
& \quad (z_2 - w_2)^{\delta_2-1} \dots (z_n - w_n)^{\delta_n-1} f(w_1, w_2, \dots, w_n) dw_1 dw_2 \dots dw_n \\
&= \mathcal{I}_1 + \mathcal{I}_2 + \mathcal{I}_3 + \dots + \mathcal{I}_{n+1} + \mathcal{I}_{n+2} + \mathcal{I}_{n+3},
\end{aligned}$$

where

$$\begin{aligned}
\mathcal{I}_1 &= \frac{1}{\Gamma(\delta_1)\Gamma(\delta_2)\dots\Gamma(\delta_n)} \int_{a_1}^{a_1+l_1} \int_{a_2}^{a_2+l_2} \dots \int_{a_n}^{a_n+l_n} (z_1 + l_1 - w_1)^{\delta_1-1} \\
& \quad (z_2 + l_2 - w_2)^{\delta_2-1} \dots (z_n + l_n - w_n)^{\delta_n-1} f(w_1, w_2, \dots, w_n) dw_1 dw_2 \dots dw_n, \\
\mathcal{I}_2 &= \frac{1}{\Gamma(\delta_1)\Gamma(\delta_2)\dots\Gamma(\delta_n)} \int_{a_1}^{a_1+l_1} \int_{a_2+l_2}^{z_2+l_2} \dots \int_{a_n}^{a_n+l_n} (z_1 + l_1 - w_1)^{\delta_1-1} \\
& \quad (z_2 + l_2 - w_2)^{\delta_2-1} \dots (z_n + l_n - w_n)^{\delta_n-1} f(w_1, w_2, \dots, w_n) dw_1 dw_2 \dots dw_n, \\
\mathcal{I}_3 &= \frac{1}{\Gamma(\delta_1)\Gamma(\delta_2)\dots\Gamma(\delta_n)} \int_{a_1+l_1}^{z_1+l_1} \int_{a_2}^{a_2+l_2} \dots \int_{a_n}^{a_n+l_n} (z_1 + l_1 - w_1)^{\delta_1-1} \\
& \quad (z_2 + l_2 - w_2)^{\delta_2-1} \dots (z_n + l_n - w_n)^{\delta_n-1} f(w_1, w_2, \dots, w_n) dw_1 dw_2 \dots dw_n, \\
& \quad \vdots \\
\mathcal{I}_{n+1} &= \frac{1}{\Gamma(\delta_1)\Gamma(\delta_2)\dots\Gamma(\delta_n)} \int_{a_1}^{a_1+l_1} \int_{a_2}^{a_2+l_2} \dots \int_{a_n+l_n}^{z_n+l_n} (z_1 + l_1 - w_1)^{\delta_1-1} \\
& \quad (z_2 + l_2 - w_2)^{\delta_2-1} \dots (z_n + l_n - w_n)^{\delta_n-1} f(w_1, w_2, \dots, w_n) dw_1 dw_2 \dots dw_n, \\
\mathcal{I}_{n+2} &= \frac{1}{\Gamma(\delta_1)\Gamma(\delta_2)\dots\Gamma(\delta_n)} \int_{a_1+l_1}^{z_1+l_1} \int_{a_2+l_2}^{z_2+l_2} \dots \int_{a_n+l_2}^{z_n+l_n} (z_1 + l_1 - w_1)^{\delta_1-1} \\
& \quad (z_2 + l_2 - w_2)^{\delta_2-1} \dots (z_n + l_n - w_n)^{\delta_n-1} f(w_1, w_2, \dots, w_n) dw_1 dw_2 \dots dw_n, \\
\mathcal{I}_{n+3} &= \frac{1}{\Gamma(\delta_1)\Gamma(\delta_2)\dots\Gamma(\delta_n)} \int_{a_1}^{z_1} \int_{a_2}^{z_2} \dots \int_{a_n}^{z_n} (z_1 - w_1)^{\delta_1-1} \\
& \quad (z_2 - w_2)^{\delta_2-1} \dots (z_n - w_n)^{\delta_n-1} f(w_1, w_2, \dots, w_n) dw_1 dw_2 \dots dw_n.
\end{aligned}$$

By applying variable transformation in  $\mathcal{I}_{n+3}$ ,

$$\begin{aligned} \mathcal{I}_{n+3}^* &= \frac{1}{\Gamma(\delta_1)\Gamma(\delta_2)\dots\Gamma(\delta_n)} \int_{a_1+l_1}^{z_1+l_1} \int_{a_2+l_2}^{z_2+l_2} \dots \int_{a_n+l_n}^{z_n+l_n} (z_1+l_1-w_1)^{\delta_1-1} \\ &\quad (z_2+l_2-w_2)^{\delta_2-1} \dots (z_n+l_n-w_n)^{\delta_n-1} \\ &\quad \times f(w_1-l_1, w_2-l_2, \dots, w_n-l_n) dw_1 dw_2 \dots dw_n \\ \mathcal{I}_{n+2} - \mathcal{I}_{n+3}^* &= \mathcal{I}_{n+4} = \frac{1}{\Gamma(\delta_1)\Gamma(\delta_2)\dots\Gamma(\delta_n)} \int_{a_1+l_1}^{z_1+l_1} \int_{a_2+l_2}^{z_2+l_2} \dots \int_{a_n+l_2}^{z_n+l_n} (z_1+l_1-w_1)^{\delta_1-1} \\ &\quad (z_2+l_2-w_2)^{\delta_2-1} \dots (z_n+l_n-w_n)^{\delta_n-1} \\ &\quad [f(w_1-l_1, w_2-l_2, \dots, w_n-l_n) - f(w_1, w_2, \dots, w_n)] dw_1 dw_2 \dots dw_n \end{aligned}$$

$$\begin{aligned} |\mathcal{I}_{n+4}| &\leq \frac{1}{\Gamma(\delta_1)\Gamma(\delta_2)\dots\Gamma(\delta_n)} \int_{a_1+l_1}^{z_1+l_1} \int_{a_2+l_2}^{z_2+l_2} \dots \int_{a_n+l_2}^{z_n+l_n} |(z_1+l_1-w_1)^{\delta_1-1} \\ &\quad (z_2+l_2-w_2)^{\delta_2-1} \dots (z_n+l_n-w_n)^{\delta_n-1} \\ &\quad \times [f(w_1-l_1, w_2-l_2, \dots, w_n-l_n) - f(w_1, w_2, \dots, w_n)]| dw_1 dw_2 \dots dw_n \end{aligned}$$

As the function  $f(z_1, z_2, \dots, z_n) \in H^v(J_1 \times J_2 \times \dots \times J_n)$  on  $[a_1, b_1] \times [a_2, b_2] \times \dots \times [a_n, b_n]$ ,

$$\begin{aligned} |\mathcal{J}_{n+4}| &\leq \frac{C \|l_1, l_2, \dots, l_n\|_2^v}{\Gamma(\delta_1)\Gamma(\delta_2)\dots\Gamma(\delta_n)} \int_{a_1+l_1}^{z_1+l_1} \int_{a_2+l_2}^{z_2+l_2} \dots \int_{a_n+l_n}^{z_n+l_n} |(z_1+l_1-w_1)^{\delta_1-1} \\ &\quad (z_2+l_2-w_2)^{\delta_2-1} \dots (z_n+l_n-w_n)^{\delta_n-1}| dw_1 dw_2 \dots dw_n \\ &= \frac{C \|l_1, l_2, \dots, l_n\|_2^v}{\Gamma(\delta_1+1)\Gamma(\delta_2+1)\dots\Gamma(\delta_n+1)} (z_1-a_1)^{\delta_1} (z_2-a_2)^{\delta_2} \dots (z_n-a_n)^{\delta_n} \end{aligned}$$

For  $(z_1, z_2, \dots, z_n) \in [a_1, b_1] \times [a_2, b_2] \times \dots \times [a_n, b_n]$ , one can get

$$\begin{aligned} |\mathcal{I}_{n+4}| &\leq \frac{C \|l_1, l_2, \dots, l_n\|_2^v}{\Gamma(\delta_1+1)\Gamma(\delta_2+1)\dots\Gamma(\delta_n+1)} (b_1-a_1)^{\delta_1} (b_2-a_2)^{\delta_2} \dots (b_n-a_n)^{\delta_n} \\ |\mathcal{I}_{n+4}| &\leq C \|l_1, l_2, \dots, l_n\|_2^v \end{aligned}$$

where

$$C = \frac{(b_1-a_1)^{\delta_1} (b_2-a_2)^{\delta_2} \dots (b_n-a_n)^{\delta_n}}{\Gamma(\delta_1+1)\Gamma(\delta_2+1)\dots\Gamma(\delta_n+1)}.$$

Now, similarly applying the above steps, the bound of  $J_1$  is found to be

$$\begin{aligned}
 |\mathcal{I}_1| &\leq \frac{1}{\Gamma(\delta_1)\Gamma(\delta_2)\dots\Gamma(\delta_n)} \int_{a_1}^{a_1+l_1} \int_{a_2}^{a_2+l_2} \dots \int_{a_n}^{a_n+l_n} |(z_1 + l_1 - w_1)^{\delta_1-1} \\
 &\quad (z_2 + l_2 - w_2)^{\delta_2-1} \dots (z_n + l_n - w_n)^{\delta_n-1}| \\
 &\quad \times |f(w_1, w_2, \dots, w_n) - f(0, 0, \dots, 0)| dw_1 dw_2 \dots dw_n \\
 &\leq \frac{C \|l_1, l_2, \dots, l_n\|_2^v}{\Gamma(\delta_1)\Gamma(\delta_2)\dots\Gamma(\delta_n)} \int_{a_1}^{a_1+l_1} \int_{a_2}^{a_2+l_2} \dots \int_{a_n}^{a_n+l_n} |(z_1 + l_1 - w_1)^{\delta_1-1} \\
 &\quad (z_2 + l_2 - w_2)^{\delta_2-1} \dots (z_n + l_n - w_n)^{\delta_n-1}| dw_1 dw_2 \dots dw_n \\
 &\leq \frac{C \|l_1, l_2, \dots, l_n\|_2^v}{\Gamma(\delta_1)\Gamma(\delta_2)\dots\Gamma(\delta_n)} \int_{a_1}^{a_1+l_1} \int_{a_2}^{a_2+l_2} \dots \\
 &\quad \int_{a_n}^{a_n+l_n} |(a_1 + l_1 - w_1)^{\delta_1-1} (a_2 + l_2 - w_2)^{\delta_2-1} \dots (a_n + l_n - w_n)^{\delta_n-1}| dw_1 dw_2 \dots dw_n \\
 &= \frac{C \|l_1, l_2, \dots, l_n\|_2^v}{\Gamma(\delta_1 + 1)\Gamma(\delta_2 + 1)\dots\Gamma(\delta_n + 1)} l_1^{\delta_1} l_2^{\delta_2} \dots l_n^{\delta_n} \\
 &\leq C \|l_1, l_2, \dots, l_n\|_2^v.
 \end{aligned}$$

where

$$C = \frac{l_1^{\delta_1} l_2^{\delta_2} \dots l_n^{\delta_n}}{\Gamma(\delta_1 + 1)\Gamma(\delta_2 + 1)\dots\Gamma(\delta_n + 1)}.$$

Similarly, the bounds of remaining integrals are obtained as

$$\begin{aligned}
 |\mathcal{I}_2| &\leq C \|l_1, l_2, \dots, l_n\|_2^v, \text{ where } C = \frac{l_1^{\delta_1} (b_2 - a_2)^{\delta_2} \dots l_n^{\delta_n}}{\Gamma(\delta_1 + 1)\Gamma(\delta_2 + 1)\dots\Gamma(\delta_n + 1)} \\
 |\mathcal{I}_3| &\leq C \|l_1, l_2, \dots, l_n\|_2^v, \text{ where } C = \frac{(b_1 - a_1)^{\delta_1} l_2^{\delta_2} \dots l_n^{\delta_n}}{\Gamma(\delta_1 + 1)\Gamma(\delta_2 + 1)\dots\Gamma(\delta_n + 1)} \\
 &\vdots \\
 |\mathcal{I}_{n+1}| &\leq C \|l_1, l_2, \dots, l_n\|_2^v, \text{ where } C = \frac{l_1^{\delta_1} l_2^{\delta_2} \dots (b_n - a_n)^{\delta_n}}{\Gamma(\delta_1 + 1)\Gamma(\delta_2 + 1)\dots\Gamma(\delta_n + 1)}.
 \end{aligned}$$

As a consequence, for a suitable constant C,

$$\begin{aligned}
 |(\mathcal{I}^\delta f)(z_1 + l_1, z_2 + l_2, \dots, z_n + l_n) - (\mathcal{I}^\delta f)(z_1, z_2, \dots, z_n)| \\
 \leq |\mathcal{I}_1| + |\mathcal{I}_2| + |\mathcal{I}_3| + \dots + |\mathcal{I}_{n+1}| + |\mathcal{I}_{n+2}| + |\mathcal{I}_{n+3}| \\
 \leq C \|l_1, l_2, \dots, l_n\|_2^v.
 \end{aligned}$$

The proof follows from Lemma 2.

**Theorem 2** *If the continuous function  $f(z_1, z_2, \dots, z_n)$  defined on  $[a_1, b_1] \times [a_2, b_2] \times \dots \times [a_n, b_n]$  with  $f(0, 0, \dots, 0) = (0, 0, \dots, 0)$  obeys Lipschitz condition, then for  $0 < \delta_1, \delta_2, \dots, \delta_n < 1$ ,*

$$\dim_{\mathcal{H}} Gr(\mathcal{I}^\delta f, J_1 \times J_2 \times \cdots \times J_n) = \dim_B Gr(\mathcal{I}^\delta f, J_1 \times J_2 \times \cdots \times J_n) = n.$$

The proof follows from Lemma 1 and Theorem 1.

**Remark 1** For any fractal function  $f(z_1, z_2, \dots, z_n)$  having box dimension  $n + 1 - v$ , the upper box dimension of its RL type fractional integral is not more than  $n + 1 - v$ .(i.e.,) If

$$\dim_B G(f, J_1 \times J_2 \times \cdots \times J_n) = n + 1 - v,$$

then

$$\overline{\dim}_B G(\mathcal{I}^\delta f, J_1 \times J_2 \times \cdots \times J_n) \leq n + 1 - v.$$

Hence,

$$\overline{\dim}_B Gr(\mathcal{I}^\delta f, J_1 \times J_2 \times \cdots \times J_n) \leq \dim_B Gr(f, J_1 \times J_2 \times \cdots \times J_n) = n + 1 - v.$$

## 4 Conclusion

In this article, the bounds for both the Hausdorff dimension and upper box dimension of the mixed RL fractional integral of a multivariate function are found to be  $n + 1 - v$ , when it satisfies Hölder condition. On the other hand, when it obeys Lipchitz condition, it is illustrated that the box dimension and Hausdorff dimension of a multivariate function are  $n$ .

## References

1. Falconer, K.: Fractal Geometry: Mathematical Foundations and Applications. John Wiley & Sons Ltd, England (1990)
2. Barnsley, M.F.: Fractals Everywhere, 2nd edn. Academic, USA (1993)
3. Banerjee, S., Hassan, M.K., Mukherjee, S., Gowrisankar, A.: Fractal Patterns in Nonlinear Dynamics and Applications. CRC Press, Boca Raton (2019)
4. Gowrisankar, A., Uthayakumar, R.: Fractional calculus on fractal interpolation function for a sequence of data with countable iterated function system. *Mediterr. J. Math.* **13**(6), 3887–3906 (2016)
5. Priyanka, T.M.C., Gowrisankar, A.: Riemann-Liouville fractional integral of non-affine fractal interpolation function and its fractional operator. *Eur. Phys. J.: Spec. Top.* **230**, 3789–3805 (2021)
6. Gowrisankar, A., Prasad, M.G.P.: Riemann-Liouville calculus on quadratic fractal interpolation function with variable scaling factors. *J. Anal.* **27**(2), 347–363 (2019)
7. Liang, Y.S.: Box dimension of Riemann-Liouville fractional integrals of continuous functions of bounded variation. *Nonlinear Anal.* **72**(11), 4304–4306 (2010)
8. Liang, Y.S., Su, W.Y.: Fractal dimension of certain continuous functions of unbounded variation. *Fractals* **25**(01), 1750009 (2017)

9. Liang, Y.S., Su, W.Y.: Riemann-Liouville fractional calculus of one dimensional continuous functions. *Sci. Sin. Math.* **46**(4), 423–438 (2016)
10. Verma, S., Viswanathan, P.: Bivariate functions of bounded variation: fractal dimension and fractional integral. *Indag. Math.* **31**(2), 294–309 (2020)
11. Chandra, S., Abbas, S.: Box dimension of mixed Katugampola fractional integral of two dimensional continuous functions. [arXiv:2105.01885](https://arxiv.org/abs/2105.01885)
12. Chandra, S., Abbas, S.: Analysis of fractal dimension of mixed Riemann-Liouville fractional integral. [arXiv:2105.06648](https://arxiv.org/abs/2105.06648)
13. Banerjee, S., Easwaramoorthy, D., Gowrisankar, A.: *Fractal Functions, Dimensions and Signal Analysis*, 1st edn. Springer, Cham (2021)
14. Verma, S., Viswanathan, P.: A note on Katugampola fractional calculus and fractal dimensions. *Appl. Math. Comput.* **339**, 220–230 (2018)
15. Verma, S., Viswanathan, P.: Katugampola fractional integral and fractal dimension of bivariate functions. *Results Math.* (2021). [arXiv:2101.06093](https://arxiv.org/abs/2101.06093)
16. Frank, B.: Tatom: the relationship between fractional calculus and fractal. *Fractals* **3**(1), 217–229 (1995)
17. Chandra, S., Abbas, S.: Analysis of mixed Weyl-Marchaud fractional derivative and Box dimensions. *Fractals* (2021). <https://doi.org/10.1142/S0218348X21501450>
18. Priyanka, T.M.C., Gowrisankar, A.: Analysis on Weyl-Marchaud fractional derivative for types of fractal interpolation function with fractal dimension. *Fractals* **29**(7), 2150215 (2021)
19. Peng, W.L., Yao, K., Zhang, X., Yao, J.: Box dimension of Weyl-Marchaud fractional derivative of linear fractal interpolation functions. *Fractals* **27**(4), 1950058 (2019)

# Stochastic Predator-Prey Model with Disease in Prey and Hybrid Impulses for Integrated Pest Management



Shivani Khare , Kunwer Singh Mathur , and Rajkumar Gangele 

**Abstract** The stochastic effect is sometimes crucial in the case of integrated pest management due to fluctuating exotic environmental and climate conditions, and it also affects the resources required for pest extinction. Hence, we extend the classical predator-prey model into an impulsive control system by incorporating disease in the prey along with a stochastic element, which helps in controlling optimal pesticide level more accurately in most economic means for pest eradication. Further in analysis, it is obtained that the solution of the proposed model is positively bounded and globally attractive. The long-term behavior of the model is examined, and the condition for pest eradication is driven. The analysis shows that pest control becomes more complex due to the high amplitude of impulsive period and higher intensities of external interference. Finally, we perform some numerical simulations to support our analytical findings and their interpretation.

**Keywords** Predator-prey model · Integrated pest management · Impulsive control · Pest eradication · Permanence · Stochastic differential equations

## 1 Introduction

Integrated pest management (IPM) is one of the most effective methods to reduce the pest level. It is also an environmentally friendly approach that relies on the combination of common-sense practices. The IPM approach mainly focuses on reducing pest damage by the most economical means and the least possible hazard to people, property, and the environment. Biological control, chemical control, mechanical control, microbial control, remote sensing are the most valuable and significant methods to

---

The research work of the first author is supported by the DST-INSPIRE Fellowship (No. DST/INSPIRE Fellowship/2019/IF190224).

---

S. Khare · K. S. Mathur (✉) · R. Gangele  
Department of Mathematics and Statistics, Dr. Harisingh Gour Vishwavidyalaya, Sagar 470003,  
Madhya Pradesh, India  
e-mail: [kmathur1709@gmail.com](mailto:kmathur1709@gmail.com)

© The Author(s), under exclusive license to Springer Nature Switzerland AG 2022  
S. Banerjee and A. Saha (eds.), *Nonlinear Dynamics and Applications*,  
Springer Proceedings in Complexity,  
[https://doi.org/10.1007/978-3-030-99792-2\\_96](https://doi.org/10.1007/978-3-030-99792-2_96)

1133



suppress the pest population. Mechanical control is a traditional method requiring more human efforts, while the chemical control is used to eradicate the pest by using chemical pesticides. But, heavy use of chemical pesticides creates more problems to the environment, and it also affects human health, i.e., overuse of DDT damage bird eggs. On the other hand, the biological control involves controlling populations of pests by releasing other living organisms that are commonly called natural predators. Microbial control with pathogens is also a part of biological control. Microbial control with the pathogen can suppress pests by releasing infected pests into the region of consideration, which is a natural process in controlling pests without harming the crop. In this paper, the hybrid approach including biological and chemical controls will be used, which is more effective in controlling pests.

Further, the mathematical models play a vital role in describing the impact of various pest control strategies in IPM systems. Mathematical modeling is recently catching a lot of attention in the field of Integrated pest management systems [14, 19]. Mathematical models have also been proposed to study the hybrid effect of biological and chemical pesticides together in the eradication of pest population [4, 8]. Moreover, some models involving chemical pesticides and disease incorporation (microbial control) in the pest population are presented in [9, 13]. Further, the impulsive differential equations serve as a tool to study the dynamic processes that are subject to a sudden change in the state of the population [10, 18]. Many researchers have developed a state-dependent impulsive differential equations system in order to study the pest control system by releasing pest controlling agents when the pest population exceeds the economic threshold level [15, 16]. Many authors considered time-dependent impulsive differential systems because sometimes pest control agents are released in a periodic manner [12, 21]. They considered either biological or hybrid approaches, e.g., biological (including microbial) and chemical control.

Besides, the real world is full of randomness. Random fluctuations occur due to drought, earthquake, flooding, harvesting fire, sudden rainfall, temperature rise. These random events affect the dynamics of the ecosystem, and these fluctuations can not be neglected. Generally, in the deterministic system, it is taken that involved parameters are constant, but due to random fluctuations, these parameters fluctuate around some average value, and this fluctuation in parameters affects the system's dynamics. Therefore, to capture the effect of random fluctuations, some authors presented a stochastic prey-predator system for integrated pest management [1, 2, 7, 11]. But generally, these models incorporate single impulsive control strategy i.e. biological control or chemical control [3, 6, 17, 20]. Hence stochastic prey-predator model, which incorporates natural enemies, disease, and chemical pesticides in an impulsive manner, is a new challenging problem to the researchers and has not been investigated yet.

Motivated from the literature, this paper considers two species predator-prey model with stochastic effect for integrated pest management. Also, we apply microbial control with the pathogen, natural enemies, and chemical control methods in an impulsive manner to suppress the pest.

The main aim of our paper is to analyze the dynamics of the proposed Impulsive Eco-epidemic prey-predator system by considering white noise and finding out the

condition for pest extinction and permanence of populations. The presented paper is organized as follows: In Sect. 2, we construct the stochastic Eco-epidemic model. Also, some assumptions of the model and essential lemmas are formulated. In Sect. 3, we investigate the susceptible pest extinction solution and the condition for the permanence of the system. Some numerical simulations are carried out to validate the theoretical results in Sect. 4. Finally, we discuss some conclusions of our proposed model and the scope of the work in the last section.

## 2 Model Development

A predator-prey model with disease in prey and two impulses for integrated pest management is proposed analyzed by Shi et al. in [13]. In this model, two compartments are considered for the pest population: Susceptible pest  $S(t)$  and Infected pest  $I(t)$ . It is considered that the pest can be suppressed with the help of a biological approach using microbial control with the pathogen and releasing of natural enemies simultaneously. However, the growth of pests and natural enemies is affected due to several random fluctuations, like, varying environmental and climate conditions which are not considered in [13] and hence the model proposed in [13] is not able to describe biological phenomena realistically. In this case, only stochastic differential equations can be used to model this biological situation. Keeping in mind the facts, we will propose a stochastic prey-predator model with disease in prey with hybrid impulsive pest management strategies with the following assumptions:

- (A1) Due to continuous environment fluctuations, the intrinsic growth rate of susceptible pest population  $r$ , natural death rate of infected pest  $d_1$  and death rate of natural enemies  $d_2$  fluctuates around some average value. We construct stochastic model by perturbing  $r \rightarrow r + \sigma_1 dB_1(t)$ ,  $d_1 \rightarrow d_1 - \sigma_2 dB_2(t)$  and  $d_2 \rightarrow d_2 - \sigma_3 dB_3(t)$ .
- (A2) Both chemical and biological control are used to suppress the pest population. It is assumed that a portion  $\delta_n$  of susceptible pest is reduced impulsively by spraying chemical pesticides while a portion  $p_n$  of infected pest and  $q_n$  of natural enemies are released impulsively at every moment of time  $t = nT$ .
- (A3) Moreover, it is considered that natural enemies consume the susceptible pests with the predation rate  $\beta_2$  with conversion efficiency rate  $k$ .

Therefore, with the above assumptions, we formulate the following stochastic prey-predator model for integrated pest management:

$$\left. \begin{aligned} dS(t) &= \left[ rS(t) \left( 1 - \frac{S(t)}{K} \right) - \beta_1 S(t)I(t) - \beta_2 S(t)N(t) \right] dt \\ &\quad + \sigma_1 S(t)dB_1(t), \\ dI(t) &= [\beta_1 S(t)I(t) - d_1 I(t)] dt + \sigma_2 I(t)dB_2(t), \\ dN(t) &= [k\beta_2 S(t)N(t) - d_2 N(t)] dt + \sigma_3 N(t)dB_3(t), \\ S(t^+) &= (1 - \delta_n)S(t), \\ I(t^+) &= (1 + p_n)I(t), \\ N(t^+) &= (1 + q_n)N(t), \end{aligned} \right\} \quad t \neq nT, \tag{2.1}$$

Here  $S(t)$ ,  $I(t)$  and  $N(t)$  denotes the population densities of the susceptible pest, infected pest and natural enemies at time  $t$ .  $\sigma_1$ ,  $\sigma_2$ , and  $\sigma_3$  are the coefficient effect of environmental stochastic perturbation on susceptible pest, infected pest and natural enemies,  $B_i$   $i = 1, 2, 3$  are independent from other standard Wiener process.

### 3 Model Analysis

This section is devoted to stating and proving our main results.

**Theorem 1** *For all  $t \in [0, \infty)$ , the model (2.1) has a unique solution  $(S(t), I(t), N(t))$  for any initial condition  $(S_0, I_0, N_0) \in R^3_+$ .*

**Proof** First we consider the model (2.1) without impulses:

$$\left\{ \begin{aligned} dS_1(t) &= \left[ rS_1(t) \left( 1 - \prod_{0 < nT < t} (1 - \delta_n) \frac{S_1(t)}{K} \right) - \beta_1 \prod_{0 < nT < t} (1 + p_n) I_1(t) S_1(t) \right. \\ &\quad \left. - \beta_2 \prod_{0 < nT < t} (1 + q_n) N_1(t) S_1(t) \right] dt + \sigma_1 S_1(t)dB_1(t), \\ dI_1(t) &= \left[ \beta_1 \prod_{0 < nT < t} (1 - \delta_n) S_1(t) I_1(t) - d_1 I_1(t) \right] dt + \sigma_2 I_1(t)dB_2(t), \\ dN_1(t) &= \left[ k\beta_2 \prod_{0 < nT < t} (1 - \delta_n) S_1(t) N_1(t) - d_2 N_1(t) \right] dt + \sigma_3 N_1(t)dB_3(t), \end{aligned} \right. \tag{3.1}$$

with the initial value  $(S_{10}, I_{10}, N_{10}) = (S_0, I_0, N_0)$ . The classical theory of stochastic differential equations without impulses suggests that there is a unique global positive solution of the system (3.1).

Let

$$S(t) = \prod_{0 < nT < t} (1 - \delta_n) S_1(t), \quad I(t) = \prod_{0 < nT < t} (1 + p_n) I_1(t), \quad N(t) = \prod_{0 < nT < t} (1 + q_n) N_1(t),$$

with the initial condition  $(S_{10}, I_{10}, N_{10}) = (S_0, I_0, N_0)$ .  $S(t)$ ,  $I(t)$ , and  $N(t)$  are continuous on every interval  $t \in (nT, (n + 1)T)$ ,  $n \in Z^+ = 0, 1, 2, \dots$

For  $S(t)$ , we have

$$\begin{aligned}
 dS(t) &= d \left[ \prod_{0 < nT < t} (1 - \delta_n) S_1(t) \right] = \prod_{0 < nT < t} (1 - \delta_n) dS_1(t), \\
 &= \left[ rS(t) \left( 1 - \frac{S(t)}{K} \right) - \beta_1 S(t) I(t) - \beta_2 S(t) N(t) \right] dt + \sigma_1 S(t) dB_1(t),
 \end{aligned}$$

for every  $n \in N$  and  $t \neq nT$ .

$$S(nT^+) = \lim_{t \rightarrow nT^+} S(t) = \lim_{t \rightarrow nT^+} \prod_{0 < iT < t} (1 - \delta_i) S_1(t) = (1 - \delta_n) S(nT),$$

for every  $n \in N$ . And

$$S(nT^-) = \lim_{t \rightarrow nT^-} S(t) = \lim_{t \rightarrow nT^-} \prod_{0 < iT < t} (1 - \delta_i) S_1(t) = (1 - \delta_n) S(nT).$$

For  $I(t)$ , we have,

$$\begin{aligned}
 dI(t) &= d \left[ \prod_{0 < nT < t} (1 + p_n) I_1(t) \right] = \prod_{0 < nT < t} (1 + p_n) dI_1(t) \\
 &= [\beta_1 S(t) I(t) - d_1 I(t)] dt + \sigma_2 I(t) dB_2(t),
 \end{aligned}$$

for every  $n \in N$  and  $t \neq nT$ .

$$I(nT^+) = \lim_{t \rightarrow nT^+} I(t) = \lim_{t \rightarrow nT^+} \prod_{0 < iT < t} (1 + p_i) I_1(t) = (1 + p_n) I(nT),$$

for every  $n \in N$ . Also,

$$I(nT^-) = \lim_{t \rightarrow nT^-} I(t) = \lim_{t \rightarrow nT^-} \prod_{0 < iT < t} (1 + p_i) I_1(t) = (1 + p_n) I(nT),$$

for every  $n \in N$ . Similarly, for  $N(t)$ , we have

$$\begin{aligned}
 dN(t) &= d \left[ \prod_{0 < nT < t} (1 + q_n) N_1(t) \right] = \prod_{0 < nT < t} (1 + q_n) dN_1(t) \\
 &= [k\beta_2 S(t) N(t) - d_2 N(t)] dt + \sigma_3 N(t) dB_3(t), \text{ for every } n \in N \text{ and } t \neq nT.
 \end{aligned}$$

$$N(nT^+) = \lim_{t \rightarrow nT^+} N(t) = \lim_{t \rightarrow nT^+} \prod_{0 < iT < t} (1 + q_i) N_1(t) = (1 + q_n) N(nT),$$

for every  $n \in N$ . Further more,

$$N(nT^-) = \lim_{t \rightarrow nT^-} N(t) = \lim_{t \rightarrow nT^-} \prod_{0 < i T < t} (1 + q_i) N_1(t) = (1 + q_n) N(nT),$$

for every  $n \in N$ . Hence, the theorem is proved.

**Theorem 2** For any initial value  $(S_0, I_0, N_0) \in R_+^3$ , there exists functions  $u(t), U(t), v(t), V(t), w(t), W(t)$  such that the positive solution of the model (2.1) satisfies the following inequalities.

$$u(t) \leq S(t) \leq U(t), \quad v(t) \leq I(t) \leq V(t), \quad w(t) \leq N(t) \leq W(t), \quad t \geq 0 \quad a.s. \tag{3.2}$$

**Proof** The model (2.1) has a positive solution, therefore,

$$dS(t) \leq \left[ rS(t) \left( 1 - \frac{S(t)}{K} \right) \right] dt + \sigma_1 S(t) dB_1(t).$$

We formulate the following equations:

$$\begin{cases} dU(t) = \left[ rU(t) \left( 1 - \frac{U(t)}{K} \right) \right] dt + \sigma_1 U(t) dB_1(t), & t \neq nT, \\ U(t^+) = (1 - \delta_n)U(t), & t = nT, \\ U(0) = S_0 \end{cases} \tag{3.3}$$

Obviously, there is a global continuous positive solution of the system (3.3) with initial value  $S_0$ .

$$U(t) = \frac{\prod_{0 < nT < t} (1 - \delta_n) \exp \left[ \int_0^t (r - 0.5\sigma_1^2) ds + \sigma_1 \int_0^t dB_1(s) \right]}{\frac{1}{S_0} + \int_0^t \prod_{0 < nT < s} (1 - \delta_n) \frac{r}{K} \exp \left[ \int_0^s (r - 0.5\sigma_1^2) d\tau + \sigma_1 \int_0^s dB_1(\tau) \right] ds}.$$

According to the comparison theorem of stochastic differential equations, we get  $S(t) \leq U(t), t \in [0, t^*), a.s.$  Now from the second equation of the model (2.1),

$$dI(t) \geq -d_1 I(t) dt + \sigma_2 I(t) dB_2(t),$$

we formulate the following equation:

$$\begin{cases} dv(t) = -d_1 v(t) dt + \sigma_2 v(t) dB_2(t), & t \neq nT, \\ v(t^+) = (1 + p_n)v(t), & t = nT, \\ v(0) = I_0. \end{cases} \tag{3.4}$$

Obviously, 
$$v(t) = \frac{\prod_{0 < nT < t} (1 + p_n) \exp[-0.5\sigma_2^2 t + \sigma_2 B_2(t)]}{\frac{1}{I_0} + d_1 \int_0^t \prod_{0 < nT < s} (1 + p_n) \exp[-0.5\sigma_2^2 s + \sigma_2 B_2(s)] ds}$$

And we get  $I(t) \geq v(t), t \in [0, t^*], a.s.$  Moreover, from the third equation of the model (2.1), we can get the inequalities,  $dN(t) \geq -d_2 N(t)dt + \sigma_3 N(t)dB_3(t)$ , we construct the following equations:

$$\begin{cases} dw(t) = -d_2 w(t)dt + \sigma_3 w(t)dB_3(t), & t \neq nT, \\ w(t^+) = (1 + q_n)w(t), & t = nT, \\ w(0) = N_0. \end{cases} \tag{3.5}$$

Obviously, 
$$w(t) = \frac{\prod_{0 < nT < t} (1 + q_n) \exp[-0.5\sigma_3^2 t + \sigma_3 B_3(t)]}{\frac{1}{N_0} + d_2 \int_0^t \prod_{0 < nT < s} (1 + q_n) \exp[-0.5\sigma_3^2 s + \sigma_3 B_3(s)] ds}$$

And we have  $N(t) \geq w(t), t \in [0, t^*], a.s.$

From second equation of the model (2.1), we have

$$dI(t) \leq \beta_1 U(t)I(t)dt - d_1 I(t)dt + \sigma_2 I(t)dB_2(t).$$

In the similar way, we get,  $I(t) \leq V(t), t \in [0, t^*], a.s.$

Here, 
$$V(t) = \frac{\prod_{0 < nT < t} (1 + p(nT)) \exp[-0.5\sigma_2^2 t + \sigma_2 B_2(t)]}{\frac{1}{I_0} + \beta_1 \int_0^t \prod_{0 < nT < s} (1 + p(nT)) \exp[-0.5\sigma_2^2 s + \sigma_2 B_2(s)] U(s) ds}$$

Besides, from the third equation of the model (2.1), we have

$$dN(t) \leq k\beta_2 U(t)N(t)dt - d_2 N(t)dt + \sigma_3 N(t)dB_3(t).$$

Obviously, 
$$W(t) = \frac{\prod_{0 < nT < t} (1 + q(nT)) \exp[-0.5\sigma_3^2 t + \sigma_3 B_3(t)]}{\frac{1}{N_0} + k\beta_2 \int_0^t \prod_{0 < nT < s} (1 + q(nT)) \exp[-0.5\sigma_3^2 s + \sigma_3 B_3(s)] U(s) ds}$$

represents the solution of the system of equations,

$$\begin{cases} dW(t) = k\beta_2 U(t)W(t)dt - d_2 W(t)dt + \sigma_3 W(t)dB_3(t), & t \neq nT, \\ W(t^+) = (1 + q_n)W(t), & t = nT, \\ W(0) = N_0. \end{cases} \tag{3.6}$$

and  $N(t) \leq W(t), t \in [0, t^*], a.s.$

The first equation of the model (2.1) follows that

$$dS(t) \geq \left[ rS(t) \left( 1 - \frac{S(t)}{K} \right) - \beta_1 S(t)V(t) - \beta_2 S(t)W(t) \right] dt + \sigma_1 S(t)dB_1(t).$$

According to the comparison system of the SDE, we have  $S(t) \geq u(t), t \in [0, t^*], a.s.$  Here,

$$u(t) = \frac{\prod_{0 < nT < t} (1 - \delta(t)) \exp \left[ (r - 0.5\sigma_1^2)t - \beta \int_0^t (V(s) + W(s))ds + \sigma_1 B_1(t) \right]}{\frac{1}{S_0} + \frac{r}{K} \int_0^t \prod_{0 < nT < s} (1 - \delta(t)) \exp \left[ (r - 0.5\sigma_1^2)s - \beta \int_0^s (V(\tau) + W(\tau))d\tau + \sigma_1 B_1(s) \right] ds}$$

and  $\beta = \max(\beta_1, \beta_2)$ . By the following inequalities, we get that,

$$u(t) \leq S(t) \leq U(t), \quad v(t) \leq I(t) \leq V(t), \quad w(t) \leq N(t) \leq W(t), \quad t \in [0, t^*], a.s.$$

Hence, the theorem is verified.

**Theorem 3** *If  $\lim_{t \rightarrow \infty} \frac{\sum_{0 < nT < t} \ln(1 - \delta_n)}{t} < 0.5\sigma_1^2 - r$ , then the susceptible pests of SDE model (2.1) with any positive initial value tend to extinction according to probability 1.*

**Proof** Consider the transformation,  $S(t) = \prod_{0 < nT < t} (1 - \delta_n)\xi(t)$ , and the lyapunov function,  $V(t) = \ln \xi(t), t \geq 0$ .

Applying *Itô* formula to the first equation of the model (2.1), we have

$$d \ln \xi(t) = \frac{d\xi(t)}{\xi(t)} - \frac{(d\xi(t))^2}{2\xi^2(t)} \leq \left[ r - 0.5\sigma_1^2 - \frac{\prod_{0 < nT < t} (1 - \delta_n)\xi(t)}{K} \right] dt + \sigma_1 dB_1(t), \quad (3.7)$$

With the help of integration between 0 and t, we obtain that

$$\ln \xi(t) = \ln(S_0) + \int_0^t \left[ r - 0.5\sigma_1^2 - \frac{S(s)}{K} \right] ds + M_1(t), \quad (3.8)$$

where  $M_1(t)$  is a martingale and  $M_1(t) = \sigma_1 \int_0^t dB(s)$ , the quadratic variation of the martingale is  $\langle M_1(t), M_1(t) \rangle = \sigma_1^2 t$ . The theory of large numbers for local martingales implies that  $\lim_{t \rightarrow \infty} \frac{M_1(t)}{t} = 0$ .

Therefore, from (3.8),

$$\sum_{0 < nT < t} \ln(1 - \delta_n) + \ln \xi(t) - \ln S_0 = \sum_{0 < nT < t} \ln(1 - \delta_n) + \int_0^t \left[ r - 0.5\sigma_1^2 - \frac{S(s)}{K} \right] ds + M_1(t).$$

We have,  $\prod_{0 < nT < t} \ln(1 - \delta_n)\xi(t) - \ln S_0 = \sum_{0 < nT < t} \ln(1 - \delta_n) + \int_0^t \left[ r - 0.5\sigma_1^2 - \frac{S(s)}{K} \right] ds + M_1(t)$ .

Therefore,  $\ln S(t) - \ln S_0 \leq \sum_{0 < nT < t} \ln(1 - \delta_n) + \int_0^t [r - 0.5\sigma_1^2] ds + M_1(t)$ .  
 According to the hypothesis,  $\lim_{t \rightarrow \infty} S(t) = 0$ .

### 4 Numerical Simulation and Discussion

This section is devoted to performing some numerical simulations to verify our theoretical findings. Here, we consider the numerical values of some parameters from realistic sources, and some are assumed in a realistic sense (see Table 1). To find the strong solution of the stochastic system (2.1), Higham introduced the Milstein method in [5]. By using this method, we transform the system (2.1) in discrete form and demonstrate our main results. Here the main aim is to investigate the effects of the impulsive time period, pulse releasing amount of chemical pesticides to harvest the susceptible pest, pulse releasing amount of infected pest, pulse releasing amount of natural enemies, and the intensity of stochastic perturbations on the integrated pest management system. The threshold which governs the permanence of all the species and pest extinction is obtained in this section. We choose the initial values  $S(0) = 5, I(0) = 3, N(0) = 3$ , controlling parameters  $\delta_n = 0.1, p_n = 0.4208, q_n = 0.4208$  and other parameters values from Table 1. Then we analyze the stochastic system numerically to validate our analytic results and to see the effect of external interference in the system. Theorem 1 shows that there exists a positive solution of the system (2.1). In order to derive numerical simulation to validate the above results, first, we choose  $\sigma_1 = \sigma_2 = \sigma_3 = 0$  in Fig. 1 and draw the time series plot of the model (2.1). In Fig. 2 we take  $\sigma_1 = \sigma_2 = \sigma_3 = 0.1$ . From Fig. 3 it can be seen that as we increase the value of noise  $\sigma_1 = \sigma_2 = \sigma_3 = 0.3$ , we found that the solution of the system (2.1) fluctuates with high amplitude. Chaos may occur, and pulse phenomena are covered, so pulse can not be produced clearly. Further, consider the system (2.1) again. By computations we get, for the parameters values  $r(t) = 0.2, \delta_n = 0.1, \sigma_1 = 0.6, T = 5$  and  $\lim_{t \rightarrow \infty} \frac{\sum_{0 < nT < t} \ln(1 - \delta_n)}{t} = -0.0211 < 0.5\sigma_1^2 - r = -0.020$ . Therefore, from the result of Theorem 3 we can determine that the pest population will extinct for these values of parameters. We can illustrate this result in Fig. 4. To see the significant effect of chemical pesticides in the suppression of susceptible pest populations, we take parameters values  $r(t) = 0.3, \delta_n = 0.1, \sigma_1 = 0.6, T = 5$ . From Fig. 5, we can analyze that the susceptible pest population is not suppressed completely. In order to eradicate the susceptible pest population, we have to increase the pulse releasing amount of chemical pesticides  $\delta_n = 0.49$  (see in Fig. 5). Moreover, we can analyze the effect of impulsive releasing amount of infected pest and natural enemies on the system (2.1) with different intensities of stochastic perturbations. We choose parameters  $r(t) = 3, \delta_n = 0.1, p_n = 0.4208, q_n = 0.4208, \sigma_1 = \sigma_2 = \sigma_3 = 0, T = 5$ . From Fig. 1 we can see that all the species coexists. If we increase pulse releasing amount of infected pest  $p_n = 1.719$  and natural enemies  $q_n = 1.719$  then suscep-



**Table 1** Description of parameters values selection for model (2.1)

Parameter	Description	Values	Unit	Source
$r$	Intrinsic growth Rate	3	day <sup>-1</sup>	[6]
$K$	Carrying capacity	12	ind	[6]
$\beta_1$	Number of susceptible pest become infected at per unit time due to direct contact with infected pest	0.3	ind <sup>-1</sup> day <sup>-1</sup>	Assumed
$\beta_2$	Attack rate of natural enemies to catch susceptible pest	0.6	ind <sup>-1</sup> day <sup>-1</sup>	[6]
$k$	Conversion efficiency of natural enemies	0.5	–	[6]
$d_1$	Death rate of infected prey	0.2	day <sup>-1</sup>	Assumed
$d_2$	Death rate of natural enemies	0.2	day <sup>-1</sup>	[6]

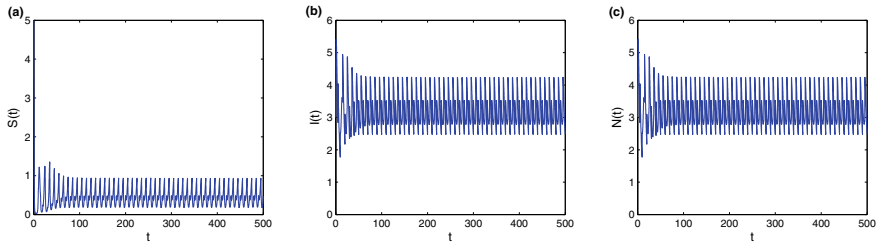


**Fig. 1** Stability analysis of system (2.1) with  $\delta_n = 0.1$ ,  $p_n = 0.4208$ ,  $q_n = 0.4208$ ,  $T = 5$ ,  $\sigma_1 = \sigma_2 = \sigma_3 = 0$ , **a–c** Population dynamics in  $t - S(t)$ ,  $t - I(t)$ ,  $t - N(t)$  planes, respectively

tible pest population will die out (see in (a–c) of Fig. 6). Also from (d–f) of Fig. 6 we can observe that if there is small stochastic perturbation in the system (2.1), then for the suppression of susceptible pest population we increase the value of  $p_n = 1.8$  and  $q_n = 1.8$  (see in (a–c) of Fig. 7). Similarly, if stochastic perturbation is large (i.e.  $\sigma_1 = \sigma_2 = \sigma_3 = 0.3$ ), then we increase the pulse releasing amount of infected pest  $p_n = 2.5$  and natural enemies  $q_n = 2.5$  to eradicate susceptible pest population completely (see in (d–f) of Fig. 7).

Further, impulsive time period and intensity of noise also affect the stochastic persistence and extinction of susceptible pest populations. In order to eradi-

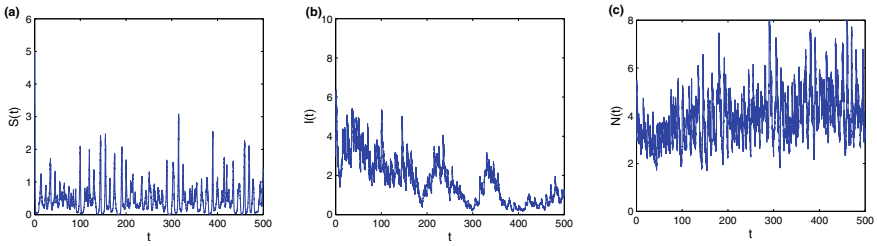


**Fig. 2** Stability analysis of system (2.1) with  $\delta_n = 0.1$ ,  $p_n = 0.4208$ ,  $q_n = 0.4208$ ,  $T = 5$ ,  $\sigma_1 = \sigma_2 = \sigma_3 = 0.1$ , **a-c** Population dynamics in  $t - S(t)$ ,  $t - I(t)$ ,  $t - N(t)$  planes, respectively

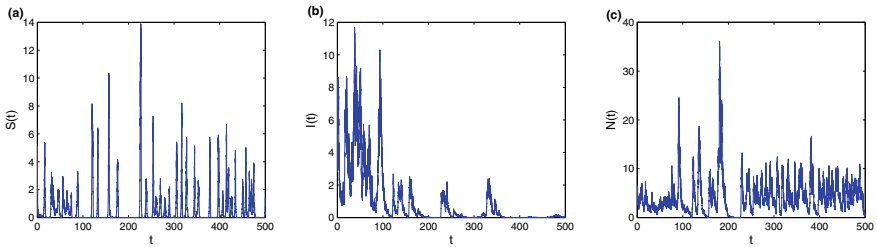


**Fig. 3** Stability analysis of system (2.1) with  $\delta_n = 0.1$ ,  $p_n = 0.4208$ ,  $q_n = 0.4208$ ,  $T = 5$ ,  $\sigma_1 = \sigma_2 = \sigma_3 = 0.3$ , **a-c** Population dynamics in  $t - S(t)$ ,  $t - I(t)$ ,  $t - N(t)$  planes, respectively

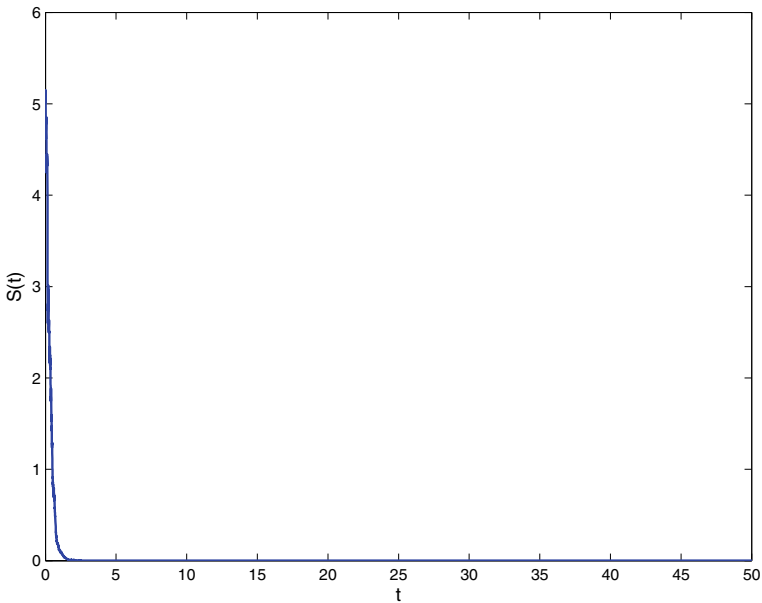


**Fig. 4** Pest population of system (2.1) with  $S(0) = 5$ ,  $r = 0.2$ ,  $\delta_n = 0.1$ ,  $\sigma_1 = 0.6$ ,  $T = 5$

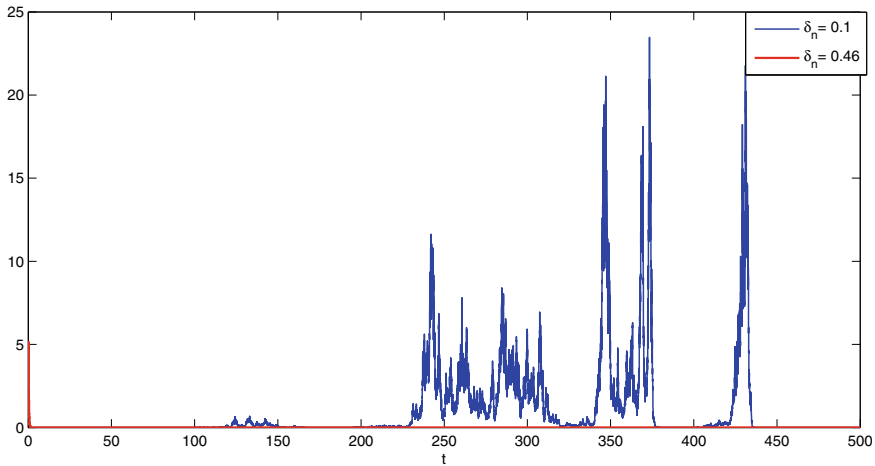


**Fig. 5** Pest population of the system (2.1) with  $S(0) = 5, r = 0.3, T = 5, \sigma_1 = \sigma_2 = \sigma_3 = 0.6$

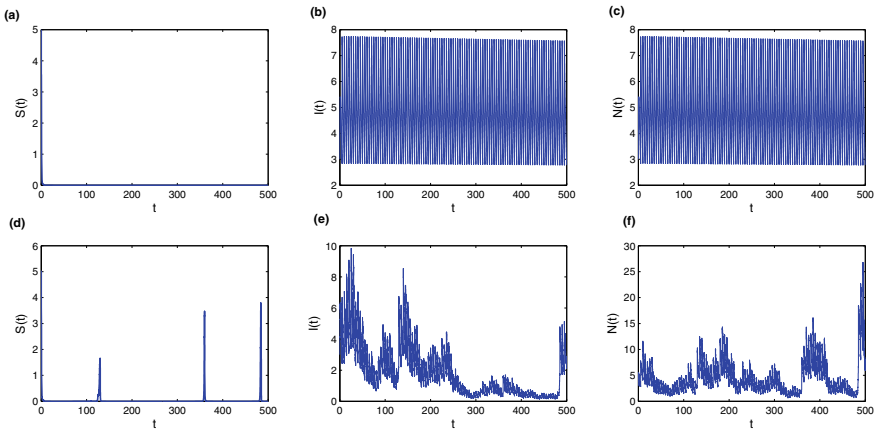


**Fig. 6** Stability analysis of system (2.1), **a–c** with  $\delta = 0.1, p_n = 1.719, q_n = 1.719, T = 5, \sigma_1 = \sigma_2 = \sigma_3 = 0$ , Population dynamics in  $t - S(t), t - I(t), t - N(t)$  planes, respectively and **(d-f)** with  $\sigma_1 = \sigma_2 = \sigma_3 = 0.1$  Population dynamics in  $t - S(t), t - I(t), t - N(t)$  planes, respectively

cate the susceptible pest population we take controlling parameters  $\delta_n = 0.1, p_n = 0.4208, q_n = 0.4208$  and the rest of the parameters are the same. If the intensity of noise is  $\sigma_1 = \sigma_2 = \sigma_3 = 0$ , then we get a threshold value for impulsive period  $T^* = 1.8285$ . From Fig. 8 we can see that for  $T = 1.7557 < T^* = 1.8285$  pest population become extinct and other populations will survives. If the intensity of noise is  $\sigma_1 = \sigma_2 = \sigma_3 = 0.1$ , then we have  $T^* = 1.7511$ . Similarly for  $\sigma_1 = \sigma_2 = \sigma_3 = 0.3$ , value of  $T^*$  will be 1.4379 (see Fig. 9). However, if the intensity of stochastic perturbation is large, then stochastic permanence of all species and pest extinction of the

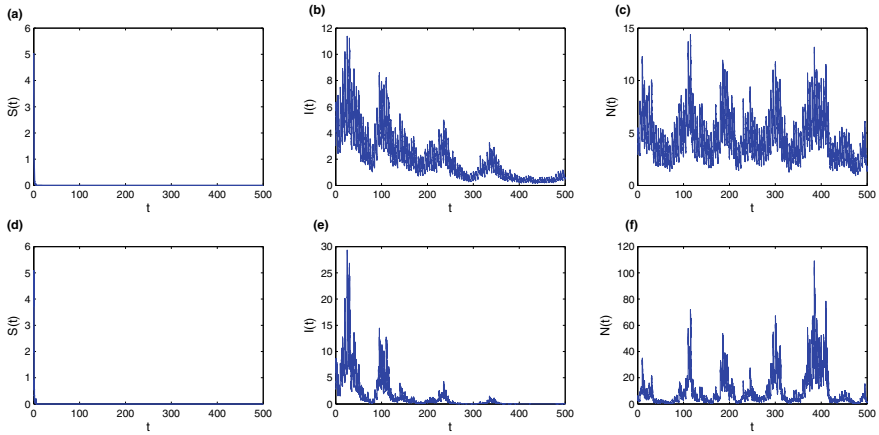


**Fig. 7** Stability analysis of system (2.1), **a–c** with  $\delta_n = 0.1, p_n = 1.8, q_n = 1.8, T = 5, \sigma_1 = \sigma_2 = \sigma_3 = 0.1$ , Population dynamics in  $t - S(t), t - I(t), t - N(t)$  planes, respectively and **d–f** with  $\delta_n = 0.1, p_n = 2.5, q_n = 2.5, T = 5, \sigma_1 = \sigma_2 = \sigma_3 = 0.3$ , Population dynamics in  $t - S(t), t - I(t), t - N(t)$  planes, respectively

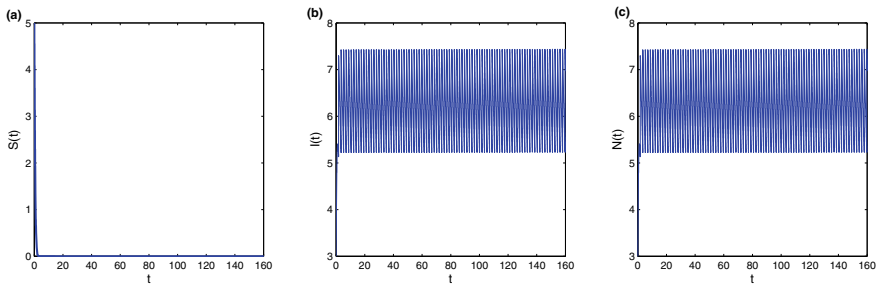


**Fig. 8** Stability analysis of system (2.1) with  $\delta_n = 0.1, p_n = 0.4208, q_n = 0.4208, T = 1.7557 < T^* = 1.8285, \sigma_1 = \sigma_2 = \sigma_3 = 0$ , **a–c** Population dynamics in  $t - S(t), t - I(t), t - N(t)$  planes, respectively

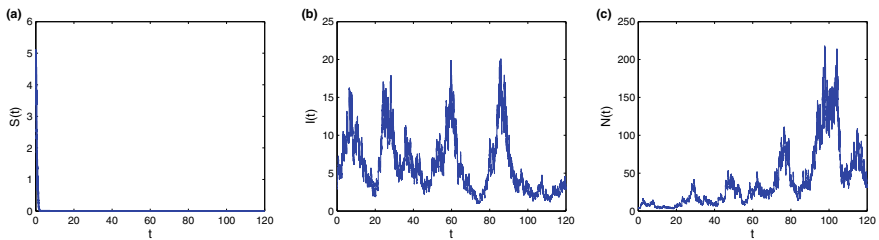


**Fig. 9** Stability analysis of system (2.1) with  $\delta_n = 0.1, p_n = 0.4208, q_n = 0.4208, T = 1.27 < T^* = 1.4379, \sigma_1 = \sigma_2 = \sigma_3 = 0.3$ , **a–c** Population dynamics in  $t - S(t), t - I(t), t - N(t)$  planes, respectively

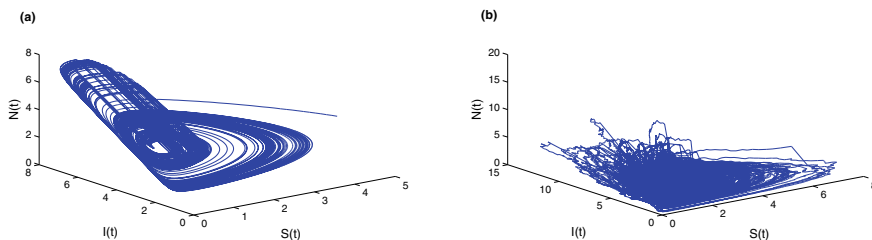


**Fig. 10** 3-D plot between: Susceptible pest, infected pest and natural enemy with  $\delta_n = 0.1, p_n = 1, q_n = 1, T = 20,$  and **a** with  $\sigma_1 = \sigma_2 = \sigma_3 = 0,$  **b** with  $\sigma_1 = \sigma_2 = \sigma_3 = 0.1$

susceptible pest population could be changed. Further, we can also get that analysis of the system (2.1) becomes more complex when the impulsive period is greater than a certain critical value. A typical chaos oscillation occurs, and pulse phenomena are covered (see Fig. 10).

### 5 Conclusion

In this paper, a stochastic prey-predator system with hybrid impulses has been proposed and analyzed. In the modeling process, we considered that pests were completely eradicated by using both biological and chemical control strategies together impulsively. We released natural enemies, infected pests, and chemical pesticides to suppress the pest population. It is also noticed that real life is full of randomness. This random fluctuation occurs in a relatively short time interval due to some random environmental factors such as flood, rainfall, harvesting, fire, etc. Generally, the species’ growth often suffers due to environmental fluctuations, and these fluctuations affect the long-term dynamics of the system. So, we can not neglect these random fluctuations, and it is essential to consider the prey-predator system with white noise. Keeping this in view, we have constructed a stochastic prey-predator model with disease in prey and a hybrid impulsive model for integrated pest management. We analyzed the dynamics of the system (2.1) and carried out some theoretical results. Theorem 1 shows that there exists a positive solution of the system (2.1). Similarly, Theorem 2 proves the permanence of the system (2.1). Moreover, By the result of Theorem 3, we obtained the condition for the pest extinction. Our analysis shows that these conditions mainly depend upon the parameters: impulsive releasing amount of chemical pesticides  $\delta_n,$  impulsive releasing amount of infected pest  $p_n,$  impulsive releasing amount of natural enemies, impulsive time-period T and the magnitude of the intensities of external interferences  $\sigma_1, \sigma_2, \sigma_3.$  If the birth rate of susceptible pests is low, then susceptible pests can be controlled by using a small amount of chemical pesticides. However, the birth rate of the susceptible pest is high, and the intensity of stochastic perturbation is large, then susceptible pest population can be suppressed by releasing both infectious pests and natural enemies. Moreover, pulse releasing

the amount of infected pests and natural enemies is also responsible for the susceptible pest extinction. The susceptible pest population can be suppressed by releasing a large amount of controlling agents. Also, if the controlling agents are released more frequently, the susceptible pest population can be eradicated completely. Our analysis also shows that pest control becomes more complex due to the high amplitude of impulsive period and higher intensities of external interference. Moreover, our analysis can help the farmer to understand the interactions of susceptible pests, infected pests, natural enemies, chemical pesticides, and environmental fluctuations to design the appropriate pest control strategies and make pest management decisions to control the pest.

## References

1. Akman, O., Comar, T.D., Hrozencik, D.: On impulsive integrated pest management models with stochastic effects. *Front. Neurosci.* **9**, 119 (2015)
2. Comar, T., Akman, O., Hrozencik, D.: Model selection and permanence in a stochastic integrated pest management model (2017)
3. Feng, T., Meng, X., Zhang, T., Qiu, Z.: Analysis of the predator-prey interactions: a stochastic model incorporating disease invasion. *Qual. Theory Dyn. Syst.* **19**(2), 1–20 (2020)
4. Gao, W., Tang, S.: The effects of impulsive releasing methods of natural enemies on pest control and dynamical complexity. *Nonlinear Anal. Hybrid Syst.* **5**(3), 540–553 (2011)
5. Higham, D.J.: An algorithmic introduction to numerical simulation of stochastic differential equations. *SIAM Rev.* **43**(3), 525–546 (2001)
6. Huang, L., Chen, X., Tan, X., Chen, X., Liu, X.: A stochastic predator-prey model for integrated pest management. *Adv. Differ. Equ.* **2019**(1), 1–10 (2019)
7. Huang, Y., Shi, W., Wei, C., Zhang, S.: A stochastic predator-prey model with Holling II increasing function in the predator. *J. Biol. Dyn.* **15**(1), 1–18 (2021)
8. Jiao, J., Chen, L.: A pest management SI model with periodic biological and chemical control concern. *Appl. Math. Comput.* **183**(2), 1018–1026 (2006)
9. Jiao, J., Chen, L., Cai, S.: Impulsive control strategy of a pest management SI model with nonlinear incidence rate. *Appl. Math. Model.* **33**(1), 555–563 (2009)
10. Lakshmikantham, V., Simeonov, P.S., et al.: *Theory of Impulsive Differential Equations*, vol. 6. World scientific (1989)
11. Li, L., Zhao, W.: Deterministic and stochastic dynamics of a modified Leslie-Gower prey-predator system with simplified Holling-type IV scheme. *Math. Biosci. Eng.* **18**(3), 2813–2831 (2021)
12. Liang, J., Tang, S.: Optimal dosage and economic threshold of multiple pesticide applications for pest control. *Math. Comput. Model.* **51**(5–6), 487–503 (2010)
13. Shi, R., Jiang, X., Chen, L.: A predator-prey model with disease in the prey and two impulses for integrated pest management. *Appl. Math. Model.* **33**(5), 2248–2256 (2009)
14. Shi, R., Tang, S., Feng, W.: Two generalized predator-prey models for integrated pest management with stage structure and disease in the prey population. *Abstr. Appl. Anal.* **2013**. Hindawi (2013)
15. Tang, S., Cheke, R.A.: State-dependent impulsive models of integrated pest management (IPM) strategies and their dynamic consequences. *J. Math. Biol.* **50**(3), 257–292 (2005)
16. Tang, S., Cheke, R.A.: Models for integrated pest control and their biological implications. *Math. Biosci.* **215**(1), 115–125 (2008)
17. Tan, X., Qin, W., Tang, G., Xiang, C., Liu, X.: Models to assess the effects of nonsmooth control and stochastic perturbation on pest control: a pest-natural-enemy ecosystem. *Complexity* **2019** (2019)

18. Wang, L., Xie, Y., Fu, J.: The dynamics of natural mortality for pest control model with impulsive effect. *J. Frankl. Inst.* **350**(6), 1443–1461 (2013)
19. Xiao, Y., Van Den Bosch, F.: The dynamics of an eco-epidemic model with biological control. *Ecol. Model.* **168**(1–2), 203–214 (2003)
20. Zhang, H., Liu, X., Xu, W.: Threshold dynamics and pulse control of a stochastic ecosystem with switching parameters. *J. Frankl. Inst.* **358**(1), 516–532 (2021)
21. Zhao, W., Liu, Y., Zhang, T., Meng, X.: Geometric analysis of an integrated pest management model including two state impulses. *Abstr. Appl. Anal.* **2014**. Hindawi (2014)

# Bifurcation Analysis of Longitudinal Dynamics of Generic Air-Breathing Hypersonic Vehicle for Different Operating Flight Conditions



Ritesh Singh , Om Prakash , Sudhir Joshi , and Yogananda Jeppu 

**Abstract** The advancements in the Hypersonic Technology have taken us a step closer to the cost effective and reliable Hypersonic flight to Space. The paper outlines nonlinear dynamical model analysis of the Air-breathing Hypersonic Vehicle (AHV) using Bifurcation Method. It shows the Bifurcation Method implementation and its application to the nonlinear dynamics and stability investigation for 3DOF Longitudinal nonlinear dynamics of the Generic AHV. Bifurcation Analysis of AHV presents a quantifiable valuation with equilibrium states throughout the whole broad flight envelop and with dynamic stability analysis for Mach Number,  $M = 0.9$ . AUTO-07p platform is used here to demonstrate the AHV flight dynamics and control analysis using the Bifurcation Technique and Continuation approach. The Bifurcation Methodology is implemented for the AHV dynamic model using AUTO-07p for different operating flight conditions with elevator deflection,  $\delta_e$ .

**Keywords** Bifurcation analysis · Longitudinal dynamics · Hypersonic vehicle

## 1 Introduction

Air-breathing Hypersonic Vehicle provides a way forward for the Hypersonic Technology in the coming decades to achieve tourism in space. Accomplishment of Hyper-X experimental vehicle during the last decade has made an increased interest in the AHV, which can lead the ultramodern dreams of rapid transportation across the world and to Space in the coming decades. Hypersonic Technology is now being developed around the world, with promising military and commercial applications, and

---

R. Singh (✉)  
Manipal University Jaipur, Jaipur 303007, Rajasthan, India  
e-mail: [ritesh.singh23@gmail.com](mailto:ritesh.singh23@gmail.com)

R. Singh · O. Prakash · S. Joshi  
University of Petroleum & Energy Studies, Dehradun 248007, Uttarakhand, India

Y. Jeppu  
Honeywell Technology Solutions, Hyderabad 500032, Telangana, India



for achieving Low Earth Orbit. The achievement with NASA Programs throughout the last seven decades has opened a new awareness for cost-effective Space entrance to many noncombatants and military missions, and provides renewed interest in Hypersonic Vehicles and its technology. The challenges with the aerodynamics of the AHV flight shows the dynamic interaction and nonlinear aerodynamics phenomena occurring at the different high speeds for the wide flight regime. Therefore, the flight dynamics of the AHV vehicle presents a challenge for the different operating flight conditions for the vehicle and shows that further dynamics analysis can be carried using the different nonlinear analysis methods. This gives a way forward to the Bifurcation Technique, which can be investigated and implemented due to the highly nonlinear AHV model, complicated aerodynamic characteristics over the whole flight regimes, large flight envelop, and significant coupling interaction.

Bifurcation approach provides a potential to significantly enhance the flight dynamics design process. The relevance of the bifurcation approach is that it may show global stability and improvements in aviation control design parameters. The nonlinear dynamical system with trim and stability analysis, may be investigated computationally using Bifurcation approaches. The bifurcation method can be used to find multiple trim points and different states which can co-exist utilizing a static categorization with control restrictions. It also forecasts system behavior utilizing several sorts of bifurcations that lead to the commencement of state dynamics, as well as information on phugoid stability for AHV dynamics analysis. Continuation algorithm implemented with the bifurcation technique delivers local stability evidence around all trim points, making the method valuable for analysis. Bifurcation method provides promising application for flight controls and its effective analysis of nonlinear phenomena occurring in the flight dynamics. When it comes to flight dynamics and control system design, using Bifurcation analysis, it proves a better nonlinear approach to be implemented, for the analysis of complex nonlinear dynamics and dynamical system with multiple trim states and control parameters.

The organization of the paper is categorized with the following sections. Section 2 presents the Bifurcation Method introduction, application and its brief literature overview. Section 3 discusses the implementation of the Bifurcation Method to the 3DOF Longitudinal AHV model using AUTO-07p platform. Section 4 discusses the Bifurcation Results of AHV for the Mach Number,  $M = 0.9$  with elevator deflection,  $\delta_e$ . And at the end, Sect. 5 deliberates the conclusion of the Method implemented.

## 2 Bifurcation Method

Bifurcation techniques are a valuable tool for numerically investigating the nonlinear effects of dynamical systems for trim and stability. With these analysis, nonlinear behavior may be better understood since it keeps track of all trim points at which equilibriums are created or destroyed, or at which the stability of equilibriums varies. This technique was first implemented for flight dynamics by [1–3] around 1982. Bifurcation analysis gives record of all critical bifurcation points for the equilibriums

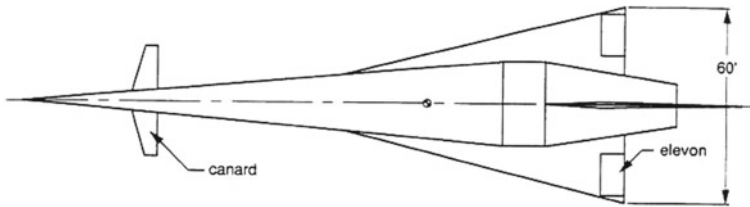


**Fig. 1** AHV model

which shows the variation of the system stability change. Analysis and application of this technique is implemented for the aircraft stability, dynamics and control for high alpha effects in [4, 5]. The method is implemented for the 6DOF aircraft models with nonlinear dynamics for different flight conditions of level, straight and turn conditions for the flight dynamics analysis by [6–9]. Hence it can be shown that this method provides fruitful way to understand the nonlinear dynamics with all information regarding the equilibrium states and can be implemented to the flight dynamics area.

The vehicle considered here is Generic Hypersonic Vehicle known as Winged Cone Model from [10], developed by NASA is presented in the Fig. 1 [10]. The model developed is based on the rigid-body hypothesis and is used for various developments such for control systems, navigation and guidance, optimization and stability for Single-Stage-To-Orbit. The propulsion model used for the vehicle is the combination of the turbojet, ramjet and scramjet, and the rocket engine used for the entire flight envelop. The hypothetically proposed ramjet and scramjet engine, integrated to the vehicle makes the model to be called as Air-breathing Hypersonic Vehicle (AHV) [11]. The nonlinear ODE (Ordinary Differential Equation) of the 3DOF longitudinal AHV flight dynamic model, given by the Eqs. (1)–(5) using [11], are used for the bifurcation method analysis. The nonlinear behavior of the AHV with complicated aerodynamic model, large flight envelop and with strong dynamic coupling gives a reasonable way to implement and apply the bifurcation technique.

The bifurcation method uses first order ODE's represented by,  $\dot{x} = f(x, u)$ , to determine the steady states for the nonlinear systems. The method uses CBA (Continuation Based Algorithm) to determine the all-possible trim equilibrium points using the software platform AUTO-07p from [12]. The CBA computes, all potential trim solutions for the system while the other control parameters are held constant and by adjusting the free control parameter. At each of the trim points, the CBA computes the local stability information. The Bifurcation Diagram provides two-dimensional depiction with calculated trim results with the function in the variable control parameter that depicts the system's overall behavior. Bifurcation Points are the stability points where trim points calculated change with each calculation. These points resemble the movements of the eigenvalues from LHS to RHS in the complex plane, indicating and representing the dynamic behavior of the system stability as unstable in nature.

### 3 Bifurcation Method Study of 3DOF AHV Model

The 3DOF longitudinal nonlinear AHV model from [13] is considered for the Bifurcation methodology implementation with the nonlinear dynamic model given by the Eqs. (1)–(5). The geometric and aerodynamic data of the AHV model is used from [13], for the development of the nonlinear aerodynamic model. The aerodynamic model developed from [14] provides changes with Mach Number and with angle-of-attack for the entire AHV flight band. The propulsion model from [14] is considered here, which is combination of the engine of turbojet, ramjet and scramjet, and rocket for the complete AHV flight. The atmosphere model considering the altitude effects for the temperature and air density from [15] is considered for the AHV model. Combining the all-sub models, and the 3DOF AHV dynamic model given by the Eqs. (1)–(5) are combined and developed as 3DOF AHV longitudinal model for the bifurcation analysis. Bifurcation with SBA is implemented with the AHV model with states considered as  $x = [V \ \alpha \ q \ \theta \ h]$  with the elevator deflection considered as input given by  $u = [\delta_e]$  and PLA (pilot lever angle) is used as the parameter  $p = [\text{PLA}]$ . Here the velocity term  $V$ , of the AHV is used as  $M$ , called as Mach number, which is obtained by the ratio of the velocity to the speed of sound. The angle-of-attack of the AHV is directly affected by the parameter, and the parameters in the SBA analysis are fixed during the simulation run. For SBA implementation to this model, the results are depicted in the terms of Bifurcation Diagram (BD) which provides in interpreting and illustrating the AHV dynamic behavior. Bifurcation with EBA is applied with the longitudinal AHV model with the dynamics given by the Eqs. (1)–(5), for the level, climb/decent and straight flight paths.

$$m\dot{V} = (T\cos\alpha - F_y - mg\sin\theta) \quad (1)$$

$$mV\dot{\alpha} = mVq - (T\sin\alpha + F_x - mg\cos\theta) \quad (2)$$

$$I_{yy}\dot{q} = M_y \quad (3)$$

$$\dot{\theta} = q \quad (4)$$

$$\dot{h} = V\sin\theta \quad (5)$$

To initiate or run the developed AUTO-07p code, we need the initial, equilibrium or starting values for the bifurcation or simulation to run. For this the equilibrium values are obtained by solving the Eqs. (1)–(5), by equating the LHS of the Eqs. (1)–(5) to zero and solving for the state values. These equilibrium values are needed for the bifurcation to implement SBA and to start the simulation or to run the code. In order to simplify the calculation  $\alpha = \theta = 0$ , and the equilibrium solution is obtained for the different Mach number,  $M$  and the altitude  $h = h_0$ , and the state equilibrium solution is obtained and is given by the Eqs. (6)–(8).

$$T(h_0) = \bar{q}SC_D \quad (6)$$

$$V_0 = \bar{q}SC_L/(mg) \quad (7)$$

$$M_y = 0 \quad (8)$$

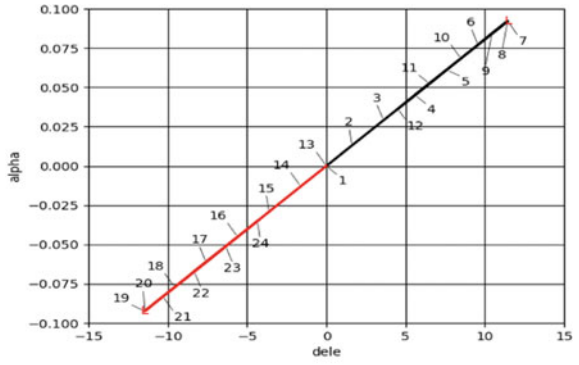
Here the term  $m$ ,  $\bar{q}$ ,  $S$ ,  $T$  are the vehicle mass, dynamic pressure, reference area and vehicle thrust. And  $C_D$  and  $C_L$ , are the aerodynamic coefficient and  $M_y$  is the pitching moment. Using the solution, given by the Eqs. (6)–(8), the drag term is made equivalent to the thrust term, and this results in the initial thrust value which can be used for the initial run. And similarly, the  $V_0$  start value for the initial run is used by the above relation  $h = h_0$ . Hence the bifurcation is carried with the states as  $\alpha$ ,  $q$  and  $\theta$ , considering the other states as fixed and constant value for the whole bifurcation run.

The different bifurcation diagrams are obtained employing the bifurcation using CBA, and all the potential trims of the AHV are computed. Using AUTO-07p, the CBA method is used to compute different trims and elevator deflection,  $\delta_e$  is varied in order to commence the continuation of the numerical simulation. Each of the bifurcation diagrams below shows the collection of equilibrium points that corresponds to the value of the specified parameter for each example. There is not at all variation with the state variables for any of the places on the curve where these solution branches are formed. When the Bifurcation Diagram is created for AUTO-07p platform, it provides altogether information of trim points in each variation with input variables. In this case, negative and positive eigen values represent the stability and instability of the dynamic system.

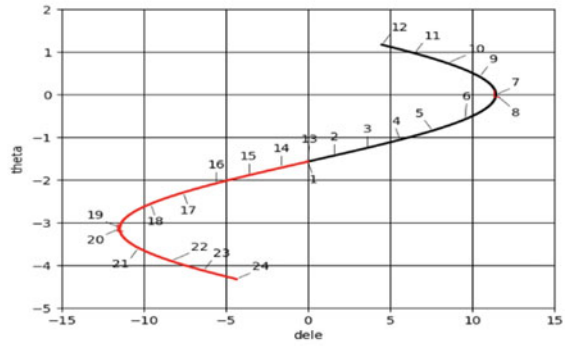
## 4 Bifurcation Results

Bifurcation analysis for the AHV at Mach number,  $M = 0.9$  and altitude,  $h = 10,000$  ft, is carried out and the Bifurcation Diagram obtained is shown in the Fig. 2, it illustrates how the equilibrium solution point shifts between  $-12^\circ$  and  $12^\circ$  deflections when the elevator deflection,  $\delta_e$  value changes. The AHV stability and bifurcation is examined by focusing on varying the value of the system parameter  $\delta_e$  and making another parameter, thrust coefficient constant. Implementing the AUTO-07p code, we observe the numerous bifurcations occurrences for the AHV's states in consideration to the parameter variation. Here the angle-of-attack,  $\alpha$  given in the Fig. 2a, when deflected for  $\delta_e$  from  $0^\circ$  to  $12^\circ$  degrees, it indicates stable behaviour for the vehicle, and when deflected from  $0^\circ$  to  $-12^\circ$  degrees down it shows stable action. The pitch angle,  $\theta$  as shown in the Fig. 2b, for the elevator deflection,  $\delta_e$ ,  $0^\circ$  to  $-12^\circ$  degrees the variation is stable between  $-4.5$  to  $1.5$  radians and for the  $-1.5$  to  $-4.25$  radians. At each of the 24 possible equilibrium points, AUTO-07p generates result demonstrating stable dynamics for all the eigenvalues. For the pitch angle,  $\theta$ , from the bifurcation

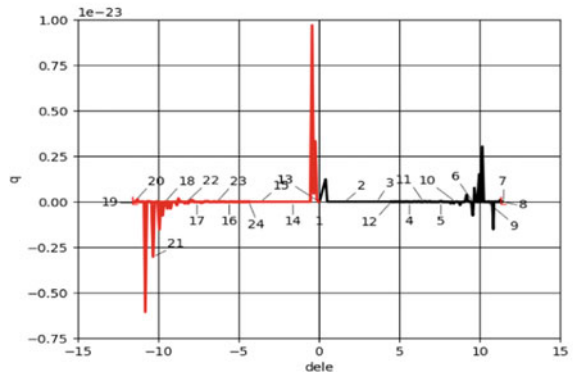
**Fig. 2** Bifurcation diagram for  $M = 0.9$



**(a)** Angle of attack with  $\delta_e$  variation



**(b)** Pitch with  $\delta_e$  variation



**(c)** Pitch rate with  $\delta_e$  variation

diagram, the points 7 and 8 in the Fig. 2b show the nose going up, whereas points 19 and 20 show the nose going down. And for the elevator deflection  $5^\circ$ , the vehicle will have  $60^\circ$  nose-down and  $60^\circ$  nose-up directional changes at various periods of the vehicle’s climb or fall. The pitch rate,  $q$  as shown in the Fig. 2c, for the elevator deflection,  $\delta_e$ ,  $0^\circ$  to  $-12^\circ$  degrees the variation is stable and when deflected  $\delta_e$  from  $0^\circ$  to  $12^\circ$  degrees, it also indicates stable behaviour for the vehicle, with ranging in a stable magnitude for the  $\delta_e$  change.

Running the AUTO-07p code for the bifurcation of AHV using CBA, we obtain the bifurcation diagram as shown in the Fig. 2. We obtain the simulation results of forward run and backward run for the implemented bifurcation method and is shown in Table 1 and Table 2 respectively. These tabular results show the bifurcation diagram data points for the different runs with iterations, indicating the different values of  $\alpha$ ,  $\theta$  and  $q$ . Here BR, PT, TY and LAB are the Bifurcation Result, Bifurcation Point, Bifurcation Type and Labelled Solution respectively. Here for different range (1 to 200) of PT’s, the forward and backward run are carried out with different iterations and corresponding L2 Norm values for the different selected parameters are determined.

It shows that the result is obtained for 200 different points with different iterations and step size at each AUTO-07p run, with LP bifurcation type is obtained at 121 run; and this indicates the presence of bifurcation point as fold for the ordinary differential equation present in the AHV dynamics.

The eigen values determined from the forward and backward run are shown for the corresponding PT for 1, 121 and 200. This shows the different eigen values with respective to the different iteration and the stability of the AHV with the Bifurcation TY. It shows the presence of Hopf function at PT 1 and Iteration 1; and Fold, BP and Hopf function at PT 121, 200 and Iteration 5, 3; with the eigen values with each iteration. The stability information can be determined with the corresponding each

**Table 1** Bifurcation result with forward run in AUTO-07p

BR	PT	TY	LAB	$\delta_e$ (rad)	L2-Norm	$\alpha$ (rad)	$\theta$ (rad)	$q$
1	1	EP	1	0.00000	1.57080	0.00E+00	- 1.570E+0	0.00E+00
1	20		2	1.61874	1.42901	1.30E-02	- 1.428E+0	2.90E-29
1	40		3	3.61065	1.25028	2.91E-02	- 1.25E+0	9.51E-31
1	60		4	5.60149	1.06042	4.51E-02	- 1.059E+0	- 2.70E-29
1	80		5	7.58995	0.84797	6.11E-02	- 8.46E-01	1.42E-27
1	100		6	9.57201	0.58508	7.71E-02	- 5.79E-01	- 1.191E-26
1	120		7	11.4416	0.09220	9.22E-02	- 3.05E-03	4.91E-27
1	121	LP	8	11.4416	0.09215	9.22E-02	1.38E-05	5.74E-28
1	140		9	10.4622	0.42539	8.43E-02	4.17E-01	7.73E-29
1	160		10	8.48822	0.73837	6.84E-02	7.35E-01	- 2.00E-27
1	180		11	6.50178	0.96809	5.24E-02	9.67E-01	- 4.068E-27
1	200	EP	12	4.51178	1.16626	3.63E-02	1.17E+00	- 2.19E-28

**Table 2** Bifurcation result with backward run in AUTO-07p

BR	PT	TY	LAB	$\delta_e(\text{rad})$	L2-Norm	$\alpha(\text{rad})$	$\theta(\text{rad})$	$q$
1	1	EP	1	0.00E+00	1.57E+00	0.00E+00	- 1.57E+00	0.00E+00
1	20		2	- 1.62E+00	1.71E+00	- 1.30E-02	- 1.71E+00	9.76E-29
1	40		3	- 3.61E+00	1.89E+00	- 2.91E-02	- 1.89E+00	3.47E-29
1	60		4	- 5.60E+00	2.08E+00	- 4.51E-02	- 2.08E+00	7.11E-28
1	80		5	- 7.59E+00	2.30E+00	- 6.11E-02	- 2.29478	- 3.05E-27
1	100		6	- 9.57E+00	2.56E+00	- 0.077102	- 2.55934	- 9.77E-27
1	120		7	- 1.15E+01	3.12E+00	- 0.092300	- 3.11735	- 3.23E-26
1	121	LP	8	- 1.15E+01	3.14E+00	- 0.092327	- 3.14158	- 3.20E-29
1	140		9	- 1.03E+01	3.59E+00	- 0.083054	- 3.59342	- 3.03E-24
1	160		10	- 8.34E+00	3.90E+00	- 0.067136	- 3.89795	- 1.03E-25
1	180		11	- 6.35E+00	4.13E+00	- 0.051132	- 4.12518	- 1.55E-26
1	200	EP	12	- 4.36E+00	4.32E+00	- 3.51E-02	- 4.32E+00	4.09E-27

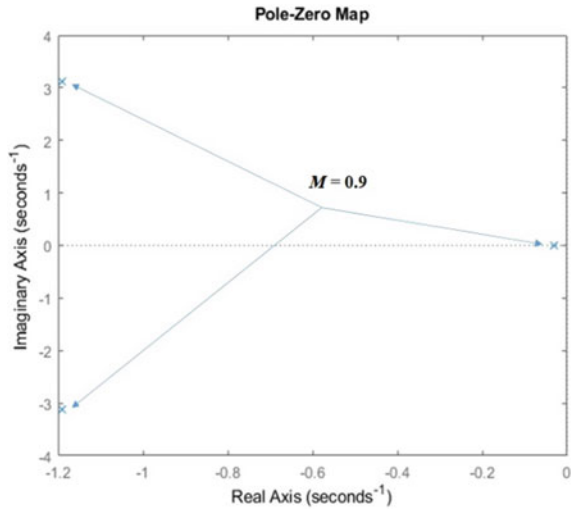
iteration with the eigen values. Considering the trim condition and iteration 1 the eigen values with the dynamic stability information are shown in Table 3 indicating the AHV stability information at the given Mach Number. It shows that there are three eigen values with one eigen value with real number and the two eigen values with complex in nature, as shown in the Table 3; and the corresponding damping ratio and the frequency at the given Mach Number is determined indicating the short period mode behaviour of the AHV.

For the eigen values considered the pole-zero plot is obtained and is shown in the Fig. 3, which outlines the stable behaviour of the AHV at the Mach Number,  $M = 0.9$  as all the poles lying at the LHS plane of the stability axis. Thus, it can be said that using the Bifurcation Method the AHV’s dynamically stability can be determined and at  $M = 0.9$  it is dynamically stable. Considering the simulation carried out for the AHV at the Mach Number,  $M = 0.9$  it shows, most stable behavior for it, using the Bifurcation Method; and their bifurcation diagrams are nonlinear in nature but are mirror images in the vertical plane and about  $\delta_e = 0^\circ$ . This shows that for the different Mach number of the AHV’s flight can be considered to determine the dynamical stability of the vehicle ranging from Mach number,  $M = 0$  to 24.

**Table 3** Dynamic stability using Bifurcation analysis for Mach Number,  $M = 0.9$

Mach No. ( $M$ )	Eigen values	Damping ratio ( $\zeta$ )	Frequency ( $\omega_n$ )	Stability
	- 3.05831E-02			
	- 1.19248E+00			
0.9	3.12365E+00	0.356	3.342	Dynamically
	- 1.19248E+00			Stable
	- 3.12365E+00			

**Fig. 3** Pole-zero plot for Mach Number,  $M = 0.9$



## 5 Conclusion

Bifurcation analysis of Longitudinal dynamics for Generic AHV model considering CBA has been implemented for AHV dynamics at Mach Number,  $M = 0.9$ , for different choices of elevator deflection and with the aim to observe the control effects. Bifurcation technique is implemented with the 3DOF longitudinal AHV model using the AUTO-07p platform for the different elevator deflection,  $\delta_e = -12^\circ$  and  $12^\circ$ . The Bifurcation Diagram obtained for the data points with different forward and backward runs with the different iterations, shows the parameter values of  $\alpha$ ,  $\theta$  and  $q$ . The forward and backward run shows the presence of Hopf function at PT 1 with iteration 1, and Fold, BP and Hopf function at PT 121, 200 and iteration 5, 3; with the eigen values with each iteration. The stability information is determined with the corresponding iteration of the eigen values, showing the dynamic stability information. The eigen values determined, indicate the short period mode behaviour of the AHV indicating the stable behaviour at the Mach Number. The Method shows the AHV's dynamically stability determined at  $M = 0.9$  is stable. This shows that for the different Mach Number of the AHV's flight, Bifurcation is promising method to determine the dynamical stability of the vehicle for the Mach number ranging from  $M = 0$  to 24. Finally, the paper outlines Bifurcation Methodology application intended for the investigation of the dynamic stability of the Generic AHV.



## References

1. Carroll, J.V., Mehra, R.K.: Bifurcation analysis of nonlinear aircraft dynamics. *J. Guid. Control. Dyn.* **5**(5), 529–536 (1982)
2. Zagainov, G.I., Goman, M.G.: Bifurcation analysis of critical aircraft flight regime. *Int. Council. Aeronaut. Sci.* 217–223 (1984)
3. Jahnke, C.C., Culick, F.E.C.: Application of bifurcation theory to the high-angle-of-attack dynamics of the F-14. *J. Aircr.* **31**(1), 26–34 (1994)
4. Guicheteau, P.: Bifurcation theory a tool for nonlinear flight dynamics. *Philos. Trans. R. Soc. Lond. Ser. A* **356**(1745), 2181–2201 (1998)
5. Goman, M.G., Zagainov, G.I., Khramtsovsky, A.V.: Application of bifurcation methods to nonlinear flight dynamics problems. *Prog. Aerosp. Sci. (Elsevier)* **33**(9–10), 539–586 (1997)
6. Khatri, A.K., Singh, J., Sinha, N.K.: Aircraft design using constrained bifurcation and continuation method. *J. Aircr. AIAA* **51**(5), 1647–1652 (2014)
7. Thomas, S., Kwatny, H.G., Chang, B.C.: Bifurcation analysis of flight control systems. In: 16th Triennial World Congress, IFAC, Elsevier, Czech Republic (2005)
8. Khatri, A.K., Singh, J., Sinha, N.K.: Aircraft maneuver design using bifurcation analysis and sliding mode control techniques. *J. Guid. Control Dyn. AIAA* **35**(5), 1435–1449 (2012)
9. Prakash, O., Singh, R.: Flight dynamics analysis using high altitude & mach number for generic air-breathing hypersonic vehicle. In: AIAA 2021-3271, AIAA Propulsion and Energy 2021 Forum, Virtual Event USA (2021)
10. Shaughnessy, J.D., Pinckney, S.Z., Mcminn, J.D., Cruz, C.I., Kelley, M.L.: Hypersonic vehicle simulation model: Winged-cone configuration. NASA Langley Research Center, NASA-TM-102610, United States (1990)
11. Keshmiri, S., Colgren, R., Mirmirani, M.: Six DoF nonlinear equations of motion for a generic hypersonic vehicle. In: AIAA Atmospheric Flight Mechanics Conference and Exhibit, AIAA, Hilton Head, South Carolina (2007)
12. Doedel, E.J., Champneys, A.R., Fairgrieve, T.F., Kuznetsov, Y.A., Sandstede, B., Xang, X.: AUTO-07p: continuation and bifurcation software for ordinary differential equations. Ver. AUTO-07p 2007, Department of Computer Science, Concordia University, Montreal, Canada (2007)
13. Keshmiri, S., Colgren, R., Mirmirani, M.: Six-DOF modeling and simulation of a generic hypersonic vehicle for control and navigation purposes. In: AIAA Guidance, Navigation, and Control Conference and Exhibit, AIAA, Keystone, Colorado (2006)
14. Keshmiri, S., Colgren, R., Mirmirani, M.: Development of an aerodynamic database for a generic hypersonic air vehicle. In: AIAA Guidance, Navigation, and Control Conference and Exhibit, AIAA, San Francisco, California (2005)
15. Roskam, J., Lan, C.T.: *Airplane Aerodynamics and Performance*, Revised Darcorporation, Lawrence, Kansas (2000)

# Multi-soliton Solutions of the Gardner Equation Using Darboux Transformation



Dipan Saha , Santanu Raut , and Prasanta Chatterjee 

**Abstract** The Gardner equation is a particular version of the extended Korteweg-de Vries (KdV) equation which presents actually the same type of characters as the standard KdV model, but it extends the range of validity to a larger domain of the parameters of the wave motion for a dynamic system. The purpose of this article is to explore a new type of multi-soliton solutions for the Gardner equation. To confirm its integrability, first, we will construct the Lax pair of the Gardner equation using Ablowitz–Kaup–Newell–Segur (AKNS) approach and finally, derive the one-soliton and two-soliton wave solutions for the Gardner equation employing the Darboux transformation method (DTM). These solutions can be extended to the generalized multi-solitary for the Gardner equation by repetition of the transformation. Some numerical graphs of one-soliton and two-soliton solutions are drawn for a clear understanding of wave motion under Gardner equation.

**Keywords** Gardner equation · Wave motion · Multi-soliton solutions · Lax pair · Darboux transformation method

## 1 Introduction

For the last few decades, nonlinear evolution equations (NLEEs) have paid a lot of interest due to their wide applications in different branches of science and engineering fields. For instance, NLEEs are substantially employed to formulate distinct problems from fluid mechanics [1, 2], plasma physics [3–5], quantum field theory, quantum mechanics [6, 7], propagation of shallow water waves [8, 9], chemical kinetics etc.

---

D. Saha (✉)

Advanced Centre for Nonlinear and Complex Phenomena, Kolkata, India  
e-mail: [dipansaha12345@gmail.com](mailto:dipansaha12345@gmail.com)

S. Raut

Department of Mathematics, Mathabhanga College, Coochbehar 736146, India

P. Chatterjee

Siksha Bhavana, Visva-Bharati, Santiniketan 731235, India

The classical Korteweg-De Vries (KdV) equation is a particular type of generic evolutionary partial differential equation which was actually addressed by Boussinesq (A) and again rediscovered by the famous Dutch mathematician Diederik Johannes Korteweg (31 March 1848–10 May 1941) and his pupil Gustav de Vries (22 January 1866-16 December 1934). KdV equation is a solvable nonlinear model which may be exactly solved by using different analytical techniques such as, Inverse scattering transform method, Backlund transformation, Hirota's bilinear approach etc. In particular, the standard KdV equation is extensively used to model weakly nonlinear long waves. Many important nonlinear features, especially, in internal unsteady internal waves in oceanic water are explored through the KdV model. In remote sensing experiments and situ measurements, it was observed that long solitary type waves are commonly appeared in density layered shallow water. But, a number of experimental observations confirm that although the KdV model effectively defines the solitary waves for a vast range of parameters however there may arise some situations when the KdV framework miserably fails, for instance as, the critical values of a particular parameter which causes the dismiss of the coefficient of the nonlinear term in the said equation. To overcome this type of difficulty, it becomes necessary to extend the KdV equation by incorporating higher-order nonlinearity instead of quadratic nonlinearity. Often, these models become meaningful in the diverse fields of applications. Considering dual nonlinearity in the KdV model, the Gardner equation arises, which claims the validity to the larger parametric zone for internal wave motion in the different physical environment. The introduction of this equation is attributed to the famous mathematician Clifford Gardner in 1968 [10]. Some excellent works on Gardner mode for modeling of internal wave in the extensive parametric domain can be found in [11]. Gardner equation is actually combination form of KdV equation and modified KdV (mKdV) equation. The Gardner equation, or the combined KdV-mKdV equation, reads

$$u_t + auu_x + bu^2u_x + cu_{xxx} = 0, \quad (1)$$

where  $u(x, t)$  presents the amplitude of the wave model and evaluates the time of the virtual displacement over the isopycnal surface,  $x$  signifies the scaled space variable along the direction of wave mode and  $t$  determines the scaled time.  $a$  and  $b$  are the coefficients of the quadratic and cubic nonlinear terms respectively whereas  $c$  presents a dispersive effect. In the present investigation, the constants  $a, b, c$  are taken as  $a = k_1c, b = k_2c$  ( $k_1, k_2$  are non-zero constants).

Many powerful methods, like Backlund transformation method [12], Inverse scattering transform method [13], Hirota method [14], pseudo spectral method [15], the tanh-sech method [16], Exp-function method [17] and the sine-cosine method [18] are used to investigate these types of equations. The Darboux transformation method (DTM) [19] is one of the most powerful and fruitful method for getting explicit solutions, which we will use in our present work.

So the outline of the present paper is as follows. In Sect. 2, we construct Lax pair of Eq. (1). Section 3 is approved for presenting the Darboux transformation of our proposed model. In Sects. 3.1 and 3.2, one-soliton and two-soliton solutions of the Gardner equation are explored respectively. Finally, the conclusions are briefly outlined in Sect. 5.

## 2 Lax Pair

In order to verify the integrability condition of a nonlinear partial differential equation, the Lax pair of a given equation is constructed. By Lax pair, we mean a set of two operators that, if they exist, implies that a nonlinear evolution equation is integrable. There is no general technique for finding the Lax pair of an integrable system. Gardner equation belongs to the class of integrable system. According to the AKNS approach [20], Lax pair of Eq. (1) is given by

$$\psi_x = U\psi = \begin{pmatrix} \lambda & u \\ -\frac{1}{6}(k_2u + k_1) & -\lambda \end{pmatrix} \psi, \tag{2}$$

$$\psi_t = V\psi = \begin{pmatrix} A & B \\ C & -A \end{pmatrix} \psi, \tag{3}$$

where

$$\begin{aligned} A &= -4c\lambda^3 - \frac{1}{3}c(k_2u^2 + k_1u)\lambda - \frac{1}{6}k_1cu_x, \\ B &= -(4cu\lambda^2 + 2cu_x\lambda + \frac{1}{3}k_2cu^3 + \frac{1}{3}k_1cu^2 + cu_{xx}), \\ C &= \frac{2}{3}c(k_1 + k_2u)\lambda^2 - \frac{1}{3}k_2cu_x\lambda + \frac{1}{18}k_2^2cu^3 + \frac{1}{9}k_1k_2cu^2 \\ &\quad + \frac{1}{18}k_1^2cu + \frac{1}{6}k_2cu_{xx}. \end{aligned}$$

Here  $\lambda$  is a parameter independent of  $x$  and  $t$ . The Lax equation is

$$U_t - V_x + [U, V] = 0,$$

which is equivalent to Eq. (1).

### 3 Construction of Darboux Transformation (DT) and Soliton Solutions of Gardner Equation

In the late 1970s, V. B. Matveev showed that the spectral problem of second-order ordinary differential equations may be improved to some important soliton equations employing a technique addressed by G. Darboux about a century ago. This method is popularly known as DTM. A number of examples for describing the continuous and discrete spectrum management in quantum mechanics are demonstrated in [21, 22] where the elementary DT and binary DT (also known as twofold elementary DT) are expressed in detail. It is also found that the  $n$ -fold Darboux transformation [23] is a  $2 \times 2$  matrix for the Kaup–Newell (KN) system. Employing  $n$ -fold DT, various types of wave solutions of the nonlinear Schrodinger (DNLS) equation, such as, periodic solution, rational traveling solution, breather solution, rogue wave, dark soliton, bright soliton, are derived explicitly from the different seed solutions. In particular, Darboux transformation provides new route to study the generalized Sawada–Kotera (SK) equation [24], the generalized TD equation, Kadomtsev–Petviashvili (KP) equation [25], the Gerdjikov–Ivanov (GI) equation etc. Here, we will employ the Darboux transformation to get multi-soliton solutions from an old solution of the Gardner equation. Starting with the trivial solution  $u = 0$  of the Gardner equation (1), one can use the Darboux transformation to obtain the soliton solutions. For  $u = 0$ , the fundamental solution of the Lax pair can be obtained as

$$\psi(x, t, \lambda) = \begin{pmatrix} e^{-4c\lambda^3 t + \lambda x} & 0 \\ e^{\frac{2}{3}ck_1\lambda^2 t + \lambda x} & e^{4c\lambda^3 t - \lambda x} \end{pmatrix} \tag{4}$$

by integrating (3). Let  $\lambda_1, \sigma_1$  be arbitrary real numbers and let

$$\gamma = \frac{e^{4c\lambda_1^3 t - \lambda_1 x} + \sigma_1 e^{\frac{2}{3}ck_1\lambda_1^2 t + \lambda_1 x}}{0 + \sigma_1 \cdot e^{-4c\lambda_1^3 t + \lambda_1 x}} \tag{5}$$

Take  $\lambda_1 \neq 0$  and  $\sigma_1 = \exp(-2\mu_1) > 0$ , then (5) becomes

$$\gamma = \gamma_1 = e^{2\mu_1 + 8c\lambda_1^3 t - 2\lambda_1 x} + e^{\frac{2}{3}ck_1\lambda_1^2 t + 4c\lambda_1^3 t}. \tag{6}$$

Now consider the gauge transformation

$$\bar{\psi}(x, t, \lambda) = D(x, t, \lambda)\psi(x, t, \lambda), \tag{7}$$

where

$$D(x, t, \lambda) = \lambda I_2 - \frac{\lambda_1}{1 + \gamma^2} \begin{pmatrix} 1 - \gamma^2 & 2\gamma \\ 2\gamma & \gamma^2 - 1 \end{pmatrix}. \tag{8}$$

For such transformation, the spectral problems (2) and (3) are transformed into

$$\bar{\psi}_x = \bar{U}\bar{\psi}, \quad \bar{\psi}_t = \bar{V}\bar{\psi}, \tag{9}$$

where

$$\bar{U} = \begin{pmatrix} \lambda & u_1 \\ -\frac{1}{6}(k_2u_1 + k_1) & -\lambda \end{pmatrix},$$

$$\bar{V} = \begin{pmatrix} \bar{A} & \bar{B} \\ \bar{C} & -\bar{A} \end{pmatrix},$$

with

$$u_1 = u + \frac{4\lambda_1\gamma}{1 + \gamma^2}, \tag{10}$$

$$\bar{A} = -4c\lambda^3 - \frac{1}{3}c(k_2u_1^2 + k_1u_1)\lambda - \frac{1}{6}k_1cu_{1x},$$

$$\bar{B} = -(4cu_1\lambda^2 + 2cu_{1x}\lambda + \frac{1}{3}k_2cu_1^3 + \frac{1}{3}k_1cu_1^2 + cu_{1xx}),$$

$$\bar{C} = \frac{2}{3}c(k_1 + k_2u_1)\lambda^2 - \frac{1}{3}k_2cu_{1x}\lambda + \frac{1}{18}k_2^2cu_1^3 + \frac{1}{9}k_1k_2cu_1^2$$

$$+ \frac{1}{18}k_1^2cu_1 + \frac{1}{6}k_2cu_{1xx}.$$

### 3.1 One-Soliton Solution

A solitary wave is a localized “wave of translation” that arises from a balance between nonlinear and dispersive effects; and also preserves its shape upon collision. The ultimate aim of the present investigation is to finding solitary waves solution for the Gardner model and for this purpose we set,  $v_1 = 2\lambda_1x - 8c\lambda_1^3t - 2\mu_1$  and  $v_2 = -\frac{2}{3}ck_1\lambda_1^2t - 4c\lambda_1^3t$ . Then from Eq. (6),  $\gamma = \gamma_1 = e^{-v_1} + e^{-v_2}$ .

By substituting this value of  $\gamma$  in (10), we obtain

$$u_1 = 0 + \frac{4\lambda_1(e^{-v_1} + e^{-v_2})}{1 + e^{-2v_1} + e^{-2v_2} + 2e^{-v_1-v_2}}$$

The equation

$$u_1 = \frac{4\lambda_1(e^{-v_1} + e^{-v_2})}{1 + e^{-2v_1} + e^{-2v_2} + 2e^{-v_1-v_2}} \tag{11}$$

is taken as the one-soliton solution of the Gardner equation.

### 3.2 Two-Soliton solution

Now if we take  $u_1$  as a seed solution, a new Darboux matrix can be constructed from  $\bar{\psi} = (\bar{\psi}_{ij})$  and a series of new solutions of the Gardner equation can be obtained.

Take constants  $\lambda_2 \neq 0$  ( $\lambda_2 \neq \lambda_1$ ) and  $\sigma_2 = \exp(-2\mu_2)$ . According to (5),

$$\bar{\gamma}_2 = \frac{\bar{\psi}_{22}(x, t, \lambda_2) + \sigma_2 \bar{\psi}_{21}(x, t, \lambda_2)}{\bar{\psi}_{12}(x, t, \lambda_2) + \sigma_2 \bar{\psi}_{11}(x, t, \lambda_2)}. \tag{12}$$

Substituting  $\bar{\psi} = D\psi = \begin{pmatrix} D_{11} & D_{12} \\ D_{21} & D_{22} \end{pmatrix} \begin{pmatrix} \psi_{11} & \psi_{12} \\ \psi_{21} & \psi_{22} \end{pmatrix}$  into Eq. (12), we have

$$\begin{aligned} \bar{\gamma}_2 &= \frac{(D_{21}\psi_{12} + D_{22}\psi_{22}) + \sigma_2(D_{21}\psi_{11} + D_{22}\psi_{21})}{(D_{11}\psi_{12} + D_{12}\psi_{22}) + \sigma_2(D_{11}\psi_{11} + D_{12}\psi_{21})} \Big|_{\lambda=\lambda_2} \\ &= \frac{D_{21}(\psi_{12} + \sigma_2\psi_{11}) + D_{22}(\psi_{22} + \sigma_2\psi_{21})}{D_{11}(\psi_{12} + \sigma_2\psi_{11}) + D_{12}(\psi_{22} + \sigma_2\psi_{21})} \Big|_{\lambda=\lambda_2} \\ &= \frac{D_{21} + D_{22} \frac{(\psi_{22} + \sigma_2\psi_{21})}{(\psi_{12} + \sigma_2\psi_{11})}}{D_{11} + D_{12} \frac{(\psi_{22} + \sigma_2\psi_{21})}{(\psi_{12} + \sigma_2\psi_{11})}} \Big|_{\lambda=\lambda_2} \\ &= \frac{D_{21} + D_{22}\gamma_2}{D_{11} + D_{12}\gamma_2} \Big|_{\lambda=\lambda_2}, \end{aligned} \tag{13}$$

where

$$\gamma_2 = \frac{\psi_{22}(x, t, \lambda_2) + \sigma_2 \psi_{21}(x, t, \lambda_2)}{\psi_{12}(x, t, \lambda_2) + \sigma_2 \psi_{11}(x, t, \lambda_2)}. \tag{14}$$

Using  $\gamma = e^{-v_1} + e^{-v_2}$  in (8) and using (4), from (7), we obtain

$$\bar{\psi}(x, t, \lambda) = \begin{pmatrix} \bar{\psi}_{11} & \bar{\psi}_{12} \\ \bar{\psi}_{21} & \bar{\psi}_{22} \end{pmatrix} = \frac{1}{L} \begin{pmatrix} P & Q \\ R & S \end{pmatrix}, \tag{15}$$

where

$$\begin{aligned} L &= 1 + e^{-2v_1} + e^{-2v_2} + 2e^{-v_1-v_2}, \\ P &= e^{-4c\lambda^3 t + \lambda x} (\lambda - \lambda_1) + e^{-4c\lambda^3 t + \lambda x} (\lambda + \lambda_1) (e^{-2v_1} + e^{-2v_2} + 2e^{-v_1-v_2}) \\ &\quad - 2\lambda_1 e^{\frac{2}{3}ck_1\lambda^2 t + \lambda x} (e^{-v_1} + e^{-v_2}), \\ Q &= -2\lambda_1 e^{4c\lambda^3 t - \lambda x} (e^{-v_1} + e^{-v_2}), \\ R &= -2\lambda_1 e^{-4c\lambda^3 t + \lambda x} (e^{-v_1} + e^{-v_2}) + e^{\frac{2}{3}ck_1\lambda^2 t + \lambda x} (\lambda + \lambda_1) \\ &\quad + e^{\frac{2}{3}ck_1\lambda^2 t + \lambda x} (\lambda - \lambda_1) (e^{-2v_1} + e^{-2v_2} + 2e^{-v_1-v_2}), \\ S &= e^{4c\lambda^3 t - \lambda x} (\lambda + \lambda_1) + e^{4c\lambda^3 t - \lambda x} (\lambda - \lambda_1) (e^{-2v_1} + e^{-2v_2} + 2e^{-v_1-v_2}) \end{aligned}$$

and hence from Eq. (12), we have

$$\bar{\gamma}_2 = \frac{X}{Y}, \tag{16}$$

where

$$\begin{aligned} X &= \frac{1}{L} [e^{4c\lambda_2^3 t - \lambda_2 x} (\lambda_2 + \lambda_1) \\ &\quad + e^{4c\lambda_2^3 t - \lambda_2 x} (\lambda_2 - \lambda_1) (e^{-2v_1} + e^{-2v_2} + 2e^{-v_1 - v_2}) \\ &\quad + e^{-2\mu_2} \{-2\lambda_1 e^{-4c\lambda_2^3 t + \lambda_2 x} (e^{-v_1} + e^{-v_2}) + e^{\frac{2}{3}ck_1\lambda_2^2 t + \lambda_2 x} (\lambda_2 + \lambda_1) \\ &\quad + e^{\frac{2}{3}ck_1\lambda_2^2 t + \lambda_2 x} (\lambda_2 - \lambda_1) (e^{-2v_1} + e^{-2v_2} + 2e^{-v_1 - v_2})\}], \\ Y &= \frac{1}{L} [-2\lambda_1 e^{4c\lambda_2^3 t - \lambda_2 x} (e^{-v_1} + e^{-v_2}) \\ &\quad + e^{-2\mu_2} \{e^{-4c\lambda_2^3 t + \lambda_2 x} (\lambda_2 - \lambda_1) \\ &\quad + e^{-4c\lambda_2^3 t + \lambda_2 x} (\lambda_2 + \lambda_1) (e^{-2v_1} + e^{-2v_2} + 2e^{-v_1 - v_2}) \\ &\quad - 2\lambda_1 e^{\frac{2}{3}ck_1\lambda_2^2 t + \lambda_2 x} (e^{-v_1} + e^{-v_2})\}]. \end{aligned}$$

Let,  $v_3 = \mu_2 + 4c\lambda_2^3 t - \lambda_2 x$ ,  $v_4 = \mu_2 + 2c\lambda_2^3 t - \frac{1}{3}ck_1\lambda_2^2 t - \lambda_2 x$ . (17)

Then by simple calculations from Eq. (16), we have

$$\bar{\gamma}_2 = \frac{\bar{X}}{\bar{Y}}, \tag{18}$$

where

$$\begin{aligned} \bar{X} &= (\lambda_2 + \lambda_1) + (\lambda_2 - \lambda_1) (e^{-2v_1} + e^{-2v_2} + 2e^{-v_1 - v_2}) \\ &\quad - 2\lambda_1 e^{-2v_3} (e^{-v_1} + e^{-v_2}) \\ &\quad + e^{-2v_4} (\lambda_2 + \lambda_1) + e^{-2v_4} (\lambda_2 - \lambda_1) (e^{-2v_1} + e^{-2v_2} + 2e^{-v_1 - v_2}), \\ \bar{Y} &= -2\lambda_1 (e^{-v_1} + e^{-v_2}) + e^{-2v_3} (\lambda_2 - \lambda_1) \\ &\quad + e^{-2v_3} (\lambda_2 + \lambda_1) (e^{-2v_1} + e^{-2v_2} + 2e^{-v_1 - v_2}) \\ &\quad - 2\lambda_1 e^{-2v_4} (e^{-v_1} + e^{-v_2}). \end{aligned}$$

According to Eq. (10),

$$u_2 = u_1 + \frac{4\lambda_2 \bar{\gamma}_2}{1 + \bar{\gamma}_2^2}$$

$$\boxed{u_2 = \frac{4\lambda_1 (e^{-v_1} + e^{-v_2})}{1 + e^{-2v_1} + e^{-2v_2} + 2e^{-v_1 - v_2}} + \frac{4\lambda_2 \bar{\gamma}_2}{1 + \bar{\gamma}_2^2}}, \tag{19}$$



where  $\bar{\gamma}_2$  is given by Eq. (18). Equation (19) is a new solution of the Gardner equation, which is taken as the two-soliton solution of the Gardner equation. Proceeding in this way finally we obtain multi-soliton solutions of the Gardner equation, but the problem is that the calculation is too tedious.

### 4 Result and Discussion

We discuss the dynamics of exact solutions (11) and (19). Some of the furnished solutions in this paper are depicted graphically for their physical appearance which stands for different types of soliton, like, kink type soliton, bell-type soliton, two kink type soliton, etc. Figure 1a, b are showing distorted kink type soliton solutions. It is interesting to note that a small transition from kink profile to bell profile follows in Fig. 1b. Figure 1c, d indicates the propagation of bell soliton in space-time domain. On the other hand, Fig. 2a shows the interaction of a kink and a solitary wave. Figure 2b signifies the interaction of two kinks and one solitary wave via the Eq. (19). This type of nonlinear phenomenon appeases due to the presence of quadratic and cubic nonlinearity along with the Burgers term. After interaction two kink waves appear, which are moving with different amplitudes as shown in Fig. 2c, d.

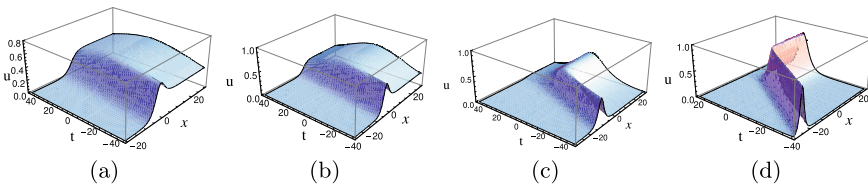


**Fig. 1** 3D profiles of the solution (11), **a** when  $\lambda_1 = 0.25; c = 0.25; \mu_1 = 0.5; k_1 = 0.5$ ; **b** when  $\lambda_1 = 0.3; c = 0.25; \mu_1 = 0.5; k_1 = 0.5$ ; **c** when  $\lambda_1 = 0.25; c = 1; \mu_1 = 0.5; k_1 = 0.5$ ; **d** when  $\lambda_1 = 0.4; c = 1; \mu_1 = 0.5; k_1 = 0.5$

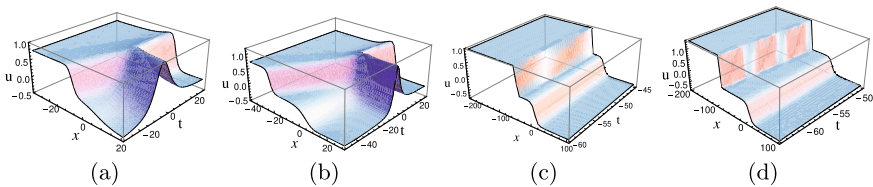


**Fig. 2** 3D Interaction of the two-soliton via solution (19) for **a** when  $\lambda_1 = 0.5; c = 0.43; \mu_1 = 0.5; k_1 = 0.5; \mu_2 = 0.5; \lambda_2 = 0.4$ ; **b** when  $\lambda_1 = 0.12; c = 0.8; \mu_1 = 0.5; k_1 = 0.25; \mu_2 = 0.5; \lambda_2 = 0.4$ ; **c** when  $\lambda_1 = 0.1; c = 0.8; \mu_1 = 0.5; k_1 = 0.5; \mu_2 = 0.5; \lambda_2 = 0.5$ ; **d** when  $\lambda_1 = 0.1; c = 0.7; \mu_1 = 0.5; k_1 = 0.5; \mu_2 = 0.5; \lambda_2 = 0.7$ .

## 5 Conclusions

The present investigation provides a new class of effective solutions of the Gardner equation which may come as a bell-shaped soliton, kink type soliton, kink bell mixed soliton depending on the choosing of the values of the nonlinear and dispersive coefficients. To the best of our knowledge, for the first time, we derive the solution of the Gardner equation employing DTM. The one-soliton and two-soliton solutions are explicitly explored and repeating the same process,  $n$  folded multi-soliton solutions can be drawn from the previous seed. The obtained solutions acquired in the proposed scheme contain many free parameters and are claimed to be fresh and further general which might bear great importance in the research area. The numerical graphs emphasized that the method utilized in this observation is of significance in nature and the obtained solution could be utilized for modeling many natural phenomena such as wave motion in a plasma environment, water wave in the oceanic platform, etc.

## References

1. Hosseinzadeh, E., Barari, A., Fouladi, F., Domairry, G.D.: Numerical analysis of fourth-order boundary value problems in fluid mechanics and mathematics. *Therm. Sci.* **14**(4), 1101–1109 (2010)
2. Antontsev, S.N., Díaz, J.I., Shmarev, S.: *Energy Methods for Free Boundary Problems: Applications to Nonlinear PDEs and Fluid Mechanics*, vol. 48. Springer Science & Business Media (2012)
3. Saha, A., Pal, N., Chatterjee, P.: Dynamic behavior of ion acoustic waves in electron-positron-ion magnetoplasmas with superthermal electrons and positrons. *Phys. Plasmas* **21**(10), 102101 (2014)
4. Raut, S., Mondal, K.K., Chatterjee, P., Roy, A.: Propagation of dust-ion-acoustic solitary waves for damped modified Kadomtsev–Petviashvili–Burgers equation in dusty plasma with a  $q$ -nonextensive nonthermal electron velocity distribution. *SeMA J.* 1–23 (2021)
5. Raut, S., Mondal, K.K., Chatterjee, P., Roy, A.: Two-dimensional ion-acoustic solitary waves obliquely propagating in a relativistic rotating magnetised electron–positron–ion plasma in the presence of external periodic force. *Pramana* **95**(2), 1–13 (2021)
6. Moshinsky, M.: Canonical transformations and quantum mechanics. *SIAM J. Appl. Math.* **25**(2), 193–212 (1973)
7. Reinisch, G.: Nonlinear quantum mechanics. *Phys. A: Stat. Mech. Appl.* **206**(1–2), 229–252 (1994)
8. Thacker, W.C.: Some exact solutions to the nonlinear shallow-water wave equations. *J. Fluid Mech.* **107**, 499–508 (1981)
9. Kânoğlu, U., Synolakis, C.: Initial value problem solution of nonlinear shallow water-wave equations. *Phys. Rev. Lett.* **97**(14), 148501 (2006)
10. Griffiths, G., Schiesser, W.E.: *Traveling Wave Analysis of Partial Differential Equations: Numerical and Analytical Methods with MATLAB and Maple*. Academic (2010)
11. Holloway, P.E., Pelinovsky, E., Talipova, T.: A generalized Korteweg–de Vries model of internal tide transformation in the coastal zone. *J. Geophys. Res.: Ocean.* **104**(C8), 18333–18350 (1999)
12. Xiao, Z.-J., Tian, B., Zhen, H.-L., Chai, J., Xiao-Yu, W.: Multi-soliton solutions and Bäcklund transformation for a two-mode KDV equation in a fluid. *Waves Random Complex Media* **27**(1), 1–14 (2017)

13. Ji, J.-L., Zhu, Z.-N.: Soliton solutions of an integrable nonlocal modified Korteweg-de Vries equation through inverse scattering transform. *J. Math. Anal. Appl.* **453**(2), 973–984 (2017)
14. Hirota, R.: Exact solution of the Korteweg-de Vries equation for multiple collisions of solitons. *Phys. Rev. Lett.* **27**(18), 1192 (1971)
15. Fornberg, B.: The pseudospectral method: comparisons with finite differences for the elastic wave equation. *Geophysics* **52**(4), 483–501 (1987)
16. Malfliet, W., Hereman, W.: The tanh method: I. Exact solutions of nonlinear evolution and wave equations. *Phys. Scr.* **54**(6), 563 (1996)
17. He, J.-H., Xu-Hong, W.: Exp-function method for nonlinear wave equations. *Chaos Solitons Fractals* **30**(3), 700–708 (2006)
18. Wazwaz, A.-M.: A sine-cosine method for handling nonlinear wave equations. *Math. Comput. Model.* **40**(5–6), 499–508 (2004)
19. Wang, X., Wang, L.: Darboux transformation and nonautonomous solitons for a modified Kadomtsev-Petviashvili equation with variable coefficients. *Comput. & Math. Appl.* **75**(12), 4201–4213 (2018)
20. Liu, L.-J., Yu, X.: Solitons and breathers for nonisospectral mKDV equation with Darboux transformation (2017). [arXiv:1710.05108](https://arxiv.org/abs/1710.05108)
21. Matveev, V.B.: Darboux transformation and explicit solutions of the Kadomtsev-Petviashvili equation, depending on functional parameters. *Lett. Math. Phys.* **3**(3), 213–216 (1979)
22. Doktorov, E.V., Leble, S.B.: *A Dressing Method in Mathematical Physics*, vol. 28. Springer Science & Business Media (2007)
23. Shuwei, X., He, J., Wang, L.: The Darboux transformation of the derivative nonlinear Schrödinger equation. *J. Phys. A: Math. Theor.* **44**(30), 305203 (2011)
24. He, G.L., Su, T.: Darboux transformation and explicit solutions for a generalized Sawada-Kotera equation. *Int. Sch. Res. Not.* **2013** (2013)
25. Nimmo, J.J.C.: Darboux transformations and the discrete KP equation. *J. Phys. A: Math. Gen.* **30**(24), 8693 (1997)

# Optical Dark and Kink Solitons in Multiple Core Couplers with Four Types of Nonlinearity



Anand Kumar, Hitender Kumar, Fakir Chand, Manjeet Singh Gautam, and Ram Mehar Singh

**Abstract** In recent years, solitons in nonlinear couplers have acquired attention of the researchers. The switching of solitons is possible using any optical logic gate. Optical switching is of particular interest due to the possibility of extremely fast switching time within the femtosecond range. In this study the dark and kink type solitons to two different types of optical multiple core couplers with four types of nonlinearities viz Kerr law nonlinearity, power law nonlinearity, parabolic law nonlinearity and dual power-law nonlinearity are extracted using the Kudryashov integration algorithm. Coupling with nearest neighbors is one example, whereas in the other case the coupling with all nearest neighbors is considered. The parametric constraint conditions, also called integrability criteria are emerging with these novel solutions and reported.

## 1 Introduction

Nonlinear optical couplers are crucial appliances that route light from the main fibre in one or more section fibres. Optical couplers have also been employed as limiters and intensity-dependent switches. Optical couplers can be manufactured as planar semiconductor devices or as dual-core single-mode fibres with solitons conveying

---

A. Kumar (✉)

Department of Physics, Chaudhary Ranbir Singh University, Jind 126102, India  
e-mail: [anandkumar@crsu.ac.in](mailto:anandkumar@crsu.ac.in)

H. Kumar

Department of Physics, Government College for Women, Gharaunda 132114, India

F. Chand

Department of Physics, Kurukshetra University, Kurukshetra 136119, India

M. S. Gautam

Department of Physics, Government College, Alewa, Jind 126111, India

R. M. Singh

Department of Physics, Chaudhary Devi Lal University, Sirsa 125055, India

© The Author(s), under exclusive license to Springer Nature Switzerland AG 2022  
S. Banerjee and A. Saha (eds.), *Nonlinear Dynamics and Applications*,  
Springer Proceedings in Complexity,  
[https://doi.org/10.1007/978-3-030-99792-2\\_99](https://doi.org/10.1007/978-3-030-99792-2_99)

1169

in each core. Multiple-core optical fibers can be used with high-powered lasers and all-optical switching between the fiber cores [1].

The study of optical solitons in nonlinear optics has attracted a lot of attention, and it's played a big part in the development of all-optical systems. Studying the dynamical behaviour of propagation of soliton along optical fibers, couplers, dense wavelength division multiplexing (DWDM) systems, metamaterials, and metasurfaces is therefore crucial to improve soliton transmission performance across long-haul optical communication networks. Many efforts have been brought in the latter half of the 19th century to solve the difficulties of optical soliton transmission by appropriate control of the fiber group dispersion. Hasegawa et al. [2] presented adiabatic dispersion control to reduce dispersive wave radiation and collision-induced frequency shift in WDM systems by altering dispersion in percentage to the soliton power. Suzuki et al. [3] utilized non-adiabatic periodic dispersion compensation to minimize integrated dispersion and transmit a 10 Gbit/s soliton signal across the Pacific without using soliton management. Smith et al. [4] shows, even though the dispersion is almost zero, a nonlinear soliton-like pulse exist in a fiber with a periodic modulation of the dispersion. The nonlinearities such as Kerr law, power law, parabolic law, and dual-power law are four forms of nonlinear media used in this investigation. The governing model for multiple core fibers with STD (spatiotemporal dispersion) in addition to the standard GVD (group velocity dispersion) is the nonlinear Schrödinger's equation (NLSE). Hence, it is essential to investigate NLSE in couplers and in fibers with the STD term incorporated. The ansatz technique [5], the Jacobi elliptic function method [7], and other methods [6, 8–10] have all been used to study optical couplers previously.

In this study, we use the Kudryashov approach [11] to handle multiple-core couplers with four different types of nonlinearities, resulting in kink and dark soliton solutions that will serve the soliton community. Kink and dark optical soliton solutions will be found alongside their existing conditions that naturally occur from the solution profiles.

Outlined of the manuscript is given as. The brief idea of Kudryashov method is presented in Sect. 2. Section 3 deals with multiple core couplers with nearest-neighbor coupling for four forms of nonlinearity. In Sect. 4, we extend our study on multiple core couplers coupling with all neighbors for four forms of nonlinearity. Section 5 allotted to graphical results. Finally, conclusions are made in Sect. 6.

## 2 A Succinct Overview of the Kudryashov Method

To present the analysis more coherently, we highlight succinctly the prime aspects of the Kudryashov method.

We acknowledge a nonlinear partial differential equation (PDE), with a physical field  $q$ , which is a function of independent variables  $x, t$  as:

$$R(q_x, q_t, q_{xx}, q_{xt}, q_{tt}, \dots) = 0, \tag{1}$$

where  $R$  is polynomial in  $q(x, t)$  Here, we briefly highlighted the steps of the method:

**Step 1:** By using  $\xi = k(x + vt)$ , Eq. (1) modify to ODE (ordinary differential equation):

$$S(q, q_\xi, q_{\xi\xi}, q_{\xi\xi\xi}, \dots) = 0 \tag{2}$$

**Step 2:** The solution of above equation can be specified in the more general form of physical field  $q(\xi)$  as:

$$q(\xi) = \sum_{n=0}^N a_n [\Psi(\xi)]^n, \tag{3}$$

with  $a_N \neq 0$  and the function  $\Psi(\xi)$  satisfying the new equation

$$\Psi(\xi) = \frac{1}{1 + \exp(\xi + \xi_0)}, \tag{4}$$

which is the solution of a special kind of Riccati equation

$$\frac{d\Psi}{d\xi} = \Psi^2(\xi) - \Psi(\xi). \tag{5}$$

**Step 3:** The integer  $N$  is defined by homogeneous balance principal in Eq. (2).

**Step 4:** Replace Eq. (3) into Eq. (2), and determine all required derivatives  $q_\xi, q_{\xi\xi}, q_{\xi\xi\xi}, \dots$  as follows

$$q_\xi = \sum_{n=0}^N a_n n \Psi^n (\Psi - 1), \tag{6}$$

$$q_{\xi\xi} = \sum_{n=0}^N n \Psi^n (\Psi - 1) [(1 + n)\Psi - n] a_n, \tag{7}$$

and so on. Replacing Eqs. (3), (6) and (7) along with (5) into Eq.(2), we attain the polynomial form as

$$S[\Psi(\xi)] = 0. \tag{8}$$

**Step 5:** Using Eqs. (8) and (4) and symbolic computer packages such as Mathematica, we found the analytic exact solutions of Eq. (1).

In the succeeding sections, we implemented the Kudryashov method to obtain dark soliton solutions for multiple core couplers in which the coupling is held with the nearest neighbors and all neighbors respectively.

### 3 Multiple-Core Couplers (Coupling with Nearest Neighbors)

This types of problems can be designated by the  $N$ -coupled NLSE with the nearest neighbor linear coupling. The dictating NLSE for multiple-core couplers (coupling with nearest neighbors) is written as

$$iu_t^{(j)} + a_j u_{xx}^{(j)} + b_j u_{xt}^{(j)} + c_j F(|u^{(j)}|^2)u^{(j)} = Q[u^{(j-1)} - 2u^{(j)} + u^{(j+1)}], \tag{9}$$

where  $1 \leq j \leq N$  and  $u^j$  denotes the optical field in the  $j$ th core. The Eq. (9) is distinguished as the coupled NLSE in which initial term represents the evolving soliton with time. The coefficients  $a_j$  are the GVD coefficients while  $b_j$  are the coefficients of STD and  $c_j$  denotes nonlinearity’s coefficients. The sign of nonlinearity is given by functional  $F$ . Here  $F$  denotes algebraic function with real-valued. The constants  $Q$  in Eq. (9) denotes the coupling coefficients in optical fibres and signifies the strength of linear coupling. Also, coupled Eq. (9) possess three integrals of motion such as energy ( $E$ ), the Hamiltonian ( $H$ ) and linear momentum ( $M$ ). To attend these coupled equations by the Kudryashov method, the following ansatz is appropriated.

$$u^j(x, t) = B_j(\xi)e^{i\phi(x,t)}, \tag{10}$$

Here,  $B_j$  ( $j = 1, 2$ ), nearest neighbour signify the amplitude component and  $v$  is the soliton’s speed, while  $\phi(x, t) = -Kx + wt + \theta$  is phase component, where  $K, w, \theta$  are the soliton frequency, wave number and phase constant respectively. Plugging ansatz (10) into Eq. (9), then the real and imaginary parts are:

$$k^2(a_j - b_j v)B_j'' + (b_j w K - w - a_j K^2)B_j + c_j F(B_j^2)B_j - Q[B_{j-1} - 2B_j + B_{j+1}] = 0, \tag{11}$$

$$-(1 - b_j K)kvB_j' + (b_j w - 2a_j K)kB_j' = 0. \tag{12}$$

From the imaginary part (12), we determine soliton speed as

$$v = \frac{b_j w - 2a_j K}{1 - b_j K}, \tag{13}$$

whenever  $1 \neq b_j K$ . The balancing principle in (11) leads to  $B_{j-1} = B_j = B_{j+1}$ , as a result, the real part Eq. (11) transformed to

$$k^2(a_j - b_j v)B_j'' + (b_j w K - w - a_j K^2)B_j + c_j F(B_j^2)B_j = 0, \tag{14}$$

In the next subsections, we examine this equation for four different sorts of non-linearity viz Kerr law, power law, parabolic law and dual power-law nonlinearities, respectively.

### 3.1 Kerr Law Nonlinearity

This is most basic kind of cubic nonlinearity which is originates from the fact that due to corresponding electric field, nonharmonic motion is shown by the bound electrons. Therefore, nonlinear responses exhibits by a light wave in an optical fiber. Hence, the induced polarization ( $P$ ) is also not linear in the electric field ( $E$ ), but includes higher-order factors in the amplitude of the electric field.  $F(u) = u$  for Kerr law nonlinearity. For multiple-core couplers (coupling with nearest neighbors) with Kerr law form nonlinearity, the executive model Eq. (9) reduces to

$$iu_t^{(j)} + a_j u_{xx}^{(j)} + b_j u_{xt}^{(j)} + c_j (|u^{(j)}|^2)u^{(j)} = Q[u^{(j-1)} - 2u^{(j)} + u^{(j+1)}], \tag{15}$$

and Eq. (14) becomes

$$k^2(a_j - b_j v)B_j'' + (b_j wK - w - a_j K^2)B_j + c_j B_j^3 = 0. \tag{16}$$

With balancing  $B_j''$  and  $B_j^3$  in Eq. (16), we have  $N = 1$ . Consequently, we reach  $B_j(\xi) = a_0 + a_1 \Psi(\xi)$ , where  $\Psi(\xi)$  satisfies the following general first and second order nonlinear differential equations:  $B_j'(\xi) = a_1 \Psi(\xi)[\Psi(\xi) - 1]$  and  $B_j''(\xi) = a_1 \Psi(\xi)[\Psi(\xi) - 1][2\Psi(\xi) - 1]$ , where  $a_0, a_1$  are constants to be determined later, such that  $a_1 \neq 0$ . Plugging the form of  $B_j(\xi)$  and their derivatives into Eq. (16) and after collecting all the terms of  $\Psi^j$  ( $j = 0, 1, 2, 3$ ) gives a set of algebraic equations which on solving by aid of Maple, we have the results:

$$a_0 = \frac{k^2(a_j - b_j v)}{c_j}, a_1 = -2a_0, w = \frac{2k^4 b_j v a_j - k^4(a_j^2 - b_j^2 v^2) + a_j K^2 c_j}{c_j(b_j K - 1)}. \tag{17}$$

Substituting Eq. (17) in Eqs. (3) and (4), we get the optical solitary wave solution for multiple core coupler with Kerr law nonlinearity (coupling with nearest neighbours) as

$$B_j(\xi) = \frac{k^2(a_j - b_j v)}{c_j} \left[ 1 - \frac{2}{1 + \exp(\xi + \xi_0)} \right], \tag{18}$$

which can be equivalently written in more simplified form using the relation  $\frac{1}{1 + \exp(\xi)} = \frac{1}{2} - \frac{1}{2} \tanh(\xi/2)$  and using Eq. (10), the optical dark solitary wave solution is specified as



$$u^j(x, t) = \frac{k^2(a_j - b_j v)}{c_j} \tanh\left(\frac{k(x - \frac{b_j w - 2a_j K}{1 - b_j K} t) + \frac{\xi_0}{2}}{2}\right) e^{i[-Kx + wt + \theta]} \tag{19}$$

This optical dark solitary wave solution will exist provided that the constraint conditions  $a_j \neq b_j v, b_j K \neq 1$  and the relation between wave number  $w$  and wave speed  $v$  from Eq. (17) can be understood as integrability condition with Kerr law nonlinearity.

### 3.2 Power Law Nonlinearity

Such type of nonlinearity is a generalized version of Kerr law and is commonly observed in nonlinear fiber optics and nonlinear plasmas. This nonlinearity can be seen in a variety of materials, such as semiconductor lasers. For this nonlinearity,  $F(u) = u^n$  where  $n$  accounts for the power-law nonlinearity factor and have  $n \neq 2$  and  $0 < n < 2$  to avoid self-focussing effect. Henceforth, the Eq. (9), for multiple-core couplers (nearest-neighbor coupling) with power-law nonlinearity will now be changed to

$$iu_t^{(j)} + a_j u_{xx}^{(j)} + b_j u_{xt}^{(j)} + c_j (|u^{(j)}|^{2n})u^{(j)} = Q[u^{(j-1)} - 2u^{(j)} + u^{(j+1)}], \tag{20}$$

and Eq. (14) leads to

$$k^2(a_j - b_j v)B_j'' + (b_j wK - w - a_j K^2)B_j + c_j B_j^{2n+1} = 0. \tag{21}$$

On setting  $B_j = U_j^{\frac{1}{n}}$  then Eq. (21) change into

$$k^2(a_j - b_j v)(nU_j U_j'' + (1 - n)(U_j')^2) + n^2 U_j^2 (b_j wK - w - a_j K^2) + c_j n^2 U_j^4 = 0. \tag{22}$$

When the powers of  $U_j U_j''$  are compared to the powers of  $U_j^4$ , the homogeneous balancing in Eq. (22) leads to  $N = 1$ . We derive the following results using the Kudryashov method's solution approach:

$$a_0 = -a_1, a_1 = \frac{3}{2} \frac{n}{(n - 1)}, w = \frac{4a_j K^2(n - 1) + 3k^2(a_j - b_j v)}{4(n - 1)(b_j K - 1)}. \tag{23}$$

Substituting Eq. (23) in Eqs. (3) and (4) and using the relation  $B_j = U_j^{\frac{1}{n}}$ , we get the optical dark solitary wave solution for multiple core coupler with power law nonlinearity as

$$u^j(x, t) = \left[ \frac{3}{2} \frac{n}{(n-1)} \left\{ 1 + \tanh \left( \frac{k(x - \frac{b_j w - 2a_j K}{1 - b_j K} t) + \frac{\xi_0}{2}}{2} \right) \right\} \right]^{\frac{1}{n}} \times e^{[i(-Kx + wt + \theta)]} \tag{24}$$

It is worth to see that the dark optical solitary wave solution (24) will satisfy the parametric constraint conditions  $n \neq 0, 1, a_j \neq b_j v, b_j K \neq 1, b_j w \neq 0$  and the relation between wave number  $w$  and wave speed  $v$  from Eq. (23) can be understood as integrability condition with power law nonlinearity.

### 3.3 Parabolic Law Nonlinearity

This is known as cubic-quintic nonlinearity which is portrayed by  $F(u) = \alpha u + \beta u^2$ , where  $\alpha$  and  $\beta$  are in overall constants that connects the two nonlinear forms. This sort of nonlinearity has significant attention after it occurs in materials such as paratoluene sulphonate that manifest fifth-order nonlinearity in response to extreme ultra-short optical pulses at 620 nm. With cubic-quintic nonlinearity, Eq. (9) for multiple-core couplers (coupling with nearest neighbors) is formulated as

$$iu_t^{(j)} + a_j u_{xx}^{(j)} + b_j u_{xt}^{(j)} + c_j (\alpha |u^{(j)}|^2 + \beta |u^{(j)}|^4) u^{(j)} = Q[u^{(j-1)} - 2u^{(j)} + u^{(j+1)}], \tag{25}$$

and Eq. (14) transformed to

$$k^2(a_j - b_j v)B_j'' + (b_j w K - w - a_j K^2)B_j + c_j(\alpha B_j^2 + \beta B_j^4)B_j = 0. \tag{26}$$

A transformation formula is used to obtain a closed form analytic solution as  $B_j = U_j^{\frac{1}{2}}$  then Eq. (26) changes into

$$k^2(a_j - b_j v)(2U_j U_j'' - (U_j')^2) + 4U_j^2(b_j w K - w - a_j K^2) + 4\alpha c_j U_j^3 + 4\beta c_j U_j^4 = 0. \tag{27}$$

From Eq. (27), we have  $N = 1$ . Using the recipe of the Kudryashov method, we obtain the following results:

$$\begin{aligned} a_0 = -a_1, a_1 &= \frac{3k^2(b_j v - a_j) - 2\alpha c_j}{k^2(b_j v - a_j)}, \\ \beta &= \frac{(b_j v - a_j)(-k^2 a_j + 2c_j \alpha + k^2 b_j v)k^2}{4[3k^2(b_j v - a_j) - 2\alpha c_j]}, \\ w &= \frac{-3(b_j v - a_j)^2 k^4 + 4(a_j K^2 + 2c_j \alpha)(b_j v - a_j)k^2 - 4c_j^2 \alpha^2}{4k^2(b_j K - 1)(b_j v - a_j)}. \end{aligned} \tag{28}$$

Replacing Eq. (28) in Eqs. (3) and (4) and setting the relation  $B_j = U_j^{\frac{1}{2}}$ , we acquire the dark optical solitary wave solution wave with parabolic law nonlinearity as

$$u^j(x, t) = \left[ -\frac{3k^2(b_j v - a_j) - 2\alpha c_j}{2k^2(b_j v - a_j)} \left( 1 + \tanh \left( \frac{k(x - \frac{b_j w - 2a_j K}{1 - b_j K} t)}{2} + \frac{\xi_0}{2} \right) \right) \right]^{\frac{1}{2}} \times e^{[i(-Kx + wt + \theta)]} \tag{29}$$

It is pointed that the dark optical solitary wave solution (29) will exist under the parametric constraint conditions  $a_j \neq b_j v, b_j K \neq 1, b_j w \neq 0$  and the relation between wave number  $w$  and wave speed  $v$  from Eq. (28) can be specified as integrability condition with parabolic law form nonlinearity.

### 3.4 Dual-Power Law Nonlinearity

Such type of nonlinearity is commonly used to explain spatial solitons in photovoltaic-photo refractive materials like as  $LiNbO_3$ . For dual-power law nonlinear media, the function  $F(u) = \alpha u^n + \beta u^{2n}$ , where  $\alpha$  and  $\beta$  are defined as real-valued constants. Equation (9), account for multiple-core couplers (coupling with nearest neighbors) with dual-power law nonlinearity as

$$i u_t^{(j)} + a_j u_{xx}^{(j)} + b_j u_{xt}^{(j)} + c_j (\alpha |u^{(j)}|^{2n} + \beta |u^{(j)}|^{4n}) u^{(j)} = Q [u^{(j-1)} - 2u^{(j)} + u^{(j+1)}], \tag{30}$$

and Eq. (14) becomes

$$k^2(a_j - b_j v) B_j'' + (b_j w K - w - a_j K^2) B_j + c_j (\alpha B_j^{2n} + \beta B_j^{4n}) B_j = 0. \tag{31}$$

It should be observed that in Eq. (31),  $\beta = 0$  recovers power-law nonlinearity, and when  $n = 1$  recovers Kerr law nonlinearity as well. However, if  $\beta \neq 0$  and  $n = 1$ , one is back in the case of parabolic law nonlinearity, which was previously explored.

On equating  $B_j = U_j^{\frac{1}{2n}}$  then Eq. (31) change into

$$k^2(a_j - b_j v) (2n U_j U_j'' + (1 - 2n)(U_j')^2) + 4n^2 U_j^2 (b_j w K - w - a_j K^2) + 4n^2 \alpha c_j U_j^3 + 4n^2 \beta c_j U_j^4 = 0. \tag{32}$$

Balancing the leading dispersive term  $U_j U_j''$  with nonlinear term  $U_j^4$  in Eq. (32), provides  $N = 1$ . Using the Kudryashov method’s solution recipe, we obtain the value of  $a_0, a_1, w$  and  $\beta$ .

$$\begin{aligned}
 a_0 &= -a_1, a_1 = \frac{n(3k^2(b_j v - a_j) - 2n\alpha c_j)}{k^2(2n - 1)(b_j v - a_j)}, \\
 w &= \frac{-3(b_j v - a_j)^2 k^4 + 8\left(K^2\left(n - \frac{1}{2}\right)a_j + n\alpha c_j\right)(b_j v - a_j)k^2 - 4n^2\alpha^2 c_j^2}{8k^2(b_j K - 1)\left(n - \frac{1}{2}\right)(b_j v - a_j)}, \\
 \beta &= \frac{(a_j + 2b_j v n - b_j v - 2a_j n)(2n\alpha c_j - k^2 a_j + k^2 b_j v)k^2}{4n^2(-2n\alpha c_j + 3k^2 b_j v - 3k^2 a_j)c_j}.
 \end{aligned}
 \tag{33}$$

Substituting these in Eqs. (3) and (4) and using the relation  $B_j = U_j^{\frac{1}{2n}}$ , we found the exact dark optical solitary wave solution as

$$\begin{aligned}
 u^j(x, t) &= \left[ -\frac{n(3k^2(b_j v - a_j) - 2n\alpha c_j)}{2k^2(2n - 1)(b_j v - a_j)} \left( 1 + \tanh\left(\frac{k(x - \frac{b_j w - 2a_j K}{1 - b_j K} t) + \frac{\xi\theta}{2}}{2}\right) \right) \right]^{\frac{1}{2n}} \\
 &\quad \times \exp[i(-Kx + wt + \theta)].
 \end{aligned}
 \tag{34}$$

It is pointed that dark optical solitary wave solution (34) will exist under the additional parametric constraint condition  $n \neq \frac{1}{2}$  and the relation between wave number  $w$  and wave speed  $v$  from Eq. (33) can be specified as integrability condition with dual power law form nonlinearity. For  $n = 1$  as a special case, we get the previously found solution (29) with parabolic form nonlinearity.

### 4 Multiple-Core Couplers (Coupling with All Neighbors)

For the pulses propagating through  $N$  coupled nonlinear fiber arrays, the governing equation for multiple-core couplers is provided in the dimensionless form as

$$iu_t^{(j)} + a_j u_{xx}^{(j)} + b_j u_{xt}^{(j)} + c_j F(|u^{(j)}|^2)u^{(j)} = \sum_{m=1}^N \lambda_{jm} u^m,
 \tag{35}$$

where  $1 \leq j \leq N$ . The Eq. (35) depicts the generic model for optical couplers wherever coupling with all neighbors is included with GVD and STD, which defines soliton passage via multiple-core optical fibers under balancing outcome of dispersion and nonlinearity. Here  $\lambda_{jm}$  in Eq. (35) renders the linear coupling coefficients in optical fibers. To approach this model by the Kudryashov method for the four types of nonlinear media, the first hypothesis is supposed to be

$$u^j(x, t) = B_j(\xi)e^{i\phi(x,t)},
 \tag{36}$$

where  $\xi = k(x - vt)$ . Replacing the hypothesis (36) into Eq. (35) and subsequently, splitting into real and imaginary parts results in

$$k^2(a_j - b_j v)B_j'' + (b_j w K - w - a_j K^2)B_j + c_j F(B_j^2)B_j - \sum_{m=1}^N \lambda_{jm} B_m = 0, \tag{37}$$

$$-(1 - b_j K)k v B_j' + (b_j w - 2a_j K)k B_j' = 0 \tag{38}$$

From the imaginary part (38), we deduce soliton speed as

$$v = \frac{b_j w - 2a_j K}{1 - b_j K}. \tag{39}$$

For all sorts of specified nonlinearity in question, the velocity of the soliton, given by (39), is constant. The balancing principle in Eq. (37) leads to  $B_j = B_m$ , as a result, the real part Eq. (37) reduces to

$$k^2(a_j - b_j v)B_j'' + (b_j w K - w - a_j K^2 - \sum_{m=1}^N \lambda_{jm})B_j + c_j F(B_j^2)B_j = 0 \tag{40}$$

From the Kudryashov method, this equation have the dark optical soliton with four types of nonlinearities.

## 5 Graphical Results and Discussion

In this section, we illustrate the graphic representation of several wave structures of the considered system. By utilizing Kudryashov method the soliton solution of optical couplers are retrieved and graphically represented in 3-D, and their contours with the selection of different parameters. The Kudryashov approach was used to examine solitary wave solutions, which are unique and different from what many other researchers have found using various methodologies.

The intensity distribution of dark solitary wave solution (19) is shown in Fig. 1 when parameter values  $a_j = 1, b_j = 1, c_j = 1, k = 1, v = 0.2, K = 2, w = 3.44,$  and  $\xi_0 = 0$ . In Fig. 2, the intensity distribution of kink solitary wave solution (24) when parameter values  $n = 3, a_j = 1, b_j = 1, c_j = 1, k = 1, v = 0.2, K = 2, w = 3.44,$  and  $\xi_0 = 0$  is depicted. In nonlinear optics, these types of propagating structures are extremely significant. Soliton has been utilized to greatly improve the transmission capabilities of Telecom lines. Solitons are well-localized structures that can travel great distances without changing shape, and optical pulses propagate in the form of solitons.

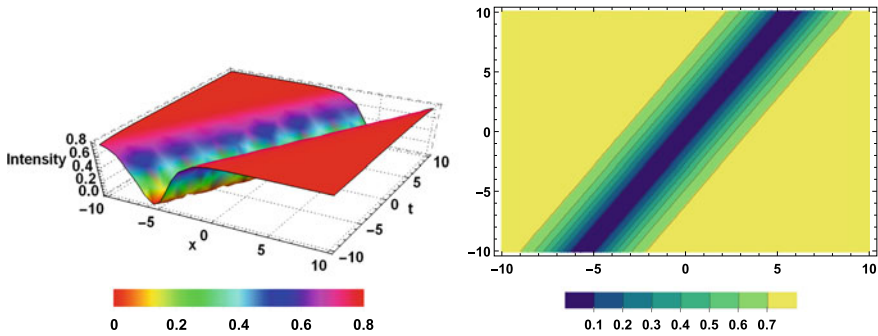


**Fig. 1** The intensity distribution of solitary wave solution (19) with parameter values  $a_j = 1$ ,  $b_j = 1$ ,  $c_j = 1$ ,  $k = 1$ ,  $v = 0.2$ ,  $K = 2$ ,  $w = 3.44$ , and  $\xi_0 = 0$

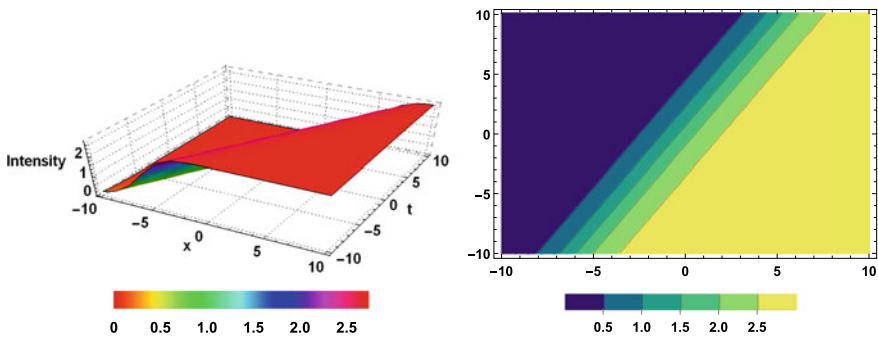


**Fig. 2** The intensity distribution of kink solitary wave solution (24) with parameter values  $n = 3$ ,  $a_j = 1$ ,  $b_j = 1$ ,  $c_j = 1$ ,  $k = 1$ ,  $v = 0.2$ ,  $K = 2$ ,  $w = 3.44$ , and  $\xi_0 = 0$

## 6 Conclusions

Optical couplers and switches are indispensable components of optical communication systems. In the present work, we obtain dark optical solitons to nonlinear directional multiple cores couplers with four different kinds of nonlinearities using Kudryashov algorithm scheme. Here, two distinctive cases were analyzed. Coupling with nearest neighbors was addressed in the first instance, while coupling with all neighbors was addressed subsequently. To ensure the existence of these solitons, the necessary constraint conditions emerge naturally. The outcomes of this paper are certainly stimulating to focus study on a diverse possibility with couplers.

## References

1. Biswas, A., Konar, S.: Introduction to Non-kerr Law Optical Solitons. CRC Press, Boca Raton (2006)
2. Hasegawa, A., Kumar, S., Kodama, Y.: Reduction of collision-induced time jitters in dispersion-managed soliton transmission systems. *Opt. Lett.* **21**(1), 39–41 (1996)
3. Suzuki, M., Morita, I., Edagawa, N., Yamamoto, S., Taga, H., Akiba, S.: Reduction of Gordon-Haus timing jitter by periodic dispersion compensation in soliton transmission. *Electron. Lett.* **31**(23), 2027–2029 (1995)
4. Smith, N., Knox, F., Doran, N., Blow, K., Bennion, I.: Enhanced power solitons in optical fibres with periodic dispersion management. *Electron. Lett.* **32**(1), 54–55 (1996)
5. Savescu, M., Bhrawy, A., Alshaery, A., Hilal, E., Khan, K.R., Mahmood, M., Biswas, A.: Optical solitons in nonlinear directional couplers with spatio-temporal dispersion. *J. Mod. Opt.* **61**(5), 441–458 (2014)
6. Mirzazadeh, M., Eslami, M., Zerrad, E., Mahmood, M.F., Biswas, A., Belic, M.: Optical solitons in nonlinear directional couplers by sine-cosine function method and Bernoulli's equation approach. *Nonlinear Dyn.* **81**(4), 1933–1949 (2015)
7. Al Qurashi, M.M., Ates, E., Inc, M.: Optical solitons in multiple-core couplers with the nearest neighbors linear coupling. *Optik* **142**, 343–353 (2017)
8. Sarma, A.K.: A comparative study of soliton switching in a two-and three-core coupler with TOD and IMD. *Optik* **120**(8), 390–394 (2009)
9. Dahiya, S., Kumar, H., Kumar, A., Gautam, M.S., et al.: Optical solitons in twin-core couplers with the nearest neighbor coupling. *Part. Differ. Equ. Appl. Math.* **4**, 100–136 (2021)
10. Vega-Guzman, J., Mahmood, M., Zhou, Q., Triki, H., Arnous, A.H., Biswas, A., Moshokoa, S.P., Belic, M.: Solitons in nonlinear directional couplers with optical metamaterials. *Nonlinear Dyn.* **87**(1), 427–458 (2017)
11. Kudryashov, N.A.: One method for finding exact solutions of nonlinear differential equations. *Commun. Nonlinear Sci. Numer. Simul.* **17**(6), 2248–2253 (2012)

# Analysis of a Variable-Order Multi-scroll Chaotic System with Different Memory Lengths



N. Medellín-Neri, J. M. Muñoz-Pacheco, O. Félix-Beltrán,  
and E. Zambrano-Serrano

**Abstract** This work presents a numerical analysis of the dynamical behavior of a multi-scroll chaotic system using variable-order calculus. In this scenario, we introduce the concept of variable-order from two approaches denominated herein as short-memory and full-memory, respectively. For the first one, the basic idea is to study the chaotic dynamics when the fractional-order changes abruptly like step-function with respect to time. The second approach is related to a smoother variation between the preceding order and the new fractional-order. To demonstrate the implications of using variable-order with distinct memory contributions, we show several numerical simulations of a multi-scroll chaotic system that contains a piecewise linear function. Numerical results are consistent with the underlying theory demonstrating the usefulness of the proposed study.

**Keywords** Variable-order · Fractional calculus · Chaos · Multi-scroll · PWL

## 1 Introduction

The chaotic behavior has remarkable characteristics such as extreme sensitivity to small variations of the initial conditions and parameters, limited trajectories in phase space, and at least, a positive Lyapunov exponent [1]. For instance, two initial trajectories that are extremely close between them, will diverge exponentially as time tends to infinite, and thereafter, have totally different evolutions. In this manner, the chaotic systems have been used in almost all fields of science and engineering, such as secure communications [2], cryptography [3], robotics [4], mechanics [5], etc.

---

N. Medellín-Neri (✉) · J. M. Muñoz-Pacheco · O. Félix-Beltrán  
Faculty of Electronics Sciences, Benemérita Universidad Autónoma de Puebla, 72570 Puebla,  
Mexico  
e-mail: [nadia.medellin@alumno.buap.mx](mailto:nadia.medellin@alumno.buap.mx)

E. Zambrano-Serrano  
Facultad de Ingeniería Mecánica y Eléctrica, Universidad Autónoma de Nuevo León, 66455 San  
Nicolás de los Garza, Nuevo León, Mexico



For several decades, it was well known that chaotic behavior requires, at least, a three-dimensional system to emerge [6], where the dimension relates to the order of their derivatives. Therefore, a  $n$ -dimensional system is a system of  $m$ th order,  $n = m, n \in \mathbb{Z}$ . However, the exception to this rule is when the order of the derivative is no longer integer but fractional (from now on we will use  $q$  when  $m \in \mathbb{R}$ ), like in  $n \neq q$  and also  $q \in \mathbb{R}$ . Fractional calculus refers to the generalization of integrals and derivatives to arbitrary order. Although this topic was proposed more than 300 years ago, it has recently been noted that the fractional calculus has superior characteristics to the conventional calculus [7]. The main reason is that the fractional-order derivatives have memory properties, giving a more convenient way to describe living and nonliving phenomena [8–12].

The three main definitions for fractional derivatives are Riemann-Liouville [13], Caputo [14], and Grünwald-Letnikov [15–17] that are equivalent under some assumptions. In literature, we can find many excellent works using fractional calculus with constant values for the fractional-order, i.e., the fractional-order  $q$  is a positive real constant that remains unchanged throughout the simulation time. As a result, memory contributions follow a power-law evolution such as the Caputo derivative with singular kernel, where past events have lower implications than recent ones. In Caputo's definition, the memory kernel is expressed in the form of a convolution integral. As seen, the fractional-order differential equations accumulate the whole past history in a weighted form, this is called the "memory effect".

However, a less researched area and still exciting is fractional calculus with variable-order. It means that the value of the fractional-order can be updated as time evolves, i.e.,  $q(t)$ . Then, the fractional-order can be defined as trigonometric, quadratic, polynomial, and constant piecewise linear functions with respect to time. Indeed, the fractional-order value can also depend on a pseudo-state of the underlying dynamical system. With the variable-order calculus, the memory contributions change with time, altering the strength of the effects of this memory. Many works have shown the importance of considering variable-order to increase the accuracy and degrees of freedom in many scientific areas. For instance, a variable-order susceptible-infected-recovered (SIR) model described the COVID19 evolution with better approximation to real data [18]. There, the memory contributions to epidemic spread were captured using a piecewise-linear fractional-order. Reference [19] offered a unified discussion of variable-order differential operators in anomalous diffusion modeling. Reference [20] reported block-based image encryption where each block has a different fractional-order using a short-memory variable-order. In mechanics, the effect of nonuniform viscoelastic frictional forces described applying variable-order to demonstrate that constant fractional-order cannot approximate the transition between the relevant dynamic regimes [21].

In this work, we present in the Eq. (5) a numerical analysis of the dynamical behavior of a multi-scroll chaotic system [22] using variable-order calculus.

A multi-scroll chaotic system can be defined as a nonlinear dynamical system that presents a chaotic attractor composed of many scrolls [23], contrary to the classical chaotic systems with only double-scroll attractors, like Lorenz, Chua, and Chen systems, to mention a few. The increased number of scrolls are originated from

nonlinear functions in the form of piecewise-linear (PWL) functions such as saturated, hysteresis, sawtooth, Heaviside, and so on [24]. As a result, the number of equilibrium points also increases, and the dynamical system has the potential to generate a multi-scroll attractor. Recently, multi-scrolls chaotic systems continue being a hot topic of research. Wu et al. proposed a new multi-scroll system that produces three distinct hidden attractors with stable equilibria and without equilibrium points [25]. Escalante-Gonzalez and Campos-Canton also reported a method for switching between hidden and self-excited multi-scroll chaotic attractors in multi-stable systems [26]. Zhang et al. introduced a multi-scroll system based on a memristive approach along with a Hindmarsh-Rose neuron model [27]. Ahmad et al. studied how to transform a multi-scroll system to the fractional calculus domain, mainly using the Caputo fractal-fractional operator [28].

The concept of variable-order is shown from two approaches denominated herein as short-memory and full-memory, respectively. For the first one, the basic idea is to study the chaotic dynamics when the fractional-order changes abruptly like step-function with respect to time. The second approach is related to a smoother variation between the initial order and the new fractional-order. Therefore, Section 2 gives the mathematical foundations of variable-order calculus. Section 3 introduces the multi-scroll chaotic system, studies the stability of equilibrium points, and presents phase portraits. Section 4 presents the proposed numerical analysis with short-memory and full-memory approaches. Numerical simulations of a four-scroll chaotic attractor are in particular analyzed. Finally, Section 5 concludes the work.

## 2 Mathematical Preliminaries

**Definition 1** Fractional calculus is a generalization of integration and differentiation to the non-integer fundamental operator  ${}_a D_t^q$ , where  $a$  and  $t$  are the limits of the operation and  $q \in \mathbb{R}$ . We have that the continuous integro-differential operator is defined as [29]:

$${}_a D_t^q = \begin{cases} \frac{d^q}{dt^q}, & q > 0, \\ 1, & q = 0, \\ \int_a^t (d\tau)^q, & q < 0. \end{cases} \tag{1}$$

Additionally, The variable-order calculus is based on the fact that the order of the derivative is not constant, for the case of study, the variation is carried out with respect to time.

**Definition 2** Let us consider  $q(t) > 0$  as a function that is limited; the fractional derivative of Caputo in its fractional-order (FO) version is defined as [19]:

$${}^C D_t^{q(t)} f(t) := \begin{cases} \frac{1}{\Gamma(q(t)-m)} \int_{t_0}^t \frac{f^m(\tau)}{(t-\tau)^{q(t)+1-m}} d\tau, & m - 1 < q(t) \leq m, \\ \frac{d^m}{dt^m} f(t), & q = m. \end{cases} \tag{2}$$

**Definition 3** Let us consider the following general form of arbitrary-order differential equation described by

$${}^C D_t^q x(t) = Ax(t) + Bu(t), \tag{3}$$

where  $x \in \mathbb{R}^n$ ,  $u \in \mathbb{R}^m$ , and  $A \in \mathbb{R}^{n \times n}$ ,  $B \in \mathbb{R}^{n \times m}$ ,  $n, m \in \mathbb{N}$ , and  ${}^C D_t^q x(t) = [{}^C D_t^q x_1(t), \dots, {}^C D_t^q x_n(t)]^T$ ,  $q \in (0, 1]$  is the fractional-order,  $t$  and  $t_0$  are the limits of operation. When the system (3) is autonomous, it can be rewritten as  ${}^C D_t^q x(t) = Ax(t)$ , with  $x(0) = x_0$ ,  $0 < q < 1$ , and  $x \in \mathbb{R}^n$ . Then, the stability analysis of the autonomous system can be expressed according to following conditions [29]:

- The system  ${}^C D_t^q x(t) = Ax(t)$  is *asymptotically stable* if and only if  $|\arg(\lambda)| > \frac{q\pi}{2}$  for all eigenvalues ( $\lambda$ ) of matrix  $A$ . In this scenario, the solution  $x(t)$  tends to 0 like  $t^{-q}$ .
- The system  ${}^C D_t^q x(t) = Ax(t)$  is *stable* if and only if  $|\arg(\lambda)| \geq \frac{q\pi}{2}$  for all eigenvalues ( $\lambda$ ) of matrix  $A$  obeying that the critical eigenvalues must satisfy  $|\arg(\lambda)| = \frac{q\pi}{2}$  and have geometric multiplicity of one.

**Definition 4** The general numerical solution of the fractional differential equation  ${}^a D_t^q w(t) = f(w(t), t)$  can be expressed as [29]:

$$w(t_k) = f(w(t_{k-1}), t_{k-1}) h^q - \sum_{j=1}^k c_j^{(q)} w(t_{k-j}), \tag{4}$$

with  $k = 1, 2, \dots, n$ ,  $n = \frac{T_f}{h}$ ,  $n \in \mathbb{N}$ ,  $h$  the time step, and  $c_j^{(q)}$  are binomial coefficients given by  $c_0^{(q)} = 1$ ,  $c_j^{(q)} = \left(1 - \frac{1+q}{j}\right) c_{j-1}^{(q)}$ .

The numerical algorithm in Definition 4 is based on the fact that for a wide class of functions, the three definitions, Caputo, Riemann-Liouville and Grünwald-Letnikov, are equivalent under the conditions [13].

### 3 Fractional-Order Multi-scroll Chaotic Systems Based on PWL Functions

Based on the chaotic system proposed in [30], we introduce the multi-scroll chaotic system with variable-order given by

$$\begin{aligned} {}^C D_t^{q(t)} x(t) &= y(t), \\ {}^C D_t^{q(t)} y(t) &= z(t), \\ {}^C D_t^{q(t)} z(t) &= -\alpha x(t) - \beta y(t) - \gamma z(t) + \phi f(x(t); k_s, h_s, p_s, q_s), \end{aligned} \tag{5}$$

**Table 1** Equilibrium points ( $EP_i$ ) of the system (5)

Function saturated series	Equilibrium points ( $EP_i$ )
$f(x; k_s, h_s, p_s, q_s) = k_s(x - ih_s) + 2ik_s$	$EP_1 = (0, 0, 0), EP_{4,5} = (\pm 2k_s, 0, 0)$
$f(x; k_s, h_s, p_s, q_s) \neq k_s(x - ih_s) + 2ik_s$	$EP_{2,3} = (\pm k_s, 0, 0), EP_{6,7} = (\pm 3k_s, 0, 0)$

where  ${}^C D_t^{q(t)}$  is variable-order Caputo’s derivative operator determined by definition (2),  $q(t)$  variable-order;  $x(t), y(t), z(t)$  are the state variables,  $\alpha = 2, \beta = 1, \gamma = 0.6, \phi = 2$ , and  $f(x; k_s, h_s, p_s, q_s)$  is a PWL function, which consists of a set of linear relationships valid in different regions as follows:

$$f(x; k_s, h_s, p_s, q_s) = \begin{cases} (2q_s + 1)k_s, & x > k_s h_s + 1, \\ k_s(x - i_s h_s) + 2ik_s, & |x - ih_s, \leq 1|, \\ & -p_s \leq i \leq q_s, \\ (2i + 1)k_s, & ih_s + 1 < x < (i + 1)h_s - 1, \\ & -p_s \leq i \leq q_s - 1, \\ -(2q_s + 1)k_s, & x < -p_s h_s - 1, \end{cases} \tag{6}$$

where  $k_s = 1$  and  $h_s = 2k_s$  are the multiplicative factors for the slopes and saturated regions,  $i \in \mathbb{Z}$ , and  $x$  is the state variable. When  $q_s = p_s = 1$ , we obtain a PWL function with 7 segments (four saturated plateaus and three slopes), to generate a 4-scroll chaotic attractor in 1D orientation on phase space. The equilibrium points ( $EP_i$ ) of system (5) are shown in Table 1. In particular, when the PWL function  $f(x; k_s, h_s, p_s, q_s) \neq k(x - ih_s) + 2ik_s$  with  $i = 1, 2, 3$  and  $k_s = 1$ , the roots of the equation (5), for the equilibrium points  $EP_{2,3}$  and  $EP_{6,7}$  are:  $\lambda_1 = -1.1833$  and  $\lambda_{2,3} = 0.2916 \pm 1.2669i$  respectively. In this manner, the minimum fractional-order  $q$ , where the multi-scroll system may present a chaotic behavior is  $q > \frac{2}{\pi} \left( \arctan \left( \frac{|\pm 1.2669i|}{0.2916} \right) \right)$ , i.e.,  $q > 0.8560$ .

### 4 Numerical Analysis of the Variable-Order-Based Memory

For simulation purposes, we herein use the numerical algorithm (4). Thus, the solution of system (5) with variable-order is given in (7). The idea is that the elements of the summation operation will be adapted for short-memory and full-memory implications.

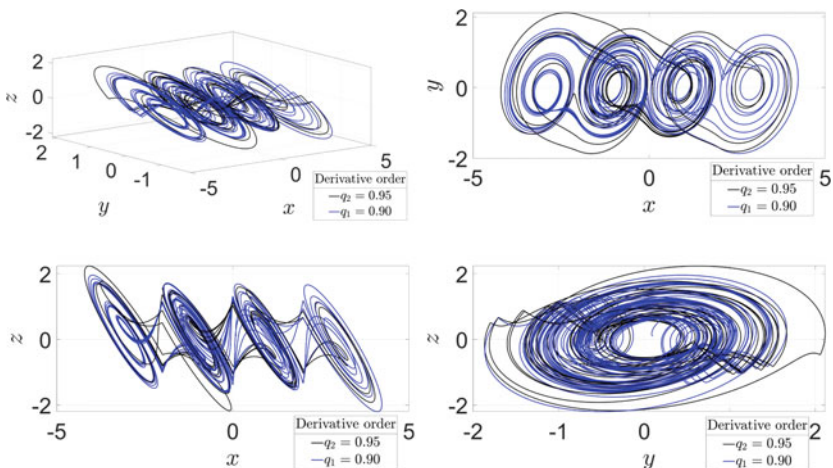


**Fig. 1** Multi-scroll chaotic attractor of system (5) applying short-memory approach with variable order:  $q_1 \in [t_0, t_1]$ , and  $q_2 \in [t_1, t_2]$

$$\begin{aligned}
 x(t_k) &= [y(t_{k-1})]h^{q(t)} - \sum_{j=1}^k c_j^{q(t)} x(t_{k-j}), \\
 y(t_k) &= [z(t_{k-1})]h^{q(t)} - \sum_{j=1}^k c_j^{q(t)} y(t_{k-j}), \\
 z(t_k) &= [-\alpha x(t_{k-1}) - \beta y(t_{k-1}) - \gamma z(t_{k-1}) + \phi f(x(t_{k-1}))]h^{q(t)} - \sum_{j=1}^k c_j^{q(t)} z(t_{k-j}).
 \end{aligned}
 \tag{7}$$

where  $x, y, z$  are the state variables,  $\alpha = 2, \beta = 1, \gamma = 0.6, \phi = 2$ , and  $f(x; k_s, h_s, p_s, q_s)$  is the PWL function,  $h$  is the integration step,  $q(t)$  is the variable-order,  $c_j$  are binomial coefficients, and  $k$  is the number of iterations.

### 4.1 Short-Memory

With the short-memory term, we mean that the simulation  $t \in [t_0, t_n]$  is divided by  $n$  intervals where each interval associates to a specific fractional-order. Considering the initial time  $t_0$  with initial condition  $x_0$ , we have  $t \in [t_0, t_1]$  and the corresponding fractional differential equation  ${}^C_{t_0} D_t^{q_0} x = f(x_0, t_0)$ . For the next interval, only the memory from  $t_1$  is considered without taking into account the initial condition  $t_0$ , i.e., the accumulated data are deleted. Thus, we obtain the updated interval  $t \in [t_1, t_2]$  and fractional differential equation  ${}^C_{t_1} D_t^{q_1} x = f(x_1, t_1)$ ; and so forth.

Figure 1 shows the resulting 4-scroll chaotic attractor using short-memory contributions with a constant PWL fractional-order  $q$ . In particular, the trajectory in blue

*color* represents the chaotic oscillator with  $q_1 = 0.90$ , while in *black color* the other fractional-order  $q_2 = 0.95$ , with a simulation time of 300s, and initial conditions [0.1, 0.1, 0.1]. The following pseudo-code gives the main instructions to implement the short-memory approach.

```

for i=1:NumberOfIterations
[t, y1]=GLMethod(Parameters, Order, AuxiliaryTime, ...
    InitialConditions);
cond=[y1(end,1), y1(end,2), y1(end,3)];
q_2=q+0.05;
Order=[q_2,q_2, q_2];
if (i==1)
yn=y1;
else
yn=[yn;y1];
end
end
    
```

### 4.2 Full-Memory

In the full-memory approach, we want to preserve all the values for the index of the summation in eq. (7). In this manner, the  $k$ th solution will depend on the whole previous values, including initial conditions  $k(0)$ . As a result, all the previously generated data since  $t_0$  are preserved and used to compute the next values for the new fractional-order. Considering the initial time  $t_0$  with initial condition  $x_0$ , we have  $t \in [t_0, t_1]$  and the corresponding fractional differential equation  ${}^C_{t_0}D^{q_0}x(t) = f(x_0, t_0)$ . For the next interval, the full memory from  $t_0$  is preserved, i.e., the data are accumulated as time evolves. Thus, we obtain the updated interval  $t \in [t_1, t_2]$  and fractional differential equation  ${}^C_{t_1}D^{q_1}x(t) = f(x_0, t_0)$ . Next, we will obtain  ${}^C_{t_2}D^{q_2}x(t) = f(x_0, t_0)$  with  $t \in [t_2, t_3]$ , and so forth. Based on this principle, we simulate again the multi-scroll chaotic system (5) with a constant PLW fractional-order  $q_1 = 0.90$  for  $t \in [0, 150s]$  and  $q_2 = 0.95$  for  $t \in [150s, 300s]$ , and initial conditions [0.1, 0.1, 0.1], as shown in Fig. 2. Similarly to the case of short-memory in the previous subsection, the following pseudo-code gives the main instructions to implement the full-memory approach:

```

function [t, Y]=GLMethod(parameter, order, simutime, Y0)
for i=2:n
if i<=15000
q=0.90;
x(i)=y(i-1)*h^q - (memoria(x, c1, i));
y(i)=z(i-1)*h^q - (memoria(y, c2, i));
z(i)=(-alpha*x(i-1)-beta*y(i-1)-gamma*z(i-1)+...
w*f_xpwl(x(i-1)))*h^q - (memoria(z, c3, i));
else
q=0.95;
x(i)=y(i-1)*h^q - (memoria(x, c1, i));
y(i)=z(i-1)*h^q - (memoria(y, c2, i));
z(i)=(-alpha*x(i-1)-beta*y(i-1)-gamma*z(i-1)+...
w*f_xpwl(x(i-1)))*h^q - (memoria(z, c3, i));
end
end
    
```

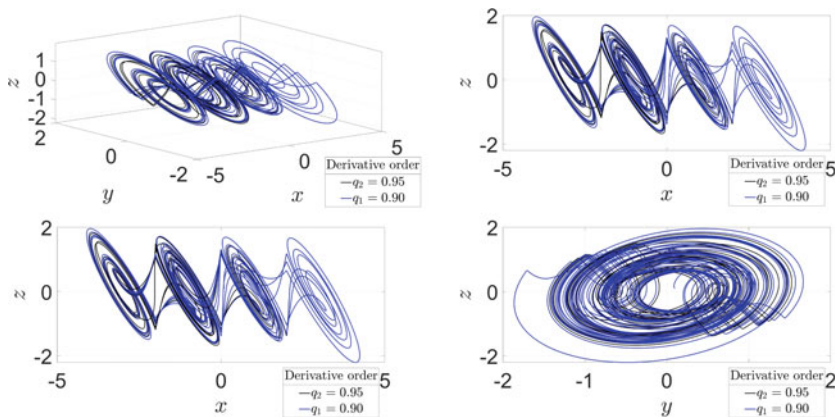


**Fig. 2** Multi-scroll chaotic attractor of system (5) applying full-memory approach with variable-order:  $q_1 \in [t_0, t_1]$ , and  $q_2 \in [t_1, t]$

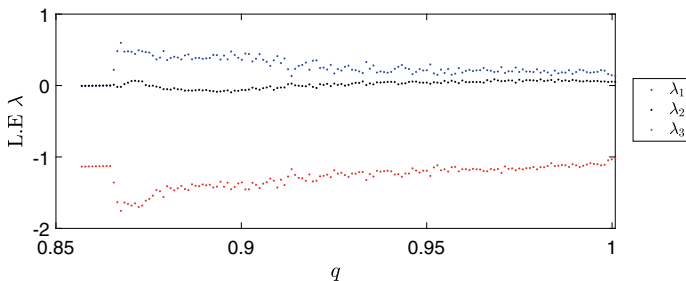


**Fig. 3** The spectrum of the Lyapunov exponents for the system (5) with  $q \in [0.8570, 0.9999]$

For the simulated chaotic attractors, we compute the Lyapunov exponent spectrum to demonstrate the chaos behavior. Figure 3 shows the Lyapunov exponents for  $q \in [0.8570, 0.9999]$  based on the Wolf’s algorithm [31]. The results confirm that in the interval  $q \in [0.8656, 0.9999]$  there is a system of chaotic dynamics with a strange three-dimensional attractor.

### 4.3 Discussion

In Fig. 4, the time evolution  $(x(t), y(t), z(t))$  of multi-scroll system (5) was computed with both short-memory and full-memory proposed approaches. While the evolution with short-memory is represented by the *blue color*, the full-memory implications are in *red color*. We observe that both solutions have a similar evolution due to the memory contributions of the fractional-order ( $q = 0.9$ ) is the same for both approaches during the first interval  $[0, 150s]$ . However, the evolution diverges for the

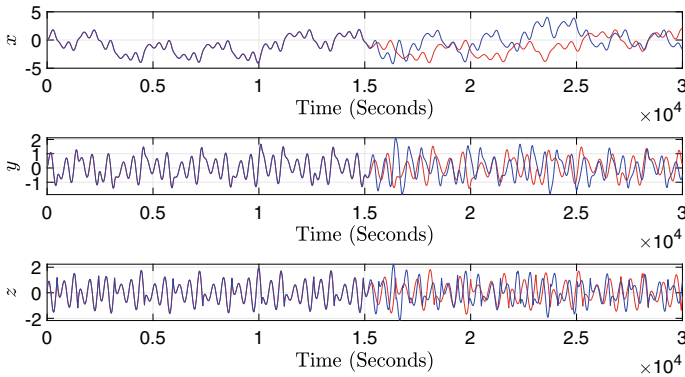


**Fig. 4** Time evolution for  $(x, y, z)$  of variable-order multi-scroll chaotic system (5) with the short-memory (blue) and full-memory (red) proposed approaches

second time interval [150s, 300s]. The reason is that each approach (short-memory and full-memory) has different characteristics. For the short-memory-based chaotic system, the initial condition in the second interval is changed to the latter value of  $(x(150), y(150), z(150))$ . It means that previous data are deleted. In the full-memory-based chaotic system, the initial conditions remains fixed to its original value  $(x(0), y(0), z(0))$ , and all previous data of the state-variables vector are accumulated with the current and next solutions.

In Fig. 5, we plot the solution of (5) for constant orders  $q = 0.9$  and  $q = 0.95$ , and variable-order  $q(t) = [q(t_0), q(t_1)]$  with short-memory order and full-memory, respectively. As expected, the variable-order oscillator with short-memory (blue trajectory) has a strong correlation with constant order  $q = 0.90$  when  $t \in [0, 150]$ ,

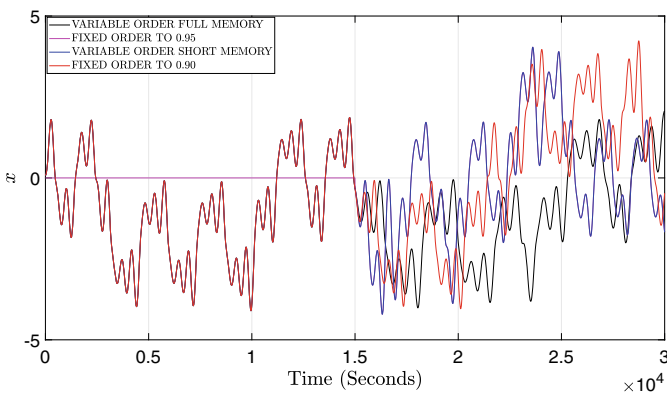


**Fig. 5** Time evolution for state-variable  $x$  of multi-scroll chaotic system (5) with: constant order  $q = 0.9$  (red), constant order  $q = 0.95$  (pink), variable-order  $q(t)$  with short-memory (blue), and variable-order  $q(t)$  with full-memory (black)



and with  $q = 0.95$  when  $t \in [150, 300]$ . On the other hand, the trajectory with full-memory (black color) has a behavior that diverges from the others once  $t \geq 150$ . This is the expected evolution because the full-memory approach considers all past values of  $q = 0.9$  to compute the solutions of recent iterations with  $q = 0.95$ .

## 5 Conclusion

Based on the variable-order theory, in this paper the numerical analysis of a multi-scroll chaotic system using short- and full-memory implications has been presented. In particular, the proposed approach considered two scenarios. The first is related to splitting the simulation time into intervals with a specific fractional-order discarding past values, whereas the latter computes the solution considering both past values from the previous fractional-order and the current values for the new fractional-order. The numerical simulations confirmed that the short-memory approach is similar to compute the solution of the chaotic systems independently and just combine them. In contrast, the full-memory strategy evolved with a distinct dynamical behavior due to including not only current values but also the past values of the fractional-order.

**Acknowledgements** N. Medellín Neri thanks CONACYT-Mexico for the given support through the Master in Sciences scholarship, number: 1072803. The authors also thank VIEP-BUAP for the support through project 100519836-VIEP2021.

## References

1. Wolf, A., Swift, J.B., Swinney, H.L., Vastano, J.A.: Determining Lyapunov exponents From a time series. *Phys. 16D* 285–317 (1985). North-Holland, Amsterdam, 18 October 1984
2. Wang, B., Zhong, S.M., Dong, X.C.: On the novel chaotic secure communication scheme design. *Commun. Nonlinear Sci. Numer. Simul.* **39**, 108–117 (2016)
3. Arroyo, D., Hernandez, F., Orúe, A.B.: Cryptanalysis of a classical chaos-based cryptosystem with some quantum cryptography features. *Int. J. Bifurc. Chaos* **27**(01), 1750004 (2017)
4. Zang, X., Iqbal, S., Zhu, Y., Liu, X., Zhao, J.: Applications of chaotic dynamics in robotics. *Int. J. Adv. Rob. Syst.* **13**(2), 60 (2016)
5. Sajid, M.: Recent developments on chaos in mechanical systems. *Int. J. Theor. Appl. Res. Mech. Eng.* **2**(3), 121–124 (2013)
6. Strogatz, S.: *Nonlinear Dynamics and Chaos: With Applications to Physics, Biology, Chemistry, and Engineering (Studies in Nonlinearity)* (2001)
7. Sun, H.G., Zhang, Y., Baleanu, D., Chen, W., Chen, Y.Q.: A new collection of real world applications of fractional calculus in science and engineering. *Commun. Nonlinear Sci. Numer. Simul.* **64**, 213–231 (2018)
8. Atangana, A., Vermeulen, P.D.: Analytical solutions of a space-time fractional derivative of groundwater flow equation. *Abstr. Appl. Anal.* **2014** (2014). Hindawi
9. Khan, A., Gómez-Aguilar, J.F., Abdeljawad, T., Khan, H.: Stability and numerical simulation of a fractional-order plant-nectar-pollinator model. *Alex. Eng. J.* **59**(1), 49–59 (2020)
10. Pandey, V.: Physical and geometrical interpretation of fractional derivatives in viscoelasticity and transport phenomena (2016)

11. Prathumwan, D., Sawangtong, W., Sawangtong, P.: An analysis on the fractional asset flow differential equations. *Mathematics* **5**(2), 33 (2017)
12. ElSafty, A.H., Tolba, M.F., Said, L.A., Madian, A.H., Radwan, A.G.: A study of the nonlinear dynamics of human behavior and its digital hardware implementation. *J. Adv. Res.* (2020)
13. Diethelm, K.: *The Analysis of Fractional Differential Equations: An Application-Oriented Exposition Using Differential Operators of Caputo Type*. Springer Science & Business Media (2010)
14. Garrappa, R., Kaslik, E., Popolizio, M.: Evaluation of fractional integrals and derivatives of elementary functions: overview and tutorial, vol. 7, *Multidisciplinary Digital Publishing Institute* (2019)
15. Podlubny, I.: *Fractional differential equations*. *Mathematics in Science and Engineering*, vol. 198. Academic, San Diego (1999)
16. Jacobs, B.A.: A new Grünwald-Letnikov derivative derived from a second-order scheme. *Abstr. Appl. Anal.* **2015** (2015). Hindawi
17. Wei, Y., Yin, W., Zhao, Y., Wang, Y.: A new insight into the Grünwald-Letnikov discrete fractional calculus. *J. Comput. Nonlinear Dyn.* **14**(4), 041008 (2019)
18. Jahanshahi, H., Munoz-Pacheco, J.M., Bekiros, S., Alotaibi, N.D.: A fractional-order SIRD model with time-dependent memory indexes for encompassing the multi-fractional characteristics of the COVID-19. *Chaos Solitons & Fractals* **143**, 110632 (2021)
19. Sun, H., Chen, W., Chen, Y.: Variable-order fractional differential operators in anomalous diffusion modeling. *Phys. A* **388**(21), 4586–4592 (2009)
20. Wu, G.C., Deng, Z.G., Baleanu, D., Zeng, D.Q.: New variable-order fractional chaotic systems for fast image encryption. *Chaos: Interdiscip. J. Nonlinear Sci.* **29**(8), 083103 (2019)
21. Coimbra, C.F.: Mechanics with variable-order differential operators. *Ann. Phys.* **12**(11–12), 692–703 (2003)
22. Deng, W., Lü, J.: Design of multidirectional multiscroll chaotic attractors based on fractional differential systems via switching control. *Chaos: Interdiscip. J. Nonlinear Sci.* **16**, 043120 (2006). <https://doi.org/10.1063/1.2401061>
23. Yalcin, M.E., Suykens, J.A.K., Vandewalle, J., Ozoguz, S.: Families of scroll grid attractors. *Int. J. Bifurc. Chaos* **12**(01), 23–41 (2002)
24. Lü, J., Han, F., Yu, X., Chen, G.: Generating 3-D multi-scroll chaotic attractors: a hysteresis series switching method. *Automatica* **40**(10), 1677–1687 (2004)
25. Wu, Y., Wang, C., Deng, Q.: A new 3D multi-scroll chaotic system generated with three types of hidden attractors. *Eur. Phys. J. Spec. Top.* **230**, 1863–1871 (2021)
26. Escalante-González, R.J., Campos-Canton, E.: Generation of self-excited and hidden multi-scroll attractors in multistable systems. *Recent Trends in Chaotic, Nonlinear and Complex Dynamics*, pp. 40–78 (2022)
27. Zhang, S., Zheng, J., Wang, X., Zeng, Z.: Multi-scroll hidden attractor in memristive HR neuron model under electromagnetic radiation and its applications. *Chaos: Interdiscip. J. Nonlinear Sci.* **31**(1), 011101 (2021)
28. Ahmad, S., Ullah, A., Akgül, A.: Investigating the complex behaviour of multi-scroll chaotic system with Caputo fractal-fractional operator. *Chaos Solitons & Fractals* **146**, 110900 (2021)
29. Petráš, I.: *Fractional Order Non-Linear Systems. Modeling, Analysis and Simulation*. Springer editorial (2011)
30. Deng, W., Lü, J.: Design of multidirectional multiscroll chaotic attractors based on fractional differential systems via switching control. *Chaos: Interdiscip. J. Nonlinear Sci.* **16**(4), 043120 (2006)
31. Wolf, A., Swift, J.B., Swinney, H.L., Vastano, J.A.: *Phys.* 16D 285–317 (1985). Department of Physics, University of Texas, Austin, Texas 78712, USA. North-Holland, Amsterdam, 18 October 1984

# Effect of DEN-2 Virus on a Stage-Structured Dengue Model with Saturated Incidence and Constant Harvesting



Kunwer Singh Mathur  and Bhagwan Kumar 

**Abstract** The effect of the DEN-2 virus on dengue infection in children and adults plays an important role. This paper proposes and analyses a nonlinear stage-structured dengue model with a saturated incidence rate and constant harvesting with primary or secondary dengue infection. We analyze the local and global stability of disease-free and endemic equilibria of the system. The disease-free equilibrium is locally and globally asymptotic stable for  $R_0 < 1$  and unstable for  $R_0 > 1$ . We also analyzed the stability of endemic equilibrium for  $R_0 > 1$ , but at  $R_0 = 1$ , the bifurcation exists, which is proven using the center manifold theory. Finally, numerical simulations are drawn to verify these theoretical results.

**Keywords** Dengue · Age-structure · Central manifold · Saturated incidence · Constant harvesting · Optimal control

## 1 Introduction

Dengue fever is the most common mosquito-borne acute arboviral (arthropod-borne viruses), caused by the bite of infected *Aedes aegypti* or *Aedes Albopictus* (also called Asian Tiger mosquito). Dengue virus infection is a leading cause of morbidity and mortality in the tropics and subtropics, mostly in urban and semi-urban areas of the world. The secondary infection of dengue in a person causes more severe complications. Sometimes, the secondary infection occurs in the form of Dengue haemorrhagic fever (DHF) or may have mild/moderate/high fever. It is also responsible for headaches, nausea, vomiting, pain in the muscles, bones, or common rashes on the skin, or most severe Dengue shock syndrome (DSS), which comprise rapid drops in blood pressure, a sudden weak pulse, suffering breathing problems, dilated pupils, cold, clammy skin, dry mouth, and restlessness. Once a patient goes into

---

K. S. Mathur (✉) · B. Kumar  
Department of Mathematics and Statistics, Dr. Harisingh Gour Vishwavidyalaya,  
Sagar 470003, Madhya Pradesh, India  
e-mail: [kmathur1709@gmail.com](mailto:kmathur1709@gmail.com)

DSS, it could be fatal within 12–24 h unless treatment is given immediately. There are four types of dengue virus (i.e., DEN-I, DEN-II, DEN-III, and DEN-IV), which are closely related to the serotypes of the virus that causes dengue infection. The four dengue serotypes, due to the infection, develop permanent immunity, probably lifelong to it, but this does not confer protective immunity against the other three serotypes. Thus, a person living in an endemic area can have as many as four dengue infections during his lifetime, one with each serotype. Moreover, the mosquitoes never recover from the infection and end their life during their infective period [7]. RT-PCR can detect the dengue viral genome in blood specimens up to day five simple precautions. There is no suitable vaccine and no immediate prospect of immunization prevention of the disease. Thus, one can say that dengue/severe dengue has no specific treatment, but the fatality rates can be lower below 1% by early detection of dengue infection and by providing proper medical care.

The transmission dynamics of infectious diseases through Mathematical modeling have been studied since a long time ago. However, the modeling of dengue disease still becomes a challenging question nowadays because of having more compartments in its mathematical model. Only a few researchers developed mathematical models for dengue disease transmission. Esteva and Vargas in [20], obtained the threshold value and the condition for the coexistence of two serotypes of dengue virus in a SIR model without including the age structure, which is not useful in the DHF outbreak of Thailand. The transmission of dengue fever is age-dependent (see, [9, 21]). Feng et al. analyzed the dengue transmission dynamics of the age-structured model [8]. Further, Suprianta is considered and investigated vaccination in a child age class models (see [1, 6]). Although, a severe manifestation of dengue infection develops in those who already have a primary infection [16]. This phenomenon should be considered in the modeling part to better present a realistic situation. Furthermore, the incidence rate will also play a key role in modeling infectious disease transmission. Many incidence rates are applicable in modeling. In the scenario of an epidemic, the bilinear incidence rate is also available, which is based on the law of mass action, which can't explain the disease dynamics [3]. Besides the bilinear incidence rate, the saturated incidence rate is more realistic in comparison to bilinear [5, 13, 18]. Therefore, we include the saturated incidence rate  $\frac{\beta A(t)V(t)}{1+\alpha V}$  which tends to a level of saturation when  $V$  gets large, here  $\alpha$  is the half-saturation constant.

Keeping in mind the above discussion, we will develop and analyze a dynamical system of nonlinear differential equations with two life stages in stage—structure form, and it is assumed that the adult has only primary dengue infection while the children under the age of 15 years have both primary and secondary infection. The presentation of the paper is as follows: In Sect. 2, a mathematical model is proposed, and in Sect. 3, the basic preliminary results including positivity and boundedness are proved. Further, the stability of equilibria is analyzed in Sect. 4 and an optimal control problem is discussed in Sect. 5. Finally, numerical simulations and conclusions are given respectively in Sects. 6 and 7.

## 2 Model Development

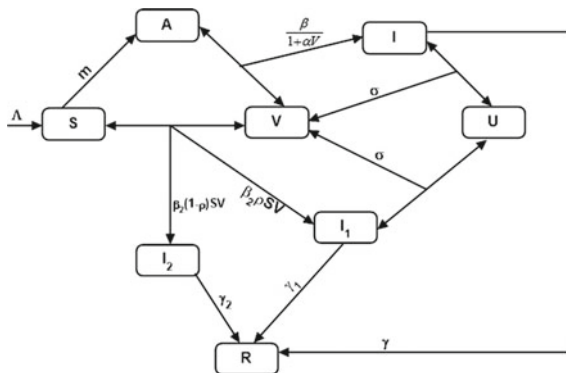
In this section, a mathematical model is proposed to study the effect of the DEN-2 virus in dengue disease transmission. The model is developed for two stages (e.g., children and adults) stage-structured population with a saturated incidence rate and constant harvesting. Let total density of host population be  $N(t)$ , in which, children population can be distinguished into two categories. Under the first category, children will not be infected by any dengue serotype DEN-I, DEN-III, DEN-IV, while in second category children may have an asymptomatic dengue infection. In this model, we will consider only second category's children population, which is divided into two compartment susceptible children  $S(t)$  and infected children. Again, infected children is divided into primary infected  $I_P(t)$  and secondary infected children  $I_S(t)$ . Here, the adult susceptible and infected populations are denoted by  $A(t)$  and  $I(t)$ , respectively, all recovered population including children and adult is represented by  $R(t)$ . Hence  $N(t) = [S(t) + I_P(t) + I_S(t)] + [A(t) + I(t)] + R(t)$ . let  $U(t)$  be the susceptible vector population and  $V(t)$  be the infected vector population such that  $M(t) = U(t) + V(t)$ . The function  $\frac{\beta A(t)V(t)}{1+\alpha V}$  represents the saturated incidence rate. Further, it is assumed that:

- (A1) The total susceptible children population is given by  $S(t) = \nu S(t) + (1 - \nu)S(t)$ ; ( $0 < \nu < 1$ ), where  $\nu S(t)$  represents the primary infection and  $(1 - \nu)S(t)$  represents the secondary infection, when children population interact with infected (DEN-II) mosquitoes.
- (A2) It is assumed that the probability of an adult being secondary infected is usually short. Therefore, we do not consider secondary infection for adults.
- (A3) It is also assumed that only the DEN-II serotype is prevalent at time  $t$ .

Here, all parameters are assumed positive.

The complete transmission dynamics is given in Fig. 1, which leads to propose the following mathematical model:

**Fig. 1** The flow diagram for dengue disease transmission



$$\begin{aligned}
 \frac{dS}{dt} &= \Lambda - \beta_1 \nu SV - \beta_2(1 - \nu)SV - mS - \mu_1 S, \\
 \frac{dI_P}{dt} &= \beta_1 \nu SV - \gamma_1 I_P - \mu_1 I_P, \\
 \frac{dI_S}{dt} &= \beta_2(1 - \nu)SV - \gamma_2 I_S - \mu_1 I_S - \mu I_S, \\
 \frac{dA}{dt} &= mS - \frac{\beta AV}{1 + \alpha V} - \mu_1 A, \\
 \frac{dI}{dt} &= \frac{\beta AV}{1 + \alpha V} - \gamma I - \mu_1 I, \\
 \frac{dR}{dt} &= \gamma_1 I_P + \gamma_2 I_S + \gamma I - \mu_1 R, \\
 \frac{dU}{dt} &= \omega_1 - \sigma U(I_P + I) - \mu_2 U - pU, \\
 \frac{dV}{dt} &= \sigma U(I_P + I) - \mu_2 V - qV.
 \end{aligned}
 \tag{2.1}$$

The model possess the following non-negative initial conditions:

$$S(0) = S_0, I_P(0) = I_{10}, I_S(0) = I_{20}, I(0) = I_0, A(0) = A_0, R(0) = R_0, U(0) = U_0, V(0) = V_0.$$

Here, descriptions of other parameters are given in Table 1.

**Table 1** Description of parameter used in model (2.1)

Parameter	Description
m	Maturation rate from child to adult
$\beta_2$	Transmission rate by which recovered children from prior asymptomatic infection by heterologous serotype are further getting secondary infection by DEN-II serotype
$\gamma_1$	The rate of recovery for the primary infected children
$\gamma_2$	The rate of recovery for the secondary infected children
$\gamma$	The rate of recovery for adults
$\mu_1$	The natural death rate for all human classes
$\mu_2$	The natural death rate of mosquitoes
$\sigma$	Transmission rate of infection to mosquitoes by primary infected children and adults
$\mu$	Disease-induced death rate for the secondary infected children
$\Lambda$	The constant recruitment rate
$\omega_1$	The recruitment rate for vector
$\beta_1$	The rate of transmission of infection
$\beta$	The rate of transmission primary infection
p, q	Constant harvesting rate

### 3 Preliminary Results

#### 3.1 Boundedness

**Lemma 1** *The System (2.1) has a positively invariant and bounded solution in the closed set:*

$$\Gamma = \left\{ (S, I_1, I_S, A, I, R, U, V) \in \mathbb{R}_+^8 : S + I_P + I_S + A + I + R \leq \frac{\Lambda}{\mu_1}, U + V \leq \frac{\omega_1}{\mu} \right\}.$$

**Proof** Consider the system of differential (2.1) in  $\mathbb{R}_+^8$  as

$$\frac{dZ}{dt} = F(t, Z(t)), Z(0) = Z_0 \in \mathbb{R}_+^8 \tag{3.1}$$

Let  $F_j(t, Z) \geq 0$  whenever  $Z \in \mathbb{R}_+^8$  and  $Z_j = 0; j = 1$  to 8. The system (3.1) has non-negative solution (see, [19]). Now, add the model equations of the host population and vector population separately, we can obtain that

$$\frac{dN}{dt} = \Lambda - \mu_1 N - vI_S, \frac{dM}{dt} \leq \omega_1 - \mu M, \tag{3.2}$$

where  $\mu = \min\{\mu_2 + p, \mu_2 + q\}$ . Accordingly,  $\limsup_{t \rightarrow \infty} N(t) = \frac{\Lambda}{\mu_1}$  and  $\limsup_{t \rightarrow \infty} M(t) \leq \frac{\omega_1}{\mu}$ . Thus,  $\Gamma$  is positively invariant and bounded.

Since the state variables  $R$  and  $U$  are not playing any role in infection dynamics, hence we can exclude these variable. Thus, the following model is considered for further analysis:

$$\begin{aligned} \frac{dS}{dt} &= \Lambda - \beta_1 vSV - \beta_2(1 - v)SV - mS - \mu_1 S, \\ \frac{dI_P}{dt} &= \beta_1 vSV - \gamma_1 I_P - \mu_1 I_P, \\ \frac{dI_S}{dt} &= \beta_2(1 - v)SV - \gamma_2 I_S - \mu_1 I_S - \mu I_S, \\ \frac{dA}{dt} &= mS - \frac{\beta AV}{1 + \alpha V} - \mu_1 A, \\ \frac{dI}{dt} &= \frac{\beta AV}{1 + \alpha V} - \gamma I - \mu_1 I, \\ \frac{dV}{dt} &= \sigma \left( \frac{\omega_1}{\mu_2} - V \right) (I_P + I) - \mu_2 V - qV, \end{aligned} \tag{3.3}$$

### 3.2 Existence of Equilibria

The disease-free state  $E_0 = (\tilde{S}, \tilde{I}_P, \tilde{I}_S, \tilde{A}, \tilde{I}, \tilde{V})$  always exists, where

$$\tilde{S} = \frac{\Lambda}{m + \mu_1}, \tilde{I}_P = 0, \tilde{I}_S = 0, \tilde{A} = \frac{m\Lambda}{(m + \mu_1)\mu_1}, \tilde{I} = 0, \tilde{V} = 0.$$

Let us denote  $\beta_3 = (\beta_1\nu + \beta_2(1 - \nu))$ . The endemic state  $E^* = (S^*, I_P^*, I_S^*, A^*, I^*, V^*)$  is given as

$$S^* = \frac{\Lambda}{V^*\beta_3 + (m + \mu_1)}; I_P^* = \frac{\beta_1\nu S^*V^*}{(\gamma_1 + \mu_1)}; I_S^* = \frac{\beta_2(1 - \nu)S^*V^*}{(\gamma_2 + \mu_1 + \nu)}; A^* = \frac{mS^*}{(\frac{\beta V^*}{1 + \alpha V^*} + \mu_1)};$$

$$I^* = \frac{\beta A^*V^*}{(1 + \alpha V^*)(\gamma + \mu_1)};$$

$V^*$  is the root of following quadratic polynomial

$$aV^{*2} + bV^* + c = 0, \tag{3.4}$$

$$a = \sigma\nu\beta_1\Lambda(\beta + \alpha\mu_1)(\gamma + \mu_1) + \beta\beta_3(\mu_2 + q)(\gamma_1 + \mu_1)(\gamma + \mu_1) + \mu_1\alpha\beta_3(\mu_2 + q)(\gamma_1 + \mu_1)(\gamma + \mu_1)$$

$$b = \sigma\beta_1\nu\Lambda\mu_1(\gamma + \mu_1) + m\beta\sigma\Lambda(\gamma_1 + \mu_1) + (\mu_2 + q)(\gamma_1 + \mu_1)(\gamma + \mu_1)(\mu_1\beta_3 + (m + \mu_1)(\beta + \mu_1\alpha)) - \frac{\sigma\omega_1}{\mu}\beta_1\nu\Lambda(\gamma + \mu_1)(\beta + \mu_1\alpha)$$

$$c = \mu_1(\mu_2 + q)(m + \mu_1)(\gamma_1 + \mu_1)(\gamma + \mu_1)(1 - R_0),$$

Let  $V_{\pm}^*$  be the roots of (3.4) then

$$V_{\pm}^* = \frac{-b \pm \sqrt{b^2 - 4ac}}{2a}.$$

Since  $a > 0$ . If  $R_0 > 1$ ,  $c < 0$ . Then it has one positive endemic state exists. If  $R_0 < 1$ ,  $c > 0$ . Then it has two real positive endemic state will exist provided  $b < 0$  and  $b^2 - 4ac > 0$ . And if  $R_0 = 1$ ,  $c = 0$ . Then one positive endemic state exist for  $b < 0$ .



### 3.3 Basic Reproduction Number

We will determine the basic reproduction number by next generation approach [10], the jacobian matrix of the system (3.3)

$$F = \begin{pmatrix} 0 & 0 & 0 & \beta_1 v \tilde{S} \\ 0 & 0 & 0 & \beta_2 (1 - v) \tilde{S} \\ 0 & 0 & 0 & \frac{\beta \tilde{A}}{(1 + \alpha \tilde{V})^2} \\ \frac{\sigma \omega_1}{\mu} & 0 & \frac{\sigma \omega_1}{\mu} & 0 \end{pmatrix}, V = \begin{pmatrix} \gamma_1 + \mu_1 & 0 & 0 & 0 \\ 0 & \gamma_2 + \mu_1 + v & 0 & 0 \\ 0 & 0 & \gamma + \mu_1 & 0 \\ 0 & 0 & 0 & \mu_2 + q \end{pmatrix}$$

clearly at  $E_0$  the next generation matrix is

$$FV^{-1} = \begin{pmatrix} 0 & 0 & 0 & \frac{\beta_1 v \Lambda}{(m + \mu_1)(\mu_2 + q)} \\ 0 & 0 & 0 & \frac{\beta_2 (1 - v) \Lambda}{(m + \mu_1)(\mu_2 + q)} \\ 0 & 0 & 0 & \frac{\beta m \Lambda}{\mu_1 (m + \mu_1)(\mu_2 + q)} \\ \frac{\sigma \omega_1}{\mu(\gamma_1 + \mu_1)} & 0 & \frac{\sigma \omega_1}{\mu(\gamma + \mu_1)} & 0 \end{pmatrix}.$$

We known that the largest eigenvalue of  $FV^{-1}$  is the basic reproduction number  $R_0$ . Which is computed as

$$R_0 = \frac{\sigma \Lambda \omega_1}{\mu(\mu_2 + q)(m + \mu_1)} \left[ \frac{\beta m}{\mu_1(\gamma + \mu_1)} + \frac{v \beta_1}{(\gamma_1 + \mu_1)} \right].$$

## 4 Stability Analysis

**Theorem 1** *The disease-free state is locally and globally asymptotically stable for  $R_0 < 1$  and unstable for  $R_0 > 1$ .*

**Proof** The jacobian matrix[J] for the system (3.3) at  $E_0$  is

$$J[E_0] = \begin{pmatrix} -(m + \mu_1) & 0 & 0 & 0 & 0 & -\frac{\beta_3 \Lambda}{\frac{m + \mu_1}{\beta_1 v \Lambda}} \\ 0 & -(\gamma_1 + \mu_1) & 0 & 0 & 0 & \frac{m + \mu_1}{\beta_1 v \Lambda} \\ 0 & 0 & -(\gamma_2 + \mu_1 + v) & 0 & 0 & \beta_2(1 - v) \frac{\Lambda}{m + \mu_1} \\ m & 0 & 0 & -\mu_1 & 0 & -\frac{\beta m \Lambda}{\mu_1(m + \mu_1)} \\ 0 & 0 & 0 & 0 & -(\gamma + \mu_1) & \frac{\beta m \Lambda}{\mu_1(m + \mu_1)} \\ 0 & \frac{\omega_1 \sigma}{\mu} & 0 & 0 & \frac{\omega_1 \sigma}{\mu} & -(\mu_2 + q) \end{pmatrix}$$

The eigenvalue of  $[J(E_0)]$  are  $-m - \mu_1, -\gamma_2 - \mu_1 - v, -\mu_1$  and other all the eigenvalue are given cubic polynomial  $\lambda^3 + B_1\lambda^2 + B_2\lambda + B_3$ . Where

$$B_1 = 2\mu_1 + \gamma_1 + \gamma + \mu_2 + q, B_2 = (\mu_2 + q)(2\mu_1 + \gamma_1 + \gamma) + (\gamma_1 + \mu_1)(\gamma + \mu_1) - \frac{\sigma \omega_1}{\mu \mu_1}(\beta_1 v \tilde{S} + \beta \mu_1 \tilde{A})$$

$$B_3 = (\mu_2 + q)(\gamma + \mu_1)(\gamma_1 + \mu_1)(1 - R_0).$$

It is clear that  $B_1 > 0$  and  $B_3 > 0$  for  $R_0 < 1$ . And

$$B_1 B_2 - B_3 = (2\mu_1 + \gamma_1 + \gamma + \mu_2 + q)(\mu_2 + q)(2\mu_1 + \gamma_1 + \gamma) + (\gamma_1 + \mu_1)(\gamma + \mu_1) + (\gamma + \mu_1)(\gamma_1 + \mu_1)(\mu_2 + q)(1 - R_0)$$

is positive if  $R_0 < 1$ . By Routh-Hurwitz criterion the polynomial has eigenvalue with negative real part if  $R_0 < 1$ . This is showing the local stability at  $E_0$ . Now by Descartes Rule of signs it has one positive eigenvalue if  $R_0 > 1$ . Hence, at  $E_0$  will be Unstable if  $R_0 > 1$ . Next we proof the system has global stability at  $E_0$ .

Let  $L(I_P, I, V) = \frac{\sigma \Lambda I_P}{(\gamma_1 + \mu_1)} + \frac{\sigma \Lambda I}{(\gamma + \mu_1)} + (\mu_2 + q)V$  be the positive definite function

$$\dot{L} = \frac{\sigma \Lambda}{\gamma_1 + \mu_1}(\beta_1 v S V - \gamma_1 I_P - \mu_1 I_P) + \frac{\sigma \Lambda}{\gamma + \mu_1}(\frac{\beta A V}{1 + \alpha V} - \gamma I - \mu_1 I) + (\mu_2 + q)(\sigma(\frac{2\omega_1}{\mu} - V)(I_P + I) - \mu_2 V - q V)$$

$\dot{L} \leq V \mu_2^2 (R_0^2 - 1) \leq 0$  for  $R_0 < 1$ . Therefore  $L(I_P, I, V)$  is Lyapunov function for  $R_0 < 1$ . At  $V = 0, \dot{L} = 0$ . Because  $E_0$  is the largest invariant set which contains the subset in which  $V=0$ . by LaSalle’s invariance principal [15], at  $E_0$  Locally and globally stable for  $R_0 < 1$ .

**Theorem 2** The system (3.3) has a locally asymptotically stable endemic state  $E^*$  for  $R_0 > 1$  and it has the forward bifurcation at  $R_0 = 1$ .

**Proof** Let  $\beta_1 = \beta_1^c$  is bifurcation parameter corresponds to  $R_0 = 1$ ,

$$\beta_1^c = \frac{\gamma_1 + \mu_1}{v} \left( \frac{\mu(\mu_2 + q)(m + \mu_1)}{\sigma \Lambda \omega_1} - \frac{\beta m}{\mu_1(\gamma + \mu_1)} \right)$$

Let  $\delta = (\delta_1, \delta_2, \delta_3, \delta_4, \delta_5, \delta_6)^T$  be a right eigenvector corresponding to the eigenvalue zero. It is given by

$$\begin{pmatrix} -(m + \mu_1) & 0 & 0 & 0 & 0 & -(\beta_1^c v + \beta_2(1 - v))\tilde{S} \\ 0 & -(\gamma_1 + \mu_1) & 0 & 0 & 0 & \beta_1^c v \tilde{S} \\ 0 & 0 & -(\gamma_2 + \mu_1 + v) & 0 & 0 & \beta_2(1 - v)\tilde{S} \\ m & 0 & 0 & -\mu_1 & 0 & -\beta \tilde{A} \\ 0 & 0 & 0 & 0 & -(\gamma + \mu_1) & \beta \tilde{A} \\ 0 & \frac{\omega_1 \sigma}{\mu} & 0 & 0 & \frac{\omega_1 \sigma}{\mu} & -(\mu_2 + q) \end{pmatrix} \begin{pmatrix} \delta_1 \\ \delta_2 \\ \delta_3 \\ \delta_4 \\ \delta_5 \\ \delta_6 \end{pmatrix} = 0$$

Solving above equation, the right eigenvector is

$$\left( \delta_1 = 0, \delta_2 = \frac{\beta_1^c v}{(\gamma_1 + \mu_1)}, \delta_3 = 0, \delta_4 = 0, \delta_5 = \frac{\beta m}{\mu_1(\gamma_1 + \mu_1)}, \delta_6 = \frac{(m + \mu_1)(\gamma + \mu_1)}{\Lambda(\gamma_1 + \mu_1)} \right).$$

Further, the left eigenvector  $v = (v_1, v_2, v_3, v_4, v_5, v_6)^T$  corresponding to the eigenvalue zero such that  $\delta \cdot v = 1$  is

$$\left( v_1 = 0, v_2 = \frac{\omega_1 \sigma \Lambda}{(\mu_2 + q)(m + \mu_1)(\gamma + \mu_1 + \mu_2 + q)}, v_3 = 0, v_4 = 0, v_5 = \frac{\omega_1 \sigma \Lambda \mu (\gamma_1 + \mu_1)}{\mu(\mu_2 + q)(m + \mu_1)(\gamma + \mu_1)(\gamma + \mu_1 + \mu_2 + q)}, v_6 = \frac{\mu \Lambda (\gamma_1 + \mu_1)}{(\mu_2 + q)(m + \mu_1)(\gamma + \mu_1 + \mu_2 + q)} \right).$$

Let  $S = x_1, I_P = x_2, I_S = x_3, A = x_4, I = x_5, V = x_6$ . The system (3.3) becomes,

$$\begin{aligned} \frac{dx_1}{dt} &= \Lambda - \beta_1 v x_1 x_6 - \beta_2(1 - v)x_1 x_6 - m x_1 - \mu_1 x_1 := f_1 \\ \frac{dx_2}{dt} &= \beta_1 v x_1 x_6 - \gamma_1 x_2 - \mu_1 x_2 := f_2 \\ \frac{dx_3}{dt} &= \beta_2(1 - v)x_1 x_6 - \gamma_2 x_3 - \mu_1 x_3 - \mu x_3 := f_3 \\ \frac{dx_4}{dt} &= m x_1 - \frac{\beta x_4 x_6}{1 + \alpha x_6} - \mu_1 x_4 := f_4 \\ \frac{dx_5}{dt} &= \frac{\beta x_4 x_6}{1 + \alpha x_6} - \gamma x_5 - \mu_1 x_5 - p x_5 := f_5 \\ \frac{dx_6}{dt} &= \sigma \left( \frac{\omega_1}{\mu} - x_6 \right) (x_2 + x_5) - \mu_2 x_6 - q x_6 := f_6. \end{aligned} \tag{4.1}$$

The partial derivatives at  $(E_0)$  are

$$\frac{\partial^2 f_2}{\partial x_6 \partial \beta_1} = \frac{v \Lambda}{(m + \mu_1)}, \frac{\partial^2 f_5}{\partial x_6^2} = -\frac{2m \Lambda \alpha}{(m + \mu_1) \mu_1}, \frac{\partial^2 f_6}{\partial x_2 \partial x_6} = \frac{\partial^2 f_6}{\partial x_6 \partial x_2} = \frac{\partial^2 f_6}{\partial x_6 \partial x_5} = \frac{\partial^2 f_6}{\partial x_5 \partial x_6} = -\sigma$$

and remaining are zero. From Theorem 4.1 [4]. The coefficient **a** and **b** are computed as,

$$\mathbf{a} = 2v_6\delta_2\delta_6 \frac{\partial^2 f_6}{\partial x_2 \partial x_6} + 2v_6\delta_5\delta_6 \frac{\partial^2 f_6}{\partial x_5 \partial x_6} + v_5\delta_6\delta_6 \frac{\partial^2 f_5}{\partial x_6 \partial x_6}, \mathbf{b} = v_2\delta_6 \frac{\partial^2 f_2}{\partial x_6 \partial \beta_1}$$

Now substitute all the partial derivatives and left and right eigenvectors we get,

$$\mathbf{a} = -\frac{2\sigma(\gamma + \mu_1)}{\mu_1(\mu_2 + q)(\gamma_1 + \mu_1)(\gamma + \mu_1 + \mu_2 + q)}(\mu\mu_1\beta_1v + \mu\beta m + \omega_1m\alpha),$$

$$\mathbf{b} = \frac{\omega_1\sigma v\Lambda(\gamma + \mu_1)}{(\mu_2 + q)(m + \mu_1)(\gamma_1 + \mu_1)(\gamma + \mu_1 + \mu_2 + q)}.$$

Clearly **a** < 0 and **b** > 0 is always. using Theorem 4.1 [4]. Forward bifurcation is possible and the *E\** is found to be locally asymptotically stable for *R*<sub>0</sub> > 1.

### 5 Optimal Control Problem

In this section, we develop an optimal control problem for the model system (2.1), control the spread of an epidemic, it is imperative to propagate awareness amongst individuals, but a successful intervention strategy reduces the number of infective individuals with minimum cost [12] an effectual way of procuring the best strategy for information propagation is using optimal control theory [11, 14]

$$J[u(t)] = \int_0^T [z_1I(t) + z_2u^2(t)]dt, \tag{5.1}$$

$$\begin{aligned} \frac{dS}{dt} &= \Lambda - \beta_1vSV - \beta_2(1-v)SV - mS - \mu_1S, \\ \frac{dI_P}{dt} &= \beta_1vSV - \gamma_1I_P - \mu_1I_P, \\ \frac{dI_S}{dt} &= \beta_2(1-v)SV - \gamma_2I_S - \mu_1I_S - \mu I_S, \\ \frac{dA}{dt} &= mS - \frac{\beta AV}{1 + \alpha V} - \mu_1A, \\ \frac{dI}{dt} &= \frac{\beta AV}{1 + \alpha V} - \frac{u(t)I}{1 + \omega I} - \gamma I - \mu_1I, \\ \frac{dR}{dt} &= \gamma_1I_P + \gamma_2I_S + \frac{u(t)I}{1 + \omega I} + \gamma I - \mu_1R, \\ \frac{dU}{dt} &= \omega_1 - \sigma U(I_P + I) - \mu_2U - pU, \\ \frac{dV}{dt} &= \sigma U(I_P + I) - \mu_2V - qV, \end{aligned} \tag{5.2}$$

with initial condition

$$S(0) \geq 0, I_P(0) \geq 0, I_S(0) \geq 0, I(0) \geq 0, A(0) \geq 0, R(0) \geq 0, U(0) \geq 0, V(0) \geq 0$$

The coefficient  $z_1$  and  $z_2$  in the cost functional are balancing coefficients transforming the integral into currency expended. The first in the cost functional represent the cost due to infection caused by epidemic and last term represent cost associated with the implementation of awareness program. Quadratic expression of control indicates non-linear cost arising at high implementation level. find an optimal control  $u^*(t)$  such that

$$J(u^*) = \min_{u \in \mathcal{U}} J(u) \tag{5.3}$$

where control set is defined as

$$Z = \{u(t) : 0 \leq u(t) \leq u_{\max}; 0 \leq t \leq T, u(t) \text{ is Lebesgue measurable}\}.$$

**Theorem 3** *There exist an optimal control  $u^* \in Z$  such that  $J(u^*) = \min[J(u)]$  corresponding to the control system (5.1)–(5.2)*

**Proof** The boundedness of solution of system (5.2) asserts the existence of solution to control system using results [17] Therefore, set of controls and corresponding state variables is nonempty. The control set is closed and convex by definition. The solution of system (5.1) are bounded above by a linear function in state and control. The integrand in the cost functional,  $z_1 I(t) + z_2 u^2(t)$  is convex on control set  $Z$ . and also there exists  $r_1, r_2 > 0$  and  $m > 1$  such that,  $z_1 I(t) + z_2 u^2(t) \geq r_1 + r_2 |u^2(t)|^m$  where  $r_1$  depends upon the upper bound of  $I(t)$  and  $r_2 = z_2$  Hence, the existence of an optimal control is established.

### 5.1 Characterization of Optimal Control Function

The Pontryagin’s Maximum Principle [2] can be used for the differential systems of adjoint variable and characterization of optimal control. we define the Hamiltonian as,

$$\begin{aligned} H(S, I_P, I_S, A, I, R, U, V, u, \lambda) = & L(S, I_P, I_S, A, I, R, U, V, u, \lambda) + \lambda_1 \dot{S} + \lambda_2 \dot{I}_P + \lambda_3 \dot{I}_S \\ & + \lambda_4 \dot{A} + \lambda_5 \dot{I} + \lambda_6 \dot{R} + \lambda_7 \dot{U} + \lambda_8 \dot{V} = z_1 I(t) + z_2 u(t)^2 + \lambda_1 (\Lambda - \beta_1 vSV - \beta_2 (1 - v)SV \\ & - mS - \mu_1 S) + \lambda_2 (\beta_1 vSV - \gamma_1 I_P - \mu_1 I_P) + \lambda_3 (\beta_2 (1 - v)SV - \gamma_2 I_S - \mu_1 I_S - \mu I_S) \\ & + \lambda_4 (mS - \frac{\beta AV}{1 + \alpha V} - \mu_1 A) + \lambda_5 (\frac{\beta AV}{1 + \alpha V} - \frac{u(t)I}{1 + \omega I} - \gamma I - \mu_1 I) \tag{5.4} \\ & + \lambda_6 (\gamma_1 I_P + \gamma_2 I_S + \frac{u(t)I}{1 + \omega I} + \gamma I - \mu_1 R) + \lambda_7 (\omega_1 - \sigma U(I_P + I) - \mu_2 U - pU) \\ & + \lambda_8 (\sigma U(I_P + I) - \mu_2 V - qV) \end{aligned}$$

where  $\lambda = (\lambda_1, \lambda_2, \lambda_3, \lambda_4, \lambda_5, \lambda_6, \lambda_7, \lambda_8)$  is known as adjoint variable. We obtain minimized cost functional subject to state variable for the given optimal control  $u^*$

and state variable there exists adjoint variable  $\lambda_i$  satisfying the following canonical equations,

$$\begin{aligned}
 \frac{d\lambda_1}{dt} &= (\beta_1 v V + m + \mu_1)\lambda_1 + (\beta_2(1 - v)V - \beta_1 v V)\lambda_2 - \beta_2(1 - v)V\lambda_3 - m\lambda_4, \\
 \frac{d\lambda_2}{dt} &= (\gamma_1 + \mu_1)\lambda_2 - \gamma_1\lambda_6 - \sigma U\lambda_7 - \sigma U\lambda_8, \\
 \frac{d\lambda_3}{dt} &= (\gamma_2 + \mu_1 + \mu)\lambda_3 - \gamma_2\lambda_6, \\
 \frac{d\lambda_4}{dt} &= \left(\frac{\beta V}{1 + \alpha V} + \mu_1\right)\lambda_4 - \frac{\beta V}{1 + \alpha V}\lambda_5, \\
 \frac{d\lambda_5}{dt} &= -z_1 + \left(\frac{u(t)}{(1 + \omega I)^2} + \mu_1 + \gamma\right)\lambda_5 - \left(\frac{u(t)}{(1 + \omega I)^2} + \gamma\right)\lambda_6 + \sigma U\lambda_7 - \sigma U\lambda_8, \\
 \frac{d\lambda_6}{dt} &= \mu_1\lambda_6, \\
 \frac{d\lambda_7}{dt} &= (\mu_2 + p)\lambda_7, \\
 \frac{d\lambda_8}{dt} &= (\mu_2 + q)\lambda_8,
 \end{aligned}
 \tag{5.5}$$

with transversality condition  $\lambda_i(T) = 0$ ,  $i=1$  to  $8$ . The Hamiltonian is minimized with respect to  $u$  at the optimal value  $u^*$ . Now from the optimality condition, we have  $\frac{\partial H}{\partial u} = 0$  at  $u = u^*$ , so

$$H = z_2 u^2 + \lambda_5 \left(\frac{-u(t)I}{1 + \omega I}\right) + \lambda_6 \left(\frac{u(t)I}{1 + \omega I}\right) + \text{terms without } u(t)$$

differentiating  $H$  with respect to  $u$  gives:

$$\frac{\partial H}{\partial u} = 2z_2 u^* - (\lambda_5 - \lambda_6) \frac{I}{1 + \omega I^*} = 0. \text{ Thus we get, } u^* = \frac{I}{2z_2(1 + \omega I^*)} (\lambda_5 - \lambda_6)$$

Now from the above findings along with the characteristics of control set  $U$ , we have

$$u^* = \begin{cases} 0 & \text{if } \frac{I^*}{2z_2(1 + \omega I^*)} < 0, \\ \frac{I^*}{2z_2(1 + \omega I^*)} & \text{if } 0 \leq \frac{I^*}{2z_2(1 + \omega I^*)} \leq 1, \\ 1 & \text{if } \frac{I^*}{2z_2(1 + \omega I^*)} > 1, \end{cases}$$

### 6 Numerical Simulation

We discuss the numerical simulation of the model as the parameters in the system (2.1) are varified in MATLAB using ODE45. We assume that arbitrary initial condition  $Y_1 = [0.8, 0.5, 0.4, 0.07, 0.1, 0.5, 20, 5]$ ,  $Y_2 = [0.6, 0.3, 0.6, 0.1, 0.6, 0.8, 22,$

12],  $Y_3 = [0.4, 0.9, 0.2, 0.4, 0.8, 5, 30, 7]$ ,  $Y_4 = [1.5, 0.1, 0.9, 2.9, 0.8, 2, 40, 20]$  and parameters value are  $m = 0.00183$ ,  $\beta_2 = 0.7$ ,  $\gamma_1 = 0.3$ ,  $\gamma_2 = 0.1428$ ,  $\gamma = 0.5$ ,  $\mu_1 = 0.0000457$ ,  $\mu_2 = 0.0714$ ,  $\sigma = 0.05$ ,  $\mu = 0.001$ ,  $\Lambda = 0.00001$ ,  $\omega_1 = 50$ ,  $\nu = 0.5$ ,  $\beta_1 = 0.005$ ,  $\beta = 0.003$ ,  $\alpha = 0.09$ ,  $p = 0.0001$ ,  $q = 0.0001$ . The basic reproduction number  $R_0 = 0.76 (< 1)$ . So,  $E_0$  exits and it is calculated as  $E_0(S, I_P, I_S, A, I, R, U, V) = (0.0345, 0, 0, 0.1234, 0, 0, 512.280, 0)$ . We can see from the projections of phase plot in  $I_P - I_S - I$  hyperplanes drawn in Figs.2 and 3, that the solution trajectories converge to the state  $E_0$ . This is showing that global stability at  $E_0$ . Now  $\beta_1 = 0.1$ ,  $\beta = 0.05$  the basic reproduction number  $R_0 = 2.1432 (> 1)$ . So,  $E^*$  will exit. And it is calculated as  $E^*(S, I_P, I_S, A, I, R, U,$

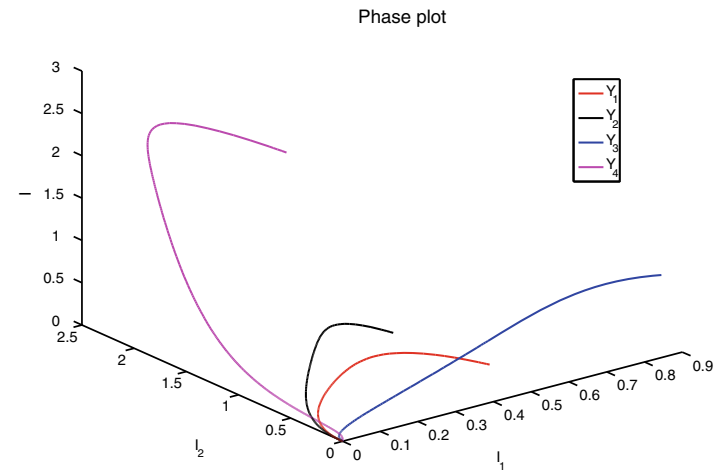


Fig. 2 A 3D  $I_P - I_S - I$  this is showing that the convergence to  $E_0$

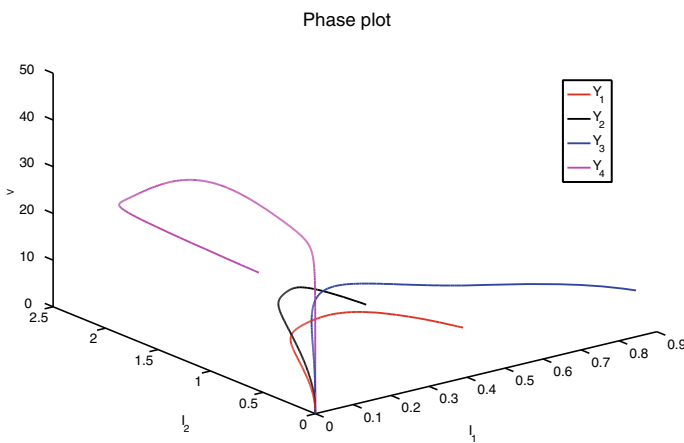
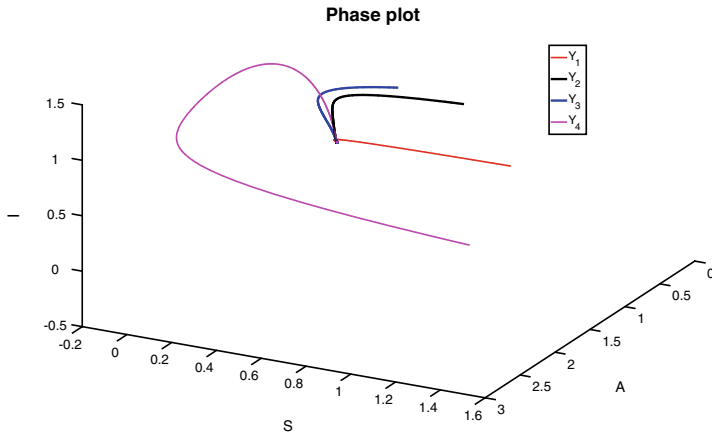
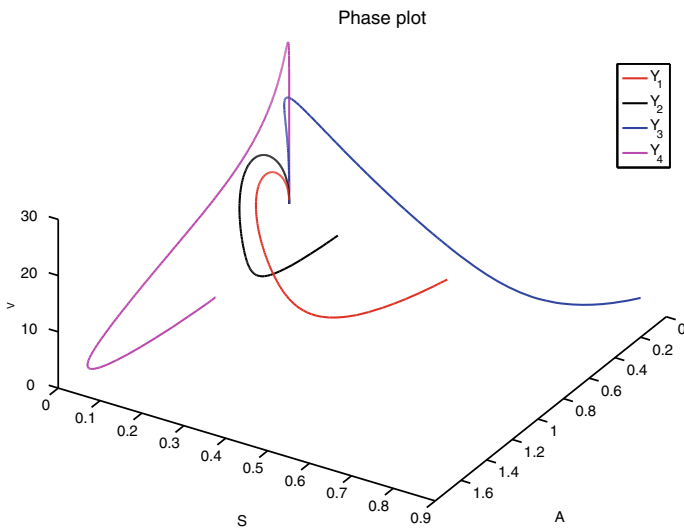


Fig. 3 A 3D  $I_P - I_S - V$  this is showing that the convergence to  $E_0$



**Fig. 4** A 3D  $A - S - I$  this is showing that the convergence to  $E^*$



**Fig. 5** A 3D  $A - S - V$  this is showing that the convergence to  $E^*$

$V) = (0.00463, 0.000001325, 0.00008542, 0.0022694, 0.0000012546, 0.24961, 512.267, 0.0032145)$ . The projections of phase plot in  $I_P, I_S, V$  hyperplanes have been drawn in Figs.4 and 5. The solution trajectories are found to converge to the state  $E^*$ , so the stability of the endemic equilibrium state.



## 7 Conclusion

We have constructed a stage-structured dengue model with a saturated incidence rate and constant harvesting to see the effect of the DEN-2 virus on the primary/secondary infection in children and adults. We have calculated the basic reproduction number  $R_0$ . It has been analyzed that the disease-free equilibrium point is locally and globally asymptotically stable for  $R_0 < 1$  and unstable for  $R_0 > 1$ . Further, locally asymptotically stable endemic state  $E^*$  for  $R_0 > 1$  and it has the forward bifurcation at  $R_0 = 1$ . An optimal control system has been constructed and by using the pontryagin maximum principle, we obtain the minimized cost function. From the numerical simulation, we verified some analytical results of the theorem. In disease dynamics, a basic reproduction number plays an essential role in controlling disease outbreaks. Here  $R_0$  is the function of harvesting coefficient  $q$  only and not dependent on  $p$ , which suggests that the harvesting of susceptible mosquitos has no impact on the dynamics. However, the harvesting coefficient  $q$  plays a crucial role in controlling dengue infection. Hence, the Govt. policies can be regulated through the basic reproduction number obtained in this paper, and the scientists can make better policies to stop the outbreak. Moreover, the endemic equilibrium point became saturated and depended on the half-saturation constant  $\alpha$ . Finally, it is concluded that the saturated incidence rate and vector harvesting rate have a more significant impact on the system's dynamics, which determines a more realistic analysis and is more practical from an epidemic point of view.

**Acknowledgements** The work is carried out under the project sponsored by Science and Engineering Research Board (SERB), New Delhi, India with file no. EMR/2017/001234.

## References

1. Alera, M.T., Srikiatkachorn, A., Velasco, J.M., Tac-An, I.A., Lago, C.B., Clapham, H.E., Fernandez, S., Levy, J.W., Thaisomboonsuk, B., Klungthong, C., et al.: Incidence of dengue virus infection in adults and children in a prospective longitudinal cohort in the philippines. *PLoS Negl. Trop. Dis.* **10**(2), e0004337 (2016)
2. Bellman, R.: *The Mathematical Theory of Optimal Processes* (1965)
3. Cai, L., Li, X., Ghosh, M., Guo, B.: Stability analysis of an HIV/AIDS epidemic model with treatment. *J. Comput. Appl. Math.* **229**(1), 313–323 (2009)
4. Castillo-Chavez, C., Song, B.: Dynamical models of tuberculosis and their applications. *Math. Biosci. Eng.* **1**(2), 361–404 (2004)
5. Chikaki, E., Ishikawa, H.: A dengue transmission model in thailand considering sequential infections with all four serotypes. *J. Infection Dev. Ctries.* **3**(09), 711–722 (2009)
6. Deen, J.L., Harris, E., Wills, B., Balmaseda, A., Hammond, S.N., Rocha, C., Dung, N.M., Hung, N.T., Hien, T.T., Farrar, J.J.: The who dengue classification and case definitions: time for a reassessment. *Lancet* **368**(9530), 170–173 (2006)
7. Enweronu-Laryea, C.C., Adjei, G.O., Mensah, B., Duah, N., Quashie, N.B.: Prevalence of congenital malaria in high-risk Ghanaian newborns: a cross-sectional study. *Malaria J.* **12**(1), 17 (2013)

8. Feng, W.J., Cai, L.M., Liu, K.: Dynamics of a dengue epidemic model with class-age structure. *Int. J. Biomath.* **10**(08), 1750109 (2017)
9. Guzmán, M.G., Kouri, G., Bravo, J., Valdes, L., Susana, V., Halstead, S.B.: Effect of age on outcome of secondary dengue 2 infections. *Int. J. Infect. Diseases.* **6**(2), 118–124 (2002)
10. Jones, J.H.: Notes on  $r_0$ . Department of Anthropological Sciences, California (2007)
11. Kandhway, K., Kuri, J.: How to run a campaign: optimal control of sis and sir information epidemics. *Appl. Math. Comput.* **231**, 79–92 (2014)
12. Kar, T., Jana, S.: A theoretical study on mathematical modelling of an infectious disease with application of optimal control. *Biosystems* **111**(1), 37–50 (2013)
13. Khan, M.F., Alrabaiah, H., Ullah, S., Khan, M.A., Farooq, M., bin Mamat, M., Asjad, M.I.: A new fractional model for vector-host disease with saturated treatment function via singular and non-singular operators. *Alex. Eng. J.* **60**(1), 629–645 (2021)
14. Kumar, B.: Role of optimal control in the smoking epidemic model with media awareness. *Int. Res. J. Moderniz. Eng. Technol. Sci.* **2**(10), 762–768 (2020)
15. LaSalle, J.P.: *The Stability of Dynamical Systems*, vol. 25. Siam (1976)
16. L'Azou, M., Moureau, A., Sarti, E., Nealon, J., Zambrano, B., Wartel, T.A., Villar, L., Capeding, M.R., Ochiai, R.L.: Symptomatic dengue in children in 10 Asian and Latin American countries. *New Engl. J. Med.* **374**(12), 1155–1166 (2016)
17. Lukes, D.L.: *Differential Equations: classical to Controlled*. Elsevier (1982)
18. Mathur, K.S., Narayan, P.: Dynamics of an [...] epidemic model with vaccination and saturated incidence rate. *Int. J. Appl. Comput. Math.* **4**(5) (2018)
19. Perko, L.: *Differential Equations and Dynamical Systems*, vol. 7. Springer Science & Business Media (2013)
20. Pongsumpun, P., Tang, I.: Transmission of dengue hemorrhagic fever in an age structured population. *Math. Comput. Modell.* **37**(9–10), 949–961 (2003)
21. Sharp, T.W., Wallace, M.R., Hayes, C.G., Sanchez, J.L., DeFraités, R.F., Arthur, R.R., Thornton, S.A., Batchelor, R.A., Rozmajzl, P.J., Hanson, R.K., et al.: Dengue fever in us troops during operation restore hope, Somalia, 1992–1993. *Am. J. Trop. Med. Hyg* **53**(1), 89–94 (1995)

# Modulational Instability Analysis in An Isotropic Ferromagnetic Nanowire with Higher Order Octupole-Dipole Interaction



T. Pavithra , L. Kavitha , Prabhu, and Awadesh Mani

**Abstract** We investigate the nonlinear spin excitation in a Heisenberg ferromagnetic nanowire with the higher order octupole-dipole interaction. In this study, the nonlinear dynamical equation of motion is obtained by a semi-classical limit employing Glauber's coherent state analysis along with Holstein-Primakoff bosonic representation for the spin operators. In the framework of linear stability analysis, we employ the Modulational Instability for the ferromagnetic nanowire with octupole-dipole interaction. It is found that the occurrence of octupole-dipole exchange interaction systematically helps to localize the excitation which improve the growth of high amplitude localized robust solitons in the ferromagnetic nanowire lattice.

**Keywords** Nonlinear excitation · Octupole-dipole interaction · Modulational instability analysis · Heisenberg ferromagnetic nanowire

## 1 Introduction

It is more interesting to study the one dimensional classical Heisenberg ferromagnetic nanowire with several types of magnetic interactions which reveals the soliton spin excitation and integrability characteristics [1, 2]. In this view, the parallel symmetry of spins in the ferromagnetic nanostructures, especially in nanowire is controlled by bilinear spin-spin exchange interaction and higher order exchange interactions like magnetic octupole-dipole and biquadratic exchange interactions found to play a predominant role in recent years [3–6]. The integrability behaviour of ferromag-

---

T. Pavithra · L. Kavitha (✉)

Department of Physics, Central University of Tamil Nadu, Thiruvavur 610 005, Tamil Nadu, India  
e-mail: [lkavitha@cutn.ac.in](mailto:lkavitha@cutn.ac.in)

Prabhu

Department of Chemistry, Periyar University, Salem 636 011, Tamil Nadu, India

A. Mani

Condensed Matter Physics Division, Indira Gandhi Centre for Atomic Research, Kalpakkam 603102, Tamil Nadu, India

netic systems in the view of biquadratic interaction is significantly established in both classically and quantum mechanically. Moriya draw out the concept of super exchange interaction to incorporate the spin-orbit coupling in a Heisenberg spin of Hamiltonian along with the biquadratic interaction, there look to be a third degree exchange interaction found to be  $(S_i \cdot S_{i+1})(S_{i+1} \cdot \vec{k})^2$ . Here ‘ $k$ ’ is fixed to be a constant vector [7–10]. Substantially, this interaction was elucidated as octupole-dipole interaction expressing the hyperfine construction of  $\Gamma_3$  ions in cubic symmetry and additionally performing as fascinating nonlinear dynamical model with higher order interactions having much attention in field of nonlinear physics. Mostly, the research works are only related with magnetic systems have been concerned to the nearest-neighbor (NN) exchange interaction [11] and only very few research works handle with the interaction of next-nearest neighbor (NNN) one. However, for numerous materials with complex structure which is essential to take into account of the NNN spin-spin interactions in the ferromagnetic system. Daniel et al. [12] has investigated the octupole-dipole interaction through Painleve singularity structure analysis, where they explored the integrable spin chain model with nonlinear spin excitation in the Heisenberg ferromagnet. Further, Bing Tang et al. [13] studied effect of octupole-dipole interaction and localization of quantum breather and soliton in the anisotropic ferromagnetic chain through quantum approach whereas they consider the localised Hatree states as quantum breathers. And also, Kavitha et al. [15] informatively studied the effective nonlinear excitation of spin in anisotropic one dimensional Heisenberg ferromagnetic lattice by semi-classical approach in the presence of octupole-dipole interaction where using soliton flipping they analyzed the magnetic switching process under the influence of octupole-dipole interaction. Recently, Djoufack et al.[14] reported the localisation of bright intrinsic localised modes in an one dimensional isotropic ferromagnets with octupole-dipole magnetic interaction. In the connection with above research works, we planning to study the energy localisation in ferromagnetic nanowire of one dimensional with the higher order octupole-dipole magnetic exchange interactions of NN and NNN spins. This paper work is arranged in a following manner. First we introduce our dynamical model: a Heisenberg spin model of ferromagnetic nanowire with first and second neighbor exchange interaction, biquadratic and octupole-dipole interactions and we derived the corresponding equations of motion. The analytical study is attribute to the exploration of Modulational Instability (MI) analysis of a plane wave generating in a ferromagnetic system of discrete lattice of nanowire and also we illustrate the existence of symmetric solitons in the spin lattice of ferromagnetic nanowire.

## 2 Hamiltonian Model of the Dynamical System

We contemplate the motion of an isotropic one dimensional ferromagnetic nanowire of  $N$  spins which can be expressed by the Hamiltonian with nearest (NN) and next nearest neighbor(NNN) higher order magnetic spin interactions

$$\begin{aligned}
H = - \sum_n & \left[ 2J_1 \left[ (\vec{S}_n \cdot \vec{S}_{n+1}) + (\vec{S}_n \cdot \vec{S}_{n+2}) \right] + 2J_2 \left[ (\vec{S}_n \cdot \vec{S}_{n+1})^2 + (\vec{S}_n \cdot \vec{S}_{n+2})^2 \right] \right. \\
& \left. + 2J_3 \left[ (\vec{S}_n \cdot \vec{S}_{n+1})(\vec{S}_{n+1} \cdot \hat{k})^2 + (\vec{S}_n \cdot \vec{S}_{n+2})(\vec{S}_{n+2} \cdot \hat{k})^2 \right] \right], \quad (1)
\end{aligned}$$

where  $\vec{S}_n = (S_n^x, S_n^y, S_n^z)$  is the spin at the lattice site  $n$  and  $\vec{S}_n \cdot \vec{S}_n = S(SH)$ . There are three types of interactions are involved in (1):

- (i) The first two expressions correspond to  $J_1$  define the bilinear NN and NNN exchange interactions in the isotropic ferromagnetic nanowire.
- (ii) The next two terms proportional to  $J_2$  represents the biquadratic interactions between first and second neighbor spin.
- (iii) The last term related with  $J_3$  express the higher order octupole-dipole spin-spin exchange interactions.

In order to demonstrate the spin excitations in spin lattice, we incorporate the boson excitations using Holstein-Primakoff modification [16].

$$\begin{aligned}
S_i^+ &= \hat{a}_i^\dagger \sqrt{2S - \hat{a}_i^\dagger \hat{a}_i}, \\
S_i^- &= \sqrt{2S - \hat{a}_i^\dagger \hat{a}_i} \hat{a}_i^\dagger, \\
S_i^z &= \hat{a}_i^\dagger \hat{a}_i - S, \quad (2)
\end{aligned}$$

where the annihilation and creation operators are represented as  $\hat{a}_i$  and  $\hat{a}_i^\dagger$  respectively which compensate the boson commutation correlation  $[\hat{a}_i, \hat{a}_j^\dagger] = \delta_{ij}$ . The number operator  $\hat{n}_i = \hat{a}_i^\dagger \hat{a}_i$  designates the spin divergence from its esteem value ( $S$ ). The ground state intimates the all magnetic spins are along in the direction of  $+z$  or  $-z$  in a ferromagnetic order. On that account, the magnetization begin to exist, which is elucidated as the nonvanishing average of  $S^z = \sum_i S_i^z$ . By developing  $\sqrt{2S - \hat{n}_i} \simeq \sqrt{2S} [1 - \hat{n}_i/S]$  to a series around the truncated excitation  $\langle \hat{n}_i \rangle \ll 2S$ , we can obtain the presiding equation for nonlinear excitations on ground states. Now, the (2) expanded as,

$$\begin{aligned}
\hat{S}_i^+ &= \sqrt{2} [\epsilon a_i - \frac{\epsilon^3}{4} a_i^\dagger a_i a_i - \frac{\epsilon^5}{32} a_i^\dagger a_i a_i^\dagger a_i a_i + O(\epsilon^7)], \\
\hat{S}_i^- &= \sqrt{2} [\epsilon a_i^\dagger - \frac{\epsilon^3}{4} a_i^\dagger a_i^\dagger a_i - \frac{\epsilon^5}{32} a_i^\dagger a_i^\dagger a_i a_i^\dagger a_i + O(\epsilon^7)], \\
\hat{S}_i^z &= [1 - \epsilon^2 a_i^\dagger a_i]. \quad (3)
\end{aligned}$$

Accordingly, behind the spin-wave approximation, we achieved the effective low-energy Hamiltonian (1) as

$$\begin{aligned}
H = - \sum_n \left[ \epsilon^2 (J_1 + J_2 + J_3) [a_{n+1}^\dagger a_n + a_{n+1} a_n^\dagger - a_{n+1}^\dagger a_{n+1} + a_n a_{n+2}^\dagger + a_n^\dagger a_{n+2} \right. \\
- a_{n+2}^\dagger a_{n+2} - a_n^\dagger a_n] - \frac{1}{4} \epsilon^4 \left[ (J_1 + J_3) [a_n a_{n+1}^\dagger a_{n+1} + a_n^\dagger a_n a_{n+1}^\dagger a_{n+1} \right. \\
+ a_n^\dagger a_n^\dagger a_n a_{n+2} - 4a_n^\dagger a_{n+2}^\dagger a_n a_{n+2} + a_n^\dagger a_n a_n a_{n+2}^\dagger + a_n^\dagger a_{n+2}^\dagger a_{n+2} a_{n+2} \\
- 4a_n^\dagger a_{n+1}^\dagger a_{n+1} a_n + a_{n+1}^\dagger a_n^\dagger a_{n+1} a_{n+1} + a_n^\dagger a_{n+1} a_n^\dagger a_n + a_{n+2}^\dagger a_n a_{n+2}^\dagger a_{n+2}] \\
+ J_2 [- 4a_{n+1}^\dagger a_n a_n a_{n+1}^\dagger - 4a_n^\dagger a_{n+1} a_{n+1} a_n^\dagger - 4a_{n+1}^\dagger a_n a_{n+1} a_n^\dagger - 4a_n^\dagger a_n a_{n+1} a_{n+1}^\dagger \\
+ 4a_n a_{n+1}^\dagger a_n a_n^\dagger + 4a_n a_{n+1}^\dagger a_{n+1} a_{n+1}^\dagger + a_n a_{n+1}^\dagger a_{n+1}^\dagger a_{n+1} + a_n^\dagger a_n a_n a_{n+1}^\dagger \\
+ a_n^\dagger a_{n+1}^\dagger a_{n+1} a_{n+1} + 4a_n^\dagger a_{n+1} a_n a_n^\dagger + a_n^\dagger a_n^\dagger a_n a_{n+1} + 4a_n^\dagger a_{n+1} a_{n+1} a_{n+1}^\dagger \\
+ 4a_n^\dagger a_n a_n a_{n+1}^\dagger + a_{n+1}^\dagger a_n a_{n+1} a_{n+1}^\dagger + a_n^\dagger a_n a_n a_{n+1}^\dagger + 4a_{n+1}^\dagger a_{n+1} a_n a_{n+1}^\dagger \\
+ 4a_n^\dagger a_n a_{n+1} a_n^\dagger + 4a_{n+1}^\dagger a_{n+1} a_{n+1} a_n^\dagger + a_n^\dagger a_{n+1} a_{n+1} a_{n+1}^\dagger + a_n^\dagger a_n^\dagger a_n a_{n+1} \\
- 4a_{n+2}^\dagger a_n a_n a_{n+2}^\dagger - 4a_n^\dagger a_{n+2} a_{n+2} a_n^\dagger - 4a_{n+2}^\dagger a_n a_{n+2} a_n^\dagger - 4a_n^\dagger a_n a_{n+2} a_{n+2}^\dagger \\
+ 4a_n a_{n+2}^\dagger a_n a_n^\dagger + 4a_n a_{n+2}^\dagger a_{n+2} a_{n+2}^\dagger + a_n a_{n+2}^\dagger a_{n+2}^\dagger a_{n+2} + a_n^\dagger a_n a_n a_{n+2}^\dagger \\
+ a_n^\dagger a_{n+2}^\dagger a_{n+2} a_{n+2} + 4a_n^\dagger a_{n+2} a_{n+2} a_{n+2}^\dagger + a_n^\dagger a_n^\dagger a_n a_{n+2} + 4a_n^\dagger a_{n+2} a_n a_n^\dagger \\
+ a_{n+2}^\dagger a_n a_{n+2} a_{n+2}^\dagger + 4a_{n+2}^\dagger a_{n+2} a_{n+2} a_n^\dagger + a_n^\dagger a_n a_n a_{n+2} + 14a_n^\dagger a_n a_n a_{n+2}^\dagger \\
+ 41a_n^\dagger a_n a_{n+2} a_n^\dagger + 4a_{n+2}^\dagger a_{n+2} a_{n+2} a_n^\dagger + a_n^\dagger a_{n+2} a_{n+2} a_{n+2}^\dagger + a_n^\dagger a_n^\dagger a_n a_{n+2} \\
- 12a_n^\dagger a_n a_{n+1} a_{n+1}^\dagger - 4a_{n+1}^\dagger a_{n+1} a_{n+1} a_n^\dagger - a_{n+1}^\dagger a_{n+1} a_{n+1} a_{n+1}^\dagger - 4a_n^\dagger a_n a_n a_n^\dagger \\
- 12a_n^\dagger a_n a_{n+2} a_{n+2}^\dagger - a_{n+2}^\dagger a_{n+2} a_{n+2} a_{n+2}^\dagger - 4a_{n+2}^\dagger a_{n+2} a_{n+2} a_n^\dagger] \Big]. \quad (4)
\end{aligned}$$

Consequently, we introduce the spin-wave approximation with some nonlinear alterations. Let us consider the P representation also called the Glauber coherent-state representation [17] described by the multiplication of the multimode coherent states  $|v\rangle = \prod_i |v_i\rangle$ , in which each element  $|v_i\rangle$  is an eigen state of the annihilation operator  $\hat{a}_i$  i.e,  $\hat{a}_i |v_i\rangle = v_i |v_i\rangle$  where  $v_i$  the coherent amplitude. The field operator sandwiched by  $|v\rangle$  can be expressed only with their diagonal components because of the coherent states are normalized and over completed. The Glauber coherent-state representation of the nonlinear (4) can be written as

$$i\hbar \frac{\partial a_i}{\partial t} = [a_i, H] = F(a_i^\dagger, a_{i+1}^\dagger, a_i, a_{i+1}). \quad (5)$$

Further, the spin dynamics are demonstrated in the view of Glauber's coherent-state representations

$$\begin{aligned}
-i \frac{dv_n}{dt} = & 2\epsilon^2 \left[ (J' + J_2) \left[ v_{n+1} + v_{n-1} + v_{n+2} + v_{n-2} - 4v_n \right] - 4J_3 v_n \right] \\
& - \frac{\epsilon^4}{4} \left[ J' \left[ 2|v_n|^2 (v_{n+1} + v_{n-1} + v_{n+2} + v_{n-2}) + v_n^2 (v_{n+1}^* + v_{n-1}^* \right. \right. \\
& + v_{n+2}^* + v_{n-2}^*) + |v_{n-2}|^2 v_{n-2} + |v_{n+2}|^2 v_{n+2} + |v_{n-1}|^2 v_{n-1} + |v_{n+1}|^2 v_{n+1} \\
& \left. \left. - 4v_n (|v_{n+1}|^2 + |v_{n-1}|^2 + |v_{n+2}|^2 + |v_{n-2}|^2) \right] + J_2 \left[ 20|v_n|^2 (v_{n+1} + v_{n-1} \right. \right. \\
& + v_{n+2} + v_{n-2}) + 10v_n^2 (v_{n+1}^* + v_{n-1}^* + v_{n+2}^* + v_{n-2}^*) + 10(|v_{n+1}|^2 v_{n+1} \\
& + |v_{n-1}|^2 v_{n-1} + |v_{n-2}|^2 v_{n-2} + |v_{n+2}|^2 v_{n+2}) - 8v_n^* (v_{n+1}^2 + v_{n-1}^2 + v_{n+2}^2 \\
& + v_{n-2}^2) - 24v_n (|v_{n+1}|^2 v_{n+1} + |v_{n-1}|^2 v_{n-1} + |v_{n-2}|^2 v_{n-2} + |v_{n+2}|^2 v_{n+2}) \\
& \left. \left. - 32|v_n|^2 v_n \right] + J_3 \left[ 8|v_{n+1}|^2 v_{n+1} + |v_{n-2}|^2 v_{n-2} + 8|v_{n+2}|^2 v_{n+2} \right. \right. \\
& - 12v_n (|v_{n-1}|^2 + |v_{n+1}|^2 + |v_{n+2}|^2 + |v_{n-2}|^2) + 16(|v_n|^2 v_{n-1} + |v_n|^2 v_{n-2}) \\
& \left. \left. + 8v_n^2 (v_{n-1}^* + v_{n-2}^*) - 48|v_n|^2 v_n \right] \right], \tag{6}
\end{aligned}$$

where  $J' = J_1 + J_3$  and the above nonlinear differential equation is in the configuration of perturbed discrete nonlinear Schrödinger equation and finding the solution to this equation is extremely tough task because of its high discreteness and nonlinearity. In this curiosity we are attracted to examine the localization of energy in discrete NN and NNN spin chain of ferromagnetic nanowire, we carryout the MI analysis.

### 3 Modulational Instability Through Linear Stability Analysis

Our motivation of the current work is to study the MI of the extended nonlinear spin waves in a ferromagnetic system consisting higher order octupole-dipole interaction. Due to the interplay between the nonlinear onsite and intersite interactions as a mechanism for changing MI and rule the localized modes occur in a nonlinear lattice. let us assume the time periodic plane wave solution is  $u_n(t) = u_0 e^{i(kn + \omega_0 t)}$ , where  $\omega_0$  designates the frequency of the plane wave and  $k$  is a wave vector. The linear stability of the nonlinear plane wave explained by looking for solutions which is in the form of adding small perturbation  $u_n(t) = u_0(1 + B_n(t))e^{i(kn + \omega_0 t)}$ , where  $B_n$  is a perturbation of small magnitude of the carrier wave. Then we assume  $B_n$  in the configuration of  $B_n(t) = B_1 e^{i(Qn - \Omega t)} + B_2^* e^{-i(Qn - \Omega^* t)}$ , here  $B_1$  and  $B_2$  represent the carrier wave amplitudes and taken as small as compared with the carrier wave parameters and the terms of complex conjugation is denoted by asterisk symbol. The frequency of modulation and wave vector are represented by  $\Omega$  and  $Q$  respectively. Upon switching the modulated spin wave into the equation of motion we achieved a system of linearly coupled equations.

$$\begin{pmatrix} -\Omega + A^+ & B \\ B & \Omega + A^- \end{pmatrix} \begin{pmatrix} B_1 \\ B_2 \end{pmatrix} = \begin{pmatrix} 0 \\ 0 \end{pmatrix} \tag{7}$$

If the determinant of the above matrix is vanishes, the equations yield only nontrivial solution, where  $B$  and  $A^\pm$  are given as follows

$$B = -\epsilon^4 u_0^2 \left[ J' \left[ \cos(k - Q) + \cos(2(k - Q)) + 2 \cos(k) + 2 \cos(2k) + \cos(k + Q) - 4 \cos(2Q) - 3 \cos(2(k + Q)) \right] + 2J_2 \left[ 6 \cos(2k) + 10 \cos(k) + 5 \cos(k - Q) + 5 \cos(2(k - Q)) + 5 \cos(2(k + Q)) - 4 \cos(4k) + 5 \cos(k + Q) - 12 \cos Q - 12 \cos(2Q) - 8 \right] + 32J_3 \left[ \cos(2k) + \cos(k) - 1 \right] \right],$$

$$A^\pm = -\omega_0 + 4\epsilon^2 \left[ (J' + J_2)(\cos(2(k \pm Q)) + \cos(k \pm Q) - 2) - 2J_3 \right] - 2u_0^2 \epsilon^4 \left[ J' \left[ 2 \cos(k \pm Q) + 2 \cos(k) + 2 \cos(2(k \pm Q)) - 2 \cos(Q) - 4 \right] + J_2 \left[ 20 \cos(k) + 20 \cos(2k) + 20 \cos(k \pm Q) + 20 \cos(2(k \pm Q)) - 8 \cos(2k \pm Q) - 8 \cos(2(2k \pm Q)) - 12 \cos(2Q) - 12 \cos(Q) - 40 \right] + J_3 \left[ 8 \cos(2k) + 8 \cos(k) + 8 \cos(k \pm Q) - 4 \cos(2Q) + 8 \cos(2(k \pm Q)) - 4 \cos(Q) - 16 \right] \right].$$

where,

$$\omega_0 = 4\epsilon^2 \left[ (J' + J_2)(\cos(2k) + \cos(k) - 2) - 2J_3 \right] - 4u_0^2 \epsilon^4 \left[ J' [\cos(2k) + \cos(k) - 2] + 2J_2 [4 \cos(2k) + 5 \cos(k) - \cos(4k) - 8] + 2J_3 [\cos(2k) + \cos(k) - 4] \right],$$

Solving (7), we obtain

$$\Omega = \frac{1}{2} \left[ 4\epsilon^2 \left[ (J' + J_2) [\cos(k - Q) + \cos(k + Q) + \cos 2(k - Q) + \cos 2(k + Q) - 2 \cos k - 2 \cos(2k) - 8] - 6J_3 \right] + 2\epsilon^4 u_0^2 \left[ 2J' (\cos(k + Q) + \cos 2(k + Q) + \cos(k - Q) + \cos 2(k - Q) - 2 \cos Q + 4 \cos(2k) + 6 \cos k + 4 \cos k + 4) - J_2 (24 \cos(2Q) + 16 \cos(4k) - 104 \cos(2k) - 20 \cos 2(k + Q) - 80 \cos k - 20 \cos(k - Q) - 20 \cos(k + Q) + 8 \cos(2k - Q) + 8 \cos(2k + Q) - 20 \cos 2(k - Q) + 12 \cos Q + 8 \cos 2(2k - Q) - 68) + J_3 (8 \cos(2k) - 12 \cos(2Q) - 4 \cos Q + 8 \cos 2(k - Q) + 8 \cos(k - Q) - 8 \cos k - 16 - 8 \cos(2Q) + 16 \cos(2k) + 32 \cos(k + Q) + 32 \cos 2(k + Q) + 32 \cos k - 16 \cos Q - 32) \right] \pm \sqrt{M^2 - \epsilon^8 u_0^4 N^2} \right], \tag{8}$$



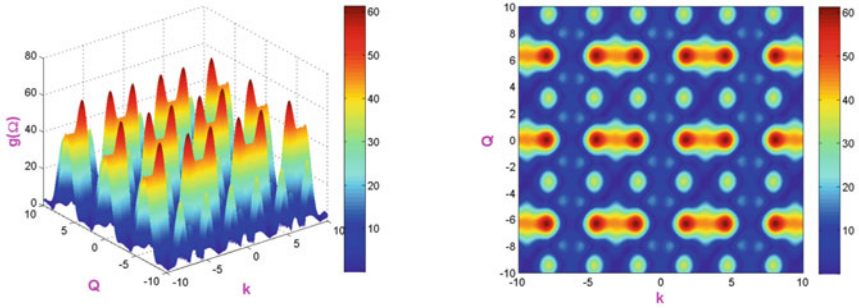
where

$$\begin{aligned}
 M = & 4\epsilon^2 \left[ 2J_3 - (J_2 + J') \left[ -2 + \cos 2(k - Q) + \cos 2(k + Q) + \cos(k + Q) \right. \right. \\
 & \left. \left. + 2 - 2 \cos k + \cos(k - Q) - 2 \cos 2k \right] \right] + 2u_0^2 \epsilon^4 \left[ J' \left[ -4 \cos Q - 10 \cos k \right. \right. \\
 & - 40 + 2 \cos 2(k - Q) + 2 \cos(k - Q) + 2 \cos(k + Q) + 2 \cos(2Q + 2k) - 16 \cos 2k \left. \right] \\
 & - J_2 \left[ -20 \cos 2(k + Q) + 8 \cos(2k - Q) + 24 \cos(2Q) - 20 \cos 2(k - Q) - 40 \cos(2k) \right. \\
 & + 8 \cos 2(2k + Q) + 24 \cos Q - 40 \cos k + 8 \cos(Q + 2k) + 8 \cos 2(2k - Q) \\
 & - 20 \cos(k - Q) + 80 - 20 \cos(Q + k) \left. \right] + J_3 \left[ -8 \cos(2k) - 8 \cos(Q) \right. \\
 & + 8 \cos(2k - 2Q) - 4 \cos(2Q) + 8 \cos(k - Q) - 16 + 8 \cos(2k) + 8 \cos(Q + k) \\
 & \left. - 4 \cos(2Q) + 48 + 8 \cos(2Q + 2k) \right] \Big], \\
 N = & J' \left[ -3 \cos 2(Q + k) - 4 \cos(2Q) + \cos 2(k - Q) + 2 \cos k + \cos(k + Q) + \cos(k - Q) \right. \\
 & \left. + 2 \cos(2k) \right] + 2J_2 \left[ 6 \cos 2k - 12 \cos 2Q + 5 \cos(k + Q) + 5 \cos 2(k - Q) \right. \\
 & \left. - 4 \cos(4k) + 5 \cos 2(k + Q) - 8 + 5 \cos(k - Q) - 12 \cos Q + 10 \cos k \right] \\
 & + 32J_3 \left[ \cos 2k \cos k - 1 \right],
 \end{aligned}$$

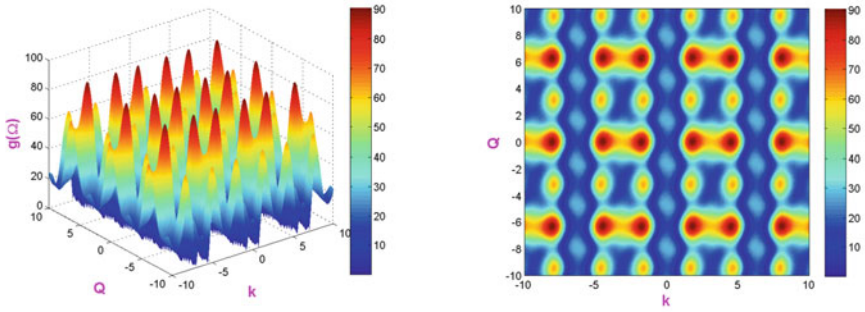
$$\begin{aligned}
 g(\Omega) & \equiv Im(\Omega) \\
 & \equiv \left[ \left[ J' \left[ \cos(k + Q) - 4 \cos(2Q) + \cos 2(k - Q) - 3 \cos 2(Q + k) + 2 \cos(2k) \right. \right. \right. \\
 & \left. \left. + \cos(k - Q) + 2 \cos k \right] + 2J_2 \left[ 6 \cos 2k - 4 \cos(4k) - 12 \cos 2Q \right. \right. \\
 & \left. \left. + 5 \cos 2(k + Q) + 5 \cos 2(k - Q) - 12 \cos Q + 5 \cos(k + Q) + 10 \cos k \right. \right. \\
 & \left. \left. + 5 \cos(k - Q) - 8 \right] + 32J_3 \left[ \cos 2k - 1 + \cos k \right] \right]^2 - \left[ 5\epsilon^2 \left[ \left[ \cos 2(k + Q) + \cos(k + Q) \right. \right. \right. \\
 & \left. \left. - 2 + \cos(k - Q) + \cos 2(k - Q) - 2 \cos k + 2 + \cos 2(k - Q) - 2 \cos 2k \right] \right. \\
 & \left. \times 2J_3 - (J' + J_2) \right] + 2u_0^2 \epsilon^4 \left[ -J_2 \left[ 24 \cos(2Q) - 40 \cos(2k) + 8 \cos(2k - Q) \right. \right. \\
 & \left. \left. - 20 \cos 2(k - Q) - 20 \cos 2(k + Q) + 24 \cos Q - 40 \cos k + 8 \cos 2(2k - Q) \right. \right. \\
 & \left. \left. - 20 \cos(k - Q) + 8 \cos(Q + 2k) - 20 \cos(Q + k) + 8 \cos 2(2k + Q) + 80 \right] \right. \\
 & \left. + J' \left[ 2 \cos 2(k - Q) + 2 \cos(k - Q) + 2 \cos(k + Q) + 2 \cos(2Q + 2k) \right. \right. \\
 & \left. \left. - 10 \cos k - 4 \cos Q - 16 \cos 2k - 40 \right] + J_3 \left[ -8 \cos(Q) - 4 \cos(2Q) \right. \right. \\
 & \left. \left. - 4 \cos(2Q) - 8 \cos(2k) + 8 \cos(2k) + 8 \cos(k - Q) + 8 \cos(2k - 2Q) - 16 \right. \right. \\
 & \left. \left. + 8 \cos(2Q + 2k) + 8 \cos(Q + k) + 48 \right] \right]^2 \Big]^{1/2}, \tag{9}
 \end{aligned}$$

here *Im* represents the imaginary term and occurrence of localized constructions in the ferromagnetic spin lattice of nanowire which are only achievable if the steady amplitude of the solution becoming unstable. Whenever  $\Omega < 0$ , the steady state solution turn out to be unstable, whereas the perturbation exponentially expands with the appreciable intensity. The gain reveals more fascinating relation of  $\Omega$  with the coupling exchange parameters  $J_1, J_2$  and  $J_3$  describing the exchange interaction and dispersive long range interactions for different values. Figure 1 depicts the stable/instable area in the plane of  $(k, Q)$  and be in tune with the influence of the

(a)



(b)



(c)

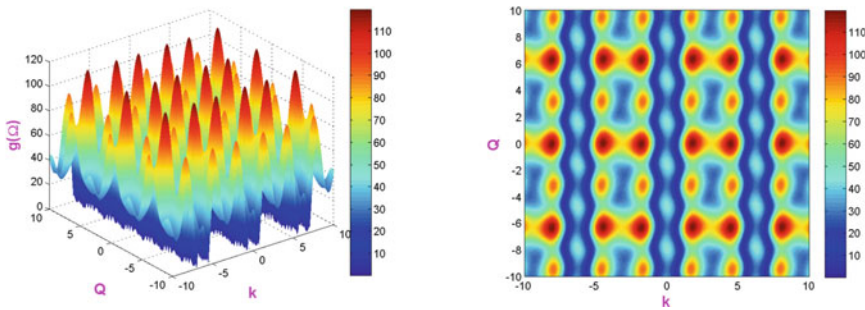


**Fig. 1** MI gain profile for (a)  $J_3 = 0.1$ , (b)  $J_3 = 0.5$ , (c)  $J_3 = 0.9$  and on all plots  $J_1 = 0.1$ ,  $J_2 = 0.2$

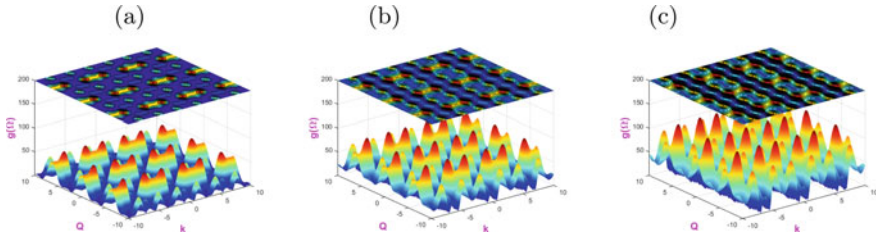


**Fig. 2** MI gain cumulative profile for (a)  $J_3 = 0.1$ , (b)  $J_3 = 0.5$ , (c)  $J_3 = 0.9$  and on all plots  $J_1 = 0.1$ ,  $J_2 = 0.2$

interaction of octupole-dipole coupling parameter denoted as  $J_3$ . In these figures, the nonlinear plane waves are reliable and stable in the dark bluish area by modulating the wavenumber  $Q$  and area with bright yellowish orange region where we expect the sudden exponential growth of the amplitude of wave which seems to be appreciable enhancement in the instability domain. Surprisingly, when we increase the octupole-dipole interaction parameter  $J_3$  from 0.1 to 0.9 units (Fig. 1a–c), the stability region becomes faded out and the generation of high amplitude, robust nonlinear solitonic waves are observed in the presence of biquadratic and bilinear interactions. Figure 2 depicts the cumulative representation of Fig. 2 as 2D and 3D plots.

## 4 Conclusion

In this investigation, we have effectively studied the modulational instability analysis of extended nonlinear solitary waves in isotropic ferromagnetic nanowire with NN-NNN higher order octupole-dipole magnetic spin interactions. The deliberated discrete nonlinear Schrödinger (DNLS) equation derived by using the spin wave approach of Glauber coherent approximation method. Then the highly discrete nonlinear complicated DNLS equation analysed through the modulational instability analysis and the result is depicted in the figures shows that control on the strength of octupole-dipole coupling exchange interaction of neighbouring spins, the place of stability/instability in the plane are predicted in which the instability region is increases with increasing of octupole-dipole interaction. The numerical simulations explore the existence of possible localized long-lived excitations of solitonic pulse in the ferromagnetic nanowire spin lattice that promote to nonlinear regime. This robust soliton expected to play a potential application in manufacturing of magnetic recording and memory devices.

**Acknowledgements** L. K. delightedly acknowledge the financial aid from DST-SERB (MTR/2017/000 314/MS), India and CSIR (03 (1418)/17/EMR-II), India in the form of Major Research Projects (MRP). L. K. and T. P. gratefully acknowledge the financial assist from UGC-DAE CSR (CSR-KN/ CRS-102/2019-20) in the configuration of a MRP.

## References

1. Huang, G., Shi, Z.P., Dai, X., Tao, R.: On soliton excitations in a one-dimensional Heisenberg ferromagnet. *J. Phys.: Condens. Matter* **42**(2), 8355 (1990)
2. Daumont, I., Dauxois, T., Peyrard, M.: Modulational instability: first step towards energy localization in nonlinear lattices. *J. Nonlinearity* **10**, 617 (1997)
3. Ivanov, B.A.: Nonlinear dynamics and two-dimensional solitons for spin-1 ferromagnets with biquadratic exchange. *Phys. Rev. B* **77**, 064402 (2008)
4. Alexey Kartsev: Biquadratic exchange interactions in two-dimensional magnets. *NPJ. Comput. Mater.* **6**, 150 (2020)
5. Christal Vasanthi, C., Latha, M.: Localized spin excitations in a disordered antiferromagnetic chain with biquadratic interactions. *Euro. Phys. J. D* **69**, 268 (2015)
6. Kavitha, L.: Modulational instability and nano-scale energy localization in ferromagnetic spin chain with higher order dispersive interactions. *J. Magn. Magn. Mater.* **404**(C), 91–118 (2016)
7. Anderson, P.W.: New approach to the theory of superexchange interactions. *Phys. Rev.* **115**, 2 (1959)
8. Anderson, P.W.: Theory of magnetic exchange interactions: exchange in insulators and semiconductors. *Solid State Phys.* **14**, 99–214 (1963)
9. Moriya, T.: Anisotropic superexchange interaction and weak ferromagnetism. *Phys. Rev.* **120**, 91 (1960)
10. Moriya, T.: New mechanism of anisotropic superexchange interaction. *Phys. Rev. Lett.* **4**, 228 (1960)
11. Huang, G., Zhang, S., Hu, B.: Nonlinear excitations in ferromagnetic chains with nearest- and next-nearest-neighbor exchange interactions. *Phys. Rev. B* **58**, 9194 (1998)
12. Daniel, M., Kavitha, L.: Soliton spin excitations in an anisotropic Heisenberg ferromagnet with octupole-dipole interaction. *Phys. Rev. B* **59**, 21 (1999)
13. Tang, Bing, Li, De-Jun., Tang, Yi.: Quantum solitons and breathers in an anisotropic ferromagnet with octupole-dipole interaction. *Int. J. Theor. Phys.* **53**, 359–369 (2014)
14. Djoufack, Z.I., Nguenang, J.P., Kenfack-Jiotsa, A.: Quantum breathers and intrinsic localized excitations in an isotropic ferromagnet with octupole-dipole interaction. *Phys. B* **598**, 412437 (2020)
15. Kavitha, L., Sathishkumar, P., Saravanan, M., Gopi, D.: Soliton switching in an anisotropic Heisenberg ferromagnetic spin chain with octupole-dipole interaction. *Phys. Scr.* **83**, 055701 (1963)
16. Holstein, T., Primakoff, H.: Field dependence of the intrinsic domain magnetization of a ferromagnet. *Phys. Rev.* **58**, 1098 (1940)
17. Roy, J.: Glauber: coherent and incoherent states of the radiation field. *Phys. Rev.* **131**, 2766 (1963)

# Study of Nonlinear Dynamics of Vilnius Oscillator



Dmitrijs Pikulins, Sergejs Tjukovs, Iheanacho Chukwuma Victor,  
and Aleksandrs Ipatovs

**Abstract** Most chaotic dynamical systems exhibit non-robust chaos when small changes of system parameters lead to abrupt jumps from chaotic to periodic motions. These unstable regimes could not be successfully utilized in practice. The detailed systematic analysis of nonlinear dynamics becomes paramount for practical applications to identify regions of robust chaos and related transitions. This paper presents an in-depth analysis of the nonlinear dynamics of a Vilnius oscillator, providing a detailed numerical study of the operational regions of Vilnius oscillator's, constructing bifurcation map and brute-force bifurcation diagrams.

**Keywords** Chaotic Oscillator · Bifurcations · Robust Chaos

## 1 Introduction

For reliable and smooth communication, accurate data must be transmitted or received robustly and securely. This, in turn, requires the implementation of specific sophisticated data-coding algorithms. It has been revealed that the required complexity could be observed in very simple dynamical systems exhibiting chaotic oscillations. In recent years, an exponential rise in computer processing power allowed modelling, predicting, and exploiting irregular dynamics of nonlinear circuits.

What benefits could chaotic communications provide that sets it apart from existing conventional systems? The answer lies in the characteristics of chaos-based communication systems: a sensitivity to initial conditions, aperiodic and noise like time series, and wide frequency bandwidth. These properties allow chaotic transmissions to have reduced interception or even detection risk.

Chaotic oscillators are simple analogue or digital circuits producing chaotic signals. Such oscillators exhibit rich dynamics and offer a wide range of applications in engineering, such as pseudo-random number generators [1], radar and sonar

---

D. Pikulins (✉) · S. Tjukovs · I. Chukwuma Victor · A. Ipatovs  
Institute of Radioelectronics, Riga Technical University, Azenes st.12, Riga, Latvia  
e-mail: [dmitrijs.pikulins@rtu.lv](mailto:dmitrijs.pikulins@rtu.lv)

© The Author(s), under exclusive license to Springer Nature Switzerland AG 2022  
S. Banerjee and A. Saha (eds.), *Nonlinear Dynamics and Applications*,  
Springer Proceedings in Complexity,  
[https://doi.org/10.1007/978-3-030-99792-2\\_103](https://doi.org/10.1007/978-3-030-99792-2_103)

1219

systems [2], switched-mode power supplies [3, 4], encryption for secure communication [5], and chaos-based communications [6–8]. Experiments on oscillatory systems using circuits simulations allow the in-depth study of phenomena and develop a wide range of practical applications.

The currently known dynamical systems frequently offer fragile chaos, meaning that the chaotic attractor has some periodic attractors in the nearby region in the parameter space [9]. This might be a concern for practical applications relying on continuous chaotic signals created by chaotic oscillators. The phase diagrams for several dynamic systems in [10] illustrate that small changes in the system parameters dramatically change its dynamics. If the chaotic attractor of a physical system meant to generate chaotic signals is fragile, the dynamics may not evolve as predicted. So, a given implementation may produce a system with parameters corresponding to a nonchaotic attractor. Even if the system starts in a chaotic state, slight changes in operational parameters caused by external stimuli or component faults may cause the transition to periodic oscillations. In practical applications, such issues may be avoided by using systems with robust chaos. Thus, it is necessary to study the parameters of oscillators in detail to determine how the system behaves in various conditions and know what regions of operation produce the most resilient chaos.

One of the chaotic systems has been presented in [11] and referenced as "Vilnius oscillator". Several papers were devoted to examining the nonlinear phenomena of this circuit [12–14]. But all of them were fragmentary and incomplete.

In this paper, an in-depth analysis of the Vilnius oscillator's nonlinear dynamics is performed to determine parameter ranges that reliably produce robust chaos.

This paper is organized as follows. The second section is devoted to the description of the schematic and analytical model of the Vilnius oscillator. The third section presents the nonlinear analysis of the dynamics of the system under study. The last section is devoted to the overall conclusions and suggestions on the applicability of this type of chaotic oscillator.

## 2 Vilnius Oscillator Model

The schematic of the Vilnius chaotic oscillator under study is shown in Fig. 1. It comprises affordable electronic components and can be implemented even on a breadboard, thus simplifying practical research. Values and part numbers of the components are summarized in Table 1.

The oscillator is built around a general-purpose operational amplifier. In the positive feedback loop, the RLC circuit is connected. A non-inverting amplifier configuration can be easily recognized in the negative feedback loop. Additional capacitor C2 and silicon diode D1 drastically change the oscillator's dynamics and transform it into a circuit with complex behaviour. The numerical study of the circuit is based on a system of differential equations, which is derived by applying general laws of circuit analysis and making several simplifications. Firstly, the equation of an ideal diode is used to describe current–voltage relations of D1:

**Fig. 1** The schematic diagram of the Vilnius chaos oscillator used in the study

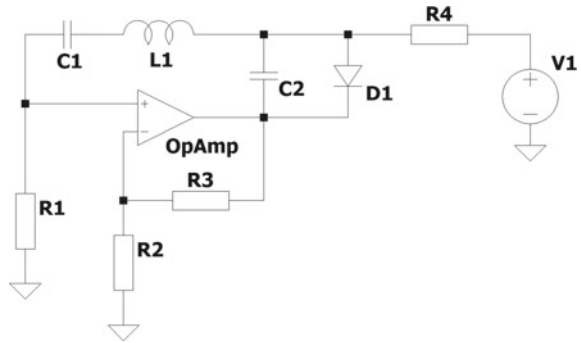


**Table 1** List of components used in the Vilnius oscillator

Component	Value or Part Number
R1	1 kΩ
R2	10 kΩ
R3	10 kΩ
R4	20 kΩ
C1	1 nF
C2	150 pF
L1	1 mH
D1	1N4148
OpAmp	TL082
V1	Laboratory power supply

$$I_D = I_S \left[ \exp\left(\frac{q \cdot V_D}{N \cdot k_B \cdot T}\right) - 1 \right] \tag{1}$$

where  $I_S$  refers to saturation current,  $q = 1.6 \times 10^{-19}$  C – the elementary charge,  $k_B$  – Boltzmann’s constant,  $T$  – the temperature in Kelvin,  $N = 1$  for an ideal diode,  $I_D$  and  $V_D$  are the current through a diode and voltage across it respectively. Equation 1 doesn’t consider parasitic capacitances of the p–n junction and equivalent resistance  $R_s$  that models resistances of neutral regions and contacts associated with an actual device. Secondly, to express the current through the  $R_4$ , it is assumed that  $R_4 \gg R_1$ . As a result, according to Ohm’s law:

$$I_{R4} = \frac{V1}{R4}. \tag{2}$$

Also, the gain of the non-inverting amplifier is expressed as:

$$k = 1 + \frac{R_2}{R_1}. \tag{3}$$

A system of ordinary differential equations describing the Vilnius oscillator is shown below:

$$C_1 \frac{dV_{C1}}{dt} = I_{L1} \quad (4)$$

$$L \frac{dI_{L1}}{dt} = (k - 1) \cdot R_1 \cdot I_{L1} - V_{C1} - V_{C2} \quad (5)$$

$$C_2 \frac{dV_{C2}}{dt} = I_{R4} + I_{L1} - I_{D1} \quad (6)$$

Furthermore, in [11], dimensionless variables and parameters are suggested for conventional numerical analysis:

$$x = \frac{V_{C1} \cdot q}{k_B \cdot T} \quad y = \frac{I_{L1} \cdot q \cdot \sqrt{\frac{L}{C_1}}}{k_B \cdot T} \quad z = \frac{V_{C2} \cdot q}{k_B \cdot T} \quad (7)$$

$$a = \frac{(k - 1) \cdot R_1}{\sqrt{\frac{L}{C_1}}} \quad b = \frac{I_{R4} \cdot q \sqrt{\frac{L}{C_1}}}{k_B \cdot T} \quad c = \frac{I_S \cdot q \cdot \sqrt{\frac{L}{C_1}}}{k_B \cdot T} \quad \varepsilon = \frac{C_2}{C_1} \quad (8)$$

These substitutions allow to use of a simplified version of the system of differential equations:

$$\frac{dx}{dt} = y \quad (9)$$

$$\frac{dy}{dt} = ay - x - z \quad (10)$$

$$\varepsilon \frac{dz}{dt} = b + y - c(e^z - 1) \quad (11)$$

In forthcoming sections,  $a$  and  $\varepsilon$  will be used as bifurcation parameters. In practical experiments or circuit simulation software, it is possible to vary  $a$  by changing the value of  $R_3$  and  $\varepsilon$  by the corresponding adjustment of  $C_2$ .

### 3 Analysis of Nonlinear Dynamics of Vilnius Oscillator

The study of nonlinear dynamics of the Vilnius oscillator requires the discrete-time model of the system. The model could be obtained numerically by sampling the variables  $x$ ,  $y$ ,  $z$ , defined by the system of nonlinear Eqs. (9)–(11). The oscillator under study is an example of an autonomous system, so it is impossible to obtain



the stroboscopic map as no external clocking element is present. Thus, the Poincare mapping is derived by sampling the variables, as the trajectory hits the plane  $y = 0$  from positive to the negative side. This mapping is used to construct bifurcation diagrams and provide the analysis of periodic or chaotic modes of operations.

First, the bifurcation map (also called the 2-parameter bifurcation diagram) is calculated for the predefined range of system parameters. This, essentially, is the graph depicting the periodic regions of regimes up to preset periodicity in the 2-parameter space. For the Vilnius oscillator, the bifurcation parameters of interest are  $a$  and  $\varepsilon$ , leaving all the other parameters fixed. The bifurcation map, depicted in Fig. 2, gives a variety of reference points to start the more detailed study of nonlinear dynamics of the oscillator, as we vary some parameters. The dashed areas depict periodic regimes, while the white area represents the periodicity  $>8$  of chaotic modes of operation.

It could be seen that for small values of  $a = 0.05-0.1$ , the system exhibits stable period-1 operation as we change  $\varepsilon$  in the whole range of interest. As we increase the  $a$  for different values of  $\varepsilon$ , the dynamics of the system change from periodic to chaotic, and in some cases, returns to periodic motions.

To provide a more detailed analysis of the nonlinear dynamics of the system, the one-parameter brute-force bifurcation diagrams are obtained, essentially as cross-sections of the bifurcation map.

The first bifurcation diagram is constructed for  $\varepsilon=0.05$  and shown in Fig. 3.

It could be noticed that for the defined parameter values, no classical period-doubling route to chaos could be observed. The stable period-1 solution suddenly becomes unstable through the period-doubling bifurcation and later recovers the stability. It could be shown that after the second period-doubling bifurcation, the

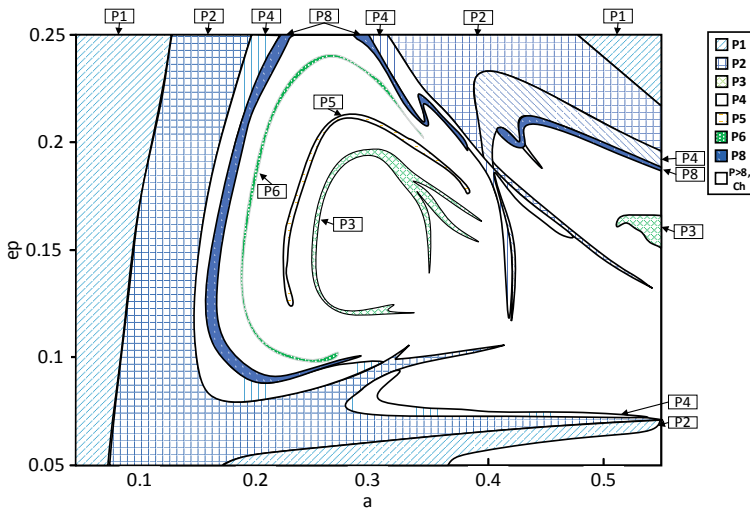
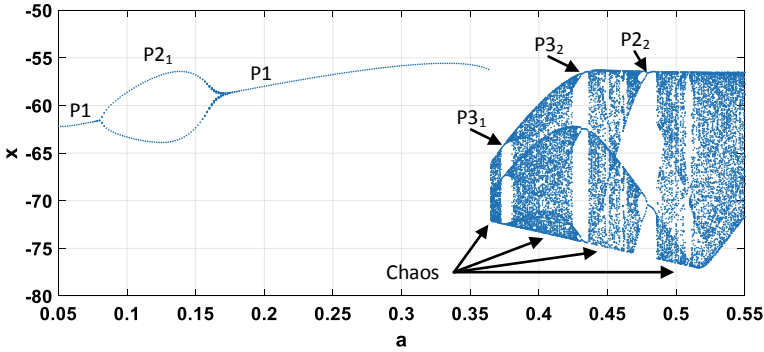


Fig. 2 The bifurcation map of Vilnius oscillator for  $b = 40$ ;  $a = 0.05-0.55$ ;  $\varepsilon = 0.05-0.25$



**Fig. 3** Brute-force bifurcation diagram for  $b = 40$ ;  $\varepsilon = 0.05$ ;  $a = 0.05\text{--}0.55$

period-1 solution is quantitatively different than that for smaller values of  $a$ . Figure 4 depicts the phase portraits in the  $x$ – $y$  plane and the system’s trajectory for  $a = 0.05$  and  $a = 0.34$ .

While the phase portraits show only insignificant changes in the system’s dynamics, as  $a$  changes, the study of the whole trajectory allows establishing the rapid growth of the amplitude of  $z$  (corresponding to the noticeable increase of voltage across the capacitor C2—see Fig. 1. and Eq. 8).

After  $a = 0.37$ , the system’s dynamics become chaotic, exhibiting the transitions to periodic windows of period-3 and period-2. Thus, from the practical point of view—the most promising chaotic regions would be for  $a = 0.38\text{--}0.42$  and  $a = 0.51\text{--}0.55$ .

To link obtained results to the physical implementation of Vilnius oscillator circuit one must keep in mind that according to Eq. 7 variable  $x$  is directly proportional to  $V_{C1}$ ,  $y$  to  $I_{L1}$ , and  $z$  to  $V_{C2}$ . Also, Eqs. 3 and 8 state that in a real circuit parameter  $a$  can be changed in the defined range, either by sweep of value of R3 or simultaneous variation of both R1 and R3. For example, to cover  $a$  range from 0.05 to 0.55, R3 must be varied from  $500\ \Omega$  to  $5.5\ \text{k}\Omega$ , which can be easily achieved using variable resistor or switching matrix of resistors with different values. In depth experimental

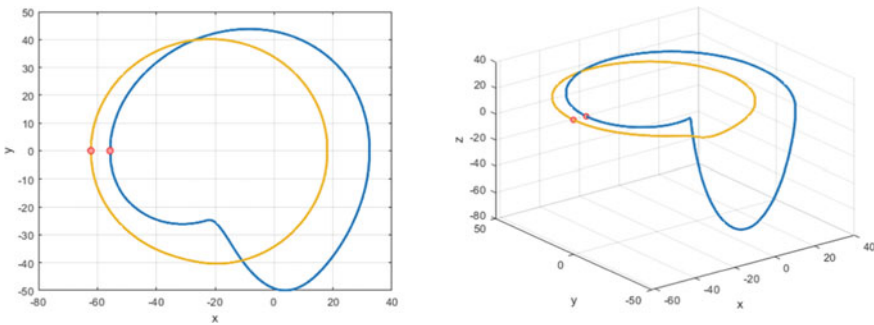


**Fig. 4** Phase portrait and trajectory of period-1 regime: for  $a = 0.05$  (yellow),  $a = 0.34$  (blue)

verification is out of the scope of this paper. The main goal of current numerical study is to identify regions of interest for both possible implementations in secure communication systems and subsequent experimental verification of the obtained results.

The following bifurcation diagram has been obtained for  $\epsilon = 0.08$  and depicts the classical period-doubling route to chaos as  $a$  is varied from 0.05 to 0.55 (Fig. 5).

The system's dynamics drastically changes for large values of  $a > 0.49$ . It could be observed that there are two different chaotic attractors – one of them with a much larger amplitude than the other one (see Fig. 6.). In practical implementations, this could lead to the intermitted jumps from the main chaotic attractor that arose from the

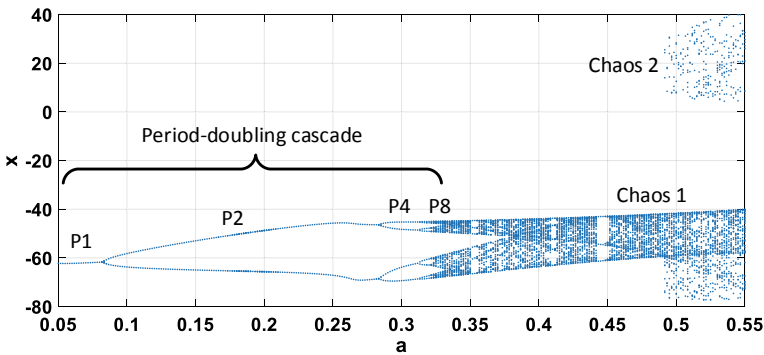


Fig. 5 Brute-force bifurcation diagram for  $b = 40$ ;  $\epsilon = 0.08$ ;  $a = 0.05-0.55$

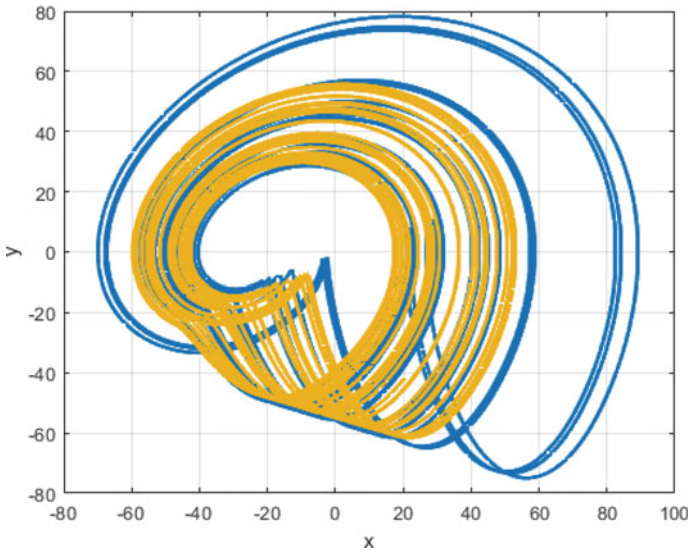


Fig. 6 Chaotic attractors for  $b = 40$ ,  $\epsilon = 0.08$ ,  $a = 0.46$  (yellow);  $a = 0.55$ (blue)

classical period-doubling cascade to the larger one, potentially leading to overvoltage and component failures. Thus, it would be desirable to avoid the operation of the Vilnius oscillator in this unsafe chaotic region.

The analysis of the bifurcation map in Fig. 2 allows the prediction of the relatively large chaotic region for a wide range of  $a$  values, as  $\varepsilon$  reaches 0.15. Figure 7 shows the brute-force bifurcation diagram, depicting chaotization of the system through the period-doubling cascade. However, unlike the chaotic region depicted, e.g. in Fig. 3, where a great variety of periodic windows is observed within the chaotic region, the diagram in Fig. 7 shows several intervals of robust chaotic oscillations (RCh<sub>1</sub>-RCh<sub>3</sub>). This means that setting system parameters with the defined ranges guarantee stable chaotic oscillations without the risk of shifting to periodic motion due to external noise or slight fluctuation in component nominal values.

Another two brute-force bifurcation diagrams were also obtained based on the bifurcation map in Fig. 2. In these cases, the value of parameter  $a$  was fixed ( $a = 0.15$  in Fig. 8 and  $a = 0.2$  in Fig. 9), and  $\varepsilon$  has been used as the bifurcation parameter of interest.

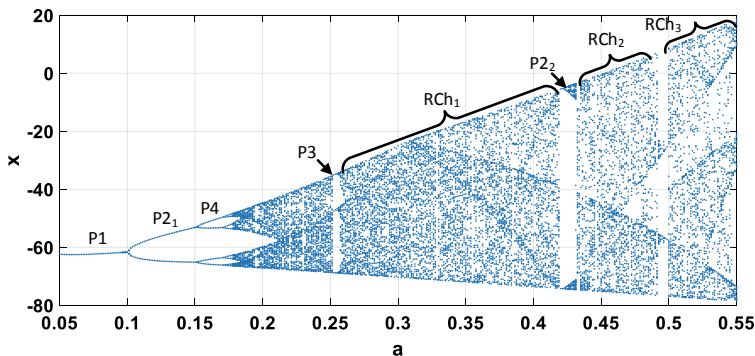


Fig. 7 Brute-force bifurcation diagram for  $b = 40$ ;  $\varepsilon = 0.15$ ;  $a = 0.05 - 0.55$

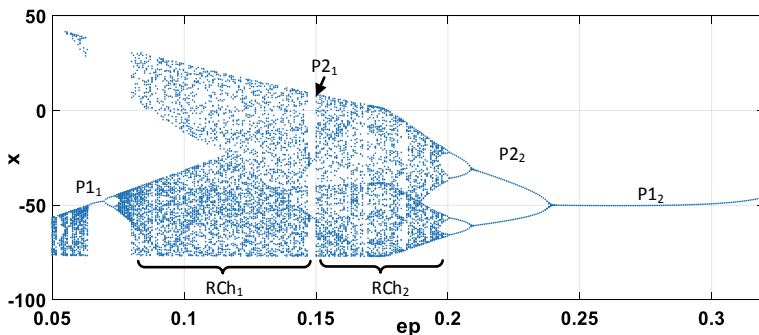
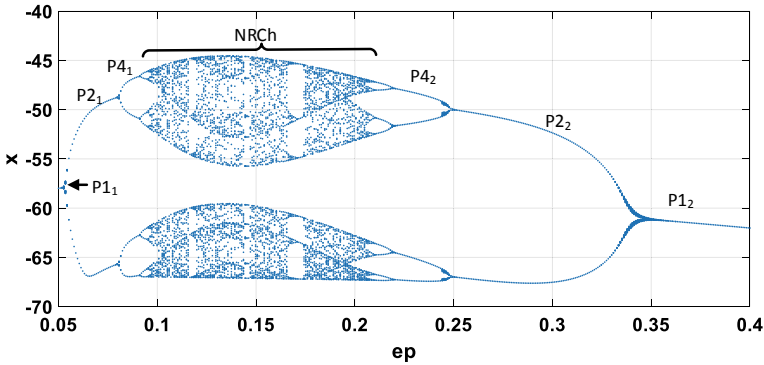


Fig. 8 Brute-force bifurcation diagram for  $b = 40$ ;  $a = 0.5$ ;  $\varepsilon = 0.05 - 0.4$



**Fig. 9** Brute-force bifurcation diagram for  $b = 40$ ;  $a = 0.2$ ;  $\varepsilon = 0.05-0.4$

The comparison of the diagrams allows us to draw important conclusions on the changes in the system’s dynamics for two values of  $a$ . In Fig. 8, the Vilnius oscillator exhibits chaotic dynamics for small values of  $\varepsilon$ . Further, it operates in the narrow period-1 window, leading to the appearance of 2 regions of robust chaotic oscillations (RCh<sub>1</sub> and RCh<sub>2</sub>) separated by a narrow period-2 window. For  $\varepsilon > 0.18$ , the transition to stable period-1 operation is observed through the inverse period-doubling cascade. Thus, the RCh<sub>1</sub> and RCh<sub>2</sub> could be used if the oscillator is supposed to provide reliable chaotic signals.

On the other hand, the similar transition from period-1 to chaos and back to period-1 is shown in Fig. 9, where  $a = 0.2$ . However, the formed chaotic region is full of stable periodic regimes (non-robust chaos- NRCh), making the oscillator not applicable as the source of chaotic oscillations.

## 4 Conclusions

As the scope of applications of chaotic systems expands, a growing number of different chaotic oscillators have been presented during several last decades. The main requirements include ease of implementation and rich nonlinear dynamics. The second point defines the necessity of the detailed numerical and experimental study of the oscillators, as frequently, even minor fluctuations of parameter values or external noises could lead to the transition from chaotic to periodic oscillations, compromising the robustness and security of the whole application.

This paper provided a detailed analysis of the nonlinear dynamics of the Vilnius oscillator in a wide parameter range. First, the usefulness of the bifurcation map has been proved, allowing the deliberate choice of parameter range, ensuring the required system’s dynamics. Second, the mentioned map has been used as the keystone for constructing detailed bifurcation diagrams, revealing the exact transitions from periodic to chaotic motions and vice-versa. The analysis of the results shows that this

oscillator could exhibit chaotic oscillations of different nature and properties: robust chaotic regions, non-robust chaotic motions, and even regions with coexisting chaotic attractors of various sizes. Thus, it has been proved that it is crucial to provide a comprehensive analysis of the system's dynamics to meet the requirements of the specific applications while utilizing the system within a feasible parameter range.

**Acknowledgements** This work has been supported by the European Regional Development Fund within the Activity 1.1.1.2 "Post-doctoral Research Aid" of the Specific Aid Objective 1.1.1 "To increase the research and innovative capacity of scientific institutions of Latvia and the ability to attract external financing, investing in human resources and infrastructure" of the Operational Programme "Growth and Employment" (No.1.1.1.2/VIAA/4/20/651).

## References

1. Dantas, W.G., Rodrigues, L.R., Ujevic, S., Gusso, A.: Using nanoresonators with robust chaos as hardware random number generators. *Chaos* **30**, 043126 (2020)
2. Carroll, T.L., Rachford, F.J.: Target recognition using nonlinear dynamics. In: Leung, H. (ed.) *Chaotic Signal Processing*, pp. 23–48. SIAM, Philadelphia (2013)
3. Deane, J.H.B., Hamill, D.C.: Improvement of power supply EMC by chaos. *Electron. Lett.* **32**, 1045 (1996)
4. Pikulins, D.: Exploring types of instabilities in switching power converters: the complete bifurcation analysis. *Elektronika ir Elektrotehnika* **20**(5), 76–79 (2014)
5. Kocarev, L.: Chaos-based cryptography: a brief overview. *IEEE Circuits Syst. Mag.* **1**, 6–21 (2001)
6. Litvinenko, A., Aboltins, A.: Chaos based linear precoding for OFDM. *RTUWO* **2015**, 13–17 (2015)
7. Litvinenko, A., Bekeris, E.: Probability distribution of multiple-access interference in chaotic spreading codes based on DS-CDMA communication system. *Elektronika Ir Elektrotehnika* **123**(7), 87–90 (2012)
8. Babajans, R., Cirjulina, D., Grizans, J., Aboltins, A., Pikulins, D., Zeltins, M., Litvinenko, A.: Impact of the chaotic synchronization's stability on the performance of QCPSK communication system. *Electronics* **10**, 640 (2021)
9. Gusso, A., Ujevic, S., Viana, R.L.: Strong chaotification and robust chaos in the Duffing oscillator induced by two-frequency excitation. *Nonlinear Dyn.* **103**, 1955–1967 (2021)
10. Gallas, J.: The structure of infinite periodic and chaotic hub cascades in phase diagrams of simple autonomous flows. *Int. J. Bifurc. Chaos* **20**, 197–211 (2010)
11. Tamaševičius, A., Mykolaitis, G., Pyragas, V., Pyragas, K.: A simple chaotic oscillator for educational purposes. *Eur. J Phys.* **26**(1), 61 (2004)
12. Tamaševičius, A., Pyragienė, T., Pyragas, K.Ė.S.T.U.T.I.S., Bumelienė, S. and Meškauskas, M.: Numerical treatment of educational chaos oscillator. *Int. J. Bifurc. Chaos* **17**(10), 3657–3661 (2007)
13. Čirjulīna, D., Pikulins, D., Babajans, R., Anstrangs, D.D., Victor, I.C., Litvinenko, A.: Experimental study of the impact of component nominal deviations on the stability of Vilnius Chaotic oscillator. In: *2020 IEEE Microwave Theory and Techniques in Wireless Communications (MTTW)*, vol. 1, pp. 231–236 (2020)
14. Babajans, R., Anstrangs, D.D., Čirjulīna, D., Aboltins, A., Litvinenko, A.: Noise immunity of substitution method-based Chaos synchronization in Vilnius oscillator. In: *2020 IEEE Microwave Theory and Techniques in Wireless Communications (MTTW)*, vol. 1, pp. 237–242. IEEE, 2020

# Classical Nonlinear Dynamics Associated with Prime Numbers: Non-relativistic and Relativistic Study



Charli Chinmayee Pal  and Subodha Mishra

**Abstract** By mapping the system of prime numbers to a physical problem, it is possible to characterise the hidden nonlinear dynamics associated with it. In order to study the properties of primes, first the single particle Schrödinger equation is solved. The wave function used in this case is constructed from the prime counting function and their interaction potential is obtained. In the corresponding classical nonlinear system, the phase trajectories and the associated fixed points which happens to be half stable and half unstable are also studied. It is interesting to note that the Lambert W function appears in connection to solutions for the fixed points as a function of energy.

**Keywords** Quantum mechanics · Wave function · Nonlinear dynamics · Prime numbers

## 1 Introduction

One can represent a dynamical system using prime numbers [1, 2] e.g a system of gas molecules that are interacting with each other. Though the prime numbers are abstract points in the number universe, they can be represented by a one-particle system with an effective potential. Many interesting works have been published recently in this direction [3–8]. In the early 1970s Billingsley et al. [7] defined a random walk problem based on the fundamental theorem of arithmetic. Julia et al. [6] proposed the idea of a non-interacting gas where a single particle may have discrete energy equal to the logarithm of  $n$ th prime number. Berry and Keating developed [3] a theory where

---

Subodha Mishra deceased on 8th January 2022.

---

C. C. Pal (✉) · S. Mishra

Department of Physics, Siksha ‘O’ Anusandhan, Deemed to be University,  
Bhubaneswar, 751030, India

e-mail: [charli.chinu@gmail.com](mailto:charli.chinu@gmail.com)

URL: <http://www.springer.com/gp/computer-science/lncs>

© The Author(s), under exclusive license to Springer Nature Switzerland AG 2022  
S. Banerjee and A. Saha (eds.), *Nonlinear Dynamics and Applications*,  
Springer Proceedings in Complexity,  
[https://doi.org/10.1007/978-3-030-99792-2\\_104](https://doi.org/10.1007/978-3-030-99792-2_104)

1229

the zeros of the Riemann zeta function are related to the eigenvalues of the system. The dynamics of this classical system were reported to be chaotic which is represented by the Hamiltonian  $H_{cl} = XP$  ( $X$  and  $P$  are position and momentum). Recently Bender et al. [4] constructed a Hamiltonian operator having eigenvalues as the nontrivial zeros of Riemann zeta function where the associated eigenfunctions obey certain boundary conditions. The classical limit of the operator is found to be exactly that predicted by Berry and Keating. All these seminal works beautifully connect and enrich quantum physics, dynamical chaos, and the prime number theory. In this work, we have taken a different approach to formulate a problem using the prime counting function [9] denoted by  $\pi(x)$ . The prime counting function  $\pi(x)$  gives the number of primes below  $x$  as the number of particles. We construct the one dimension density as  $\rho = \pi(x)/x$  and hence the corresponding wave function  $\sqrt{\rho}(x)$ . Any small smooth change in the parameter values (the bifurcation parameters) of a system causes a bifurcation in the system. It refers to a sudden qualitative change in the behavior of the dynamical system. The interaction potential between two bodies is obtained using the wave function. In the end, the relativistic and non-relativistic dynamics are studied by finding the flow trajectories, zeros, and bifurcation in that system.

## 2 Classical Dynamics: Non-relativistic

### 2.1 The Hamiltonian for Prime Number System

As discussed in the introduction, knowing the density function of primes, it is possible to construct the wave function and using the Schrodinger equation, one can map the prime number system to a dynamical system. The derivation of the interaction potential [10] is detailed in the appendix (10), which appears as  $V(x) = \frac{\hbar^2}{m} \frac{1}{4x^2} \left( \frac{1}{\ln(x)} + \frac{3}{2\ln^2(x)} \right)$ , The classical Hamiltonian [11] for a single particle system (taking  $\hbar^2/m = 1$ ) using the derived potential appears as

$$H = \frac{p^2}{2m} + V(x) = \frac{p^2}{2} + \frac{1}{4x^2} \left( \frac{1}{\ln(x)} + \frac{3}{2\ln^2(x)} \right) = E \quad (1)$$

The above classical Hamiltonian will be used to study the hidden classical non-linear dynamics [12] of the system representing primes. The variation of potential  $V(x)$  w.r.t  $x$  is plotted in Fig. 1 which shows  $V(x) = 0$  at  $x = e^{-3/2} = 0.223$  and is negative below this value of  $x$  up to  $x = 0$ . Also one can see that  $V(x = 0) \rightarrow -\infty$  and  $V(x = 1) \rightarrow \infty$ . As  $x$  increases from 1,  $V(x)$  decreases and goes to zero as  $x \rightarrow \infty$ .

Since the interaction potential (10) is determined, one can study the hidden classical dynamics characterizing prime numbers through the corresponding classical



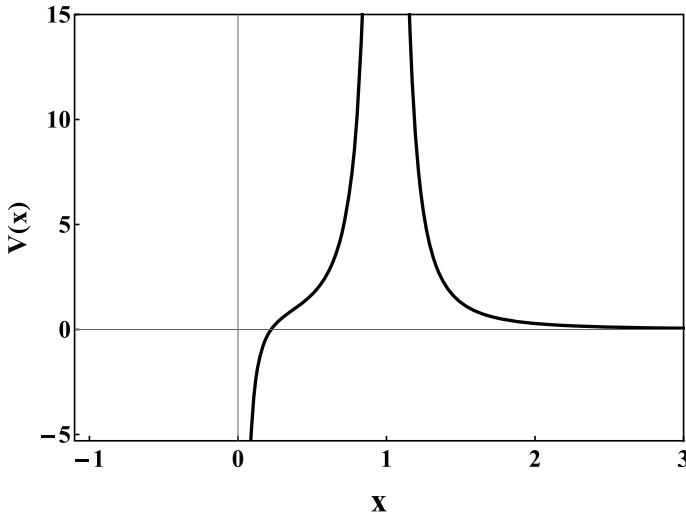


**Fig. 1** Shows the variation of potential  $V(x)$  with  $x$

Hamiltonian system. This classical study will provide the connection of prime numbers with the Lambert W functions [13] as reported earlier [14].

### 2.2 Phase Space, Trajectories and Zeroes

Now we study the classical aspects of the problem in the phase space of  $x$  and  $p$ . Since the potential function in the above Hamiltonian is nonlinear in  $x$ , where the nonlinear dynamics [12] of this system is studied here. In nonlinear dynamics the trajectories and zeroes or fixed points are very important quantities which reveal the interesting dynamics peculiar to the system. We find  $p(x)$  from the classical Hamiltonian given in (1) as

$$p(x) = \pm 2\sqrt{E - \frac{1}{4x^2}\left(\frac{1}{\ln(x)} + \frac{3}{2\ln^2(x)}\right)} \tag{2}$$

The plot between  $x$  and  $p$  for a given energy parameter  $E$  using Eq. (2) which is shown in Fig. 2. To be specific we choose  $E = -10, 0, 1, 10, 100$  and analyze those trajectories on the  $x$ - $p$  plane. We find there are only two zeroes indicated by the circles ( $x$  is a zero or a fixed point if  $\dot{x} = p = 0$  at that point). These two zeroes are half stable and half unstable fixed points. On the right branch of each of the  $x$ - $p$  plot different  $E$  of Fig. 2, if a particle has positive velocity, then it will go away from the right side zero to  $\infty$  and if it has negative velocity, it will come to that zero and stay there. On the other hand in the left branch, it is opposite in nature that is if the particle

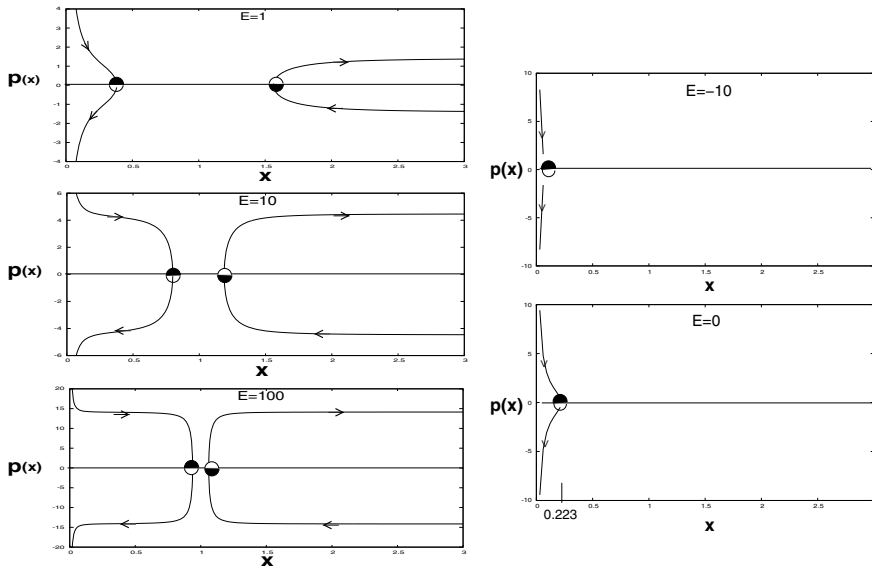


**Fig. 2** Plot of momentum  $p(x)$  as function of position  $x$  for five different values of energy  $E$ . The circles indicate the fixed points. A half full and half empty circle indicates half stable and half unstable nature of the fixed points. The two fixed points come closer as the energy increases. When energy is zero, one fixed point is at  $x_2 = 0.223$  and other one is at infinity. For negative energy the left fixed point moves towards zero from  $0.223$

has positive velocity then it will move towards the fixed point and if it has negative velocity, then it will recede from it. As is done in standard nonlinear dynamics study, stability is shown in darkness and instability in emptiness of the small circles drawn at the fixed points. We also see that as the value of energy parameter  $E$  increases, the two zeroes come closer and when  $E \rightarrow \infty$  they merge at  $x = x_1 = x_2 = 1$ . We also find, when  $E = 0$ , there is only the left branch cutting the  $x$ -axis at  $x_2 = 0.223$ , and the other one  $x_1$  is moved to infinity. As  $E$  becomes negative, the left side zero is at a value greater than 0 and less than  $x_2 = 0.223$ .

### 2.3 Bifurcation with $E$ as the Varying Parameter

As discussed in the Subsec-B, since the fixed points [12] are important in describing the dynamics, we make a detail study of these fixed points or zeroes. We see that in the Fig. 2, the two zeroes come closer as energy  $E$  increases. To find an analytic expression for the distance between the two zeroes or to study their bifurcation as a function of energy  $E$ , we first find out the positions of the two zeroes as functions of energy  $E$ . Putting  $p = 0$  in (2) we obtain Eq. (3) which is plotted in Fig. 3

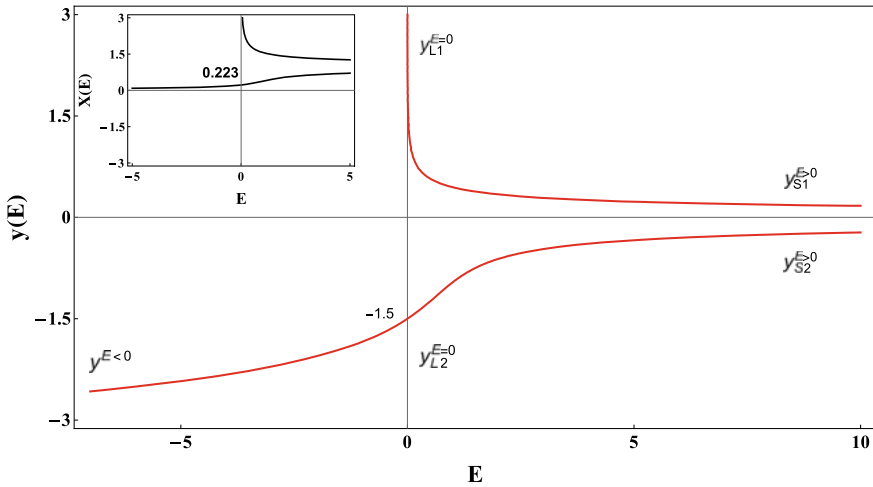


**Fig. 3** The plot is the bifurcation diagram representing the positions of fixed points in x-space and y-space defined as  $(y = \ln(x))$  as functions of energy

$$\frac{1}{\ln(x)} + \frac{1.5}{\ln^2(x)} - 4Ex^2 = 0 \tag{3}$$

The solution of (3) when  $x = e^y$  or  $(\ln(x) = y)$  and (large x or y) for any real  $E$  is given as  $y = 0.5W_n\left(\frac{1}{2E}\right)$ , ( $W_n(x)$  being the famous Lambert W function [13] corresponding to  $n = 0$  as the principal branch and other corresponds to the branch having  $n = -1$ ).

The appearance of the Lambert W function in the prime number analysis is deep rooted at different levels of analogy. It has been shown [14] recently that the prime counting function  $\pi(x)$  ( $x \rightarrow \infty$ ) is approximately equal to  $\exp(W_0(x))$  where  $W_0(x)$  is the principal branch of the Lambert W function.

### 3 Classical Dynamics: Relativistic

In order to study the relativistic dynamics of the problem we construct the relativistic Hamiltonian using the Klein-Gordon equation [10]. The K-G equation is given as

$$H = \sqrt{p^2c^2 + m^2c^4} + V(x) = E \tag{4}$$

where the first term is the relativistic kinetic energy and the  $V(x)$  is the potential used earlier in the non-relativistic analysis.

### 3.1 Phase Space, Trajectories and Zeroes

Now we study the classical aspects of the problem in the phase space of  $x$  and  $p$  when the above relativistic Hamiltonian is taken into consideration. From (4) we get

$$p(x) = \pm \sqrt{\left(\frac{E - V(x)}{c} + mc\right)\left(\frac{E - V(x)}{c} - mc\right)} \tag{5}$$

We will take  $m = 1$  and  $c = 1$  in our analysis without loss of generality. The flow shows that the dynamics is different than the corresponding non-relativistic case. The plot given in Fig. 4 shows that we have more number of trajectories and fixed points.

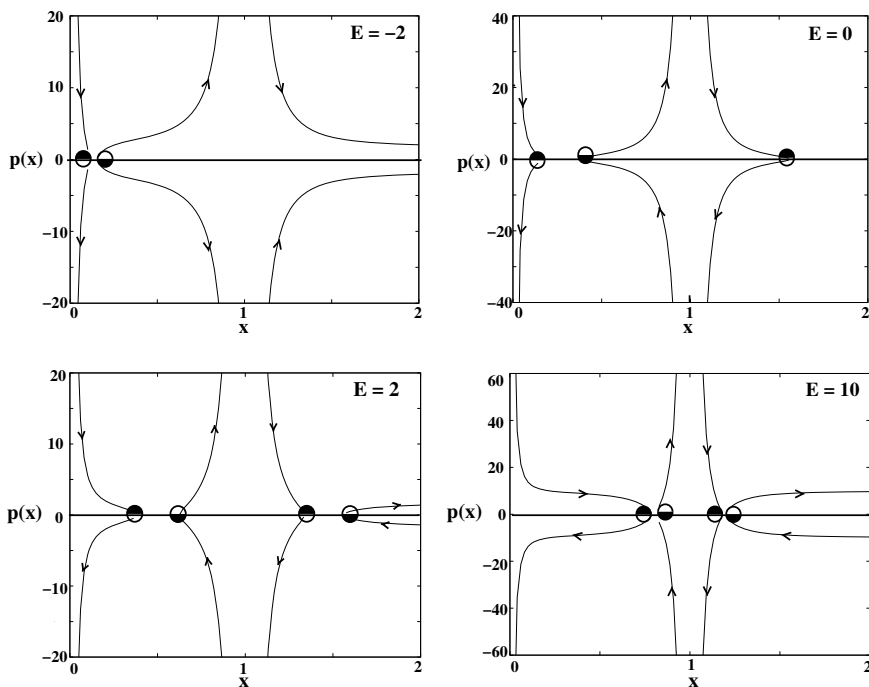


**Fig. 4** The plot represents the trajectories and the positions of fixed points in  $x$ -space as functions of energy for the relativistic case. We see that when  $E \leq -1$ , there are two fixed points,  $-1 < E < 1$ , three fixed points and when  $E > 1$  we have four fixed points but they pair up

### 3.2 Bifurcation with $E$ as the Varying Parameter

We can also study the bifurcation in the system by taking  $E$  as the varying parameter. Hence putting  $p = 0$  in (5) we get two equations which shows the bifurcation phenomenon in the system as,

$$\frac{1}{\ln(x)} + \frac{1.5}{\ln^2(x)} - 4x^2(E + 1) = 0 \tag{6}$$

$$\frac{1}{\ln(x)} + \frac{1.5}{\ln^2(x)} - 4x^2(E - 1) = 0 \tag{7}$$

These two equations are simultaneously valid. Now we have plotted the bifurcation diagram  $x = x(E)$  in Fig. 5.

We see that when  $E \leq -1$ , there are two fixed points, for  $-1 < E < 1$ , three fixed points and when  $E > 1$  we have four fixed points but they pair up (as the red and blue line).

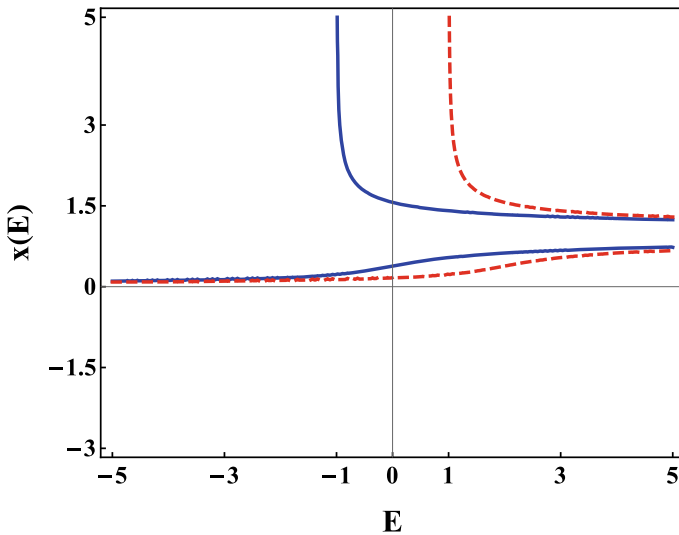


**Fig. 5** The plot is the bifurcation diagram representing the positions of fixed points in  $x$ -space as functions of energy. We see that when  $E \leq -1$ , there are two fixed points,  $-1 < E < 1$ , three fixed points and when  $E > 1$  we have four fixed points but they pair up (as the dotted red line for (6) and solid blue line for (7).)

## 4 Appendix: Derivation of the Potential

Here we construct the wave function  $\psi(x)$  of Schrodinger equation (9) through the asymptotic form of prime counting function. The prime counting function denoted as  $\pi(x)$  gives the number of primes below the real number  $x$ . if we take  $x$  as 4, then  $\pi(x) = 2$  i.e. 2 and 3. ( $\pi(x)/(x/\ln(x)) \rightarrow 1$  as  $x \rightarrow \infty$ ) becomes  $\frac{x}{\ln(x)}$  in its asymptotic form [9]. The single particle local density for prime numbers in one dimension is found to be  $\rho(x) = \frac{\pi(x)}{x} = \frac{1}{\ln(x)}$ . This gives a homogeneous distribution of the prime numbers below each value of  $x$ . In stead of considering  $\pi(x)$  which is a stair case function [3], its asymptotic form  $\frac{x}{\ln(x)}$  is used. This consideration helps in obtaining a continuous and smooth distribution of density.

The wave function is obtained to be

$$\psi(x) = \sqrt{\rho(x)} = \frac{1}{\sqrt{\ln(x)}} \quad (8)$$

We are concerned about a single particle system within a potential. So we write down the one particle Schrodinger equation [15] as

$$H\psi(x) = \left( \frac{-\hbar^2 \nabla^2}{2m} + V(x) \right) \psi(x) = E\psi(x) \quad (9)$$

In this problem, since we know the asymptotic behaviour of prime counting function, we construct a probability density associated with primes as a function of  $x$  and from that we calculate the wave function. By using this single particle wave function, we find a formula for the effective potential through which we can study the classical aspect of the prime number system. We derive [10] the potential function by using the wave function  $\psi(x)$  from the Schrodinger equation (9) (up to an additional constant and without loss of generality we have taken the constant  $E = 0$  in the  $V(x)$ ). Taking  $\hbar^2/m = 1$ , the interaction potential  $V(x)$  appears as

$$V(x) = \frac{1}{4x^2} \left( \frac{1}{\ln(x)} + \frac{3}{2\ln^2(x)} \right) \quad (10)$$

## 5 Conclusion

In conclusion, a prime number system that is equivalent to an interacting quantum many-particle system is represented by a single particle Schrodinger equation. The interaction potential is obtained and the nonlinear classical dynamics associated with this novel system are studied. We show that finding large prime numbers, which is

otherwise computationally challenging becomes easier. The fixed points associated with the classical trajectories are obtained to be half stable and half unstable. The Lambert  $W$  function appears in the solution of fixed points and is a function of energy. Thus by constructing the interaction potential for the prime number system, its properties have been investigated.

## References





1. Wells ,D.: Prime Numbers: the Most Mysterious Figures in Math, p. 56. Wiley (2005)
2. Ribenboim, P.: The New Book of Prime Number Records, 3rd edn, pp. 252–253. Springer, New York, NY (1995)
3. Berry, M.V., Keating, J.P.: The Riemann zeros and eigenvalue asymptotics. *SIAM Rev.* **41**(2), 236 (1999)
4. Bender, C.M., Brody, D.C., Muller, M.P.: Hamiltonian for the zeros of the Riemann zeta function. *Phys. Rev. Lett.* **118**, 130201 (2017)
5. Julia, B.: Statistical theory of numbers. In: Luck, J.M., Moussa, P., Waldschmidt, M. (eds.) *Number Theory and Physics*, p. 276. Springer, Berlin (1990)
6. Julia, B.: *Phys. A: Stat. Mech. Appl.* **203**(34), 425–436 (1994)
7. Billingsley, P.: Prime numbers and Brownian motion. *Am. Math. Mon.* **80**, 1099 (1973)
8. Okubo, S.: Lorentz-invariant Hamiltonian and Riemann hypothesis. *J. Phys. A* **31**, 1049 (1998)
9. Ingham, A.E.: *The Distribution of Prime Numbers*, pp. 1–3. Cambridge University Press, Cambridge (1932)
10. Griffiths, D.J.: *Introduction to Quantum Mechanics*, p. 19. Prentice Hall, New Jersey (1995)
11. Goldstein, H., Poole, C., Safko, J.: *Classical Mechanics*, 3rd edn, pp. 334–337. Addison Wesley, New York (2000)
12. Strogatz, S.H.: *Nonlinear Dynamics and Chaos*, p. 18. Perseus books, Massachusetts (1994)
13. Corless, R.M, et al.: On the Lambert  $W$  function. *Adv. Comp. Math.* **5**, 329 (1996)
14. Visser, M.: Primes and the Lambert  $W$  function. *Mathematics* **6**, 56 (2018)
15. Mishra, S., Pfeifer, P.: FAST TRACK COMMUNICATION: Schrödinger equation for the one-particle density matrix of thermal systems: an alternative formulation of Bose Einstein condensation. *J. Phys. A.: Math. Theor.* **4**(0), F243 (2007)

# **Other Fields of Nonlinear Dynamics**



# Dynamics of Chemical Excitation Waves Subjected to Subthreshold Electric Field in a Mathematical Model of the Belousov-Zhabotinsky Reaction



Anupama Sebastian , S. V. Amrutha , Shreyas Punacha ,  
and T. K. Shajahan 

**Abstract** We present a numerical study of the dynamics of spiral waves in a weak external electric field, using the Oregonator model of the Belousov-Zhabotinsky (BZ) reaction. Both free and pinned spiral waves are studied in two types of electric fields: unidirectional (DC) and Circularly Polarised Electric Field (CPEF). Both free spirals and pinned spiral waves rotate faster in the DC field. The CPEF can help a free spiral to be spatially confined. A pinned spiral period can be controlled by varying the period of the CPEF. Both DC and CPEF can unpin the pinned spiral wave, but the minimum electric field required to unpin is much less with CPEF compared to DC. Thus, CPEF is more energy efficient to unpin a pinned spiral wave.

**Keywords** Excitable medium · Spiral wave · Belousov-Zhabotinsky reaction · Subthreshold stimulation · Unpinning · Critical threshold

## 1 Introduction

Excitable systems, in general, are non-equilibrium systems with a stable resting state. They can only be aroused to a transitory excited state after crossing a certain threshold. However, perturbations below the threshold go unnoticed since they cannot set off the system to an excited state. Following the excitation, the medium returns to their resting state after a certain time period called the refractory period, during which further perturbations cannot re-excite the system. Unlike the electromagnetic waves, which obey the superposition principle, excitation waves annihilate upon mutual

---

A. Sebastian · S. V. Amrutha · S. Punacha · T. K. Shajahan (✉)  
Department of Physics, National Institute of Technology Karnataka, Surathkal, Mangalore  
575025, Karnataka, India  
e-mail: [shajahan@nitk.edu.in](mailto:shajahan@nitk.edu.in)

© The Author(s), under exclusive license to Springer Nature Switzerland AG 2022  
S. Banerjee and A. Saha (eds.), *Nonlinear Dynamics and Applications*,  
Springer Proceedings in Complexity,  
[https://doi.org/10.1007/978-3-030-99792-2\\_105](https://doi.org/10.1007/978-3-030-99792-2_105)

1241

collision. Many excitable systems exist in nature, including the heart muscles [1, 2], chicken retina [3, 4], slime-mold aggregates [5], *Xenopus* oocytes [6, 7], and Belousov-Zhabotinsky (BZ) reaction [8, 9].

One of the characteristic features of a two-dimensional excitable medium is the fascinating patterns such as rotating spiral and target waves. However, in the case of systems like the heart muscle, the high-frequency rotating spiral waves are known to disrupt the natural sinus rhythm. Furthermore, rotating spirals get stabilized once they get pinned to an obstacle. The pinned spiral waves play a key role in the progression of dynamical disorders, including cardiac arrhythmia [10, 11], and epileptic convulsions [12]. Understanding the dynamics of the pinned spiral waves is crucial to develop efficient techniques to control them.

The dynamics of spiral waves and their interaction with the external perturbations can be easily studied in the Belousov-Zhabotinsky reaction. It is an oscillating system that produces patterns by oxidizing malonic acid in the presence of a metal catalyst such as ferroin. External forcing, such as periodic illumination [13] and electric field application [14], are commonly used to study spiral dynamics. The electric field is known to influence the transport of ionic species in chemical media [15]. As a result, the spiral core drifts by forming a parallel and perpendicular component to the direction of the applied field [16]. Li et al. developed a theory of spiral wave drift caused by weak ac and polarised electric fields. Using response function theory, they derive the spiral drift velocity and direction [17]. Circularly Polarised Electric Field (CPEF) with rotational symmetry has been utilized to regulate spiral drift [18]. Frequency synchronization occurs if the CPEF and spiral are having a comparable frequency [19]. The CPEF has been used in cardiac models to investigate the control of both 2D [20] and 3D [21] pinned excitation waves. Punacha et al. proposed a theory for WEH-induced unpinning and showed that spirals can always be uninned below a threshold time period of CPEF [22]. Furthermore, a unidirectional field is used for the electrically forced release of pinned spiral waves in the BZ medium when the field strength surpasses a critical threshold (i.e., for supra-threshold fields) [23]. Previous studies, however, have not looked into how a subthreshold field, one that is below a critical threshold, interacts with free and pinned spirals in a BZ medium.

In this article, we investigate the dynamics of both free and pinned spirals in the BZ medium exposed to the subthreshold electric field. We compare the behavior of spiral waves with and without an obstacle. We find that the subthreshold electric field generates a shift in the spiral period. At greater field strengths, this effect becomes more pronounced. Compared to DC, CPEF has a lower critical threshold for unpinning, making it a more energy-efficient method to control spiral waves.

## 2 Methodology

We model the BZ reaction system using the two-variable Oregonator model [24, 25]. The activator, ‘ $u$ ’, initiates the reaction, and the inhibitor, ‘ $v$ ’, with its slow dynamics, returns the system to the resting state. Their combined effect will steer the

entire dynamics. In BZ reaction,  $u$  and  $v$  corresponds to the chemical concentration of  $HBrO_2$  and catalyst respectively. In the presence of an electric field,  $E$ , the dynamics of  $u$ , and  $v$  are given by the following equations.

$$\frac{\partial u}{\partial t} = \frac{1}{\epsilon} (u(1 - u) - \frac{fv(u - q)}{u + q}) + D_u \nabla^2 u + M_u \mathbf{E} \cdot \nabla u \tag{1}$$

$$\frac{\partial v}{\partial t} = (u - v) + D_v \nabla^2 v + M_v \mathbf{E} \cdot \nabla v \tag{2}$$

Electric field ( $E$ ) is implemented in above equations by using an advection term  $\mathbf{E} \cdot \nabla u$  and  $\mathbf{E} \cdot \nabla v$  respectively. The model parameters are  $q = 0.002$ ,  $f = 1.4$ , with diffusion coefficients  $D_u = 1.0$ ,  $D_v = 0.6$  and ionic mobilities  $M_u = 1.0$  and  $M_v = -2.0$ . The value of  $\epsilon$  is 0.01 and is used to explicitly determine the system’s excitability.

The entire  $300 \times 300$  computation domain is discretized in space into grids of uniform size  $dx = dy = 0.1$  space units (s.u). The temporal evolution is studied using the explicit forward Euler technique with a timestep,  $dt = 0.0001$  time units (t.u). Space and time are both measured in dimensionless units. A five-point Laplacian operator gives the coupling between the grids. No flux boundary conditions are imposed on the domain boundary. We use the phase-field method to implement them on the obstacle boundary [26].

An anticlockwise rotating spiral (ACW), either free or pinned to an obstacle of radius, ‘ $r$ ’ s.u, is created at the center of the domain. The diffusion coefficient  $D_u = 0.0001$  is set inside the obstacle. After five sustained rotations of the spiral wave with a period ( $T_s$ ) in the medium, we apply (i) unidirectional DC and (ii) rotating CPEF of strength  $E$ .

The DC field along the x-axis is modeled as

$$\mathbf{E}_{DC} = E \hat{i} \tag{3}$$

and we implement an anticlockwise rotating CPEF in the form

$$\mathbf{E}_{CPEF} = E \left( \cos\left(\frac{2\pi t}{T}\right) \hat{i} + \sin\left(\frac{2\pi t}{T}\right) \hat{j} \right) \tag{4}$$

where  $T$  denotes the rotational period of the CPEF. Later, we vary the pacing ratio, i.e.,  $p = \frac{T_s}{T}$  from 0.5 to 2 in the steps of 0.25 by altering the rotational period of the field. We apply an electric field until the critical threshold for pinned spirals, which is the lowest field strength for unpinning.

### 3 Results and Discussion

Our numerical study involves the interaction of the electric field of subthreshold amplitude with the rotating spiral. We consider both free and pinned spiral waves in this study.

We start with a unidirectional DC electric field in the medium oriented along the positive  $x$ -axis. A free spiral traces out a large core with increasing field strength and moves towards the positive electrode, as shown in Fig. 1a. We define the angle formed by the drift direction with the negative  $x$ -axis (represented as OX) as ' $\Theta$ ', whereas the linear distance traveled by the spiral tip in one spiral rotation is called ' $\lambda$ '. We calculate  $\lambda$  as the distance between two adjacent petals, which can also be referred to as the petal width. With the strength of the advective field, both  $\Theta$  and  $\lambda$  increases (see Fig. 1b, c). With increasing field strength,  $E$  from 0.2 to 0.8,  $\Theta$  rises quickly, reaching saturation at around 90 degrees at high field strength. Therefore, the spiral drifts precisely perpendicular to the direction of strong advective fields. The direction of spiral drift also depends on its chirality [16]. On the other hand,  $\lambda$  varies slowly with field strength. As extremely high fields lead to wave break, we limited our study up to  $E = 0.8$ .

In addition to the drift parameters, we measure the rotational period of the spiral in the presence of the DC field. The normalised spiral period,  $T_N$ , is defined as  $\frac{T_f}{T_s}$ , where  $T_s$  and  $T_f$  are the spiral periods before and after the forcing, respectively. We observe that the forcing induces an increase in  $T_N$ . When the field strength reaches

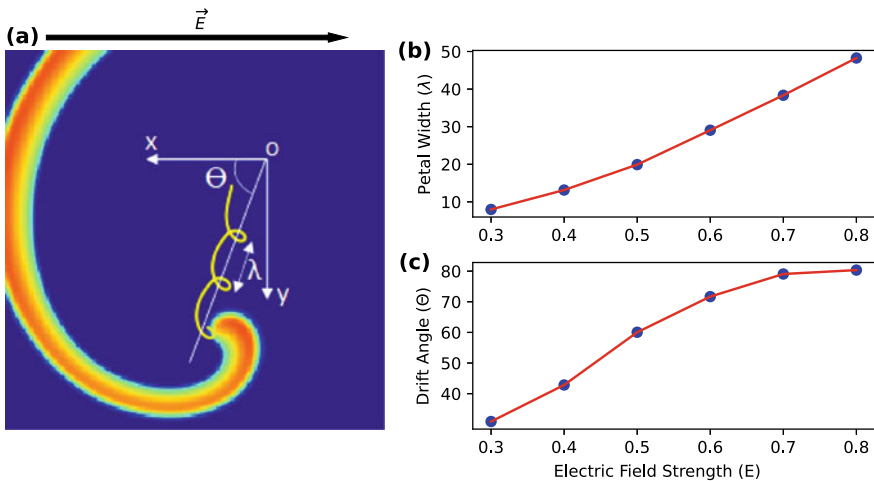


**Fig. 1** Spiral drift in the presence of DC electric field. **a** An anticlockwise rotating free spiral drifts towards the positive direction of the field by forming an angle  $\Theta$  and petal width,  $\lambda$ . The field,  $\vec{E}$  is oriented in the positive  $x$ -direction, as indicated by the thick black arrow. **b**, **c** corresponds to the variation of  $\lambda$  and  $\Theta$  with the field strength, respectively

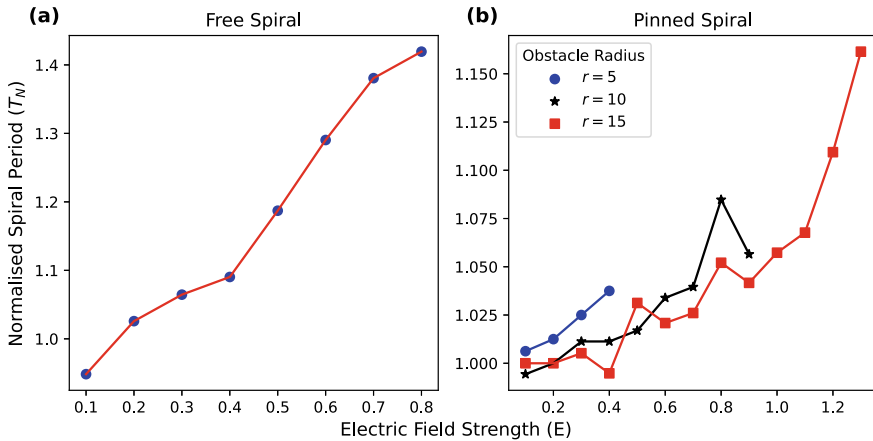


**Fig. 2** Variation of spiral rotational period with the subthreshold field strength. **a** A free spiral’s normalised time period ( $T_N$ ), which increases with field strength. **b**  $T_N$  for a pinned spiral anchored to radius,  $r = 5, 10$  and  $15$ , respectively. The field strength ( $E$ ) is varied till the wave was unpinned

$E = 0.8$ , we see a 40% increase in the spiral period as in Fig. 2a. Hence, the field inhibits spiral rotation and slows it down.

To understand how stable pinned spirals interact with the applied field, we analyze spiral waves attached to obstacles with three different radii  $r = 5, 10$ , and  $15$ . The spiral tip gets unpinned when the external forcing reaches a critical threshold [23]. We employ a field with a strength below the critical threshold to avoid unpinning. Like the free spiral, the pinned spiral attached to any obstacle of any size is slowed by the DC field. However, when compared to a free spiral, the increase in the rotational period is insignificant.

Unlike the DC field, CPEF is spatially uniform. In our simulations, we create an anticlockwise rotating CPEF with period  $T$  that has rotational symmetry with the spiral. The pacing ratio,  $p = \frac{T}{T_s}$  indicates the extent of pacing. For each strength of the electric field, we vary  $p$  from  $0.5$  to  $2$  in the steps of  $0.25$ . When subjected to CPEF, the spiral tip traces out meandering patterns if CPEF rotates too fast or too slow (see Fig. 3b). However, the motion of the free spiral tip could be spatially constrained for a range of  $p$  values closer to  $1$ , as shown in Fig. 3c. In contrast to directed drift in the DC, the rotational symmetry of the CPEF causes the spiral tip to be confined to an area in the medium.

Surprisingly, the response of the pinned spiral to the electric field is strongly influenced by the pacing ratio,  $p$ . The spiral period increases with field amplitude for overdrive pacing ( $p > 1$ ), meaning that the spiral slows down. The pacing ratio  $p > 2$ , on the other hand, does not affect the spiral dynamics (see Fig. 4). We infer that the spiral dynamics are unaffected by the exceedingly high pacing ratio. The spiral period is reduced, or the spiral advances faster when the field strength increases during underdrive pacing ( $p < 1$ ). When the spiral period and the CPEF period are

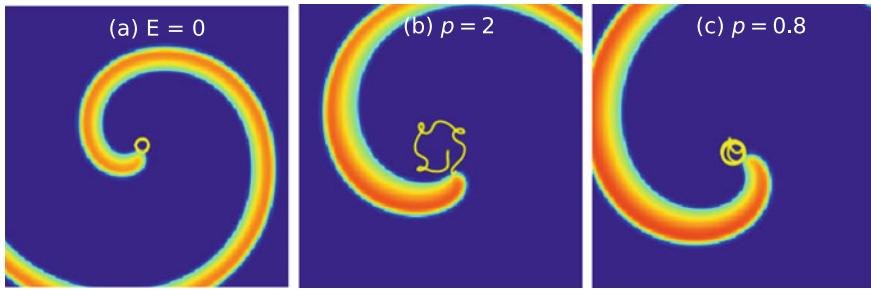


**Fig. 3** The tip trajectory of the free spiral before and after applying CPEF. **a** A free spiral, in the absence of an electric field (i.e.,  $E = 0$ ), performs rigid rotation with a small core. From the same initial phase of the spiral ( $\approx 45^\circ$ ), CPEF with field strength,  $E = 0.6$ , and pacing ratios of **b**  $p = 2$  and **c**  $p = 0.8$  is applied to the medium. Meandering occurs when  $p = 2$ , but  $p = 0.8$  results in spatial confinement

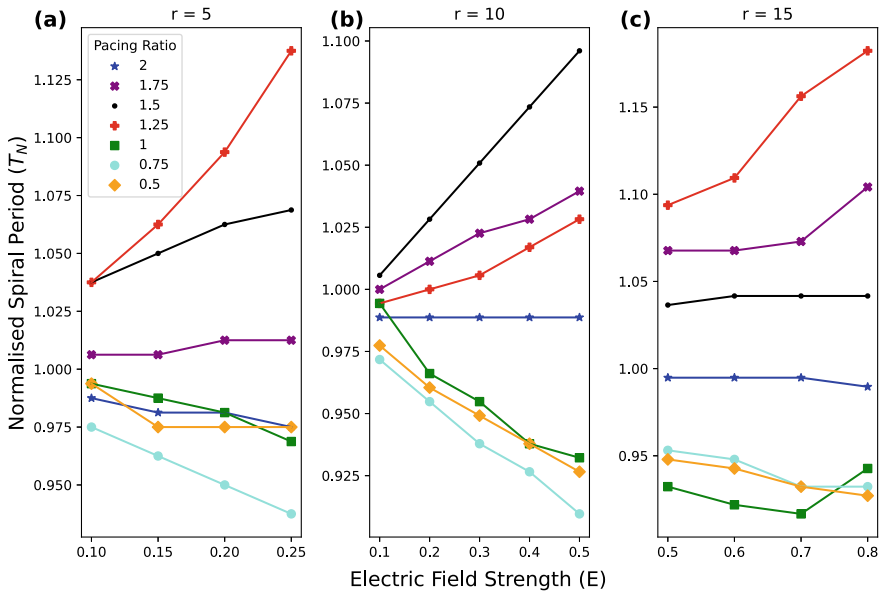


**Fig. 4** Response of pinned spiral in the presence of CPEF with different strength and pacing ratio. **a–c** Shows the change in Normalised Spiral Period ( $T_N$ ) as a function of field strength for pacing ratios  $p$  ranging from 0.5 to 2 for radii  $r = 5$ . **b** Is same as **a** for  $r = 10$ . **c** Is same as **a** for  $r = 15$ .  $T_N$  increases with the strength of the electric field for overdrive pacing and decreases for underdrive pacing

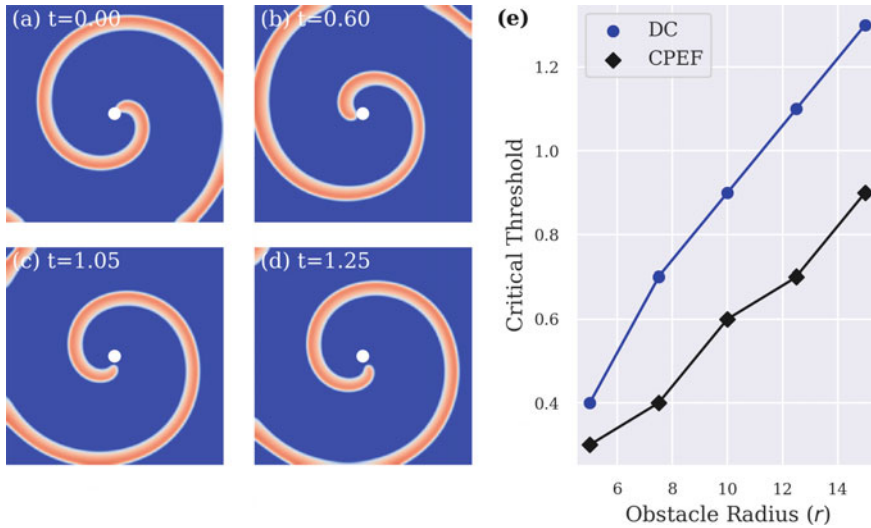


**Fig. 5 Unpinning at a critical threshold.** a–d Snapshots of DC electric field-driven unpinning from an obstacle of radius,  $r = 7.5$  at the critical threshold of strength,  $E = 0.7$ . e For both DC (dots) and CPEF with overdrive pacing (diamond), the critical threshold for unpinning is linearly related to the obstacle size. The critical threshold for DC is higher than that of CPEF

both equal ( $p \approx 1$ ), the electric field strength does not affect the  $T_N$ . Although the range of  $T_N$  varies, the trend mentioned above is followed for all obstacle sizes used in our simulation. Therefore, the spiral alters its rotational period as a response to the change in field frequency.

As the strength of the advective field increases, the pinned spiral's tip drifts away from the obstacle, a process known as unpinning. The critical threshold is the lowest field required to remove the spiral from the obstacle, which may also be thought of as the strength of the obstacle-spiral pinning interaction. In Fig. 5a–d, a DC electric field with a strength of  $E = 0.7$  induces unpinning from an obstacle with a radius of  $r = 7.5$  s.u. We investigate the critical thresholds for DC and CPEF for five obstacle sizes with radii ranging from 5 to 15. The pacing ratio is a crucial component in the case of CPEF. Underdrive pacing leads to unpinning only when the pacing ratio is very low. Moreover, unpinning at comparable frequencies ( $p \approx 1$ ) is quite difficult. As a result, we estimate the critical threshold for overdrive pacing in our simulation.

As shown in Fig. 5e, the unpinning critical threshold is directly proportional to the obstacle radius in both DC and CPEF. Furthermore, unpinning may be influenced by the initial spiral phase at field initiation. Throughout this study, we have used the same initial phase ( $\approx 45^\circ$ ) of the spiral. In addition, the critical threshold for DC is higher than that for CPEF for a spiral fixed to any obstacle size. The low critical threshold is a benefit when comparing CPEF to DC. This result helps in the efficient selection of the best low-energy control method.

## 4 Conclusion

Our numerical work focuses on the interaction of a subthreshold amplitude electric field with a rotating spiral in a BZ medium. We used both unidirectional DC and rotating CPEF to investigate how the spiral dynamics are affected by the direction and frequency of the electric field. The unidirectional DC field slows both free and pinned spirals with increasing field strength. Despite the fact that an electric field increases the spiral period with field strength, the increase in the rotational period for a pinned spiral is negligible compared to that of a free spiral. With CPEF, however, the pacing ratio plays a crucial role in defining spiral dynamics. For a range of values of pacing ratio,  $p$ , a free spiral is spatially confined by CPEF. Furthermore, the period of a pinned spiral depends on the pacing ratio of the rotating field. Underdrive pacing causes the spiral period to decrease with field strength, while overdrive pacing causes it to increase. Pacing ratios that are greater than two (i.e.,  $p > 2$ ), on the other hand, have no effect. The critical electric field for unpinning by CPEF at overdrive pacing is much lower compared to that at the DC field.

We believe our work has implications for low energy control techniques used for spiral unpinning and control in cardiac dynamics. In particular, a lower critical threshold for CPEF compared to the DC field indicate that CPEF is more energy efficient for unpinning the pinned spiral waves.

## 5 Author Contributions

A.S and S.V.A conceived the idea and planned the simulations. S.P designed the numerical study as well as the computational framework. T.K.S supervised the project and provided constructive feedback. A.S performed numerical simulations, analyzed the data, and wrote the manuscript with contributions from all authors.

## References

1. Davidenko, J.M., Pertsov, A.V., Salomonsz, R., Baxter, W., Jalife, J.: Stationary and drifting spiral waves of excitation in isolated cardiac muscle. *Nature* **355**(6358), 349–351 (1992)
2. Rostami, Z., Rajagopal, K., Khalaf, A.J.M., Jafari, S., Perc, M., Slavinec, M.: Wavefront-obstacle interactions and the initiation of reentry in excitable media. *Phys. A: Stat. Mech. Appl.* **509**, 1162–1173 (2018)
3. Gorelova, N.A., Bureš, J.: Spiral waves of spreading depression in the isolated chicken retina. *J. Neurobiol.* **14**(5), 353–363 (1983)
4. Fernandes de Lima, V.M., Hanke, W.: Relevance of excitable media theory and retinal spreading depression experiments in preclinical pharmacological research. *Curr. Neuropharmacol.* **12**(5), 413–433 (2014)
5. Siegert, F., Weijer, C.: Digital image processing of optical density wave propagation in *Dicystostelium discoideum* and analysis of the effects of caffeine and ammonia. *J. Cell Sci.* **93**(2), 325–335 (1989)



6. Lechleiter, J., Girard, S., Peralta, E., Clapham, D.: Spiral calcium wave propagation and annihilation in *Xenopus laevis* oocytes. *Science* **252**(5002), 123–126 (1991)
7. Chatterjee, M., Sain, A.: Dynamic surface patterns on cells. *J. Chem. Phys.* (2022)
8. Zaikin, A.N., Zhabotinsky, A.M.: Concentration wave propagation in two-dimensional liquid-phase self-oscillating system. *Nature* **225**(5232), 535–537 (1970)
9. Tyson, J.J.: From the Belousov-Zhabotinsky reaction to biochemical clocks, traveling waves and cell cycle regulation. *Biochem. J.* **479**(2), 185–206 (2022)
10. Fenton, F.H., Cherry, E.M., Hastings, H.M., Evans, S.J.: Multiple mechanisms of spiral wave breakup in a model of cardiac electrical activity. *Chaos: Interdiscip. J. Nonlinear Sci.* **12**(3), 852–892 (2002)
11. Alonso, S., Bär, M., Echebarria, B.: Nonlinear physics of electrical wave propagation in the heart: a review. *Rep. Progr. Phys.* **79**(9), 096601 (2016)
12. Traub, R.D., Wong, R.K.: Cellular mechanism of neuronal synchronization in epilepsy. *Science* **216**(4547), 745–747 (1982)
13. Liu, G., Wu, N., Ying, H.: The drift of spirals under competitive illumination in an excitable medium. *Commun. Nonlinear Sci. Numer. Simul.* **18**(9), 2398–2401 (2013)
14. Muñuzuri, A.P., Gómez-Gesteira, M., Pérez-Muñuzuri, V., Krinsky, V.I., Pérez-Villar, V.: Mechanism of the electric-field-induced vortex drift in excitable media. *Phys. Rev. E* **48**(5), R3232 (1993)
15. Agladze, K.I., De Kepper, P.: Influence of electric field on rotating spiral waves in the Belousov-Zhabotinskii reaction. *J. Phys. Chem.* **96**(13), 5239–5242 (1992)
16. Steinbock, O., Schütze, J., Müller, S.C.: Electric-field-induced drift and deformation of spiral waves in an excitable medium. *Phys. Rev. Lett.* **68**(2), 248 (1992)
17. Li, T.C., Gao, X., Zheng, F.F., Pan, D.B., Zheng, B., Zhang, H.: A theory for spiral wave drift induced by ac and polarized electric fields in chemical excitable media. *Sci. Rep.* **7**(1), 1–9 (2017)
18. Chen, J.X., Zhang, H., Li, Y.Q.: Drift of spiral waves controlled by a polarized electric field. *J. Chem. Phys.* **124**(1), 014505 (2006)
19. Chen, J.X., Zhang, H., Li, Y.Q.: Synchronization of a spiral by a circularly polarized electric field in reaction-diffusion systems. *J. Chem. Phys.* **130**(12), 124510 (2009)
20. Feng, X., Gao, X., Pan, D.B., Li, B.W., Zhang, H.: Unpinning of rotating spiral waves in cardiac tissues by circularly polarized electric fields. *Sci. Rep.* **4**(1), 1–5 (2014)
21. Fu, Y.Q., Zhang, H., Cao, Z., Zheng, B., Hu, G.: Removal of a pinned spiral by generating target waves with a localized stimulus. *Phys. Rev. E* **72**(4), 046206 (2005)
22. Punacha, S., Shajahan, T.K.: Theory of unpinning of spiral waves using circularly polarized electric fields in mathematical models of excitable media. *Phys. Rev. E* **102**(3), 032411 (2020)
23. Sutthiopad, M., Luengviriya, J., Porjai, P., Tomapatanaget, B., Müller, S.C., Luengviriya, C.: Unpinning of spiral waves by electrical forcing in excitable chemical media. *Phys. Rev. E* **89**(5), 052902 (2014)
24. Keener, J.P., Tyson, J.J.: Spiral waves in the Belousov-Zhabotinskii reaction. *Phys. D: Nonlinear Phenom.* **21**(2–3), 307–324 (1986)
25. Field, R.J., Noyes, R.M.: Oscillations in chemical systems. IV. Limit cycle behavior in a model of a real chemical reaction. *J. Chem. Phys.* **60**(5), 1877–1884 (1974)
26. Fenton, F.H., Cherry, E.M., Karma, A., Rappel, W.J.: Modeling wave propagation in realistic heart geometries using the phase-field method. *Chaos: Interdiscip. J. Nonlinear Sci.* **15**(1), 013502 (2005)

# Structural Transformation and Melting of the Vortex Lattice in the Rotating Bose Einstein Condensates



Rony Boral, Swarup Sarkar, and Pankaj K. Mishra

**Abstract** We numerically investigate the effect of the depth and lattice constant of square optical lattice on the vortex lattice structure of the rotating Bose-Einstein condensates. For a given angular velocity and lattice constant of the optical lattice, vortex lattice structure makes a transition from the hexagonal to the fully pinned square lattice upon increasing the pinning strength of the potential. A detailed quantitative analysis has been performed to understand the transition of the vortex lattice structure by changing the angular velocity, lattice constant and strength of the optical lattice potential. We find that the angular velocity at which the minimum potential strength is required to obtain fully pinned square vortex lattice increases upon decreasing the lattice constant of the potential with power law dependence. We also show the effect of random impurities along with pinning potential on the structure of the vortex lattice which triggers melting of the vortex lattice.

**Keywords** Optical lattice · Vortices · Abrikosov lattice · Random potential

## 1 Introduction

The experimental realization of Bose-Einstein condensates (BECs) in cold alkali-metallic gases has given an entirely new direction to the research in the cold atom physics [1]. One of the classical problem in ultracold system is to understand the genesis of the generation and dynamics of the vortices, a quantized circulation generated as a topological defect in the rotating BECs. Also the comprehensive understanding of different ordered lattice structure displayed by them upon trapping under the optical lattice has been the main thrust of the research. In last few decades the study related to the vortex lattice formation and its structural transformation in presence of different optical lattice, like square, hexagonal, rhomboid, etc. have caught a great

---

R. Boral (✉) · S. Sarkar · P. K. Mishra  
Department of Physics, Indian Institute of Technology Guwahati,  
Guwahati 781039, Assam, India  
e-mail: [rony176121108@iitg.ac.in](mailto:rony176121108@iitg.ac.in)

© The Author(s), under exclusive license to Springer Nature Switzerland AG 2022  
S. Banerjee and A. Saha (eds.), *Nonlinear Dynamics and Applications*,  
Springer Proceedings in Complexity,  
[https://doi.org/10.1007/978-3-030-99792-2\\_106](https://doi.org/10.1007/978-3-030-99792-2_106)

1251

attention of the scientific community due to the potential application of this in several other fields of the condensed matter Physics [2]. The experiments in BECs are highly tunable, so it helps to develop a better understanding of formation of pure vortex lattice and their melting in presence of the impurity. In this paper, we numerically investigate the effect of rotation and strength of the pinning potential on the lattice structure of the vortex lattice in rotating BECs.

After the first experimental realization of the vortices in BECs by the Madison Group [3] using laser stirring, the field has seen unprecedented growth at the theoretical and numerical level to unravel the underlying mechanism behind arrangements of the vortices on the lattice structure. Many theoretical investigations in BECs are based on the analysis of the vortex lattice structure and dynamics using the mean-field Gross-Pitaevskii equation. In recent years BECs trapped under the optical lattice have been used to understand many of interesting phenomena in many other fields of condensed matter physics [2]. As for as an example optical lattice are used to realize the Bloch Oscillations [4], Wannier-Stark Ladders [5], Josephson junction arrays [6], and quantum phase transition from a superfluid to a Mott-insulator [7]. There are several research groups mainly focused to investigate the effect of depth and periodicity of the optical lattice on the vortex lattice structure analytically and numerically [8, 9]. Tung et al. [10] experimentally observed the structural phase transition of the vortex lattice by rotating the condensates and investigated the effect of pinning strength of the pinning potential on transformation of the vortex lattice from the hexagonal to the square lattice structure. Pu et al. [11] showed that the structural phase transition of the vortex lattice is very highly responsive to the ratio of number of vortices with respect to the pinning sites when the condensate is trapped in harmonic and optical lattice. They also obtained that the vortex pinning increases when the vortex density matches the density of the lattice potential [12].

In recent years there are several studies that suggest a intricate nature of structural transition of the vortex lattice structures for the binary mixtures of rotating BECs trapped under optical lattice [13, 14]. William et al. [15] found that the dynamical regimes of vortex lattice depends on the depth and the periodicity of the optical lattice potential. In binary dipolar BECs such transitions between different vortex-lattice structures, like, Abrikosov lattice to square lattice, have been observed either by varying the angular velocity or by tuning the ratio of the inter- and intraspecies strengths even in absence of the optical lattice trapping [16]. In this direction Kumar et al. numerically investigated the transition of one vortex lattice to another for the dipolar rotating BECs trapped under square optical lattice and found the transition from the square to vortex sheet like structures upon tuning the ratio of the inter-species and intra-species interaction [17].

Apart from investigating the transformation between the different structure of the vortex in presence of the optical lattice, there are many studies that indicate the melting of the vortex lattice mainly induced by the random impurities present in the condensates. Mithun et al. numerically investigated the effect of the presence of Gaussian defects on the structure of vortex lattice for the rotating BECs trapped under the harmonic as well anharmonic potential and found that the beyond a certain threshold strength of the defect the vortex lattice gets melted [18]. Hu and Gu studied

squared potential pinned vortex lattice in presence of random depth optical lattice and noticed the melting of the vortex lattice structure upon increasing the depth of the random potential [19].

So far we find that lots of work in the rotating BECs which have only focused on the different structure and their transition from one structure to another. However, a comprehensive quantitative picture the factors like interaction between the vortex lattice and optical lattice, interaction between the impurities and vortex lattice responsible for melting, etc. are lacking in the literature. In this paper, we first numerically investigate the effect of the the pinning potential strength and rotation on the structure of the vortex lattice. Further using the structure factor and lattice energy of the vortex lattice we compute the minimum rotation and minimum potential strength required to perfectly pin the lattice to the optical lattice which is also associated with the structural transformation of the lattice from the hexagonal lattice structure also know as Abrikosov lattice (AL) to the pinned lattice (PL) which follow the same square lattice structure as optical lattice have. We also identify the region in the potential and rotation parameter space where there is coexistence of both AL state and PL state. We extend our analysis for the vortex lattice structure in presence of the random lattice.

The paper is organized as follows. In Sect. 2, we introduce the basic formulation of the problem and review the optical lattice pinning potential. In Sect. 3 we present the numerical procedure and simulation details to solve GP equation. In Sect. 4 we present our numerical simulation results related to effect of change in the vortex lattice structure in presence of the square optical lattice. A detailed analysis related with different nature of the vortex lattice upon change in rotation rate and strength of the pinning potential is presented. It is followed by a phase diagram that show the different nature of the vortex lattice in the potential strength and rotation parameter space. Here we also discuss the effect of addition of impurities on the vortex lattice structure. In Sect. 5, we finally conclude our observations.

## 2 Governing Equations

We consider Bose-Einstein condensate gas confined in a harmonic potential and a periodic potential in a frame rotating with an angular velocity  $\Omega$  along the  $z$ -axis. The macroscopic wave function of the condensate obeys the two-dimensional time-dependent Gross-Pitaevskii equation which is given by [12]:

$$(i - \gamma)\hbar \frac{\partial \psi}{\partial t} = \left[ -\frac{\hbar^2}{2m} \nabla^2 + V_{ext} + g |\psi|^2 - \mu - \Omega L_z \right] \psi \quad (1)$$

where,  $\psi$  is the condensate wave function,  $\nabla^2 = \partial_x^2 + \partial_y^2$ ,  $L_z = -i\hbar(x\partial_y - y\partial_x)$  is the  $z$ -component of the angular momentum operator,  $V_{ext}(x, y)$  the external optical potential which, we have chosen as a superposition of the harmonic and optical lattice potential, and  $\Omega$  is the angular velocity of the condensate along the  $z$ -axis. Here, we

have chosen both condensate and the potential rotates with the same angular velocity. The nonlinearity  $g = \frac{4\pi\hbar^2 a_s}{m}$  is the strength of interaction with  $a_s$  being the  $s$ -wave scattering length and  $m$  is the mass of the atom.  $\gamma$  denotes the dissipation due to the presence of non-condensate at finite temperature and  $\mu$  is the chemical potential of the condensate. The value of  $\gamma$  is set to be 0.03, as obtained via fitting the theoretical results with the experimental one [20]. For numerical simplification we have non-dimensionalized the above set of (1) using the scheme as  $x = a_h \tilde{x}$ ,  $t = \frac{\tilde{t}}{\omega_\perp}$ ,  $\psi = \frac{\tilde{\psi}}{a_h^{3/2}}$ , where  $a_h = \sqrt{\frac{\hbar}{m\omega_\perp}}$ , with  $\omega_\perp$  is the transverse angular frequency of harmonic trap potential. Here the variables with tilde denote the non-dimensionalized variable. In what follows for simplicity we will remove the tilde from the non-dimensionalized variables. The above changes in the variables lead to the following non-dimensional GPE

$$(i - \gamma) \frac{\partial \psi}{\partial t} = [-\frac{1}{2} \Delta + V_{ext} + g |\psi|^2 - \mu - \Omega L_z] \psi \quad (2)$$

Where,  $V_{ext} = \frac{1}{2}(x^2 + y^2) + V_{lattice}$ ,  $\Delta = \frac{\partial^2}{\partial x^2} + \frac{\partial^2}{\partial y^2}$ . The tilde is omitted for simplicity.

We have chosen the optical lattice as a superposition of the two perpendicular Gaussian beams which can be represented as

$$V_{lattice} = \sum_{n_1} \sum_{n_2} V_0 \exp\left(-\frac{|r - r_{n_1 n_2}|^2}{(\frac{\sigma}{2})^2}\right)$$

Here  $r_{n_1 n_2} = n_1 a_1 + n_2 a_2$  denotes the lattice vector with  $n_1$  and  $n_2$  number of lattice points in the  $x$ - and  $y$ - direction respectively, and  $V_0$  is the strength of the laser beam. For the square optical lattice the two lattice unit vectors are given by  $a_1 = a(1, 0)$  and  $a_2 = a(0, 1)$ . The width of the laser beam is considered to be  $\sigma = 0.65$ .

### 3 Simulation Details

We have used strange Alternate Direction Implicit-Time Splitting pseudo spectral (ADI-TSSP) method to solve the 2DGPE (2). In our numerical calculation, we consider spatial step as  $\Delta x = \Delta y = 0.1860$  and time step as  $\Delta t = 0.001$ . All the simulation runs are performed for fixed non-linearity  $g = 1000$ . Due to the non-zero value of  $\gamma$ , the time development of (2) does not conserve the norm of the wave function. In order to preserve the norm of the condensate wave function, we calculate the correction to the chemical potential in each time step as

$$\Delta\mu = (\Delta t)^{-1} \ln \left[ \int d^2r |\psi(t)|^2 / \int d^2r |\psi(t + \Delta t)|^2 \right]$$

and further run the simulation for the longer time until the stationary state is obtained. We used GPESLab, a Matlab Toolbox, for the implementation of the above numerical procedure [21].

In simulation, we first determine the ground-state wave function of the condensate in the absence of rotation and then using this ground-state wave function as the initial state of the GP equation, the equilibrium state is obtained. We analyze the vortex lattice structure using the density profile of the equilibrium condensate. We identify the structural phase transition of the vortex lattice in the presence of optical lattice using: (i) density profile of the equilibrium condensate, (ii) density profile in reciprocal space, (iii) the lattice potential energy  $\langle E_{\text{lattice}} \rangle = \int d\mathbf{r} \psi^*(\mathbf{r}) V_{\text{lattice}} \psi(\mathbf{r})$ , and (iv) the structure factor of the vortex lattice  $S(k) = \frac{1}{N_c} \sum_i n_i e^{ik \cdot r_i}$ . Here  $n_i$ ,  $r_i$ , and  $N_c$  are the winding number of individual vortices, the position of the  $i$ th vortex, and the total winding number, respectively. We calculate the above mentioned physical quantities for different optical lattice amplitude and observe the variation of them with the strength of the lattice potential.

## 4 Results and Discussion

### 4.1 Effect of Square Optical Lattice on the Vortex Lattice

In this section, we present our numerical results for the vortex lattice structure of a BECs in the presence of square optical lattice potential. In our numerical simulations, we first fix the lattice constant  $a$  of the potential and then vary the potential amplitude  $V_0$  for different angular velocities. Figure 1 depicts the density profile of the condensate in real and Fourier space for lattice constant  $a = 2.2$ , at a constant angular velocity  $\Omega = 0.8$  with increasing  $V_0$ .

As we analyze the ground state density of the condensate, we find that in the absence of optical lattice potential the single quantized vortices arranged in a Hexagonal pattern. This lattice structure is also known as Abrikosov lattice (AL) due to its similarity with the vortex lattice structure obtained in the type-II superconductor [22]. This is also observed by several other groups [23]. We notice slight distortion from the Hexagonal lattice for a sufficiently small  $V_0$ . At high pinning strength of the potential, all the vortices get pinned to the antinodes of the optical lattice potential and the vortex lattice gets transformed to the pinned lattice (PL) which is square for our case. We find that as the pinning strength of the potential is increased the resultant ground state of the vortex lattice gets transformed from AL state to the PL state.

In the bottom panel of Fig. 1, we show the reciprocal lattice structure of the vortex lattice for various pinning potential strength. In the absence of the optical

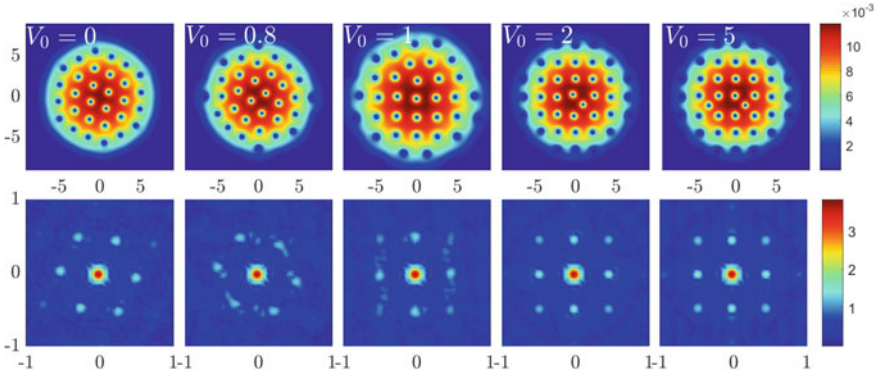


**Fig. 1** Upper panel: Density profile in real space with the variation of pinning potential strength:  $V_0 = 0.0, 0.8, 1.0, 2.0, 5.0$  (increasing strength from left to right). Bottom Panel: Fourier transform of the above density profile in  $k$  space. The density profile at  $V_0 = 0.0$  shows the Abrikosov lattice (AL) lattice structure and with increment of the  $V_0$  leads to pin the vortex lattice, for sufficient high pinning strength pinned lattice (PL) formed. Here, we used lattice constant  $a = 2.2$  and  $\Omega = 0.8$ ,  $g = 1000$

lattice potential ( $V_0 = 0$ ), the reciprocal lattice is hexagonal, as quite evident from the density plot. Upon increase of the potential strength, we find that for low optical lattice strength ( $V_0$ ) the vortex lattice gets distorted from the Hexagonal pattern at  $V_0 = 0.8$ . Upon further increase of  $V_0$  leads to the formation of distorted square pattern which becomes perfect square at  $V_0 = 2.0$ . The square lattice structure of the vortex lattice becomes more pronounced at  $V_0 = 5$ .

In order to quantify the potential strength at which the structural transformation in the vortex lattice takes place, in Fig. 2, we show the variation of structure factor profile and lattice energy with respect to  $V_0$  for different  $\Omega$ . We notice that at small rotation ( $\Omega = 0.55, 0.58, 0.62$ ), the structure factor profile and lattice energy show there exists an intermediate state where it is difficult to determine the structure of vortex lattice. This we term as the coexistence state (CS). We find that for  $\Omega = 0.55$  the CS begins at  $V_0 = 0.6$  and the vortex structure is completely pinned above  $V_0 = 1.4$ . For  $\Omega = 0.58$  and  $\Omega = 0.62$ , the CS starts from  $V_0 = 0.4$  and  $0.8$  respectively and the vortex lattice gets fully pinned above  $V_0 = 1.4$  and  $2.2$ , respectively.

The right panel of Fig. 2 shows the lattice energy and structure factor plots for relatively higher rotations ( $\Omega = 0.725, 0.8, 0.85$ ) for the lattice constant  $a = 2.2$ . For  $\Omega = 0.725$  we find that the lattice energy diminishes steadily upon increasing  $V_0$ , which suggests partial pinning of vortices. A sharp decrease in  $E_{lattice}$  is noticeable at  $V_0 = 0.6$  which indicates that the vortices are pinned above this pinning strength. Similarly, the structure factor  $S(k)$  increases successively against  $V_0$  and exhibits steady behavior above  $V_0 = 0.6$  where all vortices get attached to the pinning sites. Similar trend has been observed for  $\Omega = 0.8$  and  $0.85$  (See Fig. 2e, f).

In Fig. 3a we plot the phases of the vortex lattice in  $\Omega - V_0$  plane. We find that at  $\Omega = 0.725$  the minimum strength of potential ( $V_{min}$ ) required to get the perfectly

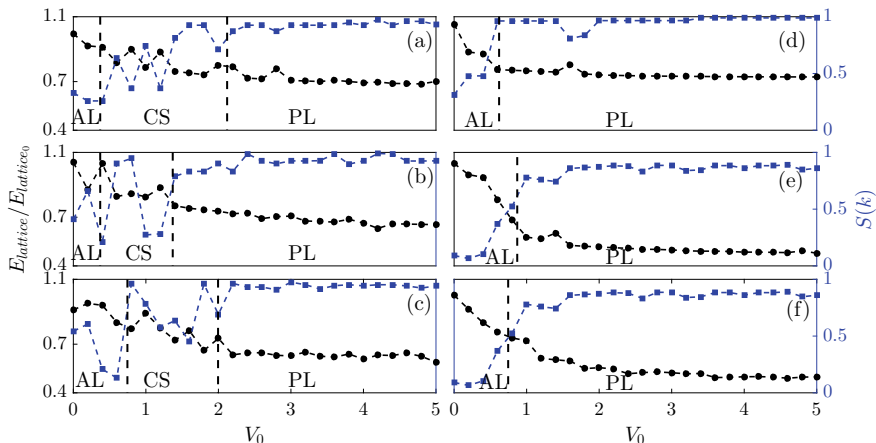


**Fig. 2** Variation of structure factor  $S(k)$  and lattice energy  $E_{lattice}$  with pinning strength  $V_0$  for different rotational frequencies: **a**  $\Omega = 0.55$ , **b**  $\Omega = 0.58$ , **c**  $\Omega = 0.62$ , **d**  $\Omega = 0.725$ , **e**  $\Omega = 0.8$ , and **f**  $\Omega = 0.85$ . The three regions are defined as Abrikosov lattice (AL), coexisting state (CS), and pinned lattice (PL). The faster rotation of the condensate can decrease the coexisting region and after a threshold value of  $\Omega$  vortex lattice makes a sharp transition from Abrikosov lattice to pinned lattice. Here, other parameters are same as Fig. 1

pinned square lattice of the vortices is 0.6. The rotation at which the minimum strength of the potential is required to perfectly pin the lattice depends upon the lattice constant of the optical lattice. We vary the lattice constant between  $a = 1.8 - 2.2$  and observe that the transformation of the vortex lattice structure against  $V_0$  for different lattice constant  $a$ . The phase diagrams for other lattice constants ( $a$ ) (does not present here) have the same nature as those for  $a = 2.2$ . In particular, there exists a rotational angular velocity at which the strength of the potential is minimum to get the pinned state. As we analyze the relation between the lattice constant  $a$  and the rotational velocity  $\Omega$  at which minimum pinning strength is required to get the pinned lattice, we find that it follows

$$a = C\Omega^d \tag{3}$$

where constant  $C = 1.76$  and  $d$  is the exponent of  $\Omega$  as shown in Fig. 3b. We find that the magnitude of  $d$  obtained for the square lattice is  $\sim -0.73$ . This implies that the pinning strength  $V_0$  takes the least value when  $a$  fulfills the above relation.



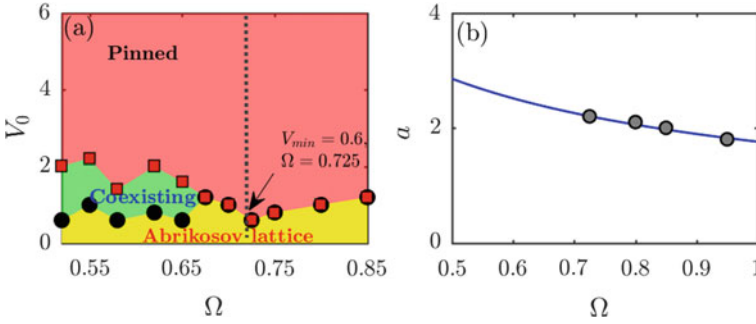


**Fig. 3** **a** Phase diagram of different lattice structures depending upon the value of  $S(k)$  obtained from Fig. 2 for different  $V_0$  at lattice constant  $a = 2.2$ . Here (yellow, green, orange) region illustrates the AL, CS, and PL domains. Dashed line annotated for finding  $\Omega$  corresponds to minimum pinning strength ( $V_{min}$ ). **b** Optimum rotational frequencies  $\Omega$  (obtained from phase diagram) for different lattice constant. Here, the solid line represents the fitted curve with (3)

## 4.2 Effect of Random Impurities on Pinned Square Lattice Structure

So far, we have presented the results in which the vortex lattice makes transformation from the Hexagonal to the square pinned lattice upon varying the strength of the potential. In this section, we present vortex lattice melting in BECs due to the random impurities or disorder in the system. Disorder is introduced in the system by the external potential associated with the random impurities. To introduce impurity, we consider a square optical lattice potential

$$V_{\text{impurity}} = \sum_{n_1} \sum_{n_2} V_{\text{imp}} \exp\left(-\frac{(x - n_1 a_{\text{imp}})^2 + (y - n_2 a_{\text{imp}})^2}{(\sigma/2)^2}\right). \quad (4)$$

Here  $n_1$  and  $n_2$  denotes the number of lattice points, respectively and  $V_{\text{imp}}$  is the strength of the impurity potential.  $a_{\text{imp}} = 1$  is the lattice constant of the impurity potential, and  $\sigma = 0.65$  is the width of the laser beam. For random impurities, the impurity potential or disorder is defined by an independent random variable uniformly distributed over  $[-V_{\text{imp}}, V_{\text{imp}}]$  at each spatial position [18]. So the total lattice potential is given by

$$V_{\text{Total}} = V_{\text{lattice}} + V_{\text{impurity}} \quad (5)$$

Here  $V_{\text{lattice}}$  is the square optical lattice potential.

In our numerical simulation, we consider rotational angular velocity as  $\Omega = 0.8$ , lattice constant  $a = 2.2$ , and nonlinearity  $g = 1000$ . We first fix the strength of the lattice potential ( $V_0 = 5$ ), and then increase the strength of the impurity potential by

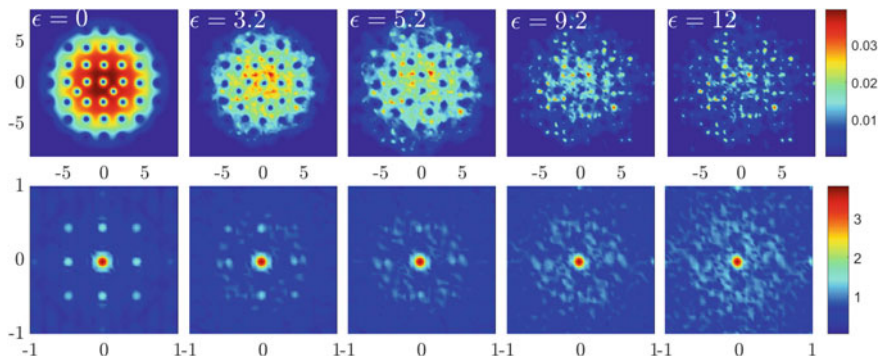


**Fig. 4** (Upper panel) Density profile in real space with the variation of impurity potential strength ( $\epsilon = 0.0, 3.2, 5.2, 9.2, 12$ ). (lower panel) Fourier transform of the above density profile in  $k$  space. The density profile at  $\epsilon = 0.0$  shows the square lattice (PL) lattice structure and with increment of the  $\epsilon$  leads to disorders in the vortex lattice, for sufficient high  $\epsilon$  pinned lattice(PL) shows melting behaviour. Here, we used lattice constant  $a = 2.2$   $\Omega = 0.8$ ,  $V_0 = 5$  and  $g = 1000$

tuning the parameter  $\epsilon$ . Here  $\epsilon = \frac{V_{\text{imp}}}{V_0}$  is the relative increase in the impurity potential strength with respect to the strength of square optical lattice potential.

In Fig. 4, we show the density profile in real and Fourier space for different  $\epsilon$ . We observe that in the absence of impurity potential, vortices are arranged in a square pattern due to lattice potential, but the square geometry of the vortex lattice is slightly distorted for a sufficiently small  $\epsilon$ . Upon further increase in  $\epsilon$  we find that the lattice structure gets fully distorted and leads to the melting of the lattice structure. The same phenomenon has been observed from the condensate density in the Fourier space, where we can see that the periodic peaks of a square lattice distorted gradually as  $\epsilon$  is increased. The detailed studies related to effect of different concentration of impurities (by varying the lattice constant of impurities) on the structure of the vortex lattice are underway and will be reported somewhere else.

## 5 Conclusion

Using the mean field model of the rotating BECs trapped in the square optical lattice we have obtained different form of vortex lattice structure like, Abrikosov, pinned square lattice, coexistence of both Abrikosov and square as the pinning strength of the potential and the rotational angular velocity of the condensate are varied. Using the structure factor and the lattice energy, we have been able to identify the minimum potential strength required to completely transform the vortex lattice from AL to PL state. We have chosen different lattice constant ( $a = 2.2, 2.0$  and  $1.8$ ) of the optical lattice potential and different rotating speed ( $\Omega = 0.55 - 0.95$ ) of the condensate. Our analysis indicate that the vortex lattice structure makes transition from the AL to PL state directly beyond a critical pinning potential strength for high angular

velocity ( $\Omega \gtrsim 0.725$ ). However, for lower angular velocity we have the presence of the AL, CL and PL state. This feature appears to be consistent with the fact that upon increasing the angular velocity the density of the vortices increases which results in perfectly pinning of the vortices. Further, we have obtained a phase of different vortex lattices in the potential strength and angular velocity parameter space for different lattice constant of the pinned potential. We find that the rotation at which minimum potential strength is required to pin the vortex lattice depends on the lattice constant of the pinned lattice. The angular velocity corresponding to that value is lowest for the lattice constant ( $a = 2.2$ ) which physically signifies that structural transformation happens perfectly when the lattice constant of the vortex lattice matches with the lattice constant of the pinning potential [12]. Finally we have investigated the effect of the random impurities on the pinned lattice of the system. We have obtained that the perfect pinned vortex lattice gets melted upon increase in the impurities strength. Similar types of melting behaviour was shown to exist for the Abrikosov lattice. In this paper we have restricted our study for the mean-field model. Using the analysis performed in this paper in other direction it would be interesting to consider the effect of the quantum fluctuation on the vortex lattice structure transformation where the vortex lattice structure have the rich variety ranging from Abrikosov lattice, square, striped, etc. upon tuning the quantum fluctuation [24].

## References

1. Davis, K.B., Mewes, M.-O., Andrews, M.R., van Druten, N.J., Durfee, D.S., Kurn, D.M., Ketterle, W.: Bose-Einstein condensation in a gas of sodium atoms. *Phys. Rev. Lett.* **75**(22), 3969–3973 (1995)
2. Morsch, O., Oberthaler, M.: Dynamics of Bose-Einstein condensates in optical lattices. *Rev. Mod. Phys.* **78**(1), 179–215 (2006)
3. Madison, K.W., Chevy, F., Wohlleben, W., Dalibard, J.: Vortex formation in a stirred Bose-Einstein condensate. *Phys. Rev. Lett.* **84**(5), 806–809 (2000)
4. Ben, D., et al.: Bloch oscillations of atoms in an optical potential. *Phys. Rev. Lett.* **76**(24), 4508–4511 (1996)
5. Wilkinson, S.R., et al.: Observation of atomic Wannier-Stark ladders in an accelerating optical potential. *Phys. Rev. Lett.* **76**(24), 4512–4515 (1996)
6. Cataliotti, F.S., et al.: Josephson junction arrays with Bose-Einstein condensates. *Science* **293**(5531), 843–846 (2001)
7. Greiner, M., Mandel, O., Esslinger, T., Hansch, T.W., Bloch, I.: Quantum phase transition from a superfluid to a Mott insulator in a gas of ultracold atoms. *Nature* **415**, 39 (2002)
8. Reijnders, J.W., Duine, R.A.: Pinning of vortices in a Bose-Einstein condensate by an optical lattice. *Phys. Rev. Lett.* **93**(6), 060401 (2004)
9. Bhat, R., Holland, M.J., Carr, L.D.: Bose-Einstein condensates in rotating lattices. *Phys. Rev. Lett.* **96**(6), 060405 (2006)
10. Tung, S., Schweikhard, V., Cornell, E.A.: Observation of vortex pinning in Bose-Einstein condensates. *Phys. Rev. Lett.* **97**(24), 240402 (2006)
11. Pu, H., Baksmaty, L.O., Yi, S., Bigelow, N.P.: Structural phase transitions of vortex matter in an optical lattice. *Phys. Rev. Lett.* **94**(19), 190401 (2005)
12. Sato, T., Ishiyama, T., Nikuni, T.: Vortex lattice structures of a Bose-Einstein condensate in a rotating triangular lattice potential. *Phys. Rev. A* **76**(5), 053628 (2007)

13. Kasamatsu, K., Tsubota, M., Ueda, M.: Vortex phase diagram in rotating two-component Bose-Einstein condensates. *Phys. Rev. Lett.* **91**(15), 150406 (2003)
14. Mithun, T., Porsezian, K., Dey, B.: Pinning of hidden vortices in Bose-Einstein condensates. *Phys. Rev. A* **89**(5), 053625 (2014)
15. Williams, R.A., Al-Assam, S., Foot, C.J.: Observation of vortex nucleation in a rotating two-dimensional lattice of Bose-Einstein condensates. *Phys. Rev. Lett.* **104**(5), 050404 (2010)
16. Kumar, R.K., Tomio, L., Malomed, B.A., Gammal, A.: Vortex lattices in binary Bose-Einstein condensates with dipole-dipole interactions. *Phys. Rev. A* **96**(6), 063624 (2017)
17. Kumar, R.K., Tomio, L., Gammal, A.: Vortex patterns in rotating dipolar Bose-Einstein condensate mixtures with squared optical lattices. *J. Phys. B: At. Mol. Opt. Phys.* **52**, 0525302 (2019)
18. Mithun, T., Porsezian, K., Dey, B.: Disorder-induced vortex lattice melting in a Bose-Einstein condensate. *Phys. Rev. A* **93**(1), 013620 (2016)
19. Hu, P., Gu, Q.: Vortices in Bose-Einstein condensates with random depth optical lattice. *J. Low Temp. Phys.* **199**, 1314 (2020)
20. Choi, S., Morgan, S.A., Burnett, K.: Phenomenological damping in trapped atomic Bose-Einstein condensates. *Phys. Rev. A* **57**, 4057 (1998)
21. Antoine, X., Duboscq, R.: GPELab, a Matlab toolbox to solve Gross-Pitaevskii equations I: computation of stationary solutions. *Comput. Phys. Commun.* **185**(11), 2969–2991 (2014)
22. Abo-Shaer, J.R., et al.: Observation of vortex lattices in Bose-Einstein condensates. *Science* **292**, 476 (2001); Haljan, P.C., et al.: Driving BEC vorticity with a rotating normal cloud. *Phys. Rev. Lett.* **87**, 210403 (2001)
23. Baksmaty, L.O., et al.: Tkachenko waves in rapidly rotating BEC. *Phys. Rev. Lett.* **92**, 160405 (2004); Mizushima, T., et al.: Collective oscillations of vortex lattices in rotating BEC. *Phys. Rev. Lett.* **92**, 060407 (2004)
24. Hsueh, C.H., Wang, C.W., Wu, W.C.: Vortex structures in a rotating Rydberg-dressed Bose-Einstein condensate with the Lee-Huang-Yang correction. *Phys. Rev. A* **102**, 063307 (2020)

# Effect of Internal Damping on the Vibrations of a Jeffcott Rotor System



Raj C. P. Shibin, Amit Malgol, and Ashesh Saha

**Abstract** The vibration characteristics of a rotor system with a rigid disc mounted in the middle of a flexible shaft are investigated in order to determine the influence of the shaft's internal damping. A well-known bulk parameter model known as the Jeffcott rotor system (JRS) is considered for the analysis. The dynamics of the system are explored using time-displacement responses, phase-plane, and frequency response graphs. The effect of rotor eccentricity and internal damping on the vibration characteristics of JRS are analysed by numerically simulating the autonomous amplitude-phase equations under simultaneous resonance conditions derived using the method of multiple scales (MMS). Among the intriguing results reported from the amplitude-frequency responses are the multiple solutions, jump events, and multiple loops. The most important finding of this paper is the destabilizing effect of internal damping beyond a critical frequency resulting in the increase of amplitude of vibrations.

**Keywords** Internal damping · Cubic nonlinearity · Jeffcott rotor system · Jump phenomenon · Multiple solutions

## 1 Introduction

Rotors are used in a wide range of applications from toys to massive turbines. Unavoidable eccentricity or mass unbalance causes rotor system to whirl along its bearing axis. For the safe operation of the machinery it is necessary to study the effects of different parameters in these lateral vibrations. Jeffcott [1] proposed the most elementary discrete model for the study of rotor vibrations and found that

---

R. C. P. Shibin · A. Malgol (✉) · A. Saha  
National Institute of Technology Calicut, Kattangal 673601, Kerala, India  
e-mail: [amitmalgol123@gmail.com](mailto:amitmalgol123@gmail.com)

R. C. P. Shibin  
e-mail: [shibinraj009@gmail.com](mailto:shibinraj009@gmail.com)

A. Saha  
e-mail: [ashesh@nitc.ac.in](mailto:ashesh@nitc.ac.in)

system can be stable at frequencies higher than critical speed. Different parameters like damping, bearing clearance, gyroscopic and hydrodynamic effects are found to have considerable effect in shaft whirling in a rotor system [2].

Damping within the system itself, termed as internal damping was also found to have an effect on the nature of vibrations of a rotor system. It is found to be stabilizing the system while operating at speeds less than a critical speed and destabilizing at higher speeds [3]. Kimball was the first to discuss the physics of internal damping in his work [4]. Later on, different internal damping models are proposed by different authors such as Dimentberg [5], Vatta and Vigilani [6] and many others. However, an extensive analysis on the effect of internal damping on the vibrations of a rotor system with different nonlinear effects is lacking in literature. Inclusion of an internal damping model proposed by Yukio and Toshio [3] and analysing its effect on a nonlinear Jeffcott rotor model is the major contribution of this paper. For performing the nonlinear analysis, method of multiple scales (MMS) is used [7–9] to obtain the autonomous amplitude and phase equations.

The rest of the paper is organized as follows. In Sect. 2, we go over the mathematical model briefly. Section 3 describes the analytical procedure for getting closed form solutions. Section 4 discusses some of the findings, while Sect. 5 concludes.

## 2 Mathematical Modeling

As illustrated in Fig. 1, the rotor model consists of a rigid disc mounted on a flexible shaft supported by bearings. The disc’s geometric centre and the shaft axis passes through point M, while the disc’s centre of gravity is represented by point G. The eccentricity of the centre of gravity G away from the geometric centre M is  $e$ .

The governing equations of the rotor system for horizontal and vertical oscillations considering the nonlinear restoring forces ( $F_{rx}$  and  $F_{ry}$ ), internal hysteretic damping forces ( $D_{ix}$  and  $D_{iy}$ ) and external damping forces ( $F_{dx}$  and  $F_{dy}$ ) are described as [1–3]

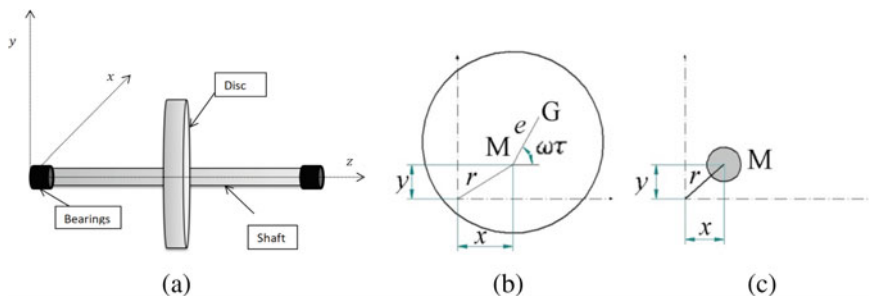


**Fig. 1** a Schematic diagram of Jeffcott Rotor System. b Cross-sectional view of disc. c Cross-sectional view of the shaft

$$m\ddot{x} + F_{dx} + F_{rx} + D_{ix} = me\omega^2 \cos(\omega\tau) \quad \text{and} \quad (1a)$$

$$m\ddot{y} + F_{dy} + F_{ry} + D_{iy} = me\omega^2 \sin(\omega\tau) - mg \quad (1b)$$

respectively, where  $mg$  is the weight of the rotor and the overdots represent the derivatives with respect to the time  $\tau$ .

The internal hysteretic damping terms along the horizontal ( $x$ -axis) and vertical directions ( $y$ -axis) are given by [3]

$$D_{ix} = \zeta^*(\dot{x} + \omega y), \quad \text{and} \quad (2a)$$

$$D_{iy} = \zeta^*(\dot{y} - \omega x) \quad (2b)$$

respectively, where  $\omega$  is the angular velocity of the shaft and  $\zeta^*$  is internal damping coefficient. The external damping forces along the horizontal ( $x$ -axis) and vertical directions ( $y$ -axis) as assumed to be similar to viscous damping terms represented by.

$$F_{dx} = c_x \dot{x}, \quad \text{and} \quad (3a)$$

$$F_{dy} = c_y \dot{y} \quad (3b)$$

respectively, where  $c_x$  and  $c_y$  are the damping coefficients.

The nonlinear restoring forces along the horizontal ( $x$ -axis) and vertical directions ( $y$ -axis) are expressed as [4]

$$F_{rx} = k_1x + k_2x(x^2 + y^2), \quad \text{and} \quad (4a)$$

$$F_{ry} = k_1y + k_2y(x^2 + y^2) \quad (4b)$$

respectively, where  $k_1$  is linear stiffness coefficient and  $k_2$  is the nonlinear stiffness coefficient.

Substituting Eqs. (2a, 2b) to (4a, 4b) in Eq. (1), we get.

$$m\ddot{x} + c_x\dot{x} + k_1x + k_2x(x^2 + y^2) + \zeta^*\dot{x} + \zeta^*\omega y = me\omega^2 \cos(\omega\tau), \quad \text{and} \quad (5a)$$

$$m\ddot{y} + c_y\dot{y} + k_1y + k_2y(x^2 + y^2) + \zeta^*\dot{y} - \zeta^*\omega x = me\omega^2 \sin(\omega\tau) - mg \quad (5b)$$

Substituting  $\ddot{x} = \ddot{y} = \dot{x} = \dot{y} = \omega = 0$  in Eqs. (5a, 5b), we obtain the static equilibrium in  $x$ -direction as  $x_{st} = 0$  and the static equilibrium in  $y$ -direction ( $y_{st}$ )

is governed by the following nonlinear equation

$$k_1 y_{st} + k_2 y_{st}^3 = -mg. \tag{6}$$

Shifting the coordinates to the static equilibrium states as  $x = x^*$ ,  $y = y_{st} + y^*$ , we obtain the governing equations in the shifted coordinates  $(x^*, y^*)$  as.

$$m\ddot{x}^* + (\zeta^* + c_x)\dot{x}^* + (k_1 + k_2 y_{st}^2)x^* + k_2 x^*(x^{*2} + y^{*2}) + 2k_2 x^* y^* y_{st} + \zeta^* \omega(y_{st} + y^*) = m e \omega^2 \cos(\omega\tau), \text{ and} \tag{7a}$$

$$m\ddot{y}^* + (c_y + \zeta^*)\dot{y}^* + (k_1 + 3k_2 y_{st}^2)y^* + k_2 y^*(x^{*2} + y^{*2}) + 2k_2(x^{*2} + 3y^{*2})y_{st} - \zeta^* \omega x^* = m e \omega^2 \sin(\omega\tau). \tag{7b}$$

Introducing the dimensionless parameters.

$$t = \omega_0 \tau, \omega_0 = \sqrt{\frac{k_1}{m}}, u = \frac{x^*}{y_{st}}, v = \frac{y^*}{y_{st}}, \zeta = \frac{\zeta^*}{\sqrt{k_1 m}}, f = \frac{e}{y_{st}}, \Omega = \frac{\omega}{\omega_0}, \omega_1^2 = 1 + \lambda, \omega_2^2 = 1 + 3\lambda, \mu_1 = \frac{c_x}{\sqrt{k_1 m}}, \mu_2 = \frac{c_y}{\sqrt{k_1 m}}, \lambda = \frac{k_2 y_{st}^2}{k_1},$$

the governing equations of the horizontally supported Jeffcott rotor system (JRS) for the horizontal and the vertical oscillations given as.

$$u'' + (\zeta + \mu_1)u' + u(1 + \lambda) + \lambda u(u^2 + v^2) + 2\lambda uv + \zeta \Omega(v + 1) = f \Omega^2 \cos(\Omega t), \text{ and} \tag{8a}$$

$$v'' + (\zeta + \mu_2)v' + v(1 + 3\lambda) + \lambda v(u^2 + v^2) + \lambda(u^2 + 3v^2) + 2\lambda uv - \zeta \Omega = f \Omega^2 \sin(\Omega t) \tag{8b}$$

where ‘ $t$ ’ is dimensionless time,  $\lambda$  is the stiffness coefficient,  $\zeta$  is an internal damping factor,  $\Omega$  is rotor speed ratio, and  $f$  is the eccentricity ratio. For the horizontal and vertical directions, respectively,  $u$  and  $v$  are displacements of the JRS,  $\mu_1$  and  $\mu_2$  are the linear damping coefficients, and  $\omega_1$  and  $\omega_2$  are the natural frequencies.

As mentioned earlier, the nonlinear analysis by the method of multiple scales (MMS) is performed to obtain the autonomous amplitude and phase equations. This MMS is performed in next section.



### 3 Method of Multiple Scales (MMS) Analysis

In this section, amplitude and phase equations corresponding to the horizontal and vertical oscillations of the rotor are derived using the method of multiple scales (MMS). Simultaneous resonance condition is considered by defining two detuning parameters  $\sigma_1$  and  $\sigma_2$  as

$$\Omega = \omega_1 + \sigma_1, \sigma_2 = \omega_2 - \omega_1 \quad (9)$$

Accordingly,  $\sigma_1$  represents the closeness of  $\Omega$  to  $\omega_1$ , and  $\sigma_2$  represents the difference between  $\omega_2$  and  $\omega_1$ .

We seek a series of the following form in the MMS:

$$u(T_0, T_1, T_2) = \varepsilon u_1(T_0, T_1, T_2) + \varepsilon^2 u_2(T_0, T_1, T_2) + \varepsilon^3 u_3(T_0, T_1, T_2) + O(\varepsilon^4), \text{ and} \quad (10a)$$

$$v(T_0, T_1, T_2) = \varepsilon v_1(T_0, T_1, T_2) + \varepsilon^2 v_2(T_0, T_1, T_2) + \varepsilon^3 v_3(T_0, T_1, T_2) + O(\varepsilon^4). \quad (10b)$$

In Eqs. (10a, 10b),  $T_0 = t$  is the fast time and  $T_1 = \varepsilon t$ ,  $T_2 = \varepsilon^2 t$ , etc. are the slow times, where  $0 < \varepsilon \ll 1$ . The time derivatives then can be written in terms of fast and slow times as:

$$\frac{d}{dt} = \frac{\partial}{\partial T_0} + \varepsilon \frac{\partial}{\partial T_1} + \varepsilon^2 \frac{\partial}{\partial T_2}, \frac{d^2}{dt^2} = \frac{\partial^2}{\partial T_0^2} + 2\varepsilon \frac{\partial}{\partial T_0} \frac{\partial}{\partial T_1} + \varepsilon^2 \left( \frac{\partial^2}{\partial T_1^2} + 2 \frac{\partial}{\partial T_2} \frac{\partial}{\partial T_1} \right). \quad (11)$$

Other system parameters are scaled according to their orders as:

$$\mu_1 = \varepsilon^2 \mu_{h1}, \mu_2 = \varepsilon^2 \mu_{h2}, f = \varepsilon^2 f_h, \zeta = \varepsilon^2 D_h \quad (12)$$

Substituting Eqs. (10a, 10b) to (12) into Eqs. (8a, 8b) and collecting coefficients of  $\varepsilon$  yield

$$O(\varepsilon) : \frac{\partial^2 u_1}{\partial T_0^2} + \omega_1^2 u_1 = 0 \quad (13a)$$

$$\frac{\partial^2 v_1}{\partial T_0^2} + \omega_2^2 v_1 = 0 \quad (13b)$$

$$O(\varepsilon^2) : \frac{\partial^2 u_2}{\partial T_0^2} + \omega_1^2 u_2 = f_h \Omega^2 \cos(\Omega T_0) - 2 \frac{\partial^2 (u_1)}{\partial T_0 \partial T_1} - 2\lambda u_1 v_1 - \Omega D_h \quad (14a)$$

$$\frac{\partial^2 v_2}{\partial T_0^2} + \omega_2^2 v_2 = f_h \Omega^2 \sin(\Omega T_0) - 2 \frac{\partial^2 (v_1)}{\partial T_0 \partial T_1} - \lambda u_1^2 - 3\lambda v_1^2 \tag{14b}$$

$$O(\varepsilon^2) : \frac{\partial^2 u_3}{\partial T_0^2} + \omega_1^2 u_3 = -\frac{\partial^2 u_1}{\partial T_1^2} - 2 \frac{\partial^2 (u_2)}{\partial T_0 \partial T_1} - 2 \frac{\partial^2 (u_1)}{\partial T_0 \partial T_2} + 2\lambda(u_1 v_2 + u_2 v_1) + \lambda u_1(u_1^2 + v_1^2) - \Omega D_h v_1 - D_h \frac{\partial u_1}{\partial T_0} - \mu_{h1} \frac{\partial u_1}{\partial T_0} \tag{15a}$$

$$\frac{\partial^2 v_3}{\partial T_0^2} + \omega_1^2 v_3 = -\frac{\partial^2 v_1}{\partial T_1^2} - 2 \frac{\partial^2 (v_2)}{\partial T_0 \partial T_1} - 2 \frac{\partial^2 (v_1)}{\partial T_0 \partial T_2} + 2\lambda(u_1 u_2 + 3v_2 v_1) - \lambda v b_1(u_1^2 + v_1^2) + \Omega D_h u_1 - D_h \frac{\partial v_1}{\partial T_0} - \mu_{h2} \frac{\partial v_1}{\partial T_0} \tag{15b}$$

The solutions of Eqs. (13a) and (13b) can be written as:

$$u_1(T_0, T_1, T_2) = A(T_1, T_2)e^{i\omega_1 T_0} + \bar{A}(T_1, T_2)e^{-i\omega_1 T_0}, \tag{16a}$$

$$v_1(T_0, T_1, T_2) = B(T_1, T_2)e^{i\omega_2 T_0} + \bar{B}(T_1, T_2)e^{-i\omega_2 T_0}. \tag{16b}$$

Substituting these solutions and eliminating secular terms by equating coefficient of  $e^{i\omega_1 t}$  to zero we get,

$$\frac{\partial A(T_1, T_2)}{\partial T_1} = -\frac{i e^{iT_1} \sigma_{h1}}{4\omega_2} f_h \Omega^2, \tag{17a}$$

$$\frac{\partial B(T_1, T_2)}{\partial T_1} = -\frac{e^{iT_1} (\sigma_{h1} - \sigma_{h2})}{4\omega_2} f_h \Omega^2. \tag{17b}$$

The remaining equations after the elimination of the secular terms are solved for  $u_2$  and  $v_2$ . All the solutions for  $u_1, v_1, u_2$  and  $v_2$  are substituted in Eqs. (15a) and (15b). Again we will get secular terms which are eliminated to get expressions for  $\frac{\partial A(T_1, T_2)}{\partial T_2}$  and  $\frac{\partial B(T_1, T_2)}{\partial T_2}$ . These expressions are quite large and not included in this work.

The time derivatives of  $A$  and  $B$  are determined using the following relations:

$$\dot{A} = \frac{dA}{dt} = \varepsilon \frac{\partial A(T_1, T_2)}{\partial T_1} + \varepsilon^2 \frac{\partial A(T_1, T_2)}{\partial T_2}, \tag{18a}$$

$$\dot{B} = \frac{dB}{dt} = \varepsilon \frac{\partial B(T_1, T_2)}{\partial T_1} + \varepsilon^2 \frac{\partial B(T_1, T_2)}{\partial T_2}. \tag{18b}$$

The final expressions for  $\dot{A}$  and  $\dot{B}$  are quite large and not shown here. The polar forms of  $A$  and  $B$  are expressed as

$$A(T_1, T_2) = \frac{1}{2} \hat{a}_1 e^{i\delta_1} = \frac{1}{2\varepsilon} a_1 e^{i\delta_1}, \tag{19a}$$

$$B(T_1, T_2) = \frac{1}{2} \hat{a}_2 e^{i\delta_2} = \frac{1}{2\varepsilon} a_2 e^{i\delta_2}. \tag{19b}$$

where  $a_1$  and  $a_2$  are the steady state amplitudes in the horizontal and vertical directions of the JRS, respectively. The corresponding phases are  $\delta_1$  and  $\delta_2$ , respectively. We can obtain the amplitude and phase equations from Eqs. (19a) and (19b) as

$$\dot{a}_1 = \frac{da_1}{dt} = 2\varepsilon \cdot \text{Re}(\dot{A})e^{-i\delta_1}, \dot{\delta}_1 = \frac{d\delta_1}{dt} = \frac{2\varepsilon}{a_1} \cdot \text{Im}(\dot{A})e^{-i\delta_1}, \tag{20a}$$

$$\dot{a}_2 = \frac{da_2}{dt} = 2\varepsilon \cdot \text{Re}(\dot{B})e^{-i\delta_2}, \dot{\delta}_2 = \frac{d\delta_2}{dt} = \frac{2\varepsilon}{a_2} \cdot \text{Im}(\dot{B})e^{-i\delta_2}, \tag{20b}$$

The final expressions for the amplitude and phase equations are obtained as

$$\dot{a}_1 = -\frac{1}{4} \frac{(-3\omega_1 + \Omega)f\Omega^2}{\omega_1^2} \sin(\phi_1) + \frac{1}{2} \frac{(-\omega_1^2 + 2\lambda)\zeta a_2 \Omega}{\omega_1^3} \sin(\phi_1 - \phi_2) - \frac{\lambda a_2^2 a_1 (4\omega_1 \lambda - 6\lambda \omega_2 + 2\omega_1 \omega_2^2 - \omega_1^3)}{8\omega_1 (2\omega_1 - \omega_2) \omega_2^2} \sin 2(\phi_1 - \phi_2) - \frac{(\mu_1 + \zeta)a_1}{2}, \tag{21a}$$

$$\dot{\phi}_1 = \frac{1}{4} \frac{(3\omega_1 - \Omega)\Omega^2 f}{\omega_1^2 a_1} \cos(\phi_1) + \frac{1}{2} \frac{(-\omega_1^2 + 2\lambda)\zeta a_2 \Omega}{\omega_1^3 a_1} \cos(\phi_1 - \phi_2) - \frac{1}{8} \frac{\lambda a_2^2 (-6\lambda \omega_2 + 4\omega_1 \lambda + 2\omega_1 \omega_2^2 - \omega_1^3)}{\omega_1 (2\omega_1 - \omega_2) \omega_2^2} \cos(2\phi_1 - 2\phi_2)$$

$$+ \frac{1}{8(4\omega_1^2 - \omega_2^2)a_1 \omega_2^2 \omega_1^3} \begin{pmatrix} 16\omega_1^4 a_1^3 \lambda^2 - 12\omega_1^4 a_1^3 \lambda \omega_2^2 - 6\omega_1^2 a_1^3 \lambda^2 \omega_2^2 \\ + 3\omega_1^2 a_1^3 \omega_2^4 \lambda + 48\omega_1^4 a_2^2 \lambda^2 a_1 + 2\omega_1^2 \lambda a_2^2 \omega_2^4 a_1 \\ - 8\omega_1^4 \lambda a_2^2 \omega_2^2 a_1 + \omega_1^2 \lambda a_2^2 \omega_2^4 a_1 - 4\omega_1^4 a_2^2 \lambda^2 \omega_2^2 a_1 \end{pmatrix}$$

$$\dot{a}_2 = \frac{1}{4} \frac{(\Omega - 3\omega_2)\Omega^2 f}{\omega_2^2} \cos(\phi_2) - \frac{1}{2} \frac{(\omega_1^2 + 2\lambda)\zeta a_1 \Omega}{\omega_2 \omega_1^2} \sin(\phi_1 - \phi_2) - \frac{\lambda a_1^2 a_2 (-2\lambda \omega_2 + 8\omega_1 \lambda - 4\omega_2 \omega_1^2 + \omega_2^3)}{8(4\omega_1^2 - \omega_2^2) \omega_2^2} \sin(2\phi_1 - 2\phi_2) - \frac{1}{2} (\mu_2 + \zeta) a_2$$

$$\dot{\phi}_2 = \sigma_1 - \sigma_2 + \frac{\lambda a_1^2 (-2\lambda \omega_2 + 8\omega_1 \lambda - 4\omega_2 \omega_1^2 - \omega_2^3)}{8(4\omega_1^2 - \omega_2^2) \omega_2^2} \cos(2\phi_1 - 2\phi_2) - \frac{(\Omega - 3\omega_2)\Omega^2 f}{4\omega_2^2} \sin(\phi_2) + \frac{(\omega_1^2 + 2\lambda)\zeta a_1 \Omega}{2\omega_2 a_2 \omega_1^2} \cos(\phi_1 - \phi_2) \tag{21d}$$

$$+ \frac{1}{8(4\omega_1^2 - \omega_2^2)\omega_1^3} \begin{pmatrix} 120\omega_1^2 a_2^2 \lambda - 12\omega_1^2 a_2^2 \omega_2^2 - 30a_2^2 \lambda \omega_2^2 \\ -4a_1^2 \omega_2^2 \lambda - 8\omega_1^2 a_1^2 \omega_2^2 + 2\omega_2^4 a_1^2 \\ 3\omega_2^4 a_2^2 + 48\omega_1^2 \lambda a_1^2 \end{pmatrix}$$

It is to be noted here that  $\dot{\phi}_1 = \sigma_1 - \delta_1$ , and  $\dot{\phi}_2 = \sigma_1 - \sigma_2 - \delta_2$ .

### 4 Results and Discussion

All the results are discussed in this section. The following set of parameter values [8] are used for all the forthcoming analysis  $\mu_1 = 0.0154$  and  $\mu_2 = 0.0247$ .

#### 4.1 Comparison of Numerical and Analytical Results

In Fig. 2, the MMS results obtained by numerically simulating the amplitude and phase Eqs. (21a–21d) are compared with the numerical simulation results of the original JRS model given by the governing Eqs. (8a, 8b). The time-displacement responses and the phase-plane diagrams in Fig. 2 show that the MMS results correlate

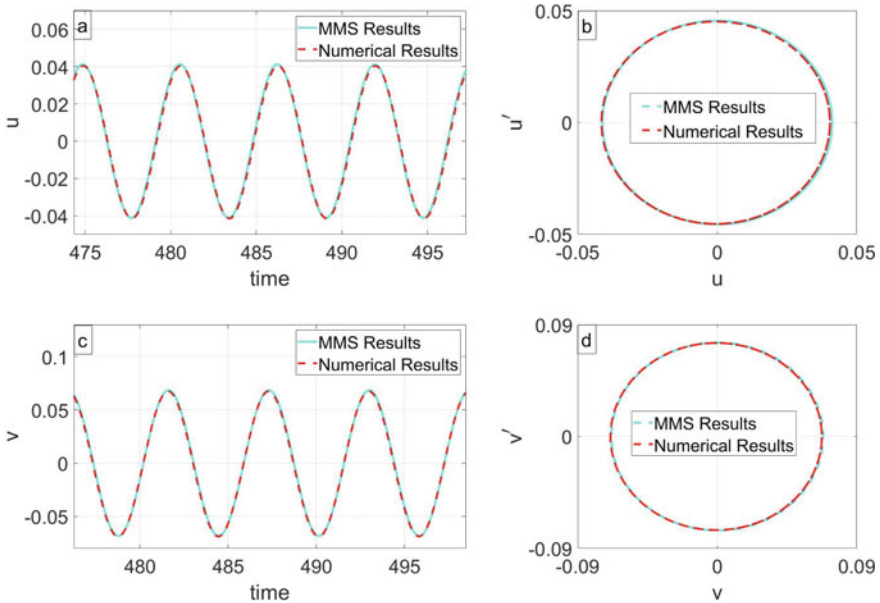


**Fig. 2** Time-displacement responses and phase plane plots of the Jeffcott rotor system for  $f = 0.025$ ,  $\zeta = 0.005$  and  $\lambda = 0.05$ . (a) and (b) for horizontal oscillations and (c) and (d) for vertical oscillations

very well with the results obtained from the original JRS model. In all the forthcoming analysis, we will use the amplitude and phase Eqs. (21a–21d) to obtain the frequency–response plots.

### 4.2 Non-Localised Oscillations

Non-Localized oscillations refer to the condition where  $a_1 \neq 0$ ,  $\phi_1 \neq 0$ ,  $a_2 \neq 0$  and  $\phi_2 \neq 0$ , i.e. both horizontal and vertical oscillations are coupled with each other. In the case of non-localized oscillations, two amplitudes  $a_1$  and  $a_2$  are evaluated simultaneously.

#### 4.2.1 Influence of Eccentricity Ratio $F$

The influence of the eccentricity ratio  $f$  on the horizontal and vertical oscillations of the JRS are shown in Figs. 3 and 4. In all of the figures, the limit point (LP) represents a change in the nature of the system solutions from stable to unstable, or vice versa. Blue colour indicates the stable solutions whereas red indicates unstable solutions. As shown in Fig. 3, a single jump phenomenon is observed for  $f = 0.015$ . The jump phenomena appears differently for horizontal and vertical oscillations. For horizontal oscillations, jump occurs close to the resonance peak, whereas for vertical oscillations, jump appears before the system reaches the resonance frequency. Furthermore, when compared to horizontal oscillations, this jump is substantially less for vertical oscillations.

Multivalued solutions with multiple loops are observed in the frequency response diagrams in Fig. 3 for the increased of the eccentricity ratio  $f = 0.05$ . The multivalued solutions and jump phenomena disappear for  $f = 0.015$  with the addition

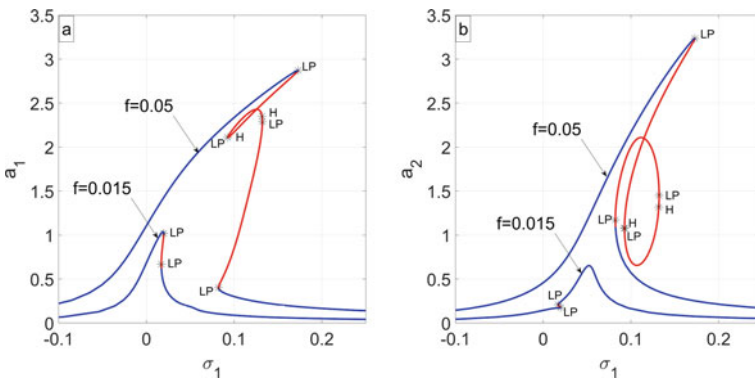


**Fig. 3** Amplitude-frequency responses of the Jeffcott rotor system for different values of  $f$ ,  $\zeta = 0$  and  $\lambda = 0.05$

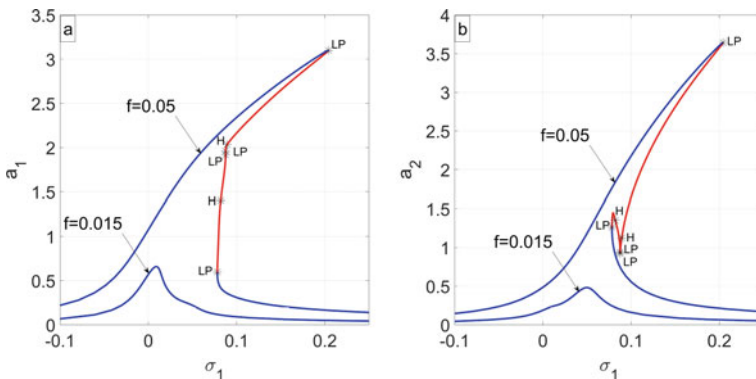


**Fig. 4** Amplitude-frequency responses of the Jeffcott rotor system for different values of  $f$ ,  $\zeta = 0.01$  and  $\lambda = 0.05$

of small amount of internal damping  $\zeta = 0.01$  as shown in Fig. 4. Moreover, the multiple loops in the frequency response plots for  $f = 0.05$  seem to disappear with the inclusion of internal damping  $\zeta = 0.01$ . However, the comparisons of Figs. 4 with Figs. 3 for  $f = 0.05$  show that the internal damping causes the resonance peaks to shift towards higher frequencies with an increase in the amplitude at resonance peak.

### 4.2.2 Influence of Internal Damping Parameter

Frequency response diagrams for two different values of internal damping factor are shown in Fig. 5 to analyse the effect of internal damping on the dynamics of the JRS. Some complicated dynamics are observed from Fig. 5. For better clarity, the stable and unstable solutions for  $\zeta = 0$  are shown by blue and red colors, and for  $\zeta = 0.025$

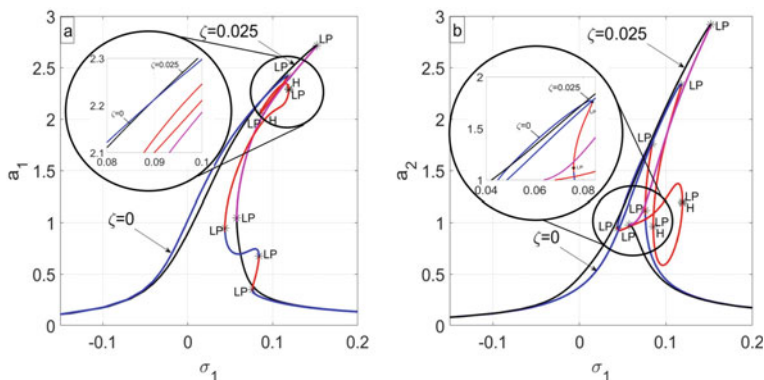


**Fig. 5** Amplitude-frequency responses of the Jeffcott rotor system for different values of  $\zeta$ ,  $f=0.04$  and  $\lambda=0.05$

by black and magenta colors, respectively. Also, zoomed views of multiple crossings near  $\sigma_1 = 0.1$  are shown at the insets of Fig. 5. It is observed from Fig. 5 that the multiple jump phenomenon and the multiple loops are eliminated with the increase of the internal damping factor from  $\zeta = 0$  to  $\zeta = 0.025$ . However, the amplitude of oscillations at resonance peaks become larger with the inclusion of internal damping in the JRS model.

It is discussed in [3] that the internal damping can have destabilizing effect on the system after a threshold speed in a sense that the effective damping of the linearized system becomes negative beyond that speed. The negative damping of the linearized system might cause an increase in the amplitude of oscillations beyond that threshold speed. A similar characteristic is shown in Fig. 5a for horizontal oscillations. For lower frequencies, amplitude of horizontal oscillations is less for  $\zeta = 0.025$  than that for  $\zeta = 0$ . The internal damping factor causes positive damping effect in this region by reducing the amplitudes of oscillations. However, with the increase in frequency beyond a certain critical value, the amplitude of horizontal oscillations become larger for  $\zeta = 0.025$ . The internal damping appear to have destabilizing effect beyond this critical value. The same conclusions cannot be drawn from the vertical oscillations shown in Fig. 5b as the amplitude of oscillations for  $\zeta = 0.025$  appear to be larger in comparison to amplitude of oscillations for  $\zeta = 0$  for the range of selected frequencies. It might happen that the critical frequency is already been crossed below the lower frequency bound shown in Fig. 5b.

## 5 Conclusions

The effects of internal damping (internal damping term  $\zeta$ ) on the vibration of a horizontally supported Jeffcott rotor system (JRS) are analyzed in this paper. Non-linear restoring force (with stiffness ratio  $\lambda$ ) is also considered in the JRS model and the effect of eccentricity ratio  $f$  is also analysed. The method of multiple scales is used to derive autonomous amplitude-phase equations in the horizontal and vertical directions. The accuracy of the MMS are verified by comparing with the results produced from numerical simulation of the original JRS equations. The influence of different parameters are analysed from the frequency response curves obtained by numerically simulating the MMS equations in 'Matcont', a numerical bifurcation toolbox based on 'Matlab'.

Internal damping reduces the occurrence of multi-jump phenomena and multiple loops in the frequency response curves. However, the peak amplitude of vibration at resonance increases with the increase of  $\zeta$ . The internal damping reduces the amplitude of horizontal vibrations upto a certain critical frequency. Above that critical frequency, the internal damping appears to be injecting energy into the system causing an increase in the amplitude of vibrations.

**Acknowledgements** This work has been supported by DST SERB - SRG under Project File no. SRG/2019/001445 and National Institute of Technology Calicut under Faculty Research Grant.

## References

1. Jeffcott, H.H.: The lateral vibration of loaded shafts in the neighbourhood of a whirling speed—the effect of want of balance. *Lond. Edinb. Dublin Philos. Mag. J. Sci.* **37**(219), 304–314 (1919)
2. Cveticanin, L.: Free vibration of a Jeffcott rotor with pure cubic non-linear elastic property of the shaft. *Mech. Mach. Theory* **40**, 1330–1344 (2005)
3. Ishida, Y., Yamamoto, T.: *Linear and Nonlinear Rotordynamics*, 2nd edn. Wiley-VCH, Germany (2012)
4. Kimball, A.L.: Internal friction as a cause of shaft whirling. *Philos. Mag. Ser.* **649**(292), 724–727 (1925).
5. Dimentberg, M.: Vibration of a rotating shaft with randomly varying internal damping. *J. Sound Vib.* **285**, 759–765 (2005)
6. Vatta, F., Vigliani, A.: Internal damping in rotating shafts. *Mech. Mach. Theory* **43**(11), 1376–1384 (2008)
7. Shad, M.R., Michon, G., Berlioz, A.: Nonlinear dynamics of rotors due to large deformations and shear effects. *Appl. Mech. Mater.* **110**(116), 3593–3599 (2012)
8. Saeed, N.A., El-Gohary, H.A.: On the nonlinear oscillations of a horizontally supported Jeffcott rotor with a nonlinear restoring force. *Nonlinear Dyn.* **88**, 293–314 (2017)
9. Yabuno, H., Kashimure, T., Inoue, T., Ishida, Y.: Nonlinear normal modes and primary resonance of horizontally supported Jeffcott rotor. *Non-linear Dyn.* **66**, 377–387 (2011)



# The Collective Behavior of Magnetically Coupled Neural Network Under the Influence of External Stimuli



T. Remi and P. A. Subha

**Abstract** We have analysed the collective behavior and synchronisation scenario under the combined effect of the magnetic coupling and external stimuli on a network of Hindmarsh Rose neurons. In the presence of constant input, the magnetic coupling induces synchrony and stabilises the equilibrium state. The periodically varying sinusoidal input enhances the synchrony in the network. The synchrony is inevitable for the signal transmission in the neurons. The external stimulus in the form of square wave has the capability to desynchronise the magnetically coupled network. The suppression of synchrony may find its relevance in clinical procedures to alleviate the symptoms of certain nervous system disorders.

**Keywords** Neural network · Linear chain · Memristor field effects · Different external stimuli

## 1 Introduction

A great effort has been carried out in studying and controlling the complex oscillatory networks in nonlinear science, with a number of practical applications [1–3]. The nonlinear models with high number of population is very common in Physics, Chemistry and Biology [4–6]. One of the many applications of nonlinear systems happens to be in neuro science as the brain comprises of several specialized areas with different functions, each being a complex network by itself and thus, is a perfect example of a complex dynamical system [7]. Different models have been proposed for biological neuronal networks which are capable of explaining all the intrinsic dynamics, response to external stimuli and collective behavior in different connection architectures [8].

---

T. Remi · P. A. Subha (✉)

Department of Physics, Farook College University of Calicut, Kozhikode 673632, Kerala, India  
e-mail: [pasubha@farookcollege.ac.in](mailto:pasubha@farookcollege.ac.in)

T. Remi

e-mail: [remi@farookcollege.ac.in](mailto:remi@farookcollege.ac.in)

The use of memristors to represent the electromagnetic field induced by the flow of ions in the neurons was proposed recently [9] and still continue to attract the researchers [10–13]. The dynamics and energy aspects of HR neurons with quadratic and cubic memristor effects have been analysed [14–16]. The impact of electromagnetic field on individual and collective dynamics of neural system is studied recently [17]. The utilisation of energy for the electrical activities in the presence of magnetic coupling and external stimuli have been studied on Hodgkin-Huxley model [18]. The hyperbolic tangent function was recognised to be easily implementable in electronic circuits and effective in numerical simulations [19, 20].

The suppression of oscillations and eventual asymptotic stabilisation of equilibrium, named as Amplitude Death (AD) has been achieved under the influence of memristor [14]. AD has been observed both theoretically and experimentally in neural networks [21, 22]. The dynamics of AD has been used to explain the temporal activity in the olfactory bulb [23]. One of the major causes of attaining AD is attributed to parameter mismatch [24–28].

The diverse firing patterns and synchronous oscillations are crucial features in neural dynamics of brains. The physiological conditions have a great influence on the electrical activity of nervous system. The collective synchrony plays an important role in the generation of both vital and pathological biological conditions. Both external and inherent stimuli constructively take part in the excitation of neural activity [29]. Zhijun Li, et al. investigated the coexistence of multiple firing patterns for different initial conditions and considering coupling strength as the sole control parameter [30]. Different methods have been employed to enhance the synchrony in the neural network owing to its vital role in signal transmission and signal processing [31, 32]. However, the unwanted synchrony among neurons which ought to have behaved independently, results in several pathological conditions [33–35]. Thus the enhancement and suppression of this synchrony is very necessary [36]. The phase synchrony in mean field coupled HR neurons with an external stimuli in form of spikes has been studied recently [37]. The external stimuli has the capability of controlling chaotic dynamics in neural network [38, 39]. However, the influence of square input on neural network is unexplored. In this work, we have analysed the capability of externally applied periodical inputs to enhance and suppress synchrony in a linear chain of HR neurons, coupled magnetically by a hyperbolic function.

The paper is organised as follows: The model is described in Sect. 2. The phase portraits and collective dynamics of the network with constant external stimulus is explained in Sect. 3.1. The control of phase space trajectories and synchrony by the combined effect of magnetic coupling and time varying external currents are presented in Sect. 3.2. Section 3.3 has been devoted to quantifying synchrony in the network with magnetic coupling and external stimuli. Section 4 concludes the study.

## 2 The Neural Network

The electromagnetic fields and externally applied stimuli are capable of altering collective electrical activities and signal propagation in a neural network. The current, induced by the change in magnetic flux across the membrane is represented by the memristor and that, due to the external stimuli are considered under three cases. The dynamical equations for a linear chain of HR neurons are described by [40, 41]

$$\begin{aligned}
 \dot{x}_i &= y_i + ax_i^2 - bx_i^3 - z_i + I - k_1\rho(\phi_i)x_i, \\
 \dot{y}_i &= c - dx_i^2 - y_i, \\
 \dot{z}_i &= r(s(x_i - x_e) - z_i), \\
 \dot{\phi}_i &= k_2x_i - k_3\phi_i + D \left( \phi_i - \sum_{\substack{j=1 \\ j \neq i}}^N \frac{W}{|i - j|} \phi_j \right), \quad i = 1, 2, \dots, N.
 \end{aligned}
 \tag{1}$$

where,  $x_i$ ,  $y_i$  and  $z_i$  represent the membrane potential, spiking variable and bursting variable of  $i^{th}$  neuron, respectively.  $y_i$  is constituted by the flow of  $Na^+$  and  $K^+$  ions and the flow of  $Ca^+$  ions constitute the  $z_i$  term. The fast oscillations of  $x_i$  and  $y_i$  correspond to spikes, whereas, the slow oscillations of the  $z_i$  variable cause burst [42]. Indices  $i, j$  and  $N$ , represent pre synaptic neuron, post synaptic neuron and total number of neurons in the network, respectively. The external current,  $I$ , is considered as a constant and two varying forms. The interaction between membrane potential,  $x_i$  and magnetic flux,  $\phi_i$  is realised with the help of memristor,  $k_1\rho(\phi_i)x_i$ , where,  $k_1$  is the magnetic coupling strength. We have considered the memory conductance term,  $\rho(\phi_i)$  as a hyperbolic form,  $\tanh(\phi_i)$  [19]. This function can be easily approximated to linear or nonlinear forms. The term  $k_2x_i$  represents the change in magnetic flux induced by membrane potential of the cell and  $k_3\phi_i$  denotes the leakage of the magnetic flux. ‘ $D$ ’ describes the field interaction between neurons. ‘ $W$ ’ represents the intensity of the field effect associated with distance between neurons. The parameters of the model are chosen as,  $a = 3.0$ ,  $b = 1.0$ ,  $c = 1$ ,  $d = 5$ ,  $r = 0.006$ ,  $s = 4.0$ ,  $x_e = -1.61$  [43],  $k_2 = 0.9$ ,  $k_3 = 0.4$ ,  $D = 0.0001$ ,  $W = 1$  [14].

## 3 Collective Dynamics and Synchronisation Scenario

The changes in the firing pattern, phase portraits and synchrony level, under the combined effect of magnetic coupling and external stimulus have been analysed. We have chosen the external stimuli in different forms (i) a constant ( $I_1$ ) and (ii) as time varying function. The time varying external inputs are considered in two different forms: (a) sinusoidal wave, given as  $I_2 = A(\sin(\omega t) + \cos(\omega t))$  with frequency,  $\omega$

and (b) square wave, represented as  $I_3 = A \mathcal{H}\left(\sin\left(\frac{2\pi t}{\rho_s}\right)\right)$ , with an interval,  $\rho_s$ .  $\mathcal{H}$  is the bi-valued Heaviside step function, whose value is zero, for negative arguments and one, for positive arguments.

### 3.1 Constant External Current

In this section, the dynamics, phase portraits and the synchrony pattern have been analysed under the memristor effect and constant external current. The dynamics and collective behavior of the network are analysed numerically by solving Eq. (1) for  $x_i(t)$ ,  $y_i(t)$ ,  $z_i(t)$  and  $\phi_i(t)$  using Runge–kutta method in step size of 0.1. Initial conditions for different neurons are chosen as,  $x_0(t)$ ,  $y_0(t)$  and  $z_0(t)$  in the range  $[-0.5, 0.5]$  and  $\phi_0(t)$  in the range  $[0,1]$ . The study of variations in  $x_i$  reveals the dynamical change induced in each neuron under the influence of magnetic coupling and external stimuli. The average of  $x_i$  over the number of neurons in the network reveals the collective behavior of the network. The average of membrane potentials is given by

$$\bar{x}(t) = \frac{1}{N} \sum_{i=1}^N x_i(t) \quad (2)$$

The dynamical change induced in a single neuron and the collective synchrony is analysed in the memristive network for different values of  $k_1$  in the presence of constant external current ( $I_1 = 2.9$ ) and is as shown in Fig. 1.

For low values of  $k_1$ , the system exhibits square wave bursting with five spikes per burst as shown in Fig. 1a. The lack of synchrony is visible from difference of  $\bar{x}$  from the individual membrane potential. We have validated the presence of plateau bursting dynamics with increase in the value of  $k_1$ , as shown in Fig. 1b. The dissimilarity in average membrane potential from the individual values represent the absence of synchrony. On further increasing the value of  $k_1$ , Fig. 1c shows AD state with no oscillations. From the studies, it is clear that magnetic coupling stabilises the system. The system is in complete synchrony as visible from the convergence of  $\bar{x}$  with the individual values. The memristor drives the system from square wave bursting to plateau bursting and to AD state, where the system exhibits complete synchrony.

The synchrony pattern in the network is further justified by the phase portraits as shown in Fig. 2. The phase space has been plotted with average membrane potential  $\bar{x}(t)$  on X-axis and membrane potential of a single neuron on Y-axis. In Fig. 2a, the phase space is dense at  $k_1 = 0.1$ , representing lack of synchrony. As the value of  $k_1$  is increased, the phase space becomes more controlled and synchronised as shown in Fig. 2b. The phase space shrinks to a single point representing stabilisation of the states, on further increase in  $k_1$ , as in Fig. 2c. The enhancement in synchrony with the increase in strength of magnetic coupling is visible from the control and shrinking of phase space.

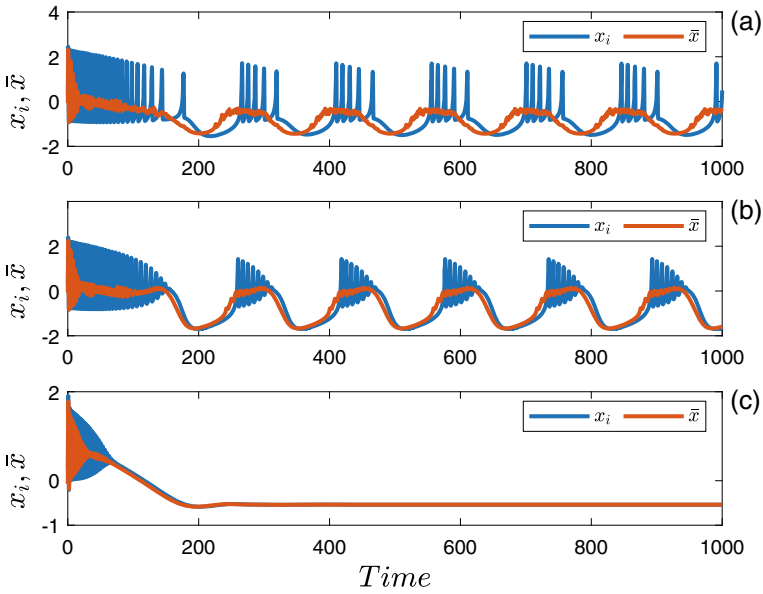


**Fig. 1** Time series of discrete and average membrane potential of the magnetically coupled neural network with constant external current ( $I = 2.9$ ). Here,  $i = 25$  and the dynamics is consistent for any neuron in the network. **a**  $k_1 = 0.1$ , **b**  $k_1 = 0.3$  and **c**  $k_1 = 1.5$

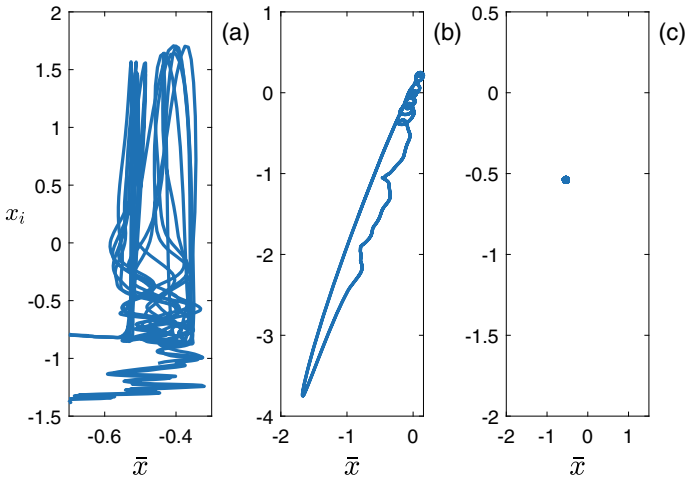


**Fig. 2** Phase portraits of neural network with magnetic coupling and constant external current ( $I = 2.9$ ). The average membrane potential is plotted in X-axis and membrane potential of single neuron on Y-axis. Here,  $i = 25$ . **a**  $k_1 = 0.1$ , **b**  $k_1 = 0.3$  and **c**  $k_1 = 1.5$

### 3.2 Time Varying External Currents

The variations in firing patterns and the collective dynamics of the network with magnetic coupling, under the influence of time varying external stimuli is analysed in this section. The time series of  $\bar{x}(t)$  for the two different external stimulus is shown in Fig. 3. In the presence of memristor and sinusoidal wave, the system exhibits square wave bursting character, as shown in Fig. 3a, for low value of input frequency,  $\omega$ . The initial transients lack complete synchrony, whereas, with evolution of time, the system attains synchrony. This is visible as the convergence of individual and average values of the membrane potential. With increase in frequency  $\omega$ , the number of spikes per burst decreases to two as shown in Fig. 3b. But the synchrony pattern is maintained. Figure 3c shows the spiking behavior under the influence of memristor and square wave. The spikes are induced in the quiescent state. The lack of synchrony is visible from the figure, by the separation of individual membrane potential from the average value. With decrease in interval of the square input, the synchrony level is even reduced, which is visible from Fig. 3d.

The phase portraits of the system with magnetic coupling and the time varying external stimulus is as shown in Fig. 4. The top and bottom panel shows the phase space of the system with sinusoidal and square inputs, respectively. In both panels, the value of  $k_1$  increases from left to right. The Fig. 4a present the influence of

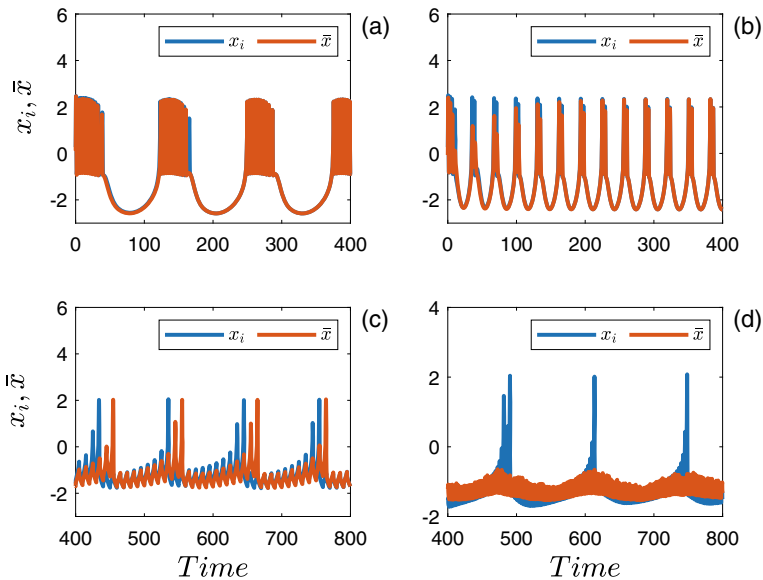


**Fig. 3** Time series of discrete and average membrane potential of the magnetically coupled neural network with time varying external stimuli. Here  $i = 25$ ,  $k_1 = 0.1$ . **a** sinusoidal input ( $A = 3$ ,  $\omega = 0.05$ ), **b** sinusoidal input ( $A = 3$ ,  $\omega = 0.2$ ), **c** square input ( $A = 3$ ,  $\rho_s = 10$ ), **d** square input ( $A = 3$ ,  $\rho_s = 3$ )

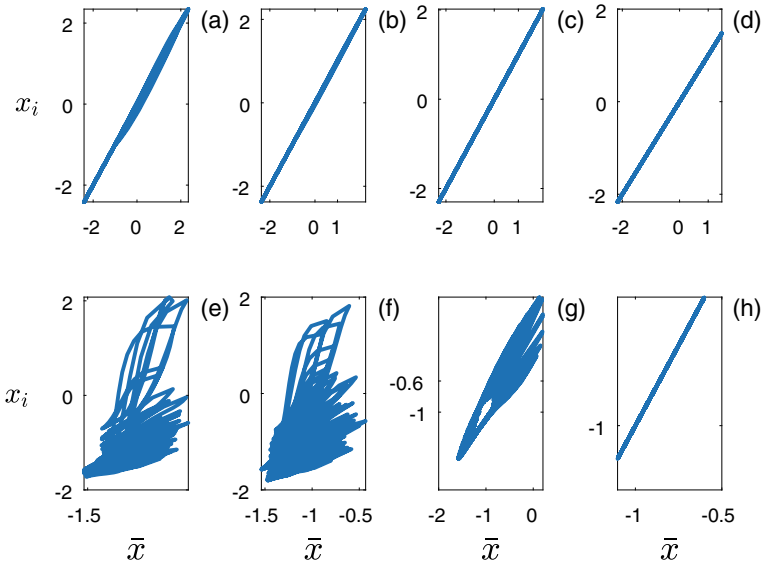


**Fig. 4** Phase space with sinusoidal (top panel) and square input (bottom panel). Here,  $i = 25$ ,  $A = 3$ ,  $\omega = 0.2$ ,  $\rho_s = 3$ . The value of  $k_1$  used are 0.1 for **a** and **e**, 0.3 for **b** and **f**, 0.7 for **c** and **g**, 1.5 for **d** and **h**

input  $I_2$  on a network with weak magnetic coupling. The phase space exhibits small dispersion. On increasing the strength of magnetic coupling,  $k_1$ , the phase space is reduced to a beeline as shown in Fig. 4b. On further increase of  $k_1$ , the synchrony in the network is preserved by the combined effect of magnetic coupling and sinusoidal input, ( $I_2$ ), observed as the straight line in phase portrait of Fig. 4c. The synchrony attained is sustained at even higher value of magnetic coupling strength, as shown in Fig. 4d. The dispersed phase portrait for low magnetic coupling strength and under the influence of square input,  $I_3$ , represents the lack of synchrony in the network, as shown in Fig. 4e. With further increase in magnetic coupling, the phase portrait is still dispersed, in the presence of square input, as shown in Fig. 4f. A slight control in the phase portrait is visible for further increase in magnetic coupling strength, as shown in Fig. 4g. At high value of magnetic coupling strength, the phase portrait is reduced to a beeline in the presence of input,  $I_3$ , as shown in Fig. 4h. Thus, it is found that the magnetic coupling helps to control the phase space in the presence of time varying external inputs. However, the control is faster in the presence of sinusoidal input compared to the square input.

### 3.3 Statistical Factor of Synchronisation

The synchrony induced by the magnetic coupling, in the presence of external stimuli is quantified using statistical factor of synchronisation [41, 44], which has the form:

$$R = \frac{\langle \bar{x}(t)^2 \rangle - \langle \bar{x}(t) \rangle^2}{\frac{1}{N} \sum_{i=1}^N [\langle x(t)_i^2 \rangle - \langle x(t)_i \rangle^2]} \tag{3}$$

where,  $\bar{x}(t)$  is given by Eq. (2) and ‘ $\langle \rangle$ ’ represent the average of the variable over time. The system attains complete synchrony when  $R = 1$  and desynchrony when  $R = 0$ .

The variation in  $R$  with  $k_1$  in the presence of different external stimuli is shown in Fig. 5a. The synchronisation factor has been calculated using (3). The blue, red and yellow lines represent the influence of constant, sinusoidal and square input on the magnetically coupled network, respectively. The amplitude of the inputs are fixed at  $A = 3$ . At low values of  $k_1$ , the value of  $R$  is about 0.5, representing partial synchrony. The synchrony obtained by the network, under the influence of constant current is found to be high compared to the square input. The high value of  $R$  obtained for even low value of magnetic coupling in the presence of sinusoidal input, represents the synchrony obtained by the network. For weakly coupled system, the synchrony obtained by the constant input lies in between square and sinusoidal input and for high values of  $k_1$ , the magnetic coupling overrides the input effects.

The variations in the  $R$  with the amplitude of the inputs is presented in Fig. 5b. The colour codes used for the inputs are similar to Fig. 5a. In the absence of any external input, the synchrony level is obtained to be about  $R = 0.85$ , as the value of  $k_1$  is fixed as 0.3. For low intensities of the inputs, the synchrony of the network is reduced from the initial value in the presence of constant input. The synchrony is even low under the influence of square input. The presence of sinusoidal input increases the synchrony in the network. With increase in the intensities of the inputs, the differences

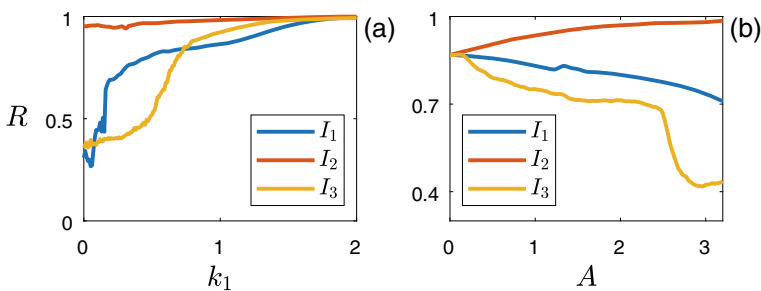


**Fig. 5** Variation of statistical factor of synchronisation with **a** magnetic coupling strength and **b** amplitude of external input, under the influence of different external stimuli. The constant input, sinusoidal and square inputs are represented by blue line, red and yellow colours respectively. **a**  $A = 3$  **b**  $k_1 = 0.3$ . Here,  $\omega = 0.2$ ,  $\rho_s = 3$



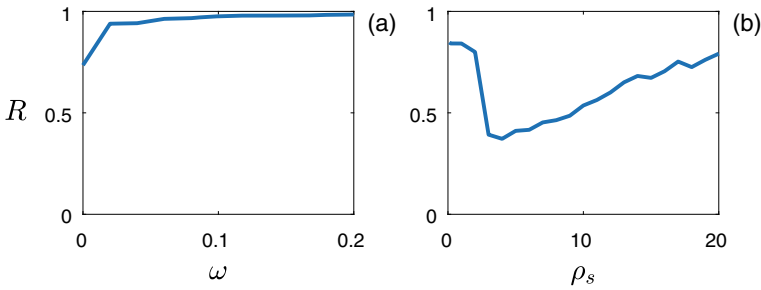


**Fig. 6** Statistical factor of synchronisation for different parameters of the time varying input. Here,  $k_1 = 0.3, A = 3$

in synchrony becomes more visible. The results obtained are in perfect agreement with the studies of Fig. 5a. At sufficiently high amplitudes of the external input, the sinusoidal input is capable of enhancing synchrony compared to the constant input. The desynchronising ability of the square input on the magnetically coupled network is also visible.

The study of synchrony pattern has been extended by varying frequencies of the inputs,  $I_2$  and  $I_3$ . The variations in  $R$  with the frequency,  $\omega$  of sinusoidal input is shown in Fig. 6a. For low value of frequency, the synchrony is quantified to be about  $R = 0.7$ . With further increase in  $\omega$ , the synchrony is also increased. Thus, the input with high frequency has a greater synchronising ability. The desynchronising ability of the square input is analysed for the variations in interval of the square input as presented in Fig. 6b. For low values of the interval,  $\rho$ , (i.e.) high frequency, the synchrony is drastically reduced. But on further increasing the interval (reducing frequency), the synchrony is increasing, representing the inability of the low frequency input to desynchronise. Thus, it is inferred that high frequency sinusoidal input and square input has the capability to synchronise and desynchronise the magnetically coupled network, respectively.

## 4 Conclusions

We have analysed a linear chain of HR neurons with magnetic coupling and external stimuli of different forms. The magnetic coupling is capable of inducing plateau bursting and amplitude death in the HR neurons with constant external input. The phase space trajectories are controlled and shrinks to a single point with the increase in magnetic coupling strength, representing synchrony and amplitude death. The synchrony is quantified using statistical factor of synchrony. The HR neural network with magnetic coupling is also analysed in the presence of sinusoidal and square waves. The dynamics of the individual neurons are square wave bursting and spiking in the presence of sinusoidal and square inputs, respectively. In the presence of time

varying external inputs, the phase space trajectories of the system are reduced to beeline, for high magnetic coupling strength. The statistical factor of synchronisation justifies the fact that, the sinusoidal input enhances synchrony and the square input suppresses the synchrony in the network, compared to the constant input. The inputs with high frequencies have greater ability to enhance and suppress the synchrony.

## References

1. Strogatz, S.H.: From Kuramoto to Crawford: exploring the onset of synchronization in populations of coupled oscillators. *Phys. D: Nonlinear Phenom.* **143**(1–4), 1–20 (2000)
2. Batista, C.A.S., Lopes, S.R., Viana, R.L., Batista, A.M.: Delayed feedback control of bursting synchronization in a scale-free neuronal network. *Neural Netw.* **23**(1), 114–124 (2010)
3. Krylov, D., Dyllov, D.V., Rosenblum, M.: Reinforcement learning for suppression of collective activity in oscillatory ensembles. *Chaos: Interdiscip. J. Nonlinear Sci.* **30**(3), 033126 (2020)
4. Kuramoto, Y.: *Chemical oscillations, waves, and turbulence*. Courier Corporation, 2003
5. Backwell, P., Jennions, M., Passmore, N., Christy, J.: Synchronized courtship in fiddler crabs. *Nature* **391**(6662), 31–32 (1998)
6. Mirollo, R.E., Strogatz, S.H.: Synchronization of pulse-coupled biological oscillators. *SIAM J. Appl. Math.* **50**(6), 1645–1662 (1990)
7. Thompson, R.F.: *The Brain: a Neuroscience Primer*. Macmillan (2000)
8. Izhikevich, E.M.: *Dynamical Systems in Neuroscience*. MIT press (2007)
9. Xu, Y., Jia, Y., Ma, J., Alsaedi, A., Ahmad, B.: Synchronization between neurons coupled by memristor. *Chaos, Solitons Fractals* **104**, 435–442 (2017)
10. Yang, J.Q., Wang, R., Wang, Z.P., Ma, Q.Y., Mao, J.Y., Ren, Y., Yang, X., Zhou, Y., Han, S.T.: Leaky integrate-and-fire neurons based on perovskite memristor for spiking neural networks. *Nano Energy* **74**, 104828 (2020)
11. Xu, L., Qi, G., Ma, J.: Modeling of memristor-based Hindmarsh-Rose neuron and its dynamical analyses using energy method. *Appl. Math. Model.* **101**, 503–516 (2022)
12. Rajagopal, K., Karthikeyan, A., Jafari, S., Parastesh, F., Volos, C., Hussain, I.: Wave propagation and spiral wave formation in a Hindmarsh-Rose neuron model with fractional-order threshold memristor synaps. *Int. J. Mod. Phys. B* **34**(17), 2050157 (2020)
13. Han, B., Yunzhen, Z., Liu, W., Bocheng, B.: Memristor synapse-coupled memristive neuron network: synchronization transition and occurrence of chimera. *Nonlinear Dyn.* **100**(1), 937–950 (2020)
14. Usha, K., Subha, P.A.: Hindmarsh-Rose neuron model with memristors. *Biosystems* **178**, 1–9 (2019)
15. Usha, K., Subha, P.A.: Energy feedback and synchronous dynamics of Hindmarsh-Rose neuron model with memristor. *Chin. Phys. B* **28**(2), 020502 (2019)
16. Usha, K., Subha, P.A.: Collective dynamics and energy aspects of star-coupled Hindmarsh-Rose neuron model with electrical, chemical and field couplings. *Nonlinear Dyn.* **96**(3), 2115–2124 (2019)
17. Zandi-Mehran, N., Jafari, S., Hashemi Golpayegani, S.M.R., Nazarimehr, F., Perc, M.: Different synaptic connections evoke different firing patterns in neurons subject to an electromagnetic field. *Nonlinear Dyn.* **100**(2), 1809–1824 (2020)
18. Wu, F.Q., Ma, J., Zhang, G.: Energy estimation and coupling synchronization between bio-physical neurons. *Science China Technol. Sci.* **63**(4), 625–636 (2020)
19. Tan, Y., Wang, C.: A simple locally active memristor and its application in hr neurons. *Chaos: Interdiscip. J. Nonlinear Sci.* **30**(5), 053118 (2020). <https://doi.org/10.1063/1.5143071>
20. Chen, M., Chen, C.J., Bao, B.C., Xu, Q.: Multi-stable patterns coexisting in memristor synapse-coupled Hopfield neural network. In: *Mem-elements for Neuromorphic Circuits with Artificial Intelligence Applications*, pp. 439–459. Academic Press (2021)

21. Saxena, G., Prasad, A., Ramaswamy, R.: Amplitude death: the emergence of stationarity in coupled nonlinear systems. *Phys. Rep.* **521**(5), 205–228 (2012)
22. Herrero, R., Figueras, M., Rius, J., Pi, F., Orriols, G.: Experimental observation of the amplitude death effect in two coupled nonlinear oscillators. *Phys. Rev. Lett.* **84**(23), 5312 (2000)
23. Monteiro, L.H.A., Filho, A.P., Chaui-Berlinck, J.G., Piqueira, J.R.C.: Oscillation death in a two neuron network with delay in a self connection. *J. Biol. Syst.* **15**, 49–61 (2007)
24. Koseska, A., Volkov, E. and Kurths, J.: Parameter mismatches and oscillation death in coupled oscillators. *Chaos: Interdiscip. J. Nonlinear Sci.* **20**(2), 023132 (2010)
25. Prasad, A.: Universal occurrence of mixed-synchronization in counter-rotating nonlinear coupled oscillators. *Chaos Solitons Fractals* **43**(1–12), 42–46 (2010)
26. Sharma, A., Shrimali, M.D.: Amplitude death with mean-field diffusion. *Phys. Rev. E* **85**(5), 057204 (2012)
27. Gjurchinovski, A., Zakharova, A., Schöll, E.: Amplitude death in oscillator networks with variable-delay coupling. *Phys. Rev. E* **89**(3), 032915 (2014)
28. Teki, H., Konishi, K., Hara, N.: Amplitude death in a pair of one-dimensional complex Ginzburg-Landau systems coupled by diffusive connections. *Phys. Rev. E* **95**(6), 062220 (2017)
29. Eteme, A.S., Tabi, C.B., Mohamadou, A.: Firing and synchronization modes in neural network under magnetic stimulation. *Commun. Nonlinear Sci. Numer. Simul.* **72**, 432–440 (2019)
30. Li, Z., Zhou, H., Wang, M., Ma, M.: Coexisting firing patterns and phase synchronization in locally active memristor coupled neurons with HR and FN models. *Nonlinear Dyn.* **104**(2), 1455–1473 (2021)
31. Dhamala, M., Jirsa, V.K., Ding, M.: Enhancement of neural synchrony by time delay. *Phys. Rev. Lett.* **92**(7), 074104 (2004)
32. Sakurai, Y., Song, K., Tachibana, S., Takahashi, S.: Volitional enhancement of firing synchrony and oscillation by neuronal operant conditioning: interaction with neurorehabilitation and brain-machine interface. *Front. Syst. Neurosci.* **8**, 11 (2014)
33. Uhlhaas, P.J., Singer, W.: Neural synchrony in brain disorders: relevance for cognitive dysfunctions and pathophysiology. *Neuron* **52**(1), 155–168 (2006)
34. Buzsáki, G.: *Rhythms of the Brain*. Oxford University Press (2006)
35. Schnitzler, A., Gross, J.: Normal and pathological oscillatory communication in the brain. *Nat. Rev. Neurosci.* **6**(4), 285–296 (2005)
36. Rosenblum, M.: Controlling collective synchrony in oscillatory ensembles by precisely timed pulses. *Chaos: Interdiscip. J. Nonlinear Sci.* **30**(9), 093131 (2020)
37. Remi, T., Subha, P.A., Usha, K.: Controlling phase synchrony in the mean field coupled Hindmarsh-Rose neurons. *Int. J. Mod. Phys. C* 2250058 (2021)
38. Lin, H., Wang, C., Yao, W., Tan, Y.: Chaotic dynamics in a neural network with different types of external stimuli. *Commun. Nonlinear Sci. Numer. Simul.* **90**, 105390 (2020)
39. Eteme, A.S., Tabi, C.B., Beyala Ateba, J.F., Ekobena Fouda, H.P., Mohamadou, A. and Crepin Kofane, T.: Chaos break and synchrony enrichment within Hindmarsh-Rose-type memristive neural models. *Nonlinear Dyn.* **105**(1), 785–795 (2021)
40. Xu, Y., Ying, H., Jia, Y., Ma, J., Hayat, T.: Autaptic regulation of electrical activities in neuron under electromagnetic induction. *Sci. Rep.* **7**, 43452 (2017). <https://doi.org/10.1038/srep43452>
41. Xu, Y., Jia, Y., Ma, J., Hayat, T., Alsaedi, A.: Collective responses in electrical activities of neurons under field coupling. *Sci. Rep.* **8**, 1349 (2018). <https://doi.org/10.1038/s41598-018-19858-1>
42. Buric, N., Todorovic, K., Vasovic, N.: Synchronization of bursting neurons with delayed chemical synapses. *Phys. Rev. E* **78**(3), 036211 (2008). <https://doi.org/10.1103/physreve.78.036211>
43. Shi, X., Wang, Z.: Adaptive synchronization of time delay Hindmarsh-Rose neuron system via self-feedback. *Nonlinear Dyn.* **69**(4), 2147–2153 (2012)
44. Qin, H., Ying, W., Wang, C., Ma, J.: Emitting waves from defects in network with autapses. *Commun. Nonlinear Sci. Numer. Simul.* **23**(1–3), 164–174 (2015). <https://doi.org/10.1016/j.cnsns.2014.11.008>

# Excitation Spectrum of Repulsive Spin-Orbit Coupled Bose-Einstein Condensates in Quasi-one Dimension: Effect of Interactions and Coupling Parameters



Sanu Kumar Gangwar, R. Ravisankar, and Pankaj K. Mishra

**Abstract** We investigate the stability of the repulsive spin-orbit (SO) coupled Bose-Einstein condensates with linear Rabi mixing by employing the Bogoliubov-de-Gennes theory. We analytically compute the eigenenergy spectrum for both non-interacting and interacting cases. The magnitude of the imaginary part of the eigenenergy has been used to characterize the dynamical instability of the condensate. We find that increase in the SO coupling ( $k_L$ ) leads to the transformation from a stable state to a single instability band then a multiple instability band. However, the effect of increase in Rabi coupling ( $\Omega$ ) is the opposite, which makes the system more stable. Further, we perform a systematic analysis to understand the effect of the variations of the interaction parameters on the instability of the spectrum. Finally, a stability phase diagram in the interspecies and intraspecies parameter plane and  $\Omega - k_L$  plane has been obtained.

**Keywords** Bose-Einstein condensates · Bogliubov-de-Gennes theory · Spin-Orbit coupling · Gross-Pitaevskii equation · Instability

## 1 Introduction

After the successful achievement of experimental realization of Bose-Einstein condensates (BECs) in the dilute atomic gases, with a lot of free parameters to control the system, it has totally given a new direction to the research in ultracold Physics.

---

WWW home page: <https://www.iitg.ac.in/pankaj.mishra/>.

---

S. K. Gangwar · R. Ravisankar · P. K. Mishra (✉)  
Department of Physics, Indian Institute of Technology, Guwahati 781039, Assam, India  
e-mail: [pankaj.mishra@iitg.ac.in](mailto:pankaj.mishra@iitg.ac.in)

© The Author(s), under exclusive license to Springer Nature Switzerland AG 2022  
S. Banerjee and A. Saha (eds.), *Nonlinear Dynamics and Applications*,  
Springer Proceedings in Complexity,  
[https://doi.org/10.1007/978-3-030-99792-2\\_109](https://doi.org/10.1007/978-3-030-99792-2_109)

1287

In BEC, the nonlinear interaction evolves from the atomic interactions, which are revealed as nonlinear terms in the Gross-Pitaevskii equation (GPE) [1]. The nonlinear interactions may be attractive or repulsive interatomic interactions.

In recent years the coupled BECs [2] have attracted the attention of the scientific community owing to its unique features of having two internal atomic states, which can be tuned to generate the multiple component BECs. Moreover, at ultralow temperatures, quantum gases allow the realizations of multi-component BECs [2–4], whose behavior is very different with respect to that of a single component BEC. The possibility of tuning a number of system parameters makes such systems ideal for studying the structure of the various phases and the nature of the phase transitions. There are lots of studies in coupled BECs system that focus on the stability region [3, 5], chaotic and unstable cycle behavior [4], etc. However, after a breakthrough experiment by Spielman and his group at NIST, who have been able to engineer a synthetic spin-orbit (SO) coupling in BECs [6], the coupled BEC field has generated renewed interests among the community. In this experiment, two Raman laser beams were used to couple hyperfine states of BECs, where the momentum transfer between atoms and lasers leads to the synthetic SO coupling [7].

In 1941, to explain the superfluid behaviour in  $^4\text{He}$  Landau developed the fundamental theory of elementary excitation. On similar line further Bogoliubov in 1947 [8] performed the analytical derivation of the excitation spectrum for the Bose gases. The collective excitation spectrum of BECs gives the basic information about the dynamics of the ultracold gases [9]. Roton-phonon-Maxon modes were found in the quasi-1D SO coupled BECs experimentally [10], and analytically [11], also the dynamical and energetic instability were investigated numerically [12]. Although there are recent works that highlight the stability/instability of the excitation spectrum of SO coupled BECs in two dimension such analysis has been lacking for 1D system where the systems exhibit interesting dynamical behaviour [13]. In this paper, we focus on the instability regions for different SO and Rabi coupling parameters while considering the repulsive inter- and intraspecies interactions between the components of condensates.

We arrange the paper in the following sequence. In Sect. 2, we develop the mathematical model and corresponding coupled Gross-Pitaevskii equations for spin-1/2 BECs. In Sect. 3 we discussed the single-particle spectrum. Section 4 we divide in three different subsections. We develop the analytical model to evaluate the excitation spectrum in the first subsection. In the next subsection, we focus on the effect of SO and Rabi couplings on the excitation spectrum of spin-1/2 BECs, and further, the effect of intra- and interspecies interactions. In Sect. 5 we present the stability phase diagrams for both cases as discussed in Sect. 4. Finally, we provide the summary of our work in Sect. 6.

## 2 The Model: Coupled Gross-Pitaevskii Equations

This section illustrates the mean-field model of spin-orbit (SO) coupled quasi-one-dimensional pseudospin-1/2 BECs. Theoretically, we can study the properties of these kinds of systems with the help of the coupled Gross-Pitaevskii equations given below (as in dimensionless form) [13]:

$$i \frac{\partial \psi_{\uparrow}}{\partial t} = \left[ -\frac{1}{2} \frac{\partial^2}{\partial x^2} - ik_L \frac{\partial}{\partial x} + V(x) + \alpha |\psi_{\uparrow}|^2 + \beta |\psi_{\downarrow}|^2 \right] \psi_{\uparrow} + \Omega \psi_{\downarrow}, \quad (1a)$$

$$i \frac{\partial \psi_{\downarrow}}{\partial t} = \left[ -\frac{1}{2} \frac{\partial^2}{\partial x^2} + ik_L \frac{\partial}{\partial x} + V(x) + \beta |\psi_{\uparrow}|^2 + \alpha |\psi_{\downarrow}|^2 \right] \psi_{\downarrow} + \Omega \psi_{\uparrow}, \quad (1b)$$

Here,  $\psi_{\uparrow}$  and  $\psi_{\downarrow}$  are the wavefunction corresponding to the spin-up and spin-down component of the condensates,  $V(x)$  is the trapping potential,  $\alpha$  and  $\beta$  are the intra- and interspecies components of the condensates respectively,  $k_L$  is SO coupling and  $\Omega$  is the Rabi coupling parameters. In the above equations (1), length is measured in units of harmonic oscillator length  $a_0 = \sqrt{\hbar/(m\omega_{\perp})}$ , time in the units of  $\omega_{\perp}^{-1}$ , and energy in the units of  $\hbar\omega_{\perp}$ , where  $\omega_{\perp}$  is the transverse direction frequency of the harmonic confinement. The SO coupling and the Rabi coupling parameters have been rescaled as  $k_L = k'_L/a_0\omega_{\perp}$  and  $\Omega = \Omega'/\omega_{\perp}$ , respectively, while the wave function is rescaled as  $\psi_{\uparrow,\downarrow} = \psi'_{\uparrow,\downarrow} a_0^{3/2}/\sqrt{N}$ . We consider the Rabi coupling as  $\Omega = |\Omega|e^{i\theta}$  that minimizes the energy when  $\Omega = -|\Omega|$  for  $\theta = \pi$  [13]. The wave functions are subjected to the following normalization condition  $\int_{-\infty}^{\infty} (|\psi_{\uparrow}|^2 + |\psi_{\downarrow}|^2) dx = 1$ .

## 3 Single-particle Spectrum

In this section, we study the single-particle spectrum of the spin-orbit coupled binary BECs, which arises by solving the coupled trapless GP equations in the absence of inter- and intraspecies interactions.

Let us consider the plane wave solution as  $\psi_{\uparrow,\downarrow} = \phi_{\uparrow,\downarrow} e^{i(k_x x - \omega t)}$ , and also  $\alpha = \beta = V = 0$ . Therefore we can write the eigenvalue problem as,

$$\omega (\phi_{\uparrow} \ \phi_{\downarrow})^T = \mathcal{L}_{sp} (\phi_{\uparrow} \ \phi_{\downarrow})^T \quad (2)$$

where,

$$\mathcal{L}_{sp} = \begin{pmatrix} \frac{1}{2}k_x^2 + k_L k_x & \Omega \\ \Omega & \frac{1}{2}k_x^2 - k_L k_x \end{pmatrix} \quad (3)$$

Which gives the single-particle spectrum as,

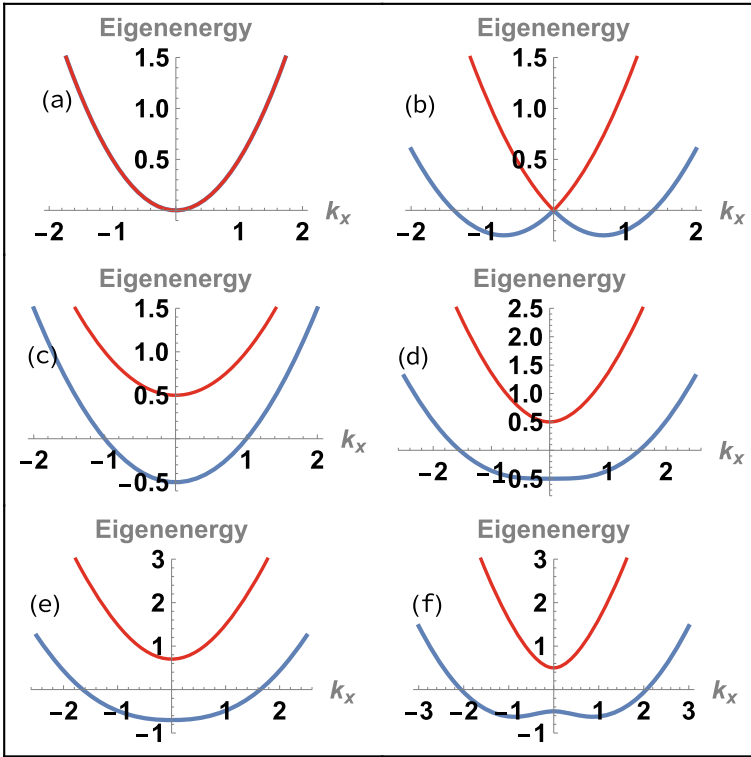


**Fig. 1** Single-particle spectrum for different combination of spin-orbit and Rabi coupling parameters **a**  $k_L = 0.0, \Omega = 0.0$  **b**  $k_L = 0.7, \Omega = 0.0$ , **c**  $k_L = 0.0, \Omega = 0.5$  **d**  $k_L = 0.7, \Omega = 0.5$ , **e**  $k_L = 0.7, \Omega = 0.7$  **f**  $k_L = 1.0, \Omega = 0.5$

$$\omega_{\pm} = \frac{1}{2} \left( k_x^2 \pm 2\sqrt{k_x^2 k_L^2 + \Omega^2} \right) \tag{4}$$

The single-particle spectrum has two solutions positive branch ( $\omega_+$ ) and negative branch ( $\omega_-$ ). The negative branch shows the transition from single minima to double minima on the variation of SO coupling for finite Rabi coupling strength, while the positive branch has single minima throughout. So mainly, in this part, we will focus on the negative branch.

For zero spin-orbit ( $k_L = 0$ ) and Rabi ( $\Omega = 0$ ) couplings, the non-degenerate parabolic spectrum occurs (see Fig. 1a). For further analysis, we introduce finite value to  $k_L = 0.7$  in the absence of Rabi ( $\Omega = 0$ ), the negative branch of the spectrum makes a transition from parabolic to double minima, which locates at the position  $k_x = \pm k_L$  (see Fig. 1b). Now we fix finite value to Rabi ( $\Omega = 0.5$ ) in the absence of the SO coupling parameter ( $k_L = 0$ ), double minima disappears, and the depth of the minima increases. We also investigate that the energy gap between negative and positive branches is  $2\Omega$  (see Fig. 1c). Since we are looking forward to the effect of

variation of SO (Rabi) with the other coupling term Rabi (SO) at some finite value, on the negative branch of the spectrum. On increasing Rabi term (see Fig. 1d and e) from  $\Omega = 0.5$  to  $\Omega = 0.7$  at fix value of SO  $k_L = 0.7$ , we analyze that the depth of minima increases, this corresponds to lowering in the energy of the system. It indicates that the system is more stable upon increase in  $\Omega$ . Again on increasing SO term from  $k_L = 0.7$  to  $k_L = 1.0$  at the fixed value of Rabi term  $\Omega = 0.5$ , we observe that the phase transition from single minimum to double minima in the negative branch of the spectrum (see Fig. 1d and f). This observation confirms the phase transition, and it will occur only when  $\Omega < k_L^2$ .

## 4 Collective Excitation Spectrum

The excitation spectrum of the condensates provides an important clue about their dynamical stability. In this section, first, we discuss the analytical results of the eigenenergy of the excitation spectrum using Bogoliubov-de Gennes (BdG) theory. It is followed by the effect of the coupling parameters on the stability of the energy spectrum.

### 4.1 Analytical Study of Excitation Spectrum

In this section, we present the analytical study of the excitation spectrum of coupled Binary BECs in the presence of SO and Rabi couplings by applying the BdG theory given by Bogoliubov in 1947. Initially, we perturb our ground state wave function  $\phi_{\uparrow,\downarrow}$  by adding a small perturbation term  $\delta\phi_{\uparrow,\downarrow}$ . After inserting this modified wave function in the coupled GP Equation, we get four different branches of the excitation spectrum. Out of four, two are positive, and two are negative. We analyze the behavior of positive and negative energy branches in the presence of SO and Rabi coupling. Elaborately, we vary the SO (Rabi) term at the fixed Rabi (SO) term. The excitation wave function to get the BdG transformation matrix is given by,

$$\psi_j = e^{-i\mu t} [\phi_j + \delta\phi_j] \quad (5)$$

$$\delta\phi_j = u_j e^{i(k_x x - \omega t)} + v_j^* e^{-i(k_x x - \omega^* t)} \quad (6)$$

Where,  $\phi_j = \sqrt{n_j} e^{i\varphi_j}$ , ( $j = \uparrow, \downarrow$ ) is the ground state wavefunction,  $u_j$ 's and  $v_j$ 's are the BdG amplitudes. Also  $n_j$  and  $\varphi_j$  is the density and phase respectively. We could calculate BdG amplitudes by substituting equation Eq. (5) in Eq. (1). Therefore,

$$\omega (u_\uparrow \ v_\uparrow \ u_\downarrow \ v_\downarrow)^T = \mathcal{L} (u_\uparrow \ v_\uparrow \ u_\downarrow \ v_\downarrow)^T \quad (7)$$



where the superscript  $T$  denotes the transpose of the matrix and  $\mathcal{L}$  is given by,

$$\mathcal{L} = \begin{pmatrix} H_1 - \mu & \alpha n_\uparrow & \beta\sqrt{n_\uparrow n_\downarrow} - \Omega & \beta\sqrt{n_\uparrow n_\downarrow} \\ -\alpha n_\uparrow & -H_2 + \mu & -\beta\sqrt{n_\uparrow n_\downarrow} & -\beta\sqrt{n_\uparrow n_\downarrow} + \Omega \\ \beta\sqrt{n_\uparrow n_\downarrow} - \Omega & \beta\sqrt{n_\uparrow n_\downarrow} & H_3 - \mu & \alpha n_\downarrow \\ -\beta\sqrt{n_\uparrow n_\downarrow} & -\beta\sqrt{n_\uparrow n_\downarrow} + \Omega & -\alpha n_\downarrow & -H_4 + \mu \end{pmatrix}$$

Where, the matrix element  $H_1, H_2, H_3, H_4$  and  $\mu$  (chemical potential) is given in the Appendix. A. The normalization condition yields  $\int (|u_j|^2 - |v_j^*|^2) dx = 1$ . The Simplified form of the BdG equation can be obtain by substituting  $\det(\mathcal{L})$  equal to zero with  $n_\uparrow = n_\downarrow = 1/2$ . Therefore we get,

$$\omega^4 + a\omega^2 + b = 0 \quad (8)$$

where the coefficients of the dispersion relation  $a, b$  are given in Appendix. B.

We calculate the eigenvalue of the matrix  $\mathcal{L}$  (see Eq. (7)). As discussed in the last section, the single-particle spectrum ( $\alpha = \beta = 0$ ) generally has a positive branch ( $\omega_+$ ) and a negative branch ( $\omega_-$ ). The positive branch exhibits single minima throughout, while the negative branch shows the phase transition from single minimum to double minima upon the variation of spin-orbit coupling at some finite Rabi coupling term. Here, we will focus on the negative branch. Note that the imaginary or complex eigenenergies indicate the dynamical instability, while the negative eigenenergy of the excitation spectrum implies that the system is energetically unstable [14]. As we are interested in investigating the effect of the different interaction and coupling parameters on the dynamical instability, we will be mainly interested in looking at the nature of the negative branch of the eigenenergy. We define the instability factor  $G = |\Im(\omega_-)|$ .

In the following, we present the effect of the couplings on the stability of the excitation spectrum.

## 4.2 Effect of SO and Rabi Coupling Parameters on the Stability of Spectrum

Recently, Ravisankar et al. [14] have analyzed the effect of the SO and Rabi couplings on the stability of the excitation spectrum for quasi two-dimension binary BECs. It has been observed while the increase in SO coupling leads the instability, increment in Rabi couplings brings the stability. In a similar line, we want to analyze the effect of variation in the couplings for a quasi-one dimension where the SO coupling acts in the same way. Figure 2 exhibits the variation of the instability ( $G$ ) along the wavenumber for different  $k_L$  with fixed  $\alpha = \beta = \Omega = 1$ . We find that the condensate is stable for  $k_L = 0$  for all ranges of the wavenumber. For small  $k_L$  ( $= 1.5, 1.75$ ) the instability appears for a band of the wavenumber. Such kind of phase transition will

**Fig. 2** Variation of the imaginary part of the eigenvalue of the excitation spectrum with  $k_x$  for different  $k_L$  with fixed  $\Omega = \alpha = \beta = 1$ . The instability region expands along  $k_x$  with increase in  $k_L$

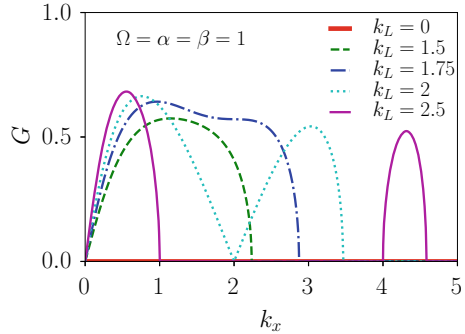
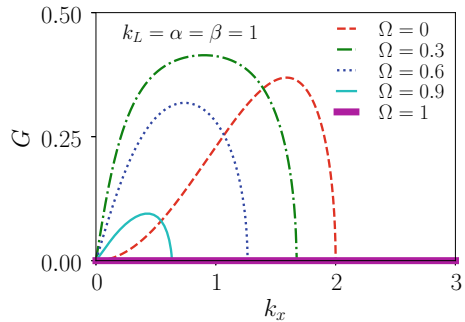


**Fig. 3** Variation of the imaginary part of the eigenvalue of the BdG spectrum with  $k_x$  for different  $\Omega$  with fixed  $k_L = \alpha = \beta = 1$ . The instability region reduce along  $k_x$  with increase in  $\Omega$



occur only for  $\Omega > k_L^2$  in the weak repulsive BECs. In particular, when  $k_L \gtrsim 1.75$  we noticed the single instability band transforms to multi-band. Upon further increase in  $k_L$  ( $= 2.0, 2.5$ ) leads to the generation of two or more wavenumber bands in which the spectrum is unstable. Note that for simplicity here we have shown the instability factor ( $G$ ) for the positive wavenumber. The behavior is symmetric about  $k_x = 0$ .

In Fig. 3 we show the variation of the instability factor ( $G$ ) along the wavenumber for different Rabi coupling ( $\Omega$ ) with fixed interaction parameters  $\alpha = \beta = 1$  and  $k_L = 1$ . For zero Rabi coupling ( $\Omega = 0$ ), the condensates lie in the stripe wave regime; thus, it has an instability band [13]. Further increase in the Rabi coupling to  $\Omega = 0.3$ , we observed that the instability bandwidth gets reduced with enhanced amplitude. However, increment in  $\Omega$  ( $= 0.6, 0.9$ ) resulted reduction in the bandwidth as well as the amplitude of the instability. Finally, we obtained the stable regime for  $\Omega \gtrsim 1$ . From the single-particle spectrum, when  $\Omega > k_L^2$ , we have a plane-wave phase which is a more stable one. Here we also confirm this through our stability analysis.

In the next section, we discuss the effect of variations of interaction parameters on the instability of the spectrum.

### 4.3 Effect of Intra- And Interspecies Interactions on the Stability of Spectrum

In the last subsection, we discussed the effect of SO and Rabi coupling parameters on the stability of the excitation spectrum; here, we present our analysis attributed to the effect of the intra- and interspecies nonlinear interaction strengths on the stability of the excitation spectrum. First we analyze the effect of intraspecies interactions ( $\alpha$ ) on the BdG spectrum for fixed SO coupling  $k_L = 2$ , and  $\Omega = \beta = 1$  (see Fig. 4). For  $k_L = 1$ , and  $\Omega = 1$ , we know that the system should be in the stable regime because it is plane wave phase as discussed in Fig. 3. Here as we are interested in analyzing the instability of the system, we choose the stripe wave regime, which is the more unstable regime. For  $\alpha = 1$ , we find two instability bands, which are maintained up to  $\alpha \lesssim 2$ . When  $\alpha > 2$ , we noticed that the two instability bands converted into a single band accompanied by a reduction in the instability amplitude. It is quite interesting that we obtain the stable regime for more repulsive intraspecies interaction strength  $\alpha = 8$  (see magenta thick solid line in Fig. 4). Overall we conclude that as we select the unstable regime, increasing  $\alpha$  makes the system enter into the stable regime.

Next, we analyze the role of interspecies interaction strength ( $\beta$ ) on the stability of the system with fixed parameters as  $k_L = \Omega = \alpha = 1$ . Here we consider the plane wave regime, which is the more stable regime, then we show the effect of increasing  $\beta$  on the stability of the system. For finite repulsive intraspecies interaction strength, we have a more stable regime (see red thick solid line in Fig. 5). When  $\beta > 1$ , we observe the appearance of the instability band. Further, we notice that the single instability band gets converted to multi-band when  $\beta > 5$ .

So far, we have discussed the effect of interactions and coupling parameters on the stability of the quasi-1D SO coupled BECs. In the next section, we will present the stability phase diagrams that we have obtained from our analysis.

**Fig. 4** Variation of the imaginary part of the eigenvalue of the excitation spectrum with  $k_x$  for different  $\alpha$  with fixed  $k_L = 2$ ,  $\Omega = \beta = 1$ . The instability region reduce along  $k_x$  with increase in  $\alpha$

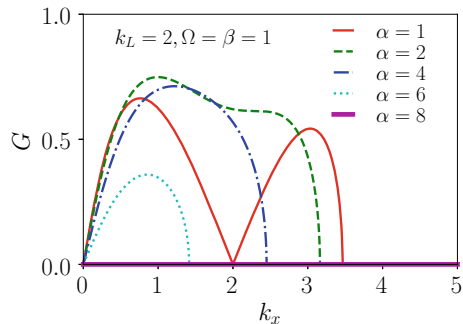
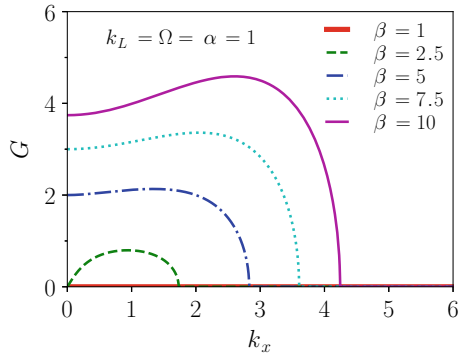


**Fig. 5** Variation of the imaginary part of the eigenvalue of the BdG spectrum with  $k_x$  for different  $\beta$  with fixed  $k_L = \Omega = \alpha = 1$ . The instability region expands along  $k_x$  with increase in  $\beta$



### 5 Stability Phase Diagrams

For better visualization of the stability of the system, we plot two different stability phase diagrams in Fig.6. The left panel is in the  $\alpha - \beta$  plane for  $\Omega = k_L = 1$  and right panel is in the  $\Omega - k_L$  plane for  $\alpha = \beta = 1$ . Both phase diagram is for the  $G$  value at  $k_x = 1$ . First, let us consider the  $\alpha - \beta$  stability phase diagram. When  $\beta < 0.9$ , we found a stable regime for all ranges of the  $\alpha$ . Afterward, we observed that the increase in  $\alpha$  with fixed  $\beta$  leads to the transformation of the unstable phase to the stable phase. However, increment of  $\beta$  for fixed  $\alpha$  results in the transformation from stable to unstable. The  $\alpha - \beta$  phase diagram clearly indicates the emergence of the more stable regime for repulsive intraspecies interaction strengths ( $\alpha$ ). On the other hand, the  $k_L - \Omega$  phase diagram shows the instability regimes (see right side Fig.6). For zero Rabi coupling ( $\Omega = 0$ ) as  $k_L$  is increased initially, the stable

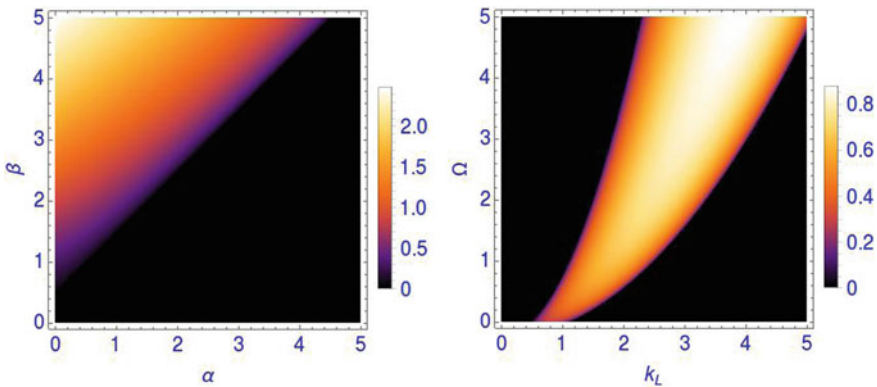


**Fig. 6** Stability and instability phases in the  $\alpha - \beta$  (left) and  $k_L - \Omega$  (right) parameter space. The fixed parameters in the left are  $\Omega = k_L = 1$  and in the left are  $\alpha = \beta = 1$ . The pseudo colour represents the  $G$  value

phase is observed, which becomes unstable for  $0.5 < k_L < 1.0$ . For  $k_L > 1.0$ , the system returns back to the stable regime. In the same line, all range of Rabi coupling behaves, which suggests that upon increasing SO coupling with fixed Rabi coupling we will have some intermediate instability regime for a short range. Recently such types of intermediate ground state phase is reported in the Ref. [15].

## 6 Conclusion

Using the Bogoliubov-de-Gennes analysis, we have analyzed the effect of the interaction and coupling parameters on the stability of the collective excitation spectrum of the SO and Rabi coupled binary BECs in quasi-one dimension. We have computed the single-particle as well the collective excitation spectrum. The absolute value of the imaginary part of the negative eigenenergy of the excitation spectrum has been used to characterize the stability of the spectrum. Our analysis shows that the increase in the SO coupling ( $k_L$ ) leads to the conversion of the single and multi-instability bands to the stable state. However, increase in Rabi coupling resulted the instability having a single-band nature. The increase in  $\alpha$  also changes the multiple instability band into single band which finally converts into stable one for strong repulsion. However, increase in  $\beta$  keeping other parameters fixed yields multiple unstable bands from a stable state. Only the amplitude to instability increases. Finally, we have obtained a stability phase diagram in  $\alpha - \beta$  and  $\Omega - k_L$  parameter space. We found that increase in  $\beta$  for a fixed value of  $\alpha$  leads the system to enter from a stable to unstable region while the effect of the increase in  $\alpha$  for fixed  $\beta$  is opposite. Similarly, we find that increase in  $k_L$  for fixed  $\Omega$  brings the system from stable to unstable phase while behavior is opposite as  $\Omega$  is increased for fixed  $k_L$ . The essential observation is that upon the increase in  $\Omega$  and  $\alpha$  alone makes the system more stable, however, increase in  $k_L$  and  $\beta$  transformed the system from stable to unstable one.

## 7 Appendix A: Elements of the BdG Matrix

$$\begin{aligned}
 H_1 &= \frac{k_x^2}{2} + k_L k_x + 2\alpha n_\uparrow + \beta n_\downarrow; & H_2 &= \frac{k_x^2}{2} - k_L k_x + 2\alpha n_\uparrow + \beta n_\downarrow \\
 H_3 &= \frac{k_x^2}{2} - k_L k_x + 2\alpha n_\downarrow + \beta n_\uparrow; & H_4 &= \frac{k_x^2}{2} + k_L k_x + 2\alpha n_\downarrow + \beta n_\uparrow
 \end{aligned}$$

and

$$\mu = \frac{1}{2} \left[ \alpha n + \beta n - \Omega \frac{n}{\sqrt{n_\uparrow n_\downarrow}} \right]$$

## 8 Appendix B: Coefficients of the BdG Excitation Spectrum

$$a = -\frac{k_x^4}{2} - 2\Omega(\alpha - \beta + 2\Omega) - k_x^2(\alpha + 2(k_L^2 + \Omega))$$

$$b = \frac{1}{16}k_x^2(k_x^2 + 2\alpha - 2\beta - 4k_L^2 + 4\Omega)(k_x^4 + 8(\alpha + \beta)\Omega + 2k_x^2(\alpha + \beta - 2k_L^2 + 2\Omega))$$

**Acknowledgements** Supported by DST-SERB (Department of Science and Technology - Science and Engineering Research Board) for the financial support through Project No. ECR/2017/002639.

## References

1. Pethick, C.J., Smith, H.: Bose-Einstein Condensation in Dilute Gases, 2nd edn. Cambridge University Press, Cambridge (2008)
2. Ho, T.-L.: Spinor Bose condensates in optical traps. *Phys. Rev. Lett.* **81**, 742 (1998)
3. Li, Y., Hai, W.: Three-body recombination in two coupled Bose-Einstein condensates. *J. Phys. A: Math. Gen.* **38**, 4105–4114 (2005)
4. Wang, Z., Zhang, X.: Ke Shen, Unstable cycle of two coupled bose-einstein condensates with three-body interaction. *J. Low Temp. Phys.* **152**, 136–146 (2008)
5. Sudharsan, J.B., Radha, R., Muruganandam, P.: Collisionally inhomogeneous Bose-Einstein condensates with binary and three-body interactions in a bichromatic optical lattice. *J. Phys. B: At. Mol. Opt. Phys.* **46**, 155302 (2013)
6. Lin, Y.J., García, K.J., Spielman, I.B.: Spin-orbit coupled Bose-Einstein condensates. *Nature (London)* **471**, 83 (2011)
7. Campbell, D.L., Juzeliūnas, G., Spielman, I.B.: Realistic spin-orbit and Dresselhaus spin-orbit coupling for neutral atoms. *Phys. Rev. A* **84**, 025602 (2011)
8. Bogolyubov, N.N.: On the theory of superfluidity. *J. Phys. (USSR)* **11**, 23 (1947)
9. Zilsel, P.R.: Liquid Helium II: the hydrodynamics of the two-fluid model. *Phys. Rev.* **79**, 309 (1950)
10. Khamehchi, M.A., Zhang, Y., Hamner, C., Busch, T., Engels, P.: Measurement of collective excitations in a spin-orbit-coupled Bose-Einstein condensate. *Phys. Rev. A* **90**, 063624 (2014). <https://doi.org/10.1103/PhysRevA.90.063624>
11. Li, Y., Martone, G.I., Pitaevskii, L.P., Stringari, S.: Superstripes and the excitation spectrum of a spin-orbit-coupled Bose-Einstein condensate. *Phys. Rev. Lett.* **110**, 235302 (2013). <https://doi.org/10.1103/PhysRevLett.110.235302>
12. Ozawa, T., Pitaevskii, L.P., Stringari, S.: Supercurrent and dynamical instability of spin-orbit-coupled ultracold Bose gases. *Phys. Rev. A* **87**, 063610 (2013)
13. Ravisankar, R., Sriraman, T., Salasnich, L., Muruganandam, P.: Quenching dynamics of the bright solitons and other localized states in spin-orbit coupled Bose-Einstein condensates. *J. Phys. B: At. Mol. Opt. Phys.* **53**, 195301 (2020). <https://doi.org/10.1088/1361-6455/aba661>
14. Ravisankar, R., Fabrelli, H., Gammal, A., Muruganandam, P., Mishra, P. K.: Effect of Rashba spin-orbit and Rabi couplings on the excitation spectrum of binary Bose-Einstein condensates. *Phys. Rev. A* **104**, 053315 (2021). <https://doi.org/10.1103/PhysRevA.104.053315>
15. Ravisankar, R., Sriraman, T., Kumar, R.K., Muruganandam, P., Mishra, P.K.: Influence of Rashba spin-orbit and Rabi couplings on the miscibility and ground state phases of binary Bose-Einstein condensates. *J. Phys. B: At. Mol. Opt. Phys.* **54**, 225301 (2021). <https://doi.org/10.1088/1361-6455/ac41b2>

# Empirical Models for Premiums and Clustering of Insurance Companies: A Data-Driven Analysis of the Insurance Sector in India



Rakshit Tiwari  and Siddhartha P. Chakrabarty 

**Abstract** The article deals with the modeling of insurance premiums and their clustering, from the paradigm of the Indian insurance sector, during a 15 year period, using data-driven regression and clustering techniques. Among three approaches considered for the predictive modeling of insurance premiums, the most effective method was determined to be the random forest approach. Interesting insights for the pre and post 2008 (financial crisis) period, revealed distinct clustering characteristics between the private and public sector insurance companies operating in India, especially in terms of consumer behavior.

**Keywords** Insurance premium · Machine learning · Regression · Clustering

## 1 Introduction

Since the solvency of an insurance company is driven by its ability to generate premiums, which must exceed the expected claims payout and other liabilities, therefore it is essential to develop predictive models of both the premium receipts, as well as the claims losses. Our analysis in this article is motivated by the somewhat minimal literature available in case of the former, as compared to the latter. The role of actuaries, while developing pricing strategies, is to assess a fair price for the insurance products they wish to sell. This however, has to be done in a manner so as to fulfill the outstanding liabilities of the insurance company, while safeguarding its solvency and reserve capital. Consequently, the actuaries must predict, with maximum possible accuracy, the total amount required to meet the claims payout. These reserves form the principal item on the insurance company's balance sheet's liability side and thus have a significant economic impact.

---

R. Tiwari · S. P. Chakrabarty (✉)  
Indian Institute of Technology Guwahati, Guwahati 781039, Assam, India  
e-mail: [pratim@iitg.ac.in](mailto:pratim@iitg.ac.in)

R. Tiwari  
e-mail: [rakshit10@alumni.iitg.ac.in](mailto:rakshit10@alumni.iitg.ac.in)

© The Author(s), under exclusive license to Springer Nature Switzerland AG 2022  
S. Banerjee and A. Saha (eds.), *Nonlinear Dynamics and Applications*,  
Springer Proceedings in Complexity,  
[https://doi.org/10.1007/978-3-030-99792-2\\_110](https://doi.org/10.1007/978-3-030-99792-2_110)

1299

In this article, we perform statistical and data analysis, on the premium data collected from the website of the Insurance Regulatory Development Authority of India (IRDAI) [1], with the objective of developing predictive models for the monthly premium collection of the insurance companies included in our dataset. The dataset available on the website of IRDAI were for 13 different companies, namely, *Royal Sundaram, Tata-AIG, Reliance General, IFFCO-Tokio, ICICI-lombard, Bajaj Allianz, HDFC CHUBB, Cholamandalam, New India, National, United India, Oriental and ECGC*.

The data that we use in this article, consists of the monthly premium amounts collected during the period of April 2003 to Dec 2017, for these 13 insurance companies mentioned above. We note here, that more detailed data was not available. Also, the issue of some anomalies and errors in some of the cells of the considered dataset, was addressed, by removing the erroneous data, so as to achieve the best possible results. Further, during the process of building a machine learning model, we followed the standard practice of training and then back-testing the model on the untrained part of the dataset. Accordingly, the training set comprised of 80% of the total data points, while the remaining 20% of the data points was used for back-testing the results, as well as finding the mean squared and root mean squared error, for comparative analysis across several types of models. The key aspect in this analysis is not just about building mathematical models, for finding results using the same, but to explain those results with the help of real life comparisons which have been discussed towards the end of the article.

Most of the modeling approaches in actuarial mathematics focus on the determination of the distribution that best fits the data. In a recent work [2], a dependent modeling framework is adopted for predictive distribution with accuracy in case of frequencies, as well as claims score, pertaining to insurance claims. In another distribution driven article [3], the authors make use of a tweedie compound Poisson model to achieve a robust prediction performance for premiums. The classification of applicants, for risk prediction in life insurance sector, is carried out by way of the supervised learning approach in [4].

## 2 Predicting the Monthly Premium Amount

We will approach the problem of predicting the monthly premium amount received by each insurance company, making use of three commonly used machine learning models. Further, we implement the models in terms of its increasing level of complexity, in order to understand whether this results in the concurrent improvement in terms of the backtesting results. The eventual goal is to ascertain whether the models and their predictive results obtained here, would be helpful in obtaining a viable prediction mechanism, for forecasting the premium amounts in the future. Accordingly, we will make use of three models, as outlined in the following subsections.



### 2.1 Linear Regression

The basis for *linear regression* model is the assumption that there exists a linear relationship between a dependent (output) variable  $y$  and several independent (input) variables  $x_1, x_2, \dots, x_n$  [5, 6]. A univariate or simple linear regression model is one where there is only one input variable, while linear regression models with multiple input variables is termed as multiple linear regression model. The most common approach of obtaining a linear regression equation, from observed data is the method of *least squares regression*. The coefficients in case of both multiple, as well single regression model, can be obtained by minimizing the sum of the least squared errors, which can be defined as  $\epsilon_i = y_i - \hat{y}_i$ , where the variable  $y$  has  $n$  observed (predicted) values, say  $y_i$  ( $\hat{y}_i$ ),  $i = 1, 2, \dots, n$ . For the sake of brevity, we state the results for multiple linear regression which can subsequently be used in case of polynomial regression model. Accordingly, we let,

$$\vec{y} = \begin{pmatrix} y_1 \\ y_2 \\ \vdots \\ y_n \end{pmatrix}, X = \begin{pmatrix} 1 & x_{11} & x_{12} & \cdots & x_{1k} \\ 1 & x_{21} & x_{22} & \cdots & x_{2k} \\ \vdots & \vdots & \vdots & \vdots & \vdots \\ 1 & x_{n-11} & x_{n-12} & \cdots & x_{n-1k} \end{pmatrix}, \vec{\beta} = \begin{pmatrix} \beta_1 \\ \beta_2 \\ \vdots \\ \beta_k \end{pmatrix} \text{ and } \vec{\epsilon} = \begin{pmatrix} \epsilon_1 \\ \epsilon_2 \\ \vdots \\ \epsilon_n \end{pmatrix}.$$

The multiple linear regression thus can be represented in the form,

$$\vec{y} = X \vec{\beta} + \vec{\epsilon}.$$

The least-squares regression approach is used to estimate the parameter  $\vec{\beta}$  by minimizing,

$$\sum_{i=1}^n \epsilon_i^2 = (\vec{y} - X \vec{\beta})^\top (\vec{y} - X \vec{\beta}),$$

which then results in,

$$\widehat{\vec{\beta}} = (X^\top X)^{-1} X^\top \vec{y}.$$

Note that the methods of regularization, is used to modify the learning algorithm (so as to achieve reduction in complexity of the regression models) by placing pressure on the absolute size of the coefficients, thereby reducing some of the coefficients to zero.

### 2.2 Polynomial Regression

We next, seek to address a key shortcoming of the linear model, namely the under-fitting, by increasing the complexity of the model, and the natural choice for the

same is to add higher powers, resulting in higher order equations [6]. Accordingly, the linear model obtained above is now represented as,

$$y_i = \sum_{j=1}^m x_i^j + \epsilon_i, \quad i = 1, 2, \dots, n.$$

Even though terms like  $x_i^j$  are present in the model, the coefficients are still linear. However, the curve we fit is going to be polynomial in nature. Therefore, *polynomial regression* is a type of linear regression in which the relationship between the input variable and output variable, is modeled as a polynomial of  $m$ -th degree. Polynomial regression matches a nonlinear relationship between the value of the input variable  $x$  and the corresponding conditional mean of the output variable  $y$ , denoted as  $E(y|x)$ . An interesting point that was observed while working with polynomial regression model, is the accuracy of the results (or equivalently, the reduction in absolute error) while back-testing results, as we select higher degree polynomials. A naive approach of selecting degree 2 polynomials till degree 10 polynomials was tested, and the same was confirmed.

### 2.3 *Random Forest Regression*

Random forest, as the nomenclature suggests, comprises of a large collection of decision trees which act collectively [7]. Each individual tree of the random forest outputs a prediction of class, with the one gaining the most votes, taken as the prediction of the model. The rationale for this impact is that the trees protect one other from their individual incorrectness (provided they do not all fail in a concurrent and consistent manner). While some trees might be incorrect, many other trees would be correct, and consequently, the trees will move in the correct direction, collectively. In our case below, we started with 10 decision trees, since this is the default value in sklearn.ensemble library [8] and slowly increased the value so that the model can learn and adapt from the training set and make better decisions.

## 3 Procedure

In this Section, we present the approach for predicting the monthly premium as elaborated in Sects. 2.1, 2.2 and 2.3.

### 3.1 *Predicting Monthly Premiums*

We will discuss the methods that were used primarily to obtain the results reported in this article. The first step was the filtering of data containing approximately 2000 data points, in order to remove the anomalies. Our main focus then was to judge the fitness of models on the test data and to suggest ways that can be used by the actuaries for projecting the growth of premiums received by the insurance firms in the future. Three modeling methods have been used in this article as described above in Sect. 2, with one of them distinctly emerging as the best choice, because of a substantial difference obtained in the mean absolute error while back-testing. Some of the standard practices of machine learning that have been used in this article are:

1. The data considered was divided in the ratio 4 : 1, between the training and the testing sets which is the standard approach adopted for machine learning programs. Also, due to the lack of availability of extensive data, as well as for the generation of a fully functional model, it is important to prioritize our limited resources, for training the model first.
2. As already noted, the data provided, comprised of monthly premiums collected across a span of 15 years. For regression purposes, we have taken the help of date ordinals, which are the standard hashed values of dates used in machine learning.
3. One of the other challenges while modeling, pertained to the choice of the degree of polynomial being used in the polynomial regression model. All polynomials from degree 2 to degree 10, were chosen one by one, and the degree which gave the least absolute error during back-testing was finally chosen.
4. Number of estimators/decision trees chosen in the random forest model was equal to 1000.

### 3.2 *Predicting the Optimum Number of Clusters for Clustering*

1. An appropriate data-frame of monthly premiums was formed to carry out the basic *K-Means clustering* [9].
2. The purpose of going forward with a basic clustering algorithm and not any advanced clustering algorithms, lies in our regression results. Since the data did not exhibit any absurd patterns, it was an optimum choice for carrying out the clustering experiment with basic algorithms.
3. In order to determine the optimum number of clusters, we used the standard *Elbow Method* [9]. The results obtained during this experiment can be seen in Sect. 4. The value of optimum clusters obtained is 2.
4. Using the same result, going forward and applying K-Means algorithm, we obtained 2 group of companies. The results obtained were on expected lines, as it segregated the 13 companies into 2 groups primarily based on their positive or negative growth of monthly premiums.

5. In order to examine the results of this experiment in a more elaborate manner, we worked around with cluster size of 3 and 4 also. This helped us in segregating organizations even further on their growth/product quality.

## 4 Results

This Section is entirely dedicated to the presentation of the results that were obtained from the data considered, and the models we have enumerated in Sect. 3. The results of the regression modeling using the random forest algorithm are presented in Fig. 1a–m, where the consistently superior performance of the random forest algorithm can be easily observed.

Using K-Means Clustering and Elbow method for finding optimum number of clusters, we were assured of that there are two optimum number of clusters present in the dataset considered, into which, we can segregate the enumerated insurance companies. Using the Elbow method, we obtained the first cluster comprising of eight companies, namely, Royal Sundaram, Tata-AIG, Reliance General, IFFCO-Tokio, ICICI-Lombard, Bajaj Allianz, HDFC CHUBB and Chalamandalam, all of which are private sector companies. The second cluster comprises of the remaining five companies, that is, New India, National, United India, Oriental and ECGC, all of which are public sector companies. The sum of the squared distances against the number of clusters are presented in Fig. 2.

When we experimented with the clustering of the companies, using different cluster sizes, we observed that the existing partition of size two, in the preceding paragraph, gets further sub-divided, on the basis of better/good performance or better/worse performance. With the number of clusters being three, the first cluster includes, Royal Sundaram, Tata-AIG, Reliance General, IFFCO-Tokio, ICICI-Lombard, Bajaj Allianz, HDFC CHUBB and Chalamandalam. The eight companies, included in the first list for three clusters, were all included in the first list for two clusters. These eight are the group of companies, who have shown an impeccable growth in period of 15 years that have been considered. The second cluster, now, comprises of four companies, namely, New India, National, United India and Oriental. These can be described as those players who suffered a major setback in 2008 but are showing signs of revival, since then. Finally, the third cluster in this case, includes just one company, that is, ECGC. It is observed from the data, that ECGC is the only company that has failed to achieve visible revival, after going through setbacks as a result of the 2008 financial crisis.

In case of cluster of size four, the first cluster includes ICICI-Lombard and Bajaj Allianz. These two companies are the ones who have an outstanding growth chart when compared to the other six companies that are in the positive growth cluster. The remaining six companies namely Royal Sundaram, Tata-AIG, Reliance General, IFFCO-Tokio, HDFC CHUBB, Chalamandalam are now a part of the second cluster out of the four clusters. The third cluster, comprises of the same cluster of public comprises, that formed the second cluster in case of three clusters, namely, New

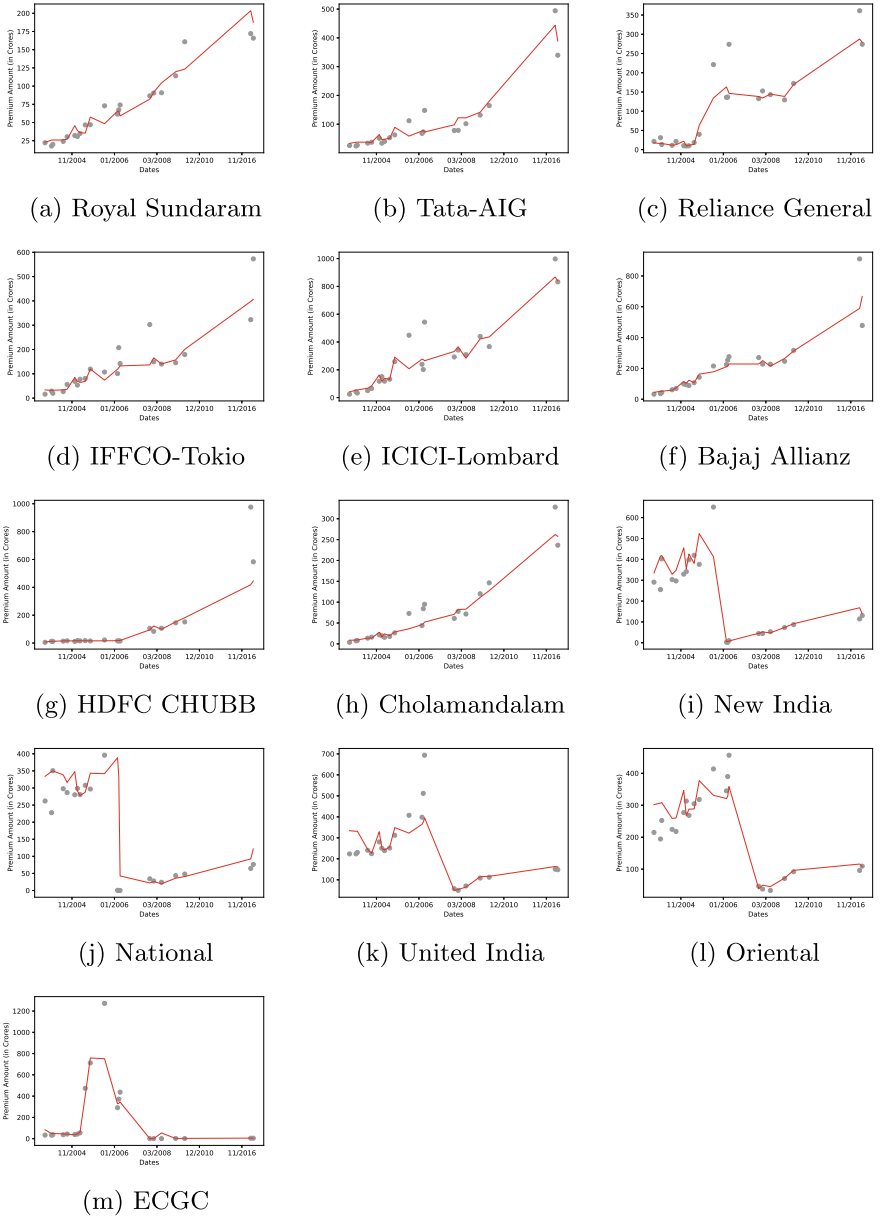


**Fig. 1** The fit to data of all the 13 insurance companies using the Random Forest Algorithm.

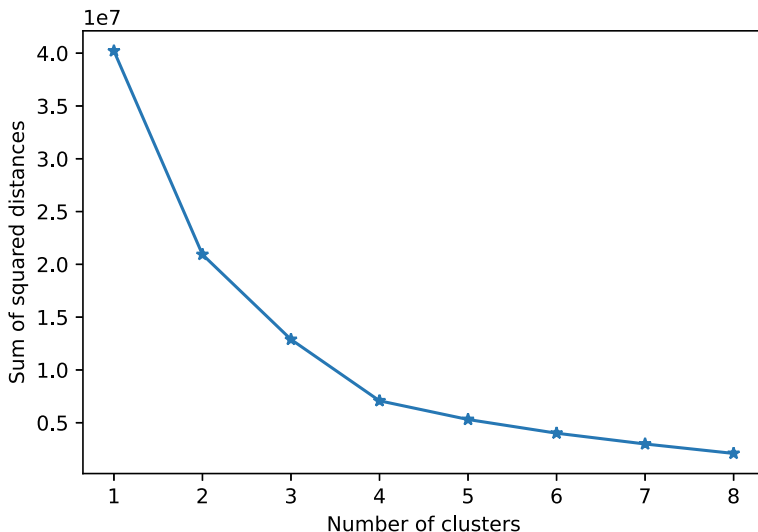


Fig. 2 The sum of squared distances against the number of clusters using the Elbow Method

India, National, United India, Oriental. Consequently, ECGC is the only company in the last of the four clusters. We observe that, the third and fourth cluster in this case, is identical to the last two clusters for the previous case of three clusters.

### 5 Discussion

It is clear that in the 15 years, for which the data was considered, the first group of companies (**for the two-cluster case**) have shown a tremendous growth, while the opposite has happened in case of the second group of companies. There are several reasons to which this happenings can be attributed to, which will be elaborated upon, in the following discussion.

One of the things that we can look at, with the help of the models, is the accuracy of our back-testing results which exhibits improvement with the increasing complexity of the model. Table 1 depicts the mean absolute error obtained using the Linear Regression (LR), Polynomial Regression (PR) and the Random Forest (RF), model in Crores.<sup>1</sup> The error data obtained from the first eight companies confirms that random forest is indeed the best model being used to predict premium amount collections in our case. Meanwhile, when we first look at the error data of last five columns in Table 1, it suggests a completely different narrative, which is actually not the case. A close look at Fig. 3 above for these companies itself, one can see a huge spike (down-fall) right around the 2007–09 period, which results in the outliers. In the context of

<sup>1</sup> 1 Crore=10 Million.

**Table 1** Mean Square Error of the Three Regression Algorithms (in Crores) for all the thirteen insurance companies

Company name	Linear regression	Polynomial regression	Random forest
Royal Sundaram	14.15	14.13	10.33
Tata-AIG	38.09	14.895	17.89
Reliance General	40.09	26.25	23.07
IFFCO-Tokio	43.61	33.15	30.79
ICICI-Iombard	77.86	41.51	40.54
Bajaj Allianz	52.93	47.88	30.14
HDFC CHUBB	92.70	32.47	37.43
Cholamandalam	25.52	12.05	11.57
New India	120.23	294.25	321.45
National	86.98	258.92	253.53
United India	105.25	197.25	197.71
Oriental	88.52	195.62	200.93
ECGC	243.73	261.99	313.92

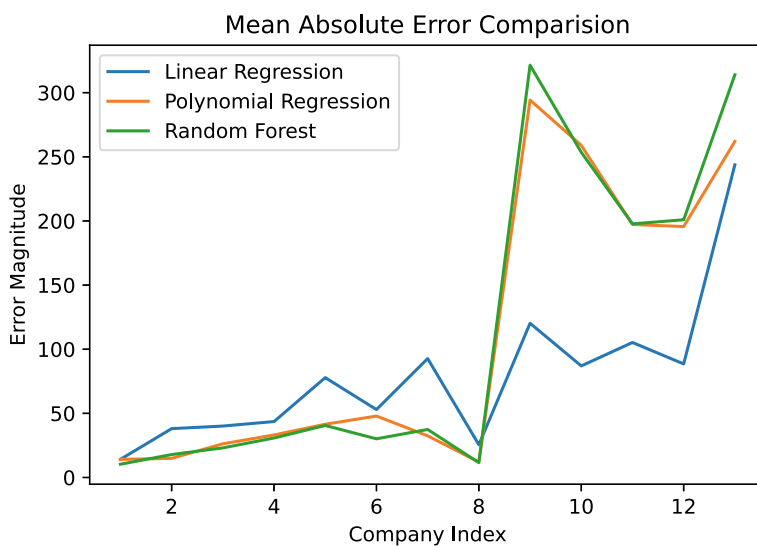


**Fig. 3** Comparison of the Mean Absolute Error using the three methods

the discussion, outliers comprise of values which exhibit significant deviation from the other data points. This deviation could be attributed to measurement inaccuracies and flaws in the experimental design, among other considerations. An outlier can be viewed as a deviation from the general trend. It is because of this reason, the data analysis obtained provides an inaccurate picture and we should rather look the graphs for judging the fitness of data, in the case of Random Forest. Accordingly, the graphical comparison is shown in Fig. 3, which highlights the heavy downfall experienced by the second group of companies (for the indices 9 – 13 in the figure), where because of outliers (as discussed above), one can observe a large deviation from truth. Also, the errors presented in Table 1 looks large, when someone discusses all these figures in Crores. The point that should be noted along with this, is that the typical figures for the monthly premium being collected is in the range of 300 – 800 Crores (as provided in our dataset), which, consequently, gives us a relative error close to 1 – 3%.

The purpose of this article is not only restricted to the determination of mathematical validity of the model to ascertain the best one, but also to effectively we can correlate the right real world reasons with what can be ascribed to the dataset. Talking first about the companies which belonged to the second cluster, one can note that they are being differentiated from other companies primarily because of the lack of growth in the last 15 years. Once we started taking a deep dive into it, which in our observation can be attributed to:

1. **Marketing:** For organizations that extensively require new customers and making sure that old customers stay onboard, one can clearly see the companies in first cluster spending extensively on marketing especially in metropolitan states which is a huge reason for their growth post the 2008 crisis. These organizations have gone out of their way, post the financial crisis to instill a deep trust between the people for using their insurance advisory.
2. **Technology:** The world is run on applications today. It is important for all the banks and financial businesses to have an online presence. Those organizations who are not having an application/website where customers can come and get the job done in one click, have faced a huge downfall must similar to what is being faced by the second cluster of companies. It may be noted that, ICICI Lombard and Bajaj Allianz are leaders, when it came to adoption of technology into their operation, especially the customer interface. In addition, both these organizations have also invested substantially on social marketing to propel their businesses online.

## References

1. IRDAI monthly insurance data. [https://www.irdai.gov.in/ADMINCMS/cms/frmGeneral\\_List.aspx?DF=MBFN&mid=3.2.8](https://www.irdai.gov.in/ADMINCMS/cms/frmGeneral_List.aspx?DF=MBFN&mid=3.2.8)
2. Lee, G.Y., Shi, P.: A dependent frequency-severity approach to modeling longitudinal insurance claims. *Insur.: Math. Econ.* **87**, 115–129 (2019)



3. Yang, Y., Qian, W., Zou, H.: Insurance premium prediction via gradient tree-boosted Tweedie compound Poisson models. *J. Bus. Econ. Stat.* **36**(3), 456–470 (2018)
4. Boodhun, N., Jayabalan, M.: Risk prediction in life insurance industry using supervised learning algorithms. *Complex Intell. Syst.* **4**(2), 145–154 (2018)
5. Schneider, A., Hommel, G., Blettner, M.: Linear regression analysis: part 14 of a series on evaluation of scientific publications. *Deutschesrztblatt Int.* **107**(44), 776 (2010)
6. Ostertagova, E.: Modelling using polynomial regression. *Procedia Engineering* **48**, 500–506 (2012)
7. Liaw, A., Wiener, M.: Classification and regression by randomForest. *R news* **2**(3), 18–22 (2002)
8. Pedregosa, F., Varoquaux, G., Gramfort, A., Michel, V., Thirion, B., Grisel, O., Duchesnay, E.: Scikit-learn: machine learning in python. *J. Mach. Learn. Res.* **12**, 2825–2830 (2011)
9. Yuan, C., Yang, H.: Research on K-value selection method of K-means clustering algorithm. *Journal* **2**(2), 226–235 (2019)

# Variations in the Scroll Ring Characteristics with the Excitability and the Size of the Pinning Obstacle in the BZ Reaction



Puthiyapurayil Sibeesh , S V Amrutha , and T K Shajahan 

**Abstract** We report the experimental results of the effects of excitability on the wave characteristics of free rotating and pinned scroll rings in the Belousov-Zhabotinsky (BZ) reaction. The experiments show that the stability of the scroll ring depends on the excitability of the medium. At low excitability, the scroll ring becomes less stable and eventually breaks up. As we increase the excitability of the medium, the time period ( $T$ ) and wavelength ( $\lambda$ ) of the excitation wave decrease while wave velocity ( $v$ ) increases. Properties of both free and pinned scroll rings change in the same way. However, at a given excitability, both the  $\lambda$  and  $v$  of a pinned scroll ring increase with the size of the obstacle. For the range of parameters chosen in our experiments, the excitability changes brought by varying reactant concentrations have a higher impact on the scroll ring properties than those induced by the size of the pinning obstacle.

**Keywords** BZ reaction · Scroll wave · Excitability · Pinning

## 1 Introduction

Excitable media support nonlinear waves that propagate as target, spiral, or scroll waves. Such waves are observed in many diverse systems including in the aggregation of *Dictyostelium discoideum* amoeba [1], the chicken retina [2], the brain [3] and the cardiac tissues [4], the Belousov-Zhabotinsky (BZ) chemical reaction [5], and the oxidation of CO on Pt surfaces [6]. In physiological tissue such self sustained spiral and scroll waves can lead to life-threatening dynamical diseases such as cardiac arrhythmias [7] or epilepsy [8].

A scroll wave is a three-dimensional manifestation of a rotating spiral wave found in the two-dimensional excitable media. While the spiral wave rotates around a single point at the tip of the spiral, the scroll wave rotates around a one-dimensional filament.

---

P. Sibeesh · S. V. Amrutha · T. K. Shajahan (✉)  
Department of Physics, National Institute of Technology Karnataka Surathkal,  
575025 Mangalore, India  
e-mail: [shajahan@nitk.edu.in](mailto:shajahan@nitk.edu.in)

© The Author(s), under exclusive license to Springer Nature Switzerland AG 2022  
S. Banerjee and A. Saha (eds.), *Nonlinear Dynamics and Applications*,  
Springer Proceedings in Complexity,  
[https://doi.org/10.1007/978-3-030-99792-2\\_111](https://doi.org/10.1007/978-3-030-99792-2_111)

1311

These filaments take the shape of a straight line or a circular ring. A scroll wave with a straight filament is a stack of two-dimensional spiral waves in parallel [9, 10]. A scroll wave with a circular closed loop as the filament is called a scroll ring. The curvature of the ring induces motion of the filament such that its radius becomes smaller and leads to the self-annihilation of the scroll ring. The collapse or shrinkage of a free scroll ring can be delayed by modifying the medium parameters. In an excitable medium, the life span of a scroll ring is short. Pinning the scroll filament to medium heterogeneities can elongate the lifetime of scroll waves [11].

The BZ reaction is one of the simplest laboratory models used to the study excitable media in which the excitation waves can be observed with naked eyes. Despite the fact that the BZ reaction is far less complex than heart tissue or any other excitable medium, they all possess similar dynamical behavior. Because of this similarity in the dynamics of excitation waves, we employ the BZ reaction as a model medium to investigate the dynamics of scroll rings. Previous studies reported that the properties of a spiral wave in a two-dimensional BZ medium modify according to the medium excitability [12], the size, and the shape of the pinning obstacle [13, 14]. The excitability of the BZ medium can be controlled by varying the initial concentrations of reactants [12]. Simulations with the Oregonator model have shown that both wave period and wavelength of a scroll wave decrease with increasing the excitability [15]. To the best of our knowledge, the dynamics of the scroll ring with the excitability and the size of the pinning obstacle is not reported so far. This article reports the dynamics of both free and pinned scroll rings in the BZ reaction by varying the excitability and the size of the pinning obstacle. In our experiments, we observed a breakup of a scroll ring filament at very low excitability. Our experimental observations show that the frequency and the wave velocity of a scroll ring increase with the excitability, whereas the wavelength decreases. As the size of the pinning obstacle increases, the time period ( $T$ ), wavelength ( $\lambda$ ), and wave velocity ( $v$ ) of a scroll ring increase for a given excitability.

## 2 Experimental Methods

We conducted experiments in chemically identical double layers of ferriin - catalyzed BZ reaction as given in [9]. Each layer of thickness 4 mm is embedded in 1.4 % w/v of agar. We performed experiments with initial concentrations of reactants as following:  $[\text{H}_2\text{SO}_4] = 0.25\text{--}0.75$  M,  $[\text{NaBrO}_3] = 1$  M,  $[\text{MA}] = 1$  M,  $[\text{SDS}] = 0.0245$  M,  $[\text{Ferriin}] = 0.025$  M. All the experiments were carried out at constant room temperature.

Spherical glass beads of diameters varying from 2 mm to 5 mm were used to pin the scroll waves. During the gelation of the first layer, two glass beads of the same size were symmetrically inserted halfway into the surface. A half-spherical wave was initiated at the center of the line joining the two glass beads by inserting the tip of a properly cleaned silver wire for a few seconds. The second layer is added above

**Fig. 1** Schematic diagram of the experiment setup: The BZ reaction medium is represented in red colour. A charge-coupled device camera kept above the medium captures the images of the reaction medium. Light source placed below enhances the imaging



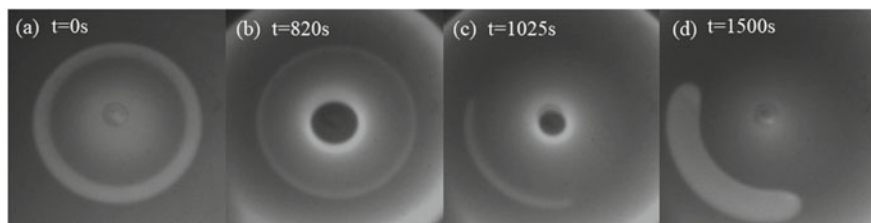
the first layer when the wavefront touches the glass beads. The half-spherical wave at the lower layer curl upwards and forms a scroll ring pinned to both the beads.

Ferriin indicator undergoes striking color difference during each excitation cycle, which allows for the optical detection of the excitation waves. The experimental medium was illuminated using a diffused white light placed below to monitor the chemical waves. The images were captured by a charge-coupled device (CCD) camera (mvBlueCougarx 120bc) positioned above the medium. A blue filter (MidOpt BP470-27) was mounted on the camera to increase the contrast between the excitation waves and the unexcited medium. The images were recorded onto a computer at 2 frames/seconds with the help of LabVIEW and the data analyzed using software developed in Python. Figure 1 depicts the schematic representation of the experiment setup.

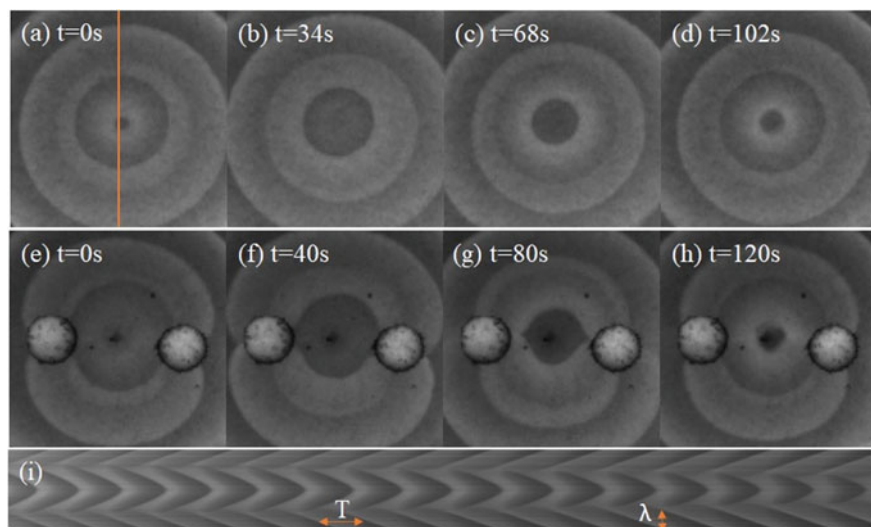
### 3 Results and Discussion

We explored the behavior of free rotating and pinned scroll rings by increasing the excitability of the BZ reaction medium. The excitability of the BZ reaction medium can be controlled by varying the concentration of the reactants ( $[H_2SO_4]$  or  $[NaBrO_3]$ ).

To vary the excitability of the medium in our experiments, we adjusted the concentration of  $H_2SO_4$  from 0.25 M to 0.75 M while maintaining the concentrations of the other reactants constant. According to the relationship suggested by Jahnke et al. [16] the excitability of the medium increases with an increase in the concentration of  $H^+$ . In a low excitable medium with  $[H_2SO_4] = 0.25$  M, the filament of a scroll ring breaks up within a short duration of time. Figure 2 represents the time evolution of a free scroll ring induced in a low excitable medium. The scroll ring breaks by the time  $t=1025s$  as shown in Fig. 2c.



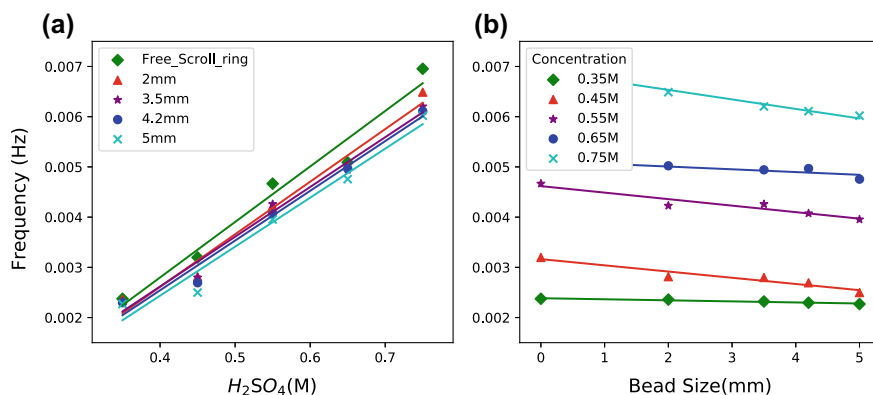
**Fig. 2** Scroll ring break up at low excitability ( $[\text{H}_2\text{SO}_4] = 0.25 \text{ M}$ ): Snapshots of a free rotating scroll ring. A complete scroll ring (a) at  $t = 0 \text{ s}$  (b) at  $t = 820 \text{ s}$  (c) the scroll ring breaks at  $t = 1025 \text{ s}$  (d) the broken scroll ring at  $t = 1500 \text{ s}$



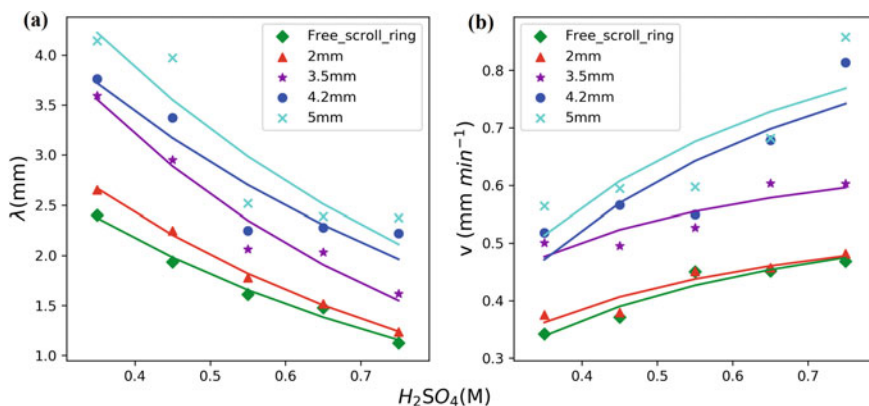
**Fig. 3** Time evolution of Scroll rings and the space time plot of the free scroll ring in BZ reaction medium ( $[\text{H}_2\text{SO}_4] = 0.75 \text{ M}$ ). (a)–(d) Free rotating, scroll ring (e)–(h) Scroll ring pinned to two spherical glass beads of diameter  $3.5 \text{ mm}$  (i) Space-time plot generated for the free rotating scroll ring along a vertical line at the center of each image in the experiment. It spans a time interval of  $41 \text{ min}$

Figure 3a–d show the snapshots of the time evolution of a free rotating scroll ring and Fig. 3e–h show snapshots of the time evolution of a scroll ring pinned to two glass beads of diameter  $3.5 \text{ mm}$  at  $[\text{H}_2\text{SO}_4] = 0.75 \text{ M}$ . Figure 3i is a space-time plot that is obtained for the free rotating scroll ring along the central vertical line (orange line in a) of the captured images for a duration of  $41 \text{ min}$ .  $T$  and wavelength  $\lambda$  of the scroll rings are calculated from the corresponding space-time plot as described in [12].

As shown in Fig. 4a (green diamond line), the frequency of the scroll rings increases as the excitability increases, and that the wavelength of the scroll rings decreases as shown in Fig. 5a (green diamond curve). Similar changes are also found



**Fig. 4** Variation of scroll ring frequency with concentration of  $H_2SO_4$  and obstacle size: (a) Frequency of the scroll ring increases with excitability. Each line corresponds to scroll ring pinned to different obstacles: free rotating scroll ring (green diamond), 2 mm glass bead (red triangle), 3.5 mm glass bead (purple star), 4.2 mm glass bead (blue dot) and 5 mm glass bead (cyan cross). (b) Frequency of the scroll ring decreases with increase in obstacle size. Each line corresponds to different excitability: 0.35 M (green diamond), 0.45 M (red triangle), 0.55 M (purple star), 0.65 M (blue dot) and 0.75 M (cyan cross)



**Fig. 5** Properties of scroll ring with concentration of  $H_2SO_4$  and obstacle size: (a) Wavelength ( $\lambda$ ) of the scroll ring decreases and (b) wave velocity ( $v$ ) increases. Both quantities increases with increase in obstacle size for a particular excitability. Each curve corresponds to scroll ring pinned to different obstacles: free rotating scroll ring (green diamond), 2 mm glass bead (red triangle), 3.5 mm glass bead (purple star), 4.2 mm glass bead (blue dot) and 5 mm glass bead (cyan cross)

in two-dimensional spiral waves [12, 17]. The wave velocity is estimated as  $\lambda/T$  [13]. As excitability increases, the wave velocity of the free scroll ring increases as shown in Fig. 5b (green diamond curve). A numerical study on a scroll wave with a straight filament pinned to a cylindrical obstacle with fixed diameter and length shows a similar trend in wave characteristics [15].

The size of the pinning obstacle influences the scroll wave dynamics. According to the experimental studies in the BZ reaction, the  $T$ ,  $\lambda$  and  $v$  of a spiral wave increases with the obstacle size [13, 14]. We used glass beads of different diameters to pin the scroll rings.

As illustrated in Fig. 4 a and b, the frequency of the pinned scroll ring increases with excitability for a certain bead size but decreases as the size of the obstacle increases. For a given excitability, the  $\lambda$  and  $v$  of a pinned scroll wave increase in proportion to the size of the obstacle. On the other hand, for a scroll ring attached to a specific obstacle size,  $\lambda$  decreases as excitability rises, while  $v$  increases (Fig. 5a and b). The change in frequency associated with the change in excitability for a given bead size is more significant than the same observed with the change in bead size for a given excitability.

## 4 Conclusions

We investigated the variations in the wave properties of the three-dimensional scroll rings by varying the concentration of sulphuric acid. We looked at the dynamics of free scroll rings and scroll rings pinned to various spherical glass beads. A scroll ring is not stable in a low excitable medium as it breaks up within a short period of time after wave initiation. When excitability increases, frequency and wave velocity increases, while wavelength decreases. Previous reports indicate that the wave properties of the spirals in the two-dimensional BZ system are modified in the same manner with changes in the concentrations of sulphuric acid and sodium bromate [12]. We also studied the scroll ring properties by varying the size of the spherical glass beads that serve as the pinning obstacle. With an increase in the size of the glass beads, the scroll ring takes a longer time to complete one rotation. This delay leads to a decrease in the frequency of the scroll ring. As a result,  $\lambda$  and  $v$  increase. Our experiments reveal that the behavior of scroll rings with variations in excitability and size of pinning obstacle is similar to that of spiral waves as previously observed. However, compared to spiral waves, scroll rings are less stable in a low excitable medium. A clear understanding and quantification of variations occurring in the wave dynamics with medium inhomogeneities will have a wide range of applications in different excitable media. Because of the similarity in the mathematical equations, the excitation waves in a wide variety of excitable media behave in similar ways. We believe our findings about scroll waves in chemical excitation waves are also applicable to other excitation waves, including the excitation waves in the cardiac tissue.

**Acknowledgements** This research was partially supported by SERB (DST) early career research grant.

## References

1. Tan, T.H., Liu, J., Miller, P.W., Tekant, M., Dunkel, J., Fakhri, N.: Topological turbulence in the membrane of a living cell. *Nat. Phys.* **16**(6), 657–662 (2020)
2. Yu, Y., Santos, L.M., Mattiace, L.A., Costa, M.L., Ferreira, L.C., Benabou, K., Rozental, R.: Reentrant spiral waves of spreading depression cause macular degeneration in hypoglycemic chicken retina. *Proc. Natl. Acad. Sci.* **109**(7), 2585–2589 (2012). <https://doi.org/10.1073/pnas.1121111109>
3. Rostami, Z., Jafari, S.: Defects formation and spiral waves in a network of neurons in presence of electromagnetic induction. *Cogn. Neurodynamics* **12**(2), 235–254 (2018)
4. Kappadan, V., Telele, S., Uzelac, I., Fenton, F., Parlitz, U., Luther, S., Christoph, J.: High-resolution optical measurement of cardiac restitution, contraction, and fibrillation dynamics in beating vs. blebbistatin-uncoupled isolated rabbit hearts. *Front. Physiol.* **11**, 464 (2020)
5. Bhattacharya, S., Iglesias, P.A.: Controlling excitable wave behaviors through the tuning of three parameters. *Biol. Cybern.* **113**(1), 61–70 (2019)
6. Kundu, S., Muruganandam, P., Ghosh, D., Lakshmanan, M.: Amplitude-mediated spiral chimera pattern in a nonlinear reaction-diffusion system. *Phys. Rev. E* **103**(6), 062209 (2021)
7. Punacha, S., Shajahan, T.K.: Theory of unpinning of spiral waves using circularly polarized electric fields in mathematical models of excitable media. *Phys. Rev. E* **102**(3), 032411 (2020)
8. Kalitzin, S., Petkov, G., Suffczynski, P., Grigorovsky, V., Bardakjian, B.L., da Silva, F.L., Carlen, P.L.: Epilepsy as a manifestation of a multistate network of oscillatory systems. *Neurobiol. Dis.* **130**, 104488 (2019)
9. Jiménez, Z.A.: Dynamical behavior of scroll rings in the presence of heterogeneities in the Belousov-Zhabotinsky excitable medium (Doctoral dissertation, The Florida State University) (2012)
10. Luengviriyaa, C., Storb, U., Lindner, G., Müller, S.C., Bär, M., Hauser, M.J.: Scroll wave instabilities in an excitable chemical medium. *Phys. Rev. Lett.* **100**(14), 148302 (2008). <https://link.aps.org/doi/10.1103/PhysRevLett.100.148302>
11. Das, N.P., Mahanta, D., Dutta, S.: Unpinning of scroll waves under the influence of a thermal gradient. *Phys. Rev. E* **90**(2), 022916 (2014). <https://link.aps.org/doi/10.1103/PhysRevE.90.022916>
12. Mahanta, D., Das, N.P., Dutta, S.: Spirals in a reaction-diffusion system: dependence of wave dynamics on excitability. *Phys. Rev. E* **97**(2), 022206 (2018). <https://link.aps.org/doi/10.1103/PhysRevE.97.022206>
13. Sutthiopad, M., Luengviriyaa, J., Porjai, P., Phantu, M., Kanchanawarin, J., Müller, S.C., Luengviriyaa, C.: Propagation of spiral waves pinned to circular and rectangular obstacles. *Phys. Rev. E* **91**(5), 052912 (2015). <https://link.aps.org/doi/10.1103/PhysRevE.91.052912>
14. Phantu, M., Sutthiopad, M., Luengviriyaa, J., Müller, S.C., Luengviriyaa, C.: Robustness of free and pinned spiral waves against breakup by electrical forcing in excitable chemical media. *Phys. Rev. E* **95**(4), 042214 (2017). <https://link.aps.org/doi/10.1103/PhysRevE.95.042214>
15. Wattanasiripong, N., Kumchaiseemak, N., Porjai, P.: Behavior of pinned scroll waves with different excitability in a simulated excitable media. *Prog. Appl. Sci. Technol.* **8**(2), 80–85 (2018). <https://ph02.tci-thaijo.org/index.php/past/article/view/243029>
16. Jahnke, W., Skaggs, W.E., Winfree, A.T.: Chemical vortex dynamics in the Belousov-Zhabotinskii reaction and in the two-variable Oregonator model. *J. Phys. Chem.* **93**(2), 740–749 (1989). <https://pubs.acs.org/doi/10.1021/j100339a047>
17. Luengviriyaa, J., Sutthiopad, M., Phantu, M., Porjai, P., Kanchanawarin, J., Müller, S.C., Luengviriyaa, C.: Influence of excitability on unpinning and termination of spiral waves. *Phys. Rev. E* **90**(5), 052919 (2014). <https://link.aps.org/doi/10.1103/PhysRevE.90.052919>



# Periodic Amplifications of Attosecond Three Soliton in an Inhomogeneous Nonlinear Optical Fiber



M. S. Mani Rajan , Saravana Veni , and K. Subramanian 

**Abstract** We show the periodic amplification of attosecond three solitons in an inhomogeneous optical fiber which is can be governed by nonlinear Schrödinger equation with higher order linear and nonlinear effects. Through AKNS method, we construct the Lax pair for higher order inhomogeneous nonlinear Schrödinger equation. Based on Lax pair, three soliton solutions are attained by means of Darboux transformation (DT) method. By properly tailoring the dispersion and nonlinear profiles, periodic amplifications of three solitons are demonstrated through some graphical illustrations. Especially, three soliton interactions are portrayed via 2D and 3D plots. Results attained through this work will be potentially useful in the field of soliton amplifications by soliton control and management. Also, we clearly observed that the impact of variable coefficients on attosecond soliton dynamics.

**Keywords** Optical solitons · Attosecond soliton · Lax pair · Darboux transformation · Soliton management · Amplification

## 1 Introduction

The controlling of optical solitons and their management in an inhomogeneous optical fiber system have been received huge attention in both theoretical and experimental research due to their enormous potential applications in long-haul communication and ultrafast signal routing systems [1–3]. The study on optical soliton shaping

---

M. S. M. Rajan (✉)

Anna University, University College of Engineering, Ramanathapuram 623513, India  
e-mail: [senthilmanirajanofc@gmail.com](mailto:senthilmanirajanofc@gmail.com)

S. Veni

Department of Physics, Amirta College of Engineering and Technology, Erachakulam Campus, Nagercoil 629901, India

K. Subramanian

Department of Physics, SRM Institute of Science and Technology, Ramapuram Campus, Chennai, India  
e-mail: [msmanirajan@aucermd.edu.in](mailto:msmanirajan@aucermd.edu.in)

and management is very important because of rapid growth of modern communication technology. In the picosecond regime, optical soliton pulse propagation in an optical fiber which governs the nonlinear Schrödinger (NLS) equation with constant coefficients [4, 5]. NLS equations are most significant models in modern nonlinear Science. However, real fiber cannot be a homogeneous in nature and because of various factors such as variation in diameter of core and lattice points, fiber medium becomes as inhomogeneous [6]. In such case, soliton propagation can be described by generalized variable-coefficient NLS equation [7]. Furthermore, there have been paid great attention on the investigation of generalized variable-coefficient NLS equations which contains dispersion, nonlinearity and some inhomogeneous terms with varying nature along the propagation axis [8]. The rapid growth of computational methods leads to the investigation for the bountiful models of nonlinear Schrödinger (NLS) with inhomogeneous terms by several researchers in various aspects like nonlinear fiber optics and nonlinear science [9, 10]. In a nonlinear fiber medium, soliton control technique can be theoretically represented by nonlinear Schrödinger model with dispersion, nonlinearity and gain or loss terms. Recently, this method of soliton control is new and important developments in the application of optical solitons for optical transmission systems which have been discussed in detail by Serkin et al. [11]. On the other hand, attosecond soliton pulses has a better performance on the transmission characteristics where higher-order linear and nonlinear effects should be taken into consideration [12].

## 2 Inhomogeneous NLS Equation with Higher Order Linear and Nonlinear Effects

To our knowledge, in real fiber systems, inhomogeneous nonlinear Schrödinger models with higher order linear and nonlinear effects are considered to describe the attosecond optical pulse transmission in an inhomogeneous fiber system. For example, in modern optical fiber communication systems, inhomogeneous profiles are varying with respect to propagation distance. Hence, we address the following generalized higher order nonlinear Schrödinger equation with variable coefficients as given below

$$i \frac{\partial E(z, t)}{\partial z} + \frac{1}{2} D_1 + \chi(z) D_2 + \beta(z) D_3 - i\gamma(z) D_4 + \delta(z) D_5 + iG(z) = 0 \quad (1)$$

where

$$D_1 = D(z) E_{tt} + 2R(z) |E|^2 E$$

$$D_2 = E_{ttt} + 6|E|^2 E_t$$

$$D_3 = E_{ttt} + 8|E|^2 E_{tt} + |E|^4 E + 4|E_t|^2 E + 6E_t^2 E^* + 2E^2 E_{tt}^*$$

$$D_4 = E_{tttt} + 10|E|^2 E_{ttt} + 10(|E|^2 E)_t + 20E^* E_t E_{tt} + 6E_t^2 E^* + 2E^2 E_{tt}^*$$

$$D_5 = E_{ttttt} + \left[ 60E^* |E_t|^2 + 50(E^*)^2 E_{tt} + 2E_{ttt}^* \right] E^2 + E \left[ 12E^* E_{tttt} + 8E_t E_{ttt}^* + 22|E_{tt}|^2 \right] + E \left[ 18E_{ttt} E_t^* + 70(E^*)^2 (E_t)^2 \right] + 20(E_t)^2 E_{tt}^* + 10E^3 \left[ (E_t^*)^2 + 2E^* E_{tt}^* \right] + 20|E|^6 E$$

$$G(z) = \frac{1}{2} \frac{W[R(z), D(z)]}{R(z), D(z)}$$

$$W[R(z), D(z)] = R(z) \frac{dD(z)}{dz} - D(z) \frac{dR(z)}{dz}$$

where  $E(z, t)$  denotes the complex envelope of incident light filed, the subscripts  $z$  and  $t$  denote respectively the partial derivatives with respect to the normalized propagation distance and retarded time.  $D(z)$  represents the GVD coefficient,  $R(z)$  is arise due to Kerr nonlinearity especially self-phase modulation which is particularly cubic nonlinearity coefficient and  $G(z)$  represents the loss (attenuation) or gain (amplification) profile.  $D_2, D_3, D_4$  and  $D_5$  are inhomogeneous coefficients of higher order dispersion and nonlinear terms. It should be emphasized that Eq. (1) not only describing the attosecond soliton propagation but also soliton control and management in an inhomogeneous fiber system. In different domain, various researchers solved many kinds of NLS equations using some mathematical techniques. In the present work, we aimed to solve inhomogeneous HNLS equations in attosecond regime.

### 3 Lax Pair

With the aid of AKNS formalism [13], matrices  $M$  and  $N$  are constructed for the Eq. (1) which can be derived from the zero-curvature equation. In order to apply the Darboux transformation, the following  $2 \times 2$  eigenvalue problem is considered. In the obtaining of soliton solutions via Darboux transformation, Lax pair plays a vigorous role.

$$\psi_t = M \psi \tag{2}$$

$$\psi_z = N \psi$$

$M$  and  $N$  matrices are can be expressed as given below for the linear eigen value problem (2)

$$M = i \begin{pmatrix} \lambda & E^*(z, t) \\ E(z, t) & -\lambda \end{pmatrix} \tag{3}$$

$$N = \sum_{j=0}^6 \lambda^j V_j$$

$$M_j = i \begin{pmatrix} A_j & B_j^* \\ B_j & -A_j \end{pmatrix} \tag{4}$$

$$A_6 = 32 \delta(z)$$

$$B_6 = 0$$

$$A_5 = 16 \gamma(z)$$

$$B_5 = 32 \delta(z) E$$

$$A_4 = -8 \gamma(z) - 16 \delta(z) |E|^2$$

$$B_4 = 16 \gamma(z) E + 16 i \delta(z) E_t$$

$$A_3 = -4 \chi(z) - 8 \gamma(z) |E|^2 - 8 i \delta(z) |E|_t^2$$

$$B_3 = -8 \beta(z) E + 8 i \gamma(z) E_t - 8 E_{tt} - 16 \delta(z) |E|^2 E$$

$$A_2 = 1 + 4 \beta(z) |E|^2 + 4 i \gamma(z) (E_t^* E - E_t E^*) + 12 \delta(z) |E|^4 - 8 \delta(z) |E_t|^2 + 4 \delta(z) (E_t^* E - E E^*)_t$$

$$B_2 = -4 \chi(z) E - 8 \gamma(z) |E|^2 E - 24 i \delta(z) |E|^2 E_t - 4 i \beta(z) E_t - 4 i \gamma(z) E_{tt} - 4 i \delta(z) E_{ttt}$$

$$A_1 = 2 \chi(z) |E|^2 + 6 \gamma(z) |E|^4 - 2 i \beta(z) (E_t^* E - E_t E^*) + 12 i \delta(z) |E|^2 (E_t E^* - E_t^* E) - 2 \gamma(z) |E_t|^2 + 2 \gamma(z) (E_{tt}^* E + E_{tt} E^*) + 2 i \delta(z) (E_t E_{tt}^* - E_t^* E_{tt} + E^* E_{ttt} - E_{ttt}^* E)$$

$$B_1 = E + 4 \beta(z) |E|^2 E - 2 i \chi(z) E_t - 12 i \gamma(z) |E|^2 E_t + 12 \delta(z) E^* E_t^2 + 16 \delta(z) |E|^2 E_{tt}$$

$$+ 4\delta(z)E^2E_{tt}^* - 2i\gamma(z)E_{ttt} + 2\beta(z)E_{tt} + 2\delta(z)E_{ttt} + 12\delta(z)|E|^4E + 8\delta(z)|EE_t|^2$$

The Eq. (1) can be obtained directly from zero-curvature equation i.e.,  $M_z - N_t + [M, N] = 0$ . In Eq. (3),  $\lambda$  being the spectral parameter in Lax pair.

### 4 Three Soliton Solutions

Using Darboux matrix  $D = \lambda I - S$  in the process of Darboux transformation method [14], explicit multi-soliton solutions can be obtained. To demonstrate the propagation of three solitons in a real fiber system, three soliton solutions with arbitrary control parameters are attained in this section. Consequently, three soliton solutions are computed via Darboux transformation technique as described below

$$E^{(3)} = 2i \frac{N_3}{D_3} \tag{5}$$

$$\begin{aligned} N_3 = & e^{2i(\theta_1 + \xi_1 t) + \sigma_1} + e^{2i(\theta_2 + \xi_2 t) + \sigma_2} + e^{2i(\theta_3 + \xi_3 t) + \sigma_3} \\ & + e^{2i(\theta_1 + \theta_1^* + \theta_2 + \xi_1 t + \xi_1^* t + \xi_2 t) + \lambda_{123}} + e^{2i(\theta_1 + \theta_1^* + \theta_3 + \xi_1 t + \xi_1^* t + \xi_3 t) + \lambda_{132}} \\ & + e^{2i(\theta_1 + \theta_2 + \theta_2^* + \xi_1 t + \xi_2 t + \xi_1^* t) + \lambda_{213}} + e^{2i(\theta_1 + \theta_3 + \theta_3^* + \xi_1 t + \xi_3 t + \xi_3^* t) + \lambda_{312}} \\ & + e^{2i(\theta_2 + \theta_2^* + \theta_3 + \xi_2 t + \xi_2^* t + \xi_3 t) + \lambda_{231}} + e^{2i(\theta_2 + \theta_3 + \theta_3^* + \xi_2 t + \xi_3 t + \xi_3^* t) + \lambda_{321}} \\ & + e^{2i(\theta_1 + \theta_2 + \theta_3^* + \xi_1 t + \xi_2 t + \xi_3^* t) + \nu_{123}} + e^{2i(\theta_1 + \theta_3 + \theta_2^* + \xi_1 t + \xi_3 t + \xi_2^* t) + \nu_{312}} \\ & + e^{2i(\theta_2 + \theta_3 + \theta_1^* + \xi_2 t + \xi_3 t + \xi_1^* t) + \nu_{231}} \\ & + e^{2i(\theta_1 + \theta_2 + \theta_2^* + \theta_3 + \theta_3^* + \xi_1 t + \xi_2 t + \xi_2^* t + \xi_3 t + \xi_3^* t) + \varphi_{123}} \\ & + e^{2i(\theta_1 + \theta_1^* + \theta_2 + \theta_3 + \theta_3^* + \xi_1 t + \xi_1^* t + \xi_2 t + \xi_3 t + \xi_3^* t) + \varphi_{231}} \\ & + e^{2i(\theta_1 + \theta_1^* + \theta_2 + \theta_2^* + \theta_3 + \xi_1 t + \xi_1^* t + \xi_2 t + \xi_2^* t + \xi_3 t) + \varphi_{321}} \end{aligned}$$

$$\begin{aligned} D_2 = & 1 + e^{2i(\theta_1 + \theta_1^* + \xi_1 t + \xi_1^* t) + \varkappa_{123}} + e^{2i(\theta_2 + \theta_2^* + \xi_2 t + \xi_2^* t) + \varkappa_{231}} + e^{2i(\theta_3 + \theta_3^* + \xi_3 t + \xi_3^* t) + \varkappa_{321}} \\ & + e^{2i(\theta_1^* + \theta_2 + \xi_1^* t + \xi_2 t) + \kappa_{123}} + e^{2i(\theta_1 + \theta_2^* + \xi_1 t + \xi_2^* t) + \kappa_{213}} + e^{2i(\theta_1^* + \theta_3 + \xi_1^* t + \xi_3 t) + \kappa_{132}} \\ & + e^{2i(\theta_1 + \theta_3^* + \xi_1 t + \xi_3^* t) + \kappa_{312}} + e^{2i(\theta_3 + \theta_2^* + \xi_3 t + \xi_2^* t) + \kappa_{231}} + e^{2i(\theta_2 + \theta_3^* + \xi_2 t + \xi_3^* t) + \kappa_{321}} \\ & + e^{2i(\theta_1 + \theta_1^* + \theta_2 + \theta_2^* + \xi_1 t + \xi_1^* t + \xi_2 t + \xi_2^* t) + \omega_{123}} + e^{2i(\theta_1 + \theta_1^* + \theta_3 + \theta_3^* + \xi_1 t + \xi_1^* t + \xi_3 t + \xi_3^* t) + \omega_{312}} \\ & + e^{2i(\theta_2 + \theta_2^* + \theta_3 + \theta_3^* + \xi_1 t + \xi_1^* t + \xi_3 t + \xi_3^* t) + \omega_{321}} + e^{2i(\theta_1 + \theta_1^* + \theta_2 + \theta_2^* + \xi_1 t + \xi_1^* t + \xi_2 t + \xi_3 t + \xi_3^* t) + \omega_{231}} \\ & + e^{2i(\theta_1 + \theta_1^* + \theta_3 + \theta_3^* + \xi_1 t + \xi_1^* t + \xi_2 t + \xi_3 t + \xi_3^* t) + \omega_{231}} + e^{2i(\theta_1 + \theta_2 + \theta_2^* + \theta_3^* + \xi_1 t + \xi_2 t + \xi_2^* t + \xi_3^* t) + \omega_{312}} \\ & + e^{2i(\theta_1 + \theta_3 + \theta_3^* + \theta_2^* + \xi_1 t + \xi_3 t + \xi_2^* t + \xi_3^* t) + \omega_{213}} + e^{2i(\theta_2 + \theta_3 + \theta_1^* + \theta_2^* + \xi_2 t + \xi_3 t + \xi_1^* t + \xi_2^* t) + \omega_{132}} \\ & + e^{2i(\theta_2 + \theta_3 + \theta_1^* + \theta_3^* + \xi_2 t + \xi_3 t + \xi_1^* t + \xi_3^* t) + \omega_{123}} \end{aligned}$$

$$+ e^{2i(\theta_1+\theta_1^*+\theta_2+\theta_2^*+\theta_3+\theta_3^*+\xi_1t+\xi_1^*t+\xi_2t+\xi_2^*t+\xi_3t+\xi_3^*t)+\Gamma}$$

$$\theta_1 = \xi_1^2 \int (D(z) - 4\xi_1 R(z) - 8\xi_1^2 \beta(z) + 16\xi_1^3 \gamma(z) + 32\xi_1^4 \delta(z)) dz$$

$$\theta_2 = \xi_2^2 \int (D(z) - 4\xi_2 R(z) - 8\xi_2^2 \beta(z) + 16\xi_2^3 \gamma(z) + 32\xi_2^4 \delta(z)) dz$$

$$\theta_3 = \xi_3^2 \int (D(z) - 4\xi_3 R(z) - 8\xi_3^2 \beta(z) + 16\xi_3^3 \gamma(z) + 32\xi_3^4 \delta(z)) dz$$

$$\xi_1 = \mu_1 + i\eta_1$$

$$\xi_2 = \mu_2 + i\eta_2$$

$$\xi_3 = \mu_3 + i\eta_3$$

$$e^{\sigma_i} = -\frac{C_{1i} \prod_j (\xi_j^* - \xi_i)}{C_{2i} \prod_{i \neq j} (\xi_j - \xi_i)}$$

$$e^{\lambda_{ijk}} = -\frac{C_{1i}^2 C_{1j} C_{1k} (\xi_j^* - \xi_j) (\xi_j^* - \xi_i) (\xi_k^* - \xi_i) (\xi_k^* - \xi_j) (\xi_i^* - \xi_k)}{C_{2i}^2 C_{2j} C_{2k} (\xi_i^* - \xi_j^*) (\xi_i^* - \xi_k^*) (\xi_i - \xi_k) (\xi_k - \xi_j)}$$

$$e^{\nu_{ijk}} = \frac{C_{1i} C_{1j} C_{1k} (\xi_i^* - \xi_i) (\xi_j^* - \xi_i) (\xi_k^* - \xi_k) (\xi_j^* - \xi_i) (\xi_i^* - \xi_j)}{C_{2i} C_{2j} C_{2k} (\xi_i^* - \xi_k^*) (\xi_k^* - \xi_j^*) (\xi_i - \xi_k) (\xi_k - \xi_j)}$$

$$e^{\varphi_{ijk}} = -\frac{C_{1i} C_{1j}^2 C_{1k}^2 (\xi_i^* - \xi_i) (\xi_i^* - \xi_j) (\xi_j^* - \xi_k^*) (\xi_i^* - \xi_k)}{C_{2i} C_{2j}^2 C_{2k}^2 (\xi_i^* - \xi_j^*) (\xi_i^* - \xi_k^*) (\xi_k^* - \xi_j^*)}$$

$$e^{\rho_{ijk}} = -\frac{C_{1i}^2 (\xi_j^* - \xi_i) (\xi_i^* - \xi_j) (\xi_k^* - \xi_i) (\xi_i^* - \xi_k)}{C_{2i}^2 (\xi_i^* - \xi_j^*) (\xi_i^* - \xi_k^*) (\xi_j - \xi_i) (\xi_i - \xi_k)}$$

$$e^{\kappa_{ijk}} = -\frac{C_{1i} C_{1j} (\xi_i^* - \xi_i) (\xi_j^* - \xi_j) (\xi_k^* - \xi_j) (\xi_i^* - \xi_k)}{C_{2i} C_{2j} (\xi_i^* - \xi_j^*) (\xi_i^* - \xi_k^*) (\xi_j - \xi_i) (\xi_k - \xi_j)}$$

$$e^{\omega_{ijk}} = \frac{C_{1i}^2 C_{1j}^2 (\xi_k^* - \xi_i) (\xi_k^* - \xi_j) (\xi_i^* - \xi_k) (\xi_j^* - \xi_k)}{C_{2i}^2 C_{2j}^2 (\xi_i^* - \xi_k^*) (\xi_k^* - \xi_j^*) (\xi_k - \xi_j) (\xi_i - \xi_k)}$$

$$e^{\theta_{ijk}} = \frac{C_{1i} C_{1j} C_{1k}^2 (\xi_i^* - \xi_i) (\xi_j^* - \xi_j) (\xi_k^* - \xi_i) (\xi_j^* - \xi_k)}{C_{2i} C_{2j} C_{2k}^2 (\xi_i^* - \xi_j^*) (\xi_k^* - \xi_j^*) (\xi_i - \xi_k) (\xi_i - \xi_j)}$$

$$e^\Gamma = \frac{C_{11}^2 C_{12}^2 C_{13}^2}{C_{21}^2 C_{22}^2 C_{23}^2}, j = 1, 2, 3.$$

By adopting particular profile for inhomogeneous functions that are present in the obtained attosecond three soliton solutions, various transmission characteristics can be investigated. Especially, with the expression of three soliton solutions (5), periodic amplification properties of attosecond three solitons to be observed by adopting periodic functions for inhomogeneous profiles in the next section.

## 5 Periodic Amplifications of Three Attosecond Solitons

The present study focused on three attosecond optical bright soliton transmission with the periodic amplification characteristics under the dispersion and nonlinearity management scheme (DNMS). Furthermore, by studying the three soliton interactions in an inhomogeneous fiber system, we can enrich the capacity of optical fiber communication system. In order to exemplify the behavior of three solitons which are transmitted under periodic amplification system, we chose the variable coefficients especially GVD parameter  $D(z)$  and Kerr nonlinearity parameter  $R(z)$  are adopted as given in the references [15–18]

$$D(z) = \frac{1}{d_0} \exp(kz) R(z) \quad (6)$$

$$R(z) = R_0 + R_1 \sin(gz)$$

Here,  $R_0$ ,  $R_1$  and  $g$  are the control parameters describing Kerr nonlinearity and  $d_0$  represent the initial peak power of the system, respectively. Here, for the sake of simplicity, control parameters are considered as  $R_0 = 0$ ,  $d_0 = 1$  and  $g = 1$ . Specifically, when  $k = 0$  in the expression (6) which corresponds to the loss less optical fiber medium (without any loss or gain).

As depicted in Fig. 1a, the evolution of three solitons is displayed which is obtained through the adopting of dispersion and nonlinearity coefficients as periodic functions. At the beginning of propagation along the  $z$ -axis, the period of oscillation is small while it is increasing significantly during the transmission of optical solitons in attosecond regime. Three solitons are got highly amplifications when propagation distance is very long. From the density plot Fig. 1b, one can conclude that three attosecond solitons are getting not only amplification but also the compressed and broadened width periodically. The snake like propagation trajectory of optical solitons is observed and this type of solitons are namely as “snake solitons”. In real optical communication network, amplified solitons may be attained through the technique of appropriately tailoring the dispersion and nonlinearity profiles which is called dispersion and nonlinearity management (DNLM) scheme. Recently, in literature, various periodic soliton amplification schemes through several methods have been suggested for numerous applications [19–23].

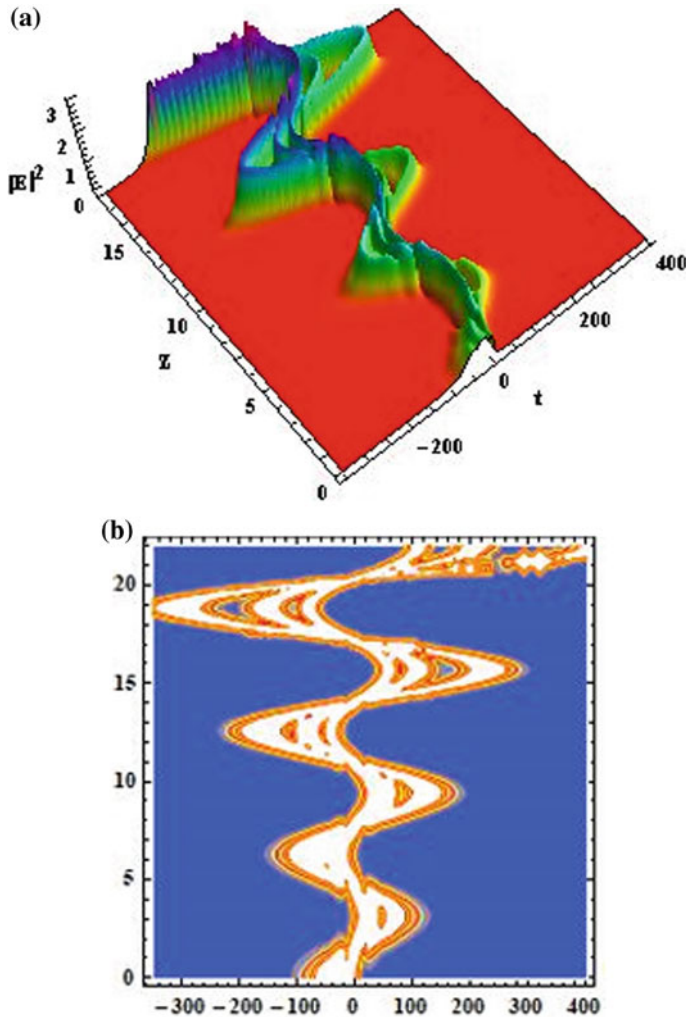


**Fig. 1** **a** Intensity profile of attosecond three solitons. The parameters are  $\mu_1 = 0.07$ ,  $\mu_2 = 0.01$ ,  $\mu_3 = 0.08$ ,  $\eta_1 = 0.08$ ,  $\eta_2 = 0.09$ ,  $\eta_3 = 0.07$ . **b** Corresponding contour plot for **a**

## 6 Conclusions

We proposed a theoretical model i.e., variable coefficient inhomogeneous NLS equation with the presence of higher order linear and nonlinear effects which governs the propagation of attosecond soliton in an inhomogeneous nonlinear optical fiber medium. Bright three soliton solutions are derived by employing the Darboux transformation method based on the constructed Lax pair. Finally, three attosecond soliton transmissions in an inhomogeneous fiber have been demonstrated graphically with



the aid of *Mathematica* software tool. By careful choices of trigonometric functions for GVD and nonlinearity parameters, periodic soliton amplification have been attained. Moreover, we observed that one can control the soliton transmission and its characteristics through adopting the dispersion—nonlinearity management scheme.

The study on simultaneous propagation of three attosecond solitons in an inhomogeneous fiber optic communication system will be used for the development of optical soliton-based switching devices and soliton shaping or management by tailoring the inhomogeneous profiles properly. The elastic interaction among three solitons offers a new way for controllable optical soliton amplification in multi soliton transmission system where ultrahigh capacity can be easily achieved. Especially, this work is useful in the study of propagation properties of attosecond soliton in an inhomogeneous fiber with the modulation of dispersion and nonlinearity. We realized that three soliton interactions effectively controlled by properly tailoring the inhomogeneous profiles in attosecond regime.

## References

1. Hasegawa, A., Kodama, Y.: Solitons in Optical Communications. Clarendon, Oxford, UK (1995)
2. Toda, H., Furukawa, Y., Kinoshita, T., Kodama, Y., Hasegawa, A.: Optical soliton transmission experiment in a comb-like dispersion profiled fiber loop. *IEEE Photon. Technol. Lett.* **9**, 1415–1417 (1997)
3. Liu, W.J., Zhang, Y., Wazwaz, A.M., Zhou, Q.: Analytic study on triple-S, triple-triangle structure interactions for solitons in inhomogeneous multi-mode fiber. *Appl. Math. Comput.* **361**, 325–331 (2019)
4. Agrawal, G.P.: Nonlinear Fiber Optics. Academic Press, San Diego (1995)
5. Tian, B., Gao, Y.T., Zhu, H.W.: Variable-coefficient higher order nonlinear Schrödinger model in optical fibers: variable-coefficient bilinear form, Bäcklund transformation, brightons and symbolic computation. *Phys. Lett. A* **366**, 223–229 (2007)
6. Serkin, V.N., Hasegawa, A.: Exactly integrable nonlinear Schrödinger equation models with varying dispersion, nonlinearity and gain: application for soliton dispersion management. *IEEE J. Sel. Top. Quant. Electron.* **8**, 418–431 (2002)
7. Serkin, V.N., Hasegawa, A., Belyaeva, T.L.: Nonautonomous solitons in external potentials. *Phys. Rev. Lett.* **98**, 074102 (2007)
8. Kruglov, V.I., Peacock, A.C., Harvey, J.D.: Exact self-similar solutions of the generalized nonlinear Schrödinger equation with distributed coefficients. *Phys. Rev. Lett.* **90**, 113902–113905 (2003)
9. Vijayalekshmi, S., Mani Rajan, M.S., Mahalingam, A., Uthayakumar, A.: Hidden possibilities in soliton switching through tunneling in erbium doped birefringence fiber with higher order effects. *J. Mod. Opt.* **62**, 278–287 (2015)
10. Serkin, V.N., Hasegawa, A., Belyaeva, T.L.: Solitary waves in nonautonomous nonlinear and dispersive systems. *J. Mod. Opt.* **57**, 1456 (2010)
11. Serkin, V.N., Belyaeva, T.L.: Optimal control of optical soliton parameters: part 1. The Lax representation in the problem of soliton management. *Quantum Electron.* **31**, 1007 (2001)
12. Prathap, N., Arunprakash, S., Mani Rajan, M.S., Subramanian, K.: Multiple dromion excitations in sixth order NLS equation with variable coefficients. *Optik* **158**, 1179–1185 (2018)
13. Ablowitz, M.J., Kaup, D.J., Newell, A.C.: Nonlinear-evolution equations of physical significance. *Phys. Rev. Lett.* **31**, 125 (1973)

14. Gu, H., Hu, H.S., Zhou, Z.X.: *Darboux transformation in Soliton Theory and Its Geometric Applications*. Shanghai Science and Technology Publishers, Shanghai (2005)
15. Mahalingam, A., Porsezian, K., Mani Rajan, M.S., Uthayakumar, A.: Propagation of dispersion nonlinearity managed solitons in an inhomogeneous erbium doped fiber system. *J. Phys. A Math. Theor.* **42**, 165101 (2009)
16. Mani Rajan, M.S.: Dynamics of optical soliton in a tapered erbium-doped fiber under periodic distributed amplification system. *Nonlinear Dyn.* **85**, 599–606 (2016)
17. Karthikeyaraj, G., Mani Rajan, M.S., Tantawy, M., Subramanian, K.: Periodic oscillations and nonlinear tunneling of soliton for Hirota-MB equation in inhomogeneous fiber. *Optik* **181**, 440–448 (2019)
18. Yao, Y., Ma, G., Zhang, X., W.J. Liu, W.J.: M-typed dark soliton generation in optical fibers. *Optik* **193**, 162997(2019)
19. Yu, W.T., Zhou, Q., Mirzazadeh, M., Liu, W.J.: Phase shift, amplification, oscillation and attenuation of solitons in nonlinear optics. *J. Adv. Res.* **15**, 69–76 (2019)
20. Mani Rajan, M.S., Mahalingam, A., Uthayakumar, A.: Observation of two soliton propagation in an erbium doped inhomogeneous lossy fiber with phase modulation. *Commun. Nonlinear Sci. Numer. Simulat.* **18**, 1410–1432 (2013)
21. Maddouri, K., Azzouzi, F., Triki, H., Bouguerra, A., Korba, S.A.: Dark-managed solitons in inhomogeneous cubic–quintic–septimal nonlinear media. *Nonlinear Dyn.* **103**, 2793–2803 (2021)
22. Liu, X., Triki, H., Zhou, Q., Liu, W.J., Anjan B.: Analytic study on interactions between periodic solitons with controllable parameters. *Nonlinear Dyn.* **94**, 703–709 (2018)
23. Wang, L., Luan, Z., Zhou, Q., Biswas, A., Alzahrani, A.K., Liu, W.J.: Effects of dispersion terms on optical soliton propagation in a lossy fiber system. *Nonlinear Dyn.* **104**, 629–637 (2021)

# Analysis of Flexoelectricity with Deformed Junction in Two Distinct Piezoelectric Materials Using Wave Transmission Study



Abhinav Singhal, Rakhi Tiwari, Juhi Baroi, and Chandraketu Singh

**Abstract** Analysis of flexoelectricity in distinct piezoelectric (PE) materials bars (PZT-7A, PZT-6B) with deformed interface in stick over Silicon oxide layer is studied analytically with the help of Love-type wave vibrations. Using the numerical data for PE material, then research achieves the noteworthy fallouts of flexoelectric effect (FE) and PE. The effect of flexoelectricity is compared first between biomaterials of piezoelectric ceramics. Dispersion expressions are procured logically for together electrically unlocked/locked conditions under the influence of deformed interface in the complex form which is transcendental. Fallouts of the research identify that contecture consisting of FE has a noteworthy impact on the acquired dispersion expressions. Existence of FE displays that the unreal section of the phase velocity rises monotonically. Competitive consequences are displayed diagrammatically and ratified with published outcomes. The outcomes of the present research done on both the real and imaginary section of the wave velocity. The comparative study between the two piezo-ceramics bars helps us to understand the properties of one piezo-material over the another and as an outcomes the significance of the present study helps in structural health monitoring, bioengineering for optimizing the detection sensitivity in the smart sensors.

**Keywords** Flexoelectricity · PZT-7A · Vibrations · Deformed Interface · PZT-6B · Deformed Interface

## Nomenclature

$\sigma$  Stress tensor

---

A. Singhal (✉) · J. Baroi · C. Singh  
School of Sciences, Christ (Deemed to Be University) Delhi NCR, Ghaziabad 201003, India  
e-mail: [ism.abhinav@gmail.com](mailto:ism.abhinav@gmail.com)

R. Tiwari  
Department of Mathematics, Babasaheb Bhimrao Ambedkar Bihar University, Nitishwar college, Muzaffarpur 842002, India

$\tau$	Higher order stress (moment stress) tensor
$\varepsilon$	Strain
$E^o$	Electric field intensity
$V^o$	Electric field gradient
$w$	Strain gradient
$D$	Electrical displacement vector
$Q^o$	Electric quadrupole tensor
$c$	Elastic tensors
$a$	Permittivity tensors
$e$	Piezoelectric tensors
$f$	Direct piezoelectric tensors
$d$	Converse piezoelectric tensors
$u$	Particle displacements
$\phi$	Electric potential
$u_i$	Mechanical displacement
$k = 2\pi/\lambda$	Wave number
$\lambda$	Wavelength
$i = \sqrt{-1}$	Imaginary unit
$c_{44}^e$	Shear modulus of the lower plate
$\rho^e$	Density of the lower plate
$\sigma^o$	Initial stress
$u^e$	Mechanical displacement of the lower plate
$\phi^e$	Electric potential of the lower plate

## 1 Introduction

The study of surface acoustic wave (SAW) propagation in piezoelectric materials based smart devices has attracted significant attention due to its distinctive applications. The SAW devices can be used as biosensors or for liquid sensing, for which the sensing layer needs to be paired with a liquid medium. To generate the SAW, an oscillating electric signal is applied to the interdigital transducer (IDT) which is designed on the surface of piezoelectric layer. Subsequently, piezoelectric crystal converts the electric signal into mechanical vibration, which another IDT receives for further processing. To fabricate metal electrodes in IDT's, complex procedure involving lithographic patterning and metal deposition along with other special equipment. Chu et al. [1] studied the vibrations in smart materials following the structures of MEMS. Singhal et al. [2] and Nathankumar kumar et al. [3] elaborated the research of seismic wave vibrations in smart materials structure where the flexoelectricity and piezoelectricity characteristics and Sahu et al. [4] extend the study of dispersion relation of wave transmission in intelligent structures.

Lately for designing composite structure, functional grading of the piezoelectric material is preferred over conventional material of same thickness due to the brittle

nature and mechanical stiffness of the material. Functional grading assists to avoid the local stress concentration and increases the bonding strength due to smooth variation of material properties. Now, currently, Othmani et al. [5] explored the results of frequency equations following the legendres polynomial approach in the distinct materials, Li et al. [6] extended the new results on the same materials and Barati [7] studied the wave transference in the nonporous materials. Arani et al. [8] mentioned the nonlinear analysis of vibrations of the microbeams rubbery soldered with a PE beam using strain gradient theory. Moreover, Singhal et al. [9] covered and extended the topic of PE material variables on shear horizontal (SH) waves continuance in multiferroic structure.

The effect of various parameter such as material gradient parameter in electrically open and short case has been studied for both FE and PE. Although several modes existing in the given range have been shown through graphs for both the dispersion and attenuation curve. The dispersion equation for considered structure for electrically open and short circuit condition have also been obtained.

## 2 Mathematical Brief Implications

Governing material equations for piezoelectricity and flexoelectricity are:

$$\sigma_{ij} = c_{ijkl}\varepsilon_{kl} - d_{ijkl}V_{kl}^o - e_{ijk}E_k^o \tag{1}$$

$$\tau_{ijm} = -f_{ijkm}E_k^o \tag{2}$$

$$D_i = a_{ij}E_j^o + e_{jki}\varepsilon_{jk} + f_{jkil}w_{jkl} \tag{3}$$

$$Q_{ij}^o = d_{klij}\varepsilon_{kl} \tag{4}$$

Here  $\tau_{ijm} = \tau_{jim}$ ,  $\sigma_{ij} = \sigma_{ji}$ , and  $Q_{ij}^o = Q_{ji}^o$ . The equation  $d = -f$  is used to derive the results. Hence,

$$\varepsilon_{ij} = \frac{1}{2}(u_{i,j} + u_{j,i}) \tag{5}$$

$$E_i^o = -\phi_{,i} \tag{6}$$

The Eqs. (2)–(6) are the main fundamental equations for the piezoelectric materials. The physical significance of the above equations in mechanical systems displays the relationship between the elastic tensors, piezoelectric tensors, and inverse piezoelectric tensors. The equilibrium is set up among all the above equations by electric field intensity and electric potential. Now:

$$w_{jkl} = \varepsilon_{jk,l} \tag{7}$$

$$V_{ij}^o = E_{i,j}^o \tag{8}$$

Also,  $V_{ij}^o = V_{ji}^o, w_{jkl} = w_{kjl}, \varepsilon_{ij} = \varepsilon_{ji}$ .

The assumption equations for the Love wave propagation are:

$$u_1^p = u_2^p = 0, u_3^p = u_3^p(x, y, t), \phi^p = \phi^p(x, y, t), \tag{9}$$

Following some considered circumstances the equation yields

$$\frac{\partial}{\partial x} \left( \sigma_{31} - \frac{\partial \tau_{311}}{\partial x} - \frac{\partial \tau_{312}}{\partial y} \right) + \frac{\partial}{\partial y} \left( \sigma_{32} - \frac{\partial \tau_{321}}{\partial x} - \frac{\partial \tau_{322}}{\partial y} \right) = \rho^p \frac{\partial^2 u_3^p}{\partial t^2} \tag{10}$$

$$\frac{\partial}{\partial x} \left( D_1^o - \frac{\partial Q_{11}^o}{\partial x} - \frac{\partial Q_{12}^o}{\partial y} \right) + \frac{\partial}{\partial y} \left( D_2^o - \frac{\partial Q_{21}^o}{\partial x} - \frac{\partial Q_{22}^o}{\partial y} \right) = 0 \tag{11}$$

The most important strain–stress relations are for the considered materials:

$$\varepsilon_{23} = \frac{1}{2} \left( \frac{\partial u_3^p}{\partial y} \right), \varepsilon_{31} = \frac{1}{2} \left( \frac{\partial u_3^p}{\partial y} \right) \tag{12}$$

$$w_{231} = \frac{1}{2} \left( \frac{\partial^2 u_3^p}{\partial x \partial y} \right), w_{232} = \frac{1}{2} \left( \frac{\partial^2 u_3^p}{\partial y^2} \right), w_{311} = \frac{1}{2} \left( \frac{\partial^2 u_3^p}{\partial x^2} \right), w_{312} = \frac{1}{2} \left( \frac{\partial^2 u_3^p}{\partial x \partial y} \right) \tag{13}$$

$$E_1^o = -\frac{\partial \phi^p}{\partial x}, E_2^o = -\frac{\partial \phi^p}{\partial y} \tag{14}$$

$$V_{11}^o = -\frac{\partial^2 \phi^p}{\partial x^2}, V_{12}^o = -\frac{\partial^2 \phi^p}{\partial x \partial y}, V_{21}^o = -\frac{\partial^2 \phi^p}{\partial x \partial y}, V_{22}^o = -\frac{\partial^2 \phi^p}{\partial y^2} \tag{15}$$

Now using the Eqs. (12)–(15) in Eqs. (1)–(4), It is obtained:

$$\sigma_{31} - \frac{\partial \tau_{311}}{\partial x} - \frac{\partial \tau_{312}}{\partial y} = c_{44} \frac{\partial u_3^p}{\partial x} + e_{15} \frac{\partial \phi^p}{\partial x} \tag{16}$$

$$\sigma_{32} - \frac{\partial \tau_{321}}{\partial x} - \frac{\partial \tau_{322}}{\partial y} = c_{44} \frac{\partial u_3^p}{\partial y} + e_{15} \frac{\partial \phi^p}{\partial y} - h_{41} \frac{\partial^2 \phi^p}{\partial x^2} + h_{41} \frac{\partial^2 \phi^p}{\partial y^2} \tag{17}$$

$$D_1^o - \frac{\partial Q_{11}^o}{\partial x} - \frac{\partial Q_{12}^o}{\partial y} = -a_{11} \frac{\partial \phi^p}{\partial x} + e_{15} \frac{\partial u_3^p}{\partial x} + (h_{41} + h_{52}) \frac{\partial^2 u_3^p}{\partial x \partial y} \tag{18}$$

$$D_2^o - \frac{\partial Q_{21}^o}{\partial x} - \frac{\partial Q_{22}^o}{\partial y} = -a_{11} \frac{\partial \phi^p}{\partial y} + e_{15} \frac{\partial u_3^p}{\partial y} - h_{52} \frac{\partial^2 u_3^p}{\partial x^2} - h_{41} \frac{\partial^2 u_3^p}{\partial y^2} \tag{19}$$

Hence, the fundamental expressions of PE material bars are:

$$c_{44} \frac{\partial^2 u_3^p}{\partial x^2} + c_{44} \frac{\partial^2 u_3^p}{\partial y^2} + e_{15} \frac{\partial^2 \phi^p}{\partial x^2} + e_{15} \frac{\partial^2 \phi^p}{\partial y^2} - h_{41} \frac{\partial^3 \phi^p}{\partial x^2 \partial y} + h_{41} \frac{\partial^3 \phi^p}{\partial y^3} = \rho^p \frac{\partial^2 u_3^p}{\partial t^2} \quad (20)$$

$$-a_{11} \frac{\partial^2 \phi^p}{\partial x^2} - a_{11} \frac{\partial^2 \phi^p}{\partial y^2} + e_{15} \frac{\partial^2 u_3^p}{\partial x^2} + e_{15} \frac{\partial^2 u_3^p}{\partial y^2} + h_{41} \frac{\partial^3 u_3^p}{\partial x^2 \partial y} - h_{41} \frac{\partial^3 u_3^p}{\partial y^3} = 0 \quad (21)$$

The following equations are arrived in the absence of flexoelectric affect:

$$u_3^p(x, y, t) = U(x)e^{ik(y-ct)}, \phi^p(x, y, t) = \Phi(x)e^{ik(y-ct)} \quad (22)$$

So, by solving Eq. (22) with mentioned below boundary conditions, dispersion relation is obtained.

### 3 Boundary Conditions (States) and Dispersion Expressions

- (1) Mechanically and electrically constraint for electrically unlocked alliance at  $x = -h_1$

$$\begin{aligned} [(\sigma_{zx} - \tau_{zxx,x} - \tau_{zxy,y}) - \tau_{zyx,y}]_{upperplate} &= 0 \\ [(D_x - Q_{xx,x} - Q_{xy,y}) - Q_{yx,y}]_{upperplate} &= 0 \end{aligned}$$

- (2) Mechanically and electrically constraint for electrically locked alliance at  $x = -h_1$

$$\begin{aligned} \text{(a)} [(\sigma_{zx} - \tau_{zxx,x} - \tau_{zxy,y}) - \tau_{zyx,y}]_{upperplate} &= 0 \\ \text{(b)} [\phi_1^p(x, y)]_{upperplate} &= 0 \end{aligned}$$

- (3) At the interface, the continuous conditions and impedance boundary condition is given at  $x = 0$  as follows

$$\text{(a)} [(\sigma_{zx} + \omega Z_1 u^p)]_{upperplate} = [(\tau_{zx} + \omega Z_1 u^e)]_{lowerplate}$$

$$\text{(b)} [D_x]_{upperplate} = [D_x]_{lowerplate}$$

$$\text{(c)} [u_3^p]_{upperplate} = [u^e]_{lowerplate} \quad \text{(d)} [\phi^p]_{upperplate} = [\phi^e]_{upperplate}$$

- (4) Mechanically and electrically state for electrically unlocked condition at  $x = -h_2$

$$(a)[\sigma_{zx}]_{lowerplate} = 0(b)[D_x]_{lowerplate} = 0$$

- (5) Mechanically and electrically state for electrically locked case at  $x = -h_2$

$$(a)[\sigma_{zx}]_{lowerplate} = 0(b)[\phi_1^e(x, y)]_{lowerplate} = 0$$

### 3.1 Dispersion Expressions

The equation called dispersion relation is obtained

$$Det[\Lambda_i]_{i=1, 2, \dots, 8}, \quad (23)$$

Therefore, to solve the Eq. (23), obtained equation can be equal to zero to determine the unknowns and hence the closed form of dispersion equation can be achieved. The values of Eq. (23) are given in Appendix 2.

The equation called dispersion relation is obtained

$$Det[\Lambda_i]_{i=1, 2, \dots, 8}, \quad (24)$$

Therefore, to solve the Eq. (24), obtained equation can be equal to zero to determine the unknowns and hence the closed form of dispersion equation can be achieved. The values of Eq. (24) are given in Appendix 4.

## 4 Numerical Discussion

Present section gives the insight of Love propagation in the piezo-composite structure. The dispersion equation is obtained in closed form. Typically, dispersion relation defines the relationship between phase velocity and wave number, but it also displays the impact of material gradient parameters on the phase velocity and attenuation (Table 1).

The consecutive Fig. 1a, b are plotted to study the results of material gradients coefficients on the Love wave phase velocity. The dimensionless variation of Love-type phase velocity increases with the increment of material gradient coefficients in both electrically open and short cases in the Fig. 1a, b. Increment in the material gradients coefficients decreases monotonically with the angular frequency ( $\omega = k_1c$ ). The Fig. 1a, b shown the phase velocity increment in the electrically closed case, but there



**Table 1** Materials values are given

	PZT-6B	PZT-7A
$C_{44}(10^9Nm^{-2})$	2.71	25.4
$\rho(10^3kgm^{-3})$	5.8	76,000
$\epsilon_{11} = \epsilon_{22}(10^{-9}Fm^{-1})$	3.6	-2.1
$\mu_{11}(10^{-6}Ns^2C^{-2})$	5	5
$e_{15}(Cm^{-2})$	4.6	9.2

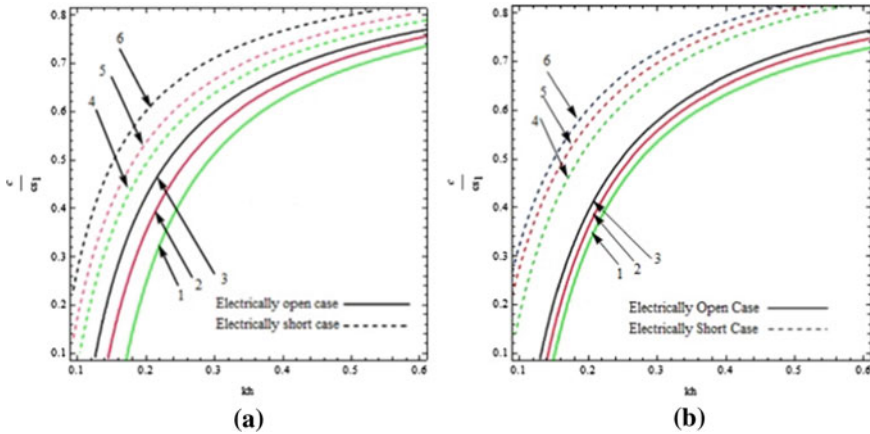


**Fig. 1 a and b** Variation of dimensionless phase velocity against dimensionless wave number for different values of material gradient of PE material gradient  $\beta$  under the influence of FE for electrically open and short cases in PZT-6B and PZT-7A materials respectively

is a less phase velocity in the electrically open case under the increment of the piezoelectric material gradient. This leads the main outcomes of the study which will be very beneficial for the material engineering.

For varied material gradients bars, the graph lines in the dispersive curves are shown in Fig. 2a, b. From the both the figs. It is concluded that the dispersive curves run towards the right and the gap between the dispersive curves of mode increases as the mode order increasing when both material gradients increase this will leads to the difference between in PZT-6B and PZT-7A. Means, phase velocity curves rise with the increase of the material plates gradients for selected wavelength and wavenumber. The graphs shown in present study quantitatively characterize the significance of individual parameters of the liquid layer as well as other parameters of piezoelectric composite on the propagation behaviour of the Love wave. It also allows the integration of SAW devices for Lab-on-chip systems. The present study may apply in the theoretical study of acoustic wave-based smart materials and non-invasive analysis of SAW devices. This model could be used in tailoring and analysing acoustic wave sensors based on Love wave and piezoelectric materials. For designing the device, the parameters like thickness of porous piezoelectric plate, the operating frequency

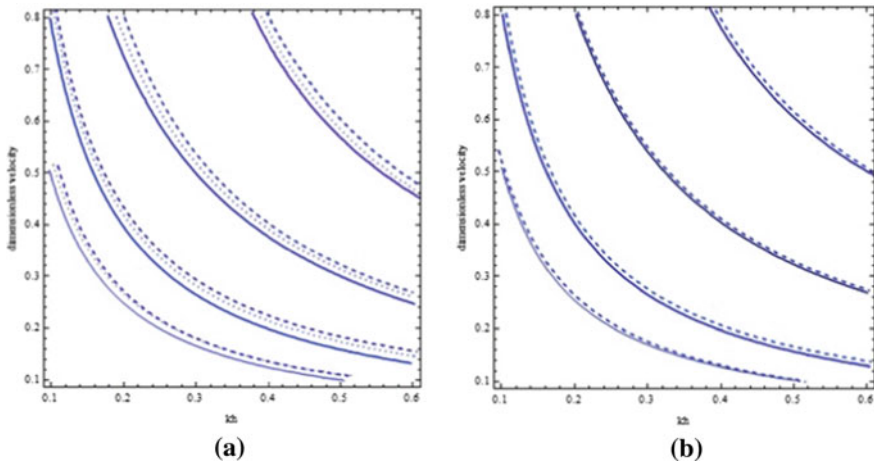


**Fig. 2 a and b** Dispersive curves of Love-type wave number for different values PE material gradient  $\beta$  under the influence of FE for electrically open and short cases in PZT-6B and PZT-7A materials respectively

which depends on wave number, the interface of two medium of composite structure are changed to optimize the structure.

## 5 Conclusions

The present article comprises the investigation of Love wave propagating in a piezoelectric biomaterial. Present study primarily focuses on the flexoelectricity and piezoelectricity, although the dispersion equation for the the materials is also established for both electrically open and short circuit conditions. The conclusions based on present study and graphical interpretation is encapsulated as follows:

- Flexoelectricity depends on the piezoelectric material gradient.
- Between piezoelectricity and flexoelectricity, from the results the flexoelectricity depends more on the materials width. This will help in enchaining the efficiency of piezo sensors.
- Higher is the material gradient value in the electric short case, higher is the phase velocity.
- The finer the functional grading, the higher is the phase velocity.
- Phase velocity and attenuation portrays completely opposite trend pertaining to a parameter when plotted against wave number.
- As an important remarks, waves phase velocity jumps high in the absence of electricity.
- The obtained results may be useful to enhance the efficiencies of IDT and Actuators.

This model could be used in tailoring and analysing acoustic wave sensors based on Love wave and piezoelectric materials. For designing the device, the parameters like thickness of porous piezoelectric plate, the operating frequency which depends on wave number, the interface of two medium of composite structure are changed to optimize the structure.

**Acknowledgements** The authors convey their sincere thanks “Department of Computational Sciences, School of Sciences, Christ (Deemed to be University) Delhi NCR Campus, Ghaziabad-201003, Uttar Pradesh, India.” for providing all necessary research facility.

**Compliance with Ethical Standards**

**Conflict of Interest:** The authors declare that they have no conflict of interest.

**Appendix 1 Secular Equation for Electrically Open Case**

$$\begin{aligned} \Lambda_{11} &= \left( Sc_{44} + e_{15} - \frac{ikh_{41}}{2} \right) s_1 e^{-s_1 h_1}, \\ \Lambda_{12} &= - \left( Sc_{44} + e_{15} - \frac{ikh_{41}}{2} \right) s_1 e^{s_1 h_1}, \\ \Lambda_{13} &= \left( Tc_{44} + e_{15} - \frac{ikh_{41}}{2} \right) s_2 e^{-s_2 h_1} \\ \Lambda_{14} &= - \left( Tc_{44} + e_{15} - \frac{ikh_{41}}{2} \right) s_2 e^{s_2 h_1}, \\ \Lambda_{21} &= \left[ -a_{11} + Se_{15} + ikS \left( \frac{h_{52}}{2} + h_{41} \right) \right] s_1 e^{-s_1 h_1} \\ \Lambda_{22} &= - \left[ -a_{11} + Se_{15} + ikS \left( \frac{h_{52}}{2} + h_{41} \right) \right] s_1 e^{s_1 h_1}, \\ \Lambda_{23} &= \left[ -a_{11} + Te_{15} + ikT \left( \frac{h_{52}}{2} + h_{41} \right) \right] s_2 e^{-s_2 h_1}, \\ \Lambda_{24} &= - \left[ -a_{11} + Te_{15} + ikT \left( \frac{h_{52}}{2} + h_{41} \right) \right] s_2 e^{s_2 h_1}, \\ \Lambda_{31} &= \left( Sc_{44} + e_{15} - \frac{ikh_{41}}{2} \right) s_1, \\ \Lambda_{32} &= - \left( Sc_{44} + e_{15} - \frac{ikh_{41}}{2} \right) s_1, \Lambda_{33} = \left( Tc_{44} + e_{15} - \frac{ikh_{41}}{2} \right) s_2, \\ \Lambda_{34} &= - \left( Tc_{44} + e_{15} - \frac{ikh_{41}}{2} \right) s_2, \Lambda_{35} = -k\alpha e_{15}, A_{36} = k\alpha e_{15}, \\ \Lambda_{41} &= \left[ -a_{11} + Se_{15} + ikS \left( \frac{h_{52}}{2} + h_{41} \right) \right] s_1, \end{aligned}$$

$$\begin{aligned} \Lambda_{42} &= -\left[-a_{11} + Se_{15} + ikS\left(\frac{h_{52}}{2} + h_{41}\right)\right] \\ s_1\Lambda_{43} &= \left[-a_{11} + Te_{15} + ikT\left(\frac{h_{52}}{2} + h_{41}\right)\right]s_2, \\ \Lambda_{44} &= -\left[-a_{11} + Te_{15} + ikT\left(\frac{h_{52}}{2} + h_{41}\right)\right]s_2, \Lambda_{47} = \varepsilon_{11}^e k, A_{48} = -\varepsilon_{11}^e k \\ \Lambda_{51} &= K_T S, \Lambda_{52} = SK_T, \Lambda_{53} = TK_T, \Lambda_{54} = TK_T, \\ \Lambda_{55} &= -(K_T + k\alpha c_{44}^e), \Lambda_{56} = (-K_T + k\alpha c_{44}^e) \\ \Lambda_{61} &= K_L, \Lambda_{62} = K_L, \Lambda_{63} = K_L, \Lambda_{64} = K_L, \\ \Lambda_{65} &= -K_L, \Lambda_{66} = -K_L, \Lambda_{67} = k\varepsilon_{11}^e, \Lambda_{77} = -k\varepsilon_{11}^e, \\ \\ \Lambda_{75} &= k\alpha e^{kah_2}, \Lambda_{76} = -k\alpha e^{-kah_2}, \Lambda_{77} = ke^{kh_2}, \Lambda_{78} = -ke^{-kh_2}. \end{aligned}$$

### Appendix 2 Secular Expressions for Electrically Unlocked Case

$$\begin{aligned} \Lambda_{11} &= \left(Sc_{44} + e_{15} - \frac{ikh_{41}}{2}\right)s_1 e^{-s_1 h_1}, \Lambda_{12} = -\left(Sc_{44} + e_{15} - \frac{ikh_{41}}{2}\right)s_1 e^{s_1 h_1}, \\ \Lambda_{13} &= \left(Tc_{44} + e_{15} - \frac{ikh_{41}}{2}\right)s_2 e^{-s_2 h_1} \\ \\ \Lambda_{14} &= -\left(Tc_{44} + e_{15} - \frac{ikh_{41}}{2}\right)s_2 e^{s_2 h_1}, \\ \Lambda_{21} &= \left[-a_{11} + Se_{15} + ikS\left(\frac{h_{52}}{2} + h_{41}\right)\right]s_1 e^{-s_1 h_1} \\ \Lambda_{22} &= -\left[-a_{11} + Se_{15} + ikS\left(\frac{h_{52}}{2} + h_{41}\right)\right]s_1 e^{s_1 h_1}, \\ \Lambda_{23} &= \left[-a_{11} + Te_{15} + ikT\left(\frac{h_{52}}{2} + h_{41}\right)\right]s_2 e^{-s_2 h_1}, \\ \Lambda_{24} &= -\left[-a_{11} + Te_{15} + ikT\left(\frac{h_{52}}{2} + h_{41}\right)\right]s_2 e^{s_2 h_1}, \\ \Lambda_{31} &= \left(Sc_{44} + e_{15} - \frac{ikh_{41}}{2}\right)s_1, \\ \Lambda_{32} &= -\left(Sc_{44} + e_{15} - \frac{ikh_{41}}{2}\right)s_1, \\ \Lambda_{33} &= \left(Tc_{44} + e_{15} - \frac{ikh_{41}}{2}\right)s_2 \end{aligned}$$

$$\begin{aligned}
\Lambda_{31} &= \left( Sc_{44} + e_{15} - \frac{ikh_{41}}{2} \right) s_1, \quad \Lambda_{32} = -\left( Sc_{44} + e_{15} - \frac{ikh_{41}}{2} \right) s_1, \\
\Lambda_{33} &= \left( Tc_{44} + e_{15} - \frac{ikh_{41}}{2} \right) s_2 \\
\Lambda_{34} &= -\left( Tc_{44} + e_{15} - \frac{ikh_{41}}{2} \right) s_2, \quad \Lambda_{35} = -k\alpha e_{15}, \\
\Lambda_{36} &= k\alpha e_{15} \Lambda_{43} = \left[ -a_{11} + Te_{15} + ikT \left( \frac{h_{52}}{2} + h_{41} \right) \right] s_2, \\
\Lambda_{44} &= -\left[ -a_{11} + Te_{15} + ikT \left( \frac{h_{52}}{2} + h_{41} \right) \right] s_2, \\
\Lambda_{47} &= \varepsilon_{11}^e k, \quad \Lambda_{48} = -\varepsilon_{11}^e k \Lambda_{51} = K_T S, \quad \Lambda_{52} = SK_T, \\
\Lambda_{53} &= TK_T, \quad \Lambda_{54} = TK_T, \quad \Lambda_{55} = -(K_T + k\alpha c_{44}^e), \\
\Lambda_{56} &= (-K_T + k\alpha c_{44}^e) \Lambda_{61} = K_L, \\
\Lambda_{62} &= K_L, \quad \Lambda_{63} = K_L, \quad \Lambda_{64} = K_L, \\
\Lambda_{65} &= -K_L, \quad \Lambda_{66} = -K_L, \quad \Lambda_{67} = k\varepsilon_{11}^e, \\
\Lambda_{77} &= -k\varepsilon_{11}^e, \quad \Lambda_{75} = k\alpha e^{k\alpha h_2}, \\
\Lambda_{76} &= -k\alpha e^{-k\alpha h_2}, \\
\Lambda_{77} &= ke^{k h_2}, \quad \Lambda_{78} = -ke^{-k h_2}.
\end{aligned}$$

## References

1. Chu, L., Dui, G., Ju, C.: Flexoelectric effect on the bending and vibration responses of functionally graded piezoelectric nanobeams based on general modified strain gradient theory. *Compos. Struct.* **186**, 39–49 (2018)
2. Singhal, A., Tiwari, R., Baroi, J., Kumhar, R.: Perusal of flexoelectric effect with deformed interface in distinct (PZT-7A, PZT-5A, PZT-6B, PZT-4, PZT-2) piezoelectric materials. *Waves Random and Complex Media* (2022). 10.1080/17455030.2022.2026522
3. Nanthakumar, S.S., Zhuang, X., Park, H.S., Rabczuk, T.: Topology optimization of flexoelectric structures. *J. Mech. Phys. Solids* **105**, 217–234 (2017)
4. Sahu, S.A., Singhal, A., Chaudhary, S.: Surface wave propagation in functionally graded piezoelectric material: an analytical solution. *J. Intell. Mater. Syst. Struct.* **29**(3), 423–437 (2018)
5. Othmani, C., Takali, F., Njeh, A., Ghozlen, M.H.B.: Numerical simulation of Lamb waves propagation in a functionally graded piezoelectric plate composed of GaAs-AlAs materials using Legendre polynomial approach. *Optik* **142**, 401–411 (2017)
6. Li, X.Y., Wang, Z.K., Huang, S.H.: Love waves in functionally graded piezoelectric materials. *Inter. J. Sol. Struct.* **41**(26), 7309–7328 (2004)
7. Barati, M.R.: On wave propagation in nanoporous materials. *Int. J. Eng. Sci.* **116**, 1–11 (2017)
8. Arani, A.G., Abdollahian, M., Kolahchi, R.: Nonlinear vibration of a nanobeam elastically bonded with a piezoelectric nanobeam via strain gradient theory. *Int. J. Mech. Sci.* **100**, 32–40 (2018)
9. Singhal, A., Baroi, J., Sultana, M., Baby, Riya.: Analysis of SH-waves propagating in multiferroic structure with interfacial imperfections. *Mech. Adv. Compos. Struct.* **9**(1), 1–10 (2022)

# A Review on the Reliability Analysis of Point Machines in Railways



Deb Sekhar Roy, Debajyoti Sengupta, Debraj Paul, Debjit Pal, Aftab Khan, Ankush Das, Surojit Nath, Kaushik Sinha, and Bidhan Malakar

**Abstract** Railways, being one of the most eminent modes of transportation used worldwide. It requires proper maintenance ensuring maximum reliability to conduct a safe journey for the passengers. Point Machines or Railway Turnouts are the vital safety assets that play a critical role in maintaining the flexibility of the rail networks. This paper provides an insightful review on the fault analysis, health monitoring and reliability analysis of point machines. A detailed review of the different technologies and algorithms proposed by the researchers, worldwide has been presented along with their current modifications for the adaptation in modern technologies. This review enables the researchers a basis for an enhanced quality and reliability in the working of point machines.

---

D. Sekhar Roy (✉) · D. Sengupta · D. Paul · D. Pal · A. Khan · A. Das · S. Nath · K. Sinha · B. Malakar  
Department of Electrical Engineering, JIS College of Engineering, Kalyani, West Bengal, India  
e-mail: [dsroy.96.00@gmail.com](mailto:dsroy.96.00@gmail.com)

D. Sengupta  
e-mail: [debajyotisengupta98@gmail.com](mailto:debajyotisengupta98@gmail.com)

D. Paul  
e-mail: [debrajpaul15@gmail.com](mailto:debrajpaul15@gmail.com)

D. Pal  
e-mail: [debjitpal741507@gmail.com](mailto:debjitpal741507@gmail.com)

A. Khan  
e-mail: [ashifkhankatwa@gmail.com](mailto:ashifkhankatwa@gmail.com)

A. Das  
e-mail: [ankush2001das@gmail.com](mailto:ankush2001das@gmail.com)

S. Nath  
e-mail: [surojitnath17@gmail.com](mailto:surojitnath17@gmail.com)

K. Sinha  
e-mail: [ksin08546@gmail.com](mailto:ksin08546@gmail.com)

B. Malakar  
e-mail: [bidhan.malakar@jiscollege.ac.in](mailto:bidhan.malakar@jiscollege.ac.in)

**Keywords** Point machine · Reliability · Rail networks · Monitoring · Algorithms · Fault analysis

## 1 Introduction

Over the last few decades railway transport has evolved into a busiest network worldwide. Vast growing railway networks and fast-moving railways has become a mass transportation system, transporting billions of passengers and cargoes daily. Enormous safety, reliability and stability is required within railway networks and transportation keeping in view of its increasing demand. This vast grown railway network requires a well driven railway traffic management system for its smooth working. Point machines plays an effective role in railway trafficking that are operated in railway turnouts and are critical elements in railway tracks. So, encountering faults of point machines and its diagnosis is an important issue to guarantee safer train journeys and has a remarkable sense in railway monitoring [1–6].

For the last few decades several researches have been done in the field of fault detection and health monitoring processes on point machines in aspects of the different railway system. The researchers from different countries of the world are united to develop effective techniques and methodologies to increase the efficiency of the reliability of a point machine. For the sake of simplicity in understanding this paper has given a brief theory on point machines, its types and working principles with technical detailing in Sect. 2. Section 3 of this paper focuses on different analysis methods of point machines which are classified into three categories: Reliability analysis, Condition monitoring and Fault analysis of point machines.

In the reliability analysis of point machine wide range of methodologies and approaches that has been proposed by the researchers worldwide are discussed. This includes methodologies like Remote Condition Monitoring (RCM) system which uses Kalman Filter method [1], Functional Redundancy Approach (FRA) for reliability estimation and Monte Carlo simulation for model designing [3], Qualitative Trend Analysis (QTA) for incipient fault detection [5], etc. The monitoring and management of point machine gives brief survey of the sensors, actuators and modelling methods used to monitor the health of point machines including condition monitoring using Discrete Wavelet Transform (DWT) [4], Principal Component Analysis (PCA) technique etc. The fault detection of point machine provides different technologies and advancements done in the field of failure detection which includes Failure Mode and Effects Analysis (FMEA) [2], Autoregressive Integrated Moving Average (ARIMA) and Autoregressive Kalman (AR-Kalman) to diagnosis and detect faults [6], etc. Therefore, this paper presents a detailed and comprehensive survey of some works done within a decade on point machine utilizing past and present technologies.



## 2 A Brief Theory About Point Machines Used in Railways

The point machine, a piece of electro-mechanical equipment with potential failure mode, is commonly used in signaling systems combining crossings, cross-overs, stock rails, rods, cranks, levers, and locking arrangements. For smooth changes in railway tracks and avoiding hazardous accidents, the role of the point machine has been considered as one of the main components in the context of the world railway system.

In detail, the function of the point machine is to unlock and operate the point switches in the exact position for detection of the correct setting of the point switch. The system mechanism includes various subsystems: motor unit including a contactor control arrangement and a terminal area, gear unit including spur-gears, worm reduction unit [7].

The inner parts of the point machine used in Railways is shown in the following Fig. 1.

### 2.1 Types of Point Machines

Point machines are broadly classified on the basis of different parameters, are as follows [7, 8]:

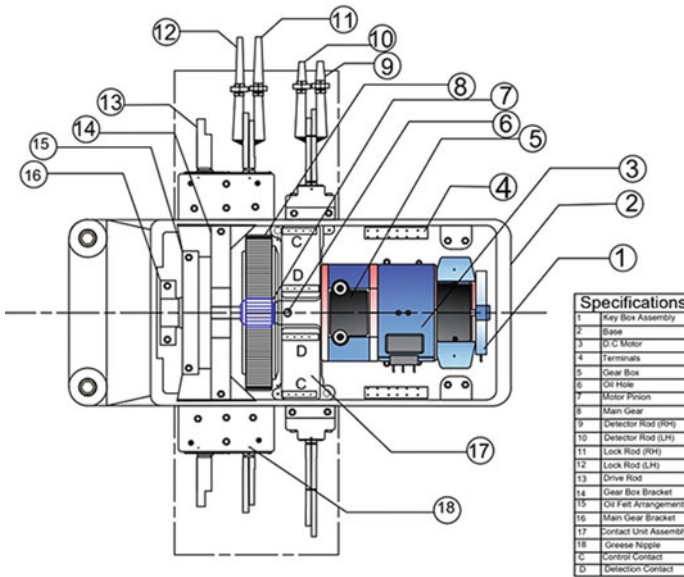


Fig. 1 Top view of inner portion of the point machine used in Railways

- i. Type of point machine on the basis of field arrangement:
  - a. Single field type point machine.
  - b. Split field type point machine.
- ii. Types of point machine on the basis of voltage rating:
  - a. High voltage type (Operating voltage of 110 V DC).
  - b. Low voltage type (Operating voltage of 24 V/ 36 V).
  - c. High Voltage AC-380 AC.
- iii. Type of point machine on the basis of speed:
  - a. High speed machine – Operating speed of 3 s.
  - b. Low speed machine – Operating speed of 5 s.
- iv. Type of point machine on the basis of locking:
  - a. Clamp type point machine.
  - b. Rotary type point machine (Siemens).
- v. Type of point machine on the basis of machine type:
  - a. Combined type point machine.
  - b. Separate type point machine.
- vi. Type of point machine on the basis of machine type:
  - a. Electro-mechanical type.
  - b. Electro-pneumatic type.
  - c. Electro-hydraulic type.

The construction of the Point Machines is shown in Fig. 2.

## 2.2 Working Principles

A point machine is the device that moves and locks the points of turnout remotely. It works under an interlocking mechanism. The electric point machine consists of two parts:

- i. One part is the point lock, which uses an electromagnet to release the lock.
- ii. The other part is the motor which moves the point blades. Both parts are electrically separated but mounted on same housing.

The sequence of operations from [7, 8] followed in the process of Railway Turnouts are as follows:

- i. When the control operator wants to change a certain switch from “straight” to “thrown” or vice versa, a signal is sent to the signaling post.
- ii. The electromagnet of the machine is energized and it releases the lock of it.

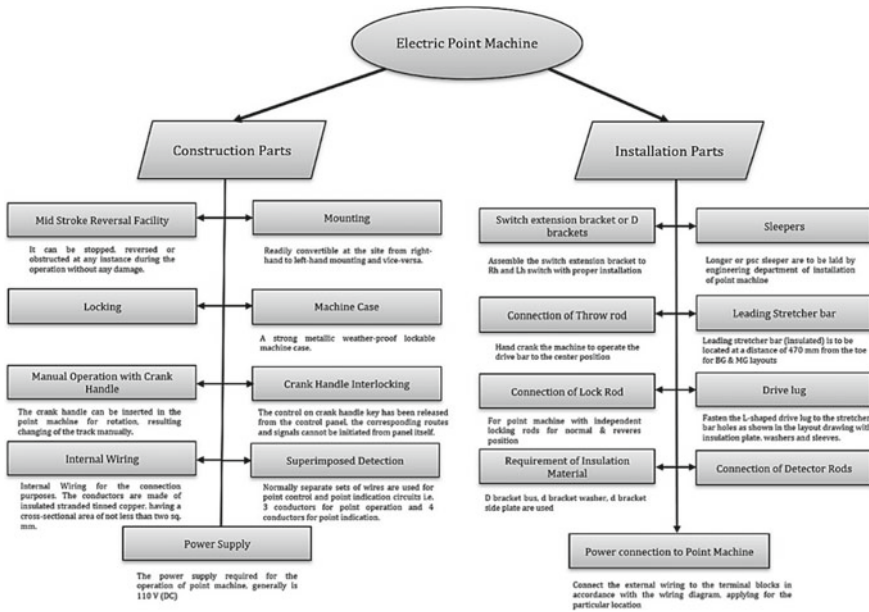


Fig. 2 Components of the point machine in Railways

- iii. The motor is powered in the desired direction and lets the points move.
- iv. At the end position, the motor gets turned off.
- v. The electromagnet gets de-energized and points in the machine gets locked.
- vi. The control operator gets confirmation of success about the change in track positions.

Henceforth, this Section briefly describes the point machines, its types and working principles used in Railways. The following table shows the technical data of motors used in different railway point machines in Table 1.

### 3 A Brief Theory About Point Machines Used in Railways

Different analyses carried out till now for the point machines are divided into the following 3 categories. Apart from these 3 categories, there may be some more categories but to keep this study simple only these three categories are considered.

**Table 1** Table consisting of technical data of motors used in different railway point machines

Salient features	Rotary type point motor	Clamp type point motor	Siemens electric point machine
Type of Motor	DC Series Split Field Motor	DC Series Split Field Motor	DC Series Split Field Motor
Voltage Rating	110 V (DC) + - 25%	110 V (DC)	110 V (DC)
Revolution Speed (RPM)	1700 + - 15%	1700 + - 15%	1700 + - 15%
Current Rating	5.3A (Max-8.5A)	5.5A	5.3A
Time of Operation	4 to 5 s	5 s Max	3–5 s
Power Rating	440 Watts	440 Watts	440 Watts
EPM Thrust	450 kg	450 kg	-
Stroke	143 mm	220 mm	143 mm
Insulation	10 M Ohm	10 M Ohm	10 M Ohm
Gear oil	SAE 30	-	-

### 3.1 Reliability Analysis of Point Machines

Before developing any hardware or methods, the priority retains in the current developments and methodology used in the twenty-first century models. In 2003, researchers from Universidad de Castilla-La Mancha, Spain in collaboration with the University of Sheffield, UK discussed a new detection technique of the gradual failure in Railway Turnouts or Point Machines, which can be managed by a RCM system, by the help of a methodology known as the Kalman Filter. By the usage of the methodology, the faults from Reverse to Normal (RN) detected 100% of faults whereas it showed 97.1% of faults in Normal to Reverse (NR) of a Point Machine [1]. In 2012, researchers from Loughborough University, UK proposed a FRA to estimate the increase in the reliability in the Railway Point Machines. The paper mainly contributes to the usage of 2P-Weibull failure distributions for the collection of field data over a long period of time and using it to model engineering fault tolerance into the existing systems [3]. In 2013, researchers from the University of Nottingham, UK, introduces research that describes the obtaining the field data of lifetime distributions of components of Switches and Crossings (S&C) and as well as on the basis of historical failure data. The paper selected the Weibull distribution as the suitable probabilistic model which was used for the collection of both time-based and utilization-based failure data resulting in efficient and cost-effective asset management [9].

In 2014, researchers from India proposed a parametric model for estimating the probability of the reliability of the Point Machines in Railways which is capable of

predicting the percentage of its failure rate. This paper frames the different types of reliability models and the procedures in the context of parametric analysis which can be applied in Indian Railway (IR) signaling systems [4]. In 2015, researchers from the University of Birmingham, UK introduces a novel algorithm that utilizes QTA for the detection and diagnosis of various incipient faults in the Point Machines, proving to be much reliable than the currently used commercial methods. The research aims to introduce various methods which are capable of reducing 30% of track Life Cycle Costs (LCCs) in the area of Condition Based Maintenance (CBM) where infrastructure operators aim to limit their maintenance costs as low as possible [5]. In 2021, researchers from the Institute of Engineering & Management, India in collaboration with the University of Greenwich, UK researched the rate of failures of different components of signaling systems, including Point Machines using analytical methods. The signaling system components (Point Machine, Track Circuit, and Signal Unit) was analyzed and developed with the help of mathematical modeling that required to increase the reliability of the signaling systems and to achieve the optimal interval inspection for the system [10].

### ***3.2 Case Studies on the Monitoring and Management of Point Machines***

In 2002, researchers from Oxford University discussed about the various sensors that are used for measuring motor driving force, driving current and voltage, temperatures and state changes etc. The data are directly collected from the sensors and processed through the operating system which remotely monitors, control and calibrates the extracted data [11]. In 2007, a paper describes about the remote condition monitoring, reliability, safety of the point machine using the Kalman filter approach. This special type of filter was basically a recursive data processing algorithm that is executed in the form of an equation. The main purpose of the Kalman filter is to filter the linear discrete data using the current sensor data in a point condition monitoring system [12]. In 2010, the authors of the paper mainly focus on the railway infrastructure and more specifically on railways point machines. By using smart techniques of the monitoring system, the problems can be predicted and be able to recover quickly. By using Artificial Intelligence (AI) and signal processing, the faults can be used to detect the faults of the point machines [13]. In 2011, [4] shows a new approach for the fault detection and diagnosis of the AC point machines used in Railways, from the University of Birmingham, UK. As electric active power can be shown as a parameter for the condition monitoring system of the AC point machines i.e., by means of the DWT. By using DWT, the original waveform is converted to multiple levels of resolution, sustaining local time information in each level of resolution. In 2012, a paper focuses on health management and condition monitoring of the point machine in the Railway [3]. This paper shows different strategies and technical architectures for the health management of the electro-mechanical point machine.

The Principal Component Analysis (PCA) was used to assess the health of the point machine. In 2013, a unique approach has been presented for fault detection and diagnosis for electric DC point machines operated on the railways in the UK. Here, the electric current is used as a main parameter for analyzing and acquiring for the DC point machine. The proposed method is dependable upon wavelet transform and Support Vector Machine (SVM). The DWT is used for feature extraction and SVM is used for the classifiers.

In 2015, a group of researchers from China had presented the improvement of the reliability, availability and maintainability, which necessitates the development of a predictive monitoring system for the fleet of point machines in the Railway industry. In the proposed monitoring system, the appropriate signals had been included and the advanced pattern was used to recognize for finding the primary indication of the point machine degradation, and a user interface for displaying and reporting the health results of the point machine [14]. In 2017, a paper describes electric current shape analysis used for condition detection of the point machine in Railway [15]. After analyzing the replacement data and labelling the shape of each replacement data, any further procedures can be undertaken. On the basis of replacement results with field replacement data, we can find the accuracy. In 2018, a paper represents a unique degradation detection method that can be used for mining and identifying the degradation state of the point machine used in Railways, researched in China. Power data is to be processed for extracting the set of features which can be used to describe the point machine properties effectively. Basically, a SVM was used to build the state classifier which can be used to identify the degradation state of the point machine in a combination with a featured map known as Self-Organizing Map (SOM). In this paper, time– frequency-based featured data were mined and a few of them were used to detect and diagnose faults based on a SVM classifier, which is used to build a preferable autonomous fault detection method, where prior knowledge of the data in CM is not vital [16]. Again, within that same year, the authors of [17] had shown their contribution by proposing a methodology known as Machine Health Assessment (MHA), which comprises both offline and online segments, for the analysis of sliding-chair degradation of Point Machines in Railways. In the offline phase, the extraction and data labeling methods were developed for diagnosing the feature selection and time-series segmentation-based fault severity whereas, in the online phase, a sliding-chair fault severity classification was studied by using supervised machine learning tools. Nevertheless, the proposed approach is only applicable if the monitoring data is readily available and if not, appropriate data imputation algorithms are to be used for the extraction of the complete data before using them for further fault detection and severity extraction. In 2019, a research paper was published that discussed the proposal of an initial fault diagnosis method of Railway Point Machines which emphasizes the mining of non-fault data and recognizing them from the assigned degradation states under diverse fault modes. Based upon extraction of data, a self-organizing feature map (SOM)-based degradation state mining method and a Particle Swarm Optimization (PSO)-SVM based classification model was proposed for various degradation conditions and to accurately identify different degradation states respectively. From the application of the esteemed method and

model on the 'SIEMENS S700K' Point Machine, it is found that the method can be used to mine different degradation level states under various fault modes and the model can easily identify the types of states with an accuracy of 97.73% [18]. In 2020, a researcher from Embedded Systems Group, CMC Americas, Inc from the United States of America discussed a new method for maintenance and diagnosis of Railway Point Machines. The method results in the reduction of costs in the examination of manual checks. Also, the method utilizes various sensors to monitor the applicable parameters of Point Machines which can be used to understand and identify the cause of a fault by studying the current situation and comparing its problems from the history of faults that occurred in it [19].

### ***3.3 Case Studies on the Fault Detection of Point Machines***

As continuous growth in railways demands target of performance with proper maintenance and failure management. In 2007, to fulfil the demand a group of researchers had published a paper focusing on maintenance and diagnosis of failure in railway track side components especially on M63 type Point Machine in the UK. They had analysed fault by signal analysis by Kalman filter model and moving average filter and constructed a comparative study about it. This study would come to a decision that moving to the average filter is a more preferable method to the Kalman filter model [12]. In 2009, researchers from Kolkata, India had developed research work on failure mode and effect analysis (FMEA) of the railway signaling systems in working mode to avoid hazardous accidents that occurred in railway tracks. This analysis would cause gradual improvements in design, classifications on a ten-grade scale had been developed in the research [2]. In 2016, a methodology had been proposed to detect the fault in point operating equipment (POE) machine in advance by measuring the current consumption of point motor. One-class Support Vector Machine (SVM) method was used in the technique to get more accuracy than other threshold-based techniques [5]. In 2016, researchers had proposed a data mining solution using audio data to diagnose and detect faults to avoid accidents. This process had gone through four different modules- two online modules and another is offline. The online module includes feature extraction and fault detection; attribute subset selection and vector machines (SVM) training are included in the offline module. To detect the fault and classify it by audio analysis, two SVM had been used and this results in cost-effectiveness and automatic detection [14].

In 2018, a group of researchers from Iran had proposed a new methodology using Stacked Autoencoders (SAE) to analyse the fault. Initially, integration of feature extraction was performed, followed by failure detection. To diagnose the fault, a trained SAE had gone through the phase of final tuning [20]. In the same year, a new method using ARIMA and AR-Kalman had been presented to diagnose and detect the faults in the point machine (S700K). In this method, signal processing including wavelet transform and statistical analysis had been presented to acquire the related data of faults in the point machine [6]. In 2019, a group of researchers from China

had presented a methodology using current signals and feature extraction approach based on locally connected autoencoder. The proposed methodology automatically acquires the informative features from raw electrical signals. For reducing the impact of the non-informative information in raw electrical signals a weighting strategy had been proposed to develop the usefulness and robustness in different features [21]. In the same year, using data from Centralized Traffic Control (CTC) systems, along with meteorological data, a methodology had been proposed to diagnose the risk factor in Point machine. In this methodology, extracting information from railway logs, presented a compact numerical representation along with algorithms of machine learning [22]. In the year 2020, a group of researchers from the UK had proposed a methodology utilizing unlabeled signal sensor data. It was claimed that it can deal with real-time faults using data pre-processing; also suitable for smart city infrastructure [19].

Henceforth, this Section describes about the existing technologies used in Point Machines in Railways in the recent decade, on the basis of Reliability, monitoring and the fault detection methods.

## 4 Conclusions

As Point Machines or Railway Turnouts are vital safety assets that play a critical role in maintaining the flexibility of rail networks, hence requiring proper maintenance procedures for reliable productivity in the field of Railways. There are different technologies developed and used currently as discussed in this paper to overcome the problem of reliability of Point Machines in Railways. In this paper the current, as well as past research, works on point machine is carefully reviewed. More specifically, the paper presents and reviews the previously published works based on the technologies implemented, application of various technologies, algorithms and methodologies, surveyed for the detection of faults, allow feasible condition monitoring and is used for increasing the reliability of the point machine.

## References

1. Márquez, F.P.G., Schmid, F., Collado, J.C.: A reliability centered approach to remote condition monitoring. A railway points case study. *Reliab. Eng. & Syst. Saf. (ELSEVIER, UK)* **80**(1), 33–40 (2003)
2. Panja, S.C., Ray, P.K.: Failure mode and effect analysis of Indian railway signalling system. *Int. J. Perform. Eng. (India)* **5**(2), 131 (2009)
3. Ardakani, H.D., Lucas, C., Siegel, D., Chang, S., Dersin, P., Bonnet, B., Lee, J.: PHM for railway system—a case study on the health assessment of the point machines. In: 2012 IEEE Conference on Prognostics and Health Management pp. 1–5. IEEE, USA (2012)
4. Atamuradov, V., Camci, F., Baskan, S., Şevkli, M.: Failure diagnostics for railway point machines using expert systems. IEEE, Spain (2011)



5. Vileiniskis, M., Remenyte-Prescott, R., Rama, D.: A fault detection method for railway point systems. *Proc. Inst. Mech. Eng. Part F: J. Rail Rapid Transit (UK)* **230**(3), 852–865 (2016)
6. Atamuradov, V., Medjaher, K., Camci, F., Dersin, P., Zerhouni, N.: Railway point machine prognostics based on feature fusion and health state assessment. *IEEE Trans. Instrum. Meas.* **68**(8), 2691–2704 (2018)
7. Handbook on Installation and Maintenance of Electric Point Machine, Indian Railways Centre for Advanced Maintenance Technology, India (2010)
8. Signal Directorate Research Designs & Standards Organisation, Indian Railways Standard Specification For Motors For Electric Point Machine, Specification No.: Irs: S 37, India (2020)
9. Rama, D., Andrews, J.D.: A reliability analysis of railway switches (NG7 2RD. UK). *Proc. Inst. Mech. Eng. Part F: J. Rail Rapid Transit* **227**(4), 344–363 (2013)
10. Kumar, N., Tee, K.F.: Reliability and inspection modelling of railway signalling systems. *Modelling (MDPI, India)* **2**(3), 344–354 (2021)
11. Zhou, F.B., Duta, M.D., Henry, M.P., Baker, S., Burton, C.: Remote condition monitoring for railway point machine. In *ASME/IEEE Joint Railroad Conference*, pp. 103–108. IEEE, USA (2002)
12. Marquez, F.P.G., Weston, P., Roberts, C.: Failure analysis and diagnostics for railway trackside equipment. *Eng. Fail. Anal. (ELSEVIER, UK)* **14**(8), 1411–1426 (2007)
13. García Márquez, F.P., Roberts, C., Tobias, A.M.: Railway point mechanisms: condition monitoring and fault detection. *Proc. Inst. Mech. Eng., Part F: J. Rail Rapid Transit (Spain)* **224**(1), 35–44 (2010)
14. Lee, J., Choi, H., Park, D., Chung, Y., Kim, H.Y., Yoon, S.: Fault detection and diagnosis of railway point machines by sound analysis. *Sensors (MDPI, Korea)* **16**(4), 549 (2016)
15. Sa, J., Choi, Y., Chung, Y., Kim, H.Y., Park, D., Yoon, S.: Replacement condition detection of railway point machines using an electric current sensor. *Sensors (MDPI, Korea)* **17**(2), 263 (2017)
16. Guo, Z., Ye, H., Dong, W., Yan, X., Ji, Y.: A fault detection method for railway point machine operations based on stacked autoencoders. In: *2018 24th International Conference on Automation and Computing (ICAC)*, pp. 1–6. IEEE, UK (2018)
17. Bian, C., Yang, S., Huang, T., Xu, Q., Liu, J., Zio, E.: Degradation detection method for railway point machines, China. [arXiv:1809.02349](https://arxiv.org/abs/1809.02349) (2018)
18. Atamuradov, V., Medjaher, K., Camci, F., Zerhouni, N., Dersin, P., Lamoureux, B.: Feature selection and fault-severity classification-based machine health assessment methodology for point machine sliding-chair degradation. *Qual. Reliab. Eng. Int. (UK)* **35**(4), 1081–1099 (2019)
19. Mistry, P., Lane, P., Allen, P.: Railway point-operating machine fault detection using unlabeled signaling sensor data. *Sensors (MDPI, UK)* **20**(9), 2692 (2020)
20. Abbasnejad, S., Mirabadi, A.: Predicting the failure of railway point machines by using Autoregressive Integrated Moving Average and Autoregressive-Kalman methods. *Proc. Inst. Mech. Eng. Part F: J. Rail Rapid Transit (Iran)* **232**(6), 1790–1799 (2018)
21. Bian, C., Yang, S., Huang, T., Xu, Q., Liu, J., Zio, E.: Degradation state mining and identification for railway point machines. *Reliab. Eng. & Syst. Saf. (China)* **188**, 432–443 (2019)
22. Doboszewski, I., Fossier, S., Marsala, C.: Data driven detection of railway point machines failures. HAL Id: hal-02407540, China (2019)
23. Panja, S.C., Ray, P.K.: Reliability analysis of a ‘point-and-point machine’ of the Indian railway signaling system. *Qual. Reliab. Eng. Int. (Wiley InterScience, India)* **23**(7), 833–848 (2007)
24. Atamuradov, V., Camci, F., Baskan, S., Sevкли, M.: Failure diagnostics for railway point machines using expert systems. In: *2009 IEEE International Symposium on Diagnostics for Electric Machines, Power Electronics and Drives*, pp. 1–5. IEEE, France (2009)
25. Asada, T., Roberts, C., Koseki, T.: An algorithm for improved performance of railway condition monitoring equipment: Alternating-current point machine case study. *Transp. Res. Part C: Emerg. Technol. (ELSEVIER, Japan)* **30**, 81–92 (2013)
26. Asada, T., Roberts, C.: Improving the dependability of DC point machines with a novel condition monitoring system. *Proc. Inst. Mech. Eng. Part F: J. Rail Rapid Transit (UK. SAGE)* **227**(4), 322–332 (2013)

27. Li, Z., Yin, Z., Tang, T., Gao, C.: Fault diagnosis of railway point machines using the locally connected autoencoder. *Appl. Sci. (China)* **9**(23) 5139 (2019)
28. Bemment, S.D., Goodall, R.M., Dixon, R., Ward, C.P.: Improving the reliability and availability of railway track switching by analysing historical failure data and introducing functionally redundant subsystems. *Proc. Inst. Mech. Eng. Part F: J. Rail Rapid Transit (SAGE, UK)* **232**(5), 1407–1424 (2018)
29. Kumar, N., Tee, K. F.: Reliability and inspection modelling of railway signalling systems. *Modelling (MDPI, UK)* **2**(3), 344–354 (2021)

# Application of a Measure of Noncompactness in $cs$ -Solvability and $bs$ -Solvability of an Infinite System of Differential Equations



Niraj Sapkota , Rituparna Das, and Santonu Savapondit

**Abstract** The theory of measure of noncompactness has been a very helpful tool in non-linear functional analysis over the years. In this paper we have examined the solvability of an infinite system of third order differential equations in the sequence space of convergent series and sequence space of bounded series using the Hausdorff measure of noncompactness. We have also used the concept of Meir-Keeler condensing operator to utilize the fixed point theory in our approach and have analysed the approach for each sequence space with suitable examples.

**Keywords** Infinite system of third-order differential equations · Measures of noncompactness · Convergent and bounded sequences

## 1 Introduction

The concepts of measure of noncompactness (MNC), in the non-linear functional analysis is used in various applications of operator theory, fixed point theory and extensively to investigate the theories of differential equations, functional integral equations and in characterizing compact operators between sequence spaces. Kuratowski [1] was first to introduce the concept of measure of noncompactness in 1930. Later Darbo [2] used this in generalising the classical schauder fixed point principle and Banach's contraction mapping principle (special variant) for condensing operators. Goldenstein and Markus [3] gave Hausdorff MNC and Istrătescu [4]

---

N. Sapkota (✉) · S. Savapondit  
Department of Mathematics, Sikkim Manipal Institute of Technology,  
Sikkim Manipal University, Sikkim 737136, India  
e-mail: [niraj.sapkota13@gmail.com](mailto:niraj.sapkota13@gmail.com)

S. Savapondit  
e-mail: [sspondit@gmail.com](mailto:sspondit@gmail.com)

R. Das  
Department of Mathematics, Pandu College, Guwahati, India  
e-mail: [ri2p.das@gmail.com](mailto:ri2p.das@gmail.com)

provided the Istrăţescu MNC. It was only in 1980 that Banás and Goebel [5] gave the axiomatic definition of the measure of noncompactness. Over the years measure of noncompactness has proven itself to be a great tools in various branches of mathematics.

In the literature, Infinite system of differential equations has been introduced by Persidskii in 1959 [6], in 1961 [7] and in 1976 [8]. Here he has coined the term “Countable systems of Differential equations”. Following this, series of other works came into existence for the solvability and existence theorems for different kinds of infinite system of calculus equations in line with our work (see, [9–16, 20–22]).

In 2011 Yueli Chen, Jingli Ren and Stefan Siegmund [17] showed the “existence of positive periodic solutions of third-order differential equations”. For this they have established a particular array of Green’s functions. The equation used here was a single equation. Borrowing the same later R. Saadati, E. Pourhadi and M. Mursaleen in 2019 [16] showed solvability for infinite set of equations of type used by Chen et al. [17] occurring simultaneously. Solvability of that infinite system was established in  $c_0$  space. Our aim is to establish the solvability conditions in the sequence space of convergent series ( $cs$ ) and bounded series ( $bs$ ) for the infinite system of third-order differential equations (ISTODE) define in section (2). For various concepts and types of MNCs one can refer to [11].

## 2 Infinite System of Third-Order Differential Equations

We introduce the following ISTODE for further work

$$\frac{d^3 k_n(\theta)}{d\theta^3} + p \frac{d^2 k_n(\theta)}{d\theta^2} + q \frac{dk_n(\theta)}{d\theta} + r k_n(\theta) = h_n(\theta, k_1(\theta), k_2(\theta), \dots), \quad (n \in \mathbb{N}) \quad (1)$$

Here we take  $h_n \in C(\mathbb{R} \times \mathbb{R}^\infty, \mathbb{R})$  as family of  $\omega$ -periodic functions with respect to  $\theta$ ;  $p, q, r \in \mathbb{R}$  are constants and  $r \neq 0$ . In this paper we will investigate the solvability conditions for  $\omega$ -periodic solutions of ISTODE (1) in  $cs$  and  $bs$  space (for definition see Sect. 3 and Sect. 4 below).

Homogeneous equations for the system (1) is  $\frac{d^3 k_n(\theta)}{d\theta^3} + p \frac{d^2 k_n(\theta)}{d\theta^2} + q \frac{dk_n(\theta)}{d\theta} + r k_n(\theta) = 0, (n \in \mathbb{N})$  and the corresponding characteristic equation is

$$\alpha^3 + p\alpha^2 + q\alpha + r = 0. \quad (2)$$

The eigen value for the Polynomial Eq.2 can have following four possibilities. (given  $r \neq 0$ ): (i)  $\alpha_1 \neq \alpha_2 \neq \alpha_3$ , (ii)  $\alpha_1 = \alpha_2 \neq \alpha_3$ , (iii)  $\alpha_1 = \alpha_2 = \alpha_3 = \alpha$ , (iv)  $\alpha_1 = u + iv, \alpha_2 = u - iv, \alpha_3 = \alpha$ , for  $u, v, \alpha \in \mathbb{R}$ . We shall seek the solvability for each case. Further, with the concept of Green’s functions one can claim that  $k \in C^3(\mathbb{R}, \mathbb{R}^\infty)$  serves as a solution of infinite system of differential equations (1) if and only if  $k \in C(\mathbb{R}, \mathbb{R}^\infty)$  acts as a solution of following integral equations

$$k_n(\theta) = \int_{\theta}^{\theta+\omega} \mathcal{K}(\theta, \eta)h_n(\eta, k(\eta))d\eta \quad (n \in \mathbb{N}). \tag{3}$$

Equation (3) is an infinite system of integral equations. Here  $\mathcal{K}(\theta, \eta)$  is a Green’s function which takes up different form in different cases of eigen values. For the varying behaviour of  $\mathcal{K}(\theta, \eta)$  for each case one may refer to [17].

### 3 Solvability of the Infinite System of Differential Equations in $cs$ Space

$cs := \left\{ k = \{(k_i)\}_{i=0}^{\infty} : \lim_{n \rightarrow \infty} \sum_{i=0}^n k_i < \infty \right\}$ . By definition  $cs$  is a space of sequences with BK and AK and also is equipped with monotone norm  $\|k\|_{cs} = \sup_n \left| \sum_{i=0}^n k_i \right|$  (see Sect.7.3. [19]). Thus with the application of formula given by Banaś and Mursaleen [11] we see that the Hausdorff measure of noncompactness for  $cs$  is

$$\chi(Q) = \lim_{n \rightarrow \infty} \left\{ \sup_{k \in Q} \left( \sup_m \left| \sum_{i=n}^m k_i \right| \right) \right\}, \quad m \geq n$$

for any  $Q \in \mathfrak{M}_{cs}$ . Further, let us state two hypothesis under which solvability of system (1) can be established:

- (H1) The operator  $h : \mathbb{R} \times cs \rightarrow cs$  defined as  $(\theta, k) \mapsto (hk)(\theta) = (h_1(\theta, k), h_2(\theta, k), \dots)$  constitutes a family  $\{(hk)(\theta)\}_{\theta \in \mathbb{R}}$  which is equi-continuous at each point in  $cs$  space, given that, each  $h_n : \mathbb{R} \times \mathbb{R}^{\infty} \rightarrow \mathbb{R}$  is  $\omega$ -periodic with respect to  $\theta$ .
- (H2) The inequality:  $|h_n(\theta, k_1, k_2, \dots)| \leq \phi_n(\theta) + \psi_n(\theta).k_n(\theta)$  holds pertaining to following conditions on  $\phi_n(\theta)$  and  $\psi_n(\theta)$ ;  $\phi_n(\theta) \mapsto \mathbb{R}$  and  $\psi_n(\theta) \mapsto \mathbb{R}$  are continuous, and  $\phi(\theta)$  defined by  $\phi(\theta) = \sum_{k \geq 1} \phi_k(\theta)$  for each  $\theta$ , is uniformly convergent to a function that vanishes identically in  $\mathbb{R}$ . And the family  $\{(\psi_n(\theta))\}_{n \in \mathbb{N}}$  in  $\mathbb{R}$  is equibounded.

Consequent upon  $\Phi := \sup\{\phi(\theta) : \theta \in \mathbb{R}\}$  and  $\Psi := \sup\{\psi_n(\theta) : n \in \mathbb{N}, \theta \in \mathbb{R}\}$  exists.

In the following subsections we shall utilise hypothesis (H1)–(H2) as a conditions for solvability in each cases.

### 3.1 Solvability in cs for Case (i)

For investigating solvability of the solution of the system 1 for the condition  $\alpha_1 \neq \alpha_2 \neq \alpha_3$  the Green’s function appearing in 3 is given by [17], for  $\eta \in [\theta, \theta + \omega]$

$$\begin{aligned} \mathcal{K}_1(\theta, \eta) &= \frac{\exp(\alpha_1(\theta + \omega - \eta))}{(\alpha_1 - \alpha_2)(\alpha_1 - \alpha_3)(1 - \exp(\alpha_1\omega))} \\ &+ \frac{\exp(\alpha_2(\theta + \omega - \eta))}{(\alpha_2 - \alpha_1)(\alpha_2 - \alpha_3)(1 - \exp(\alpha_2\omega))} + \frac{\exp(\alpha_3(\theta + \omega - \eta))}{(\alpha_3 - \alpha_1)(\alpha_3 - \alpha_2)(1 - \exp(\alpha_3\omega))} \end{aligned} \tag{4}$$

Further, considering  $0 \leq \theta + \omega - \eta \leq \omega$  and relations between  $\alpha_i$ , for  $i = 1, 2, 3$  we get,  $\sup_{\eta \in [\theta, \theta + \omega]} (\exp(\alpha_i)(\theta + \omega - \eta)) = \max\{1, \exp(\omega|\alpha_i|)\} = \exp(\omega|\alpha_i|)$ , and hence we can deduce

$$\begin{aligned} \sup_{\eta \in [\theta, \theta + \omega]} |\mathcal{K}_1(\theta, \eta)| &= (\text{let}) \mathcal{Q}_1 = \frac{\exp(\omega|\alpha_1|)}{|(\alpha_1 - \alpha_2)(\alpha_1 - \alpha_3)(1 - \exp(\alpha_1\omega))|} \\ &+ \frac{\exp(\omega|\alpha_2|)}{|(\alpha_2 - \alpha_1)(\alpha_2 - \alpha_3)(1 - \exp(\alpha_2\omega))|} + \frac{\exp(\omega|\alpha_3|)}{|(\alpha_3 - \alpha_1)(\alpha_3 - \alpha_2)(1 - \exp(\alpha_3\omega))|} \end{aligned} \tag{5}$$

**Theorem 1** *The ISTODE of the form given in Eq. 1 satisfying (H1)-(H2) falling in case  $\alpha_1 \neq \alpha_2 \neq \alpha_3$  has at least one  $\omega$ -periodic solution  $k(\theta) = (k_i(\theta)) \in cs$  whenever  $0 < \omega \mathcal{Q}_1 \Psi < 1$ , for all  $\theta \in \mathbb{R}$ .*

**Proof** From the relation (3), (4), (5) and the conditions (H2), for any  $\theta \in \mathbb{R}$  we get

$$\begin{aligned} \|k(\theta)\|_{cs} &= \sup_n \left| \sum_{i=0}^n \int_{\theta}^{\theta + \omega} \mathcal{K}_1(\theta, \eta) h_i(\eta, k(\eta)) d\eta \right| \\ &\leq \sup_n \int_{\theta}^{\theta + \omega} |\mathcal{K}_1(\theta, \eta)| \sum_{i=1}^n (\phi_i(\eta) + \psi_i(\eta) \cdot k_i(\eta)) d\eta \leq \omega \mathcal{Q}_1 (\Phi + \Psi \|k\|_{cs}). \end{aligned}$$

Hence, we get  $\|k\|_{cs} \leq \frac{\omega \mathcal{Q}_1 \Phi}{1 - \omega \mathcal{Q}_1 \Psi} = l_0$ .

Let  $k^0(\theta) = (k_i^0(\theta))$  where  $k_i^0(\theta) = 0$ . Then a closed ball  $U_0 = U(k_0, l_0)$  contains  $k$ . Now, let us consider the operator  $T = (T_i)$  on  $C(\mathbb{R}, U_0)$  defined as follows: For  $\theta \in \mathbb{R}$ ,

$$(Tk)(\theta) = (T_i k)(\theta) = \left\{ \int_{\theta}^{\theta + \omega} \mathcal{K}_1(\theta, \eta) h_i(\eta, k(\eta)) d\eta \right\}, \tag{6}$$

where  $k(\theta) = (k_i(\theta)) \in U_0$  and  $k_i(\theta) \in C(\mathbb{R}, \mathbb{R})$ ,  $\theta \in \mathbb{R}$ . Since,  $(h_i(\theta, k(\theta))) \in cs$  for each  $\theta \in \mathbb{R}$ , so we have

$$\sup_{n \rightarrow \infty} \left( \sum_{i=0}^n (T_i k)(\theta) \right) \leq \omega \mathcal{Q}_1(\Phi + \Psi \|k\|_{cs}) < \infty.$$

Therefore,  $(Tk)(\theta) = \{(T_i k)(\theta)\} \in cs$  for all  $\theta \in \mathbb{R}$ . Also,

$$\begin{aligned} (T_i k)(\theta + \omega) &= \int_{\theta + \omega}^{\theta + 2\omega} \mathcal{K}_1(\theta + \omega, \eta) h_i(\eta, k(\eta)) d\eta \\ &= \int_{\theta}^{\theta + \omega} \mathcal{K}_1(\theta + \omega, \zeta + \omega) h_i(\zeta + \omega, k(\zeta + \omega)) d\zeta \\ &= \int_{\theta}^{\theta + \omega} \mathcal{K}_1(\theta, \zeta) h_i(\zeta, k(\zeta)) d\zeta = (T_i k)(\theta). \end{aligned}$$

i.e., each  $(T_i k)(\theta)$  is  $\omega$ -periodic whenever  $k(\theta)$  is  $\omega$ -periodic. Since  $\|(Tk)(\theta) - k^0(\theta)\|_{cs} = \|(Tk)(\theta)\|_{cs} \leq l$ , thus  $T$  self maps on  $U_0$ . Also, by (H1),  $T$  and hence  $Tk$  is continuous. Now, to establish  $T$  as a Meir-Keeler condensing operator we do the following. Firstly, for any given  $\varepsilon > 0$ , we need to find  $\delta > 0$  such that

$$\varepsilon \leq \chi(U_0) < \varepsilon + \delta \implies \chi(TU_0) < \varepsilon.$$

Using Eq. (4), (3), (3), we get

$$\begin{aligned} \chi(TU_0) &= \lim_{n \rightarrow \infty} \left\{ \sup_{k(\theta) \in U_0} \left| \sum_{k \geq n} \int_{\theta}^{\theta + \omega} \mathcal{K}_1(\theta, \eta) h_k(\eta, k(\eta)) d\eta \right| \right\} \\ &\leq \mathcal{Q}_1 \lim_{n \rightarrow \infty} \left\{ \sup_{k(\theta) \in U_0} \sum_{k \geq n} \int_{\theta}^{\theta + \omega} (|\phi_k(\eta)| + |\psi_k(\eta)| |k_k(\eta)|) \right\} \\ &\leq \omega \mathcal{Q}_1 \Psi \lim_{n \rightarrow \infty} \left\{ \sup_{k(\theta) \in U_0} \sum_{k \geq n} |k_k| \right\} = \omega \mathcal{Q}_1 \Psi \chi(U_0) \end{aligned}$$

Thus, we get  $\chi(TU_0) < \omega \mathcal{Q}_1 \Psi \chi(U_0) < \varepsilon \implies \chi(U_0) < \frac{\varepsilon}{\omega \mathcal{Q}_1 \Psi}$ .

Taking  $\delta = \frac{(1 - \omega \mathcal{Q}_1 \Psi)}{\omega \mathcal{Q}_1 \Psi} \varepsilon$ , we get  $\varepsilon \leq \chi(U_0) < \varepsilon + \delta$ . Thus  $T$  is a Meir-Keeler condensing operator defined on a set  $U_0 \subset cs$ .  $T$  also satisfies all the hypothesis of Fixed point Theorem given by Aghajani et al. [18]. This shows that  $T$  has a fixed point in  $U_0$ , which is a solution of the system (1). □

$\mathcal{K}_1(\theta, \eta)$  may have different bounds depending upon the constraints on the value of  $\alpha_i$ , for  $i = 1, 2, 3$ , as described in [17]. Then,

- (E1) If  $f_1 < g_1$ , and either  $\alpha_1 > \alpha_2 > \alpha_3 > 0$  or  $\alpha_3 < \alpha_2 < 0 < \alpha_1$  holds, then  $F_3 \leq \mathcal{K}_1(\theta, \eta) \leq G_3 < 0$ .
- (E2) If  $f_2 > g_2$ , and either  $\alpha_3 < \alpha_2 < \alpha_1 < 0$  or  $\alpha_3 < 0 < \alpha_2 < \alpha_1$  holds, then  $0 < F_3 \leq \mathcal{K}_1(\theta, \eta) \leq G_3$ .

We can easily refine our Theorem 1 using the above conditions (E1)–(E2) and hypothesis (H1)–(H2) by referring to the results by Chen et al. [17] as follows:

**Theorem 2** *The ISTODE of the form given in equation (1) satisfying assumptions (H1)–(H2) along with hypothesis (E1) (resp. (E2)) has atleast one  $\omega$ -periodic solution  $k(\theta) = (k_i(\theta)) \in cs$  whenever  $\omega\Psi|F_3| < 1$  (resp.  $\omega\Psi G_3 < 1$ ), for all  $\theta \in \mathbb{R}$ .*

### 3.2 Solvability in cs for Case (ii)

For the second case where  $\alpha_1 = \alpha_2 \neq \alpha_3$ , Green’s function  $\mathcal{K}(\theta, \eta) = \mathcal{K}_2(\theta, \eta)$  (let appearing in equation (3) for investigating solvability of the solution of the system (1) is given by [17]

$$\begin{aligned} \mathcal{K}_2(\theta, \eta) = & \frac{\exp(\alpha_1(\theta + \omega - \eta))[(1 - \exp(\alpha_1\omega))((\eta - \theta)(\alpha_3 - \alpha_1) - 1) - (\alpha_3 - \alpha_1)\omega]}{(\alpha_1 - \alpha_3)^2(1 - \exp(\alpha_1\omega))^2} \\ & + \frac{\exp(\alpha_3(\theta + \omega - \eta))}{(\alpha_1 - \alpha_3)^2(1 - \exp(\alpha_3\omega))}, \quad \eta \in [\theta, \theta + \omega] \end{aligned} \tag{7}$$

Then following conditions holds true

- (E3) If  $\alpha_3 < 0 < \alpha_1 = \alpha_2$ , then  $0 < F_4 \leq \mathcal{K}_2(\theta, \eta) \leq G_4$ .
- (E4) If  $\alpha_1 = \alpha_2 < 0 < \alpha_3$ , then  $F_4 \leq \mathcal{K}_2(\theta, \eta) \leq G_4 < 0$ .
- (E5) If  $0 < \alpha_1 = \alpha_2 < \alpha_3$ ,  $\exp(\alpha_1\omega) < 1 + (\alpha_3 - \alpha_1)\omega$  then  $F_5 \leq \mathcal{K}_2(\theta, \eta) \leq G_5 < 0$ .
- (E6) If  $\alpha_1 = \alpha_2 < \alpha_3 < 0$ , and  $f_3 > 1$  then  $0 < F_4 \leq \mathcal{K}_2(\theta, \eta) \leq G_4$ .
- (E7) If  $0 < \alpha_3 < \alpha_2 = \alpha_1$ , and  $g_4 < 1$  then  $F_6 \leq \mathcal{K}_2(\theta, \eta) \leq G_6 < 0$ .

For, each notations refer to [17].

We refine our Theorem 1 for case (ii) using the above conditions (E3)–(E5) and hypothesis (H1)–(H2) by referring to the results by Chen et al. [17] as follows:

**Theorem 3** *The ISTODE of the form given in Eq. (1) satisfying assumptions (H1)–(H2) along with hypothesis (E3) (resp. (E4), (E5), (E6), (E7)) has atleast one  $\omega$ -periodic solution  $k(\theta) = (k_i(\theta)) \in cs$  whenever  $\omega\Psi G_4 < 1$  (resp.  $\omega\Psi|F_4| < 1$ ,  $\omega\Psi G_4 < 1$ ,  $\omega\Psi|F_6| < 1$ ), for all  $\theta \in \mathbb{R}$ .*



### 3.3 Solvability in *cs* for Case (iii)

For the third case where  $\alpha_1 = \alpha_2 = \alpha_3 = \alpha$  the Green's function  $\mathcal{K}(\theta, \eta) = \mathcal{K}_3(\theta, \eta)$ (let) is represented by.

$$\mathcal{K}_3(\theta, \eta) = \frac{[(\eta - \theta) \exp(\alpha\omega) + \omega - \eta + \theta]^2 + \omega^2 \exp(\alpha\omega)}{2(1 - \exp(\alpha\omega))^3} \exp(\alpha(\theta + \omega - \eta)), \quad \eta \in [\theta, \theta + \omega] \quad (8)$$

Then

(E8) If  $\alpha > 0$ , then  $F_7 \leq \mathcal{K}_3(\theta, \eta) \leq G_7 < 0$ .

(E9) If  $\alpha < 0$ , then  $0 < F_7 \leq \mathcal{K}_3(\theta, \eta) \leq G_7$ .

**Theorem 4** *The ISTODE of the form given in Eq. (1) satisfying assumptions (H1)–(H2) along with hypothesis (E8)(resp. (E9)) has atleast one  $\omega$ -periodic solution  $k(\theta) = (k_i(\theta)) \in cs$  whenever  $\omega\Psi|F_7| < 1$ (resp.  $\omega\Psi G_7 < 1$ ), for all  $\theta \in \mathbb{R}$ .*

### 3.4 Solvability in *cs* for Case (iv)

For the fourth case where  $\alpha_1 = u + iv$ ,  $\alpha_2 = u - iv$ ,  $\alpha_3 = \alpha$  the Green's function  $\mathcal{K}(\theta, \eta) = \mathcal{K}_4(\theta, \eta)$  (let) is represented by.

$$\begin{aligned} \mathcal{K}_4(\theta, \eta) = & \frac{\exp(u(\theta + \omega - \eta))[(u - \alpha)B_2(\theta) - vA_2(\theta)]}{v[(u - \alpha)^2 + v^2](1 + \exp(2u\omega) - 2 \cos(v\omega) \exp(u\omega))} \\ & + \frac{\exp(\alpha(\theta + \omega - \eta))}{(1 - \exp(\alpha\omega))[(u - \alpha)^2 + v^2]} \quad \text{for } \eta \in [\theta, \theta + \omega] \quad (9) \end{aligned}$$

Then following conditions holds true.

(E10) If  $\alpha < 0 < u, v$  and  $\frac{1 + \exp(2u\omega) - 2 \cos(v\omega) \exp(u\omega)}{\exp(2u\omega)} > \frac{[(u - \alpha)^2 + v^2](1 - \exp(\alpha\omega))^2}{v^2 \exp(2\alpha\omega)}$ , then  $0 < F_8 \leq \mathcal{K}_4(\theta, \eta) \leq G_8$ .

(E11) If  $u, \alpha < 0 < v$  and  $1 + \exp(2u\omega) - 2 \cos(v\omega) \exp(u\omega) > \frac{[(u - \alpha)^2 + v^2](1 - \exp(\alpha\omega))^2}{v^2 \exp(2\alpha\omega)}$ , then  $0 < F_9 \leq \mathcal{K}_4(\theta, \eta) \leq G_9$ .

(E12) If  $u, v, \alpha > 0$  and  $\frac{1 + \exp(2u\omega) - 2 \cos(v\omega) \exp(u\omega)}{\exp(2u\omega)} > \frac{[(u - \alpha)^2 + v^2](1 - \exp(\alpha\omega))^2}{v^2}$ , then  $F_8 \leq \mathcal{K}_4(\theta, \eta) \leq G_8 < 0$ .

(E13) If  $u < 0 < v, \alpha$  and  $1 + \exp(2u\omega) - 2 \cos(v\omega) \exp(u\omega) > \frac{[(u - \alpha)^2 + v^2](1 - \exp(\alpha\omega))^2}{v^2}$ , then  $F_9 \leq \mathcal{K}_4(\theta, \eta) \leq G_9 < 0$ .

We refine our Theorem 1 for case (iv) using the above conditions (E10)-(E13) and hypothesis (H1)-(H2) by referring to the results by Chen et al. [17] as follows:

**Theorem 5** *The IStODE of the form given in Eq. (1) satisfying assumptions (H1)–(H2) along with hypothesis (E10) (resp. (E11), (E12), (E13)) has atleast one  $\omega$ -periodic solution  $k(\theta) = (k_i(\theta)) \in cs$  whenever  $\omega\Psi G_8 < 1$  (resp.  $\omega\Psi G_9 < 1, \omega\Psi|F_8| < 1, \omega H|F_9| < 1$ ), for all  $\theta \in \mathbb{R}$ .*

### 4 Solvability of the Infinite System of Diiferential Equations in $bs$ Space

$bs := \left\{ k' = \{(k'_i)\}_{i=0}^\infty : \sup_n \left| \sum_{i=0}^n k'_i \right| < \infty \right\}$ . By definition  $bs$  is a sequence space of bounded series also equipped with the norm  $\|k'\|_{bs} = \sup_n \left| \sum_{i=1}^n k'_i \right|$  which makes it a Banach space. Also, comparing the definition between  $cs$  and  $bs$  space it becomes clear that  $cs$  is a closed subspace of  $bs$ . For the sake of clarity we shall add superscript  $*$  for anything related to  $bs$  space that are equivalent to functions and elements related to  $cs$  space.

We again state the following two conditions so as to show the solvability of the system (1) in  $bs$  space:

- (H3) The operator  $h = h' : \mathbb{R} \times bs \rightarrow bs$  defined as  $(\theta, k) \mapsto (h'k)(\theta) = (h'_1(\theta, k), h'_2(\theta, k), \dots)$  constitutes a family  $\{(h'k)(\theta)\}_{\theta \in \mathbb{R}}$  which is equi-continuous at each point in  $bs$  space, given that, each  $h'_i : \mathbb{R} \times \mathbb{R}^\infty \rightarrow \mathbb{R}$  is  $\omega$ -periodic with respect to  $\theta$ .
- (H4) The inequality:  $|h'_n(\theta, k_1, k_2, \dots)| \leq \phi'_n(\theta) + \psi'_n(\theta).k'_n(\theta)$  holds pertaining to following conditions on  $\phi'_n(\theta)$  and  $\psi'_n(\theta)$ ;  $\phi'_n(\theta) \mapsto \mathbb{R}$  and  $\psi'_n(\theta) \mapsto \mathbb{R}$  are continuous, and  $\phi'(\theta)$  defined by  $\phi'(\theta) = \sum_{k \geq 1} \phi'_k(\theta)$  for each  $\theta$ , is uniformly convergent to a function that vanishes identically in  $\mathbb{R}$ . And the family  $\{(\psi'_n(\theta))\}_{n \in \mathbb{N}}$  in  $\mathbb{R}$  is equibounded.

Consequent upon  $\Phi' := \sup\{\phi'(\theta) : \theta \in \mathbb{R}\}$  and  $\Psi' := \sup\{\psi'_n(\theta) : n \in \mathbb{N}, \theta \in \mathbb{R}\}$  exists. Do take note that the conditions for solvability in  $bs$  space is analogous to  $cs$  space. This is due to the fact that  $cs$  and  $bs$  enjoys the same norm. This fact greatly helps in shortening of proof for all the solvability cases below.

#### 4.1 Solvability in $bs$ for Different Cases

We shall reuse all the notations that we have used to shown solvability in  $cs$ . Hence, we will go straight to the theorem.

**Theorem 6** *The IStODE of the form given in Eq. 1 satisfying (H1)-(H2) falling in case  $\alpha_1 \neq \alpha_2 \neq \alpha_3$  has at least one  $\omega$ -periodic solution  $k'(\theta) = (k'_i(\theta)) \in bs$  whenever  $0 < \omega Q_1 \Psi < 1$ , for all  $\theta \in \mathbb{R}$ .*

As mentioned earlier norm for both *cs* and *bs* spaces are same and hence it becomes obvious that the proof will look similar to proof in theorem (1). Only thing noteworthy here is that the set of all solutions in *cs* space is also a subset of the set of all solutions in *bs* space.  $\mathcal{K}_1(\theta, \eta)$  may have different bounds depending upon the constraints on the value of  $\alpha_i$  for  $i = 1, 2, 3$  as described in Chen et al. [17]. By using those conditions and the hypothesis (H3)-(H4) we will refine our theorem for each case as follows:

**Theorem 7** *The ISTODE of the form given in equation (1) satisfying assumptions (H1)-(H2) along with hypothesis (E1)(resp. (E2)) has atleast one  $\omega$ -periodic solution  $k'(\theta) = (k'_i(\theta)) \in bs$  whenever  $\omega\Psi'|F_3| < 1$  (resp.  $\omega\Psi'G_3 < 1$ ), for all  $\theta \in \mathbb{R}$ .*

**Theorem 8** *The ISTODE of the form given in Eq. 1 satisfying assumptions (H1)-(H2) along with hypothesis (E3) (resp. (E4), (E5),(E6),(E7)) has atleast one  $\omega$ -periodic solution  $k'(\theta) = (k'_i(\theta)) \in bs$  whenever  $\omega\Psi'G_4 < 1$  (resp.  $\omega\Psi'|F_4| < 1, \omega\Psi'G_4 < 1, \omega\Psi'|F_6| < 1$ ), for all  $\theta \in \mathbb{R}$ .*

**Theorem 9** *The ISTODE of the form given in Eq. (1) satisfying assumptions (H1)-(H2) along with hypothesis (E8)(resp. (E9)) has atleast one  $\omega$ -periodic solution  $k'(\theta) = (k'_i(\theta)) \in bs$  whenever  $\omega\Psi'|F_7| < 1$ (resp.  $\omega\Psi'G_7 < 1$ ), for all  $\theta \in \mathbb{R}$ .*

**Theorem 10** *The ISTODE of the form given in Eq. (1) satisfying assumptions (H1)-(H2) along with hypothesis (E10)(resp. (E11), (E12), (E13)) has atleast one  $\omega$ -periodic solution  $k'(\theta) = (k'_i(\theta)) \in bs$  whenever  $\omega\Psi'G_8 < 1$  (resp.  $\omega\Psi'G_9 < 1, \omega\Psi'|F_8| < 1, \omega\Psi'|F_9| < 1$ ), for all  $\theta \in \mathbb{R}$ .*

### 5 Examples

Let us take examples and contrast the result that we got from two different spaces *cs* and *bs* space.

**Example 1** Consider the differential equation for  $(n \in \mathbb{N})$  and  $\theta \in \mathbb{R}$  :

$$\frac{d^3k_n(\theta)}{d\theta^3} - 2.1 \frac{d^2k_n(\theta)}{d\theta^2} + 5.2 \frac{dk_n(\theta)}{d\theta} - 0.5k_n(\theta) = \frac{\sin^n(\theta)}{(n+1)^3} + \sum_{j=n}^{\infty} \frac{\cos^n(\theta)k_j(\theta)}{(j^2+n^2)(nj+\pi^2)}, \tag{10}$$

**Solution 1** With the application of theory of differential equations we can find the roots of the homogeneous equation associated with equation (10) are  $\alpha_1 = 1 + 2i, \alpha_2 = 1 - 2i, \alpha_3 = 0.1$ . Now we will check  $h_n(\theta, k)$  of Eq. 10, Here,  $h_n(\theta, k) = \frac{\sin^n(\theta)}{(n+1)^3} + \sum_{j=n}^{\infty} \frac{\cos^n(\theta)k_j(\theta)}{(j^2+n^2)(nj+\pi^2)}$ . Considering  $k = (k_n) \in cs$ , we get

$$\sup_n \left| \sum_{j=1}^n h_j(\theta, k(\theta)) \right| \leq \frac{\pi^2}{6} + \frac{\pi^4}{180} \|k\|_{cs}.$$

Further, check that (H1) holds by letting  $\varepsilon > 0$  arbitrarily. Take  $k'(\theta) = (k'_n(\theta)) \in cs$  that satisfies  $\|k(\theta) - k'(\theta)\|_{cs} \leq \delta(\varepsilon) = 2(1 + \pi^2)\varepsilon$ , then

$$|h(\theta, k(\theta)) - h(\theta, k'(\theta))| \leq \frac{1}{2}(1 + \pi^2)^{-1}\delta$$

This ensures the continuity in accord with (H1).

Conditions of (H2):  $|h_n(\theta, k_1, k_2, \dots)| \leq \phi_n(\theta) + \psi_n(\theta).k_n(\theta)$  can be established by taking  $\phi_n(\theta) = (n + 1)^{-3}$  and  $\psi_n(\theta)$ , the series sum from  $j$  from 1 to  $\infty$  of the function  $\frac{1}{(j^2+n^2)(nj+\pi^2)}$ . Ofcourse, the series for  $\psi_n(\theta)$  is convergent for each  $n$ .

$$|h_n(\theta, k(\theta))| \leq \frac{1}{(n + 1)^3} + \sum_{j=n}^{\infty} \frac{|k_j(\theta)|}{(j^2 + n^2)(nj + \pi^2)} \leq \phi_n(\theta) + \psi_n(\theta)|k_n(\theta)|$$

Further, series  $\sum_{n \geq 1} \phi_n(\theta)$  converges to  $-1 + \zeta(3)$  and each  $\{\psi_n(\theta)\}_n$  is independent of  $\theta$  and hence the equiboundedness. Also  $\Psi = \sup\{\psi_n(\theta) : n \in \mathbb{N}, \theta \in \mathbb{R}\} \approx 0.0606$  With these results both conditions (H1) and (H2) is satisfied.

Now as mentioned earlier, roots of characteristic equations associated with homogeneous equation pertaining to differential equation (10) are  $\alpha_1 = 1 + 2i, \alpha_2 = 1 - 2i, \alpha_3 = 0.1$ . This implies that  $u, v, \alpha > 0$ . Consequently, given example falls under case (iv)(given in Sect. 3.4). i.e., Green’s function related to this example is given by Eq. (9). Further, since  $u, v, \alpha > 0$  and  $\omega = 2\pi$  satisfies all the conditions of (E12), we get  $F_8 \leq \mathcal{K}_4(\theta, \eta) \leq G_8 < 0$  (for all notations ref. Section 3.4). Also, it is clear that  $h_n(\theta, k)$  is  $(\omega =)2\pi$ -periodic with respect to  $\theta$ .

Upon certain approximations we also get  $\omega\Psi|F_8| \approx 0.48897 < 1$ . This would mean that all the conditions of Theorem (5) is being satisfied, and hence the infinite system of differential equations (10) has at least one  $\omega$ -periodic solution  $k(\theta) = (x_j(\theta)) \in cs$ .

Now, we are going to consider a example for  $bs$  space.

**Example 2** For  $bs$  space we consider an ISTODE as follows: for  $(n \in \mathbb{N})$  and  $\theta \in \mathbb{R}$

$$\frac{d^3k_n(\theta)}{d\theta^3} + 4.5\frac{d^2k_n(\theta)}{d\theta^2} - 3\frac{dk_n(\theta)}{d\theta} - 2.5k_n = \frac{e^{(\sin(2\theta+1))}}{(n + 1)^2} + \sin(\cos(2\theta)) \sum_{j=n}^{\infty} \frac{k_j(\theta)}{j^3}. \tag{11}$$

**Solution 2** In this example we have  $h_n(\theta, k) = \frac{e^{(\sin(2\theta+1))}}{(n+1)^2} + \sin(\cos(2\theta)) \sum_{j=n}^{\infty} \frac{k_j(\theta)}{j^3}$  Ofcourse,  $k = (k_n) \in bs$  here. Now, Checking for  $h_n(\theta, k)$  we get,

$$\sup_n \left| \sum_{i=1}^n h_i(\theta, k(\theta)) \right| \leq \frac{\pi^2}{6} (r_1 + r_2\|k\|_{bs})$$

Here,  $r_1 = \sup_{\theta} |e^{(\sin(2\theta+1))}| \approx 2.718$  and  $r_2 = \sup_{\theta} |\sin(\cos(2\theta))| \approx 0.841$  are constants. One more thing to notice here is that  $h_n(\theta, k(\theta))$  is  $\pi$ -periodic with respect to  $\theta$ . Now, take  $\|k(\theta) - k'(\theta)\|_{bs} \leq \delta(\varepsilon) = [r_2\zeta(3)]^{-1}\varepsilon$ , where, both  $k(\theta)$  and  $k'(\theta)$  belongs to *bs* space, then  $|h(\theta, k(\theta)) - h(\theta, k'(\theta))| \leq r_2\zeta(3)\delta(\varepsilon) < \varepsilon$ . Again, for  $|h_n(\theta, k(\theta))|$ , we get

$$|h_n(\theta, k(\theta))| \leq r_1(n + 1)^{-2} + r_2 \sum_{j=n}^{\infty} \frac{1}{j^3} |k_j(\theta)| \leq \phi_n(\theta) + \psi_n(\theta)|k_n|$$

By taking  $\phi_n(\theta) = r_1(n + 1)^{-2}$  and family  $(\psi_n(\theta))$  equibounded by  $r_2\zeta(3)$  we get a series  $\sum_{n \geq 1} \phi_n(\theta)$  convergent to a limit  $\frac{\pi^2 r_2}{6}$  and each member of  $(\psi_n(\theta))$  continuous and in fact a constant.

Summarizing all the results achieved so far we have  $h_n(\theta, k(\theta)) \in bs$  a  $\pi$ -periodic functions with respect to first coordinate and also satisfies conditions (H3) and (H4). Now, we look upon the homogeneous equations associated with infinite system of differential equations (11). We get roots as  $\alpha_1 = 1, \alpha_2 = -0.5$  and  $\alpha_3 = -5$ . I.e., the examples falls under case (i)(ref. Sect. 4.1). This makes clear that the Green’s function of concern is given by equation (4). Also  $37.206 = f_1 < g_1 = 42.079$ , i.e.,  $\alpha_1, \alpha_2, \alpha_3$  satisfies (E1). Hence,  $F_3 \leq \mathcal{K}_1(\theta, \eta) \leq G_3 < 0$ . Upon certain approximation we get  $\omega\Psi|F_3| = 0.9627 < 1$ . All results combined together assures that all the conditions for theorem (7) are satisfied, which in turn ensures that there exist atleast one  $\pi$ -periodic solution  $k(\theta) = (k_j(\theta)) \in bs$  for infinite system (11).

**Remark** Infinite systems of differential equations, system of Eq. (10) and system of Eq. (11) is interchangeable as an example for *cs* and *bs* space, if associated  $k(\theta) \in(cs$  or *bs*) in  $h_n(\theta, k)$  is interchanged accordingly.

**Acknowledgements** Supported by TMA Pai University Research Fund.

## References

1. Kuratowski, K.: Sur les espaces complets. *Fundamenta mathematicae* **15**, 301–309 (1930)
2. Darbo, G.: Punti uniti in trasformazioni a codominio non compatto. *Rendiconti del Seminario matematico della Università di Padova* **24**, 84–92 (1955)
3. Goldenstein, L., Markus, A.: On a measure of noncompactness of bounded sets and linear operators. *Studies in Algebra and Mathematical Analysis*, Kishinev, pp. 45–54 (1965)
4. Istrăţescu, V.I.: On a measure of noncompactness. *Bulletin mathématique de la Société des Sciences Mathématiques de la République Socialiste de Roumanie* **16**(2), 195–197 (1972)
5. Banaś, J., Goebel, K.: Measure of noncompactness in Banach space. *Lecture Notes in Pure and Applied Mathematics*, vol. 60 (1980)
6. Persidskii, K.: Countable systems of differential equations and stability of their solutions. *Izv. Akad. Nauk Kazach. SSR* **7**, 52–71 (1959)

7. Persidskii, K.: Countable systems of differential equations and stability of their solutions iii: Fundamental theorems on stability of solutions of countable many differential equations. *Izv. Akad. Nauk Kazach. SSR* **9**, 11–34 (1961)
8. Persidskii, K.: Infinite systems of differential equations, izdat (1976)
9. Mursaleen, M., Mohiuddine, S.: Applications of measures of noncompactness to the infinite system of differential equations in  $\ell_p$  spaces. *Nonlinear Anal.: Theory Methods Appl.* **75**(4), 2111–2115 (2012)
10. Mursaleen, M., Alotaibi, A.: Infinite system of differential equations in some spaces. In: *Abstract and Applied Analysis*, vol. 2012. Hindawi (2012)
11. Banaś, J., Mursaleen, M.: *Sequence Spaces and Measures of Noncompactness with Applications to Differential and Integral Equations*. Springer (2014)
12. Arab, R., Allahyari, R., Haghighi, A.S.: Existence of solutions of infinite systems of integral equations in two variables via measure of noncompactness. *Appl. Math. Comput.* **246**, 283–291 (2014)
13. Aghajani, A., Pourhadi, E.: Application of measure of noncompactness to  $\ell_1$ -solvability of infinite systems of second order differential equations. *Bull. Belg. Math. Soc.-Simon Stevin* **22**(1), 105–118 (2015)
14. Mursaleen, M., Rizvi, S.: Solvability of infinite systems of second order differential equations in  $c_0$  and  $\ell_1$  by Meir-Keeler condensing operators. *Proc. Am. Math. Soc.* **144**(10), 4279–4289 (2016)
15. Srivastava, H., Das, A., Hazarika, B., Mohiuddine, S.: Existence of solutions of infinite systems of differential equations of general order with boundary conditions in the spaces  $c_0$  and  $\ell_1$  via the measure of noncompactness. *Math. Methods Appl. Sci.* **41**(10), 3558–3569 (2018)
16. Saadati, R., Pourhadi, E., Mursaleen, M.: Solvability of infinite systems of third-order differential equations in  $c_0$  by Meir-Keeler condensing operators. *J. Fixed Point Theory Appl.* **21**(2), 1–16 (2019)
17. Chen, Y., Ren, J., Siegmund, S.: Green’s function for third-order differential equations. *Rocky Mt. J. Math.* 1417–1448 (2011)
18. Aghajani, A., Mursaleen, M., Haghighi, A.S.: Fixed point theorems for Meir-Keeler condensing operators via measure of noncompactness. *Acta Math. Sci.* **35**(3), 552–566 (2015)
19. Wilansky, A.: *Summability Through Functional Analysis*. Elsevier (2000)
20. Hazarika, B., Rabbani, M., Agarwal, R.P., Das, A., Arab, R.: Existence of solution for infinite system of nonlinear singular integral equations and semi-analytic method to solve it. *Iranian J. Sci. Technol. Trans. A: Sci.* **45**, 235–245 (2021)
21. Banaś, J., Woś, W.: Solvability of an infinite system of integral equations on the real half-axis. *Adv. Nonlinear Anal.* **10**(1), 202–216 (2021)
22. Nashine, H.K., Das, A.: Extension of Darbo’s fixed point theorem via shifting distance functions and its application. *Nonlinear Anal.: Model. Control* **27**, 1–14 (2022)

# Instabilities of Excitation Spectrum for Attractive Spin-Orbit Coupled Bose-Einstein Condensates in Quasi-one Dimension



Sonali Gangwar, R. Ravisankar, and Pankaj K. Mishra

**Abstract** In the paper, we present our analytical results to investigate the effect of spin-orbit (SO) and Rabi couplings on the excitation spectrum of attractive quasi-one dimensional binary Bose-Einstein condensates. We use Bogoliubov-de Gennes theory to analytically derive the spectrum for the non-interacting and interacting cases. The eigenvalues of the spectrum are used to identify the stability of the spectrum. First, we analyze the effect of attractive nonlinear interactions on the instability by fixing other coupling parameters. We obtain the appearance of multiple instability bands upon increase of intraspecies interaction. Similar observation is made as SO coupling strengths are increased for fixed Rabi coupling strength as  $\Omega < \Omega_c$ . For  $\Omega > \Omega_c$  we have a phase transition from unstable state to stable state. While increase in Rabi coupling with fixed  $k_L$ , the multi-band instability gets transformed to single-band instability. However, the effect of variation of interspecies interaction does not yield multiple bands. Finally, we obtain a stability phase diagram of the excitation spectrum in the coupling parameters space.

**Keywords** Bose Einstein condensates · Bogoliubov-de Gennes theory · Spin-Orbit coupling · Instability

## 1 Introduction

Since its first realization in the laboratory experiment in 2011 [1], the spin-orbit (SO) coupled Bose-Einstein condensates (BECs) have triggered unprecedented growth in the research in ultracold matter [2–4]. Owing to its highly controllable nature of the experiment it has also opened new avenues for exploration for the other fields of Physics. One of the interesting question in the field is to ascertain the different kind of excitations of the condensates which characterize the overall nature and dynamical

---

S. Gangwar · R. Ravisankar · P. K. Mishra (✉)  
Department of Physics, Indian Institute of Technology, Guwahati 781039, Assam, India  
e-mail: [pankaj.mishra@iitg.ac.in](mailto:pankaj.mishra@iitg.ac.in)  
URL: <https://www.iitg.ac.in/pankaj.mishra/>

© The Author(s), under exclusive license to Springer Nature Switzerland AG 2022  
S. Banerjee and A. Saha (eds.), *Nonlinear Dynamics and Applications*,  
Springer Proceedings in Complexity,  
[https://doi.org/10.1007/978-3-030-99792-2\\_116](https://doi.org/10.1007/978-3-030-99792-2_116)

1365

behaviour of the ground state of the system. The stability of the coupled BECs could be well understood by analyzing the elementary excitation spectrum. For example, the Bogoliubov-de Gennes (BdG) elementary excitation spectrum, much related to macroscopic quantum phenomena, namely, superfluidity and superconductivity, provides the fundamental information about the condensate dynamics. Excitation spectrum for the equal combination of Rashba-Dresselhaus 1D SO coupling [5, 6] in BECs gives rise roton-maxon structures theoretically [7, 8] and experimentally (see [9–11]). Effective study on SO coupling has played an important role in many exotic phenomena such as superfluidity [12], flat band structure in optical lattice potential [13] and ground state phase diagram. There are some works that indicate the presence of zero momentum phase [14] in quasi-1D SO coupled BECs. So far there are few studies of collective excitation study on SO coupled BEC in 2D [15]. However, such detailed studies are lacking for quasi-1D system. In this paper, we present the excitation spectrum of SO coupled BECs in quasi-1D.

SO coupled BECs can be described by coupled Gross-Pitaevskii equations. Using this we can find the single particle dispersion relation. It has two different distinct structures those are single minimum and double minima of parabola. We find that single minimum represents plane wave phase, while, the double minima corresponds to the stripe wave phase. These minima can be achieved with the help of free parameters namely SO and Rabi coupling strengths. Excitation spectrum is different from the single particle spectrum. We vary the contact inter- and intraspecies interactions and analyze their effect on the excitation spectrum. In this paper, we focus on solving the excitation spectrum and analyze its phase transition from stable to unstable state upon variation of several parameters.

The paper is organized as follows. In Sect. 2 we begin by describing the theoretical model, coupled Gross-Piteavskii equations. In Sect. 3 we present the analytical results of the Bogoliubov-de Gennes matrix and explain its excitation spectrum. The effect of interactions and coupling parameters on the stability of the excitation spectrum is demonstrated in Sect. 4, which is followed by the discussion on the stability phase diagram in Sect. 5. Finally, we conclude our paper in Sect. 6.

## 2 The Model

In this section we illustrate the mean-field model of pseudo spin-1/2 BECs in a quasi-one dimensional setting with strong transverse trap confinement. In experiments, the spin-orbit coupled BECs are created, for instance, by choosing two internal spin states of  $^{87}\text{Rb}$  atoms within the  $^5S_{1/2}$ ,  $F = 1$  ground electronic manifold, which are designated as pseudo spin-up,  $|\uparrow\rangle = |F = 1, m_F = 0\rangle$  and spin-down,  $|\downarrow\rangle = |F = 1, m_F = -1\rangle$ . Then a pair of counter propagating Raman lasers with strength  $\Omega$  (Rabi coupling) is used to couple the two states. The properties of such SO coupled BECs can be described by a set of coupled Gross-Pitaevskii equations (in dimensionless form) as [16]:



$$i \frac{\partial \psi_{\uparrow}}{\partial t} = \left[ -\frac{1}{2} \frac{\partial^2}{\partial x^2} - ik_L \frac{\partial}{\partial x} + V(x) + \alpha |\psi_{\uparrow}|^2 + \beta |\psi_{\downarrow}|^2 \right] \psi_{\uparrow} + \Omega \psi_{\downarrow}, \quad (1a)$$

$$i \frac{\partial \psi_{\downarrow}}{\partial t} = \left[ -\frac{1}{2} \frac{\partial^2}{\partial x^2} + ik_L \frac{\partial}{\partial x} + V(x) + \beta |\psi_{\uparrow}|^2 + \alpha |\psi_{\downarrow}|^2 \right] \psi_{\downarrow} + \Omega \psi_{\uparrow}, \quad (1b)$$

Here,  $\psi_{\uparrow}$  and  $\psi_{\downarrow}$  are the wavefunction corresponding to the spin-up and spin-down component of the condensates,  $V(x)$  is the one dimensional harmonic trapping potential,  $\alpha$  and  $\beta$  are the intra- and respectively interspecies nonlinear interaction strengths respectively,  $k_L$  is spin-orbit and  $\Omega$  is the Rabi coupling parameters. In the above equations (1), length is measured in units of harmonic oscillator length  $a_0 = \sqrt{\hbar/(m\omega_{\perp})}$ , time in the units of  $\omega_{\perp}^{-1}$ , and energy in the units of  $\hbar\omega_{\perp}$ , where  $\omega_{\perp}$  is the transverse direction frequency of the harmonic confinement. The SO and Rabi coupling parameters have been rescaled as  $k_L = k'_L/a_0\omega_{\perp}$  and  $\Omega = \Omega'/\omega_{\perp}$ , respectively, while the wave function is rescaled as  $\psi_{\uparrow,\downarrow} = \psi'_{\uparrow,\downarrow} a_0^{3/2}/\sqrt{N}$ . We consider the Rabi coupling as  $\Omega = |\Omega|e^{i\theta}$  that minimizes the energy when  $\Omega = -|\Omega|$  for  $\theta = \pi$  [16]. The wave functions are subjected to the following normalization condition,

$$\int_{-\infty}^{\infty} (|\psi_{\uparrow}|^2 + |\psi_{\downarrow}|^2) dx = 1, \quad (2)$$

### 3 Excitation Spectrum

The excitation spectrum provides the information about the dynamics of the condensates [15]. In this section, we present our analytical analysis of the stability of the SO coupled BECs with help of excitation spectrum. Here to understand the stability of different phases, we wish to study the excitation spectrum of plane wave solutions. This will be done by applying Bogoliubov theory. For this purpose, we assumed that homogeneous BECs with the total density of the system  $n = n_{\uparrow} + n_{\downarrow}$  is conserved and the chemical potential  $\mu$  is same for the both components [15]. Then the stationary state evolves as

$$\Psi_j = e^{-i\mu t} \left[ \psi_j + u_j e^{i(k_x x - \omega t)} + v_j^* e^{-i(k_x x - \omega^* t)} \right], \quad (3)$$

where  $\psi_j = \sqrt{n_j} e^{i\phi_j}$ ,  $j = (\uparrow, \downarrow)$  is the ground state wave functions and  $u_j$ ,  $v_j$  are the amplitudes of the two plane waves,  $n_j$ ,  $\phi_j$  are density and phase respectively of ground state wave function. The Bogoliubov coefficients  $u$ 's and  $v$ 's are obtained by substituting Eq. (3) in Eq. (1) and written as

$$\mathbf{L} \begin{pmatrix} u_{\uparrow} \\ v_{\uparrow} \\ u_{\downarrow} \\ v_{\downarrow} \end{pmatrix} = \hbar\omega \begin{pmatrix} u_{\uparrow} \\ v_{\uparrow} \\ u_{\downarrow} \\ v_{\downarrow} \end{pmatrix}, \tag{4}$$

where,

$$\mathbf{L} = \begin{pmatrix} f_1(n_{\uparrow}, n_{\downarrow}) & \alpha n_{\uparrow} & \beta\sqrt{n_{\uparrow}n_{\downarrow}} - \Omega & \beta\sqrt{n_{\uparrow}n_{\downarrow}} \\ -\alpha n_{\uparrow} & -f_2(n_{\uparrow}, n_{\downarrow}) & -\beta\sqrt{n_{\uparrow}n_{\downarrow}} & -\beta\sqrt{n_{\uparrow}n_{\downarrow}} + \Omega \\ \beta\sqrt{n_{\uparrow}n_{\downarrow}} - \Omega & \beta\sqrt{n_{\uparrow}n_{\downarrow}} & f_2(n_{\downarrow}, n_{\uparrow}) & \alpha n_{\downarrow} \\ -\beta\sqrt{n_{\uparrow}n_{\downarrow}} & -\beta\sqrt{n_{\uparrow}n_{\downarrow}} + \Omega & -\alpha n_{\downarrow} & -f_1(n_{\downarrow}, n_{\uparrow}) \end{pmatrix}, \tag{5}$$

where,

$$f_1(n_{\uparrow}, n_{\downarrow}) = \frac{k_x^2}{2} + k_L k_x + 2\alpha n_{\uparrow} + \beta n_{\downarrow} - \frac{1}{2} \left[ \alpha n + \beta n - \frac{n\Omega}{\sqrt{n_{\uparrow}n_{\downarrow}}} \right],$$

$$f_2(n_{\uparrow}, n_{\downarrow}) = \frac{k_x^2}{2} - k_L k_x + 2\alpha n_{\uparrow} + \beta n_{\downarrow} - \frac{1}{2} \left[ \alpha n + \beta n - \frac{n\Omega}{\sqrt{n_{\uparrow}n_{\downarrow}}} \right], \tag{6}$$

We consider  $n_{\uparrow} = n_{\downarrow} = 1/2$ . So using  $n = n_{\uparrow} + n_{\downarrow} = 1$ , the above quantities can be written as

$$f_1 = \frac{k_x^2}{2} + k_L k_x + \frac{\alpha}{2} + \Omega, \quad f_2 = \frac{k_x^2}{2} - k_L k_x + \frac{\alpha}{2} + \Omega,$$

The simplified form of the Bogoliubov-de Gennes equation can be obtained by substituting  $\det \mathbf{L}$  equal to zero and written as

$$\omega^4 + \Lambda\omega^2 + \Delta = 0. \tag{7}$$

where,

$$\Lambda = \frac{1}{2} \left[ -k_x^4 - 4\Omega(\alpha - \beta + 2\Omega) - 2k_x^2(\alpha + 2(k_L^2 + \Omega)) \right] \tag{8}$$

$$\Delta = \frac{1}{16} k_x^2 \left( k_x^2 + 2\alpha - 2\beta - 4k_L^2 + 4\Omega \right) \left( k_x^4 + 8(\alpha + \beta)\Omega + 2k_x^2(\alpha + \beta - 2k_L^2 + 2\Omega) \right) \tag{9}$$

### 4 Stability Analysis of the Excitation Spectrum

The single-particle spectrum ( $\alpha = \beta = 0$ ) generally have a positive branch ( $\omega_+$ ) and a negative branch ( $\omega_-$ ). Positive branch exhibits single minima throughout, while, the negative branch shows the transition from single minima to double minima upon the variation of spin-orbit coupling at some finite Rabi coupling term. We calculate the eigenvalue of the matrix  $\mathbf{L}$  (Eq. (5)). we have two positive and two negative eigen energy spectrum.

Here, we will focus on the negative branch of the elementary excitation spectrum, which plays a vital role in the transition between the different phases of the condensates. Note that the imaginary or complex eigenenergies indicate the dynamical instability, while, negative eigenenergy of the excitation spectrum implies that the system is energetically unstable [15]. As we are interested in investigating the effect of the different interaction and coupling parameters on the dynamical instability, we will be mainly interested in looking at the nature of the negative branch of the eigenenergy. We define  $G = |\Im(\omega_-)|$ , where  $\Im$  represents the imaginary part of the variable.

#### 4.1 Effect of Interactions on the Stability of Excitation Spectrum

First, we begin our discussion by analyzing the effect of the variation of the attractive nonlinear interaction on the excitation spectrum stability. In Fig. 1 we show the variation of the imaginary part of the negative branch of the eigenspectrum ( $G = |\Im(\omega_-)|$ ) along the wavenumber by fixing the other parameters as  $k_L = \Omega = 1$  and  $\beta = -1$  for different attractive intraspecies ( $\alpha$ ) interactions. For lower  $\alpha$  ( $\alpha < -4$ ) the spectrum is stable (as  $G = 0$ ) at  $k_x = 0$ , however, for  $\alpha = -4$  the spectrum shows instability at  $k_x = 0$ . The instability of the spectrum even for  $k_x = 0$  can

**Fig. 1** Variation of the imaginary part of the eigenvalue ( $G = |\Im(\omega_-)|$ ) with  $k_x$  for different range of  $\alpha$  with fixed  $k_L = \Omega = 1$  and  $\beta = -1$ . Multiple unstable bands starts appearing upon increase of attractive interaction

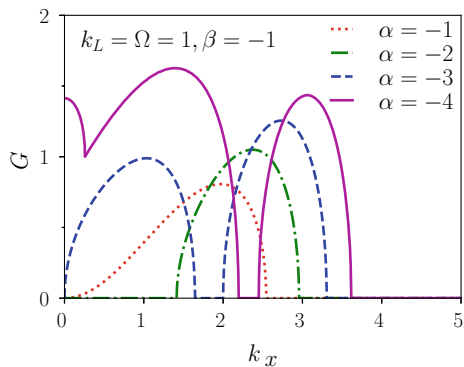
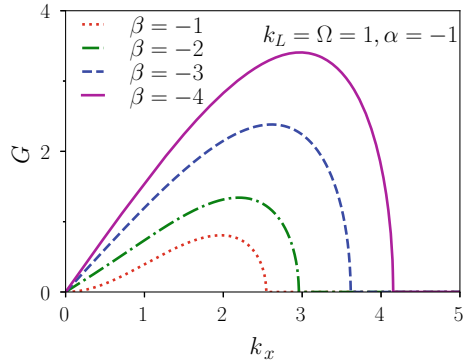


**Fig. 2** Variation of the imaginary part of the eigenfrequency ( $G$ ) with  $k_x$  for different range of  $\beta$  with fixed  $k_L = \Omega = 1$  and  $\alpha = -1$ . The instability bands become more wider upon increase in  $\beta$



be attributed to the collapsing nature of condensates at higher attractive value of  $\alpha$ . At lower  $\alpha (= -1, -2)$  the system have single instability band while for higher  $\alpha (= -3, -4)$  multiple instability band seems to appear in along the wavenumber. Note that the instability band is symmetric about  $k_x = 0$ . However, as we analyze the effect of variation in the interspecies interaction ( $\beta$ ) on the stability of the excitation spectrum we find that for all the values of  $\beta$  the system have one instability band. The wavenumber range of the instability band width and amplitude becomes wider upon increase in  $\beta$  for  $k_L = \Omega = 1$  and  $\alpha = -1$  (See Fig. 2). So we find that effect of change in  $\alpha$  and change in  $\beta$  on the stability of the excitation is different.

After discussing the effect of the interactions of the stability of the excitation spectrum now in the following we will present the effect of SO and Rabi couplings on the instability band of the excitation spectrum.

### 4.2 Effect of Coupling Parameters on the Stability of Excitation Spectrum

In Fig. 3 we show the plots of the instability strength  $G$  in the wavenumber space for different  $k_L (= 0, 1, 2, 4)$  by keeping the other coupling and interaction parameters fixed ( $\Omega = 0.25, \alpha = \beta = -1$ ). We find the presence of single instability at  $k_L = 0$ . At finite  $k_L (= 1, 2, 4)$  the spectrum shows multiple instability bands. However, as we analyze the effect of the Rabi coupling on the instability bands, we find that the multi band instability gets modified into single instability band that exhibits expansion along the wave number upon increase of  $\Omega$ . They do not split into multiple instability bands (See Fig. 4). Overall we find that the effect of Rabi coupling on the instability is opposite to those due to the SO coupling.

After discussing both interactions and coupling parameters effects on the stability of the excitation spectrum, next we move to obtain a full stability phase diagrams in interactions and coupling parameters plane.

**Fig. 3** Variation of the imaginary part of the eigenfrequency ( $G$ ) with  $k_x$  for different range of  $k_L$  with fixed  $\alpha = \beta = -1$  and  $\Omega = 0.25$

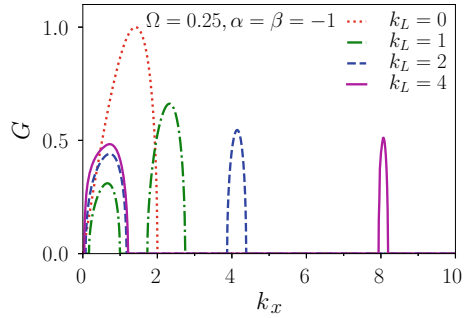
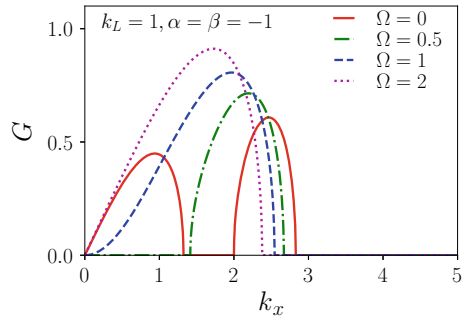


**Fig. 4** Variation of the imaginary part of the eigenfrequency ( $G$ ) with  $k_x$  for different range of  $\Omega$  with fixed  $\alpha = \beta = -1$  and  $k_L = 1$



### 5 Stability Phase Diagrams

In order to get a complete picture of the stability of excitation spectrum for the different ranges of the coupling parameters in Fig. 5 we show the imaginary part of the eigenfrequency ( $G$ ) in the  $\alpha - \beta$  plane (in left panel) and in the  $\Omega - k_L$  plane (right panel). For the left panel we fixed the parameters  $\Omega = k_L = 1$  and for right panel  $\alpha = \beta = -1$ . We have chosen  $k_x = 1$ . We have the notion that the system in the strong attractive regime of condensates gets collapsed, however, here we find the presence of a small narrow stable regime in the  $\alpha - \beta$  plane, which may be quite interesting for the experimental research. As we analyze the phase diagram in the  $\Omega - k_L$  we find that at lower  $k_L (\sim 0)$  the excitation spectrum exhibits instability for all the ranges of  $\Omega$ . However, for  $k_L \gtrsim 1$  the spectrum is unstable for small  $\Omega (\sim 0)$ . We find that the condensates become unstable upon increasing  $\Omega$  for a fixed  $k_L$ . However, the effect of increase in  $k_L$  for a fixed  $\Omega (\gtrsim 0.3)$  shows the transition from unstable to the stable phase. Overall, we find that the effect of  $k_L$  and  $\Omega$  on the excitation spectrum is quite opposite to those observed in quasi-two dimension [15]. This is due to the SO coupling present in the same components of the quasi-1D binary BECs.

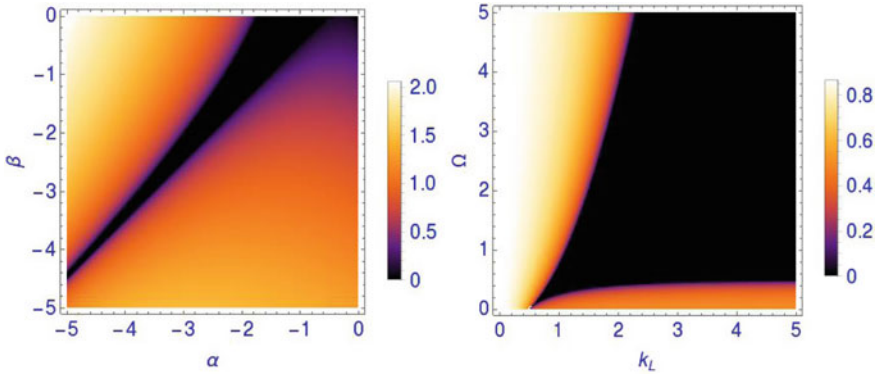


**Fig. 5** Stability phase diagram of the BdG spectrum: (left) in the  $\alpha - \beta$  plane the parameters are fixed as  $\Omega = k_L = 1$ , (right) in the  $\Omega - k_L$  plane with fixed  $\alpha = \beta = -1$ . Note that the phase diagrams are obtained for the mode  $k_x = 1$ .  $\alpha = \beta = -1$

## 6 Conclusion

In this paper, we have presented an analytical investigations of the effect of the interaction strengths and coupling parameters on the excitation spectrum of the attractive SO coupled binary BECs. We have used the Bogoliubov-de Gennes theory to analyze the excitation spectrum. The dynamical instability is characterized using the imaginary part of the negative eigenspectrum. We have obtained that the increase of intraspecies interaction leads to the formation of multiple instability bands while the increment in the interspecies interaction show the presence of only one instability band. The increase in the Rabi coupling for a fixed SO coupling ( $k_L$ ) brings multi-band instability to single-band instability in the condensates. However, the effect of  $k_L$  is opposite those of  $\Omega$ . Increase in  $k_L$  makes the condensates more stable when  $\Omega \gtrsim 0.3$ . However, for  $\Omega \lesssim 0.3$  we observed multi-band instability from single-band instability upon increase in  $k_L$  and we do not have any stable state. In this paper, we have not analyzed the nature of dynamics and the eigenvector of the eigenspectrum which give the information about the detailed correlation between the spin and density of the condensate. The study is underway.

**Acknowledgements** Supported by DST-SERB (Department of Science and Technology - Science and Engineering Research Board) for the financial support through Project No. ECR/2017/002639.

## References

1. Lin, Y.-J., Jiménez-García, K., Spielman, I.B.: Spin-orbit-coupled Bose-Einstein condensate. *Nature* **471**, 83 (2011). <https://doi.org/10.1038/nature09887>

2. Stanescu, T.D., Anderson, B., Galitski, V.: Spin-orbit coupled Bose-Einstein condensates. *Phys. Rev. A* **78**, 023616 (2008). <https://doi.org/10.1103/PhysRevA.78.023616>
3. Galitski, V., Spielman, I.B.: Spin-orbit coupling in quantum gases. *Nature* **494**, 49 (2013). <https://doi.org/10.1038/nature11841>
4. Zhai, H.: Degenerate quantum gases with spin-orbit coupling: a review. *Rep. Prog. Phys.* **78**, 026001 (2015). <https://doi.org/10.1088/0034-4885/78/2/026001>
5. Bychkov, Y.A., Rashba, E.I.: Oscillatory effects and the magnetic susceptibility of carriers in inversion layers. *J. Phys. C: Solid State Phys.* **17**, 6039 (1984)
6. Dresselhaus, G.: Spin-orbit coupling effects in zinc blende structures. *Phys. Rev.* **100**, 580 (1955). <https://doi.org/10.1103/PhysRev.100.580>
7. Martone, G.I., Li, Y., Pitaevskii, L.P., Stringari, S.: Anisotropic dynamics of a spin-orbit-coupled Bose-Einstein condensate. *Phys. Rev. A* **86**, 063621 (2012). <https://doi.org/10.1103/PhysRevA.86.063621>
8. Li, Y., Martone, G.I., Pitaevskii, L.P., Stringari, S.: Superstripes and the excitation spectrum of a spin-orbit-coupled Bose-Einstein condensate. *Phys. Rev. Lett.* **110**, 235302 (2013). <https://doi.org/10.1103/PhysRevLett.110.235302>
9. Khamehchi, M.A., Zhang, Y., Hamner, C., Busch, T., Engels, P.: Measurement of collective excitations in a spin-orbit-coupled Bose-Einstein condensate. *Phys. Rev. A* **90**, 063624 (2014). <https://doi.org/10.1103/PhysRevA.90.063624>
10. Ha, L.-C., Clark, L.W., Parker, C.V., Anderson, B.M., Chin, C.: Roton-maxon excitation spectrum of Bose condensates in a shaken optical lattice. *Phys. Rev. Lett.* **114**, 055301 (2015). <https://doi.org/10.1103/PhysRevLett.114.055301>
11. Ji, S.-C., Zhang, L., Xu, X.-T., Wu, Z., Deng, Y., Chen, S., Pan, J.-W.: Softening of roton and phonon modes in a Bose-Einstein condensate with spin-orbit coupling. *Phys. Rev. Lett.* **114**, 105301 (2015). <https://doi.org/10.1103/PhysRevLett.114.105301>
12. Zhu, Q., Zhang, C., Wu, B.: Exotic superfluidity in spin-orbit coupled Bose-Einstein condensates. *Europhys. Lett.* **100**, 50003 (2012). <https://doi.org/10.1209/0295-5075/100/50003>
13. Zhang, Y., Zhang, C.: Bose-Einstein condensates in spin-orbit-coupled optical lattices: flat bands and superfluidity. *Phys. Rev. A* **87**, 023611 (2013). <https://doi.org/10.1103/PhysRevA.87.023611>
14. Yu, Z.-Q.: Ground-state phase diagram and critical temperature of two-component Bose gases with Rashba spin-orbit coupling. *Phys. Rev. A* **87**, 051606(R) (2013). <https://doi.org/10.1103/PhysRevA.87.051606>
15. Ravisankar, R., Fabrelli, H., Gammal, A., Muruganandam, P., Mishra, P.K.: Effect of Rashba spin-orbit and Rabi couplings on the excitation spectrum of binary Bose-Einstein condensates. *Phys. Rev. A* **104**, 053315 (2021). <https://doi.org/10.1103/PhysRevA.104.053315>
16. Ravisankar, R., Sriraman, T., Salasnich, L., Muruganandam, P.: Quenching dynamics of the bright solitons and other localized states in spin-orbit coupled Bose-Einstein condensates. *J. Phys. B: At. Mol. Opt. Phys.* **53**, 195301 (2020). <https://doi.org/10.1088/1361-6455/aba661>

# **The Dynamics of COVID-19 Pandemic**



# Mapping First to Third Wave Transition of Covid19 Indian Data via Sigmoid Function



Supriya Mondal  and Sabyasachi Ghosh 

**Abstract** Understanding first and second wave of covid19 Indian data along with its few selective states, we have realized a transition between two Sigmoid pattern with twice larger growth parameter and maximum values of cumulative data. As a result of those transition, time duration of second wave shrink to half of that first wave with four times larger peak values. Realizing first and second wave Sigmoid pattern due to covid19 virus and its mutated variant— $\delta$  virus respectively, third wave was mapped by another Sigmoid pattern with three times larger growth parameter than that of first wave. After understanding the crossing zone among first, second and third wave curves due to covid19,  $\delta$  and omicron respectively, a hidden Sigmoid pattern due to mutated  $\delta+$  virus is identified in between  $\delta$  and omicron. It is really interesting that entire covid19 data of India can be easily (offcourse grossly) understood by simple algebraic expressions of Sigmoid function and we can identify 4 Sigmoid patterns due to covid19 virus and its 3 dominant variants.

**Keywords** Covid19 · Omicron · Sigmoid function · 3rd Wave

## 1 Introduction

Spreading of the novel coronavirus, covid19, from China to entire globe become so alarming that the World Health Organization (WHO) declared it as a pandemic disease on 11th March 2020 [1, 2]. The data of covid infected, recovered and death are

---

S. Mondal (✉)

MMI College of Nursing, Pachpedi Naka, Raipur 492001, Chhattisgarh, India

VY Hospital, Adjacent to Kamal Vihar (Sector 12), New Dhamtari Road, Raipur 492001, Chhattisgarh, India

e-mail: [supriyamondal.07@gmail.com](mailto:supriyamondal.07@gmail.com)

S. Ghosh

Indian Institute of Technology Bhilai, GEC Campus,

Sejbahar, Raipur 492015, Chhattisgarh, India

e-mail: [sabya@iitbhilai.ac.in](mailto:sabya@iitbhilai.ac.in)

© The Author(s), under exclusive license to Springer Nature Switzerland AG 2022

1377

S. Banerjee and A. Saha (eds.), *Nonlinear Dynamics and Applications*,

Springer Proceedings in Complexity,

[https://doi.org/10.1007/978-3-030-99792-2\\_117](https://doi.org/10.1007/978-3-030-99792-2_117)

maintained by different countries in their government based websites. Reference [3] is citing the corresponding website for India. From 2020 to now, a huge amount of works are attempted to fit the covid infected daily cases and cumulative data for predicting the their pattern. One of the successful model is SIR model [4–6], on which a large number of works can be found. Few selective works are Refs. [7–13], which focus on SIR model application for explaining Indian covid19 data as well as other countries, e.g. Ref. [14]. SIR type interaction based alternative methodologies can be found in recent Refs. [15–17]. Since the lock down is one of the preventive measurement of this epidemic spreading, so some Refs. [9, 18–23] are focused to explore this fact mathematically. Alternative methods [24–30] like regression analysis [24], population ecology [25], machine learning [26], deep learning [27] etc. This modeling estimation helps different preventive measurement related qualitative research like Refs. [31–35]. Recently, Refs. [10, 36] work on second wave data and third wave prediction. Present work is intended towards similar aims

Though SIR model is quite well cultivated model for epidemic prediction, but a simple logistic function description like Sigmoid function [37–39] can also be an easy-dealing tools to understand the same epidemic outbreak. In our earlier works [40–42], we have used this Sigmoid function framework for predicting first wave of India data. This framework is also used for understanding epidemic size of other countries, for example Refs. [38, 39, 43].

Covid19 first wave growing is initiated in India from March, 2020 and peak was noticed in Sep, 2020. Then around Jan, 2021 the daily case data quietly went down but after that a second wave growing started, whose peak was noticed around May, 2021. It was more deadly than first wave due to mutated variant -  $\delta$  virus. It also went down around June, 2021. Next, another mutated variant  $\delta+$  came into the picture with a mild spreading coverage, but another mutated variant omicron create the next level rapid growth from Jan, 2022, which can be considered as actual third wave. Present work is aimed to explain the these first, second and third waves covid19 infection data due to 3 different variants with the help of three different Sigmoid functions.

The article is organized as follows. Starting with brief formalism part of Sigmoid function, we have discussed about the steps of generating curves in the Sect. 2. Next, in results section, we have described the first and second wave curves including our third wave predicted curves. After analyzing those results, at the end we summarized our work.

## 2 Mathematical Framework

In this framework part, we will discuss quickly about the Sigmoid function which will be used to interpret covid 19 data. Then we will discuss about the steps, through which we proceed.

The form of Sigmoid function is

$$N(t) = N_0 e^{\lambda t} / \left( \frac{N_0 e^{\lambda t}}{N_m} + 1 \right), \tag{1}$$

where  $N_0$  is initial number of cases,  $\lambda$  is growth parameter,  $N_m$  is the maximum values, where cumulative case  $N(t)$  will be saturated. Here  $t$  represents number of days. Now, the time derivative of Sigmoid function is

$$\frac{dN}{dt} = \lambda N_0 e^{\lambda t} / \left( \frac{N_0 e^{\lambda t}}{N_m} + 1 \right)^2, \tag{2}$$

which is the number of new cases per day as we see in covid 19 data. Sigmoid function shows exponential behaviour in low values of  $t$  but it will saturate to a maximum values ( $N_{max}$ ) at high values of  $t$ . When we analyze its derivative or slope, then we will get first increasing and then decreasing trends after showing a peak. The peak structure of daily cases depends on three parameters  $N_m, N_0, \lambda$ . The peak time  $t_p$ , when daily cases reach its highest value, can be expressed as

$$t_p = \frac{\ln(N_m/N_0)}{\lambda}. \tag{3}$$

At  $t = t_p$  daily cases and cumulative cases are respectively

$$\left( \frac{dN}{dt} \right)_p = \frac{\lambda N_m}{4}. \tag{4}$$

and

$$N_p = N_m/2. \tag{5}$$

Above simple formalism can be useful to describe covid 19 data pattern. In India we found two waves whose cumulative and daily cases data patterns can expressed in terms of two consecutive Sigmoid functions and their time derivatives.

From the first wave of Covid 19 Indian data [3] we find out the values of  $t_{p1}$ ,  $(dN/dt)_{p1}$  and  $N_{m1}$ . These values are used in Eqs. (3) and (4) to find out the values of  $\lambda_1$  and  $N_{01}$ . Subscript 1 is added in the notations of different parameters to assign first wave case. For India and some selective states—(1) Maharashtra (MH), (2) Kerala (KL), (3) Karnataka (KA), (4) Tamil Nadu(TN), (5) Andhrapradesh (AP), (6) West Bengal(WB), those parameters are tabulated in Table 1.

Next, when we will go for corresponding second wave data, we will not get  $N_{m2}$  as it is not till finished and we can not see the second saturated cumulative values. However, we can see the  $N_{p2}$  values from data and by using Eq. (5), we can guess  $N_{m2}$  by making twice of  $N_{p2}$ . Here, subscript 2 is added in the notations of different parameters to assign second wave case. Another important point for cumulative data of second wave is that we will redefine it by subtracting first wave maximum values

**Table 1** Different parameters of Sigmoid functions, which can grossly describe covid19 first wave data of India and selective states—MH, KL, KA, TN, AP, WB

State	$\lambda_1$	$N_{m1}$	$N_{01}$	$t_{p1}$	$\left(\frac{dN}{dt}\right)_{p1}$
MH	0.05	$19 \times 10^5$	142	190	$25 \times 10^3$
KL	0.027	$10 \times 10^5$	549	278	$9 \times 10^3$
KA	0.048	$8.6 \times 10^5$	37	209	$10 \times 10^3$
TN	0.035	$8 \times 10^5$	1469	148	$7 \times 10^3$
AP	0.04	$8.8 \times 10^5$	606	182	$10 \times 10^3$
WB	0.029	$5.5 \times 10^5$	522	240	$4 \times 10^3$
India	0.045	$94 \times 10^5$	1000	192	$94 \times 10^3$

**Table 2** Same as Table 1 for second wave

State	$\lambda_2$	$N_{m2}$	$N_{02}$	$t_{p2}$	$\left(\frac{dN}{dt}\right)_{p2}$	$N_{p2} + N_{m1}$
MH	0.05	$46 \times 10^5$	350	84	$67 \times 10^3$	$42 \times 10^5$
KL	0.078	$20 \times 10^5$	648	103	$39 \times 10^3$	$20 \times 10^5$
KA	0.11	$16.8 \times 10^5$	43	96	$49 \times 10^3$	$17 \times 10^5$
TN	0.085	$16 \times 10^5$	151	109	$34 \times 10^3$	$16 \times 10^5$
AP	0.09	$10 \times 10^5$	74	106	$24 \times 10^3$	$14 \times 10^5$
WB	0.08	$9 \times 10^5$	257	102	$20 \times 10^3$	$10 \times 10^5$
India	0.08	$2 \times 10^7$	8579	96	$4 \times 10^5$	$2 \times 10^5$

$N_{m1}$ . It means that Eqs. (1) and (2) for second waves will be

$$N_2(t) = N_{02}e^{\lambda_2 t} / \left( \frac{N_{02}e^{\lambda_2 t}}{N_{m2}} + 1 \right), \tag{6}$$

and

$$\frac{dN_2}{dt} = \lambda_2 N_{02}e^{\lambda_2 t} / \left( \frac{N_{02}e^{\lambda_2 t}}{N_{m2}} + 1 \right)^2, \tag{7}$$

where  $N_{m2} = (N_{p2} - N_{m1}) \times 2$ . So knowing  $N_{m1}$ ,  $N_{p2}$  from data, we can guess about  $N_{m2}$ . Although, we should keep in mind that  $N_{m1} + N_{m2}$  is actual saturated values of second wave case, when we compare it with actual data. The parameters of second waves for India and the selective states are given in Table 2.

### 3 Results

We have described the steps, through which we have find the parameters of first and second wave of covid 19 spreading. Figure 1 shows the Sigmoid function nature of cumulative  $N$  and daily case  $dN/dt$  data of India. In the left and right panels of Fig. 1 represents the data points (squares and circles) and corresponding Sigmoid fitted curves (dotted and solid lines) in first and second waves respectively. We consider 3 main data points of daily and cumulative cases at  $t = (t_p - 2/\lambda), t_p, (t_p + 2/\lambda)$ , within which spreading become most dominant. We have taken three different values of  $\lambda = 0.04, 0.045$  and  $0.05$  to fit the three data points of first wave. In another aspect, Second wave is well fitted with one  $\lambda = 0.08$ . First waves is saturated in  $N_{m1} = 10^7$  and second waves is saturated in  $N_{m2} = 2 \times 10^7$  which are already seen in covid 19 data. They are implemented as important inputs to build corresponding Sigmoid curves.

Next, we will generate similar graphs in Figs. 2 and 3 for 6 selective states - MH, AP, WB, TN, KL and KA. In Fig. 2 we noticed that the daily cases data of MH, AP and TN in first wave are well fitted by (time derivative of) Sigmoid function but the same for WB, KA and KL are not so well fitted by Sigmoid function. On the other hand in second wave all those data are favouring the Sigmoid function, which can be seen in Fig. 3. In first wave there was no sharp peak for few states where as peak was clearly seen during second wave almost in every states. This is most probably because of rapidly growing of daily cases in second wave which was lacking for few states in first wave.

In first wave, we find the range of growth parameter  $\lambda_1 = 0.03 - 0.05$  and peak value  $\left(\frac{dN}{dt}\right)_{p1} = (0.04 - 0.25) \times 10^5$ . The state level range of growth parameter is quite close to the range of  $\lambda_1 = 0.04 - 0.05$  for entire country. Being added of state level peak values, we find  $\left(\frac{dN}{dt}\right)_{p1} \approx 1 \times 10^5$  for India. Different states

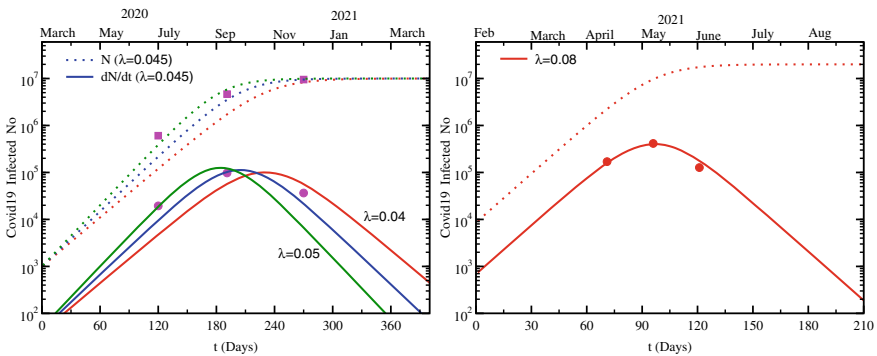


**Fig. 1** Left panel: Cumulative (squares) and daily cases (circles) data, fitted in Sigmoid curves (dotted line) and their derivatives (solid lines) for first wave. Right panel: Same for second wave

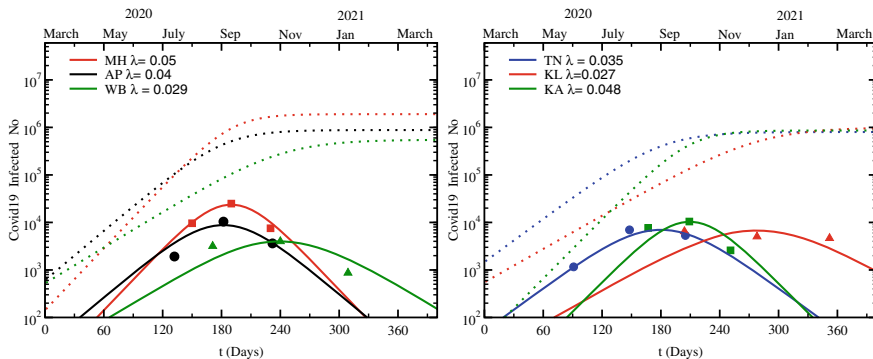


**Fig. 2** Sigmoid curves (dotted lines) and their derivatives (solid lines) for first wave in MH, AP, WB, TN, KL, KA

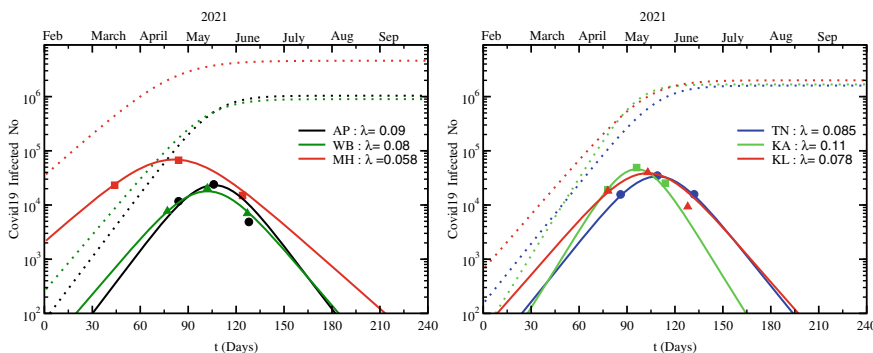


**Fig. 3** Same as Fig. 2 for second wave

shown peak value at different time points  $t_{p1}$  which are in the range of  $t_{p1} = 5 - 9$  months. India data shows the peak value around  $t_{p1} = 6.5$  months. If we analyze second wave then state level ranges are  $\lambda_2 = 0.078 - 0.1$  (excluding MH  $\lambda_2 = 0.05$ ),  $\left(\frac{dN}{dt}\right)_{p2} = (0.2 - 0.67) \times 10^5$ ,  $t_{p2} = 2.8 - 3.5$  months and India data shows at  $\lambda_2 = 0.08$ ,  $\left(\frac{dN}{dt}\right)_{p2} \approx 4 \times 10^5$ ,  $t_{p2} = 3.2$  months. If we compare first and second wave data of India and its different states, then we can notice their ratios as  $\lambda_2/\lambda_1 \approx 2$ ,  $t_{p2}/t_{p1} \approx 1/2$ ,  $N_{m2}/N_{m1} \approx 2$ . Although ratio between peak values of two waves for different states are not quite stable. As example, it is approximately 4 for India, 5 for WB, TN and 13 for KL etc. Considering India data as collective effect, we may conclude that first to second wave transition was just transition of parameters  $\lambda_1 \rightarrow \lambda_2 = 2\lambda_1$ ,  $t_{p1} \rightarrow t_{p2} = t_{p1}/2$ ,  $N_{m1} \rightarrow N_{m2} = 2N_{m1}$  and  $\left(\frac{dN}{dt}\right)_{p1} \rightarrow \left(\frac{dN}{dt}\right)_{p2} = 4\left(\frac{dN}{dt}\right)_{p1}$ .

Now let us come to the question whether we can identify the reason for occurring second wave after the first wave? Single answer of this question is really difficult but

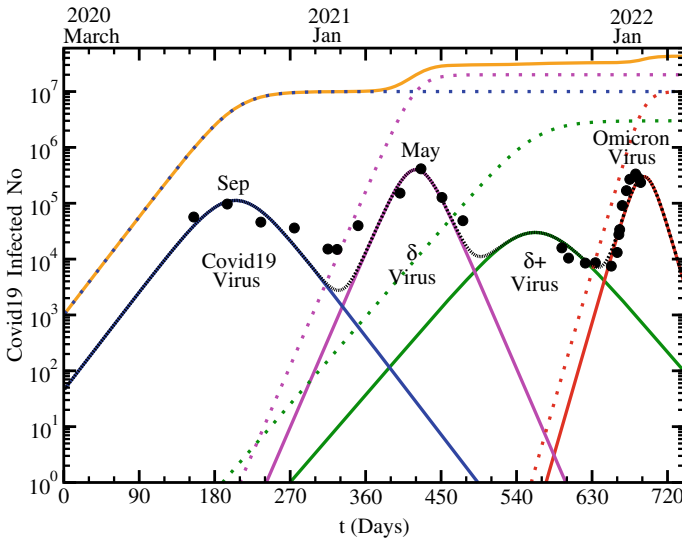


**Fig. 4** Solid (daily cases) and dotted (cumulative cases) blue (covid19), magenta ( $\delta$ ), green ( $\delta+$ ) and red (omicron) lines are plotted in log scale against time (days) axis. Brown solid and black dotted lines denote the total cumulative and daily cases respectively

mutation of virus might be considered as a dominating point. Here, we will try to understand graphically but reader should be considered that quantitative message with a very flexible way. In Fig. 4, we have drawn first and second wave daily cases curves in one portrait and we can see an overlapping/crossing zone of them around February, 2021. This is also observed in data (circles) as one can notice that second wave rising is started after Feb, 2021. We have put few selective daily cases data at  $t_{p1} - \frac{2}{\lambda_1}, t_{p1}, t_{p1} + \frac{2}{\lambda_1}, t_{p1} + \frac{4}{\lambda_1}, t_{p1} + \frac{6}{\lambda_1}, t_{p2} - \frac{6}{\lambda_2}, t_{p2} - \frac{4}{\lambda_2}, t_{p2} - \frac{2}{\lambda_2}, t_{p2}, t_{p2} + \frac{2}{\lambda_2}$ . One can notice that our Sigmoid curves for first and second waves are well fitted within  $t_{p1, p2} \pm \frac{2}{\lambda_{1,2}}$ . Outside those zones, the trends of data points and curves are going similar although bit of differences in numerical strengths are noticed. Now, assuming mutated virus as a dominating cause of second wave, let us try to describe the data as follows. After entering covid19 virus into India from March, 2020, first wave has received its peak around Sep, 2020 and then it went down until Feb, 2021. This imported covid19 virus are started to be mutated and among the different variant, delta virus [44] become more contagious than previous. We may consider this delta virus as a dominating reason for second wave, which is appeared to be started from Feb, 2021 and received peak around first week of May, 2021. Interestingly, first confirmed case of delta virus in India is observed around Oct, 2020, [45] which is quite earlier than Feb, 2021, from when second wave seems to grow. So it is quite interesting fact that the growing pattern of delta virus was hidden from Oct, 2020 to Feb, 2021. We can only see the decay pattern of first wave curve. If we extend our second wave Sigmoid curve before Feb, 2021, then we get  $N_0 \approx 1$  around Oct, 2020. Recovering this empirical point

by the simple logistic function is really very interesting fact. So if we crudely assign our first and second wave as the outcome of covid19 virus and mutated/delta virus spreading, then we can find recognize their overlapping zone.

After realizing the transition from first to second wave, we can use the idea for predicting third wave. After mutation of delta virus, recently delta plus ( $\delta+$ ) virus is first reported in India around June, 2021. Initially it was expected to be 1.5 – 2 times contagious [46, 47] than delta virus. On the basis of that speculation, a sudden grow was expected for  $\delta+$  around mid Aug-Oct, 2021 and get a peak value within Sep-Nov, 2021. Although an opposite guess was suspected in parallel [48]. In real data, we see that  $\delta+$  don't show any growing pattern within the duration June-Dec, 2021 and our hope was going toward end of the pandemic. A drastic change in data is appeared due to new variant **omicron**, which rapidly grows from first week of January, 2022 and reach its peak at the end of January, 2022 (guessed from data pattern). From June, 2021 to Dec, 2021, cumulative value was roughly saturated around  $3.5 \times 10^7$  but due to omicron, at the end of Jan, 2022, when peak value in daily cases is reached, it cumulative value reaches around  $4 \times 10^7$ . So,  $N_{p3} = (4 - 3.5) \times 10^7$  and  $N_{m3} = 2N_{p3} \approx 1 \times 10^7$ . Also, data show the peak value around  $\left(\frac{dN}{dt}\right)_{p3} \approx 3.3 \times 10^5$ , from where we can guess the  $\lambda_3 \approx 0.12$  and  $t_{p3} \approx 134$  days by using the relations

$$\begin{aligned} \left(\frac{dN}{dt}\right)_p &= \frac{\lambda N_m}{4}, \\ t_{p3} &= \frac{\ln(N_{m3}/N_{03})}{\lambda_3} \end{aligned} \tag{8}$$

respectively. This omicron Sigmoid profiles along with those of earlier variants are sketched in single graph—Fig. 4. We are getting  $t_{p3} \approx 134$  days assuming  $10^3$  daily cases in the beginning of Dec, 2021. Hence, our covid data with 3 waves can be expressed in terms of three Sigmoid functions for 3 variants—covid19,  $\delta$  and omicron, which are nicely sketched in Fig. 4. Their parameter transformation can be expressed in a single equation:

$$\begin{aligned} \lambda_1 \approx 0.04 &\rightarrow \lambda_2 \approx 0.08 &&\rightarrow \lambda_3 \approx 0.12 \\ N_{m1} \approx 1 \times 10^7 &\rightarrow N_{m2} \approx 2 \times 10^7 &&\rightarrow N_{m3} \approx 1 \times 10^7 \\ t_{p1} \approx 192 \text{ Days} &\rightarrow t_{p2} \approx 96 \text{ Days} &&\rightarrow t_{p3} \approx 134 \text{ Days} \\ \left(\frac{dN}{dt}\right)_{p1} \approx 1 \times 10^5 &\rightarrow \left(\frac{dN}{dt}\right)_{p2} \approx 4 \times 10^5 &\rightarrow \left(\frac{dN}{dt}\right)_{p3} \approx 3.3 \times 10^5. \end{aligned} \tag{9}$$

with a hidden Sigmoid profile of  $\delta+$  virus, whose parameters are roughly  $\lambda_3^{\delta+} = 0.04$ ,  $N_{m3}^{\delta+} = 0.3 \times 10^7$ . We have used index 3 with  $\delta+$  for assigning as pseudo 3rd wave by  $\delta+$ , which was actually hidden in between  $\delta$  and omicron variants due to its mild properties (probably). However, reader should notice that its presence keep the daily case data as constant during June to Dec, 2021.



## 4 Summary

In summary, present work is intended to explain the existing first, second and third waves of covid19 infection data with the help of simple logistic function, called Sigmoid function. From the data points of peak values and peak positions for daily cases of India and its selective states MH, KL, KA, TN, WB, AP, we have found the required input parameters of the Sigmoid functions. Our results grossly indicates a transition between two Sigmoid pattern with twice larger growth parameter and maximum values of cumulative data during first to second wave transition. In parallel, time duration of second wave shrink to half of that first wave and peak values of daily cases becomes four times larger. From the basic properties of Sigmoid functions, those changes can be easily realized. Realizing these first and second waves are because of Sigmoid-type spreading of covid19 and its mutated variant— $\delta$  virus, there was a speculation of third wave due to next level mutated variant  $\delta+$  virus but it shows a mild growing Sigmoid profile, for which daily cases data from June to Dec, 2021 remain almost constant. In the beginning of January, a rapid growing of third wave profile is initiated due to another mutated variant—omicron. Our guess Sigmoid profile for third wave carry 3 times larger growth parameter than first wave but its saturate cumulative value remain almost same as that of first wave. Novelty of present work may be the finding 4 different Sigmoid profiles for 4 variants to explain roughly the actual covid19 data.

**Acknowledgements** SM and SG thank to their daughter Adrika Ghosh for allowing to work in home for this project.

## References

1. WHO, Novel coronavirus (2019-nCoV) situation report - 11 (2020). <https://apps.who.int/iris/handle/10665/330776>
2. WHO, Coronavirus disease 2019 (COVID-19) situation report - 51 (2020). <https://apps.who.int/iris/handle/10665/331475>
3. Covid19 India. <https://www.covid19india.org>
4. Kermack, W.O., McKendrick, A.G.: A contribution to the mathematical theory of epidemics. Proc. R. Soc. Lond. Ser. A Contain. Papers Math. Phys. Character **115**(772), 700721 (1927). <https://doi.org/10.1098/rspa.1927.0118>
5. Hethcote, H.W.: The mathematics of infectious diseases. SIAM Rev. **42**(4), 599653 (2000). <https://doi.org/10.1137/S0036144500371907>
6. Anderson, R.M., May, R.M.: Infectious Diseases of Humans: Dynamics and Control. Oxford University Press (1992)
7. Tiwari, A.A.: Temporal analysis of covid19 peak outbreak. Epidemiol. Int. J. **4**(5), 000163, 2020. <https://doi.org/10.23880/eij-16000163>
8. Jakhhar, M., Ahluwalia, P.K., Kumar, A.A.: COVID 19 Epidemic Forecast in Different States of India using SIR Model. <https://doi.org/10.1101/2020.05.14.20101725>
9. Rajesh, A., Pai, H., Roy, V., Samonta, S., Ghosh, S.: Covid 19 prediction for India from the existing data and SIR(D) model study. <https://doi.org/10.1101/2020.05.05.20085902>
10. Ranjan Aryan, R., Mahendra, S., Verma, K.: Characterization of the second wave of COVID-19 in India. Curr. Sci. **121**(1), 85–93 (2021). <https://doi.org/10.1101/2021.04.17.21255665>

11. Ranjan, R.: Temporal dynamics of COVID-19 outbreak and future projections: a data-driven approach. *Trans. Indian Natl. Acad. Eng.* **5**, 109–115 (2020). <https://doi.org/10.1007/s41403-020-00112-y>
12. Ranjan, R.: Covid-19 spread in India: dynamics, modeling, and future projections. *J. Indian Stat. Assoc.* **58**(2), 47–65 (2020)
13. Bagal, D.K., Rath, A., Barua, A., Patnaik, D.: Estimating the parameters of susceptible-infected-recovered model of COVID-19 cases in India during lockdown periods. *Chaos Solitons Fractals* **140**, 110154 (2020). <https://doi.org/10.1016/j.chaos.2020.110154>
14. Hussain, N., Li, B.: Using R-studio to examine the COVID-19 patients in Pakistan implementation of SIR model on cases. *Int. J. Sci. Res. Multidiscip. Stud.* **6**(8), 54–59, (2020). <https://doi.org/10.13140/RG.2.2.32580.04482>
15. Singh, R.R., Dhar, A.K., Kherani, A.A., Jacob, N.V., Misra, A., Bajpai, D.: Network based framework to compare vaccination strategies. In: *International Conference on Computational Data and Social Networks*, vol. 1311, pp. 218–230. Springer, Cham (2021)
16. Kherani, A.A., Kherani, N.A., Singh, R.R., Dhar, A.K., Manjunath, D.: On modeling of interaction-based spread of communicable diseases. In: *International Conference on Computational Science and Its Applications*, pp. 576–591. Springer, Cham
17. Kherani, N.A.: If the virus respected queues, submitted in *Probability in Engineering and Information Science*
18. Bhattacharyya, A., Bhattacharyya, D., Mukherjee, J.: The connection of growth and medication of covid-19 affected people after 30 days of lock down in India. *Int. J. Sci. Res.* **9**(7) (2020). <https://doi.org/10.1101/2020.05.21.20107946>, <https://doi.org/10.36106/ijsr>
19. Bhattacharyya, A., Bhowmik, D., Mukherjee, J.: Forecast and interpretation of daily affected people during 21 days lockdown due to covid19 pandemic in India. *Indian J. Appl. Res.* **10**(5) (2020). <https://doi.org/10.36106/ijar>, <https://doi.org/10.1101/2020.04.22.20075572>
20. Adhikari, A., Pal, A.: A six compartments with time-delay model SHIQRD for the COVID-19 pandemic in India: during lockdown and beyond. *Alex. Eng. J.* **61**(2), 1403–1412 (2022). <https://doi.org/10.1016/j.aej.2021.06.027>
21. Pai, C., Bhaskar, A., Rawoot, V.: Investigating the dynamics of COVID-19 pandemic in India under lock-down. *Chaos Solitons Fractals* **138**, 109988 (2020). <https://doi.org/10.1016/j.chaos.2020.109988>
22. Sahoo, B.K., Sapra, B.K.: A data driven epidemic model to analyse the lockdown effect and predict the course of COVID-19 progress in India. *Chaos Solitons Fractals* **139**(110034), 19 (2020). <https://doi.org/10.1016/j.chaos.2020.110034>
23. Padhi, A., et al.: Studying the effect of lockdown using epidemiological modelling of COVID19 and a quantum computational approach using the Ising spin interaction. *Sci. Rep.* **10**, 21741 (2020). <https://doi.org/10.1038/s41598-020-78652-0>
24. Chauhan, P., Kumar, A., Jamdagni, P.: Regression analysis of COVID 19 Spread in India and its different states. <https://doi.org/10.1101/2020.05.29.20117069>
25. Biswas, D., Roy, S.: Analyzing COVID-10 Pandemic with a new growth model for population ecology. <https://doi.org/10.13140/RG.2.2.34847.92324/1>
26. Meghana, B.S.K., Kakulapati, V.: State-wise prevalence of covid 19 in India by machine learning approach. *Int. J. Pharm. Res.* **12**, 2 (2020). <https://doi.org/10.31838/ijpr/2020.SP2.295>
27. Arora, P., Kumar, H., Panigrahi, B.K.: Prediction and analysis of COVID-19 positive cases using deep learning models: A descriptive case study of India. *Chaos Solitons Fractals* **139**(110017), 18 (2020). <https://doi.org/10.1016/j.chaos.2020.110017>
28. Rafiq, D., Suhail, S.A., Bazaz, M.A.: Evaluation and prediction of COVID-19 in India: a case study of worst hit states. *Chaos Solitons Fractals* **139**(110014), 16 (2020). <https://doi.org/10.1016/j.chaos.2020.110014>
29. Easwaramoorthy, D., Gowrisankar, A., Manimaran, A., Nandhini, S., Lamberto, R., Santo, B.: An exploration of fractal-based prognostic model and comparative analysis for second wave of COVID-19 diffusion. *Nonlinear Dyn.* **106**, 1375–1395 (2021). <https://doi.org/10.1007/s11071-021-06865-7>

30. Gowrisankar, A., Lamberto, R., Banerjee, S.: Can India develop herd immunity against COVID-19? *Eur. Phys. J. Plus* **135**(6), 526 (2020). <https://doi.org/10.1140/epjp/s13360-020-00531-4>
31. Roy, S.: An algebraic interpretation of the spread of COVID-19 in India and an assessment of the impact of social distancing, *World J. Adv. Res. Rev.* **06**(3), 245–256 (2020). <https://doi.org/10.30574/wjarr>
32. Movsisyan, A., Burns, J., Biallas, R. et al.: Travel-related control measures to contain the COVID-19 pandemic: an evidence map. *BMJ Open* (2021) **11**(4) (2021). <https://doi.org/10.1136/bmjopen-2020-041619>
33. Kosfeld, R., et al.: The Covid 19 containment effects of public health measures a spatial difference-in-difference approach. *J. Reg. Sci.* **61**(4), 799–825 (2020). <https://doi.org/10.1111/jors.12536>
34. Kotwal, A., et al.: Predictive models of COVID19 in India: a rapid review. *Med. J. Armed Forces India.* **76**(4), 377–386 (2020). <https://doi.org/10.1016/j.mjafi.2020.06.001>
35. Bag, R., Ghosh, M., Biswas, B., Chatterjee, M.: Understanding the spatio-temporal pattern of COVID-19 outbreak in India using GIS and India's response in managing the pandemic. *Reg. Sci. Policy Pract.* **12**(6), 1063–1103 (2020). <https://doi.org/10.1111/rsp3.12359>
36. Kavitha, C., Gowrisankar, A.I., Santo, B.: The second and third waves in India: when will the pandemic be culminated? *Eur. Phys. J. Plus* **136**(5), 596 (2021). <https://doi.org/10.1140/epjp/s13360-021-01586-7>
37. Wikipedia : Sigmoid function
38. Batista, M.: Estimation of the final size of the second phase of the coronavirus epidemic by the logistic model, medRxiv 2020.03.11.20024901, <https://doi.org/10.1101/2020.03.11.20024901>
39. Batista, M.: Estimation of the final size of the COVID-19 epidemic, medRxiv 2020.02.16.20023606. <https://doi.org/10.1101/2020.02.16.20023606>
40. Mondal, S., Ghosh, S.: Fear of exponential growth in Covid19 data of India and future sketching. *Int. J. Creat. Res. Thoughts* **8**(5), 2422 (2020). <https://doi.org/10.1101/2020.04.09.20058933>
41. Mondal, S., Ghosh, S.: Possibilities of exponential or Sigmoid growth of Covid19 data in different states of India. *Indian J. Appl. Res.* **10**(6), 53–56 (2020). <https://doi.org/10.1101/2020.04.10.20060442>
42. Mondal, S., Ghosh, S.: Searching the Sigmoid-type trend in lock down period covid19 data of India and its different states. *J. Clin./Pharmaco-Epidemiol. Res.* **2**(2) (2020). <https://doi.org/10.46610/jcper.2020.v02i02.006>
43. Merzoukia, M., Bentahirb, M., Najimia, M., Chigra, F., Gala, J.-L.: The Modeling of the capacity of the Moroccan health care system in the context of COVID-19: the relevance of the logistic approach. *Bull. World Health Organ.* (2020). <https://doi.org/10.2471/BLT.20.258681>
44. <https://www.cdc.gov/coronavirus/2019-ncov/variants/variant-info.html>, <https://www.cdc.gov/coronavirus/2019-ncov/variants/variant-info.html>
45. <https://www.thehindu.com/news/international/who-says-covid-variant-in-india-of-concern/article34529654.ece>, <https://www.thehindu.com/news/international/who-says-covid-variant-in-india-of-concern/article34529654.ece>
46. Hindustantimes News: <https://www.hindustantimes.com/india-news/delta-plus-in-india-40-cases-1st-specimen-found-in-april-sample-what-we-know-so-far-101624448444003.html>
47. Hindustantimes News: <https://www.hindustantimes.com/india-news/govt-says-delta-plus-a-variant-of-concern-identifies-3-characteristics-101624405991131.html>
48. <https://www.bbc.com/news/world-asia-india-57564560>, <https://www.bbc.com/news/world-asia-india-57564560>
49. Worldometer Coronavirus: <https://www.worldometers.info/coronavirus/>

# Progression of COVID-19 Outbreak in India, from Pre-lockdown to Post-lockdown: A Data-Driven Statistical Analysis



Dipankar Mondal  and Siddhartha P. Chakrabarty 

**Abstract** In order to analyze the progression of COVID-19 outbreak in India, we present a data-driven analysis, by the consideration of four different metrics, namely, reproduction rate, growth rate, doubling time and death-to-recovery ratio. The incidence data of the COVID-19 (during the period of 2nd March 2020 to 11th September 2021) outbreak in India was analyzed, based on the estimation of time-dependent reproduction. The analysis suggested effectiveness of the lockdown, in arresting the growth and this continued for the post-lockdown period, except for the period of the setbacks resulting for the second wave. The approach adopted here would be useful in future monitoring of pandemics, including its progression.

**Keywords** Lockdown · Effective reproduction number · Estimation · COVID-19

## 1 Introduction

As of 31st October 2021, the coronavirus disease 2019 (COVID-19), first reported in Wuhan, China [1], has resulted in more than 246 million confirmed cases and nearly 4 million casualties [2]. The global pandemic resulting from the COVID-19 outbreak, was preceded by two other outbreaks of human coronavirus, in the 21st century itself, namely, the Severe Acute Respiratory Syndrome Coronavirus (SARS-CoV) and the Middle East Respiratory Syndrome Coronavirus (MERS-CoV) infections [3]. The index case for the COVID-19 outbreak in India was reported on 30th January 2020, in case of an individual with a travel history from Wuhan, China [4]. The data available on [4], suggests that during the early stages, the COVID-19 positive cases in India, was limited to individuals with a travel history involving the global hotspots of the outbreak. However, subsequently, the detected cases indicated the possibility of

---

D. Mondal · S. P. Chakrabarty (✉)  
Indian Institute of Technology Guwahati, Guwahati 781039, Assam, India  
e-mail: [pratim@iitg.ac.in](mailto:pratim@iitg.ac.in)

D. Mondal  
e-mail: [dipankarcmi@gmail.com](mailto:dipankarcmi@gmail.com)

© The Author(s), under exclusive license to Springer Nature Switzerland AG 2022  
S. Banerjee and A. Saha (eds.), *Nonlinear Dynamics and Applications*,  
Springer Proceedings in Complexity,  
[https://doi.org/10.1007/978-3-030-99792-2\\_118](https://doi.org/10.1007/978-3-030-99792-2_118)

1389

community outbreak, which resulted in the Government of India announcing a lockdown across the country, driven by the necessity of crucial step towards curbing the growth of COVID-19 in densely populated country, like India. However, given the cost of the lockdown, from both the epidemiological as well as the economic perspective, the lockdown was withdrawn in a phased manner (contingent on the situation at the local level). Accordingly, this paper presents a data-driven analysis to examine the effectiveness of the lockdown, and the dynamics of post-lockdown spread of the pandemic. In order to accomplish this, we empirically analyze four different metrics, namely, reproduction number, growth rate, doubling time and death-to-recovery ratio, which quantify the transmission rate, the growth rate, the curvature of epidemic curve, and the improvement of health care capacity, respectively.

We now give a brief summary of some of the available literature on quantitative approaches to the modeling of transmission of COVID-19 outbreak. A system of ordinary differential equation (ODE) driven model for phasic transmission of COVID-19, was analyzed for calculating the transmissibility of the virus in [5]. Kucharski et al. [1] considered a stochastic transmission model on the data for cases in Wuhan, China (including cases that originated there) to estimate the likelihood of the outbreak taking place in other geographical locations. A literature survey by Liu et al. [6], summarized that the reproductive number (and hence the infectivity) in case of COVID-19, exceeded that of SARS. A Monte-Carlo simulation approach to assess the impact of the COVID-19 pandemic in India, was carried out in [7]. In a series of recent articles, the modeling of various aspects of the outbreak in India, have been studied from the perspective of fractal based prognosis assessment [8], a prediction approach for the second and third waves [9], and the vital question of achieving herd immunity in India [10].

A key identifier for the transmissibility of epidemiological diseases such as COVID-19 is the basic reproduction number  $R_0$ , which is defined as the average number of secondary infections resulting from an infected case, in a population whose all members are susceptible. However, we seek to determine the (data-driven) time-dependent reproduction number  $R_t$ , for better clarity on the time-variability of the reproduction number, particularly in the paradigm of its dynamics, both during the phases of nationwide pre-lockdown, lockdown and post-lockdown in India. In addition, we also estimate and analyze the statistical performance of growth rate, doubling time and death-to-recovery ratio. Therefore, the paper is organized as follows. In Sect. 2, we detail the source of the data as well as the statistical approaches used for the estimation of  $R_0$  and  $R_t$ . This will be followed by the presentation of the data-driven analysis of the pre-lockdown to the post-lockdown period in Sect. 3. And finally, in the concluding remarks in Sect. 4, we highlight the main takeaways for this analysis.

## 2 Methodology for Estimating Reproduction Rate

The data of incidences used for the analysis reported in this paper was obtained from the website of India COVID 19 Tracker [4], and used for the purpose of estimation of  $R_0$ . This estimation was carried out making use of the R0 package [11] of the statistical package R. The standardized approach included in the R0 package, includes the implementation of the Exponential Growth (EG), Maximum Likelihood (ML) estimation, Sequential Bayesian (SB) method, and estimation of time dependent reproduction (TD) numbers, used during the H1N1 pandemic of 2009. The package is designed for the estimation of both the “initial” reproduction number, as well as the “time-dependent” reproduction number. Accordingly, we present a brief summary of the four approaches used in the paper.

1. *Exponential Growth (EG)*: As observed in [12], the reproduction number can be indirectly estimated from the rate of the exponential growth. In order to address the disparity in the different differential equation models, the authors observed that this disparity can be attributed to the assumptions made about the shape of the generation interval distribution. Accordingly, the choice of the model, used for the estimation of the reproduction number, is driven by the shape of the generation interval distribution. Based on the assumption that the mean is equal to the generation intervals, the authors obtained the important result of determining an upper bound, on the possible range of values of the reproduction number, for an observed rate of exponential growth, which manifests into the worst case scenario for the reproductive number. Let the function  $g(a)$  be representative of the generation interval distribution. If the moment generating function  $M(z)$  of  $g(a)$  is given by  $M(z) = \int_0^\infty e^{za} g(a) da$ , then the reproduction number is given by  $R = \frac{1}{M(-r)}$ , subject to the condition that  $\frac{1}{M(-r)}$  exists. In particular, the Poisson distribution can be used in the analysis of the integer valued incidence data [13, 14], for (discretized) generation time distribution. An important caveat is that this approach is applicable to the time window in which the incidence data is observed to be exponential [11].

2. *Maximum Likelihood (ML) Estimation*: The maximum likelihood model as proposed in [15] is based on the availability of incidence data  $N_0, N_1, \dots, N_T$ , with the notation  $N_t, t = 0, 1, 2, \dots, T$  denoting the count of new cases at time  $t$ . In practice, we take the index  $t$  in days, while noting that this indexing is applicable for other lengths of time intervals. This approach is driven by the assumption that the Poisson distribution models the number of secondary infections from an index case, with the average providing the estimate for the basic reproduction number. If we denote the number of observed incidences for consecutive time intervals by  $n_1, n_2, \dots, n_T$  and if  $p_i$  denotes the probability of the serial interval of a case in  $i$  days (which can be estimated apriori), then the likelihood function is the thinned Poisson:  $L(R_0, \mathbf{p}) = \prod_{t=1}^T \frac{e^{-\mu_t} \mu_t^{n_t}}{n_t!}$ . Note that

here  $\mu_t = R_0 \sum_{i=1}^{\min(k,t)} n_{t-i} p_i$  and  $\mathbf{p} = (p_1, p_2, \dots, p_k)$ . The absence of data from the index case can lead to an overestimation of the initial reproduction number, and accordingly a correction needs to be implemented [11].

3. *Sequential Bayesian (SB) Method*: A SIR model driven sequential estimation of the initial reproduction number was carried out by the sequential Bayesian method in [16]. It is based on the Poisson distribution driven estimate of incidence  $n_{t+1}$  at time  $t + 1$ , with the mean of  $n_t e^{\gamma(R-1)}$ . In particular, the probability distribution for the reproduction number  $R$ , based on the observed temporal data is given by  $P [R|n_1, n_1, \dots, n_{t+1}] = \frac{P [n_1, n_1, \dots, n_{t+1}|R] P [R]}{P [n_1, n_1, \dots, n_{t+1}|R]}$ , where

$P [R]$  is the prior distribution of  $R$  and  $P [n_1, n_1, \dots, n_{t+1}]$  is independent of  $R$ .

4. *Estimation of Time Dependent (TD) Reproduction*: The TD method is amenable to the computation of the reproduction numbers through the averaging over all networks of transmission, based on the observed data [17]. Let  $i$  and  $j$  be two cases, with the respective times of onset of symptoms being  $t_i$  and  $t_j$ . Further, let  $p_{ij}$  denote the probability of  $i$  being infected by  $j$ . If  $g(a)$  denotes the distribution of the generation interval, then  $p_{ij} = \frac{g(t_i - t_j)}{\sum_{i \neq k} w(t_i - t_k)}$ . Accordingly,

the effective reproduction number is given by  $R_j = \sum_i p_{ij}$ , whose average is

then given by  $R_t = \frac{1}{n_t} \sum_{t_j=t} R_j$ . In absence of observed secondary cases, a correction can be made to the time dependent estimation [18].

### 3 Data Driven Analysis of the Outbreak

The nationwide lockdown was imposed, on 25th March, 2020, with the goal of arresting the spread of infection, through strict restrictions on mass movement and encouraging social distancing, and it was expected that the spread rate would come down, along with the reduction in the possibility of community transmission. Thus, the first phase of lockdown until 14th April 2020, was extended to two more phases till 31st May, 2020. Subsequently, taking into account the economic cost of the lockdown, against the backdrop of community spread of the outbreak, a phasewise withdrawal of the lockdown was implemented, by taking into account the state of the pandemic at the local level. Accordingly, this section discusses various epidemiological aspects of the progression of the pandemic in India, from the pre-lockdown to post-lockdown, by analyzing four metrics, namely, the effective reproduction rate, the growth rate, the doubling time and the death-to-recovery ratio.



### 3.1 Analysis of Effective Reproduction Rate

One of the key mathematical indicator relied upon, in the paradigm of the spread of COVID-19 pandemic and consequent policy decisions is the effective reproduction rate (ERR) or the time-varying reproduction number. As ERR provides the information of time varying transmission rate, it would be a natural choice to measure its behaviour from the pre-lockdown, lockdown and the post-lockdown period. An analysis showed that the TD model fits well, for the Indian epidemic curve and accordingly, we discuss the results in the context of the TD-based  $R_t$ .

Figure 1a depicts the seven-day rolling ERR. It is clearly observed that, before the lockdown, the  $R_t$  was unsteady and high, but it started to decline after the commencement of the lockdown. In the first lockdown period, the overall average seven-day ERR was 1.64, which means that, during this period, if 100 individuals had COVID-19, they would have infected 164 people on an average. In the second lockdown period, the average ERR came down to 1.29, and then in the third lockdown period, the ERR further dropped to 1.21. Therefore, from the first lockdown to the end of third lockdown, the overall rate of reduction of ERR was 26%. However, after the lockdown period, the number of cases decreased gradually at first, and then increased unexpectedly. Accordingly, a sharp rise of ERR (of upto 1.14) was observed during the early March 2021 to early June 2021 (coinciding with the devastating second wave). Figure 1b displays the phase-wise<sup>1</sup> average  $R_t$ . The descriptive statistics of  $R_t$  and the corresponding confidence intervals are presented in Table 1. From these results, it can be observed that, there was a significant reduction of ERR, which continued to the early days after the lockdown was eased. But eventually, when after most of the restriction were lifted, a rise in ERR (consistent with the second wave) was observed, followed by a gradual decline.

### 3.2 Analysis of Growth Rate

The reduction of ERR should further reduce the growth rate of daily incidences. In order to see the growth rate, in a particular time period, we calculate the seven-day rolling growth rate in that period, and then take the average. Suppose that we have the daily incidence numbers,  $D(t)$ ,  $t = 1, 2, 3, \dots, 20$ , for a period of 20 days. We first compute the seven-day rolling growth rates,  $\frac{D(i + 7) - D(i)}{D(i)}$ , where  $i = 1, 2, 3, \dots, 13$ , and we get a dataset of 13 points. Finally, the simple mean of the dataset is calculated. If the seven-day average growth is 30% in a month, then the average weekly number of positive cases would have increased from 100 to 130 in that month.

---

<sup>1</sup> L0, L1, L2 and L3 imply pre-lockdown, lockdown 1, lockdown 2 and lockdown 3, respectively. PL means post-lockdown period and each PL consists of approximately 100 days.



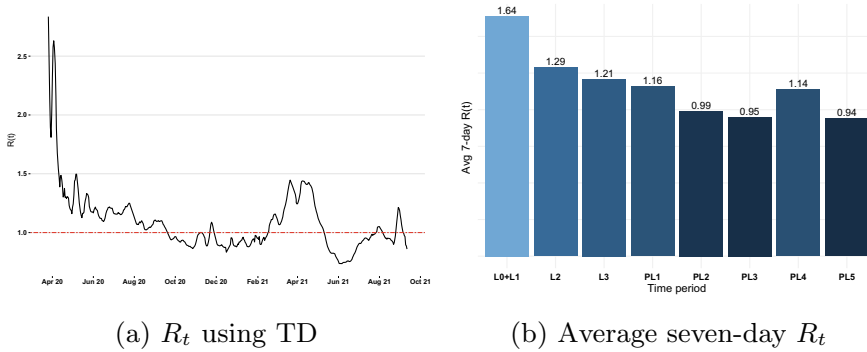


**Fig. 1** Analysis of effective reproduction rate. **a**  $R_t$  using TD, **b** Average seven-day  $R_t$

**Table 1** Effective reproduction rate during different periods

	Period	Max	Min	Mean
1	L0 + L1	2.40	1.21	1.64
2	L2	1.43	1.16	1.29
3	L3	1.30	1.16	1.21
4	PL1	1.23	1.08	1.16
5	PL2	1.10	0.87	0.99
6	PL3	1.14	0.86	0.95
7	PL4	1.43	0.74	1.14
8	PL5	1.16	0.74	0.94

The seven-day moving average of the growth rate during the period considered is presented in Fig. 2a. Figure 2b illustrates the average weekly growth rate in different time periods. In the first lockdown period (L0 + L1), the growth rate was 97%. It means that the weekly number of positive cases, increased drastically from 100 to 197 in the pre-lockdown period. The growth rate then decreased to 42% in lockdown 2 (L2). It further reduced to 22% and 32% in lockdown 3 (L3) and post-lockdown 1 (PL1), respectively. Therefore, we can conclude, that the implementation of nationwide lockdown has resulted in slowing down the growth rate of COVID-19 positive cases. With the easing of lockdown curbs, this trend continued, but then in concurrence with the second wave there was period (PL4), when the rate again showed an upward trend.

### 3.3 Analysis of Doubling Time

One of the key indicator to observe the spread of any pandemic is the doubling time. It is referred to as the time (usually counted in number of days) it takes for the total

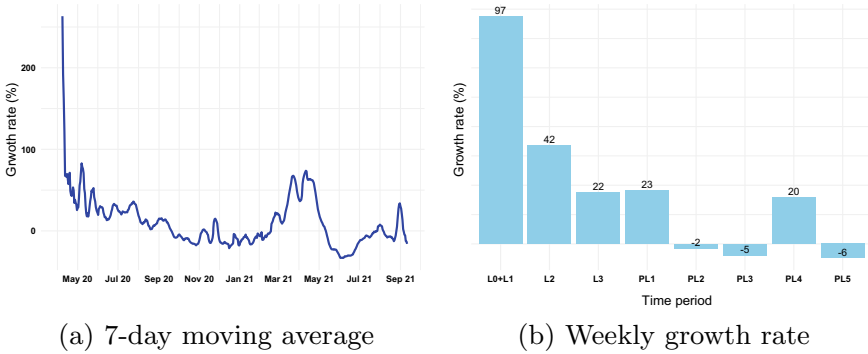


**Fig. 2** Analysis of growth rate. **a** 7-day moving average, **b** Weekly growth rate

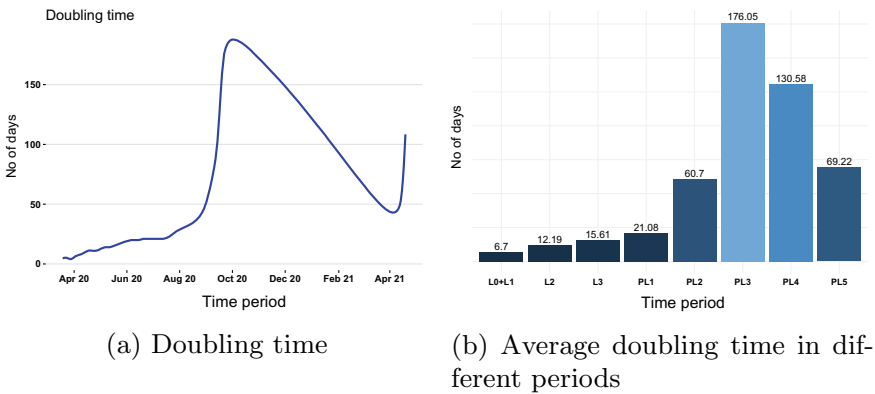


**Fig. 3** Analysis of doubling time. **a** Doubling time, **b** Average doubling time in different periods

number of cases to double. The doubling time of  $n$  days means that if there were 100 cases at day 0, then, on day  $n$ , the number of cases would be 200. The more the doubling time is, the more the possibility of achieving a flattened epidemic curve.

Figure 3a displays the doubling rate for five-day moving averages. The escalation in doubling time is easily seen from the figure. The doubling time during the third lockdown period is about 15.6 days, up from 6.7 days at the beginning of lockdown. The phase-wise average doubling timings are shown in Fig. 3b. It further increases (upto 176) in the second post-lockdown period and then falls down to 69 at the end. The increment in doubling time is clearly visible from this figure. Therefore, from these results, we infer that the doubling time has improved significantly after the enforcement of nationwide lockdown, a trend which continued until the arrival of the second wave, when the doubling time showed a steady trend of decline.

### 3.4 Analysis of Death-to-Recovery Ratio

In a pandemic, the performance of any nation’s health care system, is measured ultimately in terms of deaths and recoveries. This segment discusses the effect of lockdown on death-to-recovery ratio (DTR). The DTR is defined as a ratio between total number of deaths and total number of recoveries:

$$DTR_t = \frac{\text{Total number of deaths upto time } t}{\text{Total number of recoveries upto time } t}.$$

The DTR stipulates the clinical management ability or the efficiency of health system. It is highly important to keep the value of the DTR as low as possible. Mathematically, the closer this value is to zero, the better the efficiency of healthcare system, in dealing with the pandemic. For example,  $DTR_t = 0.5$  implies that, for every 100 recoveries, 50 infected patients would have died. The seven-day rolling DTR is plotted in Fig. 4a. It is clearly seen that the DTR has declined significantly as time has progressed. The phase-wise bar chart (Fig. 4b) also depicts the reduction of DTR over the period considered. In the pre-lockdown (L0) and the lockdown 1 (L1) periods together, the average DTR was 0.28. It was reduced to 0.12 in lockdown 2 (L2) and further declined to 0.07 in lockdown 3 (L3), which shows that, in this short period, the Indian health care system has shown significant improvement in its preparedness to tackle the COVID-19 pandemic. This trend continued well into the post-lockdown periods, not withstanding the second wave, which is a highly encouraging sign.

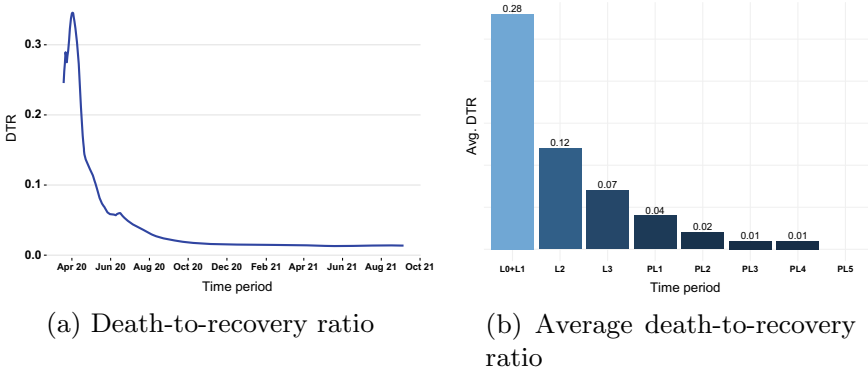


**Fig. 4** Analysis of death-to-recovery ratio. **a** Death-to-recovery ratio, **b** Average death-to-recovery ratio

## 4 Conclusion

In this paper, we have discussed the statistical analysis of the progression of COVID-19 pandemic in India, through a data-driven analysis. The goal was to ascertain the impact of the lockdown and the progression in the post-lockdown period, in terms of the intensity of the infection. Accordingly, we empirically analyzed different metrics that mainly measure the spread of infectious disease, like COVID-19. The metrics are effective reproduction rate, growth rate, doubling time and death-to-recovery ratio. For case of effective reproduction rate, it is seen that the lockdown has reduced the reproduction rate by more than 20%. The growth rate has also substantially decreased from the initial period to the end of lockdown. On the other hand, the doubling time has largely improved over the three month period. The rate of increment from pre-lockdown to lockdown 3 is nearly 123%. Finally, we described the impact on death-to-recovery ratio, which quantifies the number of death against the number of recoveries. We observed significant downfall of death-to-recovery ratio from the month of April. On average, the initial death-to-recovery of 0.28 has dipped downward to 0.08 at the third phase of lockdown. Therefore, despite rising cases of COVID-19 infection in India, the lockdown has managed to curb the spread to a great extent. Further, for the post-lockdown period, it is observed that the desirable trend for all the four metrics continued, except an adversarial trend observed, concurrently, with the devastating second wave.

**Acknowledgements** Siddhartha P. Chakrabarty was supported by Grant. No. MSC/2020/000049 from the Science and Engineering Research Board, India.

## References

1. Kucharski, A.J., Russell, T.W., Diamond, C., Liu, Y., Edmunds, J., Funk, S., Davies, N.: Early dynamics of transmission and control of COVID-19: a mathematical modelling study. *The Lancet Infectious Diseases* (2020)
2. Weekly operational update on COVID-19-3 November 2021. <https://www.who.int/publications/m/item/weekly-operational-update-on-covid-19---3-november-2021>. Retrieved 8 November 2021
3. Gralinski, L.E., Menachery, V.D.: Return of the Coronavirus: 2019-nCoV. *Viruses* **12**(2), 135 (2020)
4. India COVID-19 Tracker. <https://www.covid19india.org/>
5. Chen, T.M., Rui, J., Wang, Q.P., Zhao, Z.Y., Cui, J.A., Yin, L.: A mathematical model for simulating the phase-based transmissibility of a novel coronavirus. *Infect. Dis. Poverty* **9**(1), 1–8 (2020)
6. Liu, Y., Gayle, A.A., Wilder-Smith, A., Rocklöv, J.: The reproductive number of COVID-19 is higher compared to SARS coronavirus. *J. Travel Med.* (2020)
7. Chatterjee, K., Chatterjee, K., Kumar, A., Shankar, S.: Healthcare impact of COVID-19 epidemic in India: a stochastic mathematical model. *Med. J. Armed Forces India* (2020)
8. Easwaramoorthy, D., Gowrisankar, A., Manimaran, A., Nandhini, S., Rondoni, L., Banerjee, S.: An exploration of fractal-based prognostic model and comparative analysis for second wave of COVID-19 diffusion. *Nonlinear Dyn.* **106**(2), 1375–1395 (2021)

9. Kavitha, C., Gowrisankar, A., Banerjee, S.: The second and third waves in India: when will the pandemic be culminated? *Eur. Phys. J. Plus* **136**(5), 1–12 (2021)
10. Gowrisankar, A., Rondoni, L., Banerjee, S.: Can India develop herd immunity against COVID-19? *Eur. Phys. J. Plus* **135**(6), 526 (2020)
11. Obadia, T., Haneef, R., Boelle, P.Y.: The R0 package: a toolbox to estimate reproduction numbers for epidemic outbreaks. *BMC Med. Inf. Decis. Mak.* **12**(1), 147 (2012)
12. Wallinga, J., Lipsitch, M.: How generation intervals shape the relationship between growth rates and reproductive numbers. *Proc. R. Soc. B: Biol. Sci.* **274**(1609), 599–604 (2007)
13. Boelle, P.Y., Bernillon, P., Desenclos, J.C.: A preliminary estimation of the reproduction ratio for new influenza A (H1N1) from the outbreak in Mexico, March–April 2009. *Eurosurveillance* **14**(19), 19205 (2009)
14. Hens, N., Van Ranst, M., Aerts, M., Robesyn, E., Van Damme, P., Beutels, P.: Estimating the effective reproduction number for pandemic influenza from notification data made publicly available in real time: a multi-country analysis for influenza A/H1N1v 2009. *Vaccine* **29**(5), 896–904 (2011)
15. Forsberg White, L., Pagano, M.: A likelihood-based method for real-time estimation of the serial interval and reproductive number of an epidemic. *Stat. Med.* **27**(16), 2999–3016 (2008)
16. Bettencourt, L.M., Ribeiro, R.M.: Real time Bayesian estimation of the epidemic potential of emerging infectious diseases. *PLoS One* **3**(5) (2008)
17. Wallinga, J., Teunis, P.: Different epidemic curves for severe acute respiratory syndrome reveal similar impacts of control measures. *Am. J. Epidemiol.* **160**(6), 509–516 (2004)
18. Cauchemez, S., Boelle, P.Y., Donnelly, C.A., Ferguson, N.M., Thomas, G., Leung, G.M., Hedley, A.J., Anderson, R.M., Valleron, A.J.: Real-time estimates in early detection of SARS. *Emerg. Infect. Dis.* **12**(1), 110 (2006)

# Analysis of Fuzzy Dynamics of SEIR COVID-19 Disease Model



B. S. N. Murthy , M N Srinivas , and M A S Srinivas 

**Abstract** The objective of this article is to build an SEIR epidemic system for episode COVID-19 (novel crown) with fuzzy numbers. Mathematical models might assist with investigating the transmission elements, forecast and control of Covid-19. The fuzziness in the infection rate, increased death owing to COVID-19, and recovery rate from COVID-19 were all deemed fuzzy sets, and their member functions were used as fuzzy parameters in the SEIR system. The age lattice technique is used in the SEIR system to calculate the fuzzy basic reproduction number and the system's stability at infection-free and endemic equilibrium points. Computer simulations are provided to comprehend the subtleties of the proposed SEIR COVID-19 model.

**Keywords** SEIR · Fuzzy parameter · Fuzzy basic reproduction number · Transmission rate · Stability

## 1 Introduction

COVID-19 infection has turned into a worldwide irresistible disease and more individuals are influenced. It is spread by a COVID-19-infected person through direct interaction with another individual or through minute precipitations from a COVID-19-infected individual's mouth that are moved by another person. Almost 2.27 mil-

---

B. S. N. Murthy (✉)

Department of Mathematics, Aditya College of Engineering and Technology, Surampalem, Andhra Pradesh, India  
e-mail: [bsn3213@gmail.com](mailto:bsn3213@gmail.com)

M. N. Srinivas

Department of Mathematics, School of Advanced Sciences, Vellore Institute of Technology, Vellore, Tamilnadu, India  
e-mail: [mnsrinivaselr@gmail.com](mailto:mnsrinivaselr@gmail.com)

M. A. S. Srinivas

Department of Mathematics, Jawaharlal Nehru Technological University, Hyderabad, Telangana, India  
e-mail: [massrinivas@gmail.com](mailto:massrinivas@gmail.com)

© The Author(s), under exclusive license to Springer Nature Switzerland AG 2022  
S. Banerjee and A. Saha (eds.), *Nonlinear Dynamics and Applications*,  
Springer Proceedings in Complexity,  
[https://doi.org/10.1007/978-3-030-99792-2\\_119](https://doi.org/10.1007/978-3-030-99792-2_119)

1399

lion individuals have been diseased with the virus around the biosphere, with 0.46 million of them succumbing to it in approximately 193 nations. The best and troublesome assignment for people is to control a similar climate which they have occupied. For this reason, notwithstanding, a few rules have been given or provided and cut off points have been static that past that landscape/climate shouldn't be upset. The execution of strategies to stop the communication of the infection has been viewed as a significant test. Consequently, as we realize that numerical models are useful assets to comprehend the communication elements of irresistible infections and to kind future arranging. Various universal and virus models have been examined in previous writing, allowing us to better examine and manage the feast of transferrable diseases [1–3].

Epidemiology, the SIR model is notable, and numerous extraordinary accomplishments have been complete on that [4–6]. However, the COVID-19 disease exists an inert stage throughout which the individual is contaminated however not so far suggestive. Another portion E is acquainted in the SEIR model with portray the non-suggestive yet contaminated stage. The SEIR model has numerous renditions, and numerical medicines can be found, for example, in Diekmann [7], Hethcote [8], among others. The scientific arrangement of the SEIR model is read for the unrestricted feast of the COVID-19 contagion in [9]. A multi draining SEIR pestilence system is set up for the COVID-19 contagion with universal prevalence charges in [10]. The objective of this analysis was to create an altered SEIR compartmental numerical classical for forecast of novel corona pandemic elements considering dissimilar intercession situations which may stretch experiences on the finest mediations to lessen the plague hazard. The COVID-19 model introduced in this paper depends on a past pandemic model announced in [11–13]. Mwalili et al. [14] investigated on SEIR pandemic system for COVID-19 contamination where the resistance of the populace assumes a significant part in recovering from hatching stage to the defenseless compartment. Shikha et al. [15] concentrated on the impact of regular resistance in the SEIS pestilence system. The above examinations has made some incredible accomplishments in exploring the COVID-19 disease.

The parameters used to communicate natural systems in a numerical manner are for the most part taken as certain. A couple of endeavours have been finished by the analysts to consider the natural vulnerability in their exploration works. Because of the reasonable circumstance, fuzzy parameters in natural demonstrating ought to be utilized more every now and again than the new endeavors. The usage of fuzzy sense and fuzzy sets in organic classifications has a lot of probables, but there aren't many of them [16–19] contains a few examples of fuzzy science applications. Mishra and Pandey [20] devised and implemented a plague model with fuzzy parameters to a PC network system. A few researchers [21–23] were concentrated on the fuzzy scourge models for human irresistible disease. As of late, fuzzy hypothesis stands out enough to be noticed. Therefore, the vulnerability in this SEIR system is portrayed by fuzzy statistics.

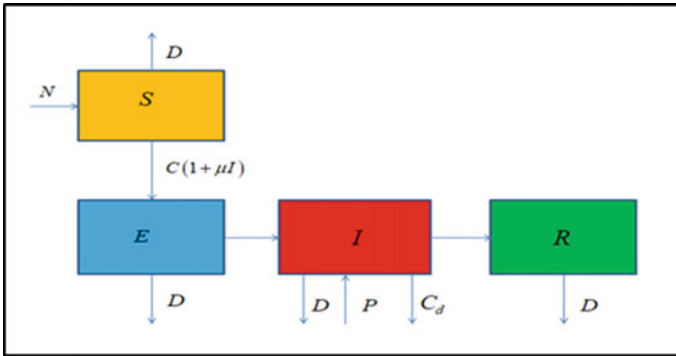


**Fig. 1** A Schematic diagram of SEIR epidemic disease COVID-19

In this article, we construct a SEIR mathematical model in regularized system in Sect. 2, we try to investigate the spread of the COVID-19 virus from a fuzzy powerful structure perspective. Because of COVID-19, the infection rate, recovery rate, and death rate due to Covid-19 are all viewed as fuzzy parameters that are based on specific infection loads. In Sect. 3, we derive fuzzy basic reproduction number and existence conditions of fuzzy SEIR were discussed. In Sect. 4, we intended the stability of SEIR fuzzy system at these equilibrium points. In Sect. 5, numerical recreations have been accessible to exemplify the investigative results. Finally, a brief conversation and inferences have been assumed in Sect. 6.

## 2 Mathematical Formulation of Proposed SEIR Model

In the present article, we recommend a SEIR Covid-19 disease system to describe the following differential equations

$$\begin{cases} \frac{dS}{dt} = N - CIS(1 + \mu I) - DS \\ \frac{dE}{dt} = CIS(1 + \mu I) - (D + \psi) E \\ \frac{dI}{dt} = P + \psi E - (D + C_d + \delta) I \\ \frac{dR}{dt} = \delta I - DR \end{cases} \quad (1)$$

where  $\Delta = N - P$  is the total population. Let S is proportion of susceptible class, E is the proportion of exposed class, I is the proportion of infected class, R is the proportion of recovered class, Let N, P is the total population, who test is negative and positive; C is the proportionality constant; D is the natural death rate of individual class;  $\mu$  is the individual lose of immunity. Figure 1 depicts transmission flow of SEIR epidemic COVID-19 disease model.



Assuming that the individuals are infected according to their Covid-19 virus load. So, in this manner the infection rate, death rate due to virus and recovery rate has been considered as fuzzy sets which rest on the corona virus consignment. Therefore, the Covid-19 virus consignment in an individual, the advanced the fortuitous of the Covid-19 virus spread in a contact interface. Let  $\Theta$  is the corona virus load class. By considering the corona virus load  $\Theta$  in each class, the parameters  $C_d(\Theta)$  is the death due to corona,  $\psi(\Theta)$  is the infection rate,  $\delta(\Theta)$  is the recovery rate can be regarded as a purpose of the corona virus consignment. Thus, the system (1) can be stretched to fuzzy SEIR classical, represented as follows

$$\begin{cases} \frac{dS}{dt} = N - CIS(1 + \mu I) - DS \\ \frac{dE}{dt} = CIS(1 + \mu I) - (D + \psi(\Theta))E \\ \frac{dI}{dt} = P + \psi(\Theta)E - (D + C_d(\Theta) + \delta(\Theta))I \\ \frac{dR}{dt} = \delta(\Theta)I - DR \end{cases} \tag{2}$$

### 3 Analysis of Fuzzy SEIR Covid-19 Model

Only two levels of headings should be numbered. Lower level headings remain unnumbered; they are formatted as run-in headings.

#### 3.1 Fuzzy Basic Reproduction Number

The fuzzy basic reproduction number  $R_0(\Theta)$  for system (2), is calculated using the next generation matrix technique [21].

$$R_0(\Theta) = \frac{C\psi(\Theta)N}{D^2(C_d(\Theta) + D + \delta(\Theta))}$$

#### 3.2 Existence of Equilibrium Points

The system (2) has two points of equilibrium, such as (i)  $E_{df}(S_0, 0, 0, 0)$  (Infection free equilibrium point), (ii)  $E_{ee}(S_*, E_*, I_*, R_*)$  (Endemic equilibrium point)

**(i) Infection free equilibrium point  $E_{df}(S_0, 0, 0, 0)$**

The disease-free equilibrium point of system (2) is found by putting  $I = I_0 = 0$ . As a result, the SEIR fuzzy system (2) has a disease-free equilibrium point  $E_{df} (\frac{N}{D}, 0, 0, 0)$

(ii) **Endemic equilibrium point**  $E_{ee} (S_*, E_*, I_*, R_*)$

The possibility of spread of COVID-19 at the endemic equilibrium point  $E_{ee} (S_*, E_*, I_*, R_*)$

where  $S_* = \frac{N}{C(1+\mu I_*)I_* - D}$ ;  $E_* = \frac{NC(1+\mu I_*)I_*}{[C(1+\mu I_*)I_* - D][\psi(\Theta) + D]}$ ;  $R_* = \frac{\delta(\Theta)}{D} I_*$

$$I_* = - \frac{(D + C_d(\Theta) + \delta(\Theta) + P(\Theta)(\psi(\Theta) + D) + \psi(\Theta)NC) + \sqrt{\Phi}}{2N(\psi(\Theta) + D)(P(\Theta) + 1)}$$

where

$$\Phi = [D + C_d(\Theta) + P(\psi(\Theta) + D) + \psi(\Theta)NC]^2 - 4\mu(\psi(\Theta) + D)(P + 1) \begin{pmatrix} C_d(\Theta) + \delta(\Theta) - D \\ P(\psi(\Theta) + D)D \end{pmatrix}$$

### 4 Stability Analysis

**Theorem 1** *At the disease-free equilibrium point  $E_{df} (S_0, 0, 0, 0)$ , system (2) is asymptotically stable locally, if  $(C_d(\Theta) + \delta(\Theta) + D) D^2 - CN\psi(\Theta) > 0$  i.e.,  $R_0 < 1$  then the  $E_{df} (S_0, 0, 0, 0)$  and if  $(C_d(\Theta) + \delta(\Theta) + D) D^2 - CN\psi(\Theta) < 0$  i.e.,  $R_0 > 1$ , then the disease free equilibrium point  $E_{df} (S_0, 0, 0, 0)$  of the system (2) is unstable.*

**Proof** The Jacobian matrix (J) is written as follows based on system (2)

$$J = \begin{bmatrix} -CI(1 + \mu I) - D & 0 & -CS - 2\mu CSI & 0 \\ CI(1 + \mu I) & -D & CS + 2\mu CSI & 0 \\ 0 & \psi(\Theta) & -C_d(\Theta) - \delta(\Theta) - D & 0 \\ 0 & 0 & \delta(\Theta) & -D \end{bmatrix}$$

At infection free equilibrium point  $E_{df} (S_0, 0, 0, 0)$ , the characteristic equation is in the form of

$$(D + \lambda)^2 \left( \lambda^2 + \lambda(C_d(\Theta) + \delta(\Theta) + 2D) + (C_d(\Theta) + \delta(\Theta) + D)D - \frac{NC}{D}\psi(\Theta) \right) = 0 \tag{3}$$

Obviously, all the roots of an equation (3) are negative if  $(C_d(\Theta) + \delta(\Theta) + D) D^2 - CN\psi(\Theta) > 0$

(i.e., if  $R_0(\Theta) < 1$ ). As a result, at the disease-free equilibrium point  $E_{df} (S_0, 0, 0, 0)$ , system (2) is locally asymptotically stable if  $\frac{C\psi(\Theta)N}{D^2(C_d(\Theta) + D + \delta(\Theta))} < 1$ . Or else, the system (2) is unstable.

**Theorem 2** At the endemic equilibrium point  $E_{ee}(S_*, E_*, I_*, R_*)$ , system (2) is asymptotically stable locally if  $\frac{C\psi(\Theta)N}{D^2(C_d(\Theta)+D+\delta(\Theta))} > 1$  (i.e.,  $R_0(\Theta) > 1$ )

**Proof** At endemic equilibrium point  $E_{ee}(S_*, E_*, I_*, R_*)$ , the characteristic equation is

$$\lambda^4 + \zeta_1\lambda^3 + \zeta_2\lambda^2 + \zeta_3\lambda + \zeta_4 = 0 \tag{4}$$

Here

$\zeta_1 = -(\sigma_{11} + \sigma_{22} + \sigma_{33})$ ;  $\zeta_2 = \sigma_{11}\sigma_{22} + \sigma_{11}\sigma_{33} + \sigma_{11}\sigma_{44} + \sigma_{22}\sigma_{33} + \sigma_{22}\sigma_{44} + \sigma_{33}\sigma_{44} - \sigma_{23}\sigma_{32}$ ;  $\zeta_3 = -\sigma_{11}\sigma_{22}\sigma_{33} - \sigma_{11}\sigma_{22}\sigma_{44} - \sigma_{11}\sigma_{33}\sigma_{44} - \sigma_{22}\sigma_{33}\sigma_{44} - \sigma_{13}\sigma_{21}\sigma_{32} + \sigma_{11}\sigma_{23}\sigma_{32} + \sigma_{23}\sigma_{32}\sigma_{44}$ ;  $\zeta_4 = \sigma_{11}\sigma_{22}\sigma_{33}\sigma_{44} + \sigma_{13}\sigma_{21}\sigma_{32}\sigma_{44} - \sigma_{11}\sigma_{23}\sigma_{32}\sigma_{44}$  where  $\sigma_{11} = -CI_*(1 + \mu I_*)$ ;  $\sigma_{13} = -CS_*(1 + \mu I_*)$ ;  $\sigma_{21} = CI_*(1 + 2\mu I_*)$ ;  $\sigma_{22} = -D - \psi(\Theta)$ ;  $\sigma_{23} = CS_*(1 + 2\mu I_*)$ ;  $\sigma_{32} = \psi(\Theta)$ ;  $\sigma_{33} = -D - \psi(\Theta) - \delta(\Theta)$ ;  $\sigma_{43} = \delta(\Theta)$ ;  $\sigma_{44} = -D$ . Clearly it is evident that  $\zeta_1 > 0$ ,  $\xi_3 > 0$ ,  $\xi_4 > 0$ ,  $\zeta_1\zeta_2 - \zeta_3 > 0$  and  $\zeta_1\zeta_2\zeta_3 - \zeta_3^2 - \zeta_1^2\zeta_4 > 0$  if  $NC\psi(\Theta) - (C_d(\Theta) + \delta(\Theta) + D)D^2 < 0$  (i.e.,  $R_0(\Theta) > 1$ ). The roots of an equation (4) have negative roots or negative real parts as per Routh-Hurwitz criteria [24]. Hence the system (2) is locally asymptotically stable at  $E_{ee}(S_*, E_*, I_*, R_*)$

## 5 Numerical Simulation

The parameters that define the rates at which individuals progress from one stage to the next, such as infection rate, death rate owing to corona virus, and recovery rate, are directly dependent on the numerical analysis of the fuzzy SEIR system. The novel corona eruption in the inhabitants will never go away (i.e.  $R_0(\Theta) < 1$ ), but it will be smaller than those who have been infected with COVID-19. The numerical simulation of Covid-19 model usages statistics on the number of Covid-19 cases in India. The initial population  $(S_0, E_0, I_0, R_0) = (1405, 821, 0.034, 0.008609)$  (in millions) and the corresponding parameters in the system (2) are  $N = 0.76$ ;  $D = 0.02$ ;  $C = 0.08960$ ;  $P = 0.07112$ ;  $\mu = 0.00009$ ;  $C_d = 0.0004 - 0.0009$ ;  $\Psi = 0.00002 - 0.00004$ ;  $\delta = 0.01 - 0.05$

The following are the observations from the above figures: Fig. 2a shows that the time series evaluation of susceptible, exposed, infected, recovered population. Figure 3a represent the variations in susceptible populations of india along with time for various values of  $\delta$ . we conclude that variation in susceptible population is more as  $\delta$  varies and which says that  $\delta$  plays a significant role on susceptible population of India. Figure 3b shows the variations in exposed populations of India for various values of  $\delta$ . We can conclude that variation in exposed population of India is more as  $\delta$  varies. So  $\delta$  variations effect the exposed of India. Figure 3c represents the infected population of variations along time for India. From this figure we conclude that variations in infected populations in India is less as  $\delta$  varies. So  $\delta$  plays a significant role as dynamic sensitive parameter on the infected populations of India. Figure 3d represents the recovered populations of India for various values of  $\delta$ . we conclude

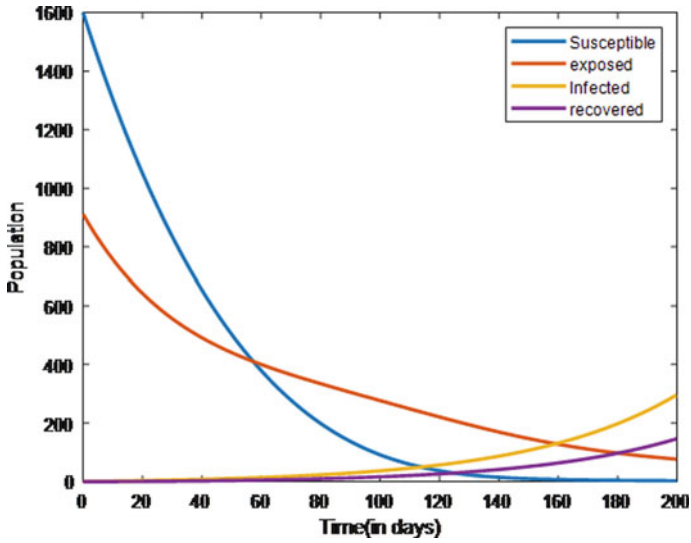


Fig. 2 Time series evaluation of population w.r.t the above set of parameter values

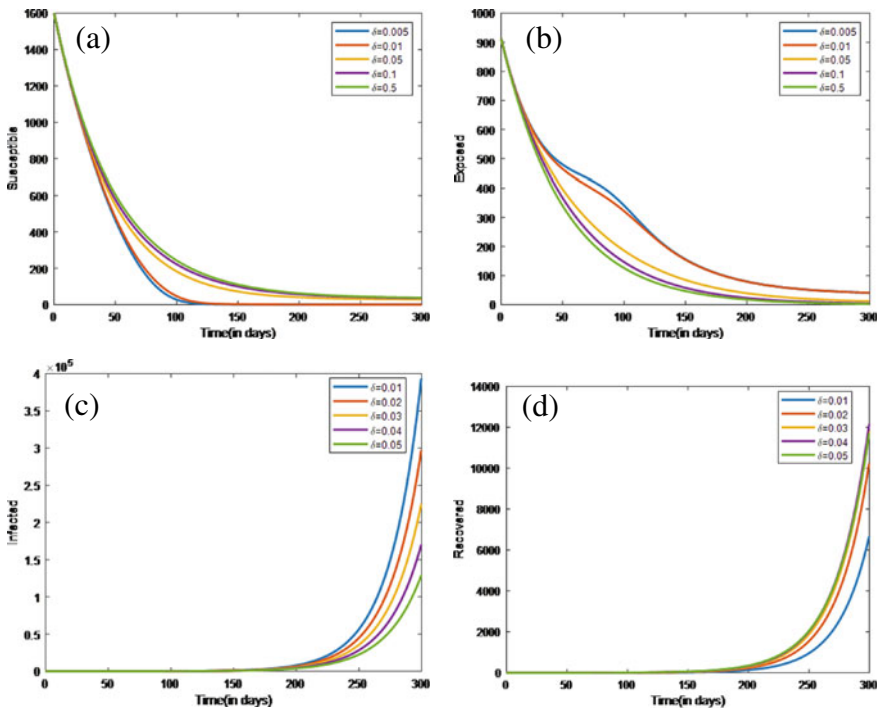
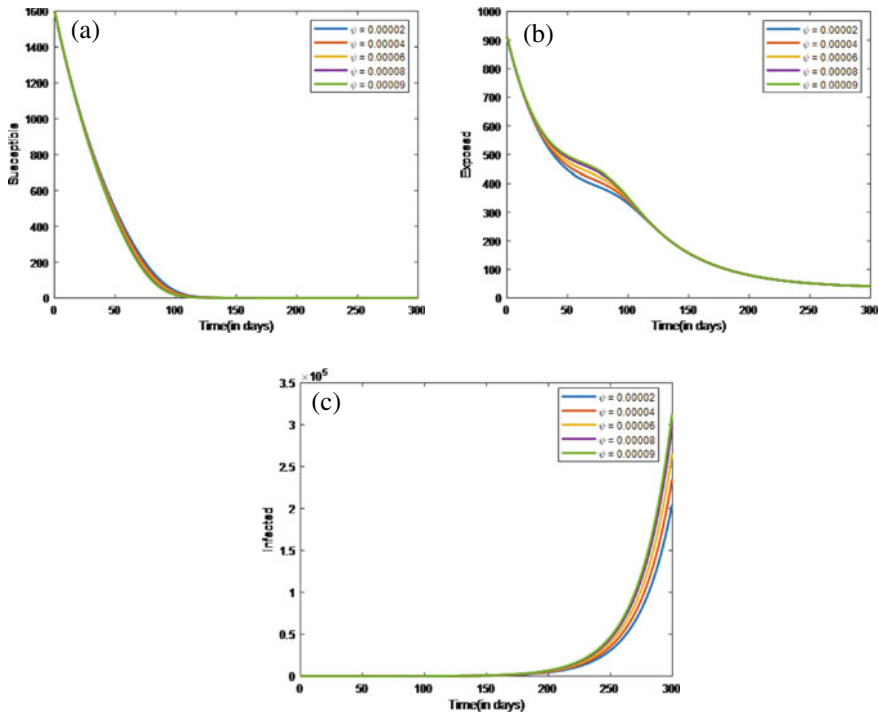


Fig. 3 a–d Time series evaluation of susceptible, exposed infected and recovered population of India where delta is varying with initial values from the above set of parameter values



**Fig. 4** **a** Time series evaluation of susceptible population of India where  $\Psi(\theta)$  is varying with initial values of above parameters. **b, c** Time series evaluation of exposed and infected population of India where  $\Psi(\theta)$  is varying with initial values of above parameters

that variations in recovered populations of India are less as  $\delta$  varies. So  $\delta$  acts as a dynamic attribute on recovered population of India. Figure 4a shows the variations in susceptible populations in India as  $\psi$  varies from 0.00003 to 0.00009. We can conclude that variations in susceptible population in India is very less. We also conclude that the attribute  $\psi$  is less dynamic in nature as it effects the susceptible populations of India. Figure 4b shows that the variation in exposed populations of India as  $\psi$  varies. We can conclude that variations in the exposed population in India almost high variations over a particular period of time in the population as we saw rapid spread of virus in a particular period. So, we conclude that  $\psi$  acts as highly dynamic on both exposed populations of India over a period of time. Figure 4c shows the variations in infected population of India as  $\psi$  varies. We conclude that the variations in infected population in India are slightly less as  $\psi$  varies. Hence we conclude that acts as a less dynamic on variations in infected population of India. As  $\delta$  is increasing susceptible population is increasing slightly but infected and exposed are decreasing because of awareness in society about precautions such as social distancing, sanitizing and usage of herbs or home medicines. Vaccination awareness and drives also place a major role in reducing number of infected population. Also

as there is less exposure of infection in society, recovered is effectively improving. Figure 4a–c shows the dynamics of susceptible, exposed and infected against time for different values of  $\psi$ . Also, it is observed that susceptible is increasing as  $\psi$  increases whereas infected and exposed are reducing because number of recoveries are going up with the help of growing immunities due to vaccination and prevention measures.

## 6 Conclusions and Remarks

The transmission dynamics of the COVID-19 outbreak are modeled with a SEIR fuzzy system in this paper. The parameters  $\Psi$ ,  $\delta$  and  $C_d$  are represented as fuzzy parameters in this study and are considered as association purposes of fuzzy numbers. These factors are dependent on the corona virus load  $\Theta$ , and their fuzzy membership functions are specified by them. For  $R_0(\Theta) < 1$  and  $R_0(\Theta) > 1$ , respectively, together the infection-free and the endemic equilibrium points are asymptotically stable locally.

**Acknowledgements** Supported by Organization Aditya College of Engineering and Technology, Surampalem, AP. and Vellore Institute of Technology, Vellore, Tamilnadu.

## References

1. Alzahrani, E., Khan, M.A.: Modeling the dynamics of Hepatitis E with optimal control. *Chaos Solitons Fract* **116**, 287–301 (2018)
2. Barros, L.C., Bassanezi, R.C., Leite, M.B.F.: The SI epidemiological models with a fuzzy transmission parameter. *Comput. Math. Appl.* **45**, 1619–1628 (2003)
3. Zhou, L., Fan, M.: Dynamics of an SIR epidemic model with limited resources visited. *Nonlinear Anal. Real World Appl.* **13**, 312–324 (2012)
4. McCluskey, C.C.: Complete global stability for an SIR epidemic model with delay- distributed or discrete. *Nonlinear Anal.* **11**(1), 55–59 (2010)
5. Bjornstad, O.N., Finkenstadt, B.F., Grenfell, B.T.: Dynamics of measles epidemics: estimating scaling of transmission rates using a time series SIR model. *Ecol. Monogr.* **72**(2), 169–184 (2002)
6. Hu, Z., Ma, W., Ruan, S.: Analysis of SIR epidemic models with nonlinear incidence rate and treatment. *Math. Biosci.* **238**(1), 12–20 (2012)
7. Diekmann, O., Heesterbeek, H., Britton, T.: Mathematical tools for understanding infectious disease dynamics. In: Princeton Series in Theoretical and Computational Biology. Princeton University Press, Princeton (2013)
8. Hethcote, H.W.: The mathematics of infectious disease. *SIAM Rev.* **42**, 599–653 (2000)
9. He, S., Peng, Y., Sun, K.: SEIR modeling of the COVID-19 and its dynamics. *Nonlinear Dyn.* **101**, 1667–1680 (2020)
10. Overton, C.E.: Using statistics and mathematical modeling to understand infectious disease outbreaks: COVID-19 as an example. *Infect. Dis. Model.* **5**, 409–441 (2020)
11. Das, P., Upadhyay, R.K., Mishra, A.K.: Mathematical model of COVID-19 with comorbidity and controlling using non-pharmaceutical interventions and vaccination. *Nonlinear Dyn.* **106**, 1213–1227 (2021)

12. Haitao, S., Zhongwei, J., Zhen, J., Shengqiang, L.: Estimation of COVID-19 outbreak size in Harbin, China. *Nonlinear Dyn.* **106**, 1229–1237 (2021)
13. Shidong, Z., Guoqiang, L., Huang, T.: Vaccination control of an epidemic model with time delay and its application to COVID-19. *Nonlinear Dyn.* **106**, 1279–1292 (2021)
14. Mwalili, S., Kimathi, M., Ojiambo, O., Gathungu, D.: Seir model for COVID-19 dynamics incorporating the environment and social distancing. *BMC Res. Notes* (2020)
15. Shikha, J., Sachin, K.: Dynamical analysis of SEIS model with nonlinear innate immunity and saturated treatment. *Eur. Phys. J. Plus* **136** (2021)
16. Jafelice, R., Barros, L.C., Bassanezei, R.C., Gomide, F.: Fuzzy modeling in symptomatic HIV virus infected population. *Bull. Math. Biol.* **66**, 1597–1620 (2004)
17. Massad, E., Burattini, M.N., Ortega, N.R.S.: Fuzzy logic and measles vaccination: designing a control strategy. *Int. J. Epidemiol.* **28**, 550–557 (1999)
18. Mondal, P.K., Jana, S., Halder, P., Kar, T.K.: Dynamical behavior of an epidemic model in a fuzzy transmission. *Int. J. Uncertain. Fuzziness Knowl-Based Syst.* **23**, 651–665 (2015)
19. Nagarajan, D., Lathamaheswari, M., Broumi, S., Kavikumar, J.: A new perspective on traffic control management using triangular interval type-2 fuzzy sets and interval neutrosophic sets. *Oper. Res. Perspect.* **6**, 100099 (2019)
20. Mishra, B.K., Pandey, S.K.: Fuzzy epidemic model for the transmission of worms in computer network. *Nonlinear Anal. Real World Appl.* **11**(5), 4335–4341 (2010)
21. Gakkhar, S., Chavda, N.C.: Impact of awareness on the spread of dengue infection in human population. *Appl. Math.* **4**(8), 142–147 (2013)
22. Phaijoo, G.R., Gurung, D.B.: Mathematical model of dengue disease transmission dynamics with control measures. *J. Adv. Math. Comput. Sci.* **23**(3), 1–2 (2017)
23. Arqub, O.A., El-Ajou, A.M., Shawagfeh, N.: Analytical solutions of fuzzy initial value problem by HAM. *Appl. Math. Inform. Sci.* **7**, 1903–1919 (2013)
24. Brauer, F., Castillo-Chavez, C.: Mathematical models in population biology and epidemiology. *Texts Appl. Math.* **2** (2012)

# Covid-19 Vaccination in India: Prophecy of Time Period to Immune 18+ Population



Anand Kumar, Agin Kumari, and Rishi Pal Chahal

**Abstract** In the present paper, we have prophesied how much time will be required to vaccinate 18+ population of India with at least one dose of COVID-19 vaccines. We have used non-linear extrapolation technique to prophecy, for this polynomial function is used for extrapolation. We have Fitted a non-linear polynomial of degree six to the cumulative vaccination data from 16 January 2021 to 24 July 2021 to estimate the required time period. Non-linear extrapolation results are depicted through the graphs, shows that the entire 18+ population will be vaccinated with at least 1 dose by mid of December of this year and 25% population will be fully vaccinated.

**Keywords** Covid-19 · Vaccination · India · Prophecy · Extrapolation

## 1 Introduction

Indian government has started vaccination drive for COVID-19 on 16 January 2021, as of 24 July 2021 over 3403.87 lacs (24.9%) population is vaccinated with at least 1 dose and over 927.63 lacs (6.8%) population is fully vaccinated with presently permitted vaccines.

Non-linear extrapolation is more reliable and inexpensive for statistical forecasts by using previous trend of data. This methodology estimates the dependent function for independent variable by interpolating a smooth nonlinear curve through all values of independent variable, using this nonlinear curve, extrapolates dependent values beyond available data. Polynomial function or rational function are used in this methodology.

---

A. Kumar (✉)

Department of Physics, Chaudhary Ranbir Singh University, Jind 126102, India

e-mail: [anandkumar@crsu.ac.in](mailto:anandkumar@crsu.ac.in)

A. Kumari

Department of Mathematics, Chaudhary Bansi Lal University, Bhiwani 127021, India

R. Pal Chahal

Department of Physics, Chaudhary Bansi Lal University, Bhiwani 127021, India



Gowrisankar et al. [1] used multifractal formalism to analyse COVID-19 data, assuming that infection rates in different countries follow a power law growth pattern. Radiom and Berret [2] constructed two models to explain the epidemic's fast-growth phase and to interpret the complete data set. Han et al. [3] studied a two-part framework, one to show repeated worldwide breakouts of COVID-19 and the other to investigate the underlying causes of recurrent outbreaks. Kavitha et al. [4] studied the SIR and fractal models on daily positive COVID-19 cases in India in order to forecast the outbreak's future trajectory. Moghadas et al. [5] constructed an agent-based model of SARS-CoV-2 transmission, and was parameterized using US statistics and COVID-19 age-specific results.

In the present paper, we have estimated how much time will be required to vaccinate 18+ population of India with at least one dose of COVID-19 vaccines. We have used non-linear extrapolation technique to prophecy, for this polynomial function is used for extrapolation. Nonlinear extrapolation method is used to prophecy as casual factors related to this kind of situation are expected to remain constant [6,7]. A non-linear polynomial of degree six is fitted to the cumulative vaccination data (vaccinated with at least 1 dose) from 16 January 2021 to 24 July 2021. A non-linear polynomial of degree five is fitted to the cumulative vaccination data (fully vaccinated) from 16 January 2021 to 24 July 2021. Non-linear extrapolation results are depicted through the graphs, shows that the entire 18+ population will be vaccinated with at least 1 dose by mid of December of this year and 25% population will be fully vaccinated.

Because COVID-19 vaccines stimulate a wide immune response including a variety of antibodies and cells, they should give some protection against new viral types. Vaccines should not be rendered fully ineffective due to changes or mutations in the virus. If any of these vaccinations prove ineffective against one or more variants, the vaccines' composition can be changed to defend against these variants. Even with minimal protection against infection, vaccination can have a significant influence on preventing COVID-19 outbreaks. To accomplish this benefit, however, ongoing adherence with non-pharmaceutical measures is required.

## 2 Modeling of Data and Fitting of Polynomial

In this section, we have constructed a table of vaccination data and fitted a suitable nonlinear polynomial for extrapolation. Table-1 contains cumulative vaccination data [8] of 18+ population of India observed on weekends for study. Figure 1 shows that a six-degree polynomial suited to the cumulative vaccination data (vaccinated with at least 1 dose) from 16 January 2021 to 24 July 2021 and a five-degree polynomial is suited to the cumulative vaccination data (fully vaccinated) from 16 January 2021 to 24 July 2021. Fitted polynomials are as follows;

$$y(x) = -0.0005x^6 + 0.0437x^5 - 1.4101x^4 + 21.153x^3 - 142.29x^2$$

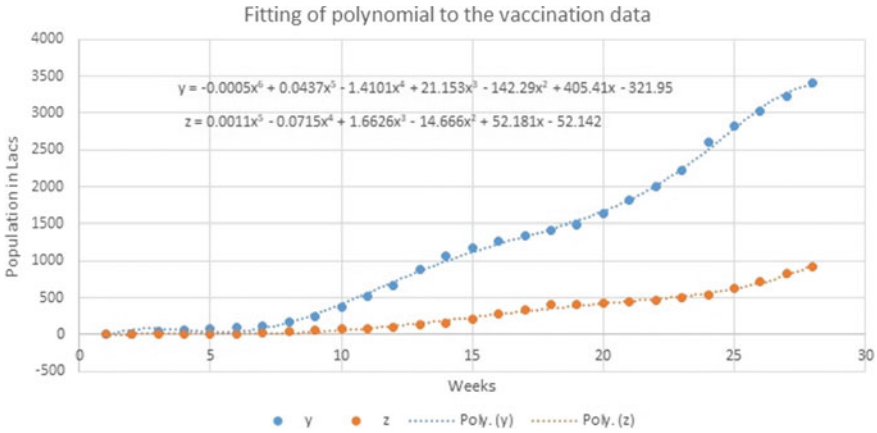


**Fig. 1** Fitting of polynomial to the vaccination data

$$y = -0.0005x^6 + 0.0437x^5 - 1.4101x^4 + 21.153x^3 - 142.29x^2 + 405.41x - 321.95$$

$$z(x) = 0.0011x^5 - 0.0715x^4 + 1.6626x^3 - 14.666x^2 + 52.181x - 52.142$$

With the help of Table 1 and Fig. 1 it is observed that in the 2nd weekend of vaccination drive the data of population vaccinated with one dose is 15 times of 1st weekend. Gradual increment in 3rd to 7th weekends, moderate increment in 8th to 10th weekends, major increment in 11th–19th weekends, significantly great increment in 20th–28th weekends, in the data of population vaccinated with one dose is observed. Gradual increment in the data of Population fully vaccinated is observed.

### 3 Extrapolation Method

In this section, we have prophesied how much population will be vaccinated with 1 or 2 dose by method of nonlinear polynomial extrapolation. We have extrapolated the values of y and z with respect to x with confidence interval 95%, i.e. weekly estimation of population vaccinated with at least 1 dose and fully vaccinated.

With the help of vaccination data given in Table 1, The extrapolated values of population vaccinated with at least 1 dose and 2 dose are obtained. From Figs. 2 and 3 and Table 2, it is observed that up to 11th December over 80 crores (almost all 18+ population) population will be vaccinated with at least 1 and about 20 crores (25% of 18+ population) population will be fully vaccinated.

**Table 1** Vaccination data at a glance in India (cumulative data observed at weekends from 16 January 2021 to 24 July 2021)

Data observed on weekends (date) (x)	Population vaccinated with at least 1 dose		Population fully vaccinated	
	in lacs (y)	in %	in lacs (z)	in %
1 (16 January)	1.99	0.0	0	0.0
2 (23 January )	15.82	0.1	0	0.0
3 (30 January )	37.44	0.3	0	0.0
4 (6 February)	57.75	0.4	0	0.0
5 (13 February )	80.45	0.6	0.07	0.0
6 (20 February )	99.64	0.7	8.73	0.1
7 (27 February )	117.88	0.9	24.54	0.2
8 (6 March)	171.68	1.3	37.54	0.3
9 (13 March)	243.07	1.8	54.31	0.4
10 (20 March)	371.25	2.7	74.79	0.5
11 (27 March)	514.41	3.8	88.28	0.6
12 (3 April)	657.39	4.8	102.40	0.7
13 (10 April)	888.86	6.5	127.09	0.9
14(17 April)	1064.31	7.8	161.91	1.2
15(25 April)	1177.95	8.6	213.90	1.6
16 (1 May)	1263.28	9.2	272.97	2.0
17 (8 May)	1333.66	9.8	341.27	2.5
18 (15 May)	1411.32	10.3	404.12	3.0
19 (22 May)	1492.19	10.9	416.22	3.0
20 (29 May)	1641.58	12.0	429.30	3.1
21 (5 June)	1809.72	13.2	445.99	3.3
22 (12 June)	1996.55	14.6	465.32	3.4
23 (19 June)	2214.93	16.2	494.15	3.6
24 (26 June)	2602.53	19.0	545.88	4.0
25 (3 July)	2822.31	20.7	620.69	4.5
26 (10 July)	3031.71	22.2	728.61	5.3
27 (17 July)	3218.93	23.6	830.37	6.1
28 (24 July)	3403.87	24.9	927.63	6.8

## 4 Discussion

In the present paper, we have obtained estimated time period to vaccinate the 18+ population in India in view of current vaccination rate. Extrapolated values of population vaccinated with at least 1 dosage and 2 dose are determined using vaccination data from Table 1 by a six-degree polynomial suited to the cumulative vaccination

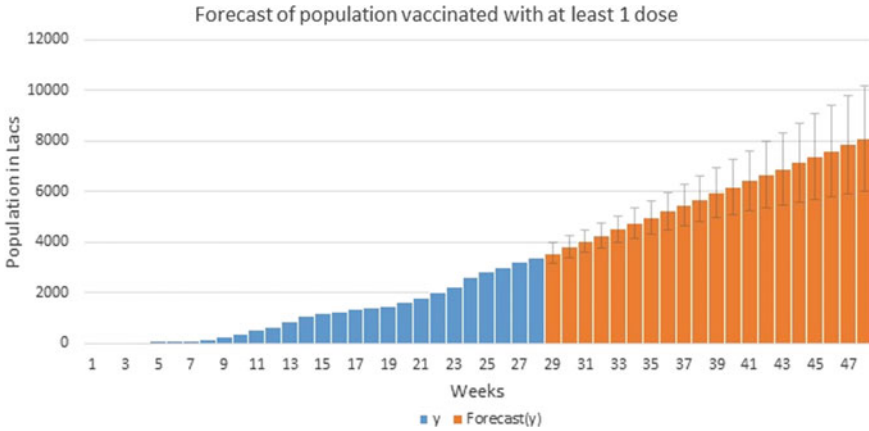


**Fig. 2** Weekly Forecast of population vaccinated with at least 1 dose from 31 July 2021 to 11 December 2021

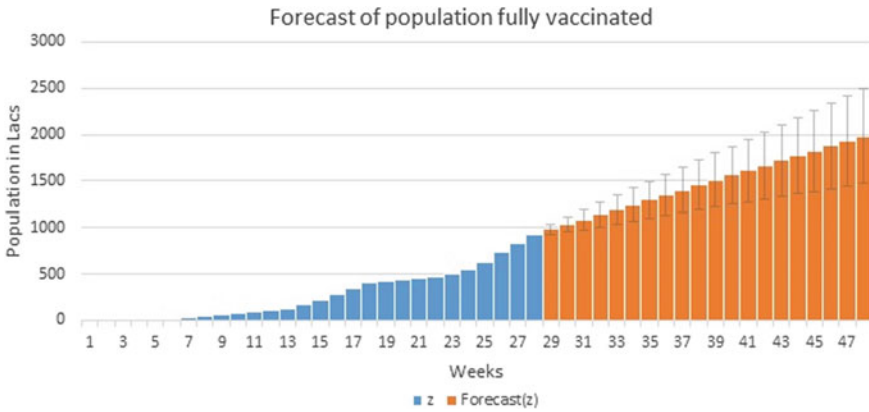


**Fig. 3** Weekly Forecast of population fully vaccinated from 31 July 2021 to 11 December 2021

data (vaccinated with at least 1 dose) from 16 January 2021 to 24 July 2021 and a five-degree polynomial is suited to the cumulative vaccination data (fully vaccinated). Figures 2 and 3 represents the weekly extrapolated forecast values of population vaccinated with 1 or full dose from 31 July 2021 to 11 December 2021 along with confidence interval. From the Table-2, It is observed that over 80 crore population will be vaccinated with at least 1 dose up to 11 December 2021 i.e. almost all population will be covered and 25% population will be fully vaccinated. COVID-19 vaccinations will provide some resistance against new virus strains since they stimulate a broad immune response that includes a variety of antibodies and cells. Vaccines should not be rendered completely ineffective as a result of virus mutations or modifications. If any of these vaccines are shown to be ineffective against one or

**Table 2** Weekly estimation of vaccinated population from 31 July 2021 to 11 December 2021 along with confidence interval

Weekends (x)	Estimated population will be vaccinated with at least 1 dose in lacs (y)	Confidence Interval (y)	Estimated population will be fully vaccinated in lacs (z)	Confidence Interval (z)
29 (31 July)	3566.17	424.00	980.31	57.15
30 (7 August)	3805.25	437.05	1033.10	84.83
31 (14 August)	4044.33	459.33	1085.88	108.94
32 (21 August)	4283.41	492.13	1138.67	131.70
33 (28 August)	4522.48	535.85	1191.45	153.93
34 (4 September)	4761.56	590.18	1244.24	175.99
35 (11 September)	5000.64	654.38	1297.02	198.12
36 (18 Sept)	5239.72	727.55	1349.81	220.44
37 (25 September)	5478.80	808.81	1402.59	243.02
38 (2 October)	5717.87	897.35	1455.38	265.92
39 (9 October)	5956.95	992.48	1508.16	289.18
40 (16 October)	6196.03	1093.62	1560.95	312.81
41 (23 October)	6435.11	1200.29	1613.73	336.84
42 (30 October)	6674.19	1312.10	1666.52	361.27
43 (6 November)	6913.26	1428.71	1719.30	386.10
44 (13 November)	7152.34	1549.84	1772.09	411.36
45 (20 November)	7391.42	1675.26	1824.87	437.03
46 (27 November)	7630.50	1804.77	1877.66	463.11
47 (4 December)	7869.58	1938.19	1930.44	489.60
48 (11 December)	8108.65	2075.36	1983.23	516.51

more variants, the vaccine's composition can be altered to protect against these variants. Vaccination, even if it provides only rudimentary protection against infection, can help avoid COVID-19 epidemics.

## References

1. Gowrisankar, A., Rondoni, L., Banerjee, S.: Can India develop herd immunity against COVID-19? *Eur. Phys. J. Plus* **135**, 526 (2020)
2. Radiom, M., Berret, J.F.: Common trends in the epidemic of Covid-19 disease. *Eur. Phys. J. Plus* **135**, 517 (2020)
3. Han, C., Li, M., Haihambo, N., et al.: Mechanisms of recurrent outbreak of COVID-19: a model-based study. *Nonlinear Dyn.* **106**, 1169–1185 (2021)
4. Kavitha, C., Gowrisankar, A., Banerjee, S.: The second and third waves in India: when will the pandemic be culminated? *Eur. Phys. J. Plus* **136**, 596 (2021)
5. Moghadas, S.M., Vilches, T.N., Zhang, K. et al.: The impact of vaccination on COVID-19 outbreaks in the United States. *medRxiv: the preprint server for health sciences*, 2020.11.27.20240051 (2021)
6. Brezinski, C., Redivo Zaglia, M.: *Extrapolation Methods-Theory and Practic*. North Holand (1991)
7. Brezinski, C., Redivo Zaglia, M.: *Extrapolation and Rational Approximation*. Springer Nature, Switzerland (2020). ISBN 9783030584177
8. <http://www.cowin.gov.in>

# COVID-19 Detection from Chest X-Ray (CXR) Images Using Deep Learning Models



Mithun Karmakar, Koustav Chanda, and Amitava Nag 

**Abstract** Due to the tremendous rise in COVID cases around the world, early detection of Covid-19 has become critical. Deep learning technology has recently sparked a lot of attention as a means of detecting and classifying diseases quickly, automatically, and accurately. The goal of this study is to develop a deep learning based automatic COVID-19 detection system for better, faster, and more accurate COVID-19 detection from chest X-Ray (CXR) images. In our work, we have used pre-trained deep learning models such as VGG16, ResNet50, DenseNet201, InceptionV3 and Xception utilizing openly accessible dataset. Experimental results show that the DenseNet201 model performs the best with more than 97% accuracy. Moreover, in terms of size, DenseNet121 is beating the rest of the models. As a results, DenseNet201 is most suitable Deep Convolutional neural networks (CNN) architecture for developing an automatic covid-19 detection tool.

**Keywords** COVID-19 · Deep learning · Deep CNN · Chest X-ray images

## 1 Introduction

In recent years, a novel coronavirus (COVID-19) arising from the coronavirus SARS-COV2 has become a global epidemic. COVID-19 was declared a pandemic by the World Health Organization (WHO) on March 11, 2020, after it had spread to over a hundred countries [1]. A novel SARS-CoV-2 variant was reported to the WHO on November 24, 2021, from South Africa. As a variant of concern, the new variant (B.1.1.529) has been officially called Omicron. As compared to the other SARS-CoV-2 variants: Alpha, Beta, Gamma, and Delta, Omicron emerges as the most noticeable and different variant among the millions of SARS-CoV-2 genomes [2].

---

M. Karmakar (✉) · A. Nag  
Department of CSE, CIT Kokrajhar, Kokrajhar, Assam, India  
e-mail: [m.karmakar@cit.ac.in](mailto:m.karmakar@cit.ac.in)

K. Chanda  
L&T Infotech, Ranaghat, India

Timely and accurate detection of Coronavirus diseases is of great importance for controlling COVID-19. Because of its high transmissibility, COVID-19 can easily be transmitted from asymptomatic to vulnerable groups. Fever, dry cough, myalgia, dyspnea, and headache are the most common symptoms of the COVID-19 [3]. In rare cases, no symptoms are also visible (asymptomatic) which makes the disease an even greater hazard to public health. The diagnosis of coronavirus is performed by conducting a reverse-transcription polymerase chain reaction (RT-PCR) test with a patient's respiratory tract or blood samples [4]. The RT-PCR is a laboratory-based COVID-19 detection procedure and takes 2–3 days to get the results, which is a long period in comparison to COVID-19's quick spread rate [5].

An alternative to RT-PCR is the rapid antigens test (RAT) which is mostly employed for large-scale testing. However, both RT-PCR and RAT have false negative rates in some cases. A useful supplement to both RT-PCR test and RAT is chest X-Rays (CXR) for the diagnosis of COVID-19 infection. The accuracy of CXR-based COVID-19 diagnosis is dependent on manual analysis and interpretation by radiologists, which can lead to inaccurate analyses due to expert radiologists and doctors who can accurately detect COVID-19 infection from chest X-Rays are in short supply in the context of the pandemic.

Based on the foregoing facts, it is essential to develop alternative, complementary, and low-cost technologies for speedy and accurate diagnosis of COVID-19. Artificial Intelligence (AI), a rapidly evolving technology, is now being used for speedy and precise diagnosis of a variety of ailments, including brain tumour detection, breast cancer detection, and so on. Deep learning, a type of artificial intelligence, has been a natural choice for use in healthcare applications such as medical image analysis in recent years. As a result, building deep learning-based computer-aided diagnostic (CAD) tools for better, faster, and more accurate COVID-19 diagnosis is worthwhile.

Advances in image processing provide an opportunity to expand its application in all areas of healthcare [6]. Applications of deep learning to medical imaging for automatic diagnosis of various diseases are growing rapidly [7, 8]. As a result, these methodologies are widely used for COVID-19 research [9]. The aim of this work is to develop a deep learning-based system for better, faster, and more accurate detection of COVID-19 from chest X-Ray (CXR) images.

The rest of the paper is organized as follows: The state-of-the-art deep Convolutional networks and the other materials and methodologies including dataset collection and preparation, required to accomplish this work are described in Sect. 2. The experimental setup as well as the results and performance analysis are provided in Sect. 3. Section 4 concludes the paper.

## 2 Materials and Methods

Deep Convolutional Neural Network (CNN) models are used in this study to reveal patterns in chest X-ray images that are imperceptible to the naked eye. The CNN is a class of Deep Learning (DL) techniques that is used to identify useful and



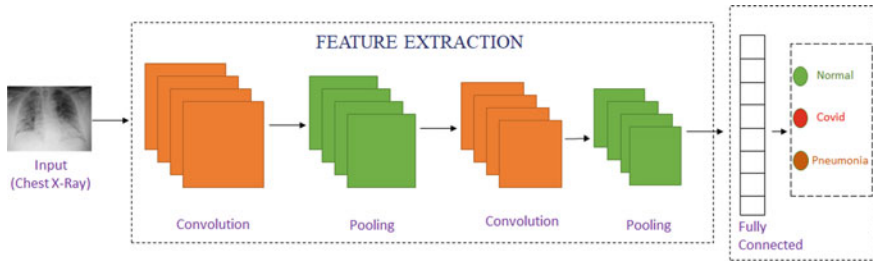


**Fig. 1** A typical Convolution Neural Network (CNN) architecture

distinctive representations of images. A typical CNN is depicted in Fig. 1. However, the fundamental issue that a deep CNN model encountered during training was a large volume of image data. This problem has been addressed using a technique known as transfer learning (TL) which is designed for the CNNs. Several pre-trained models with transfer learning that have already trained on a huge annotated image library have been designed.

Recently, a number of CNN Architectures have been proposed which are used for COVID-19 diagnosis such as VGG16 [10], ResNet50 [11], DenseNet201 [12], InceptionV3 [13] and Exception[14], etc.

We used three different classes in our work (i.e., COVID-19, pneumonia, and healthy). Figure 2 depicts the entire detection process for COVID-19. In this work, first images of chest X-rays are collected from public datasets [15]. Then, image preprocessing was done. The only preprocessing used in this study was a simple rotation of the X-ray images (from 0 to 12° clockwise or anticlockwise). Finally, pre-trained CNN models with weights from ImageNet and with the proper fine-tuning are used for classification (Fig. 3).

### 2.1 X-ray Image DataSet

In our study, we have used anterior-to-posterior (PA)/posterior-to-anterior (AP) view of CXR images as this view of radiography is widely used by radiologists in clinical diagnosis. The dataset used in our work is collected from Kaggle [15]. It consists of 12,443 images and these images are divided into three different classes- ‘Normal’, ‘Covid positive’ and ‘Viral Pneumonia’. There are 906 Covid positive images, 1345 viral pneumonia images and 10,192 normal images. These images are further split into training and testing data with a percentage ratio of 80% training data and 20% testing data.

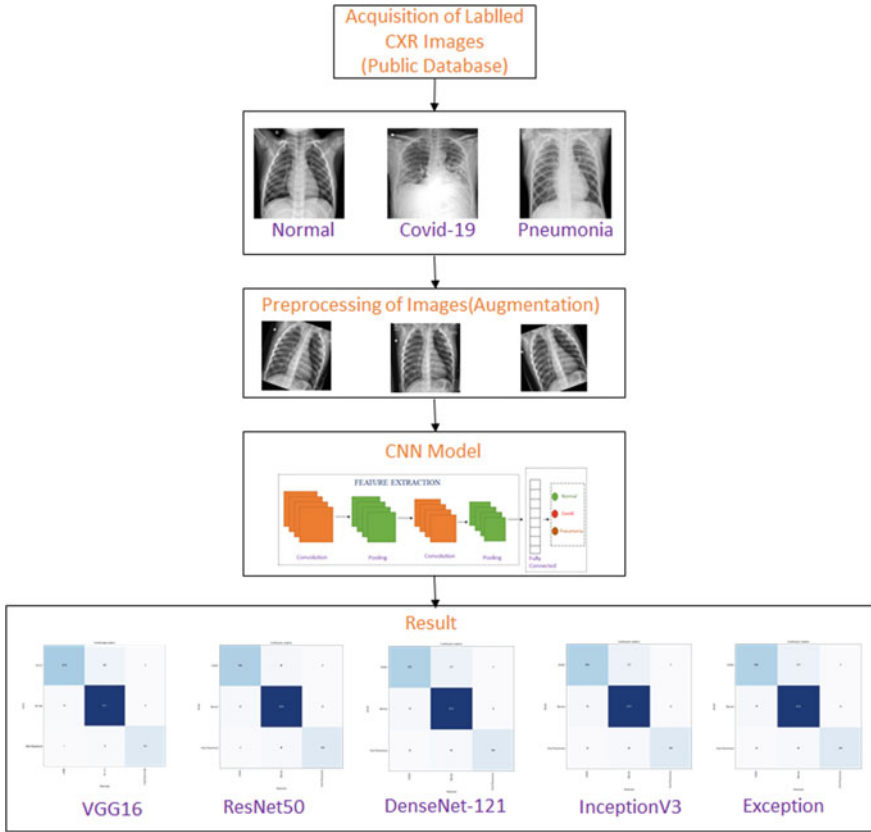


Fig. 2 Architecture of deep learning based COVID-19 diagnosis system

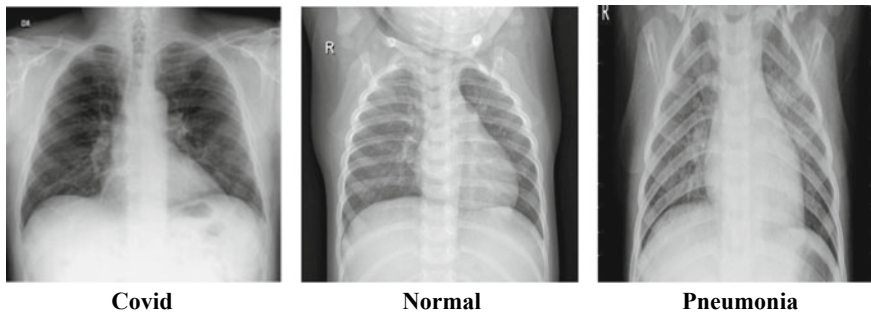


Fig. 3 Sample of X-ray images from dataset

Since the dataset is not uniform, therefore, first we have to resize the image to  $224 \times 224$  for Vgg16, ResNet50, DenseNet201 architecture, and  $299 \times 299$  for InceptionV3 and Xception architecture.

## ***2.2 Pretrained CNN Models with Fine-Tuning***

Training deep CNN models from scratch is complex as well as demand large amount of data in order to converge the model. Fine-tuning on a pre-trained CNN model can be an alternate solution. In this work, fine-tuning was performed on pre-trained CNN models such as VGG16, ResNet50, DenseNet201, Inception V3 and Xception architecture with CRX dataset [15]. The models were pre-trained with weights from ImageNet. Furthermore, the top layer of all models are truncated and a new fully-connected softmax layer is added on the top layer that used stochastic gradient descent (SGD) algorithm.

## **3 Results**

Using the datasets given in Sect. 2.1, the classification of COVID-19 against the pneumonia and normal classes is performed. The CNN models described in the Sect. 2.2 was evaluated for COVID-19 detection from CRX images. In the experiment, the dataset was divided into two halves for training and testing: 80% for training and 20% for testing.

### ***3.1 Tools Used***

We used TensorFlow 2.2.0, Python 3.7, and Google Colab graphics processing units (GPU). The CNN models used in this work are implemented using the TensorFlow 2.2.0 deep learning framework, and the training and testing procedures are carried out on the Google Colab platform.

### ***3.2 Performance Evaluation***

The performance has been evaluated in terms of classification accuracy (CA). The classification accuracy is defined as follows:

Classification accuracy (CA): It is defined as the proportion of right predictions to the total number of predictions made on a given set of data:

$$\text{Classification Accuracy (CA)} = \frac{\text{Number of unerring predictions}}{\text{Total number of predictions made}}$$

### 3.3 Results Analysis

In this work, various state-of-the-art deep CNN models such as VGG16, ResNet50, DenseNet201, InceptionV3 and Xception are used for COVID-19 identification. The results for the performance of all evaluated models are provided in Table 1. As shown in Table 1, the size of the VGG16 trained dataset weight is the largest, which is 512 MB. As a result, the VGG16 model consumes a significant amount of storage space and bandwidth, making it inefficient. The DenseNet201 model was evaluated to be the most efficient in terms of both size and performance among all the five models we trained and tested. The training and test detection accuracy are also shown in Fig. 4.

**Table 1** Experimental results of different models

	Size (MB)	Training accuracy	Test accuracy	Training loss	Test loss
VGG16	512	0.9667	0.9537	0.0920	0.1072
ResNet50	98	0.7998	0.9086	0.5369	0.2484
DenseNet201	80	0.9702	0.9704	0.2371	0.3435
InceptionV3	92	0.9398	0.9408	0.6222	0.7738
Xception	88	0.9592	0.9459	0.5204	1.0678

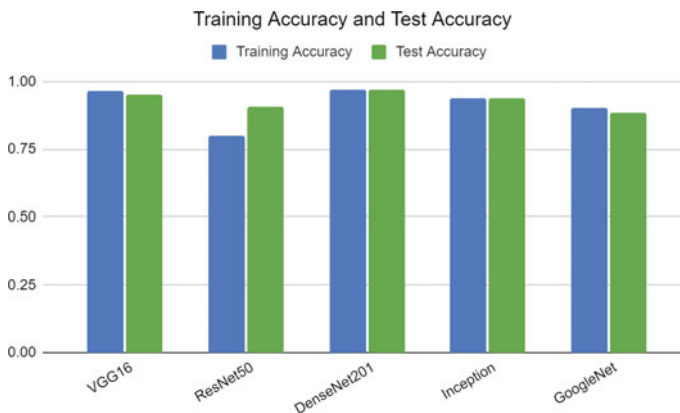


**Fig. 4** COVID-19 detection accuracy

## 4 Conclusions

The wave of Covid-19 and the continued struggle to test the patients have led to increased cases. Effective screening and early medical attention for infected patients are required to combat the covid-19. The methods that are being used are mostly manual, and thus there is a delay in testing and inaccuracy of data, and as a result, most of the time, the patient will interact with, leading to the spread of the disease. The use of deep learning to help diagnose the diseases is a mechanism that would help ensure the diagnosis are more accurate and on time. In this work, various state-of-the-art deep CNN models for COVID-19 detection classification are used. The models evaluated include VGG 16, ResNet50, DenseNets121, InceptionV3 and Xception. The experimental results show that the best performing model is DenseNets121 followed by VGG16, Xception, InceptionV3 and Resnet50. Moreover, in terms of size, DenseNet121 is beating the rest of the models. DenseNets is, therefore, a good architecture for the development of computer-aided diagnostic tools.

## References

1. Sohrabia, C., Alsafi, Z., O'Neill, N., Khan, M., Ahmed, K., Al-Jabir, A., Iosifidis, C., Agha, R.: World health organization declares global emergency: a review of the 2019 novel coronavirus (COVID-19). *Int. J.Surg.* **76**, 71e76 (2020)
2. Gowrisankar, A., Priyanka, T.M.C., Banerjee, S.: Omicron: a mysterious variant of concern. *Eur. Phys. J. Plus* **137**, 100 (2022)
3. Islam, M.M., Karray, F., Alhaji, R., Zeng, J.: A review on deep learning techniques for the diagnosis of novel coronavirus (covid-19). *IEEE Access* **9**, 30551–30572 (2021)
4. Islam, M.Z., Islam, M.M., Asraf, A.: A combined deep CNN-LSTM network for the detection of novel coronavirus (COVID-19) using X-ray images. *Informat. Med. Unlocked* **20**, 100412 (2020)
5. Naronglerdrit, P., Mporas, I., Sheikh-Akbari, A.: COVID-19 detection from chest X-rays using transfer learning with deep convolutional neural networks. In: *Data Science for COVID-19*, pp. 255–273. Academic Press (2021)
6. Altaf, F., Islam, S.M.S., Akhtar, N., Janjua, N.K.: Going deep in medical image analysis: concepts, methods, challenges, and future directions. *IEEE Access* **7**, 99540–99572 (2019)
7. Ghassemi, N., Shoeibi, A., Rouhani, M.: Deep neural network with generative adversarial networks pre-training for brain tumor classification based on MR images. *Biomed. Signal Process. Control* **57**, 101678 (2020)
8. Chowdhury, M.E.H., Rahman, T., Khandakar, A., Mazhar, R., Kadir, M.A., Mahbub, Z.B., Islam, K.R. et al.: Can AI help in screening viral and COVID-19 pneumonia? *IEEE Access* **8**, 132665–132676 (2020)
9. Bhattacharya, S., Maddikunta, P.K.R., Pham, Q.-V., Gadekallu, T.R., Chowdhary, C.L., Alazab, M., Piran, M.J.: Deep learning and medical image processing for coronavirus (COVID-19) pandemic: a survey. *Sustain. Cities Soc.* **65**, 102589 (2021)
10. Iandola, F., Moskewicz, M., Karayev, S., Girshick, R., Darrell, T., Keutzer, K.: Densenet: implementing efficient convnet descriptor pyramids (2014). [arXiv:1404.1869](https://arxiv.org/abs/1404.1869)
11. He, K., Zhang, X., Ren, S., Sun, J.: Deep residual learning for image recognition. In: *Proceedings of the IEEE conference on computer vision and pattern recognition*, pp. 770–778 (2016)

12. Zhang, X., Zou, J., He, K., Sun, J.: Accelerating very deep convolutional networks for classification and detection. *IEEE Trans. Pattern Anal. Mach. Intell.* **38**(10), 1943–1955 (2015)
13. Szegedy, C., Vanhoucke, V., Ioffe, S., Shlens, J., Wojna, Z.: ‘Rethinking the inception architecture for computer vision. In: Proceedings of the IEEE Conference on Computer Vision and Pattern Recognition, pp. 2818–2826 (2016)
14. Xception, C.F.: Deep learning with depthwise separable convolutions. In: Proceedings of the IEEE Conference on Computer Vision and Pattern Recognition, pp. 1251–8 (2017)
15. Dataset Link. <https://www.kaggle.com/tawsifurrahman/covid19-radiography-database>

# Pre-covid and Post-covid Situation of Indian Stock Market-A Walk Through Different Sectors



Antara Roy, Damodar Prasad Goswami, and Sudipta Sinha

**Abstract** Sudden and unexpected outbreak of covid-19 has left a serious impression on Indian as well as global economy. A simple way of investigating and verifying this impact is to mind the movement of stock values and consequent market swing. In this piece of work, we tried to figure out the movement pattern of stock prices in different sectors. We carefully picked some representative stocks from each of the sectors and tried to perceive their beat to beat and overall movement in the pandemic period and express through mathematical language. This study offered some interesting, valuable and to some extent 'counter-intuitive' insights.

**Keywords** Covid · Indian stock market · Pandemic · Stock values

## 1 Introduction

Recently, the entire world has gone through a very tough situation due to the sudden outbreak of deadly virus covid-19. India is not an exception. We have witnessed two consecutive waves till now and a third wave is likely to occur according to the scientists. More or less 190 countries have been affected by the pandemic situation. Economic structure around the world has abruptly been impacted for the sudden advent of corona virus. Indian stock exchange has also been more or less affected during the pandemic situation. A simple way of measuring this impact on economy is to study the stock market behavior indifferent sectors. Some similar studies have already been performed. Buszko M studied utilization of an asymmetric exponential generalized autoregressive model to reflect the asymmetric effect on conditional

---

A. Roy (✉)

Asansol Institute of Engineering and Management-Polytechnic, Asansol, India

e-mail: [royantara793@gmail.com](mailto:royantara793@gmail.com)

D. P. Goswami

Asutosh Mookerjee Memorial Institute, Sivotosh Mookerjee Science Centre, Kolkata, India

S. Sinha

Burdwan Raj College, University of Burdwan, Burdwan, India

© The Author(s), under exclusive license to Springer Nature Switzerland AG 2022

1425

S. Banerjee and A. Saha (eds.), *Nonlinear Dynamics and Applications*,

Springer Proceedings in Complexity,

[https://doi.org/10.1007/978-3-030-99792-2\\_122](https://doi.org/10.1007/978-3-030-99792-2_122)

volatility [1]. Sahoo, M. collected evidence from the Indian stock market of covid-19 impact from Nifty 50, Nifty 50 Midcap, Nifty 100, Nifty 100 Midcap, Nifty 100 small cap, and Nifty 200 [2]. Awadhi et al. investigates whether infectious diseases affect stock market returns [3]. Khaled studied the impact of the COVID-19 pandemic on retailer performance [4]. Stefano R. et al. illustrated how anticipated real effects from the health crisis, a rare disaster were amplified through financial channels [5]. Md Akhtaruzzaman examined the impact of financial contagion through financial and non-financial firms between China and G7 countries during the COVID-19 period [6]. Naveen Donthu's paper covers different industrial sectors (e.g., tourism, retail, higher education) investigating the changes in consumer behavior, businesses, ethical issues, and aspects related to employees and leadership [7]. Dayong Zhanga. et al. [8] aimed to the mapping the general patterns of country-specific risks and systemic risks in the global financial markets. It also analyzed the potential consequences of policy interventions. The article developed by Okorie et al. [9] investigated the fractal contagion effect of the COVID-19 pandemic on the stock markets. Martin Scheicher [10] studied the regional and global integration of stock markets in Hungary, Poland, and the Czech Republic.

In this paper we have considered five different sectors like automobile sector, banking sector, construction sector, finance sector, tourism sector and some corresponding stocks picked up from these sectors which are mentioned below.

## 2 Materials and Methods

We have collected dataset of individual stocks from four different sectors, the Automobile, Banking, Finance and the construction sector starting from 1st November, 2019 up to 28th December, 2021. 'Yahoo finance' has been used as the data source. The opening value of the stocks on each day has been used in this study we plotted the stock values sector-wise and observed the nature. Finally, to compare these graphs with the covid situation, we also kept an eye on the covid graph of India built from count of daily infected persons. We demonstrate the graphs of each of the sectors one by one and quantify them with Pearson's Product Moment Correlation.

### 2.1 Automobile Sector

Figure 1 shows six representative stocks in the automobile sector like Ashok Layland, TVS motors, Mahendra & Mahendra, Hero Motor and Maruti. Here, x-axis denotes time and y-axis denotes the opening share price on each day. Being in different scale, they are not clearly visible in a single graph. So, we have normalized the values to [0,1] with the formula  $\frac{x-x_{min}}{x_{max}-x_{min}}$  where x represents the time series values of stocks and plotted individual graphs in Fig. 2.



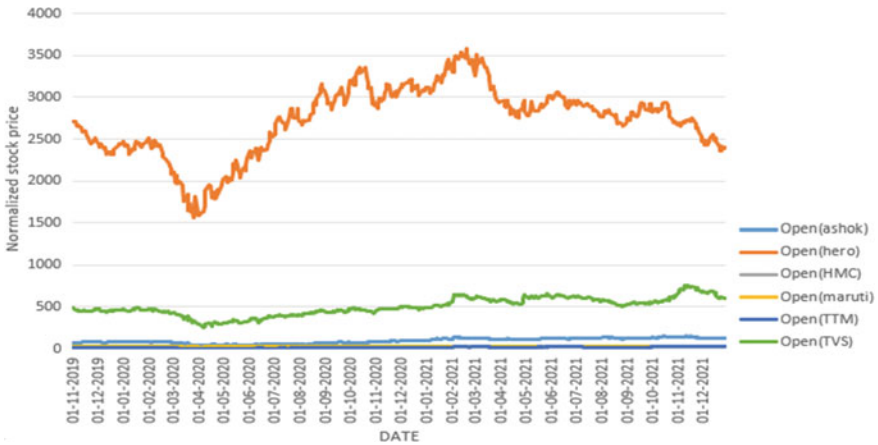


Fig. 1 Normal graph of automobile companies

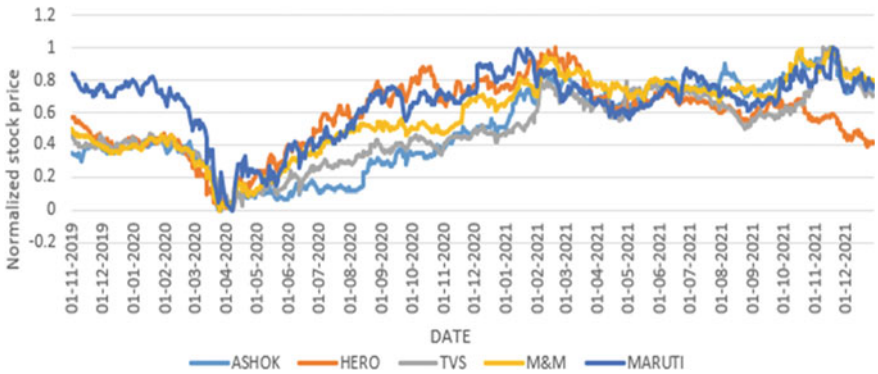


Fig. 2 Normalized graph of automobile sector

Now the graphs become comparable. This graph shows that different companies we chose, behave in a similar fashion to some extent.

To quantify this behavior, we calculated the correlation coefficients between each pair and tabulated them in Table 1.

We can observe that most of the coefficients are highly positive which explains their similar movements over time.

## 2.2 Banking Sector

The following graph presents the performance of different banks like Axis bank, Canara bank, Indian Bank, PNB, SBI and UCO bank during pandemic. Again,

**Table 1** Correlation values between automobile companies

	Ashok Layland	TVS motors	HeroMoto crop	Mahindra & Mahindra	Maruti
Ashok Layland	1	0.935084	0.5475	0.922055	0.722622
TVS motors	0.935084	1	0.561567	0.921826	0.733054
HeroMoto crop	0.5475	0.561567	1	0.731019	0.683864
Mahindra & Mahindra	0.922055	0.921826	0.731019	1	0.760863
Maruti	0.722622	0.733054	0.683864	0.760863	1

we normalized the graph as before for visual comparison and quantified through correlation coefficients presented in Table 2 (Fig. 3).

Table 2 shows a good agreement among the stocks except PNB and UCO. They also have positive correlation with others.

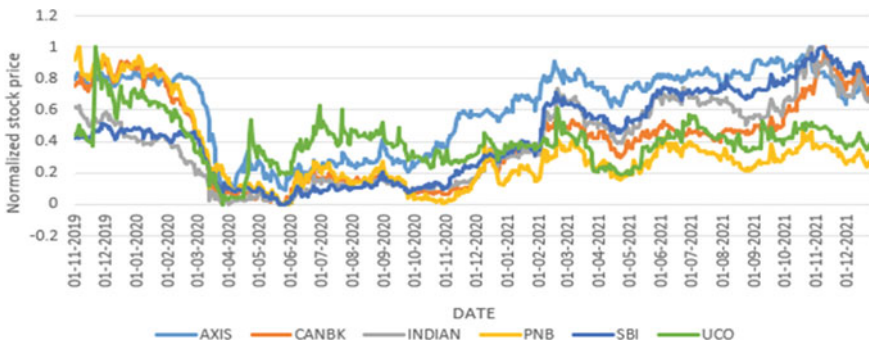


**Fig. 3** Normalized graph in banking sector

**Table 2** Correlation values between banks

	Axis bank	Canara bank	Indian bank	SBI	PNB	UCO
Axis bank	1	0.809175	0.869678	0.881935	0.591333	0.453348
Canara bank	0.809175	1	0.797292	0.767385	0.820716	0.654859
Indian bank	0.869678	0.797292	1	0.970295	0.43443	0.402588
SBI	0.881935	0.767385	0.970295	1	0.364925	0.310351
PNB	0.591333	0.820716	0.43443	0.364925	1	0.744481
UCO	0.453348	0.654859	0.402588	0.310351	0.744481	1

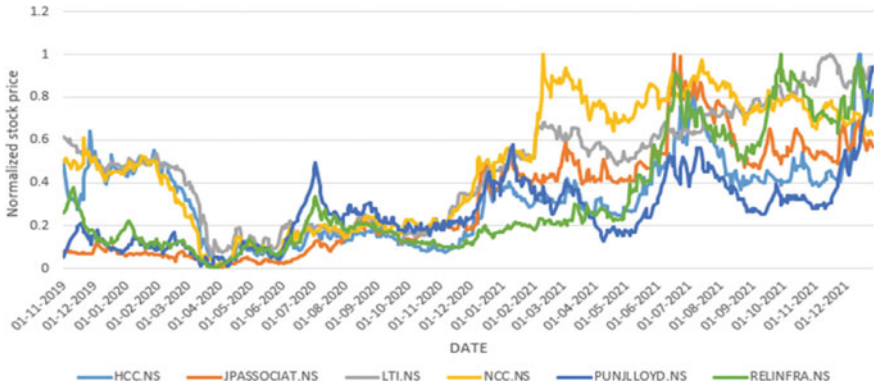


**Fig. 4** Normalized graphs in construction sector

### 2.3 Construction Sector

We follow the same protocol here and plot the normalized values of different stocks like Larsen & Toubro Ltd, NCC, Jaiprakash Associated Ltd, Punj Lloyd, Hindusthan Construction Company and Reliance infrastructure Ltd and finally calculate the correlation coefficients for the quantification purpose (Fig. 4 and Table 3).

High positive correlation values indicate their similar behavior.

### 2.4 Finance Sector

Here, we plot the normalized values of different stocks like Bajaj, LIC, Muthoot, Rhfl.NS and finally calculate the correlation coefficients for the quantification purpose (Fig. 5).

Correlation values between stocks of different finance companies are given in Table 4.

Correlation values show that except the Muthoot Finance all are in good agreement. Muthoot Finance also have positive correlation with others.

### 2.5 Travel and Tourism Sector

We follow the same protocol here and plot the normalized values of different stocks like Expedia, Mahindra Holidays and Resorts India Ltd, Thomas cook India Ltd, Tripand finally calculate the correlation coefficients for the quantification purpose.

Correlation values between stocks of different travel companies are given in Table

**Table 3** Correlation values between construction companies

	HCC	JPASSOCIATE	NCC	LTI.NS	PUNJILLOYED	RELINFRA.NS
HCC	1	0.663704	0.75423	0.812862	0.578739	0.701046
JPASSO-CIATE	0.663704	1	0.854078	0.76025	0.773943	0.830481
NCC	0.75423	0.854078	1	0.890897	0.564206	0.719297
LTI.NS	0.812862	0.76025	0.890897	1	0.568498	0.811581
PUNJLL-OYED	0.578739	0.773943	0.564206	0.568498	1	0.682547
RELINFRA.NS	0.701046	0.830481	0.719297	0.811581	0.682547	1

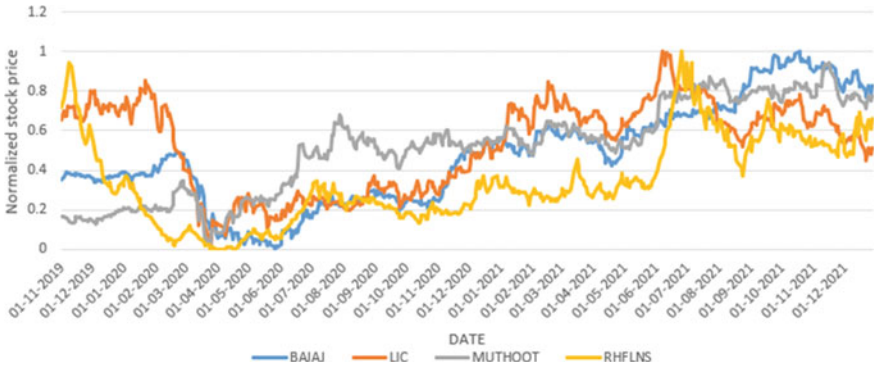


Fig. 5 Normalized graph of finance sector

Table 4 Correlation values between finance companies

	Bajaj	LIC	Muthoot	Rhfl
Bajaj	1	0.714902	0.760984	0.712494
LIC	0.714902	1	0.36199	0.647185
Muthoot	0.760984	0.36199	1	0.58674
Rhfl	0.712494	0.647185	0.58674	1

Correlation values are all positive but the correlation between EXPE and MHRILNS, THOMAS and EXPE, TRIP and THOMAS, MHRILNS and TRIP are less than 0.5 (Fig. 6).

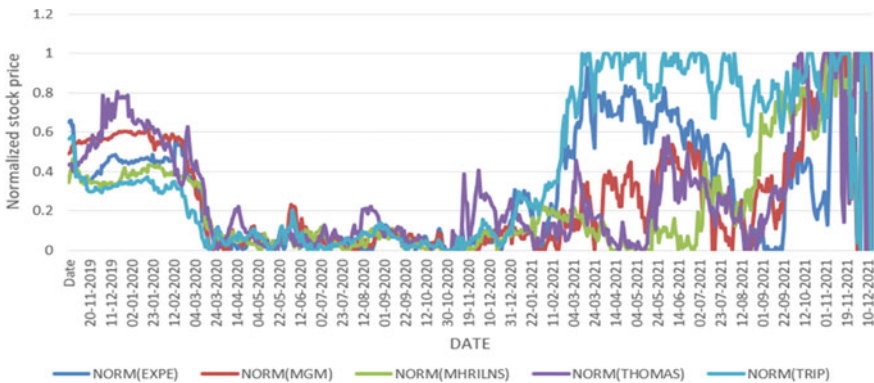


Fig. 6 Normalized graph of travel and tourism sector

**Table 5** Correlation values between tourism companies

	EXPE	MGM	MHRILNS	THOMAS	TRIP
EXPE	1	0.6699114	0.354058	0.442404	0.773126
MGM	0.6699114	1	0.702177	0.773681	0.550526
MHRILNS	0.354058	0.702177	1	0.7666008	0.404562
THOMAS	0.442404	0.773681	0.766008	1	0.317964
TRIP	0.773126	0.550526	0.404562	0.317964	1

### 3 Covid Graph

Finally, we look at the covid graph of India to have a comparison.

Figure 7 represents the typical covid curve representing daily confirmed cases, familiar to all of us having two peaks corresponding to the first and second wave of the pandemic. The first peak occurs in the middle of September and these condone occurs at the first week of May. The pandemic though started a little bit earlier, becomes clearly visible from March, 2020.

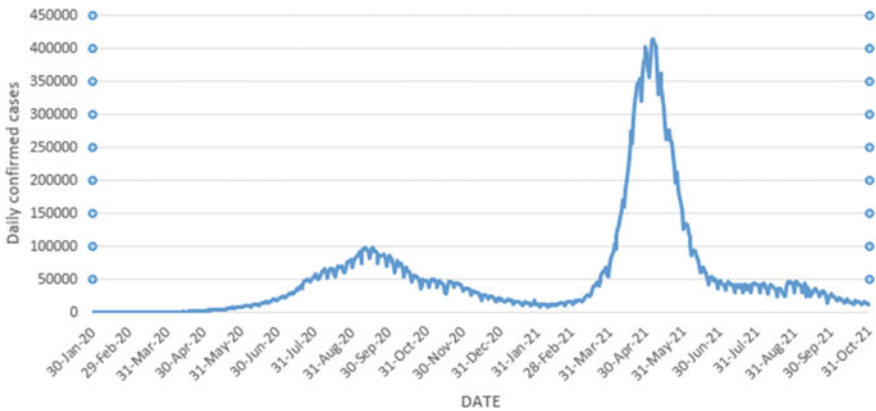


**Fig. 7** Covid graph of India

## 4 Result and Discussion

In the automobile sector, all the stock values move in a similar fashion and reaches a low value in the April, 2020. Then they start to increase and peaks in February, 2021. After that, the curves become nearly flat. This indicates that the pandemic has no impact on the automobile sector. The initial dip is probably due to ongoing recession in Indian economy which is not connected with the pandemic. The bank stocks are low in April, 2020 and journey towards this low value started long before the pandemic. They reach high in April, 2021 and then continue to increase very slowly. Both the Finance sector and the construction sector reach at minimum in April, 2020 and then start to increase. So, pandemic effect could not be found here.

## 5 Conclusion

Among the five sectors covered in this study, the Automobile, Banking, Finance and the construction sector have not been grossly influenced by the ongoing pandemic. A one-line inference can be drawn as 'the second wave has no impact and the first wave also has a very little impact' on these sectors. On the contrary, the travel and tourism sector have been grossly influenced in this time period. From 2020 march throughout the year tourism sector faced a challenging time as it experienced the lowest stock market growth. This small and illustrative study shows that different sectors behave differently in this time period. Some of them win the battle and some lose. Deeper and extensive research is necessary to find out the economic, social and behavioral counterpart behind this behavior and these parameters should be linked with the observation.

## 6 Future Research Directions

A through, elaborate and comprehensive study is necessary with large number of sample stocks chosen from diverse sectors to have an insight on the movement of stock values during the pandemic and before it. A detailed and explorative study in this regard may reveal the reasons behind the ups and downs in these sectors. If any pattern can be determined, this may reveal a causality connection among observations.

**Acknowledgements** The authors thank the editor and the reviewers for their insightful comments and constructive suggestions that substantially improved this article.

**Conflicts of Interest** The authors declares that there is no conflict of interest.

## References

1. Buszko, M., Orzeszko, W., Stawarz, M.: COVID-19 pandemic and stability of stock market-A sectoral approach. *PLOS ONE* **16**(5), e0250938 (2021)
2. Sahoo, M.: COVID-19 impact on stock market: evidence from the Indian stock market. *J. Public Aff.* **21**(4), e2621 (2021)
3. Al-Awadhi, A.M., Alsaifi, K., Al-Awadhi, A., Alammadi, S.: Death and contagious infectious diseases: impact of the COVID-19 virus on stock market returns. *J. Behav. Exp. Fin.* **27**(1), 100326 (2020)
4. Khaled, A.S.D., Alabsy, N.B., Al-Homaidi, E.A., Saeed, A.M.M.: The impact of the COVID-19 pandemic on retailer performance: empirical evidence from India. *Innovat. Market.* **16**(4), 129–138 (2020)
5. Ramelli, S., Wagner, A.F.: Feverish stock price reactions to COVID-19. *Rev. Corpor. Fin. Stud.* **9**(3), 622–655 (2020)
6. Akhtaruzzaman, M., Boubaker, S., Sensoy, A.: Financial contagion during COVID-19 crisis. *Fin. Res. Lett.* **38**, 101604 (2021)
7. Donthu, N., Gustafsson, A.: Effects of COVID-19 on business and research. *J. Bus. Res.* **117**, 284–289 (2020)
8. Zhang, D., Hu, M., Ji, Q.: Financial markets under the global pandemic of COVID-19. *Financ. Res. Lett.* **36**, 101528 (2020)
9. Okorie, D.I., Lin, B.: Stock markets and the COVID-19 fractal contagion effects. *Fin. Res. Lett.* **38**(4), 101640 (2021)
10. Martin Scheicher, F.: The co-movements of stock markets in Hungary, Poland and the Czech Republic. *Int. J. Fin. Econ.* **6**(1), 27–39 (2021)



# A Mathematical Analysis on Covid-19 Transmission Using Seir Model



Sandip Saha, Apurba Narayan Das, and Pranabendra Talukdar

**Abstract** The current work describes the scenario of Covid-19 wave by SEIR model with the aid of mathematical analysis. The SEIR model describes the present scenario using a stability point of view, namely Disease-free equilibrium (DFE) and endemic (EE) equilibrium with the aid of the next-generation matrix, to predict the possible outcomes of recovery rate, infectious growth rate, and death rate and reproduction number.

**Keywords** COVID-19 epidemic · Equilibrium state · Stability analysis

## 1 Introduction

For the first time, the novel corona virus is found in Wuhan, Hubei Province, China, in the month of December 2019 [1, 2]. The transmission of the SARS-COV-2 virus caused the pandemic and it has become the most serious issue in the present world. It spreads rapidly across the globe in a very short span of time. Now, COVID-19 become a major research object in different branches, including Biology, chemical sciences, applied mathematics, economics, and even the living space, far outside the reach of medical science. In January 30, 2020, WHO [3, 4] declared an outbreak with an international public health crisis and finally, announced a pandemic situation on March 11, 2020. Some common symptoms of COVID-19 patient are fever, shortness of breath, exhaustion and lack of smell. However, some COVID-19 patients developed pneumonia and in some cases, acute respiratory distress syndrome has been found.

---

S. Saha

Department of Mathematics, Madanapalle Institute of Technology & Science, Madanapalle 517325, Andhra Pradesh, India

School of Advance Sciences (SAS) Mathematics, Vellore Institute of Technology Chennai, Chennai 600127, Tamilnadu, India

A. N. Das · P. Talukdar (✉)

Department of Mathematics, Alipurduar University, Alipurduar 736121, West Bengal, India  
e-mail: [dinhatapt@gmail.com](mailto:dinhatapt@gmail.com)

According to the medical research, the general symptoms of sick people appear after five to six days. Some COVID-19 patient suffered shortness of breath quickly due to the lack of oxygen, hence chest X-rays, and CT scans become incompatible. The entire research community is still now trying to reveal the original fact that is going on inside the body of affected patients. Some recent investigations reported that Corona is a particular type of hypercoagulable state, which allows blood clotting in blood vessels. Kermack et al. [5], mathematically studied the characteristics of infectious diseases by employing the epidemiological statistical models and following in the works of Kermack and McKendrick [5], some eminent models to present the transmission mechanisms of some particular diseases have been proposed, such as the HIV model [6], Heathcote and Yorke [7] model to disseminate gonorrhoea [8], Ronald Ross model for controlling malaria [9], Glass network [10, 11] etc. Currently, researchers are extensively involved to develop a statistical model for identifying COVID-19. Easwar Moorthy et al. [12] analyze the fractal-based prognostic model for second wave of COVID-19. In addition, [13, 14] researchers analyzed the predication of “when will the pandemic be culminated and immunity against covid-19 in India” At this situation, it is difficult to forecast the negative impact of COVID19 by applying a single model. Shahrear et al. [15] mathematically analyzes the pandemic of COVID transmission in Bangladesh using SEQIRP model and concluded that the infection rate is proportional to the number of infected populations. In addition, it was also studied that if an effective vaccine is not available to the populations, then the rate of death percentage will rise sharply, consequently recovery rate will diminish remarkably. Based on the Russia real-time data, Tomchin et al. [16] studied the pandemic scenario of COVID-19 using SEIR model. The calculations show that the peak in the number of infected in Russia should occur no earlier than the end of May. In 2021, Hamdi et al. [17] mathematically performed the pandemic of COVID transmission in Saudi Arabia using the SEIR model with the aid of next generation matrix and stated that if the rate of transmission,  $\beta \leq 0.0000000112$ , then the number of infected cases will reduce moderately. The devastating COVID-19 pandemic situation in the whole world claims a need to develop scientific models for improving a medical preparation and monitoring the pandemic in a long-term course. From the literature survey, it has been clear that in the view of mathematical perspectives, the number of research work on COVID-19 is very less. Most of the works performed are based on SEIR model, which provides us the enough confidence to find the research gap in that field. In the present article, the impact of Covid-2<sup>nd</sup> wave is analyzed using SEIR model. For numerical understanding, several authors have utilized different software [18–21], but here, we only use the symbolic computational MATLAB software. Presently, the COVID-2<sup>nd</sup> wave not only causes the falling of health issues but also affect the social, economic, and cultural issues. The prime objective of this investigation is to narrate the pandemic situation due to COVID in the whole World. Here, SEIR model forecast some prediction with the aid of stable and unstable equilibrium states and local and global stability analysis. Based on the reproduction number [21–23], the study of the model would reveal the stable and unstable situations. At the end, sensitivity analysis for the SEIR model have been introduced with some basic phenomena

of Covid-19 such as low growth face, moderate growth face, transition face, steady and unsteady equilibrium face.

## 2 SEIR Model

The SEIR model can be treated as an extended version of the SIR model that are utilized by several authors [14–19, 24] to investigate the epidemic outbreaks. SEIR (susceptible-exposed-infectious-removed) model (Fig. 1) assumes the following relations,

- a. Susceptible (*S*) persons have never been infected by the microorganism but considered as infected person,
- b. Exposed (*E*) persons is infected by a microorganism that causes to create disease, but they are not considered as infectious, due to the passing over of the latent period of the disease,
- c. Infectious (*I*) persons are infected and they can transmit the disease to others,
- d. Removed (*R*) persons are not able to transmit that microorganism. This group contains the recovered individuals as well as the fatalities.

COVID-19 is one of the devastating pandemic that the entire human civilization has never been experienced before. In this model, it is assumed that the entire population initially belongs to a susceptible compartment. Contact rates in between the infected and suspected individuals in the population are utilized to compute the probability that a susceptible and an infectious people is in contact for a finite time and get infected. The prime difference between the SIR model and the SEIR model is that the inclusion of the exposed group to the SEIR model. The exposed group actually is a class that lies in between the susceptible group and the infectious group. It includes the people who are exposed to be infected but still are not infectious. In this model, four groups have been considered instead of three and thus, four differential equations required to describe the spread of pandemic. Susceptible class means those individuals who are at risk to be infected with the COVID-19 wave virus. The exposed group means group of those people who have been already infected with the COVID-19 virus but they have no symptoms (asymptomatic). Infectious groups are the individuals who are infected with the COVID-19 wave and also able to pass infection to susceptible persons. Finally, the recovered group are the individuals who have been already recovered. In this model, we consider that births and deaths occurred at the same rate

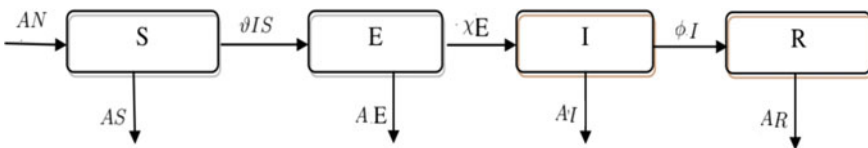


Fig. 1 Schematic diagram of SEIR model

and all the newborn are susceptible (that is, they have no inherited immunity). It is confirmed that the total population,  $N$  means that the sum of all the variables. Thus, we write

$$S(t) + E(t) + I(t) + R(t) = N \tag{1}$$

The Eq. (1) can be written in the following form:

$$s(t) + e(t) + i(t) + r(t) = 1, \tag{2}$$

where

$$s(t) = \frac{S(t)}{N}, e(t) = \frac{E(t)}{N}, i(t) = \frac{I(t)}{N}, r(t) = \frac{R(t)}{N}. \tag{3}$$

Now, we assume that the population blends homogeneously, irrespective of age, mobility or the other social factors. Thus, the following set of ODE<sup>s</sup> is considered to represent this model:

$$\frac{dS}{dt} = AN - AS - \vartheta IS \tag{4}$$

$$\frac{dE}{dt} = \vartheta IS - (A + \chi)E \tag{5}$$

$$\frac{dI}{dt} = \chi E - (A + \varphi)I \tag{6}$$

$$\frac{dR}{dt} = \varphi I - AR \tag{7}$$

We consider the parameters  $A, AS, \vartheta IS, \chi E, \vartheta > 0, \chi > 0, \varphi > 0, \psi > 0$ , which respectively denote average birth and death rate, rate at which individuals are born into the susceptible class with no passive, rate at which susceptible enters into the exposed class without being infected, the rate at which an exposed person becomes infectious, rate at which an infected individual may recover fully transmission coefficient, latency coefficient, recovery coefficient and capital death rate respectively. Initially, we assume  $(S(t = 0), E(t = 0), I(t = 0), R(t = 0)) \in \{(S, E, I, R) \in [0, N]^4 : S > 0, E > 0, I > 0, R > 0\}$ .

The equations (4)-(7) formed as

$$\frac{dS}{dt} + \frac{dE}{dt} + \frac{dI}{dt} + \frac{dR}{dt} = AN - AS \tag{8}$$

Equations (2) and (3) are plug in the equations ((4)-(7)), we find the following ODEs.

$$\frac{ds}{dt} = A - (A + \vartheta i)s \tag{9}$$

$$\frac{de}{dt} = \vartheta Ie - (A + \chi)e \tag{10}$$

$$\frac{di}{dt} = \chi e - (A + \varphi)i \tag{11}$$

The above ODEs possess a disease-free equilibrium (DFE) and an endemic equilibrium (EE).

### 2.1 Calculation of $R_0$

The Jacobian method employed for the SEIR model gives a biologically reasonable result but this method cannot provide good result in a complex compartmental model, i.e., model having large number of infected compartments, as it depends on the algebraic Routh Hurwitz conditions for stability of the Jacobian matrix. Diekmann et al. [16] proposed an alternative method and later on, it is modified by van den et al. [17], which gives a new way to determine  $R_0$  in the case of ODE compartmental model employing the next generation matrix. In this work, the method is briefly introduced and for details, readers are referred Van den et al. [19].

Let  $x = (x_1, x_2, \dots, x_n)^T$  denotes people present in each of the compartments with first  $m < n$  compartments containing infected people. We assume the existence and stability of the DFE  $x_0$  in absence of disease and the equations for  $x_1, x_2, \dots, x_n$  at the DFE effectively disassociates from the rest of the equations. For detailed discussions on the basic assumptions, see the references mentioned above. Consider the equation

$$\frac{dx_i}{dt} = F_i(x) - V_i(x), \text{ for } i = 1, 2, \dots, m \tag{12}$$

where  $F_i(x)$  denotes the rate of increase infections in the  $i^{th}$  compartment and  $V_i(x)$  expresses the rate of transitions between the  $i^{th}$  compartment and other infected compartments in other way with the assumption that  $F_i$  and  $V_i \in \zeta^2$ , and  $F_i = 0$  if  $i \in [m + 1, n]$ . Now we define

$$F = \left[ \frac{\partial F_i(x_0)}{\partial x_j} \right] \tag{13}$$

$$V = \left[ \frac{\partial V_i(x_0)}{\partial x_j} \right] \text{ for } 1 \leq i, j \leq m \tag{14}$$

Biologically,  $F$  and  $V$  represent the entry wise non-negativity and a non-singular  $M$ -matrix (see Berman and Plemmons (1994)) respectively, so  $V^{-1}$  also shows the entry wise non-negativity. If the number of infectious at the initial level be denoted by  $\Omega(0)$ , then  $FV^{-1} \Omega(0)$  defines the entry wise non-negative vector and gives the expected number of newly infected people. The  $(i, j)$ th entry of the matrix  $FV^{-1}$  denotes the expected number of secondary infections in the  $i$ th compartment supposing that infected person is introduced in  $j$  th compartment. Thus,  $FV^{-1}$  is claimed to be the next generation matrix

$$R_0 = \rho(FV^{-1}), \tag{15}$$

where  $\rho$  signifies the spectral radius. The linear stability of the DFE is confirmed by  $s(F - V)$ , where  $s$  is the maximum of the real part of the eigenvalues of the Jacobian matrix and  $s$  often known as spectral bound. Considering the notations stated above, the interrelationship between this quantity and  $R_0$  is described below in brief (for details, see the above cited references).

**Theorem 1** *If  $x_0$  is a DFE of the system*

$$\frac{dx_i}{dt} = F_i(x)V_i(x),$$

*then  $x_0$  is locally asymptotically stable if  $R_0 = \rho(FV^{-1})$ , but unstable if  $R_0 > 1$ .*

The next generation matrix is expressed using the Eqs. (9)–(11) and (18) of the SEIR Model. Here  $E$  and  $I$  represent the infected compartments.  $F$  and  $V$  are described in the DFE matrices as

$$F = \begin{bmatrix} 0 & \vartheta s_0 \\ 0 & 0 \end{bmatrix}, \text{ and } V = \begin{bmatrix} A + \chi & 0 \\ -\chi & A + \phi \end{bmatrix},$$

So  $FV^{-1}$  has the eigenvalues 0 and  $R_0$ , where

$$R_0 = \frac{\chi \vartheta s_0}{(A + \chi)(A + \phi)} \tag{16}$$

as derived biologically by the Eq. (18). Here  $\vartheta s_0$  is the rate of infection population of susceptible,  $\frac{\chi}{A + \chi}$  represents the fraction transferring from  $E$  to  $I$ ,  $\frac{1}{A + \phi}$  is the mean time in  $I$ , thus the  $(1, 1)$  entry of  $FV^{-1}$  shows expected number of the secondary infections created in compartment  $E$  by an infected people in  $E$ .

### 2.2 Local Stability

Considering the transformed sub-systems in ((4)-(6)), the local-stability is analyzed to find the disease-free equilibrium (DFE):

$$LDFE = (s, e, i), \tag{17}$$

and endemic equilibrium (DFE):

$$LEE = (s_1, e_1, i_1). \tag{18}$$

### 2.3 Disease-Free Equilibrium (DFE)

The conditions for constructing DFE is given by

$$(s_0, e_0, i_0, r_0) = \left( \frac{\gamma}{\alpha}, 0, 0, 0 \right). \tag{19}$$

There exist two infected compartments ( $e$  and  $i$ ), and it is found that the equations in two variables decide the stability of the DFE. The Eqs. (10) and (11), the Jacobian matrix at the DFE provides the characteristic equation:

$$l^2 + (2A + \chi + \varphi)l + ((A + \chi)(A + \varphi) - \chi \vartheta s_0) = 0. \tag{20}$$

All the roots of the equation will contain negative real parts (thus the DFE is linearly stable) if and only if each of the coefficient is positive, i.e.,  $\frac{\chi \vartheta s_0}{(A + \chi)(A + \varphi)} < 1$ . Here,  $\frac{\chi}{A + \chi}$  is showing the progression from exposed to infectious, and  $\frac{1}{A + \varphi}$  defines the average infectious time for taking death. In the biological understanding, the fraction is considered as reproduction number ( $R_0$ ),

$$R_0 = \frac{\chi \vartheta s_0}{(A + \chi)(A + \varphi)}. \tag{21}$$

If  $R_0 \leq 1 \Rightarrow \lim_{t \rightarrow \infty} (s(t), e(t), i(t), r(t)) = \text{DFE}$ , and for  $R_0 > 1 \Rightarrow \lim_{t \rightarrow \infty} (s(t), e(t), i(t), r(t)) = \text{EE}$ . From the Eq. (9)–(11) we find,

$$A - (A + \vartheta i)s = 0, \tag{22}$$

$$\vartheta i s - (A + \chi)e = 0, \tag{23}$$

$$\chi e - (A + \varphi)i = 0. \tag{24}$$

Therefore, the Jacobian matrix is defined as follows:

$$J = \begin{bmatrix} -(A + \vartheta i) & 0 & \vartheta s \\ \vartheta i & -(A + \chi) & \vartheta s \\ 0 & \chi & -(A + \varphi) \end{bmatrix}$$

Using Eq. (22)–(24), we find the DFE  $(s, e, i) = (1, 0, 0)$ , if we set  $i = 0$ , and the Jacobian matrix can be written as,

$$J_{DFE} = \begin{bmatrix} A & 0 & \vartheta s \\ \vartheta i & -(A + \chi) & \vartheta s \\ 0 & \chi & -(A + \varphi) \end{bmatrix}$$

Therefore from,

$$\det(J_{DFE} - \lambda I_d) = \lambda^3 + b_1 \lambda^2 + b_2 \lambda + b_3$$

where

$$b_1 = 3A + \varphi + \chi, \tag{25}$$

$$b_2 = [(A + \chi)(A + \varphi) - \vartheta \chi + A(2A + \varphi + \chi)], \tag{26}$$

$$b_3 = A[(A + \chi)(A + \varphi) - \vartheta \chi]. \tag{27}$$

The stability criteria, given in [17, 18] suggest that if  $b_1, b_3 > 0$ , and  $b_1 b_2 - b_3 > 0$ , then every roots of the characteristic equation will have negative real part that signifies a stable equilibrium. Therefore,  $R_0 < 1$  signifies a stable DFE otherwise, it becomes unstable.

### 2.4 Endemic Equilibrium (EE)

To conclude the endemic equilibrium state from the Eq. (20), we find

$$e = \frac{(A + \varphi)i}{\chi}. \tag{28}$$



Putting the above value of  $e$  in Eq. (19), we get

$$s_1 = \frac{(A + \chi)(A + \varphi)}{\vartheta \chi s_0} = \frac{1}{R_0}. \tag{29}$$

Putting the value of  $s$  in Eq. (18), we find

$$i_1 = \frac{A}{\vartheta}(R_0 - 1), \tag{30}$$

and considering the Eqs. (24)–(26), we find

$$e_1 = \frac{(R_0 - 1)A}{R_0(A + \chi)} \tag{31}$$

Therefore, we find the endemic equilibrium points as,

$$(s_1, e_1, i_1) = \left( \frac{1}{R_0}, \frac{(R_0 - 1)A}{R_0(A + \chi)}, \frac{A}{\vartheta}(R_0 - 1) \right).$$

The Jacobian matrix is written as

$$J_{EE} = \begin{bmatrix} -AR_0 & 0 & -\frac{(A+\chi)(A+\varphi)}{\vartheta} \\ A(R_0 - 1) & -(A + \chi) & \frac{(A+\chi)(A+\varphi)}{\vartheta} \\ 0 & \chi & -(A + \varphi) \end{bmatrix}$$

Thus,

$$\det(J_{EE} - \lambda I_d) = \lambda^3 + b_1\lambda^2 + b_2\lambda + b_3,$$

where

$$b_1 = (2 + R_0)A + \varphi + \chi, \tag{32}$$

$$b_2 = AR_0(2A + \varphi + \chi), \tag{33}$$

$$b_3 = A(R_0 - 1)[A^2 + A(\varphi + \chi) + \vartheta\varphi]. \tag{34}$$

From the stability criteria of Routh-Hurwitz (2013), if  $b_1, b_3 > 0$ , and  $b_1b_2 - b_3 > 0$ , then the roots possess negative real part which means the occurrence of stable equilibrium. The first two conditions remain true for  $R_0 > 1$  as  $b_1, b_3 > 0$ , and  $b_1b_2 - b_3 > 0$ . Therefore, endemic state equilibrium becomes stable if  $R_0 > 1$ , otherwise unstable. It causes the occurrence of an outbreak and the epidemic grows.

The epidemic criteria in  $R_0$ , given in (21) presents the basic reproduction value, which is the most important factor for analyzing any epidemiological model.  $R_0$ , especially shows whether an epidemic appears due to the spread of infectious diseases because  $R_0$  represents the average number of secondary infections created by one infected people during the mean period of infection in a susceptible population. If  $R_0 \leq 1$ , then on average, new infections created by one infected people over the mean course of the pandemic is less than unity, which implies the disease will disappear in no time. On the other hand, when  $R_0 > 1$ , the number of new infectious created by infected people becomes greater than unity, that causes the spread of infectious disease as an epidemic.

**Algebraic analysis of  $R_0$ :** If a plan for controlling the disease is considered for entire population, then Herd immunity is found. On the other hand, when the population contains several host types, then the strategy to control pandemic only found for one host population. For example, we consider a vector-host model of malaria where spray is applied to the mosquito vectors. To propose this Roberts et al. [18, 19] introduced a particular type of reproduction number,  $R_0$ . This type of controlling strategy influences single column/row of the next generation matrix, depending on control of impressing susceptibility or infectivity. Shuai et al. [20] recentralized this idea by singling out the entries to control and defined a target reproduction number. For example, shorten of contacts among the children can be taken as a reduction strategy for breaking out Cholera. Let us assume  $K = [k_{ij}]$  be an  $n$ th order next generation matrix (i.e.,  $K = FV^{-1}$ ) and the entries for a set  $s$  are taken as a control strategy (this may be treated either in a decreasing or an increasing manner in the entries of  $s$ . The  $(i, j)$ th element of the target matrix  $Ks$  is defined as  $k_{ij}$ , if entry  $(i, j) \in s$ , and 0 otherwise. For  $\rho(K - Ks) < 1$ , the target reproduction number is denoted as  $F_s$  and defined by

$$F_s = \rho(Ks(I_d K + Ks)^{-1}) \tag{35}$$

where  $I_d$  represents an  $n^{th}$  order unit matrix. When all the entries in a particular row/column or more rows/columns of  $K$  are selected, then the selected reproduction number is reduced to the reproduction number as narrated by Roberts et al. [14, 15]. If a fraction,  $1 - \frac{1}{F_s}$  of total population can be prevented then the disease will no longer exist.

**Theorem 2** *The solutions of SEIR model together with the initial condition become a subset in the interval  $[0, \infty)$  and  $\{s(t), e(t), i(t), r(t)\} \geq 0$  for  $0 \leq t < \infty$ .*

The right-hand sides of the SEIR model is totally continuous and locally Lipschitzian on  $t$ . The solutions  $\{s(t), e(t), i(t), r(t)\}$  together with its initial conditions also exist and become unique in the interval  $[0, \infty)$ . From the Eq. (9), we have  $[A - \vartheta i(t)s(t)] \geq 0$ , then, we find valid inequality

$$\frac{ds}{dt} \geq -As(t). \tag{36}$$

By solving the above inequality, we find

$$s(t) \geq s_0 e^{-As(t)} \geq 0. \tag{37}$$

Hence,  $s(t)$  becomes a non-negative function for all  $t$  such that,  $t \in [0, \infty)$ . In the similar way, form the Eqs. (10) and (11), we find

$$e(t) \geq e_0 e^{-(A+\chi)t} \geq 0, \tag{38}$$

$$i(t) \geq i_0 e^{-(A+\varphi)t} \geq 0, \tag{39}$$

$$r(t) \geq r_0 e^{-At} \geq 0. \tag{40}$$

Thus,  $e(t)$ ,  $i(t)$  and  $r(t)$  are all non-negative functions for all values of  $t$  such that,  $t \in [0, \infty)$  and hence the proof.

**Lemma 1** *All of the solutions of SEIR model that initiate in the zone  $[0, \infty)$  are bounded inside the domain  $\varpi$ , given by  $\varpi = \{(s, e, i, r) \in [0, \infty) : 0 \leq N(t) \leq A\vartheta\}$  as  $t \rightarrow \infty$ .*

### 2.5 Uniqueness Theorem for DFE and EE Conditions:

The general condition of DFE is given by

$$(s_0, e_0, i_0, r_0) = \left( \frac{\gamma}{\alpha}, 0, 0, 0 \right) \tag{41}$$

Therefore,  $|J_{DFE}| \neq 0$  means that the equilibrium is isolated, which means there is a disk around it that does not contain other equilibrium.  $|J_{EE}| \neq 0$ , where  $R_0 = \frac{\chi\vartheta s_0}{(A+\chi)(A+\varphi)}$ , Therefore,  $R_0$  is unique, hence the proof.

### 2.6 Global Stability of Equilibrium of the SEIR Model (Lyapunov's Stability Theorem)

The Lyapunov functions represent the scalar functions that may be utilized in order to prove the state of global stability of equilibrium. Lyapunov reports that if the function  $V(x)$  is globally positive definite as well as radially unbounded, and time derivative of  $V(x)$  is globally negative,  $V(x) < 0$  for all  $x = x^*$  then the equilibrium,  $x^*$  becomes globally stable in an autonomous system

$$\frac{dx}{dt} = f(x), \quad (42)$$

and  $V(x)$  is called the Lyapunov's function.

**Lemma 2** *In the SEIR model, DFE  $(e_0) = (\frac{A}{\beta}, 0, 0, 0)$  stands for globally stable of the DFE under the state  $R_0 < 1$ .*

**Lemma 3** *When  $R_0 \leq 1$  the DFE( $e_0$ ) becomes globally attractive.*

### 3 Conclusion

1. From the SEIR epidemiological model, it has been concluded that if the reproduction number  $R_0 > 1$ , then the disease will spread like an outbreak. The sensitivity analysis revealed that whenever the transmission rate is increased or the recovery rate is reduced, the disease will spread, but whenever the transmission rate is reduced or the recovery rate is increased, the disease will die out.
2. Every root of the characteristic equation contains negative real part that signifies a stable equilibrium and for  $R_0 < 1$  signifies a stable DFE, otherwise it becomes unstable. If  $R_0 \leq 1$ , then on average, new infections created by one infected person over the mean course of the pandemic is less than unity that implies the infectious disease will vanish. On the contrary, when  $R_0 > 1$ , the number of new infections created by one infected person becomes greater than unity, that causes the spread of infectious disease as an epidemic.

### References

1. Paul, A., Chatterjee, S., Bairagi, N.: Prediction on Covid-19 epidemic for different countries: focusing on South Asia under various precautionary measures. MdRxiv (2020). <https://doi.org/10.1101/2020.04.08.20055095>
2. Lin, Q., Zhao, S., Gao, D., Lou, Y., Yang, S., Musa, S., He, D.: A conceptual model for the coronavirus disease 2019 (COVID-19) outbreak in Wuhan, China with individual reaction and governmental action. *Int. J. Infect. Dis.* **93**, 211–216 (2020)
3. Fang, Y., Nie, Y., Penny, M.: Transmission dynamics of the COVID19 outbreak and effectiveness of government interventions: a data-driven analysis. *J. Med. Virol.* **92**(6), 645–659 (2020)
4. Bajardi, P., Poletto, C., Ramasco, J., Tizzoni, M., Colizza, V., Vespignani, A.: Human mobility networks, travel restrictions, and the global spread of 2009 H1N1 pandemic. *PloS One* **6**(1) (2011)
5. Kermack, W.O., McKendrick, A.G.: A contribution to the mathematical theory of epidemics. *Proc. R. Soc. Lond. Ser. A* **115**(772), 700–721 (1927)

6. Anderson, R.M., May, R.M.: Population biology of infectious diseases, Part 1. *Nature* **820**, 361–367 (2005)
7. Diekmann, O., Heesterbeek, P.A.: Mathematical epidemiology of infectious diseases: model building, analysis and interpretation. *Math. Comput. Biol.* **15**, 1–13 (2000)
8. Driessche, P.V., Watmough, J.: Reproduction numbers and sub-threshold endemic equilibria for compartmental models of disease transmission. *Math. Biosci.* **180**(1–2), 29–48 (2002)
9. Driessche, P.V., Watmough, J.: Further notes on the basic reproduction number. *Math. Epidemiol.* **180**(1–2), 159–178 (1945)
10. Wang, F., Yang, Y., Zhao, D., Zhang, Y.: A worm defending model with partial immunization and its stability analysis. *J. Commun.* **10**(4), 276–283 (2015)
11. Shahrear, P., Glass, L., Edwards, R.: Chaotic dynamics and diffusion in a piecewise linear equation. *Chaos* **25**(3), 033103 (2015)
12. Easwara Moorthy, D., Gowrisankar, A., Manimaran, A., Nandhini, S., Rondoni, L., Banerjee, S.: An exploration of fractal-based prognostic model and comparative analysis for second wave of COVID-19 diffusion. *Nonlinear Dyn.* **106**(2), 1375–1395 (2021)
13. Kavitha, C., Gowrisankar, A., Banerjee, S.: The second and third waves in India: when will the pandemic be culminated? *Eur. Phys. J. Plus* **136**(5), 1–12 (2021). *J. Plus* **135**
14. Gowrisankar, A., Rondoni, L., Banerjee, S.: Can India develop herd immunity against COVID-19? *Eur. Phys. J.* **6**, 1–9 (2020)
15. SMS, R., Shahrear, P., Islam, M.S.: Mathematical model on branch canker disease in Sylhet, Bangladesh. *Int. J. Math.* **25**(3), 80–87 (2017)
16. Tomchin, D., Fradkov, A.: Partial prediction of the virus COVID-19 spread in Russia based on SIR and SEIR models. <https://doi.org/10.1101/2020.07.05.20146969>
17. Hamdy, M., Youssef, A.N., Alghamdi, A.N., Alghamdi, A.M., Ezzat, A.M.: Modified SEIR model with global analysis applied to the data of spreading COVID-19 in Saudi Arabia. *AIP Adv.* **10**(12), 125210 (2020)
18. Roberts, M.G., Heesterbeek, P.J.A.: A new method for estimating the effort required to control an infectious disease. *Proc. Bio. Sci.* **270**(1522), 1359–1364 (2017)
19. Roberts, M.G., Heesterbeek, P.J.A.: Model-consistent estimation of the basic reproduction number from the incidence of an emerging infection. *J. Math. Biol.* **55**(5–6), 803–816 (2017)
20. Shuai, Z., Heesterbeek, P.J.A., Driessche, V.D.: Extending the type reproduction number to infectious disease control targeting contacts between types. *J. Math. Biol.* **67**(5), 1067–1082 (2013)
21. Blower, M.S., Dowlatabadi, H.D.: Sensitivity and uncertainty analysis of complex models of disease transmission: an HIV model. *Int. Statist. Rev.* **62**(2), 229–243 (1994)
22. Shahrear, P., Rahman, S.M.S., Nahid, M.H.: Prediction and mathematical analysis of the outbreak of coronavirus (COVID-19) in Bangladesh. *Results Appl. Math.* **10**, 1–12 (2021)
23. Ruiz Estrada, M.A.: COVID-21. Available at SSRN 3686440 (2020)
24. Sandip, S., Biswas, P., Nath, S.: Numerical prediction for spreading novel coronavirus disease in india using logistic growth and SIR models. *Eur. J. Med. Educ. Technol.* **14**(2), 1–09 (2021)

# Dynamics of Coronavirus and Malaria Diseases: Modeling and Analysis



Attiq ul Rehman and Ram Singh

**Abstract** COVID-19 has been declared a pandemic by the WHO on the 11th of Mar. 2020. This virus is believed to be born in China in 2019. The study of this disease is very complicated and challenging. In this manuscript, a fractional-order epidemic model to study the impact of COVID-19 and malaria disease has been proposed and analysed. The model is formulated with the help of fractional order by using the Caputo-Fabrizio derivative. The model is solved numerically with the help of the ABM method. The parameters which characterize the disease transmission are taken from real data of India [1]. The qualitative and quantitative behaviour of the proposed model is examined. The numerical work is performed to authenticate the analytic solutions. It is observed that the malaria disease acts as a launching pad for the COVID-19 dynamics as it weakens of humans immune system.

**Keywords** Coronavirus · Malaria · Modeling · Analysis

## Abbreviations

COVID-19 Coronavirus Diseases-19

SARS-CoV-2 Severe Acute Respiratory Syndrome Coronavirus 2

WHO World Health Organization

GHE Global Health Emergency

DDT Dichloro Diphenyl Trichloroethane

ARDS Acute Respiratory Distress Syndrome

CQ Chloroquine

HCQ Hydroxychloroquine

ABM Adams Bashforth Moulton

---

A. Rehman (✉) · R. Singh

Department of Mathematical Sciences, BGSB University, Rajouri 185234, India

e-mail: [attiq@bgsbu.ac.in](mailto:attiq@bgsbu.ac.in)

R. Singh

e-mail: [drramsinghmaths@gmail.com](mailto:drramsinghmaths@gmail.com)

© The Author(s), under exclusive license to Springer Nature Switzerland AG 2022

S. Banerjee and A. Saha (eds.), *Nonlinear Dynamics and Applications*,

Springer Proceedings in Complexity,

[https://doi.org/10.1007/978-3-030-99792-2\\_124](https://doi.org/10.1007/978-3-030-99792-2_124)

1449

C	Caputo
CF	Caputo-Fabrizio
ABC	Atangana Baleanu in Caputo sense
DFE	Disease Free Equilibrium
EE	Endemic Equilibrium
LAS	Locally Asymptotically Stable
GAS	Global Asymptotically Stable
ODE	Ordinary Differential Equation
FDE	Fractional Differential Equation
VIE	Volterra Integral Equation
PE	Predict Evaluate
CE	Correct Evaluate
PV	Predictor Value
CE	Corrector Value

## 1 General Introduction

The mathematical modeling of disease has been attracting the attention of many epidemiologists. COVID-19 was revealed to be supervised for a substantial number of pneumonia cases from China, in Dec. 2019. The number of cases has exploded in China, and then all over the world. On Dec. 31, 2019, the disease was first reported to the WHO, and on Jan. 30, 2020, this outbreak was declared a GHE, followed by a global pandemic on Mar. 11, 2020.

Fever, dry cough, and Fatigue are the most prevalent symptoms of COVID-19. Runny nose, nasal congestion, loss of taste, pains, rashes on the skin, and smell are all possible side effects. These symptoms usually appear and are modest over time. The majority of patients recover from the ailment without the need for medical treatment. All stages of people with underlying medical problems like respiratory or heart difficulties, diabetes, or weakened immune systems should be given special attention [2].

When someone with coughs, speaks, and minute droplets from the nose are transmitted from person to person, especially in improperly congested interior areas where the short-range aerosol transmission cannot be ruled out. It can also be contracted by contacting contaminated things or surfaces and then touching the eyes, nose, or mouth [3]. People who have no symptoms can to some accounts, spread the virus. But, the frequency of such transmissions is unknown.

Likewise COVID-19, malaria is a parasitic infection, transmitted by Anopheles vectors and caused by genus plasmodium parasites, that gives a notable worldwide health threat and leads to a long life-threatening illness. This disease increases mortality and mobility in these areas, causing a toxic impact on their economies and their health structures [4]. About 229 million cases of malaria and approx. 5,00,000 deaths have been reported by WHO, displaying the largest fraction of cases and the highest death [5].

It is critical to control the spread of malaria by implementing long-term and targeted interventions. These two actions should be sufficient to halt the spread of malaria [6]. Insecticide-treated fabrics, most likely vector nets, have been utilized to combat malaria. In addition, data suggest that anopheline vectors have begun to develop resistance to the pyrethroids used to treat vector nets. Indoor residual DDT pesticides and insect reflecting creams are two other options.

Drainage of standing waters is beneficial to human health. Chemoprophylaxis is applied as a prophylactic measure in endemic areas. This reduces the risk of severe maternal anemia and low birth weight in babies. However, due to a lack of *Plasmodium falciparum* tolerance, chemoprophylaxis is only marginally successful [7]. In circumstances of limited transmission, microgametocyte medicines may play a substantial role in malaria prevention. It lowers the rate of transmission. But, transgenic vectors become available, they may provide more benefits in the fight against malaria.

While both diseases can present similarly, the same symptoms they share include, but aren't controlled to, breathing problems, fever, head pain, and tiredness, that can give to a mistreat of both and vice versa, especially if the clinician data solely on signs [8]. Coronavirus had a big field of clinical signs from asymptomatic. Headache, myalgia, and vomiting are all possible symptoms. Malaria patients, on the other hand, commonly with fever, headache, and sweating, as well as fatigue, arthralgia, myalgia, nausea, and vomiting [9].

Malaria-affected people may be mistreated as COVID-19 due to the similarity of symptoms between both diseases, particularly difficulty breathing, fever, acute onset headache, and fatigue. Furthermore, both malaria and COVID-19 can cause complications such as ARDS, septic shock, as well as multi-organ failure. Dry cough, headache, and fever such as health protector patients and workers along with a long time of contact with a number of the COVID-19 peoples, is the first step in identifying a COVID-19 patient [10].

In terms of alertness locally, regionally, and internationally, a top-level of suspicion is demonstrated towards the COVID-19. Humans with fever are currently tested for COVID-19 and then return if the result is non-positive, siding the chance of malaria. The malaria consequences are toxic if a case of malaria is overlooked. Patients who are feverish and have a COVID-19 disease, on the other hand, may be screened for malaria. A single instance of the COVID-19 has the ability to show impact on 3.58 people [11]. The third situation is that a patient has both malaria and COVID-19, and the treatment, as well as diagnosis of one of these, leads to the other being missed.

The widespread utilization of CQ, HCQ, and other anti-malarial medications in malaria-positive regions, according to some researchers, explains the reverse connection between COVID-19 and malaria. It's worth noting that the ability of CQ and HCQ for the medication of COVID-19 disease has been examined since the initial SARS outbreak [12]. Some older studies elaborated on the usefulness of HCQ in the medication of SARS-CoV-2 and stated that a daily dose of four hundred milligrams of HCQ for ten days was the best treatment option. But, subsequent clinical data have recommended that HCQ for COVID-19 be given at a loading medicine of four



hundred milligrams twice on the first day, followed by two hundred milligrams every 12 hours for the next 4 days.

In this manuscript, we have presented an epidemic model of COVID-19 and malaria. As there are very few papers in which the dynamics of both diseases are studied. It is important to study the dynamics of these epidemics.

The paper organization is as follows. Basic preliminaries are in Sect. 2. The mathematical epidemic model is described in Sect. 3. Existence and positiveness are proved in Sect. 4. Stability analysis is discussed in Sect. 5. The numerical work are presented in Sect. 6. At last, the conclusion is drawn in Sect. 7.

## 2 Basic Preliminaries

Since the fractional-order derivative is the generalization of the integer-order derivative. The basic concepts and definitions of Caputo, Caputo-Fabrizio, and Atangana-Baleanu-Caputo. The Caputo derivative has been derived with the power-law type of singular non-local kernel, CF with a non-singular kernel, and ABC with Mittag-Leffler kernel memory. But in this paper, we used only the CF fractional operator since it has a non-singular kernel.

**Definition 1** For a function  $f$  from  $C^n$  space, the Caputo fractional derivative of order  $\alpha \in (n - 1, n]$  with  $n \in \mathbb{Z}^+$  is given as follow:

$${}_0^C D_t^\alpha (f(t)) = \frac{1}{\Gamma(n - \alpha)} \int_0^t \frac{1}{(t - \varphi)^{\alpha-n+1}} f^{(n)}(\varphi) d\varphi,$$

The above Caputo fractional derivative approaches the ordinary derivative when order  $\alpha$  is one.

**Definition 2** For  $a < 0$ ,  $\alpha \in (0, 1]$ , the fractional derivative with a non singular kernel, for a function  $f(t)$  of  $C^1$  space is given as follow:

$${}_0^{CF} D_t^\alpha f(t) = \frac{M(\alpha)}{1 - \alpha} \int_a^t (f(t) - f(\varphi)) \exp\left[-\alpha \frac{t - \varphi}{1 - \alpha}\right] d\varphi.$$

**Definition 3** If  $f(t)$  is differentiable then, the new derivative is called the Atangana-Baleanu in the Caputo sense as follow:

$${}_a^{ABC} D^\alpha f(t) = \frac{B(\alpha)}{1 - \alpha} \int_a^t D_t^\alpha f(\varphi) E_\alpha\left[-\alpha \frac{(t - \varphi)^\alpha}{1 - \alpha}\right] d\varphi,$$

with  $B(\alpha)$  is the normalization mapping s.t.  $B(0) = B(1) = 1$ , in which  $B(\alpha) = 1 - \alpha + \alpha/\Gamma(\alpha)$ .

**Definition 4** For order  $\alpha \in (0, 1)$ , the unchangeable point  $x^*$  is called the critical point of the below Caputo fractional-order function:

$${}_0^C D_t^\alpha(x(t)) = f(t, x(t)) \iff f(t, x^*) = 0. \tag{1}$$

To show the stability of the non-linear fractional-order systems in the insight through Lyapunov way we firstly think of the afterward results from [13].

### 3 Fractional-Order Mathematical Model Formulation

To express the epidemic model, we split the COVID-19 affected host population into four sub-classes, namely susceptible, infectious, vaccinated, and discharged individuals. The complete host population is constituted by  $\Sigma_1 = S_h + I_h + V_h + D_h$ , where  $S_h$  is COVID-19 susceptible host,  $I_h$  is COVID-19 infectious host,  $V_h$  is the COVID-19 vaccinated host and  $D_h$  is COVID-19 discharge host population. Likewise,  $\Sigma_2$  is the complete number of vectors which are further split into susceptible vectors  $S_m$ , and infected vectors  $I_m$ . So that  $\Sigma_2 = S_m + I_m$ . The mathematical model of six FDEs to relate the mechanism of the dynamical transmission of both disease as follow:

$$\begin{aligned} {}_0^C D_t^\alpha S_h &= (1 - \sigma)Z_h - \beta_h S_h I_m + \rho L_0 h - x_h S_h, \\ {}_0^C D_t^\alpha I_h &= \beta_h S_h I_m - (\eta + \kappa_h + x_h) I_h, \\ {}_0^C D_t^\alpha V_h &= \sigma Z_h + \xi \kappa_h D_h - (\rho + x_h) V_h, \\ {}_0^C D_t^\alpha D_h &= \eta I_h - (\xi \kappa_h + x_h) D_h, \\ {}_0^C D_t^\alpha S_m &= Z_m - \beta_m S_m I_h - x_m S_m, \\ {}_0^C D_t^\alpha I_m &= \beta_m S_m I_h - x_m I_m, \end{aligned} \tag{2}$$

with i.c.'s  $S_h(0) = S_{h0}, I_h(0) = I_{h0}, V_h(0) = V_{h0}, D_h(0) = D_{h0}, S_m(0) = S_{m0}$ , and  $I_m(0) = I_{m0} \geq 0$ .

The exceeding proposed epidemic model  $Z_h$  and  $Z_m$  show the new upcoming rate of host and vector populations. The proportion of vaccination during the new coming host population is represented by  $\sigma$ .  $\beta_h$  is the transmission rate between humans to mosquitoes and  $\beta_m$  is the transmission rate between mosquito to human respectively. Also, In COVID-19 affected human population class  $\eta$  represent the discharge rate,  $\kappa_h$  represent disease-induced death rate,  $\rho$  represent the loss of vaccination-induced immunity, and  $\xi$  is the parameter with modifies disease death rate of discharge hosts. The natural mortality of the host individuals is denoted by  $x_h$  and for vector  $x_m$  respectively.

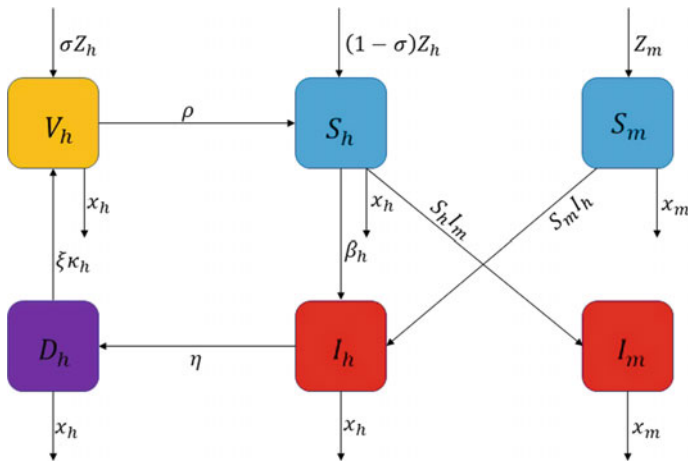


Fig. 1 Flowchart diagram of COVID-19 and malaria disease

In susceptible host population  $(1 - \sigma)Z_h$ , vaccination host  $\sigma \kappa_h$  and susceptible vector  $Z_m$  is the new upcoming rates. The rate  $\beta_h S_h I_m$  is flowing from the susceptible human individual to the infected human individual, and  $\beta_m S_m I_h$  is flowing from the susceptible mosquito individual to the infected mosquito individual, respectively. The rate  $\rho$  is the flow from vaccinated host to susceptible host,  $\eta$  is flow from  $I_h$  to  $D_h$ , and  $\kappa_h$  is from  $I_h$  to  $D_h$ . The natural death rate  $x_h$  is going out of each class of host population and  $x_m$  is going out of each class of vector population respectively. All these mentioned flowing rates of biological parameters are elaborated in Fig. 1.

### 4 Existence and Positiveness

To show the positivity of the dynamical system solution, we have  $\mathbb{R}_+^6 = \{v \in \mathbb{R}^6 : v \geq 0\}$  and  $v(t) = (S_h(t), I_h(t), V_h(t), D_h(t), S_m(t), I_m(t))^T$ . To move further, we have generalized mean value theorem.

**Lemma 1** Suppose that  $\phi \in [a, t], \forall a < t < b, f(t) \in C[a, b]$  and  $a <_0^C F D_t^\alpha f(t) \leq b$ , with  $\alpha(0, 1]$ , then  $f(t) = f(a) + \frac{1}{\Gamma(\alpha)} ({}_0^C F D_t^\alpha f)(\phi)(t - a)^\alpha$ .

Now we consider the following results.

**Theorem 1** The solution  $v(t)$  of the system (2) is exists, non-negative and will stay in  $\mathbb{R}_+^6$ .

**Proof** The existence as well as uniqueness of the fractional model can be easily demonstrated. Now to show the positive solution, it is compulsory that on each hyperplane bounding the positive orhant space to  $\mathbb{R}_+^6$ . Therefore, the proposed system (2), gives

$$\begin{aligned}
 {}_0^C D_t^\alpha S_h|_{S_h=0} &= (1 - \sigma)Z_h + \rho L_0 h \geq 0, \\
 {}_0^C D_t^\alpha I_h|_{I_h=0} &= \beta_h S_h I_m \geq 0, \\
 {}_0^C D_t^\alpha V_h|_{V_h=0} &= \sigma Z_h + \xi \kappa_h D_h \geq 0, \\
 {}_0^C D_t^\alpha D_h|_{D_h=0} &= \eta I_h \geq 0, \\
 {}_0^C D_t^\alpha S_m|_{S_m=0} &= Z_m \geq 0, \\
 {}_0^C D_t^\alpha I_m|_{I_m=0} &= \beta_m S_m I_h \geq 0.
 \end{aligned}
 \tag{3}$$

Hence, by Lemma 1, the solution will stay in  $\mathbb{R}_+^6$ , and so the biological feasible solution is given as:

$$\Sigma = \{ (S_h, I_h, V_h, D_h, S_m, I_m) \in \mathbb{R}_+^6 : S_h, I_h, V_h, D_h, S_m, I_m \geq 0 \}.$$

Afterward, we will evaluate the equilibrium points and basic reproduction number  $\mathcal{R}_0$  of the proposed model (2) in the below subsection.

### 4.1 Equilibrium Points and Estimation of $\mathcal{R}_0$

The equilibria of the system (2) are acquired by solving the system as follows.

$${}_0^C D_t^\alpha S_h = {}_0^C D_t^\alpha I_h = {}_0^C D_t^\alpha V_h = {}_0^C D_t^\alpha D_h = {}_0^C D_t^\alpha S_m = {}_0^C D_t^\alpha I_m = 0.$$

Thus, we evaluated the proposed epidemic model and found two types of critical points. The DFE point is obtained as

$$E^1 = (S_h^1, I_h^1, V_h^1, D_h^1, S_m^1, I_m^1) = \left( \frac{(1 - \sigma)Z_h}{x_h}, 0, \frac{\sigma Z_h}{\rho + x_h}, 0, \frac{Z_m}{x_m}, 0 \right).$$

Next, the EE point is obtained as  $E^2 = (S_h^2, I_h^2, V_h^2, D_h^2, S_m^2, I_m^2)$ , with

$$\begin{aligned}
 S_h^2 &= \frac{(1 - \sigma)Z_h + \rho V_h^2}{\beta_h I_m^2 + x_h}, \\
 I_h^2 &= \frac{(1 - \sigma)Z_h Z_m \beta_h \beta_m - x_h(\eta + \kappa_h + x_h)x_m^2}{\beta_m(\eta + \kappa_h + x_h)(Z_m \beta_h + x_h x_m)}, \\
 V_h^2 &= \frac{\sigma Z_h + \xi \kappa_h D_h^2}{\rho + x_h}, \\
 D_h^2 &= \frac{\eta I_h^2}{(\xi Z_h + x_h)}, \\
 S_m^2 &= \frac{Z_m}{\beta_m I_h^2 + x_m}, \\
 I_m^2 &= \frac{\beta_m Z_m I_h}{(\beta_m I_h^2 + x_m)x_m}.
 \end{aligned} \tag{4}$$

The EE point  $E^*$ , exist only if  $\mathcal{R}_0 > 1$ . The  $\mathcal{R}_0$  for the non-integer COVID-19 and malaria disease models is determined by using the next-generation technique.  $\mathcal{R}_0$  is biologically very essential and determines the global dynamical transmission of the model. The corresponding diseases matrices  $F$ (without infection) and  $V$ (with infection) are given by

$$F = \begin{bmatrix} 0 & \frac{(1 - \sigma)Z_h \beta_h}{x_h} \\ \frac{Z_m \beta_m}{x_m} & 0 \end{bmatrix}, \quad V = \begin{bmatrix} \eta + \kappa_h + x_h & 0 \\ 0 & x_m \end{bmatrix}.$$

The inverse of infected matrix  $V$  is

$$V^{-1} = \begin{bmatrix} \frac{1}{\eta + \kappa_h + x_h} & 0 \\ 0 & \frac{1}{x_m} \end{bmatrix}, \quad FV^{-1} = \begin{bmatrix} 0 & \frac{(1 - \sigma)Z_h \beta_h}{x_h x_m} \\ \frac{Z_m \beta_m}{x_m(\eta + \kappa_h + x_h)} & 0 \end{bmatrix}.$$

This above spectral radius is called the basic reproduction number of the model, and after some simplification, we have

$$\mathcal{R}_0 = \sqrt{\frac{(1 - \sigma)Z_h Z_m \beta_h \beta_m}{x_h x_m^2 (\eta + \kappa_h + x_h)}}.$$

### 5 Stability Analysis

In this section, we have presented the stability analysis of DFE results in both local as well as global stability. The Variational of the model (2) is as follows.

$$J_{E^1} = \begin{bmatrix} -x_h & 0 & \rho & 0 & 0 & \frac{-(1-\sigma)\beta_h Z_h}{(1-\sigma)\beta_h Z_h} \\ 0 & \eta + \kappa_h + x_h & 0 & 0 & 0 & \frac{x_h}{0} \\ 0 & 0 & -(\rho + x_h) & \xi\kappa_h & 0 & 0 \\ 0 & \eta & 0 & \xi\kappa_h - x_h & 0 & 0 \\ 0 & \frac{-\beta_m Z_m}{\beta_m Z_m} & 0 & 0 & -x_m & 0 \\ 0 & \frac{x_m}{\beta_m Z_m} & 0 & 0 & 0 & -x_m \\ 0 & \frac{x_m}{x_m} & 0 & 0 & 0 & -x_m \end{bmatrix}.$$

**Theorem 2** For  $q_1, q_2 \geq 0$  such that  $q_1$  and  $q_2$  are primitive root. Let  $m_1 = \alpha = \frac{q_1}{q_2} > 0$ , and  $Q = q_2$ , then  $E^1$  is LAS if  $|\arg(\lambda)| > \frac{\pi}{2Q}$ , with  $\lambda$  is the possible roots of the characteristic equation of the Variational matrix at  $E^1$  as follows:

$$\det(\text{diag}[\lambda^{m_1}, \lambda^{m_1}, \lambda^{m_1}, \lambda^{m_1}, \lambda^{m_1}, \lambda^{m_1}] - J_{E^1}) = 0. \tag{5}$$

**Proof** By the expansion of Eq. (5) we get the below equation in terms of  $\lambda$ ,

$$(-x_m - \lambda)(-\rho - x_h - \lambda)(\xi\kappa_h - x_h - \lambda)(-x_h - \lambda)[\lambda^2 + r_1\lambda + r_2], \tag{6}$$

with the coefficients are as follows:

$$r_1 = (\eta + \kappa_h + x_h + x_m), r_2 = x_m(\eta + \kappa_h + x_h)(1 - \mathcal{R}_0).$$

The arguments for the roots of the equation  $(-x_m - \lambda) = 0$  are as below:

$$\arg(\lambda_l) = \frac{\pi}{m_1} + l\frac{2\pi}{m_1} > \frac{\pi}{Z} > \frac{\pi}{2Z}, \text{ with } l = 0, 1, 2, \dots, (m_1 - 1). \tag{7}$$

Likewise, the pattern, it can be demonstrated by the arguments for the roots of other equations, and all are greater than  $\frac{\pi}{2Q}$ . Also, if  $\mathcal{R}_0 < 1$ , then the condition  $|\arg(\lambda)| > \frac{\pi}{2Q}$  is proved for all the roots of the polynomial Eq. (6). But if  $\mathcal{R}_0 > 1$ , then by the Descartes sign’s rule, there exists single root of characteristic equation with  $|\arg(\lambda)| < \frac{\pi}{2Q}$ . Hence, if  $\mathcal{R}_0 < 1$  then DFE point is LAS and if  $\mathcal{R}_0 > 1$  then DFE point is unstable.

For the case of global stability of the DFE point, we have the following theorem.

**Theorem 3** If  $\mathcal{R}_0 < 1$  then DFE point is GAS and if  $\mathcal{R}_0 > 1$  then DFE point is unstable.

**Proof** In order to obtain our result, we have the following Lyapunov function:

$$\begin{aligned}
 V(t) = & N_1 \left( S_h - S_h^1 - S_h^1 \frac{S_h}{S_h^1} \right) + N_2 I_h + N_3 \left( L_0 h - V_h^1 - V_h^1 \frac{L_0 h}{V_h^1} \right) \\
 & + N_4 D_h + N_5 \left( S_m - S_m^1 - S_m^1 \frac{S_m}{S_m^1} \right) + N_6 I_m,
 \end{aligned} \tag{8}$$

with  $N_1, N_2, N_3, N_4, N_5, N_6$  are arbitrary positive constant. By Eqs. (5) and (8), along with the system of Eq. (2) we have

$$\begin{aligned}
 {}_0^{CF} D_t^\alpha V(t) = & N_1 \left( \frac{S_h - S_h^1}{S_h} \right) {}_0^{CF} D_t^\alpha S_h + N_2 {}_0^{CF} D_t^\alpha I_h + N_3 \left( \frac{V_h - V_h^1}{V_h} \right) {}_0^{CF} D_t^\alpha L_0 h \\
 & + N_4 {}_0^{CF} D_t^\alpha D_h + N_5 \left( \frac{S_m - S_m^1}{S_m} \right) {}_0^{CF} D_t^\alpha S_m + N_6 {}_0^{CF} D_t^\alpha I_m \\
 = & x_m (\eta + \kappa_h + x_h) (\mathcal{R}_0 - 1).
 \end{aligned} \tag{9}$$

Thus, if  $\mathcal{R}_0 < 1$  then  ${}_0^{CF} D_t^\alpha V(t) < 0$ . Hence,  $E^1$  is GAS in  $\Sigma$ .

## 6 Numerical Work

In this section, we employed the ABM method to solve the dynamical system (2). The main mathematical explanation steps that occur in the mechanism are demonstrated here for the order  $\alpha \in (0, 1]$ . This is the generalization of the ordinary ABM method applied to solve numerically the first order ODEs. This appears in the category of the so-called PE and CE type because it contains calculation of the PV which is further utilization to find the CV. This aforesaid numerical method and its behaviour are well known in the area of fractional calculus as well as in applied areas [14]. To find the approximate solution to this analogy, take the below non-linear FDE.

$$D^\alpha f(t) = H(t, f(t)), t \in [0, T] \ \& \ f^{(l)} = f_0^l, l = 0, 1, \dots, n - 1, \text{ for } n = \lceil \alpha \rceil \tag{10}$$

The Eq. (10) is equivalent to the VIE:

$$f(t) = \sum_{l=0}^{n-1} f_0^{(l)} \frac{t^l}{l!} + \frac{1}{\Gamma(\alpha)} \int_0^t \frac{1}{(t-s)^{1-\alpha}} H(s, f(s)) ds. \tag{11}$$

By utilizing this algorithm on the proposed model (2), Eq. (11) can be discretized as below [15].

$$\begin{aligned}
 K_{n+1} &= K_0 + \frac{h^\alpha}{\Gamma(\alpha + 2)} \left[ ((1 - \sigma)Z_h - \beta_h K_{n+1}^p P_{n+1}^p + \rho M_{n+1}^p - x_h K_{n+1}^p) \right. \\
 &\quad \left. + \sum_{j=0}^n a_{j,n+1} ((1 - \sigma)P_h - \beta_h K_j P_j + \rho M_j - x_h K_j) \right], \\
 L_{n+1} &= L_0 + \frac{h^\alpha}{\Gamma(\alpha + 2)} \left[ (\beta_h K_{n+1}^p P_{n+1}^p - (\eta + \kappa_h + x_h)L_{n+1}^p) \right. \\
 &\quad \left. + \sum_{j=0}^n a_{j,n+1} (\beta_h K_j P_j - (\eta + \kappa_h + x_h)L_j) \right], \\
 M_{n+1} &= M_0 + \frac{h^\alpha}{\Gamma(\alpha + 2)} \left[ (\sigma Z_h + \xi \kappa_h N_{n+1}^p - (\rho + x_h)M_{n+1}^p) \right. \\
 &\quad \left. + \sum_{j=0}^n a_{j,n+1} (\sigma Z_h + \xi \kappa_h N_j - (\rho + x_h)M_j) \right], \\
 N_{n+1} &= N_0 + \frac{h^\alpha}{\Gamma(\alpha + 2)} \left[ (\eta L_{n+1}^p - (\xi \kappa_h + x_h)N_{n+1}^p) \right. \\
 &\quad \left. + \sum_{j=0}^n a_{j,n+1} (\eta L_j - (\xi \kappa_h + x_h)N_j) \right], \\
 O_{n+1} &= O_0 + \frac{h^\alpha}{\Gamma(\alpha + 2)} \left[ (Z_m - \beta_m O_{n+1}^p L_{n+1}^p - x_m O_{n+1}^p) \right. \\
 &\quad \left. + \sum_{j=0}^n a_{j,n+1} (Z_m - \beta_m O_j L_j - x_m O_j) \right], \\
 P_{n+1} &= P_0 + \frac{h^\alpha}{\Gamma(\alpha + 2)} \left[ (\beta_m O_{n+1}^p L_{n+1}^p - x_m P_{n+1}^p) \right. \\
 &\quad \left. + \sum_{j=0}^n a_{j,n+1} (\beta_m O_j L_j - x_m P_j) \right], \tag{12}
 \end{aligned}$$

where

$$\begin{aligned}
 K_{n+1}^p &= K_0 + \frac{1}{\Gamma(\alpha)} \sum_{j=0}^n b_{j,n+1} ((1 - \sigma)Z_h - \beta_h K_j P_j + \rho M_j - x_h K_j), \\
 L_{n+1}^p &= L_0 + \frac{1}{\Gamma(\alpha)} \sum_{j=0}^n b_{j,n+1} (\beta_h K_j P_j - (\eta + \kappa_h + x_h)L_j), \\
 M_{n+1}^p &= M_0 + \frac{1}{\Gamma(\alpha)} \sum_{j=0}^n b_{j,n+1} (\sigma P_h + \xi \kappa_h N_j - (\rho + x_h)M_j),
 \end{aligned}$$



$$\begin{aligned}
 N_{n+1}^p &= N_0 + \frac{1}{\Gamma(\alpha)} \sum_{j=0}^n b_{j,n+1} (\eta L_j - (\xi \kappa_h + x_h) N_j), \\
 O_{n+1}^p &= O_0 + \frac{1}{\Gamma(\alpha)} \sum_{j=0}^n b_{j,n+1} (P_m - \beta_m O_j L_j - x_m O_j), \\
 P_{n+1}^p &= P_0 + \frac{1}{\Gamma(\alpha)} \sum_{j=0}^n b_{j,n+1} (\beta_m O_j L_j - x_m P_j),
 \end{aligned} \tag{13}$$

in which  $a_{j,n+1} = \begin{cases} n^{\alpha+1} - (n+1)(n-\alpha), & j = 0, \\ (n-j)^{\alpha+1} - 2(n-j+1)^{\alpha+1} + (n-j+2)^{\alpha+1}, & j = [1, n], \\ 1, & j = n+1, \end{cases}$

and  $b_{j,n+1} = \frac{h^\alpha}{\alpha} [(n-j+1)^\alpha - (n-j)^\alpha], \quad j \in [0, n].$

Figures 2 and 3 demonstrate that  $I_h(t)$  decreases significantly with time  $t$ . In Fig. 2 it has been observed that for  $\alpha = 0.75$ , the graph of  $I_h$  increase from  $t = 10$  to  $t = 50$  and then decline significantly. Likewise for  $\alpha = 0.65$  and  $\alpha = 0.55$  we have the behaviour of  $I_h$  versus time  $t$ . This graph indicates that for large value of  $\alpha$  have shown good impact on state variables. Since  $\alpha$  has a reciprocal impact on  $I_h(t)$  and  $I_m(t)$ . In order to find a stable and convergent solution, the value of  $\alpha$  should be as small as possible and should be greater than zero. Afterwards, Fig. 4 shows the effects of  $\eta$  on  $I_h(t)$ . Since, as we increase the value of  $\eta$  the graph of  $I_h(t)$  also increases. In Fig. 5 we observe the effect of  $\rho$  on  $S_h(t)$  class. On increase of  $\rho$ ,  $S_h(t)$

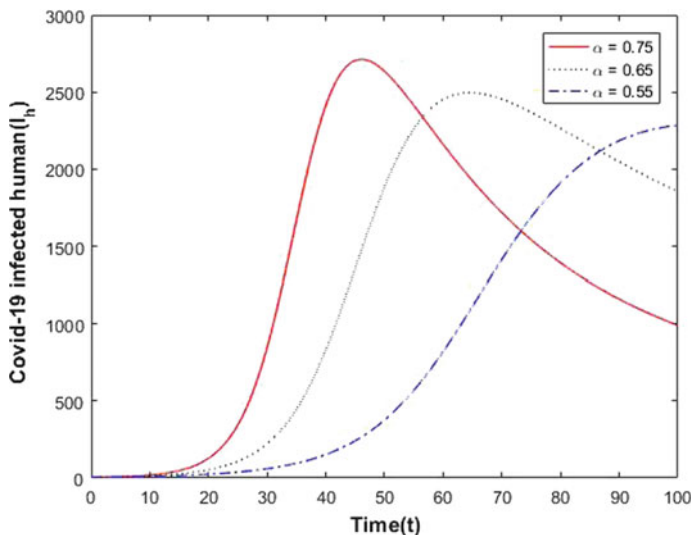


Fig. 2 Effect of  $\alpha$  on  $I_h$

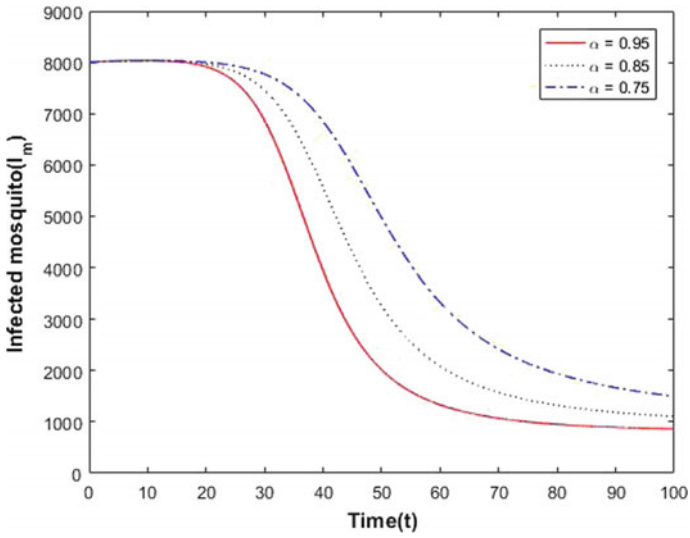


Fig. 3 Effect of  $\alpha$  on  $I_m$

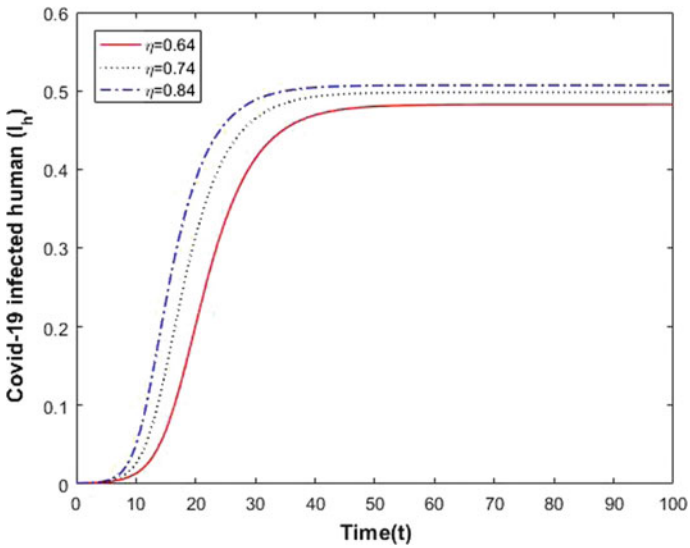


Fig. 4 Effect of  $\eta$  on  $I_h$

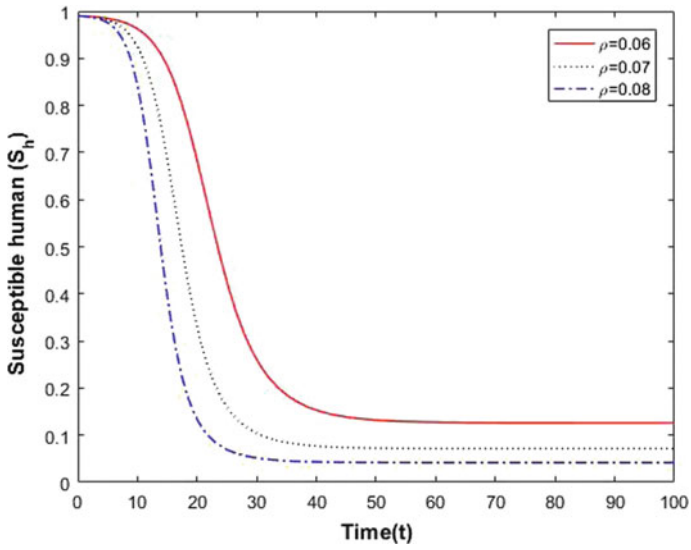


Fig. 5 Effect of  $\rho$  on  $S_h$

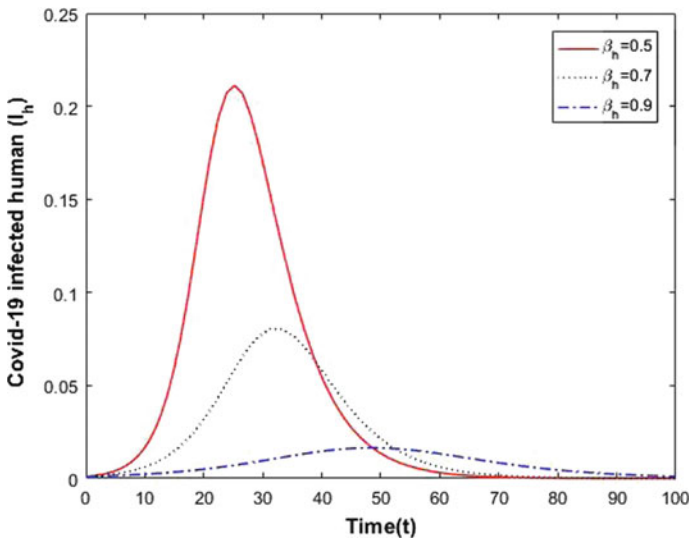


Fig. 6 Effect of  $\beta_h$  on  $I_h$

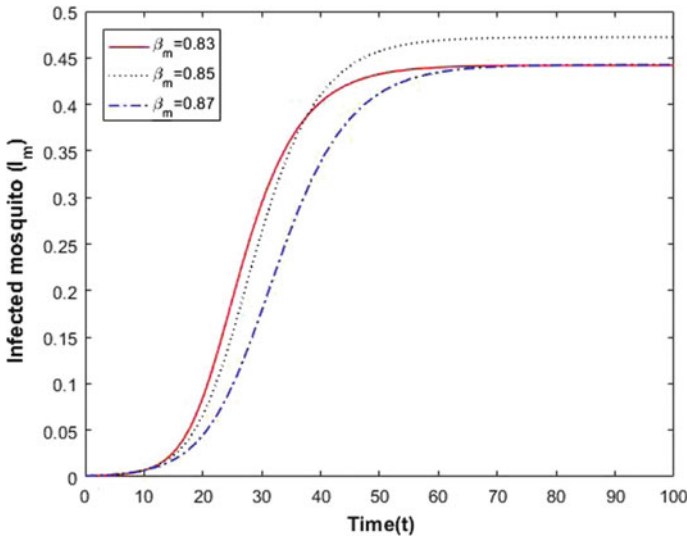


Fig. 7 Effect of  $\beta_m$  on  $I_m$

get decrease. Next, in Fig. 6 demonstrates the impact of  $\beta_h$  on the  $I_h(t)$  class. As we increase the value of  $\beta_h$ , the curves of  $I_h$  are increased. Finally, Fig. 7 shows the effect of  $\beta_m$  on  $I_m(t)$ . On the increase of  $\beta_m$ , the curves of the  $I_m(t)$  class are decreased. In Fig. 7 it has been seen that for  $\beta_m = 0.83, 0.85, 0.87$ , the graph of  $I_m$  increase from  $t = 10$  to  $t = 40$ . This show the realistic fact. As the transmission rate increase the number of infectious mosquitoes get increased in the population.

## 7 Conclusion

Malaria and Coronavirus are odd infectious diseases that wreak havoc over the world, and their route of transmission is still a mystery. We studied the dynamics of malaria and COVID-19 disease mathematically in this investigation. We computed the  $\mathcal{R}_0$  and established a stability analysis using several key theorems. Figures demonstrate the impact of non-integer order  $\alpha$  and various transmission rates graphically. Our findings are consistent with those that suggest malaria serves as a launchpad for the SARS-CoV-2 virus and causes death [16]. In the spirit of CF, we compared these several models. In the numerical work, CF is found to have even better outcomes in terms of stability than the other operators like Riemann-Liouville and Caputo.

### Concluded remark:

- It is observed that DFE is LAS when  $\mathcal{R}_0 < 1$ , and unstable if  $\mathcal{R}_0 > 1$ .
- It is also observed that for the disease model, the traditional condition of  $\mathcal{R}_0 < 1$  is not sufficient for eradication of the COVID-19 and malaria.

### Future direction:

The future direction of the study will incorporate the optimization of medical treatment for COVID-19 and malaria.

## References

1. Government of India, my gov.in/COVID-19
2. Gowrisankar, A., Rondoni, L., Banerjee, S.: Can India develop herd immunity against COVID-19 ?. *Eur. Phys. J. Plus* **135**, 526 (2020)
3. Kavitha, C., Gowrisankar, A., Banerjee, S.: The second and third waves in India: when will the pandemic be culminated ?. *Eur. Phys. J. Plus* **136**, 596 (2021)
4. Pinto, C.M.A., Machado, J.A.T.: Fractional model for malaria transmission under control strategies. *Comput. Math. Appl.* **66**(5), 908–916 (2013)
5. WHO, World Malaria Reports. MMV (2020)
6. Manda, S., Sarkar, R.P., Sinha, S.: Mathematical models of malaria - a review. *Malar. J.* **10**(1), 2–19 (2002)
7. Tumwiine, J., Mugisha, J.Y.T., Luboobi, L.S.: A mathematical model for the dynamics of malaria in a human host and mosquito vector with temporary immunity. *Appl. Math. Comput.* **189**(2), 1953–1965 (2007)
8. Chanda-Kapata, P., Kapata, N., Zumla, A.: COVID-19 and malaria: a symptom screening challenge for malaria endemic countries. *Int. J. Infect. Dis.* **94**(2020), 151–153 (2020)
9. Hussein, M.I.H., Albashir, A.A.D., Elawad, O.A.M.A., Homeida, A.: Malaria and COVID-19: unmasking their ties. *Malar. J.* **19**(457), 1–11 (2020)
10. Yu, X., Qi, G., Hu, J.: Analysis of second outbreak of COVID-19 after relaxation of control measures in India. *Nonlinear Dyn.* **106**, 1149–1167 (2021)
11. Sher, M., Shah, K., Khan, Z.A., Khan, H., Khan, A.: Computational and theoretical modeling of the transmission dynamics of novel COVID-19 under Mittag-Leffler power law. *Alex. Eng. J.* **59**(5), 3133–3147 (2020)
12. Ray, M., Vazifdar, A., Shivaprakash, S.: Co-infection with malaria and coronavirus disease-2019. *J. Glob. Infect. Dis.* **12**(3), 162–163 (2020)
13. Abdeljawad, T., Banerjee, S., Wu, G.C.: Discrete tempered fractional calculus for new chaotic systems with a short memory and image encryption. *Optik* **203**, 163698 (2020)
14. Rehman, A.U., Singh, R., Abdeljawad, T., Okyere, E., Guran, L.: Modeling, analysis and numerical solution to malaria fractional model with temporary immunity and relapse. *Adv. Differ. Equ.* **2021**, 390 (2021)
15. Li, C., Tao, C.: On the fractional Adams method. *Comput. Math. Appl.* **58**(8), 1573–1588 (2009)
16. Thakare, P., Sharma, S., Gupta, A., Lilare, N., Utpat, K., Desai, U., JM, J., Bharmal, R.N.: A Case Series on Early Virological Clearance in Malaria COVID-19 Co-infection. *Int. Clin. Case Rep.* **1**(1), 1-3 (2021)

# Design of Imidazole-Based Drugs as Potential Inhibitors of SARS-Cov-2 of the Delta and Omicron Variant



## An *in Silico* Approach

Peter Solo and M. Arockia Doss

**Abstract** 30 imidazole-based drugs were designed, prepared and optimized using Gaussian 09, and were screened for drug-likeness with SWISS-ADME server. Molecular docking was performed using MOE 09, where the designed drugs were docked with the spike glycoprotein of the Delta (B.1.617.2) and Omicron (B.1.1.529) variant of SARS CoV-2. Nafamostat and Hydroxychloroquine were used as standards in comparing the docking results. Among the designed drugs, those drugs which used Benzil and Hyroxy/methoxy-benzaldehyde as the starting compound exhibited good binding scores, and can be potential inhibitors of the Delta and Omicron variant of SARS CoV-2.

**Keywords** SARS-CoV-2 · Imidazole-based drug design · Molecular docking

## 1 Introduction

The outbreak of severe acute respiratory syndrome corona virus 2 (SARS CoV-2) continues to prevail. The detection of the new omicron variant (B.1.1.529) in south Africa has ignited fresh concern over the already contagious delta variant (B.1.617.2). On 26 November 2021, WHO has designated omicron as a variant of concern which has now spread across the entire globe [1]. Unlike the other variants, omicron has large number of mutation with 32 mutations in the spike glycoprotein [2] and 15 mutations in the receptor-binding domain (RDB) alone [3]. Computational studies have affirmed that the Omicron variant had a higher affinity for human angiotensin-converting enzyme 2 (ACE2) as compared to the delta variant due to the significant

---

**Supplementary Information** The online version contains supplementary material available at [https://doi.org/10.1007/978-3-030-99792-2\\_125](https://doi.org/10.1007/978-3-030-99792-2_125).

---

P. Solo (✉) · M. A. Doss  
Department of Chemistry, St. Joseph University, Dimapur 797115, India  
e-mail: [Solopeter82@gmail.com](mailto:Solopeter82@gmail.com)

P. Solo  
Department of Chemistry, St. Joseph's College (Autonomous), Jakhama 797001, India

© The Author(s), under exclusive license to Springer Nature Switzerland AG 2022  
S. Banerjee and A. Saha (eds.), *Nonlinear Dynamics and Applications*,  
Springer Proceedings in Complexity,  
[https://doi.org/10.1007/978-3-030-99792-2\\_125](https://doi.org/10.1007/978-3-030-99792-2_125)

1465

of mutations in the RBD regions of the spike protein [4]. Initial modelling suggests that the omicron variant is 2.8 times more infectious than the delta variant [5]. Most monoclonal antibodies are not effective against the omicron variant as they target the spike protein which has significant mutations [6].

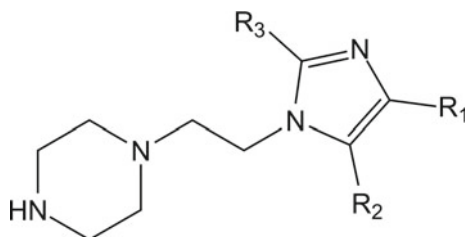
Imidazole and its derivatives forms a prominent class of hetero cyclic compounds, displaying diverse applications especially with regards to its biological and pharmacological activities. Many substituted Imidazole are found to exhibit anti-inflammatory [7, 8], anti-fungal [9, 10], anti-bacterial [11], anti-epileptic, anti-microbial [12], anti-cancer [13, 14] and anti-tubercular activities [15]. They are also found to have analgesic properties [16]. Imidazole is the main structural feature in many drugs found in the markets, namely isoconazole, ketoconazole, clotrimazole, miconazole, econazole, fluconazole, sertaconazole, eprosartan, losartan, olmesartan, metronidazole, etc. [17]. The study aims at designing imidazole-based drug in search for potential inhibitor against SARS CoV-2 using *in silico* approach.

## 2 Materials and Methods

### 2.1 Designing of Ligands

The Ligands were designed based on a published work [18] where the heterocyclic imidazole ring forms an important structural feature with regard to its pharmacological activity as antimicrobial and antifungal (Fig. 1). Alpha-diketone, aromatic aldehyde, 2-(piperazin-1-yl) ethanamine and ammonium acetate are the reactants in the synthesis of the drugs. From a synthetic point of view various derivatives of the drug were designed by replacing various substituents at R1, R2 and R3 positions. R1 and R2 are replaced by alkyl or aromatic groups using diacetyl or benzyl as reactants respectively. R3 groups can have the most number of variations as it is formed by an aromatic aldehyde. All the drugs/ligands were designed using Gaussian 09 [19]. Optimization was performed with DFT/B3LYP method using 6-31G(d,p) level of theory. The optimized structures were saved in both MOL and SDF format.

**Fig. 1** Framework for imidazole-based drug design



## **2.2 Screening of Ligands for Drug-Likeness**

The designed ligands were screened for drug-likeness with SWISS-ADME server [20], which analyses many important aspects of the drug, namely Lipophilicity, Water Solubility, Pharmacokinetics, Drug-likeness and medicinal properties of the drug. The screening for drug-likeness with Lipinski, Ghose, Veber, Egan and Muegge are all included in the SWISS-ADME server. The SDF structures of the designed-drugs were fed into the SWISS-ADME server and were converted into SMILES format which were then screened for drug-likeness.

## **2.3 SARS CoV-2 Spike Glycoprotein Target Selection and Homology Modelling**

The 3D structure for the spike glycoprotein of the delta variant (B.1.617.2), with PDB ID:7so9, was downloaded from RCSB protein data bank (<https://www.rcsb.org/structure/7SO9>). All other chains and water molecules were deleted, and only chains A, F and K of the spike glycoprotein was retained. The 3D structure for the spike glycoprotein for the Omicron variant (B.1.1.529) was not available at RCSB protein data bank, therefore, it was constructed with homology modelling using Swiss Model server [21]. The target sequence of the Omicron variant with GenBank ID UFO69279.1 (<https://www.ncbi.nlm.nih.gov/protein/UFO69279.1>) was downloaded in FASTA format from NCBI website and was pasted in Swiss Model server for the construction of 3D model. Blast and HHblits methods were used to search for template structure in the SWISS-MODEL template library. The template with PDB ID 7n1u.1.A was selected for building the 3D model. The details of the template and homology modelling results are given in Table 1.

## **2.4 Protein and Ligand Preparation**

MOE 09 docking tools [22] was used to prepared both the target proteins and all the ligands. Structure preparation of the target proteins was executed and all corrections were performed for the PDB structures of the two target proteins, i.e., Delta variant and Omicron variant. Energy minimization of the structures were performed using Amber12:EHT Force field where hydrogens and charges were added. A database of ligand containing all the 30 compounds were prepared in MDB format. Each ligand in SDF format was entered into the database after 3D protonation and energy minimization with Amber12:EHT Force field.



**Table 1** Details of template and homology modelling

SARS-CoV-2	GenBank IDs	Template	Seq identity	Method	Seq similarity	coverage	description	Qmean score
B.1.1.529	UFO69279.1	7n1u.1.A	97.00%	EM	0.61	1.0	Spike glycoprotein	-1.67

### 3 Results and Discussion

In this study, 30 imidazole-based drugs were designed in search for potential antiviral candidate for the prevailing SARS CoV-2 pandemic using *in silico* method. The drugs were designed based on published literature where the imidazole ring forms an essential structural feature for its pharmacological activity as antimicrobial and antifungal drugs. Designing and optimization of the 3D structures of the drugs were performed efficiently using Gaussian 09.

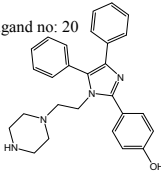
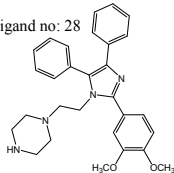
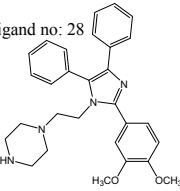
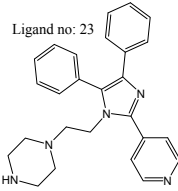
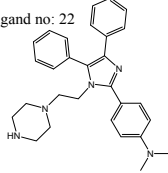
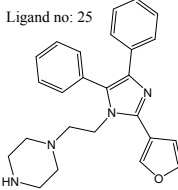
Most compounds performed very well in the screening for drug-likeness with SWISS-ADME server and there were no serious violations or alerts (S.1). The alerts were due to higher molecular mass and higher lipophilicity of some compounds to the presence of aromatic rings. All compounds showed high GI absorption and there was no Lipinski's violation. All the 30 compounds were selected to be docked with the target proteins.

The docking analysis with MOE 09 reveals that most of the designed drugs binds quite well to the target spike glycoprotein as compared to the standards (S. 1). The top 3 ligand with the best binding energy are displayed in Table 2. The designed drugs with alkyl substituents at R1 and R2 Positions (Fig. 1) did not top the list, which suggest that aromatic substituents at these positions increases ligand affinity for the target spike proteins. Ligand number 28 binds very well to both the target spike proteins exhibiting a binding affinity of  $-8.06753635$  kcal/mol for the Delta variant and  $-7.19685173$  kcal/mol for the Omicron variant.

In most of the interactions of the ligands with the active site, the imidazole ring is actively involved either through Conventional Hydrogen bond, Carbon Hydrogen bond, alkyl interactions or pi-alkyl interactions with the residues of the target site. In the docking with omicron spike protein the imidazole ring is involved in pi-alkyl interaction with ILE A:192 (ligand 20) and ILE B:192 (ligand 22) residues (Fig. 2). In the docking with delta spike protein the imidazole ring is involved in alkyl interaction with PHE K:377 residue of the target protein (ligand 23). It is also involved in convention hydrogen bond and amide pi-stacked interactions with ARG A:408 and SER K:375 residues respectively (Fig. 3). Interaction of ligand 20 with omicron variant is mainly stabilized with three conventional hydrogen bonding with THR B:390, SER B:511 and ASN B:391, and carbon hydrogen bond with THR B:390 (Fig. 2). On the other hand, interaction of ligand 28 with the delta variant is mainly stabilized by five carbon hydrogen bonds with GLY A:404, ASP F:405, GLU F:406 and PHE A:374 (Fig. 3).

Drugs which were prepared using Benzil and hydroxy/methoxy-benzaldehyde as starting compound aided the binding of the drugs with multiple favorable interactions. The hydroxyl group (ligand 20) in complex with the omicron variant is involved in two conventional hydrogen bond with SER B:511 and ASN B:391 residues (Fig. 2). In the complex with delta variant, the methoxy-groups of ligand 28 is involved in two carbon hydrogen bond with GLU F:406 and PHE A:374 residues, and alkyl interaction with LYS F:417 (Fig. 3).

**Table 2** Docking scores of the top 3 ligands with the standards

Top hits ligands docking with Omicron variant (B.1.1.529)	Docking score (kcal/mol)	Top hits ligands Docking with delta variant (B.1.617.2)	Docking score (kcal/mol)
Ligand no: 20 	-7.22973061	Ligand no: 28 	-8.06753635
Ligand no: 28 	-7.19685173	Ligand no: 23 	-7.96867609
Ligand no: 22 	-7.17171955	Ligand no: 25 	-7.96448946
Hydroxychloroquine	-6.51112795	Hydroxychloroquine	-6.40599966
Nafamostat	-7.13362694	Nafamostat	-6.89814949

The common amino acids at the binding site of the ligands with the Omicron variant are ASP B976, LEU C543, LEU C514 and LEU C515 (Fig. 2 and S. 2). At the active site of the binding of the ligands with the Delta variant, ARG A408, LYS A417, GLU A406, PHE K374, PHE K377, SER K375 and ARG K408 (Fig. 3 and S. 2), are the common amino acids. The difference in the common amino acid residues at the binding sites of the two spike protein variants reflects the enormous difference in their structure at the active site.

All common amino acids residues, accept for ASP B976, are in the receptor binding domain (RBD) which initiates viral entry into the host by binding to the cell receptor ACE2 in the aminopeptidase N [23]. Therefore, we can theoretically conclude that the designed drugs can inhibit the viral binding to ACE2 receptor.

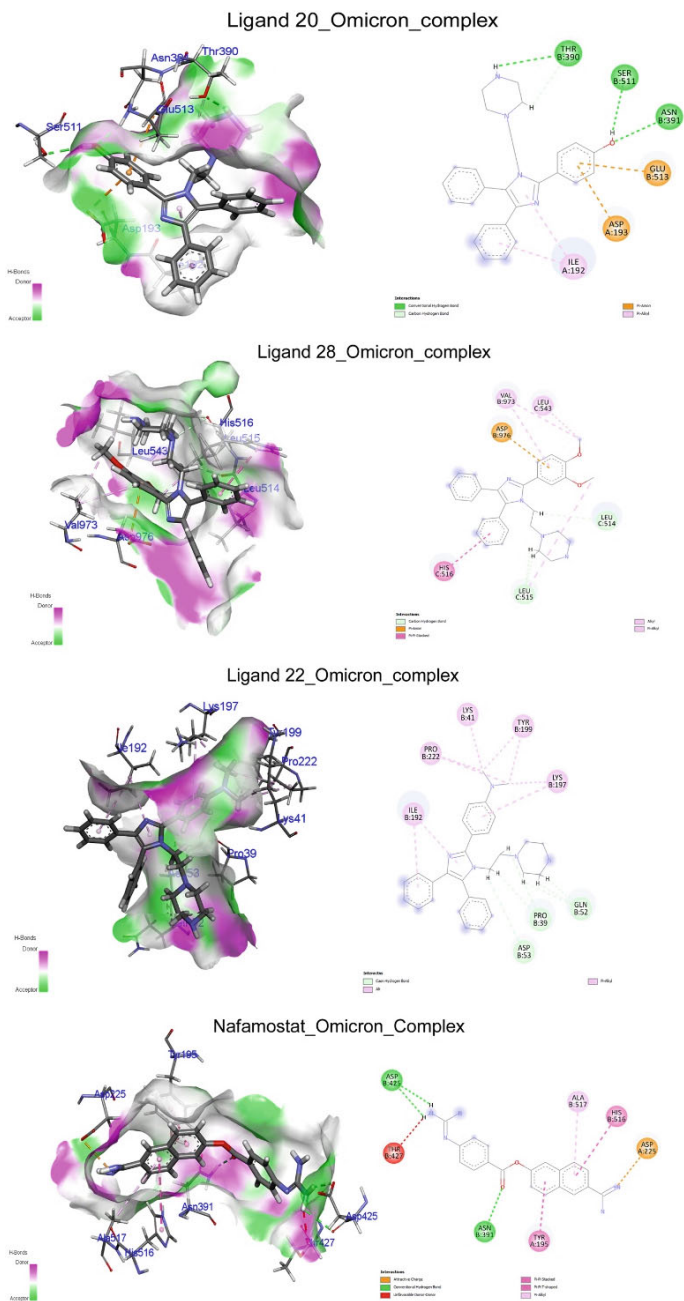


**Fig. 2** 3D and 2D structure of the docking results of ligands 20, 28, 22 and Nafamostat with Omicron (B.1.1.529) spike glycoprotein

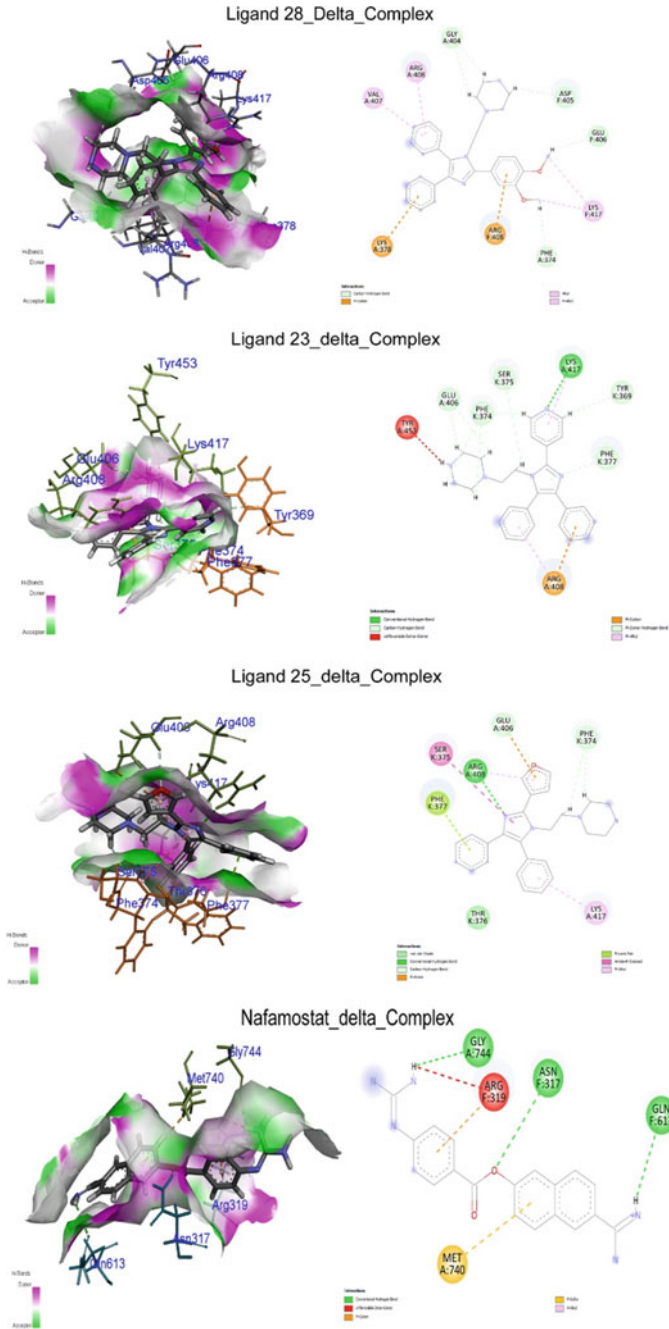


**Fig. 3** 3D and 2D structure of the docking results with ligands 28, 23, 25 and Nafamostat with Delta (B.1.617.2) spike glycoprotein

## 4 Conclusion

The study reports potential inhibitors for the SARS-CoV-2 main protease, through designing of Imidazole-based drugs and computational analysis. All the designed drugs were screened for drug-likeness using SWISS-ADME web based server. Gaussian 09 was used to design the drugs and optimization was performed using DFT/B3LYP method with 6-31G(d,p) level of theory. All the designed drugs were docked with the target spike proteins at the receptor binding domain using MOE 09. The docking results identified ligand 28 with good binding affinity for both the target proteins. The study also reports the active participation of the imidazole in the binding pockets of all the docked structures.

In silico approach for new drug discovery as potentials inhibitor against the prevailing contagious SARS CoV-2, can be a great contribution in the search for antiviral drugs for the virus, as the world is pushed to its limit with time and resources. Computational resources and software with user friendly interface are available in many open sources which can be easily utilized by those interested.

In conclusion the study reports that Imidazole-based drugs are found to bind quite effectively to the target spike proteins of Delta and Omicron variant. More Imidazole-based drugs can be designed in search for more efficient inhibitor for SARS CoV-2. In general, most heterocyclic-based drugs would display amazing pharmacological activities and hence, there are huge avenues in heterocycle-based drug designing. Further in vivo and in vitro analysis can be performed to support the conclusion made by the study.

**Acknowledgements** The authors gratefully acknowledge the support from St. Joseph University Dimapur (India) and St. Joseph's College (autonomous) Jakhama (India).

## References

1. WHO Homepage. [https://www.who.int/news/item/26-11-2021-classification-of-omicron-\(b.1.1.529\)-sars-cov-2-variant-of-concern](https://www.who.int/news/item/26-11-2021-classification-of-omicron-(b.1.1.529)-sars-cov-2-variant-of-concern)
2. Gao, S.J., Guo, H., Luo, G.: Omicron variant (B.1.1.529) of SARS-CoV-2, a global urgent public health alert!. *J. Med. Virol.* (2022). <https://doi.org/10.1002/jmv.27491>
3. Thakur, V., Radha R.K.:OMICRON (B.1.1.529): A new SARS-CoV-2 variant of concern mounting worldwide fear. *J. Med. Virol.* 1–4 (2021). <https://doi.org/10.1002/jmv.27541>
4. Kumar, S., et al.: Omicron and Delta variant of SARS-CoV-2: a comparative computational study of spike protein. *J. Med. Virol.* 1–9 (2021). <https://doi.org/10.1002/jmv.27526>
5. STATPEARLS Homepage. <https://www.statpearls.com/ArticleLibrary/viewarticle/132707>
6. Li, P., et al.: SARS-CoV-2 Omicron variant is highly sensitive to molnupiravir, nirmatrelvir, and the combination. *Cell Res.* (2022). <https://doi.org/10.1038/s41422-022-00618-w>
7. Lombardino, J.G., Wiseman, E.H.: *J. Med. Chem.* **17**(11), 1128–1188 (1974). <https://doi.org/10.1021/jm00257a011>
8. Puratchikody, A., Mukesh, D.: Antinociceptive and anti-inflammatory activities and QSAR studies on 2-substituted-4,5-diphenyl-1H-imidazoles. *Bioorg. Med. Chem.* **15**(2) (2007). <https://doi.org/10.1016/j.bmc.2006.10.025>

9. Vita, D.D., et al.: Synthesis and antifungal activity of a new series of 2-(1H-imidazol-1-yl)-1-phenylethanol derivatives. *J. Med. Chem.* **49**, 334–342 (2012). <https://doi.org/10.1016/j.jmchem.2012.01.034>
10. Heeres, J., et al.: Antimycotic imidazoles. Part 4. Synthesis and antifungal activity of ketoconazole, a new potent orally active broad-spectrum antifungal agent. *J. Med. Chem.* **22**(8), 1003–1005 (1979). <https://doi.org/10.1021/jm00194a023>
11. Ganguly, S., et al.: Synthesis, antibacterial and potential anti-HIV activity of some novel imidazole analogs. *Acta Pharm.* **61**(2), 187–201 (2011). <https://doi.org/10.2478/v10007-011-0018-2>
12. Amir, M. et al.: Design and synthesis of some azole derivatives containing 2,4,5-triphenyl imidazole moiety as anti-inflammatory and antimicrobial agents. *Indian J. Chem.* **B50**, 207–213 (2011). <http://www.nopr.niscair.res.in/handle/123456789/11029>
13. Özkay, Y., et al.: Synthesis of 2-substituted-N-[4-(1-methyl-4,5-diphenyl-1H-imidazole-2-yl)phenyl]acetamide derivatives and evaluation of their anticancer activity. *Eur. J. Med. Chem.* **45**(8), 3320–3328 (2010). <https://doi.org/10.1016/j.ejmech.2010.04.015>
14. Yadav, S. et al.: Synthesis and evaluation of antimicrobial, antitubercular and anticancer activities of 2-(1-benzoyl-1Hbenzo[d]imidazole-2-ylthio)-N-substituted acetamides. *Chem. Central J.* **12**(66) (2018). <https://doi.org/10.1186/s13065-018-0432-3>
15. Shankar, G., et al.: Novel imidazo[2,1-b][1,3,4]thiadiazole carrying rhodanine-3-acetic acid as potential antitubercular agents. *Bioorg. Med. Chem. Lett.* **22**(5), 1917–1921 (2012). <https://doi.org/10.1016/j.bmcl.2012.01.052>
16. Uçucu, Ü., et al.: Synthesis and analgesic activity of some 1-benzyl-2-substituted-4,5-diphenyl-1H-imidazole derivatives. *Il Farmaco* **56**(4), 285–290 (2001). [https://doi.org/10.1016/S0014-827X\(01\)01076-X](https://doi.org/10.1016/S0014-827X(01)01076-X)
17. Bastide, M., et al.: A comparison of the effects of several antifungal imidazole derivatives and polyenes on *Candida albicans*: an ultrastructural study by scanning electron microscopy. *Can. J. Microbiol.* **28**(10), 1119–1126 (1982). <https://doi.org/10.1139/m82-166>
18. Rajkumar, R., et al.: Synthesis, spectral characterization and biological evaluation of novel 1-(2-(4,5-dimethyl-2-phenyl-1H-imidazol-1-yl)ethyl)piperazine derivatives. *J. Saudi Chem. Soc.* **18**(5), 735–743 (2014). <https://doi.org/10.1016/j.jscs.2014.08.001>
19. Gaussian 09, Revision A.02, M. J. Frisch, Gaussian, Inc., Wallingford CT, 2016. <https://www.gaussian.com>
20. Daina, A. et al.: SwissADME: a free web tool to evaluate pharmacokinetics, drug-likeness and medicinal chemistry friendliness of small molecules. *Sci. Rep.* **7**(42717) (2017). <https://doi.org/10.1038/srep42717>
21. Waterhouse, A., et al.: SWISS-MODEL: homology modelling of protein structures and complexes. *Nucl. Acids Res.* **41**(W1), W296–W303 (2018). <https://doi.org/10.1093/nar/gky427>
22. Chemical Computing Group ULC, 1010 Sherbooke St. West, Suite #910, Montreal, QC, Canada, H3A 2R7, 2021. <https://www.chemcomp.com/Products.htm>
23. Huang, Y., et al.: Structural and functional properties of SARS-CoV-2 spike protein: potential antiviral drug development for COVID-19. *Acta Pharmacol. Sin.* **41**, 1141–1149 (2020). <https://doi.org/10.1038/s41401-020-0485-4>